



Proceeding

International Conference on Materials & Energy

May 17 – 20, 2016,
La Rochelle, France

ICOME'16
& MATERIALS
ENERGY



Contents

Welcome	3
Foreword.....	4
Conference Chairs.....	6
Scientific Committee.....	7
Organizing Committee	8
Keynotes talks	9
“Engineering interfaces and nanofluids for energy applications”, Pietro ASINARI	9
“World production and energy consumptions: what kind of mid term evolutions?”, Michel COMBARNOUS.....	9
“Trend and opportunities in wood based bio-industries”, Xavier DEGLISE.....	10
”Transformation of the electricity system to a renewables based-one: necessary political and economical regulatory framework”, Eva HAUSER.....	10
“Time-space-fractional models of anomalous diffusion: Physical basis, approximate solutions and analysis for application in material science”, Jordan HRISTOV	11
“Transition to renewable energies: a reality check”, Marcel LACROIX.....	11
List of Sessions /Contributions per session	14
Thermal Building and Optimisation.....	14
Building Materials	15
Sustainable Constructive Materials	16
Heat and Mass Transfer Optimisation (I)	17
Materials / Energy Products.....	18
Sustainable Constructive Materials (II).....	19
Heat and Mass Transfer Optimisation (II)	20
Hygroscopic & Bio-Materials / Composites.....	21
Thermal Building and Energy Storage.....	22
Energetic Systems.....	23
Constructive Materials: Mechanical Optimisation.....	24
Inner and Outer Flows	25
Safety / Reliability and Durability	26
Sponsors.....	1091





Welcome

After the success of the International Conference on Materials & Energy (ICOME'15) in the beautiful North Mediteranean city of Tétouan in Morocco, we are pleased to run the edition 2016 in the beautiful Atlantic city of La Rochelle. ICOME'16 host the Spring School of Eco-Materials dedicated to PhD and Post docs.

Natural coupling of materials and energy is a strong point of this event. This is an interconnected topics with very fecond fields of application in our modern societies.

The inter-Mediterranean link is also an important fact of this international conference and will allow a better South/North mixture allowing to share innovation and sustainable development.

The conference chairs hopes that everyone will found in this meeting an important topical interest, a great pleasure on exchanging with the both community of materials and energy.

ICOME'16 CHAIR

Prof. Rafik Belarbi

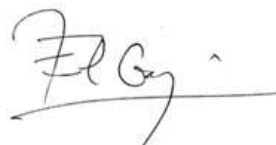


ICOME SERIE'S CHAIRS

Prof. R. Bennacer



Prof. M. El Ganaoui



Foreword

It is difficult to sketch any credible scenarios of the human future without integrating materials and energy in this matter. These two topics, which are evidently part of the DNA of human history, have always known strong interaction, often under unimagined facets and at unexpected spatial and temporal scales. Nowadays, the result is amazing. The innovation progress is obvious, anyone can observe the generation gap in communication ability and connectivity when observing a child handling technology today, as compared with his father and his grandfather.

This coupling of materials and energy became visible to all the social ladder leaning against a socio-economic aspect, directly related to the life of comfort and designing the contours of the city of tomorrow. This coupling received largely the benefit of fundamental disciplines such as mathematical and physical sciences. Abstraction keeps feeding this hidden face of continued enthusiasm of a public of all ages toward innovation that materializes through the attraction to devices (gadgets).

If the vocation of mathematics focuses on excellence by promoting measurements, accuracy and the writing of nature in equations, physics has another particular focus on energy and materials.

Physics considers energy as the ability of a system to interact with its environment and develop producing movement, radiation or heat. It collects materials like the arrangement of material to obtain the desired properties for specific applications at will.

Both looks are enough to show the complexity of the problem of studying the coupling materials/energy when it gathers heat and mass transfer phenomena specialists, electricians, civil engineers, automaticians, etc ...

The series of Conferences about Materials and Energy wants to provide an appointment, amplifying young researchers' initiatives, first by the recognition and realization of the importance of the knowledge as a base for any progress, and then by the training exercise, which has also its place in this event. A thematic school, animated by international speakers, will take place like in the previous edition in Morocco.

So many initiatives contribute to the pyramid of understanding, for it to find its meaning on the path of knowledge that has enabled man to save his spirit and accelerate his route towards progress. In their quest for truth, scientists have to deal with innovation, the social and economic cost of material/energy/systems, the different points of view, ethics, and so on.

In this sense, the reference to the universal scientist Averroes (who was born in 1126 in Cordoba, Spain, and died in 1198 in Marrakech, Morocco) through a special award, reinforces this vision of a man who puts truth beyond beliefs and allegiances of his time, intelligence beyond the interest of use: "There are vulgar conceptions quite sufficient for practical life; they should even be human food. They are not sufficient to intelligence" Averroes.



The 2016 edition, held on the Atlantic coast in La Rochelle, succeeds that of 2015 organized in the Mediterranean city of Tetouan. This edition is dedicated to two key aspects, Materials & Energy for the control of environmental impacts of transport activities and habitations. Indeed, eco-materials and sustainable buildings are an essential topic, given the current and future challenges of the energy transition and sustainable development.

This event is supported by public institutions and private organizations in order to treat problems thanks to the use of research and innovation for technologies, economy and society.

This conference will allow scientists and political leaders not only to link the themes related to energy and those dedicated to materials, but also to gather up-to-date knowledge on the latest scientific, technological and industrial advances in the two following key areas:

- Materials and especially building materials: from the eco-design of materials with a low environmental impact to the recovery of waste and by-products. This also includes the life cycle analysis and the estimates of environmental costs.

- Energy in the field of construction: energy demands of buildings, innovative packaging systems moods, energy production in the housing sector, positive energy buildings, and renewable energies.

Among the speakers there are international experts in the fields of renewable energies, energy building and sustainability of structures.

Thus, in addition to plenary lectures and sessions, the conference will bring together scientists, industrialists and industry professionals, contractors and building owners in exchange workshops on the latest fundamental know-how applied in these areas. It should be noted that the "Mini Symposia" sessions scheduled in the afternoon of May 19 will be open to the public, while the thematic school of May 17 will be open to scientists.

ICOME'16 will gather more than 250 attendees from various international institutions (European, American, Asian and African) and several industrial partners which are very sensitive to the issue of innovation to improve their competitiveness and the quality of their cities.

This event also aims to support regional and national industry through exchange moments in which local and national companies will present their projects, their innovative products and their expertise.

Furthermore, and for information, the next edition of this conference, ICOME'17, is scheduled in China in 2017.

The chairs and members of the organizing committee of ICOME 16 wish all present a great stay in La Rochelle, fruitful exchanges and may everyone find what they expect from this edition.

ICOME'16 Chairs

Prof. Rafik Belarbi
University of La Rochelle

Prof. R. Bennacer
ENS Cachan

Prof. M. El Ganaoui
University of Lorraine



Conference Chairs



Professor BELARBI Rafik, Received his engineer degree in Building Physics from School of engineers of Poitiers (ESIP) and Master of Thermal sciences from University of Poitiers, France in 1993. He obtained his PhD Thesis in civil engineering in La Rochelle University, 1998. In 1999, he joined the LEPTAB research staff laboratory and civil engineering department of La Rochelle University as Associate Professor. Actually, he is full Professor. Since 1994, he was involved in several National and International projects dealing with Heat and moisture transfer the building energy conservation. The main projects are: Pascool/Joule and Altener/Sink (passive cooling systems

modelling and their impact on the building energy consumption), PDEC/Joule II (Utilisation of Passive Draught Evaporative Cooling systems on non-domestic buildings), Joule/Thermie B, Altener/Greencode (Reglementary Frame for Renewable Energy Use in Urban Site Through Vegetation Planting and Strategic Surfacing), Altener/SolVent, and Altener/Cluster (Solar Passive Heating and Cooling), Seventh Framework Program " Marie Curie (Old Masonry Repair). His main expertise is in microstructural, thermal, physical and hydric characterization of porous building material and heat and mass transfers with application in Energy Efficiency in Buildings and Indoor Environment and durability of constructions. He is author or co-author of more than 100 papers in international journals or international conferences. He supervised 15 PhD and 13 Post-Doctoral researchers. Since October 2007, he is the Head of the Civil Engineering Department.



Pr. Dr. Ing. R. Bennacer, is an Engineer in Mechanical field (1989), and he got his PhD thesis at Pierre et Marie Curie University (Paris 6) in 1993. He worked as lecturer in the University Paris XI (1993/94), became an associate professor at Cergy Pontoise Uni. 1994 and full Professor in 2008. He moved as senior Professor to the prestigious school Ecole Normale superieure (Cachan) since 2010. He is also adjunct professor at Tianjin /comm. (University, P.R. of China). He assumed several responsibilities, director of the LEEVAM research team (2003-2007), Licence degrees (2008-2010), Aggregation title (2010-2011), Master research degree (2011-2013), Transfer and Environmental

Research Unit (CNRS LMT-Lab) (since July 2012) and dean of Civil/Environmental department (since Oct. 2012). His present research activity is within the LMT laboratory where he manages Transfer and Environmental Research Unit. His Research field covers wide spectrum and several domains. It covers the building material for energy applications or on durability aspect, renewable and energy system. The expertise covers the direct numerical simulation including CFD coupling on multi-scales. The previous approach is consolidated by analytical or reduction approach in order to identify the instabilities and global behavior bifurcation and similarity controlling parameters in multiphysics situation. He published several book chapters and more than 150 Referenced international journals.



M. El Ganaoui, is a full professor at the University of Lorraine and researcher in the Jacques Villermaux Federation for mechanics, energy and processes (FR 28 63/LERMAB). He is heading the research in energy in the Henri Poincaré Institute of Technology in Longwy. Previously, he was a teacher researcher in the University of Limoges and the SPCTS UMR 6638 CNRS laboratory where he was responsible for the Physics Department (2004-2010) and the international cooperation service (2006-2010) in the Faculty of science and technology. His research aims to understand heat and mass transfers through modeling and numerical simulation with a specific activity in the field of the solid -liquid-vapor phase change. Applications concern materials and energy and benefit to energy

systems including phenomena for sustainable building (Eco-materials). M. El Ganaoui teaches the mechanics of continuous media, heat transfers, and numerical methods. He been advisor of more than 20 Phd Thesis with strong international interaction noticeably in the Euro-Mediterranean context. He participated/managed the PAI Australia, Canada, Maghreb (Tassili, Utique, Volubilis), China (Xugangqi). El Ganaoui has participated in the Edition of more than 10 special issues and conference proceedings, co-authored over than 150 publications in journals (rank A) and participated in more than 100 international conferences including a teen that he has co-organized. He is member of the many international scientific societies in mechanics and heat transfers.



Scientific Committee

Abrudeanu M.,	Acad. Sciences	Roumania
Addou M.,	Univ. Abd. Essaadi (UAE),	Morocco
Aït-Mokhtar A.	Univ. La Rochelle	France
Alexander J. I. D.,	Case Western Reserve Univ.	USA
Bayazitoglu Y.,	Rice University,	USA
Belarbi R.,	University of La Rochelle,	France
Bennacer R.,	Ecole Normale Sup. Cachan,	France
Benim A. C.,	University of Duesseldorf,	Germany
Bensaïbi M.,	ENSTP,	Algeria
Bontoux P.,	University of Aix Marseille,	France
Bouali M.,	University of Mondragon,	Spain
Bouhadeh Kh.,	University USTHB,	Algeria
Chai J.,	School of Computing and Eng.,	UK
Coronas A.,	Universitat Rovira i Virgili	Spain
Costa V.,	University of Aveiro,	Portugal
Cotta R.,	Me Coppe UFRJ,	Brazil
De Lemos M.,	Inst. Tecno. De Aeronautica,	Brazil
Dombrovsky L.,	Inst. High Temperatures,	Russia
El Ganaoui M.,	University of Lorraine,	France
Gabsi S.,	University of Sfax,	Tunisia
Ghomari F.,	University of Tlemcen,	Algéria
Inard C.,	University of La Rochelle,	France
Khatib J.,	University of Wolverhampton,	UK
Lappa M.,	University of Napoli,	Italy
Meyer JP.,	University of Pretoria,	South Africa
Mimet A.,	Univ. Abd. Essaadi (UAE),	Morocco
Nandakumar K.,	Louisiana State Univ.,	USA
Nunzi J. M.,	Queen's University,	Canada
Oka S.,	University of Belgrade,	Serbia
Runchal A.,	CFD Inov. ACRI,	India
Sammouda H.,	University of Sousse,	Tunisia
Seghir Z.,	Ryerson University,	Canada
Viera G.,	University UCP,	Brazil
Timchenko V.,	University of NSW,	Australia
Yuen R.,	City University of Hong Kong,	Hong Kong
Zeghmati B.,	University of Perpignan,	France
Zhu Ji-Hong.,	Northwestern Polytech. Univ.,	China



Organizing Committee

Abahri K.,	Ecole Normale Sup. Cachan,	France
Aït-Mokhtar A.,	University of La Rochelle,	France
Belarbi R.,	University of La Rochelle,	France
Benabed A.,	University of La Rochelle,	France
Bennai F.,	University of La Rochelle / Univ. Bejaïa	France / Algeria
Bennacer R.,	Ecole Normale Sup. Cachan,	France
Bozonnet E.,	University of La Rochelle,	France
Chérif R.,	University of La Rochelle,	France
Djedjig R.,	University of Lorraine,	France
Dubois F.,	University of La Rochelle,	France
El Ganaoui M.,	University of Lorraine,	France
Ferroukhi M.Y.,	University of La Rochelle,	France
Hamami A.A.,	University of La Rochelle,	France
Hervaud C.,	University of La Rochelle,	France
Issaadi N.,	University of La Rochelle,	France
Issaadi-Hamitouche T.,	University of La Rochelle,	France
Khelifa M.,	University of Lorraine,	France
Moinard C.,	University of La Rochelle	France
Morsli S.,	University of Lorraine / University Of Oran	France/Algérie
Ouleghlou M.,	University of La Rochelle,	France
Turcry P.,	University of La Rochelle,	France
Younsi A.,	University of La Rochelle,	France
Zaghmati B.,	University of Perpignan,	France



Keynotes talks



“Engineering interfaces and nanofluids for energy applications”,

Pietro ASINARI

Politecnico di Torino, Italy

ABSTRACT: This talk aims to discuss some multi-scale transport phenomena at solid-liquid interfaces, which are relevant in characterizing and designing materials for energy applications. We can distinguish two broad categories: interfaces where the solid phase prevails on the liquid one and those where the opposite holds. The first category includes engineered interfaces for optimizing the water uptake (adsorption/infiltration) isotherms into solid micro-/ nano-porous materials. In this talk, I will investigate water-zeolite adsorption isotherms for thermal storage applications and water-zeolite infiltration isotherms for reverse osmosis applications. Concerning the second category, I will discuss the nanofluids, namely colloidal suspensions of engineered nanoparticles. In this case, the interfacial properties are determined by the nanoparticle surface, engineered by functionalizations, electrolytes and surfactants. The nanoparticle surface determines the properties of the solvent nanolayer effect, which is responsible of the solvation forces and consequently of the colloidal stability. In this talk, I will put some special emphasis on nanofluids for solar thermal engineering.

BIOGRAPHY: Dr. Asinari received his B.S. and M.S. (cum laude) in Mechanical Engineering in 2001 from “Politecnico di Torino”, Italy. After working as industrial consultant, he received his Ph.D. in Energetics in 2005 at the Department of Energetics. He is currently Associate Professor at the Energy Department of “Politecnico di Torino”. His research activity deals with proposing mesoscopic descriptions of phenomena, designing new numerical schemes (mainly in the framework of Lattice Boltzmann Method), developing new numerical codes (including parallel codes on large cluster facilities) and finally applying the previous tools in order to investigate the microscopic fluidics of industrial devices.



“World production and energy consumptions: what kind of mid term evolutions?”,

Michel COMBARNOUS

Laboratoire Transferts, Écoulements, Fluides, Énergétique, Talence

ABSTRACT: Starting from the evolution of world population in the next decades, needs in energy production are presented, as well as all the new tools to save energy, included in what is called now « energy transition ». After a general presentation of the overall panel of energy production devices, some renewable energies are detailed: wind energy, photovoltaic, biomasses... In conclusion, the behavior of the overall system « Continents – Oceans – Atmosphere » is presented in the same time as other general problems (water resources,...).

BIOGRAPHY: Michel Combarnous, Professor “Emeritus” at the University of Bordeaux, has been associate professor at the University of Gabès (Tunisia) (2006-2011). A specialist in fluid mechanics and energetics, he was encharged of the Department « Engineering Sciences » at CNRS (1980-1985). He is a founding member of « Académie des Technologies », and Corresponding Member of the Academy of Sciences, since 1978 (www.academie-sciences.fr)





“Trend and opportunities in wood based bio-industries”,

Xavier DEGLISE

University of Lorraine

ABSTRACT: Wood, as a major part of biomass, could be the best source able to give way, economically, to the substitution of chemicals, fuels, and bio-products in new bio-based plants that we call: bio-refineries.

In these bio-refineries, we will produce all the chemicals that we need, from woody biomass. They will allow improving numerous old processes which have been developed in the first half of the 20th century in wood chemistry (or Xylochemistry). The Xylochemicals will surely replace Petrochemicals at the end of the 21st Century.....if we are able to secure the wood procurement!

BIOGRAPHY: **Xavier Deglise, Professor “Emeritus”** UL (University of Lorraine) Nancy, France – Founder and former Director of LERMaB (Joint research Unit on Wood Material UHP/INRA/ENGREF forestry school) – Founder and Honorary Director of ENSTIB (Ecole Nationale Supérieure des Sciences et Technologies du Bois) – Former assistant Professor Laval University (Canada) – Correspondent of the French Academy of Agriculture (Wood and Forest section) – Fellow and former President of the International Academy of Wood Science IAWS – Member of the Forest Products Society, USA – Concurrent Professor at Nanjing Forestry University, P.R. of China – Honorary Professor at University of Agriculture of Warsaw, Poland – Honorary Professor at Transylvania University, Brasov, Romania – Editorial Board of the Saint Petersburg Forest Technical University, Russia – Knight of the national order of Merit – Commander in the order of the Academic Palms – Roumanie – Comité éditorial de l’Université technique forestière de Saint Petersburg, Russie – Chevalier de l’ordre national du Mérite – Commandeur des Palmes Académiques.



”Transformation of the electricity system to a renewables based-one: necessary political and economical regulatory framework”,

Eva HAUSER

IZES - Institut für ZukunftsEnergieSysteme, Germany

ABSTRACT: The whole energy system needs to undergo important transformations due to challenges stemming from climate change and actual and future resource scarcity. These transformation processes will take place on a technical but also on a societal level. Therefore, a broad understanding of the “energy system” as such and of its transformation” is needed. This lecture tries to show the technical, economical and societal challenges and to identify the links between them.

BIOGRAPHY: **Eva Hauser**, M.A., born 1972, studied political science, economic and social history and anthropogeography at the Universities of Saarbrücken and Cardiff from 1991 to 1997. She wrote her Master thesis on European Regional Policy. Afterwards, she worked as a project manager on studies about energy efficiency at Energy-Cities in Besancon in France ; later on, she worked in the management of two non-profit companies in the field of research and waste management in France. Since 2007, she is working for the research institute IZES, Saarbrücken, Germany. Her main research areas are the transformation of the electricity system to a renewables based-one, with a special focus on the necessary political and economical regulatory framework.





“Time-space-fractional models of anomalous diffusion: Physical basis, approximate solutions and analysis for application in material science”,

Jordan HRISTOV

Department of Chemical Eng., University of Chemical Tech. and Met. Bulgaria

ABSTRACT: The lecture presents the physical basis and the mathematical approach to model anomalous diffusion emerging in new materials and special processes by space and time- fractional diffusion equations. The main approaches for solution of the existing models from pure mathematical basis parallel to the approximate integral-balance method involving space-fractional derivatives of Riemann-Liouville and Caputo are presented.

BIOGRAPHY: **Professor Jordan Yankov Hristov** was graduated from Electrical Engineering (Measurements), Technical University- Sofia in 1979. He is working at the Dept. of Chemical Engineering, University of Chemical Technology and Metallurgy from Sofia. Starting from a position of a technician, even though he was a graduated engineer, he was promoted in the next 3 years to a research fellow. He has obtained his Ph. D degree in 1994 in Chemical Engineering. He was promoted in 1998 to the associate professor position and in January 2014 as a professor of Chemical Engineering. The main research area developed more than 30 years was the fluidization, especially, external field effects (magnetic or electric) for controlling the bed hydrodynamics and consequently the performed heat and mass transfer operations. He supervised 6 PhD theses and more than 25 M.Sc. theses. He published more than 135 papers and he obtained more than 700 citations. Since 2009, Professor Jordan Yankov Hristov is the Editor-in Chief of the International Review of Chemical Engineering-Rapid Communications and since 2012 he become the Editor in Chief of the International Journal on Advanced Materials and Technologies.



“Transition to renewable energies: a reality check”,

Marcel LACROIX

Université de Sherbrooke, Canada

ABSTRACT: The transition to renewable energies (REs) appears to be the way towards a more sustainable world. But REs are not necessarily sustainable. History and fundamental principles reveal that the energy transition is far more challenging than expected. The challenges are examined and the physical constraints are discussed. It is shown that if REs meet our wants, they cannot meet our needs. It is to the world to adapt to REs. Not the other way around. Are we ready for it?

BIOGRAPHY: **Marcel Lacroix** is a physicist and a professional engineer who holds a doctorate in nuclear engineering. His professional career spans more than 35 years in the private and public sectors in Canada and abroad. He has been a chief technical manager at Atomic Energy of Canada and Professor at many universities among which the Université Claude Bernard and the École des Mines in France. He is currently a full Professor at the Université de Sherbrooke and a private consultant for the power and process industry. He is the author of numerous technical publications among which textbooks on thermodynamics and popular books on energy and society.





"Synthesis and characteristics of composite phase change humidity control materials",

Menghao QIN

Centre for Sustainable Building Research (CSBR)

School of Architecture and Urban Planning, Nanjing University, China

ABSTRACT: A new kind of phase change humidity control material (PCHCM) was prepared by using PCM microcapsules and different hygroscopic porous materials. The PCHCM composite can regulate the indoor hygrothermal environment by absorbing or releasing both heat and moisture. The PCM microcapsules were synthesized with methyl triethoxysilane by the sol-gel method. The vesuvianite, sepiolite and zeolite were used as hygroscopic materials. The scanning electron microscopy (SEM) was used to measure the morphology profiles of the microcapsules and PCHCM. The differential scanning calorimetry (DSC) and the thermal gravimetric analysis (TGA) were used to determine the thermal properties and thermal stability. Both the moisture transfer coefficient and moisture buffer value (MBV) of different PCHCMs were measured by the improved cup method. The DSC results showed that the SiO₂ shell can reduce the super-cooling degree of PCM. The super-cooling degrees of microcapsules and PCHCM are lower than that of the pure PCM. The onset temperature of thermal degradation of the microcapsules and PCHCMs is higher than that of pure PCM. Both the moisture transfer coefficient and MBV of PCHCMs are higher than that of the pure hygroscopic materials. The results indicated the PCHCMs have better thermal properties and moisture buffer ability.

BIOGRAPHY: Prof. Menghao Qin is Director of the Center for Sustainable Building Research at School of Architecture and Urban Planning, Nanjing University (Top 3 in China). Prior to joining Nanjing University, he held a permanent faculty position in the School of Planning, Architecture and Civil Engineering at Queen's University in the United Kingdom, where he was champion for sustainability, and acted as the Program Director for the MSc in Sustainable Design. Dr Qin received the PhD in Building Science from the University of La Rochelle in France, and was a guest scientist at the US National Institute of Standards and Technology (NIST) in Washington DC, USA. Prof. Qin has over 18 years of research and practical experience in Building Science. He has developed advanced experimental methods, computer simulation models and environmental control technologies. He has authored/co-authored over 90 research papers, and 5 books in relevant areas.



"The effect of microstructure on the two dimensional flow of a bingham fluid in porous media",

Andrew S. REES

Department of Mechanical Engineering, University of Bath, United Kingdom

ABSTRACT: Bingham fluids exhibit a yield stress which means that they exhibit a nonzero rate of strain only when the shearing stress is larger than the yield stress. The first analysis of the flow of a Bingham fluid which might be regarded as being of relevance to porous media is that through a circular pipe, and it is what might be termed Hagen-Poiseuille-Bingham flow. The resulting variation of the mean flow with the applied pressure gradient is known as the Buckingham-Reiner relation. In recent years attention has focussed on flows through a random network of such circular capillaries in order to model realistic porous media, and the main aim has been to acquire information about



the breakthrough pressure gradient and the overall magnitude of the resulting one-dimensional flow as a function of the applied pressure gradient.

The present work extends these one dimensional (1D) analyses beginning with a presentation of some novel analytical expressions for different types of 1D media. The main focus, however, is on two dimensional (2D) networks of channels. We consider how the detailed microstructure affects how not only the amplitude of the mean flow but also its direction are dependent on the magnitude and direction of the applied pressure gradient.

First we consider various networks which tessellate the plane, namely those with square, triangular and hexagonal patterns. In each case we find that the network yields anisotropic responses to the direction of the applied pressure gradient, and this is especially so near the threshold gradient where flow may not arise in certain ranges of orientation of the applied pressure gradient but will in others. Thus we have a yield-stress induced anisotropy because all three of these networks are isotropic when filled with a Newtonian fluid. These networks become isotropic as the pressure gradient increases.

Then we consider random networks in the sense that the nodes are perturbed randomly away from those corresponding either to a square network or a triangular network. In both cases we assume that the network remains periodic overall, but that each periodic unit is itself randomly composed. We find that randomly perturbed square networks remain anisotropic even when averaged over many cases, but that triangular networks approach isotropy much more readily as the number of nodes within the periodic unit increases.

BIOGRAPHY: **Dr. Andrew Rees** is a mathematician who has been lecturing in the Department of Mechanical Engineering at the University of Bath, UK, for over 25 years. His BSc was from Imperial College, London in 1980 and his PhD, which was entitled, "Convection in Porous Media", was awarded by the University of Bristol in 1986. After a brief time at the University of Exeter as a fixed-term lecturer in Mathematics, he joined the University of Bath. His main area of research is the analysis and simulation of thermoconvective instabilities and these analytical and numerical tools are applied primarily to flows in porous media. His most recent research interest is on the modelling and simulation of flow and convection of Bingham fluids in porous media. He is the author of over 150 journal papers and is on the editorial boards of *Transport in Porous Media*, the *International Journal for Numerical Methods in Heat and Fluid Flow*, and *Computational Thermal Sciences*. Although he has pursued an academic career, he still finds time to engage in music making with two orchestras, two operatic societies, his local church choir and many other occasional groups.



List of Sessions /Contributions per session

Thermal Building and Optimisation

- 52 "Study energy consumption in residential buildings in hot humid climat in Djibouti", Mohamed Said D., Abdou Idris O., Abdoukader Ibrahim I. and Ramadan A.
- 60 "Numerical evaluation of the insulation by the mud on the thermal convection in buildings", Benachour E., Draoui B., Asnourne K., M.Hasnat and Rahmani L.
- 62 "Validation of a study on the evaluation of buildings energy north of morocco with software trnsys16", Eddib F. and Lamrani M.A.
- 73 "Heating of a greenhouse by means of a rock bed accumulator", Gourdo L., Fatnassi H., Wifaya A., Ait El Cadi R., Demrati H., Bekkaoui A., Haroune A.A. and Bouirden L.
- 80 "Analysis of exterior shading by overhangs and fins in hot climate", Idchabani R., El Ganaoui M. and Sick F.
- 87 "Energy efficiency in building: the effect of building envelope on optimal calculation of the building orientation", Kaloun S., Chihab Y. and Bencharef O.
- 97 "A simulation based-optimization method for energy efficiency of a multi-zone house integrated phase change material", Kharbouch Y., Mimet A., El Ganaoui M. and Ouhaine L.
- 104 "The study natural ventilation by using buildings windows: case study in a hot dry climate, Ghardaïa, Algeria", Hamdani M., Bekkouche S.M.A., Benouaz T., Belrabi R. and Cherier M.K.
- 123 "Study of the effect of sun patch on the transient thermal behaviour of a heating floor", Benzaama M.H., Maalouf C., Lachi M. and Mokhtari A.
- 136 "Effect of the occupant and the inside faces coating of a multi- alveolar structure on the unsteady thermal behavior of a bi-zone building", Lajimi N., Ben Taher N. and Boukadida N.
- 139 "The effects of water fountains on thermal comfort in courtyard houses in saharan regions", Benameur O. and Zemmouri N.
- 143 "Albedo effect of external surfaces on the energy loads and thermal comfort in buildings", Mansouri O., Belarbi R. and Bourbia F.
- 165 "Numerical investigation of entropy generation in a propane-air burner", Morsli S., Sabeur A. and El Ganaoui M.
- 175 "Effects of building typology on energy consumption in hot and arid regions", Tibermacine I. and Zemmouri N.
- 186 "Study of the impact of opening on the light and thermal efficiency", Hamza Cherif Y., Mokhtari A. and Benammar A.



Building Materials

- 6 "Design of an experimental device for the study of hygrothermal behavior for very hygroscopic walls", Slimani Z., Trabelsi A. and Virgone J.
- 59 "Effect of locations and thicknesses for the different material constituting a building wall", El Khattabi E., Mharzi M. and Nadah M.A.
- 64 "Heat transfer in porous building material", Bennai F., Abahri K., Belarbi R. and Tahakourt A.
- 111 "Synthesis and characteristics of composite phase change humidity control materials", Qin M. and Chen Z.
- 117 "Infrared thermography and finite element method applied to the detection of a plaster detachment", El Afi M., Belattar S. and Bouferra R.
- 125 "Experimental validation of a ham-bes co-simulation approach", Ferroukhi M.Y., Belarbi R., Limam K. and Bosschaerts W.
- 133 "Experimental assessment of the variability of concrete air permeability: repeatability, reproducibility and spatial variability", Issaadi N., Hamami A.A., Belarbi R. and Aït-Mokhtar A.
- 144 "Optimal control by using reduced order models for transfer equations", Ouleghlou M. and Allery C.
- 146 "Green wall impacts inside and outside buildings: experimental study", Djedjig R., Belarbi R. and Bozonnet E.
- 151 "Thermal transmittance comparison between multilayer walls made from hollow fired clay and plaster-granular cork bricks using electrical analogy", Raefat S., Souihel M., Garoum M. and Laaroussi N.
- 174 "Numerical analysis of heat and moisture transfer in porous material", Thi V., Mnasri F., Khelifa M., El Ganaoui M. and Rogaume Y.
- 196 "Electrical prediction of tortuosity in porous media", Merioua A., Bezzar A. and Ghomari F.
- 198 "Comparison between the permeability water and gas permeability of the concretes under the effect of temperature", Mohammed Belhadj A.H., Mahi A., Choinska M. and Khelidj A.
- 201 "Valuation of natural pozzolan for energy renovation of old buildings", Benchiheub D., Amouri C., Houari H. and Aggoune M.



Sustainable Constructive Materials

- 30 "Influence of drying conditions on hydration of cement pastes with substitution of portland cement by a recycled cement paste fine", Bordy A., Younsi A., Fiorio B. and Aggoun S.
- 34 "Effect of concrete waste quality on the compressive strength of recycled concrete", Kebaili B., Kebaili O. and Redjel B.
- 98 "Influence of recycled aggregates on the mechanical and tribological behavior of concrete", Falek K., Aoudjane K., Kadri E.H. and Kaoua F.
- 101 "Performance of dune sand concrete made using recycled materials", Azzouz L., Benabed B. and Kenai S.
- 103 "Elaboration and characterization of eco-materials made from recycled or bio-based raw materials", Thieblesson L.M., Collet F., Prétot S., Lanos C. and Kouakou H.
- 112 "Characterization of sand slag concrete", Senani M., Ferhoune N. and Guettala A.
- 115 "Comparative study of the properties of mortars with recycled glass aggregates incorporated by adding and substituting", Bentchikou M., Bouriah S., Hamdane N., Debieb F. and Boukendakdji O.
- 138 "Analysis of physical and mechanical properties of concrete containing recycled aggregate for the enhance of these aggregates", Goufi N., Kerdal K, Abidelah A., Kaid N. and Ayed A.
- 154 "Valorization of quarries marble wastes sand as an addition in cement", Berdoudi S., Hebhouh H., Belachia M. and Djebien R.
- 160 "Properties of fiber reinforced concrete using recycled aggregates", Setti B., Setti F., Hammoudi S. and Achit-Henni M.
- 178 "Mechanical and thermal characterization of stabilized earth bricks", Toure P.M., Sambou V., Faye M. and Thiam A.
- 200 "Contribution to the modeling of cracked composite panels", Beghdad H., Rahal N., Tehami M. and Souici A.



Heat and Mass Transfer Optimisation (1)

- 1 "Analytical and numerical study of double diffusive convection with sores and dufour effects in a horizontal porous layer", Abbes A., Mamou M. and Benissaad S.
- 5 "Free convection heat transfer of nanofluids into cubical enclosures with a bottom heat source: lattice boltzmann application", Boutra A., Ragui K., Bennacer R and Benkahla Y.K.
- 20 "Numerical analysis of non-premixed combustion using 2d and 3d unsteady reynolds averaged navier-stokes equations", Guessab A., Aris A., Mourad T.J. and Benamar A.
- 28 "Quantification of emissions in a turbulent diffusion flame applied to a burner", Hedef A., Mameri A., Aouachria Z. and Thabet F.
- 45 "Study of the coke combustion kinetics: the modeling of a natural phosphate calcination process", Bouatba I., Bilali L., Benchanaa M. and Elhammioui M.
- 53 "Rehafutur : insitu instrumentation for a comprehensive building analysis", Derbal R., Brachelet F., Antczak E., Defer D. and Lucas A.
- 84 "Volume reconstruction of a plane jet impinging on a slotted plate using the phase averaged method", Hamdi J., Assoum H.H., El Hassan M., Abed-Meraïm K. and Sakout A.
- 90 "Parametric study on natural convection for nanofluids in a heated chamber", Bara E.H., El Hamdani S., Bendou A. and Limam K.
- 96 "MRT-scheme applied to natural convection coupled to surface radiation in a cavity partially heated from one vertical side and cooled from above", Rehhali K., Hasnaoui M., Raji A., Alouah M. and El Mansouri A.
- 122 "Control volume finite element method for a benchmark validation of a natural convection in a square cavity", Hasnat M., Belkacem A., Kaid N. and Benachour E.
- 129 "Numerical simulation of CH₄-H₂-air non-premixed flame stabilized by a bluff body", Alliche M., Kheladi F.Z. and Chikh S.
- 152 "Hybrid FD-LBM simulations of thermosolutal convection generated in an inclined enclosure in the presence of sores and dufour effects with heatlines and masslines concepts", Hasnaoui S., Amahmid A., Raji A., Hasnaoui M. and Dahani Y.
- 211 "Phase change materials for improving the inertia thermal of building materials", Laaouatini A., Martaj N., Bennacer R., Elomari M. and El Ganaoui M.



Materials / Energy Products

- 2 "The use of pleurotus mutilus as biosorbent for nickel (ii) removal from synthetic aqueous solution in a fixed-bed column", Gherbia A., Chergui A., Yeddou A.R., Selatnia A. and Nedjemi B.
- 3 "Electronic properties of phosphorene nanoribbons", Boutahir M., Rahmani A., El Majdoub S., Fakrach B., Chadli H. and Rahmani A.
- 4 "Theoretical infrared phonon modes and band gap calculations of a bundle of two single walled carbon nanotubes", Rahmani A., Boutahir M., Fakrach B., Chadli H. and Rahmani A.
- 26 "Oxydation of a nanostructured superalloy of high temperature", Aklouche S., Adjal S. and Miroud D.
- 41 "Analytic study of oxygen diffusion in aluminum alloy at high temperature", Benantar C., Aklouche S. and Attafi S.
- 42 "Numerical modelling of HDPE behavior during 2-ECAP process using 90° and 120° dies", Mistak A. and Aour B.
- 71 "Peritectic structures proposed as materials for thermal energy storage", Achchaq F. and Palomo Del Barrio E.
- 72 "Crystallization activation of undercooled xylitol by bubbling for energy discharge process", Godin A., Duquesne M., Palomo Del Barrio E., Achchaq F. and Monneyron P.
- 94 "In situ simulation by rheed and photoemission of INAS(001) $\alpha_2(2 \times 4)$ reconstructed surface", Khachab H., Nouri A., Abdelkafi Y. and Brahmi M.
- 106 "Synthesis, characterization, electron paramagnetic resonance and uv₂visible study of perovskite layered system $[\text{NH}_3-(\text{CH}_2)_8-\text{NH}_3]_2\text{CuCl}_4$ ", Ettakni M., Aazza J., Haiki F., Kaiba A. and Khechoubi M.
- 137 "Optimization of the band gap and transmitter thickness to boost efficiency of alxga1-xas/ gaas multi-junction solar cell", Hemmani A., Nouri A. and Khechab H.
- 164 "The dolerite of tindouf basin (naga)", Bentaalla-Kaced S., Aifa T., Dermacji K. and Ould Hamou M.
- 173 "Stability study of output voltages of single stage three levels inverter for pv system in south algeria", Thameur A., Benamrane K., Benslimane T., Abdelkhalek O. and Borni A.
- 197 "Experimental test for evaluation of scc static segregation", Bensebti S.E., Chabane A., Aggoun S. and Houari H.
- 207 "Effect of tunnel junction on the indium gallium nitride multijunction tandem solar cell performances", Dennai B., Belnslimane H. and Khachab H.

Sustainable Constructive Materials (II)

- 13 "Effects of waste marble powder on rheological properties and strength of self-compacting concrete", Boukhelkhal A., Azzouz L., Belaidi A.S.E., Benabed B., Kenai S. and Kadi E.H.
- 18 "Effect of water film thickness on the rheological behavior in the presence of mineral addition with polycarboxylate superplasticizer", Adjoudj M., Boubekour T., Didouche Z., Ezziane K. and Kadri E.H.
- 69 "Microstructure characterization and numerical analysis of the mechanical behaviour of arc-sprayed composite coating", Fizi Y., Mebdoua Y., Lahmar H. and Benamar M.E.A.
- 86 "Energy consumption reduction in concrete mixing process by optimising mixing time", Ngo H-T., Kaci A., Kadri E.H., Ngo T-T, Trudel A. and Lecrux S.
- 140 "Vulnerability assessment for steel structures", Amellal O. and Bensaïbi M.
- 142 "Effect of supplementary cementitious materials (scm) on delayed ettringite formation in heat-cured concretes", Amine Y., Leklou N. and Amiri O.
- 145 "Influence of accelerated carbonation on co₂ diffusion coefficient of cement pastes", Namoulniara K., Turcyr P., Gendron F., Aït-Mokhtar A. and Meusnier J-F.
- 147 "Chemical composition of the interstitial solution of cementitious materials", Cherif R., Hamami A.A., Aït-Mokhtar A. and Meusnier J-F.
- 166 "Practical concrete rheometer with new vane geometry", Soualhi H., Kadri E.H., Ngo T-T., Bouvet A. and Cussigh F.
- 180 "Natural pozzolana addition effect on compressive strength and capillary water absorption of mortar", Deboucha W., Leklou N., Khelidj A. and Oudjit M.N.
- 182 "Influence of different amounts of natural pozzolan from cameroonian volcanic scoria on the rheological properties of portland cement pastes", Juimo Tchamdjou W.H., Cherradi T., Abidi L. and Oliveira L.
- 183 "Influence of the color of natural pozzolan from cameroonian volcanic scoria on the rheological properties of portland cement pastes", Juimo Tchamdjou W.H., Cherradi T., Abidi L. and Oliveira L.
- 189 "Hydration kinetics of compound cement in the presence of superplasticizers", Didouche Z., Ezziane K. and Adjoudj M.
- 191 "Buckling analysis of chiral single-walled carbon nanotubes using non-local timoshenko beam theory", Zidour M., Bensattalah T., Ait Amar Meziane M. and Adim B.
- 192 "Study of the effect of marble fillers substitution of cement on the rheological and mechanical characteristics of the self-compacting concrete (SCC)", Djecri N., Rahmouni Z. and Belagraa L.



Heat and Mass Transfer Optimisation (II)

- 37 "Study of laminar-turbulent transient flow conjugated with mixed convection in a vertical channel", Belaid A., Kholai O., Djebli A., Arrif T. and Boulkroune S.
- 43 "Coupled radiation and double-diffusive laminar mixed convection flow in a lid-driven cavity", Cherifi M., Benbrik A., Laouar-Meftah S. and Lemonnier D.
- 63 "Unsteady natural convection in a water filled cavity with hot partitioned wall", Zemani-Kaci F. and Sabeur A.
- 66 "Study of dynamic and thermal fields in a channel filled with an anisotropic porous matrix", Ben Aoua S., Kibboua R. and Mechighel F.
- 74 "Numerical analysis of bifurcations in thermal convection of Boger fluids saturating a porous square box", Ben Hamed H., Ouarzazi M.N., Chahtour C., Naderi P. and Beji H.
- 93 "Critical dimension of a circular heat and solute source for an optimum transfer into square porous enclosures", Ragui K., Boutra A., Bennacer R. and Benkahla Y.K.
- 95 "Numerical and analytical analysis of the thermosolutal convection in a heterogeneous porous cavity", Choukairy K. and Bennacer R.
- 132 "Effect of buoyancy ratio on unsteady double diffusive natural convection in vertical open-ended cylinder filled with porous medium", Himrane N., Ameziani D.E., El Ganaoui M. and Balistrrou M.
- 153 "Mixed convection in horizontal duct with double population lattice boltzmann method", Sahraoui N.M. and Houat S.
- 159 "Three-dimensional simulation of natural convection in cubic cavity partially filled with porous media", Habbachi F., Segni Oueslati F., Bennacer R., El Ganaoui M. and Elcafsi A.
- 168 "Simultaneous estimation of volumetric capacity and thermal conductivity of moroccan wood species from experimental flash method", Souihel M., Raefat S., Garoum M. and Laaroussi N.
- 181 "Numerical analysis of Al₂O₃/water nanofluids natural convection and entropy generation in enclosures", Boudaoud W., Sabeur A., Morsli S. and El Ganaoui M.
- 184 "Numerical simulation of flow through a porous square cylinder", Mahdhaoui H., Chesneau X. and Laatar A.H.
- 185 "Heat and mass transfers by natural convection during water evaporation in a vertical channel with a protuberance", Mchirgui O., Chesneau X. and Laatar A.H.



Hygroscopic & Bio-Materials / Composites

- 14 "Thermal conductivity and thermal degradation of cementitious mortars reinforced with doum and diss fibers", Achour A., Belayachi N. and Ghomari F.
- 35 "A dynamic simulation of the low-energy building using the wood-based material", Bahria S., El Ganaoui M., Amirat M., Hamidat A. and Ouhsaine L.
- 38 "Effect of wall orientation of the sand concrete lightened by lignocellulosic materials on the thermal inertia properties", Belhadj B., Bederina M. and Quéneudec M.
- 47 "Hygrothermal properties of hemp starch composite", Bourdot A., Moussa T., Malouf C. and Polidori G.
- 48 "On the application of carbon nanotube-based composite materials for smart design of wind turbine blades", Attaf B.
- 51 "Hemp-straw composites: thermal and hygric performances", Collet F., Prétot S. and Lanos C.
- 54 "Influence of hardener type for epoxy matrix on the mechanical behavior of composite laminates", Basaid D., Aribi C., Kadri D. and Benmounah A.
- 58 "Microscopic swelling analysis of spruce wood in sorption cycle", El Hachem C., Abahri K. and Bennacer R.
- 88 "Hydric and structural approaches for earth based materials characterization", Remki B., Abahri K., Belarbi R. and Bensaïbi M.
- 108 "Modelling of heat and mass transfer during convective drying of wood", Andrianantenaina M.H., Zeghmati B., Ramamonjisoa B.O.A. and Randriamilantoniaina Y.O.
- 109 "Characterization and comparison of thermal and hygric properties of hemp-clay composite and hemp-lime concrete", Mazhoud B., Collet F., Pretot S. and Lanos C.
- 110 "Multi-scale characterization of hygrothermal transfers in the unfired earth", Medjelekh D., Ulmet L. and Dubois F.
- 113 "Experimental evaluation of load-strain behaviour of GFRP poles under flexural loading.", Metiche S. and Masmoudi R.
- 118 "Evolution of the stress distribution in the cross-ply aged composite laminates", Khodjet Kesba M., Benkhedda A., Adda B. and Boukert B.
- 134 "Distribution of fibers and their effect on lateral deformation", Saoudi N., Saoudi B., Cherfa H. and Bezzazi B.



Thermal Building and Energy Storage

- 10 "Radiative forcing of desert aerosol observed at ouarzazate (Morocco), tamanrasset (Algeria) and ilorin (Nigeria)", Tahiri A., Diouri M. and Barkani J.
- 49 "Simulation of summer and winter microclimate and thermal comfort within urban open space in semi-arid climate", Kedissa C., Belarbi R. and Ouattas S.
- 56 "Thermal characteristic in solar air heater fitted with plate baffles and heating corrugated surface", Sahel D. and Benzeguir R.
- 57 "Crystal growth kinetics of sugar alcohols as phase change materials for thermal energy storage", Duquesne M., Godin A., Palomo Del Barrio E. and Achchaq F.
- 76 "On the semi-analytical solution of integro-partial differential equations", Hasseine A., Attarakih M., Belarbi R. and Bart H.J.
- 102 "Effect of the position of the phase change material (PCM Na₂CO₃, 10H₂O) on the solar chimney effect", Bin L., Liangliang S., Qi W., Shaoli M. and Bennacer R.
- 119 "Numerical study of transfer by convection in a lid-driven cavity with a thin pcm layer", Binous M.S., Abide S., Zeghmati B. and Hassis H.
- 149 "Numerical study of the solidification of nano-enhanced phase change material in a latent heat storage unit cooled by laminar heat transfer fluid flow", Elbahjaoui R., El Qarina H. and El Ganaoui M.
- 167 "Study of thermo physical properties of a building material based on pcm", Souci Y. and Houat S.
- 171 "Instant autovaporization as intensification way of classic distillation processes: fundamental and industrial applications", Issaadi-Hamitouche T., Besombes C. and Allaf K.
- 202 "Numerical modelling of solar drying of thin layer of wet sand", Benaouda N-E. and Zeghmati B.
- 205 "Numerical simulation of heat and mass transfers during solar drying of residual sludge: solar radiation effect", Ben Hassine N., Chesneau X. and Laatar A.H.
- 206 "Numerical study of coupled heat of and mass transfers in multilayer building materials: analysis of the effect of internal and external insulation", Mnasri F., Li M., El Ganaoui M., Khelifa M. and Gabsi S.
- 208 "A comparative study about the energetic impact of dryland residential buildings with the integration of photovoltaic system", Belahya H., Boubekri A. and Kriker A.



Energetic Systems

- 17 "Exergetic analysis and optimization regime of temperatures for absorption chiller single stage H₂O-NH₃", Adjibade M.I.S., N'Tsoukope K.E. and Thiam A.
- 22 "Performance improvement of combined organic rankine-vapor compression cycle using a serial cascade evaporation in the organic cycle", Bounefour O. and Ouadha A.
- 23 "Comparative assesment of lng and lpg in hcci engines", Djermouni M. and Ouadha A.
- 32 "Modelling of an rdc extraction column using the differential maximum entropy method (dmaxentm)", Attarakih M., Hasseine A. and Bart H-J.
- 40 "Perfrmance optimization for absorption refrigeration machine", Ben Iffa R., Bouaziz N. and Kairouani L.
- 46 "Energetic and exergetic analysis of a novel mixture for an absorption/compression refrigeration system: r245fa/dmac", Lounissi D., Bouaziz N. and El Ganaoui M.
- 50 "Experimental investigation of syngas and hydrogen", Borisut C., Zeghmati B., Satta W. and Pravitt T.
- 89 "Numerical modeling of a refreshing buried tank", Dehina K., Mokhtari A.M. and Souyri B.
- 127 "Design analysis of a mvc desalination unit powred by a grid connected photovoltaic system", Ibrahimi M., Abaoui A. and Aoura Y.
- 148 "Thermal and optical analysis of a 3.9 mwth parabolic trough solar collector operating with air at 600°C", Ait El Cadi R., Selhaoui N., Bouabid K., Gourdo L., Ihlal A., Bouirden L., Abnay B. and
- 155 "Simulation of photovoltaic installation connected to the grid with storage system", Ben Mabrouk S., H.Oueslati, Ben Mabrouk A., Zizzo G., La Cascia D., Dusonchet L., Favuzza S. and Massaro F.
- 162 "A numerical investigation of a diffusion-absorption chiller based on propylene-nonane mixture", Soli N.
- 177 "Analyze the performance of a new system which combines orc-vcc for the cogeneration", Toujeni N., Bouaziz N. and Kairouani L.
- 187 "Transient analysis of an absorption solar refrigerator with external and internal irreversibilities", Boukhchana Y., Fellaf A. and Ben Brahim A.



Constructive Materials: Mechanical Optimisation

- 7 "Influence of the pozzolanic reactivity of the slag and metakaolin on mortars", Abdelli K., Tahlaiti M., Belarbi R. and Oudjit M.N.
- 8 "Influence of the origin of metakaolin on pozzolanic reactivity of mortars", Abdelli K., Tahlaiti M., Belarbi R. and Oudjit M.N.
- 21 "The behavior of concrete based on opc cement and blended cement subjected to accelerated carbonation", Merah A., Khenfer M.M. and Quéneudec M.
- 27 "Meso-scale analysis of the aggregate size influence on the mechanical properties of heterogeneous materials using the brazilian splitting test", Al-Khazraji H., Benkemoun N., Choinska M. and Khelidj A.
- 29 "Prediction of the stiffness modulus of a polymer modified asphalt via the experimental design method", Meksen A. and Bensaïbi M.
- 39 "Effect of the glass powder and the polypropylene fibers on the characteristics of high-performance concretes", Belkadi M., Chaid R., Perrot A., Djeridi A. and Saoudi N.
- 44 "The total replacement effect of limestone powder by marble powder on the freeze-thaw resistance of the self-compacting concrete", Bensalem S., Amouri C., Houari H., Belachia M. and Belkadi A.
- 100 "Effect of sand type on performances of self-compacting concrete", Azzouz L., Benabed B., Kadri E.H. and Kenai S.
- 158 "Thermo-mechanical behavior of unfired clay bricks and fired clay bricks made from a mixture of clay and laterite", Bodian S., Faye M., Sene N.A., Sambou V., Limam O., Aubert J.E., Bal H. and
- 161 "Abrasion resistance of concrete and high strength concrete reinforced with steel fibers", Setti F., Ezziane K. and Setti B.
- 163 "Seismic vulnerability classification of roads", Adafer S. and Bensaïbi M.
- 172 "Mechanical behaviour of a structure reinforced by carbone fibers", Ayad T., Kadri T. and Rezigua A.
- 190 "Frp properties effect on numerical deformations in frp bars-reinforced concrete elements in hot zone", Zaidi A., Brahim M.M., Mouattah K. and Masmoudi R.
- 199 "Time-dependent behavior of composite steel-concrete beams with creep according eurocode 4", Rahal N., Beghdad H., Tehami M. and Souici A.
- 209 "Dynamic analysis of fiber reinforced composite beam containing a transverse crack", Hammou Y., Adjal A., Benzidane R. and Sereir Z.



Inner and Outer Flows

- 19 "Resuspension of indoor particles due to human foot motion", Benabed A. and Limam K.
- 33 "Experimental investigation of soil particles filtration process through granular porous media", Azirou S., Benamar A. and Tahakourt A.
- 79 "A cfd consol model for simulating complex urban flow", Houda S., Houda S., Belarbi R., Hasseine A. and Zemmourti N.
- 82 "Dynamics of a plane impinging jet in the presence of self-sustaining sound: correlation between the acoustic field and the transverse velocity", Assoum H.H., El Hassan M., Hamdi J., Ali M., Abed-Meraïm K. and Sakout A.
- 83 "The turbulent kinetic energy and the acoustic field in a rectangular jet impinging a slotted plate", Assoum H.H., El Hassan M., Hamdi J., Hammoud A, Abed-Meraïm K. and Sakout A.
- 85 "Finite element modeling of polydisperse flows using the direct quadrature method of moments", Janssens B., Bosschaerts W. and Limam K.
- 91 "Numerical study of transport and particle deposition inside buildings", Limam K., El Hamdani S., Abadie M., Linder G. and Bendou A
- 92 "Experimental study of particle concentrations in an underground magenta metro station of paris", Fortain A., Limam K., Cremezi Charlet C. and Linder G.
- 107 "An approach using lattice boltzmann method to simulate fluid- structure-interaction", Benamour M., Liberge E. and Béghein C.
- 128 "Validation of turbulence models for simulation of turbulent flow of air around an obstacle square section", Alliche M., Rebhi R., Mamou M. and Korichi A.
- 130 "CFD-based entropy generation analysis of multiple jets", Boussoufi M., Sabeur-Bendehina A., A.Ouadha and El Ganaoui M.
- 156 "A geometrical approach for simulating static contact angles in multiphase flows with a lattice boltzmann method", Leclair S., Abahri K., Belarbi R., Latt J., Chopard B. and Bennacer R.
- 179 "Article: numerical study of heat transfer and flow characteristics of air jet in a semi-confined cavity", Tovondrainy N., Abide S. and Zeghmati B.
- 188 "Effects of the diameter and blades orientation on the mixing tank efficiency", Kamla Y., Arab I.M., Ameer H., Bouzti M. and Kamla K.
- 194 "Numerical investigation and analysis of indoor air quality in a room based on impinging jet ventilation", Koufi L., Younsi Z., Cherif Y. and Naji H.



Safety / Reliability and Durability

- 9 "Influence of the cooling of building surfaces on the temperature of indoor air", Kaddour A. and Bekkouche S.M.A.
- 12 "Risk-eu method applied to the Algerian city of arzew to assess exposure to earthquakes", Aouane A., Rahal D., Mohammed Belhadj A.H. and Hamou K.
- 24 "Composite materials containing different polymer levels: designing & estimating durability indicators", Latroch N., Benosman A.S., Bouhamou N., Belbachir B., Taïbi H. and Mouli M.
- 36 "Experimental and computer modeling study of the diffusivity in cement-silica fume based materials", Bajja Z., Dridi W., Darquennes A. and Bennacer R.
- 68 "Seismic scenarios of Tipaza network supply", Halfaya F.Z., Djilali H.I., Bensaïbi M. and Davenne L.
- 77 "Chloride transport on partially saturated concrete media: the influence of the hydric state", Chalabi H., Bezzar A. and Khelidj A.
- 81 "Rehabilitation study of construction built in seismic zone in Algeria", Djafar Henni I. and Kassoul A.
- 105 "Seismic fragility curves of unreinforced masonry structures", Djaalil F. and Bensaïbi M.
- 116 "Seismic vulnerability index for bridges", Djemai M.C. and Bensaïbi M.
- 121 "Combined effect of temperature and sulfate attack on the durability of repair mortar based on mixture of dune-alluvial sand", Lakhdari M.F., Zaidi A., Bouhicha M. and Krobba B.
- 124 "Effect of sand nature and rate of natural pozzolana on the durability of mortars", Rouibi M., Khelafi H., Kaid N. and Ghomari M.L.
- 135 "Impact of fiber treatment on the fire reaction and thermal degradation of building insulation straw composite", Belayachi N., Hoxha D. and Ismail B.
- 157 "Fractal dimension of concrete mix gradation: a quantitative parameter for some concrete properties", Sebsadji S.K. and Chouicha K.
- 169 "Seismic vulnerability assessment of blida city", Tadjer K., Tadjer K. and Bensaïbi M.



Thermal and Building Optimisation

STUDY ENERGY CONSUMPTION IN RESIDENTIAL BUILDINGS IN HUMID HOT CLIMAT IN DJIBOUTI

Mohamed Said, D.^{1*}, Abdou Idris O.¹, Abdoukader Ibrahim I¹, Ramadan A¹.

*#Research Center at the University of Djibouti, Faculty of sciences
Street Djanaleh, B.P. 1904, Djibouti*

¹mohamed_said_darar@univ.edu.dj

ABSTRACT

The aim of this study is to develop representative building energy data sets and benchmark model for the Djibouti residential sector. The study focuses on the energy consumption for residential buildings in a typically hot humid climate in the city of Djibouti. This study reports the results of a recent field survey on the average consumption for residential buildings in Djibouti. In this survey, the energy use profiles for air conditioners, refrigeration, lighting, and appliances are described for two types of building construction in Djibouti. Aiming to use solar energy for electricity production in households, with a daily mean irradiation of 5.87 kWh/m²/day, the solar potential of Djibouti is one of the most significant in the world. Solar energy resources across the country can be developed to bring higher quality energy services to populations across the country.

INTRODUCTION

The Republic of Djibouti currently stands at a crossroads, faced with a number of critical challenges associated with the generation, distribution, and use of energy. The country remains heavily dependent on imported fossil fuels and power. This exposes it to volatile and rising oil prices, placing uncertainties on economic development, and pressing social development challenges.

In its ambitious Vision 2035, the Government of Djibouti recognizes the importance of developing these resources to meet both its economic and social development objectives. Indeed, the Government has made clear that its objective is to meet 100% of domestic demand through renewable energy by 2020. Djibouti has abundant geothermal, wind, and solar energy resources and it can be developed to bring higher quality energy services to populations.

The economic growth nourishes the demand for building space, comfort, and services, which raises the demand for residential energy.

A design with the minimum energy consumption must deal with the specific climatic conditions. Djibouti climate is called “maritime desert”. A maritime desert is a climatic region with warm humid conditions in the winter season and hot humid

weather in summer. The difference with tropical climate is the scarcity of rainfall. However, the presence of a warm sea near the city of Djibouti results in high humidity.

Red sea water temperature is between 25° C and 32° C all of the year. Many propositions have been made to make buildings with less energy consumption in Djibouti [1].

To allow the development of economic activities with less energy, efforts must focus on three areas: energy conservation, in individual behavior; energy-efficient equipment and renewable energy [2].

Literature review

Energy modelling for residential building

In the area of residential energy modelling, different methods have been applied to estimate the energy use in many countries. In the literature, the most common three methods to estimate energy use in buildings are (1) linear regression models, (2) neural networks, and (3) survey [3]. For example, Aydinalp and al. developed residential energy consumption models for the Canadian residential sector. The study used a neural network method to estimate the consumption

of appliances, lighting and space-heating and cooling components [4], others similar studies using neural network include the work of Sozen and al. in Turkey, Azadeh and al. in Iran , karatou et al. I, Greece, Gonzalez in Spain and Abdel-Aal in Saudi Arabia [5 -9]. On the other side, example using linear regression model is the work of bianco et al. tried to forecast electricity consumption in Italy [10-11]. Similar studies using linear regression include the work Ranjan in India, Abosedra in Lebanon, further in this paper. The main focus of this paper is real data and surveys of the building energy

However, considering electricity consumption, the building sector represents by far the largest share, about 90% of the country's consumption. As the following graph shows (figure 1), the service sector

Mohamed in New Zeland, Pachauri in india and Murata et al. in China [12-16].

However, the neural network method and linear regression method require validation by comparison with real data and fact patterns for existing consumption and a priori statistical analysis. Despite the importance of neural network and linear regression techniques the two methods are not investigated

consumption to build a comprehensive and detailed residential energy model

alone accounts for approximately 50% of electricity consumption, 35% for public administration and 13% for the branch of commercial buildings.

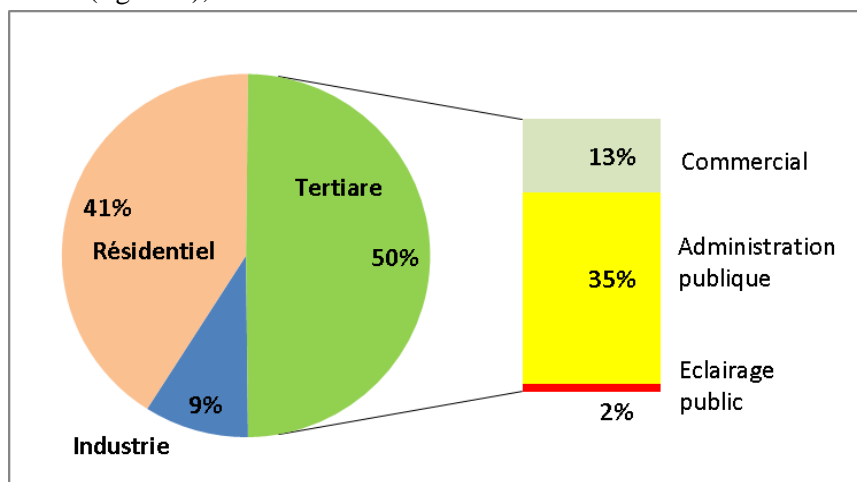


Figure 1: Sectoral distribution of electricity consumption in Djibouti – 2013 [2]

3. METHODOLOGY

3.1 Selection of representative model

The methodology implemented in this paper includes aspects which determine the energy consumption characteristic of residential building in Djibouti. The first step was to carry out a literature review on past and recent survey. The second step was to identify typical building construction and characteristics through field survey. The survey plan included a description of a comprehensive set of building construction, equipment and dimension. Several specific energy consumption issues were addressed during the on site survey. For third and final step, actions were taken to develop representative benchmark models of residential building

According to the results of the 2nd General survey of Population and Housing (RGPH) in 2009, conducted by department of the statistical studies (DISED) the total resident population is 818 159 in DJIBOUTI.

More than 70% of the population lives in urban areas, with nearly 60% in the capital city - Djibouti. Mainly three types of housing is observed in Djibouti city. Ordinary houses in lightweight sheet metal and plywood are the most representative with 60,844 units. Followed by apartments in a building and single villas constructed of concrete block Representatives in 1413 and 1477 respectively housing (DISED RGPH 2009).

For our study we have tried to define a representative model of energy consumption in residential building with single household.

3.2 Residential Building description

There are two types of building construction in Djibouti. The first one is construction with massive walls of bricks, concrete or stones. Roofs of this type of construction are generally

heavy roofs built with concrete. The second one is construction with light weight wall composed of aluminum sheet as external wall and wood sheet as internal wall. Roofs of this second type of construction are lightweight roofs (generally aluminum sheet). To avoid extreme heat, ceiling is generally provided under the lightweight roof. Nor the massive walls nor the light weight walls are generally insulated thermally in Djibouti. The present study we focus in residential building characterized by the massive wall which represent more than 50 % of electricity consumption in residential sector

3.3 Energy characteristics for residential building sector

The collected information was combined and analysed to reflect the energy performance of representative realistic situation in air conditioned residential buildings. The development of the representative residential apartments was underlined by building design characteristics and audited energy use data collected during the survey. On the basis of this set of data the building models together with hourly usage profiles and operation patterns of air conditioners and other equipment were established, representing typical residential building in Djibouti. Details of the representative building benchmark models are described in the results section.

3.4 Weather data and solar resources

3.4.1 Temperature and relative humidity

The climate of the Republic of Djibouti, controlled by the movement of anticyclones of Arabia and Libya as well as that of the intertropical convergence zone (ITCZ), is arid tropical type characterized by low annual rainfall and two seasons mainly differ by temperature. The season called "fresh" start of the

Two types of energy audit were conducted for the selected residential building during the October and December 2015. First analyses of the utility bills, and second a walk-through survey. The utility bill analysis was made prior to the walkthrough survey to become familiar in advance with the consumption patterns of residential building visited. This step helped in obtaining more accurate information from the building's occupants. A request to the electricity utility companies in city of Djibouti was made to provide the utility bills for the year 2013, 2014 and 2015. The bills were analysed and entered in spreadsheets to identify the patterns of use, peak demand and weather effects. Then the walkthrough visit major energy use equipment (air conditioners, ceiling fans, lighting, refrigerator, television, washing machine, etc)

Were identified and household members were asked about the hours of operating during summer and winter. Also the characteristic construction and layout of every visited apartment was noted. Later the utility bills for the year 2014 and 2015 were collected from utility companies.

end of October until April, when the ITCZ is south of the country, with temperatures between 20 ° C and 30 ° C, while the season hot from June to September when the ITCZ passes through the region, characterized by temperatures between 30 ° C and 45 ° C and a west wind dry, hot and loaded with sand, the Khamsin. Transition periods separate the two seasons, when the ITCZ is located at the latitude of the country, during which the climate is characterized by high temperatures (28 ° C-36 ° C), a high humidity and a no wind. In general, across the country, rainfall is extremely limited (150mm / year on average), irregular and particularly localized in time, the temperatures are very high, with annual averages between 25 ° C and 30 ° C, and relative humidity is quite high, with peaks in winter of about 90% and summer minima at around 40%.

3.4.2 Solar energy resources

With a daily mean irradiation of 5.87kWh/m²/day, the solar potential of Djibouti is one of the most significant in the world. And solar energy resources across the country can be

developed to bring higher quality energy services to populations across the country.

Djibouti has two peak periods of insolation (Mar-April, and Sept-Oct) when the diurnal variation between the minimum and maximum radiation values is small. The lowest radiation values are

observed from June to August, which coincide with the hot and humid season. However, even during these periods of low insolation, the country receives sufficient amounts of solar radiation of about 5-6 kWh/m²/day, which are still good enough for solar energy applications.

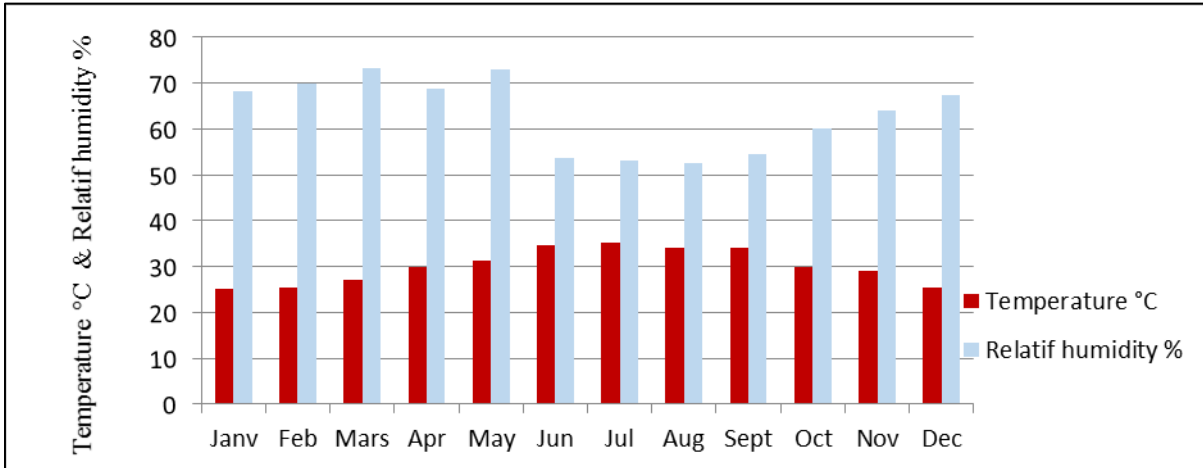


Figure 2: Average annual of the ambient temperature and the relatif humidity in the capital Djibouti-city, Source weather station of University Djibouti.

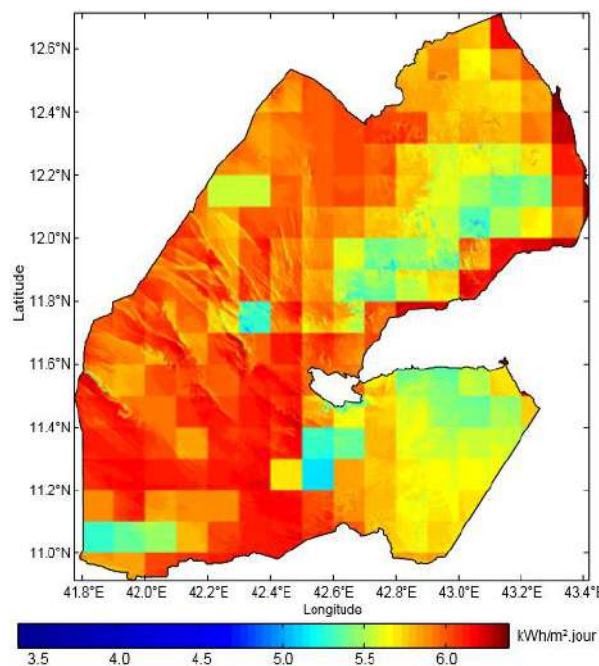


Figure 3: Annual map of average daily irradiation (kWh / m² day) in the Republic of Djibouti for the period 2008-2011 [17],

4. SURVEY RESULTS

4.1. Annual electricity use and Occupancy rates

The sample groups in this survey was 25 households. And two type of household was defined. First on is household using an air conditioner and second is household no using an air conditioner. The average consumption for typical building to be 35kWh/m²/year with air conditioner and whitout air conditioner is 15.10 kWh/m²/year. The annual energy

consumption per household is of 5050,54 kWh/year where 45% of was for air conditioning electricity using the household electricity use air conditioner. For household without air-conditioner, the annual energy consumption is 1730 kWh/year in the residential sector in Djibouti. In this survey the average people in household is 8.68 and the average occupancy density is 14,08 m² on usable floor areas per person. The occupiers are within the age range of 18-42. Most apartment occupancy would be away from home between 08:00 until 14:00. All resident would stay at home after 20:00. Most residents would stay at home on Fridays because the weekend in Djibouti.

4.5. Domestic appliance and Mechanical cooling load intensities

In this sample, more than 90% of apartments have at least three fans. The most common type is the ceiling fan besides pedestral will and table fans. The data collected in the survey shows that the average home in Djibouti has an average of 4.2 ceiling fan units. The most common fan type is the three blades (48 inch) with a speed of 330 RPM and air flow rate of 3000 CFM. The average annual operation time in Djibouti is 3285 Hours with a power of 60 Watts. The survey results indicate that apartment usage modes depend the thermal comfort level during the warm periods only fans are used and during the hot periods fan and air conditioners are used simultaneously. More than 50% of building in the sample had air conditioners (split or windows

units) serving mainly bedrooms and or living rooms. At least one AC units was found in this sample surveyed and power consumption per units is less than 1500 Watt.

4.6 Representative benchmark models to design solar energy

Representative model were constructed based on described internal load intensities and patterns. The daily operating, power demand and daily consumption of air conditioning units, ceiling fans, refrigerator, plug loads and lighting appliances in the reference model were calibrated based on the surveyed monthly utility bills. We found two representative model energy consumption for residential building. The first representative model (Table 1) based on household electricity consumption. The distribution of electricity consumption by the different domestic appliances for the representative model were realised in the figure 4. The Other represent in the table 1, the equipment like satellite decoder, mobile charge, mixer, and stereo). Solar energy could be a serious alternative in urban areas and especially for household sector. The average daily global solar irradiation is equal to 5.38 kWh/m²/day. The table 1, show the value of the parameters we need to design solar system for residential building of the two representative model energy consumption in residential building. We can see in the table 2, the electric characteristic of solar equipment we use for the two representative model were design.

Table 1; representative model of domestic appliance with air-conditioner

APPLIANCE	Number	Type (AC/DC)	Power (W)	Total Power (W)	Daily operating hours	Daily Consumption Wh/day
Lighting	6,5	220V/230V	40	240	5,8	1508
Fan	4,2	220V/230V	60	240	10	2520
Refrigerator	1	220V/230V	190	190	12	2280
Television	1	220V/230V	84	84	8	672
Air conditioning type split	1	220V/230V	1400	1400	4,75	6650
Electric iron	1	220V/230V	1000	1000	0,5	500
Others	1	220V/230V	100	100	2	200
Average consumption per day (Wh/day)						14330
Average consumption per year kWh/year						5230,45

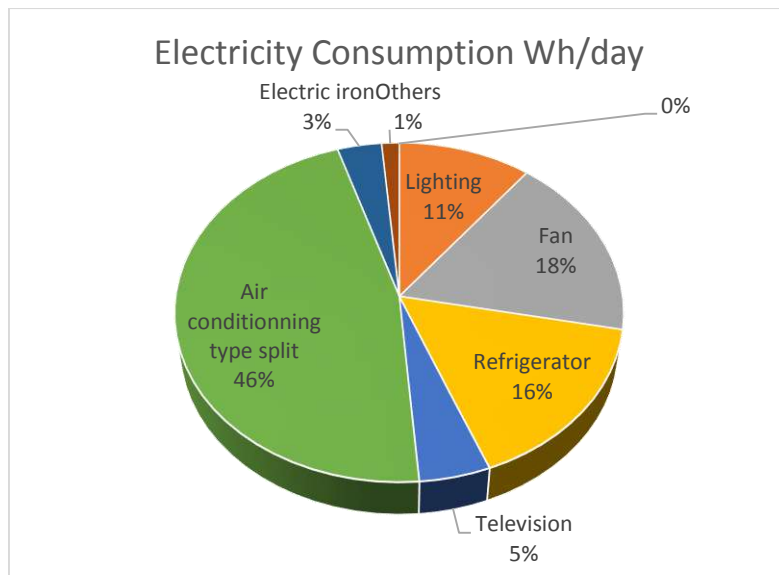


Figure 4: electricity use end by household with air-conditioner

PARAMETER	VALUE	
Irradiation kWh/m ² /day	4,4	
Battery efficiency	80%	
Lost PV efficiency (Dust & heater)	85%	
Daily Storage	2	
System Tension VDC	24	
Decharge of Deep	60%	
DESIGNATION	Household use Air-conditionner	Household Without Air -conditionner
Daily consumption (Watt hour)	14330	5078
Solar power (Watt : Wp)	4789,438503	1697,192513
Battery capacity (Amper Hour : AH)	2487,847222	881,5972222
Inverter (Watt)	3500	2000
Charge Controller (Amper : A)	110-140 A	80-110 A

Table 2: Solar energy system

5 DISCUSSION

The great need to approach the opportunities for energy efficiency in the Djiboutian residential sector requires the development of verified and update knowledge on energy performance of residential building. Therefore, the main objective of this study was to create representative models that match the electricity consumption patterns of representative residential building. Based on the surveyed residential building, the characteristics and electricity consumption patterns were analysed and the average annual building electricity use intensity was defined. During the model verification process several important lesson were learned.

First of all, the model shows that the use of air conditioners dominated the energy usage in residential buildings in the Djibouti city. Therefore, the electricity consumption patterns of residential building would be significantly affected during the extended summer period (April-october), the identifying the frequency and patterns of use of air-conditioners in relation to indoor thermal comfort should be a basic step in any future investigation.

Secondly, the study revealed that all surveyed building had a very poor thermal performance and indoor air quality. The building envelopes of most of the buildings investigated are the airtight, with single glazed opening, with non-insulated walls and without shading treatment. On the other hand, more than 60 % of building have been equipped with at least one air conditioner unit which results in peak electricity loads that the existing electricity grid cannot provide. Thus the potential in energy savings in the building sector are necessarily and in the same time high.

The survey findings revealed the most building were equipped with air conditioners, frigdes, fans and television. However, almost all appliances have no energy description labels. There must be an effort to phase out poor quality and high energy consumption product. There is a potential of energy saving in the existing building stock if high efficiency equipment and appliance are used.

The last remark is related to global climat change and the heat island effect. The increasing trend of summer

discomfort is creating on top of the current energy demand an incremental demand due to cooling. The continuation of this trend will imply a greater demand cooling in Djibouti city. This increased cooling demand is unwanted given its impacts on energy consumption and grid feeding stability and the vicious heat insland effect.

A solution to those problems might be switching to solar electric air conditioning systems to break this circle in the future. The use renewable energy technology for cooling residential building in Djibouti are investigated.

This study proves that there is sufficient evidence that energy efficiency can be improved in the building sector. Despite a great part of precious resources being wasted daily, there is an opportunity to reduce the apartment consumption of energy resources through improved end use utilisation efficiency. Improving the end-use utilisation efficiency may be achieved by improving the envelopes, operation patterns and by installing more efficient appliances.

The present study is an essential first step toward establishing models for the real application of a new energy standard in Djibouti.

CONCLUSION

Based on the data collected from surveying almost 25 residential building with different type of construction. The representative models have been constructed for the representation of typical residential building in Djibouti. The key findings from those survey have been summarised in this paper. The survey results include building physical characteristics and occupancy energy profiles. Also based on that set of data, average operating patterns of appliances were identified. These energy characteristics of residential buildings were intended to be used to model representative benchmark and reference condition of residential building in Djibouti.

The survey results show that electricity use is significantly dominated by the seasonal use of air conditioners. The use of fans reduced the total annual operation hours of air conditioners, in particular during the early and late summer periods. The average energy use per residential building is

between 16 kWh/m²/year and 36 kWh/m²/year. In addition, the frequency and pattern of use of appliances has been identified. Finally, the results presented in this paper, can provide a good basis for investigating the potential energy savings of applying the new Djiboutian energy standard.

REFERENCES

- [1] Dunham, Building for the maritime desert: climate, construction and energy in Djibouti, ISERST/VITA, 1983
- [2] UNDP Djibouti office, Rafik Missaoui. Elaboration of a strategic plan to conserve energy in Djibouti May 2014
- [3] Shady Attia, Arnaud Evrard, Elisabeth Gratia. Development of benchmark models for the Egyptian residential buildings sector. Appl Energy 2012. 01. 65
- [4] Aydinalp M. Ugursal V, fung A. Modeling of the appliance, lighting and space cooling energy consumptions in the residential sector using neural network. Appl Energy 2002; 71:87-110.
- [5] Sozen A. Arcaklioglu et al. Turkey's net energy consumption energy. Appl. Energy 2005; 81(2) : 209- 21
- [6] Azadeh A Ghaderi SF et al. A simulated-based neural network algorithm for forecasting electrical energy consumption in Iran. Energy Policy 2008; 38 (7) : 2637-44.
- [7] Karatasou S, Santamouris et al. Modeling and predicting building's energy use with artificial neural network: methods and results. Energy build 2006;38 (8) : 949-58.
- [8] Gonzalez P. Zamarreno J. Prediction of hourly energy consumption in building based on a feedback artificial neural network, Energy build 2005 ;37 (6) :595-601
- [9] Abdel -Aal RE, Al Garni AZ et al. Modelling and forecasting monthly energy consumption in eastern Saudi Arabia using abductive networks Energy 1997;22 (9) : 911-21.
- [10] Bianco V, Manca O et al. Electricity consumption forecasting in Italy using linear regression models. Energy 2009;34 (9):1413-211.
- [11] Bianco V, Manca O et al Linear regression models to forecast electricity consumption in Italy. Energy Sources, Part B: Econ Plan Policy, in press.
- [12] Ranjan M, Jain VK. Modelling of electrical energy consumption in Delhi. Energy 1999; 24 (4):351-61.
- [13] Abosedra S, Dah A, Ghosh S. Electricity consumption and economic growth, the case of Lebanon. Appl. Energy 2009;86:429-32.
- [14] Mohamed Z, Bodger P. Forecasting Electricity consumption in New Zealand using economic and demographic variables. Energy 2005; 30 (10):1833-43.
- [15] Pachauri S. An analysis of cross sectional variations in total household energy requirements in India using micro survey data. Energy Policy 2004; 32:1723-35.
- [16] Maruta A. and al. Electricity demand in the Chinese urban household sector. Appl. Energy 2008;85(12):1113-25.
- [17] PILLOT, B., MUSELLI, M., POGGI, P., HAURANT, P., HARED, I. (2013). The first disaggregated solar atlas of Djibouti: a decision-making tool for solar systems integration in the energy scheme. Renewable Energy, 57(0)

NUMERICAL EVALUATION OF MUD INSULATION ON THERMAL BUILDING COMFORT.

E. Benachour, B. Draoui, K. Asnoune, M. Hasnat and L. Rahmani
ENERGARID Laboratory, University of Tahri Mohamed - Bechar, P.O. P 417. 08000,
Road Kenedza , Bechar, Algeria

*Elhadj Benachour: Email: Benachour_elhadj@yahoo.fr

ABSTRACT

Insulation materials run the gamut from bulky fiber materials such as fiberglass, rock and slag wool, cellulose, and natural fibers to rigid foam boards to sleek foils. Bulky materials resist conductive and -- to a lesser degree -- convective heat flow in a building cavity. Rigid foam boards trap air or another gas to resist conductive heat flow. Highly reflective foils in radiant barriers and reflective insulation systems reflect radiant heat away from living spaces, making them particularly useful in cooling climates. Other less common materials such as cementitious and phenolic foams and vermiculite and perlite are also available. The Initial energy costs include the amount of energy consumed to produce the material. The long term energy cost is the economic, ecological, and social costs. Sometimes people take into consideration the energy savings or durability of the materials and see the value of paying a higher initial cost in return for a lower life time cost. so, This work presents a study of numerical simulation aiming at the role and the influence of the insulation by the mud Reduced like a local material to the town of Bechar located at the south west of Algeria (SAHARA OF Algeria), we are interested in a comparative study for pursued these goals. In this context, an analogy was used for the functions which are discretized by the finite difference method and integrated in the FLUENT software which is based on the finite volume method. The results are presented in the form of distributions of the isotherms, the streamlines, local and average Nusselt number of which the goal to study the influence on comfort.

Key words: Building material, Materials Energy, Heat transfer, Thermal convection, CFD, Laminar flow.

NOMENCLATURE

Latin symbols

g	: Gravitational acceleration	[m/s ²]
H	: Height of the cavity	[m]
L	: The length of the cavity	[m]
e	: Wall thickness	[m]
C_p	: Specific heat at constant pressure	[J / kgK]
h	: Heat transfer coefficient	[W m ⁻² K]
Nu	: Average Nusselt number	[-]
t	: Time	[s]
P	: Pressure	[Pa]
T_c	: Temperature of hot wall	[K]
T_f	: The temperature of cold wall	[K]
T	: Temperature	[K]
X, Y	: Dimensionless coordinates	[-]
U, V	: Dimensionless velocity components	[-]
Pr	: Prandtl number	[-]
Ra	: Rayleigh number	[-]

Greek letters

α	: Thermal diffusivity	[m ² /s]
β	: Coefficient of expansion	[K ⁻¹]
λ	: Thermal conductivity	[W/mK]
μ	: Dynamic viscosity	[Kg m ⁻¹ /s ⁻¹]
ρ	: Density	[Kg/m ³]
ΔT	: Temperature difference	[K]

INTRODUCTION

Actually, the fast economic growth and high standards of living imposed the world to consume large amount of conventional energy resources (fossil fuels) that drive environmental pollutions and climate changes. In addition, the dependency towards conventional energy resources will empties the sources more rapidly. Therefore, the effectiveness utilization of energy becomes a main issue recently. Various renewable energy systems were developed to enhance energy efficiency such as thermal energy storage (TES) system [1]. TES is the temporary energy storage medium for later used. It provides realistic solution to increase the efficiency of the energy utilization and management. This technology is an elegant energy technology which can be used in various industries especially building industry [2–5].

There many important factors influencing electricity use in sahara of algeria . One is economics and population growth and the other is hot weather. As expected, electricity use increased as economic activity and population, both increased. Hot weather

also increases electricity demand for air conditioning. Thermal comfort is dependent and influenced by a range of environmental factors viz. air temperature, radiant temperature, humidity, air movement, metabolic rate or human activity [6,7]. Where buildings are large consumers of energy in all countries, especially in regions with extreme climatic conditions and a substantial share of the energy goes towards heat and cool buildings [8]. The new European energy regulation now considers a high standard of thermal protection in buildings with reasonable energy consumption, satisfactory thermal comfort conditions and low operational costs [9]. Numerous studies across the world have shown the impacts of hot working environments on the working population [10–14]. In the context of climate change, and in the view of predictions made by Intergovernmental Panel on Climate Change (IPCC) [15–18], to meet occupants thermal comfort requirements traditional systems use a lot of energy. The insulation strategy provides a better thermal climate. Building insulation materials are the building materials which form the thermal envelope of a building or otherwise reduce heat transfer, but Many insulations are made from petrochemicals and may be a concern for those seeking to reduce the use of fossil fuels and oil. A significant portion and An important part of these not isolated external walls are massive solid brick walls or the thermal perceived in buildings was aimed by some research [19-22]. Insulation may be categorized by its composition (natural or synthetic materials), form (batts, blankets, loose-fill, spray foam, and panels), structural contribution (insulating concrete forms, structured panels, and straw bales), functional mode (conductive, radiative, convective), resistance to heat transfer, environmental impacts, and more. Sometimes a thermally reflective surface called a radiant barrier is added to a material to reduce the transfer of heat through radiation as well as conduction.

The choice of which material or combination of materials is used depends on a wide variety of factors. Some insulation materials have health risks, some so significant the materials are no longer allowed to be used but remain in use in some older buildings such as asbestos fibers and urea. Also, the cost can be high compared to the traditional insulation. The interior or external insulation does not often becomes the only possible solution in particular with the old buildings in the Sahara of Algeria. Hygrothermal parameters of the existing

wall material should be reported and well known for designing powerful and durable walls in the time study. First, in this paper, CFD software is used as a technique to modelling the behaviour of fluid and the thermal convection between the external wall of the house and air with different Rayleigh numbers [$10^3 \leq Ra \leq 10^6$]. This work presents a study of numerical simulation aiming at the role and at the influence of the insulation by the mud as a local material at the city of Bechar situated in the south west of Algeria, or we are interested in a comparative study for aimed these goals. We have added both concrete and adobe materials respectively, in triangular shapes. In this context, an analogy was used for the used functions which are discretized by the finite difference method and integrated in the Fluent software, which is based on the finite volume method. The validation of this procedure was confirmed by comparing some obtained results. The results are presented in the form of distributions of isotherms, Stream lines and the local Nusselt number and average Nusselt number with the aim to study the influence on comfort in buildings.

GEOMETRIC CONFIGURATION

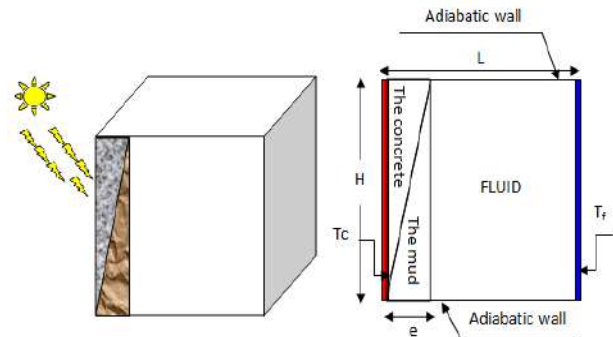


Figure 1
Schematic of the studied configuration

By giving two configurations, one to describe the wall without insulation or the exterior wall is constructed only with the concrete and the other with an insulation mud in a triangular shape. Studied the configuration is shown in Figure 1. The Temperatures imposed are experimentally captured in a day of summer in August in the town of Bechar. To model this phenomenon, we used a square cavity of length L and a height h . The left and right vertical walls of the cavity have equal temperature for the dimensionless case, respectively

$T_c = 1$, $T_f = 0$ equal to 0 for the case, and the other walls are kept adiabatic. The form factor is $A = H/L = 1$.

To simplify the problem, assume that:

- The fluid is Newtonian and incompressible.
- The heat dissipation by viscous friction is neglected.
- The Boussinesq approximation is considered

OBJECTIVES

We can express our aim for this study in the following points:

- Study the Modelling of the coupling of convection - conduction.
- Study of the effect of the distribution of the heat inside buildings on the convection.
- Comparative study between the construction of buildings with and without insulation.
- Study the effect of the Rayleigh number on the convection in building.
- Test the reliability of the insulation with the Mud as local material.

MATHEMATICAL MODEL

The fluid is assumed incompressible and obeys the Boussinesq approximation. In these cases, continuity in two dimensions and the equations governing the flow and energy is given by:

Continuity.

$$\frac{\partial U}{\partial X} + \frac{\partial V}{\partial Y} = 0 \quad (1)$$

X-momentum.

$$\frac{\partial U}{\partial t} + U \frac{\partial U}{\partial X} + V \frac{\partial U}{\partial Y} = -\frac{1}{\rho} \frac{\partial P}{\partial X} + \nu \nabla^2 U \quad (2)$$

Y-momentum.

$$\frac{\partial V}{\partial t} + U \frac{\partial V}{\partial X} + V \frac{\partial V}{\partial Y} = -\frac{1}{\rho} \frac{\partial P}{\partial Y} + \nu \nabla^2 V + g\beta \frac{\partial T}{\partial X} \quad (3)$$

Energy.

$$\frac{\partial T}{\partial t} + U \frac{\partial T}{\partial X} + V \frac{\partial T}{\partial Y} = \frac{\lambda}{\rho C_p} \nabla^2 T + \frac{1}{\rho C_p} \varphi \quad (4)$$

The derived equation of motion (2) over Y and the equation of motion (3) by contributing to x, then, after subtracting the two equations obtained, we obtain the equations dimensionless variables in writing Helmholtz in terms of vorticity and stream function formulation are as follows:

$$\frac{\partial \omega}{\partial t} + U \frac{\partial \omega}{\partial X} + V \frac{\partial \omega}{\partial Y} = \text{Pr} \nabla^2 \omega + \text{Ra Pr} \frac{\partial T}{\partial X} \quad (5)$$

$$\frac{\partial T}{\partial t} + U \frac{\partial T}{\partial X} + V \frac{\partial T}{\partial Y} = \frac{\partial^2 T}{\partial X^2} + \frac{\partial^2 T}{\partial Y^2} + \frac{\varphi}{\rho C_p a \Delta T} \quad (6)$$

$$\frac{\partial^2 \psi}{\partial X^2} + \frac{\partial^2 \psi}{\partial Y^2} = -\omega \quad (7)$$

The stream function and vorticity are related to the velocity components by the following expressions:

$$U = \frac{\partial \psi}{\partial Y}, \quad V = -\frac{\partial \psi}{\partial X} \quad \text{and} \quad \omega = \frac{\partial V}{\partial X} - \frac{\partial U}{\partial Y} \quad (8)$$

The dimensionless parameters in the equations above are defined as follows:

$$\left\{ \begin{array}{l} X = \frac{x}{H}, \quad Y = \frac{y}{H}, \quad U = \frac{u}{u_i} \\ V = \frac{v}{u_i}, \quad P = \frac{P}{\rho u_i^2}, \quad T = \frac{T - T_i}{T_c - T_i}, \quad t^* = \frac{t}{L^2 / a} \end{array} \right. \quad (9)$$

For solid, we are interested only in the following heat equation:

$$\frac{\partial T}{\partial t} = \frac{1}{a} \left(\frac{\partial^2 T}{\partial x^2} + \frac{\partial^2 T}{\partial y^2} \right) \quad (10)$$

THE THERMOPHYSICAL PROPERTIES OF THE USED MATERIALS

a) *for the concrete*

- 1) Thermal Conductivity : 1.75 (k)
- 2) Density : 2200 (kg/m³)
- 3) Specific Heat : 878 (J/kg K)

b) *for the mud*

- 1) Thermal Conductivity: 0.12 (k)
- 2) Density : 700 (kg/m³)
- 3) Specific Heat : 1000 (J/kg K)

PROCEDURE OF SIMULATION

The numerical calculation was conducted using the computer code "fluent" 6.2.13. The numerical procedure used in this work is that of finite volume.

It involves the integration of differential equations of mathematical model on finite control volumes

for the corresponding algebraic equations. The SIMPLE algorithm [24-25] was chosen for the coupling speed pressure in the Navier-Stokes equations on a staggered grid. The convective terms in all equations are evaluated using the schema apwind first order.

The discretization of the time term is made in a totally implicit scheme. The convergence of the solution is considered reached when the maximum relative change of all variables (u, v, w, p, t) between two successive time is not less than 10^4 . With an aim of following well any variation of the fields thermal and hydrodynamic, we used a uniform grid of 12126 nodes and 12317 Elements in unsteady mode.

RESULTS AND DISCUSSION

The structure of the flow, the temperature field and heat transfer through the hot wall are discussed in this section. In this study, to target the most important goal, we will show and studied the effect of the insulation by the Mud on dynamic and thermal behavior of the fluid in the cavity. Taking the Prandtl number equal to 0.71 because the fluid used is air

ISOTHERMS

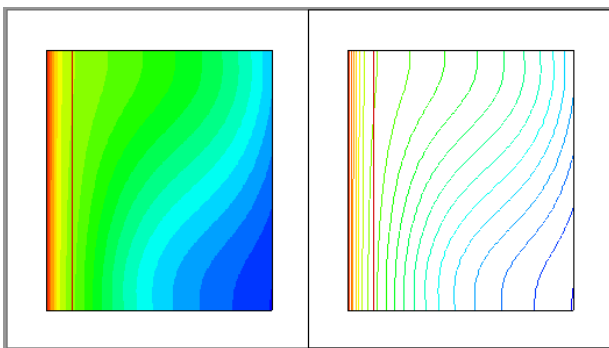
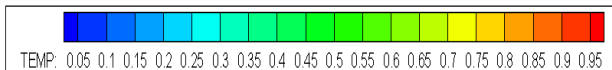


Figure 2
The Isotherms For uninsulated wall (For wall of the concrete only), $Ra=10^4$, $Pr=0.71$

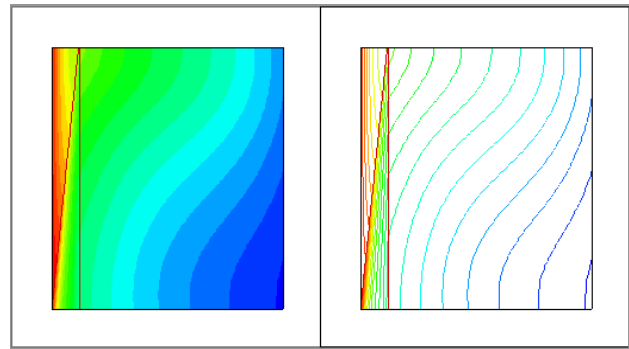
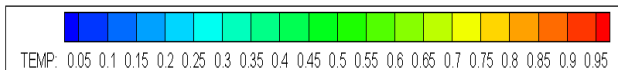


Figure 3
The Isotherms For Insulated Wall, (Mixture Wall of the concrete and the mud $Ra=10^4$, $Pr=0.71$

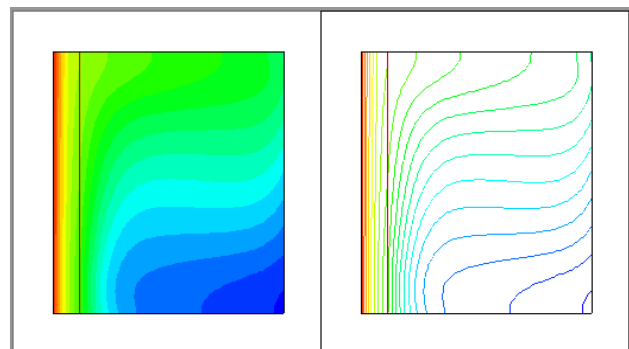


Figure 4
The Isotherms For uninsulated wall (For wall of the concrete only), $Ra=10^5$, $Pr=0.71$

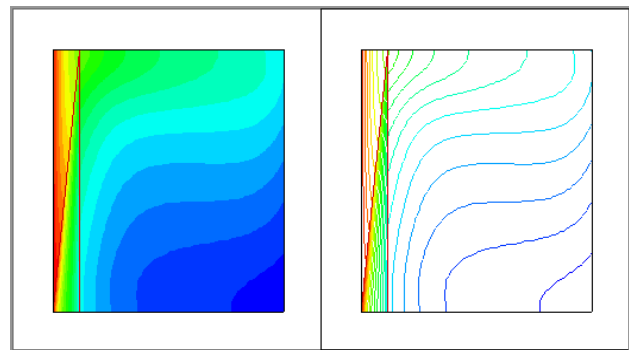


Figure 5
The Isotherms For Insulated Wall, (Mixture Wall of the concrete and the mud), $Ra=10^5$, $Pr=0.71$

The isotherms are shown in Figures [2-5]. The heat distribution in the cavity is in accordance with the fluid circulation revealed by isotherms and iso currents. Indeed we find a heating fluid from the interface, if it causes the change of the heat distribution in the cavity (see figures) for different numbers of Rayleigh For a fixed value of

the number of Prandtl equal 0.71. Gradually, as the Rayleigh number has increased, the isotherms become increasingly wavy and heat transfer increases, so the flow intensifies and natural convection is expanding and predominates (natural convection is predominant).

NUSSELT NUMBERS

Figure 6 shows the variations of average Nusselt numbers versus the different Rayleigh numbers

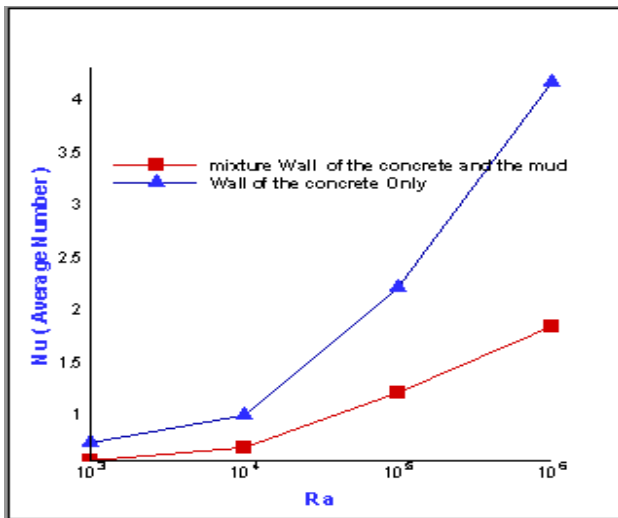


Figure 6

Profiles of average Nusselt number, for different values of $Ra=10^3, 10^4, 10^5$ and 10^6 , for uninsulated and insulated walls, $Pr = 0.71$.

Also, we report the influence of the Rayleigh number on average Nusselt number. We found a significant influence. The increase in average Nusselt number is accompanied with the increase of Rayleigh number, For both configurations studied, firstly wall built with concrete only and the second case, the wall built of concrete 50% and 50% of the mud in a triangular shape as is shown in Figure 1. consequently Improves the heat transfer. Despite it is clear that it becomes important for every increase of Rayleigh because of the change in the exchange ratio between the wall and the air, and because the inertia and the thermal resistance of the mix (concrete + mud) are large relative to the construction of walls by concrete only. A difference of around 43.22 % on average between insulated and uninsulated walls to $Ra = 10^5$, for example.

CONCLUSION

The idea of this work is based on actual events; the objective of our work was to study the behavior of the air in house with two-dimensional numerical study of natural convection or (where) laminar flow is considered on is interested by conduction or convection coupling. Solving equations governing natural convection written Helmholtz's variables ψ and ω which are discretized by the finite difference method. We validated this work for the hydrodynamic and thermal studies in the cavities where he showed good consistency. For our simulation, we presented the streamlines, isotherms and the influence of key parameters such as positioning after the interface and the number of Rayleigh, the convection. We have shown by this simulation, the following:

1. Convection affects the structure of the isotherms.
2. The temperature of the fluid increases dramatically with increase in Rayleigh number.
3. The Interior thermal isolation reduces the losses of heat and minimizes the energy needs (request of heating) and thus reduced in fact, at the same time: the invoice, consumption and pollution.
4. The Mud is insulating effective which to guarantee the comfort and the air quality inside the building
5. The interior thermal insulation helps to preserve a constant temperature in the integrality of your housing in winter or summer.
6. The Inside thermal insulation has a promising future provided that all actors, around the sector of construction are justified and motivated and conscious of the ecological and financial issues.
7. Insulation not only add insulation to the wall either inside or outside, but you can even use local materials in the Sahara of Algeria as insulation and construction material simultaneously as Adobe that are many and which can reduce the heat transfer to 43%.

REFERENCES

1. Tumirah Khadiran, Mohd Zobir Hussein, Zulkarnain Zainal, Rafeadah Rusli, Advanced energy storage materials for building applications and their thermal performance characterization: A review, *Renewable and Sustainable Energy Reviews* 57 (2016) 916–928
2. Jankowski NR, McCluskey FP. A review of phase change materials for vehicle component thermal buffering. *Appl Energy* 2014;113:1525–61

3. Memon SA. Phase change materials integrated in building walls: a state of the art review. *Renew Sustain Energy Rev* 2014;31: 870–906.
4. Zhang P, Ma ZW. An overview of fundamental studies and applications of phase change material slurries to secondary loop refrigeration and air conditioning system. *Renew Sustain Energy Rev* 2012;16: 5021–58.
5. Mondal S. Phase change materials for smart textiles – an overview. *Appl Therm Eng* 2008;28:1536–50
6. Y. Epstein, Daniel S. Moran, Thermal comfort and the heat stress indices, *J. Ind. Health* 44 (2006) 388–398
7. P.K. Latha , Y. Darshana , Vidhya Venugopal , Role of building material in thermal comfort in tropical climates – A review, *Journal of Building Engineering* 3 (2015) 104–113, June 2015.
8. The European Parliament and the Council of the European Union, the Energy Performance of Buildings, Council Directive of 2002/91/EC, 2002.
9. S.A. Arngrímsson, D.S. Petitt, M.G. Stueck, D.K. Jorgensen, K.J. Cureton, Cooling vest worn during active warm-up improves 5-km run performance in the heat, *J. Appl. Physiol.* 96 (2004) 1867–1874.
10. A. González, G. Craig, M.J. John, The cardiovascular challenge of exercising in the heat, *J. Physiol.* 586 (2008) 45–53.
11. C. Wesseling, J. Crowe, C. Hogstedt, K. Jakobsson, R.A. Lucas, D.H. Wegman, Resolving the enigma of the Mesoamerican nephropathy-men – a research workshop summary, *Am. J. Kidney Dis.* 63 (3) (2014) 396–404.
12. G.P. Bates, J. Schneider, Hydration status and physiological workload of UAE construction workers – a prospective longitudinal observational study, *J. Occup. Med. Toxicol.* 3 (2008) 21–26.
13. P. Dutta, V. Chorsiya, Scenario of climate change and human health in India, *Int. J. Innov. Res. Dev.* 2 (8) (2013) 157–160.
14. K.M. Willett, S. Sherwood, Exceedance of heat index thresholds for 15 regions under a warming climate using the wet-bulb globe temperature, *Int. J. Climatol.* 32 (2012) 161–177.
15. P.K. Latha, Y. Darshana, Vidhy Venugopal, Role of building material in thermal comfort in tropical climates, *Journal of Building Engineering*, Vol 3, September 2015, Pages 104-113
16. P.A. Schulte, H. Chun, Climate change and occupational safety and health: establishing preliminary framework, *J. Occup. Environ. Hyg.* 6 (2009) 542–554
17. R. Akhtar, Airies, Climate change and health and heat wave mortality in India, *J. Glob. Environ. Res.* 11 (2007) 51–57.
18. M.S. Mohsen and B.A. Akash, ‘Some Prospect of Energy Saving in Building’, *Energy Conversion Management*, Vol. 42, N°11, pp. 1307 - 1315, (2001).
19. M.A. Aktacir, O. Büyükalaca and T. Yılmaz, ‘A Case Study for Influence of Building Thermal Insulation on Cooling Load and Air-Conditioning System in the Hot and Humid Regions’, *Applied Energy*, Vol. 87, N°2, pp. 599 - 607, (2010).
20. L. Peeters, R. de Dear, J. Hensen and W. D’haeseleer, ‘Thermal Comfort in Residential Buildings: Comfort Values and Scales for Building Energy Simulation’, *Applied Energy*, Vol. 86, N°5, pp. 772 - 780, (2009).
21. Benachour E. and al, Effect of positioning the heating element on natural convection in a square cavity (habitat type), *international review of mechanical engineering*, vol.4N.5, July (2010).
22. Linshuang Long, Hong Ye, Effects of thermophysical properties of wall materials on energy performance in an active building, *Energy Procedia* 75 (2015) 1850 – 1855,
23. Benachour E. and al, Study of the Influence of the Mural Heating on the Convection in the Building in Arid Area, *international review of mechanical engineering (IREME)*, vol.9N.1, (2015).
24. S. V. Patankar, “Numerical Heat Transfer and Fluid Flow,” McGraw-Hill New York, (1980).
25. De Vahl Davis G, “Natural convection of air in a square cavity. A bench mark numerical solution.”, (1983).

TRNSYS VALIDATION OF A STUDY ON BUILDING'S ENERGETIQUE EVALUATION IN NORTH OF MOROCCO

F.Eddib*¹, M.A. Lamrani¹

¹UCA, FSSM, Department of Physics, LMFE, Affiliated unit to CNRST (URAC 27), B.P. 2390,
Marrakesh, Morocco

*Corresponding author: Email: farah.eddib@edu.uca.ac.ma

ABSTRACT

The study is done on an apartment of 85 m², located in Tangier. A south facing façade receives a continuous sunshine all day. The outer walls are hollow brick Double skin spaced from an air knife (10 cm), the inside walls consist of simple dividers, while the ceiling and floor are concrete 30 cm thickness.

The aim of this study is to evaluate the hygro-thermal behavior of a multi-zone apartment located in northern Morocco by using the TRNSYS16 software, and compares its results with those from a study with CODYBA software and to estimate the heating load in January and the air conditioning load for the month of august.

Meteorological data and building materials properties are those used in the north of Morocco.

NOMENCLATURE

Text: external temperature in (°C)

Trs: inside resultant temperature (°C)

Hext: external relative humidity (%)

Hint: internal relative humidity (%)

INTRODUCTION

Morocco is poorly endowed with energy resources and imports over 96% of the energy it consumes. 36% of the overall energy consumption goes to the residential and tertiary sector, the housing sector emits more than 30% of greenhouse gas (GHG) emissions responsible of global climate on global warming.

The increasing of the standard of living, and the availability of heating and air conditioning equipment at low prices, thus everyone has the possibility of heating in winter and cooling in summer. While the majority of existing electrical networks in some urban areas are not designed for these power calls, which weakens them.

In addition the demand for electricity could quadruple by 2030.

The aim of this study is to compare the simulation results of two TRNSYS16 and CODYBA software.

The study is to make a hydrothermal simulation of a local multi-zone and estimate the heating load for the

month of January and the air conditioning load for the month of August.

DESCRIPTION OF THE LOCAL

STUDIED: The study is done on a flat in the city of Tangier in northern Morocco, with an area of 85m². A south-facing façade receives a continuous sunshine throughout the day; the plan of the apartment is on (figure1)

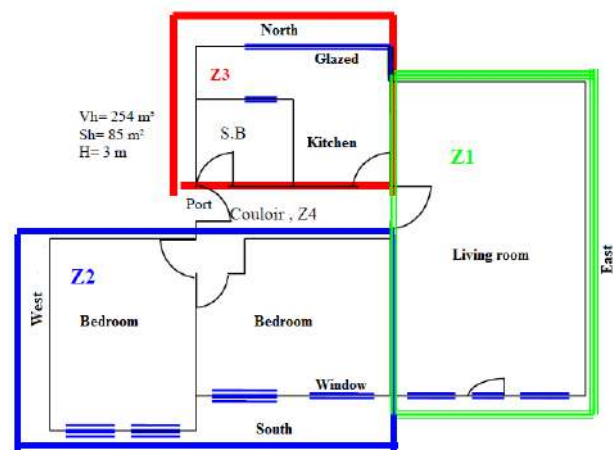


Figure1

Plan of the apartment studied

The exterior walls are brick Hollow double skin spaced from an air knife (10 cm), the interior walls are consist of simple dividers, while the ceiling and the floor are concrete 30 cm of thickness. The

structure construction in northern Morocco exterior walls appears on (figure2).

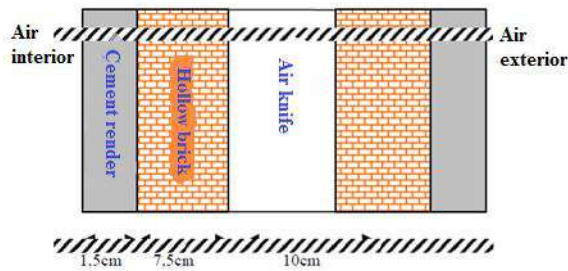


Figure2
Structure of an external wall

WEATHER DATA: Meteorological data were measured on the Tangier weather site over the two years 2003 and 2004.

BUILDING MATERIALS USED IN NORTHERN MOROCCO: There is no reference to access the average values of thermo-physical characteristics of the materials used in Morocco. In our case, we take the thermos-physical properties of construction materials used in the north from the library TRNSYS16 software that is very rich.

HYGROTHERMAL MODELING OF THE APARTMENT: TRNSYS is a particularly suitable for dynamic simulation software system, the thermal behavior of multi-zone buildings and associated systems. Because of its modular structure, it can describe complex systems with many components (types) included in its library. The TRNSYS environment comprises two sub-programs:

- TRNSYS Simulation Studio, host structure for both the development of new numerical models and implementation of dynamic simulations,
- The TRNBUILD interface, which defines the building envelope structure.

Modeling assumptions

Conditions considered for the simulations are as shows in Table 1, the air change rate is represented in table2.

Modeling in multi-zones:

In order to have a more detailed model of a house in function of their use, the studied apartment is divided into four climatic zones.

These areas are the following (figure 1)

Zone 1: The living room (Z1)

Zone 2: Bedroom 1 and 2 (Z2)

Zone 3: Kitchen and bathroom (Z3)

zone4: Hallway (Z4)

Table1
Internal loads of the apartment

Entity	Nb	power (w / unit)	unoccupied scenario
occupants	4	130	from 8h to 12h and from 14h to 18h
equipment	4	60	from 23h to 6h, 8h to 12h, and from 14h to 18h.
lamps	4	40	from 00h to 18h

Table2

The air change rate of apartment

	volume flow rate (m ³ /h)	scenario of operating
living room	90	From 8h to 14h and from 17h to 20h.
Bedroom 1 and 2	100	From 8h to 12h and from 14h to 18h.
kitchen	80	From 7h to 12h and from 14h to 22h.

RESULTS AND DISCUSSION

All the results for different parameters characterizing the atmosphere of the studied apartment (the interior temperature and humidity) will be presented as graphics and will be compared to those of the study by CODYBA.

We determine the evolution of these indicators over time, which will allow us to estimate the annual consumption for heating and air conditioning of the local.

Evolution of temperature: The figures 3 and 4 show the evolution of temperatures for the months of January.

We got changes in temperature in the various local areas.

We observed changes in these two parameters of a zone to the other, it's caused by radiation received via glass surface of this areas.

However the development of Zone 3 is higher, considering its operation.

There is a bit difference in the half of the months that caused by the difference between method of calculation for each software.

There is a similarity between temperatures in different zones with TRNSYS16 and CODYBA.

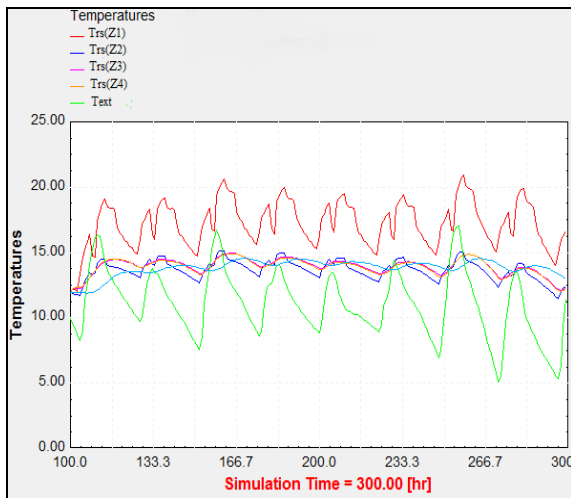


Figure3

Resulting temperature of the apartment for the month of January (01/01 to 15/01) with TRNSYS 16

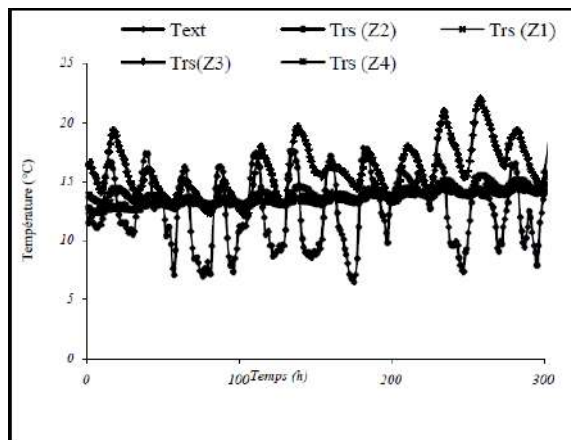


Figure4

Resulting temperature of the apartment for the month of January (01/01 to 15/01) with CODYBA

For the months of august as shown in figure 5 there is a similitude between temperature results with TRNSYS16 and CODYBA for all zones.

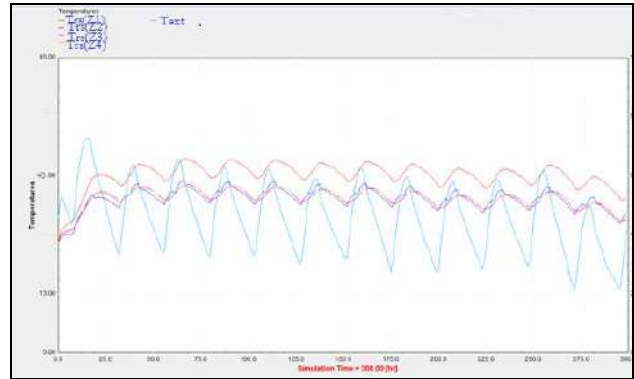
Evolution of humidity: We got changes in relative humidity in various local areas; it present presents a variation from one to another zone in multi-zone modelisation.

The humidity is maximum in zone 1 and 2 because of the ventilation. It is minimum in the zone 3 and 4 because they are regularly ventilated.

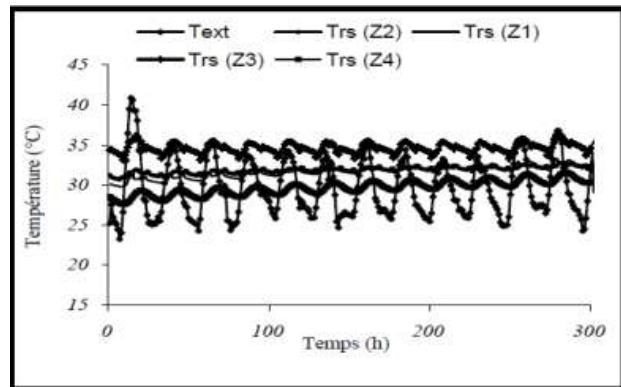
we find the same values for both software.

For the months of august we have same comments as the months of January .

The advantage of this software is to perform simulations of the evolution of different parameters characterizing the internal atmosphere of the building.



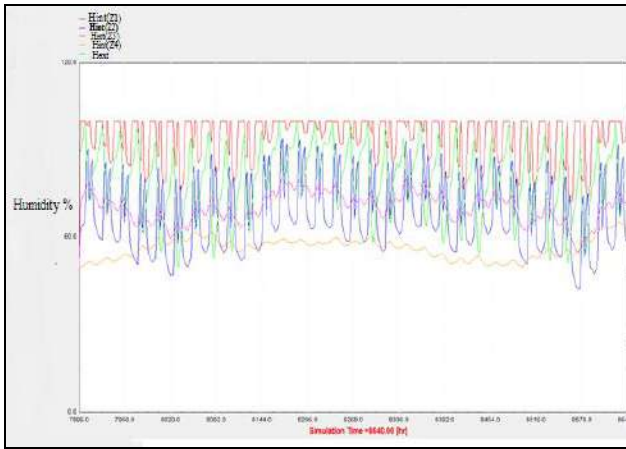
(a)Simulation with TRNSYS16



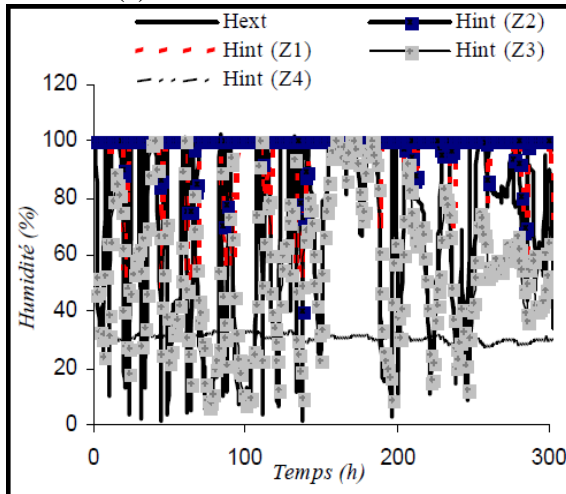
(b)Simulation with CODYBA

Figure5

Resulting temperature of the apartment for the month of august (01/08 to 15/08) for two Software.



(a) Simulation with TRNSYS16



(b) Simulation with CODYBA

Figure 6

Resulting humidity of the apartment for the month of January (01/01 to 15/01) for two software

CONCLUSIONS

TRNSYS 16 allowed us to model the building in dynamic regime.

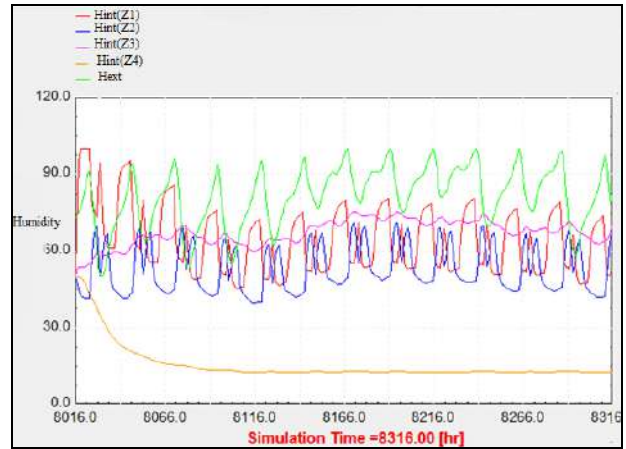
All simulations results helped us to estimate the power of heating and cooling during winter and summer periods.

To dimension an air conditioning system adequate; in January we need around 160kwh of heating energy to keep the temperature at 18°C (winter comfort), wish is higher than what they estimate with CODYBA software.

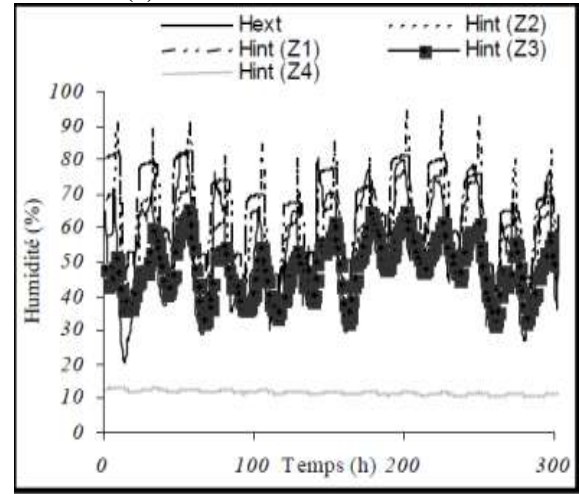
And 540kwh of cooling energy to keep the temperature at 25°C (summer comfort) wish is higher than what they estimate with CODYBA software.

This difference in results is due to the calculation methods of the two software.

the calculation method of TRNSYS is to make the heat balance on all sides, unlike the software that CODYBA considered as the rays that come through



(a) Simulation with TRNSYS16



(b) Simulation with CODYBA

Figure 7

Resulting humidity of the apartment for the month of august (01/08 to 15/08) for two software.

the window to the floor and is reflected to the other walls.

This software help to gain valuable time, an improving the reliability of the results in the study and the design of the thermal insulation, heating and air conditioning of a housing, and a study of the thermal behavior of the building.

KEYWORDS

Energy simulation, comfort heat, air temperature

REFERENCES

1. BABBAH. S, and DRAOUI. A, 2004, Evaluation Energétique des bâtiments au Nord du Maroc, Projet de Stage de Recherche, DESA, Transferts Thermiques et Energies Renouvelables, FST de Tanger, décembre.
2. BOUSSAID. S, 1990, Caractérisation physico chimique Thermo-physique et mécanique de la terre

utilisée en Construction au Nord du Maroc", Thèse de 3ème Cycle, Faculté des Sciences, Tétouan Maroc .
3.CABIROL. T, FAURE. D and ROUX. D, 1982, Chauffage de l'habitat et énergie solaire, tome 1: Confort thermique et techniques de chauffage, Charly-Yves, Edisud.
4. EL BAKKOURI. A, 1990, Caractéristique Thermo-physique et mécanique de quelques matériaux locaux utilisés dans l'isolation et la construction au Maroc: Le plâtre, le liège et la brique

creuse, Thèse de 3ème Cycle, Faculté des Sciences, Tétouan Maroc.
5.WERNER.K, and PAUL.S, 2005 TRNSYS Manuel, For Simulation Studio 4.0.
6.J.Noël, J, and J.Roux, 2004 CoDyBa Manuel d'utilisateur, Rev.1.00/Nov.
7.Fanger P.O,1982, Thermal comfort. Robert E. Kreiger publishing company. Malabar Florida.
8.Réglementation Thermique, 2000, Centre Technique des Industries Aéronautiques et Thermiques.

HEATING OF A GREENHOUSE BY MEANS OF A ROCK BED ACCUMULATOR

L.GOURDO^{1*}, H.FATNASSI², A.WIFAYA³, R.AIT EL CADI¹, H.DEMRATI¹, A. BEKKAOUTI⁴,
AAHAROUNE¹ & L.BOUIRDEN¹

¹Laboratory of Thermodynamics and Energy, Faculty of Science, Agadir

²INRA, Research Center PACA - Sophia Antipolis

³INRA, CRRA -Agadir

⁴Department of Energy and agricultural machinery-I.A.V Hassan II, Rabat-Morocco

*Corresponding author: Fax: +212 06 11 95 10 12 Email: lahoucine.gourdo@edu.uiz.ac.ma

ABSTRACT

The protected crop cultivation in the moderate climate requires heating almost every day during the season, either for raising the temperature, or for reduction of air humidity. The required amount of heat might be partially met by accumulation of excessive heat from the conversion of solar energy entering the plastic tunnel or greenhouse.

Experiments were carried out in two identical greenhouses, each with 15 m² ground area. Rocks were filled in a canal excavated and insulated in the soil of one of the greenhouses. Greenhouse air was pushed through the rock-bed by a centrifugal fan with 1000 m³/h air flow rate and controlled by two thermostats when the energy storage or release was required.

The operation of this system is as follows:

- The day when the greenhouse is warm injected excess heat in rock-bed accumulator.
- The night when the temperature of the greenhouse is very low, the heat stored in the rock-bed accumulator is discharged into the air inside the greenhouse, which will help heat the greenhouse at night.

The results of this study showed that the rock-bed system created an air temperature difference of about 1-2 °C at night, between the two greenhouses, the control one having the lower temperature. Furthermore, the rock-bed system kept the inside air temperature higher than that of outside air at night.

KEYWORDS

Agricultural Greenhouse, microclimate, heating, rock bed

NOMENCLATURE

T_{exp} : Temperature inside the greenhouse with system of heating (°C)

T_a : temperature outside the greenhouse (°C)

T_{wh} : Temperature inside the greenhouse without heating system en (°C)

U : Wind speed (m/s).

D_v : wind direction (deg)

R_{net} : Net radiation (W/m²)

R_G : Outside global radiation (W/m²)

T_{soil} : Temperature of soil surface (°C)

T_{rocks} : Temperature of inside rock bed (°C)

INTRODUCTION

A greenhouse is a structure covered with transparent materials that utilize solar radiant energy and provide optimum growing conditions for plants [1].

Heating applications in greenhouses have an important effect on the yield as well as on the quality and the cultivation time of the products. Optimization of air temperature in greenhouses is of particular

importance in relation to plant growth and development. In order to keep the greenhouse temperature considerably higher than outside temperature, heating is frequently needed during cold seasons

There are two types of agricultural solar greenhouses which utilize solar energy for heating purposes

Firstly, the passive greenhouses, which are utilized as collectors and designed for maximizing the solar heat gains by using a special cover and structure materials [2].

Secondly, the active greenhouses, which are equipped with solar systems that utilize a separated collecting system from the greenhouse with an independent heat storage system, such as adding thermal energy inside the greenhouse from an air heating system in addition to direct thermal heating [3], [4], [5] and [6].

The Classification of various systems of heating agricultural greenhouses as shown in fig 1:

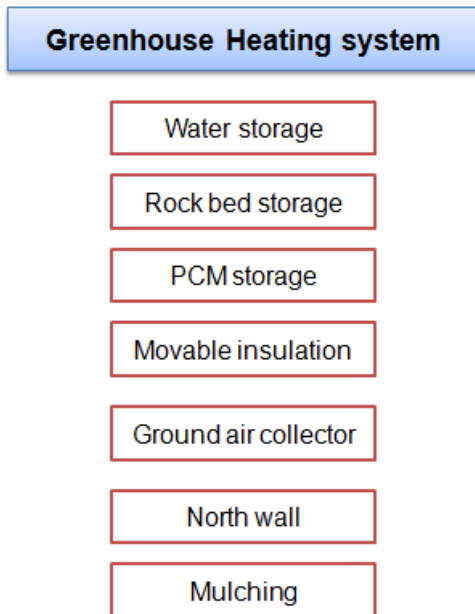


Fig 1: Classification of various systems of heating agricultural greenhouses [7].

The capacity to benefit from the excess of diurnal energy depends mainly on the investment costs related to a capture system installation and distribution of this heat. Thus, this exploitation mode is profitable if the savings in heating are higher than the installation system cost.

Greenhouse heating by a solar system is more profitable. While it is less powerful than a conventional system, it does not pollute. It cannot alone meet the total requirements for heating, and therefore it is the fuel boiler which is used as a auxiliary system and not a solar system [8].

MATERIAL AND METHODS

Site and structure of the greenhouse

The experiments were carried out in two agricultural greenhouses installed in the experimental station of Regional Center for Agricultural Research of Agadir, located near the side (30°13 Latitude, 9°23 Longitude, 80m Altitude). The experimental greenhouse has an area of 15m² (5m width by 3m length) and a height of 2.5m at gutter level and 3m at span level. The greenhouse was covered by a 200um polyethylene thermal film and the orientation of its spans was North-South, i.e., perpendicular to the prevailing wind direction (figure 1).

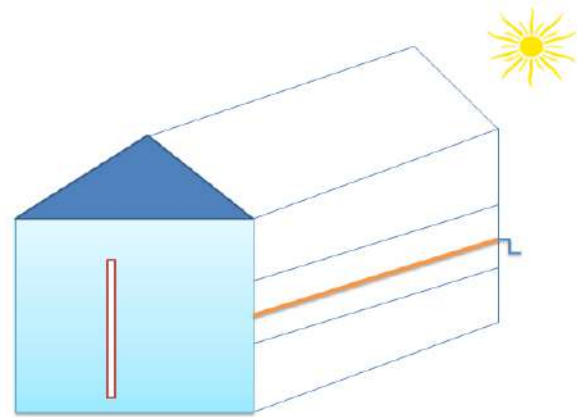


Figure 2: The greenhouse

The climate is semi-aride dominated by alternating hot and dry season and wet and temperate season with large regional nuances. Figs. 3 and 4 represent the meteorological data of the average monthly global solar radiation and ambient temperatures in a period of 2013–2014. These figures show that the highest monthly average radiation are detected in May & July (310 W / m²), and the highest monthly average ambient temperature are detected in August (24°C). The minimum monthly average radiation is 150W / m² while the minimum monthly temperature is 12°C in January.

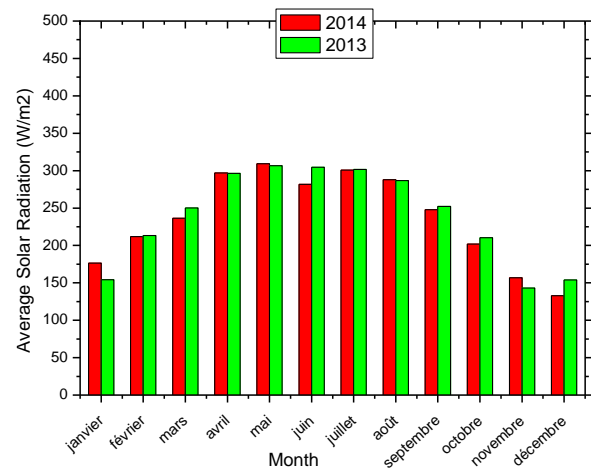


Fig. 3. Monthly variation of the global solar radiation for the 2013–2014 periods in Agadir.

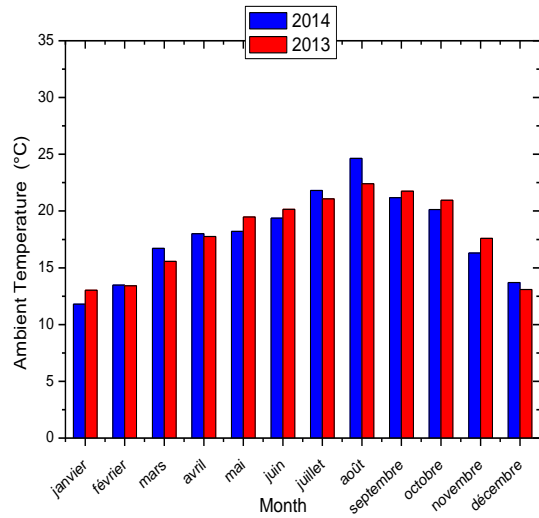


Figure 4. Monthly variation of the ambient temperature for the 2013–2014 periods in Agadir

The culture:

The crop is tomato type Pristyla. The rows are oriented North South, perpendicular to the wind direction. Irrigation is provided by a system of drop by drop.

The culture has the following characteristics:

- planting date: 28 /10/ 2015
- Total number of plants : 9
- Distances between plants : 0.4m

Experimental measurements

In order to characterize the inside climate of the greenhouse, we have measured the following parameters (Figure 4):

- Net radiation R_{net} under the plastic cover
- Air temperature T_e and Relative humidity H_r ,
- Temperature of greenhouse walls and roof, soil surface & inside rock bed ,
- wind speed U and wind direction D_v
- Outside global radiation R_G .



Fig : 107 Temperature Probe



Fig :HMP50, Temperature and Relative Humidity Sensor

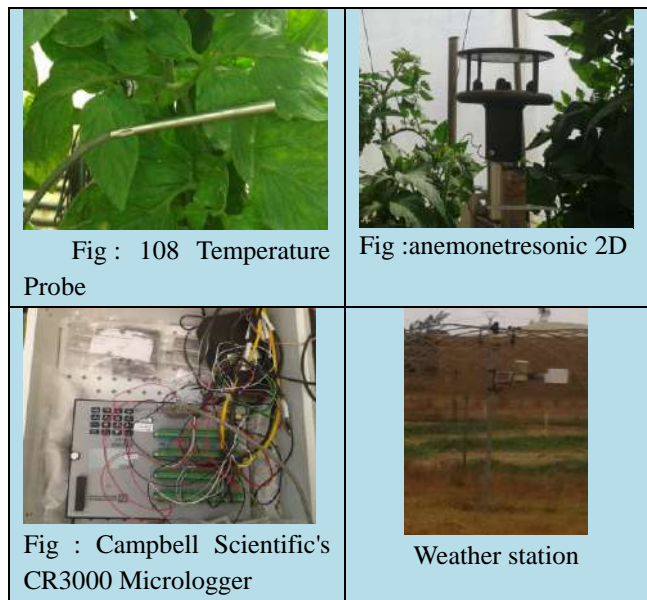


Fig : 108 Temperature Probe

Fig : anemometresonic 2D

Fig : Campbell Scientific's CR3000 Micrologger

Weather station

HEATING SYSTEM USING THE ROCK BED ACCUMULATOR

Description of the system

As it is shown in fig.4, The storage system consists of a cylindrical tube of PVC 200 mm in diameter filled with gravel diameter between 4 and 8 cm placed on the floor of the greenhouse.

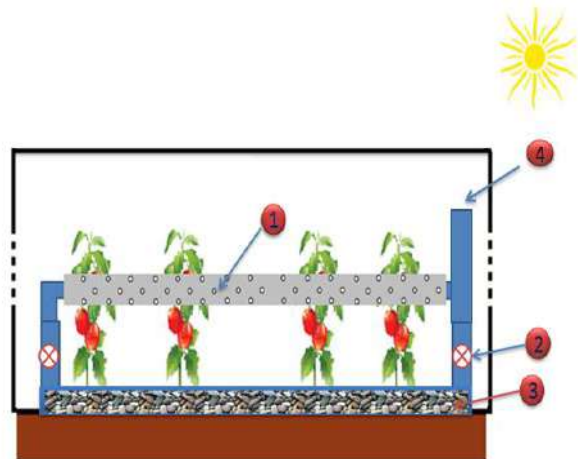


Figure 5. Schematic of the prototype with rock bed installed in the greenhouse.

During the day, excess solar heat is collected and it is recovered at night in order to satisfy the heating needs of the greenhouse. The day when the greenhouse is warm injected excess heat in rock-bed accumulator. The night when the temperature of the greenhouse is very low, the heat stored in the rock-bed accumulator is discharged into the air inside the

greenhouse, which will help heat the greenhouse at night.

In order to evaluate the benefit of using the solar heating system for the experimental greenhouse, another similar greenhouse without a heating system. Which we name the reference greenhouse, is installed next to the first one, and contains the same cultivation.

Reason choosing the rocks as storage materials?

In addition to criteria defining the suitability of a material to store sensible heat (thermo-physical properties, cost effectiveness and environmental aspect), other characteristics such as abundance, chemical and mechanical properties, as well as resistance to thermal shocks are decisive criteria for choosing the best material allowing effective thermal storage and long lifetime. Tiskatine et al. [8]. performed an petrographic and thermo-mechanical analysis on thirteen different rocks of the region at laboratory scale. The choice of these rocks is justified by the fact that they include the three major categories existing on earth. The best correlations between physico-mechanical properties have been found, and a great influence of these properties on the lifetime of rocks has been observed. The analysis of the obtained results showed that the Quartz and calcite are the principal minerals controlling rock physico-mechanical properties

Effect of the system on the internal temperature of the greenhouse

Fig 6 represents the variation of the temperatures, inside the experimental greenhouse, and inside the reference greenhouses and the ambient temperature. In order to show the effect of heating clearly, two days were chosen. It is found that the temperature of the outside air is always lower than the temperature of the air inside the greenhouse.

At night the temperature of the experimental greenhouse is higher than that of the greenhouse light, the difference may reach 1-2 ° C, and reverse the day. So this system we managed to partially heat the air inside during the night and the day it cool down.

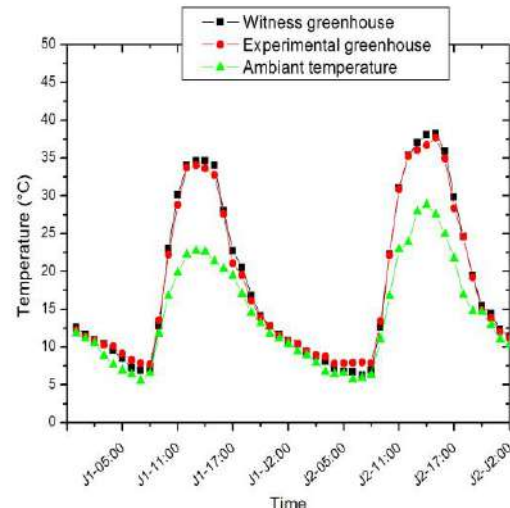


Fig 6: Ambient temperature (T_a), and air temperature inside greenhouse with (T_{exp}) and without water heating (T_{wh}) as a function of day times.

Figure (7) shows the evolution of the overall external radiation and net radiation inside the greenhouse. Global radiation in this period is maximum during the day than 670W / m² and minimum night. The net radiation in the greenhouse is highest during the day (670W / m²) and minimum night (-15W / m²).

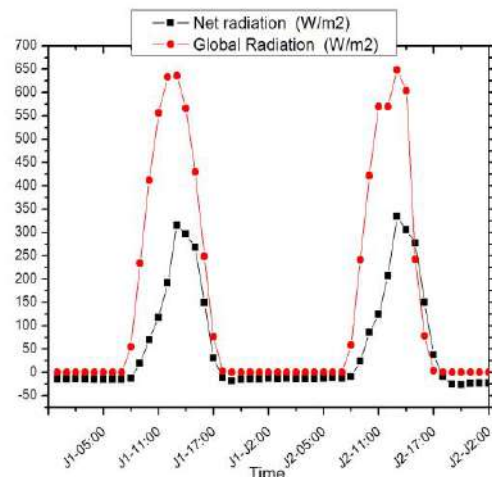


Fig 7 : Evolution of the overall external radiation (R_G) and net radiation inside the greenhouse (R_{net}).

Figure (8) shows the evolution of the temperature pebble rocks, experimental greenhouse and soil of the greenhouse.

- On the day the temperature of the air in the experimental greenhouse is higher than that of the rollers of rocks.

- At night the temperature pebble rocks is higher than that of the air inside the greenhouse, it is the heat that has been stored by the rocks during the day. This energy will be released into the air inside the greenhouse to increase its temperature overnight. It is found that the temperature difference between the rollers of rocks and the air inside the greenhouse up to 5 ° C at night, (discharge period of pebble reservoir rocks), and day the difference can reach -10 ° C (charging period pebble rocks)

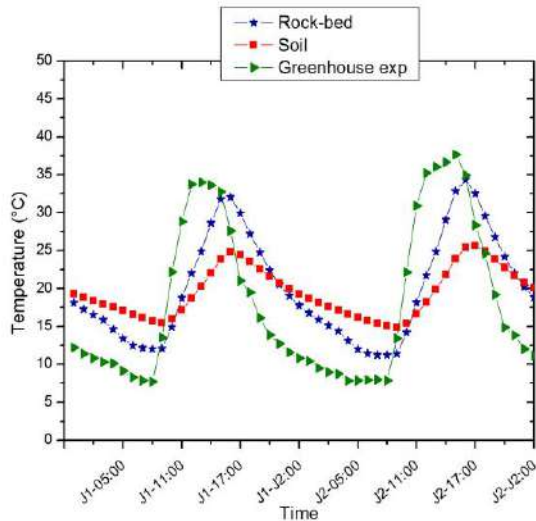


Fig 8: Evolution of the temperature pebble rocks (T_{rocks}), experimental greenhouse (T_{exp}) and soil of the greenhouse (T_{soil}).

CONCLUSIONS

For greenhouse horticulture, climate control is crucial to obtain both a high quality product and a high yield. High quality is required to meet the demands of the needs of consumers and high yield is required for economic production.

Moreover, developing efficient and economical heat storage systems and related devices is as important as developing new energy sources from the point of view of energy conservation.

This regulation system of the microclimate of the greenhouse that we tested can:

- decrease the temperature in the greenhouse during the night of 1 to 1.5 ° C compared to the greenhouse witness

- Increase the temperature of the air of the experimental greenhouse of 1 to 2 per respect to the greenhouse witness and 2 to 3 with respect to the outside.

Acknowledgement

Our thanks to the Regional Center for Agricultural

Research of Agadir. who gracefully allowed us to use their greenhouse and helped us throughout the realisation of the measurements involved in this study.

REFERENCES

- [1] N.L. Panwar, S.C. Kaushik, S. Kothari, Solar greenhouse an option for renewable and sustainable farming, *Renew Sustain Energy Rev*, 15 (2011), pp. 3934–3945
- [2] G. Bot, N. VandeBraak, H. Challa, S. Hemming, T.H. Rieswijk, G. van Straten, I. Verloot, The solar greenhouse: state of the art in energy saving and sustainable energy supply *Acta Hortic* (ISHS), 691 (2005), pp. 501–508.
- [3] V.P. Sethi, K. Sumathy, C. Lee, D.S. Pal, Thermal modeling aspects of solar greenhouse microclimate control: a review on heating technologies, *Sol Energy*, 96 (2013), pp. 56–82.
- [4] M. Santamouris, C.A. Balaras, E. Dascalaki, M. Vallindras, Passive solar agricultural greenhouses: a worldwide classification and evaluation of technologies and systems used for heating purposes, *Sol Energy*, 53 (1994), pp. 411–426
- [5] J. Korecko, V. Jirka, B. Sourek, J. Cerveny, Module greenhouse with high efficiency of transformation of solar energy, utilizing active and passive glass optical rasters, *Sol Energy*, 84 (2010), pp. 1794–1808.
- [6] G.N. Tiwari, A.K. Dubey, R.K. Goyal, Analytical study of an active winter greenhouse, *Energy*, 22 (1997), pp. 389–392
- [7] V.P. Sethi, S.K. Sharma, Survey and evaluation of heating technologies for worldwide agricultural greenhouse applications, *Sol Energy*, 82 (2008), pp. 832–859
- [8] M. Lazâar , S. Kooli , M. Hazami, A. Farhat , A. Belghith, Comparison between a solar system and a fuel boiler for greenhouse air-conditioning, *Desalination* 168 (2004) 391-396
- [9] R. Tiskatine , A. Eddemani , L. Gourdo , B. Abnay , A. Ihlal , A. Aharoune , L. Bouirden, Experimental evaluation of thermo-mechanical performances of candidate rocks for use in high temperature thermal storage, *Applied Energy*, 171 (2016), pp. 243–255.

ANALYSIS OF EXTERIOR SHADING BY OVERHANGS AND FINS IN HOT CLIMATE

Rachida Idchabani^{1*}, Mohamed El Ganaoui², Friedrich Sick³

(1) Superior National School of Mines, Av Hadj Ahmed Cherkaoui - BP 753, Agdal, Rabat, Morocco

(2) IUT Henri Poincaré, Université de Lorraine, France

(3) University of applied sciences, Berlin, Germany

*Corresponding author: Fax: 00212 537 771 055 E-mail: idchabani@enim.ac.ma

ABSTRACT

Although the Moroccan climate is generally mild and temperate, both heating in winter and cooling in summer are required to reach comfort levels in different regions. The building energy consumption related to the heating and cooling can be reduced by several solutions like the use of suitable shading. This paper presents a study of the effect of overhangs and fins on the heating and cooling energy demand in the city of Marrakech. A simulation study has been performed using the TRNSYS Simulation Program to determine the required energy for heating and cooling depending on orientation of the window and the overhangs and fins dimensions. Furthermore, practical tables, to determine rates of cooling energy reduction by using overhangs, were established.

KEYWORDS: Energy Efficiency, Building, Shading, Overhangs, Fins, TRNSYS.

INTRODUCTION

The Moroccan Energy Strategy is one of the most ambitious strategies in the Middle East and North Africa region [1]. Its intention is to establish 42% of total installed capacity from solar, wind and hydropower resources by 2020 and to promote the energy efficiency in several sectors. The building sector is targeted by this strategy, since it consumes 36% of total energy of the country [2]. This consumption is expected to increase in the future decades with demographic and economic development. Recently, on November 2015, Moroccan authorities have launched the implementation of the first national thermal regulation. It's a starting point for the integration of energy efficiency in building sector.

Furthermore, the Moroccan climate is generally mild and temperate, but to reach comfort levels in several regions, both heating in winter and cooling in summer are required. The building energy consumption related to the heating and cooling can be reduced by using insulation of building's envelope, efficient glazing, and suitable shading.

Several numerical and experimental studies have been conducted to examine the effect of various factors on building energy consumption [3-8]. Many of them focused on the effect of windows and exterior shading [7-14]. Singh and Garg [7] carried out energy rating of different window glazings available in the Indian market. Jaber and Ajib [8] studied the effects of windows' *U*-value, window orientation and windows size on annual heating and cooling energy demand considering the both energy and investment costs. Chan and Chow [9] reports the findings on the energy and environmental impact due to the provision of a balcony. Aldawoud [10]

investigated the performance and the effectiveness of electrochromic glazing to prevent unwanted solar heat gains from entering a conditioned space. Then, he compared these performances to those offered by conventional fixed exterior shading devices in identical conditions. Babaizadeh et al. [11] employed Life Cycle Assessment (LCA) to compare the effects of three different shading materials on building energy consumption and their impacts to the environment within five major climate zones defined by American Society of Heating, Refrigerating and Air-conditioning Engineers (ASHRAE). Hoffmann et al. [12] investigated twelve different coplanar shades with different geometry, material properties, and cut-off angles for two California climates: the moderate San Francisco Bay Area climate and a hot and dry Southern California climate. Jinkyun Cho et al. [13] present an integrated approach for exterior shading design analysis about energy performance and economic feasibility in a high-rise residential building (Seoul, Korea) by both numerical simulations and field mock-up test for possibility of installing. Hammad and Abu-Hijleh [14] explored the influence of external dynamic louvers on the energy consumption of an office building located in Abu Dhabi-UAE. But there is a lack of such studies for Moroccan cases since the first Moroccan thermal regulation was promulgated recently and the building energy efficiency had just taken the interest it deserves.

In the present work, we focus on the effect of exterior shading by Overhangs and Fins on heating and cooling energy demand of building in the city of Marrakech.

METHODOLOGY

Prototype building: In order to predict the solar shading effect of exterior overhangs and fins, a simulation study has been performed using the TRNSYS Simulation Program, Version 16.1. A box shaped building zone with one window, no internal gains and no ventilation is being investigated with respect to specific heating and cooling energy demands. The box dimensions are 4m x 4m x 4m. The construction is massive with 8cm polystyrene insulation. The window is a single pane window with dimensions of 1.5 m x 1.5 m. In the base case, no external shading is applied.

Climate conditions: The study is done for Marrakech city climate conditions. Climate data are available through the Meteonorm software. A typical meteorological year corresponding to Marrakech city was established.

Projection factor definition: Variations are as follows: The orientation of the window varies in 45° steps: S, SW, W, NW, N, NE, E, SE. For each orientation, the base case, four overhang and four fin situations are investigated.

This sum up to 72 simulation runs. The overhang and fin variations distinguish projection factors (PF) of 0.15, 0.25, 0.4 and 0.6.

The projection factor for overhangs is expressed as a dimensionless ratio defined as follows:

$$PF_{\text{overhangs}} = A/B \quad (1)$$

with A and B are the width of the overhang and the height of the window respectively as illustrated in Figure 1.

The projection factor for the fin is expressed as a dimensionless ratio defined as follows:

$$PF_{\text{fins}} = A/B \quad (2)$$

with A and B are the height of the fin and the width of the window respectively as illustrated in Figure 2.

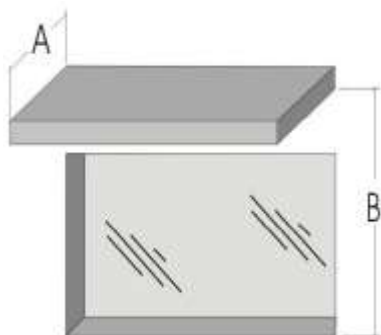


Figure 1
Definition of A and B for the projection factor in the overhang situation

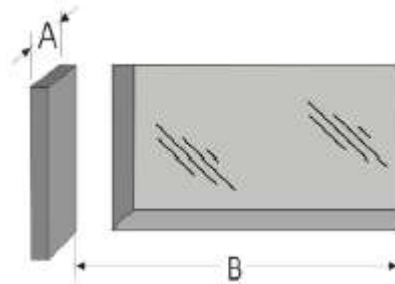


Figure 2
Definition of A and B for the projection factor in the fin situation.

The distances between the overhang and top edge of the window as well as fin and nearest side edge of the window are set to zero. The single fin is always placed in such a way that the sun is obstructed, e.g. in case of the Western wall, it is situated on the right hand side of the window viewed from outside whereas the East facing window has its fin on the left hand side.

RESULTS

The following four diagrams sum up the results for overhangs and fins. In each case, there is one diagram for the specific heating energy demand, and one for the specific cooling energy demand with set points of 20°C and 26°C, respectively. Units are kWh/(m².year).

Heating demand as Function of PF Overhang

The following diagram (figure 3) sum up the results for heating demand as function of projection factor for overhangs with set points of 20°C expressed in kWh/(m².year).

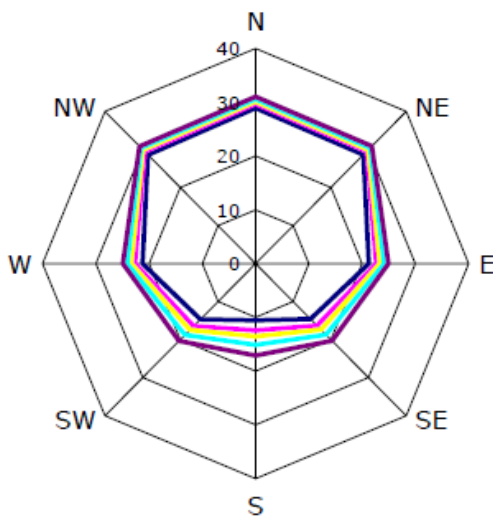
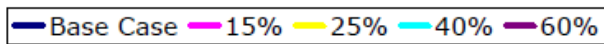


Figure 3

Influence of an overhang with varying projection factors (PF) on the heating energy demand in kWh/(m².year) as function of orientation.

It is noted that for the base case, the heating needs are more important for the North direction (about 30kWh/m².year), they are reduced by a third for the East and West direction, whereas for the South orientation, they are only about 10kWh/m².year. These heating requirements tend to increase using overhangs especially at the South orientation, SE and SW.

Cooling Demand as Function of PF Overhang

The figure 4 sum up the results for cooling demand as function of projection factor for overhangs with set points of 26°C expressed in kWh/(m².year).

For the base case, the maximum cooling requirements are registered at the direction E, W, SE and SW (56-60kwh/m².year). The orientation that records the less cooling demand is North (N) followed by the South (S), given that the use of overhangs has more impact at the last orientation.

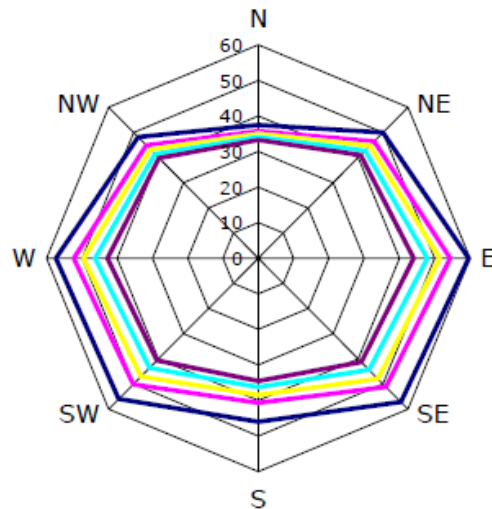
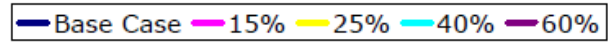


Figure 4

Influence of an overhang with varying projection factors (PF) on the cooling energy demand in kWh/(m².year) as function of orientation.

Heating Demand as Function of PF Fin

The following diagram (figure 5) sum up the results for heating demand as function of projection factor for fins with set points of 20°C expressed in kWh/(m².year).

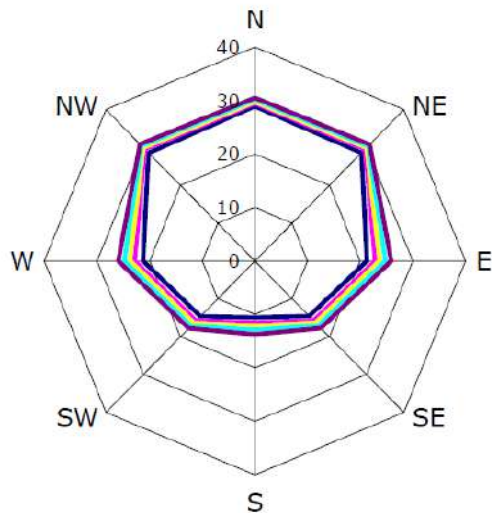
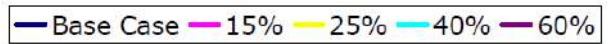


Figure 5

Influence of a side fin with varying projection factors (PF) on the heating energy demand in kWh/(m²a) as function of orientation.

The thermal behavior of the building according to the orientation follows the same logic as in Figure 3 (case of influence of an overhang), except that the impact of the fins is reduced comparing it to overhangs effect particularly for the South orientation.

Cooling Demand as Function of PF Fin

The figure 6 sum up the results for cooling demand as function of projection factor for fins with set points of 26°C expressed in kWh/(m².year).

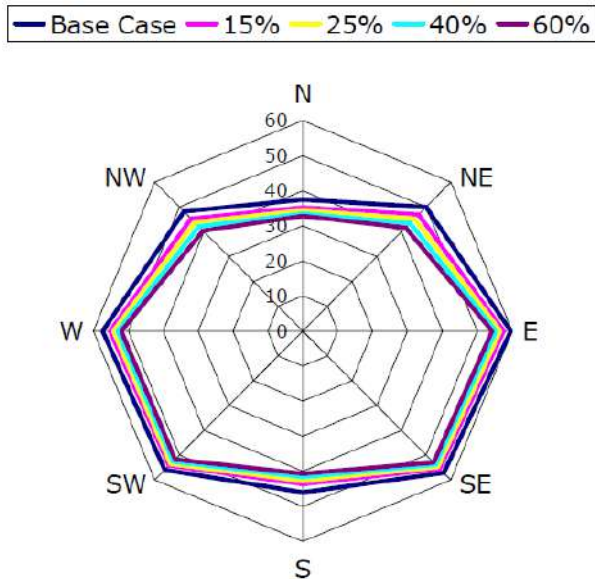


Figure 6

Influence of a side fin with varying projection factors (PF) on the cooling energy demand in kWh/(m²a) as function of orientation.

Comparing to the figure 4, the fins have less effect than the overhangs on reducing cooling requirements. The most significant reduction is recorded for directions NE and NW.

After simulating the effect of exterior shading by Overhangs and Fins on heating and cooling energy demand, we focused on cooling, because the city of Marrakech has more requirements on cooling than on the heating. For this end, we defined the shading factors.

The “shading factor” is the ratio of cooling energy reduction and base case cooling energy demand. This leads to the following tables.

Table1
Overhang Shading Factors

	Overhang Projection Factor			
	15%	25%	40%	60%
N	4.7%	6.7%	9.0%	11.1%
NE	7.1%	10.6%	14.5%	18.0%
E	8.8%	13.8%	19.7%	26.2%
SE	10.5%	16.1%	22.4%	27.9%
S	11.5%	16.4%	21.1%	24.9%
SW	10.3%	15.8%	22.0%	27.4%
W	8.7%	13.6%	19.3%	25.4%
NW	6.9%	10.3%	14.0%	17.4%

Table2
Fin Shading Factors

	Fin Projection Factor			
	15%	25%	40%	60%
N	5.8%	8.4%	10.7%	12.4%
NE	6.3%	9.4%	13.1%	16.7%
E	3.5%	5.3%	7.2%	9.0%
SE	2.9%	4.3%	5.9%	7.2%
S	5.0%	7.3%	9.6%	11.5%
SW	3.0%	4.5%	6.0%	7.4%
W	3.7%	5.5%	7.5%	9.3%
NW	6.1%	9.2%	12.7%	16.1%

These tables may be used as rough estimate of shading effects. However, it should be noted that heating energy demands go up with these measures. Therefore caution is necessary in heating dominated areas.

CONCLUSION

In recent decades, the traditional architecture has been abandoned for modern methods of construction that are not necessarily adapted to the Moroccan climate. It's the case of the city of Marrakech which was known by overhangs made with local materials (tiles). This study focus on the effect of exterior shading by Overhangs and Fins, on building heating and cooling energy demand in this city. Furthermore, practical tables to determine rates of cooling energy reduction by using overhangs were established.

REFERENCES

1. Alaa Alhamwi, David Kleinhaus, Stefan Weitemeyer, Thomas Vogt, 2015, Moroccan National Energy Strategy reviewed from a meteorological perspective, Energy Strategy Reviews, Volume 6, , Pages 39–47.
2. <<http://www.aderee.ma/index.php/fr/59efficacite-energetique/efficacite-energetique>> (accessed March 2, 2016).
3. Rachida Idchabani, Mohamed Garoum, Assia Lamzah, 2016, Thermal performance and environmental impact of residential buildings' heating in Morocco, International Journal of Sustainable Energy, Volume 35, Issue 3. pages 295-307.
4. Ilaria Ballarini, Vincenzo Corrado, 2012, Analysis of the building energy balance to investigate the effect of thermal insulation in summer conditions, Energy and Buildings 52, 168–180.
5. Mehlika N. Inanici, F. Nur Demirebilek, 2000, Thermal performance optimization of building aspect ratio and south window size in five cities

- having different climatic characteristics of Turkey, *Building and Environment* 35, 41±52.
6. Jinghua Yu, Changzhi Yang, Liwei Tian, 2008, Low-energy envelope design of residential building in hot summer and cold winter zone in China, *Energy and Buildings* 40, 1536–1546.
 7. M.C. Singh, S.N. Garg, 2009, Energy rating of different glazings for Indian climates, *Energy* 34, 1986–1992.
 8. Samar Jaber, Salman Ajib, 2011, Thermal and economic windows design for different climate zones, *Energy and Buildings* 43, 3208–3215.
 9. A.L.S. Chan, T.T. Chow, 2010, Investigation on energy performance and energy payback period of application of balcony for residential apartment in Hong Kong, *Energy and Buildings* 42, 2400–2405.
 10. Abdelsalam Aldawoud, 2013, Conventional fixed shading devices in comparison to an electrochromic glazing system in hot, dry climate, *Energy and Buildings* 59, 104–110.
 11. 14. Hamed Babaizadeh, Nasim Haghghi, Somayeh Asadi, Reza Broun, David Riley, 2015, Life cycle assessment of exterior window shadings in residential buildings in different climate zones, *Building and Environment*, Volume 90, Pages 168–177.
 12. Sabine Hoffmann, Eleanor S. Lee, Andrew McNeil, Luis Fernandes, Dragan Vidanovic and Anothai Thanachareonkit, 2016, Balancing daylight, glare, and energy-efficiency goals: An evaluation of exterior coplanar shading systems using complex fenestration modeling tools, *Energy and Buildings*, Volume 112, 15 January 2016, Pages 279–298.
 13. Jinkyun Cho, Changwoo Yoo, Yundeok Kim, 2014, Viability of exterior shading devices for high-rise residential buildings: Case study for cooling energy saving and economic feasibility analysis, *Energy and Buildings*, Volume 82, Pages 771–785.
 14. Fawwaz Hammad, Bassam Abu-Hijleh, 2010, The energy savings potential of using dynamic external louvers in an office building, *Energy and Buildings* 42, 1888–1895.

ENERGY EFFICIENCY IN BUILDING: THE EFFECT OF BUILDING ENVELOPE ON OPTIMAL CALCULATION OF THE BUILDING ORIENTATION

Soulaimane KALOUN (1), Younes CHIHAB (2), Omar BENCHAREF (1)

(1) SAEDD, EST Essaouira, UCA, Morocco

(2) FPD Safi, UCA, Morocco

PB 386 Poste Principale ESSAOUIRA, MAROC

*Corresponding author: Fax: +212 5 24 79 26 48 Email: so.kaloun@uca.ma

ABSTRACT

Energy efficiency requirements in buildings focus upon building envelope including elements, such as, walls, roofs, doors, windows. This concept plays a large role in energy efficiency standards. In addition, building orientation also plays a critical role on the thermal comfort of occupants. A review of the literature showed that there is an absence of a direct mathematical formulation for the optimal calculation of the building orientation, owed essentially to the large number of parameter to be considered, and it directs us to the methods based on the machine learning. We developed a system, which detects optimal calculation of the buildings orientation, based on the choice of the customer (Wall Area, Roof Area, Overall Height, Glazing Area, Glazing Area Distribution, Heating Load, and Cooling Load).

In order to find the most adapted algorithm to our problem, we conducted a comparative study between several classification algorithms (Bayesian Network, Neural network, Random forest...); But none of these algorithms gave a correct prediction of the orientation, which is why we opted for a hybrid system based on the reduction of the parameters with PCA and a classification system based on Random Forest K-means clustering.

INTRODUCTION

Since the implementation of the first measures in favor of energy savings after the oil crises, then with the fight against climate change, the question of the energy efficiency of buildings was always in the heart of the politics energy-climate, at an international level. Reports realized on the energy and climatic future; integrate all recommendations concerning the improvement of the energy efficiency in housing.

Energy efficiency requirements in buildings focus upon building envelope including elements, such as, walls, roofs, doors, windows) design. This concept plays a large role in energy efficiency standards. In addition, building orientation also plays a critical role on the thermal comfort of its occupants [1]. Good orientation, combined with other energy efficiency features, can reduce or even eliminate the need for auxiliary heating and cooling, resulting in lower energy bills, reduced greenhouse gas emissions and improved comfort. It takes account of summer and winter variations in the sun's path as well as the direction and type of winds, such as cooling breezes. Building orientation refers simply to the way a building is situated on a site and the positioning of windows, rooflines, and other features [2]. It is often considered to optimize the sun's capacity for daylight and heat gain in winter. Therefore, each orientation

should be treated differently to optimize the result. For example, windows facing north and south generally have good access to daylight, should be encouraged whilst windows facing west generally have excessive solar heat gain, and therefore should be minimized. Selecting the most optimal building orientation is one of the critical energy efficient design decisions that could have impact on building envelope energy performance, as it can be used to minimize the direct sun radiation into the buildings [3].

In recent years, there has been a movement to promote greater energy efficiency for buildings. Several works had been done on building energy efficiency. Lam et al [4] reported a study that investigated the impact of façade's surfaces orientation on the intensity of the direct and indirect solar radiation; findings from this study showed that the north has the lowest solar intensity. On the other hand M. Al-Tamimi et al [3] investigation describes the effect of building orientation in regards of solar radiation absorbance in exterior walls. The results show that eastern windows have more noticeable effects on increasing indoor air temperature than western windows; this can be applied to both ventilated and unventilated rooms. Moreover the objective of the work of K. M. Odunfa et al [5] was to investigate the effect of building orientation on

energy demand in buildings. They analyzed energy efficiency through different building orientations. The study established North/South building orientation as the best option for the building energy efficiency. This building orientation also ensures maximum ventilation and natural light in all climatic conditions which invariably provides comfortable living conditions inside the building. La Roche and Liggett [6] expressed in their work, as well as the others, that a climate responsive building design is important not only because of the comfort and because of the energy saving implications for its users, but also because it helps preserve valuable resources on our planet.

A review of the literature showed that there is an absence of a direct mathematical formula that'll allow us to optimally calculate the building's orientation, which is owed to the large number of parameter to be considered, and that leads us to use the methods based on machine learning.

On the basis of an experimental database, our goal is to develop a system that predicts the optimum orientation of buildings, based on the physical and energetic characteristics of the building and the clients choice of the minimum and maximum thermal loads.

CLASSIFICATION ALGORITHMS

As already mentioned the absence of a mathematical formalism, leads to no other choice but machine learning methods. We conducted a Data Mining study using the best-supervised learning classifiers (Bayesian networks, C4.5 decision trees, the Random Forest and neural networks).

Bayesian Network: The Bayesian network is a classifier based on the modeling of uncertain knowledge by learning from data. Bayesian networks represent all relationships between attributes as graphs [7-8]. In practice to each variable, we associate a node. Moreover, for each dependency relation between two variables we associate an equation to calculate the joint probabilities.

Decision Tree: The C4.5 algorithm is a supervised classification algorithm. A decision tree is a tree in the computer science sense it's the graphical representation of a classification procedure [9]. To generate of a decision tree, three questions should be answered:

1. Decide if a terminal node (leaf)

2. Select a test to be associated with a node

3. Assign a class to a leaf.

```

Begin
Initialize the empty tree;
Repeat
Decide whether the current node is
terminal
If the node is then terminal
Assign a class
If not
Select a test and create the subtree
  EndIf
Skip to the next unexplored node if
one exists
Until a decision tree
End

```

C4.5 use the training set to prune the resulting tree. The pruning criterion is based on a heuristic to estimate the actual error on a given subtree.

Rnd Tree: Rnd tree or Random Forest uses decision trees, but takes a different approach [10-11]. Rather than growing a single deep tree that is carefully managed by an analyst, Random Forest relies on aggregating the output from many trees generated randomly. That means that: we use random variable selection and random record selection to generate many decision trees. The output of the algorithm is the average output of all the trees.

Neural Network: Based on a duplication of neural connection, Artificial Neural Network (ANN) present a distinctive classifier with the ability to learn and memorize data[12]. Considered as an heuristic algorithm ANN is easy to implement, we just need to fix a few parameters (number of layer, number of neuron in each layer, learning edges,..). A neuron is a tiny processor, capable of handling a simple function; a combination of a big number of neurons can be very powerful and can smoothly handle nonlinear problems.

PROPOSED STUDY AND EXPERIMENTAL RESULTS

The Dataset: The dataset was created by Angeliki Xifara and was processed by Athanasios Tsanas in Oxford Centre for Industrial and Applied Mathematics[13]. The assessing the heating load and cooling load requirements of buildings based on the building characteristic. In our work, we consider the heating load and cooling load as client choice

like (Surface Area, Wall Area or Roof Area) and we try to predict optimal orientation based this choice.

The dataset contains eight attributes (or features, denoted by X1,X2,X3,X4,X5,X7,X8,y1,y2) and one responses (or outcome, denoted by X6). The aim is to use the nine features to predict the orientation X6.

Specifically:

Inputs:

X1 Relative Compactness

X2 Surface Area

X3 Wall Area

X4 Roof Area

X5 Overall Height

X7 Glazing Area

X8 Glazing Area Distribution

y1 Heating Load

y2 Cooling Load

Output:

X6 Orientation

Comparative Study: In this section we are going to evaluate the classification algorithms already presented (Bayesian networks, C4.5 decision trees, the Random Forest and neural networks) using the dataset to find the best classifier for our problem.

In our first test, we considered all the attributes of the Dataset as the classifiers input and of course the building orientation as output.

We used 90% of the data for learning and validation and 10% for testing. The following tables (1, 2, 3 and 4) show the results obtained for each algorithm.

Table 1

Classification rate for the Naive Bayes Classifier. With Lambda for laplacian = 0 and Homoscedasticity assumption=1. Execution time 15ms

Error rate									0.7461								
Values prediction						Confusion matrix											
Value	Recall	Precision		O1	O2	O3	O4	Sum									
o1	0	1		o1	0	84	14	94	192								
o2	0.4427	0.747		o2	0	85	14	93	192								
o3	0.0781	0.7368		o3	0	84	15	93	192								
o4	0.4948	0.7467		o4	0	83	14	95	192								

Sum						0	336	57	375	768
-----	--	--	--	--	--	---	-----	----	-----	-----

Table. 2

Classification rate for the multilayer perceptron. With 10 Neurons in the hidden layer, Validation set proportion 0.2, Learning rate 0.15, Stopping ruleMax iteration 100 and Error rate threshold 0.01

Error rate						0.75								
Values prediction						Confusion matrix								
Value	Recall	Precision		o1	o2	o3	o4	Sum						
o1	1	0.75		o1	192	0	0	0	192					
o2	0	1		o2	192	0	0	0	192					
o3	0	1		o3	192	0	0	0	192					
o4	0	1		o4	192	0	0	0	192					
				Sum	768	0	0	0	768					

Table 3

Classification rate for the C4.5 algorithm. With Min size of leaves=5 and Confidence-level for pessimistic=0.25, Number of nodes=21 and Number of leaves=11. Execution time 62ms

Error rate						0.7318								
Values prediction						Confusion matrix								
Value	Recall	Precision		O1	O2	O3	O4	Sum						
O1	0.9635	0.742		O1	185	4	2	1	192					
O2	0.0573	0.620		O2	175	11	5	1	192					
O3	0.0365	0.588		O3	179	6	7	0	192					
O4	0.0156	0.4		O4	178	8	3	3	192					
				Sum	717	29	17	5	768					

Table.4

Classification rate for the Random Forest algorithm. Execution time 1ms.

Error rate						0.5443								
Values prediction						Confusion matrix								
Value	Recall	Precision		o1	o2	o3	o4	Sum						
o1	0.9271	0.653		o1	178	7	5	2	192					
o2	0.3542	0.4237		o2	114	68	9	1	192					
o3	0.2969	0.3448		o3	112	23	57	0	192					
o4	0.2448	0.06		o4	109	20	16	47	192					
				Sum	513	118	87	50	768					

Can Clearly notice that no algorithm can predict for shore the orientation. To choose the best performance was done using Random Forest with an error rate of 54.43%.






View the results obtained in this part, the second step was to analyze the attributes and check their impact on the output.

Data analysis

We chose to work with the Principal Component Analysis (PCA) to analyze the entered data to find the entered, which composes the main axes found by the PCA[14-15]

The following table shows the main axes and their contribution decision.

Table 5.
PCA analyze of the dataset

A is	Eigen value	Difference	Proportion (%)	Histogram	Cumulative (%)
1	5.2224	3.6887	58.03 %		58.03 %
2	1.5336	0.3149	17.04 %		75.07 %
3	1.2187	0.4136	13.54 %		88.61 %
4	0.8051	0.6426	8.95 %		97.56 %
5	0.1625	0.1295	1.81 %		99.36 %

Note that the first two axes represent 75.07% of the data to be extracted from the Dataset. In addition, the use of three components allows Treaty 88%. The following table shows the composition of each main component.

Table 6
Input contribution in each PCA axis

Attribute	Axis_1	Axis_2	Axis_3	Axis_4
X4	0.981	0.028	0.101	0.064
X5	0.981	-0.003	-0.103	0.057
Y2	0.922	0.291	-0.012	0.059
Y1	0.919	0.337	0.032	0.071
X2	0.886	0.448	-0.101	0.003
X1	0.864	-0.468	0.106	0.005
X3	0.243	0.847	-0.413	-0.126
X7	0.106	0.378	0.713	0.570
X8	0.035	0.233	0.704	-0.670
Var.				
Expl.	5.222	1.534	1.219	0.805

The table shows the correlations and accumulated correlations for each attribute in relation to four main components axis.

Relying to the downgrading of the histogram of Eigen values, we will only consider the first three axis; sure, we only take into account 88% of

available inertia. However, we do not want to get a comprehensive view of the data but only build on sufficient information to produce a typology that is relevant and interpretable

By considering the first three axis, the attributes (X4, X5, Y2, Y1, X2, X1, and X3) have a correlation accumulation that exceeds 93%.

Proposed algorithm: On the basis of these results we decided to eliminate the X7 and X8 attributes and resume classification calculations.

- We will add the three main axes extracted from the principal component analysis, as additional entries.

- To increase the degree of separation we applied a clustering algorithm on the orientation column he divided the data into two classes (class 1 composed of o1 and o2 orientation and a class composed of two orientations and o3 o4. And we added the orientation class column as additional input

The following table shows the results obtained by the Random Forest algorithm applied to the improved data set:

Table.7
Classification rate for the Random Forest algorithm applied to the improved dataset.
Execution time= 15ms.

Error rate		0.2995					
Values prediction			Confusion matrix				
Value	Recall	Precision	o1	o2	o3	o4	Sum
o1	0.854	0.3518	o1 164	28	0	0	192
o2	0.536	0.2137	o2 89	103	0	0	192
o3	0.895	0.3509	o3 0	0	172	20	192
o4	0.515	0.1681	o4 0	0	93	99	192
Sum			253	131	265	119	768

First, we can notice we have lower Error rate of 0.299, second all confusion appear on elements of the same class of orientation o1 with o2 or o3 with o4.

So what we can do is to consider two class of orientation class 1(o1+o2) and class two (o3+o4). In the first step,we look for the class of orientation (class1 or class2)as the output, and then we apply the classifier again to separate o1 from o2 or o3 from o4. Table 8 the separation rate between o1 and o2.

Table. 8

Classification rate for the Random Forest algorithm applied to separate between o1 and o2.

Error rate			0		
Values prediction			Confusion matrix		
Value	Recall	1-Precision	o1	o2	Sum
o1	1	0	o1	192	0
o2	1	0	o2	0	192
			Sum	192	192

Finally, the separation between o1 and o2 or o3 and o4 was done perfectly with an error rate of 0%.

X1	X2	X3	X4	X5	Y1	Y2
...

X1	X2	X3	X4	X5	Y1	Y2	A1	A2	A3	CO
----	----	----	----	----	----	----	----	----	----	----

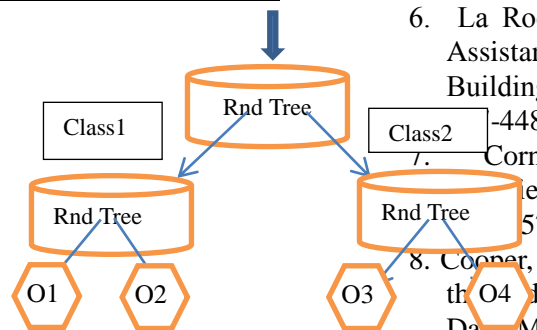


Figure.1: proposed method

CONCLUSIONS

In this paper, we propose a machine learning approach to predict building orientation based on client choices. The proposed system seems to be very effective. The only inconvenient is that we always need new data for new geographic location.

KEYWORDS

Energy Efficiency, building envelope, building Orientation, classification method,

REFERENCES

- Nicol, F. and Roaf, S. "Post-Occupancy Evaluation and Field Studies of Thermal Comfort". Building Research and Information, 33, 338-346. 2005
- UN GREEN BUILDING MANUAL NEW COMMERCIAL UPDATED 5-MAY-11
- Al-Tamimi M. et al "The Effects of Orientation, Ventilation, and Varied WWR on the Thermal Performance of Residential Rooms in the Tropics" Journal of Sustainable Development, Vol. 4, No. 2; April 2011
- Lam, J.C., Wan, K.K.W., Tsang, C.L. and Yang, L. "Building Energy Efficiency in Different Climate". Building, 01, 013, 2008
- Chunfeng, J., T. O. Odufa, V. O. Odufa. "Energy Efficiency in Building: Case of Buildings at the University of Ibadan, Nigeria", Journal of Building Construction and Planning Research, 3, 18-26, 2015
- La Roche, P. and Liggett, R. "A Web Based Assistant for the Design of Climate Responsive Buildings". Architectural Science Review, 44, 448, 2001
- Cornuéjols, A. Miclet, L. Apprentissage automatique, concepts et algorithmes, Eyrolles, 2007, 57-64.
- Cooper, G. Herskovits, E A Bayesian Method for the Induction of Probabilistic Networks from Data, Machine Learning, 9, pages 309-347, 1992.
- Quinlan. J. R. C4.5: Programs for Machine Learning. Morgan Kaufmann, San Mateo, CA, 1993.
- Breiman L., Random forests. In Machine Learning, Seiten 5-32, 2001
- Geurts, P.; Ernst, D.; Wehenkel, L. (2006). "Extremely randomized trees" (PDF). Machine Learning 63: 3. doi:10.1007/s10994-006-6226-1.
- Parizeau, M. « RESEAUX DE NEURONES » GIF-21140 et GIF-64326 Université de LAVAL 2006.
- Tsanas, A. Xifara, A. 'Accurate quantitative estimation of energy performance of residential buildings using statistical machine learning tools', Energy and Buildings, Vol. 49, pp. 560-567, 2012.
- Jolliffe, I.T. (2002). Principal Component Analysis, second edition (Springer).

15. Husson. F, Sébastien. L, Pagès J
(2009). Exploratory Multivariate Analysis y
Example Using R. Chapman & Hall/CRC The R
Series, London. 224p. isbn=978-2-7535-0938-2

A SIMULATION BASED-OPTIMIZATION METHOD FOR ENERGY EFFICIENCY OF A MULTI-ZONE HOUSE INTEGRATED PHASE CHANGE MATERIAL

Yassine Kharbouch^{a*}, Abdelaziz Mimet^a, Mohammed El Ganaoui^b, Lahoucine Ouhsaine^{a,b}

^aEnergetic Laboratory, The University of Abdelmalek Essaâdi, Tetouan, Morocco

^b LERMAB Laboratory, University of Lorraine, France

*Corresponding author: Email: kharbouch.yassine@gmail.com

ABSTRACT

This work aim to optimize the design of an air-conditioned multi-zone house integrated PCMs considering real-life conditions and under north Moroccan climate conditions. The objective of this optimization is to minimize heating and cooling loads. The methodology of this optimization is based on coupling between Energyplus® as a dynamic simulation tool and GenOpt® as an optimization tool. The results show that the obtained optimal design allows minimizing the energy consumption regarding to reference house without PCM.

Keywords : PCM, House multi-zone, simulation based optimization, energy performance.

NOMENCLATURE

PCM	Phase change material
IEE	index of energy efficiency
HVAC	Heating ventilation air-conditioning
W	watt
Q	Energy consumption
Ref	Reference
Opt	Optimal
ACH	Air change per hour
P.A	Period activity

INTRODUCTION

Building sector is one of the major energy consumers in the world, according to the international energy agency (IEA), Buildings represent about 32% of total final energy consumption [1]. In the last years, the most countries in the world has realized the importance of energy efficiency improvements in buildings by reduction of energy costs as well as integration of renewable energy systems in building .

In Morocco as in other countries, it has been to introduce progressively the concept strong concepts and techniques to a better energy efficiency in building sector, therefore a better management of energy consumption and reducing energy costs. Among the new technologies that aim to better optimize energy consumption in building, it is well known that building envelopes incorporated PCM could increase significantly thermal inertia, and limits the temperature fluctuations in the building

indoor environment, thus reducing energy consumption for air conditioning.

Several research studies have clearly shown that the PCM can improve energy performances of buildings by reducing heating and cooling loads with an energy consumption reduction rates between 5 to 30% [2] [3]. Through an experimental study, *Bouzlou and al* [4] conclude that PCM is effective for storage of heating gains, and improvement of thermal comfort in cubicle room located in Casablanca in Morocco. Furthermore, it is clear that the integration of PCMs in building requires an additional Investment. The cost-effectiveness of this Investment depends obviously on the quantity of energy saving through integration PCM in building envelope. In fact , the integration of PCM in the building depend on multiple factors, such as melting temperature, the quantity of the used PCM , and others factors that concerning global design of building (Orientation, glazing area , infiltration rate ,...etc) [5].

In this context, finding an optimal design of a residential building incorporating PCM is still a complex task because we have to take into account many parameters that allow us to describe a more accurately the thermal performance of building. The combination of a dynamic simulation building tool and an optimization tool can help to find optimal design with more efficient and faster ways [5].

By the way we aims to optimize the design of PCM-enhanced house envelope. the objective of this optimization is to maximize the energy performance of the house by minimizing energy consumption for heating and cooling. A parametric study is also presented to illustrate the impact of each variable

variation on the thermal performance of optimal design obtained .

METHODOLOGY

A simulation-based optimization was carried out by combining Energyplus® and GenOpt® tools to find the optimal design solution for a PCM-enhanced house. The optimization concerning a set of a predefined variable which are:

- The orientation of the house « α ».
- The PCM melting temperature « T_m ».
- The PCM layer thickness « e_{mcp} ».
- The glazing windows type « W_{type} ».
- The rate of glazing area « R_{gla} ».
- The air infiltration rate « R_{inf} ».
- Solar absorbance coefficient of the outside surface of the external wall « C_a ».

Simulation software Overview: The simulation was carried out by using Energyplus® software. It is a thermal dynamic simulation tool and building energy analysis and it allow calculating the indoor air temperature and energy requirements for heating and cooling to maintain a building in specified temperature conditions [6].

Optimization tool: GenOpt® (Generic Optimization) [7] is an optimization program for the minimization of an objective function (HVAC energy demands) evaluated by an external simulation software such as Energyplus®(see Figure 1). It allows determining the optimal value of each optimization variable introduced in the study. The figure 1 shows how Energyplus®(is coupled with this optimization programmer. After each iteration, Energyplus® is regularly restarted by a batch file (*.bat) embedded in GenOpt®.

DESCRIPTION OF CASE STUDY:

House prototype: the optimization was carried out for a multi-zone familial house with a surface of 64m². Six thermals zone (see figure 2) was considered in the simulation, the bedroom1, bedroom2, living room, kitchen, the entry, and the bathroom. Table 1 illustrates the structure of the

external wall. The house includes 3 fenestrated facades, and the orientation of house is defined by the surface azimuth angle α (Figure 2).

The indoor air temperature is controlled by an Ideal HVAC system with 100% convective air system and 100% efficiency. The air set-point temperature is fixed between 21°C and 23°C activated during the occupied period. The house is equipped with lamps and a set of electric equipment's. The internal loads and heat gains due to people activity, equipment and lighting devices are reported in table 2.

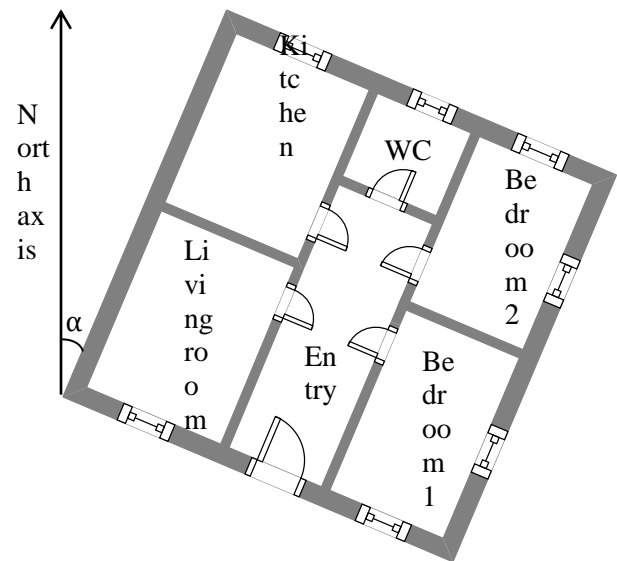
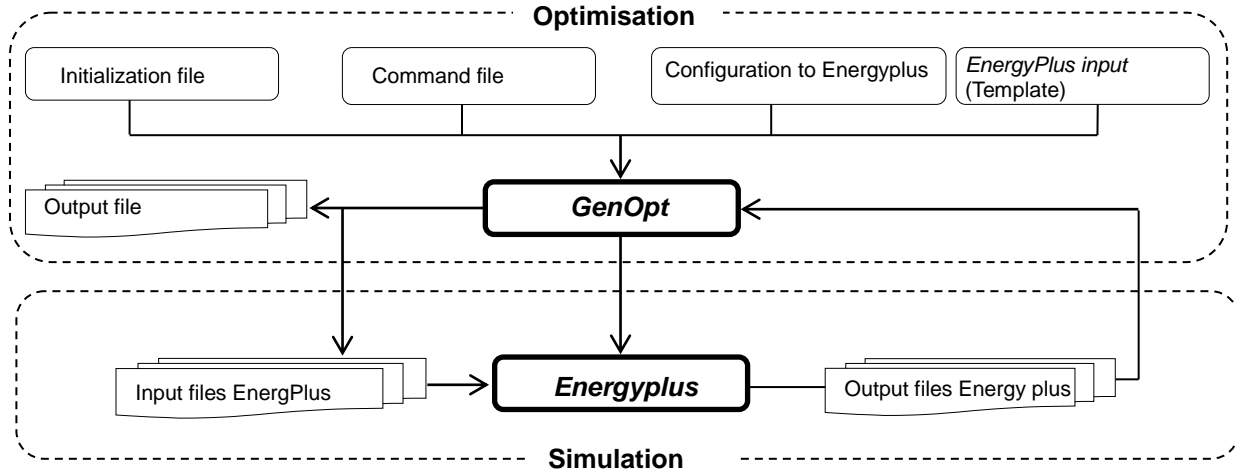


Figure 2: 2D Floor plan

Optimization variables: The variables of optimization has been defined in order to identify quality and quantity of the appropriate PCM to integrate into house envelope structure. Four PCM qualities with different melting temperatures(T_m). (20 °C, 22 °C, 24 °C, 26 °C) were used. The thickness of the PCM (e_{mcp}) layer is comprised between 0.5 cm to 2 cm. Furthermore four other variables related to design building parameters has been introduced which are able to define the energy performance of the house .

Table 3 below summarizes all of the optimization variables considered in this study.


Figure 1: Coupling principle between GenOpt and EnergyPlus

Material (layer)	Thickness (cm)	Heat capacity (j/kg °C)	Thermal conductivity (W/m °C)	Density (kg/m3)
Cement	1,5	1000	1,15	1700
Hollow brick	20	804	0,2	2732
PCM Layer	0,5 - 2	1132-15200	0,18-0,22	1400
Plasterboard	1	650	0,4	1200

Table 1: External wall structure

	Lights		Electric equipment's		Person number	People occupation		HVAC activation
	P.A (Hour)	Energy (w/m2)	P.A (Hour)	Energy (w)		P.A (Hour)	Energy (w/person)	P.A (Hour/day)
Bedroom 1	10	5	2	140	2	10	120	24
Bedroom 2	10	5	2	660	2	10	120	24
Kitchen	6	5	24	600	1	6	120	12
Living room	4	5	4	660	4	4	120	12
Entry	8	5	-	-	-	-	-	12

Table 2: Internal heat gains and HVAC system activation schedule

Optimization variable		Unit	Value/ designation
α	Orientation house (Azimuth surface angle)	(°)	-90/-45/0/45/90
T_m	PCM Melting temperature	(°C)	20/22/24/26
e_{pcm}	PCM layer thickness	(cm)	0,5/1/1,5/2
R_{glai}	The rate of glazing area	(%)	10/15/20
W_{type}	The glazing windows type	-	Double galzing/ simple glazing
R_{in}	The air infiltration rate	(ACH)	0,1/0,4/0,7/1
C_a	Solar absorptance coefficient of the outside surface of the external wall	-	0,2 /0,4 /0,6/ 0,8

Table 3: Optimization variable

PCM characteristics: Based on the physical proprieties of the *Dupont ENERGAIN®* PCM product [8], four hypothetical PCM were selected PCM_20, PCM_22, PCM_24, PCM_26 with the melting temperature, 20°C, 22°C, 24°C, 26°C Respectively. Figure 3 present the enthalpy-temperature curve for these hypothetical PCM products.

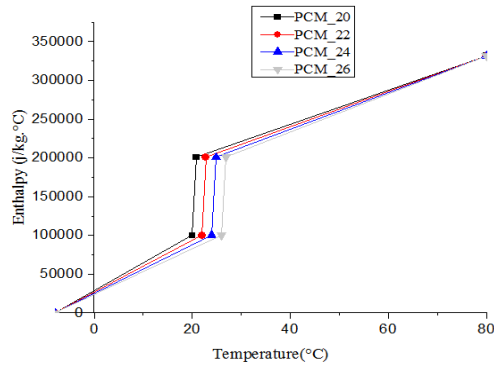


Figure 3: Enthalpy-Temperature curve

RESULTS AND DISCUSSION

The optimization results are shown in the table below.

Description variable	Valeur/Désignation
α	0
T_m	20°C
e_{pcm}	2 cm
R_{gla}	10 %
W_{type}	Double glazing
R_{in}	0,1
C_a	0,2

Table 4: Optimal design variable

According to these results, the optimum PCM melting temperature is 20°C. It would be adequate to minimize the heating and cooling demand for the moderate Mediterranean climate that distinguishes the northern region of Morocco (climate zone selected for our study).

Figure 4 shows a comparison between energy performance of optimum design obtained for a PCM-enhanced house and the energy performance of a reference house without PCM. The rate of reduction of energy consumption which is evaluated with the index of energy efficiency (IEE) (equation 1) shows clearly that the energy saving achieved through this optimum design allow to

decrease significantly heating energy demand during the-cold and swing seasons(From November to may). While, is still not significant during the heating season. In fact, it is found that from June to October, the index of energy efficiency (IEE) has a negative value which means that the PCM-enhanced house is characterized by cooling demands higher regarding to the reference house (without PCM) .

The global annual index of energy efficiency (IEE) is 3.34% which is particularly due to reduces in heating energy demand.

$$IEE(\%) = \left(1 - \frac{Q_{tot,Ref}}{Q_{tot,opt}}\right) \times 100 \quad (1)$$

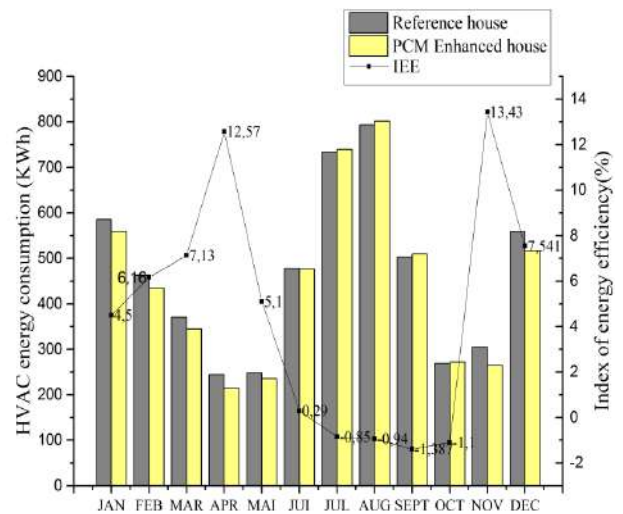


Figure 4: Monthly HVAC energy consumption for the optimal design PCM-enhanced house and the reference house.

The figure (5a, 5b, 5c, 5d, 5e, 5f) shows a parametric evaluation of the impact of the variation of each variable on the thermal performance of the optimal design obtained.

In figure (5a), it's clear that the annual heating and cooling demands increase progressively with the increase of PCM melting temperature. The same observation is valuable for the variation of the glazing area (5c), the infiltration rate (5e), and the solar absorbance of the outside surface of the external wall (5f). In fact, the low infiltration rate allows to limits the heat exchange between the indoor air and outdoor environment and therefore

reduces heat loss in winter and the overheating in summer. The solar absorbance of the outside surface

the type of glazing, the glazing area rate; the air infiltration rates; solar absorption coefficient of the

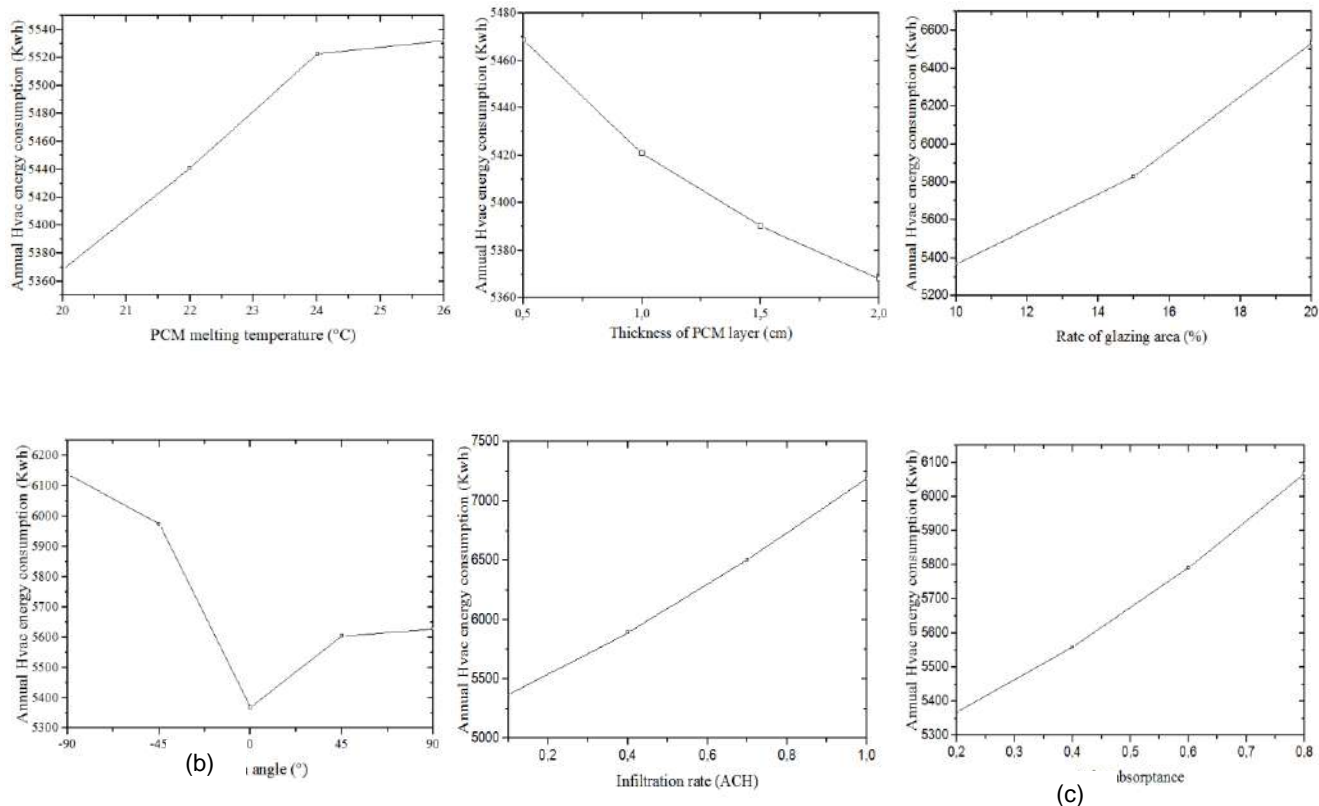


Figure 4: Impact of the variation of (a) PCM melting temperature (b) Thickness of the PCM layer (c) Rate of glazing area (d) Surface azimuth angle (e) Air infiltration rate (f) Solar absorbance of the outside surface of the external wall : on the annual HVAC energy consumption of the PCM-Enhanced house

of external the wall (cement) is related to colour that covers this surface. A light colour with a low solar absorbance is more appropriate to improve the thermal performance of the house. Furthermore, the increase the PC (d) thickness layer allows decreasing the annual heating and cooling demands (figure 5b).

CONCLUSIONS

In conclusion, the optimization methodology based on the coupling of the Genopt optimization tool and the building simulation tool EnergyPlus represents an efficient way to optimize the design of a building integrated PCM with a less time-consuming. In this study, we have chosen to limit ourselves to some variables that have a great influence on the energy performance of a house incorporating a PCM (The PCM temperature melting, The PCM thickness layer;

outer layer of the habitat). The results show the improvement of the energy performance for a house by integration the PCM and by adopting an optimal (e) sign to define the adequate (f) and quantity of the incorporated PCM as other parameters of design (The type of glazing, the glazing area rate; the air infiltration rates; solar absorption coefficient of the outer layer of the house).

ACKNOWLEDGMENTS

The authors should address their acknowledgements. to the France Institute of Rabat in Morocco for their supports .

REFERENCES

1. IEA, <https://www.iea.org/aboutus/faqs/energyefficiency/>
2. Feustel HE (1995) simplified numerical description of latent storage characteristics for phasechange wallboard. In: Indoor Environmental Program, Energy and Environment Division. Lawrence Berkeley Laboratory, University of California, Berkeley
3. Schossig P, Henning H, Gschwander S, Haussmann T (2005) Microencapsulated phase change materials integrated into construction materials. *Sol Energy Mater Sol Cells* 89:297–306
4. BOUZLOU, Yassine, MOURID, Amina, EL ALAMI, Mustapha, et al. Experimental study of heat storage in a PCM incorporated into a residential premises walls. In : Renewable and Sustainable Energy Conference (IRSEC), 2014 International. IEEE, 2014. p. 390-394.
5. SOARES, N., GASPAR, A. R., SANTOS, P., et al. Multi-dimensional optimization of the incorporation of PCM-drywalls in lightweight steel-framed residential buildings in different climates. *Energy and buildings*, 2014, vol. 70, p. 411-421.
6. Energy Plus, Energy Plus Documentation. US Department of Energy, 2010
7. LBNL (2011). GenOpt–Generic Optimization Program. Lawrence Berkeley National Laboratory. <http://simulationresearch.lbl.gov>.
8. CAO, Sunliang, GUSTAVSEN, Arild, UVSLØKK, Sivert, et al. The Effect of Wall-Integrated Phase Change Material Panels on the Indoor Air and Wall Temperature–Hot-box Experiments. In : Renewable Energy Research Conference. 2010.

The Study Natural Ventilation by Using Buildings Windows: Case Study in a Hot Dry Climate, Ghardaïa, Algeria

M. Hamdani *¹, S.M.A. Bekkouche ¹, T. Benouaz ², R. Belarbi ³ and M.K. Cherier ¹

¹ Unité de Recherche Appliquée en Energies Renouvelables, URAER, Centre de Développement des Energies Renouvelables, CDER, 47133, Ghardaïa, Algeria.

² University of Tlemcen, Algeria.

³ University of La Rochelle, France.

*Corresponding author: hamdanimaamar@yahoo.fr

ABSTRACT

Natural ventilation in buildings can create a comfortable and healthy indoor environment, and save energy used in the mechanical ventilation systems, have an important role on the balance between heating and cooling needs, It is also necessary to study the possible combinations with natural resources.

With natural ventilation the internal building structure is cooled through open windows and/or air vents, in order to provide a wind induced flow or stack effect. It is dependent on natural forces to move air through a building: so the disadvantage is that there is no direct control of the ventilation, but on the other hand it delivers low running costs and low energy usage by reducing the electrical energy used for air-conditioning.

The building design must implement simple principles based on common sense and have proven their effectiveness in traditional constructions. It must be adapted to seasonal needs (warm in winter, cool in summer) and promote maximum passive solar gain and minimize losses

In the first part of this article, the building geometry, its operation and the thermo-aerodynamics numerical model are developed under the TRNSYS-CONTAM environment are presented. In the second part, the simulation is performed for both cases; with ventilation natural night and without natural ventilation. The study will ensure the night ventilation door and window of the cell which are open from 20 pm until 8 am.

KEYWORDS

INTRODUCTION

The natural ventilation and infiltration of a building are driven by the pressure difference across the building structure between the inside and outside; this pressure difference is a result of temperature difference between inside and outside which cause a difference in air density (stack effect). With stack effect, the movement of the air is due to the temperature difference between the inside and the outdoor. The air flow is vertical along the path of least resistance [1]. In this way when the inside temperature is higher than the outside, the warmer air rises through the building and flows out at the top, while the colder outside air comes to the bottom to replace the warmer air which is rising up through the structure. The wind pressure on buildings surfaces depends on several factors, such as wind direction, speed shape of building, location, local environment

and so on. Generally the pressures are higher on the windward side and lower/negative on the leeward. In general a global effect of natural ventilation is a combination between stack effect and wind effect and it has to be supported by motorized vents to guarantee different air flows in the different periods of the days. This also depends on building height, local terrain, internal resistance to vertical air flow and flow resistance characteristics. In natural ventilation, low energy usage imposes restrictions on the shape of the building. The ventilated spaces have to be within a relatively small distance from an external wall. Moreover some drawbacks can happen. For the opening windows, such as security issues, noise and pollution are not always sufficient to ensure a ventilation rate [1]. The design phase has a fundamental importance for the building have to

PRESENTATION AND BUILDING MODELLING

The building climate is hot and dry in the summer with temperatures variation between a maximum of around 45 °C and a minimum of 20 °C, thus giving a large temperature swing. Winter temperatures vary between a maximum of 24 °C and a minimum of 0 °C. Its normal temperature in January is 10.4 °C and 36.3 °C in July. The average annual range is about 12.2 ° amplitudes of monthly average temperatures. They are more moderate in winter than in summer (average 11° in winter cons 13.5° in summer). The monthly maximum amplitudes are larger in summer than in winter fluctuates around 20 °C. Solar radiation is intense throughout the year with a maximum of 700 Wm⁻² in winter and 1000 Wm⁻² in summer, measured on the horizontal surface [6]-[10].

The study was carried out on a building in Ghardaïa. The exterior envelope, apart from contributing to the energy savings during the building life by controlling the energy exchange between indoor space and environment developed a comfortable indoor environment [6]-[10]. Fig. 2 is a schematic outline of apartment building, the house has a net area of 71.3 m², and wall heights are equal to 2.8 m while the other dimensions are shown in detail in Fig. 2. The flooring is placed on plan ground to lodge the ground floor. The concrete of the flooring is directly poured on the ground thus minimizing losses. Floor tiles are end coating resisting to corrosion and chemical agents. The roof is composed of cement slabs and concrete slab made so that it handles the load and be economical. A roof sloping of 5° allowed water evacuation through several openings. The flat roofs are considered the air infiltration in it as architectural solution. Windows and doors contribute significantly to the energetic balance. Their contribution however depends on several parameters as: local climate, orientation, frame, relative surface (window-flooring), and concealment performance during night and sunny days. In this case focus is made particularly on windows and doors dimensions and all are made of woods. The apartment has a surface of 95.74 m² with an occupied space of 71.3 m².

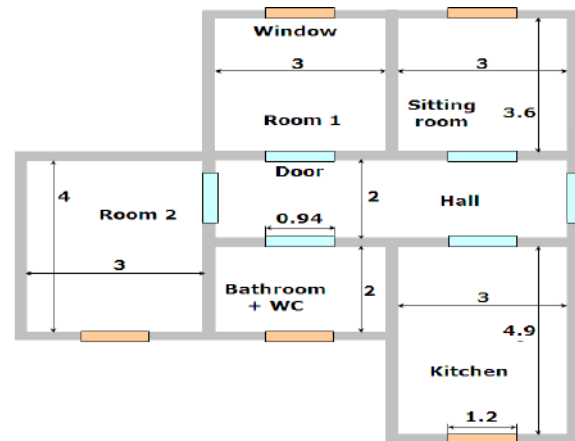


Figure 2

The house plan

In our model, the openings are on both north and south surface for the building with a main door on the East side, during the day the temperature of the outside air is greater than that of the interior. To eliminate the exchange ventilation with outdoor air, the windows and the door will be closed during the day, opened the night (the window and the door will be closed is the time or $T_{ai} < T_{ao}$ and be opened $T_{ai} > T_{ao}$) [11]. By numerical simulation of the model is determined corresponding to each case. For better ventilation of the interior during the night, the door and the window will be on two different opposite wall, it is necessary to seek their guidance for minimized heat gain. During the day the windows and the door will be closed. heat transfer is carried out as the case of an opaque member. To calculate the temperature in the inside face of the window and the door, the same method and the same steps in the case of wall are followed [6]-[10].

BUILD ENERGY MODEL IN TRNSYS

The thermal simulation of the building was performed by coupling a thermal model developed under TRNSYS and ventilation via the CONTAM software model. As illustrated in Fig. 3, the building is modeled as a single-building area in a "ventilation" model which calculates the ventilation rate and the air permeability through the casing [12].

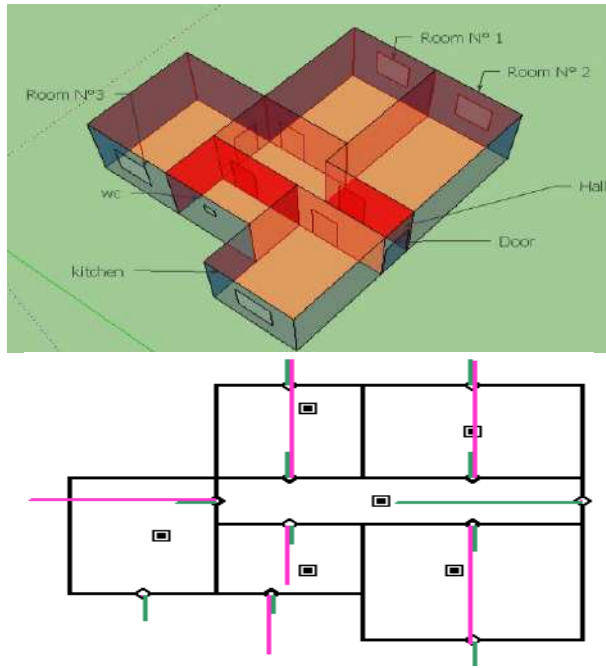


Figure 3

Airflow and pressure distributions in the six-zone calculated by CONTAM

To calculate the dynamic air infiltration rates, CONTAM is used to create the multi-zone model for the case study building. To build the multi-zone model in CONTAM, one needs to zone the building reasonably to the level that it is not too complicated while not affecting the accuracy of results. Second, we calculate the wind pressure coefficient on each surface. To calculate the wind pressure coefficient of each surface, Urban context plays a very important role in wind pressure profile calculation [12].

PRESSURE COEFFICIENT MODEL

The wind effect on the building is calculated in a multi-zone ventilation model using the wind pressure coefficient C_p . In order to convert wind speeds to pressures on the exterior surface of a building being analysed, CONTAM uses wind pressure coefficients [12]-[13].

These coefficients, typically designated as C_p , are related to the wind pressure on the exterior surface of the building p_w in (1).

$$P_w = C_p \frac{\rho v^2}{2} \quad (1)$$

Where C_p is the wind pressure coefficient (dimensionless) which is a function of wind direction and location on the exterior surface, ρ is the air density (kg/m³) and v is the wind speed (m/s) at the building height.

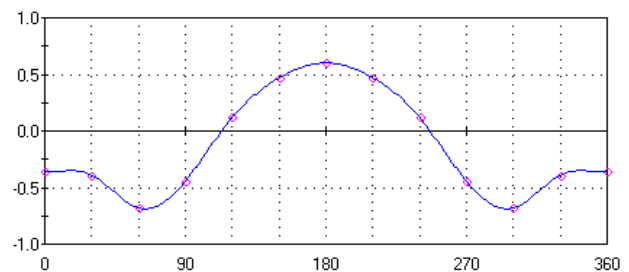
Values of the pressure coefficient depend on the building shape, the wind direction, the environment (nearby buildings and vegetation) and the specific location on the building surface (height and distance from the middle) (ASHRAE, 2005). They rely on inter- or extrapolation of generic knowledge and previously measured data in wind tunnel studies and full-scale experiments.

This correlation is based on a number of studies and yields wind pressure coefficients over a building surface as a function of wind direction. This correlation takes the form

$$C_p = C_{p0} \ln(1.2480.703 \sin(\alpha/2) - 1.175 \sin^2(\alpha) - 0.131 \sin^3 + 0.769 \cos(\alpha/2) + 0.07G^2 \sin^2(\alpha/2) + 0.717 \cos^2(\alpha/2)) \quad (2)$$

Where C_{p0} is the wind pressure coefficient on the surface towards which the wind blows in a normal direction ($\alpha = 0$), α is the wind direction measured normal to the wall, and G is the natural log of the ratio of the length of the wall to the length of the adjacent wall. To use this correlation, one needs a value for C_{p0} . Some relevant information for determining C_{p0} is given in the ASHRAE handbook chapter and other sources [4]. The correlation in (2) is the basis of the wind pressure profile libraries presented in Appendix B and described briefly.

Wind pressure coefficients on the envelope is determined for each wall depending on the angle of incidence of the wind thereon according to the model proposed by Swami et al, as shown in Fig. 4 each orientation [12]-[13].



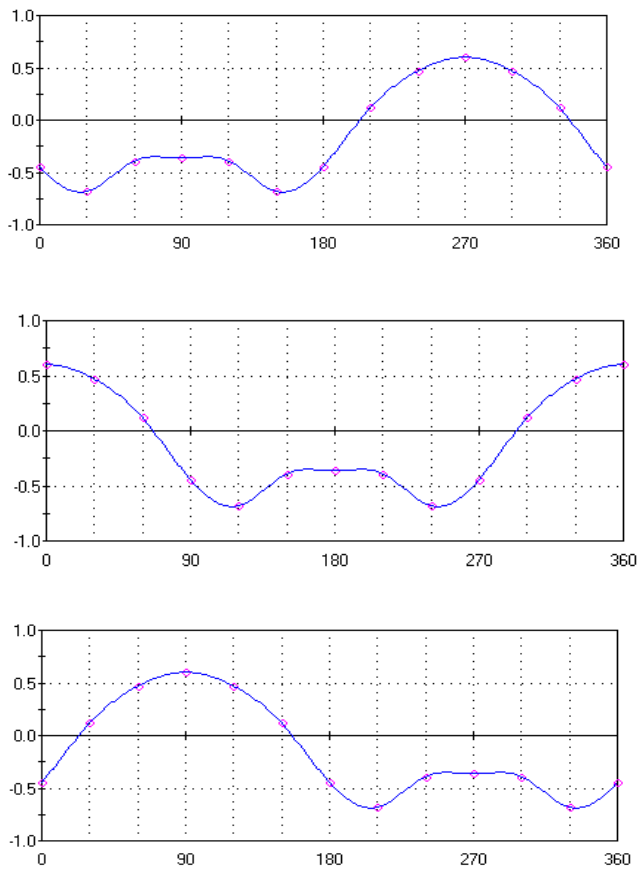


Figure 4

Plot of Wind Pressure Profile for the four wind directions

Fig. 5 shows the temperatures in the Open Space for summer days from the current model. We also note that the indoor temperature is higher than the outside at night with a difference up to 2.5°C .

The interest of the night ventilation is to use this temperature difference to create an aspiration of fresh air into the building to cool the building during the night to avoid overheating during the day effect. To assess the impact of the phenomenon, it is first necessary to study the physics of the phenomenon involved is commonly called the stack effect.

Natural ventilation gives excellent results in terms of summer comfort. The study shows that it would be wise to use this process during the summer months especially as it requires no cooling energy. The variation in the size of the opening would also improve thermal comfort.

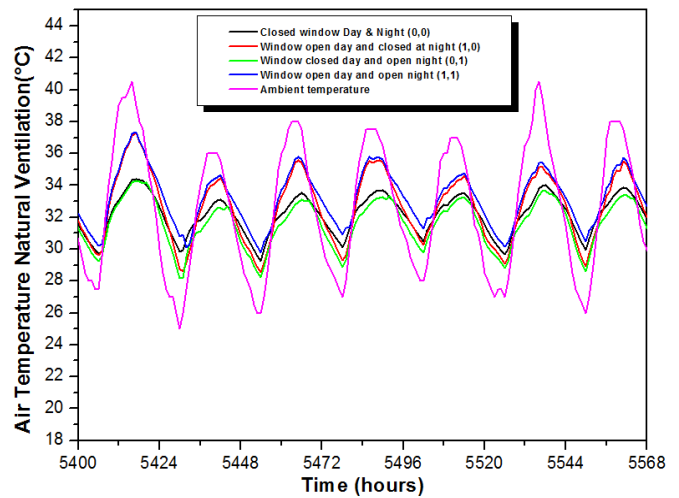


Figure 5

Comparison of indoor temperatures in scenarios with different ventilation

CONCLUSION

Thermo- aeraulic modeling is essential for establishing overall thermal performance values and understand how different assembly designs perform under different interior and exterior climate conditions. This tool is used to evaluate the performance of a proposed architecture for a real building located in a very hot climate. The object of the Natural night ventilation is to discharge a maximum during the night, the heat accumulated in the building material and for strong absorption of heat during the day this is especially building energy management regulated depending on weather conditions. It is timely today. Free cooling, which is to refresh the local at night to avoid air conditioning expenditures, provides another illustration Thus, with simulation tools.

The models are made using TRNSYS coupling with CONTAM. Four ventilation scenarios are studied to know the most thermal comfort scenario.

From the perspective of thermal engineering, windows are a special gate in the building envelope too. Their global heat transfer coefficient is typically 3 to 10 times higher than the equivalent for the opaque envelope. Therefore, they let the heat flow more easily between the indoor and the outdoor. In buildings located in climates with cold winters, the heat loss through windows can be quite significant. However, windows are also permeable to the penetration of solar radiation. Thus, if properly orientated, they can also contribute with a “free heating energy” in winter time. In the summer time,

however, the penetration of solar radiation may be a concern and contribute to overheating or increased energy demand for cooling. In the opposite trend, windows can contribute to cool the building through ventilation free-cooling, including night ventilation

REFERENCES

1. Ghjuvan Antone Faggianelli „Rafrâchissement par la ventilation naturelle traversante des bâtiments en climat méditerranéen, Université corse Pascal Paoli, Thèses 2014.
2. Barhoun Hayssam, nfluence des transferts aérauliques dans les parois sur leurs performances thermiques, 2006 , Thèses l'INSA de Lyon.
3. Bart Macquoy, Natural ventilation based bioclimatic redevelopment - 1/14 - Building transformation and improvement into an integrated energy efficient multifunctional design ,January 14th, 2014.
4. R.Lapisa, Effect of ground thermal inertia on the energy balance of commercial low-rise buildings, Building Simulation 2013, Chambéry, France.
5. Etude de l'impact des « cool roofs », de la ventilation naturelle et de l'inertie thermique du sol sur les performances énergétiques de bâtiments commerciaux), Université de La Rochelle, France.
6. S.M.A. Bekkouche, T. Benouaz, M.K. Cherier, M. Hamdani, N. Benamrane, M.R. Yaiche, Thermal resistances of local building materials and their effect upon the interior temperatures case of a building located in Ghardaïa region, Construction and Building Materials 52 (2014) 59–70.
7. M. Hamdani, S. M. A. Bekkouche, T. Benouaz, R. Belarbi, M. K. Cherier, Minimization of indoor temperatures and total solar insolation by optimizing the building orientation in hot climate, Engineering Structures And Technologies, Taylor & Francis: ISSN 2029-882X / eISSN 2029-8838 2014 6(3): 131–149, doi:10.3846/2029882X.2012.988756.
8. S. M. A. Bekkouche, T. Benouaz, M. K. Cherier, M. Hamdani, M. R. Yaiche et N Benamrane, "Influence of the Compactness Index to Increase the Internal Temperature of a Building in Saharan Climate", Elsevier, Energy and Buildings vol.66 (2013) pp. 678–687.
9. S. M. A. Bekkouche, T. Benouaz, M. K. Cherier, M. Hamdani, R. M Yaiche, R. Khanniche (2013), Influence of building orientation on internal temperature in Saharan climates, building located in Ghardaïa region (Algeria), International Scientific Journal, Thermal Science, 2013, Vol. 17, No. 2, pp. 349-364.
10. S. M. A. Bekkouche, T. Benouaz, M. R. Yaiche, M. K. Cherier, M. Hamdani, F. Chellali, Introduction to Control of Solar Gain and Internal Temperatures by Thermal Insulation, Proper Orientation and Eaves, Elsevier, Energy and Buildings vol.43 (2011) pp. 2414–2421.
11. Bencheikh Hamida, Etude et Realisation D'un Systeme de Refroidissement Passif en Utilisant une toiture radio-evaporative dans les climats chauds et arides, universite mentouri de constantine, these doctorat, 2007.
12. CONTAM,<http://www.bfrl.nist.gov/IAQanalysis/CONTAM/>.
13. D. Cóstola, B. Blocken, J.L.M. Hensen, Overview of pressure coefficient data in building energy simulation programs ,Building and enveronement,44(10),2007-2036.

Study of the effect of sun patch on the transient thermal behaviour of a heating floor

Mohammed Hichem BENZAAMA^{a, b}, Chadi MAALOUF^a, Mohammed LACHI^{a*}, Abderahmane MOKHTARI^c

^a GRESPI Laboratory - Thermomechanics (EA 4694), University of Reims Champagne-Ardenne, Reims, France)

^b LMSR Laboratory, University of Djillali Liabès, Sidi Bel Abbes, Algeria

^c LMST Laboratory, University of Science and Technology, Mohamed BOUDIAF, Oran, Algeria

*Corresponding author: Email: benzaama.hichem@hotmail.com

ABSTRACT

Solar radiation is a renewable non polluting energy source which can be used in buildings through various systems technologies. Thermal radiation, absorbed or transmitted by the walls and windows, creates a solar gain which has a direct impact on the thermal behavior in the building. Most existing thermal models neglect the effect of the evolution of the sun patch position on the heating floor which can have a great impact on the indoor thermal comfort.

In this paper, we present a 3D model to calculate the transient sun patch position and its influence on the heating floor model in order to evaluate its impact on the heating floor operating conditions and on the indoor thermal comfort under the climatic conditions of Oran City in Algeria. The sun patch is calculated using FLUENT tool whereas the room and the solar heating floor are modeled with TRNSYS software.

Using literature data, the 2 proposed models are validated and used to simulate the cases with different window orientations. Our results suggest that the displacement of the sun patch on the heating floor may lead to a superheating of the irradiated zone and it impacts the indoor thermal comfort.

Key words:

1. INTRODUCTION

To reduce the problems related to pollution by greenhouse gas emissions, the use of solar energy based systems for heating is an undeniable interest to address this issue.

Solar radiation depends on the position of the sun (altitude and azimuth). This position varies throughout the year and the day. According to this context, Athienitis et al. [1] developed a method to determine the solar radiation intensity absorbed by the inside wall surfaces of the room. They studied the influence of latitude, room geometry and the surface of the window.

Wall [2] presented the effect of solar radiation distribution in a room with a large glazed surface on

its southern wall. They compared the results of four different softwares and showed that in the case of large window areas heating requirement will be underestimated in some programs. This is mainly due to an inadequate consideration of the solar radiation through the window.

The presence of the solar patch on the floor has an impact on the thermal comfort because of local overheating over the portion receiving the direct solar beam (Trombe et al.) [3]. For this purpose Boukhris et al. [4] used a zonal method to analyze the influence of the sun patch on the calculation of the radiant temperature in two adjacent rooms. The glazing of the first room is located on the south wall whereas the window of the second room is located on the west wall. The results show a non-homogeneous temperature distribution in the region where the sunspot is located (in the first room). The

air temperature near this region is equal to 17.75°C while in the second room when there is no sun patch, the temperature is close to 15.5°C.

In an experimental study performed on the site of EDF R&D in South-West of Paris (France), Rodler et al. [5] studied the effect of the displacement of the sun patch on the walls and the floor in a well insulated room. Experimental data was used to validate a 3D numerical model.

In the case of a room equipped with a heating floor system, the entering solar radiation can generate a great level of thermal discomfort which is due to overheating. Most existing thermal models in buildings do not take into account this effect. We can cite the studies of H.Karabay et al. [6] and Khorasanizadeha et al. [7] which neglected the effect of the sun patch on the heating floor, they showed that when the temperature distribution on the floor is uniform, a better thermal comfort is provided.

In this work we investigate the effect of a solar patch on the temperature and thermal comfort conditions in a room equipped with a heating floor system under Algerian climate. Knowing the exact position of the sun patch on the floor, the temperature of the irradiated area is computed and compared to that of the unexposed area. As our modelisation is in 3 dimensions we visualize the behavior of the heated floor, and by calculating the temperature at different elevations in the room to get the level of thermal comfort.

2. MODELING AND COUPLING

In the first case we use TRNSYS software to model room envelope and the heating floor system. In this case the temperatures of the room and the floor surface are considered without taking into account the overheating of the irradiated zone.

To simulate the effect of the sun patch on air conditions over the heating floor we use FLUENT software which uses as initial conditions results obtained by TRNSYS tool. Zhai and Chen [8] classified the methods of coupling between the CFD and the ES simulation (Energy simulation) in three classes: static, dynamic and quasi-dynamic. A static coupling consists of “one-step” or in “two steps” data exchange between softwares. A dynamic

strategy of coupling consists in a continuous exchange of data for each time-step in the simulation.

Referring to these coupling methods, Gowreesunker et al. [9] used a quasi-dynamic model in his study to couple TRNSYS and CFD code (Figure 1).

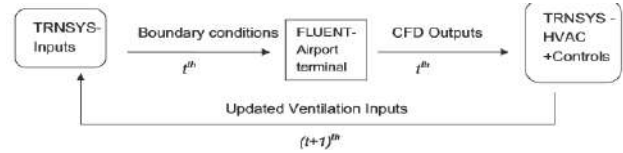


Figure 1

quasi-dynamic coupling between CFD-TRNSYS.

Based on these principles, for our case we chose the static coupling method. Data exchange has been done from TRNSYS to FLUENT: The transformed variables are: the temperatures of walls, the temperature of the glazing and the convective heat transfer coefficient of the heating floor. Heat transfer by convection from an inner surface has a major effect on thermal comfort, K. Arendt et al. [10]. Following this hypothesis, the model 80 "Type 80" on TRNSYS was used to obtain the convection coefficient of heating floor (Figure 2).

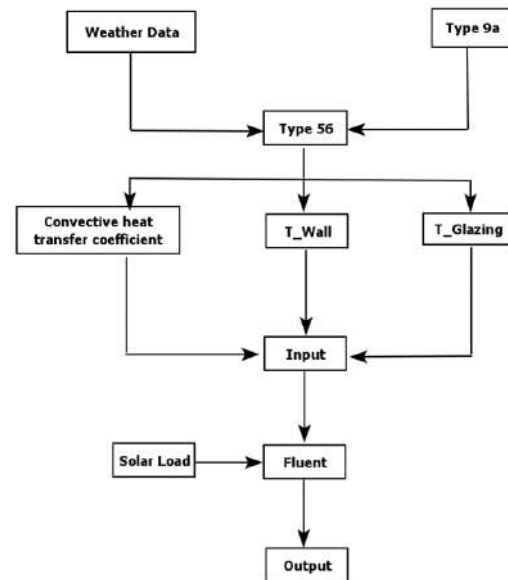


Figure 2

Illustration of the temporal coupling between TRNSYS and FLUENT.

3. VALIDATION OF THE MODELS

3.1 Validation of the model of the heating floor in TRNSYS.16

To validate the model used in TRNSYS, we compared it to the work data given by Merabtine [11] who studied numerically and experimentally a heating floor under the weather conditions of Nancy. The outdoor temperature and the heating floor inlet temperature were measured and have been included in the simulation using TRNSYS type 9a (Figure 3).

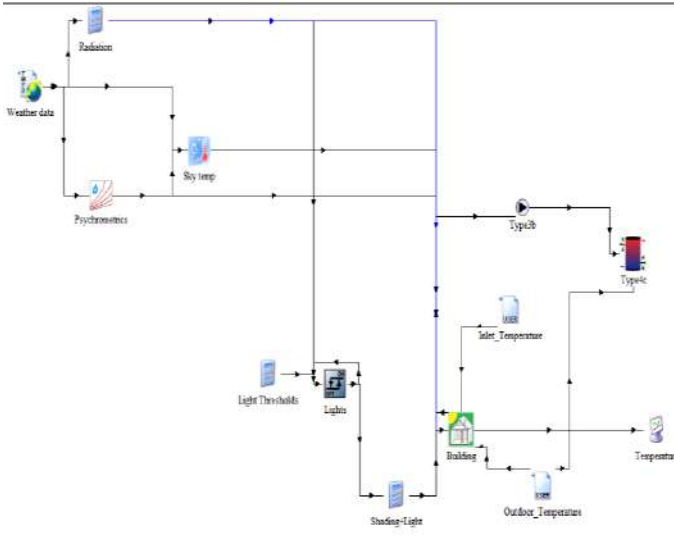


Figure 3

TRNSYS Interphase

Figure 4 shows numerical results for the floor outlet temperature and compares them to experimental measurements. A good agreement is found between the curves.

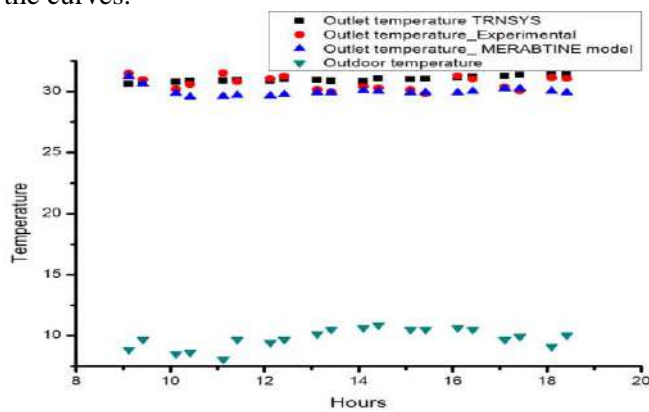


Figure 4.

Validation of the model of heating floor for the 20 of december.

3.2 Validation of the model of the sun patch in FLUENT:

The model of the sunspot established with FLUENT (CFD) is validated by comparing it to the results of Boukhris et al. [4] and to Bouia et al. [12] for a 5 m × 3 m × 3 m room with two windows situated on the southern façade. The room is oriented in the north-south direction. The validation of the model was made for two climatic conditions, Lyon and Marseille for different periods.

Table 1
Geographic coordinates.

City	Latitude	Longitude
Lyon	45,75°	4,85°
Marseille	43,30°	5,40°

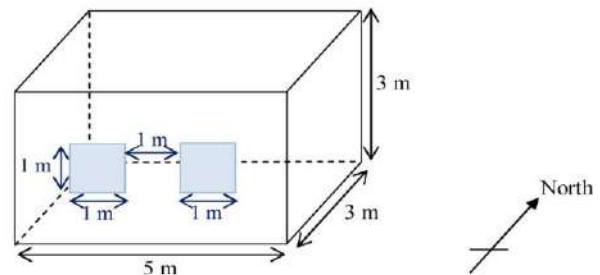
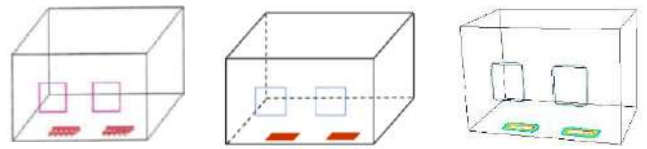


Figure 5

Shape and dimensions of the room

21/06/2002 at 4 pm Lyon

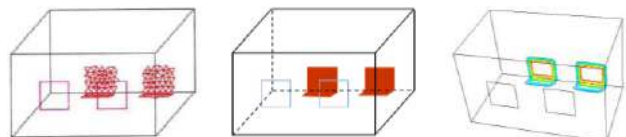


Bouia model [12] (IBPSA 2002)

Boukhris model [4] in « ZAER tool »

Sun patch model «FLUENT»

21/12/2002 at noon Lyon



Bouia model [12] (IBPSA 2002) Boukhris model [4] in « ZAER tool » Sun patch model « FLUENT »

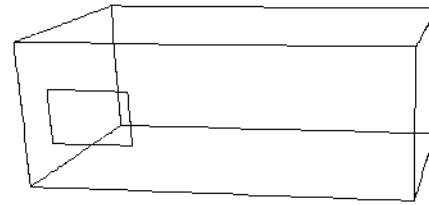


Figure 7

Geometric description of the cell

The construction of the tested cell was made to be considered as an insulated building. The vertical walls, the ceiling and the floor composition are given in the following tables:

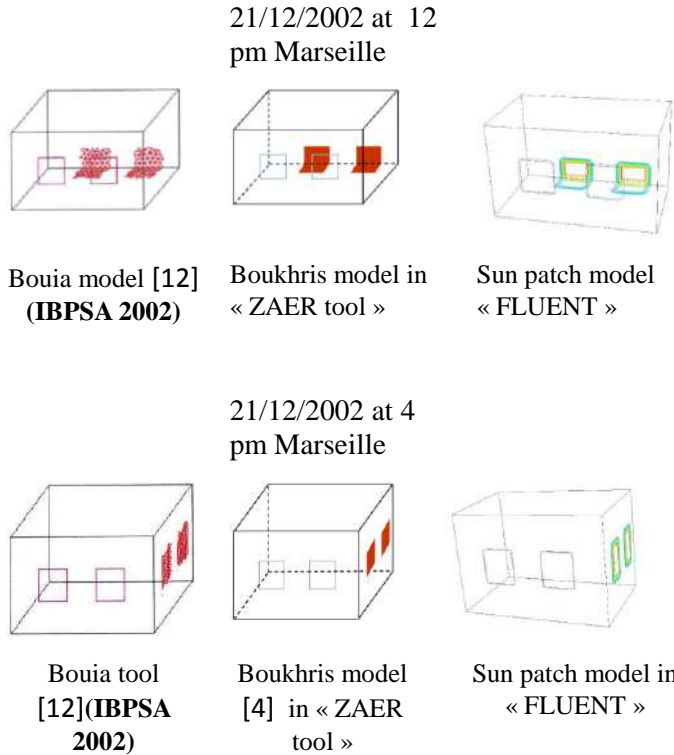


Figure 6

Validation of the model of the sun patch for Lyon and Marseille cities

Table 2

Composition of the vertical walls

Material	Thickness (cm)
Cement plaster	1 cm
Wall first Brick	10 cm
Polystyrene insulation	3.2 cm
Wall second Brick	10 cm
Plaster coating	1 cm

Table 3

Composition of the ceiling

Material	Thickness(cm)
The tightness	3 cm
Forme de pente insulation	2 cm
Hollow floor plaster	(16 + 4) cm
	1.5 cm

Table 4

Composition of the floor

Material	Thickness (m)	Conductivity λ (W/m ² k)	Capacity cp (J/Kg°C)
Gerflex Coating	0.003	0.31	1046
Dallage	0.1	1.75	920
Glass wool	0.04	0.038	1450
Concrete slab	0.1	1.75	920

4. CASE STUDY FOR ORAN CITY

4.1 Simulation in Trnsys.16

The studied cell (Figure 7) is located at the university of sciences and technology, Mohamed Boudiaf, in the locality of the commune of Es-Senia of Oran, Algeria (35.65° Northern latitude, 0.62° Western longitude). It is composed of two identical rooms of 20 m² each. They are oriented in the North-South direction and have dimensions of 4.7 m × 3.7 m × 2.7 m. It has a glazed surface of 1.2 m² located on the southern façade (Figure7).

The heating is ensured by a Co-generator Eco-power e47 producing an electric power of 1.3 KW to 4.7 KW and releasing a thermal power of 4 KW to 12.5 KW. The heat provided by the Co-generator is stored

in a thermal stratification water tank with a capacity of 1500 liters.

Figure 8 shows the evolution of the floor surface and air indoor air temperatures as simulated by TRNSYS for two days period in January for Oran city. We notice that the floor surface temperature ranges from 23°C to 24.5°C and that of air from 20°C to 22°C.

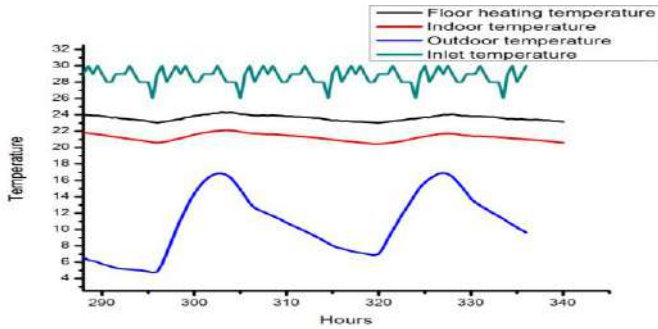


Figure 8
Simulation in TRNSYS

4.2 Effect of the sun patch on the floor heating: Coupling Trnsys.16 – Fluent

Our model has the particularity to locate the sun patch on the surface of the heating floor at different times, allowing to take into account the real distribution of the solar radiation entering in the cell. The chosen period for this simulation is January 12 at 4 pm

Table 5
Boundary conditions (12 January at 4 pm).

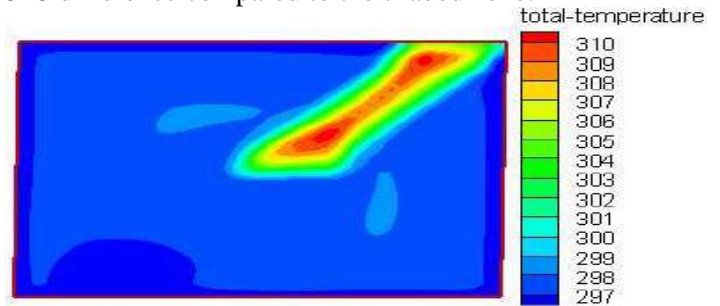
Wall	Temperature	Convection heat Coefficient (w/m ² .K)
North Wall	22.08 °C	/
South Wall	22.45 °C	/
East Wall	21.72 °C	/
West Wall	21.79 °C	/
Floor	24.29 °C	2.55
Ceiling	21.58 °C	/
Glazing	8.78 °C	/

In the figures below, we represent the influence of the displacement of the sun patch on the thermal behavior of the heating floor. The passage of the sun patch generates a rise in temperature showing local floor overheating (Fig 9.a). The temperatures of the floor surface and indoor air remain homogeneous

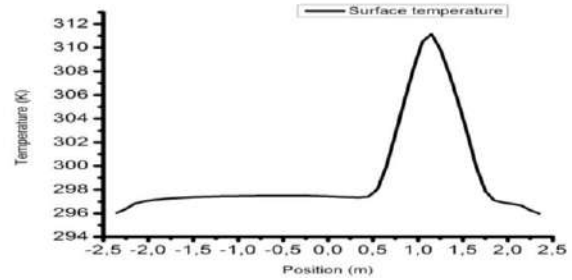
until the appearance of the sun patch on the floor. From there, the heterogeneities of temperature appear on both temperatures.

At the floor surface level, the temperature of the solar irradiated zone reaches a maximum of 36 °C (Figure 9 b) against a temperature around 25 °C for the shaded zone which is a difference of 11°C.

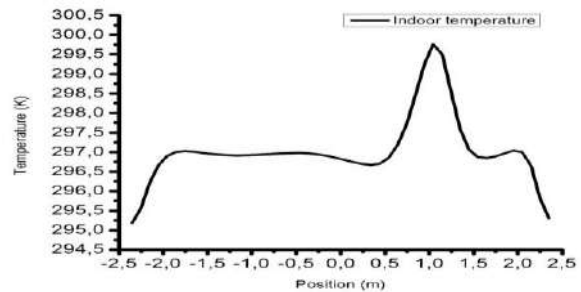
The indoor temperature is maintained at 24 °C (Fig 9.c) in the shaded zone. This temperature is greatly influenced by the passage of the sun patch and it reaches a maximum value of 27°C (Fig9.c) which is 3°C difference compared to the shaded zone.



(a)



(b)



(c)

Figure 9

Effect of the sun patch on the thermal behavior of heating floor (12 January at 4 pm) (Along the X axis).

5. CONCLUSION:

This paper presents the effect of solar patch on the thermal behavior of a heating floor under the

weather in the city of Oran (Algeria). For this purpose, a floor heating model was established in TRNSYS and validated with the results found in the literature.

The model of the sunspot is established with FLUENT software and makes it possible to locate the sun patch on the floor surface at various moments. In this case we can compare the temperature of the irradiated zone with that of the shaded zone.

The results show that the presence of the sunspot on the heated floor during a sunny day has a significant effect on the indoor air and floor surface temperatures, generating heterogeneities in temperature distribution ranging from 3°C difference for the air temperature to 11°C difference for the floor surface temperature. This model will be used to study the effect of window orientation as well as its surface on the thermal behavior of the heating floor.

REFERENCES:

- [1] A.K. ATHIENTIS, M. STYLIANOU, Method and global relationship for estimation of transmitted solar energy distribution in passive solar rooms. *Energy Sources* 13,319–336. (1991).
- [2] M. Wall, Distribution of solar radiation in glazed spaces and adjacent buildings. A comparison of simulation programs. *Energy and Buildings*, 26(2), 129–135.
- [3] A.Trombe, L.Serres, , M. Moisson. Solar radiation modelling in a complex enclosure. *Solar Energy Vol. 67, Nos. 4–6*, pp. 297–307, 1999.
- [4] Yosr Boukhris, Leila Gharbi, Nadia Ghrab-Morcos. Coupling the building simulation tool ZAER with a sunspot model. Case study in Tunis. *Energy and Buildings* 70 (2014) 1–14.
- [5] A. Rodler, J. Virgone, J.-J. Roux, J.L. Hubert. Development and validation of a three dimensional thermal transient numerical model with sun patch: Application to a low energy cell. *Energy and Buildings* 87 (2014) 425–435.
- [6] Hasan Karabay, Muslum Arıçı, Murat Sandık. A numerical investigation of fluid flow and heat transfer inside a room for floor heating and wall heating systems. *Energy and Buildings* 67 (2013) 471–478.
- [7] H. Khorasanizadeh, G.A. Sheikhzadeh, A.A. Azemati, B. Shirkavand Hadavand. Numerical study of air flow and heat transfer in a two-dimensional enclosure with floor heating. *Energy and Buildings* 78 (2014) 98–104.
- [8] Zhiqiang John Zhai, Qingyan Yan Chen, Performance of coupled building energy and CFD simulations. *Energy and Buildings* 2005;37:333-44.
- [9] B.L. Gowreesunker , S.A. Tassou, M. Kolokotroni. Coupled TRNSYS-CFD simulations evaluating the performance of PCM plate heat exchangers in an airport terminal building displacement conditioning system. *Building and Environment* 65 (2013) 132-145.
- [10] K. Arendt , M. Krzaczek, Co-simulation strategy of transient CFD and heat transfer in building thermal envelope based on calibrated heat transfer coefficients. *International Journal of Thermal Sciences* 85 (2014) 1-11.
- [11] Merabtine Abdelatif. Modélisation Bond Graphs en vue de l'efficacité _énergétique du bâtiment. *Thermics*. Université de Lorraine, 2012. French. <tel-00789679>
- [12] H. Bouia, J.J. Roux, C. Teodosiu, Modélisation de la tache solaire dans une pièce équipée d'un vitrage utilisant un maillage en surface de Delaunay, in: *Proceedings of IBPSA, France*, 2002, pp. 15–19.

EFFECT OF THE OCCUPANT AND THE INSIDE FACES COATING OF A MULTI-ALVEOLAR STRUCTURE ON THE UNSTEADY THERMAL BEHAVIOR OF A BI-ZONE BUILDING

Nour LAJIMI¹, Nour BEN TAHER², Nouredine BOUKADIDA^{3*}

¹ENI-Monastir, ²ESST-HS, ³UMSE, University of Monastir, Avenue Tahar Haddad 5000, Monastir

*Corresponding author: Fax: +216 7337 0710 E-mail: noureddine.boukadida@gmail.com

ABSTRACT

The aim of this work is to study the unsteady thermal behavior of a bi-zone building exposed to sunshine under clear sky conditions. The walls in South and West frontages are equipped with a multi-alveolar structure with a variable insulation depending on the heat flow direction. The structure has blades which are inclined relative to the horizontal direction. The results show the effects of the optical properties of the inner surfaces of the alveolar structure, the position of the alveolar structure with regard to the stone layer and the occupant on the unsteady thermal behavior of the bi-zone building.

Keywords Solar energy, bi-zone, occupant, building, alveolar structure, thermal inertia.

NOMENCLATURE

A	corporal surface	m^2
S	thermal load of the human body	$W.m^{-2}$
M	metabolism	$W.m^{-2}$
K	conduction	$W.m^{-2}$
C	convection	$W.m^{-2}$
R	GLO radiation between occupant and inner environment	$W.m^{-2}$
R _{resp}	respiration	$W.m^{-2}$
E _{evap}	evaporation	$W.m^{-2}$
T _i	real-time temperature	K
(mc) _i	heat capacity	$J.K^{-1}$
C _{i,j}	conductive and/or convective coefficient between nodes i and j	$W.K^{-1}$
K _{i,j}	radiative coupling coefficient	$W.K^{-4}$
σ	Stefan-Boltzman constant	$5,610-8 W.m^{-2}.K^{-4}$
φ _t	density of global heat transfer	$W.m^{-2}$

tilted or not active against the gravity field, others are rather interested in inclined cavities.

Taking into account the aero-thermal phenomena in the alveolar structure, D. Gutierrez [1] determined, temperature and speed fields in the alveolar according to different angles of inclination and report shape. Seki and al [2] experimentally studied the heat transfer by natural convection in a cavity of size (H=72mm, L=50mm) performed with fluid of Prandtl number (air, distilled water, refined oil). The angle of inclination takes the values: 0, ± 0,25, ± 45, ± 60 and ±70 degree. The high and low passive walls (lamellas) are constituted by an insulating material. Chochung and Trefethen [3] showed the influence of the thermal boundary conditions in cavities on transfer by examining numerically various conductance between superimposed cavities. Bairi [4] experimentally studied the natural convection in the closed alveolar structure when the active walls remain vertical. He brought out correlations of type Nusselt number according to the Grashof number for different obtained configuration by varying the angle of inclination, the report of shape and the temperature difference ΔT between both warm and cold vertical walls. He also showed the influence of the thermal boundary conditions at the level of the passive walls (lamellas) on the convective transfer. Several studies considered the unoccupied building, but others have taken into account the presence of the occupant as an internal load. The calculations become much more complicated because the building has obviously a direct influence on the subject and, in return, it is involved in the heat balance of the environment and it is very important to know how the human body reacts. To refine the calculations, several human thermoregulation

INTRODUCTION

The control of the energetic consumption of buildings is a major priority. This control requires knowledge on the energy performance of the envelope of buildings and the knowledge of the effect of different parameters that permit to save energy. Many previous works concerning the study of the thermal behavior of mono-zone or multi-zone buildings have been carried out in recent decades. Many researchers are interested in thermal behavior of the alveolar structure. Among them are those who are involved in studying rectangular cavities. Their faces are

models have been created since decades and they were coupled with thermal models of the building envelope like in the work of Thellier [5] who inserted a human thermoregulation model created by JAJ Sttolijk in TRNSYS habitat simulation program to characterize the impact of the atmosphere settings on the human physiological reactions and the influence of the presence of the occupant on the physical quantities characterizing the building as the rate of the relative humidity which allowed the prediction of thermal comfort. In this work, the calculation of the radiative exchange between the piece and a standing occupant was based on the method of MONTE CARLO to calculate view factors and the assesment of the impact of solar radiation on the thermal comfort was based on solar spot model and a view factors model developed by Mavroulakis et al. [6]. Serres et al. [7] studied the thermal supply to the human body consisting of flow absorbed by an occupant assimilated to a parallelepiped assembly, facing a bay and for different positions. In the same context of thermal comfort study and dynamic thermal simulation, Tulumoglu et al. [8] analyzed the thermal behavior of the individual and its interaction with the environment; the model was coupled to the building neglecting thermal exchanges by conduction and evaporation.

ANALYSIS AND MODELLING

Position of the problem

In this work, we are interested in studying the thermal behavior of bi-zone buildings in which walls of two zones (zone 1, zone 2) are identical (surface $S = 30 \text{ m}^2$ and volume $V = 300 \text{ m}^3$ with height, length and width of 3 m, 10 m, and 10 m respectively), and separated by a common wall on the eastern side. This wall is a polystyrene layer of 5,7 cm. Vertical walls which are placed on the south and west facing sides are composed of multi-alveolar structures (inclination angle: 60° , report shape: $R_p=1$) and a thick stone layer ($E_s=30\text{cm}$) (figure 1).

Vertical wall which is placed on the Nord facing sides and roof are composed of a wood layer, a coating layer and a thin wool layer in the middle. Floor is composed of a concrete layer, a coating layer and a thin wool layer in the middle. The thermo-physical properties of walls are given in Table 1. To solve this problem, the thermoelectricity analogy method is used [9]. The bi-zone building is occupied by two individuals at rest and taking a standing position (one in each zone), so breathing (R_{esp}) contributes only with

10% to the global exchange, conduction (K) with only 1 % (given the very small contact surface of the feet with the ground [5]), the metabolism is equal to $70 \text{ W}\cdot\text{m}^{-2}$ [7].

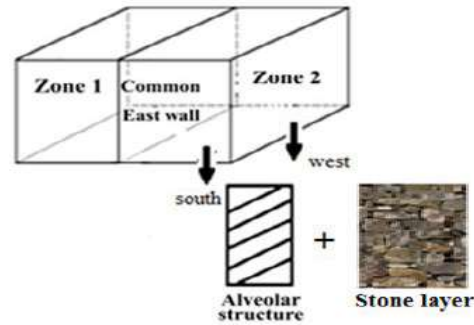


Figure 1 description of the bi-zone building

Material	$c(\text{J/Kg}\cdot\text{K})$	$\lambda(\text{W/m}\cdot\text{K})$	$\rho(\text{Kg/m}^3)$
Polystyrene	1450	0.039	18
Wood	2400	0.14	540
Stone	1000	1.4	1895
Wool	1000	0.04	30
Coating	1000	0.57	1150
Concrete	1000	1.7	2200

Table 1 Thermo-physical properties of wall components

Mathematical model

This mathematical model is based on the balance equation which can be written as:

$$(mc)_i \frac{dT_i}{dt} - S(t)A = \sum_{j=1,n} C_{i,j}(T_j - T_i) + \sum_{j=1,n} K_{i,j}(T_j^4 - T_i^4) + P_i(t)$$

Where $S(t) = M - (E_{vap} + R + C)$ and $P_i(t)$ is the absorbed part of the incident direct and diffuse solar flux by element i at the time t . The solar flux which depends on many parameters as the solar height, azimuth, declination of the sun. It is calculated for the 15th day of each month using equations (2), (3) and (4) in [10].

- Global density of heat transfer inside alveolar: We have opted for the correlation that includes convection and radiation, determined experimentally by Nouredine Boukadida and Vullierme J. J [11] in case of an angle of inclination equal to 60°C and a shape factor equal to unity:

$\varphi_t = \gamma(\Delta T)^n$ with $n=1.25$, where γ is Coefficient which depends on the heat direction

and faces emissivity of the slats (low or high emissivity).

The working assumptions

- The heat transfer is unidirectional.
- The air is considered a perfect transparent gas.
- The thermo-physical properties of materials are constant and identical for two zones.
- The air temperature inside the two zones is uniform.

We take into consideration the participation energy of the occupant.

For outdoor temperatures, we used in our calculations the average temperature per hour for the 15th day of each month of the year, taken from the weather station of the region of Sousse.

Discretization of the model and solving method

The numerical method retained is nodal method which is frequently used to study the building thermal behavior, does not require a refined mesh and integrate the concept of the fictitious node. It consists in splitting the system into multiple elements, each element is represented by a node which is affected by temperature and thermophysical properties of the element. This model, divided into 81 nodes, includes 6 faces (south, east, west, north, roof and floor). For more details, lecturer can refer to [12].

RESULTS AND DISCUSSION

Thermal behavior of multi-alveolar structures

In this case, the building is assumed to be unoccupied and the temperature of the inside air is not imposed. Figure 2 shows the evolution of the temperatures of outer and inner faces of the multi-alveolar structures which is placed on south facing wall.

When the multi-alveolar structures are placed in the inner side of the wall, the temperature of outer and inner faces have similar profiles and the temperature of the outer face takes the upper values compared to the inner face during the entire day.

When the structures are placed in the outer side of the wall, the two temperature profiles are different: the profile corresponding to the inner face has an important damping and smaller amplitude. We also note that during the night time the temperature of the inner face takes higher values compared to the outer one and during the daytime period (presence of sunlight),

profiles are reversed: the temperature of the inner face takes lower values compared to the outer face which is directly exposed to solar radiation.

So we note that the location of the multi-alveolar structures on the inner side highlights the effect of the high thermal inertia of the stone wall, the radiation sun that strikes the external surface is absorbed and converted into heat flux. This latest is transferred by conduction through the stone block and reaches the multi-alveolar structures with low value which explains the amortization of temperature at its outer and inner faces.

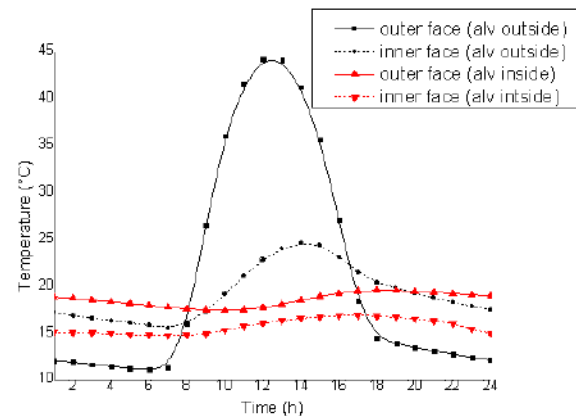


Figure 2 Evolution versus time of inner and outer faces temperatures

Effect of multi-alveolar structures positions on the inside air temperature:

Figure 3 shows that whatever the position of the multi-alveolar structures, the inside air temperature takes higher values compared to the temperature of the outside air over 24 hours and an identical phase shift of 3 hours (this is strongly linked to the high inertia of the wall). Both locations act differently on the values of the inside air temperature, the multi-alveolar structures located outside are more favorable during a cold period (January), the inner temperature varies slightly around 14°C, while it varies around 13°C when the structure is located inside. For the damping, the inside location of the structure gives a difference of 1°C between the minimum and the maximum of the inside air temperature, while the outside location gives a difference of 1.5°C.

Figs. 4 and 5 show the average power required to maintain the inside air temperature to 19 °C over 24 hours during January and the cold season. As shown, the energy consumption is lower if the multi-alveolar structures is placed outside (this saves around 400W during night time). We note that during the diurnal period there is a strong rapprochement of the two curves (between 8h and 14h) hence a low need for heating (figure 4).

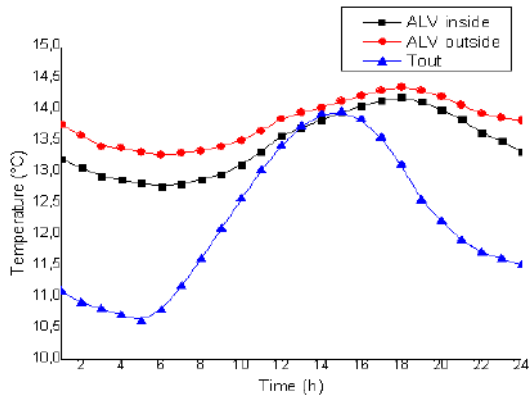


Figure 3 Evolution versus time of the inside air temperature

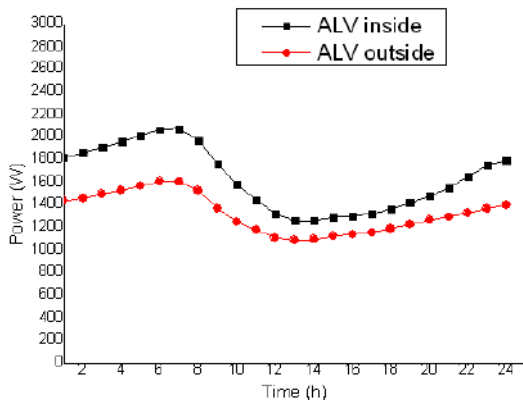


Figure 4 Evolution versus time of average heat power required in January

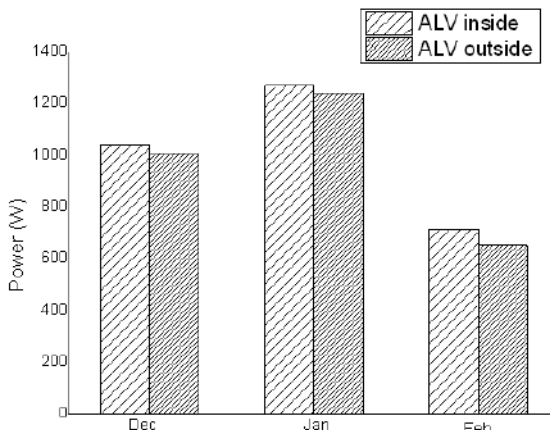


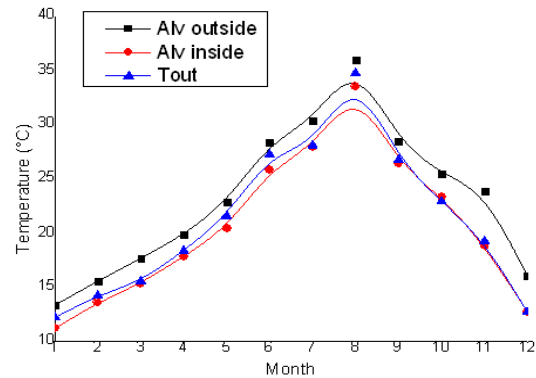
Figure 5 Average power consumption in cold season

Figure 6-a shows the evolution of:

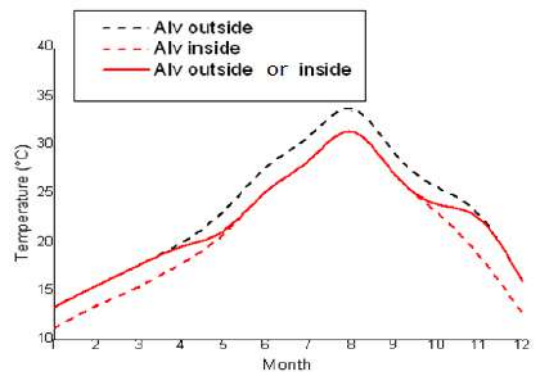
- The average annual meteorological temperature of Sousse region,
- The average inside air temperature over one year for the two locations of the multi-alveolar structure (inner and outer side). We find that these two positions are favorable for different periods, the external position is efficient during the winter (as shown in Figure 3), but during the summer,

the inner position becomes more efficient. So an optimal case which allows a desirable internal atmosphere is needed.

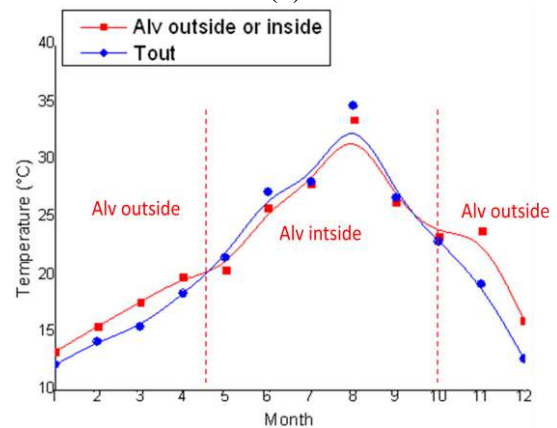
Changing the location of this structure is not possible once the wall is built, so the annual variation of the inside air temperature shows that for a cold climate, the location must be on the outer side and for a hot climate it must be on the inner side of the wall (figure 6-b and c).



(a)



(b)



(c)

Figure 6 Evolution versus time of annual inside air temperature

Effect of optical properties

Inside alveolar structure the main heat exchange takes place by radiation and convection. Radiation exchange on each vertical face depends

naturally on the emissivity of each face of the cavity. To calculate the global heat transfer coefficient inside each alveolar structure, we have opted for the correlation including convection and radiation, determined experimentally by N. Boukadida and J.-J. Vullierme [11]. Two cases are studied:

Case 1

The lower vertical face of each alveolar structure has an emissivity which is equal to 0.9 and all other faces (upper vertical face and the inclined lamellas) have an emissivity which is equal to 0.075.

Case 2

The lower vertical face of the alveolar structure has an emissivity which is equal to 0.075 and all other faces (upper vertical face and the inclined lamellas) have an emissivity which is equal to 0.9.

Figure 7 shows that there is not a big difference between the temperatures associated to those two cases (a difference of 0.2°C). Optical properties of multi-alveolar structures faces slightly affect the internal ambiance of the structure.

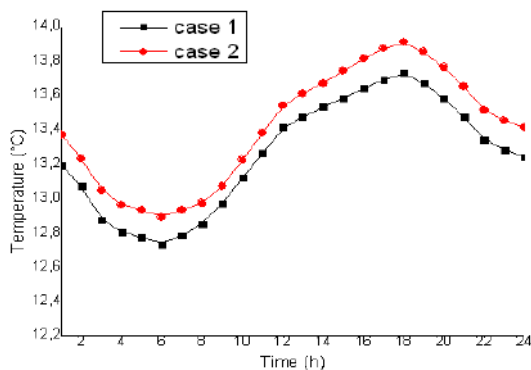


Figure 7 Evolution versus time of the inside air temperature with different optical properties of the multi-alveolar structure

Effect of energy participation of occupant

Figure 8 shows that during a winter day the individual's energy participation helps to increase the inside air temperature by 2°C (compared to an unoccupied building) over every 24 hours. Figure 9 shows that average supplied power to maintain the air temperature at 19°C in case of the occupied building by two individuals consumes less energy, we note a difference of 400W over 24 hours.

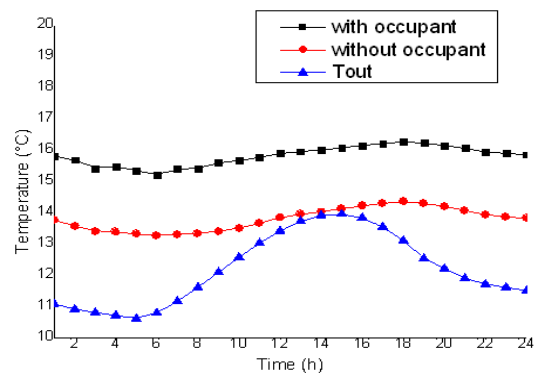


Figure 8 Evolution versus time of the inside air temperature with and without occupant

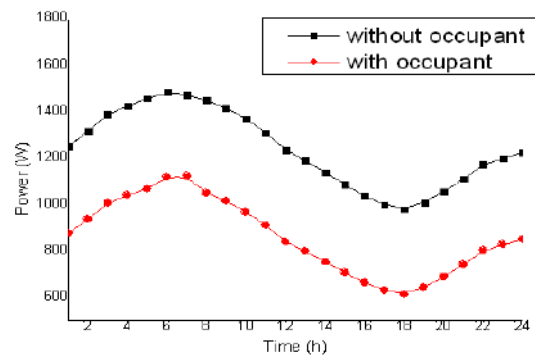


Figure 9 Evolution versus time of heat power required in January with and without occupant

CONCLUSIONS

We studied the effects of the position of multi-alveolar structure and its inner faces optical properties on bi-zone building thermal behavior. The results show that the location of this structure (inner or outer side of the wall) has an influence on its thermal behavior and highlights the effect of the thermal inertia of the stone layer. The outer position of multi-alveolar structure is more favorable during a cold period and it reduces energy consumption.

The emissivity of the inner faces of the multi-alveolar structure affects slightly the inside air temperature.

During a cold day the inside air temperature sensitively increases when the building is occupied by two individuals (one in each zone) and for an imposed temperature, the heating power decreases. This work principally shows the importance of the position of the multi-alveolar structure and the taking into account the presence of the occupant as an internal input.

REFERENCES

1. Guittierez D.V. Contribution to the theoretical and experimental study of the aero thermal

- phenomena in parallelepiped cavities with walls.
2. Fokosako. S, Yamagushi. A, An experimental study of free convective heat transfer in a parallelogrammic enclosure, ASME J. Heat Transfer 105 (1983), pp. 433- 439.
 3. Cho Chung K., Trefethen L. M., Natural convection in a vertical stack of inclined parallelogrammic cavities, Int. J. Heat Mass tranfer. 25 (1982), pp. 277-2844.
 4. Bairi A., Contribution to the experimental study of parallelogrammic sections, thesis, N° 199, University of Poitiers, France, (1984).
 5. Françoise Thellier. Modélisation du comportement thermique de l'homme et de son habitat. Une approche de l'étude de confort. Thermics. Université Paul Sabatier - Toulouse III, 1989.
 6. Mavroulakis A., Trombe A., A new semi analytical algorithm for calculating diffuse plane view factors, J.H eat Tran.120 (1) (1998) 279–282.
 7. Serres. L, Trombe.A, and Miriel. J, Flux solaires absorbés par l'occupant d'un local vitré. Prise en compte dans l'équation du confort thermique, *Int. J. Therm. Sci.* (2001) 40, 478–488.
 8. Tulumoglu. P, Nutin.A, Giuliana. S, and Feldheim. V, Modélisation et évaluation détaillée du comportement thermique du corps humain et intégration du modèle dans un bureau, Congrès Français de Thermique (SFT), Lyon, France, 2014
 9. Lajimi.N, Boukadida. N, Numerical study of the thermal behavior of bi-zone buildings. Comptes Rendus Physique Volume 16, Issue 8, Octobre 2015, pp 708–720.
 10. Lajimi.N, Boukadida.N, Performance énergétique de l'enveloppe d'un bâtiment bizones soumis à des conditions météorologiques variables, 17èmes Journées Internationales de Thermique (JITH 2015), Marseille (France), 28 - 30 Octobre 2015.
 11. J.-J. Vullierme, N. Boukadida, Experimental study of the performance of a structure with effect of thermal diode, Rev. Gen.Therm.. 324 (1988) 645–651.
 12. Boyer. H., Chabriat. J.-P, Tourr. C, and Brau. J, Thermal building simulation and computer generation of nodal models, Build. Environ. 31 (3) (1996) 207–214.

THE EFFECTS OF WATER FOUNTAINS ON THERMAL COMFORT IN COURTYARD HOUSES IN SAHARAN REGIONS

Benameur, O.*, & Zemmouri, N.

*University of Biskra, department of Architecture; University of Biskra

*Email: okbabenameur6@hotmail.com

ABSTRACT

Saharan regions have a very harsh weather conditions especially during summer season which extends from March to October. An air conditioning system is essential throughout the day in order to achieve thermal comfort conditions. Courtyard houses as a passive configuration are known to have the capacity to improve thermal conditions and the comfort of the inhabitants. However, this passive architectural thermal regulator model has been abandoned for a more sophisticated and complicated slab model. The purpose of this study is to evaluate the ability of an evaporative system, i.e. a water fountain in a typical courtyard house in achieving indoor thermal comfort. Different design configurations and scenarios have been tested including dimensions, geometry, position and depth. The simulation tool used is Ansys Fluent CFD code, combined with the Mesh generator ICEM-CFD, the software evaluates the impact of water fountain in an unsteady state through the introduction of a User Defined Functions (UDF), which was compiled in C ++. Mathematical functions have been determined using Matlab to describe the trend of air velocity, temperature and relative humidity of a typical design day in Biskra, Algeria. It is clear from the results that the evaporative cooling in hot and arid zones is very useful in reducing heat in the courtyard and interior spaces. The study shows that a house with one floor with a square centered shape courtyard, can achieve an acceptable level of thermal comfort. The polygonal courtyard shape presents an optimal configuration for houses with two stories.

Keywords: *Sahara, CFD, Evaporative cooling, Courtyard, Fountains, Fluent.*

NOMENCLATURE

k: Turbulent kinetic energy.

ϵ : The rate of dissipation of the turbulent kinetic energy.

V: Velocity.

H: Relative humidity.

T: Temperature.

INTRODUCTION

In hot and dry locations, such as Saharan regions, annual and daily fluctuations of temperature are important. The temperature amplitude between the coldest and warmest month exceeds 20°C. The Zibans region, particularly the city of Biskra (located about 400Km, Southeast of the capital Algiers), has a daily temperature range for the hot season, that nearby 22°C [1]. The use of an air conditioning system with high energy consumption is essential throughout the day in order to achieve thermal comfort conditions. The appearance of courtyard houses dating back to a distant past 6500 to 6000 years BC in the old village of "Mehrgarh", India [2]. They represent an efficient passive cooling solution in these regions, and even more if they are associated with an evaporation system. [3]

Given the growing interest in indoor thermal comfort in courtyard houses, various attempts have been made to study the impact of courtyards on natural ventilation, evaporative cooling and thermal comfort. A comparative study between the different passive cooling techniques, through numerical calculations, shows that the evaporation cooling is the most suitable technique to minimize the flow of heat in a hot climate. [3]

This study aims to evaluate quantitatively the impact of a direct evaporative system, i.e. a water fountain in hot and dry conditions of Biskra, using different design configurations including courtyard dimensions, geometry, position and depth.

Courtyard effects:

A courtyard is an enclosed semi-outdoor space we can find inside the houses. "Courtyard" word has been used as a traditional element particularly in the design of houses.

Recently it is considered a passive design strategy to moderate the climate.[4] During the hot season

courtyard provides natural ventilation, especially in hot climates. During the day, the air in courtyard becomes warmer, it rises and evacuates through the openings. Therefore, it allows good air circulation inside the adjacent building. [5]

The courtyard has several effects on light and shade, energetic consumption and thermal comfort. In diverse climates, the patio can be used as a source of lighting in the morning, especially the deep parts of houses. During winter it serves to protect the building from weather conditions such as wind. [6-7-9]

Muhaisen and Gadi demonstrated that a deep patio with different geometric shape could achieve maximum internal shaded areas during summer. During winter a shallow form seems to be advantageous to get more sun and light. [7]

In energy terms, according to El-Deeb et al., reduction of energy consumed by courtyard houses is closely linked to the increase of the depth of these courtyards (see Figure 1), through a comparative analysis of several cities that are characterized by their hot climate, which are: Khargah , Cairo, Alexandria and the city of Berlin. [8]

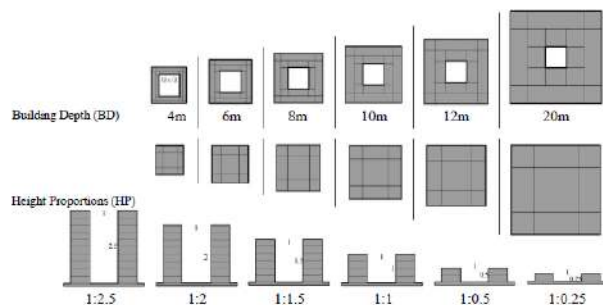


Figure 1

The relationship between the ratio of height and depth of the patio of the house [8]

For the thermal effect, Bahbudi et al. point out that a patio can be more effective for natural cooling through evaporation using vegetation and water fountains. [9]

The study by Safarzadeh and Bahador reveals that courtyards alone cannot achieve a high level of thermal comfort in hot summer hours in Tehran, Iran. [10] Additional, cooling systems are needed such as water fountains.

Water effects:

Water has a primordial importance for passive cooling. The evaporative cooling is one of the most efficient techniques used in regions with hot and dry climate. The presence of a water basin in a courtyard is very important for the reflection of light, because water is a transparent element which plays an important role in the reflection of light towards different parts of the house.[11]

Water is used as a direct and indirect evaporative cooling system in different manners. Ali established an analytical and experimental investigation to evaluate the effect of nocturnal passive cooling by the evaporation and convection of radiation in a non-isolated open tank filled with water and heat in hot regions and arid. [12] Experimental results of this study indicated that for a water depth tank ranging from 0.2 to 0.6 m, and the net passive cooling could as high as 19.7 MJ / m². Temperature values of water are increase to 18.7 °C.

Pires and co-authors have made an experimental study on an innovative passive element to refresh buildings. This device has been integrated in the building envelope in order to reduce energy consumption and the use of air conditioning systems. The proposed device has a parallelepiped shape surrounded by external walls MDF which is resistant to water with wood beams and isolated by extruded polystyrene panels and consists of an inner panel made of mortar of cement with paraffin (see Figure 2).[12]

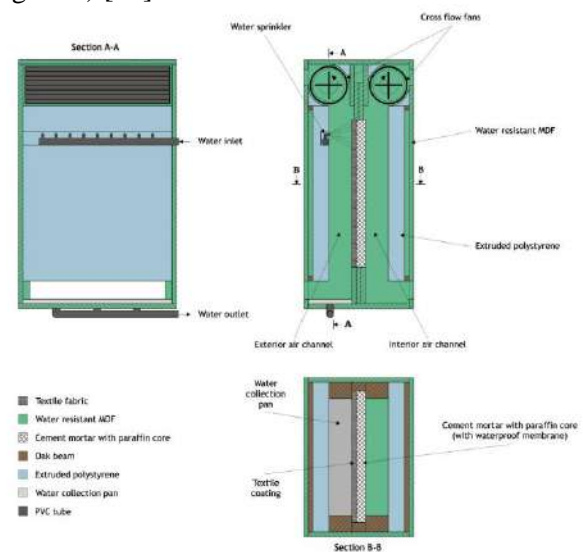


Figure 2

The proposed device components [12]

The calorimetric results have shown the ability of that device to store heat during transition phase

(solid / liquid) of paraffin due to the beneficial effect of water.

Overnight the presence of the evaporation process allows the cooling of the element core at temperatures well below the outside temperature through the night ventilation effect. [12]

During summer, the traditional house of the Mزاب region (located in the northern Sahara in Ghardaia, Algeria, 600 km south of Algiers) have porous water jars installed in patios, front of the dominant directions of cold air, this water evaporates and generates a good cooling in the interior of these homes.[13]

Through these studies, we can deduce that water has the ability to create a microclimate in hot and arid regions. There are several methods to improve these conditions.

ANALYSIS AND MODELLING

The thermal performance characteristics of courtyards, with the presence of water fountains, were analyzed according to the following design parameters: dimensions, geometry, position and depth using Ansys Fluent CFD code combined to ICEM-CFD as a mesh generator, under a typical design day representing the climatic conditions of Biskra.

The city of Biskra is characterized by a hot and dry climate, with Saharan tendency, an average temperature of 22.8°C and an average air speed of 4.4 m/s in Northwest/Southeast direction. The annual average rate of relative humidity is about 40%, while the precipitation rate is decreased and rare.

Simulation models:

The following criteria have been used in order to determine the typical house model: shape, orientation, construction materials and openness (shown on Table 1).







Generally, courtyard houses are built with heavy materials (Stone or Mud-Brick) to store heat and reduce temperature fluctuations to ensure good thermal inertia. [14]The optimal orientation in Biskra region is North-South, with an optimum percentage, about 20% of openness. An investigation by Hakmi, aims to define the dimensions and the optimal shape of the courtyard houses in Middle East, which meet the social and bioclimatic needs of their occupants, and he checked the performance of several models. He found that square and rectangle are the optimal shape for a single courtyard house. [15]

Table 1
Typical house model

Parameters	
Shape and dimensions	<i>Rectangular, 12X 16 m</i>
Floors Number	<i>One and Two levels</i>
Construction materials	<i>Mud-Brick walls (0.5m)</i>
Orientation	<i>North-South</i>
Opening (Windows)	<i>20% of the main facade</i>

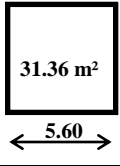
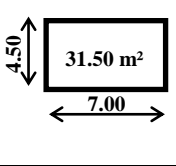
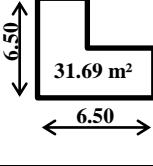
For the courtyards shape, Petruccioli, has classify courtyard houses in several types according to the functions and human needs, and grouped them into four main groups according to: a typology with one floor (DRC), a second with several floors, a third with occupancy multiple (interior balconies) and a final typology with additional modules. [16] The patio shapes used are: square, rectangular and polygonal, that could be located in the house center, or placed in an eccentric position in one of the four corners.(see Table 2)

Table 2
Matrix of simulated models

Shape	Square	Rectangular	Polygonal
	1 and 2 Levels	1 and 2 Levels	1 and 2 Levels
Centered			
Eccentric			

The courtyard surface area respects the percentage (16 to 30%) of the total typical house area [14]. Full descriptions of the courtyards models dimensions are illustrated in Table 3.

Table 3
Courtyard’s dimensions

Shape	Square	Rectangular	Polygonal
Dimensions	 <p>31.36 m² 5.60</p>	 <p>31.50 m² 7.00 4.50</p>	 <p>31.69 m² 6.50 6.50</p>

Design day concept:

Choosing a day simulation allows us to reduce the annual calculation of the phenomenon in one critical and representative day. In the region of Biskra, the 21 July presents the hottest day in the critical summer period.

The climate data used corresponds to the typical meteorological year 2005 (TMY3 2005) created based on the measured data between 2000 and 2009 proposed by the Meteonorm software. [17]

To introduce the climatic data of the design day simulation, we have to create a User Defined Functions (UDF) compiled in C ++, in order to create an unsteady state in Fluent. Mathematical functions have been determined using Matlab (Matrix Laboratory) to describe the trend of air velocity, temperature and relative humidity through the followings polynomial functions:

- Air velocity:

$$V(t) = 2.637277292e-8(t)^8 - 2.353965207e-6(t)^7 + 7.780890408e-5(t)^6 - 1.039604851e-3(t)^5 + 3.876113535e-4(t)^4 + 1.257433067e-1(t)^3 - 1.105592113(t)^2 + 3.001168339(t) + 0.343508488 \quad (1)$$

- Temperature:

$$T(t) = -5.255e-6(t)^6 + 0.0004549(t)^5 - 0.01459(t)^4 + 0.2067(t)^3 - 1.202(t)^2 + 2.739(t) + 31.66 \quad (2)$$

- Relative humidity :

$$H(t) = -6.567e-6(t)^4 + 0.0004291(t)^3 - 0.008344(t)^2 + 0.04482(t) + 0.245 \quad (3)$$

Simulation tools configurations:

ANSYS FLUENT is CFD simulation software to model fluid flow, heat transfer, and chemical reactions in complex geometries.

ICEM CFD, one of ANSYS Fluent components is an advanced extension for generating mesh and grid optimization that meets the requirements of all

engineering applications such as computational fluid dynamics and analysis structures.

In this study we have chosen a hybrid hexahedral mesh (mixed) that includes tetrahedral, pyramidal and prismatic elements, which agrees with the presence of a circular water fountain inside our simulated models.

This mesh as shown in the figure 3 is extended throughout the area and refined in a hierarchical manner from the outer walls to the walls of the courtyard and fountain.

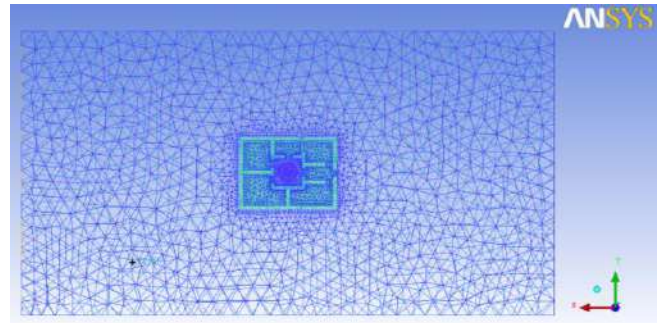


Figure 3

Hexahedral mesh of one level square centered courtyard model

The turbulence model k-ε, one of the Reynolds Averaged Navier-Stokes (RANS) is used in this study. For the boundary conditions, as already mentioned, for a transient case, the introduction of an UDF function is necessary as Velocity inlet. The water fountain jet should be configured as Velocity inlet too with a velocity magnitude of 1.27m/s, and 22°C temperature.

The symmetric parts of the calculation domain are set to Symmetry, and the outlet of the domain has been adjusted on Pressure Outlet.

RESULTS AND DISCUSSION

Courtyard shape and position:

We have decided to demonstrate the effect of water fountains only on some significant results. It's clear that the square shaped centered courtyard house represents the optimal configuration (see Figure 4). A 3 to 6°C decrease in temperature have been shown in the surrounding spaces at 2:00 pm which represents the worst weather condition.

In the rectangular shaped centered courtyard the water effect is less important (see Figure 5).

For the L-shaped centered, the evaporative cooling does not exceed patios walls (see Figure 6).

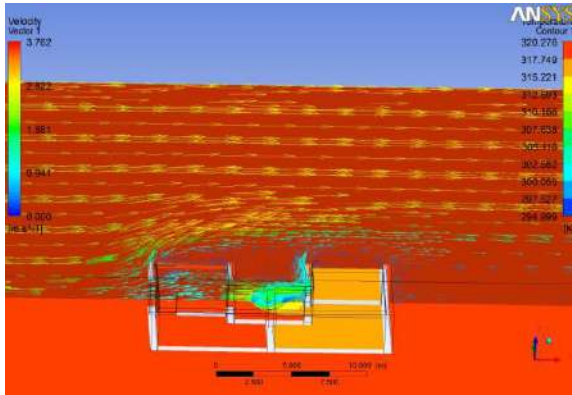


Figure 4

Velocity and temperature results in centered square courtyard with one story

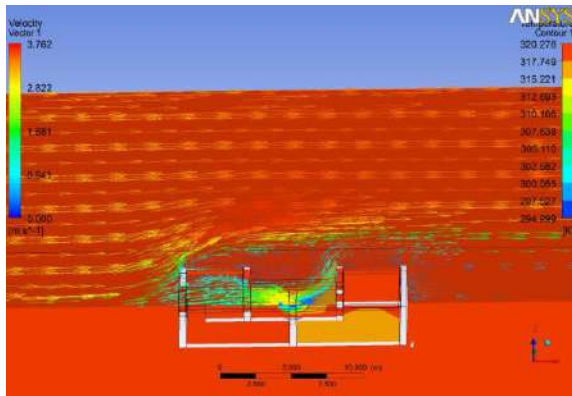


Figure 5

Velocity and temperature results in centered rectangular courtyard with one story

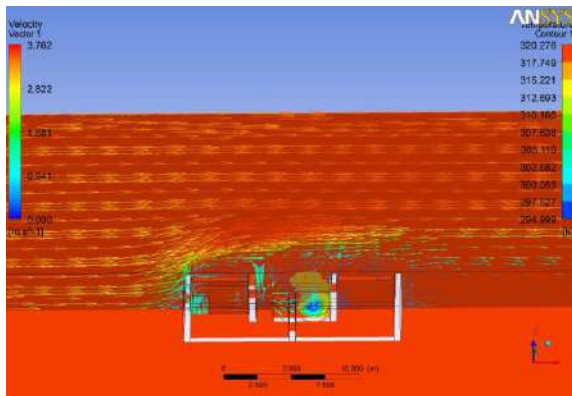


Figure 6

Velocity and temperature results in centered polygonal courtyard with one story

In the eccentric courtyards configuration, the evaporative cooling is reduced compared to the centered position.

Courtyard depth effect:

In term of depth, the “L” shaped eccentric configuration with two stories seems to give the best results.

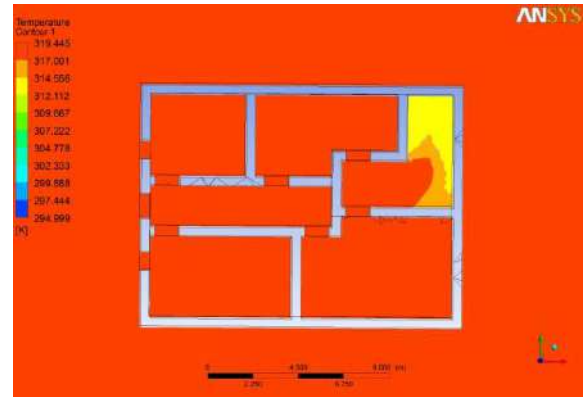


Figure 7

Temperature results in eccentric “L” shaped courtyard with two stories

CONCLUSIONS

It is clear from the results that the evaporative cooling in hot and arid zones is very useful in reducing heat in the courtyard and interior spaces.

The study shows that:

- This cooling system is efficient both in one and two stories, although a reduced effect can be noticed.
- A house with one floor with a square centered shape courtyard, can achieve an acceptable level of thermal comfort.
- The polygonal “L” shaped courtyard presents an optimal configuration for houses with two stories.

ACKNOWLEDGMENTS

Authors wish to express their deepest thanks to Dr Houda, S. and Dr Belghar, N. for their comments and useful suggestions.

REFERENCES

1. Côte, M. (2005). La ville et le désert: le Bas-Sahara algérien. Paris : Karthala.
2. Maheswari, S., & Garg, R. (2001). An Ancient Indian Architecture. CBS Publishers, 24-25.
3. Tiwari, G.N., Upadhyay, M. & Rai S. N. (1994). A Comparison of Passive Cooling Techniques. Building and Environment, 29 (1), 21-31.
4. Heidari, S. (2000). Thermal Comfort in Iranian Courtyard Housing. PHD, University of Sheffield, England.

5. El-Deeb, K., El-Zafarany, A., & Sherif, A. (2012). Effect of building form and urban pattern on energy consumption of residential buildings in different desert climates. PLEA,28, Conference, Opportunities, Limits & Needs Towards an environmentally responsible architecture. Lima, Peru.
6. Upadhyay, A. K. (2008). Sustainable Construction for the Future: Climate Responsive Design Strategies for Sydney Metropolitan Region. In Third International Conference of the Cooperative Research Centre (CRC) for Construction Innovation. Australia: Gold Coast.
7. Muhaisen, A.S., & Gadi, M.B. (2006). Shading performance of polygonal courtyard forms. *Building and Environment*, 41, 1050–1059.
8. El-Deeb, K., Sherif A., & El-Zafarany, A., (2014). Effect of courtyard Height and proportions on Energy Performance of Multi-Storey Air-Conditioned Desert Buildings. PLEA, 30, International PLEA Conference, CEPT University, Ahmedabad.
9. Bahbudi, K.T., Taleghani, M., & Heidari, S. (2010). Energy Efficient Architectural Design Strategies in Hot-Dry Area of Iran. In Best 2 Conference. USA : Hilton Portland & Executive Tower.
10. Safarzadeh.H., & Bahadori M.N. (2005). Passive cooling effects of courtyards. *Building and Environment* 40, 89–104.
11. Arjmandi, H., Tahir, M., & Shabani, M. (2010). Application of transparency to increase day lighting level of interior spaces in the dwelling apartments in Tehran—a lesson from Iranian traditional architecture. Malaysia: Editorial Board/Sidang Editor.
12. Ali, A-H.H. (2007). Passive cooling of water at night in uninsulated open tank in hot arid areas. *Energy Conversion and Management*, 48, 93-100.
13. Dutreix, A. (2010). Bioclimatisme et performances énergétiques des bâtiments. Paris : Eyrolles,1, 239.
14. Liébard A., & De Herde A. (1996). Guide de l'architecture bioclimatique, Tome 2. Paris : Observ'ER.
15. Hakmi, M. (2006). The geometry of single and multi-family. In Edwards, B., Sibley, M., Hakmi, M., & Land, P. (Eds.), *Courtyard housing past, present and future* (pp.260-279). UK: Taylor & Francis.
16. Petruccioli, A. (2006). The courtyard house: typological variations over space and time. In Edwards, B., Sibley, M., Hakmi, M., & Land, P. (Eds.), *Courtyard housing past, present and future* (pp.1-25). UK: Taylor & Francis.
17. TM3 2005, Weather Data, METEONORM software, v7.0.

ALBEDO EFFECT OF EXTERNAL SURFACES ON THE ENERGY LOADS AND THERMAL COMFORT IN BUILDINGS

Ouarda.Mansouri^{1,2,3}, Rafik.Belarbi², Fatiha.Bourbia³

1 Département d'Architecture et d'Urbanisme, Faculté des sciences de la terre, Université Badji Mokhtar, BP 12 Sidi Amar, 23000 Annaba, Algeria

2Laboratoire des Sciences de l'Ingénieur pour l'Environnement "LaSIE". Université La Rochelle, Avenue Michel Crépeau. 17042 La Rochelle Cedex 01. France

3 Laboratoire d'Architecture Bioclimatique et Environnement "ABE". Université Constantine3. Algeria
Email: wmansouri_2006@yahoo.fr

ABSTRACT

Due to climate changes which are growing through time, in addition to the building consumption that is considered to be the largest consumer of energy sector in the world, the kind of materials covering the urban areas (pavements, facades and roofs), plays a leading role in the bill consumption and thermal ambience inside and outside the building depending on the climate.

This paper presents a part of a study aimed to evaluate the effect of reflective coatings used in the building envelope on minimizing energy requirements and improving internal thermal comfort.

In Skikda city, situated in North-East of Algeria, reflecting the Mediterranean climate, a parametric study was carried out on a building, by varying its orientation, solar reflectance of its walls, thermal mass and insulation of its vertical envelope.

The results show that thermal insulation combined with high solar reflectance defined a good combination for high level comfort and decrease energy loads.

Keywords: Solar reflectance, energy loads, orientation, thermal mass, insulation, thermal comfort

INTRODUCTION

Mineralization of urban spaces and the reduction of green areas which were replaced by roads, roofs and facades whose materials absorb heat and increase the discharges of long wavelength, cause the warming of these spaces, and generate what is called the urban heat island.

To remedy this problem and try to mitigate its intensity, great interest was focused on surface materials, especially those that have a high reflectivity "high albedo" to minimize the absorption of solar radiation and therefore, reduce its restitution in long wavelength at night.

Much research has proven the positive effect of reflective materials on the urban microclimate moderation, on mitigating the outside temperatures and the increasing degrees of comfort for pedestrians and users of outdoor urban spaces [1].

What about its effect on the indoor environment and energy consumption?

Solar radiation incident on building envelope can be absorbed, reflected or transmitted. It influences exterior and interior surface temperature. Heat flux enters the building in several different modes, namely by conduction and convection through four walls, roof and floor, by convection in the form of

ventilation and infiltration, and by direct gain through glazed area of windows.

A multitude of research, old and new, experimental and numerical were conducted in this direction; showed the positive effect of reflective coatings on the mitigation of indoor temperatures and energy consumption of buildings. These solar reflective coatings can be applied to the horizontal wall "roof" by doing what is called "cool roof", or the vertical wall (facade), their application allows a reflect of maximum sunlight instead of absorbing it. This application reduces the outer surface temperature, decreases heat flow entering the building and therefore decreases the inner room temperature. Citing some work in this direction: Givoni and Hoffman [2] performed early experiments on small buildings with different exterior colors in Israel, They compared the resulting indoor temperature for unventilated buildings. They found that buildings with white-colored walls were approximately 3°C cooler in summer than when the same buildings were painted gray. Reagan and Acklam [3] done a study that shows that while changing the roof color from dark ($\alpha=0.75$) to light ($\alpha=0.35$), it does greatly reduce the roof heat gain. The reductions were 6.4% and 4.8% in July day in Tucson, Arizona, for houses with ceiling thermal resistances of 2.50 and

5.88m²k/w respectively. Taha et al. [4] simulated building cooling load reduction of 18.9% for summer days in Sacramento, California, for an albedo increase of both roof and walls from 0.30 to 0.90. Ceiling and wall thermal resistances were 5.28 and 3.35m²k/w respectively. Simulations for Sacramento indicate that whitewashing the building can result in direct saving of up to 14% and 19% on cooling peak power and electrical cooling energy, respectively. Modifying the overall urban albedo, in addition to whitewashing, can result in total savings of up to 35% and 62 % respectively. Bansal et al. [5] have studied experimentally as well as theoretically the effect of external surface colour on the thermal behavior of a building, they found that the black painted enclosure recorded a maximum of 7°C higher temperature than the corresponding white painted enclosure during hours of maximum solar radiation. Taha et al. [6] found that white electromagnetic coatings with a reflectivity of over 0.72 could be as high as 45°C cooler than black coatings with a reflectivity of 0.08, in varying reflectivity materials used in urban surfaces. Parker et al. [7] monitored six homes in Florida before and after application of high-albedo coatings on their roofs. Reduction in air-conditioning electricity consumption was measured between 11% and 43% with an average saving of 9.2kwh/day, and reduction in peak power demand (occurs between 5 and 6 pm) was 0.4–1.0kw with an average reduction of 0.7kw. Akbari et al. [8] monitored peak power and cooling energy savings from high-albedo coatings at one house and two school bungalows in Sacramento, California. They found savings of 2.2kwh/d for one house (80% of base case use), and peak demand reductions of 0.6 kw. In the school bungalows, cooling energy was reduced 3.1kwh/d (35% of base case use), and peak demand by 0.6kw. Simpson and McPherson [9], Reductions in total and peak air-conditioning load of approximately 5% were measured for two identical white (SR≈0.75) compared to gray (SR≈0.30) and silver (SR≈0.50) roofed scale model buildings in Tucson Arizona. Shariah et al. [10] carried out a series of simulations for two mild and hot climates in Jordan. They found that, as the reflectance changes from 0 to 1, the total energy load decreases by 32% and 47% for non-insulated buildings and by 26% and 32% for insulated buildings in Amman and Aqaba respectively. Cheng et al. [11] performed investigation with test cells about the effect of envelope colour and thermal mass on indoor temperatures under hot and humid weather condition. They showed that the maximum difference of inside

air temperature between a black and a white cell was about 12°C for lightweight construction. Synnefa et al. [12] demonstrated that the use of reflective coatings can reduce a white concrete tile's surface temperature under hot summer conditions by 4°C and during the night by 2°C. They also studied [13] the impact from using cool roof coatings on the cooling and heating loads and estimated the indoor thermal comfort conditions of residential buildings for various climatic conditions. The results show that increasing the roof solar reflectance reduces cooling loads by 18–93% and peak cooling demand in air-conditioned buildings by 11–27%. Zinzi et al. [14] evaluated the solar properties of ecological cool coatings and the benefit achievable for building applications for different Mediterranean localities. They showed that there is an influence of cool materials on the energy performance in all zones especially where higher insulation levels coupled with solar control lead to strong energy reductions and have consequent improvement of thermal conditions inside the built environment. Uemoto et al. [15] demonstrated that the cool colored paint formulations produced significantly higher near infrared radiation reflectance than conventional paints of similar colors, and that the surface temperatures were more than 10°C lower than those of conventional paints when exposed to infrared radiation. Shen et al. [16] performed an experimental study on the impact of reflective coatings on indoor environment and building energy consumption. They found that exterior and interior surface temperatures can be reduced by up to 20°C and 4.7°C respectively using different coatings, depending on location, season and orientation. The maximum reduction in globe temperature and mean radiant temperature was 2.3°C and 3.7°C in that order. For the conditioned case, the annual reduction in electricity consumption for electricity reached 116kwh. For their part, Bozonnet et al. [17] studied the impact of cool roofs on building thermal response in French context through experimental study which was completed by dynamic simulations. They found that cool roof decreases the mean outside surface temperature by more than 10°C, with low differences for lower temperatures, but a strong impact on the highest temperatures. The difference for the highest indoor temperature is not negligible, this is mainly due to the strong insulation consistent with building standards in France for all new building. Thus, the indoor temperature differences are very clear for the non insulated building.

ANALYSIS AND MODELLING

To estimate the effect of the reflectivity of materials (albedo) combined with other factors (orientation, Thermal mass and thermal insulation) on the annual energy needs for heating and cooling and thermal comfort, a parametric study was carried out on a building reference situated in Skikda city, in North-east of Algeria (latitude 36.54°N and a longitude of 6.52°E). This building represent the most common type of buildings in the region in a Mediterranean climate context (hot and humid in summer and mild with low amplitudes in winter). The simulations of this study are performed for 02 years by the mean of TRNSYS17 [18] “Transient System Simulation”, with a time step of one hour.

The building used in this study which represents a reference case is a parallelepiped of 10m length, 7m width and 3m high, it consists of cinderblock walls with flat roof (not accessible). We considered for these simulations that the reflectivity of the roof is fixed to a value of 0.5 but the reflectivity of the walls is changed between 0.1 and 0.9 (knowing that a perfectly reflecting or absorbing material does not exist in reality). The building orientation is varied in the range (90, 270) towards the south with step of 45°. The roof has a fixed u-value of 2.42, but wall facades are varied of 1.57 for cinderblock wall, and 1.69 for concrete wall, the two main materials used in the region. Simulations are performed with and without insulation of an air void layer of 5cm thick.

The first simulations are performed for opaque walls in order to deduce their effect, then repeated by introducing a glazed surface of 6m² to the south side of the building (percentage given by the recommendations of Mahoney tables) [19], to deduct the influence of penetration of solar radiation on the energy needs.

The window has a wooden frame with single glazing of 4mm thick, and g-value of 0.87.

Set point temperatures are 20°C and 26°C for heating and cooling respectively. Moreover, internal gains of human that define the conditions of comfort such as "clothes" and "metabolic activity" are taken from ISO7730.

Infiltration and ventilation are considered null to deduct the net effect of the reflectivity of the opaque walls on actual energy needs and the inner ambience in the absence of air sweeping.

The same simulations were repeated under free floating conditions to estimate the effect of change solar reflectance on comfort conditions in the building.

The characteristics of the different envelopes and the conditions of dynamic thermal simulation are summarized in the following table:

Table 1
Summary of the different parameters considered in the simulation

Building Element	Characteristics		
	Solar reflectivity	Orientation	U-value (w/m ² .k)
Concrete wall	0.1-0.9	90-270	1.69
Cinderblock wall	0.1-0.9	90-270	1.57
Building surface	70m ²		
Building volume	210 m ³		
Set cooling temperature	26°C		
Set heating temperature	20°C		

RESULTS AND DISCUSSION

The analysis of the results of all these simulations allowed us to highlight the effect of the reflectivity (albedo) of the opaque vertical wall on energy requirements and thermal comfort, as well as modification of this effect once the glazing introduced.

Energy loads

The analysis of the parametric study results is expressed by the following graphs according to various different parameters:

Solar reflectance effect:

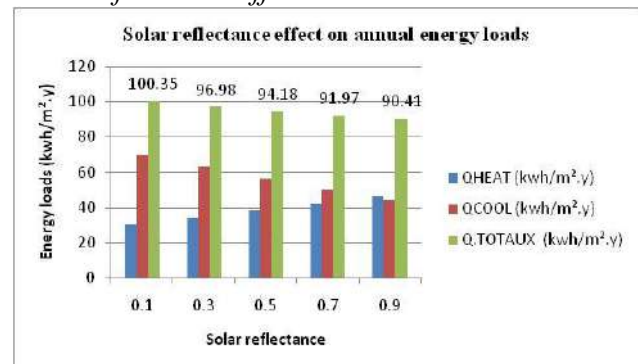


Figure 1

Solar reflectance effect on annual energy loads for cinderblock insulated building oriented South

According to the graph, we note that energy needs are inversely proportional to the values of the solar reflectivity. The reference building with a reflectivity of 0.5 presents an annual energy needs for heating of 37.81kwh/m².y, and cooling needs of 56.36kwh/m².y, which will make a total of 94.18kwh/m².y. When changing the coating of outer

surfaces of the walls by a reflective coating with a value of 0.9, the heating needs increase by 8.65kwh/m².y with a percentage of 18.61%, the need for cooling decrease by 12.41kwh/m².y, making a percentage of 22%. Hence, the total needs decreased by 3.77kwh/m².y equivalent to a percentage of about 4%.

However, the allocation of a reflectivity value of 0.1 (absorbing materials) for facade walls gives opposite results compared with the reference building. In fact, the heating needs decreased by 7.25kwh/m².y for a percentage of 19.17%. The cooling requirements increased by 13.44kwh/m².y, giving a percentage of 19.25%, hence the total requirements increased by 6.17kwh/m².y, where a percentage of 6.14%.

We can therefore conclude that the external colour of a building affects the thermal performance of the building although its impact is little in our climate.

Orientation effect:

The effect of orientation shows very small nuances between the different simulated orientations, either for heating demand, air conditioning or total requirements.

The better is the orientation 0 (South) with a minimum total annual demand of 94.18kwh/m².y. The one with the maximum demand is the orientation 45 (South-West) with total needs of 95.96kwh/m².y which is not far from the South-East orientation (315) with a value of 95.94kwh/m².y, where as two remaining orientations 90 and 270 (East and West) have exactly the same needs for heating, cooling and total needs.

Figure2 summarizes these results.

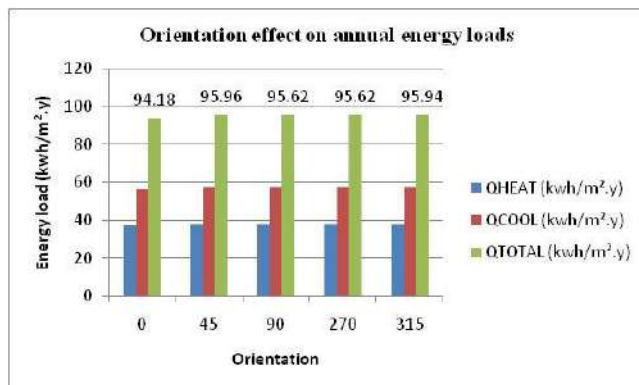


Figure2

Orientation effect on annual energy loads for building with cinderblock walls and solar reflectivity of 0.5

It can be deduced that for cinderblock walls and solar reflectance value of 0.5, the orientation of the

building plays a negligible role in mitigating the energy needs.

Type of material and insulation effect:

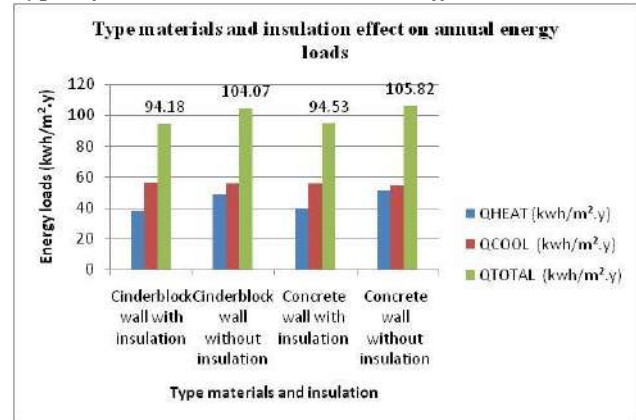


Figure3

Type materials and insulation effect on annual energy loads for solar reflectivity of 0.5 and orientation 0

The change in the constitution of the vertical wall of the building between the cinderblock wall and concrete wall gave approximately similar results. The heating requirements for buildings with cinderblock wall are 48.23kwh/m².year while for the concrete walls, they are 51.19kwh/m².y, hence an increase of 2.96kwh/m².y representing a percentage of 5.78%. The cooling needs are 55.84kwh/m².y for cinderblock walls and 54.63kwh/m².y for concrete walls, where the difference is 1.21kwh/m².y and the percentage is 2.16%. The total requirement in turn spend 104.07kwh/m².y for the first case to 105.82kwh for the second case giving a difference of 1.65%. This small difference is due to the thermal mass of the two materials which is almost nearly the same.

The effect of the insulation is estimated by comparing the same type of wall with and without insulation.

For the cinderblock wall, heating requirements when the insulation is applied are less by 10.42kwh to the needs obtained for a wall without insulation, with a percentage of 21.60%, whereas the cooling needs increased insignificantly. As consequence, the total needs decrease is 9.89kwh/m².y with a percentage of 9.5%.

For the concrete wall, the same trend is noticed, the heating needs for the insulated wall are lower than those of the uninsulated wall about 12.08kwh, where a percentage of 23.59%. The change in the field of cooling requirements is negligible, which results in a

reduction of the total needs of 11.29kwh with a percentage of 10.66% between the concrete wall with and without insulation.

Furthermore, the change in the annual energy needs for heating, cooling and total requirements between the two walls when the insulation is applied show the same trends as the change between the 2 types of walls without insulation, i.e negligible results.

This is due to the almost similarity of thermal mass of the two walls.

After introducing a window in the south wall of the building, the energy needs have changed.

For the cinderblock wall facing south, with a reflectivity of 0.5, there was a decrease in the heating needs of 6.14kwh/m².y i.e with a percentage of 16.23%. While the cooling requirements have increased of 4.79kwh/m².y with a percentage of 7.83% resulting in a decrease in total needs of 1.35kwh/m².y, so a percentage of 1.43%.

For the reflectivity of 0.1, the heating needs for the pierced wall decrease of 4.48kwh/m².y at a percentage of 14.65%. The cooling needs are increased by 3.87kwh/m².y, resulting in a percentage of 5.25%. This gives a negligible decrease in the total requirements.

For the reflectivity of 0.9, the heating requirements decreased of 8.11kwh/m².y with a percentage of 17.45%. The need for cooling increased of 5.54kwh/m².y where a percentage of 11.19%, and total requirements decreased to a very low rate of approximately 2.84%, as it is showed in the following figure.

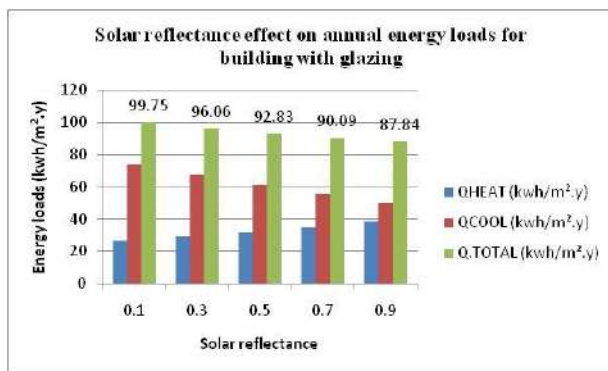


Figure4

Solar reflectance effect on annual energy loads for cinderblock insulated building oriented South with glazing

We can conclude that introducing window in the south wall can dilute the benefit effect of the high reflectance of a building envelope on the energy demand.

Thermal comfort

To estimate the summer comfort inside the building, we repeated the same simulations without air conditioning (free floating conditions), we took a temperature threshold of 27°C, beyond which we will record the numbers of hours of discomfort.

We will present the results obtained after the change in the reflectivity of the façade walls.

The number of hours of discomfort for the reference building is from 3088 hours so a percentage of 35%. As expected, increasing the reflectivity of the wall cladding decreases the number of hours of discomfort. For example, for the reflectivity value of 0.9, the number of hours of discomfort will be reduced to 2603 hours equivalent to a percentage of 30%.

And if we apply a coating with a reflectivity of 0.1, we note that the number of hours of discomfort increases to 3441 hours, resulting in a percentage of 39%.

We can conclude that the reflectivity of wall coatings materials plays a role in improving summer comfort conditions inside the building, beyond 0.5, the interior ambience is moderated by reducing the number of hours of discomfort.

CONCLUSION

The aim of this study is to estimate the effect of solar reflectivity (albedo) with other parameters on energy consumption and thermal comfort in Mediterranean climatic context.

It was found that all the parameters play an important role when they are implemented.

The best combination that could be obtained was the one with light colored coatings, applied on the outer walls of an albedo value greater than 0.5, combined with a thermal insulation.

This study has as perspective the determination of database, with the right combination of insulation, orientation, thermal mass and of course the high reflectivity coatings of the outer shell of the building, useful for stakeholders (designers, architects, policy makers ... ect) to optimize the energy balance of the building throughout the year and its corollary thermal comfort.

REFERENCES

1. Rosenfeld, A. H, Akbari, H, Bretz, S, Fishman, B. L, Kurn, D. M, Sailor, D, and Taha, H, 1995 "Mitigation of urban heat islands: materials, utility programs, updates,"

- Energy Build.*, vol. 22, no. 3, pp. 255–265.
2. Givoni, B, and Hoffman, M.E, 1968, “Effect of building materials on internal temperatures,” *Res. Report, Build. Res. Station. Tech. Haifa*.
 3. Reagan, J. A, and Acklam D. M, 1979, “Solar reflectivity of common building materials and its influence on the roof heat gain of typical southwestern U.S.A. residences,” *Energy Build.*, vol. 2, no. 3, pp. 237–248.
 4. Taha, H, Akbari, H, Rosenfeld, A, and Huang J, 1988, “Residential cooling loads and the urban heat island—the effects of albedo,” *Build. Environ.*, vol. 23, no. 4, pp. 271–283.
 5. Bansal, N. K, Garg, S. N, and Kothari, S, 1992, “Effect of exterior surface colour on the thermal performance of buildings,” *Build. Environ.*, vol. 27, no. 1, pp. 31–37.
 6. Taha, H, Sailor, D, Akbari, H, 1992, “High albedo materials for reducing cooling energy use,” *Lawrence Berkeley Lab. Rep. 31721*, vol. UC-530, Berkeley CA.
 7. Parker, D.S, Barkaszi, S.F, Sonne, J.K, 1994 “Measured cooling energy savings from reflective roof coatings in Florida,” *Phase II report, Rep. No.FSEC-CR-699-94, Florida Sol. Energy Center, Cape Canaveral, FL*.
 8. Akbari, H, Bretz, S, Kurn, D. M, and Hanford, J, 1997, “Peak power and cooling energy savings of high-albedo roofs,” *Energy Build.*, vol. 25, no. 2, pp. 117–126.
 9. Simpson, J. R, and Mcpherson, E. G, 1997, “The effects of roof albedo modification on cooling loads of scale model residences in Tucson, Arizona,” vol. 25.
 10. Shariah, A, Shalabi, B, Rousan, A, and Tashtoush, B, 1998, “Effects of absorptance of external surfaces on heating and cooling loads of residential buildings in Jordan,” *Energy Convers. Manag.*, vol. 39, no. 3–4, pp. 273–284.
 11. Cheng, V, Ng, E, and Givoni, B, 2005, “Effect of envelope colour and thermal mass on indoor temperatures in hot humid climate,” *Sol. Energy*, vol. 78, no. 4 SPEC. ISS., pp. 528–534.
 12. Synnefa, A, Santamouris, M, and Livada, I, 2006, “A study of the thermal performance of reflective coatings for the urban environment,” *Sol. Energy*, vol. 80, no. 8, pp. 968–981.
 13. Synnefa, A, Santamouris, M, and Akbari, H, 2007, “Estimating the effect of using cool coatings on energy loads and thermal comfort in residential buildings in various climatic conditions,” *Energy Build.*, vol. 39, no. 11, pp. 1167–1174.
 14. Zinzi, M, Daneo, A, and Fanchiotti, A, 2008, “Paper No 314: Optical properties and influence of reflective coatings on the energy demand and thermal comfort in dwellings at Mediterranean latitudes,” *PLEA 2008 – 25th Conf. Passiv. Low Energy Archit. Dublin, 22nd to 24th Oct. 2008*, no. 314.
 15. Uemoto, K. L, Sato, N. M. N, and John, V. M, 2010, “Estimating thermal performance of cool colored paints,” *Energy Build.*, vol. 42, no. 1, pp. 17–22.
 16. Shen, H, Tan, H, and Tzempelikos, A, 2011, “The effect of reflective coatings on building surface temperatures, indoor environment and energy consumption — An experimental study,” vol. 43, pp. 573–580.
 17. Bozonnet, E, Doya, M, and Allard, F, 2011, “Cool roofs impact on building thermal response: A French case study,” *Energy Build.*, vol. 43, no. 11, pp. 3006–3012.
 18. “TRNSYS 17”, T. S. S. P. U. Manuel, *Sol. Energy Lab. Univ. Wisconsin, Madison, USA*.
 19. Koenigsberger, O.T, Ingersoll, T.G, Mayhew, A, Szokolay, S.V, 1973 “Manual of tropical housing and building,” *Part 1. Climatic Des.*

NUMERICAL INVESTIGATION OF ENTROPY GENERATION IN A PROPANE-AIR BURNER

Souad Morsli¹, Amina Sabeur¹, Mohammed El Ganaoui²

1. Laboratoire des Sciences et Ingénierie Maritimes, Faculté de Mécanique, USTO

BP 1505 El M'naouer Oran, Algeria,

2. Lorraine University, Energetic Laboratory of Longwy, (FJV/LERMAB), Henri Poincaré Institute of Longwy, France)

ABSTRACT

Large amounts of high quality energy are spent in the chemical process industry to convert raw materials into desired products. The turbulent diffusion flames can be found in a wide variety of thermal energy production systems. The burners operating with this type of flames are used for example in combustion chambers. The need to understand the structure of these flames has been our motivation to carry out a numerical study of the turbulent aero thermo-chemistry of C₃H₈ / Air diffusion flames in a burner by using numerical simulations. Such kind of problems induces strong variation in the concerned field and the analysis has to be well conducted to understand physical phenomena. In such way the entropy generation rate was introduced in the post processing. Due to the high temperature and velocity gradients in the combustion chamber; the effects of equivalence ratio and oxygen percentage in the combustion air are investigated for different situations. In each case, combustion is simulated for the fuel mass flow rate resulting in the same heat transfer rate. Numerical calculations are performed for all cases using computational fluid dynamics code (Fluent CFD code) with integrating specific routines. The results shown that the increase of equivalence ratio corresponds to a significantly decrease in the maximum reaction rates and the maximum temperature increase with the oxygen percentage. While total entropy generation rate decreases exponentially; the ratio of the rates useful energy transfer to irreversibility therefore improves as the oxygen percentage increases. Mixing hydrogen with propane causes considerable reduction in temperature levels and a consequent reduction of CO emission.

KEYWORDS Turbulent diffusion, Entropy generation, Fluent CFD

NOMENCLATURE

Latin Symbols

Be	Bejan number
CFD	Computational fluid dynamics
C _μ , C _{ε1} , C _{ε2}	Coefficients in <i>k-ε</i> turbulence model
f _{k,j}	Specific force of volume acting on the species K in the direction i
G _k	The production of turbulent kinetic energy
<i>H</i>	Enthalpy
h _k	Specific enthalpy of the species k
h _{s,k}	Heat transfer coefficient, sensible enthalpy of species
k	Turbulent kinetic energy
<i>L</i>	Length of burner
LCV	Lower calorific value
P	Pressure
RNG	Renormalization group

<i>r</i>	Radial distance
<i>r_i</i>	Inner radius of air inlet
<i>r₀</i>	Outer radius of air inlet
<i>S_{gen}^m</i>	Volumetric entropy generation rate
<i>T</i>	Temperature
<i>u_i</i>	Velocity in direction i
<i>V_{k,i}</i>	Velocity diffusion of the species k in direction i
<i>Y_k</i>	Mass fraction of the species k

Greek Symbols

<i>δ_{ij}</i>	Kronecker delta
<i>ε</i>	turbulent energy dissipation rate
<i>ϕ</i>	Equivalence ratio
<i>Φ</i>	Viscous dissipation
<i>λ</i>	Air excess ratio
<i>μ</i>	dynamic viscosity
<i>ρ</i>	Density
<i>θ</i>	Tangential direction
<i>ρ_k</i>	Density of the species k
<i>σ_{ij}</i>	Tensor of the constraint in plan i and the direction j
<i>ω_k</i>	Production rate of the k species.

τ_{ij}	Tensor of the viscous constraints
<i>Subscripts</i>	
F	Fuel
K	Species
N	Total number of species number
o	Oxydant
p	At constant pressure
s	Sensibility (enthalpy)
v	At constant volume
r	Radial
x	Axial
Heat	Heat transfer
Air	Air
eff	Effective
fric	Friction
f	Fuel
i,j	Indices of tensor notation
in	Inlet

INTRODUCTION

Entropy generation is one of the most significant problems to overcome to optimize a system / process and its performance, and this will unfortunately remain as a crucial problem to the next generation. In this regard, better understanding of the concept of entropy and its role among various classes of thermal systems and processes with a diverse coverage is crucial. Bejan [1] focused on the different reasons behind entropy generation in applied thermal engineering where the generation of entropy destroys the available work (exergy) of a system. Therefore, it makes good engineering sense to focus on the irreversibility of heat transfer and fluid flow processes, and to try to understand the function of associated entropy generation mechanisms. Bejan [2] also conducted an extensive review on entropy generation minimization. Mahmud et al [3], Sahin [4,5], Yilbas et al [6], Shuja et al [7], Demirel et al [8], Bouras et al [9, 10] performed many studies on second law analysis and the entropy generation due to the heat transfer and fluid friction in duct flows under various conditions.

Research into transport phenomena in energy systems and applications has substantially increased during the past a few decades due to its diversity in applications. This makes the special issue a most timely addition to existing literature. It includes recent major developments in both the fundamental and applications, and provides a valuable source to researchers dealing with analysis of entropy generation in thermal systems and processes.

Combustion includes thermal, hydrodynamic, and chemical processes [11]. It starts with the mixing of fuel and oxidant, and sometimes in the presence of other species or catalysts. The fuel can be gaseous, liquid, or solid and the mixture may be ignited with a heat source.

When ignited, chemical reactions of fuel and oxidant take place and the heat release from the reaction creates self- sustained process. Turbulent combustion of hydrocarbon fuels and the incineration of various industrial by products and wastes are an integral part of many segments of the chemical process and power industries.

The main objectives in burner design are to increase combustion efficiency and to minimize the formation of environmentally hazardous emissions, such as CO, unburned hydrocarbons (HC) and NOx. Critical design factors that impact combustion include: the temperature and residence time in the combustion zone, the initial temperature of the combustion air, the amount of excess air and turbulence in the burner and the way in which the air and fuel streams are delivered and mixed [12].

This work considers the combustion of propane with air and the local entropy generation rate due to the high temperature and velocity gradients in combustion chamber using a single burner element. In order to investigate the effect of Therefore, CFD codes can serve as a powerful tool used to perform low cost parametric studies. The CFD codes solve the governing mass, momentum and energy equations in order to calculate the pressure, concentrations, velocities and temperatures fields.

MATHEMATICAL MODEL

The purpose of this simulation is to estimate numerically the rate of local entropy generation and the effect of oxygen percentage on the combustion in the combustion chamber of a burner. For this case, the combustion of fuel with air is examined at various oxygen percentages in the air by using Fluent CFD code in the combustion chamber of a burner. For this case, the combustion of propane (C_3H_8) with air, in a burner was considered. The two-dimensional axisymmetric model and geometric configuration of the burner are shown in Figure 1. As apparent from this figure, the fuel and air inlets are coaxial and merge downstream. It is assumed that the burner wall is under ambient conditions and that the walls near the air and fuel inlets are isolated. The model used for the numerical calculations include the RNG (renormalization group theory) $k-\epsilon$ for turbulent flow however for chemical species transport and reacting flow, the

eddy-dissipation model with the diffusion energy source option is adopted. The mixture (propane-air) is assumed as an ideal gas; no-slip condition is assumed at the burner element walls.

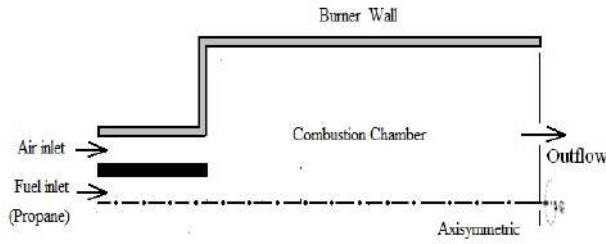


Figure 1
Geometry of the burner

The governing equations for mass, momentum and energy conservation, respectively, for the two-dimensional steady flow of an incompressible Newtonian fluid are:

Governing equations

The mass conservation equation and species transport is defined:

$$\frac{\partial \rho}{\partial t} + \frac{\partial \rho u_i}{\partial x_i} = 0 \quad (1)$$

And the mass conservation equation for k species is written as follows:

$$\frac{\partial \rho Y_k}{\partial t} + \frac{\partial}{\partial x_i} (\rho (u_i + V_{k,j}) Y_k) = \dot{\omega}_k \quad (2)$$

We defined also the momentum conservation equation

$$\frac{\partial}{\partial t} \rho u_j + \frac{\partial}{\partial x_i} \rho u_i u_j = -\frac{\partial P}{\partial x_j} + \frac{\partial \tau_{ij}}{\partial x_i} + \rho \sum_{k=1}^N Y_k f_{k,j} = \frac{\partial \sigma_{ij}}{\partial x_i} + \rho \sum_{k=1}^N Y_k f_{k,j} \quad (3)$$

And

$$\tau_{ij} = -\frac{2}{3} \mu \frac{\partial u_k}{\partial x_k} \delta_{ij} + \mu \left(\frac{\partial u_i}{\partial x_j} + \frac{\partial u_j}{\partial x_i} \right) \quad (4)$$

The energy conservation equation is defined as:

$$\frac{\partial \rho H_s}{\partial t} + \frac{\partial}{\partial x_i} (\rho u_i h_s) = \dot{\omega}_T + \dot{Q} + \frac{DP}{Dt} + \frac{\partial}{\partial x_i} (\lambda \frac{\partial T}{\partial x_i}) + \tau_{ij} \frac{\partial u_j}{\partial x_i} - \frac{\partial}{\partial x_i} (\rho \sum_{k=1}^N V_{k,i} Y_k h_{s,k}) \quad (5)$$

Two additional equations for the RNG k-ε turbulence model- The turbulence kinetic energy, k,

and the dissipation rate, ε, are determined using the following transport equations, respectively:

$$\begin{aligned} \frac{\partial}{\partial x_i} (\rho x_i k) &= \frac{\partial}{\partial x_i} (\alpha_k \mu_{eff} \frac{\partial k}{\partial x_i}) + G_k - \rho \epsilon \quad (6) \\ \frac{\partial}{\partial x_i} (\rho x_i \epsilon) &= \frac{\partial}{\partial x_i} (\alpha_\epsilon \mu_{eff} \frac{\partial \epsilon}{\partial x_i}) + \frac{\epsilon}{k} (C_{1\epsilon} G_k - C_{2\epsilon} \rho \epsilon - \chi) \end{aligned}$$

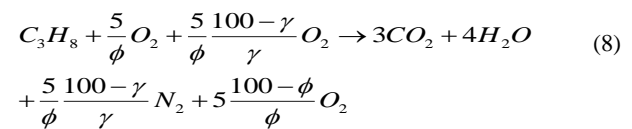
This model, based on the work of Magnussen and Hjertager, called the eddy-dissipation model. The net rate of production of species i due to reaction r, $R_{i,r}$, is given by the smaller of the two expressions below:

$$R_{i,r} = v'_{i,r} W_{\omega,i} A \rho \frac{\epsilon}{k} \min_R \left(\frac{Y_R}{v'_{R,r} W_{\omega,R}} \right) \quad (7)$$

$$R_{i,r} = v'_{i,r} W_{\omega,i} A B \rho \frac{\epsilon}{k} \left(\frac{\sum_p Y_p}{\sum_j v'_{j,r} W_{\omega,j}} \right)$$

COMBUSTION AND REACTION MECHANISM

The simplest description of combustion is that it is a process that converts the reactants available at the beginning of combustion into products at the end of the process. The most common combustion processes encountered in engineering are those which convert a hydrocarbon fuel (which might range from pure hydrogen to almost pure carbon (C), e.g. coal) into carbon dioxide (CO₂) and water (H₂O). In this study, the combustion of fuel with propane is modeled with a one-step reaction mechanism (NR=1). The reaction mechanism takes place according to the constraints of chemistry, and is defined by:



Where:

$$\begin{aligned} \phi &= 5[W_{O_2} + (100-\gamma) / \gamma W_{N_2} m_{fuel}] \quad (9) \\ &/ (W_{fuel} m_{air}) \end{aligned}$$

Entropy generation rate

In fluid flow, irreversibility arises due to the heat transfer and the viscous effects of the fluid. In these

systems, when both temperature and velocity fields are known, the volumetric entropy generation rate S_{gen}''' at each point in the system can be calculated as follows [1],

$$S_{gen}''' = (S_{gen}''')_{heat} + (S_{gen}''')_{fric} \quad (10)$$

Where $(S_{gen}''')_{heat}$ and $(S_{gen}''')_{fric}$ represent the entropy generation rates due to heat transfer and fluid friction, respectively, and are defined as:

$$(S_{gen}''')_{heat} = \frac{\lambda_{eff}}{T^2} \cdot \left[\left(\frac{\partial T}{\partial x} \right)^2 + \left(\frac{\partial T}{\partial r} \right)^2 \right] \quad (11)$$

and

$$(S_{gen}''')_{fric} = \frac{\mu_{eff}}{T} \cdot \phi \quad (12)$$

Where ϕ is

$$\phi = 2 \cdot \left[\left(\frac{\partial U_x}{\partial x} \right)^2 + \left(\frac{\partial U_r}{\partial r} \right)^2 + \left(\frac{U_r}{r} \right)^2 \right] + \left(\frac{\partial U_x}{\partial r} + \frac{\partial U_r}{\partial x} \right)^2$$

The total entropy generation rate over the volume \dot{S}_{gen} can be calculated as follows:

$$\dot{S}_{gen} = \iiint S_{gen}''' d\theta.dr.dx \quad (13)$$

Bejan number, Be , which compares the magnitude of entropy generation due to heat transfer with the magnitude of the total entropy generation, is defined by:

$$Be = \left(\dot{S}_{gen} \right)_{heat} / \dot{S}_{gen} \quad (14)$$

When $Be \gg 0.5$, irreversibility due to heat transfer dominates, while for $Be \ll 0.5$ the irreversibility due to viscous effects dominates. For $Be \cong 0.5$, entropy generation due to heat transfer is almost of the same magnitude as that due to fluid friction.

COMPUTATIONAL TOOLS

Fluent 6.3.26 [13] was chosen as the CFD computer code which uses a finite-volume procedure to solve the Navier–Stokes equations of fluid flow in primitive variables such as velocity, and pressure. It can also model the mixing and

transport of chemical species by solving conservation equations describing convection, diffusion, and reaction sources for each component species. The RNG model was used as a turbulence model in this study [14]. While the inlet velocities of air are presented in table I. The solution method for this study is axisymmetric. In order to achieve higher-order accuracy at cell faces, second-order upwind is selected.

Table1.

Inlet velocities of air for $U_f = 2.247 \text{ m/s}$ and $\dot{Q} = 1000 \text{ W}$

U air [m/s]			
λ [%]	$\phi = 0.5$	$\phi = 0.7$	$\phi = 1$
10	56.436	40.312	20.218
20	28.614	20.439	14.307
30	19.340	13.814	9.670

NUMERICAL RESULTS

Grid independency

Grid tests were adopted to ensure grid independence of the calculated results. So, the total cell number of 15000 cells was adopted. The grid distributions are uniform within each region.

RESULT AND DISCUSSION

Reactions rates

Figure 2 show the contours of reactions rates in the combustion chamber for the cases of $\phi = 0.5, 0.7, 1.0$, and oxygen percentage in air these figures. We can see that with the increase of γ these $\gamma = 10, 20$ and 30% respectively. The effect of reactions is apparent from regions contract in the axial direction however they expand in the radial direction; So, the reaction rate decreases significantly with the increase of ϕ .

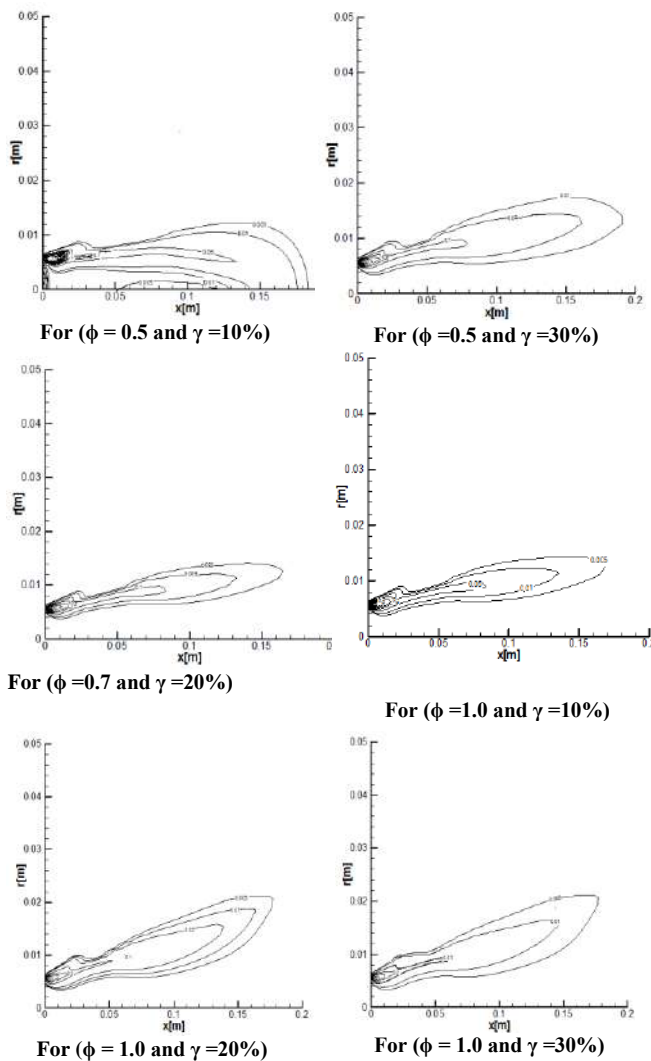


Figure 2

Contours of reactions rates for different values of equivalence ratio ϕ and oxygen percentage in air.

TEMPERATURE DISTRIBUTION

When entropy is created, a part of mechanical energy is necessarily converted into heat [15]. According to Gouy–Stodola theorem, the rate of the available work dissipation is proportional to the rate of internal entropy generation [1]. Knowing that the heat, which is released in the chemical reaction and transferred into the flowing

gas including the reactant and product molecules [16], increases the temperature of this gas. In order to view the temperature distribution, the variations of temperature along the axis of burner are plotted in figure 3.

It is very important to notice that the increase of ϕ significantly reduces the gradients so, larger temperature gradients occur in the axial direction (especially between $x = 0$ and about 0.20 m). The heat calculations performed for the each fuel case bring out that in the case of $\phi < 1$, the total heat per unit mass released in the combustion.

Consequently, the results obtained from this figures show that in the cases of $\phi < 1$, complete combustion occurs, while in the case of $\phi = 1$ it is very close to the complete combustion state.

ENTROPY GENERATION AND BEJAN NUMBER

Figure 4 presents the volumetric local entropy generation rate for different ϕ and γ , they are plotted as the logarithmic contours; high entropy is generated in the region in which the reaction rates are effective, and in which the large positive and negative temperature gradients occur in the axial and radial directions. It is apparent from that figure that the variations of ϕ and γ have an irregular effect on the volumetric local entropy generation rate distribution. These values bring out that the volumetric local entropy generation rates decrease about 10 and 5 % in the cases of $\phi = 0.5, 0.7$ and 1 Respectively, with an increase of γ from 10, 20 to 30%.

Figure 5 shows the Bejan number contours, it was clearly seen that the Bejan number (Be), is very close to 1, and this, therefore, means that the irreversibility as a result of the heat transfer dominates; it’s due to the lower value of the entropy generation rates by reason of the fluid friction respect to those due to the heat transfer.

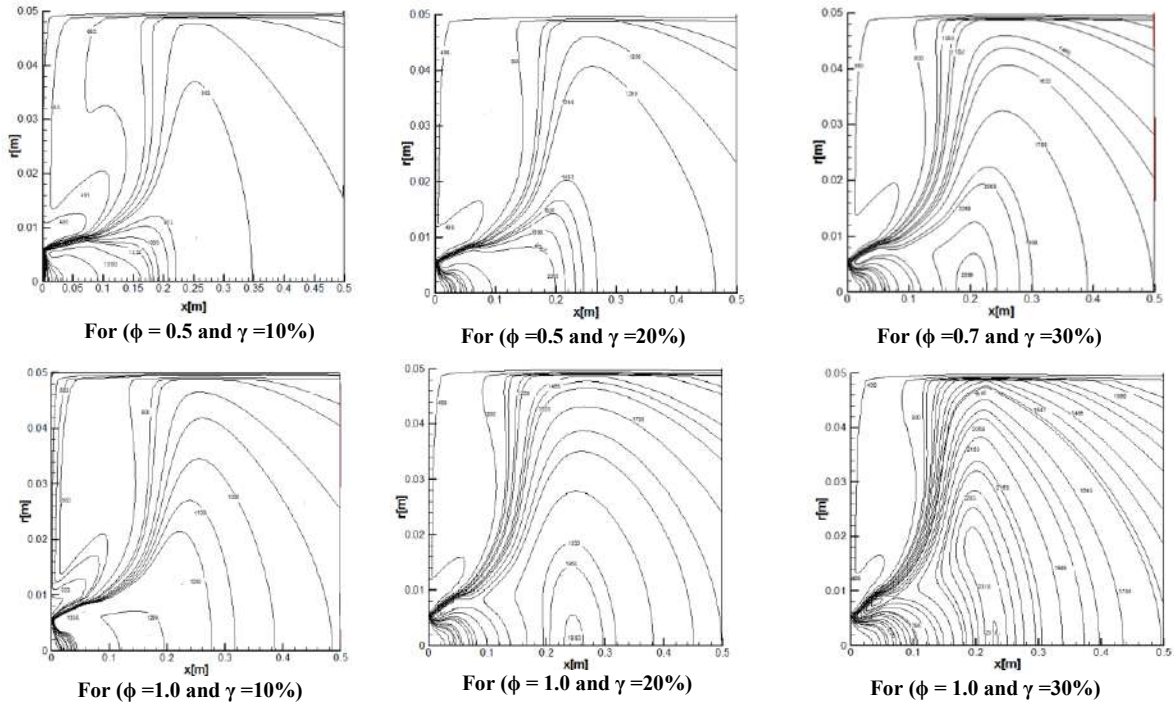


Figure 3
Temperature distribution for $\phi = 0.5$, 0.7 and 1.0 at different values of γ .

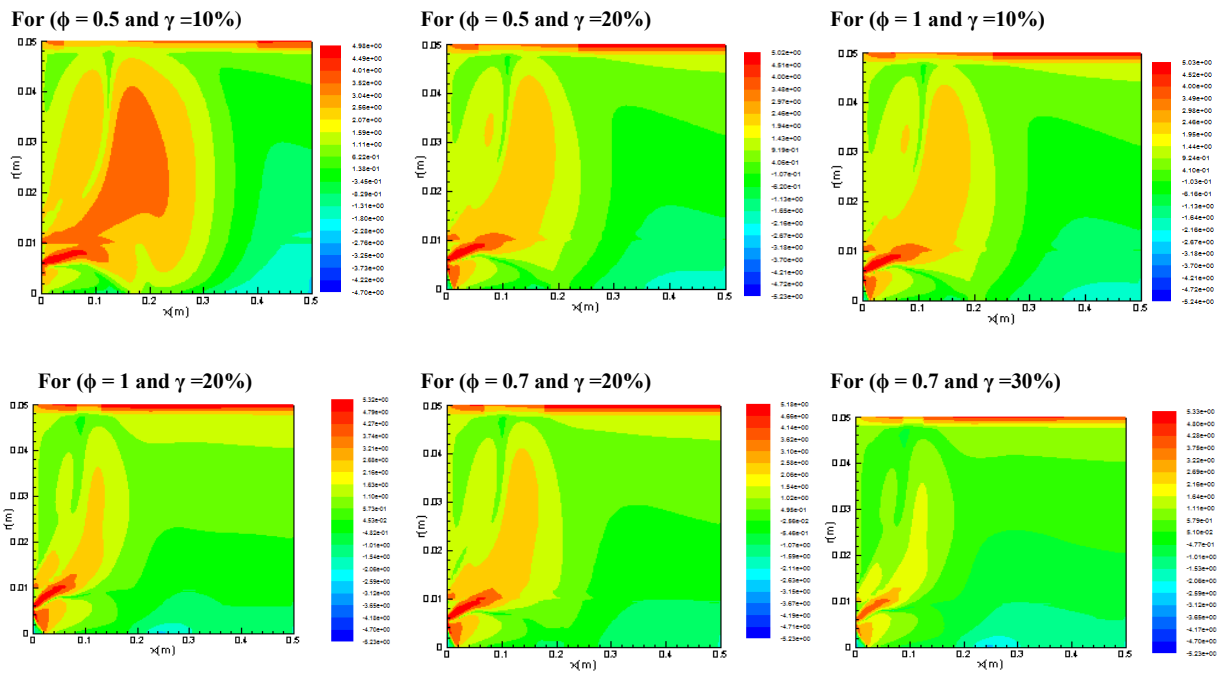


Figure 4
Logarithmic volumetric local entropy generation rate contours. For $\phi = 0.5$, 0.7 and 1.0 at different values of γ .

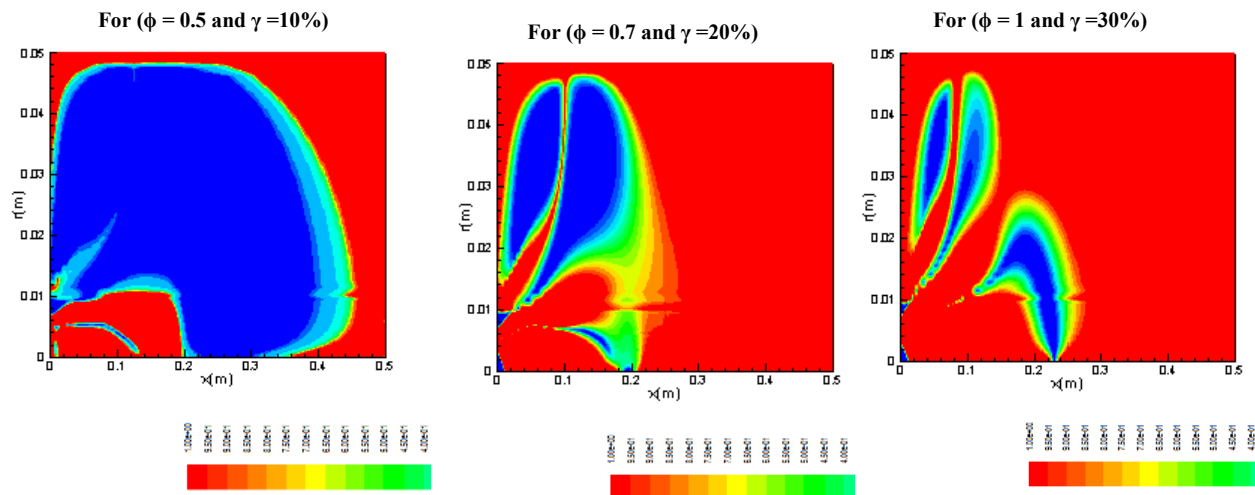


Figure 5
Bejan Number Contours

CONCLUSION

The combustion of propane with air in a burner was considered and the effect of the equivalence ratio and oxygen percentage in air was investigated, for different numerical values. The resulting local entropy generation rates due to heat transfer and fluid friction contributions were computed. The main conclusion is that:

- ❖ The increase of ϕ reduces significantly the reaction rate levels.
- ❖ In the case of $\phi < 1$, the complete combustion occurs, and the combustion in The case of $\phi = 1$ is very close to the complete combustion state
- ❖ The maximum temperatures in the combustion chamber increase with the increases of γ (from 10 to 30%) and ϕ (from 0.5 to 1.0), respectively.
- ❖ In all investigated cases, the Bejan number is very close to 1 (about 0.996). Therefore, the irreversibility due to the heat transfer dominates.

REFERENCES

adiabatic wall. *Int. J. Heat Mass Transfer*, 46, pp. 2947–2955.

1. Bejan A., 1996, *Entropy generation minimization* (Boca Raton, NY: CRC) .
2. Bejan A., 1996, Entropy minimization: the new thermodynamics of finite-size devices and finite-time processes, *J. Appl. Phys*, **79**, pp. 1191–1218.
3. Mahmud S, Fraser R.A, 2003, The second law analysis in fundamental convective heat transfer problems, *Int. J. Thermal Sci*, **42**, pp. 177–186.
4. Sahin A.Z, 1999, Effect of variable viscosity on the entropy generation and pumping power in a laminar fluid flow through a duct subjected to constant heat flux. *Heat Mass Transfer* **35**, pp. 499–506.
5. Sahin A.Z, 2000, Entropy generation in turbulent liquid flow through a smooth duct subjected to constant wall temperature. *Int. J. Heat Mass Transfer*, **43**, pp. 1469-1478.
6. Shuja S.Z., 2001, Yilbas B.S., Budair M.O, Local entropy generation in an impinging jet: minimum entropy concept evaluating various turbulence models, *Comput. Methods Appl. Mech. Eng*, **190**, pp. 3623–3644.
7. Yilbas B.S, S. Z. Shuja M. Rashid, 2003, Confined swirling jet impingement onto an
8. Demirel. Y, Kahraman. R, 1999, Entropy generation in a rectangular packed duct with wall heat flux, *Int. J. Heat Mass Transfer*, 42, pp. 2337–2344.

9. Bouras F, Soudani A, Si Ameur. A, 2012, Thermochemical study of Internal Combustion Engine, *Energy Procedia*, 18, pp.1086–1095.
10. Bouras F, Attia M. E. H. Khaldi F, 2015, Entropy Generation Optimization in Internal Combustion Engine *Environ, Process.* 2, pp. 233-242.
11. Zhou. C, 2013, Combustion. Retrieved from <http://www.eoearth.org/view/article/151315>.
12. Pinho C.E.L., Delgado J.M.P.Q, et al, 2008, *Defect and Diffusion Forum*, 273-276, pp. 144-149.
13. Fluent Inc. FLUENT 6.3.26 User's guide. (Fluent Inc), 2006.
14. Launder. B.E, Spalding D.B, 1972, *Lectures in Mathematical Models of Turbulence*. Academic Press, London, England.
15. Green A.E., Naghdi P.M, 1978, *On thermodynamics and the nature of the second law*. Lecture Notes.
16. Yapıcı. H, Kayataş. N, Albayrak. B. Baştürk, 2004, Numerical study of effect of oxygen fraction on local entropy generation in a methane–air burner *.Sadhana*, 29, Part 6.

EFFECTS OF BUILDING TYPOLOGY ON ENERGY CONSUMPTION IN HOT AND ARID REGIONS

Islam TIBERMACHINE¹, Nouredine ZEMMOURI², Department of Architecture, University of Biskra
 B.P 145 R.P Biskra 07000,Algeria
 Fax: +213 33 543 266 Email: islam.tiber@yahoo.fr

ABSTRACT

This article highlights results of an investigation which was set to determine the effects of residential buildings typology on the consumption of energy for heating and cooling under the specific climatic conditions of hot and arid regions. Five typologies similar in characteristics and living space layouts have been simulated using TRNsys version 17 code. The typologies are representative of actual urban developments constructed during the 80s in Biskra, Algeria.

The results showed that compactness, orientation have a great impact on building energy consumption in cooling and heating. In addition, the slab configuration and semi attached one seem to reduce drastically the energy loads.

KEYWORDS

Energy Consumption, Typology, Building Form, Compactness, Residential Building, TRNsys, Hot and Arid Regions.

INTRODUCTION

Building form, orientation, compactness, dimensions, geometry and construction materials has a substantial effect on energy consumption for heating and cooling in buildings. Ruano has reported that building configuration in form and orientation can reduce energy loads up to 40% [1]. Depecker [2], E.Gratia and A.De Herde [3] have stressed the fact that energy consumption is proportional to building compactness, recent research; Ross [1], showed that tall buildings tend consume more energy than low rise buildings for the same floor area and that compactness window/wall ratio and glazing type are the main factors that have greater influence on building energy consumption Al Anzi [4].

Otherwise, according to the National Agency for the Promotion and Rationalization of Energy Use (APRUE), the final energy consumption in Algeria has reached 8.5Mtoe in 2012. And the electricity consumption of the residential sector has reached 1414 Ktoe. It represents 40% of total electricity consumption, making it the largest consumer of electricity on the national level [5]

ANALYSIS AND MODELLING

The case-study: Building shape and layout considered in this paper were based on an analysis made to bring

out the most common typologies of residential apartment in average size building. The analysis revealed that 64% of these cities include slab configuration, 30.6% of them contain L floor layout, 27.4% have pavilion configuration and 12.9% contain U floor layout buildings, while buildings with courtyard represent only 3.2%.

The slab configuration has been defined as a reference for its common use in the considered urban area. Four common typologies have been studied: the pavilion, the L, the U, the courtyard shape. All these typologies are similar in characteristics: glazing area, construction materials, living space layouts and east/west main orientation. The characteristics of all typologies are summarized in the following table:

Table 1
 Characteristics of different Typologies

Typologies	Living Space (m ³)	Envelope area (m ²)	Built area (m ²)	Building Height (m)
Slab	4011,519	2077,98	397,85	10,8
Pavilion	4011,519	1905,93	198,92	21,6
L shape	4011,519	2314,39	397,85	10,8
U shape	4011,519	2631,22	411,05	10,8
Courtyard	4011,519	2937,39	424,25	10,8

We used Google sketch up plug-in to model of five configurations.

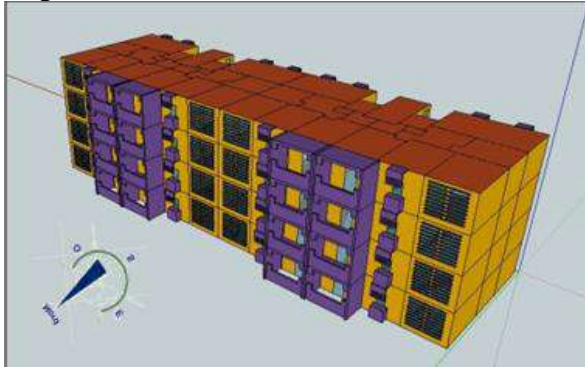
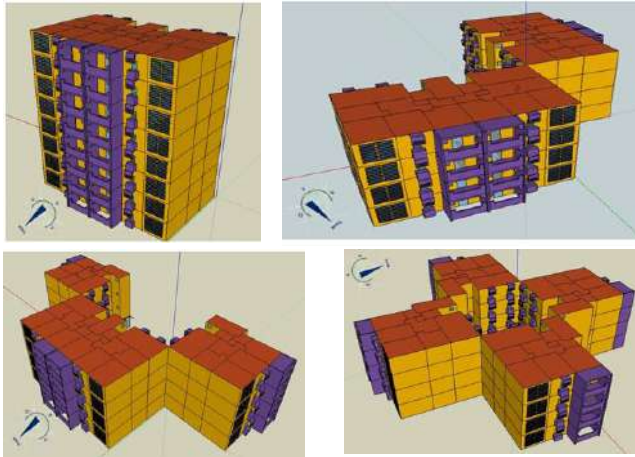


Figure 1



The slab typology modeled under trnsys3d.

Figure 2

Typologies modeled under trnsys3d. Pavilion, L, U, and courtyard shape building.

Building description: The building set as reference is four stories building situated in "HAY EL AMEL" in the west side of Biskra, with four apartments by story and two separate accesses.



Figure 3

The reference building.

The main spaces of the apartment are: a living room, two bedrooms, a kitchen, a courtyard, a lobby, a toilet, a bathroom, balcony and an entrance "sas". With the total area of 92.13m² and a ceiling height of 2.70m.

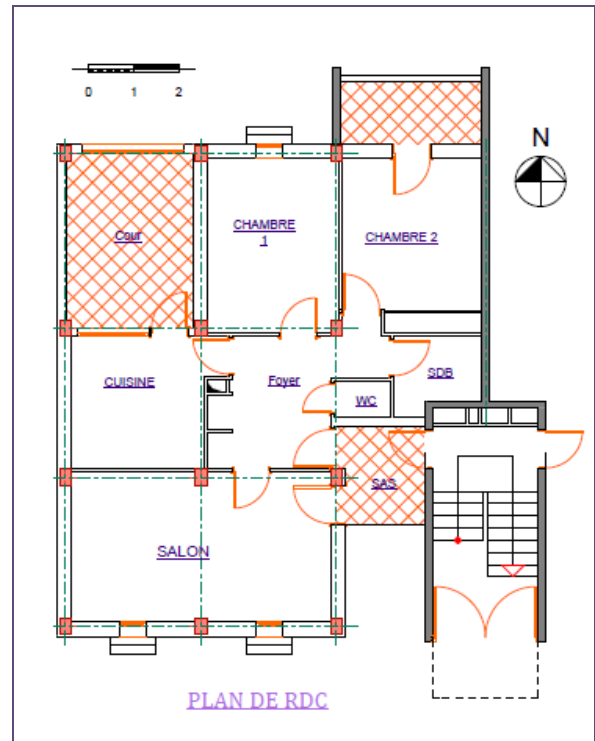


Figure 4

The ground floor layout.

The simulation procedure: In our study the TRNSYS code, version 17 was used as a tool for investigating the energy consumption. This program was developed by Solar Energy Lab (SEL), University of Wisconsin–Madison in unites state. TRNSYS is a dynamic simulation program used to simulate the behavior of transient systems: thermal and electrical energy simulation including the multi-zone buildings, it is used also to model other dynamic systems such as traffic flow, or biological processes [7]. The use of this program requires a data set, such as building proprieties and simulation conditions. These inputs must be included to simulate the models.

As mentioned above, the zoning of building is similar to the apartment layout. The required scenario "regime" in the program corresponds to a family of four persons (parents and two children). A complete weather data set of biskra for the year 2005 was used.

The calculation procedure using TRNSYS version 17 was applied for five buildings configurations for spaces with cooling and heating devices: the living room and two bedrooms. The number of all simulated zones is equal to "240 zones."

The heating and the cooling control was set to 17 °C and 27 °C.

RESULTS AND DISCUSSION

Impact of building typology on energy consumption: The energy consumption for each hour of the year was calculated automatically by TRNSYS v17, which give hourly results. The Excel program was used to calculate the annual energy consumption of heating and cooling for each zone, then for each building typology.

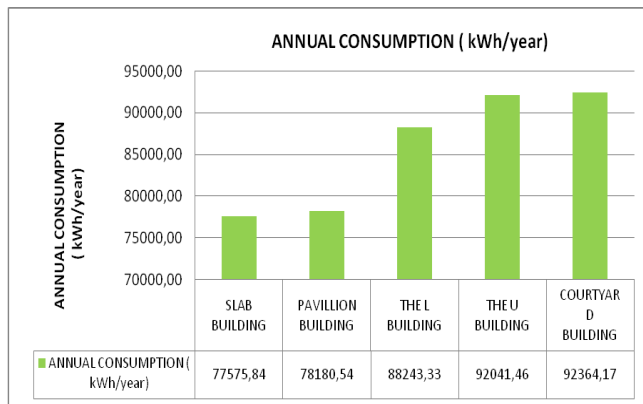


Figure 5

Annual Energy Consumption of different typologies.

After analyzing five typologies, the results show that the most efficiency typology are the slab and pavillion configurations. Whereas, the L, the U shapes and courtyard configuration are the most consumers on energy for heating and cooling.

It is noted that the slab configuration consumes "14788.33kWh/year" less than building with courtyard configuration.

To find the characteristics of different studied typologies, the impact of the following factors on energy consumption has also been investigating:

- The compactness factor.
- Building layout "mitoyenneté".
- South surface to West surface ratio.
- Roof surface to wall surface ratio.

Effect of compactness factor on energy consumption:

The studied typologies show different compactness values. The most compact configurations are the pavillion and the slab configurations. While the L, the U shapes and the courtyard configuration are the most dispersed forms.

A difference of 0.25 is found between the factor of the most compact configuration and the factor of the dispersed configuration.

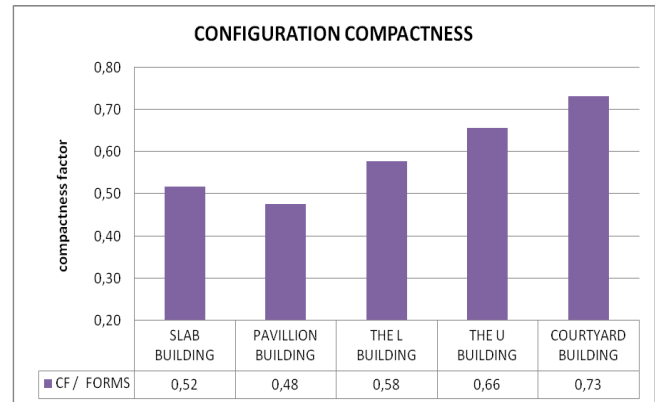


Figure 6

Compactness values of studied typologies.

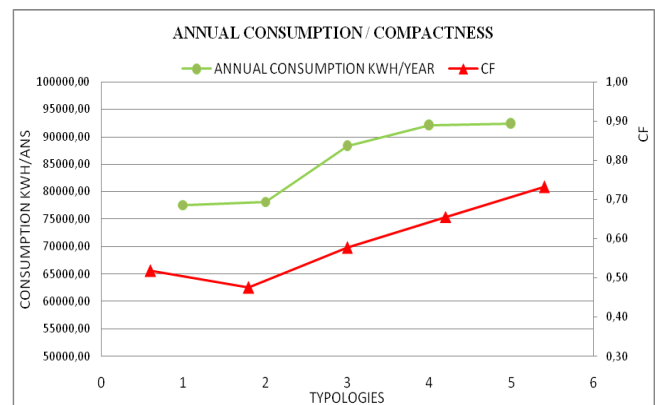


Figure 7

Compactness and global energy consumption plots.

While comparing between compactness factor and annual consumption plots, we found that compactness of shapes is important factor to increases or decreases the annual consumption in hot and arid regions.

In fact, an interval of 0.25 between the pavillion configuration and the courtyard configuration corresponds to "14183.63 kWh/year", which represents about 15.3% of reduction.

Low compactness reduce the exposition of building envelope to solar radiation and hot winds in summer, therefore, the cool loads decreases significatilly. In addition, compact configurations are less exposed to air infiltration into building in winter, which also

minimise the heat loads to set the inner comfort conditions .

Effect of building layout factor on energy consumption:

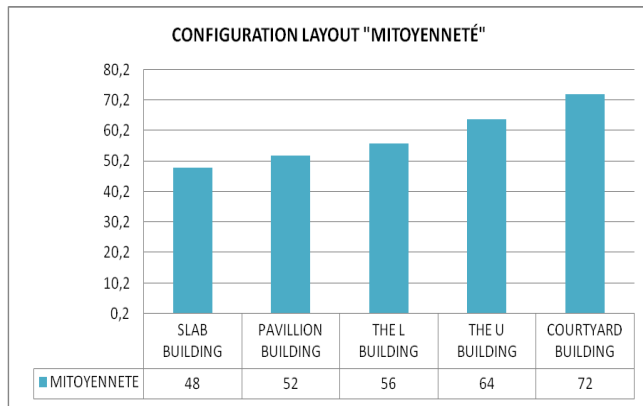


Figure 8

The number of exterior faces of studied typologies

The number of exterior faces allows to determine the number of faces counted as deperditif.

The results showed that the building with courtyard is the most deperditif configuration and the slab one is the most protected. The interval between the two configurations is equals to 24 faces.

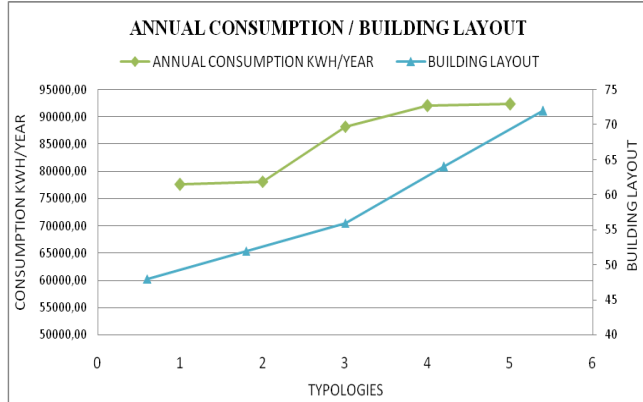


Figure 9

Building layout and global energy consumption plots.

The energy consumption is proportionally changed in fonction of the number of faces exposed to the outside. Sign of a relationship between these two factors.

The interval of «24 faces» represents an increase of 16% in energy consumption.

Effect of south surface to west surface ratio on energy consumption: This ratio was manually calculated by devising the south walls area on the west walls area. The figure 9 summarizes the obtained results.

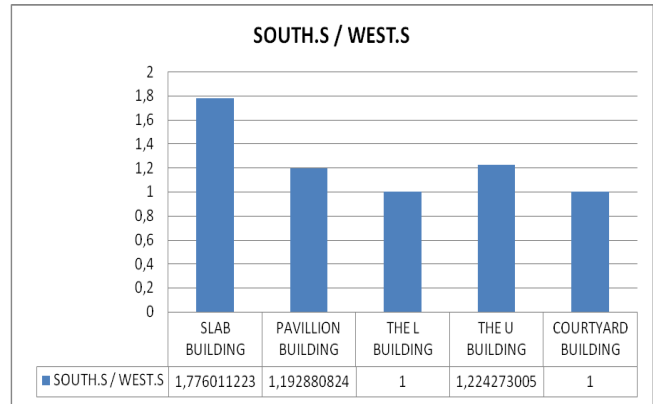


Figure 9

South surface to West surface ratio results

This factor showed that the slab configuration has the biggest area oriented forwards south with a ratio of 1.8. The interval is about 0.8 between the slab configuration and the L configuration.

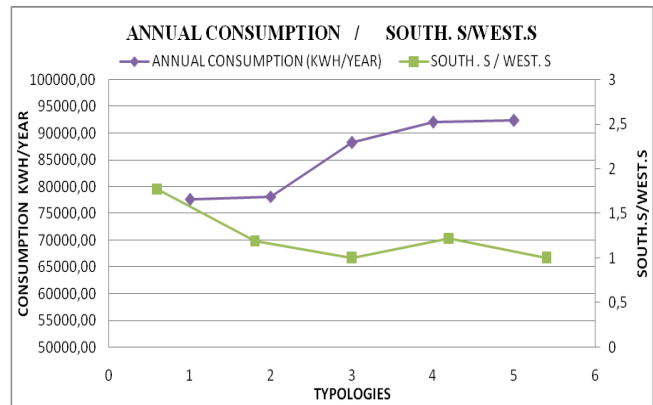


Figure 11

South surface to west surface ratio and global energy consumption plots.

A reduction of 16% on energy consumption has been noticed between the slab configuration and the L configuration.

From the figure 11, we can observe that important south walls area decreases the energy consumption, and important west walls area increases the energy consumption significantly. Indeed, building orientation forwards south can reduces the need to the heating and cooling advices because it takes into account the seasonal variations in the sun’s path as well as wind direction.

Effect of roof to wall ratio on energy consumption:

The ratio was calculated by devising the roof area on the exterior walls area. In general, high buildings have a small roof to wall ratio.

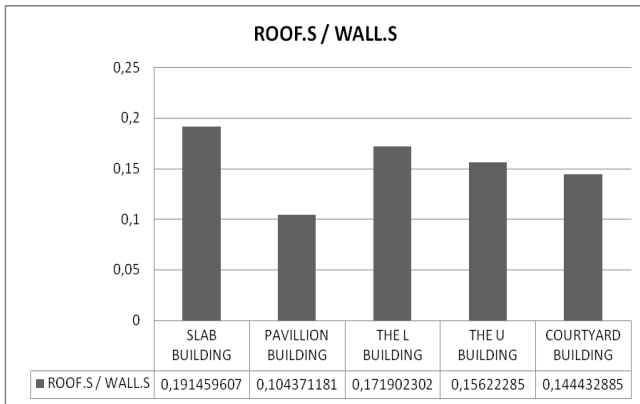


Figure 12
Roof surface to wall surface ratio results

The biggest ratio was found appertains to the slab configuration, it is about 0.19. While the smallest ratio is about 0.1 appertains to the pavilion configuration.

The interval between these two configurations is 0.09.

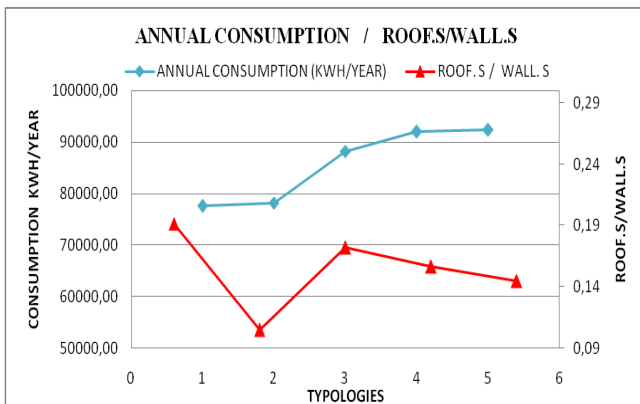


Figure 13

Roof/wall ratio and annual energy consumption plots.

The correlation between annual consumption and roof to walls ratio is not perfect. However, the energy consumption increases when "roof to walls" ratio is important in the most cases.

Buildings which have big horizontal surfaces “roof and ceiling” are the most exposed to the climatic variation. That is why, configurations with important roof to walls ratio are the most consumers on energy consumption for heating and cooling.

CONCLUSIONS

The results from recent research showed that compact forms are recommended in hot and arid regions to achieve significantly energy efficiency in buildings. However, compactness could not be the only design

factor used by architects to reduce energy consumption and loads. Many other factors are taken into consideration while designing in different environments and different climate condition such as orientation, height, building envelope configuration and layout for getting the optimal solution.

The present research showed that building slab configuration and attached building forms which in fact represent merely 64 % of residential sector in Biskra are the best option for a sustainable buildings form.

ACKNOWLEDGMENTS

The authors are grateful to the Algerian Ministry of Higher Education and Research for support.

REFERENCES

1. Iturra, E. E. M, 2011, Impact de la configuration des bâtiments scolaires sur leur performance lumineuse, thermique et énergétique. Université laval québec, pp 18.
2. Depecker, P, & al, 2001, Design of buildings shape and energetic consumption. Building and Environment, Amsterdam, Elsevier Science Ltd, pp 627-635.
3. Gratia, E, and De Herde, A, 2006, thermique des immeubles de bureaux, UCL presses universitaires de lauvain, pp.41.
4. Ourghi, R., Al-Anzi, A., Krarti, M. 2007, A simplified analysis method to predict the impact of shape on annual energy use for office buildings, Energy Conversion and Management, Amsterdam, Elsevier Science Ltd, pp 300-305.
5. www.aprue.org.dz/
6. Biskra weather station
7. TRNSYS version 17 documentation, solar energy laboratory, 2014.

STUDY OF THE IMPACT OF OPENING ON THE LIGHT AND THERMAL EFFICIENCY, IN EDUCATIONAL AREAS, ORAN ALGERIA

Y. Hamza Cherif*, A. Mokhtari, A. Benammar
Faculty of architecture and civil engineering

*Corresponding author: Email: hamzacherif.yamina@yahoo.fr

ABSTRACT

The present paper talk about, the thermal and luminous efficiency analysis of the windows components in the building design. The case study is an educational space (The room's workshop of Oran architecture school - Sciences and Technologies University; Mohamed Boudiaf - Algeria). This work raises the question of the window's conceptual design impact on indoors temperatures and lighting levels. Several parameters were considered (orientation, position, size of the windows ... etc.) to see their impact on the ambiance quality. An investigation followed on site, allows us to know the occupants (architecture students) appreciations in terms of thermal and visual comfort. To confirm the collected statements, case study simulations were done using one hand for the DIALux software for the lighting and the daylight factor calculation, and secondly the TRNSY software for indoors temperatures evolution. The comparison between the simulated rooms proves well that a rigorous conceptual study of openings (the size, the shape, the position) can have a real impact on the improvement of the levels of illumination and indoor thermal comfort.

NOMENCLATURE

Lighting (lux)

INTRODUCTION

during the last years , Algeria had lead a construction policy, where the quality is often lacking, making our buildings energy efficient. Topped the list with the residential-commercial sector, in fact in 2005 this sector accounted for 43% of final energy consumption [1]. This latter is distributed as follows: 49% electricity, 41% product gas, 10% oil products. Ensuring the lighting needs, heating and refresh the indoor environments. while the window is an interface element between the external environment and the internal environment of the building, so it is a nerve center of the building. It is a way to capture the sun's rays, which allow us to introduce light and heat, however it can also be seen as critical of any insulation, this makes it a key part of our energy consumption.

If the habitat account as an excellent place for the research on comfort, workplaces remains important, particularly educational areas. These require a minimum level of visual comfort and heat necessary to the accomplishment of the task. Especially as regards the visual comfort, indeed in the furniture is fixed workspaces, tasks demanding concentration and support evil glare, plus a minimum illumination of 500lux on the work plan must be insured [2].

To perform this work we chose to study the levels of illumination and interior temperatures at the architectural school, the aim is to check the guidelines in our latitudes avoided, recommend, and what impact plays window on visual and thermal comfort.

ANALYSIS AND MODELLING

In this study, we choose two workshops from different configuration and orientation, we analyze the design of the window in three reports: glasses Area / exteriors walls area, height bay / Local depth, Area glasses / Area floor.

Table 1 :
window geometrical study in the selected workshops

		1 st Local		2 nd Local		Ideal case
Glass area (m ²)		north	11	west	25.1	
				south	4.0	
floor area (m ²)			162.00		123.00	
Height (m)	bay		2.45		2.85	
					2.80	
Local depth (m)			10.30		11.20	
Exteriors walls area (m ²)			131.00		121.70	
Glass area / Floor area			0.07		0.24	0.20[3]
Local depth /			4.20		3.92	1.50 to 2

Height bay		3.97	[4]
Glass Area / Exteriors walls area	8.4%	23.90%	≤30% [5]

After studying the workshops openings conceptual design, we carry on some simulations. The study of luminous comfort is done with DIALUX software, using the daylight factor method that allowed us to assess the levels of illumination; while simulations indoor temperatures are made using TRNSYS, respecting building materials and rooms occupancy. We present the results of simulations [6] for the day of 21st June and 21st December as they represent critical days and correspond to workshop occupation periods.

Table 2 :
Simulation results for the two workshops for the 21st June

	Lighting Average 12pm(lux)	Daylight factor	T min (K)	T max (K)
1 st Local	142	0.7	249.18	296.69
2 nd Local	392	2	294.75	301.81

Table 3 :
Simulation results for the two workshops for the 21st December

	Lighting Average 12pm(lux)	Daylight Factor %	T min (K)	T max (K)
1 st Local	74	0.7	285.45	287.40
2 nd Local	204	2	285.93	291.70

The simulation results clearly indicate that the lighting levels are insufficient in the first local, as to the second local, even if the light levels are correct in the second case, there is a risk of overheating in summer. These results confirm the results of the investigation.

To know the window's impact on the thermal and visual comfort. We offer two solutions for each local. Given that the first place is marked by a low level of illumination we suggest to increase the glass surface in the first option will be exclusively oriented north, in the second part will be oriented north west another.

In the second room, he saw a danger of overheating, it is suggested to decrease the glass surface and the spread differently on both south and west facades.

RESULTS AND DISCUSSION

Table 4 :
window geometrical study
1st Local and the two solutions

	1 st Local	1 st Solution	2 nd Solution
Glass area (m ²)	north 11	north 32	north 21 west 11
floor area (m ²)	162.00	162.00	162.00
Height bay (m)	2.45	3.40	3.45
Local depth (m)	10.30	10.30	10.30 15.00
Exteriors walls area (m ²)	131.00	131.00	131.00
Glass area / Floor area	0.07	0.20	0.20
Local depth / Height bay	4.20	3.00	3.00 4.35
Glass Area / Exteriors walls area	8.4%	24.4%	24.4%

Table 5 :
Simulation results of 21st June
1st Local and the two solutions

	Lighting Average 12pm(lux)	Daylight Factor %	T min (K)	T max (K)
1 st Local	142	0.7	21.18	23.69
1 st Solution	383	1.8	21.36	24.81
2 nd Solution	442	2.1	21.57	25.70

Table 6 :
Simulation results of 21st December
1st Local and the two solutions

	Lighting Average 12pm(lux)	Daylight Factor %	T min (K)	T max (K)
1 st Local	74	0.7	285.45	287.40
1 st Solution	200	1.8	285.35	287.99
2 nd Solution	231	2.	285.44	288.60

The results in table 4,5 and 6 show clearly that it is possible to improve light levels in the room, while respecting the thermal comfort zone. also it seems that the most appropriate option is the second one (bilateral lighting) , because it allows a significant improvement in illumination levels, and the closest indoor temperatures of thermal comfort zones.

Table 7 :
window geometrical study
2nd Local and the two solutions

	2 nd Local		1 st Solution		2 nd Solution	
	west	east	west	east	west	east
Glass area (m ²)	25.1	4.0	15	10	10	15
floor area (m ²)	123.00		123.00		123.00	
Height bay (m)	2.85		2.70		2.70	
	2.80		2.45		2.65	
Local depth (m)	11.20		11.20		11.20	
Exteriors walls area (m ²)	121.70		121.70		121.70	
Glass area / Floor area	0.24		0.20		0.20	
Local depth / Height bay	3.91		4.14		4.14	
			4.60		4.60	
Glass Area / Exteriors walls area	23.90%		20.50%		20.50%	

Table 8 :
Simulation results of 21st June
2nd Local and the two solutions

	Lighting Average 12pm(lux)	Daylight Factor %	T min (K)	T max (K)
2 nd Local	392	2	294.75	301.81
1 st Solution	480	2.3	294.65	300.31
2 nd Solution	623	3	294.57	299.6

Table 9 :
Simulation results of 21st December
2nd Local and the two solutions

	Lighting Average 12pm(lux)	Daylight Factor %	T min (K)	T max (K)
2 nd Local	204	2	285.93	291.70
1 st Solution	250	2.3	286.13	291.62
2 nd Solution	325	3	286.26	292.05

The results in table 7,8 and 9 revealed that the second solution(glasses area 10m² west & 15m²) offer the most comfortable indoor temperatures, so we can see that in summer the gap's maximum temperatures between the original local and the 2nd solution is more than 275 K, unfortunately in winter this improvement is less marked, also this solution had the advantage to offer us the best lighting levels.

CONCLUSIONS

This study shows that the increase in glass surfaces has a greater impact on the lighting levels than on the interior temperatures, contrary to the direction which influences the temperatures, in this sense in our latitudes west orientation is avoided because it presents a risk of overheating and glare.

In the case of educational areas that require significant levels of illumination, the depth ratio of local / height = 1.5 to 2 play an important role, particularly in local background. We advise to opt for a bilateral lighting or for shallower possible spaces.

Finally we can conclude that improved lighting levels do not necessarily induces a less comfortable room temperature, just choose to select the appropriate orientation, in order to get a compromise between thermal and visual comfort)

ACKNOWLEDGMENTS

We want to thank LOCIE laboratory (Savoie University) for allowing us to use the software TRNSYS16.

KEYWORDS

windows, lighting average, temperature, daylight factor, orientation, simulation, energy efficiency,

REFERENCES

1. Ministère de l'Énergie et des Mines, 2014, *bilan énergétique national de l'année 2013*, **40**, téléchargé le 26/06/2014
2. Bruxelles Environnement, 2010, rapport technique « bâtiments exemplaires » *les risques de surchauffe, Gueldelle 100* ; www.bruxellesenvironnement.be/batimentsexemplaires, PDF téléchargé le 07/06/ 2011.
3. Mazouz, S., 2006, *Éléments de Conception Architecturale*, ed office des publications universitaires, **268**, pp, 184-188,
4. De Herde, A and Reiter, S., 2004, *L'Éclairage Naturel des Bâtiments*, presse universitaires de Louvain UCL, **265**, p.72
5. Neufert, E., 2002, *Les éléments des projets de construction*, 8e edition, Le Moniteur, **646**, pp.191.
6. Hamza Cherif, Y, 2012, *Analyse De L'efficacité Lumineuse et Énergétique Des Composantes Fenêtres dan la Conception du Bâtiment : Compromis entre Confort Thermique et Confort Visuel*, **174**, pp. 152-167, département d'architecture Usto Oran.

Building Materials

DESIGN OF AN EXPERIMENTAL DEVICE FOR THE STUDY OF HYGROTHERMAL BEHAVIOR FOR VERY HYGROSCOPIC WALLS

Zakaria Slimani¹, Abdelkrim Trabelsi^{1*}, Joseph Virgone¹

¹ Centre d'Énergétique et de Thermique de Lyon [CETHIL], UMR 5008, CNRS, INSA-Lyon, Université Lyon 1, Bât Sadi Carnot - 9 Rue de la Physique - 69621 Villeurbanne cedex, France

*Corresponding author: Fax: [+33] [0]4 72 43 88 11 Email: abdelkrim.trabelsi@univ-lyon1.fr

ABSTRACT

Simulation of Heat, Air and Moisture (HAM) transfers in building envelope is a practice which is becoming increasingly popular. This is due to the impact of moisture transfer on the energy performance of the envelope and indoor air quality as shown in the latest studies related to this subject. In this context we designed a new experimental setup which reproduces wide range of hygrothermal solicitations in building. It has a various physical measurements, which allows the understanding of hygrothermal phenomena and provide sufficient data to validate HAM models. This article present the qualification of the device and its use to understand the behavior a highly hygroscopic thermal insulating material which is fiber wood. The results highlighted heat and mass coupling effects especially the contribution of latent heat in the overall energy balance for different type of loading.

INTRODUCTION

Very hygroscopic materials such as wood and its derivatives, allow to reduce energy consumption of buildings [1]. They have also a strong capacity to fix CO₂ present in the air [2]. They would constitute a very good candidates to meet the goals and commitments of the Grenelle Environment Forum.

Numerical modeling of Heat, Air and Moisture (HAM) transfer for this type of material becomes important. This is due to strong coupling between physics and to the impact of water transfers on the energy performance for highly hygroscopic envelopes as shown in some studies on that subject [1], [2], [3].

Validation of HAM numerical simulation codes is therefore essential as these materials exhibit complex behavior and strong heterogeneities. In this context we propose to design a new experimental device for the study of hygrothermal transfers.

Different experimental benches for the study of hygrothermal transfers exist. Most of them, although allowing varied boundary conditions, focus on the study at the material scale [4], [5], or on the study of the storage/release of water [6], [7]. At the wall scale, we can cite the work of [8], [9] where the hygrothermal loading is limited to the control of a single side and [10] where no mass flux is measured.

Other, focus on the building scale where the boundary condition are not fully mastered [11], [12]. The objective of this article is to present an experimental device that goes beyond the scale of the material while offering the same opportunities in terms of hygrothermal stresses. It may thus consider multilayer walls with a surface of 1 m² with natural or even forced convection under laboratory conditions.



Figure 1
Picture of the experimental device

The experimental results ensuing come meet the need of the community for this type of data. This work was developed in the frame of the ANR project HYGRO-

BAT whose objective is to put in place a methodology for good building hygrothermal design.

EXPERIMENTAL DEVICE DESCRIPTION

The proposed device reproduces hygrothermal constraints encountered in building. It was designed on the basis of the existing experimental benches [13]. It has a rich instrumentation permitting the measurement of water and thermal fluxes. It is designed to provide an experimental observation for a better understanding of the hygrothermal phenomena and have sufficient data for validation of HAM models or even the characterization of transfer properties at the wall scale.

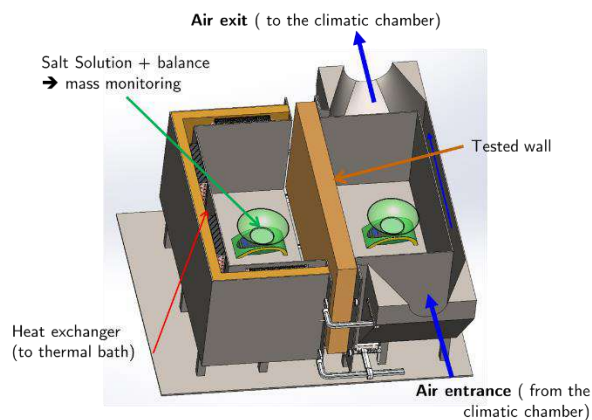


Figure 2

Descriptive scheme of the experimental device

Specifications: To characterize the behavior of buildings walls [different wall thicknesses, different materials] with regard to coupled heat and moisture loading, the proposed experimental device meets the following requirements:

- Having two compartments regulated in temperature and relative humidity separated by the wall to be studied. Thus we can consider different hygrothermal loads (constant, step...).
- Measuring the temperature and humidity fields in the two compartments [air + surface] to monitor and check the boundary conditions [stability, homogeneity contribution of the long wave radiations...].
- Measuring the temperature and humidity of fields on the surface and in the volume of the wall in order to have the response of the wall with regard to the applied loads and to check the unidirectionality of the transfer

- Measuring mass flow through the wall as well as the amount of water stored. This will achieve an overall water balance and deduce the buffering capacity of the wall.
- Measuring the heat flux at the outer surfaces and thus know the powers involved in the transfer.
- Measuring the difference in pressure between the two compartments in order to have the contribution of convection.
- Measuring the speed and condition of the air inlet and outlet of the vein to measure the water vapor flows.

The proposed device is shown in Figures 1 and 2. It helps to have the response of the wall facing static and dynamic hygrothermal loading in natural and forced convection. It is composed of two compartments with a volume of $0.5 \times 1 \times 1 \text{ m}^3$. It has more than 60 measurement points. The chosen sensors for the measurement of temperature and relative humidity inside the wall are SHT75. They have been tested to verify their durability under aggressive conditions and drift in time. They show a very good behavior even after condensation. Figure 3 shows the positions of the sensors inside the test wall and in the compartments of the device.

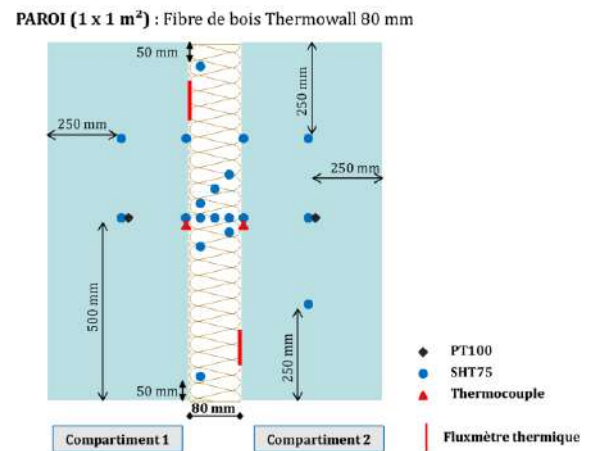


Figure 3

Cross-section of the device showing the position of the sensors

The first compartment is regulated in humidity through a Saturated Salt Solution (SSS) and in temperature using a fluid-air exchangers connected to a temperature control unit. It consists from the outside to the inside of:

- An external part
- A polystyrene insulation layer having a thickness of 60 mm
- 4 heat exchangers connected to a temperature control unit.
- An internal part with a volume of 0.5 m³ and an exchange surface of 1 m²

The two heat exchangers are arranged in counter-current for a better uniformity of temperature in the compartment. In this configuration the temperature differences are substantially constant along an exchanger.

The second compartment consists of internal and external parts allowing to have a thermal guard. It has two operation modes in natural and forced convection. The first mode is obtained with the 2 elements where the relative humidity regulation is achieved using SSS and temperature regulation through a climatic chamber [in remote mode] controlling the temperature in the thermal guard. The second mode is obtained directly with the external part and the climatic chamber that pulse conditioned air in parallel to the studied wall with an airflow control. Compartment 2 consists from the outside to the inside of:

- Thin multilayer insulation 24 [thermo-reflective insulation]
- 2 layers of hemp wool insulation with a thickness of 40 mm.
- An external compartment connected to the climate chamber by isolated air ducts [glass wool insulation of 50 mm thickness]
- An internal part similar to the compartment 1 internal part.

Heating and cooling powers of regulation systems are sufficiently large to allow to quickly reach the desired temperature. The vapor stream obtained by the SSS are limited. The mass of the used SSS for relative humidity control is about 2.5 kg and its exchange surface area is about 0.46×0.3 m². Fans are used to homogenize the humidity and temperature in each compartment.

Tests for the qualification of the bench: the qualification of the bench is a necessary step because it allows to give the uncertainty of all possible measures on this bench. This qualification has

brought on the calibration of sensors, verification of humidity and temperature regulation systems, checking balances drift, the estimation of air tightness, the estimation of the uncertainty on the position, the verification of the unidirectionality of the transfer.

This article only presents tests on regulation and the tightness of the compartments as well as the summary of the uncertainties of the measurements on the bench. Other qualification tests are on [14].

Table 1
Boundary conditions of the tests for the qualification of the bench

Compartment 1		Compartment 2	
Temperature [°C]	Relative Humidity [%]	Temperature [°C]	Relative Humidity [%]
5	43	35	76

In order to achieve regulation and air tightness tests, we have put a moisture insulated wall through a vapor barrier between the two environments with the hygrothermal conditions presented in table 1. The measures of interest are the effective conditions in terms of temperature and relative humidity as well as the SSS mass.

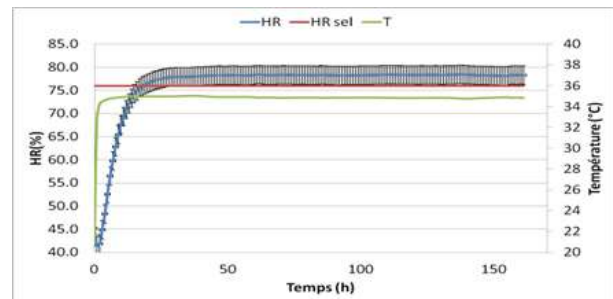


Figure 4
Evolution of temperature and relative humidity in compartment 2

Regulation system: for the sensors installed at different positions especially in height, a good homogeneity and stability of the measured values was observed. Over the last 48 hours the standard deviation of the two compartments does not exceed 0.06 °C for temperature and 0.14% for relative humidity. Note that the difference between the measured relative humidity and that displayed by the

SSS tables in this case is less than 2%. Figure 4 display temperature and relative humidity in one of the compartments.

Air tightness: to estimate the magnitude of leaks we put a vapor barrier on both sides of the wall to avoid water vapor transfer between the ambient air and the wall. The monitoring of the mass of the SSS and the relative humidity allowed us to estimate the magnitude of the leak.

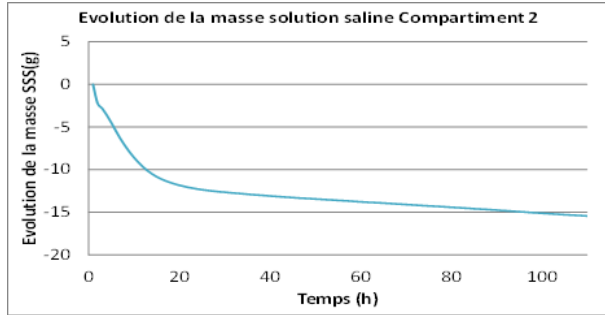


Figure 5

Evolution of the mass of the saturated salt solution for compartment 2.

During the first 20 hours [see Figure 4 and 5] there is a great evolutions of relative humidity and mass of evaporated SSS. The latter evaporates to balance the relative humidity of the ambient air [at $t = 0$, $RH = 42\%$] until to reach equilibrium at 78%. After 70 hours, despite a stable ambient air conditions, the SSS always evaporates without affecting the relative humidity of the atmosphere. This steam flow cannot be explained by the balances drift since this point has been checked. Actually, it represents the leakage of the compartments for the given operatory test conditions. It is of the order of 0.033 g/h for the compartment 2 and 0.004 g/h for the compartment 1.

Table 2
Domain and measurements uncertainties

Measurement	Domain	Uncertainty
Temperature (SHT75)	[5-45] °C	0,17°C
Relative humidity (SHT75)	[40-90] %	2 %
Temperature (Pt100)	[5 à 45] °C	0,15°C
Temperature (thermocouples)	[5-45] °C	0,16°C

Summary of the measurements uncertainties: table 2 gives a summary of hygrothermal operating

domain of the experimental device and the uncertainties on the temperatures and relative humidity's according to the type of sensor.

STUDY OF A STRONGLY HYGROSCOPIC WALL

As an example we present results for isothermal loading. This case study allow to highlight the effects of vapor transfer on the thermal behavior of a wall when latent heat effects are predominant.

The study is conducted on an 8 cm thickness wood fiber insulation. This material was characterized by different laboratories in the framework of HYGROBAT project [ANR-10-HABISOL-005-01 [15]]. Its physical properties are presented in table 3. Note that this material has a high storage capacity and a strong dependence of thermal conductivity to relative humidity showing 12% variations in the hygroscopic field unlike a non-hygroscopic material where its variation is negligible in the hygroscopic field such as brick [2]. On the other hand, this material has a high vapor diffusion coefficient. This indicates that water vapor passes through this material almost as easily than in the air.

Table 3
Hygrothermal properties of the tested wood fiber insulation

Bulk density	0.144g/cm ³
Porosity	90-99%
Water vapor permeability [kg/[Pa.m.s]	dry cup 1,43×10-10
	wet cup 3,62×10-11
Thermal conductivity λ [mW/m.K]	14,8- θ +40
	[θ : Volumetric water content %]

To see the effect of mass transfer on the heat transfer we realized a test under isothermal conditions at 20 °C with a relative humidity of 73% in the outside and 52% in the inside one. Figure 6 shows the boundary conditions to which the wall is subjected. Again a good stability of the boundary conditions is noted. The water vapor steady state is slower to reach because of the significant vapor flow needed. We had to intervene regularly to regenerate the SSS.

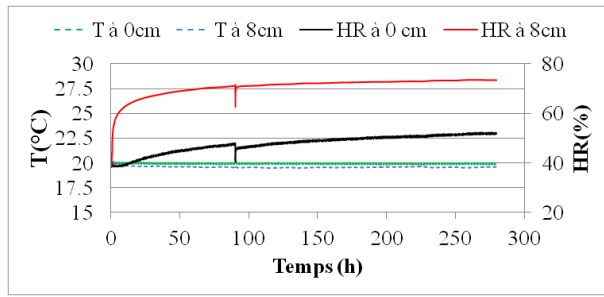


Figure 6

Temperature and humidity changes at the boundaries of the wall

RESULTS AND DISCUSSION

Figure 7 shows the evolution of the water vapor concentration in the wall at $x = 0, 2, 4, 6$ and 8 cm. This curve was obtained from the temperature and relative humidity measurements for different positions in depth of the wall. It can be seen that the wall start from a constant water vapor concentration of the order of 7 g/m^3 and evolves over time. The evolution of water vapor concentration over time is due to the boundary conditions that creates a difference between the two sides of 3.7 g/m^3 . This gradient induces a water vapor flux through the wall which has been measured through the monitoring of the mass of SSS.

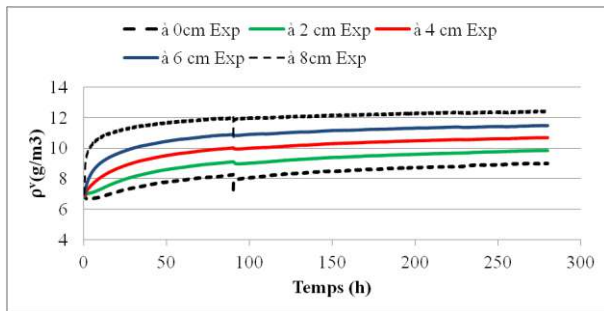


Figure 7

Evolution of the water vapor concentration in the wall at different positions

We can see in figure 8 the evolution of the mass of the SSS depending on the time in the compartments 1 and 2. The slopes of the curves allow to have the flow of moisture at the input and output of the wall. Note that the water flux based calculated over the last 24 hours is 1.15 g/h at the external side and 1.2 g/h at the inside. The difference between the two measurements is about 4.3%. It can be concluded that a pseudo-permanent regime is reached.

The algebraic sum between the two curves is the amount of stored water. The tested wall stores a large amount of water during the first 50 hours estimated to 156 g . After 12 days, this amount reaches the 327 g . Given the porous nature of the wall, the stored water cannot only be in vapor form. It is largely in a condensed form.

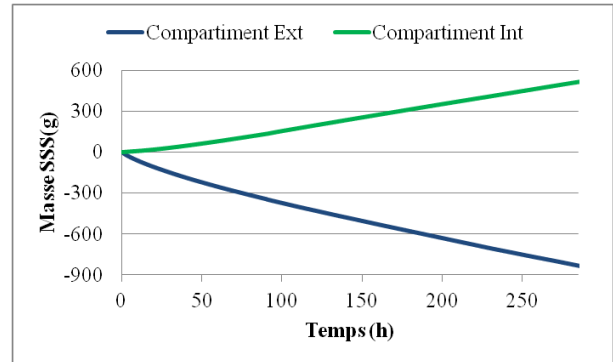


Figure 8

Evolution of the mass of the saturated salt solution in the two compartments

Figure 9 presents the evolution of the temperature in the wall over time. It may be noted a sudden increase in temperature on the outside (at 4 cm and 6 cm from the edge close to $\text{HR} = 70\%$). The temperature reaches its maximum value after 5 hours. The magnitude of the elevation is $1.7 \text{ }^\circ\text{C}$. The increase in temperature is explained by the condensation which is accompanied by a release of heat. This heat is diffused through the wall which causes dephasing found on temperatures at different positions.

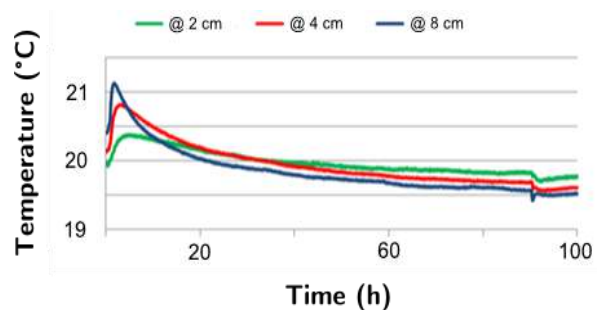


Figure 9

Temperature evolution at different position in the wall submitted to isothermal conditions with a vapor concentration gradient

The experimental results for this highly hygroscopic wall are a benchmark for validation of HAM transfer models.

CONCLUSIONS

This paper presents experimental device for the study of hygrothermal transfers in the walls of buildings. It is a laboratory device that allows the measurement of a large number of variables including water vapor flux in dynamic regime. It can also reproduce varied loads in a single tool. His qualification allowed us to show its capacity of hygrothermal regulation and assess the uncertainty of the measurements on this bench.

The case of a single-layer wall in wood fiber submitted to thermal solicitations allowed to show the interest to take into account water transfers in the study of the heat balances for a highly hygroscopic wall. Indeed, because of the latent effects of condensation of water in the wall, showed a rise in temperature that goes beyond the degree Celsius.

ACKNOWLEDGMENTS

This work has received the support of the national research agency [ANR], HYGROBAT project, ANR-10-HABISOL-005-01

REFERENCES

1. Yoshino H, Mitamura T, Hasegawa K. Moisture buffering and effect of ventilation rate and volume rate of hygrothermal materials in a single room under steady state exterior conditions. *Building and Environment*. 2009 juillet;44[7]:1418–25.
2. Le ADT. Étude des transferts hygrothermiques dans le béton de chanvre et leur application au bâtiment. Université de Reims - Champagne Ardenne; 2010
3. Teasdale-St-Hilaire A, Derome D. Comparison of experimental and numerical results of wood-frame wall assemblies wetted by simulated wind-driven rain infiltration. *Energy and Buildings*. 2007;39[11]:1131–9.
4. Qin M, Aït-Mokhtar A, Belarbi R. Two-dimensional hygrothermal transfer in porous building materials. *Applied Thermal Engineering*. 2010 Nov;30[16]:2555–62.
5. Trabelsi A, Belarbi R, Abahri K, Qin M. Assessment of temperature gradient effects on moisture transfer through thermogradient coefficient. *Building Simulation*. 2012;5[2]:107–15.
6. Talukdar P, Osanyintola OF, Olutimayin SO, Simonson CJ. An experimental data set for benchmarking 1-D, transient heat and moisture transfer models of hygroscopic building materials. Part II: Experimental, numerical and analytical data. *International Journal of Heat and Mass Transfer*. 2007 décembre;50[25–26]:4915–26.
7. Talukdar P, Olutmayin SO, Osanyintola OF, Simonson CJ. An experimental data set for benchmarking 1-D, transient heat and moisture transfer models of hygroscopic building materials. Part I: Experimental facility and material property data. *International Journal of Heat and Mass Transfer*. 2007;50[23-24]:4527–39.
8. Van Belleghem M, Steeman M, Willockx A, Janssens A, De Paepe M. Benchmark experiments for moisture transfer modelling in air and porous materials. *Building and Environment*. 2011 avril;46[4]:884–98.
9. Olutimayin SO, Simonson CJ. Measuring and modeling vapor boundary layer growth during transient diffusion heat and moisture transfer in cellulose insulation. *International Journal of Heat and Mass Transfer*. 2005;48[16]:3319–30.
10. Collet F, Pretot S. Experimental highlight of hygrothermal phenomena in hemp concrete wall. *Building and Environment* [Internet]. [cited 2014 Oct 3];
11. Piot A, Woloszyn M, Brau J, Abele C. Experimental wooden frame house for the validation of whole building heat and moisture transfer numerical models. *Energy and Buildings*. 2011 juin;43[6]:1322–8.
12. Desta TZ, Langmans J, Roels S. Experimental data set for validation of heat, air and moisture transport models of building envelopes. *Building and Environment*. 2011 mai;46[5]:1038–46.
13. Slimani Z, Trabelsi A, Virgone J, Jay J, Buathier S. Conception d'un dispositif expérimental pour l'étude des transferts hygrothermiques dans les parois très hygroscopiques. In: 32èmes rencontres universitaires de Génie Civil. Orléans; 2014.
14. Slimani Z. Analyse expérimentale et numérique du comportement hygrothermique de parois fortement hygroscopiques. Claude Bernard Lyon 1; 2015.
15. Ferroukhi MY, Abahri K, Belarbi R, Limam K, Nouviaire A. Experimental validation of coupled heat, air and moisture transfer modeling in multilayer building components. *Heat Mass Transfer*. 2015 Dec 17;1–13.

EFFECT OF LOCATIONS AND THICKNESSES FOR THE DIFFERENT MATERIAL CONSTITUTING A BUILDING WALL

EL Mehdi EL KHATTABI, Mohamed MHARZI, Mohamed Amine NADAH

ISTA-USMBA-FSDM, Fez, MOROCCO

*mehdienerg@gmail.com

ABSTRACT

In this study we examine the effect of a given wall thermal resistance on an inside temperature under dynamic regime. Our computational study is conducted to establish, for a given wall thermal resistance, how the inside temperature is influenced by the thermal characteristics, locations and thicknesses for the different materials constituting a building wall. Comparative results for three walls having identical thermal resistance are presented under Fes weather conditions.

KEYWORDS

Thermal resistance, Dynamic regime, building, Weather conditions

NOMENCLATURE

C	Thermal capacity (kJ/kg K)
h	Convective heat exchange coefficient (W/m ² K)
m	The mass of the layer (Kg)
U _v	Global exchange coefficient (W/m ² K)
t	Time, (min)
a	Absorption coefficient (%)
J	Number of days
R	Thermal resistance (°C m ² /W)
S	Wall surfaces, (m ²)
T	Temperature, °C

INDICES / EXPOSITS

Ex	Exterior
Int	Interior
ME	EST wall
cim	cement

INTRODUCTION

Evaluation of building heat loss is generally based on steady state model. Consequently the thermal inertia of walls is not been considered.

Givoni [1] suggest that inertia is a necessary recommendation for construction in warm climate to large range. Narayan [2] validate the effectiveness of the inertia under cold climate in the creation of thermal comfort and reducing energy consumption.

Other studies such as Solange [3], state that thermal inertia may also be useful in the hot and humid climate.

This research is attempted to show interest of considering energy storage in room walls. So, the comparative results of room walls, with and without energy storage at the wall, are presented for three types of walls having the same heat resistance.

DESCRIPTION OF THE BUILDING STUDIED

A 15 m² room located in Fez, whose south wall, East, North and ceiling are exposed to sunlight. Taking into account weather condition of Fez, the overall radiation incident on the vertical and horizontal walls was calculated numerically and the radiation transmitted by the glazing according to their orientation. This first result is validated by [4-5]. The south wall has a 1.68 m² surface of window and door surface 2.68 m² to the west wall, the thermo-physical properties of these materials were taken by referring to the TRNSYS library [6] and literature [7].

ANALYSIS AND MODELLING

The numerical study is based on solar and thermal models. The incident radiation on the walls is evaluated using equations reported in [8]. The following hypothesis was used:

- The day relative humidity is assumed to be constant and equal to 50%,
- The atmospheric turbidity B is equal to 0.1
- The steam saturation pressure of water is evaluated for a constant temperature room,
- The heat transfer in the wall is one-dimensional,

- The internal irradiative heat exchange is neglected,
- The convective heat transfer coefficients are constant.

The 16 heat balance equations concerning the case without energy storage at the building walls room are:

◆ Externals walls

$$\frac{dT_i}{dt} = \frac{1}{\rho_i V_i c p_i} [h_{ext} S (T_{ext} - T_i) + a_{cim} G S + h_{rciel} S (T_{ciel} - T_i) - \frac{(T_i - T_{i+1}) S}{\sum_{n=1}^{n=4} R_n} + h_{rsol} S (T_{sol} - T_i)]$$

◆ Internals walls

$$\frac{dT_{i+1}}{dt} = \frac{1}{\rho_i V_i c p_i} [-\frac{(T_i - T_{i+1}) S}{\sum_{n=1}^{n=4} R_n} + h S (T_{i+1} - T_{int})]$$

◆ Air change

$$\frac{dT_{air}}{dt} = \frac{1}{\rho_{air} V_{air} c p_{air}} [\sum_{n=1}^6 Q_{Wall} + Q_{RE} + Q_{vitre} + Q_{sol}]$$

◆ Glazing transmitted flux

$$Q_{vitre} = F_S G_{Sud} S_{sud} + U_{vitre} S_{vitre} (T_{ext} - T_{int})$$

◆ Indoor Air

$$Q_{RE} = 0.34 q_v (T_{ext} - T_{int})$$

In study with energy storage at the composite wall, the equations of heat balance are established for each layer of the wall. Hence, 4 equations are established for each wall.

RESULTS AND DISCUSSION

Constitution and the thermo-physical properties of the various walls considered are summarised on tables 1 and 2.

Table 1: Thermo-physical properties of externals walls components

	Thickness (cm)	Thermal capacity (kJ/kg K)	Thermal conductivity (W/m K)	Density (kg/m³)
Polystyrene	2-12	1.380	0.04	35
Cement mortar	1.5	1	1.15	1700
Brick	20	0.878	1.15	1800

Table 2: Thermo-physical properties of roof components

	Thickness (cm)	Thermal capacity (kJ/kg K)	Thermal conductivity (W/m K)	Density (kg/m³)
Floor tile	2	0.7	1.75	2300
Mortar	10	1	1.15	1700
Concrete	4	0.65	1.75	2100
Concrete	16	1	1.23	1300
Plaster	2	1	0.4	1500

The presented results are obtained for 1 June taken as the day type of this study. Figure 1 shows the distribution of the radiation on the various orientations of the room's walls.

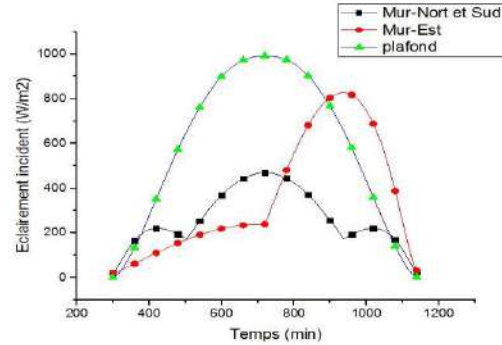


Figure 1: Incident radiation for different orientation walls (Fez 1 June)

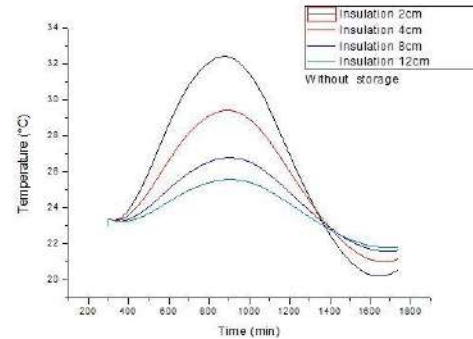


Figure.2: Variation of internal temperature with various insulation thicknesses and with no wall energy storage

As shown in figure 2 the internal temperature at mid day corresponding to 12 cm isolation was reduced about 8 °C compared to the case with 2 cm insulation. Additionally, we note that the internal temperature was insensitive to growth of insulation thicknesses over 12 cm (no represented).

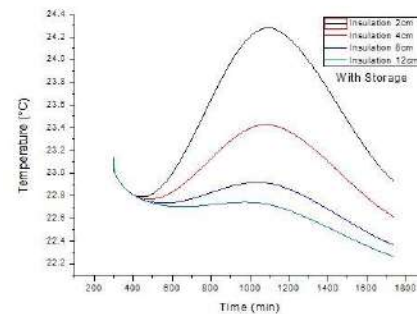


Figure.3: Variation of internal temperature with various insulation thicknesses and with wall energy storage

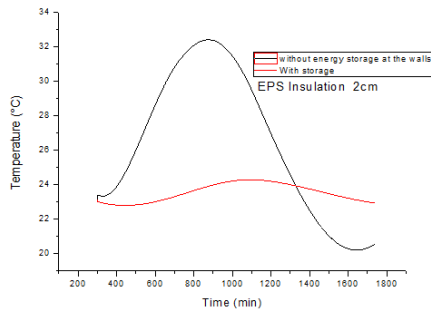


Figure.4: Dynamic regime effect on the internal temperature

Otherwise figure 3 attest that the maximum of internal temperature under all isolation thickness was less by 3 to 7 degrees if the energy storage in wall is considered. Under dynamic regime a 2 cm isolation thickness permit a reduction of 9 °C and 2 hours phase shift in comparison with the steady state case (figure 4).

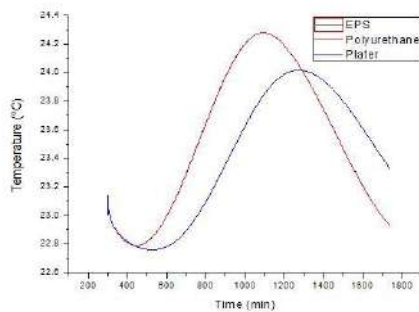


Figure.5: Internal temperature variation with different arrangement of layers of the outer wall

Table 3: Constitution and the thermo-physical properties of the others walls layers

	Thickness (cm)	thermal capacity (kJ/kg K)	Thermal conductivity (W/m K)	density (kg/m ³)
Polystyrene	2	1.380	0.04	35
Polyurethane	2	0.84	0.04	45
Plaster	20	1.00	0.40	1500

Study of three walls with a fixed thermal resistance and different layers arrangement (table 3) shows principally a 100 minutes phase shift of the internal temperature maximum in case of plaster (figure 5). Note that the EPS and polyurethane have the same thermal resistance so they emplacement in the wall provide the same effect. In comparison with the plaster layer a 20 cm thickness must be use to have an identical thermal resistance. So in this case the thickness of wall is bigger and here thermal inertia is greatest.

CONCLUSION

In the present work we have conclude that:

- ♦ Under steady stat regime, the change of layers position with the conserving of the total thermal resistance gives the same result,
- ♦ Optimum insulation is obtained with a thickness of layer insulating equal to 12 cm,
- ♦ The internal temperature variation is moderated under dynamic regime,
- ♦ Under dynamic regime a 2 cm isolation thickness permit a reduction of 9 °C and 2 hours phase shift in comparison with the steady state case

REFERENCES

1. B. Givoni, "Effectiveness of mass and night Ventilation in lowering the indoor daytime temperatures. Part I: 1993 Experimental periods", Energy and Buildings, Vol. 28, n°1, pp.25–32, 1998.
2. T. Narayan, "A Passive Courtyard Home in Jaipur, India: Design Analysis for Thermal Comfort in a Hot Desert Climate", Arizona State University. Thulasi.Narayan@asu.edu Last saved 03/02/05.
3. V.G.G. Solange, "Thermal Inertia and Natural Ventilation – Optimization of Thermal Storage as a Cooling Technique for Residential Buildings In Southern Brazil", PhD Thesis, October, 2004.
4. M.R. Yaïche, S.M.A. Bekkouche, "Design and Validation of a program for Excel Estimation of Solar Radiation Incident in Algeria. For a Totally Clear Sky "Review Renewable Energy 11, 423-436 (2008).
5. S.M.A. Bekkouche, "Thermal Behavior Modeling Some Devices Solar ", PhD in Physics and Electronics, University of Tlemcen. (May 2009).
6. Document, "TRNSYS, Version 16 User Manual".
7. Y. Jannot, "Solar Thermal", October 2003.
8. P. Bessemoulin and J. Olivieri, "The Solar Radiation and the Ultraviolet Component", Atmospheric Physics, Meteorology, Round 8, No. 31, September 2000

HEAT TRANSFER IN POROUS BUILDING MATERIAL

F. BENNAI^{1,2*}, K. ABAHRI³, R. BELARBI², A. TAHAKOURT¹¹ Laboratoire de Génie de la Construction et Architecture (LGCA), Faculté de Technologie, Université de Bejaia, 06000 Bejaia, Algérie.² LaSIE, UMR 7356 CNRS Université de La Rochelle, Avenue Michel Crépeau 17042 La Rochelle cedex1, France.³ LMT-Cachan/ENS Cachan/CNRS/Université Paris Saclay, 61 Avenue du Président Wilson, 94230 Cachan, France.

*Corresponding author: Email: fares.bennai@etudiant.univ-lr.fr

ABSTRACT

Porous media possess a complex structure on a microscopic scale and present strong heterogeneities, which makes their precise description extremely complex. The macroscopic behavior of these media is strongly dependent of mechanisms that act to the scale of these constituents. In this present work we are interested in the development of a macroscopic model of heat transfer by conduction and convection with a heat source in the porous materials. This model is established by periodic homogenization of energy conservation equations written on a microscopic scale in each phase (solid, liquid and gas). Expressions the different input parameters of model were obtained. Numerical calculations of the homogenized thermal conductivity tensor are performed on a representative three-dimensional elementary cell of the porous medium. Finally, a sensitivity study of this tensor depending of the variation of the water content of the elementary cell concerned has been performed.

Keywords Heat transfer, porous building materials

NOMENCLATURE

C	volumetric heat capacity [J/m^3k]
h_l	specific enthalpy of the liquid [J/Kg]
h_{lv}	specific enthalpy of vaporization [J/Kg]
I	identity matrix
L	characteristic macroscopic length [m]
l	characteristic microscopic length [m]
n_{ij}	normal unit vector directed from the domain Ω_i toward the domain Ω_j
n_i	volume fractions of the materials i
Pc	capillary pressure [Pa]
T	temperature [K]
t	time [s]
v	velocity [m/s]
X	dimensional space variable [m]
x	macroscopic dimensionless space variable
y	microscopic dimensionless space variable

Greek Letters

Γ	interface between two different phases
ε	scale separation parameter
λ	thermal conductivity [W/mK]
λ^{hom}	macroscopic conductivity tensor [W/mK]
ρ	density [Kg/m^3]
ω_{lg}	liquid-gas interface velocity [m/s]
Ω	period
Ω_i	part of the period occupied by the pores by mediums i [m^3]

Subscripts

s	solid
l	water liquid
g	gas
r	reference variable
$*$	dimensional variable
$\alpha = s, l$ and g	

INTRODUCTION

In order to reduce energy costs and environmental impacts related to buildings, several organizations and research laboratories have focused on the physical study of the building and its energy behavior [1]. Most materials used in building construction are porous materials with a complex structure and exhibit strong heterogeneities on the microscopic scale. Moreover, most of the phenomena involved at the microscopic scale are the origin of the phenomena presented on the macroscopic scale: the macroscopic behavior of material is strongly dependent mechanisms acting at the scale of these constituents. It is then necessary to dispose of macroscopic laws that allow us to take into account the heterogeneity and complexity of porous media and describe their overall behavior on a large scale.

One possible solution to describe these highly heterogeneous on the pore scale is to assimilate them to the equivalent continuous media on a macroscopic scale, with the same average behavior, using homogenization methods, also called scaling method or micro-macro transition.

The effective medium is then characterized by effective transport properties, or macroscopic coefficients reflecting physics at the pore scale.

The periodic homogenization method is among the most well-known and rigorous scaling methods available in literature allowing obtaining pertinent model. It is mainly based on the method of asymptotic expansions [2]. This method assumes that the microstructure of the macroscopic medium is constituted of a periodic repetition of basic elementary cells. In this work, we propose to establish the periodic homogenization of heat transport equations on the microscopic scale for the different phases of the real porous media, the recourse to the periodic homogenization well known by its reliability to achieve relevant and pertinent macroscopic models. Then, numerical simulations on a representative elementary cell of the microstructure of the studied porous medium are investigated, in order to calculate the homogenized tensor of thermal conductivity.

MICROSTRUCTURAL DESCRIPTION OF PERIODIC MEDIUM

The internal elements of the material structure constitute the microstructure that affects significantly the properties of macroscopic materials. At the macroscopic scale, many materials present a homogeneous geometry but they are in reality highly heterogeneous on a microscopic scale, especially when considering the cementitious material. Indeed, the macroscopic behavior of materials is strongly dependent on the mechanisms involved at the microscopic scale.

Figure 1 shows an example of an X-ray tomography image of cementitious material representing the heterogeneity of such material; it contains aggregates in white, cement and sand in gray and voids in black.

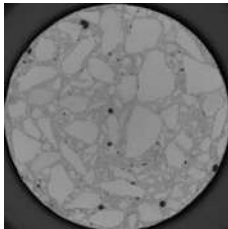


Figure 1: tomographic image obtained by X- rays of the concrete (resolution 60 μm) [3]

Considering a porous medium having a microstructure constituted of periodical repetition of an elementary cells (see Figure 2). Each cell is composed of a solid phase Ω_s^* , a liquid phase Ω_l^* and a gaseous phase Ω_g^* . The interfaces between

these various phases are Γ_{lg}^* , Γ_{sg}^* et Γ_{ls}^* ; they represent the gas-liquid, gas-solid, and liquid-solid interfaces, respectively.

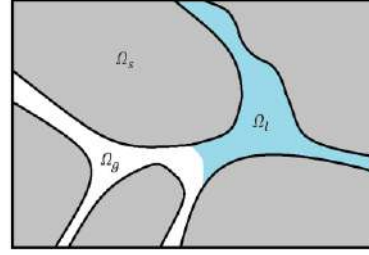


Figure 2: Example of a periodic microstructure partially saturated

MICROSCOPIC DESCRIPTION OF HEAT TRANSFER EQUATIONS:

Considering the conduction and convection heat transfer, the conservation of energy [4] in each phase can be written respectively

$$\rho_s^* c_s^* \frac{\partial^* T_s^*}{\partial t^*} - \text{div}^*(\lambda_s^* \cdot \text{grad}^* T_s^*) = 0 \quad \text{in } \Omega_s^* \quad (1)$$

$$\rho_l^* c_l^* \frac{\partial^* T_l^*}{\partial t^*} - \text{div}^*(\lambda_l^* \cdot \text{grad}^* T_l^*) + \rho_l^* c_l^* v_l^* \cdot \text{grad}^* T_l^* = 0 \quad \text{in } \Omega_l^* \quad (2)$$

$$\rho_g^* c_g^* \frac{\partial^* T_g^*}{\partial t^*} - \text{div}^*(\lambda_g^* \cdot \text{grad}^* T_g^*) + \rho_g^* c_g^* v_g^* \cdot \text{grad}^* T_g^* = 0 \quad \text{in } \Omega_g^* \quad (3)$$

The boundary conditions at the various interfaces are given by:

$$\text{Gas-liquid:} \quad T_g^* = T_l^* \quad \text{on } \Gamma_{gl}^* \quad (4)$$

$$-\lambda_g^* \frac{\partial^* T_g^*}{\partial y^*} \mathbf{n}_{gl}^* = -\lambda_l^* \frac{\partial^* T_l^*}{\partial y^*} \mathbf{n}_{gl}^* + q_{gl}^* \mathbf{n}_{gl}^* \quad \text{on } \Gamma_{gl}^* \quad (5)$$

$$\text{Gas-solid:} \quad T_g^* = T_s^* \quad \text{on } \Gamma_{gs}^* \quad (6)$$

$$\lambda_g^* \frac{\partial^* T_g^*}{\partial y^*} \mathbf{n}_{gs}^* = \lambda_s^* \frac{\partial^* T_s^*}{\partial y^*} \mathbf{n}_{gs}^* \quad \text{on } \Gamma_{gs}^* \quad (7)$$

$$\text{Liquid-solid:} \quad T_l^* = T_s^* \quad \text{on } \Gamma_{ls}^* \quad (8)$$

$$\lambda_l^* \frac{\partial^* T_l^*}{\partial y^*} \mathbf{n}_{ls}^* = \lambda_s^* \frac{\partial^* T_s^*}{\partial y^*} \mathbf{n}_{ls}^* \quad \text{on } \Gamma_{ls}^* \quad (9)$$

These terms (equations 4 to 9) represent the continuity of temperatures and heat flows on the interfaces Γ_{gl}^* , Γ_{gs}^* et Γ_{ls}^* .

In addition to the conduction and convection terms, the consumption or energy production (term source or sink) due to the phase change are added to the balance energy. In the present case this term q_{gl}^* : is a heterogeneous source of heat [5, 6] at the liquid-gas interface:

$$q_{gl}^* = \rho_g^* h_{lv}^* (v_g^* - \omega_{lg}^*) \quad (10)$$

On the other hand, the time average of each balance equation term in the phase “ i ” is given by:

$$\left\langle \frac{\partial^* T_\alpha^*}{\partial t^*} \right\rangle_i = \frac{\partial^*}{\partial t^*} \langle T_\alpha^* \rangle_i - \frac{1}{|\Omega|^*} \int_{\Gamma_{ig}^*} T_\alpha^* \omega_{ig}^* \mathbf{n}_{ig}^* d\Gamma^* \quad (11)$$

With: $\alpha = s, l$ and g

DIMENSIONAL ANALYSIS OF EQUATIONS

The dimensionless physical data are defined by dividing each variable by its characteristic value. These variables are estimated in terms of the parameter ε which represents the ratio between the characteristic microscopic length “ l ”, and the characteristic macroscopic length “ L ”. The perturbation parameter ε , verifies the scale separation condition and the existence of an equivalent medium:

$$\varepsilon = \frac{l}{L} \ll 1 \quad (12)$$

By introducing in the previous equations (1 to 11) the dimensionless variables following:

$$\begin{aligned} y &= \frac{y^*}{l} & x &= \frac{x^*}{L} & t &= \frac{t^*}{t^r} \\ \omega_{lg} &= \frac{\omega_{lg}^*}{\omega_{lg}^r} & \rho_\alpha &= \frac{\rho_\alpha^*}{\rho_\alpha^r} & v_\beta &= \frac{v_\beta^*}{v_\beta^r} \\ T_\alpha &= \frac{T_\alpha^*}{T_\alpha^r} & C_\alpha &= \frac{C_\alpha^*}{C_\alpha^r} & \lambda_\alpha &= \frac{\lambda_\alpha^*}{\lambda_\alpha^r} \\ q_{lg} &= \frac{q_{lg}^*}{q_{lg}^r} \end{aligned}$$

Where y represents the microscopic space variable, and x the macroscopic space variable. The variables indexed by “ r ” are the reference ones, supposed known. The sign * denotes the dimensional variables, and the new variables appeared without star (*) are dimensionless.

Replacing the dimensionless variables defined into the previous equations of transport (equations 1 to 11), we obtain a new dimensionless energy conservation equations:

$$P_s C_s \frac{\partial T_s}{\partial t} - \text{div}(\lambda_s \cdot \text{grad} T_s) = 0 \quad \text{in } \Omega_s \quad (13)$$

$$P_s \cdot C_1 \cdot C_l \frac{\partial T_l}{\partial t} - \lambda_1 \cdot \text{div}(\lambda_l \cdot \text{grad} T_l) + P_l C_l v_l \text{grad} T_l = 0 \quad \text{in } \Omega_l \quad (14)$$

$$P_s \cdot C_2 \cdot C_g \frac{\partial T_g}{\partial t} - \lambda_2 \cdot \text{div}(\lambda_g \cdot \text{grad} T_g) + P_l C_3 v_1 C_g v_g \text{grad} T_g = 0 \quad \text{in } \Omega_g \quad (15)$$

With: $C_\alpha = \rho_\alpha c_\alpha$

The boundary conditions on the various interfaces become:

$$\text{Gas-liquid:} \quad T_g = T_l \quad \text{on } \Gamma_{gl} \quad (16)$$

$$\lambda_3 \lambda_g \frac{\partial T_g}{\partial y} \mathbf{n}_{gl} = \lambda_l \frac{\partial T_l}{\partial y} \mathbf{n}_{gl} + N_{lv} q_{gl} \mathbf{n}_{gl} \quad \text{on } \Gamma_{gl} \quad (17)$$

$$\text{Gas-solid:} \quad T_g = T_s \quad \text{on } \Gamma_{gs} \quad (18)$$

$$\lambda_2 \lambda_g \frac{\partial T_g}{\partial y} \mathbf{n}_{gs} = \lambda_s \frac{\partial T_s}{\partial y} \mathbf{n}_{gs} \quad \text{on } \Gamma_{gs} \quad (19)$$

$$\text{Liquid-solid:} \quad T_l = T_s \quad \text{on } \Gamma_{ls} \quad (20)$$

$$\lambda_1 \lambda_l \frac{\partial T_l}{\partial y} \mathbf{n}_{ls} = \lambda_s \frac{\partial T_s}{\partial y} \mathbf{n}_{ls} \quad \text{on } \Gamma_{ls} \quad (21)$$

The average of the time derivative of each equation then becomes:

$$\left\langle C_\alpha \frac{\partial T_\alpha}{\partial t} \right\rangle = C_\alpha \frac{\partial}{\partial t} \langle T_\alpha \rangle - \frac{\mathcal{R}_T}{|\Omega|} \int_{\Gamma_{lg}} T_\alpha \omega_{lg} \mathbf{n}_{lg} d\Gamma \quad (22)$$

The following dimensionless numbers characterizing the various transfers appear naturally after the dimensional analysis of the microscopic transfer equations:

$$\begin{aligned} P_s &= \frac{C_\alpha^r l^2}{\lambda_s^r t^r} & P_l &= \frac{C_l^r v_l^r l}{\lambda_s^r} & C_1 &= \frac{C_l^r}{C_s^r} \\ C_2 &= \frac{C_g^r}{C_s^r} & C_3 &= \frac{C_g^r}{C_l^r} & \lambda_1 &= \frac{\lambda_l^r}{\lambda_s^r} \\ \lambda_2 &= \frac{\lambda_g^r}{\lambda_s^r} & \lambda_3 &= \frac{\lambda_g^r}{\lambda_l^r} & v_1 &= \frac{v_g^r}{v_l^r} \\ N_{lv} &= \frac{l}{\lambda_l^r} q_{gl}^r & \mathcal{R}_T &= \frac{t^r \omega_{lg}^r}{l} \end{aligned}$$

All these appeared parameters characterizing the various transfers considered in porous media are dimensionless number, as examples: the inverse of the number Fourier P_s , the Peclet number P_l , the ratio of thermal conductivities $\lambda_1, \lambda_2, \lambda_3$, the ratio of thermal capacities C_1, C_2, C_3 . To be reduced to a dimensionless one scale problem, we express the dimensionless numbers depending on the perturbation parameter ε . Taking into account the characteristic values and different physical phenomena and for homogenisables problems. The orders of magnitude of dimensionless numbers corresponding are then given by:

$$\begin{aligned} P_s &= \mathcal{O}(\varepsilon^2) & P_l &= \mathcal{O}(\varepsilon) & C_1 &= \mathcal{O}(1) \\ C_2 &= \mathcal{O}(\varepsilon) & C_3 &= \mathcal{O}(\varepsilon) & \lambda_1 &= \mathcal{O}(1) \\ \lambda_2 &= \mathcal{O}(\varepsilon) & \lambda_3 &= \mathcal{O}(\varepsilon) & v_1 &= \mathcal{O}(\varepsilon) \\ N_{lv} &= \mathcal{O}(\varepsilon^2) & \mathcal{R}_T &= \mathcal{O}(\varepsilon) \end{aligned}$$

MACROSCOPIC MODEL

The classical periodic homogenization [7-9] procedure consists to replace the orders of magnitude of the dimensionless numbers in the dimensionless equations (13 to 22). Then, the unknowns variables of the problem are searched in the form of an asymptotic development

depending on the perturbation parameter ε as following:

$$T_\alpha(x, y) = T_\alpha^{(0)}(x, y) + \varepsilon T_\alpha^{(1)}(x, y) + \varepsilon^2 T_\alpha^{(2)}(x, y) + \dots \quad (23)$$

Note that all the terms T_α^i in Equation (23) are y-periodic. The variables x and y are linked by $x = \varepsilon y$

The derivation operators grad and div are written:

$$grad = grad_y + \varepsilon grad_x = \frac{\partial}{\partial y} + \varepsilon \frac{\partial}{\partial x} \quad (24)$$

$$div = div_y + \varepsilon div_x \quad (25)$$

By equating to zero the factors of successive powers of ε , we obtain the coupled problems $\mathcal{P}_0, \mathcal{P}_1, \mathcal{P}_2 \dots$

The flow of the liquid is governed by the Darcy law at the macroscopic scale [10, 11]:

$$v_l = -\Lambda_{ll} \nabla(P - P_c) \quad (26)$$

Where Λ_{ll} represents the Darcy tensor defined by the expression:

$$\Lambda_{ll} = \frac{K_{rl} K_l}{\mu_l} \quad (27)$$

K_{rl} is the relative permeability of the liquid phase, K_l is the intrinsic permeability of the material and μ_l is the fluid viscosity.

The total pressure of the gas phase is considered constant, and the capillary pressure P_c is a characteristic of the porous medium, dependent on temperature, which allows us to write:

$$\nabla P_c = \left(\frac{\partial P_c}{\partial T} \right) \nabla T \quad (28)$$

The homogenized equation of heat transfer in porous media is given by:

$$(n_s C_s + n_l C_l) \frac{\partial T}{\partial t} - div_x (\lambda_s^{hom} + \lambda_l^{hom}) \nabla T + div_x \rho_l h_l \Lambda_{ll}^{hom} \left(\frac{\partial P_c}{\partial T} \right) \nabla T - h_{lv} m_g = 0 \quad (29)$$

Where h_l : is the specific enthalpy of liquid. $h_{lv} m_g$: is the macroscopic phase change rate and h_{lv} : is the specific enthalpy of vaporization. n_s and n_l are the volume fractions of the solid and liquid phases:

$$n_s = \frac{|\Omega_s|}{|\Omega|} \text{ and } n_l = \frac{|\Omega_l|}{|\Omega|}$$

Then we have:

$$C^{hom} \frac{\partial T^0}{\partial t} - div_x (a_t \nabla T) - h_{lv} m_g = 0 \quad (30)$$

Thus,

$$C^{hom} = (n_s C_s + n_l C_l) \quad (31)$$

$$a_t = \lambda^{hom} - h_l \rho_l \Lambda_{ll}^{hom} \left(\frac{\partial P_c}{\partial T} \right) \quad (32)$$

$$m_g = \frac{1}{|\Omega|} \int_{\Gamma_{lg}} \rho_g (v_g - \omega_{lg}) \mathbf{n}_{lg} d\Gamma \quad (33)$$

C^{hom} : is the macroscopic heat capacity, a_t : Corrected thermal conductivity, m_g : represents the mass evaporation rate. It is to notice that the term of phase change is a function of the velocity of the gas-liquid interface ω_{lg} . If this parameter decreases, the available interface liquid-gas for the phase change also decreases.

$$\Lambda_{ll}^{hom} = \frac{1}{|\Omega|} \int_{\Omega_l} \Lambda_{ll} \left(\frac{\partial \chi_l}{\partial y} + I \right) d\Omega \quad (34)$$

$$\lambda^{hom} = \frac{1}{|\Omega|} \int_{\Omega_s} \lambda_s \left(\frac{\partial \chi_s}{\partial y} + I \right) d\Omega + \frac{1}{|\Omega|} \int_{\Omega_l} \lambda_l \left(\frac{\partial \chi_l}{\partial y} + I \right) d\Omega \quad (35)$$

The homogenized thermal conductivity tensor is strongly dependent on the porous structure through local variables χ_s and χ_l , determined by solving the local boundary value problem in the porous medium.

Where: χ_s is periodic, of zero average on Ω_s ; and χ_l is periodic, of zero average on Ω_l . The solutions are obtained by solving on the period, the local boundary value problem is:

$$\begin{aligned} div_y \left(\lambda_s \left(\frac{\partial \chi_s}{\partial y} + I \right) \right) &= 0 & \text{in } \Omega_s \\ div_y \left(\lambda_l \left(\frac{\partial \chi_l}{\partial y} + I \right) \right) &= 0 & \text{in } \Omega_l \\ \lambda_s \left(\frac{\partial \chi_s}{\partial y} + I \right) \cdot \mathbf{n}_{gs} &= 0 & \text{on } \Gamma_{gs} \\ \lambda_l \left(\frac{\partial \chi_l}{\partial y} + I \right) \cdot \mathbf{n}_{gl} &= 0 & \text{on } \Gamma_{gl} \\ \lambda_l \left(\frac{\partial \chi_l}{\partial y} + I \right) \cdot \mathbf{n}_{ls} &= \lambda_s \left(\frac{\partial \chi_s}{\partial y} + I \right) \cdot \mathbf{n}_{ls} & \text{on } \Gamma_{ls} \\ \chi_l &= \chi_s & \text{on } \Gamma_{ls} \\ \langle \chi_s \rangle &= 0 \quad \langle \chi_l \rangle = 0 \end{aligned} \quad (36)$$

NUMERICAL APPLICATION

In this part, we concentrate on the main input parameter of the heat transfer model. Regarding the obtained model, the macroscopic thermal conductivity depends on the microstructure of the considered porous medium via the thermal conductivity (λ^{hom}) tensors calculated in the previous section. Here, we calculate this obtained by the periodic homogenization method.

Numerical solution for an elementary cell of three-dimensional geometry

Let us consider a porous medium whose microstructure consists in a periodic repetition of a three-dimensional unit cell. The studied consists of two spheres of radius $r_{c1} = 0.3805$ and $r_{c2} = 0.3899$ located in the center of the unit cell, and eighths of spheres of radius $r_s = 0.36$ located at the corners of the cell, and quarters of spheres of the same radius, located on each side of the cell (Figure 3).

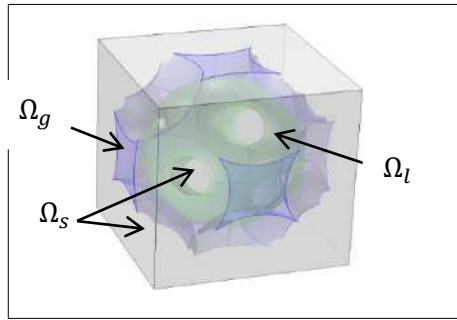


Figure 3: Elementary cell of periodic medium. The domain in green represents the liquid phase. This water layer adsorbed on the solid phase is of very small thickness ($e_l = 0.0094$), which lays to a water content of 1.5%, that corresponds to a constant relative humidity in the hygroscopic region..

By solving the local boundary value (84), the homogenized thermal conductivity tensors was calculated to determine the variables χ_s and χ_l . These local boundary value problems are solved by the finite element method by using COMSOL Multiphysics.

Resolution of the local boundary value problem on the period

Thermal conductivity tensor homogenized

The local boundary value problem to be solved in this case is:

$$\begin{aligned} \Delta_y \chi_{s_i} &= 0 \quad (i = 1,2,3) && \text{in } \Omega_s \\ \frac{\partial \chi_{s_i}}{\partial y} \cdot \mathbf{n} &= n_i && \text{on } \Gamma_{sg} \\ \frac{\partial \chi_{s_i}}{\partial y} \cdot \mathbf{n} &= \frac{\lambda_l}{\lambda_s} \left(\frac{\partial \chi_{l_i}}{\partial y} \right) n_i && (37) \\ & - \left(1 - \frac{\lambda_l}{\lambda_s} \right) n_i && \text{on } \Gamma_{ls} \end{aligned}$$

$$\begin{aligned} \chi_{s_i} &= \chi_{l_i} && \text{on } \Gamma_{ls} \\ & \langle \chi_{s_i} \rangle_{\Omega_s} = 0 && \\ \Delta_y \chi_{l_i} &= 0 \quad (i = 1,2,3) && \text{in } \Omega_l \\ \frac{\partial \chi_{l_i}}{\partial y} \cdot \mathbf{n} &= n_i && \text{on } \Gamma_{lg} \\ \frac{\partial \chi_{l_i}}{\partial y} \cdot \mathbf{n} &= \frac{\lambda_s}{\lambda_l} \left(\frac{\partial \chi_{s_i}}{\partial y} \right) n_i && (38) \\ & - \left(1 - \frac{\lambda_s}{\lambda_l} \right) n_i && \text{on } \Gamma_{ls} \end{aligned}$$

$$\chi_{l_i} = \chi_{s_i} \quad \text{on } \Gamma_{ls} \\ \langle \chi_{l_i} \rangle_{\Omega_l} = 0$$

Remind that on the solid-solid and liquid-liquid interfaces, the conditions of periodicity are applied for each component of χ_s and χ_l .

After the numerical resolution, the obtained homogenized thermal conductivity tensor is the following:

$$\lambda^{hom} = \lambda_s \begin{bmatrix} 0.76421 & 0 & 0 \\ 0 & 0.76421 & 0 \\ 0 & 0 & 0.76421 \end{bmatrix} + \lambda_l \begin{bmatrix} 0.01056 & 0 & 0 \\ 0 & 0.01056 & 0 \\ 0 & 0 & 0.01056 \end{bmatrix}$$

This unit cell considered is realistic in terms of geometric representation of the medium studied, and it also allows us to obtain a low porosity corresponding to these porous media. It is clear that the tensor homogenized of thermal conductivity is characterized by the same value in the three main directions, and this is due to the isotropy and symmetry of the considered material.

Sensitivity of the diffusion coefficient

Generally the water content affects all the hydrothermal transfer parameters [12]. These parameters include the thermal conductivity coefficient. It informs us directly on the kinetics of the transfer within the porous medium, it therefore has a major role in the prediction of thermal exchanges.

This sensitivity study allows showing the impact of varying the water content on the homogenized thermal conductivity tensor calculated in the previous section.

In this part, the homogenized thermal conductivity tensor is calculated numerically by varying the water content of 0% to 2.5%. With $\lambda_s = 2.1 \text{ W/m K}$ [12] and $\lambda_l = 0.6 \text{ W/m K}$. The results are illustrated in the following figures:

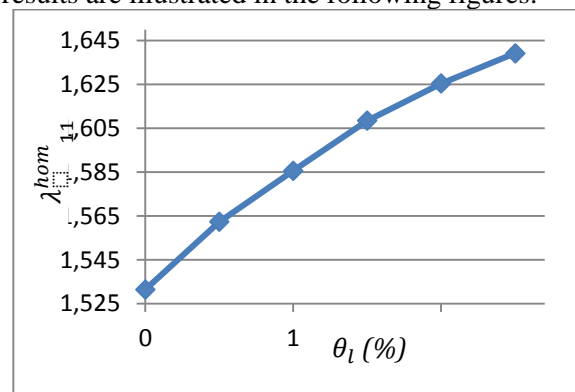


Figure 4: Variation of homogenized thermal conductivity depending on the water content θ_l

Figure 4 represents the evolution of homogenized thermal conductivity tensor deduced from numerical simulations based on the volume of water contained in the representative unit cell.

These figures show that the moisture has significant influence on the homogenized thermal conductivity tensor of the studied material: more the material is wet, the greater its isolation power is low. Indeed with increasing relative humidity, the water replaces the air, which reduces the thermal conductivity of the medium.

CONCLUSIONS

The implementation of the multiscale homogenization technique, allowed us to elaborate, from the equations written at the pore scale of the porous medium, a pertinent macroscopic model of heat transfers. The homogenization method used is based on dimensional analysis of the equations of conservation of energy at microscopically scale. The macroscopic parameters of the developed model are so defined. This method assumes that the microstructure of the porous medium consists of a periodic repetition of a certain elementary cell, called basic cell. A representative elementary cell of the porous medium was chosen in order to numerically determine the homogenized tensor of thermal conductivity. This latter depend on the geometrical properties of the cell. Finally, a sensitivity analysis has allowed us to highlight the influence of the water content of the material on the evolution of the homogenized thermal conductivity tensor. It proved that the homogenized thermal conductivity tensor is sensitive to variations of the water content of unit cell.

REFERENCES

1. Ferroukhi MY, Djedjig R, Belarbi R, Limam K, Abahri K, 2015, Effect of Coupled Heat, Air and Moisture Transfers Modeling in the Wall on the Hygrothermal Behavior of Buildings. *Energy Procedia* 78:2584–2589.
2. Bensoussan A, Lions J-L, Papanicolaou G, 1978, *Asymptotic analysis for periodic structures*. North-Holland Pub. Co.; sole distributors for the U.S.A. and Canada, Elsevier North-Holland, Amsterdam; New York: New York.
3. Darquennes A, Wang Y, Benboudjema F, Nahas G, 2015, Monitoring internal sulphate reactions by X-ray tomography. 15th Euroseminar on Microscopy Applied to Building Materials. Delft, the Netherlands.
4. Moyne C, Batsale J-C, Degiovanni A, 1988, Approche expérimentale et théorique de la conductivité thermique des milieux poreux humides—II. Théorie. *International Journal of Heat and Mass Transfer* 31:2319–2330.
5. Moyne C, Amaral Souto HP, 2014, Multi-scale approach for conduction heat transfer: one- and two equation models: Part 1: theory. *Computational and Applied Mathematics* 33:257–274.
6. Duval F, 2002, *modélisation du renouage d'un lit de particules: contribution à l'estimation des propriétés de transport macroscopiques*. INPT, Toulouse. France.
7. Auriault JL, Adler PM, 1995, Taylor dispersion in porous media: Analysis by multiple scale expansions. *Advances in Water Resources* 18:217–226.
8. Mchirgui W, Millet O, Amiri O, 2013, Modelling moisture transport for a predominant water vapour diffusion in a partially saturated porous media. *European Journal of Environmental and Civil Engineering* 17:202–218.
9. Bourbatache K, Millet O, Aït-Mokhtar A, Amiri O, 2012, Modeling the Chlorides Transport in Cementitious Materials By Periodic Homogenization. *Transport in Porous Media* 94:437–459.
10. Mchirgui W, 2012, *Modélisation des transferts hydriques dans les milieux poreux partiellement saturés par homogénéisation périodique: Application aux matériaux cimentaires*. La Rochelle. France.
11. Abahri K, 2012, *Modélisation des transferts couplés de chaleur, d'air et d'humidité dans les matériaux poreux de construction*. La Rochelle. France.
12. Trabelsi A, 2010, *Etudes numérique et expérimentale des transferts hygrothermiques dans les matériaux poreux de construction*. La Rochelle. France.

SYNTHESIS AND CHARACTERISTICS OF COMPOSITE PHASE CHANGE HUMIDITY CONTROL MATERIALS

Menghao Qin*, Zhi Chen
Center for Sustainable Building Research
School of Architecture and Urban Planning, Nanjing University
Nanjing 210093, China
*Corresponding author: Prof. Menghao Qin E-mail: mqin@nju.edu.cn

ABSTRACT

A new kind of phase change humidity control material (PCHCM) was prepared by using phase change material (PCM) microcapsules and different hygroscopic porous materials. The PCHCM composite can regulate the indoor hygrothermal environment by absorbing or releasing both heat and moisture. The PCM microcapsules were synthesized with methyl triethoxysilane by the sol–gel method. The vesuvianite, sepiolite and zeolite were used as hygroscopic materials. The scanning electron microscopy (SEM) was used to measure the morphology profiles of the microcapsules and PCHCM. The differential scanning calorimetry (DSC) and the thermal gravimetric analysis (TGA) were used to determine the thermal properties and thermal stability. Both the moisture transfer coefficient and moisture buffer value (MBV) of different PCHCMs were measured by the improved cup method. The DSC results showed that the SiO₂ shell can reduce the super-cooling degree of PCM. The super-cooling degrees of microcapsules and PCHCM are lower than that of the pure PCM. The onset temperature of thermal degradation of the microcapsules and PCHCMs is higher than that of pure PCM. Both the moisture transfer coefficient and MBV of PCHCMs are higher than that of the pure hygroscopic materials. The results indicated the PCHCMs have better thermal properties and moisture buffer ability.

INTRODUCTION

Climate change is happening; and it is mainly caused by the increase of greenhouse gas emissions. Since most of this emission increase is a result of burning fossil fuels for energy, it's critical to improve the energy efficiency to tackle the climate change. Many technologies are utilized to reduce fossil energy consumption. For example, the development of green energy, improving energy efficiency and the use of innovative passive materials are feasible methods [1-3]. The energy consumption of the heating, ventilation and air conditioning (HVAC) system accounts for 1/3 of building energy consumption. So it's essential to improve the building energy efficiency and reduce the energy consumption of HVAC systems. Using new type of building materials to passively control the indoor temperature and humidity to at a relatively stable and comfortable level is a possible way of energy saving [4, 5].

Building materials with large specific heat capacity can reduce indoor temperature fluctuations. Phase change materials (PCM) can absorb or release large amount of thermal heat, and the temperature of the materials maintain constant in phase change process.

So phase change materials can be used to regulate indoor temperature and cut down the energy consumption [5].

The moisture transfer process may cause moisture damage to construction materials. And indoor relative humidity affects the comfort and health of human body. For example, low relative humidity (RH < 30%) is related to mucous membrane, dryness of skin and throats, sensory irritation of eyes, and high relative humidity (RH > 70%) may cause rheumatic, rheumatoid arthritis, respiratory discomfort and allergies by promoting mold growth [6-9]. Previous studies [10] show people feel most comfortable when the indoor relative humidity is ranging from 50% to 60% [10]. In order to maintain a stable and comfortable indoor relative humidity, HVAC system is used to dehumidify/humidify the supply air in most building applications, which consumes a lot of energy to remove the latent heat of the moisture. Hygroscopic humidity control materials can absorb and release large account of moisture from indoor air, which means that these

materials may be used to control the relative humidity.

The main purpose of the study is to develop a new kind of passive phase change humidity control material (PCHCM), which can moderate both the indoor temperature and moisture. Several PCHCMs were prepared in the paper. The thermal properties, moisture transfer coefficient and moisture buffer value of different PCHCMs were tested, analyzed and compared.

EXPERIMENTAL

40g PCM and 5g sodium dodecyl sulfate (SDS) were added into 150ml distilled water in a beaker. The temperature of the solution was kept at 35 °C to melt the PCM, and then the solution was stirred at a rate of 600 rpm for 0.5 h with a magnetic stirrer. And then the temperature of the solution was maintained at 23 °C, and the solution was stirred for 0.5h. 40g Methyl triethoxysilane (MTES), 40g ethanol and 75ml distilled water were mixed in a beaker to form the solution. The pH of the solution was adjusted to 2–3 by adding hydrochloric acid. Then the temperature of the solution was maintained at 50 °C, and the solution was stirred at a rate of 500 rpm for 20 min by a magnetic stirrer. After the hydrolysis reaction of the MTES, the sol solution as the microencapsulation precursor was obtained.

The temperature of the prepared PCM Oil/Water emulsion was controlled at 35°C and stirred at a rate of 400 rpm. And then the PH degree of the prepared PCM Oil/Water emulsion was adjusted to 9-10 by adding ammonia solution. Then, the sol solution was dropped into the PCM Oil/Water emulsion. The mixture was kept reacting and being stirred for 2 h. The SiO₂ was formed by condensation reactions between the methyl silicate and methyl silicate. After the polymerization process of the sol mixture, the SiO₂ shell was formed on the surface of the PCM droplet. Then, the microcapsules were collected by filter paper and washed with distilled water. Then the microcapsules were dried in a low temperature vacuum oven at 0 °C for 24 h. The microencapsulated PCM with SiO₂ shell were gained, and then named as CPCM. The vesuvianite, sepiolite and zeolite are typical hygroscopic porous materials, which are often used as humidity control materials for indoor environment. We chose these three materials as the base material for the preparation of PCHCM. Firstly, the vesuvianite, sepiolite and zeolite were dried in a vacuum oven for

10 h at 100 °C. Then the CPCM was added into the vesuvianite, sepiolite and zeolite with the mass ratio of 1:4, respectively. The CPCM can influence the mechanical properties of the hygroscopic materials, which may make the bricks too loose to be formed. In this experiment, in order to obtain bricks, the mass ratio of the CPCM and hygroscopic materials was tested repeatedly. The mixtures and water with mass ratio 1:2 were stirred at a rate of 200 rpm at the room temperature for 5 min, and were formed as bricks. Then the bricks were dried in a low temperature vacuum oven at 0 °C for 48 h. The CPCM/vesuvianite, CPCM/sepiolite and CPCM/zeolite composites were acquired, and then were named as VCPCM, SCPCM and ZCPCM, respectively. The hygroscopic materials and water with mass ratio 1:2 were stirred at a rate of 200 rpm at the room temperature for 5 min, and were formed as bricks. The bricks formed by pure vesuvianite, sepiolite and zeolite will be as the control samples for the PCHCMs.

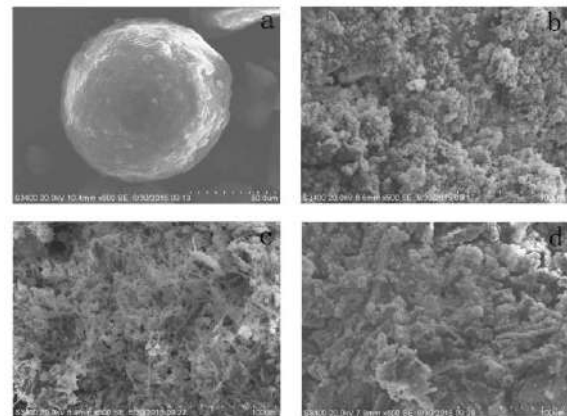


Figure 1
SEM photographs of the (a) CPCM, (b) VCPCM, (c) SCPCM, (d) ZCPCM

CHARACTERIZATIONS OF THE CPCM AND PCHCMs

The microstructure and morphology of the CPCM and PCHCMs are shown in Figure 1. As seen in Figure 1a, the microcapsules have a compact SiO₂ shell to encapsulate the PCM, and the SiO₂ shell can keep the PCM from leaking when the PCM is melted. The microcapsules have a spherical shape, and the size of the microcapsules is about 100µm. The SEM profiles of VCPCM, SCPCM and ZCPCM are shown in Figure 1b-d. It can be seen that the CPCM was dispersed in the hygroscopic materials.

Figure 2 and Figure 3 showed the DSC results of the PCM, CPCM, VCPCM, SCPCM and ZCPCM. The PCM melting process is shown in Figure 2, and the PCM solidifying process is shown in Figure 3. As can be seen in, the melting temperature and solidifying temperatures of the PCM are investigated to be 28.3°C and 24.8°C, the melting latent heat and solidifying latent heat are measured to be 146.2kJ/kg and 148.7kJ/kg, and the super-cooling degree is 3.5°C. The melting temperature of the CPCM, VCPCM, SCPCM and ZCPCM are measured to be 27.2°C, 26.9°C, 26.8°C and 27.1°C. The solidifying temperatures of the CPCM, VCPCM, SCPCM and ZCPCM are measured to be 25.0°C, 25.2°C, 25.2°C and 25.1°C respectively. The super-cooling degrees of the CPCM, VCPCM, SCPCM and ZCPCM are 2.2°C, 1.7°C, 1.6°C and 2.0°C, respectively. It can be seen that the super-cooling degrees of CPCM, VCPCM, SCPCM and ZCPCM are lower than that of the PCM. The reason is that the SiO₂ shell of the microcapsules acts as nucleation agent, which can improve the phase change process. The lower super-cooling degree is conducive to the stability of the temperature.

The melting latent heat of the CPCM, VCPCM, SCPCM and ZCPCM are 77.4kJ/kg, 14.1kJ/kg, 15.4kJ/kg and 12.9kJ/kg respectively. The solidifying latent heat of the CPCM, VCPCM, SCPCM and ZCPCM are 79.5kJ/kg, 14.4kJ/kg, 15.9kJ/kg and 13.2kJ/kg respectively. The hygroscopic materials have no phase change process, so the latent heat of the composites is lower than that of PCM.

Figure 4 showed the TGA results of the PCM, CPCM, VCPCM, SCPCM and ZCPCM. When the temperature is up to 130 °C, the thermal degradation process of the PCM occurs, and the residual weight of the PCM at 230 °C is close to zero. When the temperature is up to 175 °C, the thermal degradation process of the CPCM and PCHCMs occurs. Hence the SiO₂ shell is advantageous to form a physical protective barrier on the surface of the PCM. The protective barrier can hinder the transfer of flammable molecules to the gas phase, which means that the SiO₂ shell can protect the PCM, improve the stability of the composites and acts as a flame retardant to improve the kindling point.

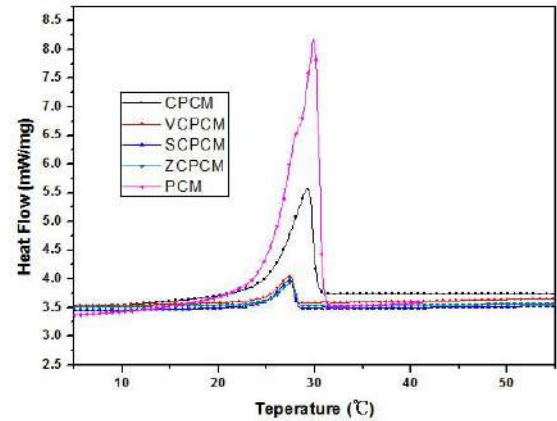


Figure 2
Melting DSC curve of PCM, CPCM, VCPCM, SCPCM and ZCPCM

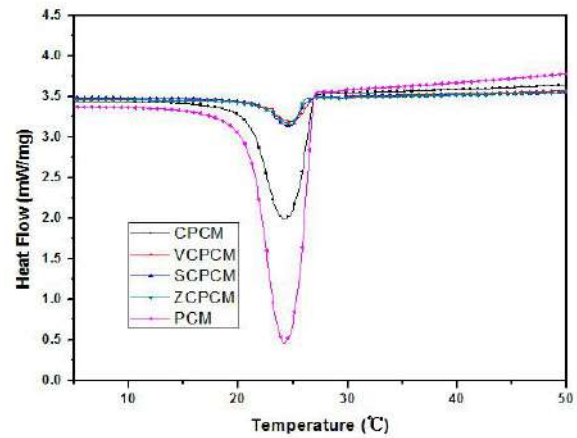


Figure 3
Solidifying DSC curve of PCM, CPCM, VCPCM, SCPCM and ZCPCM

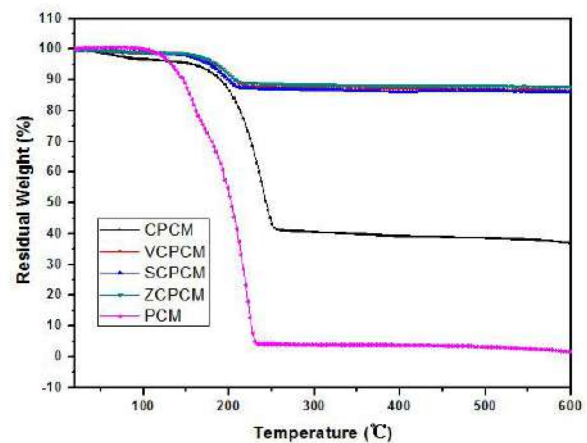


Figure 4
TGA curve of PCM, CPCM, VCPCM, SCPCM and ZCPCM

The moisture transfer coefficient was measured with classic cup method. The samples with areas of $4 \times 4 \text{ cm}^2$ were fixed in the outlet of containers, which filled with saturated NaCl solution. The saturated NaCl solution kept the RH of the air in container as 75%. And the RH outside is maintained at 54%. The difference between the RH made the water vapor transfer from one side to the other side of the sample.

The moisture transfer coefficients of vesuvianite, sepiolite, zeolite, VCPCM, SCPCM and ZCPCM are shown in Table 1. As seen in Table 1, the moisture transfer coefficients of the PCHCMs are all higher than those of the pure hygroscopic materials. The moisture transfer coefficient of VCPCM is 1.47 times higher than that of vesuvianite, the moisture transfer coefficient of SCPCM is 1.68 times higher than that of sepiolite, and that of ZCPCM is 1.83 times higher than that of zeolite. And the moisture transfer coefficients of the PCHCMs are all higher than the gypsum. The result indicates that the CPCM can improve the moisture transfer in hygroscopic materials.

Table 1

Moisture transfer coefficient of vesuvianite, sepiolite, zeolite, VCPCM, SCPCM and ZCPCM

Samples	Moisture transfer coefficient ($10^{-8} \text{ kg/m} \cdot \text{s} \cdot \text{RH}$)
Vesuvianite	8.25
Sepiolite	5.42
Zeolite	4.11
VCPCM	12.12
SCPCM	9.11
ZCPCM	7.54
Gypsum	2.4

The moisture buffer value (MBV) is defined as a characteristic of a material based on a period of moisture uptake/release [11, 12]. The practical MBV presents the amount of water vapor that is transport in or out a material per open surface during a certain period of time, when it is subjected to relative humidity variations of surrounding air. The practical moisture buffer value can be measured with an experimental set up. The samples are exposed to cyclic variations in high RH and low RH for 8h and 16h. the high RH is controlled at 75% with saturated NaCl solution, and the low RH is controlled at 33% with saturated KCl solution. The moisture uptake/release

process was alternative operated for at least 7 days, which ensure the process was stable. And the mass of the samples were measured with analytical balance.

Figure 5 and Table 2 show the MBV of the samples. It can be seen that the MBV of the PCHCMs are all higher than those of the pure hygroscopic materials. The MBV of VCPCM is 1.45 times higher than that of vesuvianite, the MBV of SCPCM is 1.44 times higher than that of sepiolite, and the MBV of ZCPCM is 1.46 times higher than that of zeolite. And the MBVs of the PCHCMs are all higher than the gypsum. The results show that adding CPCM can improve the moisture buffer ability of hygroscopic materials.

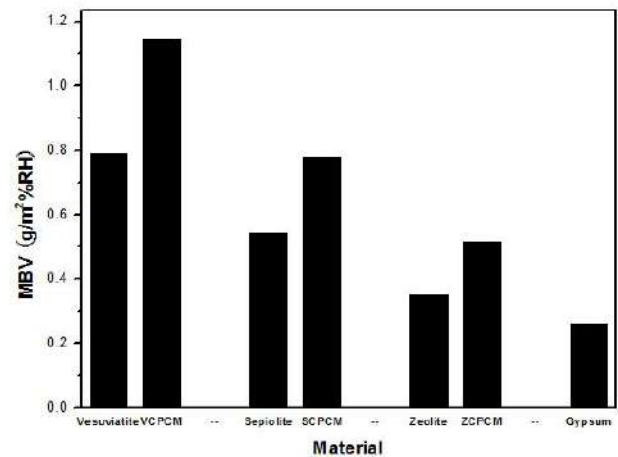


Figure 5

MBV of the vesuvianite, sepiolite, zeolite, VCPCM, SCPCM and ZCPCM

Table 2

MBV of vesuvianite, sepiolite, zeolite, VCPCM, SCPCM and ZCPCM

Samples	MBV ($\text{g/m}^2 \cdot \text{RH}$)
Vesuvianite	0.788
Sepiolite	0.542
Zeolite	0.351
VCPCM	1.145
SCPCM	0.78
ZCPCM	0.514
Gypsum	0.26

Rode [12] used five different categories to classify the MBV. The good class ranges from $1 \text{ g/m}^2 \cdot \text{RH}$ to $2 \text{ g/m}^2 \cdot \text{RH}$, the moderate class ranges from $0.5 \text{ g/m}^2 \cdot \text{RH}$ to $1 \text{ g/m}^2 \cdot \text{RH}$, and the limited class

ranges from 0.2 g/m²%RH to 0.5 g/m²%RH. It can be seen that the MBV of VCPCM is within good class and higher than that of the other two PCHCMs. The MBV of SCPCM and ZCPCM are within moderate class.

CONCLUSIONS

A new kind of phase change humidity control material was synthesized by using microencapsulated PCM and different hygroscopic porous materials. The results showed that the SiO₂ shell can reduce the super-cooling degree of PCM. The super-cooling degrees of CPCM, VCPCM, SCPCM and ZCPCM are lower than that of the pure PCM, which is advantageous to make temperature stable. The onset temperature of thermal degradation about the CPCM is higher than that of PCM, which can improve the stability of the composites and acts as a flame retardant to improve the kindling point. The CPCM also can improve the moisture transfer performance and moisture buffer ability of hygroscopic materials. The moisture transfer coefficients of PCHCMs are all higher than that of the pure hygroscopic materials, ranging from 1.47 times for CPCM/vesuvianite composite to 1.83 times for CPCM/zeolite composite. The moisture buffer values of PCHCMs are averagely 1.45 times higher than that of pure hygroscopic materials. The results also indicate that the CPCM/vesuvianite composite has a better hypothermal performance than other two PCHCMs. It has the potential to be a good energy saving material.

ACKNOWLEDGMENTS

This work was supported by the National Natural Science Foundation of China (Grant No. 51108229 and 51578278), and Research Fund for the Doctoral Program of Higher Education of China (Grant No. 20130091110053).

REFERENCES

1. Marchand, R. D, Kohn, S. C. L, and Morris, J. C, 2015, Delivering energy efficiency and carbon reduction schemes in England: Lessons from Green Deal Pioneer Places. *Energy Policy*, 84, pp. 96–106.
2. Moriarty P, and Honnery, D, 2012, What is the global potential for renewable energy? *Renew Sust Energy Rev*, 16, PP. 244-252.
3. Resch, G, Held, A, Faber, T, Panzer, C, Toro, F, and Haas, R, 2008, Potentials and prospects for renewable energies at global scale. *Energy Policy*, 36, pp. 4048-4056.
4. Lelievre, D, Colinart, T, and Glouannec, P, 2014, Hygrothermal behavior of bio-based building materials including hysteresis effects: experimental and numerical analyses. *Energy Build*, 84, pp. 617-627.
5. Saadi, S. N. A, and Zha, Z, 2013, Modeling phase change materials embedded in building enclosure: a review. *Renew Sust Energy Rev*, 21, pp. 659–673.
6. Toftum, J, Jorgensen, A. S, and Fanger, P. O, 1998, Upper limits of air humidity for preventing warm respiratory discomfort. *Energy Build*, 28, pp. 15-23.
7. Reinikainen, L. M, and Jaakkola, J. J. K, 2003, Significance of humidity and temperature on skin and upper airway symptoms. *Indoor Air*, 4, pp. 344-352.
8. Bornehag, C. G, Blomquist, G, Gyntelberg, F, Jarvholm, B, Malmberg, P, and Nordvall, L, 2001, Dampness in buildings and health, Nordic interdisciplinary review of the scientific evidence on associations between exposure to ‘Dampness’ in buildings and health effects (NORDDAMP). *Indoor Air*, 2, pp. 7-86.
9. Bornehag, C. G, Sundell, J, Bonini, S, Custovic, A, Malmberg, P, and Skerfving, S, 2004, Dampness in buildings as a risk factor for health effects, EUROEXPO: a multidisciplinary review of the literature (1998-2000) on dampness and mite exposure in buildings and health effects. *Indoor Air*, 4, pp. 243–257.
10. King, S, 1997, house dust mites and indoor climate. *Arch Sci Rev*, 40, pp. 43–47.
11. Rode, C, and Peuhkuri, R, 2006, The concept of moisture buffer value of building materials and its application in building design, In: *Proceedings of healthy buildings*, Lisbon, Portugal.
12. Rode, C, Peuhkuri, R, Time, B, Svenberg, K, and Ojanen, T, 2007, Moisture buffer value of buildings. *J. ASTM Inter*, 4, pp. 1-12.

INFRARED THERMOGRAPHY AND FINITE ELEMENT METHOD APPLIED TO THE DETECTION OF A PLASTER DETACHMENT

Mohamed EL AFI^{a*}, Sougrati BELATTAR^a, Rachid BOUFERRA^b

a) Faculty of Sciences Semlalia, Department of Physics, Marrakech

b) Faculty of Science and Technology of Marrakech, Department of Civil Engineering

*Corresponding author: Email: med.elafi@gmail.com

ABSTRACT

The inspection of inhomogeneity, delamination and all others anomalies of building is of main importance for the safety and the durability of concrete structure. Infrared thermography is one of the suitable techniques of non-destructive evaluation for the detection of defect in concrete structure in general and particularly in the habitat system. It allows a quick non-destructive testing of a given structure by studying the obtained thermal images. The main objective of these investigations is the analysis of a plaster slab containing two types of delamination: air blades and water blades. The study concerns the effect of the geometry and the size of this delamination on the surface temperature. The simulations results, using the finite element method, are presented and analyzed in form of thermographical images by interpreting different contrast in these images and the temperature spatial distribution changes.

KEYWORDS

Infrared thermography, Numerical simulation, Non-destructive testing, temperature, air blade, water blade, Concrete.

NOMENCLATURE

λ : Thermal conductivity

ρ : Density of the material

C: Heat capacity at constant pressure

t: Time

T: Temperature field

λ : Thermal conductivity

A: Square matrix of dimension [N_h , N_h]

F: Vector of N_h components

T: Vector to calculate temperatures

a: Thermal diffusivity

INTRODUCTION

The search of hidden empty of air or water in a concrete structure in general and in a wall particularly remains a main requirement in the safety and durability of these structures. The weakening of structure caused by the presence of internal detachment of layers is a very serious problem which implies many risks and damages even the breaking of the considered structure. Infrared thermography as one of the effective NDT techniques has proven to be an efficient tool in

detecting of hidden detachments. The reliability of the infrared thermography method for defect detection makes it as a widely used one for non-destructive evaluation of materials, especially in civil engineering and reinforced concrete for the identification of heat losses in building envelopes or the control of the integrity of concrete structures.

In this paper, the thermal behaviour of a detachment between a layer concrete and plaster is discussed. The presence of these defects is detected due to a temperature spatial distribution and thermographical images on the structure surface in question. The modelling of different configurations is achieved by using a numerical simulation model based on finite elements modelling (FEM). The model of a parallelepiped concrete structure of concrete and plaster containing cracks in forms of a parallelepiped and a spherical form is adopted. This structure is supposed to be excited on the higher face by a heat flux, the lower face being maintained at a constant temperature and the others faces are supposed thermally insulated. The thickness and the

position of the crack-layer and the diameter and position of the defect are studied.

DESCRIPTION OF THE MODEL

Geometrical characteristics

To illustrate the application of the TNDT method, the results of the nondestructive testing of a concrete slab of thickness $e = 150$ mm, $L = 1000$ mm, and the width $L = 1000$ mm, where a layer of plaster adhered $e = 25$ mm, length $L = 1000$ mm, and the width $L = 1000$ mm (fig.1), the slab containing 16 equidistant defects in crack are presented. Defects are parallelepiped and spherical shape.

Lines $A_1A_2, A_3A_4, A_5A_6, A_7A_8, B_1B_2, B_3B_4, B_5B_6, B_6B_7$, respectively pass by the point of co ordinates $\{(160,160,1) (760,160,1)\}, \{(160,370,3) (790,370,3)\}, \{(160,580,15) (790,580,15)\}, \{(160,790,25) (790,790,15)\}, \{(160,160,1) (160,790,1)\}, \{(370,160,3) (370,790,3)\}, \{(580,160,5) (580,790,5)\}, \{(790,160,10) (790,790,10)\}$.

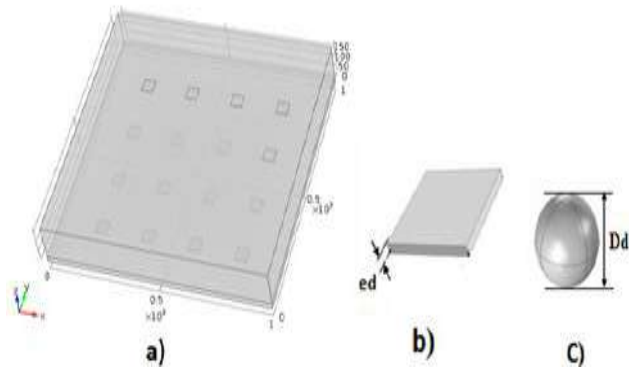


Figure1: a) 3D geometry of the slab, b) Structure of parallelepiped detachment, c) Structure of spherical detachment

Effect of the volume at constant position

To analyze the effect of the volume parameter, defects were placed at the same position p by report to the input face of plaster according to $(-oy)$ axis and of different volumes $l_d \times l_d \times e_{di}$ (l_d : the defect side and e_{di} : the variable thickness) for the parallelepiped form figure 2(b), and $kDdi^3$ (Ddi : variable diameter) for the spherical form figure3 (b).

Effect of the position at constant volume

In the same way, to analyze the effect of the position parameter, defects of the same volume were placed at different positions p_i (p_i : the variable position) by report to the input face of plaster according to $(-ox)$ axis for parallelepiped form figure 2(a), and spherical form, figure 2(d).

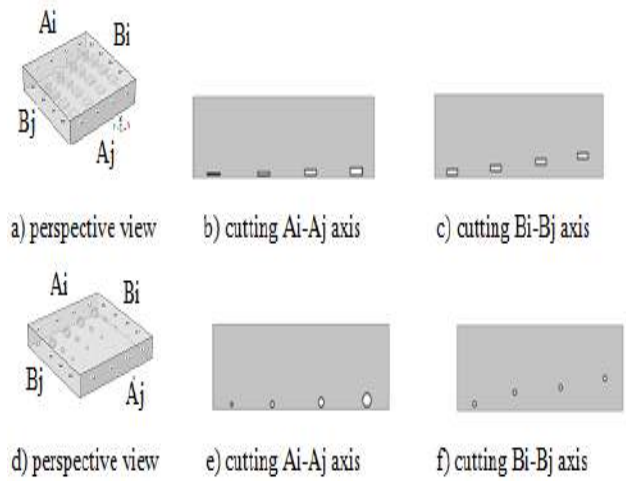


Figure 2. Defects of parallelepiped and spherical form

MATHEMATICAL MODEL

Let us consider the following thermal equation:

$$\rho C_p \frac{dT}{dt} - \text{div}(\bar{\lambda} \cdot \text{grad}T) - q = 0 \quad (1)$$

Where:

ρ : The material density

c_p : The Specific heat capacity

$\bar{\lambda}$: The thermal tensor conductivity

q : Voluminal source of heat

With the following boundary conditions:

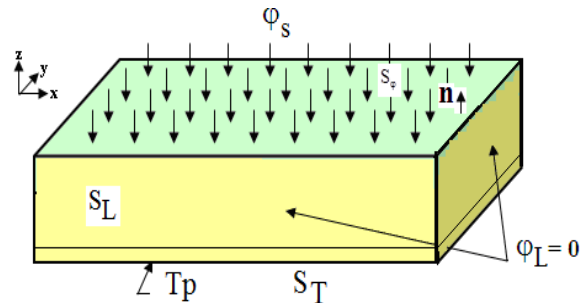


Figure 3: boundary conditions

Where:

S_L : Side surface

$\phi_L = 0$: side flow

T_p : The imposed temperature on a surface S_T

ϕ_s : The imposed flow on the input surface S_ϕ

\vec{n} : The unit vector perpendicular to S and directed towards outside

And the initial condition:

$$T(x, y, z, t_0) = T_0(x, y, z) \quad (3)$$

Numerical modeling conditions

The calculation of the thermal response is made for a concrete wall where we exposed the front surface to a constant heat flux, continuously extended of density $Q = 50 \text{ W/m}^2$. The rear face of the wall being held at a constant temperature $T_a = 19^\circ\text{C}$ which also the initial temperature of the system and for the other faces are thermally isolated ($Q = 0$).

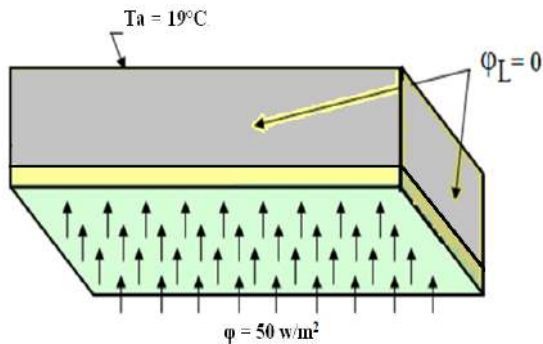


Figure 4: Numerical conditions

Thermophysical characteristics

The table 1 shows the thermophysical parameters of materials.

Table 1. Thermophysical parameters

Material	λ [W/ (m*K)]	ρ [kg/m ³]	C [J/ (kg*K)]
Air	0.0272	1.1845	100
Water	0.589	999.045	4180
Plaster	0.35	950	1000
Concrete	1.8	2300	385

SIMULATION RESULTS

Effects of the defect thickness and position

In this section, we are inserted defects of parallelepiped form and of spherical form figure 5 (a) in a concrete slab, these defects having successively (along the y axis increasing) the thickness $e_d = 1 \text{ mm}$, 3mm, 5mm and 10mm for the parallelepiped and the diameter $D_d = 16.84 \text{ mm}$, 24.28mm, 28.80 mm and 36.28 mm for the spherical forms. Each of these thickness and these diameters were placed at for different positions: $p = 1 \text{ mm}$, 3 mm, 15 mm and 25 mm from the input face.

Figure 5 (b) shows the thermographical image of concrete slab subjected to a step of heat flow in steady mode. The related images to parallelepiped or

spherical forms clearly show the colors contrast representing different levels the sample surface temperature. The contrast amplitude depends on the volume and the location of the defect in the structure. Through these thermal images one can note that the defect effect is much larger when it is close to the input surface or of a larger volume. On the thermal images, thermal spots reproduce the shape of the internal defect. The form of the task is related to the form of the internal defect.

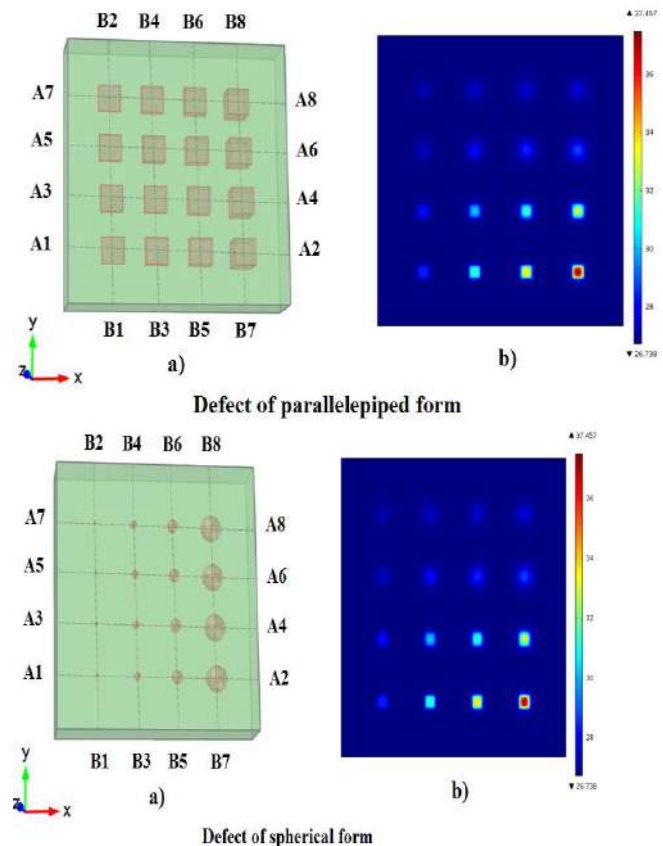


Figure 5: distribution of cracks in concrete slab (a) and thermographical images (b)

Thickness or diameter effect for a constant position

The figure 6 represents the surface temperature spatial evolution of the input concrete slab. At a constant position, the defect effect depends on the thickness or diameter of the defect for each position respectively of the crack or the air pocket.

Analysis according to A2 - A1 axis, where the defect position is constant and the volume is variable.

We can note from the images of figures (5b) that according to each axis among A₁-A₂, A₃-A₄, A₅-A₆ or A₈-A₇ axis, defects are in the same position by report to the sample input surface and that the defect who has the largest volume, it is the one who creates

the greatest temperature disturbance on the sample surface. More the defect volume increases more the peak amplitude of the sample surface spatial temperature increases and therefore it is the greatest stain on the thermographical image. This means that, at constant position, when the volume of the crack is large, the easier it is to detect, and vice versa. This phenomenon is observed for both types of defects. On the thermographical image, the size of the stain created by the defect is related to the effective defect surface seen from the input surface of the structure (projection of the defect on the input surface). The results show that for a spherical defect which has an area surface equivalent to a circular area of radius $D_d / 2$. So the corresponding stain is small compared to that of a square surface as in the parallelepiped form which makes this relatively simple to detect for small dimensions of defect.

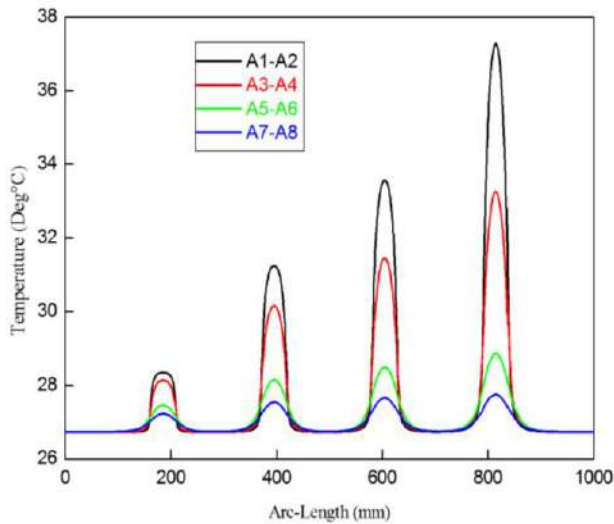


fig.6(a)

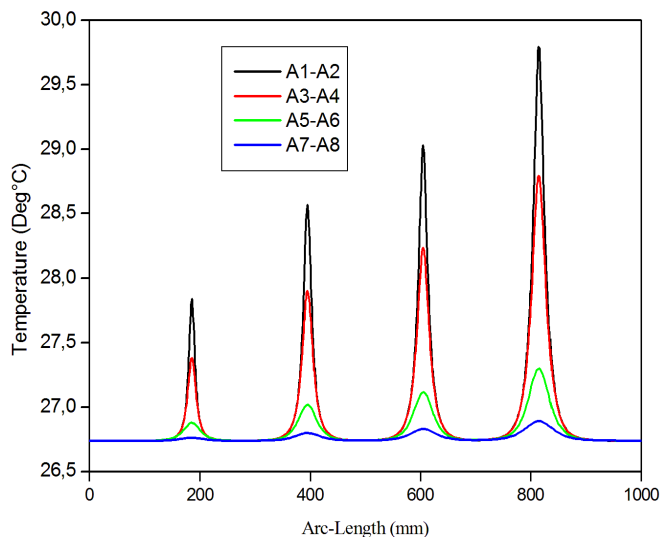


Fig.6(b)

Figure6. Effect of the crack thickness (volume), for the parallelepiped form (a) and the effect of diameter of spherical form (b), on the surface temperature profile for four defect positions, $p= 1$ mm; 5mm; 15 mm and 25 mm.

Position effect for a constant Thickness or diameter

Analysis according to B2-B1 axis, where the defect volume is constant and the defect position is variable.

The analysis of curves along the axis B2-B1, B4-B3, B6-B5 or B8-B7 illustrates the importance of the defect position in the concrete structure. In fact, ranging from the farthest defect position by report to the input surface of the sample (from B2 to B1, taking the volume as constant) to the closest one, the peak value of the temperature increases and vice versa. The same phenomenon is observed on the axis B4 - B2 ... etc.. These results show that, for a given volume, the value of the peak temperature is related to the position of the defect in the structure. Again we can conclude that, at constant volume, when the crack is the more close to the sample input surface the more easier it is to detect and vice versa.

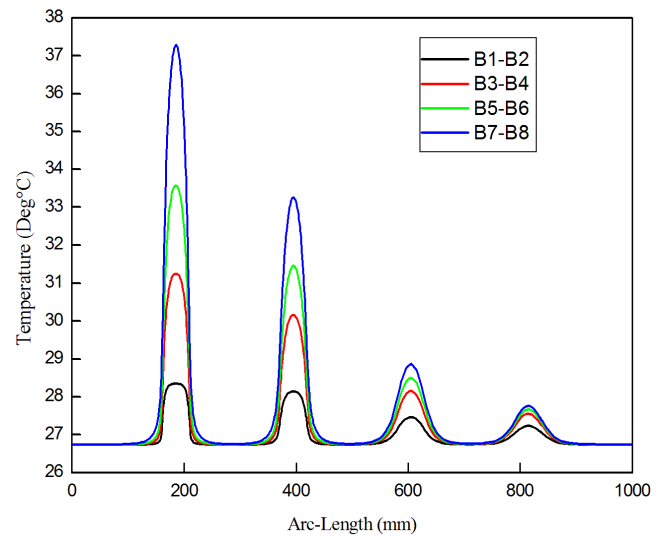


Fig.7(a)

Figure7 (a). Effect of the crack position on the surface temperature profile for four different value of crack thickness $ed= 1$ mm; 3 mm; 5 mm and 10 mm

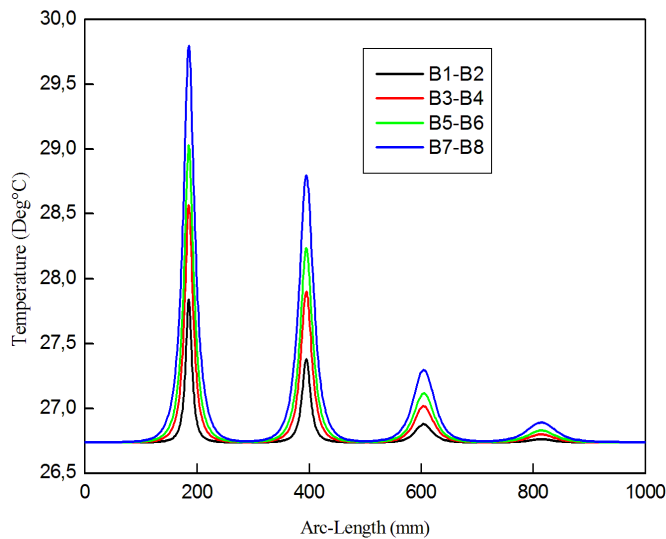


Fig.7(b)

Figure 7 (b). Effect of the crack position on the surface temperature profile for four different value of diameters $D_d = 16.84\text{ mm}$, 24.28 mm , 28.80 mm and 36.28 mm .

Effect of the thermophysical nature of defect

In this section we sought to know what will be the behavior of the system when the thermophysical characteristics of defect changes. To see what about the detectability of these defects in air compared to others known like water we performed simulations presented in Figure (8) and (9). In these simulations, the same geometry of system is taken for the case of the water.

Figure 8. Effect according to Ai-Aj Axis of the crack thickness(a) for parallelepiped form and of the defect diameter (b) for spherical form, on the surface temperature profile of the plate, for water copper and steel and for four positions $p = 1\text{ mm}$, 3 mm , 5 mm and 10 mm .

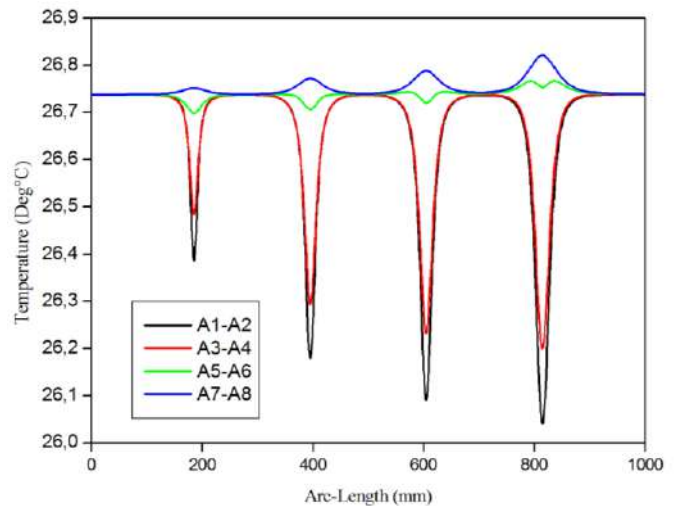
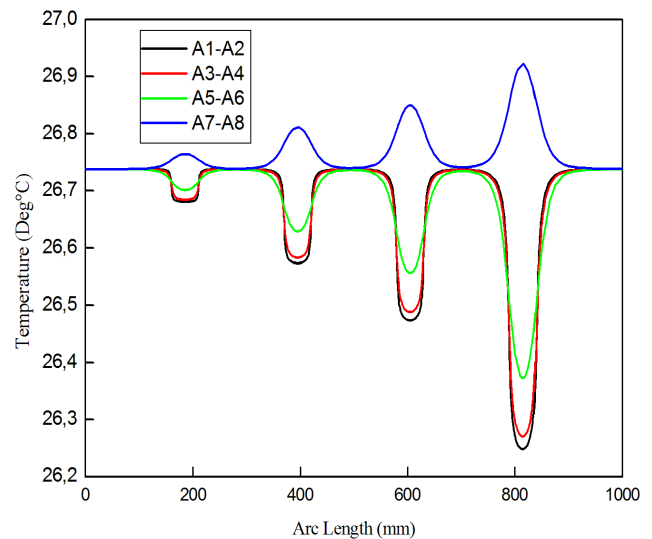


Figure 8. Effect according to Ai-Aj Axis of the crack thickness(a) for parallelepiped form and of the defect diameter (b) for spherical form, on the surface temperature profile of the plate, for water copper and steel and for four positions $p = 1\text{ mm}$, 3 mm , 5 mm and 10 mm .

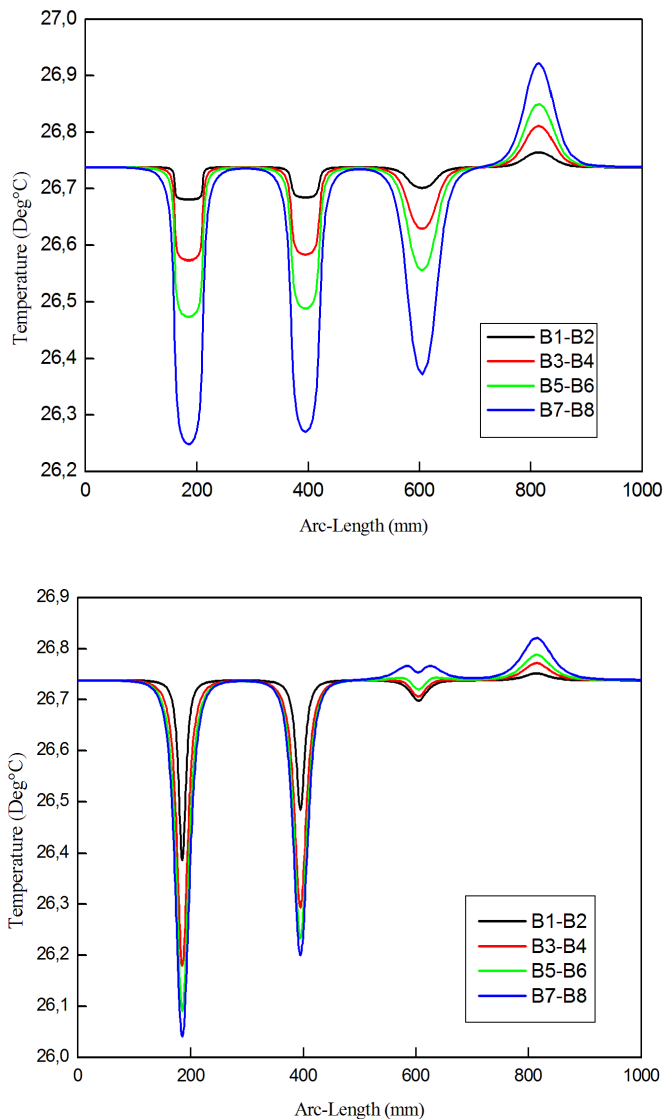


Figure 9 :

Figure 9. Effect according to Bi-Bj Axis of the position of the crack **a**): parallelepiped form and **b**): spherical form, on the surface temperature profile of the plate, for three materials: aluminum, copper and steel and for four thickness for **a**): parallelepiped form, $e_d = 1$ mm, 3 mm, 5 mm and 10 mm and the diameter **b**): spherical form $D_d = 16.84$ mm, 24.28 mm, 28.80 mm and 36.28 mm.

The same phenomena of the previous section are observed on the curves of Figure 9 when it comes to analyzing the evolution according the Bi-Bj axis.

5. Conclusion

We studied the effect of the size and position of the defects, such as cracks on the thermographical images of the input surface of a concrete slab, and it was concluded that the more the defect dimensions increase the more the defect becomes easier to detect,

and equally the more the defect is closer to the input surface the more it is easier to detect and vice versa. The comparison between the parallelepiped and the spherical form shows that there is a little temperature difference between the two forms on the plate surface and that even at the same volume for the two forms, is the defect which has the largest surface area close to the plate input surface that has the greatest effect. Results show that it is relatively easier to detect defects like cracks in the less conductive material than in more conductive one.

Références

- [1] A. Elballouti, S. Belattar, A. Obbadi, S. Sahnoun " Numerical method applied to the non-destructive characterization of the cracks in the roadways" 12th A-PCNDT 2006 – Asia-Pacific Conference on NDT, 5th– 10th Nov 2006, Auckland, New Zealand.
- [2] A; Elballouti, S. Belattar : " Numerical method applied to the non-destructive characterization of the cracks in throadways" Physical & Chemical News 35 (May 2007) 43-47.
- [3] J.Rhazi, S.Naar " Aptitude de la thermographie infrarouge à détecter les fissures et les nids d'abeille dans le béton", 12ème colloque sur la progression de la recherche québécoise sur les ouvrages d'art (2005).
- [4] S.Maillard, J.Cadith, H.Walszek, A.Dillenz " La thermographie infrarouge stimulée, une nouvelle technique de contrôle sur les lignes de production, Cofrend 2008 Toulouse, 20 – 23 mai, 2008
- [5] S.Belattar, S.Sahnoun " Thermal nondestructive testing study of a circular defect in plane structure 8th ECNDT European Conference on Nondestructive Testing Barcelona (Spain), June 17-21, 2002.

EXPERIMENTAL VALIDATION OF A HAM-BES CO-SIMULATION APPROACH

M.Y. FERROUKHI^{1,*}, R. BELARBI¹, K. LIMAM¹, W. BOSSCHAERTS²

¹ LaSIE, UMR 7356 CNRS University of La Rochelle, Avenue Michel Crépeau 17042 cedex1, La Rochelle, France

² Royal military school of Brussel, Belgium

*Corresponding author: Fax: +33546458200 Email: mohammed_yacine.ferroukhi@univ-lr.fr

ABSTRACT

High levels of humidity in buildings lead to building pathologies. Moisture also has an impact on the indoor air quality and the hygrothermal comfort of the building's occupants. To better assess these pathologies, it is necessary to take into account the heat and moisture transfer between the building envelope and its indoor ambience.

In this work, coupled heat, air and moisture transfer model in multilayer walls (HAM) was established. Thereafter, the HAM model is coupled dynamically to a building behavior code (BES). The coupling concerns a co-simulation between COMSOL Multiphysics and TRNSYS softwares.

Afterward, the HAM-BES co-simulation accuracy was verified by conducting an experimental validation using an experimental device devoted to assess the hygrothermal response of building walls under several hygrothermal conditions.

The comparison between numerical and experimental results showed good agreement with acceptable errors margins.

KEYWORDS

Heat and mass transfers, HAM-BES co-simulation, experimental validation.

NOMENCLATURE

i	Layer position in the wall from the outside to inside
T	Temperature [K]
P_v	Water vapour pressure [Pa]
P	Total pressure [Pa]
t	Time [s]
ρ_s	Dry density [kg/m ³]
C_m	Storage moisture capacity [kg/(kg.Pa)]
C_p	Heat capacity [J/(kg.K)]
L_v	Evaporation latent heat [J/kg]
λ	Thermal conductivity [W/(m.K)]
C_a	Humid air Capability [s ² /m ²]
k_m	Total moisture permeability [kg/(m.s.Pa)]
k_T	Liquid water conductivity caused by temperature gradient [kg/(m.s.K)]
k_p	Moisture infiltration coefficient [kg/(m.s.Pa)]

γ, α	Heat convection coefficient due to a water vapor pressure gradient and a total pressure gradient respectively [m ² /s]
σ	Ratio between water vapor exchange mass and the overall mass exchange [-]

INTRODUCTION

In order to reduce energy costs and environmental impacts related to buildings, several organizations and research laboratories have focused on the physical study of the building and its energy behavior. These studies allow creating different approved modeling tools for the thermal and hydric study of building as TRNSYS and Energy plus. However, the coupled heat, air and moisture transfers in the walls are generally badly represented.

To overcome this problem, and be able to better stimulate hygrothermal behavior of buildings, several approaches were proposed in recent years. Among these approaches the co-simulation, which consists to cohabit two existing softwares, one for

dynamic building simulation and the other for accurate modeling of hygrothermal behavior at the envelope. The concerned approach allows a better description of heat and moisture transfer through hygroscopic walls as an integral part of the building. In this sense, the literature reported a number of previous works among which are mentioned, hereinafter, the most important.

Tariku et al. [1] have developed a simulation environment under SimuLink named HAMFitPlus, which integrates both hygrothermal transfer models for the envelope and indoor of building. Steeman et al. [2] have conducted an integration of a 1D HAM model in a BES software (TRNSYS) for modeling the hygrothermal transfer in porous building materials. This could be achieved by coupling the HAM model equations to those of TRNSYS.

However, in the majority of carried out works in this subject, 2D and 3D modeling of coupled heat and moisture transfer is not taken into account. In this paper, a model of coupled heat, air and moisture transfer in multilayer walls was established. Subsequently, for studying the wall hygrothermal transfer effect on building energy consumption, an integration approach of envelope coupled heat, air and moisture transfer model (HAM) in a building simulation code (BES) was undertaken. Finally, an experimental setup has been established for the purpose of checking the reliability of the developed HAM-BES co-simulation platform.

HAM-BES CO-SIMULATION APPROACH

Heat, air and moisture transfer in the envelope: To accurately predict the hygrothermal behavior at the building envelope, we opted for a model based on Luikov theory [3], [4], [5], with the following assumptions:

- Local thermodynamic equilibrium between all present phases;
- Gaseous phase complies to the ideal gas law;
- Hysteresis and chemical reactions between phases were not taken into account;
- Humidity storage capacity variation with temperature change was neglected;
- Solid medium is not deformable;

The developed model considers as driving potentials the temperature for heat transfer, the total pressure for air transfer and the water vapor pressure for the hydric transfer. This allows the avoidance of discontinuity problems at the wall layer interfaces,

which is not the case with the water content. Moreover, the water vapor pressure is in direct relation with the relative humidity, which is a useful parameter with a simple and direct signification, particularly when using experimentation [6].

To realize an accurate and detailed study, we took into account in this approach, the variation of hygrothermal material properties with the water content. This especially concerns: the moisture permeability k_m [kg/(m.s.Pa)], the moisture storage capacity C_m [kg/(kg.Pa)] for hydric transfer and the thermal conductivity (λ [W/(m.K)]) for heat transfer.

The HAM model is built on heat and mass conservation laws. Eq.(1) and Eq.(2) represent both moisture (liquid and water vapor) and gaseous balances, and Eq.(3) expresses the heat balance by taking into account the heat conduction and heat advection due to moisture and total pressure gradients. It is noted that the capillary liquid transfer expressed by Darcy's law is taken into account in the HAM model. Indeed, the gradient of capillary suction is reduced to the water vapor pressure gradient and temperature gradient using Kelvin's law. Experimental validation of the proposed HAM model was undertaken in Ferroukhi et al. [7] works.

$$C_{m_i} \rho_{s_i} \frac{\partial P_v}{\partial t} = \text{div}(k_{m_i} \nabla P_v + k_{T_i} \nabla T + k_{p_i} \nabla P) \quad (1)$$

$$C_{a_i} \frac{\partial P}{\partial t} = \text{div}(k_{p_i} \nabla P) \quad (2)$$

$$C_{p_i} \rho_{s_i} \frac{\partial T}{\partial t} = \text{div}(\lambda_i \nabla T + \alpha_i \nabla P_v + \gamma_i \nabla P) + L_v \rho_{s_i} \sigma_i C_{m_i} \frac{\partial P_v}{\partial t} \quad (3)$$

HAM-BES co-simulation platform: The co-simulation approach consists on coupling a dynamic building simulation tool (TRNSYS) with a coupled heat, air and moisture transfer model implemented in COMSOL. The coupling was carried out through MATLAB which represents an integrator tool ensuring the data exchange between TRNSYS and COMSOL.

Indeed, TRNSYS is used here because it is widely used by scientific community and by engineers. In addition, its modular architecture is an advantage because it allows extending the modeling to a thermo-hydro-aeraulic modeling. This is achievable by integrating ventilation types in simulations as Comis or Contam. For the hygrothermal transfer simulation in the building's walls, COMSOL was chosen in order to have an enough fine granularity

simulation to describe the hygrothermal transfer in 2D and 3D especially in specific envelope components involving multidirectional flows such as thermal bridges.

The COMSOL/MATLAB connection is provided through the LiveLink interface [8]. Thus, the HAM model is defined in MATLAB and differential equations system is solved by the COMSOL solver. Concerning the TRNSYS/MATLAB link, it is established using the type 155 [9].

In this approach, the control of the time step was provided by the BES model (TRNSYS). Consequently, the data exchange between the two coupled softwares is made in the post-convergence to the current BES model time step during which the HAM model is solved in COMSOL with a finer time step. The diagram in figure 1 summarizes the temporal synchronization approach and data exchange strategy between the BES model in TRNSYS and the HAM model in COMSOL.

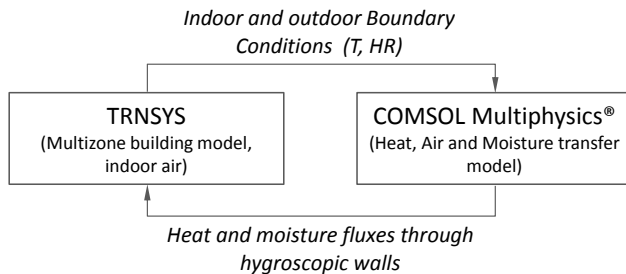


Figure 1: Dynamic co-simulation approach between HAM (COMSOL) and BES (TRNSYS) models

EXPERIMENTAL INVESTIGATION

As expected previously, an experimental device adapted to study the hygrothermal response of buildings envelopes has been developed in this work. This experimental device is used to validate the proposed HAM-BES co-simulation approach.

The experimental validation was conducted by controlling relative humidity and temperature profiles for a steady state situation.

In this work, a monolayer chipboard wall with a thickness of 6.6 cm was used. The tested thickness envelope was taken enough small to optimize the test time, given the hygrothermal transfer kinetics and especially the moisture transfer which is relatively slow.

The test principle consists on submitting the envelope to two hygrothermal controlled environments. Each compartment was made of a plywood envelope (1.5 cm) with an internal polystyrene insulation (3 cm). The inner surfaces of compartments walls were covered with sheet metal to

avoid any moisture exchange with the indoor environment.

The temperature is maintained for each ambiance with a thermostatic bath who feeds a copper heat exchange. For the relative humidity, a humidity generator was used. These apparatus are equipped with deported sensors that allow a downstream hygrothermal control (ie in the two ambiances). Figure 2 illustrate the developed experimental device.



Figure 2: Experimental device

In this experimentation, the tested wall was submitted to a constants temperatures and relative humidity gradients with conditioning the left compartment (see figure 2) at a temperature of $16\pm 1^\circ\text{C}$ and relative humidity of $80\pm 3\%$. For the right compartment (see figure 2), the temperature was controlled at $24\pm 1^\circ\text{C}$ and the relative humidity was kept free. It should be noted that the experiment lasted 20 days.

For monitoring the temperature and the relative humidity profiles along the wall during the test, hygrothermal sensors were implemented at different thickness of the wall. Regarding the small thickness of the tested envelope it is important that the sensors do not affect the hygrothermal behavior. That is why; the sensors used in this experiment (SHT75 sensors) are suited for this application as their small size provides a stable and reliable measurement. Figure 3 show the location of the used sensors in the tested wall as well as in the two compartments.



Figure 3: Sensors locations

Hygrothermal characterization for the numerical simulation: In order to examine the numerical behavior of the tested chipboard wall, an estimation of the input parameters of the developed HAM model is required.

Initially, the moisture storage capacity of the chipboard has been evaluated. This parameter was calculated from the adsorption and desorption isotherm curves of water vapor evaluated using the BELSORP-Aqua3 equipment. Figure 4 represents the adsorption-desorption curve of the chipboard.

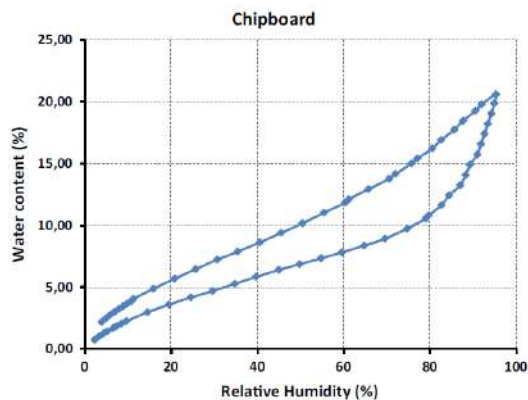


Figure 4: Adsorption and desorption isotherm curve

Similarly, the water vapor permeability has been evaluated using the Gravitest (GINITRONIC, Suisse) equipment based on the cup method according to the European Standard EN ISO 12572. The experimental procedure consists to make a regular monitoring, until equilibrium, of sample mass subjected to a water vapor pressure gradient under isothermal conditions (23°C) [10]. In this case, water vapor pressure gradient was created by imposing relative humidity of 50% and 95% between the two faces of

the tested sample. For chipboard, the obtained vapor permeability is about $1.28 \times 10^{-11} [\text{kg}/(\text{m.s.Pa})]$.

Another thermophysical parameter that should be evaluated is the thermal conductivity. It was achieved by using the Lambda-meter Ep 5000e. The test tool operates with the guarded hot plate apparatus method according to ISO 8302 DIN EN 1946-2 DIN EN 12667 and ASTM C177 (DIN 52612) norms.

In this work, the impact of the material's water content on the measured thermal conductivity was evaluated. Figure 5 shows the variation of chipboard thermal conductivity depending on its water content.

Concerning the specific heat capacity evaluation the DSC (Differential Scanning Calorimetry) method under a nitrogen flow of 50 ml/min is required. For chipboard, the measured specific heat capacity is about $1790 [\text{J}/(\text{kg.K})]$.

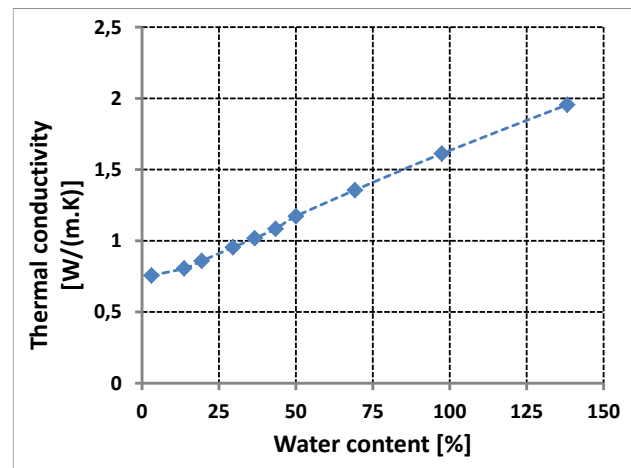


Figure 5: Thermal conductivity of chipboard

NUMERICAL SIMULATION AND VALIDATION

In order to validate the developed HAM-BES platform, the numerical resolution obtained by this tool was compared to the experimental data provided from the experimentation previously presented.

It is noted that to perform the numerical simulation task, evidently, the initial and boundary conditions are identical to those of the experiment. For a better understanding of the presented experimental results, the placements of measurement points over the experimental device were illustrated in figure 6.

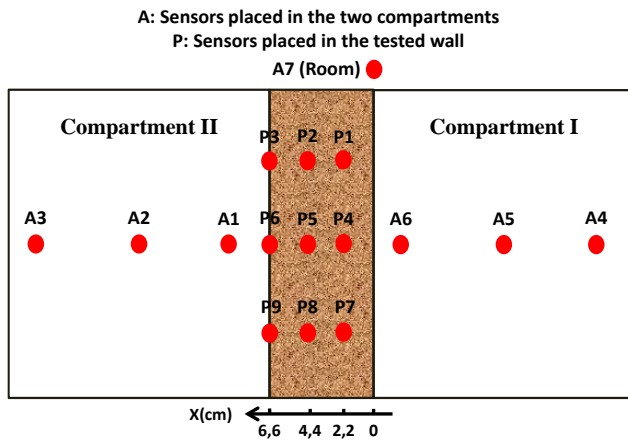


Figure 6: Sensors emplacements over the experimental device

The hygrothermal conditions imposed in the two controlled ambiances are represented in figure 7.

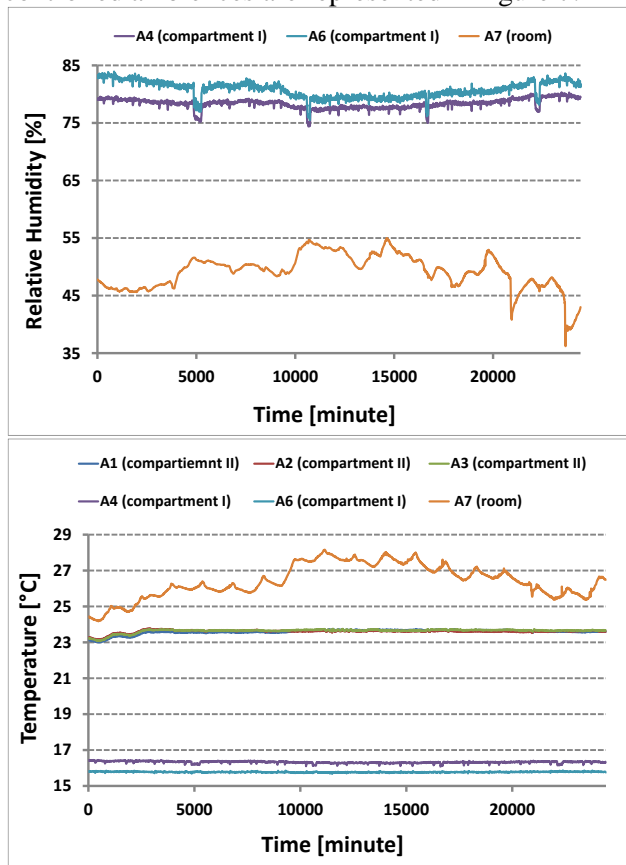


Figure 7: Imposed hygrothermal conditions in the two compartments

The numerical and experimental comparison of temperature and relative humidity distributions in the wall and the relative humidity in the compartment II are shown in figures 8 and 9.

Focusing on the temperature distribution trough the wall, the results show good agreement between the experimental data and numerical simulation. The

mean temperature deviation is about 0.2°C at a depth of 2.2cm. At 4.4cm and 6.6cm, the mean deviations are 0.35°C and 0.30°C respectively.

Concerning the comparison of the relative humidity distributions, a good agreement between predicted and measured data was observed. The mean variation reach 2%, 1.5% and 1.3% at 2.2cm, 4.4cm and 6.6 cm of depth respectively.

The same observation was noted by comparing the numerical and experimental data of the relative humidity variation in compartment II. The mean deviation over the experimentation reaches 1.6% with a maximum of 2.7% (see figure 9).

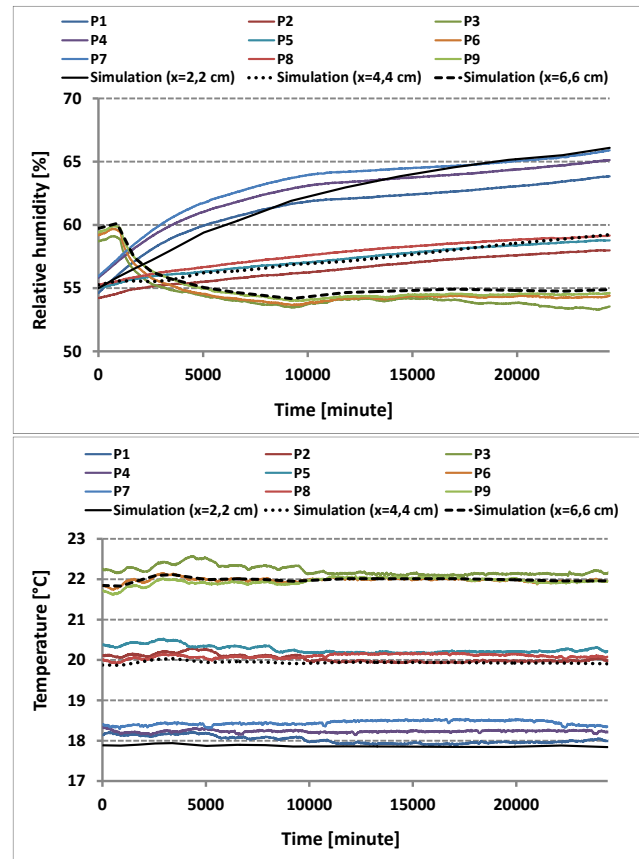


Figure 8: Comparison of numerical simulation with experimental data (temperature and relative humidity at different depths of the wall)

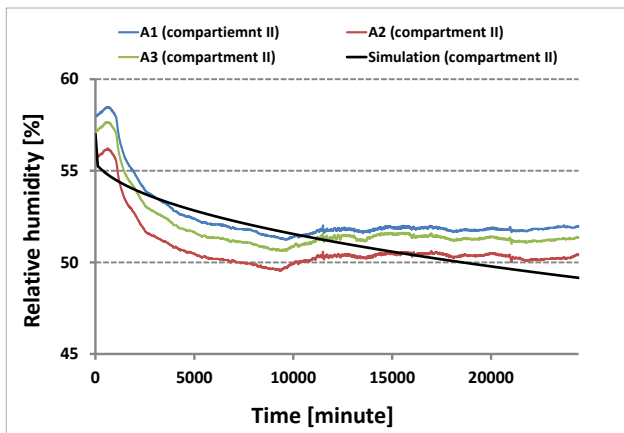


Figure 9: Comparison of numerical simulation with experimental data (Relative humidity variation in compartment II)

CONCLUSIONS

In this work, a HAM-BES co-simulation approach was developed. The coupling of the BES and HAM models was achieved through the development of a new co-simulation platform running TRNSYS and COMSOL together to perform a coupled dynamic simulation of heat, air and moisture transfer in buildings.

The efficiency of this co-simulation approach has been verified by comparisons to experimental data. This application was achieved by developing an experimental device enabling the study of hygrothermal behavior of buildings envelopes at a representative scale.

In fact, the good agreement between computed and experimental data allows to applied, with a confidently, the developed HAM-BES co-simulation platform to a realistic cases study in order to assess the impact of hygrothermal transfer in the envelope over the prediction of the indoor air quality as well as building energy consumption.

ACKNOWLEDGMENTS

This work was funded by the French National Research Agency (ANR) through the Program Sustainable Cities and Buildings (project HUMIBATex n°ANR-11-BVD).

REFERENCES

1. Tariku, F, Kumaran, K, and Fazio, P, 2010, Integrated analysis of whole building heat, air and moisture transfer, *Int. J. Heat Mass Transf*, **53**, pp. 3111-3120.

2. Steeman, M, Janssens, A, Steeman, H. J, Belleghem, M. V, and Paepe, M. D, 2010, On coupling 1D non-isothermal heat and mass transfer in porous materials with a multizone building energy simulation model, *Build. Environ*, **45**, pp. 865-877.
3. Luikov, A. V, 1966, Heat and mass transfer in capillary porous bodies, Pergamon Lond.
4. Belarbi, R, Qin, M, Ait mokhtar, A, and Nilsson, L. O, 2008, Experimental and theoretical investigation of non-isothermal transfer in hygroscopic building materials, *Build. Environ*, **43**, pp. 2154-2162.
5. Remki, B, Abahri, K, Tahlaiti, M, and Belarbi, R, 2012, Hygrothermal transfer in wood drying under the atmospheric pressure gradient, *Int. J. Therm. Sci.*, **57**, pp. 135-141.
6. Nilsson, L. O, 2003, Moisture mechanics in building materials and building components, PhD course, Lund Institute of Technology, Sweden.
7. Ferroukhi, M. Y, Abahri, K, Belarbi, R and Limam, L, 2015, Experimental validation of coupled heat, air and moisture transfer modeling in multilayer building components, *Heat Mass Transf.*, pp. 1-15.
8. Comsol Multiphysics User's Guide, Comsol Multiphysics User's Guide. 2012.
9. Solar Energy Laboratory, TRANSSOLAR Energietechnik GmbH, CSTB – Centre Scientifique et Technique du Bâtiment, et TESS – Thermal Energy Systems Specialists, *TRNSYS 17 a TRAnSient SYstem Simulation program*, vol. A3. 2010.
10. Qin, M, Belarbi, R, Ait mokhtar, A, and Nilsson, L. O, 2008, Nonisothermal moisture transport in hygroscopic building materials: modeling for the determination of moisture transport coefficients, *Transp Porous Med*, **72**, pp. 255-271.

EXPERIMENTAL ASSESSMENT OF THE VARIABILITY OF CONCRETE AIR PERMEABILITY: REPEATABILITY, REPRODUCIBILITY AND SPATIAL VARIABILITY

N. Issaadi*; A. A. Hamami, R. Belarbi, A. Aït-Mokhtar

University of La Rochelle-CNRS, LaSIE UMR 7356, Avenue Michel Crépeau 17042
La Rochelle Cedex 1

*Corresponding author: Fax: +33 546 457 223 Email: nabil.issaadi@univ-lr.fr

ABSTRACT

To study the effect of spatial variability of some influential parameters on the durability of the building envelopes, some important information are required: the mean, the standard deviation and the spatial correlation of the studied fields defined by the correlation lengths. In this paper, the characterization of the concrete spatial variability was performed which included a significant number of test allowing the characterization of concrete air permeability. For this a concrete wall of 2 m of height, 1.20 m of width and 15 cm of thickness was manufactured in laboratory in which concrete specimens were periodically taken and tested. Firstly, results repeatability was performed. For these purpose, three tests per sample was carried out in order to assess the repeatability of the measurements. Secondly, the reproducibility of the measurements was carried out by testing two samples for each cored specimen. Good repeatability of the intrinsic permeability measurements on each tested sample is recorded. Indeed, the standard deviation does not exceed $0.67 \times 10^{-17} \text{ m}^2$. Also, the concrete intrinsic permeability depends on the spatial location of the studied sample. It was found to be ranging between 2.38×10^{-17} and $5.91 \times 10^{-17} \text{ m}^2$ with an average value equal to $3.66 \times 10^{-17} \text{ m}^2$. The obtained results enable to quantify the spatial variability of concrete air permeability, particularly in terms of mean value and standard deviation. Also, it allowed highlighting the spatial correlation length of the studied fields and for probabilistic approaches regarding the prediction of the concrete durability.

INTRODUCTION

The cementitious materials, which are nowadays the most used building material, have a very complex microstructure with heterogeneous shape leading to random mechanical and physical properties. These properties are affected by different phenomena that have chemical origin such as the cement hydration or physical such as the moisture, heat and aggressive species transfers. These latter can vary considerably depending on how the concrete is manufactured, cast and conditioned. This variability will affect the material behavior in general and, particularly, his behavior regarding the transfer phenomena.

Some works have highlighted the effect of the variability of some concrete parameters on its behavior. De Larrard [1] has studied the influence of this variability on leaching of concrete and its service life when it is used for manufacturing tunnels for radioactive waste storage. They showed the interest of considering this properties variability of cementitious materials.

The present work focuses on the study of the spatial variability of concrete air permeability. This will be

used in probabilistic approaches for the prediction of hygrothermal behavior and durability. Trabelsi *et al.* [2] have studied the statistical variability of water vapor desorption isotherms. They showed their impact on the concrete drying and noticed a significant effect especially in the concrete cover. Dominguez-Minoz *et al.* [3] have studied the thermal conductivity of foams and noticed an important variability of this property. They compared other results provided by an inter-laboratories study on the hydric properties. They noticed a good reproducibility for some properties (porosity and density) when this reproducibility remains very poor for other properties such as the sorption isotherms and the resistance to the water vapor despite the used techniques are the same for the different laboratories. Feng *et al.* [4] studied the repeatability and the reproducibility of hydric properties of different materials. They concluded to a good repeatability for their results, nevertheless, the reproducibility was poor when comparing the results obtained by different laboratories. Indeed, significant differences are reported for the transport

properties due to differences of the experimental procedures and analyses monitoring conditions, when comparing the results obtained by different laboratories [3, 5-7].

The study is conducted on a concrete wall. This wall was cored at different spatial locations in order to obtain different samples. The obtained samples were used for the characterization of air permeability of this concrete. A statistical distribution laws are proposed for the description of the variability of this property. Also, repeatability and reproducibility of the results are performed.

Experimental program: To study the effect of spatial variability of some influential parameters on the hygrothermal behavior of the building envelopes, some important information are required: the mean, the standard deviation and the spatial correlation of the studied fields defined by the correlation lengths. To obtain this data, an experimental concrete wall of 2 m of height, 1.20 m of width and 15 cm of thickness was manufactured in the laboratory in which samples were cored following six vertical lines. Two lines are dedicated to air permeability tests (diameter=65 mm, height=50 mm) (lines B and E in Figure 1).



Figure 1

Specimen position in the experimental concrete wall

The used concrete was prepared with Portland-cement of type CEM I 52.5 N with 95% part of clinker. It was prepared in according to the EN 206-1 standard. Its composition is reported in Table 1.

Table 1
Composition of concrete

Constituents	Kg.m ⁻³
Cement CEM1 52.5N	350
Gravel 10/14	1201
Sand 0/4	762
Water	211.8

RESULTS AND DISCUSSION

To study the spatial variability of air permeability of the concrete composing the wall, this latter was cored periodically following the two lines B and E in order to obtain cylindrical specimens which were, then, sawn to have samples of 65 mm diameter and 50 mm thick. To verify the reproducibility of the measurements, two samples were produced by cored specimen. In this way 36 samples were obtained to perform the measurements. To ensure a radial tightness of the samples a mono-directional flow of the air and, each sample was laterally surrounded by a resin ring of about 15 mm thick.

The permeability measurement was performed using a fully automatic device composed by a “Thermicar permeameter” and a data acquisition interface. The followed method is a transitory method which principle is described by Figure 2.

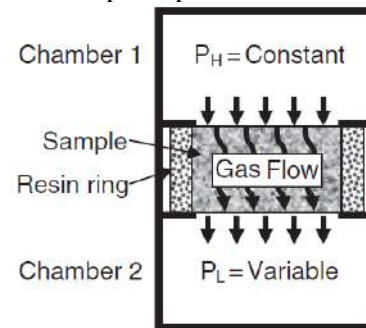


Figure 2

Schematic view of the air permeability device principle

During the measurement, carried out following the procedure described by Hamami *et al.* [8], the sample is placed between two pressure chambers and submitted to a pressure gradient. This one is generated by applying several levels of a high pressure P_H , which is kept constant (equal to one of these values: 130 – 160 – 190 – 210 and 350 kPa), at the upstream of the sample and a low pressure P_L , initially equal to 8.5 kPa, at the downstream. This low pressure varies according to the air flow through the sample.

For each high pressure applied, an apparent permeability “ K_A ” is obtained according to a modified Darcy’s law (eq. 1). The intrinsic permeability “ K_{INT} ” of the material is then calculated according to Klinkenberg [9] approach (eq. 2) which is based on the evolution of this apparent permeability “ K_A ” as a function of the

inverse mean pressure P_m (Eq. 3) (Figure 3). More detailed description of the used method is given by Hamami *et al.* [8].

$$K_A = \frac{2\mu L}{P_H^2 - P_L^2} V_L \frac{dP_L^2}{dt} \quad (1)$$

μ [Pa.s] is the air dynamic viscosity, V_L [m³] is the volume of the low pressure chamber (at the downstream of the sample) and L [m] is the sample thickness.

$$K_A = K_{INT} \beta \frac{1}{P_m} + K_{INT} \quad (2)$$

β [Pa] is the Klinkenberg factor which represents the air slip at the interface of the material pores.

$$\frac{1}{P_m} = \frac{2}{P_H + P_L} \quad (3)$$

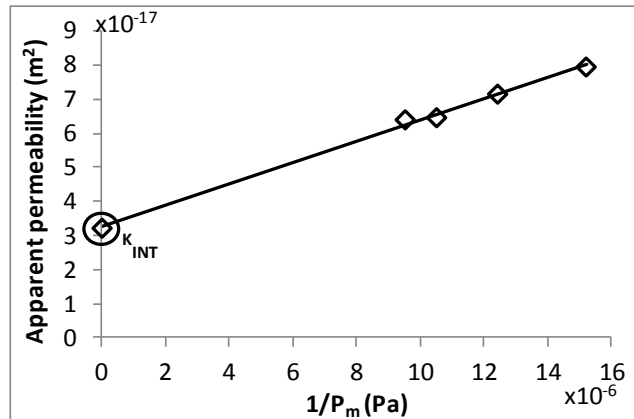


Figure 3

Intrinsic permeability determination according to Klinkenberg approach

The results of the intrinsic permeability of the two vertical lines B and E are shown on the Fig. 13. In order to properly quantify the spatial variability of the intrinsic permeability, the repeatability and reproducibility of the measurement were studied. For these purposes, three tests per sample was carried out in order to assess the repeatability of the measurements and, as previously indicated, two samples were tested for each cored specimen to assess the reproducibility of the measurements. Obtaining more than two samples of 50 mm thick per cored specimen was impossible since the thickness of the wall is equal to 150 mm (which correspond to the specimen height) and the use of more thin concrete samples (less than 50 mm thick) cannot be considered because of the device specifications. The statistical data corresponding to the results presented

in Figure 4 are reported in Table 2 (by averaging the average value of the reproducibility tests).

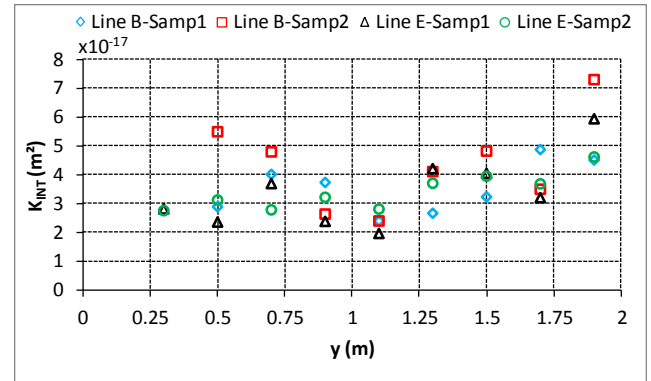


Figure 4

Intrinsic permeability following the vertical lines B and E

Table 2

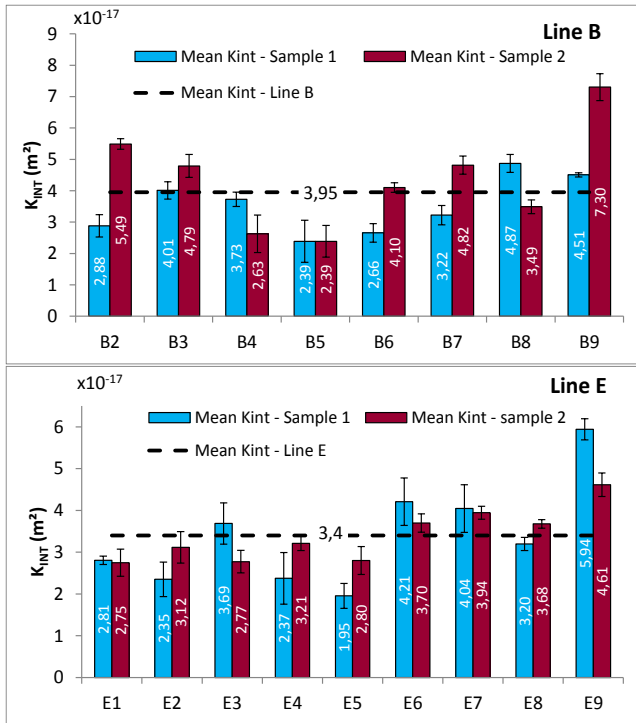
Statistical data of the air permeability for the two vertical lines B and E

	Average $\times 10^{-17}$	Standard deviation $\times 10^{-17}$	Coef of variation (%)	Min $\times 10^{-17}$	Max $\times 10^{-17}$
Line B	3.95	1.03	26.20	2.39	5.91
Line E	3.40	0.89	26.50	2.38	5.28
Both lines	3.66	0.97	26.7	2.38	5.91

The obtained results give a good repeatability of the intrinsic permeability measurements on each tested sample. Indeed, the standard deviation does not exceed $0.67 \times 10^{-17} \text{ m}^2$.

Concerning the reproducibility assessment, the results presented in Figure 5 give a comparison between the measured values of the intrinsic permeability of the two tested samples per location. Each value corresponds to the average of the three values measured on the same sample.

This Figure 5 shows that, on the one hand, an important variation is observed for the intrinsic permeability measured on two samples from the same location (B2) and, on the other hand, permeability that remain constant for the two tested samples (B5). Globally, this figure shows that the intrinsic permeability depends on the spatial location of the studied sample. The permeability decreases at the middle of the vertical line, increases a little near to the bottom of the wall and is more important at the top of this one.



Intrinsic permeability measurements reproducibility following the lines B & E

Considering these observations, one can expect that the spatial variability will be of an important impact on the wall permeability. To bring more clarifications to this question, the spatial distribution of the intrinsic permeability is associated to statistic distribution laws in order to identify the different parameters governing the spatial variability of this concrete property (Figure 6).

Figure 6 shows the variability extent of the intrinsic permeability observed on the 36 tested samples and the fitted probabilistic laws associated to this variability. The different data for the studied distribution laws are given by Table 3. The Normal and Weibull laws seems to be the most appropriated to reproduce the statistic distribution of the experimental values. These two laws present the same average of $3.65 \times 10^{-17} \text{ m}^2$ and a variance of $0.95 \times 10^{-34} \text{ m}^4$ and $1.04 \times 10^{-34} \text{ m}^4$ respectively for the Normal and Weibull law.

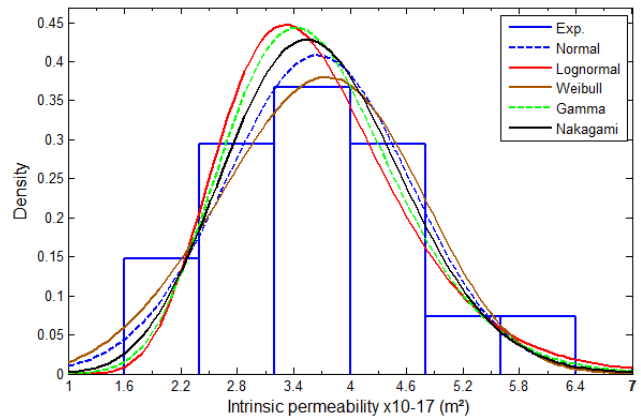


Figure 6
Intrinsic permeability distribution for concrete. The lines are the fitted proposed probabilities density

Table 3
Statistic data associated to the proposed distribution laws

Distribution Law	Normal	Lognormal	Weibull	Gamma	Nakagami
Average $\times 10^{-17}$	3.65	3.66	3.65	3.65	3.66
Variance $\times 10^{-34}$	0.95	0.94	1.04	0.85	0.86

The concrete intrinsic permeability (by just averaging the air permeability value of the repeatability test results) was found to be ranging between 1.95×10^{-17} and $7.3 \times 10^{-17} \text{ m}^2$ with an average value equal to $3.65 \times 10^{-17} \text{ m}^2$. This is in good agreement with the results obtained by [7, 10]. The results variability is reduced in the case where the reproducibility test is taken into account by averaging the average value presented in the Fig. In this case the concrete intrinsic permeability was found to be ranging between 2.38×10^{-17} and $5.91 \times 10^{-17} \text{ m}^2$ with an average value equal to $3.66 \times 10^{-17} \text{ m}^2$.

In order to perform hygrothermal and durability simulations using probabilistic approach taking into account spatial variability of the inputs parameters, it is necessary to know the spatial correlation of the studied property field. This is defined by the correlation length noted “Lc” which may enable to estimate the distance between two testing points at which the measured values become independent. It reflects the importance of the random field spatial correlation used in the probabilistic approach implementation. The higher the correlation length, more the field is strongly correlated [3]. This

parameter is identified using a variogram based on the experimental value previously presented. The variogram is a practical mean for describing the spatial correlation of measurements. On one hand, it is a tool to investigate and quantify the spatial variability of the phenomenon under study. On the other hand, most geostatistical estimation or simulation algorithms require an analytical variogram model, which can be derived from the experimental variogram [11, 12]. The variogram at the lag distance “d” is expressed as follows (Eq. 4).

$$\gamma(d) = \frac{1}{2|N(d)|} \sum_{(i,j) \in N(d)} |Y_i - Y_j|^2 \quad (4)$$

Where

$$N(d) = \{(i, j) \mid |x_i - x_j| = d\}$$

Where $\gamma(d)$ is the variogram value; Y_i is the value of the studied property at the x_i position; $N(d)$ is the set of pairs of points (i, j) such that the distance between these points is equal to d (number of pairs that satisfy this condition).

The relationship between the covariance (C) and the variogram is defined by Eq. 5. Remember that the covariance on 0 is the variance. By knowing the variogram value corresponding to each distance, we can deduce from Eq. 5 the value of the covariance. Then, it is enough to optimize the value of correlation length “Lc” in the covariance functions which can be expressed as follows (Eq. 6):

$$\gamma(d) = C(0) - C(d) \quad (5)$$

$$C(x, y) = \sigma^2 \exp\left(-\frac{\|x_i - x_j\|^2}{L_c^2}\right) \quad (6)$$

Where $C(x,y)$ is the covariance between the two points x_i and x_j . Each term C_{ij} of the covariance matrix “C” is the value of the covariance function calculated between the nodes i and j of the mesh. The vectors x_i and x_j give the position of the corresponding nodes.

Figure 7 shows a comparison between the covariance values measured on the experimental concrete wall and those obtained using the corresponding covariance functions. As indicated previously, the air permeability was evaluated according to two lines (B & E). It is presented on the y-axis the normalized

covariance relative to the variance. It is observed that the correlation length is of the order of the meter.

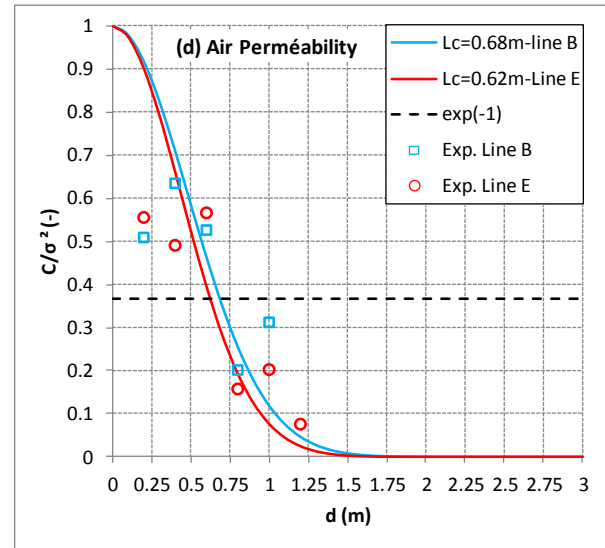


Figure 7
Correlation length identification of the air permeability

CONCLUSIONS

The main of this work is to characterize spatial variability of some influential parameters on the prediction of the hygrothermal behavior and concrete structure durability. For this, an experimental wall concrete is built in the laboratory. Several specimens are cored periodically and tested to evaluate the spatial variability of the air permeability. It is found Good repeatability of the intrinsic permeability measurements on each tested sample is recorded. Indeed, the standard deviation does not exceed $0.67 \times 10^{-17} \text{ m}^2$. Also, the concrete intrinsic permeability depends on the spatial location of the studied sample. It was found to be ranging between 2.38×10^{-17} and $5.91 \times 10^{-17} \text{ m}^2$ with an average value equal to $3.66 \times 10^{-17} \text{ m}^2$. The correlation length of the air permeability is of the order of the meter. It was found to be ranging from 0.62 to 0.68 m.

The results obtained do however constitute a database that can be used as inputs for probabilistic approaches. It can be used by considering the fitting probabilistic laws or as inputs for generating random fields by using, for example, Karhunen Loeve decomposition.

ACKNOWLEDGMENTS

This work has been supported by the French Research National Agency on the reference ANR-10-HABISOL-005 through the “Habitat intelligent et solaire photovoltaïque” programme (project HYGRO-BAT) and the Poitou-Charentes Region project through the European Fund FEDER 2007-2013 N° 33586-2011 “Development of a platform for heat and moisture characterization of green roof components”.

REFERENCES

1. T. De Larrard, *Variabilité des propriétés du béton : caractérisation expérimentale et modélisation probabiliste de la lixiviation*, ENS Cachan, 2010.
2. A. Trabelsi, A. Hamami, R. Belarbi, P. Turcry et A. Aït-Mokhtar, «Assessment of the variability of moisture transfer properties of High Performance Concrete from multi-stages drying experiment,» *European Journal of Environmental and Civil Engineering*, vol. 16, p. 352–361, 2012.
3. F. Dominguez-Munoz, B. Anderson, J. Cejudo-Lopez et A. Carrillo-Andres, «Uncertainty in the thermal conductivity of insulation materials,» *Energy and Buildings*, vol. 42, p. 2159–2168, 2010.
4. C. Feng, H. Janssen, Y. Feng et Q. Meng, «Hygric properties of porous building materials: Analysis of measurement repeatability and reproducibility,» *Building Environment*, vol. 85, pp. 160-172, 2015.
5. S. Roels, J. Carmeliet, H. Hens et O. ADAN, «Interlaboratory comparison of hygric properties of porous building materials,» *Thermal Envelope and Building Science*, vol. 27, p. 307–325, 2004.
6. S. Roels, P. Talukdar, C. James et C. J. Simonson, «Reliability of material data measurements for hygroscopic buffering,» *International Journal of Heat and Mass Transfer*, Vols. 53 sur 54, p. 5355–5363, 2010.
7. A. Aït-Mokhtar, R. Belarbi, F. Benboudjema, N. Burlion, B. Capra, M. Carcassès, J. B. Colliat, F. Cussigh, F. Deby, F. Jacquemot, T. de Larrard, J. F. Lataste, P. Le Bescop, M. Pierre, S. Poyet, P. Rougeau, T. Rougelot, A. Sellier, J. Séménadisse, J. M. Torrenti, A. Trabelsi, P. Turcry et H. Yanez-Godoy, «Experimental investigation of the variability of concrete durability properties,» *Cement and Concrete Research*, vol. 45, pp. 21-36, 2013.
8. A. A. Hamami, P. Turcry et A. Aït-Mokhtar, «Influence of mix proportions on microstructure and gas permeability of cement pastes and mortars. 42(2):490-498,» *Cement and Concrete Research*, vol. 42, pp. 490-498, 2012.
9. Klinkenberg et L. J, The permeability of porous media to liquid and gases, *Drill. Prod. Pract. Am. Pet. Inst.*, 1941, pp. 200-214.
10. C. Gallé et J. Sercombe, «Permeability and pore-structure evolution for silico-calcareous and hematite high-strength concretes submitted to high temperatures,» *Material and Structures*, vol. 34, pp. 619-628, 2001.
11. N. T. Nguyen, Z. M. Sbartai, J.-F. Lataste, D. Breyse et F. Bos, «Assessing the spatial variability of concrete structures using NDT techniques – Laboratory tests and case study,» *Construction and Building Materials*, vol. 49, pp. 240-250, 2013.
12. E. Gringarten et C. V. Deutsch, «Variogram interpretation and modeling,» *Mathematical Geology*, p. 9, 2001.

Optimal Control by using Reduced Order Models for Transfer Equations

MOURAD OULGHELOU AND CYRILLE ALLERY

LaSIE UMR CNRS 7356, Université de La Rochelle,

Pôle Science et Technologie, Avenue Michel Crépeau, 17042 La Rochelle Cedex 1, France

mourad.oulghelou@univ-lr.fr, cyrille.allery@univ-lr.fr

ABSTRACT

The purpose of optimal control is to act on a set of parameters characterizing a dynamical system to achieve a target dynamics. In order to reduce CPU time and memory storage needed to perform control on evolution systems, it is possible to use reduced order models (ROMs). The mostly used one is the Proper Orthogonal Decomposition (POD). However the need of full simulations to build a basis for each control parameter is time consuming and makes that approach still relatively expensive. In this communication, to overcome this difficulty we suggest to implement the Proper Generalized Decomposition (PGD) method within the control loop. This method is considered here as an adaptive self error corrector respectively to control variations during the optimization process. POD/ROM and PGD/ROM approaches are applied to control the flow governed by Stokes equations in a 2D lid driven cavity.

Keywords: Model reduction, PGD, Optimal control, Stokes equations

Nomenclature

\mathbf{u}	velocity vector field
p	pressure scalar field
\mathbf{f}	external forces
Ω	Physical space domain
$\partial\Omega$	Boundary of physical space domain
I	Time domain
α	temporal basis functions
Φ	temporal basis functions

1 Introduction

Model reduction in optimal control considered as suboptimal replaces the full model system by a suitable low order model which allows to express the solution in a reduced order basis, for which the optimal control problem is then solved. Consequently it is expected that only a few basis elements will provide a reasonably good description of the controlled flow. The projection of governing equations onto the selected reduced basis results in a set of differential equations with considerably smaller size than the degree of freedom arising from classical control method, and their resolution is very fast. The mostly investigated model reduction approach in optimal control is the Proper Orthogonal Decomposition (POD), see for instance [1, 2, 3]. Usually, a POD/ROM is constructed for a specific flow configuration. Consequently, the range of validity of a

given POD/ROM is generally restricted to a region of the control parameter space. In the control process, out of this region we are led to construct a new POD/ROM and consequently increasing the computational cost. To overcome this difficulty it is possible to compute a POD basis suitable for a range of parameters [4], and proceed by an interpolation method. This method is quite accurate, however it requires an important offline computational time.

Herein, we propose to apply the PGD method within the control process. This method was firstly introduced in the context of computational rheology by Ammar et al. [5], and has been further applied in a variety of applications such as solid mechanics, quantum mechanics, fluid mechanics ... In the present paper, this approach is imbedded in control loop to enrich and adapt the current spatial basis corresponding to a given control in order to obtain a new one suitable for the new parameter. The potential of either PGD/ROM and POD/ROM methods within the control loop are eventually studied on a boundary control problem of the flow governed by Stokes equations in a lid driven cavity.

2 Formulation of the problem

In this section we formulate the optimal control problem with integral constraints and review first order necessary optimality conditions.

2.1 The constrained optimal problem

Let $I = [t_i, t_f] \subset [0, +\infty[$ and $\Omega \subset \mathbb{R}^2$ a bounded domain with boundary $\partial\Omega \subset C^2$ with outward unit normal \mathbf{n} . The non dimensional Stokes equations in primitive

variables (\mathbf{u}, p) are given by

$$\begin{cases} \frac{\partial}{\partial t} \mathbf{u} - \frac{1}{Re(\theta)} \Delta \mathbf{u} + \nabla p = \mathbf{f} & \text{in } \Omega \times I \\ \nabla \cdot \mathbf{u} = 0 & \text{in } \Omega \times I \\ \mathbf{u} = \theta \mathbf{g} & \text{on } \partial\Omega \times I \\ \mathbf{u}(t_i) = \mathbf{u}^{t_i} & \text{in } \Omega. \end{cases} \quad (1)$$

Here \mathbf{u} and p are respectively the velocity vector field and the pressure scalar field (defined up to an additive constant), $Re(\theta)$ is the Reynolds number ¹, \mathbf{f} and \mathbf{u}^{t_i} are the given source term and the initial condition of the problem, and $\theta \in U_{ad}$ denotes the control parameter, where

$$U_{ad} = \{\theta \in \mathbb{R}^{+*} / \theta_{min} \leq \theta \leq \theta_{max}\}$$

Let $\mathbf{u}_0(\theta)$ be a divergence free vector field satisfying $\mathbf{u}_0(\theta) = \theta \mathbf{g}$ in $\partial\Omega$. By introducing the homogeneous velocity field $\tilde{\mathbf{u}} = \mathbf{u} - \mathbf{u}_0$, problem (1) can be reformulated to

$$\begin{cases} \frac{\partial}{\partial t} \tilde{\mathbf{u}} - \frac{1}{Re(\theta)} \Delta \tilde{\mathbf{u}} + \nabla p = \tilde{\mathbf{f}}(\theta) & \text{in } \Omega \times I \\ \nabla \cdot \tilde{\mathbf{u}} = 0 & \text{in } \Omega \times I \\ \tilde{\mathbf{u}} = 0 & \text{on } \partial\Omega \times I \\ \tilde{\mathbf{u}}(t_i) = \tilde{\mathbf{u}}^{t_i} & \text{in } \Omega. \end{cases} \quad (2)$$

with $\tilde{\mathbf{f}}(\theta) = \mathbf{f} - \frac{\partial}{\partial t} \mathbf{u}_0(\theta) + \frac{1}{Re(\theta)} \Delta \mathbf{u}_0(\theta)$.

Let $\mathcal{V} = \left\{ \mathbf{v} \in C_0^\infty(\Omega)^2 : \nabla \cdot \mathbf{v} = 0 \right\}$, and define the solenoidal spaces $H = \overline{\mathcal{V}}^{|\cdot|_{L^2(\Omega)^2}}$, $V = \overline{\mathcal{V}}^{|\cdot|_{H^1(\Omega)^2}}$ where the superscripts denote closure in the respective norms. Let V^* denote the dual space of V , and define

$$W = \left\{ \mathbf{v} \in L^2(I; V) : \mathbf{v}_t \in L^2(I; V^*) \right\}$$

$$Z := L^2(I; V) \times H$$

For $\tilde{\mathbf{u}}^{t_i}$ and $\tilde{\mathbf{f}}$ sufficiently regular, problem (2) admits a solution $(\tilde{\mathbf{u}}, p) \in W \times L^2(I; L_0^2(\Omega))$.

Starting from the flow corresponding to an initial control parameter θ_{ini} , the aim is to seek the target parameter θ_c corresponding to the target flow $\tilde{\mathbf{u}}_c$. In a mathematical setting, the goal is to solve the constrained optimization problem : Find θ^* such that the functional $\mathcal{J} : W \times U_{ad} \rightarrow [0, \infty[$ defined by

$$\begin{aligned} \mathcal{J}(\tilde{\mathbf{u}}, \theta) &= \frac{1}{2} \int_I \int_\Omega |\tilde{\mathbf{u}} - \tilde{\mathbf{u}}_c|^2 dx dt \\ &+ \frac{1}{2} \int_\Omega |\tilde{\mathbf{u}}(t_f) - \tilde{\mathbf{u}}_c(t_f)|^2 dx + \frac{1}{2} \kappa |\theta|^2. \end{aligned} \quad (3)$$

is minimized under dynamics constraints described by equations (2). Note that in equation (3), $\tilde{\mathbf{u}}_c = \mathbf{u}_c - \mathbf{u}_0$ is the target state, and $\kappa > 0$ denotes a regularization parameter.

For a compact formulation of the optimal control problem we introduce the mapping

$$e : X := W \times U_{ad} \rightarrow Z^* \quad (4)$$

defined as

$$e(\tilde{\mathbf{u}}, \theta) = \left(\frac{\partial}{\partial t} \tilde{\mathbf{u}} - \frac{1}{Re(\theta)} \Delta \tilde{\mathbf{u}} - \tilde{\mathbf{f}}(\theta) ; \tilde{\mathbf{u}}(t_i) - \tilde{\mathbf{u}}^{t_i} \right)$$

The subject boundary control problem can then be written as

$$(P) \begin{cases} \min \mathcal{J}(\tilde{\mathbf{u}}, \theta) & \text{over } (\tilde{\mathbf{u}}, \theta) \in X \\ \text{such that } \langle e(\tilde{\mathbf{u}}, \theta), z \rangle_{Z^*, Z} = 0 & \forall z \in Z \end{cases}$$

Where $\langle \cdot, \cdot \rangle_{\cdot, \cdot}$ denotes the duality product. It's worth noting that the conservation of mass, as well as the boundary condition are realized in the choice of space function W while the dynamics are described by the condition $e(\tilde{\mathbf{u}}, \theta) = 0$ in Z^* .

2.2 First order necessary optimality condition

A necessary condition for the existence of Lagrange multiplier associated to the solution of $(\tilde{\mathbf{u}}^*, \theta^*)$ of constrained minimization problem (P) is given by

Theorem 1 *Let $(\tilde{\mathbf{u}}^*, \theta^*)$ be a solution of optimization problem (P). then there exists a unique Lagrange multiplier $\xi^* \in Z$ which together with the optimal solution $(\tilde{\mathbf{u}}^*, \theta^*)$ satisfy the optimality system*

$$\begin{cases} L_{\tilde{\mathbf{u}}}(\tilde{\mathbf{u}}^*, \theta^*, \xi^*) &= \mathcal{J}_{\tilde{\mathbf{u}}}(\tilde{\mathbf{u}}^*, \theta^*) \\ &+ \langle e_{\tilde{\mathbf{u}}}(\tilde{\mathbf{u}}^*, \theta^*)(\cdot)_{W, \xi^*} \rangle_{Z^*, Z} = 0 \text{ in } W^* \\ L_\theta(\tilde{\mathbf{u}}^*, \theta^*, \xi^*) &= \mathcal{J}_\theta(\tilde{\mathbf{u}}^*, \theta^*) \\ &+ \langle e_\theta(\tilde{\mathbf{u}}^*, \theta^*)(\cdot)_{U_{ad}, \xi^*} \rangle_{Z^*, Z} = 0 \text{ in } U_{ad} \\ e(\tilde{\mathbf{u}}^*, \theta^*) &= 0 \text{ in } Z^* \end{cases} \quad (5)$$

where the subscripts in $L(\tilde{\mathbf{u}}^*, \theta^*, \xi^*)$, $\mathcal{J}(\tilde{\mathbf{u}}^*, \theta^*)$ and $e(\tilde{\mathbf{u}}^*, \theta^*)$ denote the action of first order differentiation operator ².

2.3 Gradient step descent method

To compute the optimal solution of (P), we use a gradient step descent method, It is an iterative process in which at every iteration the descent direction $d = -\mathcal{J}_\theta$ must be evaluated. In most constrained control problems the explicite form of \mathcal{J}_θ is not straight forward. In the following we describe the methodology to explicite that descent direction for problem (P).

We note by $\tilde{\mathbf{v}}$, $\tilde{\mathbf{v}}^{t_i}$, q and $\tilde{\mathbf{f}}_\theta$ respectively, the directional derivatives³ of $\tilde{\mathbf{u}}$, $\tilde{\mathbf{u}}^{t_i}$, p and $\tilde{\mathbf{f}}$ by respect to θ in a direction $\bar{\theta} \in U_{ad}$, we have

$$\begin{aligned} \mathcal{J}_\theta(\tilde{\mathbf{u}}, \theta) \cdot \bar{\theta} &= \int_I \int_\Omega (\tilde{\mathbf{u}} - \tilde{\mathbf{u}}_c) \tilde{\mathbf{v}} dx dt \\ &+ \int_\Omega (\tilde{\mathbf{u}}(t_f) - \tilde{\mathbf{u}}_c(t_f)) \tilde{\mathbf{v}}(t_f) dx + \kappa \bar{\theta} \end{aligned} \quad (6)$$

where $\tilde{\mathbf{v}}$ satisfies the boundary value problem

$$\begin{cases} \frac{\partial}{\partial t} \tilde{\mathbf{v}} - \frac{1}{Re(\theta)} \Delta \tilde{\mathbf{v}} + \nabla q = -\frac{\bar{\theta}}{\theta Re(\theta)} \Delta \tilde{\mathbf{u}} + \tilde{\mathbf{f}}_\theta & \text{in } \Omega \times I \\ \nabla \cdot \tilde{\mathbf{v}} = 0 & \text{in } \Omega \times I \\ \tilde{\mathbf{v}} = 0 & \text{on } \partial\Omega \times I \\ \tilde{\mathbf{v}}(t_i) = \tilde{\mathbf{v}}^{t_i} & \text{in } \Omega. \end{cases} \quad (7)$$

¹ $Re(\theta) = \rho \theta L / \eta$, where ρ is the density of the fluid, η is the kinematic viscosity and L is the characteristic length.

² The first order differential operator respectively to x applied to a function is denoted as $f_x = \frac{\partial}{\partial x} f$

³ The Derivative of a function f respectively to x in the direction \bar{x} is defined by : $f_x \cdot \bar{x} = \lim_{\epsilon \rightarrow 0} \frac{f(x + \epsilon \bar{x}) - f(x)}{\epsilon}$

In (6) the evaluation of \mathcal{J}_θ is not straightforward due to the inexploitable expression of $\tilde{\mathbf{v}}$. A strategy to get over this issue is to define the dual state of (2). Using this last as a bridge will allow to explicitly express the gradient of the objective functional (3). From the first equation of (5) we can derive the following dual problem

$$\begin{cases} \frac{\partial}{\partial t}\xi + \frac{1}{Re(\theta)}\Delta\xi + \nabla\pi = \tilde{\mathbf{u}} - \tilde{\mathbf{u}}_c \text{ in } \Omega \times I \\ \nabla \cdot \xi = 0 \text{ in } \Omega \times I \\ \xi = 0 \text{ on } \partial\Omega \times I \\ \xi(t_f) = -(\tilde{\mathbf{u}}^{t_f} - \tilde{\mathbf{u}}_c^{t_f}) \text{ in } \Omega. \end{cases} \quad (8)$$

It is now easy using the weak fomulations of problems (1), (7), and (8) to establish the following

$$\begin{aligned} & \int_I \int_\Omega (\tilde{\mathbf{u}} - \tilde{\mathbf{u}}_c) \tilde{\mathbf{v}} dx dt + \int_\Omega (\tilde{\mathbf{u}}(t_f) - \tilde{\mathbf{u}}_c(t_f)) \tilde{\mathbf{v}}(t_f) dx \\ &= \int_I \int_{\partial\Omega} \frac{1}{Re(\theta)} \nabla\xi \cdot \mathbf{n} \tilde{\mathbf{v}} + \pi \tilde{\mathbf{v}} \cdot \mathbf{n} \, d\sigma dt \\ & - \frac{\theta}{\theta Re(\theta)} \int_I \int_\Omega \nabla\tilde{\mathbf{u}}(\theta) \nabla\xi dx dt - \int_\Omega \xi_{t_i} \tilde{\mathbf{v}}^{t_i} dx \end{aligned} \quad (9)$$

Notice that except the last term in the equality above, all the other terms are explicite.

Suppose now that $\tilde{\mathbf{u}}^{t_i}$ satisfies the equations

$$\begin{cases} \beta\tilde{\mathbf{u}} - \frac{1}{Re(\theta)}\Delta\tilde{\mathbf{u}} + \nabla p = \tilde{\mathbf{h}}(\theta) \text{ in } \Omega \\ \nabla \cdot \tilde{\mathbf{u}} = 0 \text{ in } \Omega \\ \tilde{\mathbf{u}} = 0 \text{ on } \partial\Omega \end{cases} \quad (10)$$

where $\beta > 0$ and $\tilde{\mathbf{h}}(\theta) = \mathbf{h}(\theta) - \beta\tilde{\mathbf{u}}_0 + \frac{1}{Re(\theta)}\Delta\tilde{\mathbf{u}}_0$

Then $\tilde{\mathbf{v}}^{t_i}$ satisfies the sensibility problem ⁴

$$\begin{cases} -\beta\tilde{\mathbf{v}}^{t_i} + \frac{1}{Re(\theta)}\Delta\tilde{\mathbf{v}}^{t_i} + \nabla q = -\frac{\theta}{\theta Re(\theta)}\Delta\tilde{\mathbf{u}}^{t_i} + \tilde{\mathbf{h}}_\theta \text{ in } \Omega \\ \nabla \cdot \tilde{\mathbf{v}}^{t_i} = 0 \text{ in } \Omega \\ \tilde{\mathbf{v}}^{t_i} = 0 \text{ on } \partial\Omega \end{cases} \quad (11)$$

Using the following dual problem associated to (10)

$$\begin{cases} \beta\eta_u + \frac{1}{Re} \Delta\eta_u + \nabla\eta_p = -\xi_{t_i} \text{ in } \Omega \\ \nabla \cdot \eta_u = 0 \text{ in } \Omega \\ \eta_u = 0 \text{ on } \partial\Omega \end{cases} \quad (12)$$

we get the final explicite form of \mathcal{J}_θ given by

$$\begin{aligned} \mathcal{J}_\theta(\tilde{\mathbf{u}}, \theta) &= \frac{1}{Re(\theta)} \int_I \int_{\partial\Omega} \nabla(\xi + \eta_u) \cdot \mathbf{n} g \, d\sigma dt \\ & - \frac{1}{\theta Re(\theta)} \left(\int_I \int_\Omega \nabla(\tilde{\mathbf{u}} + \mathbf{u}_0) \nabla\xi \, dx dt \right. \\ & \quad \left. + \int_\Omega \nabla(\tilde{\mathbf{u}}^{t_i} + \mathbf{u}_0(t_i)) \nabla\eta_u \, dx \right) \\ & + \int_I \int_{\partial\Omega} (\pi + \eta_p) \mathbf{g} \cdot \mathbf{n} \, d\sigma dt - \int_\Omega \mathbf{h}'(\theta) \eta_u \, dx + \kappa\theta \end{aligned} \quad (13)$$

In numerical implementation, the evaluation of \mathcal{J}_θ is a necessary task in every iteration of the control algorithm. It requires on one hand the resolution of the stationary problems (10) and (12) to obtain $\tilde{\mathbf{u}}^{t_i}$, η_u and η_p . On the

⁴In numerical application, if $\tilde{\mathbf{u}}^i$ denotes the initial condition considered for problem (2) and dt the time step, β and \mathbf{h} might be defined as $\beta = \frac{1}{dt}$ and $\mathbf{h}(\theta) = \frac{1}{dt}(\tilde{\mathbf{u}}^i + \mathbf{u}_0)$
 $(\cdot, \cdot)_{L^2}$ denotes the L^2 scalar product

other hand the resolution of the two instationary problems (2) and (8) to obtain $\tilde{\mathbf{u}}$, ξ and π . However, in terms of CPU time, a direct simulation of (2) and (8) is too expensive, that's why we turn interest into reduced models.

3 Reduced model

To begin we denote by $(\tilde{\mathbf{u}}^1, \dots, \tilde{\mathbf{u}}^M)$ and (p^1, \dots, p^M) two ensembles of snapshots of the considered system of evolution corresponding to the time instances t_1, \dots, t_M where $[t_1, t_M] = I_M \subset I$ ($|I_M|$ is considerably smaller than $|I|$).

3.1 Proper Orthogonal Decomposition

The basic steps to construct such a decomposition using the POD method are first by building the correlation matrices K^u and K^p from the considered snapshots whose elements are given as

$$K_{ij}^u = \int_\Omega \tilde{\mathbf{u}}^i \tilde{\mathbf{u}}^j dx \quad K_{ij}^p = \int_\Omega p^i p^j dx$$

for $1 \leq i, j \leq M$. Then we compute the eigenvalues $\lambda_1, \dots, \lambda_M$ and eigenvectors $\mathbf{w}^1, \dots, \mathbf{w}^M$ of K^u , thereafter

we set $\Phi_{u,i} := \sum_{j=1}^M \mathbf{w}_j^i \tilde{\mathbf{u}}^j$ and finally we normalize $\Phi_{u,i} = \frac{\Phi_{u,i}}{\|\Phi_{u,i}\|}$. The same applies to obtain $\Phi_{p,i}$, $i=1, \dots, M$.

The function $\Phi_{u,i}$ and $\Phi_{p,i}$, $i=1, \dots, M$ constructed this way are called modes. They are mutually orthonormal and optimal in terms of their ability to represent the flow kinetic energy [6], i.e. they are optimal with respect to the L^2 scalar product in the sense that no other basis can contain more energy in fewer modes. In order to obtain a low dimensional basis that represents velocity and pressure only the first m modes corresponding to higher eigenvalues are considered. Then the velocity field and pressure are approximated as

$$\begin{cases} \tilde{\mathbf{u}}(t, x) \approx \tilde{\mathbf{u}}_m(t, x) = \sum_{i=1}^m \alpha_{u,i}(t) \Phi_{u,i}(x) \\ p(t, x) \approx p_m(t, x) = \sum_{i=1}^m \alpha_{p,i}(t, x) \Phi_{p,i}(t, x) \end{cases} \quad (14)$$

The reduced order model (ROM) of the primal problem (2) resulting from the Galerkin projection of its equations onto the selected spacial basis is given by

$$\begin{cases} \sum_{k=1}^m \left\{ (\Phi_{u,k}, \Phi_{u,l})_{L^2} \frac{d}{dt} \alpha_{u,k} - (\Delta\Phi_{u,k}, \Phi_{u,l})_{L^2} \alpha_{u,k} \right. \\ \quad \left. + (\nabla\Phi_{p,k}, \Phi_{u,l})_{L^2} \alpha_{p,k} \right\} = (\tilde{\mathbf{f}}, \Phi_{u,l})_{L^2} \\ \sum_{k=1}^m (\Phi_{u,k}, \Phi_{u,l})_{L^2} \alpha_{u,k}(t_i) = (\tilde{\mathbf{u}}^{t_i}, \Phi_{u,l})_{L^2} \\ l = 1, \dots, m \end{cases} \quad (15)$$

The same applies to obtain the ROM corresponding to the Dual problem (8). These differential equations are going to be solved in each iteration of the control algorithm to predict the flow in the whole time interval I . The POD

suboptimal control problem is summarized in algorithm 1

```

k=0:θk=θini∈Uad
while J>ε do
  1 : Solve problem (10) to obtain  $\tilde{\mathbf{u}}^{t_i}$ 
  2 : Solve Primal
  problem (2) in  $I_M \subset I$  (extract snapshots)
  3 : Compute POD primal spatial basis, solve
  the corresponding ROM and reconstruct  $\tilde{\mathbf{u}}_m$  .
  4 : Solve Dual
  problem (8) in  $I_M^* \subset I$  (extract snapshots)
  5 : Compute POD
  dual spatial basis, solve the corresponding
  ROM and reconstruct  $\eta_{u,m}$  and  $\eta_{p,m}$ .
  6 : Solve problem (12) to obtaine ( $\eta_u, \eta_p$ )
  7 : Evaluate the descente
  direction  $d_k = -\mathcal{J}_\theta$  with equation (13)
  8 : Determine
  the new control  $\theta_k = \theta_k + \rho_k d_k$  ( $\rho_k > 0$ )
end

```

Algorithm 1: POD suboptimal control algorithm

For the sake to reduce time CPU time required by steps 2 and 4 in the algorithm above, we propose the utilization of Proper Generalized Decomposition approach.

3.2 Proper Generalized Decomposition

In contrast to POD, Proper Generalized Decomposition (PGD) is considered as an a priori space time decomposition [7], i.e. it does not require previously computed data. Moreover it has the natural property of learning from its own error to approach the solution. In order to define a generalized decomposition for the mixed problem in hand, let's introduce first the following function spaces

$$\tau = L^2(I), \mathcal{V}_r = \tau \otimes V, \mathcal{P}_r = \tau \otimes L_0^2(\Omega), \mathcal{H}_r = \tau \otimes H$$

$$K = L^2(I, H_0^1(\Omega)) \times L^2(I, L_0^2(\Omega));$$

The goal is to establish (14),

$$\begin{cases} \tilde{\mathbf{u}}(t,x) \approx \tilde{\mathbf{u}}_m(t,x) = \sum_{i=1}^m \alpha_{u,i}(t) \Phi_{u,i}(x) \\ p(t,x) \approx p_m(t,x) = \sum_{i=1}^m \alpha_{p,i}(t,x) \Phi_{p,i}(t,x) \end{cases}$$

To simplify the notations we write

$$\{\tilde{\mathbf{u}}, p\} \approx \{\tilde{\mathbf{u}}_m, p_m\} = \sum_{i=0}^m \alpha_i \otimes \Phi_i \in \mathcal{V}_r \times \mathcal{P}_r$$

Let us assume that space time decomposition of order $m-1$ is known for both velocity vector field and pressure scalar function. The new couple (α_m, Φ_m) is determined so that it satisfies the double Galerkin orthogonality criteria. That is $\mathcal{S}_m(\alpha) = \Phi$ and $\mathcal{T}_m(\Phi) = \alpha$. \mathcal{S}_m and \mathcal{T}_m are respectively defined by

$$\begin{cases} \langle \mathcal{N}(\{\mathbf{u}_{m-1}, p_{m-1}\} + \alpha \otimes \Phi), \alpha \otimes \Psi \rangle_{K^*, K} = 0, \\ \langle \mathcal{N}_0(\mathbf{u}_{m-1} + \alpha_u \Phi_u), \alpha_u \Psi_u \rangle_{\mathcal{H}_r^*, \mathcal{H}_r} = 0, \\ \forall \Psi \in H_0^1 \times \mathcal{P}, \forall \Psi_u \in H \end{cases} \quad (16)$$

and

$$\begin{cases} \langle \mathcal{N}(\{\mathbf{u}_{m-1}, p_{m-1}\} + \alpha \otimes \Phi), \beta \otimes \Phi \rangle_{K^*, K} = 0, \\ \langle \mathcal{N}_0(\mathbf{u}_{m-1} + \alpha_u \Phi_u), \beta_u \Phi_u \rangle_{\mathcal{H}_r^*, \mathcal{H}_r} = 0, \\ \forall \beta \in \tau^2, \forall \beta_u \in \tau. \end{cases} \quad (17)$$

where

$$\mathcal{N}(\tilde{\mathbf{u}}, p) = \left(\frac{\partial}{\partial t} \tilde{\mathbf{u}} - \frac{1}{Re} \Delta \tilde{\mathbf{u}} + \nabla p - \tilde{f}(\theta), \nabla \cdot \tilde{\mathbf{u}} \right)$$

$$\mathcal{N}_0(\tilde{\mathbf{u}}) = \tilde{\mathbf{u}}(t_i) - \tilde{\mathbf{u}}^{t_i}$$

This problem can be interpreted as a generalized eigenvalue problem [8], and by consequence a power like method can be numerically implemented to enrich the old decomposition.

Bellow we summarize the PGD algorithm, as well as the PGD suboptimal control algorithm.

```

for m=1 to mmax do
  1 : Initialisation of α (and normalize),
  for k=1 to kmax do
    2 : Solve Φ = S(α) (16),
    3 : Solve α = T(Φ) (17) and normalize,
    4 : check convergence,
  end
  5 : Enrich
  spatial basis Ψm = span{Φ1, ..., Φm-1, Φ},
  6 : Update step : Solve Λm = T(Ψm) (Eqs.15)
  7 : Set {um, pm} = Λm · Ψm,
  8 :
  Evaluation of the residual, convergence check.
end

```

Algorithm 2: Progressive PGD algorithm with update step

The PGD suboptimal control algorithm is given as following

The PGD suboptimal control algorithm is given as following

```

k=0:θk=θini∈Uad
while J>ε do
  1 : Solve problem (10) to obtain  $\tilde{\mathbf{u}}^{t_i}$ 
  while Resp>εp do
    2 : Apply
    algorithm 2 to enrich the primal basis.
  end
  while Resd>εd do
    3 : Apply
    algorithm 2 to enrich the dual basis.
  end
  3 : Solve problem (12) to obtaine ( $\eta_u, \eta_p$ )
  4 : Evaluate the descente direction  $d_k = -\mathcal{J}_\theta$ 
  5 : Determine
  the new control  $\theta_k = \theta_k + \rho_k d_k$  ( $\rho_k > 0$ )
end

```

Algorithm 3: PGD suboptimal control algorithm.

Here Res_p and Res_d are respectively the residuals of primal and dual problems. $\epsilon > 0$, $\epsilon_p > 0$ and $\epsilon_d > 0$ are the precisions set by the user.

Remark 1 In numerical applications, to ensure a fast convergence of algorithm 1 and 3, the descent step ρ_k should be defined so that it realizes the optimal descent. One way to do so, is by verifying the Armijo descent step condition. This condition requires an evaluation of the objective functional (3) for every suggested step until it

holds. Therefore it is worth noting that in the case of reduced models, the test of Armijo condition could be done by simply conserving the spatial basis which still valide for a range of control parameters, and afterwards solving the ROMs (15) associated to neighbor control parameters generated from each proposed descent steps ρ_k .

4 Numerical experiments

4.1 Problem setup

In this section we propose to control the flow governed by Stokes equations inside a Lid driven cavity, by acting on the parameter θ of the top boundary condition.

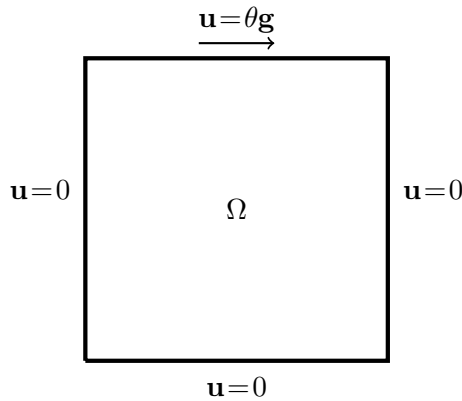


Figure 1: Studied Problem

Starting from the flow associated to different arbitrary first guesses θ_{ini} , the aim of this study is to find the target control parameter θ_c corresponding to the given velocity field $\tilde{\mathbf{u}}_c$. To achieve it, POD/ROM and PGD/ROM will be imbedded in the control algorithm. To obtain the discrete form of the problem, on one hand we use a first order impicite scheme for the time interval $I = [0,4]$ where $dt = 0.08$. On the other hand the finite element method (Taylor-Hood Q_2/Q_1) for the spatial domain $\Omega = [0,1] \times [0,1]$. Ω is subdivided to 552 quadrilaterals, which is $N_u = 2273$ and $N_p = 585$ where N_u and N_p are respectively the degree of freedom for velocity and pressure. The resulting finite dimensional saddle point problem to be solved twice (for primal and dual problems) in every control iteration with respect to control variation is of the type

$$\begin{cases} M \frac{d}{dt} u + Ru - B^t p = f \\ Bu = 0. \\ u(t_i) = u^{t_i}. \end{cases} \quad (18)$$

where M and R are the $N_u \times N_u$ mass and stiffness matrices, and B is the $N_p \times N_u$ divergence matrix. Augmented Lagrangian approach was opted in order to solve this problem.

4.2 Results analysis

Figures 2 and 3 depicts respectively the convergence behaviour to the target control as well as the evolution by respect to iterations of the objective functional. It is

obviously shown that convergence is ensured for all the considered starting control guesses and a good approximation of the desired control is reached after few iterations. Moreover, control using PGD/ROM is nearly of the same order compared with control using POD/ROM.

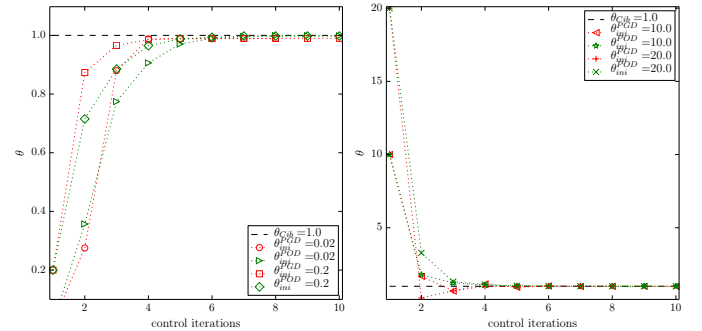


Figure 2: Convergence of control parameter for different initial guesses, $\theta_{ini} = 0.02$ and $\theta_{ini} = 0.2$ (left), $\theta_{ini} = 10$ and $\theta_{ini} = 20$ (right) with POD/ROM and PGD/ROM

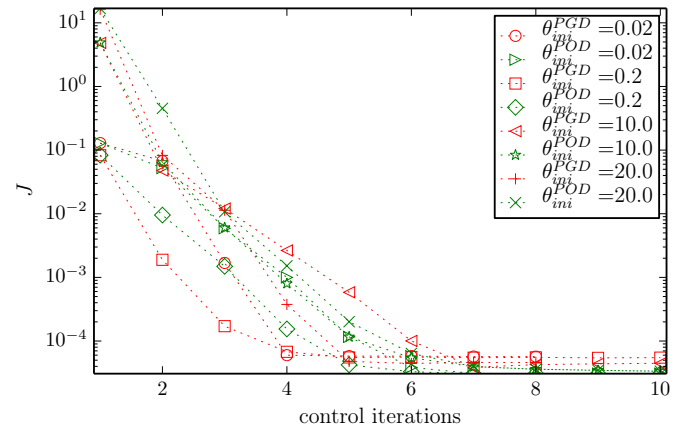


Figure 3: Evolution of objective functional \mathcal{J} versus control iterations

Table 1 contains relative errors defined as

$$Err(\mathbf{v}) = \frac{\|\mathbf{v} - \mathbf{u}_c\|_{L^2(I;L^2(\Omega))}^2}{\|\mathbf{u}_c\|_{L^2(I;L^2(\Omega))}^2} \cdot 100\%,$$

where \mathbf{u}_c is the target field that corresponds to θ_c and v is the approximated field. The percentage of errors for the two approaches is significantly small and then the resulting controlled velocity is a good approximation of the target field \mathbf{u}_c . This can also be seen in Figures 4 and 5 which represents velocity profiles in the center of cavity of the controlled velocity filed using the two approaches PGD/ROM and POD/ROM vis-a-vis to the target velocity field profiles.

Relative Errors				
θ_{ini}	0.02	0.2	10	20
$Err(\mathbf{u}_{POD})$	0.015%	0.015%	0.015%	0.015%
$Err(\mathbf{u}_{PGD})$	0.02%	0.03%	0.018%	0.019%

Table 1: Relative Errors

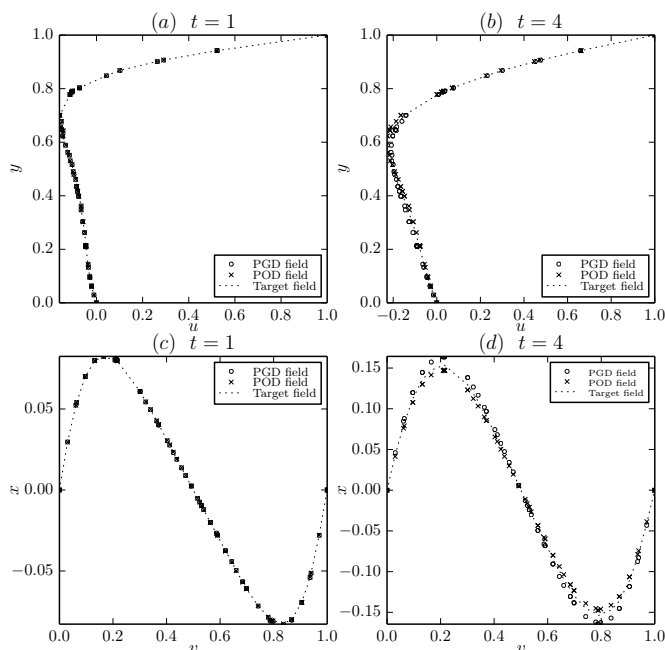


Figure 4: Comparison of controlled velocity profiles obtained by POD/ROM and PGD/ROM in the center of the cavity for $\theta_{ini}=0.2$. Figure (a) (resp (b)) represents the horizontal velocity on $x = 0.5$ and Figure (c) (resp (d)) the vertical velocity on $y = 0.5$ at the time instance $t = 1$ (resp $t = 4$).

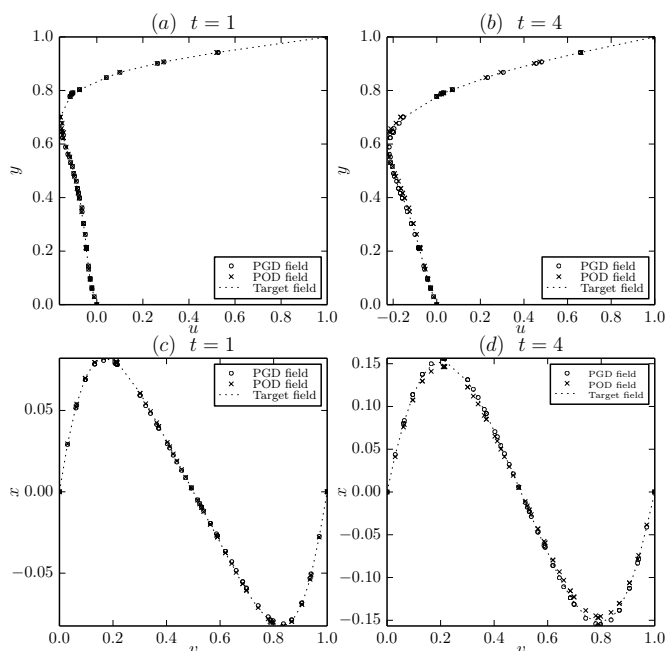


Figure 5: Comparison of controlled velocity profiles obtained by POD/ROM and PGD/ROM in the center of the cavity for $\theta_{ini}=10$. Figure (a) (resp (b)) represents the horizontal velocity on $x = 0.5$ and Figure (c) (resp (d)) the vertical velocity on $y = 0.5$ at the time instance $t = 1$ (resp $t = 4$).

Finally, Table 2 contains CPU time needed for the convergence of suboptimal control algorithms compared to the classical control. Recall that the Armijo descent step can be efficiently imbedded in PGD/ROM and POD/ROM control in a way that the convergence speeds up. Contrarily to the case of classical control where the evaluation of Armijo condition is very expensive.

Therefore the descent step considered for this last is set such that $\rho_k = \rho = 1$.

Computational CPU time				
θ_{ini}	0.02	0.2	10	20
Classical	τ_1	τ_2	τ_3	τ_4
POD	$\tau_1/2.5$	$\tau_2/33.3$	$\tau_3/5.3$	$\tau_4/8.3$
PGD	$\tau_1/7.6$	$\tau_2/90$	$\tau_3/11.1$	$\tau_4/14.3$

Table 2: Needed CPU time for suboptimal control algorithms using POD and PGD in order to attain a good approximation of target control. The CPU time is calculated compared to the classical control using full DNS simulations.

5 Conclusion

In this paper the PGD process was implemented within the boundary control problem of unsteady Stokes equations in a Lid driven cavity. In terms of CPU time, regardless the choice of the first guess θ_{ini} , numerical tests show that suboptimal control algorithms using either POD or PGD approaches are faster than the classical control algorithm. The gain in time is more important with PGD than POD. For $\theta_{ini}=0.02$, $\theta_{ini}=10$ and $\theta_{ini}=20$ the time is nearly divided by 10 and even 90 for $\theta_{ini}=0.2$ compared with the classical approach. Moreover, the convergence behaviour to the optimum as well as the obtained approximated solution endorse the fact that the PGD method has the property to adapt the reduced basis respectively to control variations.

References

- [1] M. Bergmann and L. Cordier, “Optimal control of the cylinder wake in the laminar regime by trust-region methods and pod reduced-order models,” *Computational Physics*, vol. 227, pp. 7813–7840, 2008.
- [2] S. S. Ravindran, “Constraint qualifications in maximization problems,” *Proper Orthogonal Decomposition in Optimal Control of Fluids*, 1999.
- [3] K. Ito and S. S. Ravindran, “Reduced basis method for optimal control of unsteady viscous flows,” *Computational Fluid Dynamics*, 1997.
- [4] A. Tallet, C. Allery, and C. Leblond, “Optimal flow control using a pod based reduced-order model,” *Numerical Heat Transfer, Part B*, 2016.
- [5] A. Ammar, B. Mokdad, F. Chinesta, and R. Keunings, “A new family of solvers for some classes of multidimensional partial differential equations encountered in kinetic theory modelling of complex fluids: Part ii: Transient simulation using space-time separated representations,” *Non-Newtonian Fluid Mechanics*.
- [6] L. Sirovich, “Turbulence and the dynamics of coherent structures: I, ii and iii,” *Quarterly of Applied Mathematics*, pp. 461–590, 1987.
- [7] C. Leblond and C. Allery, “A priori space-time separated representation for the reduced order modeling of low reynolds number flows,” *Computer Methods in Applied Mechanics and Engineering*, 2014.
- [8] A. Nouy, “A generalized spectral decomposition technique to solve a class of linear stochastic partial differential equations,” *Computer Methods in Applied Mechanics and Engineering*, 2007.

GREEN WALL IMPACTS INSIDE AND OUTSIDE BUILDINGS: EXPERIMENTAL STUDY

Rabah DJEDJIG^{1,*}, Rafik BELARBI², Emmanuel BOZONNET²

¹LERMAB, University of Lorraine, IUT de Longwy, 186 rue de Lorraine, 54400 Cosnes-et-Romain, France

²LaSIE, University of La Rochelle, France

*Corresponding author: Email: rabah.djedjig@univ-lorraine.fr

ABSTRACT

The experimental study of vegetated façades and their hygrothermal effects on heat loads is essential. Indeed, the complexity of thermal fluxes and airflows taking place within green walls modules under extreme climatic conditions is to date not mastered. In addition, phenomena related to buoyancy, street confinement, condensation, frost and sorption-desorption are not considered in most reliable models. This paper presents an experiment on green walls performed to apprehend their thermal and hydrological behavior and their impact inside and outside buildings. The experiment is based on a living wall set up on a reduced scale mockup of buildings and streets. Diurnal monitoring of temperature, humidity and heat fluxes variations near and within the living wall and a reference case enable us to analyze thermal effects of green façades. Measurements were performed in La Rochelle city in France

KEYWORDS

1. INTRODUCTION

Green roofs, living walls and green facades can be valuable for building energy performance and for urban microclimate mitigation [1–4]. They reduce the temperature peaks of external surfaces of buildings in summer [5,6]. Green facades affect the heat transfer through the building wall layers. Several experimental studies seek out quantifying the heat gains and losses from green walls [7–9]. Several studies estimate that green walls reduce significantly the building's cooling load during summer [2,10].

Thermo-hydric behavior of green facades is quite complex since they are influenced by their orientation and by surrounding urban environment. Compared to green roofs, experimental studies of green facades are uncommon. In Greece, temperature measurements were performed on a wall facing West and partially covered with creepers [11]. Measurements showed that vegetation cover reduces temperature peaks. Similarly, reference [12] reports a study carried out on a real building with green facade on East. In this study, greening was found to reduce

external surface temperature by about 5 ° C. Living walls with substrate imply additional issues related to water and heat transfer within the substrate. Thus, an experimental study [13] conducted in Hong Kong on a vegetated panel composed of a hydroponic medium of Rockwool and grass shows that gravity plays an important role on the vertical distribution of water in the substrate.

In urban environment, green walls thermal impacts are as important as for green roofs, especially in dense cities. When the urban structure is characterized by narrow street canyons, the radiation trapping increases the surface temperature and the reduced airflow recirculation leads to higher air temperatures. Alexandri & Jones [14] performed simulations for different canyon aspect ratios and climates. They studied a canyon with two green roofs and two green walls and found that the air temperature diminution within the canyon could reach about 10°C for a hot and arid climate. More recently, we have developed a new modeling approach to assess thermal impacts of green walls

on buildings in urban environment. A case study is presented in Djedjig *et al.*[15]. The simulated urban scene consists of a series of identical buildings and street canyons. Each building is a three story full scale building. The cooling load was compared for buildings with different aspect ratios ($H/W = 0, 0.5$ and 1.0) depending on the width of the streets. The results quantify the progressive effects of streets confinement according to the aspect ratio variation and the potential of green walls to mitigate increased cooling loads. The numerical results show that green walls installed on east and west façades of the studied building reduces by 37% the cooling load of nearby buildings with an aspect ratio equal to one and reduce it by 33% for a secluded building, for Athens summer climate.

There is still a lack of experimental data on these effects, so our study focuses on the experimental verification of such results and gives verification data for developed models. In this paper, we present an experimental approach to determining thermal impacts of green walls on buildings. The study was conducted on a reduced-scale model similar to a typical urban scene characterized by five rows of street canyons. The main objective was to assess the impact of vegetated building facades through relative comparisons with a reference building without vegetation and in real climatic conditions. The study also aimed to provide a database of experimental measurements.

2. MOCKUP DESIGN

The experimental platform consists of five rows of concrete empty tanks which stand for reduced scale buildings (Figure 1). Each row is made up of three tanks which form a block of 5 m long, 1.24 m high and 1.12 m wide. The aspect ratio of the street canyons is 1.2 and the scale reduction is approximately 1:10. The experimental bench is built on a $10 \text{ m} \times 20 \text{ m}$ terrace of concrete tiles. The canyon facades, oriented to East and West, and roofs are painted in white.

A green wall system was set up on the West façade (GWallF) of one row of buildings. The green wall growing medium consists in Chile sphagnum of 15 cm thick and is fixed on a metal grid which forms an air layer weakly ventilated of 5 cm. There are six different species of vegetation planted on the green wall. This later is watered twice a day by an

automatic drip watering system. One row of concrete tanks and one street canyon (RefC) was kept as a reference for further comparisons.



Figure 1: Experimental Mockup ClimaBat

The experiment aims to assess the impact of the vegetated envelopes on diurnal and seasonal variations in indoor and outdoor environments. Many sensors were installed to measure temperature, air humidity and solar irradiation all over the platform. The used thermocouples are type K (chromel-alumel) with an accuracy of about $0.3 \text{ }^\circ\text{C}$.

RESULTS AND DISCUSSION

Impact inside buildings: In this section we compare the temperature measurements performed inside the reduced scale buildings. The positions of the sensors whose measurements are analyzed are shown in the sketch at the top of Figure 2. There are two thermocouples that measure inside air temperatures and 12 other thermocouples placed at different locations that measure inside surface temperatures.

Figure 2 is composed of three graphs: the first compares the measurements of the temperature performed on the inner surface of the two façades facing west (the vegetated facade and the reference façade). The second graph compares the inside air temperature measurements performed within the two blocks. The third one shows the difference between the operative temperatures calculated on the basis of all previous measurements for both reference and vegetated blocks.

As we can see on the first graph, the green walls installed on the west façade decrease the inner

temperature of the facade up to 10°C (from 35°C for 25°C for example). The decrease of temperature concerns only daytime periods, at night there is no change in this temperature. The decrease in inner facade temperature leads to lower inside air temperature. In fact, the second graph of Figure 2 shows that the inside air temperature picks are lowered by about 5°C. We remind that we are considering here building blocks of 5 cm concrete depth and without any insulation.

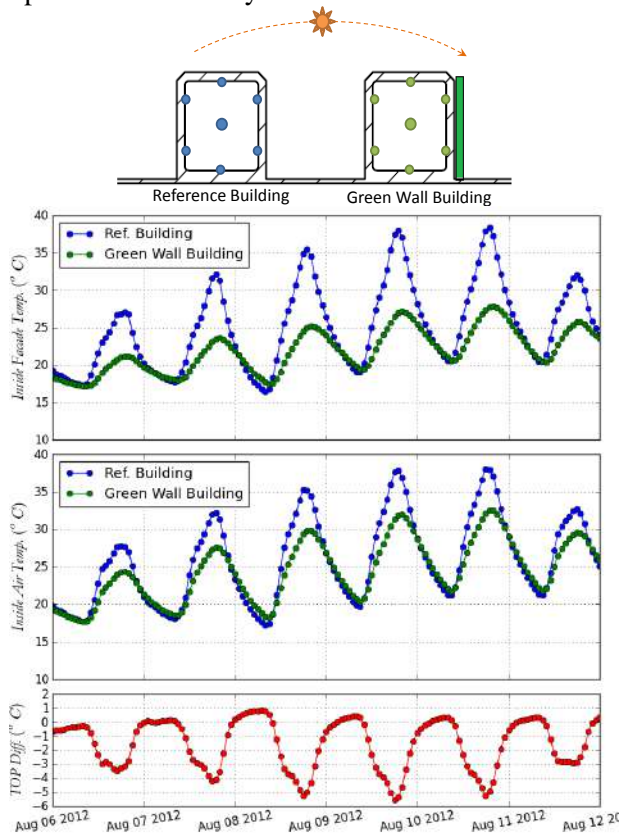


Figure 2: Comparison vegetated vs. reference building – Inside air temperature, Inner surface temperature and operative temperature

In order to assess of the green wall impacts on the indoor thermal comfort, the operative temperature inside the reference the green wall blocks have been calculated. The operative temperatures calculation is based on the temperature measurements performed inside the two building blocks. The sketch above Figure 2 shows the locations of the 7 thermocouples whose measurements have are used for each building block. Since the air motion is very low inside the mockup blocks, the operative temperature is taken equal to the mean value between the inside air temperature and the mean radiant temperature. The last part of Figure 2 shows the difference between the

operative temperatures calculated respectively for green wall building and for the reference building blocks. This temperature difference reach um 5°C in day time, a value substantially close to the measured difference in terms of inside air temperature.

Impact outside buildings: In this section we investigate the thermal impact of the green wall outside of buildings. Indeed, the green wall refreshes outdoor air temperature. In confined spaces such as street canyons, measurable reduction in air temperature takes place in summer. Measurements presented reference [3] show that the green wall tested on this experimental mockup reduce until 1.5 °C the temperature rise within the street canyon.

In this paper we focus mainly on the temperature gradient that takes place near the green walls. So we will compare the temperature variation observed through streets canyons. Concretely, we compare the difference between the temperatures measured by thermocouples T3 and T4 placed in the green wall Street to the difference between the temperatures measured by thermocouples T1 and T2 located in the reference Street (see Figure 3). It is clear that in the absence of the green wall the two curves are superimposed. On this figure, green colored area represents the deviation of the green wall street compared to the reference street. As can be seen, the compared difference is negative in morning and positive in afternoon, which is quite expected since the facades facing east warm up in morning and those facing the west heat up in the afternoon.

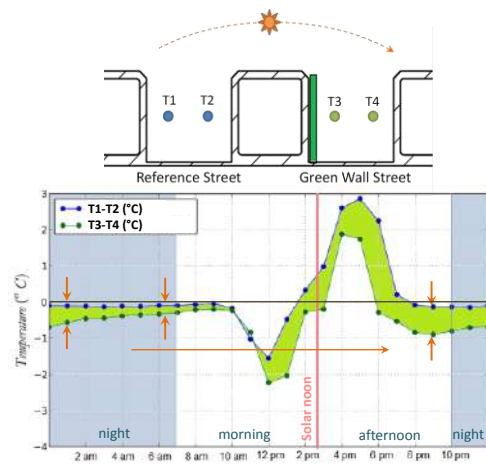


Figure 3: Comparison of temperature difference measured across street canyons

The green wall effect can be seen in the difference between the two curves. In fact, Figure 3 signifies that the green wall refreshes the air within the street by cooling the air near the facade. This is why the difference T3-T4 remains lower than the difference T1-T2 during all the day. We can see also that the cooling effect diminishes progressively during night when no irradiation on the considered walls.

CONCLUSIONS

The experimental work presented in this paper enables us to measure the thermal impact of vegetated walls inside and outside buildings. Thus, it has been shown that the green wall reduce the mean radiant and indoor air temperatures. Furthermore, the results show that the green facade cools the air near it leading to the streets cooling effect.

ACKNOWLEDGMENTS

This work was supported by the French Research National Agency on the reference ANR-09-Vill-0007-04 (project VegDUD)

REFERENCES

- [1] Saadatian, O., Sopian, K., Salleh, E., Lim, C. H., Riffat, S., Saadatian, E., Toudeshki, A., and Sulaiman, M. Y., 2013, "A review of energy aspects of green roofs," *Renewable and Sustainable Energy Reviews*, **23**, pp. 155–168.
- [2] Djedjig, R., Bozonnet, E., and Belarbi, R., 2015, "Analysis of thermal effects of vegetated envelopes: Integration of a validated model in a building energy simulation program," *Energy and Buildings*, **86**, pp. 93–103.
- [3] Djedjig, R., Bozonnet, E., and Belarbi, R., 2015, "Experimental study of the urban microclimate mitigation potential of green roofs and green walls in street canyons," *Int. J. Low-Carbon Tech.*, **10**(1), pp. 34–44.
- [4] Wong, N. H., Chen, Y., Ong, C. L., and Sia, A., 2003, "Investigation of thermal benefits of rooftop garden in the tropical environment," *Building and Environment*, **38**(2), pp. 261–270.
- [5] Jaffal, I., Ouldboukhitine, S.-E., and Belarbi, R., 2012, "A comprehensive study of the impact of green roofs on building energy performance," *Renewable Energy*, **43**, pp. 157–164.
- [6] Dvorak, B., and Volder, A., 2013, "Rooftop temperature reduction from unirrigated modular green roofs in south-central Texas," *Urban Forestry & Urban Greening*, **12**(1), pp. 28–35.
- [7] Wong, N. H., Kwang Tan, A. Y., Chen, Y., Sekar, K., Tan, P. Y., Chan, D., Chiang, K., and Wong, N. C., 2010, "Thermal evaluation of vertical greenery systems for building walls," *Building and Environment*, **45**(3), pp. 663–672.
- [8] Pulselli, R. M., Pulselli, F. M., Mazzali, U., Peron, F., and Bastianoni, S., 2014, "Emergy based evaluation of environmental performances of Living Wall and Grass Wall systems," *Energy and Buildings*, **73**, pp. 200–211.
- [9] Susorova, I., Angulo, M., Bahrami, P., and Brent Stephens, 2013, "A model of vegetated exterior facades for evaluation of wall thermal performance," *Building and Environment*, **67**, pp. 1–13.
- [10] Zinzi, M., and Agnoli, S., 2012, "Cool and green roofs. An energy and comfort comparison between passive cooling and mitigation urban heat island techniques for residential buildings in the Mediterranean region," *Energy and Buildings*, **55**, pp. 66–76.
- [11] Tsoumarakis, Assimakopoulos, V. ., Tsiros, I., Hoffman, M. E., and Chronopoulou, A., 2008, "Thermal performance of a vegetated wall During hot and cold weather conditions," Dublin.
- [12] Eumorfopoulou, E. A., and Kontoleon, K. J., 2009, "Experimental approach to the contribution of plant-covered walls to the thermal behaviour of building envelopes," *Building and Environment*, **44**(5), pp. 1024–1038.
- [13] Cheng, C. Y., Cheung, K. K. S., and Chu, L. M., 2010, "Thermal performance of a vegetated cladding system on facade walls," *Building and Environment*, **45**(8), pp. 1779–1787.
- [14] Alexandri, E., and Jones, P., 2008, "Temperature decreases in an urban canyon due to green walls and green roofs in diverse climates," *Building and Environment*, **43**, pp. 480–493.
- [15] Djedjig, R., Bozonnet, E., and Belarbi, R., 2016, "Modeling green wall interactions with street canyons for building energy simulation in urban context," *Urban Climate*, **In Press**.

THERMAL TRANSMITTANCE COMPARISON BETWEEN MULTILAYER WALLS MADE FROM HOLLOW FIRED CLAY AND PLASTER-GRANULAR CORK BRICKS USING ELECTRICAL ANALOGY

Saad RAEFAT, Mohammed Souihel, Mohammed GAROUM, Najma LAAROUSSI
Laboratory of Energy, Materials and Environment, University Mohamed V-Rabat, EST Sale
(11060, 227 Avenue Prince Héritier, Sale, Morocco)

*Corresponding author: Fax: +212 37 88 15 64 Email: saad.raefat@gmail.com

ABSTRACT

In this work a comparative study of thermal transmittance between different multilayer walls is examined numerically using the so called Combined Method recommended in the Moroccan standard NM EN ISO 6946/2007. For this purpose a special script was written in Mathematica based on the electrical analogy and where all the thermal transfers occurring across the brick were considered. Three configurations with and without air gap of 7 cm were compared. The first configuration, concerns walls made of cement render, cement mortar and three sizes of hollow clay fired bricks (3, 8 and 12 cavities). In the second one, bricks were substituted with those prepared with plaster and granular cork mixes. Finally, in this second case, plaster-granular cork was used instead of cement render. In addition, the compliance with the Moroccan Thermal Regulation of Construction (MTRC) was examined. Results show that in the third configuration, double walls (with air gap) consisting of 8 or 12 cavities bricks are in accordance with all Moroccan climatic zones of the MTRC.

KEYWORDS: Equivalent thermal transmittance; electrical analogy; hollow clay bricks; composite materials; energy saving; external wall.

NOMENCLATURE

R_c thermal resistance of convection within brick cavity, K/W
 R_r thermal resistance of radiation within brick cavity, K/W
 R_{ca} thermal resistance of the brick cavity, K/W
 R_{er} thermal resistance of external render, K/W
 R_{ir} thermal resistance of internal render, K/W
 R_{vp} thermal resistance of vertical partition, K/W
 R_{hp} thermal resistance of horizontal partition, K/W
 R_m thermal resistance of mortar joint, K/W
 R_{si} internal surface thermal resistance, K/W
 R_{se} external surface thermal resistance, K/W
 R_{up} upper thermal resistance, K/W

R_{low} lower thermal resistance, K/W
 R_g air gap thermal resistance, K/W
 e_{vp} thickness of the vertical partition, m
 A_{hp} vertical partition area, m²
 d the thickness of the air gap, m
 b the length of the air gap, m
 N_m total number of mortar joints
 N_c total number of bricks in the wall
 N_{vp} total number of vertical partitions per brick (three for 8C, four for 12C)
 N_{hp} total number of horizontal partitions per brick
 N_{vc} total number of cavities per column per brick (in vertical direction)
 N_{hc} total number of cavities per row per brick

(in horizontal direction)

Greek letters

λ_{vp} thermal conductivity of the vertical partition, W/m²K
 ε_1 the right internal surface of the air gap emissivity
 ε_2 the left internal surface of the air gap emissivity

Subscripts

12C brick of twelve cavities
 8C brick of eight cavities
 3C brick of three cavities
 PCM Phase Change material

INTRODUCTION

Red fired clay hollow bricks, being mainly used to construct building walls, have been long known to accommodate warm homes in the winter and cool dwellings during summer; in contrast, they present several disadvantages and occupy a considerable amount of building's energy demand. Therefore many recent researches proposed alternatives of the usual bricks, [1] studied the thermal behaviour of hollow clay bricks made up of paper waste and optimized their thermal performance, [2] managed to reduce the total heat transfer occurring across brick walls by 23% through placing clay protuberances inside brick cavities, also [3] improved the thermal inertia of buildings by filling bricks with PCM. The effect of the type of PCM used, its quantity and position inside the brick cavities were then evaluated. Consequently, this paper propose the use of bricks made

of a new composite material plaster-granular cork instead of fired clay bricks, this will not only guarantee a better energy efficiency inside buildings, but will also suppress the environmental pollution resulted from the fired clay manufacturing process.

MATERIALS AND METHOD

In order to evaluate the thermal performance of different bricks inside the wall, three types of hollow bricks (fig1) frequently used in Moroccan buildings are studied; coded according to their cavities number.

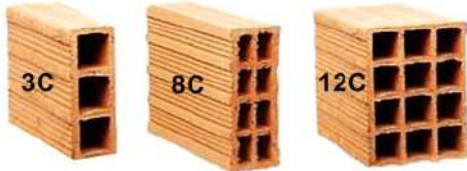


Figure 1
The different bricks studied

For easy thermal resistance determination, the representing unit cell is consisting of two superposed bricks 8C with joining mortar of 0.01m in thickness on the top and the bottom of each brick and between the two bricks, and with external and internal render of 0.02m; represented in fig 2 a.

Thermal conductivities of basic materials and of the composite material studied; picked from [4, 5], are given in table 1.

Table 1
Thermal conductivity of basic materials

Material	Thermal conductivity (W/m.K)
Fired clay	0.346
Cement mortar	0.703
Plaster- granular cork	0.101

MATHEMATICAL ANALYSIS

The method used in this work is based on the Combined Method disposed in the Moroccan standard NM ISO 6946/2007[6]. It provides an approximate rapid procedure that can be applied for inhomogeneous layers such as masonry walls. It consists of three steps described in [7].

In this method, the calculations must consider in addition of the conduction, the convection and radiation phenomena that occur within the air cavities. Assuming that:

- Thermal conductivity does not depend on temperature variation for materials studied.
- All thermal transfers are considered occurring in one dimension and under steady state conditions.

- Contrary to horizontal joints, vertical ones are neglected (their amount is neglected to the amount of bricks they are adjusting).
- Both convection and radiation in the pore space of the body brick are neglected, (since the dimensions of the pores are so small).
- The emissivity of the studied materials is considered constant ($\epsilon = 0.9$).

The thermal transmittance U (W/m².K) is determined according to [6]:

$$U_m = \frac{1}{R_{si} + R_{se} + R_m} \tag{1}$$

R_m is then calculated by averaging both R_{up} [8] and R_{low} [7]; determined by the following equations:

$$R_{up} = R_{er} + R_{ir} + \frac{1}{\frac{N_{hp}}{N_m} \left(\frac{N_{vp}}{N_{nc}} \right)} \tag{2}$$

$$R_{low} = R_{er} + R_{ir} + \frac{N_{vp}}{\frac{N_c}{R_{vp}} + \frac{N_m}{R_{m1}}} + \frac{N_{nc}}{N_b \times \left(\frac{N_{vc}}{R_{ca}} + \frac{N_{hp}}{R_{m2}} \right)} \tag{3}$$

The scheme of upper thermal resistance and lower thermal resistance decompositions is shown in fig 2b and fig 2c respectively.

Elementary thermal resistances are defined as the thickness of the partition in question divided by the product of its material thermal conductivity and its apparent section, for example, the vertical partition thermal resistance is expressed as follows:

$$R_{vp} = \frac{e_{vp}}{\lambda_{vp} \times A_{vp}} \tag{4}$$

As stated earlier, both convection and radiation phenomena occur inside the cavity, henceforth, the cavity thermal resistance is expressed as:

$$R_{ca} = \frac{1}{\frac{1}{2 \times R_c} + \frac{1}{R_r}} \tag{5}$$

The thermal resistances R_c and R_r are both determined using multiple equations, therefore they were simulated using a special script developed in Mathematica. For further details, one can consult [8].

Thermal resistances of internal and external surfaces are taken respectively as:

$$R_{si} = 1/h_{in} = 0.13 \text{ m}^2 \cdot \text{K/W} \text{ and } R_{se} = 1/h_{out} = 0.04 \text{ m}^2 \cdot \text{K/W}.$$

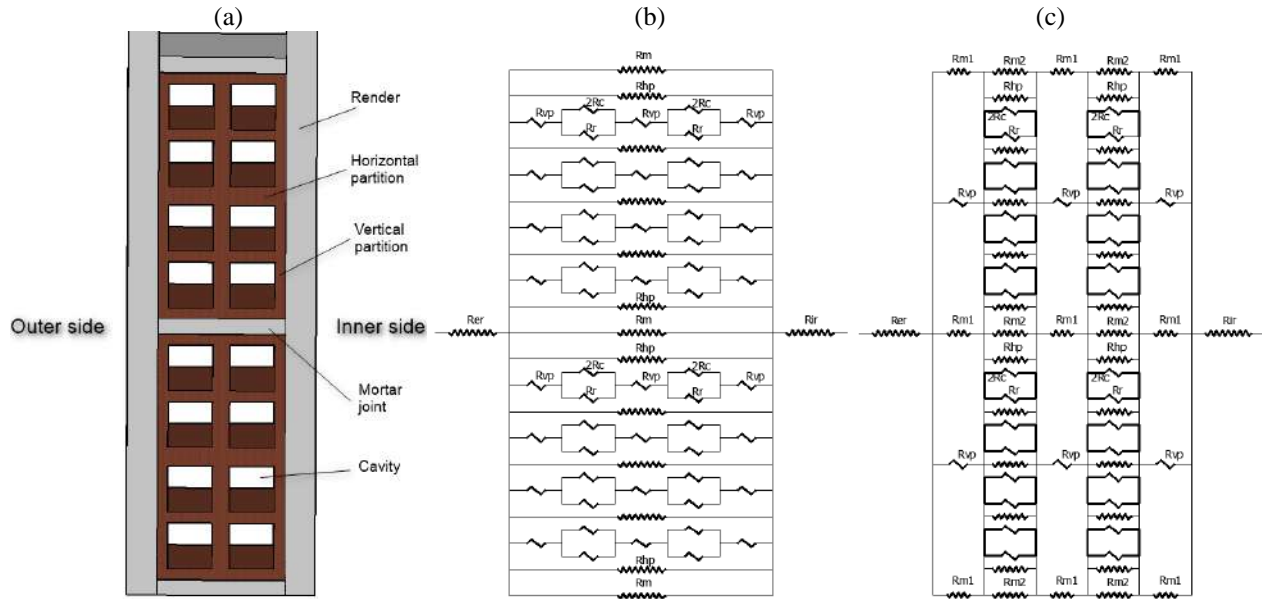


Figure 2
 (a) The representing cell for easy thermal resistance determination;
 (b) upper thermal resistance electrical analogy;
 (c) lower thermal resistance electrical analogy.

RESULTS AND ANALYSIS

Thermal transmission Comparison of tree different configurations: Tree configurations with and without air gap of 7 cm are compared, the configurations consist of:

- In the first cast, walls are made of cement render, cement mortar and hollow clay fired bricks.
- In the second one, bricks are substituted with others made of plaster- granular cork.
- Finally, in the previous case, plaster-granular cork was used instead of cement render.

For the tree configurations, the tree different bricks are compared.

Walls without air gap: In Morocco, most of exterior walls are made without air gap, this solution remains economic and occupies less space in buildings, and consequently, the thermal transmission of these walls was calculated in table 2 for the tree configurations and the tree types of bricks.

From table 2, It is clear that the higher the brick cavities the better is the overall thermal transmission of the wall, also, the thermal coefficients is getting better once we pass from a configuration to the next one, hence; the 3rd configuration represents the best thermal coefficients.

Walls with air gap: In order to ameliorate the walls thermal transmission and to ensure a better thermal efficiency inside buildings, walls are separated with an air gap of variant thicknesses (7cm in our case).

Table 2
 Thermal transmission of the different studied walls without air gap

Configuration	U _m (W/m ² .K)	Different bricks studied		
		3C	8C	12C
1 st	U _{up}	2,024	1,477	1,062
	U _{low}	2,127	1,560	1,099
	U _m	2,075	1,519	1,080
2 nd	U _{up}	1,553	1,048	0,733
	U _{low}	1,555	1,044	0,721
	U _m	1,554	1,046	0,727
3 rd	U _{up}	1,017	0,773	0,587
	U _{low}	1,018	0,771	0,579
	U _m	1,018	0,772	0,583

The thermal resistance of the air gap is calculated according to [6] and using the following equation:

$$R_g = \frac{1}{h_c + \left(\frac{1}{\epsilon_1} + \frac{1}{\epsilon_2} - 1\right) \cdot 4\sigma \cdot T_{av}^3 + \left[1 + \sqrt{1 + \frac{d^2}{b^2}} - \frac{d}{b}\right]} \quad (6)$$

And where:

$$h_c = \text{Max}[1.25 ; 0.025/d] \quad (7)$$

The thermal transmission coefficients were calculated for the different walls with air gap in the following table:

Table 3
Thermal transmission of the different studied walls with air gap

Configuration	U (W/m ² .K)	Different bricks studied		
		3C	8C	12C
1 st	U _{up}	1,161	0,821	0,569
	U _{low}	1,229	0,870	0,590
	U _m	1,194	0,845	0,580
2 nd	U _{up}	0,861	0,567	0,384
	U _{low}	0,862	0,564	0,378
	U _m	0,862	0,565	0,381
3 rd	U _{up}	0,667	0,475	0,340
	U _{low}	0,667	0,473	0,335
	U _m	0,667	0,474	0,337

It is observed from table 3 that the overall thermal transmission coefficient improvement of double walls is following the same pattern as of single walls, except that the improvement is more significant when the air gap is present.

Discussion of the compliance with the MTRC:

For the purpose of decreasing the building sector high demand, the MTRC (Moroccan thermal Regulation of Construction) [9] has recently become mandatory for the

six climatic zones presented in Morocco (fig 3). In its prescriptive approach, the thermal performance of the new dwellings is estimated knowing the thermal transmission U of their components.

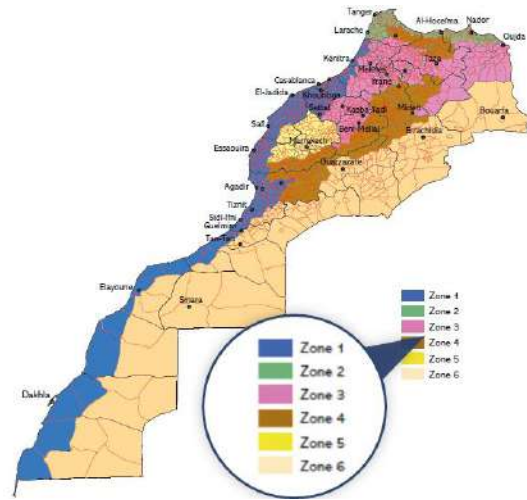


Figure 3

The six climatic Moroccan zones according to the MTRC

Indeed, in order to help building’s owners to choose between different walls configurations respecting the MTRC regardless of the Moroccan zone they are belonging to, the compliance of the different walls studied with the six climatic zones were represented in fig 4 for walls without air gap and in fig 5 for walls with air gap, according to their thermal transmission.

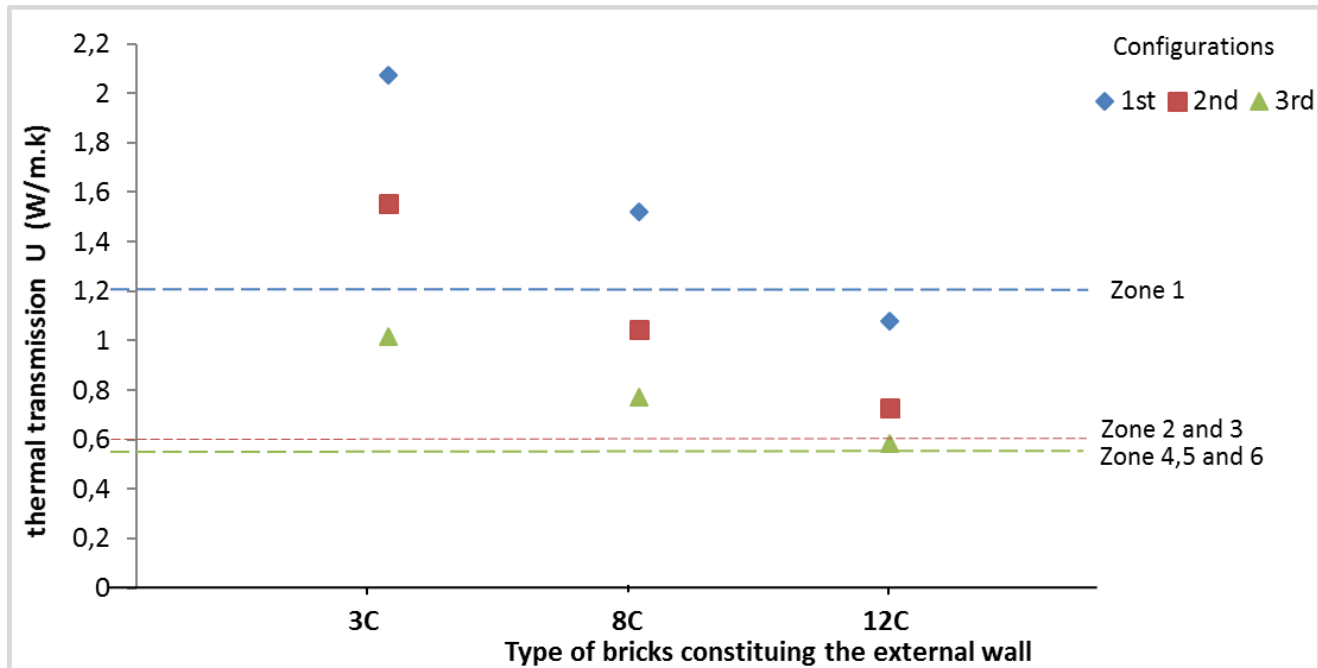


Figure 4

The compliance of the walls without air gap with the MTRC for the different configurations studied

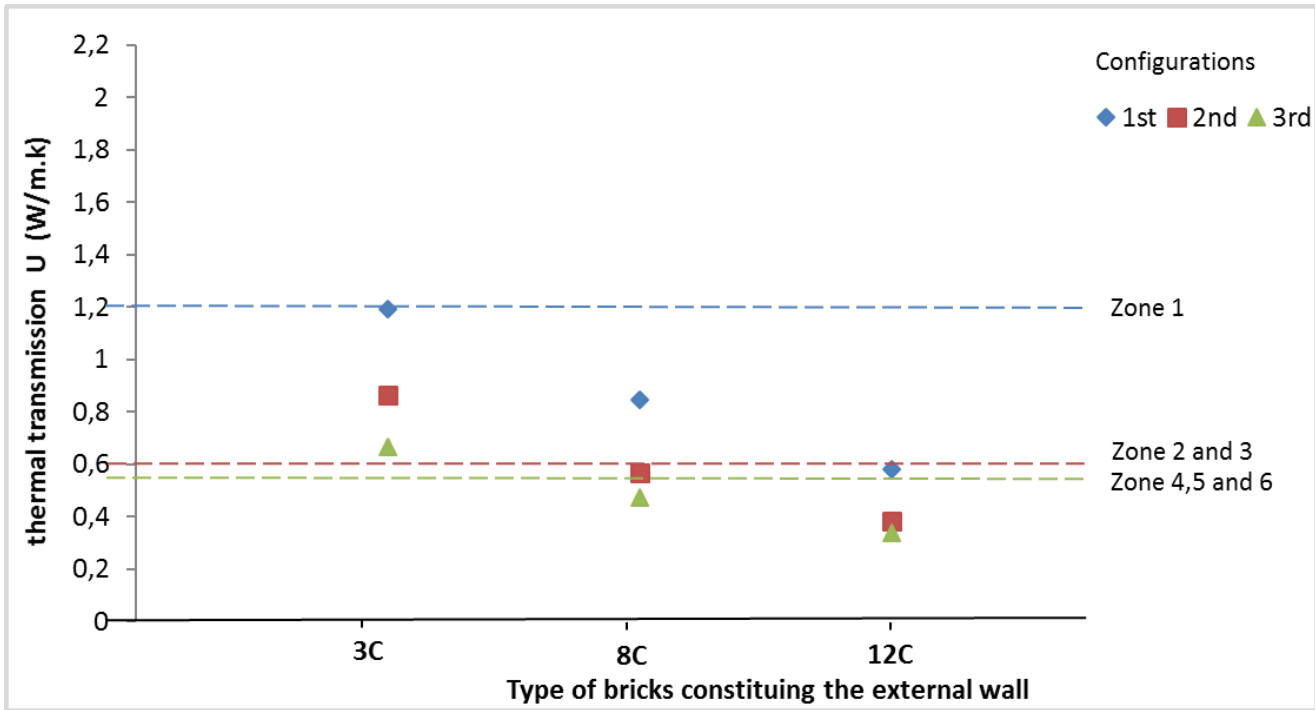


Figure 5
The compliance of the walls with air gap with the MTRC for the different configurations studied

From fig 4, for walls constituted with bricks 3C, only the third configuration is respecting the first zone’s thermal transmission. For bricks 8C, both first and second configurations are respecting the first zone, and for bricks 12C all the configurations are respecting it. Correspondingly, the third configuration is also respecting the second and the third zones for bricks 12C.

From fig 5, all the configurations are respecting the first zone’s thermal transmission for all the bricks studied, moreover, the second configuration walls of bricks 12C and the third configuration walls of bricks 8C and 12C are respecting all the six climatic zones.

The energy saving of the transition from the 1st to the 3rd configuration: In order to emphasise the thermal performance importance resulted from substituting clay bricks with bricks made of plaster-granular cork material, the energy gain was evaluated for the different walls in table 4 using (8).

$$\text{Energy_saving} = 100 \times \left(1 - \frac{U_{3rd}}{U_{1st}}\right) \quad (8)$$

From table 4 the energy saving of the transition from the 1st to the 3rd configuration increases from 40,90% (for 12C walls with air gap) up to 50,94% (for 3C walls without air gap), this will help to reduce the walls energy consumption up to the half making buildings more efficient and comfortable

Table 4: Energy saving of the transition from the 1st to the 3rd configuration:

Walls	Energy saving		
	3C	8C	12C
Without air gap	50,94%	49,18%	46,02%
With air gap	44,14%	43,91%	41,90%

Conclusion

This article has shown the interest of substituting fired clay bricks with plaster-granular cork bricks constituting walls, which represent the major surface areas of the buildings, by giving a thermal transmission coefficient comparison between different walls, for this purpose tree configurations were proposed and studied. Indeed, the 3rd configuration, which consist of a double wall composed of bricks and render made of plaster-granular cork, present the best transmission coefficient (0,337 W/m2.k for 7cm air gap’s thickness) and respect all climatic Moroccan zone’s thermal transmission. Furthermore, relevant information is obtained from calculating the energy saving of the transition from the 1st to the 3rd configuration for the different walls; the obtained results are leading to overall heat transfer reductions up to 51%. In addition, the 3rd configuration walls will be much heavier; this will decrease the total cost of buildings by reducing the required amount of reinforced concrete, by contrast this could raise some solidity for the brick wall. Accordingly,

this study needs to include furthermore the mechanical resistance determination of the studied walls.

References

1. Sutcu, M., del Coz Díaz, J. J, Álvarez Rabanal, F. P., Gencel, O., and Akkurt, S, 2014, Thermal performance optimization of hollow clay bricks made up of paper waste, *Energy and Buildings*, **75**, pp. 96-108.
2. Costa, V. A. F, 2014, Improving the thermal performance of red clay holed bricks, *Energy and Buildings*, **70**,pp. 352-364.
3. Hichem, N., Noureddine, S., Nadia, S., and Djamila, D, 2013, Experimental and numerical study of a usual brick filled with PCM to improve the thermal inertia of buildings, *Energy Procedia*, **36**.
4. Laaroussi, N., Cherki, A., Garoum, M., Khabbazi, A., and Feiz, A, 2013, Thermal Properties of a Sample Prepared Using Mixtures of Clay Bricks, *Energy Procedia*, **42** ,pp. 337-346.
5. Mounir, S., abdelhamid, K., and Maaloufa, Y, 2015, Thermal Inertia for Composite Materials White Cement-cork, Cement Mortar-cork, and Plaster-cork, *Energy Procedia*, **74**, 991-999.
6. NM. ISO6946/2007 Building components and building elements: Thermal resistance and thermal transmittance: Calculation method.
7. Raefat, S., Garoum, M and Laaroussi, N, Numerical estimation of apparent thermal resistance and transmittance of multilayer walls made from hollow clay bricks using the electrical analogy.
8. Bouchair, A, 2008, Steady state theoretical model of fired clay hollow bricks for enhanced external wall thermal insulation, *Building and Environment*, **43**, 1603-1618.
9. ADEREE, 2011, Règlement thermique de construction au Maroc, **46**.

NUMERICAL ANALYSIS OF HEAT AND MOISTURE TRANSFER IN POROUS MATERIAL

V. D. Thi^{1,2*}, F. Mnasri¹, M. Khelifa², M. El Ganaoui¹, Y. Rogaume²

¹ University of Lorraine, LERMAB, EA 4370, IUT de Longwy, 54400 Cosnes et Romain, France

² University of Lorraine, LERMAB, EA 4370, 27 rue Philippe Séguin, 88026 Epinal, France

*Corresponding author: Fax: +33 29 29 61 38 Email: vandiem.thi@univ-lorraine.fr

ABSTRACT

This paper presents a two-dimensional model to analyse the heat and moisture transfer through wood porous building materials. Transient coupled model of heat and moisture transfer in timber material under low temperature is presented. The resulting coupled model is converted to two nonlinear partial differential equations, which are then numerically solved by an implicit iterative scheme. The numerical results of temperature and moisture potential changes are compared with the experimental measurements available in literature. Predicted results demonstrate validation of the proposed theoretical model and effectiveness of the developed numerical algorithms. It is expected to provide useful information for the wood material design based on heat and moisture transfer model.

KEYWORDS Heat transfer; Moisture transfer; Porous materials; Wood; Finite element method.

1. INTRODUCTION

The behaviour of porous building material such as wood subjected to different environmental conditions is highly dependent on its material structure and chemical composition. The amounts of water present inside wood considerably influence its thermo-physical properties and geometric shape. Being porous, hygroscopic and orthotropic material, the heat and moisture transfer in timber makes a complex system of coupled mechanisms. Moreover, if the moisture content changes over time, this may induce distortions, residual stresses, and failures in timber products. In this case, almost all properties in wood as well as the wood–water relations are temperature-dependent. For these reasons, it is of particular interest to have good knowledge of these variables in various timber structures. The main objective of this article is to achieve an analysis of the heat and moisture transfers in porous materials by means of coupled model adopted for finite element analysis.

In the last decades, to improve building energy efficiency and indoor air quality, the coupled heat and moisture transfers in porous materials have been widely studied due to its presence in many industrial applications, particularly in timber buildings. Many researches have been performed such as [1-3]. To evaluate coupled heat and moisture transfer in porous building materials, Abahri et al. (2011) proposed a one-dimensional analytical model in ref [1]. Lack of

experimental and numerical results, no comparison was performed. Chang et al.(2000) also described an analytical solution to coupled heat and moisture diffusion transfer in porous materials. For the same application, the obtained results for the wooden slab are similar with other published analytical solutions using the decoupling technique [2]. Younsi et al. (2006) [3] present a mathematical model based on a set of coupled, heat and mass transfer equations presented by Luikov (1975) in ref [4]. They have also studied the effect of heat and mass transfer parameters through the Biot number on heat and moisture transfer. It was concluded that the governing dimensionless parameters have a significant influence on the kinetics of the heat and moisture transfer. To analyse the heat and moisture transfers in capillary porous media, Luikov (1966) in [5] proposed a model assuming the same analogy between moisture transport and heat transfer. This model was used by several researchers [6-7].

To solve the obtained coupled system for temperature and moisture potentials, many authors used both theoretical and numerical approaches. The solution of the governing partial differential equations depends on the considered specific problem. Generally, all approaches are based on the use of transformation functions. Chang et al. [3] have introduced a potential function corresponding to their equations system, using a change of

variables for temperature gradient and moisture rate. They used the boundary condition of Neumann type and compared their predicted results with those of Thomas et al. (1980) presented in [8].

This paper presents a numerical strategy applied to solve the partial differential equations. It concerns two-dimensional heat and moisture transfer through porous building materials. The finite element solutions were performed using the natural hygrothermal boundary conditions proposed by Abahri et al. [1] and Chang et al. [2]. A numerical approach by means of incremental finite element method will be presented. In order to validate the proposed finite element model, a numerical procedure and a staggered technique to resolve the coupling between temperature and moisture are given in details. Moreover, the comparisons of the obtained numerical results with other *analytical* models given by Abahri et al. [1], Chang et al. [2].

2. ANALYTICAL FORMULATION

Heat and moisture transfer in porous media subjected to convective boundary conditions can be modelled using Luikov's approach presented in [5]. The following assumptions are assumed in this work:

- The timber specimen is homogenous and the thermo-physical properties are constant.
- The initial values of moisture and temperature in wood were uniform.
- The shrinkage and the degradation of the timber sample were neglected.

The constitutive equations describing two-dimensional heat and moisture transfer for wood are given by [9] and [10] as follows:

Heat transfer

$$\rho c_p \frac{\partial T}{\partial t} = \lambda \left(\frac{\partial^2 T}{\partial x^2} + \frac{\partial^2 T}{\partial y^2} \right) + \rho c_m (\varepsilon \cdot h_{LV} + \gamma) \frac{\partial m}{\partial t} \quad (1)$$

Moisture transfer

$$\rho c_m \frac{\partial m}{\partial t} = D_m \left(\frac{\partial^2 m}{\partial x^2} + \frac{\partial^2 m}{\partial y^2} \right) + \delta \cdot D_m \left(\frac{\partial^2 T}{\partial x^2} + \frac{\partial^2 T}{\partial y^2} \right) \quad (2)$$

where T [K] is the temperature, m [°M] is the moisture potential, t [s] is time, x [m] and y [m] are the location coordinates, c_p [J/(kg.K)] and c_m [kg/(kg.°M)] are heat and moisture capacities of the medium, λ [W/(m.K)] and D_m [kg/(m.s.°M)] are thermal and moisture

diffusion coefficients respectively, ρ [kg/m³] is the dry solid density, ε is the ratio of vapour diffusion coefficient to coefficient of total moisture diffusion, γ [J/kg] is the latent heat, δ [kgmoisture/(kg.K)] is the thermal gradient coefficient and h_{LV} [kJ/kg] is the heat of phase change.

The associated hygrothermal boundary and initial conditions are listed below:

(a). Initial conditions

$$T(x,y,t=0)=T_0; \quad m(x,y,t=0)=m_0 \quad (3)$$

The moisture potential m is related to the moisture content M by:

$$M=c_m \times m \quad (4)$$

c_m [kg/(kg.°M)] is the specific mass capacity.

(b). Boundary conditions

$$\begin{aligned} T(x=0,y,t)=T_{in}; \quad T(x=L,y,t)=T_{out} \\ m(x=0,y,t)=m_{in}; \quad m(x=L,y,t)=m_{out} \end{aligned} \quad (5)$$

$$\begin{aligned} \frac{\partial T}{\partial y}(x,y=0,t)=0; \quad \frac{\partial T}{\partial y}(x,y=H,t)=0 \\ \frac{\partial m}{\partial y}(x,y=0,t)=0; \quad \frac{\partial m}{\partial y}(x,y=H,t)=0 \end{aligned} \quad (6)$$

Eqs. (1) & (2) are coupled heat and moisture transfer equations for porous building materials can be solved numerically by the finite element modelling.

3. FINITE ELEMENT MODELLING

The Galerkin's weighted residual method is used to discretize the space for Eqs.(1) and (2). Temperature T is selected as the state variable for heat transfer. The state variable for moisture transfer is chosen as moisture potential, denoted as m . For an element, the state variables are approximated by linearizing three node elements, for example:

$$\begin{aligned} T(x,y,t) &= \sum_{i=1}^3 N_i(x,y) \cdot T_i(t); \\ m(x,y,t) &= \sum_{i=1}^3 N_i(x,y) \cdot m_i(t) \end{aligned} \quad (7)$$

where $N_i(x,y)$ is the shape functions of triangular finite element, $T_i(t)$ is the time-dependent nodal temperatures and $m_i(t)$ is the time-dependent nodal moistures.

Applying Galerkin's weighted residual approach to Eqs. (1) and (2):

$$\rho c_p \int_{\Omega} N_i \frac{\partial T}{\partial t} d\Omega = \lambda \int_{\Omega} N_i \left(\frac{\partial^2 T}{\partial x^2} + \frac{\partial^2 T}{\partial y^2} \right) d\Omega + \rho c_m (\varepsilon \cdot h_{LV} + \gamma) \int_{\Omega} N_i \frac{\partial m}{\partial t} d\Omega \quad (8)$$

$$\rho c_m \int_{\Omega} N_i \frac{\partial m}{\partial t} d\Omega = D_m \int_{\Omega} N_i \left(\frac{\partial^2 m}{\partial x^2} + \frac{\partial^2 m}{\partial y^2} \right) d\Omega + \delta \cdot D_m \int_{\Omega} N_i \left(\frac{\partial^2 T}{\partial x^2} + \frac{\partial^2 T}{\partial y^2} \right) d\Omega \quad (9)$$

Inserting boundary conditions, applying the phase equilibrium relations and rearranging Eqs.(8) and (9), the resulting system of ordinary differential equations is obtained:

$$[C_T] \{\dot{T}\} + [K_T] \{T\} = [F_T] \{m\} \quad (10)$$

$$[C_m] \{\dot{m}\} + [K_m] \{m\} = [F_m] \{T\} \quad (11)$$

where $[C_T]$, $[K_T]$, $[F_T]$, $[C_m]$, $[K_m]$ and $[F_m]$ are corresponding matrices consisting of coefficients derived from Eqs. (8) and (9).

4. APPLICATION ON A WOOD SLAB BUILDING ENVELOPE

An application on a wood slab building envelope has been simulated using the material properties given from [1-2] which are associated to the boundary conditions described previously in section 2 are recapitulated in Table 1.

Table 1

Material properties for wood.

c_m	0.01 kg/(kg.°M)	ε	0.3
c_p	2500 J/(kg.K)	m_0	86 °M
δ	2 °M/K	m_{in}	45 °M
λ	0.65 W/(m.K)	m_{out}	4 °M
ρ	370 kg/m ³	h_{LV}	2.5×10^{-9} J/kg
D_m	2.2×10^{-8} kg/(m.s.°M)	γ	0
L	24 mm	T_{∞}	110 °C
H	60 mm	m_{∞}	4 °M
T_0	10 °C	h_c	2.25 W/(m ² .K)
T_{in}	60 °C	h_m	2.5×10^{-6} kg/(m ² .s.°M)
T_{out}	110 °C		

The Finite Element (FE) model of the wood slab of 24×60mm is modelled by 960 triangular elements consisted of 525 nodes. Figs 1 and 2 illustrate respectively the temperature and the moisture distribution in wooden slab sample at different times.

From Figs 1, it can be seen that at time $t=1000s$, a larger temperature gradient was established on 3/4 width plane of the tested specimen. During a prolonged heat transfer process (Figs 1a, 1b and 1c), the temperature distribution evolves rapidly at the beginning and then becomes stable. The temperature difference between the inner region and the outer region decreases more and more. After the heat and moisture transfer in wood slab panel, a moisture gradient was established in response to temperature gradient with maximum moisture potential in the surface region. The moisture content in the outer region decreased from 80°M moisture potential to around 70°M at time $t = 4000s$ (Fig. 2c). We also note that the moisture rate in the centre zone decreased progressively until the moisture potential reaches 70°M at time $t=1000s$ (Fig. 2b).

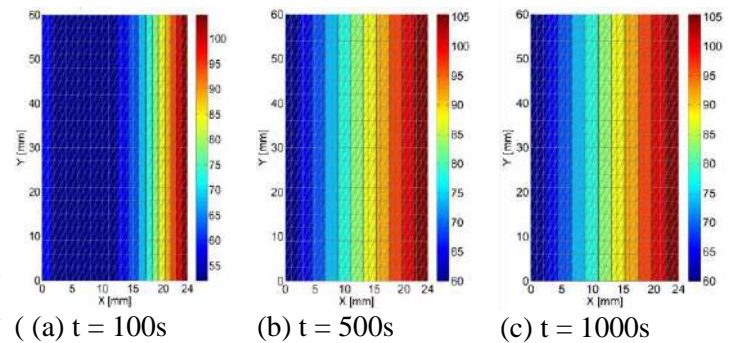


Fig. 1. Contour maps of temperature distribution at different time.

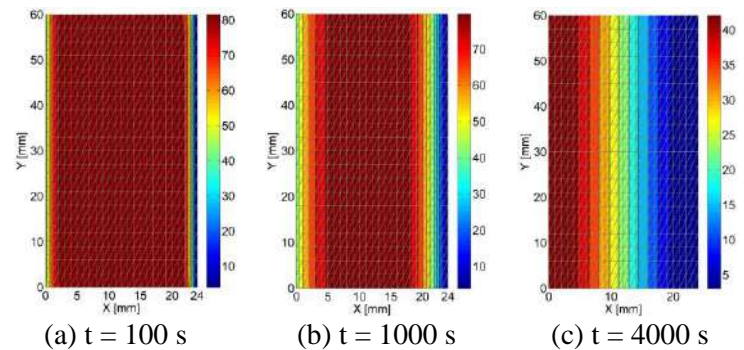


Fig.2. Contour maps of moisture potential distribution at different time.

Fig. 3 shows the temperature distribution of at the centre of wood slab ($x=12mm$). It can be seen that the temperature distributions of the three layers during the heat and moisture transfer can be divided in three different phases: I) an initial rising phase of temperature, II) a non-linear rising in temperature at the centre of wood panel and III) a quasi-stable

phase in temperature at the centre of the wall. The FE results are similar to the experimental results of Abahri et al. [1]. From a short time of 690s, the temperature is stationary and equal to 85.2°C, which is well predicted by the model.

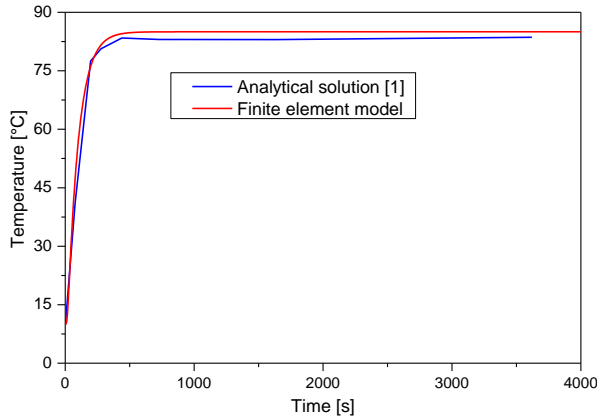


Fig. 3. Curves of temperature versus time at the centre of wood slab.

Fig. 4 shows the comparison between the analytical solution and predicted results of the moisture potential versus time at the centre of wood slab. It can be seen that the moisture potential distributions can be separated in three phases: I) an initial slightly linear increasing phase, II) a quasi-stable phase and III) a non-linear decreasing phase. There is a very good correlation between the analytical solution given in [1] and the obtained numerical results. During the heat and moisture transfer in the porous slab, the moisture potential continues to decrease with increase in time, until the end.

For the same example, the moisture evolution at the surface and at the middle of the slab are shown in Fig. 5. It can be seen that the results from the natural hygrothermal boundary conditions developed by Chang et al. [2] agree well. With regard to the moisture content profile of the wood slab at the surface and at the middle presented in Fig. 5, a good accuracy of the present model can then be verified by a very small difference around 1% between the predicted and the results obtained by Chang et al. in ref [2].

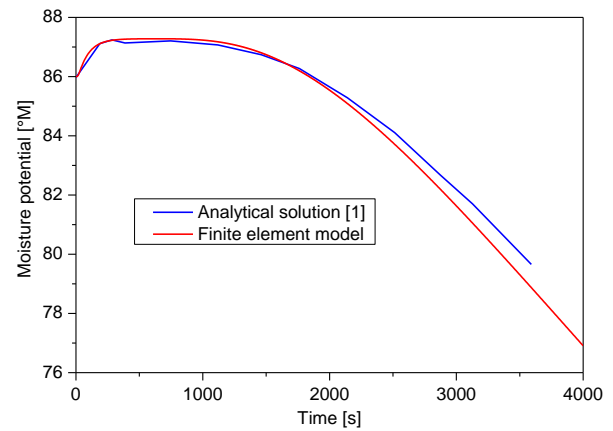


Fig. 4. Curves of moisture potential versus time at the centre of wood slab.

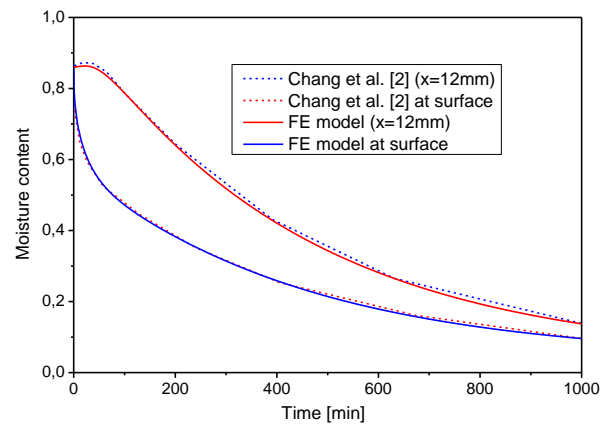


Fig. 5. Curves of moisture content versus time at two different locations.

5. CONCLUSION

The objective of this work is to propose a numerical methodology to simulate 2D heat and moisture transfer in porous building materials and to complete the work of Abahri and Chang in [1, 2] who solved this problem by using an one-dimensional analytical model. In the first step, a generalised mathematical model accounting the governing equations describing the coupled heat and moisture transfers for porous material has been formulated in detail. The associated numerical aspects in the framework of the classical Galerkin-based FE formulation are also discussed. Several finite element simulations using the natural hygrothermal boundary conditions proposed by Chang et al. [2] are conducted to compare the predicted results with the analytical and experimental measurements available in literature. The quality of the solutions obtained in terms of the hygrothermal fields' distribution, through the porous panel thickness, seems very satisfactory.

Further investigations are now under progress to extend this numerical procedure to 3D case with the hope of simulating the heat and moisture transfers in the porous building panels made by different materials and several layers under complex and severe hygrothermal conditions.

ACKNOWLEDGEMENTS

The authors acknowledge the LERMAB laboratory, which is supported by the French National Research Agency (ANR) through the Laboratory of Excellence ARBRE.

REFERENCES

1. Abahri K, Belarbi R, Trabelsi A. Contribution to analytical and numerical study of combined heat and moisture transfer in porous building materials. *Build Environ* 2011;46:1354-1360.
2. Chang W, Weng C. An analytical solution to coupled heat and moisture diffusion transfer in porous materials. *Int J Heat Mass Tran* 2000;43:3621-3632.
3. Younsi R, Kocaefe D, Kocaefe Y. Three-dimensional simulation of heat and moisture transfer in wood. *Appl Therm Eng* 2006;26:1274-1285.
4. Luikov AV. Systems of differential equations of heat and mass transfer in capillary-porous bodies. *Int J Heat Mass Tran* 1975; 8:1-14.
5. Luikov AV. Heat and mass transfer in capillary-porous bodies. Oxford: Pergamon Press; 1966. chap. 6.
6. Thomas HR, Morgan K, Lewis RW. A fully monolinear analysis of heat and mass transfer problems in porous media. *Int J Numer Meth Eng* 1980;15:1381-93.
7. Ribeiro JW. Complete and satisfactory solutions of Luikov equations of heat and moisture transport in a spherical capillary-porous body. *Int Commun Heat Mass* 2000;27:975-84.
8. Thomas HR, Lewis RW, Morgan K. An application of the finite element method to the drying of timber. *Wood Fiber* 1980;11(4):237-43.
9. Liu JY, Cheng S. Solution of Luikov equations of heat and mass transfer in capillary porous bodies. *Int J Heat Mass Tran* 1991;34:1747-54.
10. Qin M, Belarbi R. Development of an analytical method for simultaneous heat and moisture transfer in building materials utilising transfer function method. *J Mater Civil Eng ASCE* 2005;17(5):492-7

ELECTRICAL PREDICTION OF TORTUOSITY IN POROUS MEDIA

Merioua Abderrahmene, *EOLE laboratory, Civil Engineering, Tlemcen University, Algeria;*

Dr Bezzar Abdelillah, *EOLE laboratory, Civil Engineering, Tlemcen University, Algeria;*

Pr Ghomari Fouad, *EOLE laboratory, Civil Engineering, Tlemcen University, Algeria;*

BP 230 CHETOUANE Tlemcen 13000 ALGERIE

*Corresponding author: Email: merioua_abderrahmene@hotmail.com

ABSTRACT

The fluid transport phenomena in porous materials such as concrete is one of the main actions involved in the degradation of the structures lying in aggressive areas. This transport is governed by several physical and chemical parameters such as porosity, tortuosity, diffusion coefficient or concentration of chemical species. The main objective of this work is to quantify the tortuosity parameter by a non-destructive method. Tortuosity is a parameter with significant influence on the transfer and diffusion of particles in porous media. Indeed it takes account of the irregularity and sinuous transport paths in the pore structure of the material.

The experimental program focuses on applying a non-destructive method for measuring the electrical conductivity of materials as glass beads and sand with different classes, saturated with NaCl solution at different concentration. The material is placed in a PVC cell of 50 mm diameter, equipped with two stainless steel electrodes connected to the measuring circuit.

The tortuosity values obtained in this work are less than unity. This accords considerably with the values found in the literature, we also note that the variation of this parameter depends on the nature of the medium but also according to its geometrical properties.

KEYWORD Tortuosity, porosity, electrical conductivity, nondestructive measurements, transport phenomena, porous media.

NOMENCLATURE

EC: Electrical conductivity (S/m);

NaCl : Sodium Chloride;

CE_{SG} : Electrical conductivity (S/m);

n : Porosity;

S : Electrodes area (m²);

l : Distance between electrodes (m);

R_x : Electrical resistance (Ω);

CE_0 : Electrical conductivity of the pore solution (S/m);

L : Macroscopic right distance between two points (A et B);

L_e : The effective distance crossed geometrically;

A : tortuosity;

T_m : Tortuosity factor ;

τ_m : Geometric tortuosity factor;

INTRODUCTION

Porous media represent a large class of complex systems. Their pore space is very complex, with pore sizes varying in a wide range. But what really makes particular feature of porous media, is that paths they provide -for the flow of fluids - are not straight, but tortuous and sinuous. A particle must cross a path which is longer than the straight line between its original source and destination.

In the literature, the tortuosity is defined as a geometric parameter associated with hydraulic, electrical or diffusive properties [1-3]. This important parameter purely geometrical influences the transfer of particles in a porous medium. The concept of tortuosity is generally shown as a kind of factor influencing the macroscopic transport movements to reflect the complex transport paths in

porous media and characterize the structure of these environments. There are different concepts and definitions of the tortuosity known from the literature in transport through porous media [4-7]. According (Shackelford and Moore) [7], the tortuosity term (Λ) is given to the ratio of length (L) of the macroscopic straight line between two points (A and B) defining the path of a flow through a given sample, and the actual or effective distance of this flow, traversed by the solution between the same points (Figure 1), this ratio is defined as following :

$$\Lambda = \frac{L}{L_e} \quad (1)$$

With $0 \leq \Lambda \leq 1$

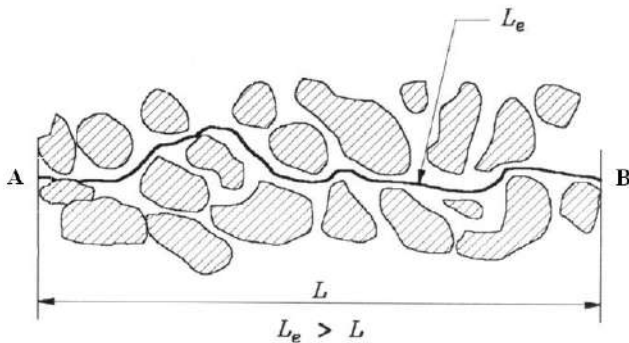


Figure 1

Tortuous diffusion path in a saturated porous medium [4].

Another form of tortuosity is known as geometric tortuosity factor (τ_m) which is equally lower than unit ($\tau_m \leq 1$), to reflect the reduction in macroscopic concentration gradient and correct not parallel direction of the effective pathways in which chemical species flow [7]. Mathematically it represents the square of tortuosity given by equation (1), defined as following :

$$\tau_m = \Lambda^2 = \left(\frac{L}{L_e}\right)^2 \quad (2)$$

For saturated porous materials, the τ_m values range from 0.01 to 0.84 and from 0.025 to 0.57 for unsaturated materials [5, 6, 8]. Bear and Epstein have presented values of his tortuosity which are also less than unity and range between 0.56 and 0.8 [9, 10].

In some cases, tortuosity parameter is defined as the inverse of equation (2), called tortuosity factor T_m , and therefore, it's will be a value greater than unity, ($\infty \geq T_m \geq 1$) [11-14], The tortuosity factor T_m is presented by the equation (3):

$$T_m = \frac{1}{\tau_m} = \left(\frac{L_e}{L}\right)^2 \quad (3)$$

This tortuosity was used for example to predict the permeability in porous media, taking a value of ($\sqrt{2}$) but also values between 1.41 and 1.58 [15]. The $\sqrt{2}$ value was also adopted for electrical measurements on fibrous media [16]. Pisani [17] found tortuosity factor between 1 and 3 for materials with porosities between 0.4 and 0.7. Another work was used to assess this tortuosity and present values between 1.03 and 1.81 for porosities which vary in the range 0.38 to 0.93, using an acoustic method on porous materials rigidified with fibers [17].

Until now, there is no technique or known measurement method wich can really estimate this factor. However, several models based on the formation factor F , (represents the effect of the microstructure located on the electrical conductivity of material, and is equal to the ratio of the conductivity of the pore solution (EC_0) on the bulk electrical conductivity EC), can connect the tortuosity factor to the electrical parameters of saturated porous material, such as electrical conductivity (EC) or electrical resistivity [14, 15, 18]:

$$T_m = n \cdot F \quad (3)$$

With n : porosity of the porous medium.

Another theoretical linear relationship established by Rhoades and Oster [19], exists between EC of a saturated porous medium, EC_0 and a tortuosity factor ≤ 1 , as shown in equation 4 [8, 20]:

$$EC = \tau_m \cdot \theta_w \cdot EC_0 + EC_{SG} \quad (4)$$

Where θ_w is the volumetric water content of the porous material. EC_S is the electrical conductivity of the solid phase.

Equation (4) provides the geometric tortuosity factor τ_m by plotting the EC saturated material according to the CE_0 (Figure 2). The slope of this curve by analogy with equation (4) represents the product ($\tau_m \cdot \theta_w$) and the intersection between the curve and the vertical axis represents the conductivity of the solid grains EC_{SG} . ($EC_{SG} = 0$ in the case of granular materials [21]).

However, electrical conduction in some materials such as clay soils occurs in pores but also on the surface of clay particles electrically charged. Indeed in the clays, the conductance at the particles may be a significant factor affecting the total conductivity of the porous medium [22].

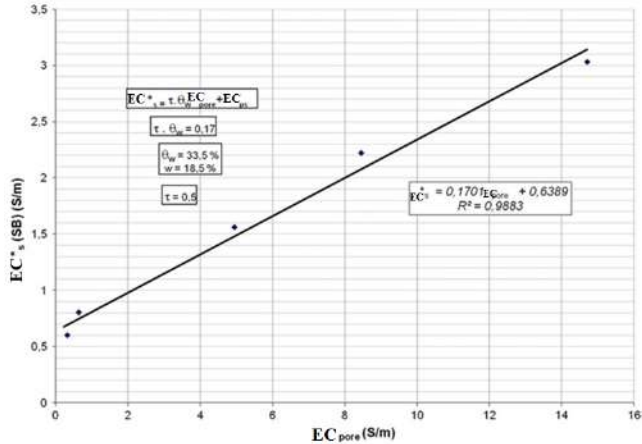


Figure 2

Geometric tortuosity factor (τ_m) obtained by of Rhodes and Oster relation [8].

There is another model that relates the geometric tortuosity with formation factor called Nernst-Einstein equation (equation 5), allowing to have influence of tortuosity on the electrical parameters of porous materials. This relation can be used for non-reactive ionic species between diffusion and ion conductivity [23-25].

$$\frac{EC}{EC_0} = n \cdot \tau_m \quad (5)$$

MATERIALS AND METHODS

Materials Used: In this work the materials used are shown in Figure 3a, 3b. First a mono spherical glass beads with known porosities having diameters of (1.5, 2, 3 and 4) mm are used. Secondly, three classes of siliceous career quartz sand also with known porosities have been studied (1 – 2 mm; 0.5 – 1 mm and 0.25 – 0.5 mm).

Tortuosity Measurement: In this part, the relation Nernst-Einstein (equation 5) was used for determining the tortuosity of each porous medium studied (glass beads and sands) depending on the formation factor which represents the ratio of the EC of saturated porous media on EC_0 of the saturated solution.



Figure 3a

The different diameters of glass beads used.



Figure 3b

(a) Sand class 1 – 2 mm, (b) sand class 0.5 – 1 mm, (c) sand class 0.25 – 0.5 mm.

For measuring EC , an electric circuit developed within our laboratory (Figure 4) for measuring an electrical resistance R_x with Ohm's law principle, this resistance will be transformed into EC according to the equation (6):

$$CE = \frac{l}{R_x \cdot S} \quad (6)$$

With l the spacing between the electrodes, S electrode area.

For glass beads and sand classes, a PVC cell of 50 mm diameter was filled to the necessary amount of material saturated with a NaCl concentration in solution of between 5 and 117 g / l.

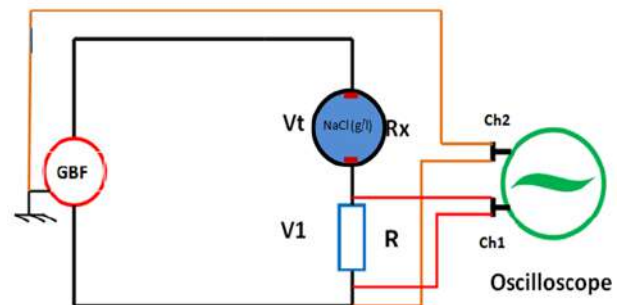


Figure 4

Circuit for the electrical measurement [26].

Regarding of EC_0 , it is measured using a digital conductivity meter (Ohaus STARTER-3000C), which was calibrated using KCl solutions (0.01, 0.1, 1) mol (Figure 5).



Figure 5

Calibration of conductimeter with a KCl solution.

RESULTS AND DISCUSSION

Figure 6 illustrates the variation in EC with the EC_0 of the tested materials (glass beads of diameter 1.5 and 2 mm and a class of sand (1-2) mm, saturated with solutions of NaCl with concentration between 5 and 117g/l. This variation is correlated by straight lines type $y=ax$, passing through the origin (for a concentration of 0 g/l, the material is dry and therefore no electrical conductivity, with correlation coefficient ≥ 0.98).

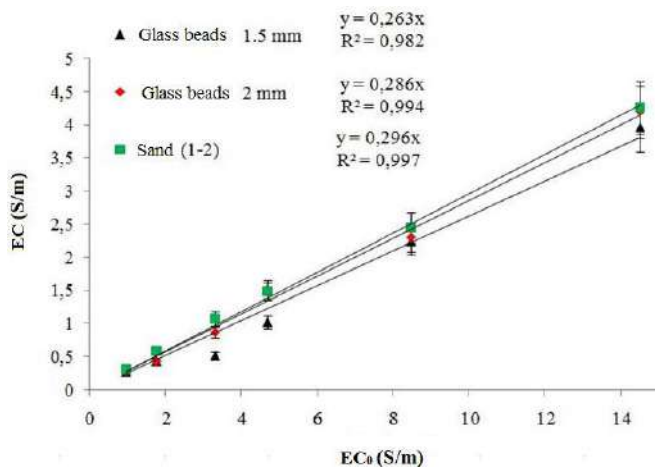


Figure 6

Variation of EC with CE_0 for the tested materials glass beads 1.5, 2mm and (1-2) mm sand class.

From analogy with the equation 5, we deduce that the straight slope is the product ($n * \tau_m$). This analogy

allows us to calculate the various tortuosity of porous media studied (table 1). The error shown in Figure 6 defines the cumulative relative uncertainty due to the electrical measurement, estimated at 9.3%.

Table 1 summarizes the results of tortuosity of porous media studied with their corresponding porosities. What we can say from these results, is that for a given medium such as glass beads, geometric tortuosity factor increases with the grain diameter and therefore with increasing porosity of the medium, phenomenon also noted in the work of (Piekaar and Clarenburg) [16] using a geometric analysis model to estimate tortuosity in fibrous porous media.

Table 1

Tortuosity measured on different studied porous media.

Porous material	Tortuosity	Porosity
Glass beads 4 mm	0.721	0.426
Glass beads 3 mm	0.702	0.42
Glass beads 2 mm	0.685	0.417
Glass beads 1.5 mm	0.639	0.411
Sand (1 – 2) mm	0.671	0.442
Sand (0.5 – 1) mm	0.662	0.438
Sand (0.25 – 0.5) mm	0.648	0.418

Tortuosity values found for glass beads vary in the interval $0.639 \leq \tau_m \leq 0.721$ for porosities ranging from 0.411– 0.426, the same trend is observed for sands with tortuosity $0.648 \leq \tau_m \leq 0.671$ for porosities between 0.418 and 0.442. We also note that this geometric factor differs depending on the nature of the porous medium; but also according to their geometrical properties (size and shape of the grains, porosity, pore distribution, etc). Shackelford found that the geometric tortuosity is <1 and τ_m values are between 0.01 and 0.84 for saturated porous media [4, 7]. We also find research of (Gillham, Robin) which deduced that the tortuosity were between 0.33 and 0.7 for saturated soils [27]. It was also shown that this geometric tortuosity factor allows to estimate the diffusion coefficients of porous media without going through diffusion tests [4, 7, 8].

CONCLUSIONS

Tortuosity remains, until now, a very complex parameter discussed in the literature due to its

impact on the phenomenon of diffusion. Tortuosity used for this work is a tortuosity less than unity (< 1). The Nernst-Einstein equation, allowed us to identify this parameter using a non-destructive electrical method through the formation factor.

This work has also enabled us to implement a very fast and easy procedure to handle, on granular media with different intrinsic characteristics, to estimate the parameter tortuosity, since it just needs to proceed to an electrical measurement with two electrodes to get an idea about the internal structure of the medium studied and understand the phenomenon of transport. This parameter also offers the possibility to deduct the diffusion coefficient of a porous medium saturated without necessity the diffusion test.

ACKNOWLEDGMENTS

The authors would like to acknowledge EOLE Laboratory (Algeria) for its financial support.

REFERENCES

- Clennell, M.B, 1997, Tortuosity: a guide through the maze. Geological Society, London, Special Publications, **122**(1): p. 299-344.
- Sahimi, M, 1993, Flow phenomena in rocks: from continuum models to fractals, percolation, cellular automata, and simulated annealing, *Reviews of modern physics*, **65**(4): p. 1393.
- Matyka, M, Khalili, A, and Koza Z, 2008, Tortuosity-porosity relation in porous media flow. *Physical Review E*, **78**(2): p. 026306.
- Shackelford, C. D, 1991, Laboratory diffusion testing for waste disposal—a review, *Journal of Contaminant Hydrology*, **7**(3), pp. 177-217.
- Shackelford, C. D, Daniel, D. E, 1991, Diffusion in saturated soil I: Background, *Journal of geotechnical engineering*, **117**(3), pp 467-484.
- Shackelford, C.D, and Daniel, D.E, 1991, Diffusion in saturated soil. II: Results for compacted clay. *Journal of geotechnical engineering*, **117**(3): p. 485-506.
- Shackelford, C. D, and Moore, S. M, 2013, Fickian diffusion of radionuclides for engineered containment barriers: Diffusion coefficients, porosities, and complicating issues, *Engineering Geology*, **152**(1), pp. 133-147.
- Bezzar, A, and Ghomari, F, 2013, Monitoring of pollutant diffusion into clay liners by electrical methods, *Transport in porous media*, **97**(2), pp. 147-159.
- Bear, J, 1972, *Dynamics of fluids in porous media*, Elsevier Publisher Company, New York, 764 pages.
- Epstein, N, 1989, On tortuosity and the tortuosity factor in flow and diffusion through porous media. *Chemical Engineering Science*, **44**(3): p. 777-779.
- Van Brakel, J, and Heertjes, P, 1974, Analysis of diffusion in macroporous media in terms of a porosity, a tortuosity and a constrictivity factor, *International Journal of Heat and Mass Transfer*, **17**(9), pp. 1093-1103.
- Jaafar, W, 2003, Influence de la carbonatation sur la porosité et la perméabilité des bétons, DEA Géomatériaux. Division Bétons et Composites Cimentaires, Section Microstructure et Durabilité du Béton, LCPC.
- Hudson, T. L, and Aharonson, O, 2008, Diffusion barriers at Mars surface conditions: Salt crusts, particle size mixtures, and dust, *Journal of Geophysical Research: Planets* (1991–2012), **113**(E9).
- Promentilla, M.A.B, and al, 2009, Quantification of tortuosity in hardened cement pastes using synchrotron-based X-ray computed microtomography, *Cement and Concrete Research*, **39**(6): p. 548-557.
- Lane, N. M, Numerical studies of flow in porous media using an unstructured approach, 2011, Southeastern Louisiana University.
- Piekaar, H. and L. Clarenburg, Aerosol filters—the tortuosity factor in fibrous filters. *Chemical Engineering Science*, 1967. **22**(12): p. 1817-1827.
- Pisani, L, 2011, Simple expression for the tortuosity of porous media, *Transport in Porous Media*, **88**(2): p. 193-203.
- Umnova, O, and al, 2005, Deduction of tortuosity and porosity from acoustic reflection and transmission measurements on thick samples of rigid-porous materials, *Applied Acoustics*, **66**(6): p. 607-624.
- Ghanbarian, B, and al, 2013, Tortuosity in porous media: A critical review, *Soil science society of America journal*, **77**(5): p. 1461-1477.
- Rhoades, J, and Oster, J, 1986, Solute content, *Methods of Soil Analysis: Part 1—Physical and Mineralogical Methods*, (methodsofsoilan1): p. 985-1006.

21. Paris, T, and al, 2003, Mise au point de sondes de mesure de conductivité électrique pour l'estimation des transferts de solutés en milieux poreux variablement saturés, Actes du 4ème colloque Géophysiques des Sols et des Formations Superficielles. UPMC, VI, Paris, p. 74-77.
22. Jackson, P. D, 1975, An electrical resistivity method for evaluating the insitu porosity of clean marine sands, Marine Georesources & Geotechnology, 1(2): p. 91-115.
23. Ait Saadi, L, 2003, Méthodologie de contrôle de l'homogénéité et de la perméabilité des barrières argileuses, Villeurbanne, INSA.
24. Blewett, J, and al, 2003, An experimental study on ionic migration through saturated kaolin, Engineering Geology, 70(3-4): p. 281-291.
25. Nokken, , and Hooton, R, 2008, Using pore parameters to estimate permeability or conductivity of concrete, Materials and Structures, 41(1): p. 1-16.
26. Neithalath, N, and Jain, J, 2010, Relating rapid chloride transport parameters of concretes to microstructural features extracted from electrical impedance, Cement and Concrete Research, 40(7): p. 1041-1051.
27. Merioua, A, Bezzar, A, and Ghomari, F, 2015, Non-destructive Electrical Methods for Measuring the Physical Characteristics of Porous Materials, Journal of Nondestructive Evaluation, 34(2): p. 1-12.
28. Gillham, R, and al, 1984, Diffusion of nonreactive and reactive solutes through fine-grained barrier materials, Canadian Geotechnical Journal, 21(3): p. 541-550.

COMPARISON BETWEEN THE PERMEABILITY WATER AND GAS PERMEABILITY OF THE CONCRETES UNDER THE EFFECT OF TEMPERATURE

Mrs MOHAMMED BELHADJ Ahlem Houaria^{1*}, Pr MAHI Abdelkader²,
Mrs CHOINSKA Marta³, Pr KHELIDJ Abdelhafid³.

1: Smart Structures Laboratory (SSL) Univ Ctr of Ain Temouchent, Po Box 284, 46000, Algeria.

2: University of Science and Technology of Oran USTOMB: Laboratory LMST, Algeria.

3: The University Nantes Angers Le Mans (L'UNAM) GEM-Research Institute of Civil Engineering and Mechanics, CNRS UMR 6183, Nantes University-IUT Saint-Nazaire, France

* Email: mb_ah1@yahoo.fr

ABSTRACT

Characterization of permeability is essential to fully describe the transport phenomena occurring in porous medium at elevated temperatures. The aim of this work is to study the evolution of the inherent gas and water permeability of concretes with temperature variations. The tests were performed on two types of concretes (ordinary and pozzolanic) using Algerian local products. Addition of natural pozzolan, promoting use of local products, with a rate of 15% was incorporated in the pozzolanic concretes and samples (11x22cm) were subjected to different temperatures (200 °C, 300° C, 400° C, 600° C and 700° C). After cooling, gas and water permeability using, respectively, CEMBUREAU and CONTROLAB permeability devices were measured and loss of mass and compressive strength were then conducted. Experimental results of permeability and mechanical strength variations are shown and pozzolanic concretes depicted better characteristics both in terms of gas and water permeability as well as compressive strength in comparison with ordinary concrete.

KEYWORDS: Permeability – ordinary concrete – pozzolanic concrete – addition – temperature.

INTRODUCTION

Available pore space and the connectivity of pores govern the ingress and transport of gases and liquids into porous materials and, consequently, the durability of these materials. The pore volume is characterized by porosity and the connectivity of pores by permeability. These two properties together govern the durability of porous materials such as concrete [1].

During their service life, concrete structures are subjected to various forms of distress due to the mechanical, thermal and chemical stress environment. Generally speaking, the service loads by themselves are not enough to cause significant degradation to the mechanical properties of structural concrete [2-3].

However, at elevated temperatures, e.g. in case of fire, in a concrete structure, the material is prone to several types of damaging effect. These damages generally result in an overall increase in porosity and permeability of the concrete [4].

Explosive spalling is known to occur in ordinary concrete and in high-performance concrete. The risk of explosion seems to increase with decreased permeability, increased moisture content, decreased tensile strength, and increased heating rate [5].

Permeability is one of the main material properties influencing spalling during a fire. The low permeability led to the increased vapor pressure during heating.

Many experimental and numerical studies have demonstrated the influence of permeability on explosive spalling [1-5]. Experimental studies of permeability were performed by employing different permeating media (gases and liquids) as well as different measurement methods, since currently there is no generally accepted testing method. Some of the laboratory measurement methods that use liquids (water) as medium are: constant head experiment [6] and falling head experiment [7-9]. The methods using gases (oxygen, nitrogen, helium) as medium are: the RILEM-CEMBUREAU method [10] and the Hassler method [7][10-12].

The majority of the experimental studies on the influence of temperature on permeability were performed in residual state, i.e. after cooling the specimens to room temperature [6]. Only very limited studies aimed at measuring permeability on heated specimens can be found in the literature [1, 6]. This is mainly due to the technical difficulties involving measurements of permeability at elevated temperatures.

The aim of this work is to study the evolution of the inherent gas and water permeability of concretes with temperature variations. The tests were performed on two types of concretes (ordinary and pozzolanic) using Algerian local products. Addition of natural pozzolan, promoting use of local products, with a rate of 15% was incorporated in the pozzolanic concretes and samples (11x22cm) were subjected to different temperatures (200

°C, 300° C, 400° C, 600° C and 700° C). After cooling, gas and water permeability using, respectively, CEMBUREAU and CONTROLAB permeability devices were measured and loss of mass and compressive strength were then conducted.

EXPERIMENTAL PROGRAM

Concrete composition and specimens preparation:

The choice of local Algerian materials was based on their abundant availability and their moderate cost.

CEMENT:

The cement used was a local ordinary Portland cement type (CEM I/ 42.5R), from the factory of ZAHANA Cement Company located in the west of Algeria. The cement complied with the Algerian standard NA 442, which is mainly based on the European EN 197-1. Its chemical properties and Mineralogical composition data are presented in Table 1 and 2.

Table 1
Chemical compositions of cement

Oxides	%
CaO	63.82.
SiO ₂	21.00
Al ₂ O ₃	4.59
Fe ₂ O ₃	3.76
SO ₃	2.20
K ₂ O	0.4
MgO	2.19
Loss in ignition insolubles	2.47 4.6

Table 2
Mineralogical (Bogue) compositions of cement

Bogue composition (%)			
C ₃ S	C ₂ S	C ₃ A	C ₄ AF
59	18	8.5	12

Natural pozzolan:

Pozzolan used is a natural pozzolan extracted from deposits in North-West Algeria (Bouhamidi deposit (Beni-Saf, Ain Temouchent, Algeria) source situated about 100 km from Oran). This pozzolan is provided in the form of crushed pumice rock type and slag diameters ranging from 50 to 100 mm. These rocks are crushed and screened to obtain the granular fractions sieving 80 µm. The chemical and physical characteristics are given in Table 3.

Table 3
Chemical compositions of Natural Pozzolan

Component	SiO ₂	Al ₂ O ₃	CaO	Fe ₂ O ₃	MgO
Ratio (%)	47.48	18.83	10.51	9.92	4.38
Component	SO ₃	K ₂ O	Na ₂ O	P.F	
Ratio (%)	0.50	0.20	0.81	3.91	

Concrete mix:

The concretes were prepared using the method of Dreux-Gorisse. The mix proportions of concrete tested in this study are given in table 4.

Table 4

Mix proportion of the concrete mixtures per cubic meter

	Control concrete BT	Pozzolanic concrete BZ 15%
aggregate 8/15 (kg)	410	410
aggregate 3/8 (kg)	837	837
Sand 0/3	632	632
Cement CEMI 42.5R (kg)	400	400
Natural pozzolan (kg)	-	60
Water	200	133
Plasticizer SP40 (kg)	-	8
W/C ratio	0.5	0.33
Weight (kg/m ³)	2479	2480

In this experimental study, one size of cylindrical concrete specimens was chosen, (11X22) cm.

Concrete cylinders were cut using a diamond blade saw to obtain 5cm-thick discs to use for gas permeability. Two discs were extracted from each central portion of the cylinder. Their thickness was measured with an accuracy of 0.1 mm. In order to have uniaxial flow of gas through the discs and to prevent any gas leakage while testing gas permeability, their curved surface was covered with aluminum adhesive.

Testing procedure:

Heating-cooling tests:

After demolding, the specimens were subjected to heating-cooling cycles (see Figure.1). Heating-cooling was done as per RILEM recommendations [33].the heating rate was kept at 1C°/min. After the maximum temperature was reached, the oven was turned off. Specimens were allowed to cool down inside the oven in order to prevent thermal shock.

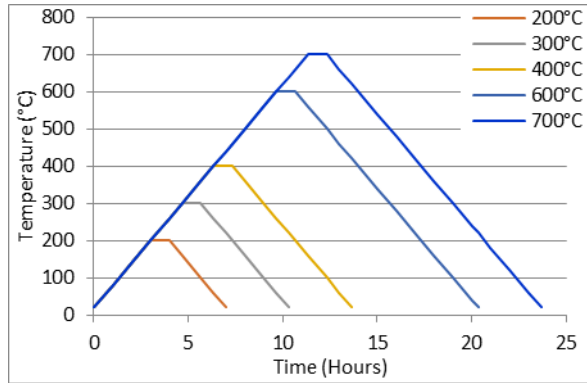


Figure 1
Heating-cooling cycles

Permeability tests:

Gas permeability:

The gas permeability was measured in the GeM laboratory (France), using a constant head permeameter, known as the CEMBUREAU permeameter, and nitrogen as the neutral percolation gas [12]. A general view of the gas permeability device is given in picture 1.



Picture 1
Gas permeameter CEMBUREAU, (GeM Laboratory – France)

The procedure of this test followed the recommendations given in [35, 36].

The apparent permeability K_a does not depend only on the pore structure of the material, but also on the applied mean pressure:

$$P_{moy} = (P_{inj} + P_{atm})/2 \quad (1)$$

Permeability measurements were carried out in an air-conditioned room ($20 \pm 1^\circ\text{C}$). Each disc was tested at five differential pressures P_{inj} ranging from

0.3 to 0.1 MPa (relative values). In order to ensure a uniaxial gas flow and prevent any gas leakage, the specimen was placed in a fitted collar and then confined during all the test by a lateral pressure (0.5 MPa) applied on the curved surface of the cylindrical specimen of concrete.

In the case of laminar flow of a compressible viscous fluid through a porous material, the apparent gas permeability, denoted K_a , can be found from direct measurement, for each differential pressure (one side of the test specimen is submitted to a constant inlet pressure P) by using Eq. (2), derived from Hagen–Poiseuille’s law when applied to compressive fluids (gases) :

$$K_a = \frac{2 \cdot \mu \cdot Q \cdot L \cdot P_{atm}}{A(P_{inj}^2 - P_{atm}^2)} \quad (2)$$

Q is the gas volume flow (m^3/S); A is the cross-sectional area (m^2); L is the thickness of the sample (m); μ is the nitrogen dynamic viscosity at 20°C ($1.75 \times 10^{-5} \text{Ns/m}^2$); P_{inj} the inlet pressure, i.e. applied absolute pressure (N/m^2); P_{atm} the atmospheric pressure (N/m^2).

Intrinsic permeability K_{int} can be obtained by considering the relation suggested by Klinkenberg which takes into account the slip of the gas molecules on the concrete pores and cracks walls in Eq. (3):

$$K_a = K_{int} \left(1 + \frac{\beta}{P_{moy}}\right) \quad (3)$$

β is Klinkenberg’s constant (bar).

Water permeability:

Water permeability characterizes the capability of saturated concrete to transport water when subjected to an applied hydraulic gradient [12]. It is usually measured in the laboratory by permeability tests based on Darcy’s law Eq. (4):

$$K_w = \frac{Q \cdot L}{A \cdot \Delta h} \quad (4)$$

Where K_w is the coefficient of water permeability (m/s); Q is the flow rate of water at the upstream side of the specimen (m^3/s); L is the thickness of the concrete sample (m); A is the permeation area of the concrete specimen (m^2) and Δh is the pressure head (water pressure expressed in terms of a water column height h) (m).

The water permeability was measured in the EOLE laboratory (Algeria), by water permeameter CONTROLAB (see Picture.2).



Picture 2
Permeameter with water (CONTROLAB)

RESULTS AND DISCUSSION

Weight loss:

For each sample, the weight loss after heating was calculated using equation Eq 5:

$$\text{Weight loss (in Kg)} = W_{bef} - W_{aft} \quad (5)$$

W_{bef} : Weight before heating

W_{aft} : Weight after heating

The study of the evolution of the weight loss during testing was initiated because of the importance of water portion in the heat transport phenomena and mass in concrete. The mass balance allowed us then to have the evolution of the mass of water evaporated depending on the temperature to 400 °C see in figure 2, beyond this temperature it allows to see the loss of chemical characteristics of concrete.

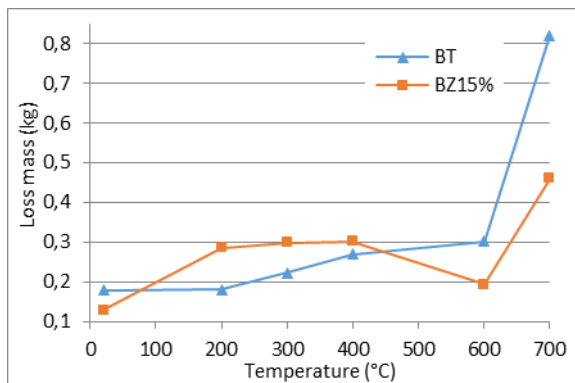


Figure 2
The loss of weight at various temperatures

The compressive strength:

The concrete specimens are subjected to simple compression. The results of tests on ordinary concrete and pozzolan concrete on heated and unheated specimens are given in figure 3.

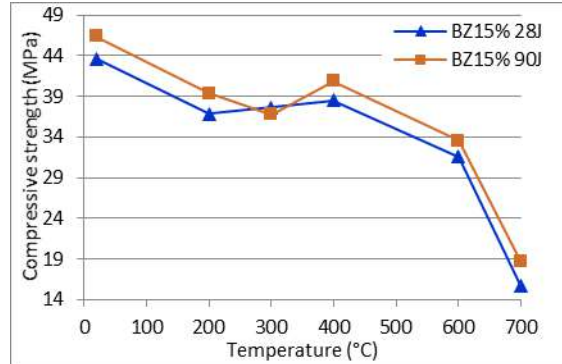


Figure 3
Evolution of the compressive strength at various temperatures

The age of concrete specimens is 90 days.

Through the results obtained, it is clear that the resistance to compression of concrete depend on the type of concrete (witness or with additions), ambient temperature that is observed (20 °C) of pozzolan concrete resistance is greater than that of the control concrete. It is found that the addition of the pozzolan increases the compressive strength of the concrete. We note that in the vicinity of 400 °C the strength of concrete pozzolan increases and there is a peak for concrete 25% added but beyond that temperature resistance decreases. This increase in resistance would be the result of the effect of additional products of hydration generated by the pozzolanic character. This gain in strength was observed by Kodur [13]

The strength loss is attributed to damage in general (internal cracking) caused by dehydration, vapor pressure and destruction of hydration products especially at the interfaces aggregate/cement paste. It is also noted when the temperature is between 200 °C and 400 °C, there is no obvious crack on the concrete as against 600 °C and they are exposed to 700 °C peeling is observed and destruction of materials.

Water permeability:

The analysis of these results shows that at room temperature the addition of pozzolan reduced

permeability compared to conventional concrete. The different concrete saw their water permeability increase to a temperature of 400 °C, then a permeability reduction is observed which can be explained by the increase of the resistance and the concentration of the hydration product at this temperature (see figure 4).

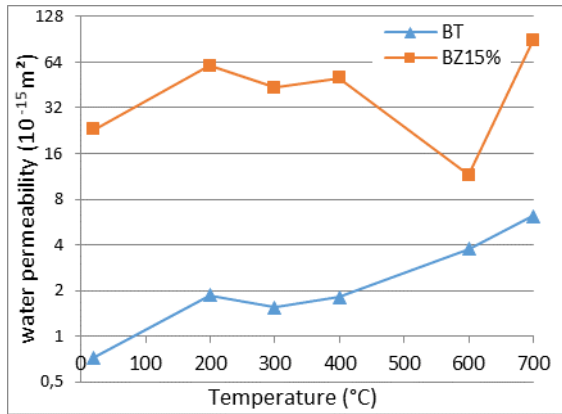


Figure 4
Evolution of the water permeability at various temperatures

Then at 600 °C a further reduction is observed for different concretes. This new reduction in permeability is due to the effect of the temperature and vapor pressure, where the walls of the cavities essentially made of hydration products collapsed and clogged flow.

Gas permeability:

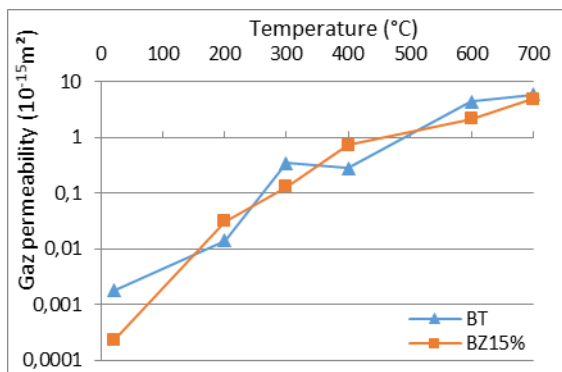


Figure 5
Evolution of the gas permeability at various temperatures

From the figure 5, it can be seen that there was severe loss in the permeability of control

concrete from $0.0018 \times 10^{-15} \text{m}^2$ at 20°C to $5.893 \times 10^{-15} \text{m}^2$ at 700°C, which is 3300% loss, and it was possibly due to the internal cracking and pore structure coarsening of concrete at high temperatures. Similar results were reported by Nomowé et al [4].

Under the same conditions, the permeability of pozzolanic concrete was less than that of the control concrete, the percentage increase being 8% at 20°C to 1.5% at 700°C.

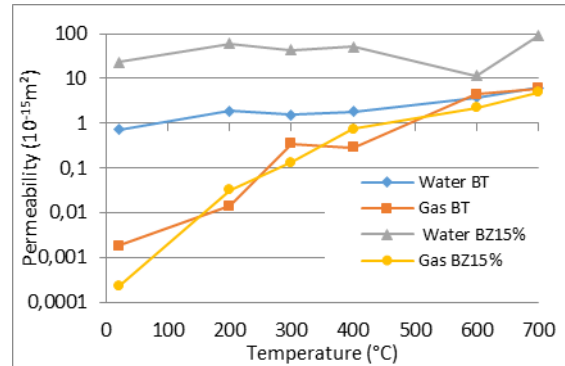


Figure 6
Comparison between water and gas permeability of concrete

Comparing the water permeability and gas permeability of the control concrete, we see that the ratio between the two permeability at 20 °C which is equal to 400%, will decrease under the effect of temperature up to 1% at 700 °C (see in figure 6). For concrete pozzolanic we see the same results, the water permeability is substantially greater than the gas permeability.

For the gas permeability is almost finds the same results as the water permeability but that was the order of magnitude is much different by contribution to the same type of concrete that is of the 10⁻¹⁹ order for gas permeability (see figure 6). This difference is due to the ease of flow of gas through the narrow pore one hand and on the other hand an amount of water is observed after heat treatment and when the water permeability tests going return to hydration in the so called rehydration phenomenon actually therefore the testing of the permeability to water gives an estimate of the permeability of concrete while testing the gas permeability is more precise.

CONCLUSION

In this paper we study the effect of high temperature on the permeability of concrete, We made a

comparison between the water permeability and gas permeability of the two types of concrete, a concrete control and a pozzolanic concrete with 15% addition of natural pozzolan,

The results of this study allowed us to draw the following conclusions:

- At room temperature, the addition of the pozzolan increases the compressive strength of the concrete relative to the control concrete.
- Adding the pozzolan has closed pores and activated the hydration phenomenon which leads to a reduction in the permeability of these concretes.
- The permeability of concrete increases with temperature, except for the temperature equal to 400 °C and 600 °C, a reduction in the permeability is observed.
- The greatest variation in permeability boots from a 600 °C heating temperature for ordinary concrete and pozzolan.
- Testing the gas permeability is more accurate than the test of water permeability.
- Can be seen from the gas permeability is significantly small in contribution to water permeability.

REFERENCES

1. Bosnjak, J., Ozbolt, J., Hahn, R., 2013, Permeability measurement on high strength concrete without and with polypropylene fibers at elevated temperatures using a new test setup, *Cem. Conc. Res.*, 53, 104-111.
2. Hoseini, M., Bindiganavile, V., Banthia, N., 2009, The effect of mechanical stress on permeability of concrete: A review, *Cem. Conc. Res.*, 31, 213-220.
3. Norris W.E., Naus D.J., Graves H.L., 1999, Inspection of nuclear power plant containment structures. *Nucl. Eng. Des.*, 192(2), 303–29.
4. Noumowe, A.N., Siddique, R., Debicki, G., 2009, Permeability of high-performance concrete subjected to elevated temperature (600°C), *Construction and Building Materials* 23, 1855-1861.
5. Castillo, C., Durrani, A.J., 1990, Effect of transient high temperature on high strength concrete, *ACI Mater. J.*, 35(1), 47–53.
6. Noumowe A.N., Clastres, P., Debicki, G., Costaz, J.L., 1996, Transient heating effect on high strength concrete. *Nucl. Eng. Des.*, 166:99–108.
7. Picandet, V., Khelidj, A., Bastian, G., 2001, Effect of axial compressive damage on gas permeability of ordinary and high performance concrete, *Cem. Conc. Res.*, 31, 1525–32.
8. Biparva, A., 2005, Permeability and durability of high volume fly-ash concrete under an applied compressive stress, M.A.Sc. PhD thesis, University of British Columbia.
9. Banthia, N., Bhargava, A., 2007, Permeability of stressed concrete and role of fiber reinforcement, *ACI Mater. J.*, 104(1), 70–6.
10. Choinska, M., Khelidj, A., Chatzigeorgiou, G., Pijaudier-Cabot, G., 2007, Effects and interactions of temperature and stress level related damage on permeability of concrete, *Cem. Conc. Res.*, 37:79–88.
11. Aubernon, C., 2011, Evolution of the permeability of concrete under stress of a serious accident: effects of mechanical loading, saturation and the nature of fluid percolating, PhD thesis, Institute of Radiation Protection and Nuclear Safety, France; [in French].
12. Kameche, Z.A., Ghomari, F., Choinska, M., Khelidj, A., 2014, Assessment of liquid water and gas permeability of partially saturated ordinary concrete, *Cons. Buil. Mat.*, 65, 551-565.
13. Kodur, V.K.R., 2000, Spalling in high strength concrete exposed to fire – concerns, causes, critical parameters and cures”, actes du congrès de l’ASCE sur les structures, Philadelphie (PA).

EVALUATION OF NATURAL POZZOLAN FOR ENERGY RENOVATION OF OLD BUILDINGS

BENCHIHEUB Djihen^A, AMOURI Chahinez^B, HOUARI Hacem^C, mostefa aggone^D

^ALaboratory Materials, Geotechnical, Housing and Urbanism University of Skikda – Algeria
Djihen_11@hotmail.com

^BLaboratory Materials and Durability of Constructions, University 1- Constantine Algeria
c.amouri@yahoo.fr

^CLaboratory Materials and Durability of Constructions, University 1- Constantine Algeria
hhouarilmcd@yahoo.fr

^DResearch Laboratory Constructions Materials, granitex Algiers - Algeria
maggoune@granitex.dz

ABSTRACT

“The Roman concrete is the most remarkable invention in the history of engineering, the Pantheon in Rome is the most impressive civil engineering works of antiquity” through this sentence admiration and research developed chemistry we try to reproduce a formulation of an old mortar using a less expensive binder and a natural resource, in order to compensate the deficit in the production of Portland cement, but as the old built a foundation stone is known by its climate comfort, Our purpose of this research is not only to formulate a mortar equivalent to the old but also to keep it or improve thermal comfort to reduce the overall consumption of buildings energetic

We have selected for our studies two binders natural pozzolan and aerated lime, we conducted tests on the thermal conductivity of different mortars developed, as well as adhesion to various substrates, was also performed mechanical tests (compression and bending) on specimens of 4 * 4 * 16 for terms of measures (7.14.28.60 days)

Keywords Natural pozzolan

INTRODUCTION

Renovation of the existing housing stock is now one of the main levers for lute against environmental changes, master the energy bill and contain global warming. Yet practice sustainable renovation of its housing is still too often a challenge for the individual who wishes to embark on this process the building sector emits the CO₂ fourth product in the world and represents half of the total primary energy consumed. Interventions in the building industry are essential. They pass in particular by retrofitting old buildings. The renovations will be done in a holistic approach, integrating in particular the issues of conservation and respect for our built heritage, protected or not. [8] The reconciliation of these environmental and cultural issues requires a better understanding of the behavior of old buildings, key point of any rehabilitation project [9]. However, the opposition "renovation or rehabilitation" is still present, because for many teachers to work and contractors, it is easier to demolish and rebuild as restore. It also claims that the renovation costs less than restoration. In fact, the choice falls on many factors: technical, economic, social, historical, aesthetic, etc. [2]. The architectural structure and thermal behavior of old buildings

require specific global studies, in order to avoid structural damages on the building and health problems for the inhabitants. Traditional or innovative techniques and materials have to be adapted, the work must be reversible and respect the heritage character of the frame. [Martin MALVY president of the Midi-Pyrénées Region, former minister] [9]. the use of lime mortar is complex assays must be very rigorous in particular the water dosage. It is possible to develop compositions (recipes) either studied the basic mortar, we can introduce minerals and / or vegetable or synthetic fiber additions: pozzolan, silica fume, slag, straw, hemp, flax, etc.

EXPERIMENTAL PROCEDURE

Pozzolan

Table 1 Chemical composition and physical characteristics of the pozzolan

Chemical composition of pozzolana										
Elem ents	Si O ₂	Al ₂ O ₃	Fe ₂ O ₃	Ca O	M gO	S O ₃	Na ₂ O	K ₂ O	Cl	PF
%	46.83	17.45	8.36	9.38	3.88	0.36	4.32	1.4	0.03	4.79
Physical characteristics of pozzolana										
Designation	Blaine specific surface (cm ² /g)		Absolute density (t/m ³)		density		Bulk density (t/m ³)			
Values	3192		2.68				0.98			

Sand

The used sand comes from the Hedna career Ain Smara. This sand has a bulk density of 1.46 t / m³, a true density of 2.6 t / m³, a 69% equivalent of sand and a fineness modulus of 2.6

Lime

The use of lime is the key to the sustainability of current restorations, cement plasters LEAD disorders such as deterioration of the stones that do not breathe, degradation of wood components in masonry (beams, floor beams etc ...)

The lime used in this study comes from the production unit el khroub the wilaya of Constantine

Table 2
Physical characteristics of lime

average particle diameter	5μ
bulk density	0.65g/cm ³
apparent surface	1.5 à 18m ² /g
crystal structure	Hexagonale
Molecular weight	74.09
Specific weight	2.342
Aspect	Fine poudre blanche inodore

The thickener

Penta EC 18 is a rapidly soluble cellulose ether in water at both a neutral and alkaline system. This feature makes it usable in the preparation of both cement and lime based plaster and gypsum plasters. It modifies their rheology by improving viscosity and water retention.

RESULTS

Thermal conductivity test

The purpose of the test is to determine the thermal conductivity of different mixtures and compare results

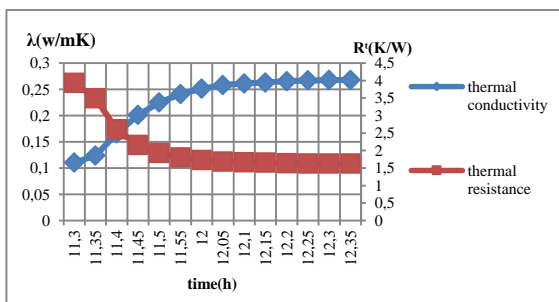


Figure 1 Evolution of conductivity and thermal resistance of lime mortar

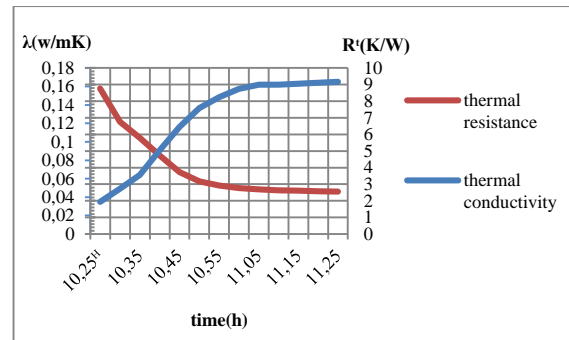


Figure 2 Evolution of conductivity and thermal resistance of the mortar of lime and pozzolan

From the results obtained it is found that the incorporation of the pozzolan and improved the heat resistance of mortar

After an hour of test time, thermal conductivity mortar (Ch + PZ) has stabilized at 0.17 W / mk, against a lime mortar and after only 15 minutes led thermal conductivity 0.11W / mK and it stabilized at 0.26W / mk after an hour of time

Adhesion test

The adhesion test was carried out CNERIB laboratory on the basis of EN 1015 to 1012, a surface portion is isolated by making an incision (Ø 5cm) in the model.

Then just stick a metal pad on the surface of the model. When the glue is dry, it has the traction device on the metal disk and sends a pull.

Finally the force required to pull it note and the type of break

The results obtained are shown in the following tables

Table 3 tearing stress and failure mode of lime mortar

Gross cement		Type of support hollow concrete block		Clay brick	
f _u (N/mm ²)	Failure mode	f _u (N/mm ²)	Failure mode	f _u (N/mm ²)	Failure mode
0.28	E	0.21	E	0.29	E
0.27	E	0.21	E	0.35	E
0.26	E	0.23	E	0.26	E
medium =0.27	/	medium =0.21	/	medium =0.30	/

Table 04 tearing stress and failure mode of the mortar of lime and pozzolan

Gross cement		Gross cement		Gross cement	
f _u (N/mm ²)	Failure mode	f _u (N/mm ²)	Failure mode	f _u (N/mm ²)	Failure mode
0.22	E	0.18	E	0.26	E
0.23	E	0.19	E	0.26	E
0.24	E	0.23	E	0.26	E
Moy=0.23	/	Moy=0.20	/	Moy=0.26	/
3		0		6	

The results of the adhesion tests are of the order of 2 N / mm^2 , it is sufficient for coating work on three types of substrates

Mechanical strength

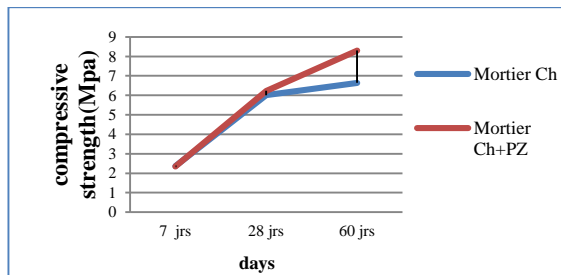


Figure 3 Compressive strength of different mixtures

From this figure, pozzolan improved compressive strength above 60 days when there was a remarkable improvement in resistance mortars Ch + PZ and this is due to the pouzzolanité these mixtures knowing pozzolan mixed with lime gives rise to HSCs and increases runoff mortar and makes it well able to harden under water and not deteriorate.

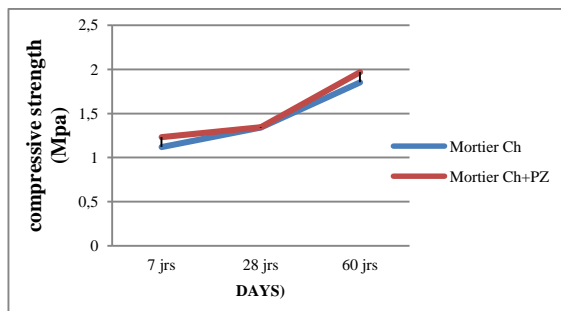


Figure 4 tensile strength by bending the different mixtures

The use of the pozzolan was beneficial to the tensile strength

CONCLUSION

According to the results obtained mortars studied are effective for the majority of the renovation mortars. The binders mortars made with lime should also include a small percentage of hydraulic additions to offset the mechanical weakness and the length of coatings curing time. This balance is the key to the sustainability of current restorations, which is why we decided to add a light, insulating stone that has by nature the main components already combined construction materials by the calories provided by volcanoes "pozzolan".

The majority of ancient masonry are heterogeneous and little cohesive: the flexibility of the lime gives the coating a low modulus. Aesthetically, the old houses are known for their harmonious façade and their integration into the local environment: the use of lime helps to regain the original state of the facades.

The materials used are local materials, and the results made mortars based pozzolan exhibit outstanding thermal insulation. This subsequently reduced the overall energy consumption of old buildings with the least cost

REFERENCES

- [1] N. BOUANANE KENTOUICHE, 2008, PATRIMOINE ET SA PLACE DANS LES POLITIQUES URBAINE ALGERIENNES, memoire pour l'obtention du diplome de magister, constantine, algerie
- [2] STAP DU CALVADOS, 2013, rehabilitation du bati ancien, <http://www.calvados.gouv.fr/>
- [3] J. KRIBECHE - YUCEF ALI, 2012, manuel des typologies constructives, architecturales et architectoniques de la vieille ville de constantine
- [4] L.MAMMAR, M.MOULI, 2009, ETUDE DE REHABILITATION D'UN IMMEUBLE VIEUX, BATI A ORAN, sbaidco – 1st international conference on sustainable built environment infrastructures in developing countries enset oran (Alegria)
- [5] RECOMMANDATIONS POUR LA RESTAURATION DES FAÇADES D'IMMEUBLES ET DES DEVANTURES COMMERCIALES DE G.MAGNE. edition caue hte vienne, p61-105
- [6] RESTAURATION DES BATIMENTS EN PIERRE, PAR MARC MAMILLAN, techniques de l'ingenieur, traite construction, doc. c 2- 150
- [7] JEAN-PAUL KURTZ, 2004, dictionary of civil engineering, *springer science & business media*,
- [8] AUP - D. GROLEAU, guide pour la rénovation énergétique des bâtiments anciens a Poitiers - Pouget consultants mars 2010
- [9] guide méthodologique pour les villes souhaitant réaliser un audit énergétique du patrimoine bâti ancien, association nationale villes et pays d'art et d'histoire.

Sustainable Constructive Materials (1)

INFLUENCE OF DRYING CONDITIONS ON HYDRATION OF CEMENT PASTES WITH SUBSTITUTION OF PORTLAND CEMENT BY A RECYCLED CEMENT PASTE FINE

A. BORDY^{1*}, A. YOUNSI², B. FIORIO¹, S. AGGOUN¹

¹University of Cergy-Pontoise, L2MGC, 5 Mail Gay-Lussac, 95031 Cergy-Pontoise Cedex, France

²University of La Rochelle, CNRS, LaSIE UMR-7356, Avenue Michel Crépeau, 17042 La Rochelle Cedex 1, France

*Corresponding author: Arthur BORDY

Tel: +33 (0)1 34 25 69 35

Email: arthur.bordy@u-cergy.fr

ABSTRACT

This paper presents the results of an experimental study conducted on cement pastes designed with partial substitution of Portland cement by a recycled cement paste fine (RCPF) obtained from crushing, grinding and sieving of a laboratory-made cement paste. As such cementitious materials may exhibit a high sensitivity to drying, in this work, the influence of conservation conditions on their hydration kinetics was studied. The cement pastes were then subjected to drying in ambiances with different temperatures and relative humidities (RH) to identify the possible presence of a RH threshold that significantly slows-down or even stops the hydration process.

The results of monitoring hydration coupled to the microstructure results showed that the effect of drying conditions on hydration kinetics of the different studied cement pastes depends on their intrinsic properties (microstructure). This could explain the lack of consensus in the literature on the drying conditions under which hydration kinetics are strongly affected.

Key words: Drying conditions, Hydration, Microstructure, Recycled fine, Cement paste.

INTRODUCTION

Designing new cementitious materials by substituting a part of their Portland cement by a fine obtained from demolition waste without any thermal pre-treatment, instead of using an ordinary mineral addition, would contribute:

- to reduce the environmental impact of these materials by reducing the amount of Portland cement and also by avoiding the heating of the recycled fine [1,2];
- to limit the systematic use of natural resources by reducing the amount of Portland cement and by avoiding the use of some mineral additions such as limestone filler [3-5];
- to limit landfill by reusing the recycled fine [6,7].

However, such cementitious materials, with low clinker contents, may exhibit a high sensitivity to drying [8]. In fact, hydration is known to be governed by various parameters intrinsic to the material, essentially related to the composition, but also by the curing conditions. This work deals then with the study of the influence of conservation conditions

(drying at different RH and temperatures) on hydration kinetics.

Cement pastes were designed with partial substitution (0 to 75% by mass) of Portland cement CEM I 52.5 N type by a recycled cement paste fine (RCPF), obtained from crushing, grinding and 80- μ m sieving of a laboratory-made cement paste. The latter was itself manufactured with the same Portland cement. The choice of using the same cement, and using a laboratory-made cement paste to generate RCPF, instead of a real demolished concrete, allows to better control the chemical composition of the recycled fine by eliminating the variability of its properties when recovered from demolished materials.

The microstructure of the so-obtained cement pastes was characterized. Then the cement pastes were subjected to drying in ambiances with different temperatures and RH to identify the possible presence of a RH threshold that significantly slows-down or even stops the hydration process.

EXPERIMENTAL PROGRAM

Materials and mixtures: Cement pastes were designed with substitution of Portland cement CEM I 52.5 N type, complying with the European EN 197-1 Standard, by a fine, denoted in the following “RCPF” (Recycled Cement Paste Fine), obtained from crushing, grinding and 80- μm sieving of a laboratory-made cement paste. The latter was itself manufactured with the same Portland cement CEM I 52.5 N type. The recycled cement paste (Table 1) was prepared with a water-to-cement ratio equal to 0.3 in order to limit bleeding and segregation, and to obtain thus a homogeneous paste.

Table 1
Recycled cement paste composition

Portland cement (C) [kg/m^3]	1606
Effective water (W) [kg/m^3]	482
W/C [-]	0.30
C/(W+C) [-]	0.77

The recycled cement paste was cast into $\text{Ø}16\text{X}32$ cm molds and stored in a room at 20 ± 1 °C for 24 hours. All cylinders were then demolded 1 day after casting and cured under water at 20 ± 1 °C for 89 days. At the age of 90 days, specimens were first crushed by compression to obtain fragments less than 15cm and then grinded in a laboratory ball mill until obtaining 80 μm powder after successive sieving. Finally, the so-obtained RCPF was stored under hermetically sealed conditions before use. Such a conservation would limit the exposition of RCPF to the atmospheric humidity and CO_2 .

Four cement pastes (Table 2) were prepared using the mix-design method described by the following equations:

$$V_C + V_F + V_W = 1\text{m}^3 \quad (1)$$

$$\frac{W}{F + C} = 0.45 \quad (2)$$

$$\frac{F}{F + C} = j \quad (3)$$

with V_C , V_F and V_W [m^3] the cement, RCPF and water volumes, respectively, W, F and C [kg] the effective water, RCPF and cement contents, respectively. The pastes are denoted P_i with i the percentage of cement substitution by mass, $i=j*100$.

Table 2
Mix proportions and properties

	P0	P30	P50	P75
Portland cement (C)	1294	894	633	313
RCPF (F)	0	383	633	939
Effective water (W)	583	575	570	564
F/(F+C) [-]	0	0.30	0.50	0.75
W/C [-]	0.45	0.64	0.90	1.80

Protocols: Cement pastes (Table 2) were cast into $\text{Ø}3\text{X}6$ cm molds maintained in rotation during the first six hours after casting (curing time). The rotating device, placed in a room at 20 ± 1 °C, limits bleeding and segregation [9]. One day after casting, the $\text{Ø}3\text{X}6$ cm cylinders were demolded:

Water porosity measurements: A first set of cylinders was sawn into $\text{Ø}3\text{X}2$ samples and stored under water at 20 ± 1 °C to measure the water porosity at the ages of 28 and 90 days. Measurements were carried out by means of water saturation under vacuum according to the French NF P18-459 Standard.

Water vapor desorption isotherm determination: A second set of cylinders was sawn into 5 mm cubic samples and stored under water at 20 ± 1 °C to determine the water vapor desorption isotherm at the age of 28 days. For each composition, some cubic samples were water saturated under vacuum and placed in sealed cells where the relative humidity was controlled by means of saturated salt solutions or silica gel (tested RH: 86, 76, 65, 55, 33, 12 and 3 %) and the temperature was kept around 20 ± 1 °C.

Thermogravimetric analysis: A last set of cylinders was sawn into 5 mm cubic samples and placed in sealed cells where the relative humidity was controlled by means of saturated salt solutions and the temperature by means of a cryostat (Table 3). The objective was to determine the influence of drying at different relative humidities and temperatures on hydration kinetics. At different ages: 1, 2, 3, 7, 14, 28 and 90 days, 5 mm cubic samples were crushed into powders of around 100 mg to assess their Portlandite content by means of thermogravimetric analysis (TGA). Tests were performed with a temperature rise of 10 °C/min from 20 to 1200 °C in a nitrogen atmosphere.

Table 3
Conservation conditions before TGA measurements

T [°C]	RH [%]			
	5	10	20	30
Magnesium nitrate	58	57	55	-
Ammonium nitrate	-	-	-	59
Sodium chloride	76	76	76	75
Ammonium sulfate	82	82	81	80
Potassium chloride	88	88	86	85
Potassium nitrate	96	95	93	91
Potassium sulfate	98	98	97	96

RESULTS AND DISCUSSION

Water porosity: The obtained porosities for both 28 and 90 days are given in Figure 1. They show that the porosity increases linearly with the substitution ratio. In fact, the higher the cement substitution ratio, the lower the clinker content. This reduces the amount of hydrates and leads thus to a high porosity. Note also that the measured porosity is lower in 90 days than in 28 days. This can be explained by the hydration which continued to clog the pores with additional hydrates. The porosity should not evolve when the cement paste has reached its ultimate degree of hydration under water.

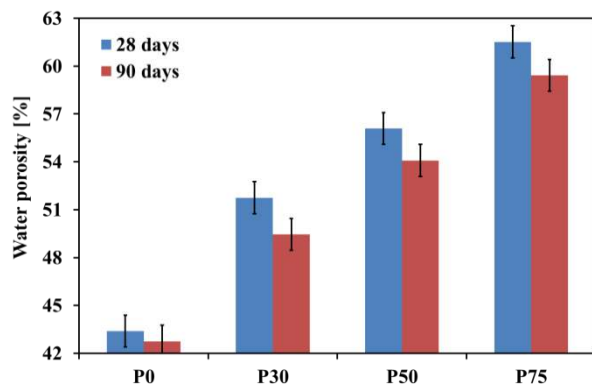


Figure 1
Water porosity at 28 and 90 days

Water vapor desorption isotherm: Figure 2 gives the water vapor desorption isotherms measured at 28 days. For a given RH, the cement paste with the coarsest microstructure has the lowest water saturation degree [10]. The paste “P0” exhibits thus the finest microstructure and “P75” the coarsest one. The curves show also that the higher the cement substitution ratio, the coarser the microstructure.

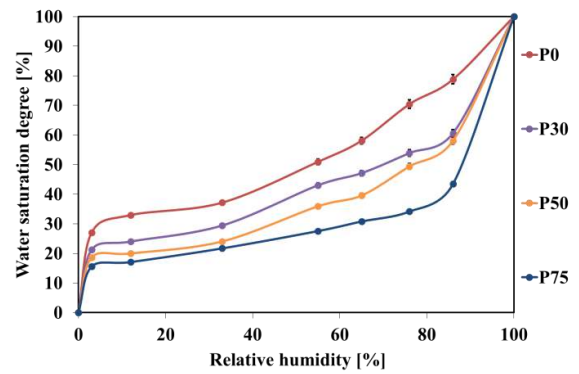


Figure 2
Water vapor desorption isotherm at 28 days

According to these previous results (Figures 1 and 2), it is possible to conclude that increasing the RCPF content increases the porosity, leads to a coarser microstructure and increases thus the moisture diffusion coefficient. In fact, Figure 3, giving an example of weight loss occurring during the isotherm measurements, shows that increasing the RCPF content accelerates the drying of the cement paste.

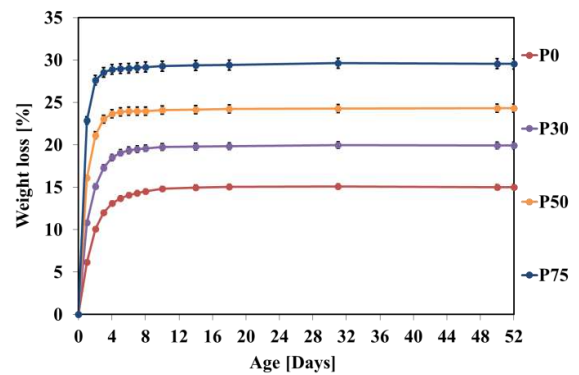


Figure 3
Weight loss due to drying for 52 days at 3 % RH

Portlandite content: The content of produced Portlandite is calculated by deducting from the total Portlandite content the initial Portlandite present in both Portland cement and RCPF.

Effect of RCPF content: Figures 4 to 8 show that whatever the ambient temperature and relative humidity, the higher the cement substitution ratio, the lower the Portlandite content. In fact, increasing the RCPF content reduces the clinker content, which decreases the hydration and leads thus to low Portlandite content [11].

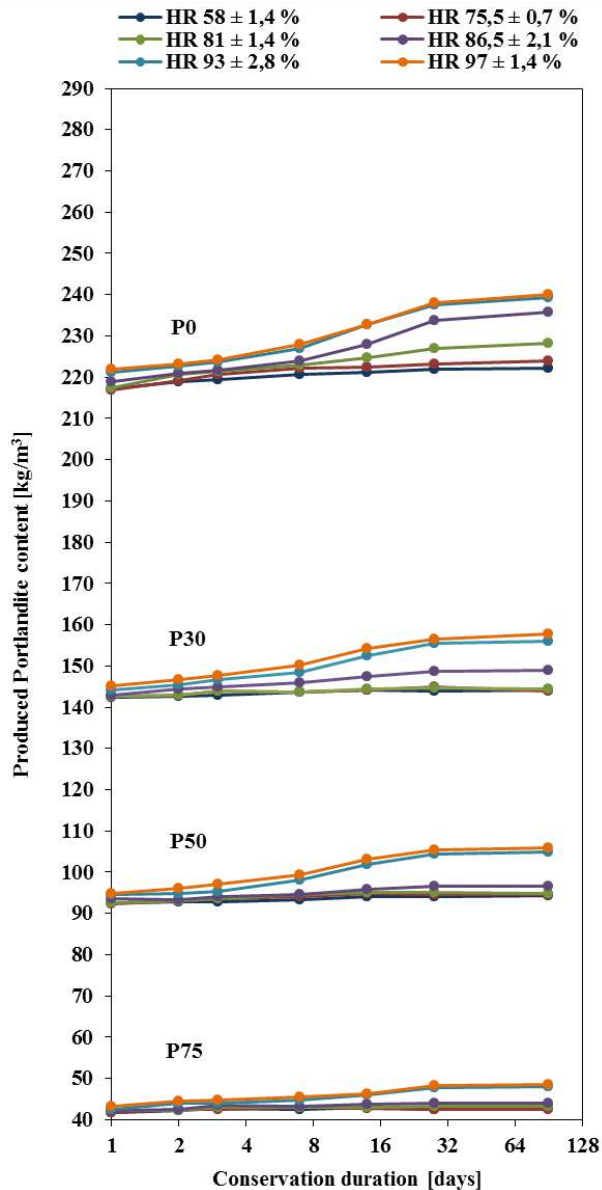


Figure 4
Produced Portlandite content versus duration of conservation at 5 °C

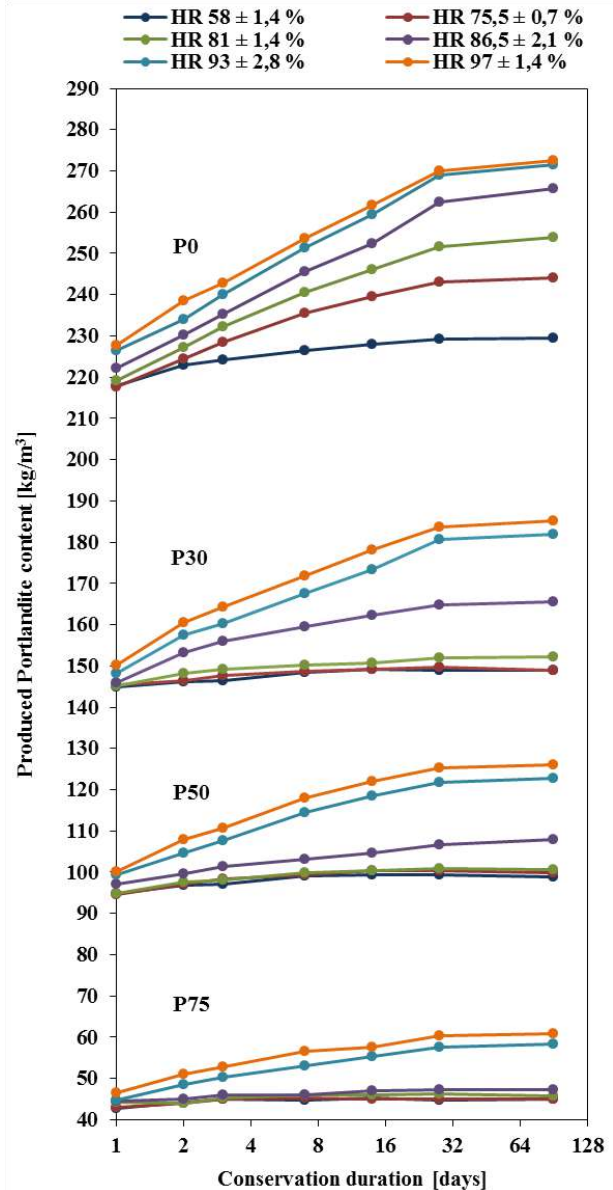


Figure 5
Produced Portlandite content versus duration of conservation at 20 °C

Effect of ambient RH: The curves of Figure 8 show that whatever the ambient temperature, the Portlandite content decreases with the ambient RH. Moreover, the RH threshold that slows down the hydration increases with the RCPF content. Indeed, the hydration of “P0” is considerably slowed down for RH lower than 58 %, while for “P75”, the hydration is stopped for RH equal to 86 %. This could be explained by the fact that “P0” has a lower moisture diffusion coefficient (due to its low porosity and fine microstructure) that reduces the drying, as mentioned previously.

Then, in order to stop the hydration of “P0”, the ambient RH must be enough low to dry the material and evaporate the water which is necessary for the hydration reactions. On the other hand, “P75” has a high moisture diffusion coefficient that allows drying even for high ambient RH. It is therefore not possible to designate a consensual ambient RH threshold that would stop the hydration kinetics of cementitious materials because it depends on parameters intrinsic to the material as porosity and pore distribution.

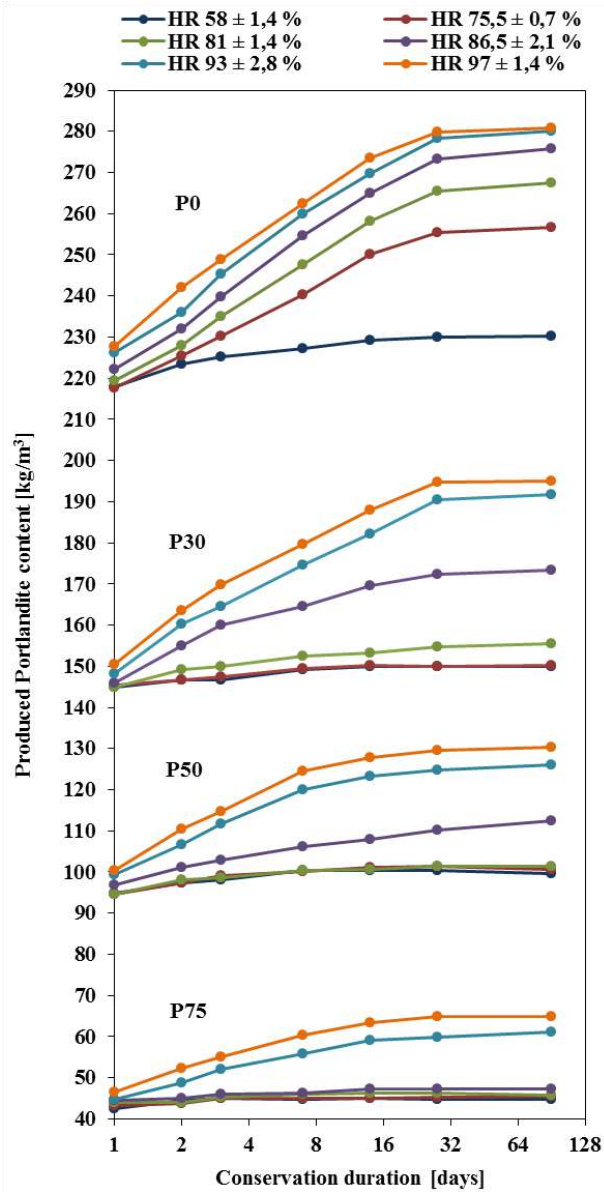


Figure 6
Produced Portlandite content versus duration of conservation at 30 °C

Effect of ambient temperature: The results of Figure 7 show that for high RH ($RH > 93\%$), increasing the ambient temperature increases the formation of Portlandite. However, for lower RH ($RH < 86\%$), the increase of temperature does not compensate enough the hydration decrease due to the water loss by drying, especially in the case of cement pastes containing RCPF (pastes with high moisture diffusion coefficient). This result is expectable since the presence of water in the cementitious material is more essential to the hydration reactions than the increase of the ambient temperature.

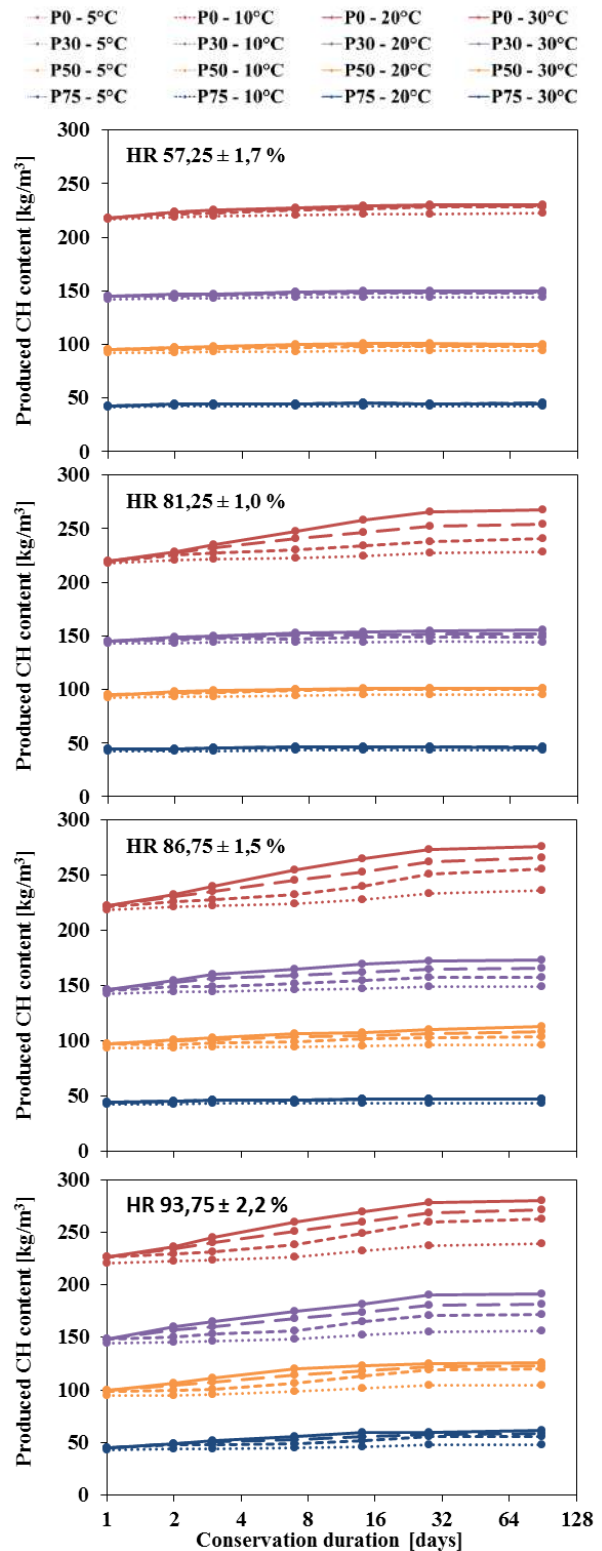


Figure 7
Produced Portlandite content versus duration of conservation at different RH

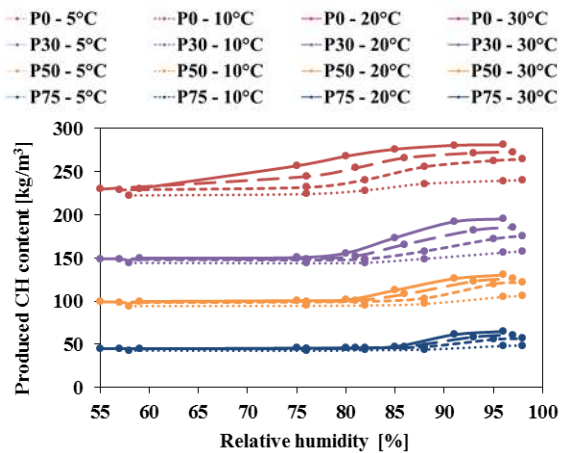


Figure 8

Produced Portlandite content in pastes conserved for 90 days at different temperatures

CONCLUSIONS

This work was devoted to the study of the influence of drying conditions on hydration of cement pastes designed with partial substitution of Portland cement by a recycled cement paste fine obtained without thermal pretreatment. Its main conclusions are:

- Water porosity measurements showed that the porosity increases linearly with the cement substitution;
- Water vapor desorption isotherm measurements showed that the microstructure becomes coarser with the cement substitution;
- Weight loss monitoring at different RH showed that the drying kinetics increases with the cement substitution;
- TGA occurred on pastes at different ages, temperatures and RH, showed that the produced Portlandite content decreases with the cement substitution;
- TGA showed also that the produced Portlandite content increases with the ambient RH and the RH threshold that slows down, or stops, the hydration increases with the cement substitution. This could explain the lack of consensus in the literature on the drying conditions (ambient RH) under which the hydration kinetics is strongly affected, because the RH threshold depends on parameters intrinsic to the material as porosity and pore distribution.

REFERENCES

1. Oksri-Nelfia, L., Mahieux, P.-Y., Amiri, O., Turcry, P., Lux, J., 2015, Reuse of recycled crushed concrete

finer as mineral addition in cementitious materials, *Materials and Structures/Materiaux et Constructions*, **13**, Article in Press.

2. Florea, M.V.A., Ning, Z., Brouwers, H.J.H., 2014, Activation of liberated concrete fines and their application in mortars, *Constr. Build. Mater.*, **50**, pp. 1-12.

3. Tam, V.W.Y., 2008, Economic comparison of concrete recycling: A case study approach, *Resour. Conserv. Recycl.*, **52**, pp. 821-828.

4. Gartner, E., and Hirao, H., 2015, A review of alternative approaches to the reduction of CO₂ emissions associated with the manufacture of the binder phase in concrete, *Cem. Concr. Res.*, **78**, pp. 126-142.

5. Flower, D.J.M., and Sanjayan, J.G., 2007, Green house gas emissions due to concrete manufacture, *Int. J. Life Cycle Assess.*, **12**, pp. 282-288.

6. Schoon, J., De Buysser, K., Van Driessche, I., De Belie N., 2015, Fines extracted from recycled concrete as alternative raw material for Portland cement clinker production, *Cem. Concr. Compos.*, **58**, pp. 70-80.

7. Hansen, T.C., 1992, *RILEM: recycling of demolished concrete and masonry*, Report of Technical Comité 37-DRC: Demolition and Reuse of Concrete, Chapman & Hall, London.

8. Younsi, A., Turcry, P., Aït-Mokhtar, A., Staquet, S., 2013, Accelerated carbonation of concrete with high content of mineral additions: Effect of interactions between hydration and drying, *Cem. Concr. Res.*, **43**, pp. 25-33.

9. Alrifai, A., Aggoun, S., Kadri, A., Kenai, S., Kadri, E., 2013, Paste and mortar studies on the influence of mix design parameters on autogenous shrinkage of self-compacting concrete, *Constr. Build. Mater.*, **47**, pp. 969-976.

10. Baroghel-Bouny, V., 2007, Water vapour sorption experiments on hardened cementitious materials. Part I: Essential tool for analysis of hygral behaviour and its relation to pore structure, *Cem. Concr. Res.*, **37**, pp. 414-437.

11. Mounanga, P., 2003, Comportement des matrices cimentaires au jeune âge : relation entre évolution chimique et déformations chimique et endogène, *XXI^{ème} Rencontres Univ. Génie Civ.*, pp. 189-198.

EFFECT OF CONCRETE WASTE QUALITY ON THE COMPRESSIVE STRENGTH OF RECYCLED CONCRETE

B. Kebaili^a, O. Kebaili^b, B. Redjel^c

^{a,c} Civil engineering laboratory, Badji Mokhtar University, BP12 23000, Annaba, Algeria

^b materials, geo-materials and environment laboratory, Badji Mokhtar University

Fax:038 87 53 97

bachir.kebaili@univ-annaba.dz

ABSTRACT

The reuse of concrete waste as a secondary aggregate could be an efficient solution for sustainable development and long-term environmental protection. The variable nature of waste concrete, with various compressive strengths can have a negative effect on the final compressive strength of recycled concrete. Accordingly an experimental test programme was developed to evaluate the effect of parent concrete qualities on the performance of recycled concrete. Three grades with different compressive strengths 10MPa, 20MPa, and 30MPa were considered in the study; moreover an unknown compressive strength was introduced as well. The trial mixes used 40% secondary aggregates (both course and fine) and 60% of natural aggregates. The compressive strength of the test concrete decrease between 15 and 25% compared to normal concrete with no secondary aggregates. This work proves that the strength properties of the parent concrete have a limited effect on the compressive strength of recycled concrete. Low compressive strength parent concrete when crushed generate a high percentage of recycled coarse aggregates with less attached mortar, and give the same compressive strength as an excellent parent concrete.

KEYWORDS: recycled, concrete, quality, strength

INTRODUCTION

Presently a huge program of construction is in progress in Algeria, with more than one million housing, basic infrastructures, as well as a 1200km east-west highway taking place. The nature and scope of the work necessities the use of vast amounts of natural aggregates for use in concretes, road construction and use engineering fill. The consequence is negative effect on the natural environment. To date concrete waste which is the result of old buildings demolition and seismic disasters has been neglected as a possible source of construction, historically, this material is treated as a waste product. Fig. 1 below shows typical unregulated landfill rubble dumping, which damages the natural landscape.

Therefore, the reuse of concrete waste would give a positive solution to the problems described above. In addition, the use of secondary aggregates would help to protect natural environment allowing a rational consumption of natural resources.

Currently in Algeria construction wastes usage stands at 5%; with the remained being dumped, thereby constituting a burden for management and environmental policy. The purpose of this research is to demonstrate the potential benefits of the using concrete waste in concrete manufacture. This has the secondary benefit of preserving the natural environment.



Figure 1
Uncontrolled concrete waste dumping (Annaba city)

Recycled concrete (RC) showed similar characteristics when compared to normal concrete (NC) with natural aggregates (NA). The percentage use of recycled aggregate concrete (RAC) for the manufacture of RC can vary from 20 to 100 %, this range of replacement has been proved to produce excellent mechanical and physical characteristics; however the compressive strength (CS)

decreases from about 20 to 25% [1]. The RAC has very high water absorption coefficient, because of the porosity induced by the attached mortar. They absorb roughly 6% [2], as a consequence the RC requires more water to achieve the same workability as NC. The increased water content is deemed responsible for the decreased of CS when compared to NC, [3] and [4].

It has been proven that the CS of RC decreases according to the level of the aggregate replacement in new concrete [2]. A secondary by-product of replaced is an increase in the water absorption coefficient, [5]. The substitution of natural sand by recycled fine aggregate (RFA) has also been studied. Published research has proven that the very high porosity of RFA can alter the long term durability of the RC. Also the compressive strength decreases, reduces by up to 30% for a 100% replacement [6]. However, replacement between the limits of 30% to 60% of RFA, has been shown to no effect on RC characteristics [7].

The increased porosity of the RC can be reduced or offset by maintaining a normal W/C ratio with the addition of plasticizing admixture, [8] who recorded the same characteristics as a NC with NA.

The effect of recycled aggregates derived from parent concrete (PC) has been analysed only by a few researchers. They showed that the fraction of the water absorption coefficient was more significant, according to the strength of PC, also the CS was related to this latter[9]. A large part of concrete waste could be recycled, but the question which arises is, is it necessary to sort out the concrete waste in accordance with their compressive strength? That, will constitute a difficult task, even impractical process; where the importance of studying the effect of PC compressive strength on the RC.

EXPERIMENTAL PROGRAM

Three categories of PC were used, low, normal, and excellent CS varying from 10MPa to 30MPa. These strengths are typical of infrastructure work in Algeria furthermore; a PC with an unknown quality was introduced to the study as a random variable.

For each category, a minimum of 12 cubes (10x10x10 cm) was manufactured. A comparison was made with a NC with compressive strength target of 20MPa. This standard material used no secondary aggregates.

The concrete waste was sourced from various concrete test Specimens not used yet from different laboratory fig. 2.

The CS is measured by crushing by crushing cylindrical concrete specimen in compression testing machine, and sorted according to their CS. The PC exhibited a wide range of compressive strength with the lower and upper limits being 10 to 40 MPa. The justification of the three RCA strength classes is shown in Table 1.



Figure 2
Test specimen as concrete waste

Table1
Compression strength ranges of parent concrete used as recycled aggregates

Excellent	Normal	Low	Concrete waste	
30.6	21.2	9.8	Strength (MPa)	1
35.1	21.5	10.2		2
34.5	21.4	11.5		3
39.2	19.8	9.6		4
41	19.6	12.1		5
34.7	19.9	10.5		6
30.5	19.9	10.8		7
30.3	20.8	11		8
33.1	19.9	9.8		9
34.7	20.2	9.9		10
36.1	21	12		11
31.8	19.7	10.9		12

Crushing of concrete

Waste concrete was broken into pieces and then crushed using a jaw crusher to sizes smaller than 20 mm fig. 3, and sieved into various sizes to produce the 03 RAC size, fine 0-5mm and coarse 5-10-20mm.

In the case of RC obtained from PC material having a CS between 30MPa and 20MPa, a decrease in CS was observed between 15% and 23% respectively. This is typical for normal when the target strength is 20MPa, as a result of the water absorption coefficient and the bond's effect at the interface between the coarse aggregate and the attached old mortar attached.



Figure 3

Jaw crusher apparatus and the machine in operation

The RAC obtained are heterogeneous, consisting of a natural coarse aggregate with attached cement mortar as shown in fig. 4.

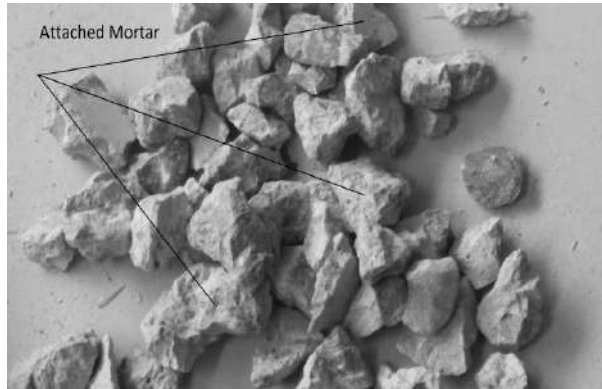


Figure 4

Crashed Recycled aggregates with attached mortar

Having obtained the grading curves a blended aggregate mixture was produced which contained 40% RAC and 60% NA including RFA. The choice of 40% RAC was deemed by the research team an adequate proportion to maximize usage without adversely affecting other concrete properties.

Concrete mix

The grading size analysis allowed estimating the concrete composition using Bolomey dosage method [8], with a target slump ranging from 40 to 70 ± 10 mm as a plastic concrete. The mix design was conceived for the second phase of concrete testing, RC and NC, taking into account different Water/Cement ratio. The target CS was 20MPa, which is required by the Algerian seismic standard. The cement contents proportion was 350kg/m³ of CEM.II 42.5. The mix was made to achieve a plastic concrete slump. Four categories of RC were undertaken, defined as RC10,

RC20, RC30 and RC for the unknown RA, obtained from the corresponding PC, low, normal, excellent and unknown CS.

The mix proportions derived from the Bolomey dosage method are shown in table 2. below.

Table 2
Amount of aggregate, cement and water

Sizes mm	NA kg	RAC kg	Cement kg	Water/Cement ratio
0/5	418	279	350	W/C=0.7 RC
5/10	172	114		W/C=0.5 NC
10/20	482	321		

The concrete manufacture was undertaken in accordance with the standard (NF P 480-1 part.1, 2014) and the consistency was determined standard (NF EN 12350 part.2, 2012). The slump test values ranged between 5 and 7cm for all recycled concrete, RC10, RC20, RC30, RC and NC, which confirms the assumption for plastic concrete.

The W/C ratio was higher for recycled concrete compared to normal concrete for the same workability of concrete; this was mainly due to the porosity of recycled aggregate and the nature of attached mortars with their higher absorption factor.

Twelve cubic specimens were prepared for each category of recycled concrete and normal concrete. The cube manufacture was made on a shaking table in accordance with the standard (NF P18-422, 1981).

Compression test

Tests on the 4 categories of RC and NC were carried out after 28 days. Compression testing was conducted on a calibrated 500kN Hydraulic press. The testing work was undertaken at constant speed as mentioned in the standard (NF EN 12390 part.3, 2012).

Results and discussion

The compressive strengths obtained from recycled concrete compared to concretes parents RC10, RC20, and RC30 are presented below figs. 6.

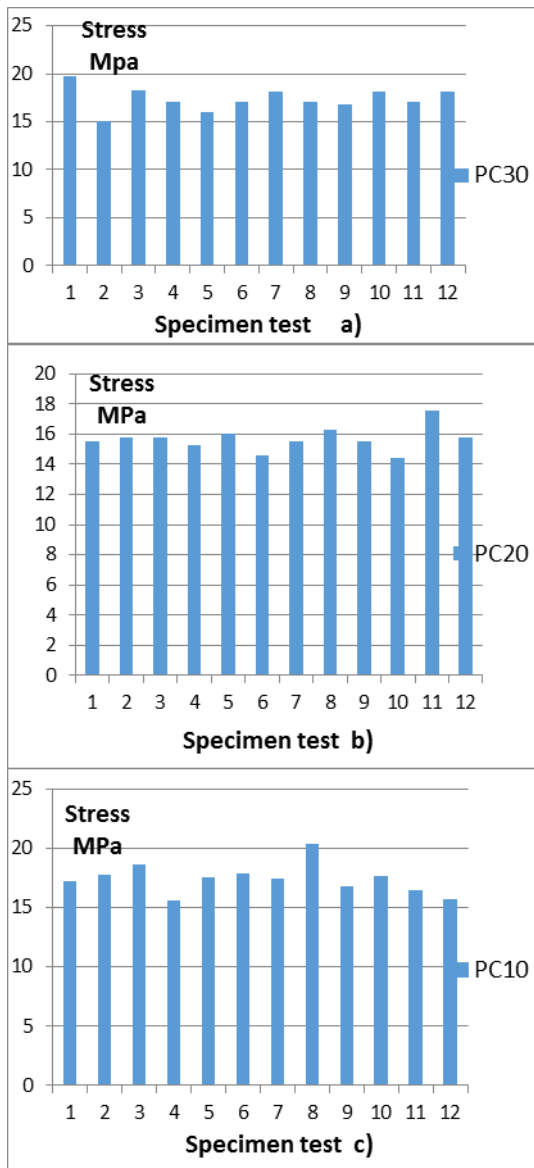


Fig 6

RC's CS for a) PC 10MPa a) b) 20 Mpa and c) 30MPa

However, the reduction in RC's CS was less significant when the PC' material CS was 10MPa. The strength reduction was 15%, the same diminution as PC30. Contrary to the general statement saying that the CS of RC is correlated to the CS of PC, when the parent concrete has a weaker CS, the RC has the same characteristics as that obtained from excellent PC. This can be explained by the mortar-aggregate bond, in the case of PC30 the mortar-aggregate bond had more strength than PC20 which is why the RC strengths obtained had good qualities. Whereas for the RC strength obtained from PC10 the compressive strength decreased by around only 15%, which is the same as the RC30.

Further investigations were needed to understand this experimental contradiction of the theoretical statement

saying more PC has lower CS, more the influence on the RC strength will be bad. In the case of PC10 the coarse aggregates obtained after crushing are more natural, having less attached mortar which tends to make the RAC more like a traditional concrete. Naturally the more attached mortar in the mix with results in a weaker zone within the matrix which will crack at significant lower stress levels. The interface if much cleaner, increasing therefore the bond between the new mortar and the RA, improving the RC's CS.

The comparative analysis of the results obtained from the different RC allowed deducing the following observations. On average the % decrease in compressive strength for the RC10, RC30 is approximately 15%, whereas for the RC20 this depletion was approximately 23%. This is contrary to what has been observed by other researchers [9] who noted that the better the PC strength was the more RC was also.

This is true when the PC has a good quality, but for weak parent concrete the effect is quite the opposite. This seems normal given that the RC10, after being crashed, gave a more traditional recycled aggregate form with less mortar attached. As a result the recycled aggregates obtained from a weak concrete have better quality than such obtained from a good quality concrete waste because of the amount of attached mortar.

For unknown parent concrete it was observed that the compressive strength decreases by less than 12%, therefore it is clear that the influence of the origin of the recycled aggregates may not be as significant as previously considered. Therefore the requirement of sorting the concrete waste related to the CS which will make the reuse of concrete waste practically more difficult and may be unable to be realized is not necessary. The variability in the scatter of the results is very similar for the entire materials tested table 4.

Table 4
Strength characteristic for different RC

N°	Average strength MPa	Standard deviation MPa	Characteristic strength MPa
NC	20.41	0.72	19.23
RC10	17.41	1.29	15.29
Reduction %	14.75	-	20.52
RC20	15.68	0.81	14.34
Reduction %	23.25	-	25.43
RC30	17.37	1.22	15.36
Reduction %	14.75	-	20.15
RC	17.96	1.15	16.06
Reduction %	12.00	-	16.47

The strength characteristics of the recycled concretes were of the same order of magnitude. The maximum variation observed was 10.70%, what is allowable for concrete as heterogeneous material, compared to the standard deviation which gives an average variation of compressive strength equal to 7.32%. The strength reduction in this case is considered to vary between 15 and 25 % as shown in fig. 9.

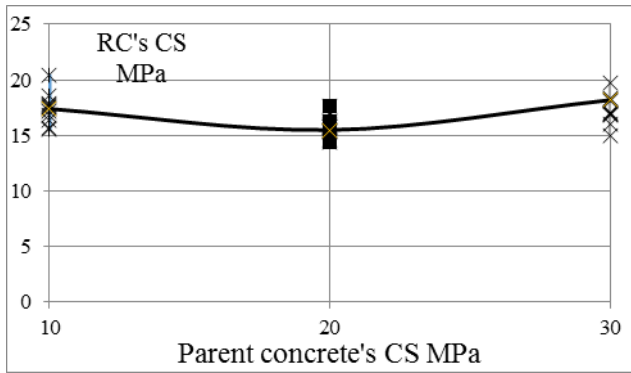


Figure 9

Compared CS for RC obtained from 10, 20, and 30 MPa PC

The results obtained for recycled concrete RC10, RC20, RC30 and the unknown RC material when compared to the target concrete shown that the parent concrete strength characteristic has a limited impact on the compressive strength of the recycled concrete. Therefore, it could be suggested that the reuse of recycled aggregate can be done without any restriction to their origin, and without any sorting. However, more testing is needed to confirm this hypothesis. It can also be stated that unknown parent concrete gives the same compressive strength as concrete RC10, RC20, and RC30, which is a confirmation of the statement given above.

3.1 Concrete mix correction

The RAC has a greater superficial porosity due to the attached mortar which affects the RC's CS. When the concrete is mixed an amount of cement powder is absorbed by the pore as a result the CS decrease relatively to the rate of substitution.

To estimate the cement powder ratio absorbed by the apparent porosity of the RA, the differential porosity between the NA and RAC was estimated after 5 minutes, which can correspond to the time of mixing the concrete fig. 10.

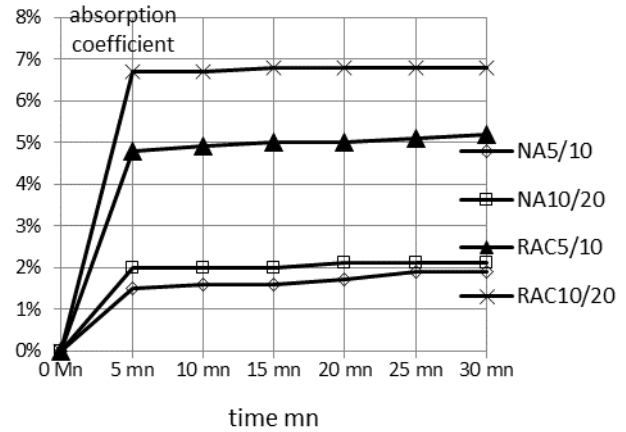


Figure 10

Absorption coefficient for RAC and NA

This can be used as a basis for the correction of cement content. The RAC porosity was determined as 6%, whereas the average NA was 2%. The difference between the two porosities can be defined as the apparent porosity of RAC. This allowed considering a 4% rate of the weight of the RAC used suitable cement content addition to improve the CS of the RC.

In this way a new recycled concrete corrected RCC mix was carried using the same proportion adding 4% of the weight of the RAC. The new mix proportions are shown in Table 5.

Table.5 Amount of additional cement content

Sizes mm	NA kg	RAC kg	Cement content correction kg	Water Litre
0/5	418	279	350+(279+114+321)*4%=403.5	W/C=0.55 RC
5/10	172	114		W/C=0.5 NC
10/20	482	321		

The slump test on the revised mix gave a subsidence between 5 and 7cm for all recycled concrete, RC10, RC20, RC30, RC and NC.

Compression testing was done for this new mix and the results established that the CS was improved by the additional cement content. The results are shown in fig. 11.

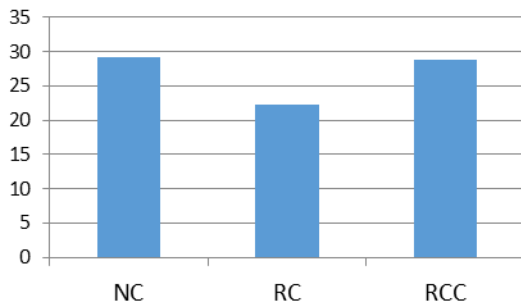


Fig. 11: CS (MPa) for NC, RC, and RCC with 4% of additional cement content.

The CS for RCC has been improved with this additional cement content. This approach potentially could be used as option to correct the recycled concrete mix made with different kind of recycled aggregate by using only the absorption coefficient of each constituent.

Conclusions

In accordance with the experimental study carried out, the main conclusions obtained are given below:

1. Low compression strength concrete crushed; give a high percentage of recycled coarse aggregates with less attached mortar.
2. The W/C ratio in recycled concrete is more important than normal concrete for the same workability. This affects the compactness of concrete, resulting in lower recycled concrete compressive strength.
3. For a given target mean strength, the achieved strength increases with an enhance on the quality of parent concrete, nevertheless in the case of low CS parent concrete the strength is not affected because of less attached mortar to coarse aggregates.
4. The percentage loss in compressive strength due to 40% recycled aggregate replacement is between 15 and 25%, but the offset in strength can be mitigated with a local correction in the cement content.
5. The potential need for parent concrete sorting could be eliminated based on this current study finding. However more testing is needed, if the findings are ratified in further works there is a potential large saving for new works in terms of environmental impact.

References:

1. Etxeberria M, Vázquez E, Marí A, Barra M, (2007) "Influence of amount of recycled coarse aggregates and production process on properties of recycled aggregate concrete", Cement and Concrete Research, Volume 37, Issue 5, May 2007, Pages 735-742, doi:10.1016/j.cemconres.2007.02.002
2. de Juan Marta Sanchez, Pilar Alaejos Gutierrez, "Study on the influence of attached mortar content on the properties of recycled concrete aggregate", Construction and Building Materials, Volume 23, Issue 2, February 2009, Pages 872-877, doi:10.1016/j.conbuildmat.2008.04.012
3. Lopez-Gayarre F, Serna P, Domingo-Cabo A, Serrano-López M.A, López-Colina C, "Influence of recycled aggregate quality and proportioning criteria on recycled concrete properties", Waste Management, Volume 29, Issue 12, December 2009, Pages 3022-3028, doi:10.1016/j.wasman.2009.07.010
4. Tabsh Sami W, Abdelfatah Akmal S, "Influence of recycled concrete aggregates on strength properties of concrete", Construction and Building Materials, Volume 23, Issue 2, February 2009, Pages 1163-1167, doi:10.1016/j.conbuildmat.2008.06.007
5. Xiao Jianzhuang, Li Jiabin, Zhang Ch, "Mechanical properties of recycled aggregate concrete under uniaxial loading", Cement and Concrete Research, Volume 35, Issue 6, June 2005, Pages 1187-1194, doi:10.1016/j.cemconres.2004.09.0
6. Khatib J.M, "Properties of concrete incorporating fine recycled aggregate", Cement and Concrete Research, Volume 35, Issue 4, April 2005, Pages 763-769
7. Talamona D, Tan Kang Hai, "Properties of recycled aggregate concrete for sustainable urban built environment", Journal of Sustainable Cement-Based Materials, Vol. 1, No. 4, December 2012, Pages 202-210, doi:10.1080/21650373.2012.754571
8. Matias D, Brito J. de, Rosa A, Pedro D, "Mechanical properties of concrete produced with recycled coarse aggregates – Influence of the use of superplasticizers", Construction and Building Materials, Volume 44, July 2013, Pages 101-109 doi :10.1016/j.conbuildmat.2013.03.011
9. Padmini A.K, Ramamurthy K, Mathews M.S, "Influence of parent concrete on the properties of recycled aggregate concrete", Construction and Building Materials, Volume 23, Issue 2, February 2009, Pages 829-836, doi:10.1016/j.conbuildmat.2008.03.006

INFLUENCE OF RECYCLED AGGREGATES ON THE MECHANICAL AND TRIBOLOGICAL BEHAVIOR OF CONCRETE

K. Falek^a, K. Aoudjane^b, E.H Kadri^c, F. Kaoua^d

^{a,b,d}Faculty of Civil Engineering, Laboratory LBE, University of Sciences and Technology Houari Boumedienne

^cDepartment of Civil Engineering, Laboratory L2MGC-EA4114, University of Cergy-Pontoise, France.
Corresponding author: aoudjanekheir@yahoo.fr

ABSTRACT

The objective of this study is to evaluate the performance of a current concrete using recycled aggregate. Physical and mechanical tests of characterization were conducted on the aggregates to better understand the effects of absorptions. An experimental program to test fresh concrete was conducted regarding the workability and tribology for different substitutions of recycled aggregates with a constant and variable W/L ratio. Mechanical strength tests were also performed. The results on aggregates clearly show a lower density for recycled aggregates which is reflected in the fresh concrete according to the substitution. The rate of porosity is important, reaching 17% with an uptake of 7%, greater than that of the natural gravel. The mechanical tests confirm low wear resistance. With a W/L constant, the drop in workability is significantly dependent on the content of the % recycled, while the mechanical strength decreases only slightly. In terms of tribology, yield interface friction (τ) increases with the percentage of recycled aggregate and the viscous constant (η) of 100% recycled, reaching twice that of natural concrete. The test with constant workability and a W/C ratio variable causes a fall in compressive strength values approaching 25%. A third formulation dosed in adjuvant, with maneuverability and constant volume of dough gives resistance values comparable to that of the reference concrete with a yield interface equivalent to that of the reference concrete and a slightly higher viscous constant.

Keywords: Recycled aggregates; workability; compressive strength; interface friction; viscous constant

INTRODUCTION

The construction sector should adapt to the sustainable development approach to meet what has become a social emergency, the preservation of the environment and natural resources. The complete recycling of concrete provides answers to these questions. The various studies on concrete made from recycled aggregates [1-2] with substitution rates from 10 to 100%, have shown that the mechanical strength compressive or tensile these concretes are acceptable until a replacement rate of 40%. These works have shown that the aggregates of different sources have different properties. The use of recycled concrete aggregate as a quality control requires aggregates because they are collected from different sources. The work on the properties of basic materials, such as shape, texture, density, absorption, moisture content, permeability, strength characteristics, harmful substances, resistance to freeze-thaw, etc. should be carefully evaluated before they are used to produce concrete [3-4]. These global properties greatly affect the properties of concrete. It would therefore be necessary to assess the effect of recycled aggregate concrete and the final work on the optimal composition of recycled aggregates to produce a desirable quality concrete [5]. Recycled

aggregates derived from crushed specimens are absorbing character and in this context a series of tests were conducted to assess the character. This relates to the absorbance values, porosity, and rate of mortar attached and on the hardness parameters. Several alternative variants of natural gravels were tested on the behavior of fresh and hardened concrete.

PROPERTIES OF AGGREGATES

It is certain that the material from a crushed concrete have different properties and therefore it is normal that important work on sorting of demolition materials must be done to get the cleanest possible aggregates. In our case we used a series of test specimens of a natural concrete class C30 from the same construction site project. The aggregates were obtained using an impact crusher. The density of the recycled aggregates is lower than that of natural reaching 10% absorption: the absorption increases to 7% depending on the class of the aggregate.

Water absorption

The water absorption is important for the recycled aggregates. In fact the "All the results show that the concrete aggregates are characterized by a strong ability to absorb water. In addition, it seems that the thinner part of the recycled aggregates absorb a higher quantity of water than the coarse particles.

Figure 1 shows the variation of the water absorption coefficient 3/8 natural aggregate (NA) and 3/8 recycled (RA) measured according to standard NF 1097-6 after 60 minutes. It is observed that the values obtained on recycled gravel are much larger than the natural.

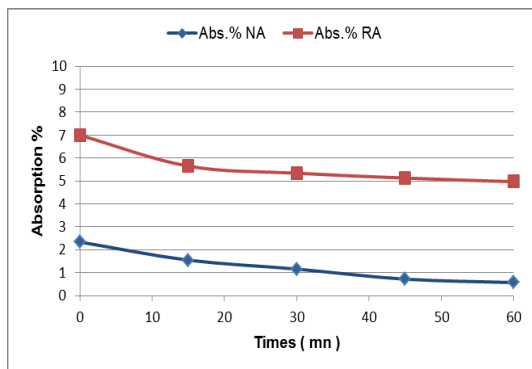


Fig.1 Absorption coefficient of natural and recycled aggregates

Porosity

The porosity rate is also higher for the GR confirming that the gravel recycled is more porous than the natural gravel. The maximum porosity rate reaching 17%, for gravel Small-scale 3/8, see Figure 2

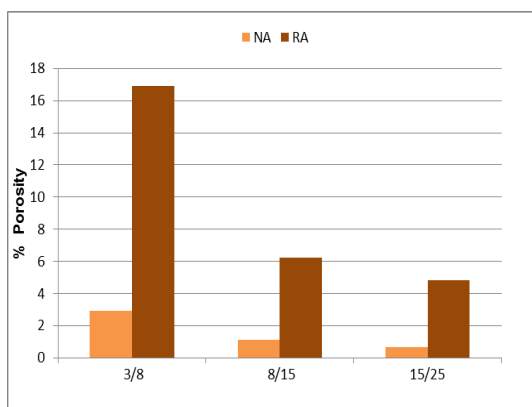


Fig. 2 The porosity variation of recycled aggregates

Adhered mortar

The recycled concrete aggregates have an irregular granular structure and, due to the mortar adhered can be a concern because it is a factor which contributes to the higher water absorption. The mortar adhered to recycled aggregates rate notes of several parameters, origin and initial compaction concrete crushing, shape and size of the aggregates and also cleaning with water or dry. The principle of the test for determining the weight percentage of cement pastes adhered to the recycled aggregates involves immersing after drying in the acid CHLORIDE 33% and an ambient temperature of 20 °. The results show the presence of a high percentage of mortar stuck to the largest aggregates for gravel 3/8 of around 37%, 32% for the 8/15 and 10% for large aggregates 15/25.

The research concluded that over 50% of recycled aggregates have joined a paste mortar [8] reported that the mortar adheres percentage depends on the size of the aggregates. In the size range of 4 / 8mm varies between 33- 55% and the range 8 / 16mm is 23-44%. These results are in line with the literature suggesting that this may vary from 25 to 65% and also depend on the method adopted for evaluating the content of mortar. This factor contributes to a large amount of water absorption in the recycled aggregates, which varies from 4 to 12% as shown in Figure 1 which in turn also depends on the size of aggregates as well as the grinding process and thus affect the compressive strength of the concrete

Abrasion

Abrasion is related to the intrinsic strength of the aggregates. Since increased abrasion%, the compressive strength decreases, and it depends on the relative strength of the concrete and the size of the aggregates. Sami [6] reported a small abrasion to a greater relative strength concrete. For the fine aggregate, which have a larger surface area, the mortar adhered to these aggregates is higher is also abrasion [7] reported that the recycled aggregates can have abrasion up 48% in case of fine aggregate and this can lead to a loss of strength in the range of 20-35%. The hardness tests have shown that for Los-Angeles coefficient of recycled aggregates, it is higher than that of natural gravel. Impact tests give higher values than to wear (micro deval).his high value is due to the amount of cement paste around the recycled aggregates crushed.

EXPERIMENTAL PROGRAM

Recycled aggregates used are all from test sample batches of the same project realization. Three-dimensional aggregates were used: 3/8, 8/15 and 15/25 mm. As for the sand there are two sands, coarse and finer, to obtain a fineness modulus close to 2.5. Concrete mixtures were prepared using the formulation method of the concrete Dreux- Gorisse, using a 380kg of cement content for 1 m³ of concrete in all mixtures. In different formulations, we used a CEM II/A 42.5 with a Blaine fineness of 3500 cm² / g.

Table1. Proportioning of the concrete mixture

Constituents (Kg/m ³)	NC	RC25	RC50	RC75	RC100
C	380	380	380	380	380
W	200	200	200	200	200
NS	351	356	361	365	370
NSf	275	283	292	300	308
NA (3/8)	138	104	69	35	0
NA(8/15)	549	412	275	137	0
NA(15/25)	412	309	206	103	0
RA(3/8)	0	56	112	167	223
RA(8/15)	0	86	172	257	343
RA(15/25)	0	120	240	360	480
S.PI (%)	0.7	0.7	0.7	0.7	0.7
Slump.(cm)	18	14	12	10	6
Rc.28(Mpa)	38	37.8	37.2	36.3	34.4

Natural and recycled Aggregates

All of recycled aggregates were manufactured from the crushing of test pieces TP from laboratory tests of C30 concrete class. They were sieved in three dimensions of groups and also to remove fine particles less than 4 mm. Gradations are shown in Figure 3.

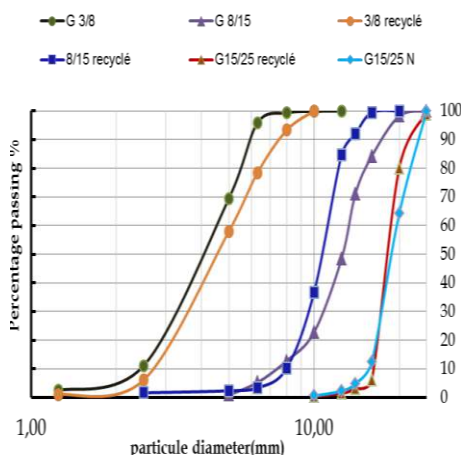


Fig.3 Grading curves of natural and recycled aggregates.

Three concrete formulation series containing RA (recycled aggregates) has been made. A first series was realized with percentage 25%, 50%, 75% and 100% of RA with a W/C ratio constant Table 1. The second series will cover the same percentage of RA, and constant workability with added water and therefore a W/C variable. The third formulation is in constant workability with a dosage of superplasticizer.

Mixture 1

Tests with W / C = Cst, without adding water. The workability of concrete with recycled aggregates for the same water content is lower depending on the replacement rate, which has been reported by many researchers, especially [7]. The slump test method used is that of the Abram's cone. It is observed in this first concrete formulation containing RA, than the value of the sag decreases according to the increase in the percentage of recycled aggregates used. The loss of maneuverability increases with the replacement rate. Water absorption test by recycled aggregates support this idea (Table 1).

Compressive strength

Replacing natural aggregates NA by recycled aggregates RA, usually involves a decrease in the compressive strength of conventional concrete. The results obtained figures 4 for use of 100% RA gives a reduction not exceeding 13%. This also results in a considerable drop in the value of subsidence, reaching 60mm to 100% RA. In this first concrete formulation based on recycled aggregates with a W/C = constant 0.526, the compressive strength of the recycled concrete is smaller than the concrete of natural aggregates. The compressive strength at 28 days, decreases with the increase of the recycled aggregates content for four different proportions (25, 50, 75 and 100%). The compressive strength although most researchers have all reported a decrease in the resistance for concrete based recycled RAC aggregates, it should be noted that the degree of reduction is related to parameters such as the type of concrete used for the manufacture of RA, the replacement rate, water / cement ratio and the moisture condition of the recycled aggregate. From the water-cement ratio, the moisture condition of RA seems to affect the compressive strength. Limited work has been made in trying to connect the power of the state of aggregates (kiln dried, air-dried, saturated dry surface, etc.).

Our tests are focused on the nature and quantity of the cement paste attached to the recycled aggregate, and the decrease in resistance has reached 13% for a degree of substitution of 100% of RA, with a workability which decreases 70%.

Mixture 2

Constant workability with added water. A second mixture is achieved by maintaining a constant slump, by addition of water according to the percentage of recycled gravel and the absorption rate. In a first method, we increased the dosage directly into the mixer through repeated trials until the mixture reaches the value of a slump (18cm) for each percentage. The second procedure who was often used to conduct the pre-wetting of the recycled aggregates with an amount of water corresponding to the difference in the absorption rate and then add the amount of water in the kneading to obtain the constant slump. The results obtained, see Figure 5, which decreases remarkably compared with that of natural concrete NC reaching 30% for a RC 100%. It is clear that the w/c ratio increases real, even if part of the water is absorbed by the old mortar attached to the recycled aggregates.

Mixture 3

With added superplasticizer. In this third formulation of concrete with recycled aggregates, workability is constant 18 ± 2 obtained through the collapse assay superplastifiant based polycarboxylates and the ratio of $W / C = 0.526$ is also constant. The decrease of the compression strength of concrete with recycled aggregates RCA by the proportions used, is less important. Indeed maximum strength loss to 100% of RA does not exceed 13%.

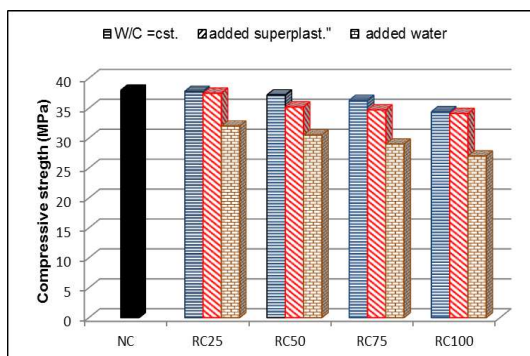
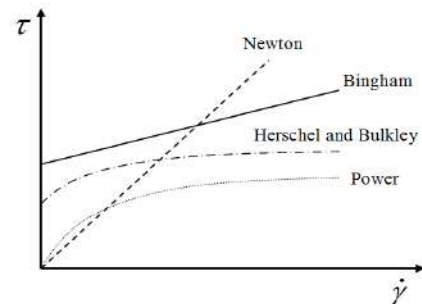


Fig.4. Compressive strength of concrete with the tree mixture

TRIBOLOGICAL

Fresh concrete is an intermediate material between a fluid and a stack wet particles. As a fluid, it has to flow to fill a volume of any shape. But only the difference of a fluid, the granular mixture, when sheared, it presents of volume that will lose the homogeneity of the mixture.

Body fluid behavior is shown from the relationship between the shear rate and shear stress.



Fluid rheology models

The current concrete, to form or plastic consistency, have a considerable dilatant behavior [8]. The rheological behavior of fresh concrete is similar to that of Bingham fluids whose constitutive law is written: The Bingham model: $\tau = \tau_0 + \mu\dot{\gamma}$

Test protocols

The rheological properties of fresh concrete are determined by the so-called rheometers, which measure the shear stress at varying shear rates. The measurement mode of resistance moment is to consider only the descent speed curve and the neglect of the climb, was used by many researchers [8]. The crude result of a test carried out with the tribometrical is in the form of $(T = T_0 + kV)$. The flow of concrete at the steel-concrete interface be written in the general form: $\tau = \tau_0 + \eta v/t$ seeks to calculate the pumping parameters (τ_0 et η) à from T_0 values T_0 and V found during the tribological test.

Results

The curves of Figures 5-6 show that the friction torques vary linearly with the speed of rotation. The observation of several tests confirms [9-10], the fact that the torque-speed curves at decreasing sense of speed are more linear than the growing sense. For concrete based on natural gravel (reference concrete) with a slump of 18 ± 2 cm, it

is noted that when the cylinder speed is low and the cylinder rub directly against the concrete, there's not been a boundary layer formation. This is supported by the importance of the slope of the torque-speed curve in this speed range. Then this slope decreases slightly due to the presence of the boundary layer. The friction interface (τ), increases with the percentage of recycled aggregates. In addition, when the rotation of the cylinder increases, the viscous constant (η) of concrete with 100% recycled aggregates, strong increases, up to double that of natural concrete. The test with constant workability and a w/c ratio variable causes a decrease in the compressive strength value approaching 25% for concrete with 100% recycled aggregates with added water and less than 13% with the addition of a superplasticizer and w/c constant curves figure 9, value of the friction torque for these two mixtures are practically confused, it gives equivalent output interface values to that of concrete reference and a slightly higher viscosity constant. The three curve corresponds to a concrete with 100% recycled gravel and sagging 6cm, the value of the friction interface increases more than 50% from the concrete with natural aggregates and three more times for the viscosity.

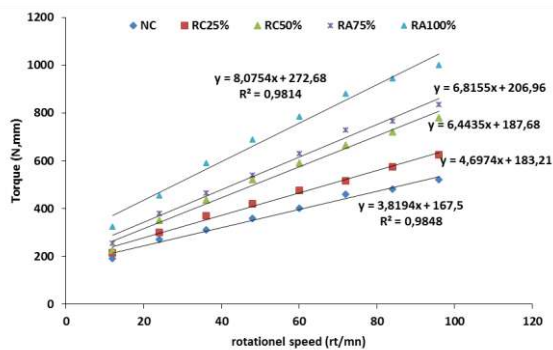


Fig. 5. Torque for % of recycled aggregates

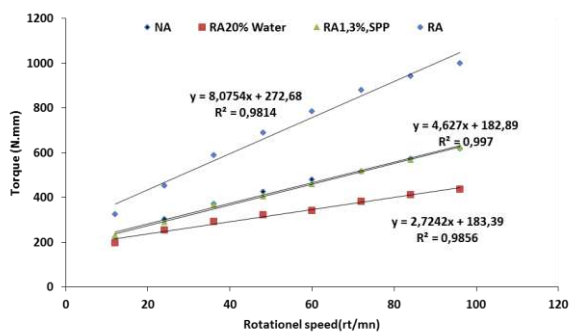


Fig. 6. Evolution of torque for 100 % of recycled

CONCLUSION

The results on the physical properties of the recycled aggregates clearly show a higher absorption capacity, a rate of porosity also important, up to 17% greater than that of the natural gravel. The mechanical tests confirm low wear resistance. With a constant ratio W / C, the reduction in workability is based on the amount of recycled, while the mechanical strength is reduced. A mixture dosed superplasticizer for the same workability, gives a lower decrease in the value of the compressive strength reaching 13%. In terms of tribology, the interface of the friction performance (τ) increases with the percentage of recycled aggregates and viscosity constant (η) of 100% recycled fibers, reaching double that of natural concrete. The test constant handling and W/C variable ratio causes a decrease in the compressive strength value approaching 25%. A third formulation dosed in adjuvant, with a workability and a constant volume of dough gives resistance values comparable to that of the reference concrete with an output interface equivalent to that of the reference concrete and a slightly greater constant to viscosity.

REFERENCES

1. Silva RV and all. 2014“ Properties and composition of recycled aggregates from construction and demolition waste suitable for concrete production” Con. Build. Mater.65, 201–217.
2. Fonseca N, de Brito J, Evangelista L. 2011“ The influence of curing conditions on the mechanical performance of concrete made with recycled concrete waste. Cem. Con. Comp. 33:637–643.
3. Gómez-Soberón JM. 2002. “Porosity of recycled concrete with substitution of recycled concrete aggregate”. Cem. Conc. Res. 32:1301–1311.
4. Kou SC, Poon CS, Etxeberria M. 2014“Residue strength, water absorption and pore size distributions of recycled aggregate concrete after exposure to elevated temperatures. Cem.Concr. Comp. 53:73–82.
5. Topçu İB, Şengel S. Properties of concretes produced with waste concrete aggregate. Cem.Concr. Res. 2004;34:1307–1312.
6. Sami W. Tabsh, Akmal S. Abdelfatah, 2009. “Influence of recycled concrete aggregates on strength properties of concrete, Construction and Building Materials.” 23. 1163–1167
7. Kadri EH, Aggoun S, De Schutter G. 2009. “Interaction between C3A, silica fume and naphthalene sulphonate superplasticiser in high

- performance concrete”. *Constr. Build. Mater.*23:3124– 3128.
8. Etxeberria M, Vázquez E, Marí A, et al. Influence of amount of recycled coarse aggregates and production process on properties of recycled aggregate concrete. *Cem. Res.* 2007;37:735–742.
9. Hamza Soualhi, El-Hadj Kadri, Tien-Tung Ngo, Adrien Bouvet, François Cussigh and Benchaa Benabed. 2015. “Rheology of ordinary and low-impact environmental concretes.” *Journal of Adhesion Science and Technology*, Vol. 29, No. 20, 2160–2175,
10. T.T. Ngo, E. Kadri, F. Cussigh and R. Bennacer, 2001. “ Measurement and modeling of fresh concrete viscous constant to predict pumping pressure.” *Canadian Journal of Civil Engineering*, vol. 38(8), pp. 944-956, 2011.

PERFORMANCE OF DUNE SAND CONCRETE MADE USING RECYCLED MATERIALS

Lakhdar AZZOUZ^a, Benchaa BENABED^b and Said KENAI^c

^a Civil Engineering Laboratory, University of Laghouat, Algeria, l.azzouz@mail.lagh-univ.dz

^b Civil Engineering Laboratory, University of Laghouat, Algeria, b.benchaa@mail.lagh-univ.dz

^c Geomaterials Laboratory, University of Blida, Algeria, sdkenai@yahoo.com

Corresponding author: +213 29145847 Email: l.azzouzlagh-univ.dz

ABSTRACT

The aim of this study presented herein is to show how useful is the use of recycled materials in the fabrication of sand dune concrete. The valorization of recycled civil engineering materials permits to solve problems that arise when considering ecological and environmental issues. It offers an economic solution that avoids the extraction of raw materials, thus contributing the preservation of the environment. Two fillers obtained from recycled materials were used; fillers of recycled bricks and limestone filler (calcareous fillers). A comparative study was carried out in order to establish the effects of the two fillers on the physical and mechanical properties of sand dune concrete. The sand used is from the Laghouat were in Algeria. The introduction of fillers mode of used materials into the concrete mix seems to provoke improvements in the physical and-mechanical properties. During the work, we examine in particular the effects of different parameters such as cure, environment and the addition of fillers on the behaviour of sand dune concrete. It has been shown that the curing realised in water gives the best results for all dosage.

Keywords: bricks, limestone, filler, concrete; dune, sand, valorization, cure, environment, conservation, physical; mechanical.

INTRODUCTION

The word of construction is the sector key in the economic activity. Today the construction in Algeria is confronted to two contradictory requirements, on one hand the reduction of building cost and on the other hand the improvement of building quality.

Algeria knows a deficit in aggregates and in particular the sand. This deficit is going to increase with measures aiming the protection of the environment as the interdiction of the utilization of beach sands. The valorization of the crushing sand and the dunes sand in the concrete can contribute to surmount this deficit. Studies of formulation and characterization have been undertaken by different researchers, however the durability of this concrete in an of the Sahara environment as well as its behavior in structure elements has not been undertaken.

This work permits to know some of features of dune sand concrete, however the main objective of this work is to know all its physical and mechanical properties, in particular the mechanical resistance and durability, while trying to improve its behavior and to valorize its constituent, as sand and fillers (bricks and chalky) that make local materials part. The valorization of recycled civil engineering materials can only give as well some encouraging results in term of economy, and ecology, that of

behavior. Our works research carried on invader to get a sand concrete based on fillers having some satisfactory features, in particular the mechanical resistance and the durability, this work is divided in five parts:

We tried to treat the different physical and mechanical features of the constituent elements of the sand concrete. We examined the evolution during the time of resistances to the compression and bending for the three types of conservation and two fashion of cure, as we have studies the influence of the fillers percentage on resistances, as well as the influence of conservation conditions on the mechanical behavior of the sand concrete.

we relies an experimental tests to study the effect of the type and percentage of filler on the stand of the sand concrete to the frost-thaw and moistening–drying as well as that capacity of water absorption.

BIBLIOGRAPHIC STUDY

The concrete of sand made until now days the object of few researches. The quoted experiences are varied: laboratory tests statistical studies, and field experiences one yard. But then, the concrete of sand seems to have a wide use in some application in the future, the technical and economic advantages of sand concretes let some foresee an important

development for the future. On the light of the bibliographic research, we note that the works on the survey of the influence of cure treatment on the durability of the sand concrete are very few. A few big principles can be extracted of the whole of the bibliography treated, that concretes of sand will be able to replace the classic concretes in some elements of structure weakly solicited, and that several application has already been achieved with success.

Properties of the concrete hardened are influenced extensively by properties of the fresh concrete that are mainly the handiness and the compactness.

The maneuverability not only depends on the W/C report, but also of the module of sand sharpness, and it especially depends on the type and the content in fine of additions. We saw that it requires more water than a classic concrete. On the other hand it appears obvious that mixture cement-sands will present a more high porosity than the porosity of the traditional concrete [1], this inconvenience is made up for by the addition of fine of good nature to improve the compactness. It is necessary to choose sands of good granular distribution therefore. It is necessary to find a compromise between the maneuverability of the concrete and its compactness [2]. The sharpness of the fine increases the compactness further and the resistance.

The resistance in compression of sand concretes is 15 to 25 MPa, and The strength to bending varies between 1,5 and 8 MPa of after already worked out certain works [2]. That value of the springiness module is weaker than the one of a classic concrete what gives to the concrete of sand a big deformability and therefore a least crack [3].

In short of other works, as the shrinking, the module of springiness, the adhesion to armatures of durability has been undertaken on the concrete of sand in comparison with a classic concrete [4, 5], which they made the object practically that of few study, the obtained results are limited to the very determined materials and the very precise compositions [6,7, 8,].

CHARACTERIZATION OF MATERIALS

Used Materials: The different Materials characterized which are the principal element of the sand concrete studies are the sand of dune, the cement, and fillers.

The sand used is the dune sand of the region (LAGHOUAT). it is characterized by its sharpness and its maximal diameter less than 0.63 mms, and own. The cement used for the whole of experimentations is type CPA 325. Two type of fillers we have use two different less than fillers types by their sharpness and their mineralogical natures has know, a filler of limestone and the second it is a filler of brick of which their maximal diameter doesn't exceed 80µm.

Properties of fresh concrete

The retained compositions used during this survey with a constant W/C ratio equal to 0,8, are represented in table 1. The Values of slumps (cone of Abrams) and the times (Vebe) obtained, are presented in tables 2 and 3. It is shown that the calcareous fine has an important effect on the workability of concrete. For the same W/C ratio, the concrete that contains the fines is generally more plastic (workable) than concrete without fines.

Table 1: Compositions of dune sand concrete (limestone and bricks fillers)

Constituent	Proportions of the constituent Kg/m ³			
	330	330	330	330
Cement	330	330	330	330
Sand	1236	1286	1336	1486
Limestone Filler	250	200	150	/
Bricks Filler	250	200	150	/
Water	264	264	264	264
Composition	B.S.C ₃	B.S.C ₂	B.S.C ₁	B.S

Table 2: slump and times (limestone fillers)

Compositions	percentage of filler (Kg/m ³)	Slum p (cm)	Time Vebe (sec)
BS	0	6.5	5
BSC ₁	150	7,2	4.7
BSC ₂	200	7.8	2.8
BSC ₃	250	8	2

Table 3: slump and times (bricks fillers)

Compositions	percentage of filler (Kg/m3)	Slum p (cm)	Time Vebe (sec)
BSB1	150	7,2	2,5
BSB ₂	200	6,2	3,5
BSB ₃	250	5,5	4,5

Table 3 shown that concrete workability decreases with the increase in bricks filler percentage. This denotes the higher water absorption capacity of the bricks filler that in turn lead to a 15 % increase in mixing water. Thus, in order to get a workable concrete (plastic) with the bricks filler an increase in mixing water is necessary.

MECHANICAL BEHAVIOR OF DUNE SAND CONCRETE

In this study the effect of age, curing environment and the duration of cure on the properties of concrete were investigated. The compressive strength was determined for 7, 14, 28 and 90 day old concrete. For each composition, curing environment or age a minimum of four specimens were tested.

In order to examine the influence of curing and the percentage and nature of fillers on the compressive strength, tests were carried out on specimens that were cured in either of the following environments: uncontrolled laboratory conditions (ENVI), in water (ENVII) and , inside a drying oven (ENVIII). The number of specimens tested was six for the compressive strength and five for the flexural strength.

Compressive strength

Sand concrete with limestone fillers

The study of the variation of the compressive strength with the age has shown that specimens cured in ENVII (in water) performed better as they gave they highest compressive strength. This can be partly explained by the fact that the hydration of cement increase with age in saturated water. Moreover, an increase in the percentage of the filler seems to act favorably on the compressive strength of concrete at the concrete ages considered.

The variation of concrete strength with age for specimens cured in ENVII is shown in Fig. 1. The highest registered values for this strength were generally obtained for a percentage of filler equal to $F_1= 150 \text{ Kg/m}^3$.

These values are:

- Rc = 14,36 MPA for 14 days of age
- Rc = 17,73MPA for 28 days of age

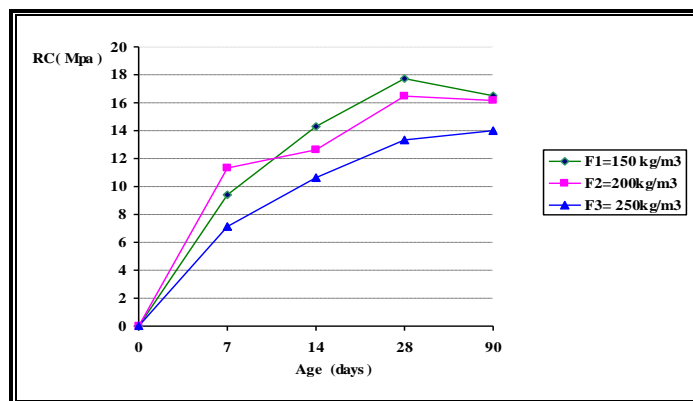


Fig. 1: variation of the compressive strength in function of age (5 days under water, BSC)

Sand concrete with brick fillers

The main conclusions drawn from specimens fabricated with different proportions of filler and cured in the previously mentioned environments are:

- curing in water improves concrete strength and increase the necessary curing time.
- Curing concrete in environment III seems to reduce the concrete strength
- The highest concrete strength at 14 and 28 days were obtained when using ENVII curing. The development of the strength with time is shown in fig. 2. The maximum registered strength are:

- Rc = 12,56 MPA for 14 days
- Rc = 14,36 MPA for 28 days

These two values correspond to a filler content equal to 150 Kg/m^3 (B1) which is the lowest percentage of filler considered.

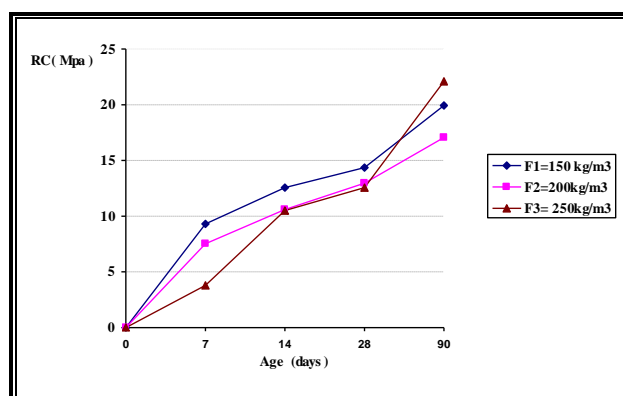


Fig. 2: variation of the compressive strength in function of age (5 days under water, BSB)

Comparative study: According to the results obtained with the two types of fillers, we note that the age of concrete acts positively on the compressive strength and this is true for all the curing environments and the filler content considered. The highest compressive concrete strength was obtained for a filler content of 150 Kg/m³. This denotes, perhaps, the existence of an optimum of the fillers content. Rapid water evaporation seems to decrease concrete strength. The increase in curing time in ENVIII decrease the strength.

Flexural strength

Sand concrete with limestone fillers :The flexural strength to bending also increases with age, which has a similar relation to the one of the strength to the compressive is gotten by the strength to bending.

The best observed strength corresponds to the test-tube maintained under water (ENV II) and correspondent to the composition BSB2 (B2 = 200 Kg/m³) of filler (figure-3.), we obtained:

T = 28 days R_f = 8,68 MPa (B.S.C2)

These flexural strength correspond practically to dosage in fine of limestone (C2 = 200 kg/m³) B.S.C2.

we obtained:

T = 28 days R_f = 6,60 Mpas (B.S.C1)

- For the environment (ENV III) (to steams it), the increase of the cure period Leads to a shift of the maximum of strength of 7 is to 14 days.

Therefore one can say that test-tubes preserved under water present the best strength to bending with regard to those preserved in steams it and the free air.

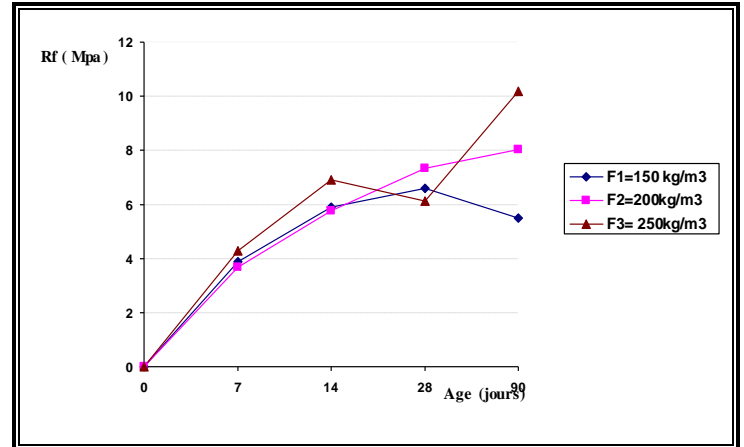


Fig 4 : variation of the flexural strength to bending in function of age(5 days under water, BSB)

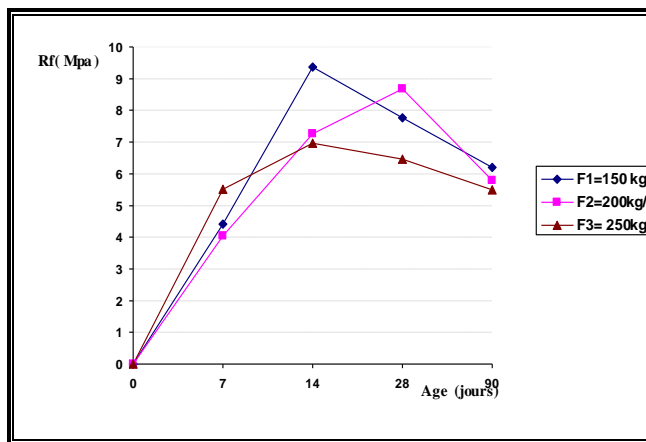


Fig. 3: evolution of the flexural strength to bending in function of age(5 days under water, BSC)

Sand concrete with brick fillers : The flexural strength to bending presents some optimal strength always to 28 days of hardening.

- The conservation under water is favorable to the increase of the flexural strength to bending for the weak dosage in filler.

- The best observed flexural strength corresponds to the test-tube maintained under water (ENV II) and correspondent to the weak dosage in filler of recycled brick (figure 4),

Comparative study: We notices, that flexural strength to the bending of sand concretes preserved in the outside air as well as to steams, are lower to the one of the same concretes of sand preserved under water lasting 7 days, this reduction of the flexural strength is owed to the impoverishment in water following its evaporation to air free of the mass of the concrete, dragging a lowering of the hydration kinetics that provokes a reduction of the flexural strength.

Concretes undergoing in a cure of 7 days in water present the high strength owed to the sufficient quantity of water that assures them the continuity of the hydration process, dragging an elevation of the strength.

With regard to the behavior of sand treaty concretes steams some, the same observation that for the strength to the compression can be made. Indeed the resistance to bending increases until 28 days, beyond this age, it either decreases, stabilize to 90 days, the fast evaporation of water is responsible of the strength fall

After different result observation we can say that, the temperature affects strength of sand concretes, and this phenomenon is much more visible than the concrete of sand contains fillers of

or the necessity to proceed has cures. The introduction of brick fillers seems to improve, strength to bending to all age of the sand concrete by contribution to fillers limestone.

Shrinkage

In order to see the effect of the temperature on the variation of the shrinking, we have follows the evolution of the test-tube shrinking to basis of limestone fillers preserved to steams it

The obtained results, show effectively, that for the same E/C ratio and the same concentration of cement, the composition of the sand concrete without filler presents the weakest shrinking.

In the case of the sand concrete with fillers of limestone preserved to steams it, in remark that the shrinking accelerates die the young age until 14 days of about 12% with regard to the concrete of sand with fillers of limestone canned food to the free area for a dosage of filler of 200 Kg/m³, then to the delay there is a reduction of 14% (figure 5).

For what is the concrete of sand with fillers of bricks preserved to the free area, the shrinking decreases according to the increase of the fillers dosage (figure 6). One notices that this shrinking and bigger than the shrinking of the sand concrete without fillers die the young age, for the concrete of sand with fillers of limestone, the evolution is different. The concrete of sand with fillers of limestone preserved to the present free area a shrinking delays until 14 days then there are an increase that passes the one of the sand concrete with fillers of bricks, to arrive to the about of 10% to 90 days.

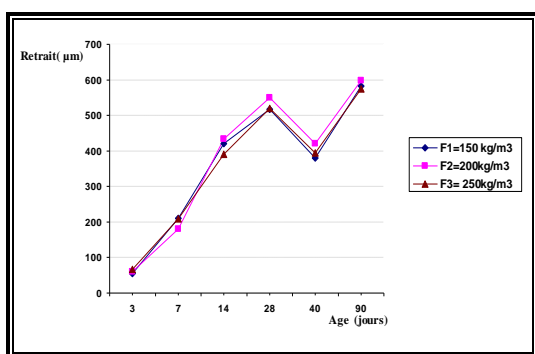


Fig 5: shrinking according to dosage of the limestone fillers (to the free air)

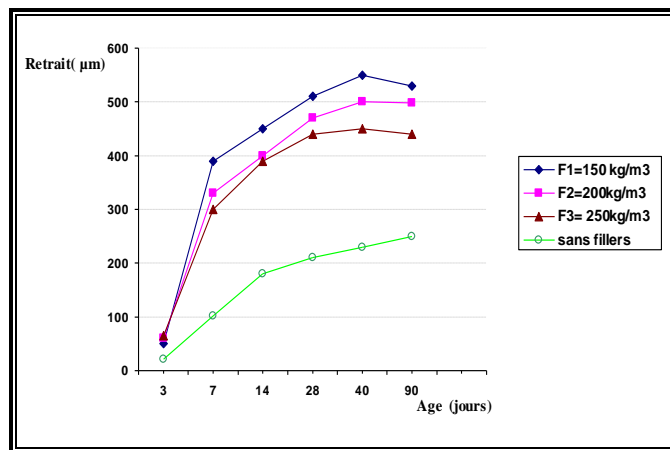


Fig 6 : shrinking according to the dosage of brick fillers (to the free air)

CONCLUSION :

In this survey we examine the influence of the conservation, the environment and the addition of fillers on the evolution of the physical and mechanical features of the dune sand concrete.

we did the experimental tests of durability to study the effect of the type and dosage in filler on the holding of the sand concrete to the frost-thaw and moistening - drying as well as that capacity of water absorption.

The introduction of fillers of garbage brick seems to provoke physical and mechanical property improvements. Among the different fashions of conservation chosen, the conservation under water appears as the best cure of the sand concrete, and this some either dosage in fillers and the age of the concrete.

This study permitted us to put on the one hand in evidence the direct influence of the fillers addition on the dune sand concrete, that essentially characterizes himself by a reduction of the shrinking and by a mechanical resistance improvement and on the other hand the considerable contribution of the treatment of the humid cure for the concrete of dune sand. Of the point of view holding screw to screw of durability tests, the survey revealed us the importance of the addition of the fine on the resistance of the material or the rate of resistance is superior to 60% in all cases. On the other hand the weak dosage in fine improvement is observed distinctly for the case of the sand concrete to basis of limestone fillers.

Finally, we show that this new materials, can replace the traditional concrete in the realization of the secondary elements of construction and also of elements carriers for structures little solicited for

the mechanical performances that are its specific but also for the economic grounds especially in the abundant local resource valorization or in the lowering of the come back. Price.

REFERENCES

1. CHAUVIN J.J.et GRIMALDI G. Les bétons de sable. Bulletin de liaison des laboratoires des ponts et chaussées (LCPC)1988;157: 9-15.
2. CHAUVILLARD G., BASSUYAUX O. Une méthode de formulation des bétons de sable à maniabilité et résistance Fixées. Bulletin de liaison des laboratoires des ponts et chaussées (LCPC) 1996; 205: 49-63.
3. GORISSE F. Etude des micro-bétons pour modèles de structures. Annales de l'institut technique du bâtiment et des travaux publics 1972 ;291.
4. Benaissa A. Déformation différées du béton de sable. Thèse de doctorat de génie civil Université de Bordeaux I, 1992.
5. CHAUVIN J.J. béton de sable Propriétés d'usage. Séminaire Franco- Soviétique sur le béton de sable. Bordeaux 1991: 79-85.
6. BENMALEK M., BALI A. Comportement du béton de sable dunaire sur des éléments d'ossature armés. Séminaire national en génie civil. M'sila 1997.
7. AMRANI Y. Béton de sable. expérience marocaine. Laboratoire public d'essais et d'étude, Maroc.
8. Benmalek M. Contribution à l'étude par béton de sable de dune pour des éléments de Structure. Thèse de magister ENP Alger 1993.

ELABORATION AND CHARACTERIZATION OF ECO-MATERIALS MADE FROM RECYCLED BIO-BASED RAW MATERIALS

*L. M. Thieblesson a) b) , F. Collet a), S. Prétot a) , C. Lanos a) , H. Kouakou b)

a) Laboratory of civil engineering and mechanical engineering, University of Rennes1,

3 rue du clos courtel-BP 90422-35704 Rennes cedex 7-France

b) STRM, Laboratory of Geomaterials, University of Félix Houphouët Boigny of Cocody,
Abidjan, Côte d'Ivoire

*Corresponding author: Email: lydie.thieblesson@univ-rennes1.fr

ABSTRACT

This project is realized in partnership between the Laboratory of civil engineering and mechanical engineering (Rennes, France) and the Laboratory of Geomaterials (Abidjan, Ivory Coast). The objectives of this work are to test the feasibility and characterize the thermohygric properties of composite materials, realized with eco-friendly raw materials and designed to make suspended ceilings or interior partition walls.

Several raw materials are considered: recycled paper (granules or cellulose wadding) and wood fibers. Aggregates or fibers are bonded with organic or mineral binder. One of the binder considered is starch, due to its availability in Ivory Coast (cassava flour). The calcium sulfate hemihydrate is also used for comparison.

The density of the produced composites ranges from 400 to 1200 kg/m³ depending on formulation. The Thermal conductivity increases proportionally with the density and ranges from 0.09 to 0.5 W/(m.K).

The characterization of hygric behavior is based on the measurement of moisture buffer value (MBV). Composites appear as moderate to excellent hygric regulators.

NOMENCLATURE

A: open surface area (m²),

K : constant l (Hot Wire),

MBV : Moisture Buffer Value (g/(m².%RH)),

q: heat flow per meter (W/m) (Hot Wire),

RH_{high/low}: high/low relative humidity level (%),

t: heating time (s) (Hot Wire),

Δm: moisture uptake/release during the period (g),

ΔT: temperature rise (°C) (Hot Wire),

λ : thermal conductivity (W/(m.K)),

ρ: density (kg/m³).

INTRODUCTION

In a context of sustainable development, green buildings aim at reducing the environmental impacts of buildings while also ensuring high indoor quality (comfortable and healthy). Bio-based or recycled raw materials can be used to reach this objective.

The objectives of this work, in partnership between the Laboratory of civil engineering and mechanical engineering (Rennes, France) and the Laboratory of Geomaterials (Abidjan, Ivory Coast), are to test the feasibility and characterize composites, realized with

eco-friendly raw materials and designed to make suspended ceilings or interior partition walls. The considered raw materials are issued from local recycled or bio-based materials. Thus, the binders considered are plaster, which is widely used in France, and starch, for its availability in Ivory Coast and its lower cost. The developed loads are made from paper waste, as this is widely available in Ivory Coast. Other cellulosic loads are also considered for comparison.

Some products made of mineral binder with recycled paper already exist [2,3]. They are often studied on acoustical and fireproofing point of view. Yeon et al. analyzed physical properties of cellulose sound absorbers produced from recycled paper [4]. Mortar with recycled paper are also developed [5]. Granules of paper are currently industrially produced and are available in bags for animal's litter [6]. Wadding cellulose is obtained from newspaper's recycling and is mainly used in bulk. Hurtado et al. investigate the properties of cellulose fiber insulation [7].

Wood fiber is a bio based material available on the market as insulation panels of conductivity around 0.04 W/(m.K) and apparent density of 110 kg/m³.

Among various binders, cassava starch is well adapted to the local context in Africa where plaster is a scarce resource. Starch is considered as one of the most promising materials for biodegradable plastics, because of its natural abundance and low cost. It can also be used as binder. As example, wholly bio-based insulation products made of hemp and starch is currently studied by Tran Le [8].

Thus, this study focuses, on the one hand, on the formulation of composites made of bio-based or recycled local resources and, on the other hand, on their hygrothermal characterization.

MATERIALS

Loads: Wood fiber and recycled paper (granules and cellulose wadding) are considered in this study. Wood fibers (quoted WF) are commonly used for thermal insulation. Fibers are fireproofed with ammonium phosphate. Commercial fibers are used in this study. They are manually carded before use. SEM examination of the fibers shows hollow fibers of 20 to 50 μm in diameter (Figure 1).

The cellulose wadding (quoted CW) is also an industrial product stemming from the recycling of newspapers. The cellulose wadding is fireproofed with boron salts. SEM examination shows a loose tangle of the cellulose wadding fibers (Figure 2).

The paper granules (quoted PG) are made of waste paper recovered after use in offices. This paper is subject to various process of transformation in the laboratory to obtain paper granules. Firstly, strips of paper are soaked in water for a few hours. Then, the wet paper is transformed in soup and after that it is wrung out to remove water before being pushed across a metal grid of small mesh in order to obtain almost spherical granules of millimeter size (Figure 3 a, b, c). SEM examination of the granules shows a compact tangle of 15 μm width fibers (Figure 3 d).

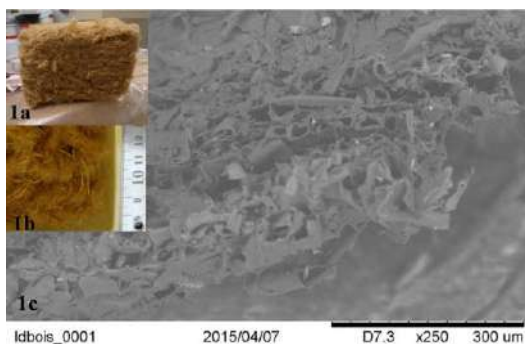


Figure 1

Wood fiber: 1a) Wood fiber panel 1b) Carded fibers
1c) SEM view

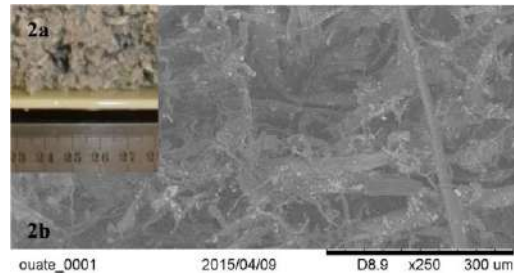


Figure 2

2a) Cellulose wadding 2b) SEM view

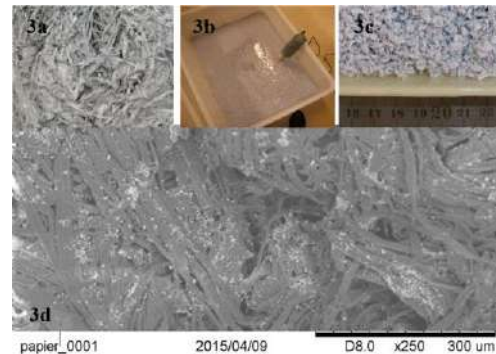


Figure 3

Paper granules: 3a) strips of paper; 3b) mixing; 3c) paper granules; 3d) SEM view

Binders: Aggregates or fibers are bonded with mineral or organic binder.

The calcium sulfate plaster (quoted P), commonly used as binder in France, is selected to allow comparisons with organic binder. The used plaster is Molda 3 Normal calcium sulfate hemihydrate from St Gobain-France. The cassava starch is a low cost material with large availability in Ivory Coast. Tests are made with commercial potatoes starch (from Roquette-France, quoted S). In hot water ($>70^{\circ}\text{C}$), the grains of starch inflate under a process of irreversible gelatinization (Figure 4).



Figure 4

Binders: 4a) plaster powder; 4b) plaster binder;
4c) starch powder; 4d) starch binder

Formulation and composite production:

Various kinds of composite materials with different loads to binder ratios are produced. The identification of composite includes the type of load (WF, CW or GP), the type of binder (P or S) and finally the water to binder mass ratio that appears in brackets.

For composites production, binders are firstly prepared: plaster powder is mixed with water or starch is prepared by adding hot water to the powder. Then, in both cases, loads are gradually added in the binder. The quantity of loads is adjusted to obtain good workability (Figure 5). After mixing, the specimens are produced by molding. The size of the molds is 28×23×7cm³. The molds are filled by the mixture and the specimens are compacted under a pressure of 0,03 MPa with a manual press (Figure 5). After compaction, the starch specimens are demolded immediately and placed in the ambient temperature of the laboratory (Figure 6). For plaster specimens, the mold removal is applied after setting.

For plaster, the influence of water to binder ratio is investigated. In this study, this ratio ranges from 0.4 to 2.5. The load to binder mass ratios ranges from 0.07 to 1.41.

First trial with starch is made with water to starch ratio of 0.83 and a paper granules to starch mass ratio of 4.17.



Figure 5

Production process: 5a) Binder mixing; 5b) Addition of the load; 5c) Mixing; 5d) Compaction

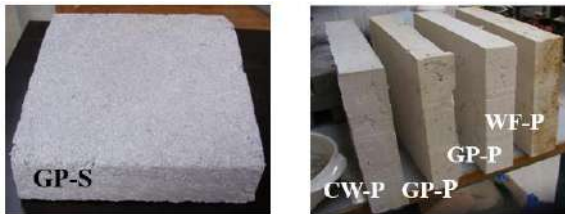


Figure 6

Produced specimens

METHODS OF CHARACTERIZATION

Hot wire method: The thermal characterization is based on the measure of the conductivity after stabilization of the specimens at 23°C and 50%RH. To avoid water migration during the measurement, a transient state method is used. The thermal conductivity λ (W/(m.K)) is measured by using the commercial CT-meter device with a five-centimeter-long hot wire (Figure 7).

The measurement is based on the analysis of the temperature rise versus heating time. The heat flow and heating time are chosen to reach high enough temperature rise (>10 °C) and high correlation coefficient (R²) between experimental data and theoretical curve (1).

$$\Delta T = \frac{q}{4\pi\lambda} (\ln(t) + K) \tag{1}$$

Where q is the heat flow per meter (W/m) and K is a constant including the thermal diffusivity of the material.

According to the manufacturer, the hot wire is well adapted for the measurement of thermal conductivities ranging from 0.02 to 5 W/(m.K) and the expected accuracy is 5%.

In this study, the heating time is 120 s and the heat flow ranges from 4.1 to 11.4 W/m.



Figure 7

CT meter

Moisture buffer value: The moisture buffer value MBV quantifies the moisture buffering ability of a material. It is measured under dynamic conditions according to the method defined in the NORDTEST project. This value relates the amount of moisture uptake (and release), per open surface area, under daily cyclic variation of relative humidity according to (2).

$$MBV = \frac{\Delta m}{A \cdot (RH_{high} - RH_{low})} \tag{2}$$

with MBV: moisture buffer value ($\text{kg}/(\text{m}^2 \text{ \%RH})$), Δm : moisture uptake/release during the period (kg), A: open surface area (m^2), $\text{RH}_{\text{high/low}}$: high/low relative humidity level (%).

The test method requires prismatic specimens to be sealed on five out of six sides. After stabilization at (23°C ; $50\% \text{RH}$), specimens are exposed to daily cyclic variations: 8 h at high relative humidity (75%) followed by 16 h at low relative humidity (33%). Stability is reached when the change in mass is the same between the last three cycles with a discrepancy lower than 5%.

Within the NORDTEST project, a round robin test was held on nine representative building materials and a classification of materials according to their MBV is proposed (Figure 8)[1].

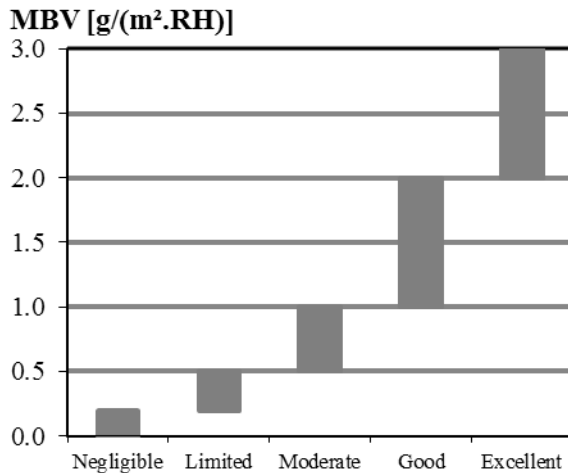


Figure 8
Nordtest project classification [1]

The device used consists in a climate chamber (Vötsch VC4060) which can be controlled in the ranges $+10$ to $+95^\circ\text{C}$ and 10 to $98\% \text{RH}$. The study is performed at 23°C . The relative humidity in the chamber is switched manually ($75\% \text{RH}$; $33\% \text{RH}$). Temperature and relative humidity are measured continuously with Sensirion SHT75 sensors and with the sensor of the climate chamber. The air velocity is measured in the surroundings of the specimens: the vertical velocity is in the range 0.07 – 0.14 m/s and the horizontal one is 0.1 – 0.4 m/s. The specimens are weighed out of the climatic chamber five times during the adsorption period and two times during the desorption one. The weighing instrument reading is 0.01 g, and its linearity is 0.01 g. The accuracy of the moisture buffer value is thus about 5%.

RESULTS AND DISCUSSION

Physical characterization:

To ensure good workability, the quantity of water used in the mix increases with the mass of loads (figure 9).

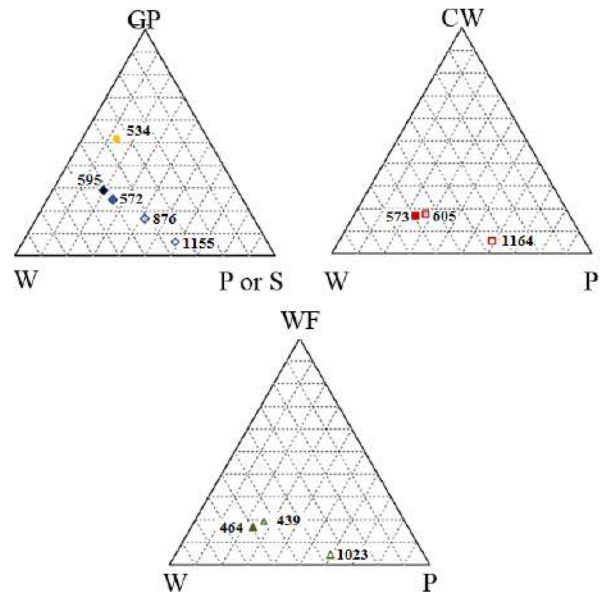


Figure 9
Mass ratios of the components and apparent densities (kg/m^3) of composites

After production, the specimens are naturally dried at 23°C $50\% \text{RH}$. They are regularly weighed until stabilization. The typical drying time is about 15 days whatever the composite formulation (figure 10). Then, the apparent density is calculated from measuring and weighing the specimens. The densities range from 400 to 1200 kg/m^3 for the composites made with plaster binder, depending on formulation and particularly on the water to binder mass ratio. For the composites made of paper granules and starch, the density is about 500 kg/m^3 (figure 9).

It is shown that the apparent density decreases as the amount of water or loads is increasing.

For equivalent water to binder and load to binder mass ratios, the apparent density is the lowest for the composites with wood fibers and similar for the composites with cellulose wadding or paper granules. It may be linked with a highest rate of trapped air during mixing of wood fibers composites and fibers arrangements.

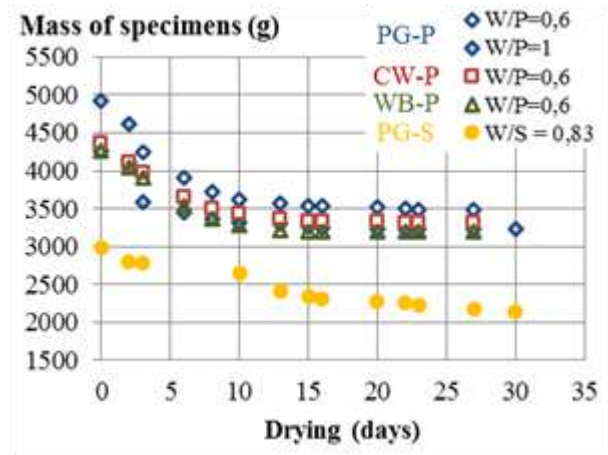


Figure 10
Mass of the specimens during drying

Thermal characterization: Thermal conductivity increases proportionally with the density (figure 11). Indeed, for the water to plaster ratio equal to 0.6 and paper granules or cellulose wadding composites, the specimens densities range between 1000 and 1200 kg/m³ and the conductivity is about 0.45 W/(m.K). At high level of plaster in the composite, the kind of load do not affect the conductivity. The measured value is slightly lower than the values commonly used for plaster only (about 0.48 W/(m.K) for 1100 kg.m³ in the French standard).

For densities between 550 and 610 kg/m³, the thermal conductivity ranges from 0.16 to 0.19 W/(m.K) as expected for this range of densities. Finally, the conductivity of wood fibers composites whose density is around 450 kg/m³ is about 0.09 W/(m.K). This may also be linked with a higher rate of trapped air during mixing.

The composite made of starch and paper granules has a thermal conductivity of 0.18 W/(m.K). This value is in the range of thermal conductivity obtained for composites made with plaster, with the same range of density.

The composites showing the lowest densities can thus be used for distributed insulation.

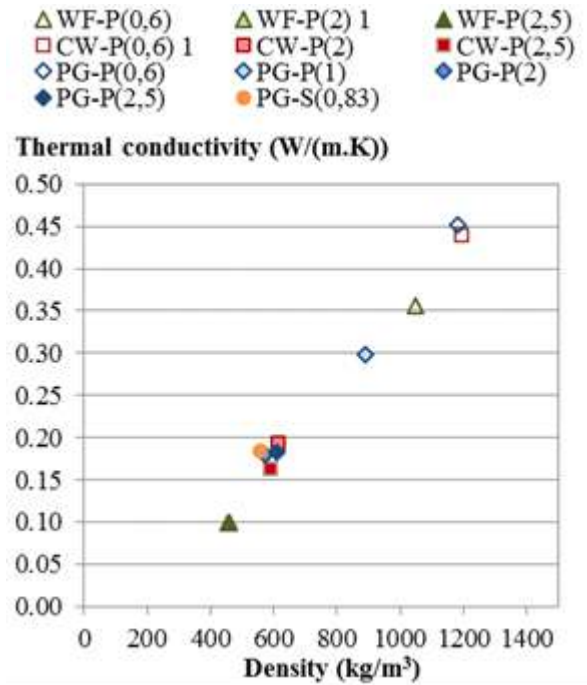


Figure 11
Thermal conductivity of materials versus density at (23°C; 50%RH)

Hydric characterization: Plaster and starch specimens, initially stabilized at 23°C 50 %HR, are first submitted to absorption phase. The discrepancy between mass variations during the cycles becomes lower than 5 % between the second and the third cycles (figure 12). The MBV is thus calculated with cycles 3 to 5.

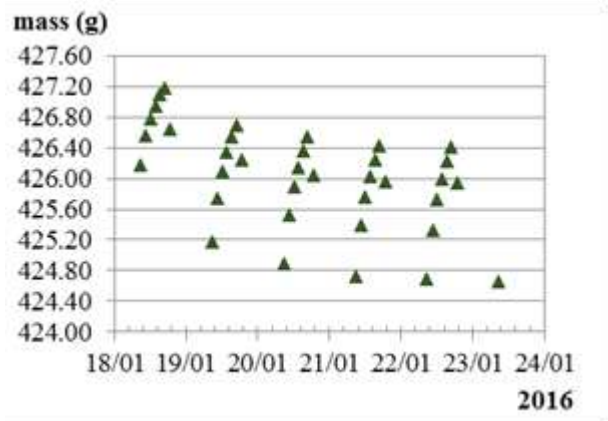


Figure 12
Moisture uptake and release: example of WF-P (2.5), specimen 3

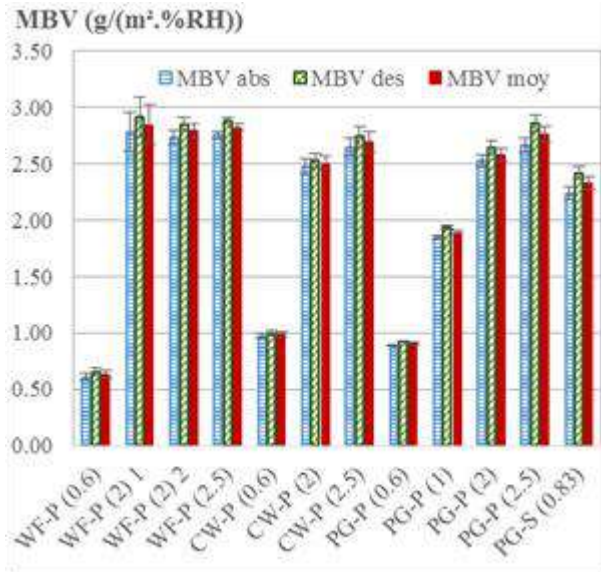


Figure 13
Moisture Buffer Value (MBV) in absorption,
desorption and average for all composites

Figure 13 gives the Moisture Buffer Value in absorption, desorption and average for all kinds of composites. For all composites, the desorption value is greater than the absorption one. This can be explained by a decreasing trend of the mass uptake/release curve before stabilization (Figure 12).

For specimen with plaster binder, when the water to plaster mass ratio is 0.6, the MBV ranges from 0.61 to 0.97 g/(m²·%RH) with the three kinds of loads. These composites have moderate ability to damp ambient relative humidity variations. This is probably due to their low porosity. They are slightly better hygric regulators than gypsum with MBV about 0.60 g/(m²·%RH) [1].

When the water to binder mass ratio is 1, with paper granules, the MBV is 1.89 g/(m²·%RH)). This composite is a good hygric regulator.

Finally, when water to binder mass ratio is higher than 2, the MBV is higher than 2.50 g/(m²·%RH)) for all kinds of loads. All these composites are excellent hygric regulators. For water to plaster mass ratio of 2, the load to binder ratio is similar for the three kinds of loads. For these composites, wood fiber composites are the best ones, probably due to a different porosity network.

Paper granules - starch composites are also excellent hygric regulators, their MBV is 2.33 g/(m²·%RH)).

CONCLUSION

This study investigates the feasibility of composites made from paper (paper granule, cellulose wadding) and bio-based materials (wood fibers) bonded with plaster or starch. It is shown that to ensure good workability, the water content increases with load content.

Whatever the kind of loads, the density of composites decreases when water ratio increases. The density obtained with wood fiber is lower, probably in link with higher entrapped air.

The thermal conductivity of composites ranges from 0.09 to 0.45 W/(m.K). The lightest composites can be used as distributed insulation.

The developed composites (with starch and with plaster) are excellent hygric regulators when the water to plaster ratio is higher than 2.

Finally, these study will be completed with mechanical characterization. The great interest of such composites is encouraging to go on with the development of starch composites.

REFERENCES

1. Rode, C., 2005, Moisture buffering of Building Materials, Report BYG-DTU R-126, ISSN 1601 – 2917, ISBN 87-7877-195.
2. European technical advice, fermacel greenline, ATE-03/0050
3. www.armstrong.fr/plafonds
4. Yeon Jun-Oh et al., 2014, Physical properties of cellulose sound absorbers produced using recycled paper, *Constr. Build. Mater.*, 70, pp. 494–500
5. Aciu et al., 2014, Recycling of Paper Waste in the Composition of Plastering Mortars, *Procedia Technology*, Volume 12, Pages 295-300
6. <http://www.pettex.co.uk/>
7. Hurtado PL and al., 2016, A review on the properties of cellulose fibre insulation, building and environment, v96, pp170-177.
8. Tran Le A.D. et al., Experimental investigation on the mechanical performance of starch–hemp composite materials, *Construction and Building Materials* 61, 2014, p106–113

CHARACTERIZATION OF SAND SLAG CONCRETE

Meriem SENANI¹, Nouredine FERHOUNE², Abdelhamid GUETTALA¹

¹University of Mohamed Khider Biskra, Algeria

² University of Larbi Ben M'hidi, Algeria

*Corresponding author: senani_meriem@hotmail.fr

ABSTRACT

In this study, we sought to use the crystallized sand slag of blast furnace in the production of ordinary concrete. The natural sand is partially or totally substituted by the crystallized sand slag in the composition of concrete. The characterization of these concretes was made based on their mechanical properties: compressive strength, tensile strength as well as durability: capillary, absorption of water and shrinkage. The results show that the percentage of crystallized sand slag has an important effect on the mechanical properties of concrete. The comparison of different characteristics study in this work shows the benefits of use of crystallized sand slag in the composition of concrete compared with ordinary concrete, which confirm the possibility to use the crystallized sand slag in the manufacturing of concrete.

KEYWORDS

Concrete sand slag, crystallized sand slag, natural sand, performance, mechanical proprieties, hydraulic proprieties.

INTRODUCTION

Crystallized slag from blast furnace of the El Hadjar steel complex, Algeria, can be identified as a new building material in the preparation of concrete. The uses of industrial waste as a substitute material helps save a large share of natural resources and protect the environment. The crystallized slag was used as an aggregate in the composition of concrete core of rectangular thin welded steel tubes subjected to axial or eccentric load performed by Fehoune Nouredine and al [1, 2, 3]. The crystallized slag aggregate was used also in the manufacturing of concrete in the composite stubs with I shaped steel section study by Zeghiche Jahid and al in 2012 [4]. The concrete sand slag has not fact object a comprehensive study to identify his different properties. A Few studies have been made on the characterization of this concrete, for this, we conducted a comparative study between concretes containing crystallized sand slag and ordinary concrete. In this work, we have characterized the different mechanical proprieties and study the durability of sand slag concrete. All

results obtained were compared to the proprieties of ordinary concrete.

MATERIALS CHARACTERIZATION

Cement and water: The cement used in this study is commercial Portland (CEM II) class 42.5 MPa from cement factory of Hajar Elsoud Skikda (Algeria). The chemical and mineralogical compositions of the cement are presented in Tables 1. The apparent density of cement used in the manufacturing of concrete is 1100 kg/m³ and his specific density is 3000 kg/m³, the fineness measured of this cement is between 3200-3400 cm²/g. The water used in the composition of concrete study in this work is tap water at a temperature of 20 ± 2C°. Its quality conforms to the requirements of standard NFP 18-404.

Sand: The sand used (0/2.5 mm) in this study is from Tébéssa quarry (Algéria),and crystallized slag sand (0/3.15mm) from blast furnace of the el Hadjar steel complex, Algeria. The chemical compositions

and the physical properties of the sands are presented in Tables 2 and 3. All properties were measured by following standards NF P18-553, NF P18-555, NF P18-597 NF P18-598, and NF P18-560. The morphologies and grading curves of the different sands before and after correction are given in Figure. 1.

Gravel: We used fractions of crushed stone (5/12.5 mm) from the Souk Ahras region (Algeria). The Apparent density measured is 1300.0 kg/m³, the specific density is 2500 kg/m³ and coefficient of Los Angeles is equal to 23.04% (hard). The properties were measured by NF P18-560, NF P18-554, and NF P18-573. The grading curves of the gravels are given in figure 1. The physical properties of gravel and sand used in the composition of concrete are presented in Table 1 and 2.

Mineral addition: In this study, we used slag was essentially obtained by grinding by-products of the industry of blast furnace steel El-Hadjar (Algeria). The compositions and physical properties of the addition are shown in Tables 3. The comparison between physical proprieties of slag and cement we finding an important note is that the slag fineness is greater than that of cement.

Concrete mix design: Concrete mixes containing either natural or crystallized slag sands were studied and compared. Three different mix designs were investigated for the concrete with natural and crystallized slag sand (figure 2). The first of these was a control mix and did not contain any granulated blast furnace slag, and is designated by BO. Two of the mixes contained 100% replacement of natural sand with crystallized slag sand is designated by BSI and one contained 28 % natural sand and 72% crystallized slag sand , is designated by BSII. The complete proportions for the mixes BO, BSI, BSII are given in table 4.

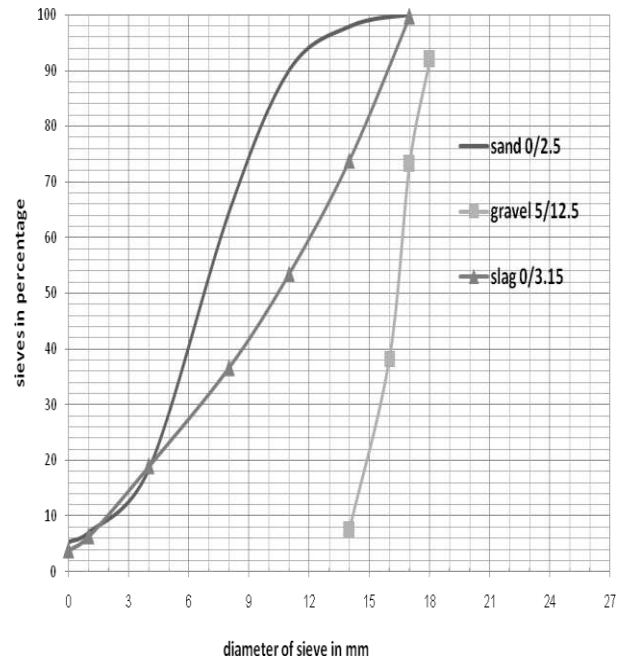


Figure 1
Grading curves of gravels



Figure 2
Concrete specimens

Table 1
Physical properties of sands

Sand type	Apparent density (kg/m ³)	Specific density (kg/m ³)	Porosity in percentage	in fines Modulus (M.F)	Water content in percentage	ES in percentage
-----------	---------------------------------------	---------------------------------------	------------------------	------------------------	-----------------------------	------------------

Dune sand (0/2.5mm)	1610	2650	40	2.21		90.52
Crystallized sand slag (0/3.15mm)	1570	2630	41	3.1	0.35	88.52

Table 2
Physical properties of gravel

Gravel type	Apparent density (kg/m ³)	Specific density (kg/m ³)	Porosity in percentage	Water content in percentage	Property	Absorption coefficient in percentage
gravel (5/12.5mm)	1300	2500	48	0.79	2	2.55

Table 3
Physical properties of the addition

Addition type	slag
(apparent density) (kg/m ³)	1257
Masse volumique absolue (kg/m ³)	2955.3
Finesse (cm ² /g)	5501.9

Table 4
The mix proportions and properties

Compositions	Unit	Mix1	Mix2	Mix3
Cement CPJ 42.5	Kg/m ³	350	300	300
Water/Cement calculated	-	0.5	0.81	0.61
Water/Cement real	-	0.55	0.88	0.88
Sand Dune 0/ 2.5	Kg/m ³	725.59	-	500
Slag granulated 0/3.15	Kg/m ³	-	1540 (100%)	1275
Gravel 5/12.5	Kg/m ³	1070.67	-	-

RESULTS AND DISCUSSION

Concrete slump: The test of concrete slump was performed in accordance with standard NFP18-451. The experimental concrete slump was evaluated by measuring the slump of the fresh concrete with an Abrams cone. The three types of concrete: concrete BO, BSI slag sand concrete, and slag concrete BSII are formulated with a plastic consistency, with a slump of about 6 ± 1 . Figure 3 shows the different results of real and calculated water/cement ration of three type of concrete study here. The ratio water/cement is quasi-proportional and can be explained by the cavities found in crystallized slag which absorb water.

Density: The search for a high compactness or density is justified to have good mechanical properties. The density is determined using the standard NF EN 12350-6, as for a conventional concrete, the density of slag sand concrete depends on its formulation and its implementation. Normally density obtained on wet concrete is equal or greater than 2.4.

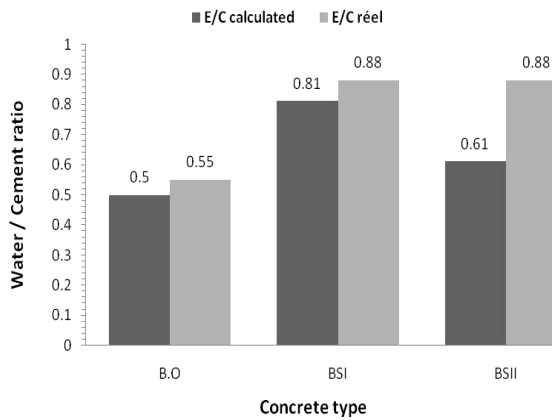


Figure 3

Variation of water / cement ration of different concrete type

The density obtained for the three concretes study here, is 2.55 for BO concrete, and is equal to 2.529 for BSI concrete, and finally 2.455 for BSII concrete. The results of density obtained in this study are shown in figure 4.

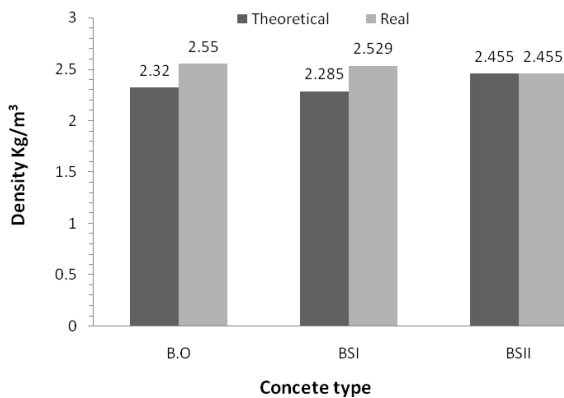


Figure 4

Density of different concretes

Compressive strengths: The compressive strengths are estimated on cubic samples of concrete with dimension ($100 \times 100 \times 100 \text{ mm}^3$). The characterization of the compressive strengths of concrete was carried out in 28 days; using a 500kN compressive hydraulic testing machine. The value of the considered compressive strength constitutes the average of the results from six specimens. The compression test was conducted in accordance with standard NF P 18-406. Results show that the compressive strength of concrete BO and BSI is a bit higher than that of concrete mix BSII, this can be explained by the best binding paste-granulate and the surface texture of the aggregate used manufacturing of BO and BSI concrete. The

decrease rate of compressive strength of concrete BSII at 28 days compared to two other concrete studies in this work is between 3% and 4%. The evaluation of the compressive strength of three types of concrete study here was found proportional to the time of conservation, and the compressive strength begins to stabilize after 90 days of conservation as shown in figure 5.

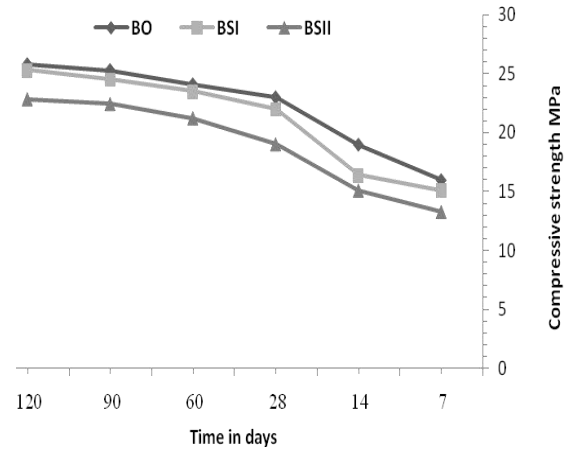


Figure 5

Compressive strength of concrete axis title to the right

Tensile strength: The Tensile strength is determined using the standard BS 1881 (figure 6). The splitting tensile strengths of the concrete mixes are compared in figure 8. The results obtained show that the largest recorded value of the tensile strength is that of concrete BSI who's the natural sand is completely replaced by the sand slag in the composition. The rate of the tensile strength increase for mix BSI compared to that of mix BO is almost 100%; this can be explained by the better behavior of paste-granulate content 100% of sand slag in the case of traction force.

Three-point bending strength: The bending test by three points was performed according to ASTM D 790-81. The bending strength represented in the figure 8 is the average of six samples tested specimens for each type of concrete study here. We note that the BSI concrete with natural sand is completely replaced by the slag sand has a higher bending strength than that of ordinary concrete BO. The growth rate of strength is 42% in this case, meaning that the concrete BSII has better bending strength compared to ordinary concrete BO. By against, the BSII concrete has a bending strength that it is within the range of two concrete strength

resistance of BSI and BO (Figure7).

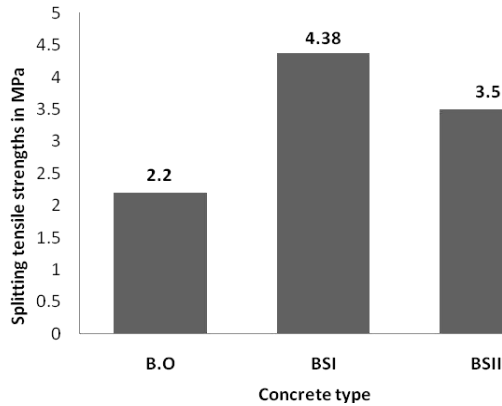


Figure 6
Tensile strength of concrete

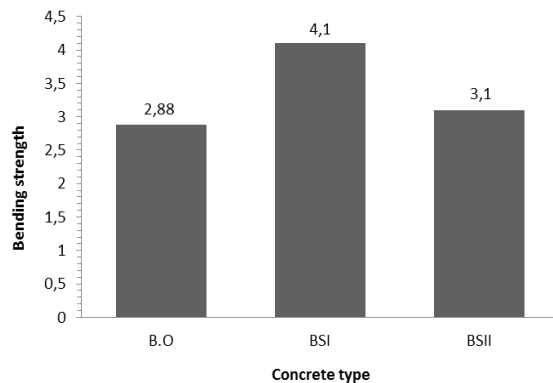


Figure 7
Bending strength of concrete

Capillarity: The capillarity is determined using the standard NF P 18-502. The results presented in figure 10 are the average of six prismatic specimens $70 \times 70 \times 280 \text{ mm}^3$. These results show that the capillary rise is low for concrete BSI ($C = 0.37\%$) and BSII ($C = 0.28\%$) compared to ordinary concrete BO ($C = 0.47\%$). From these results we can conclude that the use of crystallized slag as sand in the manufacturing of concrete does not increase the permeability (Figure 8).

Water absorption by immersion: The result is the average of six prismatic specimens $70 \times 70 \times 280 \text{ mm}^3$, the water absorption in percentage is equals to 5.43 for BSI concrete and 7.15 in the cases of BSII concrete. We can note that the percentage of water absorption by immersion of both BO and BSI concrete are very close, which means they have the same characteristic of water absorption. The results registered are presented in figure 9; we see that ordinary concrete BO has a water absorption

coefficient higher than that of other type of concrete study here.

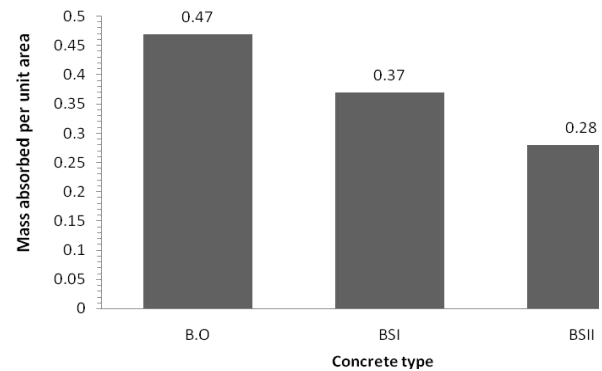


Figure 8
Capillarity of concretes

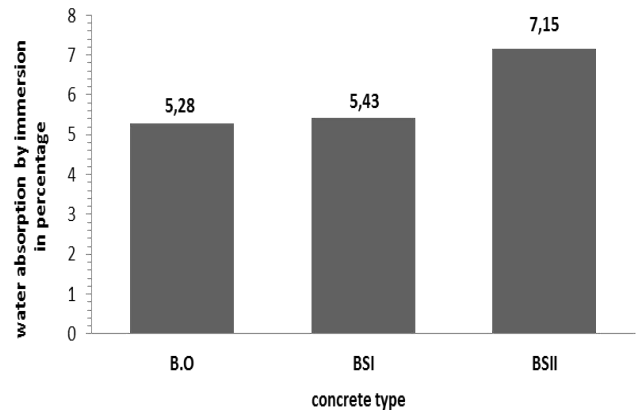


Figure 9
Water absorption by immersion of concretes

Weight loss according concrete age: Weight losses for concrete based on the sand slag of blast furnace BSI and BSII are the weakest. This is explained by the fact that part of the mixing water is chemically combined with slag fine and participates in the hydration reactions. As against the ordinary concrete BO, have higher weight loss rates. All results of Weight loss depending on the concrete age are presented in figure 10.

Hydraulic shrinkage: The shrinkage is determined using the standard NF P 15-433. The evolution of hydraulic shrinkage over time of the three concretes is shown in figure 11. It can be see that overall values of hydraulic shrinkage of sand slag concrete with high dosage of granulated slag are lower and remain close to the limits of the current values of ordinary concrete BO. This can be explained by the strong compactness obtained

for the sand slag concrete.

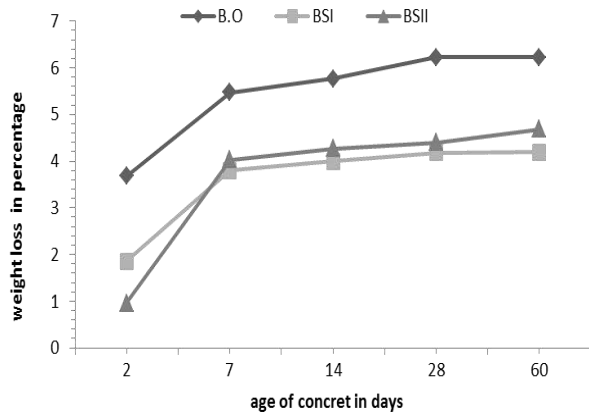


Figure 10

Water absorption by immersion of concretes

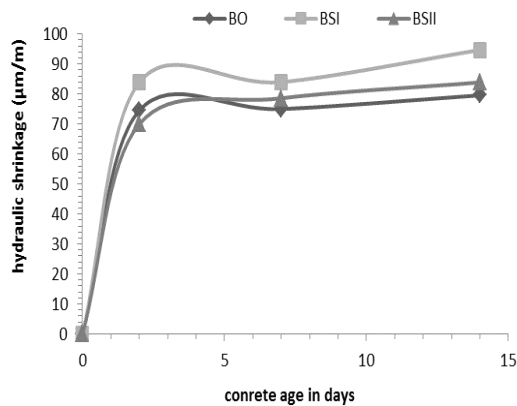


Figure 11

Hydraulic shrinkage of different concretes

CONCLUSIONS

Sand concrete represent a new family of concretes whose performances evolve according to several independent parameters. This study highlighted the role and influence of certain parameters namely: the dosage, the nature and size of the sand on the characteristics of the concrete slag sand, fresh and hardened.

The characterization of slag sand concrete were made from their mechanical properties: compressive strength and tensile strength, as well as their durability: the capillary water absorption and hydraulic shrinkage. By analyzing the results we can conclude several positive points:

- The high compactness achieved by adding sand slag in suitable proportions provides gains in compressive and tensile strength.
 - The use of granulated slag as sand in the composition of concrete can meet two objectives

that have a direct relationship to the cost of concrete: minimize the amount of cement in the concrete composition and increasing the mechanical characteristic of concrete.

- The amount of mixing water used in concrete sand slag is important because of the high water absorption by the crystallized slag sand.
- The use of crystallized sand slag granulated in the composition of concrete can give an economic interest in reducing the cost of concrete and may intervene in the environmental protection of this blast furnace waste.

REFERENCES

1. N. Ferhoune, J. Zeghiche, "Experimental behaviour of concrete filled rectangular thin welded steel stubs (compression load case)", *Comptes rendus mecanique*, N°340, 2012, pp 156-164.
2. N. Ferhoune, "Experimental behaviour of cold-formed steel welded tube filled with concrete made of crushed crystallized slag subjected to eccentric load", *Thin-walled structures*, N°80, 2014, pp 159-166.
3. N. Ferhoune, J. Zeghiche, "Numerical analysis of cold-formed steel welded tube filled with concrete made of crystallized slag aggregate", *Mechanics & Industry*, N°16-112, 2015, pp 1-13.
4. J. Zeghiche, "Further tests on thin steel and composite fabricated stubs", *Journal of Constructional Steel Research*, N° 81, 2013, pp 124–137.
5. L. Alexandre and J L. Sebileau, "The blast furnace slag", edited by the technical center and promotion of slags, 1988.
6. R. Dupain, L. Anchon and JC. Saint Aroman, "Aggregates, soils, cement and concrete", *Characterization of Civil Engineering Materials by Laboratory tests*, Paris, 2004.

COMPARATIVE STUDY OF THE PROPERTIES OF MORTARS WITH RECYCLED GLASS AGGREGATES INCORPORATED BY ADDITION AND SUBSTITUTION

M. Bentchikou^{1*}, S Bouriah¹, N. Hamdane¹, F. Debieb², O. Boukendakdji²

¹LMP2M Laboratory, Université Yahia Farès de Médéa, Algérie, ²LME Laboratory, Université Yahia Farès de Médéa, Algérie

*Corresponding author: Fax: +21325785155 E-mail: bentchikou_moham@yahoo.com

ABSTRACT

An investigation carried out from mirror artisans shows that in the region of Médéa in Algeria and in the absence of a factory of glass making, an important glass quantity is generated by this activity but not exploited and eventually throws in the landfill. This study is a contribution to the valuation of this waste in the manufacturing of mortar either by substitution of the aggregates of the sand by the glass, or by addition. Six (6) different proportions (0 (reference), 25, 35, 50, 75 and 100%) of recycled glass as mass substitution of sand and three (3) others taken as addition to the reference formulation were used.

A comparison of the properties of the material made with one or the other method (substitution or addition) was realized, and some durability aspect was investigated.

By working either on constant workability or with constant W/C ratio, a comparative plan and a discussion of the properties in the fresh and hardened states, sometimes good for one case but bad for others were clarified.

At 28 days, the optimum in terms of mechanical strength was achieved for the mortar with 35% substitution and with 10% addition of recycled glass.

Key words: Mortar, Waste Glass, Physical, Mechanical, Characterisation.

INTRODUCTION

The recycling of used materials has become an important issue as it is a suitable way to preserve natural raw materials that are increasingly rare, reduce landfills and save energy [1,2].

The construction sector is one of the most absorber of recycling wastes and many research works on the use of waste glass as substitution of sand aggregates or Portland cement have been done [3-6].

Kiang Hwee T. & Hongjian Du [1] have tested 4 composition up to 100% of sand substitution by waste glass; they found a reduction of the flowability and density of mortar, while its air content increase and the mechanical properties were compromised. This behaviour is comparable to other research program [7-8].

In this part of the study, we examine the possibility of making a mortar with recycled glass supplied by artisan glaziers, once by substituting the sand by the glass and in another time by adding glass quantity to the mixture. Then, this material is mechanically and physically characterized.

EXPERIMENTAL DETAIL

Waste flat glass sourced from a local glaziers' artisans is used for the manufacturing of a glass mortar (GM). The glass in fraction of 25, 35, 50, 75 and 100 % substitutes a mass of sand. Samples were characterized in both the fresh state by examining the density, the air content and the fluidity and in the hardened state (flexural and compressive strength), shrinkage and swelling. An important aspect of durability for this type of material is the alkali-silica reaction (ASR) which has also been considered in this study.

Materials: Ordinary Portland cement OPC CEM II/A 42.5 was used.

The chemical composition of OPC is given in Table 1.

In this study, recycled glass (RG) with a fineness modulus of 3.83, and 2.49 g/cm³ of density is used. It's chemical composition is given in Table 1.

The natural fine aggregate used was corrected from rolled and crushed sand with fineness modulus of 2.50 and a density of 2.63 g/cm³. No superplasticizer was used.

Table 1
Chemical composition of OPC & glass (%)

	SiO ₂	Al ₂ O ₃	Fe ₂ O ₃	CaO	MgO	Na ₂ O	K ₂ O
OPC	21.91	5.19	2.94	60.41	1.60	0.16	0.54
Glass	72.5	1.5	0.1	9.3	3	13	0.3

Mixtures preparation, casting and curing: the mortar mixed is cast in moulds 4x4x16 cm³. 24 h after, samples are demoulded and stored for a cure, in water with 20 C° ± 2 C° or in the free air (24 C° ± 2 C° according to the nature of the test).

It should be noted that for the same percentage of substitution, two types of mortars are studied, once by maintaining a flowability constant (10s) and another time by keeping the water/cement ratio (w/C) constant (0.5).

Mix proportions of different type of mortar are cited by M. Bentchikou & all [9]

Tests and measurements: Tests on fresh properties of GM, include flow test, air content test and fresh density are conducted respectively.

Tests on the cast specimens include shrinkage, and water absorption test and flexural & compressive strength that were conducted according to NF EN 196 –1 at 7, 28, and 90 days, respectively. All testing was carried out in room temperature from 20 to 28 °C. Test results are given below.

RESULTS AND DISCUSSION

Results of the various tests of the density, incorporated air content and mechanical tests, carried out on the mortars made according to the various combinations referred to above are given below:

Unit weight :

As shown in Fig. 1, when the glass sand replacement amount is increased, the mortar unit weight is reduced compared with the reference Mortar without glass (MTsc) because the glass sand unit weight is lower than that of general sand, thus leading to a reduction in the mortar unit weight for all types of mortar prepared with substitution of glass (M25-M100%) or with addition (MA10-M30%).

These results are in the same range with those presented by P. Penacho & all [7].

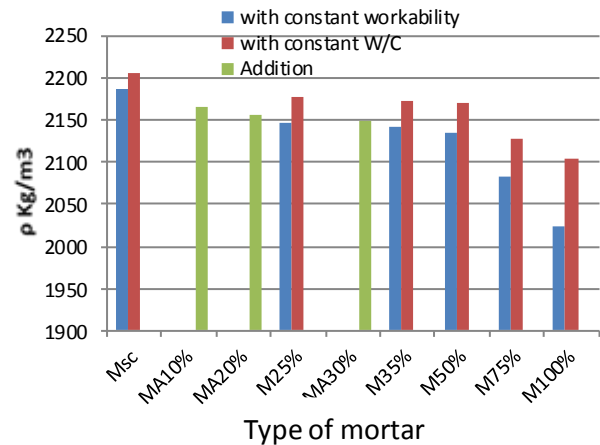


Figure 1

Variation of the unit weight of the 3 types manufactured glass mortars.

Incorporated air content: by comparing the results of these modified mortars (obtained by partial replacement of natural aggregate by glass waste) with those for a conventional mortar (0% waste incorporation), Fig. 2 enables us to conclude that the incorporated air content increased with the replacement of sand by glass aggregates in an almost linear relationship ($R^2 \approx 0.99$).

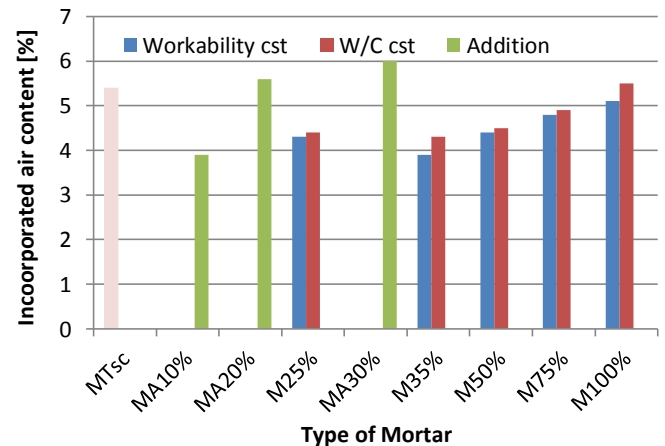


Figure 2

Variation of the air content of the 3 types manufactured glass mortars.

This result also explains the decrease in bulk density in the fresh mortars. The trend may be justified by the change in internal structure due to the waste incorporation.

The same tendency is observed for the composition produced with addition of glass waste (10, 20 & 30%) to the conventional mix.

Flexural and Compressive Strength : Results of Flexural and compressive strength determined at 7, 14 and at 28 days after moulding are grouped on figures 3, 4, 5, 6, 7 and 8 respectively for the 2 types of mortar (substitution & addition) and for the 2 types of preparation (at constant workability and constant W/C).

Flexural Strength:

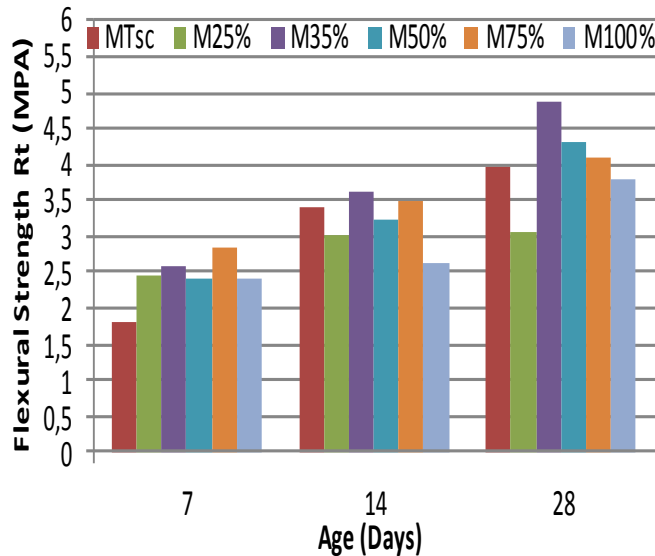


Figure 3

Flexural strength Vs. time of cure for the 6 compositions with glass substitution prepared with constant workability.

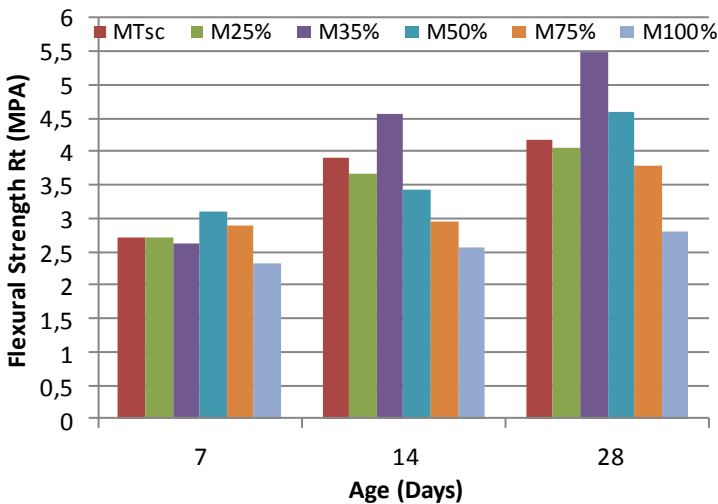


Figure 4

Flexural strength Vs. time of cure for the 6 compositions with glass substitution prepared with constant W/C.

The substitution of sand aggregates by glass improves flexural strength compared to the reference mortar (0%). The best result is got for 35%.

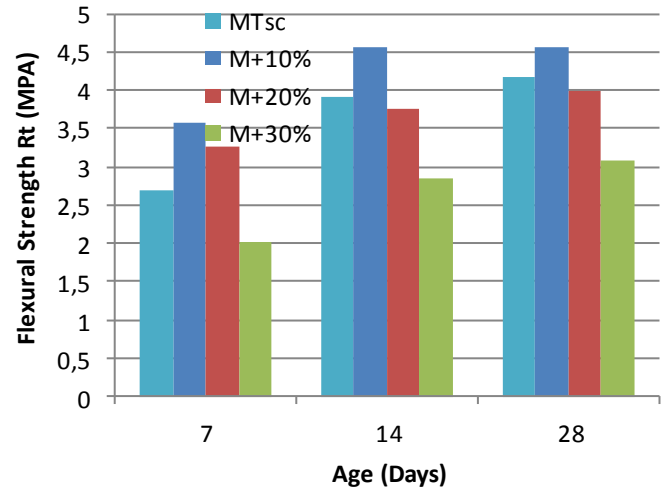


Figure 5

Flexural strength Vs. time of cure for the 4 compositions with glass addition prepared with constant workability.

From 7 to 28 days flexural strength increase not as the result found by Kiang Hwee & all [8], where there is not a significant difference between the strength at 7 and 28 days.

Compressive Strength: From the graphs below we see a continuous increase of the compressive strength with time. This increase is due to the hydration of the cement over time; which causes changes in compactness.

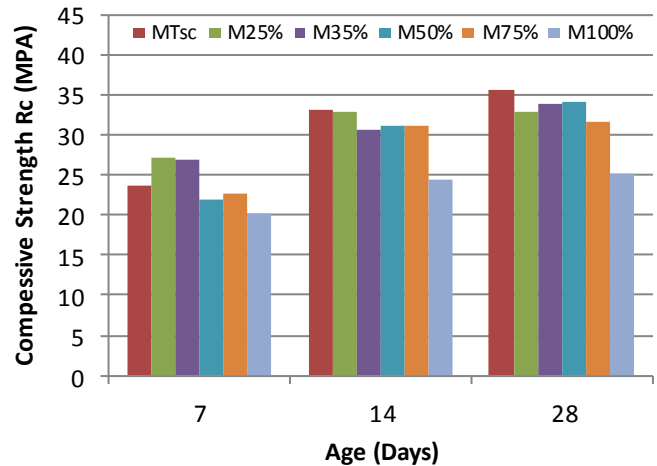


Figure 6

Compressive strength Vs. time of cure for the 6 compositions with glass substitution prepared with constant workability.

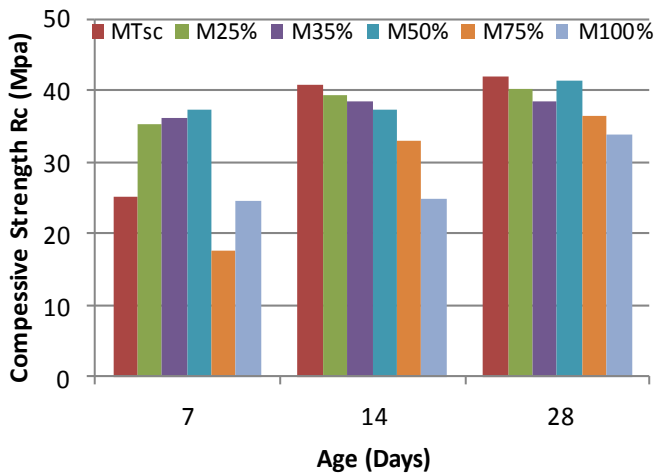


Figure 7

Compressive strength Vs. time of cure for the 6 compositions with glass substitution prepared with constant W/C.

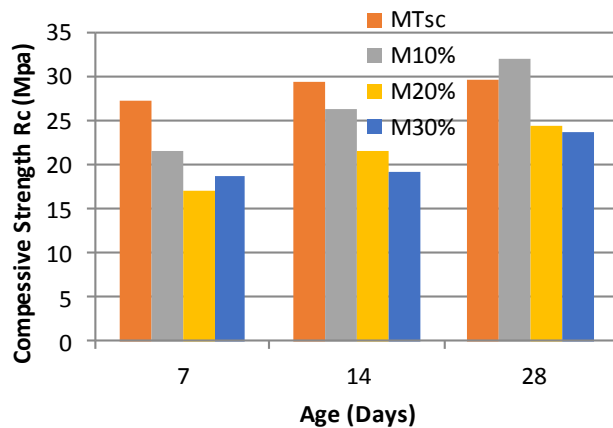


Figure 8

Compressive strength Vs. time of cure for the 4 compositions with glass addition prepared with constant workability.

For all substituted glass fractions, there has been a decrease in the compressive strength in comparison with the control mortar (0%). We note that for 100% aggregates sand replaced by WG, resistance drop is estimated at 28% and 19% respectively for mortar with constant workability and constant W/C.

CONCLUSIONS

By fixing workability at 10 s, we note that:

The amount of air entrained in the mortar, achieved by constant workability is lower than that of mortar made with constant W/C. in all cases the glass mortar is lighter than control mortar.

At 28 days the optimum in terms of resistance is achieved for the mortar with 35% substitution and with 10% addition of recycled glass.

By fixing W/C at 0.5, we note that:

The mechanical strengths of mortars with constant W/C are more important than resistance of mortars with constant workability.

REFERENCES

1. Kiang Hwee T. & Hongjian Du, 2013, Use of waste glass as sand in mortar: Part I – Fresh, mechanical and durability properties, *Cement & Concrete Composites*, 35 pp. 109–117
2. Mehta PK. 2001, reducing the environmental impact of concrete. *Concr Int* 23(10), pp. 61–6.
3. Polley C, Cramer SM, Cruz RV, 1998, Potential for using waste glass in Portland cement concrete. *J Mater Civ Eng* 10(4), pp. 210–9.
4. Jin W, Meyer C, Baxter S, 2000, “Glascrete” – concrete with glass aggregate. *ACI Mater J* 97(2), pp.208–13.
5. Shayan A, Xu A, 2004, Value-added utilization of waste glass in concrete. *Cem Concr Res* 34(1), pp.81–9.
6. Taha B, Nounu G, 2009, Utilizing waste recycled glass as sand/cement replacement in concrete. *J Mater Civ Eng* 21(12) (2), pp709–21.
7. Penacho P, de Brito J, Veiga R, 2014, Physico-mechanical and performance characterization of mortars incorporating fine glass waste aggregate, *Cement & Concrete Composites* 50, pp. 47–59.
8. Kiang Hwee T, Hongjian D, 2013, Use of waste glass as sand in mortar: Part I – Fresh, mechanical and durability properties, *Cement & Concrete Composites* 35, pp.109–117.
9. Bentchikou M, Bouriah S, Hamdane N, Debieb F, Boukendakdji O, 2015, Du verre recycle dans le Mortier, The 3rd International Workshop on Waste Management and Sustainable Development, October 7, 8, 9 - 2015 *ATLAS RIF HOTEL Tangier, Morocco*

ANALYSIS OF PHYSICAL AND MECHANICAL PROPERTIES OF CONCRETE CONTAINING RECYCLED AGGREGATES

N.Goufi¹, D.Kerdal¹, A. Abidelah², N. Kaid², K. Ayed², Goufi Nourredine³

¹Laboratory of mechanical structures and stability of construction LM2SC

²Laboratory of materials soil and thermal LMST

³USTOMB département de Génie Civil Oran, Algérie

Email: n_goufi@yahoo.fr

ABSTRACT

The use of aggregates from recycling of demolition products can contribute to the solution of the storage problem of waste, contributing to the reduction of pollution of the environment, preserving natural resources, reducing the cost of construction and finally solve the problem of supply of sand and gravel.

The use of recycling concrete aggregates requires the characterization of physical - chemical properties of these aggregates, the determination of mechanical performance of recycled aggregate concrete and the understanding of the rheology of these new concretes.

In this work, we present the values of some characteristics of recycled aggregate concrete that are analyzed by comparison with an ordinary concrete.

Recycling materials covered in this study come from the demolition of buildings in Oran (ALGERIA).

The observation of the evolution of compressive strength and loss weight are particularly important factors for a first characterization of the developed material. The values found show that it is important to standardize the use of such aggregates in concrete.

Finally, the values of deformation modulus are compared with those of analytical expressions proposed by the EC2. It turns out that, the relations proposed by the EC2 provide satisfactorily the mechanical properties and the stress strain curve of the elaborated concrete.

INTRODUCTION

Sustainable development has become a strategic issue for the construction industry in its various dimensions because of the direct impact on the building materials. The production of these materials generates CO₂ emissions, is energy consuming and as well as causing the depletion of natural raw materials generates great quantities of waste during construction and demolition[1].

At the end their useful life, structures of civil engineering constitute a major source of recycled aggregates after their demolition especially as the cost of landfill is in constant increase [2, 3]. Recycling aggregates therefore can be one of the solutions to the problem of resource depletion and waste storage.

Recuperating the cement paste after treatment of the aggregates can also lead to minimize the CO₂ impact attributed to the manufacture of cement.

The introduction of recycled aggregates in concrete is

already done in some European countries such as Denmark, England, Germany and other industrialized countries such as Australia and Japan [4, 5]

In Algeria, although there is a large deficit in aggregates and cement that amounts to about 20% of the quantities needed, the wastes generated by the construction industry and the demolition that are important in volume are not valorized [6]. After the seism of 1982 that struck the region of CHLEF (ALGERIA), a campaign for promoting the wastes generated by the collapsed constructions was undertaken in collaboration with the Scientific and technical Centre of Belgian Building (S.C.T.C) [6].

The use of these materials requires the quantification of their impact on the behavior of concrete in the fresh and hardened state across the identification of mechanical, thermal, porometric and rheological properties.

Currently, the EN206-1 norm allows a reuse of recycled aggregates in the production of fresh

concrete, but in a proportion not exceeding 30% (in reinforced concrete) depending on the characterization of the recycled granulates [6]. The present study, by presenting the result of some physical and mechanical parameters of concrete based on recycled aggregates, attempts to contribute to the recovery of such waste.

STUDY OF CONCRETE MADE WITH RECYCLED AGGREGATES

Several research works [7, 8, 9] have studied the replacement of some or all the natural gravels by recycled aggregates in concrete. The recycled concrete aggregates differ from natural aggregates by their composition. Indeed, the recycled concrete aggregate is a composite material in which the two principal components shown in figure 1 are [10]:

- Natural aggregates crushed partially,
- Crushed hydrated paste cement coating the natural aggregates.



Figure1

Compositions of recycled aggregate concrete

In this article, we present the results of some of the characteristics of a concrete made with natural aggregate replaced entirely by recycled aggregate.

MATERIALS AND EXPERIMENTAL PROCEDURES

Materials

Cement: Cement used is the CEM II / B 42.5 type that conforms to the NF EN 42.5 norm. The Blaine specific surface, SSB = 3600 cm² / g. The chemical analysis of the cement is given in the table 1.

Table 1
Chemical analysis of used cement

Elements	SiO ₂	Al ₂ O ₃	Fe ₂ O ₃	CaO
(%)	18.92	4.35	3.58	62.34
Elements	MgO	SiO ₂	Free CaO	Fire loss
(%)	1.30	1.72	0.62	6.38

Tap water is used for mixing.

Aggregates: Two families of aggregates were used. Crushed aggregates obtained from ordinary concrete samples and recycled aggregates resulting from the crushing of concrete waste. These wastes were recovered after the demolition of several buildings located in the city of Oran in Algeria. These aggregates were prepared in 3 steps as shown in figure 2.

- 1- Manual preliminary crushing by using a hammer
- 2- Automatic Crushing by a mechanical crusher;
- 3- Sifting for getting 3-8 mm and 8/15 mm aggregates;



a) Product of demolition

b) Crushed aggregates



c) Aggregates 3/8

d) Aggregates 8/15

Figure 2

Steps of recycled aggregates preparation

The main characteristics of the aggregates used are given in Table 2. Analysis of the results shows that the recycled aggregates have a lower density than natural aggregates but a greater absorption capacity than natural aggregates.

Table 2
Main characteristics of used aggregates

Characteristics	Natural aggregate	
	Gravel 3/8	Gravel 8/15
Mva (Kg/m ³)	1.56	1.60
Mvs (Kg/m ³)	2.65	2.67
Absorption %	2.45	4.90
Characteristics	Recycled aggregate	
	Gravel 3/8	Gravel 8/15
Mva (Kg/m ³)	1.12	1.20

Mvs (Kg/m ³)	2.39	2.52
Absorption %	6.05	4.75
Characteristics	Sand (crushed)	
Mva (Kg/m ³)	1.36	
Mvs (Kg/m ³)	2.63	
Fineness modulus	2.95	

Note that the materials have previously been washed and the recycled aggregates were put in water for more than 24 hours for saturation [6, 11, and 12]. The grading curves of the materials used are shown in the following figure.

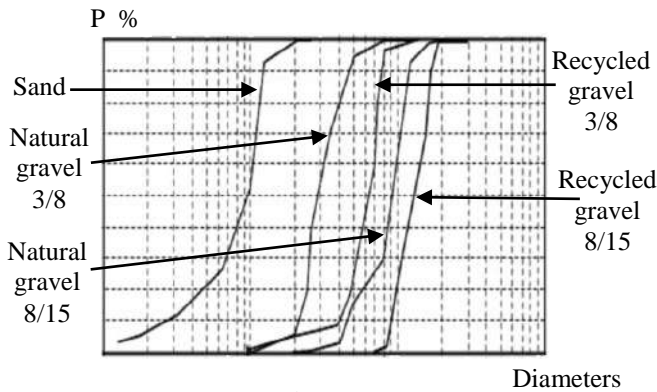


Figure 3
Grading curves of aggregates

EXPERIMENTAL PROCEDURES

For the purposes of the study, 16x32 cm² cylinders were prepared in order to characterize the compressive strength and the modulus of elasticity of concrete made with natural and recycled aggregates. The formulation of these concretes is based on the Dreux Gorisse method [13]. The main parameter of formulation taken into consideration in the study is consistency. Therefore the quantity of cement was kept constant. The amount of water was adjusted until the desired consistency was obtained.

It should be noted that the quantity of calculated water does not represent the total amount but the value of efficient water. During mixing the water is introduced in 3 phases. The details of formulations are given in Table 3.

Table 3
Formulating concrete (% of Constituents)

Composition in %	Cement	Sand	Gravel 3/8	Gravel 8/15
Ordinary concrete	15.36	23.43	5.79	45.63
Recycled concrete	15.36	23.82	4.98	45.03
Composition en %	eau	E/C	Water added	E/C corrected

Ordinary concrete	9.59	0.62	0	9.59
Recycled concrete	10.22	0.66	0.96	0.73

All samples were stored at controlled hygrometry and temperature (T = 20 ° C, HR = 95%) during 24 hours. After 24 hours, the samples are kept in water.

ANALYSIS OF RESULTS

Abrams Slump cone

This parameter allowed us to correct the quantity of water in the concrete based on recycled aggregates. The values found are given in Table 4.

Table 4
Values of the Abrams slump cone

Ordinary concrete		Recycled concrete	
Before correction	After correction	Before correction	After correction
7.8	-	3.8	7.5

The analysis of results, shows that for the same ratio W / C, the workability of a concrete made of 100% recycled aggregates (recycled concrete) is weaker than that of a concrete of natural aggregate because of the important capacity of absorption of the recycled aggregates [14, 15].

Densities and absorption

The results of the characteristics determined in Table 1 show that the density of recycled concrete is less than that of concrete made with natural aggregates while their absorption is more important. These differences are attributed to a higher porosity of the recycled aggregate concrete compared to that of ordinary concrete [16, 17]. The change in mass of the test specimens as a function of time is given in the following Figure 4.

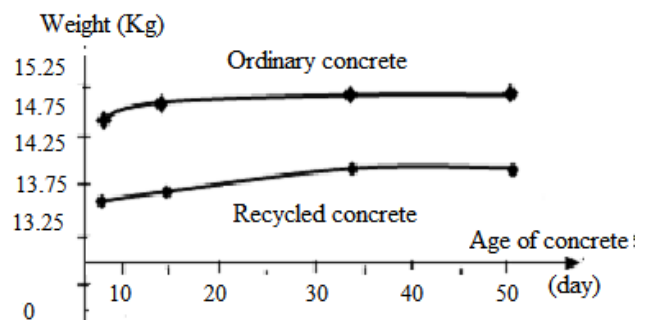


Figure 4
Weight Variation of ordinary and recycled concrete according to the age

The analysis of figure 4 shows an increase of the weight of the ordinary and recycled concrete of 16x32 cm² specimens. At the age of 28 days, the mass of the specimens was 14.98 Kg and 13.85Kg respectively. These values lead to densities equal to 2328.28 and 2152.66 Kg/m³. The value the density of recycled concrete is less than that of ordinary concrete because of the mortar that remains stuck to the aggregates. These values are in agreement with those of previous research works that found that the value of the density of concrete made with recycled aggregates lies generally between 2000 and 2200 kg / m³ [18].

Mechanical performance

The evolution of compressive strengths of concretes studied is presented in what follows.

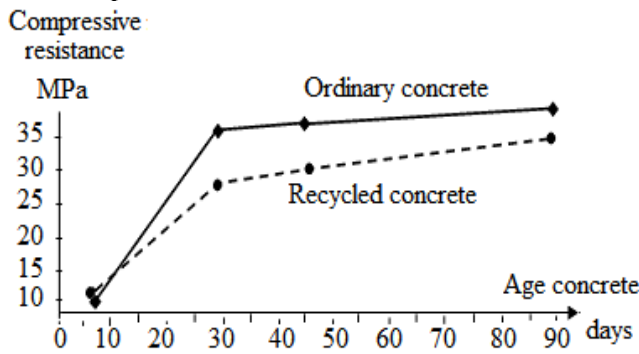


Figure 5
Variation of compressive strengths of concretes studied

Analysis of figure 5 shows that the studied concretes have the same kinetic evolution of resistance over time. However, the values of the compressive strength of concrete made with natural aggregates are superior to those of recycled concrete aggregate. This difference is equal to 16% at 28 days and rises to 18% at the age of 45 days. This lower value of resistance of concrete made with recycled aggregate is attributed to the greater porosity in the recycled aggregate concrete, a bad interface aggregate / binder (figure 6) and the quality of concrete recycling aggregates.



(a) (b)

Figure 6
Facing concrete with natural (a) and recycled aggregates (b)

Modulus of deformation

The deformation modulus is one of the important characteristics of concrete. Its determination gives an idea of the behavior and the stiffness of the material. The following table gives the values of this parameter and the corresponding stress and strain of the specimens tested.

Table 5
Values of deformation modulus

Concrete	Stress (MPa)	Strain (%)	Deformation Modulus (GPa)	Value of EC2	Difference %
Ordinary	34,82	0,101	34,46	29,642	16,26
Recycled	27,48	0,096	28,67	26,83	6,86

The analysis of results shows that the modulus of deformation of the recycled concrete aggregate has a value lower than that of ordinary concrete. Like the BAEL, Eurocode 2 [19] considers only the use of natural aggregates and does not mention the use of recycled aggregates. The following formula given in the Eurocode 2 was used to calculate the modulus of deformation from the compressive strength.

$$E = 17553(f_c/10)^{0.42}$$

With

E: Deformation modulus

f_c: Compressive strength.

These values are very close to the experimentally measured values.

CONCLUSION

The study was conducted to assess the effect of the incorporation of recycled concrete aggregates on the mechanical and physical properties of concrete. The following conclusions can be drawn:

Concrete made with recycled aggregates is less dense than the concrete with natural aggregates. This is due to the adhesion between the old mortar stuck on recycled aggregates and the new product.

The absorption of concrete made with recycled aggregates is higher than that of the concrete based on natural aggregates due to greater porosity.

The use of recycled material did not significantly affect the strength development. But values of the compressive strengths of concrete made with natural aggregates are superior to those of recycled concrete aggregate due to the nature of the used aggregates.

So, the results obtained shows that the characteristics of recycled concrete aggregate although lower than those of normal concrete are still acceptable and that the recycled aggregates can be used in making ordinary concrete. However further research studies of recycled concrete must be carried out in order to understand the link between the properties of concrete and aggregates from crushed concrete, and to control the quantity and quality of the cement paste present on the original aggregate. It is also necessary to study shrinkage and durability of concrete made from recycled aggregates if we want to popularize its use. Finally, an effort must be carried on "selective sorting out" of the different inert waste generated by the demolition of construction in order to avoid their mix.

REFERENCES

1. Pedro D, de Brito J, Evangelista L, 2014, Influence of the use of recycled concrete aggregates from different sources on structural concrete, construction and building Materials, **71** pp.141-151.
2. Recyc-Quebec, 1999, Guide d'information sur le recyclage des matériaux secs.
3. Rubaud M, Pasquet J.F, Bourgeois F, 2006, Recyclage des matériaux de construction : les filières pour préserver l'environnement. Géosciences, n°1
- 4 Charonnat Y, Marsot A, Pitsch C, 1990, Recyclage du béton de ciment. Bulletin de Liaison Ponts et Chaussées, spécial XVI, Chaussées en béton.
5. Hansen TC, 1992, Recycling of demolished concrete and masonry. In: RILEM 06. E et FN SPOON, London
- 6 Kenai S, Debieb F, 2011. Caractérisation de la durabilité des bétons recyclés à base de gros et fins granulats de briques et de béton concassés. Materials and Structures **44** pp.815–824
7. Corinaldesi V, 2010, Mechanical and elastic behavior of concretes made of recycled-concrete coarse aggregates. Construction and Building Materials pp.1616–1620
8. Casuccio M, Torrijos M.C, Giaccio G, Zerbino R, 2008, Failure mechanism of recycled aggregate concrete. Construction and Building Materials **22** pp. 1500–1506
9. González FB, Martínez AF, Carro LD, Seara PS, 2011, Stress–strain relationship in axial compression for concrete using recycled saturated coarse aggregate. Construction and Building Materials, **25** pp. 2335–2342
10. Padmini A.K, Ramamurthy K, Mathews M.S, 2009, Influence of parent concrete on the properties of recycled aggregate concrete. Construction and Building Materials, **23**, pp. 829-836
11. Québaud M, 1996, Caractérisation des granulats recyclés-Etude de la composition et du comportement de béton incluant ces granulats. Thèse de doctorat. Université d'Artois, France.
12. Mefteh H, Kebaili O, Oucief H, Berredjem L. et Arabi N, 2013, Influence of moisture conditioning of recycled aggregates on the properties of fresh and hardened concrete, Cleaner Production, **54** pp.282-288.
13. Dreux, G, and Festa, J, 1998, *Nouveau Guide du Béton*. Huitième édition. Eyrolles, Paris
14. Assia D.T, 2011, Determining the water absorption of recycled aggregates utilizing hydrostatic weighing approach. Construction and building materials.
15. Tam V.W.Y, 2005, New approach in measuring water absorption of recycled aggregates. Construction and Building Materials **35** pp. 1195-1203
16. Padmini A.K, Ramamurthy K, Mathews M.S, 2009, Influence of parent concrete on the properties of recycled aggregate concrete. Construction and Building Materials **23** pp. 829-836
17. Gomez S.J.M.V, 2002, Porosity of recycled concrete with substitution of recycled concrete aggregate. An experimental study. Cement and Concrete Research, **32** pp.1301– 1311
18. Topçu I. B, Sengel S, 2004, Properties of concretes produced with waste concrete aggregate. Cement and Concrete Research. **34** pp. 1307-1312.
19. George W, Elhem G, 2013, Eurocode 2 : Application aux bétons à graviers recyclés. 31èmes Rencontres de l'AUGC, E.N.S. Cachan

VALORIZATION OF QUARRIES MARBLE WASTES SAND AS AN ADDITION IN CEMENT

Said.Berdoudi*¹ H.Hebhoub².M.Belachia².R.Djebien²

1. Laboratory of Mining Engineering, National School Polytechnic of Algiers, Alger

2. LMGHU laboratory, Department of Civil Engineering Skikda University.

126 lotissement 01 El Arrouch Skikda

*Corresponding author: Email: berdoudisaid@yahoo.fr

ABSTRACT

Valorization and recycling of quarries waste may offer interesting advantages and solutions in order to preserve the environment and should be considered as a supplementary source of construction materials.

The main objective of this study is to technically show the possibility to recuperate the sand marble wastes as a substituted addition in the cement and mortar. The aggregate used in this study is a sand of marble wastes (excess loads of sand exposed to bad weather conditions) of the quarry derived from Fil-fila marble (Skikda, east of Algeria). The basis of this study is the effect of marble waste sand fillers substitution in the cement paste and mortar (5, 10, 15 and 20%) with the same fineness of the cement, to compare the results obtained through control samples (0%) of cement paste properties in the fresh condition and the mechanical performances of mortar in the hardened condition.

The results show that the introduction of marble waste sand fillers led to improve the consistency, increases the time of start and end of setting until 15% of the substitution rate without affecting the stability of the cement. For the mechanical properties, the study shows an increase in the compressive strength at 7 days for 5% of the substitution rate, while for the flexural strength the best performance is obtained for 5 and 10%.

Key words: Waste, Sand, valorization, marble, substitution, cement.



Fig1: Declassified powder of Fil-fila quarry (Algeria)

INTRODUCTION

Algeria has a large deficit in building materials, especially cement and sand, the demand rises annually to more than 15 million cubic meters of sand.

The quarries of granite and marble provided a large amount of scrap masses and waste, also the crushing plants generate a very large amount of waste consisting essentially of powders and slurries, the storage of such wastes in the deposits favours air pollution, [1].contamination of water sources and rural land, therefore it is necessary to remove these products, to enhance and reuse them again.

The main objective of this study is to contribute to the reuse of white marble waste sand (dust) of the Fil-fila career in cement manufacturing.

2. CHARACTERIZATIONS OF THE USED MATERIALS

The used materials for this period are:

- Cement CEM1 class 42.5 coming from the cement works of HADJAR SOUD Company,
- Fillers of Marble waste sand are obtained by grinding in a standard normalized ball.

- The mortars are prepared with standard sand CEN according to the norm EN 196-1, this natural siliceous sand with an apparent voluminal mass of 1.63 g/Cm³ and an absolute density mass of 2.5g/Cm³, this sand is inert from a chemical point of view with fineness module of 2.33.

With the results listed in Table 1 and according to the chemical analysis, we find that the marble waste sand are limestone fillers (98, 67 CaCO₃). The addition of marble waste sand fillers in cement leads to increase the CaO quantity. This increase gives a

lot of C3S; it also reduces the quantity of C2S, C3A and C4AF.

Table 1
Characteristics of used materials

Characteristics	CEMI	marble wastes sand fillers
Absolute density (g/cm^3)	3,33	2,79
Surface Blaine (Cm^2/g)	3200	3200
CaO	61,31	55,29
Al_2O_3	5,45	0,14
Fe_2O_3	3,54	0,09
SiO_2	22,73	0,53
MgO	0,48	0,2
Na_2O	0,19	0,00
K_2O	0,63	0,01
Cl ⁻	0,035	0,025
SO_3	2,44	0,04
Loss on ignition	2,45	43,40
Insoluble residue	0,85	0,035
CaO (free)	0,4	--
MS	2,52	--
MAF	1,54	--
LSF	0,88	--
MH	1,93	--
C3S	28,14	--
C2S	38,71	--
C3A	8,45	--
C4AF	10,76	--
CaCO_3	--	98,67

3. EXPERIMENTAL PROGRAM

In the experimental program, we study the substitution of a cement part by the marble wastes sand additions, through varying the substitutions rate (0%, 5%, 10%, 15%, 20%).

3.1 Campaign 1: Manufacturing starting from cement CEM I and marble wastes sand fillers of cement pastes with substitutions rates (0%, 5%, 10%, 15%, 20%).

The constants and variables parameters are water/cement ratio which is equal to 0,27 and the substitution rate respectively. Tests made in this company are consistency, setting and steadines

3.2 Campaign 2: Manufacturing starting from cement CEM I and marble wastes sand fillers of mortars with substitutions rates (0%, 5%, 10%, 15%, 20%). The constants and variables parameters are water/cement ratio which is equal to 0,5 and sand, substitution rate respectively. Tests on hardened mortar samples are compressive and tensile strength in flexion at 2, 7, 28, and 90 days.

4. EFFECT OF RECYCLED FILLERS ON THE CEMENT PASTE CHARACTERISTICS.

4.1 Consistency

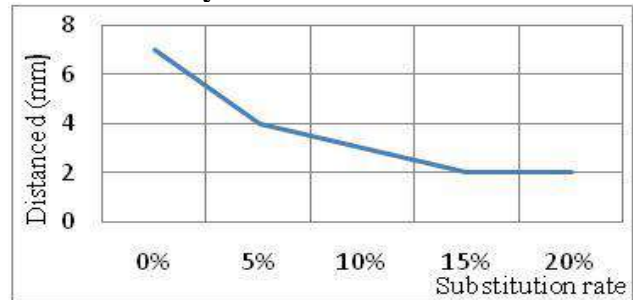


Figure 2: Variation of the consistency according to the substitution rate

For specific surface (Blaine) marble waste sand fillers equal to specific surface (Blaine) cement, the penetration of the probe « Vicat » is a decreasing function with the degree of substitution, the bad consistency is obtained for the sample cement (cement rich in C3A) [2].; the addition of marble waste sand fillers led to improved the consistency of the cement paste [3].

4.2 Start and end of setting

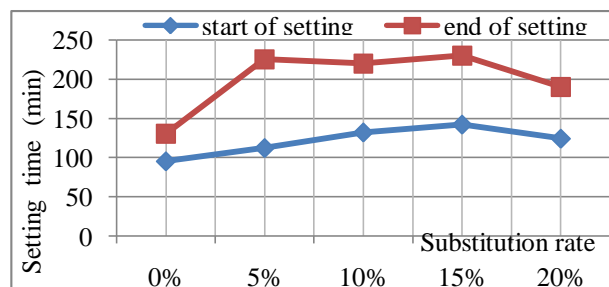


Fig 3: Variation of time of start and end of setting according to the substitution rate.

Figure 3 shows that for W / C constant, the start and end of setting times vary depending on the substitution rate, minimum values are obtained for the sample cement (presence of large quantities of the C3A giving a quick time of setting) [2] and the maximum values are obtained for a substitution rate of 15% for marble waste sand.

4-3 Steadiness

Figure 4 show that the introduction of marble waste fillers does not affect the stability of the cement paste whatever the rate of substitution and the fineness of grinding.

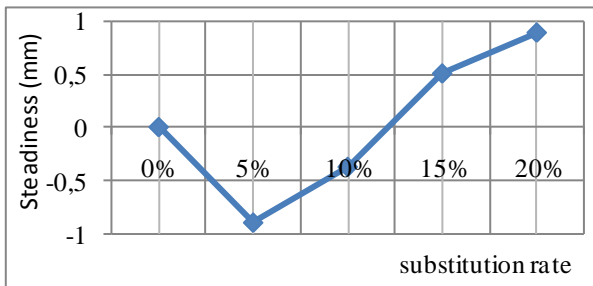


Figure 4: Variation of steadiness according to the substitution rate

5. EFFECT OF RECYCLED FILLERS ON THE MORTAR CHARACTERISTICS

5.1. Compressive strength

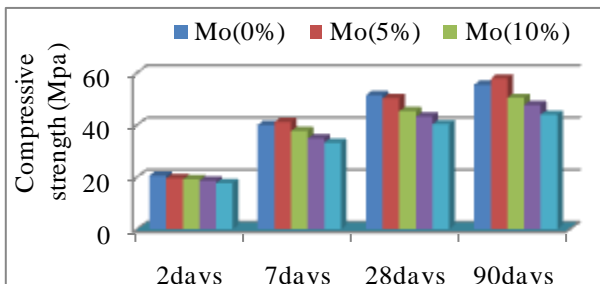


Figure 5: Influence of substitution rate on the compressive strength

Up to 7 days, the best performance is obtained for the mortar with 5% substitution rate. The introduction of 5% of marble waste sand leads to increase the compressive strength, this can be explained by the increase of CaO which promotes hydration of the C3S [3], Beyond 5%, the behavior of the different formulations is the same for all ages.

Between 2 and 7 days the change in the strength is important compared to 7d, 28d and 90 days, this can be explained by the presence of CaO in large quantities which offers very high strengths at short term. The strength increases with age [4].

5.3. Flexural strength

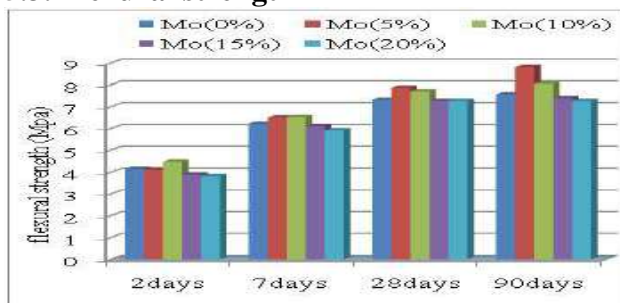


Figure 6: Influence of substitution rate on the flexural strength

Generally, the behavior of the flexural strength (Figure 6) is the same as in compression;

The variation is less between 28 and 90 days compared with 2 and 7 days.

CONCLUSIONS

The study shows that:

-The bad consistency is achieved for the sample cement; adding the marble waste sand, duct improved the consistency of the cement paste; they cause a decrease in the C3A quantity.

- The introduction of marble wastes sand fillers accelerates the mechanical strengths of mortars at a young age.

-The introduction of marble waste leads to increase cohesion.

-The mechanical strength decreases with increasing of the substitution rates (beyond of 5%)

ACKNOWLEDGMENTS

The authors would like to thank the staff of the Civil Engineering Laboratories at the Skikda University and National school of Algiers for their assistance and support during the course of this research. Also, the GICA Company (HDJAR EL SOUD), for their generous financial support.

REFERENCES

1. H.Hebhoub, M.Belachia and R. Djebien 2013,Introduction of sand marble wastes in the composition of mortar, Structural Engineering and Mechanics, Vol. 49, No. 4 (2014) 491-498
2. A.Messan: Contribution to the study of thin Structure out of Mortar Behavior at Very Early Age. Doctoral thesis, Montpellier, 2006.
3. Caré, S, linder,R Baroghel Bouny,V De Larrard, F and Charonnat, Y., 2002, Effect of Mineral Admixtures on Concrete use Properties. Experience plan and Static Analysis, LCPC. ouvrage d'art OA33.
4. Benia, M., 2011, Influence of Specific Surface Cements with Mineral Additives on the Mechanical Behavior of Mortar and Concrete Using Local Materials, Magister memoy, Msila University, Algeria.

PROPERTIES OF FIBER REINFORCED CONCRETE USING RECYCLED AGGREGATES

B. SETTI ^{1*}, F. SETTI ², S. HAMMOUDI ³, M. ACHIT-HENNI ³

¹ Geomaterials Laboratory Materials Science and Environment, University of Hassiba Ben-bouali, Chlef, BO: 151, Chlef, 02000, Algeria.

² Geomaterials Laboratory, University of Hassiba Ben-Bouali Chlef, Algeria.

³ Laboratory Materials Science and Environment, University of Hassiba Ben-bouali, Chlef, Algeria.

*Corresponding author: Email: setti_ba@yahoo.fr

ABSTRACT

Environmental protection is fundamental, it is directly related to the survival of human beings, fauna and flora. Parameters such as the environment, nature conservation and sustainable development play an important role in meeting modern requirements for construction.

The depletion of natural sources of aggregates, stricter laws on environmental protection and the problems of waste disposal are all factors that promote the recycling of materials démolition public works and engineering works civil. Cette study aims to highlight the possibility of using waste as aggregates for concrete reinforcement. In addition to conventional tests such as analysis of the particle size, the density measurement and the test Los Angeles, physical characterization tests on mechanical and recycled aggregates (gravel), the influence of the addition metal fibers in concrete aggregates recycled with different percentage of replacing natural aggregates was studied in fresh and hardened concrete.

KEYWORDS

Recycled Aggregates, Fiber Reinforced concrete, Environment, Concrete, Mechanical Properties, replacement rates.

INTRODUCTION

The ecological thrust imposed to take account of the environment is avoiding

The ecological thrust needed to take account of the environment, eliminating waste and by-products

which often unsightly deposits may lead to some pollution of the natural environment which will require the mobilization of very large capital. Developing countries including Algeria lags far behind in the management of such waste; they are

often abandoned in landfills causing environmental impact. Concrete represents 75% by weight of the buildings, the result is that the majority of demolition waste is concrete [1]. In the context of sustainable development, it is desirable to think of recycling aggregates [2, 3, 4]. The majority of aggregates applications recycled from demolition products are mainly in the road sector, but a better understanding of concrete behavior, including such aggregates can contribute to the development of this application [5, 6]. However, work on demolition materials as replacement aggregates are not or inconclusive. They are considered "non-standard aggregates." They are believed to have a negative impact on the durability of concrete [7,8]. The high water absorption of recycled aggregate is attributed to the presence of old mortar bonded aggregates. [9] It generally appears that the use of recycled aggregate concrete decreases drop from concrete containing natural aggregate for the same W / C [10, 11]. This decline would collapse due to the large absorption and angularity of recycled aggregates. Moreover, qualification and development of demolition materials depend on the pollutant content (plaster, wood, plastic, paper

...) and acceptability is fixed compared to their level of contaminants. [12] This can be improved by treatment before the development of recycled aggregates. It is generally recognized that for a conventional formulation of the concrete and a replacement of 100% of the natural aggregate, a reduction in compressive strength is observed. Several researchers have found a 10% decrease of the 28-days strength of concrete in this case [13]. Like several other properties of the concrete, it is observed that the tensile strength of the concrete decreases as the rate of replacement of natural aggregate by recycled granulate increases [11, 14]. this experimental study is to value the contribution of steel fibers in concrete aggregates from demolition. The influence of concrete based on recycle aggregates (gravel) with different percentage of substitution and in the presence of metal fibers, on the fresh and hardened concrete was studied

MATERIAL COMPOSITION OF CONCRETE

Cement: Portland cement concrete is a compound CPJ-CEM II / A 42.5; manufactured by ECDE of cement Chlef.

Table 1
Composition of the cement used.

Chemical composition (%).							
CaO	Al ₂ O ₃	Fe ₂ O ₃	MgO	SO ₃	K ₂ O	PAF	SiO ₂
62,14	4.2	3.55	0.62	2.19	0.42	1.84	22.6
Minéralogique composition (%).							
C ₃ S	C ₂ S	C ₃ A	C ₄ AF				
41.8	3.33	5.1	10.7				

Sand: The sands used are the sands called "sands rolled" .

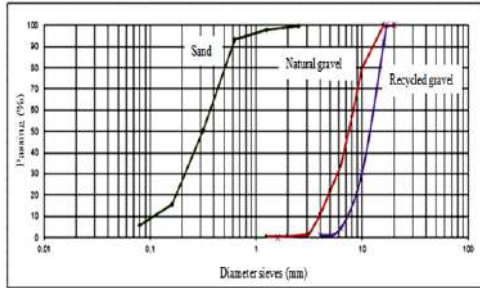


Figure 1
Curve size

The natural aggregates and recycled aggregate:

Aggregates must have a good size. The diameter of the aggregates varies from smallest to largest. They can be:

- Natural broken (quarry rocks) or recycled aggregates (crushed concrete), manufactured in the laboratory.
- LOS Anglos coefficient for natural gravel = 0.28
- LOS Anglos coefficient for recycled gravel = 0.3

Table 2
Identification of natural and recycled aggregates used

Guy	Class	Code	Nature	Source
Natural gravel	3/15	NG	Crushed limestone	Career
Recycled gravel	3/15	RG	Crushed concrete	Made in laboratory


Adjuvant: Adjuvant is chemicals incorporated into fresh concrete in small quantities. They improve the properties of the concretes and mortars to which they are added. The

adjuvant that we used is a super plasticizer manufactured by GRANITEX called MEDAFLOW 145.

Metal fibers: The fibers used are metal fibers made from drawn steel wire, marketed by the company under the name Sika Dramix (METAL FIBRE RC-80/50-BN). They have hooks at both extremities. They are connected and separated into contact with water in order to ensure their distribution in the concrete.

The different properties of the fibers are summarized in (Table 3) as follows:

Table 3
Caractéristiques of fiber Dramix

Form					
Length (mm)	Diameter (mm)	Slenderness Ratio (l/d)	Tensile strength (MPa)	Nb of fiber per kg	
50	0.62	80	1100	8168	

Mixing Procedure and preparation of test specimens:

Experimental program: The various concrete we have made in this study are shown in Table 4.

Table 4
Designation of tested concretes

CFM	Concrete metal fiber
CFR25	Concrete fiber with 25% recycled aggregates and 75% natural aggregates
CFR50	Concrete fiber with 50% recycled aggregates and 50% natural aggregates
CFR75	Concrete fiber with 75% recycled aggregates and 50% natural aggregates
CFR100	Concrete fiber with 100% recycled aggregates

Preparation of test specimens: In the tests carried out for studying the concrete, two types of specimens were used:

*Cylindrical specimens of dimensions 16x32 cm; whose height is equal to two times the diameter for the compression tests.

*Prismatic specimens of size 7x7x28 cm, according to the flexural tensile tests. So the total is 120 samples. Crushing were carried out at 7, 14, 28 days.

define the optimal mixing of the various aggregates that are available, as well as the cement content, water and adjuvant in order to achieve a concrete which are those desired qualities and in particular, the workability and the resistance.

In order to study the rheological and physico-mechanical properties of steel fiber concrete using recycled aggregates, we examined five types of concretes (Table.4), concretes were made by the method Dreux-Gorisse [15].

Concrete formulation: The formulation of the concrete is to

Table 5
Assays weight of components (kg / m³)

Designation Component	CFM	CFR25%	CFR50%	CFR75%	CFR100%
Cement	400	400	400	400	400
Sand	750	750	750	750	750
Gravel N	1019	764.3	509.5	254.7	/
Gravel R	/	254.7	509.5	764.3	1019
Fiber	38.9	38.9	38.9	38.9	38.9
Water	240	240	240	240	240
Adjuvant	20	20	40	60	80

Testing:

Tests on fresh concrete:

Abrams cone slump: Controlling the workability is performed by the slump test cone Abrams (Slump test), which is the test most used because of its ease and reproductive on site.

This test is used to control the percentage of water in the made

concrete. It consists in measuring the sagging of a concrete cone under the effect of its own weight after the lifting of the Abrams cone vertically. We take the average of three successive trials.

The use of recycled aggregates decreases concrete slump versus a concrete containing natural aggregate for the same W / C ratio. This decline

would collapse due to the large absorption and angularity of recycled aggregates. Indeed, to avoid this problem and the dosage of superplasticizer was increased when the recycled gravel rate increases.

Table 6
Subsidence of concretes used.

Concrete type	subsidence (cm)
CFM	4,5
CFR 25%	5
CFR 50%	5
CFR 75%	5,5
CFR 100%	11,16

Tests on hardened concrete:

Compression Test: It is carried out on cylindrical specimens (16 * 32) cm, using a hydraulic press capacity of 3000 KN.

Bending test: This test is performed on samples 7x7x28 cm prismatic. To measure the flexural tensile strength we use the method of 3 points (three points bending).

RESULTS AND INTERPRETATION

Compressive strength: In Table 7, the represented values of the compressive strength is an average made on three values of concretes CFM, CFR25% CFR50% CFR75% and CFR100%. The compressive strength increases proportionally with time, although the rate of change is not similar for the different concrete mixtures.

The maximum value of the compressive strength at 28 days is 27.44 MPa obtained in the concrete BFR75%. The minimum value of the compressive strength at 28 days is 23.2 MPa obtained in the recycled aggregate concrete without BF. This can be explained by the strength of the concrete is influenced by the form of aggregates with the fibers, so the adhesion strength between the recycled fibers and the gravel with cement paste is larger than those of natural gravel with the fibers. In the long term, the resistance of blends of recycled gravel and the fibers are greater than the mixture with natural gravel base and the fibers, which confirms that the granularity of the recycled gravel provides better cohesion than the recycled gravel-based matrix with the fibers.

Table 7
Compressive strength

Strength Concrete	Strength (MPa) 7 days	Strength (MPa) 14 days	Strength (MPa) 28 days
CFM	19.80	21.22	23.20
CFR25%	18.95	19.52	23.65
CFR50%	19.80	23.20	24.44
CFR75%	26	26.48	27.44
CFR100%	25.46	26.31	27.16

Bending strength: In Table 8, the represented values of the tensile strength is an average made on three values of BF concretes BFR25% BFR50% BFR75% BFR100%.

The mixed substitution does not obey the law of mixtures; the two partial substitutions are not cumulative. It is noted that the interaction of the

different effects is accentuated depending on the age of loading and the stress.

Table 8
Bending strength

Strength Concrete	Strength (MPa) 7 days	Strength (MPa) 14 days	Strength (MPa) 28 days
CFM	5.05	5.69	7.16
CFR25%	5.32	5.96	6.42
CFR50%	5.60	7.16	7.16
CFR75%	5.51	5.51	6.61
CFR100%	4.77	5.51	7.89

The maximum value of the tensile strength by bending at 28 days is 7.89 MPa obtained in the concrete BFR100%. The minimum value of the tensile strength by bending at 28 days of 6.82 MPa is obtained in the concrete BFR25%. This can be explained by the tensile strength of the fiber-reinforced concrete recycled aggregate base is influenced by the texture of the aggregate, so the adhesion strength between the fibers and recycled gravel and cement paste is larger than those of without natural aggregates and recycled fibers.

CONCLUSION:

- The strong water absorption rate of recycled aggregates complicates the implementation of the concrete.
- The addition of recycled aggregates in reinforced concrete, as a percentage (75% GR), providing a maximum increase in compressive strength; beyond 75% of the compressive strength decreases, while the percentage of (100%) of GR gives a better tensile strength (flexural).
- The blends of partially substituted aggregates give the best performance

in fresh and cured concrete than or completely substituted by reference.

-The replacement rate of 100% of natural aggregate has in most cases a negative effect on the compressive strength and beneficial for bending resistance.

-This study sheds light on the utilization of by products and should help ultimately to the establishment of concrete formulation of rules-based alternative aggregates.

REFERENCES

1. Ramachandran, V-S, 1981. utilisation des déchets et sous-produits comme granulats du béton. CBD-215-F, conseil national de recherches Canada.
2. Petkovic G., Engelsen C. J., Håøya A.O., Breedveld G., 2004. Environmental impact from the use of recycled materials in road construction: method for decision-making in Norway. Resources, Conservation and Recycling, 42, pp. 249–264
3. Levy S. M., Helene P., 2004, Durability of recycled aggregates concrete: a safe way to sustainable development, Cement and Concrete Research, 34, pp.1975–1980.
4. Oikonomou N.D., 2005. Recycled concrete aggregates. Cement & Concrete Composites. 27, pp.315–318
5. Buyle-Bodin F., Zaharieva R.H., 2002. Influence of industrially produced recycled aggregates on flow proper ties of concrete.

- Materials and Structures, 35, pp. 504-509
6. Poon C. S., Chan D., 2007. The use of recycled aggregate in concrete in Hong Kong', Resources, Conservation and Recycling, 50, pp. 293-305
 7. Wirquin E., Zaharieva R.H., Buyle-Bodin F., 2000. Utilisation de l'absorption d'eau des bétons comme critères de leur durabilité - Application aux bétons de granulats recyclés, Materials and Structures, 33, pp. 403-408
 8. Tu T. Y., Chen Y. Y., Hwang C.L., 2006. Proper ties of HPC with recycled aggregates, Cement and Concrete Research, 36, pp. 943–950
 9. Juan M. S., Gutiérrez P.A., Study on the influence of attached mortar content on the proper ties of recycled concrete aggregate, Construction and Building Materials, 23 (2009) 872-877
 10. Butler, L., West, J. S. et Tighe, S. L. (2011). The effect of recycled concrete aggregate properties on the bond strength between RCA concrete and steel reinforcement. Cement and Concrete Research, volume 41, numéro 10, p. 1037-1049.
 11. Chakradhara Rao, M., Bhattacharyya, S. K. et Barai, S. V. (2011). Influence of field recycled coarse aggregate on properties of concrete. Materials and Structures/Materiaux et Constructions, volume 44, numéro 1, p. 205-220.
 12. Hussain H., Levacher D., Recyclage de béton de démolition dans la fabrication des nouveaux bétons', Proceeding, XXIemes Rencontres Universitaires de Génie Civil, La Rochelle, France, (2003) 425-432.
 13. Rahal, K. (2007). Mechanical properties of concrete with recycled coarse aggregate. Building and Environment, volume 42, numéro 1, p. 407-415.
 14. Kou, S. C. et Poon, C. S. (2012). Enhancing the durability properties of concrete prepared with coarse recycled aggregate. Construction & Building Materials, volume 35, p. 69-76.
 15. Dreux G., Festa J., Nouveau guide du béton et ses constituants, Edition Eyrolles, 8eme édition, 1998.

MECHANICAL AND THERMAL CHARACTERIZATION OF STABILIZED EARTH BRICKS

Pape Moussa TOURE*, Vincent SAMBOU, Mactar Faye, Ababcar Thiam
Laboratoire d'Energétique Appliquée (LEA), Ecole Supérieure Polytechnique (ESP), Université Cheikh
Anta Diop (UCAD)
BP 5085 Dakar-Fann, Dakar, Sénégal.

*Corresponding author:

Fax: +221338255594

Email: papemoussa.toure@ucad.edu.sn

ABSTRACT

In Senegal, soil is used in construction with a misunderstanding of the thermal and mechanical properties. The lifespan of building considerably depends of the mechanical properties of construction materials used. The thermal properties of construction materials have considerable influence on the energy performance of the building. This work deals with the determination of thermal and mechanical properties of soil bricks stabilized with cement produced by five handicraft manufacturers. For the mechanical characterization, we determine the compressive strength of bricks using a mechanical press. The thermal characterization is to determine thermal capacity and thermal conductivity of bricks by asymmetrical transient Hot Plate method. The results show that vibrated bricks have a compressive strength of about 1.6 MPa and a thermal conductivity of about $0.8 \text{ W}\cdot\text{m}^{-1}\cdot\text{K}^{-1}$. The compressed bricks have better compression strength of about 2 MPa and a thermal conductivity of about $0.7 \text{ W}\cdot\text{m}^{-1}\cdot\text{K}^{-1}$.

KEYWORDS

Characterization, stabilized, thermal, mechanical, brick, thermal effusivity, thermal conductivity, compressive strength.

NOMENCLATURE

a	Thermal diffusivity(m^2s^{-1})
C	Thermal capacity per area unit ($\text{J}\cdot\text{m}^2\cdot\text{K}^{-1}$)
c	Specific heat($\text{J}\cdot\text{kg}^{-1}\cdot\text{K}^{-1}$)
E	Thermal effusivity($\text{W}\cdot\text{m}^2\cdot\text{k}^{-1}\cdot\text{s}^{1/2}$)
e	Thickness of sample (mm)
Fc	Compression strength(MPa)
p	Laplace parameter
Rc	Contact thermal resistance ($\text{m}^2\cdot\text{K}\cdot\text{W}^{-1}$)
w	water content

Greek Symbols

ψ	Quadratic error between experimental and theoretical curves
ρc	Thermal capacity ($\text{J}\cdot\text{m}^{-3}\cdot\text{K}^{-1}$)
Φ	Laplace transform of the flux
θ	Laplace transform of the temperature

Subscripts

exp	Experimental
mod	Model
h	Heating element
i	Insulating blocks

INTRODUCTION

The lifespan of building depends considerably on the mechanical properties of construction materials used. The thermal properties of construction materials have considerable influence on the energy performance of the building both in terms of thermal inertia or insulating property. The conception of a sustainable building requires knowledge of the mechanical and thermal properties of construction materials to use.

Many studies have been published concerning the characterization of mechanical and thermal properties of materials.

Aigbomian and Fan [1] develop a new building material using sawdust, waste paper and Tradical lime. Their results showed that lightweight sustainable blocks can be produced with good insulating, density ranging from 356 to 713 kg/m³ and compressive strength from 0.06 to 0.80 MPa. Millogo et al. [2] conducted an investigation to determine the physical and mechanical properties of Hibiscus cannabinus fibers used in the fabrication of Pressed Adobe Blocks (PABs). Muntohar. [3] showed that compressive and flexural strength of clay brick are improved by adding of lime and rice husk. Alavez-Ramirez et al. [4] evaluated the effects of the addition of Lime and sugar cane bagasse ash on the mechanical properties of compacted soil blocks. F. Gouny et al. [5] have worked on the pull-out and shear mechanical behavior of laboratory assemblies of wood, geomaterial binder and two different types of earth brick. Benmansour et al. [6] have studied the thermal and the mechanical performance of a new material composed with natural cement, sand and date palm fibers. Mounir et al. [7] determined the thermal properties of clay by combining it with cork, using the asymmetrical hot plate and the flash methods. Daniel Maskell et al. [8] have demonstrated the improvement of the compressive strength of extruded earth, with a range of cement or lime contents and three initial curing temperatures. Bal *et al.* [9] conducted an experimental study of thermal properties of laterite bricks with millet waste as additive material.

In all these characterization works, materials have been fabricated in laboratory only in framework of study. This research work is a mechanical and thermal characterization of stabilized earth bricks produced by five different handicrafts manufacturers constructing buildings witnesses with these bricks.

I. DESCRIPTION OF THE EXPERIMENTAL PROTOCOL

1. MANUFACTURING PROCESSES

For anonymity, the five manufacturers are named respectively A, B, C, D and E. The brick manufacturing process is the same for the manufacturers B, C, D and E. Bricks of these manufacturers are compressed while those of

manufacturer A are vibrated. The details of the compositions of these earth bricks are in Table 1.

Table1: Mixture proportions of brick

Manufacturers	Laterite(%)	Sand(%)	Cement(%)
A	90	0	10
B	74	20	6
C	62	30	8
D	67	27	6
E	67	25	8

2. MECHANICAL CHARACTERIZATION METHOD

The compressive strength is measured using a compression machine with 0.05 kN of precision and a loading speed of 2 kN/s. This test consists of subjecting a brick to a simple compression until failure as illustrated in Figure 1.

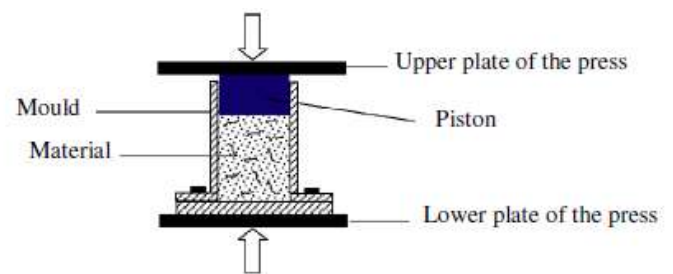


Fig.1. Schema of the mold used for the manufacture of brick [11].

3. THERMAL CHARACTERIZATION METHOD

The thermal capacity and the thermal conductivity of bricks are measured using the hot plate device. The asymmetrical experimental device represented schematically in Figure 2 was adopted. A plane heating element having the same section (100×100 mm²) as the sample is placed under the sample (100×100×10 mm³). A thermocouple is stuck on the lower face of the heating element. The sample is placed between two extruded polystyrene blocks with a thickness of 50 mm; these blocks are set between two aluminum blocks with a thickness of 40 mm. A heat flux step is sent into the heating element and the transient temperature $T(t)$ is recorded. Since the thermocouple is in contact with polystyrene that is a deformable material, the presence of the thermocouple does not increase the

thermal contact resistance between the heating element and the polystyrene. Furthermore, since polystyrene is an insulating material, this thermal resistance will be neglected.

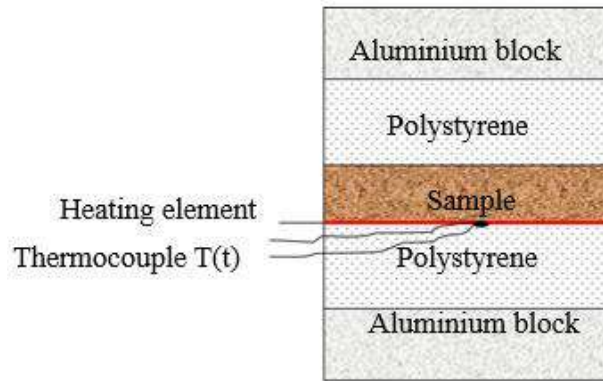


Fig.2. Schema of the experimental hot plate device [10].

The theoretical model originates from the integral transform treatment of the heat equation [10], is modeled with the hypothesis that the heat transfer remains unidirectional 1D at the center of the sample during the experiment. The recording processing of $T(t)$ is realized by supposing that the heat transfer at the center of the heating element is 1D. Considering the very low value of the heat flux reaching the aluminum blocks through the polystyrene and their high thermal capacity, their temperatures are supposed equal and constant.

Within these hypotheses, one can write:

$$\begin{bmatrix} \theta \\ \Phi_{01} \end{bmatrix} = \begin{bmatrix} 1 & 0 \\ C_h & 1 \end{bmatrix} \begin{bmatrix} 1 & R_c \\ 0 & 1 \end{bmatrix} \begin{bmatrix} A & B \\ C & D \end{bmatrix} \begin{bmatrix} A_i & B_i \\ C_i & D_i \end{bmatrix} \begin{bmatrix} 0 \\ \Phi_1 \end{bmatrix} = \begin{bmatrix} A_1 & B_1 \\ C_1 & D_1 \end{bmatrix} \begin{bmatrix} 0 \\ \Phi_1 \end{bmatrix} \quad (1)$$

$$\begin{bmatrix} \theta \\ \Phi_{02} \end{bmatrix} = \begin{bmatrix} A_i & B_i \\ C_i & D_i \end{bmatrix} \begin{bmatrix} 0 \\ \Phi_1 \end{bmatrix} \quad (2)$$

$$\Phi_0 = \frac{\phi}{p} = \Phi_{01} + \Phi_{02} \quad (3)$$

θ is the Laplace transform of the temperature $T(t)$, Φ_{01} the Laplace transform of the heat flux density living the heating element (upstream), Φ_{02} the Laplace transform of the heat flux density living the heating element (downstream), Φ_0 the Laplace transform of the total heat flux density produced in the heating element, Φ_0 the heat flux density produced in the heating element, C_h the thermal capacity of the heating element per area unit:

$C_h = \rho_h c_h e_h$; R_c the thermal contact resistance between the heating element and the sample, Φ_1 the Laplace transform of heat flux density input on the upper aluminum block, Φ_2 the Laplace transform of heat flux density input on the lower aluminum block.

$$A = D = \cosh\left(e\sqrt{\frac{\rho c p}{k}}\right); B = \frac{\sinh\left(e\sqrt{\frac{\rho c p}{k}}\right)}{\sqrt{k\rho c p}} \quad (4)$$

$$C = \sqrt{k\rho c p} \sinh\left(e\sqrt{\frac{\rho c p}{k}}\right); A_i = D_i = \cosh\left(\sqrt{\frac{p}{a_i}}e_i\right) \quad (5)$$

$$B_i = \frac{\sinh\left(\sqrt{\frac{p}{a_i}}e_i\right)}{k_i\sqrt{\frac{p}{a_i}}}; C_i = k_i\sqrt{\frac{p}{a_i}} \sinh\left(\sqrt{\frac{p}{a_i}}e_i\right) \quad (6)$$

E is the sample thermal effusivity, ρc the sample thermal capacity, e the sample thickness, k_i the polystyrene thermal conductivity, a_i the Polystyrene thermal diffusivity, e_i the polystyrene thickness.

Combining those five equations, the system leads to:

$$\theta(p) = \frac{\Phi_0(p)}{\frac{D_1}{B_1} + \frac{D_i}{B_i}} \quad (7)$$

The principle of the method is to estimate the value of the parameters ρc and k of the sample that minimizes the sum of the quadratic error $\psi = \sum_{j=0}^N [T_{\text{exp}}(j) - T_{\text{mod}}(j)]^2$ between the experimental curve and the theoretical curve calculated with relation (7). The inverse transformation is performed using the De Hoog algorithm [11].

4. RESULTS AND DISCUSSION

4.1. MECHANICAL RESULTS

The results of mechanical test are shown in Table 2.

Table2: Mechanical characterization results

Manufacturers	ρ (kg/m ³)	Fc (MPa)
A	1757	1.65
B	1950	2.50
C	1818	2.10

D	1805	2.10
E	1889	2.60

The vibrated bricks (manufacturer A) have a lower density and a lower compressive strength of about 1.6 MPa. The compressed bricks (manufacturer B, C, D, and E) have a mean value of density of about 1865 kg/m³ and the mean value of compression strength is about 2.3 MPa. The difference between vibrated and compressed bricks can be explained by the manufacturing process. The vibrated bricks are not compacted or the compact increases the compressive strength of the brick. Despite the difference of the composition of compressed bricks, the standard deviation of compression strength is about 0.3 MPa. The low standard deviation show that the mean value of compression strength is enough representative. These results show that compressed bricks can be used as structural wall.

4.2. THERMAL RESULTS

The results of thermal test are shown in Table3.

Table3: Thermal characterization results

Manufacturers	w	ρc	k
A	1.2	$1.65 \cdot 10^6$	0.81
B	1.6	$1.98 \cdot 10^6$	0.69
C	1.3	$1.93 \cdot 10^6$	0.72
D	2.0	$2.0 \cdot 10^6$	0.72
E	1.6	$1.91 \cdot 10^6$	0.72

The vibrated bricks (manufacturer A) have the lower thermal capacity of about $1.6 \cdot 10^6 \text{ Jm}^{-3}\text{K}^{-1}$ and the high thermal conductivity of about $0.8 \text{ W.m}^{-1}\text{K}^{-1}$. The compressed bricks (manufacturer B, C, D, and E) have a mean value of thermal capacity of about $1.9 \cdot 10^6 \text{ J.m}^{-3}\text{K}^{-1}$ and a mean value of thermal conductivity of about $0.7 \text{ W.m}^{-1}\text{K}^{-1}$. The standard deviation of thermal capacity and thermal conductivity are respectively $0.04 \cdot 10^6 \text{ J.m}^{-3}\text{K}^{-1}$ and $0.01 \text{ W.m}^{-1}\text{K}^{-1}$.

5. CONCLUSIONS

It is clear that the use of construction materials with more favorable mechanical and thermal properties greatly increases the lifespan of building and reduces the heat gain. For that, a great knowledge of the characteristic of the construction materials can be used and introduced by designers in the estimation of the sustainable building. For this purpose, the mechanical and thermal characterization of stabilized earth bricks from five different handicrafts

manufacturers is done. The measurements essentially give compressive strength, thermal capacity and thermal conductivity. The results show that vibrated bricks have a compressive strength of about 1.6 MPa and a thermal conductivity of about $0.8 \text{ W.m}^{-1}\text{K}^{-1}$. The compressed bricks have better compression strength of about 2 MPa and a thermal conductivity of about $0.7 \text{ W.m}^{-1}\text{K}^{-1}$.

These results provide the necessary information to the manufacturers for optimal use of these building materials. This work allows a better valuation of these local building materials.

ACKNOWLEDGMENTS

The authors wish to thank Mr Doudou DEME, Mr Mactar SECK, Mr Mamadou SECK and Mr Elhadji DIOP for their support.

REFERENCES

1. Eboziegbe Patrick Aigbomian, Mizi Fan : Development of Wood-Crete building materials from sawdust and waste paper, *Construction and Building Materials* 40, (2013) 361–366
2. Younoussa Millogo, Jean-Claude Morel, Jean-Emmanuel Aubert, Khosrow Ghavami, Experimental analysis of Pressed Adobe Blocks reinforced with Hibiscus cannabinus fibers, *Construction and Building Materials* 52 (2014) 71–78
3. Agus Setyo Muntohar, Engineering characteristics of the compressed-stabilized earth brick, *Construction and Building Materials* 25 (2011) 4215–4220
4. Rafael Alavez-Ramirez , Pedro Montes-Garcia , Jacobo Martinez-Reyes, Delia Cristina Altamirano-Juarez , Yadira Gochi-Ponce, The use of sugarcane bagasse ash and lime to improve the durability and mechanical properties of compacted soil blocks, *Construction and Building Materials* 34 (2012) 296–305
5. F. Gouny , F. Fouchal, O. Pop , P. Maillard , S. Rossignol, Mechanical behavior of an assembly of wood–geopolymer–earth bricks, *Construction and Building Materials* 38 (2013) 110–118
6. Nadia Benmansour, Boudjemaa Agoudjil, Abdelkader Gherabli, Abdelhak

- Kareche, Aberrahim Boudenne, Thermal and mechanical performance of natural mortar reinforced with date palm fibers for use as insulating materials in building, *Energy and Buildings* 81 (2014) 98–104
7. Soumia Mounir, Youssef Maaloufa, Abou bakr Cherki, Abdelhamid Khabbazi, Thermal properties of the composite material clay/granular cork, *Construction and Building Materials* 70 (2014) 183–190
 8. Daniel Maskell, Andrew Heath, Pete Walker, Inorganic stabilisation methods for extruded earth masonry units, *Construction and Building Materials* 71 (2014) 602–609
 9. Harouna Bal, Yves Jannot, Nathan Quenette, Alain Chenu, Salif Gaye, Water content dependence of the porosity, density and thermal capacity of laterite based bricks with millet waste additive, *Construction and Building Materials* 31 (2012) 144–150
 10. N. Laaroussia, A. Cherki, M. Garoum, A. Khabbazi, A. Feiz, Thermal properties of a sample prepared using mixtures of clay bricks, *Energy Procedia* 42 (2013) 337 – 346
 11. Guettala A, Abibsi A, Houari H. Durability study of stabilized earth concrete under both laboratory and climatic conditions exposure, *Construction and Building Materials* 20 (2006) 119–127

CONTRIBUTION TO THE MODELING OF CRACKED COMPOSITE PANELS

BEGHDAD Houda^{1,a}, RAHAL Nacer^{2,a,*}, TEHAMI Mohamed^{1,a}, SOUCI Abdelaziz^{2,a}

²Civil Engineering department, USTO BP 1505 M'Naouer, Oran 31000 Algeria

¹Civil Engineering department, University of Mascara, Algeria

^aLaboratory of mechanical structure and construction stability (LM2SC), USTO, Oran 31000 Algeria

*N. RAHAL: Email: rahnac2002@yahoo.fr

ABSTRACT

The purpose of this study is to model a stiffened panel having a longitudinal crack in a bidirectional tensile loading. According to the laws of linear fracture mechanics, it was found that the stress concentration is always located at the tip of the crack. In order to stop, delay or reduce the spread and stress concentration, it is better to use high-performance materials such as composites. In addition, the stiffeners may be employed to optimize the total weight, the increase panel strength and relaxation of the stress concentration at the tip of the crack. In this context, we account on the proposal for an Ansys modeling for the study of the crack propagation in a composite laminate panel. Our modeling take into account the effect of the load intensity, the influence of the presence and location of the stiffeners, the crack inclination angle end and the influence of the material properties. Following the satisfactory results obtained by the proposed modeling, our work can be used as a basis for the repair of cracked laminated composite panels after a possible shock.

1. INTRODUCTION

The shipbuilding industry is increasingly interested in the use of composite materials. It is no longer just small pleasure boats, but also military vessels (ships composite), passenger vessels (bridges sandwich material) etc. Unfortunately, and unlike steel, many uncertainties remain concerning the mechanical behavior of the composites. One of the important aspects of the behavior of the composites is their resistance to impact and therefore damages and cracks resulting [1, 2]. The study of tensile strength of the composite materials is a much more complex than analysis of elastic or viscoelastic properties. Indeed, the development of a crack depends on several parameters intrinsic to the material such as the geometrical and mechanical properties of the structure, or extrinsic as the extent of the crack or the nature of the loads applied [3, 4]. All these parameters should be taken into account in the computer simulation, so as to allow the study of the static crack growth in a stiffened panel. According to the process of degradation of composites, we can have the micro cracks appear in the matrix, the fibers that break (brittle or ductile fracture), the debonding are created at the interfaces of lamination appear without causing the ruin of the room [5].

Much research has focused on the behavior of composite panels. In this context, we can mention the work of Kadid. A [6] proposed a model to describe the behavior of composite panels stiffened but not cracked. In their research, Dexter et al [7] analyzed the crack growth effect on the behaviour of the long box girders with welded stiffeners. The model aims

to assess the stress intensity factor based on the mechanical superposition of the linear-elastic fracture solutions, taking into account the typical motifs of residual stresses in the stiffened panels. The study of the effect of fracture in stiffened panels, subjected to lateral pressure, has been the subject of work provided by Vishwajeet et al [8] and Riccio et al [9] using various samples of stiffened and unstiffened panels subjected to lateral pressure. In order to study the propagation of fracture behaviour of stiffened and unstiffened specimens subjected to lateral pressure, an experimental and FE analysis is presented by Željko BOZICA et al [10]. Puhui et al [11] studied the behavior of a unidirectional composite damaged under static loading and fatigue. The model is part of the mechanical damage.

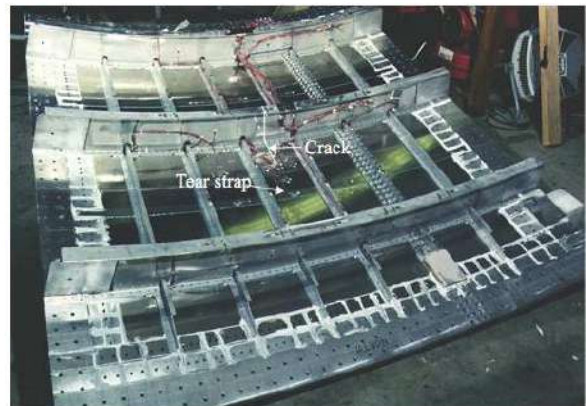


Figure 1: Cracks in aeronautics construction panels

As a continuity of the research mentioned above, we expect the proposal for an Ansys modeling for the study of the crack propagation in a composite panel. In addition, For Reasons of reinforcement stiffeners can be placed to delay or stop the spread of this crack. The position, dimensions and loading the Applied are the hand evaluated parameters for linear modeling of our composite laminate panel.

2. MODELING

The purpose of this work is to model a stiffened panel with a crack at its center. This panel is simply supported on its contour and exposed to a bi-directional loading. Because of the axial symmetry and the symmetry of the load, it was only considered the quarter panel. This technique allows reducing the grid and activating the calculation time. In order to block the propagation of this crack, two stiffeners are arranged in longitudinal and transverse direction. The panel is made completely of a composite graphite/epoxy with the mechanical characteristics data in Tables 1 and 2.

Table 1 : Mechanical properties of a composite Graphite/Epoxy

E_1 (GPa)	E_2 (GPa)	E_3 (GPa)	G_{12} (GPa)	G_{13} (GPa)	G_{23} (GPa)	ν_{12}	ν_{13}	ν_{23}
130	10	10	4.85	4.85	3.62	0.31	0.31	0.52

Table 2 : Resistance of a graphite epoxy composite

X_T (MPa)	X_C (MPa)	Y_T (MPa)	Y_C (MPa)
1933	1051	51	141

E_1, E_2, E_3 : are longitudinal deformation modulus in the directions 1, 2 and 3.

G_{ij} : are the transverse deformation of modulus.

ν_{ij} : are the Poisson's ratios.

X_T : tensile strength in direction 1.

X_C : compressive strength in direction 1.

Y_T : tensile strength in direction 2.

Y_C : compressive strength in direction 2.

Our structure is modeled by ANSYS software. The proposed panel is six degrees of freedom at each

node with a symmetrical lamination of eight layers [0/90/45/-45] of uniform thickness of 0.125mm. Figure 3 shows the mesh structure with the fastening methods and loading conditions.

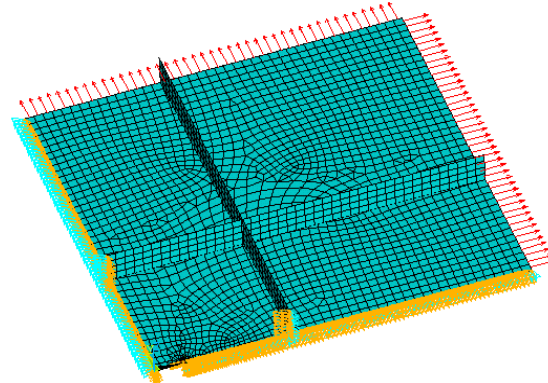


Figure 2 : Simply supported panel under a bi-axial tensile loading

3. STUDY PARAMETERS

Behavioral study the parameters of our panel, composite laminate, bidirectional cracked under tensile loading are:

3.1 Effect of the intensity of the load

To illustrate the evolution of the stresses along the panel and can follow the behavior as a function of applied load, was performed a gradual increase in the load of $P=5$ MPa at $P=100$ MPa. Thereafter, it traces the evolution of the longitudinal stress σ_x (Fig. 3), the transverse stress σ_y (Fig. 4) and the equivalent stress σ_{equi} (Fig. 5), along the panel for a progressive variation of the applied load. In all the figures, it is clear that the stress is always highest at the tip of the crack. The presence of the longitudinal and transverse stiffeners generates a fluctuating stresses. Moreover, the gradual increase of the load generates a sizeable increase in stress. For example, to equivalent stress, the maximum value at the point of crack password 39,605 MPa for a load $P = 5$ MPa to 792,103 MPa for a load $P = 100$ MPa.

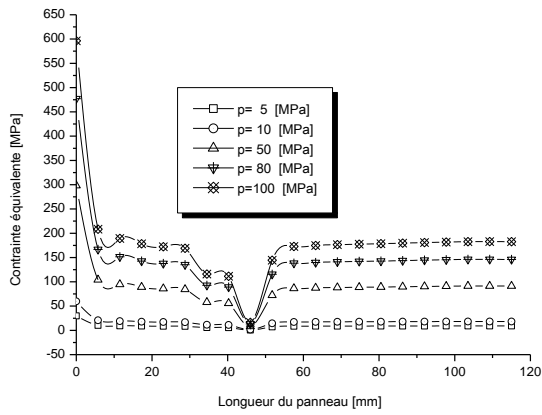


Figure 3 : Variation of the longitudinal strain as a function of load

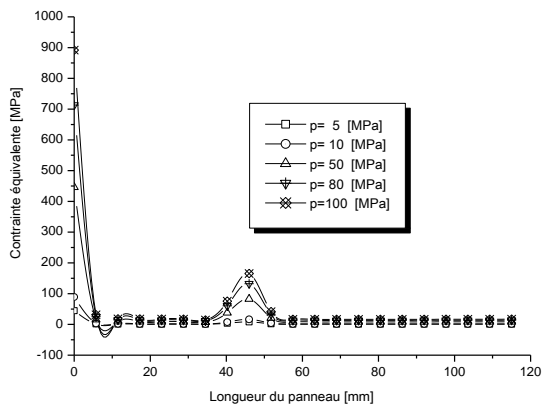


Figure 4 : Variation of the transverse stress as a function of load

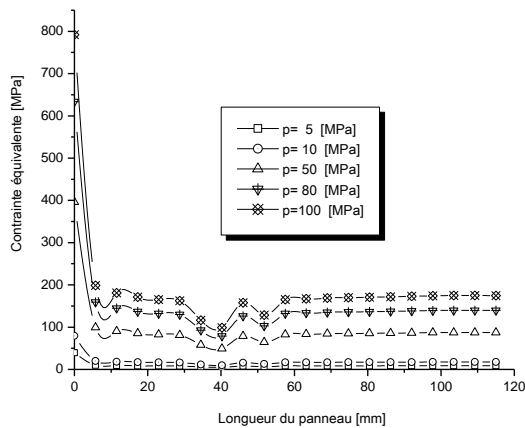


Figure 5 : Variation of the equivalent stress as a function of load

3.2 Influence stiffeners

3.2.1 Influence Effect of the presence of stiffeners

To test the effect of the presence of the stiffeners on the evolution of the equivalent stress at the crack tip, we have plotted in figure 6. This figure shows the

change in the equivalent stress according to the increase of the load applied for four types of panels: 1- plate without stiffening; 2- longitudinal stiffening 3- transversal stiffening; 4- bidirectional stiffening. From this figure, it is clear that for low loads, the stiffeners have no effect on the evolution of this constraint. A superposition of the curves is observed up to a load of 10 MPa. Above this load, a clear distinction begins to appear between the four curves. For maximum load ($P = 100$ MPa), the location of the stiffening in the transverse direction allows a net reduction of this constraint, because it offers almost similar results to those of a stiffening in both directions. The worst case is that of a longitudinal stiffening because it hardly affects the equivalent stress; that is to say, the values are almost equal to those of a plate without stiffening. It is obvious that for a load $P = 100$ MPa, the equivalent stress = 876 MPa. This stress is reduced to 792 MPa if the stiffeners are placed in the transverse direction.

Table 3 : Comparison between the equivalent stress and the weight of each panel

Type panel	Equivalent stress (MPa)			
	PNR	PRL	PRT	PRTL
maximum value	876.01	863.21	798.86	792
Percentage added compared to PNR	0%	-1.46%	-8.81%	-9.59%

Type panel	Total weight of the panel (Kg)			
	PNR	PRL	PRT	PRTL
maximum value	0.08451	0.09113	0.09113	0.09788
Percentage added compared to PNR	0%	+7.83%	+7.83%	+15.82%

PNR : Panel Unstiffened.
 PRL : panel with longitudinal stiffener.
 PRT : panel with transverse stiffener.
 PRTL : panel with transverse and longitudinal stiffeners.

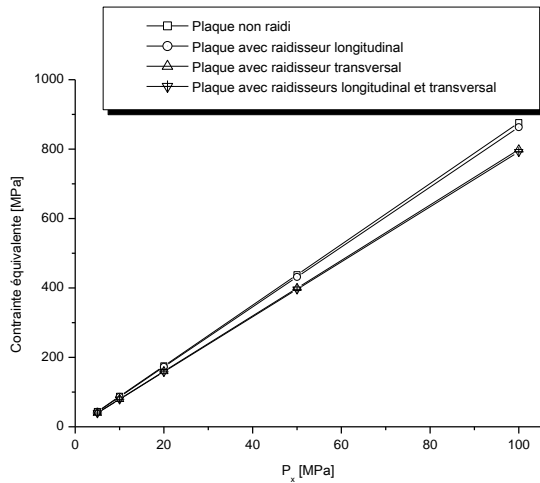


Figure 6 : Constraint equivalent to the crack tip for the four types of panels.

3.2.2 Influence of the position of the stiffeners

To reduce stress concentration at the bottom of the crack and stop or delay the spread of the crack, it is essential to find an appropriate position of the stiffener. Therefore, the location of the stiffeners relative to the location of the crack is a determining factor for minimizing or stress relaxation at the bottom of the crack.

In this context, varying the transverse stiffeners position that the distances 0, 40, 80 and 120 mm from the end of the panel. It is obvious that a high stress concentration is located at the crack tip. This stress concentration is less important with the approximation of the stiffeners to the tip of the crack. The evolution of the equivalent stress according to the panel length for different positions transverse stiffeners. From this figure, we notice that the stress takes a peak at the bottom of the crack (maximum stress). Subsequently, it has an asymptotic value $\sigma = 50\ 081$ MPa. The position of the stiffeners gives rise to fluctuations constraints ($\sigma = 409.52$ MPa for a spacing of 40 mm, $\sigma_{eq} = 396.05$ MPa for a spacing of 80 mm and $\sigma = 431.23$ MPa for the spacing of the end).

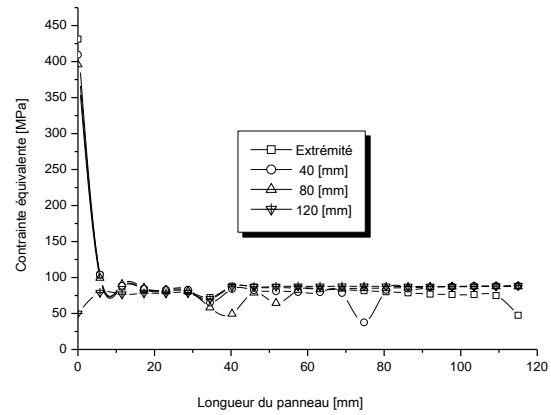


Figure 7 : Variation of the equivalent stress as a function of the position of the transverse stiffener under a load

3.2.3 Influence of the thickness of stiffeners

In order to relax the stress concentration at the crack tip, we will try to keep this constant times- it the position of the stiffeners, but their thickness varies only following the same stacking sequence data initially. The problem is therefore to double the thickness of each layer. Figures 18-21 represent the mesh panel with different thicknesses stiffeners (1.0 mm, 2.5 mm, 3.75 mm, 5.0 mm).

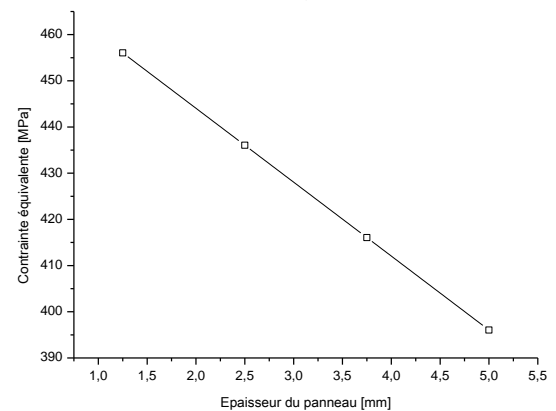


Figure 8 : Variation of the equivalent stress according to the variation of the thickness

3.3 Influence of the orientation of the crack

The variation in the position and thickness of the stiffeners are not the only parameters affecting this stress concentration. For this, is varied progressively panel tilt angle without changing the stacking sequences and applied loads. Now we vary the angle of orientation of 0° to 90° in steps of 15° . Figures 24 to 30 illustrate the variation of the equivalent stress for angles of directions 0° , 15° , 30° , 45° , 60° , 75° and 90° . Of all of the figures, it is obvious that a

high stress concentration is located at the tip of the crack.

To better Quantify this variation, we present the Evolution of the equivalent stress at the crack tip based on the panel orientation angles. From this figure, it is evident That $\theta = 75^\circ$ angle of orientation Provides the minimum constraints contre has $\theta = 0^\circ$ orientation Generates a high concentration of stresses. The Therefore, it is desirable to carry out an orientation of 75° for better relaxation of stress concentration.

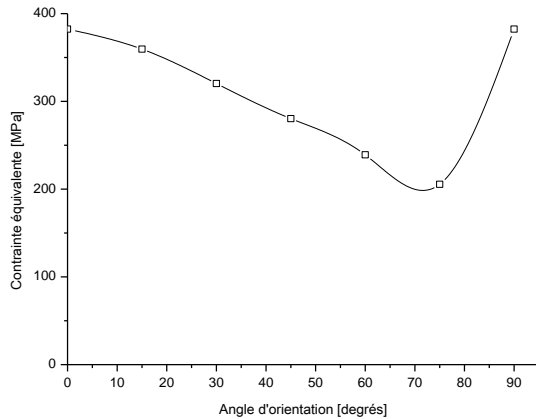


Figure 9 : Variation of the equivalent stress according to the inclination angle of the crack

3.4 Influence of material properties

To check the effect of the nature of the materials on the stress concentration at the crack tip, four kinds of materials are proposed (IM6/epoxy, E-glass/epoxy, graphite/epoxy, Kevlar). To see the effect of the choice of materials, the figure 32 is a plot that illustrates the evolution of the equivalent stress along the panel. From this figure, it is clear that E-glass/epoxy material offers minimal constraints ($\sigma=353.34$ MPa). By cons, a Kevlar material produces a high concentration of stresses of 406 MPa.

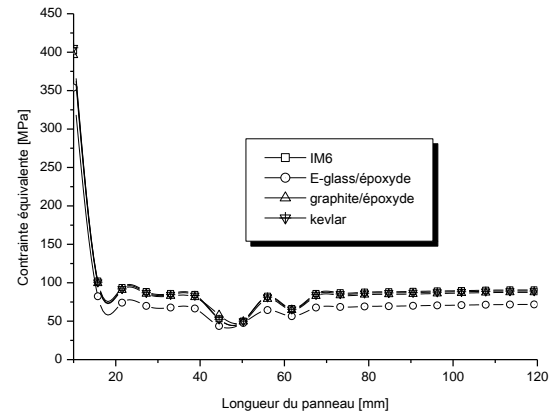


Figure 10 : variation of the equivalent stress based on material properties.

4. CONCLUSION

For this work, the linear behavior of stiffened panels laminated composite having a longitudinal crack in bidirectional load was analyzed. The study was performed using ANSYS software, and provides a basis for the repair of laminated composite panels cracked after a possible shock.

From the results, it turned out that for this type of panels, the crack propagation is related:

- the nature of the load.
- fixing the conditions.
- the geometry of the panel.
- orientation of the crack.
- the type of materials.
- the change in the equivalent stress is proportional to the applied load.
- the maximum equivalent stress is always on the cutting edge of the crack.
- the presence of the stiffeners creates slight fluctuation constraints.

The location of the stiffening in the transverse direction is more dominant because they:

- contribute to blocking the propagation of the crack.
- allow a significant reduction in weight compared to the stiffeners arranged in two directions.
- for loads of low intensity, the stiffeners have no effect on the behavior of our panel.

In order to minimize the stress concentration at the bottom of crack, stop and even delay the spread of the crack, it is recommended to place the transverse stiffeners in the vicinity of the tip of the crack.

Increasing the thickness of the stiffener has a considerable effect on the relaxation of the stress concentration at the crack tip, but in part against it

gives an additional weight. In addition, it was observed that the stresses are significantly influenced by the fiber orientation angles.

For future recommendations include provision for patches for repairing cracked panels. In order to ensure structural stability, there is also address the buckling of panels and the stiffening sheet-peeling associated.

5. REFERENCES

- [1] Agarwal. B and Davis. R. C: Minimum Weight Designes for Hat stiffened composite panels under axial Compression. NASA-TN D-7779, National Aeronautics and Space Administ-ration, Washington, D.C, Nov (1974)
- [2]Valery V. Vasiliev: Mechanics and analysis of composite Materials. First edition, (2001).
- [3]Berthelot. J .M: Matériaux composites Mécanismes de rupture et endommagement des matériaux composites. 3ème édition, (1995).
- [4]Payan. J: Etude du comportement de composites stratifiés sous chargement statique et de fatigue. Thèse de doctorat, Université d'Aix-Marseille, (2004).
- [5]Bertolini. J: Contribution à l'analyse expérimentale et théorique des ruptures de structures composites en post-flambement par décollement de raidisseurs. Thèse de doctorat de l'université de Toulouse, (2008).
- [6] Abdelkrim Kadid: Stiffened plates subjected to uniform blast loading. Journal of civil engineering and management 2008 14(3): 155–161
- [7] Dexter, R.J., Pilarski, P.J., Mahmoud, H.N: Analysis of crack propagation in welded stiffened panels. International Journal of Fatigue 25, (2003)1169-1174.
- [8] Vishwajeet. S. B., Mohammad. K and Ramji. M: Optimization of circular composite patch reinforcement on damaged carbon fiber reinforced polymer laminate involving both mechanics-based and genetic algorithm in conjunction with 3D finite element analysis. Journal of Composite Materials, September 2014; vol. 48, 22: pp. 2679-2695.
- [9] Riccio. A., Raimondo. A., Di Caprio. F and F Scaramuzzino: Delaminations buckling and growth phenomena in stiffened composite panels under compression- Part II: a numerical study. Journal of Composite Materials, September 2014; vol. 48, 23: pp. 2857-2870
- [10] Željko Božić, S. Schmauder: Fracture modeling of damaged stiffened panels under lateral pressure load. Procedia Materials Science 3 (2014) 1129 – 1134
- [11] Puhui. C., Zhen. S and Junyang. W: Damage tolerance analysis of cracked stiffened composite panels. Journal of Composite Materials, October 2001; vol. 35, 20: pp. 1815-1843.

Heat and Mass Transfer Optimisation (1)

ANALYTICAL AND NUMERICAL STUDY OF DOUBLE DIFFUSIVE CONVECTION WITH SORET AND DUFOUR EFFECTS IN A HORIZONTAL POROUS LAYER

Abbes Attia^{1*}, Mahmoud Mamou² and Smail Benissaad¹

¹Laboratoire d'Énergétique Appliquée et de Pollution, Département de Génie Mécanique, Université des Frères Mentouri-Constantine, Route Ain El Bey, Constantine 25017, Algérie

²Aerodynamics Laboratory, National Research Council Canada, Ottawa, Ontario, Canada, K1A 0R6

*Corresponding author: Email: attia.abbas@gmail.com

ABSTRACT

In this work Dufour and Soret effects on natural double diffusion convection in a horizontal porous layer have been studied numerically using a finite difference method. A uniform heat and mass fluxes are applied on the horizontal walls while the vertical walls are impermeable and adiabatic. The Darcy model along with the Boussinesq approximation is assumed in the problem formulation. The governing parameters of the problem are the thermal Rayleigh number, R_T , the buoyancy ratio, N , the Lewis number, Le , the aspect ratio of the cavity, A , and the Dufour, D_u , and Soret, S_r , coefficient. For a shallow enclosure, a closed form analytical solution was derived assuming zero convection wave number, which is still valid near criticality. The effects of Dufour and Soret on the heat and mass transfer rates and on the flow intensity are studied, and their effects on the onset of subcritical, supercritical and oscillatory convection were also investigated.

Keywords Double diffusion convection, porous media, analytical and numerical solution, Soret and Dufour effects.

NOMENCLATURE

A aspect ratio.
 D_{CT} cross-diffusion coefficient due to T' component.
 D_{CS} cross-diffusion coefficient due to S' component.
 D solute diffusivity.
 g gravitational acceleration.
 H' height of the porous enclosure.
 j' constant mass flux per unit area.
 K permeability of porous media.
 L' length of the porous enclosure.
 Le Lewis number, α_p/D .
 N buoyancy ratio, $\beta_S \Delta S^* / \beta_T \Delta T^*$.
 Nu Nusselt number.
 q' constant thermal flux per unit area.
 R_{TC}^{sub} subcritical Rayleigh number.
 R_{TC}^{sup} supercritical Rayleigh number.
 R_T thermal Rayleigh number,
 $g \beta_T K \Delta T^* H' / \nu \alpha_p$.
 Sh Sherwood number.
 S dimensionless concentration,
 $(S' - S'_0) / \Delta S^*$.
 ΔS^* concentration difference, $j' H' / D$.
 T dimensionless temperature,
 $(T' - T'_0) / \Delta T^*$.
 ΔT^* temperature difference, $q' H' / k$.

t dimensionless time, $t' \alpha_p / \sigma H'^2$.
 (u, v) dimensionless velocity components,
 $(u' H' / \alpha_p, v' H' / \alpha_p)$.
 (x, y) dimensionless coordinates,
 $(x' / H', y' / H')$.

Greek Symbols

α_p thermal diffusivity of the saturated porous medium.
 β_S solutal expansion coefficient.
 β_T thermal expansion coefficient.
 k thermal conductivity of the saturated porous medium.
 ε normalized porosity, ε' / σ .
 ε' porosity of the porous medium.
 ν kinematic viscosity of fluid.
 $(\rho c)_f$ heat capacity of the fluid.
 $(\rho c)_p$ heat capacity of the saturated porous medium.
 σ heat capacity ratio, $(\rho c)_p / (\rho c)_f$.
 Ψ dimensionless stream function.

INTRODUCTION

Combined heat and mass transfer by natural convection has received considerable attention recently, due to its importance in many natural and engineering applications. A comprehensive review of the phenomena of double diffusion convection can be found in Huppert and Turner

[1]. Double diffusive convection in porous media is encountered in many applications, among them are the migration of moisture in fibrous insulation, contaminant transport in saturated soil, underground disposal of nuclear wastes and electro-chemical and drying processes. Mass-diffusion (Dufour effect) and thermo-diffusion (Soret effect) could be encountered in double diffusive convection and their effects could be significant, see for instance, Nield and Bejan [2] and Vafai [3]. Dufour effect was found to be significant in gas mixtures with very light (H_2 , He) and medium molecular weight (N_2 , air). In liquid mixtures, Soret effect was found to be strong as stated by Platten and Legros [4] and in most liquid mixtures the Dufour effect was negligible. The effects of buoyancy ratios, Rayleigh numbers and Soret and Dufour coefficients on double diffusion convection in a horizontal cavity were studied numerically by Jin Wang et al [5]. The coupling–diffusive interaction was found to have a significant effect on heat transfer and mass transfer rate. In a horizontal porous layer heated and salted from below at constant temperature and solute, for opposing buoyancy forces, Gaikwad et al [6] concluded that a positive/negative Soret parameter destabilizes/stabilizes the system in the stationary/oscillatory mode. However, the Dufour parameter destabilizes the system in both stationary and oscillatory modes. Both Soret and Dufour parameters increases the Nusselt number and Sherwood number, Benano-Melly et al. [7] studied numerically and experimentally the problem of thermo-diffusion in an initially homogeneous mixture submitted to a horizontal thermal gradient. Their numerical results showed that, depending on the Soret number value, multiple convective flow patterns could develop in the presence of counter-acting thermal and solutal buoyancy forces. The Soret effect on convection in a horizontal porous cavity submitted to cross gradients of temperature and concentration was considered by Bennacer et al. [8]. Their results showed that, when the vertical concentration gradient was stabilizing, multiple steady-state solutions became possible over a range of buoyancy ratios which was strongly dependent on the Soret parameter. Bahloul et al. [9] considered the double-diffusive and Soret-induced convection in a shallow horizontal porous layer. The stability of the parallel flow solution was studied and the threshold for Hopf bifurcation was determined.

In the present study, both Soret and Dufour effects on double diffusive convection in a shallow porous layer were considered in the

presence of vertical thermal and solute concentrations gradients. The Soret and Dufour effects on the heat and mass transfer were investigated and explicit expressions were derived for the thresholds of the onset of subcritical and supercritical convection using a parallel flow assumption.

MATHEMATICAL FORMULATION

The schematic representation of the system under consideration is shown in Fig. 1. It consists of a two-dimensional enclosure of width L' and height H' . The left and right side walls are assumed to be adiabatic and impermeable, while the top and the bottom walls are subject to constant heat, q' , and mass, j' , fluxes. The convective motion in the homogeneous isotropic porous medium is assumed to be governed by the Darcy law for which the form drag and viscous effects are negligible.

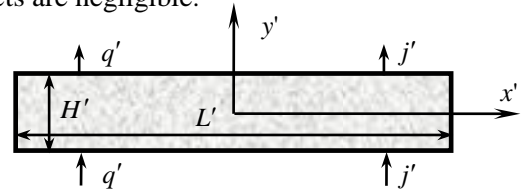


Figure 1
Flow configuration.

The dimensionless governing transport equation describing stream function, energy and mass in the porous medium are written as follows:

$$\nabla^2 \Psi = -R_T \left(\frac{\partial T}{\partial x} + N \frac{\partial T}{\partial x} \right) \quad (1)$$

$$\frac{\partial T}{\partial t} + u \frac{\partial T}{\partial x} + v \frac{\partial T}{\partial y} = \nabla^2 T + D_u \nabla^2 S \quad (2)$$

$$\varepsilon \frac{\partial S}{\partial t} + u \frac{\partial S}{\partial x} + v \frac{\partial S}{\partial y} = \frac{1}{Le} (\nabla^2 S + S_r \nabla^2 T) \quad (3)$$

where the stream function Ψ is defined such that

$$u = \frac{\partial \Psi}{\partial y}, \quad v = -\frac{\partial \Psi}{\partial x} \quad (4)$$

By considering the total heat and mass fluxes on the active walls, the corresponding dimensionless boundary conditions are derived as follows:

$$\left. \begin{aligned} y = \pm \frac{1}{2}, \Psi = 0, \quad \frac{\partial T}{\partial y} + D_u \frac{\partial S}{\partial y} = -1, \quad \frac{\partial S}{\partial y} + S_r \frac{\partial T}{\partial y} = -1 \\ x = \pm \frac{A}{2}, \Psi = 0, \quad \frac{\partial T}{\partial x} = \frac{\partial S}{\partial x} = 0 \end{aligned} \right\} \quad (5)$$

where A is the aspect ratio of enclosure defined as $A = L' / H'$.

The dimensionless parameters governing the problem are the Rayleigh number, R_r , the Lewis number, Le , the buoyancy ratio, N , the normalized porosity, ε , the Dufour coefficient, D_u , and the Soret coefficient, S_r , which are defined as follows.

$$\left. \begin{aligned} R_r &= \frac{g\beta_T K \Delta T^* H'}{v\alpha_p}, \quad Le = \frac{\alpha_p}{D} N = \frac{\beta_S \Delta S^*}{\beta_T \Delta T^*} \\ \varepsilon &= \frac{\varepsilon'}{\sigma}, \quad D_u = \frac{D_{CS} \Delta S^*}{\alpha_p \Delta T^*}, \quad S_r = \frac{D_{CT} \Delta T^*}{D \Delta S^*} \end{aligned} \right\} \quad (6)$$

In the presence of the Dufour and Soret effect, the heat and mass transfer rates are expressed in term of the Nusselt and Sherwood numbers, defined as follows:

$$Nu = \frac{1}{\Delta T + D_u \Delta S}, \quad Sh = \frac{1}{\Delta S + S_r \Delta T} \quad (7)$$

where $\Delta T = T_{(0,-1/2)} - T_{(0,1/2)}$ and $\Delta S = S_{(0,-1/2)} - S_{(0,1/2)}$ are respectively the temperature and concentration differences evaluated at the centre of the enclosure ($x=0$).

ANALYTICAL SOLUTION

In the present problem, the above governing equations can be solved analytically using the parallel flow approximation when the aspect ratio of the cavity is very large ($A \gg 1$), see Mamou [10]. For this situation, the flow in the central region of the cavity becomes parallel to the horizontal walls of the cavity and both of the temperature and concentration profiles are characterized by a linear stratification in the horizontal direction leading to the following simplification:

$$\Psi(x,y) \approx \Psi(y) \quad (8)$$

$$T(x,y) = C_T x + \theta_T(y) \quad (9)$$

$$S(x,y) = C_S x + \theta_S(y) \quad (10)$$

Using these approximations together with the boundary conditions (5) and substituting into the governing equations (1)-(3), we obtain

$$\Psi(y) = \Psi_0 (1 - 4y^2) \quad (11)$$

$$T(x,y) = C_T x + \frac{C_T - C_S D_u Le}{3(1 - D_u S_r)} \Psi_0 (3y - 4y^3) - a_T y \quad (12)$$

$$S(x,y) = C_S x + \frac{C_S Le - S_r C_T}{3(1 - D_u S_r)} \Psi_0 (3y - 4y^3) - a_S y \quad (13)$$

where Ψ_0 is the value of Ψ at the centre of the porous layer which is defined as:

$$\Psi_0 = \frac{1}{8}(C_T + NC_S).$$

The constants a_T and a_S are defined as:

$$a_T = (1 - D_u)/(1 - D_u S_r) \quad \text{and} \quad a_S = (1 - S_r)/(1 - D_u S_r),$$

and C_T and C_S are constant gradients of temperature and solute concentration in the x -direction, respectively. The constants are determined by considering zero energy and species balances across any transversal cross section of the cavity.

$$C_T = \frac{4b\Psi_0 [2b(a_T - D_u a_S Le) + Le^2 \Psi_0^2]}{3[(2b + \Psi_0^2)(2b + Le^2 \Psi_0^2) - D_u S_r (2b - Le \Psi_0^2)^2]} \quad (14)$$

$$C_S = \frac{4b\Psi_0 [2b(a_S Le - a_T S_r) + Le \Psi_0^2]}{3[(2b + \Psi_0^2)(2b + Le^2 \Psi_0^2) - D_u S_r (2b - Le \Psi_0^2)^2]} \quad (15)$$

Substituting the above expressions of C_T and C_S in the expression of Ψ_0 , we obtain the following polynomial expression:

$$\Psi_0 [Le^4 \Psi_0^4 - 2bLe^2 d_1 \Psi_0^2 - b^2 d_2] = 0 \quad (16)$$

with

$$\left. \begin{aligned} d_1 &= R_r^* Le (Le + N) - (1 + Le + 2Le D_u S_r) \\ d_2 &= 4R_r^* Le^2 [1 + NLe - (D_u + NS_r)(Le + 1) \\ &\quad + D_u S_r (Le + N)] - 4Le^2 (1 - D_u S_r)^2 \end{aligned} \right\} \quad (17)$$

where

$$R_r^* = R_r/12, \quad b = b_0(1 - D_u S_r) \quad \text{and} \quad b_0 = 15/16.$$

Equation (16) shows that five solutions are possible, one of which is null and corresponds to the fluid rest state solution or pure diffusion:

$$\Psi_0 = 0 \quad (18)$$

The other four convective solutions are given by:

$$\Psi_0 = \pm \sqrt{\frac{b_0}{Le}} \sqrt{d_1 \pm \sqrt{d_1^2 - d_2}} \quad (19)$$

where two of them (with positive sign within the square root expression) are stable and the two others (with negative sign) are unstable. The positive and negative sign outside the square root indicate that the flow circulation could be clockwise or counter-clockwise.

Substituting Eqs. (12) and (13) in Eqs. (7), the Nusselt and Sherwood numbers become:

$$Nu = \frac{3}{3 - 2C_T \Psi_0}, \quad Sh = \frac{3}{3 - 2C_S Le \Psi_0} \quad (20)$$

NUMERICAL SOLUTION

The numerical solution of the full governing equations is obtained using a second-order finite-

difference method. The discretized form of the energy and concentration equations (2)-(3) were solved using a time-accurate scheme based on the alternating direction implicit method (ADI) and the flow motion equation (1) was solved using a successive over relaxation method (SOR). A grid sensitivity study was performed using a grid size ranging from 60×80 to 80×240 , see Table 1. The results indicate that, for a refined grid, there is a relative difference of 0.4 % for the stream function and less than 1 % for the heat and mass transfer rates. Thus a grid of 80×240 was found to be enough to simulate accurately the convective flow.

Table 1

Grid sensitivity study for $R_T = 100$, $Le = 2$, $N = 1$,
 $D_u = 0.1$, $S_r = -0.1$ and $A = 10$.

	Numerical solution				Analytical solution
	60×120	80×160	80×220	80×240	
	4.696	4.699	4.698	4.698	4.696
Nu	4.242	4.253	4.245	4.242	4.228
Sh	5.696	5.744	5.757	5.757	5.742

RESULTS AND DISCUSSION

Typical numerical results in terms of streamlines, isotherms and isolines are presented in Figure 2, from top to bottom respectively, for $R_T = 50$, $Le = 2$, $N = -0.5$, $S_r = 1.1$, $D_u = 0.2$ and $A = 10$. From these results, it is clear that for a shallow cavity ($A \gg 1$) the flow in the core region of the enclosure is essentially parallel while the temperature and concentration are linearly stratified in the horizontal direction.

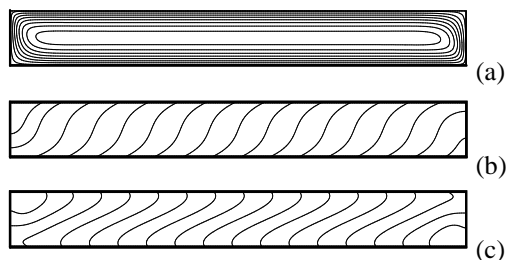


Figure 2

Streamlines (a), isotherms (b) and isolines (c) for $R_T = 50$, $Le = 2$, $N = 0.5$, $S_r = 1.1$, $D_u = 0.2$ and $A = 10$.

Figure 3(a)-(b) shows the stream function, temperature and concentration distributions in the centre of the cavity with a very good agreement between the numerical and the analytical results. For constant Dufour effect, the evolution of the flow intensity, Ψ_o , the Nusselt, Nu , and the

Sherwood, Sh , numbers with R_T is presented in Figure 4 for $Le = 2$, $N = -1$, $D_u = 0.2$ and various values of S_r (1.1, 0.55 and 0.45). Figure 4(a) shows that there was only one convective stable solution for $S_r = 1.1$ (pitchfork bifurcation), occurring at supercritical Rayleigh $R_{TC}^{sup} = 3.8$. In the range of Soret number $0.45 < S_r < 0.55$ the analytical solution predicted the existence of two stable solution (solid line) and unstable one (dashed line), showing the existence of subcritical flows where the bifurcation occurred at a saddle-node point characterized by a finite amplitude convection. The subcritical Rayleigh number is obtained from the condition $d_1 > 0$ and $d_1^2 + d_2 = 0$. The evolution of Nu and Sh with R_T are presented in Figure 4(b)-(c). Generally, at large R_T , far from criticality, it could be seen that the heat transfer rate increased with increasing S_r , however a reverse trend was seen for the mass transfer rate. There was a strange behavior of the Sh number which dropped below unity very close to the onset of supercritical convection for $S_r = 1.1$.

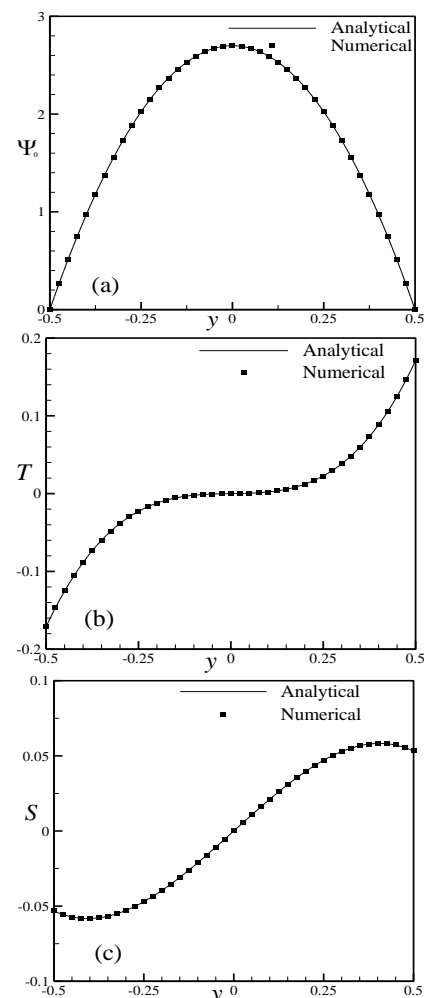


Figure 3

Stream function (a), temperature (b) and concentration (c) profiles at the centre of the

cavity for $R_T = 50$, $Le = 2$, $N = 0.5$, $S_r = 1.1$,
 $D_u = 0.2$ and $A = 10$.

As discussed above, for $S_r = 0.55$ and $S_r = 0.45$, two types of subcritical bifurcation occurred. For $S_r = 0.55$, the bifurcation was characterized by two saddle node points: The first ($R_T^{sub} = 43.64$) represented the onset of subcritical convection at finite amplitude and the other one ($R_T^{sup} = 59.40$) characterized the onset of supercritical convection at zero amplitude. For $S_r = 0.45$, the pure subcritical convection occurred at finite amplitude convection ($R_T^{sub} = 63.18$) and characterized only by a single saddle node point. For a constant Soret coefficient, $S_r = 0.2$, the Dufour effect on the flow intensity, and on the heat and mass transfer rates is displayed in Figure 5. To illustrate the three types of bifurcations, three values of $D_u = -0.45$, -0.2 and 0.02 are considered. For $D_u = -0.45$, the bifurcation is purely supercritical, and the onset of convection occurred at $R_T^{sup} = 16.57$. For $D_u = -0.2$, a double bifurcation occurred leading to two saddle node points. The first subcritical bifurcation occurred a pure subcritical bifurcation occurred at decrease in the Dufour coefficient induced an at $R_T^{sub} = 45.56$ and the second one which is supercritical occurred at $R_T^{sup} = 81.12$ and at zero amplitude. The later could be viewed as a backward supercritical bifurcation.

For $D_u = 0.02$, $R_T^{sub} = 77.78$ without any connection to the onset of supercritical state. Overall, above criticality, as shown in Figure 5, the increase in the flow intensity, and in the heat and mass transfer rates. The present study is relied on the parallel flow assumption for the determination of the onset of subcritical and supercritical convection. The assumption is regarded as a nonlinear stability analysis that was able to predict the threshold of subcritical convection that usually occurs at finite amplitude flows.

The assumption was also valid for predicting the onset of supercritical convection thresholds, which occurred at zero amplitude convection. Also, it is important to mention that the current approach was based on steady state convection. However, unsteadiness occurrences near the onset of convective flows are well known in double diffusive convection. Therefore, to complete the present analysis, a linear stability analysis is required to examine any occurrence of overstable flows below the of supercritical

convection. The analysis will be presented in a journal paper to be published in the near future.

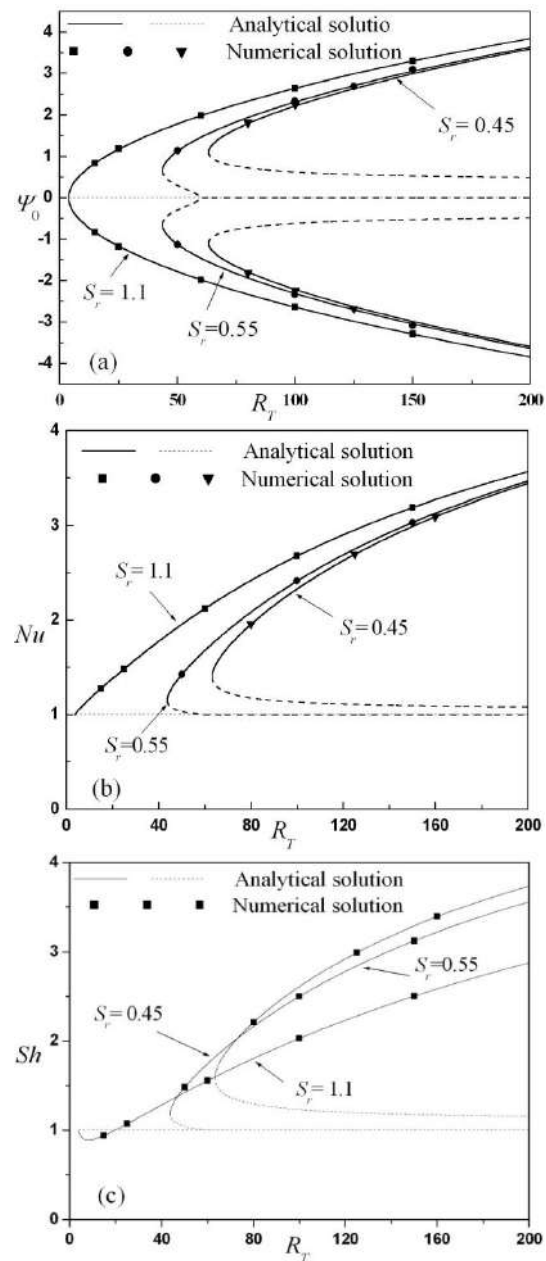


Figure 4

Bifurcation diagrams of (a) stream function, (b) Nu and (c) Sh versus R_T for $S_r = 0.45, 0.55$ and 1.1 ,
 $Le = 2$, $N = -1$ and $D_u = 0.2$.

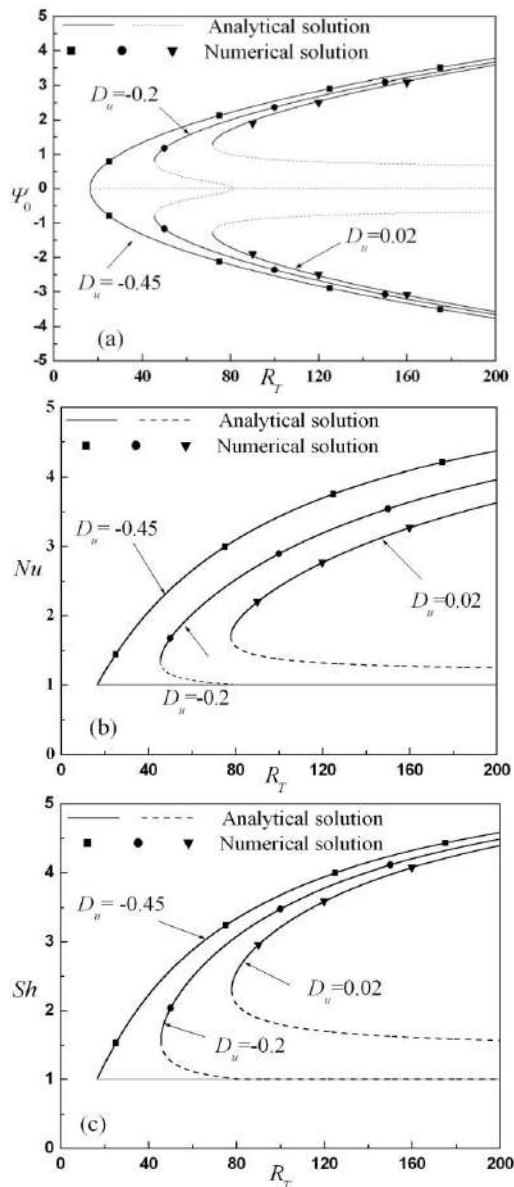


Figure 5

Bifurcation diagram of (a) stream function, (b) Nu and (c) Sh versus R_T for $D_u = -0.45, -0.2$ and 0.02 , $Le=2$, $N=-1$ and $S_r = 0.2$.

CONCLUSION

Double diffusive convection induced in a horizontal porous layer subject to uniform fluxes of heat and mass was studied analytically and numerically in the presence of Soret effect and Dufour effect. The analytical solution, based on the parallel flow approximation, was determined for the case of shallow enclosure. The influence of governing parameters on the Nusselt and Sherwood numbers were predicted and discussed.

The main features predicted by the analytical solution were confirmed by the numerical solutions of the full governing equations. It is

observed that the Soret and Dufour effects modify considerably the occurrence of the convective flow, and the heat and mass transfer rates. Three types of bifurcations were captured in the present analysis, depending on the Soret and Dufour coefficients. The first bifurcation occurred at zero amplitude characterizing the onset of supercritical convection. The second one is a mixture between subcritical bifurcation occurred at finite amplitude followed by a backward supercritical bifurcation. The third one is a pure subcritical bifurcation that occurred also at finite amplitude convection but with no connection to any supercritical state.

REFERENCES

- [1] Huppert, H. E., and Turner, J. S., 1981, "Double-diffusive convection," *J. Fluid Mech.*, 106, pp. 299-329.
- [2] Nield, D. A., and Bejan, A., 2006, *Convection in porous media*, 3rd Springer-Verlag, New York.
- [3] Vafai, K., 2005, *Hand book of porous*, 2nd Edition.
- [4] Platten, J. K., and Legros, J. C., 1984, *Convection in liquids*. New York: Springer.
- [5] Jin, W., Mo, Y., and Yuwen, Z., 2014, "Onset of double-diffusive convection in horizontal cavity with Soret and Dufour effects," *Int. J. Heat and Mass Transfer.*, 78, pp. 1023-1031.
- [6] Gaikwad, S. N., Malashetty, M. S., Rama Prasad, K., 2009, "Linear and Non-linear Double Diffusive Convection in a Fluid-Saturated Anisotropic Porous Layer with Cross-Diffusion Effects," *Transp Porous Med*, 80, pp. 537-560.
- [7] Benano-Melly, L. B., Caltagirone, J. P., Faissat, B., Montel, F., and Costeseque, P., 2001, "Modeling Soret coefficient measurement experiments in porous media considering thermal and solutal convection," *Int. J. Heat and Mass Transfer.*, 44, pp.1285-1297.
- [8] Bennacer, R., Mahidjiba, A., Vasseur, P., Beji, H. and Duval, R., 2003, "The Soret effect on convection in a horizontal porous domain under cross temperature and concentration gradients," *Int. J. Numerical Methods for Heat and Fluid Flow.*, 13, pp. 199-215
- [9] Bahloul, A., Boutana, N. and Vasseur, P., 2003, "Double-diffusive and Soret induced convection in a shallow horizontal porous layer," *J. Fluid Mech.*, 491, pp. 325-352.
- [10] Mamou, M., and Vasseur, P., 1999, "Thermosolutal bifurcation phenomena in porous enclosures subject to vertical temperature and concentration gradients," *J. Fluid Mech.*, 395, pp. 61-87.

FREE CONVECTION HEAT TRANSFER OF NANOFUIDS INTO CUBICAL ENCLOSURES WITH A BOTTOM HEAT SOURCE: LATTICE BOLTZMANN APPLICATION

A. BOUTRA^{1,2,*}, K. RAGUI¹, R BENNACER³, and Y.K. BENKAHLA¹

¹Laboratory of Transport Phenomena, USTHB, Algiers, Algeria.

²Preparatory School of Science and Technology, Algiers, Algeria.

³ LMT - ENS Cachan - CNRS - Paris Saclay University, 94230 Cachan, France

(BP. 32 El Alia, 16111 Bab Ezzouar, Algiers, Algeria;

61, Av du Président Wilson 94235 Cachan Cedex, France)

*Corresponding author: Fax: +213 21 20 77 67 Email: aeKnad@yahoo.fr

ABSTRACT

The main purpose of this work is to investigate the hydrodynamic and thermal characteristics of an Ag-water nanofluid into a cubical enclosure, including a heat source which located at the center of the bottom wall. Due to its crucial role in the characterization of the main transfer into such configurations, the effect of some parameters is widely inspected. It consists the Rayleigh number (103 to 106), the solid volume fraction (0% to 10%), the width ($10\% \leq w \leq 40\%$) and height of the heat source ($10\% \leq h \leq 50\%$). To do so, a numerical code based on the Lattice-Boltzmann method, coupled with a finite difference one, is utilized. The latter has been validated after comparison between the present results and those of the literature. It is to note, at the end, that the three dimensions D3Q19 model is adopted based on a cubic Lattice, where each pattern of the latter is characterized by nineteen discrete speeds.

KEYWORDS

NOMENCLATURE

a Coefficient in external forces ($= g \beta$)
 a_{ij} Coefficients in Equation (12)
 c Cold
 c_s Sound velocity in the Lattice ($c_s = 1/\sqrt{3}$)
 C_p Specific heat at constant pressure, ($J \text{ kg}^{-1} \text{ K}^{-1}$)
 f fluid
 f_{eq} Equilibrium distribution Function
 F_{ext} External Force
 f_i Distribution Function
 h Hot
 k Thermal conductivity, ($W \text{ m}^{-1} \text{ K}^{-1}$)
 $H_{x,y,z}$ Enclosure dimensions, (m)
 m_j Moments
 nf Nanofluid
 Nu Mean Nusselt number
 Pr Prandtl number ($Pr = \nu/\alpha$)

s Solid particles
 S_j Relaxation rate
 t Time, (s).
 T Temperature, (K)
 Ra Rayleigh number, ($= 2T_0 H^3 a / \nu k$)
 u Horizontal velocity component, (m)
 v Vertical velocity component, (m)
 w Depth velocity component, (m)
 x, y, z Dimensional Cartesian coordinates, (m)
 X, Y, Z Dimensionless coordinates,
 ($X = x/H, Y = y/H, Z = z/H$)
 α Thermal diffusivity, ($m^2 \text{ s}^{-1}$)
 β Thermal expansion coefficient, (K^{-1})
 θ Dimensionless temperature
 ω_i Coefficients of the equilibrium function
 ρ Density, ($kg \text{ m}^{-3}$)
 φ Nanoparticles volume fraction
 ε Energy square

ν Kinematic viscosity, $m^2 s^{-1}$
 Ω Collision Operator

INTRODUCTION

Natural convection phenomena inside enclosures are relevant to a wide range of industrial processes or environmental situations. It has been the subject of a very intense research activity over the past decades [1-5]. The most innovative, (and most promising), technique is the injection of nanoscale particles into the base fluid such as the Ag, Al_2O_3 , Cu, CuO and TiO_2 , nanoparticles, to enhance the heat transfer rate in engineering systems.

Some papers deals with free convection in differentially heated enclosures were very helpful [6-7], a review of the literature indicates that numerous geometries were investigated [8-13]. Even though there have been these numerous investigations, under many configurations and boundary conditions, relatively few studies were documented by taking into account the third dimension. As such, this paper presents a comprehensive numerical investigation of a nanofluid natural convection inside a cubical enclosure, having a temperature gradient generated by the side walls and a bottom heat source. The numerical study is developed using the coupling between Lattice Boltzmann method and finite difference method [14, 15].

Referring to papers of Santra *et al.* [8] and many others, the nanoparticles with a high thermal conductivity (such the Ag and Cu) produce a significant enhancement of heat transfer rate. Thus, the use of the Ag nanoparticles is considered in our investigation.

Noted that the Brownian motion is not taken into consideration in our study since the nanoparticles size is assumed to be greater than 40 nm.

PROBLEM STATEMENT

The system considered in this paper is shown in Fig. 1. The system consists of a cubical enclosure with cold-sides walls, having an isothermal solid source with width 'w' and height 'h', which located at the center of the bottom wall. The bottom, top, front and rear side walls are assumed to be insulated.

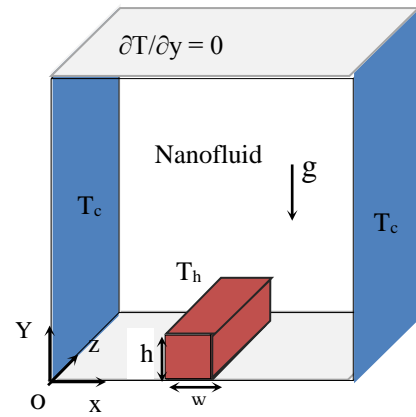


Figure 1. Simulation domain with its boundary conditions.

The thermo-physical properties of the base fluid and the spherical Ag nanoparticles are given in Table 1. Constant thermo-physical properties are considered for the nanofluid whilst the density variation, in the buoyancy term, was determined using the Boussinesq approximation, [16].

Table 1. Thermophysical properties of the base fluid and the Ag nanoparticles, Pr = 6.2.

Thermophysical properties	Base fluid (water)	Ag
C_p ($J kg^{-1} K^{-1}$)	4179	230
ρ ($kg m^{-3}$)	997.1	10500
k ($W m^{-1} K^{-1}$)	0.613	418
β (K) 10^5	21	1.65

MATHEMATICAL FORMULATION

The nanofluid density, noted as ρ_{nf} , heat capacity $(\rho C_p)_{nf}$, thermal expansion coefficient $(\rho \beta)_{nf}$, and thermal diffusivity α_{nf} , may be defined respectively, as follows [13]:

$$\rho_{nf} = (1 - \phi) \rho_f + \phi \rho_s \quad (1)$$

$$(\rho C_p)_{nf} = (1 - \phi) (\rho C_p)_f + \phi (\rho C_p)_s \quad (2)$$

$$(\rho \beta)_{nf} = (1 - \phi) (\rho \beta)_f + \phi (\rho \beta)_s \quad (3)$$

$$\alpha_{nf} = \frac{k_{nf}}{(\rho C_p)_{nf}} \quad (4)$$

For the effective dynamic viscosity μ_{nf} , and the effective thermal conductivity k_{nf} , Brinkman [17] and Maxwell-Garnetts models [18] are employed, respectively, as:

$$\mu_{nf} = \frac{\mu_f}{(1 - \phi)^{2.5}} \quad (5)$$

$$\frac{k_{nf}}{k_f} = \frac{(k_s + 2k_f) - 2\varphi(k_f - k_s)}{(k_s + 2k_f) + \varphi(k_f - k_s)} \quad (6)$$

The dimensionless conservation equations, describing the transport phenomenon inside the cube, can be written as follows:

$$\nabla \cdot \vec{V}' = 0 \quad (7)$$

$$\frac{\partial \vec{V}'}{\partial t} + (\vec{V}' \cdot \nabla) \vec{V}' = -\vec{\nabla} P + \frac{\mu_{nf}}{\rho_{nf} \alpha_f} \nabla^2 \vec{V}' + \frac{(\rho\beta)_{nf}}{\rho_{nf} \beta_f} Ra Pr \theta \quad (8)$$

$$\frac{\partial \theta}{\partial t} + (\vec{V}' \cdot \nabla) \theta = \frac{\alpha_{nf}}{\alpha_f} \nabla^2 \theta \quad (9)$$

where V' is the velocity component U in X direction, V in Y direction and W in the Z one. $Ra = (g \beta \Delta T H^3 / \alpha_f \nu_f)$ is the Rayleigh number, $Pr (= \nu_f / \alpha_f)$ is the Prandtl number.

LATTICE BOLTZMANN METHOD

Regarding the Lattice Boltzmann equation for nanofluids, a nineteen-velocity model on a three-dimensional lattice, noted as D3Q19, is utilized [19]. For the adopted dynamic model, two successive phases are taken into account; starting with the first one which expresses the propagation of particles from nodes to their neighbors, and continuous with the second one, so-called as the collision, where particles on the same lattice redistribute and relax into their quasi-equilibrium. The particles distribution equation can be expressed as follows:

$$\frac{\partial \vec{f}}{\partial t} + \vec{c} \cdot \nabla \vec{f} = \left(\frac{\partial \vec{f}}{\partial t} \right)_{scat} \quad (10)$$

where $f(x, c, t)$ is the distribution function depending on the particle velocity \vec{c} at a location (x) and a time (t) . According to Guo et al. [15], the right side term of particles distribution equation displays the diffusion process when the new equilibrium distribution is rebuilt after the collision.

Function of the location (x) and the time (t) , the fluid shape can be defined as particles populations vector, noted as f_i , where $i = 0, 1, 2, \dots, 18$. Thus, the discrete distribution equation can be given as:

$$f_i(x + c_i \Delta t, t + \Delta t) = f_i(x, t) + (\Omega f)_i \quad (11)$$

where (f_i) is the space vector based on the discrete velocity set and Ω is the collision operator. Noted that a primary discrete velocity sets will be created then from the set of 18 vectors pointing from the

origin to the above neighbors and the zero vector $(0,0,0)$.

The space vector, f_i , is constructed using the moment of the last. The relationship between two spaces is defined by means of the below equation, when the coefficient a_{ij} is calculated using the particle velocity c_i .

$$m_j = \sum_i a_{ij} f_i \quad (12)$$

where the corresponding 19 moments m_j (0, 1, 2, ..., 18) are: the mass density ($m_0 = \rho$), the kinetic energy independent of the density ($m_1 = e$), the kinetic energy square independent of the density and kinetic energy ($m_2 = \varepsilon = e^2$), the momentums ($m_{3;5;7} = j_{x;y;z}$), the energy flux independent of the mass flux ($m_{6;8;10} = q_{x;y;z}$), and the symmetric traceless viscous stress tensor ($m_9 = 3 p_{xx}$, $m_{11} = p_{yy} = p_{zz}$, with $p_{xx} + p_{yy} + p_{zz} = 0$, $m_{13;4;15} = p_{xy;yz;zx}$).

The two vectors of quadratic order, m_{10} and m_{12} , have the same symmetry as the diagonal part of the traceless tensor p_{ij} , while the other three vectors of cubic order are parts of a third rank $m_{16;17;18}$ tensor, with the symmetry of $j_k p_{nm}$. The diagonal collision matrix S_{ij} is given as:

$$S_{ij} = \begin{pmatrix} 0, s_1, s_2, 0, s_4, 0, s_4, 0, s_4, s_9, s_{10}, \\ s_9, s_{10}, s_{13}, s_{13}, s_{13}, s_{16}, s_{16}, s_{16} \end{pmatrix} \quad (13)$$

Note that relaxations are related to the dynamic viscosity [20].

About the energy equation, and because of the nonexistence of non-linearity, the finite-difference scheme is found more required than the LBE-scheme. The relation between the temperature and flow fields is found to be as far as the force in the y -direction, which arises with the temperature gradient, is introduced. The later is thus, used in the y -velocity calculations, as shown in the advection term in the energy equation cited below:

$$\frac{\partial T}{\partial t} + \vec{V} \cdot \nabla T = k \Delta T \quad (14)$$

At the end, it is worth to denote that the mean Nusselt number computed along the side walls is obtained through the following expressions:

$$Nu = \left(\frac{k_{nf}}{k_f} \right) \int_0^H \int_0^H (\partial T / \partial x)_{x=0, \text{ or } H} dy dz \quad (15)$$

where k_{nf} and k_f are the nanofluid and the base fluid thermal diffusivity, respectively.

RESULTS AND DISCUSSION

The presented results are generated for different dimensionless groups, such as the Rayleigh number ($10^3 \leq Ra \leq 10^6$), the solid volume fraction (0% to 10%), the width ($0.1 \leq w \leq 0.4$) and height of the obstacle ($0.1 \leq h \leq 0.5$). The Prandtl number is fixed at 6.2. The predicted hydrodynamic and thermal fields' variables are presented through the Streamlines, the temperature Iso-surfaces. The average Nusselt number is also represented in order to supply useful information about the influence of each parameter, quoted above, on heat transfer enhancement.

The performance of the using code via the 3D natural convection problem is established by comparing predictions with other numerical results, namely those of Fusegi *et al.* [21] and Frederick *et al.* [22]. By taking into account the same hypotheses, Table. 2 demonstrate a comparison of the mean Nusselt number computed inside the Air cube. As we can see, the present results and those of Fusegi *et al.* and Frederick *et al.* are in excellent agreement with a maximum discrepancy of about 2%.

Table 2. Average Nusselt number obtained with our computer code and those of references [21, 22], $Pr = 0.71$.

	Fusegi <i>et al.</i> [17]	Frederick <i>et al.</i> [18]	Present Work
10^3	1.085	1.071	1.071
10^4	2.100	2.057	2.062
10^5	4.361	4.353	4.367
10^6	8.770	8.740	8.761

Figure 2 illustrates temperature Iso-surfaces (a), streamlines and Isotherm plots (b) for different values of the Rayleigh number (Ra). For low values of the Rayleigh number ($Ra \leq 10^4$), the flow is not very significant and heat exchanges are then dominated by conduction mode (conductive regime). However, for high values of the Rayleigh number ($Ra \geq 10^5$) flow intensifies and convective exchanges prevail resulting in a convective regime.

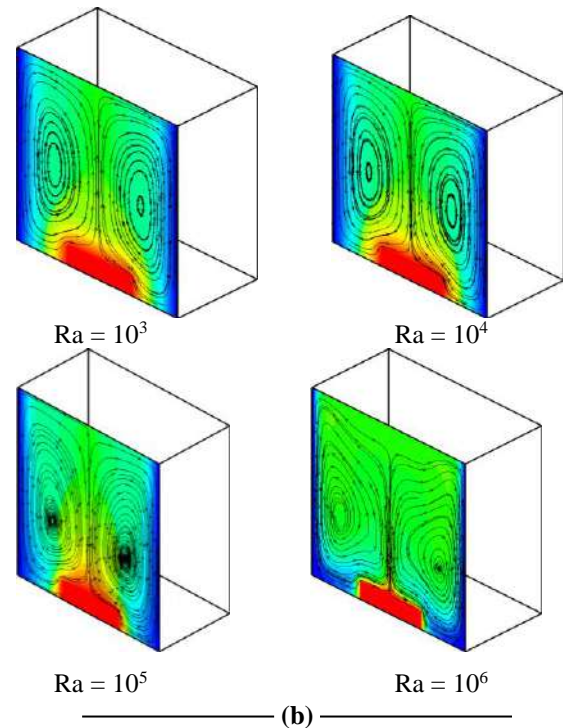
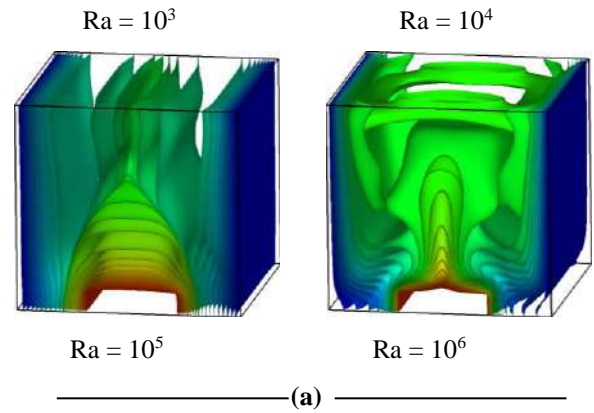
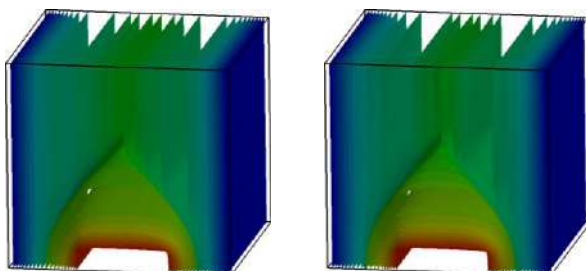


Figure 2: Temperature Iso-surfaces (a), streamlines and Isotherm plots (b) of nanofluid for various values of the Rayleigh number, $W = 0.4$, $h = 0.1$ and $\phi = 0$.

Figure 3, present the temperature Iso-surfaces (a) and the streamlines with Isotherm plots (b) for different values of various widths of the heat source. $Ra = 10^6$.

Gradually, as the width of the heat source increases the flow of convective fluid intense, and consequently, the thermal boundary layer (and figuratively close cold side walls) becomes thin, making it the heat transfer more important.

The variation of the mean Nusselt number as function of the height of the obstacle, for different values of the Rayleigh number nanoparticles volume fraction ($\phi = 0$) and ($\phi = 0.1$), is shown in Fig. 4. The mean Nusselt number is found as an increasing

function of the nanoparticles volume fraction, and increases by increasing the Rayleigh number. Additionally, It appears that the average Nusselt number increases when the height of the obstacle increases

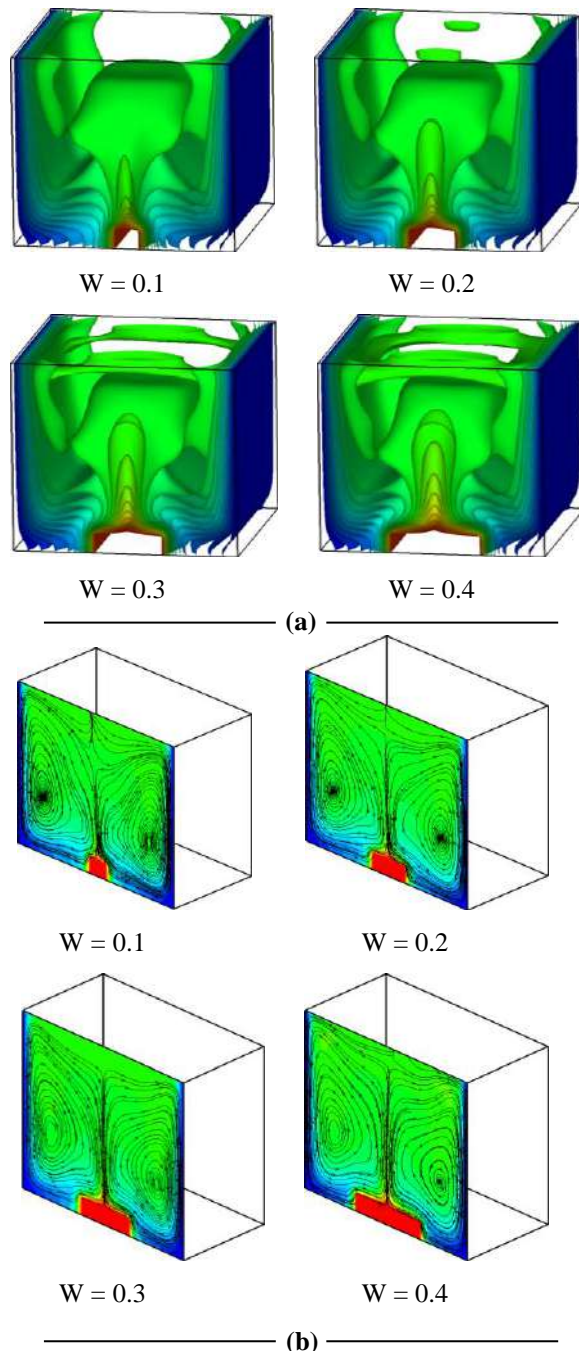


Figure 3 : Temperature Iso-surfaces (a), streamlines and Isotherm plots (b) of nanofluid for various values of the width W , $Ra = 10^6$ and $h = 0.10$.

Figure 5 shows the evolution of the average Nusselt number according to the variation of the source' height for different widths (elevating W from 0.1 to

0.4). It appears that the average Nusselt number increases so, by increasing the high of the heat source, specially with using the nanoparticles inside.

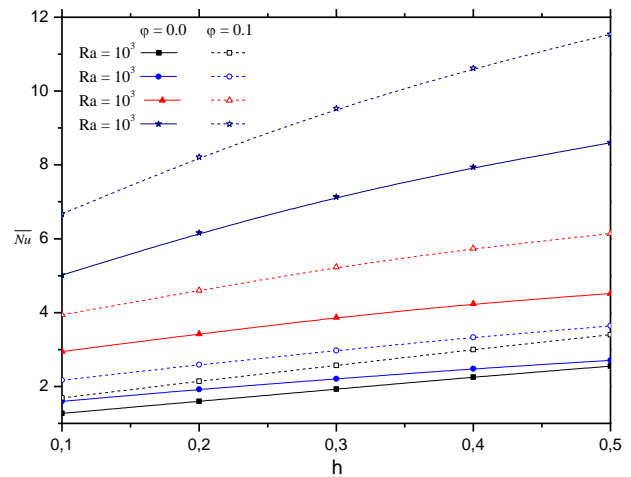


Figure. 4 Variation of the mean Nusselt number with the source height for various values of Rayleigh number and nanoparticles volume fraction.

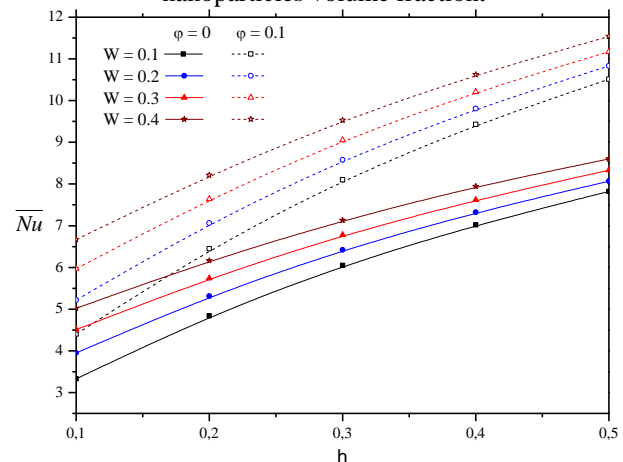


Figure 5: Variation of the mean Nusselt number, with the source height for various values of the width, and two different nanoparticles volume fraction $\phi = 0$ and $\phi = 0.1$.

CONCLUSIONS

The analysis of natural convection phenomenon inside a cubical enclosure, including heated source which located at the center of the bottom wall was realized in this paper. Taking into account the effects of various parameters, such as the Rayleigh number, the nanoparticles volume fractions, and the width and height of the obstacle, the results may be summarized as follows: The heat transfer enhancement is consequent to the dispersion of solid nanoparticles into the base fluid and increases by increasing the nanoparticles volume fraction, the latter is an increasing function of the increase Rayleigh number, the width and height of the bottom heat source.

REFERENCES

1. Koseff, J.R, and Street, R.L, 1984, Visualization of a shear driven three dimensional recirculating flow, *J. Fluids Eng*, **106**, pp. 21-29.
2. Barakos, G; and Mitsoulis, E,1994, Natural convection flow in a square cavity revisited: laminar and turbulent models with wall functions, *Int. J. Num. Methods Fluids*, **18**, pp. 695-719.
3. Calcagni, B; Marsili, F; Paroncini, M, 2005, Natural convective heat transfer in square enclosure heated from below, *Appl. Thermal Eng*, **25**, pp. 2522-2531.
4. Jou, R.Y; Tzeng, S.C, 2006, Numerical research of nature convective heat transfer enhancement filled with nanofluids in rectangular enclosures, *Int. Commun. Heat Mass Transfer*, **33**, pp. 727-736.
- [5] Moraveji, M.K; Darabi, M; Haddad, S.M.H; and Davarnejad, R, 2011, Modeling of convective heat transfer of a nanofluid in the developing region of tube flow with computational fluid dynamics. *Int Commun.Heat Mass Transfer*, **38**, 1291-1295.
- 6 Choi, S.U.S, 1995, *Enhancing Thermal Conductivity of Fluids with Nanoparticles, in Developments and Applications of Non-Newtonian Flows*, American Society of Mechanical Engineers, New York, **231**, pp. 99-105.
7. Wang, X, Xu, X, Choi, S.U.S, 1999, Thermal conductivity of nanoparticle-fluid mixture , *J. Thermophysics Heat Transfer*, **13**, pp. 474-480.
8. Santra, A.K, Sen, S, Chakraborty, N, 2009, Study of heat transfer due to laminar flow of copper–water nanofluid through two isothermally heated parallel plates , *Int. J. Thermal Sciences*, **48**, pp.391-400.
9. Lelea, D, 2011, The performance evaluation of Al₂O₃/water nanofluid flow and heat transfer in microchannel heat sink , *Int. J. Heat Mass Transfer* **54**, pp. 3891-3899.
10. Ghasemi, B, Aminossadati, S.M, 2009, Natural convection heat transfer in an inclined enclosure filled with a water-CuO nanofluid, *Numer. Heat Transfer Part A*, **55**, pp. 807-823.
11. Ogut, E.B, 2010, Heat transfer of water-based nanofluids with natural convection in an inclined square enclosure , *J. Thermal Science and Technology*, **30**, pp. 23-33.
12. Kahveci, K, 2010, Buoyancy driven heat transfer of nanofluids in a tilted enclosure , *J. Heat Transfer*, **132**, pp. 01-12.
13. Khanafer, K, Vafai, K, Lightstone, M, 2003, Buoyancy-driven heat transfer enhancement in a two-dimensional enclosure utilizing nanofluids , *Int. J. Heat Mass Transfer*, **46**, pp. 3639-3653.
14. Ameziani, D.E, Guo, Y, Bennacer, R, El Ganaoui, M, Bouzidi, M, 2010, Competition between Lid-Driven and Natural Convection in Square Cavities investigated with a Lattice Boltzmann Method , *Comput. Thermal Sciences*, **02**, pp. 269-282.
15. Guo, Y, Bennacer, R, Shen, S, Ameziani, D.E, Bouzidi, M, 2010, Simulation of mixed Convection in a slender rectangular cavity with a Lattice Boltzmann Method , *Int. J. Numer. Meth. heat Fluid Flow*, **03**, pp. 227-248.
16. Bejan, A, 2004, *Convection heat transfer*, John Wiley & Sons, Inc., Hoboken, New jersey, USA.
17. Brinkman, H.C, 1952, The viscosity of concentrated suspensions and solutions, *J. Chem. Physics*, **20**, pp. 571-581.
18. Maxwell, J.C,1873 , *A Treatise on Electricity and Magnetism*, Vol. II, Oxford University Press, Cambridge, U K, **54**.
19. d’Humières, D, 1992, Generalized lattice-Boltzmann equations, in *Rarefied Gas Dynamics: The theory and simulations*. In: B.D. Shizgal and D.P. Weaver, Editors, AIAA Progress in astronautics and aeronautics, **159**, pp. 450-458.
20. Fallah K; Khayat, M; Borghei, M.H Ghaderi, A, Fattahi, E, 2012, Multiple-relaxation-time lattice Boltzmann simulation of non-Newtonian flows past a rotating circular cylinder, *J. Non-Newt. Fluid Mech*, **177**, 01-14.
21. Fusegi T; Hyun, J.M; Kuwahara, K; Farouk, B,1991, A numerical study of three-dimensional natural convection in a differentially heated cubical enclosure, *Int. J. Heat Mass Transfer*, **34**, pp. 1543-1557.
22. Frederick, R.L; Moraga, S.G, 2007, Three-dimensional natural convection in finned cubical enclosures, *Int. J. Heat Fluid Flow*, **28**, pp. 289-298.

NUMERICAL ANALYSIS OF NON-PREMIXED COMBUSTION UNING 2D AND 3D UNSTEADY REYNOLDS AVERAGED NAVIER-STOKES EQUATIONS

GUESSAB Ahmed^{1*}, ARIS Abdelkader¹, MOURAD Taha Janan², BENAMAR Ali¹

¹Laboratoire de Recherche en Technologie de Fabrication Mécanique, Ecole Nationale Polytechnique d'Oran 31000, Algérie;

²Laboratoire de Mécanique, Procédés et Processus Industriels (LMPPI), Ecole Nationale Supérieure d'Enseignement Technique de Rabat, Maroc

*Corresponding author: Fax: +213 41 290 789 Email: med_guessab@yahoo.fr

ABSTRACT

Turbulent swirling flow in can-type model of a gas turbine combustor is computationally investigated. Computations were performed using the commercial finite-volume code ANSYS-FLUENT. As the basic modeling strategy, a two and three-dimensional Unsteady Reynolds Averaged Navier-Stokes (URANS) approach is applied, employing a differential Reynolds Stress Turbulence model (RSM and SST k- ω). Numerical predictions of the mean flow field showed a large inner recirculation zone and an outer recirculation zone which represents a typical result of confined swirl flames. Mean velocity vector plots showed that the inner recirculation zone is formed by two counter rotating vortex pair, while instantaneous velocity vector plots showed clearly the existence of many small vortex in that zone.

KEYWORDS

Gas turbine combustor, 2D URANS RSM, 3D URANS RSM, Fluent

INTRODUCTION

Numerical simulations of the flows in gas turbine combustors had become an unavoidable way to accelerate the design of this type of modern engines and optimize their performances: reducing fuel consumption, limiting noise and air pollution, avoiding combustion instabilities...etc.

The simulations also facilitate the understanding and the visualization of physical phenomena often inaccessible by the experimental measurements.

The use of numerical tools for simulating unsteady combustion phenomena still presents some issues; the Reynolds Averaged Navier-Stokes (RANS) approach, also in its time-resolved form, URANS, has been proven of not being capable of resolving all time and space scales, which play crucial roles in highly turbulent unsteady combustion. Swirling lean premixed flames are frequently used in modern gas turbine combustors since they offer a possibility of controlled flame temperature and thus favorable

thermal NO_x emissions and avoid intrusive methods disturbing flow field.

Combustion requires the effective mixing of fuel and oxidizer. For premixed flames, mixing takes place in a separated mixing chamber. This type of burner imposes the danger of a flashback of the flame into the mixing chamber. Another possibility is the mixing of fuel and air within the burner chamber. This prevents the danger of flashbacks, but homogeneous mixing is more difficult to achieve.

A method often used in practical burners is the application of the swirling flows to improve mixing. In the swirl burner natural gas freely propagates into the burner chamber in the axial direction and is surrounded by the combustion air flow which has radial and tangential velocity components (swirl) in addition to the axial flow. The resulting flow field is strongly turbulent. Hot burned gases are transported back to the nozzle by internal recirculation in the flame and thus ensure effective mixing and stable ignition conditions. Swirling flows have been the

subject of intensive experimental, analytical and numerical investigation over many years [1-2-3-4 ,5]. The application of swirling flows in industrial gas turbine combustors is of particular interest to the current work. The goal of actual study is flame behavior according to transit natural gas turbulent flame evolution is analyzed using commercial code ANSYS-FLUENT with URANS Simulation model to treat turbulence coupling to partially premixed model to treat combustion. Models are applied to a three-dimensional geometry; they gave suitable results and were able to describe a detailed flow field. Results of the mean as well as the time-dependent numerical predictions of the turbulent vortex structures were presented.

GEOMETRY

The basic geometry of the gas turbine can-type combustor chamber is shown in Fig. 1. The flame is stabilized by a low swirl number ($S = 0.6$). The size of the combustor is 590 mm in the Z direction, 250 mm in the Y direction, and 230 mm in the X direction. The primary inlet air is guided by vanes to give the air a swirling velocity component. The total surface area of primary main air inlet is 57 cm^2 . The fuel is injected through six fuel inlets in the swirling primary air flow. There are six small fuel inlets, each with a surface area of 0.14 cm^2 . The secondary air is injected in the combustion chamber through six side air inlets each with an area of 2 cm^2 . The secondary air or dilution air is injected at 0.1 m from the fuel injector to control the flame temperature and NO_x emissions. The can-type combustor outlet has a rectangular shape with an area of 0.0150 m^2 .

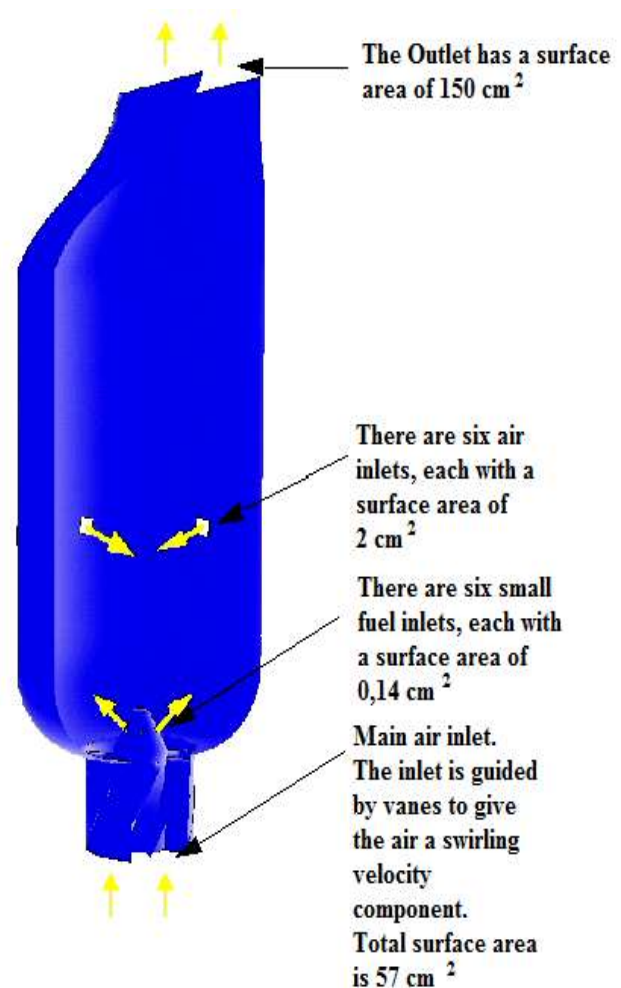


Figure 1
Computational domain

MODELING AND NUMERICAL SIMULATION

Conservation equations governing reactive flows resolved by the numerical code ANSYS-FLUENT [6] actual investigations are: mass, momentum, species and energy conservation equations using several models described below with finite volume methods. Gambit post-processor [7] is a generator used to generate high quality 3-D meshes for CFD simulations. It creates tetrahedral, pyramids and prisms in 3D meshing mode. Generally these are the regions where we expect maximum gradients in our fluid flow. Moreover the grids should also be fine enough to resolve the geometry accurately. We cannot have the smallest grid size throughout the whole geometry as that would increase the computational time significantly.

Thus we would like to have a finer mesh in regions where the geometry is complex and also where we expect higher gradients in the flow field variables. Periodic boundary conditions can significantly reduce our computational domain. If a model is axis-symmetric then instead of meshing and solving the entire 3D model we can simply cut out a wedge from the solid part and use periodic boundary conditions. A view of the grid system is shown in Fig. 2. The mesh is generated by automatic method and its main quality specifications are summarized in Table 3. A 3D URANS-RSM procedure is applied [8], [9].

For comparison, the Shear Stress Transport (SST) model is also applied within the 3D URANS formulation for assessing the performance of RSM vs. SST. The RSM and SST models are also applied within a 2D-axisymmetric URANS formulation, and the results are compared with 3D URANS ones. For the temporal discretization, a second-order Euler scheme is employed. The time step size is chosen in such a way that the cell Courant number while sufficiently resolving important physical time scales such as the eddy turnover time. In combustor flow applications, the Eddy Dissipation Concept (EDC) of Magnussen and Hjertager [10] is used as the combustion model. The oxidation of fuel, which is assumed to be methane, is represented by a four-step global reaction mechanism of Jones and Lindstedt [11]. The flow and thermal variables are defined by the boundary conditions on the boundaries of the studied model. Mass-flow inlet conditions are applied at the two inlets in the burner and one in the combustor for secondary air inlet. Out flow boundary condition is applied at the exit of the combustion chamber and the walls are treated as constant wall temperature. The walls are stationary with no-slip conditions applied on the wall surface. The detailed and typical data boundary conditions are summarized in the Table 4 below. The specific heat of the species is temperature and mixture dependant. The physical properties are defined for the mixture material and the constituent species. The flow is considered unsteady and 2D/3D, used parameters in the numerical simulation using ANSYS-FLUENT code are shown in Table 3 with the pressure-based solver [1] which is an algorithm that belongs to a general class of methods called projection method and SIMPLEC scheme proposed by [1] with second order solver algorithms pressure based are available as isolated algorithm. Geometries produce high levels of turbulence and enhanced mixing rates. The nozzle used in can-type combustor in this study has axial type swirler, as illustrated in Fig. 4. Swirl

generator is characterized by eight-fixed vanes in the annular nozzle with a fix angle in the trailing edge; the definition assumed for the swirl number is the relation between the flow-averaged-azimuthal velocity and the corresponding axial velocity.

Table 1
The Jones-Lindstedt mechanism (4-step)

JL1	$\text{CH}_4 + 0.5\text{O}_2 \rightarrow \text{CO} + 2\text{H}_2$
JL2	$\text{CH}_4 + \text{H}_2\text{O} \rightarrow \text{CO} + 3\text{H}_2$
JL3f	$\text{H}_2 + 0.5\text{O}_2 \rightarrow \text{H}_2\text{O}$
JL3r	$\text{H}_2\text{O} \rightarrow \text{H}_2 + 0.5\text{O}_2$
JL4	$\text{CO} + \text{H}_2\text{O} \leftrightarrow \text{CO}_2 + \text{H}_2$ (forward)

Table 2
Rates equations of the original Jones-Lindstedt mechanism: units in [m], [s], [Kmol], [J] and [K]

Eq.	Rates equations [Kmol/(m ³ .s)]
JL1	$\frac{d[\text{CH}_4]}{dt} = 4.4 \times 10^{11} e^{-1.26 \times 10^8 / (RT)} \cdot [\text{CH}_4]^{0.5} [\text{O}_2]^{1.25}$
JL2	$\frac{d[\text{CH}_4]}{dt} = 3.0 \times 10^8 e^{-1.7 \times 10^8 / (RT)} \cdot [\text{CH}_4] [\text{H}_2\text{O}]$
JL3f	$\frac{d[\text{H}_2]}{dt} = 6.8 \times 10^{15} T^{-1} e^{-1.67 \times 10^8 / (RT)} \cdot [\text{H}_2]^{0.25} [\text{O}_2]^{1.5}$
JL3r	$\frac{d[\text{H}_2\text{O}]}{dt} = 1.255 \times 10^{17} T^{-0.877} e^{-4.095 \times 10^8 / (RT)} \cdot [\text{H}_2]^{-0.75} [\text{O}_2] [\text{H}_2\text{O}]$
JL4	$\frac{d[\text{CO}]}{dt} = 2.75 \times 10^9 e^{-8.4 \times 10^7 / (RT)} \cdot [\text{CO}] [\text{H}_2\text{O}]$

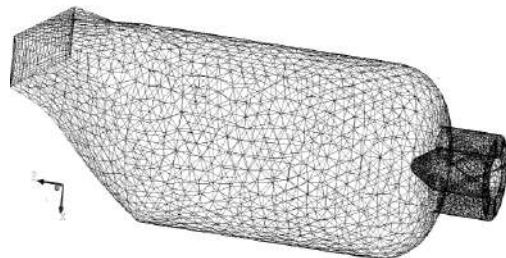


Figure 2
3D grid system

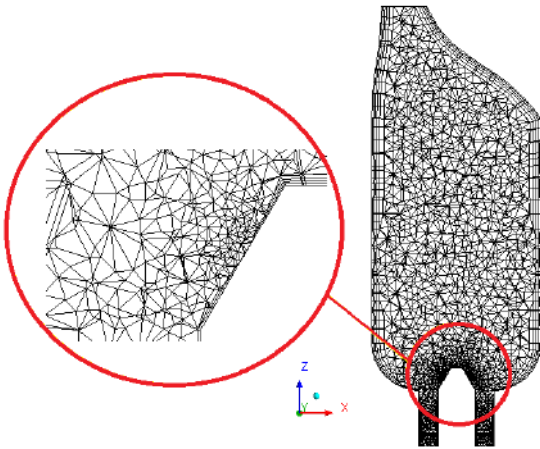


Figure 3

Mech geometry of gas turbine can-type combustor (midaxial vertical plane)

Table 3
Mech statistics

Number of Nodes:	31433
Number of Elements:	106651
Tetrahedra:	74189
Pyramids:	1989
Wedges:	30473
Extents:	
min x, max x:	-0.11314 [m], 0.11314 [m]
min y, max y:	-0.125 [m], 0.125 [m]
min z, max z:	-0.138145 [m], 0.45 [m]
Max Edge Length Ratio:	21.1566
Volume:	0.0186368 [m ³]

Table 4
Boundary conditions

	Type	values
Primary air inlet	Mass flow inlet	U = 10 m/s; Q = 0.0688875kg/s D _h = 85 mm. T = 300K It = 10%
Fuel inlet	Mass flow inlet	U = 40 m/s; Q = 0.00218033kg/s D _h = 4.2 mm. T = 300K It = 10%
Secondary air inlet	Mass flow inlet	U = 6 m/s; Q = 0.00845225kg/s D _h = 16 mm. T = 300K It = 10%
Combustion chamber exit	Outflow	
Walls of combustion chamber	Wall	T = 320 [k]

RESULTS AND DISCUSSION

Detail plots of the instantaneous velocity field, in a section near the inlet, predicted by the 2D and 3D URANS-RSM and SST k-w methods are shown in Figure 4 and 5. In this section, 2D and 3D URANS modeling the Reynolds Stress Model (RSM) and the Shear Stress Transport model (SST) are compared for ability to predict flow field. The radial profiles of the time-averaged circumferential velocity components extracted 50 mm above the injector inlet, figure 4, reveal that case 3D-URANS RSM, overestimates the negative circumferential velocity on the axis in comparison to case 3D-URANS SST k-w by approximately 5% (in the interval of -0.075m and +0.075m). Then again, case 3D-URANS RSM captures the intensity of the flow between the inner and outer shears better, figure 4, and also the shape of the ORZ is better reproduced from the profiles extracted for case 3D-URANS RSM. All test cases show the right penetration of the ORZ in the chamber: at $x = 50$ mm, the ORZ is not present anymore, figure 5. Due to the contraction of the chamber into the exhaust canal rectangular a peak of velocity was registered next to the outlet. A similar comparison for $z = 0.2$ m is provided in Fig. 5. Based on the profiles of time-averaged axial velocity at $z = 0.05$ m, one can see that 3D URANS SST k-w overpredicts the size and intensity of the recirculation zone compared to 3D URANS RSM (Fig. 4). Comparing the time-averaged circumferential velocity profiles, one can observe that 3D URANS RSM predicts a more confined vortex core with substantially higher velocities compared to 3D URANS SST k-w. for the comparison of time-averaged circumferential velocities by 3D URANS RSM and 3D URANS SST k-w, similar trends are observed, also for $z = 0.2$ m. The 2D URANS SST k-w results predict an even larger recirculation zone and a broader vortex core compared to 3D URANS SST k-w. It is already mentioned above that no convergence could be obtained by 2D URANS RSM, which can be seen as the manifestation of ability of RSM to capture low frequency flow unsteadiness. The 2D URANS RSM results displayed in the figures predict a qualitatively complete different W velocity field, implying a region of forward flow (central jet) enveloped by a recirculation zone. The circumferential velocity profiles of 2D URANS RSM also differ considerably from those of 3D URANS RSM.

The all cases 2D-URANS, reveals better profiles for time averaged circumferential velocity.

This comparison shows the importance of three-dimensional effects combined with flow unsteadiness. Generally, the time averaged characteristics of the flow field were very well captured by all numerical simulations.

Figure 6, gives the temperature contours in a central cross section of the combustion chamber for six instantaneous time steps $t=0.15s$, $t=0.25s$, $t=0.35s$, $t=0.55s$, $t=0.65s$ and $t=0.95s$. The time evolution of the flame in size and position can be clearly observed in the sequence of 6 images presented in Figure 6. In fact, initially at $t=0.15s$, flames are present in the center of the combustion chamber. Then at $t=0.55$ the flames moves upstream and approach each other. At $t=0.65s$ they are partially mixed and finally at $t=0.95s$, they are totally mixed to form two relatively big flame.

The simulation reported by case 3D-URANS SST k-w investigated the possible improvements in the simulation due to chemical kinetics effects. Since using very large reaction models would lead to a too high computational effort. The flame of the model combustor can be considered as a technically premixed flame. Because the fuel admission holes are positioned between the inner and outer swirler, so that fuel and air can premix to a certain extent before arriving in the primary reaction zone.

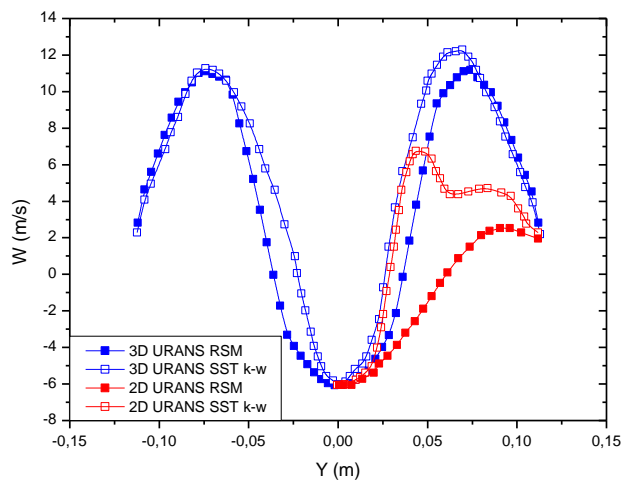


Figure 4

Time-averaged circumferential velocity profiles for different turbulence models along a line at $z = 55mm$

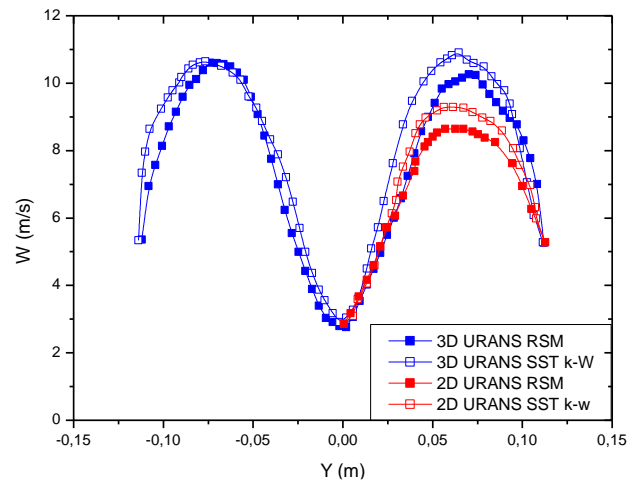


Figure 5

Time-Averaged circumferential velocity profiles for different turbulence models along a line at $z = 0.2m$

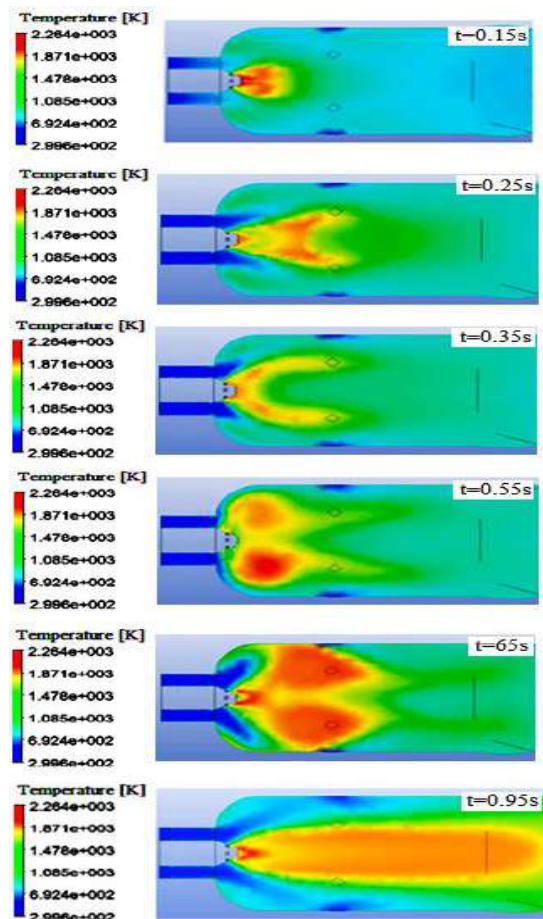


Figure 6

Contours plot of time – averaged temperature in [K], in meridial plan (Oyz) of the combustion chamber with 3D URANS SST k-w

CONCLUSION

Turbulent swirling flow in can-type combustor model of a gas turbine combustor is computationally investigated. As the basic modeling strategy, a 3D unsteady RANS/URANS approach is applied, employing a differential Reynolds Stress Turbulence Model (RSM/.....). A highly unsteady and 2D/3D flow structure, the vortex breakdown and a precessing vortex core are observed.

Main findings can be summarized as:

- For obtaining a sufficiently stationary time-averaged flow field, the time-averaging time should be about 5 times the integral time scale.
- Differences between 3D URANS RSM and 3D URANS SST k-W are rather substantial. The larger differences are observed for the time-averaged circumferential velocity profile, as the former predicts a more intense vortex core with higher maximum velocities.
- 2D URANS (RSM/SST K-w) results may only be used for purely qualitative purposes.
- 2D URANS RSM did not lead to converged results. 2D URANS RSM leads to substantially different results compared to 3D URANS RSM.

REFERENCES

1. Benim A. C., Cagna M., Joos F. and Wiedermann A.: Computational analysis of turbulent swirling flow in water model of a gas turbine combustor (2009). Proceeding of 6th International conference on computational heat and mass transfer, May 18-21, 2009, Guangzhou, China 243.
2. Selvakuma K., M., Young Kim, 2014, "Combustion and emission characteristics in a can-type combustion chamber", International Journal of Mechanical, Aerospace, Industrial and Mechatronics Engineering, Vol. 8, No: 7, pp. 1300–1303.
3. Widenhorn A., B. Noll and M. Aigner (2010), Numerical Characterization of a Gas Turbine Model Combustor High Performance Computing in Science and Engineering '09 ,Part 4, 179-195.
4. Khelil, A., Naji, H., Loukarfi, L., Mompean, G., 2009, "Prediction of a high swirled natural gas diffusion flame using a PDF model", Fuel, Vol. 88, Issue 2, pp. 374–381.
5. Lysenko D. A. and Solomatnikov A. A. (2006), Numerical analysis of aerodynamics and hydraulic loss in the GTE'-150 combustion chamber of gas-turbine power plant with the use of the Fluent suite, Journal of Engineering Physics and Thermophysics, Vol. 79, No. 4.
6. ANSYS, Inc. ANSYS FLUENT v14.0: User's Guide; Theory Guide; UDF Manual, November 2010.
7. Gambit v2.4, <http://www.ansys.com>.
8. Launder, B. E., Reece, G. J. and Rodi, W. (1975): Progress in the development of a Reynolds-stress turbulence closure, J. Fluid Mechanics, Vol. 68, pp. 537-566.
9. Speziale, C. G., Sarker S., Gatski, T. B. (1991): Modelling the pressure-strain correlation of turbulence, J. Fluid Mech., V. 227, pp. 245-272.
10. B. F. Magnussen. "On the Structure of Turbulence and a Generalized Eddy Dissipation Concept for Chemical Reaction in Turbulent Flow". Nineteenth AIAA Meeting, St. Louis 1981.
11. Jones, W.P.; Lindstedt, R.P. "Global Reaction Schemes for Hydrocarbon Combustion". Combustion and Flames, 1988, 73, 233-249.
12. Widenhorn A., B. Noll and M. Aigner (2010), Numerical Characterization of a Gas Turbine Model Combustor High Performance Computing in Science and Engineering '09 ,Part 4, 179-195.
13. F. R. Menter, Scale-Resolving Simulations in ANSYS CFD, November 2015. www.ansys.com
14. Spotts N., Unsteady Reynolds-averaged Navier-Stokes simulation of inlet distortion in the fan system of a gas-turbine aero-engine. These: Colorado state University, 2015, 146 pages, N° 160655. <http://search.proquest.com/docview/1758252282>
15. Hunter, W., Nishino, T. & Willden, R. H. J. (2015) "Investigation of tidal turbine array tuning using 3D Reynolds-averaged Navier-Stokes simulations," International Journal of Marine Energy, Vol. 10, pp. 39-51. <http://dx.doi.org/10.1016/j.ijome.2015.01.002>
16. Sarlak, H., Nishino, T. & Sørensen, J. N. (2015) "URANS simulations of separated flow with stall cells over an NREL S826 airfoil," 13th International Conference of Numerical Analysis and Applied Mathematics (ICNAAM 2015), Rhodes, Greece, Sep. 2015.

QUANTIFICATION OF EMISSIONS IN A TURBULENT DIFFUSION FLAME APPLIED TO A BURNER

Amar HADEF^{1*}, Abdelbaki MAMERI¹, Zeroual AOUACHRIA², Fouzi THABET³

¹Département de physique, Université d'Oum El Bouaghi 04000 Algérie

²Laboratoire de Physique Energétique Appliquée, Université de Batna 1 05000 Algérie

³DBFZ, Torgauer Straße 116, D-04347 Leipzig, Germany

*Corresponding author: Fax: +213 32685310 Email: Hade_f_am@yahoo.fr

ABSTRACT

Nitrogen oxides NO_x are pollutants that spread along important distances and affect eco systems. Particular attention is paid to these emissions, which are originated by three factors: free radicals concentration, flame temperature and residence time.

This work is a CFD analysis of the NO_x production in a diffusion turbulent combustion of methane and air. Relation between the dilution of primary air with CO₂ and emissions levels is stressed. It is shown that the emissions can be reduced by 90% by diluting primary air.

KEYWORDS

Combustion, flame, scalar dissipation rate, flamelet.

NOMENCLATURE

T	temperature, K
P	pressure, Pa
Y	mass fraction
Z	mixture fraction
K	turbulent kinetic energy, m ² s ⁻²
H	enthalpy, J kg ⁻¹
h ⁰	enthalpy of formation, J kg ⁻¹
C _p	specific heat coefficient at pressure constant, Jkg ⁻¹ K ⁻¹
Greek letters	
ε	dissipation rate of turbulent kinetic energy, m ² s ⁻³
μ	dynamic viscosity
φ	global equivalence ratio
ρ	density, kgm ⁻³
χ	scalar dissipation rate, s ⁻¹
Superscripts	
~	Favre-averaged
–	Reynolds-averaged
“	fluctuations

1. INTRODUCTION

Accumulation in the atmosphere of certain gases by the industrial activities is likely to involve important modifications of the climate and to compromise the perennality of the biosphere.

Most of domestic and industrial energy responsible of pollution is produced via combustion processes [1], which emits extremely toxic species, such as carbon

monoxide (CO) and nitrogen oxides (NO_x). The turbulent diffusion flames are widely used in the industrial field especially in ovens. Therefore, the reduction of the polluting emissions became a priority in order to satisfy the world standards.

Several techniques allow the reduction of the polluting emissions in burners. We can cite the staged combustion technique [2], the selective non catalytic reduction (SNCR) technique and the mixture dilution by flaring gases technique [3]. Despite the disadvantages of carbon dioxide stated by Du et al. [4], these techniques show that the addition of CO₂ in fuel or the combustive has chemical and thermal effects on the reduction of thermal NO and the reduction of the soot formation. The researches conducted by Liu et al., [5] and Park et al., [6] show that the reaction

$CO_2 + H \rightarrow CO + OH$ is responsible of the chemical effect in the dilution by CO_2 , therefore the radicals OH and NO are reduced with a significant rate by means of dilution beside combustive [5].

This work constitutes a CFD contribution to the quantification of the polluting emissions of a turbulent diffusion flame diluted by CO_2 with a volume range from 0% to 24%, where the upper value represents the extinction limit of the flame.

2. GEOMETRICAL CONFIGURATION OF THE PROBLEM AND BOUNDARY CONDITIONS

The burner is formed by a central jet of diameter $D=7.2$ mm which injects a mixture of methane-air (25% vol. CH_4 , 75% vol. air) with a Reynolds number of 22400. The jet is surrounded by a set of small pilot flames spread over a diameter of 18.2 mm. This burner is plunged in a flow of air.

The initial speed of the central jet is 49.6 m/s, that of the pilot flame is 11.4 m/s and that of the air is 0.9 m/s [7].

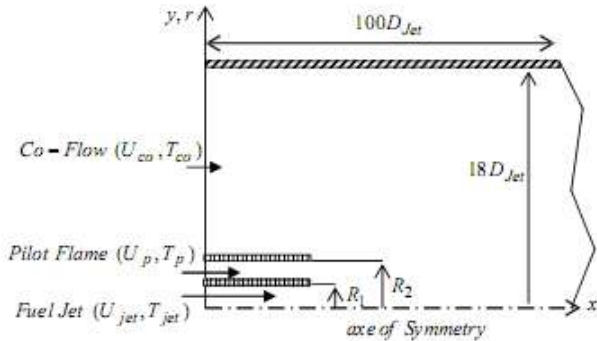


Figure 1
Geometry of the combustion chamber

The kinetic energy of the turbulence [8] of the flow of air and its rate of dissipation [9] are expressed by

$$\bar{k} = 2 \left(\bar{u}'^2 + 2\bar{v}'^2 \right) \quad (1) \quad \varepsilon = \frac{\bar{k}^{3/2}}{0.3D_h} \quad (2)$$

3. Combustion model

In this study, the laminar flamelet approach is used, where the mixture fraction Z is defined by:

$$Z = \frac{\phi Y_F - \frac{Y_O}{Y_{O,0}} + 1}{\phi + 1} \quad (3)$$

with ϕ

$$\phi = \left(\frac{Y_{F,0}}{Y_{O,0}} \right) / \left. \frac{Y_F}{Y_O} \right|_{st} \quad (4)$$

For such a mixture the fraction takes values ranging between 0 and 1 ($Z = 1$ for fuel and $Z = 0$ for oxidant). In the previous equations, Y_F represents the mass fraction of fuel and Y_O the mass fraction of oxidant.

The flame is located in the stoichiometric plane where:

$$Z = Z_{st} = \frac{1}{1 + \phi} \quad (5)$$

The structure of the laminar flamelet is given by the resolution of the conservation equations of the chemical species (by adopting a reactional mechanism) and that of energy [10].

$$-\frac{\rho \chi}{2Le_k} \frac{\partial^2 Y_k}{\partial Z^2} = \dot{\omega}_k \quad (6)$$

$$-\frac{\rho \chi}{2} \frac{\partial^2 T}{\partial Z^2} = \frac{1}{C_p} \sum_{k=1}^N h_k \dot{\omega}_k \quad (7)$$

The equations of the flamelet are solved by supposing that Lewis number $Le_n = 1$ for all the species. The two input parameters are the fraction of mixture (Z) and the rate of scalar dissipation stoichiometric (χ_{st}). With this approach, the functional dependence of the scalar rate of dissipation with the fraction of mixture $\chi(Z)$ is parameterized par χ_{st} .

This value acts as an external parameter, which is imposed on the structure of the flamelet by the field of fraction of mixture. A set of discrete values of χ_{st} is used in which the limits are represented by $\chi_{st} = 0$ at the equilibrium and $\chi_{st} = \chi_q$ at the extinctions. Moreover, the effect of the loss of heat within the limits of extinction is not taken into account. [11].

Under the non-adiabatic conditions, the temperature field is then obtained from the enthalpy in an iterative way (Eq (3) below.) for a range of values of average enthalpy \tilde{H} .

$$\tilde{H} = \sum_n \tilde{Y}_n \tilde{H}_n \quad (8)$$

and

$$\tilde{H}_n = \int_{T_{ref}}^T c_{p,n} dT + h'_n(T_{ref}, n) \quad (9)$$

with $C_{p,n}$ is the species n specific heat at constant pressure, which is function of the temperature.

$h'_n(T_{ref}, n)$ is the enthalpy of formation of species n at the temperature of reference.

The PDF (Probability Density Function) required by the fraction of mixture is of Beta type, it is controlled by the transport equation of the fraction of mixture Z and its variance.

The stationary solution is stored in tables containing the profiles of temperature and the mass fractions of all the chemical species in function of the mixture fraction, its variance and its stoichiometric scalar dissipation rate. The average density is calculated from the law of perfect gases:

$$\frac{1}{\bar{\rho}} = \frac{RT}{\bar{P}} \sum_n (\tilde{Y}_n / MW_n) \quad (10)$$

In this equation \bar{P} is the average pressure, R the universal constant of gases and W_n the molar mass of species n.

Consequently, the average temperature, mass fraction and the density are given by:

$$\tilde{T}(\tilde{Z}\tilde{Z}^2, \tilde{H}, \tilde{\chi}_{st}) \quad (11)$$

$$\tilde{Y}_n(\tilde{Z}\tilde{Z}^2, \tilde{\chi}_{st}) \quad (12)$$

$$\bar{\rho}(\tilde{Z}\tilde{Z}^2, \tilde{H}, \tilde{\chi}_{st}) \quad (13)$$

The coupling of the chemistry and the flow field is carried out via the fraction of mixture, its variance, the scalar dissipation stoichiometric rate and the enthalpy, which are provided starting from calculations of field of flow. In fact, in code CFD, the equations transports are solved for the fraction of mixture and its variance.

These equations are closed by the assumption of the gradient of diffusion (first order closure) for scalar turbulent flows:

$$\frac{\partial}{\partial t}(\bar{\rho}\tilde{Z}) + \frac{\partial}{\partial x_i}(\bar{\rho}\tilde{u}_i\tilde{Z}) = \frac{\partial}{\partial x_i} \left(\frac{\mu_t}{Sc_t} \frac{\partial \tilde{Z}}{\partial x_i} \right) \quad (14)$$

$$\frac{\partial}{\partial t}(\bar{\rho}\tilde{Z}^2) + \frac{\partial}{\partial x_i}(\bar{\rho}\tilde{u}_i\tilde{Z}^2) = \frac{\partial}{\partial x_i} \left(\frac{\mu_t}{Sc_t} \frac{\partial \tilde{Z}^2}{\partial x_i} \right) +$$

$$C_g \mu_t \frac{\partial \tilde{Z}}{\partial x_i} \frac{\partial \tilde{Z}}{\partial x_i} - \bar{\rho}\tilde{\chi}$$

where Sc_t is the Schmidt number turbulent (it takes a value of 0.85). The C_g constant takes a value of 2.86. χ is the scalar dissipation average rate, its modeling is based on the effect of the stretching and the fluctuations of the fraction of mixture :

$$\tilde{\chi} = C_d \frac{\varepsilon}{k} \tilde{Z}^2 \quad (16)$$

with $C_d = 2.0$.

The transport equation for the averaged enthalpy, \tilde{H} , is also solved in code CFD:

$$\frac{\partial}{\partial t}(\bar{\rho}\tilde{H}) + \frac{\partial}{\partial x_i}(\bar{\rho}\tilde{u}_i\tilde{H}) = \frac{\partial}{\partial x_i} \left(\frac{\mu_t}{Pr_t} \frac{\partial \tilde{H}}{\partial x_i} \right) + S_h \quad (17)$$

with Pr_t the number of turbulent Prandtl (it takes a value of 0.85), S_h is the source term due to the radiation.

4. CHEMICAL MODEL

The choice of the chemical kinetics is based on the tests of Davidenko in which the performances of the chemical mechanisms mentioned in table 1 were compared in various configurations of shock tube and the well-stirred reactor. The results showed that the chemical mechanisms tested lead to similar results. On the other hand, Pitsch et al. [14] showed that the GRI mech mechanisms are also able to predict the mass fractions of CO and CO₂. Taking account of these results and in order to reduce the amount of calculations without weakening the exactitude of the predictions, the chemical mechanism GRI mech 3 is adopted.

5. RADIATION MODEL

The radiation is taken into account in the energy equation (15) by the approach of the optically thin body. The absorption coefficients of H₂O, CO₂ and CO are taken starting from an adjustment for calculations of narrow band by using RADCAL [16], as reported in [15].

6. FLAMELET BASED NO_x MODEL

In this work, the modeling of NO_x is carried out in the phase of post-processing. A single transport equation for the average mass fraction of NO with a source term is solved after obtaining convergent solution of the flow and the mixture of field through calculations of turbulent flow.

$$\frac{\partial}{\partial t}(\bar{\rho}\tilde{Y}_{NO}) + \frac{\partial}{\partial x_j}(\bar{\rho}\tilde{u}_j\tilde{Y}_{NO}) = \frac{\partial}{\partial x_j}\left(\frac{\mu_t}{\sigma_{NO}}\frac{\partial\tilde{Y}_{NO}}{\partial x_j}\right) + \tilde{\omega}_{NO} \quad (18)$$

where the number of turbulent Prandtl σ_{NO} is regarded as being 0.7.

During calculations of flamelet, for a given value of the dissipation scalar rate, the total production rate of NO is calculated and compiled with the other reactive scalars according to the fraction of mixture. The source terms laminar are then integrated into the supposed β -PDF for obtaining the average of the source term $\tilde{\omega}_{NO}$.

7. GAS-PHASE GOVERNING EQUATIONS AND NUMERICAL METHOD

The fields of flow and mixture are studied in 2D in an axisymmetric geometry. The effects of turbulence are modeled by the model with two transport equations ($k-\varepsilon$). On the basis of the report that the standard model ($k-\varepsilon$) over-estimates the rate of round widening out of the jets. This over-estimation can come from the growth of the size of the swirls and the acceleration of their destruction related to the axisymmetric effects. Priest [17] takes into account this effect by proposing an additional term of production of dissipation to the transport equation of ε , proportional to the swirling stretching. A transport equation for the average enthalpy is solved with the radiation source term. Instead of solving the transport equations of several species, the equations of the fraction of mixture and its variance are solved. Then the species are obtained from a table calculated as a preliminary by the model of the flamelets. The solution of the transport equations is made using the Current FLUNT 6 CFD code [18].

The equations that describe the reactive turbulent flow are of convective diffusion type with a source term. These equations are converted into algebraic equations by discretization with UpWind diagram [19], the simple algorithm is used for speed-pressure coupling, and finally the solution of the algebraic system of equations is obtained by using the Thomas algorithm.

8. RESULTS AND DISCUSSION

8.1. Validation of the procedure of calculation:

Figure 2 shows the profiles of the fraction of mixture and the temperature along the central line. The axial decrease of the fraction of mixture is well reproduced and the measured temperatures are estimated with a

reasonable precision. However, the fraction of mixture and the temperature are slightly underestimated between $x=100$ mm and $x=350$ mm which can be related to uncertainties in the profile speed of entry [20].

These results show that calculation by the approach of the flamelet and the model $k-\varepsilon$ correctly predicts the form of the flame, its height and the distribution of the temperature.

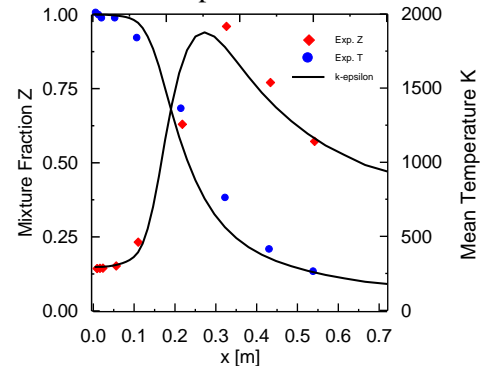


Figure 2
Centerline mixture fraction and temperature in flame

8.2 Study of the effect of dilution by CO₂ on the thermal field :

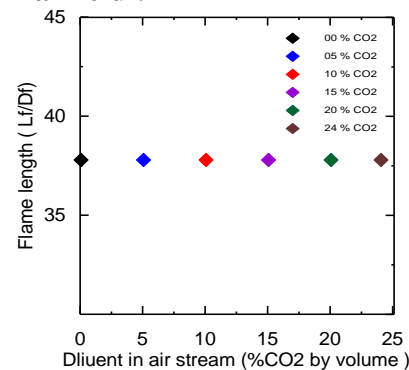


Figure 3
Effect of dilution over the length of the flame

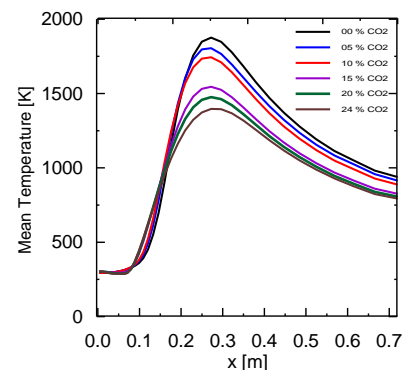


Figure 4
Profile of the temperature on the axis of symmetry.

Figure 3 shows that the position of temperature axial peak $x_{T_{max}}$, used for the determination length of flame L_f ($L_f=x_{T_{max}}$), keeps the same axial position with the increase in dilution. Contrary to the length of the flame, the maximum of temperature decreases according to CO_2 added about 24%.

Figure 4 represents the axial profiles of temperature for the various percentages of dilution by the CO_2 species. It is noted that the axial evolution of temperature keeps the same track for the five cases.

Dilution does not affect the axial profiles in the zone close to the outlet of the central methane tube, contrary, its effect appears especially starting from $x > 0.2m.$.

8.3 Study of the effect of dilution by CO_2 on the field of the species

such as H, O, CO and the HCN will appear gradually and increase to reach maximum values in the zone of reaction as the profiles show (figures 5,6,7 and 8). the behavior of their mass fractions is similar. The effect of dilution by CO_2 is very significant for the various species, it generates an important reduction. For the species H (Fig. 5) the reduction is about 73%, for the species O (Fig.6) it is about 60%, and for the specie CO is reduced almost with the same rate Fig. 7.

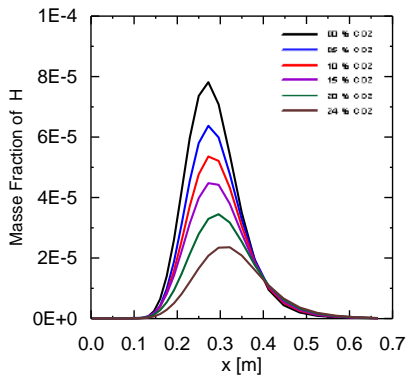


Figure 5

Profile of the mass fraction of H on the axis of symmetry

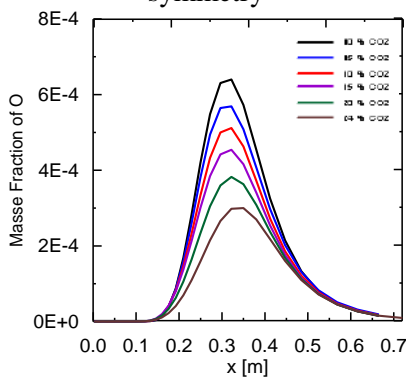


Figure 6

Profile of the mass fraction of O on the axis of symmetry

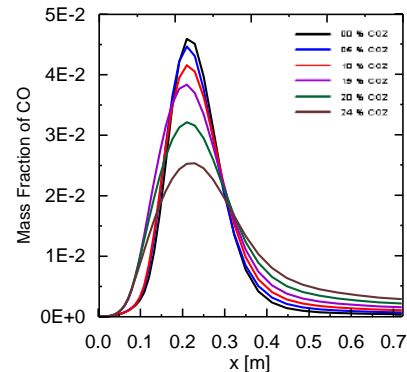


Figure 7

Profile of the mass fraction of CO on the axis of symmetry

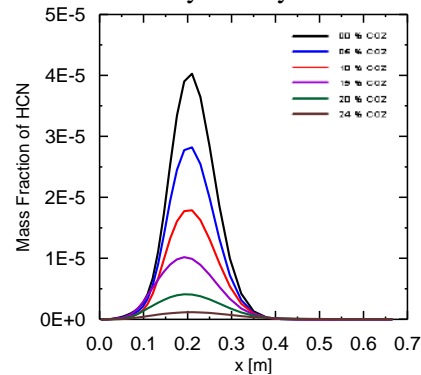


Figure 8

Profile of the mass fraction of HCN on the axis of symmetry

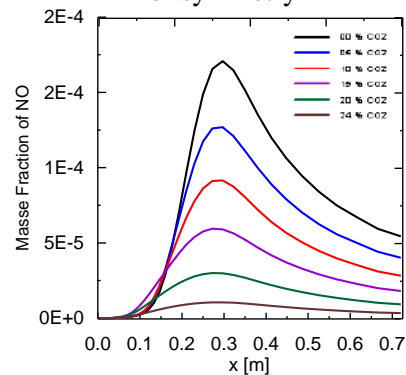


Figure 9

Profile of the mass fraction of NO on the axis of symmetry.

We notices that the most important variations are around the point $x = 272$ mm, i.e. to the maximum of the variables. It is the zone of the face of flame ($T=T_{max}$). The none existent species in the mixture

In the rich face of the flames, the carbonaceous radicals (CX) can easily break the nitrogen molecule following the reaction $N_2 + \dot{C}H \rightarrow \dot{N} + HCN$ with activation energy of 50 Kcal/mole. Due to that, the species HCN (Fig.8) is formed in a very narrow zone on the axis of the flame with a considerable growth, then it is dissociated quickly with the temperature diminution.

The nitric oxide will appear and increase gradually starting from the point $X = 150$ mm to reach maximum values in the zone of reaction as show it Fig 9, downstream from the flame front, the concentration of this species decreases to reach its normal value at the outlet.

CONCLUSIONS

The rate of formation of NO can be reduced approximately 93% by using a dilution by CO₂ of the primary education air that an injection vitiated (swirl) or sheared primary education air which feed the burner.

In spite of dilution impacts on the reduction of the maximum temperature of the flame which is about 25% its length remains constant.

The dilution in the air stream with CO₂ leads to a greater reduction of the concentrations of the important radical species, such as O, H, CO and the HCN which generates the reduction of NO directly.

REFERENCES

1. Tomlin, A.S., 2007, Can combustion technologies reduce our impact on both the global climate and local air quality, 3 ème Congrès Européen de Combustion (ECM), Crete, Grèce.
2. Faivre, V, 2003, Etude expérimentale et numérique du contrôle actif de jets dans les chambres de combustion, Thèse de doctorat de l'institut polytechnique de Toulouse, Toulouse, France.
3. Pesenti, B, 2006, Caractérisation numérique et expérimentale d'un brûleur à gaz à swirl variable : Longueur de flamme, transfert thermique et production de NOx , Thèse de Doctorat en Sciences appliquées, Faculté polytechnique de MONS, Bruxelles, Belgique.
4. Du, D.X., Axelbaum. R.J, and Law, C.K., 1990, The influence of carbon dioxide and oxygen as additives on soot formation in diffusion flames.

Proceedings of the 23 rd International Symposium on Combustion, The Combustion Institute, 1501.

5. Liu, F., Guo, H., Smallwood, G.J., and Gulder , O, 2001. The chemical effects of carbon dioxide as an additive in an ethylene diffusion flame: implications for soot and NO formation, *Combustion and Flame* **125**,778.
6. Park, J., Lee, K.H., and Kim, K.S., 2002 b.,Dilution effect of air stream on NO emission characteristic in H₂/Ar counterflow diffusion flame, *International Journal of Energy Research* **26**,473.
7. <http://www.sandia.gov/TNF/pilotedjet.html>
8. Schneider, Ch., Dreizler, A Janickaa, E.P. Hassel, 2003,Flow field measurements of stable and locally extinguishing hydrocarbon-fuelled jet flames, *Combustion and Flame* **135**, 185–190
9. Mamerie, A. 2009, Numerical study of turbulent premixed combustion methane/air enriched with hydrogen. PhD Thesis University of Orleans Paris France.
10. Mameri,A. , Tabet,F., and HadeF. A, 2015, Simulation of biogas counter flow diffusion flame Under Serval operation condition of composition and pressure international, Book of procceding 12-15 Novembre conference on sustainable development, Belgrad,165-172.
- 11.Mameri.A and Tabet.,F, 2016 Numerical investigation of counter-flow diffusion flame of biogase hydrogen blends: Effects of biogas composition, hydrogen enrichment and scalar dissipation rate on flame structure and emissions, *international journal of hydrogen energy* , **41**(3),2011–2022
- 14 Pitsch H, 2000, Unsteady flamelet modelling of differential diffusion in turbulent jet diffusion flames, *Combust Flame*,**123**:358–74.
15. <http://www.ca.sandia.gov/tdf/Worhshop/Submodels.html#Rad>.
16. Grosshandler W.L, 1993, NIST technical note, vol. **1402**. NIST.
17. Pope, S.B, 1978, An explanation of the turbulent Round-Jet/Plane-Jet anomaly, *AIAAA J*, **16**(3),279–81.
18. Fluent 6.3 user's guide, Septembre 2006.
- 19.Patankar, S.V.,1985. Numerical Heat Transfer and Fluid Flow, Hemisphere, Washington, D.C.
- 20.Kleiveland R.N,2005, Modelling of soot formation and oxidation in turbulent diffusion flames. Ph.D. thesis, Norwegian

STUDY OF THE COKE COMBUSTION KINETICS: THE MODELING OF A NATURAL PHOSPHATE CALCINATION PROCESS

Ikbal BOUATBA, Latifa BILALI, M'barek BENCHANAA, Mustapha ELHAMMIUI

¹Laboratoire de Recherche « Réactivité des Matériaux et Optimisation des Procédés : REMATOP». Université Cadi Ayyad, Faculté des Sciences Semlalia, Avenue Prince Moulay Abdellah, B.P. 2390, 40000 Marrakech, Maroc.
ikbalboutba@gmail.com

ABSTRACT

The study of the coke combustion kinetics has been achieved by using isothermal thermogravimetry (TGA/TDA) under an oxidizing atmosphere. The goal is the determination of kinetic parameters required for modeling of coke combustion process during the calcination process of natural phosphate.

In order to analyze the effects of heating rate and temperature on the change in the rate of coke combustion reaction, various experiments were carried out at temperatures ranging from 650 to 1050°C and various heating rates in the area 1-50 °C/min.

The experimental results show that:

The organic matter of the coke combustion reaction starts only after a latency period, which varies depending on the temperature and the speed of heating. The duration of the combustion also depends on the evolution of these two parameters.

The percentage of organic matter burned coke, in thermal equilibrium, is always of the order 98%.

If the temperature corresponding to the maximum rate of coke combustion is increased, the kinetics of this reaction becomes slower when increasing the heating rate.

The application of the Friedman's method the thermogravimetric curves allows deducing the values of the apparent activation energy and the pre-exponential factor.

Keywords: Phosphate ore, Coke, Kinetic, Calcination, Combustion, Energy.

INTRODUCTION

Coke has become as a result of significant progress in the distillation of oil, a material for multiple uses and a very important energy source, particularly in the phosphate treatment processes at the phosphate calcination that is based on the dissociation thermally carbonates, in a temperature range between 700 and 1000°C, the progress of this reaction requires an amount of energy supplied by the exothermic reaction of coke combustion.

A study of representative samples of coke combustion kinetics is conducted using a thermogravimetric apparatus ATG / ATD in conditions close to those existing in industrial furnaces (variable heating rate and variable temperature) in order to optimize the energy consumption at the level of the calcination and obtaining a calcined phosphate better.

The kinetics of the combustion of coke was the subject of several research published in the scientific literature.

This work is devoted to the analysis of experimental results obtained by TGA/DTA, from heterogeneous kinetic methods to acquire data, such as the rate constant, activation energy and pre-exponential factor ...) to understand the reaction mechanism involved in the combustion.

ANALYSIS AND MODELLING

Characterization of coke

Coke used in this study was provided by the Centre for Studies and Research on the Chérifien Phosphates Office Group.

The results of his immediate analysis, elemental and physical characteristics are given in Tables 1, 2 and 3.

Immediate analysis allows evaluation of the moisture content, volatiles, fixed carbon and ash. Moisture was determined by measuring the weight loss of a sample dried in an oven for one hour at 105°C. The ash content was evaluated from the residue of the combustion of a coke sample at a temperature of 800°C. The volatile matter was determined by the weight loss of a sample maintained at a temperature of 900°C under nitrogen. Fixed carbon is obtained by difference.

Table 1 Results of the studied coke immediate analysis

Compound	% by mass
Humidity	0.79
Volatile matter	12.9%
Ash	2
Fixed carbon	83.31

Table 2 Results of the studied coke elemental analysis

Element	% by mass
C	85.13
H	3.62
N	1.62
S	7

Elemental analysis was performed using the CHNS-CERPHOS unit

Table 3 Values of density, specific surface area and studied coke porosity

Density (kg m ⁻³)	1.41
Specific surface area (m ² g ⁻¹)	0.36
Porosity (%)	99.5

The density of the coke studied was determined using autopycnomètre 1320. The pore surface area was measured using a mercury prosimètre.

Experimental technique

The experimental study of the coke combustion kinetics was carried out using the thermogravimetric apparatus Rheometrix Scientific STA 1500. try has been made on the initial mass 18 mg, at different temperatures 650, 750, 850, 950 and 1050°C at various heating rates, 1, 5, 10,50°C / min and an air flow rate 100ml/min.

RESULTS AND DISCUSSION

Thermogravimetric analysis

Coke combustion was carried out at a temperature 1000°C with a heating rate of 5°C /min under an air flow 100ml/min and an initial mass of 18mg.

The result of the thermogravimetric analysis and differential is shown in Figure 1. Including the curves represent the total loss of mass and heat flow during the combustion of coke as a function of temperature.

The analysis of these curves shows that the combustion of coke:

- Through a single step in the temperature range 390-630°C.
- The curve of the differential thermal analysis shows a single exothermic peak between 277-650°C corresponds to the combustion of organic matter in the coke;
- The percentage of lost mass is around 98%.

During this, after several tests at different heating rates, it should be noted that when increasing the rate of heating, the maximum temperature which is the combustion speed of the coke increases (Table 4).

Table 4 Temperature maximum combustion of coke (Tmax)

Sample	1 ° C/mi	5 ° C/mi	50 ° C/mi
Coke	460 ° C	510 ° C	600 ° C

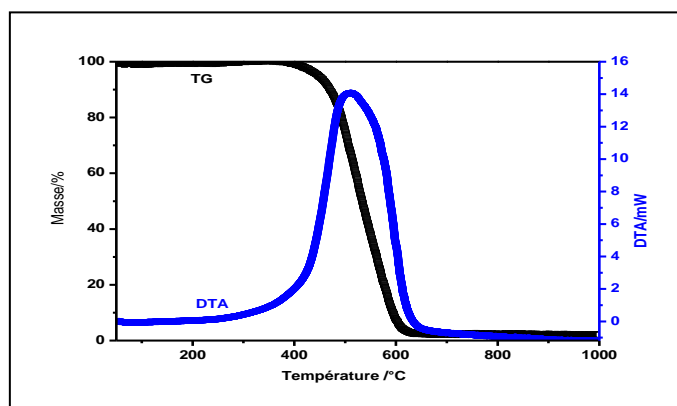


Fig. 1. Analysis Thermogravimetry and differential of the coke under air (5°C/min)

According to several experimental try carried out, it was noted that the reaction of the coke combustion takes place in the temperature range 250-600 ° C.

This leads us to consider the following results in this range.

Temperature effect on the evolution of the combustion reaction degree progress

Isotherms progress curves $\alpha = f(t) T$, express the variation of the degree progress α as a function of time are shown in Figure 2.

The analysis of these curves shows that:

i / - whatever the temperature, the curves tend towards the same combustion stage.

ii / - the percentage of the organic material, in combustion equilibrium is still of the order 98%.

iii / - the organic matter combustion reaction of the coke begins only after a latency period, which varies depending on temperature.

4i / - the duration of the reaction also depends on the evolution of the temperature.

5i / - from the first 30 minutes, each curve can be described by a parabolic shape.

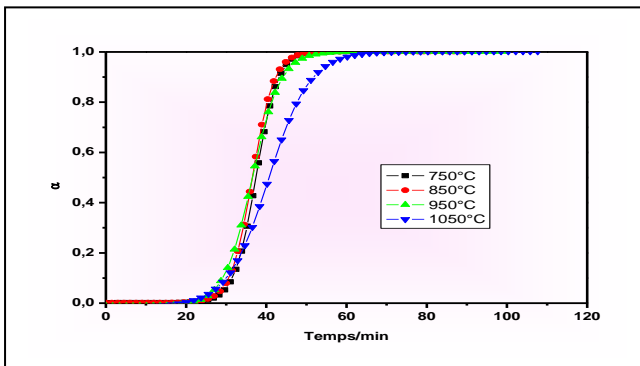


Fig. 2. Evolution of the rate of the combustion progress time for different temperatures with a 10 °C/min heating speed

Effect of the heating rate on the degree progress of the combustion reaction

The results reflect the evolution over time of the promotion rate $\alpha = f(t) \beta$ for different heating rates: $\beta = 1^\circ\text{C}/\text{min}$; $\beta = 5^\circ\text{C}/\text{min}$; $\beta = 10^\circ\text{C}/\text{min}$; $\beta = 50^\circ\text{C}/\text{min}$. the maximum combustion temperature is $T_{\text{max}} = 1,050^\circ\text{C}$. Figure 3.

The analysis of the results shows that:

i / - always tend to bend the same a combustion bearing whatever the heating rate. The percentage of burnt organic matter is still on the order of 98%.

ii / - these curves can be described by two different speeds depending on the heating rate.

For the low heating rate; they have the sigmoid shape and their inflection points are at lower feed rates.

This form changes to become quasi-sigmoid at high heating rates.

iii / - over the heating rate, the higher the combustion kinetics becomes slower.

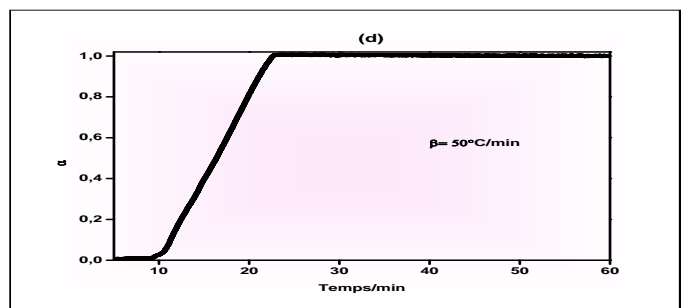
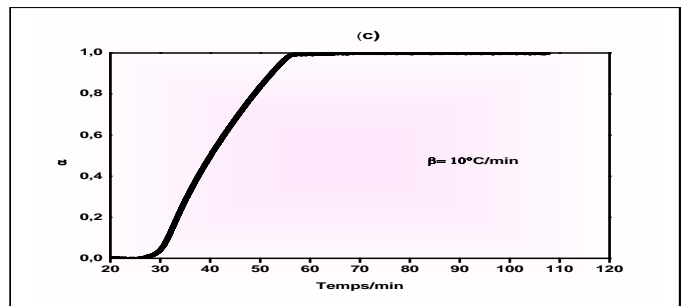
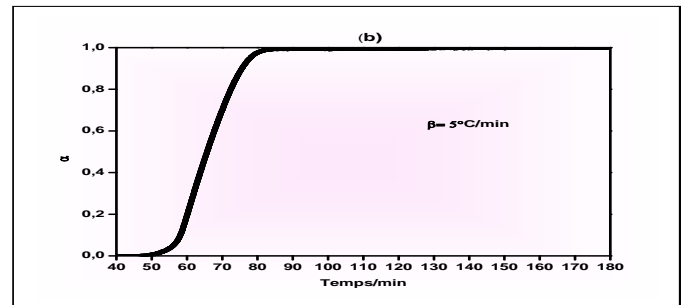
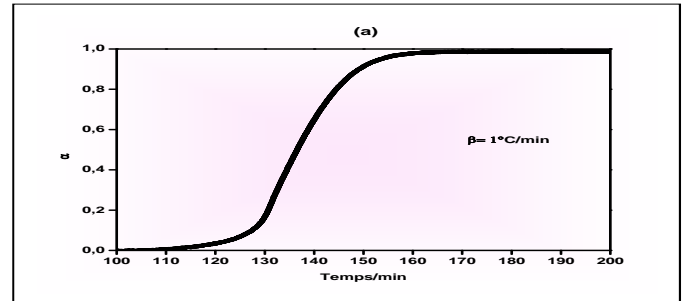


Fig. 3. Evolution of the coefficient of progress over time for different speeds of heating ($\beta = 1^\circ\text{C}/\text{min}$, $\beta = 5^\circ\text{C}/\text{min}$, $\beta = 10^\circ\text{C}/\text{min}$ and $\beta = 50^\circ\text{C}/\text{min}$) at $T_{\text{max}} = 1000^\circ\text{C}$

To seek the dominant kinetic regime in the case of non-isothermal combustion of coke, several experiments were made at different temperatures. The progress curves $\alpha = f(t) \beta$ were traced

according to the maximum temperature for different temperatures as shown by curves $\alpha = f(T)$ β shown by Figures 4, 5, 6, 7 and 8.

We found that most of the heating rate, the higher the combustion kinetics becomes increasingly slow for different try.

This is explained by the fact that the volatiles once quickly released from the solid mass of coke, provide protection around the particle, this protection is consumed slowly with oxygen until now too thin, the particle oxygen attacks.

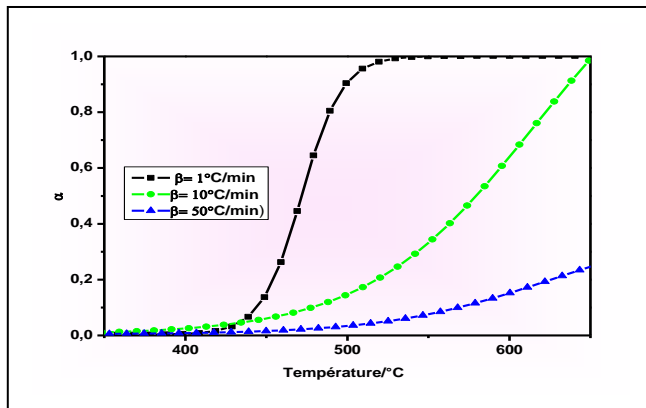


Fig. 4. Evolution of the coefficient of progress according to the temperature for different speeds of heating ($\beta = 1^\circ\text{C}/\text{min}$, $\beta = 10^\circ\text{C}/\text{mi}$ and $\beta = 50^\circ\text{C}/\text{mi}$) at $T_{\text{max}} = 650^\circ\text{C}$

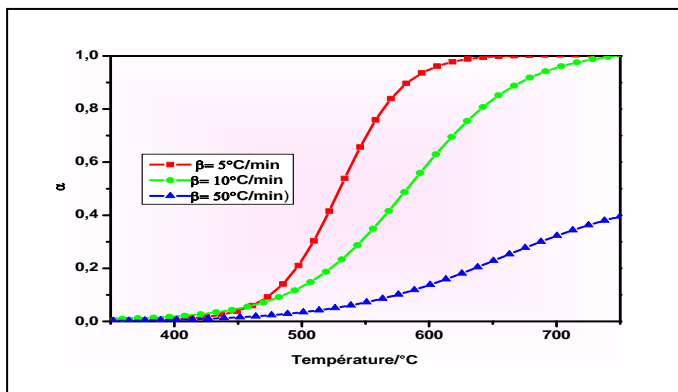


Fig. 5. Change in the coefficient of progress according to the temperature for different speeds of heating ($\beta = 5^\circ\text{C}/\text{min}$, $\beta = 10^\circ\text{C}/\text{mi}$ and $\beta = 50^\circ\text{C}/\text{mi}$) at $T_{\text{max}} = 750^\circ\text{C}$

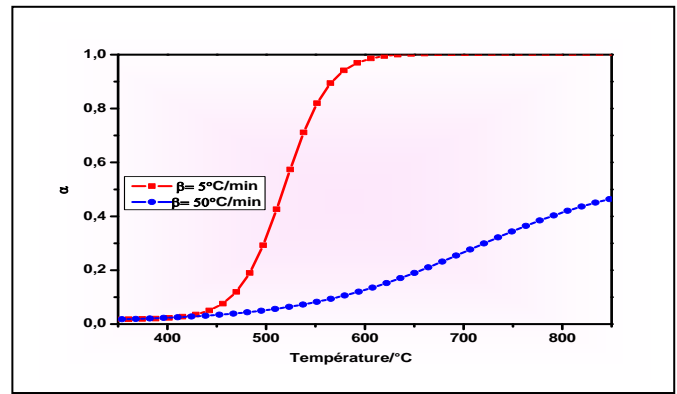


Fig. 6. Evolution of the coefficient of progress according to the temperature for two-speed heating ($\beta = 5^\circ\text{C}/\text{min}$ and $\beta = 50^\circ\text{C}/\text{mi}$) at $T_{\text{max}} = 850^\circ\text{C}$

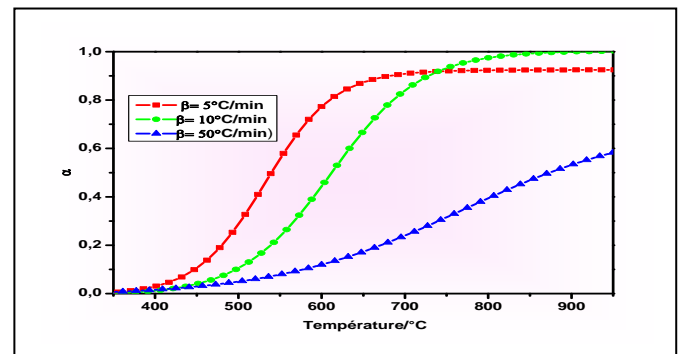


Fig. 7. Evolution of the coefficient of progress according to the temperature for different speeds of heating ($\beta = 5^\circ\text{C}/\text{min}$, $\beta = 10^\circ\text{C}/\text{mi}$ and $\beta = 50^\circ\text{C}/\text{mi}$) at $T_{\text{max}} = 950^\circ\text{C}$

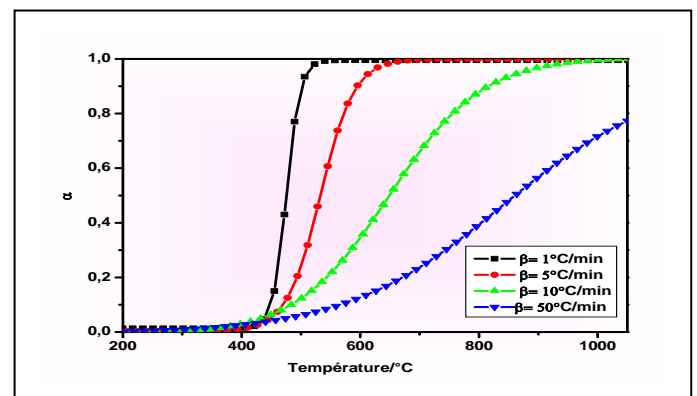


Fig. 8. The coefficient of progress based on the temperature for different speeds of heating ($\beta = 1^\circ\text{C}/\text{min}$ $\beta = 5^\circ\text{C}/\text{min}$, $\beta = 10^\circ\text{C}/\text{mi}$ and $\beta = 50^\circ\text{C}/\text{mi}$) $T_{\text{max}} = 1050^\circ\text{C}$

The overall kinetics of the coke combustion

At a heating rate of 5°C / min, the coke combustion begins at temperature 292°C with a minimum speed of combustion 0.106 mg / min to reach thereafter to a maximum value of 5.540 mg / min at the temperature 410°C. Figure 10

The speed of this reaction can be controlled by one or a combination of processes:

- Chemical process between the solid reactant (carbon) and the reactive gas (oxygen), which occur at low temperatures (350-500°C) [1-6].
- Transfer Process (Dissemination of material and heat) through the gas layer surrounding the coke particles and pores of the solid, which take place at high temperatures (600-1400°C) [1, 3, 6, 7].

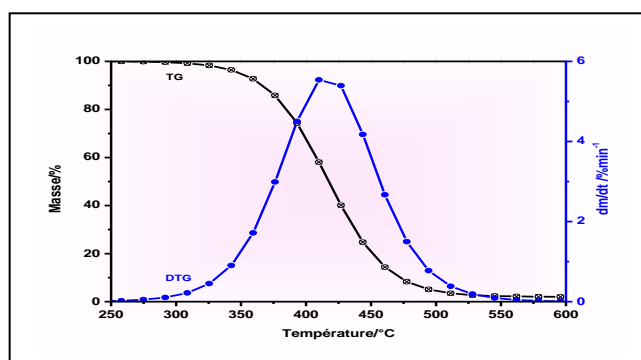


Fig. 9. Derivative of thermogravimetric analysis of coke combustion for a maximum temperature 1000°C and 5°C/min heating speed

CONCLUSIONS

The organic matter of the coke combustion reaction starts only after a latency period, which varies depending on the temperature and the speed of heating. The length of the combustion also depends on the evolution of these two parameters;

- The percentage of organic material burnt coke is always about 98%;
- When increasing the heating rate, the maximum temperature corresponding to the maximum speed of burning coke increases;

- The higher the speed, the higher heating kinetics becomes slower this is explained by the fact that the combustion of volatiles vapor goes first before oxygen finds time to attack the grain coke.

- At a heating rate of 5°C/min, the activation energy and pre-exponential factor found from the Friedman's method, respectively, are of the order of 31.78 kJ / mol and $\ln(K) = 7.37$ in the temperature range 242-613°C. these values are significantly different from that of the literature. This difference is due to the nature of the raw material (coke) used in the experimental study and the mathematical model of the kinetic adopted for the treatment of experimental results.

REFERENCES

- [1] R.J. Hamor, I.W. Smith, R.J. Tyler, Kinetics of combustion of a pulverized brown coal char between 630 and 2200°K. *Combust. Flame* 1973; 21:153.
- [2] L.C. Lin, M.D. Deo, F.V. Hanson, A.G. Oblad, Nonisothermal analysis of the kinetics of the combustion of coked sand. *Ind. Eng. Chem. Res.* 1991; 30 (8): 1795.
- [3] L.D. Smoot, P.J. Smith, *Coal Combustion and Gasification*, NewYork 1985; 77.
- [4] S. Dutta, C.Y. Wen, R. J. Belt, Reactivity of Coal and Char. 1. In *Carbon Dioxide Atmosphere*. *Ind. Eng. Chem. Process Des. Dev.* 1977; 16 : 20.
- [5] M. Boumahmaza, Étude cinétique de la gazéification d'un charbon du Maroc (anthracite de Jerada) par thermogravimétrie. Approche de modélisation de la réaction, thèse de doctorat d'État, faculté des sciences, Rabat, Morocco 1991.
- [6] I.W. Smith, D.J. Harris, M.G. Valix, D.L. Trimm, Mass Transport and Carbon Reactivity at High Temperature. *Fundam. Issues in Control of Carbon Reactivity* 1991; 192: 49.
- [7] J.E. Hustad, D.Vareide, O.K. Sonju, Burning rates of coke particles in the freeboard above a fluidized bed reactor. *Combust. Flame* 1991; 85 (1-2) : 232.

REHAFUTUR – INSITU INSTRUMENTATION FOR A COMPREHENSIVE BUILDING ANALYSIS.

Radhouan DERBAL^a; Franck BRACHELET^a; Emmanuel ANTCZAK^a; Didier DEFER^a; Alain LUCAS^b.

^aUniv. Artois, EA 4515, Laboratoire de Génie Civil et géo-Environnement (LGCgE), Béthune, F-62400, France

^bAssociation Création Développement Eco-Entreprises (Cd2e), Base du 11/19 - 62750 Loos-en-Gohelle, France

*Corresponding author: Tel: +33 3 2163 7128 Email: radhouan.derbal@gmail.com

ABSTRACT

The building industry is called to a generalised use of eco friendly materials for a climate change limitation. In this context, the EU project ‘Rehafatur’ aims to promote the use of bio-based materials in building. Thus, a traditional north France house was renovated using 8 bio-based materials and was instrumented. The instrumentation allows different parameters monitoring during several months and seasons. In this article, we present an over view of the project and the first recorded data. Then, we focus on the south-east wall data to apply an inverse heat transfer method. The method was developed and applied in our laboratory, it allows thermophysical properties estimation.

NOMENCLATURE

C	Volumetric heat capacity	$J K^{-1} m^{-3}$
T	Temperature	$^{\circ}C$
t	Time	s
x	Space (Thickness)	m
λ	Thermal Conductivity	$W K^{-1} m^{-1}$
α	Thermal Diffusivity	$m^2 s^{-1}$
p	Parameters array	
F	Objective function	

INTRODUCTION

Recently COP21 and Paris agreement were achieved. Building is one of the major axes of reduction in energy consumption and greenhouse gas emissions. In this context, Rehafatur 1 is one of the multiple demonstration sites of the EU project called Cap’Em. The project was achieved thanks to partners (Cd2e - sustainable activities organisation- , Maisons et Cités -social housing landlord-, Ekvation -Cluster- and others). All participants aim to promote the use of bio-based materials in building through this project. It is also considered as a reference in hygrothermal buildings’ studies in the actual conditions of renovation: north France old mining houses, more than 100 000 units. Rehafatur 1 concerns the

rehabilitation of a 20’s built mining engineer house using at least 8 bio-based materials. It is now considered as a close to passive establishment open to public [1] (Figure 1).



Figure 1

Rehafatur - North France mining house: before and after renovation.

The original constructions’ walls were non-insulated traditional north France bricks based. Now, roof and walls thermal performances are enhanced thanks to an interior insulation by using: hemp concrete bloc (HCB), cellulose wadding, sheep, linen and wood wools. The actual work aims to share an in situ

experience. The first months' data and the first conclusions made on its light are exposed.

INSTRUMENTATION

To analyse the building behaviour a complete instrumentation was performed. The building was instrumented during renovation using more than 50 sensors. Thus, 70 parameters are monitored to study the building behaviour for a middle term: 2 years. The building is equipped with an Air Handling Unit (AHU) for an optimum inside air quality and energy exchange between the in and out air. 6 sensors were placed in the basement nearby the AHU for temperatures, relative humidity (RH%) and air velocity monitoring at different locations of the unit (Figure 2). A compact Local Telemetry Unit is used to record the building consumptions. Thus, power consumption at different locations is monitored.

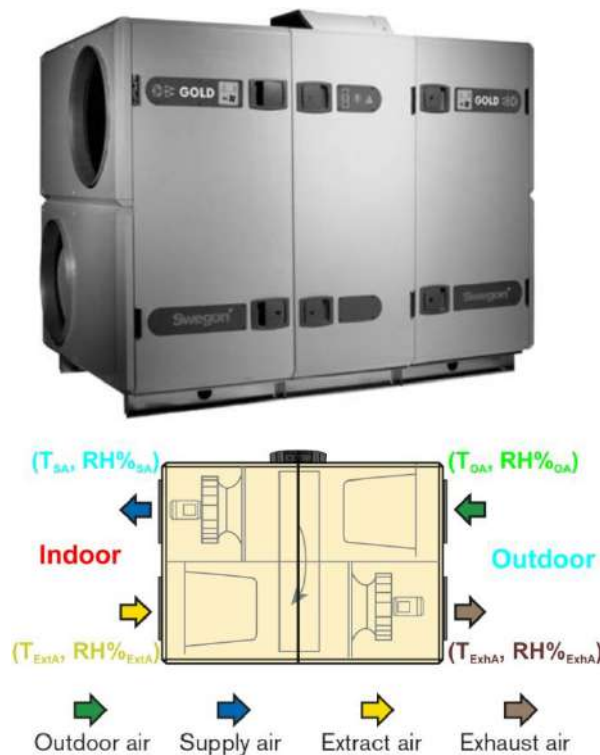


Figure 2
Air Handling Unit -Glod RX- details

In the same time, the four buildings' facades were similarly instrumented. Each wall was equipped with heat flux meters and thermocouples placed at the inside, outside and at the insulation/brick interface. Hygrothermal sensors were also placed at the interfaces (Figures 3 and 4).

The inside building temperatures and RH% in addition to CO₂ amounts are all monitored at different

locations. The outside temperatures and RH% are also recorded (Figure 5).

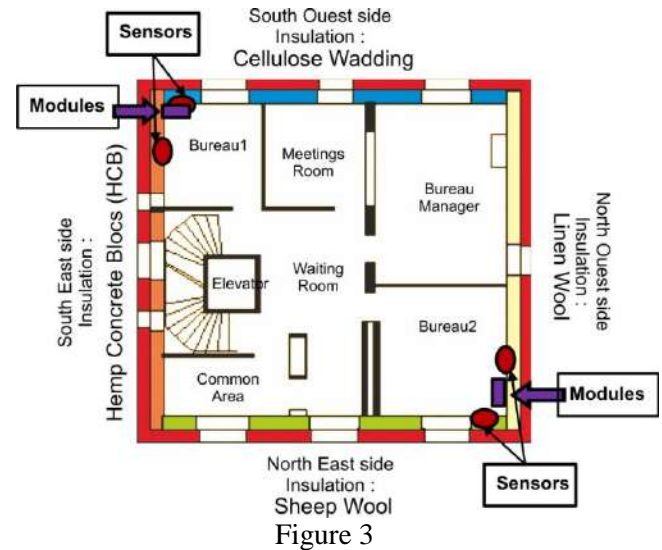


Figure 3
First floor sensors and modules positions

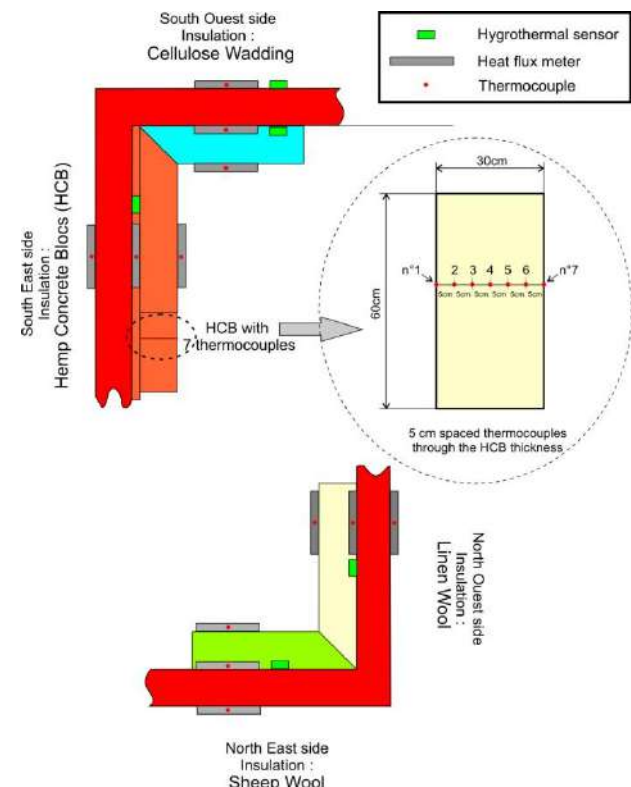


Figure 4
Walls instrumentation details.

An instrumentation network was imagined to gather the whole data in one accessible monitor. Thus, a programmable display monitor is used to communicate with the measurement network, record different physical variables and display live results (Figure 6).

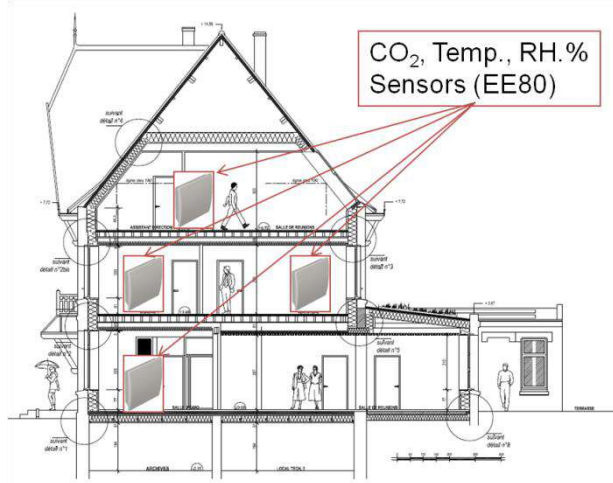


Figure 5
CO₂, Temperature and Relative Humidity sensors locations in the house.

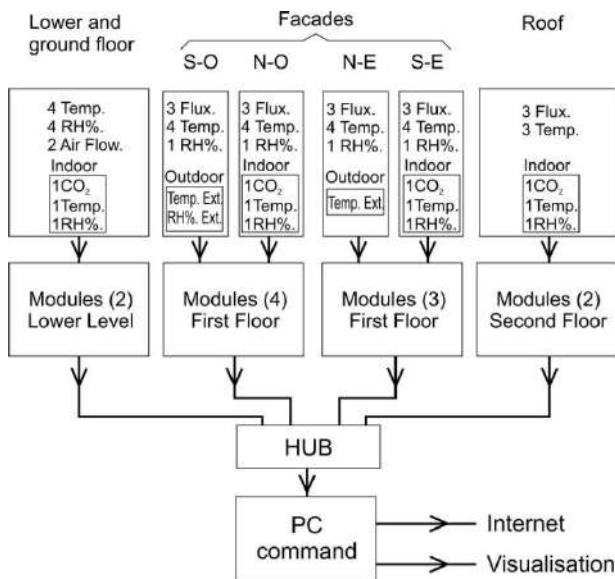


Figure 6
Instrumentation network details.

In addition, 7 thermocouples were placed at different locations through HCB thickness (Figures 4 and 7). Thus, an In situ LGCgE developed method application is being possible.

ANALYSIS AND MODELLING

The developed method is based on an inverse heat transfer analysis using experimental tests and a numerical model [2]. In fact, the recorded in situ temperatures thanks to the 7 thermocouples ($T_{meas\ i}$, $i=1,\dots,7$) are compared in an optimisation algorithm with the model simulated temperatures to predict the HCB behaviour. At this stage, the method is applied

to estimate the thermophysical properties (ThPs) of the hemp concrete. Next, prior laboratory tests will allow defining the correlation between materials' ThPs and their moisture content. Using future several months' available data will allow us estimating the HCB hydric state. Thus, its hydric and thermal properties will be estimated during the 2 years data exploitation.

Numerical basis of the inverse heat transfer developed method is exposed hereafter.

First, a direct heat transfer model is implemented on Matlab® to solve the heat equation (equation 1). The direct model inputs are: initial ($T_{ini}(x)$) and boundary conditions ($T_1(t)$ and $T_7(t)$) and the user initial ThPs (λ_0 : thermal conductivity and C_0 : volumetric heat capacity). The initial HCB temperature is determined thanks to the first recorded temperatures through the material's thickness (Figure 7). HCB boundary recorded temperatures allow determining the boundary conditions. A heat flow meter setup (please refer to EN 12667, EN 13939 and previous work [3]) allow us to determine the materials' ThPs in laboratory. The model outputs are: simulated temperatures (T_{sim}) through the HCB thickness (1D). For more information about the experimental setup or the model validation and sensitivity study, please refer to our previous work [4].

$$C \frac{\partial T}{\partial t} = \lambda \frac{\partial^2 T}{\partial x^2} \quad \text{or} : \quad \frac{\partial T}{\partial t} = \alpha \frac{\partial^2 T}{\partial x^2} \quad (1)$$



Figure 7
HCB instrumentation details: 7 equidistant thermocouples and 6 supposed layers

The model simulated temperatures are compared to recorded temperatures in an iterative optimisation algorithm implemented on Matlab®. Thus, an objective function (equations 2 and 3) is minimised and new thermal properties are estimated over the 6 supposed layers (Figure 7). When at least one stop criterion is satisfied, the iterations stop and optimum

ThPs are reached (Figure 8). Next, the inverse heat analysis results and first recorded data are exposed.

$$f_j(\mathbf{p}) = \frac{T_{meas j} - T_{sim j}(\mathbf{p})}{\max(T_{meas j}) - \min(T_{meas j})} \quad (2)$$

$$F(\mathbf{p}) = \sum_j (f_j(\mathbf{p}))^2 \quad (3)$$

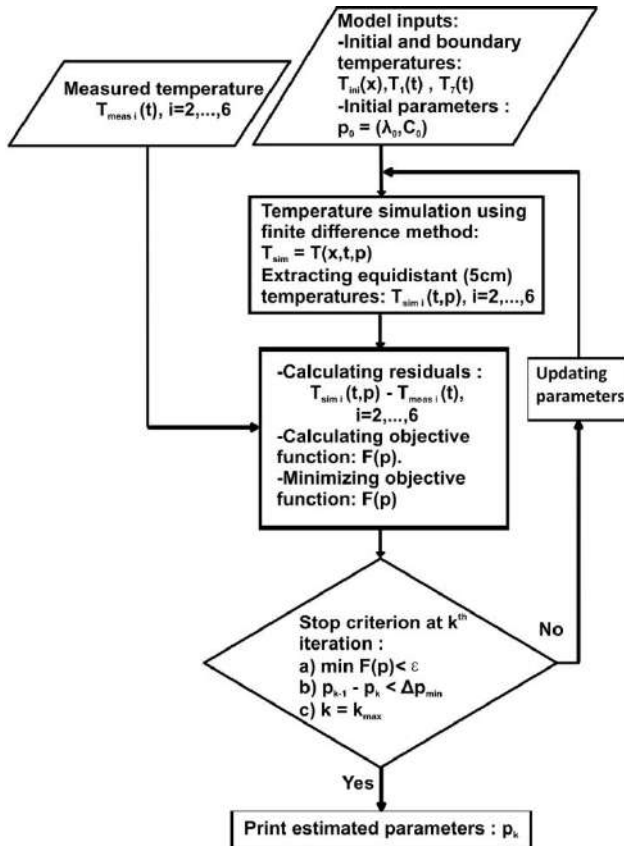


Figure 8

Inverse analysis diagram: ThPs estimation

RESULTS AND DISCUSSION

In this section, the building envelope recorded parameters are exposed. Then, the inverse developed method results are exposed and discussed. The rest of recorded parameters are still being analysed.

The results of the most instrumented side (S-E wall) are presented.

Heat flux (locations: outside, interface and inside: Figure 4) evolution during the first months is presented on Figure 9. The heat flux sign convention is: positive for heat gain (ex: incident radiation) and negative for heat loss. The temperatures at the same locations, during the same period, are presented on Figure 10. During the summer afternoons the S-E wall is exposed

to solar radiation and heat flux reach high values up to 566W/m². High temperatures up to 43°C are recorded. The attenuation of the most part of incident radiation takes place through the 34cm bricks thickness where the estimated thermal lag reach values up to 12 hours. Thus, bricks large thickness plays an important role in building indoor comfort during hot periods. This comfort is being analysed thanks to the hygrothermal sensors and recorded ambient temperature and RH%. The recorded data (Figure 9) will allow in a future analysis to estimate the S-E wall heat loss per year.

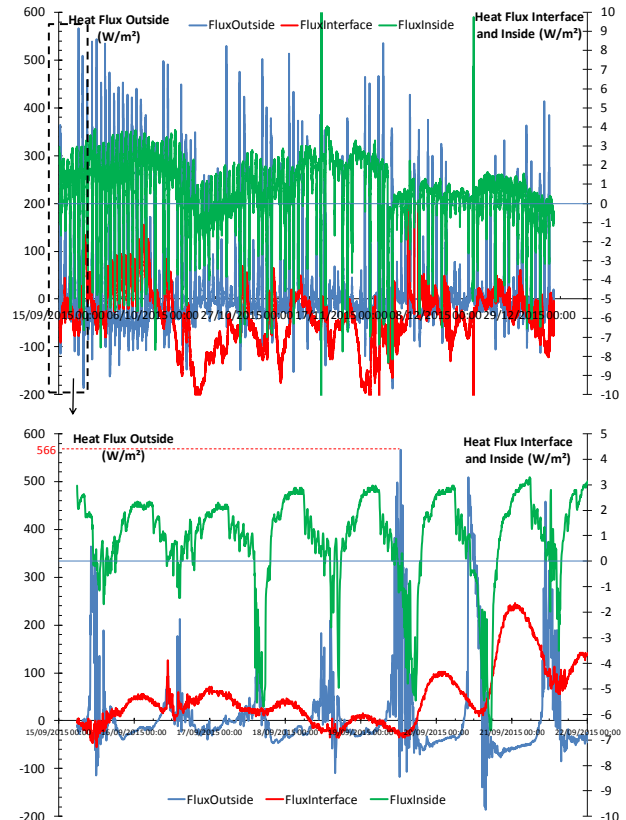


Figure 9

S-E wall: recorded heat flux at the three locations: Outside, interface and inside

Hygrothermal probe placed at the interface (Figure 4) provides important information about the condensation risk at this location. Thanks to the recorded temperature and RH% the dew point evolution is estimated and also the condensation's risk (Figure 11). The chosen period present a supposed high risk, when passing from hot to cold periods. As shown on Figure 11, until now, no real condensation risk has been recorded. The future analysis of cold period data will allow us to define if the condensation occurs at the interface and the most risky points.

The recorded data through the HCB thickness thanks to the 7 thermocouples is shown on Figure 12. This corresponds to the measured temperatures “ T_{meas} ” on the diagram (Figure 8). Result of the inverse method is shown on Figure 13. One can see the curve fitting between simulated and measured temperatures at the Tc6 position (Figure 7) during the first week recorded data (Sep 15th to Sep 22nd).

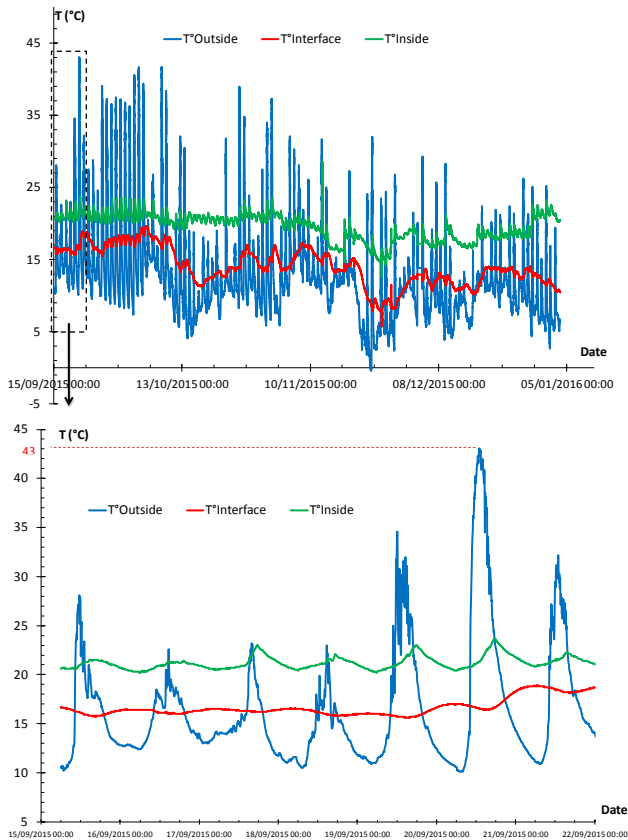


Figure 10

S-E wall: recorded temperatures at the three locations

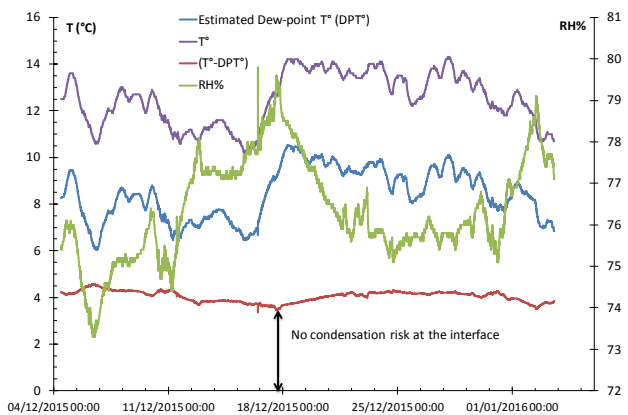


Figure 11

Temperature and RH% at the interface: Estimated Dew Point Temperature and condensation risk

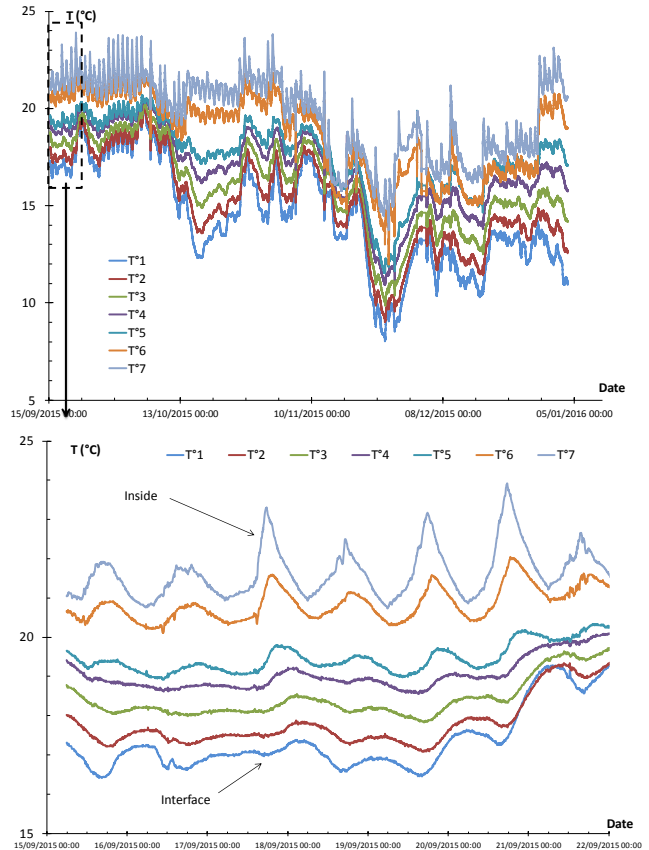


Figure 12

Recorded temperatures through the HCB thickness

First week recorded data is used to estimate the ThPs of the instrumented HBC. The estimation is repeated for all the analysed data: from Sep 15th to Nov 4th. The rest of data is being analysed. Estimated ThPs evolution is presented on Figures 14, 15 and 16. One can see the variation of thermal conductivity, volumetric heat capacity and deduced thermal diffusivity. The thermal diffusivity through the HCB is not constant; it is time and space dependent. Its minimum values are estimated for the layer 6: location of the highest temperatures. The maximum thermal diffusivity values are estimated for the layer 1 location of low temperatures and thus high relative humidity. 20.41% is the mean relative deviation between the minimum and the maximum thermal diffusivity values. This is due to the high water and water vapour diffusivities compared to the HCB dry bulk. In a future analysis, the hydric material state will be estimated, and thus, its moisture content evolution.

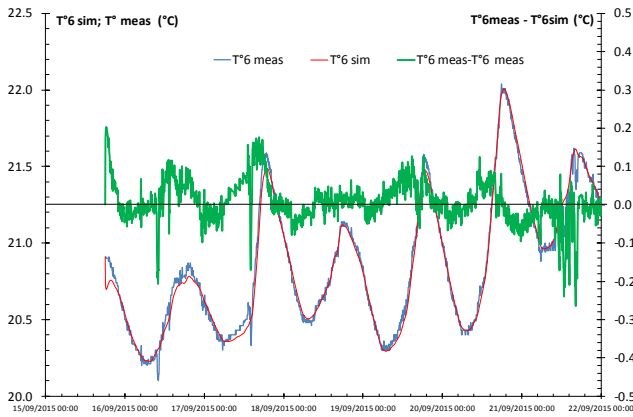


Figure 13

Inverse analysis results: curve fitting in Tc6 position

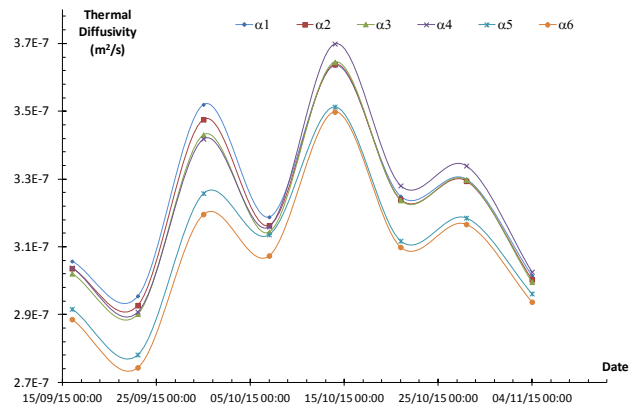


Figure 16

Estimated Thermal diffusivity

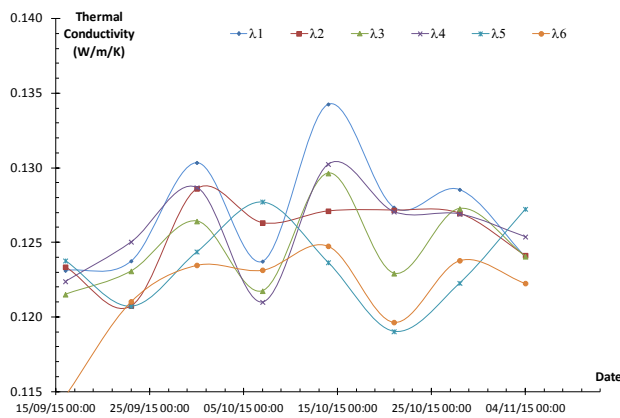


Figure 14

Estimated thermal conductivity

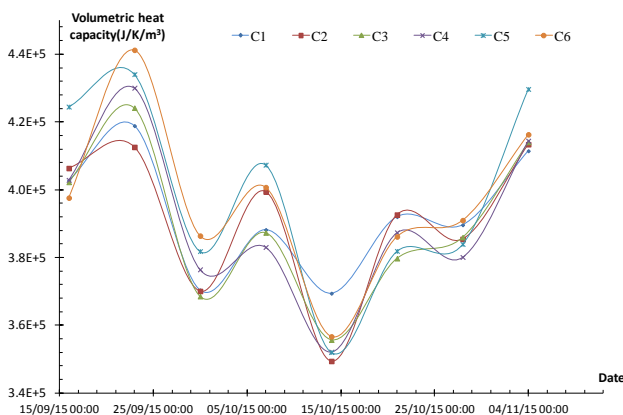


Figure 15

Estimated Volumetric heat capacity

CONCLUSIONS

The EU project (Rehafutur) is presented in this paper. A North France traditional mining engineer house was renovated and instrumented. The instrumentation and the first months' recorded data are presented. A laboratory developed inverse method is described and its results presented. The applied method allows monitoring the thermophysical properties of an instrumented Hemp Concrete Bloc "HCB" during several weeks. Next analysis will allow estimating the moisture content of studied HCB.

ACKNOWLEDGMENTS

The authors gratefully acknowledge the partners: Cd2e, Ekvation, Maisons et cites, and others support for Rehafutur project.

REFERENCES

- [1] REHAFUTUR (Web site). Cd2e - Ekvation.
- [2] Özişik N, Orlande HRB. Inverse Heat Transfer: Fundamentals and Applications. London: Taylor & Francis; 2000.
- [3] Derbal R. Développement d'une méthode inverse de caractérisation thermique : application à l'estimation des propriétés thermophysiques et hydriques des matériaux de construction. Béthune: Université d'Artois; 2014.
- [4] Derbal R, Defer D, Chauchois A, Antczak E. A simple method for building materials thermophysical properties estimation. Construction and Building Materials. 2014;63:197-205.

VOLUME RECONSTRUCTION OF A PLANE JET IMPINGING ON A SLOTTED PLATE USING THE PHASE AVERAGING METHOD

Jana Hamdi¹, Hassan Assoum², Mouhammad El Hassan², Kamel Abed-meraim¹, Anas Sakout¹

¹ Laboratoire des Sciences de l'Ingénieur pour l'Environnement (LaSIE), University of La Rochelle, Avenue Michel Crépeau, Pôle Sciences et Technologies, 17000 La rochelle, France

² Beirut Arab University (BAU), Tripoli Branch, Lebanon

*Corresponding author: Email: jana.hamdi@univ-lr.fr

ABSTRACT

Impinging jets are widely used in ventilation systems in order to improve indoor air quality and energy consumption. Thus the flow dynamics involved in these configurations is very important and should be understood and controlled. In the present study, a plane jet issuing from a rectangular nozzle and impinging on a slotted plate was investigated experimentally by means of 3D-stereoscopic PIV. The velocity field was experimented for thirty parallel planes. The whole field was obtained by interpolation between planes and a 3D reconstruction of the flow was obtained by using the phase averaging technique applied to each of the instantaneous fields. Self-sustained tones generated in this configuration were measured simultaneously with the PIV fields by the use of a microphone. The obtained acoustical signal was used as reference in the phase averaging technique.

NOMENCLATURE

H	height of the jet (mm)
L	nozzle to plate distance (mm)
L_z	width of the jet (mm)
u	Transversal velocity (m/s)
v	Longitudinal velocity (m/s)
w	Transversal normal velocity (m/s)
Re	Reynolds number
ν	kinematic viscosity of air (m^2/s)
T_0	Average period of acoustic signal (s)

INTRODUCTION

In several configurations, the fluid dynamics can be a source of noise as well as airflow discomfort. The acoustic noise is due to the self-sustaining tones which are a result of the energy transfer between the aero-dynamic and the acoustic fields. In fact, lots of studies were done in the domain of a flow past a circular cylinder. For such a configuration turbulence properties, vortex dynamics and the wall shear stress were studied in 2D as well as in 3D such as in [1], [2] and [3] by means of PIV, stereoscopic PIV known as 3C-PIV or SPIV and time resolved PIV known as TRPIV. Whereas, for a plane jet impinging a slotted plate the essential studies were done in 2D. Assoum

[4] have studied the vortex dynamics and the self-sustained tones as well as the aero-acoustic coupling in a plane jet impinging a slotted plate [5]. In addition, these studies have shed light on the different regimes of the flow according to the initial conditions. On the other hand, the main structures for this type of flow are the kelvin-Helmholtz vortices which result from the convective instability in the shear layer. Thus, at a high Reynolds number, the flow presents a dual character of organized and random fluctuations. For this reason, the phase averaging technique was implemented for this class of flow in order to decompose it into its coherent and turbulent parts. Our study is based on the 3D analysis of the vortex dynamics for a plane jet impinging a slotted plate, for this reason the use of 3C-PIV technique which provides the transversal normal velocity was necessary. The principle of the 3C-PIV technique as well as the different stereoscopic configurations are described and detailed in [6]. In the present paper, a plane jet was investigated by means of 3C-PIV for a $Re=4458$ which correspond to a noisy configuration. In order to study the noisy 3D configurations and analyse correlations between sound production and deformation of vortex structures that impinge the slotted plate, we performed a volume reconstruction

of the time resolved SPIV planes. Thirty parallel planes were investigated by means of stereoscopic PIV, and the phase averaging technique was applied to each of the 3C-PIV plane fields. Afterwards, an interpolation between the plane fields has led to a reconstructed volume. We will start first by a representation of the experimental set-up, then in the following section we will describe the phase averaging technique and will present the obtained results.

EXPERIMENTAL SET-UP

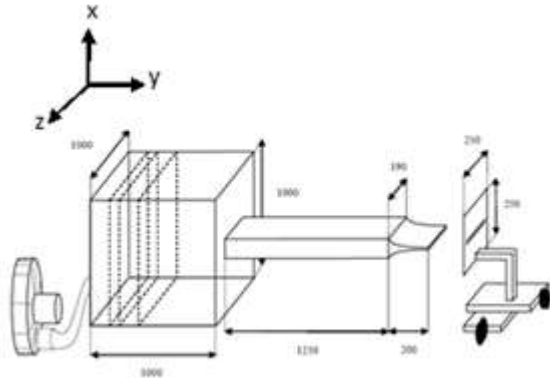


Figure 1: Jet flow facility

Jet flow facility

The experimental setup of our study as displayed in

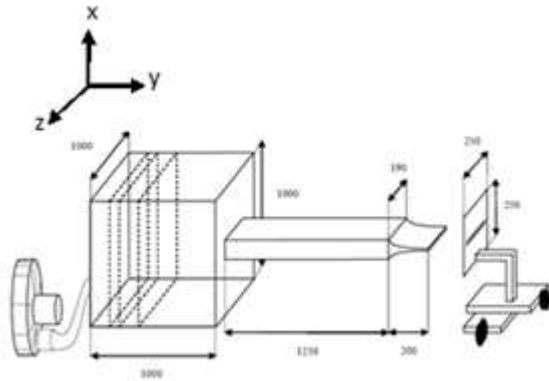


Figure 1, is designed to allow measurements of 3D velocity field using SPIV. The air flow is generated by a compressor which is commanded by a controller. This controller is in charge of the flow velocity, it was fixed on the fifth position corresponding to an initial velocity of 7 m/s. The air flow crosses a settling chamber and a rectangular tube extended by a rectangular convergent creating by that a free jet such that $H=10$ mm and $L_z=190$ mm. The formed jet hurts a slotted plate having the same dimensions as the convergent outlet and perfectly aligned with that. The nozzle to plate distance is 40 mm. The Reynolds

number is equal to 4458 at a temperature of 23 °C, Assoum [7] has showed that for a confinement of $L/H=4$ this Reynolds number corresponds to a noisy configuration as shown in the figure below.

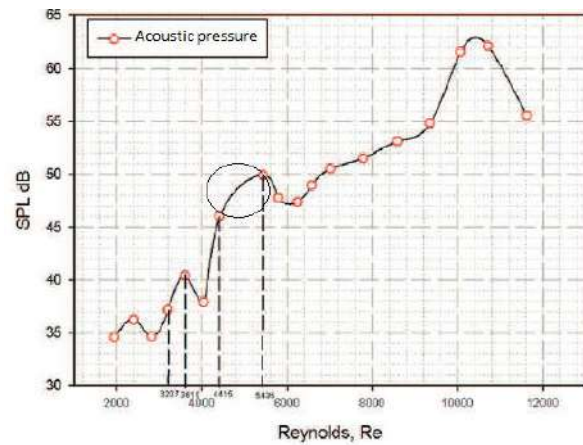


Figure 2: Acoustic pressure in function of Reynolds number for $L/H=4$

Stereoscopic 3C- PIV

Three components PIV acquisitions were carried out using as shown in Figure 4: (1) two cameras Phantom V711 of 1 MPixel resolution and 7530 Hz frequency mounted normally to the laser plane sheet, and a laser generated by a ND: YLF Litron laser of 30 mJ energy per pulse and 527 nm wavelength. The laser beam is focused into an optical fibre (2) which generates a plane sheet as shown in Figure 3.

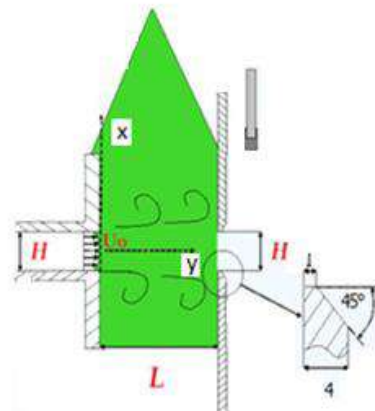


Figure 3: Laser plane sheet

In addition, the two camera axes are rotated such that the two axes intersect the object plane at the system axis. Furthermore, the object, the lens and the image planes should be collinear so that they satisfy the Scheimpflug condition which ensures that all particles should be in good focus in the image plane. The air jet flow illuminated by the laser sheet

is seeded with small olive oil droplets, of $2 \mu\text{m}$ in diameter, provided by a liquid seeding generator. The acquisition frequency of the PIV system is 5000 Hz that is a total of 2500 pair of images were acquired. Simultaneously, the sound pressure is investigated by the use of a microphone (4) placed behind the slotted plate far from the fluctuations of the flow. The sampling frequency of the B&K Free-Field $\frac{1}{2}$ " Type 4189 microphone is equal to 5000 Hz. The synchronization between the laser and both cameras is done by a LaVision high-speed controller, and the synchronization with the acoustic signal is performed by a data acquisition card: National Instruments. The data acquisition and its post processing are performed with Davis 8.3.0 software. From the other hand, the optical fibre generator of plane laser sheet as well as both cameras are fixed on a displacement system (3). This displacement system was necessary to obtain more than one plane, that is, to satisfy the strategy of our study based on the reconstruction of thirty parallel planes.



Figure 4: Experimental set-up

In fact, thirty parallel planes are investigated by means of 3C-PIV. Each of these planes is obtained by a position of the laser plane sheet where initially the displacement system is fixed at a position P0 corresponding to the middle plane of the plate. Afterwards, this system is moved forward by 2 mm for the first sixteen planes and by 5 mm for the rest reaching by that the plane P98 corresponding to an

outside position of the nozzle and distant of 98 mm from the middle plane.

DATA ANALYSIS

SPIV Plane: P0

Our study is based on the analysis of the vortex dynamics in the reconstructed field. In order to have a profound understanding of the mechanisms, we will show first the results obtained in one of the parallel planes. A good example was the middle plane P0. The images were processed by a multi-grid algorithm correlation and the final grid is composed of $3 \times 32 \times 32$ pixel size interrogation window with 75% overlap. This PIV vector calculation was necessary due to the fact that the phase averaging technique is based on the instantaneous acquisitions of vector fields. Figure 5 represents an instantaneous vector field which is chosen for a representative instant of the formation of vortices.

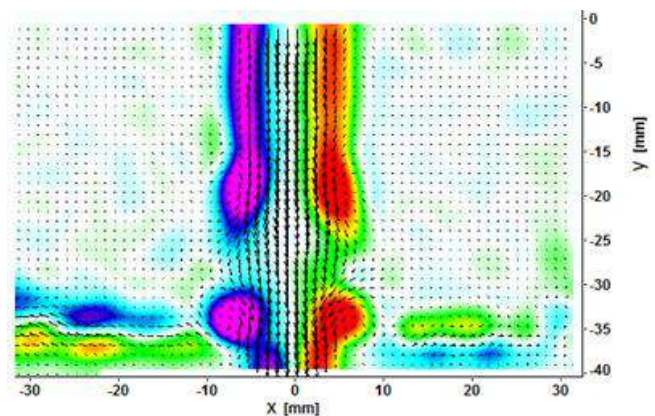


Figure 5: PIV vector field and vorticity in colors
Plane P0

As mentioned earlier, our main purpose is to study the evolution of the transversal velocity w , normal to the parallel planes in order to understand the dynamics of vortices in the studied volume. As for the moment, the available technique is the TR-SPIV, so we started by an investigation of parallel planes and then chose to perform a volume reconstruction of the flow. The 3D field was obtained by an interpolation between the parallel planes while the reconstruction of the flow was obtained by using the phase averaging technique applied to each of the instantaneous fields. We will start by a brief explanation of the phase averaging technique, afterwards the application and the results of this processing will be presented.

Phase averaging

The phase averaging is a technique of conditional sampling of PIV data acquisitions. It is based on a synchronised acquisition between the laser measurements and a trigger signal which is periodic and characteristic of the vortex shedding. Thus the phase average measurements are obtained by a post-processing of the data acquisition.

Concept:

As a consequence of the regular large-scale vortex shedding process, the wake flow contains dominant quasi-periodic component. This characteristic of the periodic component of the flow can be represented by the triple decomposition of Reynolds and Hussain [8]. Actually, for Reynolds and Hussain [8] any instantaneous flow property can be decomposed into a mean component, a periodic fluctuation and a chaotic one as follows:

$$U_i = \bar{U} + \tilde{U}_i + u'_i,$$

where \bar{U} is the mean velocity, \tilde{U}_i is the quasi-periodic fluctuation and u'_i is the random fluctuation. In addition, $\tilde{U}_i = \tilde{U}(x, \varphi + 2\pi n)$ where n is an arbitrary integer and φ the phase angle of the periodic component of the trigger signal. As in our study, the kelvin Helmholtz instability is of the global type that is the velocity has a strong quasi-periodic component at every point in the flow. This periodic property allows the application of the phase averaging technique in order to represent the coherent flow motion described by the vortex formation and the shedding process. This quantity is therefore composed of the mean and periodic component. In other terms, as defined in [9] the phase average is the average, for every point of the space, of a quantity U realised for a given value φ of the trigger signal. Consequently, knowing φ the phase average can be represented as a conditional average, as follows:

$$\langle U_i \rangle = \bar{U} + \tilde{U}_i = \lim_{N \rightarrow \infty} \frac{1}{N} \sum_{n=0}^N U^i(t) I_\varphi^i(t),$$

with $I_\varphi^i(t)$ is equal to 1 if the phase of the flow is φ at t , and 0 if not.

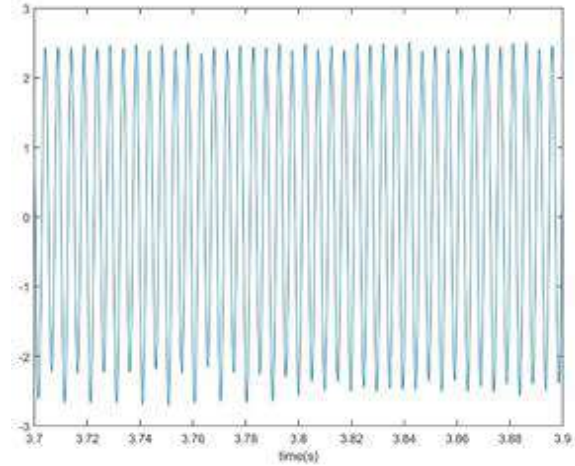


Figure 6: Acoustic signal - plane P0

Trigger signal and phase identification:

In order to apply the phase average technique to the instantaneous velocity fields realizations provided by the TR-SPIV, the phase of each instantaneous field should be determined. There are two ways for the phase determination, the first is by the use of an external phase indicator called a trigger signal and the second method is by using an extraction of the realization itself. The trigger signal should be a good indicator of vortex shedding. Several choices were exploited in the domain of a flow past a circular cylinder such as the pressure signal as used by Cantwell & Coles [10] and Perrin [11]. In the case of a plane jet impinging a slotted plate the acoustic signal was chosen as trigger signal as in Assoum [4]. Similarly to Assoum [4] we chose the acoustic signal as a trigger. The acoustic signal, as mentioned in the previous section, was measured by a microphone placed behind the plate so that it won't be affected by the turbulent fluctuations. On the other hand, this signal represents a strong quasi-periodic component as shown in Figure 6. In fact, the controller of the air flow was fixed on its fifth position after verifying the sinusoidal shape of the acoustic signal for this position. Moreover, Perrin [12] detailed the different criterion for the phase identification where for a periodic flow the phase is defined as the time lag between phase reference and the studied moment. The phase reference is the maxima of the acoustic signal. Since our flow is periodic, the phase was the time lag between the maxima of the acoustic signal and the studied instant.

Application:

This section is performed under MATLAB. As explained previously, the phase averaging technique

is based on a phase identification. At first, the trigger signal was analysed and stored. For each of the parallel planes, we applied a sequence of steps to the acoustic signal. The procedure is divided as follows:

- First we eliminate the negative part of the trigger signal.
- Second we detect the maxima of the signal by a quadratic interpolation. Figure 7 illustrate the cut off and the peak detection of the acoustic signal procedure for the plane P0.
- Finally the intervals of time corresponding to the time lag between the maxima and the studied instant are stored in a MATLAB file as t_{parabol} .

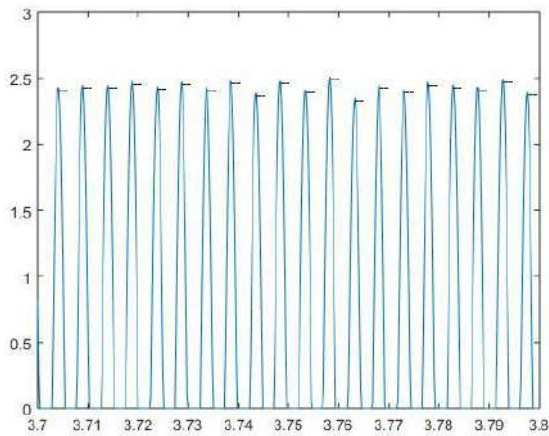


Figure 7: Peak detection of acoustic signal

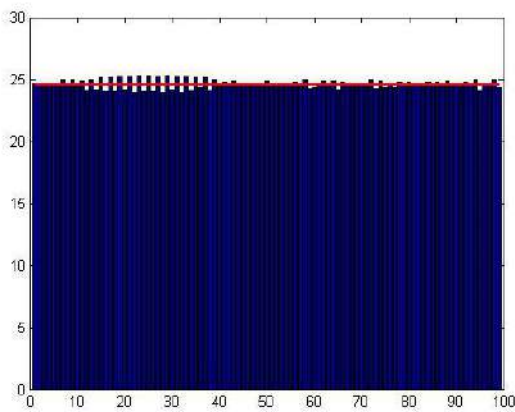


Figure 8: Period histogram in blue and average period in red

Note that the histogram shown above was carried out by conditioning the acoustic signal by a band-pass filter without phase shift and then by identifying the maxima. An index of the degree of periodicity can be given by the standard deviation σ_T of the periods normalized by the average period T_0 . For the chosen

signal this degree was $\frac{\sigma_T}{T_0} = 1.42\%$ which is a good indication of convergence of the periods.

On the other hand, the PIV field acquisition are processed. The velocity signal is decomposed in portions delimited by the time intervals t_{parabol} . The portions are then superposed after normalisation of the time intervals. Furthermore, the average of the velocity on all the unique period is then calculated. This procedure is repeated for the thirty planes and for every point of the plane field.

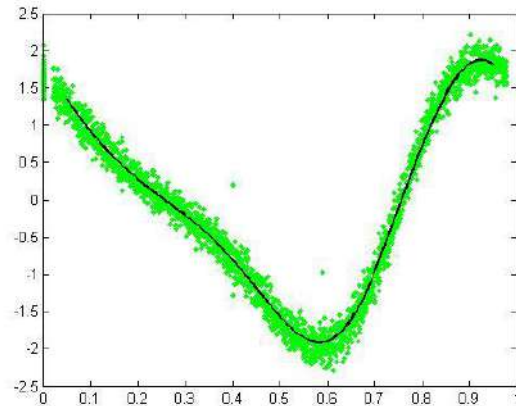


Figure 9: Superposition of the transversal velocity portions in green, phase averaged in black

The procedure explained above is summarized in Figure 9. In this figure, the x-axis represents the normalized time intervals where the y-axis the transversal velocity of the plane P0 for a point representative of the passage of vortices.

Results:

After interpolation of the reconstructed field,

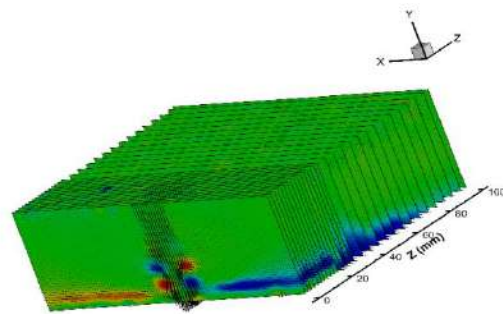


Figure 10 shows the reconstructed planes.

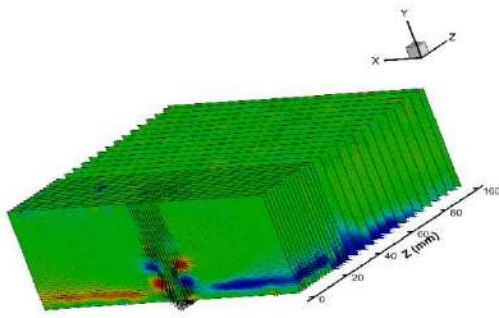


Figure 10: Longitudinal 3D Stereo-PIV planes, Transverse velocity in colours and velocity field in vectors

CONCLUSIONS

In the present study the jet flow was studied for a confinement of $L/H=4$ and for a Reynolds number of $Re=4458$. Thirty parallel planes were investigated by means of stereoscopic PIV. The planes were reconstructed by application of the phase averaging technique. The applied method is based on a post-processing of PIV data acquisitions. The acoustic signal was took as trigger signal. The phase identification was determined from the trigger signal. The reconstructed planed were accorded by an interpolation between planes. The obtained volume is to be studied.

The analysis of the transversal velocity normal to the parallel planes is one of our perspectives. The vortex dynamics of this component will be analysed by a detection of vortices using several methods such as vorticity and lambda 2 criterion. In addition, the frequency of vortices at the edge of the nozzle is to be valued using the temporal evolution of the transversal velocity.

KEYWORDS

Impinging jet, volume reconstruction, phase averaging, stereoscopic PIV, time resolved PIV, self-sustained tones, trigger signal

REFERENCES

[1] M. E. Hassan, H. H. Assoum, R. Martinuzzi, V. Sobolik, K. Abed-Meraim, and A. Sakout, 'Experimental investigation of the wall shear stress in a circular impinging jet', *Phys. Fluids 1994-Present*, vol. 25, no. 7, p. 077101, Jul. 2013.

[2] M. E. Hassan, H. H. Assoum, V. Sobolik, J. Vétel, K. Abed-Meraim, A. Garon, and A. Sakout, 'Experimental investigation of the wall shear stress and the vortex dynamics in a circular

impinging jet', *Exp. Fluids*, vol. 52, no. 6, pp. 1475–1489, Feb. 2012.

- [3] R. Perrin, M. Braza, E. Cid, S. Cazin, A. Barthet, A. Sevrain, C. Mockett, and F. Thiele, 'Obtaining phase averaged turbulence properties in the near wake of a circular cylinder at high Reynolds number using POD', *Exp. Fluids*, vol. 43, no. 2–3, pp. 341–355, Aug. 2007.
- [4] H. H. Assoum, M. El Hassan, K. Abed-Meraim, and A. Sakout, 'The vortex dynamics and the self sustained tones in a plane jet impinging on a slotted plate', *Eur. J. Mech. - BFluids*, vol. 48, pp. 231–235, Nov. 2014.
- [5] H. H. Assoum, M. E. Hassan, K. Abed-Meraim, R. Martinuzzi, and A. Sakout, 'Experimental analysis of the aero-acoustic coupling in a plane impinging jet on a slotted plate', *Fluid Dyn. Res.*, vol. 45, no. 4, p. 045503, 2013.
- [6] A. K. Prasad, 'Stereoscopic particle image velocimetry', *Exp. Fluids*, vol. 29, no. 2, pp. 103–116, Aug. 2000.
- [7] Hassan ASSOUM, 'Etude expérimentale des couplages entre la dynamique d'un jet qui heurte une plaque fendue et l'émission sonore générée', Université de la rochelle, La rochelle, 2013.
- [8] W. C. Reynolds and A. K. M. F. Hussain, 'The mechanics of an organized wave in turbulent shear flow. Part 3. Theoretical models and comparisons with experiments', *J. Fluid Mech.*, vol. 54, no. 02, pp. 263–288, Jul. 1972.
- [9] P. G. N. FORESTIER and L. JACQUIN, 'Evaluation de moyennes de phase dans un écoulement au-dessus d'une cavité résonante', *6ème congrès francophone de vélocimétrie laser*, Sep-1998.
- [10] B. Cantwell and D. Coles, 'An experimental study of entrainment and transport in the turbulent near wake of a circular cylinder', *J. Fluid Mech.*, vol. 136, pp. 321–374, Nov. 1983.
- [11] R. Perrin, E. Cid, S. Cazin, A. Sevrain, M. Braza, F. Moradei, and G. Harran, 'Phase-averaged measurements of the turbulence properties in the near wake of a circular cylinder at high Reynolds number by 2C-PIV and 3C-PIV', *Exp. Fluids*, vol. 42, no. 1, pp. 93–109, Nov. 2006.
- [12] R. PERRIN, 'Analyse physique et modélisation d'écoulements incompressibles instationnaires turbulents autour d'un cylindre circulaire à grand nombre de Reynolds', Thèse, Université de Toulouse, 2005.

PARAMETRIC STUDY ON NATURAL CONVECTION OF NANOFUIDS IN A HEATED CHAMBER

El hafad BARA¹, Sakina EL HAMDANI¹, A. BENDOU¹, Karim LIMAM²

1 LMPEE, ENSA d'Agadir, BP 1136, Agadir, Maroc

2 LaSIE FRE-CNRS 3474, av. M. Crépeau 17042 La Rochelle Cedex 1 France

*El hafad BARA: Fax: +33 5 46 45 82 41 Email: elhafadbara@gmail.com

ABSTRACT

In this work, we conducted a numerical study of laminar natural convection in a closed cavity. The top and the bottom of the cavity are adiabatic, the upper part of the left wall is subjected to a hot temperature T_H , and the lower part of the right wall is subjected to a cold temperature T_C . The governing equations were discretized by the finite volume method using the power law schema. The dynamic viscosity and the effective thermal conductivity of the nanofluid are approximated respectively by the model of Brinkman and Maxwell Garnetts. Numerical simulations are performed using pure water and a mixture of water and nanoparticules (Al_2O_3 , Cu et TiO_2) for a Rayleigh Number from 10^3 to 10^6 and a fraction of nanoparticules between 0 and 0.1. The results obtained shows that the heat transfer improves if we increase the volume fraction of the nanoparticules and de Rayleigh Number.

NOMENCLATURE

C_P	Specific heat, J.(Kg.K) ⁻¹
u, v	Dimensional velocity components, m.s ⁻¹
P	Dimensionless pressure
Pr	Prandelt number
Ra	Rayleigh number
Num	Average Nusselt number
H	Enclosure lengh, m
x, y	coordinates, m
p	Dimensional pression, Pa
T	Dimensional temperature, K
k	Thermal conductivity, W.(m.K) ⁻¹
g	Gravity acceleration, m.s ²
X, Y	Dimensionless coordinates
U, V	Dimensionless vilocity components
Greek sympols	
α	Thermal diffusivity, m ² .s ⁻¹
θ	Dimensionless temperature
ψ	Dimensionless streamline
β	coefficient of thermal expansion, K ⁻¹
ϕ	Particle volume fraction
ρ	Density, Kg.m ⁻³
μ	Dynamic viscosity, N.m ⁻² .s
ν	Kinetic viscosity, m ² .s

Subscripts

H	Hot
C	Cold
f	Fluid(pur water)
nf	Nanofluid
np	Nanoparticle
a	Average

max Maximum

INTRODUCTION

Heat transfer by natural convection is used in various industrial processes such as cooling of electronic equipment, solar technology, safety of nuclear reactors, biology, medical diagnostics, water treatment... etc. Regarding the applications in the field of heat transfer, studies conducted over the past ten years have shown that under certain conditions, the addition of nanoscale particles in a fluid (called then nanofluid) such as Aluminum oxide particles (Al_2O_3), copper oxide (CuO), copper (Cu) or carbon nanotubes in water could increase the heat transfer compared to the case of the pure substance (water), by modifying significantly the thermal conductivity of the carrier fluid.

Several recent studies have been conducted on the natural convection of nanofluids, for example, Khanafer et al. [1], Jou and Tzeng [2], Hwang et al. [3], Ho et al. [4], Abu-Nada and Oztop [5], Mohamed Elhatab [6], Ghasemi et al. [7], Mahmoudi [8], Putra et al. [9], Li and Peterson [10], Wen and Ding [11], Ho et al.[12], Santra et al.[13], and Esmail [14] .All these studies demonstrated that the increase of the volume fraction improves heat transfer. A numerical study of natural convection in rectangular enclosures partially heated was carried out by Hwang et al. [3], and also Ho et al. [4], Abu-

Nada and Oztop [5], Mohamed El Hatab [6] and Ghasemi et al. [7]. In the present work, we study numerically the stationary laminar natural convection of water-Al₂O₃, water-Ti₂O₃ and water-Cu mixture into a squared enclosure.

Problem formulation and solving method

The geometry of the studied case is shown in Figure 1. It is mainly based on a squared enclosure of length H, filled with a homogeneous mixture of water and the nanoparticle Al₂O₃. The upper 1/3 of the left wall is maintained at a constant temperature T_H, and the lower 1/3 of the right wall is maintained at a constant temperature T_C. The other surfaces are all adiabatic. The base fluid used is Newtonian; the flow is two-dimensional, laminar and stationary. The viscous dissipation is negligible and the thermo-physical properties of the nanofluid are constant, except for the change of density, which is estimated by the Boussinesq approximation. The thermophysical properties of pure fluid and nanoparticles are summarized in Table 1.

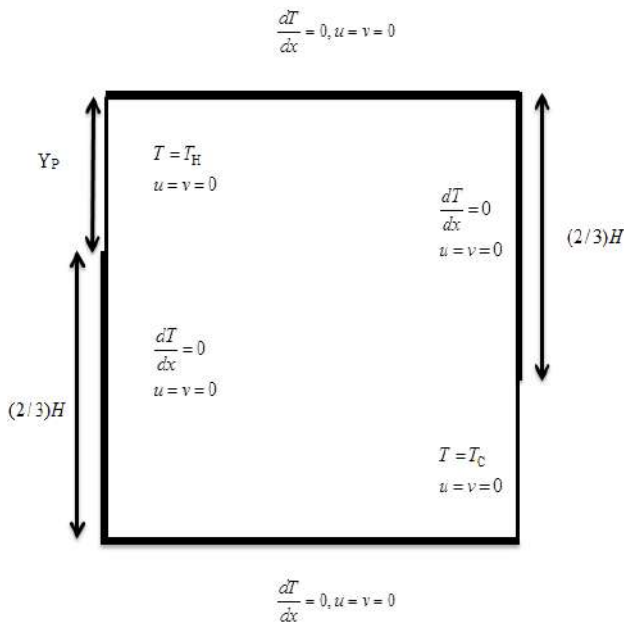


Figure 1

Sketch of the studied configuration and boundary conditions

Table 1

Thermophysical properties of water and the other nanoparticles

	Pr	P (Kg/m3)	C _p (J/Kg.K)	K (W/m.K)	β×10 ⁻⁵ (K ⁻¹)
Pur	6,2	997,1	4179	0,613	21

water					
Al ₂ O ₃	-	3970	765	40	0,85
Cu	-	8933	385	400	1,67
Ti ₂ O ₃	-	4250	686,2	8,9538	0,9

The governing equations for a laminar and steady flow in the case of natural convection of a nanofluid, in dimensionless form are written as follows:

$$\frac{\partial U}{\partial X} + \frac{\partial V}{\partial Y} = 0 \tag{1}$$

$$U \frac{\partial U}{\partial X} + V \frac{\partial U}{\partial Y} = -\frac{\partial P}{\partial X} + \frac{\mu_{nf}}{\rho_{nf} \alpha_f} \left(\frac{\partial^2 U}{\partial X^2} + \frac{\partial^2 U}{\partial Y^2} \right) \tag{2}$$

$$U \frac{\partial V}{\partial X} + V \frac{\partial V}{\partial Y} = -\frac{\partial P}{\partial Y} + \frac{\mu_{nf}}{\rho_{nf} \alpha_f} \left(\frac{\partial^2 V}{\partial X^2} + \frac{\partial^2 V}{\partial Y^2} \right) + \frac{(\rho\beta)_{nf}}{\rho_{nf} \beta_f} Ra_f Pr_f \theta \tag{3}$$

$$U \frac{\partial \theta}{\partial X} + V \frac{\partial \theta}{\partial Y} = \frac{\alpha_{nf}}{\alpha_f} \left(\frac{\partial^2 \theta}{\partial X^2} + \frac{\partial^2 \theta}{\partial Y^2} \right) \tag{4}$$

The variables of the preceding equations are made dimensionless as follows:

$$X = \frac{x}{H}, \quad Y = \frac{y}{H}, \quad U = \frac{uH}{\alpha_f}, \quad V = \frac{vH}{\alpha_f}, \quad P = \frac{(p + \rho_f g y) H^2}{\rho_{nf} \alpha_f^2} \tag{5}$$

$$\theta = \frac{T - T_f}{T_c - T_f}, \quad Ra = \frac{g \beta_f H^3 (T_c - T_f)}{v_f \alpha_f}, \quad Pr = \frac{\nu_f}{\alpha_f}$$

The properties of the nanofluid are calculated by the following equations:

$$\rho_{nf} = (1 - \Phi) \rho_f + \Phi \rho_{np}$$

$$\alpha_{nf} = k_{eff} / (\rho C_p)_{nf}$$

$$(\rho C_p)_{nf} = (1 - \Phi) (\rho C_p)_f + \Phi (\rho C_p)_{np} \tag{6}$$

$$(\rho\beta)_{nf} = (1 - \Phi) (\rho\beta)_f + \Phi (\rho\beta)_{np}$$

The dynamic viscosity and the effective thermal conductivity of the nanofluid are modeled respectively by the Brinkman model [15] and Maxwell-Garnetts [16].

$$\mu_{nf} = \frac{\mu_f}{(1 - \Phi)^{2.5}} \tag{7}$$

$$k_{eff} = k_f \left[\frac{(k_{np} + k_f) - 2\Phi(k_f - k_{np})}{(k_{np} + k_f) + \Phi(k_f - k_{np})} \right] \tag{8}$$

The average Nusselt number (Nu_a) of the hot wall is expressed as follows:

$$Nu_a = \frac{1}{Y_p} \int_{H-y_p}^H NudY \tag{9}$$

where, the local Nusselt number of the hot wall is defined as follows:

$$Nu = - \left. \frac{k_{eff}}{k_f} \frac{d\theta}{dX} \right|_{X=0} \quad (10)$$

In order to estimate the improvement of the heat transfer in nanofluids compared to pure fluid, we define the heat transfer rate (E) as follows:

$$E(\%) = \frac{Num_{\Phi} - Num_{\Phi=0}}{Num_{\Phi=0}} \times 100 \quad (11)$$

NUMERICAL SOLUTION

The system of equations (1-4) given below associated with boundary conditions is solved numerically using the finite volume method [17], while adopting the power law as resolution scheme. The velocity and pressure are coupled by SIMPLEC algorithm. The raster scan method, with Thomas algorithm is used for the iterative solution of the equation system. To study the influence of the mesh, we calculated the average Nusselt number (Nu_a) on the heated portion of the hot wall for six uniform grids. The results are related to water- Al_2O_3 mixture ($\Phi = 0.06$, $Ra = 10^5$) and are presented in Table 2. From this table, it appears that the grid 121×121 is fine enough for the numerical simulations.

The program we have developed to solve the basic equations has been validated, taking as reference certain numerical studies in the literature in the case of a square cavity filled with air to $Pr = 0.7$ and $Ra = 10^5$, where a temperature gradient is imposed between the two vertical walls and top and bottom walls are adiabatic. The value of the number of Nu_a our simulation were compared with those obtained by De Vahl Davis [18] (Figure 2), and for greater certainty we compared the change in temperature for the position $Y = 0.5$ along the X axis compared with experimental results from Krane and Jesse [19] and numerical results from Khanafer et al. [20] (Figure 3). It is clear that this code is in good agreement with other works found in the literature.

Table 2

Average Nusselt number of the hot wall for different meshes.

Mesh	91×91	101×101	121×121	141×141
Nu_a	2.9951	2.9868	2.9827	2.9819

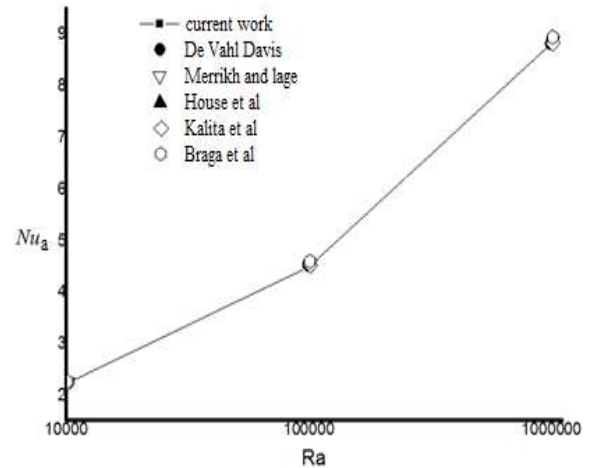


Figure 2

Comparison of Average Nusselt number with other literatures

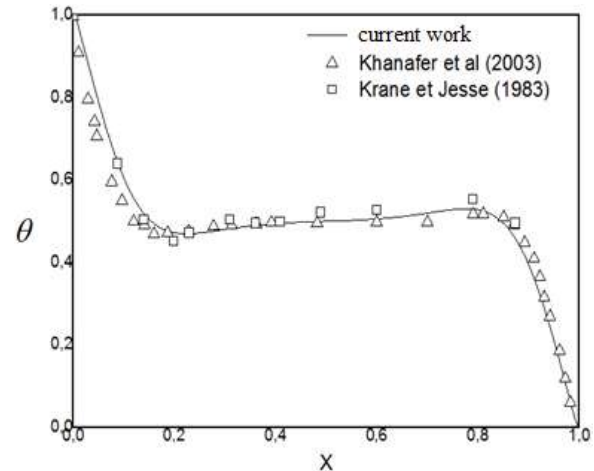


Figure 3

Comparison of temperature distribution at $Y=0.5$ along X with other literatures ($Ra=10^5$ and $Pr=0.7$)

RESULTS AND DISCUSSION

The results presented in this work were obtained for water as pure fluid $Pr = 6.2$, the mixtures water- Al_2O_3 , water-Cu and water- TiO_2 while varying the Rayleigh number (Ra) from 10^3 to 10^6 and the volume fraction of nanoparticles (Φ) from 0 to 0.1.

Figure 4 represents the streamlines (right) and isotherms (left) for pure water as fluid and different nanofluids for $\Phi = 0.06$ and $Ra = 10^5$ to study the effect of different nanoparticles on the dynamic and thermal transfers. From this figure we conclude that pure water and various mixtures have the same dynamic and thermal behavior. The flow is unicellular and the cells expand horizontally as well as a symmetrical flow for all nanofluids. It is also noted that the thermal field is marked by a horizontal stratification within the cavity and by

high thermal gradients on the active walls that is to say, the hot and cold portions of the vertical walls, which means that the heat transfer by convection to the dominance large Rayleigh number.

The vertical component of the velocity (V) of a flow along the horizontal centerline of the cavity, is shown in Figure 5 using different nanofluids for $Ra = 10^5$ and $\Phi = 0.03$. The velocity profiles show that the cell circulates clockwise and the vertical velocity component is insensitive to the type of nanoparticles in the base fluid. This is due only to the use of the formula Brinkman for calculating the dynamic viscosity of nanofluid which takes into account only the volume fraction of the nanoparticles that is not its nature.

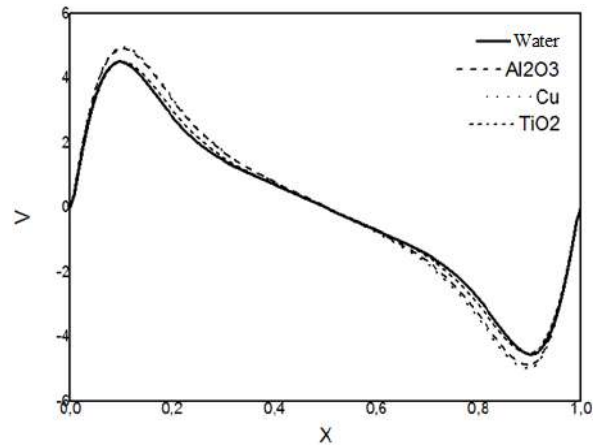


Figure 5

Profile of the vertical component of the velocity at $Y = 0.5$ for pure water and different nanofluids

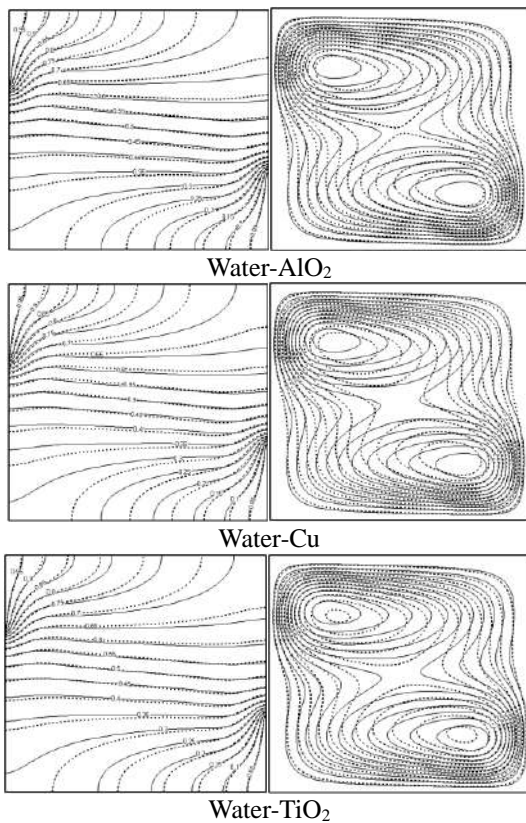
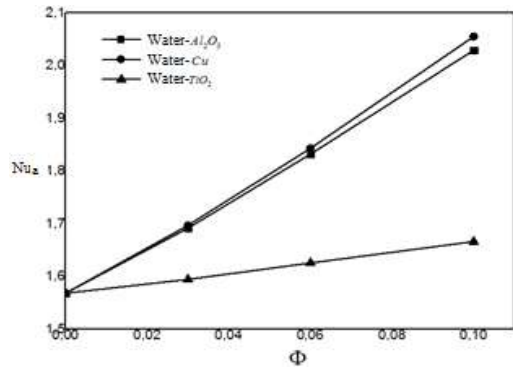


Figure 4

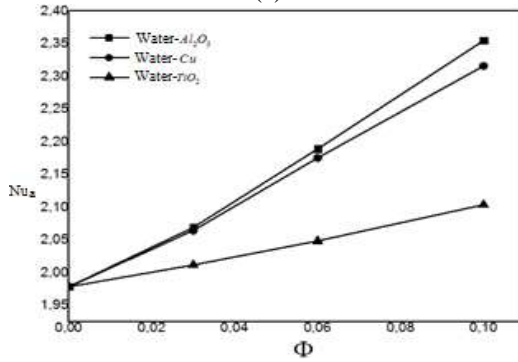
Streamlines (right) and isotherms (left) for pure water and for different nanofluids (continuous lines for pure water and the dotted lines for nanofluids)

In Figure 6 we will present the variation of average Nusselt number (Nu_a) as a function of volume fraction of nanoparticles (Al_2O_3 , TiO_2 and Cu) for different values of the Rayleigh number. From this figure we conclude that for a given volume fraction, Nu_a increases with the increase of the Rayleigh number. On top of that, the number of Nu_a increases with the volume fraction of nanoparticles to any value taken by the Rayleigh number. This increase can be explained by the improvement of the effective thermal conductivity of nanofluid (made by adding the nanoparticles to the base fluid), when the volume fraction of the nanoparticles increases. This figure also shows the effect of nanoparticles on the type of variation in the Nu_a , heat transfer is maximum for copper, since it has the highest thermal conductivity compared to TiO_2 and Al_2O_3 .

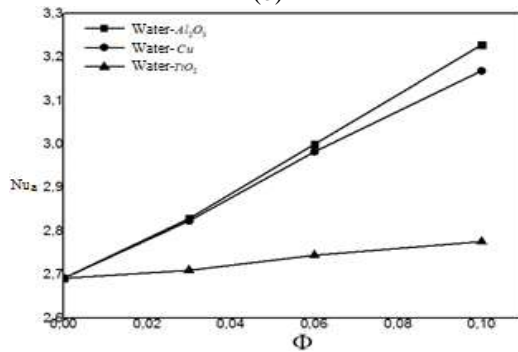
Figure 7 illustrates the heat transfer ratio (E) as a function of the Rayleigh number for different volume fractions of nanoparticles ($\Phi = 0.03, 0.06$ and 0.10), showing the improvement of heat transfer provided by the different types of nanofluids (Al_2O_3 , Cu , and TiO_2) relative to the base fluid, that is water in this. We note that for all types of nanofluids, the ratio E is maximum for $Ra = 10^3$ and minimum for $Ra = 10^4$. This means that the effect of nanoparticles is more important to the low Ra than high Ra . This result is obvious because the thermal conductivity of nanofluids has no great influence on the dominant convective transfer on high Rayleigh number, contrary to the low Ra where the transfer by conduction dominates.



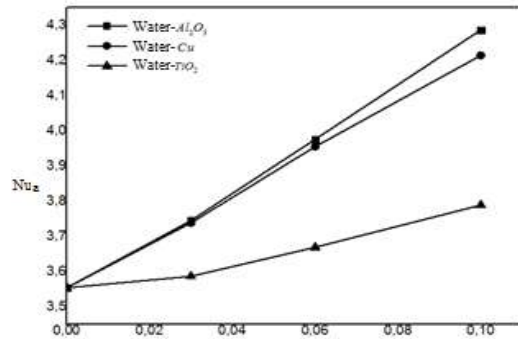
(a)



(b)



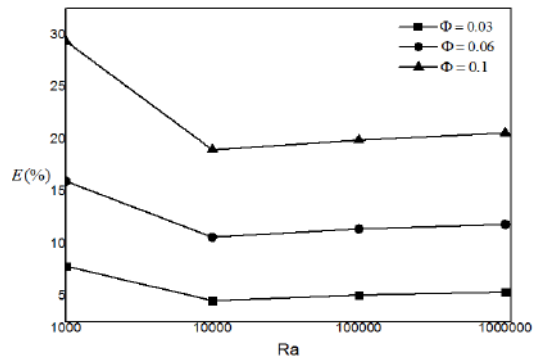
(c)



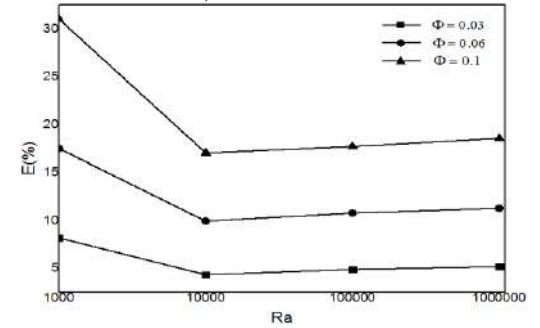
(d)

Figure 6

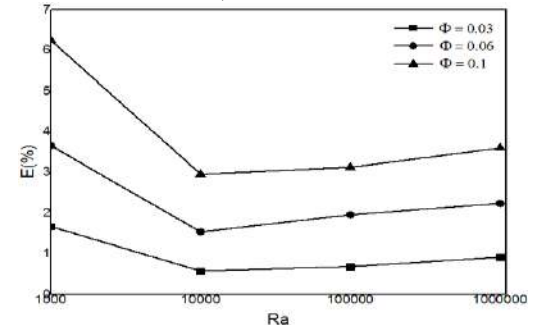
Variation of Nu_a as function of Φ for different nanoparticles, (a) $Ra=10^3$, (b) $Ra=10^4$, (c) $Ra=10^5$, (d) $Ra=10^6$.



a) Water- Al_2O_3



b) Water-Cu



c) Water- TiO_2

Figure 7

Heat transfer ratio ($E(\%)$) for different nanofluids.

CONCLUSIONS

In this work, the problem of transfer of heat by natural convection of nanofluids confined in a squared enclosure has been solved numerically. A temperature gradient is imposed between the two vertical walls (hot side and cold side), while the top and bottom walls are adiabatic. The influence of certain parameters like the volume fraction of nanoparticles, the type of nanoparticles and the Rayleigh number on heat transfer were investigated. This study allowed us to come out with the following conclusions that confirm the results obtained by the other literatures that studied the same problem with the same conditions but in different configurations:

- The heat transfer rate increases with the increase of the volume fraction of nanoparticles and the Rayleigh number (average Nusselt).
- The effect of nanoparticles on heat transfer is more important at low Rayleigh number (the dominance of heat transfer by conduction).
- Heat transfer with the presence of copper nanoparticles is improved compared to the results obtained with nanoparticles of Al_2O_3 or TiO_2 .

KEYWORDS

Nanofluid, Heat transfer, Natural convection, numerical study, finite volume.

REFERENCES

1. K. Khanafer, K. Vafai et M. Lightstone, Buoyancy-Driven Heat Transfer Enhancement in a TwoDimensional Enclosure Utilizing Nanofluids, *International Journal of Heat and Mass Transfer*, Volume 46, Pages 3639–3653, 2003.
2. R.Y. Jou et S.C. Tzeng, Numerical research of nature convective heat transfer enhancement filled with nanofluids in rectangular enclosures, *Int. Comm. Heat Mass Transfer*, Volume 33, Pages 727–736, 2006.
3. K.S. Hwang, J.H. Lee et S.P. Jang, Buoyancy-driven heat transfer of water based Al_2O_3 nanofluids in a rectangular cavity, *Int. J. Heat Mass Transfer*, Volume 50, Pages 4003–4010, 2007.
4. C.J. Ho, M.W. Chen et Z.W. Li, Numerical simulation of natural convection of nanofluid in a square enclosure: Effects due to uncertainties of viscosity and thermal conductivity, *Int. J.*, Volume 51, Pages 4506–4516, 2008.
5. E. Abu-Nada et H.F. Oztop, Effects of inclination Angle on natural convection in enclosures filled with Cuwater Nanofluid, *int. J Heat. Fluid Flow*, Volume 30, Pages 669-678, 2009.
6. M. El hatab, R. Mir, Y. El hammami, Numerical simulation of natural convection of nanofluid in a square enclosure with a protruding isothermal heater, *International Journal on Heat and Mass Transfer – Theory and Application*, vol 2, 2014, pp., 1-8.
7. B.S. Ghasemi et M. Aminossadati, Periodic natural convection in a nanofluid-filled enclosure with oscillating heat flux, *International Journal of Thermal Sciences*, Volume 49 Pages 1–9, 2010.
8. Mahmoodi, M., “Numerical Simulation of Free Convection of a Nanofluid in L-Shaped Cavities, *International Journal of Thermal Sciences*, Vol. 50, No. 9, 2011, pp. 1731–1740.
9. Putra, N., Roetzel, W., and Das, S. K., “Natural Convective of Nanofluids,” *Heat and Mass Transfer*, Vol. 39, Nos. 8–9, 2003, pp. 775–784.
10. Li, C. H., and Peterson, G. P., “Experimental Studies of Natural Convection Heat Transfer of $\text{Al}_2\text{O}_3/\text{DI}$ Water Nanoparticle Suspensions (Nanofluids),” *Advances in Mechanical Engineering*, Paper 742739, 2010.
11. Wen, D., and Ding, Y., “Formulation of Nanofluids for Natural Convective Heat Transfer Applications,” *International Journal of Heat and Fluid Flow*, Vol. 26, No. 6, 2005, pp. 855–864.
12. Ho, C. J., Liu, W. K., Chang, Y. S., and Lin, C. C., “Natural Convection Heat Transfer of Alumina-Water Nanofluid in Vertical Square Enclosures: An Experimental Study, *International Journal of Thermal Sciences*, Vol. 49, No. 8, 2010, pp. 1345–1353.
13. Santra, A. K., Sen, S., and Chakraborty, N., “Study of Heat Transfer Augmentation in a Differentially Heated Square Cavity Using Copper–Water Nanofluid,” *International Journal of Thermal Sciences*, Vol. 47, No. 9, 2008, pp. 1113–1122.
14. Esmaeil, K. K., “Numerical Feasibility Study of Utilizing Nanofluids in Laminar Natural Convection Inside Enclosures,” *Heat and Mass Transfer*, Vol. 49, No. 1, 2013, pp. 41–54.
15. H.C. Brinkman, The viscosity of concentrated suspensions and solutions, *J. Chem. Phys.*, Volume 20, Pages 571–581, 1952.
16. J.C. Maxwell, *A Treatise on Electricity and Magnetism*, Clarendon Press., U.K, 1891.
17. G. De Vahl Davis, Natural convection of air in a square cavity, a benchmark numerical solution, *Int. J. Numer. Methods Fluids* 3 (1962) 249–264.
18. Patankar, S.V., “*Numerical Heat Transfer and Fluid Flow*”, Hemisphere Publishing Corporation, Taylor and Francis Group, New York, (1980).
19. R.J. Krane, J. Jessee, Some detailed field measurements for a natural convection flow in a vertical square enclosure, in: *1st ASME-JSME Thermal Engineering Joint Conference*, 1 (1983) 323–329.
20. K. Khanafer, K. Vafai, M. Lightstone, Buoyancy-driven heat transfer enhancement in a two-dimensional enclosure utilizing nanofluids. *Int. J. Heat Mass Transfer* 46 (2003) 3639–3653.

MRT-SCHEME APPLIED TO NATURAL CONVECTION COUPLED TO SURFACE RADIATION IN A CAVITY PARTIALLY HEATED FROM ONE VERTICAL SIDE AND COOLED FROM ABOVE

K. REHHALI ^{1*}, M. HASNAOUI ¹, A. RAJI ², M. ALOUAH ¹ and A. EL MANSOURI ¹

¹UCA, FSSM, Department of Physics, LMFE, Affiliated unit to CNRST (URAC 27), B.P. 2390, Marrakesh, Morocco

²Sultan Moulay Slimane University, FST Beni-Mellal, LAMET, Department of Physics, B.P. 523, Béni-Mellal, Morocco

*Corresponding author: Email: khaoula.rehhali@edu.uca.ac.ma

ABSTRACT

A two-dimensional modeling is performed to study natural convection coupled with radiation in a square cavity partially heated from one vertical side and cooled from above. The simulation of flow and heat transfer is achieved by adopting the MRT scheme of the Lattice-Boltzmann method. In this work we focus on qualitative and quantitative effects engendered by the coupling between the surface radiation and natural convection in the studied configuration. The obtained results are presented in terms of streamlines, isotherms, heatlines and average Nusselt number.

This preliminary study shows that the MRT-LBM method can be used to simulate faithfully the heat transfer by natural convection coupled to radiation. The contribution of the radiation to heat transfer should be considered since its effect is far from negligible, even more; it outweighs that of convection depending on the value of Rayleigh number.

KEYWORDS

Lattice Boltzmann method, MRT Scheme, natural convection, surface radiation.

NOMENCLATURE

c_x, c_y	discrete velocity of the particle located at $r = (x, y)$	Δr	distance between two neighboring D2Q9 network nodes
f	vector of distribution functions	s	vector of the relaxation rate
F_y	buoyancy force	Δt	time step
g	vector of distribution functions relative to temperature	T	temperature
L	Length of the square cavity	T_c	temperature of the cold wall
g	gravitational acceleration	T_h	temperature of the hot wall
Nu	Nusselt number	T_{ref}	reference temperature
m	vector of the moments of distribution functions	ΔT	difference temperature
m^*	vector of moment after the crash phase	u	x component of velocity
m^{eq}	vector of moments in equilibrium	v	y component of velocity
M	transition matrix	Greek symbols	
Pr	Prandtl number	β	expansion coefficient
Ra	Rayleigh number	ε	emissivity (radiation)
		Ω	collision operator
		Ψ	stream function
		ρ	density

Subscripts

cv	convective
r	radiative
tot	total

INTRODUCTION

The study of natural convection in closed rectangular cavities still arouses much interest given its omnipresence in daily life and in many industrial applications such as cooling of electronic components, thermal building, metallurgical industry, etc. An important part of the literature in this field is summarized in books by Bejan [1] and Yang [2]. Most previous works on the problem of natural convection concern cases of enclosures subjected to horizontal temperature gradients (differentially heated cavities) or vertical temperature gradients (Rayleigh-Bénard configurations). However, situations where the active walls may be subject to various types of non-uniformities in the temperature are numerous and encountered in many practical situations. Therefore, the literature review shows that researchers have not ignored the case of partially heated cavities or containing one or more heat sources. This type of heating is closer to reality and can lead to specific behaviors that induce flow and heat transfer which are very different from those encountered when the entire wall of a cavity is heated or when a heat flux is used. In this context, there can be mentioned numerical study of Valencia and Frederick [3] which numerically analyzed the natural convection of air in a square cavity with partially active walls. They found that the heat transfer rate increases when the heater is placed in the middle of the wall. The effect of the position of the heating element on a given wall has been discussed by several authors. However, in the majority of works on the thermal convection involving a partial heating, the contribution of radiation has been neglected. This neglect may be justified only if the wall emissivity is low or when the maximum differences of temperatures involved are not significant. Under actual operating conditions, the thermal radiation is generally present, and is strongly coupled to the natural convection. Among the earliest studies on the coupling between the convection and heat radiation in rectangular cavities, we can cite the contribution of Larson and Viskanta [4]. Their results show that the contribution of the radiation heat transfer is greater than that of natural convection. The objective of this work is to experiment the Lattice-Boltzmann method with the MRT scheme to address a

convection-radiation coupling problem in a square cavity partially heated. Some illustrative results for the combined effects of the position of the active element, wall's emissivity and Rayleigh number are presented. Saravanan and Sivaraj [5] investigated natural convection combined with surface radiation in an air-filled cavity with a centrally placed thin heated plate. It was shown that the presence of radiation renders temperature distribution uniform within the cavity and leads to a reduction of the temperature difference between the insulated walls. Emissivity, Rayleigh number, and plate length have a positive impact on the overall heat transfer across the cavity. Very recently, the effect of surface radiation on transient natural convection in a differentially heated cavity with one vertical wavy wall has been studied numerically by Sheremet and Miroschnichenko [6]. It has been found that the average total Nusselt number at the vertical wavy wall is an increasing function of Rayleigh number, surface emissivity and shape parameter for the concave undulations and a decreasing function of the undulations number and shape parameter for the convex undulations.

MATHEMATICAL FORMULATION

Problem Description: The problem studied is a two-dimensional heat transfer in a square cavity filled with air. The geometry under consideration and coordinates are sketched in Figure 1.

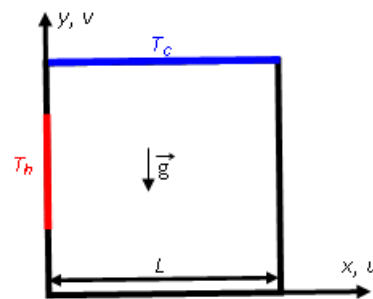


Figure 1
Schematic representation

The cavity is cooled from above and partially heated from the left side. The heated portion is placed at three different positions on the left vertical wall which are namely High-Position, HP, Centered-Position, CP, and Low-Position, LP. The remaining walls are considered adiabatic. The active element covers the half of the left wall. The study is performed for a wide range of Rayleigh number (10^3

$\leq Ra \leq 10^6$) and the emissivity of the inner surfaces ($0 \leq \varepsilon \leq 1$) by setting constant the Prandtl number ($Pr = 0.71$) and the temperature difference ($\Delta T = 30$ K). The obtained results are presented in terms of streamlines, isotherms, heatlines and average Nusselt numbers.

Lattice-Boltzmann Method: Using the Lattice-Boltzmann method [7] to simulate fluid flows is based on the resolution of the following Boltzmann equation:

$$f(r + c\Delta t, t + \Delta t) - f(r, t) = \Omega(f) \quad (1)$$

The MRT scheme considers that the propagation phase occurs at the microscopic level in the space formed by the discrete velocities c_k ($k=0, \dots, 8$) while the collision phase takes place in a macroscopic space formed by the moments of the distribution functions. The transition between these two areas is provided by a transition matrix M [8]:

$$m = Mf \quad (2)$$

In the crash phase, the moments that don't retain themselves undergo relaxation to an equilibrium state according to the relation:

$$m^* = m - s(m - m^{eq}) \quad (3)$$

The moments which are conserved are changed by the presence of the buoyancy force, and are obtained as:

$$m_\rho^* = m_\rho = \rho \quad (4)$$

$$m_u^* = m_u = \rho u \quad (5)$$

$$m_v^* = m_v = \rho v + F_y \quad (6)$$

After the propagation phase, macroscopic values are then calculated from the new values of moments:

$$\rho = \sum_{k=0}^8 f_k = m_0 \quad (7)$$

$$u = \frac{1}{\rho} \sum_{k=0}^8 f_k \cdot c_{x,k} = \frac{m_u}{\rho} \quad (8)$$

$$v = \frac{1}{\rho} \sum_{k=0}^8 f_k \cdot c_{y,k} = \frac{m_v}{\rho} \quad (9)$$

The boundary conditions are treated with the standard regimen of "bounce".

MRT similar scheme is used to calculate the temperature values at each point of the cavity by considering the D2Q5 network model with 5 discrete velocities only. These values are given by:

$$T = \sum_{k=0}^4 g_k \quad (10)$$

The cavity is divided into elementary surfaces having as centers nodes. The radiosity and the corresponding view factors are determined by adopting the same approach as the one used by Raji and al. [9].

In natural convection, the buoyancy force is obtained as a result:

$$F_y = \rho g \beta (T - T_{ref}) \quad (11)$$

RESULTS AND DISCUSSION

Numerical code validation: The validation of the MRT-LBM code was performed against the numerical results of Wang et al. [10] obtained in the case of a differentially heated square cavity whose interior walls are assumed to be gray, diffuse and opaque and having the same value of emissivity. As it is seen in Table 1, the agreement observed between our results and those published in reference [10] is excellent; the maximum relative deviation registered remains less than 0.1% in terms of mean Nusselt number.

Table 1

Numerical code validation for $\varepsilon = 0.8$ and $Ra = 10^6$.

	Nu_{cv}	Nu_r	Nu_{tot}
LBM-MRT	7.818	11.255	19.073
Ref [8]	7.815	11.265	19.08
Difference	0.03%	0.08%	0.03%

Effect of the position of the thermally active portion:

Typical streamlines, isotherms and heatlines illustrating the effect of the position of the active heating element are presented in Figure 2 for $Ra = 10^6$ and $\varepsilon = 0$. It can be seen that for the three considered positions of the heating element (LP, CP and HP), the resulting flow patterns consist of a monocellular clockwise cell occupying the available space in the cavity. However, the position of the active element has a noticeable impact on the fluid circulation since the upward moving of the heating element drives to an important slowdown of the fluid flow circulation. Quantitatively, the intensity of the flow undergoes a relative decrease of about 31 % when the heating element is moved from the lower position to the higher one. This tendency is accompanied by an improvement of the heat transfer from $Nu_{cv} = 5.91$ for Lower-Position to $Nu_{cv} = 7.66$ for Higher-Position.

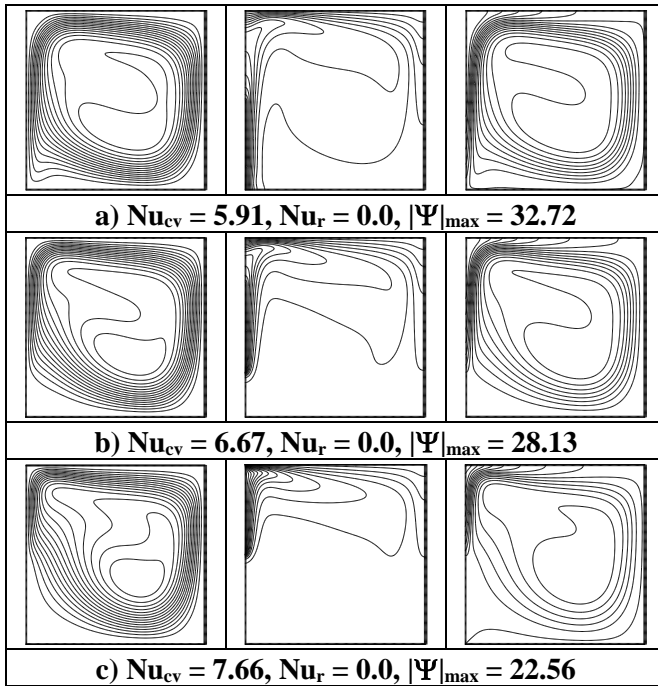


Figure 2

Streamlines, isotherms and heatlines for $Ra = 10^6$ and $\varepsilon = 0$: a) LP, b) CP and c) HP.

Walls emissivity effect: The effect of the emissivity of the walls on the average Nusselt numbers, evaluated at the horizontal cooled wall is displayed in figure 3. The Rayleigh number and the temperature difference are fixed at $Ra = 10^6$ and $\Delta T = 30$ K, respectively. It can be seen from this figure that the convective heat transfer is weakly affected by the increase of the emissivity of the wall. In fact, the convective Nusselt number, Nu_{cv} , is seen to follow a small decrease with the emissivity for the LP and CP configurations while for the HP configuration, Nu_{cv} undergoes a slight increase with the emissivity. In the case of radiative component, figure 3 shows that Nu_r is logically more sensitive to the increase of the emissivity. The radiative heat flux increases significantly with the emissivity of the walls. A comparison between radiation and convection contributions to the overall heat transfer shows that the contribution of radiation to the total heat transfer is significant. This contribution becomes more important than that of natural convection once the emissivity value becomes close to 1 for LP and CP, but for HP, the contribution of convection to the total heat transfer remains more important than that of radiation.

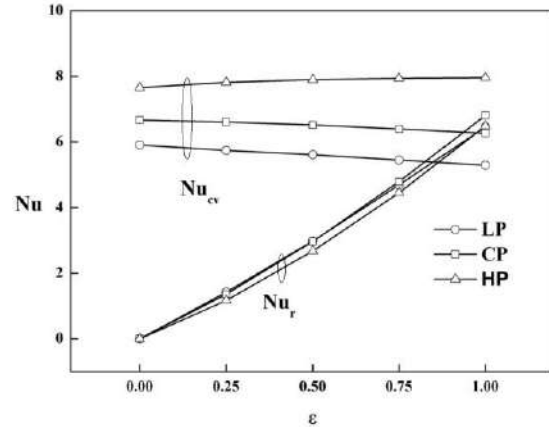


Figure 3

Effect of the emissivity ε on the Nusselt numbers Nu_{cv} and Nu_r for the LP, CP and HP configurations.

In order to illustrate the effect of the emissivity of the walls on the flow structure and heat transfer, we present in figure 4 streamlines, isotherms and heatlines for the HP configuration. Compared to the case of pure convection ($\varepsilon = 0$) in figure 2c, figure 4, obtained for $\varepsilon = 1$, shows that the wall's emissivity leads to an important qualitative change of the flow structure and temperature distribution within the cavity. The unicellular flow structure, observed in the absence of radiation persists and we assist to the formation of two small cells, of less importance, in the lower corners of the cavity. In terms of heat transfer, the total Nusselt number, $Nu_{tot} = Nu_{cv} + Nu_r$, undergoes an increase of about 89 % when the value of the emissivity changes from 0 to 1.

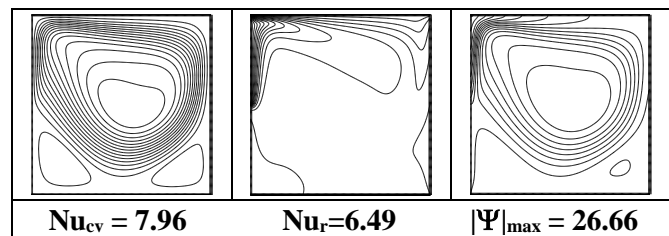


Figure 4

Streamlines, isotherms and heatlines in the case of the HP configuration for $Ra = 10^6$ and $\varepsilon = 1$.

Rayleigh number effect: The effect of the Rayleigh number on streamlines, isotherms, and heatlines is illustrated in figure 5 for the HP configuration. For $Ra = 10^4$, the streamlines indicate a monocellular clockwise rotating flow (Figure 5a). The flow intensity is relatively small indicating a

relative slow convective motion ($|\Psi|_{\max} = 4.29$). The corresponding isotherms are spaced indicating a weak heat exchange between the active element and the confining fluid. By increasing the Rayleigh number, the flow structure undergoes significant changes. For the higher considered value of the Rayleigh number, $Ra = 10^6$, Figure 5c shows a large increase in the intensity of flow ($|\Psi|_{\max} = 22.56$). The distribution of heatlines is seen to be similar to the path of the streamlines due to the dominance of the convective heat transfer. The corridor followed by the open lines is narrowed towards the walls under the expansion of the inactive zone characterized by the closed lines.

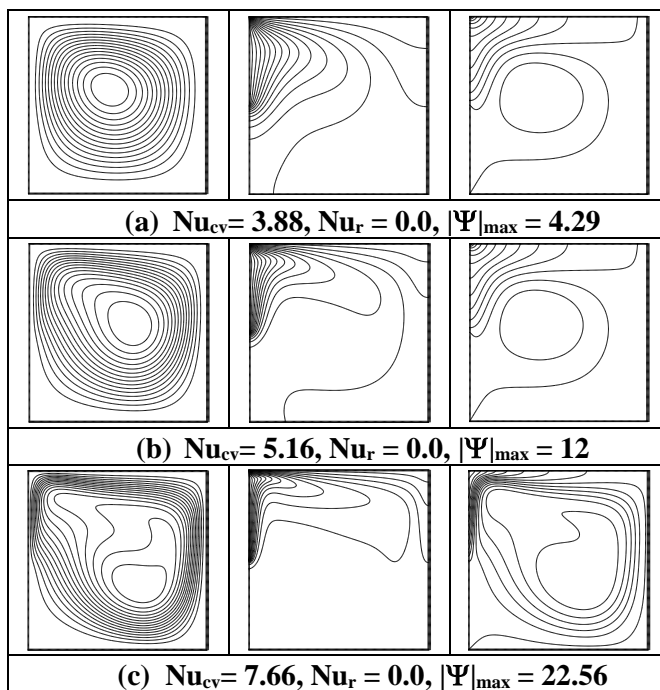


Figure 5

Streamlines, isotherms and heatlines for the HP configuration and $\varepsilon = 0$: (a) $Ra = 10^4$, (b) $Ra = 10^5$ and (c) $Ra = 10^6$.

Variations versus the Rayleigh number Ra , of the total Nusselt number, resulting from contributions of convection and radiation, evaluated along the heated element, are presented in figure 6 for the three different positions of the heating element and for two values of ε . The behavior of this evolution is the same even for $\varepsilon = 0$ and also for $\varepsilon = 1$ with increasing slopes by increasing the emissivity. It can be also noted that for the two different values of the emissivity of the walls, the total Nusselt number increases when the active heating element is moved upward.

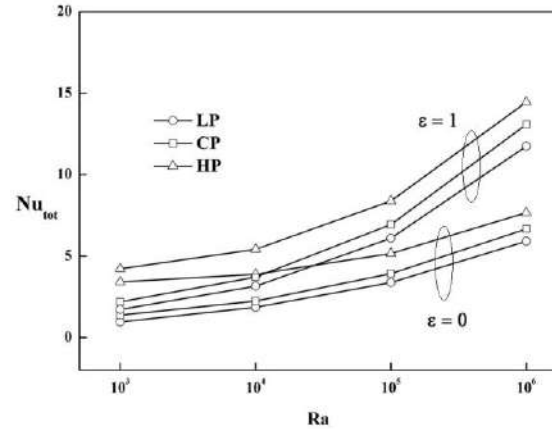


Figure 6

Evolution of Nu_{tot} versus Rayleigh number for LP, CP, HP and different values of walls emissivity.

CONCLUSIONS

A numerical investigation on natural convection coupled with radiation in a square cavity was carried out by adopting the MRT scheme of the Lattice-Boltzmann method. A discrete heating is applied on the left vertical wall and the upper horizontal wall is uniformly cooled. The numerical simulations revealed that the radiation contributes importantly to the enhancement of the overall heat transfer. Its contribution to the overall heat transfer is found generally to be not negligible. Also, it is found that the heat transfer is increased when the heating element is moved upward even in the absence or in the presence of the radiation effect. Finally, the MRT-LBM was successfully experimented to study a problem involving the coupling between natural convection and walls' radiation.

REFERENCES

1. Bejan, A, 1995, Convection heat transfer, 2nd ed., John Wiley and Sons, New York.
2. Yang, K.T., 1987, Natural convection in enclosures, in: S. KaKaç, R.K. Shah, W.Aung (éds). Handbook of single-phase convective heat transfer, Chap. Wiley, New York, **13**, pp. 1-51.
3. Valencia, A, and Frederick, R.,L., 1989, Heat transfer in square cavities with partially active vertical walls, Int. J. Heat Mass Transfer **32**, pp. 1567–1574.
4. Larson, D.W. and Viskanta, R, 1976, Transient combined laminar free convection and radiation in a

rectangular enclosure, *J. Fluid Mech., Part 1*, **78**, pp. 65-85.

5. Saravanan, S. and Sivaraj, C, 2013, Coupled thermal radiation and natural convection heat transfer in a cavity with a heated plate inside, *Int. J. Heat Fluid Flow*, **40**, pp. 54–64.

6. Sheremet, M.A. and Miroshnichenko, I.V, 2016 Effect of surface radiation on transient natural convection in a wavy-walled cavity, *Numerical Heat Transfer, Part A*, **69**, pp. 369-382.

7. Mohamad, A.,A., 2007, *Applied Lattice Boltzmann method for transport phenomena, Momentum Heat Mass Transfer*, Sure Print, Calgary.

8. Bouzidi, M, d’Humières, D., Lallement, and P ,Luo, L.S, 2001, Lattice Boltzmann equation on a two-dimensional rectangular grid, *J. Computational Physics*, 172, pp. 704-7017.

9. Raji, A. and Hasnaoui, M, 2001. Combined mixed convection and radiation in ventilated cavities, *Engineering Computations*, 18, pp. 922-949

10. Wang, H, Xin, S and Le Quéré, P., 2006. Étude numérique du couplage de la convection naturelle avec le rayonnement de surfaces en cavité carrée remplie d’air, *C.R.Mécanique*, 344, pp. 48-47

CONTROL VOLUME FINITE ELEMENT METHOD FOR A BENCHMARK VALIDATION OF A NATURAL CONVECTION IN A SQUARE CAVITY

Hasnat Mohammed, Abdellah Belkacem, Kaid Noureddine, Benachour elhadj

Laboratory of energy in arid areas (ENERGARID), Faculty of Science and Technology, University of
BECHAR, BP 417, 08000 BECHAR.

*Corresponding author: Email: mohammed.hasnat@yahoo.fr

ABSTRACT

The formulation written in terms of the primitive variables using co-located equal-order Control-Volume based Finite Element Method (CVFEM), for a benchmark validation of natural convection in a square cavity. The computer Fortran code that have been developed in the context of this work using all forms of dimensionless equations to allow a quick and easy comparison the results with the benchmark solution of De Vahl Davis numerical works and other works. The problem considered, is for a two-dimensional flow, for a Prandtl number of 0.71 using Boussinesq approximation. The results taken into account are the stream function, velocities and heat transfer, which are obtained at Rayleigh numbers of 10^3 , 10^4 , 10^5 and 10^6 .

Keywords: CVFEM, Equal-order Control-Volume-based, Benchmark validation, Rayleigh number, Natural convection

NOMENCLATURE

Length	b	m
Coordinates Cartesian	x, y	m
Pressure	P	Pa=N/m ²
Velocity		
Components in Cartesian	u, v	m/s
Temperature absolute	T	K
Density Mass(=M/V)	ρ	Kg/m ³
Diffusivity, Thermal (=k/ ρC_p)	α	(m ² /s)
Coefficient of Volume Expansion	β	K ⁻¹
Streamline function	Ψ	-

DIMENSIONLESS GROUPS

Cartesian	$X = x/b$ $Y = y/b$
Pressure	$P_m = P b^2 / \rho \alpha^2$
Velocity	$U = ub/\alpha$ $V = vb/\alpha$
Temperature	$\theta = (T - T_0) / (T_p - T_0)$ $Pr = \nu/\alpha$

Prandtl Number	
Rayleigh number	$Ra = g\beta\Delta T b^3 / \alpha\nu$
Nusselt number	$Nu = \nabla\theta \cdot n$
Average Nusselt number	$Nu_{moy} = \int_0^1 Nu \cdot dY$
Spatial gradient operator	∇
Outward unit normal vector at $X=0$	n

INTRODUCTION

Natural convection heat transfer in a square cavity is important in many engineering applications, such as nuclear reactor insulation, ventilation of rooms, solar energy collection and crystal growth in liquids. Therefore, many investigations have been carried out to study the interaction between the hydrodynamic and thermal effects theoretically used a method for the numerical solution, for a great variety of parameters.

Many papers on this problem have been published with numerical results obtained mainly by finite differences and the Reynolds number has been slowly pushed upwards [1],[2], [3], [4], [5]. A complete analysis of the solutions by numerical computations were given by Vahl Davis [6] for laminar natural convection in an enclosed rectangular cavity. Later Vahl Davis [7] presented a solution second-order, central difference approximations were used mesh refinement and extrapolation led to solutions for $10^3 \leq Ra \leq 10^6$. Vahl Davis and Jones [8] have presented a number of contributed solutions to the problem of laminar natural convection in a square cavity have been compared

with what is regarded as a solution of high accuracy. Reading of Stevens [9] work, is based on the solution of the derivation of vorticity and power lines, for the formulation of primitive equation of the equations of motion, of energy and continuity for an incompressible fluid. Use of boundary vorticity formula or iterative fulfillment of the no-slip boundary condition is avoided by application of the finite element discretization and a displacement of the appropriate discrete equations. Solution is obtained by Newton-Raphson iteration of all equations simultaneously. A similar study was documented by T. Fusegi and al [10] a high-resolution, finite-difference numerical study is reported on natural convection in a square cavity. The internal Rayleigh number varies in the range $10^9 < Ra_L < 10^{10}$, while the external Rayleigh number is set at $Ra_E = 5.10^7$ for most computations. C. Wan and al [11] has proposed the problem of a new benchmark quality solution for the buoyancy-driven cavity by discrete singular convolution (DSC) for the numerical simulation of coupled convective heat transfer problems. The problem is solved by two completely independent numerical procedures. One is a quasi-wavelet-based DSC approach, while the other is a standard form of the Galerkin finite-element method. The objective of Guo.Y and Bathe. K.-J. [12] is to present the results obtained using the 9-node quadrilateral element in ADINA, and it was used with various meshes. A. Dalal and al. [13] states that natural convection occur in the vicinity of inclined square cylinder in the range of ($0^\circ \leq \theta \leq 45^\circ$) inside an enclosure having horizontal adiabatic wall and cold vertical wall figure out by cell-centered finite volume method, which is used to calculate two dimension Navier-stokes equation for incompressible laminar flow. Basak et al. [14] have reported the effect of temperature boundary conditions (Constant temperature and sinusoidally varying) on the bottom wall for Ra varying from 10^3 to 10^5 for both the Prandtl numbers of 0.7 and 10. This paper presents a solution of a natural convection in a square cavity problem based on extending the co-located equal-order Control-Volume-based Finite Element Method (CVFEM) by Lamoureux and Baliga [15]. As an advantage of the present method is the use of primitive variables which facilitates the application of the boundary conditions. To validate the present method of solution, the results are analyzed and compared with Vahl Davis.[7] benchmark solution and Ismail and Scalon [16].

GOVERNING EQUATIONS

The non-dimensional governing equations for the natural convection in a square cavity are given by two-dimensional incompressible Navier-Stokes and energy equation in primitive variable form as

Continuity equation:

$$\frac{\partial U}{\partial X} + \frac{\partial V}{\partial Y} = 0 \quad (1)$$

X-momentum equation:

$$U \frac{\partial U}{\partial X} + V \frac{\partial U}{\partial Y} = -\frac{\partial P_m}{\partial X} + \text{Pr} \left[\frac{\partial^2 U}{\partial X^2} + \frac{\partial^2 U}{\partial Y^2} \right] \quad (2)$$

Y-momentum equation:

$$U \frac{\partial V}{\partial X} + V \frac{\partial V}{\partial Y} = -\frac{\partial P_m}{\partial Y} + \text{Pr} \left[\frac{\partial^2 V}{\partial X^2} + \frac{\partial^2 V}{\partial Y^2} \right] + Ra \cdot \text{Pr} \cdot \theta \quad (3)$$

Energy equation:

$$U \frac{\partial \theta}{\partial X} + V \frac{\partial \theta}{\partial Y} = \frac{\partial^2 \theta}{\partial X^2} + \frac{\partial^2 \theta}{\partial Y^2} \quad (4)$$

Where $\text{Pr} = \frac{\nu}{\alpha}$, Prandtl number, and

$$Ra = \frac{g \beta \Delta T b^3}{\alpha \nu}, \text{ the Rayleigh number.}$$

The geometry is shown in Figure 1. For this problem, the appropriate boundary conditions are

$$U = V = 0 \quad \text{on all boundaries}$$

$$\theta = 1 \text{ on } X = 0, \theta = 0 \text{ on } X = 1$$

$$\partial \theta / \partial Y = 0 \text{ on } Y = 0, 1 \text{ (adiabatic horizontal walls)}$$

The definition for local Nusselt number is:

$$Nu = \nabla \theta \cdot n \quad (5)$$

Also shown, are the average values again found using Simpson's rule, which exaggerates the variation of Nu with X.

$$Nu_{\text{moy}} = \int_0^1 Nu \cdot dY \quad (6)$$

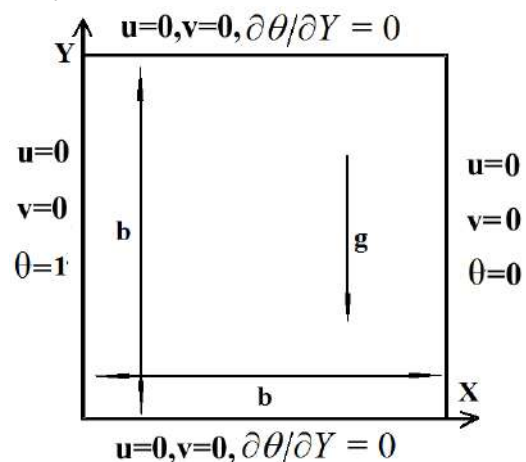


Figure 1

Geometry of natural convection in a square cavity

The calculation domain ($b/10 \times b/10$), is first divided into three-node triangular elements unstructured grid i.e. irregular-shaped. The centroid of each triangular element is then joined to the midpoints of its sides. Thereby dividing each triangular element into three equal areas (regardless of the shape of the triangular element). Collectively, these areas form non overlapping contiguous polygonal cross sections of the control volumes, each associated with a node in the finite-element mesh, A. Lamoureux and R. Baliga[15].

NUMERICAL METHOD

In each triangular element, the diffusion coefficient is Prandtl number in x -and y-direction components of momentum, respectively, and one energy equation, are evaluated at the centroid and assumed to prevail over that element. The volumetric source term, $Ra.Pr.\theta$ is stored at the vertices of the triangular elements and assumed to prevail over the corresponding portions of the control volumes within that element.

In the proposed CVFEM, all of the dependent primitive variables (U, V, P, θ) are stored at the same nodes (co-located) and interpolated linearly over the same elements (equal-order) proposed by Baliga and Patankar [17]. Prakash and Patankar [18], Schneider and Raw [19], [20]. Equations (2), (3) and (4) contain a convective flux and a diffusive flux. In this investigation, interpolation functions were used to obtain algebraic approximations to the terms that represent convective transport across the control-volume faces, mass-weighted skew upwind interpolation (MAW). The MAW scheme is an adaptation of a positive-coefficient scheme for quadrilateral elements, introduced by Schneider and Raw [19], to triangular elements with the sub-control volumes previously defined.

RESULTS AND DISCUSSION

To show efficiency and accuracy of CVFEM, the following quantities are calculated and compared with available data in the literature.

$|\Psi|_{mid}$ the stream function at the mid-point of the cavity.

U_{max} the maximum horizontal velocity on the vertical mid-plane of the cavity (together with its location).

V_{max} the maximum vertical velocity on the horizontal mid-plane of the cavity (together with its location).

Nu_{moy} the average Nusselt number throughout the cavity.

Nu_{max} the maximum value of the local Nusselt number on the boundary at $x = 0$ (together with its location).

Nu_{min} the minimum value of the local Nusselt number on the boundary at $x = 0$ (together with its location).

Table 1
Numerical results of Natural Convection in Square Cavity for $Ra = 10^3$

	$ \Psi _{mid}$	U_{max} Y	V_{max} X
Bench mark (Position)	1.174	3.649 0.813	3.697 0.178
Ref [7] Error (Position)	1.174 0.00%	3.589 1.64% 0.811	3.629 1.84% 0.811
Ref [16] Error (Position)	1.159 1.28%	3.645 0.11% 0.814	3.695 0.05% 0.178
Present study Error (Position)		3.623 0,71% 0.814	3.670 0.73% 0.175

Table 2
Numerical results of Natural Convection in Square Cavity for $Ra = 10^4$

	Nu_{max} Y	Nu_{min} Y	Nu_{moy}
Bench mark (Position)	3.528 0.143	0.586 1	2.243
Ref [7] Error (Position)	3.603 2.13% 0.165	0.610 4.10% 1	2.212 1.38%
Ref [16] Error (Position)	3.529 0.03% 0.15	0.592 1.02% 1	2.256 0.58%
Present study Error (Position)	3.526 0.05% 0.140	0.595 1.53% 1	2.241 0.08%

Table 3

Numerical results of Natural Convection in Square Cavity for $Ra = 10^5$

	$ \Psi _{mid}$	U_{max} Y	V_{max} X
Bench mark (Position)	9.111	34.73 0.855	68.59 0.066
Ref [7] Error (Position)	9.702 6.49%	36.46 4.98% 0.854	62.79 8.46% 0.075
Ref [16] Error (Position)	8.786 3.57%	33.421 3.77% 0.853	70.44 2.70% 0.0672
Present study Error (Position)	9.247 1.49%	35.153 1.21% 0.854	68.195 0.57% 0.065

Table 4

Numerical results of Natural Convection in Square Cavity for $Ra = 10^6$

	Nu_{max} Y	Nu_{min} Y	Nu_{moy}
Bench mark (Position)	17.925 0.037	0.989 1	8.800
Ref [7] Error (Position)	14.215 20.70% 0.124	1.749 76.85% 1	9.027 2.58%
Ref [16] Error (Position)	15.601 12.97% 0.09	0.971 1.82% 1	8.934 1.52%
Present study Error (Position)	17.142 4.36% 0.040	1.087 9.90% 1	8.774 0.29%

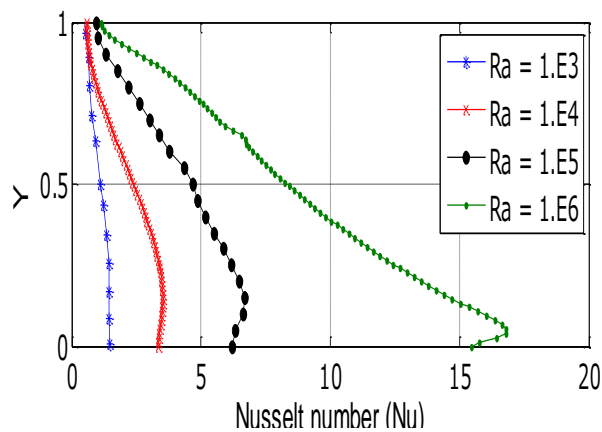


Figure 2

Local Nusselt number variation by CVFEM simulations: hot wall, $10^3 \leq Ra \leq 10^6$

Table 1 to table 4, shows the predicted values from the present solution as compared with the benchmark solution, the solution due to Vahl Davis [7] and Ismail and Scalon [16] for different values of Rayleigh numbers and using an unstructured grid of (11×11) . The analysis of the results in table 1 to table 4, show that the predictions from the present method indicate smaller errors as compared with Vahl Davis and Ismail results except for the Rayleigh number 10^3 to 10^6 . As the Rayleigh number is increased the errors associated with the solution also increase reaching values of about 4.36% (present study) as compared to 20.70% from the present (Vahl Davis). These errors can be reduced without any difficulties by using finer grid size.

Figure 2 elucidates the local Nusselt number distribution along the hot wall obtained by using the CVFEM. There is a greater transfer of heat from the lower bottom of the hot wall to the fluid. This rate of transfer of heat from the wall to the fluid, and vice versa, increases with the Rayleigh number. Local Nu is maximum at a point close to the bottom of the hot wall and minimum at the top.

CONCLUSIONS

We have developed in this work the CVFEM method for resolution of advection-diffusion equation for solving the convective heat transfer in laminar flow. We have used equal order interpolation functions for the pressure and velocity components which can handle the pressure-velocity coupling of the problem, for the resolution of the discretized equations. Our results were compared with those obtained by other numerical methods. The method yields results very similar to those obtained with other methods.

REFERENCES

- [1] Joye, D. D., 1996, "Comparison of aiding and opposing mixed convection heat transfer in a vertical tube with Grashof number variation," *Int. J. Heat Fluid Flow*, **17**(95), pp. 96–101.
- [2] Sprenger, C., 1999, "Book Reviews," pp. 1251–1263.
- [3] Bozeman, J. D., and Dalton, C., 1973, "Numerical study of viscous flow in a cavity," *J. Comput. Phys.*, **12**(3), pp. 348–363.
- [4] de Vahl Davis, G., and Mallinson, G. D., 1976, "An evaluation of upwind and central difference approximations by a study of recirculating flow," *Comput. Fluids*, **4**(1), pp. 29–43.
- [5] Greenspan, D., 1969, "Numerical Studies of

- Prototype Cavity Flow Problems,” *Comput. J.*, **12**(1), pp. 88–93.
- [6] DAVIS, V., 1968, “LAMINAR NATURAL CONVECTION IN AN ENCLOSED RECTANGULAR CAVITY,” **I**, pp. 1675–1693.
- [7] DAVIS, V., 1983, “natural convection of air in a square cavity a bench mark numerical solution,” **3**(July 1982), pp. 249–264.
- [8] Davis, G. D. E. V., and Jones, I. P., 1983, “natural convection in a square cavity: a comparison exercise,” **3**(July 1982), pp. 227–248.
- [9] Stevens, W. N. R., 1982, “finite element , stream function-vorticity solution of steady laminar natural convection,” (January).
- [10] Torn Fusegi, J. M. H. & K. K., “natural convection in a differentially heated square cavity with internal heat generation,” (September 2013), pp. 37–41.
- [11] Wan, D. C., Patnaik, B. S. V, and Wei, G. W., 2001, “a new benchmark quality solution for the buoyancy-driven cavity by discrete singular convolution,” (March).
- [12] Guo, Y., and Bathe, K.-J., 2002, “A numerical study of a natural convection flow in a cavity,” *Int. J. Numer. Methods Fluids*, **40**(8), pp. 1045–1057.
- [13] Dalal, A., Eswaran, V., and Biswas, G., 2008, “A Finite-Volume Method for Navier-Stokes Equations on Unstructured Meshes,” *Numer. Heat Transf. Part B Fundam.*, **54**(3), pp. 238–259.
- [14] Basak, T., Roy, S., and Balakrishnan, A. R., 2006, “Effects of thermal boundary conditions on natural convection flows within a square cavity,” *Int. J. Heat Mass Transf.*, **49**(23-24), pp. 4525–4535.
- [15] Lamoureux, A., and Baliga, B. R., “Improved Formulations of the Discretized Pressure Equation and Boundary Treatments in Co-Located Equal-Order Control-Volume Finite-Element Methods for Incompressible Fluid Flow,” (January 2013), pp. 37–41.
- [16] Ismail, K. A. R., and Scalon, V. L., 2000, “A finite element free convection model for the side wall heated cavity,” *Int. J. Heat Mass Transf.*, **43**(8), pp. 1373–1389.
- [17] Baliga, B., and Patankar, S., 1983, “A control volume finite-element method for two-dimensional fluid flow and heat transfer,” *Numer. Heat Transf.*, **6**(3), pp. 245–261.
- [18] Prakash, C., and Patankar, S., 1985, “A control volume-based finite-element method for solving the Navier-Stokes equations using equal-order velocity-pressure interpolation,” *Numer. Heat Transf.*, **8**(3), pp. 259–280.
- [19] Schneider, G. E., and Raw, M. J., 1986, “Skewed, Positive Influence Coefficient Upwinding Procedure for Control-Volume-Based Finite-Element Convection-Diffusion Computation,” *Numer. Heat Transf.*, **9**(1), pp. 1–26.
- [20] Schneider, G. E., and Raw, M. J., 2007, “control volume finite-element method for heat transfer and fluid flow using colocated variables — 1 . computational procedure,” (March 2013), pp. 37–41.

NUMERICAL SIMULATION OF CH₄ -H₂-AIR NON-PREMIXED FLAME STABILIZED BY A BLUFF BODY

ALLICHE Mounir*, KHALADI Fatma Zohra², CHIKH Salah²

1- *Laboratoire de Mécanique Physique et Modélisation Mathématique (LMP2M), Université de Médéa, Quartier Ain Dheb, Medea, 26000, Medea, Algeria*

2- *Laboratoire de Transports Polyphasiques et Milieux Poreux (LTPMP), Université de Technologie Houari Boumediene, Alger, Algeria*

*Corresponding author: Fax: +213 25 78 52 53 Email: alliche.mounir@univ-medea.dz

ABSTRACT

The aim of this study is to perform a numerical simulation of a non-premixed turbulent flame of methane-air enriched by hydrogen. The selected axisymmetric configuration is composed of a central injector of methane-hydrogen mixture surrounded by a bluff-body, which is surrounded by a co-axial air jet. The Ansys CFX software is used to solve the equations governing turbulent reactive flow (Navier Stokes averaged). The Turbulence is modeled using the k- ϵ model. The EDM (Eddy Dissipation model), then the FRC model (Finite Rate Combustion) combined with EDM are used to modeling the combustion phenomena. The results show some concordance with the temperature profile given by experience to a hydrogen rate of 50%.

KEY WORDS: *Non-premixed combustion, Hydrogen enrichment, EDM and FRC models, Ansys CFX.*

INTRODUCTION

Over the past three decades, there has been considerable effort in the world to develop and introduce alternative transportation fuels to replace conventional fuels such as gasoline and diesel, environmental issues, most notably air pollution and limited availability of conventional fuels are among the principle driving forces behind this movement. Thus, if one tries to find for the definition of perfect fuel, hydrogen probably satisfies most of the desirable characteristics of such a fuel. Plentiful and clean burning, hydrogen has very high-energy content. [1, 2]

Due to difficulties in conducting spatially resolved measurements of combustion characteristics in devices, the numerical simulation can be cost effective approach to study the combustion mechanism. In this work, Computational Fluid Dynamics (CFD) based numerical simulations have been performed to study the combustion of non-premixed turbulent hydrogen-air mixture in cylindrical chamber with Co-Current Injector. The performance of the combustor is evaluated by using Ansys CFX under adiabatic wall condition at various equivalence ratios and mass flow rates of Methane/hydrogen/air.

The present work try to study the fundamentals of Computational Fluid Dynamics (CFD), Numerical modeling, combustion phenomenon and various aspects in order to use them for solving the realistic problems. This study allows us:

- The understanding of the basics of Hydrogen-oxygen reaction mechanism, its combustion and the geometry of the cylindrical chamber used in this study is very important for simulating Methane-Air combustion system enriched by Hydrogen.
- To develop a two-dimensional numerical mesh and flow model which adequately and accurately represent the physical model of combustion chamber and is simple enough to limit the amount of computational time for obtaining a solution.
- The objective of this study is to find and apply appropriate model that improve the simulation of combustion with the commercial CFD as Ansys CFX.
- Generate numerical data/solutions, which correlate as much as possible with the experimental data for various conditions including

equivalence ratios, mass flow rates of hydrogen-air mixture.

In the same context, Zhuyin Ren [3] presents a numerical simulation of a non-premixed combustion flame methane-air enriched by hydrogen, stabilized by a recirculation zone created by an obstacle or a bluff-body : a simple approach in which we apply a different combustion model to see if the same results were been obtained. Zhuyin Ren [3] uses a reduced description with chemical tabs implemented in FLUENT is combined with the EDC model (Eddy Dissipation Concept) considers that a moderate or chemistry with model PDF (probability density function) for combustion. We decided, in the simulation of combustion, for EDM in its infinitely fast chemistry limited compared to the scale of the turbulent times. Then for model Combined EDM/FRC, firstly, that it is valid for several reactions classified from a low to a high number of Damköhler (slow or fast chemistry compared to the scale of the turbulence time) and secondly, reaction rates are firstly calculated for each model separately and then the minimum of both is used. This procedure is applied to each reaction separately, so that when the level in one-step, would be limited by the chemical kinetics, certain other steps would be limited by the turbulent mixing at the same time and in the same physical position. [4].

Our approach is a first step in choosing the appropriate mesh following a test of several types of mesh, with an infinitely fast chemistry, applying the EDM model for the combustion of methane-air flame. Then, we compare the methane-air flame at the hydrogen-air flame.

In the other hand, we compare the application of EDM model to combined EDM/FRC model for simulating the combustion of an air- methane sulfonate flame enriched by hydrogen. The results of our calculations are presented in the form of temperature profiles.

Hydrogen as a fuel

Hydrogen is a colorless, odorless, tasteless, and nonpoisonous gas under normal conditions on Earth. It typically exists as a diatomic molecule. Hydrogen is the most abundant element in the universe, accounting for 90 percent of the universe by weight. However, it is not commonly found in its pure form. [1, 2, 5].

In other hand, Hydrogen has several important chemical properties that affect its use as a fuel:

- It readily combines with oxygen to form water, which is necessary for life on this planet.
- It has a high-energy content per weight (nearly 3 times as much as gasoline), but the energy density per volume is quite low at standard temperature and pressure. Volumetric energy density can be increased by storing the hydrogen under increased pressure.
- Hydrogen is highly flammable; it only takes a small amount of energy to ignite it and make it burn. It also has a wide flammability range, meaning it can burn when it makes up 4 to 74 percent of the air by volume.
- Hydrogen burns with a pale-blue, almost-invisible flame, making hydrogen fires difficult to see.
- The combustion of hydrogen does not produce carbon dioxide (CO₂), particulate, or sulfur emissions.
- Hydrogen can be produced from renewable resources, such as by reforming ethanol, (this process emits some carbon dioxide) and by the electrolysis of water, (electrolysis is very expensive).
- Energy Content for 1 kg of Hydrogen = 424 Standard Cubic Feet (Reacting with oxygen to form water).
- Higher Heating Value = 141,600 KJ and Lower Heating Value = 119,600 KJ

The properties of hydrogen are largely listed in reference [6] with conventional fuels i.e. Gasoline & Diesel and other alternative fuels such as CNG, LPG, and Biogas. From this table, the limits of flammability are one of the most important properties of a fuel. These parameters are a measure of the range of the fuel/air ratios over which an engine can operate. Hydrogen has wide range of flammability in comparison with other fuels. One of the significant advantages is that hydrogen engine can run on a lean mixture. When engine is run on slightly lean mixtures fuel economy is greater and the combustion reaction is more complete. Additionally, the final combustion temperature can be lowered by using ultra-lean mixtures, reducing the amount of NO_x emissions. Indeed, the minimum energy required for ignition for hydrogen is about an order of magnitude less than that required for gasoline. This enables hydrogen engines to run well on lean mixtures and ensures prompt ignition. Unfortunately, since very

little energy is necessary to ignite a hydrogen combustion reaction, and almost any hydrogen/air mixture can be ignited due to wide limits of flammability of hydrogen, hot gases and hot spots on the cylinder can serve as sources of ignition, creating problems of premature ignition and flashback [7].

HYDROGEN COMBUSTION

In the combustion chamber, the combustion flame is typically extinguished at certain distance from the cylinder wall due to heat losses called as quenching distance. For hydrogen, the quenching distance is less than that of gasoline, so that flame comes closer to the wall before it is extinguished. Thus, it is more difficult to quench a hydrogen flame than a gasoline flame. [8]

The flame speed of hydrogen is nearly an order of magnitude higher than that of gasoline. For stoichiometric mixtures, hydrogen engines can more closely approach the thermodynamically ideal engine cycle. At leaner mixtures, the flame velocity decreases significantly.

In other hand, one the reasons for which we are interested in hydrogen is because its chemistry is considered a starting point for the more complex hydrocarbon chemistry. It is important to stress that in the auto ignition stages of any flame, the fuel air mixture may follow a low temperature reaction mechanism and in the latter stages, an explosive reaction due to the increase in temperature and/or pressure causing the operating point to shift between the regions of the explosion limits of a stoichiometric mixture.

GEOMETRY AND CONFIGURATION

In our study, we adopted the geometry of Zhuyin Ren [3] with the same conditions of entry of fuel and air: methane-hydrogen is surrounded by a bluff-body and an air co-flow.

The diameter of the bluff-body, D_b , is 0.05 m and the jet is 0.0036 m. The computational domain is shown in Figure 1. Origin coordinate system is taken at the center of the output plane of the jet.

The numerical conditions selected for calculating a non- premixed turbulent flame stabilized by bluff-body are :

- An axial velocity of fuel 118 m / s with a 10% turbulence intensity and Hydraulic diameter is 0.0036 m to 300K temperature.
- An air concurrently 40 m/s [9] with a 10%

turbulence intensity and Hydraulic diameter equal to 0.25 m at a temperature of 300 K.

The domain is discretized with a mesh multizone: hexahedral prisms with 10954 to 10051 nodes.

MATHEMATICAL MODELING

In Computational Fluid Dynamics, we model the physical system involving fluid flow within the definite boundaries by the set of mathematical equations usually in differential form and obtain the numerical solution of these governing equations describing the fluid flow by the use of computational methods.

The governing equations may include: the set of the Navier-Stokes equations, continuity equation, and any additional conservation equations, such as energy or species concentrations. The fluid flow is modeled by the governing equations, which show the effect of the governing phenomena on the fluid flow. These governing phenomena may include conduction, convection, diffusion, turbulence, radiation and combustion. The following is brief description of the governing equations. [10]

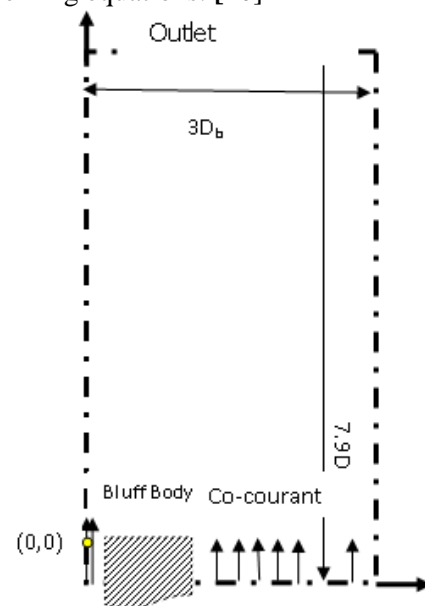


Figure 1. Schematic Diagram of the Combustion Chamber

Continuity Equation

Considering the law of conservation of mass the continuity equation,

$$\frac{\partial \rho}{\partial t} + \mathbf{u} \cdot \text{div}(\rho) + \rho \cdot \text{div}(\mathbf{u}) = 0 \quad (1)$$

In the given equation the first term is the rate of change of density. In the second and the third terms the divergence div is the flux density or flux/volume. The first two terms show the two ways the density of the fluid element changes. If we assume the incompressibility condition i.e. density of the fluid is constant, the above equation reduces to, $\text{div}(\mathbf{u})=0$.

Momentum Equations

Also known as Navier and Stokes equations, these are derived for a viscous flow and give the relationships between the normal/shear stresses and the rate of deformation (velocity field variation). We can obtain these equations by making a simple assumption that the stresses are linearly related to the rate of deformation (Newtonian fluid), the constant of proportionality for the relation being the dynamic viscosity of the fluid. Following is stated the Navier and Stokes equation for i -th coordinate direction,

$$\frac{\partial(\rho u_i)}{\partial t} + \frac{\partial(\rho u_i u_j)}{\partial x_j} = -\frac{\partial p}{\partial x_i} + \frac{\partial \tau_{ij}}{\partial x_j} + F_i \quad (2)$$

Where τ_{ij} is the viscous force tensor and F_i represents a body force in the i -th coordinate direction. In practical situations of combustion, all fluids are assumed as Newtonian and the viscous stress tensor is:

$$\tau_{ij} = \mu \left\{ \frac{\partial u_i}{\partial x_j} + \frac{\partial u_j}{\partial x_i} \right\} - \frac{2}{3} \mu \delta_{ij} \left\{ \frac{\partial u_k}{\partial x_k} \right\} \quad (3)$$

Where μ is the molecular viscosity, which depends on the fluid. The Kronecker delta is $\delta_{ij}=1$, if $i=j$, 0 otherwise.

Species Equation

$$\frac{\partial(\rho Y_\alpha)}{\partial t} + \frac{\partial(\rho u_j Y_\alpha)}{\partial x_j} = -\frac{\partial J_j^\alpha}{\partial x_j} + w_\alpha \quad (4)$$

Where n is the number of species, J_j^α is the molecular diffusivity flux of the species α in the j -th coordinate direction, w_α is the mass reaction rate of this species per unit volume, and Y_α is the mass fraction of species α .

The diffusive flux, J_j^α , can be approximated by:

$$J_j^\alpha = -\frac{\mu}{Sc_\alpha} \frac{\partial Y_\alpha}{\partial x_j} = -\rho D_\alpha \frac{\partial Y_\alpha}{\partial x_j} \quad (5)$$

where Sc_α is the Schmidt number of the species α , defined as:

$$Sc_\alpha = \frac{\mu}{\rho D_\alpha} \quad (6)$$

Where D is the molecular diffusivity of the species α relative to the other species.

Standard k-ε turbulence model

In this simple model, two additional transport equation are solved for the two turbulence quantities viz. the turbulent kinetic energy k and the energy dissipation rate ϵ . These two quantities are related to the primary variables and can give a length scale and time scale to form a quantity with dimension of \mathbf{v}_T , thus making the model complete (no more flow-dependent specifications are required). This is a widely used model in CFD simulations.

$$\bar{k} = \frac{1}{2} \bar{u}^2 \quad (7)$$

The balance equation for k is:

$$\frac{\partial \bar{\rho} \bar{k}}{\partial t} + \nabla \cdot (\bar{\rho} \tilde{u} \bar{k}) = -(2/3) \bar{\rho} \bar{k} \nabla \cdot \tilde{u} + \sigma : \nabla \tilde{u} + \nabla \cdot \left\{ \left[\frac{\mu_{eff}}{\rho k} \right] \nabla \bar{k} \right\} - \bar{\rho} \bar{\epsilon} + \bar{w}^s \quad (8)$$

BOUNDARY CONDITIONS

The inlet temperature of hydrogen and air is considered uniform at 300 K. A fixed, uniform velocity 90 m/s is specified at the hydrogen inlet. Axis-symmetric boundary conditions are applied along the central axis of the combustion chamber. At the exit, a pressure outlet boundary condition is specified with a fixed pressure of 1.01325×10^5 Pa. At the chamber wall, no-slip boundary condition and no species flux normal to the wall surface are applied. The thermal boundary condition on the chamber wall is taken as adiabatic wall condition.

RESULTS AND DISCUSSION

A number of numerical simulations have been performed to study the combustion phenomena under adiabatic wall conditions when hydrogen air mixture changes from lean to rich and at different mass flow rate of mixture.

The first step was a choice of the mesh to discretize the volume occupied by the fluid, a mesh that ensures convergence of the numerical procedure. To achieve this were tested several types of mesh. For testing of the mesh, methane-air combustion was simulated without adding hydrogen with EDM (Eddy dissipation model). The figures below show the evolution of the temperature for each type of mesh.

Figure 2 shows that for an axial section of the injector very close (a) the change in temperature is almost the same regardless of the mesh type. But away from the injector, this trend changes from one mesh to another (a) and (b) except for the multizone mesh with three types of mapped mesh (b).

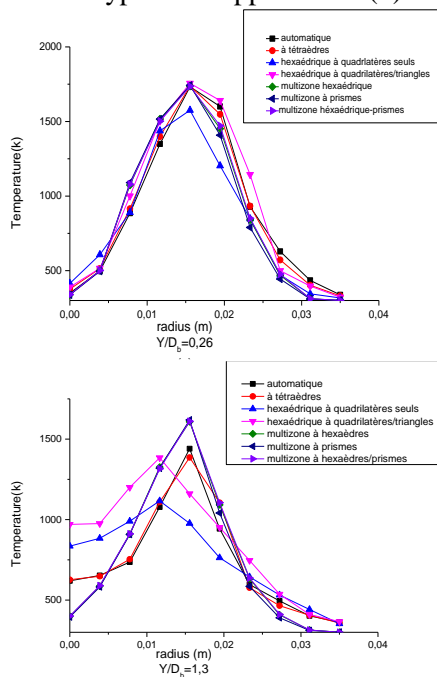


Figure 2. Temperature Profiles for different mesh

Figure 3 shows clearly that the clearly change in the temperature curve is better represented by a multizone mesh than by automatic mesh. Indeed, in the first case we see that the temperature logically evolves in an increasing manner from one section to another to exit the chamber. While this trend is not stable in the second case: decreasing between 0.26, 0.6 and 1.3 and 1.8 de 1.3 increasing then decreasing from 1.8 to exit the combustion chamber.

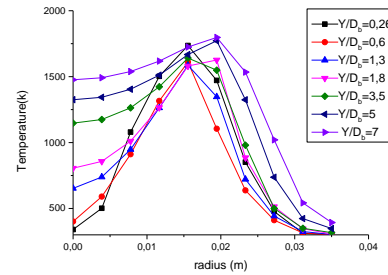


Figure 3. Temperature Profiles for different positions in the axial centerline

Figure 4a shows an asymmetric shape of the iso-contours in a hexahedral-dominated meshing, and this is the case in all types tested mesh, except for the multizone mesh where the shape of the iso-contour is axisymmetric as shown in Figure 4b.

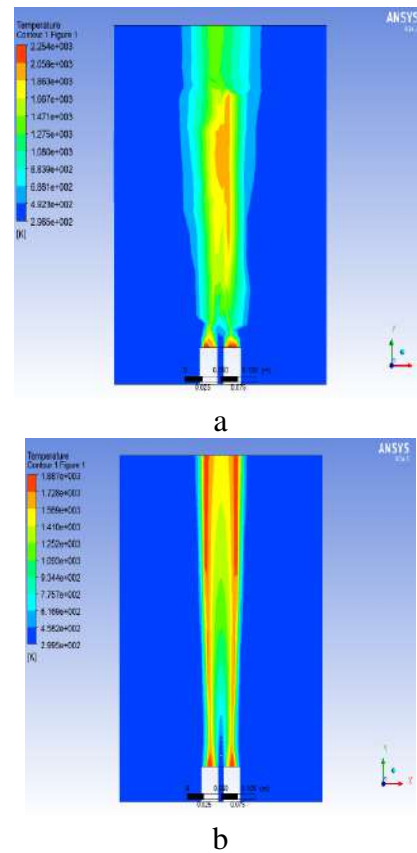


Figure 4. Temperature iso-contours for different mesh: (a) Method for dominance hexahedral: mesh free only quadrilateral faces, (b) Method Multizone with a mapped hexahedral mesh / prism

From the above we see that the evolution of the temperature is homogeneous and uniform axisymmetric for multizone mesh (prism, hexahedral) or no uniform (hexahedral prisms) than for other types of mesh. In addition, it does not require a lot of computing time compared to

other types of mesh (500 iterations against 1000). That is why we opted for the multizone mesh. Only between uniform and non-uniform mesh, we choose the latter.

HYDROGEN-AIR FLAME

The Figure below shows the temperature iso-contours in a hydrogen-air flame with the same basis as those of air methane: an asymmetrical shape of a flame that seems blown but where the maximum temperature is substantially greater than that of methane-air (2273 k / 1887k).

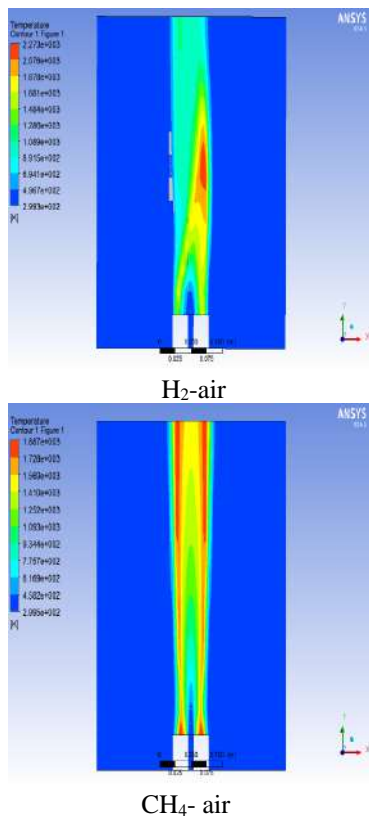


Figure 5. Temperature iso-contours for Hydrogen-Air and Methane-Air Flames

The Figure shows the contours of temperature (K) on the cross section along central axis of combustion chamber at stoichiometric air fuel ratio (at $\Phi=1$). It shows the gas temperature distribution along the central axis. It can be seen from this Figure that the highest temperature is obtained at the exit of combustion chamber. The flame temperature can be as high as 2365K, which is almost the same as the adiabatic flame temperature of the Combustion of non-premixed stoichiometric hydrogen-air mixture.

ENRICHMENT WITH HYDROGEN

The figure 6 below clearly illustrates the difference in the radial variation in temperature between three types of flames: air-methane, hydrogen-air and methane-hydrogen-air. Although the initial temperature and that at the end of combustion (flame resistance to extinction?), the Figure shows that hydrogen flame, is higher than in a methane flame, the widest radial development of this temperature is observed only away from the injector. (Fig 6d).

As to the radial profile of the temperature of a methane-air flame, enriched with 10% hydrogen, it coincides with that of a methane-air flame without addition of hydrogen but with a slight increase of the temperature in the first flame. Indicating the effect of enrichment with hydrogen, ie the percentage remains suitable for the adopted configuration.

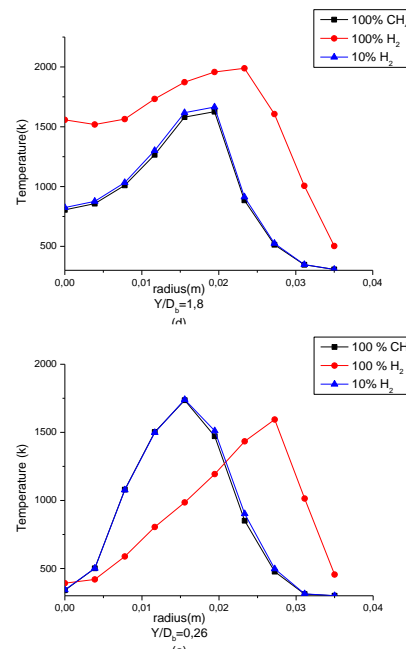


Figure 6- Radial Profile of for different sections and three flames types

Figure 7 shows the evolution of the temperature in a methane-air flame enriched with hydrogen at different enrichment levels. We notice a significant difference in the evolution of temperature increases with increasing hydrogen content when combustion is simulated model combined with EDM/FRC. A slight increase when combustion is simulated with the EDM model. However, the maximum temperature may decrease when the proportion of hydrogen exceeds 50% (Figure 9). The temperature

iso-contours (Figure 8) for each percent of added hydrogen confirm this imbalance: the flame loses its axially symmetrical shape and homogeneous and appears blown. The best percentage of hydrogen addition would be a priori 50% a result confirmed by [3].

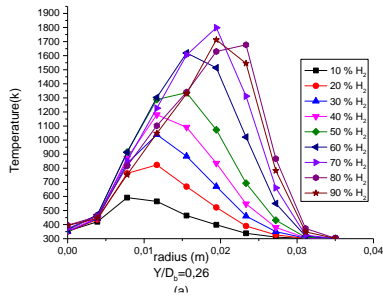


Figure 7. Radial temperature profile for different percentages Hydrogen Combustion added simulated with the model EDM / FRC combined

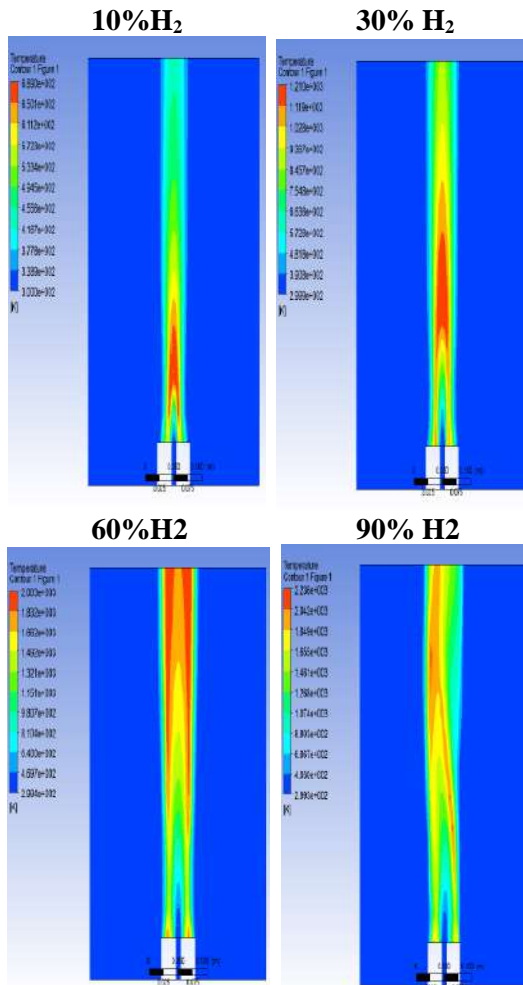


Figure 8. Iso-contours of temperature for different hydrogen percentages Added: Combustion simulated by EDM / FRC Combined

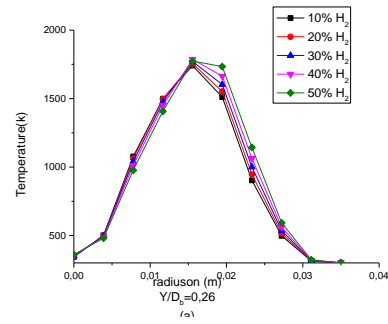


Figure 9. Temperature evolution for different percentages of Hydrogen added: Simulated Combustion with EDM

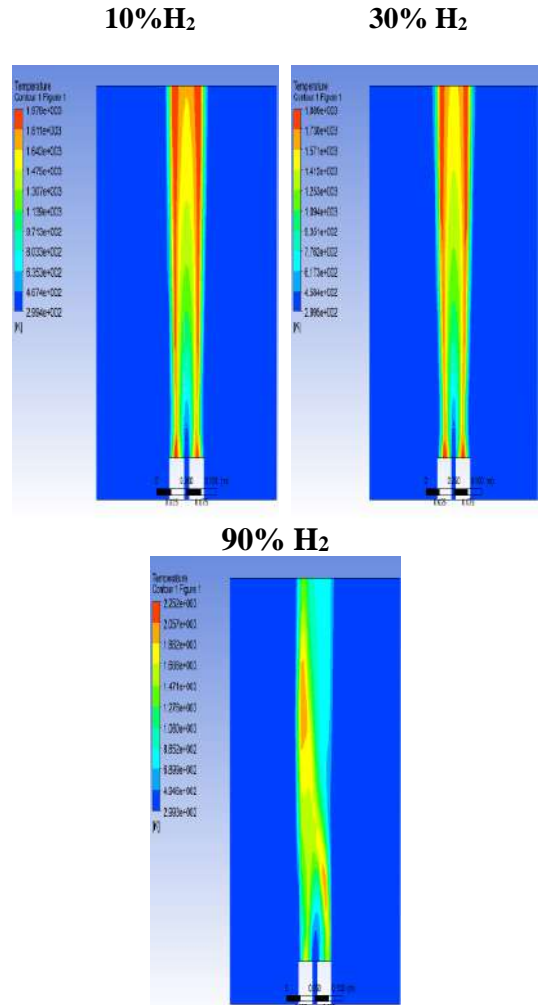


Figure 10. Iso-temperature contours for different percentages of added hydrogen simulated combustion by EDM

COMPARISON WITH EXPERIMENT

The question is what model is best for simulating this flame? For this, a comparison is made with experimental data from [3]. The figure 11 shows a good agreement with simulation and experiment

results. The combined model EDM/FRC give better result than simple EDM model in the outlet zone of the combustion chamber. Near the burner region, the EDM model can be used with an acceptable precision.

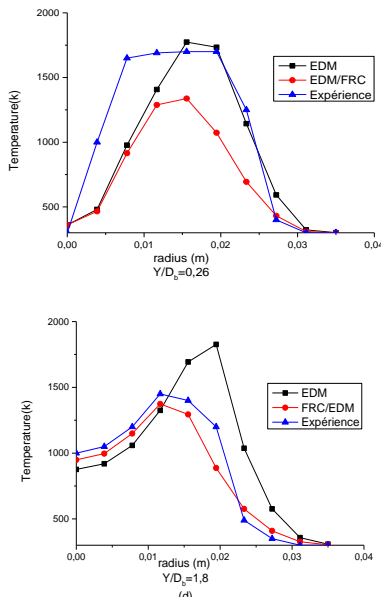


Figure 11: Radial profile of the temperature of a methane-air flame enriched with 50% hydrogen

CONCLUSION

In this work, the CFD based combustion simulations have been applied to analyze the combustion characteristics of non-premixed hydrogen-air in a 2D combustor. The CFD simulations, taking in to account the coupling of fluid dynamics, heat transfer and detailed chemical kinetics, are used to investigate the effects of various operating conditions. The combustor performance is evaluated by predicting the temperatures of exit gas of the combustor and outer wall of the combustor. To make the combustor operable, the heat output should meet the design criteria, the wall temperature should be lower than the material allowable temperature and the exit gas temperature should be high enough.

In other hand, this study presents a numerical simulation of a non-premixed turbulent flame of methane-air enriched by hydrogen. The selected axisymmetric configuration is composed of a central injector of methane-hydrogen mixture surrounded by a bluff-body, which is surrounded by a co-axial air jet. The EDM (Eddy Dissipation model), then the FRC model (Finite Rate Combustion) combined with EDM are used to

modeling the combustion phenomena. The results show some concordance with the temperature profile given by experience to a hydrogen rate of 50%.

REFERENCES

1. Das L.M., Hydrogen-oxygen reaction mechanism and its implication to hydrogen engine combustion, 21:703-715 International Journal of Hydrogen Energy, 1996
2. S. Verhelst, R. Sierens, Hydrogen engine-specific properties, International Journal of Hydrogen Energy 26 (2001) 987990.
3. Zhuyin Ren, Graham M. Goldin, Varun Hiremath et Stephen B. Pope, "Simulations of a turbulent non-premixed flame using combined dimension reduction and tabulation for combustion chemistry ", Elsevier, 1er septembre 2012.
4. Jingsong Hua, MengWu, Kurichi Kumar, Numerical simulation of the combustion of hydrogenair mixture in micro-scaled chambers. Part II: CFD analysis for a micro-combustor 60:3507-3515, chemical engineering science, 2005.
5. Belahomley Sauvi, Introduction aux combustibles et à la combustion, Édition Technip, Paris, 1981.
6. Sources Gaz De France, Carburants et Moteurs, Guibet, Combustibles gazeux (oct 93)
7. CFX –Solver modeling Guide
8. R. Mouangue, M. Obounou, " Simulation numerique d'une flamme de diffusion turbulente h2/air ", Phys. Chem. News 50 (2009) 69-78
9. John GRONDIN," Etude du mélange et de la combustion dans les flammes-jets subsoniques à haute vitesse : influence des vitesses, des densités et de la composition du combustible", Thèse de doctorat, ENSMA Poitiers, 7 janvier 2010.
10. BORGHI. R., 1988, Turbulent combustion modelling, Prog. Energy Comb. Sci., 14 245
11. Mounir Alliche, Pierre Haldenwang, Salah Chikh, Extinction conditions of a premixed flame in a channel, Combustion and Flame, 157 (2010), 1060-1070.

HYBRID FD-LBM SIMULATIONS OF THERMOSOLUTAL CONVECTION GENERATED IN AN INCLINED ENCLOSURE IN THE PRESENCE OF Soret AND DUFOUR EFFECTS WITH HEATLINES AND MASSLINES CONCEPTS

Safae Hasnaoui*, A. Amahmid, A. Raji⁽¹⁾, M. Hasnaoui, Y. Dahani

Cadi Ayyad University, Faculty of Sciences Semlalia, LMFE, Unit affiliated to CNRST (URAC 27) BP
2390, Marrakech, Morocco

⁽¹⁾Sultan Moulay Slimane University, Faculty of Sciences and Technics, Physics Department, Laboratory of
Flows and
Transfers Modelling (LAMET), B.P. 523, Béni-Mellal 23000, Morocco

*Corresponding author: safae.hasnaoui@edu.uca.ac.ma

ABSTRACT

An hybrid Lattice-Boltzman finite-difference method is proposed to assess the impact of the inclination angle of the cavity on thermosolutal natural convection of a binary fluid confined in a square cavity differentially heated and salted from two opposite walls with constant temperatures and concentrations. This method seems more flexible in implementing additional effects and apparently more efficient than the classical CFD methods. The study is conducted in the case of aiding buoyancy forces and many other controlling parameters. Results obtained showed important qualitative and quantitative effects of the governing parameters on fluid flow and heat and mass transfer characteristics. The heatlines and masslines concepts are also implemented to obtain additional details on heat and mass transfer processes.

Keywords: Heat transfer, Numerical study, Lattice-Boltzmann method, Soret and Dufour effects, Inclined enclosure.

NOMENCLATURE

Du	Dufour parameter
g	Gravitational acceleration
H	Height of the square cavity
Le	Lewis number
N	Buoyancy ratio
Pr	Prandtl number (ν/κ_{11})
R_T	Thermal Rayleigh number
Sr	Soret parameter
f	Vector of distribution functions
c	Discrete velocity of the particle located at r
F_y	Buoyancy force

Greek

β	Volume expansion coefficient
θ	Dimensionless temperature
γ	Inclination angle
ν	Fluid kinematic viscosity
μ	Fluid dynamic viscosity
Ψ	Nondimensional stream-function

INTRODUCTION

Convective transport phenomena both in fluids and porous media have attracted the attention of

researchers through the decades due to numerous applications involving these phenomena in industrial and environmental fields including, but not limitative to, underground diffusion of nuclear waste, oil reservoir analysis, petroleum extraction, mineral material migration, separation of mixtures, etc. Particularly, coupled heat and mass transfer by natural convection in a fluid confined in a rectangular cavity has been the object of numerous studies during the last decades due to the importance of this process which is observed in many geophysical and natural systems of practical interest. The coupling between the energy equation and that characterizing the conservation of species through Dufour and Soret parameters strengthens the interaction between the thermal and solute fields even when the fluid is at rest.

The literature review on double diffusion shows that numerous studies were conducted on rectangular enclosures [1-3]. The literature inspection reveals also that the Dufour effect plays a negligible role in liquids, but its effect is prominent in gaseous mixtures. Soret and Dufour effects were in reality often neglected, since they are of a smaller order of magnitude when compared to the effects described by Fourier's and Fick's laws despite the exceptions.

To be more precise, the Soret effect engenders the separation of species in many mixtures while the Dufour effect should be not neglected in mixtures between gases since its impact could be of considerable importance. Even from a purely fundamental point of view, the Soret effect (may be more than the Dufour effect) has an interest justified by different specific behaviors engendered by its presence. More specifically, the bifurcation occurrence, the multiplicity of solutions and the hysteresis cycles are examples of phenomena that may accompany the implication of the Soret effect in a large category of problems in double-diffusive natural convection. Comparatively, and from a theoretical point of view (to be limited only to this aspect), the impact of Dufour effect on such phenomena remains less elucidated. Several studies have been conducted in our team on thermosolutal convection in the presence of the Soret effect [4-6]. In these studies, analytical solutions have been the main concern in porous horizontal [4], vertical [5] or inclined [6] cavities. The literature review shows also the existence of some works on thermosolutal convection in the presence of both Soret and Dufour effects in rectangular geometries (or confined fluids in general) [7-9]. However, the studies addressing both Soret and Dufour effects remain scarce in the literature compared to those addressing the Soret effect solely.

In view of the existing, the main objective of this contribution is to experiment the hybrid LBM-FDM to solve a natural thermosolutal convection problem in an inclined enclosure in the presence of Soret and Dufour effects.

MATHEMATICAL FORMULATION

A schematic of the physical problem and the associated boundary conditions are shown in Figure 1 with $T_1 > T_0$ and $S_1 > S_0$. The non-active boundaries of the cavity are considered adiabatic and impermeable to the mass transfer. The confined mixture is considered Newtonian and the flow is assumed incompressible and laminar. The velocity problem is governed by the Boltzmann equations (1) for the momentum equation using the BGK approximation [10] and the Boussinesq approximation while the equations of advection-diffusion of temperature and concentration are solved separately using an explicit finite-difference technique [11]. The Lattice-Boltzmann equation in

the presence of an external force \mathbf{F} can be written for the flow field as follows:

$$f_k(r + c_k \Delta t, t + \Delta t) = f_k(r, t) - \omega_k \left(f_k(r, t) - f_k^{eq}(r, t) \right) + F_k \Delta t \quad (1)$$

The model of He and Luo [12], used in this work to treat the incompressible case, is the most popular [13]. Thereby, the local equilibrium distribution function, $f_k^{eq}(r, t)$ known also as Maxwell's distribution function, is obtained as:

$$f_k^{eq}(r, t) = \omega_k \rho \left[1 + 3 \frac{\vec{c}_k \cdot \vec{u}}{c^2} + 4.5 \frac{(\vec{c}_k \cdot \vec{u})^2}{c^4} - 1.5 \frac{\vec{u} \cdot \vec{u}}{c^2} \right] \quad (2)$$

With ρ being the density, \vec{c}_k the discrete velocities for the D2Q9 scheme and ω_k is the weighting factor. The Boussinesq approximation is introduced in the discrete external force using the following expression:

$$F_k = 3\omega_k F = 3\omega_k \rho g \beta \left((T - T_m) + N(S - S_m) \right) c_{ky} \quad (3)$$

Where $T_m = (T_H + T_C)/2$, $S_m = (S_H + S_C)/2$, β is the thermal expansion coefficient and c_{ky} is the projection of the microscopic velocity \vec{c}_k on the y axis.

The macroscopic quantities which are the density, ρ , and the velocity, \vec{u} , can be obtained by using the following formulas:

$$\begin{cases} \rho(r, t) = \sum_{k=0}^{k=8} f_k(r, t) \\ \rho \vec{u}(r, t) = \sum_{k=0}^{k=8} \vec{c}_k f_k(r, t) \end{cases} \quad (4)$$

The Chapman-Enskog procedure was used to link the kinematic viscosity and the thermal diffusivity to the relaxation time.

The energy and species equations can be grouped as a single equation under the following form:

$$\frac{\partial \Gamma}{\partial t} = u \frac{\partial \Gamma}{\partial x} + v \frac{\partial \Gamma}{\partial y} = \kappa_1 \left(\frac{\partial^2 \Gamma}{\partial x^2} + \frac{\partial^2 \Gamma}{\partial y^2} \right) + \kappa_2 \left(\frac{\partial^2 \chi}{\partial x^2} + \frac{\partial^2 \chi}{\partial y^2} \right) \quad (5)$$

Where Γ represents $T/(S)$ and χ represents $S/(T)$ if equation (5) is the equation of energy/(conservation of species). The coefficients κ_1 and κ_2 are respectively thermal diffusivity and translating the coupling to Dufour effect or mass diffusivity and translating the coupling to Soret effect depending if Eq. (5) represents the conservation of energy or the conservation of species.

Equation (5) was discretized at the Boltzmann scale using a similar approach to that proposed by Lallemand and Luo [11] with $\Delta t = \Delta x = \Delta y = 1$. This method is explicit and conditionally stable.

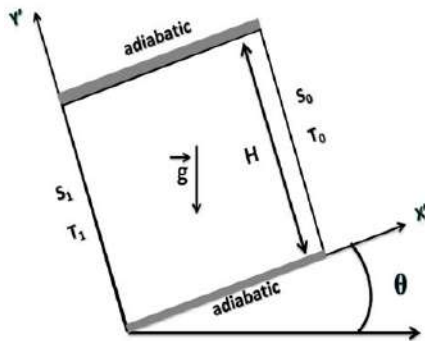


Figure 1
Studied configuration

Validation of the numerical code: The numerical code was validated against a classical finite difference method (the Alternate Direction Implicit method). This method was used to solve the governing equations, which are namely, the dimensionless equations of vorticity, energy and concentration written in their transient forms. The iterative Point-Successive-Over-Relaxation (PSOR) technic was used to solve the dimensionless stream function equation (to satisfy the continuity equation). Comparative results between both methods (not shown here) in the case of aiding buoyancy forces and different values of Sr , Du and inclination angle γ have shown an excellent agreement. Other complementary tests relative to the conservation of energy and species were systematically checked with success at each code running. Finally, it is to specify that all the results presented here were obtained with a grid of 101×101 . The choice of this grid was based on preliminary tests using finer grids which have not led to a noticeable change in the results, instead they have led to a substantial increase in the computing time.

RESULTS AND DISCUSSION

The results presented in this study are obtained in the case of a cavity heated and salted from opposite sides for different values of Sr (-0.5, 0 and 0.5) combined to Du (-0.5, 0 and 0.5) and γ (-60° , -30° , 0° , 30° and 60°). The effect of Soret and Dufour parameters and the inclination angle on fluid flow and heat and mass

transfer characteristics is illustrated for $Pr = 10^5$, $Pr = 0.71$, $Le = 2$ and $N = 1$.

Streamlines, isotherms, iso-concentration lines, heatlines and masslines: These structures obtained for $Sr = Du = -0.5$ are illustrated in Figs. 2a and 2b corresponding respectively to $\gamma = -30^\circ$ and 0° . It is shown that the monocellular structure of the flow, observed for $Du = Sr = 0$ (not presented here), is still conserved even in the presence of Soret and Dufour effects. However, its intensity undergoes a considerable reduction. More precisely, for $\gamma = 0^\circ$

(-30°), $|\Psi_{min}|$ drops from 9.44/(4.94) to 5.74/(2.80) when the couple (Du, Sr) passes from $(0, 0)$ to $(-0.5, -0.5)$. Also, the flow intensity is nearly halved when the inclination passes from 0° to -30° . In fact, the inclination -30° puts the lightest fluid (i.e. the fluid located next to the left active wall) at a higher altitude compared with the heaviest fluid located next to the right active wall. Such a situation reduces the strength of the buoyancy forces which leads to a reduction of the flow intensity. The most important changes undergone by the flow when the cavity is tilted by -30° are observed in the vicinity of the center line, parallel to the inactive walls. A little away from this zone, we can see that the particles paths resembles somewhat to lozenges whose long sides are tilted with respect to the inactive wall. The consequence of this new structure are clearly visible on the isotherms and iso-concentration. In fact, the stratification of the isotherms and iso-concentrations observed a little away from the cavity boundaries is not parallel to the inactive walls (as it is the case for $\gamma = 0^\circ$). As a result, the temperature and concentration gradients parallel to the inactive walls are not cancelled outside the hydrodynamic boundary layer. In these conditions, it is not expected to observe the classical thermal and solutal boundary layers in the cavity; this will be clearly confirmed by the plot of the temperature and the concentration profiles (see the next paragraph). The heatlines and masslines of Figs. 2 show clearly how heat and solute are transported from the left active wall towards the right active one. It is seen that the heat and solute are mainly extracted from the lower half of the left active wall and evacuated through the upper half of the right active one. The presence of an inert zone (zone not contributing to transport phenomena) occupying more than the half of the cavity (i.e. the zone of closed lines) results from the relatively important effects of convective transport.

Recall that, in the absence of convection, the inert zone disappears and the heatlines and masslines consist of straight lines parallel to the inactive walls. A qualitative comparison of the heatlines and masslines indicates that the paths followed by the solute resemble more the paths of the fluid particles (a little away far from the solid boundaries). In fact, as the solutal diffusivity is lower than the thermal one ($Le > 1$), convection affects more the solute transport. It should be noted that, in regions where convection has dominant effects, the convective component of heat and/or solute flux is dominant. Hence, the heatlines and/or masslines coincide with the trajectories of the fluid particles.

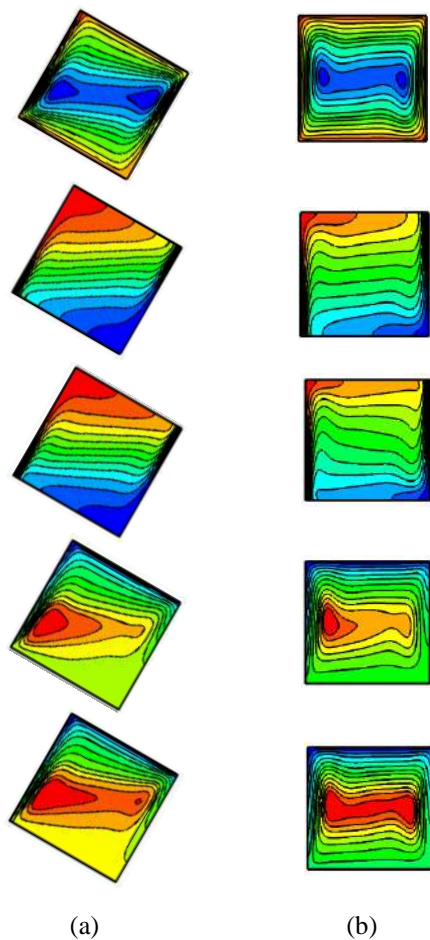


Figure 2

From top to bottom: Streamlines, isotherms, iso-concentrations, heatlines and masslines for $Sr = Du = -0.5$ and $\gamma = -30^\circ$ (a) and 0° (b).

Mid-height profiles: The influence of negative values of Soret and Dufour parameters are illustrated in Figs. 3a to 3c respectively for velocity, temperature and concentration profiles at mid-height

of the cavity for $Ra = 10^5$ and $\gamma = 0^\circ$ and -30° . It is seen in Fig. 3a, that these negative values of the parameters Sr and Du lead to an important attenuation of the extremum values of velocity and this, for both inclinations. In addition, for given values of Sr and Du , the negative inclination engenders also a decrease of the extremum value of velocity in comparison with $\gamma = 0^\circ$. In addition, the velocity profile remains insensible to the cavity inclination and Soret and Dufour parameters in the central part of the cavity where the velocity is almost cancelled. The situation is different in the case of the temperature profile where it is seen in Fig. 3b that the inclination has a considerable effect on this profile while the impact of the parameters Sr and Du is seen to be limited. In fact, for $\gamma = -30^\circ$, the effect of Soret and Dufour acts slightly on the temperature profile by increasing more the temperature gradients in the vicinity of the vertical walls. From a certain distance of the active walls, this effect decreases while approaching the center of the cavity. For $\gamma = 0^\circ$, the temperature profile exhibits a boundary behavior in the presence and in the absence of the Soret and Dufour effects but the latter improve the temperature gradients within the boundary layers zones. Outside the boundary layer region, the Soret and Dufour effect disappears completely and the temperature profile becomes horizontal; behavior characteristic of a classical thermal boundary layer. In the case of concentration, we note some similarity (to a certain limit) with the behavior of temperature vis-à-vis of the inclination and the Soret and Dufour effect. In fact, for $\gamma = 0^\circ$, we observe also the existence of a boundary layer for concentration with a linear but not horizontal profile outside the boundary layer region. In the latter region, we observe also that the concentration profile is insensible to the Soret and Dufour effect. Finally, in the case of $\gamma = -30^\circ$, it is seen from the profiles of Figs. 3b and 3c that the temperature and concentration variations are considerable even in the core region (outside the velocity boundary layer). This result confirms the observations already formulated in the discussion of the streamlines and iso-solutes.

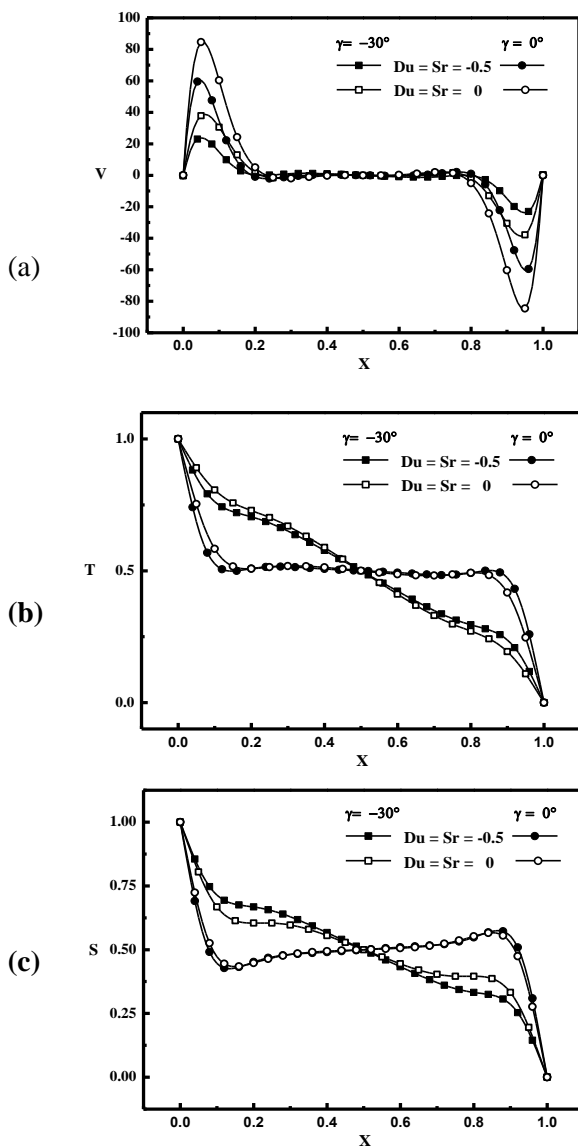


Figure 3

Profiles at mid-height of the cavity for various values of γ , Du and Sr : profiles of velocity (a), temperature (b) and concentration (c).

Concentration and temperature gradients: The profiles of the temperature and concentration gradients at mid-height of the enclosure are presented respectively in Figs. 4a and 4b. These profiles show that the temperature and concentration gradients are too small in the core region compared to the ones obtained in the vicinity of the active walls for zero inclination. However, for the inclination -30° , we can observe that the temperature gradient in the core is close to unity and it is about two to three times higher in the vicinity of the active walls for the combination considered for the Soret and Dufour parameters. A similar trend is observed for the

concentration gradient but with an increase in the gap between the value obtained in the core and that obtained at the active walls. This difference is mainly due to the ratio of thermal and solutal diffusivities which is higher than unity ($Le = 2$). Another information to be deduced from Figs. 4a and 4b is the intensification of the temperature gradients under the Soret and Dufour effects for the combination $Sr = Du = -0.5$ for both 0° and -30° inclinations (in the case of the concentration gradient we observe a slight attenuation for -30°). Note that, for the same combination, the heat and mass transfers are reduced by the Soret and Dufour effects as it will be discussed later.

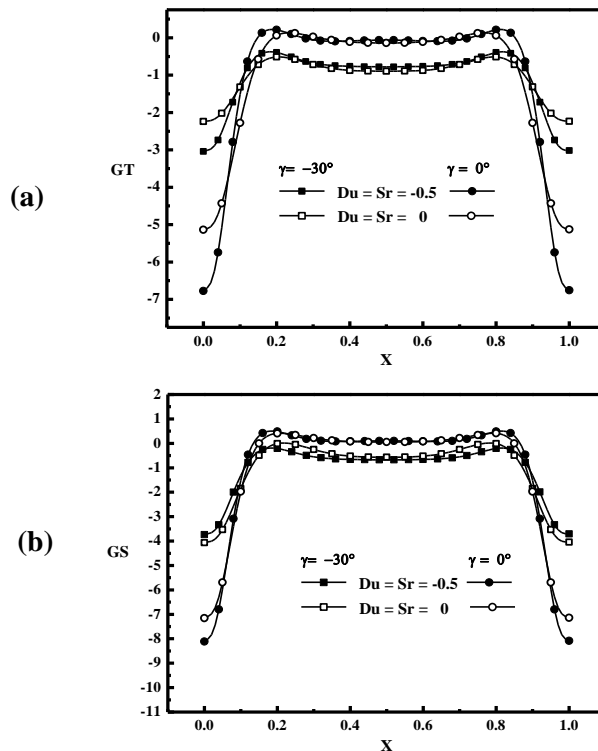


Figure 4

Gradients at mid-height of the cavity for various values of γ , Du and Sr : gradients of temperature (a) and concentration (b).

Mean Nusselt and Sherwood numbers: The variations of the Nusselt and Sherwood numbers with the inclination γ are presented respectively in Figs. 5a and 5b in the absence ($Du = Sr = 0$) and in the presence ($Du = Sr = -0.5$) of the Soret and Dufour effects. It is seen that the variations of the inclination parameter γ affect considerably/(weakly) the heat and mass transfers in the range $-60^\circ \leq \gamma \leq 0^\circ$ / ($0^\circ \leq \gamma \leq 60^\circ$). Quantitatively, $Nu/(Sh)$ is multiplied by 4.3 / (0.9) when γ passes from -60° to 0° , while it changes only by 2% when γ

passes from 60° to 0° . The presence of the Soret and Dufour effects is found to attenuate considerably the heat and mass transfers. At $\gamma = 60^\circ$, for example, the value of $Nu/(Sh)$ is divided by 1.68/1.52 when the couple (Du, Sr) passes from $(0, 0)$ to $(-0.5, -0.5)$. Note that the mass/(heat) flux induced by the Soret/(Dufour) effect is opposite to the one induced by the concentration/(temperature) gradient for negative value of $Sr/(Du)$. This why we observe an attenuation of the heat and mass under Soret and Dufour effects in this study. Finally, it should be mentioned that the flow becomes unsteady periodic for the inclination 60° ; the data reported on the Nusselt and Sherwood figures are average values calculated over several flow cycles.

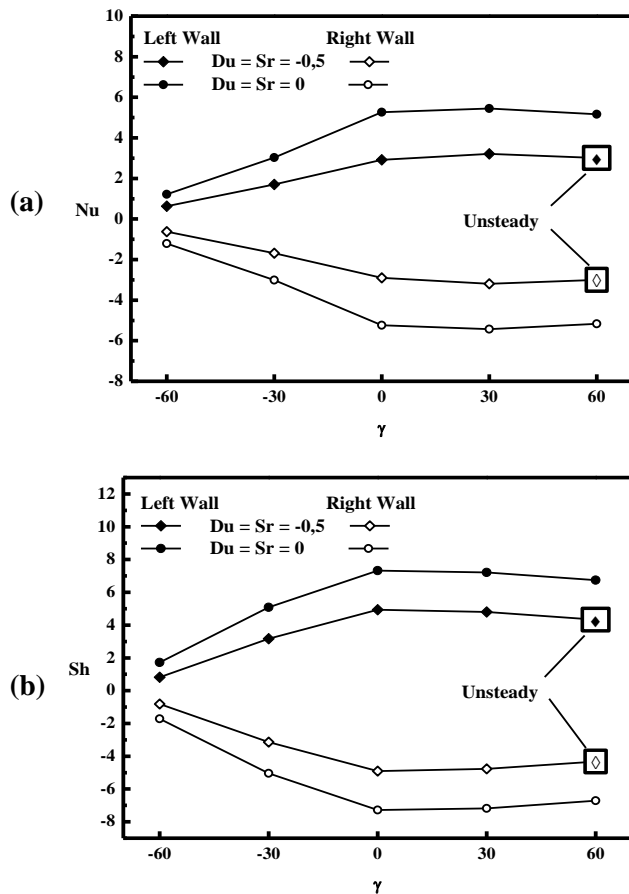


Figure 5

Variations, vs. γ , of the average Nusselt (a) and Sherwood (b) numbers on both vertical sides of the cavity for different values Du and Sr .

Conclusions

Thermosolutal natural convection induced in an inclined cavity in the presence of Soret and Dufour

effect is studied numerically using a hybrid finite difference-Lattice Boltzmann method (FD-LBM). The latter was validated successfully against classical methods based on the resolution of Navier-Stokes equations. It is shown that the combined effect of Soret and Dufour parameters and the inclination angle may lead to important changes in the heat and mass transfer characteristics. An inclination of -30° combined with $Sr = Du = -0.5$ reduces the flow intensity to one third and the Nu/Sh to almost 45%/(38%). An increase of the inclination in the range 0° to 60° has not considerable effect on Nu and Sh .

REFERENCES

- Gobin, D. and Bennacer, R. Cooperating thermosolutal convection in enclosure-II. Heat transfer and flow structure, *Int. J. Heat Mass Transfer*, **39**, pp. 2683-2697, 1996.
- Mamou, M. Vasseur, P. Bilgen, E. and Gobin, D. Double-diffusive convection in an inclined slot filled with porous medium, *Eur. J. Mechanics, B/Fluids*, **14**, pp. 629-652, 1995.
- Amahmid, A. Hasnaoui, M. Mamou, M. and Vasseur, P., Double-diffusive parallel flow induced in a horizontal Brinkman porous layer subjected to constant heat and mass fluxes: analytical and numerical studies, *J. Heat Mass Transfer*, **35**, pp. 409-421, 1999.
- Bourich, M. Hasnaoui, M. Amahmid, A. and Mamou, M., Onset of convection and finite amplitude flow due to Soret effect within a horizontal sparsely packed porous enclosure heated from below, *Int. J. Heat Fluid Flow*, **26**, pp. 513-525, 2005.
- Er-Raki, M. Hasnaoui, M. Amahmid, A. and Mamou, M., Soret effect on the boundary layer flow regime in a vertical porous enclosure subject to horizontal heat and mass fluxes, *Int. J. Heat Mass Transfer*, **49**, pp. 3111-3120, 2006.
- Rtibi, A. Hasnaoui, M. and Amahmid, A., Analytical-numerical study of optimal separation of species in an inclined Darcy-Brinkman porous cavity saturated with a binary mixture, *Acta Astronautica*, **98**, pp. 71-85, 2014.
- Nithyadevi, N. and Yang, R.J., Double diffusive natural convection in a partially heated enclosure with Soret and Dufour effects, *Int. J. Heat Fluid Flow*, **30**, pp. 902-910, 2009.
- Nithyadevi, N. and Yang, R.J., Magneto convection in an enclosure of water near its density maximum with Soret and Dufour effects, *Int. J. Heat Mass Transfer*, **52**, pp. 1667-1676, 2009.
- Wang, J. Yang, M. and Zhang, Y., Coupling-diffusive effects on thermosolutal buoyancy convection in a horizontal cavity, *Num. Heat Transfer, Part A*, **68**, pp. 583-597, 2015.

10. Bhatnagar, P.L., Gross, E.P. and Krook, M.K., A model for collision process in gases. I: Small amplitude processes in charged and neutral one-component system, *Phys. Rev.*, **94**, Issue 3, pp. 511-525, 1954.
11. Lallemand P. and Luo, L.S., Hybrid Finite-difference thermal Lattice Boltzmann equation, *Int. J. Modern Physics B*, **17**, Issue 1 no 2, pp. 41-47, 2003.
12. He, X. and Luo, L.S., Lattice-Boltzmann Model for the Incompressible Navier-Stokes Equation, *J. Statistical Physics*, **88**, no 3/4, pp. 927-944, 1997.
13. Mohamad, A.A. and Kurzmin, A., A critical evaluation of force term in lattice Boltzmann method, natural convection problem, *Int. J. Heat Mass Transfer*, **53** pp. 990–996, 2010.

PHASE CHANGE MATERIALS FOR IMPROVING THE INERTIA THERMAL OF BUILDING MATERIALS

A. Laaouatni^{1, 2, *}, N. Martaj¹, R. Bennacer³, M. Elomari² and M. El Ganaoui⁴

¹ EPF Campus de Troyes 2, rue F. Sastre 10430 Rosières-près-Troyes, France

² Université Cadi Ayyad, Laboratoire LAEPT, Marrakech, Maroc

³ LMT CNRS UMR 8535, Ecole Normale Supérieure de Cachan, Cachan, 61 Av du Président, Wilson 94235 Cachan Cedex, France

⁴ Université de Lorraine, Laboratoire Lermab, IUT Henri Poincaré de Longwy, 186 rue de Lorraine, 54400 Longwy - Cosnes et Romain, France

*Corresponding author: Email: amine.laaouatni@ced.uca.ac.ma

ABSTRACT

A solution based on the incorporation of a phase change material with ventilation tubes is proposed. This coupling is tested on a building material "concrete block" to increase the thermal inertia of the buildings wall. In the first part of the study, an experimental device is designed to compare the thermal response of different configurations depending on the condition of the tubes (open, closed, ventilated). The second part is a numerical simulation conducted using the COMSOL Multiphysics software on a three-dimensional model. The results show the suitability of the new solution to ensure a large thermal inertia of a building.

KEYWORDS: Phase Change Materials, PCM, Latent heat storage, Thermal inertia, Building

NOMENCLATURE

Latin letters

C_p	specific heat at constant pressure (J/kgK)
h	convective heat transfer coefficient (W/m ² K)
k	thermal conductivity (W/mK)
T	temperature (K)
t	time (s)
T_{sl}	phase change temperature (K)

Greek letters

δ_M	the activation function of the material, 0 or 1
ρ	density (kg/m ³)

Subscript

app	apparent
e	external
f	face
i	internal
l	liquid
PCM	phase change material
s	solid

INTRODUCTION

In the current context, energy problem and environmental balance are widely imposed in all areas of human life. Emissions of greenhouse gases and increasing the consumption of fossil fuels greatly influence energy balance. However, the world is mobilizing increasingly for identifying these issues. The industrial sector and the construction sector are presented among the largest consumers of energy.

In the building sector, the constraints are increasing, the economic aspect requires that construction be more lightly. The sensitive storage in the thick walls can improve occupant comfort, but the need to reduce the walls thickness affects considerably the thermal inertia of the building elements. Several works have been developed to solve this problem [1]. Among the solutions, the use of the latent heat storage properties.

The integration of phase change materials (PCMs) in the building began in 1940. Since then, this principle is used in many applications related to thermal comfort in the building and also in the thermal storage applications [2].

The contribution of the phase change material appears in the large storage capacity by latent heat. When they are integrated into building elements, this ability intervenes to create a thermal phase shift between the storage and release of energy and amortization that would minimize the needs on air conditioning. During the summer period, operation is effective to absorb heat peaks due to daytime outdoor temperatures. The incorporation of PCM, in the various structural components, is done in several ways including: Direct incorporation, impregnation of building materials, the incorporation of the capsules filled with PCM in the construction elements. However, the constraint that arises is the possibility of leakage of PCM in liquid phase. This problem has promoted the use of mixtures with polymers in order to have gels, which gives a mechanical stability during melting [3-10].

This work is part of use of stabilized PCM and presents a study on an integrated building solution, developed to increase the thermal inertia of the building envelope. This component is a hollow "concrete block " filled with PCM (mechanically stable in the liquid state). This new system includes vertical ventilation tubes to control the loading/unloading interior energy. We study the thermal behavior of this coupling. The study is addressed both on the plane, experimental and numerical, to highlight the effectiveness of this solution and allow control of the temperature inside the building.

DESCRIPTION OF THE EXPERIMENTAL DEVICE

System block / PCM / Ventilation: The concrete block used is a commercial hollow block having the following dimensions: 50 cm x 20 cm x 9.5 cm. Consisting of 3 rectangular cavities whose geometric characteristics: length, width and height are respectively 13 cm, 6.5 cm and 17 cm.

The tubes used are on PVC, with a diameter of 2 cm and a thickness of 1 mm (Fig. 1). Two holes are made in the base of three cavities in order to place the six tubes. The PCM is incorporated directly in the molten state (temperature higher than the sol-gel temperature). The volume of the PCM in each cavity is equal to 1140 cm³. The Figure 2 shows a photograph of the resulting system.

The PCM used is a mixture of a paraffin and a styrene-type polymer. This mixture has a high mechanical stability, which is important to prevent

leakage problems. The paraffin used is a commercial product having a melting temperature of 28 °C and a latent heat of 245 kJ/kg. The normalization of the manufacturing process as well as the characterization of this material are being optimized.

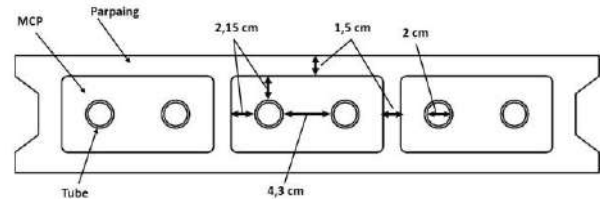


Figure 1. Description of the disposition of the tubes in the concrete block



Figure 2. Photography of the block filled with PCM and ventilated tubes

Experimental procedure: A device shown schematically in Figure 3, is used to study the thermal dynamics of the block subject to thermal constraints. This device comprises:

- a heating system based on a silicone resistance in form of flexible plate, that allows for an acceptable contact for good heat transfer on one of side surfaces of the block.
- 8 K-type thermocouples placed at half height on the same transverse plane and in the different module areas as described in Figure 3 (thermocouple characteristics: 0.5 mm weld diameter, response time 5 s, incertitude ± 1.5 °C, measurement range -50 to 650 °C).
- small fans having the same diameter as the tubes to control the intra-tube air flow (air velocity in the pipe is between 0 and 1 m/s) (fan characteristics: power 0.45 W, debit 0.085 m³/min, rotation speed 104.72 rad/s).
- polystyrene insulation system (Fig. 4) was placed on all surfaces except the second side surface that is left in direct contact with the ambience (ambient temperature in the

laboratory), this limits heat loss and ensures a unidirectional transfer.

- a data acquisition system consists of two cards of National Instruments is used. It allows to monitor the evolution of temperature with 8 thermocouples.
- a relay board to program the heating cycle (temperature) to be imposed. The acquisition program was developed on LabVIEW.

The heating resistor has been adapted through preliminary tests and a power of 462 W/m^2 allows a temperature rise from 20 to $64 \text{ }^\circ\text{C}$ on the heated side after approximately 5 hours. This increase is adopted to test the different configurations. The laboratory temperature slightly fluctuates around $20 \text{ }^\circ\text{C}$ during the experiment. The injection of air through ventilation is done immediately after stopping the heating.

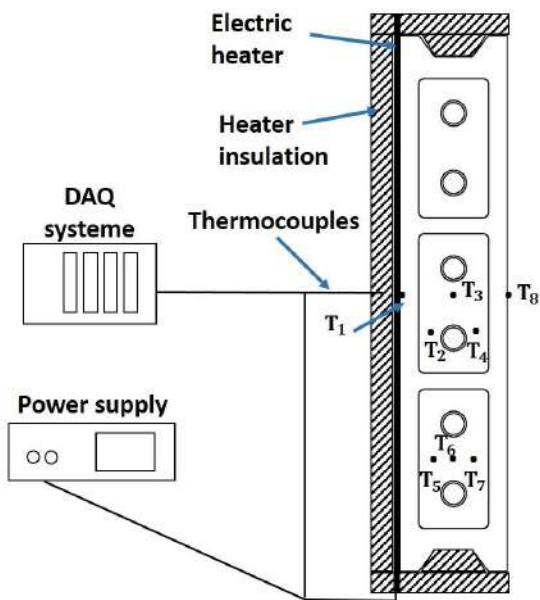


Figure 3. Schematic representation of the experimental bench



Figure 4. Photography of the experimental

device

EXPERIMENTAL RESULTS

The experimental approach adopted allows tracking temperatures for 24 hours. This approach responds to the thermal behavior of the PCM, as it allows the temperatures within the PCM to stabilize. In the results presented here, a comparison is done between the three cases closed tubes: Open tubes, tubes with ventilation.

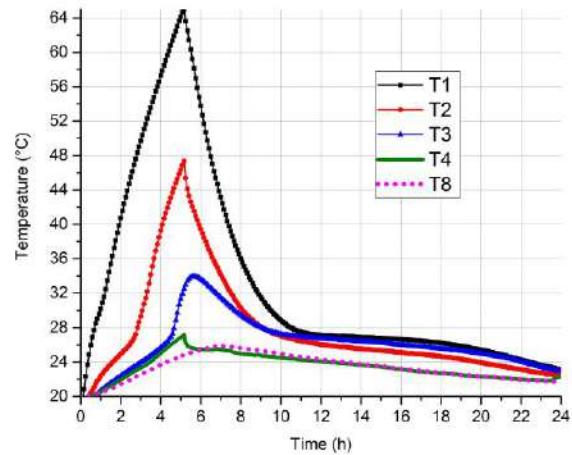


Figure 5. Time evolution of the temperature inside the concrete block filled PCM and intra-ventilated by the tubes

Figure 5 shows the temperatures recorded by the five thermocouples (T1, T2, T3, T4 and T8). We note the linear trend of temperature across all probes with a phase shift related to the progression of the heat flow in the different materials. When stopping the heating, the temperatures drop after 2h30 to stabilize around the phase change temperature. The rapid response of the temperature obtained by the thermocouple T4 shows the effect of ventilation on improving energy release. The temperature variations show that the system is equivalent to a resistance-capacitance in the case without ventilation. In the case with ventilation, the behavior can be represented by a shunt resistor which describes the flow in the middle of the system. The calculation of the characteristic time for various temperatures shows the improvement of thermal inertia. This experiment shows both the influence of the use of PCM for increasing the thermal inertia of the element and also the role of the tubes to increase the heat exchange surface within the PCM. The temperature on the inner face rises slightly to $26 \text{ }^\circ\text{C}$ before stabilizing.

In order to highlight the action of the tubes on the behavior of PCM, we compared on figure 6, the temperatures before and after the tube in the three studied cases. The temperature curves obtained by the thermocouple T2, show that the difference between the levels of the temperatures achieved is 1 to 2 °C, with a more rapid response by ventilation. This part of the PCM is too influenced by the heated face. In the other side of the tube, the temperature level decreases to about 20 °C, a very important phase shift which marks the contribution of PCM/tube coupling. In both cases, tubes closed and open tubes, the temperatures converge towards a bearing in the range of phase change temperatures. For the response in case with ventilation, temperature does not exceed the melting threshold, it quickly drops from 27 to 25 °C before continuing to room temperature.

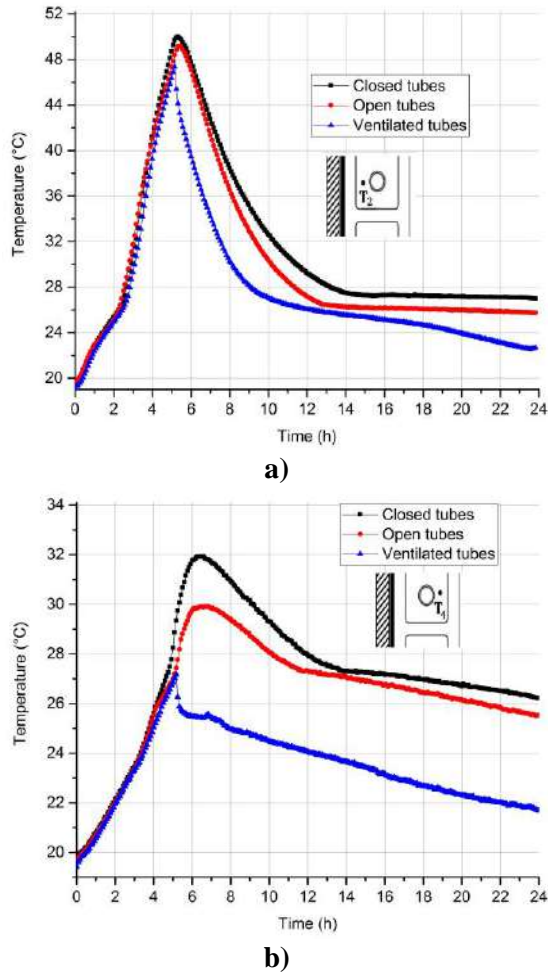


Figure 6. Temperature variation in the PCM: **a)** between the heated face and the tube **b)** between the tube and the side in contact with the ambient air

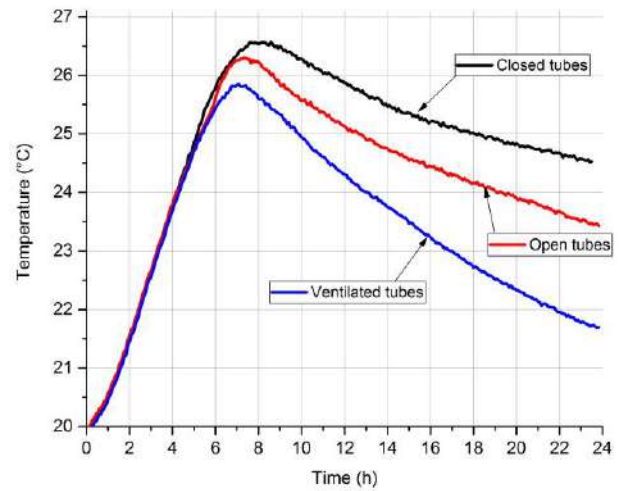


Figure 7. Evolution of the temperature on the side face of the block

Figure 7 shows the evolution of the temperature on the side face of the block, the analysis, performed on the temperatures within the concrete block, explains the behavior on the side in contact with the ambient air. Here, the influence of the atmosphere of the laboratory is important. We note that the system behavior highlighting appears clearly in the PCM near the side in contact with ambient air. Knowing that laboratory temperature does not correspond to a temperature of comfort.

NUMERICAL SIMULATION

To simulate the behavior of the system, a 3D modeling with finite element was developed using the simulation software COMSOL Multiphysics. Heat transfer in the PCM is based on use of the method of the apparent heat capacity. The equation governing heat transfer is:

$$(\rho C_p)_{app} \left(\frac{\partial T}{\partial t} + u \cdot \delta_M \nabla T \right) = \nabla(k \nabla T) \quad (1)$$

Where ρ , C_p and k are the intrinsic characteristics of the material of the middle concerned, u is the velocity field and δ_M the activation function of the material with 0 or 1 respectively in the solid and the fluid.

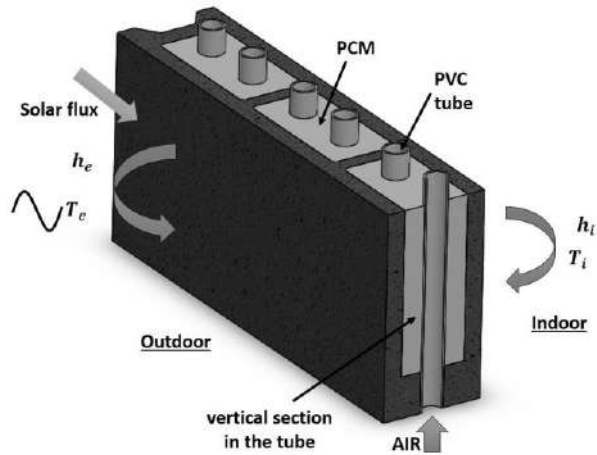


Figure 8. Schematic explication of the thermal module and the boundary conditions for the simulation 2

Two simulations were conducted, the first simulates the conditions imposed in the experimental protocol to validate the results. The second simulation uses real boundary conditions of a Mediterranean climate in summer. Outside, a solar flux and a sinusoidal temperature (between 20 and 39 °C). Inside, a comfortable temperature of 25 °C is imposed by an air conditioning device. The exchanges by convection with surrounding environments are included on both surfaces, internal and external, with convective coefficients estimated by correlation to a low air speed ($h_e = 17 \text{ W/m}^2\text{K}$ and $h_i = 8 \text{ W/m}^2\text{K}$). Air Injection is carried out from the time when the outside temperature is strictly less than the melting temperature of the PCM.

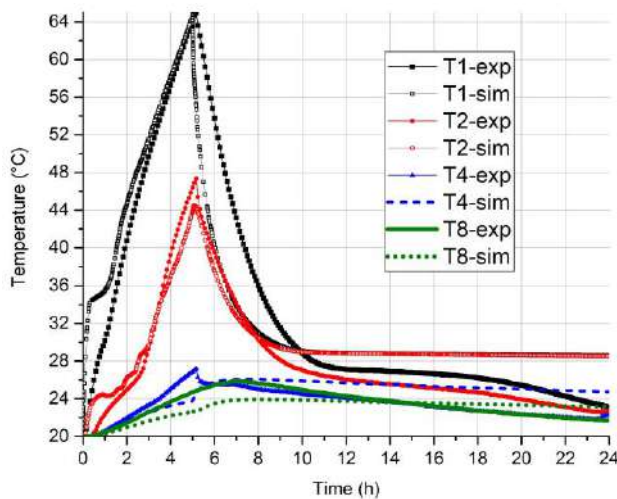


Figure 9. Comparison of temperature variations obtained numerically and experimentally

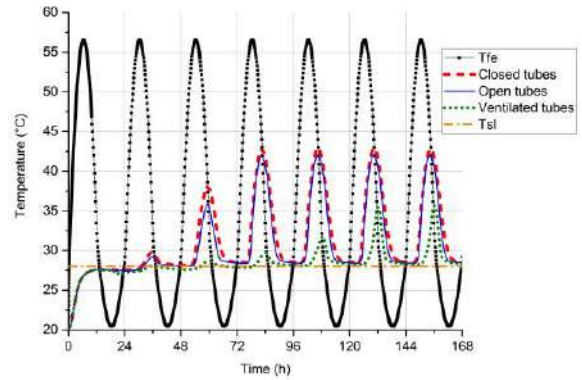


Figure 10. Evolution of the temperature on the inner side of the block for each configuration

Figure 9 shows the comparison between the results from the simulation and those obtained by experiment. We remark a small difference between these data, which is probably due to the heating resistance that does not have a uniform power over the whole surface of the block. Thus, the influence of thermal insulation, which is not ideal to eliminate heat loss. In general, good agreement between the simulation and experiment is observed, which is used to validate the model.

For the second simulation, Figure 10 shows the evolution of the temperature on the inner side of the block for all three cases: tubes closed, open tubes and with ventilation speed of 1 m/s. Comparison with the temperature on the outside shows that in addition to the contribution of PCM, the addition of ventilation tubes saves 6 °C on the inner side with respect to the maximum temperature. Stabilization of the minimum temperature on the inside rises to 4 days, the integration of PCM imposes a level of the temperature around the temperature of phase change T_{sl} .

CONCLUSIONS

The study described in this paper is part of a project whose goal is to achieve optimal walls made from concrete block filled with PCM and ventilated tubes. The goal is to increase the thermal inertia of the walls to absorb thermal stresses imposed from the outside. The proposed coupling is based on the thermal properties of PCM with the principle of increasing the exchange surface by ventilated tubes. The functioning of the system prevents the rapid increase of the peaks daytime temperatures and destocking by injecting air at night.

An experimental study was conducted to highlight the thermal behavior of this system. The results

confirms that the insertion of the paraffin with the tubes allows to have a temperature level around the temperature of phase change and therefore the damping applied thermal stresses. In perspective, we will envisage to test the influence of the variation of the air velocity and improving the control of temperature imposed by the heating system.

The 3D numerical simulations were conducted using the COMSOL Multiphysics software. The first simulation shows good agreement between the experimental and numerical results. An improvement can be obtained by better adapting of the heating system. The second simulation is based on summer discomfort conditions. The results confirm, on the one hand, the contribution of PCM for controlling temperatures within that construction element and on the other hand, the influence of the addition of the splines on the overall response and in particular on the side interior walls. This simulation will be the base of a predictive tool to optimize this coupling.

REFERENCES

1. Zhou D, Zhao C Y and Tian Y 2012 Review on thermal energy storage with phase change materials (PCMs) in building applications *J. Appl. Energy* **92** 593-605.
2. Ahmad M, Bontemps A, Sallée H and Quenard D 2006 Experimental investigation and computer simulation of thermal behaviour of wallboards containing a phase change material *J. Energ. Building* **38** 357-366.
3. Kuznik F, David D, Johannes K and Roux J J 2011A review on phase change materials integrated in building walls *J. Renew. Sustainable Energy Rev.* **15** 379-391.
4. Royon L, Karim L and Bontemps A 2013 Thermal energy storage and release of a new component with PCM for integration in floors for thermal management of buildings *J. Energ. Building* **63** 29-35.
5. Kadri H, Aggoun S, Bennacer R and Bouvet A 2009 *Stockage de l'énergie dans les matériaux de construction* (Congrès de Mécanique, Marrakech).
6. Royon L 2012 *Amélioration énergétique de dalles alvéolées par l'intégration d'un MCP stable mécaniquement* (XXXe Rencontres AUGC-IBPSA Chambéry, Savoie).
7. Khudair A M and Farid M M 2004 A review on energy conservation in building. Applications with thermal energy storage by latent heat using phase change materials *J. Energ. Convers. Manag.* **45** 263-275.
8. Ceron I, Neila J and Khayet M 2011 Experimental tile with phase change materials for building use *J. Energ. Buildings* **43** 1869-1874.
9. Cabeza L F, Castell A, Barreneche C, De Gracia A and Fernandez A 2011 Materials used as PCM in thermal energy storage in buildings: A review *J. Renew. Sustainable Energy Rev.* **15** 1675-1695.
10. Hasse C, Grenet M, Bontemps A, Dendievel R and Sallée H 2011 Realization, test and modelling of honeycomb wallboards containing a phase change material *J. Energ. Building* **43** 232-238.
11. Ahmad M, Bontemps A, Sallée H and Quenard D 2006 Thermal testing and numerical simulation of a prototype cell using light wallboard coupling vacuum isolation panels and phase change material *J. Energ. Building* **38** 673-681.

Materials / Energy Products

THE USE OF PLEUROTUS MUTILUS AS BIOSORBENT FOR NICKEL (II) REMOVAL FROM SYNTHETIC AQUEOUS SOLUTION IN A FIXED-BED COLUMN

Abdelali Gherbia^{a, b, *}, Abdelmalek Chergui^{a, c}, Ahmed Réda Yeddou^a, Ammar Selatnia^{a, c},
Boubekeur Nadjemi^a

^aLaboratoire d'Etude et de Développement des Techniques de Traitement et d'Épuration des Eaux et de Gestion Environnementale LEDTEGE, Ecole Normale Supérieure, Kouba KOUBA BP 92, Alger.

^bDépartement de Sciences et Techniques, Faculté de Technologie, Université de Laghouat, Alger.

^cEcole Nationale Polytechnique, Département Génie de l'Environnement, 10 Avenue Hassen Badi, BP 182, El Harrach, Alger. Algérie.

*Corresponding author: Fax: +213 21 52 29 73 Email: abdelali98111@yahoo.fr

ABSTRACT

This study used an industrial waste, *pleurotus mutilus* to produce biosorbent for nickel (II) metal ion removal in a fixed-bed column. The biosorbent properties were characterized by using Potentiometric titration and Fourier transform infrared spectroscopy (FTIR). The adsorption capacities were determined through Thomas and Yoon-Nelson's models for various pH values, in order to obtain the best adequacy of column data and to determine the characteristic parameters of the column. The models were found appropriate for describing the biosorption process of the dynamic behaviour of the *pleurotus mutilus* in column. The elution efficiency for nickel (II) metal ion desorption from *pleurotus mutilus* was determined for 0.1 M HCl, exhibited elution efficiencies greater than 78%.

INTRODUCTION

Industrial mining sites are one of the prominent sources of heavy metal pollutants, which are transported by run-off water and contaminate water sources. Heavy metal pollution causes significant environmental problems due to the toxic effects of metals, it can bind to the surface of microorganisms and may even penetrate inside the cell. The microorganisms use chemical reactions to digest food and their accumulation throughout the food chain leads to serious ecological and health problems [1, 2].

Physical and chemical techniques have been widely used for removal of heavy metals from industrial wastewater, such as chemical precipitation, chemical oxidation or reduction, ion-exchange, filtration, electrochemical treatment, reverse osmosis, membrane technologies and evaporation recovery [3]. The conventional methods have some limitations [4, 3]. One of the major problems linked to these methods is when the metals are in the range of 1-100 mg L⁻¹ because they are expensive and can themselves produce other waste problems. This has limited their industrial applications [5]. Biosorption offers an economically feasible technology for efficient removal from aqueous solution.

The aim of this work is to develop a cheap technology for the removal of nickel (II) ions in a fixed-bed column from synthetic aqueous solutions onto *pleurotus mutilus* as biosorbent, which is inexpensive and widely available source of biomass. Effect of pH was studied. Both Thomas and Yoon-nelson's models were used to analyze the column experimental data and to determine the characteristic parameters of the column. The possibility of regeneration of *Pleurotus mutilus* biomass was also studied.

MODELING AND ANALYSIS OF COLUMN DATA

Thomas's model and Yoon and Nelson's model, were used to analyze the column performance for the removal of nickel (II) from aqueous solution [6-8].

The linearized form of Thomas's model can be expressed as follows:

$$\ln\left(\frac{C_0}{C} - 1\right) = \frac{K_{Th}Q_0M}{F} - K_{Th}C_0t \quad (1)$$

Where k_{Th} is the kinetic constant in (l mg⁻¹ h⁻¹), Q_0 is the maximum adsorption capacity (mg g⁻¹), t is the time for biosorption (h), F is the

volumetric flow rate (ml min^{-1}) and M is the sorbent mass (g).

The kinetic coefficient k_{Th} and the maximum adsorption capacity of the bed Q_0 can be determined from a plot of $\ln[(C_0/C)-1]$ against t .

The linearized form of the Yoon and Nelson's model is as follows:

$$\ln\left(\frac{C}{C_0 - C}\right) = K_{\text{YN}}t - \tau K_{\text{YN}} \quad (2)$$

Where k_{YN} the rate constant (ml min^{-1}), τ is the time required for 50(%) adsorbate breakthrough (h) and t is the breakthrough time (h).

The overall sorption zone (Δt) is the difference between the bed exhaustion time t_e and breakthrough time t_b were calculated from the breakthrough curve.

Total amount of nickel sent to column (m_{total}) is calculated as follows.

$$m_{\text{total}} = \frac{C_0 \cdot F \cdot t_e}{1000} \quad (3)$$

The removal efficiency $R(\%)$ can be calculated from the ratio of the sorbate mass biosorbed to the total mass of sorbate sent to the column, as follows.

The removal efficiency:

$$R(\%) = \frac{m_{\text{ad}}}{m_{\text{total}}} \cdot 100 \quad (4)$$

The area below the desorbed metal concentration versus time plots, obtained through numerical integration, can be used to find the metal mass desorbed m_d . The elution efficiency $E(\%)$ can be calculated as follows .

$$E(\%) = \frac{m_d}{m_{\text{ad}}} \cdot 100 \quad (5)$$

The column uptake (Q_{col}) can be calculated by dividing the total mass of biosorbed sorbate (m_{ad}) by the mass of the biosorbent (M). The mass biosorbed of sorbate is calculated from the area above the breakthrough curve (C vs. t) is obtained through numerical integration, multiplied by the flow rate [9, 10].

EXPERIMENTAL

Preparation of Biomass

Antibiotic fermentation produces large amounts of semi-solid, *Pleurotus mutilus* is a waste product from the production of *Pleuromutilin* antibiotic veterinary obtained from SAIDAL Antibiotic (Médéa-Algeria) which is normally disposed by incineration. This biomass was washed several times with distilled water to eliminate impurities and dried at 60°C for 24 h to constant weight. It was, then, crushed using a mortar and sieved using a sifter RETCH (model: AS 200) in order to select a fraction biomass with particle diameters between 315 and $400\mu\text{m}$.

Characterization of Biomass

a) Potentiometric titration of Biomass

For each titration, a constant mass of *Pleurotus mutilus* biomass 1 g was placed in contact with 50 ml of 0.1 mol L^{-1} NaNO_3 as background electrolyte for all the experiments titration, at

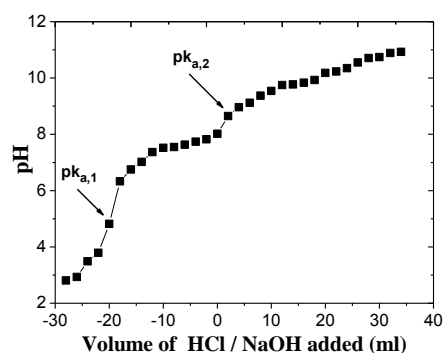


Figure 1
Potentiometric titration curve of *Pleurotus mutilus*

room temperature, the Flasks were continuously stirred during 2 hours at 200 rpm. After adding a definite volume of 0.1 N NaOH or HCl into each flask containing the biomass suspension. Flasks were agitated for 24 h.

Figure 1 shows two inflection points at approximately pH 4.97 and 8.18, which corresponds to pK_a values of two groups, may be carboxyl and saturated amine. These groups are likely to be responsible for nickel (II) metal ion biosorption.

b) Surface charge density

Figure 2 shows the variation of surface charge density of *Pleurotus mutilus* as a function of pH, was calculated according to the following equation [11, 12].

$$\sigma = \frac{f(C_a - C_b + [OH^-] - [H^+])}{S \cdot a} \quad (6)$$

where σ is the surface charge density ($C\ m^{-2}$), f is the faraday constant ($C\ mol^{-1}$), C_a and C_b are the concentrations ($mol\ L^{-1}$) of the acid and base added to the suspension, $[OH^-]$ and $[H^+]$ are the concentrations of OH^- and H^+ measured from the pH of the solution, a is the concentration of the *Pleurotus mutilus* biomass in the solution ($g\ L^{-1}$), and S is the specific surface area of the sample ($m^2\ g^{-1}$).

Figure 2 shows that the surface is charged positively in the acidic pH range below the PZC (at around pH 8) as the number of $-NH_3^+$ groups predominate over the $-COO^-$ groups. With the increase in pH, the concentration of $-NH_3^+$ would decrease and $-COO^-$ concentration would increase. The concentrations of the two would become equal to each other at the PZC [$-NH_3^+ = -COO^-$]. Negatively charged above the PZC as the number of $-COO^-$ groups predominate over the $-NH_3^+$ groups [$-COO^- > -NH_3^+$], this effect is certainly caused by the ionization of the carboxylic groups at higher pH values.

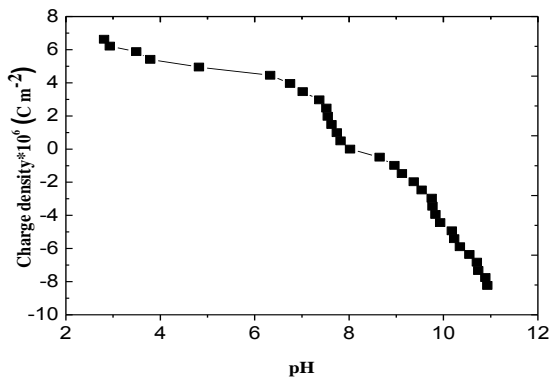


Figure 2

Variation of surface charge density of *Pleurotus mutilus* as a function of pH

c) Ion exchange capacity of Biomass

Cation and anion exchange properties of the biomass were studied, the calculation of ion exchange capacity q ($meq\ g^{-1}$) was calculated by the following equation [13].

$$q = \frac{C_{a,b}(V_1 - V_2)}{1000m} \quad (7)$$

Were $C_{a,b}$ ($mole\ L^{-1}$) is the concentration of the acid/base, V_1 (mL) the volume of added HCl/NaOH in *Pleurotus mutilus* experiment at defined value of pH, V_2 (mL) the volume of

added HCl/NaOH in blank experiment at the same pH and m (g) is the mass of *Pleurotus mutilus* biomass. The ion exchange capacity of *Pleurotus mutilus* is presented in Figure. 3. According to Figure 3, the cation exchange capacity of *P. mutilus* biomass was higher than $0.003\ meq\ g^{-1}$, while the anion exchange capacity was higher than $0.0027\ meq\ g^{-1}$.

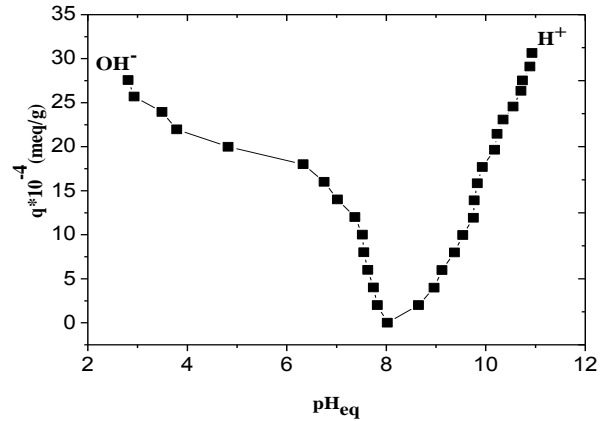


Figure 3

Curve of the ion exchange capacity of *Pleurotus mutilus* as a function of pH

d) FTIR analysis of biomass

From the figure 4 the broad stretching absorption band at $3438\ cm^{-1}$ representing $-OH$ groups of the β -glucose and $-NH$ stretching of the protein and chitin-chitosan in the biomass. This indicates that there is a possibility of metal binding in carboxyl and amino groups. The bands observed at around $2924\ cm^{-1}$ are ascribed to the symmetric and asymmetric stretching of C-H bond of the $-CH_2$ and $-CH_3$ groups. The band at around $1640\ cm^{-1}$ indicates that assigned to C=O stretching vibration coupled to N-H deformation of the amide I group of protein and chitin-chitosan. The deep band at around $1085\ cm^{-1}$ could be assigned to the O-C-O stretching of sugars.

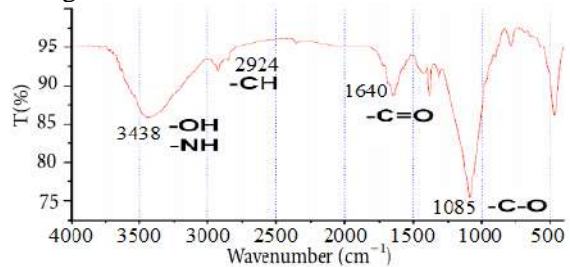


Figure 4

FTIR spectra of *Pleurotus mutilus* biomass

Fixed-bed column biosorption study

a) Experimental procedure

The experiments were carried out in glass column of 18 cm length and 1.6 cm internal diameter, which filled with 10.0 g of *Pleurotus mutilus*. Porous sheets were attached at the bottom of the column and the top of the bed in order to support the fungi bed, to ensure uniform liquid distribution into the column and to avoid the loss of biomass. Figure 5 shows the schematic diagram of the column. The initial ion concentrations of 50 mg L⁻¹ was prepared by diluting 1 g L⁻¹ of stock Nickel solution, which was obtained by dissolving NiCl₂ · 7H₂O in distilled water and the pH of each test solution was adjusted to the required value with 0.1M of HCl or NaOH solutions, Nickel (II) solution was pumped upward through the column at flow rate of 20 ml min⁻¹ by a peristaltic pump. Samples were collected from the exit of the column at regular intervals and analyzed using flame atomic absorption spectrophotometer (Shimadzu AAS. Model: AA-6300-P/N 206-51800) at wavelength 232 nm.

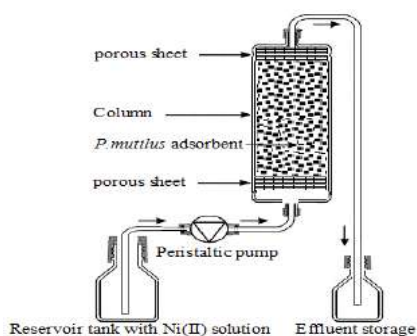


Figure 5

Schematic diagram of experimental column

b) Effect of initial solution pH on breakthrough curves

The value of pH is an important environmental factor influencing not only site dissociation, but also the solution chemistry of the heavy metals which strongly influence the speciation of the heavy metals [7, 14-16]. The experiments were carried out at initial Ni (II) concentration of 50 mg/L, particle size of adsorbent of 315-500 μm and pH values 2.0, 4.0 and 6.0.

Figure 6 shows the effect of pH values on adsorption of Nickel onto *P. mutilus* using a plot of (C_t/C_0) versus time (t). As shown in Figure

6, when the value of pH was 2.0, the value of C_t/C_0 reached 0.96 in 3h but the breakthrough curve of the pH 4.0 and 6.0 was not more than 0.45 and 0.18 in the same time, respectively. Obviously, with an increase of pH in the influent, the breakthrough curves shifted from left to right, which indicates that more Ni (II) can be removed (table. 1). It would spend more time reaching the saturation.

The results suggested that with the increasing of pH in experimental condition, the adsorption capacities increase. The surface of *P. mutilus* may contain a large number of active sites, as the pH increased from 4 to 6, the ligands such as carboxylate groups were deprotonated, increasing the negative charge density on the biomass surface, thus enhancing the binding metal cations via ion exchange mechanism, but the high pH value can cause precipitation of metal complexes. On the other hand, at pH 2, the carboxylic and amino groups become protonated and, thus, are no longer available to attract metal ions from solutions [16].

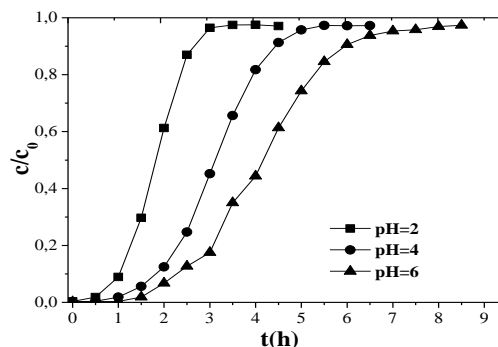


Figure 6

Breakthrough curve of the effect of pH values on biosorption of Ni (II) onto *P. mutilus* ($F = 20$ ml min⁻¹, $C_0 = 50$ mg L⁻¹ and 25°C).

c) Application of the Thomas and Yoon-Nelson models

Thomas and Yoon-Nelson's models were applied to investigate the breakthrough behavior of Ni (II) from synthetic aqueous solution onto *Pleurotus mutilus* in a fixed-bed column. The parameters of Thomas's model were determined by the slope and intercept of the linear plots of $\ln[(C_0/C_t)-1]$ versus time t . Analysis of the regression coefficients indicated that the regressed lines provided excellent fits to the experimental data with R^2 values ranging from 0.97 to 0.99. According to Table 2 the values of Q_0 increased and k_{Th} decreased with increasing of the values of pH. On the other hand, the

maximum solid-phase concentration of solute Q_0 very similar to Column uptake Q_{col} values obtained through numerical integration, indicating that Thomas's model fits excellently to the experimental data. Also, the parameters predicted from Yoon-Nelson's model at different pH are presented in Table 2. The rate constant k_{YN} decreased and the time required for

obtained by using Thomas's model are 50% adsorbate breakthrough τ increased with increasing of the values of pH. Also, the regressed lines of the experimental data fit well with Yoon-Nelson's model indicating that Yoon-Nelson model is also appropriate to describe the adsorption of *p. mutilus* in fixed bed column.

Table 1
Column data and parameters obtained at different values of initial pH.

pH	F (ml min ⁻¹)	t_b (h)	t_e (h)	V_{eff} (L)	m_{ad} (mg)	m_{total} (mg)	Q_0 (mg/g)	R (%)
2	20	0.47	3.6	4.32	93.0	216.27	09.30	43.03
4		0.98	6.3	7.92	197.7	358.72	17.97	55.11
6		1.57	8.5	10.2	259.7	511.34	25.93	50.78

Table 2
Parameters predicted from Thomas and Yoon-Nelson models at different pH.

pH	Thomas parameters			Yoon-Nelson parameter			
	K_{Th} (L mg ⁻¹ h ⁻¹)	Q_0 (mg g ⁻¹)	R^2	K_{YN} (min ⁻¹)	τ (min)	$\tau_{50\% exp}$ (min)	R^2
2	0.0549	11.47	0.991	0.0866	37.78	37.16	0.991
4	0.0342	19.86	0.957	0.1064	52.27	48.18	0.957
6	0.0247	28.71	0.979	0.1145	78.20	72.29	0.979

50% adsorbate breakthrough τ increased with increasing of the values of pH. Also, the regressed lines of the experimental data fit well with Yoon-Nelson's model indicating that Yoon-Nelson model is also appropriate to describe the adsorption of *pleurotus mutilus* in fixed bed column.

d) Regeneration studies

Desorption of nickel (II) from *P. mutilus* was also studied. 0.1 M of HCl solution was pumped through the column in order to remove the nickel (II) from *P. mutilus* biomass at different flow rates; the concentration of nickel was measured until dropped to a value around zero. The results are presented in the figure 7 and 8.

CONCLUSIONS

This study demonstrated that *P. mutilus* constitute a promising material for the development of a low cost biosorption technology the removal of nickel (II) from aqueous solutions in a fixed-bed column. The results showed that both Thomas's and Yoon-Nelson's models were found suitable to predict

the adsorption performance for Ni (II) adsorption in a fixed-bed column.

P. mutilus can be regenerate with 0.1 M HCl and used again after the desorption process.

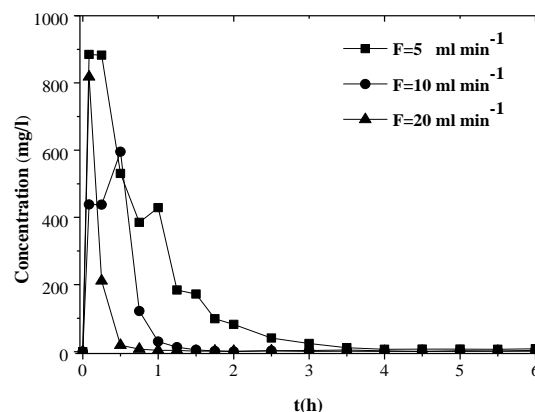


Figure 7

Elution curves for desorption of nickel with 0.1 M HCl at different flow rates at different flow rates ($F_1=5$, $F_2=10$ and $F_3=20$ ml min⁻¹)

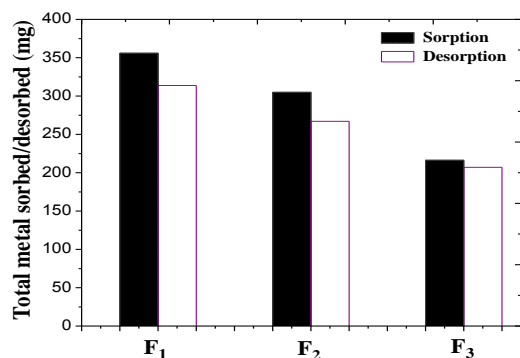


Figure 8

Amounts of adsorbed and desorbed nickel (II) at different flow rates (F₁=5, F₂= 10 and F₃= 20 ml min⁻¹)

KEYWORDS: Heavy metal, Biosorbent, Adsorption capacity, Fixed-bed, Regeneration.

REFERENCES

- [1] Malik, A, 2004, Metal bioremediation through growing cells. *Environmental International*, **30**, pp. 261-278.
- [2] Ahluwalia, S. S, and Goyal, D, 2007, Microbial and plant derived biomass for removal of heavy metals from wastewater, *Bioresource Technology*, **98**, pp. 2243–2257.
- [3] Sud, D, Mahajan, G, and Kaur, M.P, 2008, Agricultural waste material as potential adsorbent for sequestering heavy metal ions from aqueous solutions – A review. *Bioresource Technology*, **99**, pp. 6017-6027.
- [4] Srivastava, N. K, and Majumder, C. B, 2008, Novel biofiltration methods for the treatment of heavy metals from industrial wastewater: a Review. *J. Hazardous Materials*, **151**, pp. 1-8.
- [5] Nourbakhsh, M, Sag, Y, Ozer, D, Aksu, Z., Katsal, T, and Calgar, A, 1994, A comparative study of various biosorbents for removal of chromium(VI) ions from industrial wastewater. *Process Biochemistry*, **29**, pp. 1-5.
- [6] Kundu, S, and Gupta, A. K, 2007, As (III) removal from aqueous medium in fixed bed using iron oxide-coated cement (IOCC): Experimental and modeling studies. *Chemical Engineering Journal*, **129**, pp. 123-131.
- [7] Han R, Zhang J, Zou W, Xiao H, Shi, J, and Liu, H, 2005, Biosorption of copper (II) and lead (II) from aqueous solution by chaff in a fixed-bed column. *J. Hazardous Materials*, **133**, pp.262-268.
- [8] Aksu, Z, 2005, Application of biosorption for the removal of organic pollutants: a review. *Process Biochemistry*, **40**, pp. 997-1026.
- [9] Volesky, B, Weber, J, and Park, J. M, 2003, Continuous-flow metal biosorption in a regenerable *Sargassum* column. *Water Research*, **37**, pp. 297-306.
- [10] Lodeiro, P, Herrero, R, and Sastre de Vicente, M. E, 2006, The use of protonated *Sargassum muticum* as biosorbent for cadmium removal in a fixed-bed column, *J. Hazardous Materials*, **137**, pp. 244-253.
- [11] Mustafa, S, Dilara, B, Nargis, K, Naem, A, and Shahida, P, 2002, Surface properties of the mixed oxides of iron and silica. Source: *Colloids and Surfaces A: Physicochemical and Engineering Aspects*, **205**, pp. 273-282.
- [12] Partey, F, Norman, D, Ndur, S, and Nartey, R, 2008, Arsenic sorption onto laterite iron concentration: Temperature effect. *J. Colloid and Interface Science*, **321**, pp. 493-500.
- [13] Chubar, N, Carvalho, J. R, and Correia, M. J. N, 2004, Crok biomass as biosorbent for Cu (II), Zn (II) and Ni (II). *Colloids and surfaces A: Physicochem. Engineering Aspects*, **230**, pp. 57-65.
- [14] Esposito, A, Pagnanelli, F, and Veglio, F, 2002, PH-related equilibria models for biosorption in single metal systems. *Chemical Engineering Sciences*, **57**, 307-13.
- [15] Crini, G, and Badot, P. M, 2008, Application of chitosan, a natural aminopolysaccharide, for dye removal from aqueous solutions by adsorption processes using batch studies: a review of recent literature. *Progress polymer Science*, **33**, pp. 399-447.
- [16] Vijayaraghavan, K, and Yun, Y. S, 2008, Bacterial biosorbents and biosorption. *Biotechnology Advances*, **26**, pp. 266-291.

ELECTRONIC PROPERTIES OF PHOSPHORENE NANORIBBONS

M. Boutahir, AH. Rahmani, S. EL Majdoub, B. Fakrach, H. Chadli and A. Rahmani*

Laboratoire d'Etude des Matériaux Avancés et Applications (LEM2A), Université Moulay Ismail, FSM-ESTM-FPE, BP 11201, Zitoune, 50000 Meknes, Morocco.

*Corresponding author: Email: a.rahmani@fs-umi.ac.ma

ABSTRACT

Few-layer black phosphorus [1], a new elemental 2D material recently isolated by mechanical exfoliation, is a high-mobility layered semiconductor with a direct bandgap that is predicted to strongly depend on the number of layers.

We perform a comprehensive first-principles study of the electronic properties using tight-binding model [2] of phosphorene nanoribbons and multilayer phosphorene. Our calculations show that multilayer phosphorene sheets are semiconductors with their bandgaps decreasing with increasing the number of multilayers. For zigzag phosphorene nanoribbons (z-PNRs) are metals, regardless of the ribbon width while armchair phosphorene nanoribbons (a-PNRs) are semiconductors with indirect bandgaps and the bandgaps are insensitive to variation of the ribbon width.

INTRODUCTION

Recently, a new 2D material, namely, layered black phosphorus or phosphorene [1], has been isolated in the laboratory through mechanical exfoliation from bulk black phosphorus and has immediately received considerable attention [2]. It turns out that phosphorene possess some remarkable electronic properties as well. For example, it is reported that phosphorene has the drain current modulation up to 10^5 and carrier mobility up to $1000 \text{ cm}^2\text{V}^{-1}\text{s}^{-1}$, which makes phosphorene a potential candidate for future nanoelectronic applications [3]. Phosphorene also has a direct bandgap which can be modified from 1.51 eV for a monolayer to 0.59 eV for a five-layer [4]. Moreover, the p-type black phosphorene transistor has already been integrated with the n-type MoS2 transistor to make a 2D CMOS inverter [5].

Our goal in this communication is to apply the above mentioned tight-binding model for phosphorene zigzag and armchair nanoribbons and calculate the band structure and quantum conductance of the ribbons and compare the results with other more sophisticated calculations. Then, we examine the effect of the application of transverse electric field on the band structure and quantum conductance of both zigzag and armchair nanoribbons.

ANALYSIS AND MODELLING

The tight-binding Hamiltonian recently proposed for this system [6] is given by

$$H = \sum_{i,j} t_{ij} C_i^+ C_j \quad (1)$$

where summation is over the lattice sites, and t_{ij} are the hopping integrals between i th and j th sites, and C_i^+ and C_j represent the creation and annihilation operators of electrons on sites i and j , respectively. These hopping integrals between a site and its neighbours are shown in Fig. 1.

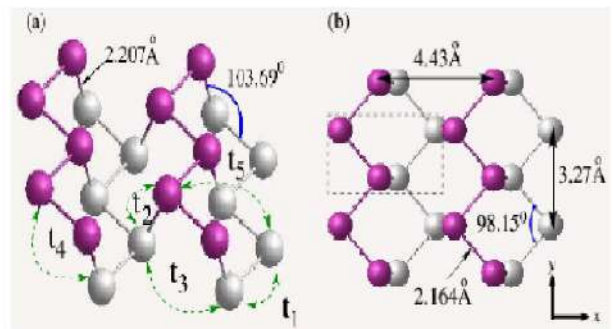


Figure 1: (a) Crystal structure and hopping integrals t_i of a single layer phosphorene for the tight-binding model. (b) Top view. The dark (grey) balls represent phosphorus atoms in the upper (lower) layer. The dotted rectangle represents a primitive unit cell containing four atoms. The parameters for the bond angles and unit cell lengths are taken from [7].

The connections in each zigzag chain in the upper or lower layer are representing the t_1 hoppings, and the connections between a pair of upper and lower zigzag chains represent the t_2 hopping integrals. t_3 is between the nearest sites of a pair of zigzag chains in the upper or lower layer, and t_4 is the hopping between the next nearest neighbour sites of a pair of the upper and lower zigzag chains. t_5 is the hopping between two atoms on upper and lower zigzag chains that are farthest from each other.

The explicit values of these hopping's as suggested by [6] reads $t_1 = -1,220$ eV, $t_2 = 3,665$ eV, $t_3 = -0,205$ eV, $t_4 = -0,105$ eV, and $t_5 = -0,055$ eV.

The special character of this model is that the second hopping integral is positive. This implies zigzag chains with negative t_1 hoppings along the chains and positive t_2 hoppings that connect these chains. For zigzag nanoribbons, the eigen-states of the transverse modes, which characterize the behaviour of the states as edge states or bulk states are along both t_1 and t_2 connections. As depicted in Fig. 1 the unit cell of phosphorene is a rectangle containing four phosphorus atoms.

RESULTS AND DISCUSSION

A) One-dimentional phosphorene

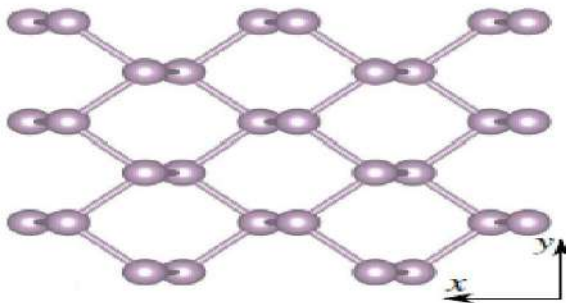


Figure 2: Top view of the crystal structure of monolayer BP

In Fig. 3, we show the band structures of monolayer. One can see that in the case of the monolayer, all spectral features remain essentially the same as for bulk BP, with the exception of the gap between the VB and CB, which also appears at the point, but has a significantly higher value (1.60 eV).

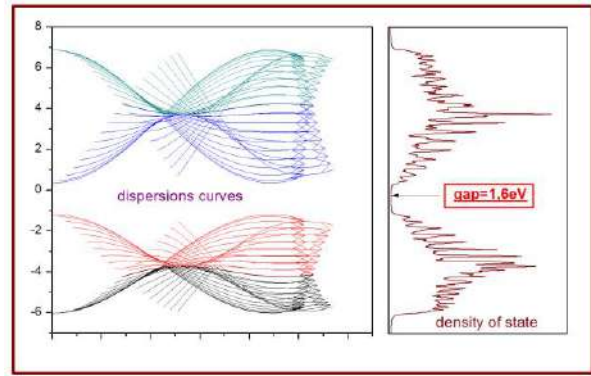


Figure 3: The band structures of monolayer of black-phosphorene.

B) One-dimentional phosphorene nanoribbons

In the next step we study the dependence of the electronic properties of the aPNRs and zPNRs.

The band structure (shown in Fig. 4) for the aPNRs, it is clear that the size of the band gap for the ribbon is determined by the position of the conductance band (CB) and valence band (VB). The electronic states associated with the VB and CB states are located in the bulk of the ribbon. Since the Fermi energy is located in the band gap, all aPNRs are semi-conductors independent of their ribbon width.

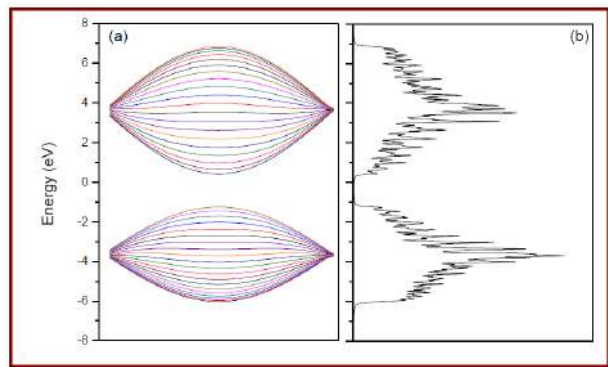


Figure 4: The band structures of monolayer of aPNRs.

We also calculated the change of the band gap of aPNRs as a function of different widths (Shown in Fig. 5). The band gap uniformly decreases. By increasing the aPNR width the band gap decreases much faster. This is due to the fact

that the electrostatic potential difference is proportional to the ribbon width.

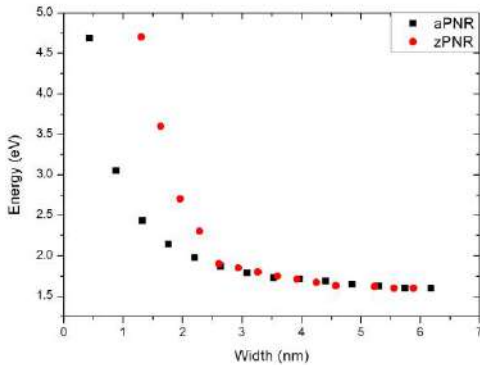


Figure 5: The band gap of zPNRs and aPNRs as a function of ribbon width

Now we focused on the structure band of zPNRs (Fig. 6). Like in aPNRs it is clear that the size of the band gap for the ribbon is determined by the position of the conductance band (CB) and valence band (VB). Since the Fermi energy is located in the band gap, all zPNRs are semi-conductors independent of their ribbon width.

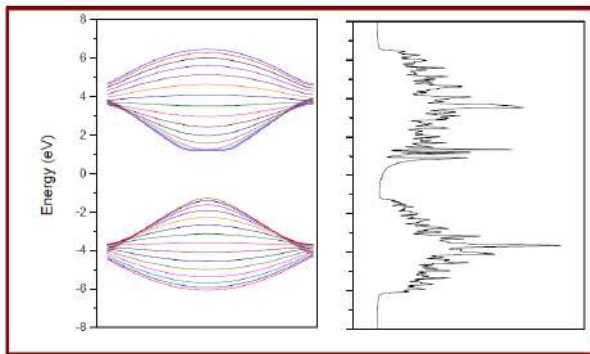


Figure 6: The band structures of monolayer of zPNRs.

As in aPNRs, we calculated the change of the band gap of zPNRs as a function of different widths (Shown in Fig. 5). By increasing the zPNR width the band gap decreases much faster. This is due to the fact that the electrostatic potential difference is proportional to the ribbon width.

CONCLUSION

We presented in this paper, the electronic properties of a black-phosphorene and the aPNRs and zPNRs nanoribbons. We found that the band gap in black-phosphorene is around 1.6eV and the band gap in aPNRs and zPNRs uniformly decreases by increasing the width. Our numerical results based on a five parameter tight-binding model for PNRs show that zPNRs and aPNRs are always semiconductors independent of their ribbon width. Our results based on the relatively simple tight-binding model are in good agreement with first-principle calculations and this suggests that this model can provide a reasonable basis for studying the electronic properties of this system.

References

1. Appalakondaiah, S.; Vaitheeswaran, G.; Lebegue, S.; Christensen, N. E.; Svane, A. Effect of van der Waals interactions on the structural and elastic properties of black phosphorus. *Phys. Rev. B* 2012, 86, 035105.
2. Buscema, M.; Groenendijk, D. J.; Blanter, S. I.; Steele, G. A.; van der Zant, H. S.; Castellanos-Gomez, A. Fast and broadband photoresponse of few-layer black phosphorus field-effect transistors. *arXiv preprint arXiv:1403.0565* 2014.
3. Li, L.; Yu, Y.; Ye, G. J.; Ge, Q.; Ou, X.; Wu, H.; Feng, D.; Chen, X. H.; Zhang, Y. Black phosphorus field-effect transistors. *Nat Nano* 2014, advance online publication.
4. Qiao, J.; Kong, X.; Hu, Z.-X.; Yang, F.; Ji, W. Few-layer black phosphorus: emerging direct band gap semiconductor with high carrier mobility. *arXiv preprint arXiv:1401.5045* 2014.
5. Liu, H.; Neal, A. T.; Zhu, Z.; Luo, Z.; Xu, X.; Tománek, D.; Ye, P. D. Phosphorene: An Unexplored 2D Semiconductor with a High Hole Mobility. *ACS Nano* 2014.
6. Rudenko, A. N. and Katsnelson, M. I. , *Phys. Rev. B* 89, 201408 (2014).
7. Castellanos-Gomez, A. ; Vicarelli, L. ; Prada, E. ; Island, J. O. ; Narasimha-Acharya, K. L. ; Blanter, S. I. ; Groenendijk, D. J. ; Buscema, M. ; Steele, G. A. ; Alvarez, J. V. ; Zandbergen, H. W. ; Palacios, J. J. and van der Zant, H. S. J. ; *2D Materials* 1, 025001 (2014).

THEORETICAL INFRARED PHONON MODES AND BAND GAP CALCULATIONS OF A BUNDLE OF TWO SINGLE WALLED CARBON NANOTUBES

AH. Rahmani, M. Boutahir, B. Fakrach, H. Chadli and A. Rahmani*

Laboratoire d'Etude des Matériaux Avancés et Applications (LEM2A), Université Moulay Ismail, FSM-ESTM-FPE, BP 11201, Zitoune, 50000 Meknes, Morocco.

*Email : a.rahmani@fs-umi.ac.ma

ABSTRACT

Recently a bundle of two Single Walled Carbon Nanotubes (SWCNTs) have been synthesized using the chemical vapor deposition method and named this Nano system, dimer. The homogeneous (two identical SWCNT) and inhomogeneous (non-identical SWCNT) dimers of SWCNTs are characterized by a weak van der Waals interaction between the neighboring carbons of its two constituting SWCNTs. In this paper, we report the calculation results of infrared active modes in dimer of SWCNTs. The spectra calculations are performed using the spectral moment's method (MMS). We present the evolution of the dimers of SWCNTs Infrared spectrum as a function of the diameter and chirality of the two interacting nanotubes. The results are useful for the interpretation of the future experimental data of dimer of carbon nanotubes. In the second part of this paper, we investigated the electronic properties of bundle of SWCNTs and the effect of coupling between nanotubes on charge transfer processes.

KEYWORDS: Carbon nanotube, Raman, Infrared, Dimer, charge transfer, MMS.

NOMENCLATURE

MMS: spectral moment's method

SWCNT: Single Walled Carbon Nanotubes

INTRODUCTION

Since the discovery of carbon nanotubes [1], they are attracting growing interest from the international scientific community because of their intrinsic properties. Carbon nanotubes can be metallic or semiconducting, and offer many possibilities for creating nanoelectronics devices. Many experimental and theoretical studies have been conducted on their vibrational properties.

Carbon nanotubes continue to grow since their discovery, these improvements are due to the development of synthesis techniques. Recently, the most promising method to produce carbon nanotubes on an industrial scale is the catalytic vapor chemical deposition (CVD) [2]. The principle of the CVD involves the decomposition of a carbon source in a gas phase, usually a hydrocarbon (methane, ethane, ethylene or acetylene are commonly used), carbon monoxide and ethanol on the catalyst particles metal (usually iron, cobalt or nickel). The method is very flexible since, depending on the catalyst system used and the operating conditions, it is possible to produce either nanofibers either single walled carbon nanotubes or multi-walled.

Raman spectroscopy is one of the most powerful tools for investigating the vibrational properties of materials in relation to their structural and electronic

properties [3]. Infrared spectroscopy of carbon nanotubes has been neglected since the infrared activity is related to a dynamic dipole moment that is weak. Nevertheless, a number of optical phonons are active in infrared through transient dipole, creating a surprising number of phonon mode bands. The objective of this work is to calculate the Infrared active modes in dimers of carbon nanotubes. Calculations are performed for different possible configurations such as: armchair-armchair, zigzag-zigzag and armchair-zigzag. We report the evolution of infrared spectrum dimers according to diameter, chirality and the length of the two interacted nanotubes. The results are useful in the interpretation of future experimental Infrared data of dimers of SWCNTs.

MODEL AND METHODS

A dimer consists of two SWCNTs greatly spaced by intermolecular distance d . The interactions between the carbon atoms at the surface of SWNT are described using the force constants model introduced by Saito [1998] and previously used to calculate the Raman and Infrared spectra of SWNTs [3,4,5]. Van der Waals interaction between the two tubes is described by the Lennard-Jones potential, given by the following expression:

$$U_{LJ} = 4\epsilon[(\sigma/R)^{12} - (\sigma/R)^6] \quad (1)$$

The values of the Lennard-Jones parameters were chosen as $\epsilon=2.964$ meV and $\sigma=0.3407$ nm. The energy calculations performed using the Lennard-

Jones potential show that the optimal SCNT-SCNT distance d in dimers is around 0.34 nm.

The intensity of the infrared absorption spectrum is given by the following expression:

$$I_{\alpha}(\omega) = \frac{\omega}{nc} \sum_j \frac{|a_{j\alpha}|^2}{2\omega_j} \left(\delta(\omega - \omega_j) - \delta(\omega + \omega_j) \right) \quad (2)$$

with

$$a_{j\alpha} = \sum_{k\alpha} \frac{q_k}{\sqrt{m_k}} e_j(k\alpha) \quad (3)$$

Where n and c are respectively the indice of the material and speed of light, respectively, ω_j and $e_j(k\alpha)$ are respectively the frequency and the $(k\alpha)$ component of the displacement amplitude for the k^{th} (α is cartesian coordinate) in the j^{th} mode. q_k is the effective charge and m_k is the mass of the k^{th} atom. To enhance the IR response of nanotubes, dynamical effective charges on tied carbon atoms were fixed at $q_A=+1$ and $q_B=-1$ for a given A-B bond.

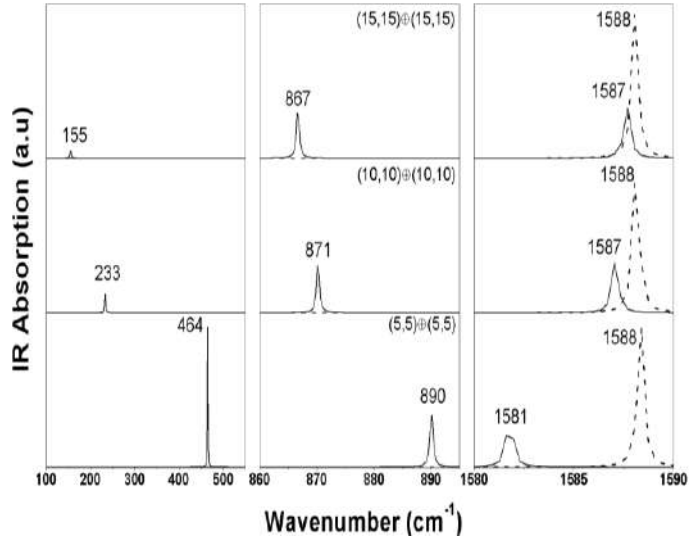
The usual method to calculate the IR spectrum consists of injecting in the previous expressions the values of ω_j and $e_j(k\alpha)$ obtained by direct diagonalization of the dynamical matrix of the system. However when the system contains a large number of atoms, as for long dimer of SWNT, the dynamical matrix is very large and its diagonalization fails or require long computing time. By contrast, the spectral moment's method [Rahmani 2002] allows the Infrared spectrum of very large harmonic systems to be directly computed without any diagonalization of the dynamical matrix.

In the electronic part of this paper we employ a tight-binding (TB) Hamiltonian including four orbitals per atom to study the electronic properties of dimers. In which the σ - π electron hybridization can be included [6-7]. The model Hamiltonian is in reference [8].

RESULTS AND DISCUSSION

First, we focus on the infrared spectra of infinitely homogeneous dimers are obtained by applying periodic conditions on the unit cells of the two SWNTs. In order to identify all infrared active-modes, we present in figure 1 the calculated $I_x(\omega)$ (solid line) and $I_z(\omega)$ (dashed line) for (5,5)-(5,5), (10,10)-(10,10) and (15,15)-(15,15) armchair-armchair dimers. Spectra are displayed in the breathing-like phonon modes

(BLM), intermediate and tangential-like phonon modes (TLM) regions. We found that the frequencies in the BLM and TLM regions of dimers significantly differ from those calculated for SWCNTs. Depending on the polarization, we found that if the diameter increases, the peaks corresponding to BLM mode and those of the intermediate region are downshifted. Regarding the TLM region, the peaks corresponding to the polarization $I_x(\omega)$ are up-shifted, while the IR



spectrum ZZ (dashed line) undergoes no change.

Figure 1

The calculated $I_x(\omega)$ (solid line) and $I_z(\omega)$ (dashed line) infrared spectra of homogeneous (5,5)-(5,5), (10,10)-(10,10) and (15,15)-(15,15) armchair-armchair dimers in the BLM (left), intermediate (middle) and TLM (right) regions.

In the case of Zigzag-Zigzag dimers (Figure 2), we found that if the diameter of carbon nanotubes increases, the peaks corresponding to BLM mode and those of the intermediate region are downshifted.

Regarding the TLM mode, the peaks corresponding to the spectrum $I_x(\omega)$ are downshifted, while the peaks corresponding to the spectrum $I_z(\omega)$ are up-shifted. This behavior is opposite to that of armchair-armchair dimers.

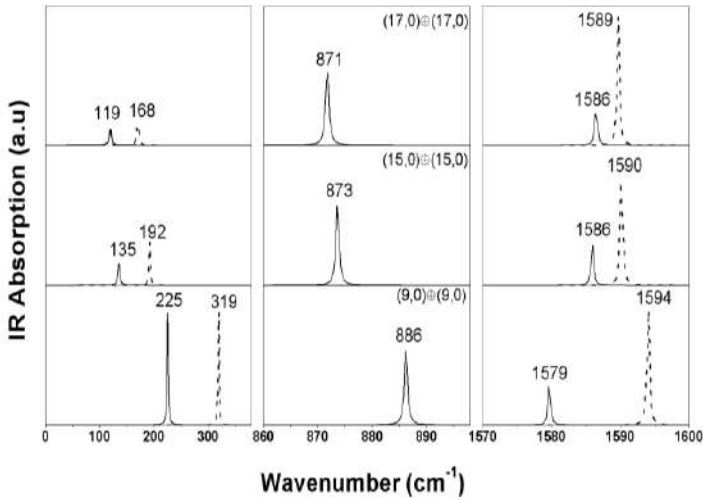


Figure 2

The calculated $I_x(\omega)$ (solid line) and $I_z(\omega)$ (dashed line) infrared spectra of homogeneous (9,0)-(9,0), (15,0)-(15,0) and (17,0)-(17,0) zigzag-zigzag dimers in the BLM (left), intermediate (middle) and TLM (right) regions.

In the case of dimer samples, it seems reasonable to consider that the two SWCNTs may not be identical. This hypothesis is supported by the observations supported in ref [3]. In the following, we calculated the infrared spectra of inhomogeneous dimers such as armchair-zigzag.

zigzag dimers. We found that if the diameter increases, the peaks corresponding to RBLM mode and those of the intermediate region are downshifted and the all spectrum present the three modes in RBLM region one mode of the armchair and two modes of zigzag single-walled carbon nanotubes. In the TLM region, we found four modes two peaks corresponding to the spectrum $I_x(\omega)$ (solid line) and the two others corresponding to spectrum $I_z(\omega)$ (dashed line). From figure 3 the two peaks of $I_x(\omega)$ (resp. $I_z(\omega)$) spectrum are up shifted (resp. downshifted) if the diameter increases.

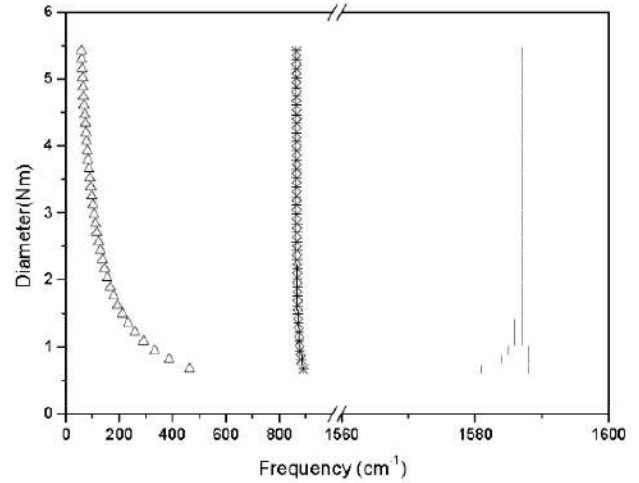


Figure 4

Diameter dependence of the frequencies of the main infrared active modes for armchair-armchair.

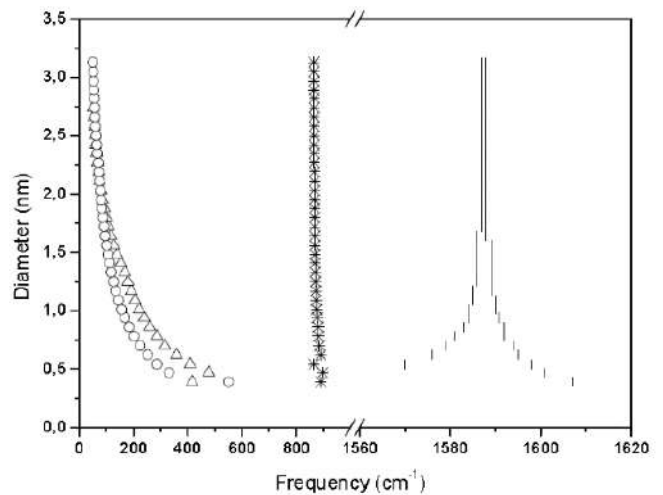


Figure 5

Diameter dependence of the frequencies of the main infrared active modes for zigzag-zigzag:

In figure4 we discuss the dependence with the diameter of an armchair-armchair, in RBLM region we found one mode is downshifted when the diameter

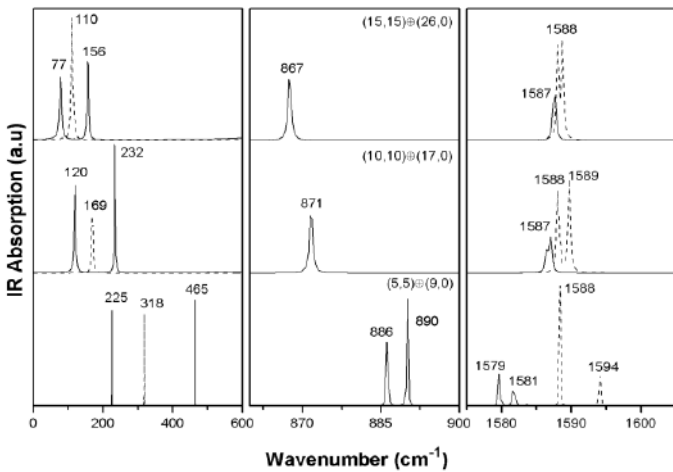


Figure 3

$I_x(\omega)$ (solid line) and $I_z(\omega)$ (dashed line) absorption spectra of inhomogeneous (5,5)-(9,0), (10,10)-(17,0) and (5,7,15)-(26,0) armchair-zigzag dimers in the BLM (left), intermediate (middle) and TLM (right) regions.

In figure 3, are displayed the infrared spectra of (5,5)-(9,0), (10,10)-(17,0) and (15,15)-(26,0) armchair-

increases. Also the RBLM modes downshift in zigzag-zigzag (figure 5).

Notice that as in SWCNT, the BLM's are not significantly dependent on the chirality of the tube. In the TLM region, when the tube diameter increases, an upshift of TLM's modes around 1589 cm^{-1} of large diameter (figure4). In the Zigzag-Zigzag dimer (figure5), the TLM's modes are downshifted. As in SWCNT, the TLM region is very sensitive to the chirality of the tubes.

Carbon nanotubes represent a new class of materials for investigating fundamental one dimensional (1D) physics and for exploring nanoelectronics and molecular electronics. Among the many interesting properties exhibited by nanotubes, it is the electronic properties that are arguably the most significant characteristic of this material. A SWNT can be either metallic or semiconducting, depending only on diameter and chirality, while the local carbon-carbon bonding remains constant. They are characterized by two types of bond, in analogy with graphene, which exhibits so-called planar sp^2 hybridization. Among the four valence orbitals of the carbon atom (the $2s, 2p_x, 2p_y$ and $2p_z$ orbitals, z perpendicular to the sheet), the (s, p_x, p_y) orbitals combine to form in-plane σ (bonding or occupied) and σ^* (antibonding or unoccupied) orbitals (Figure7).

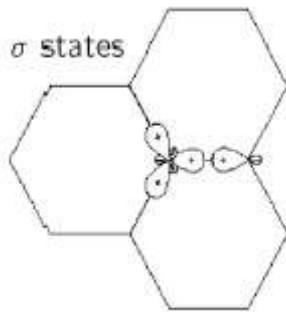


Figure 6

The σ bonds in the carbon hexagonal network connect the carbon atoms and are responsible for the binding energy and the elastic properties of the graphene sheet.

Using the tight-binding model we present the band structures and densities of states of two SWNTs (8,6) and (9,7) and after we present the density of states of (8,6)-(9,7) dimer.

As the nanotubes are one dimensional, their Brillouin zone is one dimensional as well with zone edges usually labeled X. The nanotube band structure is therefore represented along the Γ X direction.

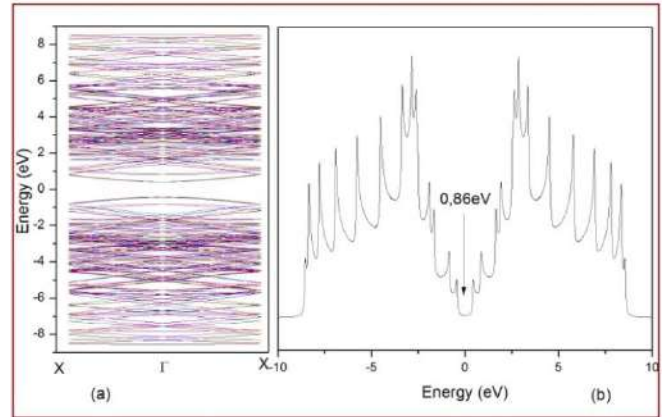


Figure 7

Band structure and density of states for (8,6) nanotube. The Fermi level is located at zero energy.

The electronic band structure and density of states of (8,6) nanotube are presented in Figure 8.

We observe two bands (conduction band and valence band). The figure 8 (a) show that the conduction band and the valence band separate by a gap equal a 0.86 eV so we conclude that the (8,6) tube is a semiconducting tube. The same thing with (9,7) tube that we present the electronic band structure and density of states in Figure 9 the gap of (9,7) tube is 0.74 eV.

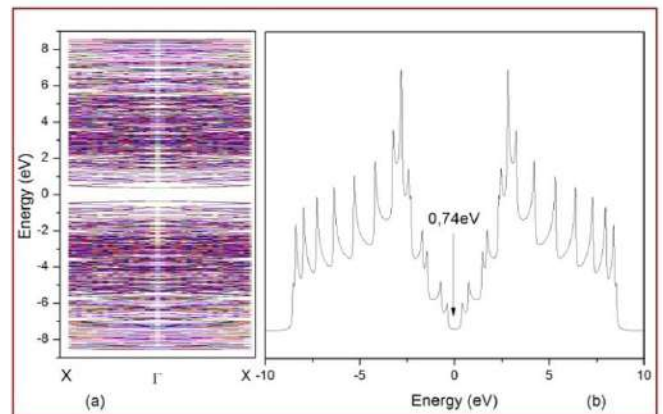


Figure 8

Band structure and density of states for (8,6) nanotube. The Fermi level is located at zero energy.

The Figure 9 shows the electronic band structure and density of states of (8,6)-(9,7) dimer with intertube distance equal a 3.4 \AA , so charge transfer from the tube to other tube took place.

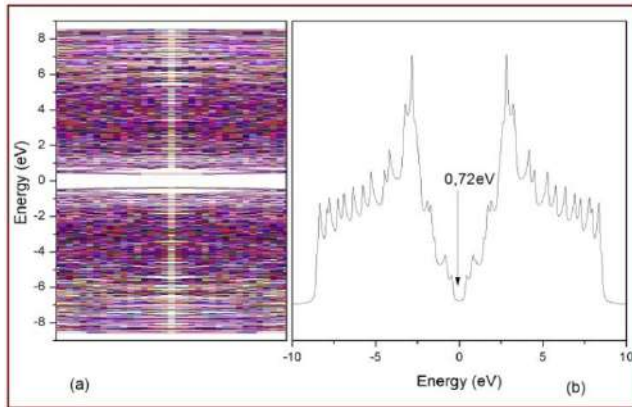


Figure 9

Band structure and density of states for (8,6)-(9,7) dimer. The Fermi level is located at zero energy

CONCLUSION

In this work, using the spectral moment's method, the Infrared spectra of homogeneous and inhomogeneous dimers of SWCNTs are calculated. The effect of coupling between nanotubes on the Infrared spectrum in dimers is identified. The dependence of the Infrared spectra as a function of the diameter and chirality of SWCNTs is predicted. An investigation of the finite-size effects on the infrared spectra of dimers is actually in progress.

In the second part, we presented the electronic properties of a Sc-Sc dimer and the charge transfer effect caused by this interface is stated. Sc-M and M-M SWNT dimer interfaces are under studies.

REFERENCES

1. S Iijima Nature, 1991, 354 56-58.
2. J-L Sauvajol, D. Levshov, T. Michel, M. Paillet, X.T. Than, H.N. Tran, R. Arenal, A. Rahmani, M. Boutahir, A-A. Zahab, 2014, Coupled Vibrations in Index-Identified Carbon Nanotubes, MRS Spring Meeting.
3. A. Rahmani, J. L. Sauvajol, S. Rols and C. Benoit, 2002, Phys. Rev. B, 66, 125404-125412.
4. A. Rahmani, J. L. Sauvajol, J. Cambedouzou and C. Benoit, 2005, Phys. Rev. B, 71, 125402-125408.
5. K. Sbai, A. Rahmani, H. Chadli, J. L. Bantignies, P. Hermet and J. L. Sauvajol, 2006, J. Phys. Chem. B, 110, 12388-12393.
6. J.C. Charlier, Ph. Lambin, T.N. Ebbesen, 1996, Phys. Rev.B 548377.
7. H.S. Sim, C.J. Park, K.J. 2001, Chang, Phys. Rev.B 63073402.
8. J. Lu, and S. Wang, 2007, Phys. Rev.B 76 233103.

OXIDATION OF A NANOSTRUCTURED SUPERALLOY OF HIGH TEMPERATURE

S.Aklouche-Benouaguel¹, S.Adjal¹, D.Miroud²

¹ Laboratoire des Transports Polyphasiques et dans les Milieux Poreux.
LTPMP. USTHB Algérie

² Laboratoire de Génie des Matériaux. LGM, USTHB, Algérie

*Corresponding author: Email: mesadz@yahoo.fr

ABSTRACT

In this work, we are interested in an analytical, numerical and experimental study of the oxidation kinetics of a nickel-based super alloy developed by powder metallurgy and used in the disks of turbine blades. The rate constant and evolution in the oxidation forehead were determined analytically and based Fick's diffusion equation. This equation is solved by the method of finite volumes with an iterative method. In the experimental part we have considered the case of powdered material and when it is compacted. We have examined the behavior of the material by thermo gravimetric analysis for two periods namely the transitional period when the temperature increases over time and the period where the temperature is maintained constant. The results showed at 700 ° C and the powder state the mass gain is equal to 0.09%. For the compacted material it is equal to 0.14%.

Keywords Nano materials / dry Corrosion / thermo gravimeter.

NOMENCLATURE

$a(x,t)$: Concentration of oxygène

$b(x,t)$: Solute concentration of Chromium

$c(x,t)$: Solute concentration of iron

D_0 : Oxygene diffusion coefficient

D_1 : Chrome diffusion coefficient

D_2 : Iron diffusion coefficient

x : Diffusion distance [cm]

P_{CrOn1} : Dissociation pressure of chromium oxide

P_{FeOn2} : Dissociation pressure of iron oxide

P_{O_2} : Oxygen pressure

ξ_1 : The front of oxidation of chromium oxide

ξ_2 : The front of oxidation of iron oxide

INTRODUCTION

Powder metallurgy is a real technological leap for the mechanical characteristics and the production of complex geometries. The sectors involved in nanotechnology are energy, automotive, construction, clothing, cosmetics and food. Applications have been developed, in surgery, in the treatment of cancers, molecular imaging, medical devices and tissue engineering. The metal foam obtained by powder metallurgy has a pore microstructure isolated superior resistance to those interconnected pores. This type of structure, closed cell is particularly suitable for applications requiring a combined weight reduction at a high energy absorption capacity. Nickel based alloys are very important materials in engineering. They

have good toughness and a resistance to hot oxidation, chipping and many corrosive environments. These alloys are very commonly used in combustion systems such as municipal waste incinerators. The study of high-temperature corrosion is a highly interdisciplinary subject at the interface of the physical chemistry of ceramic-metallic materials and mechanical, it operates in areas where failures often have a financial cost, environmental or human high. Knowledge and understanding of corrosion, aging and damage are essential to predict the lifespan. The high temperature oxidation designates the corrosive reaction between the metal and oxygen. Experimental studies exist to explain the behavior of nickel alloys at high temperatures. There are few studies that investigated on the phenomenon (high temperature corrosion) in the world of nanomaterials. A number of researcher have been interested to the high temperature corrosion of nickel-based alloys, to the characterization of degradation, to an inter diffusion and local electronic properties of passive films which can be formed during the oxidation the development of new alloys and finally to the numerical Modeling at high temperature of corrosion. Effects of water vapor on high temperature oxidation of a chromia nickel-based alloy have been investigated by Rolland [1]. Morphological analysis showed the presence of more plastic chromite layers with a porosity distributed throughout the thickness of the layer for the tests carried out in the presence of water vapor. The oxide layers are then more adherent. Delabrouille [2] has worked on the characterization by

transmission electron microscopy and the stress corrosion cracking of nickel-based alloys: Trials traction showed that the higher the chromium content of the alloy increases, the sensitivity decreases, the sensitivity to stress corrosion cracking (SCC) is practically modified above 25% chromium. Massoud [3] studied the nanostructure and local electronic properties of passive films formed on pure nickel and stainless steel Fe-Cr-Ni. They have showed the local variations in gaps anionic or cationic gaps in the grain boundaries of the various passive layers formed. Trindade, et al., [4] have studied numerically the high-temperature corrosion. This simulation was designed for predicting the lifetime of the components; Finite differences are used to treat the diffusion kinetics on the one hand and the concept of local thermodynamic equilibrium on the other. The agreement between experimental observations and simulation results revealed the potential of the numerical modeling for application to complex corrosion process. Vialas [5] has devoted his work on deterioration by high temperature oxidation and interdiffusion coating systems / nickel based superalloy. The oxidation kinetics of three superalloys were determined by thermogravimetric analysis at 900 ° C and 1150 ° C. Cyclic oxidation tests "long term", of 15000h (300h cycles) at 900 ° C and 1050 ° C, as well as cyclic oxidation "short term" test of 1800h (1h cycles) at 1050 ° C. in humid air, were carried out. The "long term" tests are used to accelerate damage to systems and provide data for modeling. The monitoring of microstructural and chemical changes in coating systems / superalloy, helped refine the data to be used for prevision model Laghoutaris [6] presented an investigation on stress corrosion of Alloy 600 in primary middle in réactors pressurized water. He has proposed the mechanisms of Corrosion Under Stress Alloy 600 (>72% Ni, 14% Al 17% Cr, 6% to 10% Fe and other <1%) in primary middle Reactor Pressurized Water (REP).

This model allows to take into account the role of parameters related to the material (defect, strain, type of grain boundary) and the environment (hydrogen content, temperature) which affect the kinetics of diffusion of oxygen in oxide at the grain boundaries of the alloy and for chromium in the alloy grain boundaries. Lecallier, [7] worked on a nickel base superalloy obtained by powder metallurgy. Its objective was the modernization of the M88 engine SNECMA using new materials in the field of aeronautics including high pressure turbine disks. The study focused mainly on microstructures prepared

nuances. Andrew et al,[8] were interested in analyzing the consequences of oxidation at 950 ° C in alloys based on Nickel, near the alloy-oxide interface. The study was done by comparing the analytical model of Wagner with the numerical model Feulvarch. In this work, we were interested to study the oxidation kinetic at high temperature analytically, numerically and experimentally of a porous nanomaterial based with nickel with the diffusion phenomenon represented by the second law of Fick.

ANALYSIS AND MODELLING

To calculate kinetic constants and changes in the oxidation front, we are based on the second law of Fick.

Analytical analysis

The speed of propagation of the oxidation front is determined by solving the equations of the second law of FICK:

$$\frac{\partial a}{\partial t} = D_0 \frac{\partial^2 a}{\partial x^2} \quad (1)$$

$$\frac{\partial b}{\partial t} = D_1 \frac{\partial^2 b}{\partial x^2} \quad (2)$$

$$\frac{\partial c}{\partial t} = D_2 \frac{\partial^2 c}{\partial x^2} \quad (3)$$

To carry out this study, a first simplification of the problem, has been applied by some authors, JP Castin, M .Grosbras, M.Cahoreau [9], is to assume that in the vicinity of the oxide particles, the respective concentrations of oxygen, first element addition and second addition element (a_1 , a_2 , b_1 and c_1) take constant values and satisfy the relations.

$$P_{S1} = (a_1)^{n_1} b_1 \quad \text{and} \quad P_{S2} = (a_2)^{n_2} c_1$$

With n_1 and n_2 are stoichiometric coefficients. The form of the solutions of the equations of the second law of Fick is given by:

$$F = A + B \cdot \operatorname{erf}\left(\frac{x}{2\sqrt{D_j t}}\right) \quad (4)$$

D_j is the species diffusion coefficient ($j = 1 \dots m$) [cm^2 / s].

$$\operatorname{erf}(\theta) = \frac{2}{\sqrt{\pi}} \int_0^\theta e^{-x^2} dx$$

A and B are constants to be determined from the boundary conditions such as is illustrated in Figure 1 and Figure 2.

Figure 1 illustrates the application of the boundary conditions for the diffusion of oxygen in the MBC matrix.

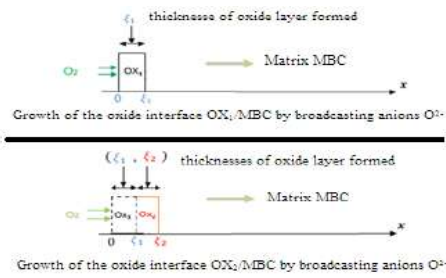


Figure 1 distribution of oxygen in the matrix MBC

Figure 2 presents the growth of the oxide layer of the first and second alloying element.

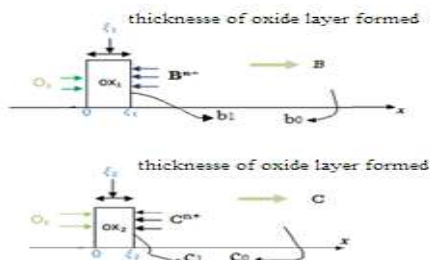


Figure 2 growth of the oxide layer

To determine the kinetic constant, you have to write that the amount of oxygen consumed in the oxidation fronts equals n_1 or n_2 multiplied by the quantity of atoms of the first or second element adding arriving at ξ_1 and ξ_2 respectively .

$$\lim_{\varepsilon \rightarrow 0} D_0 \left(\frac{\partial a}{\partial x} \Big|_{\xi_1+\varepsilon} - \frac{\partial a}{\partial x} \Big|_{\xi_1-\varepsilon} \right) = n_1 D_1 \lim_{\varepsilon \rightarrow 0} \frac{\partial b}{\partial x} \Big|_{\xi_1+\varepsilon}$$

$$\lim_{\varepsilon \rightarrow 0} D_0 \left(\frac{\partial a}{\partial x} \Big|_{\xi_2+\varepsilon} - \frac{\partial a}{\partial x} \Big|_{\xi_2-\varepsilon} \right) = n_2 D_2 \lim_{\varepsilon \rightarrow 0} \frac{\partial c}{\partial x} \Big|_{\xi_2+\varepsilon}$$

We get the final expression of the constant oxidation kinetics.

$$K = \sqrt{\frac{2D_0 a_0 (1 - \alpha)}{n_1 b_0 (1 - \beta) + n_2 c_0 (1 - \gamma)}} \tag{5}$$

We have used MATLAB logiciel

Numerical Modelisation

In this part we have developed a Fortran language computer program to estimate the rate constant and the oxidation front. We chose to work in cylindrical coordinates. The numerical study based on the finite volume consists of the distribution of the concentration of oxygen in unsteady without source term in a porous medium as a cylinder of radius r . We adopted the following simplifying assumptions: the

material is isotropic, diffusion is two dimensional, the transitional arrangements and porosity equal to one.

The general equation dimensional mass transfer in polar coordinates and transient is as follows:

$$\frac{\rho \partial C}{\partial t} = \frac{1}{r} \frac{\partial}{\partial r} \left(r D \frac{\partial C}{\partial r} \right) + \frac{1}{r} \frac{\partial}{\partial \theta} \left(D \frac{\partial C}{\partial \theta} \right) \tag{6}$$

control volume taken into consideration is the following:

$$\delta V = [(r + \delta r)^2 - r^2] \delta \theta = \frac{1}{2} \delta r^2 \delta \theta + r \delta r \delta \theta$$

For our calculations, we opted for a non-uniform mesh and an external layer of the cylinder.

Experimental technology

We conducted thermogravimetric analysis and differential thermal analysis (TGA / DTA) on samples in powder form and compacted form, to assess the impact of the porosity of the compacted samples. We made a compactage matrix, and it is very important to choose the material used for manufacturing of the matrix, which can withstand pressures up to 30 MPa. Heat treatment at the surface (to approximate the case of cementation), allowed us to have a matrix that resists compaction operations to our fine powder up to 15MPa.

RESULTS AND DISCUSSION

Analytical results

In Figure 3, we represent an evolution of the oxidation kinetics.

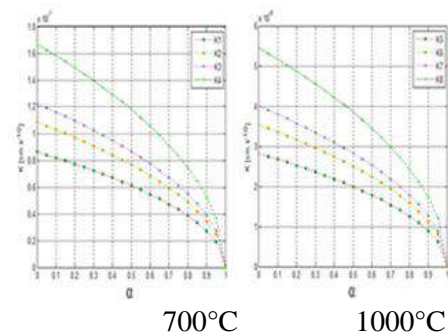


Figure 3 representation of the rate constant

We note that for a constant value of the initial concentration of oxygen and for a constant ratio of concentration of the first addition element as well as a variable ratio of concentration of the

second additive elements, the value of the constant of the kinetics of oxidation increases.

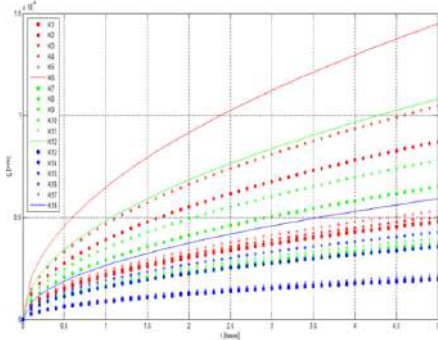


Figure 4 representation of oxidation forehead (1000°C)

The resulting curves have a parabolic shape and have two areas: a linear area corresponding to the rapid oxidation where the slope is very pronounced, therefore, the oxidation rate is very important. An area where the oxidation rate tends to stabilize.

Numerical Results

Evolution of oxygen concentration in cylindrical coordinates, and a function of time.

Figure 5 shows an evolution of the concentration of oxygen in cylindrical coordinates (r, θ) and a function of time for T = 700° C.

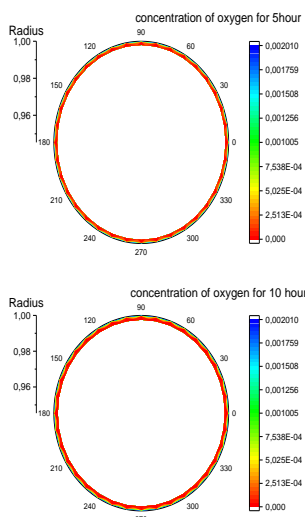


Figure 5 evolution of oxygen concentration versus at 700 °C.

The figure 6 shows the evolution of the concentration of oxygen in cylindrical coordinates (r, θ) and a function of time T = 1000 °C

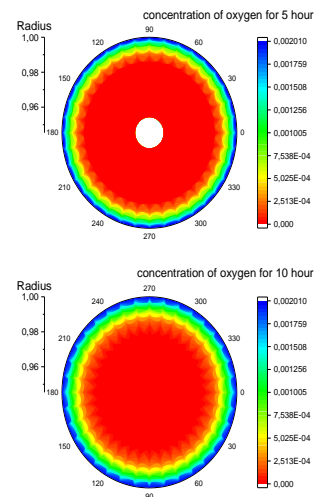


Figure 6 evolution of oxygen concentration versus time at 1000 ° C.

Figures 5 and 6 represent an evolution of the concentration of oxygen for values of the radius (0.94 , 1).This values are choose for a better visualization of the diffusion of oxygen in the outer layers because the diffusion is inside.The choice of 5 hours was imposed by experimentation while for 10 Hours we visualize better the phenomenon.

Evolution of the oxygen concentration as a function of radius and time

We have represented an evolution of the oxygen concentration as a function of radius for different values of time and temperature in figure 7.

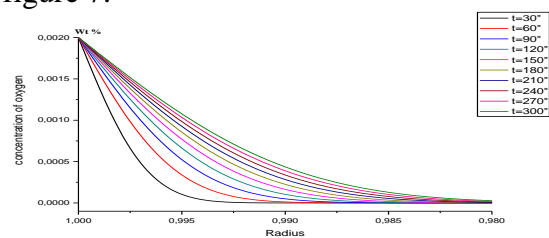


Figure 7 evolution of oxygen concentration as a function of radius and time at 1000 ° C.

We find that the more one moves towards the center, the oxygen concentration is less important. Also, beginning of oxidation, the diffusion of oxygen is very important which stabilizes over time.

We represente an evolution of the front of oxidation in figure 8.

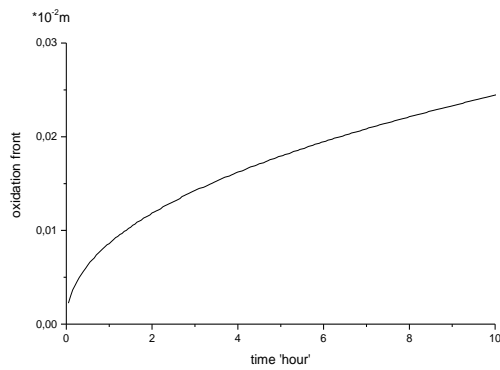
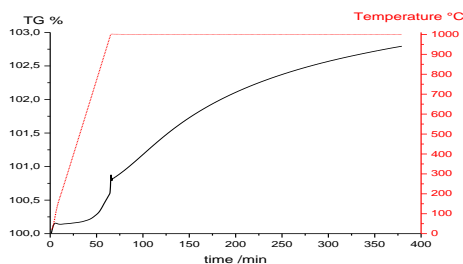


Figure 8 Evolution of the oxidation front to 1000 °C

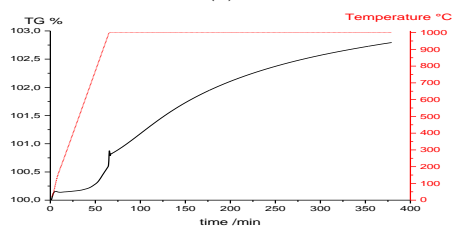
We note that an evolution of the oxidation front is parabolic. The analytical results are consistent with numerical results. The values are very close to analytics to 1000 °C and 700 °C

Experimental Results

The results of thermogravimetry for a temperature 1000 °C are represented in Figure 9 for the powder form and compacted respectively.



(a)



(b)

Figure 9 Gain mass: (a) powder, (b) powder compacted

For 1000°C, the mass gain for the transitional period is far lower compared to the stabilization period. Phenomena are reversed for the compacted powder.

Micrographs and Microanalyses of the alloy

in the raw mass uptake curve and thermal differential analysis Microanalysis carried out on the powder allowed us to deduce the chemical composition shown in Figure 10.

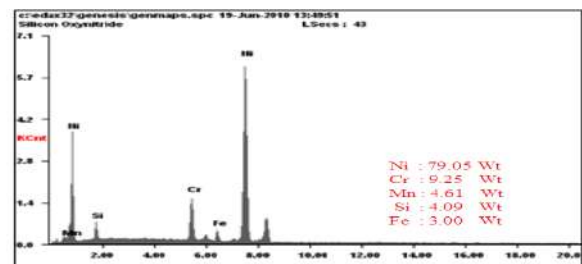


Figure 10 microanalysis EDS of the 'powder

Observation of the powder to the raw state, with the scanning electron microscope, we determine the morphology and the distribution size of the powder. It is composed mainly of spheres with different sizes ranging from the microscale and the nanoscale. The powder is a porous nanostructured material made of nickel

Micrographic observations after oxidation at 1000°C of alloy compacted.

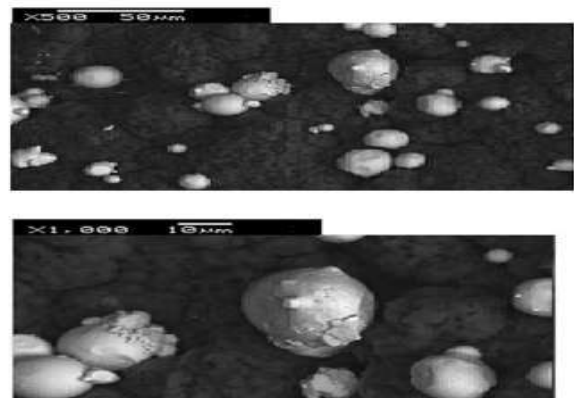


Figure 11 micrographic observation of the compacted powder after oxidation at 1000°C

The scanning electron microscope on the surface of the samples showed that there are nickel particles in the non-oxidized form which confirms the hypothesis of selective internal corrosion

Profile of the evolution of oxygen diffusion into the sample center

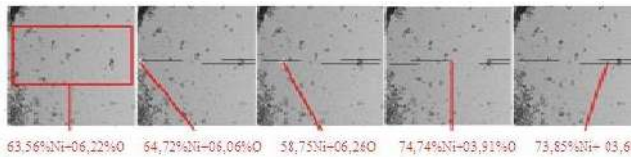


Figure 12 observation scanning electron microscope with a progressive microanalysis to the center of the alloy oxidized at 1000 ° C after polishing.

We performed microanalyses towards the center of the sample. The figure 12 shows that the concentration of oxygen is important to the surface and becomes zero at the center

CONCLUSION

Work undertaken involves the study of the oxidation of a nickel-based powder obtained by powder metallurgy, and used in the discs of the turbine blades. The oxidation has been studied analytically, numerically and experimentally. The study has the following results:

Analytical calculation

The formation of the oxide and the kinetic constant are important when the initial concentration of oxygen is high. The resulting curves have a parabolic shape and have two areas: a linear area corresponding to the rapid oxidation where the slope is very pronounced, therefore, the oxidation rate is very important. An area where the oxidation rate tends to stabilize. We noted that the oxidation front is more important to a low oxygen concentration ratio and high concentration ratios for the two additions elements. We concluded that to prevent significant deterioration it is best to avoid this case, conversely to have a slow deterioration it is preferable to be in this case.

Numerical calculation

We find that the more one moves towards the center, the oxygen concentration is less important. Profiles of oxygen concentration change linearly during the first simulation time. During the last appearance time, it becomes linear, and is zero at the same point, they may correspond to saturation concentrations of the oxide formed. The concentration tends to be canceled by going increasingly to a significant depth.

Experimental Part.

At 700 ° C the weight gain for the transitional period and the period stabilization are equivalent for the powder. The scanning electron microscope for the compact MB40 show that the oxidation is very important: to 700°C we notice

the iron oxide formation. To 1000°C there is appearance of two distinct layers around the high concentration of nickel particle. This particle is in a totally oxide environment. The microanalyses performed reveal a diffusion of oxygen to the sample surface which is very important. Subsequently, we conducted a polishing so that we can observe oxidation and an oxygen diffusion within the samples.

REFERENCES

1. Rolland, R., 2012, Study of the influence of water vapor on high temperature oxidation of a chromic-forming alloy based on nickel. PhD Thesis University Blaise Pascal. .
2. Delabrouille, F., 2004, TEM characterization of stress corrosion cracking of nickel-based alloys: Influence of chromium content and chemistry of the environment: Ph.D. Thesis Polytechnic of Toulouse.
3. Massoud, T., 2012, Nanostructure and local electronic properties of passive layers on nickel and stainless steel. Thesis University Pierre & Marie Curie
4. Trindade, VB., U. Krupp, and HJ. Christ, 2008 Computer-based Simulation of High-Temperature Corrosion Phenomena. J. Braz. Chem. Soc., Vol. 19, N° 1, pp.157-161.
5. Vialas, N., 2004, Study of the deterioration by oxidation at high temperature and inter diffusion systems coating / super alloy based on nickel: life prediction. Ph.D. thesis Polytechnic National Institute of Toulouse.
6. Laghoutaris, P., 2009, Stress corrosion cracking of the alloy 600 primary mid pressurized water reactors: contribution to understanding the mechanisms. Thesis National School mines Paris.
7. Augustin-Lecallier, I., 2011, Development of new nickel base super alloys MP for turbine disc, PhD Thesis, National School of Mines of Paris.
8. André, N., 2012, Investigation of the physico-chemical evolution of the substrate at the high temperature oxidation of Ni-Cr alloys model low chromium and alloy model Ni-16CR-9Fe, Memory Master at the University of St. Etienne
9. J. P. Castin, M. Grosbras, M. Cahoreau, 1993, Oxydation interne d'alliages ternaires : Cu-Sn-AL, URA 131 du CNRS, Poitiers,

ANALYTIC STUDY OF OXYGEN DIFFUSION IN ALUMINUM ALLOY AT HIGH TEMPERATURE

C. BENANTAR ¹, S.AKLOUCHE-BENOUAGUEF ², S.ATTAFI ¹

¹: Laboratoire Technologie des Matériaux, LTM, USTHB, Algeria

²: Laboratoire des Transports Polyphasiques et Milieux Poreux, LTPMP USTHB, Algeria

Corresponding author: chaouki.benantar@gmail.com / Tel: +213 555 822 600

ABSTRACT

Aluminum 6061 is a metal alloy used in various fields such as the nuclear, naval and Aérospatiale industry. [7] Actually, the problem of corrosion at high temperatures has become inseparable from any use of metallic materials in the nuclear industry. In this work, we are interested in the high temperature oxidation phenomena of Al-Mg-Si alloy with analytical method. We proposed an analytic model that translates the alloy oxidation by diffusion phenomena; this model is governed by Fick's second law. The solution of the equation leads us to the calculation of the kinetic constant that depends on different parameters mainly the concentration coefficient a_0 , T , α , β and Y the parameter set gives us a view about the oxidized layer depth that we represented in a 3D curves where we can determine the depth for very long duration of the oxidation. This study contributes to determine analytically the behaviour of the material after long periods of oxidation.

Key words: Aluminium 6061, Diffusion, high temperature, oxidation, Fick's law, Kinetic constant.

NOMENCLATURE

$a(x,t)$: oxygen concentration

$b(x,t)$: G Solute concentration (Magnesium)

$c(x,t)$: S Solute concentration (Silicon)

D_0 : oxygen diffusion coefficient

D_1 : Magnesium diffusion coefficient (G)

D_2 : Silicon diffusion Coefficient (S)

D : Macroscopic diffusion coefficient [cm/s]

C : Diffusion Species Concentration [g/cm³]

X : Diffusion Distance [cm]

$|\Delta G_{SO_2}| > |\Delta G_{GO_1}| > |\Delta G_{AO_1}|$

$PAO_n > PO_2 > PGO_{n1}$

$PAO_n > PO_2 > PSO_{n2}$

PO_2 : Pressure of Oxygen

ξ_1 : oxidation front for GO_{n1}

ξ_2 : oxidation front for SO_{n2}

P_{O_2} : Partial Pressure of dioxygen (atm)

P_0 : Atmospheric Pressure (1 atm)

J : Atom flux [mole.cm⁻².s⁻¹ or g.cm⁻².s⁻¹]

α : Lattice parameter [\AA^0]

γ : Poisson Coefficient

ΔS_D : Entropy [J/mole K]

ΔH_D : Diffusion activation Enthalpy [J/mole K]

R : Gas constant [J/ mole K]

T : Absolute Temperature [K]

INTRODUCTION

At present, the high temperature corrosion problem has become inseparable from any use of metallic materials. We propose in this work an analytical model that reflects the oxidation of the alloy by oxygen diffusion phenomenon. This model is governed by the two diffusion laws of FICK. The dry corrosion is the result of the attack of a metal by a hot gas at high temperatures. The reaction that occurs is of the form:

A (Solid Metal) + B (Gaseous Reagent: O_2) \rightarrow AB (Solid Product). It is a complex reaction between a solid and a gas. The thermodynamic and kinetic aspects will be considered. [1][2]

Oxidation kinetics Aspect: [3] To study the oxidation phenomenon, it is essential to know the kinetics with which the oxidation process predominates. We study essentially the kinetics of

the process, since the metal or the alloy in question is thermodynamically unstable, and also the oxidation mechanism. This oxidation occurs by adding oxygen atoms to the surface of the material. The mass generally increases in a proportional manner to the amount of oxidized material.

The equations of FICK:[4][8]The basic relationship for the diffusion defines the flow of atoms in motion. It is the number of atoms per time unit passing through the unity of a plane perpendicular to the flow direction. We will write the first equation of FICK:

$$J = -D \frac{\partial c}{\partial x}$$

Generally, the diffusion coefficient measurements can only be performed at elevated temperature where atoms are highly mobile and travel macroscopic distances. The first equation of FICK allows calculation of D in the case of a steady state, ie when the gradient is constant in time. But in the case of the transitional process we find the second equation by writing that throughout the volume, there is conservation of matter, we have:

$$\frac{\partial c}{\partial t} = -\frac{\partial J}{\partial x} \text{ (Conservation Equation)}$$

by combination with other equations we obtain the second law of FICK:

$$\frac{\partial c}{\partial t} = D \frac{\partial^2 c}{\partial x^2}$$

ANALYSIS AND MODELLING

1 Analytical modelling of the diffusion:

We Consider an alloy AGS, A as the base metal, S the second summing element and SO_{n2} its oxide. G having the GO_{n1} oxide and A having the AO_n oxide. Obtaining these oxides depends on meeting the following conditions:

- 1- oxides formation enthalpies must satisfy the following condition:
 $|\Delta G_{SO_{n2}}| > |\Delta G_{GO_{n1}}| > |\Delta G_{AO_n}|$
- 2- oxides dissociation tensions at the oxidation temperature should be as follows:
 $PAO_n > PO_2 > PGO_{n1}$ and $PAO_n > PO_2 > PSO_{n2}$
- 3- The oxygen diffusion rate in the alloy must be greater than that of G and S, otherwise the oxidation will happen at the surface. The kinetics of the simultaneous oxidation of two solutes has been described by Van Rooijen and al. [5][6] whose fundamental aspects are

as follows: During the internal oxidation treatment, oxygen diffuses from the surface (x = 0) in the direction of the positive x (semi-infinite alloy). Both oxides generally have different affinities for oxygen. We assume that the element S is oxidized first, after a time t the positions of oxidation fronts ξ_1 for GO_{n1} and ξ_2 for SO_{n2} are like $\xi_1 < \xi_2$. The model that calculates the oxidation fronts propagation speeds is based on solving the equations of the second law of FICK:

$$\frac{\partial c}{\partial t} = D \frac{\partial^2 c}{\partial x^2}$$

In our case, the law of FICK applies as follow:

$$\frac{\partial a}{\partial t} = D_0 \frac{\partial^2 a}{\partial x^2} \dots\dots\dots (1)$$

$$\frac{\partial b}{\partial t} = D_1 \frac{\partial^2 b}{\partial x^2} \dots\dots\dots (2)$$

$$\frac{\partial c}{\partial t} = D_2 \frac{\partial^2 c}{\partial x^2} \dots\dots\dots (3)$$

This study is mainly based on the simplification model adopted by J.Pcastin et Al [5], which consists in considering that the concentrations of oxygen and G are constant values in the vicinity of the oxide particles GO_{n1}, the respective constants a' and b' are related by the solubility product that is a function of the temperature:

$$PS_1 = (a')^{n1}.b'$$

The solubility product for SO_{n2} would be:

$$PS_2 = (a')^{n2}.c'$$

n1 and n2 are stoichiometric coefficients

For this calculation method the boundary conditions are defined as follows:

For t=0 :

For x ≤ 0 => a = a₀

For x > 0 => a = 0

For x ≥ 0 => b = b₀

For x ≥ 0 => c = c₀

For t > 0 :

For x = 0 => a = a₀

For x → ∞ => b = b₀

For x → ∞ => c = c₀

The progress of the oxidation front in binary alloys is a parabolic function of time which is written as follows: $\xi = k\sqrt{t}$

In our case the oxidation fronts ξ_1 and ξ_2 related to G and S solutes will be:

$$\begin{aligned} \xi_1 &= k_1\sqrt{t} \\ \xi_2 &= k_2\sqrt{t} \end{aligned}$$

The kinetics of oxidation will be characterized by determining the two constants k_1 and k_2 . Equations solutions (1) (2) and (3) are given by:

$$F = \alpha_i + \beta_i \cdot \text{erf} \left(\frac{x}{2\sqrt{D_j t}} \right)$$

α_i and β_i ($i=1\dots n$): constants to be determined from the boundary conditions

D_j : Species Diffusion Coefficient

t : Time

erf: Error Function

α and β are constants to calculate following the initial and boundary conditions, So the solutions of the equations 1,2 and 3 are :

2 Oxidation front of the S element ($x \geq \xi_2$) :

$$c(x, t) = \alpha_1 + \beta_1 \text{erf} \left(\frac{x}{2\sqrt{D_2 t}} \right)$$

Initial and boundary conditions:

$$c(x, t) = c_0 \text{ quand } x \rightarrow \infty$$

$$c(x, t) = c' \text{ quand } x = \xi_2 = k_2\sqrt{t}$$

$$c(x, t) = c_0 - (c_0 - c') \left[\frac{\text{erfc} \left(\frac{x}{2\sqrt{D_2 t}} \right)}{\text{erfc} \left(\frac{k_2}{2\sqrt{D_2}} \right)} \right] \dots\dots\dots(4)$$

3 Oxidation front of the G element ($x \geq \xi_1$)

$$b(x, t) = \alpha_2 + \beta_2 \text{erf} \left(\frac{x}{2\sqrt{D_1 t}} \right)$$

Initial and boundary conditions:

$$b(x, t) = b_0 \text{ quand } x \rightarrow \infty$$

$$b(x, t) = b' \text{ quand } x = \xi_1 = k_1\sqrt{t}$$

$$b(x, t) = b_0 - (b_0 - b') \left[\frac{\text{erfc} \left(\frac{x}{2\sqrt{D_1 t}} \right)}{\text{erfc} \left(\frac{k_1}{2\sqrt{D_1}} \right)} \right] \dots\dots\dots(5)$$

4 Oxidation front of the A element:

The study of the diffusion and concentration of the oxygen in our model is in three areas thus three cases of boundary conditions

4-1 The first case where $0 \leq x \leq \xi_1$:

$$a(x, t) = \alpha_3 + \beta_3 \text{erf} \left(\frac{x}{2\sqrt{D_0 t}} \right)$$

The initial and boundary conditions are:

$$a(x, t) = a_0 \text{ quand } x = 0$$

$$a(x, t) = a'_1 \text{ quand } x = \xi_1 = k_1\sqrt{t}$$

$$a(0, t) = \alpha_3 + \beta_3 \text{erf}(0) = a_0$$

$$\text{erf}(0) = 0 \text{ hence: } \alpha_2 = a_0$$

$$a(x, t) = a_0 - (a_0 - a'_1) \left[\frac{\text{erf} \left(\frac{x}{2\sqrt{D_0 t}} \right)}{\text{erf} \left(\frac{k_1}{2\sqrt{D_0}} \right)} \right] \dots\dots(6)$$

4-2 The second case where $\xi_1 \leq x \leq \xi_2$:

$$a(x, t) = \alpha_4 + \beta_4 \text{erf} \left(\frac{x}{2\sqrt{D_0 t}} \right)$$

The initial and boundary conditions are:

$$a(x, t) = a'_1 \text{ Quand } x = \xi_1 = k_1\sqrt{t}$$

$$a(x, t) = a'_2 \text{ Quand } x = \xi_2 = k_2\sqrt{t}$$

$$a(x, t) = a'_1 - (a'_1 - a'_2) \frac{\text{erf} \left(\frac{x}{2\sqrt{D_0 t}} \right) - \text{erf} \left(\frac{k_1}{2\sqrt{D_0}} \right)}{\text{erf} \left(\frac{k_2}{2\sqrt{D_0}} \right) - \text{erf} \left(\frac{k_1}{2\sqrt{D_0}} \right)} \dots\dots(7)$$

4-3 Third case where $x \geq \xi_2$:

$$a(x, t) = \alpha_5 + \beta_5 \text{erf} \left(\frac{x}{2\sqrt{D_0 t}} \right)$$

The initial and boundary conditions are:

$$a(x, t) = a'_2 \text{ Quand } x = \xi_2 = k_2\sqrt{t}$$

$$a(x, t) = 0 \text{ Quand } x \rightarrow \infty$$

$$a(x, t) = a'_2 \frac{\text{erfc} \left(\frac{x}{2\sqrt{D_0 t}} \right)}{\text{erfc} \left(\frac{k_2}{2\sqrt{D_0}} \right)} \dots\dots\dots(8)$$

To determine k_i ($i=1,2$), simply believe that the amount of oxygen consumed in the oxidation fronts is n_i times the amount of atoms (G or S) arriving at ξ_i . In practice we have:

$$\frac{D_0}{D_1} \text{ and } \frac{D_0}{D_2} \text{ are big in the order of } 10^3$$

$$\text{EXP} \left(\frac{k_i^2}{4D_0} \right) = \text{EXP} \left(\frac{k_i^2}{4D_0} \right) \approx 1$$

From which:

$$k_1 = k_2 = \sqrt{\frac{2D_0(a_0 - a'_1)}{n_1(b_0 - b'_1) + n_2(c_0 - c')}}}$$

5 The parameters involved:

In our study we took the parameter set that is summarized in the table below

Table 1

Set of parameters used to calculate the different values of the rate constant K and the evolution of the oxidation front ξ

Kinetic Constant	Concentration Coefficient a_0	Concentration Ratio β	Concentration Ratio Y
K1	10^{-4}	β_1	Y1
K2	10^{-4}	β_1	Y2
K3	10^{-4}	β_1	Y3
K4	10^{-4}	β_2	Y1
K5	10^{-4}	β_2	Y2
K6	10^{-4}	β_2	Y3
K7	10^{-4}	β_3	Y1
K8	10^{-4}	β_3	Y2
K9	10^{-4}	β_3	Y3
K10	2.08×10^{-4}	β_1	Y1
K11	2.08×10^{-4}	β_1	Y2
K12	2.08×10^{-4}	β_1	Y3
K13	2.08×10^{-4}	β_2	Y1
K14	2.08×10^{-4}	β_2	Y2
K15	2.08×10^{-4}	β_2	Y3
K16	2.08×10^{-4}	β_3	Y1
K17	2.08×10^{-4}	β_3	Y2
K18	2.08×10^{-4}	β_3	Y3
	the concentration ratios of the values involved are:	$\beta_1 = 0.05$ $\beta_2 = 0.45$ $\beta_3 = 0.85$	Y1 = 0.15 Y2 = 0.50 Y3 = 0.95

RESULTS AND DISCUSSION

1- RESULTS OF THE ANALYTICAL PART

Diagram representation of the evolution of kinetic constant:

1-1- Evolution of the kinetic constant K as a function of α :

To view the various changes in the kinetic constant K as a function of α , we have developed a program in Matlab. We based on the phenomenon of diffusion of the two Fick's laws, and on the set of the parameters mentioned in Table 1.

The results are shown by curves for two initial oxygen concentrations $a_0=10^{-4}$ and $a_0=2.08 \times 10^{-4}$

- $K(\alpha)$ for $a_0 = 10^{-4}$:

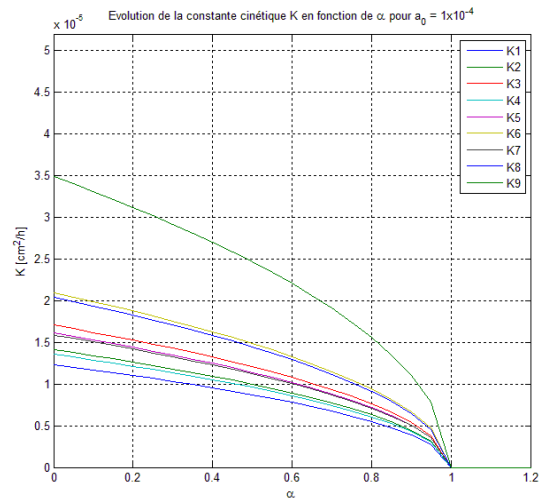


Figure 1

Superposition of different graphs of the evolution of the kinetic constant $K(\alpha)$ for $a_0=10^{-4}$, $\beta_1 = 0.05$, $\beta_2 = 0.45$, $\beta_3 = 0.95$, $Y_1=0.15$, $Y_2=0.50$ and $Y_3=0.85$

- $K(\alpha)$ for $a_0 = 2.08 \times 10^{-4}$:

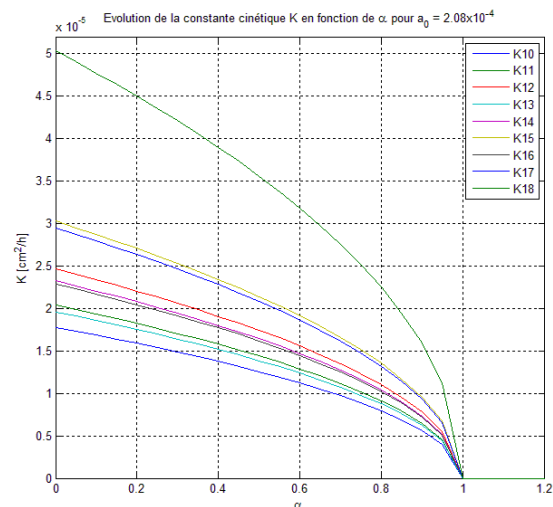


Figure 2

Superposition of different graphs of the evolution of the kinetic constant $K(\alpha)$ for $a_0 = 2.08 \times 10^{-4}$, $\beta_1 = 0.05$, $\beta_2 = 0.45$, $\beta_3 = 0.95$, with $Y_1 = 0.15$, $Y_2 = 0.50$ and $Y_3 = 0.85$

1-2- Evolution of the kinetic constant K as a function of α and the concentration a_0 :

To better observe the evolution of the kinetic constant K we added a range of variation in the value of a_0 , and this by taking it between an initial value equal to zero and a limit value equal to 3.5×10^{-4} .

The three-dimensional representations of the following figures are taken to the set of parameters β and Y previously indicated. Some examples:

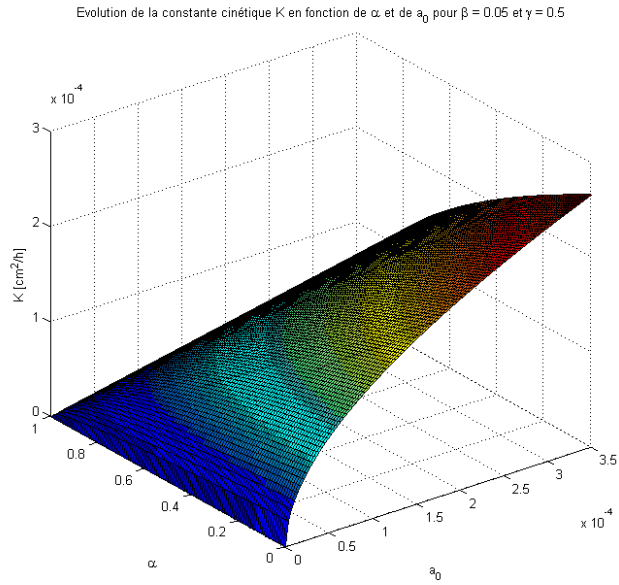


Figure 3

Evolution of the kinetic constant K as a function of α and a_0 for $\beta=0.05$ and $Y=0.5$

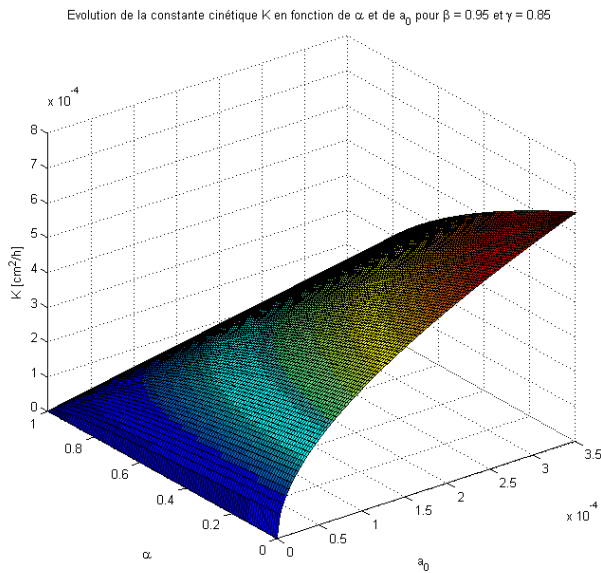


Figure 4

Evolution of the kinetic constant K as a function of α and a_0 for $\beta=0.95$ and $Y=0.85$

1-3- Evolution of the oxidation front ξ function of time and α for a set of parameters β and Y for $a_0=10^{-4}$ and for $a_0=2.08 \times 10^{-4}$:

In this part of the study we will represent the evolution of the oxidation front ξ function of time (hours), and α coefficient for the set of parameters we chose.

The following figures give us an overview of the possible values of the thickness of the oxidized layer on a time interval up to 100 hours.

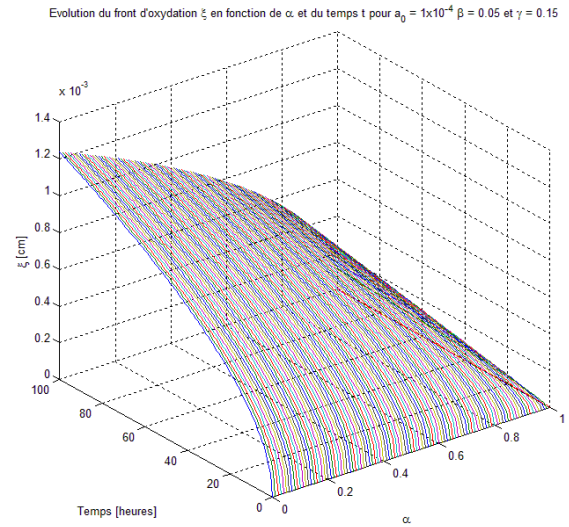


Figure 5

Evolution of the oxidation front ξ in function of time t (hours) of the coefficient α for values of $\beta=0.05$ and $Y=0.15$

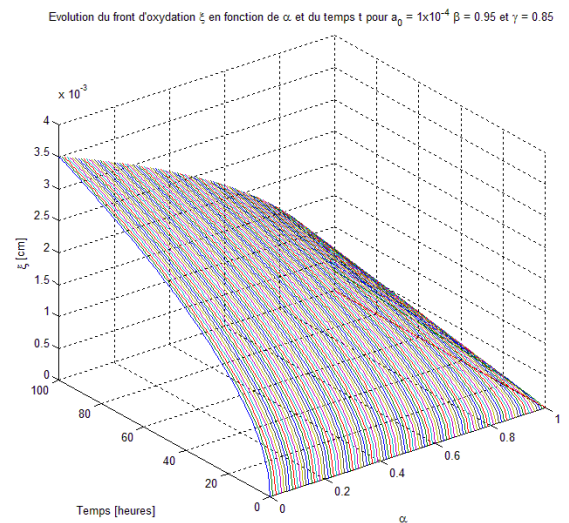


Figure 6

Evolution of the oxidation front ξ in function of time t (hours) of the coefficient α for values of $\beta=0.95$ and $Y=0.85$

CONCLUSION

The representation of the evolution of the oxidation front ξ function of time and α shows that the thickness of the oxidation front, as well as the concentration of the initial oxygen a_0 vary in a proportional manner. We can see that for small values of beta and gamma, K_{si} takes a maximum value of 1.23×10^{-3} for $a_0 = 10^{-4}$, while for $a_0 = 2.08 \times 10^{-4}$, it takes a value greater than or equal to 1.78×10^{-3} .

This is still valid for large values of beta and gamma close to one, where I can see that K_{si} takes a maximum value of 3.5×10^{-3} for $a_0 = 10^{-4}$, while that value is 5×10^{-3} for $a_0 = 2.08 \times 10^{-4}$.

The observation of the evolution profiles obtained in 3D nous allows us to see paraboloid surfaces resulting from an alignment of K_{si} parabolic evolution curves in the direction of evolution of alpha, this shape is the same for all the evolution figures for the different parameters beta and gamma that we have introduced into the MATLAB calculation program and that gave us the results shown in figures 5 et 6.

The results of the analytical study give us values and curves that extend over an oxidation time interval of 100 hours at 500°C temperatures. This gives us an idea about the values that can take the oxidation kinetic constant and the evolution of the oxidation front ξ for extended time periods of degradation, experiments that are not possible to conduct practically (months, years).

This study is only a first step in the study of the degradation of AL6061 aluminum alloy at high temperature. A deeper study may reveal more truths about the behavior of this alloy during high temperature oxidation.

REFERENCES

- [1] J.Benard, A.Michel, J.Philibert, J.Talbot
General Metallurgy. Second Edition, Masson, Paris 1984.
- [2] C.Chaussin, G.Hilly
Metallurgy, Tome I, Metallic Alloys. Tenth edition 1978.
- [3] M.F.Ashby, D.R.H.Jones

Materials I Properties and Application.
IUT, Engineering School, Dunod, Paris, 1998.

- [4] D.Landolt
Corrosion and Chemistry of Surfaces,
Materials Treaty.
Polytechnic and University Press,
Romande, 1994.
- [5] J.P.Castin, M.Grosbras, M.Cahoreau
Internal Oxidation of ternary alloys
Cu-Sn-Al
Physical Metallurgy Laboratory,
URA 131 du CNRS, Poitiers, 1993
- [6] VA. Van Rooijen, E.W. van Royen, J. Vrijen
and S. Radeiaar, Acta Met. 23 (1975) 987.
- [7] S. Vincent et al.
Microstructural evolution of two Aluminium
6061 alloys during the elaboration steps,
20th French congress of mechanic 2011.
- [8] Pr. Pierre GUIRALDENQ
Diffusion in metals, metals and alloys study:
metallic state, Techniques de l'Ingénieur,
Metallic materials treaty, p102, 1994.

NUMERICAL MODELLING OF HDPE BEHAVIOR DURING 2-ECAP PROCESS USING 90° AND 120° DIES

MITSAK Ali, AOUR Benaoumeur

Laboratory of Applied Biomechanics and Biomaterials, National Polytechnic School of Oran, BP1523
EL M'naour, Oran, 31000, Algeria

*Corresponding author: Fax: +213 41 29 00 95 Email: ben_aour@yahoo.fr

ABSTRACT

In this work, a numerical and experimental investigation of a typical semi-crystalline thermoplastic polymer (high density polyethylene (HDPE)) during two turn Equal Channel Angular Pressing (2-ECAP) using 90° and 120° dies has been presented. The warping of the extruded samples has been also highlighted experimentally. The material parameters of an elasto-viscoplastic constitutive law were identified using compressive tests at different temperatures and strain rates. The effects of the main parameters, such as, the channel angles, the dimensions of the intermediate channel, the friction and the temperature have been analyzed. Finally, to confirm the numerical results, two dies composed of one elbow (1-ECAP) and two elbows (2-ECAP) have been manufactured and tested. It was found that the warping obtained using 2-ECAP die is more reduced than that of 1-ECAP die even with several passes.

INTRODUCTION

Equal channel angular pressing (ECAP) is an effective tool to impose large plastic strains. The process, developed firstly by Segal et al. [1], has attracted considerable interest as a method to improve the material properties by super plastic deformation. Indeed, this process involves simple shear deformation that is achieved by pressing the workpiece through a die containing two channels of equal cross-section that meet at a predefined angle. This method has been proved to be very effective in producing ultrafine grain size in metallic materials [2-4] and a significant molecular orientation in the case of polymeric materials [5-16] with accompanying enhancement in mechanical properties.

According to our knowledge, this process was first applied to polymers by Sue and Li [5]. They showed that the ECAP process is efficient in altering the morphology of a linear low density polyethylene (LLDP). Sue et al. [6] have been reported that for ECAP to be effective, it is necessary that the extrusion be held at temperatures slightly below the glassy transition in the case of polycarbonate (PC). For the same polymer, Li et al. [7] confirmed that the mechanical properties can be tailored by extruding the material via various processing routes and different number of passes. The effect of molecular anisotropy on the impact strength of polycarbonate (PC) was examined by Xia et al. [8]. They found that the enhancement of the impact resistance is directly

related to the changes in molecular orientation induced by ECAP process. According to Xia et al., [9], the crystallinity and molecular orientation have been identified as two important factors affecting the dynamic mechanical properties of the ECAP-oriented semicrystalline polyethylene terephthalate (PET). An improvement of bending and torsional storage modulus was found. Creasy and Kang [10] studied fibre fracture during ECAP process of short fibre-reinforced thermoplastics. They found that the fibre length can be controlled and oriented by setting the process temperature below the melting point of the polymer crystallites. On the other hand, the effect of different ECAP routes on the tensile, fracture toughness, flexural, and ballistic impact properties of polymethylmethacrylate (PMMA) was investigated by Weon et al. [11]. The process was also used to modify the aspect ratio and orientation of clay nanoparticles in nylon-6/clay nanocomposites by Weon and Sue [12]. A fruitful discussion was reported by Wang et al. [13] on lamellar formation and relaxation in simple sheared polyethylene terephthalate (PET) using the in-situ time resolved synchrotron Small-Angle X-ray Scattering (SAXS) technique. More recently, numerical and experimental investigations were achieved to highlight the effects of the main geometrical and processing parameters on the viscoplastic behaviour of polymers during ECAP process [14-16].

The major motivation of this work is to investigate the behavior of a high density polyethylene using 2-

ECAP in order to improve the level and the homogeneity of the plastic strain and to highlight the reduction of the sample warping. To achieve this objectives, the paper was organized as follows. The elastic-viscoplastic constitutive law and its identification using compressive tests at different strain rates and different temperatures are presented respectively in sections 2 and 3. Section 4 introduces details on the finite element modeling. The numerical results obtained for the effects of friction and temperature on the plastic strain distribution using two dies of 90° and 120° are presented in section 5. Section 6 gives a comparison between the experimental results obtained using 1-ECAP and 2-ECAP dies. Finally, section 7 gives the main remarks.

CONSTITUTIVE MODEL

The large plastic deformation of the polymer under study (HDPE) is characterized by a strain rate dependent yield followed by a strain hardening. Various constitutive laws, basing on micromechanical or phenomenological considerations [17,18], were developed to describe the specific behavior of polymers. In this paper, a phenomenological constitutive model was used to describe the behavior of the studied material [15]. It is based on the additive decomposition of the strain rate tensor \mathbf{d} into an elastic part \mathbf{d}^e and a viscoplastic part \mathbf{d}^{vp} as:

$$\mathbf{d} = \mathbf{d}^e + \mathbf{d}^{vp} \quad (1)$$

The elastic strain rate tensor \mathbf{d}^e is given by:

$$\mathbf{d}^e = \mathbf{C}^{-1} \tilde{\boldsymbol{\sigma}} \quad (2)$$

$$\tilde{\boldsymbol{\sigma}} = \dot{\boldsymbol{\sigma}} - \mathbf{W}\boldsymbol{\sigma} + \boldsymbol{\sigma}\mathbf{W} \quad (3)$$

Where $\tilde{\boldsymbol{\sigma}}$ the Jaumann derivative of the Cauchy stress tensor is $\boldsymbol{\sigma}$ based upon the spin tensor \mathbf{W} and \mathbf{C} is the fourth-order isotropic elastic modulus tensor:

$$C_{ijkl} = \frac{E}{2(1+\nu)} \left[(\delta_{ik}\delta_{jl} + \delta_{il}\delta_{jk}) + \frac{2\nu}{1-2\nu} \delta_{ij}\delta_{kl} \right] \quad (4)$$

where E , ν and δ are respectively Young's modulus, Poisson's ratio and Kronecker-delta symbol.

The viscoplastic strain rate tensor \mathbf{d}^{vp} can be expressed by the following relationships:

$$\mathbf{d}^{vp} = \frac{3}{2} \left\langle \frac{\boldsymbol{\sigma}' - R}{K} \right\rangle^n \frac{\boldsymbol{\sigma}'}{\sigma_e} \quad (5)$$

$$\boldsymbol{\sigma}' = \boldsymbol{\sigma} - \text{tr}(\boldsymbol{\sigma})/3\mathbf{I} \quad (6)$$

$$\sigma_e = \sqrt{3/2 \boldsymbol{\sigma}' \boldsymbol{\sigma}'} \quad (7)$$

where K and n are the viscosity parameters, $\boldsymbol{\sigma}'$ is the deviator stress tensor, σ_e is the equivalent stress, and R is the isotropic hardening defined by a simple phenomenological evolution law as follows:

$$R = h \left(1 + \frac{\varepsilon^p}{\varepsilon_0} \right)^m \quad (8)$$

$$\varepsilon^p = \int_0^t \dot{\varepsilon}^p d\tau = \int_0^t \sqrt{2/3 \mathbf{d}^{vp} \mathbf{d}^{vp}} d\tau \quad (9)$$

with ε^p is the equivalent viscoplastic strain, ε_0 is the initial yield strain, m and h are the hardening parameters.

FITTING EXPERIMENTAL DATA

In order to simulate the plastic flow behavior of HDPE during 2-ECAP process, using finite element analysis, a series of compressive tests on HDPE specimens were carried out to identify the parameters of the elastic-viscoplastic constitutive law presented in the previous section. The HDPE material was provided by Goodfellow© company as a cylindrical bar of 10 mm diameter and length of 1000 mm, with a number-average molecular weight $M_n = 10$ kg.mol⁻¹ and a weight-average molecular weight $M_w = 70$ kg.mol⁻¹. The experimental tests were performed on an electromechanical testing machine (Instron® 5800) with a load-cell of 10 kN at different temperatures ($T=25, 40, 60$ and 80°C) and strain rates ($10^{-2}, 10^{-3}$ and 10^{-4} s⁻¹). Noting that the plates of the testing machine were well lubricated, so that the friction effect at the contact surfaces with the specimen is negligible. During tests, the values of cross-head displacement, force and time were recorded by the computer using Bluehill software. The experimental stress-strain curves obtained from compressive tests on HDPE are shown in Fig. 1. Compression strain and stress are plotted as positive values. It can be seen that the mechanical response of HDPE is nonlinear with an evident transition from elastic to inelastic stage.

The constitutive equations introduced in section 2 were used to predict the non-linear behavior of HDPE at large strains. In addition to the Young's modulus and Poisson's ratio, the constitutive equations contain four parameters to be determined: K , n , m and h . They were identified using a least squares regression fitting method. The Young's modulus E was deduced from the slope of the initial linear portion of the compression stress-strain curve. The Poisson's ratio ν was taken equal to

0.38. Table 1 gives the values of the identified material parameters. Figure 1 gives the comparison between the experimental data (in symbols) and the elasto-viscoplastic constitutive model (in solid lines) for HDPE at 25°C (Fig. 1a), 40°C (Fig. 1b), 60°C (Fig. 1c) and 80°C (Fig. 1d). As it can be seen that a fairly good agreement is obtained between the experimental data and the theoretical constitutive elastic-viscoplastic law.

Table 1. The material parameters for HDPE at different temperatures.

T [°C]	E [Mpa]	K [Mpa]	n [-]	h [Mpa]	m [-]
25	500	31.2	7.8	3.15	0.88
40	280	20	8.3	5	0.7
60	150	10.7	10.2	5.5	0.65
80	130	5.7	11.17	6	0.45

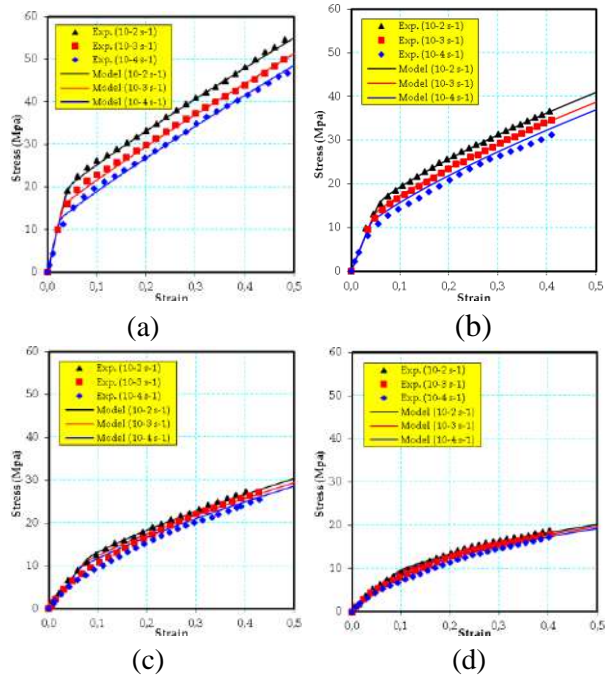


Figure 1. Stress-strain curves of HDPE for various temperatures: (a) room temperature (25 °C), (b) 40 °C, (c) 60 °C, (d) 80 °C.

FINITE ELEMENT MODELLING

The simulations were carried out using the finite element software MSC.Marc under plane-strain conditions. The sample dimensions were 10mm (width) × 10mm (thickness) × 110mm (length). The dies geometry was taken with channel angle $\Phi_1 = \Phi_2 = \Phi = 90^\circ$ (and 120°) and the two outer corners angles have been fixed to 10° . A radii $r = 2\text{mm}$ has been taken at the inner corners. Noting that these

values have been selected according to the previous study undertaken by Aour et al. [19]. Initially, the friction coefficient between the sample and the die channels was assumed to be zero, implying frictionless condition (for the first tests).

The die and the ram were considered as rigid bodies in the modeling. A displacement of 110mm was assigned to the ram in the extrusion direction. According to the theoretical [4] and experimental [20] analysis, the isothermal condition can be fulfilled at low pressing speeds. So, all simulations were performed with a ram speed of 0.1mm/s, which generates negligible heat due to the plastic deformation [19]. The sample behaviour was considered as being elastic-viscoplastic. In order to control the plastic strain distribution, the selected cross-section was taken at 15mm below the second inner corner (see Fig. 2).

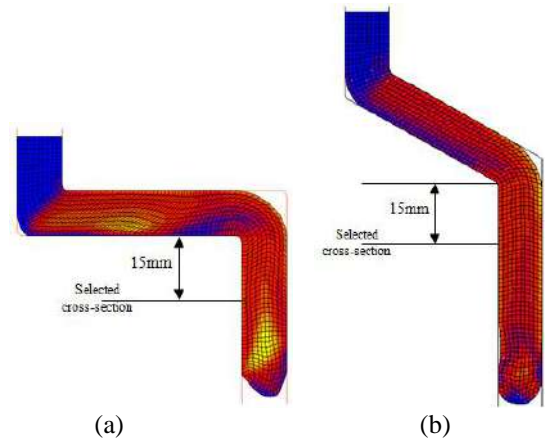


Figure 2. Illustration of the finite element meshes of the samples and the selected cross-section for the measurement in the case of: (a) 90° die and (b) 120° die.

RESULTS AND DISCUSSION

Equivalent Plastic Strain Distribution: In ECAP process the homogeneity of the plastic strain distribution in the bulk material during successive passes is very important. The aim of this section is to determine the optimal conditions which allow us to improve the homogeneity of the plastic strain distribution in terms of the thickness (t) and the length (L) of the second channel for the two-elbow tool.

Case of 90° die: Figure 3 shows the equivalent plastic strain distribution for four different lengths $L = \{20, 30, 40, 50\text{mm}\}$ with a section of $w \times t =$

10×10mm² and an inner corner radii of 2mm. It can be observed that the plastic strain is not uniform at the end of the samples. However, at the middle, the homogeneity of the plastic strain is relatively improved especially after the second pass except in the case of L=20mm. This is due to the phenomenon of folding which is much more pronounced when the second channel length is low (L = 20mm).

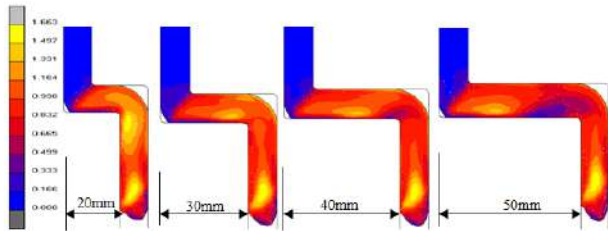


Figure 3. Equivalent plastic strain contours for HDPE samples during 2-ECAP process using 90° die for different lengths of the second channel.

For more details, we have shown in Figure 4, the distribution of the equivalent plastic strain in terms of the distance from the bottom along the selected cross-section of the sample (see Fig. 2) for each thickness with different lengths of the second channel. It can be seen that the low equivalent plastic strain is obtained when the length L= 50mm for all cases. However, the high level of plastic strain is obtained when the length L= 30mm for t = 8, 10 and 12mm while for t = 6 mm the high level of plastic strain is obtained when the length L= 40mm.

It is worth nothing that the variation factor is an important parameter, which can be related to the strain homogeneity (i.e. the higher is its value, the more important is the heterogeneity of the deformation) [21]. So, in order to quantify the degree of the plastic strain homogeneity, a statistical analysis has been carried out by introducing the standard deviation and the variation factor V, defined as the ratio of the standard deviation to the average strain as

$$V = \frac{1}{\varepsilon_{ave}} \sqrt{\frac{1}{N} \sum_{i=1}^N (\varepsilon_i - \varepsilon_{ave})^2} \times 100(\%) \quad (10)$$

where ε_i is the equivalent plastic strain value of a given integration point along the sample width, ε_{ave} is the arithmetic average of the equivalent plastic strain values computed on N integration points.

The maximum punch force required, the maximum and the average values of the equivalent plastic stain given by the numerical solution as well as the variation factor and the standard deviation calculated

according to the different geometries are presented in Table 2. It can be remarked that the maximum punch force increases with the increase of the second channel thickness.

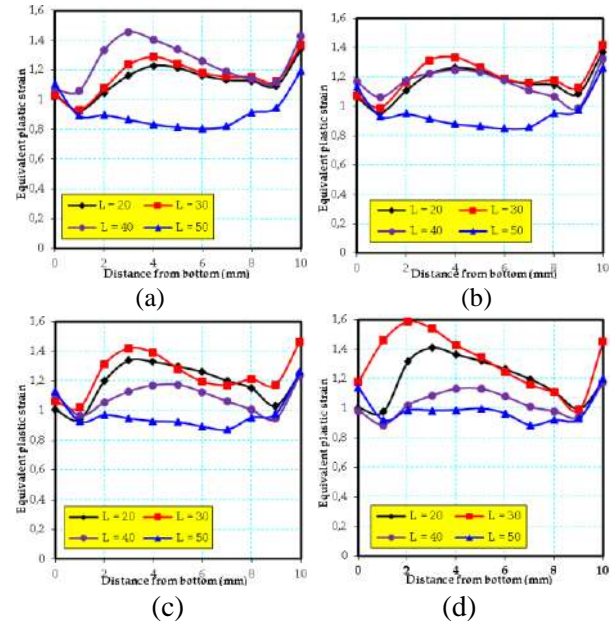


Figure 4. Distribution of the equivalent plastic strain along the selected cross-section for different lengths and thicknesses of the second channel in the case of 90° die.

Table 2. Evolution of the punch force, the equivalent plastic strain and the variation factor in terms of t and L in the case of 90° die.

t (mm)	L (mm)	F _{max} (kN)	ε_{ave}	Stand. deviat.	V (%)
6	20	9.675	1.138	0.106	9.285
	30	9.512	1.166	0.116	9.980
	40	9.675	1.259	0.143	11.340
	50	9.747	0.926	0.121	13.069
8	20	12.765	1.173	0.105	8.948
	30	12.710	1.208	0.117	9.712
	40	12.700	1.167	0.093	7.962
	50	12.710	0.970	0.121	12.467
10	20	15.697	1.187	0.129	10.903
	30	15.810	1.251	0.136	10.891
	40	15.724	1.093	0.087	7.923
	50	15.794	0.989	0.110	11.164
12	20	17.855	1.197	0.148	12.356
	30	19.073	1.320	0.183	13.881
	40	18.938	1.040	0.087	8.333
	50	19.008	0.999	0.095	9.478

Nonetheless, the average plastic strain varies from 0.926 to 1.320 for all cases. However, by considering the variation factor, it can be concluded that the best homogeneity of the plastic strain distribution was obtained when the **thickness t = 10mm and the length L = 40mm**. Moreover, one

can note that the more heterogeneous plastic deformation is obtained with a thickness of 12mm and a length of 30mm.

Case of 120° die: The same simulations have been carried out for the case of 120° die and the obtained results are depicted in figure 5. It can be seen that the equivalent plastic strain distribution is relatively uniform and homogeneous compared to that of 90° die. In order to give more details, we presented in figure 6 the evolution of the equivalent plastic strain in terms of the distance from the bottom along the selected cross-section of the sample for each thickness with different lengths of the second channel. It can be observed that the low equivalent plastic strain is obtained when the length $L = 50\text{mm}$ for all cases. However, the high level of plastic strain is obtained when the length $L = 20\text{mm}$ and $t = 10$ or 12mm while when $t = 6$ and 8mm the high level of plastic strain is obtained when the length $L = 30\text{mm}$. Table 3 shows the values of the maximum punch force required, the maximum and the average values of the equivalent plastic strain given by the numerical solution as well as the variation factor and the standard deviation calculated according to the different geometries in the case of 120° die.

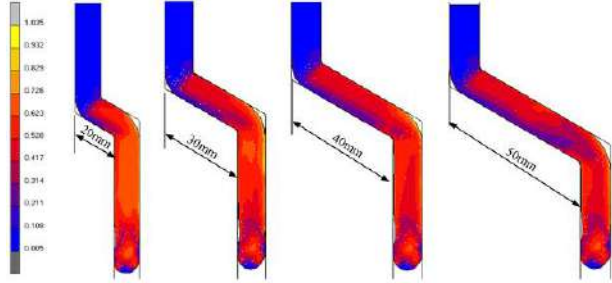


Figure 5. Equivalent plastic strain contours for HDPE samples during 2-ECAP process using 120° die for different lengths of the second channel.

It can be observed that the maximum punch force decreases with the decrease of the second channel thickness. Furthermore, the limits of the average plastic strain varies from 0.581 (at $t = 6\text{mm}$ and $L = 50\text{mm}$) to 0.675 (at $t = 10\text{mm}$ and $L = 20\text{mm}$) for all the presented cases. By taking into account the variation factor criterion, it can be deduced that the best homogeneity of the plastic strain distribution was obtained when the **thickness $t = 10\text{mm}$ and the length $L = 20\text{mm}$** .

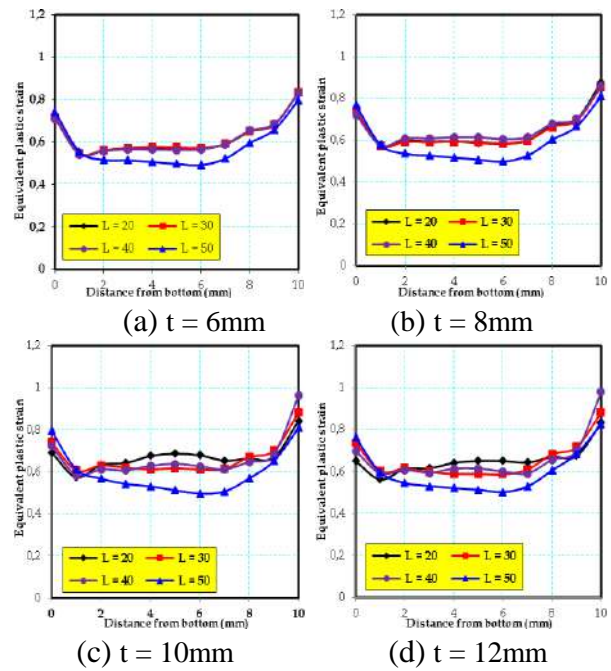


Figure 6. Distribution of the equivalent plastic strain along the selected cross-section for different lengths and thicknesses of the second channel in the case of 120° die.

Table 3. Evolution of the punch force, the equivalent plastic strain and the variation factor in terms of t and L in the case of 120° die.

t (mm)	L (mm)	F_{max} (kN)	ϵ_{ave}	Stand. deviat.	V (%)
6	20	2.575	0.624	0.084	13.502
	30	2.618	0.625	0.084	13.421
	40	2.683	0.620	0.086	13.824
	50	2.624	0.581	0.100	17.280
8	20	3.651	0.647	0.089	13.763
	30	3.590	0.643	0.084	13.126
	40	3.612	0.656	0.078	11.899
	50	3.622	0.596	0.103	17.354
10	20	4.518	0.675	0.062	9.176
	30	4.429	0.665	0.081	12.137
	40	4.405	0.666	0.101	15.160
	50	4.396	0.600	0.105	17.546
12	20	5.556	0.656	0.063	9.654
	30	5.571	0.657	0.088	13.396
	40	5.503	0.659	0.109	16.508
	50	5.495	0.602	0.105	17.417

Effect of Friction: In the above sections, we have assumed that the friction between the sample and the tool walls is negligible (i.e. frictionless condition). In this section, the friction effects on the equivalent plastic strain distribution and the pressing force are analyzed on the optimised geometries of 2-ECAP tools (with $t = 10\text{mm}$ and $L = 40\text{mm}$ for 90° and $t = 10\text{mm}$ and $L = 20\text{mm}$ for 120° die). The friction between the tool and the

sample is modelled with Coulomb friction law. The computations have been performed with three friction coefficients $f = \{0.1, 0.2 \text{ and } 0.3\}$. Figures 7a and 7b show respectively the plastic strain distribution across the sample thickness for the dies of 90° and 120° . It can be seen that the friction influences significantly the homogeneity and the magnitude of the equivalent plastic strain in the extruded material (HDPE). Indeed, more the friction coefficient increases, more is the increase of the plastic strain.

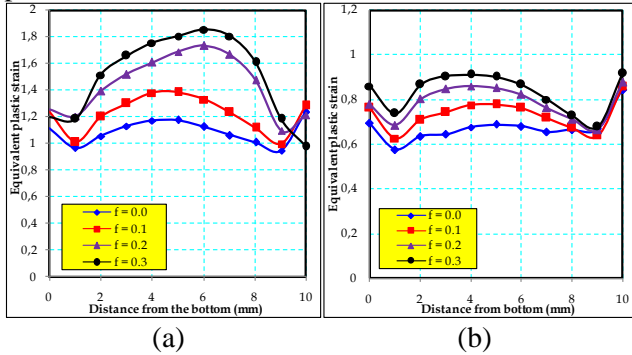


Figure 7. Illustration of friction effect on the equivalent plastic strain distribution in the case of: 90° die (a) 120° die.

Effect of Temperature: In order to analyze the sensitivity of the equivalent plastic strain distribution in terms of the temperature, the computations were performed for four values of $T = \{25, 40, 60 \text{ and } 80^\circ\text{C}\}$ at a constant ram speed of 0.1 mm/s and under frictionless conditions. The simulations are conducted using both dies with their optimized geometries ($t=10\text{mm}$ and $L=40\text{mm}$ for 90° die and $t = 10 \text{ mm}$ and $L = 20 \text{ mm}$ for 120° die). The distributions of the equivalent plastic strain along the sample thickness as a function of the temperature are shown in Fig. 8a for 90° die and Fig. 8b for 120° die. It can be seen that the temperature strongly influences the magnitude of the equivalent plastic strain (the higher is the temperature, the lower is the plastic strain). Furthermore, in the case of 90° die, one can notice that the distribution of the plastic strain is highly temperature sensitive at low temperatures, whereas this effect becomes insignificant beyond a certain temperature as illustrated in Fig. 8a, where the results at 60 and 80°C are almost identical. However, in the case of 120° die, the plastic strain decreases with the increase of the temperature.

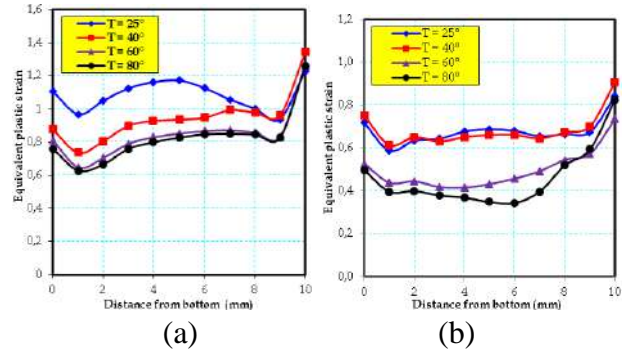


Figure 8. Effect of the temperature on the evolution of the equivalent plastic strain in the case of: (a) 90° die and (b) 120° die.

EXPERIMENTAL TESTS OF ECAP

After an optimization study of the geometrical parameters, a 2-ECAP device with a channel angle $\Phi = 120^\circ$, a thickness $t = 10 \text{ mm}$ and an intermediate channel with a length $L = 20 \text{ mm}$ was designed and manufactured (Fig. 9a).

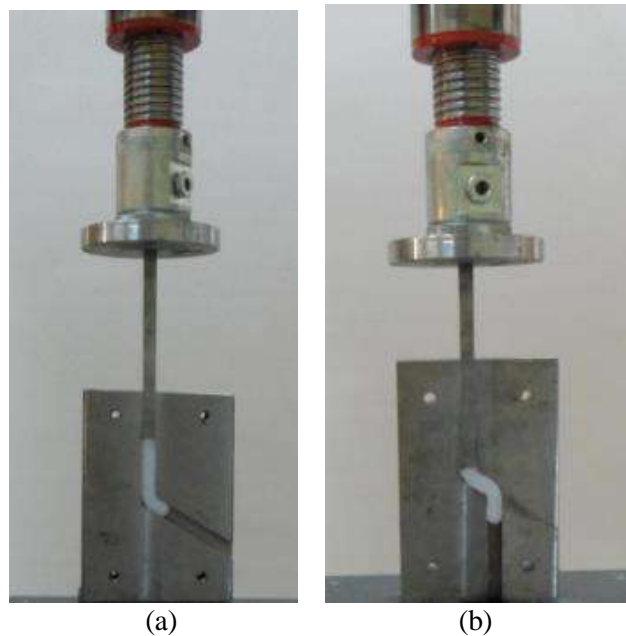


Figure 9. Experimental study of HDPE behaviour using 120° die with: (a) one elbow (1-ECAP) and (b) two elbows (2-ECAP).

In order to make a comparison between the deformed samples using 1-ECAP and 2-ECAP, another tool with one elbow and the same channel angle ($\Phi=120^\circ$) was also designed and manufactured (Fig. 9b). For both dies, the lengths of the entrance and exit channels are respectively 85mm and 80mm . ECAP samples of $10\text{mm} \times 10\text{mm}$

cross-section and 70mm in length were cut from commercially HDPE plates in the same direction, then surfaced simultaneously on the cutting facets and polished. Next, the HDPE samples were annealed in vacuum at 120°C for 2h. Note that the widths and the thickness of the channels and the samples are the same, but with a clearance fit. All the ECAP tests were performed with a ram speed of 0.07mm/s and at the room temperature of 25°C. The warping of the extruded samples obtained by using the both dies (1-ECAP with route C and 2-ECAP) has been quantified in this experimental part. Noting that, route C involves a rotation of 180° after each pass. Fig. 10 shows pictures of HDPE samples that have undergone one pass using 1-ECAP and 2-ECAP and four passes (route C) using 1-ECAP and two passes with 2-ECAP die. The obtained results for 1-ECAP and 2-ECAP are listed in table 4 and illustrated in figure 10. The maximum curvature (warping) of the sample was quantified by measuring the height of the sample before and after extrusion. For a similar number of passes through the elbows, it was found that the minimum warping is always obtained using 2-ECAP die. Furthermore, the warping obtained for two passes using 2-ECAP die is less than the half of that obtained using four passes with 1-ECAP die.

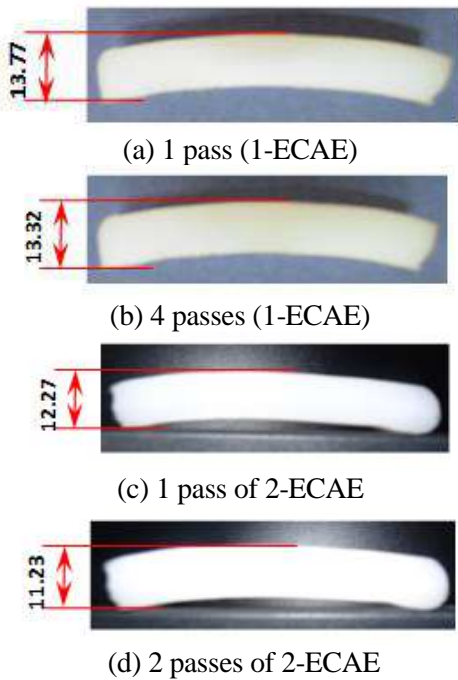


Figure 10. HDPE samples extruded at room temperature after (a) one and (b) four passes using 1-ECAP die and (c) one and (d) two passes using 2-ECAP die with a channel angle of 120°.

Table 4. Maximum values of the curvature of HDPE samples obtained by 1-ECAP and 2-ECAP dies with a channel angle of 120°.

Type of the die	Height before extrusion Hb (mm)	Height after extrusion Ha (mm)	Curvature $Cu = Ha - Hb$ (mm)
1 pass (1-ECAP)	9.85	13.77	3.92
2 passes (1-ECAP)	9.85	13.28	3.43
1 pass (2-ECAP)	9.82	12.27	2.45
3 passes (1-ECAP)	9.85	13.45	3.60
4 passes (1-ECAP)	9.85	13.32	3.47
2 passes (2-ECAP)	9.82	11.23	1.41

CONCLUSIONS

In the present work, the finite element method has been used to provide fruitful information for the optimization of the geometrical parameters in order to manufacture 2-ECAP tool which allows simultaneously an improvement of the level of the plastic strain and a significant reduction of the warping. The simulations have been performed on HDPE samples using two turn ECAP process with channel angles of 90° and 120°. It was found that the length of the second channel, the friction and the temperature play a significant role on the homogeneity of the plastic strain distribution and the magnitude of the pressing force required for extrusion.

We noticed that the best homogeneity of the plastic strain distribution was obtained when the second channel has a thickness $t = 10$ mm and a length $L = 40$ mm in the case of 90° die, however, in the case of 120° die, the optimal dimensions are $t = 10$ mm and $L = 20$ mm.

A significant sensitivity of friction conditions on the plastic strain distribution has been found especially for 90° die. Indeed, the higher is the friction coefficient, the higher is the level of the plastic strain. So, in order to reduce the friction effect on the magnitude of the pressing force, it is advised to use an appropriate lubricant during the process.

During 2-ECAP process, the temperature increase leads to lower plastic strain in the sample and a higher variation factor. In the particular case of HDPE samples, room temperature processing is favored, unless force limitations on the equipment require heating.

Finally, in order to combine the modelling analysis of the deformation behaviour of HDPE samples with experimental tests two dies with a channel angle of 120° have been designed and manufactured. The first with only one elbow, however, the second is composed of two elbows according to the results of the numerical optimization. It was found that the use of two-turn ECAP tool contributes significantly on the reduction of the warping without the use of the back pressure.

REFERENCES

1. Segal, V. M., 1995, Materials processing by simple shear, *Mater. Sci. Eng.* **A197**, pp. 157-164.
3. Beyerlein, I.J., Tomé, C. N., 2004 Analytical modeling of material flow in equal channel angular extrusion(ECAE), *Mater. Sci. Eng.*, **A380**, pp. 171-190.
4. Kim, H. S, Estrin, Y, 2005, Microstructural Modelling of Equal Channel Angular Pressing for Producing Ultrafine Grained Materials, *Mater. Sci. Eng.*, **A 410–411**, pp. 285–289.
5. Sue, H.J, Li C. K. Y, 1998, Control of orientation of lamellar structure in linear low density polyethylene via a novel equal channel angular extrusion process, *J. Mater. Sci. Lett.*, **17**, pp. 853-856.
6. Sue, H.J., Dilan, H., Li C.K.Y., 1999, Simple shear plastic deformation behaviour of polycarbonate plate due to the equal channel angular extrusion process. I: Finite element methods modelling, *Polym. Eng. Sci.*, **39**, pp. 2505-2515.
7. Li, C. K. Y, Xia, Z.Y, Sue, H.J., 2000, Simple shear plastic deformation behaviour of polycarbonate plate. II: Mechanical property characterization, *Polymer*, **41**, pp. 6285-6293.
8. Xia, Z, Sue HJ, Hsieh A. J., 2001, Impact fracture behaviour of molecularly orientated polycarbonate sheets, *J. Appl. Polym. Sci.*, **79**, pp. 2060-2066.
9. Xia, Z, Sue, H. J., Hsieh, A.J., Huang, J. W. L., 2001, Dynamic mechanical behaviour of oriented semi-crystalline polyethylene terephthalate, *Journal of Polymer Science, Part B: Polymer Physics*, **39**, pp. 1394-1403.
10. Creasy, T. S., Kang, Y.S., 2005, Fibre fracture during equal-channel angular extrusion of short fibre-reinforced thermoplastics, *J. Mater. Process. Technol.*, **160**, pp. 90-98.
11. Weon, J. I, Creasy, T.S., Sue, H.J., Hsieh, A.J., 2005, Mechanical behaviour of polymethylmethacrylate with molecules oriented via simple shear, *Polym. Eng. Sci.* **45**, pp. 314-324.
12. Weon, J.I., Sue, H.J., 2005, Effects of clay orientation and aspect ratio on mechanical behavior of nylon-6 nanocomposites, *Polymer* **46**, pp. 6325-6334.
13. Wang, Z. G., Xia, Z.Y., Yu, Z.Q., Chen, E.Q., Sue, H.J., Han, C.C., Hsiao, B.S., 2006, Lamellar formation and relaxation in simple sheared poly(ethylene terephthalate) by small-angle X-ray scattering, *Macromolecules*, **39**, pp. 2930-2939.
14. Zaïri, F., Aour, B., Gloaguen, J.M., Naït-Abdelaziz, M., Lefebvre, J.M., 2008, Steady plastic flow of a polymer during ECAE process: experiments and numerical modeling, *Polymer Engineering Sciences*, **18**, pp. 1015-1021.
15. Aour, B., Zaïri, F., Gloaguen, J.M., Naït-Abdelaziz, M., Lefebvre, J.M., 2009, Finite element analysis of plastic strain distribution in multi-pass ECAE process of high density polyethylene, *J. Manuf. Sci.*, **E131** pp. 1-11.
16. Bouaksa, F., Ovalle, Rodas, C., Zaïri F., Stoclet G., Naït-Abdelaziz M., Gloaguen J.M., Tamine T., Lefebvre J.M., 2014, Molecular chain orientation in polycarbonate during equal channel angular extrusion: Experiments and simulations, *Computational Materials Science*, **85**, 244-252.
17. Tervoort, T.A., Smit, R.J.M., Brekelmans, W.A.M., Govaert, L., 1998, A constitutive equation for the elasto-viscoplastic deformation of glassy polymers, *Mech. Time-Depend. Mater.*, **1**, pp. 269-291.
18. Boyce, M.C., Socrate, S., Llana, P.G., 2000, Constitutive model for the finite deformation stress-strain behavior of poly(ethylene terephthalate) above the glass transition, *Polym.*, **41**, pp. 2183-2201.
19. Aour, B., Zaïri, F., Gloaguen, J.M., Naït-Abdelaziz, M., Lefebvre, J.M., 2008, A channel angular extrusion of a polymer, *Int. J. Mech. Sci.*, **50**, pp. 589-602.
20. Yamaguchi, D., Horita, Z., Nemoto, M., Langdon, T.G., 1999, Significance of Adiabatic Heating in Equal-Channel Angular Pressing. *Scr. Mater.* **41**, pp. 791–796.
21. Aour, B., Zaïri, F., Gloaguen, J.M., Naït-Abdelaziz, M., Lefebvre, J.M., 2006, Numerical investigation on equal channel angular extrusion process of polymers, *Comput. Mater. Sci.* **37**, pp. 491-506.

A PROPOSITION OF PERITECTIC STRUCTURES AS CANDIDATES FOR THERMAL ENERGY STORAGE

F. Achchaq^{1*}, E. Palomo del Barrio¹.

¹ Université de Bordeaux, I2M-site ENSAM, Esplanade des Arts et Métiers, 33 405 Talence, France

*Corresponding author: Fax: [+33 5.56.84. 54.36](tel:+33556845436) Email: fouzia.achchaq@u-bordeaux.fr

ABSTRACT

Peritectic structures are proposed as candidates for thermal energy storage in solar power plants. According to the evolution of Concentrated Solar Plants (CSP) technologies, the development of a new technology for ultra-compact Thermal Energy Storage (TES) over an extended range of temperatures is required. Identification, synthesis, analysis and characterization of innovative advanced materials should allow reaching outstanding energy density, long term stability, reasonable investment and could also enhancing heat transfers. All these assets make the 'peritectics' very appealing potential candidates for heat storage. In this work, a theoretical study based on phase diagrams modeling is performed to investigate the possible use of binary peritectic structures. It has been shown that peritectics can provide significantly increased energy density compared to simple melting/solidification processes, mainly because they involve chemical reactions. These materials could hence represent a very innovative and promising route for ultra-compact heat storage over a wide range of temperatures [300 - 700°C].

NOMENCLATURE

ROMAN LETTERS	
T_p	Peritectic temperature
$\Delta T_{L \rightarrow P}$	Temperature between the liquidus and the solidus points
E_p	Energy density related to the peritectic reaction
$E_{L \rightarrow P}$	Energy density related to
ΔH	Enthalpy change related to the peritectic reaction
$\Delta H_{L \rightarrow P}$	Enthalpy change added between the liquidus and the solidus points
ACRONYMS	
CSP	Concentrated Solar Plant
LHS	Latent Heat Storage
PCM	Phase Change Material
TCS	Thermo-Chemical Storage
THS	Thermochemical Heat Storage

INTRODUCTION

Thermochemical Heat Storage (THS) is intensively studied because it is a nearly lossless way of storing energy when the chemical reaction materials are stored separately and because it could provide high values of volumetric energy density. Currently, THS can provide the highest heat storage followed by Latent Heat Storage (LHS) and then, by Sensible Heat Storage for the same amount of material [1]. Various kinds of gas-solid reaction systems are under investigation: dehydrogenation of metal hydrides (80-400°C), dehydration of metal hydroxides (250-800°C), decarboxylation of metal carbonates (100-

950°C), and thermal desoxygenation of metal oxides (600-1000°C) [2]. The enthalpy of reaction is usually extremely high, 400-1100 kWh/m³ depending on the temperature, which makes THS a very promising alternative. However, their feasible volumetric energy density is between 200 and 500 kWh/m³ only, because of several requirements such as the full interaction needed between the reactant materials or the impact of internal and external conditions of the thermochemical systems on the productivity rate, for instance [1]. THS development is, thus, still in a fundamental, laboratory stage and far from any proven design and material to be transferred to a relevant scale.

This work aims at participating to the development of a new kind of materials which are able to combine the melting/solidification processes with chemical reactions. Contrary to gas-solid reactions in which chemical reactants have to be separated, the liquid and the solid phases involved in peritectic formation separate and recombine by themselves. Moreover, the peritectic structures work at atmospheric pressure both in charge and in discharge. As a result, simple storage concepts, like one-single tank with storage material in bulk and embedded heat exchanger, could be applied.

CONCEPT AND EXPLANATION

The proposal is based on a ground-breaking idea consisting in using chemical compounds formed during the peritectic transition, in which thermal

energy is stored by two consecutive processes: a melting/solidification process and a liquid-solid chemical reaction. Thus, the so-called 'peritectics' present the major asset of combining sensible heat, latent heat and reversible chemical reaction.

Peritectic structures are formed by a reversible chemical reaction in which a liquid phase (L) reacts with a primary solid (α) on cooling to produce a new solid phase (β). Three classes of peritectic phase diagram have been identified based on the shape of the peritectic (β) solid-solution region [3] as shown in Fig. 1.

1. Type A system where the $\beta/\alpha + \beta$ solvus and the β -solidus have slopes of the same sign. The phase β formed during the peritectic reaction is a solid solution of one of the system components
2. Type B system where the slopes have opposite signs. As in Type A, the phase β formed is a solid solution of one of the system components
3. Type C system where the β -phase has a limited composition, referred as stoichiometric peritectic compound.

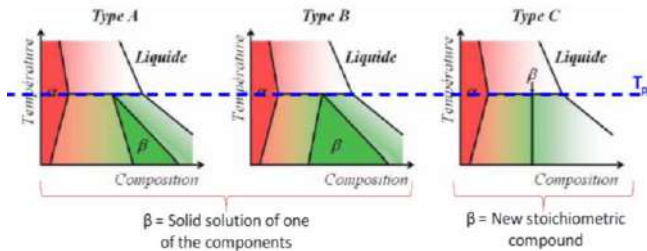


Figure 1

Types of peritectic structures [3]

The capacity of peritectic compounds to combine sensible, latent and thermochemical heat during their heating/cooling process at atmospheric pressure suggest a possibility to reach interesting values of associated energy density. Theoretically, the peritectic structure forms/melts at a defined temperature and the reversible chemical reaction occurs at the same defined temperature. The case of Type C systems suggest also that there is a possibility to manage with the new stoichiometric compounds in almost the same easy way as eutectic ones but with a higher potentiality. Fig. 2 sketches the phase diagram of a binary system (A/B) with one stoichiometric compound β formed during the peritectic transition $L + \alpha \rightarrow \beta$. It allows describing how energy is stored/delivered when heating/cooling the (A/B) system at the stoichiometric composition $C_{\beta p}$.

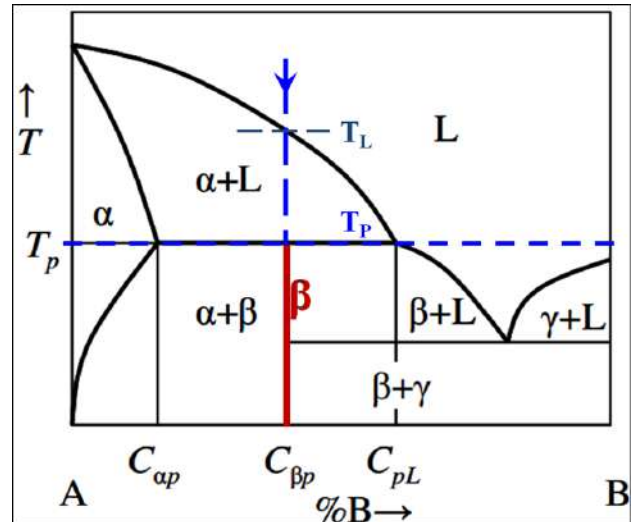


Figure 2

Phase diagram with one stoichiometric peritectic compound β

A more detailed description is provided in Fig. 3.

- On cooling (discharge process), the pro-peritectic phase α (s) starts to nucleate when the liquid phase reaches the liquidus temperature T_L , then it grows from T_L to T_p . At the peritectic temperature T_p , the remaining liquid phase reacts with α (s) to form β (s).
- On heating (charging process), the solid β (s) decomposes at temperature T_p into a liquid phase L and the solid α (s). Then, the solid α (s) melts also from temperatures T_p to T_L .

The energy is hence stored/delivered by two consecutive processes:

- i) an incongruent melting/solidification (latent heat) from T_p to T_L ,
- ii) and a liquid/solid chemical reaction (peritectic transition) at temperature T_p .

To summarize, a peritectic structure forms by means of at least three mechanisms: peritectic reaction, peritectic transformation and direct precipitation. The second mechanism is the slowest one because the transformation takes place by atoms diffusion through the peritectic solid. If the diffusion rate is small, for instance, less than 10^{-13} m²/s for substitutionally dissolved alloying elements in face-centered cubic metals, the time for peritectic transformation will be unrealistically large. The final structure obtained at the end of the cooling process will be out of equilibrium, with not complete annihilation of the pro-peritectic phase. Hence, the amount of energy delivered will be less than the theoretical value.

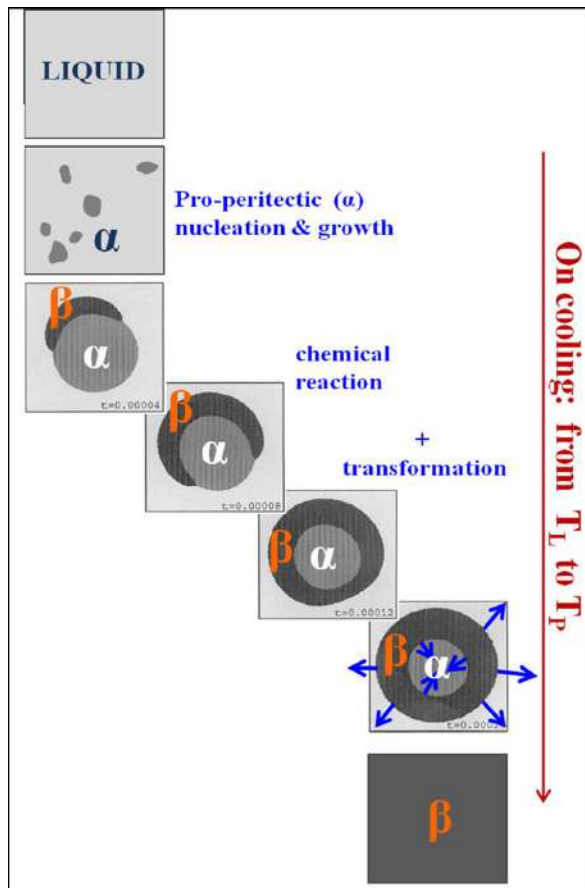


Figure 3

Different steps involved in peritectic transition on cooling

SCREENING METHODOLOGY

The screening focuses, on the one hand, on the 300-700°C temperature range, which allows covering a wide spectrum of significant applications. For instance, this range includes the interval 300-400°C which matches fully with the operating temperature range of Rankine cycle. The range above 400°C up to 700°C is also taken into account in order to propose, from the scientific viewpoint to begin, the potential materials with the suitable capacity to encounter the requirements of the CSP systems in development and with higher thermal efficiency (~650°C).

On the other hand, it focuses on the volumetric energy density superior to 200 kWh/m³ since the best THS systems today have an effective energy density between 200-500 kWh/m³ with an energy restitution preferably at constant temperature. Consequently, a review of the thermophysical properties of binary compositions with potential heat storage were performed. For this preliminary work, the multicomponent systems (ternary systems and more)

were not considered as well as those made of radioactive elements.

Software employed

FactSage 6.4® software has been used for an extensive search and selection of stoichiometric peritectic structures providing energy density superior to 200 kWh/m³ in the range of temperatures from 300°C to 700°C. This software, established on Calphad method [4], allows the calculation of optimized temperature-composition phase diagrams as well as the related thermodynamic functions and parameters using Gibbs free energies.

Out of 635 binary systems analyzed, 145 have at least one stoichiometric peritectic compound. The selection was performed within the same interval 300-1100°C performed by Kotzé with metallic PCMs in [5]. The review was performed using the set of evaluated and optimized thermodynamic databases for inorganic systems; in particularly molten salt, light metal alloy, oxide, high-T oxycarbonitride FactSage 6.4® databases.

Scientific criteria

Considering first the peritectic reaction step, the main thermophysical properties required for heat storage materials at constant temperature are:

i) the peritectic temperature T_p which must correspond to the working temperature of the in developing storage systems and ii) the gravimetric enthalpy change ΔH corresponding to the formation of the peritectic compound (β) at the defined temperature T_p . The conversion into the volumetric energy density E has been performed taking into account the density ρ such as $\rho = \rho_{min}(\rho_\beta, \rho_{L/\alpha})$ at the temperature T_p .

Then, considering the latent heat process related to the pro-peritectic phase formation from T_p to T_L , the associated volumetric energy densities $E_{L \rightarrow p}$ over a range of temperature $\Delta T_{L \rightarrow p}$ (from peritectic temperature to corresponding liquidus temperature) have been also calculated. In this latter case, the density ρ is such as $\rho = \rho_{min}(\rho_{L/\alpha}, \rho_L)$ at the liquidus temperature T_L . All parameters have been calculated assuming that the binary system solidifies under normal equilibrium conditions.

RESULTS AND DISCUSSION

The results of the preliminary screening of different chemical classes carried out are depicted in Fig.4. The full squares represent the peritectic compounds whilst the empty squares represent the eutectic ones.

Fig. 4 shows the enthalpy change versus temperature. Even if stoichiometric peritectics are not as common as eutectics, they appear in many binary systems. At first sight, the enthalpy change related to the peritectic reaction seems not to be so interesting and, hence the peritectic structures do not clearly distinguish from eutectics.

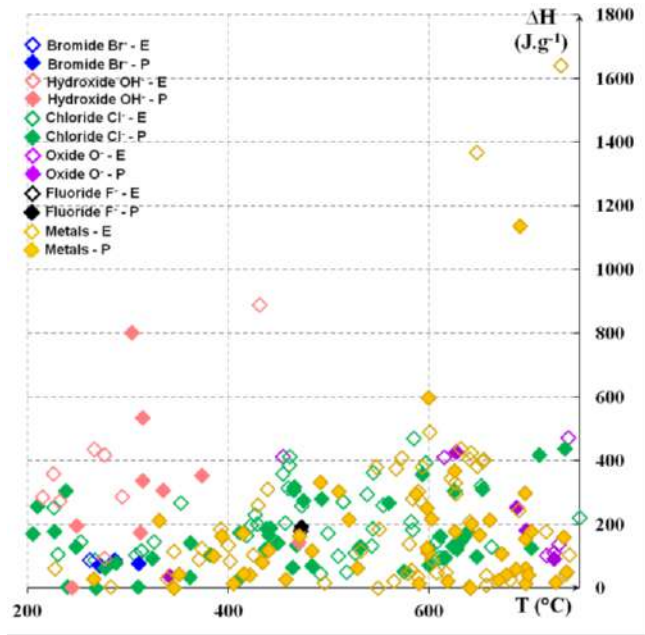


Figure 4

Peritectics map of enthalpy change vs. temperature during the peritectic reaction

The corresponding volumetric energy density E has been then calculated taking into consideration the density ρ of the studied system such as $\rho = \rho_{min}$ (ρ_{β} slightly below the peritectic temperature at the stoichiometric composition $C_{\beta P}$, $\rho_{L/\alpha}$ slightly above the peritectic temperature at the stoichiometric composition $C_{\beta P}$ (Fig. 2)) in order to avoid an overestimation. The map of energy density versus peritectic temperature presented in Fig.5 shows that peritectics can compete with eutectics from the effective energy density viewpoint. In this case, the energy density provided by the liquid/solid chemical reaction (peritectic transition) leading to the studied peritectic structures lies within the interval 200-400 kWh/m³ most of the time.

Therefore, the densities of the system around the transition line of interest (solidus line) are crucial since they inform on the minimum storage volume required.

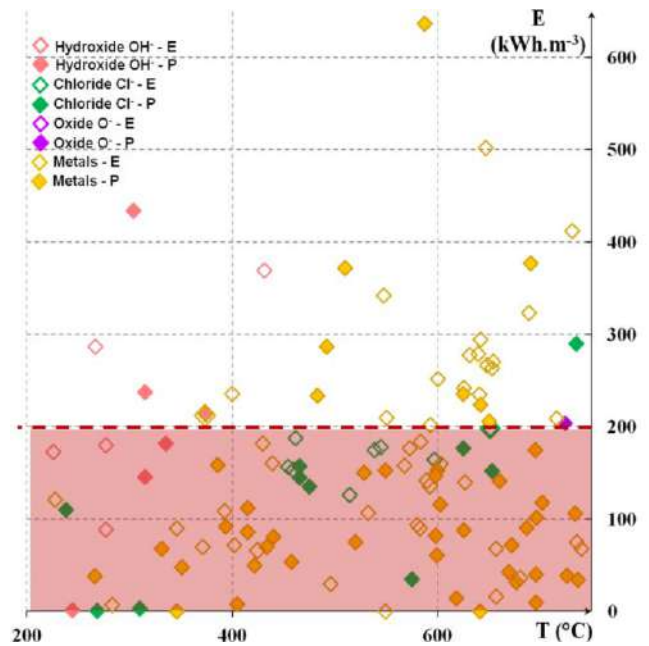


Figure 5

Peritectics map of the related energy density vs. temperature

A few peritectic structures of interest have been selected from the previous map and the effective energy density $E_{L \rightarrow P}$ due to the latent heat part have been calculated and added to the energy of the peritectic reaction. This time, the densities of the system around the liquidus line have been considered. For each binary system, both energy densities versus temperature are represented in Fig. 5.

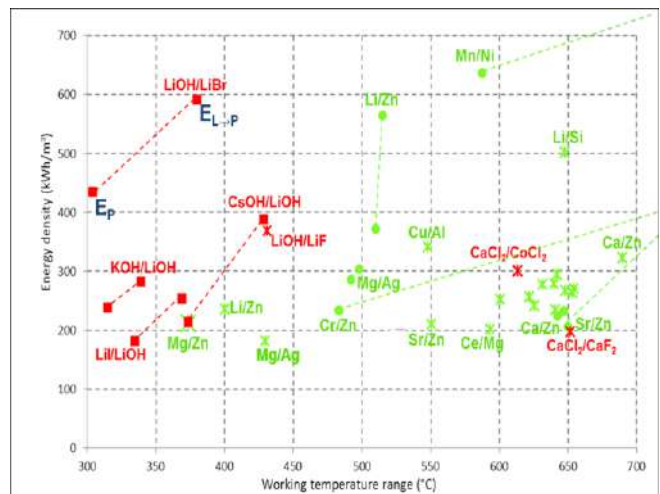


Figure 5

Peritectics map of the effective energy density vs. temperature taking into account the energy provided over the temperature range (peritectic temperature - corresponding liquidus temperature)

First, it can be noticed that the selected systems are mainly salt- and metallic-based alloys. Then, the

effective energy density reaches now the range of 400-650 kWh/m³ which means that these values become then quite as interesting as those of gas-solid reactions under investigation in the world; which make peritectics attractive for large-scale TES applications.

Table 1 and Table 2 give more detailed information on some peritectics of the map (Fig. 5) which could participate to develop the performances of CSPs intended for work in the field of high temperatures as it has been done in several works [6, 7].

Table 1

Peritectic temperature, enthalpy change and energy density of some binary systems related to peritectic reaction

Binary system A/B	T _p (°C)	ΔH (J.g ⁻¹)	E _p (kWh.m ⁻³)
LiBr/LiOH	303.90	803	434
KOH/LiOH	314.82	535	238
LiI/LiOH	334.93	308	182
CsOH/LiOH	373.63	354	214
Cr/Zn	483.12	118	234
Mg/Ag	491.94	332	286
Li/Zn	510.02	304	372
Mn/Ni	587.35	297	637
Ce/Mg	625.22	368	235
Ca/Zn	642.05	201	224
Sr/Zn	649.97	167	206
Li/Si	690.57	1136	377
CaCl ₂ /CaF ₂	734.94	438	290

Table 2

Temperature range and total energy density between the solidus and liquidus points of the same binary systems

Binary system A/B	ΔT _{L→P} (°C)	E _{L→P} (kWh.m ⁻³)
LiBr/LiOH	76	591
KOH/LiOH	24	283
LiI/LiOH	34	253
CsOH/LiOH	55	388
Cr/Zn	483	679
Mg/Ag	6	304
Li/Zn	5	565
Mn/Ni	493	1642
Ce/Mg	4	239
Ca/Zn	5	232
Sr/Zn	83	349
Li/Si	20	467
CaCl ₂ /CaF ₂	98	402

The proof of the concept has been achieved at the laboratory scale through the theoretical and

experimental study of Li₂K(OH)₃ peritectic structure, detailed in [8]. It has been shown experimentally that its onset temperature equals 312°C and its corresponding enthalpy change reaches 484 J/g. Moreover, the onset temperature of Li₂K(OH)₃ remains unchanged over the 100 cycles whilst the composite enthalpy change is improved and tends even to increase with cycling.

CONCLUSION

Peritectic structures can provide effective volumetric energy density comparable and even higher to that of the best solid-gas reactions under development. Moreover, as the expected volumetric energy density is much higher than that of currently used phase-change materials, the investment cost should be lower than that of latent heat storage technologies and probably close to that of the cheapest sensible heat storage systems. Contrary to solid-gas reactions, peritectic structures do not require complex storage system technology. They offer, therefore, a chance to achieve compact TES at attractive investment cost.

ACKNOWLEDGMENTS

The authors would like to thank all partners involved in TESLAB/ABENGOA SOLAR for their financial support.

REFERENCES

1. Aydin D., Casey S.P., Riffat S., 2015, The latest advancements on thermochemical heat storage systems, *Renewable and Sustainable Energy Reviews*, **41**, pp.356-67.
2. Pardo P., Deydier A., Anxionnaz-Minvielle Z., Rougé S., Cabassud M., Cognet P., 2014, A review on high temperature thermochemical heat energy storage, *Renewable and Sustainable Energy Reviews*, **32**, pp.591-610.
3. St. John D. H., Hogan L. M., 1987, *Acta Metall.* 35 171; Titchener A P, Spittle J A 1974 *Met. Sci.* 8 112]
4. Saunders N., Miodownik A.P, 1998. *CALPHAD Calculation of Phase Diagrams-A comprehensive guide*. Pergamon Press
5. J.P. Kotzé, T.W. von Backstrom, P.J. Erens, 2013, High temperature thermal energy storage utilizing metallic phase change materials and metallic heat transfer fluids., *ASME: Journal of Solar Energy Engineering*, **135**, 035001, pp.16.
6. Kenisarin M.M., 2010, High-Temperature phase change materials for thermal energy

- storage, *Renewable and Sustainable Energy Reviews*, **27**, pp.724-737.
7. Liu M., Steven Tay N.H., Bell H., Belusko M., Jacob R., Will G., Saman W., Bruno F., 2016, Review on concentrating solar power plants and new developments in high temperature thermal energy storage technologies, *Renewable and Sustainable Energy Reviews*, **53**, pp.1411–1432.
 4. 8. F. Achchaq, E. Palomo del Barrio, A. Renaud, S. Ben-Khemis, 2015, Characterization of $\text{Li}_2\text{K}(\text{OH})_3$ as material for thermal energy storage at high temperature, The 13th International Conference on Energy Storage Greenstock, China.

BUBBLE AGITATION AS A NEW LOW-INTRUSIVE METHOD TO CRYSTALLIZE GLASS-FORMING MATERIALS

A. Godin^{1*}, M. Duquesne², E. Palomo del Barrio³, F. Achchaq³, P. Monneyron³.

¹ CNRS, Esplanade des Arts et Métiers, 33 405 Talence Cedex, France

² Institut National Polytechnique de Bordeaux, 16 avenue Pey Berland, 33607 Pessac Cedex, France

³ Université de Bordeaux, Esplanade des Arts et Métiers, 33 405 Talence Cedex, France

*Corresponding author: Fax: +33 5.56.84.54.36 Email: alexandre.godin@u-bordeaux.fr

ABSTRACT

Xylitol is a very promising Phase Change Material (PCM) for long-term thermal energy storage at low to medium temperatures due to its low melting temperature, its high energy density, its high and stable undercooling allowing long-term storage with reduced thermal losses. However, the activation of the energy discharge process (crystallization activation) is difficult and the subsequent crystallization rates (discharge powers) are very low.

To overcome such problems, a simple and efficient technique is proposed. It consists in bubbling undercooled Xylitol using a gas until it crystallizes and the recalescence phase is completed. The mechanisms activating the crystallization are presented in this paper and the bubbling performances are experimentally investigated.

NOMENCLATURE

ROMAN LETTERS

C_p	Xylitol specific heat
f_s	Solid fraction
H	Melting enthalpy
L_m	Xylitol latent heat
T	Temperature of the melt at time t
T_0	Initial temperature of the melt (also referred as starting/working temperature)
T_∞	Room temperature, air inlet temperature
V	Volume of the melt

ACRONYMS

<i>PCM</i>	Phase Change Material(s)
<i>SA</i>	Sugar alcohols
<i>ca</i>	Circa (approximately)

INTRODUCTION

Considering the major current energy and economic issues, the development of new PCM for solar seasonal energy storage, matching the building applications requirements, constitutes a technological challenge. The ideal PCM must have a melting temperature inferior to 100°C, a high energy density (> 100 kWh.m⁻³) for the compactness of the storage system and a large undercooling in order to limit heat losses over the long term storage. It must also be

cheap, stable, non-toxic and extracted from renewable sources. Currently, many PCM are available in the market for thermal energy storage applications [1,2] but only salt hydrates fit with long-term storage. Indeed, their stable and high undercooling allows reducing thermal losses. Compared to them, SA present several advantages like no separation, no segregation, no corrosion etc. Among SA, Xylitol has a high potential: its melting point is inferior to 95°C which allows using cheap solar collectors; its latent heat is superior to 263 J.g⁻¹ and its total energy density is 4-5 times higher than that of water (110-150 kWh.m⁻³ whereas it is approximately 30 kWh.m⁻³ for water on a seasonal basis). Moreover, Xylitol has a high and very stable undercooling, allowing long-term storage with limited thermal losses and negligible risk of spontaneous discharge. Finally, it has an acceptable cost (< 3 €/kg) and is available in the market.

Unfortunately, the discharge process of Xylitol is difficult because of its high viscosity and the subsequent crystallization rates are very low. In this work, different techniques to crystallize Xylitol have been considered. Local cooling fails to trigger nucleation because the activation energy for atoms diffusion and rearrangement at the solid-liquid interface is very high in Xylitol. Seeding allows activating Xylitol crystallization, even in cases with very high undercooled melts. However, the effect of

seeding on crystallization is too local and the subsequent crystal growth rates are too low for the application. This technique lead to low heat release rate and too long discharge times. High-power ultrasounds (450 W) also allow crystallizing Xylitol. However, the crystallization rates are also too low for this technique to become appropriate at the storage system scale. Solvents addition does not contribute to accelerate Xylitol crystallization [3]. Mechanical agitation could be a solution to discharge the storage system when necessary and at appropriate speeds. However, this intrusive technique would require a specific reactors design leading to a significant extra-cost.

In this paper, we propose bubbling as a simple and efficient technique to activate Xylitol crystallization and to allow high enough crystal growth rates. As far as we know, the use of a bubbling technique to activate the nucleation of undercooled melts and to accelerate their crystallization rates has never been studied, despite the extensive researches on bubble columns in the last few decades (e.g. recent reviews [1,2]) or the use of bubbling to enhance paraffin heat transfer [4].

EXPERIMENTAL TECHNIQUES

Sample: Xylitol was purchased from Roquette (batch E089X, purity 98.43%).

Experimental means: The used liquid/gas reactor is a cylindrical glass vessel of 85 mm of diameter and 105 mm of height, equipped with thermocouples. It is filled with melt Xylitol up to 60 mm height (Fig.1). Air bubbles are generated at the bottom of the vessel by a single tube connected to a pump (tube inner diameter: 3 mm).

Experiments: Two kinds of experiments were performed. In all the performed experiments, melt Xylitol is conditioned as follows: 100°C overnight in an oven to melt it, then, cooled down to the working temperature during 1h30 to 2h. Once the working temperature reached, bubble agitation is started. Initial temperature of the melt (T_0) varies from 34°C to 71°C. The air is injected at room temperature (air inlet temperature: $T_\infty \sim 25^\circ\text{C}$). The air injection flow rate is $Q = 80$ l/h.

First experiments consist in observing and reaching an overall understanding. Once it starts, the bubbling is observed using a CDD camera (Genie HM1024: image capture rate from 0.1 to 117 fps in 1024 x 728 active resolution, Fig.1). In the second kind, the experiments are carried out using the exact same means, sample and protocol except that, this time, the

glass vessel is thermally insulated. This insulation prevents to observe Xylitol behavior during bubbling. The set-up is completed with two thermocouples located close to the wall of the vessel, one in the vicinity of the air inlet and the other one at the opposite side. Xylitol thermal response during bubbling is recorded by the two thermocouples previously mentioned. These experiments allow studying bubbling performances.

OVERALL VIEW OF THE CRYSTALLIZATION PROCESS

Numerous experiments were performed in order to get an overall view of the crystallization process by bubbling. The pictures in Fig.1 show (from the left to the right side) the activation and progress of the crystallization in experiments carried out at $T_0 = 75^\circ\text{C}$.

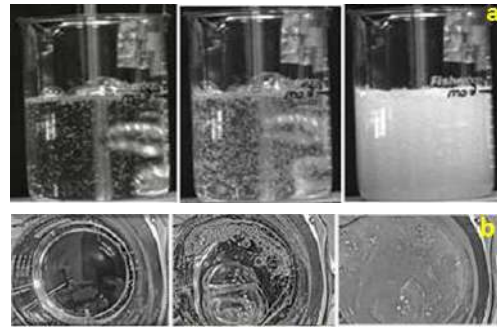


Figure 1

Snapshots at different times of the Xylitol crystallization process activated by air bubbling
a) side view; b) top view.

Whatever the initial thermal conditions, the crystallization process has the following general characteristics:

- Bubbles are formed at the submerged orifice of the tube. They grow first, detach from the orifice and rise in the melt up to the liquid free-surface. The bubbles generation is periodic and induces an oscillatory motion of the liquid, with a major circulation cell in the entire column.

- At the liquid free-surface, the bubbles burst and generate daughters bubbles (Fig.1). Part of these bubbles are caught by the fluid and entrained by the flow cell (Fig.2a). As it can be seen in Fig.1, the small bubbles are dispersed within the liquid and their amount increases with time.

- After some stirring time of the mixture "bubbles/melt Xylitol", the latter starts to crystallize. Crystallization begins on the bubble surface (Interface air/Xylitol), then progresses in the outward direction forming a spherical solid shell. Fig.2c shows the reactor at a quite advanced stage of

the crystallization process, where numerous spherical solid particles can be observed in suspension. A picture of one of these solid particles (~1 mm-diameter) is shown in Fig.2b. A magnified image of the cross-section of this particle is in Fig.2d. A hole can be noticed in the center of the solid sphere, obtained *via* the crystallization on the bubble surface.

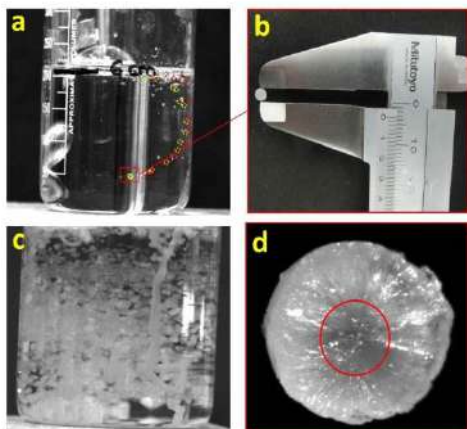


Figure 2

Pictures of Xylitol crystallization:

- a) liquid circulation cell dragging small air bubbles;
- b) solid particle formed by crystallization on the bubbles surface;
- c) numerous solid particles observed in suspension at an advanced stage of the crystallization process; and
- d) magnified image of the cross-section of a solid particle.

As mechanical agitation, stirring by bubbling is able to activate the nucleation of Xylitol in extended and highly spatially resolved areas. The efficiency of the crystallization process will be obviously dependent on the number of nucleation produced sites as well as the extent and the homogeneity of their dispersion within the melt. Besides, this technique is a low intrusive technique and, consequently, easy to implement in standard storage containers.

BUBBLING PERFORMANCES ANALYSIS

A typical thermal response of Xylitol during bubbling is depicted in Fig.3.

Three different periods can be clearly distinguished:

- The induction period, from the beginning of bubbling to the beginning of crystallization. In an adiabatic reactor, the temperature of the melt should be constant during this period. In practice, it slightly decreases due to thermal losses which both occur, by conduction through the vessel wall and by convection due to air bubbling.
- The recalescence period, during which Xylitol crystallizes and its temperature rises. In a perfectly insulated system, Xylitol should reach the

melting point and the crystallization process should stop at that moment. However, due to thermal losses, the maximum temperature reached by Xylitol is slightly inferior to the melting point and the crystallization can progress beyond this point. From now, we consider that the reach of Xylitol maximum temperature corresponds to the end of the recalescence period.

- The end-period, during which crystallization (if any) is driven by heat extraction due to thermal losses.

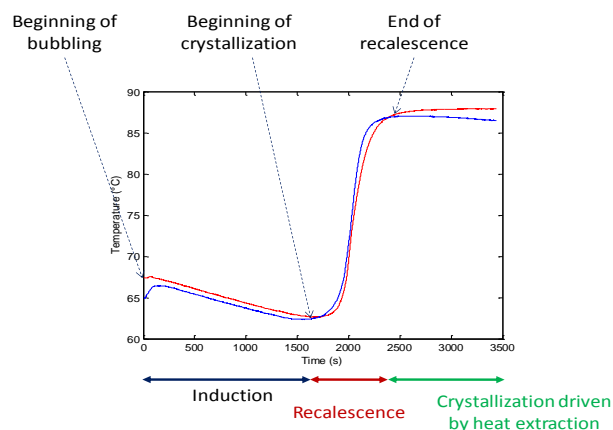


Figure 3

Xylitol thermal response typically observed during bubbling.

Eight experiments were carried out at initial temperatures ranging from 34°C to 71°C. Xylitol thermal behaviors recorded in these experiments are represented in Fig. 4a. The starting point of the curves represents the end of the induction period (time corresponding to the crystallization beginning). The legend of the curves indicates the melt temperature (T_0) at the crystallization beginning. Xylitol course on an enthalpy-temperature chart is depicted in Fig.4b. The continuous black line represents Xylitol enthalpy function by melting. Xylitol enthalpy function has been calculated from measurements of specific heat, latent heat and melting point (Eq 6&7 in Appendix). The enthalpy of undercooled Xylitol is represented by the discontinuous black line. Colored lines correspond to Xylitol enthalpy evolution during bubbling in the different experiments carried out (one curve by experiment). The crystallization beginning is indicated by a circle on the discontinuous black line. In a perfectly insulated system, the trajectory of the melt on the enthalpy-temperature chart must be a horizontal line (constant enthalpy) joining the crystallization temperature to the melting point. Because of the thermal losses, the

observed trajectories are not horizontal lines but show a slight decrease of enthalpy with temperature. Moreover, the maximum temperature achieved is below the melting point. The maximum achieved temperature tends to decrease when the initial undercooling of the melt increases. This should indicate that thermal losses are mainly due to bubbling. Indeed, considering that the air is injected at room temperature and that the residence time of primitive bubbles increases with the viscosity of the melt, the thermal losses are expected to be higher in the experiments carried out at higher undercooling degree.

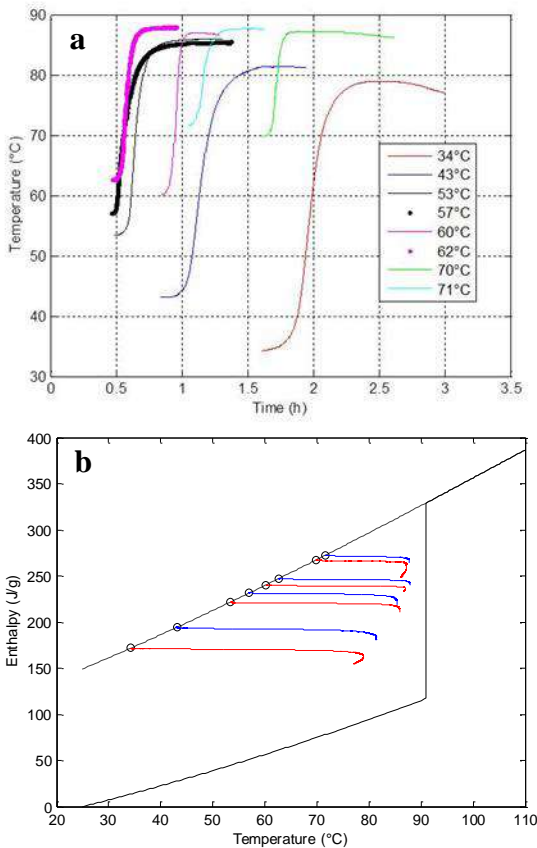


Figure 4

- a) Xylitol thermal evolution during the different bubbling experiments (one curve by experiment); b) Xylitol course on the enthalpy-temperature chart.

From the recorded temperature data, the evolution of the solid fraction over time as well as the total crystallization rate can be estimated (Eq 1-5 in Appendix). They are depicted in Fig.5 a&b. The crystallization progresses slowly at the very beginning, then accelerates up to a maximum crystallization rate, and the rhythm of crystal production reduces afterwards. Beyond the recalescence period, the crystallization rate is such

that power delivered by solidification equals the thermal losses of the system. The maximum value of the observed crystallization rates ranges between *ca* 3 min⁻¹ to *ca* 6 min⁻¹.

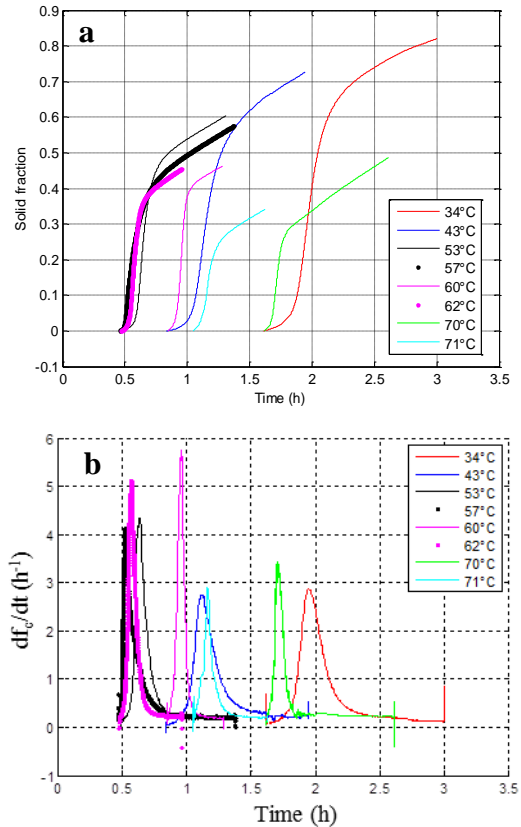


Figure 5

- a) Time evolution of the solid fraction during the different bubbling experiments (one curve by experiment); b) time behavior of the total crystallization rate during the same experiments (one curve by experiment).

In Fig. 6a is represented the mean crystallization rate (Eq. 8 in Appendix) observed in the experiments carried out. The highest mean crystallization rate is superior to 0.02 min⁻¹ and is obtained at approximately 60°C. The mean crystallization rate initially increases with the undercooling, reaches a maximum and then slows down as the temperature is further decreased. This behavior is in agreement with the measurements of Xylitol crystal growth carried out under isothermal conditions using optical microscopy (Fig 6.b, see also ICOME 2016, M. Duquesne). The similitude between the shape of the curves representing the variation of the mean crystallization rate in the reactor and the growth velocity of the crystals of xylitol as a function of the temperature support the hypothesis that once nucleation on the bubble surface occurs, subsequent

crystal growth is exclusively determined by the Xylitol properties and the local undercooling.

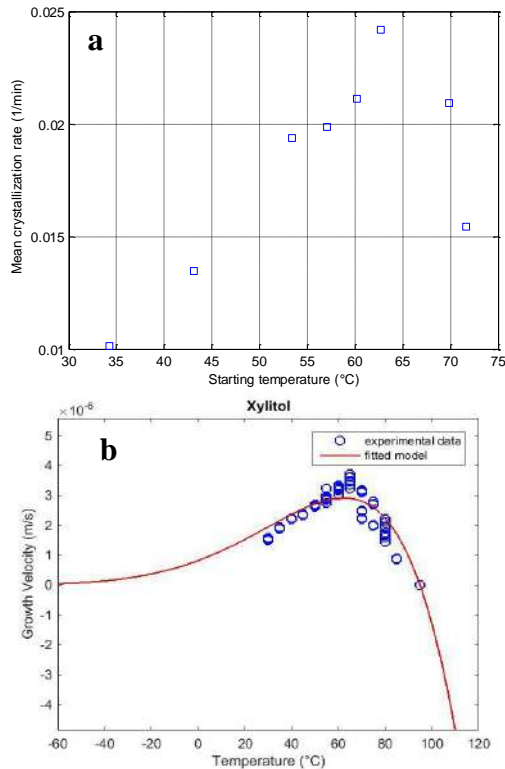


Figure 6

a) Mean crystallization rate of Xylitol in the reactor as a function of the starting temperature; b) growth velocity of Xylitol crystals measured under isothermal conditions by optical microscopy.

Xylitol crystallization is studied in a thermally insulated reactor which allows quantifying bubbling efficiency through key parameters such as the induction nucleation and recalescence times. They are represented in Fig.7 as a function of the starting temperature T_0 . The symbols represent the measured values whereas continuous lines are polynomial fits allowing highlighting trends. The recalescence time progressively decreases with the starting temperature, going from *ca* 75 min at the lowest temperature to *ca* 15 min at the highest one. This behavior is in agreement with the fact that the amount of solid phase produced during the recalescence increases with decreasing temperature (see enthalpy chart in Fig. 4.b).

The induction time ranges from *ca* 100 min to *ca* 30 min. Contrary to the recalescence time, the induction time shows a minimum at *ca* 55°C.

This behavior is a bit surprising. Indeed, the melt viscosity being lowered, a decrease in induction time should be expected with an increase in temperature.

However, when the starting temperature of the melt increases, the heat exchange between the injected air and the melt is enhanced because the size of the bubbles, for the same gas flow rate, diminishes.

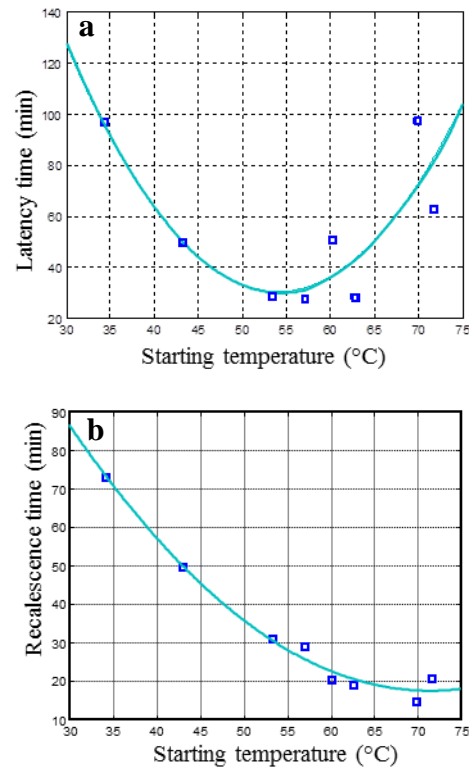


Figure 7

a) Induction time and b) recalescence time as a function of the starting temperature. Measurements (symbols) and regression lines (continuous lines)

CONCLUSION

In this paper, bubbling is presented as an innovative and efficient technique to activate the crystallization of highly viscous undercooled Xylitol. This low intrusive technique is easy to implement in standard storage containers.

It has been shown that Xylitol crystallization occurs on the surface of the small bubbles generated at the liquid surface when primitive bubbles burst. Once dispersed within the reactor by the liquid flow, they act as nucleation sites. The bursting of the primitive bubbles at the free liquid surface with production of daughters is hence a necessary condition for Xylitol crystallization. Besides, the efficiency of the crystallization process will be obviously dependent on the number of nucleation produced sites as well as the extent and the homogeneity of their dispersion within the melt.

Using bubbling techniques allows reaching 3 to 6 min⁻¹ as maximum crystallization rates. The highest mean crystallization rate is superior to 0.02 min⁻¹ and is obtained at approximately 60°C. Besides, it has been noticed that the observed crystal growth rates are exclusively determined by the local undercooling and Xylitol properties. The recalescence time goes from *ca* 75 min at 34°C temperature to *ca* 15 min at 71°C. The induction time ranges from *ca* 100 to 30 min (at *ca* 55°C). Storage at approximately 50-60°C could provide the best balance between the induction time, the crystallization rates and the maximum reachable temperature.

Additional research carried out on bubbling is required to pave the way for bubbling conditions optimization.

ACKNOWLEDGMENT

The authors acknowledge the financial support of the European Commission for subsidizing FP7 SAM.SSA Project.

REFERENCES

1. Agyenim, F., Hewitt, N., Eames, P., and Smyth, M., 2010, A review of materials, heat transfer and phase change problems formulation for latent heat thermal energy storage systems, *Renewable and Sustainable Energy Reviews*, **14**, pp.615-628.
2. Cabeza, L.F, Castell, A., Barreneche, C., de Garcia, A., Fernandèz, A.I, 2011, Materials used as PCM in thermal energy storage in buildings: a review, *Renewable Sustainable Energy Rev*, **15** (3), pp.1675-1695.
3. Seppala, A., Merilainen, A., Wikstrom, L., Kauranen, P., 2010, *Experimental Thermal and Fluid Science*, **34**, pp.523-527.
4. Velraj, R., Seeniraj, R.V., Hafner, B., Faber, C., Schwarzer, K., 1999, Heat transfer enhancement in a latent heat storage system, **65** (3), pp.171-180.

APPENDIX: DATA TREATMENT

We assume that the temperature of the melt is uniform at every time. In such condition, the energy balance within the melt during the induction period can be written as:

$$V\rho c_p \frac{dT}{dt} = -hA(T - T_\infty) \Rightarrow \frac{dT}{dt} = -k(T - T_\infty) \text{ with } k = \frac{hA}{V\rho c_p} \quad (1)$$

where ρc_p is its thermal capacity and hA is the thermal losses coefficient. According to Eq.1, the thermal behavior of the melt during the induction period can be written as:

$$(T - T_\infty) = (T_o - T_\infty) \exp(-kt) \quad (2)$$

where the coefficient k is determined fitting Eq.2 to experimental data.

During the recalescence period, the energy balance of the melt is given by the equation:

$$V\rho \frac{dH}{dt} = -hA(T - T_\infty) \quad (3)$$

Considering the relationship between enthalpy, temperature and solid fraction, Eq.3 becomes:

$$V\rho c_p \frac{dT}{dt} - V\rho L_m \frac{df_s}{dt} = -hA(T - T_\infty) \quad (4)$$

We can hence write:

$$\frac{df_s}{dt} = \left(\frac{c_p}{L_m} \right) \left[\frac{dT}{dt} + k(T - T_\infty) \right] \quad (5)$$

Once parameters c_p , L_m and k are known, the crystallization rate (df_s/dt) and the solid fraction can be estimated by Eq.5.

Xylitol enthalpy function has been calculated from measurements of specific heat, latent heat and melting point as follows:

$$H(T) = \begin{cases} c_{p(s)}(T - T_{ref}) & T < T_m \\ c_{p(s)}(T - T_{ref}) + L_m & T = T_m \\ c_{p(s)}(T - T_{ref}) + L_m + c_{p(l)}(T - T_{ref}) & T > T_m \end{cases} \quad (6)$$

with:

$$c_{p(s)} = -3.9 \times 10^{-6} T^2 + 5.953 \times 10^{-3} T + 1.267 \quad (J / g / ^\circ C)$$

$$c_{p(l)} = -2.345 \times 10^{-5} T^2 + 6.547 \times 10^{-3} T + 2.578 \quad (J / g / ^\circ C)$$

$$T_{ref} = 25^\circ C, T_m = 91^\circ C, L_m = 267 J / g$$

The enthalpy of undercooled Xylitol is given by:

$$H(T) = c_{p(s)}(T - T_{ref}) + L_m + c_{p(l)}(T - T_{ref}) \quad T < T_m \quad (7)$$

The mean crystallization rate is defined as:

$$\text{Mean Crystallization Rate} = \frac{f_s(t_{end})}{\Delta t} \quad (8)$$

where $f_s(t_{end})$ represents the solid fraction in the reactor at the end of the recalescence period and Δt is the duration of the recalescence.

REFLECTION HIGH-ENERGY ELECTRON-DIFFRACTION AND PHOTOEMISSION STUDY DURING MOLECULAR-BEAM-EPITAXY GROWTH OF INAS(001) $\alpha_2(2 \times 4)$ SURFACE

H. Khachab^{1,2*}, A. Nouri^{2,3}, Y. Abdelkafi^{1,2}, M. Barhmi²

1:LPDS laboratory, University TAHRI Mohamed – Béchar, BP 417 Béchar, Algeria

2: Department of Sciences of Matter, Faculty of Sciences exact, University of TAHRI Mohamed, Bechar,, BP 417 Bechar, Algeria

3: LabMat Laoratory, BP 1523 EL-M'naouer Oran 31000 Algeria

* Corresponding author: Fax +(213)49238993, Email : khachab_hamid_2000@yahoo.fr

ABSTRACT

The Molecular Beam Epitaxy (MBE) is a growth technique to manufacture electronic devices with excellent quality. In sprint of some minor disadvantages; MBE is one of recent and promising of epitaxial growth techniques. The advantage of this growth technique is based on its ability to control and possibility of following the surface growth in real time. The Reflection High Energy Electron Diffraction (RHEED) intensity is used to sample the surface structure, it allows a very good control of the thicknesses of very thin layers with excellent quality. Our study focuses on the modeling and simulation of the epitaxial growth by Molecular beam epitaxy of InAs using the Kinetic Monte Carlo methods (KMC). The in situ characterization (in real time) was achieved by Photoemission and RHEED simulation

The studied model treats the growth of In and As species including different microscopic processes; absorption, desorption, diffusion, incorporation.

NOMENCLATURE

E: The diffusion barrier energy(eV)

R: The hopping barrier energy ()

v: The atom vibration (s-1)

n: nearest – neighbor.

Es: The substrate barrier (eV)

En: The energy contribution from each nearest – neighbor (eV)

I_{RHEED} : The RHEED intensity (ua)

θ_n : The rate coverage (ua)

$h_i(t)$: The height of the site (i,j)

$\sigma_h(t)$: The degree of surface roughness (ua)

INTRODUCTION

MBE is a versatile crystal growth technique for growing thin epitaxial structures made of semiconductors, metals or insulators.

This technique is particularly suitable for III-V and II-VI semi-conductors such as the GaAs, it also used

for stack different materials, with an excellent quality crystalline [1-3].

Since last three decades the study of the InAs (001) surface have been make a lot of interest by several experimental and theoretical studies because it is the basic element in the structure of the most part of the electronic components multilayers [4, 5, 6].

The objective of our work is the modeling and the simulation of InAs (001) $\alpha_2(2 \times 4)$ reconstructed surface based on the model of the reconstruction GaAs(001) $\beta_2(2 \times 4)$ [4.6].

This model includes all the microscopic details such as: the atomic process of the island growth, surface reconstruction, the zinc blende structure and the different kinetic properties of the growth [4, 8].

In this simulation, we discuss the results of the InAs homoepitaxy and the observations during growth using RHEED and photoemission simulation [6, 7, 9].

MODELING OF GAAS (001) $\alpha_2(2 \times 4)$ RECONSTRUCTED SURFACE

GaAs(001) $\beta_2(2 \times 4)$ reconstructed surface model

The GaAs (001) surface is one of the most studied semiconductor surfaces, it has attracted much interest for both experimental and theoretical studies [8].

The composition of the grown epilayer and its doping level depend on the relative arrival rates of the constituent elements and dopants, which in turn depend on the evaporation rates of the appropriate sources. The growth rate of typically $1 \mu\text{m/h}$ (1 monolayer/s) is low enough that surface migration of the impinging species on the growing surface is ensured. Consequently, the surface of the grown film is very smooth. [1-3]

Itoh [4] presented a simulation model based on the zinc blend (001) structure for homoepitaxial GaAs (001) growth.

Both in thermodynamic equilibrium and over a wide range of growth conditions, the GaAs (001) surface forms the $\beta_2(2 \times 4)$ reconstruction, each (2×4) unit cell is built up from two (2) As dimers and two (2) missing dimers in the top most layer and missing Ga pair in the second Fig. 1 [4-9].

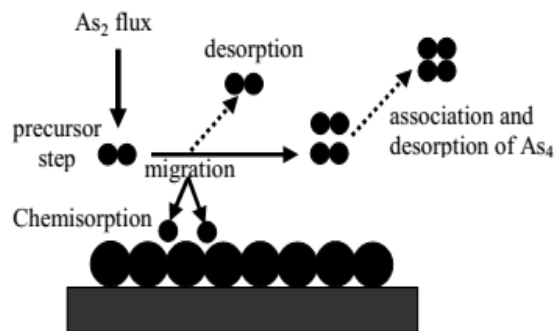


Figure 1
GaAs surface growth [4,5]

The kinetic process of Itoh model included in the simulation is as follows [6, 8-16].

1. Deposition randomly of Ga atoms.
2. Diffusion of Ga atoms on the surface.
3. Incorporation of Ga adatoms; if a Ga adatom reaches a strongly bound site.
4. As₂ flux into the precursor state become As₂*.
5. Absorption of As₂ into surface sites as As₂ dimers.

6. Desorption of As₂*; there are two As₂* desorption events with different rates in our model, depending on the chemical environment, the As₂ is bounded by:
 - a) Desorption into the vacuum.
 - b) Desorption from a surface site into the precursor state.
7. Diffusion of As monomers after the breaking of the As – dimer bond

Simulation of InAs $\alpha(2 \times 4)$ reconstructed surface

The observations obtained by STM show that the surface of InAs(001) is similar to a structure of GaAs(001). This structure consists of two atomic forms; the first is the regular reconstruction $\beta_2(2 \times 4)$, while the other is composed by Frank (simple lines) of the dimers of arsenic [5].

Yamaguchi and Horikoshi have proposed a new atomic structure called $\alpha(2 \times 4)$ which is represented on the Figure 2.

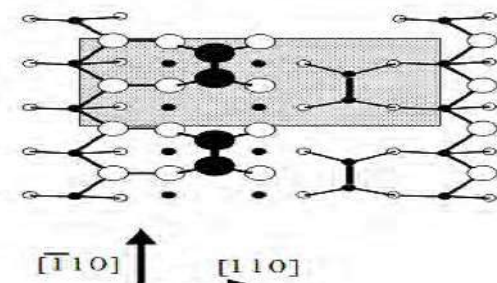


Figure 2
Side and plan views of the $\alpha_2(2 \times 4)$ reconstruction of InAs (001) [5]

In this approach, we have used the $\beta_2(2 \times 4)$ reconstructed model to simulate InAs homoepitaxial growth with support of some variations, such as the arsenic dimers and the interaction energies [4-6, 9]

KINETIC MONTE CARLO

About 30 years ago, KMC simulation started to be used for the study of kinetic processes (Binder 1979, Binder and Kalos 1979). The aim of KMC is to reproduce faithfully non-equilibrium or relaxation processes [8-11]. KMC simulation has been widely used in modeling epitaxial crystal growth. This is because it allows easy implementation of a wide range of atomistic kinetic processes whose rates can be determined from first principles [8]. The KMC simulation of homoepitaxy GaAs (001) growth has been based on simple cubic solid – on – solid (SOS) model. This model has explained a number of surface morphologies [6]. The key parameter in the

KMC method is the hopping barrier energy R of each atom from a site to a neighbor site on the surface:

$$R = \nu e^{-\frac{E}{k_n T}} \tag{1}$$

Where E is the diffusion barrier energy [13]. E depends only upon the initial nearest-neighbor environment of the migrated atom.

$$E = E_s + nE_n \tag{2}$$

E_s : The substrate barrier and E_n the contribution from each nearest – neighbor bond formed parallel to the substrate.

In the conventional used SOS model, surface adatoms can have a maximum of five bonds, one to the underlying atom and four to nearest neighbor atoms in the surface plane, so can take any value between 0 to 4 [6, 8-12].

The principle of calculation routine is shown in the chart below Fig.3

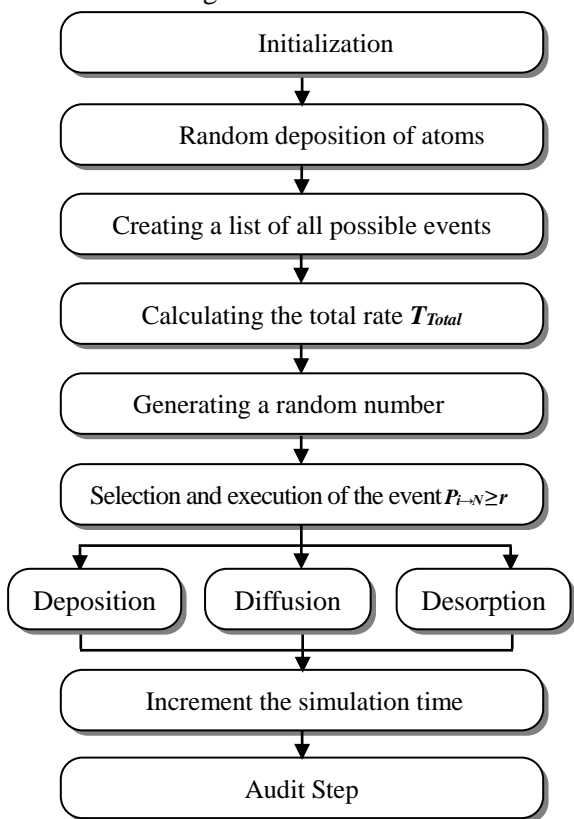


Figure 3

Principle of calculation on KMC simulation of InAs (001) α_2 (2x4) reconstructed surface [9, 12].

RESULTS AND DISCUSSION

Surface Morphology

The results of KMC simulations of InAs(001) α_2 (2x4) surface morphology are obtained for typical condition in MBE growth (flows In=0.1 ml/s, flux As=0.4 ml/s and T=385°C). The Figure 4 represents the evolution as a function of time of the morphology of InAs(001) α_2 (2x4) reconstructed surface in a cluster of (100x100) atoms during deposition of two bilayers (3 monolayers).

White (grey, black) circles denote layer number n ($n+1, n+2$); i.e. In (As, In) atoms.

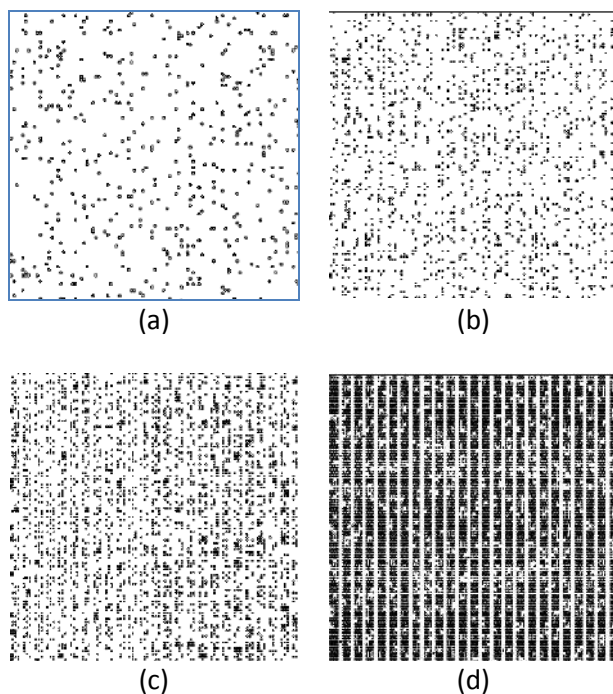


Figure 4

Surface morphology of InAs cluster of dimension (100x100) obtained by a KMC simulation for different values of coverage. (a) In deposition, (b) As deposition, (c) In and As diffusion and (d) In diffusion

The reconstruction α_2 (2x4) of InAs(001) begins by the initial deposition (random) of the In Atoms (Fig 4(a)). Then, the deposition of the As atoms Fig 4 (b). In the Fig (c), we show the diffusion of In and As atoms (dimer pair As). Finally in Fig 4 (d), the edges creation is very remarkable, and this becomes even clearer for the coverages greater than 40% [9].

In situ simulation

The important advantage of MBE is the in situ monitoring possibility during growing.

To examine the validity of the KMC results, a simulation in situ RHEED and photoemission simulations were carried out. These two techniques are very used to follow the evolution of the surface morphology during growth.

RHEED intensity: RHEED is one of the most powerful tools used to see the flatness and atomic structure of the surface during growth. Furthermore, intensity oscillation of the RHEED signal accurately measures the growth rate in Å/sec [13-15].

In the case of a two-dimensional (2D) growth mode, the main information provided by the analysis of the RHEED pattern are the surface reconstruction and the growth rate [6, 9, 15].

The RHEED intensity is given by [13, 14]:

$$I_{RHEED} = \left| \sum_n (\theta_n - \theta_{n+1}) (j)^n \right|^2 \quad (3)$$

Where θ_n , θ_{n+1} are the rate coverage of even (In) and odd (As) layers (respectively).

Under such condition, the specular beam intensity of RHEED is inversely related to the degree of surface roughness which is calculated by [16]:

$$\sigma_h(t) = \sqrt{\left(\frac{1}{N} \sum_i (h_i(t) - \langle h(t) \rangle)^2 \right)} \quad (4)$$

Where N is the number of lattice sites, h_i is the height of the site (i,j) and $\langle h(t) \rangle$ is the average height of the atoms expressed in monolayer unit and given by:

$$\langle h(t) \rangle = \frac{1}{N} \sum_i h_i(t) \quad (5)$$

The Figures 5 and 6 show the KMC simulation of the RHEED intensity and surface roughness variation for α_2 (2x4) InAs (001) reconstructed surface depending on the number of diatomic layers and time respectively. The growth conditions are In flow = 0.1mL / s, As flow = 0.4ml/s.

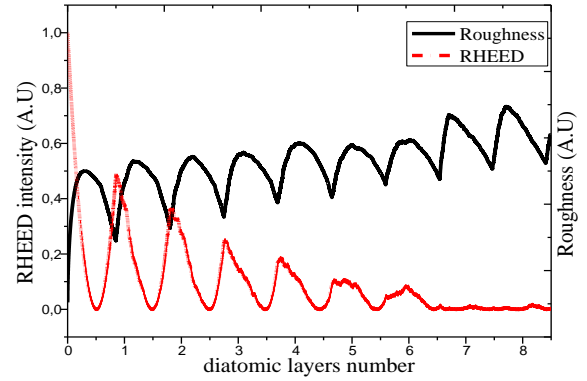


Figure 5

Variation of the roughness surface and e RHEED intensity of the InAs (001) α_2 (2x4) reconstructed surface depending on the number of diatomic layers.

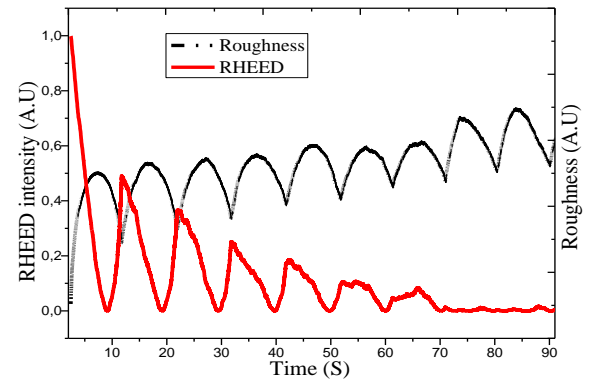


Figure 6

Variation of the roughness surface and e RHEED intensity of the InAs (001) α_2 (2x4) reconstructed surface depending on the time.

Figures 5 and 6 show that the amplitude of the RHEED oscillations decreases with time (number of diatomic layer) because the layers are not formed, and it is noted successively, that the second layer can start to grow before the first layer is not complete. Therefore increase the roughness in the course of the time [6, 12].

In our simulation, we have seen the creation of multiple layers simultaneously (creation of 2 to 5 diatomic layers at once). This is well observed in Figure 7 and 8 which represent the variation in the coverage rate of In, As and InAs according to time.

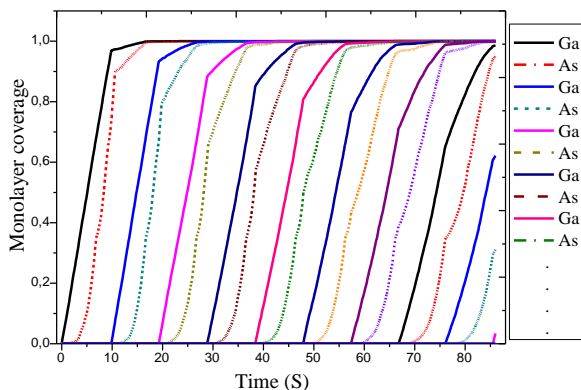


Figure 7

Monolayer rate coverage (In and As) of the InAs (001) α_2 (2x4) reconstructed surface (100 x 100) at 385°C

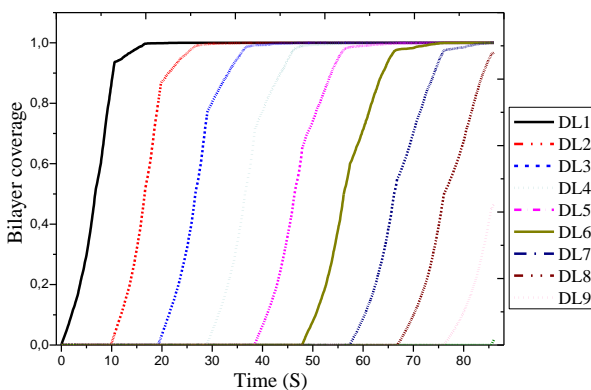


Figure 8

Bilayer rate coverage of the InAs (001) α_2 (2x4) reconstructed surface (100 x 100) at 385°C

We notice the creation of 5 layers at the same time, but with a different cover rate. This also reflects a tridimensional mode.

There is therefore an increase of the roughness average over of time. In this type of growth, the roughness does not increase but the oscillation disappears, this is due because the growth is done by advances in the marches.

So we can see that this type of growth can change their appearance over the time, the 3D growth is favored versus the 2D one.

Photoemission current phenomena: The photoemission phenomenon depends on the chemical nature and the structural of absorbed atoms [16]. The

photoemission current is proportional to the number of dangling bonds of In atoms. Experimentally the growth takes place for arsenic rich conditions. So the As atoms control the growth. In addition, the In atoms are more electropositive than As atoms which implies a decrease in surface energy and therefore a significant emission of photoelectrons [16-18].

In Figures 9 and 10, we postpone the photoemission current variation of the InAs (001) α_2 (2x4) reconstruction surface as a function of layers number (diatomic layers) and time respectively.

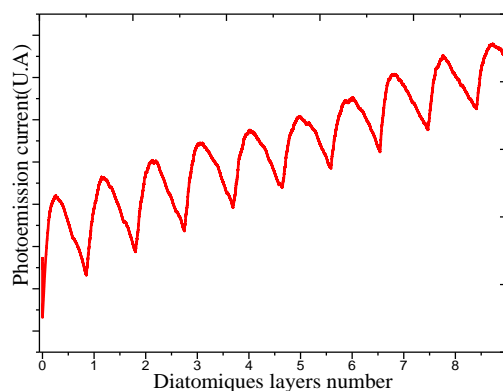


Figure 9

Variation of photoemission current of the InAs (001) α_2 (2x4) reconstructed surface depending on the number of diatomic layers

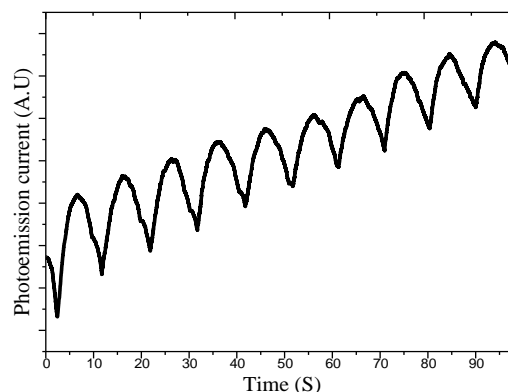


Figure 10

Variation of photoemission current of the InAs (001) α_2 (2x4) reconstructed surface depending on time.

These two figures show a fast increase of the photoemission current, which is justified by the increase in the number of connections due to charge transfer from In surface atoms to As ones. This indicates that the InAs(001) growth is done by the three-dimensional islands formation. We note that experimentally, the conditions for the layers growth of InAs are extremely difficult.

We also observe that the maximum of the photoemission current oscillations coincides with the half diatomic layer and the minimum with the diatomic layer [9,12,15] (the contrary case with the RHEED signal) with a small offset.

By comparing the RHEED intensity with that of the photoemission current, we note that these two oscillations have the same period which corresponds to a diatomic layer.

CONCLUSIONS

We have studied the atomic morphologies of the InAs (001) $\alpha 2$ (2x4) reconstruction surface simulated by Kinetic Monte Carlo simulation, the results were characterized by Reflection High-Energy Electron Diffraction intensity and photoemission current.

In this study we have taken into account all the growth process: deposition, diffusion, incorporation, absorption and desorption of In and As Atoms.

This work has confirmed that the growth of the InAs surface reconstruction begins by a layer-by-layer growth then it changes the shape to a growth in 3 dimensions after the deposition of several layers. This type of growth is called Step flow.

As perspective to this work, additional works focus on the same model, with other growth modes such as heteroepitaxy and by the use of other of characterization techniques such as Low Energy Electron Diffraction, X-ray Diffraction would be very beneficial.

KEYWORDS

MBE, Kinetic Monte Carlo, InAs, reconstruction, roughness, Reflection High Energy Electron Diffraction, Photoemission.

REFERENCES

1. Farrow, R.F.C. 1995, *Molecular beam epitaxy*, Noyes publications.
2. Müller.G, Métois.J.J and Rudolph.P, 2004, *Crystal Growth*, Elsevier.
3. Byrappa. K and Ohachi.T, 2002, *Crystal Growth technology*, Springer.
4. Itoh. M, 2001, Atomic-scale homoepitaxial growth simulations of reconstructed III–V surfaces, *Progress in Surface Science* 66, Elsevier, pp.53–153.
5. Itoh. M, 2000, *Atomic – scale homoepitaxial growth simulation of reconstructed III-V surfaces*, thesis, Osaka university.
6. Khachab. H, 2010, *Modélisation de la croissance épitaxiale par jets moléculaires (MBE) avec la méthode de Monte Carlo cinétique (KMC)*, doctorat thesis; Tlemcen university.
7. Abdelkafi. Y, 2009, *Modélisation et simulation de l'épitaxie par jets moléculaires*, Magister thesis, Bechar University.
8. Kratzer. P, Penev. E and Scheffler. M, 2002, First-principles studies of kinetics in epitaxial growth of III–V semiconductors, *Appl. Phys. A* 75, pp.79–88.
9. Khachab. H, Abdelkafi.Y, Belghachi. A and Barhmi. M, 2012, Simulation in situ par RHEED et photoémission de la reconstruction $\alpha\alpha 2$ (2x4) de InAs(001) avec la méthode de Monte Carlo cinétique, *Annales des sciences et technologies*, Ouargla university, Vol 4 N° 2, pp.121-128.
10. Andrea. C.L and Kotrla. M, 1997, Theory and simulation of crystal growth, *J. Phys. Condens. Matter* 9, pp. 299-344
11. Landau. D. P and Binder. K, 2000, *A guide to monte carlo simulation in statistical physics*, Cambridge university press, Cambridge.
12. Khachab. H, Abdelkafi. Y and Belghachi. A, 2010, kinetic monte carlo (KMC) simulation of GaAs(001) $\beta 2$ (2x4) reconstructed surface and Characterization, *Defect and Diffusion Forum* Vols. 297-301, pp.308-317.
13. Braun. W, 1999, *Applied RHEED; Reflection High-Energy Electron Diffraction during crystal growth*, Springer.
14. Huhtamaki. T, Jahma. M.O and Koponen. I. T, 2007, A simple model for quantifying the degree of layer-by-layer growth in low energy ion deposition of thin films, *Nuclear Instruments and Methods in Physics Research B* 264, pp.55–60.
15. Khachab. H, Abdelkafi. Y and Belghachi. A, In situ simulation by RHEED of GaAs (001) $\beta 2$ (2x4) reconstructed surface, 2009, *International Conference on Information and Multimedia Technology*, pp.517,IEEE conference serie.

16. N.Fazouan, 2001, *Simulation de suivi in situ par photoémission de la dynamique de croissance épitaxiale de semiconducteurs III-V*, doctorat thesis, Ibn Tofail university, Morocco.
17. Djafari Rouhan. M, Fazouan. N, Gue.A. M and Estève. D, 1995, Simulation of thin film growth and in situ characterization by RHEED and photoemission', *Vacuum*, volume 46, numbers 8-10, pp. 931-934.
18. Fazouan. N, Djafari Rouhani. M, Gue. A. M and Esteve. D, 1996, Simulation of photoemission current to monitor the thin film growth', *Surface Science* 352-354, pp. 1022-1026.

SYNTHESIS, CHARACTERIZATION, ELECTRON PARAMAGNETIC RESONANCE AND UV-VISIBLE STUDY OF PEROVSKITE LAYERED SYSTEM [NH₃-(CH₂)₈-NH₃]₂CuCl₄

Mahmoud ETTAKNI¹*, Jaouad AAZZA¹, Fatima HAIKI¹, Abdellah KAIBA² and Mostafa KHECHOUBI¹

¹Moulay Ismail University, Faculty of Sciences, Laboratory of Materials and Modelisation, Physics Department, B.P. 11201 Zitoune. 5000 Meknes, Morocco.

²Prince Sattam bin Abdulaziz University, College of Sciences and Humanities, Physic Department, P.O. Box 83, Al-Kharj 11942, Saudi Arabia

*Corresponding author: Email: m.ettakni@umi.ac.ma

ABSTRACT

Perovskite Layer compounds with the general formula (C_nH_{2n+1}NH₃)₂MX₄ or [NH₃(CH₂)_nNH₃]₂MX₄ where M is a divalent metal atom and X an halogen (M = Cu, Mn, Zn, Co, Cd...) (X = Cl, Br...) are lamellar type structures with a particular properties due to the hybrid of organic and inorganic parts. In this work, we have synthesized the compound [NH₃-(CH₂)₈-NH₃]₂CuCl₄, we present the synthesis method and we studied, by X-ray powder diffraction, the crystallographic structure of the obtained compound: it crystallize in a monoclinic system and the cell parameters are a= 5.3230(15) Å, b= 13.4714 (40) Å, c= 5.1414(13) Å, β = 91.832 (32)°: The compound is also investigated by means of Infra-Red spectroscopy, Electron Paramagnetic Resonance (Electron Spin Resonance ESR) and UV-Visible spectroscopy. The ESR study shows a typical signal for distorted octahedral site and for a Ferro Magnetic Resonance (FMR). The absorption spectrum of UV-Visible spectroscopy shows bands due to Charge Transfer Transitions from the ligand orbitals (pσ and pπ) to the half-occupied d orbital.

KEYWORDS

1-INTRODUCTION

The organic–inorganic perovskites are one of the most extensively studied crystalline families of hybrids which offers an important opportunity to combine useful properties from two chemical realms, organic and inorganic compounds, within a single molecular scale composite [1]. Among these compounds, the 2D layered perovskites: (R-NH₃)₂MX₄ and (NH₃-R-NH₃)MX₄, where R is an aliphatic or aromatic ammonium cation, M is a divalent metal that can adopt an octahedral or tetrahedral coordination, and X is a halogen: Cl, Br or I. These bis (n-alkylammonium tetrahelo metallates) form lamellar type structures in which the sheets of corner-shared MX₆ octahedral are sandwiched between a pair of layer of n-alkylammonium chains. The cavities between the octahedral are occupied by the NH₃ groups which are attracted to the MX₆ by hydrogen bonds N-H...X. the organic groups R self-assemble via π - stacking interaction (when the organic group contains aromatic groups), through Van der Waals force or

hydrogen bonding when the organic group contains acid function [2]. So, the perovskite layers are typical “Sandwich” system because of the regular alternation of inorganic and hydrocarbon regions that consist of long chain alkylammonium groups ionically bonded to an inorganic support [3,4] (figure 1)

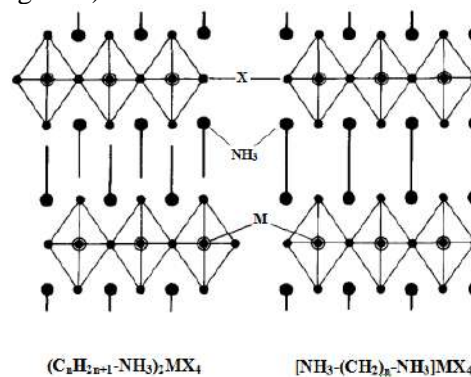


Figure 1

Schematic representation of 2D-layered perovskites

These compounds are the origin of a number of useful and peculiar properties due to the organic layer, to the inorganic layer and to the organic inorganic hybrids [1]. In fact the studies have shown that these perovskite layers are among the Phase Change Material (PCM) good for Thermal Energy Storage (TES) because of the solid-solid transition [5]. In addition, Balamurugan *et al.* and Wei Ning *et al.* have studied the electrical behavior and the magnetic properties for some layered organic inorganic hybrids [6-8].

Several papers studied structural characterization of some organic inorganic hybrids like perovskite system [1,2,5,9,15,16]. Indeed, as known the crystallography plays a crucial role to understand the structural behavior of materials and make relationship structure properties. In this manuscript, we present powder X-ray diffraction at room temperature of two (2D) organic inorganic like perovskite system $[\text{NH}_3-(\text{CH}_2)_8-\text{NH}_3]_2\text{CuCl}_4$, Infra-Red spectroscopy, Electron Paramagnetic Resonance (Electron Spin Resonance ESR) and UV-Visible spectroscopy.

2-Synthesis

A powder finely crushed of the diamine $\text{NH}_2-(\text{CH}_2)_8-\text{NH}_2$ is prepared then 0,5g of the powder is dissolved in a small quantity of distilled water and the obtained solution is made under regular and weak agitation during at least half an hour. Gaseous HCl (obtained from concentrated H_2SO_4 poured; drop with drop; on solid NaCl) is dissolved (barboté) in the diamine solution in order to form the diamine chloride ($\text{NH}_2-(\text{CH}_2)_8-\text{NH}_2, 2\text{HCl}$). Finally, the compound $[\text{NH}_3-(\text{CH}_2)_8-\text{NH}_3]\text{CuCl}_4$ is prepared from 1M of the aqueous solution of ($\text{NH}_2-(\text{CH}_2)_8-\text{NH}_2, 2\text{HCl}$) and 1M of an aqueous solution of CuCl_2

3-X-ray Powder diffraction and Infrared spectroscopic investigation

The structure of the obtained compound is investigated by means of X-ray powder diffraction (XRD) and Infra-Red spectroscopy (FTIR).

3.1-X-ray powder diffraction

The indexed X-ray diffraction powder pattern of this compound is shown in Figure 2. The program Dicvol04 [17-19] is used to determine unit parameter cell. The best solution to index the well-defined peaks (10) in the range $3^\circ - 38^\circ$ gives the monoclinic

cell, with $a = 5.3230(15) \text{ \AA}$, $b = 13.4714(40) \text{ \AA}$, $c = 5.1414(13) \text{ \AA}$, $\beta = 91.832(32)^\circ$ and volume 368.49 \AA^3 . The Figures of merit $M(10) = 76.5$ and $F(10) = 56.9(0.0068, 26)$. The indexation of this diffractogram show layered structure in direction to the big axis c . To confirm this result structural resolution from X-ray single crystal diffraction is now in progress and will be published in a future paper.

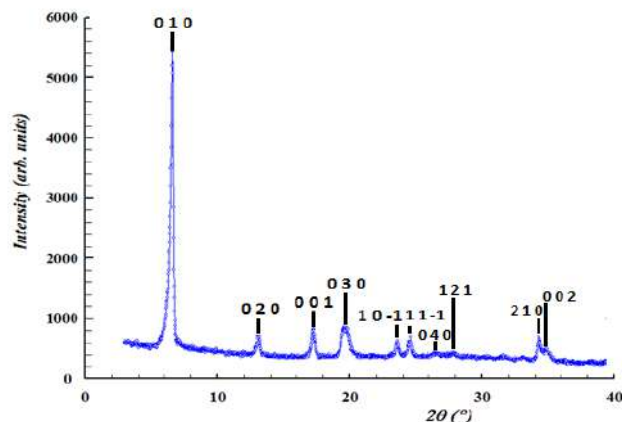


Figure 2
Indexed Diffractogram of
 $[\text{NH}_3-(\text{CH}_2)_8-\text{NH}_3]\text{CuCl}_4$

3.2-Infra-Red spectroscopy

The perovskite compound was also investigated by Fourier Transform Infra-Red Spectroscopy (FTIR). The spectrum of the layer perovskite compound is divided in two ranges: Intern vibration modes of the organic cation in the range of frequency [$4000 \text{ cm}^{-1} - 400 \text{ cm}^{-1}$], and extern vibration modes of the organic cation with the intern and extern vibration modes of the anion in the range [$<400 \text{ cm}^{-1}$]. Figure 3 present the intern vibration modes of the organic cation $[\text{NH}_3-(\text{CH}_2)_8-\text{NH}_3]^{2+}$. The principal vibrations are listed below:

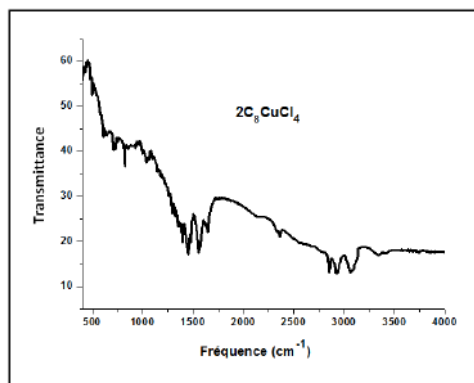


Figure 3
IR spectrum of $[\text{NH}_3-(\text{CH}_2)_8-\text{NH}_3]\text{CuCl}_4$

- 3332 cm⁻¹ Alongated vibration of (OH)
- 2924, 3063 cm⁻¹ Asymmetric and symmetric stretching modes of (NH₃⁺)
- 2663, 2887 cm⁻¹ Asymmetric and symmetric stretching modes of -(CH₂)-
- 1646, 1559 cm⁻¹ Asymmetric and symmetric deformation modes of (NH₃⁺)
- 1063 cm⁻¹ twisting modes of (NH₃⁺)
- 1037 cm⁻¹ rocking modes of (NH₃⁺)
- 820 cm⁻¹ stretching modes of C-C-C

4. Electron Spin Resonance

Electron Paramagnetic Resonance or Electron Spin Resonance (ESR) is a very sensitive tool that provides information about lattice symmetry and structure. It reflects the environment of the paramagnetic ion [10]. ESR has been proved to be a useful tool for the study of magnetic correlations in magnetic materials [8]. Our complex contains Cu²⁺ ions, which make it active to the ESR. Indeed; Cu(II) has nine valence d electrons resulting in one unpaired electron in the dx²-y² orbital in the ground state. This is perturbed by application of an external magnetic field and can be studied by Electron Spin Resonance [11].

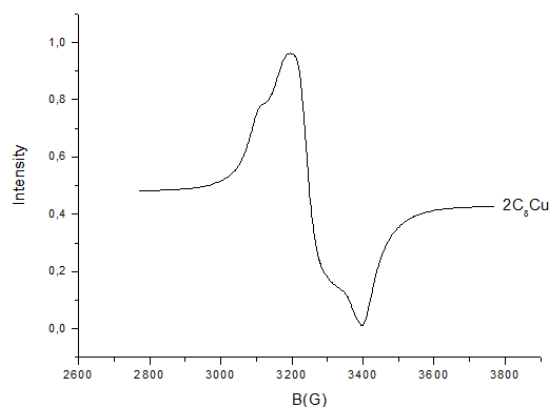


Figure 4
ESR spectrum of [NH₃-(CH₂)₈-NH₃]CuCl₄

The signal is large and asymmetric (figure 4), typical for distorted octahedral site [12], also typical for a Ferro Magnetic Resonance (FMR). More, the FMR line split into two lines and the signal appears to be composed of two overlapped spectral lines. For the splitting, the appearance of an additional FMR line is similar to the FMR behavior of coupled FM layers separated by nonmagnetic spacer layers [7], and it is caused by the presence of relatively large local field (H local) of the ferromagnetic domain. In addition,

the hyperfine structure doesn't show up, which means that the interaction between the single electron and the nucleus of the copper does not take place. So, the linking Cu---Cl has an ionic character. Indeed, these results were already observed in other papers [13, 14].

5. UV-VISIBLE

The spectrum (figure 5) presents two absorption bands, the first one at 338nm and the second one at 398nm, these bands are Charge Transfer Transitions. Indeed, at higher photon energy (UV-Vis), electrons are excited from the filled ligand-centered orbitals to the half-occupied d orbital, producing ligand to metal charge transfer transitions. The first band at 338nm represents the charge transfer transition from the pσ ligand to the half-occupied d orbital and the second band at 398nm represents the transition from the pπ ligand to the half-occupied d orbital.

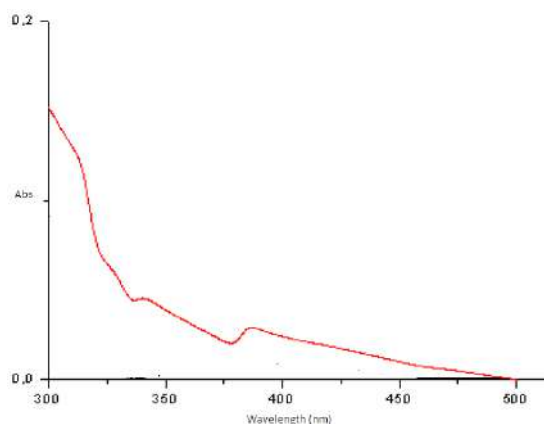


Figure 5
UV-Visible absorption spectrum of
[NH₃-(CH₂)₈-NH₃]CuCl₄

CONCLUSION

In summary, we have synthesized an organic inorganic compound with a layer structure [NH₃-(CH₂)₈-NH₃]CuCl₄, we have started the structural investigation by X Ray powder diffraction, the compound crystallizes in a monoclinic system and the cell parameters are a = 5.3230(15) Å, b = 13.4714 (40) Å, c = 5.1414(13) Å, β = 91.832 (32)°. It shows a layered structure in direction to the big axis c. By Fourier Transform Infra-Red Spectroscopy we have detected the principal vibrations. The obtained compound was also investigated by Electron Paramagnetic Resonance (Electron Spin Resonance ESR) and UV-Visible spectroscopy. The ESR study

shows a typical signal for distorted octahedral site and for a Ferro Magnetic Resonance (FMR). The absorption spectrum of UV-Visible spectroscopy shows bands due to Charge Transfer Transitions from the ligand orbitals ($p\sigma$ and $p\pi$) to the half-occupied d orbital

REFERENCES

- 1 Elmebrouki, K., S. Tamsamani, J. Aazza, M. Khechoubi and A. Khmou, 2011. Synthesis and characterization of new materials like perovskite $[\text{NH}_3-(\text{CH}_2)_n\text{NH}_3]\text{ZnCl}_4$ ($n = 8$ et 10). *J. Asian Scientific Research*, **1(4)**, pp 216-219.
- 2 Ettakni;M. Kaiba.A; Aazza.J; Haiki.F and. Khechoub.M ,2015;Synthesis and structural investigations of layered perovskite system: $[\text{NH}_3-(\text{CH}_2)_3\text{-COOH}]_2 \text{MCl}_4$ (M= Cd, Hg); *Journal of Asian Scientific Research*, , **5(9)**, pp 473-481.
- 3 Aazza.J, Elmebrouki.K, Khechoubi.M and. Khmou.A, 2013 Electron spin resonance (esr) study of four perovskite layer compounds $[\text{NH}_3-(\text{CH}_2)_3\text{-COOH}]_2 \text{CuCl}_4$, $[\text{CH}_3-(\text{CH}_2)_7\text{-NH}_3]_2 \text{CuCl}_4$, $[\text{NH}_3-(\text{CH}_2)_8\text{-NH}_3]\text{CuCl}_4$, AND $[\text{NH}_3-(\text{CH}_2)_{10}\text{-NH}_3]\text{CuCl}_4$; *Journal of Asian Scientific Research*, **3(11)**, pp1072-1077.
- 4 Aazza.J, Elmebrouki.K., Ettakni.M., Khechoubi.M and Khmou.A, 2013 Uv-visible absorption study of some perovskite layer compounds; *Journal of Asian Scientific Research*, **3(11)**, pp1078-1082.
- 5 Tamsamani.S, Aazza.J, Elmebrouki.K., Khechoubi.M., Khmou.A and Kaiba.A, 2011. Thermal and structural study of a perovskite layer $[\text{NH}_3(\text{CH}_2)_3\text{COOH}]_2\text{CdCl}_4$. *J. Asian Scientific Research*, **1(4)**, pp 212-215.
- 6 Balamurugan, K., N. Harish Kumar, J. Arout Chelvane and P.N. Santhosh, 2009. Room temperature ferromagnetism in Fe-doped BsSnO_3 . *J. Alloys and Comounds*, **472**, pp 9-12.
- 7 Wei Ning, Da-qian Liao, Xiang-qun Zhang, Zhao-hua Cheng and Young Sun, 2009. Anisotropic spin correlations in bilayered $\text{La}_{1.1}\text{Sr}_{1.9}\text{Mn}_2\text{O}_7$ investigated by electron spin resonance. *J. Solid State Communications*, **149**, pp 400-403.
- 8 Wei Ning, Fen Wang, Xiang-Qun Zhang, Zhao-Hua Cheng and Young Sun, 2009. Ferromagnetic spin fluctuations in antiferromagnetic $\text{Pr}_{1-x}\text{Ca}_x\text{MnO}_3$: An ESR study. *J. Magnetism and Magnetic Materials*, **321**, pp 88-90.
- 9 Elmebrouki. K., Khechoubi.M, Kaiba.A, Belaaraj.A, Mondieig.D and Negrier.P.2013; Preparation, crystal structure and characterization of inorganic-organis hybrid perovskite $[\text{NH}_3(\text{CH}_2)_{10}\text{NH}_3]\text{ZnCl}_4$; *Journal of Asian Scientific Research*, **3(5)**, pp 454-461.
- 10 Glinchuk, M.D. and R.O. Kuzian, 2007. ESR spectrum peculiarities in a nano-thin perovskite film. *J. Physica B*, **389** ,pp 324-241.
- 11 Edward, I.S., 2006. Spectroscopic Methods in Bioinorganic Chemistry: Blue to Green to Red Copper Sites. *Inorg Chem.*, **45**, pp 8012-8025.
- 12 Le Nestour, A, 2006, Corrélation structure – propriétés d’absorption UV-Vis-IR associée aux états de valence du cuivre dans des oxydes à base de zinc de type spinelle et wurtzite. Thèse. Université Bordeaux I.
- 13 Heslop, R. B. and Robinson, P.L., 1973, *Chimie inorganique*, Flammarion Médecine, Science Paris.
- 14 Durupthy C, 1993,. *Chimie inorganique*, Hachette Supérieur.
- 15 Mitzi, D. B, Chondroudís, K, Kagan, C.R, 1999,. Design, structure, and optical properties of organic-inorganic perovskites containing an oligothiophène chromophore. *Inorg. Chem.*, **38**, pp 6246-6256.
- 16 Zheng, Y. Y., Wu, G., Deng, M., Chen, H. Z., Wang, M., & Tang, B. Z, 2006. Preparation and characterization of a layered perovskite-type organic-inorganic hybrid compound $(\text{C}_8\text{NH}_6\text{-CH}_2\text{CH}_2\text{NH}_3)_2\text{CuCl}_4$. *Thin solid films*, **514(1)**, pp127-131.
- 17 Boulitif, A. and Louer, D,. *J. Appl. Cryst*, 2004, **37**, pp. 724-731
- 18 Louer, D. and Louer, M, 1972. *J. Appl. Cryst.*. **5**, pp. 271-275.
- 19 Boulitif, A, and Louer, D, 1991, *J. Appl. Cryst.* **24**, pp. 987-993

OPTIMIZATION OF THE BAND GAP AND TRANSMITTER THICKNESS TO BOOST EFFICIENCY OF $Al_xGa_{1-x}As$ / GaAs MULTI-JUNCTION SOLAR CELL

Abderrahmane. HEMMANI¹, Abdelkader NOURI^{1,2*}, Hamid KHACHAB¹

1: Department of Sciences of Matter, Faculty of Sciences exact, University of TAHRI Mohamed, Bechar,, BP 417 Bechar, Algeria

2: LabMat Laoratory, BP 1523 EL-M'naouer Oran 31000 ALGERIE

*Corresponding author: Fax: +(213)49238993 Email: nouri_32@yahoo.fr

ABSTRACT

Multi-junction solar cell (MJSC) are widely studied for their high efficiency in comparison with simple-junction ones, but despite this advantage they have many losses which decrease their efficiency. They are due, among other, to the photon excess energy loss, the non-absorption phenomena and the carrier recombination. In this study the optimization of the band gap and the transmitter thickness are opted to minimize these losses. An efficiency of about 24.9% is obtained under a solar spectrum of AM1.5.

NOMENCLATURE

n: The negative type region of pn diode
 p: The positive type region of pn diode
 Eg: The band gap energy of semi-conductor (eV)
 J_{ph} : The total photocurrent density (A/m^2)
 J_n : The emitter photocurrent in the p region (A/m^2)
 J_p : The base photocurrent in the n region (A/m^2)
 J_d : The photocurrent in the depletion region (A/m^2)
 Δn : The excess electron concentration in p region (m^{-3})
 δ_p : The thickness of p region (m)
 κ : The light absorption coefficient (m^{-1})
 F: The incident photon flux at surface (W/m^2)
 S_n : The electron surface recombination velocity (m^2)
 D_n : The electron diffusion coefficient (m^2/s)
 τ_n : The electrons lifetime (s)
 L_n : The electron diffusion length (m)
 R: Reflection coefficient
 Δp : The hole excess concentration (m^{-3})
 δ_n : The thickness of n region n (m)
 S_p : The hole surface recombination velocity (m^2)
 D_p : The hole diffusion coefficient (m^2/s)
 τ_p : The hole lifetime (s)

S_p : The back surface recombination velocity(m^2)

L_p : The hole diffusion length (m)

AM: The Air Mass coefficient

W: The depletion region thickness

INTRODUCTION

Many losses occurred in simple junction solar cell such intrinsic losses, due to photon excess energy loss ($h\nu > E_g$) and to the unabsorbed photon ($h\nu < E_g$) [1-3]. To minimize these losses there has been extensive study focused on the study of MJSC structure during the last three decades [4,5].

Among the solutions to reduce losses in solar cell the use of the mechanically stacked solar cells (MSSC), in such structure a high photon absorption is ensured when the cells are placed in such a way that their gap are in descending order from top to bottom. Therefore the top solar cell absorbs the photon of high energy and avoids thermal recombination. In MSSC structure the spectral response is extended and well divided on cells therefore the efficiency will improved [6,7].

In the present work the effect of $Al_xGa_{1-x}As$ /GaAs top solar cell energy gap and emitter thickness on photocurrent is opted to improve efficiency conversion. By varying the energy gap therefore the spectral response of all cells, so their photocurrent, will be improved. By the same

optimization policy we tend to improve the photocurrent by varying the top cell thickness, this one allow more photon absorption. Based on the obtained values of the thickness and the band energy gap, the optimal photocurrent will be corresponds to the best efficiency.

MATHEMATICAL MODEL

The Figure 1 shows the schematic diagram of the multi-junction solar cell. The two junctions are deposited in decreasing order of band gap in order to allow the top solar cell to absorb the photons of high energy from solar spectrum firstly. The photons of lower energy not absorbed previously will be absorbed by the second, this configuration avoid the loss energy by thermalization [8,9]

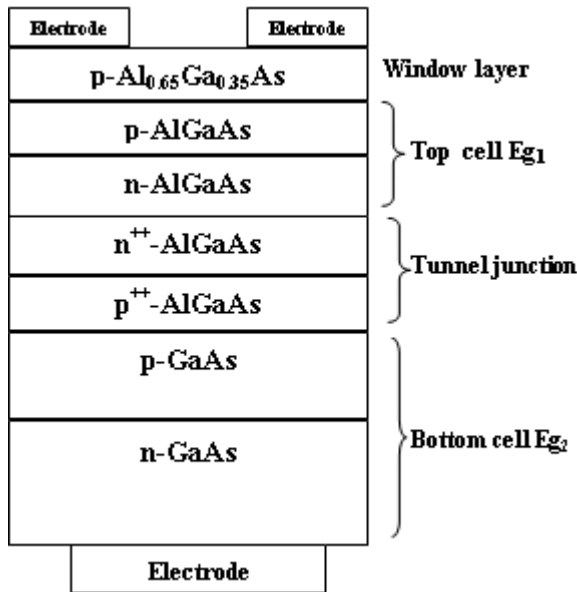


Figure 1:
Structure of the $\text{Al}_x\text{Ga}_{1-x}\text{As}/\text{GaAs}$ MSSC.

The flowing table summarized the parameters of the two solar cells initially used to calculate photocurrent of the MSSC of Figure 1[10,11].

Table 1
Initial parameters of the $\text{AlGaAs}/\text{GaAs}$ MSSC solar cell.

Cell	Top	Bottom
Acceptor concentration (cm^{-3})	2.10^{17}	2.10^{17}
Donor concentration (cm^{-3})	2.10^{17}	2.10^{17}
Intrinsic concentration (cm^{-3})	2.10^3	2.1×10^6

Electron mobility	6000	9340
Hole mobility	200	450

In order to investigate the influence of band gap energy on the optimum energy conversion in $\text{Al}_x\text{Ga}_{1-x}\text{As}/\text{GaAs}$ MSSC the total photocurrent density J_{ph} in each cell is evaluated based on the total current in standard p-n junction.

This current is given by [12, 13]:

$$J_{ph}(\lambda) = J_p(\lambda) + J_n(\lambda) + J_d(\lambda) \quad (1)$$

The emitter photocurrent is given by:

$$J_n = qD_n \left(\frac{dn_p}{dx} \right)_{\delta_p} \quad (2)$$

Which lead to the following expression:

$$J_n = \frac{qF(1-R)\alpha L_n}{\kappa^2 L_n^2 - 1} \times \left[\frac{\left(\frac{S_n L_n}{D_n} + \kappa L_n \right) - \exp(-\kappa x_j) \left(\frac{S_n L_n}{D_n} \cosh \frac{\delta_p}{L_n} + \sinh \frac{\delta_p}{L_n} \right)}{\frac{S_n L_n}{D_n} \sinh \frac{\delta_p}{L_n} + \cosh \frac{\delta_p}{L_n}} - \kappa L_n \exp(-\kappa \delta_p) \right] \quad (3)$$

Where $L_n = \sqrt{D_n \tau_n}$

The photocurrent density in the depletion region is expressed by:

$$J_d = qF(1-R)\exp(-\kappa \delta_p) [1 - \exp(-\kappa W)] \quad (4)$$

The photocurrent density at base region is given by:

$$J_p = -qD_p \left(\frac{d\Delta p}{dx} \right)_{\delta_p + w} \quad (5)$$

Which lead to the following expression:

$$J_p = \frac{qF(1-R)\kappa L_p}{\kappa^2 L_p^2 - 1} \exp(-\kappa(\delta_p + w)) \times \left[\frac{\frac{S_p L_p}{D_p} \left[\cosh \frac{\delta_n}{L_p} - \exp(-\kappa \delta_n) \right] + \sinh \frac{\delta_n}{L_p} + \kappa L_p \exp(-\kappa \delta_n)}{\frac{S_p L_p}{D_p} \sinh \frac{\delta_n}{L_p} + \cosh \frac{\delta_n}{L_p}} \right] \quad (6)$$

Where $L_p = \sqrt{D_p \tau_p}$.

The total photo-current density J_{ph} is obtained by integrating the current density $J_{ph}(\lambda)$ on the whole range of the solar spectrum.

3. RESULTS AND DISCUSSIONS

3.1 The spectral response:

In order to connect the conversion efficiency to the photocurrent, it is very useful to show the spectral response range of each separate cell.

In figure 2 we show the variation of spectral response curve of the two cells. The photons with wave length from 0.24 to 0.68 μm are absorbed by the top cell that is why the spectral response of the second cell is low in this range.

So the bottom cell is adapted to absorb photons in the range of wave length from 0.68 to 0.87 μm .

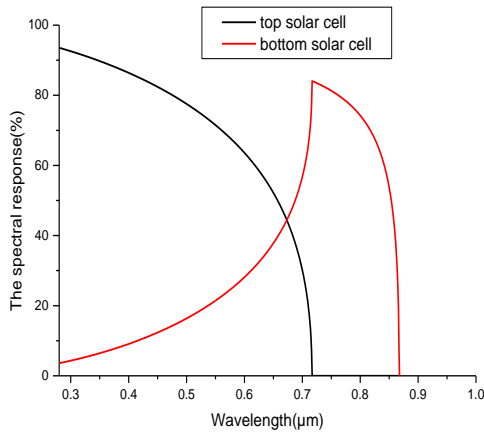


Figure.2:

The spectral response for the two solar cells

These remarks allow us to distribute each wave length range suitable for each cell, then to calculate the appropriate photocurrent.

3.2 Photocurrent optimization:

Now, by varying x in formula of $\text{Al}_x\text{Ga}_{1-x}\text{As}/\text{GaAs}$ material composition we can variate the energy gap therefore the spectral response of the two cells and their photocurrent. The following figure shows the variation of the photocurrent density of each cell depending on the energy band gap of the top cell.

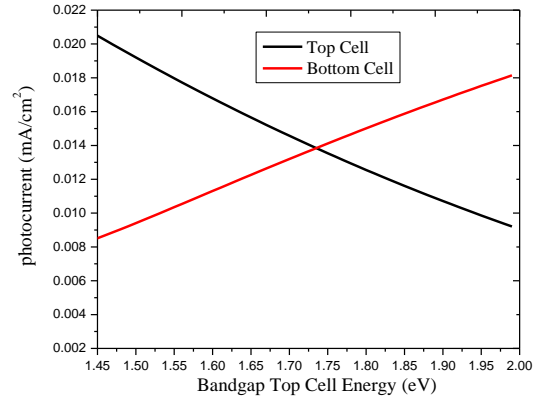


Figure 3:

The variation of photocurrent versus band gap top cell energy

The two cells are connected in series so the total current is that the smallest [14], we tend to increase this one. In figure 3 we show, for top cell band gap low energy, the photocurrent is decreasing. On the other hand the photocurrent of the bottom is increasing, this is mainly due to the reduction the range of the spectral response of the top cell and the increasing for the bottom cell. Form the curve we have optimum value of I_{ph} which is the intersection of the two currents. This means that the value of $E_g = 1.733\text{eV}$ is the optimal value to achieve an optimal photocurrent of $13.81\text{mA}/\text{cm}^2$ thereby give the better efficiency of the MSSC.

By the same optimization policy we tend to improve the photocurrent by varying the top cell thickness, this one allow more photon absorption. The figure 4 shows the variation of photocurrent versus the top cell thickness.

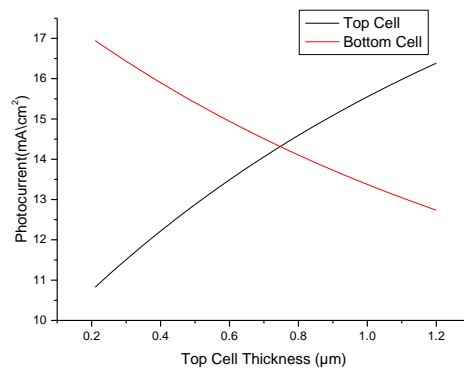


Figure 4:

The variation of photocurrent versus top cell thickness

From the intersection of the photocurrent spectra of the figure 4 the optimum value of thickness which gives a photocurrent of 14.33mA/cm^2 is $0.747\mu\text{m}$. So there is improvement of photocurrent of about 3.6% more.

3.3 The Energy gap optimization:

In this section the efficiency versus top cell band gap and its thickness is evaluated. Based on the obtained values of the thickness and band energy, of optimal photocurrent we try to see if it corresponds to the best efficiency.

Figure 5 shows the variation of the efficiency of MSSC cell according to the variation of the band gap of the top cell. The maximum of efficiency of about 24.3% is obtained for the same value of top cell band gap Energy of 1.73 eV.

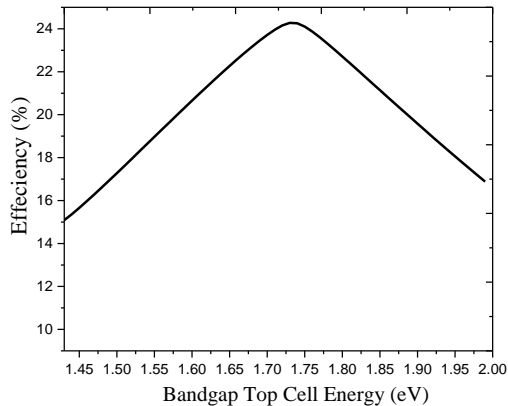


Figure 5:

The variation of efficiency versus top cell bandgap

This value is agree with the value already find from figure 3.

The variation of efficiency against top cell thickness is evaluated to display the optimum value of thickness. The figure 6 shows this variation.

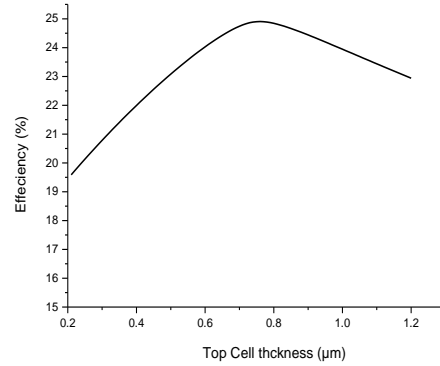


Figure 6:

The variation of efficiency versus top cell emitter thickness

By the same way, we look for the value of the thickness that corresponds to the best efficiency. From the figure 6 the efficiency is improved to maximum of 24.9% for a thickness of $0.747\mu\text{m}$ so of 2.4% more.

CONCLUSIONS

In the present work the effect of AlGaAs/GaAs top solar cell thickness and energy gap on photocurrent is opted to evaluated the improve efficiency and to avoid losses in Multi-junction solar cell

An optimization of top solar cell thickness and energy gap are opted for. The photocurrent of 14.33mA/cm^2 has been achieved for the emitter thickness of $0.747\mu\text{m}$, by the same way the optimal value of photocurrent is obtained for the top cell band gap energy of 1.73 eV. An efficiency of 24.9% is obtained for AM1.5 solar spectrum. As a perspective we can also optimize the donors concentration and the acceptors and to study the solar cell for sun concentration system.

KEYWORDS Multi-junction, Bandgap, Top Cell Thickness, Photocurrent, Optimization, Efficiency, $\text{Al}_x\text{Ga}_{1-x}\text{As/GaAs}$.

REFERENCES.

1. M. Dhankhar, O. Pal Singh, V.N. Singh, 2014, Renewable and Sustainable Energy Reviews, **40**, pp 214-223.

2. T. Frijnts, S. Kühnapfel, S. Ring, O. Gabriel, S. Calnan, J. Haschke, B. Stannowski, B. Rech, R. Schlatmann, 2015, *Solar Energy Materials and Solar Cells*, **143**, pp 457-466.
3. M. Berginski, J. Hüpkés, A. Gordijn, W. Reetz, T. Wätjen, B. Rech, M. Wuttig, 2008, *Solar Energy Materials and Solar Cells*, **92**, pp 1037-1042
4. M. Limpinsel, A. Wagenpfahl, M. Mingeback, C. Deibel, and V. Dyakonov, 2010, *Phys. Rev. B* **81**, pp 085203
5. A. P. Kirk and M. V. Fischetti, 2012, *Phys. Rev. B* **86**, pp 165206.
6. H. Tan, P. Babal, M. Zeman, A. H.M. Smets, 2015 *Solar Energy Materials and Solar Cells*, **132**, pp 597-605
7. N. López, L. A. Reichertz, K. M. Yu, K. Campman, and W. Walukiewicz, 2011, *Phys. Rev. Lett.* **106**, pp 028701.
8. R. R. King, D. Bhusari, A. Boca, D. Larrabee, X.-Q. Liu, W. Hong, C. M. Fetzer, D. C. Law, and N. H. Karam 2010, 25th European Photovoltaic Solar Energy Conference, Valencia, Spain, Sep. 6-10.
9. R. R. King, D. C. Law, K. M. Edmondson, C. M. Fetzer, G. S. Kinsey, H. Yoon, R. A. Sherif, and N. H. Karam, 2007, *Appl Phys Lett*, **90**, pp 183516.
10. Goldberg Yu.A. 1999, *Handbook Series on Semiconductor Parameters*, vol.2, M. Levinshtein, S. Rumyantsev and M. Shur, ed., World Scientific, London, , pp. 1-36.
11. S. Adachi, 1985, *J. Appl. Phys.*, **58**, no.3, pp.R1-R29.
12. E. Lorenzo, 1994 ‘Solar Electricity: Engineering of Photovoltaic System’, Progensa, Sevilla,.
13. Shive, J.N., 1959, *Semiconductor Devices*, Van Nostrand, Princeton, New Jersey .
14. Sarah R. Kurtz, P. Faine and J. M. Olson, 1990, *J. Appl. Phys.* **68**, pp 1890.

Échelle stratigraphique	Bassin de Bechar		Bassin de Reggane		Bassin de Tindouf	
	Basal	Top	Basal	Top	Basal	Top
PERMIEN (Laramien)	Les formations supérieures à l'Alger					
DEVONIEN	<ul style="list-style-type: none"> Devonien inférieur Devonien moyen Devonien supérieur 					
PROTÉROZOÏQUE						
PRÉCAMBRIEN						

Figure 3

Stratigraphic correlations between the different formations of Precambrian and Paleozoic sedimentary basins of south-western Algeria (Bechar, Reggane and Tindouf). [1], [2], [3], [4], [5], [7], [13], [14] and [16]

STRUCTURAL ASPECT

The pericratonic Tindouf basin in relation to the West African Craton, is asymmetric depression, having a very quiet south flank with a slight dip not exceeding and a northern flank highly structured and extremely faulted. This fault system is represented by the main major faults trending E-W and other NE-SW. This basin has been very affected by tectonic events from the Pan-African event to the late Hercynian event [6]. All these events were superimposed, the main event Hercynian gives the final structural character to this basin with some recent readjustments.

Toward east the axes have a dominant NW-SE direction, called Ougartienne. Toward north and west the structural axes take an E-W direction called Anti Atlassique (Fig. 2).

THE DOLERITE IN THE TINDOUF BASIN

The Paleozoic series of Tindouf basin have experienced dolerite intrusions affecting the Cambrian formations and particularly the upper Devonian (Famennian) (Fig. 3). they are set up in the surrounding rock as sills and dykes and are linked to global tectonic characterizing the West African Craton in response to the opening dated Jurassic of the Central Atlantic. A few meters of metamorphic contact affecting the Paleozoic host rocks proving the

intrusive nature of these dolerites, is described by different studies.

According to the well results, the magmatism seems to be less pronounced in the southern part of Tindouf basin but it is more prolific in the northern part of the basin where it is reported an intense tectonic activity.

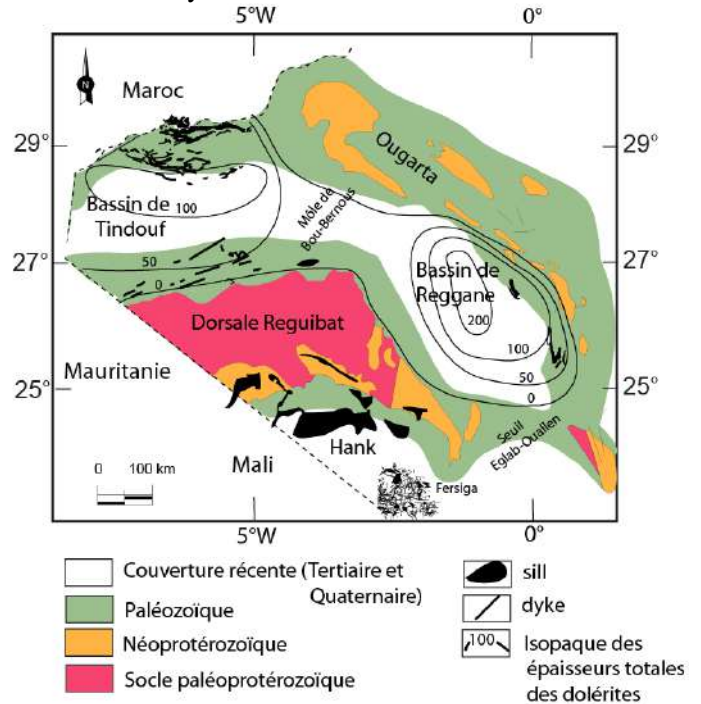


Figure 4.

Map isopachs total thicknesses of dolerite subsurface basins of Tindouf and Reggane [5].

Two major features as structural axis are related in Tindouf basin, the first one trending W-E, (Anti Atlas direction), has been reasonably explored by seismic & drilling & some gas & oil shows are reported.

The second one is located in the south, where drilling, despite absence of traps, revealed also many gas & oil shows.

In the central part, another axis oriented NW-SE (Ougarta direction), is described, it was explored by two stratigraphic wells TIN-1 and TIN-2.

A gas coming was recorded from the TIN-1 Upper Devonian (Strunian) sandstones; these sandstones are associated with a thick bench of dolerite (about 67 m) (Fig. 4). A second bench of dolerite was also identified just above the Strunian-Tournaisian limit (Fig. 5). This gas coming was questionable & according to the TIN-1 survey completion report done in 1962, the geologists have tried to find a

relationship between the sandstone strata & the dolerite wall rock.

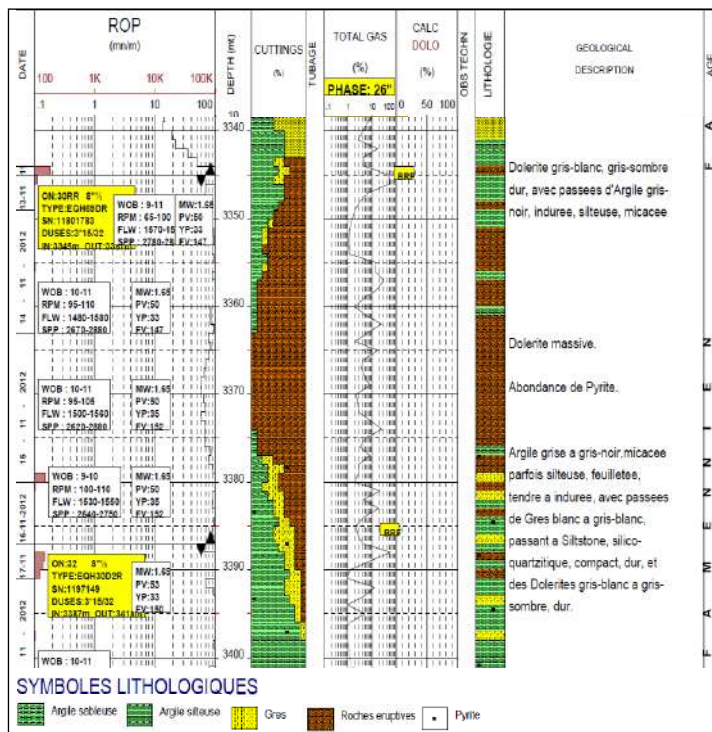


Figure 5
Masterlog -TIN-2

Dolerite in Strunian @ [2327-2391 m], [8] and [9].

(At the Dolerites bench, two (02) peaks of gas when the circulation of the bottom (BRF) of the plug which is rated at the log of total gas).

None coming of gas, such as found in TIN-1, was recorded during the drilling of the TIN-2 in 2012, these two holes are 40 km distant from each other.

The description of the TIN-1 sandstone (and dolerite bench) where was recorded gas coming, reported the presence of fractures which improving the gas flow. So it was decided to study all dolerite benches encountered by TIN-1 & TIN-2 wells, [8], [9].

For both TIN-1 & TIN-2 wells, two groups of dolerite are recognized in the Strunian and the Famennian.

A gas shows were also recorded (master log of TIN-2) during penetrating of the Famennian dolerites benches (Fig. 5).

When drilling TIN-2 well, they encountered the same dolerite bench occurring at the same level of Famennian of TIN-1; and an unmeasured gas flow was recorded after test achievement.

COMPARISON WITH INTRUSION DOLERITIC REG-1 AND REG-2 (BASIN DE REGGANE)

The neighbor pericratonic basin Reggane has also experienced an intense activity intrusive affecting the Paleozoic series of Upper Devonian and Carboniferous (Fig. 2 and 3).

Two wells REG-1 & REG-2 drilled respectively in 1979 and 1980 in the extreme North-West part of the Reganne basin in the vicinity of Bou Bernous saddle are encountered the dolerites.

During a test conducted in REG-2, 1500 m³ of dry gas was recorded from the Famennian affected by 114 m of this diabase intrusion, [8] and [9].

COMPARISON WITH DEPOSIT FORMS BY RESERVOIRS GRANITIC OFFSHORE VIETNAMESE (CUU LONG BASIN).

The geological setting of these dolerites can be compared and correlated to the granitic reservoirs in the Cuu Long basin of Vietnamese offshore.

This basin is tertiary rift formed in the early Oligocene & located in offshore southern Vietnam [12].

The Miocene inversion has intensified the fracturing of the granite basement where several reservoirs were identified and all give good oil flow after hydraulic fracturing.

The porosity is less than 5% and the permeability ranges from 0 md à 1000 md, the average depth of the top of these fractured granite reservoirs is from 2500 m to 4000 m.

The source rock of the Mesozoic granitic reservoirs is formed by excellent argillaceous bedrocks.

The reserves of oil are ranging from 100 to 400 mmb with a good rates from 2000 to 4000 BBL.

The life cycle of this basin is considered as challenge, it's generally ranging from 1 to 13 years and depends on several factors (the importance of fractures, the hydrocarbon column, the reserves in place and the production rate).

The Tertiary clastic reservoirs was the initial exploration objective in this basin, while the granitic reservoir was investigated coincidentally and became after the discoveries, the main target in this area.

The case study of the Cuu Long basin confirms that the magma reservoirs, contrary to the general believe, can be a very good reservoir for gas or/ & liquid hydrocarbons.

However to evaluate the potential of these reservoirs, the resistivity logs must be analyzed. The resistivity of igneous rocks is generally very high, but in case of presence of fractures and hydrocarbons, the drop in the resistivity is recorded. Furthermore the solidified magma could be more subject to fracture.

It is recommended to look for such reservoirs with such potential: (i) define the area of maximum of fractures and (ii) find the presence of a good source rock adjacent to reservoir.

Recall that these two conditions can be met in South-West Algeria basins Tindouf and Reggane , [5].

CONCLUSIONS AND RECOMMENDATIONS

In this report we have attempted to provide an answer about the behavior of igneous rock and particularly the dolerite as hydrocarbon reservoirs in the NAGA area of Tindouf Basin.

Three paragraphs were discussed:

- A summary of the results of TIN-1 and TIN-2 wells of Tindouf basin.
- A comparison with the neighboring basin of Reggane where the Paleozoic series has logged an intrusive activity affecting mainly the Paleozoic Upper Devonian and Carboniferous.
- A case study and a summary for hydrocarbon prone, worldwide, associated with igneous rocks.

Indeed, the magmatic rocks is spreading throughout the world, but a few are considered as hydrocarbons bearing rocks.

Generally, only shows & very low flow rates are recorded from these kind of reservoirs. Furthermore, it's well known that the igneous rocks form the best reservoir when they have been exposed on the surface and have undergone any tectonic event that led to the creation of fractures and while remaining in contact with mature source rocks.

Dolerites observed in Tindouf and Reggane basins showed an unmeasured gas flow (TIN-1 / Tindouf) and gas shows or low flow rates (REG-1 / Reggane: 1500 m³ / Gas Day).

The phenomenon associated with the dolerite is:

- Magma absorbing layer containing the bedrock.
- The host rock and magma became one body.
- The gas contained in the source rock form gas bubbles, filling the pores with gas & generating a vesicular porosity.

As soon as the bedrock magma mixing is carried out and after cooling, often fractures appear in these igneous rocks.

In our case, compaction can force the hydrocarbons within the Famennian source rock to move in new formed reservoir.

As a case study the Cuu Long offshore basin, located in Vietnam, shows that the magma reservoirs, contrary to the popular believe, can be a very good reservoir for gas or/& liquid hydrocarbons [12].

To evaluate the potential of these kind of reservoirs, we learn also from this study it is necessary to analyze the resistivity logs.

Indeed, the resistivity of igneous rocks stay high, but in the presence of fractures and hydrocarbons, the drop in the resistivity is logged.

After cooling the solidified magma became subject to fractures, it is recommended to search for such potential reservoirs to find the maximum of fractures and the good source rock communicating with these reservoirs. Recall, these two conditions could be met in the Southwest Algerian basins Tindouf and Reggane.

Around Naga area (Tindouf Basin), the resistivity data of the Strunian and Famennian was analyzed.

No resistivity drop is reported. However it should be noted that the Naga region has been the site of intense fracturing.

As recommendations, we suggest to explore the North of Naga, it remains an interesting area, structurally faulted. To rule on the existence of oil potential in these igneous rocks, it would be appropriate to take a pilot wells in the area. This would allow for an assessment of the dolerite reservoirs in contact with the source rock using the appropriate logs i.e.: imaging of the resistivity (fractures characterization & fractures orientation), the neutron-capture spectroscopy (measure mineral composition) and the magnetic resonance log (fluid characterization). Following, if the existence of hydrocarbons is confirmed, consider if needed a hydraulic fracturing program.

REFERENCES

1. Ait-Kaci-Ahmed, A., Moussine-Pouchkine, A., 1994. Les formations cambriennes de Fersiga (Sud-Ouest du Tanezrouft) : nouvelle interprétation de la sédimentation glaciaire et post-glaciaire sur le craton ouest-africain. *Bulletin du Service Géologique de l'Algérie* 5, p. 3-21.
2. Aliev, M., Ait Laoussine, N., Avrov, V., Aleksine, G., Barouline, G., Lakov-lev, B., Korj, M., Kouvykine, J., Makarov, V., Mazanov, V.,

- Medvedev, E., Mkrtchiane, O., Moustafinov, R., Oriev, L., Oroudjeva, D., Oulmi, M., Saïd, A., 1971. Structures géologiques et perspectives en pétrole et en gaz du Sahara algérien. *Altamira-Rotopress, S.A., Madrid, Espagne*, p.275.
3. Bertrand-Sarfati, J., Moussine-Pouchkine, A., Ait-Kaci-Ahmed, A., 1996. Subdivisions stratigraphiques nouvelles dans la couverture néoproterozoïque au Nord-Est du bassin de Taoudenni (Algérie). In : L. Bitam et J. Fabre (Eds.), *Géodynamique du craton ouest africain central et oriental : héritage et évolution post-panafricains. Mémoires du Service Géologique de l'Algérie* 8, p. 63-90.
 4. Bitam, L., Gourvenec, R., Robardet, M., 1996. Les formations paléozoïques anté-carbonifères du sous-bassin de Djebilet (flanc sud du Bassin de Tindouf, Nord-Ouest du Sahara algérien). In : L. Bitam et J. Fabre (Eds.), *Géodynamique du craton ouest africain central et oriental : héritage et évolution post-panafricains. Mémoires du Service Géologique de l'Algérie* 8, p. 15-22.
 5. Chabou, M.C., 2001. Etude pétrographique et géochimique du magmatisme mésozoïque de l'Ouest de la plate-forme saharienne. Mémoire de Magister, Ecole Nationale Polytechnique, Alger. p.180.
 6. Chabou, M.C., Sebaï, A., Feraud, G., Bertrand, H., 2007. Datation $^{40}\text{Ar}/^{39}\text{Ar}$ de la Province magmatique de l'Atlantique Central dans le Sud-Ouest algérien. *Comptes Rendus Géoscience* 339, p. 970–978.
 7. Fabre, J., Arnaud-Vanneau, A., Belhadj, Z., Monod, Th., 1996. Evolution des terrains méso-cénozoïques d'une marge à l'autre du craton ouest-africain, entre le Tanezrouft (Algérie) et l'Adrar de Mauritanie. In : L. Bitam et J. Fabre (Eds.), *Géodynamique du craton ouest africain central et oriental : héritage et évolution post-panafricains. Mémoires du Service Géologique de l'Algérie*, 8, p. 187-229.
 8. Final drilling reports of Tindouf Wells.
 9. Final drilling reports of Reggane Wells.
 10. Gevin, P., 1960. Etudes et reconnaissances géologiques sur l'axe cristallin Yetti-Eglab et ses bordures sédimentaires. *Service de la Carte Géologique de l'Algérie*, p.328.
 11. Jerram, D.A., Widdowson, M., 2005. The anatomy of Continental Flood Basalt Provinces: geological constraints on the processes and products of flood volcanism. *Lithos*, 79, p. 385-405.
 12. Nguyen Du and Hung Van, 2004, Petroleum Geology of Cuu Long Basin - Offshore Vietnam, Le1 Search and Discovery Article #10062.
 13. Seddiki, A., Remaci-Benaouda, N., Cottin, J.Y., Moine, B.N., Ménot, R.N., Perrache, C., 2004. The volcano-sedimentary Boukaïs inlier (south-western Algeria): evidence for lithospheric thinning during the Late Neoproterozoic. *Journal of African Earth Sciences* 39, p. 257–266.
 14. Soulaïmani, A., Bouabdelli, M., Piqué, A., 2003. L'extension continentale au Néoproterozoïque supérieur-Cambrien inférieur dans l'Anti-Atlas (Maroc). *Bulletin de la Société géologique de France* 174, p. 83-92.
 15. Peucat, J.J., Capdevila, R., Drareni, A., Mahdjoub, Y., Kahoui, M., 2005. The Eglab massif in the West African Craton (Algeria), an original segment of the Eburnean orogenic belt: petrology, geochemistry and geochronology. *Precambrian Research* 136, p. 309-352.
 16. Wec Algeria, 2007. Petroleum geology of Algeria. p. 1-93.

STABILITY STUDY OF OUTPUT VOLTAGES OF SINGLE STAGE THREE LEVELS INVERTER FOR PV SYSTEM IN SOUTH ALGERIA

¹T. Abdelkrim, ¹K. Benamrane, ²T. Benslimane, ³O. Abdelkhalek, ¹A. Borni

¹Unité de Recherche Appliquée en Energies Renouvelables, URAER, Centre de Développement des Energies Renouvelables, CDER, 47133, Ghardaïa, Algeria

²Electrical Engineering Department, University Mohamed Boudiaf of Msila, Algeria

³Department of Electrical Engineering, University Mohammed Tahri of Bechar, Algeria
tameur2@yahoo.fr, kbenamrane47@yahoo.fr

ABSTRACT

In this study, three-phase, stand-alone single stage neutral point clamped inverter for PV system is designed and simulated. In order to obtain the inverter output voltage at constant value under variation of PV voltage and load, the reference voltage vector of the voltage source inverter is determined by using two algorithms realizing the correction of amplitude and the selection of the redundancy to apply. A real data of global solar irradiance measured on horizontal plane and ambient temperature obtained by a radiometric station installed in Ghardaïa city in south Algeria are used. Simulation results show that the designed inverter produce a stable voltage all the day despite the variation of both solar irradiation and load. Total harmonic distortion level is 3.42% and this value is in the limits of the international standards.

KEYWORDS Solar irradiation, PV, Multi-level inverter, NPC, SVPWM.

NOMENCLATURE

<i>SVPWM</i>	Space vector pulse width modulation
<i>RVVAC</i>	Reference voltage vector amplitude correction
V^*	Reference voltage vector
r	Modulation index
V_{rms}	Root mean square value of output voltage
V_{rmsref}	Root mean square reference value of output voltage
Er_{rms}	Error between the root mean square value of output voltages at times t and the reference
Er_{rms21}	Error between the root mean square values of output voltages at times t and $(t-1)$
V_a, V_b, V_c	Output inverter voltages
T_1, T_2, T_3	Times conduction
<i>RS</i>	Redundancie Selection
i_{c1}, i_{c2}	Capacitors current
U_{c1}, U_{c2}	Capacitors voltage
I_{pv}	Photovoltaic array current
i_a, i_b, i_c	load currents
$V1-V6$	Inverter vectors with redundant state.
$G1-G2$	Vectors group

P_i	Possibilities
<i>GHI</i>	Global horizontal irradiance
<i>DHI</i>	Diffuse horizontal irradiance
<i>DNI</i>	Direct normal irradiance
T_a	Ambient temperature
R, L	Resistor and inductor

INTRODUCTION

Because of the greenhouse effect and the shortage of fossil fuels, the demand for renewable energy has increased significantly over the years. From different types of renewable energy sources, solar and wind energies have become popular and demanding due to advancement in power electronics technologies equipment and techniques. Solar energy converted to electricity via photovoltaic panels is used today in many applications as they have the advantages of being maintenance and pollution free [1]. These photovoltaic modules are used as power plant to the grid connected systems, photovoltaic pumping, and also in domestic use with storage systems. This last application allows the user has to sell the excess electricity produced it does not consume.

Solar irradiation intensity on Algerian territory indicates that Algeria has a strong solar potential

source (Fig. 1) [2-3]. Ghardaïa is a dry and arid city in the south, characterized by a great sunshine (more than 3,000 hours per year) where the mean annual of the global solar irradiation measured on horizontal plane exceeds 20 MJ/m². This great potential of solar energy can be used to produce electricity and reduce fossil fuels to preserve the environment [4].

Solar-powered photovoltaic panels convert the sun's rays into electricity. The type and number of converters used depend on the specified application. In this paper, authors are interested in supplying an Alternative Current (AC) load. In this case one or more than one stage converter can be used (Fig. 2) [5].

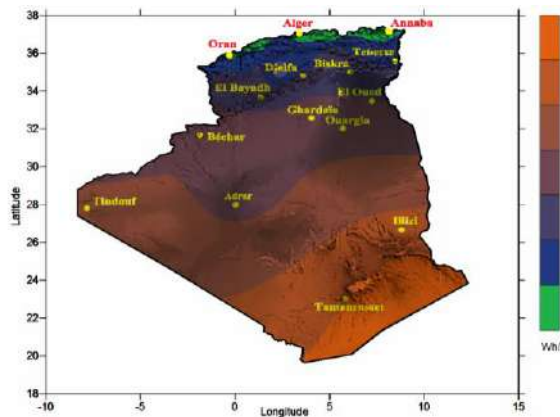


Figure 1

Average annual global solar irradiation received on a horizontal plane

The multilevel converters concept was established in the early 1980s when the Neutral Point Clamped (NPC) structure, the capacitor clamped (or Flying Capacitor (FC)) structure and the cascaded H-bridge (CHB) structure were proposed [6]. These new converters are finding increased attention in academia and industry as one of the best choices of electronic power conversion for medium and high power applications [7-9]. But these converters have a voltage unbalance problem in the DC bus [10]. Many solutions in the literature were proposed to solve this problem like the use of linear or nonlinear regulators [11], add additional circuit [12] or applied SVPWM associated to redundant switching states [13].

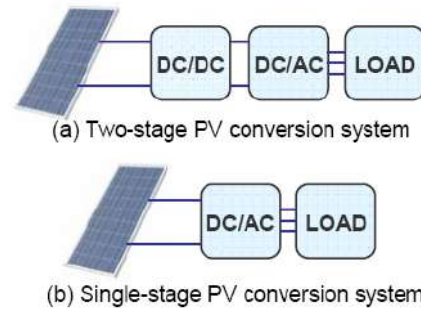


Figure 2

PV conversion systems

This paper study the conversion of solar energy to electricity via cascaded photovoltaic array-three levels inverter as presented in figure 3. In this case two problems must be solved to get a stable output voltage. These problems are the unbalance of DC capacitors voltage and the variations of photovoltaic array voltage. As solution, authors propose two new algorithms to maintain the output voltage equal to its reference. The first use the redundant states of vectors with a new algorithm that takes into account the variations of both photovoltaic array and load currents. In the second, we apply a proportional regulator of inverter modulation index to keep at stable value the root mean square output voltage.

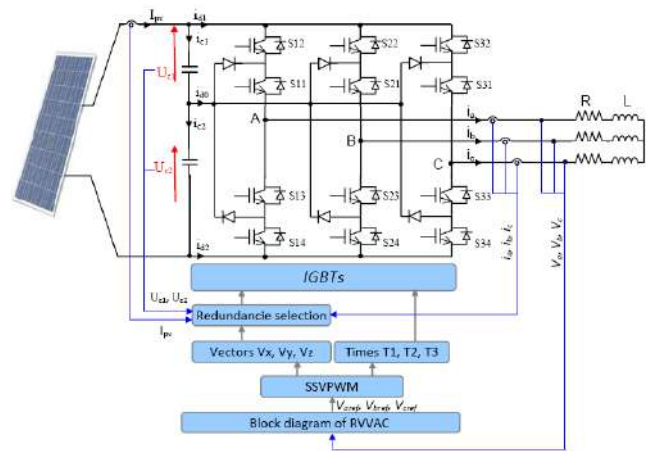


Figure 3

Photovoltaic array-three levels inverter

THREE LEVELS INVERTER CONTROL

Reference Voltage Vector Amplitude Correction (RVVAC)

In this part, a proportional regulator of modulation index r of three levels inverter is used. The reference voltage vector of inverter is given by:

$$V^* = \begin{pmatrix} V_{aref} \\ V_{bref} \\ V_{cref} \end{pmatrix} = \begin{pmatrix} r \times V_m \times \sin(\omega t) \\ r \times V_m \times \sin(\omega t - 2\pi/3) \\ r \times V_m \times \sin(\omega t - 4\pi/3) \end{pmatrix} = r \times V_m \begin{pmatrix} \sin(\omega t) \\ \sin(\omega t - 2\pi/3) \\ \sin(\omega t - 4\pi/3) \end{pmatrix} \quad (1)$$

$$\text{Where: } v_m = \frac{\sqrt{3}}{2} \quad \text{and} \quad 0 < r < 1$$

This algorithm consists to correct the reference amplitude voltage vector (modulation index r) after each 20ms. The voltage $V_{rms(t)}$ at time (t) is compared to its previous $V_{rms(t-1)}$ (time ($t-1$)) and also compared to V_{rmsref} and based to the errors obtained; the new modulation index r is calculated as presented below.

$$\begin{cases} \text{if } Er_{rms} > 0 \Rightarrow r_{(t+1)} = r_{(t)} - P_r(t) \\ \text{if } Er_{rms} < 0 \Rightarrow r_{(t+1)} = r_{(t)} + P_r(t) \\ \text{if } Er_{rms} = 0 \Rightarrow r_{(t+1)} = r_{(t)} \end{cases} \quad (2)$$

$$\text{Where: } Er_{rms} = V_{rms(t)} - V_{rmsref} \quad (3)$$

$$V_{rmsref} = 230V$$

$$\text{And } P_r(t) = |Er_{rms}| / (Er_{rms21} \times P_r(t-1)) \quad (4)$$

Er_{rms} : error between the root mean square value of output voltages at times t and the reference.

$P_r(t)$ is the amplitude correction of r at time t . It is limited by a constant value P_{rmax} .

$V_{rms(t)}$: root mean square value of output voltage at time t

The error between the root mean square values of output voltages at times t and ($t-1$) Er_{rms21} is defined:

$$Er_{rms21} = |V_{rms(t)} - V_{rms(t-1)}| \quad (5)$$

The block diagram of the reference vectors amplitude correction is presented in Fig. 4.

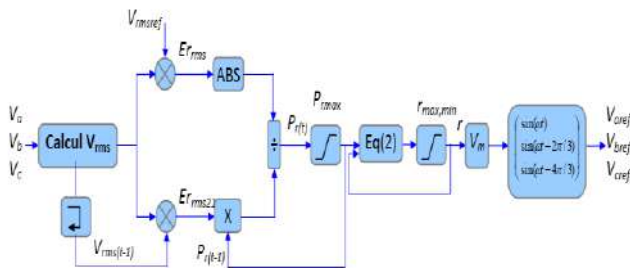


Figure 4
Block diagram of RVVAC

Reference voltage vector selection: In this work, we applied the Simplified Space Vector Pulse Width Modulation (SSVPWM) of three levels inverter. This

simple and fast method divides the space vector diagram of three levels inverter (Fig 5) into six small hexagons. Each hexagon is space vector diagram of two levels inverter, as shown in figure 6.

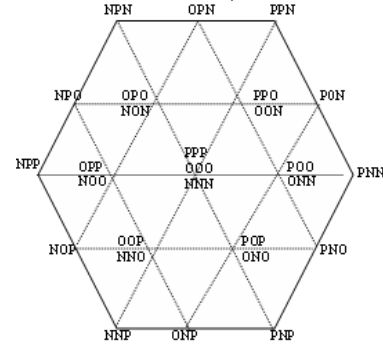


Figure 5

Space vector diagram of a three levels inverter

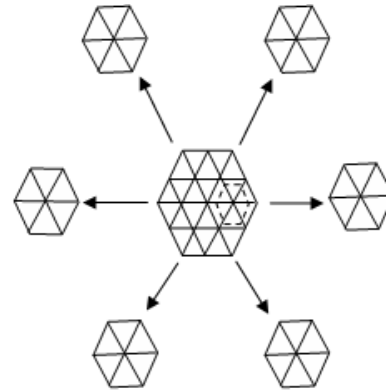


Figure 6

Decomposition of space vector diagram of a three levels inverter to six hexagons

Redundancy Selection (RS): To choose the redundancy to be used to balance the DC bus, we must know the impact of each one on capacitors voltages. The following steps present the detail of this algorithm.

Step 1: This step consists in definition of the relationship between capacitors current (i_{c1} and i_{c2}), photovoltaic array current I_{pv} and load currents i_a , i_b and i_c (Fig. 3) for each vector with redundant states (6).

$$\begin{cases} i_{c1} = I_{pv} - F_{11}^b \times i_a - F_{21}^b \times i_b - F_{31}^b \times i_c \\ i_{c2} = I_{pv} + F_{10}^b \times i_a + F_{20}^b \times i_b + F_{30}^b \times i_c \end{cases} \quad (6)$$

F_{ij}^b : are the connection functions of half legs.

Tables I resume relationships between capacitors, photovoltaic array and load currents for vectors with redundant state.

Step 2: To reduce the size of control algorithm, the second step consists in constituting vectors groups that have the same disposition in Tables 1 the equations S1, S2 and S3. Two groups have been constituted.

- Group 1 (G1): V1, V3, V5.
- Group 2 (G2): V2, V4, V6.

Table 1
Relationships load currents, photovoltaic array current and capacitor currents

Vectors		i_{c1}	i_{c2}	$S1=$	$S2=$	$S3=$	
V1	a	ONN	S3	S1	$I_{pv+ib+ic}$	I_{pv-ia}	I_{pv}
	b	POO	S2	S3			
V2	a	PPO	S1	S3	$I_{pv-ia-ib}$	I_{pv+ic}	I_{pv}
	b	OON	S3	S2			
V3	a	NON	S3	S1	$I_{pv+ia+ic}$	I_{pv-ib}	I_{pv}
	b	OPO	S2	S3			
V4	a	OPP	S1	S3	$I_{pv-ib-ic}$	I_{pv+ia}	I_{pv}
	b	NOO	S3	S2			
V5	a	NNO	S3	S1	$I_{pv+ia+ib}$	I_{pv-ic}	I_{pv}
	b	OOP	S2	S3			
V6	a	POP	S1	S3	$I_{pv-ia-ic}$	I_{pv+ib}	I_{pv}
	b	ONO	S3	S2			

Step 3: This step consists to analyzing the influence of each redundancies of constituted groups on capacitors voltages variations. From Table 2, it can remark that all vectors depend on three equations S1, S2 and S3. Considering the photovoltaic array current $I_{pv} > 0$, we can obtain three possibilities P_i of load variation (7).

$$\begin{cases} P_i = P_1 \text{ if } S1 > 0, S2 < 0 \\ P_i = P_2 \text{ if } S1 < 0, S2 > 0 \\ P_i = P_3 \text{ if } S1 < 0, S2 < 0 \end{cases} \quad (7)$$

Table 2
The vectors group

Vectors		i_{c1}	i_{c2}
G1	a	S3	S1
	b	S2	S3
G2	a	S1	S3
	b	S3	S2

Applying these possibilities of load variations, we obtain the capacitors voltages increasing or decreasing as presented in Table 3.

Table 3
Effect of redundancies of groups G1 and G2 on capacitors voltages

Groups	Redundancy	possibilities	U_{c1}	U_{c2}
G1	a	P1	↑	↑
		P2	↑	↓
		P3	↑	↓
	b	P1	↓	↑
		P2	↑	↑
		P3	↓	↑
G2	a	P1	↑	↑
		P2	↓	↑
		P3	↓	↑
	b	P1	↑	↓
		P2	↑	↑
		P3	↑	↓

Step 4: This step consists to select the redundancy to be used to cancel the unbalance in capacitor voltages (Table 4).

Table 4
Selected redundancy for groups G1, G2

Groups		G1			G2		
Derivation	Possibilities	P1	P2	P3	P1	P2	P3
		1	$U_{c1} < U_{c2}$	a	a	a	b
2	$U_{c1} > U_{c2}$	b	b	b	a	a	a

SIMULATION RESULTS

To test the performance of proposed control, a real data of solar irradiation and temperature profiles obtained by a radiometric station installed in Ghardaïa city (32°26'N 03°46'E) are used (Fig. 7). The simulation steps are presented in the following Table 5.

Table 5
Simulation steps

$T = 09^h00$	$R=0\Omega, L=0H, RS \text{ OFF, RVVAC ON}$
$T = 09^h25$	$R=50\Omega, L=0.1H, RS \text{ OFF, RVVAC ON}$
$T = 09^h35$	$R=50\Omega, L=0.1H, RS \text{ ON, RVVAC ON}$
$T = 11^h25$	$R=10\Omega, L=0.1H, RS \text{ ON, RVVAC ON}$
$T = 13^h05$	$R=100\Omega, L=0.1H, RS \text{ ON, RVVAC ON}$

Fig. 8 presents the Global Horizontal Irradiance $GHI (W/m^2)$, the Diffuse Horizontal Irradiance $DHI (W/m^2)$, the Direct Normal Irradiance $DNI (W/m^2)$ and the ambient Temperature $T_a (^\circ C)$ of January 31 2013. We note that January 31 is a nice day without atmospheric perturbation. The GHI is more than $700 W/m^2$ and temperature is between $12^\circ C$ and $25^\circ C$.

Fig. 9-(a) presents that the photovoltaic array voltage V_{pv} is stable up to 16^h , after start decreasing because the decreasing of solar Irradiance less than $400 W/m^2$

DC bus voltages U_{c1} , U_{c2} , are equal after using the redundant vectors of the proposed algorithm at $T=09^h35$ (Fig. 9-(b)).

As presented in figure 10-(a), the variation of modulation index r after using the regulator allows to maintain the root mean square output voltage V_{rms} stable and around its reference $V_{rmsref} = 230V$ (Fig. 10-(b)).

Fig. 11 presents the first phase load current i_a . This current increase at $T = 11^h25$ after variation of resistor from $R=50\Omega$ to $R=10\Omega$. After that decrease from $i_a=7A$ to $i_a=2.2A$ a result of the load variation.

The output voltage and its spectral analysis are illustrated in figure 12. It is shown that the total harmonic distortion is less than 4%.



Figure 7
Radiometric devices (Sun tracker)

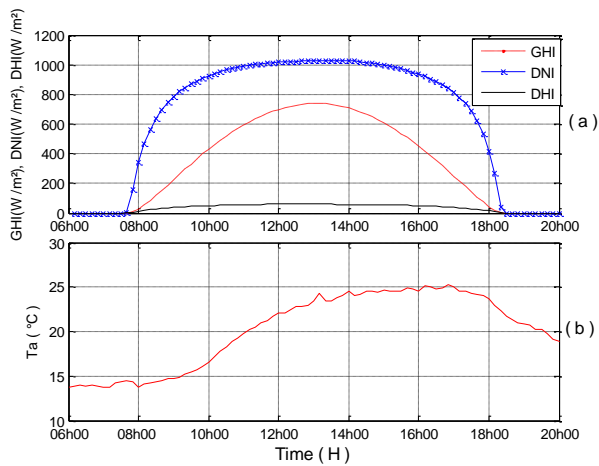


Figure 8
(a)- Global Horizontal Irradiance (GHI), Diffus Horizontal Irradiance (DHI), Direct Normal Irradiance (DNI),
(b)-Ambient Temperature (T_a)

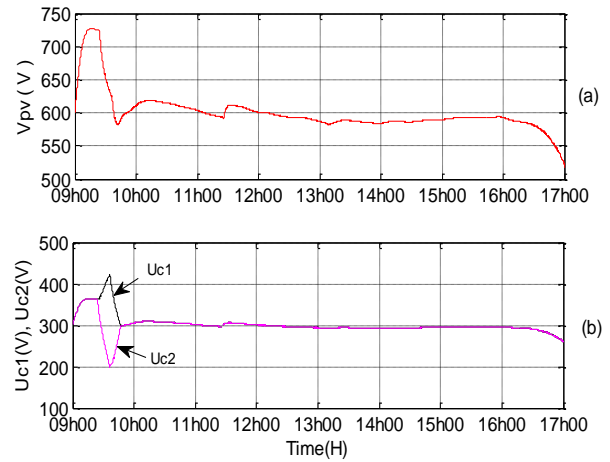


Figure 9
(a)- Photovoltaic array voltage V_{pv}
(b)- DC bus voltages U_{c1} , U_{c2}

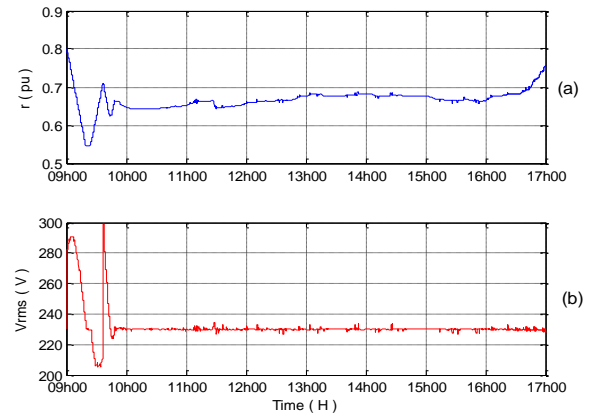


Figure 10
(a)- Modulation index r ,
(b)- Root mean square voltage V_{rms}

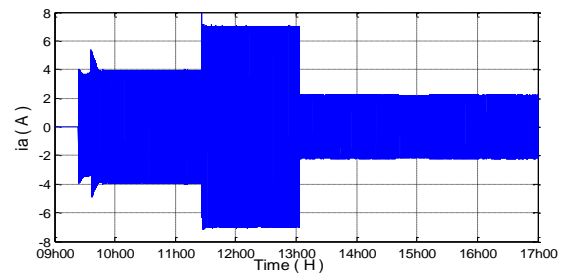


Figure 11
Load current i_a

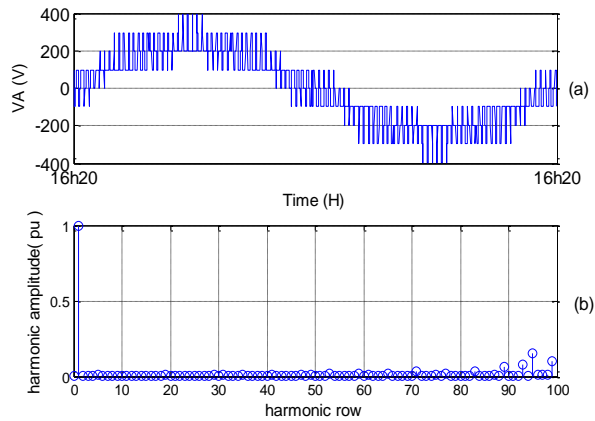


Figure 12

Output voltage V_a and its spectral analysis,
 $THD = 3.42\%$

CONCLUSION

In this study, a regulation method of output voltage of three-phase three-level NPC inverter of stand-alone PV system is designed and simulated. Two algorithms were presented and used to correct the amplitude and select the redundancy of reference voltage vector. This last is set by proposed algorithms in order to maintain all the time the root mean square voltage around its reference. From a real data obtained by a radiometric station installed in Ghardaïa city, it is seen from simulation that the inverter output voltage is stable despite the variation of both solar irradiation and load. Also, THD value of the voltages is 3.42% and this value is in the limits of international standards. With proposed solution, we do not need to introduce a DC/DC converter to stabilize the DC bus consequently the size and the cost of the system are decreased and total efficiency is increased.

REFERENCES

- Selvaraj, J, and Rahim, N. A, 2009, Multilevel inverter for grid-connected PV system employing digital PI controller, *IEEE Transactions on industrial electronics*, **56**, pp. 149-158.
- Yaiche, M.R., Bouhanik, A, Bekkouche, S.M.A, Malek, A, and Benouaz, T, 2014, Revised solar maps of Algeria based on sunshine duration, *Energy Conversion and Management*, **82**, pp. 114-123.
- Benamrane, K, Benslimane, T, Abdelkhalik, O, Abdelkrim, T, 2015, New Algorithms for Stability of Output Voltages of Stand-Alone Single Stage Five Levels Inverter in South Algeria PV System, *The Mediterranean Journal of Measurement and Control*, **11**, pp. 444-453.
- Gairaa, K, and Benkacali, S, 2011, Analysis of solar radiation measurements at Ghardaïa area, south Algeria, *Energy Procedia*, **6**, pp. 122-129.
- Ozdemir, S, Altin, N, Sefa, I, 2014, Single stage three level grid interactive MPPT inverter for PV systems, *Energy Conversion and Management*, **80**, pp. 561-572.
- Nabae, A, and Akagi, H, 1981, A new neutral-point clamped PWM inverter, *IEEE Trans. Ind. Appl*, **IA-17**, pp. 518-523.
- Franquelo, L. G, Rodriguez, J, Leon, J. I, Kouro, S, Portillo, R, and Prats, M. A. M, 2008, The age of multilevel converters arrives, *IEEE Ind. Electron. Mag.*, **2**, pp. 28-39.
- Rodriguez, J, Franquelo, L. G, Kouro, S, Leon, J. I, Portillo, R. C, Prats, M. A. M, and Perez, M. A, 2009, Multilevel converters: An enabling technology for high-power applications, *Proc. IEEE*, **97**, pp. 1786-1817.
- Kouro, S, Malinowski, M, Gopakumar, K, Pou, J, Franquelo, L. G, Bin, W, Rodriguez, J, Perez M. A, and Leon, J. I, 2010, Recent Advances and Industrial Applications of Multilevel Converters, *IEEE transactions on industrial electronics*, **57**, pp. 2553-2580.
- Maswood, A. I, Gabriel O. H. P, and Al Ammar, E, 2013, Comparative study of multilevel inverters under unbalanced voltage in a single DC link, *Power Electronics IET*, **6**, pp. 1530-1543.
- Du, E, He, L, Li, X, and Ma, Y, 2010, Neutral point potential balance of three-level inverter based on parameters self-tuning fuzzy logic control strategy, *IECON 2010 - 36th Annual Conference on IEEE Industrial Electronics Society*, pp. 2863-2867.
- Chibani, R, Berkouk E. M, Boucherit M. S, 2009, Five-Level NPC VSI: Different Ways to Balance Input DC Link Voltages, *ELEKTRIKA*, **11**, pp. 19-33.
- Abdelkrim, T, Berkouk, E.M, Benamrane, K, and Benslimane, T, 2012, Study and control of five-level PWM rectifier-five-level NPC active power filter cascade using feedback control and redundant vectors, *Turkish Journal of Electrical Engineering and Computer Sciences*, **82**, pp. 655-677.

EXPERIMENTAL TEST FOR EVALUATION OF SCC STATIC SEGREGATION

Bensebti S.E1., Chabane A1, Aggoun S.2, Houari H.1

1Laboratory MDC, University Mentouri of Constantine, Algeria.

2Laboratory L2MGC, University of Cergy Pontoise, Cergy Pontoise, France

*Corresponding author: Fax: +213 31 80 82 81 Email: s_bensebti@yahoo.fr

ABSTRACT

A Self-Compacting Concrete (SCC) is by definition one that, due to its own weight, pours and sets in place in the most complex reinforced moulds. It is important to note that the material must not undergo any form of segregation, whether “dynamic”, i.e. when it occurs during flowing, or “static”, i.e. when it occurs in the mould after compaction of different materials in the concrete. In this paper, study of static resistance segregation of self-compacting concretes is presented. Experimental assessment of segregation is carried out by procedure, which is realized in this paper. This procedure is similar to column test but different cylinder geometry and splitting is carried out at the end of setting. For each of the different mixtures studied, we also measure the slump flow, the filling ratio (L-box test), the screen stability and the V-funnel flowing time. The results obtained show that in the case of SCC, specific tests must be carried out to assess static segregation, especially when slump flow is above 70 cm. This study also shows that it is possible to obtain high quality SCC (with no risk of segregation) with screen stability test values in the region of 30%, which are much greater than the usual 15% [AFGC 2000].

Keywords *Self compacting concrete, limestone filler, segregation, slump flow.*

INTRODUCTION

Self-Compacting Concrete “SCC” is a new form of concrete, which can fill all the corners of formwork without vibration. In order to ensure this property, the SCC must have a great fluidity, a good resistance to segregation and does not have to present any form of blocking. [Nagataki and al.1995] [Su and al.2001]. A good resistance to segregation allows a regular distribution of coarse aggregates in all levels of element. In other words, concrete should not undergo any form of segregation, neither horizontal, nor vertical. Horizontal segregation can occur during the flow of concrete at more or less important distances. It is also amplified by possible blockings of coarse aggregates in the vicinity of reinforcements. Vertical segregation (figure1), also called static segregation, comes from decantation of coarse aggregates at the bottom of concrete volume and is caused almost by a bad past mix-design. [Khayat 1999] [Sedran 1999] [Trudel 1996]. These two forms of segregation must be studied during the mix design and can be avoided by adoption of an adequate composition [Bensebti and al. 2006] [Okamura and al.2003]. The L-box test simulates concrete flow in a reinforced formwork [AFGC 2000]. This test makes possible to check appearance or not of material blocking at reinforcement level. An appreciation of static segregation can be carried out by using results of sieve test [AFGC 2000]. When concrete constitutes a stable mixture static risk of segregation is less.

However, this proceeding manner remainders an indirect and subjective appreciation of static segregation. A new procedure of test allowing a direct appreciation of resistance to static segregation of SCC is presented in this paper.

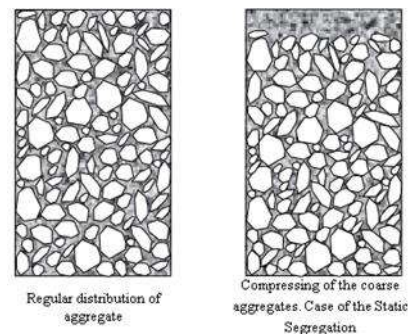


Figure 1 Static segregation in a volume of concrete

EXPERIMENTAL STUDY OF STATIC SEGREGATION

The publications in static segregation of SCC field are not numerous. However we can quote the work of V.K. Bui and al [Bui and al.2002] which presented a fast method to test the segregation resistance of SCC. It is proposed the use of a device similar to that of “Compacting Factor” to appreciate the vertical segregation [AS 1983] [Bui and al.2002]. Sidky, Legrand and Barrioulet [Sidky and al.1982] developed a test for ordinary concretes, which consists in filling and vibrate a mould of concrete (425 mm height

and 187 mms interior diameter of the mould) (figure 2). They separate then the concrete in five equal layers using separators incorporated in the container. Each layer is analyzed paste mass and aggregates mass in order to determine a coefficient of segregation S_i which indicates the content in aggregates.

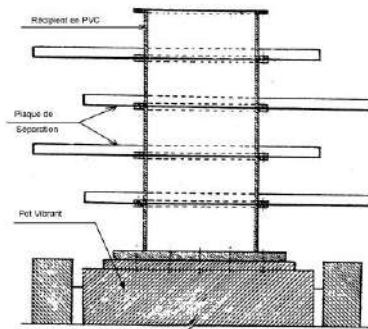


Figure 2 Experimental equipment used by Sidky, Legrand and Barrioulet.

Segregation coefficient is the relationship between the aggregate concentration of a layer, compared to initial concentration. Thus, $S_i > 1$ indicates an enrichment of aggregates while $S_i < 1$, indicates an aggregate impoverishment.

The Japanese method of cylinder [Umehara and al.1994] is also used. It's a similar method to that of Sidky and al. However, the container is a cylinder 500 mm height on 200 mm diameter (figure 3). The ratio between the aggregate mass in the upper part A and the aggregate mass in the lower part B expresses the degree of segregation.

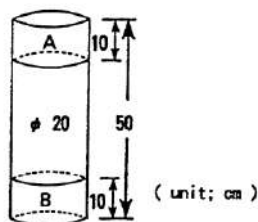


Figure 3 Cylinder for the measurement of segregation resistance.

It should be noted also that French Association of Civil engineering [AFGC 2000] recommends, for the characterization of resistance to segregation, the “test of stability into the sieve”. This test consists, to fill a bucket with 10 liters of SCC, to wait 15 minutes, then to pour on a sieve (5 mm of opening and 315 mms diameter) 4,8 kg of concrete. After 2 minutes, the quantity of paste passing through the sieve is weighed. The ratio between the weight of paste having crossed the sieve and the initial weight of the sample,

determines the tendency to segregation of SCC [The European Guidelines 2005].

A segregation-controlled design methodology was introduced for SCC by [Aaron W. S. and al.2001]. This theory suggests that aggregate segregation is governed by yield stress, viscosity, and density of cement paste matrix. So, for a given aggregate particle size distribution and volume fraction, the rheology and density of the cement paste matrix dictate the fluidity and segregation resistance of concrete.

Using an experimental setup, the influence of rheology of concrete on the settlement of aggregate was studied by [Petrou M. F., Wan B. and al. 2000]. The mortar is placed in a stainless-steel tank, and the surface exposed to air is flattened. Then a stone with aluminum plate attached to its upper side is placed gently on the surface of the mortar. Depth to which the stone sank in the mortar is measured.

Using nuclear medicine techniques, a unique experimental method for monitoring aggregate settlement in concrete was presented by [Petrou M. F, Harries K.A. and al.2000]. Real-time images of aggregate settlement due to vibration were presented.

STATIC SEGREGATION INDEX TEST

The methodology that we propose in this paper for studying our various mixtures is inspired from the work of Sidky and the Japanese method of the cylinder. The interest of our method is the fact that the operation of separation of various concrete layers is carried out after the complete stabilization of the system (at the end of setting). This stabilization makes it possible to handle easily the test-cylinder without any risk of concrete flow. Errors due to material losses during separation and weighing are thus negligible.

The column used in the testing method proposed is a cylinder 400 mm height and 110 mm diameter. The various steps of experimentation are illustrated in figure 4 and are:

- Concrete filling of the column is done in only one operation, by using a bucket and by pouring the concrete from a 10 cm height, approximately. This manner unified of filling of the column allows to eliminate the effect of the segregation which could be occur during the casting (dynamic segregation)
- After a latency (close to the end setting time), the column is separate in three equal parts (upper part, medium part and lower part)

- After washing then weighing each part, the mass ratio determines the dry ratio > 5mm compared to total mass of the considered part,
- Contents of aggregates of each part (G_{higher} , G_{medium} and G_{lower}) are given by the relationship between the mass of dry aggregates compared to the total mass of considered part.

One defines then an Index of Static Segregation “ISS” by the relation:

$$ISS = \frac{G_{higher}}{G_{lower}}$$

With:

G_{lower} : Cross aggregate content of lower part,

G_{higher} : Cross aggregate content of higher part,



Figure 4 Steps of Static Segregation Index test:

MATERIALS

Materials used are:

- a calcareous crushed gravel 8/15, density 2,7 g/cm³ and 1,35% absorption,
- a calcareous crushed sand 0/5, density 2,67 g/cm³ and 1,1% absorption,
- a sea sand 0/3, density 2,66 g/cm³ and 0,9% absorption,
- CEM/II 42.5 cement, 28 days strength of 42.5 MPa, specific Blaine area of 3891 cm²/g, absolute density of 3.1 g/cm³,
- A superplasticizer,

- a calcareous filler, density 2,7 g/cm³, the average diameter of the particles is 19 μm (98% of the fillers have a diameter lower than 200 μm and 26% of fillers have a diameter lower than 10 μm).

EXPERIENCES PROGRAM

The objective consists in validating the presented experimental procedure in order to compare results obtained to results of the recommended tests. The parameters of study chosen are:

1. The nature of sand “rolled or crushed”,
2. Calcareous filler proportion expressed by the ratio “Fillers/Binder”,
3. Water proportioning expressed by the ratio “Water/Binder”.

By fixing superplasticizer content to saturation, mix design of concrete was led according to the recommendations of the Okamura’s Japanese method [Okamura and al. 1995] [Okamura 1997] [Okamura and al. 2003].

The Coarse aggregate content is fixed at 50% of its compactness and sand content to 40% of mortar volume. The composition of the paste is deduced starting from the parameters selected Water/Binder and Fillers/Binder.

For each composition (of the 23 compositions studied), we calculated an Index of Static Segregation “ISS” and the whole of following measurements: Slump flow, stability on the sieve, the L-Box test and flow time in the V-funnel. Visual appreciations of concrete stability are also noted. The appreciation concerns essentially the depth of cement paste throughout the perimeter of concrete after the slump flow test and sweating.

RESULTS AND DISCUSSION

According to the AFGC recommendations, a SCC must present at the same time a slump flow equal to or higher than 60 cm, a filling rate with L-Box equal to or higher than 80% and stability on the sieve lower than 15%. When stability on the sieve is between 15 and 30%, the composition is regarded as critical and it is necessary to carry out specific tests of segregation.

Initially, it should be noted that all our studied concretes presented a slump flow higher than 60 cm and L-box filling rate higher than 80% (except the SCC13 and 14). These results make it possible to note that the whole of these concretes has an acceptable fluidity and does not present

risk of blocking. The essential point to check thus relates to the static segregation.

Visual appreciation of concretes (in term of stability, sweating and segregation) during various tests enabled us to note good stability of all concretes whose value with sieve was lower than 30%. One can note that all these concretes present an ISS lower or equal to 5.

Thus, one can say that when the difference of content of aggregates in the column does not vary of more than 5%, concrete can be regarded as acceptable.

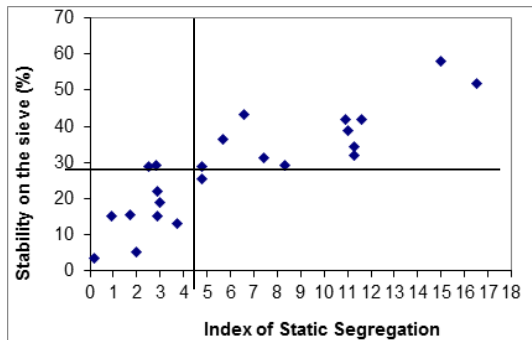


Figure 5 Relation between stability on the sieve and ISS

All the concretes located in the rectangle delimited by stability on the sieve of 30% and an index of segregation “ISS” of 5 (figure 5) are SCC of good quality and have a good segregation resistance.

We can note also, that for 30% stability on the sieve the concrete resistance to segregation is critical. Because, we can see that on figure 5, for stability equal to 30%, ISS is varying between 3 and 12.

Hence, one can estimate that the limitation to 15% of stability on the sieve, by AFGC, is too severe. This value can easily be increased without much risk to 20% or 25%.

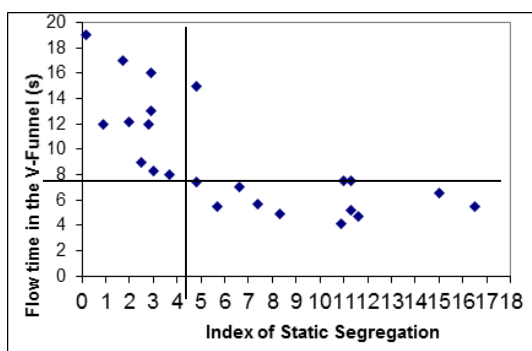


Figure 6 Relation between the flow time into V-funnel and ISS

Figure 6 shows that flow test with V-Funnel does not make it possible to assess the tendency to static segregation of SCC. One can note on this figure that for 8 seconds ISS can vary from 3 to 11. However, it is useful to note that:

- When flow time into V-funnel is lower than 8 seconds, the static segregation is systematic and very important.
- When this time is higher than 10 seconds, the risk of static segregation is very thin.

By analyzing results represented in figure 7, one can note that static risk of segregation starts to become important only when slump flow exceeds 70 cm.

Thus one can admit that it is not necessary to carry out tests for determination of index of static segregation if the made concretes present slump flow lower or equal to 70 cm.

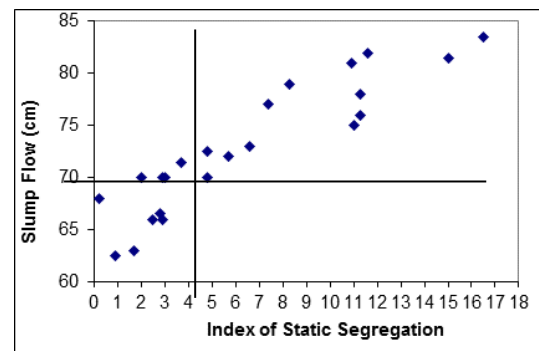


Figure 7 Relation between the slump flow and ISS.

CONCLUSION

Since SCC presents a very important fluidity, static risk of segregation is an essential parameter to consider. Thus, it is very important to check the stability of the granular system in the mass of the concrete. This kind of segregation is not visible and can be detected in structures only by very particular techniques. Irregular distribution of aggregates into the mass of concrete implies directly a differential strength.

It is true that static segregation

On the basis of the results obtained, we can advance the following conclusions:

1. It arises that the limit of ISS to obtain a good SCC is about 5. However, it is necessary to make complementary tests by adopting other parameters of study in order to refine the results on limiting value of this index,
2. For concretes whose slump flow is lower than 70 cm, the risk of static segregation is very tiny,
3. The limitation of stability on the sieve to 15% is rather severe and one can admit a value of 20% without any risks.

Static segregation in SCC means that aggregate particles sank in mortar. It is not clear whether coarse aggregate settle in concrete only during placement or after placement. Also, during placement, it is not clear whether the coarse aggregate settles all the time or no. [Petrou M. F, Harries K.A. and al.2000]. In order to ensure that all the granular system is stabilized we analyze the concrete sample (column) after setting time. So, a new static segregation control method is introduced for SCC.

Finally, the proposed method is an interesting simple procedure. It allows, by realizing simple tests, a direct appreciation of the static segregation of SCC. It would be important to carry out others test, using other materials and other size of column, in order to develop the current method.

REFERENCES

- AFGC (Association Française de Génie Civil), “Bétons Auto-plaçants. Recommandations provisoires”, July 2000.
- Aaron W. Saak, Hamlin M. Jennings, and Surendra P. Shah, “New methodology for designing self-compacting concrete”, *ACI Materials Journal*, November-December 2001
- AS (Australian Standard) AS 1012, Method for testing concrete, Section 2, Method 2, Compacting Factor Test, 1983.
- Bensebti S., Aggoun S. et Houari H., “Influence du dosage en eau et en filler calcaire sur la ségrégation statique des bétons autoplaçants”, *Fifth International Conference on Sciences of Materials (CSM5)*, may 17-19 2006, Beyrouth, Liban
- Bensebti S., Aggoun S. et Houari H., Duval R., La ségrégation statique dans les bétons autoplaçants « mise en place d’une procédure expérimentale », *Annales du Bâtiment et des Travaux Publics*, N°2-3, Avril-Juin 2007, Editions ESKA, pp 22-28
- Bui V. K., Montgomery D., Hinczac I. and Turner K., “Rapid testing method for segregation resistance of self-compacting concrete”, *Cement and Concrete Research* 32 (2002), pp.1489-1496.
- Lin Shen, Hamed Bahrami Jovein, Mo Li, “Measuring static stability and robustness of self-consolidating concrete using modified Segregation Probe”, *Construction and Building Materials*, Volume 70, 15 November 2014, Pages 210-216
- Lin Shen, Hamed Bahrami Jovein, Zhihui Sun, Qian Wang, Wenmei Li, “Testing dynamic segregation of self-consolidating concrete”, *Pages 465-471, Construction and Building Materials*, Volume 75, Pages (30 January 2015)
- Nagataki S. and Fujiwara H., “Self-compacting property of highly flowable concrete”, *Second CANMET/ACI International Symposium on Advances In Concrete Technology*, Las Vegas, ACI SP 154-16, June 1995, pp.301-314.
- Okamura H. and Ouchi M., “Self-compacting concrete”, *Journal of Advanced Concrete Technology*, Vol, 1, No. 1, April 2003 pp.5-15.
- Okamura H. and Ozawa K., Mix design for self compacting concrete, *Concrete library of JSCE*, N°: 25, June 1995
- Okamura H., *Self-Compacting High-Performance Concrete*, *Concrete International*, V. 19, No. 7, July 1997, pp 50-54.
- Sedran T., “Rhéologie et rhéométrie des bétons : Application aux bétons autonivelants”, *Thèse de Doctorat de l'Ecole Nationale des Ponts et Chaussées*, mars 1999.
- Sidky M., Legrand C. et Barrioulet M.: “Influence de la concentration en granulats et du temps sur la ségrégation interne dans le béton frais”, *Materials and Constructions*, vol 15, n°85, 1982, pp.11-19.
- Su N., Hsu K-C. and Chai H-W., “A simple mix design method for self-compacting concrete”, *Cement and Concrete Research* 31 (2001), pp.1799-1807.
- The European Guidelines for Self-Compacting Concrete, *Specification, Production and Use*, May 2005.
- Trudel A., “Maniabilité, uniformité et comportement structural du béton autonivelant à haute performance”, *Mémoire de Maîtrise ès Sciences Appliquées. Spécialité : Génie Civil*. Université de Sherbrooke, CANADA, Avril, 1996.
- Umehara H., Uehara T., Enomoto Y. and Oka S. “Development and usage of lightweight high performance concrete”, *International Conference on High Performance Concrete*, ACI SP 149 supplementary papers Singapore, 1994, pp.339-353.
- Petrou M. F., Wan B., Gadala-Maria F., Giri Kolli V. and Harries K.A., “Influence of mortar rheology on aggregate settlement”, *ACI Materials Journal*, July-August 2000
- Petrou M. F., Harries K.A., Gadala-Maria F. and Giri Kolli V., “A unique experimental method for monitoring aggregate settlement in concrete”, *Cement and Concrete Research* 30 (2000), pp.809-816.

EFFECT OF TUNNEL JUNCTION ON THE INDIUM GALLIUM NITRIDE MULTIJUNCTION TANDEM SOLAR CELL PERFORMANCES

DENNAI Benmoussa *, BENSLIMANE H and KHACHAB H

Department of S M, Faculty science, University of TAHRI MOHAMED Bechar, Algeria

* Email: deennai_benmoussa@yahoo.com.

ABSTRACT

During the past few years a great variety of multi-junction solar cells has been developed with the aim of a further increase in efficiency beyond the limits of single junction devices. $\text{In}_x\text{Ga}_{1-x}\text{N}$ is one of a few alloys that can meet this key requirement. While in mechanically stacked multi-junction (MJ) cells the subcells usually have separate contacts, monolithic MJ cells are epitaxial grown on one substrate and the sub cells are interconnected in series by tunnel diodes leading to a standard two-terminal contact.

This paper describes the role of the tunnel junction's in InGaN tandem solar cells. Two tandem solar cells the $\text{In}_x\text{Ga}_{1-x}\text{N} / \text{In}_x\text{Ga}_{1-x}\text{N}$ the first without tunnel junction and second with tunnel junction $\text{In}_x\text{Ga}_{1-x}\text{N}$ are selected for simulate the overall characteristics of the AMPS-1D. Our calculation shows that the efficiency can be improved from 17% for a tandem solar cell without tunnel junction up to 23.21% for a tandem solar cell with tunnel junction obtained in 1-sun AM1.5 illumination and at room temperature, using realistic material parameters.

KEYWORDS: InGaN Solar Cell; multi-junction; tunnel junction; AMPS-1D; simulation.

INTRODUCTION

The major loss processes of thermalization and non-absorption can be largely eliminated if the energy of the absorbed photon is marginally higher than the band gap of the cell material. This leads to the concept of the tandem cell [1], where multiple cells are used with different band gaps, each cell converting a narrow range of photon energies close to its band gap as shown in Figure 1.

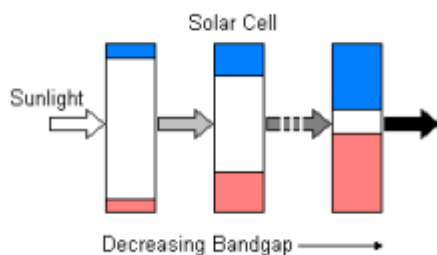


Figure 1
Concept of tandem cell

The high-gap cells are stacked on the top, which efficiently absorb the high-energy photons, transmitting the lower energy photons to the cells with lower band gaps. Earlier tandem cells used in

space applications were mechanically stacked and individually probed. With the improvement in growth technology, individual cells are monolithically grown on top of each other. Such devices function in series with only two probes for external connection, while they are internally connected through tunnel-junctions, which display ohmic characteristics. Performance of a tandem increases as the number of cells in the stack increases, with a direct sunlight conversion efficiency of 86.8% calculated for an infinite stack of independently operated cells under maximum concentration. However, increasing the number of stacks adds complications and makes the tandem sensitive to the irradiating spectrum as these individual cells have to be connected in series with low Ohmic contact resistance and have to be current matched.

Recently, $\text{In}_x\text{Ga}_{1-x}\text{N}$ alloys have become very potential for high performance MJ solar cells. Because the band gap of $\text{In}_x\text{Ga}_{1-x}\text{N}$ alloys can be varied continuously from 0.7 to 3.4 eV. This provides an almost perfect fit to the full solar spectrum offering a unique opportunity to design MJ solar cells using a single ternary alloy

system. This will be technologically very significant because of easy fabrication, similarity in thermal expansion coefficient, electron affinity and lattice constant. In addition, InN based alloys are predicted to show high nobilities and lifetime of charge carriers and superior resistance against irradiation damage. These all make $\text{In}_x\text{Ga}_{1-x}\text{N}$ alloys very promising for high performance solar cells.

In order to evaluate the possibilities of these alloys, we tried, in this work, to model and simulate tandem cells made of two $\text{In}_x\text{Ga}_{1-x}\text{N}$ junctions without and with tunnel junction a one dimensional simulation program called a analysis of microelectronic and photonic structures (AMPS-1D).

In this work, calculations were all performed under 1-sun AM1.5 illumination and a temperature of 300 K using the one diode ideal model, and for convenience, several simplifying assumptions were made, including no reflection losses and no surface recombination velocity.

MODELLING AND SIMULATIONS

Analytical model

The total of the photo current density from single cells under illumination is given by:

$$j_{ph} = j_n + j_p + j_w \quad (1)$$

Where: j_n The photo current density in the base region is expressed by:

$$J_n = -eD_n \left. \frac{d\Delta n}{dx} \right|_{x=w_e+w} \quad (2)$$

J_p The photo current density in the emitter region is expressed by

$$J_p = -eD_p \left. \frac{d\Delta p}{dx} \right|_{x=w_{e1}} \quad (3)$$

J_w The photo current density in space charge layer pn is expressed by

$$j_w = I_o \exp(-\alpha(\lambda)w_e)[1 - \exp(\alpha(\lambda)w)] \quad (4)$$

The open circuit voltage is given by

$$V_{CO} = \frac{kT}{q} \times \text{Log} \left\{ 1 + \frac{I_{ph}}{I_o} \right\}$$

PV characteristic

The power supplied to the external circuit by the solar cell under illumination depends on the load resistor (external resistor placed across the cell). This power is maximum for an operating point (P_m (I_m , V_m)) of the current-voltage curve. To this point we can write after approximations

$$V_{mp} = V_{CO} - \frac{K.T}{q} \cdot \log \left(1 + \frac{q.V_{mp}}{K.T} \right) \quad (6)$$

$$I_{mp} = \left[I_{ph} + j_0 \left(e^{\frac{qV_{mp}}{KT}} - 1 \right) \right] \quad (7)$$

The cell conversion efficiency is usually taken to be:

$$\eta_{mk} = \frac{P_{\max k}}{P_{in}} = \frac{I_{mk} \cdot V_{mk}}{P_{in}} \quad (8)$$

P_{in} is the total incident solar power.

For maximum efficiency, each cell should be operated at its optimal J-V parameters, which are not necessarily equal for each cell. If they are different, the total current through the solar cell is the lowest of the tow. By approximation, it results in the same relationship for the short-circuit current of the multi-junction mode tandem solar cell:

$$I = \min (I_{mk}) \quad (9)$$

An operating voltage V_{mk} and power output will be obtained

$$P_k = V_{mk} \cdot \min (I_{mk}) \quad (10)$$

The total conversion efficiency to be

$$\eta = \frac{\sum_{k=1}^n P_k}{P_{in}} \quad (18)$$

Parameters for the simulation

Material parameter equations used for the simulation of the $\text{In}_x\text{Ga}_{1-x}\text{N}$ SCs.

✓ Band gap[2]

$$E_g(x) = 0.7x + 3.4(1 - x) - 1.43(1 - x) \quad (11)$$

✓ Electron affinity [8,9]:

$$\chi = 4.1 + 0.7(3.4 - E_g) \quad (12)$$

✓ Absorption coefficient

$$\alpha(\lambda) = 2.2 \times 10^5 \sqrt{(1.24/\lambda) - E_g} \quad (13)$$

✓ Effective density of states in the conduction band [8]

$$N_c = [0.9x + (1 - x)2.3] \times 10^{18} \quad (4)$$

✓ Effective density of states in the valence band [4]

$$N_v = [5.3x + (1 - x)1.8] \times 10^{19} \quad (5)$$

✓ Relative permittivity [8]:

$$\epsilon_r = 14.6x + (1 - x)10.4 \quad (6)$$

✓ Carrier mobility [10] :

$$\mu_i(N) = \mu_{min,i} + \frac{\mu_{max,i} + \mu_{min,i}}{1 + (N/N_{g,i})^{\gamma_i}} \quad (7)$$

The above formulae with asterisk are obtained from the linear fitting of the corresponding parameters of InN and GaN. The carrier mobility of InGaN is assumed to be similar to GaN, where $i = n, p$ denotes electrons and holes, respectively, and N the doping concentration, while the model parameters $\mu_{min,i}$, $\mu_{max,i}$, $N_{g,i}$ and γ_i depend on the type of semiconductor [10].

Table 1

Model parameters used in the calculations of the carrier mobility.

Type of carriers	$\mu_{max,i}$ ($\text{cm}^2\text{V}^{-1}\text{S}^{-1}$)	$\mu_{min,i}$ ($\text{cm}^2\text{V}^{-1}\text{S}^{-1}$)	$N_{g,i}$ (cm^{-3})	γ_i
Electrons	100	55	2E17	1
Holes	170	3	3e17	2

$\text{In}_x\text{Ga}_{1-x}\text{N}$ tandem cells comprising two, three, four, five, six and seven junctions were simulated. The energy gap and indium fraction for $\text{In}_x\text{Ga}_{1-x}\text{N}$ alloys

computed for a six junction are given in table

OPTIMAL DEVICE STRUCTURE

The major objectives of numerical modeling and simulation in solar cell research are testing the validity of proposed physical structures, geometry on cell performance and fitting of modelling output to experimental results. Any numerical program capable of solving the basic semiconductor equations could be used for modeling thin film solar cells. The fundamental equations for such numerical programs are (i) Poisson's equation for the distributions of electric field (ϕ) inside the device and (ii) the equation of continuity for conservation of electrons and holes currents. [5]

The AMPS-1D program has been developed for pragmatically simulate the electrical characteristics of multi-junction solar cells. It has been proven to be a very powerful tool in understanding device operation and physics for single crystal, poly-crystal and amorphous structures. To date, more than 200 groups worldwide have been using AMPS-1D for solar cell design [6]. One-dimensional AMPS-1D simulator has been used to investigate the effect of different top cell layers. The structure of conventional $\text{In}_{0.52}\text{Ga}_{0.48}\text{N} / \text{In}_{0.84}\text{Ga}_{0.16}\text{N}$ solar cell is shown in Fig.1. The tunnel junction $\text{In}_{0.65}\text{Ga}_{0.35}\text{N}$ layers thickness was varied from 0.01 μm to 0.05 μm and the change of performance parameters are observed.

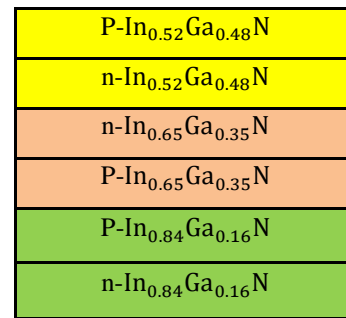


Figure 1

Cascade solar cell $\text{In}_{0.52}\text{Ga}_{0.48}\text{N} / \text{In}_{0.84}\text{Ga}_{0.16}\text{N}$ structure used for the modeling

The base parameters used for different structures adopted from some standard references are shown in Table 2:

Table 2
Description of the special paragraph styles

Layers Parameters	P- In _{0.52} Ga _{0.48} N	n- In _{0.52} Ga _{0.48} N	n- In _{0.65} Ga _{0.35} N	P- In _{0.65} Ga _{0.35} N	P- In _{0.84} Ga _{0.16} N	n- In _{0.84} Ga _{0.16} N
Thickness (μm)	0.1	0.2	0.005	0.005	0.1	0.15
Dielectric constant, ε	12.58	12.58	13.13	13.13	13.93	13.93
Electron mobility μ _n (cm ² /Vs)	685	685	685	685	685	685
Hole mobility μ _p (cm ² /Vs)	153	153	153.3	153.3	153.3	153.3
Carrier density, n or p (cm ⁻³)	1*10 ⁺¹⁷	1*10 ⁺¹⁷	1*10 ⁺¹⁹	1*10 ⁺¹⁹	1*10 ⁺¹⁷	1*10 ⁺¹⁷
Optical band gap, E _g (eV)	1.64	1.64	1.32	1.32	0.94	0.94
Effective density, N _c (cm ⁻³)	1.57*10 ⁺¹⁸	1.57*10 ⁺¹⁸	1.39*10 ⁺¹⁸	1.39*10 ⁺¹⁸	1.12*10 ⁺¹⁸	1.12*10 ⁺¹⁸
Effective density, N _v (cm ⁻³)	3.62*10 ⁺¹⁹	3.62*10 ⁺¹⁹	4.075*10 ⁺¹⁸	4.075*10 ⁺¹⁸	4.74*10 ⁺¹⁹	4.74*10 ⁺¹⁹
Electron affinity, χ (eV)	5.33	5.33	5.56	5.56	5.82	5.82

RESULTS AND DISCUSSION

Total efficiency versus tunnel junction layer thicknesses:

The simulation work has been performed aiming to compare the different types of cell structure made by changing thickness of The tunnel junction emitter layers In_{0.65}Ga_{0.35}N-P and base layers In_{0.65}Ga_{0.35}N-N to find out best structure for higher efficiency and more stable -In_{0.52}Ga_{0.48}N / In_{0.84}Ga_{0.16}N solar cells. The effect of tunnel junction on performance such as effect on general performance parameters, quantum efficiency (QE), shunt and series resistance, light and dark I-V characteristics

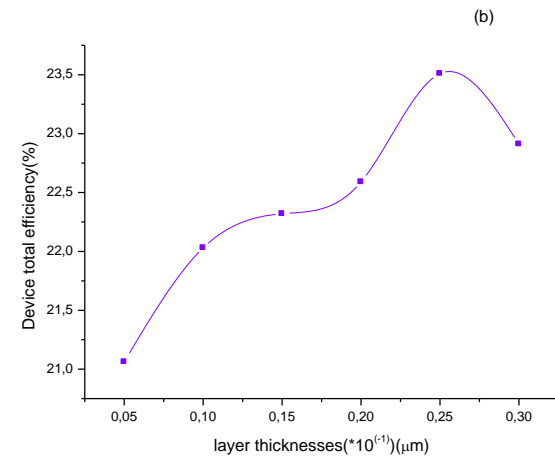
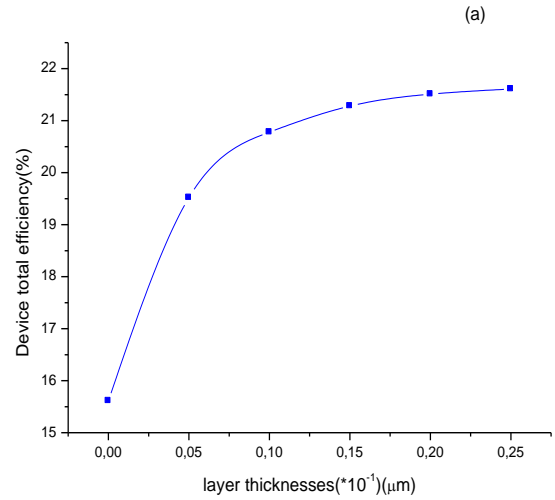


Figure 3
Device total efficiency versus tunnel junction layer thicknesses: (a) emitter layer p, (b) base layer n.

Figure 3 (a) shows the device total efficiency. The sum of the efficiency of top and bottom cells) versus the thickness of the emitter layer of the tunnel junction. The results on the Figure2 show that the optimum thickness is 0.02 microns. Figure 2 (b) shows the device total efficiency versus the thickness of the base layer of the tunnel junction cell.

The results indicate that the optimum thickness is about 0.050 microns for the tunnel junction.

Device operation

The current-voltage and power-voltage characteristics generated by the -In_{0.52}Ga_{0.48}N /In_{0.84}Ga_{0.16}N optimized device under the AM1.5G spectrum and one sun are displayed in figure 4 for multi-junction solar cell. The

corresponding PV parameters (open-circuit voltage V_{oc} , short-circuit current I_{sc} , fill-factor FF and efficiency (η) are all summarized in Table 3

Table 3
Parameters PV of the optimized GaAs /Ge device

Parameters photovoltaic	$V_{oc}(V)$	$I_{sc}(A)$	FF	$\tau(\%)$
	1,18	0.022	0.891	23.21

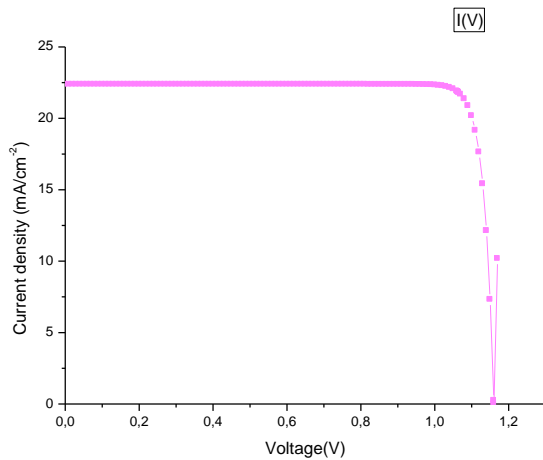


Figure 3
Current density-voltage characteristics GaAs /Ge device

CONCLUSIONS

In this investigation, we have shown that a relatively thin double-junction GaAs /Ge device can achieve a remarkably high power output. An extended spectral coverage due to a careful choice of the materials and optimization of the thickness and doping levels of each layer led to an enhanced overall power output from the $In_{0.52}Ga_{0.48}N / In_{0.84}Ga_{0.16}$ cascade device. Under the standard solar spectrum and one sun, the efficiency of the device is 23.21%,

ACKNOWLEDGMENTS

We would like to acknowledge the use of AMPS-1D program that was developed by Dr. Fonash's group at Pennsylvania State University (PSU)..

REFERENCES

Put references here.

- [1] Green, M. A. (2005). Third generation photovoltaics, Berlin, Springer..
- [2] Wu J, Walukiewicz W, Yu K M, Ager J W III, Haller E E, Lu H, Schaff W J, Saito Y and Nanishi Y 2002 Appl. Phys. Lett. 80:3967)
- [3] Xiao H L, Wang X L, Wang J X, Zhang N H, Liu H X, Zeng Y P, Li J M and Wang Z G 2005 J. Cryst. Growth 276:4011.
- [4] S. Jacobs and C. P. Bean, "Fine particles, thin films and exchange anisotropy," in Magnetism, vol. III, G. T. Rado and H. Suhl, Eds. New York: Academic, 1963, pp. 271–350.
- [5] Jani O, Honsberg C, Asghar A, Nicol D, Ferguson L, Doolittle A and Kurtz S 2005 31st IEEE Photovoltaic Specialists Conf. (Lake Buena Vista, FL, 2005) pp 37–42.
- [6] R. Nicole, "Title of paper with only first word capitalized," J. Name Stand. Abbrev., in press.
- [7] Zhang, X. B. et al., "Simulation of $In_{0.65}Ga_{0.35}N$ single-junction solar cells," J. of Phys. D: Appl. Phys. 40, 7335-7338 (2007)..
- [8] Hamzaoui, H., Bouazzi, A. S. and Rezig, B., "Theoretical possibilities of $In_xGa_{1-x}N$ tandem PV structures," Sol. Energy Mater. Sol. Cells 87, 595-603 (2005).
- [9] Levinshtein, M. E., Rumyantsev, S. L. and Shur, M. S., [Properties of Advanced Semiconductor Materials], Wiley, Chichester, UK, 1–90 (2001).
- [10] Li, N., "Simulation and Analysis of GaN-based Photoelectronic Devices," Dissertation (in Chinese), Institute of Semiconductors, Chinese Academy of Sciences, Beijing, 3 (2005).
- [11] Li, N., "Simulation and Analysis of GaN-based Photoelectronic Devices," Dissertation (in Chinese), Institute of Semiconductors, Chinese Academy of Sciences, Beijing, 3 (2005).

Sustainable Constructive Materials (II)

EFFECTS OF WASTE MARBLE POWDER ON RHEOLOGICAL PROPERTIES AND STRENGTH OF SELF-COMPACTING CONCRETE

BOUKHELKHAL A^{*,1}, AZZOUZ L¹, BELAÏDI A S E¹, BENABED B¹, KENAI S², Kadri EH³

¹Laboratory of research of civil engineering, University of Ammar Telidji, Laghouat, Algeria

²Geo-materials Laboratory, University of Blida, Algeria

³Laboratory L2MGC, University of Cergy Pontoise, F9500 Cergy Pontoise, France

*Corresponding author: a.boukhelkhal@lagh-univ.dz

ABSTRACT

Self-Compacting Concrete (SCC) is known, as it is highly fluid concrete that can flow and be placed in formwork under its own weight without requirement of vibration or compaction. This fluidity is obtained with the use of high paste volume and superplasticizer. The paste of SCC is made principally of Portland cement, which is the most expensive component of concrete. As a result, the cost production of SCC is higher compared to the conventional concrete. However, to reduce the cost production of SCC, the binder is often a binary even ternary compound: Portland cement mixed with limestone fillers, blast furnace slag, natural pozzolana, silica fume, fly ash, etc. The aim of this work is to study the effect of the reuse of waste marble powder (WMP) as a supplementary cementations material on the rheological properties and strength of SCC. In the experimental investigation, the rheological properties of SCC were measured using the slump flow and J-ring tests. The obtained results show that a substitution ratio of 20% of the marble powder in SCC enhances their fresh properties. At the hardened state, the use of the marble powder decreases the mechanical strengths of SCC.

Keywords: Marble powder, SCC, Reology, Compressive strength.

INTRODUCTION

Self-compacting concrete (SCC) or Self-consolidating concrete (SCC) are very fluid so they flow and fall into place under the effect of gravity without need of compaction or vibration and give homogeneous concrete and resistant to segregation and bleeding. The use of SCC was not stopped because it has special and interesting properties at fresh state such as deformability, passing ability and resistance to segregation, despite the extra cost caused by the use of a large amount cement and the superplasticizer adjuvant. However, to make use of the SCC more practical and economical, the solution consist to include mineral additives in the composition of the SCC by partially replacing cement. The incorporation of minerals admixtures in SCC improves fresh and hardened characteristics of SCC [1, 2]. In fact, the use of supplementary cementitious materials provides a better workability and cohesiveness by improving the grain-size distribution and particle packing [3]. On other hand, using of fine materials having different grain-size and morphology enhances the compactness and reduces the risk of cracking relatively to the heat hydration of Portland cement improving therefore the performance of SCC at long-term [4]. Belaidi [5] was reported the positive effect of the marble powder as fine materials on the rheological properties of SCC when it is used in combination with natural pozzolana.

The aim of this study is to examine the effect on waste marble powder as fine materials on some

engineering properties of SCC. In fact, this material is locally available following the development of the industry of marble in Algeria.

EXPERIMENTAL PROCEDURE

Material properties

waste marble powder subject of this study is a waste resulting from cutting, shaping and lustration of marble stones. The cement used in this study is an artificial Portland cement (CEMI) class 42.5. The physico-chemical properties of WMP and cement are given in.

As fine aggregate (FA), an alluvial sand was used, it is characterized by granular class of 0/5, and a continuous size. For coarse aggregate (CA), two classes were used 3/8 and 8/15. The physical properties of the aggregate are shown in Table 2.

In order to determine particle size distribution of marble powder, laser distribution analysis was carried out (Figure 1). The results indicated that the particle size of marble powder is less them 100 μm and 90% of particles of marble powder have a diameter lower them 20 μm .

Table 1 Chemical composition and physical properties of cement and waste marble powder

Component (%)	Cement	Waste marble powder
SiO ₂	20.14	0.42
CaO	63.47	56.01
MgO	2.12	0.12
Al ₂ O ₃	3.71	0.13
Fe ₂ O ₃	4.74	0.06
SO ₃	2.67	0.01
K ₂ O	0.47	0.01
TiO ₂	0.21	0.01
Na ₂ O	0.69	0.43
P ₂ O ₅	0.06	0.03
Loss ignition	1.72	42.78
Specific gravity	3.1	2.7
Finesses (cm ² /g)	3300	3600

Table 2 Physicals properties of aggregate

Aggregate	FA	CA	CA
	0/5	3/8	8/15
Absorption Coefficient (%)	0.59	1.56	2.26
Density	2.6	2.61	2.54
Water content (%)	0.03	0.17	0.13

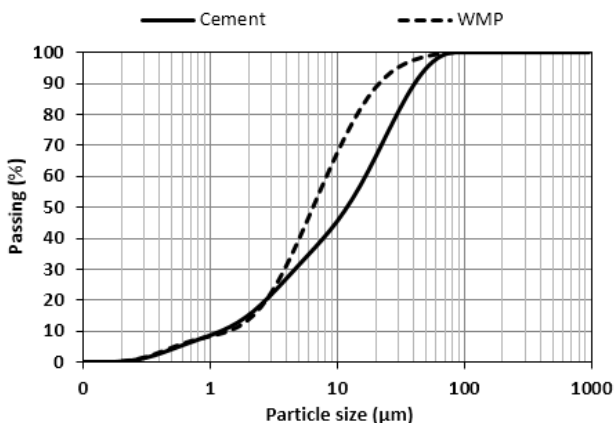


Figure 1 Particle size distribution of cement and waste marble powder

Mix design

six mixtures are considered to study the effect of waste marble powder on some properties of SCC. The binder content, water / binder ratio and dosage of superplasticizer are taken equal to 470Kg/m³, 0.4 and 0.9%, respectively. The control mix contains only the cement, while other mixtures include in addition the waste marble powder at different substitution levels (5, 10, 15, 20 and 25%). The compositions of different mixtures are presented in.

Test Protocol

Fresh concrete

The slump flow and J-ring tests were conducted to characterize the filling and passing abilities of fresh SCC. In these tests, the final diameter of the concrete sample through two directions was measured (Figure 2 and

Figure 3). For self-compacting concrete, values ranging between 65 and 80 cm are recommended [6]. The flow time T₅₀, which is the time necessary to reach the circle of 50cm of diameter, is also competed.

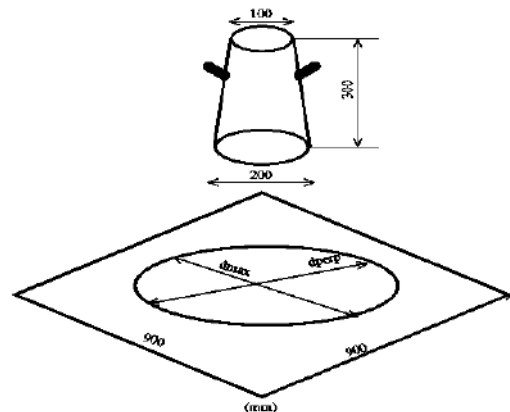


Figure 2 Schematization of the slump flow test

In order to evaluate the passing ability and the risk of blocking of SCC, the difference between slump (medium unconfined) and J-ring (medium confined) flow diameters was calculated. Difference values inferior to 2.5cm indicated that the mix has a good passing ability, values ranging between 2.5 and 5cm are the synonym of a partial blocking, the passing ability is very poor if the difference values were superior to 5cm [7]. It can be evaluate also the passing capacity in J-Ring test by measuring the height difference B_J (difference of heights between the concrete inside and outside the ring). The passing ability depends of the height difference, a low value (less than 1cm) is the sign of a good passing ability to pass, while a high value is synonymous of poor passing ability. To calculate the height difference, it is necessary to measure the height of the concrete sample in five points, one in the inside (center of concrete sample) and the other outside of the ring. The height difference is given by the following expression:

$$B_J = \frac{\Delta h_{x1} + \Delta h_{x2} + \Delta h_{y1} + \Delta h_{y2}}{4} - \Delta h_0 \quad (1)$$

It can be noted that it is possible to evaluate the trend to segregation or bleeding of SCC throw

visual control. This test gives an idea about the homogeneity of the mixture by observing the process of flow and the edges of the concrete sample. The presence of a layer of water or irregular distribution of coarse aggregate is a sign of bleeding or segregation.

Hardened concrete

The compressive strength can be measured on cylindrical or prismatic specimen in accordance with standard NF P18-430 [8]. In our case, six pieces of three prismatic specimens (7×7×28cm³) that were previously crushed by bending, were tested. The specimen is subjected to an increasing load until fracture using a hydraulic press having a capacity of 2000kN.

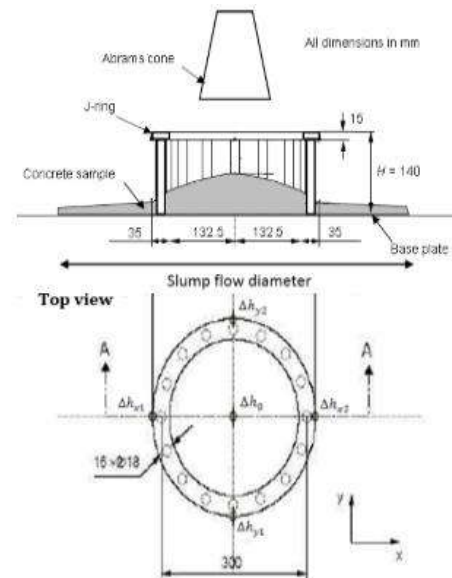


Figure 3 J-Ring flow test

Table 3 Mix proportions of SCC

Materials (Kg/m ³)	Mixes		
	0WM P	5WM P	10WM P
Cement	470	448	426
% of WMP	0	5	10
Waste marble powder	0	22	44
Sand 0/5	882.9	882.9	882.9
Gravel 8/15	553	553	553
Gravel 3/8	277	277	277
Water	188	188	188
Superplastizer	4.23	4.23	4.23
w/p	0.4		

Materials (Kg/m ³)	Mixes		
	15WM P	20WM P	25WM P
Cement	404	381	359
% of WMP	15	20	25
Waste marble powder	66	89	111
Sand 0/5	882.9	882.9	882.9
Gravel 8/15	553	553	553
Gravel 3/8	277	277	277
Water	188	188	188
Superplastizer	4.23	4.23	4.23
w/p	0.4		

RESULTS AND DISCUSSION

Fresh concrete

Figure 4 presents the variation of the slump flow with and without J-ring versus the content of WMP. The results obtained show that the incorporation of WMP increases the slump flow of SCC in the two mediums. Furthermore, the difference in slump flow (without - with J-Ring), for all mixtures is less than 2.5 cm, which is significant, according to ASTM c1621, that these mixtures have good capabilities to flow through confined medium [7]. The difference in slump flow of 0WPM; 5WPM; 10WPM; 15WPM; 20WPM and 25WPM is 2; 1.9; 1.6; 1.5; 1.2 and 1.8, respectively.

Exception 25WPM mix, it can be concluded that increasing the amount of WPM decreases the height difference. Consequently, the flow capacity increases.

The variation of flow times of T₅₀ s with and without J-Ring versus the WPM content is illustrated in Figure 5. There is a reduction of flow time with increasing the amount of WPM substituted. It can be remarked that the flow time in the unconfined medium is small compared to the confined medium, which is due to the presence of the metal bars that tend to block the flow of concrete. It was observed that all the mixtures have a flow time T₅₀ less than 2 s. These values are outside the target area 2 ÷ 5 s [9]. Similar values were however obtained in France with homogeneous SCC, which do not present a segregation or bleeding [10].

The effect of WPM on the height difference of SCC is shown in Figure 6. The results indicate a decrease in the difference of heights with increasing the content of PM. the height difference values are in the range of 1.15 and 1.55 cm. Decreasing of the height difference is the sign of increasing of the flow capacity.

The visual control of different compositions is shown in Figure 7. It can be seen from this figure that the mixes obtained with a WPM content varying between 5 and 20% are fluid and homogeneous, while the mix contains 25% of WPM presents a great risk of bleeding. The presences of bleeding in this mixture affect also the hardened properties and durability.

Hardened concrete

Erreur ! Source du renvoi introuvable. shows the evolution of compressive strength with age of the compositions tested.

By analyzing the results, it is possible to make the following observations:

- ♣ The strength of all mixes increases progressively with increasing maturing age;
- ♣ Due to its cement content, the control mix has, for all ages, the highest strength;
- ♣ With the same amount of the binder, the substitution of the cement by the WPM decreases the strength of SCC;
- ♣ The compressive strength of 0WMP; 5WMP; 10WMP; 15WMP; 20WMP and 25WMP mixes at 28 days is 37.2; 36.7; 34.5; 28.8; 26.1 and 23.60 MPa, respectively. After 90 days, these values are 47.8; 43; 39.63; 38.35; 37.20 and 34,48MPa.
- ♣ In comparison with the reference mixture, the strength of 5WMP; 10WMP; 15WMP; 20WMP and 25WMP mixture decreases by 1.25; 7.26; 22.58; 29.75 and 36.56% at 28 days and 13.17; 22.18; 25.60; 28.70 and 36.02 at 90 days.
- ♣ The 20WMP composition containing a cement content of 380kg/m³ has a similar strength to that of conventional concrete at 28 days (approximately 26MPa).

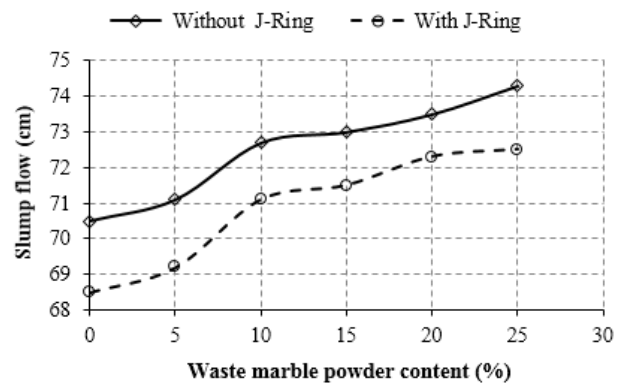


Figure 4 Effect of WPM on the slump flow of SCC

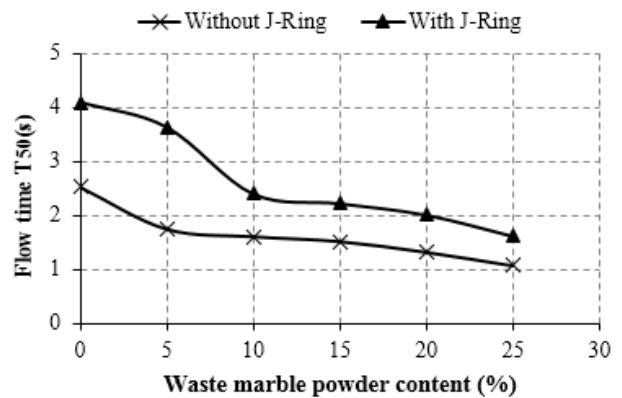


Figure 5 Effect of WPM on the flow time of SCC

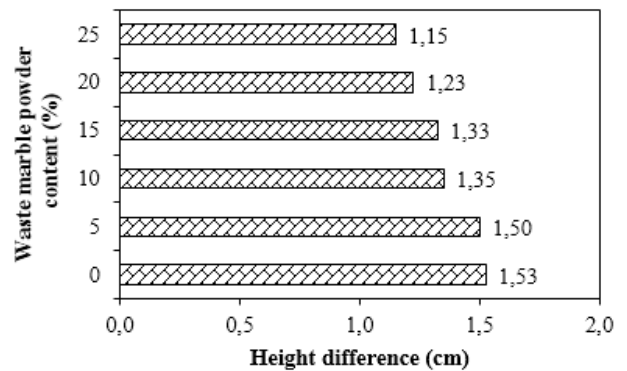


Figure 6 Evolution of the height difference of SCC

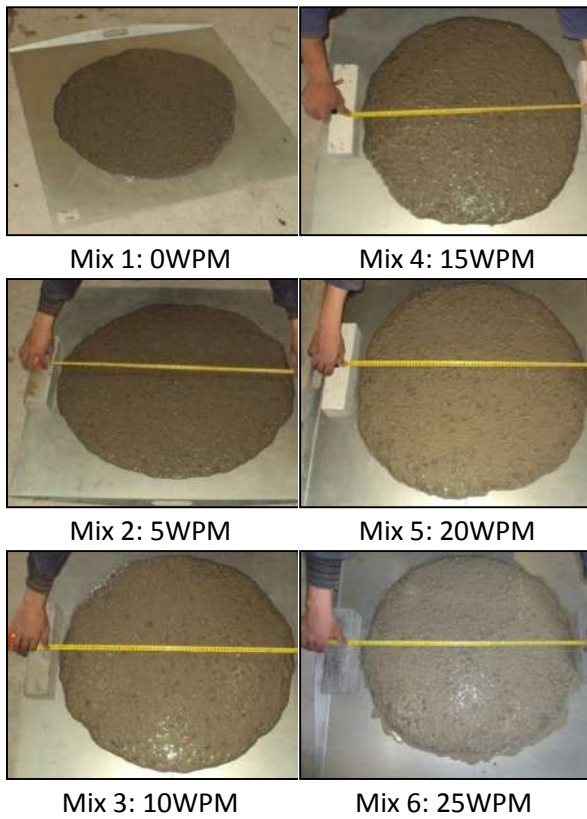


Figure 7 Visual control of SCC mixes

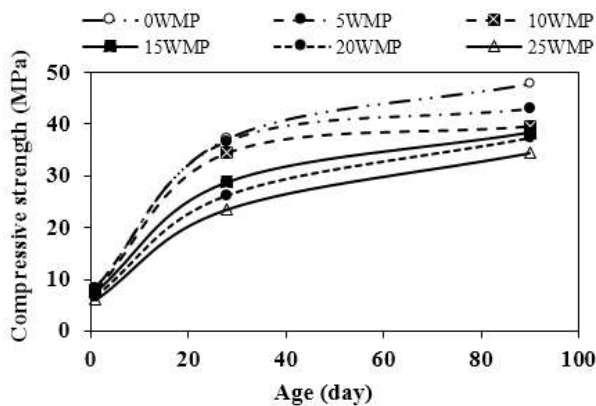


Figure 8 Evolution of compressive strength

Table 3 Properties of SCC made with waste marble powder

Parameter	Mixes						
	0W PM	5W PM	10W PM	15W PM	20W PM	25W PM	
Slump flow (cm)	70,5	71,1	72,7	73	73,5	74,3	
Flow time T ₅₀ (s)	2,53	1,75	1,61	1,52	1,32	1,07	
Slump flow with J-Ring	68,5	69,2	71,1	71,5	72,3	72,5	
Flow time T ₅₀ with J-Ring	4,09	3,63	2,4	2,22	2,01	1,62	
Height difference	1,53	1,50	1,35	1,32	1,22	1,15	
Compressive strength (MPa)	1j	8,35	8,18	7,98	7,70	6,70	6,10
	2	37,2	36,7	34,5	28,8	26,1	23,6
	8j	0	3	0	0	3	0
	9	47,8	42,9	39,6	38,3	37,2	34,4
	0j	8	8	3	5	0	8

CONCLUSIONS

Following the results obtained in this work, we can draw the following conclusions:

- The use of marble powder as a mineral addition in SCC is very advantageous in both fresh and hardened state.
- Substitution of marble powder by cement has a beneficial effect on the properties of BAP in the fresh state such as deformability and passing ability. For the homogeneity, SCC containing 5 to 20% of WMP are homogeneous, beyond 20%, the SCC present a high risk of bleeding.
- In the hardened state, the partial replacement of cement by the marble powder decreases the compressive strength. At 28 days, a range of strength varying from 23-37 MPa was obtained. These results allow the use of each replacement level in a defined application. For example, SCC containing a WMP content of 20% can be used in a structure when the desired resistance is of the order of 25MPa. For an other application requiring a strength of 35MPa a substitution rate of 10% appears to be adequate.

REFERENCES

[1] M. Sonebi, "Medium strength self-compacting concrete containing fly ash: modeling using factorial experimental plans.," *Cement Concrete Research*, vol. 34, no. 7, pp. 1199-208, 2004.

[2] A. S. E. Belaidi, S. Kenai, E.-H. Kadri, H. Soualh and B. Benabed, "Effects of experimental ternary cements on fresh and hardened properties of self-compacting concretes," *Journal of Adhesion Science and Technology*, 2015.

-
- [3] M. Sonebi and P. J. Bartos , "Hardened SCC and its bond with reinforcement," in *Proceeding of First International RILEM Symposium on Self-Compacting Concrete (PRO 7)*, Stockholm, Sweden, 13-15 September, 1999.
- [4] O. Boukendakdji, E. H. Kadri and S. Kenai, "Effects of granulated blast furnace slag and superplasticizer type on the fresh properties and compressive strength of self-compacting concrete," *cement and concrete composites*, vol. 34, no. 4, p. 583–590, 2012.
- [5] A. S. Belaidi , L. Azzouz , E. Kadri and S. Kenai, "Effect of natural pozzolana and marble powder on the properties of self-compacting concrete," *Construction and Building Materials*, vol. 31, p. 251–257, 2012.
- [6] EFNARC, "Specification and Guidelines for Self-compacting Concrete," Norfolk, UK, February 2002.
- [7] C. ASTM, "Standard Test Method for Passing Ability of Self-Consolidating Concrete by J-Ring," *American Society for Testing and Materials*, 2009.
- [8] AFNOR, *Béton et constituants du béton*, 5 ed., vol. 2, 2002.
- [9] EFNARC, "Specification and Guidelines for Self-compacting Concrete," Norfolk, UK, February 2002.
- [10] L. Soderland and C. Claeson, "Brite-EuRam project: rational production and improved workingenvironment through using self-compacting concrete," 2000.

EFFECT OF WATER FILM THICKNESS ON THE RHEOLOGICAL BEHAVIOR IN THE PRESENCE OF MINERAL ADDITION WITH POLYCARBOXYLATE SUPERPLASTICIZER

M³hamed ADJOUJ^{1,2,3}, Toufik BOUBEKEUR^{1,2}, Zahia DIDOUCHE^{1,2}, Karim EZZIANE², El Hadj KADRI³

1: University of Tissemsilt, 38000, Tissemsilt (Algeria)

2: Laboratory Geomaterials, University Hassiba Benbouali, 02000, Chlef, (Algeria)

3: Laboratory L2MGC, University of Cergy Pontoise, F9500 Cergy Pontoise, (France)

*Corresponding author: Fax: +21327799435 Email: adjoudj@hotmail.fr

ABSTRACT

In the manufacture of mortar or concrete, the water should be more than sufficient to fill the voids between the solid particles of cement and fine aggregate while the volume of the paste should be more than sufficient to fill the voids between the particles solid fine and coarse aggregates. So we should have enough water to cover all the fine particles and enough paste to cover all aggregates. Therefore it can be assumed that water film thickness and paste film thickness have major effects on the rheology of the mortar. In this study, we try to apply this approach to understand the rheological properties of mortar in combination with the amount and type of mineral and organic additives used.

KEYWORDS: Mineral addition, Mortar, Rheology, Superplasticizer, Yield stress, water film thickness.

NOMENCLATURE

QUANTITY	SYMBOL	COHERENT SI UNIT
voids ratio	μ	
water ratio	μ_w	
excess water	μ'_w	
specific surface area of the solid particles	SSS	m ²
effective surface area	SSS'	m ²
water film thickness	EFE	μm
effective water film thickness	EFE'	μm
surface areas of OPC	SSc	cm ² /g
surface areas of SF	SSd	cm ² /g
surface areas of fine aggregate	SSa	cm ² /g
volumetric ratios of OPC, SF and fine aggregate to the total solid volume	α_c, α_d and α_a	
correction coefficients	β_c, β_d and β_a	

1. INTRODUCTION

In 1968, Powers [1] proposed the approach of the thickness of the paste surrounding the aggregates like responsible for the mechanical properties of the concrete and its workability. Later, Helmuth [2] concluded that water film thickness surrounding cement particles governs the consistency of the cement paste. In a paste of fresh cement, it is determined that the water film thickness has the principal effect on its rheological behavior. In a mortar, it is added the thickness of the paste surrounding the aggregates as a second factor controlling the rheological behavior. Finally, the thickness of the mortar surrounding the large aggregates may help explain the rheological behavior of concrete. [3, 4] Recent studies on the compactness of granular mixtures concluded that the water film thickness is primarily responsible governing the rheological behavior of cement pastes [5,6], mortars, [7] and concrete [3]. It is well established that the compactness of the granular mixture and thickness of the film of water covering the solid grains, control the consistency and fluidity of mortar and concrete.

2. EXPERIMENTAL PROGRAM

2.1. Materials

Ordinary Portland cement (OPC) was used for all the mixtures and its chemical composition and physical properties are given in Table 1. The sand used in the mortars mixture is standard sand for cement mortar according to NF P 15-403 [8]. The mineral addition used is silica fume (SF). The chemical compositions and physical properties of silica fume is given in Table 1. The specific surface areas of the OPC, SF and fine aggregate were calculated as 4000 cm²/g, 18200 cm²/g and 21 cm²/g, respectively. A polycarboxylic-based superplasticizer (SP) was used in all mixtures with a specific gravity of 1.07, a solid content of 30% and a pH of 7.

2.2. Mixture proportion

Rheological properties of mortar are investigated according to the dosage of superplasticizer and silica fume content. The mortar was mixed with water for W/C ratio of 0.55. This value was chosen after making several mixes with different W/C and cementitious materials contents. Several dosages of each superplasticizer were used in the range of 0, 0.2, and, 0.4%. The quantity of silica fume was added by replacing a part of cement with the same mass of silica fume, with dosage ranged from 0% to 30% of binder (cement + silica fume). The whole sample preparation and testing procedures were carried out in a laboratory at a temperature maintained at 20 ± 2 °C.

2.3. Determination of WFT

Based on the packing density result, the voids ratio of the particle system may be determined as:

$$\mu = \frac{1 - \emptyset_{max}}{\emptyset_{max}} \quad (1)$$

Table 1
Chemical analysis and physical properties of
cementitious materials used.

Chemical	Cement	SF
----------	--------	----

constituent	(%)	(%)
SiO ₂	19.8	92
Al ₂ O ₃	5.14	0.3
Fe ₂ O ₃	2.3	0.8
CaO	64.9	0.3
MgO	0.9	1.1
SO ₃	3.4	0.2
K ₂ O	2.1	1.6
Na ₂ O	0.05	0.7
Blain fineness (cm ² /g)	4000	18200
C ₃ S	58	–
C ₂ S	13	–
C ₃ A	10	–
C ₄ AF	7	–

Where μ is the voids ratio (the ratio of the volume of voids in the bulk volume to the solid volume of the solid particles) and \emptyset_{max} is the maximum solid concentration of the solid particles. From the voids ratio so determined, the excess water ratio of the mortar can be evaluated as:

$$\mu'_w = \mu_w - \mu \quad (2)$$

Where:

μ'_w is the excess water ratio and μ_w is the water ratio (same as the W/S ratio by volume) of the mortar. This excess water ratio has the physical meaning of being the amount of excess water in the mortar per solid volume of the particles. Meanwhile, the specific surface area of the solid particles (defined as solid surface area per unit solid volume) in the mortar SSS can be calculated as:

$$SSS = \alpha_c SS_c + \alpha_d SS_d + \alpha_a SS_a \quad (3)$$

In which SS_c , SS_d and SS_a are respectively the specific surface areas of OPC, SF and fine aggregate, whereas α_c , α_d and α_a are respectively the volumetric ratios of OPC, SF and fine aggregate to the total solid volume. With the values of μ'_w and SSS so obtained, the WFT may be calculated as:

$$WFT = \frac{\mu'_w}{SSS} \tag{4}$$

Table 2
Evaluation of water film thickness effective of mortar containing various amounts of silica fume with polycarboxylate superplasticizer

1	2	3	4	5	6	7	8	9	10
SF (%)	SP (%)	OPC (g)	SF (g)	Water (g)	Sand (g)	SSS' (m2)	WFT' (µm)	WFT'' (µm)	τ (Pa)
0		630	0			669690	5.226	5.226	12.59
10	0	567	63			681219	5.137	5.137	15.52
20		504	126			692748	5.052	5.052	18.34
30		441	189			704277	4.969	4.969	26.31
0		630	0			669690	5.226	5.364	6.41
10	0.2	567	63	350	1890	681219	5.137	5.273	7.5
20		504	126			692748	5.052	5.186	10.95
30		441	189			704277	4.969	5.101	19.5
0		630	0			669690	5.226	5.502	2.32
10	0.4	567	63			681219	5.137	5.409	5.16
20		504	126			692748	5.052	5.319	8.82
30		441	189			704277	4.969	5.232	9.55

2.4. Determination of effective surface area

SSS'

To find a reliable relationship between the thickness of the water film and the rheological parameters, it has been proposed a new effective expression of the specific surface of the solid particles. This expression takes into account the effect of the strong interaction between the different components of the mixture on the compactness of the mixture. By introducing correction factors of each solid addition are:

$$SSS' = \beta_c \alpha_c SS_c + \beta_d \alpha_d SS_d + \beta_a \alpha_a SS_a \tag{5}$$

With β_c (cement), β_d (addition) and β_a (aggregate) correction coefficients determined by regression analysis from experimental results. The effective thickness of the water film will be given simply by the ratio of mixing with water on the effective surface area of the solid

material.

$$WFT' = \frac{\mu_w}{SSS'} \tag{6}$$

3. RESULTS AND DISCUSSION

3.1. Effects of *WFT* and *SF* content on yield stress

Table 2 presents the results of testing of rheological parameters of mortar containing different amounts of silica fume. Columns 1 and 2 show the rate of silica fume and the organic additive contained in mortar. Against by the columns 3, 4, 5, and 6 include the weight proportions used in the formulation of each mortar. Taking into account the particle size distribution data of the solids and their specific surfaces such as 4000 cm² / g for the cement, 18200 cm² / g to silica fume and 21 cm² / g for sand, can be deduced the overall surface area of the solid mixture described in column 7. The film of water that surrounds these solid grains is assessed on the column 8 by the ratio of the amount of mixing water (column 5) on the surface area of solid grains (column 7). By correlating between the water film values and the yield stress found, the results shown are obtained in Figure 1. A logarithmic relationship was chosen to express the variation of the rheological parameter based on the water film; this relationship is expressed as follows:

$$\tau = a \ln(EFE) + b \tag{7}$$

The correlation is very low and its coefficient takes values less than 0.4. For improving this correlation was applied the value of the water film expressed by the effective surface area and described by equations 5 and 6 depending on the experimental values of water film. By the least squares method, we got the correction parameters β_i solids and k_{sp} describing the effectiveness of superplasticizer PC. The results of the new thickness of the water film are summarized in column 9 and their correlation with the values obtained from the threshold is shown in Figure 2, where the correlation coefficient increases from 0.4 to 0.92.

$$\tau = a \ln(EFE'') + b \tag{8}$$

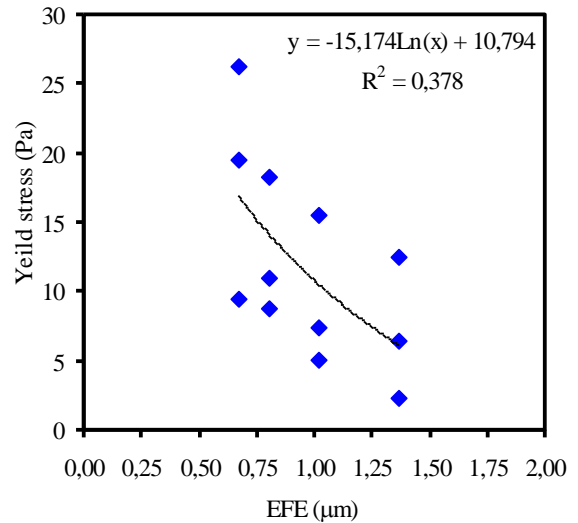


Figure 1
Correlation between the yield stress and water film thickness

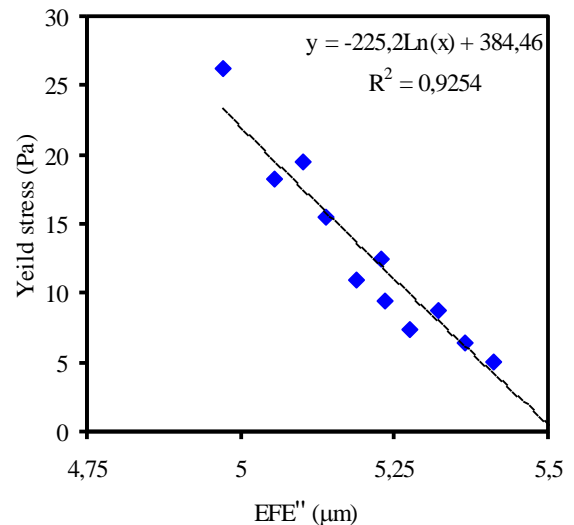


Figure 2
Correlation between the yield stress and water film thickness effective

CONCLUSIONS

In general, the yield stress decreases with increase in the thickness of the water film. This is very visible in the results presented by varying the dosage of superplasticizer and silica fume content. It can be concluded that when the mixing amount of water creates a thick water film, the shear induced in the mixture decreases thereby promoting its flow. This thickness of the water film is dependent on the type of addition used.

More the addition contains fine particles, the greater its effect on rheology is therefore where the best correlation was obtained for these additions. The variation in the rheological behaviour is related to the amount and type of superplasticizer. Its repulsion effect does the same as the thickness of the water film. The efficiency coefficient introduced into the expression 8 translated how an adjuvant helps to amplify the thickness of water and its positive value shows its compatibility with the cement used. Kwan and Fung [7,9] found that the packing density increases 0.662-0.707 by adding 1% polycarboxylate. This action is beneficial for the liberation of water trapped and the increase in thickness of water.

REFERENCES

1. Powers, T.C, 1968, the Properties of Fresh Concrete. New York, USA, John Wiley & Sons, p.664.
2. Helmuth, R.A, 1980, Structure and rheology of fresh cement paste, 7th International Congress of Chemistry of Cement, Sub-theme VI-0. p. 16–30.
3. Kwan, A.K.H, and Li, Y, 2014, Combined effects of water film, paste film and mortar film thicknesses on fresh properties of concrete, Construction and building materials, vol 50, ,pp.598- 608.
4. Li, Y, Kwan, A.K.H, 2014, Ternary blending of cement with fly ash microsphere and condensed silica fume to improve the performance of mortar, Cement and Concrete Composites, Vol 49, pp. 26-35
5. Kwan, A.K.H, and Wong, H.H.C, 2008, Effects of packing density, excess water and solid surface area on flowability of cement paste, Advances in cement research, 20, 1–11.
6. Zhang, Z, Zhang, B, Yan, P, 2016, Comparative study of effect of raw and densified silica fume in the paste, mortar and concrete, Construction and Building Materials, 70, 549–559.
7. Kwan, A.K.H, Fung, W.W.S, 2012, Roles of water film thickness and SP dosage in rheology and cohesiveness of mortar, Cement and concrete composites, vol, 34, pp.121–130.
8. NF P 15-403, 1996, standard sand, standard mortar, AFNOR, Paris.
9. Li , Leo G, Kwan, A.K.H, 2015, Effects of superplasticizer type on packing density, water film thickness and flowability of cementitious paste, Construction and Building Materials, vol, 86, pp.113–119.

MICROSTRUCTURE CHARACTERIZATION AND NUMERICAL ANALYSIS OF THE MECHANICAL BEHAVIOUR OF ARC-SPRAYED COMPOSITE COATING

Yazid FIZI *¹, Yamina MEBDOUA¹, Hadj LAHMAR¹, Mohamed El Amine BENAMAR²

¹ Centre de Développement des Technologies Avancées, Cité 20 août 1956, BP.17 Baba Hassen, Algérie

² Saad Dahlab University of Blida, Soumaa Street, P.O. Box 270, Blida 09000, Algeria

*Corresponding author: Fax: +213 21 35 10 39 Email: yfizi@cdta.dz

ABSTRACT

Arc-sprayed deposits are increasingly being used in a wide variety of industries. In order to understand, predict, and improve the reliability of coated devices, it is necessary to characterize their mechanical properties. Few researchers have therefore attempted to simulate the correlation between a thermal spray microstructure and mechanical properties of these coatings. Instrumented micro-indentation and meshing in the Object Oriented Finite Element (OOF2) program was combined with a nonlinear finite element analysis to determine elastic-plastic properties of an arc sprayed FeCNiBSi-(W/Ti)C composite coatings. Three elastic-plastic parameters are extracted, in a non-linear optimization approach, fully integrated with FE analysis, using results from a single indentation curve.

KEYWORDS

Instrumented indentation, arc-spray, composite coating, OOF2, Inverse analysis, finite element, mechanical behavior.

NOMENCLATURE

INTRODUCTION

The determination of the mechanical properties in thermal sprayed coatings is quite complicated, and often contradictory mechanical properties are reported. Non-destructive experimental procedures have been increasingly used to determine the mechanical properties of materials. In particular, instrumented indentation tests have been used to measure the depth of penetration of an indenter into a test piece. The results of such tests can be used not only to obtain and to interpret the hardness of the material but also to provide information related to near surface mechanical properties and the deformation behavior of bulk solids and coating, in this method, a hard tip of known geometry is applied perpendicular to the surface of the tested material; the depth of the penetration is continuously followed taking into account the applied load. A characteristic curve penetration-strength is obtained for both loading and unloading penetrator. This is different from conventional indentation which cannot take into account, a possible relaxation of the material and measures only the plastic deformation from residual indentation imprints.

Instrumented indentation technique emerges as an attractive technique for measuring the mechanical

properties of materials of small volume, and it is convenient, quick, and inherently simple without extensive effort of sample preparation in comparison with conventional tensile or compression experiments [1-4]. An instrumented indentation test (IIT) can, opposite to a tensile test, qualify local properties. In recent years, a number of methods based on both experimental and numerical studies have been proposed to extract the elastic-plastic properties from the indentation data. Finite element analysis (FEA), based on domain discretization, was developed to analyze indentation test. Dao et al. [1] and Bucaille et al. [5] used FEA to study instrumented sharp indentation and proposed analytical expressions of elastoplastic properties based on the FEA results. For example, Cheng and Cheng [6] used dimensional and finite element analyses to evaluate the mechanical properties of the materials from conical indentation problems. Microstructures of thermally sprayed coatings are complex ensembles of pores, cracks and different material phases. Few researchers have therefore made an attempt to simulate the correlation between a thermal spray microstructure and mechanical properties of these coatings [7].

The complexity of a thermal sprayed microstructure makes it difficult to model and simulate by classical analytical or numerical techniques and thus very

appropriate for this approach. Instrumented micro-indentation and meshing in the Object Oriented Finite Element (OOF2) program was combined with a nonlinear finite element analysis to determine elastic-plastic properties of an arc sprayed composite coatings. Three elastic-plastic parameters (modulus young's E , yield stress σ_y and work hardening exponent n) are extracted, in a non-linear optimization approach, fully integrated with FE analysis, using results from a single indentation curve.

EXPERIMENTAL PROCEDURE

Sample fabrication: In this research study, a twin wire arc spraying (TWAS) (ARCSpray 234-Metallization Company) was employed to spray FeNiBSi-(W/Ti)C coatings. The Metco 8297 cored wire with a diameter of 1.6 mm (Sulzer Metco, Switzerland) was used as wire feedstock material. The coatings were sprayed on grit blasted and cleaned carbon steel substrate cylindrical form with 25 mm in diameter and 5mm in thickness applying a voltage of 30 V, a current of 220 A, and air pressure of 6 bar with a spraying distance of 140 mm.

Metallographic investigation: X-ray energy dispersive spectroscopic (EDS) and SEM observations of the coating microstructure studies revealed the presence of porosity and oxides, it can be seen that all coatings consisted of lamellas built up from composite splats, unmolten particles. The carbides are also bounded with these Fe-rich phases. The exposed Fe-rich surfaces however were in contact with oxygen at high temperature, resulting in surface oxide layers around the particles, which became incorporated into the coatings, see Figure1[8]. The oxide layers can be clearly seen as dark gray layers between the lamellae and porosity as black spots (Figure 2.(a)).

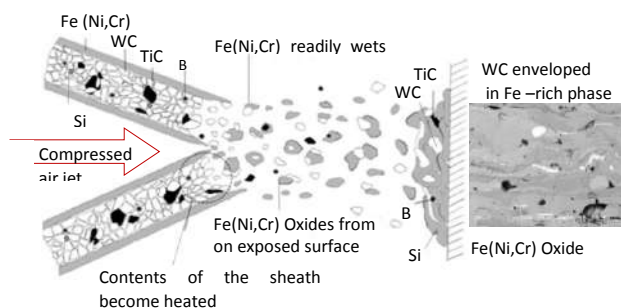


Figure 1 Schematic diagram showing the physical actions of sprayed particles during the EAS process
Mechanical Characterization

Indentation test: To explore the feasibility and robustness of the optimisation algorithm in real-life applications, it is appropriate to consider an experimental load–displacement curve test to extract the material properties. In this case, Experimental load–displacement curves for AISI 316 coating used in this study are based on microindenter Z2.5 with a Vickers tip.

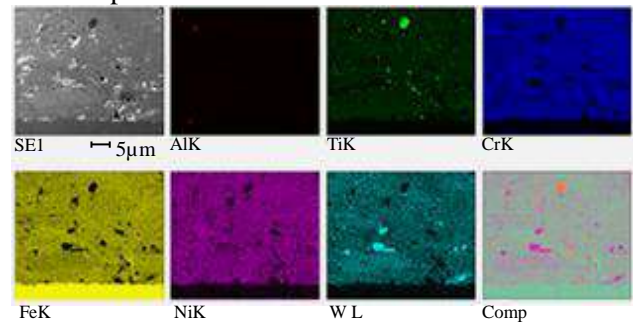


Figure 2

EDX analysis of an arc-sprayed composite coating

A Zwick/Roell equipment, with a resolution of $\pm 0.01\%$ in force and $0.02 \mu\text{m}$ in displacement, was used. The experiment was displacement controlled with an indentation velocity of $8.3 \mu\text{m/s}$. When the maximum available depth was reached, the indenter was held for 15 seconds, and then moved back with the same velocity. A Vickers indenter with a maximum load of 5N was used. The load–displacement curve was recorded continuously and elastic modulus determined from the unloading curve according to the Oliver and Pharr method [9].

FEA MODEL

In this study, the finite element simulations were performed using the commercial finite element code ABAQUS®. Contacts between indenters and composite coating are modeled. The methodology to create such a model is based on three independent steps. In the first step a digital microstructure cross section is made. In the second step this image is imported into the object-oriented finite-element analysis program OOF2 and a mesh constructed. The last step considers development of a nonlinear elastic-plastic simulation model of micro-indentation in the finite element software ABAQUS®.

The OOF2 Model

Construction of finite element models from real micrographs: The OOF2 model was created from an image of a microstructure cross-section. Polished sections were therefore prepared for microscopy analysis. The microstructure image was determined with an SEM. The digital image of the cross-section, consisting of 304 x 291 pixels, was imported into the program OOF2; an object oriented finite element program, developed at the Centre for Computational and Theoretical Material Science (CTCMS) at NIST. A typical cross-section is shown in Figure 4.

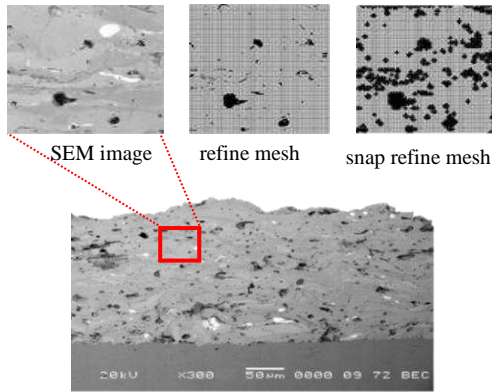


Figure 4

Typical examples of OOF models based on SEM morphological images of composites coating

Indentation model: Instrumented indentation was performed using the finite element software ABAQUS®. The overall objective with the FEA model is to predict the elastic-plastic material behavior, namely, stress-strain relationship based on load-displacement relationships determined through indentation, that is, through inverse analysis. The Vickers indenter was modeled with semi-vertical angle of 68°. At the very tip of the indenter, a spherical rounding with a radius of 5 μm was constructed because of the fact that no real indenter can be ideally sharp. During the loading step, the rigid cone indenter moves downwards along the z-direction and penetrates the foundation up to the maximum specified depth. In the second step, the indenter then taken back to the initial position. The contact between the indenter and the material is assumed to be perfect and without friction.

Material model: The plastic behaviour of the materials used in the numerical simulations was modelled considering that the stress and plastic strain, a power law strain hardening curve has been

used. The stress-strain (σ - ϵ) relationship [10] is assumed to be:

$$\sigma = \begin{cases} E\epsilon & \text{for } \sigma \leq \sigma_y \\ K\epsilon^n & \text{for } \sigma > \sigma_y \end{cases} \quad (1)$$

where K is a strength coefficient. Considering continuity at the initial yield point,

$$\sigma_y = E\epsilon = K\epsilon^n \quad (2)$$

such that

$$K = E^n \sigma_y^{1-n} \quad (3)$$

In ABAQUS® input file; a discrete set of points was required to represent the uniaxial stress-strain data, rather than specifying the work-hardening exponent n . Therefore, the set of plastic strain values varied from 0 to 0.2 with an increment of 0.02 in order to specify the plastic stress-strain data in ABAQUS®.

The friction coefficients at the contact between the indenter and the top surface of the bulk material were assumed to be zero, since friction had a negligible effect on the indentation process [5]. The presence of the substrate material was ignored in the analyses, as the indentation depth was shallow enough to regard the influence of the substrate material.

Application of inverse analysis in indentation

problem: There are four material parameters, namely, E , σ_y , n and ν , to be defined for an elastic-plastic material. For simplicity, the value of Poisson's ratio (ν) for composite is assumed to 0.3. A number of optimization techniques have been used by researchers [11, 13] to determine material properties from indentation load-displacement curves tests. In this study, a non-linear optimization technique is devised within the MATLAB®, which provides an excellent interface to FE codes such as ABAQUS®.

The inverse analysis based on Levenberg-Marquardt (LM) method is used to estimate two material properties. The LM method is described extensively in [14] and its use within the context of this work is illustrated by the flow chart shown in Figure.5. Essentially, it processes the experimental

data and attempts to obtain the best estimates for unknown state variables based on least-squares theory. The inverse analysis is based on the minimization of a cost functional measuring the discrepancy between the measured data and the one computed from the direct problem model. The expression of this cost functional for the indentation test can be expressed as in Eq. (4).

$$J(U) = \frac{1}{2} \sum_{i=1}^N [F_i^{comp}(U) - F_i^{meas}]^2 \quad (4)$$

Where $F_i^{comp}(U)$ and F_i^{meas} are respectively the reaction forces on the indenter obtained from measurement and computation of the direct problem. U is a vector that contains the unknown parameters, $U^T = [E, \sigma_y, n]$, and N is the number of measurements.

EXPERIMENTAL RESULTS

Two experimental indentation curves, corresponding to maximum and minimum values of determined E-modulus are shown in Figure 6.

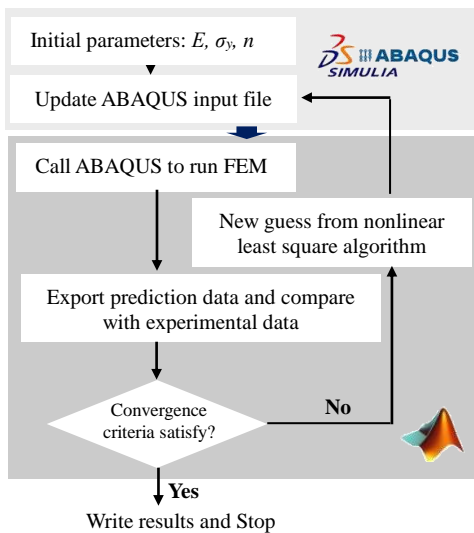
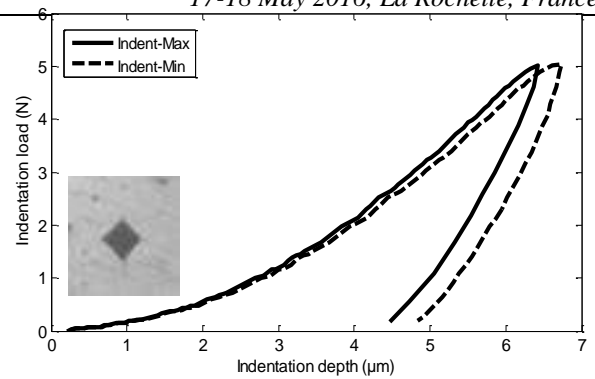


Figure 5

Flow chart of the optimization algorithm used to determine the mechanical properties

The two curves coincide at the beginning but deviate at the high force points, this may be due to micro-cracks, which could be created progressively under the indenter when the load increases. Also, probably for the same reason, the penetration depth of the indenter increases with porosity.

Figure 6



Experimental results from indentation tests corresponding to maximum and minimum values of the E-modulus

SIMULATION RESULTS

Finite Element Analysis: Modeling instrumented indentation was performed using the finite element software ABAQUS®.

The specimen was modeled as an axisymmetric geometry with four-node axisymmetric quadrilateral continuum elements with reduced integration (CAX4R). The specimen was meshed with a total of 1818 axisymmetric elements. A fine mesh density was used around the area of contact indenter coating, this density became coarser as one moves away from this zone. The Arbitrary values of E , σ_y , and n , have been chosen as initial values and the optimization algorithm has been used to find the optimized parameter from which the best fit between the experimental and predicted load–displacement loops can be achieved. The objective function is the error in the force–depth curves between the experiment and FEA. The method attempts to obtain the best estimate, based on least-squares theory, for unknown state variables. The material parameters that lead to the best fitting agreement represent the behavior of the coating. Figure 7 shows the force–depth curve from the experiment and the simulation with the initially and optimum material properties.

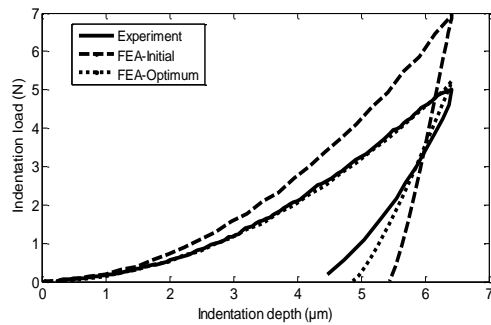


Figure 7

Comparison between experimental and simulation data for indentation curve, initial and optimized results

Table 1 shows the comparison between the results of the identification procedures of Hollomon and Ludwig laws.

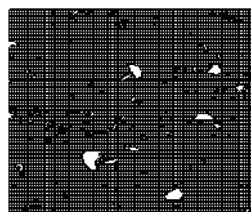
Table 1
Result of the identification procedures

Ludwik model [13]			
E (GPa)=E _{exp}	σ _y (MPa)	K (GPa)	m
137.02	1700	3.08	0.29
Hollomon model			
E (GPa)	σ _y (MPa)	n	
122.04	1691.80	0.38	

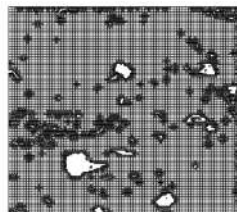
The material parameters that lead to the best fitting agreement can be considered to represent the constitutive behavior of the coating.

Experimental and numerical study [15] shows that stress–strain estimated curve can be approximated by Ludwik law ($\sigma = \sigma_y + K\varepsilon_p^n$).

Object-Oriented Finite Element Analysis: Two models of the approach are provided: one simulation with refine mesh OOFEA-1 and another with snap refine mesh OOFEA-2 (Figure 8). The substrate was not included in the FEA model. The OOF2 model is utilized to study the effect of porosity on the relationship between indentation load and displacement.



Model EF1 (a)



Model EF2 (b)

Figure 8

Finite element simulation model of composite coating, (a) refine mesh, (b) snap refine mesh

Figure 9 shows the maximum reaction force from FEA is slightly higher than the experimental data. In addition, there are differences between the experimental data and FE solutions at the end of unloading portion and it is expected that the accuracy of the optimization results will be affected by these differences. On the contrary, an analysis based on the OOF mesh, a good agreement between the experimental curve and corresponding predicted curves can be seen.

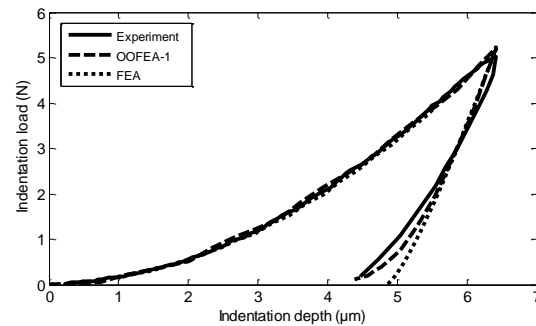


Figure 9

Comparison between experimental and simulation data for indentation curve, FEA and OOFEA results

Two OOFEA indentation curves derived in this study corresponds to model EF1 and model EF2 are shown in Figure 10. Both curves show the oscillation at the beginning of the loading step. This oscillation can be explained by the mesh density used around the contact indenter-coating. It is well known that Vickers hardness HV is about $3\sigma_{0.08}$, which corresponds to about three times of the flow stress at $\varepsilon=0.08(8\%)$ [1,16]. This means that the measured HV can predict one point on the stress and strain curve (the flow stress of $\sigma_{0.08}$).

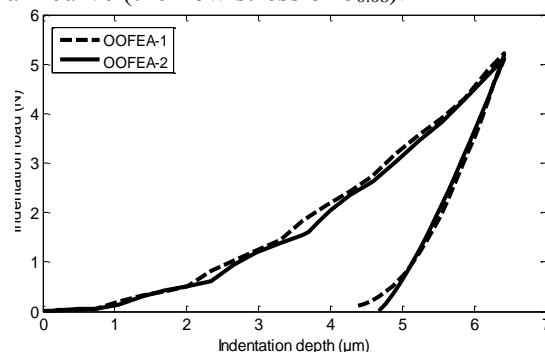


Figure 10

Indentation response of composite coating by object-oriented finite element analysis

The optimization results are summarized in Table 2 where the sensitivity of the proposed algorithm is demonstrated by changing three parameters at a time. This HV measurement yields the $\sigma_{0.08}$ of 1925.86 MPa. On the contrary, the estimated stress-strain curve with OOFEA-1 gives us $\sigma_{0.08}$ of 1813.55 MPa, showing the good agreement each other. Thus, the present approach for stress-strain behavior estimation is validated by this HV measurement.

Table 2

Three-parameter optimization for FEA and OOFEA

FEA		
E (GPa)	σ_y (MPa)	n
122.04	1691.80	0.38
OOFEA-1		
E (GPa)	σ_y (MPa)	n
87.29	904.38	0.32
OOFEA-2		
E (GPa)	σ_y (MPa)	n
111.80	1499.80	0.33

The material parameters that defined by this analysis (OOFEA-1) represent the behavior of the coating. The Von-mises stress for the model EF1 is presented in Figure 11. Stress concentrations at the indenter tip can clearly be seen.

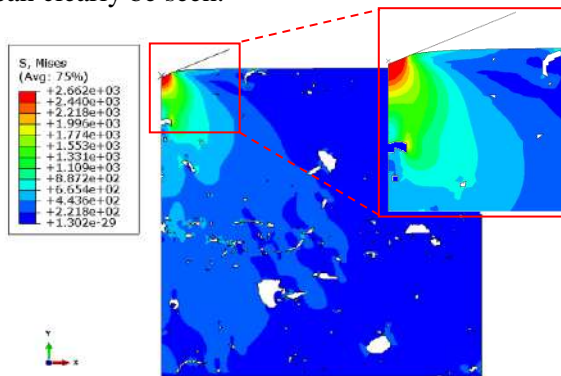


Figure 11

Simulated von Mises stress distribution under the indenter

CONCLUSIONS

In this work, the TWAS-sprayed FeCNiBSi-(W/Ti)C coatings was investigated with regard to micro-indentation tests. A mechanistic approach was proposed for extracting the mechanical properties of the cored composite coating. The approach was based on the combination of micro-indentation experiment,

finite element and inverse analysis techniques. In a future work, it should be interesting to develop and evaluate a methodology based on the combination of OOF and a nonlinear finite element analysis to simulate the interfacial indentation test.

REFERENCES

1. Dao, M., Chollacoop, N., Van Vliet, K. J., Venkatesh, T. A., and Suresh, S., 2001, Computational Modeling of the Forward and Reverse Problems in Instrumented Sharp Indentation, *Acta Mater*, **49** (19), pp.3899–3918.
2. Ogasawara N, Chiba N, Chen X, 2009, A simple framework of spherical indentation for measuring elastoplastic properties, *Mech. Mater*, **41**, pp. 1025-1033
3. A. Yonezu, H. Akimoto, S. Fujisawa, X. Chen, 2013, Spherical indentation method for measuring local mechanical properties of welded stainless steel at high temperature, *Mater. Des.* **52**, pp.812-820.
4. Xu B, Chen X, 2010, Determining engineering stress-strain curve directly from the load-depth curve of spherical indentation test. *J. Mater. Res.* **25**, pp. 2297–2307.
5. Bucaille, J. L, Staussb, S, Felderc, E, and Michler, J, 2003, Determination of Plastic Properties of Metals by Instrumented Indentation Using Different Sharp Indenters, *Acta Mater*, **51**(6), pp. 1663–1678.
6. Cheng, Y. T, and Cheng, C. M, 1999, Scaling Relationships in Conical Indentation of Elastic-Perfectly Plastic Solids, *Int. J. Solids Struct*, **36** (8), pp.1231–1243.
7. Michlik, P. and Berndt C, 2006, Image-based extended finite element modeling of thermal barrier coatings, *Surf & Coat Tech*, **201**(6), pp. 2369-2380.
8. Fizi Y, Mebdoua Y, Lahmar H, Lakhdari R, 2015, Object-Oriented Finite Element and Inverse Analysis to Determine Elastic-Plastic Properties of an Arc-Sprayed Composite Coating. *Congrès Français de la Mécanique CFM*, Lyon, France,
9. Oliver, W.C, Pharr, G.M, 1992. An improved technique for determining hardness and elastic-modulus using load and displacement sensing indentation experiments, *Journal of Materials Research* **7** (6), pp. 1564–1583.
10. Dieter G.E. *Mechanical metallurgy*, 1976, 2nd Ed, Mc Graw-Hill, New York, 26-27
11. Sun G, Xu F, Li G, Huang X, Li Q, 2014, Determination of mechanical properties of the

- weld line by combining micro-indentation with inverse modeling. *Computational Materials Science*, **85**, pp. 347–362
12. Buljak V, Bocciarelli M, Maier G, 2014, Mechanical characterization of anisotropic elastoplastic materials by indentation curves only. *Meccanica*, **49**, pp. 1587–1599
 13. Moya C.K.S, Bocciarelli M, Ringerc S. P, Ranzia G , 2011, Identification of the material properties of Al 2024 alloy by means of inverse analysis and indentation tests, *Materials Science and Engineering, A* **529**, pp. 119– 130
 14. Schnur D.S, Zabarás N, 1992, An inverse method for determining elastic material properties and a material interface, *Int. J. Numer. Methods Eng.* **33**, pp. 2039–2057
 15. Fizi Y, Mebdoua Y, Lahmar H, Djeraf S, Benbahouche S, 2015, Adhesion of FeCrNiBSi-(W-Ti)C wire-arc deposited coatings onto carbon steel substrates determined by indentation measurements and modeling, *Surf & Coat Tech*, **268**, pp. 310-316
 16. Tabor D, *Hardness of Metals*, 1951, Charendon Press, Oxford

ENERGY CONSUMPTION REDUCTION IN CONCRETE MIXING PROCESS BY OPTIMISING MIXING TIME

Hai-Thong Ngo¹, Abdelhak Kaci^{1,*}, El-Hadj Kadri¹, Tien-Tung Ngo¹, Alain Trudel², Sylvie Lecrux²

¹University of Cergy-Pontoise, L2MGC, 95000 Cergy-Pontoise, France

²Cemex France, Centre Technique National, 94150 Rungis, France

*Corresponding author: Fax: +331 3425 6941 Email: abdelhak.kaci@u-cergy.fr

ABSTRACT

Mixing process plays a very important role in the concrete microstructure which defines the quality of the final product. The improvement of energy efficiency during this process can help to reduce energy consumption and production costs, without affecting product quality. However, the current concrete mixing practice using an equal mixing time for all batches of each concrete mix design may lead to unnecessary mixing time and energy waste.

The present study investigates the benefit of the mixing time optimisation for energy consumption reduction during the concrete mixing process. For this purpose, a reliable method based on mixing power evolution is devised to calculate the shortest necessary mixing time (stabilisation time) of each concrete batch. The batch mixing energy consumption is also determined, through the use of power consumption and the duration of mixing cycle.

Experimental data obtained from 17 concrete batches of two mix designs produced in a full-scale concrete plant were analysed to figure out the energy consumption difference between the current mixing process of a single mixing time and the one of mixing time optimisation. The research results show that by optimising the mixing time, energy consumption is reduced by about 17% in comparison with the traditional mixing process. Productivity gains are significantly marked by obtaining a reduction in average mixing time of 32%.

NOMENCLATURE

- SCC : self-compacting concrete
- Ts : stabilisation time of power curve (s)
- Tm : mixing time (s)
- ΔT : mixing time difference between the mixing process of a single mixing time and the one of mixing time optimisation (s)
- ΔE : energy consumption difference between the mixing process of a single mixing time and the one of mixing time optimisation (Wh)

INTRODUCTION

Concrete is produced from the combination of aggregates (sand and gravel), cement, water and chemical admixtures. The ready-mixed concrete production includes two main processes: dry batch process and central mix concrete process (also called wet batch process). In dry batch process, concrete components are weighed individually and loaded directly into the truck's drum mixer which then performs mixing during transportation to the job site. On the other hand, in central mix concrete, raw materials are mixed in the concrete plant by a

stationary mixer. Fresh concrete is then transferred to the job site via a truck mixer. While the truck-mixing plant is popular in North America, the entire ready-mixed concrete production in Europe and Japan takes place at central plants [1]. Two important factors affecting the cost of ready-mixed concrete are raw material cost and cost of transportation. Apart from these costs, energy cost occupies a relatively large share of costs in overall manufacturing. Hence, energy saving becomes a vital issue in the concrete industry. This paper focuses on the energy saving for concrete production in central mix plant. As the mixing process represents a key role in the product's microstructure which defines the quality of the final product, in this paper, emphasis is put on the mixing energy consumption.

In several concrete plants, mixing energy requirements are determined by the power consumption curve (power consumption vs. mixing time) which is recorded and used to monitor the concrete evolution during mixing. Given the variability of aggregate water content during

industrial production, the use of this curve enables controlling batch water content and then regulating this composition in the mixing truck by adjusting the amount of water to be added in following batches [2, 3]. Indeed, when the mixing power measurement reaches a plateau (i.e. no significant change in power consumption), it is considered that concrete homogeneity is reached [4] and the water content of the mixed batch can be estimated. Besides, by tracking the time required to attain the power consumption stabilisation, different concrete mix designs need different mixing times to achieve optimum flowability [5]. This remark is also valid for the same given concrete mix design, i.e. different mixing times are required for batches containing different water contents.

However, the current mixing process consists of setting an equal mixing time for all batches within a given mix design in order to assure obtaining a compliant concrete for a majority of plant outputs. Such a production strategy may lead to unnecessary mixing time and energy waste when the mixing time needed to produce a homogeneous and uniform mix is less than that programmed in the concrete recipe. In this context, the authors propose a method of mixing time optimisation by setting the shortest necessary mixing time (stabilisation time of power consumption) as the sufficient mixing time of each concrete batch. The proposed method is compared with the current one of a single mixing time through experimental data obtained from a number of concrete batches within a full-scale concrete plant with the aim to advance in quantifying the difference in mixing times and energy consumptions. The authors strive to reduce mixing time and mixing energy consumption by limiting mixing time for each concrete batch to just what is adequate.

EXPERIMENTAL METHODS

Concrete composition

In this study, a total of 17 batches from different mix designs have been analyzed. Two self-compacting concrete recipes, i.e. an innovative concrete that does not require vibration for placing and compaction (SCC-A and SCC-B see Table 1) are mainly introduced and the water content was varied from one batch to the next. In order to reduce the water content of a concrete while maintaining a constant workability, a superplasticizer was added to the mixture. Total water content is presented in Table 1. The total water in the mixture includes the moisture of aggregates, the water added to the batch and the

water content in additives. The sand moisture is measured for each batch through a microwave moisture probe. The gravel moisture is considered constant during all the day of production. It should be noted that the concrete flowability is dependent on the effective water content which corresponds to the difference between the total water and the water absorbed by the aggregates. The water absorbed by sand and gravel equals to 6 L/m³ for SCC-A, 5.9 L/m³ for SCC-B.

Table 1
Concrete compositions

Component (kg/m ³)	SCC-A	SCC-B
Cement	295	311
Limestone filler	85	109
Sand 1 (0/4)	300	332
Sand 2 (0/4)	552	522
Gravel (4/14)	886	854
Superplasticizer	4.37	5.28
Total water	184-202	185-206
Water-cement ratio	0.62	0.60
Number of batches	8	9

Experimental procedure

The experimentation is carried out in a full-scale concrete plant equipped with a 2 m³ concrete pan-mixer. The loading cycle set by the plant operator in this concrete plant is as follow: gravel and sand (natural moisture) are first introduced into the mixer. The loading of fines (cement and filler) then occurs after about 10 s. Liquid components are sprayed onto the upper part of the mixture in 9 to 11 s approximately, after 20 s of dry mixing of aggregates and fine elements. The mixing time (T_m) is defined as the duration of mixing after completed filling of water and superplasticizer until emptying begins. For two SCC mix designs tested here, the mixing time is fixed at 100 s before discharging in a truck mixer. This T_m value is set long enough to avoid incomplete mixing.

The mixer motor power consumption evolution with mixing time (wattmeter curve) was recorded by data-acquisition equipment. The power indication represents the nominal output percentage of the mixer motor (75 kW). An example of a power

consumption curve including the loading sequence of a concrete batch is given in Figure 1.

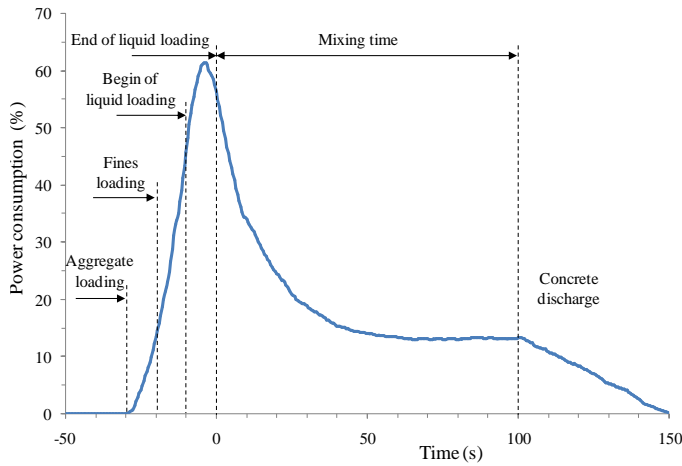


Figure 1

Power mixing and loading sequence of a concrete batch in the concrete plant

Calculation of the stabilisation time

According to some researches [6-9], the optimal fresh concrete properties are obtained and the concrete can be discharged when the stabilisation time T_s is reached. This time is defined as the time needed for the power consumption curve becomes stationary. It can be considered as the maximum efficient mixing time. Regarding the present study, the power consumption and its fluctuation in time are used to determine the moment at which the mixing power is stable (Figure 2). This fluctuation is assessed herein by calculating the standard deviation of twenty consecutive power measurements.

The stabilisation time is taken as the time when the power standard deviation is equal to a threshold value called ϵ . By observing and analysing all considered experimental power curves, when the power standard deviation decreases below ϵ set at 0.15% in absolute value, there is no longer strong fluctuation in mixing (Figure 4). For the majority of these power curves, setting the threshold value at 0.15% ensures that all subsequent values always remain below this one. The chosen criterion also allows getting a minimum value of 55 s for T_s among the mixtures tested here. This time is the minimum mixing time recommended by the French standard for SCC mix design [10].

The end-point of the stabilisation time in the power to time chart is called the "stabilisation point". After this point, the workability of all concrete mixes is considered optimal.

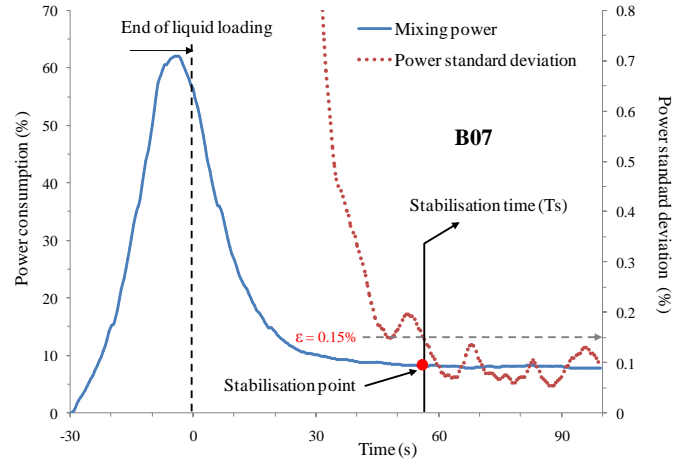


Figure 2

Power consumption and its standard deviation during the mixing of the concrete B07 are used to determine the stabilisation time

RESULTS AND DISCUSSION

Measures for time and energy saving

With the introduction of the stabilisation time of power curves for optimising the mixing time, the reduction of the mixing time can be made and quantified thanks to the mixing time difference (ΔT) between the whole mixing time T_m and the stabilisation time T_s . The energy consumption difference (ΔE) is then determined as the product of the average power consumption during ΔT and the ΔT value. Figure 3 shows an example of the determination of ΔT and ΔE .

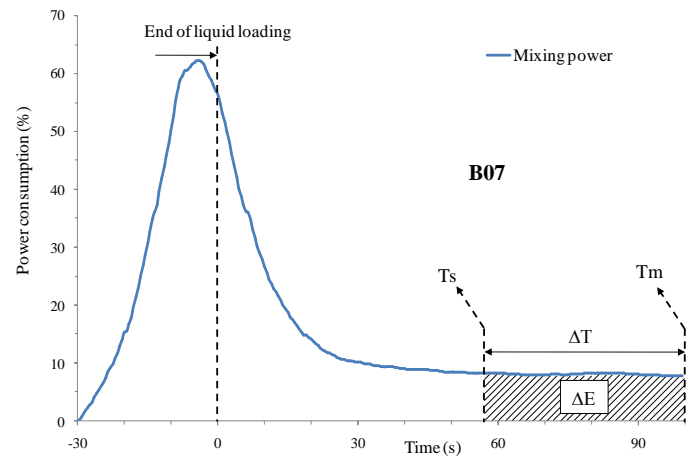


Figure 3

Energy consumption difference (ΔE) and mixing time difference (ΔT) of the concrete B07

Table 2 expresses the measurement results of stabilisation time, mixing time and mixing energy consumption differences for all concrete batches. For each concrete mix design, the results indicate the significant effect of total water content on the mixing time: the higher the water content, the smaller the stabilisation time. Indeed, more added water in the mix allows reducing the interparticle friction and increasing their mobility. This means that less mixing time and mixing energy are necessary to mix the particles. As a consequence, compared with the current process of a single, constant mixing time, the mixing time saving is greater for batches with higher water content. Nevertheless, there is no clear effect of concrete water content on the energy consumption difference. The reason is because of the dependence of the energy consumption on both mixing time and power consumption. An increase in concrete water content results in a reduction of mixing power consumption and an increase in mixing time difference.

Table 2
Values of total water, stabilisation time (Ts), energy consumption difference (ΔE) and mixing time difference (ΔT) obtained from 17 SCC batches

Mix design	N° batch	Total water (L/m ³)	Ts (s)	ΔT (s)	ΔE (Wh)
SCC-A	B01	199	55.0	45.0	95.6
	B02	193	66.5	33.5	86.5
	B03	191	69.5	30.5	83.2
	B04	184	89.0	11.0	37.4
	B05	192	71.0	29.0	65.3
	B06	187	79.5	20.5	60.2
	B07	202	57.0	43.0	75.3
	B08	198	59.0	41.0	75.2
SCC-B	B09	195	62.0	38.0	97.4
	B10	200	57.0	43.0	77.0
	B11	189	66.0	34.0	93.5
	B12	190	78.5	21.5	65.8
	B13	185	80.0	20.0	62.9
	B14	199	68.5	31.5	68.1
	B15	203	57.0	43.0	76.1
	B16	186	85.0	15.0	43.4
	B17	206	55.0	45.0	77.2

In any case, the improvement of the current mixing process allows shortening the mixing time which leads to the reduction of energy consumption. Table 3

shows the measurement results of total mixing energy consumption and mixing time of two SCC mix designs in the current mixing process. The total energy consumption of 8 SCC-A batches is 3489 Wh and 3688 Wh in the case of 9 SCC-B batches shown in the table. The total mixing time is 800 s for SCC-A and 900 s for SCC-B. For the calculation of energy consumption during mixing, we focus only on power consumption measurements after the end of liquid loading which is also the beginning of the mixing time.

Table 3
Results of total mixing energy consumption and total mixing time of two mix designs (SCC-A, SCC-B)

Mix design	Number of batches	Total mixing energy consumption (Wh)	Total mixing time (s)
SCC-A	8	3489	800
SCC-B	9	3688	900

Table 4 demonstrates measurement results for time and energy savings of these two concrete mix designs after optimising the mixing process. As presented in the table, the mixing time is reduced by 32 % for both two concrete mix designs since the stabilisation time is used as the sufficient mixing time. Moreover, the reduction of mixing time enables us to reduce energy consumption by 17 % for SCC-A and by 18 % for SCC-B. These results show that approximately 17 % of energy reduction and 32% of mixing time reduction from the current mixing process are achieved. In addition, it is pointed out that, the reduction rate of mixing energy consumption is smaller compared to that of mixing time. This is because during the mixing time, the mixer power consumption is higher before the stabilisation time is reached.

Table 4
Result of the reduction of mixing energy consumption and mixing time compared to the current mixing process

Mix design	Number of batches	Reduction of mixing energy consumption (%)	Reduction of mixing time (%)
SCC-A	8	17	32
SCC-B	9	18	32
Total	17	17	32

Stabilisation line

Five power curves are illustrated in the mixing power to mixing time chart (Figure 4) which also represents the stabilisation points for 17 tested concretes. It can be observed that the stabilisation points are located on a master line called "stabilisation line" which is mainly linear. After the intersection of this line and the power curves, power consumption does not change significantly (i.e. power standard-deviation smaller than 0.15%). Thus, further mixing is not necessary when the mixer power consumption curve reaches the stabilisation line. Therefore, the prior determination of this line may allow reducing to a minimum mixing time which ensures optimum productivity in the concrete manufacturing.

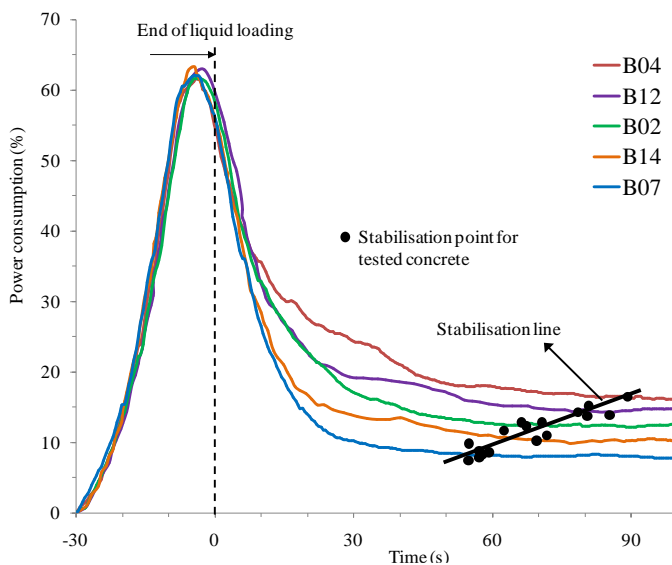


Figure 4

Five power curves and stabilisation points for all tested concretes (SCC-A and SCC-B)

CONCLUSIONS

In this paper, energy consumption is reduced in the mixing process of concrete manufacturing by optimising the mixing time. The method of mixing time optimisation consists of defining a stabilisation time of power consumption which is recorded during mixing. When the stabilisation time is taken as a sufficient mixing time of each concrete batch, a reduction of mixing time and mixing energy consumption can be made.

For a given mixing process, the stabilisation points indicating potential production "end-points" are located on a stabilisation line within the power-to-mixing time chart. The calibration of the stabilisation line depends on mixing and loading systems. Further research will aim to implement this kind of curve into

the concrete production process in order to improve the online survey and the quality control of concrete production.

KEYWORDS

Mixing time, energy consumption, mixer power measurement, stabilisation time, concrete plant, self compacting concrete

ACKNOWLEDGMENTS

The authors would like to thank Cemex companies for technical and financial support of the research work.

REFERENCES

- [1] Lobo, C. L., Gaynor, R. D., 2006, Ready Mixed Concrete. West Conshohocken, United States, International Standard Worldwide, Significance of Test and Properties of Concrete and Concrete Making-Materials.
- [2] Lê, N. D., 2007, Amélioration de la régularité du béton en production. Doctoral Thesis of Ecole des Ponts ParisTech.
- [3] Cazacliu, B., Ventura, A., 2010, Technical and environmental effects of concrete production: dry batch versus central mixed plant. *Journal of Cleaner Production*. 18 (13) 1320-1327.
- [4] Chopin, D., Cazacliu, B., De Larrard, F., Schell, R. d., 2007, Monitoring of concrete homogenisation with the power consumption curve. *Materials and Structures*. 40 (9) 897-907.
- [5] Rupnow, T. D., Schaefer, V. R., Wang, K., Hermanson, B. L., 2007, Improving Portland Cement Concrete Mix Consistency and Production Rate Through Two-Stage Mixing. National Concrete Pavement Technology Center.
- [6] Chopin, D., de Larrard, F., Cazacliu, B., 2004, Why do HPC and SCC require a longer mixing time? *Cement and Concrete Research*. 34 (12) 2237-2243.
- [7] Lowke, D., Schiessl, P., 2005, Effect of mixing energy on fresh properties of SCC, in: *Proceeding of 2nd North American Conference on the Design and Use of Self-Consolidating Concrete (SCC2005) and the 4th International RILEM Symposium on Self-Compacting Concrete*, Chicago, USA.
- [8] Mazanec, O., Schießl, P., 2008, Mixing time optimisation for UHPC, in: *Proceedings of the second international symposium on ultra high performance concrete*, Kassel, pp. 401-408.
- [9] Mazanec, O., Lowke, D., Schießl, P., 2010, Mixing of high performance concrete: effect of concrete composition and mixing intensity on mixing time. *Materials and Structures*. 43 (3) 357-365.
- [10] AFNOR, Janvier 2015, Référentiel de certification : Béton prêt à l'emploi.

SEISMIC VULNERABILITY ASSESSMENT FOR STEEL STRUCTURES

Amellal Omar, Bensaïbi Mahmoud

Department of Civil Engineering, University Blida 1, Blida, Algeria

Email: amellalomar@gmail.com

Department of Materials and Structures, Ecole Nationale Supérieure des Travaux Publics,

National School of Built and Ground Works Engineering, Kouba, Algiers, Algeria

Email: bensaibim@yahoo.co.uk

ABSTRACT

Seismic vulnerability analysis of steel structures requires some basic information on their mechanical and structural properties. The present study aims to quantify the seismic vulnerability of steel structures, through the use of a vulnerability index. The first step to do so is the identification of the main parameters that play an important role in the seismic vulnerability of such structures. Then using seismic feedback experience, weighting coefficients of each parameter are determined. An expression of the vulnerability index is given and based on the obtained value a building under study is classified as safe or unsafe according a proposed classification. A vulnerability index program (VIP) is developed in order to classify steel structures. This program is used to study several examples. The results are satisfactory comparing with in situ observations.

KEYWORDS: Seismic vulnerability, Steel structures, Vulnerability index, Seismic parameters.

NOMENCLATURE

R: Behavior Factor

Ki: Weighting Factor Ki

VI: vulnerability index

INTRODUCTION

Steel structures offer an advantage against the seismic stress due their lightness and ductility. These structures can suffer significant damage after an earthquake, [1,2].

The assessment of the seismic vulnerability of steel structures has been the subject of several studies HAZUS, RISK-UE, and RADIUS. Where vulnerability curves have been established using vulnerability index [3,4,5]. This index is calculated on the assumption of some parameters having an influence on the seismic behaviour of steel constructions and allowing description of seismic quality of such constructions [6].

These methods do not consider all influencing parameters, so in order to improve the existing index and to quantify more accurately the seismic behavior of such structure a vulnerability index method was developed [7-10].

VULNERABILITY INDEX METHOD

The parameters that have a significant influence on the seismic vulnerability of steel frame structures are given here after.

Selected parameters: these parameters are determined based on post-seismic observations and seismic experience feedback. The parameters taken into account are:

- | | |
|-----------------------------------|--------------------------|
| 1- Ductility | 8- Plan regularity |
| 2- Bearing capacity | 9- Modifications |
| 3- Assemblage | 10- Elevation regularity |
| 4- General maintenance conditions | 11- Pounding effect |
| 5- Type of soils | 12- Ground conditions |
| 6- Floor | 13- Roof |
| 7- Buckling | 14- Details |

Among these parameters, Ductility, Bearing capacity and Buckling need calculation, the other parameters are related to the in situ observation. In this paper, only Ductility is presented because it is an important and complex parameter.

Ductility: Under a strong earthquake, steel frame structures undergo plastic deformations, due to their faculty of dissipation of energy. Indeed, they have the ability to resist greater strain than the design one.

To take into account these plastic deformations, the seismic codes consider a reducing factor called “Behavior Factor” defined by the coefficient ‘R’ according to the Algerian seismic code (RPA 99 version 2003). The R values are given in table 1.

Table 1

Ductility according the Behavior Factor for Steel Frame Structures

Ductility level	Value of "R"
High Ductility: Class A	[6 – 4 [
Average Ductility: Class B	[4 - 2 [
Low Ductility: Class C	≤ 2

Quantification of each parameter: Weighting factors for each parameter are proposed on table 2. These factors are determined on a basis of a statistical data containing more than 300 constructions damaged by different earthquakes (Ain Temouchent (1999) and Boumerdes (2003)). For each parameter and each considered class, a coefficient (k_i) is identified expressing its seismic quality.

The “Details” parameter was specified as follows: studwork, dividing walls, balconies, railing, cornices, chimneys, ventilation space, electrical network, gas network, water network and sewage network.

Table 2
Weighting Factor “ K_i ”

N	Parameters	Classes/ K_i		
		Class A	Class B	Class C
1	Ductility	0.00	0.08	0.15
2	Bearing capacity	0.02	0.07	0.09
3	Assemblage	0.02	0.06	0.15
4	General maintenance conditions	0.08	0.06	0.08
5	Type of soil	0.03	0.04	0.05
6	Floor	0.03	0.04	0.05
7	Buckling	0.03	0.06	0.08
8	Plan regularity	0.03	0.04	0.05
9	Modifications	0.03	0.04	0.05
10	Elevation regularity	0.03	0.04	0.05
11	Pounding effect	0.03	0.04	0.05
12	Ground conditions	0.03	0.04	0.05
13	Roof	0.03	0.04	0.05
14	Details	0.03	0.04	0.05

Three classes are defined for each parameter. Each considered parameter can belong to one of the three defined classes A, B, and C. These classes are declined as follows:

Class A expresses a parameter inducing a good behaviour of the structure during an earthquake, *Class C*, expresses a parameter inducing a bad behaviour of the structure during an earthquake, *Class B* expresses an intermediate behaviour of the structure during an earthquake. The vulnerability index, VI, of a construction is expressed according to formula (1):

$$VI = \sum_{i=1}^{14} k_i \quad (1)$$

According to the obtained value for the vulnerability index, three vulnerability classes Green, Orange and Red are proposed, table 3:

Table 3
Vulnerability Index Classes

Class	Green	Orange	Red
VI	[0.36 – 0.54[[0.54 – 0.85[[0.85 – 1]

The first class associated to the green colour classifies the construction as resistant with no requirement to any repairs.

The second class associated to the orange colour classifies the construction as moderately resistant requiring reinforcement.

The third class associated to the red colour classifies the construction to be a construction with low resistance requiring demolition.

ELABORATED CHART

In situ observations on structures are important information required to assess the vulnerability of steel frame structures. An investigation chart for a survey was elaborated. The chart contains:

1. General data
2. Geometric characteristics
3. Information on the structural system
4. Information on the ground
5. Details on the non structural elements
6. General maintenance conditions

DEVELOPED PROGRAM

A program called Vulnerability Index Program "VIP using Delphi was elaborated providing the vulnerability index values for steel frame structures.

It uses the elaborated chart in order to estimate the coefficient of the different parameters and classify the structures.

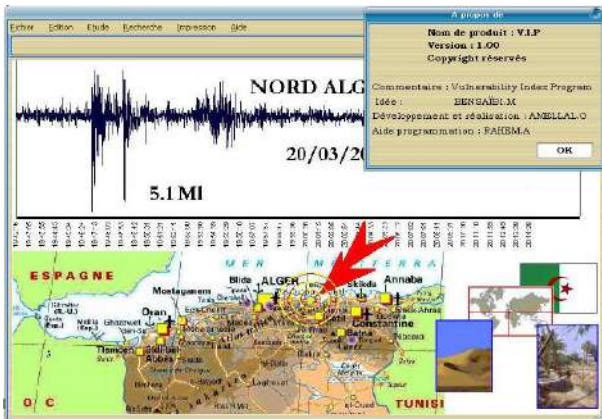


Figure 1
Front page of the VIP.

APPLICATION

Several examples have been treated. Here in, are two case studies presented as an example.

Case study one: It is a Zinc production manufacture built in 1949 and located in the West part of Algeria. The following figures show the damage undergone by this structure.



Figure 2
Damage in the bracing system.



Figure 3
Corrosion of columns.



Figure 4
Damage in the assembly system.



Figure 5
Damage in beams and floors.



Figure 6
Collapse of a floor.

The results given by the program are given in table 4.

Table 4
Manufacture parameters vulnerability

N°	Parameters	Class	Ki
1	Ductility	B	0.08
2	Bearing capacity	C	0.09
3	Assemblage	C	0.15
4	General maintenance conditions	C	0.08
5	Type of soil	B	0.04
6	Floor	C	0.05
7	Buckling	C	0.08
8	Plan regularity	C	0.05
9	Modifications	A	0.03
10	Elevation regularity	C	0.05
11	Pounding effect	B	0.04
12	Ground conditions	A	0.03
13	Roof	C	0.05
14	Details	C	0.05

A vulnerability index of 0.87 was found, this indicates that the structure belong to the red class. The conclusions provided by the Structural Engineering Control (CTC: official organization in charge of control in Algeria) suggest the demolition and the rebuilt of the manufacture according the latest standards.

So, the two conclusions are in adequacy.

Case study two: It is about a manufacture inaugurated in 1975, and composed of four parts: manufacture, storage, maintenance and administration. It should be noted that the process of manufacturing zinc liberates H₂SO₄ which is very harmful to the metal, as it accelerates the corrosion process. This manufacture built near the sea on sandy

soils and limited to the south by a high cliff. Photos below were taken on site during our visit.



Figure 7
Deformation of bracing system and buckling column.



Figure 8
Lack of bolts in the assembly system.



Figure 9
Cracking 45 degrees to both directions and both side of joint.

The VIP gives the following results:

Table 5
Result of the application of the Zinc manufacture

N°	Parameters	Class	Ki
1	Ductility	B	0.08
2	Bearing capacity	B	0.07
3	Assemblage	B	0.06
4	General maintenance conditions	B	0.06
5	Type of soil	C	0.05
6	Floor	B	0.04
7	Buckling	B	0.06
8	Plan regularity	C	0.05
9	Modifications	A	0.03
10	Elevation regularity	C	0.05
11	Pounding effect	C	0.05
12	Ground conditions	C	0.05
13	Roof	B	0.04
14	Details	C	0.05

The program gives $VI=0.76$, so the structure is classified Orange. This appears in concordance with in situ observations.

CONCLUSIONS

A vulnerability index method for steel structure has been developed and presented in this study. Elaborated specially for steel structures, it gives reasonable results regarding the influence of the different parameters such as Ductility, Bearing capacity and Buckling on the seismic behaviour of steel structure.

A classification has been established; the results from this classification are in accordance with the one done in situ. As a result, this classification can be used by engineers to reduce seismic risk and casualties in case of an earthquake.

ACKNOWLEDGMENTS

The authors wish to thank the director B. Kdroussi, the director of Technical Control of Construction (CTC/ Ouest Tlemcen), and A. Rahim, for their help in developing the computer program (VIP).

14. Mebarki, A., Boukri, M., Laribi, A., Farsi, M., 2014, "Seismic vulnerability: theory and application to Algerian buildings" Journal of

REFERENCES

1. Jerez Barbosa, R. S, march, 2011, "Seismic vulnerability of buildings: Response and damage assessment" thesis of Ph.d, university Paris-est, Paris, France.
2. Règles parasismiques Algériennes RPA 99 modifiées en 2003, 2003, Algérie.
3. Règles de Conception et de Calcul des Structures en acier CCM 97, 1997, Algérie.
4. Davidovici, V., 1999, "Construction en Zone Sismique", Publisher the Moniteur. Paris, France.
5. RISK-UE., 2003, An advanced approach to earthquake risks scenarios with applications to different European towns, WP4 : Vulnerability of current building, EVK4-CT-2000- 00014.
6. National Institute of Building Sciences, "Hazards risk assessment program", 1997, USA.
7. OYO Corporation, RADIUS methodology, IDNDR, (1999).
8. Nollet, M.J., 2004, "Evaluation de la Vulnérabilité Sismique des Bâtiments Existant ", cahier technique de l'ETS, Ecole de Technologie Supérieure Université du Québec, Montréal, Canada.
9. Akkase, M .N., 2006, Thoughts on Concepts of Seismic Hazards, Vulnerability and seismic Risk, 9th European confer on Earthquake engineering Vol X.
10. Lang. K., 2002, Seismic Vulnerability of Existing Building, thesis of doctorat, Swiss Federal institute of technology, Zurich, Suisse.
11. Yakut, A., Altuğ Erberik, M., Sucuoğlu, H., & S. Akka, 2014, " Rapid Seismic Assessment Procedures for the Turkish Building Stock, " Geotechnical, Geological and Earthquake Engineering. Volume 26, pp 15-35, 2014.
12. Ghasemi Azadkhani, M. J., Ahmadi Disfani, Y., & Reza Tavassoli, M. 2014, "Evaluating Earthquake Disaster Management in the Worn Urban, " Journal of Civil Engineering and Urbanism, Vol 4, Issue 1: 41-46 ,ISSN-2252-0430.
13. Gueguen, P. Lagomarismo, S. & Cattari, S, 2013, "Seismic Vulnerability of structures," published in Great Britain and the United States.

seismology, ISSN 1573-157X, vol. 18, no2, pp. 331-343.

15. Maio, R., et al., october (2015) "Seismic vulnerability of building aggregates through

- hybrid and indirect assessment techniques “,in Bulletin of Earthquake Engineering , volume 13, issu 10, pp 2995-3014.
16. Mehdi S., Mohsen ,G.A., and Naghmeh, P.L., July 30, 2015, “ Developing seismic vulnerability curves for typical Iranian buildings“ Proceedings of the Institution of Mechanical Engineers, Part O: Journal of Risk and Reliability, December 2015; vol. 229, 6: pp. 627-640.
17. Alessandra ,A., Marisa, P., November 2015 “ Seismic nonstructural vulnerability assessment in school buildings “ Natural Hazards, Volume 79, Issue 2, pp 1333-1358.
18. Seong- Hoon H., Ahmed, E., Samy, A., and Dimitrios G. Lignos, 25– 27 May 2015 «EARTHQUAKE LOSS ASSESSMENT OF STEEL FRAME BUILDINGS DESIGNED IN HIGHLY SEISMIC REGIONS »,5th ECCOMAS Thematic Conference on Computational Methods in Structural Dynamics and Earthquake Engineering M. Papadrakakis, V. Papadopoulos, V. Plevris (eds.),Crete Island, Greece.
19. Amellal, O., Bensaibi, M., Decembre 2015 “Estimation de la vulérabilité sismique des structures en charpentes métalliques” 9^{eme} colloque AFPS, à Marne-La-Vallée, Paris, France

EFFECT OF SUPPLEMENTARY CEMENTITIOUS MATERIALS (SCM) ON DELAYED ETTRINGITE FORMATION IN HEAT-CURED CONCRETES

Yasser AMINE, Nordine LEKLOU, Ouali AMIRI*

LUNAM Université, Université de Nantes – POLYTECH Nantes

GeM, CNRS UMR 6183, Research Institute in Civil Engineering and Mechanics, 58 rue Michel Ange BP 420 44606 Saint Nazaire cedex, France

*Corresponding author: Fax: + 33(0)2 40 90 50 90 E-mail: ouali.amiri@univ-nantes.fr

ABSTRACT

Delayed Ettringite Formation (DEF) is an internal sulfate attack caused by early age heating to a temperature of over 70 °C. In this paper, the effect of multiple mineral admixtures (Fly ash, metakaolin and natural pozzolan) of different nature or origins (two of each admixture) on the expansion of cylindrical concrete caused by DEF was investigated. For this purpose, a portion of cement was replaced by natural admixture with 15% dosages by fine admixture. The results obtained highlighted the significant effects of fly ash on DEF and the correlation existing between the expansion of the heat-cured concrete specimens and the evolution of their mechanical properties.

Keywords Ettringite, Concrete

INTRODUCTION

The Delayed ettringite formation (DEF) is an internal sulphate attack that can occur in the cementitious materials that were subjected to temperatures higher than 70°C at early age (1), (2). This heating may be due to the thermal heating of concrete during the prefabrication or the exothermicity of the hydration process of the cement in the case of massive concrete parts. Successive disorders, like swelling due to the DEF correspond to multi-directional cracking phenomena, leading to a decrease in mechanical performance and durability of concrete gradient (1); (3); (4). Previous studies have shown that some pozzolanic additions were effective in preventing the delayed ettringite formation. Ramlochan et al. (5) found that a small proportion of metakaolin ($\geq 8\%$) is able of reducing or eliminating the long-term expansion related to DEF. According to the authors, this is due to the high content of Al_2O_3 in the metakaolin and the leaching effect of reducing the alkali hydroxide of the pore solution. As for blast furnace slag, substituting rate of the cement required to remove the long-term expansion with the majority of cements is about 25%. But higher rates may be needed if used cements have very high levels of sulfate or alkaline. Fly ash required to suppress expansion depends on their composition. Fly ash with low concentrations of lime appear to be more effective when used with low substitution rate (15-25%), while the fly ash with a high concentration of lime can be effective to more degree of substitution high (25-35%). In one hand, more recently, studies of Nguyen *et al.* (4); (6) the natural pozzolan effect on the DEF

indicate that the fineness of the natural pozzolan significantly affects the kinetics of expansion due to DEF: a finely blended natural pozzolan used in partial replacement of cement can be reduced or even eliminate the expansion of DEF. In other hand, the substitution of the cement by the coarse natural pozzolan is not only ineffective, but also accelerates the expansion phenomenon (4). According to these authors, this could be explained by at least three factors: 1) pozzolanic reactions that reduce the amount of hydroxide, 2) reducing the amount of sulfates in the mortar due to the reduction of cement content, and 3) the high content of Al_2O_3 in the natural pozzolan. In addition, the fineness of the pozzolan, which determines the microstructure of the material indirectly influences the delayed ettringite formation. However, studies on the effects of mineral admixtures on the DEF are still relatively rare. In this context, the experimental study presented in this article aims to study the effect of different kinds of additions on the expansion of the concrete caused by DEF.

EXPERIMENTAL STUDY

Materials

As previously mentioned, the aim of this article is to study the effects of multiple mineral admixtures (Fly ash, metakaolin and natural pozzolan) on the risk of delayed ettringite formation, we have used admixtures of different nature or origins. The recent work of Nguyen V. H (4) on mineral admixtures showed potentials in reducing this risk. Therefore, we continued his

work and extended the study to know the influence of the nature of each admixture. This means using admixtures of different origins. The cement used in this study was a CEM I 52.5 N CE CP2 NF conformed to the European standard EN 197-1 was used. The Mineralogical composition supplied by the manufacturer (Lafarge), is: 60.6% of C₃S; 14.5% of C₂S; 8.1% of C₃A; C₄AF of 9.8% and 5.3% of gypsum. The elementary chemical composition of this cement is given in Table 1. The aggregates used were siliceous aggregates from quarry Palvadeau (NF aggregate, non-alkali reactive), using granular ranges between 0/4 mm (sand) and 4/12.5mm (gravel). The mineral admixtures used in this study were (fly ash: Fa1 and Fa2, metakaolin: Mk1 and Mk2 and natural pozzolan: Pz1 and Pz2). They were blended in order to increase their pozzolan activity. The chemical compositions of these admixtures are given in table 1. The pozzolanic activity index, aside with the other physical properties are given in table 2.

Table 1 Chemical compositions of cement and mineral admixtures

	Cement	Pz1	Pz2	Mk1	Mk2	Fa1	Fa2
	%	%	%	%	%	%	%
SiO ₂	20.07	49.5	46.83	95.46	93.16		
Al ₂ O ₃	4.86	18	17.45			82.9	85.4
Fe ₂ O ₃	3.07	10	8.36	-	-		
CaO	64.25	7.5	9.38	0.002	0.36	2.05	4.24
MgO	0.95	5.5	3.88	0.04	0.04	-	-
SO ₃	3.55	0.06	0.36	0.03	0.14	0.24	0.51
K ₂ O	1.00	2.5	1.40				
Na ₂ O	0.18	4.5	4.32	<1.03	<0.01	3.21	2.08
Eqv. Na ₂ O	0.85						
LOi		1.6	4.79	1.41	1.63		

Table 2 Physical properties and pozzolanic activity of admixtures

	Pz1	Pz2	Mk1	Mk2	Fa1	Fa2
Real density (g/cm ³)	2.94	2.61	2.3	2.5	2.43	2.38
Blain specific area (cm ² /g)	4600	4400			4680	4550
BET specific area (m ² /g)			15.75	16		
Pozzolanic activity 7d	27	40,4			>75%	>75%
Pozzolanic activity 28d	32.2	46,5	0.905	0.91	>85%	>85%
Pozzolanic activity 90d	46.4	51.8	0.912	0.928		

The concrete mix design was inspired by the GranDuBé project (7). We used cylindrical specimens (ϕ 11cm×L 22cm) because this type of test shows a more significant swelling than prism samples according GranDuBé (7). Cement substitution additions were incorporated into the concrete mass with a substitution rate of 15%. The mass proportions of the various constituents are given in Table 3.

Table 3 Concrete mix design

Kg/m ³	Ba	BaPz1	BaPz2	BaMk1	BaMk2	BaFa1	BaFa2
Aggregate 8/12.5	907	907	907	907	907	907	907
Aggregate 4/8	195	195	195	195	195	195	195
Sand 2/4 mm	202	202	202	202	202	202	202
Sand 1/4 mm	189	189	189	189	189	189	189
Sand 0/0.315 mm	98	98	98	98	98	98	98
Water	201	201	201	201	201	201	201
Cement	424	360	360	360	360	360	360
Admixture	0	64	64	64	64	64	64

Procedures

As shown in the literature, the concrete curing temperature plays a key role in the development of ettringite (8); (9). Therefore, we subjected our concrete specimens a thermal cycle of long duration represented by Figure 1

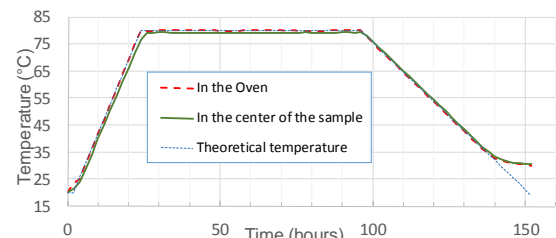


Figure 1 Heat treatment

The heat treatment applied to concrete samples shown in figure 1 is representative of a heat release of a massive concrete element. It was used by Renaud Pierre Martin and Nguyen V. H. (10); (4). Thermocouples were embedded in advance in our samples to check changes in temperature during the cycle. A programmable oven (heat chamber) was used to generate the thermal cycle. During the heat treatment, the molds were sealed tightly by cellophane to prevent the loss of water and thereby maintain a relative humidity close to saturation (90-100%). The specimens were then removed from the mold and stored in water containers at 20±1°C where the water is frequently renewed during the study. The frequency of water renewal is once a week

during the first eight weeks, then once every two weeks until the twenty fourth week, and then once every month. The volume of water with respect to the volume of the sample is kept under 1.5 to limit leaching effects (11).

Experimental methods

In this study we did two main non-destructive measurements which are: 1) Longitudinal expansion, which is measured with deformer ball. There are three generators in each cylindrical specimen. Each point on the graph is obtained from the average expansions measured on three specimens. 2) Resonance frequency measurements of each concrete specimen were performed to determine the dynamic modulus of elasticity of material. This technique gives access to mechanical properties. This self-oscillation frequency of the material is linked to the dynamic modulus of the material by the following equation:

$$f_{longi} = \frac{1}{2L} \sqrt{\frac{E_{dyn}}{\rho}}$$

f_{longi} : longitudinal self-oscillation frequency [s⁻¹]

L : height of the specimen [m]

E_{dyn} : dynamic longitudinal elastic modulus [GPa]

ρ : density of specimen [kg.m⁻³]

In addition to these measurements, we measured the apparent porosity with the evacuation method. This test is based on the procedure of AFREM (12).

RESULTS AND DISCUSSION

Heat of hydration

A microcalorimeter TAM Air isothermal was used to measure the heat flux of reaction and the reaction kinetics of binding at the early age. For each binder paste, two samples of approximately 4 to 5 grams are collected at the end of mixing, weighed (0.01 g) and introduced into plastic vials. The sealed vials are then placed in the device and the acquisition is started. Each test is conducted in the first 3 days of hydration. The first flow measurement is performed immediately after mixing.

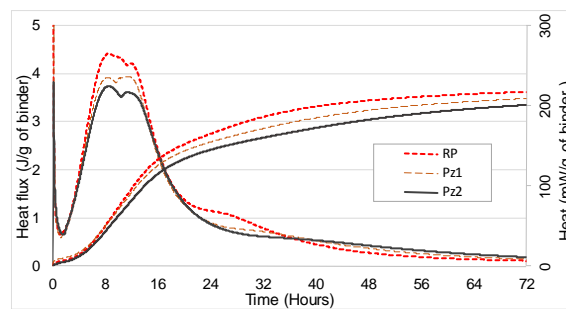


Figure 2 Heat of hydration of binders with $w/b = 0.35$ for cement pastes with pozzolan.

Figures 2 to 4 show the heat flux of hydration of cement pastes mixed with 15% of each used admixture and also show the results of a reference paste (RP) made of 100% of cement. In all these pastes, the binder has w/b ratio equals to 35%.

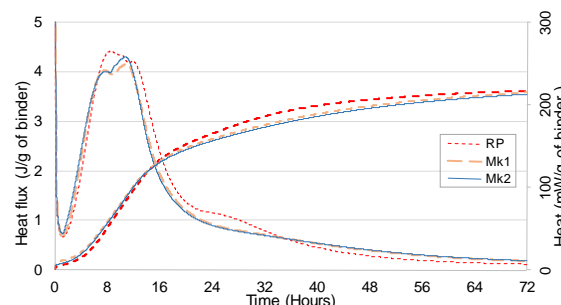


Figure 3 Heat of hydration of binders with $w/b = 0.35$ for cement pastes with metakaolin

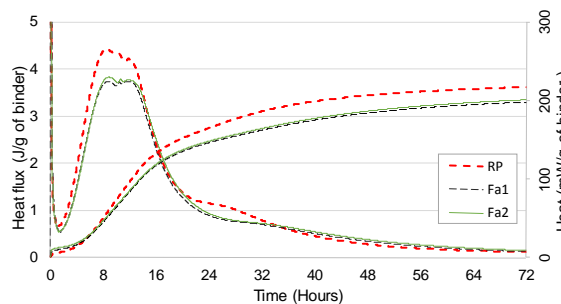


Figure 4 Heat of hydration of binders with $w/b = 0.35$ for cement pastes with fly ash

-The substitution of cement by fine natural pozzolan (figure 2) led to a slight acceleration of the heat flow (a slight shift of the 2nd and 3rd pic to the left) and to a reduction of heat flux and the total heat of hydration during 72 hours. This decrease is related to the combination of the effect of the pozzolanic reaction of the fine natural pozzolan cement. Pz1 release more heat than Pz2, it could be due to its higher fineness. -The hydration kinetics of the pastes made with metakaolin (figure 3) is significantly different from those made with natural pozzolans. We observe that during the period of acceleration of

hydration, the greater heat flux is faster compared to other additives. Furthermore, the total released heat in the first 16 hours is almost higher than that of the reference paste. According Frias (17) this acceleration of the heat flux is primarily due to the combination of the effect of the pozzolanic reaction of metakaolin and accelerating cement hydration.

-The substitution of cement by fly ash (figure 4) decreases the maximum value of the heat flux released and prolongs the dormant period of about thirty minutes compared to the reference sample RP. This leads to a reduction of the released heat in mixtures incorporating the fly ash. The results indicate that FA retards hydration mainly in the dormant and acceleration periods. FA is believed to be inert at this very early stage (18).

Expansion results

Figures 5 to 7 show the expansion curves of reference concrete (Ba) and concretes made with additives (Pz; Mk and Fa).

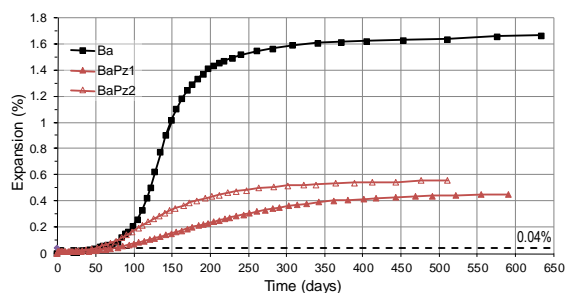


Figure 5 Expansion of concrete prepared with pozzolan

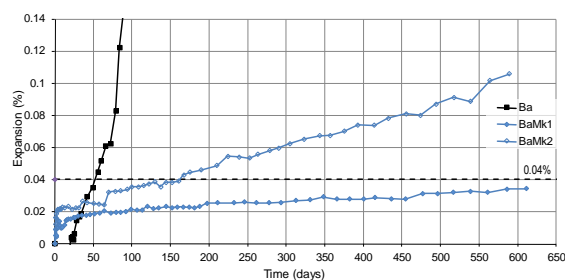


Figure 6 Expansion of concrete prepared with metakaolin

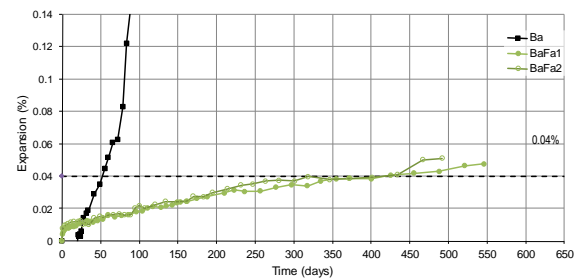


Figure 7 Expansion of concrete prepared with fly ash 1 and 2

It is noted first that reference concrete specimens (Ba) and the specimens made up with 15% natural pozzolan (Pz1; Pz2) show significant swelling (greater than 0.04%) measured at 60 days and observed that the evolution of expansions grows as sigmoid. An expansion of 0.04% is an arbitrary threshold which has already been used in the literature (13) to highlight a significant expansion. This 15% rate of substitution is not sufficient to stop the DEF which is consistent with the literature (4). In the other hand, fly ashes (Cv1; Cv2) have an inhibiting effect. No swelling even after 550 days, which is consistent with the literature (4). While Mk2 starts to expand after 160 days, the Mk1 hasn't shown any expansion yet even after 550 days of immersion. Finally, in terms of kinetics, the concrete samples made up with natural pozzolan Pz2 began swelling earlier than with the Pz1. The high content of sulfate Pz2 can be the cause of the fast swelling. Metakaolin is more efficient than pozzolan in controlling the DEF, this might be because of high content of Al_2O_3 and the small content of equivalent Na_2O , which reduces SO_3/Al_2O_3 (2); (19). Generally, we notice three phases of expansion in degraded specimens: 1- Incubation phase, where ettringite fills in the existent pores. 2- The acceleration phase, where the specimens crack and expand due to the internal pressure of ettringite. 3- Finally, the stabilization phase where the ettringite fills in the cracks. These results confirm previous experimental studies (1); (4); (14); (15); (16).

Mechanical results

Figures 8 to 10 show the evolution of dynamic elastic modulus. Figure 11 show the Compressive strength (R_c).

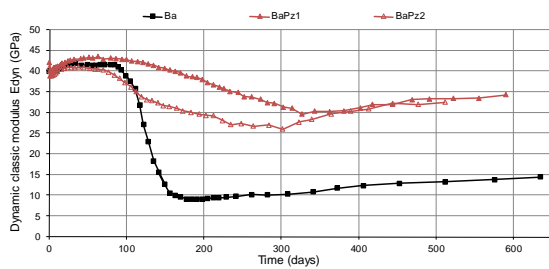


Figure 8 Dynamic elastic modulus of concrete prepared with pozzolan

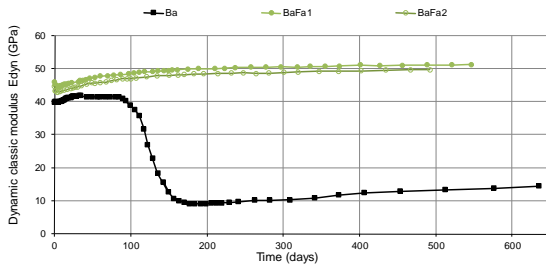


Figure 9 Dynamic elastic modulus prepared with fly ash

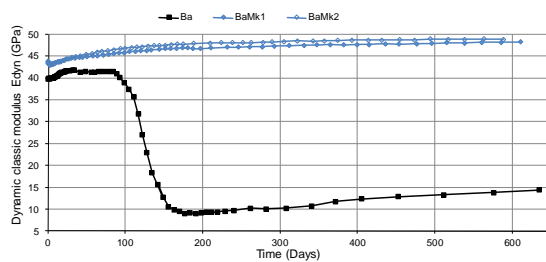


Figure 10 Dynamic elastic modulus prepared with metakaolin

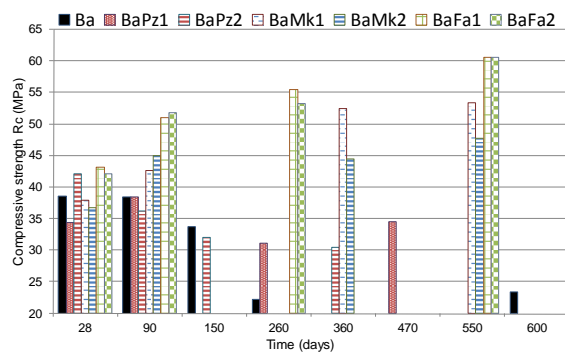


Figure 11 Compressive strength (Rc)

We can distinguish multiple forms of curves. In specimens that have shown no significant expansion ($<0.1\%$): the dynamic elastic modulus tends to improve with time. It's due to hydration. Figure 11 shows increasing compressive strength of these specimens. When expansion become more than $0.1-0.2\%$, we can see the decreasing dynamic elastic modulus. As the expansion accelerate, there are a brutal decrease in mechanical properties. We can see it clearly with

Ba. As the expansion stabilize, there are some increase in dynamic elastic modulus. This could be due to the ettringite filling the pores and cracks in degraded concrete. A slight improvement in compressive strength is also noted.

Porosity results

Figure 12 shows the porosity accessible to determined using hydrostatic weighing of concrete specimens in form of discs at specific points in time. These points were not pre-determined. Contrariwise, they cover the different phases of the degradation of concrete.

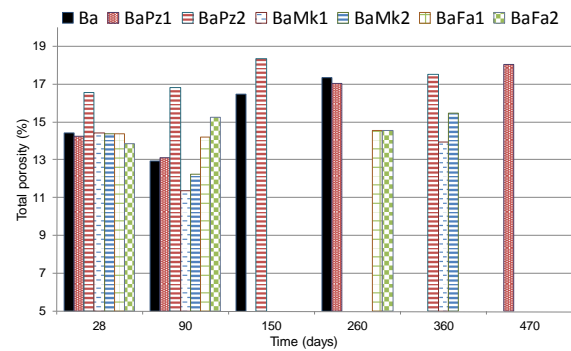


Figure 12 Apparent porosity of specimens

We can see a slight decrease of porosity between 28 days and 90 days. because of continuous hydration of concrete and filling the pores by hydrates. In degraded specimens, we notice a fast increase of porosity followed by a decrease. This confirm the mechanical results and increase of E_{dyn} in the later phase (stabilization).

Conclusions

This work is devoted to the study of the influence of additions on ettringite in concrete. The results allow us to draw the following main conclusions:

- The cement substitution rates by 15% natural pozzolan whatever the nature of that pozzolan (Pz1 or Pz2), is not sufficient to inhibit DEF.
- Cement substitution rate by 15% of metakaolin (Mk1, Mk2) is not enough, it depends on the chemical nature of addition. If it contains high content of SO_3 ,
- Cement substitution rate by 15% of fly ash (Fa1; Fa2) is enough to control long-term expansion (over 550 days).
- The nature of mineral admixture is a very important factor in determining the possibility of protecting from DEF or not, containing more SO_3 and alkaline increase the risk of expansion.

REFERENCES

1. Pavoine A. (2003), « *Evaluation du potentiel de réactivité des bétons vis-à-vis de la formation différée de l'ettringite* », thèse de doctorat, Université Pierre et Marie Curie-Paris VI
2. Taylor H.-F.-W., Famy C., Scrivener K.-L. (2001), "Delayed ettringite formation in heat cured Portland cement mortars". Cement and Concrete Research, Vol. 31, p. 683-693
3. Zhang, Z., Olek, J., & Diamond, S. (2002). "Studies on delayed ettringite formation in early-age, heat-cured mortars: I. Expansion measurements, changes in dynamic modulus of elasticity, and weight gains". Cement and concrete Research, 32(11), 1729-1736.
4. Nguyen V. H. PH.d thesis « *Effet d'addition minérale sur l'apparition de la Réaction Sulfatique interne : étude paramétrique, développement et optimisation de méthodes accélérés* », University of Nantes 2013.
5. Ramlochan T., Zacarias P., Thomas M.D.A., Hooton R.D., « *The effect of pozzolans and slag on the expansion of mortars cured at elevated temperature, Part I: Expansive behaviour* », Cement and Concrete Research, vol. 34, n°8, 2003, p. 1341-1356.
6. Nguyen V.H., Leklou N., Aubert J-E; Mounanga P., "The effect of natural pozzolan on delayed ettringite formation of the heat-cured mortars", Construction and Building Materials, Vol. 48, 2013, p. 479-484
7. Arliguie, G., & Hornain, H., « *GranDuBé : Grandeurs associées à la Durabilité des Bétons* ». Presse des Ponts, 2007.
8. Stark, J., & Bollmann, K. « *Delayed ettringite formation in concrete*. NORDIC CONCRETE RESEARCH-PUBLICATIONS-, 23, 4-28.
9. Divet L. « *Les réactions sulfatiques internes au béton : contribution à l'étude des mécanismes de la formation différée de l'ettringite* », PH.d thesis, Conservatoire National des Arts et Métiers de Paris
10. Martin R.-P., 2010, PH.d thesis « *Analyse sur structures modèles des effets mécaniques de la Réaction Sulfatique Interne du béton* » University Paris Est
11. X. Brunetaud, L. Divet, D. Damidot, « *Impact of unrestrained delayed ettringite formation induced expansion on concrete mechanical properties* » Cem Concr Res, 38 (2008), pp. 1343–1348
12. AFREM, A. (1997). *Méthodes recommandées pour la mesure des grandeurs associées à la durabilité*. Compte rendu des Journées Techniques AFPC-AFREM: Durabilité des Bétons, Toulouse, 11-12.
13. Petrov N., Tagnit-Hamou A., « *Is microcracking really precursor to DEF and consequent expansion?* », ACI Materials Journal, vol. 101, n°6, 2004, p. 442-447.
14. Leklou N., « *Contribution à la connaissance de la réaction sulfatique interne* », Ph.d thesis, University of Paul-Sabatier Toulouse III, 2008.
15. Brunetaud X. « *Etude de l'influence de différents paramètres et de leurs interactions sur la cinétique et l'amplitude de la réaction sulfatique interne au béton* », Ph.d thesis, Ecole Centrale des Arts et Manufactures de Paris.
16. Famy, Charlotte, "Expansion of Heat-Cured Mortars", Ph.D. Thesis, Department of Materials, Imperial College of Science, Technology, and Medicine, University of London, September 1999.
17. Frias, M. et al. "The effect that the pozzolanic reaction of metakaolin has on the heat evolution in metakaolin-cement mortars." Cement and Concrete Research 30.2 (2000): 209-216.
18. Langan, B. W., K. Weng, and M. A. Ward. "Effect of silica fume and fly ash on heat of hydration of Portland cement." Cement and Concrete Research 32.7 (2002): 1045-1051.
19. Heinz D., Ludwig U. (1987). Mechanism of secondary ettringite formation in mortars and concretes subjected to heat treatment. in J.M. Scanlon (ed.), *Concrete Durability: Katherine and Bryant Mather International Conference ACI SP-100*, p.2059–2071.

INFLUENCE OF ACCELERATED CARBONATION ON CO₂ DIFFUSION COEFFICIENT OF CEMENT PASTES

K. Namouniara, Ph. Turcry*, F. Gendron, A. Aït-Mokhtar, J.-F. Meusnier
University of La Rochelle, LaSIE UMR CNRS 7356, Avenue M. Crépeau, 17000 La Rochelle

*Corresponding author: Ph. Turcry Email: philippe.turcry@univ-lr.fr

ABSTRACT

Carbonation is one of the most common ageing phenomena of reinforced concrete structures. The effective diffusion coefficient of CO₂ is a key-parameter in the prediction of long term behavior of concrete. In existing carbonation models, the CO₂ diffusion coefficient is usually obtained from empirical relationships. The latter are a priori not valid for ‘modern materials’, such as concretes with high content of mineral additions. To better characterize this transfer property for any kind of cement based materials, an experimental set-up was developed. The present paper deals with results obtained using this set-up.

An experimental campaign was carried out in order to investigate the influence of binder type and accelerated carbonation on the CO₂ diffusion coefficient of cement pastes. The latter were prepared with various water/binder ratios and two binder types, namely a Portland cement and a mix of Portland cement and BFS. A series of samples was carbonated before diffusion tests.

For a given type of binder, the CO₂ diffusion coefficient increases, as expected, with porosity. When non-carbonated, pastes containing BFS are much less diffusive than pastes made with only CEMI. The influence of the accelerated carbonation depends on the binder type: the diffusion coefficient of BFS pastes is higher after carbonation while it tends to be lower for CEMI pastes. The observed evolutions of the diffusion coefficient are well correlated with changes in pore structure due to carbonation.

These results highlight the need of diffusion coefficient models designed for each type of materials.

KEY WORDS: *cementitious materials, gas diffusion, carbonation, blast furnace slag.*

INTRODUCTION

Among ageing phenomena of reinforced concrete structures, carbonation is undoubtedly the most current, since it results from the fixation of atmospheric carbon dioxide. The consecutive drop of the interstitial solution pH increases the risk of steel corrosion due to their depassivation.

A way to evaluate the performance of concrete is to model the carbonation process to predict the long-term behavior. Most of carbonation models are based on two key-phenomena: carbonation reactions of hydrates and diffusion of gaseous CO₂ [1-5]. In the case of carbonation in atmospheric conditions, the diffusion should be the governing phenomenon, since the characteristic time of diffusion is much longer than those of chemical reactions (which are often assumed to be instantaneous).

In literature models, the effective diffusion coefficient of CO₂ is derived from empirical relationships deduced by fitting experimental data.

The latter were mainly obtained by gas diffusion tests on carbonated samples of materials made with Portland cement.

In the case of materials containing mineral additions, the relationship giving the diffusion coefficient as a function of microstructural parameters (porosity, water saturation degree) should be different from that calibrated for Portland cement based materials. Indeed, additions such as ground granulated blast furnace slag (BFS) result in a porous structure far different from that obtained in the case of Portland cement [6]. Thus, a single model is not enough to predict the diffusion coefficient for various materials.

Moreover, beyond the influence of the binder, carbonation it-self has an effect on pore structure and thus on transfer properties, e.g. [7]. Models of CO₂ diffusion coefficient should take into account parameters depending on the carbonation state.

To address the influence of binder and carbonation on CO₂ diffusion, an experimental set-up was

developed for the measurement of the CO₂ diffusion coefficient of cement pastes.

In the present paper, the developed device and its experimental validation are described. This device was used as a mean to assess the influence on the diffusivity of parameters such as porosity, binder nature and carbonation. This work was carried out on CEMI pastes and BFS/CEMI pastes with different water / binder ratios. Results of this investigation are exposed and analyzed.

METHODS AND MATERIALS

Measurement of CO₂ diffusion coefficient (D):

The experimental set-up in Figure 1 was developed to determine the effective diffusion coefficient of CO₂. The core of the device is composed by two chambers, which are assembled by screwing. The sample inserted in-between is cylindrical, 30 mm in diameter. Its thickness may vary from 5 to 30 mm. For a one-dimensional diffusion, a fast-setting resin ring is molded around the perimeter of the sample leaving free the flat faces. The total diameter (sample + resin) is 60 mm. Two rubber rings of 5 mm in thickness are placed on each side of the tested sample.



Figure 1

Two-chambers diffusion cell, sample and rubber rings.

At the beginning of the test, CO₂ is injected in the upper chamber. The latter is connected to a bubbler which evacuates any overpressure. The CO₂ concentration in the upper chamber (denoted C_{up}) is kept constant by a gas analyzer. Under the concentration gradient, CO₂ diffuses from the upper to the lower chamber. After a given test duration (t_i), the CO₂ concentration in the lower chamber (C_{down}) is determined using a gas analyzer operating in a closed circuit. Note that C_{down} is measured only punctually. This protocol was preferred to continuously measure which would require a permanent pumping of gas

through the analyzer and would create a vacuum in the lower chamber.

Once C_{down} is obtained at t_i , the test is stopped and the sample removed from the diffusion cell. After a period of at least $2t_i$, all the procedure is repeated for another duration t_{i+1} . Finally, the determination of the diffusion coefficient is carried out through the acquisition of several couples ($t_i, C_{down} / C_{up}$).

To determine the CO₂ diffusion coefficient, we use an inverse analysis with two assumptions. First, the gas flow is supposed to be controlled by Fick's Second Law. Second, the diffusion coefficient is assumed to be not depending on the concentration.

For a given value of D , the Fick equation is solved with the finite differences method. Dirichlet boundary conditions are used:

- upstream, the concentration is taken equal to C_{up} ;
- downstream, the concentration, initially equal to zero, is taken constant during a time step and re-computed at the end of the latter using the Fick's first law to take into account the increase of the concentration in the lower chamber.

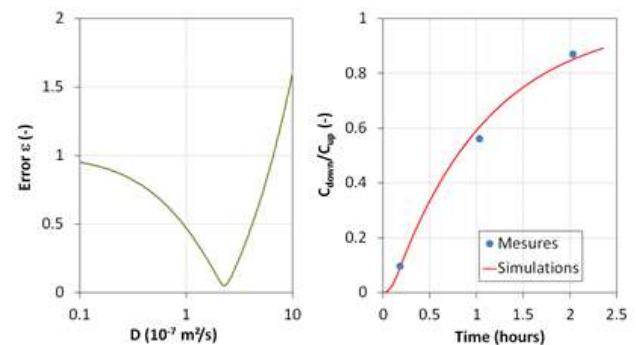


Figure 2

Evolution of the error between computed and measured concentrations as a function of D (left).

Comparison of the measured values and the computed ones for the diffusion coefficient minimizing the error (right).

A comparison is done between the computed relative concentrations (C/C_{up}) in the lower chamber and the measured ones (C_{down}/C_{up}) at different times t_i . For that, an error is calculated. Finally, the diffusion coefficient is determined by minimizing this error. Figure 2 gives an example of the inverse analysis procedure.

More details of our methods can be found in [8].

Studied materials: Experiments were carried out on hardened pastes made with CEMI 52.5 type

cement (from Lafarge, La Couronne, France) and ground granulated blast furnace slag (from Ecocem, Moerdijk, Netherlands). Mix-proportions of pastes are given in Table 1. In the following, pastes made with only cement are denoted “OPC pastes” while pastes containing both cement and BFS are denoted “BFS pastes”.

Diffusion experiments were also carried out on five limestone samples. Their porosities are between 10 to 25%. The tested samples were discs (30 mm in diameter, 10 mm in thickness).

Table 1
Mass proportions of the studied pastes

	OPC pastes			BFS pastes	
	C3	C4	C5	L3	L5
W/(C+BFS)	0.30	0.40	0.50	0.32	0.53
BFS/(C+BFS)	0	0	0	0.75	0.75

Materials preconditioning: Before any diffusion measurement, the samples were water-saturated under vacuum. Their masses and volumes were then determined. A part of the samples was oven-dried at 105° C until mass stabilization.

In order to investigate the influence of carbonation, a series of discs was carbonated before diffusion tests. For this purpose, these samples were first oven-dried at 45°C so as to sufficiently reduce the degree of water saturation. In the case of C5 and L5 pastes, this thermal treatment lasted 2 days. In the case of C3, C4 and L3 pastes, another pretreatment was used instead of a direct oven-drying which would have resulted in a too low degree of saturation and would have limited carbonation [9]. C3, C4 and L3 discs were therefore placed in desiccators at 45°C and around 50% RH. After the thermal treatment, all disks were submitted in an accelerated carbonation chamber to a CO₂ concentration of 50% at 20°C and 53% RH. During carbonation, samples masses were monitored. Pastes were assumed to be fully carbonated when the mass becomes constant.

Before diffusion tests, all samples were oven-dried at 105°C until mass stabilization and conserved à 3% RH.

Other characterizations: The porosity of all discs was obtained according to the French standard NF P18-459. The pore size distribution was investigated through mercury intrusion on cubic samples of around 2 cm square [10]. Gas permeability was measured using the device fully described in [11].

Samples for permeability measurements were also oven-dried at 105°C.

RESULTS AND DISCUSSION

Porosity: Figure 3 gives the porosity of the studied pastes. Before carbonation, porosity increases, as expected, with the water/binder ratio, for a given binder. For the same initial water/binder volume ratio, the BFS pastes have a higher porosity than the OPC pastes, which is confirmed in literature, e.g. [12].

Carbonation results in a significant drop in porosity. This phenomenon is usually explained by carbonates precipitation [13]. As shown by [14], the reduction in porosity is mainly due to the carbonation of the CSH.

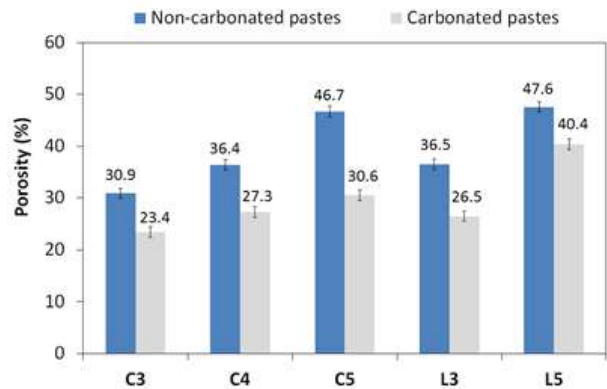


Figure 3
Porosities of the studied pastes, before and after carbonation (from water soaking).

Influence of the pore structure on the diffusion coefficient: For a given material type (limestone, non-carbonated OPC or BFS paste), the CO₂ diffusion coefficient is well correlated to the porosity as shown in Figure 4. However, for a given porosity, two materials may have very different diffusivities. The case of the limestone samples highlights this fact: although the limestone samples are less porous than the cement pastes, their diffusion coefficients are equal or even higher than those of pastes. It is also interesting to note that the BFS pastes have lower diffusion coefficient than the OPC pastes having the same water/binder ratio.

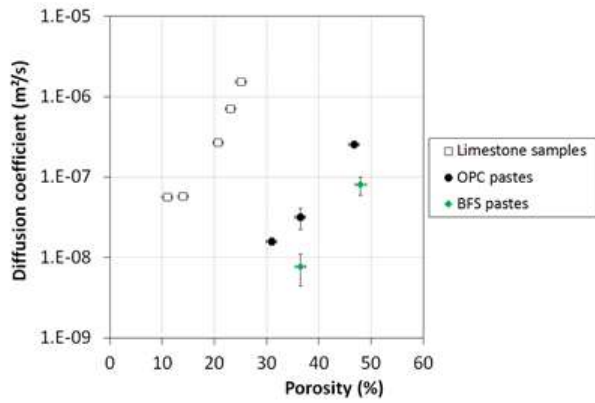


Figure 4
CO₂ diffusion coefficients of limestone and non-carbonated pastes versus porosity.

The transfer properties are not only dependent on the porosity but also on the properties of the pore structure. For instance, Figure 5 gives the pore size distribution determined by mercury intrusion for C4 and L3 pastes and a limestone sample. These data confirm that the coarser the pore structure is, the lower the diffusion coefficient.

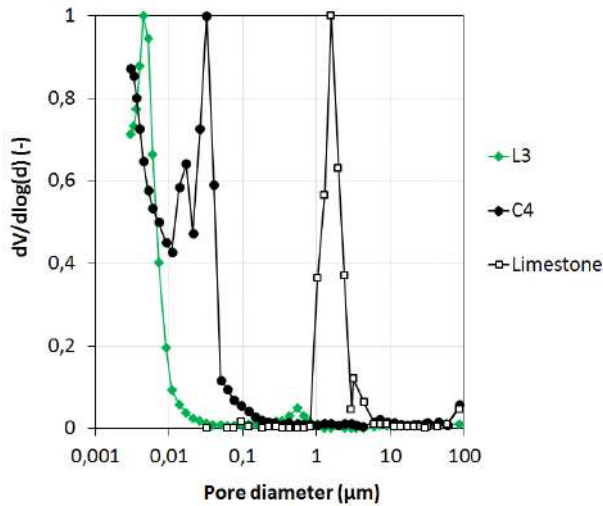


Figure 5
Pore size distributions from mercury intrusion

To go further, a rather good correlation is shown in Figure 6 between diffusion coefficient and gas permeability, which is a transfer property usually correlated to porosity and pore size distribution [11].

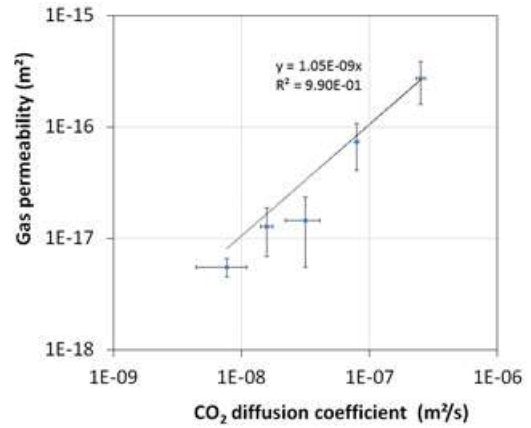


Figure 6
Correlation between CO₂ diffusion coefficient and gas permeability of non-carbonated pastes.

Influence of carbonation on the diffusion coefficient: While carbonation significantly reduces the porosity of all the tested pastes, as shown previously, its effect on the diffusion coefficient is however very unsystematic (Figure 7).

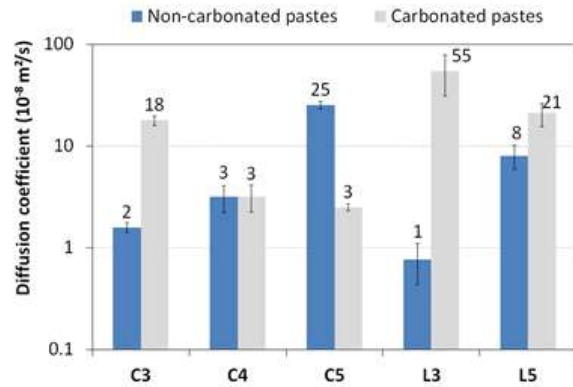


Figure 7
Influence of accelerated carbonation on the CO₂ diffusion coefficient of the studied pastes.

Only the case of the C5 paste is consistent with the porosity clogging, since its carbonation results also in a reduction of the diffusivity. For the other pastes, no change is observed (C4) or, conversely, a net increase in the coefficient (C3, L3 and L5) is observed. The absence of correlation between porosity clogging and diffusivity change has already been shown in the case of other transfer properties. For instance, an increase in chloride diffusion coefficient [7] or in water permeability [15] was observed consecutive to carbonation of cement pastes.

Figure 8 gives for instance the pore size distribution before and after carbonation, for C5 and L5 pastes. This shows that the evolution of the diffusivity consecutive to carbonation can be explained by changes in porous structure. Indeed, the pore size distributions are very different after carbonation. In most cases, the main pore mode is shifted to smaller diameters but coarser pores can also be observed. This trend is very strong for BFS pastes.

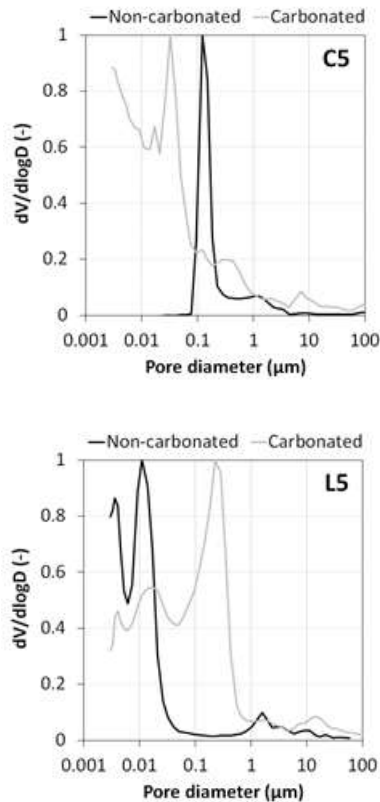


Figure 8

Pore size distributions determined by mercury intrusion before and after carbonation.

Carbonation strongly modifies the porous structure of the pastes. The beneficial effect of the porosity clogging may be offset by the coarsening of the porous network which becomes a priori more connected.

Another phenomenon has also an impact on our results. After accelerated carbonation, cracks appeared on the surface of some samples. Figure 9 gives the example of a L5 paste sample (cylinder submitted to a unidirectional carbonation). On this sawn section, crossing cracks can be seen. Note also that the carbonation ‘front’ is very irregular (carbonated areas are in white while no-carbonated

ones appear in black). The cracking of our samples, which is mainly observed for the BFS pastes (L3 and L5) and the OPC paste (C3), is a priori a consequence of a carbonation shrinkage, probably combined with a drying shrinkage due to the preconditioning at 45°C before carbonation and the oven-drying at 105°C before diffusion test.

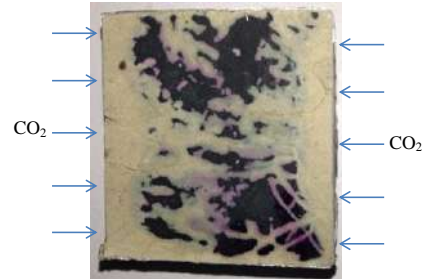


Figure 9

View of a sawn section of a cylindrical sample of the L5 paste (3 cm in diameter and 3 cm in length) after 5 days of accelerated carbonation. Surfaces in contact with CO₂ are indicated by arrows.

Carbonation shrinkage could be increased by the CO₂ concentration used in our experiments, i.e. 50%, since such high concentration leads to different carbonates products than those obtained for natural carbonation, especially in the case of slag [16]. However, cracking of pastes made with BFS cement (CEMIII type) was also observed by [15] after an accelerated carbonation with a lower CO₂ concentration, i.e. 3%, which was shown by the authors to be quite representative of a natural carbonation.

CONCLUSIONS

An experimental set-up was developed for the measurement of CO₂ diffusion coefficient, a key-parameter for the modeling of cementitious materials carbonation. This procedure was partly validated by showing the diffusive nature of the measured phenomenon. It was applied to the study of different cement pastes, carbonated or not, oven-dried at 105°C. A significant influence of the binder nature was observed. Non-carbonated, pastes with a high content of blast furnace slag are less diffusive than Portland cement pastes. However, once carbonated by an accelerated protocol at 50% CO₂, BFS pastes become much more diffusive. Although it leads to a porosity reduction, carbonation modifies strongly the porous structure and can result in

cracking. This confirms that any model to predict CO₂ diffusion coefficient should depend on both the binder nature and the carbonation state. Our results could also question the relevance of accelerated carbonation tests carried out with high CO₂ concentration for materials made with BFS.

ACKNOWLEDGMENTS

The authors acknowledge the “Région Poitou-Charentes” for funding the PhD Thesis of K. Namoulniara.

REFERENCES

- Kim, S. F. and Low, F. (1997). Liquid Film Cooling at High Temperature, *J. Film Cooling*, 122, pp. 21-26.
- Schlichting, H., (1979). *Boundary-Layer Theory*, 7th edition, McGraw-Hill, New York.
- Papadakis, V.G., Vayenas, C.G., and Fardis, M.N. (1991). Fundamental modeling and experimental investigation of concrete carbonation. *ACI Materials Journal*, 88, 363–373.
- Saetta, A.V., Schrefler, B.A., and Vitaliani, R.V. (1993). The carbonation of concrete and the mechanism of moisture, heat and carbon dioxide flow through porous materials. *Cement and Concrete Research*, 23, 761-772.
- Omikrine, O., Aït-Mokhtar, A., Turcry, Ph., Ruot B. (2012). Consequences of carbonation on microstructure and drying shrinkage of a mortar with cellulose ether. *Construction and Building Materials*, 34, 218-225.
- Thiéry, M., Villain, G., Dangla, P., and Platret, G. (2007). Investigation of the carbonation front shape on cementitious materials: Effects of the chemical kinetics. *Cement and Concrete Research*, 37, 1047-1058.
- Peter, M.A., Muntean, A., Meier, S.A., and Böhm, M. (2008). Competition of several carbonation reactions in concrete: A parametric study. *Cement and Concrete Research*, 38, 1385–1393.
- Younsi, A., Turcry, Ph., Rozière, E., Aït-Mokhtar, A., and Loukili, A. (2011). Performance-based design and carbonation of concrete with high fly ash content. *Cement and Concrete Composites*, 33, 993-1000.
- Ngala, V.T., and Page, C.L. (1997). Effects of carbonation on pore structure and diffusional properties of hydrated cement pastes. *Cement and Concrete Research*, 27, 995–1007.
- Namoulniara, K., Turcry, Ph., Aït-Mokhtar, A., (2016). Measurement of CO₂ effective diffusion coefficient of cementitious materials, *European Journal of Environmental and Civil Engineering*, DOI: 10.1080/19648189.2015.1132011.
- Turcry, Ph., Oksri-Nelfia L., Younsi, A., and Aït-Mokhtar, A. (2014). Analysis of an accelerated carbonation test with severe preconditioning. *Cement and Concrete Research*, 57, 70-78.
- Aït-Mokhtar, A. Amiri O., Dumargue P. and Sammartino S. (2002). A new model to calculate water permeability of cement-based materials from MIP results, *Advances in Cement Research*, 14, 43-49.
- Hamami, A.A., Ph. Turcry, Ph., and Aït-Mokhtar A. (2012). Influence of mix proportions on microstructure and gas permeability of cement pastes and mortars. *Cement and Concrete Research*, 42, 490-498.
- Chen, W. (2007). *Hydration of slag cement - Theory, Modeling and Application*, PhD thesis, Twente University.
- Omikrine-Metalssi, O., Aït-Mokhtar, A., Turcry, Ph., and Ruot, B. (2012). Consequences of carbonation on microstructure and drying shrinkage of a mortar with cellulose ether, *Construction and Building Materials*, 34, 218-225.
- Morandea, A., Thiéry, M., and Dangla, P. (2015). Impact of accelerated carbonation on OPC cement paste blended with fly ash. *Cement and Concrete Research*, 67, 226–236.
- Auroy, M., Poyet, S., Le Bescop, P., Torrenti, J.M., Charpentier, Th., Moskura, M., and Bourbon, X. (2015). Impact of carbonation on unsaturated water transport properties of cement-based materials, *Cement and Concrete Research*, 74, 44–58.
- Bernal, S.A., Provis, J.L., Brice, D.G., Kilcullen, A., Duxson, P., van Deventer, J.S.J. (2012). Accelerated carbonation testing of alkali-activated binders significantly underestimates service life: The role of pore solution chemistry. *Cement and Concrete Research*, 42, 1317–1326.

CHEMICAL COMPOSITION OF THE INTERSTITIAL SOLUTION OF CEMENTITIOUS MATERIALS

R. Chérif*; A.A. Hamami; A. Aït-Mokhtar, J-F Meusnier
LaSIE, UMR-7356, CNRS, Université de La Rochelle, Avenue Michel Crépeau,
17042 La Rochelle Cedex1

*Corresponding author: Fax: +33 5 46 45 82 41 Email: rachid.cherif@univ-lr.fr

ABSTRACT

The durability of the reinforced concrete structures is conditioned by the mechanical behaviour of materials used as well as their physico-chemical one against aggressive species attacks. This latter concerns especially the transfer of these aggressive species in the material porosity such as the diffusion of marine salt, the carbonation, the external sulfate attack, etc...

It is necessary to understand all the mechanisms of transfer which occur during the penetration of these species. The present study focuses on the case of chloride ions transfer through cementitious materials.

The transfer mechanism depends on the physical and chemical interactions of chlorides with the cementitious matrix and the others species in the pore solution. In order to well understand these transfer phenomena, a prior chemical investigation of the interstitial solution composition is necessary.

In this work, we study this interstitial solution of cementitious materials manufactured with Portland cement and blended one containing four types of mineral additions. Investigations were carried out, according to the age of the material and the hydration degree, on pore solution obtained by extraction from cement pastes. Results are useful for the use as initial and boundary conditions in multi-species models of transfer, mainly in chloride ingress in cementitious materials.

INTRODUCTION

The porosity of cementitious materials contains a liquid named the interstitial solution. This one is responsible of the transfer of the aggressive species such as chlorides [1–3] and sulfates [4, 5], as well as the leaching of alkaline.

The chemical composition of the interstitial solution is very important since it govern the ion mobility and the migration process, in particular, the diffusion under a concentration gradient of chlorides coming from the seawater and deicing salts within cementitious materials. When these chloride ions reach the rebar with a so-called critical concentration, they cause their depassivation and corrosion.

Among the important parameters describing the interstitial solution, we distinguish the ionic strength, the pH, the concentration of each component and the redox potential to determine the oxidation state of the multivalent elements.

In a study of the chemical composition of the pore solution, Andersson et al [6] showed that the pore solution of the cementitious materials is influenced by the type of cement and the mineral addition used. For this, they studied the chemical composition of pore solution extracted from seven different cement pastes with a W/B (Water/Binder) of 0.5. The author distinguished that the interstitial solution is composed mainly of sodium ions, potassium and calcium. An important difference is noticed between the pore solution extracted from paste 1 (containing Portland cement) and paste 2 (Portland cement produced in France) and paste 3 (Cement resistant to sulfates). The cement paste rich in silica contains the weakest concentration of Na⁺ and K⁺ while the pastes of cement rich in aluminum and fly ash are very low in calcium.

Nevertheless, the studies on the chemical composition of the interstitial solution of cementitious materials are still relatively rare. In this context, the experimental work presented in this paper has two objectives. The first one is to analyze the chemical composition of the interstitial

solution of cement pastes. The second is to study the evolution of this chemical composition

EXPERIMENTAL PROTOCOL

Materials

Cement: For this study, an ordinary Portland cement (CEM I 52.5 NR in respect with European standard NF EN 197-1) is used. It is characterized by a Blaine specific surface of 4050 cm²/g and an absolute density of 3.8 The fractions mass of the principal clinker phases provided by the manufacturer (Calcia, Bussac-France) are 65% C3S, 13% C2S, 7% C3A, 13% C4AF et 4.9% gyps.

The chemical composition of this cement is given in Table 1

Mineral additions: Different mineral additions were chosen. These additions were used as substituent of the cement as follows: 30% of fly ash, 75% of blast furnace slag, 25% limestone filler and 10% silica fume. Pozzolanic index and chemical composition of these additions are given in Table2.

The objectives of the choice of these additions are: 75% of the slag bring major modifications to the interstitial solution of cementitious materials, particularly the physical fixation of the chloride ions at the walls of the pores and the layers of CSH during migration tests [7]. Fraay et al [8] showed that in case of use of 30% fly ash, only 50% of the amount used react at the end of the first year.

According to Perraton et al [9], the use of silica fume is from 5 to 10% of substitution in mass of

according to the hydration degree.

cement. With more than 10% the replacement is useless and the performance of the material decreases.

Table 2: properties of mineral additions used.

	Fly ash	Slag	L_Filler	S_Fume
Component	Content (%)	Content (%)	Content (%)	Content (%)
SiO ₂	85.53	33.3	0.30	89.00
Al ₂ O ₃		12.50	-	-
Fe ₂ O ₃		0.40	-	-
CaO	5.10	41.50	-	1.00
Chlorides	0.013		0.001	0.10
SO ₃	0.59	0.50	0.01	2.00
K ₂ O	2.00	-	0.01	-
Na ₂ O	1.95	-		1.00
Density	2.21	2.89	2.70	2.24
Blaine specific Surface (m ² /kg)	405	450	498	-
Pozzolonic index Ca(OH) ₂ (%) consumpti	0.75	-	0.79	-

Table 1: Chemical composition of the cement

Chemical composition	SiO ₂	Al ₂ O ₃	Fe ₂ O ₃	CaO	MgO	SO ₃	K ₂ O	Na ₂ O	Na ₂ O _{eq}	Fire loss
Content (%)	20.50	5.00	3.90	64.20	1.10	2.50	0,29	0.05	0.24	1.40

Studied mixes: Cement pastes with a medium W/B are chosen for this work in order to facilitate the pore solution extraction. A performance-based approach was used in order to determine the amount of substitution for each mineral addition. This method takes into account the pozzolanic index of each addition. The compositions of the cement pastes used are presented in Table 3.

Table 3: Composition of cement pastes used.

Component (Kg/m ³)	REF	Fly ash	Slag	L_Filler	S_Fume
A/C	0.00	0.43	3	0.35	0.11
W/B	0.50	0.40	0.44	0.38	0.47

Experimental procedure

TGA: The thermogravimetric analysis is used for the determination of the hydration degree following the method described by Mounaunga [10]. The latter was adapted for eco-materials containing mineral additions.

Water porosity: The porosity accessible to water is determined following a hydrostatic weighing according to the standard NFP 18-459. This method is very simple and practicable on a wide variety of materials.

Mercury porosity: Mercury porosimetry allows the measurement of pore size distribution leading to the critical diameter. The test of a mercury porosimetry is based on the physical principle that a non-wetting liquid enters the pores open under an applied pressure. The method is based on the Laplace law linking the mercury injection pressure to the diameter of the pore. Considering the pores as cylindrical, the diameter is calculated from the applied pressure following Washburn law [11].

Chloride diffusion : The objective of this test is to determine the effective coefficient of diffusion at steady state regime. An electric field of 300V/m is applied between the two faces of the sample in order to accelerate the transfer phenomenon.

Interstitial solution extraction: To extract the interstitial solution from the cement pastes, a press (OPICAD) is used. For this purpose of the press piston is inserted in the cylindrical chamber above the cement paste sample (5cm diameter and 7cm height). The pressure necessary to extract the pore solution is applied using a standard compression testing machine.

The solution from the pores is collected through a channel located at the bottom of the device using a syringe to avoid any contact of the solution with air.

Chemical analysis of pore solution: The analysis of the pore solutions is performed by ionic chromatography at latest 24 hours after their extraction in order to avoid a possible carbonation. A dilution of 40 times is necessary to analyze the sodium and potassium, however, to analyze other species we put 1 ml of the pore solution in 5 ml of distilled water.

RESULTS AND DISCUSSION

Water and mercury porosity:

Figure 1 shows the results of total porosity of each sample at the age of 9 months.

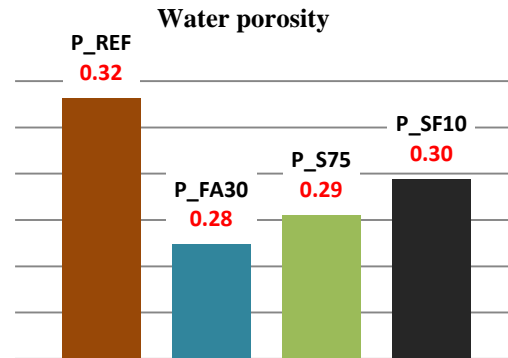


Figure 1: water porosity of the various samples after 9 months of hydration.

In Figure 2 we present the evolution of the pore sizes distribution of each material according to its age. The materials were tested at two ages (3 and 9 months).

According to the Figure 3, one can notice that as from 3 months, the hydration influences slightly the evolution of the pore size distribution, especially for the reference paste. For eco-pastes, we distinguish a small difference in the results, particularly for the paste with fly ash. This latter can be explained by the slow pozzolanic reaction with the portlandite to form more CSH which causes a slower modification of the microstructure.

Chlorides diffusion: The diffusion coefficient of the different materials was determined at steady state. It is based on the chloride ion flux measured at the downstream compartment. The effective chloride diffusion coefficient D_{eff} (m^2/s) can be calculated from equation (1) [12]

$$D_{eff} = \frac{RT}{z_{Cl^-} F} \frac{L \Delta C}{E \Delta t} \frac{V_a}{AC_0} \left(1 - e^{-\frac{z_{Cl^-} FE}{RT}} \right) \quad (1)$$

Where V_a (m^3) is the volume of the downstream solution; ΔC (mol/m^3) is the increase of the chloride concentration in the downstream compartment during a migration time Δt ; A (m^2) is the section of the sample. L (m) is the thickness of the sample; C_0 (mol/m^3) is the concentration of chloride ions in the upstream solution; E (V) is the potential difference at the sample terminals; F , z_{Cl^-} , R and T represent the Faraday constant, the valence of chloride, the

perfect gas constant and the absolute temperature (K).

The diffusion coefficients obtained for the materials studied are summarized in the Table 4.

Table 4: Diffusion coefficients of the materials studied ($m^2.s^{-1}$).

P_REF	P_FS10	P_CV	P_L75
1.2×10^{-11}	6.36×10^{-11}	0.52×10^{-11}	0.73×10^{-11}

Extraction: In order to study the composition of the pore solution, two materials were used. The solution was obtained by pressing and then analyzed using ion chromatography as previously mentioned. The obtained results are shown in Table 5.

From these results, we find that the pore solution of a cementitious material contains mainly sodium and potassium.

A high concentration of sulfates and calcium was also observed. However, the magnesium concentration remains very low, especially for reference paste. The paste based on limestone filler is rich on sulfates and calcium compared to the reference paste, especially for calcium where we distinguish a difference of 20 times.

We noticed an amount of chlorides in the limestone filler paste which can come from the cement composition or mixing water. Distilled water will be used to mix the materials in order to avoid this problem.

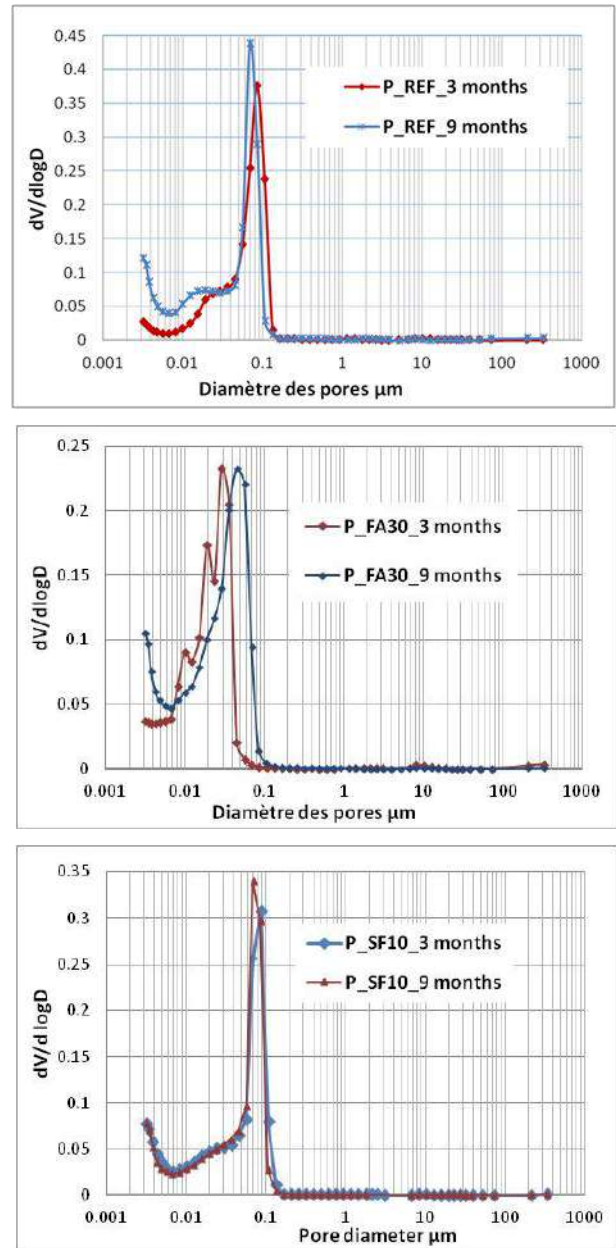


Figure 3: Pore sizes distribution of the cement pastes tested.

Table 5: Chemical composition of pore solution of cementitious materials

Conc (mg/l)	Sulfate	chlorides	Sodium	Potassium	Calcium	Magnesium
P-REF	22.511	27.466	243.825	2143.620	38.940	7.516
P_LF	64.082	34.449	1035.897	4903.215	162.617	5.446

Table 6: Interstitial solution of reference paste in time.

Concentration (mg/l)	Hydration degree	Sulfate	chlorides	Sodium	Potassium	Calcium	Magnesium
P-REF_14 days	71430	32.259	36.594	275.970	3514.776	78.643	12.240
P-REF_28 days	76.310	22.511	27.466	243.825	2143.620	38.940	7.516

Evolution of the chemical composition of the interstitial solution according to hydration:

From Table 6, we observed a very significant reduction in alkali concentration. This can be explained by the phenomenon of leaching. It is due to the concentration gradient between the interstitial solution and the conservation one. To avoid this phenomenon, the studied materials will be conserved in a solution similar to that they contain and obtained by extraction.

The alkali leaching modifies the pH of the interstitial solution. Thereafter, the CSH release the sulfates physically fixed. These latter, the chlorides and calcium react with anhydrous cement in particular the C_3A and the C_4AF to form other hydrates such as the ettringites and friedel salt. This explains the reduction of these ions concentration of the interstitial solution.

CONCLUSION: A characterization of some cementitious materials was made in order to use the properties as inputs in chloride transfer models.

In this work, the chemical composition of the interstitial solution was studied. It contains mainly sodium and potassium and changes according to age of the cementitious material because of leaching and the chemical reactions between the ionic species - in particular the sulfates and the chlorides- and anhydrous cement.

The pore solution contains a remarkable amount of sulfates and calcium. These two species cannot be neglected in multispecies transfer models, unlike models of the literatures which are based on the monovalent ions.

REFERENCES

- [1] A. Aït-Mokhtar, O. Amiri, O. Poupard, and P. Dumargue, "A new method for determination of chloride flux in cement-based materials from chronoamperometry," *Cem. Concr. Compos.* vol. 26, no. 4, pp. 339–345, May 2004.
- [2] V. Baroghel-Bouny, T. Chaussadent, and A. Rharinaivo, "Experimental investigations on binding of chloride in cementitious materials, in Chloride Penetration Into Concrete," Saint-Rémy-les-Chevreuses, France, 1995.
- [3] H. Friedmann, O. Amiri, A. Aït-Mokhtar, and P. Dumargue, "A direct method for determining chloride diffusion coefficient by using migration test," *Cem. Concr. Res.*, vol. 34, no. 11, pp. 1967–1973, Nov. 2004.
- [4] N. Leklou, J. Aubert, and G. Escadeillas, "Microscopic observations of samples affected by the delayed ettringite formation (DEF)," *Mater. Struct.* vol. 42, pp. 1369–1378, 2009.
- [5] X. Brunetaud, L. Divet, and D. Damidot, "Impact of unrestrained Delayed Ettringite Formation-induced expansion on concrete mechanical properties," *Cem. Concr. Res.*, vol. 38, pp. 1343–1348, 2008.
- [6] K. Andersson, B. Allard, M. Bengtsson, and B. Magnusson, "Chemical composition of cement pore solutions," *Cem. Concr. Res.*, vol. 19, no. 3, pp. 327–332, May 1989.
- [7] O. Amiri, A. Aït-Mokhtar, P. Dumargue, and G. Touchard, "Electrochemical modelling of chloride migration in cement based materials Part I: Theoretical basis at microscopic scale," *Electrochimica Acta*, vol. 46, pp. 1267–1275, 2001.

- [8] A. L. Fraay, J. Bijen, and Y. de Haan, "The Reaction of Fly Ash in Concrete. A Critical Examination," *Cement and Concrete Research*, vol. 19, pp. 235–246, 1989.
- [9] D. Perraton, P. Aitcin, and D. Vezena, "Permeability of Silica Fume Concrete," *Am. Concr. Inst.*, no. SP-108, pp. 63–84, 1988.
- [10] P. Mounounga, "Étude expérimentale du comportement de pâtes de ciment au très jeune âge: hydratation, retraits, propriétés thermophysiques," Université de Nantes, France, 2003.
- [11] A. Aït-Mokhtar, O. Amiri, P. Dumargue, and A. Bouguerra, "On the applicability of Washburn law: study of mercury and water flow properties in cement-based materials," *Mater. Struct.* no. 37, pp. 107–113, 2004.
- [12] O. Amiri, A. Aït-Mokhtar, P. Dumargue, and G. Touchard, "Electrochemical modelling of chlorides migration in cement based materials. Part II: Experimental study—calculation of chlorides flux," vol. 46, pp. 3589–3597, 2001.

PRACTICAL CONCRETE RHEOMETER WITH NEW VANE GEOMETRY

Hamza Souahli^{1*}, El-Hadj Kadri¹, Tien-Tung Ngo¹, Adrien Bouvet¹, François Cussigh².

¹ Laboratory L2MGC, University of Cergy Pontoise, F9500 Cergy Pontoise, France

² VINCI Construction - 61, avenue Jules Quentin 92730 Nanterre Cedex - France

*Corresponding author: Fax: +33 31 25 69 41 Email: Hamza.souahli@u-cergy.fr

ABSTRACT

This paper presents the development of a practical vane rheometer to estimate concrete plastic viscosity and yield stress (rheology).

The apparatus can be used not only in the laboratory but also on construction site. In this study, new blade geometry was proposed to minimize the effect of segregation of concrete during testing and also to expand the range of concrete workability ranging from a slump of approximately 7 cm and concretes with important plastic viscosity like concretes with mineral addition to fluid concrete.

The apparatus was tested with many experimental programs in which many rheological parameters of concrete compositions were calculated. The obtained results validated the rheometer test procedure and confirmed that the test results are reliable.

Keywords: Vane rheometer, concrete, rheology, plastic viscosity, yield stress.

INTRODUCTION

With the development of new concretes such as self-compacting concrete (SCC) and high performance concrete (HPC) and environmental friendly concretes, the control of rheological parameters (yield stress, plastic viscosity) in order to optimize the implementation of these concretes becomes crucial. It is therefore necessary to develop new methods of characterization of the rheological parameters not only in the laboratory but also on construction site.

Empirical tests such as slump and L-Box allow the measurement of these materials but provide little or no information about their viscosity or their behavior under shearing. In this context, rheometers adapted to these fluids have been developed: ICAR [1; 2]; Two points test [3; 4]; IBB [5; 6], BML [7; 8]; BTRheom [9; 10]; The MCR [11]. These rheometers can differentiate the rheological behavior of different concretes [12; 13].

Recently, two test campaigns were conducted to compare different rheometers [12; 13]. The first was performed on 12 low workability and plastic concrete with rolled or crushed aggregate and fillers, and the second campaign on 16 concretes including a majority of self-compacting concrete mixes. The results of the first campaign are reported in Figure 1. The results of the second campaign are similar to those of the first one.

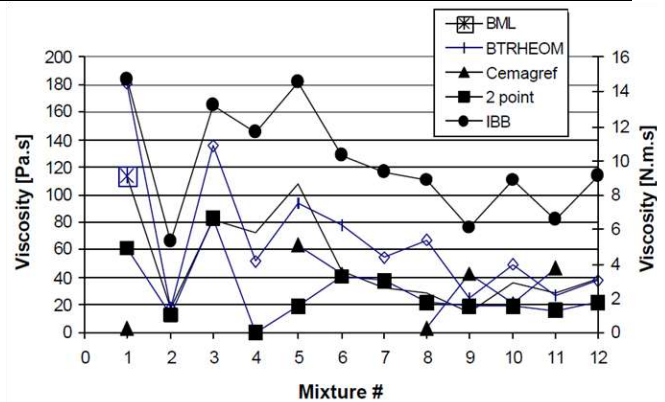


Figure.1.

Values of rheological parameters (K and μ) identified on the 12 concretes studied by [12] with different devices

These studies conclude that the parameters identified by each unit cannot be considered as intrinsic because values vary in significant proportions depending upon the equipment. However, these studies confirm the Bingham behavior of these fresh concretes [4-6; 13-32] which can be described as follows:

$$\tau = \tau_0 + \mu \dot{\gamma} \quad [\text{Eq.1}]$$

where

τ (Pa) is the shear stress, τ_0 (Pa) is the yield stress, μ (Pa.s) is the plastic viscosity and $\dot{\gamma}$ (1/s) is the shear rate.

Based on existing concrete rheometers, the objective of this work is to develop a portable rheometer

adapted to fresh concrete, with a relevant test protocol providing accurate and inexpensive rheological measurements. New blade geometry was used to minimize the effect of segregation of concrete during testing and also to expand a wide range of concrete workability. This device should be applicable on construction site and in the laboratory in order to meet the demand of the industry. It must be capable of measuring a flow curve or performing a stress growth test and should be appropriate for a wide range of concrete workability with a slump of approximately from 7 cm to fluid concrete, and concretes with important plastic viscosity such as concrete with mineral additions.

METHOD TESTS

In this study a new rheometer apparatus developed in our laboratory was used [21, 22]. The rheometer is composed of three main parts (Fig.2): an agitator with speed electronic control for recording the torques via an RS232; a container and a steel vane.

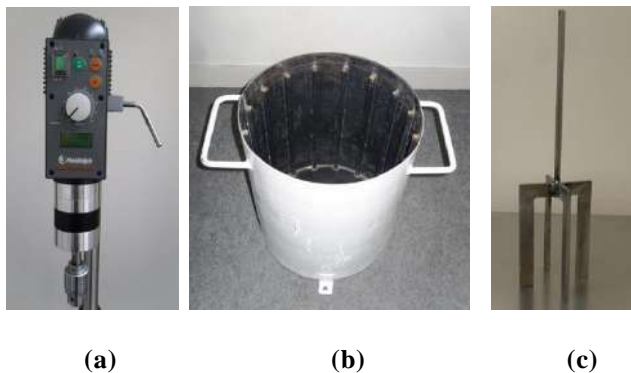


Figure 2. Rheometer components : (a) agitator ; (b) container ; (c) vane

The measurements are performed with the velocity profile defined in Fig.3 [22, 23].

1st step: Filling concrete into the container. It is done by three layers. Each layer receives 25 strokes of stitching using a rod.

2nd Step: Positioning of the blade. The blade is centered and swooped down on the concrete until the level concrete and leaving a layer of concrete of 10 cm thick below the blade.

3rd Step: Measuring torques (M). They correspond to torques to be imposed to maintain speeds in phase bearing when the container is filled with concrete.

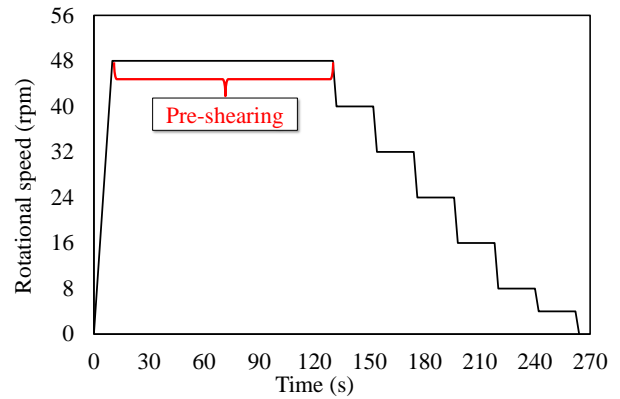


Figure 3. The remain velocity profile

The exploitation of the measurements is to determine the rheological parameters τ_0 and μ from the obtained measured torques ($M_i - \Omega_i$). This allows, by assimilating the behavior of concrete at a Bingham fluid (Eq.1).

The calculation of the Bingham model parameters of yield stress and plastic viscosity is based on the Reiner-Riwlin equation (Eq.2),

$$\Omega = \frac{M}{4\pi h\mu} \left(\frac{1}{R_1^2} - \frac{2\pi h\tau_0}{M} \right) - \frac{\tau_0}{2\mu} \ln \frac{M}{2\pi h\tau_0 R_1^2} \quad [\text{Eq.2}]$$

Where: Ω = rotational speed (rad/sec); M = torque (N.m); h = vane height (m); R_1 = vane radius (m); R_2 = outer container radius (m); μ = plastic viscosity (Pa.s); τ_0 = yield stress (Pa).

The equation 2 can be solved with a non-linear optimization. The calculation begins with the supposition of the plastic viscosity and yield stress values. For each measured speed-torque point from the test data, the radius at which flow ceases is calculated based on Eq. 2 using the guessed values of τ_0 and μ . For each point, the "calculated rotational speed" is calculated by Eq.2. The mean squared error (Eq.3) is calculated for all points as the difference between the "calculated rotational speed" and the "measured rotational speed".

$$mse = \frac{\sqrt{(\Omega_{calculated} - \Omega_{measured})^2}}{n} \quad [\text{Eq.3}]$$

The rheological parameters (τ_0 and μ) are determinate by minimization of the value of mse.

MATERIALS AND EXPERIMENTAL PROGRAMME

Several aggregate sizes within the range of 6 mm to 20 mm were used and the sand size range was between 0 mm and 4 mm.

The aggregates and sand specific gravity is 2.5. Ordinary Portland cement CEM I 52.5, slag (S), fly ash (V) and limestone filler (F) were used. A polycarboxylate superplasticizer (SP) type was used.

Tow series of experimental tests were investigated (table 1). The first program (series 1) was used to validate the repeatability of the developed rheometer. The second one (series 2) was used to validate the apparatus the reproducibility tests.

Table 1
Concrete mixture compositions

Name	W/C	C (kg/m ³)	S (kg/m ³)	V (kg/m ³)	L (kg/m ³)	SP (%)	W (kg/m ³)	Ag (kg/m ³)	Sd (kg/m ³)	Slump (cm)
BO 1	0.50	350				0.2	175	1044	815	9
BO 2	0.40	375				1.8	150	997	789	18
BES			225							17
BEV	0.40	150		225		1.4	150	1054	823	18
BEL					225					17

RESULTS AND DISCUSSION

After choosing the final version and defined the procedure of rheometer, tests of repeatability and reproducibility were performed to validate the apparatus. Repeatability tests were used to check if the results obtained from the apparatus are similar for the same concrete. Reproducibility tests were used to check if two identical rheometers give similar results for the same concrete.

Verification of repeatability of the rheometer:

In order to check the repeatability of the test, three tests were done with similar concretes BO1 and BO2 Table 1 (series 1).

The results presented in Figures 4 and 5 show clearly that the friction torque varies linearly with the speed.

The linear variation of torque- rotational speed curves and the small standard deviation (9% for plastic viscosity – Table 3) for the obtained rheological parameters proved that the repeatability of the test is good. Hence, it can be concluded that the configuration of the apparatus and the proposed test procedure allows obtaining repeatable results.

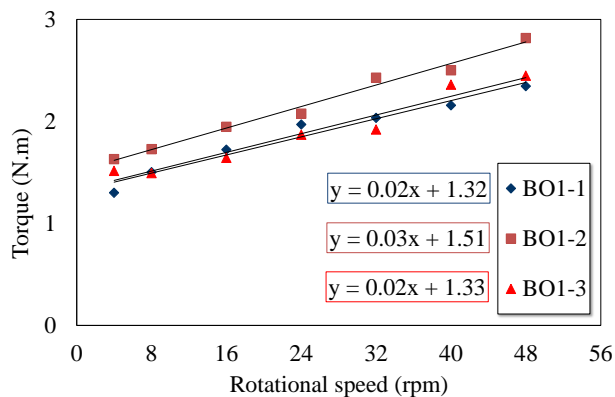


Figure 4. Torque at different rotational speeds for the repeatability test of the concrete BO1

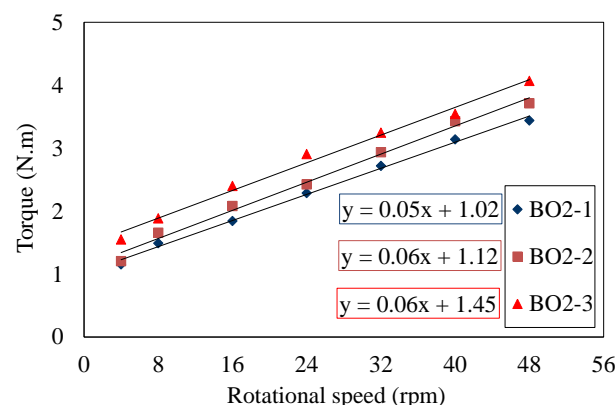


Figure 5. Torque at different rotational speeds for the repeatability test of the concrete BO2

Table 2
Variation coefficients of the rheological parameters of the repetitive tests

	BO1 - 1	BO1 - 2	BO1 - 3	Standard deviation	Variation coefficient
τ_0 (Pa)	402.05	440.1	413.6	19.51	0.047
μ (Pa.s)	23.42	27.1	24.8	1.85	0.074
	BO2 - 1	BO2 - 2	BO2 - 3	Standard deviation	Variation coefficient
τ_0 (Pa)	267.31	267.13	299.89	18.86	0.068
μ (Pa.s)	73.97	77.48	78.17	2.25	0.029

Verification of the reproducibility of the rheometer:

In order to check the reproductibility of the test, two identical rheometers were assembled to test simultaneously different concretes.

Each concrete (BES, BEL and BEV) whose compositions are given in the Table 1 (series 2) was tested at the same

time on the two apparatus by two different operators. The same procedure was strictly applied for both apparatus.

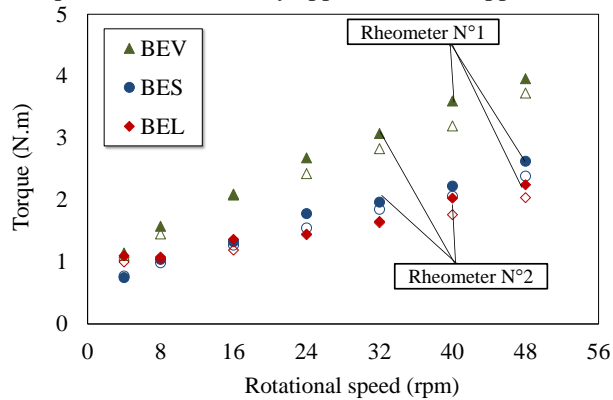


Figure 6. Torque at different rotational speeds for the repeatability test of the concrete BO2

The obtained results (Figure 6) show that the curves obtained by the two rheometers are all linear and are very close to each other. In addition, the rheological parameters (μ , τ_0) corresponding to each rheometer are obtained with a low coefficient of variation (5.8% for viscosity and 3.1% for yield stress – Table 3). Hence, this confirms the reproducibility and also repeatability of the tests.

Table 3

Variation coefficients of the rheological parameters of the reproductibility tests

	BES1 Rheo1	BES1 Rheo2	Standard deviation	Variation coefficient
τ_0 (Pa)	187.4	169.1	12.95	0.073
μ (Pa.s)	54.4	52.7	1.20	0.022
	BEV1 Rheo1	BEV1 Rheo2	Standard deviation	Variation coefficient
τ_0 (Pa)	237.73	238.94	0.86	0.004
μ (Pa.s)	99.74	87.45	8.69	0.093
	BEL1 Rheo1	BEL1 Rheo2	Standard deviation	Variation coefficient
τ_0 (Pa)	256.9	231.27	18.14	0.074
μ (Pa.s)	30.6	31.2	0.42	0.013

CONCLUSIONS

A rheometer was developed to meet the industrial needs for a reliable device that measures the rheological parameters of fluid concrete with good precision and high stability.

The developed rheometer has the same operating principle of the ICAR device and Estellé et al.'s rheometer, the difference being the geometry of blade and the speed profile.

This apparatus is designed for mobile use on site and in laboratories at a reasonable cost.

The used blade (U shaped and reversed) makes it possible to reduce the vibration of the apparatus, obtain more stable measurements, to minimize the segregation of the concretes during the test and to expand the range of concrete workability ranging from a slump of approximately 7 cm and concretes with important plastic viscosity like concretes with mineral addition to fluid concrete.

The tests show that the rheometer measurements are repetitive with a low coefficient of variation (0.05) When the same parameters are measured by two identical concrete rheometers, piloted by two different operators, the tests are reproductive with a low coefficient of variation (0.04).

REFERENCES

- Koehler EP, Fowler DW: Development of a portable rheometer for fresh Portland cement concrete. ICAR Report 105-3F. Aggregates foundation for technology, research and education. (2004).
- Koehler EP, Fowler DW, Ferraris CF, Amziane S. New portable rheometer for fresh self-consolidating concrete. ACI Mater J 2006; 233: 97-116.
- Tattersall G.H, Bloomer SJ. Further development of the two-point test for workability and extension of its range. Mag Con Res 1979; 31: 202-210
- Banfill PFG. Additivity effects in the rheology of fresh concrete containing water-reducing admixtures. Constr Build Mater 2011; 25(6): 2955-2960
- Lacombe P, Beaupré D, Pouliot N. Rheology and bonding characteristics of self-leveling concrete as a repair material. Mater Struct 1999; 32(8): 593-600.
- Jiong Hu, Kejin Wang. Effect of coarse aggregate characteristics on concrete rheology. Constr Build Mater 2010; 25(3):1196-1204
- Wallevik OH, Saasen A, Gjorv OE. Effect of filler materials on the rheological properties of fresh concrete. ACI Mater J 1995;92(5):524-28.
- Wallevik O H, Gjorv O E. Development of a coaxial cylinder viscometer for fresh concrete, Properties of Fresh Concrete. Proceedings of the rilem colloquium, Chapman & Hall, Hanover; 1990: 213-224.
- De Larrard, F, Szitkar, J.C., Hu, C, Joly, M, Design of a rheometer for fluid concretes, RILEM Workshop Special Concretes Workability and Mixing 201-208, 1993.
- Hu C, De Larrard F, Sedran T, Boulay C, Bosc F, Deflorenne F: Validation of BTrheom: the new

- rheometer for soft-to-fluid concrete, *Mater Struct* 1996; 29: 620-631.
11. Wen-Chen Jau , Ching-Ting Yang. Development of a modified concrete rheometer to measure the rheological behavior of conventional and self-consolidating concretes. *Cem Conc Compos* 2010. 32: 450-460.
 12. Banfill P, Beaupre D, Chapdelaine F, de Larrard F, Domone P, Nachbaur L, et al. Comparison of concrete rheometers: international tests at LCPC (Nantes, France). In: Ferraris CF, Brower LE, editors. NISTIR 6819, National Institute of Standards and Technology, USA; 2001.
 13. Beaupre D, Chapdelaine F, Domone P, Koehler E, Shen L, Sonebi M, et al. Comparison of concrete rheometers: international tests at MB. In: Ferraris CF, Brower LE, editors. NISTIR 7154, National Institute of Standards and Technology, USA; 2004.
 14. Tattersall G H, Application of rheological measurements to practical control of concrete, *Proceedings of the International Conference on "Rheology of Fresh Cement and Concrete"*, Liverpool, pp. 270-280, 1990.
 15. Banfill PFG. Rheological methods for assessing the flow properties of mortar and related materials. *Constr Build Mater* 1994; 8(1):43–50.
 16. Ferraris CF, De Larrard f. Testing and Modelling of Fresh Concrete Rheology, NISTIR 6094, National Institute of Standards and Technology, 59 p, 1998.
 17. De Larrard F, Sedran T. Mixture-proportioning of high-performance concrete, *Cem Conc Res* 2002; 31(11): 1699–1704.
 18. Golaszewski J, Szwabowski J. Influence of superplasticizer on rheological behaviour of fresh cement mortars, *Ceme Concr Res* 2003. 34(2): 235-248.
 19. Wallevik J E. Relationship between the Bingham parameters and slump. *Cem Conc Res* 2006. 36(7): 1214- 1221.
 20. Estellé P., Lanos C.: High torque vane rheometer for concrete: principle and validation from rheological measurements. *Appl. Rheol*, 22 (2012) 12881.
 21. Estellé P, Lanos C, Perrot A. Processing the couette viscometry data using a Bingham approximation in shear rate calculation. *J Non Newtonian Fluid Mech* 2008. 154: 31-38.
 22. Soualhi H, Kadri E-H, Ngo T-T, Bouvet A, Cussigh F. Rheology of ordinary and low-impact environmental concretes, *Journal of Adhesion Science and Technology*. 2015; Vol. 29, No. 20: 2160–2175.
 23. Soualhi H, Kadri E-H, Ngo Tt, Bouvet A, Cussigh F, Tahar Z-A: Design of portable rheometer with new vane geometry to estimate concrete rheological parameters. *Journal of Civil Engineering and Management*, 2016, DOI:10.3846/13923730.2015.1128481.

NATURAL POZZOLANA ADDITION EFFECT ON COMPRESSIVE STRENGTH AND CAPILLARY WATER ABSORPTION OF MORTAR

Walid Deboucha^{a,b*}, Nordine Ieklou^a, Abdelhafid Khelidj^a, Mohamed.N Oudjit^b

a LUNAM University, University of Nantes - IUT Saint-Nazaire, GeM, CNRS UMR 6183, Research Institute in Civil Engineering and Mechanics, France.

b Built environment laboratory « LBE », Faculty of civil engineering, University of Sciences and technology Houari Boumediene, 16111, Algiers, Algeria.

*Corresponding author: Fax: + 33(0)2 40 17 81 60 Email: walid.deboucha@etu.univ-nantes.fr

ABSTRACT

The cement manufacturing is the one of the factors that pollutes the atmosphere in the industrial sector. The common way to reduce this pollution is using mineral additions as partial replacement of Portland cement. Particularly, natural pozzolana (NP) is a component in which they can be used to decrease the rate of pollution. The main objective of this experimental work is the study of the effect of substituting cement with natural pozzolana up to 40% on compressive-flexural strength and capillary water absorption of cement mortar. Validation of the results was performed by early age and long term tests. Tests of isothermal calorimetry on paste specimens, and of Mercury intrusion porosimetry on mortar specimens, were performed. The results obtained in the present research showed that the higher dosages of natural pozzolana added could be the principal parameter of such decrease in strength at early and medium term. Further, this increase of incorporated addition has been believed to reduce the capillary water absorption.

KEYWORDS

Natural pozzolana, mortar, strength, capillary absorption.

INTRODUCTION

Building materials is the third-largest CO₂-emitting industrial sector in the world, most of which are related to concrete manufacturing [1]. Cement produced to the concrete manufacturing is taking a considerable rate of about 5 to 7 % from the total CO₂ generated [2]; and an average of 0.8–1 ton of CO₂ is emitted per one ton of Portland cement [3]. This ratio is corresponding to a high energy consumption during the calcination of limestone. The application and use of mineral additions in mortar and concrete have been widely studied in recent decades to reduce the cement consumption and improve the resistance and durability of their composites, because of the substitution of this material in rates of 8–10% [4,5]. In addition, Studies have shown that the replacement of Portland cement with mineral additions in concrete may prove to be technically feasible solutions to improve good performance, diminishing costs of production and reducing local environmental impact [6,7], as NP which is the subject of the present work.

Natural pozzolana (NP) has been widely used as supplementary cementing materials, especially in regions where there is a lack of other pozzolana such as fly ash, slag and silica fumes. Possible technological benefits from the use of natural pozzolana in concrete include enhanced impermeability and chemical durability, reduced in heat evolution and increase in ultimate strength [8,9]. The NP has been successfully applied in Algeria, particularly in cement factories and as addition to mortar and concrete.

Measurements of the capillary absorption of mortar and concrete were used as an indication of durability. A number of published articles on the effect of using NP as Portland cement replacements in the development of capillary water absorption on mortar and concrete. M. Ghrici et al. [10] reported that the concrete mixtures containing 30% NP have lower value of capillary water absorption coefficient compared to the control concrete.

In the work presented here, effects of natural pozzolana on the capillary water absorption and

compressive-flexural strength of mortar are investigated.

EXPERIMENTAL STUDY

Materials

The mortar mixtures were prepared with CEM-I 42, 5 N Ordinary Portland cement (OPC) conforming to the requirements specified in NA 442 [11], with a fineness of 367 m²/kg, natural pozzolana (NP) used in this work was obtained from Beni-Saf quarry in the west of Algeria. The NP was grounded in a laboratory mill to a specific surface of 500 m²/kg. The Chemical and physical properties of cement and natural pozzolana used are summarized in Table 1. X-ray diffraction patterns and identified phases of cement and NP are shown in Figs. 1 and 2 respectively.

A standard sand with maximum particle size of 2 mm has been used for mortar mixes design.

Table 1

The chemical composition and physical characteristics of the cement and natural pozzolana

Chemical composition (%)	OPC	NP
SiO ₂	21.57	46.66
Al ₂ O ₃	4.37	17.74
Fe ₂ O ₃	5.27	8.69
CaO	64.31	11.01
MgO		4.14
SO ₃	1.62	0.04
K ₂ O	0.38	1.10
Na ₂ O	/	5.07
Cl	0.01	0.01
LOI	0.98	8.94
Physical characteristics		
Specific gravity	3.16	2.38
Blaine (cm ² /gr)	3670	5500
Initial setting time (min)	177	-
Final setting time (min)	277	-
Expansion (mm)	0.5	-

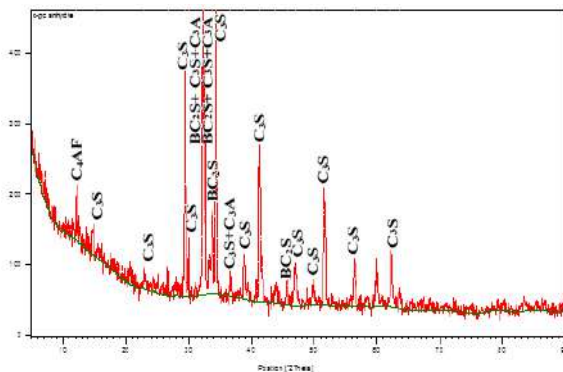


Figure 1
X-ray diffraction of cement

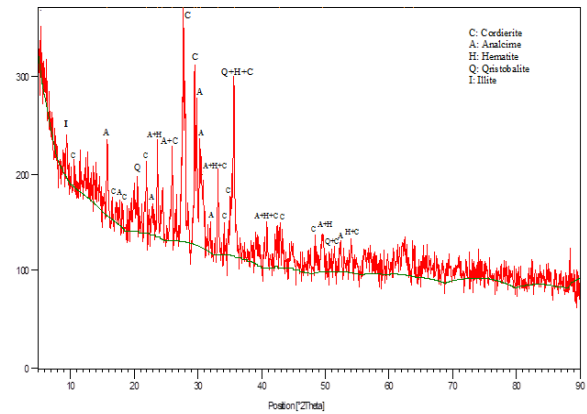


Figure 2

X-ray diffraction of natural pozzolana

Specimens

Five mixtures in total were prepared by varying the NP contents. The mixture proportion for mortar is given in Table 2. The mortar was cast into 40 mm × 40 mm × 160 mm moulds. Immediately After casting the test specimens were left in the moulds and covered with glass plate then placed in the humidity cabinet for at least twenty four hours. The hardened mortar was then demoulded and immersed in a water bath maintained at 20-21 °C until the age of testing.

Table 2

Mortar mix details

Code	Cement g	Addition g	Sand g	Water g
MR	450	0	1350	225
M10NP	360	45	1350	225
M20NP	315	90	1350	225
M30NP	270	135	1350	225
M40NP	438.75	180	1350	225

Testing procedures

Test on paste: in order to evaluate the hydration kinetics of the binders with natural pozzolana (NP) used in the mortars, heat flow of hydration was performed at 20°C in TAM Air isothermal calorimeter device. Immediately after pastes mixing, two samples with weights of 4-6g were taken from the mixture having E/B of 0.35 and were placed into standard plastic vials and then loaded into the isothermal calorimeter. The paste mixtures were noted according to their rate of substitution by NP as PR, P10NP, P20NP, P30NP and P40NP, respectively.

Tests on mortar: the compressive-flexural strength; was performed in accordance to the procedure given by French standard NF EN 196-1 [12]. The strength

value was determined as the average of three specimens test.

The durability performance of mortar was performed by means of two tests: (1) capillary water absorption and (2) mercury intrusion porosimetry.

For capillary water absorption, mortars prism of 40 mm×40mm×160mm were prepared and tested according to German Standard DIN 52-617[13]. After twenty eight days, the specimens were removed from the water curing medium and kept in a drying oven at 105 °C for 24 hours until getting a constant weight. The specimens were coated with the epoxy resin on their lateral surfaces to ensure uni-axial water absorption and immersed in water such that their cut surfaces would be submerged in water at a depth of 5 mm. The mortar specimens were weighted before and after submerging for 5, 15, 30, 60, and 150 minutes. The capillary water absorption coefficient was calculated from the following formula: $Q/A=S\sqrt{t}$, where Q/A is the amount of absorbed water per unit surface (kg/m^2); A is the area of the specimen in contact with water in (m^2); t is the time elapsed; S is the capillarity water absorption coefficient ($\text{kg}/\text{m}^2/\text{min}^{1/2}$).

The pore volume and pore size distribution of different mixtures were investigated by mercury intrusion porosimetry technique using a Micromeritics Autopore 9500 series IV with pressure capacity of 206 MPa. The data were analyzed by using the equation of Washburn as follows:

$$p = - \frac{4\gamma \cdot \cos \theta}{D}$$

Where p is the pressure of mercury injection, D the pore diameter, θ the contact angle which was taken to be 140° and γ is the surface tension which was taken to be 0.480 N/m . the test was done on about 3 cm^3 mortar specimens after drying at 40°C . The test was carried out on twenty eight days of curing.

RESULTS AND DISCUSSION

Isothermal calorimetry

The isothermal test results of heat flow rates and total heat of pastes made with natural pouzzolana and reference Portland cement paste are illustrated in Fig. 3. It can be seen from Fig.3 that the heat flow of mixture containing 10% of natural pouzzolana is somewhat higher ($\approx 2\%$) at the first approximately 9 hours compared to reference paste. Beyond this rate, the replacement of the cement by the NP induces a slight reduction in heat flow, e.g., the values of the

principal peak of P10NP, P20NP and P40NP are 102.34%, 99% and 97.84% of control paste mixture respectively (PR). As shown in Fig. 3, a delay in the appearance of the principal peak of hydration of cement pastes containing 20% and 30% NP compared to that of the reference cement paste. These results confirm that the incorporation of small amount of NP improve the cement hydration at short term. Cyr et al. [14] explained the improvement of the hydration of cement with the addition of the small amount of mineral additions at short-term by the effect of heterogeneous nucleation (physical effect). Indeed, Erdoğan et al. [15] found that the dormant period of cement paste made with 6% NP decreases. Moreover, the value of the principal peak is higher than that of control paste.

During the next approximately 24 hours, the heat flow of all mixtures decreases and the hydration reaction enters dormant period. Then the reaction begins low reactivity period and the heat flow decreases to a low level. After 25 hours, it can also be noticed that, the heat flow of control paste falls below the heat rate of NP pastes.

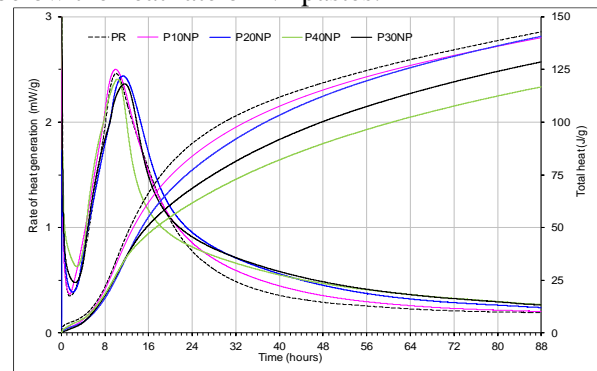


Figure 3

Hydration heat development (total heat evolved)

The Fig.3 also shows the total evolved heat for reference paste and pastes with NP. The figure shows that the total heat decreases when the substitution rate of NP increases. The total heat of NP mixes is in the range of 98%-80% of control mix. The minimum total heat is developed by mix containing 40% of NP. The reduction of total heat may related to the dilution effect of the supplementary cementitious materials [16], when the amount of cement decreases with increase of NP dosage.

The total heat of NP mixtures is in a good agreement with the investigations on mortar and concrete which confirms the trends of compressive strength of mortar at early ages. Compared to reference mix,

the mixture containing 40% of NP has the lower total heat, corresponding to the lower compressive strength of mortar at two days.

Compressive strength

The development of compressive and flexural strengths of mortar mixtures with NP additions are illustrated in Fig. 4 and Fig. 5. At all age, a reduction of compressive-flexural strength with increase of NP rates is noticed, this reduction is more pronounced for mortar mixture containing 30% and 40% of NP as cement replacement. The compressive strength for reference mortar after 28 and 90 days of curing was found to be 50.75 and 58.4MPa respectively. Similarly, the compressive strength measurement for 40 NP was found to be 27.5MPa and 36.4MPa respectively at 28 and 90 days of curing. It is the fact that compression strength is increased with increasing of curing period.

Y. Senhadji et al [17] found that mortars with 15%, 20% and 25 % of NP as cement replacement decrease the compressive strength by 9%, 11% and 17% respectively, at 90 days, in comparison with mortar mixture without NP. The results of compressive strength at early age are consistent with previous studies, which have shown that NP does not contribute notably to the early strength development of cementitious systems [18]. This could be explained by the slowness of the pozzolanic reactions between the glassy particles in the NP and the C-H. The pozzolanic reaction with C-H occurs slowly because C-H has first to be produced as a result of the hydration of Portland cement.

In our case, it was observed that the incorporation of NP leads to resistance drop for all age and all substitution rates and as it was observed in the results of heat hydration that the substitution of cement by 10% of NP can contribute to the hydration kinetics. Here, another explanation must be required. In cement chemistry, it is recognized that there are two types of calcium silicate (C-S-H) in the cementitious systems with additions [19]. The properties of these Latters can affect the macroscopic behavior of the mortar and concrete. Indeed, in the literature and from the work of Constantinides and Ulm [20] and Vandamme and al. [21], the density of the C-S-H has a significant effect on the mechanical properties. By nanoindentation test, they found that the C-S-H with a high density has a high modulus of elasticity, therefore, the resistance increases. Indeed, the compressive strength of mortars containing NP is in a good consistency with the investigation on

mortars using the dynamic elastic modulus test (Table.3).

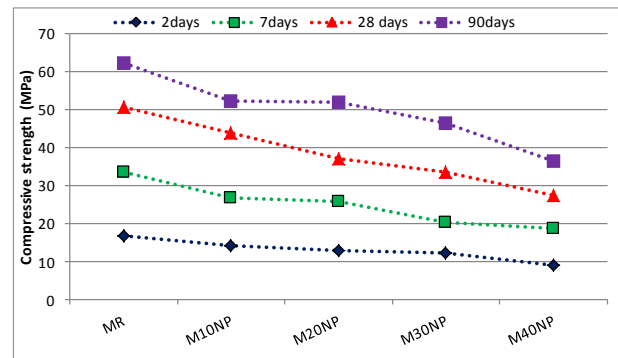


Figure 4 The effect of natural pozzolana on the compressive strength at various ages

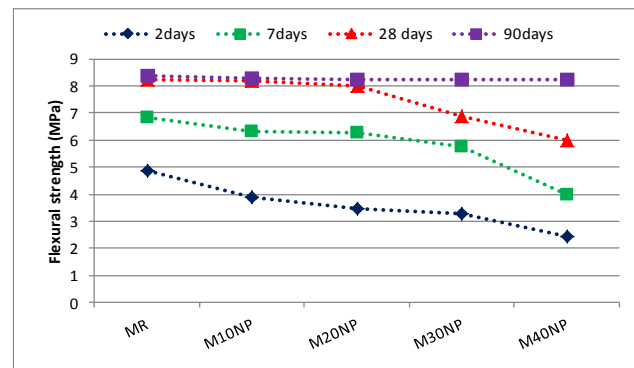


Figure 5 The effect of natural pozzolana on the flexural strength at various ages

Table 3 Dynamic elastic modulus of mortars at 90days

mixes	E_{dyn} (GPa)
MR	38.22
M10NP	36.73
M20NP	36.62
M30NP	35.81
M40NP	33.39

Capillary water absorption

Capillary water absorption results of NP mortar mixtures at the age of 28 days are presented in Fig. 6. It is noticeable from the Fig.6 that the highest capillary water absorption of 9.625 kg/m² was observed at the control mortar mixture. The incorporation of NP are remarkably effective when decreasing the capillary water absorption in mortar mixtures, particularly, mortar with 40 % of NP decreases the capillary water absorption by 45 % compared to mortar mixture without NP.

The evolution of capillary water absorption coefficient of mortars contained different amounts of NP is presented in Fig.7. The capillary absorption

coefficient results are also significantly influenced by the binder combination used. In the comparison to the mortar without addition, capillary water absorption coefficient is improved through the use of 40% NP as cement replacement is noticed for this mix. In this case, pores in the bulk paste or in the interfaces between aggregate and cement paste are filled by this mineral admixture. The capillary pores were reduced by the formation of secondary C–S–H gel due to the pozzolanic reaction, and hence the reduction in the capillary absorption coefficient of mortar. [22].

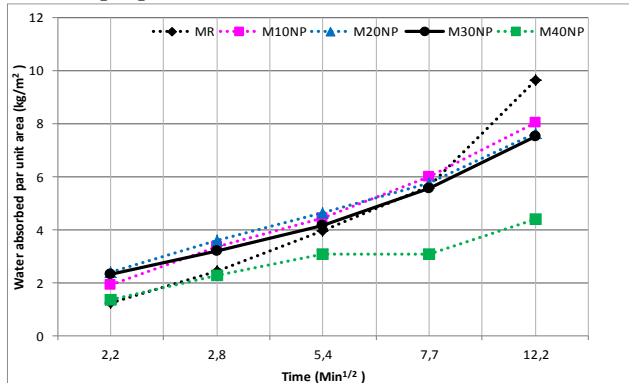


Figure 6 Water absorbed per unit area of natural pozzolana mortars at 28 days

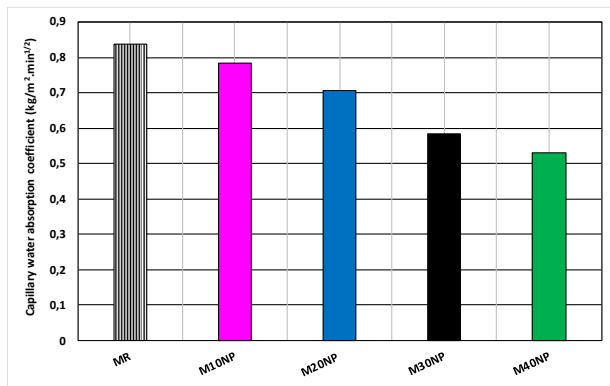


Figure 7 Capillary water absorption coefficient of natural pozzolana mortars (kg/m².min²)

Mercury intrusion porosimetry

The effect of NP on the pore size distribution of mortar at 28 days is shown in Fig8. An observation can be drawn from this figure is that the pore size distribution is affected by the NP and its rate of incorporation. As shown in the Fig.8, the mortar mixtures containing 10% and 20% of NP exhibit nearly dominant pore size to that of the reference mortar. However, the dominant pore size of the mortar mixtures containing 30% and 40% of NP are shifted to the right side of reference mortar. The dominant pore size of reference mix is 0.04 μ m

whereas a value of 0.05 μ m is obtained for the mixes containing 30% and 40% of NP.

Concerning the pore volume, it can be seen that the reference mortar and the mortars made with 10% and 20% of NP show a similar pore volume. However, the volume pore of the mortars containing 30% and 40% of NP is slightly higher than that of mortar without NP. This may occur due to the dilution effect. It should be noted that the mortar mixtures containing NP have relatively larger volume of small pores than (<0.02 μ m), as compared to the mortar without NP. This effect is directly related to different amounts of C–S–H formed [23]. The secondary C-S-H formed can decrease the interconnected pores which may explain the capillary water absorption results.

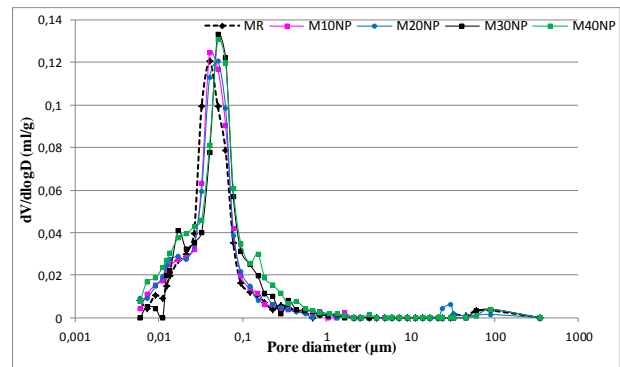


Figure 8 Pore size distribution of natural pozzolana mortars

CONCLUSIONS

The following conclusions could be drawn from the results obtained in this investigation:

- 1- At all ages of tests, the incorporation of natural pozzolana reduces the compressive strengths of mortar compared to the control mortar.
- 2- The use of NP as cement replacement improved the capillary water absorption by the most compared to the control mortar mixture.
- 3- Investigation by Isothermal calorimetry and Mercury intrusion porosimetry are in good agreement with the results of compressive strength and capillary water absorption.

REFERENCES

1. Unstats. , 2010, Greenhouse Gas Emissions by Sector , United Nation Statistical Division, New York, USA.
2. Malhotra, V.M., 2000, Role of supplementary cementing materials in reducing greenhouse gas emissions, in: O.E Gjorv, K Sakai (eds.), Concrete technology for a sustainable development in the 21st century, London, pp. 226–235.
3. Radonjanin, V., Malešev, M., Marinković, S., Al Malya, A. E., 2013, Green recycled aggregate concrete, *J. Construction & Building Materials*, **47**, pp. 1503–1511.
4. Habeeb, G.A., and Mahmud, H.B., 2010, Study on properties of rice husk ash and its use as cement replacement material, *J. Material Research*, **13**, pp. 185-190.
5. Akram, T., Memon, S., Obaid, H., 2009, Production of low cost self compacting concrete using bagasse ash, *J. Construction Building Materials*, **23**, pp. 703-712.
6. Chindaprasirt, P., Rukzon, S., 2008, Strength, porosity and corrosion resistance of ternary blend Portland cement, rice husk as fly ash mortar, *J. Construction Building Materials*, **22**, pp. 1601-1606.
7. Vaičiukynienė, D., Vaitkevičiūsa, V., Kantautas, A., Sasnauskas, V., 2012, Utilization of byproduct waste silica in concrete-based materials, *J. Materials Research*, **15**, pp. 561-567.
8. Mehta, P.K., 1981, Studies on blended Portland cements containing Santorin earth, *J. Cement & Concrete Research*, **11**, pp. 507–518.
9. Ramachandran, V.S., 1996, *Concrete Admixture Handbook: Properties, Science and Technology*, 2nd edition, Elsevier Science.
10. Ghrici, M., Kenai, S., Said-Mansour, M., 2007, Mechanical properties and durability of mortar and concrete containing natural pozzolana and limestone blended cements, *J. Cement & Concrete Composites*, **29**, pp. 542–549.
11. NA 442, 2005, Cement Composition, specifications and conformity criteria for common cements, Algerian standard, Alger, Algeria,
12. NF EN 196-1, 2006, methods of testing cement - Part 1: Determination of strength, French standard, Paris, France.
13. DIN 52 617, 1987, Determination of the Water Absorption Coefficient of Building Materials, Germany.
14. Cyr, M., Lawrence P., Ringot, E., 2005, Mineral admixtures in mortars Quantification of the physical effects of inert materials on short-term hydration, *J. Cement & Concrete Research*, **35**, pp. 719–730.
15. Erdoğan, S., Derya, Ö., Tokyay, M., 2014., Effect of Pozzolan Content and Fineness on Early Hydration of Interground Blended Cements, *J. Advanced Concrete Technology*, **12**, pp. 101-110.
16. Mounanga, P., Irfan M., Khokhar, A., El Hachem, R., A., Loukili, 2011, Improvement of the early-age reactivity of fly ash and blast furnace slag cementitious systems using limestone filler, *J. Materials & Structures*, **44**, pp. 437–453.
17. Senhadji, Y., Escadeillas, G., Mouli, M., Khelafi, H., 2014, Influence of natural pozzolan, silica fume and limestone fine on strength, acid resistance and microstructure of mortar, *J. Powder Technology*, **254**, pp. 314–323.
18. Ghrici, M., Kenai, S., Mansour-Said, M., El-Hadj Kadri, A., 2006, some engineering properties of concrete containing natural pozzolana and silica fume, *J. Asian Archit. Building. Engineering*, **02**, pp. 349–354.
19. Oudjit, M., Aroudj, K., Bali, A., 2007, Influence des fumées de silice sur l'évolution de L'hydratation des pâtes de chaux ou de Ciment Portland, *J. Materials and Structures*, **40**, pp. 703–710.
20. G., Constantinides and Ulm F., 2004, The effect of two types of C-S-H on the elasticity of cement-based materials: Results from nanoindentation and micromechanical modeling, *Cement & Concrete Research*, **34**, pp. 67–80.
21. M., Vandamme, F., Ulm, P., Fonollosa, 2010, Nanogranular packing of C–S–H at substochiometric conditions, *J. Cement & Concrete Research*, **40**, pp. 14–26.
22. Deboucha, W., Oudjit, M.N., Bouzid, A., Belagraa, L., 2015, Effect of incorporating blast furnace slag and natural pozzolana on compressive strength and capillary water absorption of concrete, *Procedia Engineering*, **108**, pp. 254–61
23. DeBelie N., Kratky J., Van-Vlierberghe, S.V., 2010, Influence of pozzolans and slag on the microstructure of partially carbonated cement paste by means of water vapour and nitrogen sorption experiments and BET calculations. *J. Cement & Concrete Research*, **40**, pp. 1723–33.

INFLUENCE OF DIFFERENT AMOUNTS OF NATURAL POZZOLAN FROM CAMEROONIAN VOLCANIC SCORIA ON THE RHEOLOGICAL PROPERTIES OF PORTLAND CEMENT PASTES

Willy Juimo^{1,2,*}, Toufik Cherradi¹, Larbi Abidi¹ and Luiz Oliveira³

¹Mohammadia School of Engineer, Mohammed V University of Rabat, Morocco

²Higher Institute of the Sahel, University of Maroua, Cameroon

³C_MADE-Centre of Materials and Building Technologies, University of Beira Interior-Covilhã, Portugal

*Corresponding author: Phone: +212 6 32 96 75 44 Email: hermannjuimo@gmail.com

ABSTRACT

This work is concerned with assessing the influence of natural pozzolan from Cameroonian volcanic scoria on the rheological properties of blended Portland Cement (PC) pastes. The objective of this paper is to examine the evolution of rheological properties (Yield stress and plastic viscosity) in cementitious materials with addition of natural pozzolan (NP). The rheological properties of blended cement-based materials depend strongly on mixture proportions and the characteristics of the components. In this study, design of experiments is used to investigate the influence of ratio of PC/NP on the yield stress and viscosity of blended pastes. Both rheological parameters are seen to vary over several orders of magnitude for the evaluated design space. Physical characteristics of the powders, such as total particle densities and total particle surface area, are computed for each NP. A set of pastes specimens was made with 0%, 25%, 35% and 45% of NP replacement. NP from Cameroonian volcanic scoria with four different colors (black, dark red, red and yellow) were used. Rheological properties of the prepared pastes were measured using a rotational rheometer (Viskomat NT). The results showed that the yield stress and plastic viscosity of cement pastes were generally decreased when the NP replaced part of the cement. The reduction of yield stress is around 3.72 to 29.04% for 25% of replacement, 21.12 to 44.26% for 35% of replacement and -1.99 to 58.96% for 45% of replacement all regardless of NP color. The reduction of viscosity is around -7.60 to 26.57% for 25% of replacement, 16.67 to 34.23% for 35% of replacement and 37.5 to 56.26% for 45% of replacement all also regardless of NP color. However, NP exhibited a significant reduction of yield stress and viscosity when amount of replacement is higher than 25%. The results also showed that the inclusion of yellow NP at replacement levels of 25% and 45% resulted in an increase of yield stress and viscosity for 1.99% and 7.60% respectively.

KEY WORDS: *Volcanic scoria ; Natural pozzolan ; blended Portland cement pastes ; rheological properties.*

INTRODUCTION

Concrete is the most widely used human-made commodity on the planet; about 25 billion metric tonnes are produced globally each year [1-3]. The production of one tonne of cement requires 60-130 kg of fuel oil or its equivalent and about 105 kWh of electricity, depending on the cement type and production process, whereas the average CO₂ emissions ranges from 0.60 to 1 tonne of CO₂ per cement tone [2-4]. Although the production process is still very energy consuming, cement is the most widely used construction material today. Due to the regulations, policies and environmental sustainability, the need for energy consumption decrease, as well as for CO₂ emission lowering, implied the pure cement replacement from

supplementary cementitious materials (SCM), which are used in order to produce what is generally called as “blended cements”. Increased volume fractions of SCM, such as volcanic pozzolans, fly ash and slag produce more environmentally-sustainable concretes, and also yield mixtures with high workability, ultimate strength, and durability [5]. The most common SCM are natural pozzolans (NP), generally derived from volcanic origins and artificial pozzolans, which are mainly industrial by products/wastes, such as fly ash, different type of metallurgical slags and silica fume. Blending PC with pozzolanic admixtures is an effective way to improve workability, strength and durability (lower permeability, resistance to chlorides and sulfates, mitigation of alkali silica reaction) [4,5].

The rheological properties of cement paste are critical to the field performance of concrete in terms of its slump, flow, and workability. Also the rheological properties of fresh concrete are related to cement hydration and chemical interactions in the cement paste system [6,7]. In addition, the rheological properties of concrete are also dependent on the shape and gradation of the aggregates contained in the mixture. But the evolution of the rheological properties at early ages depends almost entirely on the cement paste. The rheology of cement paste is strongly influenced by mixture proportions and material characteristics, including water-to-cementitious materials ratio by mass (W/C), SCM additions, and the fineness of the powder materials. The current study focuses on the latter two of these parameters, while maintaining a constant volume fraction of water in all investigated mixtures [8,9].

Cameroon is rich in NPs, materials originated from volcanic eruption. The pumice used in this study is coming from "Djoungo". Volcanic scoria of locality of "Djoungo" on the plain of Tombel (Longitude: 9°37'32" East Latitude: 4°35'16" North) are the pozzolan which has been of the greatest number of studies. The "Djoungo" pozzolan, purplish black and brick red, clean, without clay, are exploited because of their privileged geographical location (near the railway and seaport). These are fragments of vesicular magma of low density (<1), internal structure constituted by cells and more or less tight pore. The ability to use these materials in manufacture of lightweight concrete can be an important economic asset. It is characterized by a high content of vitreous components and its high pozzolanic reactivity is mainly attributed to the high content of active SiO_2 ; it can react with calcium hydroxide released during the hydration of cement to produce C-S-H gels [10-13].

The present paper focuses on the rheological of binary blended cement, produced by PC and NP.

The rheological properties of mixtures containing portland cement replacements of finely-ground basaltic ash (NP) from "Djoungo", Tombel, Littoral region, Cameroon was here investigated. In the laboratory experiments, binary PC-NP mixtures with finely ground 25, 35 and 45 mass% NP (25%NP, 35%NP and 45%NP) were used.

MATERIALS AND METHODS

Materials: A PC of class CEM I 42.5 provided from a ready-mixed plant from Covilhã-Portugal was used for this study. The volcanic scoria samples were extracted from the site of "Djoungo" in Cameroon on January 2015. The samples have been kept in plastic bags and then packed in cartons and sent to Rabat (Morocco) by plane (Fig. 1).

The reduction of volcanic scoria samples was performed, in the "Laboratoire Traitement des Minerais of Département des Mines of Ecole Nationale Supérieure des Mines de Rabat (ENSMR) by crushing. Samples of volcanic scoria were dried, pulverized at $50\ \mu\text{m}$ (Fig. 2).

Optical micrographs from petrographic investigations of crushed sand-sized particles of the volcanic scoria, which is similar to other Cameroonian volcanic scoria provide a qualitative assessment of the various glass and crystal components available for pozzolanic reaction in the experimental powders. The chemical and mineralogical characterization of "Djoungo" scoria samples were realized through overall chemical analysis and X-ray analysis (XRD) on obtained by crushing powders (grain size $63\text{-}80\ \mu\text{m}$) by several authors [10-12]. The bulk chemical composition of the volcanic scoria powder indicates a NP (Table 1).



Figure 1
Packaging of specimens

The powders Particle Size Distributions (PSD) and rheological behaviour of the pastes was performed in Centre of Materials and Building Technologies (C_Made), University of Beira Interior-Covilhã, Portugal. The PSD of powders was performed using a LS 230 laser granulometer (Coulter LS) of which analytic range extends from $0.40\ \mu\text{m}$ to $2000\ \mu\text{m}$. The differential PSD of the pastes and of the cement powder was investigated in deionized water, pure ethyl alcohol, a synthetic pore solution and in air, in order to study the influence of the media. The analysis time was 1 min for all the media used and the speed of pump is reduced to the minimum in order not to destroy the agglomerates. The PSDs

obtained were expressed in a percent by volume and are normalized to 100%.

A Micromeritics Accupyc 1330 Gas pycnometer instrument was used for density of the natural pozzolan samples measurements.

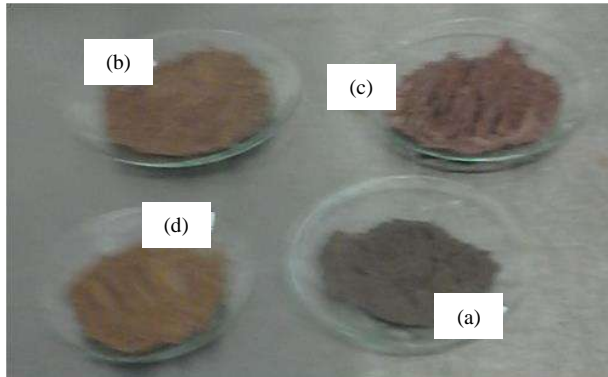


Figure 2

Different powders obtained : (a) Black , (b) Dark red, (c) Red and (d) Yellow powder

Table 1
Chemical analysis of "Djoungo"

Ref.	[10]	[11]	[12]	[1,14]
Code	DVS	ZD	DB1	ACI
SiO ₂	45.57	44.04	45.79	43–72
Al ₂ O ₃	15.94	15.26	15.68	9–20
Fe ₂ O ₃	12.81	12.77	12.83	1–12
CaO	8.97	9.29	9.60	1–15
MgO	5.76	7.00	6.26	0.50–7
MnO	-	0.17	0.17	/
Na ₂ O	3.28	5.64	3.54	0.5–11
K ₂ O	1.03	1.35	1.39	0.2–8
SO ₃	-	0.01	-	0–1.40
TiO ₂	2.11	2.87	2.84	/
P ₂ O ₅	-	0.53	0.60	/
L.O.I.	0.20	1.10	0.31	0.20–19

Note: DB1, DVS and ZD are name's codes using by authors respectively in reference [10], [11] and [12] ACI : American Concrete Institute [1].

Methods :

Cement paste mixing procedures: Thirteen different cement paste mixtures were prepared according to the mixture proportions shown in Table 2. The mixing equipment used consists in a twisted mixing anchor blade adapted to a Stuart, SS 30 mixer and a stainless steel beaker. The cement suspensions were prepared by adding the powder to water and admixture in the beaker, and then by mixing at a speed during 1 min 30 s.

Table 2

Mixture proportions by mass fraction (grams)					
Mix	Cement (C)	NP	Water (W)	W/C	W/(C+NP)
0%	900	-	500	0.56	-
25%	675	225	500	0.74	0.56
35%	585	315	500	0.85	0.56
45%	495	405	500	1.01	0.56

Determination of rheological properties: The rheological behavior of non-Newtonian fluids such as cement paste, mortar, or concrete is often characterized by two parameters, yield stress τ_0 , and plastic viscosity μ , as defined by the Bingham equation (Eq. (1)) :

$$\tau = \tau_0 + \mu \dot{\gamma} \quad (1)$$

Where: τ is the shear stress (Pa) and $\dot{\gamma}$ is the shear strain rate (s⁻¹).

Amziane et al. [15] showed that the Bingham relationship becomes complex when the cement paste is close to setting, resulting in aberrations such as a negative plastic viscosity calculated using Eq. (1). Consequently, an improved method to monitor the evolution of the yield stress at early ages was determined to be stress growth measurements. In addition to measurements of the shear stress, rheological property measurements can be used to determine the dynamic viscosity of a material sheared at a known shear rate [16,17]. Eq. (2) may be used to describe the viscosity of pastes at early ages.

$$\eta = \frac{\tau}{\dot{\gamma}} \quad (2)$$

Where η describes the viscosity (Pa s) of a material subject to a shear stress at a known shear strain rate, $\dot{\gamma}$ (s⁻¹), and τ is the shear stress applied by the rheometer on the material (Pa).

The rheological behavior of the pastes was characterized using a stress-controlled shear rotational rheometer (Viskomat NT). The employed configuration is constituted by two coaxial relatively rotatable cylinders. The material is placed in the inner cylinder (Fig.3). The temperature was fixed to 25 °C. The viskomat NT is a versatile rotational viscosimeter for determining the workability of fine grained building materials such as cement paste, mortar, fine concrete, plaster etc. with maximum particle size of 2 mm. We can obtain information on: flow curves and rheological parameters temperature dependent workability properties ; stiffening behavior as a function of time and stirring speed

effects of concrete admixtures and mineral blending agents on workability. The viskomat NT is delivered with two standard probes for mortar and cement paste. Cement paste probe made of stainless steel is used. This probe is used for cement paste and mortar with a maximum particle size of 0.5 mm. A scraper made of hardened stainless steel is also used.

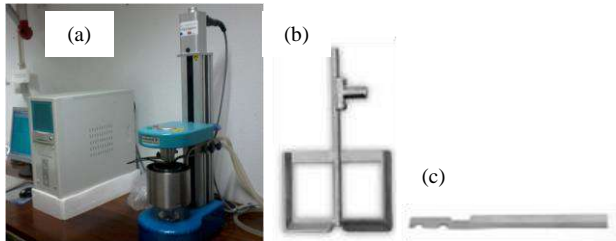


Figure 3

(a) Rotational rheometer (Viskomat NT), Rheometer used, (b) Cement paste probe and (c) Scraper

For the measurement loop, the shear rate ranged from 0 s^{-1} to 120 s^{-1} , as determined by analytical calculation from the rotational speed. To first homogenize the specimen, an increasing shear rate up to 120 s^{-1} was imposed (performed) during 180 s (6 minutes), before executing the loop of increasing and then decreasing the shear rate (Fig.4). The rheology of cement-based materials was described by the yield stress determined with the Bingham model applied between 0 s^{-1} and 120 s^{-1} . Each formulation of paste was analyzed on three different samples.

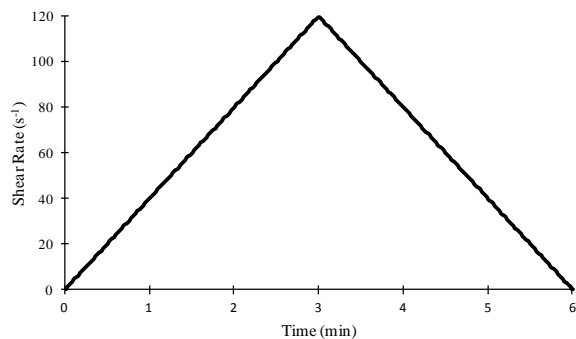


Figure 4

Evolution of Shear rate during measurement

RESULTS AND DISCUSSION

Particle sizes distributions of NP powders in different liquid media are shown in Figure 5. Indeed, their size ranges from sub-micronic dimensions (finest particles observed show a diameter about 0.40–50 μm) to a maximum size of around 50 μm . Figure 5

shows that the size particle of four powders used is approximate similar. Each shown result is the average of three individual measurements. Each result is the average of three individual measurements. Physical properties of NP samples are shown in Table 3.

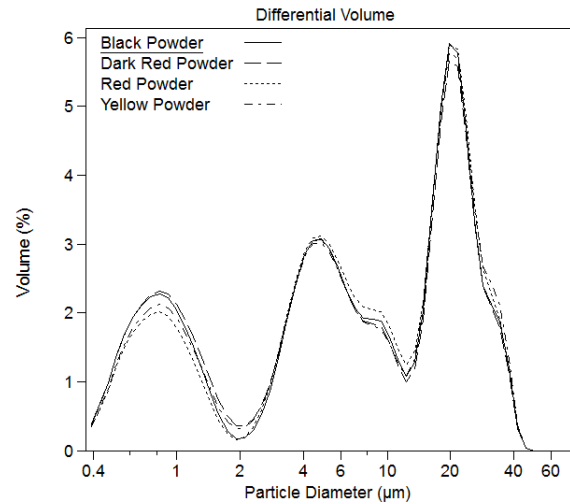


Figure 5

Particle size distributions by volume differential of the four natural pozzolan powders used

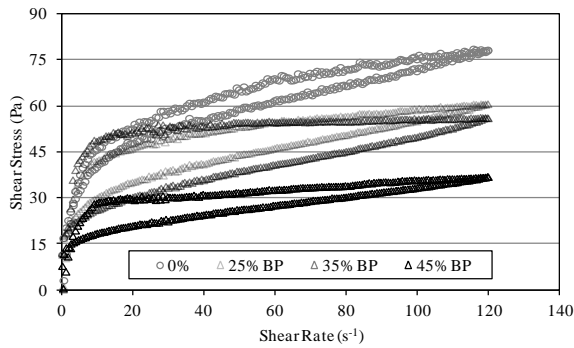
Table 3

Physical properties of natural pozzolan samples				
NP	BP	DRP	RD	YP
Density/Specific gravity (g/cm^3)	-	2.9809	3.0794	-
Mean particle size (μm)	5.998	5.726	6.456	6.210
d_{10}^a	25.90	25.71	26.26	26.66
d_{25}^a	19.70	19.46	19.96	20.01
d_{50}^a	7.179	6.587	7.839	7.365
d_{75}^a	2.512	1.722	3.231	2.723
d_{90}^a	0.745	0.746	0.785	0.772
Specific Surface Area (cm^2/g)	8401	8631	7708	8059

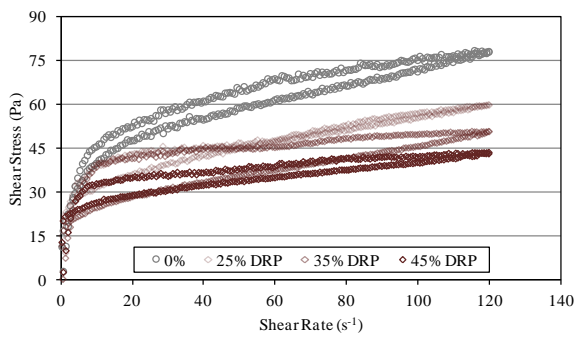
^a d_{10} , d_{25} , d_{50} , d_{75} and d_{90} values indicate the diameter size at which 10%, 25%, 50%, 75% or 90% of particles are larger than, i.e., $d_{10}=25.90$ means that 10% of all particles were $>25.90 \mu\text{m}$ diameter.

Figure 6 shows rheograms obtained after rheological measurements for different replacements by natural pozzolans. The shear stress variation at different amounts is illustrated on the figure. This variation decreases with the increase of pozzolan replacement level. This encourages their uses in 25%

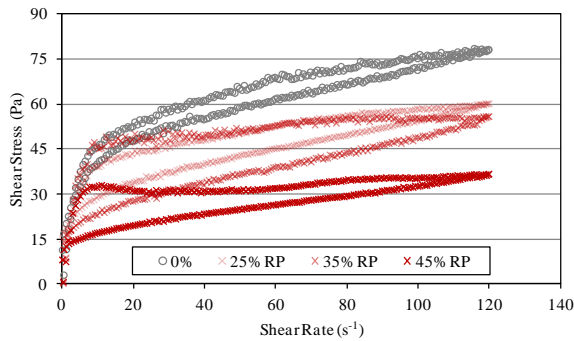
replacement level without color considerable and risk of loss of the ultimate shear stress.



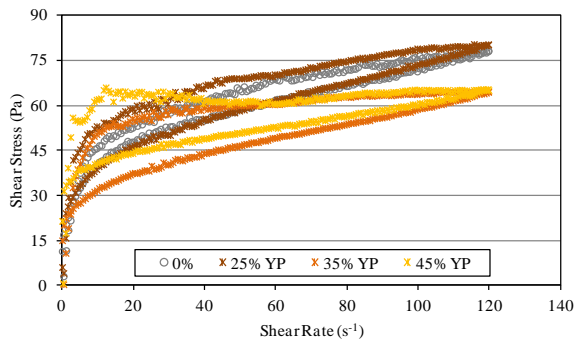
(a) Black Powder (BP)



(b) Dark Red Powder (DRP)



(c) Red Powder (RP)

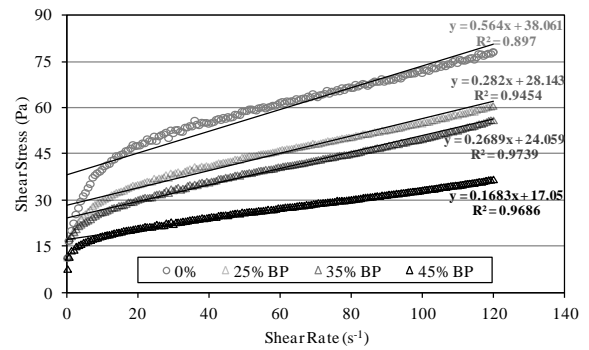


(d) Yellow Powder (YP)

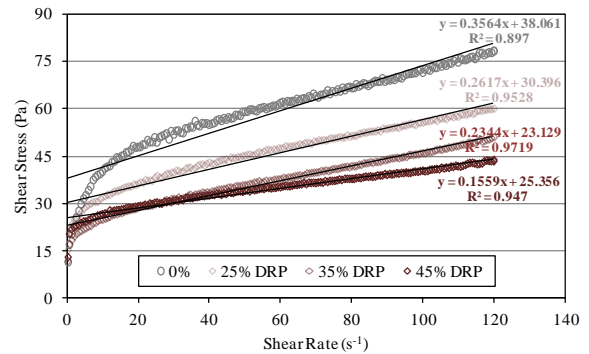
Figure 6

Rheograms obtained for different amounts of NP

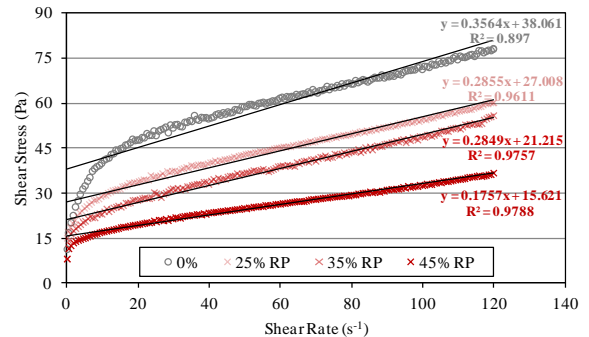
According to the results the evolution of the ultimate shear stress follows a hysteresis law. The rheological parameters, namely yield stress and viscosity, were calculated from the measured shear stress-shear rate curves for each of the mixtures in Table 2 by linear regression. A typical shear stress vs. shear rate curve for the descending data is provided (Fig.7). These descending curve data were fitted to a linear equation using ordinary least squares regression to determine a slope (plastic viscosity) and an intercept (yield stress), according to a Bingham model. The correlation coefficients (R^2) for these regressions ranged between 0.897 and 0.9788 with an average value of 0.9546 (Table 4).



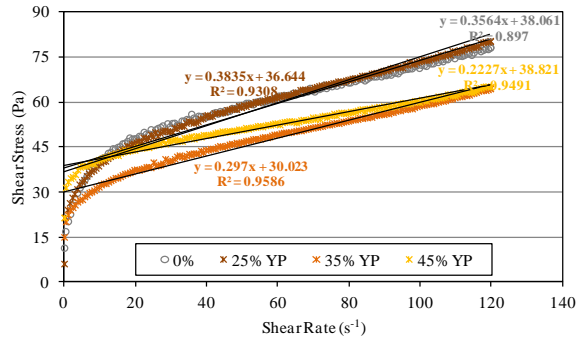
(a) Black Powder (BP)



(b) Dark Red Powder (DRP)



(c) Red Powder (RP)



(d) Yellow Powder (YP)

Figure 7

Typical descending branch shear stress vs. shear rate curve obtained for different amounts of NP

The evaluated yield stresses and viscosities by linear regression are provided in Table 4. Each of the two parameters ranged over about two orders of magnitude, indicating the strong influence of NP on rheological properties. Separate detailed discussions for yield stress and viscosity follow.

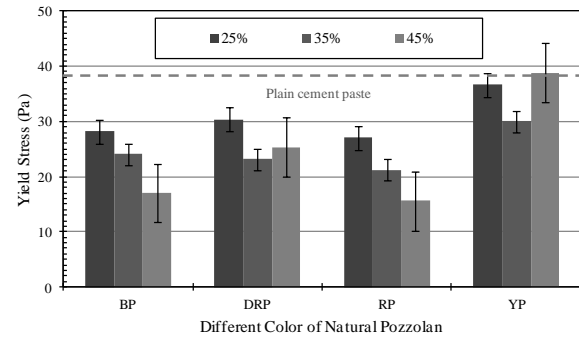
Table 4

Yield stress and viscosity determined for each blended cement paste mixture.

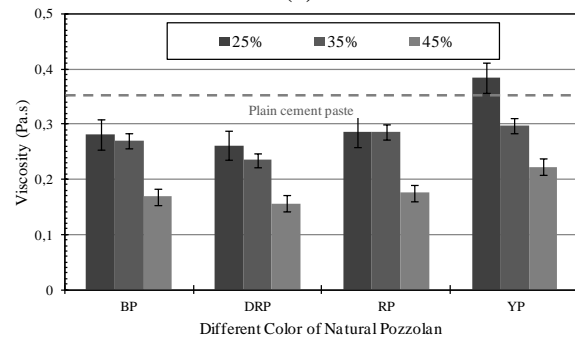
Paste Mix.	Yield Stress τ_0 (Pa)	% $\Delta(\tau_0)$	Viscosity μ (Pa·s)	% $\Delta(\mu)$	Coef. (R ²)
0%	38.061	-	0.3564	-	0.8970
25% of replacement					
BP	28.143	26.06	0.2820	20.88	0.9454
DRP	30.396	20.14	0.2617	26.57	0.9528
RP	27.008	29.04	0.2855	19.89	0.9611
YP	36.644	3.72	0.3835	-7.60	0.9308
35% of replacement					
BP	24.059	36.79	0.2689	24.55	0.9739
DRP	23.129	39.23	0.2344	34.23	0.9719
RP	21.215	44.26	0.2849	20.06	0.9757
YP	30.023	21.12	0.2970	16.67	0.9586
45% of replacement					
BP	17.050	55.20	0.1683	52.78	0.9686
DRP	25.356	33.38	0.1559	56.26	0.9470
RP	15.621	58.96	0.1757	50.70	0.9788
YP	38.821	-1.99	0.2227	37.51	0.9491

In Figure 8, it is observed that the replacement of PC by 25, 35 and 45% NP resulted in an decrease of shear stress of relative to the shear stress of specimen containing no supplementary material excepted the replacement of PC by 45% of yellow NP. Further replacement of NP beyond 25% replacement resulted in a slight decrease in the shear stress. It is interesting

to see that among all the mixes made, the one containing 5% NP. The increase in the yield stress of specimens due to replacement of NP can be attributed to the improved bridging between particles. On the other hand, the observed decrease in the yield stress of the specimens due to the replacement of PC by NP can be explained by the fact that larger replacement (small than 25%) leads to a surplus of the small-sized fraction, which begins to move apart PC grains, causing unpacking of the system and thus leading to a considerable increase in the strength of the system.



(a)



(b)

Figure 8

(a) Yield Stress and (b) Viscosity of the cement paste as a function of dosage natural pozzolan

CONCLUSIONS

In conclusion, it is possible in the near future to be able to reduce the number of tests on concrete necessary for the development of formulations having a fixed workability. Mineral additives can be selected in the laboratory by testing cement paste or mortar. An experiment would determine the rheological characteristics required for cement paste and mineral addition proportion to obtain the required workability of concrete. Lots of work needs

to be done to validate the results obtained on the cement paste with the addition of natural pozzolan. In this study case both yield stress and viscosity are strongly dependent on the ratio of the powders employed in preparing a blended cement/natural pozzolan paste with a constant volume fraction of water.

ACKNOWLEDGMENTS

This work was conducted in the “Laboratoire Traitement des Minerais of Département des Mines of Ecole Nationale Supérieure des Mines de Rabat (ENSMR) and in the Centre of Materials and Building Technologies (C_Made) of Department of Civil Engineering and Architecture at University of Beira Interior. The authors gratefully acknowledge the support from these laboratories that has made this research possible. They would like to thank Prof. Abílio Silva for its assistance in making the particle size distribution measurements presented in this study. In addition, they would also like to acknowledge the assistance of Mr. Jorge Bento in experimental testing.

REFERENCES

1. ACI, 2002, Use of Raw or Processed Natural Pozzolans in Concrete, ACI Committee 232, Manual of Concrete Practice ACI 232.1.
2. N. Lemonis, P.E. Tsakiridis, N.S. Katsiotis, S. Antiohos, D. Papageorgiou, M.S. Katsiotis, M. Beazi-Katsioti, 2015, Hydration study of ternary blended cements containing ferronickel slag and natural pozzolan, *Construction and Building Materials* 81, pp.130-139.
3. K. Celik, M.D. Jackson, M. Mancio, C. Meral, A.-H. Emwas, P.K. Mehta, P.J.M. Monteiro, 2014, High-volume natural volcanic pozzolan and limestone powder as partial replacements for portland cement in self-compacting and sustainable concrete, *Cement & Concrete Composites* 45, pp.136-147.
4. WBCSD-CSI, 2009, Cement Industry Energy and CO₂ Performance “Getting the Numbers Right” Washington, DC.
5. Kastis D, Kakali G, Tsivilis S, Stamatakis MG, 2006, Properties and hydration of blended cements with calcareous diatomite. *Cement and Concrete Research* ; 36(10):1821-6.
6. Dale P. Bentz, Chiara F. Ferraris, Michael A. Galler, Andrew S. Hansen, John M. Guynn, 2012, Influence of particle size distributions on yield stress and viscosity of cement-fly ash pastes, *Cem. and Concrete Research* 42, pp.404-409.
7. C.F. Ferraris, N.S. Martys, 2003, Relating fresh concrete viscosity measurements from different rheometers, *Journal of Research of the National Inst of Standards and Tech* 108 (3), pp. 229-234.
8. A. Papo, L. Piani, R. Ricceri, 2010, Rheological properties of very high-strength Portland cement pastes: influence of very effective superplasticizers, *Int. Journal Chem. Eng.* , 6829147 pp.
9. S.H. Lee, H.J. Kim, E. Sakai, M. Daimon, 2003, Effect of particle size distribution of fly ash-cement system on the fluidity of cement pastes, *Cement Concrete Research* 33, pp.763-768.
10. Bidjocka C, 1990, Conception de bétons légers isolants porteurs. Applications aux pouzzolanes naturelles du Cameroun, Thèse de doctorat, INSA de Lyon, 167p.
11. Billong N, Melo U C, Njopwouo D, Louvet F and Bonnet J P, 2013, Physicochemical characteristics of some Cameroonian pozzolans for use in sustainable cement like materials, *Material Science. and Application*, 4, pp. 14-21.
12. Tchakouté K H, 2013, Elaboration et caractérisation de ciments géopolymères à base de scories volcaniques, PhD Thesis, UY I, 170 p.
13. Wandji P, Tsafack JPF, Bardintzeff JM, Nkouathio DG, Kagou Dongmo A, Bellon H, Guillou H, 2009, Xenoliths of dunites, wehrlites and clinopyroxenites in the basanites from Batoke volcanic cone (Mount Cameroon, Central Africa): Petrogenetic implications. *Mine. & Petro*, 96, 81-98.
14. Kaid N, Cyr M, Julien S and Khelafi H, 2009, Durability of concrete containing a natural pozzolan as defined by a performance based approach, *Constr. and Building Materials*, 23, pp. 3457-3467.
15. S. Amziane, C.F. Ferraris, 2007, Cementitious paste setting using rheological and pressure measurements, *ACI Mat. J.* 104 (2) pp. 137-145.
16. Gaurav Sant, Chiara F. Ferraris, Jason Weiss, 2008, Rheological properties of cement pastes: A discussion of structure formation and mechanical property development, *Cement and Concrete Research* 38, pp. 1286-1296.
17. Q.D. Nguyen, D.V. Boger, 1992, Measuring the flow properties of yield stress fluids, *Annual Review of Fluid Mechanics* 24, pp. 47-88.

INFLUENCE OF THE COLOR OF NATURAL POZZOLAN FROM CAMEROONIAN VOLCANIC SCORIA ON THE RHEOLOGICAL PROPERTIES OF CEMENT PASTES

Willy Juimo^{1,2,*}, Toufik Cherradi¹, Larbi Abidi¹ and Luiz Oliveira³

¹Mohammadia School of Engineer, Mohammed V University of Rabat, Morocco

²Higher Institute of the Sahel, University of Maroua, Cameroon

³C_MADE-Centre of Materials and Building Technologies, University of Beira Interior-Covilhã, Portugal

*Corresponding author: Phone: +212 6 32 96 75 44 Email: hermannjuimo@gmail.com

ABSTRACT

The color of volcanic scoria is related to the oxydation state of iron, ferric iron to ferrous iron and the red hot zones for colder black areas (cooling longer or shorter during the ballistic trajectory). This work is concerned with assessing the color influence of natural pozzolan (NP) from Cameroonian volcanic scoria on the rheological properties of blended Portland Cement (PC) pastes. The objective of this paper is to examine the evolution of rheological properties (Yield stress and plastic viscosity) in cementitious materials with addition of NP. The rheological properties of blended cement-based materials depend strongly on mixture proportions and the characteristics of the components. In this study, design of experiments is used to investigate the influence of color and ratio of PC/NP on the yield stress and viscosity of blended pastes. Both rheological parameters are seen to vary over several orders of magnitude for the evaluated design space. Physical characteristics of the powders, such as total particle densities and total particle surface area, are computed for each NP. A set of pastes specimens was made with 0%, 25%, 35% and 45% of NP replacement. NP from Cameroonian volcanic scoria with four different colors (black, dark red, red and yellow) were used. Rheological properties of the prepared pastes were measured using a rotational rheometer (Viskomat NT). The results showed that the yield stress and viscosity of cement pastes were generally decreased when the NP replaced part of the cement. The reduction of yield stress is around 26.06 to 55.20% for replacement by black powder (BP), 20.14 to 39.23% for replacement by dark red powder (DRP), 29.04 to 58.96% for replacement by red powder (RP) and -1.99 to 21.12% for replacement by yellow powder (YP) all regardless of amount of NP. The reduction of viscosity is around 20.88 to 52.78% for replacement by BP, 26.57 to 56.26% for replacement by DRP, 19.89 to 50.70% for replacement by RP and -7.60 to 37.51% for replacement by YP all regardless of amount of NP. However, replacement by BP, DRP and RP exhibited a significant reduction of yield stress and viscosity. But the replacement YP exhibited generally a slow reduction. The results also showed that the inclusion of YP at replacement levels of 25% and 45% resulted in an increase of yield stress and viscosity for 1.99% and 7.60% respectively.

KEY WORDS: *Volcanic scoria ; Natural pozzolan color ; blended Portland cement pastes ; rheological properties.*

INTRODUCTION

Despite the notable progress during the last decades, cement sector not only has been one of the most energy intensive industries in the world, but accounts for around 5% of the global green house gas emissions, because of the burning of fossil fuels during sintering process in rotary kiln and due to the limestone decomposition, the main constituent of the raw meal. Portland cement production currently accounts for 7% (2.1×10^9 tonnes) of anthropogenic

carbon dioxide (CO₂) emissions annually, resulting mainly from production of cement clinker, the active binding ingredient of concrete [1-4]. Because kiln-fired Portland cement is an energy-intensive material, requiring 4–5 GJ per tonne of cement [2,3], about half of these emissions occur through combustion of fossil fuels. The remaining emissions result from calcination of limestone: one kg of portland cement clinker releases 0.87 kg of CO₂ to the atmosphere [4]. Although the production process is still very energy consuming, cement is the most

widely used construction material today. Due to the regulations, policies and environmental sustainability, the need for energy consumption decrease, as well as for CO₂ emission lowering, implied the pure cement replacement from supplementary cementitious materials (SCM), which are used in order to produce what is generally called as “blended cements”. Increased volume fractions of SCM, such as volcanic pozzolans, fly ash and slag produce more environmentally-sustainable concretes, and also yield mixtures with high workability, ultimate strength, and durability [5]. The most common SCM are NP, generally derived from volcanic origins and artificial pozzolans, which are mainly industrial by products/wastes, such as fly ash, different type of metallurgical slags and silica fume. Blending Portland cement with pozzolanic admixtures is an effective way to improve workability, strength and durability (lower permeability, resistance to chlorides and sulfates, mitigation of alkali silica reaction) [4,5].

The rheological properties of cement paste are critical to the field performance of concrete in terms of its slump, flow, and workability. Also the rheological properties of fresh concrete are related to cement hydration and chemical interactions in the cement paste system [6,7]. In addition, the rheological properties of concrete are also dependent on the shape and gradation of the aggregates (coarse and fine) contained in the mixture. But the evolution of the rheological properties at early ages depends almost entirely on the cement paste. The rheology of cement paste is strongly influenced by mixture proportions and material characteristics, including water-to cementitious materials ratio by mass (W/C), supplementary cementitious material (SCM) additions, and the fineness of the powder materials. The current study focuses on the latter two of these parameters, while maintaining a constant volume fraction of water in all investigated mixtures [8,9].

Cameroon is rich in NPs, materials originated from volcanic eruption. The pumice used in this study is coming from “Djoungo”. Volcanic scoria of locality of “Djoungo” on the plain of Tombel (Longitude: 9°37'32" East Latitude: 4°35'16" North) are the pozzolan which has been of the greatest number of studies. The “Djoungo” pozzolan, purplish black and brick red, clean, without clay, are exploited because of their privileged geographical location (near the railway and seaport). These are fragments of vesicular magma of low density (<1), internal structure constituted by cells and more or less tight

pore. The ability to use these materials in manufacture of lightweight concrete can be an important economic asset. It is characterized by a high content of vitreous components and its high pozzolanic reactivity is mainly attributed to the high content of active SiO₂; it can react with calcium hydroxide released during the hydration of cement to produce C–S–H gels [10-13].

The present study focuses on the rheological of binary blended cement, produced by PC and NP.

The rheological properties of mixtures containing portland cement replacements of finely-ground basaltic ash (NP) from “Djoungo”, Tombel, Littoral region, Cameroon was here investigated. In the laboratory experiments, binary PC-NP mixtures with finely ground 25, 35 and 45 mass% NP (25%NP, 35%NP and 45%NP) were used.

MATERIALS AND METHODS

Materials: A PC of class CEM I 42.5 provided from a ready-mixed plant from Covilhã-Portugal was used for this study. The volcanic scoria samples were extracted from the site of “Djoungo” in Cameroon on January 2015. The samples have been kept in plastic bags and then packed in cartons and sent to Rabat (Morocco) by plane (Fig. 1).



Figure 1

(a) Packaging and (b) volcanic scoria sample

The reduction of volcanic scoria samples was performed, in the “Laboratoire Traitement des Minerais of Département des Mines of Ecole Nationale Supérieure des Mines de Rabat (ENSMR) by crushing. Samples of volcanic scoria were dried, pulverized at 50 μm (Fig.2). Optical micrographs from petrographic investigations of crushed sand-sized particles of the volcanic scoria, which is similar to other Cameroonian volcanic scoria provide a qualitative assessment of the various glass and crystal components available for pozzolanic reaction in the experimental powders. The chemical

and mineralogical characterization of "Djoungo" scoria samples were realized through overall chemical analysis and X-ray analysis (XRD) on obtained by crushing powders (grain size 63-80 μ m) by several authors [10-12]. The bulk chemical composition of the volcanic scoria powder indicates a NP (Table 1).

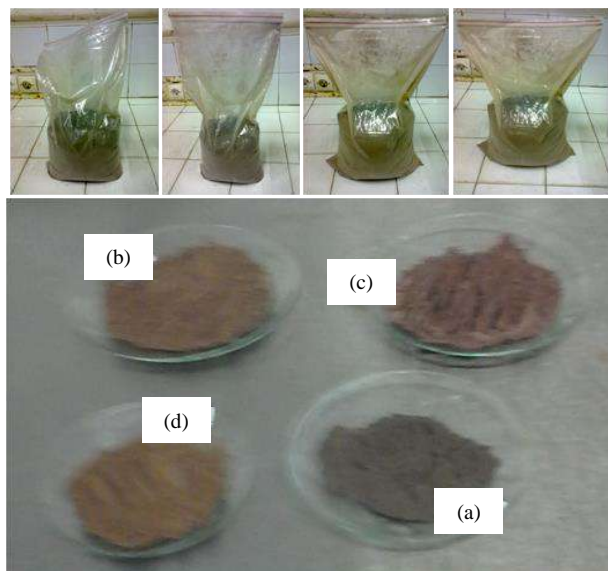


Figure 2

Packaging and different powders obtained: (a) Black, (b) Dark red, (c) Red and (d) Yellow powder

Table 1
Chemical analysis of "Djoungo"

Ref.	[10]	[11]	[12]	[1,14]
Code	DB1	DVS	ZD	ACI
SiO ₂	45.79	45.57	44.04	43–72
Al ₂ O ₃	15.68	15.94	15.26	9–20
Fe ₂ O ₃	12.83	12.81	12.77	1–12
CaO	9.60	8.97	9.29	1–15
MgO	6.26	5.76	7.00	0.50–7
MnO	0.17	-	0.17	/
Na ₂ O	3.54	3.28	5.64	0.5–11
K ₂ O	1.39	1.03	1.35	0.2–8
SO ₃	-	-	0.01	0–1.40
TiO ₂	2.84	2.11	2.87	/
P ₂ O ₅	0.60	-	0.53	/
L.O.I.	0.31	0.20	1.10	0.20–19

Note: DB1, DVS and ZD are name's codes using by authors respectively in reference [10], [11] and [12] ACI : American Concrete Institute [1].

The powders particle size distributions and rheological behaviour of the pastes was performed in Centre of Materials and Building Technologies (C_Made), University of Beira Interior-Covilhã, Portugal. The particle size distribution (PSD) of powders was performed using a LS 230 laser granulometer (Coulter LS) of which analytic range extends from 0.40 μ m to 2000 μ m. The differential PSD of the pastes and of the cement powder was investigated in deionized water, pure ethyl alcohol, a synthetic pore solution and in air, in order to study the influence of the media. The analysis time was 1 min for all the media used and the speed of pump is reduced to the minimum in order not to destroy the agglomerates. The PSDs obtained were expressed in a percent by volume and are normalized to 100%. A Micromeritics Accucyc 1330 Gas pycnometer instrument was used for density of the natural pozzolan samples measurements.

Methods:

Cement paste mixing procedures: Thirteen different cement paste mixtures were prepared according to the mixture proportions shown in Table 2. The mixing equipment used consists in a twisted mixing anchor blade adapted to a Stuart, SS 30 mixer and a stainless steel beaker. The cement suspensions were prepared by adding the powder to water and admixture in the beaker, and then by mixing at a speed during 1 min 30 s.

Table 2
Mixture proportions by mass fraction (grams)

Mix	Cement (C)	NP	Water (W)	W/C	W/(C+NP)
0%	900	-	500	0.56	-
25%	675	225	500	0.74	0.56
35%	585	315	500	0.85	0.56
45%	495	405	500	1.01	0.56

Determination of rheological properties: The rheological behavior of non-Newtonian fluids such as cement paste, mortar, or concrete is often characterized by two parameters, yield stress τ_0 , and plastic viscosity μ , as defined by the Bingham equation (Eq. (1)) :

$$\tau = \tau_0 + \mu \dot{\gamma} \quad (1)$$

Where: τ is the shear stress (Pa) and $\dot{\gamma}$ is the shear strain rate (s^{-1}).

Amziane et al.[15] showed that the Bingham relationship becomes complex when the cement paste is close to setting, resulting in aberrations such as a negative plastic viscosity calculated using Eq. (1). Consequently, an improved method to monitor the evolution of the yield stress at early ages was determined to be stress growth measurements. In addition to measurements of the shear stress, rheological property measurements can be used to determine the dynamic viscosity of a material sheared at a known shear rate [16,17]. Eq. (2) may be used to describe the viscosity of pastes at early ages.

$$\eta = \frac{\tau}{\dot{\gamma}} \quad (2)$$

Where η describes the viscosity (Pa s) of a material subject to a shear stress at a known shear strain rate, $\dot{\gamma}$ (s^{-1}), and τ is the shear stress applied by the rheometer on the material (Pa).

The rheological behavior of the pastes was characterized using a stress-controlled shear rotational rheometer (Viskomat NT). The employed configuration is constituted by two coaxial relatively rotatable cylinders. The material is placed in the inner cylinder (Fig. 3). The temperature was fixed to 25 °C. The viskomat NT is a versatile rotational viscosimeter for determining the workability of fine grained building materials such as cement paste, mortar, fine concrete, plaster etc. with maximum particle size of 2 mm. We can obtain information on : flow curves and rheological parameters temperature dependent workability properties ; stiffening behavior as a function of time and stirring speed effects of concrete admixtures and mineral blending agents on workability. The viskomat NT is delivered with two standard probes for mortar and cement paste. Cement paste probe made of stainless steel is used. This probe is used for cement paste and mortar with a maximum particle size of 0.5 mm. A scraper made of hardened stainless steel is also used.

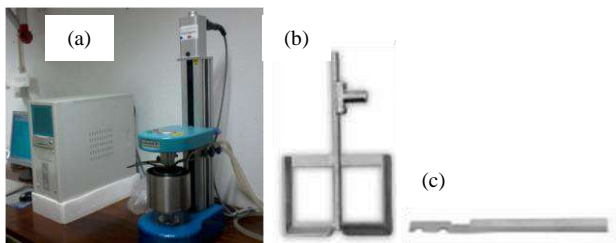


Figure 3

(a) Rotational rheometer (Viskomat NT), Rheometer used, (b) Cement paste probe and (c) Scraper

For the measurement loop, the shear rate ranged from 0 s^{-1} to 120 s^{-1} , as determined by analytical calculation from the rotational speed. To first homogenize the specimen, an increasing shear rate up to 120 s^{-1} was imposed (performed) during 180 s (6 minutes), before executing the loop of increasing and then decreasing the shear rate (Fig.4). The rheology of cement-based materials was described by the yield stress determined with the Bingham model applied between 0 s^{-1} and 120 s^{-1} . Each formulation of paste was analyzed on three different samples.

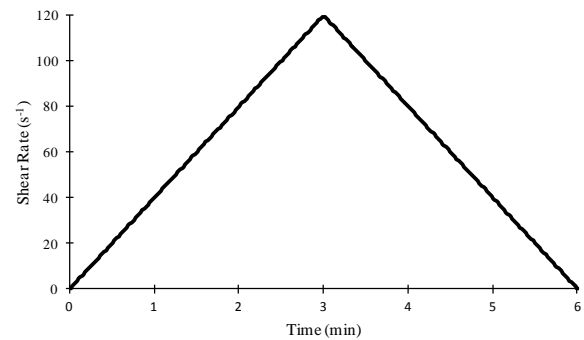


Figure 4

Evolution of Shear rate during measurement

RESULTS AND DISCUSSION

Particle sizes distributions of the cement powder and cement pastes in different liquid media are shown in Figure 5. Indeed, their size ranges from sub-micronic dimensions (finest particles observed show a diameter about 0.40–50 μ m) to a maximum size of around 50 μ m. Figure 5 shows that the size particle of four powders used is approximate similar. But we have a small different of volume percentage between four different NP powders. The considerable different is observed for particle size from 0.40 to 20 μ m (Fig.5). The origin of this different could be the color of NP. Each shown result is the average of three individual measurements.

Physical properties of natural pozzolan samples are shown in Table 3.

Volcanic scoria's of different colors have been crushed in the same conditions, but figure 5 shows different from particle size distributions of the powders obtained. This difference may be due to the

color difference volcanic scoria. The influence color on the particle size could be also identified on the rheological properties of PC/NP pastes.

Figure 6 show rheograms obtained after rheological measurements for different replacements by natural pozzolans. They illustrate the shear stress variation at different amounts. This variation decreases with the increase of pozzolan replacement level. At 25% of replacement, YP have no considerable influence on rheological properties of PC paste. BP, DRP and RP have about a similar affect.

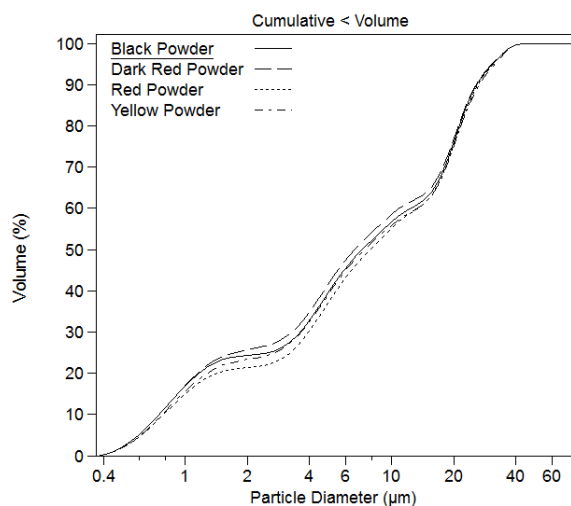


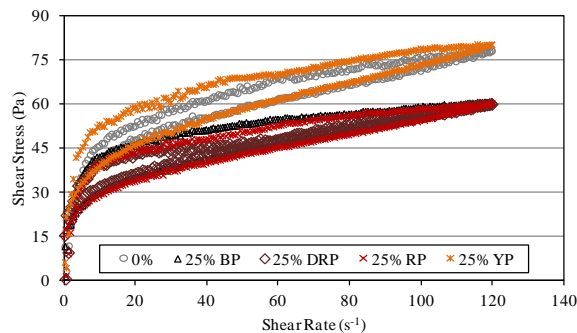
Figure 5 Particle size distributions by volume cumulative of the four natural pozzolan powders used

Table 3 Physical properties of natural pozzolan samples

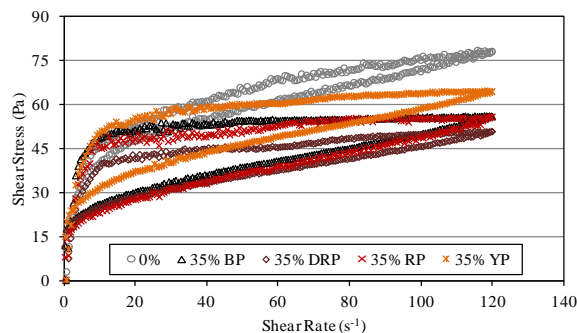
NP	BP	DRP	RD	YP
Density/Specific gravity (g/cm ³)	-	2.9809	3.0794	-
Mean particle size (µm)	5.998	5.726	6.456	6.210
d ₁₀ ^a	25.90	25.71	26.26	26.66
d ₂₅ ^a	19.70	19.46	19.96	20.01
d ₅₀ ^a	7.179	6.587	7.839	7.365
d ₇₅ ^a	2.512	1.722	3.231	2.723
d ₉₀ ^a	0.745	0.746	0.785	0.772
Specific Surface Area (cm ² /g)	8401	8631	7708	8059

^a d₁₀, d₂₅, d₅₀, d₇₅ and d₉₀ values indicate the diameter size at which 10%, 25%, 50%, 75% or 90% of particles are larger than, i.e., d₁₀= 25.90 means that 10% of all particles were >25.90 µm diameter.

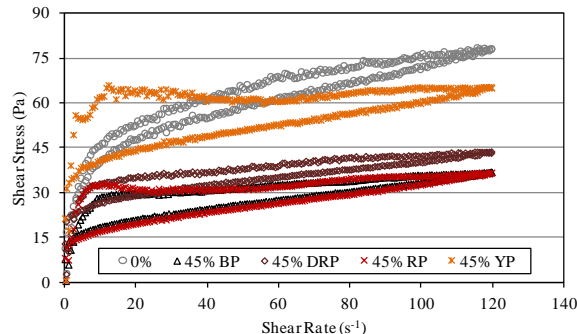
According to the results the evolution of the ultimate shear stress follows a hysteresis law. The rheological parameters, namely yield stress and viscosity, were calculated from the measured shear stress-shear rate curves for each of the mixtures in Table 2 by linear regression. A typical shear stress vs. shear rate curve for the descending data is provided (Fig.7). These descending curve data were fitted to a linear equation using ordinary least squares regression to determine a slope (plastic viscosity) and an intercept (yield stress), according to a Bingham model. The correlation coefficients (R²) for these regressions ranged between 0,897 and 0,9788 with an average value of 0.9546 (Table 4).



(a) 25% of replacement



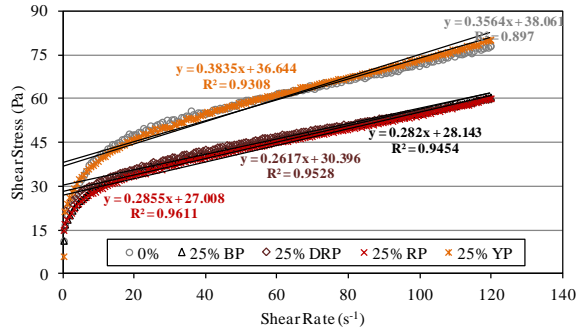
(b) 35% of replacement



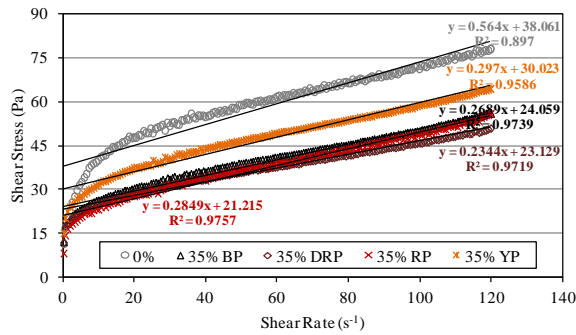
(c) 45% of replacement

Figure 6
Rheograms obtained by replacement of different natural pozzolans colors.

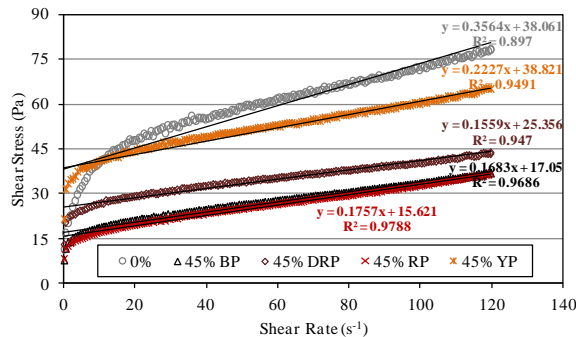
The evaluated yield stresses and viscosities by linear regression are provided in Table 4. Each of the two parameters ranged over about two orders of magnitude, indicating the strong influence of NP on rheological properties. Figure 8 shows linear evolution of yield stress and plastic viscosity of the cement paste as a function of NP amount.



(a) 25% of replacement



(b) 35% of replacement



(c) 45% of replacement

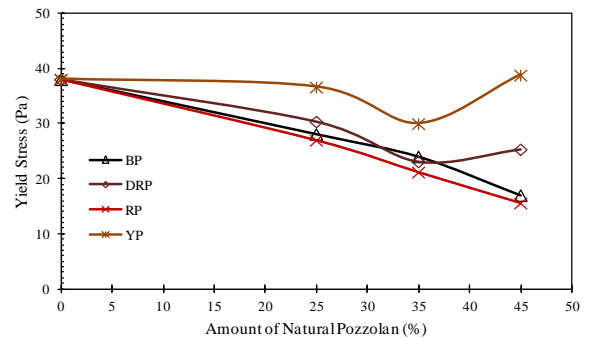
Figure 7

Typical descending branch shear stress vs. shear rate curve obtained for replacement of different NP.

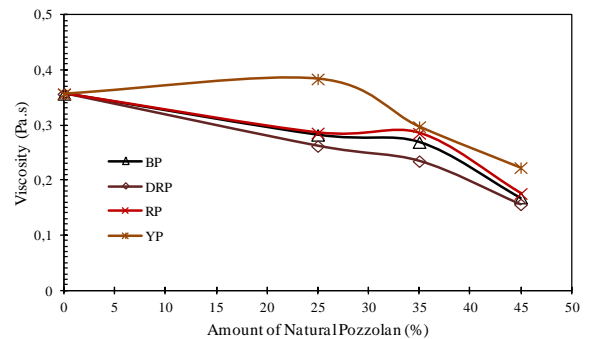
Table 4

Yield stress and viscosity determined for each blended cement paste mixture.

Paste Mix.	Yield Stress τ_0 (Pa)	% $\Delta(\tau_0)$	Viscosity μ (Pa·s)	% $\Delta(\mu)$	Coef. (R ²)
0%	38.061	-	0.3564	-	0.8970
Black Powder (BP)					
25%	28.143	26.06	0.2820	20.88	0.9454
35%	24.059	36.79	0.2689	24.55	0.9739
45%	17.050	55.20	0.1683	52.78	0.9686
Dark Red Powder (DRP)					
25%	30.396	20.14	0.2617	26.57	0.9528
35%	23.129	39.23	0.2344	34.23	0.9719
45%	25.356	33.38	0.1559	56.26	0.9470
Red Powder (RP)					
25%	27.008	29.04	0.2855	19.89	0.9611
35%	21.215	44.26	0.2849	20.06	0.9757
45%	15.621	58.96	0.1757	50.70	0.9788
Yellow Powder (YP)					
25%	36.644	3.72	0.3835	-7.60	0.9308
35%	30.023	21.12	0.2970	16.67	0.9586
45%	38.821	-1.99	0.2227	37.51	0.9491



(a)



(b)

Figure 8

Linear evolution of (a) Yield Stress and (b) Viscosity of the cement paste as a function of NP amount.

CONCLUSIONS

In conclusion, it is possible in the near future to be able to reduce the number of tests on concrete necessary for the development of formulations having a fixed workability. Mineral additives can be selected in the laboratory by testing cement paste or mortar. An experiment would determine the rheological characteristics required for cement paste and mineral addition proportion to obtain the required workability of concrete. Lots of work needs to be done to validate the results obtained on the cement paste with the addition of natural pozzolan. In this study case both yield stress and viscosity are strongly dependent on the color and ratio of the NP powders employed in preparing a blended cement/natural pozzolan paste with a constant volume fraction of water.

ACKNOWLEDGMENTS

This work was conducted in the “Laboratoire Traitement des Minerais of Département des Mines of Ecole Nationale Supérieure des Mines de Rabat (ENSMR) and in the Centre of Materials and Building Technologies (C_Made) of Department of Civil Engineering and Architecture at University of Beira Interior. The authors gratefully acknowledge the support from these laboratories that has made this research possible. They would like to thank Prof. Abílio Silva for its assistance in making the particle size distribution measurements presented in this study. In addition, they would also like to acknowledge the assistance of Mr. Jorge Bento in experimental testing.

REFERENCES

1. ACI, 2002, Use of Raw or Processed Natural Pozzolans in Concrete, ACI Committee 232, Manual of Concrete Practice ACI 232.1.
2. N. Lemonis, P.E. Tsakiridis, N.S. Katsiotis, S. Antiohos, D. Papageorgiou, M.S. Katsiotis, M. Beazi-Katsioti, 2015, Hydration study of ternary blended cements containing ferronickel slag and natural pozzolan, *Construction and Building Materials* 81, pp.130-139.
3. K. Celik, M.D. Jackson, M. Mancio, C. Meral, A.-H. Emwas, P.K. Mehta, P.J.M. Monteiro, 2014, High-volume natural volcanic pozzolan and limestone powder as partial replacements for portland cement

- in self-compacting and sustainable concrete, *Cement & Concrete Composites* 45, pp.136–147.
4. WBCSD-CSI, 2009, Cement Industry Energy and CO₂ Performance “Getting the Numbers Right” Washington, DC.
5. Kastis D, Kakali G, Tsivilis S, Stamatakis MG, 2006, Properties and hydration of blended cements with calcareous diatomite. *Cement and Concrete Research* ; 36(10):1821–6.
6. Dale P. Bentz, Chiara F. Ferraris, Michael A. Galler, Andrew S. Hansen, John M. Guynn, 2012, Influence of particle size distributions on yield stress and viscosity of cement–fly ash pastes, *Cem. and Concrete Research* 42, pp.404–409.
7. C.F. Ferraris, N.S. Martys, 2003, Relating fresh concrete viscosity measurements from different rheometers, *Journal of Research of the National Inst of Standards and Tech* 108 (3), pp. 229–234.
8. A. Papo, L. Piani, R. Ricceri, 2010, Rheological properties of very high-strength Portland cement pastes: influence of very effective superplasticizers, *Int. Journal Chem. Eng.* , 6829147 pp.
9. S.H. Lee, H.J. Kim, E. Sakai, M. Daimon, 2003, Effect of particle size distribution of fly ash–cement system on the fluidity of cement pastes, *Cement Concrete Research* 33, pp.763–768.
10. Bidjocka C, 1990, Conception de bétons légers isolants porteurs. Applications aux pouzzolanes naturelles du Cameroun, Thèse de doctorat, INSA de Lyon, 167p.
11. Billong N, Melo U C, Njopwouo D, Louvet F and Bonnet J P, 2013, Physicochemical characteristics of some Cameroonian pozzolans for use in sustainable cement like materials, *Material Science. and Application*, 4, pp. 14-21.
12. Tchakouté K H, 2013, Elaboration et caractérisation de ciments géopolymères à base de scories volcaniques, PhD Thesis, UY I, 170 p.
13. Wandji P, Tsafack JPF, Bardintzeff JM, Nkouathio DG, Kagou Dongmo A, Bellon H, Guillou H, 2009, Xenoliths of dunites, wehrlites and clinopyroxenites in the basanites from Batoke volcanic cone (Mount Cameroon, Central Africa): Petrogenetic implications. *Mine. & Petro*, 96, 81-98.
14. Kaid N, Cyr M, Julien S and Khelafi H, 2009, Durability of concrete containing a natural pozzolan as defined by a performance based approach, *Constr. and Building Materials*, 23, pp. 3457-3467.

15. S. Amziane, C.F. Ferraris, 2007, Cementitious paste setting using rheological and pressure measurements, *ACI Mat. J.* 104 (2) pp. 137–145.
16. Gaurav Sant, Chiara F. Ferraris, Jason Weiss, 2008, Rheological properties of cement pastes: A discussion of structure formation and mechanical property development, *Cement and Concrete Research* 38, pp. 1286–1296.
17. Q.D. Nguyen, D.V. Boger, 1992, Measuring the flow properties of yield stress fluids, *Annual Review of Fluid Mechanics* 24, pp. 47–88.

Hydration kinetics of compound cement in the presence of superplasticizers

Zahia Didouche^{1*}, Karim Ezziane², Mhamed Adjoudj¹

¹Tissemsilt.University Center, Algeria.

²Geomaterials Laboratory, Hassiba Benbouali University, Chlef, Algeria

*Corresponding author: Fax: 00 213 27 72 72 34, mail: zahiadidou@yahoo.fr

ABSTRACT

The use of certain organic additives in the production of mortar and concrete influences the hydration kinetic and the amount of total heat. This results in a modification of certain properties, namely mortar workability, mechanical strength and durability. Three superplasticizers were used; a polynaphthalene sulphonate (PNS), a melamine resin (PMS) and a polycarboxylate (PC). They have been incorporated with various amount in a standardized mortar based on cement limestone. The measured heat flow is significantly influenced by the type and dosage of superplasticizer especially for low dosage. The PNS is incompatible with this type of cement registering a decrease of strength but the PMS and the PC modify the kinetics of hydration with significant heat generation and improved mechanical strength.

KEYWORDS

Cement, hydration, Compressive strength, superplasticizer.

NOMENCLATURE

C: total thermal capacity of the calorimeter and the specimen (J/°C).

m_c : the cement mass (g).

$\Delta\theta$: the mortar heating difference to the ambient temperature (°C).

α : the total calorimeter thermal loss coefficient (J/h.°C).

T: the hydration time (h) .

Q: The hydration heat by gram of cement (J/g).

INTRODUCTION

The polymers affect the interface between the particle surface and the pore solution and influence the physical properties such as viscosity and the yield stress of the paste. The superplasticizers dispersion effect is related to adsorption, which depends on several factors such as the amount of C₃A and alkali in the clinker, the cement fineness as well as the type and dosage of calcium sulfate used to regulate the cement setting [1,2]. Their presence in the mortar influences the flow and the degree of hydration and the amount of hydration products formed [3]. By incorporating naphthalene sulfonate to a portland

cement, Yunsheng Z. and al. [4] found that the time to reach the acceleration period and the peak heat is delayed but the value of the exothermic heat of all mortars are similarly at three days. For others increasing the melamine dosage from 1% to 2% of the ordinary portland cement increases the temperature and delays the dormant period without delaying the exothermic peak [5]. Shin and al. [6] concluded that polycarboxylates delayed the initial hydration for a long time, when the chain length decreases with increasing molecular weight.

The aim of this study was to evaluate the mechanical and calorimeter behaviors of blended cement in presence of three types of superplasticizer, in order to choose the most compatible product to the country's climate.

EXPERIMENTAL STUDY

Material used: The cement used in this research is blended cement (CEM II / 42.5) containing 12% of limestone powder (Table 1).

Table 1
Cement characteristics

chemical characteristic	mineralogical and physical characteristics
PAF (4.49%)	C3S (41.8%)
SiO ₂ (21.14%)	C2S (33.3%)
Al ₂ O ₃ (5.66%)	C3A (5.1%)
Fe ₂ O ₃ (3.27%)	C4AF (10.7%)
CaO (62.3%)	Finesse de Blaine
MgO (0.74%)	3600 (cm ² /g)
SO ₃ (1.58%)	
K ₂ O (0.81%)	
Na ₂ O (0.11%)	
CaO _{libre} (0.7%)	

This cement is used to make a mortar based on standard sand. Three types of superplasticizers were used; the first based on polynaphthalene sulphonates (PNS), the second based on melamine resin (PMS) and the third is based on polycarboxylate (PC). These superplasticizers are diluted in the mixing water and incorporated in the mortar composition with different dosages.

Confection mortars

The mixtures for measuring the heat of hydration and mechanical strength are made at a constant temperature of 20 °C with various amounts of superplasticizer by subtracting the amount of water present in the superplasticizer from mixing water amount used for each test.

Equipment used : Prismatic mortar specimens having 40x40 mm dimensions were used for the study of compressive strength. Specimens were cast in steel moulds and kept in a moist room at 20 °C for 24 h. Demoulding took place after one day and specimens were placed in water at 20 °C for a total curing period until the day of testing. Compressive strength was determined at the age of 2, 7, 14, 28 and 90 days .

Hydration heat tests were carried out by using the method based on the Langavant Calorimeter. This semi-adiabatic method consists of quantifying the heat generated during cement hydration using a thermally isolated bottle. Since the exterior conditions are very influential, the test was carried out in air-conditioned room at 20±2 °C. The temperature measurements were made up to 5 days, since the heat increase is observed to be very low at later ages. The temperature results are used to calculate the hydration heat developed by the test sample. The hydration heat of the mortar was the

combination of the accumulated heat in the calorimeter and the heat dispersed in the environment. At time t, the hydration heat q by gram of cement is obtained by the formula:

$$Q = \frac{C}{m_c} \Delta\theta + \frac{1}{m_c} \int_0^t \alpha \Delta\theta dt$$

RESULTS AND DISCUSSION

Hydration heat: From figure 1, it is observed for early hours that control mortar releases more heat than adjuvanted samples. After 6 hour of hydration, low dosages of PNS release more water, promote hydration grains and produce more heat compared to the higher amounts which delay the contact of the cement particles with mixing water and cause a decrease in the final heat. The appearance of the principal peak in the heat flow is observed at 5.75 h for the control mortar with a magnitude of 26.68 J/g/h which increases by increasing the dosage of PNS until 48.04 J/ g/h recorded at 7 h for 1.2%. Over this dosage flow value decreases and the dormant period is extended. From this, we can say that the polynaphthalene sulphonates (PNS) plays a significant role as a setting retarder. This is conform to results found by Kadri and Duval [7]. Who have deduced that the addition of 0.6% to 5.5% of naphthalene sulphonates at cement mortar extends the dormant period from 2 to 14 hours followed by reduction of the exothermic peak. Similarly, Pirazzoli and al. [8] found that the addition of a PNS to the C3S paste increases the dormant period and reduces the length of the acceleration period.

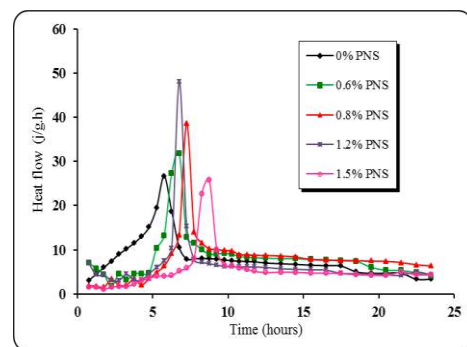


Figure 1
PNS effect on flow heat of the mortar.

The addition of PMS at different dosages to cement mortar increases the heat quantity released for all

ages compared to cement control, more significantly for low concentrations Flow curves are nearly overlaid and differ only by their amplitudes (figure2).The value of heat peak reaches 23.5 j/g/h for a substitution of 1.5% PMS, keeping the same kinetics as that of a control mortar. From this, we can conclude that the PMS has no effect on the setting or on the hydration kinetics. This is in line with Brandstetr and al. [5], where increasing dosage of melamine from 1% to 2% in ordinary Portland cement induces a gradual extending of the dormant period without delaying the exothermic peak. By adding polycarboxylate (PC), the appearance of the peaks is delayed and magnitude increases to reach 50 j / g/h at 8.25h for 1.5% PC (Figure 3).

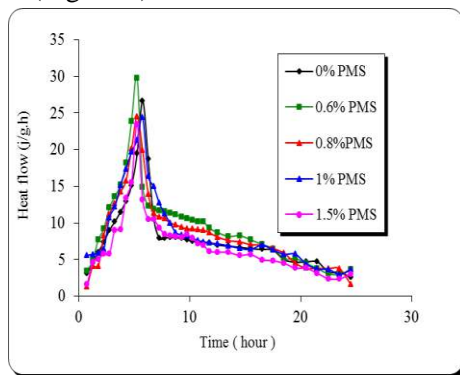


Figure 2

PMS effect on flow heat of the mortar.

This is conforms to the work of several researchers [1, 6]. Similarly, Zingg and al. [9] concluded that the heat flow is more delayed and the dormant period is extended in presence of a short molecular chain and high density of polycarboxylate.

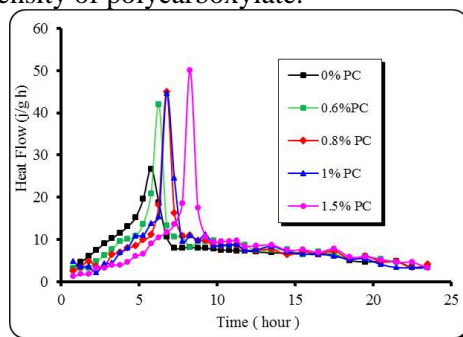


Figure 3

PC effect on Flow Heat of the mortar.

Compressive strength: The value of the reference mortar compressive strength is much higher than that of the samples with superplasticizer for all ages

(figure 4). An increase in the PNS dosage from 0.6% to 1.5% reduces the compressive strength from 35 Mpa to 21 Mpa measured at 90 days. This result affirms the incompatibility of PNS with limestone Portland cement compound which resulted in a decrease of workability when the dosage exceeds 0.6%. This confirms the results found by other researchers [8] when products hydration of the C3S paste adjuvanted with naphthalene formaldehyde sulfonate (PNS) have a small volume compared to the products hydration of a cement with water. In order to confirm the incompatibility of PNS with this type of cement, specimens were subjected to test absorption. The weight of the samples immersed in water was measured for 90 days. The result affirms that the weight gain of the adjuvanted mortar specimens is much higher than the control mortar. This absorption is also important when the PNS dosage is high, which may explain the strength drop obtained. This is similar to results found by Khatib [10]. Who said that an increase of dosage from 1% to 2% of PNS greatly reduces compressive strength. Similarly, Ramli and Akhavan Tabassi [11] and Baghabra Al-Amoudi and al. [12] concluded after testing a mortar admixture that the permeability increases when the amount of water absorption increases, therefore the compressive strength decreases.

The values of compressive strengths recorded for mortars adjuvanted by 0.6% and 1% PNS are closed to those

given by the control mortar at all ages and tend to be improved at long-term (90 days).

Compressive strength of the Mortar decreases respectively from 44.7 to 43.2, 41.9 and 35.2 Mpa, by adding 0.6, 1 and 1.5% of PMS (figure 5).

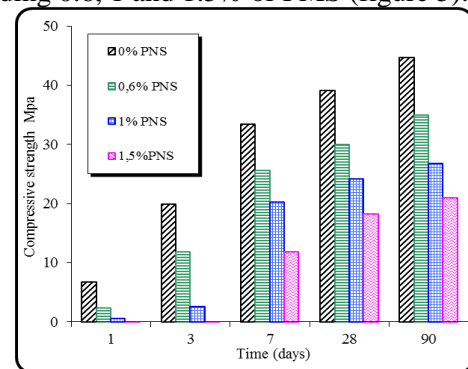


Figure 4

Effect of Polynaphtalene on Compressive Strength of mortar.

This can have a direct relationship with the maximum workability obtained for 1% PMS. Which coincides with the findings of Brandstetr and al. [5] who reported that the efficiency of the melamine resin is observed at low concentrations (<1%) where maximum strength is obtained with just 0.5% for mortar tested at 1, 15 and 28 days.

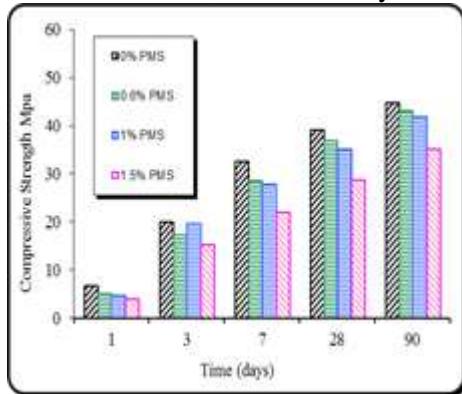


Figure 5

Effect of Polymelamine on Compressive Strength of mortar.

The incorporation of polycarboxylate (PC) to cement mortar improved workability of this last and enhanced its compressive strength at all age tested (figure 6). At 90 days, the mortar strength reaches respectively 44.7, 47.3, 48.7 and 53.1 Mpa by adding 0.6, 1 and 1.5% of PC. This is conforms to results of Puertas and al. [1] who reported that the use of superplasticizer based on polycarboxylate at low concentrations improves the compressive strength by reducing the porosity of the paste.

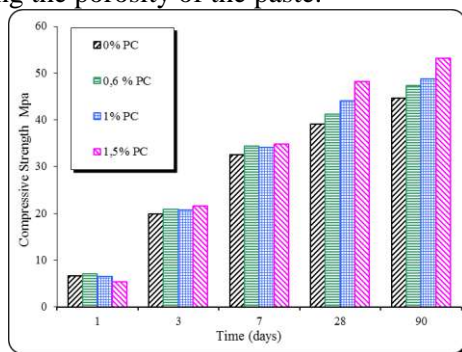


Figure 6

Effect of polycarboxylate on Compressive Strength of mortar.

CONCLUSIONS

It is obvious that the type and composition of the additive, and even its mode of action, strongly influence its effectiveness and its saturation amount

[13]. As can be noted that the fluidity of PC is larger than that of PMS and PNS whatever the dosage used.

A good workability is obtained by using a compound Portland cement limestone, adjuvanted with low dosages PNS (0.6%) for the melamine resin (PMS) an appropriate dosage of 1% is found. While polycarboxylate (PC) may be most compatible with this type of cement and more efficient to improve the fluidity of the paste all the dosages used.

The heat of all mortars adjuvanted by the PC is higher than the reference mortar for all ages. This delays the initial hydration of cement increases the flow of heat and delays the dormant period by increasing the dosage.

The polynaphthalenesulphonate (PNS) is incompatible with this type of cement and causes strength loss. But the addition of the melamine resin (PMS) at low doses (0.6%) improves the strength. However the incorporation of Polycarboxylate (PC) greatly increases the compressive strength which may reach values higher than the control cement.

REFERENCES

1. Puertas F., and Santos H., Palacios M., Martinez-Ramirez S., 2005, Polycarboxylate superplasticiser admixtures: effect on hydration, microstructure and rheological behaviour in cement pastes, *Advances in Cement Research*, **17**, pp. 77–89.
2. Bjornstrom J., and Chandra S., 2003. Effect of superplasticizers on the rheological properties of cements, *Materials and Structures / Matériaux et Constructions*, **36**, pp. 685-692.
3. Knapen E., and Gemert Van D., 2009, Cement hydration and microstructure formation in the presence of water-soluble polymers, cement and concrete research, **39**, pp.6-13.
4. Yunsheng Z., and Wei S., Sifeng L., 2002, Study on the hydration heat of binder paste in high-performance concrete, *Cement and Concrete Research*, **32**, pp.1483 -1488 .
5. Brandstetr J., and Polcer J., Kratky J., Holesinsky R., avlica J., 2001, Possibilities of use of isoperibolic calorimetry for assessing the hydration behavior of cementitious systems, *Cement and Concrete Research*, **31**, pp.941-947.
6. Shin J.Y., and Hong J.S., Suh J.K., Young-Seak L., 2008, Effects of polycarboxylate-type superplasticizer on fluidity and hydration behavior of cement paste, *Korean J. Chem. Eng.*, **25**, **6**, pp.1553-1561.

7. Kadri E.H., and Duval R., 2009, Hydration heat kinetics of concrete with silica fume, *Construction and Building Materials*, **23**, pp. 3388–3392.
8. Pirazzoli I., and Marcella A., Silvia C.; Bruno M.; Rodorico G., Ridi F., Baglioni P., 2005, The influence of superplasticizers on the first steps of tricalcium silicate hydration studied by NMR techniques, *Magnetic resonance imaging*, **23**, pp. 277-284 .
9. Zingg A., and Winnefeld F., Holzer L., Pakusch J., Becker Stefan F. R., Gauckler L., 2009, Interaction of polycarboxylate-based superplasticizers with cements containing different C3A amounts, *Cement and Concrete Composites*, **31**, pp.153-162 .
10. Khatib J.M., 2008, Performance of self-compacting concrete containing fly ash, *construction and building materials*, **22**, pp. 1963–1971.
11. Ramli M., and Akhavan Tabassi A., 2012, Effects of polymer modification on the permeability of cement mortars under different curing conditions: A correlation study that includes pore distributions, water absorption and compressive strength, *Construction and Building Materials*, **28**, pp. 561–570.
12. Baghabra Al-Amoudi Omar S., and Al-Kutti Walid A., Shamsad A., Maslehuddin M., 2009, Correlation between compressive strength and certain durability indices of plain and blended cement concretes, *Cement and Concrete Composites*, **31**, pp. 672–676 .
13. Hallal A., and Kadri E.H., Ezziiane K., Kadri A., Khelafi H., Combined effect of mineral admixtures with superplasticizers on the fluidity of the blended cement paste, *Construction and Building Materials*, **24**, pp. 1418–1423.

BUCKLING ANALYSIS OF CHIRAL SINGLE-WALLED CARBON NANOTUBES USING NON-LOCAL TIMOSHENKO BEAM THEORY.

ZIDOUR Mohamed^{1,2,*}, BENSATTALAH Tayeb^{1,2}, Mohamed AIT AMAR MEZIANE¹ and ADIM Belkacem¹

¹University of Ibn Khaldoun, BP 78 Zaaroura, 14000 Tiaret, Algeria.

²Laboratoire of Matériaux and Hydrology, University of Sidi Bel Abbés, BP 89 Ben M'hidi, 22000 Sidi Bel Abbés, Algeria.

*Corresponding author: Email: zidour.mohamed@yahoo.fr

ABSTRACT

Using the non-local elasticity theory, Timoshenko beam model has been implemented to investigate the elastic buckling of chiral single-walled carbon nanotubes (SWCNTs) under axial compression. According to the governing equations of non-local Timoshenko beam model, the analytical solution is derived and the solution for non-local critical buckling loads is obtained. Influence of non-local small-scale coefficient, the vibrational mode number, the chirality of carbon nanotube and aspect ratio of the (SWCNTs) on non-local critical buckling loads of the (SWCNTs) are studied and discussed.

The results indicate the dependence of non-local critical buckling loads on the chirality of single-walled carbon nanotube with increase the non-local small-scale coefficient, the vibrational mode number and aspect ratio of length to diameter.

Key Words: Single-walled carbon nanotubes; Buckling; Non-local elasticity; chirality; small-scale.

INTRODUCTION

Since the single-walled carbon nanotube (SWNT) and multi-walled carbon nanotube (MWNT) are found by Iijima [1, 2]. Recent studies have indicated that carbon nanotubes (CNTs) possess superior electronic, thermal and mechanical properties [3, 4], others studies have showed that they have good properties so they can be used for nanoelectronics, nanodevices and nanocomposites [5, 6].

Due to difficulties encountered in experimental methods to predict the responses of nanostructures under different loading conditions, and molecular dynamics (MD) simulations are limited to systems of computation, the continuum mechanics methods are often used to investigate some physical problems in the nanoscale [7, 8]. Recently, the continuum mechanics approach has been widely and successfully used to study the responses of nanostructures, such as the static [9, 10], the buckling [11, 12], free vibration [13, 14], wave propagation [15, 16] and thermo-mechanical analysis of (CNTs) [17, 18]. More recently, Yoon et al. [19] examine resonant frequencies and obtain vibrational modes of an individual multi-walled carbon nanotube embedded inside an elastic medium. Murmu and Adhikari [20] have analyzed the longitudinal vibration of double nanorod systems using the non-

local elasticity. Yakobson et al. [21] utilize a continuum shell model to predict the buckling of a single-walled carbon nanotube and their results are compared with molecular dynamics simulations.

The study of the buckling behavior of (CNTs) is a major topic of current interest, which is used to understand the dynamic behaviour of (CNTs) further. Several experimental works have been performed to investigate the deformation of single- and multi-walled nanotubes under high pressure (Thomsen et al and Elliott et al) [22, 23]. Continuum elastic-beam models have been widely used to study the critical buckling loads in (CNTs). For example, Ranjbartoreh et al [24] investigated the buckling behavior and critical axial pressure of double-walled carbon nanotubes with surrounding elastic medium using the numerical method based on the classical theory of plates and shells and the Galerkin method. Ranjbartoreh et al [25] presented the variations of the critical axial forces for the inner and outer tubes of a (DWCNT) for different buckling modes. Their results indicated that the critical axial force for the inner tube of a (DWCNT) was almost twice that of an (SWCNT). A molecular dynamics simulation (Odegard et al. [26]; Zhang et al. [27]) are also utilized to investigate the buckling behavior of nanotubes.

Among the most widely pursued methods to simulate the behavior of nanomaterials is the atomistic molecular dynamics (MD) approach. This approach represents the dynamics of atoms or molecules of the materials by a discrete solution of Newton's classical equations of motion. The inter-atomic forces required for the equations of motions are obtained on the basis of interaction energy functions. Jin et al. [28] used (MD) and force-constant approach and reported the Young's modulus of (SWCNTs) to be about 1236 ± 7 GPa. Cornwell and Wille [29] used the (MD) with the Tersoff–Brenner potential [30] to obtain the Young's modulus of (SWCNTs) about 0.8 TPa. In this study the Young's modulus of SWCNTs using (MD) simulation obtained by Bao WenXing et al [31] is used in the formulations, when the Young's moduli of (SWCNTs) are in the range of 929.87 ± 11.5 GPa. These results are in good agreement with the existing experimental results.

This study is concerned with the use of the non-local Timoshenko elastic beam model to analyse the non-local critical buckling loads of single-walled carbon nanotubes (SWCNTs). The solution for critical loads is obtained. Influence of the chirality of carbon nanotube, non-local small-scale coefficient, the vibrational mode number, and aspect ratio of the (SWCNTs) are studied and discussed.

GEOMETRY OF SINGLE-WALLED CARBON NANOTUBE (SWCNT):

A single-walled carbon nanotube (SWCNT) is theoretically assumed to be made by rolling a graphene sheet (Fig.1). The fundamental structure of carbon nanotubes can be classified into three categories as zigzag, armchair and chiral in terms of the chiral vector (\vec{C}_h) and the chiral angle θ shown in (Fig.1).

The chiral vector can be expressed in terms of base vectors (\vec{a}_1) and (\vec{a}_2) (Fig.1):

$$\vec{C}_h = m\vec{a}_1 + n\vec{a}_2. \quad (1)$$

where the integer pair (n, m) are the indices of translation, which decide the structure around the circumference.

The relationship between the integers (n, m) and the chiral angle is given by [32]:

$$\theta = \arccos \frac{2n+m}{2\sqrt{(m^2+n^2+mn)}} \quad (2)$$

According to different chiral angles, (SWCNTs) can be classified into zigzag ($\theta = 0^\circ$), armchair ($\theta = 30^\circ$) and chiral tubule ($0^\circ < \theta < 30^\circ$) (Fig. 2).

The relationship between the integers (n, m) and the diameter of (SWCNTs) is given by [33]:

$$d = a\sqrt{3(n^2 + m^2 + nm)} / \pi, \quad (3)$$

where (a) is the length of the carbon–carbon bond which is (1.42 \AA).

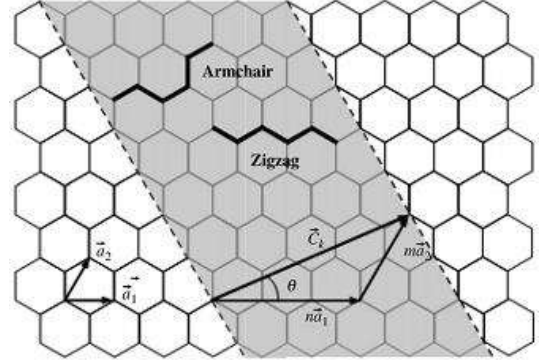


Fig. 1: Schematic diagram of the chiral vector and the chiral angle.

NONLOCAL TIMOSHENKO BEAM MODELS OF (SWCNTS):

The theory of nonlocal continuum elasticity proposed by Eringen [34,35] assumed that the stress at a reference point is considered to be a functional of the strain field at every point in the body. In the limit when the effects of strains at points other than x are neglected, one obtains classical or local theory of elasticity. For homogeneous and isotropic elastic solids, the constitutive equation of non-local elasticity can be given by [35]

Non-local stress tensor t at point x' is defined by

$$\sigma_{ij,j} = 0$$

$$\sigma_{ij}(x) = \int K(|x-x'|, \tau) C_{ijkl} \varepsilon_{kl}(x') dV(x'), \quad \forall x \in V \quad (4)$$

$$\varepsilon_{ij} = \frac{1}{2}(u_{i,j} + u_{j,i})$$

where C_{ijkl} is the classical, macroscopic stress tensor at point x' , σ_{ij} and ε_{ij} are stress and strain tensors respectively. $K(|x-x'|, \tau)$ is the kernel function and ($\tau = e0a/l$) is a material constant that depends on internal and external characteristic length (such as the lattice spacing and wavelength), where $e0$ is a constant appropriate to each material, a is an internal characteristic length, e.g., length of C–C bond, lattice parameter, granular distance, and l is an external characteristic length.

Non-local constitutive relations for present nano beams can be approximated to a one-dimensional form as

$$\left(1 - e0a^2 \frac{\partial^2}{\partial x^2}\right) \sigma_x = E \varepsilon_x \quad (5)$$

$$\left(1 - e0a^2 \frac{\partial^2}{\partial x^2}\right) \tau_{xz} = G \gamma_{xz} \quad (6)$$

where E and G are the Young's and shear modulus, respectively, and γ is the shear strain. Thus, the scale coefficient ($e0a$) in the modelling will lead to small-scale effect on the response of structures at nano size. In addition, $e0$ is a constant appropriate to each material, and a is an internal characteristic length of the material (e.g., length of C-C bond, lattice spacing, granular distance).

The expressions of the axial strain and the shear strain are [36]

$$\varepsilon_x = z \frac{\partial \psi}{\partial x} \quad (7)$$

$$\gamma_{xz} = \psi - \frac{\partial w}{\partial x}$$

where ψ is the rotation angle of cross-section of the beam and w is the transverse displacement.

The shear force and the bending moment can be defined by:

$$M = \int_A z \sigma_x dA \quad (8)$$

$$T = \int_A \tau_{xy} dA$$

Based on Eqs. 5, 6, 7 and 8 the bending moment M and the shear force T for the non-local model can be expressed as

$$\left(1 - e0a^2 \frac{\partial^2}{\partial x^2}\right) M = EI \frac{d\psi}{dx} \quad (9)$$

$$\left(1 - e0a^2 \frac{\partial^2}{\partial x^2}\right) T = \beta GA \left(\psi - \frac{dw}{dx}\right) \quad (10)$$

where $I = \int_A z^2 dA$ is the moment of inertia, A is the cross-section area of the beam, and β a correction factor depending on the shape of the cross-section of the considered beam.

From the free body diagram of an infinitesimal element of a beam structure subjected to an axial loading, P , the force equilibrium equations in vertical direction and the moment on the one-dimensional structure can be easily provided follows:

$$\frac{dT}{dx} = -P \frac{dw}{dx} \quad \text{and} \quad \frac{dM}{dx} = T \quad (11)$$

where M and V are the resultant bending moment and the resultant shear force, respectively, P is the axial compression.

Based on Eqs. (9), (10) and (11), the following relation can be obtained:

$$M = EI \frac{d\psi}{dx} + e0a^2 P \frac{d^2 w}{dx^2} \quad (12)$$

$$T = \beta AG \left(\psi - \frac{dw}{dx}\right) + e0a^2 P \frac{d^3 w}{dx^3} \quad (13)$$

Substituting equations (12) and (13) into equations (11) and eliminating ψ yield the following differential equation of a Timoshenko beam considering the non-local effects.

$$EI \frac{d^4 w}{dx^4} - \left(1 - e0a^2 \frac{d^2}{dx^2}\right) \left(1 - \frac{EI}{\beta AG} \frac{d^2}{dx^2}\right) P \frac{d^2 w}{dx^2} = 0 \quad (14)$$

Since finding an analytical solution is possible for simply supported boundary conditions for the present problem, the (SWCNT) beam is assumed simply supported. as a result, the boundary conditions have the following form [37]:

$$w = W \sin(\lambda x), \quad \lambda = \frac{N\pi}{L} \quad (15)$$

Where (W) is the amplitude of deflection of the beam and (N) is the vibrational mode number.

Substitution of Eq. (15) into Eq. (14) gives the critical buckling loads via nonlocal Timoshenko beam model:

$$P = \frac{EI \lambda^2}{\left(1 + e0a^2 \lambda^2\right) \left(1 + \frac{EI}{\beta AG} \lambda^2\right)} \quad (16)$$

RESULTS AND DISCUSSIONS

Based on molecular dynamics (MD) simulation, the Young's moduli used in this study of three types of single-walled carbon nanotubes (SWCNTs), armchair, zigzag and chiral tubules, are calculated by Bao Wen Xing et al [31]. They numeric results are in good agreement with the existing experimental ones [38]. Bao et al, indicate that the Young's moduli of SWCNTs are in the range of 929.87 ± 11.5 GPa (Table 1), when the Young's moduli of SWCNTs are weakly affected by the tube radius and tube chirality.

Table 1: lists the values of Young's modulus for different chiral angles using MD simulation [31]

(n,m)	diameter (nm)	Young's modulus (GPa)
Armchair		
(8,8)	1,0848	934.960
(10,10)	1,3560	935.470
(12,12)	1,6272	935.462
(14,14)	1,8984	935.454
(16,16)	2,1696	939.515
(18,18)	2,4408	934.727
(20,20)	2,7120	935.048
Zigzag		
(14,0)	1,0960	939.032
(17,0)	1,3309	938.553
(21,0)	1,6441	936.936
(24,0)	1,8789	934.201
(28,0)	2,1921	932.626
(31,0)	2,4269	932.598
(35,0)	2,7401	933.061
Chiral		
(12,6)	1,2428	927.671
(14,6)	1,3917	921.616
(16,8)	1,6571	928.013
(18,9)	1,8642	927.113
(20,12)	2,1921	904.353
(24,11)	2,4269	910.605
(30,8)	2,7165	908.792

To investigate the critical buckling loads of (SWCNTs), the results including the effect of nonlocal small-scale coefficient, the vibrational mode number and aspect ratio of the (SWCNTs). In addition, the critical buckling loads of different chiral angle of (SWCNTs) are compared in order to explore the effect of chirality. based on the formulations obtained above with the nonlocal Timoshenko beam models, the critical buckling loads of single-walled carbon nanotubes (SWCNT's) are discussed here. The parameters used in calculations of (SWCNT) are given as follows: the effective thickness of (CNTs) taken to be 0.34 nm [31], the mass density $\rho = 2.3 \text{ g/cm}^3$ [14] and poisson ratio $\nu = 0.19$.

In the present study, the (figs. 3–5) illustrate the dependence of the non-local critical buckling load on the chirality of carbon nanotube for different values of small-scale coefficient and vibrational mode number of the (SWCNTs). The ratio of the length to the diameter, L/d , is 30. The scale coefficients $e_0a = 0, 0.5, 1, 1.5$ and 2 nm are considered. It is clearly seen from (Figs. 3–5) that the most notable feature is that the results based on the local and non-local theories are almost the same for small mode numbers. However, it is observed that as the mode number

increases, the difference becomes obvious. This significance of nonlocal effects in higher modes is attributed to the influence of small wavelength for higher modes. For smaller wavelengths, interactions between atoms are increasing and these loads to an increase in the nonlocal effects.

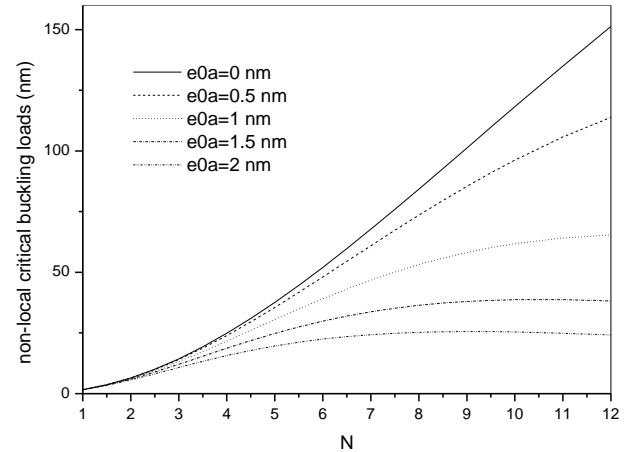


Fig. 3: Relation between the critical buckling load and the mode number (N) of zigzag (14,0) carbon nanotube, with different scale coefficients (e_0a). The value of (L/d) is 30.

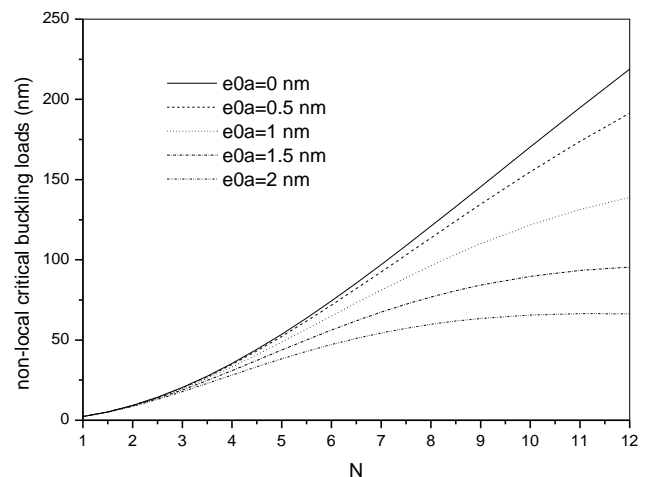


Fig. 4: Relation between the critical buckling load and the mode number (N) of chiral (16,8) carbon nanotube, with different scale coefficients (e_0a). The value of (L/d) is 30.

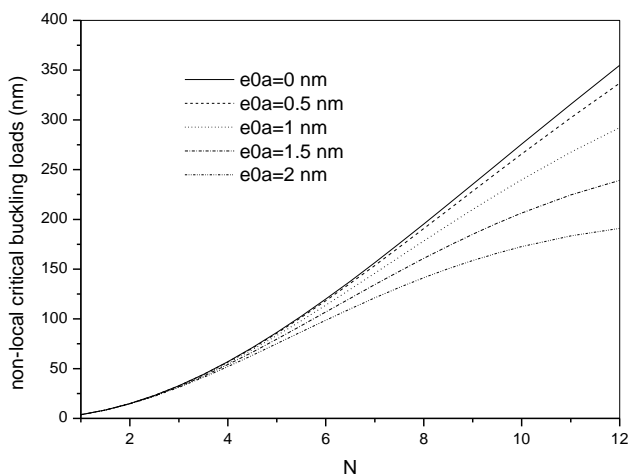


Fig. 5: Relation between the non-local critical buckling load and the mode number (N) of armchair (20,20) carbon nanotube, with different scale coefficients (e_0a). The value of (L/d) is 30.

In addition, the local Timoshenko beam model, which does not consider the small scale effects ($e_0a=0$), will give a higher approximation for the critical buckling load. But the non-local Timoshenko beam model will present an accurate and reliable result. The values of critical buckling load increases with increasing the values of mode number for zigzag (14,0), chiral (16,8) and armchair (20,20) carbon nanotube respectively. It can be seen that the ranges of the non-local critical buckling loads for these chirality of carbon nanotube are quite different. In Fig. 5, the range is the largest for armchair (20,20), but the range is the smallest for zigzag (14,0) in Fig. 3. The reason for this difference is that the increasing or decreasing of carbon nanotube diameter.

The effect of aspect ratio (L/d) on the non-local critical buckling loads for various chirality of carbon nanotube is demonstrated in (fig 6) with fundamental mode and nonlocal parameter $e_0a= 2$ nm. In these figure, we present a comparison between the effect of armchair (20,20), chiral (16,8) and zigzag (14,0) chirality of carbon nanotube respectively on the non-local critical buckling loads. In the calculations, The critical buckling load gets reduced as one transit from the armchair (20,20) to the chiral (16,8) and then, zigzag (14,0) chirality, when the diameter of nanotube is decreasing. This reduction in the critical buckling load is most pronounced when the nanotube is short.

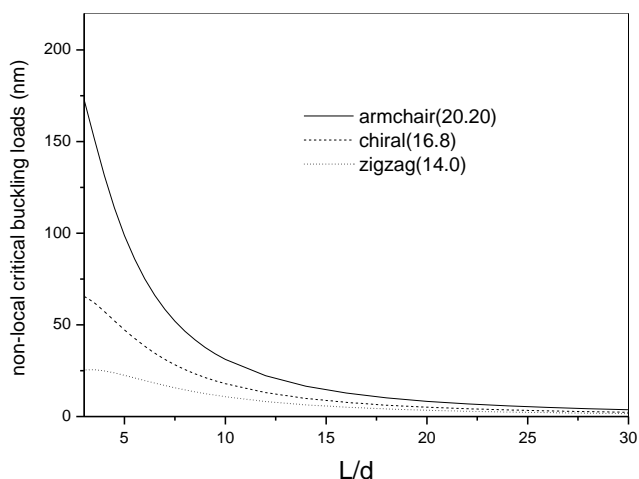


Fig. 6: effect of aspect ratio and chirality of carbon nanotube on the Non-local critical buckling load in fundamental mode and scale coefficient ($e_0a=2$ nm).

CONCLUSIONS:

This paper studies the non-local critical buckling loads analysis of (SWCNTs) based on the non-local Timoshenko beam theory. Influence of non-local small-scale coefficient, the vibrational mode number, the aspect ratio and different zigzag, chiral and armchair chirality of carbon nanotube (SWCNTs) on the critical buckling loads of (SWCNTs) are studied and discussed.

Based on non-local Timoshenko beam theory the theoretical formulations include the small scale effect, the vibrational mode number, the aspect ratio and the chirality number of carbon nanotube. The governing equations and the boundary conditions for the (SWCNTs) are solved and the non-local critical buckling loads are obtained. According to the study, the results showed the dependence of the critical buckling loads on the chirality of carbon nanotube, small-scale coefficients', Aspect Ratio and mode number. However, it is observed that as the mode number increases, the small-scale effect on the critical buckling loads will be clearly. The reason of nonlocal effects in higher modes is attributed to the influence of small wavelength when the interactions between atoms are increasing and these loads to an increase in the nonlocal effects.

In addition, the critical loads also are affected by the armchair, chiral and zigzag chirality, when the diameter of carbon nanotube is increasing or decreasing. This affection in the critical buckling load is most pronounced for short nanotube. The reason for this phenomenon is that a carbon nanotube with smaller diameter has a larger

curvature, which results in a more significant distortion of (C–C) bonds and low critical loads.

The presented investigation may be helpful in the application of CNTs, such as nanoelectronics, nanodevices, mechanical sensors and nanocomposites.

ACKNOWLEDGMENTS

This research was supported by the Algerian national agency for development of university research (ANDRU) and university of sidi bel abbes (UDL SBA) in Algeria.

REFERENCES

1. S.Iijima; Helical microtubules of graphitic carbon; *Nature* (1991);354: 56–8.
2. S. Iijima, T. Ichihashi; Single-shell carbon nanotubes of 1 nm diameter; *Nature*, 363, 603 (1993).
3. M.S.Dresselhaus, P.Avouris; Carbon nanotubes: synthesis, structure, properties and application; *Top Appl Phys* (2001);80:1–11.
4. Bachtold Adrian, Hadley Peter, Nakanishi Takeshi, Dekker Cees; Logic circuits with carbon nanotube transistors; *Science* (2001);294(5545):1317–21.
5. H.Dai, J.H.Hafner, A.G.Rinzler, D.T.Colbert, R.E.Smalley; Nanotubes as nanoprobe in scanning probe microscopy; *Nature* (1996);384: 147–50.
6. E.T.Thostenson, Z.Ren, T.W.Chou; Advances in the science and technology of carbon nanotubes and their composites; a review. *Composites Science and Technology* (2001);61:1899–912.
7. E.W.Wong, P.E.Sheehan, C.M.Lieber; Nanobeam mechanics: elasticity, strength, and toughness of nanorods and nanotubes; *Science* (1997);277:1971–5.
8. Ru CQ; Elastic buckling of single-walled carbon nanotube ropes under high pressure; *Physical Review B* (2000);62:10405–8.
9. X. Wang, H. Cai; *Acta Mater.* 54 (2006) 2067.
10. J.N. Reddy, S.D. Pang; *J. Appl. Phys.* 103 (2008) 023511.
11. Q. Wang, V.K. Varadan, S.T. Quek; *Phys. Lett. A* 357 (2006) 130–135.
12. K. Amara, A. Tounsi, I. Mechab, E.A. Adda Bedia; *Appl. Math. Model.* 34 (2010) 3933–3942.
13. Y. Zhang, G. Liu, X. Han; *Phys. Lett. A* 340 (2005) 258–266.
14. A. Benzair, A. Tounsi, A. Besseghier, H. Heireche, N. Moulay, L. Boumia; *J. Phys. D* 41 (2008) 225404.
15. L. Wang, H. Hu; *Phys. Rev. B* 71 (2005) 195412.
16. Y.G. Hu, K.M. Liew, Q. Wang; *J. Appl. Phys.* 106 (2009) 044301.
17. T. Murmu, S.C. Pradhan; *Comput. Mater. Sci.* 46 (2009) 854–859.
18. T. Murmu, S.C. Pradhan; *Comput. Mater. Sci.* 47 (2010) 721–726.
19. J. Yoon, C.Q. Ru, A.Mioduchowski; Vibration of an embedded multiwall carbon nanotube; *Compos. Sci. Technol.* 63, (2003) 1533-1545.
20. T. Murmu, S. Adhikari; *Physica E* 43 (2010) 415–422.
21. B.I.Yakobson, C.J.Brabec, J.Bernholc; Nanomechanics of carbon tubes: instabilities beyond linear response; *Phys. Rev. Lett.* 76, 2511e2514; (1996).
22. C.Thomsen, S.Reich, H.Jantoljak, I.Loa, K.Syassen, M.Burghard, G.S.Duesberg, S.Roth; Raman spectroscopy on single- and multi-walled nanotubes under high pressure; *Appl. Phys. A* 69, 309-312 (1999).
23. J.A.Elliott, J.K.W.Sandler, A.H.Windle, R.J.Young, S.P.Shaffer; Collapse of single-wall carbon nanotubes is diameter dependent; *Phys. Rev. Lett.* 92 (095501) (2004).
24. A.R. Ranjbartoreh, A. Ghorbanpour, B. Soltani; *Physica E* 39 (2007) 230.
25. A.R.Ranjbartoreh, G. X.Wang, A.Ghorbanpour Arani and A.Loghman; Comparative consideration of axial stability of single- and double-walled carbon nanotube and its inner and outer tubes; *Physica E*, (2008), 41, 202–208.
26. G.M.Odegard, T.S.Gates, L.M.Nicholson, K.E.Wise; Equivalent-continuum modeling of nano-structured materials; *Compos. Sci. Technol.* 62, 1869-1880 (2002).
27. H.W.Zhang, L.Wang, J.B.Wang; Computer simulation of buckling behaviour of double-walled carbon nanotubes with abnormal interlayer distances; *Comput. Mater. Sci.* 39, 664 (2007).
28. Y. Jin, F.G. Yuan, *Compos. Sci. Technol.* 63 (2003) 1507.
29. C.F. Cornwell, L.T. Wille, *Solid. State. Commun.* 101 (1997) 555.
30. D.W. Brenner, *Phys. Rev. B* 42 (1990) 9458.
31. Bao, W.X., Zhu, Ch.Ch., Cui, W.Zh. Simulation of Young's modulus of single-walled carbon nanotubes by molecular dynamics. *Physica B* 352, (2004) 156–163.
32. Michele Meo, Marco Rossi, Prediction of Young's modulus of single wall carbon nanotubes by molecular-mechanics; *Composites Science and Technology* 66 (2006) 1597–1605.
33. Y.Tokio; Recent development of carbon nanotube; *Synth Met* (1995);70:1511–8.
34. A.C. Eringen; *Nonlocal Polar Field Models*; Academic Press, New York, (1976).
35. A.C. Eringen; *J. Appl. Phys.* 54 (1983) 4703.
36. J.D. Achenbach; *Wave Propagation in Elastic Solids*, North-Holland Publishing Company, Amsterdam (1973).
37. Yi-Ze Wang, Feng-Ming Li, Kikuo Kishimoto; Scale effects on thermal buckling properties of carbon nanotube; *Physics Letters A* 374 (2010) 4890–4893.
38. J.Z. Liu, Q.S. Zheng, Q. Jiang; *Phys. Rev. Lett.* 86 (2001) 4843.

STUDY OF THE EFFECT OF MARBLE FILLERS SUBSTITUTION OF CEMENT ON THE RHEOLOGICAL AND MECHANICAL CHARACTERISTICS OF THE SELF-COMPACTING CONCRETE (SCC)

N. DJEBRI¹, Z. RAHMOUNI^{2*} and L. BELAGRAA^{3,**}

¹Department of Civil Engineering, M'Sila University, Algeria

²Department of Civil Engineering, Development of Géomaterials Laboratory, M'Sila University, BP 819 RP 28000 M'sila, Algéria

³Department of Civil Engineering, M'Sila University, Algeria,

** Laboratory of Materials and Electronic Systems, Faculty of Sciences and Technology, B B Arreridj University, (34 062), Algeria.

Fax: +35 55 64 53 Email: rahmouniz@yahoo.fr (corresponding author)

ABSTRACT

The self-compacting concretes (SCC's) are characterized by their high fluidity so that they could be placed without any vibration. The effect of fillers addition on the behavior of SCC in fresh and hardened state is of great importance. This incorporation of marble waste fillers aims to preserve the environment from one side and a wider use of these materials from another.

The present research experimental program examines the effect of the partial substitution of cement with marble fillers on the characteristics of self-compacting concrete in fresh and hardened state. Thus, the marble fillers (MF) was introduced into the composition of self-compacting concretes at dosages of 10%, 20% and 30%. Three Water/Cement ratios of 0.4, 0.5 and 0.6 were maintained for the studied mixtures. The one with 100% of cement served as a control concrete mix.

KEYWORDS

Self-Compacting Concrete (SCC), Marble Fillers (MF), Mechanical proprieties, rheological characteristics, environment.

NOMENCLATURE

SCC, refers to Self-Compacting Concrete.

MF, refers to Marble Fillers.

BAP0, refers to SCC as control mix without MF.

BAP1, refers to SCC with 10 % MF and W/C=0.4.

BAP2, refers to SCC with 10 % MF and W/C=0.5.

BAP3, refers to SCC with 10 % MF and W/C=0.6.

BAP4, refers to SCC with 20 % MF and W/C=0.4

BAP5, refers to SCC with 20 % MF and W/C=0.5

BAP6, refers to SCC with 20 % MF and W/C=0.6.

BAP7, refers to SCC with 30 % MF and W/C=0.4.

BAP8, refers to SCC with 30 % MF and W/C=0.5.

BAP9, refers to SCC with 10 % MF and W/C=0.6.

$R_{(c)}$, refers to compressive strength of concrete.

R_{tf} , refers to tensile strength of concrete.

W(%), refers to the absorption of concrete.

P(%), refers to the porosity of concrete.

INTRODUCTION

The self-compacting concrete was developed in Japan in 1988, It represents one of the most important advances in the technology of concretes in the last two decades.

The SCC can be considered as a material of high performance, which passes by under the influence of its own weight without any mechanical vibration, to adapt itself in a desired shape, even in the case of a very small spacing between the steel reinforcement. The easy placement under only the effect of the gravity, required a very high fluidity of materials but It is as well essential as the concrete preserves a satisfactory stability and a perfect homogeneity.

These two contradictory properties are obtained by a high quantity of fine particles of fillers coupled with a high water cement ratio W/C corresponding to a fixed dosage of super-plasticizer admixture.

The local materials in any region of the world form the first natural product of construction appropriate to this region given that It was able to resist the climatic changes of the same region in the past. Algeria with its vast area includes a heterogeneousness of local materials which deserve to be valued, like the dune sand, clays, tuff, the marble powder and others which are still up to now under valorized.

Topcu et al, (2009) investigated the effect of waste marble powder on the properties of SCC. It was concluded that the fresh properties had not been affected up to 200 Kg/m³ marble dust content, mainly the workability. It was reported that the air content increased by using marble waste in the SCC mixtures. The mechanical properties at hardened state had decreased for a higher dosage of marble addition above this level. Consequently, if the positive effect of marble dust incorporation is to be considered on fresh and hardened state of SCC a new method could be developed for dosages of marble waste below 200 Kg/m³ [1].

Other researchers pointed out that using marble powder in the SCC formulated revealed higher strength at a given water cement ratio compared to traditional concrete mix. The mean strength for SCC mixes with marble powder was 25 % higher than reference concrete [2]. A similar conclusion was observed for SCC containing limestone and chalk powders [3].

According to the research work undertaken by Corinaldesi and al (2010) on the use of marble powder as a substitution of cement and sand for SCC mortars and concretes, they noted that 10 % replacement of marble powder proved to be effective in assuring good cohesiveness of mortars and concrete at fresh state. But in terms of mechanical performance the 10 % substitution of sand by marble powder provided maximum compressive strength at the same workability level compared to the reference mixture after 28 days of age. Moreover, an even more positive effect of marble powder was noticed at early ages, due to its physical filler ability [4].

Recent studies on the use of marble powder combined with pozzolana for SCC formulation is reported to enhance the rheological properties of mortars and concrete based on this addition for ternary cement. However, a reduction of compressive

strength was observed with pozzolana and marble addition compared to control concrete [5].

For this frame of idea, the use of the marble waste fillers in the composition of the SCC, the present research work investigated the marble waste fillers incorporation to see the effect of such addition on the properties of SCC when using a dosage up to 30 % of marble powder addition in the due formulation of SCC mixtures. Also, the generated marble waste could be with a positive impact on the environment level by the valuation of the local materials in concrete composition in the field of the construction from one hand, reducing the dust and gas emissions in the atmosphere when used as cement replacement from another.

EXPERIMENTAL PROGRAMME

Materials: The used Cement is CPJ 42.5 and 32.5 delivered from the Lafarge cement plant (Hammam Dalaa wilaya of M'Sila, 250 Km from Algiers) with a specific density of 3,1. As Aggregates, the originally siliceous sand resulting from OUED MAITER in the region of Boussaâda wilaya of M'Sila was used. Two fractions of limestone crushed gravel (3/8, 8/16) from COSIDER quarry from local region of Bordj Bou Arreridj were utilized. Marble fillers powder of fraction 0.08 mm having a density 2.67 was kept at variable dosages for the experimental program. The super-plasticizer MEDAPLAST SP40 from GRANITEX manufacturer in Algiers and mixing water from the laboratory of civil engineering for concrete mixtures formulation were used.[6]

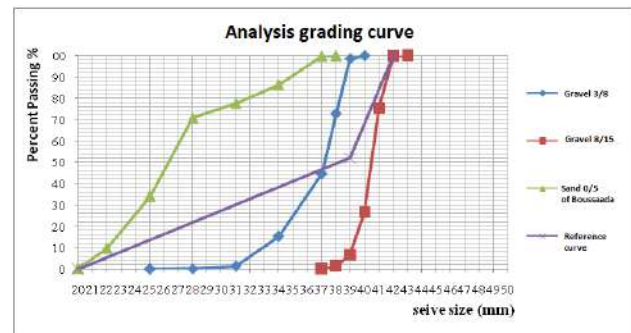


Figure 1

Analysis grading curve of aggregates (sand and gravel).

Composition of SCC mixtures: The necessary conditions allowing to guarantee the self-compacting and easy placing while based on compositions proposed in the specialized literature

were respected in the due formulation of SCC mixtures [8- 11].

It is a question of a choice the proportions of constituents in one cubic meter (1 m^3) of concrete by having the following parameters, a proportional of gravel to sand relationship of G/S equal to one ($G/S= 1$) and a water cement W/C ratio of 0.4, 0.5 and 0.6

A determined dosages for the additions such as the superplastizier (1.7 % of the weight of cement) and a variable percentages 10, 20 and 30 % of marble fillers were maintained for this program.

To be able to compare the performances of various concretes independently of the cement factor, we fixed the dosage of the latter at $420 \text{ kg} / \text{m}^3$. A total of ten mixtures beside a control concrete mix (100 % cement) were prepared.

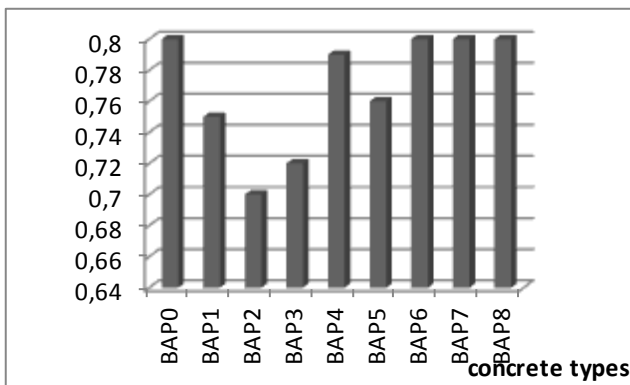


Figure 2

L box test results for the different concretes types

RESULTS AND DISCUSSION

Fresh state: The characteristic tests at fresh state of concrete were realized following the batching as recommended by the French Association of Civil Engineering (AFGC, 2000) : the flow table, the flow in the box L and the sieve stability in the aim of estimating the fluidity and the static and dynamic segregation of the SCC mixes [6].

Figure 2, shows the results obtained for the L box test.

The test is exploited through the occupancy rate relationship of the concrete heights in bottom and in the beginning of the box which must as a rule be upper to 0,8 according to the recommendations (AFGC, 2000).

The BAP 7, BAP 8 and the BAP 9 ($W / C=0.6$) are more fluid than the other concrete types, because of the higher W/C ratio.

The mixtures with marble fillers presented

occupancy rates closer to the control mix, one can say that the partial replacement of the cement by the marble powder reaching 30 % has no effects on the mobility of the concrete in a confined medium independently of the water cement ratio W/C.

Flow test : The values of the flow diameter are usually fixed between 60 and 75 cm for SCC mixtures.

It can be noticed that the values of the spreading of control mix (without addition of marble fillers) is 70 cm . While for the concretes with addition is situated between 55 to 60 cm for the SCC mixtures with $W / C=0.4$, (61 to 67 cm, 69 to74 cm for $W/ C=0.5$ and 69 to 74 cm for mixes with $W/ C=0.6$, consequently. These values show that most of the tested compositions present a spreading upper to 60 cm, that expresses greater fluidity. This high fluidity could be attributed to the use of the dosage of superplastizier (1,7 % of the weight of the binder).

For the same ratio of W/C, the partial substitution of a part of cement by marble fillers leads to a lower fluidity, hence a limited flow table diameter of the SCC mixture, in comparison with the witness. However, this increase of the powder marble dosage is resulting greater values for the flow diameter but rest lower than that of the control one (BAP0). Finally, at the dosage of 30 % the concrete with the bigger fluidity (BAP9) having a W/C ratio equal to 0.6 in regards to other SCC types with additions and It is similar to the control mix. One could conclude that the introduction of the marble fillers has no meaning effect on the spreading of the tested SCC types.

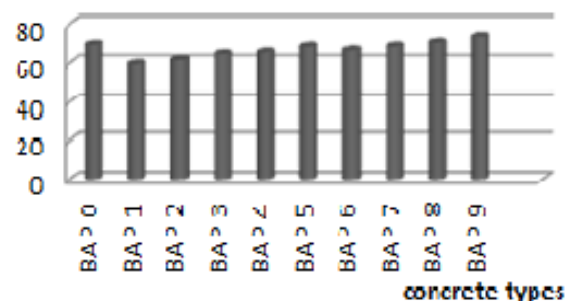


Figure 3

Flow table test results for the different concrete types.

Segregation index: The percentage in weight of slurry having crossed the sieve compared with the

weight of the initial sample expresses the stability of the concrete.

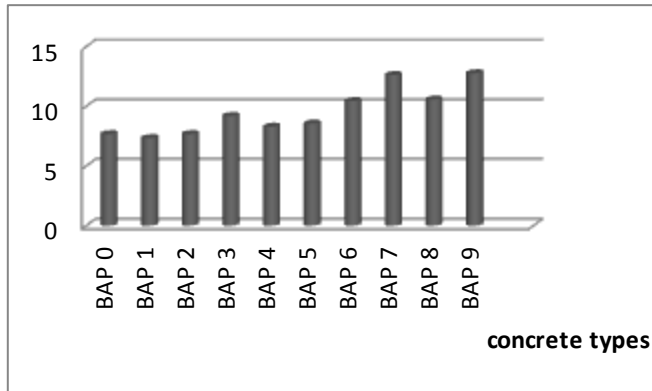


Figure 4

Segregation index test for the different concrete types.

From figure 4, the results obtained showed that, we notice that the SCC's present an index of segregation inferior to 15 % for both types the concrete witness mix and concretes of marble powder additions, this reflect a sufficient stability. Concretes having a value of the resistance in the segregation lower than 15 % offers a self compacted concrete of very good quality. The increase of the substitution amount of the cement by the marble fillers of 10 %, 20 % and 30 %, respectively; leads to a successive reduction in the quantity of necessary water to obtain the SCC satisfying the characteristics recommended by the AFGC. This gives some explanation by the fact that the filler of marble in addition to the physical role could contribute to an improvement of fluidity when coupled to the superplastizier admixture used SP 40. the due fact the partial replacement of a part the cement by the marble fillers gives a mixture with a less water demand.

Hardened state:

The Compressive strength $R_{(c)}$: The mechanical response in compression test allows to control the quality of the hardened concrete. It is about the most common current methods used so far.

It can be observed that for all the SCC mixtures the compression resistance increases with the age of the concrete in a normal development of strength according to the age of testing 7, 14 and 28 days (figure 5).

It is noticed that the dosage of the ratio $F / C=20$ %, this gives higher compression resistance relatively to

the SCC mixtures with $F/C = 10$ % and $F / C=30$ %.

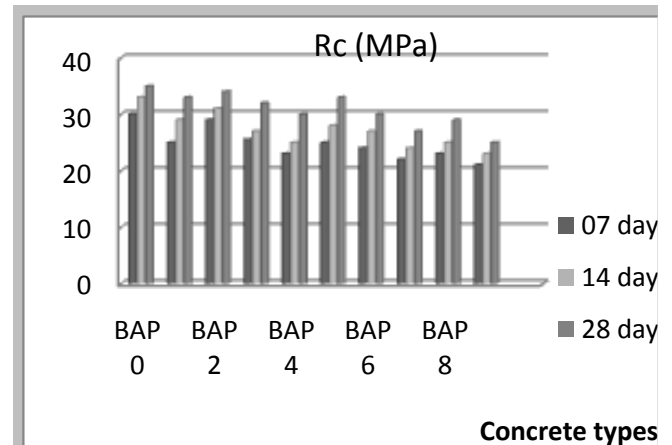


Figure 5

The compressive strength (R_c) for the different concrete types at 7, 14 and 28 days age.

The compressive strength of the SCC with addition of marble fillers are lower than that of the control mix at the age of 7, 14 and 28 days whatever is the water cement ratios adopted in the experimental program. This decrease of the resistance in compression is translated by the fact that the content of replacement introduced which led to the reduction of hydrates components hydrates in the cement based material, these are responsible on the strength development in the SCC matrices with marble powder addition.

It is evident that the increase of W/C ratio is more resulting a reduction in the of strength, nevertheless; the witness mix resistance remains high compared to those containing the marble fillers addition. So, no activity as inerte constituents could be attributed to the marble powder but in regards to its physical role of filling the voids in concrete matrix. This permit the acquiring of SCC mixtures with acceptable performances.

Tensile strength (R_{tf}): It can be observed that for all the SCC mixtures the tensile strength resistance increases with the age in a normal development trend (figure 6).

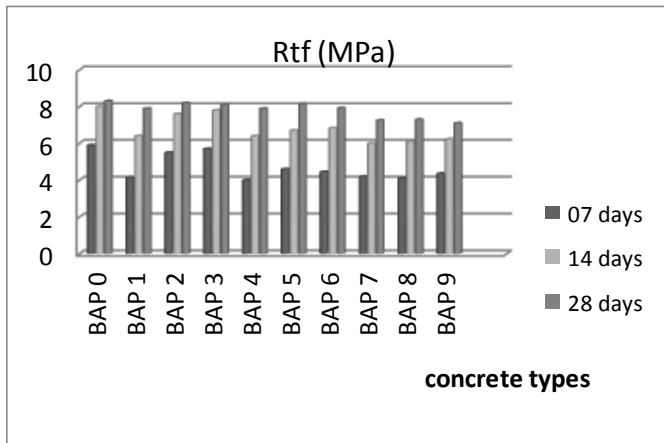


Figure 6

The tensile strength for the different concrete types.

The increase at a dosage of 20 % is remarkable for the tensile strength of this mix compared to 10 % and 30 % percentages of marble fillers SCC mixes. The addition of filler of marble led to the reduction of the tensile strength in regards to the witness concrete at the age of 7, 14 and 28 days for three water cement ratio used so far. As reported for the compressive strength all this is translated by the fact that the content of the SCC mixtures of inert replacement addition of MF instead of the active clinker.

Absorption test: It is marked in this test the influence of water cement ratio W/C regarding the SCC concrete absorption rate.

From figure 7, the marble fillers dosage increases the absorption of SCC mixes in comparison with witness concrete (without addition). This may be due to the increase of water demand of these mixes to achieve the required fluidity.

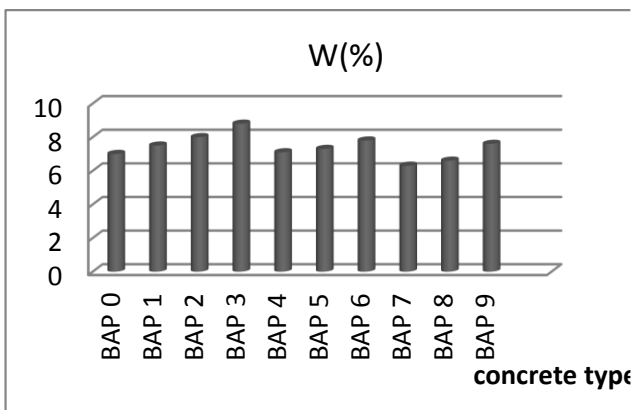


Figure 7

The absorption W (%) as a function of concrete types.

Porosity test: The obtained results for porosity test are reported in the following figure 8. It can be noticed from figure 8, that the increase of the dosage of marble fillers causes a decrease of the porosity of the concrete at the percentage of 10 % of fillers by compared to the concrete witness mix. The latter type is with a great homogeneity and low air content.

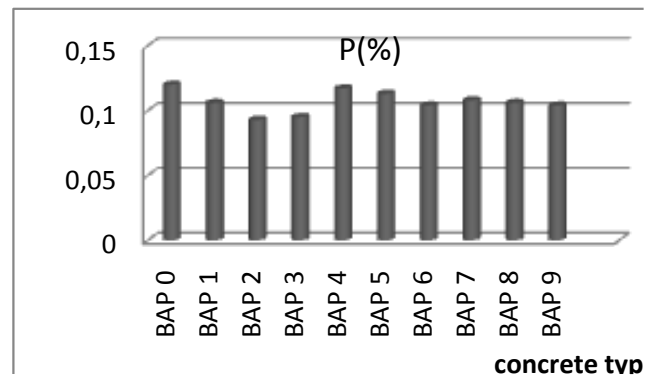


Figure 8

The porosity for the different concrete types.

CONCLUSION

Self-compacting concretes are extremely fluid allowing the easy placement by gravitation and without vibration. These concretes are distinguished from traditional concretes by their properties in the fresh state: high fluidity, stability and robustness. These exceptional particularities impose a higher dosage of cement in the paste; thus, limiting the frictions between aggregates. The additions of limestone fillers are always present in the paste of the cement, they get good handiness's, leading to a denser cement matrix, which allows to keep reasonable heat release during the hydration process.

This experimental study highlighted the possibility of using the marble waste as addition in the composition of the SCC. The characteristic tests undertaken on fresh concretes proved satisfactory fluidity and good stability acquired properties at dosages of marble fillers reaching 30 %.

At hardened state, the SCC with marble fillers percentage of 20 % presented acceptable strengths.

REFERENCES

[1] Topcu I B., Belir, T., and Uygunoglu T., 2009, effect of marble dust content as filler on properties

of self-compacting concrete, *Construction and building Materials*, 23, Elsevier, pp. 1947-1953.

[2] Alyamac K E And Ince R., 2009, A preliminary concrete mix design for SCC with marble powders, *Construction and building Materials*, 23, Elsevier, pp. 1201- 1210.

[3] Zhu W., Gibbs J C., 2005, Use of different limestone and chalk powders in self-compacting concrete, cement and *Concrete Research*, 35, pp. 1457-1462.

[4] Corinaldesi V., Moriconi G and Naik T R., 2010, Characterization of marble powder for its use in mortar and concrete, *Construction and Building Materials*, 24, Elsevier, pp. 113-117.

[5] Belaidi A SE., Azzouz L., Kadri E and Kenai S., 2012, Effect of natural pozzolana and marble powder on the properties of self-compacting concrete, *construction and Building Materials*, 31, Elsevier, pp. 251-257.

[6] Dreux G. et .Festa J., 2000 , *Nouveaux guide du béton et de ces constituants*, Ed. Eyrolles.

3. Dupain R., Lanchon R., Saint-Arromain J.C., *Granulats, sols, ciments et bétons*, Ed Casteilla, 2000.

[7] AFGC, Association française de Génie Civil, *Les bétons autoplaçants: Recommandations provisoires*, 2000.

[8] Behim M., Boucetta A., 2009. Effet des additions micronisées sur l'écoulement des bétons autoplaçants (Laitier de haut fourneau, filler calcaire et poudre de verre), 1st International Conference on Sustainable Built Environment Infrastructures in Developing Countries ENSET Oran, Algeria 12-14, October 2009.

[9] Assié S., 2004. Durabilité des bétons autoplaçants. Thèse de doctorat. l'INSA de Toulouse, France.

[10] Turcry, P., 2004. Retrait et fissuration des bétons autoplaçants –Influence de la formulation. Thèse de doctorat. Université de Nantes, France.

[11] Diederich, P., 2010. Contribution à l'étude de l'influence des propriétés des fillers calcaires sur le comportement autoplaçant du béton. Thèse de doctorat. Université Toulouse III - Paul Sabatier, France.

Heat and Mass Transfer Optimisation (II)

STUDY OF LAMINAR-TURBULENT TRANSIENT FLOW CONJUGATED WITH MIXED CONVECTION IN A VERTICAL CHANNEL

A. Belaid ^{*1,2}, O. Kholai¹, A.Djebli³, T. Arrif^{1,2}, S. Boulkroune¹

¹ Laboratory of transport engineering and environment, Institute of Mechanic, Constantine University, Road of Ain ElBey, Constantine 25001, Algeria.

² Unité de Recherche Appliquée en Energies Renouvelables, URAER, Centre de Développement des Energies Renouvelables, CDER, 47133, Ghardaïa, Alegria.

³ Unité de Développement des Equipements Solaires, UDES, Centre de Développement des Energies Renouvelables, CDER, 42415, Tipaza, Alegria

b_fetouh@yahoo.fr

ABSTRACT

In this paper the transient descendant laminar- turbulent flow for the mixed convection of air in a vertical channel heated by uniform Temperatures from the outside surface of central zone of the channel wall is presented numerically using a 2D model and boussinesq's assumption, The solution of this mathematical model is based on the masse conservation equation, Navier-Stocks equation and energy conservation equation then the finite volume method is used in order to discrete the governing equations. The *SIMPLE* algorithm handles the coupling of velocity-pressure. The numerical simulations for fixed Reynolds numbers $Re = 100$, and Grashof ($103 \leq Gr \leq 105$) to study the effects of the wall thickness and the heated part of the wall on the behavior of flow regime.

NOMENCLATURE

H channel width
K Wall-to-fluid thermal conductivity ratio ($=k_w/k_f$)
L nondimensional length of the channel
g gravity acceleration
U nondimensional transverse velocity
V nondimensional longitudinal velocity
X nondimensional transverse coordinate
Y nondimensional longitudinal coordinate

Greek Symbols

Δ channel thickness
 θ nondimensional temperature
 τ nondimensional time

Non-dimensional Numbers

Gr Grashof number based on the channel
Pr Prandtl number
Re Reynolds number

INTRODUCTION

Unsteady Mixed convection in vertical heated tube has received considerable attention because in industrial and engineering applications, especially in relation to the use of automatic control devices for accurate regulation of fluid systems involving heat exchange devices. In power plates the thermal transients resulting from unsteadiness in the thermal behavior can significantly affect their control systems. These transients may be

accidental as in the case of power surge and pump failure etc. In order to design such apparatuses and to predict their off design performance, it is necessary to obtain an exact description of the velocity, and temperature distributions under all operating conditions. But despite wide investigations there are still many cases, which are not well understood and difficult to predict.

Many researchers studied numerical and experimentally mixed convection in a vertical tube, on the behavior of flow regime laminar and turbulent. However, few researchers have studied details that would characterize transient regime.

Among the first who have studied experimentally transition from laminar to turbulent regimes in a vertical tube [1] and [2]. After them [3]. Use a technique, which allows direct visualization of fluid flow-phenomena, observed the presence of recirculation cells and of laminar-turbulent transitions at low values of the Reynolds number for fully developed flow in a closed-loop thermosiphon with uniform heat flux boundary condition. A. Behzadmehr and al. [4] deals with an analysis of the nature of the temperature and velocity fluctuations using experimental data obtained at $Re= 1000, 1300$ and 1600 over a wide range of the Grashof numbers.

A signal analysis is presented to show the details that could characterize onset of laminar–turbulent transition.

There are a number of authors who studied numerical, Wei-Mon yan. [5] study is to investigate the transient mixed convection heat transfer in vertical tube flows. Fusegi and al [6] investigated the combined effect of the oscillatory through-flow and the buoyancy on the heat characteristics of a laminar flow in a periodically grooved channel. Mai and El Wakhil. [7] Have studied the problem of upward vertical pipe flow with step change in the inlet temperature and velocity. Their results show a dissymmetry of the velocity profile and temperature between the positive and negative steps change.

Some researchers Omara and Abboudi. [8], Su and al. [9] have found that both heat conduction in the wall and wall heat capacity have an important role on the transient conjugated heat transfer. In Wang and al. [10] in a numerical study of fully developed flow in and vertical pipes investigated the effect of axial conduction and identified the regime of reversed flow occurrence for various Prandtl numbers in the $Pe-Gr/Re$ coordinates. In recent years, the M. Boumaza, A. Omara. [11] Presented a numerical analysis of the effects of wall and fluid axial conduction, physical properties and heat capacity of the pipe wall on the transient downward mixed convection in a circular duct experiencing a sudden change in the applied heat flux on the outside surface of a central zone.

The aim of this study is to deal with the conjugate heat transfer problem of the unsteady mixed convection in vertical tube partially heated. The goal of this work is to study the effects of the wall thickness and the heated part of the wall on the behavior of flow regime.

Problem description and mathematical formulation:

Figure.1a shows a schematic of the problem under study. Both walls have two identical flush-mounted, symmetric and discrete heat sources of length L_u , with uniform surface temperature T_w . All other channel walls are assumed to be adiabatic.

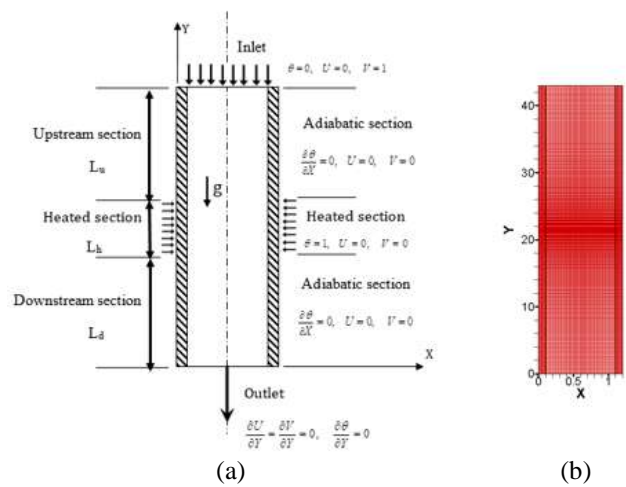


Figure 1 Geometrical configuration and grid distribution of the considered problem

A forced flow is injected with uniform velocity v_0 and ambient temperature T_0 . Flow is assumed unsteady and laminar. It is also assumed that the properties of the fluid are constant, with negligible viscous dissipation, while the density varies according to Boussinesqu approximation. The governing equations and boundary conditions for the transient conjugated heat conduction and laminar mixed convection are as follows:

$$\frac{\partial U}{\partial X} + \frac{\partial V}{\partial Y} = 0$$

$$\frac{\partial U}{\partial \tau} + U \frac{\partial U}{\partial X} + V \frac{\partial U}{\partial Y} = -\frac{\partial P}{\partial X} + \frac{1}{Re} \left[\frac{\partial}{\partial X} \left(\frac{\partial U}{\partial X} \right) + \frac{\partial}{\partial Y} \left(\frac{\partial U}{\partial Y} \right) \right]$$

$$\frac{\partial V}{\partial \tau} + U \frac{\partial V}{\partial X} + V \frac{\partial V}{\partial Y} = -\frac{\partial P}{\partial Y} + \frac{1}{Re} \left[\frac{\partial}{\partial X} \left(\frac{\partial V}{\partial X} \right) + \frac{\partial}{\partial Y} \left(\frac{\partial V}{\partial Y} \right) \right] + \frac{Gr}{Re^2} \theta$$

$$\frac{\partial \theta}{\partial \tau} + U \frac{\partial \theta}{\partial X} + V \frac{\partial \theta}{\partial Y} = \frac{1}{Re Pr} \left[\frac{\partial}{\partial X} \left(\frac{\partial \theta}{\partial X} \right) + \frac{\partial}{\partial Y} \left(\frac{\partial \theta}{\partial Y} \right) \right]$$

Where Gr , Re , Pr numbers are defined as:

$$Gr = \frac{g \beta (T_w - T_0) H^3}{\nu_0^2}, \quad Re = \frac{V_0 H}{\nu_0}, \quad Pr = \frac{\mu_0 Cp}{k}$$

Following dimensionless parameters are used in the above equations:

$$X = \frac{x}{H}, \quad Y = \frac{y}{H}, \quad \tau = \frac{t}{HN_0}, \quad U = \frac{u}{V_0}, \quad V = \frac{v}{V_0}, \quad P = \frac{p^*}{\rho V_0^2}, \quad \theta = \frac{T - T_0}{T_w - T_0}$$

Dimensionless boundary conditions can be defined

- $U = 0, V = -1, \theta = 0$ at $Y = 0$
- $\frac{\partial V}{\partial Y} = \frac{\partial U}{\partial Y} = \frac{\partial \theta}{\partial Y} = 0$, at $Y = L_u + L_h + L_d = L$
- $\theta = 1$ at $X = 0, L_u \leq Y \leq L_u + L_h$

$$X=H+2\Delta, \quad L_u \leq Y \leq L_u + L_h$$

- $\frac{\partial \theta}{\partial X} = 0$ at

$$X=0, \quad 0 \leq Y \leq L_u \text{ and } L_u + L_h \leq Y \leq L$$

$$X=H+2\Delta, \quad 0 \leq Y \leq L_u \text{ and } L_u + L_h \leq Y \leq L$$

Numerical method:

The governing equations were discretized by the finite volume method on a staggered mesh and the SIMPLE algorithm was used for the treatment of velocity-pressure coupling. In this work, we will use power-law scheme described by Patankar [12], because it requires less computing time and provides better stability of the numerical solution. Discretization has given us a system of nonlinear algebraic equations; the solution requires the use of an iterative numerical method by using double sweep algorithm THOMAS. After you study a grid independence, the 370 x 60 grid is therefore considered suitable for the present study Figure 1b. An optimal nondimensional time step of $\Delta\tau = 10^4$ was used for all the computations.

Validation

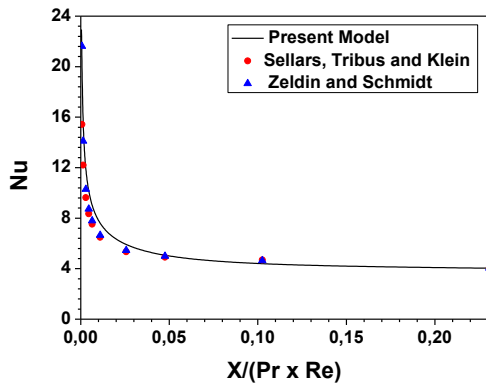


Figure 2

Comparison of local Nusselt numbers for mixed convection

In order to validate the computer code, by comparing its predictions with numerical and experimental results. Figure 2 shows a comparison of our calculated values for the axial evolution of the local Nusselt number for mixed convection in a vertical tube with the experimental results of Zeldin and Schmidt [13], Marnier and McMillan [14], shows that the model computer code is reliable. They can therefore be used with confidence for the study of the problem under consideration.

RESULTS AND DISCUSSION

The influence of the buoyancy on the global structure of the flow was examined with for fixed Reynolds numbers $Re = 100$ and varying Grashof number ($10^3 \leq Gr \leq 10^4$). The effects of the wall thickness and the heated part of the wall on the behavior of flow regime were studied.

Figure 3 presents the thermal field in the case of $Gr = 1 \times 10^4, 1.5 \times 10^4, 2 \times 10^4, 2.65 \times 10^4, 3 \times 10^4$ and 3.5×10^4 . It was observed that the isotherms are concentrating next the heated part showing a maximum heat exchange. Concerning the streamlines Figure 4, it has been noted that for $Gr = 1 \times 10^4$, the streamlines are presented with vertical lines almost parallel. The domination of the forced convection didn't allow the apparition of the recirculation zones. From $Gr = 1.5 \times 10^4$, recirculation zones appear and their length increase as Gr increases.

From the value of the Grashof number 2.65×10^4 , the isotherms are concentrated around each heated section with slight change in the curvature which increases as the Grashof number increases in such way that dissymmetry is obtained with Y axe, this indicates the existence of the instability. So, it can be remarked that the instability begins when the critical value of the Grashof number is between 2.65×10^4 and 3×10^4 . The appearance of recirculation zones can be explained by the contrast between the direction of buoyancy forces and viscous forces near the heated part. Recirculation zone appears with the critical value of Grashof number. Beyond this value, the number of recirculation zones and their length increases as Grashof number increases.

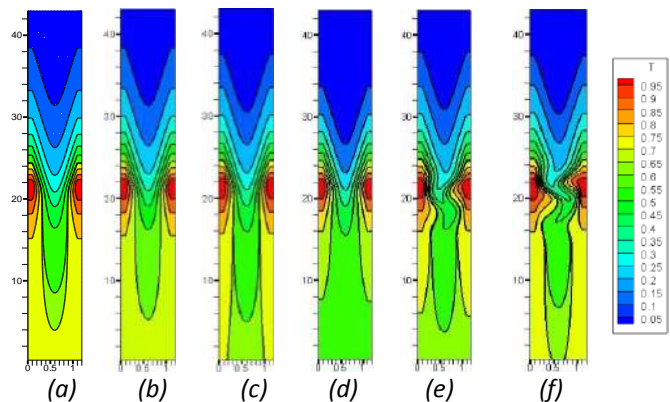


Figure 3

Isotherms in the case of $L_h=1, \Delta=0.1$ and $Re=100$:
 a) $Gr=1.0 \times 10^4$, b) $Gr=1.50 \times 10^4$, c) $Gr=2.0 \times 10^4$, d) $Gr=2.65 \times 10^4$, e) $Gr=3.0 \times 10^4$, f) $Gr=3.5 \times 10^4$.

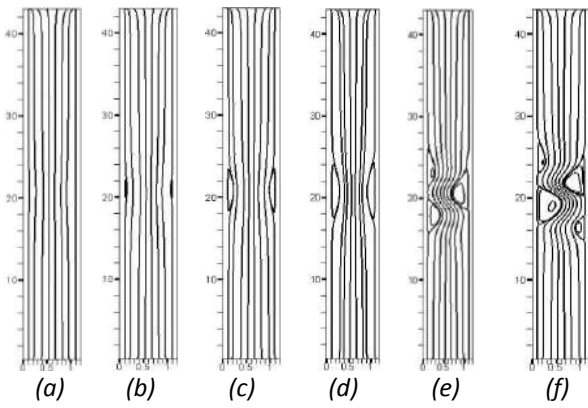


Figure 4

Stream function in the case of $L_h=1, \Delta=0.1$, a) $Gr=1.0 \times 10^4$, b) $Gr=1.50 \times 10^4$, c) $Gr=2.0 \times 10^4$, d) $Gr=2.65 \times 10^4$, e) $Gr=3.0 \times 10^4$, f) $Gr=3.5 \times 10^4$

Effects of the wall thickness on the behavior of flow regime

Figure 5 shows a temporal variation of the velocity U at the central point of the channel for a Δ thickness equal to 0.05 for different values of the Grashof number. It is clear that above the value of $Gr = 2.51 \times 10^4$ the regime is stable, by cons below this value the system is disturbed (unstable), hence the critical point of the value of the Grashof number for this thickness ($Gr_c = 2.5 \times 10^4$). For other thicknesses we have found that there is a change in the critical value of the Gr ($Gr_c = 2.65 \times 10^4$ for $\Delta = 0.1$, $Gr_c = 2.79 \times 10^4$ for $\Delta = 0.15$, $Gr_c = 2.94 \times 10^4$ for $\Delta = 0.2$).

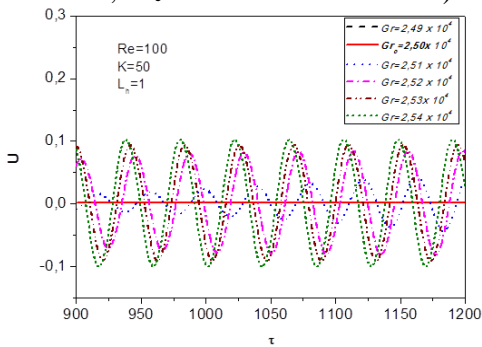


Figure 5

Time variations of velocity with heated portion $L_h=1$ at the point center of the Tube, for $\Delta=0.05$.

Figure 6 represents the thermal field in the channel with a heated section length equal to $L_h = 1$, with different values of thickness and Grashof number. For each values of the thickness, the values of Grashof number are taken less than the critical value. For the all cases, isotherms are concentrated around every heated section and the dynamic field is

represented with streamlines for the same Richardson numbers. It has been remarked the presence of two recirculation zones each one adhered to a heated part. The recirculation zone next the left heated part has a clockwise rotation, on the contrary, the recirculation zone next the right heated part has the opposite direction. Symmetry is observed with the vertical midline. This indicates stability for all cases studied. The two-recirculation zones become larger as the thickness increase.

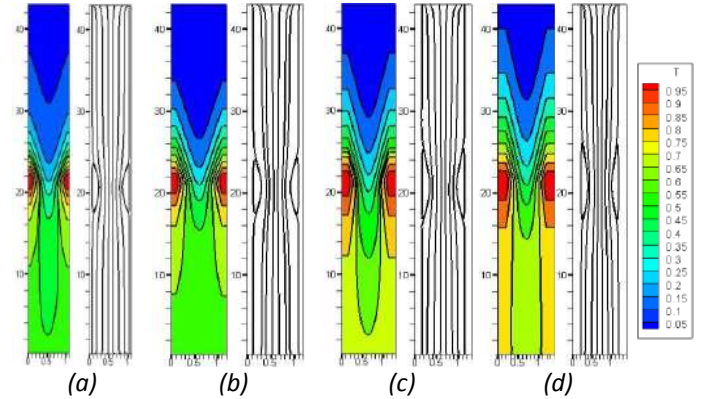
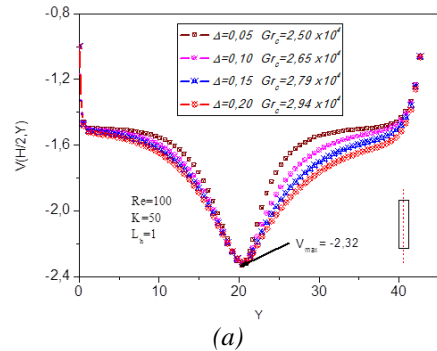
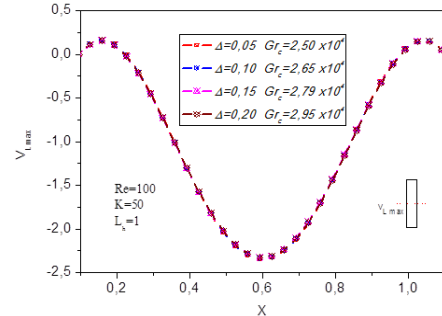


Figure 6

Isotherms and Stream function in the case of $L_h=1$, for different thickness: a) $\Delta=0.05, Gr=2.5 \times 10^4$, b) $\Delta=0.1, Gr=2.65 \times 10^4$, c) $\Delta=0.15, Gr=2.79 \times 10^4$, d) $\Delta=0.2, Gr=2.94 \times 10^4$.



(a)



(b)

Figure 7

Vertical and horizontal Velocity profile at the center of the tube for different thickness and of critical Gr_c .

Figures 7. represent the vertical and horizontal profiles at the center of channel with a heated part length equal to $L_h=1$, with different values of thickness and Grashof number. For each values of thickness, the values of the Grashof number are taken less than the critical values.

When the thickness of the wall changes, the critical point where all profiles are identical can be found, this is caused by the increasing of Richardson number, which lead to the increase of the recirculation zones size. The recirculation zones work as an obstacle and lead to the fluid velocity increase reaching the maximal velocity $V_{max}=-2.32$ in the center of the channel as shown in Figure 7a.

Effects of the heated part of the wall on the behavior of flow regime

Figure 8 represents the temporal variation of the velocity U in the central point of the channel for the value of the length of the heated section $L_h=0.25$ for different values of the Grashof number.

It is clear that above the value of $Gr = 2.75 \times 10^4$ the regime is stable, by cons below this value the system is disturbed (unstable), hence the critical point of the value of the Grashof number for this length of the heated section ($Gr_c = 2.75 \times 10^4$).

For other values of the L_h we have found that there's a change in the critical value of the Grashof number ($Gr_c = 2.65 \times 10^4$ for $L_h = 0.1$, $Gr_c = 2.57 \times 10^4$ for $L_h = 0.2$, $Gr_c = 2.54 \times 10^4$ for $L_h = 0.3$).

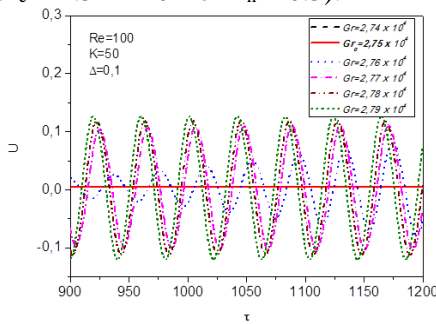


Figure 8

Time variations of velocity with thickness $\Delta=0.1$ at the point center of the Tube, for $L_h = 0.25$.

Figure 9 shows the streamlines and isotherms in channel for different values of the length of the heated section and Grashof number. Two recirculation zones were created near the heated section and growing in length with the heated section length increase and the Grashof number decrease simultaneously. Isotherms are concentrated near the heated section and getting

larger with the heated section length increase and Symmetry with the vertical midline is remarked.

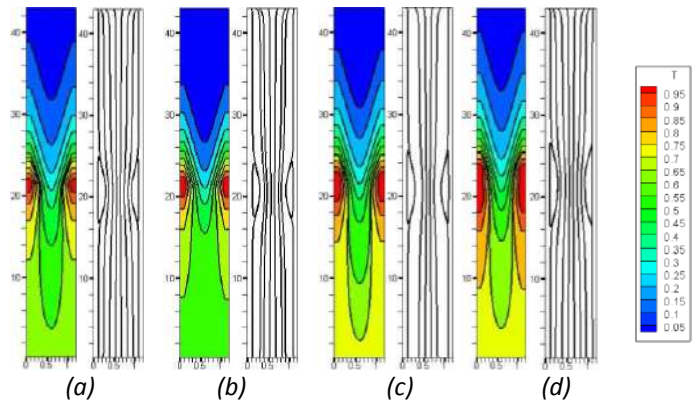
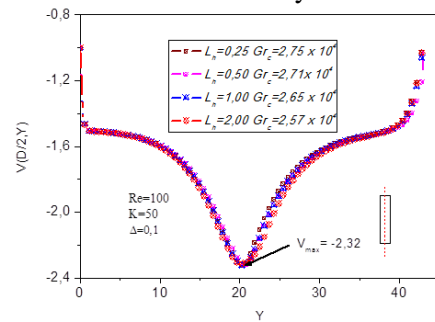


Figure 9

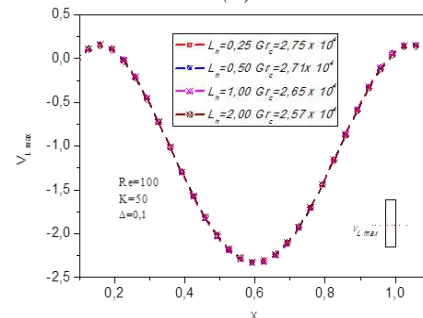
Isotherms and Stream function in the case of $\Delta=0.1$, for different length of heated portion:

- a) $L_h = 0.25$, $Gr = 2.75 \times 10^4$, b) $L_h = 1.0$, $Gr = 2.65 \times 10^4$,
- c) $L_h = 2.0$, $Gr = 2.57 \times 10^4$, d) $L_h = 3.0$, $Gr = 2.54 \times 10^4$.

Figures 10 show the vertical and horizontal velocity profiles at the center of channel with different values of the heated section and Grashof number length. For each values of the heated section length the Grashof number less than the critical values are taken. The profiles in all cases are identical and they have the same curvature and maximal velocity $V_{max} = -2.32$.



(a)



(b)

Figure 10

Vertical and horizontal Velocity profile at the center of the tube for different heated portion and of Gr_c .

CONCLUSIONS

The principal motivation on this work is the contribution and the understanding of the phenomena of dimensional mixed convection in a vertical tube, which represent an important section in the study field of heat transfer. The heated parts in the vertical wall are in constant temperature. Results obtained from deferent simulations were analyzed and show:

- The size of the circulation area increase with the increasing of the Gr number and the role of an obstacle, which decrease the flow area.
- The increasing of the heated part provoke the instability of the flow on the contrary the increasing of the thickness of the tube provoke the stability of the flow.

REFERENCES

1. Scheele, G.F, Rosen, E.M, Hanratty, T.J, 1960, Effects of natural convection on transition to turbulence in vertical pipes, *Can. J. Chem. Eng.* **38**, pp. 67–73.
2. Scheel, G.F, Hanratty, T.J, 1962, Effect of natural convection on stability of flow in vertical pipe, *J. Fluid Mech*, **98**, pp. 244–256.
3. Bernier, M.A, Baliga, B.R, 1992, Visualization of upward mixed-convection flows in vertical pipes using a thin semitransparent gold-film heater and dye injection, *Int. J. Heat. Fluid Flow* **13**, pp. 241–249.
4. Behzdmehr, A, Laneville, A, Galanis, N, 2008, Experimental study of onset of laminar-turbulent transition in mixed convection in a vertical heated tube, *Int J. Heat and mass transfer* **51**, pp. 5895-5905.
5. Yan, W.M, 1992, Transfirt mixed convection hear transfer in vertical pipe flews, *Int. Comm. Heat Mass Transfer*, **19**, pp 89–101.
6. Fusegi, T, 1996, Mixed convection in periodic open cavities with oscillatory through flow, *Num. Heat Transfert*, part A **29**, pp. 33-47.
7. Mai, T.H, El Wakhil, N, 1999, Heat transfer in a vertical tube with a variable flow. *International Journal of Thermal Sciences*, **38**, pp. 277–283.
8. Omara, A, Abboudi, S, 2006, Transient heat transfer analysis laminar flow. *Numerical Heat Transfer, Part A* **1**, pp. 1–24.
9. Su, H, Li, Q, Zhug, Y, 2011, Fast simulation of a vertical U tube heat exchanger using a one dimensional transient numerical model, *Numerical Heat transfer*, **60**, pp. 328–346
10. Wang, M, Tsuji, T, Nagano, Y, 1994, Mixed convection with flow reversal in the thermal entrance region of horizontal and vertical pipes, *Int. J. Heat Mass Transfer*, **37**, pp. 2305–2319.
11. Boumaza, M, Omara, A, 2013, Numerical investigation of transport phenomena properties on transient heat transfer in a vertical pipe flow, *Journal of King Saud University*
12. Patankar, S.V, 1980, *Numerical heat transfer and fluid flow*, Hemisphere, Washington DC,
13. Zeldin, B, and Schmidt, F.W, 1972, Developing Flow with Combined Forced-Free Convection in an Isothermal Vertical Tube, *J. Heat Transfer*, **94**, MAY, pp. 211-223
14. Marner, W.J, and McMillan, H.K, 1970, Combined Free and Forced Laminar Convection in a Vertical Tube With Constant Wall Temperature, *J. Heat Transfer*, **92**, pp. 559-562.

COUPLED RADIATION AND DOUBLE-DIFFUSIVE LAMINAR MIXED CONVECTION FLOW IN A LID-DRIVEN CAVITY

Mohammed Cherifi¹, Abderrahmane Benbrik^{*1}, Siham Laouar-Meftah¹ and Denis Lemonnier²

¹M'Hamed Bougara University, Faculty of Hydrocarbons and Chemistry, 35000 Boumerdès, Algeria

²Institut Pprime, CNRS, ENSMA, University of Poitiers, Poitiers Futuroscope, France

*Corresponding author: Fax: +213 24795254 Email: Abderrahmane.benbrik@univ-boumerdes.dz

ABSTRACT

In the present study, the effect of volumetric gas radiation on mixed double diffusive convection in a lid-driven square cavity is investigated numerically. The vertical boundary walls are maintained at different but uniform temperatures and concentrations gradients in order to create cooperating flow. The horizontal walls are thermally insulated and impermeable to mass transfer. The walls of the enclosure are assumed to be opaque, diffuse and grey. The flow behavior is analyzed when the top wall moves right side at a constant velocity and the other walls remains stationary. The cavity is filled with grey gas mixture considered as absorbing, emitting and not scattering medium. The governing differential equations are solved by a finite-volume method, by adopting the SIMPLE algorithm for pressure–velocity coupling. The discrete ordinate method is used in modeling the radiative transfer equation. Results were presented in the form of isotherms, isoconcentrations, velocities profiles and heat and mass transfer for various values of Richardson number (Ri), Buoyancy ration (N), and optical thickness (τ).

KEYWORDS: Double-Diffusion, Laminar Mixed Convection, Volumetric Radiation, Discrete Ordinate Method, Lid-Driven Enclosure.

INTRODUCTION

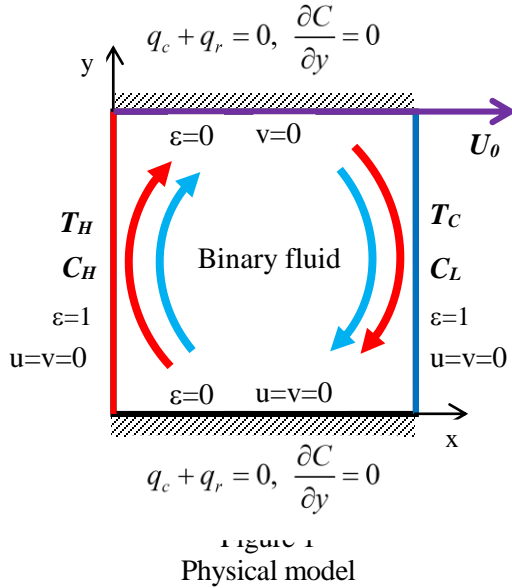
The problem of the double diffusion in binary mixtures combined to the radiation was seldom addressed in the past. Rafeivand [1] was the first to consider the coupling between double diffusive natural convection and gas radiation. The fluid enclosed in a differentially heated rectangular cavity, was regarded as a gray gas whose absorption was proportional to the local pollutant concentration. Mezrhab et al. [2] conducted a numerical study of double-diffusion convection coupled to radiation in a square cavity filled with participating gray gas. Mixed convection problem with lid-driven flows in enclosures have been studied for various geometry configuration in the past. Various thermal and flow boundary conditions have been considered. Teamaha et al. [3] performed a numerical simulation of double-diffusive mixed convective flow in rectangular enclosure with insulated moving lid. However, the effect of radiation was often neglected in the majority of the available studies. The problem of combined mixed convection and radiation is complex. In our case of combined double diffusive mixed convection and radiation it involves the interaction between the combining temperature and concentration buoyancy forces (double diffusion), forced convection induced by the shear force due to lid movement and surface-volumetric radiation. Among the few studies

in this field, Belmiloud et al. [4] conducted a numerical study of mixed convection coupled to surface radiation in a square cavity with a lid-driven (moving top wall), where the cavity were filled with air (non-participating medium). Mahapatra [5] have investigated the interaction of mixed convection in two-sided lid driven differentially heated square enclosure with radiation in presence of radiatively absorbing, emitting and scattering gray medium. They noticed that for buoyancy–aiding flow, in the presence of radiation, the flow becomes stronger and the heat transfer enhances. The authors of the reference [6] studied the effect of radiation heat transfer on mixed convection in a lid-driven trapezoidal cavity filled with a gray participating medium. The walls were considered black.

According to the fact that, there is no study dealing with combined double diffusive mixed convection and volumetric radiation in lid driven cavity, in the present study, we focus on the effect of volumetric gray gas radiation on double diffusive mixed convection in differentially heated square enclosure, with moving top wall, filled with binary mixture and subject to cooperating buoyancy and shear force.

ANALYSIS AND MODELLING

The studied physical system is represented in Figure 1. It consists in a square cavity of width L , filled with binary mixture. The vertical walls of cavity are black and maintained at constant temperatures ($T_H > T_C$) and concentration ($C_H > C_L$). The horizontal walls are adiabatic, impermeable and perfectly reflective. The top wall moves right side at a constant velocity U_0 .



Governing Equations

In this paper the flow considered is assumed to be two-dimensional, steady and laminar. The fluid in the cavity is a mixture of binary fluid. This fluid is assumed Newtonian, incompressible, with constant thermophysical properties and satisfying the Boussinesq approximation. Under these assumptions, the fluid motion is described by the following set of non-dimensional equations:

$$\frac{\partial U}{\partial X} + \frac{\partial V}{\partial Y} = 0 \quad (1)$$

$$U \frac{\partial U}{\partial X} + V \frac{\partial U}{\partial Y} = -\frac{\partial P}{\partial X} + \text{Pr} \left(\frac{\partial^2 U}{\partial X^2} + \frac{\partial^2 U}{\partial Y^2} \right) \quad (2)$$

$$U \frac{\partial V}{\partial X} + V \frac{\partial V}{\partial Y} = -\frac{\partial P}{\partial Y} + \text{Pr} \left(\frac{\partial^2 V}{\partial X^2} + \frac{\partial^2 V}{\partial Y^2} \right) + \text{Ra} \cdot \text{Pr} (\theta + NS) \quad (3)$$

$$U \frac{\partial \theta}{\partial X} + V \frac{\partial \theta}{\partial Y} = \left(\frac{\partial^2 \theta}{\partial X^2} + \frac{\partial^2 \theta}{\partial Y^2} \right) - \frac{\Theta_0}{\text{Pl}} \nabla \cdot \mathbf{Q}_R \quad (4)$$

$$U \frac{\partial S}{\partial X} + V \frac{\partial S}{\partial Y} = \frac{1}{\text{Le}} \left(\frac{\partial^2 S}{\partial X^2} + \frac{\partial^2 S}{\partial Y^2} \right) \quad (5)$$

The divergence of the radiative heat flux $\nabla \cdot \mathbf{Q}_R$ in the energy equation (5) is the radiation energy vector flux, given by [2]:

$$\nabla \cdot \mathbf{Q}_R = \tau(r) [\varphi(r) - G(r)] \quad (6)$$

Where $\tau(r)$ is the optical thickness in the medium at any position r , $\varphi(r)$ is the emissive power and $G(r)$ stand for the incident radiation at the point r . $\varphi(r)$ and $G(r)$ are given by:

$$\varphi(r) = \left[\frac{\theta(r)}{\phi} + 1 \right]^4; \quad G(r) = \int_{4\pi} \hat{I}(r, s) d\Omega$$

\hat{I} is the dimensionless radiation intensity ($\hat{I} = I / \sigma T_0^4$) in the direction s . I is the local radiation intensity. It is obtained by solving the radiative transfer equation (RTE). For an absorbing, emitting and non scattering gray medium, the RTE is given as [7]:

$$\mu \frac{\partial \hat{I}(r, s)}{\partial X} + \eta \frac{\partial \hat{I}(r, s)}{\partial Y} + \tau(r) \hat{I}(x, y, s) = \tau(r) \frac{\varphi(r)}{4\pi} \quad (7)$$

The following dimensionless parameters are defined.

$$X = \frac{x}{L}, \quad Y = \frac{y}{L}, \quad \theta = \frac{(T - T_0)}{(T_H - T_C)}, \quad T_0 = \frac{T_H + T_C}{2}, \quad S = \frac{(C - C_0)}{(C_H - C_L)}$$

$$C_0 = \frac{(C_H + C_L)}{2}, \quad \phi = \frac{T_0}{(T_H - T_C)}, \quad U = \frac{uL}{\alpha}, \quad V = \frac{vL}{\alpha}$$

$$P = \frac{p + \rho_0 g y b^2}{\rho_0 \alpha^2}, \quad \text{Ri} = \frac{Gr}{\text{Re}^2}, \quad \text{Re} = \frac{U_0 L}{\nu}, \quad \text{Pr} = \frac{\nu}{\alpha}, \quad \text{Pl} = \frac{k}{4\sigma L T_0^3}$$

$$U_0 = \sqrt{\frac{\text{Ra} \cdot \text{Pr}}{\text{Ri}}}, \quad Q = \frac{q_r}{4\sigma T_0^4}, \quad \text{Ra} = \frac{g\beta(T_H - T_C)L^3}{\nu\alpha}$$

$$N = \frac{\beta_c(C_H - C_L)}{\beta_r(T_H - T_C)}$$

Where U_0 lid-driven plate velocity

Boundary Conditions

The boundary conditions for the considered problem are as follows:

Left wall ($X = 0$): $\theta = 0.5, S = 0.5, U = V = 0$

Right wall ($X = 1$): $\theta = -0.5, S = -0.5, U = V = 0$

Bottom wall ($Y = 0$): $q_c + q_r = 0, \frac{\partial S}{\partial Y} = 0, U = V = 0$

Top wall ($Y = 1$): $q_c + q_r = 0, \frac{\partial S}{\partial Y} = 0, U = U_0, V = 0$

For an enclosure with opaque, emitting and diffusely reflecting walls, the boundary conditions used for solving the radiative transfer equation are:

$$\hat{I}_w(X, Y, \bar{\Omega}) = \varepsilon_w \frac{\sigma T_w^4}{\pi} + \frac{1 - \varepsilon_w}{\pi} \int_{\bar{\Omega}' < 0} |\bar{n} \cdot \bar{\Omega}'| \hat{I}(X, Y, \bar{\Omega}') d\Omega' \quad (8)$$

Where ε_w is the emissivity of the surface, \bar{n} is the unit normal vector, $\bar{\Omega}$ is the direction of the outgoing radiation intensity, and $\bar{\Omega}'$ is the incoming direction associated with the elementary solid angle $d\Omega'$ [2].

Heat and Mass Transfer

The average Nusselt numbers (convective, radiative and total) numbers at vertical walls are defined as follows [8]:

$$\overline{Nu}_c = \frac{1}{(T_h - T_c)} \int_0^L \left| \frac{\partial T}{\partial x} \right|_{x=0 \text{ or } L} dy \quad (9)$$

$$\overline{Nu}_R = \frac{1}{\lambda(T_h - T_c)} \int_0^L \left| q_R^{net} \right|_{x=0 \text{ or } L} dy$$

(10)

$$\overline{Nu}_t = \overline{Nu}_c + \overline{Nu}_R$$

(11)

$$\overline{Sh} = \frac{1}{(C_H - C_L)} \int_0^L \left| \frac{\partial C}{\partial x} \right|_{x=0 \text{ or } L} dy \quad (12)$$

NUMERICAL PROCEDURE

The governing equations and the associated boundary conditions are solved numerically using the finite volume method. The diffusion terms in the governing equations are discretized using the central difference scheme (CDS); while, a power scheme is employed for the convective terms. A staggered non uniform grid system together with the SIMPLE algorithm is adopted to solve for the pressure and the velocity components. The discrete ordinate method is used in modeling the radiative transfer equation. The physical domain is discretized into a non-uniform Chebyshev grid (161x65), which ensures thin grid spacing close the walls, and a coarser mesh system in the core region. The discretized equations are iteratively solved by using an ADI scheme, until the satisfaction of the following convergence criterion:

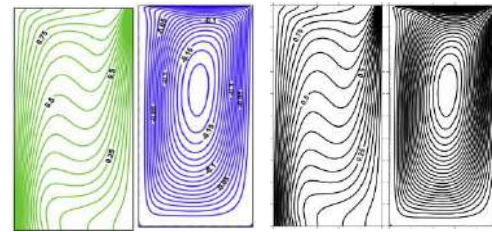
$$\frac{\sum_{i,j} |\Phi_{i,j}^n - \Phi_{i,j}^{n-1}|}{\sum_{i,j} |\Phi_{i,j}^n|} \leq 10^{-6}$$

Where Φ represents a dependent variable U, V and θ , the indexes i, j indicate a grid point; and the index n the current iteration at the finest grid lever.

Additionally, reliable numerical results were obtained by performing energy over the physical domain.

Validation of Computational Model:

The study is compared with an earlier work on double-diffusive mixed convective flow in rectangular enclosure with insulated moving lid was performed by Teamaha et al. [3]. The Comparison of results is illustrated in Fig. 2. The figure shows good agreement. Combined Double diffusive convection with gray gas radiation was also considered for validation against results provided Rafieivand [1] and Mezrhab et al. [2]. The average Nusselt number, according to the optical thickness, obtained agrees within a maximum relative error of 0.7% (at $Ra=5 \times 10^6$, $N=4$; $Pr=0,71$; $Pl=0,02$; $\theta=1.5$, $\tau=\tau_0(C^*(M)+0.5)$, $SN=8$).



(a) Teamaha et al.[5] (b) Present results

Figure 2

Comparison of isotherms and streamlines with Teamaha et al. [3]

$Gr=10^5$, $Pr=0.7$, $Le=1$, $N=1$ and $Ri=1$.

RESULTS AND DISCUSSION

Conditions of Simulation:

The configuration under consideration is a square cavity of side L, filled with a binary mixture. The left and right vertical walls are maintained isothermal at the hot temperature $T_H=580K$ and the cold temperature $T_C=530K$, respectively. The top wall is moving right side what makes thermal and mass buoyancy forces and shear forces in the same movement direction (cooperating case). The velocity of the moving wall is constant calculated as function of Richardson number.

The mathematical model developed in the previous section was used to investigate the mutual interaction between the radiation and the double diffusive laminar mixed convection flow in a lid-driven cavity. In this study, the Prandtl number, Rayleigh number, Planck number and Lewis number were held fixed to $Pr = 0.71$, $Ra = 5.10^6$, $Pl = 0.02$ and $Le = 1$. In all the computations, the reference pressure of the mixture is 1 atm and the thermo-physical properties of the mixture are taken to be constant and evaluated at the mean temperature $T_0=(T_H+T_C)/2$ and the mean concentration $C_0(C_H+C_L)/2$.

To solve the radiative transfer equation using the DOM method [8], it was used the S8 quadrature set.

In order to analyze the effects medium radiation (participating medium) on the double-diffusive mixed convection, three values of optical thickness are considered (0.1, 1 and 5). In this study, we have considered that the absorption coefficient depends on the local pollutant concentration: $\kappa(r) = \kappa_0[C(r)/C_H]$. This assumption leads to the following expression [1]: $\tau(r) = \kappa_0(S + 0.5)$.

The Reynolds number is varied by varying the lid velocity U_0 , to achieve the required Richardson number $Ri=1$ and $Ri=10$. the buoyancy ratio is studied with positive values $N=1$ and $N=4$ (assisting flow).

Flow Patterns Results:

From the previous studies, the effect of the Buoyancy ration (N) and the Richardson number (Ri) on the fluid flow and heat transfer in the absence of radiation is well known. Therefore, this study will focus on the role of volumetric radiation on the double diffusive laminar mixed convection. The effect of both Buoyancy ration and Richardson number as well as the optical thickness on double-diffusive mixed convection in a lid-driven square enclosure, are examined.

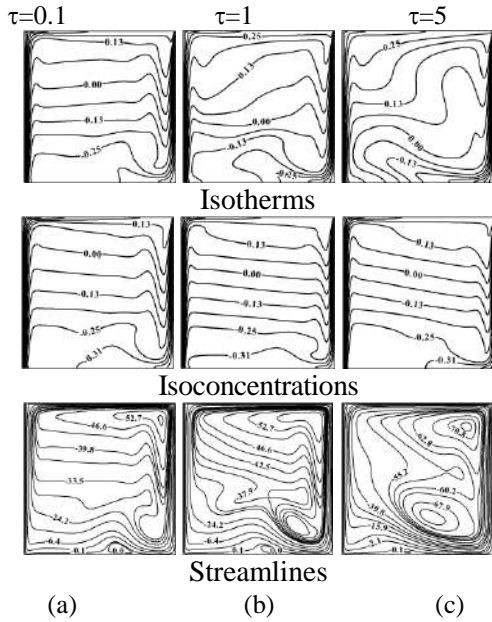
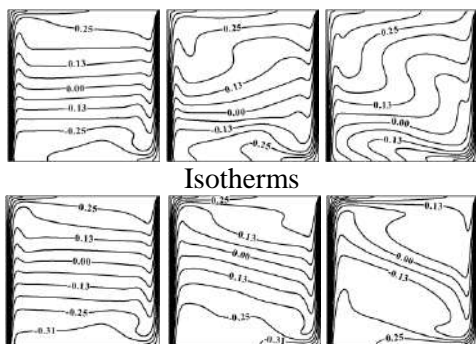


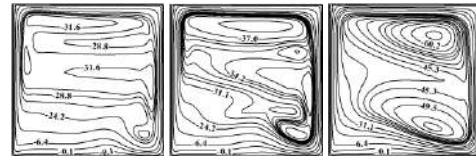
Figure 3

Isotherms Isoconcentrations and Streamlines for $N=1$ and $Ri=1$. (a) $\tau=0.1$; (b) $\tau=1$, (c) $\tau=5$

Figure 3 shows the isotherms, isoconcentrations and streamlines for the different values of the optical thickness in the case where $N=1$ and $Ri=1$. As it is seen the radiation modifies the distribution of the temperatures more than the distribution of the concentration. The streamlines are considerably affected by the increasing of τ .



Isoconcentrations

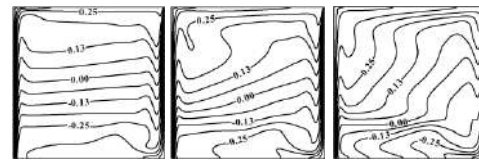


Streamlines

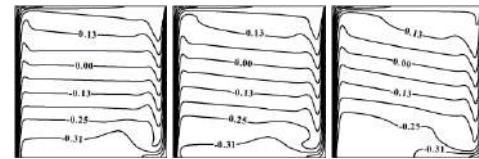
(a) (b) (c)

Figure 4

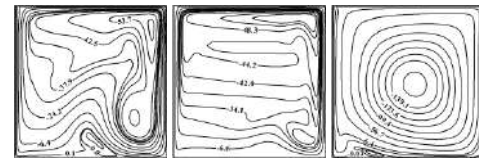
Isotherms Isoconcentrations and Streamlines for $N=1$ and $Ri=10$. (a) $\tau=0.1$; (b) $\tau=1$, (c) $\tau=5$



Isotherms



Isoconcentrations



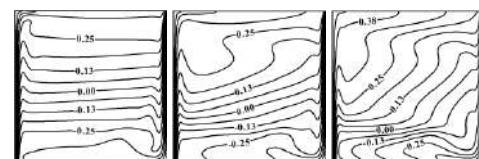
Streamlines

(a) (b) (c)

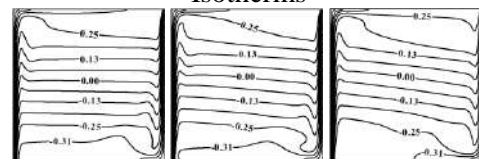
Figure 5

Isotherms Isoconcentrations and Streamlines for $N=4$ and $Ri=1$. (a) $\tau=0.1$; (b) $\tau=1$, (c) $\tau=5$

The increase of the Richardson number to $Ri=10$ in figure 4 shows that the effect of radiation is more accentuated because the shear forces due to the moving top wall are weak.



Isotherms



Isoconcentrations

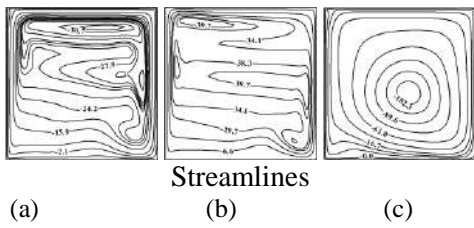


Figure 6

Isotherms Isoconcentrations and Streamlines for $N=4$ and $Ri=10$. (a) $\tau=0.1$; (b) $\tau=1$, (c) $\tau=5$

When the buoyancy ration increases $N=4$ (fig. 5, 6), i.e. when the mass forces are more dominant, for both values of Richardson number (1 and 10), the radiation has less effect on the dynamics and flow.

Effect of Radiation on Thermal Field:

The overall changes in the temperature field for different values of buoyancy ration, Richardson number and radiative transfer are displayed in Fig. 7 and 8. In all studied cases, as the opacity increases, the temperature at the median plane ($Y=0.5$) of the cavity increases. The temperatures are higher for the case when the mass buoyancy forces dominate.

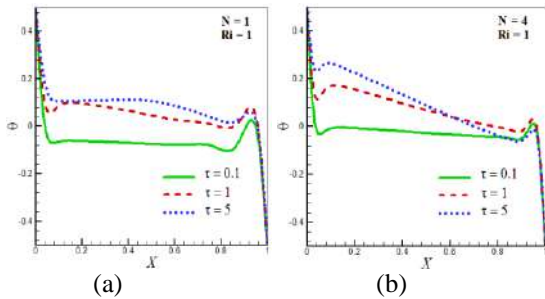


Figure 7

Temperature at midium plane $Y = 0.5$ for $Ri=1$. (a) $N=1$; (b) $N=4$

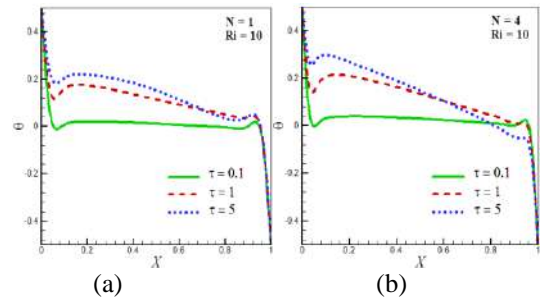


Figure 8

Temperature at midium plane $Y = 0.5$ for $Ri=10$. (a) $N=1$; (b) $N=4$

For the case of $Ni = 4$ and $Ri = 10$, where where the shear forces are neglected, a part of this contribution

of heat will be evacuated by convection along the cold wall.

Effect of Radiation on the Dynamic Field:

To examine the flow in the cavity, velocity profiles at vertical centerline are produced and presented in fig. 9 and 10. Fig.9 shows the horizontal velocity for $N=1$ and $Ri=1$. The effect of radiation is seen in the bottom of the cavity for higher value of the opacity. For $N=4$, the effects of gas radiation is negligible.

Fig. 10 shows that as Richardson number increases, at $\tau=5$, the flow is more accelerated for the case of $R=1$, when the thermal buoyancy forces dominates. But when the mass buoyancy forces increase ($N=4$) this trend weakens.

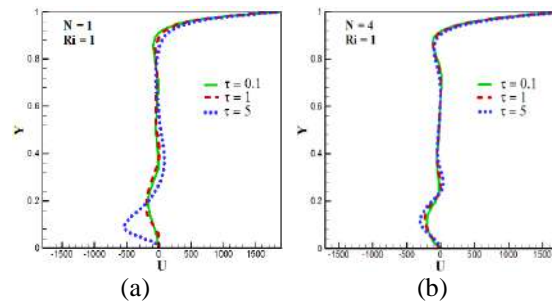


Figure 9

Horizontal velocity at median plane $X = 0.5$ for $Ri=1$. (a) $N=1$; (b) $N=4$

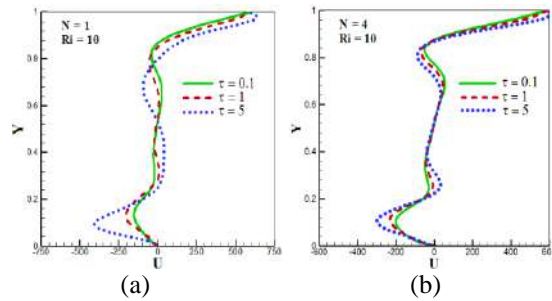


Figure 10

Horizontal velocity at median plane $X = 0.5$ for $Ri=10$. (a) $N=1$; (b) $N=4$

Heat and Mass Transfer:

The variations of total Nusselt numbers as functions of buoyancy ration and Richardson number for the three cases of the medium opacity are shown in table 1. As can be seen, the increase of buoyancy ratio leads to the increase of the heat transfer for all the value of the optical thickness. While the increase of the Richardson number leads to the decrease of heat transfer.

Table 1
Average total Nusselt number (Nu_t)

Buoyancy ratio (N)	Richardson number (Ri)	Optical thickness (τ)		
		0.1	1	5
1	1	55.68	50.56	40.31
	10	54.21	47.87	37.06
4	1	59.78	53.69	41.53
	10	58.42	51.23	38.16

The same tend of variations of total Sherwood numbers is seen in table 2 as the Nusselt number.

Table 2
Average Sherwood number (Sh)

Buoyancy ratio (N)	Richardson number (Ri)	Optical thickness (τ)		
		0.1	1	5
1	1	18.28	17.98	17.40
	10	17.13	16.95	16.49
4	1	22.55	22.50	22.43
	10	21.44	21.44	21.43

CONCLUSIONS

The effect of volumetric gas radiation on mixed double diffusive convection in a lid-driven square cavity is investigated numerically. It has been performed for three cases characterized by different value of the medium opacity. Two modes of flow, according to the buoyancy ration N and two modes of heat transfer regime characterized by the Richardson number have been considered.

In a view of results, the main finding can be summarized as follows:

The increasing of the opacity of the medium modifies the distribution of the température, concentration.

For $N > 1$, when buoyancy forces dominates, volumetric radiation has less effect on the dynamics and flow. As the opacity increases, the température at the median plane of the cavity increases.

For $Ri > 1$, dynamic field become sensitive to volumetric radiation of the medium. The flow is decelerated and the variation of the optical thickness is more noticed.

As the opacity of the medium increases, the heat and mass transfer are enhanced with the increasing of the buoyancy ration.

The decrease of the Richardson number leads to the decrease of the heat and mass transfer for all the value of the optical thickness.

ACKNOWLEDGMENTS

This work was supported by a research grant (CNEPRU project: Code: J0300320120030) from Ministry of Higher Education, Algeria.

REFERENCES

- Rafieivand, M., 1999, Etude Numérique de la Convection de Double Diffusion en Présence de Rayonnement en Cavité Rectangulaire, Ph.D. thesis, Université de Poitiers, Poitiers, France.
- Mezrhab, A. Lemonnier, D., Meftah S. and Benbrik, A., 2008, Numerical study of double-diffusion convection coupled to radiation in a square cavity filled with a participating grey gas, *J. Phys. D: Appl. Phys.*, 41, pp.195501-195517.
- Teamaha, M. A., El-Maghlany, W. M., 2010, Numerical Simulation of Double-Diffusive Mixed Convective Flow in Rectangular Enclosure with Insulated Moving Lid, *Int. J. of Thermal Sciences*, 60, pp. 1625-1638.
- Belmiloud, M. A. and Chemlou, N. S., 2015, Numerical study of mixed convection coupled to radiation in a square cavity with a lid-driven *Inter. J. of Mechanical, Aerospace, Industrial, Mechatronic and Manufacturing Engineering* Vol:9, No:107.
- Mahapatra, S. K., 2014, Mixed Convection inside a Differentially Heated Enclosure and its Interaction with Radiation-an Exhaustive Study, *Heat Transfer Engineering*, 35:1, pp. 74–93.
- Mohammadi, M., Gandjalikhan Nassab, S. A., 2015, The combined heat transfer of radiation and mixed convection analysis in a lid-driven trapezoidal cavity, *J. of theoretical and applied mechanics*, 53, 3, pp. 643-652.
- Modest, M. F., 2003, *Radiative Heat Transfer*, 2ed., Academic Press, San Diego.
- Meftah, S., Ibrahim, A., Lemonnier, D., Benbrik, A., 2009, Coupled radiation and double diffusive convection in non-gray air-CO₂ and air-H₂O mixtures in cooperating situations, *Numer. Heat Transfer, Part A* 56, pp. 1-19.
- Fiveland, W. A., 1984, Discrete Ordinates Solution of the Radiation Transport Equation for Rectangular Enclosures, *J. Heat Transfer* 103, pp. 699-706.

Unsteady natural convection in a water filled cavity with hot partitioned wall

Farah Zemani*, Amina Sabeur-Bendehina*

Laboratoire des Sciences et Ingénierie Maritimes, Faculté de Génie Mécanique, Université des Sciences et de la Technologie Mohamed, Boudiaf d'Oran, B.P. 1505 Oran El-M'naouar, 3-1000 Oran, Algérie

Email : zemanifarah@live.fr

ABSTRACT

The main objective of this work is to study numerically the unsteady natural convection phenomena in water filled rectangular enclosure with hot partitioned wall.

The fluid flow and the heat transfer described in terms of continuity, linear momentum and energy equations were predicted by using the finite volume method. Streamlines, isotherms and local Nusselt number time evolution are presented for all investigated values. The aspect ratio of the geometry, Prandtl number are fixed at 0.24, 6.64, respectively, for different partitions lengths; however the Rayleigh number values were ranging from 10^6 to $3,77 \times 10^9$ in order to observe the transition regime. Representative results illustrating the effects of the partition length for the heat transfer and the thermal boundary layer are also reported and discussed. The obtained results show that the presence of the partition on the hot wall affects both heat transfer and fluid flow. It was found that the average Nusselt number increases with increase in the Rayleigh number. Also, as the dimensionless partition length increases, the flow speed within the partitioned enclosure decreases. Moreover, the features of the unsteady flow induced by the presence of partitions are characterized and the mechanisms responsible for the unsteadiness are discussed.

Keywords: Natural Convection, unsteady regime, partial partitions, Rayleigh Number, Nusselt Number, Partitions Length

NOMENCLATURE

g	gravitational acceleration (m/s^2)
h	convective heat transfer coefficient ($W/m^2 K$)
H	height of the enclosure (m)
L	width of the enclosure (m)
Nu	Nusselt number
p	pressure (N/m^2)
Pr	Prandtl number
Ra	Rayleigh number
T	temperature (K)
T_h	temperature of the hot surface (K)
T_c	temperature of the cold surface (K)
T_0	initial temperature (K)
T_m	average temperature (k)
ΔT	Temperature variation, $T_h - T_c$ (k)
U	velocity component in x direction (m/s)
V	velocity component in y-direction (m/s)
x, y	Cartesian coordinates (m)
W	partition thickness
L	partition length
Greek symbols	
k	thermal conductivity of fluid ($W/m k$)
α	thermal diffusivity (m^2/s)
β	coefficient of volumetric expansion ($1/K$)
θ	dimensionless temperature, $(T - T_0)$
μ	dynamic viscosity ($N s/m^2$)
ρ	fluid density (kg/m^3)
Subscripts	
C	cold
H	hot
0	initial

INTRODUCTION

Natural convection flows in a differentially heated cavity are usually encountered in various industrial applications such as heat exchangers, nuclear reactors, cooling of electronic equipment and thus the studies of natural convection flows in the cavity have been extensively reported in the literature over the past decades.

Batchelor [1] has shown that the heat transfer through the cavity is dominated by conduction for sufficiently small Rayleigh numbers. However **De Vahl Davis** [2] et al has focused on the steady natural convection flow in the cavity. On the other hand, **Patterson et al** [3] studied unsteady natural convection in a rectangular cavity with instantaneous cooling and heating of two opposite vertical sidewalls. They concluded that the flow had a strong dependence on the Prandtl number and cavity aspect ratio.

Yucel et al [4] indicated in their numerical analysis of laminar natural convection in enclosures with fins attached to an active wall that with increasing number of fins the heat transfer first reaches a maximum and then approaches a constant, which is not affected by the number of fins. At low Rayleigh numbers, the heat transfer rate increases with the

increasing number of fins and the fin length. But, at higher Rayleigh numbers, the heat transfer rate can be decreased or increased by properly choosing the number of fins and the fin lengths.

The transition of the thermal boundary layer from start-up to a quasi-steady state in a side-heated cavity is observed using a shadowgraph technique is also investigated by **Xu et al [5]**. A significant feature of the transition revealed from the present flow visualization is the formation of a double-layer structure along the sidewall at the entrainment development stage. It was believed that the reverse flow in the double-layer structure is the likely cause responsible for the unstable travelling waves at the quasi-steady state. They performed a direct numerical simulation of unsteady natural convection in a differentially heated cavity with a thin fin of different lengths on a sidewall at the Rayleigh number of 3.8×10^9 . They found that the fin length significantly impacts on the transient thermal flow around the fin and heat transfer through the finned sidewall in the early stage of the transient flow development.

Numerical investigations of transient natural convection flow through a fluid-saturated porous medium in a rectangular cavity with a convection surface condition were conducted by **Pakdee et al [6]**. The exposed surface allows convective transport through the porous medium, generating a thermal stratification and flow circulations. They found that the heat transfer coefficient, Rayleigh number and Darcy number affect considerably the characteristics of flow and heat transfer mechanisms and the flow pattern is found to have a local effect on the heat convection rate.

The two-dimensional laminar natural convective transient flow characteristics in a differentially heated air-filled tall cavity with gradual heating are investigated both experimentally and numerically for various parameters such as Rayleigh number and temperature difference by **Kolsi et al [7]**. The results revealed that as the Rayleigh number increases the flow becomes unstable. Also, the flow characteristics are observed to be multi-cellular and time variant especially at high Rayleigh numbers.

In addition to the above-mentioned earlier studies, comprehensive investigations of the natural convection flows in the cavity with a partition on the sidewall have been reported in the recent literature. The effects of the size, material and position of the partitions on the natural convection flows in the cavity have been paid much attention. In most of these studies, the thickness of the partition is considered to be

sufficiently small in comparison with the fin partition and thus the fin length is the major geometric parameter for controlling the natural convection flows in the cavity.

Frederick et al [8] reported in their study that the heat transfer through the finned sidewall is reduced as the fin length increases due to the depression of the natural convection flows adjacent to the finned sidewall.

The transition from a steady to an unsteady flow induced by an adiabatic fin on the side walls was also carried out by **Xu et al [9]** they demonstrated that the fin may induce the transition to an unsteady flow and the critical Rayleigh number for the occurrence of the transition is between 3.72×10^6 and 3.73×10^6 . Thus **Paul et al [10]** treated the Effect of an adiabatic fin on natural convection heat transfer in a triangular enclosure by numerical simulations.

Rahman et al [11] investigated the unsteady natural convection heat transfer in an isosceles triangular enclosure filled with Al_2O_3 nanoparticles. Their study was performed using the finite element method and the most important of their finding was the increasing of the heat transfer with addition of nanoparticle and increasing of the Rayleigh number. The aim of this investigation is to simulate the unsteady natural convection in a differentially heated cavity with a different length of partitions on the hot wall. The present work is an extension of the work already established by **Xu et al [12]** which they treated similar cavity. The side walls are assumed to be differentially heated and the flat top and bottom walls are considered as adiabatic. The thermal and flow behavior and heat transfer characteristics have been studied for various Rayleigh number and partition lengths. The working fluid media is water with Prandtl number of 6.64 and Rayleigh number ranging from 10^6 to 3.77×10^9 . The wave features of the thermal flows around the partition are characterized and discussed in this paper.

ANALYSIS AND MODELLING

Problem Position and mathematical formulation:

The two-dimensional rectangular computational domain and boundary conditions are shown in Fig. 1. The domain which is $H=0.24$ m high by $L=1$ m long is considered. One partition is placed in the mid height of the hot wall, the partitions length has

been changed ($l=L/16, L/8, L/4, L/2$); however, the partition thickness was fixed at $w=H/12$.

With $T_h = 303,55K$ and $T_c = 287,55K$ then $T_m = 295,5K$ and $\Delta T = 16K$

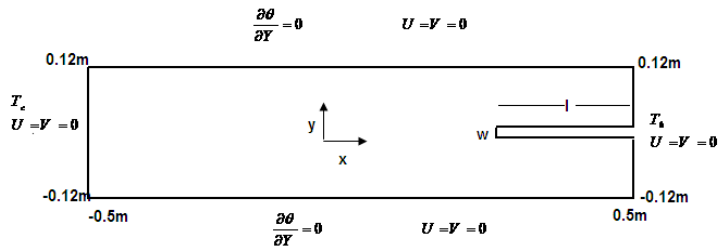


Figure 1

Schematic of the computational domain and boundary conditions

The governing equations (Navier Stokes and energy equations with the Boussinesq approximation) of the transient natural convection flows are written as

$$\frac{\partial u}{\partial x} + \frac{\partial v}{\partial y} = 0 \quad (1)$$

$$\frac{\partial u}{\partial t} + u \frac{\partial u}{\partial x} + v \frac{\partial u}{\partial y} = -\frac{\partial p}{\partial x} + \frac{Pr}{Ra^{1/2}} \left(\frac{\partial^2 u}{\partial x^2} + \frac{\partial^2 u}{\partial y^2} \right) \quad (2)$$

$$\frac{\partial v}{\partial t} + u \frac{\partial v}{\partial x} + v \frac{\partial v}{\partial y} = -\frac{\partial p}{\partial y} + \frac{Pr}{Ra^{1/2}} \left(\frac{\partial^2 v}{\partial x^2} + \frac{\partial^2 v}{\partial y^2} \right) + PrT \quad (3)$$

$$\frac{\partial T}{\partial t} + u \frac{\partial T}{\partial x} + v \frac{\partial T}{\partial y} = \frac{1}{Ra^{1/2}} \left(\frac{\partial^2 T}{\partial x^2} + \frac{\partial^2 T}{\partial y^2} \right) \quad (4)$$

Where

$$Ra = \frac{g\beta L_{ref}^3 \Delta T}{\mu \alpha} \quad \text{and} \quad Pr = \frac{\mu}{\rho} \quad (5)$$

The average Nusselt number is defined as follows:

$$Nu = - \int_0^L \frac{h \cdot y}{k} dy = \frac{h \cdot L}{k} \quad (6)$$

The governing equations are implicitly solved using a finite volume PISO algorithm. All second derivatives and linear first derivatives are approximated by a second-order center-differenced scheme. The advection terms are discretized by a QUICK scheme as described in the paper of .Xu [13]. The time integration is by a second-order backward difference method. The discretized equations are iterated with under relaxation factors. A fine non-uniform grids concentrated in the proximity of the partition is constructed. This grid shows that the numerically generated results are consistent with the corresponding experiments. Nevertheless, a further grid dependence test has been conducted on two grids 563×199 and 596×259 due to the slight variation between the current configuration and the earlier configuration reported in [13].

RESULTS AND DISCUSSION

In order to obtain insights into the steady and unsteady flow adjacent to a partitioned wall, numerical simulations for different Rayleigh number values and partitions length are carried out. The partition is an important factor to determine the transition of natural convection flows in the cavity to a steady or unsteady regime. Figure 2 illustrates time series of the calculated temperatures at the point ($x= 0.498, y= 0.09$) identified in the vertical boundary layer for different partitions length for high Rayleigh number ($Ra=3.77*10^9$). It was clearly seen that the peaks are generated called leading edge effect (LEE). The temperature is oscillatory in unsteady state.

It means that the transition from a steady to unsteady flows occurs as the Rayleigh number increases. It was also noticed that the partition ($L/16$) induces stronger perturbations than the other partitions.

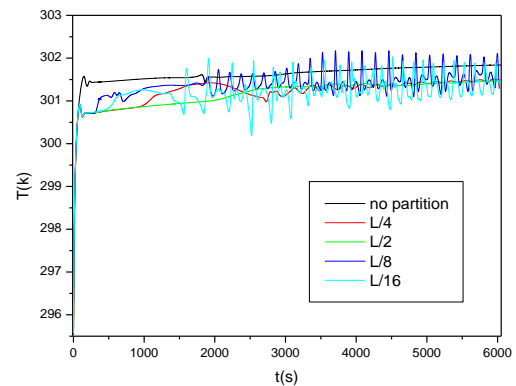


Figure 2

Temperature versus time, plotted at point (0.498, 0.09) for $Ra = 3.77*10^9$ at different partition lengths

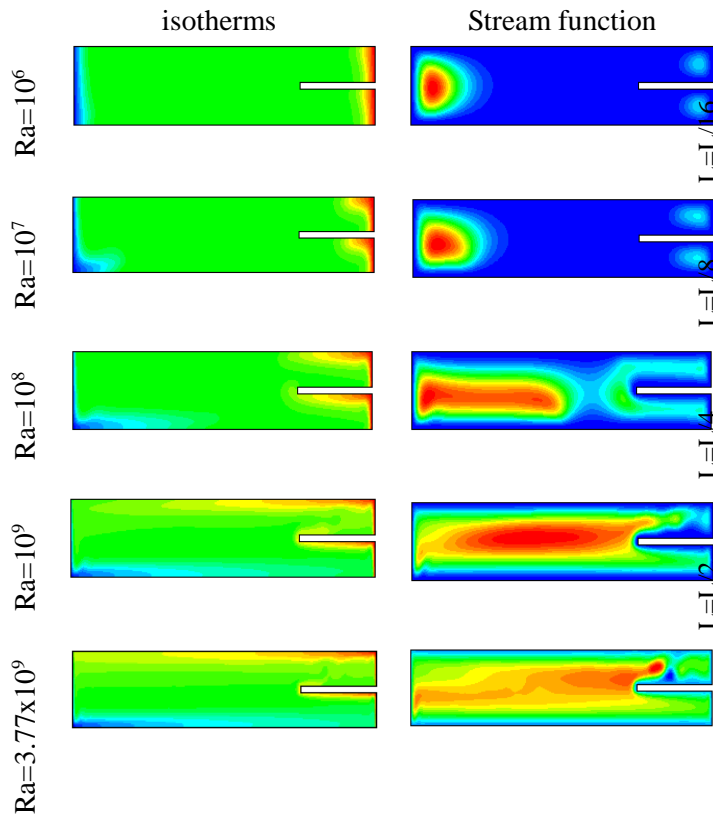


Figure 3

Isotherms and streamline contours for different Rayleigh number at $t=60000$ s for $l=L/4$.

In order to observe the flow dependence on the Rayleigh number, Figure 3 presents a set of isotherms and streamlines for different Rayleigh numbers and for $L/4$ partition length. It was clearly seen that the flow is steady if the Rayleigh number is lower than a critical value; however an increase of the Rayleigh number values the flow becomes unsteady and a lot of perturbations are developed around the partition. The same behavior was also observed for the streamlines contours.

Figure 4 shows the thermal flow contours in both early and quasi steady stage for all partitions length tested. It was clearly seen that the partition length has an important effect thus the flow depends systematically on the partition length. The flow may very smooth near the partition and the oscillation of the shedding flow disturbs the thermal boundary layer which eventually approaches a periodic flow. This phenomenon was observed in the cavity with the $L/2$ partition length. As time increases, the position of separation moves further away from the hot wall. The shedding flow separating from the partition induces two peaks wave, and the two peaks eventually merge into a single one while they propagate downstream.

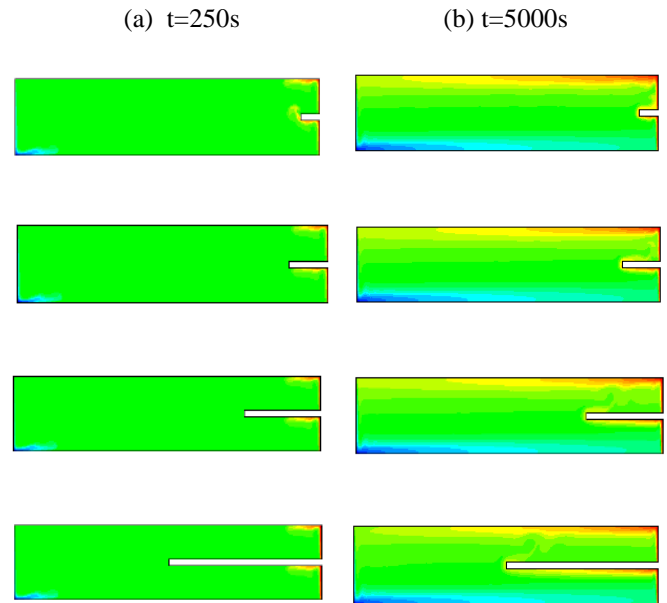


Figure 4

Thermal flows, (a) in the early stage, (b) in the quasi-steady stage, for different partitions length.

The mean Nusselt number along the hot partitioned wall versus time was plotted for different Rayleigh numbers value and different partitions length. The perturbations induced by the oscillation of the thermal flow around the partition have more room to grow. As a consequence, the heat transfer through the partitioned hot wall is notably enhanced so the presence of partition on the hot wall shows a promising result for the enhancement of the heat transfer through a differentially heated cavity.

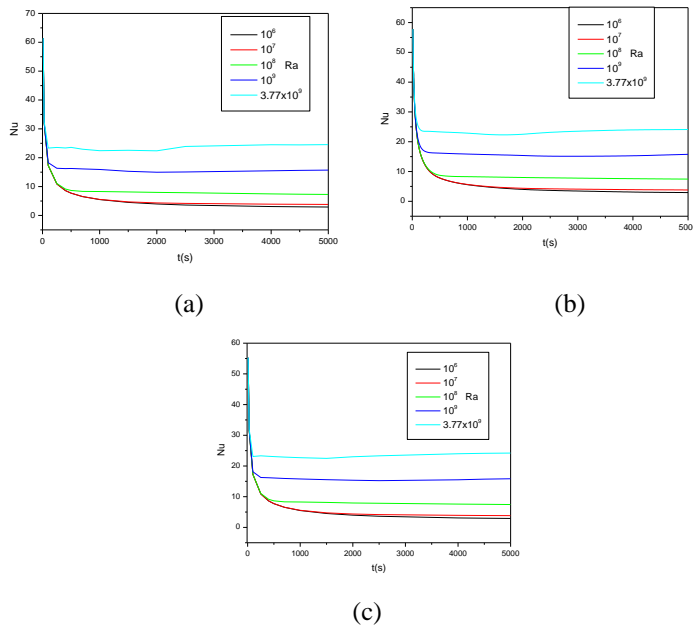


Figure 5

Mean Nusselt number, Nu along the hot wall versus time for different Rayleigh number and different partition length (a) $l=L/8$, (b) $l=L/4$ and (c) $l=L/2$

CONCLUSIONS

In order to control the heat transfer through the sidewall, the problem of transient natural convection in a differentially heated cavity with a partition on the heated sidewall has been investigated in this paper. It was important to note that the partition may significantly change the transient natural convection flow. The transition of the natural convection may be classified into three stages: an initial stage, a transitional stage and a quasi steady stage. The numerical results have demonstrated also that the partitions on the sidewall may play an important role in controlling the transient natural convection and heat transfer through a differentially heated cavity in the present Rayleigh number range (the order of 10^9). It was also noticed that the perturbation induced by the partition enforces the convection and enhances the heat transfer through the sidewalls.

ACKNOWLEDGMENTS

The authors wish to thank the members of the Scientific Committee **ICOME 16** for the time that will be provided to review the papers.

REFERENCES

1. Bachelor G.K., 1954, Heat transfer by free convection across a closed cavity between

vertical boundaries at different temperatures. *Quart. Appl.Math.* 12, 209-233.

2. G. De Vahl Davis, 1983, Natural convection of air in a square cavity: a bench mark numerical solution, *Int. J. Numer. Meth. Fluids* 3, 249–264.
3. Patterson, J.C., Armfield, S.W, 1990, Transient features of natural convection in a cavity, *J. Fluid Mech.*, 219, 469-497.
4. Yucel. N, Turkoglu.H, 1998, Numerical analysis of laminar natural convection in enclosures with fins attached to an active wall, *Heat and Mass Transfer* 33, 307-314
5. Xu.F, Patterson.J.C, Lei.C, 2005, Shadowgraph observations of the transition of the thermal boundary layer in a side-heated cavity, *Experiments in Fluids*, 38: 770–779 DOI 10.1007/s00348-005-0960-1
6. Pakdee. W, Rattanadecho.P, 2006, Unsteady effects on natural convective heat transfer through porous media in cavity due to top surface partial convection, *Applied Thermal Engineering* 26, 2316–2326 .
7. Kolsi.L, Ben Hamida.M.B, Hassen.W, Kadhim Hussein.A, Borjini.M.N, S. Sivasankaran, Saha.S.C, Awad.M.M, Fathinia.F, Ben Aissia.H, 2015, Experimental and Numerical Investigations of Transient Natural Convection in Differentially Heated Air-Filled Tall Cavity, 30-43, 2015 doi: 10.11648j.ajme.20150102.12
8. R.L. Frederick, 1989, Natural convection in an inclined square enclosure with a partition attached to its cold wall, *Int. J. Heat Mass Transfer* 32, 87e94.
9. Xu .F, Patterson. J.C and C. Lei, 2007, .natural convection adjacent to a sidewall with three fins in a differentially heated cavity ANZIAM J.48,CTAC, PP C806-C819
10. Paul.S.C, Saha.S.C, Gu .Y. T, 2013, Effect of an adiabatic fin on natural convection heat transfer in a triangular enclosure, 1(4): 78-83, doi: 0.11648, 0104.16
11. Feng Xu, Suvash V.Saha, 2014, Transition to an unsteady flow induced by a fin on the sidewall of a differentially heated air filled square cavity and heat transfer *International Journal of Heat and mass Transfer* 71, 236-244

12. M.M. Rahman , Hakan F. Öztop , S. Mekhilef , R. Saidur , Khaled Al-Salem, 2014, Unsteady natural convection in Al₂O₃–water nanoliquid filled in isosceles triangular enclosure with sinusoidal thermal boundary condition on bottom wall *Superlattices and Microstructures* 67, 181–196
13. F. Xu, J.C. Patterson, C. Lei, 2009, Transition to a periodic flow induced by a thin fin on the sidewall of a differentially heated cavity, *Int. J. Heat Mass Transfer* 52, 620-628.

NUMERICAL STUDY OF THE DYNAMIC AND THERMAL FIELDS IN A CHANNEL PARTIALLY FILLED WITH AN ANISOTROPIC POROUS MATRIX

¹Salah Ben aoua, ²Rachid Kibboua, ³Farid Mechighel

1,3LR3MI Laboratory, Faculty of sciences of engineering, BP 12, University of Annaba 23000, Algeria

2University of Sciences and Technologies Houari Boumediene USTHB, LTPMP/FGMGP, BP 32 El Alia, Algiers 16111, Algeria;

Corresponding author: bensalah101@gmail.com

ABSTRACT

This work consists of a numerical study of a laminar stationary forced convection inside a flat horizontal channel partially filled with a porous medium, it is assumed that the porous medium is anisotropic hydrodynamically, and the walls are maintained at a constant heat flux. The model of Darcy-Brinkman-Forchheimer is used to describe the flow in the porous region. The numerical finite volume method is used for solving the equations of conservation of mass and momentum and energy, and the associated boundary conditions. The present work aims specify the nature of the convective motions in anisotropic porous medium.

Key Words: Porous media, anisotropic, forced convective flow, Darcy-Brinkman-Forchheimer equation.

NOMENCLATURE

C_p : specific heat ($J Kg^{-1} K^{-1}$)
 Da : Darcy number ($=K_1/H^2$)
 e_p : thickness of the porous layer
 E : dimensionless thickness of the porous layer
 f : friction factor
 F : Forchheimer coefficient
 $(fRe)_L$: local friction coefficient in the established region
 h : coefficient of convective exchange ($W m^{-2} K^{-1}$)
 H : height of half of the channel
 J : kinematic viscosity ratio ($=\nu_{eff}/\nu_f$)
 k : thermal conductivity ($W m^{-1} K^{-1}$)
 K_1, K_2 : permeabilities along the two main axes of the porous matrix
 $[K]$: tensor of permeability
 K^* : anisotropic permeability ratio ($=K_1/K_2$)
 l : channel length (m)
 L : dimensionless length of the channel
 Nu : Nusselt number ($=2hH/k_f$)
 p : pressure ($N m^{-2}$)
 Pr : Prandtl number ($=\nu_f/\alpha_f = (\mu C_p)_f/k_f$)
 R_c : thermal conductivities ratio ($=k_{eff}/k_f$)
 R_μ : viscosity ratio ($=\mu_{eff}/\mu_f$)
 Re : Reynolds number ($=\rho_f \bar{u} H / \mu_f$)
 T : temperature ($^{\circ}C$)
 \vec{V} : velocity vector

Greek symbols

ν : kinematic viscosity ($m^2 s^{-1}$)
 μ : dynamic viscosity ($kg m^{-1} s^{-1}$)
 ρ : density ($Kg m^{-3}$)
 ε : porosity of the porous medium
 θ : anisotropy angle ($^{\circ}$)
 α_f : thermal diffusivity ($k_f/(\rho C)_f$)

1- INTRODUCTION

In recent years considerable research efforts have been devoted to the study of heat transfer by natural or forced convection into cavities filled with a porous medium saturated by a fluid, due to widespread applications in modern technologies [1-4].

A substantial part of theoretical and experimental investigations of heat transfer by convection in porous media have treated the case of isotropic materials [4, 8-11], other studies treated the heat transfer by convection in porous anisotropic media [12]. However, in many practical situations, porous materials are anisotropic in mechanical as well as in their thermal properties.

In this study we present a hydrodynamic and thermal analysis of a steady, laminar incompressible flow within a channel, partially or completely filled with an anisotropic porous medium.

2- ANALYSIS AND MODELLING

2.1- Presentation of the physical system:

The physical system studied here is illustrated in the (figure 1).

The system consists of two horizontal and parallel flat plates of length (l) separated by a distance $2H$. Both the top and the bottom plate are maintained at a constant heat flux q_w . The axis (ox') is positioned on the bottom wall, from which an axial symmetry axis (oy') is taken. The channel contains a porous layer with thickness ' e_p ' in half of the channel, and saturated with a fluid such as the porous medium is characterized by an anisotropic permeability and an isotropic thermal conductivity. Permeabilities along the two main axes of the porous matrix are denoted by K_1 and K_2 , and the anisotropy ratio is then defined as $K^* = K_1/K_2$. The orientation angle ' θ ' is defined as the angle between the horizontal direction and the main axis of the permeability K_2 . The fluid enters the channel at a uniform temperature and a uniform velocity (equals to the dimensionless velocity).

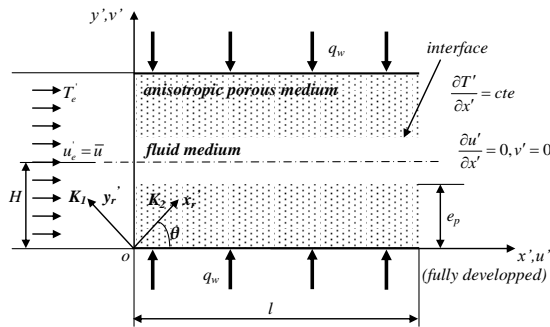


Figure 1: Physical model and coordinate system.

In the present model, we adopt the following assumptions:

For the flow field: the flow is steady laminar and two-dimensional, the fluid is Newtonian and incompressible, and no volume forces were considered. For the thermal field: the radiation heat transfer is negligible; neither viscous dissipation nor internal heat source were considered.

Furthermore, the fluid is in *local thermal equilibrium* with the solid matrix and the thermal properties for both the fluid and the solid matrix are constants.

2.2- Governing equations:

Fluid flow: To formulate the governing equations we use the Navier-Stokes equations in the fluid region and the Darcy-Brinkman-Forchheimer [1] equation in the porous region.

Those equations can be formulated in the main reference system (x', y') using rotating matrices connecting the components of the velocity vector of a coordinate system (x_r', y_r') to a coordinate system (x', y').

2.3- Dimensionless form of the governing equations:

After using dimensionless variables, the dimensionless form of the governing equations are:

Fluid flow: For both the fluid and the porous region the dimensionless continuity equation is as follows:

$$u \frac{\partial u}{\partial x} + v \frac{\partial v}{\partial y} = 0 \quad (1)$$

In the fluid region

$$u \frac{\partial u}{\partial x} + v \frac{\partial u}{\partial y} = -\frac{\partial p}{\partial x} + \frac{1}{\text{Re}} \left(\frac{\partial^2 u}{\partial x^2} + \frac{\partial^2 u}{\partial y^2} \right) \quad (2)$$

$$u \frac{\partial v}{\partial x} + v \frac{\partial v}{\partial y} = -\frac{\partial p}{\partial y} + \frac{1}{\text{Re}} \left(\frac{\partial^2 v}{\partial x^2} + \frac{\partial^2 v}{\partial y^2} \right) \quad (3)$$

In the porous region

$$u \left[\begin{array}{l} \frac{\partial u}{\partial x} + v \frac{\partial u}{\partial y} = -\varepsilon^2 \frac{\partial p}{\partial x} + \varepsilon^2 \frac{J}{\text{Re}} \left(\frac{\partial^2 u}{\partial x^2} + \frac{\partial^2 u}{\partial y^2} \right) \\ \frac{\varepsilon^2}{\text{Re Da}} (K^* \cos^2 \theta + \sin^2 \theta) \\ + \frac{F \varepsilon^2}{\sqrt{Da}} (\sqrt{K^*} \cos^2 \theta + \sin^2 \theta) \sqrt{u^2 + v^2} \\ \frac{\varepsilon^2}{\text{Re Da}} (K^* - 1) \sin \theta \cos \theta \\ + \frac{F \varepsilon^2}{\sqrt{Da}} (\sqrt{K^*} - 1) \sin \theta \cos \theta \sqrt{u^2 + v^2} \end{array} \right] u \quad (4)$$

$$v \left[\begin{array}{l} \frac{\partial v}{\partial x} + v \frac{\partial v}{\partial y} = -\varepsilon^2 \frac{\partial p}{\partial y} + \varepsilon^2 \frac{J}{\text{Re}} \left(\frac{\partial^2 v}{\partial x^2} + \frac{\partial^2 v}{\partial y^2} \right) \\ \frac{\varepsilon^2}{\text{Re Da}} (K^* - 1) \sin \theta \cos \theta \\ + \frac{F \varepsilon^2}{\sqrt{Da}} (\sqrt{K^*} - 1) \sin \theta \cos \theta \sqrt{u^2 + v^2} \\ \frac{\varepsilon^2}{\text{Re Da}} (K^* \sin^2 \theta + \cos^2 \theta) \\ + \frac{F \varepsilon^2}{\sqrt{Da}} (\sqrt{K^*} \sin^2 \theta + \cos^2 \theta) \sqrt{u^2 + v^2} \end{array} \right] v \quad (5)$$

Energy equation:

In the fluid region

$$u \frac{\partial T}{\partial x} + v \frac{\partial T}{\partial y} = \frac{1}{\text{Pr Re}} \left(\frac{\partial^2 T}{\partial x^2} + \frac{\partial^2 T}{\partial y^2} \right) \quad (6)$$

In the porous region

$$u \frac{\partial T}{\partial x} + v \frac{\partial T}{\partial y} = \frac{R_c}{\text{Pr Re}} \left(\frac{\partial^2 T}{\partial x^2} + \frac{\partial^2 T}{\partial y^2} \right) \quad (7)$$

Dimensionless boundary conditions:

In dimensionless form the boundaries conditions can be written as follows:

$$\text{For } x = 0 \quad \begin{cases} u = 1, & v = 0 \\ T = 0 \end{cases} \quad (8a)$$

$$\text{For } x = \frac{l}{H} = L \quad \begin{cases} \frac{\partial u}{\partial x} = 0, & \frac{\partial v}{\partial x} = 0 \\ \frac{\partial T}{\partial x} = 0 \end{cases} \quad (8b)$$

$$\text{For } y = 0 \quad \begin{cases} u = 0, & v = 0 \\ \frac{\partial T}{\partial y} = -\frac{1}{R_c} \end{cases} \quad (9a)$$

$$\text{For } y = 1 \quad \begin{cases} \frac{\partial u}{\partial y} = 0, & v = 0 \\ \frac{\partial T}{\partial y} = 0 \end{cases} \quad (9b)$$

$$\text{For } y = \frac{e_p}{H} = E \quad \begin{cases} u_f = u_p, & v_f = v_p \\ \frac{\partial u_f}{\partial y} = R_\mu \frac{\partial u_p}{\partial y}, & \frac{\partial v_f}{\partial y} = R_\mu \frac{\partial v_p}{\partial y} \\ T_f = T_p, & \frac{\partial T_f}{\partial y} = R_c \frac{\partial T_p}{\partial y} \end{cases} \quad (10)$$

2.4- Definition of other required parameters:

After using dimensionless variables

The *coefficient of friction* for fluid flow is defined as:

$$f (\text{Re})_{2H} = 4 \left(\frac{\bar{u} \times 2 \times H}{\nu_f} \right) (-\partial p / \partial x) \quad (11)$$

$$= 8 \text{ Re} (-\partial p / \partial x)$$

We define the *Nusselt number* as follows:

$$N_u = \frac{4H q_w}{k_f (T_w' - T_m')} \quad (12)$$

3. NUMERICAL RESOLUTION AND VALIDATION

For the resolution of the resulting system of coupled equations and boundary conditions associated we

opted used a numerical method based on the finite volume method [6].

In order verify the reliability of the code we presented a comparison of the velocity profile with Poiseuille flow for a high number of Darcy ($\text{Da} = 10^5$). Our numerical results are compared with previous investigations in the literature; mainly we perform the following validations:

- The first validation with the analytical study [7] of a flow established between two horizontal flat plates, maintained at a constant heat flow (Poiseuille).
- The second validation study with Degan et al. [5] for established flow between two flat plates maintained at a constant heat flow and filled with a dynamic anisotropic porous medium (the model used in this solution is the Darcy-Brinkman model).

As shown in tables 1 and 2 a good agreement is achieved between our numerical results and the numerical/analytical results in the literature in both cases.

Table 1: Comparison between our numerical and analytical study [7]

Controlling Number	Present numerical study		Analytical study [7]	
	u_{\max} (m/s)	Nu	u_{\max} (m/s)	Nu
10^5	1.4823	8.3204	1.5000	8.2350

Table 2: Comparison between numerical study and Degan et al. [5] investigation

Controlling Number	Present numerical study		Degan et al. [5]	
	u_{\max} (m/s)	Nu	u_{\max} (m/s)	Nu
10^{-1}	1.3241	8.9364	1.3367	8.8612

4- RESULTS AND DISCUSSION

All calculations were performed with the values of the following parameters:

Effect of anisotropic permeability ratio

For ($\text{Da} = 10^{-3}$, and $\theta = 0^\circ$, and a dimensionless thickness of the porous layer $E = 0.6$).

Figure 1 shows the effect of the permeability ratio K^* on speed profile, we observe with permeability

ratio $K^* < 1$, when the permeability in the direction of the flow is greater than the transverse direction, The trend is reversed when the permeability in the direction of flow lower than that in the transverse direction ($K^* > 1$), the porous layer offer more resistance compared to the isotropic case ($K^* = 1$).

The maximum speed is reached on the axis of symmetry of the channel; the highest being that of the case where $K^* > 1$ and the lowest that of the case where $K^* < 1$.

Table 3: Parameters used in the numerical calculations

the aspect ratio (L/H)	50
the porosity (ϵ)	0.9
the Prandtl number (Pr)	0.7
the Reynolds number (Re)	100
the ratio of the thermal conductivities	(Rc=1) and (Rc=10)
the kinematic viscosity ratio (J)	1
the Forchheimer coefficient (F)	0
the number Darcy (Da)	between (10^{-4} and 10^{-1})
the thickness of the layer E	0 (fluid case), 0.2, 0.4, 0.6, 0.8, 1 (totally porous case)
the anisotropy angle	($\theta = 0^\circ, 30^\circ, 45^\circ, 60^\circ, 90^\circ, 120^\circ, 150^\circ$ and 180°)

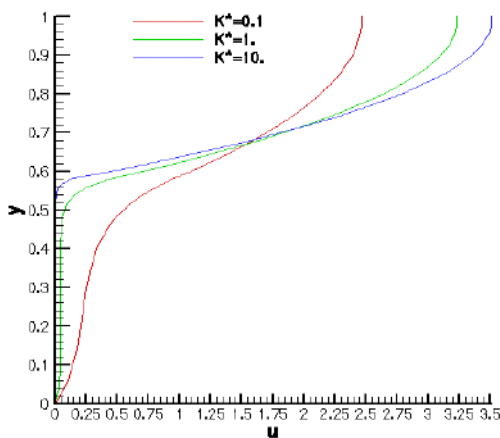


Figure 1: The speed profile for different values of K^* , and for ($\theta = 0^\circ$, $E = 0.6$, and $Da = 0.001$).

The effect of K^* on the temperature profile is shown in Figure 2, a decrease in the dimensionless temperature is observed for $K^* = 0.1$ (difference between the temperature and that of the wall is low) and an increase in the dimensionless temperature for $K^* = 10$ when compared with the isotropic case

($K^* = 1$), the difference between the temperature and that of the wall for the various curves is more important compared to completely porous channel.

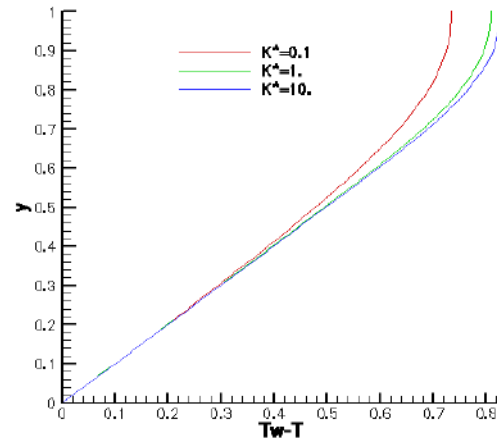


Figure 2: the temperature profile for different values of K^* , and for ($\theta = 0^\circ$, et $E = 0.6$, et $Da = 0.001$).

Effect of the angle of anisotropy

With ($Da = 10^{-2}$, and $E = 0.6$ and $K^* = 0.25$ ($K^* < 1$)), the results (not shown here) indicate that the velocity in the porous region is maximum when $\theta = 0^\circ$ (permeability in the direction of the flow is greater), and minimum when $\theta = 90^\circ$. Thus, the velocity on the central axis of the channel (fluid region) is maximum when $\theta = 90^\circ$.

For the temperature profile (not shown here), we observe a minimum difference between the temperature and the temperature of the wall for $\theta = 0^\circ$, and maximum for $\theta = 90^\circ$.

The effects of the inclination angle θ on the velocity profile (not shown here) for $K^* = 5$ ($K^* > 1$), fixing $Da = 10^{-2}$ and $E = 0.6$,

The results indicate that the velocity in the porous region is maximum when $\theta = 90^\circ$ (permeability in the direction of flow is greater), and minimum when $\theta = 0^\circ$. In fluid region we note that the situation is reversed.

For the temperature profile (not shown here), we observe temperature minimum values for $\theta = 90^\circ$ (the temperature approaches the temperature of the wall), and maximum for $\theta = 0^\circ$ (the temperature deviates from the temperature of the wall)

Variation of the friction coefficient with the thickness of the porous layer E

Figure 3 shows that the friction coefficient is an increasing function of the thickness E . For a given thickness E , the highest coefficient of friction

corresponds to a ratio of permeability $K^* > 1$, that is to say when the permeability in the direction of flow is lower than the transverse direction.

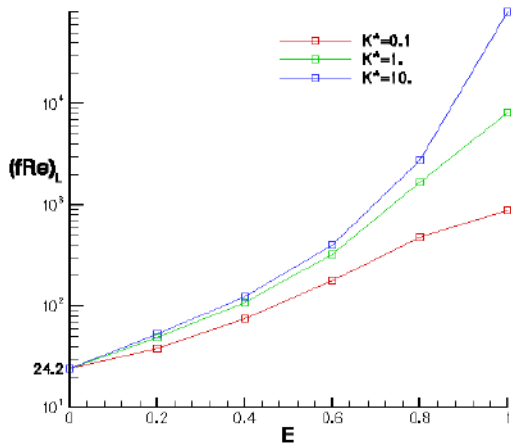


Figure 3: Variation of the friction coefficient with the thickness of the porous layer E for different K^* , $\theta = 0$, and $Da = 10^{-3}$.

Variation of the Nusselt number as a function of the thickness of the porous layer E :

The figure 4 illustrates the variation of the Nusselt number for the same condition; it is found that the Nusselt number decreases with the increase in the thickness E to reach a minimum value for a given thickness E . This optimum thickness depends on the ratio of permeability K^* .

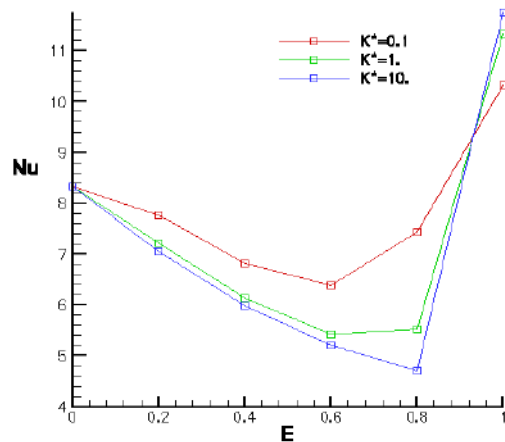


Figure 4: Variation of the Nusselt number as a function of the thickness of the porous layer E for different K^* , $\theta = 0^\circ$, $Da = 10^{-3}$, $R_c = 1$.

In contrast for $R_c=10$, the Nusselt number becomes an increasing function in terms of the thickness of the porous layer E , for a given thickness E , the most greater Nusselt number is obtained for a permeability ratio $K^* < 1$, such as the values are most greater than the case of $R_c = 1$ (Fig.5).

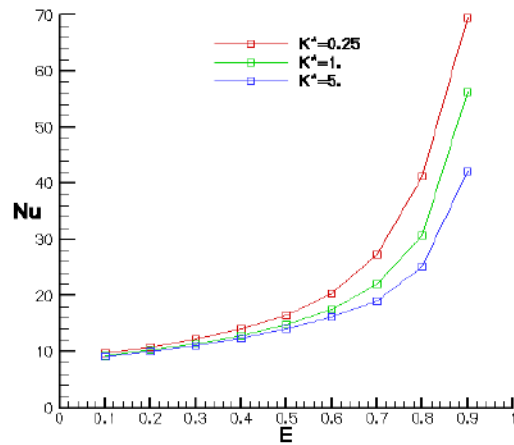


Figure 5: Variation of the Nusselt number as a function of the thickness of the porous layer E for different K^* , $\theta = 0^\circ$, $Da = 10^{-3}$, $R_c = 10$.

Effect of Darcy number and the angle of anisotropy on the Nusselt number:

In figure 6, the thickness of the porous layer is fixed ($E=0.6$), the results indicate that for $K^* = 0.25$, convective transfer is minimum with 90° , but it is maximum at 0° and 180° . The inverse is true for $K^* = 5$.

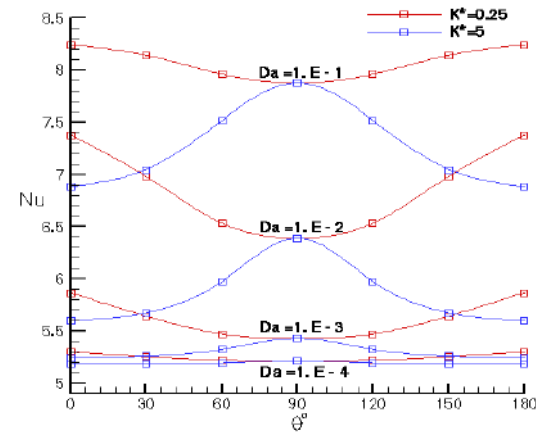


Figure 6: Effect of Darcy number Da and the angle θ of anisotropy on the Nusselt number for ($K^* = 0.25$ and $K^* = 5$), and ($E = 0.6$).

Combined effect of the angle of anisotropy, the Darcy number Da and the thickness E on the friction coefficient

Figure 7 shows that the coefficient of friction varies in proportion to the thickness E and also with the angle θ , for $K^* = 0.25$.

The combined effect of the thickness and the anisotropy angle with $K^* = 0.25$ is depicted in Figure 8. The Nusselt number decreases with the increase of the thickness E until a minimum value

for a given thickness E , this tendency reverses exceeding this thickness and exceeds the purely fluid case.

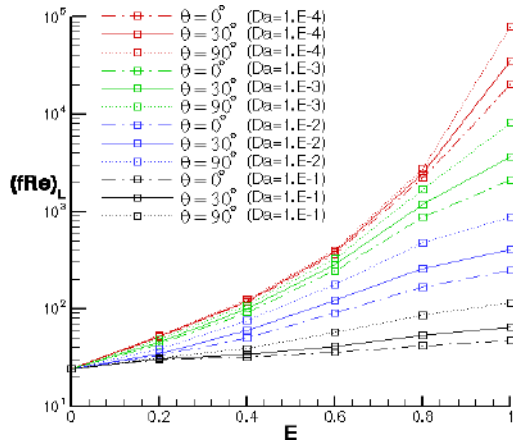


Figure 7: Combined effect of the angle of anisotropy, the Darcy number Da and the thickness E on the friction coefficient in the established region, for ($K^* = 0.25$)

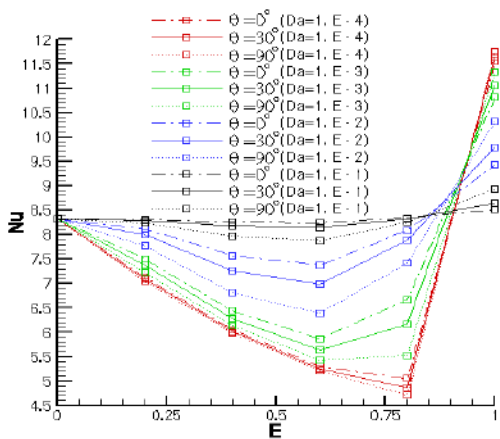


Figure 8: Combined effect of the angle of anisotropy, the Darcy number Da and the thickness E on the Nusselt number in the established region for ($K^* = 0.25$)

5- CONCLUSIONS

In conclusion we cite the following results:

-The use of a partially porous channel reduce the coefficient of friction and increase the heat transfer coefficient in the case of a thermal conductivity ratio $R_c > 1$ (mainly $R_c = 10$).

-For a given thickness E and a zero angle of orientation, the highest friction coefficient corresponds to a ratio of permeability $K^* > 1$; and for an orientation angle of 90° , the highest friction coefficient corresponds to a ratio of permeability $K^* < 1$; that is to say when the permeability in the

direction of flow is lower than the transverse direction.

-The Nusselt number decreases with the increase in the thickness E to reach a minimum value for a given thickness E when $R_c = 1$.

-When $R_c = 10$, the Nusselt number becomes an increasing function of the thickness of the porous layer E . For a given thickness E , the highest Nusselt number is obtained for a ratio of permeability $K^* < 1$.

In perspective, we propose to study the case of a channel where the porous medium is placed in the center channel, a specific study with a thermally anisotropic porous layer, with varying thermo physical properties, and with a non-local thermal equilibrium.

REFERENCES

- [1] K. Vafai, *Handbook of Porous Media*, 2nd Ed. (2005).
- [2] Nield, D. A and Bejan, A. (1992). *Convection in porous media*. Springer-Verlag, New York.
- [3] M. Kaviany, *Principals of heat transfer in porous media*, Springer –Verlag, 2nd Ed. New York 1995.
- [4] D.A. Nield, A.Bejan, *Convection in Porous Media*, Springer, 2nd Ed. (1999)
- [5] G. Degan, S. Zohoun, P. Vasseur. (2002). Forced convection in horizontal porous channels with hydrodynamic anisotropy, *International Journal of Heat and Mass Transfer* 45, 3181–3188
- [6] S.V. Patankar, *Numerical Heat Transfer and Fluid Flow*, 1980, McGraw-Hill, New York.
- [7] F.P. Incropera, D.V. DeWitt, T.L. Bergman, A.S. Lavine: *Introduction to heat transfer*, USA (2007).
- [8] Bear, J. (1972). *Dynamics of fluids in porous media*, Elsevier Pub. Company, Inc, New York.
- [9] Ingham, D. B. and POP, I. (1998). *Transport Phenomena in Porous Media*, Pergamon
- [10] A.V. Kuznetsov. *Analytical investigation of forced convection from a flat plate enhanced by a porous substrate* (1999) Acta Mech. 137, 211-223
- [11] O Cekmer · M Mobedi · B Ozerdem, I Pop, *Fully Developed Forced Convection in a Parallel Plate Channel with a Centered Porous Layer*. Transp Porous Med (2012) 93:179–201
- [12] I.S. Shivakumara, Jinho Lee, A.L. Mamatha and M. Ravisha, *Boundary and thermal non-equilibrium effects on convective instability in an anisotropic porous layer*, Journal of Mechanical Science and Technology 25 (4) (2011) 911-921.

NUMERICAL ANALYSIS OF BIFURCATIONS IN THERMAL CONVECTION OF BOGER FLUIDS SATURATING A POROUS SQUARE BOX

H. Ben Hamed^a, M.N. Ouarzazi^b, C. CHahtour^a, P. Naderi^a, H. Beji^a

a. Laboratoire des Technologies Innovantes, EA 3899, Université de Picardie Jules Verne, Avenue des Facultés, 80025 Amiens, France

b. Laboratoire de Mécanique de Lille, UMR CNRS 8107, Université de Lille I, Bd Paul Langevin, 59655 Villeneuve d'Asq, France

*Ben Hamed Haïkel: Tél: +33651579973 Fax: +33 3 2295 6889 Email: haykel.benhamed@u-picardie.fr

ABSTRACT

We report numerical results on bifurcations in natural thermal instability for a Boger fluid saturating a porous square cavity heated from below. The modified Darcy law based on the Oldroyd-B model was used for modeling the momentum equation. In comparison to Newtonian fluids, two more dimensionless parameters are introduced, namely the elasticity number and the ratio between retardation and relaxation times. The analysis of the basic state revealed the existence of a codimension-two bifurcation point in the viscoelastic parameter space, where both stationary and oscillatory instabilities occur simultaneously. The dynamics associated with the nonlinear interaction between the two kinds of instabilities is analyzed. By increasing the Rayleigh number above its critical value a first Hopf bifurcation may develop. This result may explain the observed transition from oscillatory to stationary convection in a few existing laboratory experiments when the Rayleigh number is increased. Numerical simulations performed in a parameter space far from the codimension-two point indicated a rich dynamics which is not predicted by the normal form analysis. In particular, we found that an intermittent oscillation regime may exist with steady state before the emergence of a secondary Hopf bifurcation for relatively high values of Rayleigh number.

KEYWORDS Porous media, thermal convection, viscoelastic fluids, Boger fluids, Heat transfer.

NOMENCLATURE

The units correspond to the dimensional variables with d as superscript.

x, z Coordinate system

H, H^d Side of the square box [m]

u, w, u^d, w^d The velocity components [m/s]

g Gravity acceleration [m/s^2]

C Heat capacity [J/K]

T, T^d Temperature [K]

K Permeability [m^2]

\mathfrak{R} Rayleigh Darcy number $\mathfrak{R} = Ra \times Da$

\square_0 Reference state

\square_s Solute

\square_p Polymer

\square_f Filtration

\square_c Critical

\square_{NL} Nonlinear

Exponents

\square^d Dimensional variable

\square^n nth time step

\square^{osc} Oscillatory

\square^{st} Stationary

Greek symbols

β Volumetric expansion [K^{-1}]

κ Thermal diffusivity [$m^2 s^{-1}$]

ψ Stream function

σ Heat capacity ratio between solid and liquid phases

ρ Density [kg/m^3]

ν Kinematic viscosity [$m^2 s^{-1}$]

μ Dynamic viscosity [$Pa \cdot s$]

γ Deformation tensor [s^{-1}]

τ Stress tensor [Pa]

$\lambda_i; \lambda_i^d$ Relaxation ($i = 1$) and retardation ($i = 2$) times [s]

$\Gamma = \frac{\lambda_2}{\lambda_1} = \frac{\mu_s}{\mu_s + \mu_p}$ Characteristic ratio

INTRODUCTION

The knowledge and the control of the behavior of instabilities in non-Newtonian fluids are of interest in many fields of science and engineering. In particular, viscoelastic fluids can be found in a great number of applications such as those in bio-engineering and in pharmaceutical and petroleum industries, among others. Most of the existing studies dealing with viscoelastic fluids focus either on hydrodynamic instability under isothermal conditions [1], or on thermal instabilities [2-10]. In the latter case, linear stability analysis reveals that the onset of natural convection of viscoelastic fluids can be oscillatory instead of stationary, depending on the fluid elasticity. This

Subscripts

behavior was confirmed by the experimental results [7] of Kolodner using DNA suspensions. Without DNA suspensions no oscillations on any time scale were observed in these control experiments. In the presence of DNA suspensions, experiments reveal that the first convective instability is oscillatory. Even though buoyancy-driven instabilities in viscoelastic fluids have been extensively studied for clear fluid media, the same cannot be said about their counterparts in the presence of a porous matrix. This is probably due to the crucial problem of the formulation of the constitutive equations regarding viscoelastic fluid flows in porous media.

Boger fluids are named after D.V. Boger [11], where he described the ideal fluid for experimentation as a fluid that is "highly viscous and highly elastic at room temperature and at the same time is optically clear". Boger fluids are elastic fluids with constant the viscosity ratio $\Gamma = \frac{\mu_s}{\mu_s + \mu_p} = 0.75$. They are dilute aqueous or organic polymer solutions where shear thinning caused by the polymers can be ignored. The best application to date for Boger fluids is to solve the problem of disposal of wastes produced in the processing of bauxite into alumina used in aluminum production. With Boger fluids, a protocol was developed to convert the caustic red bauxite mud into a thick matter that could still flow down pipes avoiding the dangers of tubes erupting and leading to a more sustainable practice. To our knowledge, free convection of Boger fluids saturating porous media has not been the subject of numerical investigations. In this paper, we determine by numeric experimentation the bound between rest state, and first and the second Hopf bifurcation.

The system: We consider a square box filled with a Boussinesq Boger liquid saturating a porous square cavity. Horizontal boundaries are assumed perfectly heat conducting and subjected to constant temperatures; T_0^d on the bottom and T_1^d on the top, with $T_1^d < T_0^d$. The vertical walls are considered impermeable and adiabatic. The equilibrium between the filtration velocity and the pressure gradient is instantaneous in Newtonian flows. However, for viscoelastic fluids, the equilibrium can only be reached after a certain time. This characteristic time is called relaxation time λ_1^* . Also, the material forgets its initial form after unloading some of its elastic energy into kinetic energy at a second characteristic time called the retardation time λ_2^* with $\lambda_2^* \leq \lambda_1^*$. Typical liquids having viscoelastic behavior are solutions composed of a Newtonian solvent and polymeric solute. Thus, we define the non-dimensional ratio Γ as:

$$\Gamma = \frac{\lambda_2}{\lambda_1} = \frac{\lambda_2^d}{\lambda_1^d} = \frac{\mu_s}{\mu_s + \mu_p} = \frac{\mu_s}{\mu} \quad (1)$$

Where μ_s , μ_p and μ are respectively the solvent, the polymer and the solution viscosities; it is clear that $0 \leq \Gamma \leq 1$. The

limit $\Gamma = 0$ recovers a purely elastic fluid or the so-called Maxwell fluid, and the limit $\Gamma = 1$ corresponds to a Newtonian fluid. Several approaches exist for modeling the rheological behavior of viscoelastic fluids. The Oldroyd-B model is one of the most frequently present in literature.

We transform the equations of motion to the dimensionless form using the following reference scales: H^d for Lengths, $H^{d^2} \kappa^{-1}$ for time, $T_0^d - T_1^d$ for temperature, and κH^{d-1} for velocities.

Using the double curl procedure to drop the pressure, and the stream function formulation $\psi = \int u dz = - \int w dx$ to express incompressibility, the final normalized system is written as:

$$\begin{cases} \sigma \partial_t T = (\partial_x^2 + \partial_z^2 - u \partial_x - w \partial_z) T & (2.a) \\ (1 + \lambda_1 \partial_t) \mathcal{H} = \Re(1 + \lambda_1 \Gamma \partial_t) \partial_x T & (2.b) \\ (\partial_x^2 + \partial_z^2) \psi = \mathcal{H} & (2.c) \\ T(x, 0) = 1; \quad T(x, 1) = \partial_x T(0, z) = \partial_x T(1, z) = 0 \\ \psi(x, z) = 0 \text{ for all boundaries} & (2.d - e) \end{cases}$$

Where $\Re = g\beta\Delta T K H / (\nu \kappa)$ is the Darcy-Rayleigh number, and \mathcal{H} is the harmonic function of ψ . Equations (2.d) and eq. (2.e) state respectively that horizontal walls are subjected to imposed temperatures and the vertical walls are adiabatic and that the borders of the square box are impermeable. The heat transfer rate is expressed in terms of the bulk-averaged Nusselt number defined as:

$$Nu = - \left\langle \int_0^1 \partial_z T \Big|_{z=0} dx \right\rangle \quad (3)$$

Where, the angle brackets indicate the long-time average.

Numerical method: The system (2.a,b,c) subjected to conditions (2.d,e) has been numerically solved using finite difference discretization with regular mesh.

Equation (2.a) subjected to conditions (2.d) is solved by the ADI method. To solve the equation (2.b); the space derivative of temperature is approximated by a standard second-order centered scheme, and its temporal derivative is obtained by means of (2.a). Using the already obtained temperature fields T^n and T^{n+1} , equation (2.b) becomes an ordinary temporal differential equation. We resolve it with a second order Runge-Kutta method. To find the stream function; we discretize the Poisson equation (2.c) by a standard centered second order scheme, and resolve it by the successive over-relaxation method (SOR). We use the Chebyshev acceleration in order to reduce the required total number of iterations.

RESULTS AND DISCUSSION

In this section, we present the main results dealing with bifurcations arising in a porous square box heated from below and saturated by a Boger fluid. Fig. 1 shows the steady or oscillatory nature of the convection pattern together with the transition lines between these patterns in the $(\lambda_1, \mathfrak{R})$ plane. Generally, Boger fluids follow the same dynamics as viscoelastic fluids. Nevertheless, it is the experimenter's viscoelastic fluid by excellence. In other hand, it has three interesting properties:

When $\lambda_1 < 2/\pi^2$ the Newtonian mechanism dominates, and the rest state loses its stability in favor of stationary convection at $\mathfrak{R} = 4\pi^2$.

For $\lambda_1 > 2/\pi^2$, the preferred mode at the onset of convection is an oscillatory one. Critical Rayleigh number varies from $\mathfrak{R}_c = 4\pi^2$ at $\lambda_1 = 2/\pi^2$ to $\mathfrak{R}_c = 3\pi^2$ at very large λ_1 . This means that no convection can develop if $\mathfrak{R}_c \leq 3\pi^2$ regardless of the λ_1 value. The neutral line of the transition to first oscillatory zone is given by the equation:

$$\mathfrak{R}_c = \frac{2}{\lambda_1} + 3\pi^2$$

For very large λ_1 , this oscillatory mode of convection still dominant up to $\mathfrak{R} = 47.2$ where a transition to a steady state occurs. The steady mode of convection persists in the interval $47.2 < \mathfrak{R} < 160$. Note that the extension of that interval becomes more important when $\lambda_1 \rightarrow 2/\pi^2$. Finally when \mathfrak{R} increases outside this interval, a secondary Hopf bifurcation occurs giving rise to a new oscillatory mode of convection.

Compared to a Newtonian fluid which loses its stability at $\mathfrak{R} = 4\pi^2$, the stability diagram of fig. 1 shows that the effect of the elasticity in a Boger fluid becomes significant if the relaxation time is greater than $2/\pi^2$. We propose table 1 as a simple complementary way in order to summarize different convection patterns that can be observed in a Boger fluid.

Table 1: Boger fluids behavior

Rayleigh number	$\lambda_1 < 2/\pi^2$	Rayleigh number	$\lambda_1 > 2/\pi^2$
$\mathfrak{R} > 4\pi^2$	Steady state	$\mathfrak{R} > 160$	Oscillatory zone II
		$47.2 < \mathfrak{R} < 160$	Steady state
$\mathfrak{R} < 4\pi^2$	Rest state	$3\pi^2 < \mathfrak{R} \leq 47.2$	Oscillatory zone I
		$\mathfrak{R} \leq 3\pi^2$	Rest state

Fig. 2 shows the time evolution of Nu for $\lambda_1 = 2/\pi^2$ (fig. 2 a, b) and $\lambda_1 = 0.3$ (fig. 2 c-h). These figures illustrate the nature of the convective pattern in each region of the $(\lambda_1, \mathfrak{R})$ plane. In particular, the nonlinear dynamics in the neighborhood of the codimension-two bifurcation $(\lambda_1^*, \mathfrak{R}^*) = (2/\pi^2, 4\pi^2)$ is recovered as predicted by weakly nonlinear theory. Specifically, we note that the temporal

transition to the oscillatory zone II is associated with a spatial transition from one cell to two-cell convective flow.

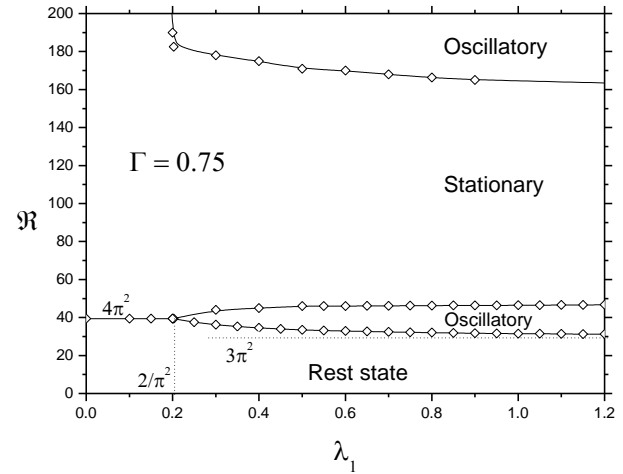
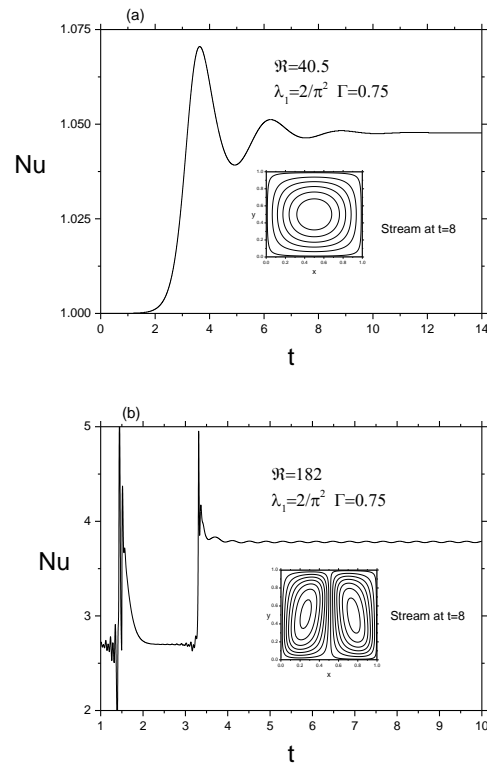


Figure 1: General stability diagram for Boger fluids



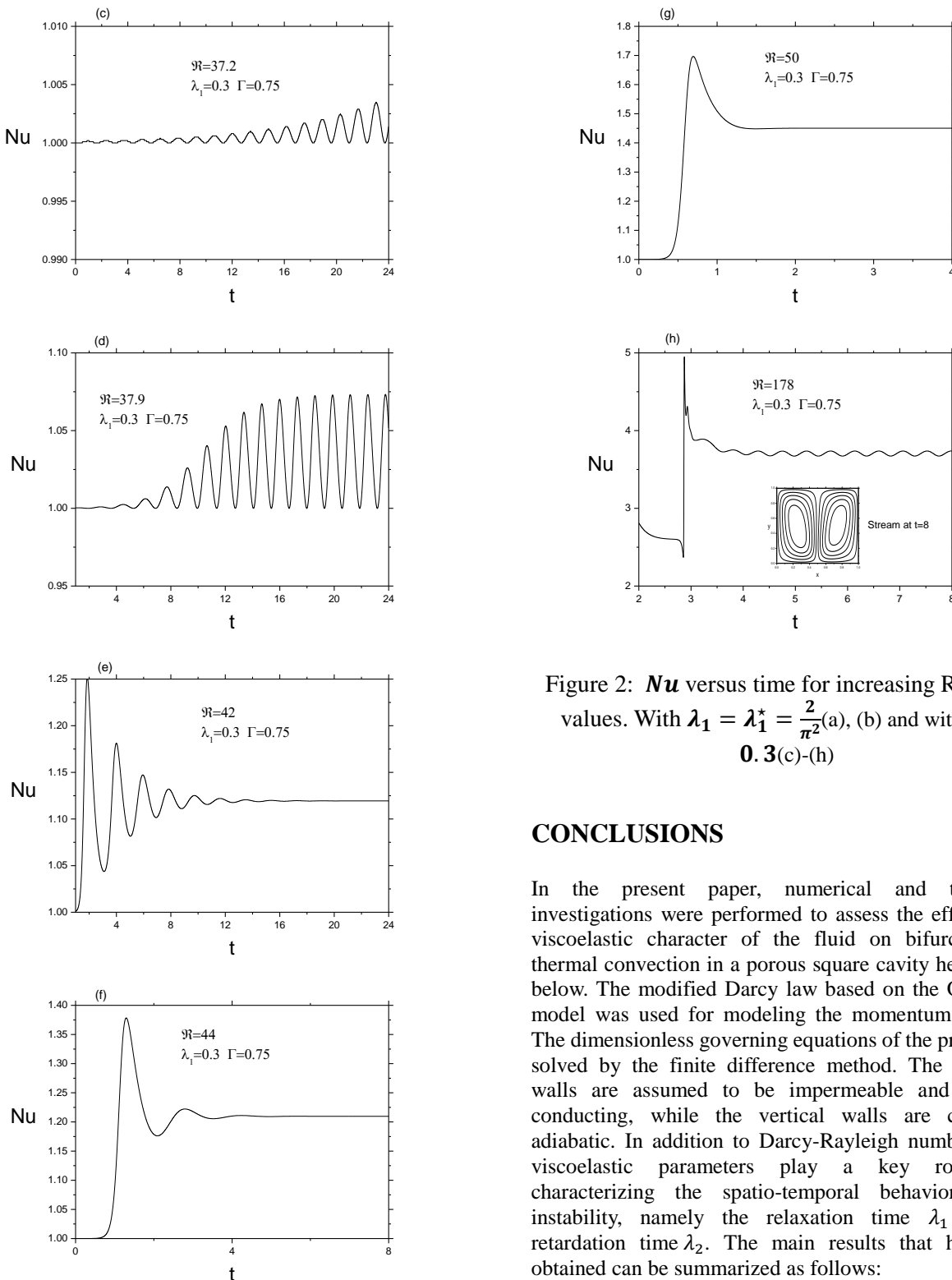


Figure 2: Nu versus time for increasing Rayleigh values. With $\lambda_1 = \lambda_1^* = \frac{2}{\pi^2}$ (a), (b) and with $\lambda_1 = 0.3$ (c)-(h)

CONCLUSIONS

In the present paper, numerical and theoretical investigations were performed to assess the effect of the viscoelastic character of the fluid on bifurcations of thermal convection in a porous square cavity heated from below. The modified Darcy law based on the Oldroyd-B model was used for modeling the momentum equation. The dimensionless governing equations of the problem are solved by the finite difference method. The horizontal walls are assumed to be impermeable and perfectly conducting, while the vertical walls are considered adiabatic. In addition to Darcy-Rayleigh number \mathfrak{R} two viscoelastic parameters play a key role when characterizing the spatio-temporal behavior of the instability, namely the relaxation time λ_1 and the retardation time λ_2 . The main results that have been obtained can be summarized as follows:

In the weakly elastic regime (i.e. $\lambda_1 \leq \lambda_1^*$ or $\lambda_2 \geq \lambda_2^*$) the fluid elasticity has no effect on the instability properties and the non-Newtonian fluid behaves as a Newtonian fluid. The stationary mode of convection dominates the dynamics independently of the prescribed values of Darcy-Rayleigh number used in this study (\mathfrak{R} up to 200).

In contrast to weakly elastic regime, a secondary bifurcation from oscillatory to a steady state may occur provided that either λ_1 do not exceed a particular value λ_1^{**} for a prescribed value of λ_2 or λ_2 remains less than a particular value λ_2^{**} for a fixed value of λ_1 . In this moderately elastic regime, both the elastic and viscous characters of the fluid act together, in addition to the heating in the destabilisation phenomena. Moreover, in the parameter space where this secondary transition is possible, it is found that near the codimension-two bifurcation point, the threshold Rayleigh number obtained numerically agrees very well with the nonlinear threshold determined analytically. Numerical simulations performed with high Rayleigh number in moderately elastic regime reveal that the system may experience a third transition to a second Hopf bifurcation where the steady state convection is replaced by a new oscillatory mode of convection. It is also shown that in the vicinity of the second Hof bifurcation line, the system experiences an intermittent evolution between a steady state and an amplified oscillatory state.

REFERENCES

1. M. Zhang, I. Lashgari, T.A. Zaki, L. Brandt, Linear stability analysis of channel flow of viscoelastic Oldroyd-B and FENE-P fluids, *J. Fluid Mech.* 737, 249-279(2013).
2. T.Green III, Oscillating convection in an elasticoviscous liquid, *Phys. Fluids.* 11, 1410–1413 (1968).
3. CM.Vest, VS. Arpaci, Overstability of a viscoelastic fluid layer heated from below, *J. Fluid Mech.* 36, 613–623 (1969).
4. M. Sokolov, R. I. Tanner, Convective stability of a general viscoelastic fluid heated from below”, *Phys. Fluids.* 15, 534-539 (1972).
5. S. Rosenblat, thermal convection in a viscoelastic liquid, *J. Fluid Mech.* 21, 201-223 (1986).
6. H. M. Park, H. S. Lee, Hopf bifurcations of viscoelastic fluids heated from below, *J. Non-Newtonian Fluid Mech.* 66, 1–34 (1996).
7. P. kolodner, Oscillatory convection in viscoelastic DNA suspensions, *J. Non-Newtonian Fluid Mech.* 75, 167-192 (1998).
8. J. Martinez-Mardones, R. Tiemann, D. Walgraef, Thermal convection thresholds in viscoelastic solutions, *J. Non-Newtonian Fluid Mech.* 93, 1-15 (2000).
9. Z.Li, R. E. Khayat, Finite-amplitude Rayleigh-Bénard convection and pattern selection for viscoelastic fluids, *J. Fluid Mech.* 529, 221–251 (2005).
10. S. C. Hirata, L. S. de B. Alves, N. Delenda, M. N. Ouarzazi, Convective and absolute instabilities in Rayleigh-Bénard-Poiseuille mixed convection for viscoelastic fluids, *J. Fluid Mech.* 765, 167–210 (2015).
11. J. Niu, C. Fu, W.Tan, Thermal convection of a viscoelastic fluid in an open-top porous layer heated from below, *J. Non-Newtonian Fluid Mech.* 165, 203-211 (2010).

CRITICAL DIMENSION OF A CIRCULAR HEAT AND SOLUTE SOURCE FOR AN OPTIMUM TRANSFER INTO SQUARE POROUS ENCLOSURES

K. RAGUI^{1,*}, A. BOUTRA^{1,2}, R BENNACER³, Y.K. BENKAHLA¹

¹Laboratory of Transport Phenomena, USTHB, Algiers, Algeria.

²Preparatory School of Science and Technology, Algiers, Algeria.

³ LMT - ENS Cachan - CNRS - Paris Saclay University, 94230 Cachan, France.

(BP. 32 El Alia, 16111 Bab Ezzouar, Algiers, Algeria;

aeknad@yahoo.fr, rachid.bennacer@ens-cachan.fr, youbenkahla@yahoo.fr).

*Corresponding author: Fax: +213 21 20 77 67 Email: ragui-karim@live.fr

ABSTRACT

The present work refers to the investigation of natural convection into a partitioned porous enclosure, driven by cooperating thermal and solutal buoyancy forces. The side walls are maintained at a uniform temperature and concentration, lower than that of a circular heat and solute source, which located at the center of the porous square, the rest of the horizontal walls are kept insulated. The physical model for the momentum conservation equation makes use of the Brinkman extension of the classical Darcy equation, the set of coupled equations is solved using the finite volume method and the SIMPLER algorithm.

To account for effects of the main parameters such the buoyancy ratio; Lewis and porous thermal Rayleigh numbers; as well as the source dimension, heat and mass transfer characteristics are widely inspected and then new powerful correlations are proposed, which predict within $\pm 1\%$ the numerical results. Noted that the validity of the used code was ascertained by comparing our results with experimental data and numerical ones already available in the literature.

KEYWORDS Double-diffusive convection/ square porous enclosure/ circular source/ finite volume approach/ powerful correlations.

NOMENCLATURE

C	Dimensional mass fraction
d	Circular source' diameter, [m]
\mathcal{D}	Mass diffusivity, [m ² s ⁻¹]
Da	Darcy number, K/H^2
H	Cavity height, [m]
K	Porous medium permeability, [m ²]
Nu	Mean Nusselt number
p	Pressure, [Pa]
P	Dimensionless pressure, $(p/\rho_{fluid} \beta \Delta T H)$
Sh	Mean Sherwood number
T	Dimensional Temperature, [K]
u, v	Velocity components, [m s ⁻¹]
U, V	Dimensionless velocity components, u (or v)/ $(\rho_{fluid} \beta \Delta T H)^{1/2}$
x, y	Cartesian coordinates, [m]
X, Y	Dimensionless Cartesian coordinates, x (or y)/H.

Greek letters

α	Thermal diffusivity, [m ² s ⁻¹]
β_T	Thermal expansion coefficient, [K ⁻¹]
β_C	Solutal expansion coefficient

ϕ Dimensionless concentration

θ Dimensionless temperature

Subscripts

h Hot
c Cold

INTRODUCTION

Double-diffusive natural convection analysis into a porous medium has been the subject of a very intense research activity over the past forty decades, due to the importance of related industrial and technological applications such fibrous insulating materials, heat exchangers, catalytic reactor and some modes of assisted oil recuperation [1], to name but a few.

With both temperature and concentration gradients present to drive the fluid flow, an increased number of transport configurations was possible; with parallel or perpendicular gradients; and the body forces augmenting or opposing [2-8].

In the main idea to predict heat and mass transfer into such configurations, powerful correlations were

proposed. Back to 1987, Trevisan and Bejan [9] projected the thermal and solutal transfer, quantified by Sherwood and Nusselt numbers, as function of the thermal Rayleigh and the Lewis numbers as well as the aspect and the buoyancy ratios. In 1990 Lin *et al.* [10] proposed Nusselt and Sherwood correlations as function of the thermal Grashof number and that, for small values of the buoyancy ratio ($|N| < 5$). In 1993, Bennacer [11] suggested a general correlation for mass transfer inside square enclosures, which may be used in a wide range of the porous thermal Rayleigh number, the buoyancy ratio and the Lewis number as well.

In 2016, Ragui *et al.* [12] proposed general correlations for thermosolutal convection into square enclosures which including a central bottom source.

Motivated by these works and the practical applications of the double-diffusive convection, this paper will discuss the results of the latter into a porous square included a heat and solute circular source, mounted at the center, to bring up at the end some powerful correlations that may be used in many industrial applications, especially in cooling cylindrical fuel assemblies and predicting pollutants spreading into heat exchangers.

PROBLEM STATEMENT

The studied configuration, shown in Fig. 1, consists of a cold (less concentric) side-walls of a porous enclosure, which containing a heat and solute circular source, mounted in its centre. The fluid filled the porous medium is assumed to be Newtonian, its thermophysical properties are presumed to be constant except the density variation, in the buoyancy term, which depends linearly on both the local temperature and concentration.

$$\rho_{(T,C)} = \rho_0 [1 - \beta_T (T - T_0) - \beta_C (C - C_0)] \quad (1)$$

where β_T and β_C are the thermal and solutal expansion coefficients:

$$\beta_T = -\frac{1}{\rho_0} \left(\frac{\partial \rho}{\partial T} \right)_p, \beta_C = -\frac{1}{\rho_0} \left(\frac{\partial \rho}{\partial C} \right)_p \quad (2)$$

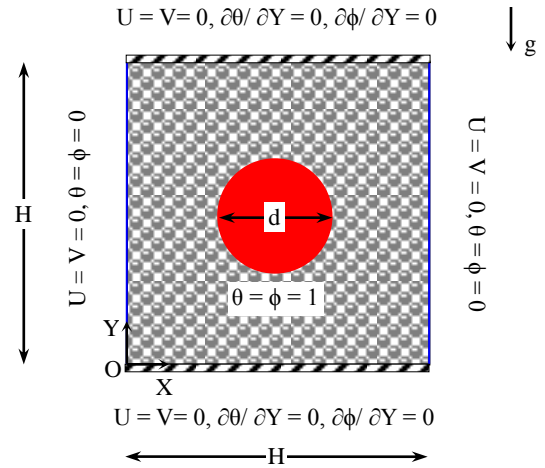


Figure 1 Simulation domain with its boundary conditions. The solid matrix is supposed to be isotropic, homogeneous and in thermal equilibrium with the fluid. The permeability of the porous medium K is kept uniform, when the porosity ϵ is about 40%. The dimensionless conservation equations describing the transport phenomenon inside the porous square can be written as:

$$\frac{\partial U}{\partial X} + \frac{\partial V}{\partial Y} = 0 \quad (3)$$

$$\frac{1}{\epsilon^2} \left(U \frac{\partial U}{\partial X} + V \frac{\partial U}{\partial Y} \right) = -\frac{\partial P}{\partial X} - \frac{Pr}{Da} U + Pr \left(\frac{\partial^2 U}{\partial X^2} + \frac{\partial^2 U}{\partial Y^2} \right) \quad (4)$$

$$\frac{1}{\epsilon^2} \left(U \frac{\partial V}{\partial X} + V \frac{\partial V}{\partial Y} \right) = -\frac{\partial P}{\partial Y} - \frac{Pr}{Da} V + Pr \left(\frac{\partial^2 V}{\partial X^2} + \frac{\partial^2 V}{\partial Y^2} \right) + Ra Pr (\theta + N \phi) \quad (5)$$

$$U \frac{\partial \theta}{\partial X} + V \frac{\partial \theta}{\partial Y} = \left(\frac{\partial^2 \theta}{\partial X^2} + \frac{\partial^2 \theta}{\partial Y^2} \right) \quad (6)$$

$$U \frac{\partial \phi}{\partial X} + V \frac{\partial \phi}{\partial Y} = \frac{1}{Le} \left(\frac{\partial^2 \phi}{\partial X^2} + \frac{\partial^2 \phi}{\partial Y^2} \right) \quad (7)$$

where Da is the Darcy number, Le is the Lewis number, N is the buoyancy ratio, Pr and Ra are the Prandtl and the thermal Rayleigh numbers.

The average rate of heat and mass transfer across the side walls are expressed in dimensionless form by the Nusselt and Sherwood numbers:

$$|Nu \text{ (or Sh)}_{\text{Vertical walls}}| = \int_0^1 \left(\frac{\partial \theta \text{ (or } \phi)}{\partial X} \right) \Big|_{\text{wall}} dY \quad (8)$$

NUMERICAL PROCEDURE AND VALIDATION

The governing conservation equations are discretized in space using the finite volume approach, when the convection-diffusion terms were treated with a Power-Law scheme. The resulting

algebraic equations, with the associated boundary conditions, are then solved using the line by line method. As the momentum equation is formulated in terms of the primitive variables (U, V and P), the iterative procedure includes a pressure correction calculation method, namely SIMPLER [13], to solve the pressure-velocity coupling. Noted that the convergence criterion for temperature, concentration, pressure, and velocity is given as:

$$\frac{\sum_{j=1}^m \sum_{i=1}^n |\xi_{i,j}^{t+1} - \xi_{i,j}^t|}{\sum_{j=1}^m \sum_{i=1}^n |\xi_{i,j}^{t+1}|} \leq 10^{-5} \quad (9)$$

where m and n are the numbers of grid points in the x - and y -directions, respectively. ξ is any of the computed field variables, and t is the iteration number.

The performance of the using code via the double-diffusive natural convection problem in a confined porous medium is established by comparing predictions with other numerical results and experimental data, and by verifying the grid independence of the present results. First, the present results are consistent with previous computations, namely those of Hadidi *et al.* [14]. By taking into account the same hypotheses, Table 1 demonstrates a comparison of the mean Nusselt and Sherwood numbers computed with various values of the buoyancy ratio. As we can see, the present results and those of Hadidi *et al.* are in excellent agreement with a maximum discrepancy of about 2%.

Table 1. Average Nusselt and Sherwood numbers obtained with our computer code and those of Hadidi *et al.* $Ra = 10^6$, $Pr = 7$, $Da = 10^{-4}$, $Le = 10$.

N	Hadidi <i>et al.</i> [13]		Present Work	
	Nu	Sh	Nu	Sh
0	2.83	10.25	2.79	10.29
10	3.95	26.30	3.91	26.33
15	4.57	29.75	4.56	29.81

To ascertain the numerical code validity with the inner circular results, those obtained by Kim *et al.* [15] for a cold enclosure containing a centered hot cylinder have been selected. Fig. 2 displays the comparison between the numerical Kim *et al.* predictions and the present ones in term of streamlines and Isotherm plots, Table 2 illustrates the obtained mean Nusselt number and both; Kim *et al.* and Sheikholeslami *et al.* [16], for various Rayleigh

values. A great agreement between our results and both works is reported, what validates our code via the circular shape.

Then, to check the numerical code validity with experimental results, those obtained by Weaver and Viskanta [17] for an Ethanol/Nitrogen binary fluid have been selected. Fig. 3 displays the comparison between the experimental data and both, the numerical Weaver and Viskanta predictions and the present ones in term of velocity contours. Once again, the numerical results show a good qualitative concordance with the experimental data and a great agreement with the numerical Weaver and Viskanta predictions.

In order to determine a proper grid for the numerical simulations, a grid independence study is conducted for the convection phenomenon inside the porous

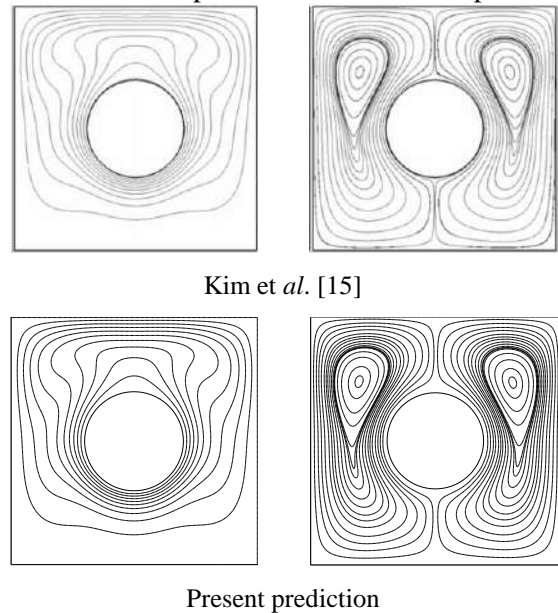


Figure 2. Comparison between the present results and those reported by Kim *et al.* [15], $Pr = 0.71$.

Table 2. Mean Nusselt number obtained by the present solution and previous works [15, 16], for various Rayleigh numbers, $Pr = 0.71$.

Ra	Kim <i>et al.</i> [15]	Sheikholeslami <i>et al.</i> [16]	Present work	$\Delta(\%)$
10^3	4.95	4.97	4.97	0.42
10^4	5.03	5.09	5.05	0.40
10^5	7.71	7.67	7.72	0.13

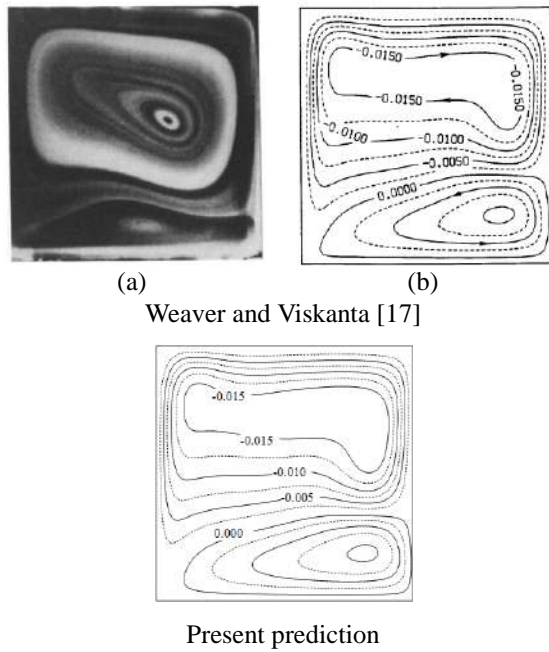


Figure 3. Ethanol/Nitrogen binary fluid in a square cavity, (a): $Gr = 1.157 \cdot 10^6$, $N = -2.335$, $Pr = 0.802$, $Sc = 0.555$. (b): $Gr = 1.121 \cdot 10^6$, $N = -2.328$, $Pr = 0.802$, $Sc = 0.557$. squares previously shown in Fig. 1. Several mesh distributions ranging from 161^2 to 401^2 were tested and the mean Sherwood number of the squares, for the above uniform grids, is presented in Fig. 4. It is observed that a 201^2 uniform grid is adequate for a grid independent solution. However, a fine structured mesh of 241^2 is used to avoid round-off error for all other calculations in this investigation.

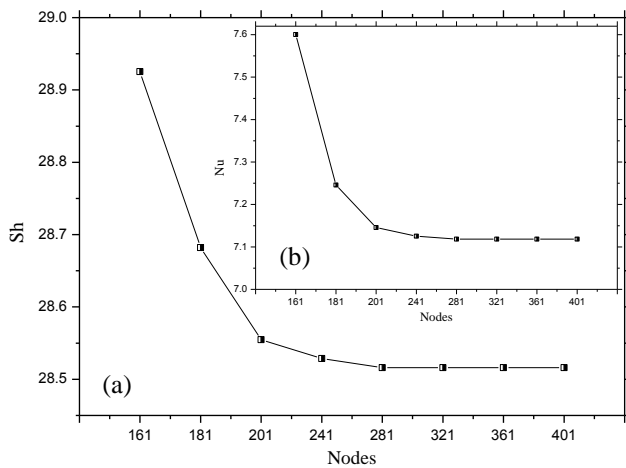


Figure 4. Mean Sherwood (a) and Nusselt numbers (b) of the porous enclosure for different uniform grids. $Da = 10^{-3}$, $Le = 10$, $N = 10$, $Ra^* = 100$, $d = 0.40$.

RESULTS AND DISCUSSION

The range of parameters that has been examined in this study concerns the cooperating buoyancy forces domain. The value of the buoyancy ratio has been taken from 0 to 30 and that, for various values of the porous thermal Rayleigh number ($Ra_T Da$), which ranging from 100 to 2000. The Lewis number has been taken between 10 and 300. The source diameter has been taken between 10% and 90% the enclosure length, when both the Prandtl and the Darcy numbers are fixed at 10 and 10^{-3} , respectively.

Impact of Lewis Number buoyancy ratio

When the buoyancy ratio and the source diameter are fixed at 10 and 0.20, respectively, the results illustrated in Fig. 5 have been obtained for two different values of Lewis number such as 10 and 100, respectively.

By presenting the profile of the vertical velocity ratio V/V_{max} , in the mid-plane of the enclosure, side by side with the temperature and the concentration profiles, it is found that the flow driven by buoyancy near the side-walls is due primarily to concentration gradient; as the temperature variation is insignificant, which is not the same near the circular source where; the buoyancy effect is caused by the combined effect of the temperature and the concentration variations.

The increase in Lewis number causes the diminution of the thickness of the mass boundary layer near the active walls unlike the temperature one, what enhances accordingly the computed local Sherwood value and decrease the Nusselt one.

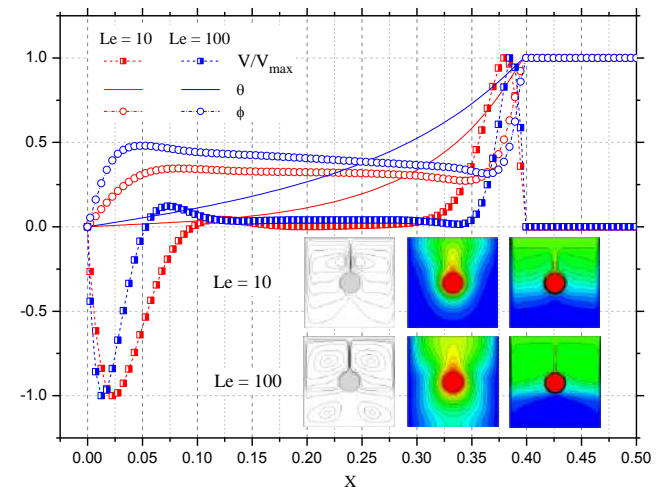


Figure 5. V/V_{max} , θ and ϕ profiles at the mid-section of the enclosure for various values of Lewis number. $Da = 10^{-3}$, $N = 10$, $Ra^* = 100$, $d = 0.20$.

When the Lewis number is fixed at 10, Fig.6 displays the impact of the buoyancy ratio on the flow field, side by side with the temperature and the concentration. As for the last one, (Fig.5), and near the side-walls, the flow driven by buoyancy is due primarily to concentration gradient; as the temperature variation still insignificant. Near the circular source, the buoyancy effect is caused by the combined effect of the temperature and the concentration variations.

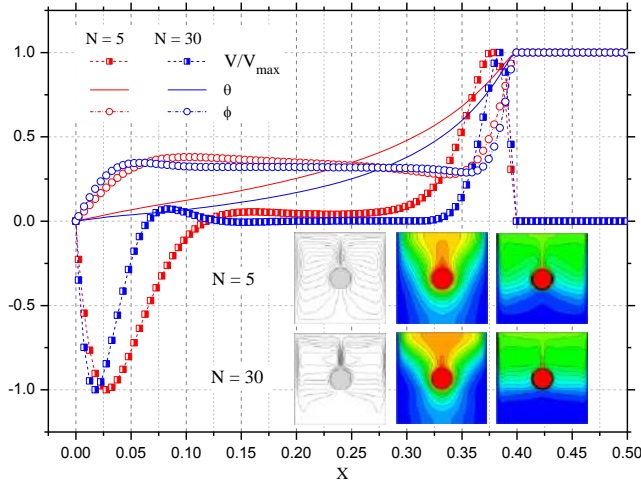


Figure 6. V/V_{\max} , θ and ϕ profiles at the mid-section of the enclosure for various values of buoyancy ratio. $Da = 10^{-3}$, $Le = 10$, $Ra^* = 100$, $d = 0.20$.

The increase in the buoyancy ratio makes the thermal and the solutal boundary layers thinner near the active walls, what improves the local transfer characteristics (i.e. local Nu and Sh) into these regions and so the overall thermosolutal transfer into the porous enclosure.

Impact of the source' diameter

As far as the source diameter effect is conducted, Fig.7 displays the thermal and solutal transfers as a function of the source geometry which reported by the aspect ratio (d/H) and that, for various values of the Lewis and buoyancy ratio, ($Ra^* = 100$).

For a given value of Le (or N as well), a further increase in the aspect ratio to 0.80 causes a significant improvement in thermosolutal convection, as the latter controls this phenomenon into the porous square. Going far with its value, the use of an aspect ratio greater than '0.80' die out the impact of Lewis and buoyancy ratio on the mean heat transfer as the conductive regime will take control.

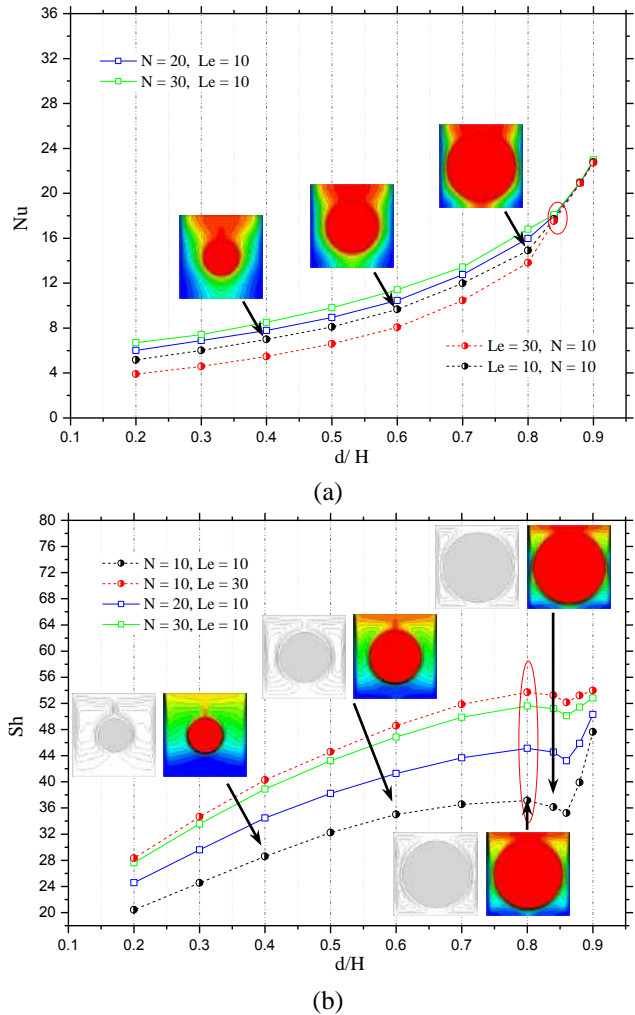


Figure 7. Mean Nusselt (a) and Sherwood numbers (b) as a function of the source diameter. $Da = 10^{-3}$, $Ra^* = 100$. After this critical value, (i.e. $d/H = 0.80$), the Sherwood number decreases a little before starting another increase. This reduction may relate to the fluid mass which is very low and that, raison of the enhancement of the source diameter. The increase in the Sherwood number once again can be related to the pure diffusion regime, which can be reached by using an important aspect ratio such 0.90.

Proposed correlations

Summarizing our numerical predictions, (Fig. 8(a,b)) and by taking into account the previous observations, new powerful correlations that give the heat and mass transfers into the porous square can be proposed as:

$$Sh|_{N \geq 0} = 0.7524 \left[\frac{Ra^* Le (N+1)}{(1 - (d/H))^3} \right]^{0.3258} \quad (10)$$

$(R^2 = 0.998)$

$$Nu|_{N>0} = 3.338$$

$$+ 1.7144 \text{ Log} \left[\left(\frac{Ra^* |N|}{Le} (d/H)^{2.2} \right)^{0.48} \right] \quad (11)$$

$$- 0.034 \left\{ \text{Log} \left[\left(\frac{Ra^* |N|}{Le} (d/H)^{2.2} \right)^{0.48} \right] \right\}^2$$

$(R^2 = 0.991)$

The last ones, made using the solutal Rayleigh number $Ra^* Le (N+1)$ and the aspect ratio d/H , are available for a Lewis number ranging from 10 to 300, a buoyancy ratio taking between 0 and 50, a porous thermal Rayleigh number in between 100 and 2000, and an aspect ratio in between 0.20 and 0.80.

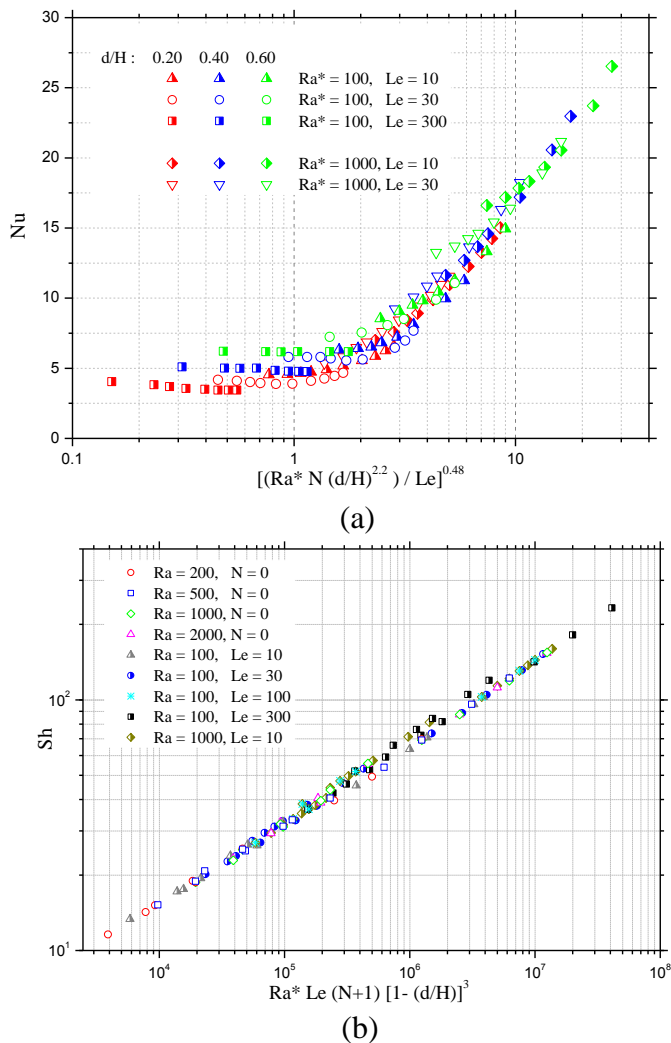


Figure 8. Proposed model for the mean Nusselt (a) and Sherwood numbers (b).

CONCLUSION

A numerical investigation of double-diffusive natural convection phenomenon inside a square Darcy-Brinkman porous enclosure, having a centered circular source was realized in this paper.

In general; heat and mass transfers seems to be severely affected by the source diameter as well as the governing parameters such the buoyancy ratio, the Lewis and the porous thermal Rayleigh numbers.

Then, new powerful Sherwood and Nusselt correlations, which display the heat and mass transfer inside the square, are expected with a precision of about 2%. Note that the present investigation doesn't take into account effects of other parameters such as the porosity and the Darcy number, what provide guidance for future work.

REFERENCES

1. Nield, D.A and Bejan, A, 1992, Convection in porous media, Springer, Berlin.
2. Ostrach, S,1980, Natural convection with combined driving forces, Phys-Chemical Hydrodynamic, **01**, pp. 233-247.
3. Kamotani, Y, Wang, L.W, Ostrach, S, Jiang, H.D, 1985, Experimental study of natural convection in shallow enclosures with horizontal temperature and concentration gradients, Int. J. Heat Mass Transfer, **28**, pp. 165-173.
4. Lee, J, Hyun, M.T, Kim, K.W, 1988, Natural convection in confined fluids with combined horizontal temperature and concentration gradients, Int. J. Heat Mass Transfer, **31**, pp. 1969-1977.
5. Benard, C, Gobin, D, Thevenin, J, 1989, Thermosolutale natural convection in a rectangular enclosure: Numerical Results, in Heat Transfer in Convective Flows, ASME, R. K. Shah, Ed., pp. 249-254, New York.
6. Han, H, Kuehn, T.H, 1989, A numerical simulation of double diffusive natural convection in a vertical rectangular enclosure, in Heat Transfer in Convective Flows, ASME, R.K. Shah, Ed., pp. 149-154, New York.
7. Chang, J, Lin, T.F, 1993, Unsteady thermosolutal opposing convection of liquid-water mixture in a square cavity- II: Flow structure and fluctuation analysis, Int. J. Heat Mass Transfer, **36**, pp. 1333-45.
8. Chen, F, 1993, Double-diffusive fingering convection in a porous medium, Int. J. Heat Mass Transfer, **36**, pp. 793-807.
9. Trevisan, O, Bejan, A, 1987, Heat and mass transfer by high Rayleigh number convection in a porous medium

- heated from below, *Int. J. Heat Mass Transfer*, **30**, pp. 2341-2356.
10. Lin, T.F, Huang, C.C, Chang, T.S, 1990, Transient binary mixture natural convection in a square enclosure, *Int. J. Heat Mass Transfer*, **33**, pp. 287-299.
 11. Rachid, B, 1993, Thermosolutal convection: fluid flow and heat transfer numerical simulations, Ph.D. Thesis, Pierre and Marie Curie, Paris.
 12. Ragui, K., Boutra, A., Benkahla, Y.K., 2016, On the Validity of a Numerical Model Predicting Heat and Mass Transfer in Porous Squares with a Bottom Thermal and Solute Source: Case of Pollutants Spreading and Fuel Leaks, *Mechanics & Industry* : Forthcoming, Accepted: 14/11/2015.
 13. Patankar, S.V, 1980, Numerical heat transfer and fluid flow, Mc Grow, New York.
 14. Hadidi, N, Ould Amer, Y, Bennacer, R, 2013, Bi-layered and inclined porous collector: Optimum heat and mass transfer, *Energy*, 51, pp. 422-430.
 15. Kim, B.S., Lee, D.S., Ha, M.Y., Yoon, H.S., 2008, A numerical study of natural convection in a square enclosure with a circular cylinder at different vertical locations, *Int. J. Heat Mass Transf.* **51**, pp. 1888-1906.
 16. Sheikholeslami, M., Gorji-Bandpy, M., Pop, I., Soheil, S., 2013, Numerical study of natural convection between a circular enclosure and a sinusoidal cylinder using control volume based finite element method, *Int. J. Thermal Sci.* **72**, pp. 147-158.
 17. Weaver, J.A, Viskanta, R, 1992, Natural convection in binary gases driven by combined horizontal thermal and vertical solutal gradients, *Exp. Thermal Fluid Sci.*, **5**, pp. 57-68.

NUMERICAL AND ANALYTICAL ANALYSIS OF THE THERMOSOLUTAL CONVECTION IN AN HETEROGENEOUS POROUS CAVITY

Khadija CHOUKAIRY ^{1*}, Rachid BENNACER ²

¹ Université Hassan 1 Settat, Laboratoire IPOSI, Equipe Energétique, Ecole Nationale des sciences appliquées
Khouribga, Maroc

² Ecole Normale Supérieure (ENS)-Cachan - Dpt. GC/LMT, France

*Corresponding author: (khadijachoukairv@yahoo.fr)

ABSTRACT

This study carries the natural thermosolutal convection induced in heterogeneous porous media. The configuration considered is cartesian. The horizontal and vertical walls are submitted to different mass and heat flows. The equations which govern this type of flow are solved numerically by using the finite volume method. The flow is considered two-dimensional and laminar. The model of Darcy and the approximation of the Boussinesq are taken into account. The parameters which control the problem are the thermal Darcy-Rayleigh number, R_T , the buoyancy ratio, N , the Lewis number, Le , the aspect ratio of the enclosure, A and the local permeability ratio, K_r . The flow fields, temperature and concentrations are given for various values of the local permeability. The effects of increasing the local permeability, the thermal Darcy-Rayleigh number R_T and the lateral heating on the heat and mass transfer are discussed. These numerical results were confirmed analytically by using the parallel flow approximation. A good agreement was found between the two analytical and numerical approaches, which confirm the validity of the analytical approach in such heterogeneous domain. The flow intensity and transfer increase with the increase of the permeable heterogeneity of the domain.

KEYWORDS

NOMENCLATURE

A aspect ratio of the enclosure, L/H
 a lateral heating intensity
 b vertical heating intensity
 C_s dimensionless concentration gradient in x -direction
 C_T dimensionless temperature gradient in x -direction
 g gravitational acceleration
 H height of the enclosure
 j constant mass flux per unit area
 K dimensionless resistivity of the porous medium
 K_r reference resistivity
 L width of the cavity
 Le Lewis number, α/D
 N buoyancy ratio, $\beta_s \Delta S / \beta_T \Delta T'$
 n constant controlling the permeability heterogeneity, Eq. (5)

Nu Nusselt number
 q constant heat flux, per unit area
 R_T thermal Rayleigh number
 S dimensionless concentration $(S' - S'_a) / \Delta S'$
 Sh Sherwood number
 T dimensionless temperature, $(T' - T'_0) / \Delta T'$
 (u, v) dimensionless velocity, $(u' / (\alpha/H), v' / (\alpha/H))$
 (x, y) dimensionless coordinate system, $(x'/H, y'/H)$

Greek symbol

α fluid thermal diffusivity, $\lambda / (\rho C)_f$
 β_s solutal expansion coefficient
 β_T thermal expansion coefficient
 ν kinematic viscosity
 ρ fluid density
 $(\rho C)_f$ fluid heat capacity

- $(\rho C)_p$ saturated porous medium heat capacity
- σ heat capacity ratio, $(\rho C)_p / (\rho C)_f$
- Ψ dimensionless stream function, Ψ' / α
- Ψ_0 dimensionless stream function at the center of the cavity

SUBSCRIPT

- S solutal
- 0 refers to the center of the cavity
- T temperature

INTRODUCTION

Natural convection in fluid saturated porous media occurs in many engineering systems and in nature. It includes the disposal of waste material, drying processes, migration of moisture contained in fibrous insulation, grain storage installations, food processing, chemical transport in packed-bed reactors, contamination transport in saturated soil, etc., see for instance Alavyoon [1], and Montel [2]. Most investigation of this topic are concerned with the case of isotropic porous media with different configuration (Cartesian, Cylindrical) in transient and steady state, Choukairy [3], Bennacer [4]. However, in several applications the porous materials present macroscopically heterogeneity or anisotropy. Natural convection in such heterogeneous porous media has received relatively little attention despite its broad range of applications. Castinel and Cambarnous [5] have considered the variable permeability for the study the flow through a porous medium. Both experimental and theoretical results were reported by those authors for the case of a layer with impermeable boundaries. The same configuration was considered by McKibbin [6], Nilsen and Storesletten [7], for various boundary conditions.

The study of such effect on the mixed convection in semi infinite porous medium bounded by horizontal surfaces has been considered by Hassanien [8]. It was found that a variable permeability tends to increase the heat transfer rate. The effect on an anisotropic permeability of arbitrary orientation on the convective heat transfer in a vertical cavity heated isothermally from the sides was investigated numerically by Zhang [9]. The same configuration was considered by Degan [10] for the case of constant applied heat fluxes on the vertical walls of the enclosure. The results indicate that a maximum (minimum) heat transfer occurs when the porous matrix is oriented with its principal axis with higher permeability parallel (perpendicular) to the vertical direction.

The main purpose of this work is to study the natural convection in a porous layer incorporating the permeability variation especially the increase close to the horizontal surfaces. The horizontal and vertical walls are maintained at different mass and heat conditions. The parallel flow

approximation was applied and validated numerically using finite-volume approach.

MATHEMATICAL MODEL

Consider a fluid-saturated, porous layer enclosed in a rectangular cavity of length L and height H as illustrated on Fig.1. The origin of the coordinate system is located at the center of the cavity. The two horizontal walls of the cavity are exposed to uniform heat (q) and solute (j) fluxes. The vertical walls are subjected to uniform heat flux ($a \times q$), where a is constant values. All the boundaries are impermeable. It is assumed that the flow is incompressible laminar and the fluid is Newtonian.

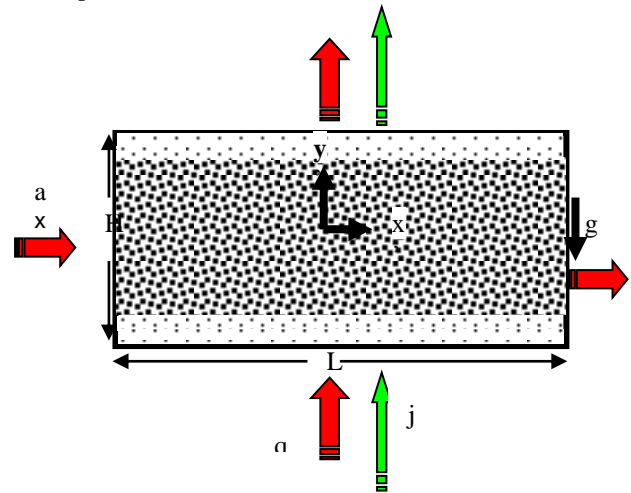


Figure 1: Geometry of the problem

The problem is considered as two-dimensional. The Boussinesq approximation is assumed to be valid. The thermo physical properties of the fluid are assumed to be constant, except the density ρ of the mixture is related to the temperature and solute concentration by a linear equation of state:

$$\rho(T', S') = \rho_r [1 - \beta_T(T' - T'_0) - \beta_S(S' - S'_0)] \quad (1)$$

where β_T and β_S are the thermal and solutal relative density variation respectively and ρ_r is the reference density computed at $T' = T'_0$ and $S' = S'_0$.

The porous matrix is assumed to be rigid and in thermal equilibrium with the fluid.

The dimensionless equations describing conservation of momentum, energy and concentration are given respectively by:

$$\frac{\partial u}{\partial x} + \frac{\partial v}{\partial y} = 0 \quad (2)$$

$$\nabla \left[\frac{1}{K_r(y)} \nabla \Psi \right] = -Rt \frac{\partial(T+NS)}{\partial x} \quad (3)$$

$$u \frac{\partial T}{\partial x} + v \frac{\partial T}{\partial y} + \frac{\partial T}{\partial t} = \nabla^2 T \quad (4)$$

$$u \frac{\partial S}{\partial x} + v \frac{\partial S}{\partial y} + \varepsilon \frac{\partial S}{\partial t} = Le^{-1} (\nabla^2 S) \quad (5)$$

In the present study it is assumed that the permeability of the porous medium changes with the depth, increasing from the bulk to the horizontal surfaces of the layer in the following way Fig.2:

$$K_r(y) = 1 + 4 * (2 * y)^n = 1 + 4 * (2 * y)^{1/b} \quad (6)$$

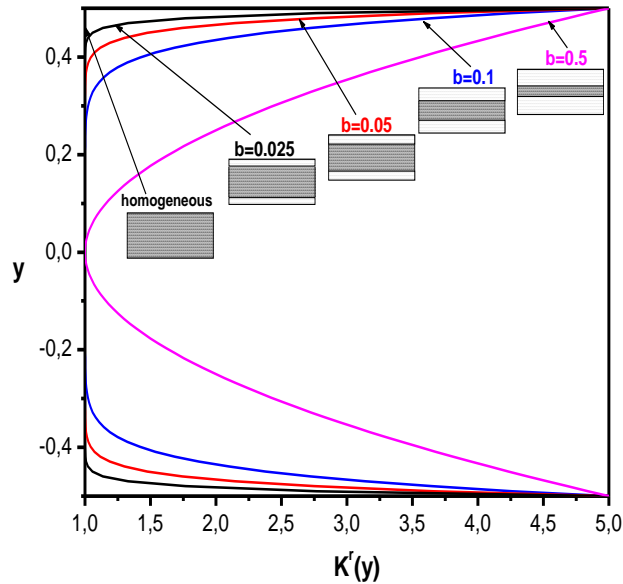


Figure 2: Permeability of the porous media versus the depth for different b values.

The above equations were obtained using the following dimensionless quantities

$$(x, y) = \frac{(x, y)}{H} \quad (u, v) = \frac{(u, v)H}{\alpha} \quad (7)$$

$$T = \frac{(T - T_0)}{\Delta T} \quad \text{where} \quad \Delta T' = \frac{qH}{\lambda} \quad (8)$$

$$S = \frac{(S - S_0)}{\Delta S} \quad \text{where} \quad \Delta S' = \frac{jH}{D} \quad (9)$$

$$\psi = \frac{\psi'}{\alpha} \quad K_r(y) = \frac{K'(y)}{K_r^0} \quad \varepsilon = \frac{\phi}{\sigma} \quad (10)$$

where α is the fluid mixture thermal diffusivity, σ heat capacity ratio, λ the thermal conductivity, q and j are respectively the constant heat and mass fluxes applied on the system. K' is permeability of the porous medium, K_r^0 the reference resistivity at the center of the layer and ϕ the porosity of the porous medium.

The stream function ψ' is defined by: $u' = -\frac{\partial \psi'}{\partial y'}$ and

$$u' = -\frac{\partial \psi'}{\partial y'}, \quad \text{such that the conservation of mass is}$$

satisfied.

The dimensionless parameters that characterize the problem in the equations (4)-(6) are:

$$Rt = \frac{g\beta\Delta TH}{\kappa\alpha\nu}, \quad N = \frac{Gr_s}{Gr_T} = \frac{\beta_s \Delta S'}{\beta_T \Delta T'}, \quad A = \frac{L}{H'} \quad (2a)$$

$$Le = \frac{Sc}{Pr} \quad \text{where} \quad Pr = \frac{\nu}{\alpha} \quad \text{and} \quad Sc = \frac{\nu}{D} \quad (11b)$$

where Rt , N , A and Le are the thermal Darcy-Rayleigh number, the solutal to thermal buoyancy ratio, the domain aspect ratio and the Lewis number, respectively.

The dimensionless boundary conditions on the vertical walls and horizontal surfaces are as follows:

$$x = \pm \frac{A}{2} \quad \frac{\partial T}{\partial x} = \alpha \quad \text{and} \quad \frac{\partial S}{\partial x} = 0 \quad (3a)$$

$$y = \pm \frac{1}{2} \quad \frac{\partial T}{\partial y} = -1 \quad \text{and} \quad \frac{\partial S}{\partial y} = -1 \quad (12b)$$

The Nusselt and Sherwood numbers are evaluated by:

$$Nu = \frac{1}{\alpha} \quad (4a)$$

$$Sh = \frac{1}{\Delta S} \quad (13b)$$

where $\Delta T = \left(T \left(x, -\frac{1}{2} \right) - T \left(x, +\frac{1}{2} \right) \right)$ and

$\Delta S = \left(S \left(x, -\frac{1}{2} \right) - S \left(x, +\frac{1}{2} \right) \right)$ are, the average

temperature and concentration difference between the two horizontal surfaces, respectively.

NUMERICAL MODEL

The governing equations (2) to (5) were solved by using the control volume finite difference method described by Patankar [11]. SIMPLER algorithm is employed to solve the equations in primitive variables.

Non uniform grids are used in the program, allowing fine grid spacing near the boundaries. Calculations were necessary to check the accuracy. Convergence with mesh size was verified by employing coarser and finer grids on selected test problems. The typical grid points in the present study were (101 x 51).

The convergence criterion was based on the average residue of the continuity equation and the average quadratic residues of each governing equation evaluated on the whole computational domain. It was assumed that convergence was reached when the maximum error was within machine error (10^{-9}).

The computer code was validated with the result available in literature. The comparison was observed to be very good

ANALYTICAL SOLUTION

In this section, an analytical solution is developed for the case of $A \gg 1$, by using the parallel flow approximation.

For this situation, we have:

$$\Psi(x, y) \approx \Psi(y) \tag{5}$$

$$T(x, y) = C_T x + \theta_T(y) \tag{6}$$

$$S(x, y) = C_S x + \theta_S(y) \tag{7}$$

where C_T and C_S are unknown constant temperature and

concentration gradients, in x -direction, and θ_T and θ_S are

the temperature and concentration profiles in the vertical direction, respectively.

Substituting Eqs. (14-16) into Eqs. (3-5) yields the following set of equations:

$$\frac{1}{k_r(y)} \frac{d^2 \Psi}{dy^2} + \frac{d}{dy} \left(\frac{1}{k_r(y)} \right) \frac{d \Psi}{dy} = -E \tag{8}$$

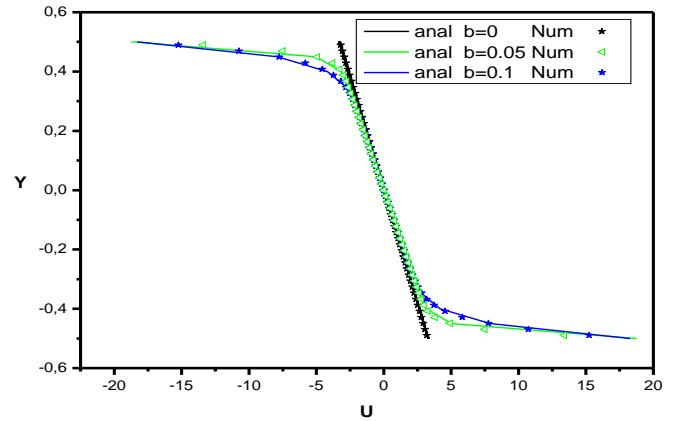
$$\frac{d^2 \theta_T}{dy^2} = C_T \frac{d \Psi}{dy} \tag{9}$$

$$\frac{d^2 \theta_S}{dy^2} = Le C_S \frac{d \Psi}{dy} \tag{10}$$

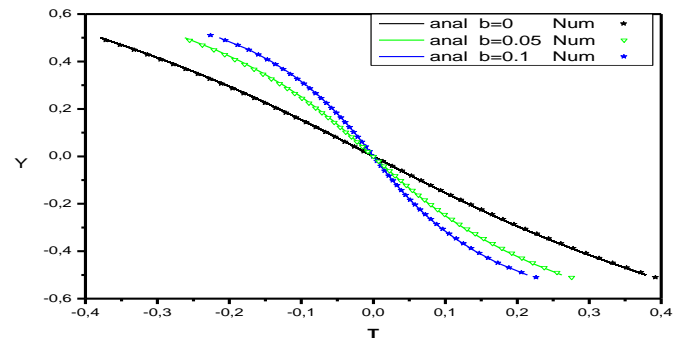
$$\text{where } E = Rt(C_T + NC_S) \tag{11}$$

RESULTS AND DISCUSSION

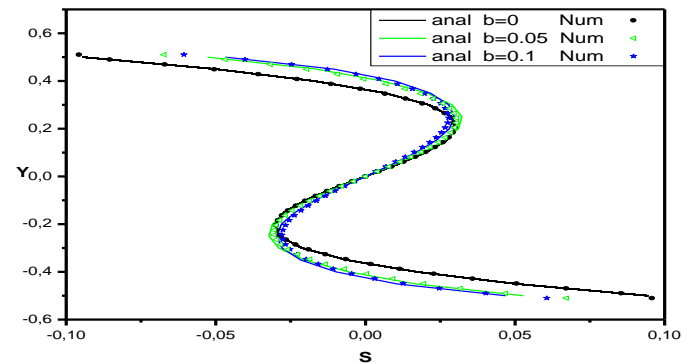
The distribution of velocity component (u), temperature (T) and concentration (S) profiles in the vertical mid-plane of the cavity for different values of heterogeneous resistivity parameter b and for $Rt=15$, $N=0.1$, $Le=10$, $a=0.05$ are represented on Fig.3. The numerical results are represented by dotted symbols on the other hand the analytical results are by solid lines. The results show that two results (analytical and numerical) are in excellent agreement. These profiles are anti-symmetrical for all values of b (Eq.5). The homogeneous cases ($b=0$) correspond to a porous layer with a constant permeability for which the velocity, temperature and concentration profiles varies linearly with y with respect to the center of the layer. Such linear velocity behavior is a consequence slip boundary condition and Darcy flow. As the values of b is increased, the flow resistance is lower in the top and bottom part of the layer the flow intensity is promoted in this region Fig.3a. As a result, Fig.3b-c indicates that both the temperature and concentration increase at the top and the bottom of the layer.



(a)



(b)



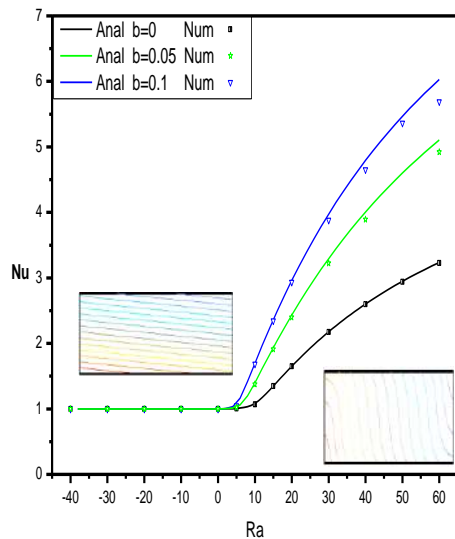
(c)

Figure 3: Profiles of Horizontal velocity component (a), Temperature(b) and Concentration(c) in the vertical mid-plan for different values of b ($Rt = 15$).

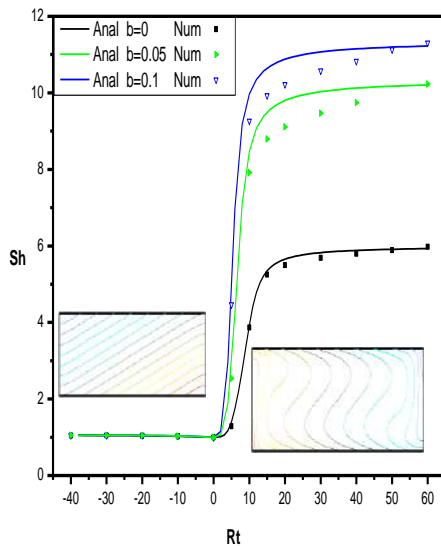
Fig. 5 illustrates the effect of the Rayleigh number Rt and b on Nu and Sh for $a=0.05$, $Le=10$ and $N=0.1$.

For Fig.5a, and for $Rt < 0$, the heat and mass effect are cooperating, and they are in the same direction as the forces of gravity, so the fluid is at rest state with corresponding diffusive heat and mass transfer like shows

it the isotherm and isoconcentration in top graphs. When $Rt > 0$, the heat and mass effect are cooperating, and they are in the opposite direction as the forces of gravity, the flow is destabilizing.



(a)



(b)

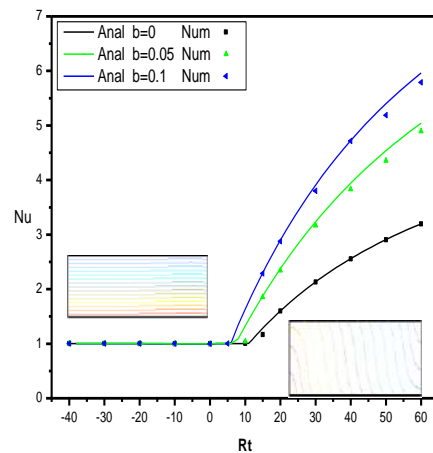
Figure 3: Effect of Rt and b on the Nusselt Number Nu (a) and Sherwood number Sh (b) for $N=0.1$

Fig6 illustrates the effect of the Rayleigh number Rt and b on Nu and Sh for $a=0.05$, $Le=10$ and $N=-0.1$.

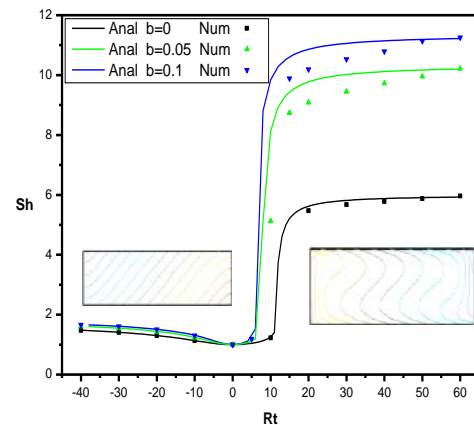
The mass and heat effect are acting in opposite direction. For $Rt < 0$, the heat transfer and the forces of gravity are in the same direction, so the heat transfer is stabilizing, what corresponds to a diffusive transfer (see the isotherm in top graphs), on the other hand the mass transfer is

destabilizing. When $Rt > 0$, the heat transfer and the forces of gravity are in the opposite direction, so the heat transfer is destabilizing, on the other hand the mass transfer and the forces of gravity are in the same direction, so the mass transfer is stabilizing

The influence of parameter b on the heat and mass transfer rates is observed to be significant. Thus, it's observed that the increase of b from 0 to 0.1. All the curves indicate that the mass transfer tend asymptotically toward constant values that depend upon the variable permeability parameter b .



(a)



(b)

Figure 6: Effect of Rt and b on the Nusselt Number Nu (a) and Sherwood number Sh (b) for $N=-0.1$

CONCLUSIONS

In this paper, the effect of the hydraulic heterogeneity on natural convection in a rectangular cavity is investigated. The two horizontal walls of the cavity are exposed to uniform heat and solute fluxes. The vertical walls are

subjected to uniform heat flux. The analytical result shows a good agreement with a numerical result. The influence of the Rayleigh number, inhomogeneity b and the buoyancy ratio N on the Nusselt number (Nu) and Sherwood number (Sh) are also analyzed numerically and analytically. It's found that the heat and mass transfer are doubled while passing from the homogeneous case ($b=0$) to the heterogeneous case ($b=0.05, b=0.1$).

References

1. Alavyoon,F., Eklund,A., Bark,F.H, Simonsson,D, 1991, Theoretical and experimental studies of free convection and stratification of electrolyte in a lead-acid cell during recharge. *I. Electrochim. Acta*;14 :2153-2164.
2. Montel F, 1994, Importance de la thermodiffusion en exploration et production petrolieres. *Entropie*, 184/185: 86-93.
3. K.Choukairy , R.Bennacer, 2006, 'The effects of porous block on transient natural convection' *Mecanique and Industrie*, 7,pp. 573-578.
4. Bennacer R., Beji H., and Mohamad A.A, 2003, Double Diffusive Natural Convection in a Vertical Multilayer Saturated Porous Media, *International Journal of Thermal Sciences.*: **42**, 141-151.
5. Castinel, G. and Combarous, M.,1974, Critère d'apparition de la convection naturelle dans une couche poreuse anisotrope, *C. R. Acad. Sci. Paris B278*: 701-704.
6. McKibbin, R.,1984, Thermal convection in a porous layer: effects of anisotropy and surface boundary conditions, *Trans. Porous Media* 1 271-292
7. Nilsen, T.; Storesletten, L.,1990, An analytical study on natural convection in isotropic and anisotropic porous channels, *J. Heat and Transfer*; 112: 396-401
8. .Hassanien IA, Salama AA, Elaiw AM, 2003, Variable permeability effect on vortex instability of mixed convection flow in a semi-infinite porous medium bounded by a horizontal surface. *App. Math. Comp*, 146: 829-847
9. Zhang, X.,1993, Convective heat transfer in a vertical porous layer with anisotropic permeability, Proc. 14th Canadian Congr. *Applied Mechanics*, 2: 579-580
10. Degan G., Beji H., Vasseur P. and Robillard L.,1998, Effects of anisotropy on the development of convective boundary layer flow in porous media, *Int. Comm. Heat Mass Transfer*; 25, 8: 1159-1168
11. Patankar S, 1980, Numerical heat transfer and fluid flow. Hemisphere, Washington, DC.

Effect of buoyancy ratio on unsteady double diffusive natural convection in vertical open-ended cylinder filled with porous medium.

N. Himrane^{1,*}, D.E. Ameziani², M. El Ganoui³, M. Balistrrou¹

¹ : UMBB- Faculté des sciences de l'ingénieur (FSI)

Laboratoire Energétique Mécanique et Ingénierie (LEMI)

²: USTHB – Laboratoire des transports polyphasiques et milieu poreux (LTPMP)

³: Université de Lorraine – Laboratoire IUT de Longwy - LERMA

* Corresponding Authors: nabil.himrane@gmail.com

ABSTRACT

The effect of a buoyancy ratio on the double-diffusive natural convective flow in a vertical, open ended, porous cylinder has been investigated numerically. The medium is the seat of a chemical reaction formulated by reducing the Arrhenius law to a linear approach. Two types of boundary conditions have imposed on lateral wall of enclosure, namely a constant temperature and a sinusoidal time variation temperature. The numerical results show that the flow behavior strongly depend on the buoyancy ratio values. Three types of flows take place, chimney flow with and without fluid recirculation and top aspiration flow. Further, the effect of buoyancy ratio (N) at which the different flow types occur is significantly influenced by the thermal Rayleigh number (Ra), aspect ratio (A), reaction rate (Ak), and dimensionless temperature amplitudes (XA). The relative heat transfer enhancement between sinusoidal and constant wall temperature depend on the controlling parameters and it is particularly sensitive to the buoyancy ratio. The relative heat transfer enhancement between sinusoidal and constant wall temperature is profoundly affected by the buoyancy ratio, thermal Rayleigh number and dimensionless amplitude.

Keywords: Double-diffusive convection, porous medium, open-ended channel.

NOMENCLATURE

A Aspect ratio, $A=R/H$
 Ak Scaled lumped effective reaction rate
 Bi_r Heat transfer Biot number
 Bi_m Mass transfer Biot number
 C_p Specific heat at constant pressure
 C Dimensionless concentration
 D Species diffusivity, $m^2 s^{-1}$
 h Heat transfer coefficient at the cylinder exit,
 H Cylinder height, m
 k Thermal conductivity
 K Porous medium permeability
 Le Lewis number, $Le = \alpha_f / D_{eff}$
 Nu Nusselt number
 N Buoyancy ratio
 P Dimensionless pressure

R Dimensionless radial coordinate
 Ra Thermal Rayleigh number
 Ra_c Solutal Rayleigh number
 R_k Conductivity ratio, $R_k = k_{eff} / k_f$

T Dimensionless temperature
 T Dimensionless time
 U Dimensionless longitudinal velocity
 V Dimensionless radial velocity
 X Dimensionless axial coordinate
 XA Dimensionless amplitude

Greek letters
 A Thermal diffusivity, $m^2 s^{-1}$
 μ Dynamic viscosity, $kg m^{-1}s^{-1}$
 ρ Fluid density, $kg m^{-3}$
 σ Heat capacity ratio, $\frac{(\rho C_p)_{eff}}{(\rho C_p)_f}$
 ε Porosity
 τ Dimensionless period

INTRODUCTION

Double-diffusive convection in porous media is encountered in many geophysical and engineering applications. Many studies have been carried out on natural convection heat and mass transfer experimentally and numerically in enclosures. Nield [1] was the first to investigate double diffusive

convection in a porous medium using linear stability theory for various thermal and solutal boundary conditions. An extension of the analysis of Nield was carried by Taunton *et al.* [2] in order to more completely characterize the onset of convection in an infinite horizontal porous medium stratified by temperature and concentration. Shipp *et al.* [3,4] performed a detailed analysis on double-diffusive convection in a vertical annulus. The effects of thermal Rayleigh number, Lewis number and buoyancy ratio are investigated on flow transition and flow reversal for fixed values of radius ratio, aspect ratio and Prandtl number. Bennacer *et al.* [5] numerically investigated the double-diffusive natural convection in a vertical enclosure filled with a saturated anisotropic porous medium. They found that the anisotropic properties of the porous medium considerably modify the heat and mass transfer rates from that expected under isotropic conditions. The influence of other factors such as thermal stratification effect Ratish *et al.* [6], anisotropy Bennacer *et al.* [7] and a non-Newtonian power law fluid Ching-Yang [8] on double diffusive natural convection in porous enclosures have also been investigated. In the literature, few studies were interested to the double diffusive natural convection in porous open geometry. This problem is particularly difficult to solve numerically. In fact, the flow rate of the fluid in the channel is imposed indirectly by the intensity of the heated wall. The effect of two types of the limit conditions in the external wall of the vertical open ended and porous cylinder has been investigated by Himrane *et al.* [9]. The aim of the present work is to investigate numerically the problem of unsteady double diffusive natural convection in vertical enclosure opened at both ends and filled with a saturated porous medium.

Mathematical formulation

The physical domain of the flow through the vertical open ended, and porous cylinder is given in figure 1.

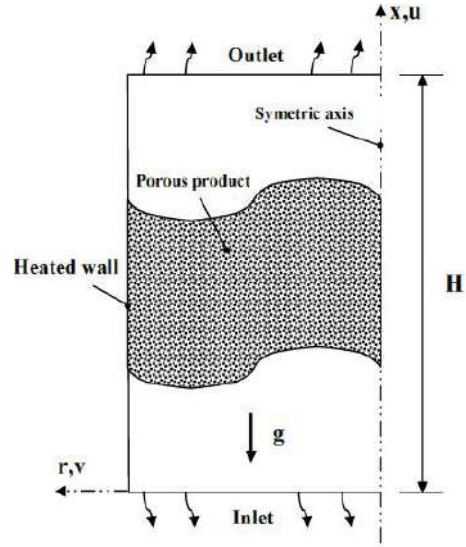


Figure 1 Geometrical configuration

It is assumed that the flow in the cylinder is axis-symmetric, allowing a two-dimensional approach. The porous medium is considered to be homogeneous, isotropic and saturated with a single phase fluid, which is in thermal equilibrium with the solid matrix. The Boussinesq's approximation is used to formulate the density distortions in the domain. The thermal/concentration dependency of the density ρ is given by the relation:

$$\rho(T', C') = \rho_0 [1 - \beta_T (T' - T'_{amb}) - \beta_C (C' - C'_{amb})] \quad (1)$$

The chemical reaction is formulated, by reducing the Arrhenius law to a linear approach under the assumption that the thermal maximum gradient is low [10]. The Darcy flow model is assumed to be valid. The analysis is performed in terms of non-dimensional parameters. To this end, the non-dimensionalization of the governing equations and boundary conditions is carried out using the following scaling:

$$L_{ref} = H; \Delta T_{ref} = T'_h - T'_{amb}; P_{ref} = \left(\frac{\mu \cdot \alpha_f}{K} \right)$$

$$U_{ref} = \frac{\alpha_f}{H}; t_{ref} = \left(\frac{H^2}{\alpha_f} \right); \Delta C_{ref} = C'_{amb} - C'_0 \quad (2)$$

The dimensionless quantities are :

$$(x, r) = \frac{(x', r')}{L_{ref}}; (U, V) = \frac{(U', V')}{U_{ref}}; T = \frac{T' - T'_h}{\Delta T_{ref}};$$

$$C = \frac{C' - C'_0}{\Delta C_{ref}}; P = \frac{P' - P'_{amb}}{P_{ref}} \text{ and } t = \frac{t'}{t_{ref}} \quad (3)$$

The resulting dimensionless continuity, concentration and energy equations are as follows:

$$\frac{\partial^2 P}{\partial X^2} + \frac{1}{r} \frac{\partial}{\partial r} \left(r \frac{\partial P}{\partial r} \right) = Ra \left(\frac{\partial T}{\partial X} + N \cdot \frac{\partial C}{\partial X} \right) \quad (4)$$

$$U = Ra \left(T + N \cdot C \right) - \frac{\partial P}{\partial x} \quad (5)$$

$$V = - \frac{\partial P}{\partial r} \quad (6)$$

$$\sigma \frac{\partial T}{\partial t} + \left(U \frac{\partial T}{\partial X} + V \frac{\partial T}{\partial r} \right) = R_k \left(\frac{\partial^2 T}{\partial X^2} + \frac{1}{r} \frac{\partial}{\partial r} \left(r \frac{\partial T}{\partial r} \right) \right) \quad (7)$$

$$\varepsilon \frac{\partial C}{\partial t} + \left[U \frac{\partial C}{\partial z} + V \frac{\partial C}{\partial r} \right] = \frac{1}{Le} \cdot \left[\frac{\partial^2 C}{\partial x^2} + \frac{1}{r} \frac{\partial}{\partial r} \left(r \frac{\partial C}{\partial r} \right) \right] + Ak(T - C) \quad (8)$$

The dimensionless initial and boundary conditions are then given by

Initially (at t=0) :

$$P(x, r, 0) = 0, \quad T(x, r, 0) = 0, \quad C(x, r, 0) = 1 \quad (9)$$

At t>0 :

$$P(0, r, t) = P(1, r, t) = 0 \quad (10)$$

Owing to the symmetry requirement at the centerline (r=0) and the impermeable lateral surface of the cylinder, it follows that:

$$\frac{\partial P}{\partial r} \Big|_{(x, 0, t)} = 0 ; \quad \frac{\partial C}{\partial r} \Big|_{(x, 0, t)} = 0 ; \quad \frac{\partial T}{\partial r} \Big|_{(x, 0, t)} = 0 \quad (11)$$

$$\frac{\partial C}{\partial r} \Big|_{(x, A, t)} = 0 ; \quad \frac{\partial P}{\partial r} \Big|_{(x, A, t)} = 0 \quad (12)$$

The lateral wall temperature can be described by a sinusoidal time variation, such that:

$$T(x, A, t) = 1 + XA \sin \left(\left(\frac{2\pi}{\tau} \right) t \right) \quad (13)$$

To consider the interaction between the natural convection through the porous domain and the external ambient fluid, we use the following conditions:

For the top surface (exit):

If U>0 (outgoing flow):

$$\frac{\partial T}{\partial x} \Big|_{(1, r, t)} = -Bi_T T(1, r, t); \quad \frac{\partial C}{\partial x} \Big|_{(1, r, t)} = -Bi_m C(1, r, t) \quad (14a)$$

If U<0 (ingoing flow):

$$T(1, r, t) = 0; \quad C(1, r, t) = 1 \quad (14b)$$

For the bottom surface (entry):

If U>0 (ingoing flow):

$$T(0, r, t) = 0; \quad C(0, r, t) = 1 \quad (15a)$$

If U<0 (outgoing flow):

$$\frac{\partial T}{\partial x} \Big|_{(0, r, t)} = Bi_T T(0, r, t) ; \quad \frac{\partial C}{\partial x} \Big|_{(0, r, t)} = Bi_m C(0, r, t) \quad (15b)$$

Heat transfer rate:

Heat transfer through the system is represented in term of local Nusselt number defined as:

$$Nu(x, t) = \frac{\partial T(x, r, t)}{\partial r} \Big|_{r=A} \quad (16)$$

The space averaged Nusselt number along the cylinder which is defined as:

$$Nu = \langle Nu(t) \rangle = \int_0^1 Nu(x, t) \cdot dx \quad (17)$$

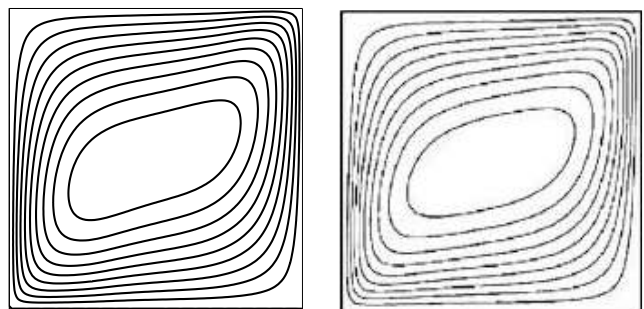
and the time averaged total Nusselt number is given by

by

$$Nu_m = \langle \overline{Nu} \rangle = \frac{1}{\tau} \int_0^1 Nu(t) \cdot dt \quad (18)$$

Validation of the numerical method

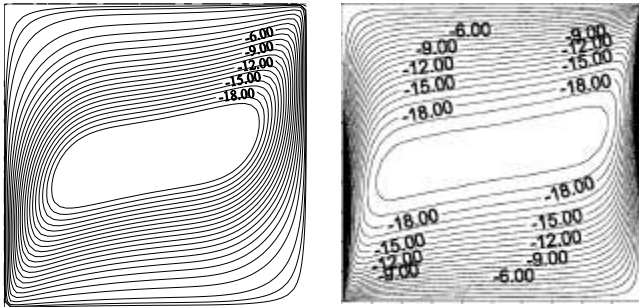
The governing equations with the associated initial and boundary conditions were solved numerically using the finite volumes method described by Patankar [11]. Note the results reported in this work are obtained using at least 81×81 irregular grid distribution. The numerical model is verified adopting the classical Darcy natural convection problem in a square porous cavity with isothermal vertical walls and adiabatic horizontal walls, for Ra= 10² and Ra= 10³.



Présent résultats

H. Hadim [2006]

Ra=10⁺²



Présent résultats Baytas et Pop [2002]
 $Ra=10^{+3}$

Figure 2. Streamlines function

A good agreement between the obtained and reported results was observed.

RESULTS AND DISCUSSION

The numerical results are presented in this section with the main objective of investigating the effect of a buoyancy ratio on the double-diffusive natural convective flow in a vertical, open ended, porous cylinder.

Effect of buoyancy ratio in the constant wall temperature case $X_A=0$:

Figure 3 gives a final diagram summarizing the flow behavior with the controlling parameters (N , Ra , A and Ak). One of the first findings is that the reaction existence extends the area of appearance of the phenomenon of recirculation for the range of the considered thermal Rayleigh number. It should be mentioned that for pure heat convection, when the buoyancy ratio is null, ($N=0$), the reaction existence does not affect the limit between the chimney natural convection and the perturbed fluid circulation.

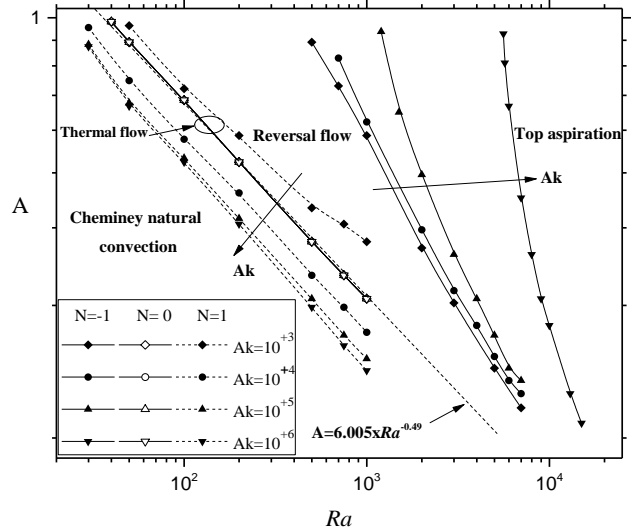


Figure 3 diagram of the onset of the different flow types for constant wall temperature ($Ra - A$) for different value of N and Ak .

This limit can be approximated by a power law expression like: $A=f(Ra^{-0.49})$. The same linear trend (of various tilt) could be observed in the low values of a and high values of ak in the aiding double diffusive flow case ($N = 1$), contrary to the opposing double diffusive flow case ($N = -1$) where this linear limit is observed in the low values of Ak .

In order to present the influence of various control parameters over the heat transfer, we present the Figure 4 which illustrates the evolution of the average heat transfer (Nu_m) for the three values of $N = 0, 1$ and -1 over considered thermal Rayleigh range.

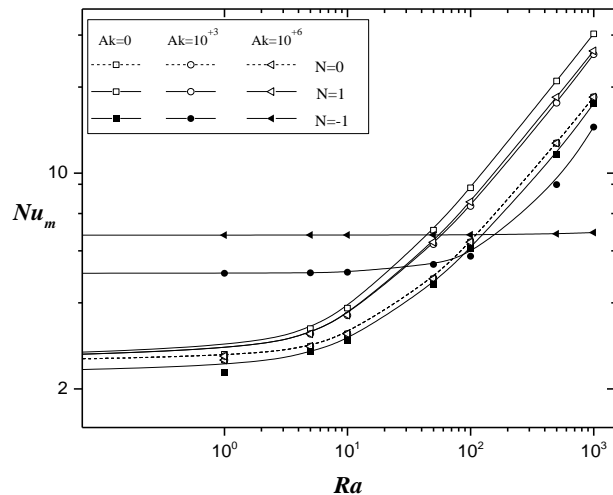


Figure 4 Average Nusselt number (Nu_m) versus Ra , for different value of Ak and N .

We found that there is competition between thermal and mass buoyancy forces. For low thermal Rayleigh values (Ra) the obtained results give the bearings with a constant Nusselt. Once the Ra exceeds a critical value, a exponential variation regime of Num has installed. This variation depends on the value of the chemical reaction rate (Ak). Note that the mass buoyancy forces dominate the buoyancy forces due to heat transfer in the case of the opposing double diffusive flow ($N = -1$) and a high value of the chemical reaction rate in the considered thermal Rayleigh range.

Effect of buoyancy ratio in the sinusoidal wall temperature case:

Figure 5 shows the temporal evolution of the average Nusselt number for high dimensionless amplitude ($XA = 0.9$) compared to the constant temperature case $XA = 0$ for various values of thermal Rayleigh number Ra , in the case of pure thermal convection flow ($N = 0$), a buoyancy ratio $N = 1$ and $N = -1$. Note that the time steps (1, 2, 3 and 4) shown in this figure correspond respectively to the temporal position over the sinusoidal wall temperature ($t_0, t_0+\tau/4, t_0+\tau/2$ and $t_0+3\tau/4$).

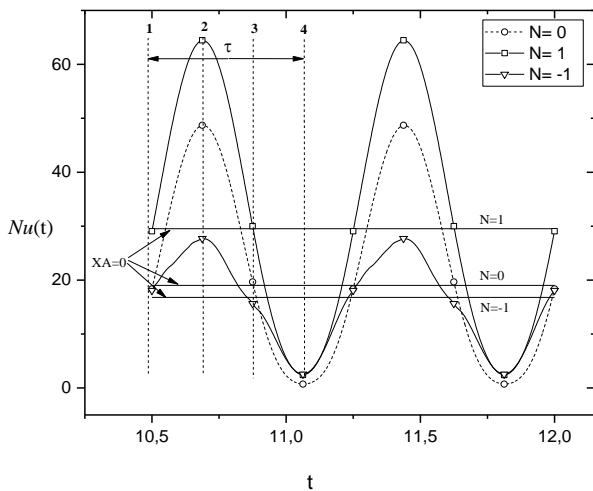


Figure 5. The space averaged Nusselt number evolution for different buoyancy ratio, $N (Ra=10^{+3}, XA=0.9, Ak=0, A=1)$

The obtained results shows that the heat transfer follow a periodic evolution in the same period as the wall heating around the stationary heating case ($XA = 0$). The aiding double diffusive flow case ($N = 1$) is more favorable for better heat transfer. We obtained a

dissymmetry of periodic evolution compared to the case of constant wall temperature for different values of buoyancy ratio. It is clear that this dissymmetry is in favor of the heating phase. It is probably due to the oscillations increasing which gives peaks in heat transfer due to the agitation of the fluid. Note that a phase difference is obtained between the heat transfer and the wall temperature for the three considered cases ($N = -1, 0$ and 1) and it is more pronounced in the opposing double diffusive flow case ($N = -1$).

Figure 6 illustrates the effect of buoyancy forces ratio on the relative heat transfer enhancement $(Nu_T - Nu_{stat}) / Nu_{stat}$ (the average Nusselt number over the period compared to the case of heat transfer with constant wall temperature) for different dimensionless amplitude values. It is found that increasing the value of the thermal Rayleigh number increases the relative difference in the case of pure thermal convection flow ($N = 0$) and The aiding double diffusive flow ($N = 1$). Conversely to the case $N = -1$ (the opposing double diffusive flow case), the increasing of thermal Rayleigh number (Ra) decreases the difference (68% and 16% for Ra values respectively, 0 and 10^{+2}). Note that for a high value of thermal Rayleigh number ($Ra = 10^{+3}$) and the dimensionless amplitude the relative difference becomes to the favor of the stationary case which gives negative values.

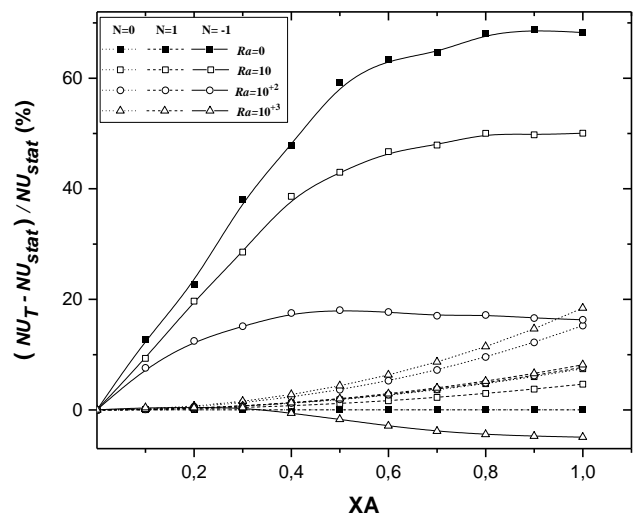


Figure 6 Influence of buoyancy ratio and temperature oscillation on the relative heat transfer

CONCLUSIONS

In this paper, we have numerically investigated the unsteady double diffusive natural convection of porous medium in vertical open-ended cylinder. Two types of boundary conditions have imposed on lateral wall of enclosure, namely a constant temperature and a sinusoidal time variation temperature. Due to the great number of control parameters involved in the present problem, only the main controlling parameters, such as buoyancy ration, thermal Rayleigh number, reaction rate, dimensionless amplitude and aspect ratio were investigated in order to gain new insights into the flow patterns and the heat transfer enhancement. Three types of flows take place, chimney flow with/without fluid recirculation and top aspiration flow. However, the flow behavior and the heat transfer are strongly depends on the controlling parameters. Increasing the value of the thermal Rayleigh number increases the relative difference in the case of pure thermal convection flow ($N = 0$) and The aiding double diffusive flow ($N = 1$). Conversely to the case $N = -1$ (the opposing double diffusive flow case), the increasing of thermal Rayleigh number (Ra) decreases the difference. Note that for a high value of thermal Rayleigh number the relative difference becomes to the favor of the stationary case which gives negative values.

REFERENCES

1. Nield, D.A, 1968, Onset of thermohaline convection in a porous medium. *Water Resource Research* **11** pp. 553-560.
2. Taunton, J., Lightfoot, E., Green, T, 1972, Thermohaline instability and salt fingers in a Porous medium, *Physics of Fluids* **15** pp. 748-753.
3. Shipp, P.W, Shoukri, M, Carver, M.B, 1993, Double diffusive natural convection in a closed annulus, *Numerical Heat Transfer, Part A: Application* **24** pp. 339–356.
4. Shipp, P.W, Shoukri, M, Carver, M.B, 1993, Effect of thermal Rayleigh and Lewis numbers on double diffusive natural convection in closed annulus, *Numerical Heat Transfer, Part A: Application* **24** 451–465.
5. Bennacer, R, Tobbal, A, Beji, H, Vasseur, P, 2001, Double diffusive convection in a vertical enclosure filled with anisotropic porous media, *Int. J. Thermal Science* **40** pp. 30–41.
6. Rathish Kumar, B. V, Singh, P, Bansod, V. J, 2002, Effect of thermal stratification on double-diffusive natural convection in a vertical porous enclosure, *Numerical Heat Transfer. Part A: Application* **41** pp. 421-447.
7. Bennacer, R, Mohamad, A. A, EL Ganaoui, M, 2005, Analytical and numerical investigation of double diffusion in thermally anisotropy multilayer porous medium, *Int. J. Heat and mass transfer* **41** pp. 298-305.
8. Ching-Yang, C, 2006, Natural convection heat and mass transfer of non-newtonian power law fluids with yield stress in porous media from a vertical plate with variable wall heat and mass fluxes, *International Communications in Heat and Mass Transfer* **33** pp. 1156–1164.
9. Himrane, N, Ameziani, D. E, Bouhadef, K, Bennacer, R, 2014, Storage silos self ventilation: Interlinked heat and mass transfer phenomenon, *Numerical Heat Transfer. Part A: Application* **66** pp. 379-401.
10. Jupp, T. E and, Woods, A. W, 2003, Thermally driven reaction fronts in porous media, *Journal of Fluid Mechanics* **484** pp. 329-346.
11. Patankar, S.V, 1980, *Numerical Heat Transfer and Fluid Flow*. Hemisphere/McGraw-Hill, New York.

MIXED CONVECTION IN HORIZONTAL DUCT WITH DOUBLE POPULATION LATTICE BOLTZMANN METHOD

N. Mahfoud SAHRAOUI, Samir HOUAT
Laboratory of MNEPM, MSMPT group,
 University of Abdelhamid Ibn Badis of Mostaganem,
 Bp300, 27000 Mostaganem, Algeria
sabd.08@hotmail.com, sa_houat@yahoo.fr

ABSTRACT

In the present work, a study of mixed convection in a horizontal duct heated from below is numerically investigated for $Pr = 0.71$, Rayleigh numbers of $Ra = 10^3 - 10^4$ and Reynolds numbers of $Re = 10-100$. The thermal lattice Boltzmann method (TLBM) is used with a combination of D2Q9 and D2Q5 lattice models for the dynamic field and the thermal field respectively. A comparison of our results with the existing data is presented for an aspect ratio $B = L/H = 20$, a Reynolds number $Re = 10$, Rayleigh $Ra = 10^4$ and Peclet number $Pe = 20/3$. The streamlines and isotherms are presented for different Reynolds numbers, Reynolds effect and Rayleigh effect are discussed.

KEYWORDS

Convection, numerically simulation, thermal lattice Boltzmann method.

INTRODUCTION

Mixed convection in a horizontal rectangular channel heated from below is motivated by its wide several areas of engineering, such as: chemical vapor deposition (CVD), the cooling of electronic equipments, heat exchangers ...ect.

This physical phenomenon results from the superposition of two convective sources: a gradient of pressure (driving of the forced convection) and a vertical gradient of the temperature (driving of natural convection).

Several work has been done in this field both experimentally and numerically, H.Ben Hamed et al [1] studied the stability of the Poiseuille Benard flow within a rectangular duct, they demonstrated that the critical Rayleigh number depends on the Peclet number and the length of the domain. L. Boutina et al [2] carried out a numerical simulation of mixed convection air cooling of electronic equipments mounted in an inclined channel where they showed the effect of the Reynolds number, the inclination

angle of the channel, the dimension of the heat source and the spacing between them on the improvement of the heat transfer.

Evans and Paolucci [3] presented a two dimensional computation investigation of mixed convection channel heated from below, where the isotherms, the vortices and the streamlines were plotted $Re = 10$, $Ra = 10^4$, $B = L/H = 20$ and a $Pe = 20/3$, a benchmark solution was also proposed for open boundary flows. A numerical investigation of forced convection in a plane channel with a built-in triangular prism was presented by Abassi et al [4], they also simulated the Poiseuille Benard flow case and compared it with benchmark solutions.

The lattice Boltzmann method (LBM), originated from the lattice gas automata [5]-[6], is a powerful technique for simulating fluid flows and associated transport phenomena. Various numerical simulations have been performed [7]-[8], using different models to investigate thermal systems [9]. The LBM method is a mesoscopic approach that solves the Boltzmann equation (BE) with the BGK

(Bhatnagar–Gross–Krook) approximation [10]. In comparison with the conventional numerical schemes, the advantages of LBM lie mainly in the simplicity of the calculation procedure as well as the implementation of boundary conditions and others. The approach used in this work is the double distribution function formulation (double population lattice Boltzmann method) [11]; it uses two different distribution functions; one for the flow field (velocity and density) and the other for the temperature field, this model is usually used to simulate thermal fluid flow [12].

The objective of this numerical study is to simulate laminar two-dimensional mixed convection in a rectangular horizontal channel heated from below using the TLBM method with double population method by comparing our data with those of the literature, the Rayleigh and Reynolds effects are discussed and streamlines, isotherms, vortices and velocity profiles are plotted for Reynolds numbers of 50 and 100.

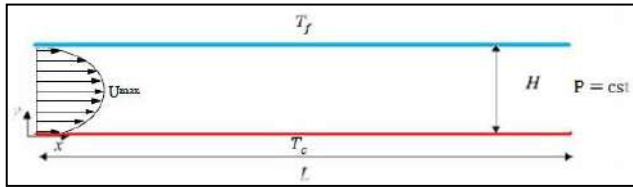


Figure 1
Physical configuration

Thermal lattice Boltzmann method (TLBM):

A thermal lattice Boltzmann double population method is considered [13], two sets of independent distribution functions are used, f and g , for the flow and the temperature fields respectively.

The time evolution equation for the mass and momentum conservations can be written as follows:

$$\begin{aligned} f_i(\mathbf{x} + \mathbf{c}_i \Delta t, t + \Delta t) - f_i(\mathbf{x}, t) \\ = -\frac{1}{\tau_v} [f_i(\mathbf{x}, t) - f_i^{eq}(\mathbf{x}, t)] + \delta F \end{aligned}$$

The time evolution equation for energy conservation is given by:

$$\begin{aligned} g_i(\mathbf{x} + \mathbf{c}_i \Delta t, t + \Delta t) - g_i(\mathbf{x}, t) \\ = -\frac{1}{\tau_T} [g_i(\mathbf{x}, t) - g_i^{eq}(\mathbf{x}, t)] \end{aligned}$$

Where \mathbf{c}_i are the discrete particle velocity vectors, Δt is the lattice step time which is set to unity. τ_v and τ_T are the relaxation time for the flow and temperature respectively, δF is the buoyancy force term applied with The Boussinesq approximation, f_i^{eq} and g_i^{eq} are the local equilibrium distribution functions for the flow field and the temperature field respectively.

The two-dimensional nine velocities model (D2Q9) for the flow, and D2Q5 for the temperature are considered.

For the D2Q9 model:

$$\mathbf{c}_i = \begin{cases} (0,0) & i = 1 \\ c[\cos(\frac{i-1}{2}\pi), \sin(\frac{i-1}{2}\pi)] & i = 2,3,4,5 \\ \sqrt{2}c[\cos(\frac{i-5}{2}\pi + \frac{\pi}{4}), \sin(\frac{i-5}{2}\pi + \frac{\pi}{4})] & i = 6,7,8,9 \end{cases}$$

For the D2Q5 model:

$$\mathbf{c}_i = \begin{cases} (0,0) & i = 1 \\ c[\cos(\frac{i-1}{2}\pi), \sin(\frac{i-1}{2}\pi)] & i = 2,3,4,5 \end{cases}$$

The kinematic viscosity ν and the thermal diffusivity α are respectively related to the relaxation time by:

$$\alpha = \left(\tau_T - \frac{1}{2}\right), \quad \nu = \left(\tau_v - \frac{1}{2}\right) c_s^2 \Delta t$$

Where: $c_s = c/\sqrt{3}$ is the lattice speed of sound.

The macroscopic density ρ , the velocity and the temperature can be calculated in terms of these variables by:

$$\begin{aligned} \rho &= \sum_{i=1}^9 f_i \\ \rho u &= \sum_{i=1}^9 f_i c_i \\ T &= \sum_{i=1}^5 g_i \end{aligned}$$

VALIDATION

A code based on the thermal lattice Boltzmann method was developed in order to validate the Poiseuille Rayleigh Benard flow Fig.1, in case of an

aspect ratio of $B = 20$, a Peclet number $Pe = 20/3$, a Reynolds number $Re = 10$ and a Rayleigh number $Ra = 10^4$.

A grid dependence was carried out to determine the sufficient mesh for our case, where the mesh sizes used range from 41×801 up to 91×1801 as shown in Fig.2.

The mesh 17×1401 was adopted for the current computation.

The comparison of our results with other references shown in table I, demonstrate good accuracy of our numerical code, were the errors in the space and time average Nusselt number are 0.56% for Abassi et al [4], 0.30% for Evans et al [3] and 0.92% for Comini et al [14].

It should be pointed out that results reported on table I are referred to a domain twice as long as that shown in the figures.

Table 1

Poiseuille Rayleigh Benard flow: $Re = 10$, $Pe = 20/3$ and $Ra = 10^4$

Reference	Present	Abassi et al [4]	Evans et al [3]	Comini et al [14]
$\langle \overline{Nu} \rangle$	2.5503	2.536	2.558	2.574

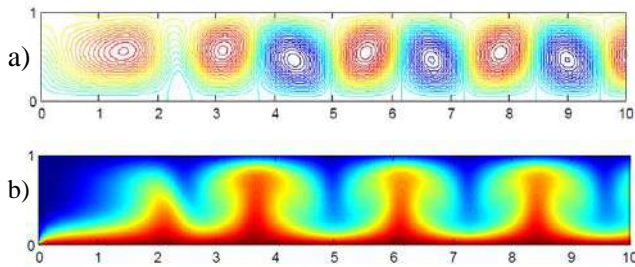


Figure 2
Solution fields at $t=t_T$ for $Re = 10$:
a) streamlines, b) Temperature.

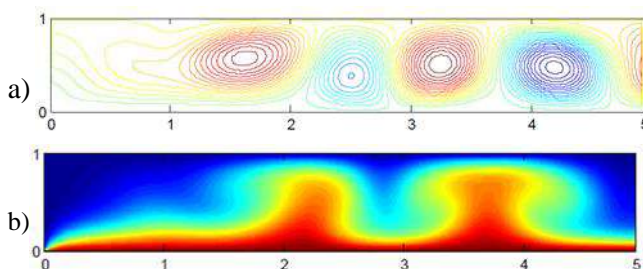


Figure 3
Solution fields at $t=t_T$ for $Re = 50$:
a) Streamlines, b) Temperature.

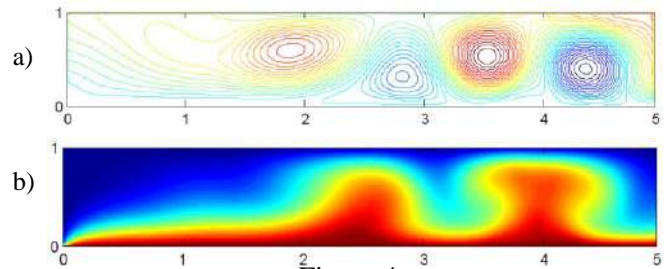


Figure 4
Solution fields at $t=t_T$ for $Re = 100$:
a) Streamlines, b) Temperature.

RESULTS AND DISCUSSION

Fields plots of streamline, temperature contours, over the first half of the computed domain for a Reynolds number $Re = 10$, are shown in Fig.2, at a time t_T which correspond to a minimum in the temperature at the position $x = 5.0$, $y = 0.5$. This moment is chosen arbitrarily [3].

At this value of time are obtained, the rest of the results for Streamline and temperature contours corresponded at $Re = 50$ and $Re = 100$ as shown in Fig.3 and Fig.4 respectively, it is clear that the nature of the flow is periodic.

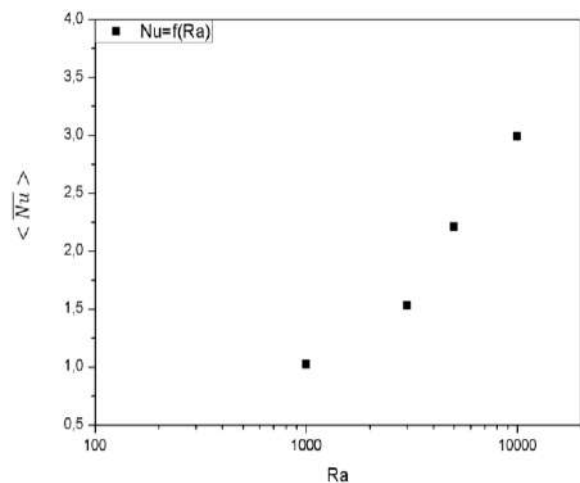


Figure 5
Rayleigh effect, $Ra = 10^3 - 10^4$

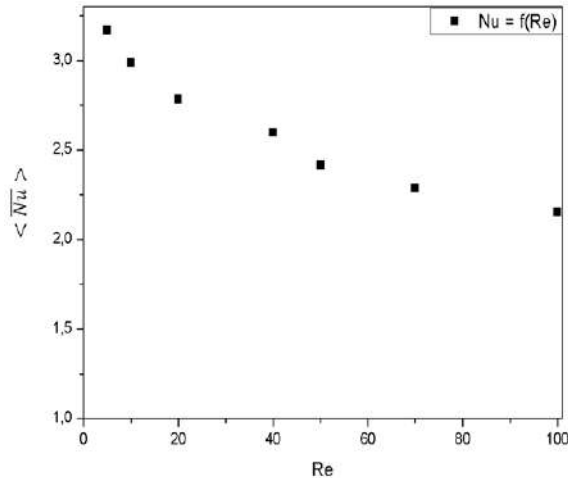


Figure 6
Reynolds effect, $Re = 10 - 100$

We studied the effect of Rayleigh number on the heat transfer in this type of flow (Figure 5) and the influence of the variation of Reynolds number between 10 and 100 (Figure 6). It is noted that the transfer of heat increases when the rayleigh number increases and the Reynolds is fixed. And that the heat transfer decreases with the increase of Reynolds number.

CONCLUSIONS

In this paper, a numerical investigation of the mixed convection in a horizontal channel uniformly heated from below was presented.

The thermal lattice Boltzmann method was used. The results obtained during the validation have demonstrated the accuracy and reliability of the TLBM method, and the good agreement between the results obtained with those found in the literature. This shows the ability of the thermal lattice Boltzmann method TLBM to reproduce this type of flow, including good numerical stability and the ability to handle convection heat transfer problems.

REFERENCES

1. Ben Hamed, H et al, 2008, Poiseuille Rayleigh-Bénard problem in a horizontal duct of finite length in streamwise direction: stability analysis, *Progress in Computational Fluid Dynamics*, **8** (6), pp 342–350.
2. Boutina, L et al, 2011, Numerical simulation of mixed convection air-cooling of electronic components mounted in an inclined channel, *Applied thermal engineering* **31**(11), pp 2052–2062.
3. Evans G., Paolucci S, 1990, The Thermoconvective Instability of Plane Poiseuille Flow Heated from below: A Benchmark Solution for Open Boundary Flow, *International Journal Numerical Method in Fluids* **11**(7), pp 1001–1013.
4. Abbassi H., Turki S and Nassrallah S, 2001, Mixed convection in a plane channel with a built-in triangular prism, *International Journal of Thermal Sciences* **40**, pp 649–658.
5. Rivet, J and Boon, J, 2001, *Lattice Gas hydrodynamics*, Cambridge University Press.
6. Dieter and Wolf-Gladrow, 2000, *Lattice-gas cellular automata and lattice Boltzmann models: an introduction*, Berlin Heidelberg, Springer-Verlag,.
7. Mezrhab., Jami M., Abid C., Bouzidi M., Lallemand P., 2006, Lattice-Boltzmann modeling of natural convection in an inclined square enclosure with partitions attached to its cold wall, *International Journal of Heat and Fluid Flow* **27**(3), pp 456–465.
8. Shan X., 1997, Simulation of Rayleigh-Benard convection using a Lattice Boltzmann method, *Phys. Rev. E*, **55**, pp 2780–2788.
9. Peng, Y et al, 2003, Simplified thermal lattice Boltzmann model for incompressible thermal flows, *Phys. Rev. E* **68**, pp 026701–1–026701–8.
10. Shi, Y, Zhao, T, and Guo, Z, 2004, Thermal lattice Bhatnagar–Gross–Krook model for flows with viscous heat dissipation in the incompressible limit, *Phys. Rev. E* **70**, 066310.
11. He X., Shan S and Doolen G. D, 1998, A novel thermal model for the lattice boltzmann method in incompressible limit, *J. Comp. Phys.*, **146**, pp 282–300.
12. Parmigiani, C. Huber, B. Chopard, J. Latt, and O. Bachmann, 2009, Application of the multi distribution lattice Boltzmann approach to thermal flows, *Eur. Phys. J. Special*, **171**, pp 37–43.
13. He, X, Chen, S and Doolen, G, D, 1998, A novel thermal model for the lattice Boltzmann method

in incompressible limit, *J. Comput. Phys.***146**, pp 282.

14. Comini G., Manzan M., Cortella M., 1997, Open Boundary Conditions for the Stream Function of Unsteady Laminar Convection. *Numerical Heat Transfer, Part B*, **31**, pp 217-234.

Three-dimensional simulation of natural convection in cubic cavity partially filled with porous media

¹Fatma HABBACHI, ²Fakhreddine S. OUESLATI, ³Rachid BENNACER, ⁴Med GANAOUI and ¹Afif ELCAFSI

¹Université Tunis El Manar, Faculté des Sciences de Tunis (FST), LETTM, TUNISIA.

²Ecole Nationale d'Ingénieurs de Carthage (ENICarthage), Charguia II Tunis, TUNISIA .

³Ecole Normale Supérieure de Cachan, Dpt. Génie Civil, Cachan, France.

⁴Université de Lorraine, LERMAB/Institut Carnot, Cosnes et Romain, France

*Corresponding author: Fax: +216 71 941 579 Email: Fakhreddine.Oueslati@fst.rnu.tn

ABSTRACT

This paper reports a numerical study with three-dimensional flows, in an enclosure domain partially filled with a central cubic porous media. The right and left vertical walls are considered at different temperature, the other walls are adiabatic. The study found that the fluid flow and heat transfer are governed by the dimensionless thickness of the porous layer, and the thermal conductivity ratio of the porous media to that of the fluid. The complex obtained flow structure and corresponding heat and mass transfer (velocity, temperature profiles) are discussed at unsteady state. The numerical results are reported in terms of stream trace, isotherms and averaged Nusselt number.

KEYWORDS Natural convection, three-dimensional, porous media, out thermal equilibrium.

NOMENCLATURE

Da	Darcy number,
g	Gravitational acceleration,
L	Length of the enclosure,
k	Thermal conductivity
K	Permeability of the porous medium
Nu	Average Nusselt number.
P'	Dimensional pressure
P	Dimensionless pressure,
Pr	Prandtl number,
Ra	Rayleigh number,
T	Dimensionless temperature,
T'	Dimensional temperature,
t	Dimensional time,
(u',v',w')	Dimensional components of the velocity
(u,v,w)	Dimensionless components of the velocity,
(x',y',z')	Dimensional coordinate system
(x,y,z)	Dimensionless coordinate system,

Greek Symbols

α ;	Effective thermal diffusivity,
β_T ;	Coefficient of thermal expansion,
$\tilde{\lambda}$	Thermal conductivity ratio,
ν	Kinematics viscosity,
ρ	Fluid density,
ε	Porosity
e	Dimensional size of porous media
η	Dimensionless size of porous media,
ΔT	Temperature difference

Subscripts

Eq	Equivalent
C	Cold
H	Hot
S	Solid
F	Fluid
0	Refers to a reference state

INTRODUCTION

Fluid flow and heat transfer in saturated porous media has received a considerable attention and has been the subject of much intensive research numerically, mathematically and experimentally. This interest is due to the fact that this kind of structure is encountered in various engineering and geophysical problems, such as oceanography, geophysics, design of heat exchangers, hydrology, biology and chemical processes (see, for instance [1-2]). In particular these problems where heat transfer takes place in a confined enclosure partially filled with porous medium have many applications, such as: thermal insulation, solar collectors with a porous absorber, thermal energy storage system [3]. Despite the rise in power of means of study, there are still of gaps, in terms of acquaintance fundamental and understanding of phenomena of heat transfer in systems include porous media. Most

of the published studies on natural convection in composite systems deal with cases in two dimensional and the buoyancy forces are due to the variations of temperature (for thermally driven flow). A good match was found with experimental and numerical results with the work of [4]. They showed that the condition on the separating interface has a significant effect on the flow field and heat transfer in such composite enclosure. Many researchers analyzed the heat transfer in multilayer geometrical, horizontal saturated porous layer and an overlying fluid layer has been investigated using the Darcy-Brinkman flow [5]. Natural convection in vertical enclosures containing simultaneously a fluid and a porous layer was investigated [6]. The numerical results show good agreement with experiments conducted utilizing various glass beads, fluids and test-cell sizes. The effect of fluid layer thicknesses on the Nusselt number has been numerically investigated for various Rayleigh and Darcy numbers.

Validation the results of numerical study based on the single-domain approach for the dynamic balance at the interface between the fluid filled regions and porous media, have been investigated by comparison of their results with those existing in the other publications, a good match was found. Recent numerical study has been conducted to investigate three-dimensional, steady, conjugate heat transfer of natural convection and conduction in a vertical cubic enclosure within which a centered, cubic, heat-conducting body generates heat [7]. The numerical results are presented and analyzed in terms of streamlines, isotherms, lines and average Nusselt number.

This paper presents a study of three dimensions numerical studies on natural convection partially filled with central porous layer. Moreover we have examined the effect of the third direction on the flow, heat transfer in comparison with the simplified approach. A parametric variation effect of the thickness of the porous layer and the thermal conductivity ratio (porous media/fluid) on the structure flow and the rate of heat transfer are presented. The obtained results are discussed based on the stream traces, isotherms, and average heat transfer.

MATHEMATICAL FORMULATION

A schematic of the system considered in this paper is shown in Fig. 1. The system consists of a cube with sides of length L , within which another cubic porous with sides of

length e is centered. The left and right side walls are isothermal at respective temperatures of T_h and T_c , whereas the other walls are adiabatic. The thermo physical properties of the incompressible fluid are taken to be constant except for the density variation in the buoyancy terms, where the Boussinesq approximation applies as:

$$\rho = \rho_0 \{1 - \beta_T \Delta T'\} \text{ with } \beta_T = -1/\rho_0 (\partial \rho / \partial T')_p$$

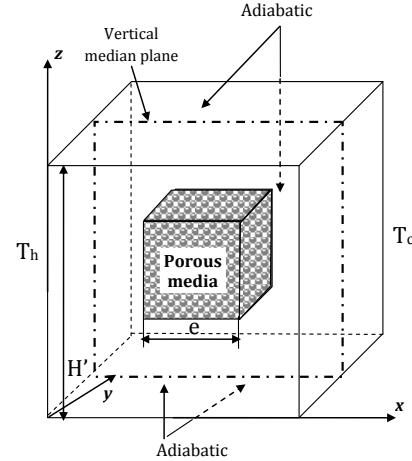


Figure 1

Physical domain model and coordinates system

In the present study a one-domain approach has been retained, with a unique momentum conservation equation. To solve the conservation governing equations, of continuity, momentum and energy in dimensionless form, respectively separately for each layer, the equations are combined into one set by introducing the following binary parameter: $a = (1, 0) / (\text{porous media}, \text{fluid media})$

$$\nabla \cdot \vec{V} = 0 \quad (1)$$

$$\{a/\varepsilon + (1-a)\} \partial \vec{V} / \partial t + \{a/\varepsilon^2 + (1-a)\} (\vec{V} \cdot \nabla) \vec{V} = -\nabla P + \text{Pr} \left(-a \vec{V} / Da + Ra \cdot \nabla^2 \vec{V} + Ra \cdot T \cdot \vec{k} \right) \quad (2)$$

$$\sigma \frac{\partial T}{\partial t} + \vec{V} \cdot \nabla T = \nabla \cdot \left(\{a(\tilde{\lambda} - 1) + 1\} \nabla T \right) \quad (3)$$

$$\text{With } \tilde{\lambda} = \lambda_{eq} / \lambda_f; \quad \lambda_{eq} = \lambda_s (1 - \varepsilon) + \varepsilon \lambda_f$$

The boundary conditions for the governing equations are the non-slip condition on the solid surfaces and the impermeability there of as well as all the walls of the cavity are assumed adiabatic ($\vec{V} = 0$ and $\nabla T \cdot \vec{n} = 0$), except the vertical walls are subjected to uniform conditions of temperature:

$$\left. \begin{aligned} T = 1, 0 \text{ at } x = 0, 1; 0 \leq y \leq 1, 0 \leq z \leq 1 \\ \partial T / \partial y = 0 \text{ at } y = 0, 1; 0 \leq x \leq 1, 0 \leq z \leq 1 \\ \partial T / \partial z = 0 \text{ at } z = 0, 1; 0 \leq x \leq 1, 0 \leq y \leq 1 \end{aligned} \right\} \quad (4)$$

At the interface between the two layers (porous-fluid), we used the fluxes continuity conditions.

$$\left. \begin{aligned} (x, y, z) &= \left(\frac{1-\eta}{2} \text{ and } \frac{1+\eta}{2} \right) \\ \Rightarrow \Phi_{mp} &= \Phi_f, \quad \varphi(\Phi)|_{mp} = \varphi(\Phi)|_f \end{aligned} \right\} \quad (5)$$

Where Φ may correspond to P, u, v, w, T and φ could be the heat flux. The results for the total heat transfer rate across the enclosure given by Nusselt number defined as:

$$\overline{Nu} = \frac{\overline{h}L}{\lambda_f} = -\frac{1}{A} \int_0^A \left(p(\tilde{\lambda}-1)+1 \right) \cdot \frac{\partial T}{\partial x} \Big|_{x=1} \text{ or } \Big|_{x=0} dy dz \quad (6)$$

NUMERICAL METHOD

The differential equations (1)–(3) governing the natural convection in the physical model are transformed into a system of algebraic equations with the use of the control volume approach. The SIMPLE algorithm [10] is used to couple momentum and continuity equations. The QUICK scheme is considered for the assessment of convective terms. The system of algebraic equations is solved iteratively by means of the Thomas algorithm. Convergence is controlled in terms of the relative error for the variables P, u, v, w and T on each control volume. We used the technical multigrid of 82^3 nodes to accelerate numerical computing, was selected on the basis of grid sensitivity.

RESULTS AND DISCUSSION

Interestingly initially to examine the intervals of the governing dimensionless parameters Rayleigh (Ra), Darcy (Da), and thermal conductivity ratio ($\tilde{\lambda}$) used in the works. To conserve laminar flow, the calculation was performed in all the work for $Ra=10^5$ and $Da=10^{-6}$ respectively. The dimensionless thickness of the porous layer (η) was varied from 0% to 100%, where the limit of 0% compatible with pure natural convection situation, while 100% represents pure conduction in the porous media, with the Nusselt number equal to 1. The focus is placed on results for a thermal conductivity ratio (porous media/fluid) $\tilde{\lambda}$ varies from 1 to 100. The effect of parameters variation, cited below, on the average heat transfer and the flow structure are analyzed and discussed.

Effect of thickness of the porous layer

Streamlines and Isotherms: Streamlines and isotherms are displayed in Figure 2. These contour plots are displays to explain the flow and heat transfer characteristics and to help the results of the average Nusselt numbers in explaining the physical phenomena (show the next section). In all cases, the stream traces show a cell rotating

clockwise about the porous layer, their intensity decreases with increase of the thickness of the porous layer.

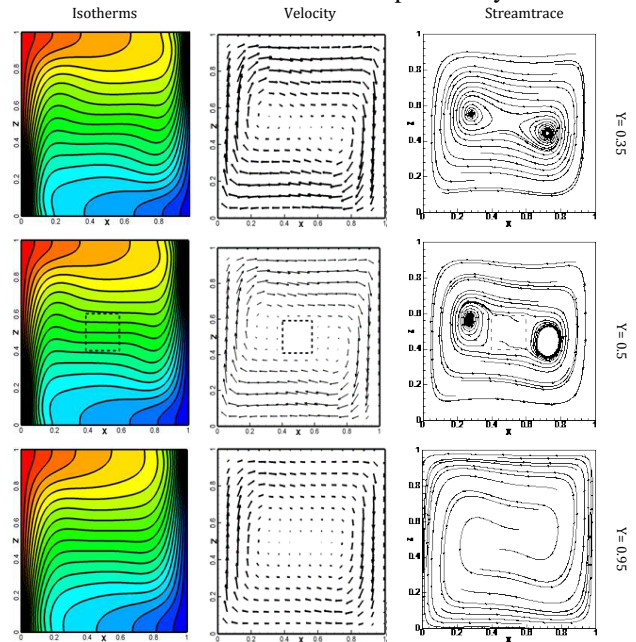


Figure 2

Isotherm, velocity and streamtrace plots for $\eta=20\%$ in the $(x-z)$ plane

For $\eta=20\%$ a comparison with case without a porous media (not shown here) reveals that the bloc porous has relatively little influence on the flow. Indeed: in pure natural convection at this Rayleigh number, the central core of the fluid region is almost stagnant. This stagnant region approximately coincides with bloc porous. As a result, the Nusselt numbers for this case almost identical from the corresponding pure natural convection value. In this case, the isotherms in the porous media are almost horizontal, indicates that heat is conducted vertically through the bloc porous, from the higher temperature fluid in the upper flow to the lower temperature fluid in the lower flow.

For a situation with a large thickness of the porous layer value of η , a significant flow obstruction in the porous layer is awesome, and the flow is mainly diffusion in the porous layer. For this purpose, the fluid circulation is more favorable, and the natural convection is more pronounced in the fluid layer. It can be seen in figure 3.

The figures reveal that the flow preserves symmetry for all values of η investigated, the flow started to bifurcate and complex flow patterns were predicted, they found that the spiral flow is sensitive to the lateral boundary conditions.

Figure 4 illustrates the temperature profiles at the vertical median plane $z=0.5$ for, $\tilde{\lambda}=1$ and for different thicknesses of the porous layer (η), confirms the thermal property described above. Accordingly, for the low thickness of the porous layer, the temperature gradients

are well pronounced on the profiles, which reveal a totally convective situation with stratification in the cavity core. Indeed for $\eta=50\%$ profile show a strong gradient thermal so that for $\eta=75\%$ show a diffusive profile.

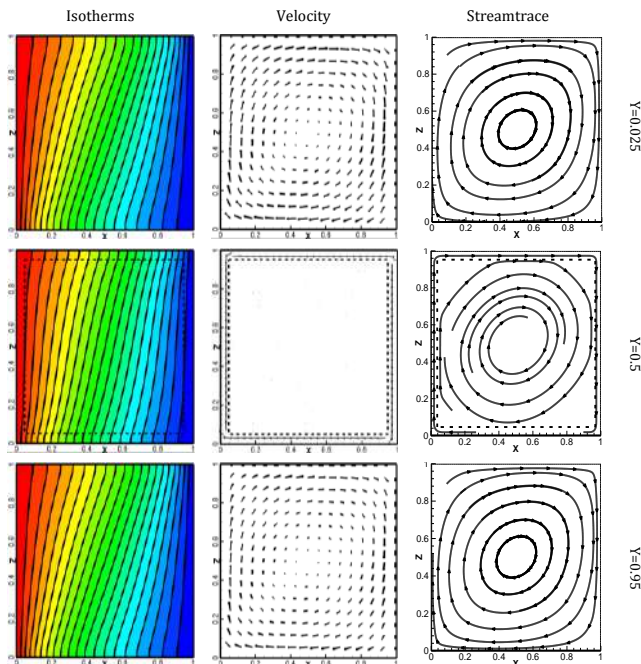


Figure 3

Isotherm, velocity and streamtrace plots for $\eta=90\%$ in the (x-z) plane

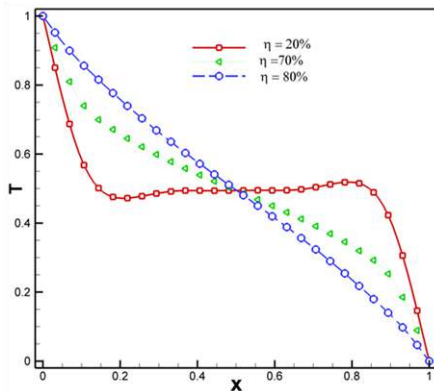


Figure 4

Temperature profile at mid height plane of the enclosure vs different values of η in the (x-z) plane

This is well illustrated by the profiles of vertical and horizontal profiles of velocity in transverse plan (x-z), Figure 5. Each profile presents two peaks at the vicinity of the vertical wall that increase by approaching the middle of the cavity, and decrease near the vertical wall. The profiles show that the flow does not circulate in the core of the

cavity which explains the importance of the edge effect. The velocity profile in the porous region is almost linear.

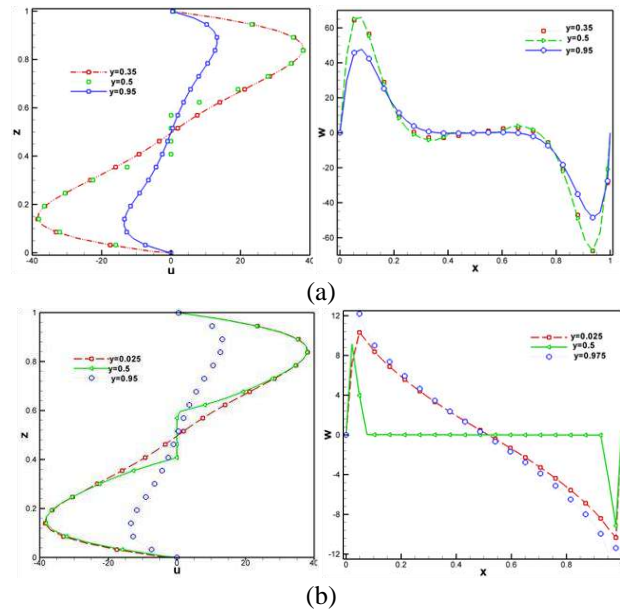


Figure 5

Dimensionless velocity components (u,w) in (x-z) plane for $\eta=20\%$ (a) and $\eta=90\%$ (b).

Moreover, the velocity profiles illustrate the symmetric propriety; each profile presents two maximums that decrease with increase in the thickness of the porous layer. For $\eta=90\%$ of totally porous cavity, the velocity profiles are almost linear, which indicates that the flow tends toward purely conductive situations.

Nusselt Numbers: Nusselt numbers as a function of the dimensionless thickness of the porous media are shown in Figure 6. Results are presented for $\tilde{\lambda}=1$.

Therefore, the Nusselt numbers tends into a single value when, the thickness of the porous layer approaches zero, corresponding to pure natural convection. Similarly, as the thickness of the porous media approaches unity, the flow tends toward a purely conductive situation through the body. As discussed earlier, the porous media block has low influence on the natural convection flow, when their size approaches the size from the almost stagnant central core, present in natural convection in an enclosure without porous media. Indeed, the porous media has only a small effect on average Nusselt number up to almost $\eta=70\%$. Above that value of η , the decrease is steeper and is predominantly due to the suppression of the natural convection flow.

This figure shows three distinct zones: a first zone is purely diffusive indicates a very low flow is illustrated by the isotherms which are almost parallel, a third zone with convective flow in major part indicates that the heat transfer is very important and an intermediate zone is

characterized by a strong increase in Nusselt number according to the thermal conductivity ratio law in the following form:

$$Nu = 1.64 \times \tilde{\lambda}^{0.315}$$

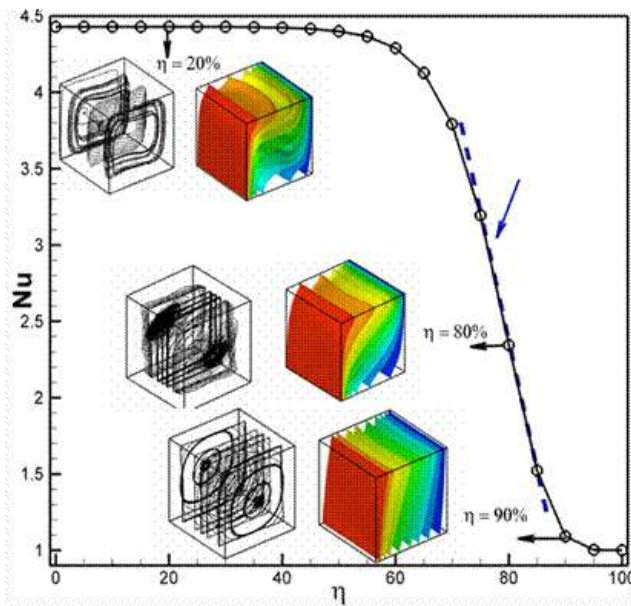


Figure 6

The evolution of the average Nusselt number (Nu) versus various values of η

Influence Thermal Conductivity Ratio

Streamlines and Isotherms: The effect of the thermal conductivity ratio $\tilde{\lambda}$, where it's varied from 1 to 100 for thickness of the porous layer $\eta=80\%$, on the isotherms and stream trace are displayed in figures 7.

Due to the large size of the porous media, the natural convection flow is much weaker than in $\eta < 80\%$. The different thermal conductivities, an important influence on the isotherms in the fluid and the porous layer.

For $\tilde{\lambda}=10$, the isotherm indicate that heat transfer is almost one-dimensional across the enclosure. Due to the high thermal conductivity of the porous media, the fluid at each position in the horizontal passages has almost the same temperature as the porous media.

The low thermal conductivity of the fluid in the vertical flow acts as a thermal barrier for the heat transfer across the enclosure. The latter clearly seen from, the different spacing of the isotherms in the porous media and the vertically flowing fluid. This is illustrated by the temperatures profiles in the vertical mid-plane $y=0.5$ and $\eta=80\%$, Figure 8.

Nusselt Numbers: The effect of $\tilde{\lambda}$ on the Nusselt number is shown in Figure 9. As discussed earlier, the thickness of the porous layer has relatively little influence on the natural

convection flow, as long as it is not much larger than the almost stagnant central core present during natural convection in a cubic enclosure without a porous media.

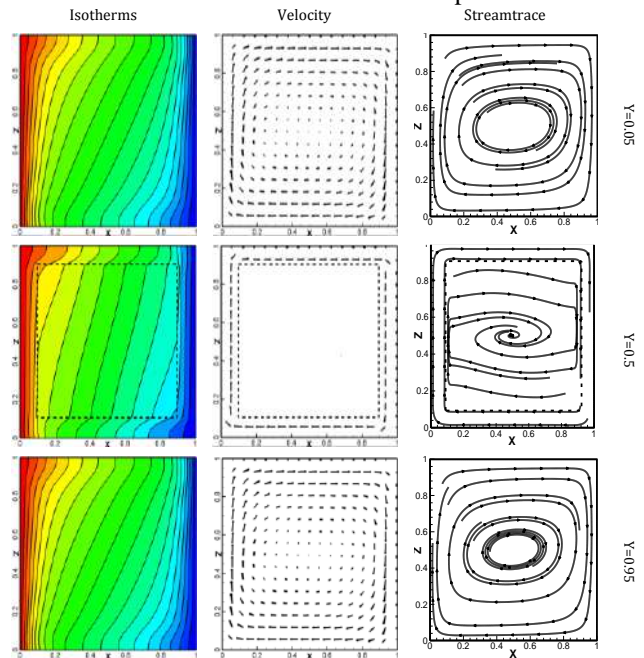


Figure 7

Isotherm, velocity and streamtrace plots for $\eta=80\%$ and $\tilde{\lambda}=10$ in the (x-z) plane

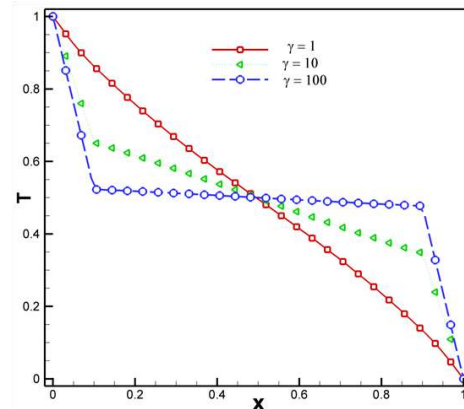


Figure 8

Temperature profile at mid height plane of the enclosure vs different values of $\tilde{\lambda}$ in the (x-z) plane

But for $\eta > 80\%$, the Nusselt number first increases a meaningful way above to the pure natural convection value, and then slightly low, until attains its maximum. Whereas most of the change takes place between thermal conductivity ratios of $\tilde{\lambda}=0.1$ and $\tilde{\lambda}=100$.

The figure reveal that the Nusselt number, which characterizes the heat transfer, increase with increasing of the thermal conductivity ratio($\tilde{\lambda}$) in when the thickness of the porous media is great then 70%. In fact the interaction

between the solid matrix of the porous media and the fluid it's more significant for a large porous media core induced a very low flow and decline the convective flow in major.

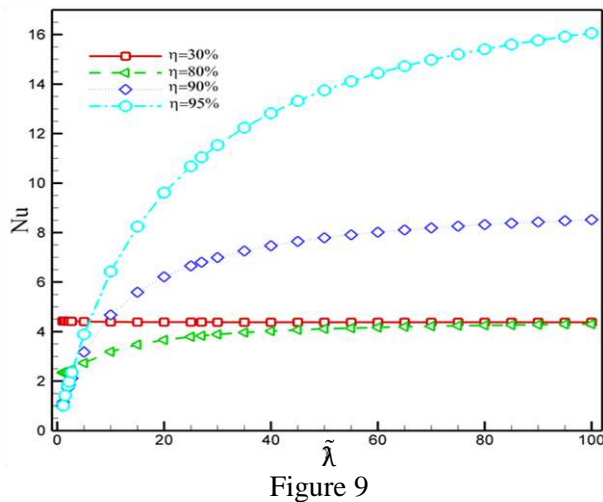


Figure 9
The evolution of the average Nusselt number (Nu) versus $\tilde{\lambda}$ and different values of η

CONCLUSIONS

The current investigation is a numerical study which conducted to investigate the steady, three-dimensional heat transfer and fluid flow characteristics in a cubic enclosure containing a centered cubic porous media heat conducting. After a detailed study, of the heat and fluid flow phenomena revealed by the numerical experiments, the following major conclusions can be tired:

- A Numerical code was developed to simulate the three-dimensional conjugate heat transfer and fluid flow problem of natural convection in a thermal non-equilibrium approach.
- The stream traces, which traduce the fluid flow, and isotherm distributions illustrate a very complicated three-dimensional patterns, due to the existence of a conducting heat transfer and flow from the centered cubic porous media.
- The Nusselt number is not significantly different from the one for pure convection without a block porous at the same Rayleigh and Darcy Numbers, up to a thickness of the porous layer that coincided with the stagnant fluid core present in an enclosure without a porous media.
- The variation of Nusselt number with body size is significantly influenced by the ratio of the thermal conductivity of the porous media to that of the fluid.

ACKNOWLEDGMENTS

This work is supported by our laboratory LETTM of the Sciences Faculty of Tunis at University of Tunis El Manar.

REFERENCES

1. D. A. Nield and A. Bejan, *Convection in Porous Media*. Springer, Berlin. (2006)
2. Viskanta R., Bergman T.L., Incropera F.P., Double diffusive natural convection, in: S. Kakac, W. Aung, R. Viskanta (Eds.), *Natural Convection: Fundamentals and Applications*, Hemisphere, Washington, DC (1985) pp.1075-1099.
3. Baytas A.C., Ingham D.B., Pop I., Double diffusive natural convection in an enclosure filled with a step type porous layer: non-Darcy flow, *International Journal of Thermal Sciences* 48 (2009) 665-673.
4. Beckerman c., Ramadhyani S., Viskanta S., Natural convection flow and heat transfer between a fluid layer and a Porous layer inside a rectangular enclosure heat transfer laboratory, School of Mechanical Engineering, Purdue university, West Lafayette, in 47907.
5. House John m., Christoph Beckemann, Theodore Smith; Effect of a centered conducting body on natural convection heat transfer In an enclosure, *Numerical Heat Transfer, part a*, vol. 18, pp. 213-225, 2014.
6. Goyeau B., Lhuillier D., Gobon D., Momentum transfer at a fluid-porous interface, *International Journal of Heat and Mass Transfer* 46(2003) 4047-4081.
7. Jun Yang, Yuan cheng Wang, Xiao jing Zhang, Yu Pan, Effect of Rayleigh numbers on natural convection and heat transfer with thermal radiation in a cavity partially filled with porous medium, *International Conference on Building Energy and Environment (COBEE)*, *Procedia Engineering* 121 (2015) 1171 – 1178.
8. M.Y. Ha, M.J. Jung, A numerical study on three-dimensional conjugate heat transfer of natural convection and conduction in a differentially heated cubic enclosure with a heat-generating cubic conducting body, *International Journal of Heat and Mass Transfer* 43(2000) 4229-4248.
9. Bennacer R., Tobbal A., Beji H., Vasseur P., Double diffusive convection in a vertical enclosure filled with anisotropic porous media, *International Journal of Thermal Sciences* 40 (2001) 30-41.
10. N. V. Patankar, *Numerical Heat Transfer and Fluid Flow*, Hemisphere, Washington, D.c., 1980.

SIMULTANEOUS ESTIMATION OF VOLUMETRIC CAPACITY AND THERMAL CONDUCTIVITY OF MOROCCAN WOOD SPECIES FROM EXPERIMENTAL FLASH METHOD

*Mohammed SOUIHEL, Saad RAEFAT, Mohammed GAROUM, Najma LAAROUSSI
Laboratory of Energy, Materials and Environment, Mohamed V University-Rabat, EST SALE
(227 Avenue Prince Héritier, SALE, MOROCCO)

*Corresponding Author: Tel: +212 6 59 42 73 61 Email: mohammed-souihel@hotmail.fr

ABSTRACT

In order to minimize the high energy demand in building sector, the first Moroccan Thermal Regulation of Construction (MTRC) has been officially mandatory. Therefore, for the buildings energy design and performance, thermal properties of building components (wall, roofs, windows ...) must be known.

In this work, dry samples made from several Moroccan and imported wood species, widely used in wood-based materials (window, door ...), were tested in order to estimate their volumetric capacity and thermal conductivity. The simultaneous numerical inverse estimation of these two thermophysical properties has been performed using the flash method and introducing a new approach based on several numerical global minimization procedures. It should be noticed that for the samples studied a comparison was made between thermal conductivities estimated values and standard ones.

Keywords: Thermal Diffusivity, Thermal Conductivity, Volumetric Capacity, Thermophysical Characterization, Construction Materials.

NOMENCLATURE

λ	The thermal conductivity, [W/mK]
a	The thermal diffusivity, [m ² /s]
h_1 and h_2	The global heat exchange coefficients on both sides of the sample, [W/m ² .K]
$Q_0.f(t)$	The finite pulse with duration t_d and Q_0 is the finite amount of heat brought to the front boundary ($x=0$).
$f(t)$	The time dependence of the heat generation. (For all measurements t_d is kept equal to 2s), [s]
e	The thickness of the sample, [m]
bi_1 and bi_2	The Biot numbers
ρ	The density, [Kg/m ³]
c	The thermal capacity, [J/Kg.K]
p	Laplace transform
MTRC	Moroccan Thermal Regulation of Construction
T_{ma}	Adiabatic Limit temperature, [K]
S	The surface of the sample, [m ²]

the real energy consumption using software programs based on standard data.

However, as there are so many materials that are specific to the Moroccan context, it is still difficult to estimate the effective behavior of buildings. While there is no thermal properties database available of the Moroccan construction materials currently, the aim of this research is to dress a detailed characterization of one Moroccan material in order to make thermal studies in buildings more significant. Related studies were investigated such as in [1] who performed experimental measurements of thermal conductivity using the heat flow meter and transient plane source technique, or in [2] who measured all of the thermal diffusivity, specific heat, and thermal conductivity of 13 species of wood using the laser flash, also [3] measured thermal conductivity for ash, oak, silver wattle, poplar, and beech, and managed to determine their corresponding coefficients. Reference [4] presented and discussed data sets of wood thermal properties differing in their complexity, the predicted temperatures were then compared to the experimental data obtained for European beech and Scots pine wood, and finally [5] performed transient simultaneous measurements of thermal conductivity and diffusivity of Swedish wood with the plane source technique.

Consequently, in this article, the thermophysical properties of two Moroccan species Cedar and Walnut and two imported ones Oak and Red Deal

INTRODUCTION

For the sake of making the new Moroccan buildings in accordance with the MTRC, calculations and simulations are done to estimate

are investigated. Their diffusivities were measured using the flash experimental method and their thermal conductivities and volumetric capacities were estimated using a specific numerical approach.

MATERIALS AND METHOD

Samples description: The samples studied are square pieces of Moroccan Cedar and Walnut and imported Oak and Red Deal wood as showed in fig 1.

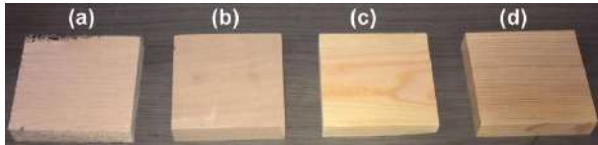


Figure 1

The different wood samples studied (a) Oak (b) Walnut (c) Red Deal (d) Cedar.

Standard thermal conductivities of wood samples studied taken from [6, 7] are given in Table 1. Further in this article, these values will be compared with the thermal conductivities measured experimentally.

Table 1
Thermal conductivity of basic materials

Material	Thermal conductivity $Wm^{-1}K^{-1}$
Cedar	0.12
Walnut	0.13
Oak	0.23
Red Deal	0.12

Method description: To determine the thermal diffusivity of the samples studied, the experimental method used in our approach is the flash method. It consists on the emission of a thermal flow generated by high temperature lamps. When the steady regime is established, this radiation is applied on the front face of the sample for a short time. In order to visualize the evolution of the rear face temperature, a thermocouple connected to an acquisition system is stuck on it. The temperature profile is then recorded by specific software. This setup is reproduced several times in order to obtain three satisfying curves.

The figure 2 shows the principle of the flash method.

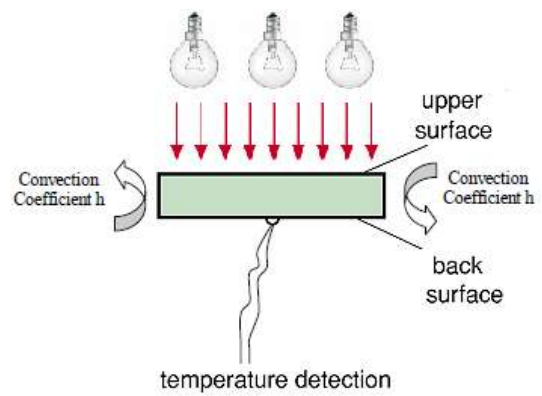


Figure 2

The schematic of the flash method

Samples preparation: The important condition which has to be satisfied in the flash method is the complete absorption of the thermal flow by the sample studied. Therefore, we have covered the samples by a black thin painting in order to avoid the flow penetration.

Moreover, the sample must be in dry state, that's why the samples were introduced into a stove for several days in order to remove their humidity. To verify that all the moisture present in the sample is totally extracted, many separate measures of masses have been made. Then, the samples have been kept in plastic bags, once their mass became constant, to avoid any humidity absorption until the measurements time.

THEORITICAL HYPOTHESIS

In order to minimize the lateral losses, the samples lateral parts were insulated using expanded polystyrene. Consequently, the only thermal exchanges the samples are confronted to were the convective ones with the front and the rear face. In addition to that, the thermal impulsion will be assimilated to a square function due to the flash duration applied to all measures which is equal to 2s. Finally, the thermal conductivity is considered independent of the temperature variation because the temperature on the rear face has a low elevation.

MATHEMATICAL ANALYSIS

After the flash is applied, the thermal flow passes through the wood sample and the rear face temperature starts increasing until attending its maximum. Thus, and according to the hypothesis considered in this paper, the sample studied corresponding to a thermal balance could be described by the following system:

$$\left\{ \begin{array}{l} \frac{\partial^2 T(x,t)}{\partial x^2} = \frac{1}{a} \frac{\partial T}{\partial t} \\ -\frac{\partial T(x,t)}{\partial x} \Big|_{x=0} = -h_1 \cdot T(0,t) + Q_0 \cdot f(t) \\ \frac{\partial T(x,t)}{\partial x} \Big|_{x=e} = h_2 \cdot T(e,t) \\ f(t) = \begin{cases} \frac{1}{t_d} & , 0 \leq t \leq t_d \\ 0 & , t_d \leq t \end{cases} \\ T(x,0) = 0 \end{array} \right. \quad (1)$$

The Laplace transform of (1) allows expressing the solution of the temperature in the Laplace space as:

$$T(e,p) = T_{ma} \cdot F(p) \frac{e^2}{a} \cdot \frac{1}{\left[\frac{(b_{i1} \cdot b_{i2}) A(p)}{\sqrt{e^2/p}} + (b_{i1} + b_{i2}) B(p) + A(p) \sqrt{e^2/p} \right]} \quad (2)$$

With:

$$\begin{aligned} A(p) &= \text{Sinh} \left(\sqrt{\frac{e^2}{a} p} \right) \\ B(p) &= \text{Cosh} \left(\sqrt{\frac{e^2}{a} p} \right) \end{aligned} \quad (3)$$

$$\begin{aligned} b_{i1} &= \frac{h_1 e}{\lambda} \\ b_{i2} &= \frac{h_2 e}{\lambda} \end{aligned} \quad (4)$$

F(p) is the Laplace transform of (1):

$$F(p) = \frac{1 - e^{-p \cdot t_d}}{p \cdot t_d} \quad (5)$$

As the objective of the study is to determine the thermophysical properties of the samples studied, we have proceeded to a numerical estimation of thermal diffusivity, volumetric capacity and thermal conductivity based on several numerical global minimization procedures.

In fact, considering (1), in adiabatic conditions when losses are neglected, it is admitted that the thermal flow transferred to the sample is corresponding to the flow which enables the sample to reach its maximum temperature, which is the limit adiabatic temperature T_{ma} . The script developed on Mathematica allows:

- Obtaining the time dependence f(t) of the temperature on the rear face by inverting numerically (1). For this purpose, the

numerical method Gaver–Stehfest [8] was chosen for its swiftness and its easier numerical implementation.

- Determining simultaneously the parameters related to the theoretical model predicting T_{th} namely T_{ma} (6), the diffusivity a and the Biot numbers b_{i1} and b_{i2} by minimizing the quadratic distance (7) between the theoretical model stemming from the numerical inversion and the experimental thermogram.

$$T_{ma} = \frac{Q_0}{\rho c S e} \quad (6)$$

$$M = \sum_{(i=1)}^N \left[T_{exp}(t_i) - T_{th}(e, T_{ma}, a, b_{i1}, b_{i2}, t_i) \right]^2 \quad (7)$$

- And finally estimating the thermal conductivity and volumetric capacity by evaluating Q_0 . For this purpose, an iron sample with known thermophysical properties was used.

RESULTS AND DISCUSSION

Density: The apparent density was easily deduced from the samples dimensions and dry masses, all these parameters are presented in the following table:

Table 2: Measured density of wood samples studied

Sample	thickness (cm)	Dimensions (mm ³)	Mass (g)	Density (Kg/m ³)
Oak	2.05	101x097x020	128.8	641.3
Cedar	2.05	101x097x020	097.1	483.4
Walnut	2.20	101x097x022	119.4	553.9
Red Deal	1.80	101x097x018	090.7	514.3

It is clear from Table 2 that the lighter wood type is Cedar, followed by Red Deal and Walnut respectively, by contrast, Oak is the heaviest one with density equal to 641 Kg/m³.

Thermal diffusivity: Table 3 represents the calculated diffusivities using the known Parker and Dgiovanni models, in addition, a third diffusivity value was returned using Mathematica script.

Table 3: Thermal diffusivity of the samples studied

Sample	Estimated diffusivity a 10 ⁻⁷ (m ² .s ⁻¹)
--------	---

	Dgiovanni method	Parker method	Present study
Cedar	1.6	2	1.6
Oak	1.74	1.95	1.67
Walnut	2.14	2.37	2.65
Red Deal	1.62	2	1.56

It is noticed that the thermal diffusivity values estimated from the Global minimization method are closer to those obtained using the Dgiovanni model which take into consideration lateral losses.

Estimated volumetric capacity, thermal conductivity and adiabatic temperature:

According to the previous models, the table 4 summarizes the results of the estimated limit adiabatic temperature, thermal conductivity and volumetric capacity of the different specimens studied.

Table 4: Estimated thermal properties of the samples studied

Sampl e	Estimated adiabatic limit temperatur e (°C)	Estimated volumetri c capacity $\text{jm}^{-3}\text{K}^{-1}$ (10^6)	Estimated thermal conductivit y $\text{Wm}^{-1}\text{K}^{-1}$
Cedar	2	0.69	0.11
Oak	1.58	0.88	0.15
Walnut	2	0.65	0.17
Red Deal	1.35	1.16	0.18

From Table 4, it is obvious that Red Deal has the greatest volumetric capacity and thermal conductivity, in return, Cedar disposes of the lowest ones. Also, we observe that the estimated thermal conductivities are close to the standard ones presented earlier in Table 1, which proves the validity of the adopted mathematical procedure, the slight difference between the two parameters is related to the variety of the experimental and numerical methods adopted.

CONCLUSION:

This paper has presented an experimental thermophysical characterization of four wood species using the flash method. For this purpose, five thermophysical properties were evaluated, the density was directly computed knowing the samples dimensions and dry masses, the thermal diffusivity was performed according to three different mathematical numerical models and the

adiabatic limit temperature, the thermal conductivity and the volumetric capacity were estimated using a specific Mathematica script. The validity of the introduced numerical approach, based on the global minimization, was confirmed through a comparison between thermal conductivities estimated values and standard ones. Moreover, this approach proved to be faster than usual known experimental methods such as hot plate and guarded hot plate, which generally take a considerable time to reach steady state. Nevertheless, this study needs to include furthermore an additional experimental method to be applied on the same studied samples in order to compare the derived thermophysical properties from both numerical and experimental studies.

REFERENCES:

1. Z.-T. Yu, X. Xu, L.-W. Fan, Y.-C. Hu, and K.-F. Cen, 2011, Experimental measurements of thermal conductivity of wood species in china: Effects of density, temperature, and moisture content," *For. Prod.* **61**, no. 2, pp. 130–135.
2. Harada, T., T. Hata, and S. Ishihara, 1998, Thermal constants of wood during the heating process measured with the laser flash method, *Journal of Wood Science*, **44**, pp. 425-431.
3. Kol, H. S, 2009, The transverse thermal conductivity coefficients of some hardwood species grown in Turkey, *Forest products journal*, **59**, p. 58.
4. Olek, W., Weres, J., and Guzenda, R, 2003, Effects of thermal conductivity data on accuracy of modeling heat transfer in wood, *Holzforschung*, **57**, pp.317-325.
5. Suleiman, Larfeldt, Leckner, and Gustavsson, M, 1999, Thermal conductivity and diffusivity of wood, *Wood Science and Technology*, **33**, pp.465-473.
6. Zimmermann, P. Zimmerman and D. J. Lef, V. Loubet, 2011, Guide régional des matériaux éco-performants.
7. N. Satiné and J. Roy, 1992, Dessin Colisage Classe d'usage : Mise en œuvre DÉCLARATION DE PERFORMANCE, **33**, pp. 33–34.
8. Stehfest, 1970, Numerical inversion of Laplace transforms. Communications of the Association for Computing Machinery.

NUMERICAL ANALYSIS OF AL₂O₃/WATER NANOFLUIDS NATURAL CONVECTION AND ENTROPY GENERATION IN ENCLOSURES

Boudaoud Warda¹, Sabeur Amina¹, Morsli Souad¹, El Ganaoui Mohammed²

1. Laboratoire des Sciences et Ingénierie Maritimes, Faculté de Mécanique, USTO

BP 1505 El M'naouer Oran, Algeria,

2. Lorraine University, Energetic Laboratory of Longwy, (FJV/LERMAB), Henri Poincaré Institute of Longwy, France)

ABSTRACT

The aim of this work is to analyze the natural convection phenomena and entropy generation of water-based Al₂O₃ nanofluids in square enclosure. The simulated domain corresponds to a square cavity heated from below and cooled from the top. The left and right walls are heated up to a height $H = (3/4)W$ and are adiabatic in the remaining part $(1-H)$. Numerical investigations have been carried out based on coupled partial differential equations of momentum and energy which are solved using finite volume method. The effective thermal conductivity of the nanofluid was expressed by the Maxwell-Garnett model however the dynamic viscosity was calculated according to the Brinkman formula. The obtained results were presented by average Nusselt number, streamlines, isotherms and entropy generation with various pertinent parameters, namely, Rayleigh number ($10^0 \leq Ra \leq 10^6$), volumetric fraction of nano-particles ($1\% \leq \phi \leq 4\%$). It was found that the heat transfer increases with the increase of Rayleigh number and volume fraction. The choice of these parameters is important to obtain maximum enhancement of heat transfer with minimum entropy generation.

KEY WORDS: Natural convection, Nanofluids, Entropy generation, volumetric fraction.

NOMENCLATURE

Latin Symbols

Be	Bejan number
CFD	Computational fluid dynamics
Cp	Specific heat
g	gravitational acceleration
h	Heat transfer coefficient
H	Dimensionless heating height
k	Thermal conductivity
L	Dimension of cavity in x direction
Nu	Nusselt number
P	Pressure
Pr	Prandtl number
Ra	Rayleigh number

S_{LHF}	local entropy generation due to heat transfer
S_{LFF}	local entropy generation due to fluid friction
S_T	Total entropy generation due to heat transfer and fluid friction
T	Temperature
U	Axial velocity
V	Radial velocity
W	Dimension of cavity in y direction

Greek Symbols

α	Thermal diffusivity
----------	---------------------

β	thermal expansion coefficient
ϕ	volume fraction of particles
μ	dynamic viscosity
ρ	Density
θ	dimensionless temperature, $\frac{(T - T_r)}{(T_h - T_c)}$

Subscripts

c	Cold wall
f	Base fluid
h	hot wall
nf	Nanofluid
p	Particles

INTRODUCTION

Free convection fluid flow and heat transfer is an important phenomenon. Its apply in different applications such as heat exchangers, cooling of electronics equipments, crystal growth, solar collector, ventilation, heating and cooling of rooms.

Usual fluids, such as water, engine oil and ethylene glycol are used generally as heat transfer fluids, the mixture of metallic or non metallic nanoparticles with traditional fluids in order to augment the heat transfer efficiency, called nanofluids, The efficiency of heat transfer by using the nanofluids is increased since the thermal conductivity of the metallic nanoparticles is superior

than that of the traditional fluids. Conventional heat transfer fluids exhibit poor heat transfer performance due to their low convection of nanofluid thermal conductivities. Many research activities have been carried out in the past to improve the thermal properties of these fluids by seeding a small quantity of highly thermally conductive solid in it [1]. The study of natural convection heat transfer within systems using nanofluids has been carried out in differentially heated enclosures. Khanafer et al. [2] numerically investigated the natural convection heat transfer of a copper–water nanofluid in a differentially heated square cavity. They found that the heat transfer rate increases with an increase in the nanoparticle volume fraction at any given Rayleigh number in their study

Nanofluid is used as the medium as a replacement for base fluid, step by step, researchers began to experimentally and numerically investigate the natural it has been more than 100 years that the thermal conductivity enhancement of conventional fluids by the suspension of solid particles, in size of millimeter and micrometer, has been well known [3]. Ho et al [4] found that Enhancement in the dynamic viscosity, counteracting that in the thermal conductivity, of the nanofluid can thus play as a crucial factor and should be taken into account when accessing its heat transfer efficacy for natural convection in enclosures. Kefayati [5,6] studied natural and mixed convection of nanofluids in a differentially heated cavity. He concluded that, by increasing the nanoparticle concentration the average Nusselt enhances. Moreover, he found that the effects of nanoparticles on the average Nusselt number drop as power-law index enhances in different Rayleigh and Hartmann numbers. Massimo Corcione [7, 8] investigated the effects of diameter and type of the nanoparticles on the heat transfer rate. He found that, the heat transfer enhancement increases when increasing the nanoparticle volume fraction up to an optimal particle loading at which the amount of heat transferred across the enclosure has a peak. In addition, his results indicated that, the heat transfer enhancement at the optimal particle loading increases as the average temperature of the nanofluid increases and the size of the suspended nanoparticles decreases. Similar observation was reported by Garoosi et al. [9] who numerically investigated laminar natural convection of nanofluid in a square cavity. Studies on entropy generation of heat transfer in nanofluid filled energy systems are extremely limited. In this context, Shahi et al. [10] performed a numerical study on entropy generation due to natural convection of a nanofluid that consists of water and Cu in a cavity with a protruded heat

source. They used finite volume method and solved the equations for different Rayleigh numbers, solid concentration and heat source location. Their results showed that the maximum value of Nusselt number and minimum entropy generation are obtained when heat source mountains in the bottom horizontal wall. Singh et al. [11] present a theoretical investigation of the entropy generation analysis due to flow and heat transfer in nanofluids. They considered the most common alumina–water nanofluids as the model fluid. They observed that at lower tube diameter, flow friction irreversibility is more significant and at higher tube diameter thermal irreversibility is more. For both laminar and turbulent flow, there is an optimum diameter at which the entropy generation rate is the minimum for a given nanofluid.

The main objective of the present work is to numerically explore the fundamental fluid flow and heat transfer characteristics for natural convection of the water– Al_2O_3 nanofluids in square enclosure.

MATHEMATICAL MODEL

Fig 1 shows the geometrical configuration under consideration. This studied enclosure is very important because used as a simplified model for crystal growth problems (known as Bridgman configuration) [12, 13, 14, 15]. It is a two-dimensional square cavity heated from below and cooled from the top. For the side walls $\frac{3}{4}$ are maintained at a hot temperature and the $\frac{1}{4}$ of the side walls is adiabatic model. The temperature driven flow in this work is considered as laminar and results are carried out by employing single method.

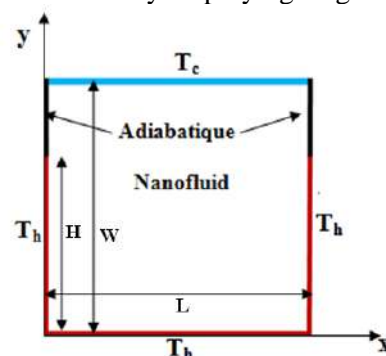


Figure 1

Geometrical configuration of the two-dimensional square cavity.

The equations governing steady state laminar natural convection fluid flow and heat transfer are described below in terms of primitive variables. The set of equations was written in dimensionless form as follows:

GOVERNING EQUATIONS

Continuity equation:

$$\frac{\partial U}{\partial X} + \frac{\partial V}{\partial Y} = 0 \tag{1}$$

Momentum equation:

$$U \frac{\partial U}{\partial X} + V \frac{\partial U}{\partial Y} = -\frac{\partial P}{\partial X} + \text{Pr} \left(\frac{\partial^2 U}{\partial X^2} + \frac{\partial^2 U}{\partial Y^2} \right) \tag{2}$$

$$U \frac{\partial V}{\partial X} + V \frac{\partial V}{\partial Y} = -\frac{\partial P}{\partial Y} + \text{Pr} \left(\frac{\partial^2 V}{\partial X^2} + \frac{\partial^2 V}{\partial Y^2} \right) + \text{RaPr}\theta \tag{3}$$

Energy equation

$$U \frac{\partial \theta}{\partial X} + V \frac{\partial \theta}{\partial Y} = \left(\frac{\partial^2 \theta}{\partial X^2} + \frac{\partial^2 \theta}{\partial Y^2} \right) \tag{4}$$

Where the Rayleigh number Ra, and the Prandtl number Pr, are:

$$\text{Ra} = \frac{g\beta_f (T_h - T_c)W^3}{\alpha_f \nu_f}, \quad \text{Pr} = \frac{\nu_f}{\alpha_f} \tag{5}$$

The boundary conditions for equations (1)-(4) are specified as follows:

$$\theta(0, Y) = 1$$

$$\theta(0, Y) = \theta(1, Y) = 1 \quad \text{for } 0 \leq Y \leq H$$

$$\left. \frac{\partial \theta}{\partial X} \right|_{(0,Y)} = \left. \frac{\partial \theta}{\partial X} \right|_{(1,Y)} = 0 \quad \text{for } H \leq Y \leq 1$$

$$\theta(X, 1) = 0$$

The effective thermo-physical properties of the nanofluids are estimated by different formulas available in the literature. The formulas chosen for the thermo-physical properties of the nanofluid in this work are as follow.

Density:

$$\rho_{nf} = (1 - \phi)\rho_f + \phi\rho_p \tag{6}$$

Thermal expansion coefficient:

$$\beta_{nf} = (1 - \phi)\beta_f + \phi\beta_p \tag{7}$$

Specific heat:

$$Cp_{nf} = \frac{1}{\rho_{nf}} \left[(1 - \phi)\rho_f Cp_f + \phi\rho_p Cp_p \right] \tag{8}$$

Thermal conductivity:

In order to approximate the effective thermal conductivity of nanofluid; the Maxwell-Garnett formula is chosen as follows:

$$k_{nf} = k_f \left[\frac{2 + k_{pf}^* + 2\phi(k_{pf}^* - 1)}{2 + k_{pf}^* - \phi(k_{pf}^* - 1)} \right] \tag{9}$$

With

$$k_{pf}^* = \frac{k_p}{k_f} \tag{10}$$

Dynamic viscosity:

The Brinkman's formula [16] is used to calculate the dynamic viscosity

$$\mu_{nf} = \mu_f (1 - \phi)^{-2.5} \tag{11}$$

The thermo-physical properties of base fluid and nanoparticles are resumed in table I.

Table I
Thermo-physical properties of base fluid and nanoparticles

The local heat transfer coefficient ($Nu_{h,nf}$) at the hot wall of the cavity is presented as:

Property	Base fluid (water)	Nanoparticle (Al2O3)
Density (kg/m ³)	997.1	3600
Specific heat (J/kg k)	4179	765
Thermal conductivity (W/mk)	0.605	46
Dynamic viscosity (kg/ms)	8.91*10 ⁻⁴	-----
Thermal expansion coefficient (k ⁻¹)	2.1*10 ⁻⁴	6.3*10 ⁻⁶

$$Nu_{h,nf} = \frac{h_{nf}L}{k_{nf}} \tag{12}$$

ENTROPY GENERATION RATE

According to the dimensionless parameters defined above and local thermodynamic equilibrium of the linear transport theory, the dimensionless local entropy generation due to heat transfer and the fluid friction (S_{LHT} and S_{LFF} respectively) for a two-dimensional heat and fluid flow in the cartesian coordinates in explicit form can be written as:

$$S_{LHT} = \left(\frac{\partial\theta}{\partial X}\right)^2 + \left(\frac{\partial\theta}{\partial Y}\right)^2 \tag{13}$$

$$S_{LFF} = \varphi \left\{ 2 \left[\left(\frac{\partial U}{\partial X}\right)^2 + \left(\frac{\partial V}{\partial Y}\right)^2 \right] + \left[\left(\frac{\partial U}{\partial Y}\right) + \left(\frac{\partial V}{\partial X}\right) \right]^2 \right\} \tag{14}$$

The total local entropy generation is the summation of S_{LHT} and S_{LFF} .

$$S_L = S_{LHT} + S_{LFF} = \left(\frac{\partial\theta}{\partial X}\right)^2 + \left(\frac{\partial\theta}{\partial Y}\right)^2 + \varphi \left\{ 2 \left[\left(\frac{\partial U}{\partial X}\right)^2 + \left(\frac{\partial V}{\partial Y}\right)^2 \right] + \left[\left(\frac{\partial U}{\partial Y}\right) + \left(\frac{\partial V}{\partial X}\right) \right]^2 \right\} \tag{15}$$

Where φ is the parameter determining the contributions of heat transfer and friction contributions to the entropy generation namely the irreversibility distribution ratio :

$$\varphi = \frac{S_{LFF}}{S_{LHT}} \tag{16}$$

The total entropy generation due to heat transfer and fluid friction (S_{THT} and S_{TEF} , respectively) are obtained by integrating the local entropy generation over the system volume:

$$S_{THT} = \int_V S_{LHT} dV; S_{TEF} = \int_V S_{LFF} dV; \tag{17}$$

$$S_T = S_{THT} + S_{TEF}$$

The local Bejan number indicates the strength of the entropy generation due to heat transfer irreversibility:

$$Be = \frac{S_{LHT}}{S_L} \tag{18}$$

At $Be \gg 1/2$, the irreversibility due to heat transfer dominates; at $Be \ll 1/2$, the irreversibility due to viscous effects dominates; finally, at $Be = 1/2$, the heat transfer and fluid friction irreversibilities are equal. The heat transfer irreversibility is the only origin of the entropy generation at $Be = 1$; at $Be = 0$, the fluid friction irreversibility is the only origin of the entropy generation.

COMPUTATIONAL AND CALCULATIONS TOOLS

The numerical code was validated by comparison with the numerical results for the

GRID INDEPENDENCE

The geometry and the grid were generated using preprocessor called Gambit. It is an integrated preprocessor for CFD analysis. The mesh file was further exported to Fluent. In this work, the grid independence study was carried out with four different grid sizes (48*48, 70*70, 90*90 and 121*121). These studies are performed for pure water. The results are compared in terms of Nusselt number which is in a good agreement with the Ho et al [3] work. So the grid 120*120 is chosen for further computations.

Table2
Validation of the Grid

Grid	Nu
48 × 48	4.52
70 × 70	4.59
90 × 90	4.518
120 × 120	4.706
Ho et al [3]	4.605

VALIDATION

Table3
Comparison of Nusselt numbers

Ra	Present Work	Ho et al [4]	Lai et al [16]	Yu et al [17]	Tanmay et al [18]
10^3	1.113	1.161	1.154	-----	1.103
10^4	2.265	2.021	2.330	2.244	2.287
10^5	4.706	4.605	4.728	4.439	4.867
10^6	9.194	9.051	9.118	8.024	-----

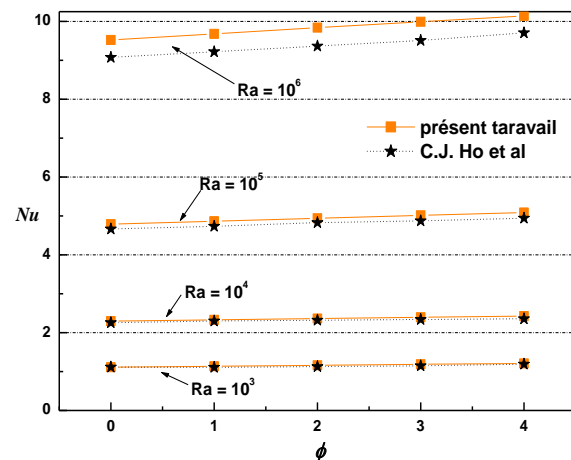


Figure 2

Representation of the Nusselt number as a function of the volume fraction of Al₂O₃ for different Rayleigh number. benchmark results [4, 18, 19, and 20] at different Rayleigh numbers as shown in Table 3. As seen

there is a good agreement between the benchmark solutions for the averaged Nusselt number and the present work. Also an excellent accord is apparently displayed between the present results and Ho et al [4] for the averaged Nusselt number at the hot wall of the enclosure for different volume fractions (figure 2).

RESULTS AND DISCUSSION

Streamlines and isotherms

In the present work, we investigate the effects of the thermal Rayleigh number (Ra), nanoparticle volume fraction on natural convection heat transfer in square cavity of water-Al₂O₃ nanofluid, due to the several cases studied, the work was carried out in this section only for the square enclosure AR = 1, with Ra = 10², 10⁴ and 10⁶ and for volumetric fraction $\phi = 0\%$ and 3%. Numerical simulation has been carried out. In this study the results indicate that the heat transfer feature of a nanofluid increases

remarkably with the volume fraction of nanoparticles.

Figures 4 and 5 illustrate comparison of the streamlines and isotherms contours between the nanofluid ($\phi = 3\%$) and the base fluid ($\phi = 0\%$) at different values of Ra = 10², 10⁴ and 10⁶, respectively.

As the volume fraction increases, the velocity components of nanofluid increase as a result of an increase in the energy transport through the fluid. The effect of the volume fraction on the streamlines and isotherms of nanofluid for various Rayleigh numbers is shown in Figs. 3(a) and 4(a). In the absence of nanoparticles ($\phi = 0\%$), The flow consists of two vortex counter-rotating as a dominant characteristic of the fluid flow inside the cavity, As the Rayleigh number increases, as shown in Figs. 3a and 4a and ($\phi = 0\%$), the vortex counter-rotating tends to becomes elliptic for (Ra = 10⁴) and (Ra = 10⁶). As the volume fraction increases, the velocities at the center of the cavity increase as a result of higher solid– fluid transportation of heat.

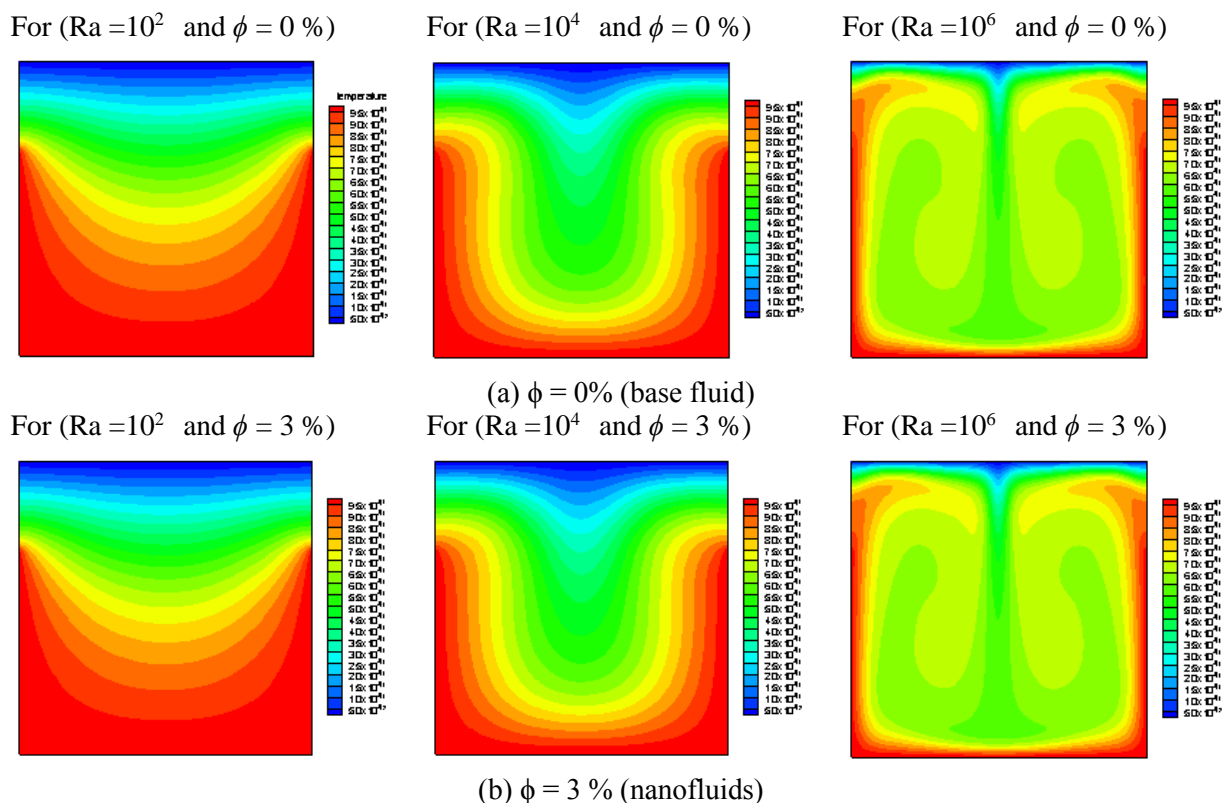


Figure 3

Temperature contours for $\phi = 0\%$ (base fluid) and $\phi = 3\%$ (nanofluids) at different values of Ra (10², 10⁴ and 10⁶).

The isotherms in Fig. 4 show that for (Ra = 10⁶) isotherms breaks up into two contra-rotating the isotherms breaks down with an increase in the volume fraction for higher Rayleigh numbers. As

the volume fraction increases, the velocities at the center of the cavity increase as a result of higher solid– fluid transportation of heat.

Nusselt number

conductivity also increases. This implies that an increase in volume fraction produces an increment in irreversibility due to heat transfer; it is interesting

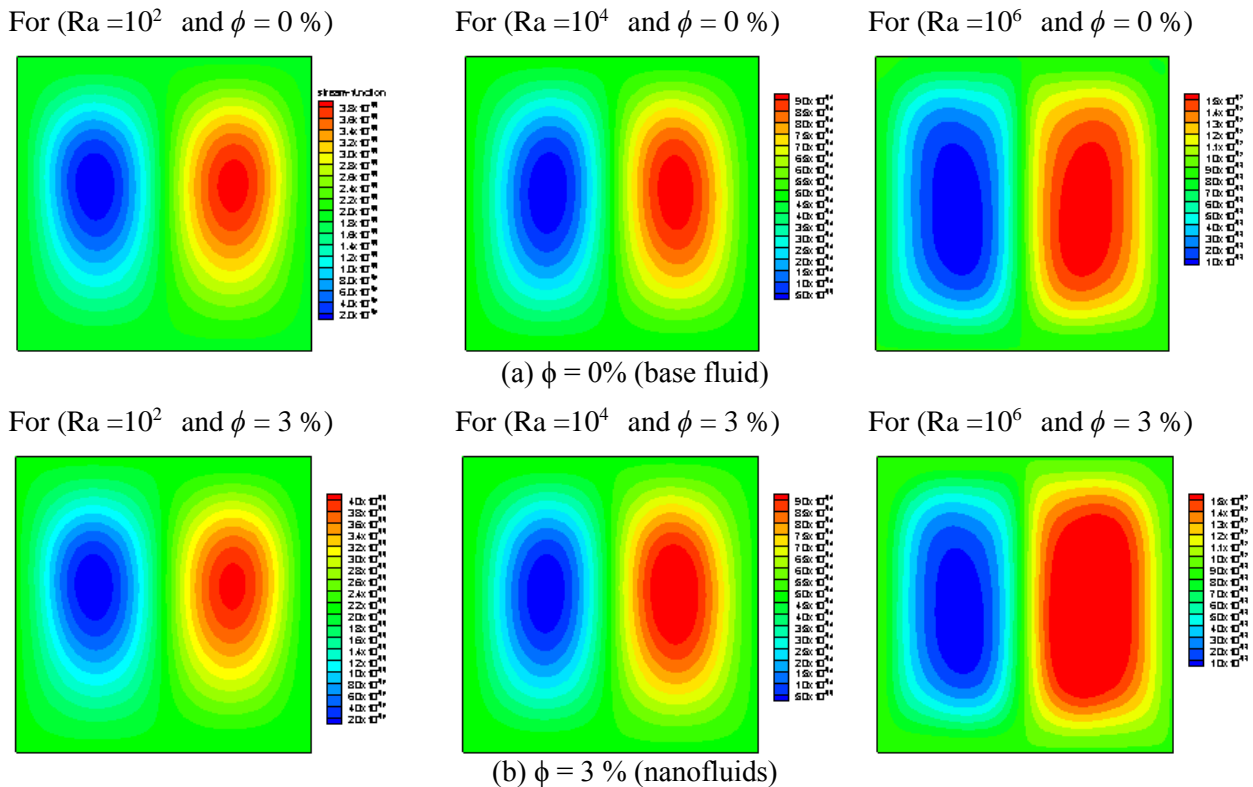


Figure 4

Streamlines contours for $\phi = 0\%$ (base fluid) and $\phi = 3\%$ (nanofluids) at different values of Ra (10^2 , 10^4 and 10^6).

The averaged Nusselt number at the bottom wall $Nu_{p,b}$ and upper wall $Nu_{p,h}$ are illustrated in Fig. 5 for the different volume fraction of the nanoparticles at different Rayleigh numbers.

In general, the results show that the average Nusselt number increases as the Rayleigh number increases due to the strengthened buoyant flow. The averaged Nusselt number exhibits a monotonic variation with the volumetric fraction of nanoparticles.

Entropy generation

The distribution of local entropy generation due to heat transfer and fluid friction irreversibility for pure fluid as well as nanofluid is shown in Figures 7,8 for different volume fraction nanoparticles and Rayleigh number. Our result shows that with the increase of Rayleigh number the heat entropy generation increases due to the increase in

buoyancy effect for which the irreversibility due to heat transfer increases, with the increase of nanoparticle volume fraction, the effective thermal

to note that the entropy generation decreases linearly with the increase of nanoparticle.

The Variation of entropy generation with Rayleigh number for different volume fraction in the case of heat entropy which has the lowest value of entropy generation in $Ra = 10^4$. As mentioned before, the heat entropy generation increases with increasing Ra number due to more heat transferred into flow and consequently higher temperature gradient. In other words, the temperature gradient and entropy generation due to heat transfer concentrates along the walls. The presence of nanoparticles plays a more significant role in reducing entropy at Ra number equal to 10^4 .

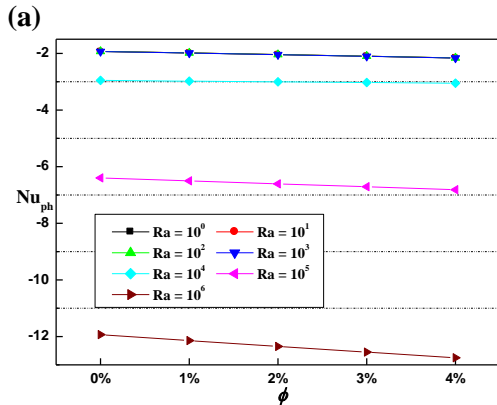
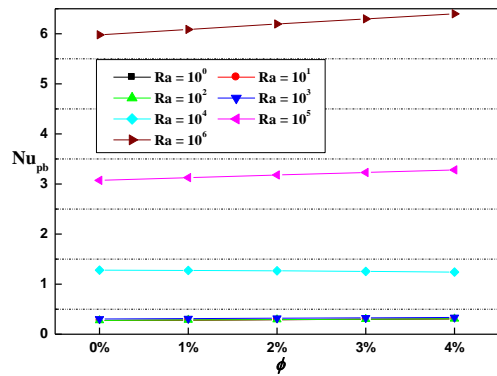


Figure 5

Variation of averaged Nusselt number with volumetric fraction for different Rayleigh number (a) bottom wall (b) upper wall.

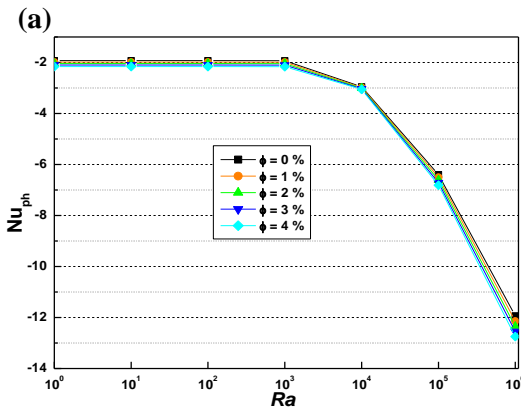
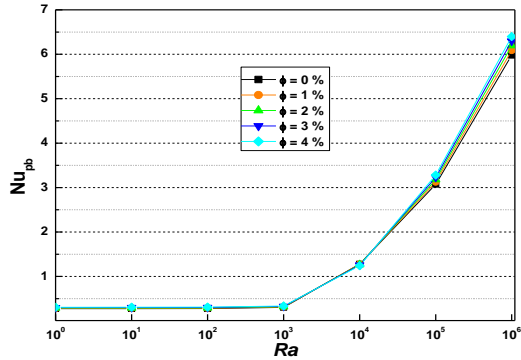


Figure 6

Variation of averaged Nusselt number with Rayleigh number for different volume fraction (a) bottom wall (b) upper wall.

Entropy generation

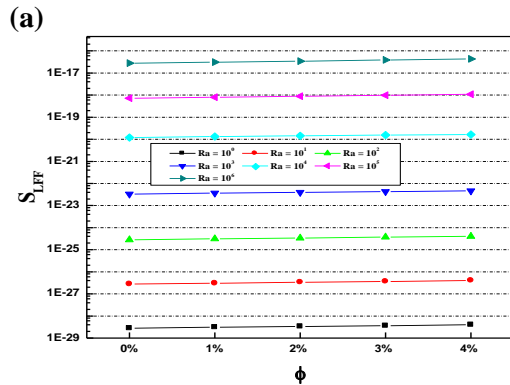
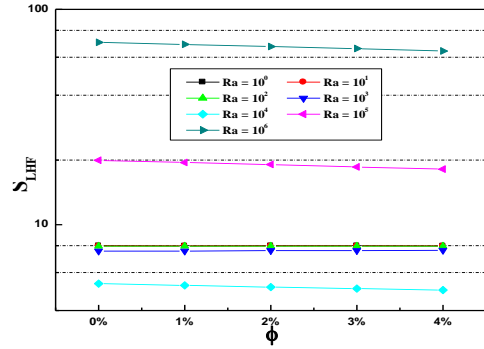


Figure 7

Variation of entropy generation with volumetric fraction for different Rayleigh number (a) heat entropy (b) viscous entropy.

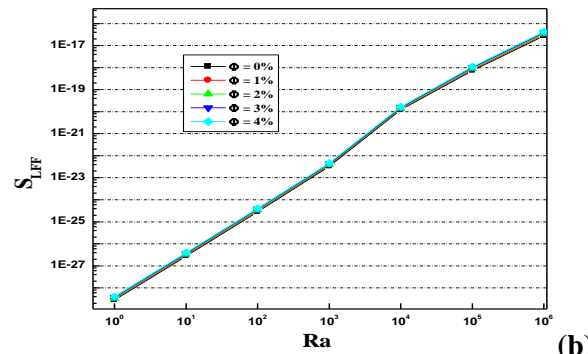
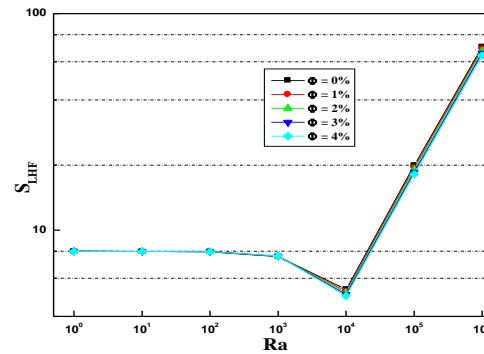


Figure 8

Variation of entropy generation with Rayleigh number for different volume fraction (a) heat entropy (b) viscous entropy.

CONCLUSION

In this paper, natural convection heat transfer performance and entropy generation of Al₂O₃/water nanofluid in a two-dimensional enclosure is studied numerically in single-phase way by open source CFD simulations via Fluent for a range of Rayleigh number and volume fractions. Results show that the average Nusselt number increases with the increase of Rayleigh number and the volumetric fraction. Compared to pure water, Al₂O₃/water nanofluid is found to have upper average Nusselt number along the heating wall because the increased conductivity is playing dominant role to increase heat convection by impeding the nanofluid flow.

Also the influence of adding nanoparticles to pure fluid, different volume fractions of nanoparticle, entropy generation is studied. The main results can be expressed as follows:

By adding nanoparticle into pure fluid, the entropy generation decreases.

The role of adding nanoparticle in reducing entropy generation is more pronounced at higher Ra numbers (10^4)

Increasing Ra number results in increase in average Nu number and entropy generation.

The results have shown that for the Rayleigh numbers considered in this study ($Ra = 10^0 \sim 10^6$), the mean Nusselt number increases and the total entropy generation decreases with an increasing volume fraction of nanoparticles.

Acknowledgments

The first author acknowledges his training period in the University of Lorraine (IUT of Longwy) permitting the achievement of the present work.

REFERENCES

- Ahuja, A.S, 1975, Augmentation of heat transfer in laminar flow of polystyrene suspensions, *J. of Applied Physics*, **46**, pp. 3408-3416.
- Khanafer, K, Vafai K, M. Lightstone, 2003, Buoyancy-driven heat transfer enhancement in a two-dimensional enclosure utilizing nanofluids, *Int. J. Heat Mass Transfer* **46**, pp. 3639–3653.
- Lee S, Choi SUS, Li S, Eastman J.A, 1999, Measuring thermal conductivity of fluids containing oxide nanoparticles, *ASME. J. Heat Transfer*, **121**, pp. 280–9.
- Ho. C.J, Chen. M. W, Li. Z.W, 2008, Numerical simulation of natural convection of nanofluid in a square enclosure: Effects due to uncertainties of viscosity and thermal conductivity, *Int. J. of Heat and Mass Transfer*, **51**, pp. 4506–4516.
- Kefayati. G.H.R, 2015, FDLBM simulation of mixed convection in a lid-driven cavity filled with non-newtonian nano fluid in the presence of magnetic field, *Int. J. Therm. Sci*, **95**, pp. 29–46.
- Kefayati. G.R, 2015, Magnetic field effect on heat and mass transfer of mixed convection of shear-thinning fluids in a lid-driven enclosure with non-uniform boundary conditions, *J. Taiwan Inst. Chem. Eng*, **51**, pp. 20–33.
- Corcione. M, Cianfrini. M, Quintino. A, 2015, Enhanced natural convection heat transfer of nanofluids in enclosures with two adjacent walls heated and the two opposite walls cooled. *Int. J. Heat Mass Transfer*, **88**, pp. 902–913.
- Corcione. M, 2011, Rayleigh-Bénard convection heat transfer in nanoparticle suspensions, *Int. J. Heat Fluid Flow*, **32**, pp. 65–77.
- Garoozi. F, Bagheri. G, Talebi. F, 2013, Numerical simulation of natural convection of nanofluids in a square cavity with several pairs of heaters and coolers (HACs) inside, *Int. J. Heat Mass Transfer*, **67**, pp. 362–376.
- Shahi M, Mahmoudi AH, Raouf AH, 2011, Entropy generation due to natural convection cooling of a nanofluid, *Int. Commun Heat Mass Transfer*, **38**, pp. 972–83.
- Singh PK, Anoop KB, Sundararajan T, Das SK, 2010, Entropy generation due to flow and heat transfer in nanofluids. *Int. J. Heat Mass Transfer*, **53**, pp. 4757–67.
- Bennacer. R, El Ganaoui. M, Leonardi. E, 2006, Symmetry breaking of melt flow typically encountered in a Bridgman configuration heated from below, *Original Research Article Applied Mathematical Modelling*, **30**, pp. 1249-1261.
- Kaenton. J, Semma. E, Timchenko. V, El Ganaoui. M, Leonardi. E, De Vahl Davis. G, 2004, Effects of anisotropy and solid/liquid thermal conductivity ratio on flow instabilities during inverted Bridgman growth, *Int. J. of Heat and Mass Transfer*, **47**, pp. 3403-3416.
- El Ganaoui.M, Bontoux. P, 1999, Gravity effects on solidification: The case of an unsteady melt affecting the growth interface, *Advances in Space Research*, **24**, pp. 1423-1426.
- El Ganaoui. M, Bontoux. P, Morvan. D, 1999, Localisation d'un front de solidification en interaction avec un bain fondu instationnaire, *Comptes Rendus de l'Académie des Sciences-Series IIB-Mechanics-Physicsastronomy*, **327**, pp. 41-48.
- Brinkman. H. C, 1952, The viscosity of concentrated suspensions and solution, *J. Chem. Phys*, **20**, pp. 571–581.
- Fluent Inc. FLUENT 6.3.26 User's guide. (Fluent Inc), 2006.

18. Feng-Hsiang Lai, Yue-Tzu Yang, 2011, Lattice Boltzmann simulation of natural convection heat transfer of Al₂O₃/water nano fluids in a square enclosure, *Int. J. of Thermal Sciences*, **50**, pp. 1930-1941.
19. Zi-Tao Yu, Wei Wang, Xu Xu, Li-Wu Fan, Ya-Cai Hu, Ke-Fa Cen, 2011, A numerical investigation of transient natural convection heat transfer of aqueous nano fluids in a differentially heated square cavity, *Int. Communications in Heat and Mass Transfer*, **38**, pp. 585–589.
20. Tanmay Basak, Ali J. Chamkha, 2012, Heatline analysis on natural convection for nanofluids confined within square cavities with various thermal boundary conditions, *Int. J. of Heat and Mass Transfer*, **55**, pp. 5526–5543.

NUMERICAL SIMULATION OF FLOW THROUGH A POROUS SQUARE CYLINDER

Hamza Mahdhaoui^{1,2}, Xavier Chesneau¹ and Ali Hatem Laatar²

¹ LAMPS, Université de Perpignan Via Domitia, 52 Avenue Paul Alduy 66860 Perpignan - France

² LETTM, Département de physique, Faculté des sciences de Bizerte, Université de Carthage, 7021 Jarzouna - Bizerte Tunisia

*Corresponding author: Xavier Chesneau: Fax: +33468662075 Email: chesneau@univ.perp.fr

ABSTRACT

Flow through porous media occurs in various engineering applications such as heat exchangers, cooling of gas turbine. Therefore, the heat transfer phenomenon through the porous medium is also interesting for many engineering applications. In this paper, a two-dimensional laminar flow around and through a porous square cylinder is studied numerically. The transfers in the channel and the porous medium are respectively described by the classic equations of forced convection and the Darcy-Brinkman-Forcheimer model. After the code validation, we have studied the effects of the Darcy and Reynolds numbers on several hydrodynamics parameters such as wake structure and streamlines.

KEYWORDS

NOMENCLATURE

C_F	Forchheimer coefficient $C_F = 1.75 / (150 \mathcal{E}^2)$
Da	Darcy number = K / h^2
h	height of the cylinder
L_D	distance between rear face of the cylinder and the outflow boundary (m)
Nu	local Nusselt number
K	permeability (m^2)
L_R	length of recirculation region (m)
Pr	Prandtl number
Re	Reynolds number = $\rho U_0 h / \mu$
T	dimensionless temperature
U, W	velocity ($m s^{-1}$)

Greek symbols

μ	dynamic viscosity ($kg m^{-1} s^{-1}$)
ρ	density ($kg m^{-3}$)
\mathcal{E}	porosity
X, Z	dimensionless coordinates
β	aspect ratio, = h/H

INTRODUCTION

The flow through porous media frequently occurs in various technological system such as cooling system for LED backlight module, heat exchanger, cooling

system for electronic component, thermal insulation, nuclear reactors, drying processes... Many numerical and experimental works are devoted to the flows around a fixed square cylinder. The flow around a square cylinder generates the apparition of Von Karman vortices from $Re_c = 60$. This value was found by Breuer et al. [1] and Korichi et al. [2]. A. K. Dhiman et al. [3] have simulated the two-dimensional mixed convection of an air flow in a horizontal channel. The isotherms and the streamlines were obtained for different values of Reynolds, Prandtl and Richardson numbers. They notice a coincidence between drag and lift coefficient profiles. The vortex shedding behind a porous square cylinder was studied by Jue [4]. His results have revealed that the vortex shedding is delayed with an increase of the Darcy number. Another research work concerning the flow around and through a porous square cylinder has been realized by Dhinakaran and Ponmozhi [5]. They have also investigated numerically the fluid flow and the heat transfer around and through a porous square cylinder. They show that the drag coefficient and wake length, for porous square cylinder, approaches the corresponding case of a solid square

cylinder for very low Darcy numbers, typically at values around 10^{-6} .

The objective of the present work is, therefore, to study, in detail, the flow and thermal field around and through a porous square cylinder and to estimate the effects of the Reynolds and Darcy numbers on different physical parameters such as the Nusselt number, the wake structure, the velocity distribution and the streamlines. Moreover, those parameters are compared with those obtained for a solid square cylinder.

PROBLEM FORMULATION

Equations

The square cylinder, of height, h , is symmetrically placed on the channel axis as indicated in Fig. 1. The upstream face of the square cylinder is located at a distance $L_u = 5h$ from the inlet. The distance between the porous medium and the outlet is equal to $L_D = 29h$. The values of L_u and L_D are those recommended by S. Dhinakaran et al. [5].

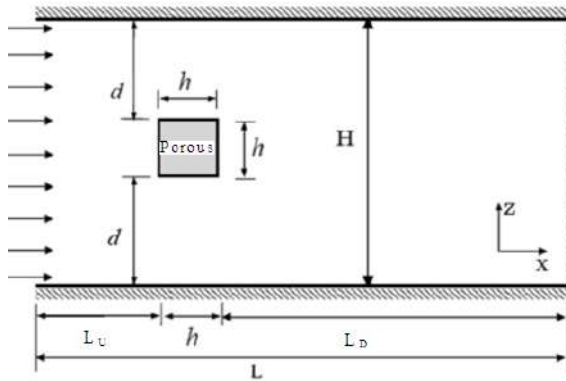


Figure 1

Schematic diagram of the problem

In this study we have considered a two-dimensional incompressible and laminar flow. Also, we have supposed that the porous cylinder is homogeneous and isotropic. The dimensionless equations can be written in the following form:

$$\left\{ \begin{aligned} \frac{\partial U}{\partial X} + \frac{\partial W}{\partial Z} &= 0 \\ \frac{1}{\varepsilon} \frac{\partial U}{\partial \tau} + \frac{U}{\varepsilon^2} \frac{\partial U}{\partial X} + \frac{W}{\varepsilon^2} \frac{\partial U}{\partial Z} &= -\frac{\partial P}{\partial X} + \frac{1}{\varepsilon \text{Re}} \left(\frac{\partial^2 U}{\partial X^2} + \frac{\partial^2 U}{\partial Z^2} \right) - \frac{U}{\text{Re} \cdot \text{Da}} - \frac{C_f}{\sqrt{\text{Da}}} (\sqrt{U^2 + W^2}) U \\ \frac{1}{\varepsilon} \frac{\partial W}{\partial \tau} + \frac{U}{\varepsilon^2} \frac{\partial W}{\partial X} + \frac{W}{\varepsilon^2} \frac{\partial W}{\partial Z} &= -\frac{\partial P}{\partial Z} + \frac{1}{\varepsilon \text{Re}} \left(\frac{\partial^2 W}{\partial X^2} + \frac{\partial^2 W}{\partial Z^2} \right) - \frac{W}{\text{Re} \cdot \text{Da}} - \frac{C_f}{\sqrt{\text{Da}}} (\sqrt{U^2 + W^2}) W \\ \frac{\partial T}{\partial \tau} + \frac{U}{\varepsilon} \frac{\partial T}{\partial X} + \frac{W}{\varepsilon} \frac{\partial T}{\partial Z} &= -\frac{\partial P}{\partial X} + \frac{1}{\text{Re} \text{Pr}} \left(\frac{\partial^2 T}{\partial X^2} + \frac{\partial^2 T}{\partial Z^2} \right) \end{aligned} \right.$$

The dimensionless variables are defined as follows:

$$X = \frac{x}{H}, Z = \frac{z}{H}, \tau = \frac{t}{H/U_0}, U = \frac{u}{U_0}, W = \frac{w}{U_0}, \\ P = \frac{p}{\rho U_0^2}, T = \frac{\theta}{\theta_0}, \text{Pr} = \frac{\nu}{\alpha}, \text{Re} = \frac{U_0 H}{\nu}$$

Boundary conditions

The boundary conditions must be specified to solve the equations. The velocity over the cross-section at the inlet has an uniform profile (U_0), whereas at the outlet section the flow is considered as fully developed. Thus, the dimensionless boundary conditions can be written as follows:

At the inlet section: $U = 1, W = 0, T = 0$

At the outlet section: $\frac{\partial U}{\partial X} = 0, \frac{\partial W}{\partial Z} = 0, \frac{\partial T}{\partial X} = 0$

At the walls: $U = 0, W = 0, \frac{\partial T}{\partial Z} = 0$

Numerical resolution

The equations are integrated by a finite-volume method and then solved by using the projection method. We use a second-order Adams-Bashforth implicit scheme for the time term. The convective and diffusive terms are discretized using QUICK and central differencing schemes, respectively.

Fig.2. shows the grids. A non-uniform structured mesh of 258×178 is used with a refinement near the walls to capture the strong gradients of temperature and velocity. The choice of step time was imposed by the precision and the numerical stability ($\Delta \tau = 2.10^{-3}$).

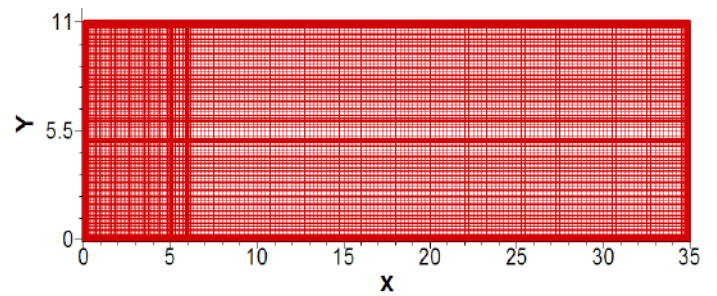


Figure 2

Non-uniform mesh distribution in the computational domain.

RESULTS AND DISCUSSION

Validation

To validate our numerical code, we have compared our results with the results of Dhinakaran and

Ponmozhi [5] who have studied the heat transfers from a porous square cylinder to a flowing fluid. The figure 3 shows the wake length after the porous cylinder as a function of the Reynolds number. We can see, on this figure, that our results are in good agreement with those of Dhinakaran and Ponmozhi.

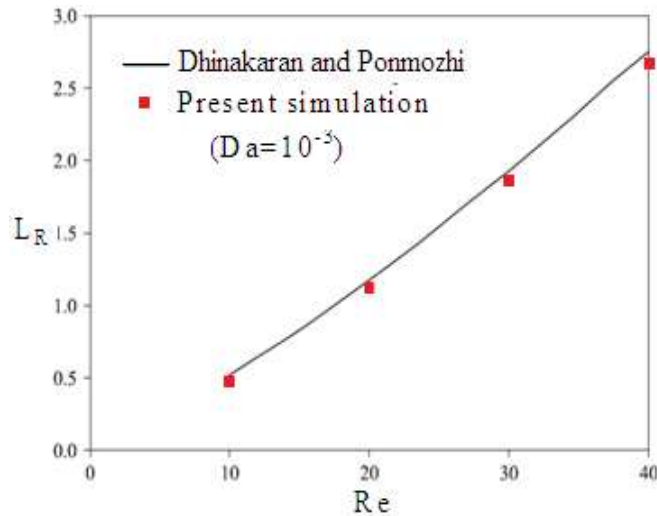


Figure 3: Variation of the wake length as a function of Reynolds number for the porous square cylinder at $Da = 10^{-3}$.

We have also validated our numerical code by comparing the local Nusselt numbers obtained in this work and those obtained by the previous authors. This comparison is presented on Fig. 4 where AB represents the frontal face and CD the rear face. We can see a good agreement for the Nusselt numbers on all the cylinder faces.

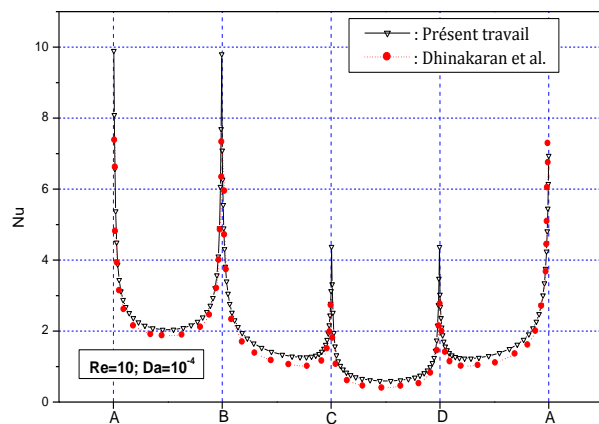


Figure 4: Time-averaged local Nusselt number around the square cylinder.

Results

The effects of the Darcy number on the flow structure are illustrated on the Fig. 5 for a Reynolds number equal to 10.

For a Darcy number equal to 10^{-2} (Fig. 5 a), the flow penetrates the porous cylinder with a low resistance. Like that, the streamlines are weakly deformed and there is not recirculation zone after the porous cylinder. With a diminution of the Darcy number (Fig. 5 b and c) the streamlines are separated in two zones located on the top and below of the porous cylinder. Just after the cylinder, there is a recirculation zone and then a reattachment of the flow.

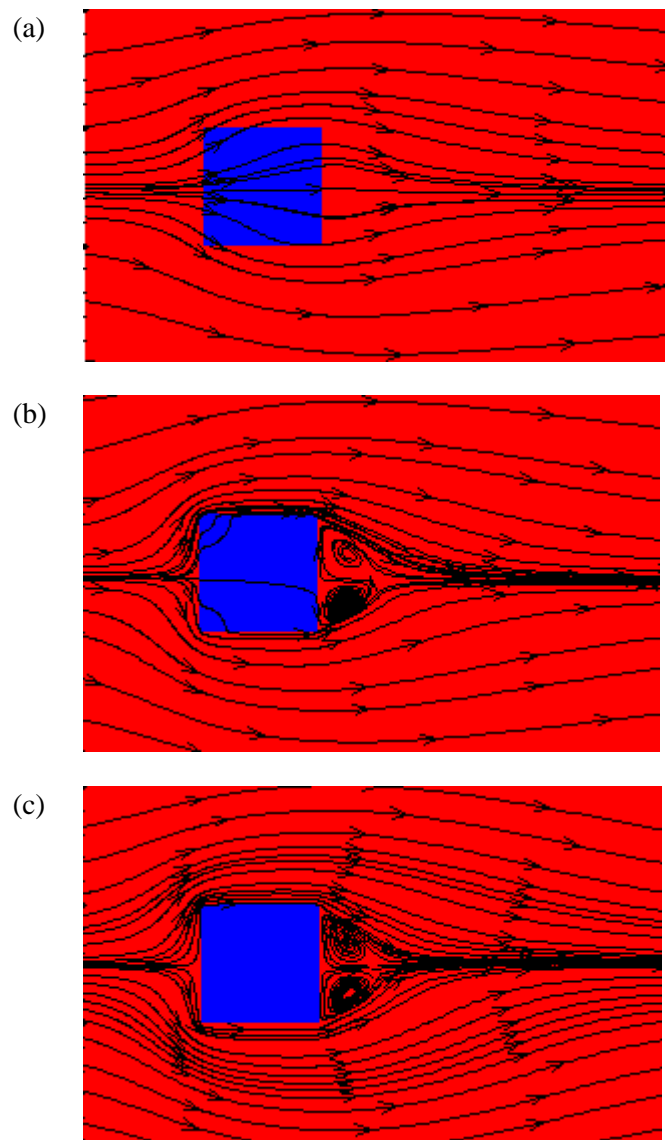


Figure 5: streamlines through and around the porous square cylinder for different Darcy numbers (a= 10^{-2} ; b= 10^{-4} ; c= 10^{-6}) at $Re=10$

Fig. 6 shows the distribution of the time-averaged local Nusselt number Nu around the square cylinder with time for different aspect ratios (1/11, 1/8, 1/5) and for $Re=40$. On the front face (A-B), the values of the Nusselt number are maximum, because the temperature gradients are more important in the inlet zone of the channel. Along the upper (B-C) and the lower (D-A) face, the Nusselt number decreases, because the air temperature increases and the temperature gradient between the porous surface and the air flow, in its vicinity, decreases. On the rear face, the nusselt number takes a low and constant value. This is due to the fact that the rear face is just before the recirculation zone. The aspect ratio has a slightly effect on the local Nusselt number (Figure 6). This influence can be better seen on the figure 7, which represents the average Nusselt number as a function of the aspect ratio. In fact, the Nusselt number increases slightly with the aspect ratio because an augmentation of the aspect ratio corresponds to a diminution of the height of the channel and then the porous medium is more enclosed.

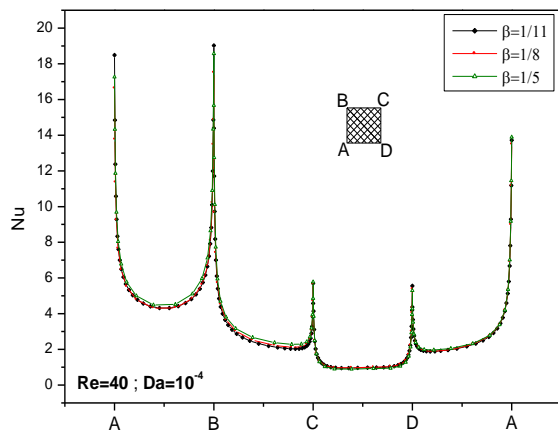


Figure 6: Time-averaged local Nusselt number around the square cylinder for different aspect ratios.

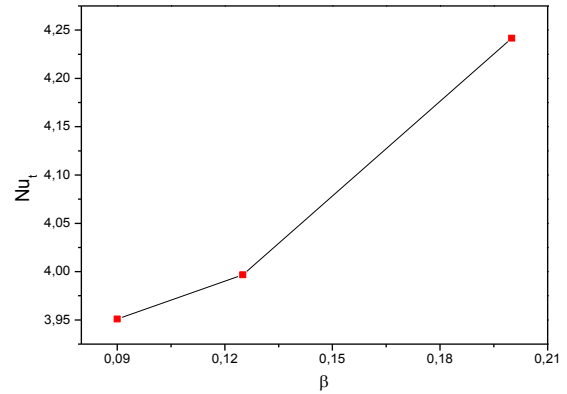


Figure 7: Variation of average nusselt number for different aspect ratios at $Da = 10^{-4}$.

On the figure 8, we have represented the average Nusselt number as a function of the Reynolds number for a fixed value of the Darcy number equal to 10^{-4} . As we can see, the Nusselt number increases linearly with the Reynolds number. This result was expected because an augmentation of the Reynolds number corresponds to an augmentation of the convection transfers between the surface of the porous medium and the air flow in its vicinity.

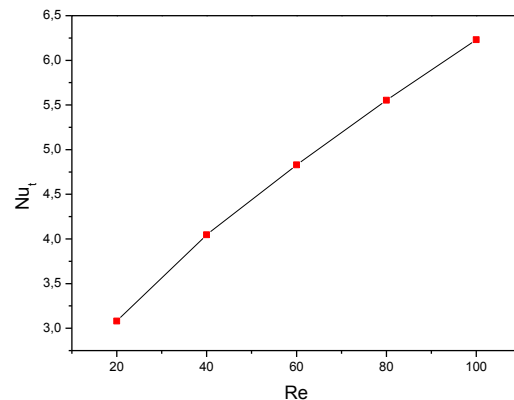


Figure 8: Variation of average Nusselt number as a function of the Reynolds number for the porous square cylinder at $Da = 10^{-4}$.

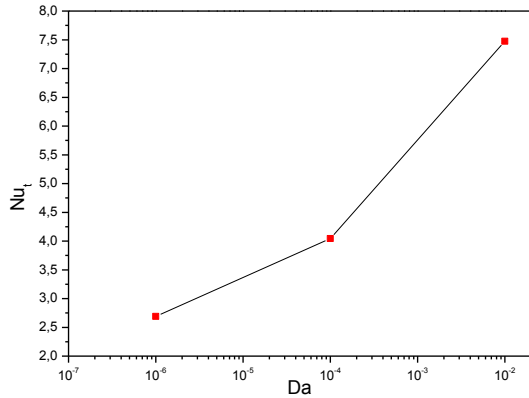


Figure 9: Variation of average Nusselt number for different Darcy numbers at $Re = 40$.

On the figure 9, we have represented the average Nusselt number as a function of the Darcy number. We can see that the average Nusselt number is very influence by a change of the Darcy number. The average Nusselt number increases with an augmentation of the Darcy number. In fact, with an augmentation of the Darcy number, the flow passes around and through the porous medium. Furthermore, the exchange surface with a porous medium is more important than for a solid medium and so the heat transfers also.

CONCLUSION

The flow structure and the heat transfers in a channel with a porous square cylinder are numerically investigated. The effects of the Darcy number, the Reynolds number and the aspect ratio are explored.

The results show principally that:

- For a low Darcy number, there is a recirculation zone after the porous medium.
- The heat transfers are slightly influenced by the aspect ratio.
- There is an increase of the heat transfers with an increase of the Reynolds number.

REFERENCES

- [1] M. Breuer, J. Bernsdorf, T. Zeiser, F. Durst, 2000, Accurate computations of the laminar flow past a square cylinder based on two different methods: lattice-Boltzmann and finite-volume, *International Journal of Heat and Fluid Flow*, Volume 21, Pages 186-196.
- [2] A. Korichi et L. Oufir, 2007, Etude numérique de l'écoulement instationnaire et du de transfert de chaleur autour d'un conduite de section carré dans un canal, *Sciences & Technologie*, N°25, Pages 55-61.
- [3] A.K. Dhiman, R.P. Chhabra and V. Eswaran, 2008, Steady mixed convection across a confined square cylinder, *International Communications in Heat and Mass Transfer*, Volume 35 Pages 47–55.
- [4] Jue T. 2004, Numerical analysis of vortex shedding behind a porous square cylinder. *Int J Numer Methods Heat Fluid Flow*;14(5):649–63.
- [5] S. Dhinakaran, J. Ponmozhi, 2011, Heat transfer from a permeable square cylinder to a flowing fluid, *Energy Conversion and Management* 52, 2170–2182.

HEAT AND MASS TRANSFERS BY NATURAL CONVECTION DURING WATER EVAPORATION IN A VERTICAL CHANNEL WITH A PROTUBERANCE

A. BOUTRA^{1,2,*}, K. RAGUI¹, R BENNACER³, and Y.K. BENKAHLA¹

Olfa Mechergui, Xavier chesneau and Ali Hatem Laatar
LAMPS, Université de Perpignan Via Domitia, 52 Avenue Paul Alduy 66860-Perpignan-France
LETTM, Département de physique, Faculté des Sciences de Bizerte, Université de Carthage, 7021
Jarzouna-Bizerte

*Corresponding author: Olfa Mechergui: Fax: +33605642027 Email: olfaamechergui@gmail.com

ABSTRACT

The internal natural convection occurs in various engineering process as evaporator, surfaces cooling Due to the importance of this phenomenon in various industrial sections much attention has been paid by researchers on the heat and mass transfers by natural convection in a vertical channel with plane walls. This paper deals with a numerical study of heat and mass transfers by natural convection occurring during water evaporation in a corrugated vertical channel. This channel is asymmetrically (or symmetrically) heated with a uniform heat flux density. The unsteady equations in two dimensional of Navier-Stokes, energy and species are integrated by a finite volume approach and then solved using the projections method. The aim of this work is to conduct a detailed numerical study to analyze the effects of physical parameters such as the flux density imposed at the wall and the relative humidity. The numerical results show the distributions of the axial velocity, of the temperature and of the concentration. We also represent the Nusselt and Sherwood numbers.

KEYWORDS

Corrugated vertical channel, protuberances, natural convection, Nusselt number, heat and mass transfers, numerical simulation, evaporation, liquid film.

NOMENCLATURE

A	protuberance length (m)	Ra	Rayleigh number
a	protuberance width (m)	Sc	Schmidt number
L	channel length (m)	Sh	Sherwood number
b	channel width (m)	T	temperature
C	water vapor mass fraction	u, w	velocity components along x, z, (ms ⁻¹)
C _p	specific heat (J kg ⁻¹ K ⁻¹)	M _v	molar mass of vapor (kg mol ⁻¹)
D	mass diffusivity (m ² s ⁻¹)	Nu	Nusselt number
g	gravitational acceleration (m s ⁻²)	X*, Z*	dimensionless cartesian coordinates
Gr	Grashof number	Greeks symbols	
H _r	relative humidity	β _T	coefficient of thermal expansion (K ⁻¹)
M	mass flow rate	β _M	coefficient of mass expansion (K ⁻¹)
L _v	latent heat of evaporation (J kg)	α	thermal diffusivity (m ² s ⁻¹)
M _a	molecular weight of air (kg mol ⁻¹)	λ	thermal conductivity (W m ⁻¹ K ⁻¹)
Nu _L	latent Nusselt number	μ	dynamic viscosity (Kg m ⁻¹ s ⁻¹)
Nu _s	sensible Nusselt number	ν	kinematic viscosity, μ/ρ (m ² s ⁻¹)
p	pressure, (Pa)	ρ	density (kg/m ³)
Pr	Prandtl number	x, z	cartesian coordinates,(m)
q	heat flux density, (w/s ²)	Indices	

* dimensionless temperature
 ref referency
 w wall

INTRODUCTION

The evaporation of liquids driven by the thermal and mass free convection is frequently encountered in engineering processes and natural environment.

The steady natural convection flows, induced by the buoyancy forces in vertical ducts have been extensively investigated [1-4]. Aung and Worku [1] have studied the flow reversal in a vertical channel with walls asymmetrically heated. It has been shown [2] that when the wall temperatures are unequal, a flow reversal occurs if the magnitude of the buoyancy force (parameter Gr/Re) exceeds a certain threshold value.

The effects of mass diffusion on thermal and mass natural convection flow have been widely investigated for the flat plates positioned vertically and more recently for the inclined position [5-8]. Yan and Soong [7] have studied numerically the evaporation of water along an inclined plate. The influences of the inclined angle, of the heat flux density applied to the wall, of the inlet film thickness and of the velocity, on the transfers, have been clarified. Mammou et al. [8] have presented a numerical study of heat and mass transfers, in laminar regime, from an inclined flat plate with a dry zone inserted between two wetted zones. They have concluded that the inclination angle has a small influence on the local Nusselt and Sherwood numbers. On the other hand, the profiles of the velocity, of the temperature and of the water vapor concentration are highly affected by the length of the dry zone. A detailed numerical analysis of the heat and mass transfers in an air flow over a falling liquid film, with some experimental measurement, was performed by Tsay et al.[9]. Their results show that the cooling of liquid film mainly caused by latent heat transfer is connected with the vaporization of the liquid film. They mentioned that a flow reversal is possible when the inlet temperature of the liquid is much higher than the ambient temperature.

To enhance the performances of the transfers in a heated vertical channel, several modified configurations have been proposed. Some authors have added straight adiabatic extensions at the upstream and downstream of the channel [10-11]. Others have placed internal objects like auxiliary plates [12-13] or obstructions [14-15]. One of the most attractive techniques used to enhance convective heat transfers in a channel is to use wavy

walls. The corrugation interrupts the hydrodynamics and thermal boundary layers and forms a recirculation zone between the corrugations; at the reattachment point the velocity is more important and consequently generates an increase of the convective heat transfers. Experimental and numerical studies about heat and mass transfers by forced convection in an asymmetric convergent-divergent channel with wavy walls have been made. The results show that mass transfer rate is enhanced by a combination of flow separation and flow oscillation which contribute to mix the fluid [16, 17].

In the present study a detailed numerical study was performed to investigate the heat and mass transfers in natural convection by using finite-volume method. The effects of heat flux density, of the relative humidity and of the size of protuberance are analysed.

The working fluid is air, with a Prandtl number $Pr = 0.71$. The aspect ratio of the channel was kept constant ($L/b = 10$).

ANALYSIS AND MODELLING

The aim of this paper is to study numerically the natural convection in an asymmetrically or symmetrically heated vertical corrugated channel.

Figure 1 schematically shows the two-dimensional physical system. The studied configuration is composed of two parallel plates forming a vertical channel in which the air can circulate. The left wall contains a rectangular protuberance (length A , width a) and heated at a uniform heat flux density q . The right wall is thermally insulated. The height of the channel plates is L whereas the distance between them is b . All the thermo physical properties are assumed to be constant.

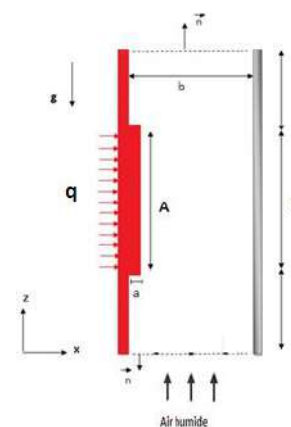


Figure 1. Geometrical configuration

To study the mass diffusion effects in natural convection, the liquid film on the wetted wall is assumed to be extremely thin, so that, it can be regarded like the boundary conditions for heat and mass transfers. The results from the present analysis are only valid for the limiting condition of extremely thin liquid films. By introducing the Boussinesq approximation, the laminar natural convection can be described by the Navier-Stokes equations in two dimensions written, in dimensionless form, as follows:

$$\begin{aligned} \frac{\partial U^*}{\partial X^*} + \frac{\partial W^*}{\partial Z^*} &= 0 \\ \frac{\partial U^*}{\partial \tau^*} + U^* \frac{\partial U^*}{\partial X^*} + W^* \frac{\partial U^*}{\partial Z^*} &= -\frac{\partial P^*}{\partial X^*} + \text{Pr} \left(\frac{\partial^2 U^*}{\partial X^{*2}} + \frac{\partial^2 U^*}{\partial Z^{*2}} \right) \\ \frac{\partial W^*}{\partial \tau^*} + U^* \frac{\partial W^*}{\partial X^*} + W^* \frac{\partial W^*}{\partial Z^*} &= -\frac{\partial P^*}{\partial Z^*} + \text{Pr} \left(\frac{\partial^2 W^*}{\partial X^{*2}} + \frac{\partial^2 W^*}{\partial Z^{*2}} \right) \\ &+ \text{Pr}^2 (Gr_T T^* + Gr_M C^*) \\ \frac{\partial T^*}{\partial \tau^*} + U^* \frac{\partial T^*}{\partial X^*} + W^* \frac{\partial T^*}{\partial Z^*} &= \left(\frac{\partial^2 T^*}{\partial X^{*2}} + \frac{\partial^2 T^*}{\partial Z^{*2}} \right) \\ \frac{\partial C^*}{\partial \tau^*} + U^* \frac{\partial C^*}{\partial X^*} + W^* \frac{\partial C^*}{\partial Z^*} &= \frac{\text{Pr}}{Sc} \left(\frac{\partial^2 C^*}{\partial X^{*2}} + \frac{\partial^2 C^*}{\partial Z^{*2}} \right) \end{aligned}$$

The dimensionless variables are defined as follows:

$$\begin{aligned} X^* &= \frac{x}{b}, \quad Z^* = \frac{z}{b}, \quad U^* = \frac{u}{V_{ref}}, \quad W^* = \frac{w}{V_{ref}}, \quad P^* = \frac{p}{P_{ref}}, \\ \tau^* &= \frac{t}{t_{ref}}, \quad V_{ref} = -\frac{\lambda}{\rho b c_p}, \quad P_{ref} = -\frac{\lambda^2}{\rho b^2 c_p^2}, \\ t_{ref} &= -\frac{\rho b^2 c_p}{\lambda}, \quad T^* = \frac{(T - T_{in})}{(qb/\lambda)}, \quad C^* = \frac{(\omega - \omega_{in})}{(qb/L_v D \rho)} \end{aligned}$$

The governing dimensionless parameters appearing in the above equations are the Schmidt number, the Prandtl number and the thermal and mass Grashof number:

$$\begin{aligned} \text{Pr} &= \frac{c_p \nu \rho}{\lambda}, \quad Gr_T = \frac{g \beta_T (\Delta \theta)_0 (b_{ref})^3}{\nu^2}, \quad (\Delta \theta)_0 = (qb/\lambda) \\ Sc &= \frac{\nu}{D}, \quad Gr_M = \frac{g \beta_M (\Delta C)_0 (b_{ref})^3}{\nu^2}, \quad (\Delta C)_0 = (qb/L_v D \rho) \end{aligned}$$

The Navier Stokes equations are solved with the following boundary conditions:

- At the inlet and the outlet :

$$\text{If } W < 0 \quad \frac{\partial W^*}{\partial Z^*} = \frac{\partial U^*}{\partial Z^*} = \frac{\partial T^*}{\partial Z^*} = \frac{\partial C^*}{\partial Z^*} = P^* = 0$$

$$\text{If } W > 0 \quad \frac{\partial W^*}{\partial Z^*} = U^* = T^* = C^* = 0, \quad P^* = -0.5 \left(\frac{1}{\Delta} \int W^* dX^* \right)$$

With Δ is the length of the outlet section where the air is incoming into the channel.

- At the channel wall:

$$U^* = W^* = \frac{\partial T^*}{\partial X^*} = \frac{\partial C^*}{\partial X^*} = 0$$

- At the protuberance surface:

$$\begin{aligned} -\frac{\partial T^*}{\partial X^*} + \rho L_v V_e V_{ref} &= 1, \quad C^* = \frac{(\omega - \omega_{in})}{(qb/L_v D \rho)}, \quad W^* = 0, \\ U^* = \pm V_e^* &= -\frac{\text{Pr}(\Delta C)_0}{Sc(1-\omega_p)} \frac{\partial C^*}{\partial X^*} \end{aligned}$$

With V_e^* : Estimated water evaporation velocity by Lee et al. (1977): This velocity has been deduced for a permanent flow regime with a small variation in the thickness of the liquid film along the plate.

- On the side faces of the protuberance:

$$\frac{\partial T^*}{\partial Z^*} = \frac{\partial C^*}{\partial Z^*} = 0, \quad U^* = 0, \quad W^* = 0$$

The heat transfers between the wetted wall and the humid air decomposes in two flux: the sensible and latent heat fluxes.

$$q_s = -K \frac{\partial T}{\partial x} \Big|_{x=0}, \quad q_L = -\frac{D \rho L_v}{1-\omega_p} \frac{\partial \omega}{\partial x} \Big|_{x=0}$$

Therefore, the sensible and latent Nusselt numbers are:

$$Nu_s = -\frac{1}{(T_p^* - T_m^*)} \frac{\partial T^*}{\partial X^*}$$

$$Nu_L = -\frac{D \rho L_v (\Delta C)_0}{qb} \frac{1}{(1-\omega_p)(T_p^* - T_m^*)} \frac{\partial C^*}{\partial X^*}$$

We define also the Sherwood number who characterizes the mass transfers:

$$Sh = -\frac{1}{(\omega_p^* - \omega_m^*)} \frac{\partial C^*}{\partial X^*}$$

RESULTS AND DISCUSSION

1- VALIDATION OF THE RESULTS

To achieve the objectives, it is necessary to define a well appropriate methodology to establish a valid digital program that can simulate all phenomena involved. The prior validation of the computer code by comparing our results with those of literature is

needed to assess its accuracy and verify its ability to study this problem.

In the present study, the computer code was validated with the results available from the literature [Nicolas Galanis, 2012] for thermal and mass transfers developing in mixed convection.

In addition, good agreement was found between our calculations and those from the numerical study Nicolas Galanis et al. 2012 for heat and mass transfers in mixed convection. Finally, Figure 2 shows a comparison of the latent Nusselt number profiles calculated by Nicolas Galanis et al. and our results. The difference between corresponding results is less than 4%. All these comparisons validate the model including the Boussinesq approximation and the numerical procedure used for its solution.

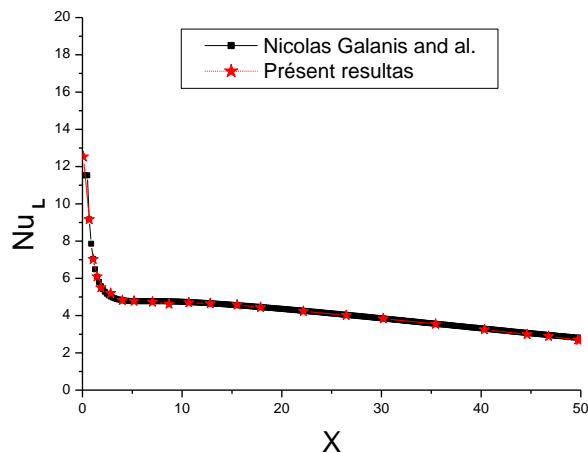


Figure 2. Comparison between our results and those from Nicolas Galanis et al., 2012 for $T_{in} = 303.15K$, $T_p = 298.15K$ and $H_r = 30\%$.

2- RESULTS

We present, in this paper, the effect of the heat flux density applied to a single wetted protuberance on one of the walls of a vertical channel, constituted of two parallel plates. One of the plates is adiabatic while the other presents a wetted protuberance of length $A=L/2$ and a width equal to $a=b/10$ and heated by a heat flux density. After and before this protuberance, the channel wall is considered not wetted and adiabatic. The results are obtained for a temperature and humidity at the inlet of $T=25^\circ C$ and $H_r=30\%$.

The figure 3 represents the evolution of the axial velocity profile along the channel for a heat flux density equal to 200 Wm^{-2} . Before the protuberance, the velocity profile is symmetric and parabolic.

Along and after the protuberance, the flow is accelerated on the side of the channel where there is the protuberance. This acceleration is due to the increase of the thermal and mass buoyancy forces. This acceleration on one side generates a flow deviation which gives way to a reversed flow, with negative velocity and incoming by the outlet. This analysis is confirmed on the figure 4 which represents the streamlines inside the channel. We can see the vertical streamlines from the inlet channel until the beginning of the protuberance. After, the streamlines move away from the adiabatic wall and give way to a reverse flow.

The figure 3b shows the temperature profile at different height in the channel, for a heat flux density equal to $q=200\text{ Wm}^{-2}$. Before the protuberance, the temperature in the channel does not increase because the right and left walls are adiabatic. Along the protuberance, the fluid temperature increases only in the vicinity of the protuberance because the heat flux density is not enough to heat the total width of the channel. The reversed flow is due to this dissymmetry of the temperature.

The figures 5 and 6 represent respectively the temperature and the mass fraction along the protuberance surface. As expected,, the temperature increases along the surface and with the heat flux density. This augmentation of the temperature generates an augmentation of the buoyancy forces and it follows an increase of the velocity in the vicinity of the surface. The mass fraction, at the surface of the protuberance, has the same evolution that the temperature because at the surface, the fluid is considerate as saturated.

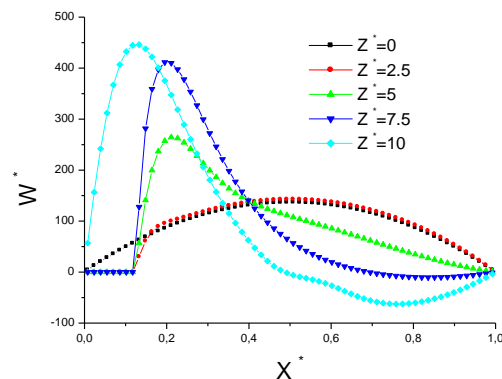


Figure 3a. Axial profiles of the vertical component velocity with $q=200\text{ Wm}^{-2}$

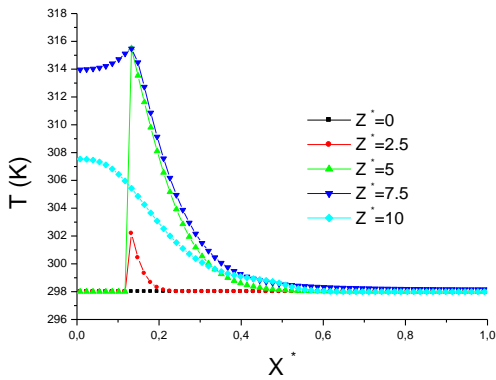


Figure 3b. Axial profiles of the temperature with $q=200Wm^{-2}$

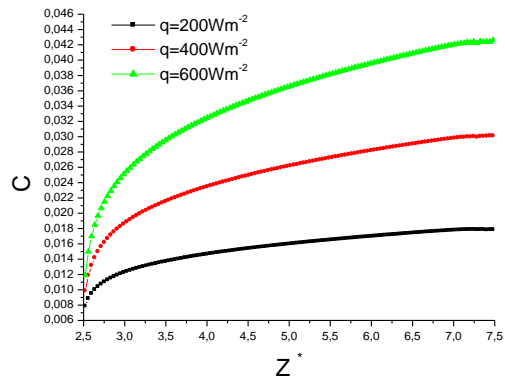


Figure 6. Variation of the mass fraction along the wetted plate for different heat flux densities

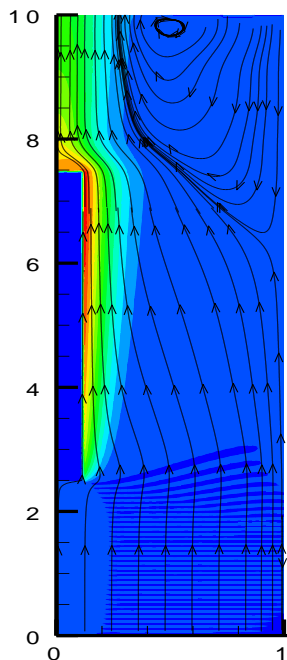


Figure 4. Streamlines and vertical velocity field for $q=200Wm^{-2}$

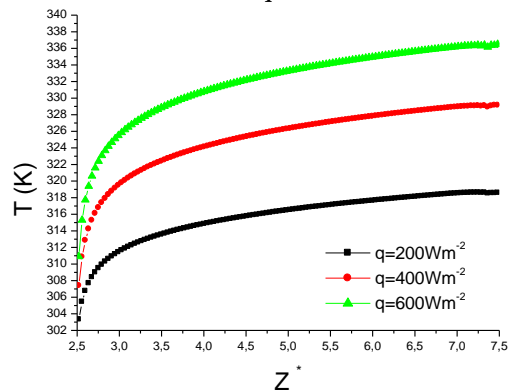


Figure 5. Variation of the temperature along the wetted plate for different heat flux densities

On the figure 7, we have represented the evaporation velocity, along the protuberance surface, for a heat flux density equal to $200 Wm^{-2}$. We can see that this evaporation velocity increases along the protuberance. This evolution is due to the fact that, at the surface, the fluid is considered as saturated and it follows that the concentration at the surface increases along the protuberance. In order to analyze the influence of the inlet humidity, we have represented, on this figure, the evaporation velocity for three inlet humidity. We can see, that an increase of the humidity generates a decrease of the evaporation velocity. This is due to the fact that the mass fraction gradient between the protuberance surface and the fluid in its vicinity is less important. That means that, for a same heat flux density, an increase of the inlet humidity generates a decrease of the heat transfers by latent mode and also an increase of the transfers by sensible mode.

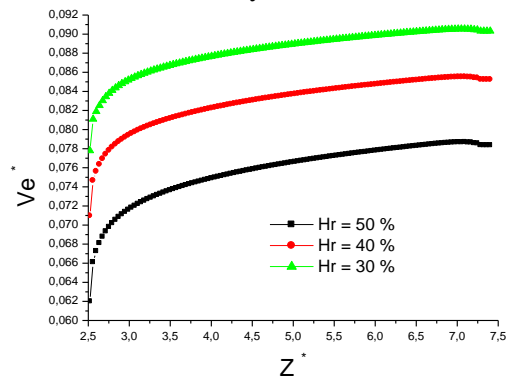


Figure 7. Evolution of the evaporation velocity along the protuberance

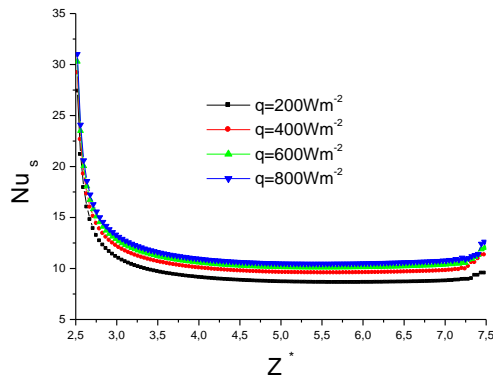


Figure 8. Variation of the sensible Nusselt number for different heat flux densities

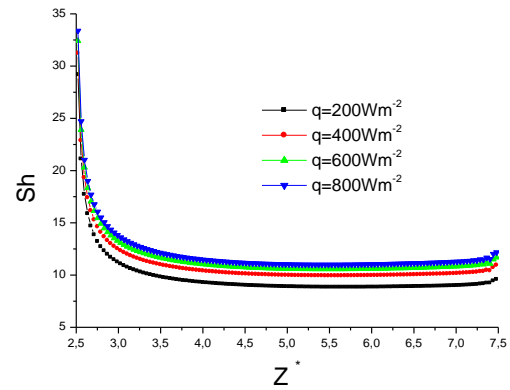


Figure 9. Variation of the Sherwood number for different heat flux densities

On the figures 8 and 9, we present the evolutions of the Sherwood number and of the sensible Nusselt number, for different heat flux densities. We can see that the Sherwood and Nusselt numbers have the same evolution along the protuberance and increase with an augmentation of the heat flux density. An augmentation of the heat flux generates an increase of the temperature and the mass fraction at the surface, it follows an increase of the heat and mass transfers and then of the Nusselt and Sherwood numbers.

We also note that, the maximum value for Nusselt and Sherwood numbers is obtained at the beginning of the protuberance. This is due to the fact that, at the beginning of the protuberance, the temperature and mass fraction gradients between the surface and the fluid, in its vicinity, are the most important.

CONCLUSIONS

We have numerically investigated the heat and mass transfers by natural convection in a channel with a wetted and heated protuberance. The results show, principally, the influence of the heat flux density, apply to the protuberance surface, on the heat and mass transfers represented by the Nusselt and Sherwood numbers. We have also analyzed the flow structure and the mass fraction and temperature profiles.

REFERENCES

- [1] W. Aung, G. Worku, Developing flow and flow reversal in a vertical channel with asymmetric wall temperatures, *ASME J. Heat Transfer* 108 (1986) 299-304.
- [2] W. Aung, G. Worku, Theory of fully developed combined convection including flow reversal, *ASME J. Heat Transfer* 108 (1986) 485-488.
- [3] A.M. Dalbert, F. Penot, J.L. Peube, Convection naturelle laminaire dans un canal vertical chauffé à flux constant, *Int. J. Heat Mass Transfer* 24 (9) (1981) 1463-1473.
- [4] C. Prakash, Y.D. Liu, Buoyancy induced flow in a vertical internally finned circular duct, *ASME J. Heat Transfer* 107 (1985) 118-123.
- [5] B. Gebhart, L. Pera, The nature of vertical natural convection flows resulting from combined buoyancy effects of thermal and mass diffusion, *Int. J. Heat Mass Transfer* 14 (1971) 2025-2050.
- [6] M. Vachon, Etude de l'évaporation en convection naturelle, Thèse de doctorat, Université de Poitiers, 1979.
- [7] W.M. Yan, C.Y. Soong, Convective heat and mass transfer along an inclined heated plate with film evaporation, *Int. J. Heat Mass Transfer* 38 (7) (1995) 1261-1269.
- [8] M. Mammou, M. Dagenet, G. Le Palec, Numerical study of heat and mass transfer from an inclined flat plate with wet and dry zones, *Int. J. Heat Mass Transfer* 35 (9) (1992) 2277-2287.
- [9] Y.L. Tsay, T.F. Lin, W.M. Yan, Cooling of a falling liquid film through interfacial heat and mass transfer, *Int. J. Multiphase Flow* 16 (5) (1990) 853-865.
- [10] K.T. Lee, Natural convection in vertical parallel plates with an unheated entry or unheated exit, *Numer. Heat. Transfer A* 25 (1994) 477e493.

- [11] A. Campo, O. Manca, B. Morrone, Numerical analysis of partially heated vertical parallel plates in natural convective cooling, *Numer. Heat. Transfer A* 36 (1999) 129-151.
- [12] A. Andreozzi, O. Manca, Thermal and fluid dynamic behavior of symmetrically heated vertical channels with auxiliary plate, *Int. J. Heat Fluid Flow* 22 (2001) 424-432.
- [13] S. Taieb, A.H. Laatar, J. Balti, Natural convection in an asymmetrically heated vertical channel with an adiabatic auxiliary plate, *Int. J. Therm. Sci.* 74 (2013) 24-36.
- [14] G. Tanda, Natural convection heat transfer in vertical channels with and without transverse square ribs, *Int. J. Heat Mass Transfer* 40 (1997) 2173-2185.
- [15] G. Desrayaud, A. Fichera, Laminar natural convection in a vertical isothermal channel with symmetric surface-mounted rectangular ribs, *Int. J. Heat Fluid Flow* 23 (2002) 519-529.
- [16] G. Wang and S. P. Vanka, Convective Heat Transfer in Periodic Wavy Passages, *Int. J. Heat Mass Transfer*, vol. 38, no. 17, pp. 3219–3230, 1995.
- [17] Y. Asako, H. Nakamura, and M. Faghri, Heat Transfer and Pressure Responses to Rounding of Peaks in Converging-Diverging Duct, vol. 52, no. 477, pp. 2170–2176, 1986.

Hygroscopic and Bio-Materials / Composites

THERMAL CONDUCTIVITY AND THERMAL DEGRADATION OF CEMENTITIOUS MORTARS REINFORCED WITH DOUM AND DISS FIBERS

Achour Abderraouf ^{1,*}, Belayachi Naima ², Ghomari Fouad ¹

¹ EOLE laboratory , Department of Civil Engineering, University of Tlemcen, BP 230, 13000 Tlemcen, Algeria

² Université d'Orléans, INSA-CVL, PRISME, EA 4229, 8 Rue Léonard de Vinci, 45072 Orléans cedex 2, France

*Corresponding author: E-mail: achourabderraouf@yahoo.com

ABSTRACT

The growing need for the reduction of energy consumption in the building has prompted scientist and engineers to find materials with low cost and low energy consumption for their production, and during their service. Therefore, a large number of materials based on natural fibers and various matrices (polymers, cement, soil...) are utilized for different applications. This work present a focus on the development of natural fiber mortar with the aim to exploit abundant plant wastes in mountainous regions in Algeria. In this context, we choose to investigate on the laboratory, the effect of the addition of xerophytic fibers of two plants: Doum (dwarf palm) (*Chamaerops humilis*) and Diss (dis grass) (*Ampelodesmos mauritanicus*) on the thermal properties of Portland cement mortars prepared with different fiber-binder ratio. Thermal conductivity measurement is performed after curing period of 28 days for different degree of saturation using hot wire method. Thermogravimetric (TG) analyzer coupled with differential scanning calorimetry (DSC) was used to study the thermal degradation and combustion characteristics of the materials. The results show a significant effect of the fibers addition on thermal conductivity of the composites. Therefore, increasing the content of vegetable fibers in mortars resulted in an increase of their weight loss at high temperatures. Similarly, the addition of the fiber promotes the absorption of heat by the composite and affects its combustion process.

KEYWORDS: Cementitious materials, Fibers, Doum, Diss, Thermal properties

INTRODUCTION

The use of new building materials based on natural fibers is one of different actions developed these last years both for the low environmental impact and the low energy consumption. It is known that for most countries, the building sector is accountable for a largest part of global energy consumption, a large part of waste and greenhouse gas emissions [1,2]. Among several solutions proposed to reduce the energy consumption and environmental impact, special attention is focused on the development of insulation building materials with low thermal conductivity, low GHG emission, and low waste generation. Thermal performance materials significantly increase the energetic efficiency of buildings. The manufacture of bio-composites with local lost natural fibers participates to reducing another part of energy consumption and GHG emission [3]. Natural fibers are usually agricultural residue or lost natural plants present several

advantages such as low density, high porosity, low cost. In addition, these natural fibers are recyclable and biodegradable for a better waste management. They become the best candidates for this mission of insulating material.

In Algeria, there are resources for this type of fibers in the forestry sector that are not currently used and they can be promoted for the development of building materials.

The main objective of this work is the investigation of the behavior of the composite based on two plants; Doum (*Chamaerops humilis*) et Diss (*Ampelodesma mauritanicum*) available in mountainous regions in Algeria for their promotion in building sector [4]. These fibers have been already studied and used for reinforcing polymer matrix [5]. The composites are manufactured with different mass fraction for the study of the effect of the fibers addition on their thermal conductivity and their thermal degradation. Thermal conductivity measurements have been performed for different

drying times to evaluate the effect of water content on thermal properties. Thermogravimetric tests coupled with scanning differential calorimetry are also performed to study the effect of the fibers addition on the degradation and mass loss of the composites at high temperature. DSC tests can also quantify the heat absorbed or emitted during thermal degradation process.

MATERIALS AND METHODS

Materials: The composites studied in this investigation are based on the Doum, Diss fibers and classical cement mortars.

Diss fiber: (*Ampelodesmos mauritanicus*, Poaceae) is a natural plant grows in the north of Africa, in Greece and Spain [6]. This is a very fibrous wild plant. The Diss fiber has a tensile strength about 100 MPa, and Young Modulus of 2.17 GPa. The density of this fiber is about 0.85 with a prickly structure which offer a better adhesion between the fibers and the cement binder [6, 7].

Doum fiber : is extracted from the dwarf palms (*Chamaerops humilis*, Arecaceae), grow naturally in the Mediterranean countries. The leaves of this fiber are used for making hats, brooms, ropes. The Doum fiber shows the better mechanical properties, with the tensile strength of 140 MPa and Young Modulus of 6 GPa [8, 9].

Composite Manufacture: the samples used for the laboratory tests of this investigation are prepared with different ratio fiber/binder (here are presented the results for only 0, 0.5, 1, 1.5, 2, 3 and 4 %). With higher percentage, the fibers agglomerate and the mixture becomes difficult. In order to improve the fiber durability and the adhesion, the Diss fibers are treated with 3% of NaOH solution against 1% only for the Doum fibers. The choice of these amount of NaOH has been examined in a previous study [10, 11 and 12]. The mortar used like reference is a classical normalized mortar noted MT. The mixture proportions of the mortar according to the standard (EN 196-1) with (450 ± 2 g of cement; 1350 ± 5g of sand and 225g of water).

The size of the fibers used for the mixture is 1 cm for the two types of fibers Doum and Diss. This size is used to improve the mixture and the homogenization of the fibers in the cementitious matrix. The thickness of the fibers is 1.5 mm for the Diss fibers and 0.4 mm for the Doum fibers. The composite is manufactured according to the mixture procedure

given by Kriker and al. [13] to facilitate fiber dispersion in the cementitious matrix. First, the fibers are immersed in 10 % of global water volume for 5 minutes. Then, the sand is mixed with 30 % of water for 30 seconds. The wet fibers are added with 30 % of water and mixed for three (03) minutes. Finally, the cement is added with the remaining water quantity and mixed for 150 seconds. A series of 40 mm x 40 mm x 160 mm are cast for four composites (mortar based on Diss fibers : MDISSP15 and MDISSP40; mortar based on Doum fibers: MDOUMP15 and MDOUM40). Samples are left to cure in water for 28 days before the tests)

Thermal conductivity measurement: In order to examine the effect of the water content on the thermal conductivity of the composites, all samples are saturated according the AFPC-AFREM procedure [14]. Thermal conductivity is measured after the total saturation and after different drying period in an oven at 60 °C. The test is performed with NEOTIM FPC2 conductivitymeter according the standard (ASTM D5930-97).

TG-DSC measurement: in the objective to study the thermal degradation and the combustion of the produced composite, thermogravimetric analysis coupled with the scanning differential calorimetry is performed by using the apparatus (LINSEIS STA PT 1000). Samples are heated to a temperature of 1000 °C with a rate of 5 °C/min. The DSC analysis will quantify the heat exchange and identify the nature of the decomposition reaction.

RESULTS AND DISCUSSION

The change in thermal conductivity as a function of mass fraction of fibers after 192 hours of drying is presented in figure 1. The results show that the greater degree of inclusion of these plant fibers in the studied mortars and thermal conductivity of composites decrease. Indeed, the loss of thermal conductivity mortar reinforced with 4% of DISS and DOUM fibers is 40% and 33% respectively compared to the control mortar. These results are in agreement with the literature [15, 16]. This is due to the increased porosity of the cured mortar related to the high capacity of water absorption of vegetable fibers which have a swelling character in contact with water, which reduces the conductivity.

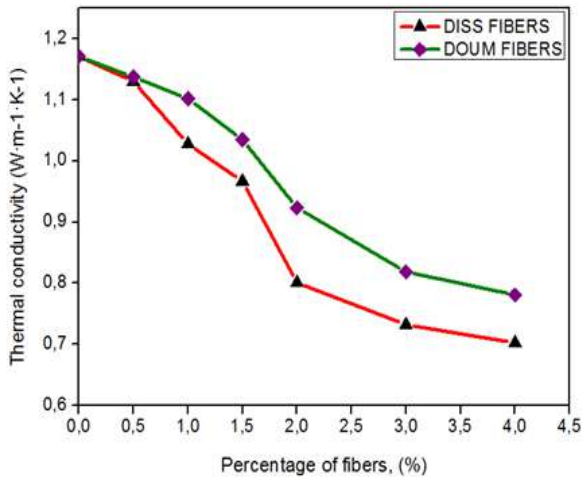


Figure 1

Evolution of thermal conductivity of the composites as a function of mass fraction of fibers after 192 hours of drying

The evolution of thermal conductivity as a function of water content is present in figure 2. We can see that the thermal conductivity decrease with increasing duration of drying mortar product. Thus, the thermal conductivity of mortars with 4% of the fibers of DISS and DOUM to decrease by about 33% and 31%, respectively, after the last drying compared the first value (saturation). This is shown that the content is an important role on the thermal conductivity. These results are consistent with literature [15].

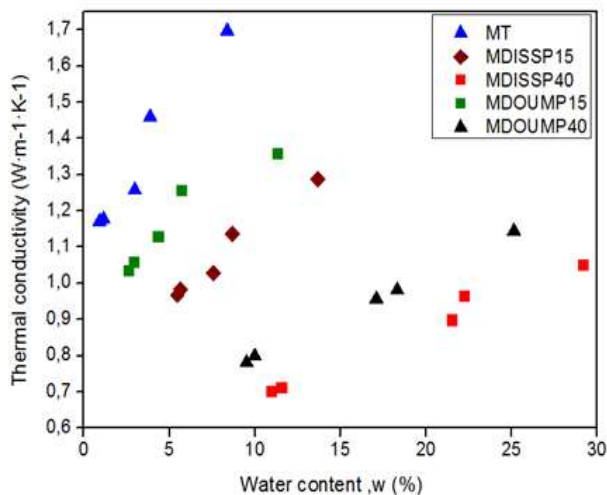


Figure 2

Evolution of thermal conductivity of the composites vs the water content for different composites

Thermogravimetric analyzes were performed in order to study the changes (weight loss) introduced by high temperatures on the chemical constituents of the study material. The TGA results were derived to identify the decomposed components. We can observe in figure 3, that all the samples compared to the literature [17, 18 and 19] have a first peak corresponding to a first loss of mass, located between 108 and 131°C due to the evaporation of water molecules and dehydration of C-S-H and ettringite. The mortars with fibers show a second peak which does not appear in the control mortar curve. This peak located between 280 and 290°C due of a thermal decomposition of pectin and hemicelluloses of fiber component that was used to produce fiber mortars [15]. A third peak between 450 and 470 °C due of the decomposition Portlandite. A fourth major peak is from about 830 °C due to the decomposition of calcite present in the aggregates as well as in carbonated Portlandite.

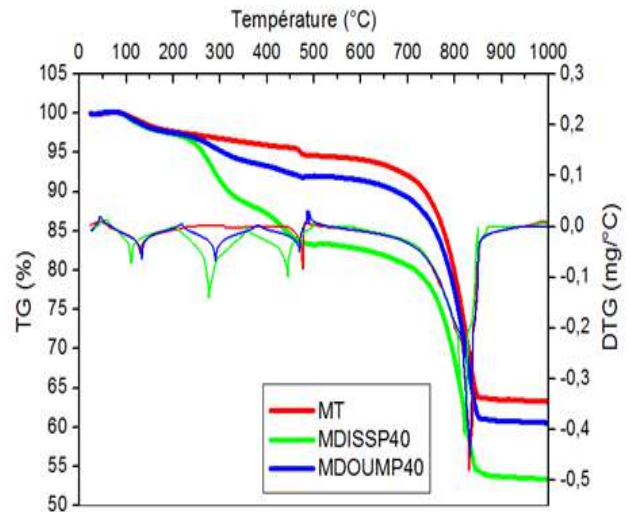


Figure 3

Evolutions of TG and DTG as function of temperature for different composite

To study the characteristics of the combustion of materials analysis that is to say the measurement of the amount of heat absorbed or can to be freed during the reaction, analysis by differential scanning calorimetry were used. The results, presented in table 1, represent the maximum peak of temperature and the enthalpy in curves of differential scanning

calorimeter. It can be seen from table 1 that the control mortar showed two peak (1 and 2) with a value of negative enthalpy -52.34 J/g and -33.38J/g, which means that this chemical reaction is an exothermic reaction which releases heat.

However, the fibers based mortar MDISSP40 and MDOUMP40 showed peak with values of the positive enthalpy which mean that the chemical reaction is an endothermic reaction that absorbs heat. These results shows that the addition of the fiber promotes the absorption of heat by the composite which has a beneficial effect on the reduction of the combustion process when fire.

Table 1

Comparison between the maximum peak of temperature and the enthalpy in curves of differential scanning calorimeter

Peak Number	MT	MDISSP40	MDOUMP40
1	T(°C)	148.6	294.9
	Entaphy (J/g)	-52.34	220.37
2	T(°C)	470.4	448.6
	Entaphy (J/g)	-33.83	337.45
3	T(°C)	822.5	817.6
	Entaphy (J/g)	38.49	64.60

CONCLUSIONS

From the experimental results, we can draw the following conclusions :

The incorporation of plant fibers is very beneficial to reduce the thermal conductivity of the composite product with a decrease that reached 40% for the composite with Diss fibers relative to the reference mortar, which allows obtaining a material with insulating properties closer than that of insulator.

The water content plays a very important effect on thermal conductivity. Analysis TGA is an effective medium to determine the behavior of the composite overlooked to high temperatures , the first mass loss of composites is produced at temperature between 108 and 131 °C while the great mass loss of materials is produced when the temperature reaches 830 °C.

The differential scanning calorimetry analyses (DSC) showed that the addition of fibers has a favorable influence on the heat absorption what which reduces the combustion process when fire.

REFERENCES

1. Essabir, H., Elkhaoulani, A., Benmoussa, K., Bouhfid, R., Arrakhiz, F., and Qaiss, A, 2013, Dynamic mechanical thermal behavior analysis of doum fibers reinforced polypropylene composites . *Materials and Design* , **51**, pp.780-788.
2. Flatt, R. J., Roussel, N., and Cheeseman, C. R ,2012, Concrete: An eco material that needs to be improved . *Journal of the European Ceramic Society* , **32**, pp. 2787-2798.
3. Maalouf, C., Le, A. T., Umuragirwa, S., Lachi, M., and Douzane, O, 2014, Study of hygrothermal behaviour of a hemp concrete building envelope under summer conditions in France . *Energy and Buildings* , **77**, pp. 48-57.
4. Pacheco-Torgal, F., and Jalali, S, 2011, Cementitious building materials reinforced with vegetable fibres: A review . *Construction and Building Materials* , **25**, pp. 575-581.
5. Sellami, A., Merzoud, M., and Amziane, S, 2013, Improvement of mechanical properties of green concrete by treatment of the vegetables fibers . *Construction and Building Materials* , **47**, pp. 1117-1124.
6. Merzoud, Mouloud., Salah. Fertikh, Mohamed Fouzi. Habita, and Abdelhacine. Gousamia. "Influence des absorptions par immersion et par capillarité sur les propriétés physicomécaniques." *INVACO2* , Rabat ,Maroc, 2011.
7. Yahiaoui, Lamia. "Caractérisation d'un composite à la rupture à base des fibres végétales (Diss)." *Université Ferhat Abbas - Setif (Algérie)*, 2011.
8. Hamza, Sabrine, Houda Saad, Bertrand Charrier, Naceur Ayed, and Fatima Charrier-El Bouhtoury,2013,Physico-chemical

- characterization of Tunisian plant fibers and its utilization as reinforcement for plaster based composites *Industrial Crops and Products* ,**49** , pp. 357-365.
9. Zbidi, F., S. Sghaier, M. Nedjma, and M. Zidi ,2009, Influence of alkaline and enzymatic treatments on the properties of Doum Palm Fibers and composite, *Applied sciences*, pp. 366-371.
 10. Oudiani, A. El, Y. Chaabouni, S. Msahli, and F. Sakli, 2011, Crystal transition from cellulose I to cellulose II in NaOH treated Agave americana L. fiber. *Carbohydrate Polymers* ,**86**, pp. 1221-1229.
 11. Raj, Gijo., Eric. Balnois, Christophe. Baley, and Yves . Grohens , 2011, Role of polysaccharides on mechanical and adhesion properties of flax fibers in Flax/PLA biocomposite. *International Journal of Polymer Science*.
 12. Izani, M.A. Norul, M.T. Paridah, U.M.K. Anwar, M.Y. Mohd Nor, and P.S. H'ng , 2013, Effects of fiber treatment on morphology, tensile and thermogravimetric analysis of oil palm empty fruit bunches fibers . *Composites Part B: Engineering* ,**45**, pp. 1251-1257.
 13. Kriker, A., A. Bali, G. Debicki, M. Bouziane, and M. Chabannet ,2008 , Durability of date palm fibres and their use as reinforcement in hot dry climates , *Cement and Concrete Composites* ,**30** , 639-648.
 14. GranDuBé, Grandeurs associées à la Durabilité des Bétons, Presses des Ponts et Chaussées2007. (381 pp.).
 15. Naima Belayachi, Dashnor Hoxha and Iuliia Redikultseva. "Etude Comparative du comportement hygrothermique des matériaux à base de fibres végétales "33èmes Rencontres de l'AUGC, Anglet, France, 2015.
 16. Abani, S., F. Hafsi, A. Kriker, and A. Bali. ,2015, Valorisation of Date Palm Fibres in Sahara Constructions , *Energy Procedia* ,**74** , 289-293.
 17. Magniont, Camille. "Contribution à la formulation et à la caractérisation d'un écomatériau de construction à base d'agroressources." Université de Toulouse, 2010.
 18. Bouasker, M., Belayachi, N., Hoxha, D. and Al-Mukhtar, M, 2014, Physical Characterization of Natural Straw Fibers as Aggregates for Construction Materials Applications, *Materials*, **7**, 3034-3048.
 19. Sedan, David. "Etude des interactions physico-chimiques aux interfaces fibres de chanvre/ciment. Influence sur les propriétés mécaniques du composite." Université de Limoges, 2007.

A DYNAMIC SIMULATION OF THE LOW-ENERGY BUILDING USING THE WOOD-BASED MATERIAL

S. Bahria*^{1,2}, M. El Ganaoui³, M. Amirat², A. Hamidat¹, L. Ouhsaine³

¹Centre de Développement des Énergies Renouvelables, CDER, 16340, Algiers, Algeria

²LMFTA Laboratory, Faculty of Physics, USTHB University, Bab Ezzouar, Alger, Algeria.

³LERMAB Laboratory, Lorraine University, IUT de Longwy, 54400 Cosnes et Romainm, France

*Corresponding author: Email: s.bahria@cder.dz

ABSTRACT

This paper presents a dynamic simulation of the low-energy building using TRNSYS software. Heating, Ventilation and Air Conditioning (HVAC) needs evaluation has been conducted for an eco-cottage prototype (within wood-based material) situated in the region of Lorraine (France). Afterward, an analysis is carried out based on different materials of construction and in different climatic zones in order to improve the building performances. The results show that our model saves about 50% of the total energy needs in the cottage. Further the moisture barriers can improve considerably the thermal comfort properties.

KEYWORDS *Low-energy building, TRNSYS software, wood-based material, dynamic simulation*

INTRODUCTION

Residential buildings account for about 40% of total energy use. There is therefore great interest in improving building performance [1]. In this context an eco-cottage is being built in Longwy University Institute of Technology (IUT). A first steps in research process for energy efficiency field. The goal is to create an eco village for a full-scale study. This first construction was created by a partnership between IUT and IsolHABITAT Belgian Company based in Liège. The cottage is built with IzoLox system, insulating shuttering blocks composed by polystyrene part and another wood chips (90%), concrete (9%) and liquid glass (1%).

kuznik et al [2] developed a new TRNSYS Type to model the thermal behavior of an external wall with PCM. Asadi et al [3] investigated a multi-objective optimization scheme (a combination of TRNSYS, GenOpt and MATLAB) to optimize the retrofit cost, energy savings and thermal comfort of a residential building.

In this work, a study has been achieved to compare thermal performances on building materials. Our paper is organized as fellow: the first paragraph represents a methodology to optimize and calculate the thermal loads within dyanamic constraints and for different insulations types. The second part, a developed model has been used to study the different cases and finally results have also been analysed and discussed.

METHODOLOGY

Geometrical description: The eco-cottage area is 24.75m², it's composed by a single room with a door on the north side of 1.5m² (double glazed) and three windows with the same area (0.42m²), the first at the east and two at the south side, the roof is slanted by 5 ° to south for the evacuation of waters rain Figure.1. The eco-cottage is located in Longwy city (Lorraine, north east of France) the altitude of the city is 300 m. The latitude and longitude of Longwy are 49.52 °N and 5.769° E.

The monthly average temperature ranges from 0.1°C in January to 17.5 °C in July. The average temperature during the year is 9.3°C [4]. Data of minimum and maximum temperature presented in Figure.2.

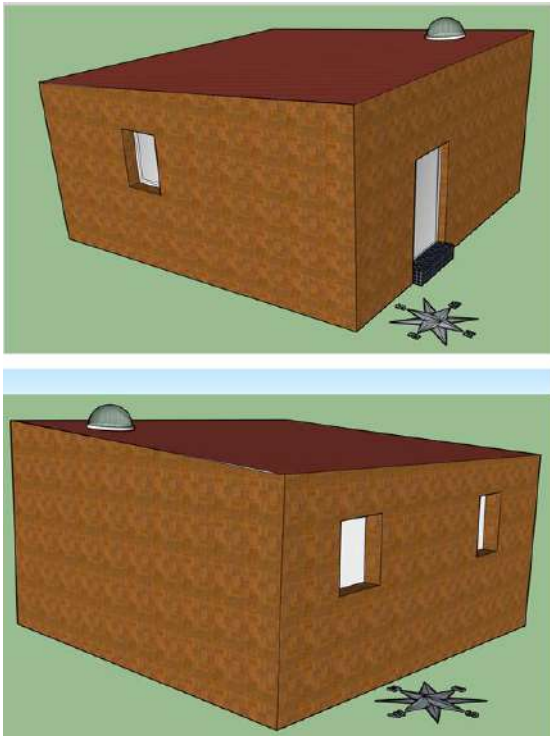


Figure. 1
The eco-cottage geometry.

In Table 1, the description of construction materials is given for floor, external walls, and roof.

Table 1
Description of the construction materials

	Layer type	Density [Kg/m ³]	Thermal conductivity [kJ/h m K]	Heat capacity kJ/kg.K
Roof	OSB panel	620	0.468	2.1
	Wood wool	50	0.1404	2.1
	Air gap	1	0.325	1.227
	Plasterboard	790	1.155	0.801
External Walls	ISB panel	675	0.396	2.45
	Neopor	15	0.1224	1.4
	Concrete	2300	6.318	0.92
	ISB panel	675	0.396	2.45
Floor	Concrete slab	2300	6.318	0.92
	EPS polystyrene	25	0.142	1.38
	Floor tile	2300	6.137	0.7

TRNSYS [5] is a transient system simulation program used to simulate the behavior of transient

systems. In this study the following data is entered in the simulation program structure:

- Air Flows: The infiltration rate is fixed at 0.6 air changes per hour during all the times.
- Gains: in this study we don't take into account gains from people and lights.
- Heating: The room is maintained at 20 degrees Celsius during occupied hours and at 15 degrees other times. The storage area is unheated.
- Cooling: the air conditioner is which turns on if the temperature rises above 26 degrees Celsius.
- Ground temperature: the Type 77 is used to calculate the mean ground surface temperature for the year.
- The Typical Meteorological Year (TMY2) file type has been generated with Meteonorm (7 version) [6] and used in TRNSYS computations.

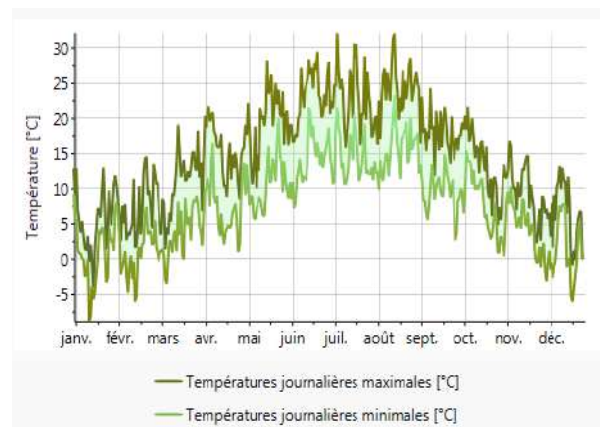


Figure. 2
Data of the minimum and maximum temperature in Longwy city as generated with Meteonorm.

CASE STUDIES

The seven investigated cases were the same dimensions as the reference case except it differ in external wall composition, thermal insulation and window glazing. The cases are represented as follows:

- Case1: In the external Walls, the Neopor is replaced by an air gap of 5 cm.
- Case2: In the external Walls, the Concrete is replaced by hollow brick of 15 cm.

- Case3: In the external Walls, the Neopor is replaced by a Wood wool insulation of 15 cm.
- Case4: Single glazing is used for all window and door. The external walls are composed by the same materials as the reference case.
- Case5: double glazing is used for all window and door. The external walls are composed by the same materials as the reference case.
- Case6: On the floor, EPS polystyrene is replaced by a mortar layer (2 cm). The external walls are composed by the same materials as the reference case.

RESULTS AND DISCUSSION

For All cases, yearly energy requirements are calculated by dividing the sum of the heating and cooling monthly loads by the total surface area of the eco-cottage. The results are reported in Figure.4. For the reference case. The total heating and cooling achieve 1842 kWh per year correspond to 74kWh/m². We can regroup the seven studied cases into two main categories.

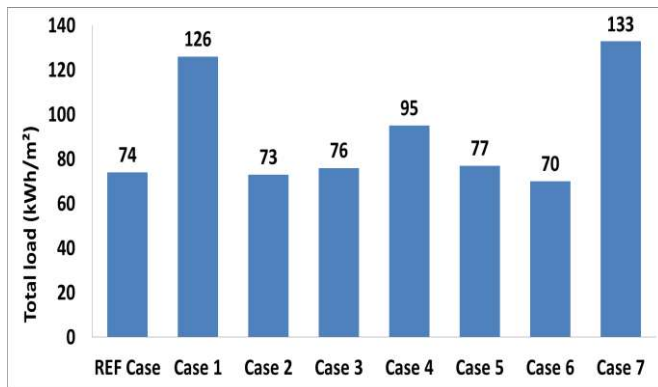


Figure. 3
Total energy requirements for all Case studies

The first one represents all cases that are close to the reference case. While the second one regroups the cases that have low building envelop performances and it represents high energy demands relatively to the reference case. For the first category that contains four cases (2, 3, 5 and 6). Case 2 can reduce significantly the construction costs by replacing concrete wall by hollow brick. While case 3 shows less improvements by using Wood wool insulation (2.6%). Further it have a suitable environmental impact regarding Neopor material insulation. On the

other hand the use of double glazing is sufficient to limit heat losses despite the triple glazing is the best one, but it is more expensive that’s why case 5 is preferable than the sixth case.

The second category contains case 1, 4 and 7. Case 1 represents 41% of the energy demands increasing without Insulation. The fourth case has 22% of supplement energy demands regarding the referring cases. The seventh case represent floor without insulation and caused 44% of energy demands.

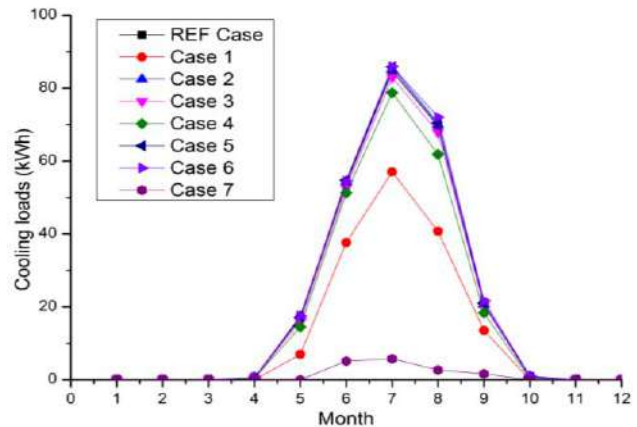


Figure. 4
Monthly cooling loa

We can observe that the first category for both figures 4 and 5 that almost cases could be beneficial in winter as approved in figure 3, but they could not be a suitable scenario in summer season. While the second category shows the inverse behavior of the first one. These results can be explained as the following reasons:

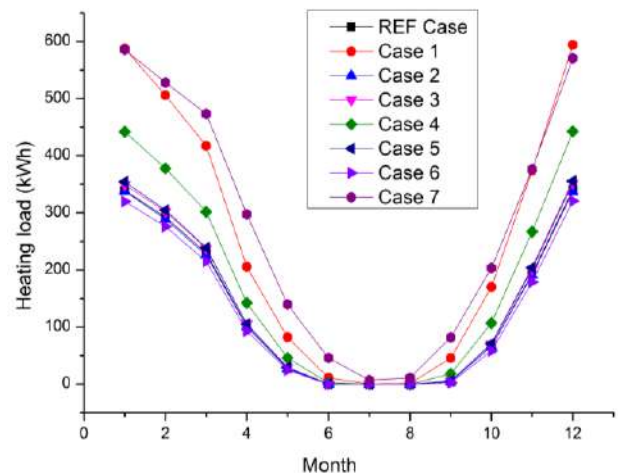


Figure. 5
Monthly heating load

The floor insulation has a good effect in winter while in summer could not be preferred because it limits the ground freezing effect.

The wall insulation could reduce heat losses to environment in winter season. But it limits heat evacuation in the summer according to high thermal inertia. The same effect can be observed in the windows when it comes to double and triple glazing.

CONCLUSIONS

In this paper, a dynamic simulation of a simple cottage building based on wood wall has been carried out using TRNsys software. Different cases have been investigated in matter of eco-construction materials. However, the insulation reduces significantly total energy demand, but it doesn't lead heat evacuation in summer season. Thus from this study it can be concluded that a natural ventilation mechanism is recommended in order to enhance energy efficiency in the building. Furthermore, towards a low material costs we conclude that double glazing window should be more reliable than triple glass and using hollow brick instead concrete wall. In other side wood wool is recommended to be used rather than neopore that can contribute to environmental damages.

ACKNOWLEDGMENTS

I would like to express my gratitude to LERMAN Laboratory and U.I.T of Longwy (Lorraine University) for their support.

REFERENCES

- [1] A. Hakansson, M. Höjer, R. J. Howlett, and L. C. Jain, Eds., *Sustainability in Energy and Buildings*, vol. 22. Berlin, Heidelberg: Springer Berlin Heidelberg, 2013.
- [2] F. Kuznik, J. Virgone, and K. Johannes, "Development and validation of a new TRNSYS type for the simulation of external building walls containing PCM," *Energy Build.*, vol. 42, no. 7, pp. 1004–1009, juillet 2010.
- [3] E. Asadi, M. G. da Silva, C. H. Antunes, and L. Dias, "A multi-objective optimization model for building retrofit strategies using TRNSYS simulations, GenOpt and MATLAB," *Build. Environ.*, vol. 56, pp. 370–378, Oct. 2012.
- [4] "LONGWY - Map of Longwy 54400 France." [Online]. Available: [http://www.map-](http://www.map-france.com/Longwy-54400/)

[france.com/Longwy-54400/](http://www.map-france.com/Longwy-54400/). [Accessed: 14-Feb-2016].

- [5] "TRNSYS 16 a Transient System simulation program." [Online]. Available: <http://sel.me.wisc.edu/trnsys/>. [Accessed: 04-Mar-2016].
- [6] "Meteonorm 7 software." [Online]. Available: http://meteonorm.com/images/uploads/downloads/mn71_software.pdf. [Accessed: 11-May-2015].

EFFECT OF WALL ORIENTATION OF THE SAND CONCRETE LIGHTENED BY LIGNOCELLULOSIC MATERIALS ON THE THERMAL INERTIA PROPERTIES

B. Belhadj^a, M. Bederina^a & M. Quéneudec^b

a. LMRS, University Amar Telidji, BP 37 G, 03000 Laghouat (Algeria)

b. EPROAD, University of Picardie Jules Verne, 80000 Amiens (France)

*Corresponding author: Email: bbelkacem21@yahoo.fr

ABSTRACT

The development of new lightweight concrete based on the valorisation of local materials and waste in construction is an environmental and sustainable approach. In this context, the composite studied is a sand concrete (dunes and alluvial) lightened by lignocellulosic materials to improve its thermo-physical properties. The objective of this study is to investigate the effect of the orientation of an exterior wall made with this material in an arid environment on the thermal inertia of properties, namely the time lag (Φ) and the decrement factor (f).

The first part of the experimental study has focused on the determination of the optimum composition of sand concrete using lignocellulosic materials. The content of lignocellulosic materials was 35 kg/m³ (30 kg/m³ wood shavings and 5 kg/m³ barley straws). This composition was chosen to achieve an acceptable level of compaction and workability. The second part of the study was to determine the thermal properties of the sand concrete without lignocellulosic materials (SC-W-LM) and sand concrete containing lignocellulosic materials (SC-LM). Finally, a numerical simulation using the EnergyPlus software was made to study the effect of wall orientation designed in the town of Laghouat (south of Algeria).

The results obtained show that the addition of lignocellulosic materials has improved the thermal properties of sand concrete namely: thermal conductivity, specific heat and thermal diffusivity. The results of numerical simulation are consistent with the literature. The favorable orientations are the east and the south and the unfavorable orientations are the north and the west. However, the east orientation has the longest time lag. The advantage of these results is comparable with concrete having improved thermophysical properties.

KEYWORDS: Lightweight sand concrete, Wall orientation, Thermal inertia, Time lag, Decrement factor.

NOMENCLATURE

ρ	Density (kg/m ³).
k	Thermal conductivity (W/mK).
cp	Specific heat (J/kgK).
a	Thermal diffusivity (m ² /s)
T_e	Temperature of outside wall surface (°C).
T_o	Temperature of inside wall surface (°C).
Φ	Time lag (h).
f	Decrement factor.
t	Time (h).

1. INTRODUCTION

Sustainable building design requires the improvement of thermal comfort and reducing energy consumption. The most important design parameters that affect thermal comfort and energy conservation in the building are: the thermophysical properties of the construction material of the envelope built, the

site, orientation of the building, distance between buildings and forms [1].

It should be noted that the construction material of the exterior wall of the building is characterized by a complex issue that depends on various criteria such as thermophysical properties of materials and construction technique of the wall in an arid environment.

In this context, the development of eco-materials in construction is an environmental and sustainable approach, whose stakes are: in terms of climate change (reduction of greenhouse gases), in terms of saving natural resources, in terms health and comfort [2]. However, among the objectives of the incorporation of lignocellulosic materials in the cement matrix composites is to get a lightweight concrete which is an important research topic because of its insulating properties [3].

The composite is then studied a sand concrete lightened by addition lignocellulosic materials to improve its thermophysical properties.

The importance of the first experimental part of this work is limited to the search for the optimal composition of an eco-sand concrete lightened by lignocellulosic materials which is the best compromise between the consistence of fresh concrete and density. However, two types of concretes were studied, namely: the sand concrete without lignocellulosic materials (SC-W-LM), which represents the reference concrete and the optimum composition of sand concrete with lignocellulosic materials (SC-LM) which lignocellulosic materials content is from 35 kg/m³ [4].

The objective of this work is to study the effect of the wall orientation (case of double wall) realized by the two studied concrete on thermal inertia properties in an arid region that is the town of Laghouat, south of Algeria. This region is characterized by a hot and dry climate in summer with large daily temperature variations. For this, a numerical simulation study was conducted to determine the two properties of the thermal inertia, that is, thermophysical properties of the wall, namely the time lag (Φ) and the decrement factor (f). Note that in hot, dry climates, a long time lag or the dephasing (Φ) and a low decrement factor (f) provide thermal comfort for occupants when the outside temperature is hot [5].

2. EXPERIMENTAL

2.1. Materials:

The two types of sand used are local dune sands (DS) that cover a very large part of southern Algeria and the alluvial sand (AS) is extracted from M'zi river crossing Laghouat region. The sands are used in admixture in a weight ratio determined by correcting the granulometric curve of alluvial sand, in the thin part, by adding sand dune. The mass ratio AS/DS = 1.7 [6], where AS: is the alluvial sand with a maximum diameter (5 mm) and DS: is the dune sand with a maximum diameter (0.63 mm).

For sustainable building solutions, cement commonly used is the Portland limestone cement (CPC) type CPJ CEM/II AL 42.5 R. The CPC is a new efficient cement class energy and provides a similar performance that of conventional Portland cement with CO₂ to manufacture up to 10% less.

The choice of mineral additions used in this study was inspired by the literature and is based on economic and environmental considerations. The objective is to reduce the use of cement and

consequently reduce CO₂ emissions. The content of mineral additions is 10% by weight of cement (1/3 limestone, 1/3 natural pozzolan and 1/3 hydraulic lime). Limestone fillers are also used in the concrete composition.

The adjuvant used is MEDAPLAST-type SP 40, complies with EN 934-2. This is a superplasticizer high range water reducer for obtaining high quality concretes and mortars.

Barley straw used is an environmentally friendly material, renewable and available in large quantities. The straw (stubble) used comprises about 70% of flaws in tubular form and 30% straw into fibers and straw blankets Figure1(a,b). This mixture represents the composition of the natural mixture of straw.

As regards the wood shavings have woodworking wastes Figure 1 (c) found in large quantities and can constitute an environmental discomfort to the extent where they are burned CO₂. The water absorption coefficient of the lignocellulosic materials is 330%.



a) Tubular straw b) Fiber straw c) Wood shavings

Figure 1

General aspect of lignocellulosic materials

2.2. Composition of concretes:

In this study, the addition of lignocellulosic materials is performed by substitution with sand. The value of the ratio sand/lignocellulosic materials is determined by the formula of absolute volumes. The content for lignocellulosic materials is limited to a content of 35 kg/m³, given its favorable effect on workability with a slump of 6 cm Abrams cone. In summary the different values of the materials used for the manufacture of the studied concretes are summarized in Table 1.

Table 1

Compositions of the studied concretes [4]

Types studied concretes	SC-W-LM	SC-LM
Sand (kg/m ³)	1316	1150
Cement (kg/m ³)	315	315
Additions minerals (kg/m ³)	35	35
Limestone filler (kg/m ³)	135	135
Total water (l/m ³)	210	255
Lignocellulosic materials (kg/m ³)	0	35
SP* (%)	2	2

* Percentage based on weight of cement and mineral additions.

3. NUMERICAL SIMULATION

3.1. Time lag and decrement factor:

In this study, the heat flux through the wall is assumed in one direction (x) and depends on the time (t). For this problem, the equation of heat transfer by conduction is, therefore, a function of (T, t, x), it is written as follows [5]:

$$k \frac{\partial^2 T}{\partial x^2} = \rho c_p \frac{\partial T}{\partial t}, \tag{1}$$

where (k) is the thermal conductivity, (ρ) is the density and (cp) is the specific heat of the material constituting the wall. To solve this problem, two boundary conditions and an initial condition are required [5]:

$$k \left(\frac{\partial T}{\partial x} \right)_{x=0} = h_i [T_{x=0}(t) - T_i], \tag{2}$$

$$k \left(\frac{\partial T}{\partial x} \right)_{x=L} = h_o [T_{sa}(t) - T_{x=L}(t)].$$

where h_i is the coefficient of heat transfer by convection to the inside wall surface, h_o is the coefficient of heat transfer by convection from the outside wall surface, $T_{x=0}$ is the temperature of the inside wall surface, $T_{x=L}$ is the temperature of the outside wall surface, T_i is the temperature of the chamber and $T_{sa}(t)$ is the sol-air temperature.

The time lag (Φ) and the decrement factor (f) are two very important factors of the wall, which determine the thermal storage capacity for materials. They are shown schematically in Figure 2.

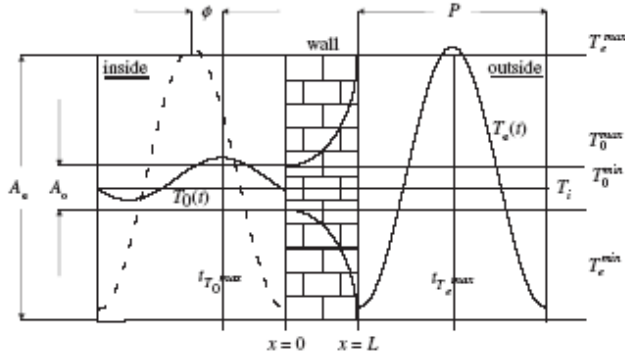


Figure 2

Schematic representation time lag (Φ) and decrement factor (f) [5]

The time it takes the heat flux to propagate to the outside surface to the inside surface, is named "time lag" or "dephasing". It is calculated by the following equation [5,7]:

$$\Phi \begin{cases} t_{T_0^{max}} > t_{T_e^{max}} \rightarrow t_{T_0^{max}} - t_{T_e^{max}} \\ t_{T_0^{max}} < t_{T_e^{max}} \rightarrow t_{T_0^{max}} - t_{T_e^{max}} + P \\ t_{T_0^{max}} = t_{T_e^{max}} \rightarrow P \end{cases} \tag{3}$$

with (Φ): time lag in hours;

$t_{T_e^{max}}$: Time when the temperature of outside surface of the wall is maximum;

$t_{T_0^{max}}$: Time when the temperature of inside wall surface is maximum.

During the propagation of the flow of heat from the outside wall surface to the inside wall surface for a period P (24 hours), its amplitude will decrease according to the thermophysical properties of materials. This means that when the flow reaches the inside surface of the wall, it will have considerably lower amplitude than the amplitude of the external surface of the wall [5,7]. The decrement factor (f) is determined by the following equation:

$$f = \frac{A_o}{A_e} = \frac{T_o^{max} - T_o^{min}}{T_e^{max} - T_e^{min}}, \tag{4}$$

Where are the amplitudes of the heat flow in the surfaces, inside and outside of the wall. It should be noted that the heat flux on the outside wall surface, includes the temperature of the outside air combined periodically with solar radiation and convection between the air of the exterior wall surface and the outside air.

3.2. Simulation Software:

In this study, the simulation was made for a day of summer 2013 in which the maximum and minimum outdoor temperature are respectively 42.5°C and 25.2°C, for a supposed wall located in the town of Laghouat, in southern Algeria (Latitude 33.80°N, Longitude 2.87°E and Altitude 765 m). This study is made for two types of wall designed with the studied concretes.

The thickness envisaged for the double wall without coatings is 25 cm (10 cm concrete + 5 cm air-gap + 10 cm concrete) and the double wall with coatings (27 cm) [8]. By using the EnergyPlus software (Version 1.2.2.030), we can get through time, in hours of the day, the temperature of the outside wall surface, the temperature of the inside wall surface and the temperature of the indoor air of cell "test Chamber" whose dimensions are (2x2x2,5 m). The envelope of the cell has a dimension door (0.60 x 1.70 m) in the wall oriented to the south.

4. RESULTS AND DISCUSSION

4.1. Physical and Mechanical Properties:

The results of the physico-mechanical properties of the studied concretes are shown in Table 2.

Since the studied concretes are intended for the construction of the housing built in arid environments, the main thermal interpretation of results will focus on the values of the thermal diffusivity. This thermal property characterizes the concept of thermal inertia, the value of which is interesting for the concrete (SC-LM) with a 35.46% reduction compared to concrete base (SC-W-LM). Furthermore, and as expected, when the density decreases, the compressive strength also decreases.

Table 2
Physical and mechanical properties
of the studied concretes

Concrete type	SC-W-LM	SC-LM
Thermal conductivity (W/mK)	1.40	1.00
Specific heat (J/kgK)	1209	1821
Thermal diffusivity 10^{-6} (m ² /s)	0.578	0.373
Dry density (kg/m ³)	2003	1470
Compressive strength (MPa)	21.58	8.88

4.2. Effect of orientation of the wall:

In arid environments, the advantage is in favor of the double wall due to the reduced values of the decrement factor in different orientations [8]. The study of the effect of wall orientation was made for double wall without coatings. The simulation results shown in Figures 3-6 and equations (3 and 4) are used to calculate the time lag (Φ) and the decrement factor (f) of the various walls (SC-LM). Summary the results of the simulation are reported in Table 3 with the various improvements.

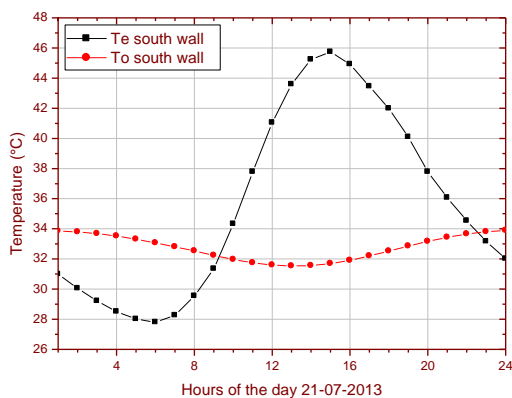


Figure 3
Temperature of outside and inside wall surface
by (SC-LM) of south orientation

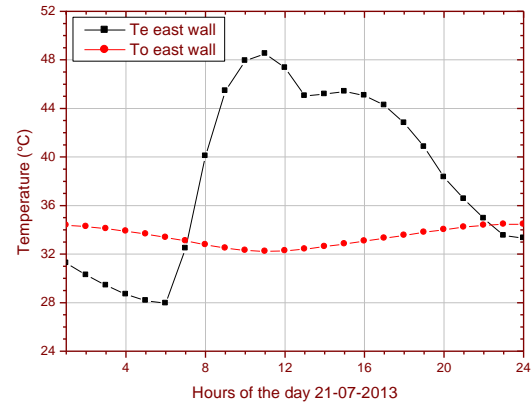


Figure 4
Temperature of outside and inside wall surface
by (SC-LM) of east orientation

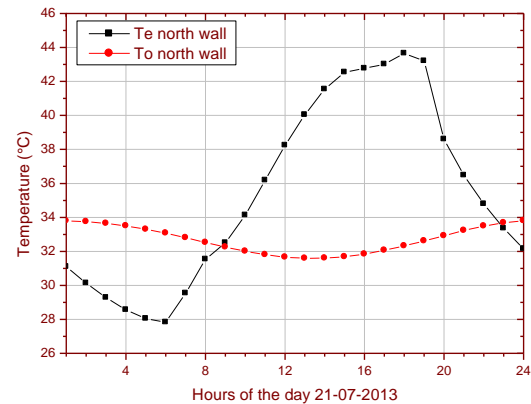


Figure 5
Temperature of outside and inside wall surface
by (SC-LM) of north orientation

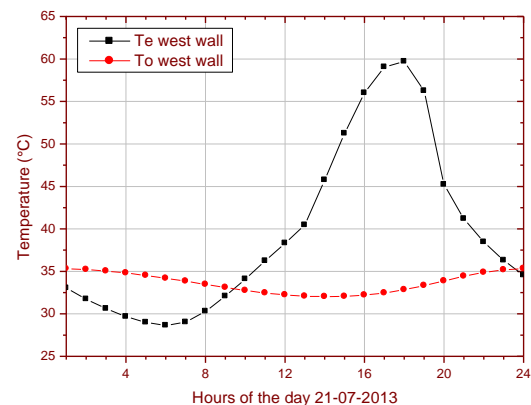


Figure 6
Temperature of outside and inside wall surface
by (SC-LM) of west orientation

Table 3
Time lag and decrement factor for different orientations of the double wall without coatings

Wall		SC-W-LM	SC-LM	Improvement
South	Φ (h)	8	9	+1(h)
Wall	f	0.177	0.131	-25.98%
East	Φ (h)	12	13	+1(h)
Wall	f	0.146	0.108	-26.02%
North	Φ (h)	6	6	-
Wall	f	0.188	0.139	-26.06%
West	Φ (h)	5	6	+1(h)
Wall	f	0.146	0.106	-27.39%

The best compromise between the time lag and the decrement factor for the double wall without coatings for the two studied concrete are the south orientation and the east orientation, when considering the time lag that is ≥ 8 hours according to the climatic zone [9]. However, the unfavorable orientations are the north and the west. The advantage of the results is in favor of concrete with improved thermophysical properties. Note that the long time lag is the benefit of the orientation east, which is consistent with the literature [8,10,11].

4.3. Effect of the addition of the coatings:

The addition of the exterior and interior coating thickness of 1 cm each increases the thickness of the double wall from 25 to 27 cm. Thermophysical properties of cement mortar as the exterior coating ($k = 1.4 \text{ W/mK}$, $cp = 1200 \text{ J/kg.K}$ and $\rho = 2100 \text{ kg/m}^3$) and the plaster as the interior coating ($k= 0.05 \text{ W/mK}$, $cp=1000 \text{ J/kg.K}$ and $\rho = 1300 \text{ kg/m}^3$). According to the simulation results summarized in Table 4 with various improvements, the favorable orientations that represent the best compromise between the time lag and the decrement factor for double wall with exterior and interior coatings are the south, the east and the north orientation for (SC-LM).

Table 4
Time lag and decrement factor for different orientations of double wall with coatings

Wall		SC-W-LM	SC-LM	Improvement
South	Φ (h)	9	9	-
Wall	f	0.157	0,114	-27.38%
East	Φ (h)	12	13	+1(h)
Wall	f	0.134	0,100	-25.37%
North	Φ (h)	6	8	+2(h)
Wall	f	0.168	0,121	-27.97%
West	Φ (h)	6	7	+1(h)
Wall	f	0.128	0,091	-28.90%

This explains the beneficial effect of the interior and exterior coatings for concrete having improved thermophysical properties. These results are better than the results of an exterior wall of barley straw sand concrete [8], because the time lag (Φ) ≥ 8 h for all orientations except the orientation west with (Φ) = 7 h, but the time lag remains, nevertheless, acceptable because it is very close to the recommended time.

4.4. Analysis of results:

4.4.1. Climate zoning: For better thermal comfort with reduced energy consumption, so you have the spaces according to their energy needs, that is to say, the need to develop a "climate zoning" by combining the habitable spaces following the south orientation and the east. However the service areas (buffer zones) of the north orientation and west. Moreover, this finding on the preferred orientation is consistent with the recommendation of the literature [8,9].

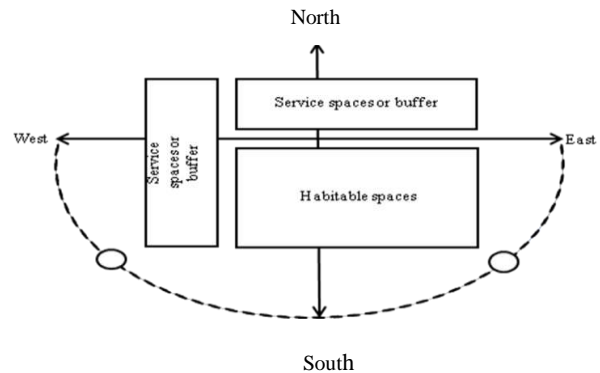


Figure 7
Climate zoning [9]

4.4.2. Advatange and focus of the lightweight sand concrete:

The development of a new eco-sand concrete based on lignocellulosic materials, which is considered as an insulating-bearer lightweight sand concrete, may led to many benefits, such as the use of local materials that are available in large quantities and at low cost, reuse of industrial waste, the reduction of CO₂ emissions, durability of building materials and finally reducing the energy consumption during the production phase and operating through the development of a material constituting the exterior wall of a building possessing a long time lag and a low decrement factor.

Indeed, in arid environments, this type of lightweight concrete allows to minimize the impact

of external climate factors and thus contribute to improve the level of thermal comfort with reduced energy consumption. Note that the materials developed are interesting by their thermal behavior. Their mechanical characteristics also allow a compatible design with modern constructions.

CONCLUSIONS

The results presented herein show that the addition of lignocellulosic materials (with the studied proportion) considerably improves the thermophysical properties of the sand concrete. The thermal conductivity and the thermal diffusivity were reduced by 28.57% and 35.46% while the specific was increased by 50.62%.

Based on numerical simulation, one can conclude that the determination of the two thermal properties, ie, the time lag and the decrement factor is very important to know, because they determine the thermal inertia of the exterior wall. The results of numerical simulation are consistent with the literature. The advantage of these results is in favor of the concrete with improved thermophysical properties (light material), from where the material can face the vagaries of adverse weather conditions.

However, the requirements of a durable construction is to minimize the external climatic effects and therefore minimize energy consumption, it is therefore necessary to provide eco-materials having reduced thermal conductivity and high specific heat in order to have a high thermal inertia.

Finally, it should be noted that the results are encouraging, promising in the eco-design option and are widely incentives to promote this type of lightweight sand concrete, as it is possible to design passive houses using the two basic principles of bioclimatic architecture: thermal inertia and orientation. This approach that we can qualify as eco-architectural, contributes favorably to improve the level of thermal comfort and the economy of energy in houses in arid environments such as the south of Algeria.

REFERENCES

1. G. Manioglou, Z. Yilmaz. Energy efficient design strategies in the hot dry area of Turkey. *Building and Environment*. 43 (2008) 1301-1309.
2. G. Escadeillas, Eco materials in construction: challenges and prospects, in: Seventh Edition of the Scientific Meetings of the Group Francophone for Research and Training on Concrete (RF)²B, 19–20 June Toulouse, France, 2006 (In French).
3. M. Khazma, A. Goullieux, R.M. Dheilly, B. Laidoudi, M. Queneudec. Impact of aggregate coating with a PEC elastomer on properties of lightweight flax shive concrete. *Industrial crops and Products*. 33 (2011) 49–56.
4. B. Belhadj, M. Bederina, N. Montrelay, J. Houessou, M. Quéneudec. Effect of substitution of wood shavings by barley straws on the physico-mechanical properties of lightweight sand concrete. *Construction and Building Materials*. 66 (2014) 247–258.
5. H. Asan, Investigation of wall's optimum insulation position from maximum time lag and decrement factor. *Building and Environment*. 32 (2000) 197–203.
6. M. Bederina, M.M. Khenfer, R.M. Dheilly, M. Quéneudec. Reuse of local sand : effect of limestone filler proportion on the rheological and mechanical properties of different sand concretes. *Cement and Concrete Research*. 35 (2005) 1172–1179.
7. H. Asan, Numerical computation of time lag and decrement factors for deferent building materials. *Building and Environment*. 41 (2006) 915–920.
8. B. Belhadj, M. Bederina. Z. Makhloufi. A. Goullieux, M. Quéneudec. Study of the thermal performance of an exterior wall of barley straw sand concrete in an arid environment. *Energy and Buildings*. 87 (2015) 166-175.
9. S. Mazouz. *Elements of Architectural Design*. Office of University Publications, Algeria, 2004 (In French).
10. K.J. Kontoleon, E.A. Eumorfopoulou, The influence of wall orientation and exterior surface solar absorptivity on time lag and decrement factor in the Greek region. *Renewable Energy*. 33 (2008) 1652–1664.
11. L.E. Mavromatidis, M. El Mankibi, P. Michel, M. Santamouris, of time lags and decrement factors for wall complexes including multilayer thermal insulation, in two different climatic zones. *Applied Energy*. 92 (2012) 480–491.

ENERGETIC AND EXERGETIC ANALYSIS OF A NOVEL MIXTURE FOR AN ABSORPTION/COMPRESSION REFRIGERATION SYSTEM: R245fa/DMAC

D. LOUNISSI¹, *Nahla BOUAZIZ¹ and M. GANAOU²

¹Unité de Recherche Energétique & Environnement, Ecole Nationale d'Ingénieurs de Tunis. Université de Tunis El Manar, BP37, le Belvédère 1002, Tunisie.;

²Université de Lorraine, IUT Henri Poincaré de Longwy/GTE – Lermab Longwy

* Nahla BOUAZIZ: Fax: +216 71 874 688 Email: nahlabouaziz@yahoo.fr

ABSTRACT

In this work, an energetic and exergetic investigations of an upgraded frigorific system, operating with a novel organic pair R245fa/DMAC (1,1,1,3,3-Pentafluoropropane/N,N'-dimethylacetamide) are performed. Working fluids are selected due to their low GWP. Results relative to the new couple are compared with those relative to the classical water/ammonia working fluids. Investigated parameters are the COP, the irreversibility and the exergetic efficiency. Results show that the performance coefficient of the system working with the new fluids is similar to that relative to the Ammonia/Water system with an optimum value about 45%. Furthermore, the system using the new couple uses lower threshold temperatures, between 60°C and 80°C for optimum COP, which allows the use of low temperature energy sources. Results of the exergetic analysis indicate that irreversibility of the system working with R245fa/DMAC is lower than that of the system working with Ammonia/Water of about 10kW, for 3kW as refrigeration power. So is the exergetic efficiency. It is noted from this study that the major gain brought by this new pair is the diminution of the threshold temperatures.

Key words: Absorption/compression, exergetic analysis, hybrid heat pump, organic absorbents.

NOMENCLATURE

COP	Coefficient of Performance
P	Pressure (bar, Pa)
T	Temperature (K, °C)
x	mass fraction
Ex_D	Exergy destruction.
\dot{m}	Mass flow rate (kg.s ⁻¹)
\dot{W}	Work transfer rate (W)
\dot{Q}	Heat transfer rate (W)
Ex	Specific exergy of a stream (kJ.kg ⁻¹)
h	Specific enthalpy of a stream (kJ.kg ⁻¹)
s	Specific entropy of a stream (kJ.kg ⁻¹ .K ⁻¹)
f	Specific solution circulation factor
η_{ex}	Exergetic efficiency
η_{is}	Isentropic efficiency

Subscribes

i	= Component or stage i
T	= Total
0	= Reference
2	= intermediate
v	= Vapor
EV	= Evaporator
COMP	= Compressor
GE	= Generator
ECH	= Solution exchanger

AB	= Absorber.
SR	= Rich solution
SP	= Weak solution

INTRODUCTION

The cooling and refrigeration cycles are mostly based on mechanically driven vapor compression. The cooling demand in countries with a hot climate leads to a peak in electricity consumption; consequently, the use of alternative technologies should be encouraged. One possibility consists in the modification of absorption cycles [1]. Their principal advantages compared to mechanically driven compression cycles are summarized to the following: a) no contribution to the destruction of the ozone layer and to the global warming effect because of the natural refrigerants use, b) little energy consumption, because the compression cycles are thermally driven (Herold et al., 1996; Ziegler, 2002) [2,3] and c) absence of moving parts in, some circulating pumps. Absorption cycles use a working couple consisting of a refrigerant and an absorbent. In generally being water-lithium bromide, (LiBr), or ammonia-water. The basic absorption cycle structure is the single effect, having four basic components: absorber, generator, evaporator and condenser. Absorption refrigerators are

commercially available and perform stable operation under part-load conditions, but their coefficient of performance (COP) values are relatively low compared to vapor compression refrigerators (Lee SF and Sherif SA, 2001) [4].

However, combined cycles of vapor compression/absorption refrigeration system can provide high COP. Several works on combined cooling system or absorption refrigerator (mainly on the cooling performance analysis and optimization) have been carried out (Lee SF and Sherif SA, 2001; Arora and S.C.Kaushik, 2009) [4,5]. In general, performance analysis of these systems is investigated using energy analysis method, based only on the first law of thermodynamics (energy balance) by means of the coefficient of performance (COP). Unfortunately, this approach is of limited use in view of the fact that it fails to make out the real energetic losses in a refrigerating system. For example, it does not identify any energetic losses occurring during the throttling process though there is a potential pressure drop and this can be predicted only through entropy or exergy analysis. Distinction between reversible and irreversible processes was first introduced in thermodynamics through the concept of 'entropy' (Dincer and Cengel, 2001) [6]. Thus, in contrast to energetic approach, the exergy analysis, which takes into account both the first and the second thermodynamics laws, assists the evaluation of the magnitude of the available energy losses in each component of the refrigeration system and the worth of energy from a thermodynamic point of view. In thermal design decisions, utilisation of the second law of thermodynamics is very well referenced (Bejan, 1994, 1995, 1996) [7-9]. In addition, the exergy analysis allows explicit presentation and improved comprehension of thermodynamic processes by quantifying the effect of irreversibility occurring in the system along with its location. Some studies have carried out exergy analysis (Lee SF and Sherif, 1999; Ravikumar et al., 1998) [10,11] pertaining to single, double and multiple-effect absorption refrigerating systems that use LiBr/H₂O or NH₃/H₂O (Anand and Kumar, 1987) [12], in these three last references was carried out irreversibility analysis of single and double-effect systems under the following conditions: condenser and absorber temperatures 37.81 °C, evaporator temperature 7.21 °C and generator temperature 87.81 °C for the single effect and 140.61 °C for the double-effect system. In these studies, there was neither computed the optimum generator temperature nor calculated the exergetic efficiency for the operation of series flow

double-effect system. (Lee and Sherif, 1999) [10], have presented the second law analysis of various double-effect lithium bromide water absorption chillers and computed the COP and the exergetic efficiency as well. It is obvious from literature that exergy investigation as regards compression/absorption heat pumps has not been carried out. This motivates the present investigation.

The aim of this work is to present a theoretical energetic and exergetic analysis of an absorption/compression frigorific system, operating with a novel organic couple R245fa/DMAC (1,1,1,3,3-Pentafluoropropane/N,N'-dimethylacetamide). All energetic and exergetic results are compared to NH₃/H₂O hybrid machine. The effects of the compressor discharge pressure and the generator temperature on system performances are examined. Exergy loss of the heat pump was evaluated for several working conditions. It is hoped that these results could serve as a source of reference for designing and selecting new absorption refrigeration systems, developing new working fluid pairs and optimizing suitable operating conditions.

HEAT PUMP PRESENTATION

The heat pump, subject of this study, is a combination between the conventional absorption one and the compression one. A compressor is injected into the cycle, upstream the absorption part, in order to ameliorate the absorption process (figure1).

The system operates at three pressure levels; the refrigerant vapor leaving the evaporator (1) is at the lower pressure (PEV). It is compressed by an isentropic transformation (2) to an intermediate pressure (P2) and finally, injected into the absorber. The rich solution going from the absorber (3) is heated by the poor one coming from the bottom of the generator (5) by a solution heat exchanger. The condenser and the generator operate at the third level of pressure (PCD) which is the condensation pressure.

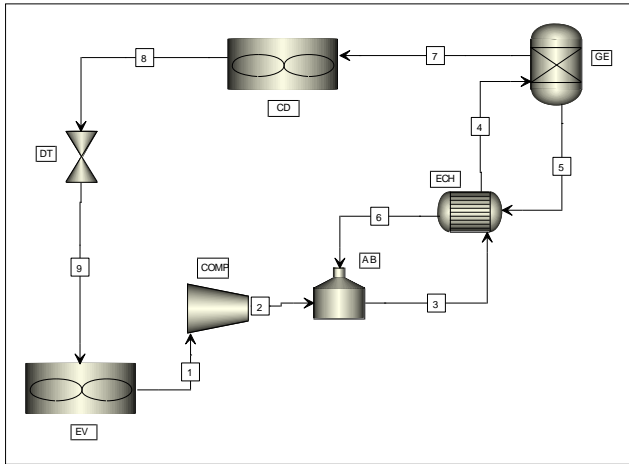


Figure 1
One stage hybrid cycle

ANALYSIS AND MODELLING

Numerical analysis of the system was performed using the Aspen plus software. Thermodynamic properties of the binary mixture were determined using the Van Laar equation of state for the liquid phase and the Virial equation of state for the vapor one where the second virial coefficient is determined by the Hayden and O'Connell method. This method was used in a previous work for similar working refrigerant/absorbent couple [13]. It has been established that this method is efficient for determining thermodynamic properties for this type of refrigeration mixtures.

Energy and mass model: The mass balances in this cycle governing the three present substances: weak solution, rich solution and refrigerant gas are given by:

$$\dot{m}_{SR} = f \cdot \dot{m}_{NH_3} \quad (1)$$

$$\dot{m}_{Sp} = (f - 1) \cdot \dot{m}_{NH_3} \quad (2)$$

Where f is the specific solution circulation factor for the cycle:

$$f = \frac{x_V - x_{SP}}{x_{SR} - x_{SP}} \quad (3)$$

\dot{m}_{SR} , \dot{m}_{Sp} and \dot{m}_{NH_3} are consecutively the rich solution, the weak solution and the gas mass flow rates. Installation contains five principle components: Condenser, evaporator, generator, absorber and compressor.

Energy balance for each installation component is presented by the following equation:

$$\dot{Q}_i = \sum(\dot{m} \cdot h)_{output} - \sum(\dot{m} \cdot h)_{input} \quad (4)$$

The compressor duty is determined by the equations below:

$$\dot{W}_{real} = \dot{W}_{is} / \eta_{is} \quad (5)$$

$$\dot{W}_{real} = \dot{m}_{NH_3} (h_3 - h_2) \quad (6)$$

So, we can conclude from "Eq (4)" and "Eq (5)", the value of the steam enthalpy at the compressor outlet.

Were the isentropic efficiency η_{is} is given by [14, 15]:

$$\eta_{is} = 0.874 - 0.0135 \cdot \tau \quad (7)$$

$$\tau = \frac{P_{comp-out}}{P_{comp-in}} \quad (8)$$

Coefficient of performance is deduced from the following expression, [16-19]:

$$COP = \frac{\dot{Q}_{EV}}{(\dot{Q}_{GE} + \dot{W}_{real})} \quad (9)$$

Exergy model: The exergy balance is based on exergy destruction method, were it is calculated for each component as follow [20]:

$$Ex_{Di} = \sum(\dot{m}Ex)_{in} - \sum(\dot{m}Ex)_{out} \pm \sum(Ex\dot{Q}) \pm \sum\dot{W} \quad (10)$$

The first two terms on the right-hand side represent the exergy of streams entering and leaving the control volume. Both third and fourth terms are the exergy associated with heat transfer \dot{Q} from the source maintained at a constant temperature T and is equal to the work obtained by the Carnot engine operating between T and T_0 , and is therefore equal to maximum reversible work that can be obtained from heat energy \dot{Q} . The last term is the mechanical work transferred to or from the control volume.

$Ex\dot{Q}$ is the thermal exergy and expressed as follow [21]:

$$Ex\dot{Q} = \dot{Q}(1 - T_0/T) \quad (11)$$

We can also express the exergy loss in terms of exergetic efficiency; it is the rate between the inlet exergy and the outlet one [23]:

$$\eta_{ex} = \frac{\text{outlet system exergy}}{\text{intletsystèmeexergy}} \quad (12)$$

Third level heading: Several assumptions were taken into account in the exergetic study:

- Kinetic and Potential exergy are neglected.
- All transformations are in a steady state.
- Pressure and heat losses in the system component are neglected.
- The exchange temperature is the input and the output logarithmic mean temperature.

- The reference temperature and pressure P_0 and T_0 are 1atm and 25°C, respectively.

RESULTS AND DISCUSSION

In the present study simulation of the absorption/compression cycle was done by Aspen Plus flow sheet simulator like shown before in Figure1.

A comparative study between two working mixtures is carried out; simulation was done for a refrigeration capacity of about 3kW for both systems.

In figure 2 is shown the COP evolution versus the generator temperature. Different condensation temperatures are used for the R245fa/DMAC system, while the COP of the NH₃/H₂O system is presented only for a temperature of 30°C. The results are given for the same compression ratio of about 3.

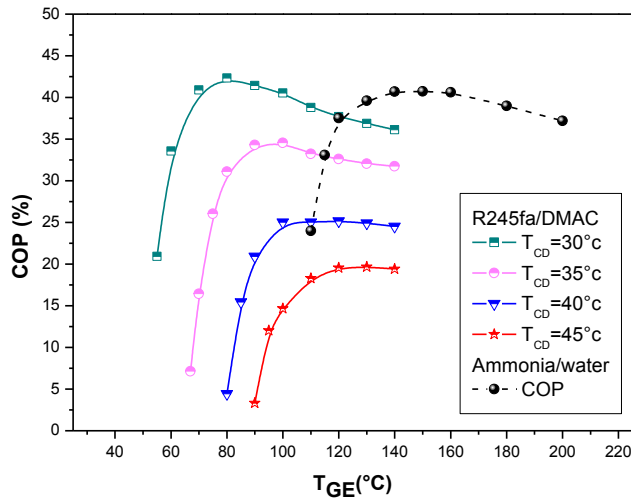


Figure 2
COP evolution versus T_{GE} for various T_{CD} for the two mixtures

COP of this hybrid one stage system is about 42% when working with NH₃/H₂O and it can achieve the same value with the new proposed mixture R245fa/DMAC for a lower generator temperature. In fact, the maximal COP for the classic couple is achieved for a generator temperature of 140°C when that of the proposed couple is achieved for only 80°C.

Figure 3 presents the irreversibility of the system for the two working mixtures and for the same conditions as figure 2. The first remarked result, is that irreversibility of the system working with the proposed couple is lower than that caused by the classic one of about 10kW. Irreversibility is reduced when the condensation temperature decreases and when increasing the generator temperature. Its

optimum values are obtained between 70°C and 110°C as generator temperature.

In figure 4 is presented the exergetic efficiency of the whole hybrid system working with the proposed mixture at the previous same working conditions.

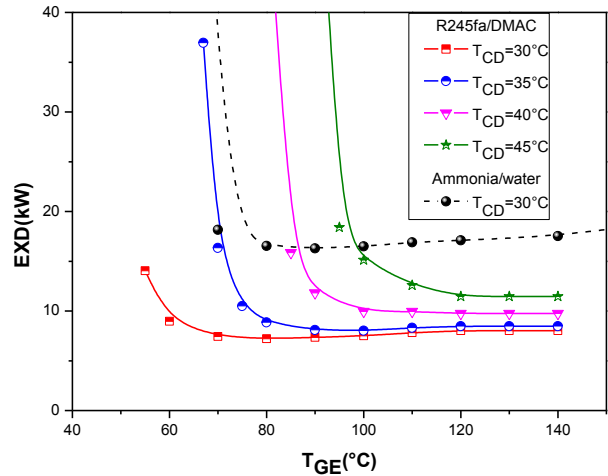


Figure 3
Irreversibility evolution versus T_{GE} for various T_{CD} for the two mixtures

Results show that optimal exergetic efficiency value of the system is achieved for a condensation temperature of 30°C and at 70°C only as generator temperature. For the worse working conditions ($T_{CD}=45°C$) the optimum value is obtained at 100°C. From the figure 4, it is clear that the exergetic efficiency of the system decreases for the high generator temperature unlike the COP behavior.

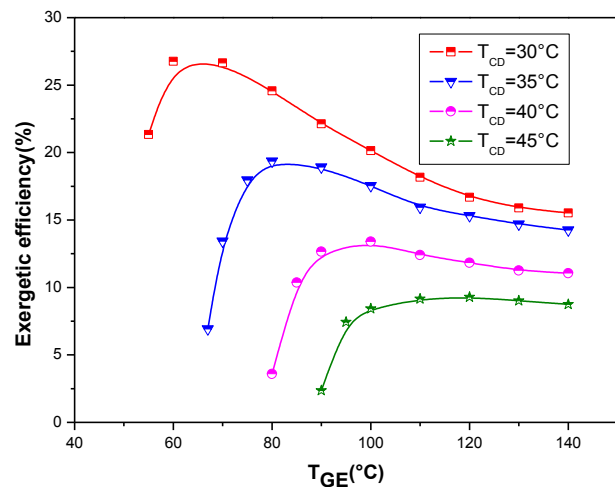


Figure 4
Exergetic efficiency evolution versus T_{GE} for various T_{CD} for R245fa/DMAC

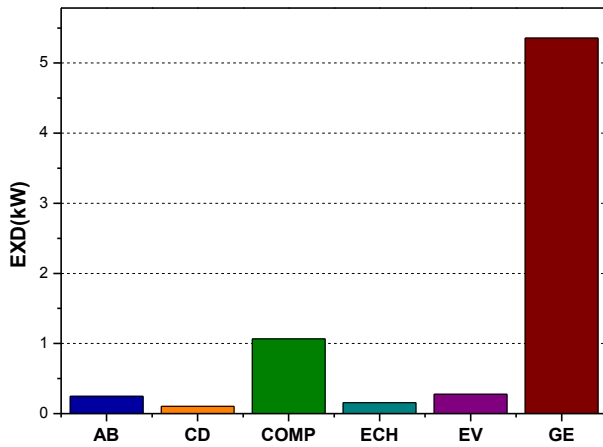


Figure 5
Part of irreversibility for each
Component of the system

Figure 5 presents the part of each component in the total irreversibility of the system. Results are generated for a generator temperature of 80°C and a condensation temperature of 30°C.

From figure 5, the great part of the system irreversibility is caused by the generator, about 5,2kW from 7,5kW as total irreversibility. This result is predicted because of the high working pressures and temperatures of this component.

Some efforts have to be provided to decrease the irreversibility of the generator.

In the next part, the effect of the compression ratio on the system performances is studied.

Figure 6 presents both of the COP and the exergetic efficiency versus the compressor discharge pressure (P_{INT}) for a condensation temperature of 30°C and 80°C as generator one.

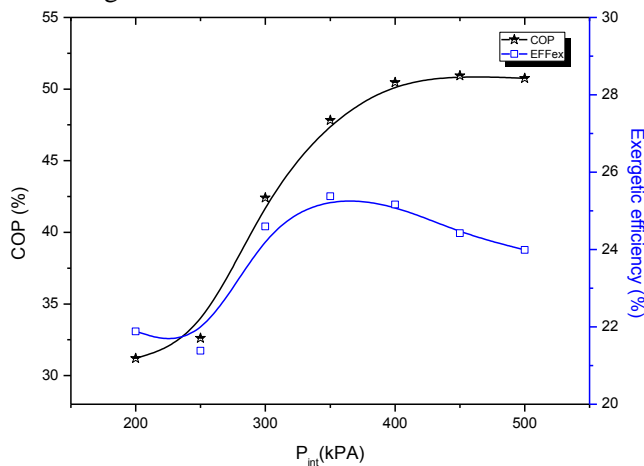


Figure 6
COP and η_{ex} versus P_{INT}

The COP of the system increases when the compressor discharge pressure increases. It can

achieve 52% as optimum value from a pressure of about 400kPa, knowing that it is for a generator temperature of 80°C which is a low temperature next to those used in classic absorption systems using ammonia/water.

Even exergetic efficiency is ameliorated for a higher intermediate pressure (compressor discharge one). Its optimum value (25%) is obtained for P_{INT} =350kPa, after this pressure it decreases again unlike the COP behavior which stabilizes for the high pressures.

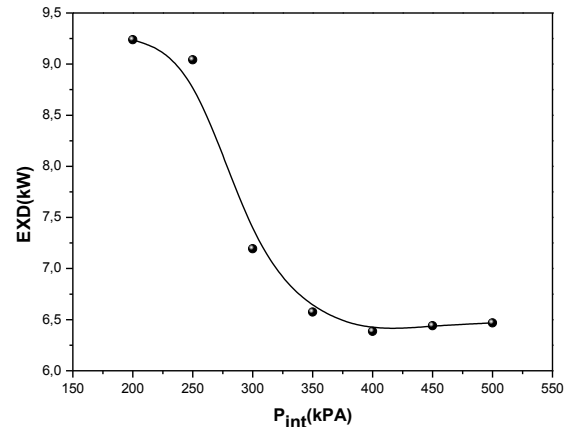


Figure 7

Total irreversibility of the system versus P_{INT}

In figure 7 is presented the total irreversibility evolution versus the intermediate pressure. It is clear from this figure that the irreversibility decreases significantly with the increase of this pressure. The minimum irreversibility is achieved from an intermediate pressure of 400kPa.

CONCLUSIONS

In this work, simulation of a hybrid compression/absorption one stage refrigeration system has been elaborated with two couples by Aspen Tech software, the classical one: water/ammonia and DMAC/R245fa(1,1,1,3,3-Pentafluoropropane /N, N' dimethylacetamide) and exergetic analysis was developed to evaluate the possibility of using this new couple. Conclusions of this study are drawn below:

- Energetic performances of the system are conserved with the new couple R245fa/DMAC while providing lower generator temperatures for the system (from 50°C to 75°C), optimum functioning states are obtained for generator temperatures varying from 80°C to 110°C with given COP of 52%, which makes this couple a good option for solar source use.

- Working with the proposed mixture allows working in lower pressures (from 300kPa to 1800kPa for Ammonia/water and from 100kPa to 600kPa for R245fa/DMAC) which can make the machine safer and easily realizable.
- The new proposed couple is reducing irreversibility of the system, exergy loss is reduced from 16kW with ammonia/water system to 7.5 kW with the R245fa/DMAC one for a refrigeration power of 3kW.
- The proposed new working mixture, not only can solve the toxicity problem of the ammonia use, but also adapt the system to low temperatures sources thanks to its low generator temperatures.

REFERENCES

1. Bouaziz N, Ben Iffa R, Kairouani L. Performance of a water ammonia absorption system operating at three pressure levels. *J Mech Eng Res* 2011; 3(4):120-7.
2. Herold K, Radermacher R, SA K. Absorption chillers and heat pumps. Boca Raton, Florida: CRC Press; 1996.
3. Ziegler F. State of the art in sorption heat pumping and cooling technologies. *Int J Refrig* 2002; 25: 450-9.
4. Lee SF, Sherif SA. Second law analysis of various double effect lithium bromide/water absorption chillers. 2001. ASHRAE Transactions; AT-01-9-5:664-673.
5. Arora A, Kaushik SC. Theoretical analysis of LiBr/H₂O absorption refrigeration systems. *Int J Energy Res* 2009; 33:1321-40.
6. Dincer I, Cengel YA. Energy, entropy and exergy concepts and their roles in thermal engineering. *Entropy* 2001; 3:116-49.
7. Bejan A. Entropy generation through heat and fluid flow. 2nd Ed. New York: Wiley; 1994.
8. Bejan A. Convection heat transfer. New York: Wiley; 1995
9. Bejan A. Entropy generation minimization. Boca Raton, FL: CRC Press; 1996.
10. Lee SF, Sherif SA. Second law analysis of multi effect lithium bromide/water absorption chillers. 1999. ASHRAE Transactions; Ch-99-23-3:1256-1266.
11. Ravikumar TS, Suganthi L, Samuel AA. Exergy analysis of solar assisted double effect absorption refrigeration system. *Renew Energy* 1998;14 (Nos. 1-4):55-9.
12. Anand DK, Kumar B. Absorption machine irreversibility using new entropy calculations. *Sol Energy* 1987; 39 (3):243-56.
13. D. Lounissi, Nahla Bouaziz and Lakdar Kairouani. An exergetic study of a new hybrid heat pump based on R124/DMAC mixture for solar cooling. *Int. J. Exergy*, Vol. 17, No. 4, 2015.
14. Brunin, O., M. Feidt and B. Hivet, (1997), Comparison of the working domains of some compression heat pumps and a compression-absorption heat pump. *International Journal of Refrigeration*, 20, 308-318.
15. L. Kairouani and E. Nehdi, (2005), Thermodynamic Analysis of an Absorption/Compression Refrigeration System Using Geothermal Energy. *American Journal of Applied Sciences* 2 (5), 914-919.
16. A.A. Godarzi, M.Jaliliana, J. Samimi, A. Jokar and M.A. Vesaghi, (2013), Design of a PCM storage system for a solar absorption chillerbased on exergoeconomic analysis and genetic algorithm. *International Journal of Refrigeration* 36, 88-101.
17. S.A. Adewusi, Syed M. Zubair, (2004). Second law based thermodynamic analysis of ammonia–water absorption systems .*Energy Conversion and Management* 45, 2355–2369.
18. J. Wang, G. Chen and H. Jiang, (1998), Study on a solar-driven ejection absorptionrefrigerationcycle. *International Journal of Energy Research*, 22, 733-739.
19. M.M. Talbi and B. Agnew, (2000), Exergy analysis: an absorption refrigerator using lithiumbromide and water as the working fluids. *Applied Thermal Engineering* 20, 619–630.
20. N. Bouaziz, D. Lounissi, L. Kairouani and M. El Ganaoui, Exergetic Analyses of a Particular Absorption Cooling System, *Defect and Diffusion Forum Vols. 326-328* (2012) pp 641-646
21. G.Q. Chen, Z.H. Qi, (2007), Systems account of societal exergy utilization: China 2003, ecological modeling, 208, 102–118.
22. Nahla Bouaziz, D. Lounissi, Energy and exergy investigation of a novel double effect hybrid absorption refrigeration system for solar cooling. *International journal of hydrogen energy*, 40 (2015) 13849-13856.

ON THE APPLICATION OF CARBON NANOTUBE-BASED COMPOSITE MATERIALS FOR SMART DESIGN OF WIND TURBINE BLADES

Brahim Attaf

CMS Ecotechnology, Composite Materials and Structures;
39 Boulevard Charles Moretti, 13014 Marseille - France

Corresponding author: Email: b.ataf@wanadoo.fr

ABSTRACT

The aim of this paper is to optimize and improve the wind turbine blade material properties using carbon nanotubes (CNTs), arranged in the form of continuous fibres and embedded in a polymer matrix. The main choice of these nano-materials is believed to be related to the ultra-high-performance indices in terms of specific stiffness and specific strength and other physicochemical properties such as thermal and electrical conductivity. These competitive advantages make CNTs attractive candidate for the reinforcement of composite wind turbine blades. With this great innovation, modern wind industries are strongly interested in the development of this technology for building offshore wind turbines that are capable to produce ultra-mega sources of clean energy. In addition, CNTs have the potential to be used as sensors for monitoring the internal health of the blade structure.

Key words: CNTs; wind energy; composite blades; innovative design; sustainable development

INTRODUCTION

Given that wind energy is a key solution responding to the sustainable development challenges through tackling air pollution, greenhouse gas emissions and various industrial wastes, the technological interest to develop bigger and more powerful machines is becoming nowadays a major concern for worldwide wind turbine manufacturers [1,2]. Thereby obtaining a high power output depends mainly on the swept area of the rotating blades: the larger the size of the blades, the more energy is captured. However, these blades are considered as critical components which must be designed strong enough to perform safely in operating conditions, withstand severe static and/or dynamic loadings to which they will be exposed throughout their service life, and survive the maximum resistance fatigue [3]. To achieve these requirements, glass and/or carbon fiber-reinforced composites [4,5] are used in such structural applications due to their good performances in terms of stiffness and strength coupled with minimum weight. Further to these notable properties, recent advances in nanotechnology have led to the development of a new class of composite materials based on carbon nanotubes (CNTs) in the form of continuous fibres [6]. These CNT-fibres are intended to replace the standard glass and carbon fibres due to their ultra-high-performance indices in terms of specific stiffness (E/ρ) and specific strength (σ/ρ)

and other physicochemical properties such as thermal and electrical conductivity (see Fig.1).

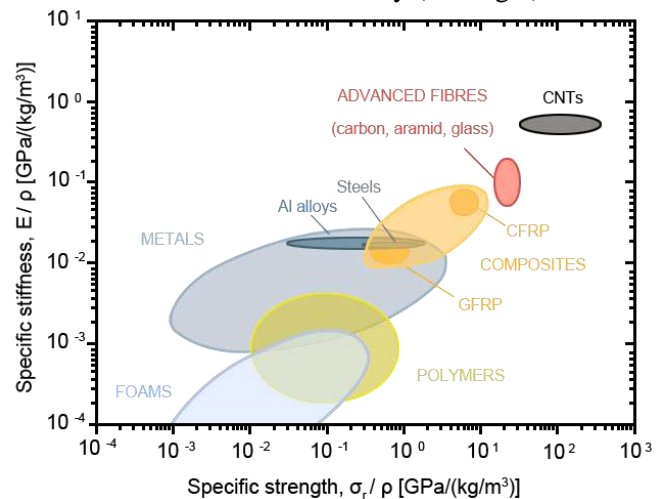


Fig. 1 Specific strength vs. specific stiffness for some composite materials [7, 8]

For instance, the strength of these fibres can be several times higher than standard carbon fibres and weigh much less for an equivalent cross-section.

All of these advantages have made CNTs attractive candidate for the reinforcement of future composite wind turbine blades. In addition, CNTs have the potential to be used as sensors for structural health monitoring and control of the blade behaviour under

extreme loading.

In order to ensure ecological sustainability of this new generation of composite materials, further studies are still needed to be undertaken in this field before starting the qualification and certification processes.

It is in the context of global efforts to fight against climate change for which this paper has been developed enabling the improvement of design process of future wind turbine blades; this will providentially offer great potential for the development of clean energy and will guarantee a new security of energy supply. Furthermore, the paper aims to support the EU's triple energy target (3×20 EU's energy objectives) that is expected to be achieved by 2020, namely: (i) a 20% reduction in greenhouse gas emissions; (ii) a 20% rise in the share of renewable energies; and (iii) a 20% reduction in energy consumption.

CHIRALITY AND GEOMETRY OF CNTS

CNT materials are based on graphite which is the stable form of carbon at ordinary temperature and pressure (e.g., pencil tip), where its molecular structure consists of an intercalated stacking of non-compact hexagonal honeycomb sheets; each sheet is separated by 0.336 nm along its normal direction (see Fig. 2a). An isolated single sheet of graphite is defined as free-standing graphene whose chemical formula is C_n (Fig. 2b)

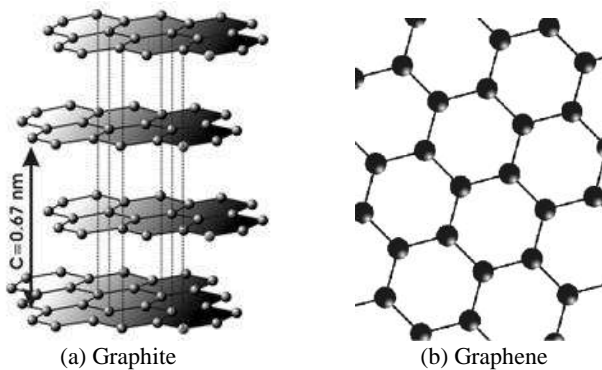


Fig. 2 Graphite and graphene molecular structures

The CNTs are obtained by rolling graphene sheets on themselves as illustrated in Fig. 3.

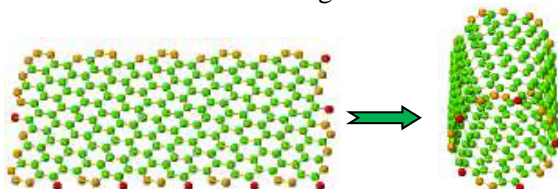


Fig. 3 Rolling up a graphene sheet into a CNT

Depending on the cut of the graphene sheet with respect to the referential coordinate system ($O; \vec{a}_1, \vec{a}_2$) defined in the hexagonal lattice as illustrated in Fig. 4, several geometries of CNTs can be obtained using the chiral vector ($\vec{C}_k = n \cdot \vec{a}_1 + m \cdot \vec{a}_2$). In general, there are three types of CNTs which are called: (i) armchair (when $n=m$), (ii) zigzag (when $m=0$) and (iii) chiral (when $n \neq m$), as shown in Fig. 5.

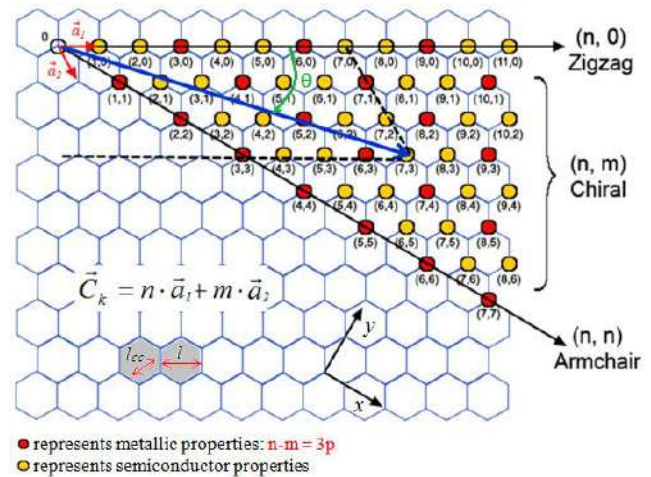


Fig. 4 Chirality and geometry of CNTs

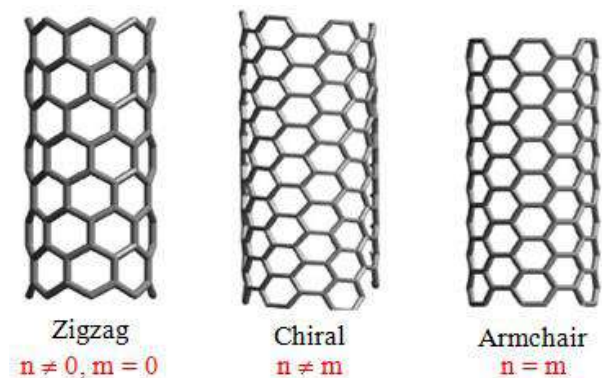


Fig. 5 Different geometric configurations of CNTs

In addition, the electrical properties of CNTs can be classified either metallic or semiconductor in accordance with the indices (n, m). Consequently, the armchair CNTs are always metallic. Whereas, the zigzag and chiral CNTs may be either metallic or semi-conductor; they are metallic when the condition ($n-m = 3p$), where p is an integer. This situation is well explained and presented in Fig. 4, where the red solid circles represent metallic CNTs and yellow solid circles represent semi-conductor CNTs. Moreover, it should be noted that this rule of electrical properties remains applicable only for certain nanotube diameters due to the significant

effects generated by small curvature in small diameters.

FORMULATIONS AND CONSTITUTIVE EQUATIONS

Integration of CNTs in wind blades: In general, CNTs can be a single-walled carbon nanotube (SWNTs) or multi-walled carbon nanotubes

(MWNTs) as shown in Fig. 6a. The diameter of CNTs is ranging from 1-80nm; whereas the length can reach several micrometres. With these nanometric dimensions, a very high aspect ratio (i.e., length-to-diameter) can be provided. Such unique characteristics contribute significantly to the improvement of the durability of the blade structure.

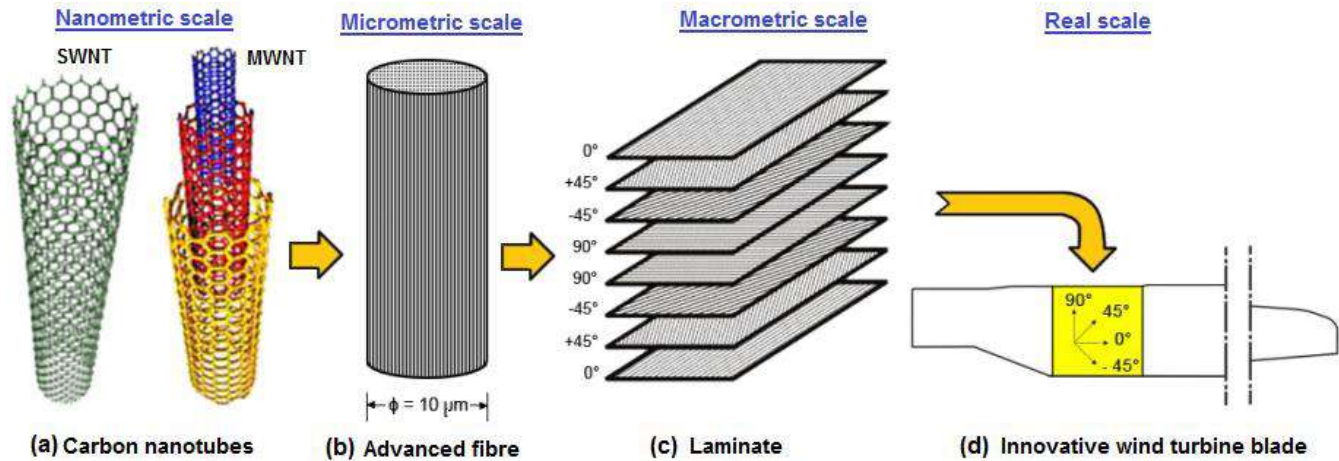
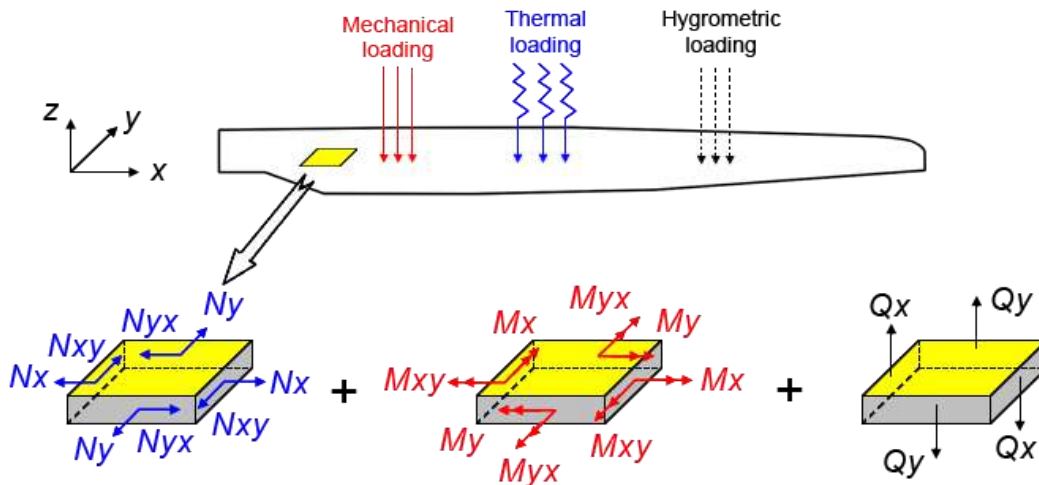


Fig. 6 Application of CNT-based continuous fibres for future design of ultra-mega wind turbine blades

Constitutive equations: The state of the structural problem is illustrated in Fig.7, where the blade structure (onshore or offshore) is assumed to be subjected to three main types of loading; these are:

- (i) mechanical loading (high wind forces, weight, ..),
- (ii) thermal loading (temperature variation) and
- (iii) hygrometric loading (moisture and seawater exposure) [9, 10].



When thermal and moisture effects besides mechanical loading are taken into consideration in the structural analysis, the constitutive relations for an unsymmetrically *n*-layered composite plate, assumed to be extracted from the blade structure,

with transverse shear deformations can be written in compact matrix form as [11, 12]:

$$\begin{Bmatrix} N \\ \dots \\ M \end{Bmatrix}_{xyz} = \begin{bmatrix} A_{ij} & B_{ij} \\ \dots & \dots \\ B_{ij} & D_{ij} \end{bmatrix} \begin{Bmatrix} \varepsilon_0 \\ \dots \\ \kappa \end{Bmatrix}_{xyz} - \begin{Bmatrix} N^{\Delta T} \\ \dots \\ M^{\Delta T} \end{Bmatrix}_{xyz} - \begin{Bmatrix} N^{\Delta m} \\ \dots \\ M^{\Delta m} \end{Bmatrix}_{xyz} \quad (1a)$$

$$\{Q\}_{xyz} = \{F_{ij}\} \{\gamma\}_{xyz} \quad (1b)$$

$$(A_{ij}, B_{ij}, D_{ij}) = \sum_{k=1}^n \int_{z_{k-1}}^{z_k} (\bar{Q}_{ij})_k (1, z, z^2) dz \quad (i,j=1,2,6)$$

$$F_{ij} = \delta_{ij} \sum_{k=1}^n \int_{z_{k-1}}^{z_k} (\bar{Q}_{ij})_k dz, \quad (i,j=4,5)$$

where:

N is the in-plane forces vector;

M is the bending/torsional moments vector;

Q is the out-of-plane forces vector;

ε^0 is the mid-plane strains vector;

κ is the curvatures vector;

γ is the transverse shear strain vector;

A_{ij} is the extensional stiffness matrix;

B_{ij} is the coupling stiffness matrix;

D_{ij} is the bending stiffness matrix;

F_{ij} is the transverse shear stiffness matrix;

ΔT represents the variation of temperature;

Δm represents the variation of moisture;

$(\bar{Q}_{ij})_k$ is the k -th ply stiffness matrix;

δ_{ij} is the transverse shear correction factor.

Considering that the transverse shear effect is neglected, the variations of temperature and moisture are kept constant and the values of N and M at each point of the blade structure are known, the strains ε^0 and curvatures κ can be calculated using Eq.(1a).

Transforming the in-plane stresses from the laminate coordinate system (x,y) to the ply coordinate system $(1,2)$ via the transformation matrix $[T]$ gives the following relationship:

$$\{\sigma\}_{1,2}^{(k)} = [T]^{(k)} \left[\bar{Q}_{ij} \right]^{(k)} (\{\varepsilon_0\} + z\{\kappa\}) \quad (3)$$

Difficulties inherent to transverse shear deformation, material anisotropy, blade geometry and boundary conditions constitute a complex and tedious analysis, which makes it impossible to provide exact values via a mathematical solution. To overcome these difficulties, numerical solutions using finite element method (FEM) and experimental investigations are the only approaches that can be employed.

SOME RESULTS AND DISCUSSION

The FEM is one of the numerical methods that can provide approximate solutions enabling optimum design process to be achieved at low cost. Numerical results on the blade structural behaviour show that stress concentrations occur within the transition zone: a zone characterised by a shift of the blade section geometry from “circular shape” to “airfoil shape”. Consequently, during stress analysis a particular attention must be paid on this transition zone with the object to assess and avoid the failure condition of individual plies. For this purpose, several criteria of ply failure have been developed and are available in composite materials literature, namely: Tsai-Hill, Tsai-Wu and Hoffman criteria.

For instance, the non-failure criterion in the state of plane stress (i.e., $\sigma_3 = \tau_{13} = \tau_{23} = 0$) of each ply constituting the upper and lower blade surfaces is checked using Tsai-Hill criterion, given by the following equation [11]:

$$\left(\frac{\sigma_1^{(k)}}{\bar{\sigma}_1^{(k)}} \right)^2 + \left(\frac{\sigma_2^{(k)}}{\bar{\sigma}_2^{(k)}} \right)^2 - \frac{\sigma_1^{(k)} \sigma_2^{(k)}}{(\bar{\sigma}_1^{(k)})^2} + \left(\frac{\tau_{12}^{(k)}}{\bar{\tau}_{12}^{(k)}} \right)^2 < 1 \quad (2)$$

where,

$\bar{\sigma}_1^{(k)}$ is the maximum tensile (compressive) failure stress in the 1-direction,

$\bar{\sigma}_2^{(k)}$ is the maximum tensile (compressive) failure stress in the 2-direction and

$\bar{\tau}_{12}^{(k)}$ is the maximum shear failure stress in the 1-2 plane.

Figure 8a illustrates a case study of a stress concentration within the blade transition zone. The numerical results correspond to the k -th ply among the other plies constituting the blade structure when this latter is subjected to static loading. Failure plies are those for which the failure criterion, given by Eq. (2) is greater than the limit value of 1 (i.e., 100%).

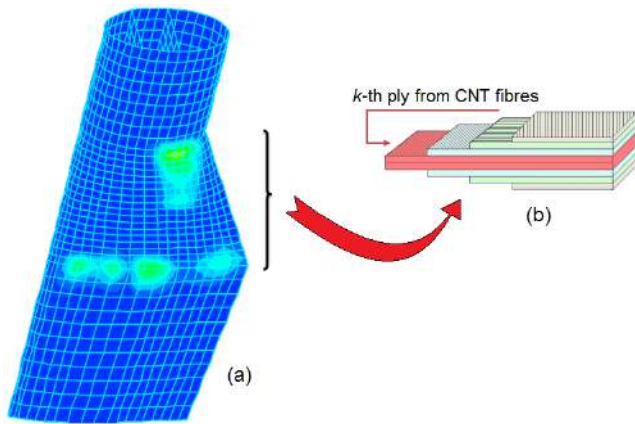


Fig.8 Blade transition zone: (a) stress concentration for the k -th ply; (b) replacement of the k -th ply by a CNT ply

To overcome this situation and avoid possible failure risk from happening, the over-stressed ply which was initially made of classical fibres is replaced by another ply of unidirectional continuous fibres made of single-walled carbon nanotubes, as shown in Fig.8b. With this alternative solution, the analysis deals with the case of hybrid composite blade made of two types of fibre reinforcements. In addition to that feature, the ply made of CNT fibres can play through its excellent electrical and thermal properties the role of active sensor as a means to obtain information about the structural blade behaviour when subjected to severe static and dynamic loading, including hygrothermal expansion and contraction.

CONCLUSION

To minimise the effect of global warming and leave a more stable environment for future generations, each country with windy areas is encouraged to play an active role in boosting research, innovation and creativity in the field of onshore and offshore wind energy. In this context, composite materials based on carbon nanotube as unidirectional continuous fibres are intended to occupy a predominant place in the modern industry of wind turbine blades. Indeed, these materials offer attractive advantages in terms of specific stiffness, specific strength and other physicochemical properties that are not achievable with classical fibres. However, besides these advantages, the notion of ecodesign has to be integrated in all design stages for sustainable and eco-friendly production of composite wind turbine blades. In fact, companies that are engaged towards the implementation of environmental management system (EMS) are encouraged to boost their activities on:

- the development of clean manufacturing processes by reducing VOC emissions;
- the development of new high-performance CNT-materials with cost effective and eco-friendly;
- the creation of specific standards for life-cycle assessment of blades based on CNT-composites;
- the implementation of strong cooperative activities between the university, research centres and the industry;
- the encouragement of innovative technology transfer whilst maintaining the protection of industrial and intellectual property;
- the development of university-entrepreneur training partnerships (UETPs) to form more technical engineers in the wind energy sector.

REFERENCES

- [1] Kamp, L.M., Smits, R.E.H.M., Andreisse, C.D. 2004, Notion on Learning Applied to Wind Turbine Development in the Netherlands and Denmark, *Energy Policy* **32**, pp. 1625-1637
- [2] Justin, T., 2008, New Record: World's Largest Wind Turbine (7+ Megawatts), in News, Renewable Power, available on line at: <http://www.metaefficient.com/news/new-record-worlds-largest-wind-turbine-7-megawatts.html>
- [3] Freebury, G., Musial, W., 2000, Determining Equivalent Damage Loading for Full-Scale Wind Turbine Blade Fatigue Tests, in: the 19th American Society of Mechanical Engineers (ASME) Wind Energy Symposium, Reno, Nevada
- [4] Attaf, B., Hollaway, L., 1990, Vibrational Analyses of Glass Reinforced Polyester Composite Plates Reinforced by a Minimum Mass Central Stiffener, *Composites* **21** (5), pp. 425-430.
- [5] Hollaway, L., Attaf, B., 1989, On the Vibration of Glass/Polyester Composite Stiffened and Unstiffened Rectangular Plates, Chinese Society of Aeronautics, in: 7th International Conference on Composite Materials, Beijing, pp. 435-444.
- [6] Wang, X., et al., 2013, Ultrastrong, Stiff and Multifunctional Carbon Nanotube Composites, *Materials Research Letters*, Vol.1, No 1, pp. 19-25

-
- [7] Hart, A., J., 2009, Nanocomposites and Fibers, Lectures/Tutorials - University of Michigan, ME599-002, Michigan.
- [8] National Academy of Sciences Report (2005), <http://www.nap.edu/catalog/11268>.
- [9] Attaf, B., 2010, Eco-conception et Développement des Pales d'Eoliennes en Matériaux Composites," Revue des Energies Renouvelables - 1^{er} Séminaire Méditerranéen sur l'Energie Eolienne, Algeria, pp. 37-48.
- [10] Attaf, B., 2010, Structural Ecodesign of Onshore and Offshore Composite Wind Turbine Blades," 1^{ère} Conférence Franco-Syrienne sur les Energies Renouvelables, 24-28 Oct., Damascus, Syria.
- [11] Jones, R. M., 1999, *Mechanics of Composite Materials*, 2nd edition, Taylor & Francis, Philadelphia
- [12] Saarela, O., 1994, Computer Programs for Mechanical Analysis and Design of Polymer Matrix Composites, Prog. Polym. Sci., vol. 19, pp. 171-201

HEMP-STRAW COMPOSITES: THERMAL AND HYGRIC PERFORMANCES

F. Collet*, S. Prétot, C. Lanos

Laboratoire de Génie Civil et Génie Mécanique, Equipe Matériaux Thermo Rhéologie, Université de Rennes 1

IUT Génie Civil-Construction Durable - 3, rue du Clos Courtel, BP 90422, 35704 Rennes, France

*Corresponding author: Fax: +33 (0) 2 23 23 40 51 Email: florence.collet@univ.rennes1.fr

ABSTRACT

The European ISOBIO project aims to develop new bio-based building insulating materials which contribute to reduce environmental impacts of buildings. The developed materials shall have low embodied energy and low carbon footprint and shall contribute to reduce energy needs of buildings and to ensure high hygrothermal comfort of users. This study investigates the valuation of agro resources as bio-based aggregates and as binding material to produce wholly bio-based composites. The developed composites are made of hemp shiv glued with wheat straw. After a feasibility study which investigates several ways to use wheat straw as a gluing material and several hemp to wheat straw ratio, three hemp-straw composites are selected. Specimens are produced to characterize thermal and hygric properties of developed composites. They show interesting thermal and hygric properties as they have low thermal conductivity (0.071 to 0.076 W/(m.K)) and they are excellent hygric regulators (MBV > 2 W/(m².%RH)).

NOMENCLATURE

A: open surface area (m²),
 C: constant including the thermal diffusivity of the material (Hot Wire),
 CV : coefficient of variation (%),
 k : thermal conductivity (W/(m.K)),
 MBV : Moisture Buffer Value (g/(m².%RH)),
 q: heat flow per meter (W/m) (Hot Wire),
 RH_{high/low}: high/low relative humidity level (%),
 t: heating time (s) (Hot Wire),
 Δm: moisture uptake/release during the period (g),
 ΔT: temperature rise (°C) (Hot Wire),
 ρ: density (kg/m³),
 σ: standard deviation.

INTRODUCTION

This study is part of the European ISOBIO project which aims to develop new bio-based building insulating materials. The aim is to reduce the embodied energy of materials while also reducing the total energy needs of buildings and allowing high hygrothermal comfort of users. Two kinds of products will be developed within ISOBIO project: insulating panels and bio-based insulating composites to be implemented on-site. The project focuses on the

valuation of agro resources as bio-based aggregates or as binding material. Five agro resources are considered in ISOBIO project: wheat, rape, hemp, flax and corn cob. They are available as straw, fiber, shiv or dust.

This study investigates the development of bio-based composites to be used to produce insulating panels. This first investigation considers only one kind of bio-based aggregate (hemp shiv) and one kind of agro resource as binding material (wheat straw). The aim is to attest the feasibility of such composites and to qualify their hygrothermal performances, in link with the objectives in term of reduction of energy needs of buildings and in term of hygrothermal comfort of users.

MATERIALS AND METHODS

Developed materials: This study focuses on the valuation of agro resources as bio-based aggregates and as binding material to produce a wholly bio-based composite.

For this first investigation, hemp shiv are used as aggregates and wheat straw is considered as gluing material. Polysaccharide is also used as reference gluing material.

Actually, hemp shiv are commonly used to produce hemp composites with lime based binders or, more recently, with PLA (Polylactic acid) or with starch [1] [2] [3]. The aggregates used to produce the composites are commercial hemp shiv (Chanvribat from LCDA Les Chanvrières de l’Aube – France). Their bulk density is about 100 to 110 kg/m³. Their particle size distribution, measured by sieving, are given figure 1. The mean width of shiv (D50) is 4 mm for Chanvribat and the width/length ratio is about 4.

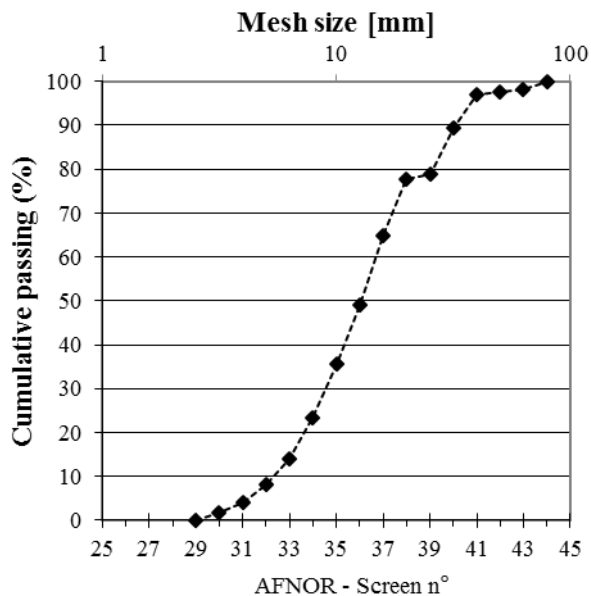


Figure 1

Particle Size Distribution of Chanvribat hemp shiv

As mentioned in [4], the lignin within the straw and other herbaceous crops acts together with hemicellulose as a perfect natural adhesive for straw and any other cellulosic materials. Thus, wheat straw is expected to be convenient as binding material with hemp shiv. In this study, several ways to use wheat straw as a gluing material are tested, varying the hemp to wheat straw ratio and thermal activation step. Firstly, wheat straw is finely chopped and mixed with hemp shiv. The dry mix is then moistened and processed under pressure and heat. It is shown (figure 2) that to ensure good cohesion using the same thermal treatment, a minimum of 15% of wheat straw is required in the dry mix. Then, the selected mix proportioning consists in 20% of hemp shiv and 20% of straw powder.

Once the gluing effect of straw powder is attested, complementary tests are made using a wheat straw infusion. For confidentiality reasons, no more details are given on the production process. After production process optimization, composite specimens are produced. Four kinds of composites are considered: three hemp-straw composites and one hemp-polysaccharide composite (table 1). For each composite, three specimens 10 centimeters in diameter and about 7 cm high are produced (figure 3). The developed composites show quite low density, ranging from 166 to 188 kg/m³ (table 2). For the same process, the composite with highest hemp content show lower density (B2 vs B1).

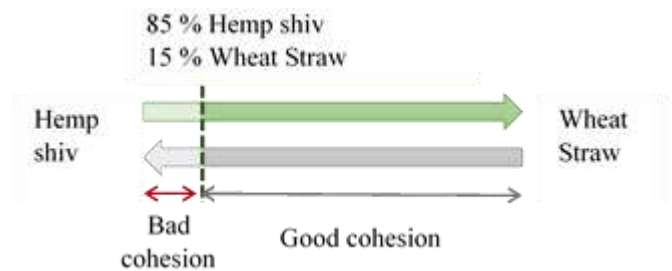


Figure 2

Cohesion versus formulation of composites hemp shiv-straw powder

Table 1

Formulation of composites (ratio of dry mix)

	35	B1	B2	S2
Hemp shiv	80 %	80 %	85 %	90.5 %
Milled wheat straw	20 %			
Infused wheat straw		20 %	15 %	
Polysaccharide				9.5 %



Figure 3

Developed composites

Table 2

Apparent density of composites: average value (ρ_{av}), standard deviation (σ_{ρ}), coefficient of variation (CV_{ρ})

	35	B1	B2	S2
ρ_{av} (kg/m ³)	179.8	187.9	165.9	181.6
σ_p (kg/m ³)	13.2	3.6	3.4	2.8
CV _{ρ} (%)	7.4	1.9	2.0	1.5

Thermal characterization: The thermal characterization is based on the measurement of thermal conductivity after stabilization at 23°C, 50%RH in climate chamber. In order to limit water migration during the test, the measurement is performed with a transient method: Hot Wire. This method is based on the analysis of the temperature rise versus heating time.

$$\Delta T = \frac{q}{4 \cdot \pi \cdot k} (\ln(t) + C) \quad (1)$$

Where ΔT is the temperature rise (°C), q is the heat flow per meter (W/m) and k is the thermal conductivity (W/(m.K)), t is the heating time (s) and C is a constant including the thermal diffusivity of the material.

The measurement is performed with the sensor sandwiched between two specimens. The heat flow and heating time are chosen to reach high enough temperature rise (>10°C) and high correlation coefficient (R^2) between experimental data and fitting curve. In this study, the commercial CT Meter device is equipped with a five centimeters-long hot wire. The power used is 142 mW and the heating time is 120 seconds. These settings allow meeting the previous requirements (temperature increase higher than 10°C and high R^2 value). According to the manufacturer, the expected accuracy is thus better than 5%. For each formulation, three pairs of specimen are considered by combining differently the three specimens (A&B, A&C, and B&C). The thermal conductivity of a pair of specimens is the average of three values with a coefficient of variation (ratio of the standard deviation to the average value) lower than 5%. The thermal conductivity of a formulation is the average of the values of the three pairs of specimens.



Figure 4
Experimental device for the measurement of Thermal Conductivity.

Hygic characterisation: The hygic characterization is based on the measurement of the moisture buffer value (MBV) of materials which characterizes their ability to moderate the variations of indoor humidity in buildings.

The moisture buffer value is measured following the Nordtest protocol [5]. Specimens are sealed on all but one surfaces. After stabilization at 23°C, 50%RH, specimens are exposed to daily cyclic variation of ambient relative humidity (8 hours at 75%RH and 16 hours at 33 %RH) in a climate chamber (Vötsch VC4060). The moisture buffer value is then calculated from their moisture uptake and release with:

$$MBV = \frac{\Delta m}{A \cdot (RH_{high} - RH_{low})} \quad (2)$$

Where MBV is the moisture buffer value (g/(m².%RH)), Δm is the moisture uptake/release during the period (g), A is the open surface area (m²), $RH_{high/low}$ is the high/low relative humidity level (%).

Temperature and relative humidity are measured continuously with sensor SHT75 and with sensor of the climatic chamber; the air velocity in the surroundings of the specimens ranges from 0.1 to 0.4 m/s for horizontal velocity and is lower than 0.15 m/s for vertical one.

The specimens are weighed out of the climatic chamber five times during absorption period and two times during desorption one. The readability of the balance is 0.01 g, and its linearity is 0.01 g. The accuracy of the moisture buffer value is thus about 5%.

For each formulation, the MBV is measured on the three specimens and the MBV of the formulation is the average value of the three specimens.



Figure 5
Experimental device for the measurement of Moisture Buffer Value.

RESULTS

Thermal characterization: Figure 6 gives an example of the increase of temperature versus neperian logarithm of heating time during the measurement with hot wire. Table 3 and figure 7 provide the average value, the standard deviation and the coefficient of variation of thermal conductivity of studied composites.

For all tests, the correlation coefficient between experimental data and fitting curve is very close to one, higher than 0.9997. More, for each composite, experimental values are very close to each other. The coefficient of variation is lower than 3 % between the nine measurements (three pairs and three measurements by pair). This induces great confidence in thermal conductivity values.

The thermal conductivities of developed composites, after stabilization at 23°C, 50%RH, range from 0.071 to 0.076 W/(m.K). As shown on figure 7, the thermal conductivity increases with density. Whatever the kind of composite (glued with straw or with polysaccharide), the thermal conductivity show the same tendency. So, the way of gluing hemp shiv doesn't seem to much impact thermal conductivity.

Compared with thermal conductivity obtained with hemp-lime composites, these values are lower, mainly thanks to lower density. Actually, for hemp-lime composites, Collet and Prétot [6] found thermal conductivity of 0.093 and 0.120 W/(m.K) at 23°C, 50%RH, with respective density of 260 and 390 kg/m³. De Bruijn and Johansson [7] studied the thermal conductivity of two lime-hemp mixes at 15%RH and 65%RH. At 65%RH, they give thermal conductivity values of 0.116 and 0.100 W/(m.K)

when the densities are respectively 394.8 and 298.1 kg/m³. For hemp-PLA composite, the thermal conductivity ranges from 0.085 W/(m.K) at 260 kg/m³ to 0.120 W/(m.K) at 350 kg/m³ [2]. These values meet the same trend curve as developed composites. Moreover, the developed composites show thermal conductivity close to the value obtained by Tran le [3] on hemp-starch composite. Actually, at dry state, he finds a thermal conductivity of 0.062 W/(m.K) with a density of 176 kg/m³. Finally, the main impacting factor on thermal conductivity of hemp composites is thus the density of composite.

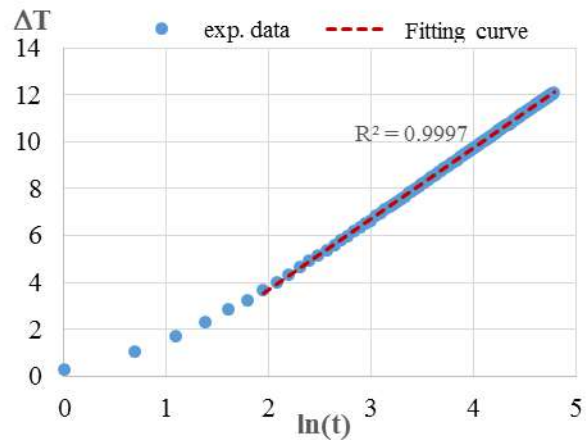


Figure 6
Example of increase of temperature versus neperian logarithm of time

Table 3
Thermal Conductivity of composites: average value (k_{av}), standard deviation (σ) and coefficient of variation (CV)

	35	B1	B2	S2
k _{av} (mW/(m.K))	0.0747	0.0759	0.0714	0.0736
σ (mW/(m.K))	0.0016	0.0019	0.0013	0.0020
CV (%)	2.09	2.56	1.82	2.70

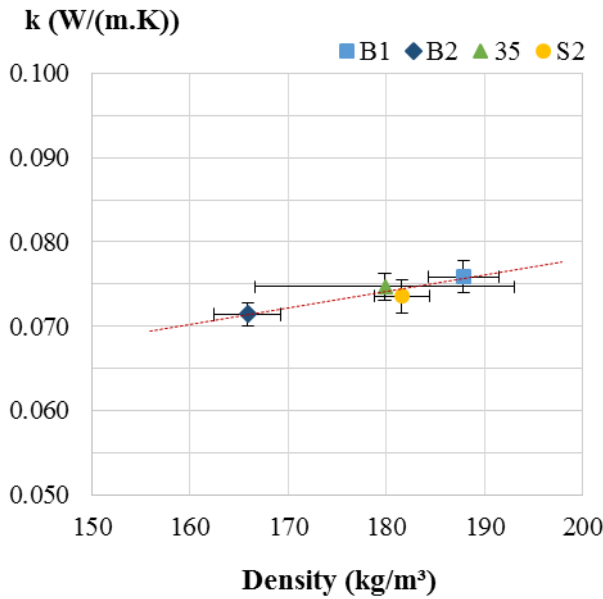


Figure 7

Thermal conductivity of composites (W/(m.K)) versus density at 23°C, 50%RH

Hygic characterization Figure 8 shows the ambient relative humidity and temperature in the climate chamber during the test. The mean value of relative humidity (RH) is slightly lower than 75 % during absorption (about 72.9 %) and slightly higher than 33% during desorption (about 33.3%) because the door of the climate chamber is regularly open to weigh specimens (peak on the curve).

Figure 9 gives as example the moisture uptake and release of specimen S2-A. For all specimens, the change in mass shows less than 5 % of discrepancy for cycles 3 to 5. The moisture buffer value is thus calculated from cycles 3 to 5.

Table 4 and figure 10 summarize the Moisture Buffer Values obtained in absorption, desorption and on average for the four kinds of composites. The standard deviations are very low, leading to coefficients of variation lower than 2% (and generally lower than 1 %).

The average MBV ranges from 2.20 to 2.42 g/(m².%RH). According the Nordtest classification [5], all these composites are thus excellent hygic regulators (MBV>2 g/(m².%RH)).

As shown on figure 10, the Moisture Buffer Value is not impacted by the density of composite. On the opposite, the three composites glued with straw have similar MBV while the composite made with polysaccharide shows slightly higher MBV. Thus, the kind of binder slightly impacts MBV.

Compared with other hemp composites, the developed composites are in the high range of MBV.

For hemp-lime composite MBV ranges from 1.94 to 2.24 g/(m².%RH) [8][2], while for hemp-PLA, the MBV is about 1.77 g/(m².%RH) [2].

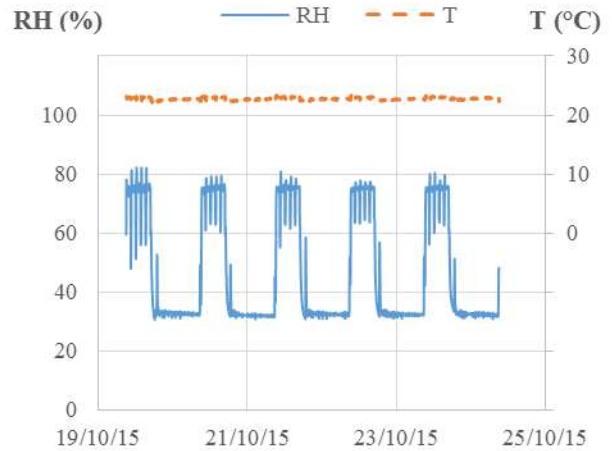


Figure 8

Monitored Relative Humidity and Temperature in the climate chamber during MBV test

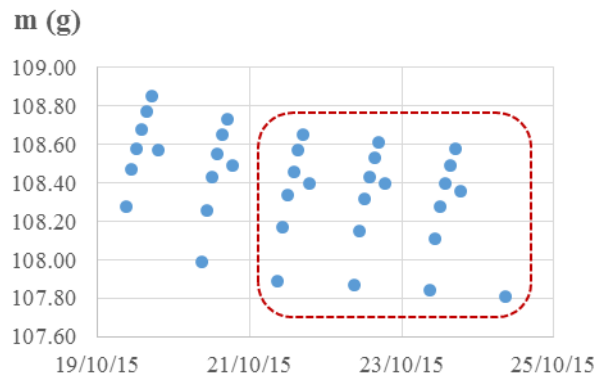


Figure 9

Moisture uptake and release for specimen S2-A

Table 4

Moisture Buffer Value of composites in absorption, desorption and average: average value and standard deviation

	35	B1	B2	S2
MBV abs (g/(m².%RH))	2.23 ± 0.02	2.17 ± 0.03	2.21 ± 0.02	2.36 ± 0.01
MBV des (g/(m².%RH))	2.30 ± 0.02	2.23 ± 0.02	2.24 ± 0.01	2.47 ± 0.01
MBV av. (g/(m².%RH))	2.27 ± 0.02	2.20 ± 0.03	2.22 ± 0.02	2.42 ± 0.01

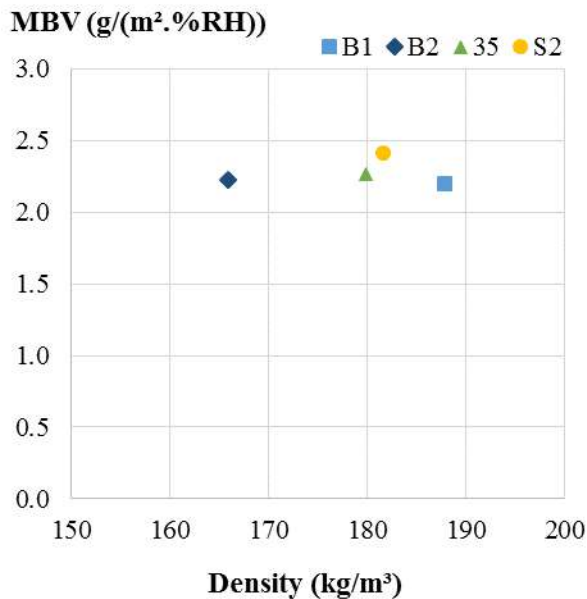


Figure 10
Average Moisture Buffer Value of composites
(g/(m².%RH)) versus density

CONCLUSION This study shows that wheat straw can be used as gluing material to produce hemp-straw composites. To ensure good cohesion, the dry mix should include 15% at least of wheat straw (and 85 % of hemp shiv). The density of developed composite ranges from 165 to 190 kg/m³. The thermal properties are interesting, as the thermal conductivity of developed composites is quite low (0.071 to 0.076 W/(m.K)). More, the developed composites are excellent hygric regulator, with MBV higher than 2.20 g/(m².%RH).

These results are thus encouraging. They meet the objectives of the project as the developed composites are fully bio-based and show thermal and hygric performances which contribute to reduce energy needs of building and to ensure hygrothermal comfort of users.

The composite mechanical characterization will complete this study to show the full efficiency of the proposed solution.

ACKNOWLEDGMENTS

This project has received funding from the European Union's Horizon 2020 research and innovation programme under grant agreement No. 636835 - See more at: <http://isobioproject.com/>

REFERENCES

1. Amziane S. and Arnaud L., Bio-aggregate-based Building Materials, Applications to Hemp Concrete, ISTE Ltd and John Wiley & Sons, Inc, 2013
2. Collet F., Prétot S., Mazhoud B., Bessette L., Lanos C., Comparing hemp composites made with mineral or organic binder on thermal, hygric and mechanical point of view, First International Conference on Bio-based Building Materials, ICBBM 2015, Clermont Ferrand, 21-24 juin 2015, e-ISBN PRO99 : 978-2-35158-154-4.
3. Tran Le A.D., Etude des transferts hydrothermiques dans le béton de chanvre et leur application au bâtiment (in french), PhD thesis, Université de Reims Champagne-Ardenne, November 2010.
4. Ghaffar S. H., Fan M., Lignin in straw and its applications as an adhesive, International Journal of Adhesion & Adhesives, 48, 92–101, 2014.
5. Rode, C.; Moisture buffering of Building Materials, Report BYG•DTU R-126, ISSN 1601 – 2917, ISBN 87-7877-195, 2005.
6. Collet F., Prétot S., Thermal conductivity of hemp concretes: variation with formulation, density and water content, Construction and Building Materials , 65, pp 612–619, 2014, DOI information: 10.1016/j.conbuildmat.2014.05.039.
7. de Bruijn P., Johansson P., Moisture fixation and thermal properties of lime-hemp concrete, Construction and Building Materials, 47, pp 1235-1242, 2013.
8. Collet F., Chamoin J., Prétot S., Lanos C., Comparison of the hygric behaviour of three hemp concretes, Energy and Buildings, 62, pp 294-303, 2013.

INFLUENCE OF HARDENER TYPE FOR EPOXY MATRIX ON THE MECHANICAL BEHAVIOR OF COMPOSITE LAMINATES

DJ. Basaid, C. Aribi, DJ. Kari, A. Benmounah
Research Unit: Materials, Processes and Environment
University of Boumerdes
FSI, City Frantz Fanon, 35000 Boumerdes, Algeria
Corresponding author: Tel: +213 558662148 Email: basaid-d@airalgerie.dz

ABSTRACT

This study is a part of a work in progress on the mechanical behavior of laminate in various modified epoxy matrix. we begin with a laminate six folds with fiberglass taffeta, and epoxide matrix cross linked by aliphatic Amine and bear the name MEDAPOXY STR, this resin appears in the form of a kit of two elements to know the monomer and the hardener with the report weight of 0,67. The treatment of the results shows that the reticulation of monomer by these Amine is incomplete what provokes a plastic domain on the mechanical behavior of the matrix, concerning laminate them developed, the results show that the elastic domain is depend of the elasticity of fibers used and not of that of the matrix. The control by ultrasound is maybe considered as a way of calculate and follow-up of the parameters elastic of the elaborate laminate.

Keywords Epoxy, aliphatic Amine, cross-linked, ultrasound, creep test, cyclic tensile test

NOMENCLATURE

σ - Normal stress (MPa)
 ε - Normal strain (%)
E - Modulus of elasticity (GPa)
 ν - Poisson ratio
 ΔT - Temperature change ($^{\circ}C$)
 α - Coefficient of thermal expansion ($^{\circ}C$)
 V_L - propagation velocity of the longitudinal wave
 V_T - the propagation velocity of the transverse wave
 ρ - Density of material (kg/m^3)
t- Time of creep (min)
 T_g - Glasses temperature
 τ_0, τ -crosslinking percentages for matrix untreated and heat treated

INTRODUCTION

The performances of composite materials are influenced by the properties of the matrix used; the latter maintains the form desired and the protection of the reinforcements against the external attacks. The epoxy resins present good physicochemical performances [1]. The reticulation of this matrix is carried out by several family of the acids amines, the choice of hardener is carried out according to several parameters bound by the method of working, as well as the field of use, consequently, viscosity, the gel time and the characteristics in a solid state will be changed[2]. In the literature, we noticed that the work on the characterization of laminates are based on types and architecture of reinforcements on the one hand [3], and of the epoxy matrix influenced by his properties of another shares [4]

[5], in this context, the creep behavior is strongly influenced by the viscoelastic properties of resin and the characteristics of fibers. In the case of the GFRP the creep limit is 0, 3 F U (F U = tensile strength), in the case of the CFRP and aramid (AFRP) the rupture limit to the creep of 0, 70 F U according to recommendations' of the ACI 440.4R04 [6].

The objective of this work is based on the physic mechanical study of a laminate based on epoxy matrix solidified by aliphatic amine and glass fiber of the type E.

MATERIALS AND TECHNIQUES

Materials used

The matrix used is epoxy nature; the monomer is of the DGEBA type whose the equivalent epoxy by chemical proportioning equal 186,38 g/mol, cross-linked by aliphatic amine with a report/ratio weight of 0.67, the set carries the trade name MEDAPOXY STR.

The reinforcement used is a class E glass fiber; its weaving is of type taffeta, the characteristics of the wick in warp and weft direction are identical. The weight is of the order of 500 g per square meter.

Elaboration of material

The specimens of STR matrix molded in machined aluminum mold to give the dumbbell shape geometrical in accordance with ISO 527, then, after remolding, the cross-linked test pieces subjected to a thermal treatment of 80 C for 8

hours in order to increase the degree of crosslinking. [7]

The laminated plates are worked out by the infusion method (complete replacement of the void by the resin), the plate remains in depression by the pump until the cross-linked of the matrix; then, it is put into an oven at 80 C for eight hours. The specimens are cut in rectangular from elaborate plates, as recommended by the standard ASTM D 3039. The samples are provided with aluminum heels

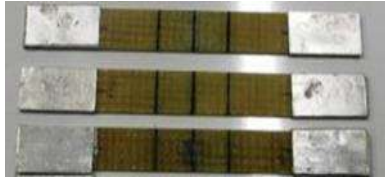


Figure 1
Prepared tensile specimens

Experimental device

Thermal analysis DTA and TGA are carried out using apparatus of the mark STA NETZSCH (Simultaneous Thermal Analysis) 409. The latter is based, on the one hand, to the differential measure of the heating effect using thermo electrical effect and, on the other hand, to the measure of the fall of mass under the effect of the temperature [8]. This technique belongs to the standard NF-EN 31357-2 (plastic Analyses calorimetric differential). The analysis is carried out on two types of sample. The first type is cross-linked without undergoing heat treatment, while the second type is cross-linked with the preceding heat treatment. The speed of heating during the tests of the thermal analysis is of 10 C/min. for these tests, we took as reference an empty capsule. The tensile tests of STR matrix are carried out on a universal machine of Zwick/Rolle type provided with a sensor of force of 10 kN and with an extensometer. Computer with a software testXpert version 12.0 controls this machine.

Concerning the laminates, the tensile tests are carried out at ambient temperature on a universal machine of type Zwick/Rolle 250 on the level of the unit of research Ur-MPE, equipped with a sensor of force of capacity 250 kN and with an extensometer; this machine is controlled by computer using the software TestXpert version 9.0. The mass rate of the reinforcement is determined by the method of the loss on ignition, according to standard NF T 57-571 (applicable to the tablecloths, wire and laminates of glass). The test-tube is of form prismatic; the latter is weighed first once at the ambient temperature (My). Then, it is

placed in a furnace at 600 C during 1 hour in order to burn the resin. The reinforcement remaining is then weighed (MF). The mass rate of reinforcement is determined by the following formula:

$$T_m = (M_f / M_a) \quad (1)$$

The creep tests were carried out on the universal Machine 250 kN for a load of “0.5σ” during 100 hours in mode of relieving and creep what makes it possible to carry out the model semi logarithmic for the prediction.

This model is largely used to describe the tension temps relationship FRP under a constant load and proved reliable like an effective means to characterize and to predict the behavior depend on the time of FRP [9] [10]. The general form of the model semi logarithmic curve is:

$$\varepsilon = \varepsilon_0 + A \ln(t) \quad (2)$$

Where ε is the total deformation of creep and ε_0 is the initial elastic strain, A = coefficient related to the level of the matter and the stress.

For ε_0 can be obtained by the constraint and the durable modulus of elasticity, it is important to determine the values of A by the method of the adjusted curve

The cyclic tests are carried with an intensity increase step by step, the first stage starts starting from 50 MPa, for each cycle increases the force it max of 2 MPa until failure

The method of nondestructive testing of laminated composite plates, by vibration ultrasound (longitudinal and transverse). The method used is said by contact (the transducers are directly in contact on both sides of the plate to be analyzed). The longitudinal wave is obtained simply while placing the transducer transmitting center frequency of 2 MHz on with dimensions of the plate, while on the other side one places the receiver of center frequency of 4 MHz

One measures the time of flight in the sample and knowing the distance between the transducers; one easily deduces from it the propagation velocity of the wave in our material. The mechanical properties are in relation to the density and longitudinal and transverse speed [11].

$$V_T = \sqrt{\frac{E \cdot (1 - \nu)}{\rho \cdot (1 + \nu) \cdot (1 - 2\nu)}} \quad (3)$$

$$V_T = \sqrt{\frac{E}{2\rho \cdot (1 + \nu)}}$$

From these formulas, one as follows deduces the properties from elasticity:

$$E = \rho V_T^2 \frac{3V_L^2 - 4V_T^2}{V_L^2 - V_T^2} \quad (4)$$

$$v = \frac{1}{2} \frac{V_L^2 - 2V_T^2}{V_L^2 - V_T^2} \quad (5)$$

RESULTS AND DISCUSSION

Characterization of the matrix

The results of DTA and the TGA of the samples without and with cooking station enables us to determine the temperature of vitreous transition T_g and the fall from mass $\Delta M/M_0$, the results are presented on the table below.

Table1
Results of Thermal analysis

	without heat treatment	With heat treatment
T_g	99,6	137,12
$\Delta M / M_0$	-1,40%	-1,04%

The analysis results show that the glass transition temperature of the heat-treated matrix (post-curing) is higher than that of the untreated matrix. With a full $T_{g\infty}$ crosslinking temperature of the EDGBA resin between 150°C and 200°C, one can calculate the rate of advance of the reticulation by the relation that is based on the diagram of the temperature, the transition, and the time [12].

$$\Delta\tau = \frac{\tau - \tau_0}{\tau_0} * 100 \quad (6)$$

$$\tau = \frac{t_g}{t_{g\infty}} \times 100 \quad (7)$$

From the equations (6) and (7), one can calculate the increase in the crosslinking percentage

$$\Delta\tau = \frac{\frac{t_g}{t_{g\infty}} - \frac{t_{g0}}{t_{g\infty}}}{\frac{t_{g0}}{t_{g\infty}}} \times 100 = \frac{t_g - t_{g0}}{t_{g0}} \times 100 \quad (8)$$

By applying the preceding formula, we obtained for this matrix: $\Delta T = 37,67\%$, this improvement is explained of made that in the ordinary cases, the tertiary amines are steric congestion, and some functional groups remain without crosslinking, the treatment by temperature makes it possible to facilitate molecular mobility and decreases this steric hindrance [13].

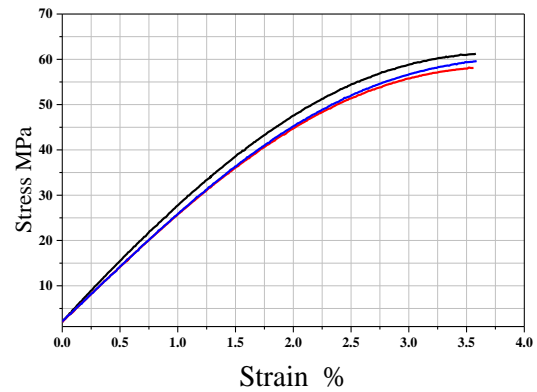


Figure 2
Tensile Behavior of the matrix STR

Figure 3 presents behavior in traction of dumbbell test pieces containing the STR matrix, an elastoplastic behavior of the matrix that is characterized by a Young modulus of 2.53 GPa and a deformation of 3.6%

Characterization of reinforcement

The reinforcement used is a glass fiber oiled of type E with an armor of the taffeta type.

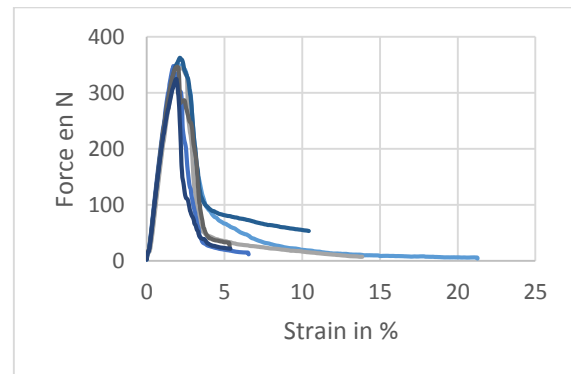


Figure 3
Tensile Behavior of the wicks in glass fiber

The calculation of the shrinkage consists in measuring the deformation of the wicks in the two directions, starting from the tensile test; the deformation is presented in the form of shrinkage. Various measurements show that the values of the undulations are equal in the two directions. The average value of the shrinkage is about 2%. During these tests, the slip of fibers in the wick is due to the oiling, which protects them from brutal shearing. The majority of fibers break with the maximum loading, except for some fibers that slip between them. What explains the appearance of a residual force until the total rupture that varies from 10 with 100N.

The linear part of the curves in the directions chains and screen is identical. One can deduce from it that the wicks used for the two directions (warp and weft) are identical or of present the same characteristics mechanics.

This deduction is confirmed by the comparison between these results and measurements carried out of shrinkage.

Characterization of the laminate

The density is determined according to the method A of standard NF T 51-561. The results obtained from the measurements on three samples give us the average value of 1.9314 g / cm³. The mass ratio is determined by the method of the loss on the ignition, according to standard NF T 57-571 "equations (1)"

Table 2
Values of the mass ratio

Composites containing matrix STR		
Mm	Mf	Rf
7,2147	5,6527	78,35
5,7451	4,5179	78,64
6,3221	4,9413	78,16

By applying the law of the mixtures one can deduce the volume fraction from the reinforcements knowing the densities of the composite (ρ_c) and the fiber which is already calculated ($\rho_f = 2,56\text{g/cm}^3$). One obtains the F_v value = 59, 13%.

The tensile tests are carried out at ambient temperature on a universal machine of type Zwick 250



Figure 5
Breaking mode by tensile test of laminate

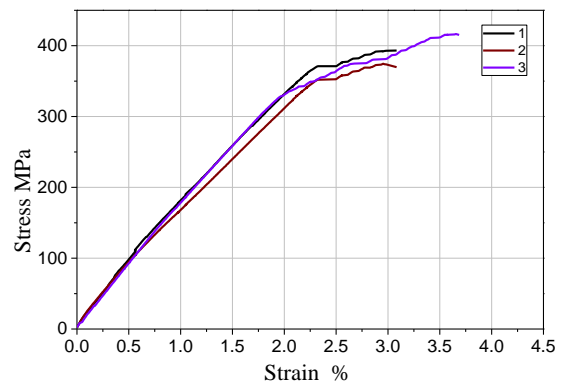


Figure 4
Tensile Behavior of laminates based STR resin

The elasticity of the laminate STR is between 0 and 2%. This value represents the shrinkage of the reinforcement used, the obtained Young's modulus of 17.85 GPa. The plastic range is characterized by two phenomena as shown in Figure 7, namely, delamination and the rupture starting from deformation of 3%. The elastic deformation of the matrix is noted here that is less than the shrinkage of the fibers used which gives us a value of deformation around 2%, which remains within the range of elasticity of the laminate composite; the matrix is not in its elastic range.

The creep test protocol is to apply 50% of stress of breakage during 100 hours, figure seven present the evolution of deformation and module according to time

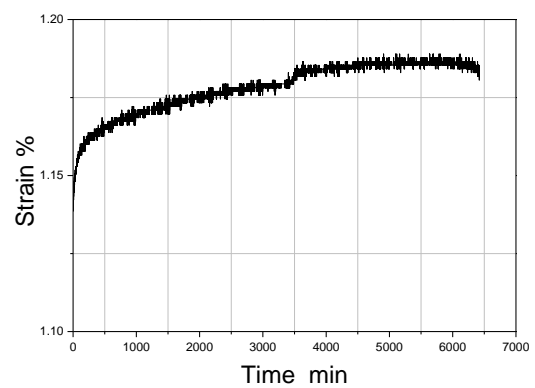


Figure 6
Creep strain at 50% of ultimate stress

With determination coefficient $R^2 = 0.9488$ logarithmic model creep behavior is given by

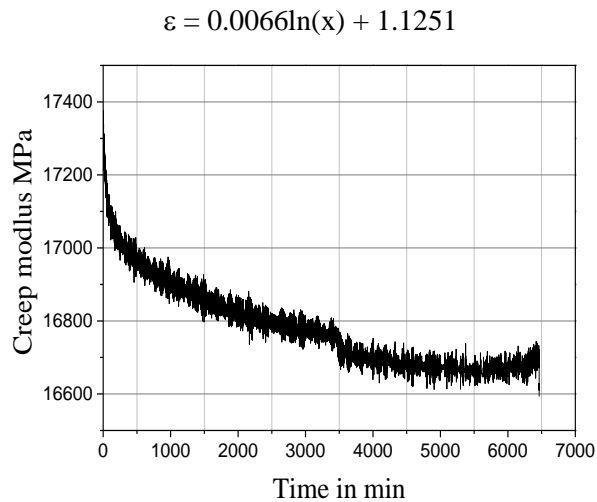


Figure 7
Creep modulus versus time

The creep modulus in function of time is shown in Figure 7, the variation of this module is in connection with the evolution of deformation knowing that the constraint is fixed in time, in correlation with the previous formula may deduct the evolution of creep modulus in time by:

$$E = E_0 / 0.0066\ln(t)$$

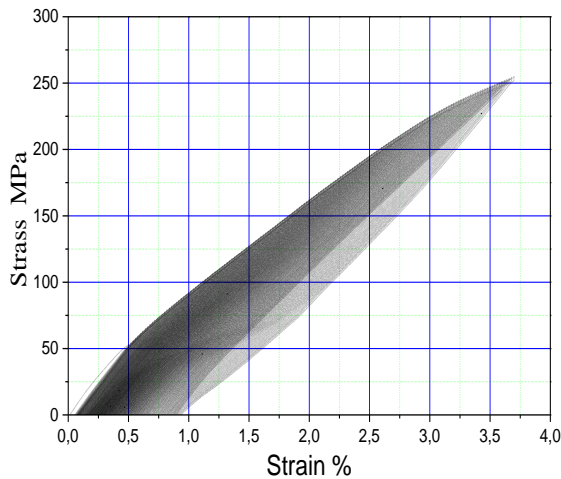


Figure 8
Cyclic tensile test

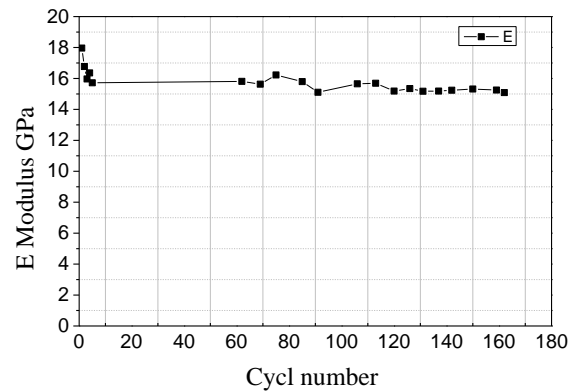


Figure 9
Creep modulus versus time

The results do not show a drastic change in the Young's modulus, but a remarkable decrease of tensile strength, we note the same deformation of the static test, which shows that the failure mechanism may be caused by brutal propagation of micro-cracks or delamination to some level of load. The test of nondestructive testing of laminated composite plates, by using the acoustic waves in the directions transverse and longitudinal gives us the following figure 9, speed is directly given by dividing the thickness of the work piece (course path by wave) by the time passed during this course.

From these echoes, one determines transverse speed, longitudinal speed and the Young modulus by using the equations (3), (4) and (5); the following table presents these values.

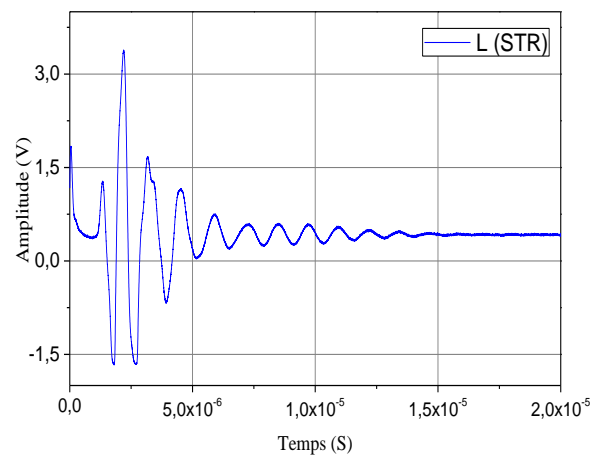


Figure 9
Propagation of longitudinal wave

Table 3

Values of ultrasonic velocity and modulus

matrix composites STR		
V_L (m/s)	V_T (m/s)	E (GPa)
1886,55	1082,67	17,25

The Young modulus obtained for the laminates at base of STR matrix are respectively lower by 0, 60 GPa compared to the results of the destructive tests. These differences are due to what follows:

The agent of coupling which can generate attenuations of the ultrasonic waves; the specimen surface quality; the porosity of composite materials.

This measurement technique method is said of the building site.

These variations are lower than 4%, which makes it possible to accept the values obtained starting from measurements by ultrasound, and see the usefulness of this technique to determine the mechanical characteristics without destroying the parts analyzed

CONCLUSIONS

The general axis of our set of themes is articulated around the mechanical behavior of laminate at base of the epoxy matrix vitrified by mixture with different hardeners, within this framework, we started with the use of an aliphatic amine. This mechanism of reticulation allows obtaining a matrix with an elastoplastic behavior, the elastic strain is lower than 2%, and this value presents the shrinkage glass fibers used in the form of weaving taffeta.

The results obtained show the need for heat treatment in the case of a reticulation by aliphatic amines, which are characterized by their high reactivity.

With regard to the mechanical behavior, the elastoplasticity of the epoxy matrix shows that the rate of reticulation is partial because these types of materials are in general thermo hardening with a three-dimensional vitrified network.

Laminates elaborate presents an elastic behavior being able to reach a value of 2%, whereas the matrix in this phase is under plastic deformation, this anomaly is the source of several findings on the creep behavior or relaxation in the elastic range.

The nondestructive testing carried out shows its utility as a means of calculation and elastic study of the parameters of material.

REFERENCES

- Jean-Pierre Pascault and Roberto, J. J. Williams, 2010. Epoxy Polymers. WILEY-VCH Verlag GmbH & Co. KGaA, Weinheim ISBN: 978-3-527-32480-4.
- Haward, R. N. and Young. R. J. Eds., 1989. The Physics of Glassy Polymers, 2nd Ed., Chapman & Hall, London.
- F. Dal Maso et J. Meziere, Calcul des propriétés élastiques des tissus utilisés dans les matériaux composites, Oil & Gas Science and Technology - Rev. IFP 53 6 (1998) 857-870.
- Gillham, J.K. Curing, Encyclopedia of Polymer Science and Engineering 4, Wiley-Interscience 2nd edition 1986.
- C. Barrere and F. Dal Maso, Résines époxy réticulées par des polyamines : structure et propriétés, Oil & Gas Science and Technology - Rev. IFP V. 52, Numéro 3, Mai-Juin 1997.
- [9] ACI 440.4R-04. Prestressing Concrete Structures with FRP Tendons, American Concrete Institute, 2004.
- Edward M. Petrie, Epoxy Adhesive Formulations, McGraw-Hill Professional Publisher DIO: 10.1036/0071455442, 2005, ISBN 0071455442.
- John M. Barton. The application of differential scanning Calorimetry (DSC) to the study of epoxy resin cure reactions. Advances in Polymer Science, 72:111–154, 1985
- R. Ho, Handbook of Univariate and Multivariate Data Analysis and Interpretation With SPSS, Chapman & Hall/CRC, Boca Raton, Florida, 2006.
- P. Meshgin, K.K. Choi, M.M.R. Taha, Experimental and analytical investigations of creep of epoxy adhesive at the concrete-FRP interfaces, Int. J. Adhes. Adhes. 29 (1) (2009) 56–66.
- M. WANIN, Évaluation non destructive de la qualité des matériaux (Partie 1), Techniques de l'Ingénieur M 4 130 – 2.
- S. Gan, J.K. Gillham, R.B. Prime, A Methodology for characterizing reactive coatings: time-temperature-transformation (TTT). Analysis of the competition between cure, evaporation and thermal degradation for an epoxy-phenolic system, J. Appl. Polym. Sci., 37,803-816 (1989).
- M. Aufray, Caractérisation physico-chimique des interfaces époxydamine/oxyde ou hydroxyde métallique et de leurs constituants, Thèse de doctorat, École doctorale des matériaux de Lyon (2005).

MICROSCOPIC SWELLING ANALYSIS OF SPRUCE WOOD IN SORPTION CYCLE

C. El Hachem^{1*}, K. Abahri¹, R. Bennacer¹

¹ LMT, ENS-Cachan, CNRS, Université Paris Saclay, 61 avenue du Président Wilson, F-94230 Cachan, France

*Corresponding author: Phone: +33 01 4740 6827 Email: elhachem@lmt.ens-cachan.fr

ABSTRACT

Depending on drying or humidification conditions, spruce wood tends respectively to shrink or swell, because of internal mechanical stresses that cause microscopic morphological changes.

In the present paper, an experimental campaign is performed at the microscopic scale, in order to study the structural changes caused by relative humidity solicitations along the sorption cycle, for both early wood and latewood phases.

That is why many specimens were scanned at different relative humidity levels using X-ray tomography. Relative humidity conditioning was successful by designing a specific device adapted to tomography. The obtained resolution using X-ray tomography was 3.3 μ m/pixel. After that, the reconstructed volumes were post-treated using adapted software to spruce wood, iMorph.

Fibers' thicknesses' and pores' diameters' have been calculated at each humidity state. These results have given much better understanding of the localized phenomena that take place at the fiber's scale.

INTRODUCTION

Use of wood is essentially based on its energetic performances. In construction, spruce wood is particularly used for isolation and mechanical purposes, being a material that guarantees all functions: structural, thermal isolation and acoustic isolation.

Upon age, spruces grow by reproducing through layering. Each layer represents one year cycle in which early wood grows in spring and early summer, followed later by the latewood development [1]. However, spruce wood is a hygroscopic material, which makes it very sensitive to humidity, especially when subjected to high relative humidity levels. At the macroscopic scale, sorption and desorption cycles are respectively marked with swelling and shrinkage [2]. Actually, these macroscopic dimensional changes are the consequences of many microscopic coupled phenomena, related to moisture and heat transfers, to the anisotropic and heterogeneous morphology, as well as the swelling and shrinkage stresses fields of fibers [3].

Although some authors achieved studies concerning the microscopic role of complex wood fiber

interaction on swelling and shrinkage [4], these phenomena has not been mastered yet. On the other hand, some authors evaluated wood fiber mechanical behaviors. For example, [5] treated the internal wood's structure influence on its water-resistance. In addition, [6] evaluated the axial compression of spruce wood. [7] has made a three point bending test on spruce wood. These works treat wood and more specifically fiber's responses due to either hygric or mechanical solicitations.

Hence the necessity of conducting new experimental campaigns, in order to have much better understanding of localized fiber's behaviors when subjected to humidity conditioning. Once the literature is provided with enough information describing these phenomena, all the experimental results will serve to develop a representative model on the microscopic scale.

In this paper, an experimental work has been achieved at the microscopic scale, concerning spruce wood swelling evaluation along the sorption cycle. A new device has been designed in order to maintain a constant relative humidity while scanning. Then, after achieving the tomography scans, the corresponding volumes were reconstructed and post processing was performed using iMorph software.

Pores' diameters, fibers' thicknesses, and porosity were calculated for each relative humidity level, which led to have access to all these parameters' evolutions along the sorption cycle.

MATERIALS AND METHODS

On the microscopic scale, spruce wood is a heterogeneous material that contains tracheids, parenchyma and pores. Early wood cells are characterized by having relatively large cavities and thin walls. During a cycle, the transition from early wood to latewood is marked by the tendency of the cells reproduction to have smaller diameters and thicker walls. At the end of a cycle, latewood is characterized by the smallest cavities and the thickest walls [8] (Fig. 1).

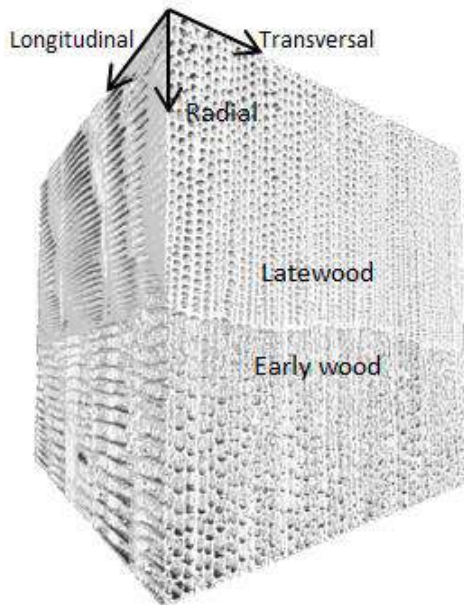


Fig. 1: 3D view of wood specimen containing both early wood and latewood phases.

Specimen preparation: First of all, and in order to select the correct specimens' dimensions, a morphological study was achieved. Early wood and latewood structural properties were studied by some researchers. For example, [9] calculated the walls' thickness of spruce wood for the transition early wood/latewood in tangential and radial directions, and respectively found average values of 2.99 μm and 3.16 μm . These authors calculated also the diameter of the tracheids for the same transition of wood in tangential and radial directions, and respectively found average values of 35.3 μm and 35 μm . [1] calculated a diameter of 50 μm for the tracheids of early wood. [1] calculated also a porosity of 79% for early wood and 27% for latewood.

Taking into consideration the small tracheids' thicknesses and pores' diameters, a high resolution in the tomograph was required. Therefore, in order to have access to the material's microstructure, small specimens were prepared. The specimens were taken from early wood and from the transition latewood/early wood. This choice was made to compare both types of wood, as well as to quantify the influence of the latewood/early wood discontinuity on the hygric transfer. In addition, the repeatability of each test was verified, by testing three specimens for each essay, with the same imposed conditions. Six spruce wood specimens of dimensions 3x3x20 mm^3 were prepared. The tracheids' direction, noted as well the longitudinal direction, was along the 20 mm side. Three of those specimens contained a part corresponding to the latewood/early wood discontinuity and the rest were cut from the early wood phase. All the scanned samples were without decay, knots and obvious defects.

Concerning the protocol of moisture's influence on the morphological properties of spruce wood, the specimens had to be conditioned at maintained relative humidity levels and constant 25°C temperature. Firstly, the conditioning was achieved by using oven drying at 50°C (for dried condition only) and saline solutions. The sorption cycle is studied, and the adapted relative humidity levels are: 60% RH, 72% RH and 95% RH. These values cover sufficiently the sorption cycle, and more specifically the hygroscopic zone (from 60% to 95%), and allows quantifying the swelling phenomenon at the microscopic scale through pores and solid granulometries comparison, and porosity evaluation.

Every time a specimen is subjected to new relative humidity conditions, it undergoes microstructural changes, due to the evolution of the water content distribution caused by the sorption phenomenon. Once the water content and distribution in a specimen don't evolve anymore, it is considered to have reached its mass equilibrium, and is ready to be scanned. Therefore, for each moisture stage, a regular monitoring of mass sample in time is undertaken. The mass equilibrium depends on the relative mass expression, which is function of the specimen's mass at times t and $t-24$ hours, noted $m(t)$ and $m(t-1)$ respectively, and should verify condition (1) [10]:

$$\frac{m(t) - m(t-1)}{m(t)} < 0.01 \quad (1)$$

Adapted X-ray Tomography for RH conditioning:

As already mentioned, X-ray tomography was used in this work, in order to have access to the localized details within the material [11]. X-ray tomography is a non-destructive method, which allows having 3D images of a defined volume. The resolution of those images is function of many parameters, like the distance between the source and the specimen. This parameter is directly related to the dimensions of the specimen. In this study, all the specimens were scanned with the tomograph X50 at LMT Cachan, and the resolution reached was $3.3 \times 3.3 \times 3.3 \mu\text{m}^3$. With such voxel size, the different heterogeneities in this material could be finely identified, like pores and fibers.

On the other hand, considering that wood is a weakly absorbing material, a special treatment was required to perform imaging scans. Therefore, many tomography tests were achieved and analyzed. A choice of using a low voltage of 80 kV and an emission current of $50 \mu\text{A}$ were selected for all the tests treated later on in this study.

Beside the used tomography parameters, it was primordial to isolate the tested specimen from all hygric transfer through the scan. Actually, the most important condition to obtain clear images, is that the specimen don't have to move while scanned, and specifically don't have to be subjected to microscopic morphological changes. This happens because the specimen is subjected to a new relative humidity level, which makes it look for a new mass equilibrium. In our study, the specimens should have small dimensions in order to have a high resolution in the tomograph, and each one should conserve its moisture content level during the scan.

Thus, the challenge here was to maintain constant relative humidity conditions for such small dimensions of specimen. In addition, another challenge in this study was to refix the specimen at its initial position inside the tomograph, in order to succeed the comparisons protocol between many scans. For that, a new device adapted to X-ray tomography concerning such dimensions of specimens was designed (Fig. 2). It was made using the 3D printer. This device is constituted of a tube attached from one side to the rotation device and from the other side to a piece on which another piece where the specimen was glued should rely inside the tomograph, and a cover. The cover was put inside the conditioning room with the specimen. When the specimen reached its mass equilibrium, it was covered inside the conditioning room, and taken inside the tomograph to be scanned. That way, the

specimen should remain in the same humidity atmosphere while scanning, and the transfers were minimized as much as possible. After achieving many scans, this technique has led to very satisfying results and clear volume reconstructions.

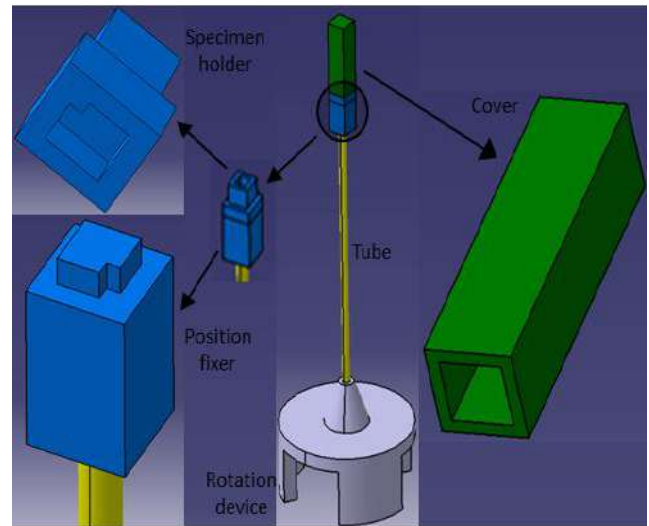


Fig. 2: Device adapted to maintain the sample's conditioning inside the tomograph.

Once the volume reconstruction has been completed, the post-processing has been made using iMorph software [12]. Pores' and fibers' granulometries have been calculated, and they refer respectively to pores' diameters and fibers' thicknesses distributions. The corresponding results permit to verify the local morphological changes due to many hygric solicitations.

RESULTS AND DISCUSSION

Wood is a multiphase material. It contains air, liquid water and vapor. Unfortunately, water is hierarchically distributed inside. Hence, it is essential to use a powerful procedure in order to distinguish these phases and how this water interacts with the material solid matrix. The obtained resolution of $3.3 \times 3.3 \times 3.3 \mu\text{m}^3$ in the tomograph, was sufficient to distinguish the different heterogeneities of this material. The fibers and the pores were easily identified.

Taking into consideration the anisotropy and heterogeneity of spruce wood microstructure, it is evident that the hygric transfer in this material can favor a direction among others. For example, the transfers' kinetic toward longitudinal direction is surely faster than the one toward transversal and radial directions. Therefore, it is essential to study the hygric transfers at the microscopic scale, and

understand the hygric and mechanical coupling, leading to wood swelling.

Swelling analysis: In this part, the swelling due to hygric solicitations is investigated. Three early wood specimens and three specimens with latewood/early wood discontinuity were treated, at dried and controlled relative humidity conditions of 0%, 60%, 72% and 95%.

The pores' diameters and fibers' thicknesses of an early wood specimen at all the RH levels are respectively presented in Fig. 3 and Fig. 4.

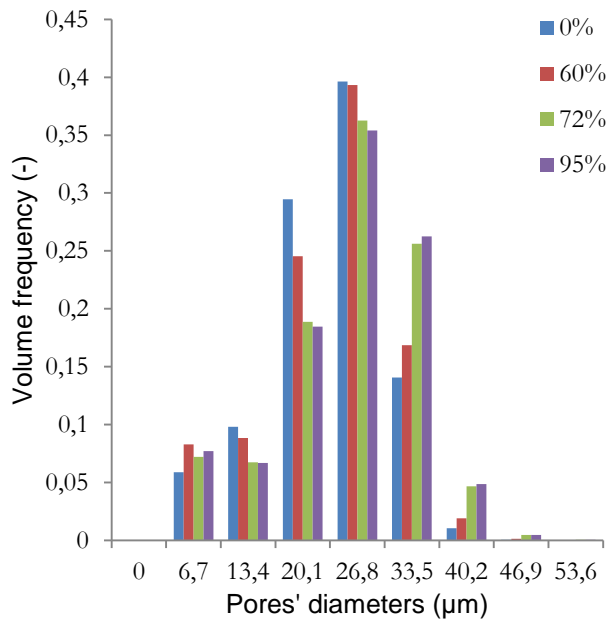


Fig. 3: Pores' diameters' distribution of an early wood specimen at different relative humidity levels.

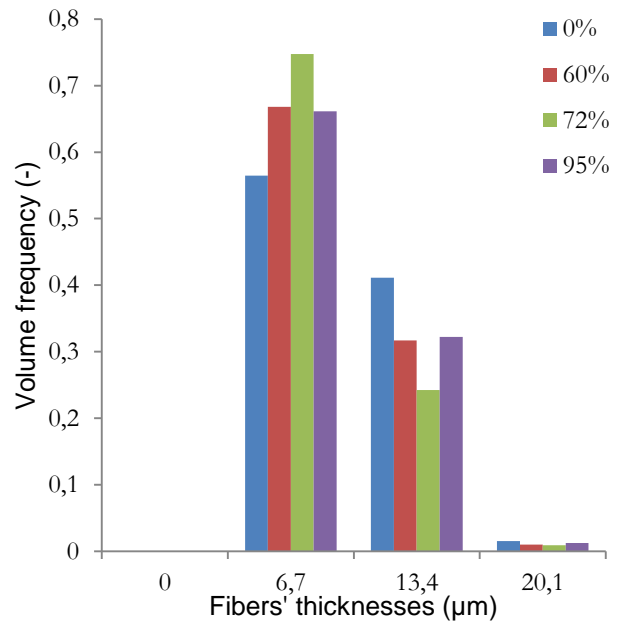


Fig. 4: Fibers' thicknesses' distribution of an early wood specimen at different relative humidity levels. Concerning the pores' diameters distribution, it is remarkable (Fig. 3) that for all the RH levels, the average early wood pores' diameter is 26 µm. On the other hand, comparing the results of 0% RH, 60% RH and 72% RH, it is evident that bigger is the RH, more the pores' diameters' distribution tends to contain much more big pores, and much less small pores. Concerning the fibers' thicknesses distribution, when the RH gets higher, the fibers' thicknesses decrease.

Comparing these results to the ones corresponding to 95% RH, it appears that the pores' diameters' distribution at 95% RH increases and the fibers' thicknesses' distribution increases.

After that, the same treatment was made concerning the specimen with latewood/early wood transition. The corresponding pores' diameters and fibers' thicknesses at 60%, 72% and 95% RH are respectively presented in Fig. 5 and Fig. 6.

These figures show the same evolution (Fig. 5 and Fig. 6), concerning either pores' diameters or fibers' thicknesses for 60% and 72% RH. When the RH increases, the corresponding pores' diameters distribution tends to have bigger pores.

All results show that the early wood and latewood fibers' behavior don't differ in terms of distribution evolution along sorption cycle.

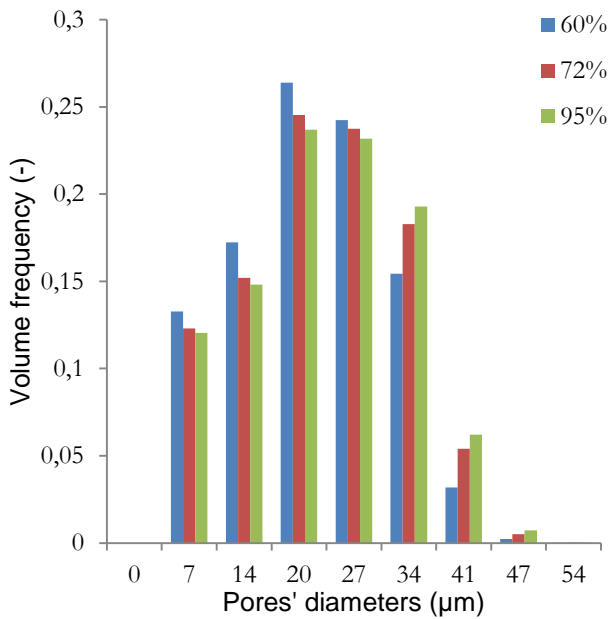


Fig. 5: Pores' diameters' distribution of a specimen with latewood/early wood transition at different relative humidity levels.

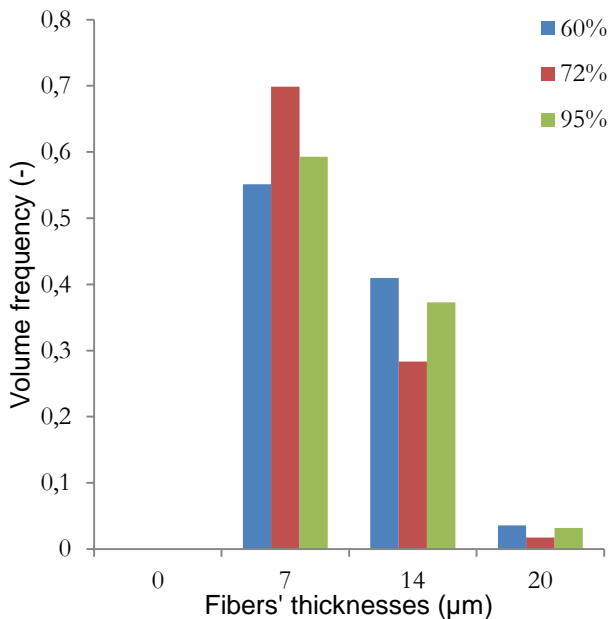


Fig. 6: Fibers' thicknesses' distribution of a specimen with latewood/early wood transition at different relative humidity levels.

The physical explanation for the results corresponding to 0%, 60% and 72% RH is that when the fibers absorb water, they swell, which leads to have an increasing pores' diameter. On the other hand, the fiber's Poisson ratio leads to have a contraction perpendicular to the swelling direction, and the fibers' thicknesses decrease. Because of all these mechanical phenomena, resulting from hygric solicitations, the pores' diameters get bigger, and the fibers' thicknesses get smaller. However, this

microscopic behavior is the cause of the macroscopic swelling.

Concerning the 95% RH, the results for all specimens are coherent. On the other hand, they are not easy to interpret, especially that at 95% RH, the fibers contain free water, because of the high water content. A conceivable hypothesis that explains these results is that the free water within the material influences the scan's reconstruction especially that this water is either in pores' or fibers' voxels. However, this remains a question that needs a precise answer, especially that the results' interpretation at high relative humidity level can be improved by using other adapted techniques.

CONCLUSIONS

In this work, an experimental procedure has been achieved, concerning spruce wood microscopic behavior when subjected to different relative humidity conditions along the sorption cycle. This work describes very well the hygro-mechanical coupling of localized fibers.

The results show that until a relative humidity of 72%, the fibers absorb water, which make them swell. On the other hand, they present a retraction perpendicularly to the swelling direction. Therefore, the structural consequences are that fibers' thicknesses decrease, and the pores' diameters increase.

For higher relative humidity state, the results don't present the same tendency. This may be because of the presence of free water within the material.

REFERENCES

1. Sedighi-Gilani, M, Boone, M.S, Mader, K, Schwarze, F.W.M.R, 2014, Synchrotron X-ray micro-tomography imaging and analysis of wood degraded by *Physisporinus vitreus* and *Xylaria longipes*, *Journal of Structural Biology*, 187, pp. 149-157.
2. Virta, J, Koponen, S, and Absetz, I, 2006, Measurement of swelling stresses in spruce (*Picea abies*) samples, *Building and Environment* 41, pp. 1014-1018.
3. Rafsanjani, A, Lanvermann, C, Niemz, P, Carmeliet, J, et al., 2013, Multiscale analysis of free swelling of Norway spruce, *Composites: Part A*, 54, pp. 70-78.
4. Rafsanjani, A, Derome, D, Wittel, F.K, and Carmeliet, J, 2012, Computational up-scaling of anisotropic swelling and mechanical behavior of

- hierarchical cellular materials, *Composites Science and Technology*, 72, **pp.** 744-751.
5. Li, W, Bulcke, J.V, Mannes, D, Lehmann, E, et al., 2014, Impact of internal structure on water-resistance of plywood studied using neutron radiography and X-ray tomography, *Construction and Building Materials*, 73, **pp.** 171-179.
 6. Gindl, W, and Teischinger, A, 2002, Axial compression strength of Norway spruce related to structural variability and lignin content, *Composites: Part A*, 33, **pp.** 1623-1628.
 7. Forsberg, F, Sjö Dahl, M, Mooser, R, Hack, E, et al., 2010, Full Three-Dimensional Strain Measurements on Wood Exposed to Three-Point Bending: Analysis by Use of Digital Volume Correlation Applied to Synchrotron Radiation Micro-Computed Tomography Image Data, *Strain*, 46, **pp.** 47-60.
 8. Trechsel, H.R, 2001, *Moisture Analysis and Condensation Control in Building Envelopes*, ISBN 9780803120891, ASTM International.
 9. Trtik, P, Dual, J, Keunecke, D, Mannes, D, et al., 2007, 3D imaging of microstructure of spruce wood, *Journal of Structural Biology*, 159, **pp.** 46-55.
 10. EN ISO 2001, 2001, *Hygrothermal performance of building materials and products - Determination of hygroscopic sorption properties*, ISO12571.
 11. Mayo, S.C, Chen, F, and Evans, R, 2010, Micron-scale 3D imaging of wood and plant microstructure using high-resolution X-ray phase-contrast microtomography, *Journal of Structural Biology*, 171, **pp.** 182-188.
 12. Brun, E, Vicente, J, Topin, F, Occelli, R, et al., 2009, *Microstructure and Transport Properties of Cellular Materials: Representative Volume Element*, *Advanced Engineering Materials*, 10, **pp.** 805-810.

HYDRIC AND STRUCTURAL APPROACHES FOR EARTH BASED MATERIALS CHARACTERIZATION

Boudjemaa REMKI^{1,2}, Kamilia ABAHRI³, Rafik BELARBI², Mahmoud BENSAIBI²

¹E.N.ST.P, Garidi Kouba, 16051 Alger

²Université de La Rochelle, LaSIE UMR 7356 CNRS, Avenue Michel Crépeau 17042 La Rochelle Cedex 1
France

³LMT, ENS-Cachan, CNRS, Université Paris Saclay, 61 avenue du Président Wilson, F-94230 Cachan,
France

*Corresponding author: Fax: +33 1 47 40 74 65 Email: kamilia.abahri@lmt.ens-cachan.fr

ABSTRACT

The earth-based material considered in this work is called Stabilized Earth Brick (SEB). Two distinguish type of SEB were examined: SEB5-Tu and SEB5-Te; their difference refers to the freestone, or the red earth composition. Firstly, a morphological characterization has been done by comparing two different approaches: the water porosity test and the mercury porosimetry which provide access to the material porosity and the pore size distribution.

Then, the sorption-desorption isotherm were carefully evaluated for each SEB type. The dynamic gravimetric method was selected for such measurement. Further, theoretical modeling of the sorption desorption isotherm was investigated; here the model parameters allow more accurate interpretation of experimental results.

Most of these measurements provided the hygric and structural characteristics relating to the SEB materials and a comparison of their characteristics depending on the variation of their compositions.

KEYWORDS

Porosity, experimental characterization, sorption desorption isotherm, Stabilized Earth Brick, moisture storage capacity.

INTRODUCTION

The objectives set for builders are mainly related to minimize energy costs, improve the comfort inside the living space by using sustainable and inexpensive materials. So, materials based on earth respond to the problem of natural resources' depletion and were, naturally, used for millennia. However, the major drawback of their use is their low resistance to erosion by rain and their tendency to swell or shrink after a number of humidification or drying cycles. The resulting dimensionless variations lead generally to dramatic modification of the thermophysical properties of these materials. To overcome these difficulties, a compaction of tempered based-earthed mixture is recommended to increase the material strength. Also, the addition of small stabilizers quantities such as cement, lime and bitumen is well

adopted to reduce its water sensitivity. The resulting material is then called Stabilized Earth Brick (SEB). Two distinguish type of SEB were examined here (SEB5-Tu and SEB5-Te); their difference refers to the cement, freestone, and sand percentages.

The thermophysical properties of these materials and their impact on the hygrothermal behavior and consequently the thermal building comfort have been little investigated by researchers. In other manner, characterizing correctly materials, involves precise answer one the essential properties and how accurate they must be defined to perform the heat and mass energy impact questions.

The studied materials' are porous structure within which water, liquid or vapor may migrate, be stored or returned to the indoor environment. The non-regulation of the humidity rate inside the

compartment is a major cause of damage to the walls of the building; in fact, besides the problems of durability that can be generated, the thermal performances are substantially modified.

That's why, in this study we propose in a first step to characterize the SEB materials porosity and morphology, to better identify the microstructure of these material since the macroscopic behavior of materials is highly dependent on the mechanisms involved at the microscopic scale. Then, a hygrothermal characterization is performed through the measurement of the sorption desorption isotherm. The determination of these characteristics allow, in a future step, to perform simulations based on the HAM models [1, 2, 3] to predict the behavior of the walls in SEB and improving building efficiency energy.

EXPERIMENTAL CHARACTERIZATION

Studied material: Two categories of Stabilized Earth Brick (SEB) materials were selected for the present study (see table 1). They were classified by the National Center for Studies and Research for integrated Building in Algiers (CNERIB) [4].

Despite their thermal insulation performance and low cost, these materials, different from conventional one, are little used. The improvement of earth materials becomes today possible du to two important actions that are chemical stabilization and compaction process. Stabilization step reduces the pore volume and thus increases the strength of the SEB. On the other side, compaction ste, using a manual or semi-industrial press, induces an increase in the density of the material and also contributes to the mechanical strength.

The manufacturing process follows the classical screening stages, blending, compacting and molding. The detailed composition of the tested SEB materials is shown in Table 1. The detailed compositions are referenced to the CNERIB [5].

Table 1
Compositions of the studied materials

SEB 5	70% of sand	25% of toffee	5% of
Tu	(0.2-0.8mm)	(0.2mm)	cement
SEB5	70% of sand	25% of red	5% of
Te	(0.2-0.8mm)	earth	cement
		(0.2mm)	

Microstructural characterization method:

Mastering SEB's structural morphology is primordial; to better understand its response when subjected to hygrothermal solicitations. In fact, several studies have shown the close link between the topology of the environment and these hygrothermal transfers [6, 7]. Among the most influential parameters on these transfers, we find the porosity and the pore size distribution.

Two main experimental protocols were used and compared to evaluate this parameter: water porosity and mercury intrusion porosimetry.

Water porosity: The water porosity is measured according to the protocol defined by the AFPC-AFREM [8] and its expression is given by (1):

$$\varepsilon_{eau} = \frac{M_{sat} - M_{sec}}{\rho_{eau} V_0} \quad (1)$$

Where, M_{sec} is the mass of the sample in the dry state (kg), M_{sat} is the mass of the sample in the saturated state (kg), ρ_{eau} is the water density (kg/m^3) and V_0 is the total volume of the sample (m^3) obtained by geometrical measurement or by hydrostatic weighing.

M_{sec} was measured after drying in a ventilated oven at 45°C instead of 105°C to avoid degradation of the microstructure of the SEB material. The dry mass is reached when the relative weight loss does not exceed 0.05% after 24 hours in the oven.

In addition to the porosity, we can also calculate the density of the material ρ and the moisture content u in the saturation (100% relative humidity) by the following expressions:

$$\rho = \frac{M_{SEC}}{V_0} \quad (2)$$

$$u = \frac{M_{sat} - M_{sec}}{M_{sec}} \quad (3)$$

Mercury intrusion porosimetry (MIP): Mercury intrusion porosimetry method is widely used for investigating the materials texture at different scales: micro, meso and macroscopique. It provides access to the porosity of the sample, bulk density, or distribution of pore size.

The test involves injecting mercury into the sample by successive levels of pressure; at equilibrium, the volume of the injected mercury is measured automatically. The method is based on the model of parallel cylindrical pores with different radii. The pore diameter is thus determined by Laplace's law:

$$d = -\frac{4\gamma_{Hg}}{P_c} \cos\theta \quad (4)$$

Where, γ_{Hg} is the surface tension of mercury (the used value is 0.00485 N/cm), θ is the contact angle between mercury and the porous solid (the used value is 130°), P_c is the mercury capillary pressure up to 411Mpa.

The tests were performed using the manufacturer's porosimeter Micromeritics type Autopore III9420. It covers a range of pores varying from 0.003 to 360 μ m.

Sorption desorption isotherm: The characterization of the hygric behavior of a porous material is often presented in terms of isothermal sorption and desorption in the hygroscopic domain. These curves express the variation of water content u according to the Relative Humidity RH . The shape of these curves depends especially on the porosity, the particle size and the mineralogical composition of the sample.

These curves remain poorly studied, on the SEB materials, given the slow kinetics of transfer by using the conventional method of salt solutions [9]. Thus, the recourse to other methods to reduce the time for obtaining these curves by dynamic tests is much appropriated. The used equipment in our case is the Dynamic Vapor Sorption (DVS).

In the measurement protocol, we define the levels of relative humidity in adsorption and desorption cycle at a given temperature and we fixed the mass controlling criterion $\frac{dm}{dt} \leq 2.10^{-4}$, that depends on the relative humidity stage too.

In order to understand the hydrothermal behavior of the two SEB materials, the curves of sorption-desorption isotherms were plotted for the two samples, previously crushed, having masses of 0.924g for SEB 5Tu and 0.834 g for the SEB 5Te.

RESULTS AND DISCUSSION

This section is devised into three parts. The first one corresponds to the water and mercury porosity evaluation and comparison that were extended to the standard materials (High performance concrete and clay brick); the second one corresponds to the sorption desorption isotherm analysis. Further, theoretical modeling of the sorption desorption isotherm was investigated; here the model parameters allow more accurate interpretation of experimental results.

Porosity: The table 2 shows the results of water porosity, Mercury Intrusion Porosity (MIP) and material density.

We notice a difference between the water porosity and the MIP. This latter, in most cases, relatively presents lower porosities values. This reflects the fact that the porosity by mercury intrusion covers only a narrow range of pores compared to that by water intrusion. On the other side, the bulk densities are obtained in the same range.

Table 2
Materials characteristics

Material test		Density(kg/m ³)		Porosity (%)	
		Water Porosity	Mercury intrusion porosity	Water Porosit y	Mercury intrusion porosity
SEB 5Tu	5	1936.27	2145.80	33.83	33.29
SEB 5Te	5	2201.38	2266.10	32.44	31.65

Porosities of the SEB materials are represented in Fig. 1 (between 30% and 35%) and compared to those of baked clay bricks (25 to 34%) and high performance concrete where the porosity varies from 10 to 15%. A significant gap was registered between these two latter.

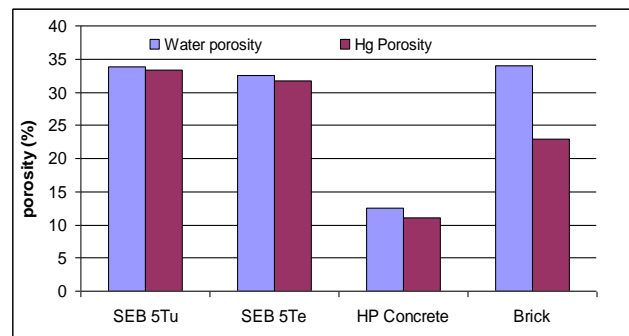


Figure 1

Comparison of porosity of various materials obtained by water porosimetry and mercury intrusion

The differences between the MIP and the water porosity are less important for the SEB materials and concretes unlike the clay brick. In the latter case, the clay particles fuse during the firing time and often have a porous space with a high specific surface area attributed to an effect of micro-

roughness of walls rather than an effective pore volume. This explains the fact that the mercury porosity is much lower than water porosity.

Fig. 2 shows the pore size distribution of the two studied SEB materials. It covers a wide range of pore sizes from 0.03 μm to 300 μm . Both materials cover the range of macropores but the difference lies in the fact that SEB 5Tu is bimodal. This is certainly related to its composition, in which, we note the presence of limestone which is composed mainly of calcite ($\approx 50\%$). This preponderance could explain the appearance of a separate mode, the addition of cement and sand in the composition introduces an additional porosity. However, the SEB 5Te contains the red earth, which consists of silica, alumina, kaolin and iron oxide (red color comes from the presence of the latter). In this case, the physicochemical interactions between these various components make that the porosity is obtained on a single mode.

The SEB 5Te presents one main mode between 0.1 μm and 1 μm , on the other side, two main modes were distinguished for the SEB 5Tu, they are between 0.03 μm and 0.1 μm and between 12 μm and 20 μm , respectively. These results show that the SEB 5Te is fully macroporous, while SEB 5Tu has mesoporous preponderance with macro porous tendency.

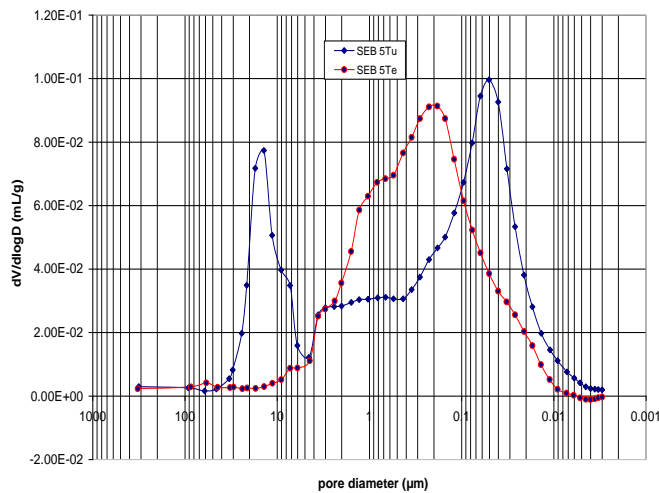
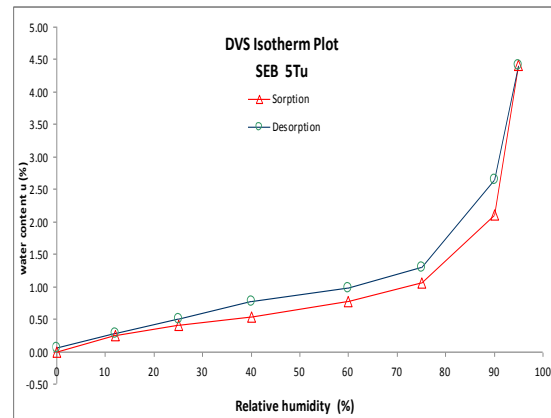


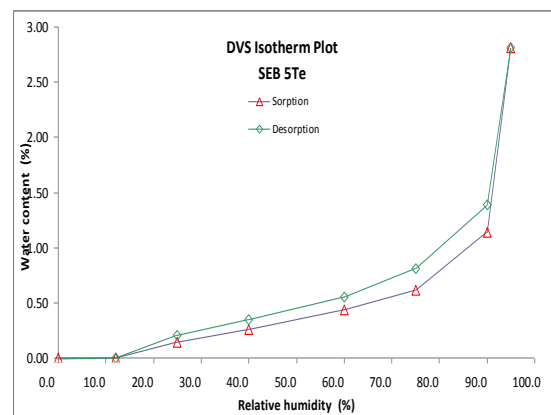
Figure 2
SEB material's pore size distribution

Adsorption-desorption kinetics: Figures (3a) and (3b) present the sorption-desorption isotherm at 25°C for bricks SEB 5Tu and SEB 5Te, respectively. The tests were conducted on samples of equivalent masses at 0.92g and 0.83g, respectively. The

maximum obtained water contents, at RH = 95%, reached 4.5% for the SEB 5Tu and 2.8% for SEB 5Te. The saturation and super-saturation capillary (liquid phase) regimes are not reached by the DVS method because; it's asking a very long time to reach equilibrium levels. As indication, the water content at saturation, measured by the water porosity test, is around of 17.53% and 14.74% for samples of SEB 5Tu and SEB 5Te, respectively. The difference in behavior of both materials is due to their porosity: the pore size distribution is wider and the specific surface is larger for the SEB 5Tu due to its bimodal pores morphology (mesopores and macropores) which favors water adsorption. In fact, the porous structures play different role during adsorption and desorption cycle: the phenomenon of capillary condensation appears for the higher relative humidity, and distribution of pore sizes, in this case, plays a very important role. Distribution space and connectivity, in turn, determine desorption.



(a)



(b)

Figure 3

Curves of sorption-desorption isotherms

According to the figures (3), the difference in water content at equilibrium between sorption and desorption over the entire range of relative humidity present a hysteresis of type H3 for such SEB materials. This difference is minimal in comparison with other materials such as concrete [9] and reflects, in part, the amount of water strongly bound.

The shape of sorption curves is similar for both SEB materials: after a slight dip to 12% relative humidity, there is an almost linear variation of water content till 80% RH. Between 80 and 95% HR, the increase is very significant: a factor of 4.5 and 3, respectively, for the SEB 5Tu and SEB 5Te is observed (the water content increases from 1% to 4.5% and 2.8%).

The interpretation of the obtained adsorption desorption isotherms can be based on the classification described by Brunauer et al [10]. and adopted by the IUPAC [11]. Indeed, as has been previously noted, two inflection points were found (around 12% and 80%) on adsorption curves (Figures 3(a) and 3(b)). It's reflected in the fact that isotherm is of type II according to the classification of IUPAC [11].

Modeling of the sorption desorption isotherm:

Literature gives a considerable number of models describing the adsorption [12]. Models BET, GAB and GDW are most used in the civil engineering community and are all based on the theory of Langmuir:

- The model BET (Brunauer, Emmett and Teller) predicts that the adsorption occurs on identical sites energetically; this implies the consideration of homogeneous surfaces and several layers can be superimposed on the first adsorbed layer [10]. The BET model equation is then written as following:

$$u = \frac{u_m CRh}{(1 - Rh)(1 + (C - 1)Rh)} \quad (5)$$

With; u is the water content at equilibrium and Rh is the relative humidity, u_m is the water content at saturation of the monolayer and C is a kinetic constant due to the adsorption of the first layer.

- The GAB model (Guggenheim-Anderson-de Boer) is applicable in several areas. In comparison with the BET model, an additional parameter is introduced that takes into account the heat adsorbed by the molecular layers [12]:

$$u = \frac{u_m CKRh}{(1 - KRh)(1 + K(C - 1)Rh)} \quad (6)$$

Where, K is a kinetic constant due to the multi-molecular adsorption.

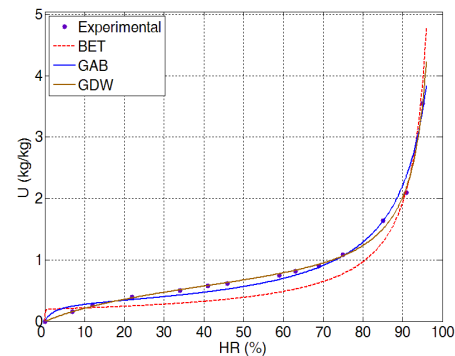
- The model GDW (Generalised D'Arcy and Watt) supposes that many molecules of water vapor can be adsorbed on each molecule along the secondary sites of adsorption [12]:

$$u = \frac{u_m KRh(1 - k(1 - \omega)Rh)}{(1 + KRh)(1 - kRh)} \quad (7)$$

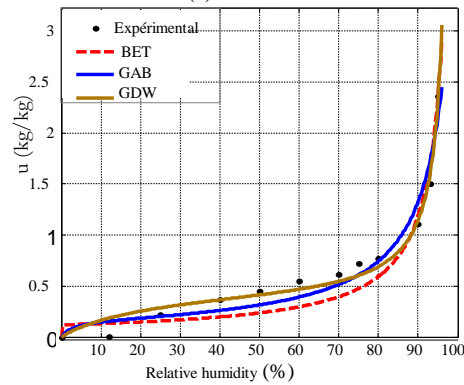
Here, ω is the rate of molecules adsorbed on primary sites which are converted into secondary sites. K and k are constants related to the adsorption kinetics of primary and secondary sites.

These three models complete the interpretation of the experimental results; in particular, the use of these models allows one to express analytically the capacity of storage humidity C_m .

Figures 4(a) and (b) show, respectively, the comparison of sorption isotherms for the two materials SEB 5Tu and SEB 5Te obtained experimentally and those obtained by the three models described above.



(a) BTS 5Tu



(b) BTS 5Te

Figure 4

Water vapor adsorption isotherms of SEB materials

Regarding these results, it seems that the GDW model is best suited to reproduce the experimental results of sorption isotherm for the SEB materials.

CONCLUSIONS

In this work, some characteristics on two stabilized earth bricks (SEB), having different compositions, were studied and compared. It appears that the hygric behavior of material, specifically the change in water content, is highly depending on the ambient relative humidity and the material porosity. These parameters strongly modify the coefficients used in macroscopic models of coupled transfer of heat and moisture in unsaturated porous media. Indeed, for example, knowing that the conductivity of water is thirty times greater than that of dry air, the water present in the material, following the condensation of steam, will therefore change its conductivity overall.

The experimental values of moisture at equilibrium showed that the sorption isotherms of SEB are type II. The hysteresis phenomenon is relatively small presence compared to other materials such as concrete.

The experimental results can serve as input parameters for physical simulations to evaluate the hydrothermal performance of the SEB buildings envelopes.

REFERENCES

1. Belarbi, R, Ait-Mokhtar, A, Qin, M and Omikrine, O, 2006, Development of simplified approach to model the moisture transfer of building materials, *European Journal of Environment and Civil Engineering*, 10/9, pp.1033-1048.
2. Belarbi, R, Ait-Mokhtar, A, Nilsson, L., O, 2008, Nonisothermal moisture transport in hygroscopic building materials: modeling for the determination of moisture transport coefficients, *Transport in Porous Media*, 72(2), pp. 255-271.
3. Qin, M, Belarbi, R, Ait-Mokhtar, A, Nilsson, L., O, 2009, Coupled heat and moisture transfer in multi-layer building materials, *Construction and Building Materials*, 23(2), pp.967-975.
4. CNERIB (Centre National d'Etudes et de Recherches Intégrées du Bâtiment), *Projet d'efficience énergétique dans le secteur de la construction en Algérie*, <http://www.med-enec.Com/>.
5. CNERIB, 2009, *Recommandations pour la production et la mise en œuvre des bétons de terre stabilisée*, Alger.
6. Crausse, P, Laurent, J., P and Perrin, B, 1996, Influence des phénomènes d'hystérésis sur les propriétés hydriques de matériaux poreux, *Revue Générale Thermique*, 35, pp.95-106.
7. Dian, J., F, 2013, *Equilibre et transferts en milieux poreux*, These, Université Joseph Fourier, France.
8. AFPC, A. 1997, *Compte-rendu des journées techniques AFPC-AFREM durabilité des bétons. Méthodes recommandées pour la mesure des grandeurs associées à la durabilité*, 65, pp. 121-125.
9. Trabelsi, A, 2010, *Etudes numérique et expérimentale des transferts hygrothermiques dans les matériaux poreux de construction*, Thèse de doctorat, Université de La Rochelle.
10. Brunauer, S, Emmet, P. H., Emmet and Teller, E, 1938, Adsorption of Gases in Multimolecular layers, 60(2), pp. 309-319.
11. Sing, K., S, 1985, Reporting physisorption data for gas/solid systems. In *Pure and applied chemistry, Fundamentals of Adsorption, Proceedings of the Engineering Foundation Conference*, 75, pp. 603-619.
12. Furmaniak, S., Terzyk, A., P and Gauden, P., A, 2007, The general mechanism of water sorption on foodstuffs - importance of the multitemperature fitting of data and the hierarchy of models, *Journal of Food Engineering*, 82(4), pp. 528-535,

Modelling of heat and mass transfer during convective drying of wood

ANDRIANANTENAINA Marcelin Hajamalala¹, B. Zeghmati³, B.O.A. RAMAMONJISOA², Randriamilantoniaina Yves Odon¹

¹ Laboratoire de Physique Appliquée de l'Université de Fianarantsoa,
B.P. 1264, 301 Fianarantsoa, Madagascar

² Laboratoire de Recherche Appliquée Multidisciplinaire de l'Université de Fianarantsoa,
B.P. 1264, 301 Fianarantsoa, Madagascar

³ Université de Perpignan Via Domitia
52 avenue Paul Alduy - 66860 Perpignan Cedex, France

Corresponding author: hajamalalaa@yahoo.fr

ABSTRACT

The model of heat and mass transfer during wood drying used here is deduced from Philip-Devries's theory. 2-D equations for coupled heat and mass conservation equations for wood are solved to study the transient heat and mass transfer during wood sample drying. The model equations based on temperature and moisture content parameters are solved numerically by the Finite Difference Implicit Method and the algebraic equations system are solved by the THOMAS algorithm. The simulation of the proposed model allows the assessment of the effect of the heat and mass transfer within wood. A parametric study was also carried out to determine the effects of several parameters such as initial moisture content, initial temperature and the sample thickness on the temperature and moisture content distributions within the samples during drying.

KEYWORDS: Wood drying, wood, heat and mass transfer, Philip-Devries's model

NOMENCLATURE

Latin symbols

C_p	Specific heat of material	$[J.kg^{-1}K^{-1}]$
D_T	Mass phase transport associated to a temperature gradient	$[m^2.s^{-1} K^{-1}]$
D_{TV}	Vapor phase transport associated to a temperature gradient	$[m^2.s^{-1} K^{-1}]$
D_X	Mass phase transport associated to a moisture gradient	$[m^2 s^{-1}]$
D_{XV}	Vapor phase transport associated to a moisture gradient	$[m^2 s^{-1}]$
L	: length of the sample	$[m]$
L_V	Latent heat of vaporization	$[J.kg^{-1}]$
Pr	: Prandtl number	
Re	: Reynolds number	
Sc	: Schmidt number	
Sh	: Sherwood number	
T_1	: Drying air temperature,	$[K]$
X	: Moisture content dry basis,	$[kg\ water/kg\ dry\ solid]$

X_0	: Initial moisture content,	$[\%]$
X_1	: Drying air moisture,	$[\%]$

Greek symbols

α_q	: Convective heat transfer coefficient,	$[W.m^{-2}K^{-1}]$
α_m	: Convective mass transfer coefficient,	$[kg.m^{-2}.s^{-1}.m^{-1}]$
λ	: Thermal conductivity	$[W.m^{-2}K^{-1}]$
ρ	: Solid density	$[kg.m^{-3}]$
ρ_l	: Liquid density	$[kg.m^{-3}]$
Ω	: Boundary surface for convective heat and mass transfer	

INTRODUCTION

Drying is a classical example of transport in porous media, and the modelling of this process has been the subject of great interest for many years[1-5]. Wood is a fascinating biological porous material that is both anisotropic and heterogeneous. Its structure is rather complex, however, it is well known and thoroughly documented in the literature[6].

To date a number of comprehensive two-dimensional (2-D) models are available for studying the drying process. These models have been applied in the domains of wood drying [7,8,9,10] and building materials, such as brick [11]. These models have provided the drying engineer with fundamental knowledge that has increased the understanding of the process and allowed new and innovative drying operations to be proposed.

Our contribution consists in the theoretical study of two dimensional heat and mass transfer during the drying of wood. The model used is drawn from the work of Philip-Devries's theory [12] with two variables(temperature, moisture content).

A parametric study was also carried out to determine the effects of several parameters such as initial moisture content, initial temperature and the sample thickness on the temperature and moisture content distributions within the samples during drying.

ANALYSIS AND MODELLING

The process of drying of wood involves simultaneous transport of heat, and mass through a porous medium. The problem considers a sample of wood exposed to convective heating in an inert atmosphere.

Assumptions

- ✓ The binary mixture (air flow and vapor flow) is considered as an ideal gas.
- ✓ The flow of drying air is laminar
- ✓ The steam movement by gravity and hydraulic conductivity are neglected
- ✓ The heat and mass transfer are two-dimensional and physical properties of the porous material are constant.

The model of heat and mass transfer in an unsaturated porous media through classical mechanism of vapor diffusion and liquid movement by capillarity is described by J.R.Philip, D.A. De Devries model [12].

Heat transfer

$$\rho C_p \frac{\partial T}{\partial t} = Div((\lambda + \rho_l L_v D_{TV}) \nabla T + \rho_l L_v D_{XV} \nabla X) \quad (1)$$

Mass transfer

$$\frac{\partial X}{\partial t} = Div(D_T \nabla T + D_X \nabla X) \quad (2)$$

where : $D_T = D_{TL} + D_{TV}$ and $D_X = D_{XL} + D_{XV}$

The system of equations expressed in the referential (Oyz) :

$$\rho C_p \frac{\partial T}{\partial t} = \frac{\partial}{\partial y} \left(\lambda_{yy}^* \frac{\partial T}{\partial y} + \rho_l L_v D_{XV} \frac{\partial X}{\partial y} \right) + \frac{\partial}{\partial z} \left(\lambda_{zz}^* \frac{\partial T}{\partial z} + \rho_l L_v D_{XV} \frac{\partial X}{\partial z} \right) \quad (3)$$

$$\frac{\partial X}{\partial t} = \frac{\partial}{\partial y} \left(D_T \frac{\partial T}{\partial y} + D_X \frac{\partial X}{\partial y} \right) + \frac{\partial}{\partial z} \left(D_T \frac{\partial T}{\partial z} + D_X \frac{\partial X}{\partial z} \right) \quad (4)$$

Where : $\lambda^* = \lambda + \rho_l L_v D_{TV}$

Initial and boundary conditions

Initially the wood has some prescribed moisture content and temperature,

at time $t = t_0$: $X(y,z,t_0) = X_0$ and $T(y,z, t_0) = T_0$

The transverse (z-direction) and radial (y-direction) directions of the wood are considered in the analysis and a two-dimensional mathematical model is constructed. In this study the porous material (wood) is assumed as being a rigid, homogeneous, and anisotropic structure that has some portion of its void space occupied by liquid water.

The shaded region, $0 < z < L_2$, and $0 < y < L_1$, represents the wood being dried by forced convection of hot dry air. The faces $z = L_1$ and $y = L_2$ are exposed to the external drying conditions fixed characteristics (temperature, velocity and humidity), while the faces $z = 0$, and $y = 0$, are considered as symmetry planes(Impermeable side). It is assumed that no mass and heat is transferred across that surface of the drying material. The figure 1 shows the geometry of the wood sample.

The boundary conditions at Ω is:

$$-\lambda^* \frac{\partial T}{\partial n} - \rho_l L_v D_{XV} \frac{\partial X}{\partial n} = \alpha_q (T - T_1) + \alpha_m L_v (X - X_1) \quad (5)$$

$$-\left(D_T \frac{\partial T}{\partial n} + D_X \frac{\partial X}{\partial n} \right) = \alpha_m (X - X_1) \quad (6)$$

Where n is the spatial direction (y,z).

Mass transfer coefficient α_m and heat transfer coefficient α_q are determined from the expressions for laminar flow [13], respectively:

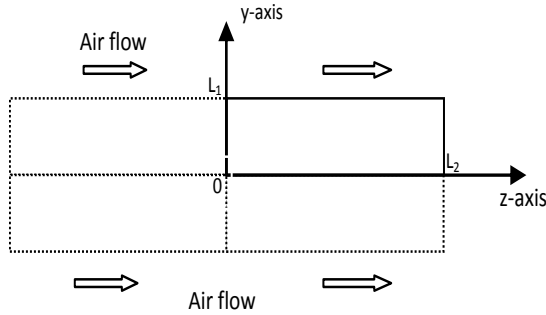


Figure 1

Physical configuration and computational domain

$$Nu = \frac{\alpha_q L}{\lambda_{air}} = 0,664 Re^{0,5} Pr^{0,33} \quad (7)$$

$$Sh = \frac{\alpha_m L}{D} = 0,664 Re^{0,5} Sc^{0,33} \quad (8)$$

Numerical formulation

To facilitate the numerical solutions of these differential equations, the following dimensionless variables are introduced :

$$y' = \frac{y}{L} \quad z' = \frac{z}{L} \quad \alpha = \frac{\lambda}{\rho C_{ps}} \quad \tau = \frac{\alpha t}{L^2}$$

$$\theta = \frac{T - T_0}{T_1 - T_0} \quad X' = \frac{X - X_1}{X_0 - X_1}$$

The coupled system of two non-linear partial differential equations is expressed such as:

$$\begin{cases} \frac{\partial \theta}{\partial \tau} = A_{\theta y1} \frac{\partial^2 \theta}{\partial y'^2} + A_{\theta z1} \frac{\partial^2 \theta}{\partial z'^2} + A_{Xy1} \frac{\partial^2 X'}{\partial y'^2} + A_{Xz1} \frac{\partial^2 X'}{\partial z'^2} \\ \frac{\partial X'}{\partial \tau} = A_{\theta y2} \frac{\partial^2 \theta}{\partial y'^2} + A_{\theta z2} \frac{\partial^2 \theta}{\partial z'^2} + A_{Xy2} \frac{\partial^2 X'}{\partial y'^2} + A_{Xz2} \frac{\partial^2 X'}{\partial z'^2} \end{cases}$$

The numerical solution technique employed to solve the coupled system of two non-linear partial differential equations with boundary conditions is performed by finite differences method according to implicit scheme.

The final form of the discretized coupled system of two non-linear partial differential equations is expressed by the following:

$$\begin{cases} A\theta_{(i-1,j)}^{(n)} + B\theta_{(i,j)}^{(n)} + C\theta_{(i+1,j)}^{(n)} = \theta_{(i,j)}^{(n-1)} + D \\ A'X'_{(i-1,j)}{}^{(n)} + B'X'_{(i,j)}{}^{(n)} + C'X'_{(i+1,j)}{}^{(n)} = X'_{(i,j)}{}^{(n-1)} + D' \end{cases}$$

At each time, the Tri Diagonal Matrix Algorithm of Thomas (TDMA) is used to solve the algebraic systems of temperature and humidity. The governing equations are solved numerically with FORTRAN. The simulated results is obtained for the existing data in the literature as plywood[14].

RESULTS AND DISCUSSION

The dimensions of the wood sample were 5-6 cm in the radial and 50 cm in the transverse direction, which implied a computational domain of 2.5-3 cm x 25 cm. Initially the board was assumed to be at the ambient temperature of 25 °C and average moisture content 80% and 120%.

The physical properties of the chosen material is shown in table 1.

Table 1 : Physical properties of material

Symbol	Plywood [14]
ρ , kg/m ³	445
C_p , J/kg K	1880
λ , W/m K	0.091
L_v , J/kg	2.5x10 ⁶
D_T , m ² /s K	10 ⁻¹¹
D_{TV} , m ² /s K	5x10 ⁻¹¹
D_X , m ² /s	4.5x10 ⁻⁷
D_{XV} , m ² /s	4.5x10 ⁻⁷

Figure 2 shows the time evolution of average temperature and moisture content during drying of the sample. During process, the temperature increases and the average moisture content decreases almost linearly with time, due to the influence of gas temperature. Evaporation of liquid moisture takes place from the wood sample surface by absorbing the heat of vaporization. The moisture migrates toward the external wood surfaces by means of capillary flow under the influence of moisture content gradient.

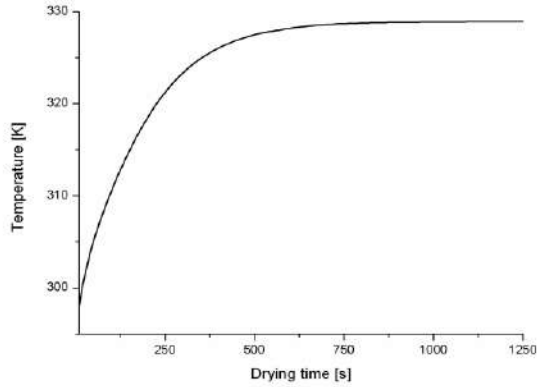


Figure 2(a)
Time evolution of average temperature profiles
Wood dimension : 3x25cm

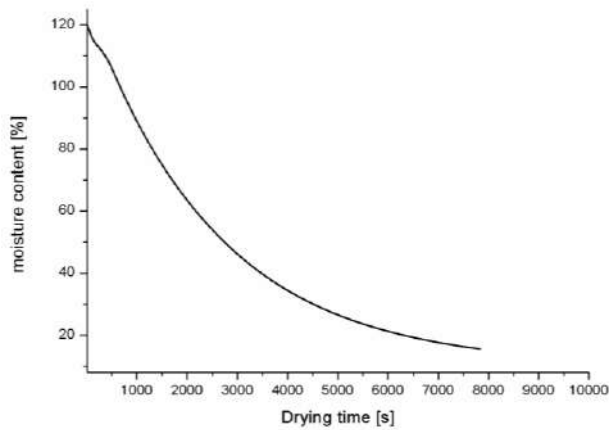


Figure 2(b)
Time evolution of average moisture content profiles
Wood dimension : 3x25cm

As expected, the drying process is as fast as the board width is small, fig. 3.

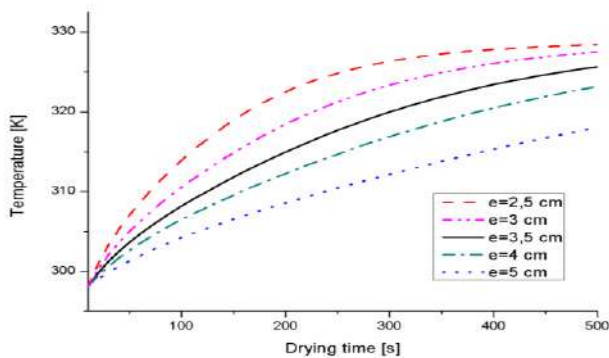


Figure 3(a)
Effect of sample thickness on the temperature

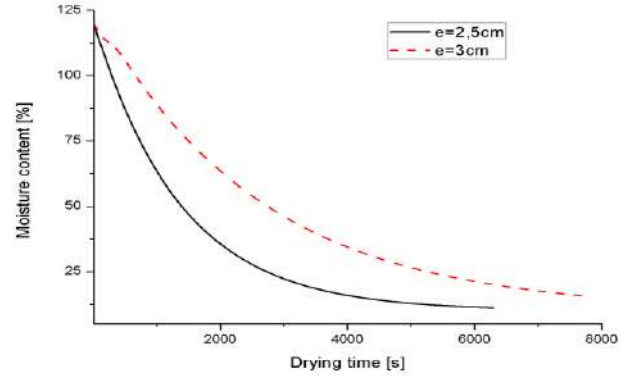


Figure 3(b)
Effect of sample thickness on the moisture content

A series of simulations were carried out at different initial average moisture contents (X_0) of 80%, and 120% keeping the other conditions constant. The influence of initial moisture content of wood on temperature and moisture content vs. time data is presented in fig. 4. It can be seen from the figure that there are slight differences between the temperatures of the samples: lower the initial moisture content of the sample, higher is the temperature. Clearly, vaporization has a cooling effect. Since the humidity of the gas is kept constant, high initial moisture content means higher moisture gradients at the surface. Therefore, vaporization rate at the surface will be higher for the sample with high moisture content which leads to lower temperatures. As expected, the time necessary for moisture removal is greater if the initial moisture content of the sample is higher when the other treatment conditions are kept constant.

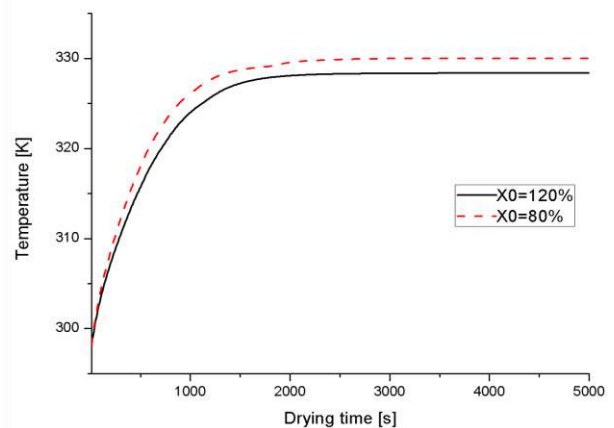


Figure 4(a)
Effect of initial moisture on the temperature
Wood dimension : 2.5x25cm

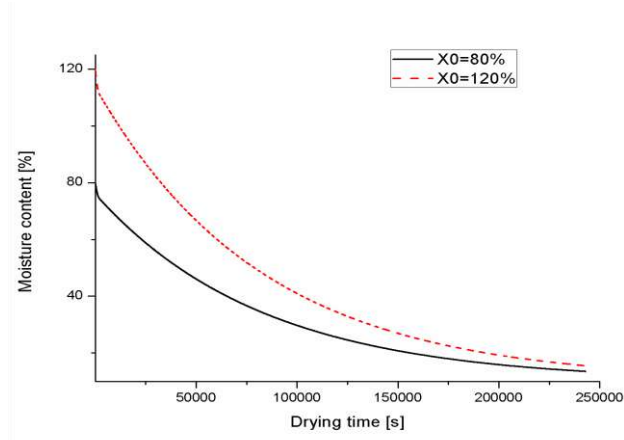


Figure 4(b)

Effect of initial moisture on the moisture content
Wood dimension : 2.5x25cm

Figure 5 shows the time evolution of average temperature and moisture content during drying of the sample with different airflow temperature. Drying process is as quick as the airflow temperature is large.

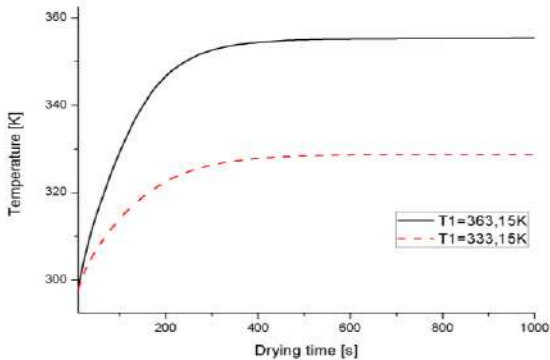


Figure 5(a)

Effect of Airflow temperature on the temperature
Wood dimension : 2.5x25cm

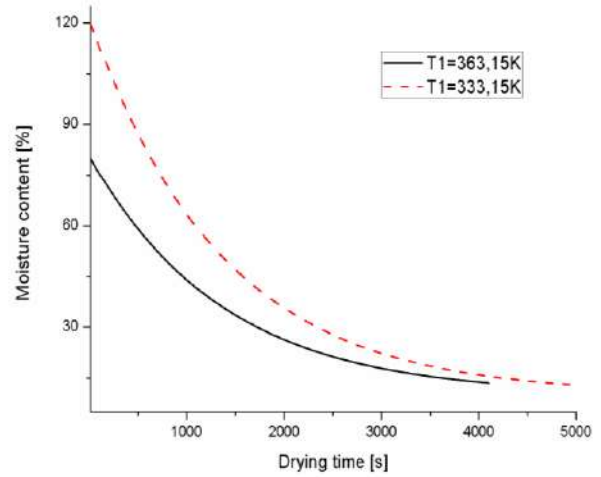


Figure 5(b)

Effect of Airflow temperature on the moisture content.
Wood dimension : 2.5x25cm

CONCLUSIONS

A coupled heat and mass transfer model has been used to accomplish a better understanding of the drying process of wood and to determine its influence on several parameters that control the process. This study is carried out by solving 2-D Philip and De Devries model. FORTRAN software was used to solve the coupled system of partial differential equations.

ACKNOWLEDGMENTS

The authors wish to thank the French government for the financial support of this work within the BGF 2015.

REFERENCES

1. Whitaker, S, 1995, Simultaneous heat, mass and momentum transfer in porous media: A theory of drying. *Advances in Heat Transfer*, Vol. **13**. Academic, Press New York, 1977, pp. 119-203.
2. Degiovann, A, and Moyne, C, 1992, Conductivité thermique de matériaux poreux humides: Evaluation théorique et possibilité de mesure. *Int . J. Heat Mass Transfer* **30**(11), 2225-2245

3. Perré, P, 1987, Le Séchage convectif de bois résineux: choix, validation et utilisation d'un modèle. *Thèse de Doctorat de L'Université Paris*, vii.
4. Turner, I. W, The modelling of combined microwave and convective drying of a wet porous material. Ph.D. Thesis, University of Queensland, Australia
5. Turner, I, W, A two-dimensional orthotropic model for simulating wood drying processes. *J. Appl. Math. Modelling*, in press
6. Siau, J.F, 1984 *Transport Processes in Wood*, Springer-Verlag.
7. Perré, P, A. Degiovanni, 1990, Simulations par volumes finis des transferts couplés en milieu poreux anisotropes: séchage du bois à basse et à haute température, *Int. J. Heat and Mass Transfer* **33** (11), pp. 2463-2478.
8. Perré, P, and Turner, I, 1996, The use of macroscopic equations to simulate heat and mass transfer in porous media, in: Turner, I., Mujumdar, A.S, (Eds.), *Mathematical Modeling and Numerical Techniques in Drying Technology*, Marcel Dekker, New York.
9. Fahyr, C., Rasmuson, A, 1994, Numerical simulation of superheated steam drying of wood chips, in: V. Rudolph, R.Keey, A.S, Mujumdar (Eds.), *Drying 94, Proceedings of the 9th International Drying Symposium*, Gold Coast, Australia, pp. 727-734 (Part B)
10. Couture, F, Fabrie, P, Puiggali, J.R, 1995, An alternative choice for the drying variables leading to a mathematically and physically well described problem, *J. Drying Technology* **13** (3), pp. 519-550
11. Boukadida, N, Nasrallah S. B., 1995, Two-dimensional heat and mass transfer during convective drying of porous media, *J. Drying Technology* **13** (3), pp. 661-694
12. Philip, J.R, and De Devries, D.A, 1957, Moisture movement in porous material under temperature gradients. *Transactions of American Geophysical Union* . Vol.38 N°2.
13. Incropera, F. P, and DeWitt, D. P, 2002 *Fundamentals of Heat and Mass Transfer*, John Wiley & Sons, New York, USA.
14. Talukdar, P. T, Olutmayin S.O, Osayintola, O.F, and Simonson, C.J, 2007, An experimental data set for benchmarking 1D, transient heat and moisture transfer models of hygroscopic building materials. *International Journal of Heat Transfer*, **50**(23-24), pp.4527-4539.

CHARACTERIZATION AND COMPARISON OF THERMAL AND HYGRIC PROPERTIES OF HEMP-CLAY COMPOSITE AND HEMP-LIME CONCRETE

B. Mazhoud*, F. Collet, S. Pretot, C. Lanos

Laboratoire de Génie Civil et Génie Mécanique, Equipe Matériaux Thermo Rhéologie, Université de Rennes 1

3, rue du Clos Courtel, BP 90422, 35704 Rennes, France

*Corresponding author: Fax: +33 (0) 2 23 23 40 51 Email: brahim.mazhoud@univ-rennes1.fr

ABSTRACT

This study investigates the use of clay as binder in hemp composite and compares hemp-clay composite to hemp-lime concrete. The clay is produced from washing mud from gravels production site. Two clay drying temperatures are used. The thermal properties are measured with a hot wire method at 23°C, 50%RH and the hygric characterization is based on the measurement of Moisture Buffer Value at 23°C. Performances obtained on clay blocks, hemp-clay composite and hemp-lime composite are compared. The results show that the two clay drying temperatures do not impact on the thermal conductivity nor on the moisture buffer value of clay blocks. Hygro-thermal performances of hemp-clay and hemp –lime composites with the same densities are quite similar. These materials act as excellent hygric regulators. Performances measured separately on hemp and clay reveal an interesting synergetic effect in the case of hemp-clay composite leading to a higher ability to the moisture buffering. Such material can be advantageously used in buildings to reduce energy needs of building and to moderate indoor humidity variations.

INTRODUCTION

In a context of sustainable development, bio-based building materials are developed to replace conventional products in order to reduce the impact on environment. Bio-based materials are relevant because they are made from renewable raw materials and allow carbon storage during their growing [1]. Among them, hemp based materials have been studied a lot these last years because hemp shiv have many advantages (renewal, recycling, carbon sequestration...) [1] [2] [3] [4] [5] [6] [7] [8]. Up to now, many researches have been conducted on hemp concrete [9] [10]. This material is usually composed of hemp shiv with lime based binder. In such material, the LCA exhibit that the lime is the more impacting component [2].

In order to reduce the environmental impact of hemp composite, this study aims to replace lime based binder by natural clay binder. Actually, the overall environmental impact of this binder is low: the resource is available in large quantities, the energy required to extract, transform and produce materials from earth is extremely low and it is a recyclable material. More, this material is highly interesting on hygric point of view, due to its capacity to regulate

ambient relative humidity [11]. On thermal point of view, clay is not a good thermal insulator, but the coupling with hemp shiv should reduce the composite thermal conductivity.

The formulation of hemp-clay composite is based on the target density (the same as hemp-lime concrete for wall application). The analysis of thermal and hygric performances is based on comparison between experimental results of hemp-clay composite, hemp-lime concrete, hemp shiv and clay.

MATERIALS

Hemp shiv: The shiv used are commercial products Chanvribat (from LCDA France). Their bulk density is about 100 to 110 kg/m³. Their particle size distribution, measured by sieving, is given Figure 1. The mean width of shiv (D50) is 4 mm. The width/length ratio is about 4.

Binders: Two binders are considered in this study: natural clay binder and lime based binder (used as reference).

The natural clay used corresponds to a washing mud taken from a gravels production site. After decanting, the mud is dried in an oven. After drying, the material is milled with a knife mill. The powder

is then sieved with a square mesh of 0.2 mm side to remove the larger particles. Two drying temperatures are used: 100 ° C and 40 ° C. Actually, the higher temperature allows faster drying. The aim is to check if the drying temperature does impact hygric and thermal properties of clay binder

The lime-based binder used is a commercial product (Tradical BCB PF70 – BCB France) commonly used to produce hemp concrete. This binder is made of 75% of hydrated lime, 15% of hydraulic binder and 10% of pozzolanic binder.

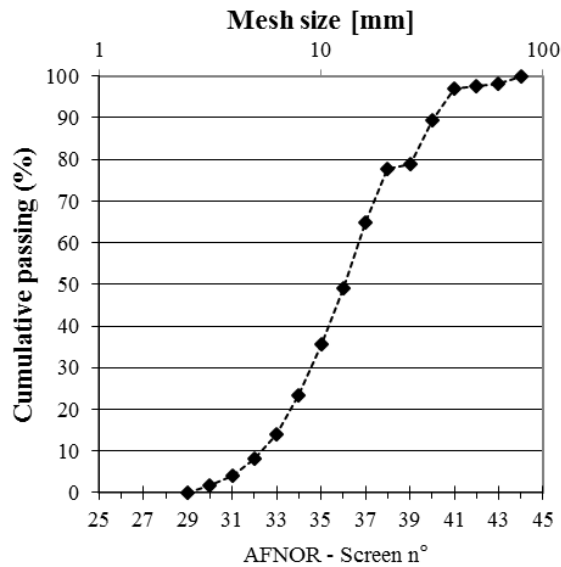


Figure 1
Particle size distribution of shiv

Formulations:

For this study, two types of clay blocks are produced by molding. One is manufactured with mud dried at 40°C (quoted C40) and the other is manufactured with mud dried at 100°C (quoted C100). Clay and water are mixed with water to binder mass ratio of 0.4. Molds are filled with the mixture and the material is manually compacted. After drying, the densities of blocks are quite the same (1680 kg/m³).

The hemp-clay composite (quoted HCC) is made with clay made from mud dried at 100°C. The hemp to clay ratio is estimated regarding traditional mix of hemp concrete used for wall applications. Thus, the target density is around 400 kg/m³. The composite is produced by moulding. Then, hemp shiv and clay binder are mixed with hemp to binder mass ratio of 0.75. Water content is adjusted to obtain a satisfactory workability. The water to clay ratio is 0.7. Moulds are filled with the mixture and the

composite is manually compacted. The density of hemp-clay composite is about 383-387 kg/m³.

The hemp- lime concrete (quoted HLC) is realized with Tradical BCB PF70 binder. Hemp to binder ratio is 0.5 and the hemp-lime concrete is applied with spray technic with water to binder ratio of 0.8. The components of each formulation are given table 1.

For thermal and hygric studies, specimens are selected to be representative of the material (density and homogeneity). The sizes and densities of the specimens are given in Table 2.

For solid materials (clay, hemp-clay composite and hemp-lime concrete), the numbers of specimens used are: (i) three for the moisture buffer value, (ii) three for the thermal properties. For clay and hemp-clay composite, the same specimens are used for thermal and hygric characterization.

Table 1
Composition of the studied materials

Ref.	Binder	Hemp shiv	Hemp/binder mass ratio
C40	Clay (dried at 40°C)	-	-
C100	Clay (dried at 100°C)	-	-
HCC	Clay (dried at 100°C)	Chanvribat	0.75
HLC	Lime based binder (Tradical 70)	Chanvribat	0.5

Table 2
Density at (23°C, 50%RH) of specimens

Ref.	Number of specimens	Density (kg.m ⁻³)	Size 1×L×h (cm)
C40	3	1684±7	10×10×5
C100	3	1675±5	10×10×5
HCC	3	385±2	10×10×7
HLC	6	426±12	15×15×7

METHODS

Thermal properties: The thermal property investigated is the thermal conductivity. It represents the ability of a material to conduct heat under temperature gradient and steady state conditions.

The thermal conductivity is measured at 23°C, 50%RH. In order to limit water migration during the test, the measurements are performed with a transient state method: hot wire. The measurement is based on the analysis of the temperature rise versus heating time. The heat flow and heating time are chosen to reach high enough temperature rise (>10°C) and high correlation coefficient (R^2) between experimental data and fitting curve. In this study, the commercial CT meter device is equipped with a 5 centimeters-long hot wire.

For clay, hemp-clay composite and hemp-lime concrete, the measurement is performed with the sensor sandwiched between two specimens. The contact surface of specimens is as flat as possible in order to ensure the thinner air layer between specimens. In this study, the used heating time is 120 s for all materials and the power is 0.142 W for the two types of clay, 0.689 W for hemp-clay composite and 0.23 W for hemp-lime concrete. The size of the specimen is bigger than the probe volume which is about 2.5 cm in radius (infrared photography taken immediately after measurement). This allows the hypothesis of infinite surrounding (assumed in the hot wire model). For each material, three pairs are formed from the three specimens. The thermal conductivity of a pair of specimens is the average of five values with a variation coefficient lower than 5%. The thermal conductivity of one material is the average value of results obtained on the three pairs.

For hemp shiv, the hot wire is sandwiched between two samples placed in two jackets to control bulk density during the measurement (figure 2). The heating power is 0.159 W and the heating time is 60 s.



Figure 2

Thermal conductivity measurement of hemp shiv with Hot wire

Hygic characterization: The hygic characterization is based on the measurement of the moisture buffer value MBV of the materials which quantifies their ability to moderate the variations of indoor relative humidity in buildings. It is measured according to the method defined in the NORDTEST project [12]. This value relates the amount of moisture uptake (and release), per open surface area, under daily cyclic variation of relative humidity according to equation (1).

$$MBV = \frac{\Delta m}{A(RH_{high} - RH_{low})} \quad (1)$$

Where MBV is the Moisture Buffer Value ($g/(m^2 \cdot \%RH)$), Δm is the moisture uptake / release during the period (g), A is the open surface area (m^2) and $RH_{high/low}$ are the high/low relative humidity level (%).

Within the NORDTEST project, a round robin test was performed on nine representative building materials. It gives initial results and leads to a classification of moisture buffer values from negligible to excellent (Figure 3).

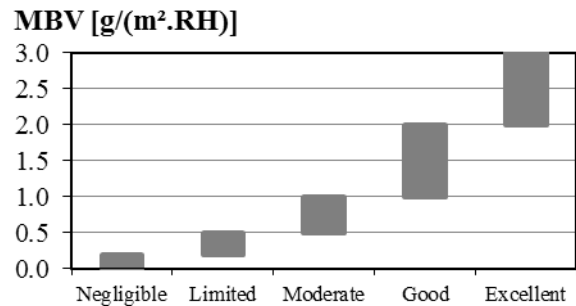


Figure 3

Nordtest project Classification [12]

After stabilization at (23°C; 50% RH), specimens are exposed to daily cyclic variations: 8 hours at high relative humidity (75%) followed by 16 hours at low relative humidity (33%). The test goes on until the change in mass Δm is the same between the last three cycles with less than 5% of discrepancies. For each specimen, the MBV is thus the average value calculated from the last 3 cycles. The MBV of the materials is thus the average value of the three specimens.

The device used for MBV test is a climate chamber Vötsch VC4060 with a temperature range from +10 to +95 °C and a relative humidity range from 10 to 98 % RH. The relative humidity is switched manually according to the (8 hours at 75 %RH; 16

hours at 33%RH) scheme. Temperature and relative humidity are measured continuously with Sensirion SHT75 sensors and with the sensor of the climate chamber. The air velocity is measured in the surroundings of the specimens: the vertical velocity is lower than 0.14 m/s and the horizontal one ranges from 0.1 to 0.4 m/s. The specimens are weighed out of the climate chamber five times during the absorption period and two times during the desorption period. The weighing instrument reading is 0.01 g, and its linearity is 0.01 g. The accuracy of the moisture buffer value is thus about 5%.

For solid material, the test method requires prismatic specimens to be sealed on five out of six sides. The exchange area is higher than 100 cm² for each specimen, and the total exchange area is higher than 300 cm² by material.

For hemp shiv, aggregates are placed in a container. The exchange area is 116 cm². The bulk density of hemp shiv is checked to be representative.

RESULTS AND DISCUSSION

Thermal properties: For all the measurements, the correlation coefficient between experimental data and fitting curve is very close to 1 (higher than 0.9996) and the coefficient of variation between experimental data is lower than 4%.

Figure 4 gives the thermal conductivity of studied materials versus density at (23°C; 50%RH). The thermal conductivity globally increases with density.

Hemp shiv has the lowest thermal conductivity (0.067 W/(m.K)) due to its low density (113 kg/m³) and, thus, its high porosity.

The clay shows the highest values of thermal conductivity. This was expected as clay has the highest density. The two clay have similar thermal conductivity (0.605 W/(m.K) at 1684 kg/m³ for C40 and 0.612 W/(m.K) at 1673 kg/m³ for C100). This result show that the drying temperatures do not impact the thermal conductivity.

The hemp-clay composite HCC shows lower thermal conductivity than hemp-lime concrete HLC (respectively 0.085 W/(m.K) at 385 kg/m³ and 0.139 W/(m.K) at 422 kg/m³). The thermal conductivity is thus mainly dependent on density and is also slightly impacted by the type of binder.

Compared with other bio-based building material, studied hemp-clay composite and hemp-lime concrete shows lower thermal conductivity than the values obtained from the relationship (2) established by Cerezo for hemp concrete [4]. This can be

explained by the lower hemp to binder ratio utilized by cerezo.

$$\lambda = 0.0002\rho + 0.0194 \quad (2)$$

Finally, studied hemp-clay composite has similar thermal conductivity as straw-clay studied by Labat ($\lambda=0.088$ W/(m.K); $\rho=381$ kg/m³) [14].

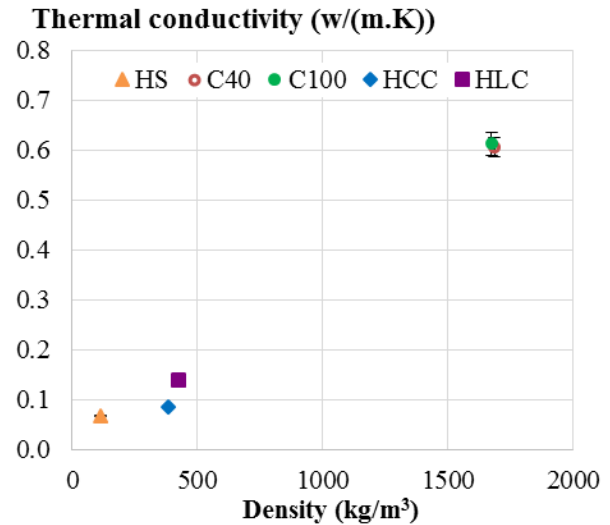


Figure 4
Thermal conductivity of materials versus density at (23°C; 50%RH)

Hygic characteristics: Figure 5 shows the ambient relative humidity in the climate chamber during the test. The average value of relative humidity (RH) is slightly lower than 75 % during absorption (about 74.13 %) and slightly higher than 33% during desorption (about 35.2 %) because the door of the climatic chamber is regularly open to weigh specimens (peak on the curve). The step changes in relative humidity are achieved within 30 minutes from low to high RH and within one hour from high to low RH. This induces a nearly square wave of relative humidity. It was shown in [13] that the time needed to achieve the step in relative humidity has a limited influence on the moisture buffer value (less than 5 %) even when it takes one hour and a half to achieve the required relative humidity.

Figure 5 also gives an example of moisture uptake and release during the MBV test. For all materials, the measures performed on the three specimens give similar results for moisture uptake and release and thus for moisture buffer value.

Figure 6 gives the average value of the moisture buffer value calculated from cycles 3 to 5 in adsorption, desorption and average for the all materials. The value is very slightly higher in desorption than in adsorption. Actually, after stabilization at 23°C; 50%RH, the test begins under adsorption at 75% RH. These conditions are higher than the average of the quasi steady state conditions that arise after some cycles. There is thus a declining tendency in the variation of mass (Figure 5) which induces higher value in desorption than in adsorption. These two values are approaching each other after repeated cycles.

According to the NORDTEST project classification, all the studied materials are excellent hygric regulators ($MBV > 2 \text{ g}/(\text{m}^2 \cdot \%RH)$).

The Moisture Buffer Value of hemp shiv is $2.30 \text{ g}/(\text{m}^2 \cdot \%RH)$. The MBV of clay is $2.06 \pm 0.04 \text{ g}/(\text{m}^2 \cdot \%RH)$ for C40 and $2.08 \pm 0.03 \text{ g}/(\text{m}^2 \cdot \%RH)$ for C100. The tested drying temperatures do not impact the moisture buffering ability of clay. The hemp-clay composite shows higher value of MBV than shiv and than clay ($2.68 \text{ g}/(\text{m}^2 \cdot \%RH)$). This underlines the coupling effect of the two components. Actually, figure 7 shows that the MBV is not related to the density. This value is both linked to moisture transfer and storage capacity of the material. It is thus dependent on the porosity of the material and on the connectivity in the porous structure. This is the reason why the MBV of hemp-clay composite is higher than the MBV of hemp shiv and than the MBV of clay.

More, hemp-clay composite is also better hygric regulator than hemp-lime concrete. Actually, the MBV of hemp-lime concrete is $2.15 \text{ g}/(\text{m}^2 \cdot \%RH)$. This result is in the range of values given for several hemp concretes by Collet et al. [10] (1.94 to $2.15 \text{ g}/(\text{m}^2 \cdot \%RH)$), Tran Le [15] (experimental value $1.99 \text{ g}/(\text{m}^2 \cdot \%RH)$ and analytical value $2.35 \text{ g}/(\text{m}^2 \cdot \%RH)$) and Rahim [16] ($2.02 \text{ g}/(\text{m}^2 \cdot \%RH)$) for similar formulation.

These results on moisture buffer value of hemp-clay composite underline their interest on hygric point of view. The combination of hemp shiv together with an earthen matrix allows reaching performances even better than those obtained with hemp-lime concrete (figures 6 and 7). This could be attributed to the very good hygric characteristics of clay binder that largely overtops usual mineral binders [11].

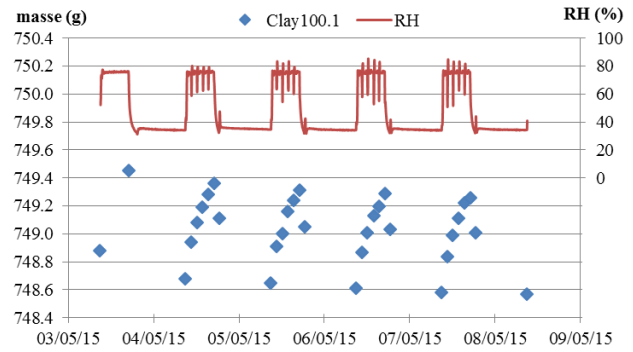


Figure 5
Ambient relative humidity during the test and example of moisture uptake and release

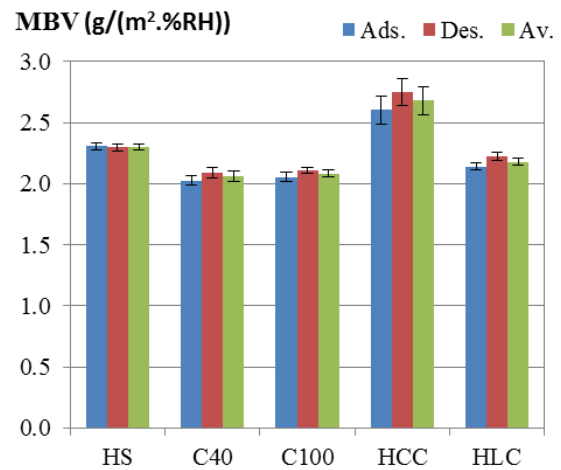


Figure 6
Moisture Buffer Value of studied materials at 23°C – Adsorption, Desorption, Average.

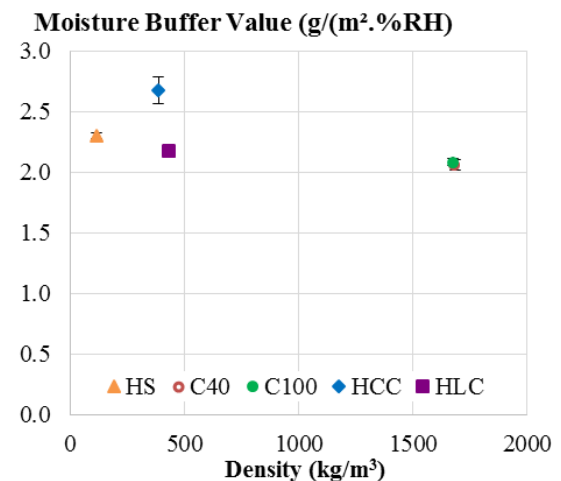


Figure 7
Moisture Buffer Value of materials versus density at (23°C; 50%RH)

CONCLUSIONS

This study investigates the use of clay as binder in hemp composite and compares hemp-clay composite to hemp-lime concrete.

Results show that the drying temperatures do not impact thermal and hygric properties of clay. Thus, composites can be produced with clay dried at 100°C, leading to a fastest drying.

The density of developed hemp-clay composites can be similar to the density of hemp-lime concrete used for wall application adjusting the mix proportioning.

The thermal conductivity is mainly dependent on density but is also slightly impacted by the kind of binder.

As well hemp-lime concrete as hemp-clay composite are excellent hygric regulators. The moisture buffering ability of hemp-clay composite is higher than that of hemp-lime concrete (respective MBV values: 2.68 and 2.15 g/(m².%RH)). It is underlined that the high performance of hemp-clay composite is due to the synergetic effect of hemp and clay on connected porosity.

Finally, hemp-clay composite seems to be an interesting material to be used for building envelop. Actually, it can contribute to reduce energy needs of building and to ensure hygrothermal comfort of users.

REFERENCES

1. Amziane, S., and Arnaud, L., 2013, Bio-aggregate-based Building Materials, Applications to Hemp Concrete, ISTE Ltd and John Wiley & Sons, Inc.
2. Pretot, S., et al., 2014, Life cycle assessment of a hemp concrete wall: impact of thickness and coating, *Building and Environment*, **72**, pp. 223–231
3. Boutin, M.P, et al., 2005, Analyse du cycle de vie de: Compounds thermoplastiques chargés fibres de chanvre et Mur en béton de chanvre banché sur ossature en bois ,INRA Lille.
4. Cerezo, V., 2005, Propriétés mécaniques, thermiques et acoustiques d'un matériau à base de particules végétales: approche expérimentale et modélisation théorique, Ecole Nationale des Travaux Publics de l'Etat, Institut National des Sciences Appliquées de Lyon.
5. Collet, F. and Pretot, S., 2012, Experimental investigation of moisture buffering capacity of sprayed hemp concrete, *Construction and Building Materials*, **36**, pp. 58–65.
6. Collet, F., and Pretot, S., 2014, Thermal conductivity of hemp concretes: Variation with formulation, density and water content, *Construction and Building Materials*, **65**, pp. 612–619.
7. Evrard, A., 2006, Sorption behaviour of Lime-hemp concrete and its relation to indoor comfort and energy demand, in: 23rd Conference on passive and low energy architecture, Geneva, Switzerland; pp.6–8.
8. Tran Le, A.D., et al., 2010, Transient hygrothermal behaviour of a hemp concrete building envelope. *Energy and Buildings*, **42**, pp. 1797–1806.
9. Laurent, A., and Etienne, G., 2012, Experimental study of parameters influencing mechanical properties of hemp concretes, *Construction and Building Materials*, **28**, pp. 50–56.
10. Collet, F., et al., 2013, Comparison of the hygric behaviour of three hemp concrete. *Energy and Building*, **62**, pp. 294–303.
11. Cagnon, H, et al., 2014, Hygrothermal properties of earth bricks, *Energy and Buildings*, **80**, pp. 208–217.
12. Rode, C., 2005, Moisture buffering of Building Materials, Report BYG-DTU R-126, ISSN 1601 – 2917, ISBN 87-7877-195.
13. Roels, S., and Janssen, H., 2005, Is the moisture buffer value a reliable material property to characterize the hygric buffering capacities of building materials? Working paper A41-T2-B-05-7 for IEA Annex 41 project, Whole Building Heat, Air and Moisture Response, Trondheim.
14. Labat, M., et al., 2016, From the experimental characterization of the hygrothermal properties of straw-clay mixtures to the numerical assessment of their buffering potential, *Building and Environment*, **97**, pp. 69–81.
15. Tran Le, A.D, 2010, Etude des transferts hygrothermiques dans le béton de chanvre et leur application au bâtiment, PhD thesis, Université de Reims Champagne- Ardenne, [in French].
16. Rahim, M., et al., 2015, Characterization of flax lime and hemp lime concretes: Hygric properties and moisture buffer capacity. *Energy and Building*, **88**, pp. 91–99

MULTI-SCALE CHARACTERIZATION OF HYGROTHERMAL TRANSFERS IN THE UNFIRED EARTH

MEDJELEKH Dalel^{1-2*}, ULMET Laurent¹, DUBOIS Frédéric¹

¹Université de Limoges, Groupe d'Etude des Matériaux Hétérogènes, 19300 Egletons, France

² Université Mentouri, Ecole d'Architecture, Laboratoire d'Architecture Bioclimatique et d'Environnement A.B.E, 25000 Constantine, Algérie

*Corresponding author: Fax: +33 5 55 93 45 01 Email: dalel.medjelekh@yahoo.fr

ABSTRACT

In front of the building energy issues and environmental impact bound, it appears that the earth envelopes are a promising track in terms of improving thermal comfort, indoor air quality, energy consumption and indoor humidity regulation. For this purpose, a characterization of hygrothermal transfers in the unfired earth has been conducted with a multi-scale experimental and numerical approach. Thus, monitoring of one inhabited house, built in earth/straw was the characterization focus at the first scale. The study on the material scale allowed to characterize the properties related to the heat and mass transfer. The hygrothermal coupling has been the subject of a specific study via a dual-climate test chamber at an earth wall scale. Finite differences FD and finite elements FE implementations have resulted in a detailed analysis of transfers across tested earth wall with a reduction work of order required to limit the calculation time. Emphasis is placed on the effects of moisture brought in indoor environments in order to validate a digital tool developed in this work.

KEYWORDS: Multi-scale characterization, unfired earth, heat and mass transfers, experimentations, numerical simulations.

NOMENCLATURE

q Heat flux (W/m^2) ; C_p Heat Capacity (specific, constant p) ($J/kg K$) ; L Length (m), W width (m), H height (m), M Masse (g) ; k Thermal Conductivity (W/mK), T Absolute Temperature (K) ; t Time (s), RH Relative Humidity (%) ; w Moisture content (kg/kg) ; p_{vs} Saturated vapor pressure (Pa),
 δ Water vapor permeability ($kg.s^{-1}.m^{-1}.Pa^{-1}$)

INTRODUCTION

Several experimental monitoring in different climates (northern Europe, Mediterranean regions or Africa) have demonstrated that unfired earth constructions have a high potential in the hygric regulation and the damping of relative humidity fluctuations in buildings [1-2-3]. Moreover, the coupling between heat and mass transfer process modifies the thermal inertia and the energy consumption in terms of heating and air conditioning [3-4], thus improving the thermal comfort [3]. On the other hand, the environmental profile of the unfired clay bricks was judged excellent when compared to typical concrete

[5] or to the fired brick, under the production process (grey energy and transportation) [6-7].

For this purpose, a characterization of hygrothermal transfers in the unfired earth has been conducted with a multi-scale experimental and numerical approach. Thus, monitoring of one inhabited house, built in earth/straw under hot climate was the characterization focus at the first scale. A heat transfer model and mass coupled starting from a mathematical model is then developed using two approaches FD/FE at wall and envelope levels. At this scale, the properties related to the heat and mass transfer of unfired earth bricks are characterized in order to supply, eventually, the established model. The hygrothermal coupling has been the subject of a specific study via a dual-climate test chamber at an earth wall scale. FD/FE implementations have resulted in a detailed analysis of transfers across tested earth wall with a reduction work of order required to limit the calculation time. Emphasis is placed on the effects of moisture brought in indoor environments in order to validate a digital tool

developed in this work. Figure 1 illustrates the approach adopted.

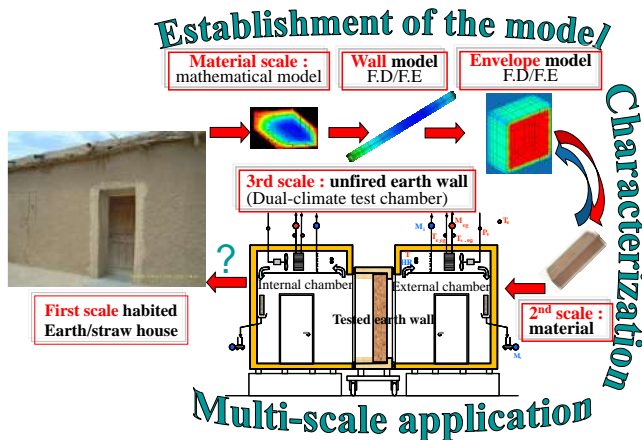


Figure 1

Adopted approach

MATERIAL AND METHODS

First scale (inhabited house): At the first characterization scale, an introverted house, built of earth and straw under hot and hyperarid climate of Barika in Algeria was selected for the monitoring of 15 months, Figure 2. Readings of temperature and relative humidity were taken every fifteen minutes using LogTag sensors in two rooms opening onto a courtyard: the living room (S-E) and bedroom 2 (N-W). For the sampling of external climatic conditions, a third sensor has been placed under protection at the S-E facade.

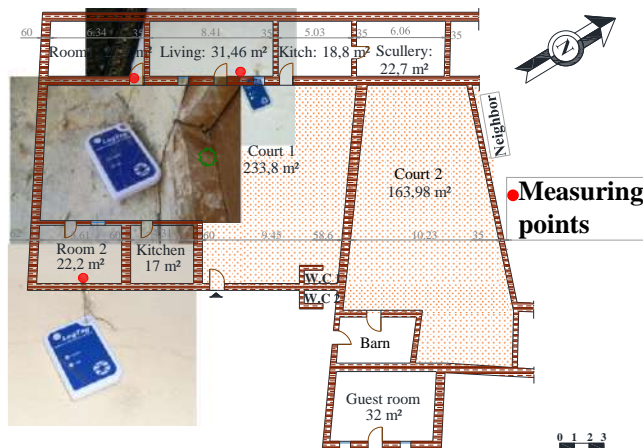


Figure 2

Plan of earth-straw house and measuring points

Second scale (material): At this scale, three half unfired earth bricks of dimensions: $L \times W \times H = 107$

$\times 57 \times 107$ mm have followed a dissociated characterization, thermal and hygric.

Sorption isotherm: Identification of sorption isotherms is based on the identification of the content equilibrium moisture for each relative humidity level in adsorption and desorption. To obtain the complete sorption isotherms using the gravimetric method, a follow in the climatic chamber by regular weighing of the samples, Figure 3, was performed according to the chosen following hygric path :

- Sampling is first conditioned in the atmosphere of the laboratory (+/- 20 °C, +/- 50% RH) ;
- An adsorption phase at 95% RH and at a constant temperature at 20 °C ;
- Two desorption phases at 65% RH and 50% RH at 20 °C of constant temperature ;
- Sample passage in the oven at 103°C for optimum drying and measuring the dry mass M_s ;
- Three levels of adsorption at 50% RH, 65% RH and 80% RH at 20 °C.

The evolution of the average moisture content \bar{w} is derived from the evolution of the wet mass M_h according to the following expression :

$$\bar{w} = \frac{M_h - M_s}{M_s} \quad (1)$$



Figure 3

Unfired earth bricks samples, weighing and followed in the climate test chamber

Characterization of the heat transfer properties (conductivity, specific heat and density):

At each stabilization of RH level during measurement of sorption isotherms, thermal conductivity measures of unfired earth bricks were carried out using the hot disk method, Figure 4. This technique, based on the principle of Transient Plane Source (TPS) gives direct access to the thermal conductivity [8]. A fine probe is placed between two blocks of the material being measured. The probe consists of a nickel wire coiled in the shape of a double-spiral and inserted into a Kapton film. The probe

simultaneously plays a role of surface heat source (Joule effect) and of a sensor measuring the temperature rise, via the measurement of the electrical resistance of the wire.



Figure 4

Measure of thermal conductivity by hot disc method

Also, the dry heat capacity C_p measure of unfired earth bricks was performed by the C80 Calvet calorimeter (Setaram), of differential type. Samples were ground and then placed in an oven for 24 hours at 110° C of temperature. In parallel, the experience of white (empty cell) was launched in advance for a period of 48 hours. On leaving the oven, the sample is weighed with an electronic balance of high precision. The sample cell is then inserted into the calorimeter with a rod for the data processing, Figure 5.



Figure 5

Measure of dry heat capacity: crushed sample in the oven, weighing, introduction into the cell and data processing

As to the dry density of the unfired earth bricks was measured directly on the tested samples.

Third scale (wall): This scale represents the intermediate dimension to pass from the material scale at the complete envelope scale. In addition, the actual dimensions regarding the mass and heat transfer must be able to characterize the one hand, diffusion properties, but also its interaction with the heat transfer. A wall of 2.5m of side and 10cm of thickness, composed of unfired earth bricks braced by a wooden frame is tested in response to dynamic thermal hydric sollicitation using a dual climate chamber, Figure 5.

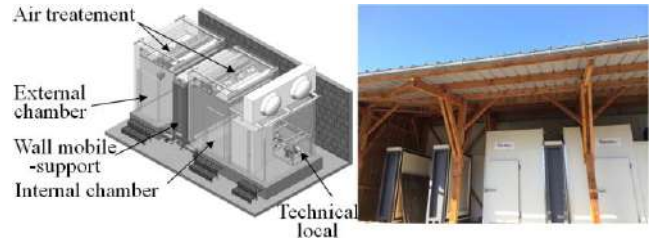


Figure 6

Dual climate test chamber

When built, the wall was instrumented in two parts, left and center, of 5 sensors each, incorporated into the bricks at different depths in order to measure thermal and moisture gradients during the various tests. Spaced 10 mm into the thickness, the sensors were arranged at mid-height of the wall in the provided cavities, Figure 7. The instrumentation is complemented by surface temperature sensors. The measures of temperature and relative humidity of the both rooms are taken by the computer control system.

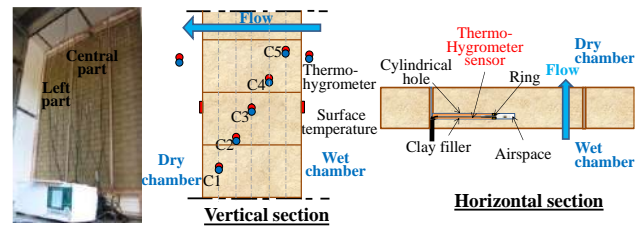


Figure 7

Monitoring and measuring points of the earth wall

RESULTS AND DISCUSSION

Monitoring of inhabited house: Living room's ambient temperature offers stability with an average amplitude of 3.8 K. It falls in late day and follows the external temperature due to the free-cooling. An amortization of 10.6 K was recorded after 4hr 45min between the outer peak temperature (46.4°C) and the indoor temperature (35.8°C), Figure 8. The time lag and amortization phenomena are obviously due to the high thermal inertia. Amortization is caused by the insulating effect of earth/straw component. It's a hygroscopic material that combines both, a macroporosity due to the imperfect arrangement of the earth particles and a microporosity of straw vegetal fibers [9]. The time lag is mainly due to the effect of large thickness of walls and roof (60-45cm).

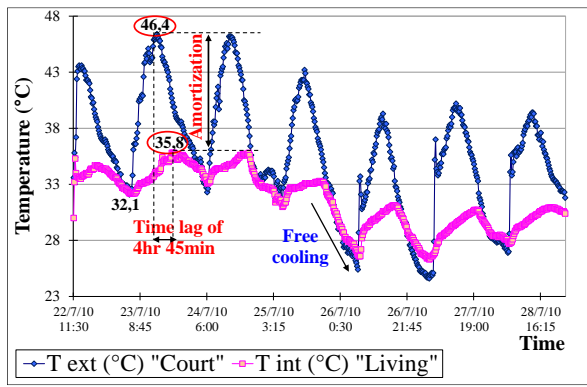


Figure 8

Hourly variation of outdoor and indoor temperature in the south east living room (summer period)

Because of the climate aridity, the outdoor relative humidity is below 20%RH. In the living room, relative humidity is significantly higher (Figure 9) as the earth regulates well the indoor conditions. Study of hygrothermal properties of earth bricks has confirmed their ability to regulate the internal moisture [10].

For passive cooling purposes, the users claim that they pour 4 buckets water of 20 liters and that they allow for an hour or more to dry the floor after. Small replicas succeed each time the peaks in the indoor specific humidity (16.82 g/kg). Chores performed between 9 am and 11 am are followed by a ventilation period (fans operating) that brings down the specific internal humidity (13.41 g/kg). Just after the closing of windows, another peak (14.7 g/kg) is reached caused by a restitution of the water vapor of the envelope hygroscopic material. A rate of 2.12 g/kg was recorded after 5hr 45min, Figure 9. This amount of water released, however small, improves the thermal comfort sensation.

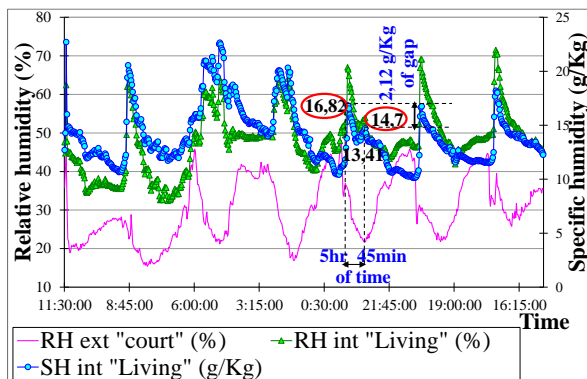


Figure 9

Hourly variation of relative and specific humidity in the living room (summer period)

Modeling tool:

Coupled transfer equations: A mathematical model is developed according two approaches FE under Cast3M and DF under VBA (Excel) in models of wall and zone. The idea was to compare the results of both approaches, if they match, the model established in this case, is validated. The two models are powered by the heat and mass materials properties and the boundary conditions of the real climate. Figure 10 summarizes the various transfer forms and storage: thermal and mass in liquid and vapor form, and the interactions between them.

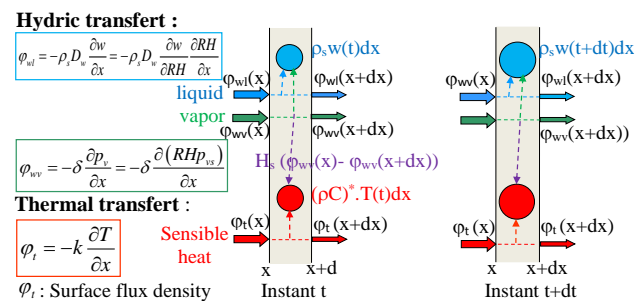


Figure 10

Schematic representation of the thermal and hygric balance on an infinitesimal slice of material

Two equations of thermal and hygric balance express the coupled transfer, assuming that one is in the hygroscopic field, liquid water is neglected. The driving potential are T (K) and RH ($0 \leq RH \leq 1$). The first equation (2) expresses the energy stored or restored which is equal to the thermal conduction balance more Q_t , the thermal source of sorption heat ($H_s = 2500 \text{ kJ.kg}^{-1}$). The second equation (3) expresses the hygric distribution balance.

$$(\rho C) \cdot \frac{\partial T}{\partial t} = \vec{\nabla} (k \cdot \vec{\nabla} T) + Q_t \quad (2)$$

With : $Q_t = H_s \cdot \vec{\nabla} (\delta \cdot \vec{\nabla} (RH \cdot p_{vs}))$

$$\rho_s \left(\frac{\partial w}{\partial RH} \right) \cdot \frac{\partial RH}{\partial t} = \vec{\nabla} (\delta \cdot p_{vs} \cdot \vec{\nabla} RH) + \vec{\nabla} (\delta \cdot RH \cdot \vec{\nabla} p_{vs}) \quad (3)$$

A strong assumption consist that in any point of the material, the hygroscopic equilibrium is reached, i.e. that weight water content w of material corresponds to the moist air relative humidity RH in the network of voids, according to the sorption isotherms.

Characterization at material scale

Sorption isotherm: The model proposed by Merakeb [11], based on the thermodynamics of the water phase equilibrium linked with its saturated vapor pressure is used. The relationship is given as a function of the water content and relative humidity:

$$w = w_s \exp(\varphi \ln(RH)) \exp(aRH) \quad (4)$$

With w_s : equilibrium moisture (at 100% RH) ; φ and a : calibration parameters of the isotherms curve.

The obtained isotherm of sigmoidal shape of the earth bricks has a hysteresis loop moderately marked and slightly open, according to the earth hygroscopicity degree. The theoretical isotherms fits well with the experimental isotherms depending the identification of the model parameters used, Figure 11.

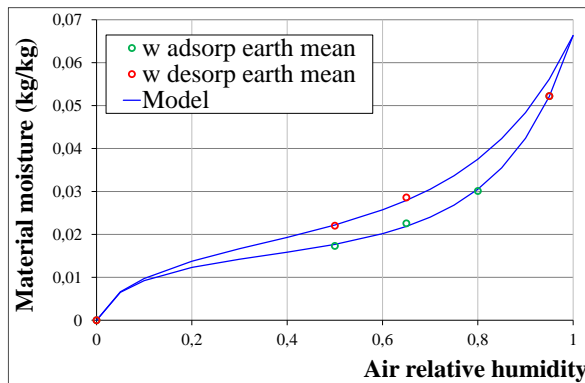


Figure 11

Sorption isotherms of unfired earth brick identified from the levels points

Diffusion properties: To identify material diffusion properties by exploiting the sorption kinetics, the experimental curves of water content variation are integrated in a minimization procedure of the discrepancies between measurements and calculation by FE model. The vapor permeability δ is supposed dependent on the humidity (nonlinear Fick's law):

$$\delta(w) = \delta_0 \cdot \exp(f \cdot w) \quad (5)$$

For unfired earth bricks, the values of δ_0 (anhydrous permeability) is 7.48×10^{-12} , f (nonlinearity parameter) of 76.3. This identification method allows to obtain a continuous variation law of vapor permeability as a function of water content, Figure 12.

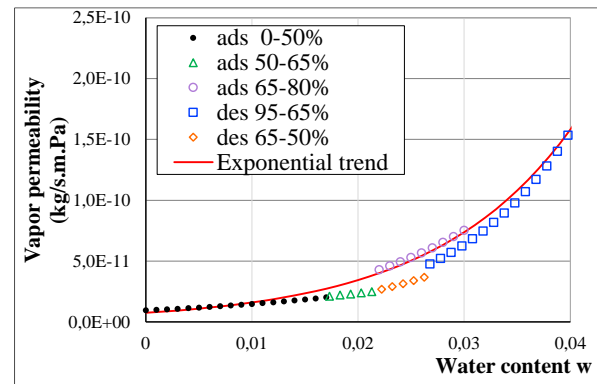


Figure 12

Vapor permeability as a function of water content

Heat transfer properties: Table 1 below gives the measured thermal properties of unfired earth bricks.

Table 1

Thermal properties of tested unfired earth bricks.

Conductivity k (W/mk)	Density ρ (kg/m ³)	Specific heat C_p (J/kg K)
0.77-0.95	1761.9-1797.6	817.62 (40°C) - 877.59 (100°C)

Characterization at material scale

Modeling of the experimental conducted at the tested wall in the dual climate chamber is based on a FE simulation (Cast3M). To limit the calculation induced time, firstly, by the incremental form of resolution and loops of convergence between the thermal and hygric resolution, the spatial discretization, while being three-dimensional, is devoted to a wall strip, of 10 mm² surface. In terms of boundary conditions, temperatures and relative humidity of both chambers are imposed via the thermal and hygric convection exchanges. Along the four faces (in the thickness of the wall), outgoing thermal and hygric flows are null.

Finite element implementation: implementation of heat and mass transfer equations is performed in Cast3M by diverting "Translin" procedure developed for the transfer of non-linear heat allowing to solve, incrementally, the partial differential equation:

$$a(T) \cdot \frac{\partial T}{\partial t} = \vec{\nabla} \cdot (b(T) \cdot \vec{\nabla} T) + Q \quad (6)$$

Thus, the incremental algorithm is used for solving the heat transfer equation recalled below:

$$\rho \cdot C \cdot \frac{\partial T}{\partial t} = \frac{\partial}{\partial x} \left(\lambda \cdot \frac{\partial T}{\partial x} \right) + H_s \cdot \frac{\partial}{\partial x} \left(\delta \cdot \frac{\partial (H_v \cdot P_{vs})}{\partial x} \right) \quad (7)$$

The mass transfer equation is:

$$\rho_s \cdot \frac{\partial \omega}{\partial RH} \cdot \frac{\partial RH}{\partial t} = \frac{\partial}{\partial x} \left(\delta \cdot \frac{\partial (RH \cdot P_{vs})}{\partial x} \right) + \frac{\partial}{\partial x} \left(\delta \cdot RH \cdot \frac{\partial P_{vs}}{\partial x} \right) \quad (8)$$

To optimize the parameters materials introduced into model, a simplex algorithm has helped to minimize the gap between numerical and experimental results.

The simulation presented relates to the solicitation by multiple slots RH imposed in the wet chamber of the enclosure at 23°C. The dry chamber is kept at 50% RH and 23°C. The first slot is at 90%RH for half an hour followed by a free regime for 6 days, then by stabilization at 50%RH. The latest successive jumps are at 80%RH with an offset of 30 min, which is also followed by a hygric regulation interruption. The hygric response is accentuated depending on the sensor location in earth wall, Figure 13. The moisture damping is highlighted according to the depth moisture penetration in the wall. The simulation gives a good behavior with gaps to experimental surveys, less than 3%RH. Temperature profiles show the moisture gradient effect on the sorption heat, Figure 14.

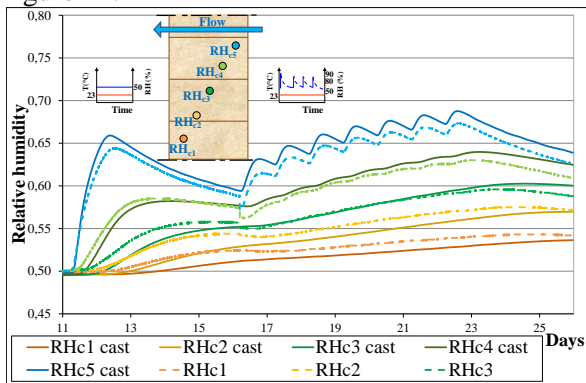


Figure 13

Measured and modeled hygric profiles

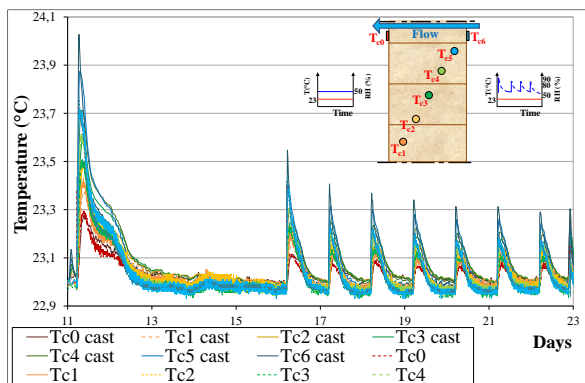


Figure 13

Measured and modeled temperature profiles

CONCLUSIONS

This work has allowed to study via the experimental and numerical approaches, the thermal behavior of the unfired earth. The first level of characterization with the monitoring of the earth/straw house shows that the envelope with this material regulates the ambient air humidity by the effect of "hygric buffer". It also provides a good heat insulation in summer by the thermal inertia effect, and therefore it reduces the energy consumption.

At the centimetric scale of material, an experimental characterization was conducted, suited to the established numerical model. Thus, a reverse method was developed to characterize the intrinsic properties of hygric diffusion for unfired earth. This scale has allowed the characterization of the diffusion process by incorporating non-linear hygric behavior and the sorption isotherms.

The metric scale of the wall via the dual-climate chamber has permitted to characterize the thermal hygric coupling. Using a FE code, although expensive in calculation time, allowed to consider the energy exchanges at the middle of the wall.

The final motivation of this study aimed in perspective, is to apply the transfer coupled model established at the inhabited house scale.

ACKNOWLEDGMENTS

The authors would like to acknowledge Pr. Rachid Bennacer from ENS Cachan (Paris), Benoît Nait Ali from GEMH (Limoges) and CTMNC from Limoges.

REFERENCES

1. T. Padfield, 1999, The role of absorbent building materials in moderating changes of relative humidity, Ph.D. thesis, University of Denmark.
2. D. Allinson, M. Hall, 2010, Hygrothermal analysis of a stabilised rammed earth test building in the UK, Energy and Buildings 42, 845–852.
3. D. Medjelekh, L. Ulmet, F. Dubois, 2013, Effet du comportement thermo-hydrigue de l'enveloppe hygroscopique sur le confort thermique de l'habitat: cas de la terre et la paille, XIème Colloque CIFQ 2013 : 3-5 june, Reims, France.

4. S. Liuzzi, M.R. Hall, P. Stefanizzi, S.P. Casey, 2013, Hygrothermal behaviour and relative humidity buffering of unfired and hydrated lime-stabilised clay composites in a Mediterranean climate, *Building and Environment* 61 82-92.
5. F. Collet, L. Serres, J. Miriel, M. Bart, 2006, Study of thermal behaviour of clay wall facing south, *Building and Environment* 41, 307–315.
6. J.E. Oti, J.M. Kinuthia, J. Bai, 2009, Engineering properties of unfired clay masonry bricks, *Engineering Geology* 107, 130–139.
7. J.C. Morel, A. Mesbah, M. Oggero, P. Walker, 2001, Building houses with local materials: means to drastically reduce the environmental impact of construction, *Building and Environ.* 36 1119-26.
8. S.E. Gustafsson, 1991, Transient plane source techniques for thermal conductivity and thermal diffusivity measurements of solid materials, *Review of Scientific Instruments* 62, 3, 797-804.
9. D. Medjelekh, 2015, Caractérisation multi-échelle du comportement thermo hydrique des enveloppes hygroscopiques, PHD thesis, Limoges University.
10. H. Cagnon, J.E. Aubert, M. Coutand, C. Magniont, 2014, Hygrothermal properties of earth bricks, *Energy and Buildings* 80, 208–217.
11. S. Merakeb, F. Dubois, C. Petit, 2009, Modeling of the sorption hysteresis for wood, *Wood Science and Technology*, 43(7-8), 575–589.

EXPERIMENTAL EVALUATION OF LOAD-STRAIN BEHAVIOUR OF GFRP POLES UNDER FLEXURAL LOADING.

Slimane Metiche* & Radhouane Masmoudi**

* University of Sciences & Technology Houari Boumediene,
BP 32 El-Alia, Bab-Azzouar, Algiers, Algeria.

** University of Sherbrooke, Québec, Canada.

*Corresponding author: Fax: +213 21 24 79 04 Email: Slimane.Metiche@USherbrooke.ca

ABSTRACT

Glass Fibre Reinforced Polymer (GFRP) poles offer several properties advantageous to applications in overhead power line and telecommunications networks. Their high strength-to-weight ratio and light weight contribute to reduce installation and transportation costs, and make them more interesting alternatives than poles made of traditional materials. The use of GFRP poles is not new. A number of manufacturers are already involved in the production of such poles. The research in this field, however, is very limited. An extensive research project is currently carried out at the University of Sherbrooke to develop and evaluate the flexural behaviour of lightweight fibre reinforced polymer (FRP) poles. The strains of Composite Materials can be evaluated experimentally and is particularly useful in verifying a failure criteria or a theoretical model of complex geometry. These experimental results allowed determining the state of strains on both sides of the GFRP poles at different height levels and at the opening as well as determining the maximum ultimate strains at failure and their respective corresponding critical positions.

INTRODUCTION

The mechanical behaviour of Fibre-Reinforced Polymer (FRP) materials is a topic that has attracted several researchers in recent years. These materials have very high strength-to-weight ratios, and because of this they are steadily being selected over metal alloys in a variety of structural applications. While many studies have addressed the material failure and buckling of thin-walled sections such as I-beams, box beams, etc., made from composite materials [1] ; [2], very few studies have been conducted on the behaviour of tapered sections [2]. The behaviour of scaled FRP models of transmission poles under cantilever loading conditions was investigated by Lin [3]. The four specimens tested were of prismatic circular hollow cross-section. The outside diameter of the poles was 76 mm and the wall thickness was 6 mm. These were fabricated by filament winding strips of pultruded sheets arranged in circular pattern. According to the test results, a linear behaviour of the FRP poles was observed up to failure. Experimental and analytical studies were carried out [4]; [5] to validate the predicted ultimate loads for tapered filament wound FRP scaled poles subjected to cantilever bending. The results of this study show

that the stiffness and the strength of FRP poles as well as the mode of failure depend mainly on their wall thickness. While a local buckling failure was observed for thin walled samples, compression and tension failures were observed for samples with more significant thicknesses. The fibre orientation has a significant effect on the performance of FRP poles. The same performance of FRP poles having high fibre volume fraction can be achieved by using less fibre volume fraction but with changing the fibre orientation towards the longitudinal direction [6] and the incorporation of circumferential layers tend to increase the critical ovalisation load [7]. Using high proportions of circumferential layers, to fabricate filament winding FRP laminates, leads to a lower tensile strength and a higher ultimate strain [6]. More tests, however, are required to determine the optimum values of fibre angle and fibre volume fraction. A research project is currently carried out at the University of Sherbrooke (Quebec, Canada) and the main objective is to study the full-scale flexural Behaviour of fibre-reinforced polymer (FRP) tapered poles manufactured by the filament winding process, in order to optimize the design and to propose improvement of the manufacturing process [8]; [9]; [2].

EXPERIMENTAL PROGRAM

Mechanical bending tests under lateral loading were performed on 22 full-scale prototypes of FRP poles with length ranging from 5 to 12 m. The FRP poles having hollow circular cross section and variable wall thickness were produced with the filament winding process, using epoxy resin reinforced with E-glass fibres. Each type of the poles tested in this study is constituted by three zones where the geometrical and the mechanical properties are different in each zone. The difference of these properties is due to the number of layers used in each zone and the fibre orientation of each layer. The mechanical and physical properties of the fibres and the resin are presented in Table 1. The characteristics and configuration of the tested poles are presented in Table 2. Two types of fibres (Type A & Type B) are used to evaluate their effects on the flexural behaviour, the only difference between both fibre types is the linear density as shown in Table 1. All test prototypes have been tested in flexural bending up to failure. The analysis of the different failure modes was presented in previous works [2]; [8].

Table 1
Properties of Fibres and Resin.

Properties	Glass	Glass	Epoxy resin
	fibres type A	fibres type B	
Tex (*) (g/km)	1100	2000	-
Density (g/cm ³)	2.6	2.6	1.2
Modulus of elasticity (GPa)	80	80	3.38
Shear modulus (GPa)	30	30	1.6
Poisson's ratio	0.25	0.25	0.4

(*): In the fibre industry the *tex* indicates the weight in gram of a 1000 m long single fibre (linear density).

Each type of pole tested in this study is constituted by three zones, where the geometrical and the mechanical properties are different in each zone. The difference of these properties is due to the different number of layers used in each zone and the fibre orientation of each layer. The fibre content of each prototype, expressed in volume ratio V_f was determined experimentally by pyrolysis tests [2]. It should be mentioned that all the prototypes presented in this study are single segment and were fabricated

with extra reinforcing provided around the principal holes except for the prototypes 17-B-3-C and 17-A-3-C. On the other hand, there was no extra reinforcing provided around the hole located under the ground line. All the holes were cut at the manufacturer site after the poles were fabricated. A new test-setup (Figure 1) was designed and built according to the recommendations of the Standards ASTM D 4923-01[10]; and ANSI C 136.20-1990 [11] as well as the Proposed California Test 683-1995[12]. A 225 KN load-capacity cell was used while the displacement rate of the bridge crane was 12 mm/sec (Figure 2). The deflection of the FRP poles was measured with a draw wire transducer (DWT) at $h_c/4$; $h_c/2$ as well as under the load application position (Figure 2), where h_c is the cantilever length or free length of the pole. Electrical strain gages were placed on the two sides of the poles (compression and tension), near the ground line support (level 0), at $h_c/8$, $h_c/4$, $h_c/2$, $3/4h_c$ as well as at the principal maintenance opening zone (Figure 3). The strain gages were used to monitor the longitudinal strain (ϵ_x), the circumferential strain (ϵ_y) and the strain at 45° from the longitudinal axis of the pole. The values of these three types of strains were used to determine the shear strain (γ_{xy}) using Equation 1 [13]. At the principal maintenance opening zone, the strain gages were placed in “Front”, “Behind”, “Left”, “Right” of the hole (Figure 3.a) as well as “Under” the hole (Figure 3.b).

$$\gamma_{xy} = 2\epsilon_{at45^\circ} - \epsilon_x - \epsilon_y \quad (\text{Equation 1})$$



Figure 1
Full-scale test setup.

Table 2
 Characteristics and Configuration of the Tested Poles.

Pole Id. And samples		h _{Total} * (mm)	h _{Supported} * (mm)	Bottom-Top diameters (mm)
17-B-3-C	2	5093	914	150-76
17-A-3-C	2	5093	914	150-76
18-B-3-C	2	5398	914	155-76
18-B-3-T	2	5398	914	155-76
20-B-4-C	2	5994	1219	164-76
33-B-5-C	2	10 058	1524	261-114
35-B-5-C	2	10 566	1524	270-114
40-A-5-C	2	12 090	1524	291-114
40-B-5-C	1	12 090	1524	291-114
40-B-5-T	1	12 090	1524	291-114
29-B-5-C	1	8738	1524	247-114
18-B-4-C	1	5398	1219	155-76
18-B-4-T	2	5398	1219	155-76

Pole Id. And samples	Principal hole (AGL)**			
	Dimensions (mm)	Location (mm)	Positioning	
17-B-3-C	2	64x127	610	Comp.
17-A-3-C	2	64x127	610	Comp.
18-B-3-C	2	102x305	762	Comp.
18-B-3-T	2	102x305	762	Tension
20-B-4-C	2	102x305	1372	Comp.
33-B-5-C	2	102x305	1219	Comp.
35-B-5-C	2	102x305	1219	Comp.
40-A-5-C	2	102x305	1219	Comp.
40-B-5-C	1	102x305	1219	Comp.
40-B-5-T	1	102x305	1219	Tension
29-B-5-C	1	64x127	457	Comp.
18-B-4-C	1	102x305	457	Comp.
18-B-4-T	2	102x305	457	Tension

(*) h_{Total}: Total length of the pole, h_{Supported}: Supported length, (**) AGL: Located Above Ground line.

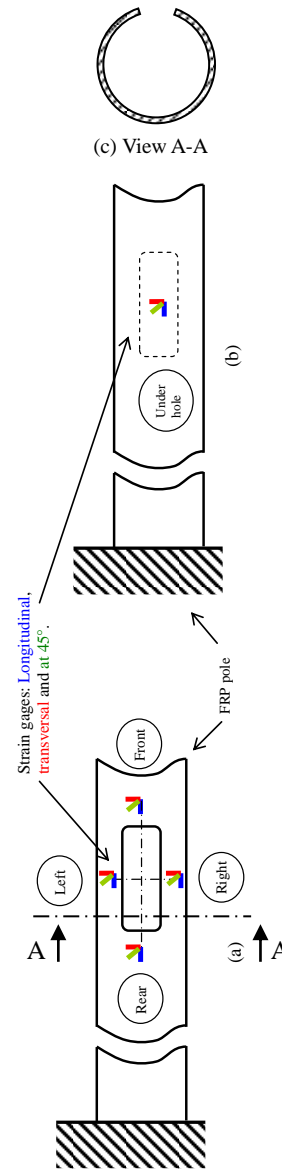


Figure 3.
 Strain gages positions.

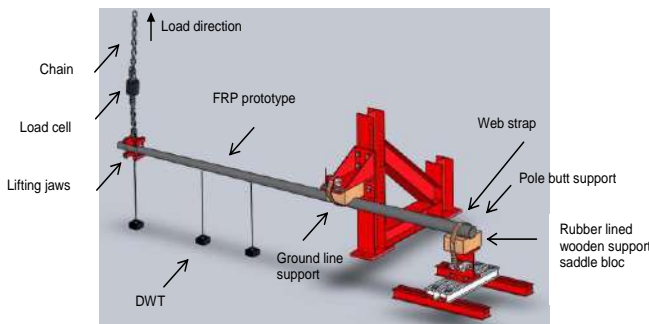


Figure 2.
 Schematic drawing of the full- scale test setup.

RESULTS AND DISCUSSION

Load – longitudinal strain behaviour

The Figure 4 shows a typical load – longitudinal strain curves at the ground line level (level 0) of the prototype 29-B-5-0-(1). During the bending test the prototype was loaded up to (5712 N) which represents 93% of the failure load, then unloaded to its initial state before the test, then loaded up to failure (6142 N). The curves in Figure 4 show that the load - longitudinal strain behaviour under lateral loading was practically linear-elastic.

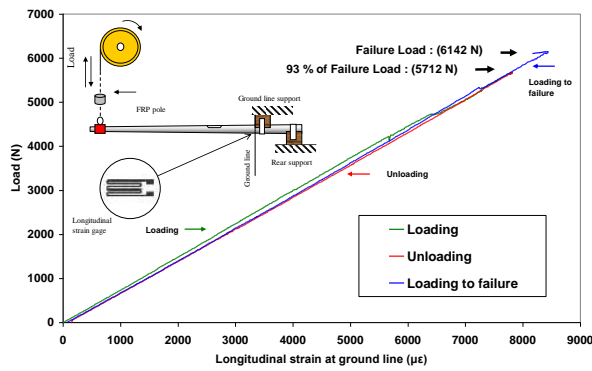


Figure 4.

Load - longitudinal strain curve, typical linear elastic behaviour.

Strain analysis, levels (0, $h_c/8$, $h_c/4$, $h_c/2$ and $3/4 h_c$)

Typical load – strain curves (longitudinal ϵ_x , transversal ϵ_y , at 45° and shear γ_{xy}) respectively at height levels (0, $h_c/4$, $h_c/2$ and $3/4 h_c$) were drawn. The ultimate strains at failure are presented on Table 3. It should be noted that the behaviour of two prototypes tested in the same test conditions and for the same parameter was almost identical indicating good repeatability of the tests.

Longitudinal strains

Table 3 shows that the ultimate longitudinal strain at failure recorded on the tension side of the pole was higher (in absolute value) than that recorded on the compression side respectively for the levels (0, $h_c/2$ and $3/4 h_c$), while the opposite was observed at the level ($h_c/8$). The curves load – longitudinal strain (Figure 5) show a linear behaviour up to failure regardless of the pole’s side considered (tension or compression). The longitudinal strains recorded during loading and at failure on the pole’s compression side (Figure 5) and (Table 3) respectively at levels (0, $h_c/8$; $h_c/2$ and $3/4 h_c$) can be ranked from highest to lowest (in absolute values) as follows: $h_c/8$, 0, $h_c/2$, $3/4 h_c$ for the prototypes 20-B-4-C and 0, $h_c/4$, $h_c/2$, $3/4 h_c$ for the other prototypes. It should be noted that the compression longitudinal strains recorded at $h_c/8$ were higher than those recorded at the level 0 for the prototypes 20-B-4-C. This confirms the compression failure mode at this level for the prototypes 20-B-4-C [2] and can be attributed to the high compression stress at the level $h_c/8$. The longitudinal strains recorded on the pole’s tension side can be ranked from the highest to the

lowest (in absolute values) as follows: 0; $h_c/8$; $h_c/2$, $3/4 h_c$.

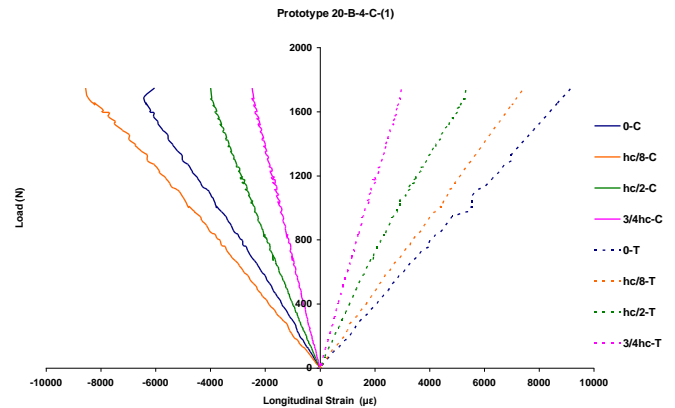


Figure 5.

Typical Load – Longitudinal Strain (Prototype 20-B-4-C- (1))

Transversal or hoop strains

Table 3 shows that the ultimate transversal strain at failure recorded on the tension side of the pole was higher (in absolute value) than that recorded on the compression side respectively for the levels (0, $h_c/8$, $h_c/2$ and $3/4 h_c$). The curves load – transversal strain show a non-linear behaviour either on tension side or compression side of the pole. The transversal strains recorded during loading and at failure on the pole’s compression side respectively at levels (0, $h_c/8$; $h_c/2$ and $3/4 h_c$) can be ranked from highest to lowest (in absolute values) as follows: 0, $h_c/8$, $3/4 h_c$, $h_c/2$. The transversal strains recorded on the pole’s tension side can be ranked from highest to lowest (in absolute values) as follows: 0; $h_c/8$; $h_c/2$, $3/4 h_c$.

Shear strains

The values of the longitudinal strain (ϵ_x), the circumferential strain (ϵ_y) and the strain at 45° from the longitudinal axis of the pole were used to determine the shear strain (γ_{xy}) using Equation 1 [13]. Figure 6 shows that the Load – shear strain curves are linear up to about 50% of the failure load. The maximum shear strain was recorded at the ground line level (level 0) on the compression pole’s side and had a value of $4496\mu\epsilon$.

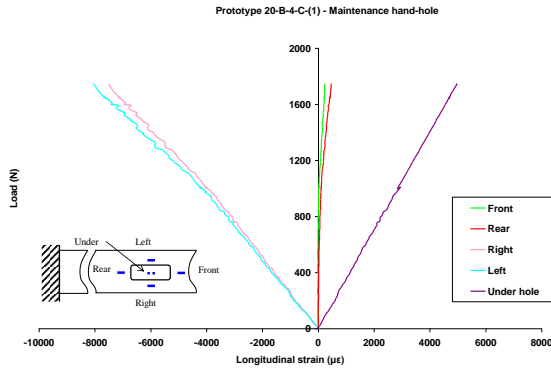


Figure 6. Typical Load – Longitudinal Strain (Opening zone, Prototype 20-B-4-C-(1))

Strain analysis at the maintenance opening zone

The present investigation allowed drawing the load – strain curves (longitudinal ϵ_x , transversal ϵ_y , at 45° and shear γ_{xy}) at the maintenance opening zone. The ultimate strains at failure are presented on Table 3. The curves load-longitudinal strains as well as the curves load – transversal strains of the hole’s opposite zones have the same shape. It should be noted that the behaviour of two prototypes tested in the same test conditions and for the same parameter was almost identical indicating good repeatability of the tests.

The curves load-longitudinal strains shows that during the loading and up to failure the longitudinal strains recorded on the Left or Right of the maintenance opening are (in absolute values) larger than those recorded in Front or Behind or Under the opening. This indicates that the most critical longitudinal strains at the principal opening zone are located on the sides (Left & Right) of the opening. the curves load – transversal strains shows that during the loading and up to failure the transversal strains recorded under the maintenance opening are (in absolute values) larger than those recorded around the hole (in Front or Behind or Left or Right of the opening). This indicates that the most critical transversal strains at the principal opening zone are located under the opening. During the loading and up to failure the longitudinal strains are larger (in absolute values) than the transversal strains considering the same location except on Front location and Behind location where the opposite was observed. These two locations (Front and Behind) of the opening seem to be insensitive to longitudinal strains.

Table 3. Ultimate Strains at Failure. Prototype 20-B-4-C-(1).

Position	LONGITUDINAL STRAINS ($\mu\epsilon$)	
Pole’s side		
	Compression	Tension
ALONG THE POLE		
0	-6037	9187
h_c/8	-8561	7461
h_c/2	-3987	5342
3/4h_c	-2468	2980
OPENING ZONE		
Front	241	-----
Rear*	464	-----
Right	-7517	-----
Left	-8048	-----
Under	-----	4974
Position	TRANSVERSAL STRAINS ($\mu\epsilon$)	
Pole’s side		
	Compression	Tension
ALONG THE POLE		
0	2057	-5324
h_c/8	904	-4384
h_c/2	545	-2986
3/4h_c	734	-1898
OPENING ZONE		
Front	-1730	-----
Rear*	-1920	-----
Right	2412	-----
Left	2384	-----
Under	-----	-3089
Position	STRAINS AT 45° ($\mu\epsilon$)	
Pole’s side		
	Compression	Tension
ALONG THE POLE		
0	-4238	3019
h_c/8	-3123	1580
h_c/2	-1663	985
3/4h_c	-813	499
OPENING ZONE		
Front	-791	-----
Rear*	-1177	-----
Right	-2886	-----
Left	-3341	-----
Under	-----	579

(*): Rear position of the maintenance opening coincides with h_c/4. h_c is the cantilever height of the prototype.

This can be attributed to the presence of the opening which constitutes a discontinuity of the material. The transverse strains are however generated by the flattening (ovalisation) of the pole at the maintenance opening zone. The curves load – shear strains shows that the Load – shear strain curves at the principal opening are linear up to about 50% of the failure load. The maximum shear strain was recorded at the left of the opening and had a value of $1018\mu\epsilon$.

CONCLUSIONS

In this paper, the full-scale flexural Behaviour of Fibre Reinforced Polymer (FRP) tapered poles manufactured by the filament winding process was experimentally investigated. Different types of FRP poles, having different geometrical properties and made of epoxy resin reinforced with E-glass fibres were subjected to full scale flexural static testing. Each type of the poles tested in this study is constituted by three zones where the geometrical and the mechanical properties are different in each zone. The difference of these properties is due to the different number of layers used in each zone and the fibre orientation of each layer. Pyrolysis tests and scanning electron microscope analysis were used in this investigation to determine the fibre and the matrix volume ratio as well the stacking sequences of the different pole's zones. Electrical strain gages were placed on the two sides of the poles (compression and tension), near the ground line support (level 0), at $h_c/8$, $h_c/4$, $h_c/2$, $3/4h_c$, where h_c is the cantilever length or free length of the pole, as well as at the principal maintenance opening zone. The strain gages were used to monitor the longitudinal strain (ϵ_x), the circumferential strain (ϵ_y) and the strain 45° from the longitudinal axis of the pole. The values of these three strains were used to determine the shear strain (γ_{xy}). At the principal maintenance opening zone, the strain gages were placed in "Front", "Behind", "Left", "Right", as well as "Under" the hole. The values of ultimate strains recorded at failure on both sides (compression and tension) at different height levels of the poles as well as at the maintenance opening zone were presented in this paper. This experimental investigation of the strains allowed determining the load – longitudinal strain (ϵ_x) behaviour, load – transversal strain (ϵ_y) behaviour and load – shear strain (γ_{xy}) behaviour of the FRP poles. This study allowed also knowing the state of strains on both sides of the prototypes at different height levels and at the maintenance opening zone as well as determining the maximum

ultimate strains at failure and their respective corresponding positions.

Considering the strains occurring at levels (0, $h_c/8$, $h_c/4$, $h_c/2$ and $3/4 h_c$) the following conclusions can be drawn:

- The behaviour of two prototypes tested in the same test conditions and for the same parameter was almost identical indicating good repeatability of the tests.
- The load - longitudinal strain (ϵ_x) behaviour under lateral loading was linear elastic.
- As expected, longitudinal strain gages on the compression side of a given prototype were subjected to compression and transversal strain gages were subjected to tension. The opposite was observed on the tension side of the prototype.
- Without considering the hand hole, the maximum longitudinal strains ($\epsilon_{x \max}$) at the failure occur usually at the ground line level (level 0) or at the level $h_c/8$.

Considering the strains occurring at the maintenance opening, the following conclusions can be drawn:

- Good symmetry of the longitudinal strains (respectively the transversal strains) has been generally observed between the opposite sides around the maintenance opening.
- Around the maintenance opening, the longitudinal strains are greater than the transverse strains (during loading and up to failure) except for front and back of the opening where the longitudinal strains are much smaller than the transverse strains. These two zones (front and rear) seem insensitive to longitudinal strains. This can be attributed to the presence of the opening which constitutes a discontinuity of the material. The transverse strains are however generated by the flattening (ovalisation) of the pole at the maintenance opening zone. Critical positions for longitudinal strains were at the sides (right or left) or below the hole while critical positions for transverse strains were at the front or behind the hole.

ACKNOWLEDGMENTS

The research reported in this paper was partially sponsored by the Natural Sciences and Engineering Research Council of Canada (NSERC). The authors

also acknowledge the contribution of the Canadian Foundation for Innovation (CFI) for the infrastructure used to conduct testing. Special thanks to the manufacturer (FRE Composites Inc., St-André-d'Argenteuil, Québec, Canada) for providing FRP poles. The opinion and analysis presented in this paper are those of the authors.

REFERENCES

1. Barbero, E. J. and Raftoyiannis, I. G. (1993), "Euler Buckling of Pultruded Composite Columns. *Composite Structures*," vol. 24: 139-147.
2. Metiche, S. and Masmoudi, R. (2010a), *Comportement à la flexion de nouveaux poteaux en matériaux composites-Évaluation expérimentale et théorique*. Sarrebruck, Allemagne : Éditions Universitaires Européennes, 270 p.
3. Lin, Z. M. (1995), "Analysis of Pole-Type Structure of Fiber-reinforced Plastics by Finite Element Method," *Ph. D. thesis*. University of Manitoba, Manitoba, Canada.
4. Polyzois, D., Ibrahim, S. and Raftoyiannis, I. G. (1999), "Performance of fiber-reinforced plastic tapered poles under lateral loading," *Journal of composite materials*, vol. 33: 941-960.
5. Ibrahim, S. (2000) *Performance Evaluation of Fiber-Reinforced Polymer Poles for Transmission Lines*. Ph. D Thesis, Department of Civil and Geological Engineering, University of Manitoba, Winnipeg, Manitoba, Canada.
6. Metiche, S. and Masmoudi, R. (2010b) "Tensile properties of new glass fiber reinforced composite laminates produced by the filament winding wet technique" 8th Joint Canada-Japan Workshop on Composites, École de technologie Supérieure & Industrial Materials Institute, Québec, Canada, July 26-29, 2010.
7. Ibrahim, S. and Polyzois, D. (1999), "Ovalisation analysis of fiber-reinforced plastic poles," *Composite Structures*, vol. 45: 7-12.
8. Metiche, S. and Masmoudi, R. (2007), "Full-Scale Flexural Testing on Fiber-Reinforced Polymer (FRP) Poles," *The Open Civil Engineering Journal*, vol. 1: 37-49.
9. Masmoudi, R., Mohamed, H. and Metiche, S. (2008), "Finite Element Modeling for Deflection and Bending Responses of GFRP Poles," *Journal of Reinforced Plastics and Composites*, 6 (27): 639-658.
10. American Society for Testing and Materials ASTM D 4923 – 01. (2005), "Standard Specification for Reinforced Thermosetting Plastic Poles", in *Annual Book of ASTM Standards*, vol. 08.02, West Conshohocken, USA: ASTM International, pp. 726-735.
11. American National Standard Institute. (2005), "Fiber-Reinforced Plastic (FRP) Lighting Poles". American National Standard for Roadway Lighting Equipment, USA. C 136.20.
12. California Department of Transportation (1995), "Proposed California Test 683, Method for testing deflection and bending strength of fiber-reinforced plastic poles", New York, State of California, USA.
13. Bazergui, A., Bui-Quoc, T., Biron, A., McIntyre, G., Laberge, C. (2003) *Résistance des matériaux*, Québec, 3^e édition, Presses Internationales Polytechnique, 715 p.

EVOLUTION OF THE STRESS DISTRIBUTION IN THE CROSS-PLY AGED COMPOSITE LAMINATES

Khodjet-Kesba Mohamed^{1*}, Benkhedda Amina¹, Adda Bedia², Boukert billel¹

¹ Laboratoire des sciences aéronautiques, Institut d'aéronautique et des études spatiales, Algérie

² Laboratoire matériaux et hydrologie, université Sidi Belabes, Algérie

*Corresponding author: Email: mkhojet@hotmail.fr

ABSTRACT

The purpose of this paper is to investigate the progressive transverse cracking across the width of cross-ply laminates, subjected to uniaxial tensile loading under hygrothermal aging in the transient mode (desorption case). Two analytical models were used to evaluate the stress distribution, Shear Lag and the variational approach. The results were compared with finite element analysis published by Berthelot and al. These comparisons show that a complete parabolic variation of displacement gives a good approximation of the stress distribution obtained by finite element analysis. Furthermore the cracked cross ply laminate is submitted to transient conditions of temperature and moisture. The obtained results show that the hygrothermal environment has a significant effect on the stress distribution especially at the higher crack density.

INTRODUCTION

The evolution of the transverse cracking in the 90° layers was characterized in 1977 by Reifsnider [1] and Garrett and Bailey [2] for cross-ply laminates loaded in the 0° ply direction by static or fatigue traction test. Then developed in many analyses in the literature [3,4,5] where they provide a means of evaluating the different hypotheses of the approaches and their consequences on the material properties of the cracked laminates. The modeling of transverse cracking is generally schematized by the models which make the analysis of the shear transfer between fiber and matrix [6,7,8,9,10] with the assumption that the mechanical loading is transferred between the layers to 0° and 90° via a fine layer located at the interface between the layers. The authors [11,12,13,14,15] propose a law of evolution of the transverse cracking which considers that the normal ply stresses in load direction are constant over ply thickness. The approximate solution is obtained by minimizing complementary energy in the two layers of the laminate.

In this paper, two analytical models have been studied and compared with the finite element method, the shear-lag model modified by introducing the stress perturbation function and the variational approach, are used to predict the effect of transverse

cracks on the stress distribution. Then, the longitudinal stress reduction due to transverse ply cracking in cross ply laminate when this latter is initially exposed to the hygrothermal aging submitted to transient and non-uniform moisture concentration distribution is taken into account. The obtained results illustrate well the dependence of the stress distribution on the cracks density and hygrothermal conditions.

STRESS DISTRIBUTION ANALYSES

Shear-Lag model: The problem to solve is the problem of elasticity of the cracked laminate. Like any elasticity problem, the exact solution is to look in the elementary cell of the displacement and stress field, at each point satisfying the equilibrium equations, strain-movement relations, the compatibility conditions, the continuity conditions at the borders and the behavior laws in 0° and 90°-layers. We consider a symmetric cross-ply laminate which is subjected to uniaxial loads. It is assumed that the 90° ply has developed continuous intralaminar cracks in fiber direction which extend from edge to edge in the z direction. The cross ply laminate is characterized by $2.t_{90}$ the width of 90° ply, t_0 the width of 0° ply and the spacing between two cracks is $2.l_0$ (Fig. 1).

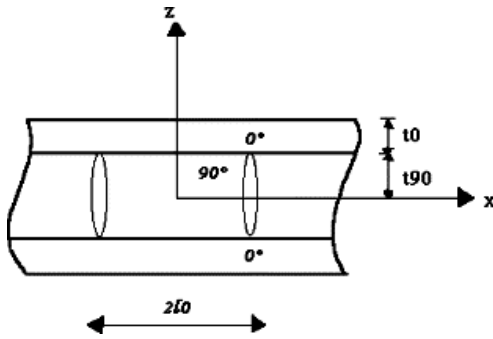


Figure 1

Transverse cracked cross ply laminate and geometric model.

The longitudinal displacement in both layers 0° plies and 90° ply is [10]:

$$u_0(x, z) = \bar{u}_0(x) + f(z)A_0(x) \quad (1)$$

$$u_{90}(x, z) = \bar{u}_{90}(x) + \left(z^2 - \frac{t_{90}^2}{3}\right)A_{90}(x) \quad (2)$$

Where $\bar{u}_0(x)$ and $\bar{u}_{90}(x)$ are the average longitudinal displacements in 0° plies and the 90° ply, respectively.

$A_0(x)$, $A_{90}(x)$ and $f(z)$ to be determined.

The shear stress $\tau(x)$ at the interface between layers 0° and 90° is:

$$\tau(x) = \frac{3G}{t_{90}} [\bar{u}_0(x) - \bar{u}_{90}(x)] \quad (3)$$

The generalized shear modulus G is done by:

$$G = \frac{G_{xz}^{90}}{1 - 3 \frac{G_{xz}^{90}}{G_{xz}^0} \frac{f(t_{90})}{t_{90} f'(t_{90})}} \quad (4)$$

The equilibrium of longitudinal forces in an element of the 90° layer leads to:

$$\frac{d\bar{\sigma}_{xx}^{90}}{dx} = -\frac{1}{t_{90}} \tau(x) \quad (5)$$

The average longitudinal displacement in 0° plies and the 90° ply are linked to the average longitudinal stress σ_c applied to a cross ply laminate by:

$$\alpha \bar{\sigma}_{xx}^0(x) + \bar{\sigma}_{xx}^{90}(x) = (1 + \alpha) \sigma_c \quad (6)$$

Where α is the stacking parameter of layer 0° and 90° :

$$\alpha = \frac{t_0}{t_{90}} \quad (7)$$

Stress strain relations in the 0° layers and 90° layer are taken in the forms:

$$\bar{\sigma}_{xx}^0 = E_0 \cdot \bar{\varepsilon}_{xx}^0 \quad \text{with} \quad \bar{\varepsilon}_{xx}^0 = \frac{d\bar{u}_0}{dx} \quad (8)$$

$$\bar{\sigma}_{xx}^{90} = E_{90} \cdot \bar{\varepsilon}_{xx}^{90} \quad \text{with} \quad \bar{\varepsilon}_{xx}^{90} = \frac{d\bar{u}_{90}}{dx} \quad (9)$$

Where E_0 and E_{90} are the Young's moduli of the 0° and 90° layers, respectively.

Taking into account the relations (3), (5), (8) and (9), the classical differential equation will be:

$$\frac{d^2 \bar{\sigma}_{xx}^{90}}{dx^2} - \lambda^2 \bar{\sigma}_{xx}^{90} = -\frac{E_{90}}{E_x^0} \sigma_c \cdot \lambda^2 \quad (10)$$

$$\lambda^2 = \frac{3G(t_0 + t_{90})E_x^0}{t_{90}^2 t_0 E_0 E_{90}} \quad (11)$$

The Young's modulus of the undamaged laminates

E_x^0 is given by the law of mixtures:

$$E_x^0 = \frac{\alpha E_0 + E_{90}}{1 + \alpha} \quad (12)$$

Finally, the stress and displacement distribution are expressed in the form:

$$u_0(x, z) = \bar{u}_0(x) + \sigma_c \frac{E_{90}}{E_x^0} \frac{1}{G_{xz}^0 f'(t_{90})} \eta \frac{\sinh \eta a \frac{x}{l}}{\cosh \eta a} f(z) \quad (13)$$

$$u_{90}(x, z) = \bar{u}_{90}(x) + \sigma_c \frac{E_{90}}{E_x^0} \frac{1}{2G_{xz}^0 t_{90}} \eta \frac{\sinh \eta a \frac{x}{l}}{\cosh \eta a} \left(z^2 - \frac{t_{90}^2}{3}\right) \quad (14)$$

$$\bar{\sigma}_{xx}^0(x, z) = \bar{\sigma}_{xx}^0(x) + \sigma_c \frac{E_0 E_{90}}{E_x^0 G_{xz}^0 t_{90} f'(t_{90})} \eta^2 \frac{\cosh \eta a \frac{x}{l}}{\cosh \eta a} f(z) \quad (15)$$

$$\bar{\sigma}_{xx}^{90}(x, z) = \bar{\sigma}_{xx}^{90}(x) + \sigma_c \frac{E_{90}^2}{2E_x^0 G_{xz}^0} \eta^2 \frac{\cosh \eta a \frac{x}{l}}{\cosh \eta a} \left(\frac{z}{t_{90}} - \frac{1}{3}\right) \quad (16)$$

$$\tau(x) = \sigma_c \frac{E_{90}}{E_x^0} \eta \frac{\cosh \eta a \frac{x}{l}}{\cosh \eta a} \quad (17)$$

Variational approach: There is another method, relatively simple, the variational approach [11-12], which satisfies equilibrium and all boundary and

interface conditions to find an optimal approximation to the principle of minimum complementary energy. By assumption, normal stress in load direction σ_{xx} are constants depending on the thickness (z) and the width (y) in the 90° and 0° layers respectively. They may be expressed in the form:

$$\sigma_{xx}^{90} = \sigma_{90}(1 - \phi_1(x)) \quad (18)$$

$$\sigma_{xx}^0 = \sigma_0(1 - \phi_2(x)) \quad (19)$$

Where σ_{90} is the stress in 90° layer before cracking, calculated by laminated plate theory for undamaged cross ply. $\frac{\sigma_{90}}{\sigma_c} = \frac{E_{90}}{E_x^0}$

σ_0 is the stress in 0° layer before cracking, calculated by laminated plate theory for undamaged cross ply. $\frac{\sigma_0}{\sigma_c} = \frac{E_0}{E_x^0}$

ϕ_1, ϕ_2 are unknown functions.

Next, we denote

$$\phi_1(x) = \phi(x) \quad (20)$$

And express $\phi_2(x)$ in term of $\phi(x)$ due to equilibrium condition in x direction:

$$\sigma_0 t_0 \phi_1(x) + \sigma_{90} t_{90} \phi_2(x) = 0 \quad (21)$$

Final expression for complementary energy will be in form of :

$$u_c = \frac{1}{2} \sigma_{90}^2 t_0^2 \int_{-a}^a \left(C_{00} \phi^2 + C_{02} \phi \frac{d^2 \phi}{d\xi^2} + C_{22} \phi \left(\frac{d^2 \phi}{d\xi^2} \right)^2 + C_{11} \left(\frac{d\phi}{d\xi} \right)^2 \right) d\xi \quad (22)$$

Where,

$$C_{00} = \frac{1}{E_{90}} + \frac{1}{\alpha E_0} \quad (23)$$

$$C_{02} = \frac{\nu_{90}}{E_{90}} \left(\alpha + \frac{2}{3} \right) - \frac{\alpha \nu_0}{3E_0} \quad (24)$$

$$C_{22} = \frac{1}{60E_{90}} (\alpha + 1)(3\alpha^2 + 12\alpha + 8) \quad (25)$$

$$C_{11} = \frac{1}{3} \left(\frac{1}{G_{90}} + \frac{\alpha}{G_0} \right) \quad (26)$$

$$a = \frac{l}{t_{90}} \quad (27)$$

Finally, the distribution of stress can be expressed in the form:

$$\frac{\sigma_{xx}^{90}}{\sigma_c} = \frac{E_{90}}{E_x^0} (1 - \phi_1(x)) \quad (28)$$

$$\frac{\sigma_{xx}^0}{\sigma_c} = \frac{E_0}{E_x^0} \left(1 + \frac{E_{90}}{E_0} \frac{1}{a} \phi_1(x) \right) \quad (29)$$

RESULTS FOR STRESS DISTRIBUTION

We present numerical examples for stress distribution based on analytical models (shear lag and variational approach). The results are compared with finite elements method for glass/epoxy laminate [10]. The material properties of the chosen composite are summarized in Table 1.

Table 1

Material properties of composite used in calculations for glass/epoxy laminate [10].

E_L (Gpa)	E_T (Gpa)	G_{LT} (Gpa)	G_{TT} (Gpa)	ν_{LT}	V_f
42.31	13.2	4.41	3.5	0.3	0.7

Variation of longitudinal stress across the thickness:

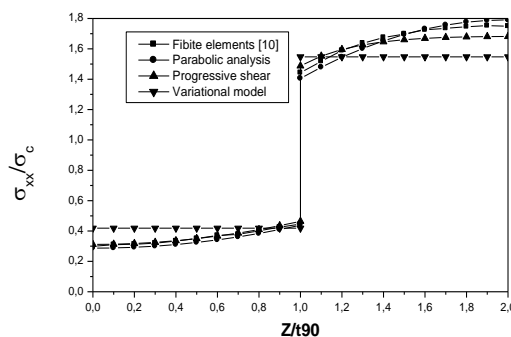


Figure 2

Variation of longitudinal stress σ_{xx} across the thickness of $[0/90]_s$ laminates with $a=2.5$ and $V_f=0.7$

The results obtained by the analytical models are compared with the finite element method published by Berthelot [10]. When the crack density increases (Fig. 2 $a = 2.5$), the first results show an increase in the longitudinal stress through the thickness of the layer at 90° and 0° due to the shear behavior of layers. Then the longitudinal stress tends to be constant, which corresponds to traction of layer. This status of traction is more easily achieved when the longitudinal modulus E_0 of the layer is high and the cracking aspect ratio "a" is low. The variational model is constant across the thickness of layers and for different cracking aspect ratio. This justified that the variational model depends only on the longitudinal coordinate. The complete parabolic variation of longitudinal

displacement in both 0° and 90° layers shows good agreement with the results from the finite element analysis [10].

Variation of longitudinal stress along the laminate: A gap is visible between the three models when we have a small cracking aspect ratio ($a = 2.5$ in Fig. 3). The Longitudinal stress is much lower than σ_{90} . New cracks are formed without or with only a small increase of the applied load for low crack density, then for large crack density, the propagation of cracks cannot take place and this is justified by the saturation status. At the crack plane, the longitudinal stress decreases and vanishes. As previously, the results deduced from the complete parabolic shear-lag analysis are in good agreement with the finite element results.

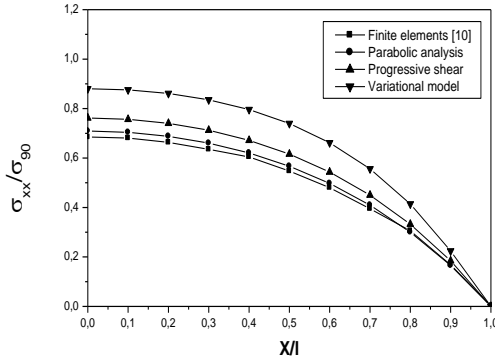


Figure 3

Variation of longitudinal stress σ_{xx} along the length of $[0/90]_s$ laminates with $a=2.5$ and $V_f=0.7$

Variation of interlaminar shear stress along the laminate : In Figure 4, it can be observed that the results of interlaminar shear stress at the interface deduced from the complete parabolic model is similar to the finite element model in large range $0 \leq x / l \leq 0.6$. The results differ in the crack plane, where only the finite element analysis satisfies the stress free boundary condition at the crack tip.

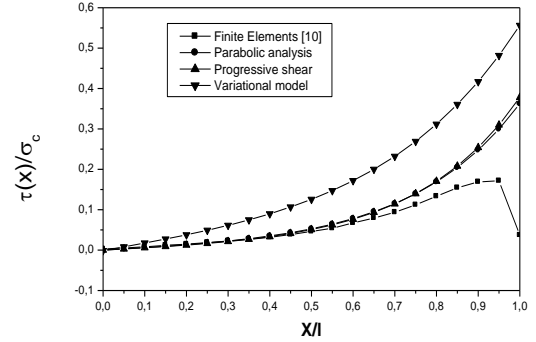


Figure 4

Variation of interlaminar shear stress τ along the length of $[0/90]_s$ laminates with $a=2.5$ and $V_f=0.7$

MODELING HYGROTHERMAL AGING

The study, here has been focused on longitudinal stress reduction due to transverse ply cracking in cross ply laminate when this latter is initially exposed to the hygrothermal aging submitted to transient and non-uniform moisture concentration distribution. Tsai [16] proposes the adimensional temperature T^* , which is the essential parameter for evaluation of the hygrothermal effect in stress distribution:

$$T^* = \frac{T_g - T_{opr}}{T_g - T_{rm}} \quad (30)$$

Where T_g is the glass transition temperature, T_{opr} is the operating temperature and T_{rm} is the room temperature. We further assume that moisture suppresses the glass transition temperature T_g^0 by simple temperature shift.

$$T_g = T_g^0 - gc \quad (31)$$

The initial moisture concentration C_{init} is uniform at $t=0$. Both sides of the plate are suddenly exposed to a zero moist environment (Fig. 5). The moisture concentration inside the plate is described by Fick equation with diffusivity D_z .

$$\frac{\partial C}{\partial t} = D_z \frac{\partial^2 C}{\partial z^2} \quad (32)$$

With the initial conditions:

$$C=C_{init} \text{ for } -h/2 \leq z \leq h/2 \text{ et } t=0$$

$$C=0 \text{ for } z=-h/2 ; z= h/2 \text{ et } t>0$$

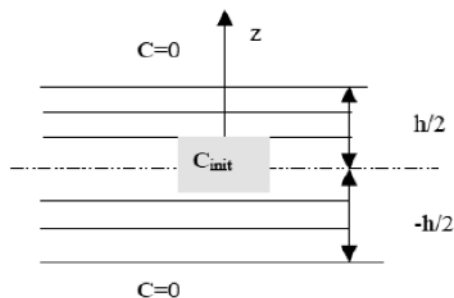


Figure 5
Desorption phase

The initial conditions being uniform and the boundary conditions are constant, the unidimensional solution of Fick equation can be expressed as [17-18]:

$$C(z_k, t) = \left[\frac{4C_{init}}{\pi} \sum_{n=0}^{\infty} \frac{(-1)^n}{(2n+1)} \cos\left(\frac{(2n+1)\pi z_k}{h}\right) \exp\left(\frac{-D_z(2n+1)^2 \pi^2 t_{init}}{h^2}\right) \right] \quad (47)$$

Effect of hygrothermal conditions on the longitudinal stress across the thickness: A small reduction in the longitudinal stress across the 0° layer is observed with the increase in temperature and moisture. On the other side a reverse behavior of the longitudinal stress is noticed across the 90° layer.

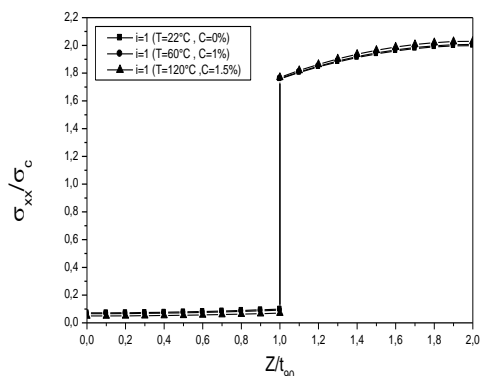


Figure 6

Hygrothermal effect on longitudinal stress σ_{xx} across the thickness of $[0/90]_s$ laminates with $a=2.5$ and $V_f=0.7$

Effect of hygrothermal conditions on the longitudinal stress along the laminate: A reduction in the longitudinal stress in the layer 90 is being much lower than σ_{90} in the case of increasing in temperature and moisture (Fig. 7) and for high crack densities on a large part of the crack spacing ($0 \leq x/l \leq 0.7$). Then the longitudinal stress decreases

and vanishes at the crack plane. The hygrothermal effect is more observed with increasing of the cracking aspect ratio.

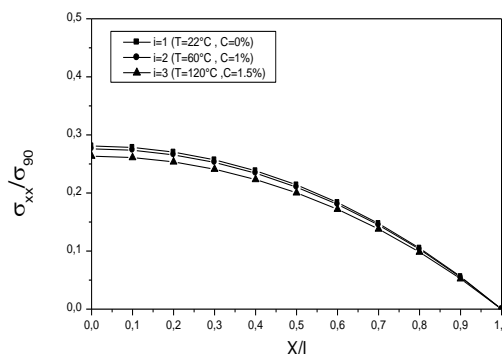


Figure 7

Hygrothermal effect on the longitudinal stress σ_{xx} along the length of $[0/90]_s$ laminates with $a=1$ and $V_f=0.7$

Effect of hygrothermal conditions on the interlaminar shear stress along the laminate: At the crack tip, we noticed a maximum reduction of interlaminar shear stress deduced from complete parabolic shear-lag analysis with increasing temperature and moisture for the absorption case.

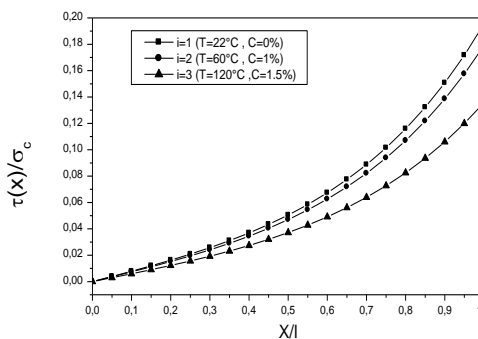


Figure 8

Hygrothermal effect on the interlaminar shear stress τ along the length of $[0/90]_s$ laminates with $a=2.5$ and $V_f=0.7$

With a small cracking aspect ratio (Fig. 8), the results show a remarkable influence of hygrothermal conditions for interlaminar shear stress on a large part of crack spacing ($0.2 \leq x/l \leq 1$). A maximum rate of reduction, approximately 30% is observed between cracked cross-ply under standard environment ($i=1$) and the other under high temperature and moisture ($i=3$). The hygrothermal

effect in the case of desorption, makes very interesting the study of the interlaminar shear stress on the cross-ply composite laminates with transverse cracking and delamination between the 0° and 90° layers.

CONCLUSION

At high crack density, only a parabolic variation of longitudinal displacement in 0° and 90° layers give a good approximation of the stress distribution obtained by finite element analysis, which makes this method more useful for studying the transverse cracking multiplication and modeling the hygrothermal aging. In the second part of this study, the cracked cross-ply laminate is exposed to the hygrothermal aging submitted to transient and non-uniform moisture concentration distribution. The results show a small influence of hygrothermal conditions depending on crack density for the longitudinal stresses across the thickness and along the laminate. On the other side, it has been observed a large influence of temperature and moisture on the reduction of the interlaminar shear stress along the laminate. This makes very attractive the study when we want to see the hygrothermal effect on the mechanical properties of composite laminates with intra- and interlaminar damage.

REFERENCES

1. Reifsnider, K.L., 1977, Some fundamental aspect of the fatigue and fracture response of composite materials" Processing of 14th annual society of engineering science meeting, Lehigh University, Bethlehem, Pa (USA), pp. 14-16.
2. Garret, K.W. and Bailey, J.E., 1977, Multiple transverse fracture in 90° cross-ply laminates of a glass fibre-reinforced polyester. *J. Mater. Sci.*, **12**, pp. 157-168.
3. L. Boniface & S.L. Ogin, 1989, Application of the Paris equation to the fatigue growth of transverse ply cracks, *Journal of Composite Materials*, **23**, pp. 735-754
4. S.E. Groves, C.E. Harris, A.L. Highsmith, D.H. Allen & R.G. Norvell, 1987, An experimental and analytical treatment of matrix cracking in cross-ply laminates, *Experimental Mechanics*, **22**, pp. 73-79.
5. R.P. Hanison & M.G. Bader, 1983, Darnage development in CFRP laminates under monotonic and cyclic stressing, *Fibre Science and Technology*, **18**, pp. 163-180.
6. Lee, I.M. Daniel, I.M., 1990, Progressive transverse cracking of cross ply composite laminates, *Journal of composite material*, **24**, pp. 1225-43.
7. Ogin, S.L, Smith, PA and Beaumont, P.W.R., 1987, Matrix cracking and stiffness reduction during fatigue of $(0/90)_s$ GFRP laminate, *Composite science and technology*, **22**, pp. 23-31.
8. Mast, P.W, Nash, G.E, Michopoulos, J.G, 1995, Characterization of strain induced damage in composite based on the dissipated energy density, *Theoretical and applied fracture mechanics*, **2**, pp. 71-125.
9. J-M. Berthelot, J-F. Le Corre, 1999, Modelling the transverse cracking in cross-ply laminates: application to fatigue, *Composites*, **30**, pp. 569-577.
10. Berthelot, J.M., 1997, Analysis of the transverse cracking of cross-laminates: a generalized approach. *J. Compos. Mater.* **31**, pp. 1780-1805.
11. Hashin, Z., 1985, Analysis of cracked laminates: a variational approach. *Mech. Mater.* **4**, pp. 121-136.
12. Hashin, Z., 1986, Analysis of stiffness reduction of cracked cross ply laminates. *Engineering Fracture Mechanics*, pp. 771-778.
13. J.A. Nairn, 1989, The strain energy release rate of composite microcracking: a variational approach, *Journal of Composite Materials*, **23**, pp. 1106-1129.
14. J.L. Rebière & D. Gamby, 1992, Analytical and numerical analysis of transverse cracking in a cross-ply laminate. Influence of the constraining effect, *Composite Structures*, **20**, pp. 91- 101.
15. J. Varna & L.A. Berglund, 1992, A model for prediction of the transverse cracking strain in cross-ply laminates, *Journal of Reinforced Plastics and Composites*, **11**, pp. 708-728
16. Tsai, S.W., 1988, *Composite Design*, Think Composites, fourth ed. Dayton, OH, USA.
17. A. Benkhedda, A. Tounsi and E.A. Adda bedia, 2008, Effect of temperature and humidity on transient hygrothermal stress during moisture desorption in laminated composite plates, *Composite Structure*, **82**, pp. 629-635.
18. C.H. Shen et G. S. Springer, 1981, Moisture absorption and desorption of composite materials, *Environmental effects on composites materials*, ed. G.S. Springer, Technomic Publishing Co., Lancaster, PA.

DISTRIBUTION OF FIBERS AND THEIR EFFECT ON LATERAL DEFORMATION

Nacira SAOUDI ^{1,*}, Brahim SAOUDI ², Hayet CHERFA ³, Boujemaa BEZZAZI ⁴

¹ University of BOUIRA, UR_MPE, Laboratory LRME Boumerdes , Algeria

² University of Science Jijel Algeria

³ University of Science and Technology Houari Boumediene, Algeria,

⁴ Unité de recherche UR_MPE ,Laboratory LRME ,University Boumerdes Algeria

* Corresponding author : saoudinacira@gmail.com

ABSTRACT

In literature researches, generally the effects of addition fibers even different shape or length in concrete all prove increasing properties and study concrete reinforced fibers behavior. In this purpose we add our experimental results.

The aim of this investigation was to study the formulation, factors influencing the mechanical compressive properties of steel-fiber-reinforced concrete with mixing two kind length of fiber in different volume fraction contents. The specially designed fiber is widely used in engineering because it can help to improve the bonding strength of fiber and the interface quality.

The parameters and fatigue performances of SFRC are investigated by an experimental program consisted on flexion, compression loading (Extensometers) tests of SFRC. The specimen cylinder size tested is: 16*32 cm.

The distributions of fiber at different sections are depending on percentage or concentration of fiber length and also deformation lateral is important regarding the quantities.

KEYWORDS

Steel fiber. compressive strength, lateral deformation Concrete.formulation.

NOMENCLATURE

SFRC: Steel fiber reinforced concrete

ADVA; Superplasticizers

INTRODUCTION

The concrete strengthened by fibers gives new materials, on which it is advisable to specify and to quantify the mechanical behavior.

The purpose of this work is the realization of significant tests on specimens of steel fiber concrete in order to characterize the behavior of the latter. The fixe parameter used during formulation concrete determined by workability, so we adjusted quantity of Superplasticizers in order to obtain by slump test same value for all batches. And we search relation between distribution of these fibers, homogeneous and mechanical behavior, knowing that during formulation fibers dimensions don't fluctuate as well as sand cement and grains, difference displacement of small and longer fibers length 15mm and 60mm,

for the first it give's ductility for concrete at small percentage then forms urchin , but for the second it curves. In order to answer or clarify the effect of fibers volume fraction, length and distribution on the lateral deformations, we characterize by test of extensometers compressive.

Materials : The materials used in this research KADDARA career coarse aggregate with a particle density of 2.72 kg/dm³, sand with a particle density of 2.63 kg/dm³.Maximum particle size of the sand and coarse aggregate was 0/3 mm and 3/8 mm respectively 15 mm.The type of cement used in all concrete series was CEM I 42.5R coming from MSILA and its properties are presented in Table 1. A modified polycarboxylate polymer based superplasticizer ADVA Flow 390 was also used at varying contents fixing workability parameter to produce concretes with a slump in the range of 14±0,5cm.

Concrete with 15 mm Steel fiber length was used throughout the study at varying contents. Physical and mechanical properties of SFRC, provided by the manufacturer, are presented in Table 2.

Table 1: Cement Characteristics

Characteristics	Results
Normal Consistence	25.81(%)
Start grip	161(min)
End grip	244(min)
SSB	4162(Cm ² /g)
Masse specifics	3.1(g/cm ³)

Table 2: Steel fiber characteristics

Fibers	SF1
Lengths [mm]	15 ± 3mm
Diameter [mm]	0.12±0.01mm
L Hooked end [mm]	/
anchorage	Simple
slenderness	L/d=15/0.12

As summarized in Table 3, a total of mixtures 7 were prepared with constant cement content of 400 kg/m³ and one w/c ratio of 0.4. Steel fiber was added at different mixing percentage (0,5 - 0,75-1-1,25-1,5-1,75-2)% of steel fibers.

Mixing was performed in a 120 l capacity pan mixer with a vertical rotation axis and fresh concrete properties were determined immediately after the mixing. . After demolding, all the specimens dedicated to instantaneous mechanical tests at 28 days, conserved at air ambience.

Plural batches were cast for flexion tensile specimens 7× 7× 28 cm (in bending) , cylindrical specimens 16×32 cm three for compressive extensometers .

Table 3 Composition of concrete for all batches

Fibers %	0/3 kg	3/8 kg	8/15	cement	water	Addition ///
0,5-0,75-1-1,25-1,5-1,75-2	623	243	881kg	400kg	160l	

MECHANICS TEST

Formulation of SFRC: In this work, the formulation of the concrete is carried out according to the method of DREUX-GORRIS.for the content

fiber we studied [0, 0,5%, 0,75% 1%, 1,5%, 2%]of fiber , and. During formulation we notice difficulty of workability with increasing volume fraction of steel[1] and dispersion of fiber so non homogeneous of distribution, So time of mixing were different between batches.

In this study, an evaluation of performances is presented for the differences mixtures. using one basic composition for different batches, a series of mechanical characterization tests in flexion tensile and in compression extensometers were performed in order to obtain a relation between contain fiber , lateral deformation ,flexion strength of the Steel fiber concrete reinforced

Compressive Extensometer: The specimens devoted to compression tests were equipped with extensometers for strain measurement and were stored in the test room in air ambience until loading at 28 days, measured in laboratory (University Bouira Algeria) on test specimen dimensions 16×32cm.



Figure 1: Picture of specimens

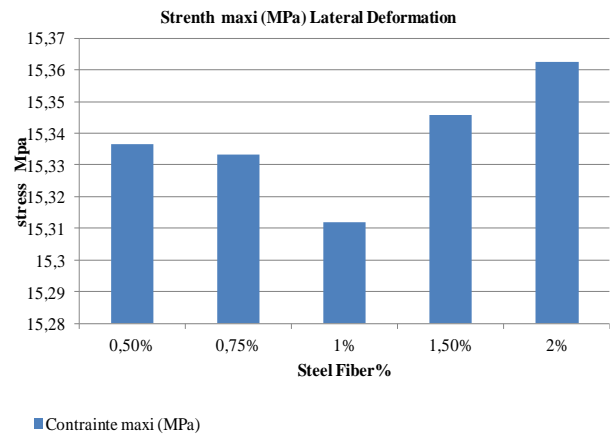


Figure 2: Stress compressive extensometer SFRC for % fiber.

We noticed from figure 2 that for 1,5% an 2% necessary high stress to deform the specimen 16*32 and unregister lateral deformation ,which are

confirmed in split tensile (figure 3) and by Y. Mohammadi and al[4] were the results confirm that there is an increase in the compressive strength varying from 3% to 26% on addition of fibers to the concrete mix .

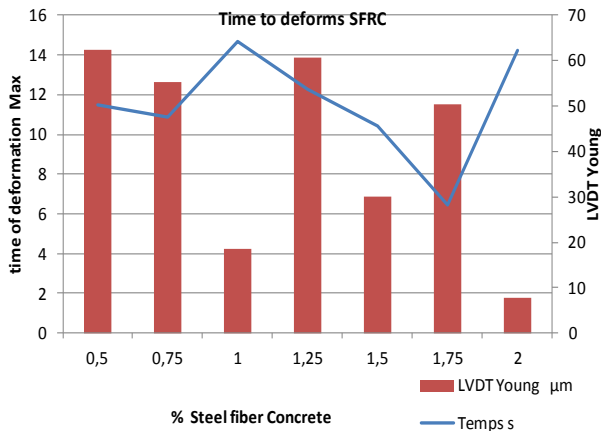


Figure 3: time of strength crushing in relation stress compressive

In this figure we observed that for 1 and 2% of steel fiber , for small LVDT Young it take time enough but for 0,5% SRFC , in few seconds it deforms high quantity.

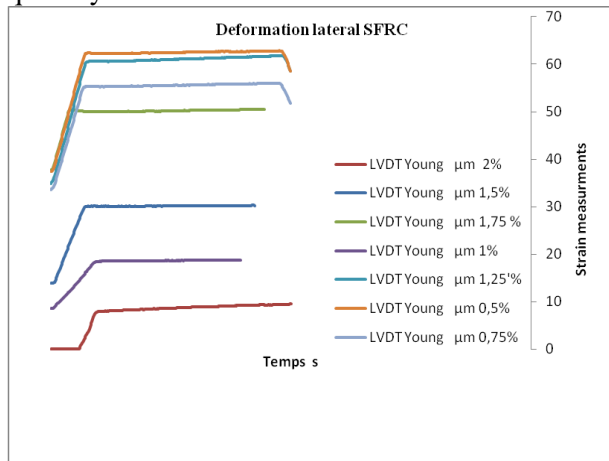


Figure 4: lateral deformation of steel fiber concrete different percentage

Different results in term of compressive extensometers are grouped in figure 4 , were concluding that for concrete 2% specimen resist best than others , so take much time to start deforms , that explained about important ductility of SFRC .

In this graphs SFRC lateral deformation increase with increasing of volume fraction, example the low deformation lateral obtained for 2% SFRC and the

high LVDT Young is unregistered on 0,5% SFRC deformation obtained at few seconds.

Flexural Tensile strength: The level at which the addition of steel fibers influences the mechanical properties of the concrete was shown to be dependant

on various parameters like material and aspect ratio of the fibers, their volume fraction in the mix, and loading rate [6,7]. Flexural toughness is an important parameter that is widely assessed to observe the influence of fibers on the post-cracking response of the concrete composites. Toughness indices were shown to increase with increasing fiber dosage, with an optimum value present for fiber volume fraction [7,8].

In this part we have studied flexural tensile test at 28 days, after that we calculated and studied the distribution (position) of Steel in section of specimens 7*7*28 to explain the relation between different parameters as can be seen in Figure 5.

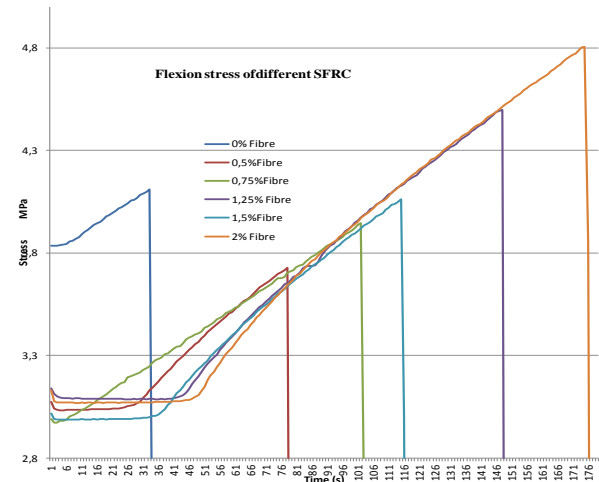


Figure 4: flexion Tensile strength of concrete.

We notice clearly increasing of flexion tensile strength, even though with small percentage, the improvement appears. Comparing with the concrete none reinforced, all the steel reinforced concrete proved performance with increasing fraction volume of steel. The percentage of 2% of fiber presented good characteristics and homogenization between fiber and matrix of concrete means all the steel fiber covered sufficiently. But with the proportioning of 1,75% a question perhaps during laboratory conditions or during formulation. And provided the presence effect of fibers in the matrix, maximum increase in flexural strength taken 20% for 2% volume fraction of fibers, Y Mahammadi [5] and al confirm the maximum increase of 100% was obtained for concrete but long fibers at a fiber volume fraction of 2.0%.

For other SFRC resists more time than the plain concrete which weak at 31seconds, it te 4 to 5 time the moment of plain concrete.

Distributions of fibers: we have analyzed the flexion sections of each specimen after flexural test, and report their fibers coordinates.

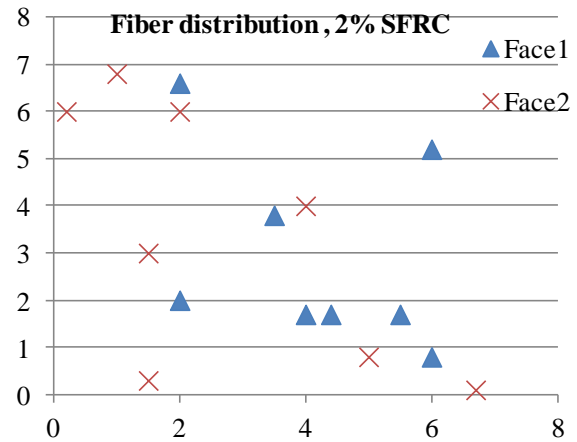
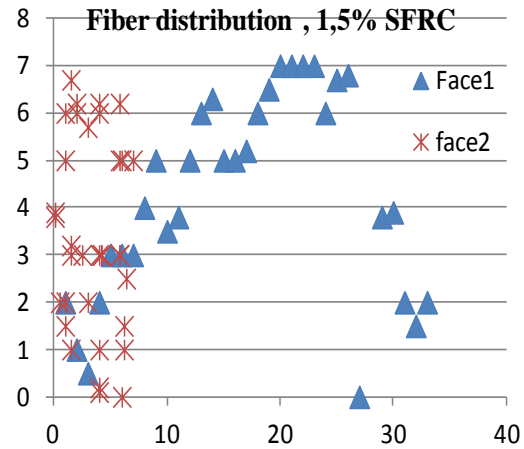
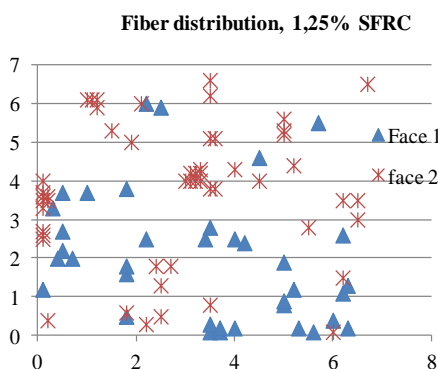
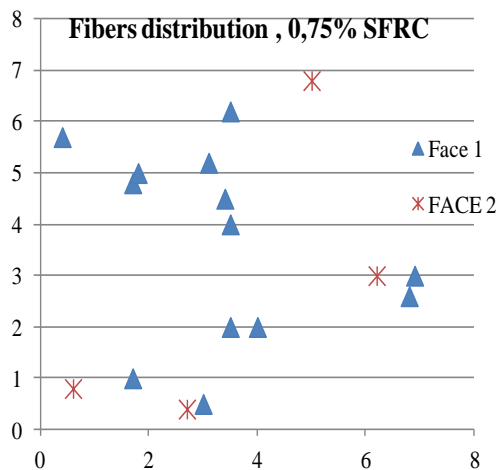


Figure 5 : sections of specimen tested on flexural tensile and distribution fibers.

This sections explain the results obtained before on the flexural test, if we observed (figure 4) SFRC with 1,25% volume fraction is better than 1,5%, because of distributions is saturated and only on one part of the section, but for 1,25% regarding saturated but all area of the section have steel fiber. We remark that a good distribution is presented in 2% of steel fiber and this contain is the best value in flexion tensile, compressive and extensometers, this section is not saturated on all surface, in the opposite specimen of 1,5% SFRC the distribution is only in one part of the section .and number of fiber in two part is equal on the 2% contain.

For SFRC with 1,5% volume fraction this distribution induce to stop the lateral deformations if this quantity reproduced in each section, opposite of SFRC with 1,25% volume fraction this distribution induce to stop the lateral deformations but the quantity is not sufficient to reproduce the

same section distribution, as 2% volume fraction this distribution can reproduce in each section.

CONCLUSIONS

The first important result is that fiber with 15mm length, without hook or undulation, the percentage given improvement is 2% , we notice difficulty in formulation to take workability as fixe parameters, and searches about quantity of Superplasticizers given same collapse 14cm at slump test results. Lateral deformation depends on distribution of fibers if it is the same on the total longer of specimen, but for flexural deformations it depends on the middle section.

We notice an increase of the flexural tensile strength and also an improvement of compressive strength, as confirmed with Y Mohamadi and al best performance given by the concrete containing 2.0% volume fraction of fibers followed by concrete containing 1.5% volume fraction and 1.0% volume fraction of fibers.

For this program, the improvement is not because of fibers only, also the quantity of superplasticizer has significant role and time of mixing.

REFERENCES

1. Malika Malou, Influence of introduction of Steel Fibers on the behavior Postponed from a Matrix Cimentaire. Characterization - monotonous Behavior - Microstructure, PhD Thesis, 2007, University Constantine Algiers.
2. Tianyu Xie, Togay Ozbakkalogl, Behavior of steel fiber-reinforced high-strength concrete-filled FRP tube columns under axial compression, *Engineering Structures* 90 (2015) 158–171
3. Bensaid Boulkebatche, Comportement des betons fibres a la flexion, influences des fibres et de la resistance à la compression, 31rencontres de l'AUGC, ENS Cachan 29au 31 2013.
4. Mohammadi Y., Impact resistance of steel fibrous concrete containing fibers of mixed aspect ratio *Construction and Building Materials* 23 (2009) 183–189 Elsevier
5. Mohammadi Y. Behaviour of steel fibre reinforced concrete in flexural fatigue. Ph.D. Thesis, Department of Civil Engineering, IIT Roorkee; November 2002. p. 304.],
6. Toutanji H, Bayasi Z. Effects of manufacturing techniques on the flexural behaviour of steel fibre-reinforced concrete. *Cem Concr Res* 1998;28(1):115–24.
7. Mohammadi Y., Singh SP, Kaushik SK. Properties of steel fibrous concrete containing mixed fibres in fresh and hardened state. *Construct Build Mater* 2008;22(5):956–65.
8. Altun F, Haktanir T, Ari K. Effects of steel fiber addition on mechanical properties of concrete and RC beams. *Construct Build Mater* 2007;21(3):654–61.

Thermal Building and Energy Storage

RADIATIVE FORCING OF DESERT AEROSOL OBSERVED AT OUARZAZATE (MOROCCO), TAMANRASSET (ALGERIA) AND ILORIN (NIGERIA)

A. TAHIRI¹, M. DIOURI^{1*}, J. BARKANI²

¹Department of physics, University Mohamed First,
Faculty of science, 60020 Oujda, Morocco

²Laboratoire des Sciences de l'Ingénieur - LSI, Faculty Polydisciplinaire of Taza,
University Sidi Mohamed Ben Abdellah, Fez, Morocco

*Corresponding author: m.diouri@fso.ump.ma

ABSTRACT

The desert aerosol confirmed influences on climate. Its direct effect on the latter is observed through diffusion and absorption phenomena of solar and terrestrial radiation. The indirect effect is manifested in the cloud formation process where the aerosol act as condensation nuclei and thus alter their optical properties.

This study is based on network data AERONET / PHOTONS* initiated by Laboratory's research teams of Atmospheric Optics Lilles and NASA since more than twenty years. From the collected data, we can analyze the aerosol radiative forcing calculated at ground surface and at the top of the atmosphere at Ouarzazate (Morocco), Tamanrasset (Algeria) and Ilorin (Nigeria). The aerosol radiative forcing obtained at the land surface and at the top of the atmosphere (120 km altitude) are calculated for 2012 using the radiative transfer model from the measurements of the aerosol spectral optical depth carried out by sun photometers.

The monthly average values obtained at ground surface range from -178 W/m^2 and -10 W/m^2 with peaks recorded in July (Ouarzazate), March (Tamanrasset) and January (Ilorin), characterized by a regionally significant load of desert aerosol on these periods. At the top of the atmosphere, monthly averages recorded a variation from -60.91 W/m^2 to $+2.36 \text{ W/m}^2$ with a minimum value observed in Ilorin on March. The passages from negative to positive values for Ouarzazate ,Tamanrasset can be explained for spring and summer by the influence of the large proportion of coarse particles mode which characterize regional desert aerosol of storms observed at this time. Coarse particles scatter a significant radiation to the Earth's surface. In autumn and winter the influence of clouds can explain these inversions. The impact of desert aerosol on radiative forcing of these desert areas shows a general trend towards regional cooling with the values that may be below -230 W/m^2 at the Earth's surface in summer and below -100 W/m^2 on top of the atmosphere in spring and summe

KEYWORDS

Desert aerosol, Sun-photometer, Aerosol optical Depth, Aerosol radiative forcing.

INTRODUCTION

The Sahara desert is the most important source of mineral dust in the Northern Hemisphere. North African dust is injected into the atmosphere through resuspension processes at the source areas, may be transported particularly with dust storms at different altitudes (up to 7km) to different areas in the world [5]. Mineral dust particles are one of the main

constituents of the atmospheric aerosol which influence the radiation budget of the atmosphere. The evaluation of the dust-radiation interaction is essential for climate forcing assessment at both local and regional scales. However, large uncertainties still remain in assessing the dust climate impacts. One of the major sources of the large uncertainties in dust radiative forcing is associated with dust optical and physical properties due to the

complexity in dust size distribution and mineral composition [4].

Remote sensing results of dust optical properties indicate that dust is nearly non-absorbing [3], while earlier laboratory measurements suggested dust to be partly absorbing at visible wavelengths [4]. Many measurements campaign in desert zone were conducted in the past, the recent one with SAMUM consortium undertaken on May-June 2006 at Ouarzazate and Zagora (Morocco) close to Sahara gives very important description including chemical and physical properties of desert aerosol near ground and at different altitude levels during its transport [2]. The omnipresence of dust causes a direct radiative forcing, but the magnitude (its sign and its global significance) is discussed subject [1]. This study is developed on AERONET (AERosol RObotik NETwork, <http://aeronet.gsfc.nasa.gov/>) network data concerning the radiative forcing of desert aerosol in three representative desert areas (Table 1) for the year 2012.

SITES AND METEOROLOGY

Ouarzazate, the site is associated with the weather station. Ouarzazate is a small town with almost no industrial activity. It is located in the southeast of the Atlas and the northwestern Sahara. With a pre-Saharan climate characterized by low rainfall and hot and dry summer. The average maximum temperature is 40°C and the average minimum is 25°C (July). In January, the minimum and maximum average temperatures are respectively 2°C and 16°C, at night, the temperature can drop to -4°C. In the spring, clouds with exceptional storms are rare. The desert winds (Sirocco and Chergui) play an important role in the Ouarzazate climate.

Tamanrasset instrument site is located on the roof of the Regional Meteorological Center (Algeria). This area, free of industrial activities, is in the high lands of the Algerian Sahara (home of the Kel Ahaggar Tuareg). Tamanrasset has a hot desert climate, with very hot summers and mild winters. There is very little rain throughout the year.

Ilorin, the site is located on the roof of the Department of Physics, on the campus of the University of Ilorin, Nigeria, in sub-Sahel Africa. It is positioned at the upper tip of the Guinea Savannah zone under the influence of the annual alternating southward and northward passages of the Inter-Tropical Convergence Zone (ITCZ). During the 'dry season' (November -February) when the ITCZ

appears slightly south or north of Ilorin, the prevailing north-easterly wind, known as the 'Harmattan', brings in Saharan dust air. The dust plumes originate from the Bodel Depression in the Chad Basin. This is a climatically important region due to its location in a desert transition zone and because of the influence of the dusty Harmattan wind which is persistent for prolonged periods of time, and characterized by steady dusty conditions with high aerosol loading.

Table 1
AERONET site locations

Sites	Coordinates	Elevation
Ouarzazate	30.92°N, 6.91°W	1136 m
Tamanrasset	22.79°N, 5.53°E	1377 m
Ilorin	08.32°N, 4.34°E	0350 m

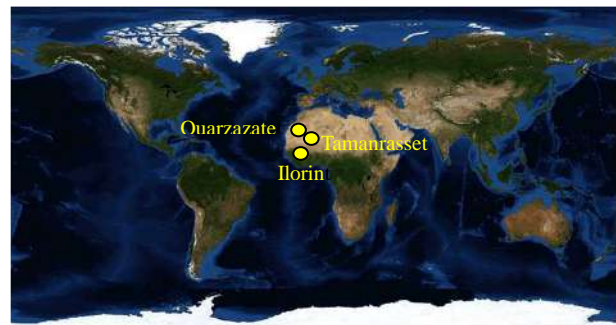


Figure 1
Desert aerosol station locations

Aerosol Radiative Forcing (ARF)

Aerosol radiative forcing at ground surface is defined as the instantaneous increase or decrease of the net radiation flux due to an instantaneous change of aerosol atmospheric content. The atmosphere free of aerosols (Clear atmosphere) is the reference case. Thus, the ARF values can be derived from the following expression:

$$ARF = (F^{\downarrow} - F^{\uparrow}) - (F_0^{\downarrow} - F_0^{\uparrow})$$

Where F and F_0 denote the global irradiances with aerosol and without aerosol respectively. The arrows indicate the direction of the global irradiances, \downarrow indicating downward irradiance and \uparrow indicating upward irradiance.

The monthly means ARF values is ranged from -180 W/m² to -10 W/m² (Figure 2). The negative value at surface reveals that the desert dust aerosol reduced

significantly the solar radiation at the ground level producing a large surface cooling.

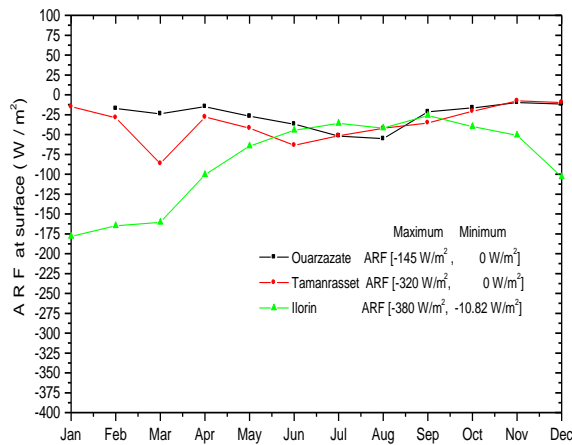


FIGURE 2

Monthly mean of ARF at ground surface (2012)

The aerosol radiative forcing at top of atmosphere are given in figure 3. The monthly means ARF values is ranged from -60 W/m^2 to $+2.7 \text{ W/m}^2$, and aerosol radiative forcing at the top of the atmosphere is near 0 W/m^2 as it was observed in our previous study on the whole terrestrial desert stations [6]. The passages from negative values to positive values can be explained by the greater amount of the radiative energy available that has been reflected by cirrus clouds.

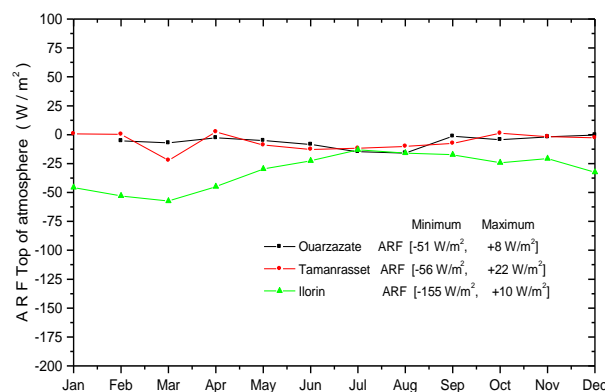


Figure 3

Monthly mean of ARF at top of atmosphere (2012)

CONCLUSIONS

The monthly average values of the aerosol radiative forcing observed at top of atmosphere

ranges from -60 to $+2.7 \text{ W/m}^2$, the negative values indicates an increase of the scattered back light to space inducing thus a significant Earth-atmosphere cooling, while the positive values indicate a greater amount of radiative energy reflected by cirrus.

The values of the aerosol radiative forcing observed at surface varies between -180 to -10 W/m^2 , are fairly representative of the importance of forward diffusion of particle coarse modes which induce desert aerosol decrease in net flux at ground surface. The impact of the studied desert aerosol on radiative forcing showed a general trend towards regional cooling with negative values close to zero at the top of the atmosphere and on average around -80 W/m^2 at surface. However, we register negative values more pronounced in Nigeria below -180 W/m^2 at surface and -60 W/m^2 on top of the atmosphere that can be explained by the high atmospheric desert aerosol load and biomass combustion that observed at this region in January.

ACKNOWLEDGMENTS

Authors want to thank all P.I of AERONET Sites: Emilio Cuevas-Agullo, Taoufik Zaidouni and Rachel T. Pinker.

REFERENCES

- [1] Y. Balkanski, M.Schulz, T. Claquin and S. Guibert. Reevaluation of mineral aerosol radiative forcings suggests a better agreement with satellite and AERONET data, *Atmos.Chem. Phys.*, 7(1), 81-95, 2007.
- [2] K. Kandler, L et al. Size distribution, mass concentration, chemical and mineralogical composition and derived optical parameters of the boundary layer aerosol at Tinfou, Morocco, during SAMUM 2006. *Tellus* (2009), 61B, 32-50.
- [3] Y. J. Kaufman, D. Tanré et al. A satellite view of aerosols in the climate system, *nature*, 419 (6903), 215-223, 2002.
- [4] I. N. Sokolik, and Toon, O.B. Incorporation of mineralogical composition into models of the radiative properties of mineral aerosol from UV to IR wavelengths, *J. Geophys. Res.*, 104, 9423-9444, 1999.
- [5] M. Tesche et al. Vertical profiling of Saharan dust with Raman lidars and airborne HSRL in

Southern Morocco during SAMUM, *Tellus B*, 61, 144-164, 2009.

[6] Abdelouahid Tahiri and Mohammed Diouri. Aerosol Radiative Forcing of Desert Regions. *Environmental Sciences*, Vol. 3, 2015, no. 1, 17-29. <http://dx.doi.org/10.12988/es.2015.4118>.

Simulation of summer and winter microclimate and thermal comfort within urban open space in semi-arid climate

Kedissa Chahrazed^{a,b,c}, Belarbi Rafik^b, Outtas Saliha^c

^a Faculty of Earth Sciences and Architecture, Larbi Ben M'Hidi university, Oum-el-Bouaghi, 04000, Algeria

^b Laboratoire de Sciences de l'Ingénieur pour l'Environnement, LaSIE, University of La Rochelle, France

^c Laboratoire d'Architecture Bioclimatique et Environnement, ABE, Constantine 3 University, Algeria

*Corresponding author: Email: archi_bio2005@yahoo.fr

ABSTRACT

Outdoor thermal comfort in urban spaces is as an important contributor to pedestrians' health. This latter is also important through its influence on the energy use of buildings. These issues are likely to become more acute as increased urbanization and climate change increase the urban heat island effect. However, urban planning shall be able to provide for different urban environments many urban forms that produce various microclimates with different comfort situations for pedestrians. This study tries to find configurations of urban open spaces, mainly urban plaza and courtyard. It does so by analyzing the influence of geometry parameter that benefit both outdoor and indoor. To achieve this goal, open spaces are analyzed by field measurements and simulation for a typical hot and cold days in the semi-arid climate of Ali Mendjeli -Constantine -Algeria. The present paper discusses the results of simulation. Envi-met 3.1 programs is used for simulating outdoor air temperature, mean radiant temperature (T_{mrt}), wind speed and relative humidity, whereas RayMan pro 2.1 is used for converting these data into Physiological Equivalent Temperature (PET). Models with various geometries are evaluated according to aspect ratio H/W, the geometrical indicator. The results show that duration of direct sun, mean radiant temperature and wind speed, which are influenced by urban form, play the most important role in thermal comfort.

Keywords: Urban microclimate, urban geometry, public courtyard, thermal comfort, Envi-met, PET.

1. INTRODUCTION

In recent years, microclimate has become an important issue in urban planning because it has an impact on outdoors thermal comfort related to health and well being for citizens and human activities. Furthermore, comfortable outdoor spaces have a significant bearing on comfort conditions of the indoor ambience, when their demand is significantly increased as result of exposure to uncomfortable outdoor conditions. Those in turn have put an immense pressure on the energy demand in the cities [1] and consequently amplify the phenomenon of urban heat island [2]. Several definitions of thermal comfort exist considering subjective and psychological dimension [3] or physiological dimension [4].

In this way, needs and preference regarding thermal comfort differ from seasons and also depend on human factors (gender, age, body shape), activity level, clothing and psychological aspects.

Because this differences, urban geometry, should offer a reasonable thermal range in spaces, instead of attempting to create an exact thermal condition where

user will find comfort depending on individual dispositions [5].

Nevertheless, it is important to establish criteria for outdoor comfort in order to evaluate urban microclimatic conditions and to provide a design reference.

2. BACKGROUND

Urban geometry and thermal properties of urban surfaces have been found to be the two main parameters influencing microclimate [6-9] and therefore thermal comfort. Urban geometry it also defined that is much more important at the micro-scale than thermal behavior of materials and albedo effects [10]. In fact, it determines the thermal environment by controlling: distribution of shaded and sunny areas determined by the orientation and heights of buildings, furthermore the air flows generated by the porosity of the space to the wind. The interactions between urban geometry and surface properties under a specific climate generate microclimates. These interactions were first discussed by Olgyay and Oke [11, 12]. Givoni [13]

discussed the thermal impact of urban typologies in different climates and arrived at general design guidelines. He writes that architectural forms, surface materials and urban morphology (compactness, elongations, etc.) can affect the microclimate environment. Steemers et al. [14] proposed six archetypical generic urban forms for London and compared the incident solar radiation, built potential and daylight admission. They concluded that large courtyards are environmentally adequate in cold climates, where under certain geometrical conditions they can act as sun concentrators and retain their sheltering effect against cold winds. Muhaisen [15] analyzes the impact of different design configurations of courtyards based on shading simulations. This study found that shading conditions of courtyards are highly influenced by formal proportions, location latitude and climatic conditions. In another related study, Muhaisen and Gadi [16] show that the proportion and geometry of courtyards play influential roles in improving the shading performances, hence, deep courtyard forms with any geometry in summer and shallow forms in winter are recommended. Berkovic et al. [17] using simulation program conducted study on urban courtyard in hot-dry climate, investigated summer thermal comfort, and showed that, although the air temperature difference between shaded and unshaded areas was only 0.5 °C, the mean radiant temperature was different up to 30°C.

3. METHODOLOGY

As knowing, the design parameters that determine the insolation of any open space are the height of the building around it, its orientation and proportions.

This paper considers the mutual interaction between courtyard geometry and solar access to urban open space in purpose to examine and evaluate the effects of their width (W) and building height (H) on the solar access for different orientation. Since this can only be achieved hypothetically, numerical modeling and computer simulation were adopted in this study.

3.1. Sun exposure: is aimed by proportioning the courtyard internal envelope to ensure adequate solar ratio accessibility in winter for warming up both ground and building surfaces and providing sufficient shadow in summer. Using Ray Man Pro 2.1 software we assumed that:

- At least half of the surface ground is exposed to the sun at the winter solstice

- Its sunshine during the summer solstice is half of his daily hour's sunshine duration (14h.24' / 2)

The rectangular form was choosing since it represents the typical form in Algerian neighborhood layout.

3.2. Size of open space: By means of simple volumetric modeling of urban space in this step considered closed to avoid wind effect since the main objective of study is highlighting the role of geometry on thermal comfort.

The orientations of open spaces correspond to the orientation of the length-wise axis. Four directions were considered: N-S, E-W, NE-SO and NO-SE.

This scenario is concentrated on dependency of microclimatic situation of the open space on its aspect ratio H/W.

To create several H/W ratios, the proportions of models varying in length and width from 30 to 135m with steps of 15m. The high varying from 3 to 72 m with steps of 3m (one storey)

3.3. Thermal comfort: To assess it, we use Envimet 3.1 microclimatic tool to measure air temperature, relative humidity, wind speed and The mean radiant temperature (T_{mrt}) using the location data [18]. Outdoor microclimate is calculated at the height of 1.2m. The simulated data calculated by Envi-met are used as inputs in RayMan Pro 2.1 to assess thermal comfort of pedestrian's. This study adopted physiological equivalent temperature (PET) a thermal comfort index expressed in (°C) which takes into account all the environmental parameters influencing thermal comfort: temperature, radiation, humidity and wind speed. PET index has point scales, from very cold to very hot, combining individual parameters (metabolism 80 w, and clothing resistance 0.9 clo) and T_{mrt} (Fig.1). This T_{mrt} has strongest influence on PET index. [19]. It is defined as the uniform temperature of a hypothetical spherical surface surrounding the subject that would result in the same net radiation energy exchange with the subject as the actual, complex radiative environment [20].

3.4. The study parameters: This study was carried out in New-town Ali Mendjeli, Constantine,

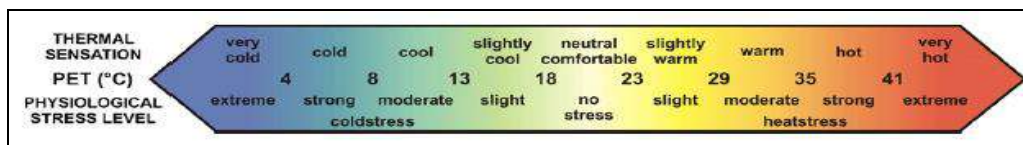


Figure. 1: PET scale for human thermal sensation and stress levels (based on Matzarakis and Mayer 1996)

characterized by a semi- arid climate, hot and dry in the summer with an average maximum temperature of 36°C, cold and humid in winter with an average maximum temperature of 7°C. The main wind direction is the North-west in winter and North in summer with an average speed reaching 2.1 m/s. Simulations are performed at initial time 00h, for typical days 21st of December, the short day of year the ($T_{air} = 6^\circ$, wind speed = 4.1 m/s, wind direction = 320°C, relative humidity = 87%) and the 21st of June, the longest day of the year and representing the summer season ($T_a = 25^\circ\text{C}$, wind speed = 1 m/s, wind direction = 0°, relative humidity = 57%). These latter represent the extreme cases which may take place throughout the year. Ground and wall Albedo are, respectively, 0.25, and 0.5.

4. RESULTS AND DISCUSSIONS

4.1. Sun exposure: The first phase begins with a solar exposure analysis for a central point in the middle of each configuration. 560 models were simulated. We sum the results at (Fig.2):

- For the same H / W ratio and orientation, different configurations have the same duration of sunshine.
- The E- W direction provides a long duration of sunshine either in winter than the summer.
- NE- SW receives sun radiation mostly in afternoon to opposite the NW-SE witch receive sunshine in early morning.
- The N- S direction receives the shortest duration of sun radiation in summer.

Taking into account the cold and warm seasons, only the spaces included in the range $0.4 \leq H / W \leq 0.6$, and oriented N-S satisfy our assumption related to solar radiation exposure.

4.1. Outdoor thermal comfort: to assess thermal comfort situations related in urban geometries within the above determined range $0.4 \leq h / w \leq 0.6$.

The largest ratio $H/W = 0.1$ of the open space S1 is compared with the ratios from the above determined

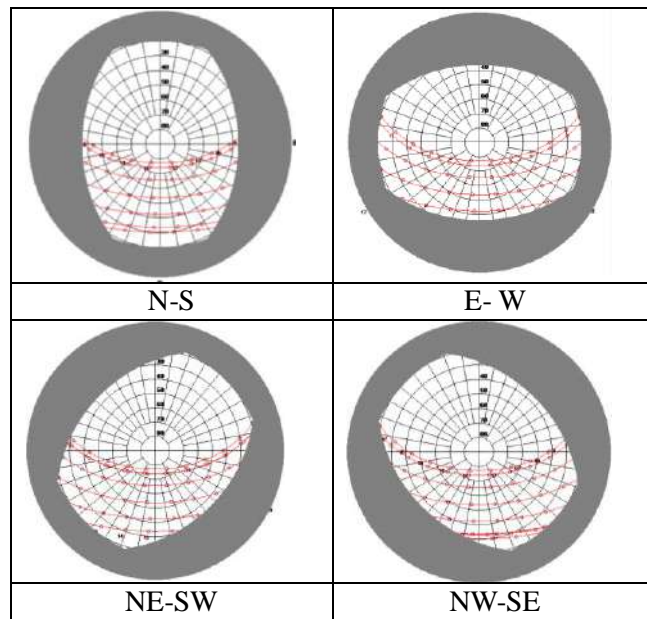


Figure.2: Sunshine duration of H/W= 0.4 ratio geometry related to various orientations.

range: 0.4, 0.5 and 0.6 corresponding, respectively, to deep open spaces S2, S3 and S4 (Fig.3)

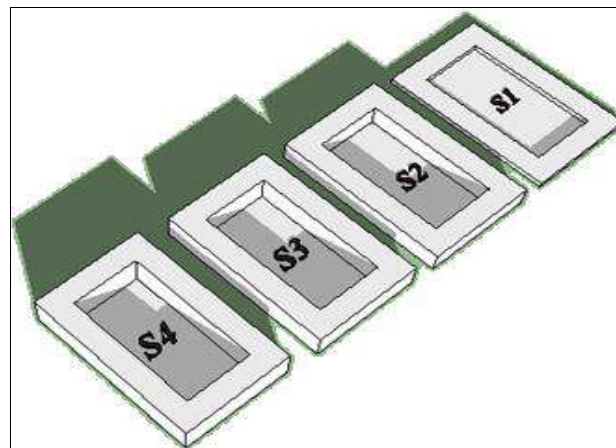


Figure.3: S1, S2, S3 and S4's geometries.

It may be noted, the length axes of these geometries are two times longer than there widths.

Figure 4, 5, 6 and 7 display spatial and temporal distribution of T_{mrt} and PET at the centre point of the four cases in winter and summer.

We can notice the high resemblance between the T_{mrt} and PET variations since radiation is the main factor determining comfort in these closed spaces.

4.1.1. Winter: At the night, the modeling T_{mrt} results showed a strong correlation between the H/W ratio and T_{mrt} , as proven by Andrade [21], due to the enclosure and reducing energy exchanges between the ground and the sky. The maximum T_{mrt} value, -0.1°C , occurs in the deepest station S4. Its difference with the station S1 is 5.7°C (Fig.4). A strong cold stress is felt. PET values are 1°C in S4 and 3.4°C in S1 (Fig.5).

At 8h and 16h, i.e. an hour after sunrise (7h45') and an hour before sunset (17h 18'), the radiation balance is still negative, this explains the variations of T_{mrt} at the start and end of the day. The maximum difference between S1 and S4 is 1.7°C at 8h and 1°C at 16h.

When the spaces receive the direct radiations, in between 8h and 16h, the T_{mrt} values increase rapidly reaching their maximum at noon. The recorded values in the three stations S2, S3, S4 are almost identical, about 33.9°C . The difference is 2.5°C with station S1.

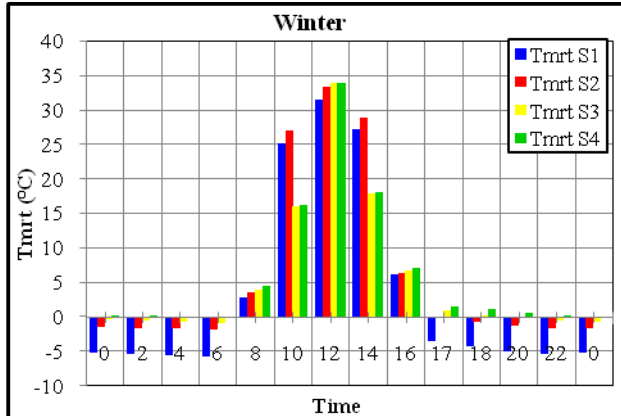


Figure.4: winter T_{mrt} Variations in open spaces.

The PET values vary between 1.6 and 17°C where the shallowest model S1 represents the highest thermal stress against the deepest profiles with a longer period of comfort (Fig.4,5). The maximum PET in S1 is 9.2°C and in the S4 is 17°C . The decline of temperature for the two deeper spaces S3 and S4 occurred much more sharply after 14h, about 35°C , when the centre points are shaded from the solar rays by the surrounding vertical surfaces. at the hottest time of the day, the PET difference between S1 and S2 is 7.8°C .

The calculation reveals a negative correlation

between the H/W and the PET ($R^2 = 0.96$). this result demonstrates the interest deep geometries for human thermal comfort in winter.

However, it should be mentioned that the PET evaluates the real thermal sensation without taking into account the adaptation by clothing that could restore thermal comfort.

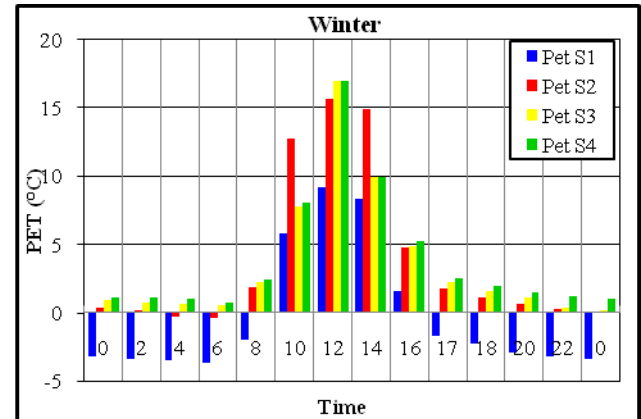


Figure.5: winter PET Variations in open spaces.

4.1.2. Summer results: In whole period of simulation, the patterns of T_{mrt} and PET are almost similar for the deep cases S2, S3 and S4. However, considerable differences are observed with the shallow case S1.

At the night time, The T_{mrt} differences at the four stations are very low. The highest value, 14°C , occur at 2h in S4, the difference is 1.3°C with S1, and only 0.4°C with the other stations. The maximum value recorded of the PET is 17.5°C in S1 corresponding to slightly cold and 18.6°C in the other three spaces corresponding to comfortable (Fig.1,7). The minimum PET is reached at 6h with a maximum difference of 3°C between S1 and S4.

At 8h, T_{mrt} increases rapidly in the shallow space S1, almost 26.6°C highest than the deep profiles since the centre area of them, is still protected from the direct radiations. It culminates at 16h, 70.1°C . However, during the critical period of 12h to 14h, the T_{mrt} in S1 is in average 6.4°C lower than the rest. These results are inconsistent with the amounts of the incident radiations on shallow open space.

It is explained by the differential heating of a ground surfaces and wind speed. In the three other stations, T_{mrt} increases at 10h and culminates at 14h with about 66.8°C value. A difference of 4°C with S1 is observed.

In the afternoon a rapid decrease is caused by the shadow projection of walls on the receptors. This decrease reached at 18h: 35.9 , 33.4 , 32.1 and 40.3°C in ,respectively, S4, S3, S2 and S1. These

results inform us about the shadow ability to decrease T_{mrt} and rapid cooling power of shallow configuration. The conditions are similar for all cases at the following time.

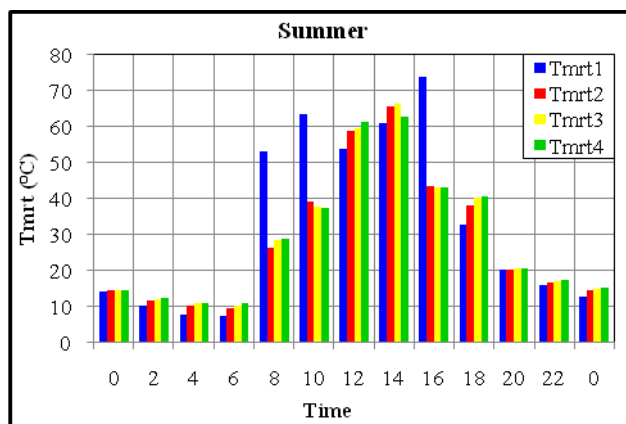


Figure.6: Summer Tmrt Variations in open spaces.

As illustrated in fig.7, PET values of the four locations, at the daytime, is above the upper comfortable limit range of 23°C (Fig.1).

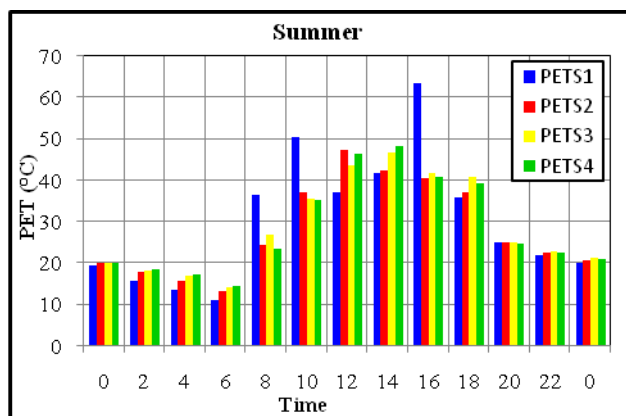


Figure.7: Summer PET Variations in open spaces.

After 10h until 14h when solar radiation and ground radiation are at their maximum, The cooling capacity of the surfaces are reduced for high ratio consequence of important storage of infrared radiations amplified by lack of effective ventilation (wind speed = 0 m/s) as proven by De Souza and Eliasson [22,23]. In this period, Station S4 has a maximum value of PET to 48.3 ° Corresponding to a state of extreme heat stress (Fig.1) against 63.3° C to station S1 at 16h with wind speed = 0.7 m / s. This reveals ability of the height ratios of urban spaces to reduce significantly the extreme changes in the thermal sensation.

Nevertheless, Variances of PET between shaded and sunny areas, great reduced to the shallow space, just 2.1 °C during the period of overheating (Fig.8),

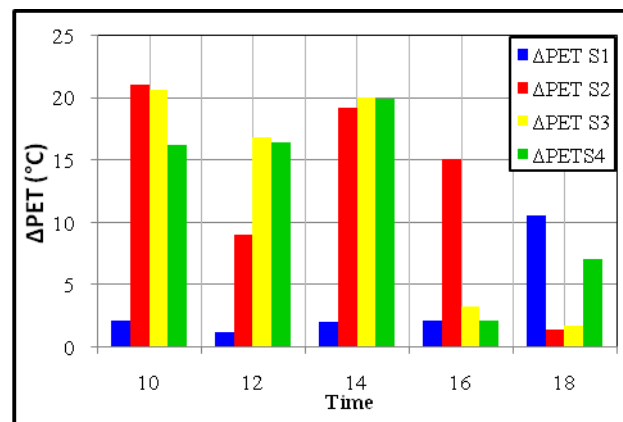


Figure.8: maximum differences temperatures between shaded and sunny areas in summer time.

reach 20°C for deep geometries, as found by Berkovic [17] providing so several adjustment situations to the users.

the calculation reveals a positive correlation between the H/W and the PET ($R^2 = 0.61$). This results demonstrate the interest of deep geometries for human thermal comfort in summer, compared to shallows, even in the lack of ventilation.

5. Conclusion

Urban morphology has a discordant seasonal effect on thermal comfort, with demand for compactness in summer, to secure protection from the sun, and openness in winter to provide solar access.

The focus of this research is on outdoor spaces exposed to direct solar radiations in the aim for estimating thermal ambience created only by its geometry according to its aspect ratio H/W.

By assuming reasonable solar exposure conditions in rectangular open spaces for both cold and hot seasons, a margin $0.4 \leq H / W \leq 0.6$ combined with N-S orientation of the open space is determined by simulation.

Comparison of the thermal environment provided by these ratios with a shallow space has proven effectiveness in winter. But providing high thermal comfort in summer time is hard to achieve in these fully exposed spaces to solar radiations during Overheated period. The interest of the geometry with high H/W ratio in the safeguarding of human thermal comfort is recognized only with the combination of a good ventilation of space.

Besides the various thermal comfort situations offered by shaded areas in these deep spaces for user spaces, a thermally comfortable duration could be substantially increased once the open spaces performance is optimized through porosity of wind ,

and dynamic solutions, such as trees, water pool,...etc.
 Future research will look at the thermal conditions of these latter and asses their effectiveness for improving the outdoor thermal performance even during critical hours of the day. It focuses also on the impact of urban open space geometry on the indoor thermal conditions and energy performance of surrounding buildings.

REFERENCES

1. Khandaker, S.A., 2003, Comfort in urban spaces: defining the boundaries of outdoor thermal comfort for the tropical urban environments, *Energy and Building* 35, pp.103-110.
2. Akbari, H., Konopacki, S., 2004, Energy effects of heat-island reduction strategies in Toronto, Canada. *Energy* 29, pp.191-210.
5. Nikolopoulou, M, Baker N, Steemers K., 2001, Thermal comfort in outdoor urban spaces: understanding the human parameter, *Sol energy*, 70(3), pp.227-35
4. Fanger, P.O., 1970, *Thermal comfort*, Danish Technical Press. Copenhagen
5. Lindberg, F., 2007, Modeling the urban climate using a local governmental geo-database, *Meteorological Applications*, 14 (3) s, pp.263-273.
6. Oke, T.R, 1988, Street design and urban canopy layer climate, *Journal of Energy and Buildings*, pp.103-113
7. Eliasson, I, 1990/ 91, urban geometry, surface temperature and air temperature, *Energy and Buildings*, 15- 16, pp.141- 145.
8. Böhm, R., 1998, Urban bias in temperature time series, *Climatic change*, 38, pp.113- 128.
9. Arnfield, A.J., 2003, Two decades of urban climate research: a review of turbulence, exchanges of energy and water, and the urban heat island, *International Journal of Climatology*, 23:1-26
10. Steemers, K., Nikolopoulou, M., Crowther, D., Dubiel, J., Baker, N., 1998, Radiation absorption and urban texture, *Building Research and Information*, 26(2), pp. 103- 112.
11. Olgyay, V., 1963. *Design with Climate*. Princeton University Press, Princeton, NJ.
12. Oke, T.R., 1987, *Boundary Layer Climates*. Routledge, New York.
13. Givoni, B., 1998, *Climate Considerations in Building and Urban Design*. Wiley
14. Steemers, K., Baker, N., Crowther, D., Dubiel, J., Nikolopoulou, M., Ratti, C., 1997, City texture and microclimate, *Urban Design Study*. 3, pp.25-50
15. Muhaisen, AS., 2006, shading simulation of the courtyard form in different climatic regions. *Build Environ*, 41(12), pp1731-41.
16. Muhaisen, AS., Gadi MB., 2006, Shading performance of polygonal courtyard forms, *Build Environ*; 41(8), pp.1050-9
17. Berkovic, S., Yezioro, A., Bitan, A., 2012, Study of thermal comfort in courtyards in a hot arid climate. *Sol Energy*, 86, pp.1173-86
18. Envi-met 3.1 manual online, <http://envi-met.com>
19. Matzarakis, A., Mayer, H., 1996, Another kind of environmental stress: thermal stress. *WHO Newsletter* 18, pp.7-10
20. Matzarakis, A., Frank Rutz, F., Mayer, H., 2007, Modelling radiation fluxes in simple and complex environments - application of the RayMan model, *International Journal of Biometeorology*, 51, pp.323-334.
21. Andrade, H., 2003, Microclimatic variations of thermal comfort in Lisbon city district, the 5th international conference on urban climate, Lodz, Poland.
22. De Souza, L., 2005, Incorporating sun paths for solar analysis in the 3Dskyview extension, CUPUM, The 9th international conference, London
23. Eliasson, I., 1996, Urban nocturnal temperatures, street geometry and land use, *Atmospheric environment*, 30(3), pp.379 -392.

THERMAL CHARACTERISTIC IN SOLAR AIR HEATER FITTED WITH PLATE BAFFLES AND HEATING CORRUGATED SURFACE

Djamel Sahel*¹, Redouane Benzeguir²

¹Département des Sciences Technique-Faculté de la Technologie,
Université Amar Thilidji-Laghout, Algérie

^{1,2}Laboratoire des Carburant gazeux et Environnent, Faculté de Génie mécanique Université des Sciences et de la Technologie, Mohamed Boudiaf-Oran, BP 1505, El-M'Naouer, Oran 31000, Algérie.

*Corresponding author: djamel_sahel@ymail.com

ABSTRACT

This paper presents a numerical investigation of heat transfer and friction factor characteristics in a solar air heater channel fitted with upper corrugated surface/wall and baffle series placed on a lower wall along the length of the channel. The corrugated surface/wall characterized by heating corrugated surface ratio (HCSR) varied from 0 to 0.5. The baffle series defined by blockage ratio (BR) fixed in 0.5. The fluid flow and heat transfer behaviors are presented for Reynolds numbers based on the hydraulic diameter of the channel ranging from 8000 to 20000. The computations are based on the finite volume method, and the SIMPLE algorithm has been implemented. The present results show that the heat transfer rate and friction factor increase with the raise of Reynolds number. The best thermal performance factor observed at HCSR=0.5 tends to 2.7 at highest Reynolds number.

KeyWords: corrugated surface, baffle, heat transfer, friction factor.

INTRODUCTION

Many thermal applications need a raised performance such as heat exchangers, solar collectors and other engineering's installation. The feeble thermal efficiency of thermal applications due to the presence of laminar sub-layers decreases the thermal transfer execution. For decades, one method using in various thermal installations is baffles or ribs placing in the cooling channels or channel heat exchangers because this ribs restrict development hydrodynamic and thermal boundary layers and create turbulence near the wall leading to an increase in thermal transfer rate.

Several experimental and numerical investigations have been carried out to study the effect of several geometrical parameters in solar air heater channels or different ribbed ducts on heat transfer and friction factor. In general, the geometry parameters used for design of baffled or ribbed channels are the attack and orientation angle, channel aspect ratio (AR), blockage ratio (BR), baffle pitch ratio (PR) and baffle arrangement.

The V baffle shape is presents in literature for generation of the vortex in channels. [1-5]. Singh et al. [6] used mathematical model for predicting the energetic efficiency of a solar air heater having the discrete V-down rib roughened absorber plate. They plotted the curves of optimum rib-roughness

parameters. Lanjewar et al. [7] investigated experimentally the heat transfer and friction factor characteristics of solar air heater rectangular duct roughened with W-shaped ribs. They concluded that the Nusselt number increases whereas friction factor decreases. Promvong et al. [8], Sriromreun et al. [9] they showed that the friction and enhancement factors dependent of the baffle height, pitch and Reynolds number. For investigate periodic laminar flow and heat transfers in channel, Sripattanapipat et al. [10] proposed diamond-shape baffles with different attack angles (5 to 35°). They found that the order of heat transfer enhancement is about 200%–680% for using the diamond baffles. However, this augmentation of heat transfer is associated with enlarged friction loss ranging from 20 to 220 times above the smooth channel. Dutta et al. [11] noted in an experimental work that the thermal transfer rate depends on the position, the orientation and the geometry of the second baffle. Promvong et al. Promvong. [12], Promvong et al. [13] led to a combination between the attack angle, and V-shape baffle, they showed that this combination increases in thermal transfer rate and associated friction factor for different values of blockage ratio

The surfaces roughness in baffled channels is present in several experimental and numerical studies. Eiamsa-ard et al [14] examine numerically

to the turbulent forced convection in a two-dimensional channel with periodic transverse grooves on the lower channel wall. The computations based on a finite volume method. They used four turbulence models: the standard $k-\varepsilon$, the Renormalized Group (RNG) $k-\varepsilon$, the standard $k-\omega$, and the shear stress transport (SST) $k-\omega$ turbulence models. They found that the RNG and the $k-\varepsilon$ turbulence models generally provide better agreement with available measurements than others and concluded that the $k-\varepsilon$ model is selected to use in prediction of this complex flow.

This paper presents a numerical investigation of the effect of the combination between the heat transfer corrugated surface and plate baffle on the thermal performances in a bi dimensional channel. The corrugated surface/wall is characterized by heating surface corrugated ratio (hcs/lcs). The lower surface/wall fitted with plate baffle. For this design, the flow passes on the inferior baffles and creates recirculation, separation and reattachment zones on the upper surface/wall.

FLOW CONFIGURATION AND MATHEMATICAL FORMULATION

Baffle and channel geometry

The system studied in this work is a bi-dimensional horizontal channel fitted with upper corrugated wall and baffle series placed on a lower wall along to the channel length (L) as shown in Fig. 1. The heating corrugated surface/wall characterized by heating corrugated surface/wall ratio (HCSR), where HCSR is the ratio between the height of corrugated surface/wall (hcs) and the length of corrugated surface/wall (lcs=H). For the upper wall, the dimensions is known where (e) is the baffles thickness fixed with $0.04H$, b is the baffle height, H fixed with 0.05 m, is the height of channel and b/H is known as the blockage ratio (BR). The distance between the baffles is set to s in which s/H is defined as the spacing ratio (S) equal to H. These dimensions allow studying the effect of HCSR which varied between 0 to 0.5.

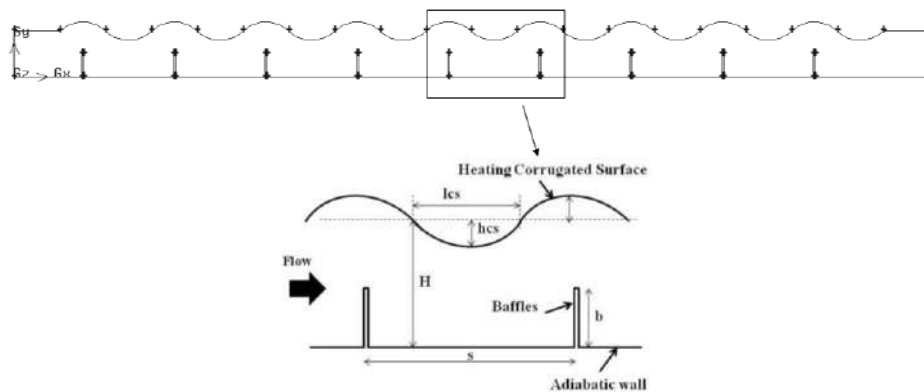


Figure 1
Problem geometry

Governing equations

A computer code is used to perform numerical simulations of incompressible turbulent flow bi-dimensional horizontal channel fitted with upper corrugated wall and baffle series placed on a lower wall according to the length of the channel by solving the Reynolds averaged Navier–Stokes (RANS) equations and the energy equation.

Continuity Equation

$$\frac{\partial}{\partial x_i}(\rho u_i) = 0 \quad (1)$$

Momentum equation

$$\frac{\partial}{\partial x_i}(\rho u_i u_j) = -\frac{\partial P}{\partial x_i} + \frac{\partial}{\partial x_i} \left[\mu \left(\frac{\partial u_i}{\partial x_j} - \overline{\rho u_i' u_j'} \right) \right] \quad (2)$$

Where u' is a fluctuating component of velocity.

Energy equation

$$\frac{\partial}{\partial x_i}(\rho u_i T) = \frac{\partial}{\partial x_j} \left((\Gamma + \Gamma_t) \frac{\partial T}{\partial x_j} \right) \quad (3)$$

The RNG $k-\varepsilon$ model is very effective for prediction of heat Transfer and pressure loss in baffled channel. [3, 14]. The RNG-based $k-\varepsilon$ turbulence model is derived from the instantaneous Navier–Stokes equations, using a mathematical technique called “renormalization group” (RNG) methods. All the governing equations were discretized by the first order upwind numerical scheme, decoupling

with the SIMPLE algorithm and solved using a finite volume method. For closure of the equations, the RNG k-ε model was used in the present study. The solutions were converged when the normalized residual values were less than 10⁻⁵ for all variables but less than 10⁻⁷ only for the energy equation. The friction factor, *f* is computed by pressure drop, Δ*P* across the length of the channel, *L* as

$$f = \frac{1}{\left(\frac{L}{D}\right)} \frac{\Delta P}{\frac{\rho \bar{U}^2}{2}} \quad (7)$$

For the thermal behaviors, the calculations based on the Nusselt number, is given by

$$Nu = \frac{1}{L} \int Nu_{(x)} dx \quad (8)$$

The thermal enhancement factor η is defined by

$$\eta = (Nu/Nu_0)/(f/f_0)^{1/3} \quad (9)$$

Where *Nu*₀ and *f*₀ stand for Nusselt number and friction factor for the smooth channel, respectively.

Grid independence test

The different computational domains are resolved by triangular meshes. For this channels flow, irregular grid was applied throughout the domain. Grid independent solution is obtained by comparing the solution for different grid levels. It is found that the difference in heat transfer coefficient between the results of grid system of about 87.600, 94.100 and 110.200 cells which is less than 2%. Considering both convergent time and solution precision, the grid system of 87.600 was adopted for the computational models.

RESULTS AND DISCUSSION

Verification of results for smooth channel

The verification of results in this work based on the Nusselt number and friction factor obtained from the present smooth channel are compared with Dittus-Boelter and Blasius correlations, respectively.

$$Nu = 0.023 Re_D^{0.8} Pr^{0.4} \quad \text{For } Re \geq 10^4 \quad (10)$$

$$f = 0.316 Re^{-1/4} \quad \text{For } 2.10^3 < Re < 10^5 \quad (11)$$

Fig. 2a and b show, respectively, a comparison of Nusselt number and friction factor obtained from the present study with those from Eqs. (10) and (11). In the figures, the present results reasonably agree well within ±2.9% and ±6.6% for both

friction factor correlation of Blasius and Nusselt number correlation of Dittus-Boelter, respectively.

FLOW STRUCTURE

Figs. 3 and 4 shows that the flow front of the lower baffle separates in three recirculation zones: a large central recirculation zone or a central vortex, a small one at the corner behind the lower wall baffle and a small one at the corner in front of the upper wall baffle.

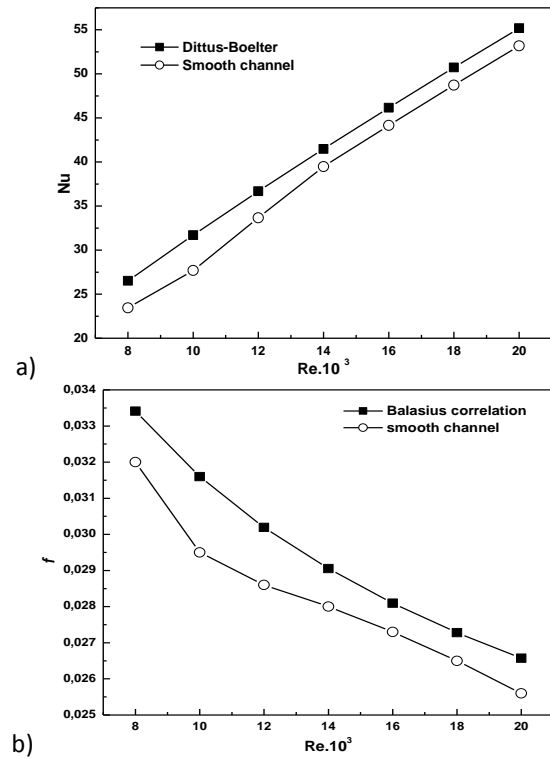


Figure 2 Verification of (a) Nusselt number and (b) friction factor for smooth channel

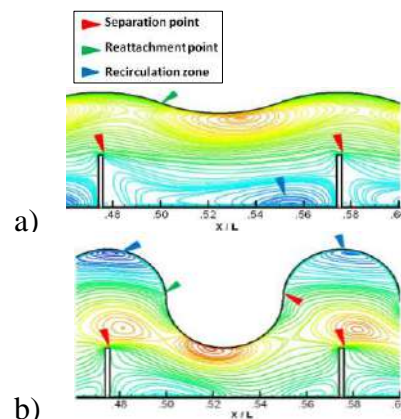


Figure 3 Corrugated surface effect on the flow structure: a) HCSR=0.1, b) HCSR=0.6

The central vortex or recirculation zone behind of the lower baffle causes the fluid to strongly rotating motion. For the corrugated surface/wall, the formation of reattachment point in the inferior part of corrugated surface/wall due to the flow acceleration in the zone to locate at the top of inferior baffles. The recirculation zone creates on the higher part of the corrugated surface/wall due to the separation of the flow on the lower part level of the corrugated surface/wall where the lower part plays a baffle role. Thus, the presence of the baffle

leads to longer flow path and high strength of central vortex due to changing in its orientation. Fig. 3 shows the lower baffles and corrugated Surface/wall effect on the flow structure for the section $0.46 \leq x/L \leq 0.60$. Fig 3.a shows the absence of recirculation zones on the upper wall (corrugated surface) caused by the absence of separation points. On the other hand, in Fig 3.b the vortex zones to appear clearly on the higher parts of corrugated surface/wall.

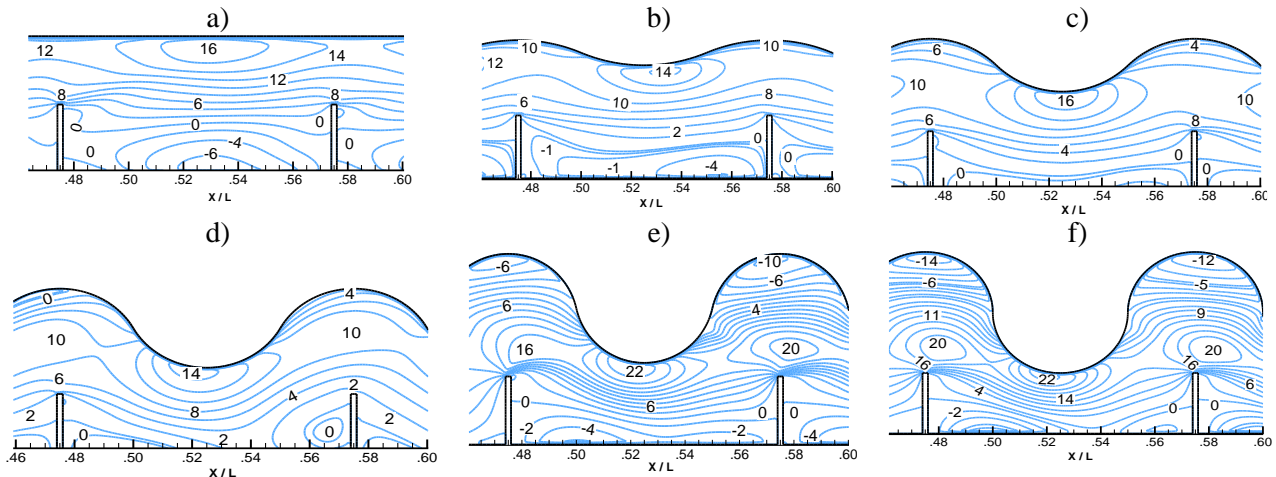


Figure 4
Axial velocity streamlines: a) HCSR=0, b) HCSR=0.1, b) HCSR=0.2, c) HCSR=0.3, d) HCSR=0.4, e) HCSR=0.5, f) HCSR=0.6

Fig. 4 presents axial velocity streamlines around baffle and corrugated surface for the various geometry for the section $0.46 \leq x/L \leq 0.60$ at $Re = 8000$, blockage ratio (BR) and spacing ratio(S) fixed in 0.5 and 1 respectively. This figure exhibits the following phenomena:

- Formations of the recirculation zones appear clearly in the large zone to locate between two successive baffles.
- For the corrugated surface; the recirculation zones is appear in the first time from HCSR = 0.3. Thus, these zones clearly appear in the cases of HCSR = 0.4 and 0.5. This phenomena caused by the formation of separation points of the flow on the corrugated wall where the inferior parts of corrugated surface played the baffles role.

HEAT TRANSFER

Fig. 5 displays the variation of Nusselt number ratio, Nu/Nu_0 with Reynolds number for different HSCRs. In the figure, the Nusselt number ratio tends to increase with the rise of Reynolds number from 8000 to 20,000 for all HSCR values. The higher HSCR value results in the increase in the Nu/Nu_0 value. The use of the corrugated

surfaces/walls with the $BR = 0.5$ achieve heat transfer rate of about 0.9–6.8 times higher at than the smooth channel with no baffle with Reynolds number values.

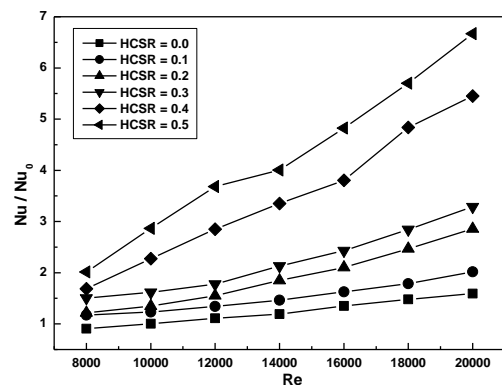


Figure 5
Variation of Nu / Nu_0 with Reynolds number for various baffled channels

PRESSURE DROP

Fig. 6 shows the variation of the friction factor ratio, f/f_0 with the Reynolds number value and shows that the friction factor ratio tends to increase

with raising in the HSCRs and Reynolds number. The corrugated surfaces provide a considerable increase in the f/f_0 than the heated plate wall at the same operating condition.

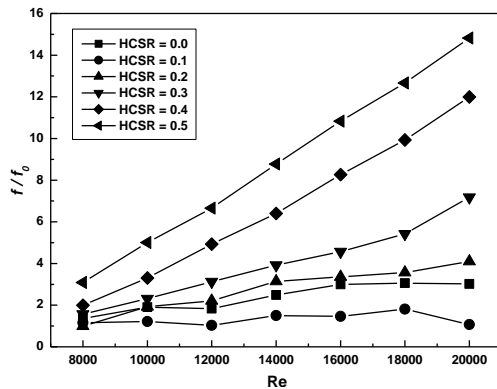


Figure 6
Variation of f / f_0 with Reynolds number for various baffled channels

But the friction factor of the $HSCR = 0$ is larger than that the $HSCR = 0.1$ case, caused by the improvement of the flow pass section between the inferior baffle extremity and the upper corrugated wall without change in the flow structure and increase in turbulence intensity. The friction factor for $HSCR = 0.5$ appears to be about 3-15 times higher than that for the smooth channel.

PERFORMANCE EVALUATION

Fig. 7 shows the variation of thermal enhancement factor for solar air heater bi dimensional channel fitted with plate baffle and heating corrugated surface/wall.

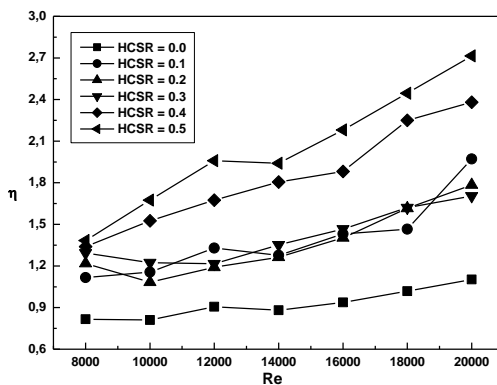


Figure 7
Thermal enhancement factor for various baffled channels

In the figure, the enhancement factor of both the HSCRs tends to increase with the rise of Reynolds number. The enhancement factor for the $HSCR = 0.1$ presents a feeble value of enhancement factor and increase with the Re , indicating that the

corrugation of heat transfer wall is advantageous with flow structure and heat transfer execution. For all the HSCRs; the enhancement factors vary between 0.8 and 2.7, depending on Reynolds number values. The case of $HSCR = 0.5$ present a better enhancement factor is about 2.7 at the highest Reynolds number.

CONCLUSIONS

A numerical study has been conducted to investigate air flow friction and heat transfer behaviors in a solar air heater channel fitted with upper heating corrugated wall and plate baffles placed on the lower wall. Numerical investigation effected for turbulent flow regime, where Reynolds number varied from 8000 to 20000. The results show that the Nusselt number and friction factor increases with the rise of Reynolds number and HSCR values. In general, the values of friction factor and Nusselt number are higher as compared to those for plate wall. This is due to change in flow characteristics because of plate baffle/heating corrugated wall shapes that causes flow separation, reattachments and generation of recirculation zones. The case of $HSCR = 0.5$ present better heat transfer rate is varied from 2 to 6.8 time depending with Reynolds number, however, this augmentation of heat transfer associates pressure loss from 3 to 15 time compared with smooth channel. The case of $HSCR = 0.5$ present a better enhancement factor is about 2.7 at the highest Reynolds number.

NOMENCLATURE

- b Baffle Height, (m)
- B RBlockage ratio, (b/H)
- D Hydraulic diameter, (m)
- f Friction factor
- h Heat transfer coefficient, ($W m^2 K^{-1}$)
- H Channel Height, (m)
- hcs Height of corrugated surface,(m)
- HCSR Heating corrugated surface ratio, (hcs/lcs)
- G_K Turbulent kinetic energy production
- K Turbulent kinetic energy, ($m^2 s^{-2}$)
- k_f Thermal conductivity, $W m^{-1} K^{-1}$
- lcs Length of corrugated surface, (lcs=H),(m)
- L Channel Length, (m)

Greek letter

- η Thermal enhancement factor
- ρ Density, $kg m^{-3}$

REFERENCES

- [1] Dong Hyun Lee, Dong-Ho Rhee, Kyung Min Kim, Hyung Hee Cho, Hee Koo Moon. Detailed measurements of heat/mass transfer with continuous and multiple V-shaped ribs in rectangular channel. *Energy*, vol. 34, pp. 1770–1778, (2009).
- [2] Wei Peng, Pei-Xue Jiang, Yang-Ping Wang, Bing-Yuan Wei. Experimental and numerical investigation of convection heat transfer in channels with different types of ribs. *Applied Thermal Engineering*, vol. 31, pp. 2702-2708, (2011).
- [3] Pongjet Promvonge, Wayo Changcharoen, Sutapat Kwankaomeng, Chinaruk Thianpong. Numerical heat transfer study of turbulent square-duct flow through inline V-shaped discrete ribs. *International Communications in Heat and Mass Transfer*, vol. 38, pp. 1392–1399, (2011).
- [4] Pongjet Promvonge, Withada Jedsadaratanachai, Sutapat Kwankaomeng, Chinaruk Thianpong. 3D simulation of laminar flow and heat transfer in V-baffled square channel. *International Communications in Heat and Mass Transfer*, vol. 39, pp. 85–93, (2012).
- [5] V.S. Hans, R.P. Saini, J.S. Saini. Heat transfer and friction factor correlations for a solar air heater duct roughened artificially with multiple v-ribs. *Solar Energy*, vol. 84, pp.898–911,(2010).
- [6] Sukhmeet Singh, Subhash Chander, J.S. Saini. Exergy based analysis of solar air heater having discrete V-down rib roughness on absorber plate. *Energy* 37 (2012) 749-758.
- [7] Atul Lanjewar, J.L. Bhagoria, R.M. Sarviya. Heat transfer and friction in solar air heater duct with W-shaped rib roughness on absorber plate. *Energy*, vol. 36, pp.4531-4541,(2011).
- [8] P. Promvonge, C. Khanoknaiyakarn, S. Kwankaomeng, C. Thianpong. Thermal behavior in solar air heater channel fitted with combined rib and delta-winglet. *International Communications in Heat and Mass Transfer*, vol. 38, pp. 749–756, (2011).
- [9] Parkpoom Sriromreun, Chinaruk Thianpong, Pongjet Promvonge. Experimental and numerical study on heat transfer enhancement in a channel with Z-shaped baffles. *International Communications in Heat and Mass Transfer*, vol. 39, pp. 945–952, (2012).
- [10] Somchai Sripattanapipat, Pongjet Promvonge. Numerical analysis of laminar heat transfer in a channel with diamond-shaped baffles. *International Communications in Heat and Mass Transfer*, vol. 36, pp. 32–38, (2009).
- [11] Prashanta Dutta, Akram Hossain. Internal cooling augmentation in rectangular channel using two inclined baffles. *International Journal of Heat and Fluid Flow*, vol. 26, pp. 223–232, (2005).
- [12] Pongjet Promvonge. Heat transfer and pressure drop in a channel with multiple 60° V-baffles. *International Communications in Heat and Mass Transfer*, vol. 37, pp. 835–840, (2010).
- [13] Pongjet Promvonge, Sutapat Kwankaomeng. Periodic laminar flow and heat transfer in a channel with 45° staggered V-baffles. *International Communications in Heat and Mass Transfer*, vol. 37, pp. 841–849, (2010).
- [14] Smith Eiamsa-ard, Pongjet Promvonge. Numerical study on heat transfer of turbulent channel flow over periodic grooves. *International Communications in Heat and Mass Transfer*, vol. 35, pp. 844-852, (2008).

CRYSTAL GROWTH KINETICS OF SUGAR ALCOHOLS AS PHASE CHANGE MATERIALS FOR THERMAL ENERGY STORAGE

M. Duquesne^{1*}, A. Godin², E. Palomo del Barrio³, F. Achchaq³.

¹ Institut National Polytechnique de Bordeaux, 16 avenue Pey Berland, 33607 Pessac Cedex, France

² CNRS, Esplanade des Arts et Métiers, 33 405 Talence Cedex, France

³ Université de Bordeaux, Esplanade des Arts et Métiers, 33 405 Talence Cedex, France

*Corresponding author: Fax: +33 5 40 00 66 68 Email: marie.duquesne@enscbp.fr

ABSTRACT

Among bio-based materials, Sugar Alcohols (SA) are very promising Phase Change Materials (PCM) for thermal energy storage at low temperatures due to their low melting temperature, their high energy density, their high and stable undercooling allowing long-term storage with reduced thermal losses. When heating is needed, the storage system is discharged by activating SA crystallization and its discharge power depends on the SA crystal growth kinetics. This work aims at measuring and modeling crystal growth rates in undercooled melts of SA according to the temperature and determining the involved crystal growth mechanisms. Crystal morphologies and morphological transitions are also observed and discussed.

NOMENCLATURE

ROMAN LETTERS

$C_{1,2}$	Fit Parameters
f	fraction of interface sites (active growth sites)
k	Pre-factor
k_B	Boltzmann constant
L	Diffusion jump distance
R	Universal gas constant
v	Crystal growth velocity
T	Temperature at the crystal-melt interface (bulk temperature)
T_m	Liquidus temperature
T_0	Working temperature (bulk temperature)

GREEK LETTERS

η	Viscosity of the liquid
ΔH_{ls}	Latent heat of melting
ΔS_a	entropy difference
ΔT	undercooling $T_m - T$ (with T , the temperature at the crystal-melt interface)

ACRONYMS

PCM	Phase Change Materials
SA	Sugar alcohols
TES	Thermal Energy Storage

INTRODUCTION

Considering the current energy and economic issues, the development of new PCM for solar seasonal energy storage, matching building applications requirements, constitutes a technological challenge. Major assets of SA for these Thermal Energy Storage (TES) applications are their melting temperature (368-391K) which allows using cheap solar collectors, their outstanding energy density (4-5 times superior to the water energy density on a seasonal basis), which can lead to highly compact systems, and their high and stable undercooling allowing long-term storage with reduced thermal losses. Crystal growth kinetics of SA are an important issue for TES applications and are studied in this work.

MATERIALS & EXPERIMENTAL METHODS

Samples: The crystal growth of four pure sugar alcohols (Erythritol, Xylitol, Adonitol and L-Arabitol) has been studied in this work. Tab. 1 summarizes their specific information.

Table 1
Specific product information for the studied SA

SA	CAS number	Provider	Purity (%)
Erythritol	149-32-6	Cargill	99.5
L-Arabitol	7643-75-6	Stanford Chemicals	98
Adonitol	488-81-3	Sigma Aldrich	≥99
Xylitol	87-99-0	Roquette	98.43

Their melting temperature and energy density are listed in Tab.2. The latter and other (viscosity, density, conductivity etc.) properties as well as their measurements are detailed in [1].

Table 2
Melting point and Latent heat of the studied SA

SA	Melting Temperature (K)	Latent heat (J/g)
Erythritol	391	340.00
L-Arabitol	376	230.00
Adonitol	373	250
Xylitol	368	267.00

The sample consists in 300 mg of SA deposited on a microscope glass with no control of the thickness. This sample is prepared as follows: 1) the product is first molten in a vessel; and 2) the molten product is then poured on the glass slide.

Experimental means: The main elements of the set-up are a CCD camera and a heating/cooling system for temperature control.

The heating/cooling stage is a layered structure including, from the bottom to the top: i) a cooling element, which is kept at constant temperature during the experiments; ii) a flat heating element (80 mm x 115 mm x 1 mm), which is an electric resistance (4.7 Ω) placed between a copper layer and a layer made of kapton; iii) a metallic plate (80 mm x 115 mm x 10 mm) which is provided with a K-type thermocouple for temperature control. The heating element is controlled to heat the sample according to a predefined temperature pattern, whereas the metallic plate acts as a thermal diffuser.

The used camera is a high speed camera (Genie HM1024) and allows image capture rate from 0.1 fps to 117 fps in 1024x768 active resolution. The highest spatial resolution is about 4 μm. The set-up allows working temperatures ranges from ambient

temperature to 200°C and a maximum cooling rate of 10°C/min. This set-up is also mounted on a vibration free solid support

Experiments: The sample is initially in the liquid state at temperature below the melting point (undercooled melt) and the tests are carried at constant bulk temperature. The heating/cooling system is used to reach the selected working temperature (T_0) on the aluminium plate and to keep it constant thereafter. The sample is then placed on the aluminium plate and we wait until thermal equilibrium is reached. The studied SA and the corresponding ranges of working temperatures are given in Tab.3.

Afterwards, the crystallization is initiated with a small seed placed in the middle of the studied product. The small seeds used to activate the crystallization are carefully prepared: 1) the same product as the studied one is first molten in a vessel; 2) droplets of it are deposited on a glass slide 3) in contact with the glass slide, heterogeneous nucleation occurs generating semi-spherical crystallized droplets; 4) once crystallized, they are measured and only the ones of diameters ranging from 200 to 300 μm with a regular semi-spherical shape are used to activate the crystallization.

Table 3
List of the studied SA and the working temperatures

SA	Working temperatures
Erythritol	From 50°C to 110°C, every 5°C
L-Arabitol	From 40°C to 90°C, every 5°C
Adonitol	From 28°C to 93°C, every 5°C
Xylitol	From 30°C to 85°C, every 5°C

Data treatment: The movies recorded during the experiments are then processed in order to determine crystal growth rates using the data processing developed in [2].

RESULTS & DISCUSSION

Crystal growth kinetics: The experiments carried out show that the SA crystal growth is interface-controlled with diffusion-limited kinetics. The modern form of Wilson-Frenkel model for crystal growth hence applies and is written as follows [1,3]:

$$v = \frac{2k_b T}{\pi \eta(T) l^2} f \exp\left(-\frac{\Delta S_a}{R}\right) \left[1 - \exp\left(-\frac{\Delta H_b \Delta T}{RT_m T}\right)\right] \quad (1)$$

It is adapted to the crystallization rate of glass-forming materials, where the mobility of the atoms limits the growth rate (diffusion-limited kinetics). In these materials a rearrangement of the configuration and positions of the other atoms in the liquid is required for an atom or molecule to join the crystal. This rearrangement process is therefore thermally activated with the same activation energy as the liquid diffusion and the decrease of the viscosity.

Fig.1 presents the graphs of crystal growth velocities of the four studied SA according to the bulk temperature.

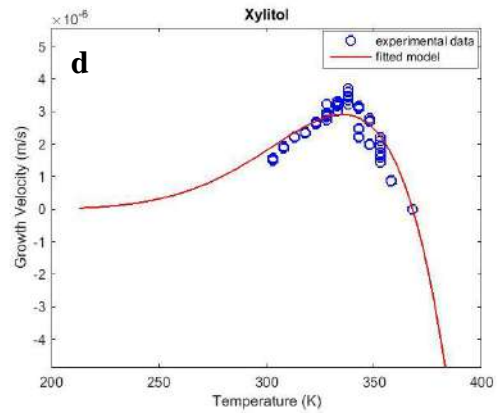
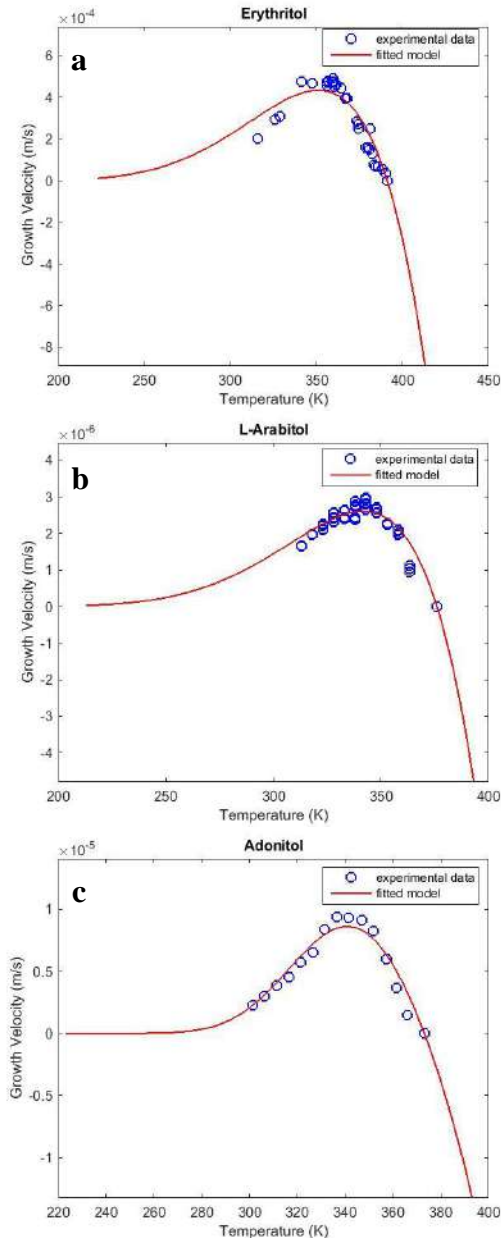


Figure 1

Graphs of crystal growth velocity vs. bulk temperature for a) Erythritol b) L-Arabitol c) Adonitol d) Xylitol.

The crystal growth rate is zero at the liquidus temperature. As the temperature decreases, the growth rate increases to a maximum up to a temperature at which the term including the activation energy drastically increases. Below this latter temperature, the growth rate decreases as the activation energy term begins to dominate.

Tab.4 shows the maximum crystal growth velocity, obtained using Wilson-Frenkel model, at the corresponding temperature for each SA. Erythritol crystallization appears to be much faster than the one of the other SA. Indeed, the crystal growth rate of Adonitol, Xylitol and L-Arabitol is two orders of magnitude inferior to Erythritol one. Adonitol is a bit faster than L-Arabitol and Xylitol. The obtained growth rates for Adonitol, L-Arabitol and Xylitol seem too low for the application. They lead to low heat release rates and too long discharge times. Erythritol presents very interesting crystal growth rates which could match the required energy discharge powers.

Table 4

List of the studied SA and the working temperatures

SA	Temperature (K)	Maximum Growth velocity (m/s)
Erythritol	351	435.2
L-Arabitol	342	2.6
Adonitol	341	8.6
Xylitol	335	2.9

Active growth sites & crystal morphologies:

The modern form of Wilson-Frenkel model is used here to investigate the temperature dependence of

the fraction f of interface sites that are active growth sites. From Eq.1, we can hence write:

$$kf = \frac{v\eta(T)}{(2k_B T / \pi) \left[1 - \exp\left(-\frac{\Delta H_{ls} \Delta T}{RT_m T}\right) \right]} \quad (2)$$

$$\text{with } k = \frac{1}{l^2} \exp\left(-\frac{\Delta S_a}{R}\right)$$

By assuming that the entropy difference, ΔS_a , and the diffusion jump distance, l , are not functions sensitive to the temperature, the pre-factor k can be considered as a constant. Then, Eq. 2 can be used to analyze the temperature dependence of f . This equation can also be used to distinguish which mechanism controls the interface reaction, because f has a different temperature dependence for each mechanism. The mechanism of growth may be defined as the manner in which atoms or molecular groups attach to the growing crystal surface. Two broad categories of mechanisms can be distinguished: continuous and lateral. The continuous mechanism operates when molecules can attach to the crystal surface at essentially any site (rough surfaces), allowing the interface to advance uniformly. For continuous growth, f is generally assumed to be large and independent of the temperature. Lateral growth occurs when a crystal surface is essentially atomically flat (smooth surfaces). Two idealized types of lateral mechanisms can be distinguished: surface-nucleation and screw dislocation. In the surface-nucleation mechanism, it is assumed that molecules can attach only at the edges of one-molecule-thick-layer on the crystal surface. Each layer is initiated by one or more one-molecule-thick-nucleii. Its formation obeys the classical laws of nucleation kinetics. In such case, the density of active growth sites f depends on the density of growth sites provided by the nucleation process. However, defects in the crystal structure can help to form new layers, so that a nucleation process is not necessary for growth. For instance, a screw dislocation that ended at a surface provides a continuous step on a surface for growth. The fraction f of active sites for growth is now proportional to the undercooling [3,4].

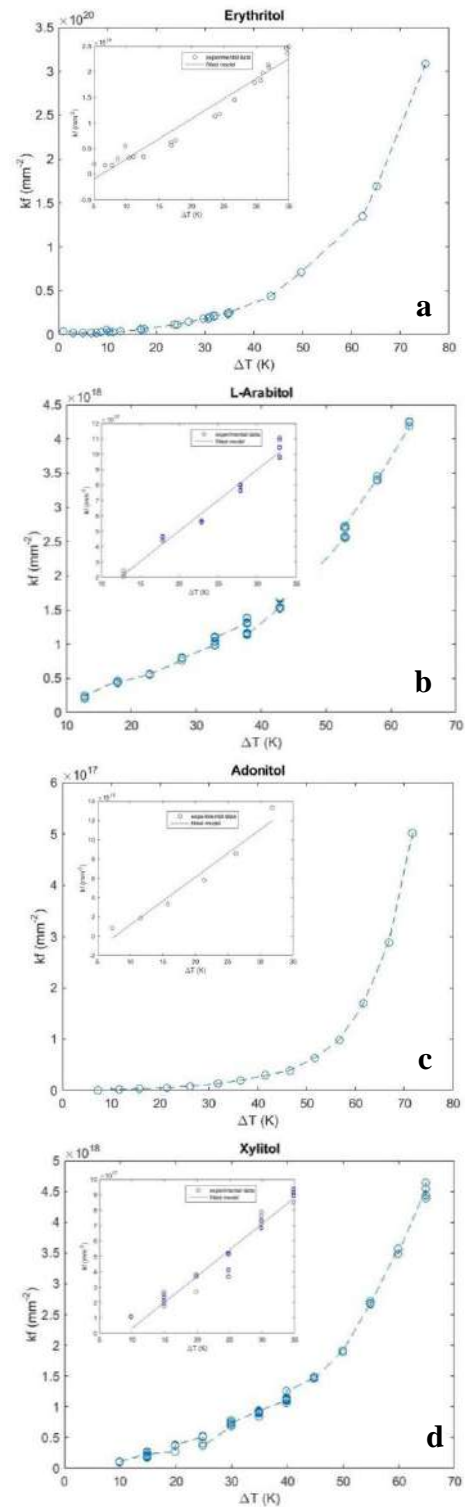


Figure 2
Temperature dependence of the density of active growth sites. Plot of kf , the density of active growth sites vs the undercooling ΔT for a) Erythritol b) L-Arabitol c) Adonitol d) Xylitol.

Fig.3 shows pictures of SA crystal morphologies at different undercooling degrees.

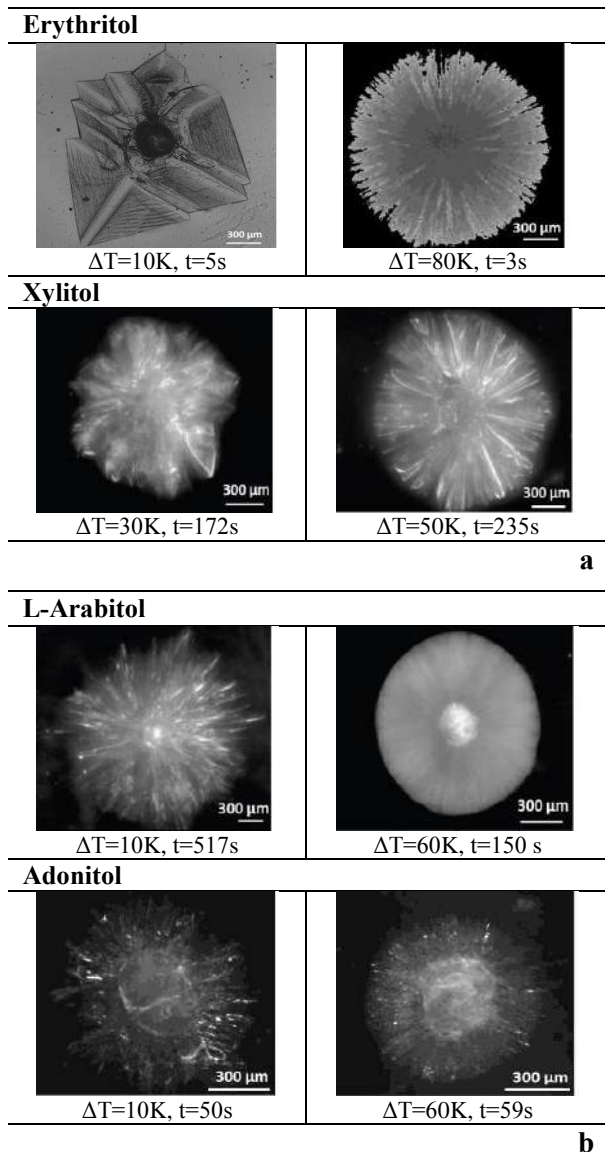


Figure 3

Pictures of the SA crystal morphologies at small (left raw) and high (right raw) undercooling degree: a) faceted dendritic morphologies b) dense branching morphologies

Using the measured values for the crystal growth velocity v (data in Fig.1), the temperature dependence of f has been calculated using Eq. 2. As shown in Fig.2 (left side, inset), for all the studied SA, at small undercoolings ($\Delta T < 40$ K), the fraction f of active sites for growth increases linearly with the undercooling, in accordance with the theory of growth on screw dislocations. Then the density of active growth sites increases dramatically. At small undercoolings the defect density determines the density of active growth sites and at large undercooling ($\Delta T > 50$ K) another mechanism takes

over. This second mechanism could be either surface nucleation or a continuous mechanism due to increased roughness of the edge of the steps or both.

As it can be seen in Fig. 3, among the tested SA, Xylitol and Erythritol present faceted dendritic morphologies whereas Adonitol and L-Arabitol present dense branching ones. In both cases, the morphology of the crystal-melt interface is also changing with undercooling. At small undercoolings, faceted interfaces with large facets are observed for Erythritol and Xylitol and respectively large branches, for L-Arabitol and Adonitol. With progressively larger undercoolings, the size of the facets, respectively branches, decreases. At high undercoolings, the morphology of the interface is spherulitic and its roughness is probably also increased for all SA.

In Fig.4 is represented the logarithm of kf against to the inverse of temperature. It can be seen that there is a quite good linear relationship between $\ln(kf)$ and $1/T$. Therefore, the following model has been adjusted to the data (red line in Fig.2):

$$kf = C_1 \exp\left(\frac{C_2}{T}\right) \quad (3)$$

The crystal growth velocity is hence approached by

$$v = C_1 \exp\left(\frac{C_2}{T}\right) \frac{2k_B T}{\pi\eta(T)} \left[1 - \exp\left(-\frac{\Delta H_b \Delta T}{RT_m T}\right)\right] \quad (4)$$

Table 5
Fit parameters for each studied SA

SA	C_1 (mm ⁻²)	C_2 (K ⁻¹)
Erythritol	$9.9043 \cdot 10^8$	$8.4956 \cdot 10^3$
L-Arabitol	$4.2964 \cdot 10^{10}$	$5.8085 \cdot 10^3$
Adonitol	$8.0792 \cdot 10^3$	$9.5747 \cdot 10^3$
Xylitol	$2.5890 \cdot 10^9$	$6.5214 \cdot 10^3$

The blue line in Fig.2 represents the crystal growth velocity calculated using Eq.4. The fit parameters are estimated and listed in Tab.5.

The agreement with measurements is quite good. We notice the importance of a detailed analysis of the interface temperature when discussing the temperature dependence of experimentally determined growth rates. Indeed, the red line in Fig. 3 corresponds to Eq.4 in which C_1 , C_2 and v are obtained using the values of the bulk temperature.

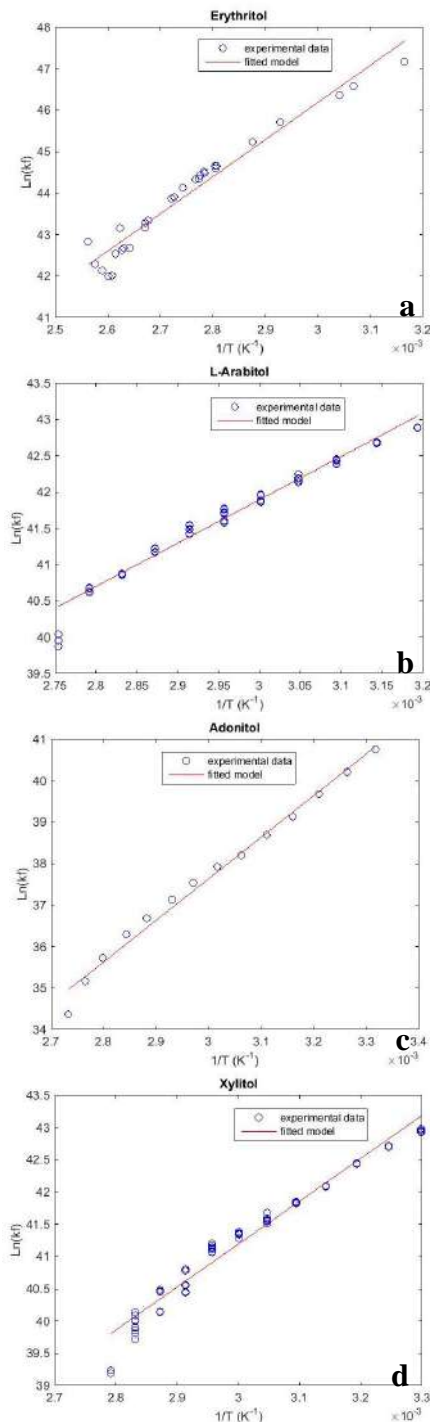


Figure 4

Plot of $\ln(kf)$ vs the undercooling ΔT for a) Erythritol b) L-Arabitol c) Adonitol d) Xylitol.

CONCLUSION

A study of crystal growth kinetics of SA and of the involved mechanisms according to the temperature has been performed. The experiments carried out show that the SA crystal growth is interface-controlled with diffusion-limited kinetics. The

modern form of Wilson-Frenkel model, adapted to the crystallization rate of glass-forming materials, presents a good agreement with the measured kinetics. It has also been proved that SA growth mechanisms, kinetics and crystal morphologies depend on the bulk temperature. Increasing the undercooling degree lead to morphological transitions. SA interfaces are smooth at small undercoolings (screw dislocations) and become rough at high ones (either surface nucleation or a continuous mechanism).

Regarding seasonal energy storage, the obtained growth rates for Adonitol, L-Arabitol and Xylitol seem too low (maximum velocities 2-9 $\mu\text{m/s}$). Indeed, they lead to low heat release rates and too long discharge times. On the contrary, Erythritol presents very interesting crystal growth rates (maximum velocity > 400 $\mu\text{m/s}$ maximum). Therefore, Erythritol could be a very promising candidate for TES applications. The other studied SA could be used in seasonal energy storage applications but a method (such as bubbling, see ICOMÉ 2016, A. Godin) to activate their crystallization in extended and highly spatially resolved areas would be required.

ACKNOWLEDGMENT

The authors acknowledge the financial support of the European Commission for subsidizing FP7 SAM.SSA Project.

REFERENCES

- Godin, A., Palomo del Barrio, E., Duquesne, M., et al., 3 April 2014, Summary of measured physical properties. In: 4th Progress Meeting, FP7 project-SAM.SSA-Work Package, Bucharest.
- Godin, A., Duquesne, M., Palomo del Barrio, E., Morikawa, J., 2015, Analysis of crystal growth kinetics in undercooled melts by infrared thermography, Quantitative InfraRed Thermography Journal, DOI: 10.1080/17686733.2015.1066133
- Jackson, K.A., 2004, *Kinetics processes. Crystal Growth, Diffusion, and Phase Transitions in Materials*, Wiley-VCH Verlag GmbH & Co. KGaA, Weinheim.
- Herlach, D.M., Galenko, P., Holland-Moritz, D., 2007, *Metastable solids from undercooled melts*, Pergamon materials series. Amsterdam.

On The Semi-Analytical Solution of Integro-Partial Differential Equations

A. Hasseine^{a,1}, M. Attarakih^b, R. Belarbi^d, H.-J. Bart^e

^aLaboratory LAR-GHYDE, University of Biskra, Algeria

^bFaculty of Eng. &Tech., Chem. Eng. Dept. The University of Jordan 11942-Amman, Jordan

^dLaboratory of engineering sciences for environment (LaSIE), University of La Rochelle, France

^eChair of Separation Science and Technology, Center for Mathematical Modeling, Kaiserslautern University, P.O. Box 3049, D-67653 Kaiserslautern, Germany

*Corresponding author: Email: hasseine@yahoo.fr

ABSTRACT

The breakage and aggregation processes in batch systems had attained highly interest in applied mathematics and engineering fields. In this work, we developed analytical solutions of the particle breakage and aggregation using the population balance equation (PBE) in batch flow systems. To allow explicit solutions, we approximated the particle breakage and aggregation mechanisms by assuming functional forms for breakage and aggregation kernels. In this framework, the Adomian decomposition method (ADM), variational iteration method (VIM) and homotopy perturbation method (HPM) were used to solve the population balance model. These semi-analytical methods overcome the crucial difficulties of numerical discretization and stability that often characterize previous solutions of the PBEs. The obtained results in all cases showed that the predicted particle size distributions converge exactly in a continuous form to that of the analytical solutions using the three methods.

Keywords: Population balance model, Adomian decomposition method, variational iteration method, homotopy perturbation method.

NOMENCLATURE

$n(v, t) dv$ number of particles in size range
 $n_m(v, t)$ solution components
 v, v' particle volumes

Greek letters

$\beta(v/v') dv$ fractional number of particles formed in the size range to +d formed upon breakage of particle of volume v'
 $\Gamma(v')$ number of particles in the size range to +d disappearing per unit time by breakage
 $\omega(v, v')$ aggregation frequency between two particles of volumes v and v'

crystallization[4,5], polymerization[6-8], aerosol[9], granulation[10–13], and biological [15].

The continuous distribution of particles for PBE in batch system is usually described by a number density function $n(v, t)$, which represents the number of particles within a differential volume size range per unit volume of latex. The rate of change of the particle number density is described by a nonlinear integro-partial differential population balance equation for one-dimensional[16-18]

$$\frac{\partial n(v, t)}{\partial t} = \int_0^{\infty} \beta(v/v') \Gamma(v') n(v', t) dv' + \frac{1}{2} \int_0^v \omega(v-v', v') n(v-v', t) n(v', t) dv' - \Gamma(v) n(v, t) - \int_0^{\infty} \omega(v, v') n(v, t) n(v', t) dv. \quad (1)$$

with the initial condition $n_0(0, v) = n_0(v) \geq 0$.

INTRODUCTION

Nonlinear integro-partial differential equations are encountered in various fields in applied mathematics[1,2] and engineering[3]. For example, population balance equation (PBE) is used to describe various kinds of phenomena such as

Here it is assumed that at any instant the number of particles $n(v, t)$ depends only on time and one internal coordinate, which is the particle volume v .

where: $\Gamma(v)$ and $\omega(v, v')$ are the breakup and aggregation frequencies, respectively, and $\beta(v/v')dv$ is the number of daughter particles having a volume in the range from v to $v + dv$ formed upon breakup of the particle of volume v' . The first two terms on the right hand side represent particle formation due to breakup and aggregation succeeded by two terms which represent particle loss due to breakup and aggregation.

Numerical solution of the above PBE (1) is difficult due to the integral and the non-linear behavior of the source term. There are only few numerical techniques available in the literature to compute the complete property distribution. Some numerical techniques can be found in the following literature [19-25], these series of papers on the available numerical methods were discussed up to the mid-eighties to find efficient and stable numerical methods for solving the population balance equation, such as the fixed-and moving pivot methods, Dual Quadrature Method of Generalized Moments (DuQMoGeM), and Cumulative Quadrature Method of Moments (CQMOM).

In recent years, several methods have drawn particular attention, such as the Adomian decomposition method [26], the variational iteration method [27], and the homotopy perturbation method [28]. The main advantage of the techniques are the most transparent methods of solution of (PBEs) and can be coupled with an optimization algorithm to solve inverse problems of the estimation of properties of building materials because they provide immediate and visible symbolic terms of both analytical and numerical solutions to linear as well as nonlinear integro-partial differential equations without linearization or discretization.

We propose in this work these three semi analytical methods as a novel converging sequence of continuous approximations to the particle number density function with new breakage and aggregation kernels, which a solution to the PBE.

THE ADOMIAN DECOMPOSITION METHOD

In this section we consider the model equation of the form:

$$L u + Ru + Nu = g(t), \quad (2)$$

where L is the linear operator usually containing the highest-ordered partial derivative which is assumed to be easily invertible, R is the linear remainder operator and N represents the nonlinear term, and $g(t)$ the source term.

Operating with L^{-1} on (2) and using the given conditions we have the canonical form:

$$u = u_0 - L^{-1}(Ru + Nu) \quad (3)$$

The nonlinear operator Nu can be decomposed by an infinite series of polynomials given by

$$Nu = \sum_n A_n \quad (4)$$

where A_n 's are the Adomian polynomials given by

$$A_n = \frac{1}{n!} \frac{d^n}{d\lambda^n} \left[N \left(\sum_{i=0}^{\infty} \lambda^i u_i \right) \right]_{\lambda=0} \quad n=0, 1, 2, \quad (5)$$

The Adomian decomposition method [26] assumes that the unknown function $u(t, v)$ can be expressed by the sum

$$u = \sum_{i=0}^{\infty} u_i. \quad (6)$$

The solution of the linear PDEs in the form (3) with the initial value

$$u_0 = f(v), \quad (7)$$

can be determined by the series (6) with the Adomian recursion scheme

$$u_{n+1}(v, t) = -L^{-1}Ru_n - L^{-1}A_n, \quad k \geq 0. \quad (8)$$

THE VARIATIONAL ITERATION METHOD

Consider the following functional equation:

$$Ln + Nn = g(x, t), \quad (9)$$

where L is a linear operator, N a nonlinear operator and $g(x, t)$ a source term.

According to the VIM, we can construct a correction functional as follows:

$$n_{n+1}(x, t) = n_n(x, t) + \int_0^t \lambda(\xi) (Ln_n(x, \xi) + N\tilde{n}_n(x, \xi) - g(x, \xi)) d\xi, \quad (10)$$

where λ is a general Lagrangian multiplier which can be identified optimally via the variational theory and \tilde{n}_n is a restricted variation which means $\delta\tilde{n}_n = 0$ [27]. Consequently, the solution is given by $n(x, t) = \lim_{n \rightarrow \infty} n_n(x, t)$.

THE HOMOTOPY PERTURBATION METHOD

To represent the procedure of this method, let us consider the following function:

$$A(u) - f(r) = 0, r \in \Omega \tag{11}$$

with the boundary conditions

$$B(u, \frac{\partial u}{\partial n}) = 0, r \in \partial\Omega \tag{12}$$

where A and B are general differential operator and boundary operator, respectively. $f(r)$ is a known analytical function and $\partial\Omega$ is the boundary of the domain Ω .

After dividing the general operator into a linear part (L) and a nonlinear part (N), Eq. (11) can be rewritten as

$$L(u) + N(u) - f(r) = 0. \tag{13}$$

According to the HPM, we construct a homotopy in the form

$$H(v; p) = L(v) - L(u_0) + pL(u_0) + p[N(v) - f(r)] = 0,$$

or

$$H(v; p) = (1 - p)[L(v) - L(u_0)] + p[A(v) - f(r)] = 0, \tag{14}$$

Where $r \in \Omega$ and $p \in [0, 1]$ is an embedding parameter, u_0 is an initial approximation of Eq.(11) which satisfies the boundary conditions Eq.(12). In HPM, one can use the embedding parameter as a small parameter. Therefore, the basic assumption is that the solution of Eq.(14) can be expressed as a power series in p :

$$v = v_0 + pv_1 + p^2v_2 + \dots \tag{15}$$

The approximate solution of Eq. (11), therefore, can be readily obtained:

$$u = \lim_{p \rightarrow 1} v = v_0 + v_1 + v_2 + \dots \tag{16}$$

APPLICATIONS

In all the following case studies, we will apply the Adomian decomposition method, variational iteration method and the homotopy perturbation method to solve the population balance equation, and present the analytical results to verify the effectiveness of these methods.

Aggregation only with multiplicative kernel

$$\omega(v, v') = vv' \text{ and } n_0 = e^{-v}$$

Consider the problem in the continuous system as given by Eq.(1) with $\omega(v, v') = vv'$:

$$\frac{\partial n(v, t)}{\partial t} = \frac{1}{2} \int_0^v (v - v') v' n(v - v', t) n(v', t) dv' - \int_0^\infty vv' n(v, t) n(v', t) dv'. \tag{17}$$

Homotopy perturbation method

To solve the Eq. (17) by the HPM, we can construct the following homotopy:

$$hp_1 = (1 - p) \left(\frac{\partial n(v, t)}{\partial t} - \frac{\partial n_0(v, t)}{\partial t} \right) + p \left(\frac{\partial n(v, t)}{\partial t} - \frac{1}{2} \int_0^v (v - v') v' n(v - v', t) n(v', t) dv' + \int_0^\infty vv' n(v, t) n(v', t) dv \right). \tag{18}$$

Substituting Eq. (15) into Eq. (18) and equating the coefficients of p with the same power, one gets

$$\frac{\partial n_1(v, t)}{\partial t} - \frac{1}{2} \int_0^v (vv' n_0(v - v', t) n_0(v', t) - v^2 n_0(v', t) n_0(v - v', t)) dv + \int_0^\infty vv' n_0(v, t) n_0(v', t) dv = 0, \tag{19}$$

$$\frac{\partial n_2(v, t)}{\partial t} - \frac{1}{2} \int_0^v \left(v^2 n_1(v - v', t) n_0(v', t) - v^2 n_1(v', t) n_0(v - v', t) + vv' n_1(v', t) n_0(v - v', t) + vv' n_0(v', t) n_1(v - v', t) \right) dv - \int_0^\infty (vv' n_0(v, t) n_0(v', t) + vv' n_0(v, t) n_1(v', t)) dv = 0, \tag{20}$$

$$\frac{\partial n_3(v, t)}{\partial t} - \frac{1}{2} \int_0^v \left(v^2 n_1(v - v', t) n_1(v', t) + vv' n_1(v', t) n_1(v - v', t) - v^2 n_2(v', t) n_0(v - v', t) + vv' n_2(v', t) n_0(v - v', t) + v^2 n_2(v - v', t) n_0(v', t) + vv' n_0(v', t) n_2(v - v', t) \right) dv - \int_0^\infty (vv' n_1(v, t) n_1(v', t) + vv' n_0(v, t) n_2(v', t) + vv' n_2(v, t) n_0(v', t)) dv = 0, \tag{21}$$

The corresponding solutions for the above system of equations are the series solution which is given as

$$n_1(v) = e^{-v} t \left(-v + \frac{v^3}{12} \right), \tag{22}$$

$$n_2(v) = e^{-v} t^2 \left(\frac{v^2}{2} - \frac{v^4}{12} + \frac{v^6}{720} \right), \quad (23)$$

$$n_3(v) = e^{-v} t^3 \left(-\frac{v^3}{2} + \frac{v^5}{24} - \frac{v^7}{720} + \frac{v^9}{120960} \right). \quad (24)$$

➤ **Variational iteration method**

We apply variational iteration method to Eq. (17) where its iteration formula reads

$$n_{n+1}(v) = n_n(v) - \left[\int_0^t \left(\frac{\partial n_m(v,t)}{\partial t} - \frac{1}{2} \int_0^v (v-v') v' n_m(v-v', t) dv' + \int_0^\infty v v' n_m(v,t) n_m(v',t) dv' \right) dt, \right. \\ \left. \frac{\partial n_m(v,t)}{\partial t} = \int_v^\infty \beta(v/v') \Gamma(v') n(v',t) dv' - \Gamma(v) n(v,t). \right] \quad (30)$$

From this scheme we calculate the solution components recursively as follows:

$$n_1(v) = e^{-v} + e^{-v} t \left(-v + \frac{v^3}{12} \right), \quad (25)$$

$$n_2(v) = e^{-v} + e^{-v} t \left(-v + \frac{v^3}{12} \right) \\ + e^{-v} t^2 \left(\frac{v^2}{2} - \frac{v^4}{12} + \frac{v^6}{720} \right) \dots, \quad (26)$$

$$n_3(v) = e^{-v} + e^{-v} t \left(-v + \frac{v^3}{12} \right) + e^{-v} t^2 \left(\frac{v^2}{2} - \frac{v^4}{12} + \frac{v^6}{720} \right) \\ + e^{-v} t^3 \left(-\frac{v^3}{2} + \frac{v^5}{24} - \frac{v^7}{720} + \frac{v^9}{120960} \right) \dots \quad (27)$$

The general term for the two methods is:

$$n_m(v) = \frac{v^{3m} t^m}{(m+1)! \text{Gamma}[2m+2]}. \quad (28)$$

Then the exact solution is given by:

$$n(v) = \sum_{m=0}^{\infty} \frac{v^{3m} t^m}{(m+1)! \text{Gamma}[2m+2]} = \\ e^{-(1+t)v} \text{HypergeometricPFQ} \left[\left\{ \right\}, \left\{ \frac{3}{2}, 2 \right\}, \frac{tv^3}{4} \right], \quad (29)$$

where HypergeometricPFQ is the generalized hypergeometric function.

The above analytical solution is the same as that derived by [28] using the Laplace transform methods. It should be noted that the authors didn't find the exact solution of (17) for the same form of the aggregation kernel by the Adomian decomposition method and then gave only approximate series solution.

Fig. 1 shows the particle number density for initial time, t=0.5 and t=1 are as predicted using HPM and VIM methods. Our graph shows that these semi

analytical solutions are very close to the exact one, which was determined by the Laplace method [28].

5.2. Breakage only

In this section we consider the particle breakage with general frequency $\Gamma(v) = v^k$ and daughter particle distribution $\beta(v/v') = \frac{kv^{k-2}}{v'^{k-1}}$ where Eq.(1)

$$\frac{\partial n_m(v,t)}{\partial t} = \int_v^\infty \beta(v/v') \Gamma(v') n(v',t) dv' - \Gamma(v) n(v,t). \quad (30)$$

With $n_0(v) = v e^{-v}$ as an initial distribution.

➤ **Adomian decomposition method**

We find the solution to (28) by the recursive relationship of ADM as follows:

$$n_{n+1}(v) = \int_0^t \left(\int_v^\infty \beta(v/v') \Gamma(v') n_m(v',t) dv' - \Gamma(v) n_m(v,t) \right) dt, \\ m=0,1,2\dots \quad (31)$$

Then, the first few terms of the decomposition series are given by

$$n_1(v) = e^{-v} t \left(k + \frac{2k}{v^2} + \frac{2k}{v} - v \right) v^k, \quad (32)$$

$$n_2(v) = e^{-v} t^2 \left(-k - \frac{2k}{v^2} - \frac{2k}{v} + \frac{v}{2} \right) v^{2k}, \quad (33)$$

$$n_3(v) = e^{-v} t^3 \left(\frac{k}{2} + \frac{k}{v^2} + \frac{k}{v} - \frac{v}{6} \right) v^{3k}, \quad (34)$$

➤ **Variational iteration method**

Following the same procedure as VIM's for calculating the Aggregation, we obtain the following iteration

$$n_1(v) = v e^{-v} + e^{-v} t \left(k + \frac{2k}{v^2} + \frac{2k}{v} - v \right) v^k, \quad (35)$$

$$n_2(v) = v e^{-v} + e^{-v} t \left(k + \frac{2k}{v^2} + \frac{2k}{v} - v \right) v^k + \\ e^{-v} t^2 \left(-k - \frac{2k}{v^2} - \frac{2k}{v} + \frac{v}{2} \right) v^{2k}, \quad (36)$$

$$n_3(v) = v e^{-v} + e^{-v} t \left(k + \frac{2k}{v^2} + \frac{2k}{v} - v \right) v^k + \\ e^{-v} t^2 \left(-k - \frac{2k}{v^2} - \frac{2k}{v} + \frac{v}{2} \right) v^{2k} + e^{-v} t^3 \left(\frac{k}{2} + \frac{k}{v^2} + \frac{k}{v} - \frac{v}{6} \right) v^{3k}. \quad (37)$$

The components $n_4(v), n_5(v), \dots$ can be easily

determined. The general term of the series of the two methods is given by

$$n_i(v) = e^{-v} \frac{(-t)^i}{i!} \left(ik - \frac{2ik}{v^2} - \frac{2ik}{v} + v \right) v^{ik}. \quad (38)$$

The exact solution is obtained as

$$n(v) = \sum_{i=0}^{\infty} e^{-v} \frac{(-t)^i}{i!} \left(ik - \frac{2ik}{v^2} - \frac{2ik}{v} + v \right) v^{ik} = e^{-v-tv^k} \frac{(v^3 + 2ktv^k + 2ktv^{k+1} + ktv^{2+k})}{v^2}. \quad (39)$$

It should be noted that we have treated only the problems with exact solutions. However, an approximate solution can be obtained for any breakage and aggregation kernels if the solution of the problem exists.

Fig. 2 presents the comparison of the number density distributions at time $t=0.05$ for the cases of $k=2$ and 3 corresponding respectively to the parabolic and cubic breakage rates. Clearly this comparison shows that the parabolic breakage rate gives much production of particles than for cubic breakage rate.

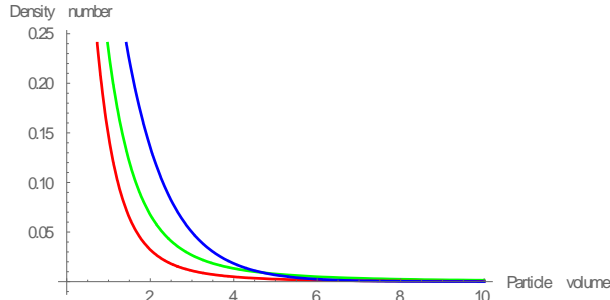


Figure 1. Aggregation with product kernel, and an exponential feed distribution.

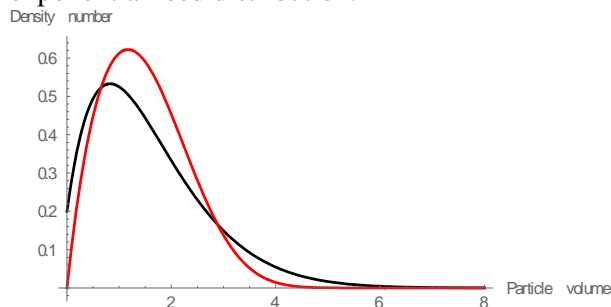


Figure 2 .Breakage with parabolic and cubic breakage rates at $t=0.05$, and an Gaussian feed distribution.

CONCLUSIONS

In this paper, Adomian decomposition method (ADM), variational iteration method (VIM) and homotopy perturbation method (HPM) have been successfully applied to find the solution of the population balance equation involving particle breakage and aggregation. Solution of population balance equation shows that the results of proposed methods are in agreement with each other. The results obtained here clearly show, that these semi analytical methods, are capable of solving population balance equation, without any restrictive assumptions or transformations, that may change the physical behavior of the problem. The comparison between VIM and HPM with Adomian decomposition method (ADM) shows that VIM and HPM are more effective and convenient to use and overcomes the difficulty arising in calculating of the Adomian polynomials that mostly require tedious algebraic calculations. Moreover, the VIM requires the valuation of the Lagrangian multiplier λ . In general these semi analytical methods can be widely used in mathematical, physical and engineering problems regarding to the classical methods, due to their simplicity and efficiency.

REFERENCES

1. A. Hasseine, A. Bellagoun, H.J. Bart, Analytical solution of the droplet breakup equation by the adomian decomposition method, *Appl. Math. Comput.* 218(2011) 2249–2258.
2. A.Hasseine, H.J.Bart, Adomian decomposition method solution of population balance equations for aggregation, nucleation, growth and breakup processes. *Appl. Math. Modelling.*39(2015) 1975–1984.
3. A. Hasseine, S. Senouci, M. Attarakih and H.-J. Bart, Application of two analytical approaches for the solution of the population balance equations: Particle breakage process. *Chemical Engineering & Technology. Chem. Eng. Technol.* 2015, 38, No. 9, 1574–1584.
4. C.Y. Ma, X.Z. Wang, K.J. Roberts, Multi-dimensional population balance modeling of the growth of rod-like L-glutamic acid crystals using growth rates estimated from in-process imaging, *Adv. Powder Technol.* 18 (2007) 707–723.
5. R. Gunawan, I. Fusman, R.D. Braatz, High resolution algorithms for multidimensional

- population balance equations, *AIChE J.* 50 (2004) 2738–2749.
6. Y. Yao, Yi-Jun He, Z.H. Luo, L. Shi, 3D CFD-PBM modeling of the gas–solid flowfield in a polydisperse polymerization FBR: The effect of drag model, *Adv. Powder Technol.* (2014).
 7. R.M. Ziff, E.D. McGrady, The kinetics of cluster fragmentation and depolymerisation, *J. Phys. A: Math. Gen.* 18 (1985) 3027–3037.
 8. P.J. Blatz, A.V. Tobolsky, Note on the kinetics of system manifesting simultaneous polymerization depolymerization phenomena, *J. Phys. Chem.* 49 (1945) 77.
 9. M.Z. Jacobson, Analysis of aerosol interactions with numerical techniques for solving coagulation, nucleation, condensation, dissolution, and reversible chemistry among multiple size distributions, *J. Geophys. Res.* 107 (D19) (2002) 4366, <http://dx.doi.org/10.1029/2001JD002044>.
 10. Z. Ning, Distinct element simulation of impact breakage of lactose agglomerates. modeling of coating in a jet-fluidized bed, *Adv. Powder Technol.* 18 (2007) 311–327.
 11. K.P. Hapgood, M.X.L. Tan, D.W.Y. Chow, A method to predict nuclei size distributions for use in models of wet granulation, *Adv. Powder Technol.* 20 (2009) 293–297.
 12. M.L. Eggersdorfer, S.E. Pratsinis, Agglomerates and aggregates of nanoparticles made in the gas phase, *Adv. Powder Technol.* 25 (2014) 71–90.
 13. A. Chaudhury, A. Kapadia, A.V. Prakash, D. Barrasso, R. Ramachandran, An extended cell-average technique for a multi-dimensional population balance of granulation describing aggregation and breakage, *Adv. Powder Technol.* 24 (2013) 962–971.
 14. A. Hasseine, Z. Barhoum, M. Attarakih, H.-J. Bart, Analytical solutions of the particle breakage equation by the Adomian decomposition and the variational iteration methods. *Advanced Powder Technology* 26 (2015) 105–112.
 15. F. Srieenc, Cytometric data as the basis for rigorous models of cell population dynamics, *J. Biotechnol.* 71 (1999) 233–238.
 16. S. Kumar, D. Ramkrishna, On the Solution of Population Balance Equations by Discretization—III. Nucleation, Growth and Aggregation of Particles, *Chem. Eng. Sci.*, 52 (1997) 4659–4679.
 17. K.J. Valentas, A.R. Amundson, Breakup and coalescence in dispersed phase systems, *Ind. Eng. Chem. Fundamen.* 5 (1966) 533–542.
 18. W. Podgórska, J. Bałdyga, Scale-up effects on the drop size distribution of liquid liquid dispersions in agitated vessels, *Chem. Eng. Sci.* 56 (2001) 741–746.
 19. D. Ramkrishna, The status of population balances, *Rev. Chem. Eng.* 3 (1985) 49–95.
 20. M. Kostoglou, A. J. Karabelas, Evaluation of zero order methods for simulating particle coagulation, *J. Colloidal Interface Sci.* 613 (1994) 420–431.
 21. S. Kumar, D. Ramkrishna, On the solution of population balance equations by discretization – I. A fixed pivot technique, *Chem. Eng. Sci.* 51 (1996a) 1311–1332.
 22. S. Kumar, D. Ramkrishna, On the solution of population balance equations by discretization—II. A moving pivot technique, *Chem. Eng. Sci.* 51 (1996b) 1333–1342.
 23. S. Kumar, D. Ramkrishna, On the Solution of Population Balance Equations by Discretization—III. Nucleation, Growth and Aggregation of Particles, *Chem. Eng. Sci.*, 52 (1997) 4659–4679.
 24. Attarakih, M. (2013) Integral formulation of the population balance equation: Application to particulate systems with particle growth. *Computers & Chemical Engineering*, 48, 1–13.
 25. Santos, F. P., Senocak, I., Favero, J. L. & Lage, P. L. C. (2013). Solution of the population balance equation using parallel adaptive cubature on GPU. *Computers & Chemical Engineering*, 55, 61–70.
 26. G. Adomian, *Solving Frontier Problems of Physics: The Decomposition Method*, Kluwer Academic, Dordrecht, 1994.
 - [27. J.H. He, A new approach to nonlinear partial differential equations, *Comm. Nonlinear Sci. Numer. Simul.* 2 (1997) 203–205.
 28. J.H. He, Homotopy perturbation technique, *Comput. Methods Appl. Mech. Eng.* 178 (1999) 257–262.
 29. R. Singh, J. Saha, J. Kumar, Adomian decomposition method for solving fragmentation and aggregation population balance equations. [Journal of Applied Mathematics and Computing](#) June 2015, Volume 48, Issue 1, pp 265–292.

EFFECT OF THE POSITION OF THE PHASE CHANGE MATERIAL (PCM $\text{Na}_2\text{CO}_3 \cdot 10\text{H}_2\text{O}$) ON THE SOLAR CHIMNEY EFFECT

Liu Bin^a, Shan Liangliang^a, Wang Qi^a, Mao Shaoli^a, Rachid Bennacer^{a,b}

^aTianjin Key Lab of Refrigeration Technology, Tianjin University of Commerce Tianjin, 300134, People's Republic of China

^bENS-Cachan Dpt GC/ LMT,61, Av du Président Wilson 94235 Cachan Cedex France

*Corresponding author: E-mail: lbtjcu@tjcu.edu.cn

ABSTRACT

To reduce the energy consumed by ventilation in a building is a critical task for the related researchers. Using the solar chimney effect to obtain the nature ventilation at day time is possible. Here a hybrid wall with PCM was provided, and the effect of the position of PCM in the hybrid wall on the solar chimney effect was studied. The thickness of PCM was 1cm, the air gap was 30cm and the power of the simulation solar light was 780W. The results show that when PCM was in front of absorber, the temperature of the air in the gap was higher than that of the air with a PCM behind the absorber. As for the air velocity in the gap, when the simulation solar light was turn on, the air velocity with PCM in front of the absorber was higher than that of the air with PCM behind the absorber. While when the simulation solar light was turn off, the air velocity with PCM in front of the absorber was lower than that of the air with PCM behind the absorber. It is interesting to guide the construction of the hybrid wall.

Keywords Hybrid wall; chimney effect; PCM; nature ventilation; building energy consumption; position.

NOMENCLATURE

\dot{m} the air mass flow rate, kg/s

ρ the air density, kg/m³

\bar{V} the average air velocity at the hybrid wall cross-section, m/s

INTRODUCTION

The energy consumption of the ventilation is one important part of the total energy consumed by buildings, it is one of the feasible method to realize the nature ventilation by the solar chimney effect, which is one of the hottest research topics in the energy utilization [1]. In solar chimneys, the solar radiation is utilized to enhance the natural ventilation in buildings, which is resulted from the fact that the density of the air inside the solar chimney will be reduced for a temperature rise caused by the heat adsorption of the air.

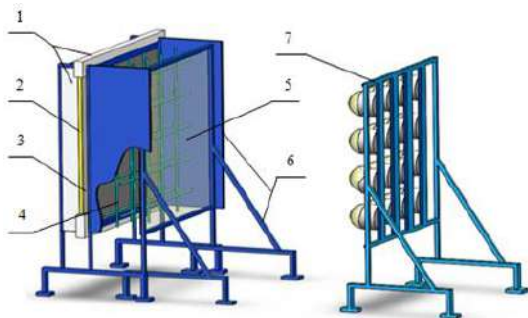
Some experiments and theoretical investigations have been carried out to study the effects of geometry, inclination angle and meteorological parameters on the ventilation performance of solar chimneys [2~6]. But the nature ventilation resulted from the solar chimney effect has one critical shortage that there will be no nature ventilation at night when there is no solar light. In order to solve the problem, some researchers began to use the hybrid wall including the phase change materials (PCM) to improve the solar chimney effect. In the solar chimney, PCM is

used as the heat storage. In day time, PCM absorbs heat and stores it, while at night, PCM releases heat and maintains the solar chimney effect. There are many kinds of PCM which can be used in the hybrid wall, including water based materials, salt hydrate, eutectic, paraffin, fatty acid and so on [7-8]. Different researchers carried out some studies on the chimney effect according to the thermal properties of PCM. Li and Liu [7-10] experimentally and numerically studied the PCM (paraffin wax RT 42) solar chimney and obtained good agreements. They found that the application of high effective thermal conductivity of PCM can further improve the performance of the chimney under lower solar radiation. Liu [11] carried out the experiment of the solar chimney effect with different thickness PCM ($\text{Na}_2\text{CO}_3 \cdot 10\text{H}_2\text{O}$) and find the thickness had an important effect on the nature ventilation performance of the hybrid wall. While for the hybrid wall used as the heat storage, the position of PCM in the hybrid wall also has an important on the chimney effect performance. There is few study about that. At here, it focus on the effect of the position of PCM on the chimney effect.

EXPERIMENTAL SETUP

The experimental setup was installed in one large laboratory with a temperature of $20 \pm 2^\circ\text{C}$, The setup included two parts as shown in Fig.1 The first part was the chimney part including the 100

mm Polyurethane insulation, the PCM($\text{Na}_2\text{CO}_3 \cdot 10\text{H}_2\text{O}$) layer, the absorber (10mm cement sand plaster), the frame for sensors, the glass and the experimental frame. The position of PCM and the absorber can be exchanged. The PCM layer can be adjusted according to the experimental requirement, in this paper the thickness of PCM was 10mm. The gap between the glass and the absorber can be changed from 5mm to 600mm. In the study, the depth of the gap was 300mm, the width was 1000mm and the height was 1000mm also. The second part is the heating part. A solar simulator has been designed as the heat source to reproduce solar radiation in this experiment. The light source consists of 12 indoor heating lamps (Model DAAIC) and the light intensity of the lamps is controlled by a contact voltage regulator (Model TDGC2-3) with a variable range from 60 V to 160 V, in this study the voltage was 140 V (780W). The wavelength of the lamps is measured by USB200 fiber spectrometer and ranges from 0.34 μm to 1.03 μm . More details about the heating part was specified in reference [3]. The distance between the chimney and the solar simulator was 1000mm.



1:100mm Polyurethane insulation; 2: PCM $\text{Na}_2\text{CO}_3 \cdot 10\text{H}_2\text{O}$; 3: absorber (9.5mm cement sand plaster); 4:the frame for sensors; 5:glass; 6:experimental frame; 7:solar simulator

Fig.1 schematic diagram of the experimental setup

In this study, the PCM was $\text{Na}_2\text{CO}_3 \cdot 10\text{H}_2\text{O}$ for a low melting temperature with a melting temperature 360C. In the solar chimney, in order to avoid the component separation of $\text{Na}_2\text{CO}_3 \cdot 10\text{H}_2\text{O}$, it was divided into small size with a width and height of 30mm \times 30mm shown in Fig.2.

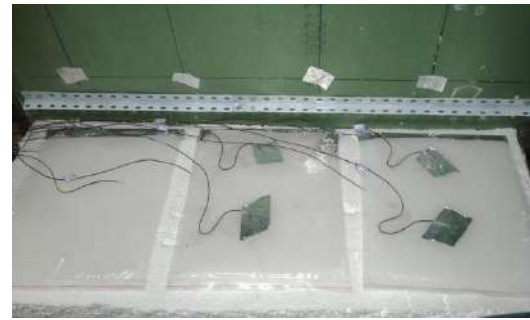


Fig.2 PCM of $\text{Na}_2\text{CO}_3 \cdot 10\text{H}_2\text{O}$ integration and the probes

The measuring positions of the temperature, the air velocity were shown in Fig.3. In order to avoid the reverse effect at the gap outlet, the measuring position of the outlet was located a distance of 125mm from to outlet. In order to get the temperature distribution of different components of the solar chimney, 128 copper constantan thermocouples with an accuracy of $\pm 0.2^\circ\text{C}$ were used. As for the air velocity, the multichannel anemometer (Model 1560) with an accuracy of ± 0.01 m/s was used, whose range is from 0m/s to 10 m/s.

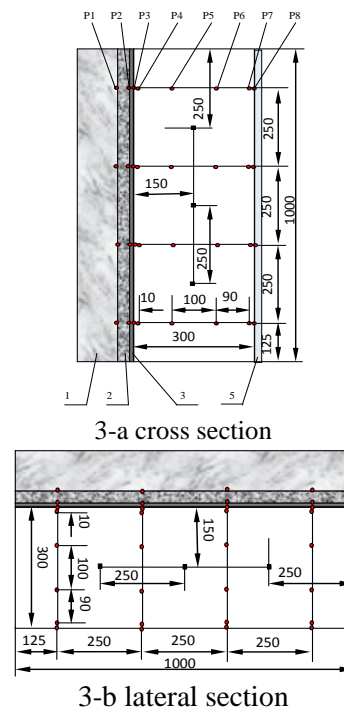


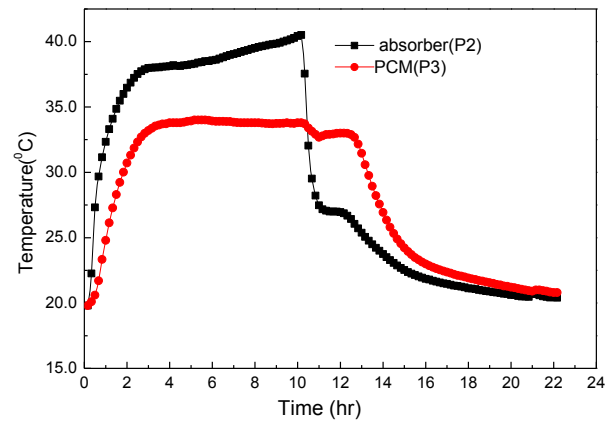
Fig.3 measuring position of sensors
1: insulator; 2: PCM; 3: absorber; 5: glass;
●:Temperature sensor; ■ :air velocity sensor

RESULTS AND DISCUSSION

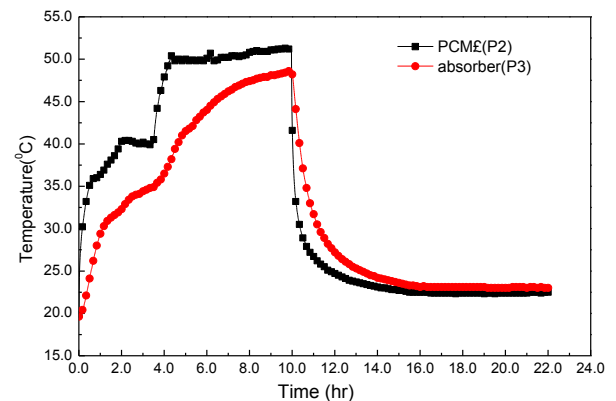
Comparison of the temperature development of PCM the absorber

Fig.4 shows the temperature development of PCM the absorber at two different position of PCM. From 4-a, we can find that the temperature of the absorber was higher than that of PCM. The development of both of PCM and absorber increased quickly in a short time in the beginning three hours when it was being charged, and the absorber had a higher increasing rate than PCM had. The reason is that the absorber absorbed heat from the radiation firstly, but for its low heat capacity, so the temperature of the absorber increased quickly. Because PCM was behind of the absorber, so its temperature increasing rate was smaller than that of the absorber. After three hours heat charging, the temperature of PCM reached the beginning melting temperature, so the temperature of PCM almost kept at a constant value, while the temperature of the absorber still increased slowly. When the heat charging stopped, the temperature of the absorber was reduced quickly from 430C to 270C in one hour, and the temperature of PCM also reduced a little about 10C to reach the solidification temperature. When PCM reached the solidification temperature, both temperature of the absorber and PCM were kept at a constant temperature. After that, both of them began to reduce slowly to the environment temperature, but were always higher than that of the environment, which would resulted in the chimney effect after heat charging. From Fig4-b, it shown a different temperature development of the absorber and PCM compared to Fig.4-a. First, the temperature of the absorber and PCM increased quickly in one hour after the charging beginning, then the increasing rate was reduce. And after that, the temperature of PCM was kept at a constant value, while the temperature of the absorber still increased slowly. Then the temperature of PCM increased quickly to a constant value about 500C, and the temperature of the absorber still increased quickly. In Fig.4-b, PCM was fixed in front of the absorber, it was directly heated by the radiation heat. When the temperature of PCM reached the melting temperature, it began to melt. In theoretically, the temperature of PCM should be kept at a constant value. But when the radiation heat was larger than the melting latent heat of PCM, and the conductivity of PCM and the absorber were enough, the temperature of PCM would still increase slowly as in Fig.4-b. When

the melting was finishing, the temperature of PCM increased again quickly until to reach the steady state. Because the absorber was behind of PCM, it's temperature was always lower than that of PCM, but it would be increased to get a balance between PCM and the absorber. When the radiation heat was stopped, the temperature of PCM reduced quickly, and there was not the solidification stage with a constant temperature. The main reason was that the convection heat was higher than the solidification heat.



4-a the heated surface temperature development of PCM and absorber when PCM was behind of the absorber at the height of 750mm



4-b the heated surface temperature development of PCM and absorber when PCM was in front of the absorber at the height of 750mm

Fig.4 the heated surface temperature development of PCM and absorber

The air temperature distribution in the air gap

Fig.5 shows the air temperature distribution in the air gap from the absorber or PCM to the glass when the charging time was five hours. It will find that the air temperature in the gap when PCM was in front of the absorber was higher than

that of the air in the gap when PCM was behind the absorber. The main reason is that PCM stored more heat when PCM was in front of the absorber. From Fig.4, we can find that the temperature of PCM was higher than that of the absorber. And as for the glass temperature, both of them are almost the same. So under the effect of the coupling glass and the absorber or PCM, the air temperature will be different. When PCM was in front the absorber, it had higher temperature, so the air temperature in the gap was higher.

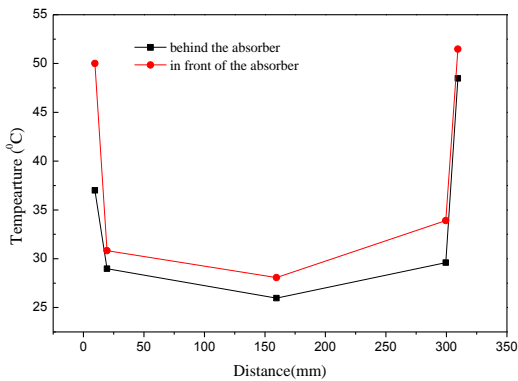


Fig.5 the distribution of the air temperature in the air gap

The air velocity and the air mass development in the air gap

Fig.6 shows the air velocity and the air mass flow rate development during the whole experimental time. For the air mass flow rate, it is calculated as equation (1).

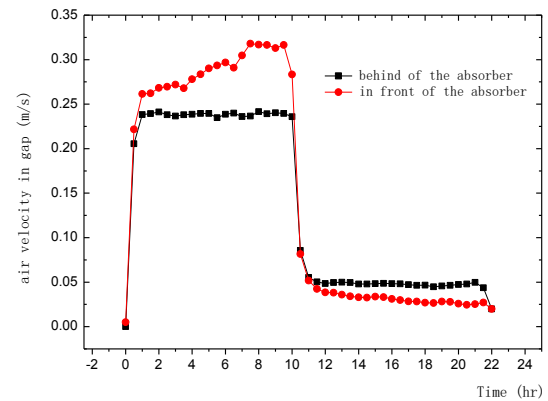
$$\dot{m} = \int_0^A \rho \times V \times dA = \rho \times \bar{V} \times dA \quad (1)$$

Where \dot{m} is the air mass flow rate, kg/s, ρ is the air density, kg/m³, \bar{V} refers to the average air velocity at the hybrid wall cross-section, m/s.

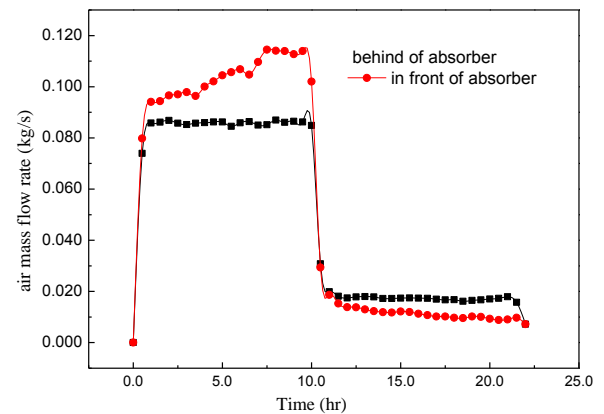
From Fig.6, it can be found the development tendency of both the air velocity and the air mass flow rate is the same, so the air velocity is analyzed. During the heat charging time, the air velocity increased continuously when PCM was in front of the absorber, and was higher than the value when PCM was behind of the absorber. From Fig.4, we have found that the temperature of the position of P2 with PCM in front of the absorber was higher than the temperature of the position of P2 with PCM behind the absorber, which meant a bigger temperature difference between the air in the gap and the wall surface. A bigger temperature difference will result a large chimney effect. So the air velocity in the air gape with PCM in front of the absorber was large, which also resulted in the larger air mass flow rate. During the discharging time, the air velocity

with PCM in front of the absorber was lower than the value with PCM behind of the absorber, which meant a lower air mass flow rate as shown in Fig.6-b. During the discharging time, PCM was cooled quickly, and the stored heat was transferred in a short time at the beginning of the discharging. So during the whole time of the discharging, the temperature difference between the air in the gap and PCM surface was lower, and a smaller chimney effect was caused shown in Fig.6-b in the discharging time.

From Fig.6, it provides a selection to arrange PCM in the solar hybrid double wall. If we want to adjust the nature ventilation resulted from the chimney effect, PCM should not be heated by the radiation heat directly. PCM fixed in the middle of the hybrid wall can store the heat effectively, and will discharge the heat a long time at the night which will result a stronger nature ventilation at night.



6-a the air velocity development



6-b the air mass development

Fig.6 air velocity and air mass development

CONCLUSIONS

To improve the nature ventilation at night is an important way to reduce the energy consumed by the mechanical ventilation. Here the position of PCM in the hybrid wall on the chimney effect is

discussed, the temperature development, the air velocity development and the air mass flow rate development were discussed. By the experiments, we can conclude when PCM is heated by the radiation heat directly, The temperature difference between the heat surface and the air in the gap will be higher than the temperature difference of PMM behind of the absorber. If the density of the radiation heat is enough, the heat surface temperature of PCM will rise directly with a short time of constant temperature (melting temperature) depending the conductivity of PCM and the convection resulted from the chimney effect in the charging time. While in the discharging time, the heat surface temperature of PCM will decrease quickly without a time of constant temperature (solidification temperature). For a good energy storage, PCM should not been heated by the radiation heat.

REFERENCES

1. X.Q. Zhai, Z.P. Song, R.Z. Wang et al, A review for the applications of solar chimneys in buildings[J], *Renewable and Sustainable Energy Reviews*,2011,15: 3757~3767
2. Shuangping Duana, Chengjun Jing, Ensheng Longa, Transient flows in displacement ventilation enhanced by solar chimney and fan, *Energy and Buildings*,2015,103: 124-130
3. Bin Liu, Xiaoyan Ma, Xiaolin Wang et al, Experimental study of the chimney effect in a solar hybrid double wall, *Solar Energy* ,2015,115:1–9
4. Haiwei Jing, Zhengdong Chen, Angui Li, Experimental study of the prediction of the ventilation flow rate through solar chimney with large gap-to-height ratios, *Building and Environment*,2015, 89: 150~159
5. Mehran Ghalamchi, Alibakhsh Kasaeian, Mehrdad Ghalamchi, Experimental study of geometrical and climate effects on the performance of a small solar chimney, *Renewable and Sustainable Energy Reviews*, 2015,43:425-431
6. Ahmed Abdunabi Imran, Jalal M. Jalil, Sabah T. Ahmed, Induced flow for ventilation and cooling by a solar chimney, *Renewable Energy* ,2015, 78 :236-244
7. Yongcai Li, Shuli Liu. Experimental study on thermal performance of a solar chimney combined with PCM [J]. *Applied Energy*, 2014,114: 172–178.
8. Yongcai Li, Shuli Liu. Numerical study on thermal behaviors of a solar chimney incorporated with PCM[J], *Energy and Buildings*,2014, 80:406–414.
9. Yongcai Li, Shuli Liu, Ashish Shukla, Experimental analysis on use of thermal conductivity enhancers (TCEs) for solar chimney applications with energy storage layer[J], *Energy and Buildings* 2016,116 : 35–44
10. Shuli Liu, Yongcai Li, An experimental study on the thermal performance of a solar chimney without and with PCM[J], *Renewable Energy*2015, 81 :338-346
11. Liu Bin, Li Peng, Ma Xiaoyan, et al, Chimney effect of hybrid double-wall with different thickness of PCM $\text{Na}_2\text{CO}_3 \cdot 10\text{H}_2\text{O}$, *Energy Procedia*, 2015,75:521-526.

NUMERICAL STUDY OF TRANSFER BY CONVECTION IN A LID-DRIVEN CAVITY WITH A THIN PCM LAYER

Binous Mohamed Sabeur, Abide Stéphane, Zeghmati Belkacem, Hassis Hédi
Laboratoire de Mathématiques et physique, EA 4217, Université de Perpignan Via Domitia, 52 Avenue
Paul Alduy, 66860 Perpignan; France

Ecole Nationale d'ingénieurs de Tunis, BP 37, LE BELVEDERE 1002, Tunis, Tunisie

*Corresponding author: Fax: +00 33 4 68 66 22 34 Email: med.sabeur.binous@gmail.com

ABSTRACT

A numerical method to solve transfer equations in a thin phase change material (PCM) layer in contact with a solid material or a fluid is presented. This numerical method is applied to predict the heat transfer in a lid-driven cavity which one of its vertical plane wall is covered with a thin layer of PCM. The mathematical and numerical modeling will be first presented, then the boundary condition associated to the PCM wall is formulated in term of “Signorini boundary condition”. The numerical method proposed to solve this formulation is validated by a test case.

Key words: Forced convection, Lid-driven cavity, Heat transfer, Phase change material, Signorini problem.

NOMENCLATURE

C_p = specific heat ($J\ kg\ K^{-1}$)
 H = height (m)
 L_m = latent heat ($J\ kg^{-1}$)
 L_{ref} = reference length (m)
 Nu_m = average Nusselt number
 Nu_c = local Nusselt number
 P_r = Prandtl number
 q'' = heat flux density ($w\ m^{-2}$)
 q_c = non dimensional diffusive flux
 Q'' = non dimensional heat flux
 Re = Reynolds number
 u_{ref} = reference velocity ($m\ s^{-1}$)
 T = temperature (K)
 T_m = melting temperature (K)

Greek symbols

ρ = density ($kg\ m^{-3}$)
 μ = dynamic viscosity (Pa s)
 k = thermal conductivity ($W\ m^{-1}\ K^{-1}$)
 α = thermal diffusivity ($m^2\ s^{-1}$)
 ν = cinematic viscosity ($m^2\ s^{-1}$)
 λ = liquid fraction
 θ = non dimensional temperature

INTRODUCTION

In the last decades the use of PCM has been extensive in various fields such as: building's to improve their thermal inertia, thermal protection of electronic devices in order to limit the peak of temperature, increase battery life time, solar power plants, etc. The common goal of all these applications is the heat energy storage. Heat energy storage not only reduces the mismatch between the supply and the demand, but also improves the performance and reliability of energy systems, hence plays a crucial role in the future energy needs [1,2]. Phase change materials (PCMs) usually provide a large amount of heat, due to phase change during charging and discharging [3-5]. Due to the rise of computer-aided modeling, several numerical methods for solving phase change problems have been developed. A phase change problem is more generally characterized by a moving melting front which splits the domain into a liquid and a solid phase. The overall phenomena are described by heat transfer equations and involves latent heat terms. The well-known “Stefan problem” [6-8] which is well-studied since more than 100 years, illustrates this kind of phase change phenomena. Two types of numerical method have been developed to these problems. Firstly, the interface tracking of the melting front is based on Lagrangian description of

the interface. On the other hand, a derived formulation of the heat equation, namely enthalpy method [9-10], is based on a Eulerian description thanks to the introduction of the liquid fraction. In our work, we consider a PCM thin layer on the boundary of a fluid domain; we formulate this by means of “Signorini formulation” and we propose a new numerical method. The mathematical and numerical modeling is first presented and numerical results dealing with a lid-driven heated cavity which one of its vertical plane wall is covered with a thin layer of PCM is next investigated to highlight the potential of this method.

ANALYSIS AND MODELLING

Let us consider a lid-driven cavity containing an incompressible fluid (Fig-1). The left wall of the cavity is covered with a thin layer of PCM and is subjected to a pulsating heat flux. The top wall is moving with a non-dimensional velocity U , a constant temperature is imposed on the right wall of the cavity while the bottom wall is adiabatic (See Fig-1). The equations that govern transfer in the fluid by forced convection and conduction in the PCM layer are linked at the vertical wall by conditions of temperature and heat flux continuities. The Obereck-Boussinesq approximation is used to relate density to temperature variation, and to link in this way the temperature field “ θ ” to the flow field [11,12]. The flow inside the cavity is governed by the Navier-Stokes equations which are given in their non-dimensional following form:

$$\frac{\partial u}{\partial x} + \frac{\partial v}{\partial y} = 0 \quad (1)$$

$$\frac{\partial u}{\partial t} + u \frac{\partial u}{\partial x} + v \frac{\partial u}{\partial y} = -\frac{\partial p}{\partial x} + \frac{1}{R_e} \left(\frac{\partial^2 u}{\partial x^2} + \frac{\partial^2 u}{\partial y^2} \right) \quad (2)$$

$$\frac{\partial v}{\partial t} + u \frac{\partial v}{\partial x} + v \frac{\partial v}{\partial y} = -\frac{\partial p}{\partial y} + \frac{1}{R_e} \left(\frac{\partial^2 v}{\partial x^2} + \frac{\partial^2 v}{\partial y^2} \right) + \theta \quad (3)$$

$$\frac{\partial \theta}{\partial t} + u \frac{\partial \theta}{\partial x} + v \frac{\partial \theta}{\partial y} = -\frac{\partial p}{\partial x} + \frac{1}{P_r R_e} \left(\frac{\partial^2 \theta}{\partial x^2} + \frac{\partial^2 \theta}{\partial y^2} \right) \quad (4)$$

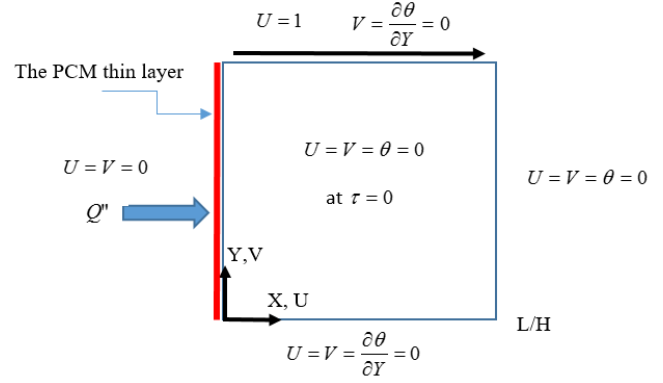


Figure 1: Lid-driven heated cavity

In equations (1-4) the dimensionless parameters are based on: the length scales $L_{ref} = H$; the reference

$$\text{velocity } u_{ref} = \frac{2g\beta H}{\alpha L q''}, \quad \text{and} \quad \Delta T_{ref} = 1,$$

$$0 \leq \theta = T - T_c \leq 1, \quad P_r = \frac{\nu}{\alpha}; \quad R_e = \frac{uL}{\nu};$$

For heat transfer by conduction in the PCM layer, we assumed that its thickness is small in comparison with L_{ref} , its thermal inertia is neglected and the heat transfer occurs only in the normal direction to the vertical wall. A thermal balance at the interface fluid-PCM leads to:

$$(q_c - j) \cdot n = \rho L_m \lambda' \quad \text{on } \Gamma_{PCM} \quad (5)$$

Where \mathbf{q}_c is the diffusive flux, \mathbf{j} the imposed heat flux, \mathbf{n} the outward normal, L_m the latent heat, ρ the density, and λ' the time derivative of the liquid fraction. So, the melting-solidifying model in the PCM is given by a system of inequalities:

$$\begin{cases} \lambda = 0 & \text{if } T \leq T_m \\ \lambda = 1 & \text{if } T > T_m \\ 0 \leq \lambda \leq 1 & \text{if } T = T_m \end{cases} \quad (6)$$

This model can be divided into the two following models

$$\begin{cases} (T_m - T)\lambda = 0 \\ T_m - T \geq 0 \\ \lambda \geq 0 \end{cases} \quad (7) \quad \begin{cases} (T - T_m)(1 - \lambda) \\ T - T_m \geq 0 \\ 1 - \lambda \geq 0 \end{cases} \quad (8)$$

Equations (7) describe the mushy-solid phase change and the equations (8) the mushy-liquid phase change. This boundary condition is similar to one of Signorini mechanical contact problem [12]. The literature revealed a recent numerical method of Signorini problem developed by Zhang and Zhu [13]. This method used to solve the Signorini boundary condition over the Laplace equation is based on an iterative method. This method is retained for this work.

NUMERICAL METHODOLOGY

Our boundary formulation is different from that of the Signorini boundary condition, developed by Zhang and Zhu by the lake of normal derivative term in our formulation. So, first we try to get closer to their formulation in order to use their iterative algorithm. Then, we proceed the time discretization of equation (5) expressed on equations (7) and (8). This discretization at each time step leads to the Signorini boundary condition on Γ_{PCM} that is the PCM boundary of the solid part as follow as:

$$\begin{cases} (T_m - T^{n+1})(a - b\nabla T^{n+1}.n) = 0 \\ T_m - T^{n+1} \geq 0 \\ a \geq b\nabla T^{n+1}.n \end{cases} \quad \text{on } \Gamma_{PCM} \quad (9)$$

and the liquid part as follow as

$$\begin{cases} (T_m - T^{n+1})(b\nabla T^{n+1}.n - (a - 1)) = 0 \\ T^{n+1} - T_m \geq 0 \\ b\nabla T^{n+1}.n \geq a - 1 \end{cases} \quad \text{on } \Gamma_{PCM} \quad (10)$$

Where $a = \lambda^n - \frac{\Delta t}{\rho L_m} j^{n+1}.n$ and $b = \frac{\Delta t}{\rho L_m} k$.

(9) and (10) are indeed complementary. The special feature of this formulation is that the two parts are valid in the mushy zone, which allows us to exchange between the two parts. In the next section, we present the iterative algorithm of resolution for the implicit scheme proposed.

The method of solving the boundary condition is based on the projection method presented by Zhang and Zhu [13]. They propose to introduce a fixed point equation to solve the non-linear boundaries. We present the resolution of the solid part. For a constant $c > 0$, the equation of the solid phase is equivalent to the following fixed point equation:

$$T_m - T - [T_m - T - c(a - b\nabla T.n)]_+ = 0 \quad (11)$$

With $[x]_+ = \max(x, 0)$. According to Zhang and Zhu, an iterative scheme is proposed as follows:

$$T^{(k+1)} = T_m - [T_m - T - c(a - b\nabla T.n)]_+ \quad (12)$$

The iterative steps are:

Step 1

Initially, the boundary condition on Γ_{PCM} is set to $T^{(0)} = T_m$ and a first solution is guessed with solving the heat equation.

Step 2

The part of Γ_{PCM} which is defined by $S_d = \{x \in \Gamma_{PCM}, T_m - T^{(k)} - c(a - b\nabla T^{(k)}.n) \leq 0\}$ is computed. On this part, Dirichlet condition is prescribed while on its complement compared to Γ_{PCM} Robin condition is considered.

Step 3

A new approximation of elliptic boundary value problem is computed:

$$\begin{cases} \Delta T^{(k+1)} + \frac{\rho C_p}{\Delta t} T^{(k+1)} = \rho C_p \frac{T^n}{\Delta t} & \text{in } \Omega \\ T^{(k+1)} = g & \text{on } \Gamma_D \\ \nabla T^{(k+1)}.n = f & \text{on } \Gamma_N \\ T^{(k+1)} = T_m & \text{on } S_d \\ T^{(k+1)} cb - \nabla T^{(k+1)}.n = T^{(k)} - ca & \text{on } \Gamma_{PCM/S_d} \end{cases}$$

Step 4

If the convergence criterion $\|T^{(k+1)} - T^{(k)}\| < \varepsilon$ is

reached, the next liquid fraction λ^{n+1} is updated and a new time step is performed. Otherwise go to step2. Regarding the liquid part of the boundary condition the calculation algorithm is the same, replacing a by a-1 in the algorithm.

VALIDATION

In order to validate the proposed numerical method, we consider a one dimensional case which allows us comparisons with standard methods. So, we consider the heat conduction problem in a solid bar which the left end is covered by a thin layer of PCM. The temperature at the left end of this bar is imposed. Consequently, a conductive heat transfer takes place in the rod and there occurs a phase change phenomenon in the PCM layer. The transfer equations in the PCM thin layer and the rod are coupled by temperature and flux continuities at the interface rod-PCM. In the solid bar, heat transfer is governed by the unsteady heat conduction equation and in the PCM domain heat transfer is described by enthalpy method (Voller method) [14]. To validate our model, the average interface temperature calculated with our numerical method and the multi-domain [15] are compared. Indeed, the testing physical model is a rod of length 10 cm with a thermal diffusivity $\alpha=2.61 \cdot 10^{-4} \text{ m}^2/\text{s}$. Computations are carried out with four PCM thickness ($e=2 \text{ cm}$, $e=1 \text{ cm}$, $e=0.5 \text{ cm}$ and $e=0.1 \text{ cm}$). It should be noted that the heat energy stored is defined by $L_v \times e=55000 \text{ J m} / \text{kg}$, is constant. It should be highlighted that our numerical code is able to reproduce the time evolution of the average temperature at the interface rod-PCM. The average interface temperature obtained by multi-domain method and by our method are very close as the PCM thickness decreases (Fig-2). This results validate our method for a thin PCM layer thickness. We can also observe that the phase change occurs at melting temperature of the selected PCM whatever the phase change as melting or solidifying.

In the next section, this new boundary condition is applied in a fluid dynamic problem.

The lid-driven cavity in figure (1) is considered now. Regardless the PCM boundary conditions, the Navier-Stokes equations are discretized by means of second order finite difference defined on a staggered grid. Then, the semi-implicit scheme of Adams Bashforth/Crank Nicholson is considered as time discretization. The velocity/ pressure coupling is overcoming by the projection method [16]. The method of solution for the linear systems resulting of these discretization's is based on multigrid solver. We consider the numerical method dealing with the PCM heat transfer equation, which is coupled with Navier-

Stokes equations. Then, we consider a thin PCM layer on the left wall of the square enclosure.

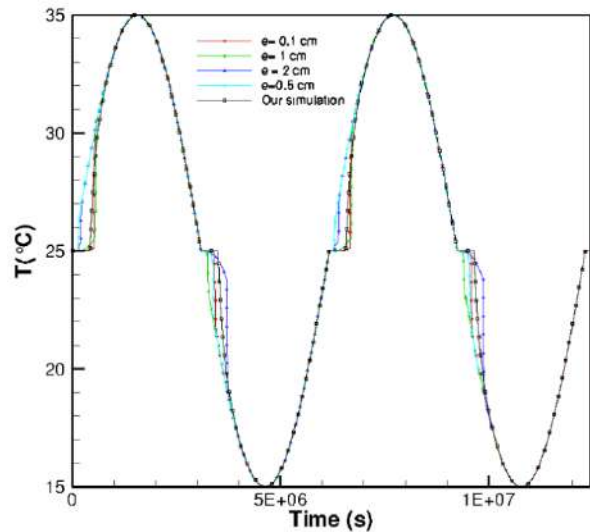


Figure 2: evolution of average interface rod-PCM temperature versus time.

RESULTS AND DISCUSSION

Computations have been performed for Prandtl number $Pr = 0.7$ as well as a rectangular heat flux function $q''(t)$ which is applied on the left wall with a dimensionless frequency $f=0.01$. The figure 3 presents the evolution of the average temperature versus time along the left wall and figure 4 the evolution of the local Nusselt number versus time at right wall for four Reynolds number $Re=400$, $Re=600$, $Re=800$ and $Re=1000$. The heat energy storage is set to $150000 \text{ J m} / \text{kg}$. It can be seen that a periodic behaviour is retrieved even if a PCM layer is added on the left wall. We observe a sinusoidal evolution of the average temperature and the local Nusselt number versus time. For a Reynolds number $Re=400$, the amplitude of the average temperature is varying between 0.176 and 0.2 and for $Re=1000$ between 0.12 and 0.168. The amplitude of the local Nusselt number for $Re=400$ is varying between 0.81 and 0.92 and for $Re=1000$ is in the range 0.87 and 1.12. So, if Reynolds numbers increase, the amplitudes of the average temperature and the local Nusselt number increase. This evolution during time remains in phase. It can be concluded that the variation of the Reynolds number has an impact on the amplitude of the average temperature along the

left wall and the amplitude of the local Nusselt number along the right wall.

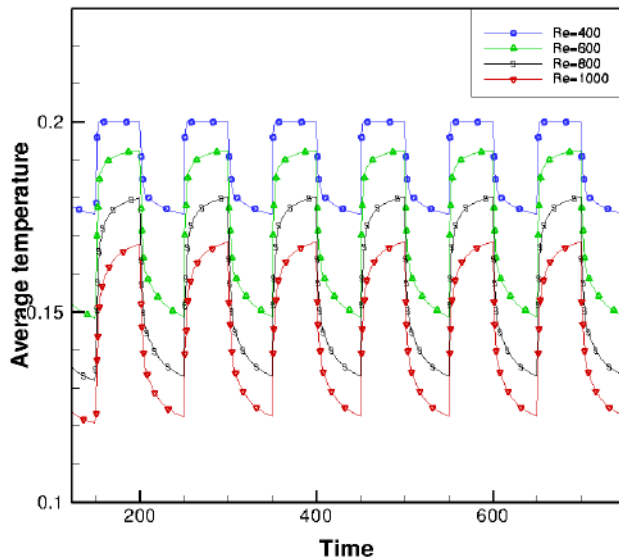


Figure 3 : Evolution of the left wall average temperature versus time.

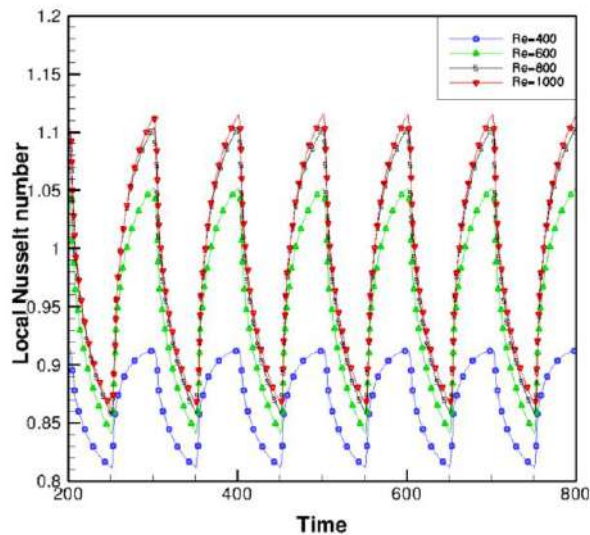


Figure 4 : Evolution of the right wall local Nusselt number.

CONCLUSIONS

A numerical method for predicting heat transfer by conduction in PCM layer and material as a rod or fluid is presented. The numerical method is suitable for heat transfer by conduction and convection transfer along a plane wall recovered by a thin thickness PCM layer. So, this numerical method can be easily coupled with different modes of heat transfer as conduction or convection. This numerical method has been applied first to a rod which one end

is covered by a thin PCM layer and next to a lid-driven cavity with a vertical wall covered by a thin PCM layer thickness on the left wall. It has been shown that the Reynolds number reduces the difference between the maximum and minimum values of the average temperature and the local Nusselt number.

REFERENCES

- 1.H.P. Garg, S.C. Mullick, A.K. Bhargava, 1985, Solar Thermal Energy Storage, D. Reidel. Publishing Co.
- 2.V.V Sharma, C.R, Tyagi, D, Chen, C. Buddhi, 2009 Review on thermal energy storage with phase change materials and applications materials and applications, *Renew. Sustain. Energy Rev.* **13**, pp 318-345.
3. J. Stekli, L. Irwin, R. Pitchumani, 2013, Technical challenges and opportunities for concentrating solar power with thermal energy storage, *J. Therm. Sci.Eng. Appl.* **5**, 0210111-02101112.
4. B. Zalba, J.M. Mar, L.F. Cabeza, H. Mehling, 2003, Review on thermal energy storage with phase change: materials, heat transfer analysis and applications, *Appl. Therm. Eng.* **23**, pp, 251-283
5. U. Herrmann, D.W. Kearney, 2002, Survey of thermal energy storage for parabolic trough power plants, *J. Sol. Energy-T ASME* **124**, pp, 145-152.
6. A.F. Regin, S.C. Solanki, J.S. Saini, 2008 Heat transfer characteristics of thermal energy storage system using PCM capsules: a review, *Renew. Sust. Energy Rev.* **12**, pp 2438-2458.
7. W.D. Steinmann, R. Tamme, 2008, Latent heat storage for solar steam systems, *J. Sol. Energy-T ASME* **130**, 011004-011005.
8. L.I. Rubinstein, 1971, The Stefan Problem, *Translations of Mathematical Monographs*, **27**, American Mathematical Society, Providence, Rhode Island.
9. Weihuan Zhao, A.F. Elmozughi, A. Oztekin, S. Neti, 2013, Heat transfer analysis of encapsulated phase change material for thermal energy storage, *Int. J. Heat Mass Transfer*, **63**, 323–335.

10. N.R. Vyshak, G. Jilani, 2007, Numerical analysis of latent heat thermal energy storage system, *Energy Convers. Manage.*, **48** (7), 2161–2168
11. J. Boussinesq, 1903, *Théorie Analytique de la chaleur 2*, Gauthier-Villars, Paris.
12. S. V. Patankar, 1980, *Numerical Heat Transfer and Fluid Flow*, Hemisphere, Washington, D.C
13. Shougui Zhang, Jialin Zhu, 2013, A projection iterative algorithm boundary element method for the Signorini problem, *Engineering Analysis with Boundary Elements*, **37**, (1), (2013), 176-181.
14. Stéphane Abide, Stéphane Viazzo, 2005, A 2D compact fourth-order projection decomposition method, *Journal of Computational Physics*, **206** (1), 252–276
15. V.R. Voller, 1987, A heat balance integral method based on an enthalpy formulation, *International Journal of Heat and Mass Transfer*, **30**, (3), 604-607
16. Daniel X. Guo, 2015, Modified fully discretized projection method for the incompressible Navier–Stokes equations, *Applied Numerical Mathematics*, **96**, 187-202
17. J. L. Lage, A. Bejan, 1993, The resonance of natural convection in an enclosure heated periodically from the side, *International Journal of Heat and Mass Transfer*, **36**, (8), 2027-2038

NUMERICAL STUDY OF THE SOLIDIFICATION OF NANO-ENHANCED PHASE CHANGE MATERIAL IN A LATENT HEAT STORAGE UNIT COOLED BY LAMINAR HEAT TRANSFER FLUID FLOW

* Radouane ELBAHJAOU¹, Hamid EL QARNIA¹, Mohammed EL GANAOU²

¹Cadi Ayyad University, Faculty of Science Semlalia, Department of Physics, Fluid Mechanics and Energetic Laboratory (affiliated to CNRST, URAC 27), Marrakesh, B.P. 2390, Morocco

²Lorraine University, Energetic Laboratory of Longwy, (FJV/LERMAB), Henri Poincaré Institute of Longwy, France

*Corresponding author: Email: radouane.elbahjaoui@ced.uca.ac.ma

ABSTRACT

Latent heat storage units (LHSU) using phase change materials (PCMs) are very interesting for thermal energy storage applications due to their absorption / release of great amount of energy at a substantially constant phase transition temperature. However, the PCMs are characterized by a low thermal conductivity, which limits the heat exchange rate and slowed the melting/solidification rate of these materials. This paper presents a numerical investigation of heat transfer during solidification process of PCM in a rectangular LHSU unit through dispersion of high conductivity nanoparticles. The storage unit consists of a number of vertically oriented plates of Nano-enhanced phase change material (NEPCM) separated by rectangular channels in which flows a heat transfer fluid (HTF). A two dimensional mathematical model is considered to investigate numerically the LHSU thermal performance. The solidification problem was formulated using the enthalpy porosity method. The finite volume approach was used for solving equations. The numerical model has been validated by experimental, theoretical and numerical results available in literature. The effects of nanoparticles volumetric fraction on the heat transfer rate have been investigated.

KEYWORDS

Nano-enhanced phase change material (NEPCM), Phase change material (PCM), Nanoparticles, Latent heat storage unit (LHSU), Solidification, Enthalpy method.

NOMENCLATURE

c specific heat (J/kg K)
d NEPCM slabs thickness (m)
f liquid fraction
g gravity (m/s^2)
h volumetric enthalpy (J/m^3)
H height of the NEPCM slabs (m)
k thermal conductivity (W/m K)
 \dot{m} HTF mass flow rate (kg/s)
 N_c number of HTF channels
p pressure (Pa)
q heat charging rate (W)
T temperature ($^{\circ}C$)
t time (s)
u, v velocity components (m/s)
x, y Cartesian coordinates (m)
w thickness of the HTF channels (m)
Greek symbols
 α thermal diffusivity (m^2/s)
 ϕ volumetric fraction of nanoparticles

β coefficient of thermal expansion of liquid (K^{-1})
 μ dynamic viscosity ($N\ s/m^2$)
 ν cinematic viscosity (m^2/s)
 ΔH latent heat of fusion (J/kg)
 ρ density (kg/m^3)
 ψ stream function (m^2/s)
 Ψ dimensionless stream function ($=\psi/\alpha_{m,l}$)
Subscripts
e inlet
f HTF
o melting
s solid
l liquid
m PCM
n nanoparticles
nm NEPCM

INTRODUCTION

Thermal energy storage systems (TESS) are practical to store heat and extend the operational

time of thermal systems. Among of such TESS, those storing heat using phase change materials (PCMs) have become an appealing method to conserve produced energy. These materials (PCMs) are becoming increasingly attractive because of their high storage density and their storage / release heat at a substantially constant temperature. However, their main disadvantage is the low thermal conductivity, which limits heat transfer exchange and causes poor melting / solidification rates. Latent heat storage systems (LHTS) using PCMs have been used in several applications such as solar heating and cooling [1-3], building envelopes [4-8] and electronic cooling [9-12]. Therefore, a number of studies on LHSS including experimental, analytical and numerical investigations were performed by many researchers for the last 20 years.

De Gracia, Navarro [13] used a numerical model to study the thermal performance of a space heating and cooling system during the charge process. The studied storage system is composed of phase change material (PCM) panels placed inside the air chamber of a ventilated façade. Liu, Belusko [14] studied numerically the thermal performance of a flat slab phase change thermal storage (PCTS) unit stored thermal energy transferred from several heat transfer fluids (HTFs). They used a validated mathematical model to predict the HTF outlet temperature, liquid fraction and heat transfer rate during both charging and discharging processes. Osterman, Butala [15] used phase change material (RT22HC) as thermal energy storage to reduce energy consumption in buildings. The proposed storage unit consists of 30 plates of PCM placed in a heat transfer fluid (air) flow. Bechiri and Mansouri [16] performed an analytical investigation of LHSS composed of several PCM flat slabs separated by laminar HTF flow. The results show that the obtained solution gives a good estimation during charging and discharging operational modes. Halawa and Saman [17] conducted a numerical study of an air LHSS consisting of a number of one dimensional slabs. The effects of air mass flow, air gaps, slab dimension and charge/discharge temperatures difference on the air outlet temperature and heat transfer rate of LHSS have been studied.

In the best of knowledge of the authors, the solidification of nano-enhanced phase change materials (NEPCM) inside vertical slabs separated by rectangular channels through which HTF (water) flows has not extensively studied by researchers. The

proposed work is motivated by the need to intensify heat transfer and accelerate discharging operational mode in latent heat storage units (LHSU) which can be integrated to solar thermal systems to extend their operational times and enhance their thermal performances.

NUMERICAL MODEL

The system under investigation consists of (N_c+1) vertical slabs of phase change material (PCM: Paraffin wax P116) dispersed with high conductivity nanoparticles (Al_2O_3), separated by N_c rectangular channels through which a HTF flows as shown in Figure 1a. A representative volume in the LHSU, which is repetitive, is chosen. The solution domain is shown in Fig. 1b. It consists of a NEPCM rectangular enclosure of width, $d/2$, and height, H , and a HTF channel of width, $w/2$. The LHSU contains a volume of 0.1 m^3 filled with NEPCM. The initial temperature of the superheated liquid NEPCM is 60°C . The mass flow rate and the inlet temperature of the HTF are 0.3 kg/s and 22°C , respectively. The number of HTF channels in the LHSU is 10 and the width of each channel is 6 mm. Numerical calculations were performed for water as a HTF and Paraffin wax (P116) dispersed with nanoparticles (Al_2O_3) as a Nano-PCM. The thermal properties of HTF, PCM and nanoparticles (Al_2O_3) are summarized in Table 1.

The density, specific heat and latent heat of the NEPCM are defined as follows:

$$\rho_{nm} = \phi\rho_n + (1-\phi)\rho_m \quad (1)$$

$$c_{p,nm} = \frac{\phi(\rho c_p)_n + (1-\phi)(\rho c_p)_m}{\rho_{nm}} \quad (2)$$

$$\Delta H_{nm} = \frac{(1-\phi)(\rho\Delta H)_m}{\rho_{nm}} \quad (3)$$

(3)

The dynamic viscosity and thermal conductivity of the NEPCM are given as follows:

$$\mu_{nm} = \frac{\mu_m}{(1-\phi)^{2.5}} \quad (3)$$

$$k_{nm} = k_{\text{eff}} + k_d \quad (4)$$

where k_{eff} is the thermal conductivity of the stagnant NEPCM and k_d corresponds to the conductivity enhancement term which represents the Brownian motion. They are considered as follows:

$$k_{\text{eff}} = \frac{k_n + 2k_m - 2(k_m - k_n)\phi}{k_n + 2k_m + (k_m - k_n)\phi} k_m \quad (5)$$

$$k_d = C^* (\rho c_p)_{nm} \sqrt{u^2 + v^2} d_n \quad (6)$$

Where d_n is the diameter of nanoparticles ($d_n = 45$ nm) and C^* is an empirical constant evaluated according to the work of Wakao and Kagueli [18].

The modeling of the thermal and flow characteristics of the LHSU is made using the governing conservation equation of energy for HTF, continuity, momentum and energy equations for NEPCM. The flows in HTF channels and liquid NEPCM are assumed laminar and two-dimensional. The HTF and liquid phase of PCM are incompressible and Newtonian. For the HTF (water) circulating in channels, the flow is assumed hydro-dynamically fully developed. The thermo-physical properties are assumed to be constant except for the density of liquid phase of NEPCM according to the Boussinesq approximation. The enthalpy–porosity approach was used for the formulation of phase change problem [19].

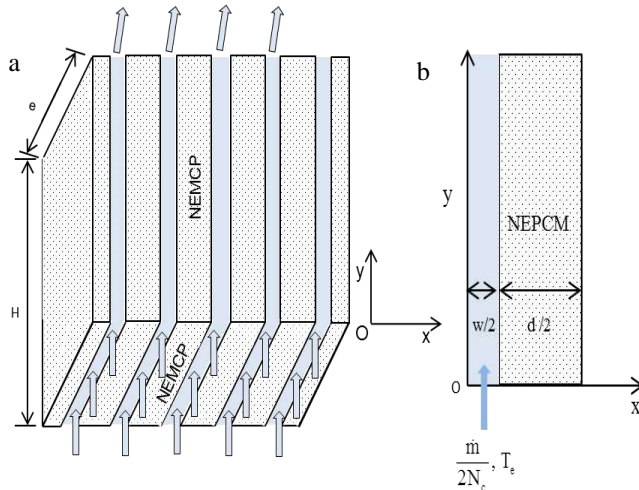


Figure 1

- (a) Latent heat storage unit (LHSU)
 (b) Computational domain

Table 1

Thermal properties of HTF, PCM and nanoparticles

Property	HTF (water)	Paraffin Wax	Al ₂ O ₃
Density (kg/m ³)	989	802	3600
Specific heat (J/kg K)	4180	2510	765
Thermal	0.64	0.36(l),0.24(s)	36

Property	HTF (water)	NEPCM	Al ₂ O ₃
conductivity (W/m K)			
Dynamic viscosity (kg/m s)	577×10 ⁻⁶	1.3×10 ⁻³	-
Latent heat (kJ/kg)	-	226	-
Melting temperature (°C)	-	47	-

Consequently, the two dimensional system of equations can be expressed as follows:

For HTF

$$\frac{\partial T_f}{\partial t} + \frac{\partial (v_f T_f)}{\partial y} = \frac{\partial}{\partial x} (\alpha_f \frac{\partial T_f}{\partial x}) + \frac{\partial}{\partial y} (\alpha_f \frac{\partial T_f}{\partial y}) \quad (7)$$

$$\text{where } v_f = \frac{3}{2} V_{moy} (1 - (\frac{x}{w/2})^2).$$

For NEPCM

Continuity equation:

$$\frac{\partial (\rho_{nm} u_{nm})}{\partial x} + \frac{\partial (\rho_{nm} v_{nm})}{\partial y} = 0 \quad (8)$$

Momentum equations:

$$\frac{\partial (\rho_{nm} u_{nm})}{\partial t} + \frac{\partial (\rho_{nm} u_{nm} u_{nm})}{\partial x} + \frac{\partial (\rho_{nm} v_{nm} u_{nm})}{\partial y} = -\frac{\partial p}{\partial x} + \frac{\partial}{\partial x} (\mu_{nm} \frac{\partial u_{nm}}{\partial x}) + \frac{\partial}{\partial y} (\mu_{nm} \frac{\partial u_{nm}}{\partial y}) + S_u \quad (9a)$$

$$\frac{\partial (\rho_{nm} v_{nm})}{\partial t} + \frac{\partial (\rho_{nm} u_{nm} v_{nm})}{\partial x} + \frac{\partial (\rho_{nm} v_{nm} v_{nm})}{\partial y} = -\frac{\partial p}{\partial y} + \frac{\partial}{\partial x} (\mu_{nm} \frac{\partial v_{nm}}{\partial x}) + \frac{\partial}{\partial y} (\mu_{nm} \frac{\partial v_{nm}}{\partial y}) + S_v \quad (9b)$$

Energy equation:

$$\frac{\partial (\rho_{nm} h)}{\partial t} + \frac{\partial (\rho_{nm} u_{nm} h)}{\partial x} + \frac{\partial (\rho_{nm} v_{nm} h)}{\partial y} = \frac{\partial}{\partial x} (\frac{k_{nm}}{c_{p,nm}} \frac{\partial h}{\partial x}) + \frac{\partial}{\partial y} (\frac{k_{nm}}{c_{p,nm}} \frac{\partial h}{\partial y}) + S_h \quad (10)$$

with

$$S_u = -C \frac{(1-f)^2}{(f^3 + b)} u_m \quad (10a)$$

$$S_v = -C \frac{(1-f)^2}{(f^3 + b)} v_{nm} + \rho_{nm} g \beta (T_{nm} - T_0) \quad (11b)$$

$$h = \int c_{nm} dT_{nm} \quad (10c)$$

$$S_h = -\rho_{nm} \Delta H_{nm} \frac{\partial f}{\partial t} \quad (11d)$$

where f is the local liquid fraction and h is the sensible specific enthalpy.

Initial and boundary conditions:

$$t = 0 \quad T_f = T_{nm} = T_0, \quad u_{nm} = v_{nm} = 0 \quad (12a)$$

$$x = 0 \quad \frac{\partial T_f}{\partial x} = 0 \quad (12b)$$

$$x = w/2 \quad k_{nm} \frac{\partial T_{nm}}{\partial x} = k_f \frac{\partial T_f}{\partial x}, \quad u_{nm} = v_{nm} = 0 \quad (12c)$$

$$y = 0 \quad T_f = T_e, \quad \frac{\partial T_{nm}}{\partial y} = 0, \quad u_{nm} = v_{nm} = 0 \quad (12d)$$

$$x = w/2 + d/2 \quad \frac{\partial T_{nm}}{\partial y} = 0, \quad u_{nm} = 0, \quad \frac{\partial v_{nm}}{\partial x} = 0 \quad (12e)$$

$$y = H \quad \frac{\partial T_f}{\partial y} = 0, \quad \frac{\partial T_{nm}}{\partial y} = 0, \quad u_{nm} = v_{nm} = 0 \quad (12f)$$

RESULTS AND DISCUSSION

The streamlines describing the flow field in the liquid NEPCM at times: $t = 1$ min, 10 min, 34 min and 56 min for $\phi=0\%$ and 10% are shown in Figs.2a-2d and Figs.3a-3b, respectively. With the start of the HTF circulation between the slabs, a large anticlockwise cell develops and decreases in size as solidification progresses. It should be noted that compared to the case of $\phi=10\%$, the maximum value of streamline function is achieved for $\phi=0\%$ which indicates that the dispersion of nanoparticles in PCM enhances the conduction and causes a decrease in the effect of natural convection.

The temperature distribution in the liquid NEPCM at the same times: $t = 1$ min, 10min, 34 min and 56 min for $\phi=0\%$ and 10% are shown in Figs.4a-4d and Figs.5a-5b, respectively. At the early stages, the heat transfer is controlled by natural convection and therefore the isotherms are distorted in the liquid NEPCM. The effect of natural convection decreases with increasing time which promotes heat transfer by conduction mode. Consequently, the isotherms in the NEPCM enclosure become nearly parallel to the vertical heat exchanger wall. It should be noted that the comparison between Figs. 4 and 5 shows that the minimum temperature is achieved for $\phi=10\%$.

The effect of the volumetric fraction of nanoparticles on the time wise variation of the liquid fraction is shown in Fig. 6. It can be seen, from this figure, that the liquid fraction decreases with increasing time. The results also show that the solidification time decreases with the increase of the nanoparticle volumetric fraction.

The effect of the volumetric fraction of nanoparticles on the time wise variation of the heat transfer rate is

shown in Fig. 7. As shown in Figure 7, the heat transfer rate goes through three stages. The first stage begins with the start of the discharge process where the heat transfer rate increases to reach a maximum value. Larger maximum value corresponds to higher volumetric fraction of nanoparticles. In the second stage, the heat transfer rate undergoes a nonlinear decrease until it reaches the zero value. In the third stage (steady state regime), the heat transfer rate remains constant and equal to zero. This behaviour is due to the fact that there is no heat exchange between HTF and NEPCM in this stage and the NEPCM temperature has become equal to the HTF inlet temperature.

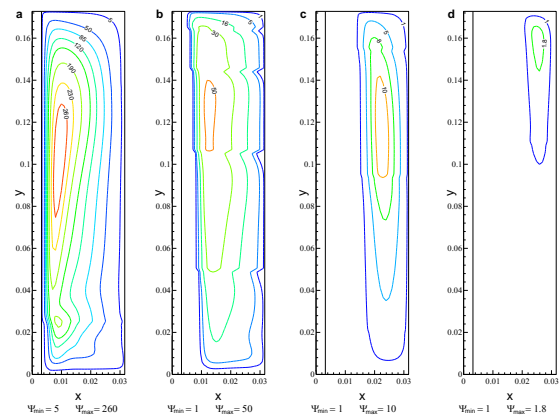


Figure 2

Streamlines for $\phi=0\%$ at (a) $t=1$ min, (b) 10 min, (c) 34 min and (d) 57 min.

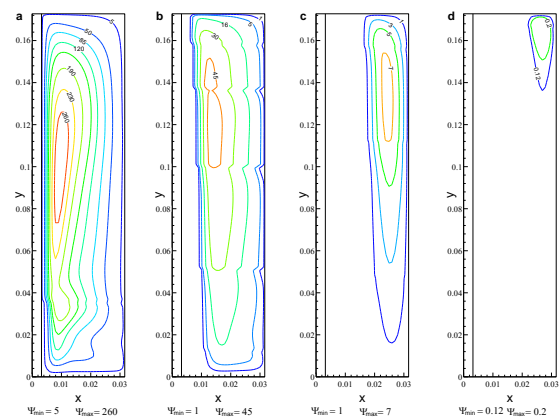


Figure 3

Streamlines for $\phi=10\%$ at (a) $t=1$ min, (b) 10 min, (c) 34 min and (d) 57 min

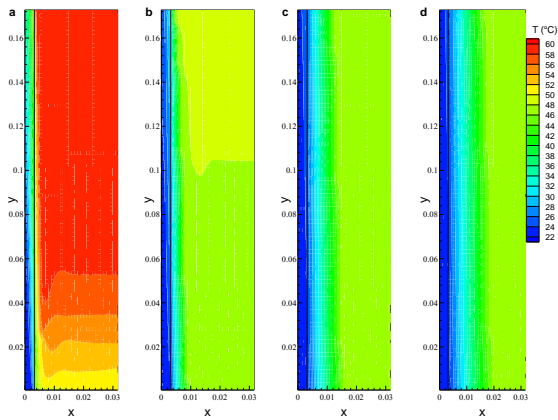


Figure 4

Isotherms for $\phi=0\%$ at (a) $t=1$ min, (b) 10 min, (c) 34 min and (d) 57 min

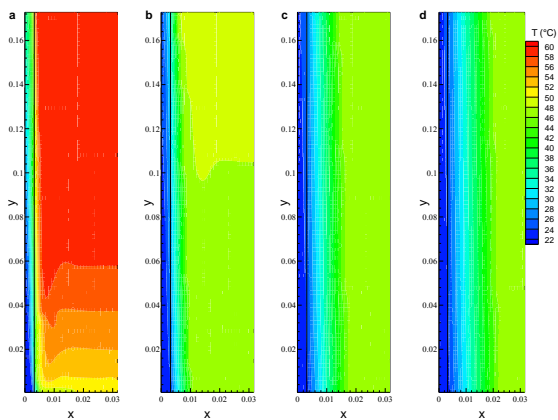


Figure 5

Isotherms for $\phi=10\%$ at (a) $t=1$ min, (b) 10 min, (c) 34 min and (d) 57 min

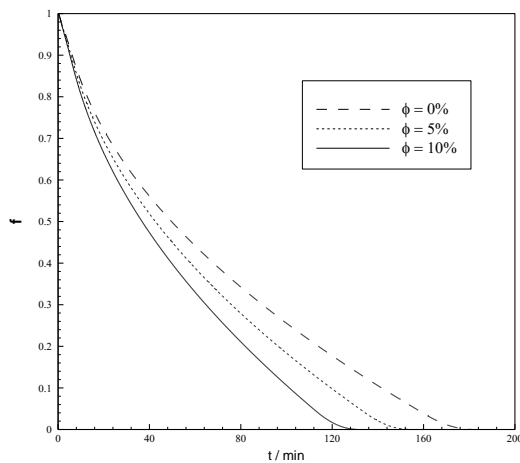


Figure 6

Time wise variation of the liquid fraction

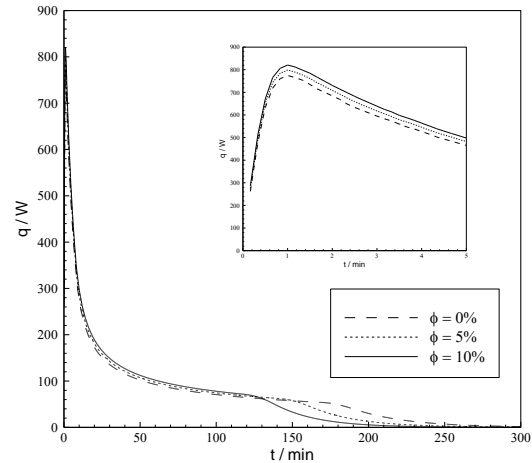


Figure 7

Time wise variation of the heat transfer rate

CONCLUSIONS

In the present research study, solidification of Nano-enhanced phase change material in a rectangular latent heat storage unit (LHSU) has been studied numerically. A mathematical model based on the conservation equations of mass, momentum and energy has been developed to investigate the effect of the volumetric fraction of nanoparticles.

The following conclusions are drawn:

- The dispersion of high conductivity nanoparticles in a pure PCM enhances the heat transfer rate;
- The solidification time decreases with the increase of the volumetric fraction of nanoparticles.

REFERENCES

1. Alawadhi, E. M., Alqallaf, H. J., 2011, Building roof with conical holes containing PCM to reduce the cooling load: Numerical study, *Energy Conversion and Management*, 52, pp.2958-64
2. Das, S., Dutta, T. K., 1993, Mathematical modeling and experimental studies on solar energy storage in a phase change material, *Solar Energy*, 51, pp.305-12
3. Jiang, F.Wang, X., Zhang, Y., 2011, A new method to estimate optimal phase change material characteristics in a passive solar room, *Energy Conversion and Management*, 52, pp.2437-41
4. Feldman, D.Banu, D.Hawes, D., Ghanbari, E., 1991, Obtaining an energy storing building material by direct incorporation of an organic phase change material in gypsum wallboard, *Solar Energy Materials*, 22, pp.231-42

5. Peippo, K.Kauranen, P., Lund, P. D., 1991, A multicomponent PCM wall optimized for passive solar heating, *Energy and Buildings*, 17, pp.259-70
6. Scalat, S.Banu, D.Hawes, D.Parish, J.Haghighata, F., Feldman, D., 1996, Full scale thermal testing of latent heat storage in wallboard, *Solar Energy Materials and Solar Cells*, 44, pp.49-61
7. Shilei, L.Guohui, F.Neng, Z., Li, D., 2007, Experimental study and evaluation of latent heat storage in phase change materials wallboards, *Energy and Buildings*, 39, pp.1088-91
8. Zhou, G.Yang, Y.Wang, X., Zhou, S., 2009, Numerical analysis of effect of shape-stabilized phase change material plates in a building combined with night ventilation, *Applied Energy*, 86, pp.52-9
9. El Qarnia, H.Draoui, A., Lakhali, E. K., 2013, Computation of melting with natural convection inside a rectangular enclosure heated by discrete protruding heat sources, *Applied Mathematical Modelling*, 37, pp.3968-81
10. Shatikian, V.Ziskind, G., Letan, R., 2008, Numerical investigation of a PCM-based heat sink with internal fins: Constant heat flux, *International Journal of Heat and Mass Transfer*, 51, pp.1488-93
11. Wang, Y.-H., Yang, Y.-T., 2011, Three-dimensional transient cooling simulations of a portable electronic device using PCM (phase change materials) in multi-fin heat sink, *Energy*, 36, pp.5214-24
12. Yang, Y.-T., Wang, Y.-H., 2012, Numerical simulation of three-dimensional transient cooling application on a portable electronic device using phase change material, *International Journal of Thermal Sciences*, 51, pp.155-62
13. De Gracia, A.Navarro, L.Castell, A., Cabeza, L. F., 2015, Energy performance of a ventilated double skin facade with PCM under different climates, *Energy and Buildings*, 91, pp.37-42
14. Liu, M.Belusko, M.Steven Tay, N. H., Bruno, F., 2014, Impact of the heat transfer fluid in a flat plate phase change thermal storage unit for concentrated solar tower plants, *Solar Energy*, 101, pp.220-31
15. Osterman, E.Butala, V., Stritih, U., 2015, PCM thermal storage system for 'free' heating and cooling of buildings, *Energy and Buildings*, 106, pp.125-33
16. Bechiri, M., Mansouri, K., 2013, Exact solution of thermal energy storage system using PCM flat slabs configuration, *Energy Conversion and Management*, 76, pp.588-98
17. Halawa, E., Saman, W., 2011, Thermal performance analysis of a phase change thermal storage unit for space heating, *Renewable Energy*, 36, pp.259-64
18. Wakao, N., Kaguei, S., 1982, *Heat and Mass Transfer in Packed Beds* Gordon and Breach Science Publications, New York,
19. Voller, V. R., Prakash, C., 1987, A fixed grid numerical modelling methodology for convection-diffusion mushy region phase-change problems, *International Journal of Heat and Mass Transfer*, 30, pp.1709-19

STUDY OF THERMO PHYSICAL PROPERTIES OF A BUILDING MATERIAL BASED ON PCM

O.Youcef SOUCI, Samir HOUAT

Laboratory of MNEPM , MSMP group, University of Abdelhamid Ibn Badis of Mostaganem, Bp300, 27000 Mostaganem, Algeria

Corresponding authors: souci_youcef@yahoo.fr, sa_houat@yahoo.fr,

ABSTRACT

This work is based on the approach of a numerical study of the thermo physical property of the hollow brick used in buildings.

This material is filled by a material with phase change (PCM) that is proposed to increase the thermal inertia of the walls in buildings. Numerical calculation using in this study is based on the finite elements methods which make possible to determine thermo physical property such as effective thermal conductivity and heat capacity equivalent.

KEYWORDS: hollow brick, PCM, Thermo physical properties, finite element method

NOMENCLATURE

C_p : Specific heat capacity (J/kg·K)

T : Temperature (K)

L_f : Latent heat of fusion, (J/kg)

λ : Thermal conductivity W/m.K

ρ : Density (kg/m³)

f : The melted fraction

t : Time (h)

φ : Flux density (W/m²)

w : Thickness of material (m)

Subscript

l : Liquid

eff : Effective

s : Solid

e : equivalent

is : Inside

m : Melting point

os : Outside

INTRODUCTION

Nowadays, energy and environment are the two keys in the development of human beings.

Energy production and consumption is the main driving force of all urban and industrial activities.

More than 80% of world energy is provided by combustion of fossil fuels.

In addition, 16% of the total energy consumption is provided by nuclear power and the remaining 4%

includes other forms, such as hydro, wind and solar energy. It is worth to note that a well developed country with enormous energy sources and proper energy management systems can have an improved economic status than its neighboring developing countries. On the other hand, it can be seen that the demand for energy will tend to grow as the economies of the developing world rises simultaneously.

To overcome these problems that are facing the world today, in the twenty-first century, some measures have been taken by the industrialized countries. So The Europe 2020 strategy sets three objectives for climate and energy policy, to be reached by 2020 [1].

- Reducing GHG emissions by at least 20 % compared with 1990 levels;
- Increasing the share of renewable energy in final energy consumption to 20 %; and
- Moving towards a 20 % increase in energy efficiency.

The achievement of these objectives through a reduction in energy consumption and the increased production of energy called "renewable" (solar, geothermal, wind etc ...).

The building (residential and tertiary sectors) in 2010 consumes about 40% of total world energy [2]. In Algeria, the proportion is 39% and the construction sector is the largest consumer of energy [3]. Much of

this consumption comes from heating and cooling systems which ensure a compatible internal temperature with comfort conditions.

From this perspective, it is timely to propose systems for correcting the thermal design of buildings to obtain situations of well being. Among the proposed solutions: wall insulation and roof [4], the use of light colors on the external surfaces [5], and the use of energy storage devices in the building structure [6]. This last technique requires the phase-change materials (PCMs) and offers the opportunity to achieve good energy efficiency and also reduce the environmental impact associated with the use of conventional energy.

The advantage of the integration of PCM is to allow the storage of a large amount of energy as latent heat in a small volume through the melting of these materials, then return in an ambient medium to solidification.

Indeed, a perfect knowledge of thermo physical properties of a PCM and the measurement method are essential to properly analyze a storage system by latent heat, validate models and predict the effectiveness of PCMs [7]. According to some authors, the data provided by the manufacturer may sometimes be incorrect and usually optimistic [8].

Initially, this work is based on the presentation of a numerical study to determine the proprieties thermo physiques of this material proposed for building walls with using COMSOL [9] based on the fine elements method.

DESCRIPTION OF MATERIALS:

The PCM is introduced during its manufacture in the cavities of a hollow brick. The hollow brick consists of 8 holes as dimension (thickness, width, length) 10x20x30 cm. For the cavity in this material has a parallelepiped section (3.5 x 3.5 cm²) and 30 cm in length (Figures 1).

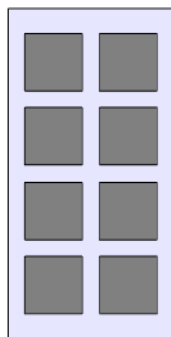


Figure 1
Hollow brick wall

The PCM used in this study is paraffin (n-octadecane).

The composition of the paraffin-polymer mixture is optimized so as to completely eliminate the potential leakage of the PCM in the liquid state. To the melting phase, the onset temperature is 26 ° C; the temperature at the peak is 27.6 ° C and latent heat of fusion is 243.5 kJ / kg.

These values are consistent with the results already achieved and those in the literature [10]. The thermo physical characteristics of hollow brick and PCM are shown in Table 1.

In this study, the heat transfer is considered in one dimensional. The material is assumed homogeneous and isotropic. All thermo physical properties were kept constant but may be different in the liquid and solid phases (conductivity and specific heat) and no convective heat-transfer in the liquid PCM phase.

Table 1
Characteristics of PCM and hollow brick

	Density (kg/m ³)	Thermal Conductivity (W/m.K)	heat capacity (J/kg.K)
PCM (solid)	865	0.358	1934
PCM (liquid)	780	0.148	2196
hollow brick	1600	0.7	840

The mathematical formulation of this problem following the implementation of the enthalpy balance is:

$$\rho C \frac{\partial T}{\partial t} + \varepsilon \rho L_f \frac{\partial f}{\partial t} = \lambda \frac{\partial^2 T}{\partial x^2} \quad (1)$$

With: $\varepsilon=0$: The case of a construction or PCM material (liquid or solid phase).

$\varepsilon=1$: PCM molten at $T = T_m$,

The equations of the system (1) above, associated with the boundary conditions (internal and external surfaces) is solved numerically using the finite element method (COMSOL).

The indoor environment is still considered held at a constant temperature $T_{is} = 20^\circ\text{C}$. On the outer face of the wall is imposed a linear increase in temperature from 20 ° C to 50 ° C for 15 hours (up shift = 2 ° C / h) then the temperature is maintained from the outside at 50 ° C for 9 hours.

NUMERICAL VALIDATION:

Before presenting the numerical results, the numerical code is validated by comparison with an experimental solution available in the literature [11].

In this experimental work, they studied the phase change of the PCM in the melting and in the solidification process.

In this validation we will take into account only the part of melting. The experimental setup consists to study an alveolar slab incorporated by PCM. This last is paraffin with melting point equal to 27°C.

On the bottom face of the slab a linear rise is imposed in temperature of 20 °C to 35 °C for one hour (Rate of rise = 1.25 °C / hr) and then maintains the temperature of the bottom face at 35°C for 6 hours.

Their top side is in direct contact with the atmosphere of the laboratory room to $T_{is} = 20\text{ °C}$.

Figures 2 show the comparison between our numerical results with the results that were obtained in the experimental on the variation in the temperature of bottom and top surfaces of the slabs.

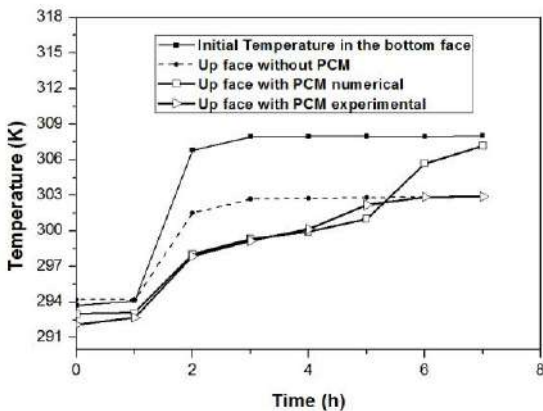


Figure 2

Temperature at the interfaces of the slab

As shown in Figure 2, when the temperature is lower than 300 K (Temperature of melting), the numerical result agrees well with the experimental measurements but when the PCM transforms to its liquid state, we observed that the temperature deduced numerically increasing more rapidly than of the experimental.

This difference can be explained by the presence of natural convection in the experimental cases by

against we neglect its effect in our numerical study.

In a general way, we see that our numerical model is valid to predict results which are closer to reality when the natural convection in the liquid phase of PCM will be neglect.

RESULTS AND DISCUSSION

To clarify the influence of PCM a comparative study was established between the temperatures in the two sides of the hollow brick.

In the first case, the hollow brick is incorporated by PCM and in the second part is the reference case (material without PCM).

The result of this comparison is shown in the figures 3.

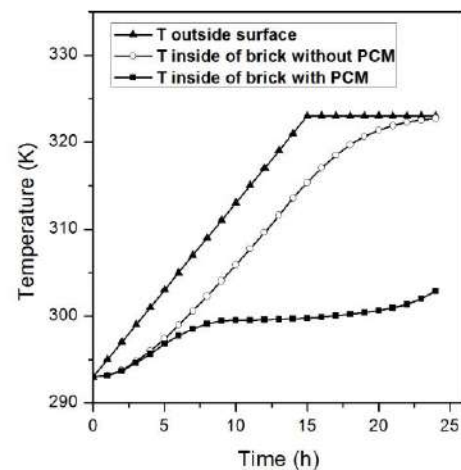


Figure 3

Temperature variation surfaces
According to time

It is found that the temperature level in the reference case is higher than the first case when material is incorporated by PCM for similar conditions.

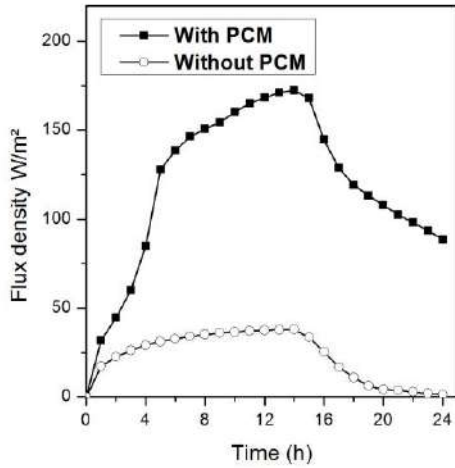
This numerical study clearly highlights the effect of PCM in the thermal inertia of this material.

The variation of the temperature between two sides of the hollow brick with PCM is much slower than the reference case. This is due to thermal losses in the hollow brick during the melting of PCM.

To calculate the thermo physical properties, it's required to study the difference between the flux density in the both sides of the material incorporated by PCM and comparing it with the reference case. The result is presented in figures 4.

It is clear that the heat losses are very important in the hollow bricks with PCM compared to the reference case and this is due to the large accumulation of heat in this material.

In the following of our work we are going to determine the equivalent values of thermo physical properties of the hollow brick with PCM.



Figures 4

The difference between flux density in the hollow brick with and without PCM

For the equivalent specific heat:

In our case we have only a fraction f of the material changes therefore the equivalent heat capacity condition can be written:

$$C_{pe}' = C_p \pm L_f \times \frac{\partial f}{\partial T} \quad (2)$$

L_f As the latent heat of change of state and f is the melted fraction of material that changes state.

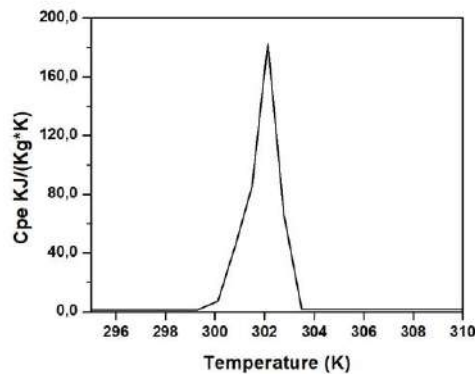


Figure 5

The equivalent thermal capacity of hollow Brick with PCM

It's observed a strong augmentation in C_{pe} of the hollow brick during the process of melting of PCM. The value of C_{pe} is varied from 300 K to 303 K (range of melting temperature).

To determine the thermal conductivity in the solid state, it's required to impose a temperature difference between two faces of the material until reaching the steady state.

The relation below provides faster access to the value of the effective conductivity in the solid state:

$$\lambda_{eff} = \frac{\varphi \times w}{\Delta T_s} \quad (3)$$

w : Thickness of material

ΔT_s : Temperature difference between T_{os} and T_{is}

when $T_{os}, T_{is} < T_m$.

In the same way, for the determination of the liquid conductivity, the material is subjected to a temperature difference. This time, the temperature levels in the two sides are higher than the melting temperature:

$$\lambda_{eff} = \frac{\varphi \times w}{\Delta T_l} \quad (4)$$

ΔT_l : Temperature difference between T_{os} and T_{is}

when $T_{os}, T_{is} > T_m$.

The result of the effective thermal conductivity is shown in Table 2.

TABLE 2
The effective thermal conductivity

Effective Conductivity	Brick +PCM
λ_{eff} W/m. K phase solid	0.5
λ_{eff} W/m. K phase liquid	0.33

CONCLUSION:

A numerical simulation based on the finite element method was undertaken to study the thermal characteristics in the melting process of a phase change material (PCM 27) incorporated in hollow brick and compare it with the reference case (without PCM).

We noticed that the steady state is reached much later when the wall is filled with PCM. Paradoxically, the material being introduced is more heat conductive than the wall without PCM. This result is explained by a large accumulation of heat in the PCM particularly when phase change.

This study demonstrated also the possibilities for thermal characterization of materials containing phase change materials from a numerical simulation.

buildings. *Energy and Buildings*, 68, pp.703-706.

REFERENCES

1. Conseil de l'union européenne, 2007, Rapport CUN du 8 et 9 mars, paragraphe 32, Bruxelles.
2. Zhu N., Ma Z. and Wang S., 2009, Dynamic characteristics and energy performance of buildings using phase change materials: A review, *Energy Conversion and Management*, 50, pp. 3169-3181.
3. Aprue, 2010, Bilan de la consommation énergie finale en Algérie. Agence de promotion et de rationalisation de l'utilisation de l'énergie, affiliée au ministre de l'énergie et des mines.
4. Barrios G., Huelsz G., Rojas J., 2012, Thermal performance of envelope wall/roofs of intermittent air-conditioned rooms. *Applied Thermal Engineering* 40, pp.1-7.
5. Granja A.D., Labakiny L.C., 2003, Influence of external surface color on the periodic heat flow through a flat solid roof with variable thermal resistance. *Int. J. Energy Res*, 27, pp.771–779.
6. Amir M., Lacroix M., Galanis N., 1999, Comportement thermique de dalles chauffantes électriques pour le stockage quotidien. *Int. J. Therm. Sci*, 38, pp.121-131.
7. Arkar C., Medved S., 2005, Influence of accuracy of thermal property data of a phase change material on the result of a numerical model of a packed bed latent heat storage with spheres, *Thermo chimica Acta*, 438, No 1-2, pp.192-201.
8. Tyagi V, Buddhi D., 2007, PCM thermal storage In buildings: A state of art. *Renewable and Sustainable Energy, Reviews*, 11, No 6, pp. 1146-1166.
9. COMSOL Multiphysics, User's guide v3.2, 2005, <http://www.comsol.com/>
10. Farid M., Khudhair A., Razack S., Al-Hallaj S., 2004, A review on phase change energy storage: materials and applications, *Energy Conservation and Management*, 45, pp.1597–1615.
11. Karim, L., Barbeon, F., Gegout, P., Bontemps, A., and Royon, L., 2014. New phase change material components for thermal management of the light weight envelope of

Instant Autovaporization as Intensification Way of Classic Distillation Processes: Fundamental and Industrial Applications

Tassadit Issaadi-Hamitouche*, Colette Besombes, Karim Allaf

University of La Rochelle; Laboratory of Engineering Science for Environment LaSIE - UMR-CNRS 7356. Research Unit of "Intensification of Industrial Eco-Processes". Avenue Michel Crepeau, 17042 La Rochelle Cedex 01 (France).

tassadit.hamitouche@univ-lr.fr

*Corresponding author: Email: tassadit.hamitouche@univ-lr.fr

ABSTRACT

In the present work, the new extraction process of Détente Instantanée Contrôlée DIC was studied, developed, optimized and compared to the conventional hydrodistillation method for the extraction of essential oils of sandalwood. DIC was used as a thermomechanical treatment, DIC subjecting the product to a high-pressure saturated steam. The DIC cycle ends with an abrupt pressure drop towards vacuum, and this instantly leads to an autovaporization of sandalwood volatile compounds. An immediate condensation in the vacuum tank produced a micro-emulsion of water and essential oils. Thus, an ultra-rapid cooling of residual leaves occurred, precluding any thermal degradation. Response surface methodology RSM was used with a 2-parameter 5-level Design of Experiments (DoE). The structure with a slight destruction of cell walls after DIC treatment. The operating parameters (independent variables) were the treatment time t , and the number of pressure drops C , whilst the main response was the extraction of extraction efficiency EE of volatile compounds. RSM Statistical analysis allowed comparing this process with conventional hydrodistillation unit operation in terms of total yields of essential oil. The most important differences between the two essential oils were reflected in the yields, with 1.14 as against 1.23 g EO/100 g of raw matter, and in the extraction time, with 5 min as against 24 hours for respectively the DIC and the hydrodistillation operations. These differences have been previewed through the fundamental analysis based on both concept of thermodynamics of instantaneous transformations and calculation of the volatility as well as on Darcy similar transfer law was used to explain the main results.

KEY WORDS: *Intensification, Instant Autovaporization, Volatility, Instant Controlled Pressure Drop DIC, Distillation Paradoxical Stage*

INTRODUCTION

Sandalwood is considered one of the most valuable trees in the world (1), Sandalwood oil is an essential oil obtained by the distillation of the heartwood and roots of the plant *Santalum album* (family – Santalaceae). *S. album* is a hemiparasitic tree of great economic value, growing in Southern India, Sri Lanka, Australia and Indonesia. Its trunk contains resins and essential oils particularly the α and β santalols, santalenes and many other minor sesquiterpenoids (2). These sesquiterpenoids are responsible for the unique sandalwood fragrance. A number of aromatic and phenolic compounds have also been identified in the oil *S. album* (3). The quantity of oil produced in a tree varies considerably according to location (environmental factors) and age of the tree, even in nearly identical growing conditions (2). It should also be noted that santalol

composition can vary depending on the method of oil extraction, sections of a single tree. The international standard (ISO 3518, 2002) for sandalwood oil and similar authorities stipulate a minimum of 90% w/w santalol (as free alcohol) in the oil (4).

Sandalwood oils are essential oils commonly used as fragrances for body oils and incense as well as in medicines and cosmetics. Sandalwood oils have many well-known health benefits in traditional medicinal systems such as Ayurveda, as antiseptic, antipyretic, antiscabietic, diuretic, expectorant, stimulant, and for the treatment of bronchitis, dysuria, urinary infection, and in gonorrhoeal recovery.

Sandalwood oils are usually extracted by steam distillation (5). However, solvent extraction can be performed on chips of sandalwood (6). It would present numerous disadvantages (5). Therefore,

various other alternatives were tested. Thus Marongiu and al.(7), Piggott and al (8) used supercritical or subcritical fluid for extracting and fractioning essential oils. Microwave-assisted extraction was also used as new innovative techniques (9). They offer some advantages regarding kinetics and preservation of the chemical composition, but as far as we know, no industrial development has been achieved and all applications are still at the laboratory or pilot scale.

In this context, it was proposed to carry out a comparative study of the extraction of the essential oils of the sandalwood using two different methods: traditional hydrodistillation and the innovative technology of Détente Instantanée Contrôlée DIC (French, for instant controlled pressure drop). DIC was defined in 1988 (10) and has been studied, developed, optimized and used at industrial scale for various applications such as drying and decontamination, texturing, the extraction of non-volatile molecules such as flavonoids (11) and of volatile compounds (12-15). In the present work, we studied DIC, as essential oil extraction process. A preliminary thermodynamic study allowed us to determine the relative or absolute volatility of each compound versus temperature. The hydrodistillation was performed as references to compare the DIC extraction yields and kinetics.

MATERIELS AND METHODS

Raw Material: The bark of the sandalwood tree used in this study, was provided by the company BAHAVE (Nantes, France). Its was originally from Australia and harvested in avril 2013. Its initial moisture content was 11 g H₂O/100 g dry matter, with average diameter of 2mm.

Assessment protocol: In the present study we had examine the effects of the total heating time (t) and the number of cycles (C) as DIC operating parameters (independent parameters), regarding the extraction efficiency EE considered as the main response parameter (dependent variable). The principle objective was to identify separately the impacts of evaporation and autovaporization phenomena. An experimental design was built intervening t and C; the first must be correlated to the evaporation process while the second one must reveal the effect of the autovaporization by itself. This investigation was achieved according to the protocol shown in Figure. 1. The treatments by

hydrodistillation were performed as references to compare the DIC extraction yields and kinetics. An adequate statistical treatment of the data issued from the experimental work carried out in the present article allowed us to study, analyze, optimize and model the DIC extraction of essential oils.

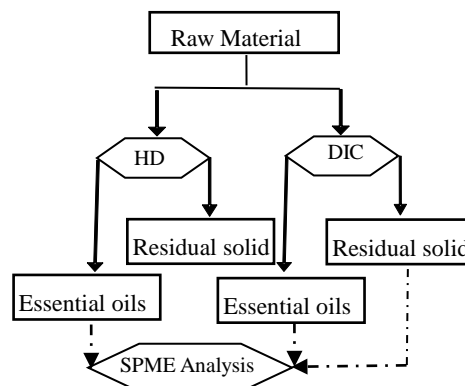


Figure.1. Protocol treatment of sandalwood chips oil extraction

Hydrodistillation: The hydrodistillation equipment used was a modified Clevenger, in accordance with conventional hydrodistillation protocols, 50 g of raw material was immersed in 500 mL of distilled water in a 1 L distillation flask. The extraction of essential oils was performed out from the first drop of distillate until no more essential oil was obtained. The essential oil yield (Y) is defined as the ratio of the mass of the oil obtained (M_{EO}) to the dry of sandalwood chips (M_{dm}):

$$Y (\%) = \frac{M_{EO}}{M_{dm}} \quad (1)$$

Laboratory scale (DIC) process: The reactor we used was a 18 l processing vessel with a heating jacket; thermal treatment in this vessel was achieved using saturated steam with a pressure varying from 0,1 MPa up to 0,6 MPa, which means a temperature between 100 and 160°C. A 1600 l vacuum tank with cooling water jacket is connected with a water ring vacuum pump allowing the vacuum to be maintained at 5 kPa. A pneumatic valve ensures an “instant” connection between the vacuum tank and the processing vessel; it can open in less than 0.2 s. Some other valves control the flow of steam and compressed air within the processing vessel. (Figure 2).

DIC treatment: In the present study, the raw sandalwood was directly put in the DIC reactor-processing vessel. After placing the raw material in

the treatment vessel and closing it, a first vacuum stage (about 5 kPa) was established in order to remove the air presented in the vessel and, thus to assure close contact between the surface of the sample and the steam to be injected just after (Figure 3. phase c).

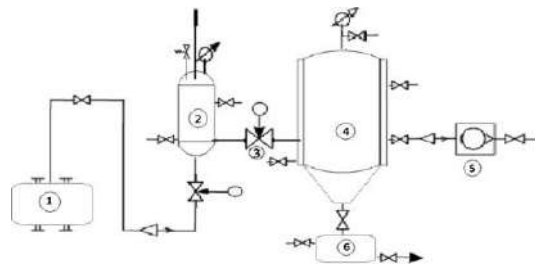


Figure.2. Schematic diagram of DIC system. (1: boiler; 2: processing vessel; 3: quick pneumatic motion valve; 4: vacuum tank; 5: vacuum pump; 6: tank of liquid).

High pressure saturated steam used in our case was 0.6 MPa according to the experiment design (Table 1), and the product temperature to 160 °C. This stage lasted 10–300 s and ended by an abrupt pressure drop towards a vacuum (5 ± 0.2 kPa) by opening the pneumatic valve V3 (Figure.2), which assured a decompression rate higher than 1 MPa s⁻¹

In our case, several DIC-cycles were carried out and atmospheric pressure was established after the final pressure drop. Figure. 3 gives the flow-sheet of this treatment. In our case, during the total thermal treatment time (phases d of various cycles), a part of essential oils must evaporate; the instant pressure drops towards a vacuum would normally simultaneously provoke an autovaporization of a part of water and volatile molecules (essential oils), and an instantaneous cooling of the product immediately stoppes its thermal degradation.

Statistical and experimental design protocol: Response surface methodology (RSM) method with a five-level central composite rotatable experimental design method was adopted. In the present study, the saturated steam pressure used kept constant at 0.6 MPa and the two DIC operating parameters we studied were the total heating time t , and the number of pressure drops C , (Table 1).

Moisture content just before DIC treatment was maintained constant (11±0.3 g H₂O/100 g dry matter). DIC treatment experiments were then carried out using the operating conditions described in Table 3.

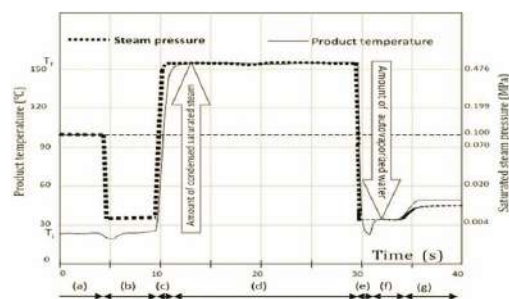


Figure.3. Temperature and pressure history of a cycle of DIC extraction: (a) Sample at atmospheric pressure; (b) initial vacuum; (c) saturated steam injection to reach the selected pressure; (d) constant temperature corresponding to saturated steam pressure; (e) abrupt pressure drop towards vacuum; (f) vacuum; (g) releasing to the atmospheric pressure. Evolution vs time of the product and vessel temperatures (±0.5 °C) during a 1 cycle-DIC treatment (16)

Table 1 Independent variables used in response surface methodology at a fixed steam pressure value

parameters	Coded level				
	-α	-1	0	+1	+α
number of cycles	2	5	12	19	22
treatment time (s)	120	240	600	960	1080

The statistical treatment of results was executed using the analysis design procedure of Statgraphics Plus software for Windows (1994, version 4.1, Levallois-Perret, France). Variance (ANOVA) was performed to determine significant differences between independent variables, and Pareto charts were introduced as well as general trends, response surface, empirical model coefficients, and R² were determined. The dependent variables had concerned process performances : the response was expressed with a second order polynomial model of independent variables:

$$Y = \beta_0 + \beta_1 t + \beta_{11} t^2 + \beta_2 C + \beta_{22} C^2 + \beta_{12} tC + \varepsilon$$

where Y was the response, $\beta_0, \beta_1, \beta_{11}, \beta_2, \beta_{22},$ and β_{12} were the regression coefficients, C, t were the independent variables, ε was random error. Response surface methodology could be used to optimize the operating parameters by coupling various studied responses.

The extraction efficiency EE considered as the main response parameter (dependent variable) was calculated from SPME analysis by summing the areas, carried out on untreated sandalwood chips

(raw material) and residual solid after DIC treatments, as:

$$EE(\%) = \frac{EO \text{ in raw material} - EO \text{ in DIC solid residue}}{EO \text{ in raw material}}$$

Analysis by GC/MS with solid-phase microextraction (SPME) :The volatile molecules present in the untreated solid samples, as well as in DIC treated samples were analyzed through SPME system (model CombiPal, CTC Analytics AG, Zwingen, Switzerland) connected with a GC-MS system. Comprising a Varian GC 3800. equipped with a capillary column VARIAN, with an apolar phase (polydimethylsiloxane) model VF-5ms (30m× 0,25 mm× 0,25 mm), was connected to a mass spectrometer Saturn 2100T, equipped with a sample tray of the CombiPaL (Cie Varian, Les Ulis, France).

In this study, a 75µm CAR/PDMS Fuses Sillica fiber was used.The SPME parameters including the sample mass, extraction temperature, extraction time, and desorption time were respectively: 1 g, 70 °C, 30 min and 10 min. GC analysis conditions were optimized, with helium used as carrier gas, at a constant rate of 1 ml/min. The column temperature was 70 °C for 6 min; it increased to 120 °C at 15°C/min, from 120 to 200 at 3 °C/min, and 25 °C/min up to 250 °C. The detection, and transfer temperature was 230 °C and 250 °C respectively.

Compounds were identified by comparing their mass spectral fragmentation patterns with those stored in the data bank MS from National Institute of Standards and Technology (NIST). For each compound on the chromatogram, percentage of peak area relative to the total peak areas from all compounds was determined and reported as the relative amount of that compound.

RESULTS AND DISCUSSION

Hydrodistillation: The study of the kinetics of extraction of essential oil by hydrodistillation reveals extraction increases with time to reach after 160 hours of extracting a level of stability. (Figure 4).

The partial pressures of water and other volatile compounds inside the holes of the plant considered as porous material closely depend on the temperature

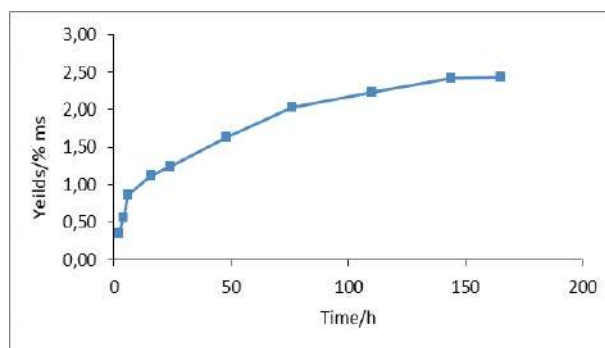


Figure.4. Kinetics of hydrodistillation of sandalwood

through the thermodynamic liquid/gas equilibrium of the mixture of the volatile molecules.(12) . Therefore we sought to determine the thermodynamic properties of liquid-vapor equilibrium of each compound of sandalwood. The vapor pressure at various temperatures of the various compounds was determined using the ACD / I-Lab (ACD / Labs 2010-2014). These data then plot the relative volatility of each compound relative to the water Figure 5. The results show a relative volatility whose evolution is significant depending on the temperature. Thus, in the field of hydrodistillation, the temperature is 100 ° C, and the relative volatility is less than 0.004. This aspect of very low relative volatility explains the low kinetic evaporation extraction.

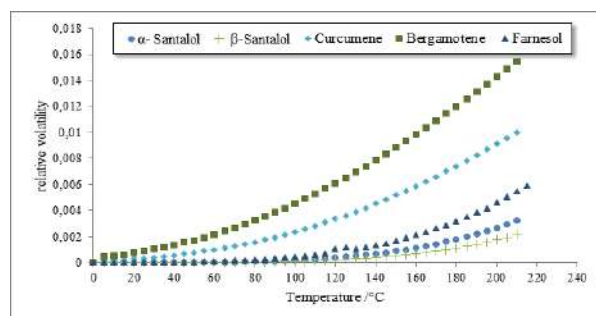


Figure.5 Relative volatility of sandalwood volatile compounds vs water

Comparative extraction yields of hydrodistillation extraction and DIC: These both values of hydrodistillation and DIC yields were underestimated, the first would be due to the condenser problems whereas the second would concern some amount of essential oils linked on the vacuum tank wall. However, these values were able to prove the ability of DIC to extract very quickly much higher yields of sandalwood essential oils.

Table 2 Yield of essential oils obtained using DIC extraction in comparison with conventional hydrodistillation.

	DIC	Hydrodistillation
Yields (g EO/100 g dm)	1,14	1,23
Total heating time	5min	24h

DIC optimization statistical and experimental design protocol: As shown in Table 3, we performed a central composite experimental design. The number of DIC cycles and total heating time were taken as independent parameters it allowed analyzing and determining the importance of the Autovaporisation and evaporation respectively. The extraction efficiency EE% determined on each solid residue after DIC experimental design by SPME was considered as the main response parameter.

The mathematical relationship obtained with the statistical package Statgraphics was a polynomial equation representing the quantitative effect of process variables and their interactions on the measured response EE.

The response surfaces allowed us to represent the total effect of operative parameters. RSM optimization was used to show the impact of the operative factors in terms of extraction efficiency EE (Figure. 8). Thus, it was possible to identify the highest and the quickest DIC extraction process through the operation efficiency. Here, it was clear that the number of cycles (revealing the impact of the pressure drops) was the only factor to have a profound effect.

The values of the coefficients of C and t were related to the effect of these variables on the response EE (Figure.6). A positive value represented an effect that favors the operation, while a negative value indicated an antagonistic effect.

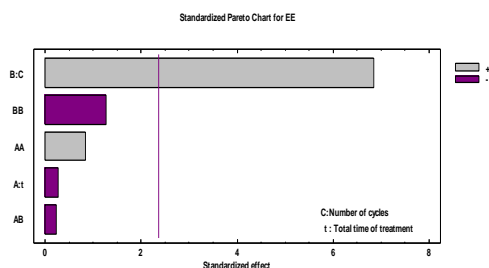


Figure.6 Standardized Pareto chart for EE (%)

This mathematical relationship is listed below:

$$EE (\%) = 15,6644 - 0,0218008t + 4,54692C + 0,0000199396t^2 - 0,000341237tC - 0,0729185C^2$$

With $R^2 = 87,62\%$

The optimized operative conditions with the goal to maximize the extraction efficiency EE was calculated as an optimum value of 77,17%, for 120 s as a total thermal treatment time t, and 22 as a theoretical value of the number of cycles C. These t and C optimized values were substituted and used in experimental trials carried out at 0.6 MPa as saturated steam pressure P, total thermal treatment time t = 330 s, and C = 22 cycles, which means 15 s of thermal treatment time for each cycle.

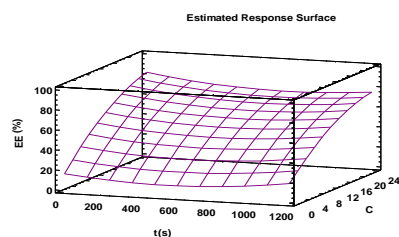


Figure.7 The response surfaces to represent the total effect of operative parameters

CONCLUSION

The present research work confirmed the high relevance of DIC treatment as extraction process. At both fundamental and experimental points of view, this study allowed the DIC extraction process to be defined as a mainly autovaporization phenomenon; the contribution of evaporation to the extraction of essential oils was established to be very weak even negligible in the usual DIC processes. The natural structure of some plants such as sandalwood prevents an easy conventional essential oil extraction. The extraction performed by hydrodistillation (HD) showed that a slow process.

ACKNOWLEDGMENTS

The authors wish to thank la Communauté d'Agglomération de La Rochelle (CDA) for financial support for this research.

Table 3 DIC extraction trials with extraction efficiency

	1	2	3	4	5	6	7	8	9	10	11	12	13
Total time (s)	600	1080	600	600	960	960	600	240	240	600	120	600	600
Time per cycle (s)	50	90	27	50	51	192	50	48	13	50	10	300	50
Number of cycles	12	12	22	12	19	5	12	5	19	12	12	2	12
Efficiency (%)	47,54	48,32	69,51	40,97	71,03	38,06	63,22	31,28	67,69	55,34	59,92	15,43	50,12

REFERENCES

1. Fox, J. E. D, 2000, Sandalwood: The royal tree, *Biologist* 47, 31-34.
2. Jones, C. G., Plummer, J. A., and Barbour, E. L., 2007, Non-destructive sampling of Indian sandalwood (*Santalum album* L.) for oil content and composition, *J. Essent. Oil Res.* 19, 157-164.
3. Kim, T. H., Ito, H., Hayashi, K., Hasegawa, T., Machiguchi, T., and Yoshida, T, 2005, Aromatic constituents from the heartwood of *Santalum album* L, *Chemical and Pharmaceutical Bulletin* 53, 641-644.
4. ISO 3518 (2002), Oil of sandalwood (*Santalum album* L.), International Organization for Standardization.
5. Misra, B. B., and Dey, S, 2012, Differential Extraction and GC-MS based Quantification of Sesquiterpenoids from Immature Heartwood of East Indian Sandalwood Tree, *Journal of Natural Sciences Research* 2, 29-33.
6. Hasegawa, T., Toriyama, T., Ohshima, N., Tajima, Y., Mimura, I., Hirota, K., Nagasaki, Y., and Yamada, H, 2011, Isolation of new constituents with a formyl group from the heartwood of *Santalum album* L, *Flavour Fragrance J.* 26, 98-100.
7. Marongiu, B., Piras, A., Porcedda, S., and Tuveri, E, 2006, Extraction of *Santalum album* and *Boswellia carterii* Birdw. volatile oil by supercritical carbon dioxide: influence of some process parameters, *Flavour Fragrance J.* 21, 718-724.
8. Piggott, M. J., Ghisalberti, E. L., and Trengove, R. D, 1997, Western Australian sandalwood oil: Extraction by different techniques and variations of the major components in different sections of a single tree, *Flavour Fragrance J.* 12, 43-46.
9. Tran, V. N, 2006, Sandalwood Microwave Characterisation and Oil Extraction, in *Advances in Microwave and Radio Frequency Processing*, pp 119-128, Springer.
10. Allaf, K., and Vidal, P, 1989, Feasibility study of a new process of drying/swelling by instantaneous decompression towards vacuum, Chemical Engineering Department, University of Technology of Compiègne, Compiègne, France.
11. Amor, B. B., Lamy, C., Andre, P., and Allaf, K. , 2008, Effect of instant controlled pressure drop treatments on the oligosaccharides extractability and microstructure of *Tephrosia purpurea* seeds, *Journal of Chromatography A* 1213, 118-124.
12. Allaf, T., Tomao, V., Besombes, C., and Chemat, F, 2013, Thermal and mechanical intensification of essential oil extraction from orange peel via instant autovaporization, *Chemical Engineering and Processing: Process Intensification* 72, 24-30.
13. Berka-Zougali, B., Hassani, A., Besombes, C., and Allaf, K, 2010, Extraction of essential oils from Algerian myrtle leaves using instant controlled pressure drop technology, *Journal of Chromatography A* 1217, 6134-6142.
14. Besombes, C., Berka-Zougali, B., and Allaf, K. ,2010, Instant controlled pressure drop extraction of lavandin essential oils: Fundamentals and experimental studies, *Journal of Chromatography A* 1217, 6807-6815.
15. Kristiawan, M., Sobolik, V., and Allaf, K, 2008, Isolation of Indonesian cananga oil using multi-cycle pressure drop process, *Journal of Chromatography A* 1192, 306-318.
16. Allaf, T., and Allaf, K, 2014, Instant controlled pressure drop (D.I.C.) in food processing : from fundamental to industrial applications.

Numerical and Experimental Study of a Modular Solar Dryer Coupled to a Parabolic Trough Solar Concentrator for Agricultural Product

N.Benaouda^{1, a}, B.Zeghmami²

¹ Centre de Développement des Energies Renouvelables, CDER ; BP 62 Route de l'Observatoire, Bouzaréah, 16340, Algiers, Algeria

² Université de Perpignan via Domitia, Laboratoire de Mathématique et Physique (LA.M.P.S.), EA 4217, F66860 Perpignan, France

^{a)} Corresponding author: nbenaouda@gmail.com

^{b)} zeghmami@univ-perp.fr

ABSTRACT. A numerical and experimental study has been carried out to investigate the performance of a modular solar dryer using a parabolic trough collector to produce the required heat for drying agricultural products. The modular solar dryer consists of a parabolic trough solar collector, a water-air heat exchanger and a drying chamber. The solar concentrator system has been constructed and tested without tracking device. The parabolic trough solar concentrator was oriented north-south and tilted from the horizontal at an angle equal to the latitude of the location (Algiers latitude $\beta=36^\circ$). Tomato slices have been used in this study. The drying experiments have been performed for two air flow velocities and several air drying temperature in order to determine the drying velocity and the characteristic drying curve. A drying program based on thermal and mass balances on components of the cabinet dryer was developed and implanted in the TRNSYS software. Mathematical models describing the other components of the drying system are included in the TRNSYS library. Simulations are carried out for meteorological data of Algiers (Algeria). The results show that the parabolic trough solar collector gives drying air temperature in the range 60-90°. The air drying temperature, drying efficiency and collector system efficiency increases with increasing the flow rates of the air and water. The simulation results are in good agreement with experimental data. The discrepancies between experimental and numerical results are inferior to 8%. The drying duration required for reducing moisture from 80% to 10.5 % (Wet basis) is less than five hours and the drying efficiency is about 80%.

INTRODUCTION

Various works have been reported on mathematical models and computer programs to simulate the performance of drying systems to estimate the solar drying curves and drying rate and investigate the efficiencies of the solar drying system. Equations for predicting the drying process and the air solar collector functioning are solved using numerical methods such as (Nodal method, Euler method, Finite element method, characteristic methods, etc.). Several researchers and engineers in solar drying technologies are conducted their own models to simulate the Various works have been reported on mathematical models and computer programs to simulate the performance of drying systems to estimate the solar drying curves and drying rate and investigate the efficiencies of the solar drying system. Equations for predicting the drying process and the air solar collector functioning are solved using numerical methods such as (Nodal method, Euler method, Finite element method, characteristic methods, etc.). Several researchers and engineers in solar drying technologies are conducted their own models to simulate the drying system behavior prior to their prototype implementation. The computer software's are used in engineering design to get simulation results of a solar system efficiently in a very short time, which consists of several connected components. A large number of drying parameters, calculations, tables and graphs can be carried out by computer programs that simulate theoretical approaches to be easily converted to practical works. The simulation software's such as

(TRNSYS, SIMULINK-MATLAB, etc.), have the great advantage of increasing the prediction of the long-term (multi-year) performance of the solar system as proposed in this work. TRNSYS remains one of the most simulation software with flexible open source and facilitates the addition to the program of mathematical models not included in the standard TRNSYS library. There are many applications in the literature of this software in solar energy applications. In the following we present some works which have used TRNSYS for conducting parametric studies to simulate the behavior of the drying systems and solar water heating systems. A.Gama et al. [2] performed a study in both design and construction of a parabolic trough solar concentrator without tracking the sun. The TRNSYS software was used to simulate the thermal performance of a system consisting of a closed loop (with water) and its use for heating sanitary water, storage tank with heat exchanger. The results showed that the outlet temperature of the fluid (water) does not exceed 100° C for several values of water flow rate. B.Ringeisen et al. [3] investigated the effectiveness of adding a concave solar concentrator built from low-cost, locally available materials to a typical solar crop dryer. The solar dryer is wooden structures covered with transparent plastic film and contains several wooden trays to withstand the tomato slices. The focal line of the concentrator is directed towards the solar dryer. The results would tend to show that the addition of a solar concentrator can help to increase drying efficiency by increasing drying rate of tomato slices and did not negatively affect tomato quality and reducing drying time by 21% compared the

direct mode solar drying system. N.Benaouda et al. [4] conducted a numerical and experimental study of an indirect forced convection solar drying system of bay leaves using a simulation program, written in FORTRAN and integrated to TRNSYS software. The TRNSYS software was used to simulate the thermal performance of the solar drying system composed of a solar collector, drying chamber and of an auxiliary heater. The results showed that the return on investment is about 2 years for a sale price of dried leaves equal to 4.02 (USD) per kg, a solar fraction and an efficiency of the solar collectors equal respectively to 60% and 75%. The useful heat gain currently can be achieved by using a flat-plate collectors and concentrators, since collectors' efficiency depends on the irradiation, materials, heat transfer characteristics and ambient weather condition; the collector performances depending on these parameters was investigated by various authors [1-4]. In the case of a flat plate collector, the performance-related results depend principally on the absorber that heats the air flowing in its vicinity. Many works [5] show that adding a single or double panel of glass cover for greenhouse effect, in which air flows above, below, or both sides of the absorber plate and/or heat exchange absorber surface enhance the thermal performance of these collectors, that operate with an outlet air temperature between 10-30°C according to a drying conditions [6]. However, in the case of a modular solar dryer with flat-plate solar collectors for heating the air drying, the air temperature, outlet the collector is not sufficiently high for an efficiency of the dryer. Consequently, these solar dryer systems are made by an auxiliary source to produce the required heat for drying agricultural products, usually electrical, with a high price and a precarious availability in agricultural areas. Without the auxiliary heating, the solar drying is slower, low flow rate to achieve the air temperature; collecting area is large enough to reach the desired temperature, etc. To our knowledge, the most dryers for food products and vegetables work in optimum drying temperatures ranging between 60 and 85 °C [7]. In order to fulfill the requirements of the air drying temperature, the air mass flow rate must be decreased, usually causing a significant decrease of the performance of solar collectors. In addition, during the day the outlet air temperature of the flat plate solar collector evolution has a bell shape with a maximum value at midday (solar time) [8]. The drying performance is depending generally on the drying conditions such as air temperature or flow rate and collector efficiency can be enhanced by using, for instance, a system composed of a parabolic trough solar concentrator, Liquid-Air Heat Exchanger and a ventilator to move the drying air in the dryer chamber. This system will certainly bring an alternative to operating without an electrical heater and can easily achieve air drying temperature of 60-90°C with the great values of air flow rate, allowing to adjust the mean drying parameters for an efficiency drying process [2]. So, this paper is about a numerical study of a modular solar dryer composed of a parabolic trough solar concentrator, an air-water heat exchanger and a dryer cabinet. The parabolic trough collector has been designed, fabricated and tested. The modular solar dryer is connected to the parabolic trough solar concentrator, which is placed on a north-south axis

so that the troughs can track the sun from east to west [9]. The product to dry is tomato slices. The dried slices tomatoes are an essential ingredient in cooking for many preparations such as sauces, pizzas, etc. Computer subprograms for a cabinet dryer is constructed based on a transient theoretical analysis and are added to the TRNSYS environment. The aim of this work is to use TRNSYS tool to simulate the functioning of the modular solar dryer in the Algiers weather conditions in order to determine notably its thermal efficiency.

MATERIALS AND METHODS

Drying system

The modular solar dryer, as shown in Figure 1, consists of a parabolic trough solar collector, a water-air heat exchanger and a drying chamber. The parabolic trough solar collector which can be used for domestic applications as hot water is composed of an aluminum foil sheet with a shape of a parabolic cylinder for reflecting and concentrating solar radiations onto a copper tube with $\varnothing 25$ mm outside diameter. This tube, considered as the absorber of the trough solar collector, is located at the focus line of the parabolic cylinder and is surrounded by a glass for lowering convective heat loss from the collector pipe. The space between the tube and the glass cover is evacuated. The parabolic trough solar collector can rotate about a single axis of rotation east-west oriented (the rate of rotation is 15 degrees per hour), and is seasonal or monthly tilt adjusted. The fluid is supplied by the parabolic trough solar collector flows via a circulation pump (type WILO Star, 3 Speed) through the closed primary circuit of a heat exchanger. This heat exchanger is consisted of copper tube coils and of aluminum fins for increasing the heat exchange rate. Automatic air vents are installed at a high point in the system for removing the air contained in the solar circuit (Figure 1a) and to keep constant pressure in this circuit. An expansion tank (2litre capacity, low pressure) is in a closed loop heating. Its function is to absorb the expansion of water in the solar loop (Figure 1a) when the water reaches the boiling point and limit also the pressure in the solar circuit. A second open circuit of air is linked with the dryer chamber by operating the centrifugal flow fan (Type BA12C37T-2, operating temperature -10 C to + 70 C, Power: 19 ~ 21W) through this heat exchanger; the hot air produced is then fed into the drying chamber. The drying chamber is a parallelepiped enclosure of dimensions 0.93 m \times 0.65 m cross-sectional areas and 1.9 m height whose walls are composed of galvanized iron plate. Vertical, top and bottom walls as well as the door are insulated using polyurethane foam of thickness equal to 60 mm. The access to the inside of the drying chamber is via an insulated door (0.93 m \times 1.9 m). There are ten trays (L = 0.02, W = 0.01 m). The tray is made of a wood frame of thickness equal to 0.005 m and a perforated aluminum sheet. The distance from the bottom of this drying chamber to the bottom tray is about 20 cm and a distance of 20 cm among each tray. The bottom side (drying loop) of this chamber is a circular tube (15 cm in diameter) connected to a centrifugal fan (220 V, 0.1 kW). The air circuit of a heat exchanger is connected to the centrifugal fan with a

stainless tube. A PT100 platinum sensor placed at the entrance of the drying chamber allows to specify the desired air temperature (T_{dry}). This temperature is depending on the flow rate of each fluid (air and water). The flow rates can be varied between 1.0 and 2.0 $m^3 h^{-1}$

and 0.1 and 0.3 $kg s^{-1}$ respectively, using a ventilator speed controller (Inline Duct Vortex Blower Exhaust Control 1800W) and a flow pump control system integrated into the pump.

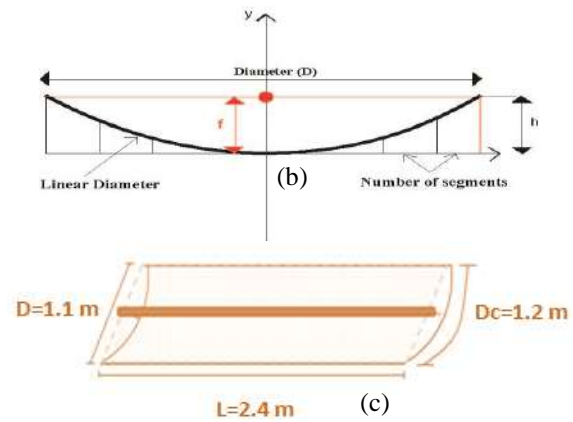
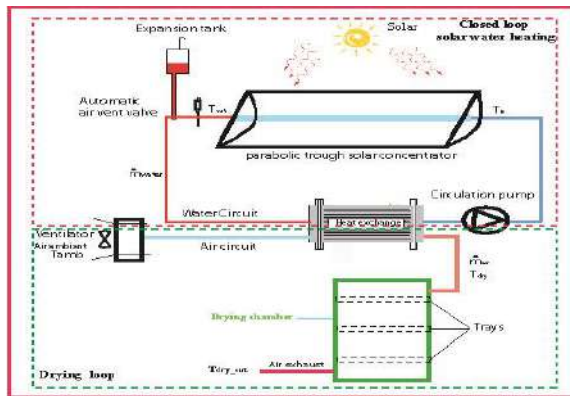


FIGURE 1. (a) Synoptic views of solar drying system (b) and

(c): The schematic of the Collector design

Experimental test on a Parabolic Trough Solar Concentrator

Collector (Trough design)

A pilot trough-receiver unit is developed from the standard reflective stainless steel sheets (2.4 m × 1.2 m). The desired focal length of the concentrating parabolic trough has been obtained using the software "Parabola calculator" [10]. This software, based on the parabolic equation developed by Price et al [11], needs the parabola dimensions: Diameter (D), depth (h) and the number of body segments (Ns) from the user and displays the focal length (f), the volume, the fLength/Diam (f/D) and the coordinates x; y of each body segment (figure 1b-c). The parabolic equation is expressed in Cartesian coordinates as:

$$X^2 = 4fy \tag{1}$$

From equation (1), the height of the parabola in terms of the focal length and aperture diameter is:

$$(a/2)^2 = 4f h \tag{a} \quad \text{Or: } f = a^2/16h \tag{b} \quad (2 \text{ a-b})$$

The geometrical concentration C_g is defined by the ratio between the area of the collector aperture $A_{Aperture}$ and the surface area of the receiver $A_{absorber-tube}$. The concentration factor C_f is:

$$C_f = \frac{A_{aperture}}{A_{absorber_tube}} = \frac{2DL}{2\pi rL} = \frac{D}{\pi r} = \frac{2.4}{3.1416 \cdot 0.025} = 30.55 \tag{3}$$

A solar concentrator system has been constructed and tested without tracking device. The parabolic trough solar concentrator was oriented north-south and tilted from the horizontal at an angle equal to the latitude of the location (Algiers latitude $\beta = 36^\circ$). To know the full benefit of the system, we carried out tests on the system. These experiments, carried out during July 2014, are intended to measure during the day long the outlet water temperature (T_w), the ambient temperature (T_a) and air drying temperature (T_{dry}). The hourly global solar radiation sequences (G_t) are also recorded.

TABLE 1. Geometrical data of the PTC

Item	Sample	Value
Diameter	D	2.4 m
Aperture	a	1 m
The concentrator height	h	0.25 m
Receiver diameter	d	3.8 cm
Focal length	f	0.25 m
Geometrical C_f	C_f	30.55

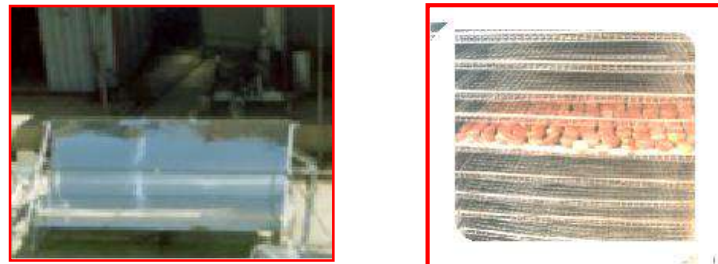


FIGURE 2. (a) Parabolic trough solar concentrator realized in Algiers, Algeria, (b) Detail of drying trays with tomatoes

Product to be dried (Tomato slices)

The tomatoes, greenhouse-grown, were procured from local-market and stored in a refrigerator maintained at 6°C until the drying experiments. Before starting the experiment, tomatoes of size 60–80 g were maintained at ambient temperature during approximately one hour. The tomatoes were washed with water and sliced into circular discs of 4–6 mm thicknesses using a hand-operated adjustable mechanical slicer. The sliced tomatoes were placed on trays in a single layer and dried using the modular solar dryer described previously (figure 2b.). The dry weight of the tomato was determined by using a vacuum oven at 70°C for 24 h [12]. Triplicate samples were used for the determination of moisture content and the average values were reported.

Mathematical modeling (Transfers equations)

Solar collector

The linear parabolic concentrator, Type 536, in the TESS's library (Thermal Energy System Specialists) [13] was used to simulate the energy useful and outlet water temperature. Refer to "Solar Engineering of Thermal Processes", by Duffie and Beckman [9] for more information on the modeling of these collectors. The solar inputs for this collector should be output from the TYPE 16 radiation processor operating in modes 2 or 3 for tracking surfaces. This subroutine requires an external data file which contains the incidence angle modifiers as a function of incidence angle (up to 10°). The subprograms compute the evolution during the time of the outlet air temperature through the air solar collector, and the useful energy delivered at the outlet of the collector.

The energy balances on the collector components give the following equation:

$$\alpha \tau I_b A_{\text{Aperture}} = \varepsilon \sigma (T_{\text{absorber}}^4 - T_{\text{amb}}^4) A_{\text{Absorber_tube}} + U_L (T_{\text{absorber}} - T_{\text{amb}}) A_{\text{Absorber_tube}} + Q_u \quad (4)$$

$$\text{Thermal energy extracted from the collector: } Q_u = Q_{\text{absorber}} - Q_{\text{losses}} \quad (6)$$

$$\text{With } Q_{\text{losses}} = U_L A_{\text{absorber_tube}} (T_m - T_{\text{amb}}), \quad T_m = \left[(T_{\text{out_w}} + T_{\text{in_w}}) / 2 \right] \quad (7)$$

$$Q_{\text{solar}} = I_b A_{\text{aperture}} \quad (a) \quad \text{and} \quad Q_{\text{absorber}} = \tau \alpha Q_{\text{solar}} \quad (b) \quad (8 \text{ a-b})$$

The calculation of the overall loss coefficient (U_L) based on convection and radiation. For the assumption that the area between the cover (glass) and the receiver (absorber) tube is a stagnant quantity of air, U_L is one be found out from the following equation:

$$U_L = \frac{\dot{m}_w c_{pw} (T_{\text{out_w}} - T_{\text{in_w}})}{A_{\text{absorber_tube}} (T_m - T_{\text{amb}})} \quad (9)$$

The useful heat is related to the flow rate can also be defined on the base of the water temperature differentials between inlet and outlet as [9]: $Q_u = \dot{m}_w c_{pw} (T_{\text{out_w}} - T_{\text{in_out}})$ (10)

The solar collector efficiency is defined as [9]:

$$\eta_c = \frac{\dot{m}_w c_{pw} (T_{\text{out_w}} - T_{\text{in_w}})}{Q_{\text{solaire}}} \quad (11)$$

With the determination of the optical efficiency and overall loss coefficient, we obtain the following relationship the optical efficiency is depending on the

$$\eta_{\text{optical}} = \tau \alpha - \eta_c = \tau \alpha - U_L \frac{(T_m - T_{\text{amb}})}{I_b C_f} \quad (12)$$

With A_{Aperture} and $A_{\text{Absorber_tube}}$, the collector aperture and the absorber tube area; Q_u the useful heat and Q_{losses} the heat loss by radiation, convection and conduction; Q_{solar} , Q_{absorber} the solar energy incident on the area of the absorber tube and the heat absorbed by the black absorber area; $T_{\text{out_w}}$, $T_{\text{in_w}}$, water inlet and outlet temperatures; T_{absorber} and T_{amb} , temperature of absorber and the ambient; I_b the incident beam radiation; τ and α the transmittance and the absorption coefficient; ε the emissivity of the absorber tube; σ the Stefan- Boltzmann constant ($5.67 \times 10^{-8} \text{ W / m}^2\text{K}^4$); m_w the water mass flow rate (kg/s).

Heat Exchanger

The TRNSYS component of Type 5g (Shell and Tube) is used for modeling the air- water heat exchanger. The water outlet temperature is calculated by F.P Incropera and D.P Dewitt [14].

$$T_{w,\text{out}} = T_{w,\text{in}} - \varepsilon \left(\frac{C_{\text{min}}}{C_{\text{pw}}} \right) (T_{w,\text{in}} - T_{a,\text{in}}) \quad (13)$$

Where:

- C_{min} : minimum capacity rate of one the fluid (water or air) $J K^{-1}$
- C_{pw} : specific heat capacity of water ($J kg^{-1}K^{-1}$)
- $T_{w,out}$: outlet water temperature (K)
- $T_{w,in}$: inlet water temperature (K)
- $T_{a,in}$: inlet air temperature (K)
- $T_{a,out}$ (T_{dry}) : outlet air temperature (K)
- ϵ : heat exchanger effectiveness
- m_a, m_w : air and water mass flow rate ($kg s^{-1}$)

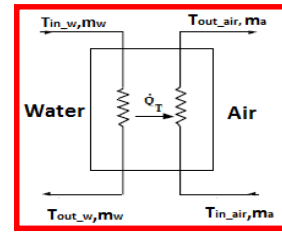


FIGURE 4. Heat Exchanger schematic

Cabinet dryer (component program developed)

The system is modeled using the time-dependent energy and mass balances. We suppose that (a) there is a one-dimensional heat-flow across the components of the solar collector and the drying cabinet perpendicular to the air flow direction; (b) there are no shrinkage and no chemical reactions during drying; (c) the thermal properties of the product, the air and their moisture content are constants in the range of temperature considered, the

ground temperature is equal to the ambient temperature, the air is transparent to the solar radiation and its thermal inertia is negligible. The dryer chamber is divided, respectively, into N slices perpendicular to the air flow rate direction. From the drying air, the temperature computed in the *i*th slice is supposed to be the inlet one of the following slice. The thermal properties of the product, the air and their moisture content are constants in the range of temperature considered.

General equation:
$$m_j C_{pj} \frac{\partial T_j}{\partial t} = \sigma_{sj} + \sum_{k=1}^n \left(h_{r,j-k} + h_{c,j-k} + h_{d,j-k} \right) (T_k - T_j) \tag{14}$$

Dryer:
$$\dot{m}_a C_{pa} (T_a - T_a^*) = S_{pr} h_{c,a-pr} (T_a - T_{pr}) + \Delta S_{wi} h_{c,a-wi} (T_a - T_{wi}) + m_{dry} L_v \frac{\partial X}{\partial t} \tag{15}$$

Tomato slices:
$$m_{pr} C_{p-pr} \left(\frac{\partial T_{pr}}{\partial t} \right) = h_{cv,pr-a} \Delta S_{pr} (T_a - T_{pr}) - m_{dry} L_v \chi \left(\frac{\partial X^*}{\partial t} \right)_0 \tag{16}$$

$\left(\frac{\partial X^*}{\partial t} \right)_0$ is the initial drying rate expressed in kg per $kg^{-1}dm s^{-1}$, χ and $\left(\frac{\partial X^*}{\partial t} \right)_0$ obtained from drying kinetics' experiments (given in Table. 2). The input data are meteorological data, initial, final moisture content and equilibrium moisture of the slices tomato. The drying efficiency is the ratio between the thermal energy utilized for the drying and the thermal energy available for the drying. The solar fraction is defined as the useful energy supplied by the collector divided by the thermal energy available for the drying [1, 4]:

$$\eta_D = \frac{m_v L_v}{Q_D} \tag{a} \quad f = \frac{Q_u}{Q_D} \tag{b} \tag{17 a-b}$$

Trnsys simulation

We use the TRNSYS software (version 17) [15] to simulate the functioning of the modular solar dryer. All components described above and parameters needed

for the simulation were introduced in this software as shown in Figure 5. Multiple simulations are done for several values of air drying temperatures and air drying velocities. The simulations are performed for the following operational conditions and assumptions (Table 1):

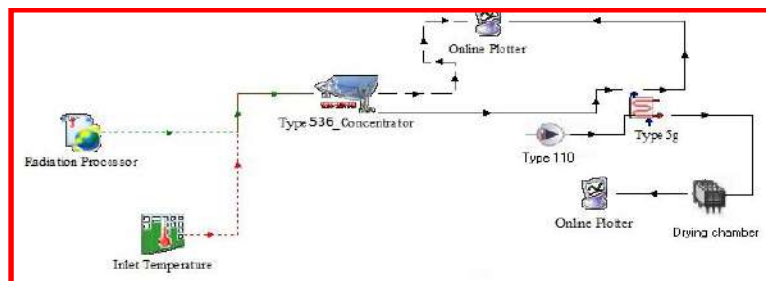


FIGURE 5. Schematic diagram of solar drying system in assembly panel of TRNSYS simulation studio

Economic analysis

An economic analysis is necessary to support decision-making the choice of a modular solar drying connected to a parabolic trough solar concentrator for slices tomatoes. In this work we choose a succinct model and we focused

this study on the payback period of the modular solar dryer presented above. This analysis is focused on the payback period. The great advantage of the payback period is that it is simple and is an excellent tool for engineers and technical staff in research to choose among proposals without going through a detailed economic analysis [16].

We adopted the following assumptions. The rates (Insurance, maintenance, etc. was assumed to be constant during the useful life of the system, (ii) the inflation rate is neglected (iii) the costs and gains are annual, (iv) the operating costs include electrical consumption for pump and ventilator, labor, insurance, maintenance and repair costs. (v) Costs and income are annual; (vi) The revenue is achieved by selling the dried tomato slices. The life of the system is assumed to be 15 years. First, we calculate the average annual net income (total income-costs). The payback period is the time in which the initial investment is expected to be recovered from the net income generated by the modular solar dryer.

The favorable conditions as the ambient temperature and solar heat flux density, also the availability of tomato throughout the year in Algeria location allow using the solar dryer almost all the year (250 days). The costs and the main economic parameters based on the economic situation in Algeria are shown in Table 4. Using this data, the payback period, which is the time in which the initial

investment is expected to be recovered from the net income generated by the modular solar dryer, was calculated using the formula below [16].

$$\text{Payback period} = \frac{\text{Initial investment}}{\text{Annual Net Undiscounted Benefits}} \quad (18)$$

RESULTS

Drying Kinetics of Tomato Slices (Experimental study)

In this study, convective drying kinetic of tomato slices was conducted in order to identify the characteristic parameters of tomato slices. The effect of air velocity of several air drying temperatures and two air velocities of 0.5 and 1.0 ms⁻¹ is shown in Figure 3.

TABLE 2. Drying characteristic of tomato slices

Parameters	Values / Relationship	Unit	R ²	FitStdEr r
Moisture content (kg water/kg dm)	X ₀ =16.6, X _f =0.140			
Constant drying rate phase (CDRP)(-dX*/dt) ₀	0.0017 × (T _s -T _h) V ^{1.58}	-	0.933	0.013
reduced drying rate	χ=-3.109X* ⁵ + 8.344X* ⁴ - 7.49X* ³ + 1.751X* ² + 1.48X* + 0.022	-	0.963	0.025
X _{eq} at T=40-50°C	-0.060+3.198H _r -10.114H _r ² + 8.77H _r ³ +8.77H _r ⁴	(kg water /kg dm)	0.997	0.032
X _{eq} at T=50-60°C	0.005+0.807H _r -2.580H _r ² + 2.355H _r ³ + 2.055H _r ⁴	(kg water /kg dm)	0.978	0.021

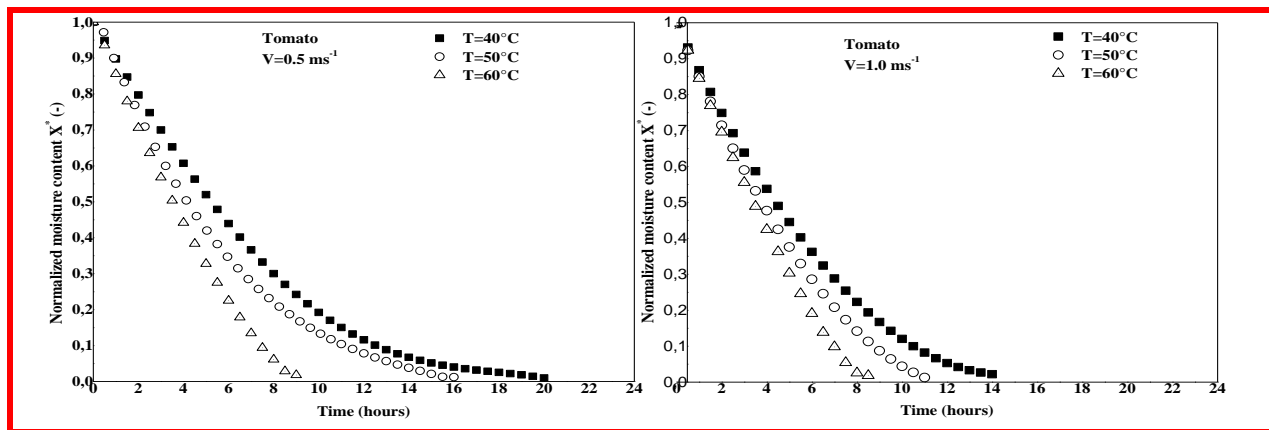


FIGURE 3. The drying kinetics of tomato slices

A variation of the moisture content of tomato slices over drying time for different temperatures and air drying flow rate is shown in Figure 3. It will be noted the absence of the constant drying phase. This result is in agreement with the drying of various food products which do not exhibit constant rate drying phase [1, 17]. According to the results of the authors mentioned above [1, 17], the drying duration decreases with the increase on the one hand of the air drying velocity on the other hand of the air drying temperature.

Simulation

Parabolic Trough Solar Concentrator

The figure 6 b-c shows the effect of the air flow rate on the outlet air temperatures of the parabolic trough solar concentrator during June, July and August. We observe an increase of this temperature when the air flow rate decreases. In fact, the flow rates of air and water were adjusted to 50, 20 kg h⁻¹ respectively, in order to obtain a drying air temperature in a the range 60-80°C, values recommended for the drying of tomato slices. The

water outlet air temperature decreases as these days' months and consequently the outlet air temperature

decrease as the air flow increases. The collector efficiency as a function of $(T_m - T_{amb})/G_t$ is illustrated by Figure 6a.

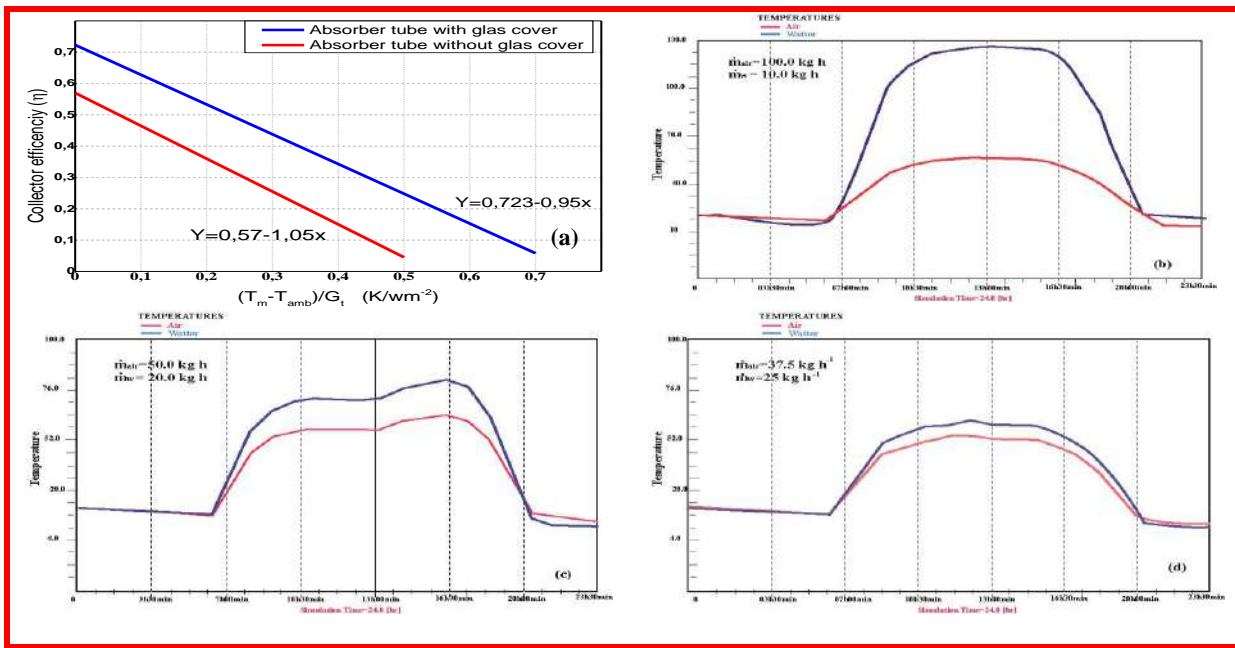


FIGURE 6. (a) Collector efficiency for a parabolic trough solar concentrator. (b), (c) and (d) Water outlet temperature of a evacuated glass receiver, and drying temperature, with local time for a typical day in July and different flow rates.

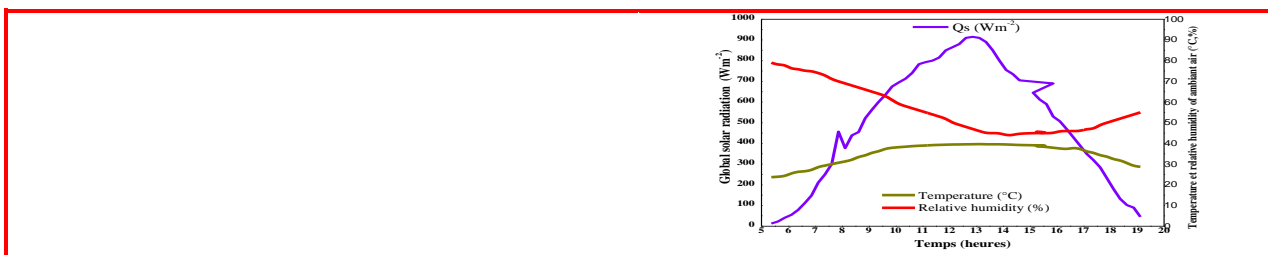
Drying efficiency and solar fraction

When the amount of heat needed for the drying process is supplied by a parabolic trough solar concentrator, the solar fraction and the drying efficiency are during the year, superior to those obtained with a typical flat plate solar collector (Figure 7). We note from this figure that during summer the drying efficiency and the solar fraction reach respectively 90% and 100 %.

Experimental

A period of one clear sky days (14th July) has been selected for measuring all required temperature, as was mentioned previously for modular solar dryer by using a

parabolic trough solar concentrator as shown in figure 1. As we have seen in figure (8 a-b) the performance of the parabolic trough solar concentrator is high for July days, although the solar radiation and ambient temperatures are lower than those of the winter days. The ambient temperature is in the range 25-38°C, while the total solar radiation is 480 Wm⁻² at 9:00 am reaching about 900 Wm⁻² at solar noon then decreases after solar noon gradually. In Figure 10, it can be noted that that experimental results are close to those obtained from simulations for the drying conditions given in Table 3. The parabolic trough solar concentrator can provide an air low rate of 50 kg h⁻¹ at a temperature varying between 60 and 80 ° C during five hours. This will fully ensure the drying of the tomato slices. These results are promising for this configuration of a parabolic cylindrical without a sun tracking system.



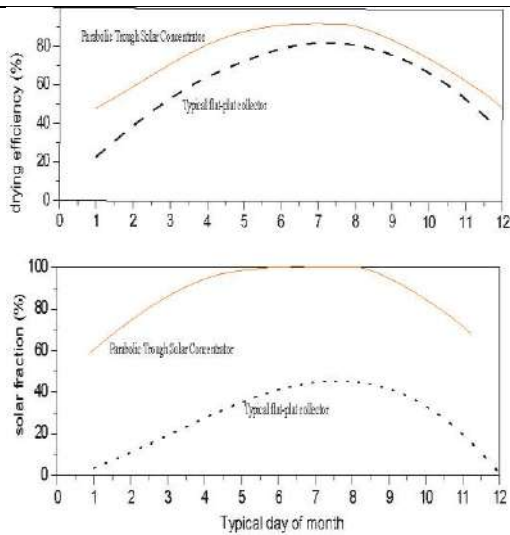


FIGURE 7. Monthly evolution of the drying performance during the drying tomatoes the dryer is connected to parabolic trough solar concentrator and to a typical flat-plate collector

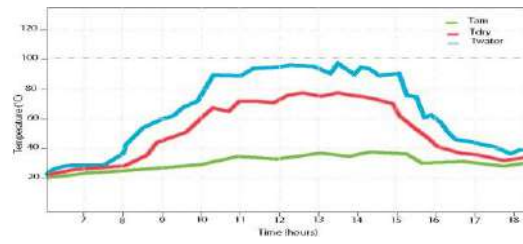


FIGURE 8. (a) Hourly weather data variation. (b) Ambient temperature, water outlet temperature of an evacuated glass receiver, and drying temperature, with local time for 14/07/2014 clear July day in Algiers (a flow rate mwater = 20 kg h⁻¹ and mair = 50 kg h⁻¹)

Payback analysis

The payback period is very small (1.004 years) compared to the life of the modular solar dryer (15 years), so the solar dryer will dry tomato slices free of cost for almost its entire life period.

TABLE 3. Simulation parameters and assumption

Item	Conditions or assumption
Location	Algiers, Algeria
Crop	Tomatoes
Air temperature drying	60 and 70 °C
Relative humidity	20-40 %
Air drying velocity	0.5, and 1 m s ⁻¹
Drying period	June, July and August
Initial moisture content	0.937 to 1.083 kg w kg ⁻¹ dm
Final moisture content	0.05236 to 0.07921 "
Drying time	4-6 hours
Air flow rate	10-100 kg h ⁻¹
Water flow rate	10-25 kg h ⁻¹

TABLE 4. Payback period of the modular solar dryer

costs/ income	Number / rate	DZD
Modular solar dryer {Collector, Dryer chamber with trays, Pump Ventilator, Exchanger, Various Capacity of dryer	Σ	119000
Capacity of dryer	20 kg	
Weight Coefficient of tomato β	0.2	
Drying cycle	4-6 hours	
Depreciation	1	119000
Life of dryer	15 years	
Cost of maintenance 2.5% of	2,50%	2975
Labor cost (430*6*250)	430/h	645000
Repair costs 2.5% of (119000)	2,50%	2975
Cost of assurance 2% of (119000)	2%	2380
Cost of fresh tomatoes (10	10 DZD	75000
Electric cost (4 semesters)	800	3200,00
Total cost	Σ	731530
Price for dried tomato (120 ×20	120	850000
Total income		850000
Net income		118470

Note. 1.01 US Dollar = 100DZD

$$\text{Payback period} = \frac{119000}{118470} = 1.004$$

CONCLUSION

Experimental and numerical studies of a modular solar dryer with cylindrical-parabolic concentrating effect have been carried out. The numerical study based on heat and mass balances has enabled us to develop a mathematical model to control the outlet temperature of the collector. The experimental study has allowed the determination of the air and the water flow rates for suitable drying conditions. The parabolic trough solar collector system provides all the heat needs for the drying process. The performance evaluations show that the drying time required, reducing the moisture content of the tomato

slices from 80% to 10.5 % (Wet basis) is less than five hours with a drying efficiency of 90%. The economic evaluation was done according to the criterion of the payback period. The payback period was very small 1.004 years compared to the life of the dryer estimated at 15 years.

REFERENCES

1. N.Benaouda, B.Zeghmami, X.Chesneau, « Etude expérimentale et théorique d'un Séchoir Solaire Modulaire pour Denrées Agroalimentaires », 17èmes Journées Internationales de Thermique

- (JITH 2015), Marseille (France), 28 - 30 Octobre 2015.
2. A.Gama, M.Haddadi et A.Malek, Etude et réalisation d'un concentrateur cylindro-parabolique avec poursuite solaire aveugle, *Revue des Energies Renouvelables* Vol. 11 N°3, pp. 437 – 451,2008.
 3. B. Ringeisen, D. M. Barrett and P. Stroeve, Concentrated solar drying of tomatoes, *Energy for Sustainable Development* 19 (2014), pp. 47–55.
 4. N. Benaouda, B. Zeghmati, X.Chesneau, A.Khellaf, performances evaluation of a modular solar dryer, 19th International Drying Symposium (IDS 2014),Lyon, France, August (2014), pp. 24-27.
 5. René Tchinda, “A review of the mathematical models for predicting solar air heaters systems”, *Renewable and Sustainable Energy Reviews*, Volume 13, Issue 8, (2009), pp. 1734-1759.
 6. M. Dagueuet, *Les séchoirs solaires: théorie et pratique*, UNESCO, Paris, 1985.
 7. Arun S. Mujumdar, *Handbook of Industrial Drying*, CRC Press, 4th enhanced edition, 2014
 8. N.Benaouda, , B.Zeghmati, , and A.Khellaf, , Experimental study and simulation of a solar dryer for spearmint leaves (*Mentha spicata*), *International Journal of Ambient Energy*, Volume 36, Issue 2, 2015.
 9. J. A.Duffie, , and W. A.Beckman, , *Solar Engineering of Thermal Process*, New York (John Willey & Sons), 1991.
 10. Freeware Program, solar parabola calculator designer <http://mscir.tripod.com/parabola/>,
 11. Price. H., E. Lupfert, D. Kearney, E. Zarza, G.Cohen, R. Gee and R. Mahoney, *Advances in Parabolic Trough Solar Power Technology*. J. Solar Energy Eng. Vol.124, pp.109-125, 2002.
 12. Wolf,W., W.E.L.Spiess, and G.Jung. Standardization of Isotherm Measurements (costproject 90 and 90 BIS), In D.Simatos, and J.L.Multon (ed.) *Properties of Water in Foods in Relation to Quality and Stability*. Martinus Nijhoff, Boston, pp. 661-679, 1985.
 13. Tess Documentation Library, chapter 10.Solar Library Technical Reference, type 536: linear parabolic concentrating solar collector, pp536.1-5
 14. F.P.Incropera, and D.P.Dewitt, *introduction to heat transfer*, 3rd ed., john wiley and sons, new York, 1996.
 15. Solar Energy Laboratory, University of Wisconsin-Madison, USA et.al.; TRNSYS 16 – a Transient System Simulation program, (2013), <http://sel.me.wisc.edu/trnsys/user-resources/index.html>
 16. R.Neufville, *Applied Systems Analysis. Engineering planning and technology management* McGraw-Hill Publishing Company, New York, USA, 1990.
 17. Ibrahim Doymaz, Air-drying characteristics of tomatoes, *Journal of Food Engineering*, Volume 78, pp. 1291–1297, 2007.

NUMERICAL SIMULATION OF HEAT AND MASS TRANSFERS DURING SOLAR DRYING OF SEWAGE SLUDGE: SOLAR RADIATION EFFECT

Nidhal BEN HASSINE^{1,2*}, Xavier CHESNEAU¹, Ali. Hatem LAATAR²

¹ Laboratoire de Mathématiques et Physique, Université de Perpignan Via Domitia, Perpignan, France.

² Laboratoire d'Énergétique et Transferts Thermique et Massique, Faculté des Sciences de Bizerte, Bizerte, Tunisie.

*Corresponding author: Fax: +33468662234 Email: benhassinenidhal@gmail.com

ABSTRACT

The drying of sewage sludge is a current environmental problem, not sufficiently described in the literature. Hence, the aim of this work is a numerical study of heat and mass transfers during solar drying of residual sludge. This sludge is assimilated to a porous medium and exposed to a forced convection laminar flow within a horizontal channel. The transfers in the channel and the porous medium are respectively described by the classic equations of forced convection and the Darcy-Brinkman-Forchheimer model. The implicit finite difference method is used to discretize the governing differential equation system. The algebraic systems obtained are solved using the Gauss, Thomas and Gauss-Seidel algorithms. To determine the drying rate, we associate a drying kinetics model. We particularly studied the effects of solar radiation intensity on the space-time evolution of temperature, velocity and mass fraction at the porous medium-fluid interface. Moreover, the evolutions of the Nusselt numbers are represented to characterize the transfers at the sludge surface. This work is completed by a drying kinetics study. Indeed, we represent the effect of solar radiation on the space-time evolution of the drying rate.

KEYWORDS

Heat transfer, mass transfer, solar drying, sewage sludge.

NOMENCLATURE

T	temperature (<i>K</i>)
u	longitudinal velocity (<i>m/s</i>)
v	transverse velocity (<i>m/s</i>)
c	mass fraction
x	longitudinal coordinate (<i>m</i>)
y	transverse coordinate (<i>m</i>)
t	time (<i>s</i>)
L	channel length (<i>m</i>)
H	channel height (<i>m</i>)
e	thickness of the sludge (<i>m</i>)
Ms	dry mass (<i>kg</i>)
D_v	vapor diffusion coefficient (m^2/s)
L_v	latent heat of vaporization (J/kg)
q	solar flux density (W/m^2)
k	permeability of porous medium (m^2)
C_f	Forchheimer coefficient
Re	Reynold number ($Re = \frac{\rho U_0}{\mu}$)
Pr	Prandtl number ($Pr = \frac{\nu}{\alpha}$)

Sc	Schmidt number ($Sc = \frac{\nu}{D_v}$)
Da	Darcy number ($Da = \frac{k}{H^2}$)
Xs	Water content in dry base (<i>kg water/kg Ms</i>)
Hr	relative humidity (%)

Greek symbol

α	thermal diffusivity ($m^2.s^{-1}$)
λ	thermal conductivity ($W.m^{-1}.K^{-1}$)
ν	kinematic viscosity ($m^2.s^{-1}$)
ϕ	porosity of porous medium
ρ	density ($kg.m^{-3}$)
Ω	vorticity (s^{-1})
ψ	stream function ($m^2.s^{-1}$)

Subscript

f	fluid
p	porous
0	Ambient

Superscript

*	dimensionless variable
---	------------------------

INTRODUCTION

The energy required to be provided to evaporate 1 kg of water is very important, it is in the order of 4180 J/kg. For this, the use of renewable energy and not expensive during the process of sewage sludge drying, as solar energy, is necessary to reduce energy consumed. To achieve this objective, we need to master the mechanisms of heat and mass transfers in the solar drying operation.

In this context, many scientific works are focused on this phenomenon. Among these studies we cite the work of H. Amadou et al. [1], which provides a numerical model of the drying kinetics based on the concept of the characteristic curve. The comparison between the results of this model and those obtained by laboratory experiments shows an excellent accordance. R. Slim [2] has realized a numerical model of the sludge drying taking into account the climatic conditions. He has found the optimal operating cycle for the heat pump which is used for the ventilation of the greenhouse. To define the optimal parameters for improve the heat and mass transfers during the evaporation of a saturated porous layer, Y. Chou et al. [3] have conducted a numerical study of the effects of different parameters as Reynolds number and the layer porous thickness on the temperature, vapor mass fraction, sensible and latent Nusselt numbers and evaporation rate at the interface. They have shown that an increase of the Reynolds number generates an intensification of the heat and mass transfer. R. Font et al. [4], have conducted a series of laboratory experiments on drying sludge where the temperature and the velocity of drying air are not constant. These experiments have shown that, whatever the conditions, there is crust formation on the sludge surface. These same authors have developed a numerical model of the drying kinetics that takes into account the crust formation. The results obtained by this model are in agreement with the experiments. Using a recent engineering approach known as REA (Reaction Engineering Approach), Putranto et al. [5] have modeled the convective drying of sewage sludge. Their model determines the activation energy of the sludge from the drying rate which has been previously determined by experiment. The comparison of the results obtained by this new model with experimental datas of the literature shows its effectiveness.

In this work, we propose to provide a further contribution to previous work already done on this subject. So, the present work is a numerical study

of the solar drying of sewage sludge in laminar forced convection where the solar radiation and the ambient temperature vary during the day.

POSITION OF THE PROBLEM

The system considered in this work is a horizontal channel where the upper wall is transparent to the solar radiation. The bottom is a porous medium, which has the characteristics of sewage sludge. This sludge is exposed to a forced laminar flow with a parabolic velocity profile, a temperature T_0 , a relative humidity H_{r0} and a constant pressure P_0 at the inlet (Figure 1).

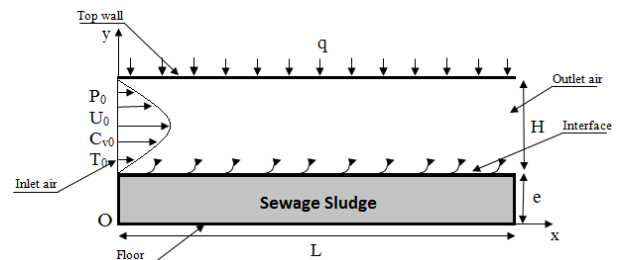


Figure 1: Geometric configuration

In order to simplify the problem, the following assumptions are made:

- The transfers are laminar and two-dimensional ;
- The fluid is Newtonian and incompressible ;
- The viscous dissipation is neglected ;
- The Soret and Duffour effects are neglected ;
- The Boussinesq approximation is retained ;
- The air water vapor mixture is a perfect gas ;
- The air-porous media is at local thermodynamic equilibrium ;
- The porous medium is isotropic.

PROBLEM FORMULATION

Conservation equations: To generalize the results, the equations are written in dimensionless forms. The variables used to obtain the dimensionless variables are the height of the channel and the inlet conditions (the velocity, the temperature and the moisture content)

In the channel: For a two-dimensional case in Cartesian coordinates, the system of equations for heat and mass transfers by forced convection may be formulated by the following dimensionless form:

- Conservation of mass

$$\frac{\partial u_f^*}{\partial x^*} + \frac{\partial v_f^*}{\partial y^*} = 0 \quad (1)$$

– Conservation of X-momentum

$$\frac{\partial u_f^*}{\partial t^*} + u_f^* \frac{\partial u_f^*}{\partial x^*} + v_f^* \frac{\partial u_f^*}{\partial y^*} = -\frac{\partial P_f^*}{\partial x^*} + \frac{1}{Re_f} \left(\frac{\partial}{\partial x^*} \left(\frac{\partial u_f^*}{\partial x^*} \right) + \frac{\partial}{\partial y^*} \left(\frac{\partial u_f^*}{\partial y^*} \right) \right) \quad (2)$$

– Conservation of energy

$$\frac{\partial T_f^*}{\partial t^*} + u_f^* \frac{\partial T_f^*}{\partial x^*} + v_f^* \frac{\partial T_f^*}{\partial y^*} = \frac{1}{Re_f Pr_f} \left(\frac{\partial}{\partial x^*} \left(\frac{\partial T_f^*}{\partial x^*} \right) + \frac{\partial}{\partial y^*} \left(\frac{\partial T_f^*}{\partial y^*} \right) \right) \quad (3)$$

– Conservation of species (water vapor)

$$\frac{\partial C_f^*}{\partial t^*} + u_f^* \frac{\partial C_f^*}{\partial x^*} + v_f^* \frac{\partial C_f^*}{\partial y^*} = \frac{1}{Re_f Sc_f} \left(\frac{\partial}{\partial x^*} \left(\frac{\partial C_f^*}{\partial x^*} \right) + \frac{\partial}{\partial y^*} \left(\frac{\partial C_f^*}{\partial y^*} \right) \right) \quad (4)$$

with:

$$Re_f = \frac{HU_0}{\nu_f} ; Pr_f = \frac{\nu_f}{\alpha_f} ; Sc_f = \frac{\nu_f}{D_v} ; \alpha_f = \frac{\lambda_f}{\rho_f C_p}$$

Where all the air property ($\nu_f, D_v, \lambda_f, \rho_f, C_p$) are variable.

In the porous medium: In order to ensure the momentum conservation in the porous medium we use the model of Darcy-Brinkman-Forchheimer [6]. In order to overcome the difficulty posed by the boundary conditions to impose on the pressure to solve the momentum equation in porous medium, it is written using the formulation of stream function-vorticity [7]. In this formulation the continuity equation is satisfied automatically. So the transfer equations in the porous medium are:

– Stream function equation

$$\frac{\partial^2 \Psi^*}{\partial x^{*2}} + \frac{\partial^2 \Psi^*}{\partial y^{*2}} = -\Omega^* \quad (5)$$

– Vorticity equation

$$\frac{1}{\phi} \frac{\partial \Omega^*}{\partial t^*} + \frac{u_p^*}{\phi^2} \frac{\partial \Omega^*}{\partial x^*} + \frac{v_p^*}{\phi^2} \frac{\partial \Omega^*}{\partial y^*} = -\frac{1}{Re_p Da} \Omega^* - \frac{C_f}{\sqrt{Da}} \sqrt{u_p^{*2} + v_p^{*2}} \Omega^* + \frac{1}{\phi Re_p} \left(\frac{\partial^2 \Omega^*}{\partial x^{*2}} + \frac{\partial^2 \Omega^*}{\partial y^{*2}} \right) \quad (6)$$

– Energy conservation

$$\frac{\partial T_p^*}{\partial t^*} + u_p^* \frac{\partial T_p^*}{\partial x^*} + v_p^* \frac{\partial T_p^*}{\partial y^*} = \frac{1}{Re_p Pr_p} \left(\frac{\partial}{\partial x^*} \left(\frac{\partial T_p^*}{\partial x^*} \right) + \frac{\partial}{\partial y^*} \left(\frac{\partial T_p^*}{\partial y^*} \right) \right) \quad (7)$$

With:

$$u_p^* = \frac{\partial \Psi^*}{\partial y^*} ; v_p^* = -\frac{\partial \Psi^*}{\partial x^*} ; Re_p = \frac{HU_0}{\nu_p} ; Pr_f = \frac{\nu_p}{\alpha_p} ; Da = \frac{K}{H^2}$$

Initial conditions: Initially ($t^*=0$) the temperature, the pressure and the water vapor concentration are

uniform in the channel. Inside, the porous medium, the temperature and the water content are also uniform.

Boundary conditions:

For the channel: At the channel inlet:

$$u_f^* = 6[y^* - y^{*2}] ; v_f^* = 0 ; C_f^* = 1 ; T_f^* = 1$$

At the upper surface of the channel:

$$u_f^* = 0 ; v_f^* = 0 ; \frac{\partial C_f^*}{\partial y^*} = 0 ; \frac{\partial T_f^*}{\partial y^*} = 0$$

At the outlet of the channel:

$$\frac{\partial u_f^*}{\partial x^*} = 0 ; \frac{\partial v_f^*}{\partial x^*} = 0 ; \frac{\partial T_f^*}{\partial x^*} = 0 ; \frac{\partial C_f^*}{\partial x^*} = 0$$

For the Porous medium: At the right and left walls of porous medium:

$$u_p^* = 0 ; v_p^* = 0 ; \frac{\partial T_p^*}{\partial x^*} = 0$$

For the boundary conditions of the stream function and vorticity, we consider:

$$\frac{\partial \Psi^*}{\partial x} = 0 ; -\Omega^* = \frac{\partial^2 \Psi^*}{\partial x^{*2}}$$

Similarly, for the bottom wall:

$$u_p^* = 0 ; v_p^* = 0 ; \frac{\partial T_p^*}{\partial y^*} = 0 ; \frac{\partial \Psi^*}{\partial y} = 0 ; -\Omega^* = \frac{\partial^2 \Psi^*}{\partial y^{*2}}$$

For the fluid-porous medium interface:

$$\mu_f \frac{\partial u_f^*}{\partial x^*} = \mu_p \frac{\partial u_p^*}{\partial x^*} ; v^* = -\frac{1}{Re_f Sc_f} \frac{1}{\left(\frac{1}{C_0} - (C_f^*)_{y^*=\frac{e}{H}} \right)} \left(\frac{\partial C_f^*}{\partial y^*} \right)_{y^*=\frac{e}{H}}$$

The vapor concentration at the interface can be calculated by:

$$C_f^* = \frac{1}{C_0} \left(\frac{M_v P_{vs}}{M_v P_{vs} + M_a (P_g - P_{vs})} \right)$$

P_{vs} is the equilibrium vapor pressure at the interface temperature which is given as:

$$P_{vs} = 10^{[17.443 - \frac{279.5}{T} - 3.968 \times \log(T)]}$$

For the stream function and vorticity boundary conditions to the fluid-porous medium interface, we consider:

$$\frac{\partial \Psi^*}{\partial x^*} = v_p^* ; -\Omega^* = \frac{\partial^2 \Psi^*}{\partial y^{*2}} + \frac{\partial^2 \Psi^*}{\partial x^{*2}}$$

The heat balance at the interface air-porous medium gives us:

$$H. q / T_0 = \lambda_p \left(\frac{\partial T_p^*}{\partial y^*} \right) - \lambda_f \left(\frac{\partial T_f^*}{\partial y^*} \right) - L_v \frac{\rho_f D_v}{T_0 \left(\frac{1}{C_0} - (C^*)_{y^*=\frac{e}{H}} \right)} \left(\frac{\partial C^*}{\partial y^*} \right)_{y^*=\frac{e}{H}}$$

The daily evolutions of the global solar radiation and the ambient air temperature are approximated by sinusoidal functions:

$$q(h) = A \sin \left[\frac{\pi}{\Lambda} (h - h_s) \right]$$

$$T_0(h) = \frac{T_{0 \max} + T_{0 \min}}{2} - \frac{T_{0 \max} - T_{0 \min}}{2} \sin \left(\frac{2\pi h}{\Lambda} - \phi \right)$$

Where A is the maximum intensity of the solar radiation, h_s is the sunrise hour and h is the time in hours.

Λ is the sunshine duration and ϕ is the phase shift between the maximum of the temperature and global solar radiation.

The daily variations in temperature of the ambient air and the global solar radiation are approximated by two Gaussians. We consider a delay of two-hour between the two evolutions. The sunshine duration is 14 hours.

Drying kinetics model: To determine the drying rate, we adopt the model of the drying kinetics of sewage sludge defined and validated by H. AMADOU [1]. This model is based on the concept of characteristic curve [8].

$$\left(-\frac{dX}{dt} \right)_{t^*+\Delta t^*} = \left(-\frac{dX}{dt} \right)_1 f(Xr)$$

where : $f(Xr) = A_1 Xr + A_2 Xr^2 + A_3 Xr^3$
is the reduced drying rate.

$$Xr = \frac{X - X_{eq}}{X_{cr} - X_{eq}} \text{ the reduced water content}$$

$$X_{eq} = k \left(\frac{Hr}{1 - Hr} \right)^n \text{ the equilibrium water content [9]}$$

$\left(-\frac{dX}{dt} \right)_1$ is the constant phase rate.

A_1 , A_2 , A_3 , k and n were determined experimentally by H. AMADOU [1]. The values are presented in Table 1.

Table 1: model parameters

Parameter	Value
k	0.0938
n	0.484
A_1	2.37
A_2	-3.30
A_3	1.92

NUMERICAL RESOLUTION AND VALIDATION

Numerical resolution: For the two media (fluid and porous), the transfer equations are discretized implicitly by using a finite difference method. The numerical resolution is realized by the Gauss and Thomas algorithms in the fluid medium and by the Thomas and Gauss-Seidel algorithms in the porous medium. The considered mesh is regular and rectangular in the two media. In our case, we have considered a mesh for the channel with 121 nodes in the X-direction and 201 nodes in the Y-direction. For the porous medium, we have taken a mesh with 121 nodes in the X-direction and 41 nodes in the Y-direction

Validations: The computational code has been validated for the two media. We compare our results with those of Mohamad [10] in the case of heat transfer by forced convection in a horizontal channel filled with a porous medium whose walls are maintained at constant temperature. For the flow, we have compared our evolution of average Nusselt number with that obtained using the correlation developed by Sieder and Tate [11] in the case of a laminar flow in a horizontal duct where the walls are at a constant temperature. For the two cases, the maximum difference does not exceed 4%.

RESULTS AND DISCUSSION

The results, below, illustrate the effect of the variation of maximum solar radiation intensity on the drying process. They are obtained for an ambient air relative humidity $Hr=50\%$ and a Reynolds number $Re=1000$. These results are taken at one pm of the day of half drying. Four maximal values of the solar radiation intensity have been used ($q_{\max}=500 \text{ w/m}^2$, $q_{\max}=700 \text{ w/m}^2$, $q_{\max}=850 \text{ w/m}^2$ and $q_{\max}=1000 \text{ w/m}^2$).

Thermal and mass transfers: The figure 2 shows the evolutions of temperature, mass fraction and dimensionless vapor velocity at the sludge surface for different maximum solar radiation intensities. As expected, the surface of the sludge heats up with the intensification of solar radiation. This increase of surface temperature generates an increase of the mass fraction at the surface and an increase of the evaporation velocity at the surface.

Moreover, in this figure we note that the temperature evolutions have a minimum value at the inlet of the greenhouse and increases along the channel. The mass fraction and the evaporation velocity at the surface of the sludge have the same evolution that the temperature.

In order to better analyze the effect of maximum solar radiation on the mechanism of heat and mass transfers, we presented in Figure 3 the evolutions of the sensible and latent Nusselt numbers at the sludge surface for different maximum solar radiation intensities.

We can see on these figures that the mass and heat transfers are more important at the inlet of the greenhouse. This is due to the fact that, at the inlet, the temperature gradient and mass concentration gradient between the surface of the sludge and the air in its vicinity are important. After the entrance zone, the air humidity and the air temperature have increased and the gradients of temperature and mass fraction at the sludge surface are less important. It follows that the Nusselt number decreases along the greenhouse.

We can also see, on those figures, that the latent Nusselt number is more important than the sensible one, which means the predominance of transfers by latent mode.

Drying kinetics: On the figure 4, we have presented the evolution of the drying rate along the sludge surface for different maximum solar

radiation intensities. As expected, the intensification of solar radiation generates an increase of the sludge drying rate

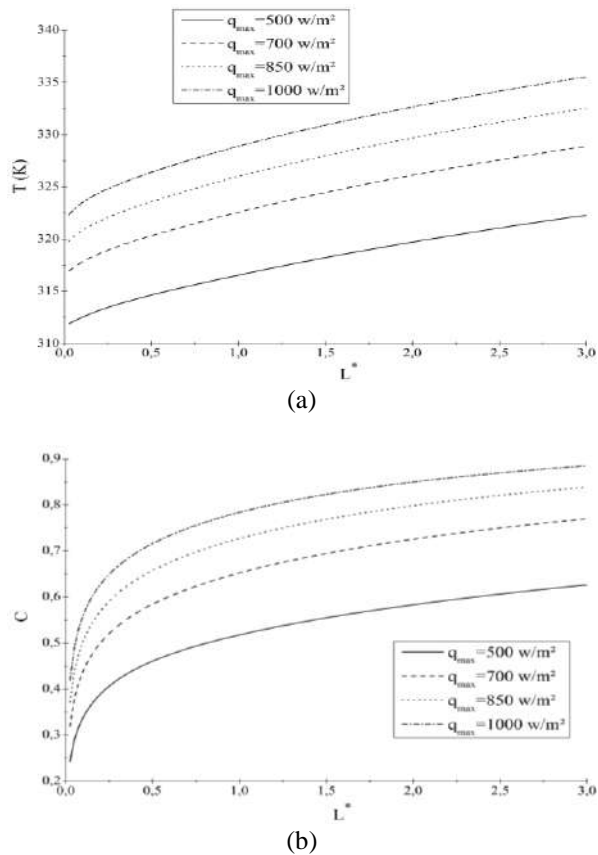


Figure 2: Evolution of the temperature and the mass fraction at the sludge surface

Moreover, we note that for a moderate solar radiation, the maximum of the sludge drying rate is located at the entrance of the greenhouse and then decreases continuously to a constant value at the outlet. For a high solar radiation, the sludge drying rate decreases in the entrance zone of the greenhouse and then increases in the outlet zone. This can be explained by the fact that the water content is more important in the outlet zone.

On the figure 5, we have represented the evolution of the drying rate during one day for different maximum solar radiation intensities. Gradually, with the increasing of solar radiation during the day, we note that the drying rate also increases, but with a time delay which corresponds to the time required to heat up the sludge and increase the evaporation.

The maximum of the drying rate is obtained at 14 hours, two hours after the maximum solar radiation, after this maximum it decreases with the time.

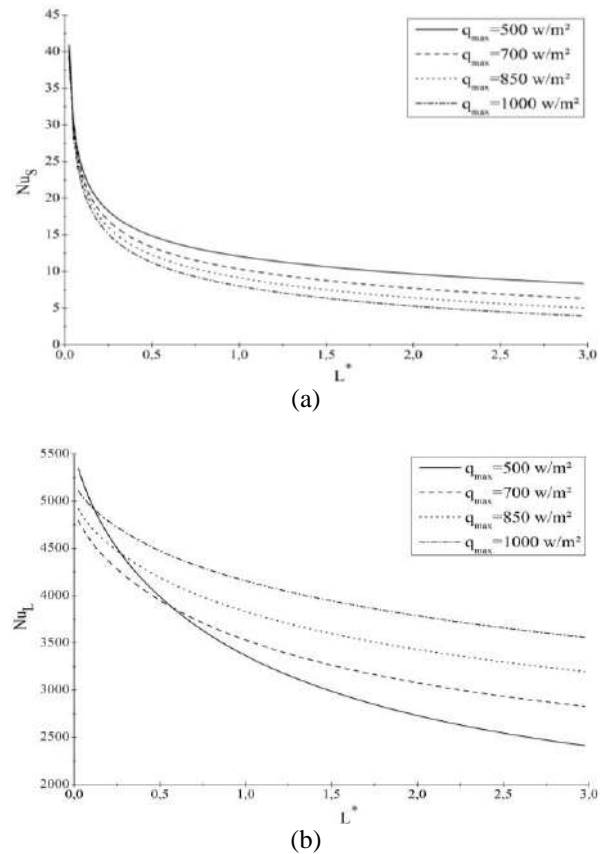


Figure 3: Evolution of the local sensible and latent Nusselt numbers at the sludge surface

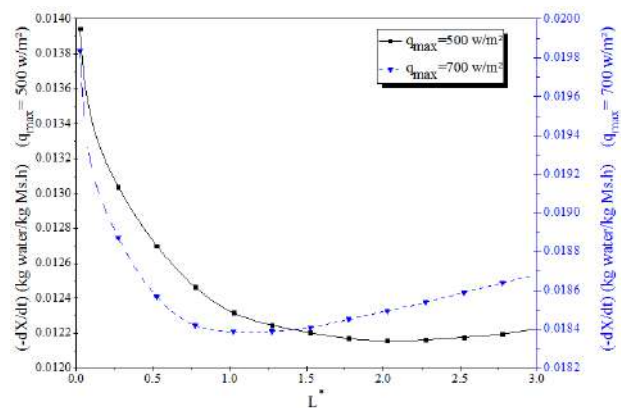


Figure 4: evolution of the drying rate along the sludge surface

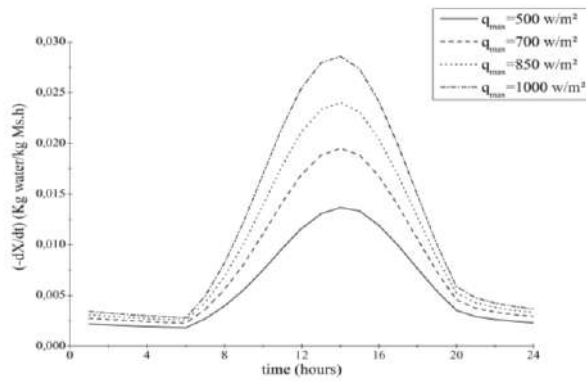


Figure 5: drying rate evolution during one day

We also note that during the night, in the absence of solar radiation, the drying rate is not equal to zero. Even in the night, there is evaporation because the surface temperature of the sludge is always important.

CONCLUSION

This paper presents a two dimensional numerical study of heat and mass transfers during solar drying of sewage sludge. The solar radiation intensity and the ambient air temperature are supposed variable during the day. The results show principally that:

- The temperature, the mass fraction and the evaporation velocity at the sludge surface increases with the solar radiation intensity
- The heat and mass transfers at the sludge surface are maximum at the greenhouse inlet.
- The latent heat transfer increases with the solar radiation while sensible heat decreases.
- The drying rate increases when the solar radiation is intensified.

REFERENCES

- [1] H. Amadou, *Modélisation du Séchage Solaire sous Serre des Boues de Station d'Épuration Urbaines*, PhD Thesis, ULP Strasbourg 1, (2007).
- [2] R. Slim, *Etude et Conception d'un Procédé de Séchage Combiné de Boues de Stations*

d'Épuration par Énergie Solaire et Pompe à Chaleur, PhD Thesis, Ecole des Mines de Paris, (2007).

- [3] Y. Chou, R. Yang, *The Evaporation of a Saturated Porous Layer Inside an Inclined Airflow Channel*, International Journal of Heat and Fluid Flow 28, 407-417, (2006).
- [4] R. Font, M.F. Gomez-Rico, A. Fullana, *Skin effect in the heat and mass transfer model for sewage sludge drying*, Separation and Purification Technology 77, 146-161, (2011).
- [5] Aditya Putranto and Xiao Dong Chen, *A simple and effective model for modeling of convective drying of sewage sludge: the reaction engineering approach (REA)*, Procedia Chemistry 9, 77-87, (2014).
- [6] M. Swati, R. D. Prativa, B. Krishnendu & G. C. layek *Forced convective flow and heat transfer over a porous plate in a Darcy-Forchheimer porous medium in presence of radiation*, Meccanica, vol 47, pp, 153-161, (2012).
- [7] E. F. Nogotov, B. M. Berkovsky & W.J. minkowycz, *Application of Numerical Heat Transfer*, Mc Graw-Hill book company, chapter 4, 99-130, (1978).
- [8] Van Meel, *Adiabatic Convection Batch Drying with Recirculation of Air*, Chemical Engineering Science, Vol 9, pp 36-44, (1957).
- [9] C. R. Oswin, *The Kinetics of Package Life*. International Chemical Industry, 65, 419-421, (1946).
- [10] A.A. Mohamad, *Heat Transfer Enhancements in Heat Exchangers Fitted with Porous Media Part I: Constant Wall Temperature*, International Journal of Thermal Sciences 42, 385-395, (2003).
- [11] Sieder, E. N., and Tate, G. E., *Heat Transfer and Pressure Drop of Liquids in Tubes*. Industrial & Engineering Chemistry, vol. 28, no. 12, pp. 1429-1435, (1936).

NUMERICAL STUDY OF COUPLED HEAT OF AND MASS TRANSFERS IN MULTILAYER BUILDING MATERIALS: ANALYSIS OF THE EFFECT OF INTERNAL AND EXTERNAL INSULATION

Faiza Mnasri^{1,3}, Mengya Li¹, Mohammed El Ganaoui¹, Mourad Khelifa², Slimane Gabsi³

¹University of Lorraine, LERMAB, EA 4370, IUT de Longwy, 54400 Cosnes et Romain, France

²University of Lorraine, LERMAB, EA 4370, ENSTIB Epinal, France

³Environment Research Unit, Catalysis and Process Analysis, National School of Engineers of Gabes,
Tunisia

*Corresponding author: faiza.mnasri@univ-lorraine.fr

ABSTRACT

In this paper, we propose to study the coupled phenomena of heat and moisture transfers in bio-based materials. We are interested in an innovative building composite material, which named as AKU-IBS. This new material contributes to the construction of passive building. In order, to describe the hygrothermal behavior of this panel, a mathematical model has been developed. This model couples the heat transfer and moisture diffusion, also takes into account the thermo physical properties and the boundary conditions of temperature and relative humidity of the composite. Therefore, a multiple series of hygrothermal calculations on several cases of wall are proposed. Firstly, the case of internal insulation when an insulating Neopor material is exposed at the interior of the wall. In the second case, we propose the opposite; the insulation is used at the exterior of the wall. Initially, the temperature and relative humidity of the wall are at 20°C and 50% respectively. The hygrothermal behavior of this configuration is evaluated under a periodic climate outside condition. This evaluation is carried out for a summer and a winter seasons. Finally, to compare the hygrothermal behavior on insulation by exterior or by interior, we proposed to evaluate the exchange of heat and air at the interface. The evolution of the temperature field and the moisture content was processed.

NOMENCLATURE

C_m	Moisture storage capacity [kg/(kg.Pa)]
C_p	Heat capacity [J/(kg.K)]
λ	Thermal conductivity [W/m.K]
ω	Moisture content [kg/kg]
ε	Porosity [-]
δ	Gradient moisture potential [m ² .Pa/(s.°M)]
ρ	Density of material [kg/m ³]
D_m	Total moisture permeability[kg/(m.s.Pa)]
χ	Water saturation degree [-]
h_{lv}	Latent heat of vaporization [J/kg]
e	Thickness [cm]
n	Layer number
ext	External ambience
int	Internal ambience
0	Initial condition
H	Relative Humidity [%]
T	Temperature [°C]
t	Time [s]

INTRODUCTION

The hygrothermal behavior of envelopes affect on indoor comfort and the consumption of energy in building. Moreover, it depends on thermal and hydric proprieties of the wall components and building materials which constituted this wall [1]. In this context, bio-based materials are becoming the subject of several studies in order to understand and characterize their hygrothermal behavior [2, 3].

The study of the heat and moisture transfers in porous building materials can involve several levels of scale [4]. The scale of component which concerns the composition of the wall represents the second level of research. At this scale, two types of configurations can be represented: simple or multilayer wall. For the simple wall, it is a monolayer without coating while the multilayer system is a wall covered with one or more coating layers. The coating and the other outer layers play an important role in hygrothermal behavior of the wall [5]. The external layers limit the flow of air and

moisture through the biobased materials walls and have an impact on the heat conduction [6]. However, the comprehension of the heat transfer physic and the diffusion of vapor and liquid water within a material is complex. It can be analyzed by two types of research: numerical simulation and experimentation investigation. Collet et al.[7], have showed in their experimental investigation about three types of bio-based concrete, that the vapor diffusion occurred homogeneously throughout the material thickness and that the framework does not disturb the hygrothermal behavior of the wall. Evrard et al.[8] studied by simulation, the hygrothermal behavior of different wall systems subjected to different variations in temperature and moisture. Ait Oumeziane et al. [9], as Samri D.[10] proposed in their numerical investigation the consideration of air transfers and hysteresis sorption-desorption. In fact, taking account of air transfer leads to a better distribution of water vapor within the hemp concrete and the curve of sorption-desorption improves the representation of the actual storage of moisture in the material. However, it is often noted that the simulations and the experiments are carried out simultaneously [11]. This allows a comparison and validate the model on which the simulation is based. In this paper, we present a numerical investigation about the transient hygrothermal behavior in a multilayer configuration on concrete combined with a bio-based building composite named IBS-Aku panel [12], which is exposed at the interior and at the exterior of the structure. This wall is insulated by a polystyrene insulating. The hygrothermal behavior of this configuration is evaluated under different dynamic conditions for two seasons (summer and winter) in the region of Longwy. Initially, the temperature and relative humidity of the wall are at 20°C and 50% respectively. The evaluation of the performance of insulation will be established by comparing between the internal and the external insulation.

MATHEMATICAL MODEL:

Governing equations

Literature disposed multiple models about the coupled phenomena of heat and moisture transfers in porous materials. In this present paper, we propose a bidimensional model, which the moisture is transported under liquid and vapor phases. The governing partial differential equations of this heat and mass transfer model through a multilayer wall are given by the following equations:

$$\rho_n C_{p_n} \frac{\partial T}{\partial t} = \text{div}(\lambda_n \nabla T + \delta_n \nabla \omega) + h_{iv} \rho_n \chi \frac{\partial \omega}{\partial t}$$

$$\rho_n C_{m_n} \frac{\partial \omega}{\partial t} = \text{div}(D_{m_n} \nabla W + D_{m_n} \varepsilon_n \nabla T)$$

Boundary conditions

The structure of this envelope is composed of four layers: L_1 and L_4 represent the IBS panel with a thickness of 3.5 cm, L_2 is the polystyrene insulating and L_3 is the concrete layer. These two last layers have the same thickness as 10 cm (see Fig. 1).

At the interface between two materials inside the wall, the distributions of temperature and relative humidity are continuous and the contact is supposed perfect. The current model does not consider the radiation on the surfaces.

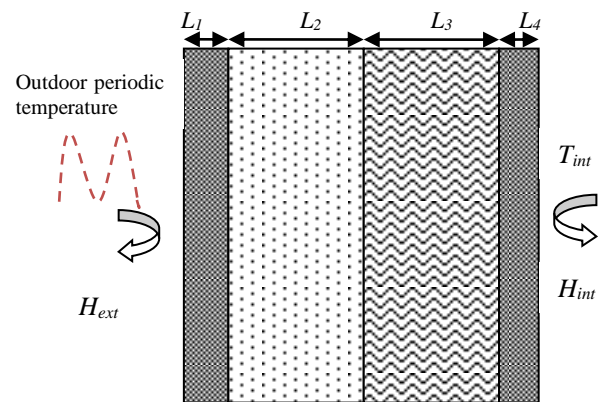


Figure 1

Multilayer configuration of the wall

The boundary conditions are corresponding to exterior solicitations for two seasons; winter (January) and summer (July) in the region of Longwy (see Fig.2). The temperature inside is fixed at 23°C for the two cases. The calculations were carried out for a one week period of time.

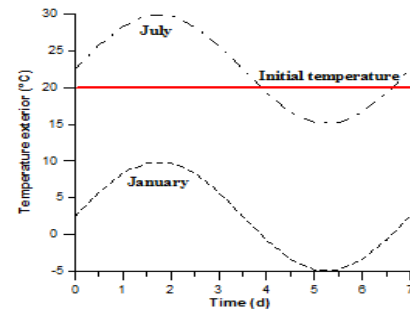


Figure 2

Exterior boundary conditions of temperature

For relative humidity, the comfort zone is between 40% and 80%. The same initial conditions are

considering for both envelope of the building ($T_0=20^\circ\text{C}$ and $H_0=50\%$).

According the above analysis, the boundary conditions can be given as follows:

$$\lambda \frac{\partial T(x, y, t)}{\partial t} \Big|_{x=0/July} = 7.5 \sin\left(\frac{2\pi}{7}t\right) + 22.5$$

$$\lambda \frac{\partial T(x, y, t)}{\partial t} \Big|_{x=0/January} = 7.5 \sin\left(\frac{2\pi}{7}t\right) + 2.5$$

$$H(x, y, t) \Big|_{x=0} = 80\%$$

$$H(x, y, t) \Big|_{x=n} = 40\%$$

$$\lambda \frac{\partial T(x, y, t)}{\partial t} \Big|_{x=n} = 23^\circ\text{C}$$

Where: $n = L_1 + L_2 + L_3 + L_4$

MATERIALS AND CASE OF STUDY

The objective of this study is to evaluate the hygrothermal behavior of a multilayer building envelope. This behavior is associated to the hydric and the thermal proprieties of materials implemented. In this case, we propose to study a new structure distributed by a Belgian company SYSTEM'BAT [12]. It is based on a formwork system, named ISOL+ST, which is a monolithic technology of construction where the walls and slabs are concreted in prepared casing panels of wood chips.



Figure 3
Composition of structure ISOL + ST

The basic material of this structure is the IBS-Aku panel, which is a biobased material, with a 3.5 cm thick. It is composed by an 89% of wood chips and 10 % of cement. The system proposed, is a double reinforcements of IBS-AKU panels, which are an external and internal porters of our structure, separated by a layer of concrete and insulated by Neopor polystyrene.

The hygrothermal proprieties of these materials constituted our multilayer wall are presented in the following table:

Table 1
Hygrothermal proprieties of materials

Materials	L	ρ	λ	Cp	D_m
Panel IBS	3.5	675	0.11	1880	$9.55 \cdot 10^{-13}$
Concrete	10	2500	1.2	840	$1.64 \cdot 10^{-12}$
Polystyrene	10	15.8	0.034	1470	$3.44 \cdot 10^{-12}$
unity	cm	kg/m^3	w/m.K	J/kg.K	kg/m.s.Pa

RESULTS AND DISCUSSION

This study is a numerical investigation by simulation in order to describe the evolution of temperature and relative humidity gradients in the wall. However, we propose to evaluate the effect of thermal insulation for two cases: internal insulation, external insulation for a better prediction of the performance of insulation. This analysis consists to pose once the insulating polystyrene on the outside of the concrete layer and once on the inside of this layer for the internal insulation case.

The simulation results show the temperature and relative humidity profiles, in each layers of the wall for different cases of insulation and two cases of seasons.

Summer season

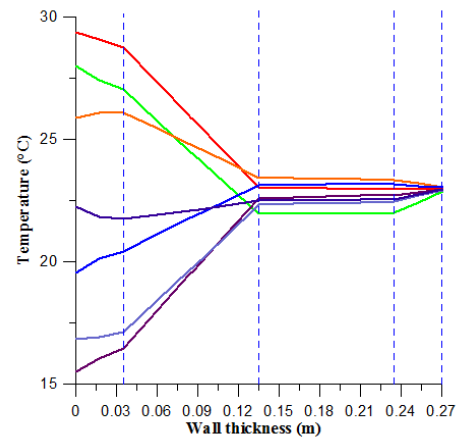


Figure 4
External insulation: Evolution of the Temperature in the wall

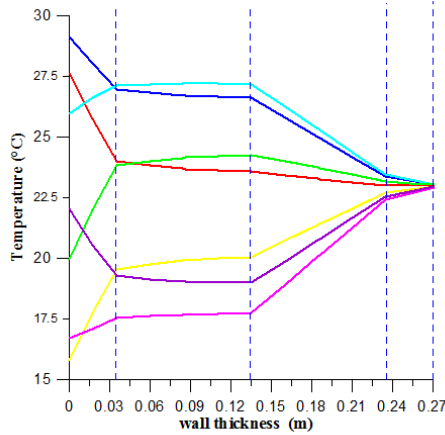


Figure 5

Internal insulation: Evolution of the Temperature in the wall

Winter season

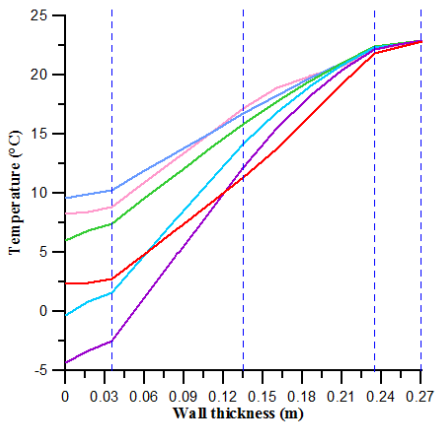


Figure 6

External insulation: Evolution of the Temperature in the wall

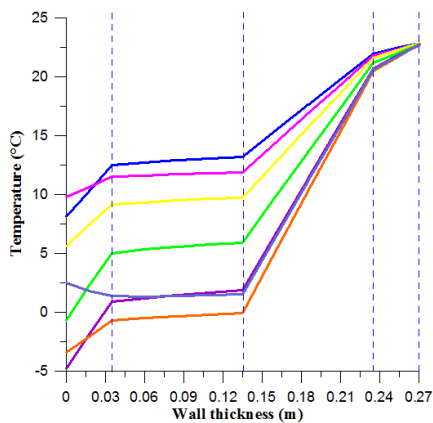


Figure 7

Internal insulation: Evolution of the Temperature in the wall

By analyzing these figures from Figure 4 to Figure 5, we can note that the temperature profiles change allure for all four layers as a result of the difference in intrinsic properties of each material. The variation of the temperature curve in the wall thickness is between 15 and 30 °C for the summer season and between -5 and 25°C. The low temperatures in the thickness of the wall at the interface of junction with the insulator can increase the potential of degradation on the wall.

The external and internal formwork panels IBS-AKU posed at the two extremes sides have a same hygrothermal performance characterized by a high thermal resistance which prevents the passage of the cold or the heat and thus the maintenance of indoor thermal comfort. This combination of polystyrene with wood-cement panel is applied for construction parts and builds a healthy home of high energy efficiency. In fact, the lightness of this polystyrene insulation block limits the physical constraints.

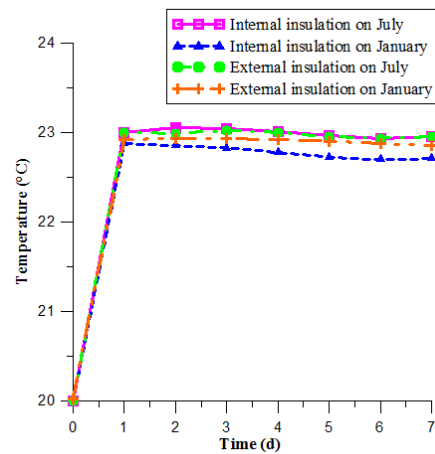


Figure 8

Evolution of temperature in the time for different cases of study

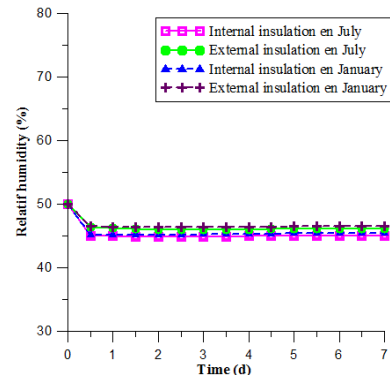


Figure 9

Evolution of relative humidity in the time for different cases of study

These two figures (Figure 8 and Figure 9) show that the temperature and relative humidity profiles in the interior surface, in summer for the two cases of insulation, have almost the same performance; but in winter it can be seen that the external insulation have a better performance than the internal insulation. So, this combination of IBS blocks with polystyrene insulation provides a thermal inertia for greater comfort in summer and winter in the construction.

CONCLUSIONS

In order to study the influence of thermal insulation in a multilayer wall, a coupled heat and moisture transfer transient model was proposed in this paper. Relative humidity and temperature were chosen as the driving potentials. The coupled heat and moisture transfer through walls under periodic boundary conditions were simulated for two seasons (summer and winter). The analyze of the effect of internal or external insulation show that external insulation have a better performance in the multilayer building envelope proposed in this study.

KEYWORDS

Building materials, IBS-Aku panel, Multilayer configuration, exterior insulation, interior insulation

ACKNOWLEDGMENTS

We would like to thank the System' BAT company.

REFERENCES

1. L. Amel, and al. "Experimental thermal characterization of bio-based materials (Aleppo Pine wood, cork and their composites) for building insulation," *Energy Build.*, Jan. 2016.
2. R. S Coutts, A review of Australian research into natural fiber cements composites. *Cement and Concrete Composites*, 27(5), 518-526. (2005).
3. D. Lelièvre. Simulation numérique des transferts de chaleur et d'humidité dans une paroi multicouche de bâtiment en matériaux biosourcés (Doctoral dissertation, Université de Bretagne Sud). (2015)
4. CSTB, & FCBA. Synthèse de l'étude hygrothermique des parois à ossature bois. (2011).
5. Daouas, N., Hassen, Z., & Aissia, H. B. Analytical periodic solution for the study of thermal performance and optimum insulation thickness of building walls in Tunisia. *Applied Thermal Engineering*, 30(4), 319-326. (2010).
6. Shea, A., Lawrence, M., & Walker, P. Hygrothermal performance of an experimental hemp–lime building. *Construction and Building Materials*, 36, 270-275. (2012).
7. F. Collet, S. Prétot, C. Lanos.. Etude expérimentale du comportement hygrothermique d'une paroi en blocs de beton de chanvre avec ossature en bois. 29ème rencontres universitaires de génie civil. (pp 258-267). (2011).
8. A. Evrard, A. De Herde. Hygrothermal Performance of Lime–Hemp Wall Assemblies. *Journal of Building Physics Online First*. (November 26, 2009)
9. Y. Ait Oumeziane. Modélisation du transfert de chaleur et de masse : impact de la perméabilité à l'air et de l'hystérésis pour le béton de chanvre. 29ème rencontres universitaires de génie civil. (2011)
10. D. Samri. Thèse: Analyse physique et caractérisation hygrothermique des matériaux de construction: approche expérimentale et modélisation numérique. ENTPE. (p.284). N° d'ordre : 2008-ISAL-0067 (2008)
11. Qin, M., Belarbi, R., Ait-Mokhtar, A., & Nilsson, L. O. Coupled heat and moisture transfer in multi-layer building materials. *Construction and building materials*, 23(2),967-975. (2009).
12. Catalogue Données d'application ISOL+ST IBS - AKU: <http://www.isolhabitat.be/accueil>

A COMPARATIVE STUDY ABOUT THE ENERGETIC IMPACT OF DRYLAND RESIDENTIAL BUILDINGS WITH THE INTEGRATION OF PHOTOVOLTAIC SYSTEM

Hocine BELAHYA^{1*}, Abdelghani BOUBEKRI¹, Abdelouahed KRIKER²

¹Université Kasdi Merbah Ouargla, Laboratoire de Développement des Energies Nouvelles et Renouvelables dans les Zones Arides et Sahariennes, Faculté des Sciences Appliquées, Ouargla 30000, Algeria

²Université Kasdi Merbah Ouargla, Laboratoire d'Exploitation et Valorisation des Ressources Naturelles en Zones Arides, Faculté des Sciences Appliquées, Ouargla 30000, Algeria

*Corresponding author: E-mail: belahya.hocine@univ-ouargla.com ; bhocine30@gmail.com

ABSTRACT

Nowadays, the Algerian energy consumption among the residential sector ranks first. The national energetic consumption is growing in an inordinate way because the Algerian state has launched a massive plan of housing construction without taking in consideration the legislation of energy performance. In addition, the simultaneous change of users requirements to maintain their comfort, especially in summer, which leads to a large amount of electricity consumption through using air conditioning. In the actual study, we focused on the seasonal consumption of air conditioning system that varies according to the degree of comfort and air-conditioned area. In Ouargla city, in the south of Algeria, the analysis of historical energetic data shows that the cooling system of the building consumes more than 63% of the total energy per year in the average. To decrease this considerable seasonal energy consumption, the building energy performance should be improved by two solutions. The passive solution is through the optimization of the envelope, while the active solution is the integration of PV system. Obtained results, through the analysis of simulation showed that 172 kWh/m² is consumed by the cooling system which represents more than 70% of the total energy consumption in Hollow Brick envelope. However, in the performance envelope (3D panel) the integration of photovoltaic panels in the roof can reduce seasonal energy consumption until to 87.4 kWh/m² per year which represents more than 50% of the total energy consumption. In the case of (3D panel) we can save the half 50% of the total energy consumption.

Keywords Energy consumption, Envelope building, Hollow Brick, 3D panel, Dry land, BIPV

NOMENCLATURE

3DP 3D Panel
BIPV Building Inegrated PhotoVoltaic
CEEC Continuous Electric Energy Consumption
CGEC Continuous Gas Energy Consumption
EXPS Extruded polystyrene
HB Hollow Brick
PV Photovoltaic
SEEC Seasonal Electric Energy consumption
SGEC Seasonal Gas Energy consumption

INTRODUCTION

Nowadays, energy consumption through the residential launched a huge plan of housing construction without taking into account the legislation of energy performance [2-4].

Algeria holds one of the largest solar potential in the world. It is valued at more than 3,000 hours of sunshine per year and 5 kWh of daily energy received on a horizontal surface on most part of the country and more than 3,500 hours in the Saharan region [5]. Thus in summer, this situation is added to simultaneous changing of user's requirements to maintain their comfort.

Buildings face problems of discomfort, mainly due to the overheating phenomenon and the facades exposure to sector ranks first [1]. 42% of national consumption could grow by exaggerated way because the Algerian state has solar radiation. These lead to a large amount of electricity consumption by using air conditioning. Available results in current literature show that annual energy consumption could be saved by choosing optimal orientation and using insulation of walls and roofs of sun protection during hot season [6-9]. Bioclimatic design can minimize the seasonal energy consumption; it refers to the reduction of energy consumption without causing a decrease in the level of comfort [10]. Some published simulation results show that protection against solar radiation and glare has a great influence on the arid climate [11-14].

Energy consumption could be divided into two types; the first one is the continuous energy consumption of equipments which are working during the year as lighting, fridge, TV and other equipments. The second one represents the seasonal equipments which are used for air conditioning, cooling and heating.

The present paper aims to compare between two buildings envelope and integrate PV system; the first one is hollow brick which is very common used in this region, the second one is high performance energy envelope which is 3D panel. The best strategic combination of construction that must be applied to improve the performance of buildings consists to using solar panels as an insulator against the direct sunlight and glare especially in the summer which reduced the seasonal energy consumption for cooling; secondly PV systems can choose either to feed the generated electricity into the distribution grid and receive compensation in the form of e.g. a feed-in tariff or to directly use it at the installation site (self-consumption) and thus reduce the amount of energy purchased from an electric utility. It is common to combine these two options, i.e. to directly use as much of the locally generated electricity as possible and feed excess energy into the public grid [15, 16].

DATA COLLECTION

SITE METEOROLOGICAL DATA

Ouargla city is located 800 km southern from Algiers the capital Fig.1. It is one of the most important cities of Algeria and the main source of wealth. It is known as the oil and the oasis capital. It is difficult for people to deal with a lot of natural obstacles, particularly the hard climate that is characterized by high temperatures, low rainfall and low humidity, especially in summer. The values of the average temperature are shown in Fig. 2.



Figure 1. Geographical situation of Ouargla city

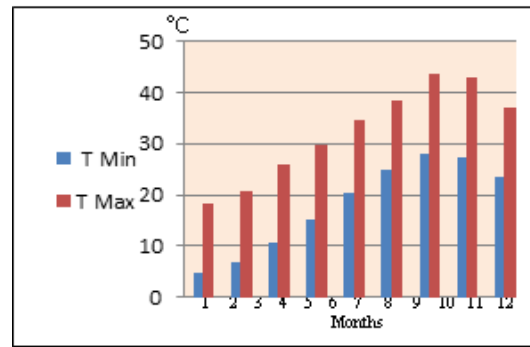


Figure 2. Average monthly temperature in Ouargla

REFERENCE HOUSE CHARACTERISTICS

To estimate yearly energy consumption, 100 houses are taken from 5 different zones to be more representative in the real sample, in order to improve the yearly average energy consumption; we depend in the selection on a reference type house which has all the characteristics of the buildings in this region (Table 2). Detailed model of the reference house has been implemented in TRNSYS [17]. This software calculates the yearly simulations by using the time step for one hour.

HISTORY OF CONSUMPTION IN REFERENCE HOUSE

In this study, we noticed that the maximum load penetrates the building envelope through its roof and walls. Air conditioning system consumes a large proportion of the generated electrical energy and it increases the fuel consumption which causes more environmental pollution. We depend in our study on two types of electrical energy consumption; the first is seasonal consumption which is the value of the seasonal consumed energy (air conditioning in summer and heating in winter), while the continuous consumption is the value of the yearly consumed energy. The historical energetic data analysis of one year shows that the cooling system of the building counts more than an average of 63% of the total energy consumption. The following figure 3 shows the continuous and seasonal consumption of electric energy in the 5 zones of Ouargla. The continuous and seasonal electric consumption per subscriber represented in Fig. 3 revealed that the proportion of the continuous electrical energy consumption stays almost constant at five zones with a value of 30% and seasonal consumption of electrical power of 70%.

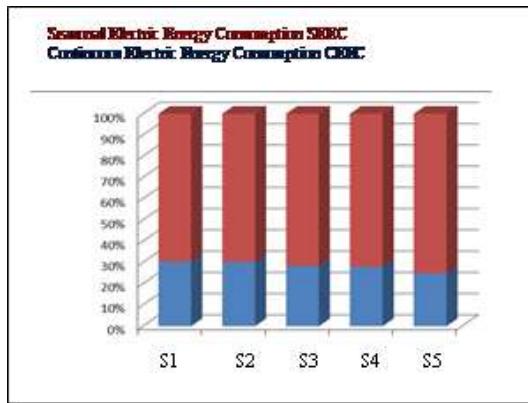


Figure 3. Continuous and seasonal electric energy consumption

HOUSING DESIGN OPTIMISATION

The function of building envelope is to separate physically the building interior from the external environments. Therefore, it serves as an external protection to the indoor environment while facilitating as climate control at the same time [18]. External wall materials in our chosen sample are the hollow brick (Fig. 4) this category of materials has a high thermal mass by absorbing heat from the solar radiation and transferring it to the interior. The other category materials are 3D panel insulation envelope, with superior thermal insulation (Fig. 5). The table 1 shows more detail.

The plan design in prototype simulation is shown in Fig. 6. With 100m² area this design is selected as reference house in the present study. The annual results from the insulated house 3D panel envelope and Hollow Brick are shown in Table 1. We used TRNSYS program to simulate energy consumption in Ouargla climate; then we obtained in the case of 3D panel the total energy consumption is 87 kWh/y m² vs 172 kWh/y m² for Hollow Brick.

The plan design in prototype simulation is shown in Fig. 6. With 100m² area this design is selected as reference house in the present study. The annual results from the insulated house 3D panel envelope and Hollow Brick are shown in Table 1. We used TRNSYS program to simulate energy consumption in Ouargla climate; then we obtained in the case of 3D panel the total energy consumption is 87 kWh/y m² vs 172 kWh/y m² for Hollow Brick.

Fig. 7 and Fig. 8 show the monthly energetic performance of the two studied cases. These figures show a slightly better performance of the 3D panel envelope. In this case of insulation compared with the case of the reference house. The 3D panel envelope is able to reduce the

seasonal energy consumption to the half i.e. 50 %.

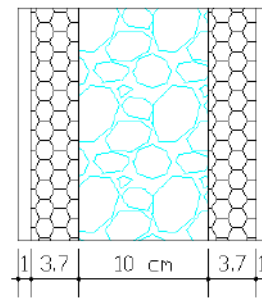


Figure 4. 3D panel wall (Insulated house)

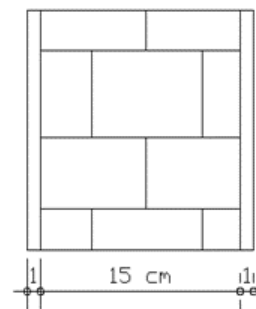


Figure 5. Hollow Brick (Reference house)

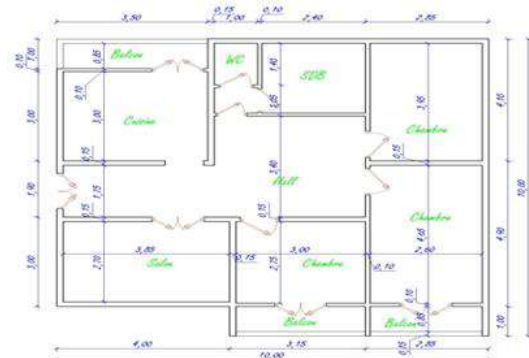


Figure 6. Typical house plan 100m² area

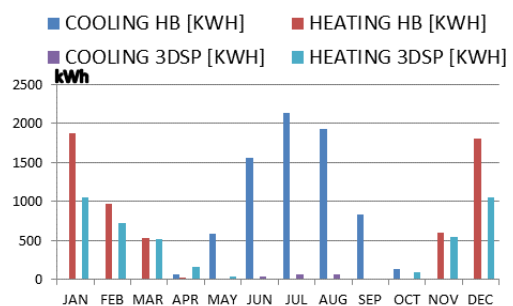


Figure 7. Seasonal Consumption HB vs 3DP

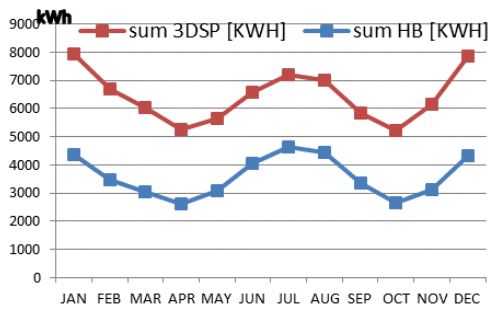


Figure. 8. Total Energy Consumption HB vs Energy 3DP

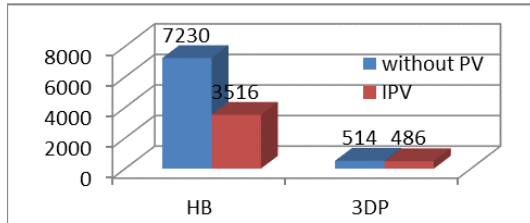


Figure 9. Arid climate 3D panel case.

Table 1 The yearly energy consumption for Hollow Brick and 3D Panel

	Continues Consumption (kWh)	Seasonal Consumption		Total (kWh/year m ²)
		Cooling (kWh)	Heating (kWh)	
Hollow Brick	2500	7230	5814	172
3D Panel	2500	514	4852	87

Table 2 Thermo physical properties for envelopes building

Material	K (W/mK)	ρ (kg/m ³)	C _p (J/ kg K)
Concrete [19]	1.731	2243	840
Hollow Brick [20]	0.62	1600	840
EPS [19]	0.029	35	1213
Plaster [20]	0.72	1865	840

Table 3 The Investment and price for HB and 3DP for on grid

Total power	On grid	
	price kwh	investment*
Hollow Brick 6 kW	11.8 DZD/kwh	1 000 400.00 DZD
3D panel 1 kW	12.7 DZD/Kwh	278 000.00 DZD

*110.05 DZA=1\$ (March, 11th 2016)

ECONOMICAL ANALYSIS OF THE INTEGRATION OF PHOTOVOLTAIC SYSTEM IN THE ROOF

Photovoltaic (PV) generation is one of the most rapidly growing renewable energy sources, and is regarded as an appealing alternative to conventional power generated from fossil fuel [21-23]. The Integration of PV in the roof can reduce the seasonal energy consumption. The simulation results show that protections against solar radiation and glare have a great influence on the arid climate 3D panel case (Fig.9). The integration of photovoltaic panel reduces the seasonal cooling energy consumption from 514 kWh to 486 kWh, it represents about 6%. In the second case of the Hollow Brick, the integration of PV panel reduces the seasonal cooling energy consumption from 7230 kWh to 3516 kWh which represents 48.63%.

CONCLUSIONS

This study attempts to design a new residential building in the dry lands, by using the photovoltaic solar panels. The objective is to optimize thermal comfort in summer, and to reduce the need of the seasonal energy consumption through air conditioning. The analysis of the total energy consumption in Hollow Brick envelope, which is common, shows that the total energy consumption is 172 kWh/m², and more than 70% is consumed by cooling system. However in the high performance envelope (3D panel) the integration of photovoltaic panels in the roof as protector against solar radiation can reduce seasonal energy consumption until to 87.4 kWh/m² per year, which reduce the total energy consumption to 50%.

The main obstacle for the integration PV system is its high capital cost of investment. It requires a long-term strategy, energetic legislation and standards to encourage it. However, we can overcome this obstacle by injecting the excess unused PV electricity on the grid which can contribute to the overall economic feasibility. Net metering is beneficial for the residents because it excludes their need to purchase an expensive and unwieldy battery storage system. Net metering can also prove advantages for utilities because it helps to have peak loads, which generally coincide with maximum PV power production. Net metering can also reduce the price of kWh and make BIPV competitive project against the classical electric one.

REFERENCES

- [1] Ministry of energy and mines, Renewable Energy and Energy Efficiency Program, Algiers, March 2011
- [2] Stratégie et Veille, Recueil trimestriel de l'hebdomadaire/2008/Sonelgaz/DGDS/DS.
- [3] A. Ghezloun and all Actual case of energy strategy In Algeria and Tunisia, *Energy Procedia* 74 (2015) 1561 – 1570
- [4] M. Missoum and all, Impact of rural housing energy performance improvement on the energy balance in the North-West of Algeria, *Energy and Buildings* 85 (2014) 374–388
- [5] Renewable Energy development Center (CDER) Algeria, <http://www.cder.dz>
- [6] Passivhaus Primer: Designer's Guide, a Guide for the Design Team and Local Authorities (2013) www.passivhaus.org.uk
- [7] Seyedeh zahra Mirrahimi and all, The effect of building envelope on the thermal comfort and energy saving for high-rise building sin hot-humid climate, *Renewable and Sustainable EnergyReviews*53 (2016)1508–1519
- [8] Niccolo Aste and all, The influence of the external walls thermal inertia on the energy performance of well insulated buildings, *Energy and Buildings* 41 (2009) 1181–1187
- [9] I. Mandilaras and all, Thermal performance of a building envelope incorporating ETICS with vacuum insulation panels and EPS, *Energy and Buildings* 85 (2014) 654–665
- [10] P. Daniela, and al., Impact of energy efficiency measures on the economic value of buildings, *Applied Energy* 89 (2012) 454–463.
- [11] Architectural solutions to increase the energy efficiency of buildings *Journal of Civil Engineering and Management*,18 (1) (2012), pp.71–80
- [12] Sabine Hoffmann, Balancing daylight, glare, and energy-efficiency goals: An evaluation of exterior coplanar shading systems using complex fenestration modeling tools, *Energy and Buildings* Volume 112, 15 January 2016, Pages 279–298
- [13] Iason Konstantzos Experimental and simulation analysis of daylight glare probability in offices with dynamic window shades, *Building and Environment* Volume 87, May 2015, Pages 244–254
- [14] Barbara Szybinska Matusiak, Glare from a translucent façade, evaluation with an experimental method, *Solar Energy*, Volume 97, November 2013, Pages 230–237
- [15] Ying-Chieh Chan and all, A systematic method for selecting roller shade properties for glare protection, *Energy and Buildings*, Volume 92, 1 April 2015, Pages 81–94
- [16] Zahedi A. Areview of drivers, benefits, and challenges in integrating renewable energy sources into electricity grid. *Renew Sust Energ Rev* 2011;15: 4775–9.
- [17] TRNSYS. TRNSYS 17 Reference Manual. Solar Energy Laboratory, University of Wisconsin-Madison; 2012
- [18] Ralegaonkar RV,Gupta R. Review of intelligent building construction: a passive solar architecture approach. *Renew Sustain Energy Rev* 2010 ;14 (8):2238–42.
- [19] Meral Ozel, Thermal performance and optimum insulation thickness of building walls with different structure materials, *Applied Thermal Engineering*, Volume 31, Issues 17–18, December 2011, Pages 3854–386, 3SET 2010 Special Issue
- [20] Sami A. Al-Sanea and all, Heat Transfer Characteristics and Optimum Insulation Thickness for Cavity Walls, *Journal of Thermal Envelope and Building Science* January 2003 26: 285-307
- [21]J. Jung and al. Local steady-state and quasi steady-state impact studies of high photovoltaic generation penetration in power distribution circuits. *RenewableandSustainableEnergyReviews*43(2015)569–583
- [22] United States Department of Energy. Sun Shotvision study. Report DOE/GO-102012- 3037. http://www1.eere.energy.gov/solar/sunshot/vision_study.html; 2012.
- [23] Thornton A,Monroy CR. Distributed power generation in the United States. *Renew Sust Energ Rev* 2011;15:4809–17.
- [24] Jochen Linssen and all Techno-economic analysis of photovoltaic battery systems and the influence of different consumer load profiles; *Applied Energy* xxx (2015)
- [25] Muiyiwa S. Adaramola Techno-economic analysis of a 2.1 kW rooftop photovoltaic-grid-tied system based on actual performance *Energy Conversion and Management* 101 (2015) 85–93

Energetic Systems

EXERGETIC ANALYSIS AND OPTIMIZATION REGIME OF TEMPERATURES FOR ABSORPTION CHILLER SINGLE STAGE H₂O-NH₃

Mohamed Izzedine Serge ADJIBADE ^{*a}, Kokouvi Edem N'TSOUKPOE^b, Ababacar THIAM ^a, Christophe AWANTO ^c, Dorothé AZILINON ^a

^a Laboratoire d'Energétique Appliquée (LEA), Ecole Supérieure Polytechnique, Université Cheikh Anta Diop (UCAD), BP 5085 Dakar-Fann, Sénégal

^b Laboratoire Energie Solaire et Economie d'Energie (LESEE), Institut International d'Ingénierie de l'Eau et de l'Environnement (2iE)

^c Laboratoire d'Energétique et de Mécanique Appliquée (LEMA), Ecole Polytechnique d'Abomey-Calavi, Université d'Abomey-Calavi (UAC)

*Corresponding author: Email: amihad007@yahoo.fr, mohamed.adjibade@ucad.edu.sn

ABSTRACT

Single stage absorption chillers using H₂O-NH₃ have received increasing research interest in recent years, in order to make them competitive with conventional refrigeration machines. This work presents a study on the performance of such tri-thermal machines, used for negative temperature refrigeration. The objective is to determine the values of the system operating temperatures that minimize the irreversible losses in the various heat exchangers. To do this, the overall exergy efficiency of the system has been expressed as a function of the various operating temperatures. This objective function is to be maximized. The results show that the cycle is more thermodynamically efficient when the absorption cooling system is operated at a low evaporation temperature (lower than 0 °C). Thus, the exergy efficiency is maximal and varies from 0.46 to 0.52 for an evaporation temperature ranging from 0 to -15 °C, the heat source temperature from 75 °C to 120 °C and condensation/absorption temperature around 30 °C.

KEYWORDS: absorption chiller; exergy; thermodynamic irreversibility; exergetic efficiency; water-ammonia.

NOMENCLATURE

h	specific enthalpy (kJ•kg ⁻¹)
I_r	irreversibility (kW)
\dot{m}	mass flow (kg•min ⁻¹)
P	pressure (kPa)
\dot{Q}	flow of heat exchanged (kW)
s	specific entropy (kJ•kg ⁻¹ •K ⁻¹)
\dot{S}	entropy generation (kW•K ⁻¹)
T	temperature (°C)
\dot{W}	power (kW)
X	ammonia mass fraction

Symbol

θ	Carnot coefficient
η	exergetic efficiency
ψ	specific exergy (kJ•kg ⁻¹)
$e_{x,D}$	exergy destroyed by the process (kJ•kg ⁻¹)

Subscripts

a	Reference
c	Condenser
e	intake cooling water or chilled water
g	heat source
p	ammonia-poor solution
r	ammonia-rich solution
s	outlet cooling water or chilled water
sys	system
o	evaporation

INTRODUCTION

Cold generation is mainly achieved by compression refrigeration machines, which require large energy consumption. In addition, these machines use, for their operation, refrigerants that deplete the ozone layer or contribute to a considerable extent to the increase in the greenhouse effect.

Many industries generate heat from fossil fuels for their processes. After use, this heat is released in to the environment as waste. Waste heat can be used to operate an absorption system for cold production [1].

Absorption chillers have several advantages compared to compression machines and appear as a promising alternative [2] for cold generation, with various advantages:

- use of thermal energy (thermal effluents, solar, biogas, etc.)
- use of environmentally friendly refrigerants
- low maintenance due to the absence or the presence of very few mechanical moving parts; therefore, they exhibit limited operating cost
- limited electricity consumption and hence, limited operating cost

The power consumption required to operate the pump of an absorption system, only electrical elements of the system, is less than 1 % of the cooling capacity, unlike the compression systems that require at least 20 to 50 % cooling capacity [3].

LITERATURE REVIEW

The performance of absorption chillers depends not only on the performance of various heat exchangers of the system but also on the thermodynamic and chemical properties of the used fluids. A number of researchers have used either COP, exergy efficiency or both to analyze absorption cooling systems. A particular attention is given to simple effect absorption cooling system [1, 4-11].

Zhi-Gao-Lin Nuo Sun and Xie [4] worked on an experimental study of the performance of a small combined cold and power (SCCP) for air conditioning system with micro gas turbine. A double-effect absorption refrigeration unit LiBr-H₂O is used in their work. A burner is installed in the double-effect absorption chiller, which is used to increase refrigerating capacity of the absorption chiller when air-conditioning needed more cooling load. The output temperature of chilled water and cooling water is respectively 7°C and 35 °C. Primary energy rate (PER) and comparative saving of primary energy (Δ_{SCCP}) demand are used to evaluate the performance of the system. PER and Δ_{SCCP} of the system are 0.867% and 12.3% with burner working, and 0.726% and 19.4% with no burner working, respectively.

Martinez and Pinazo [5] employed a statistical method in order to improve the initial design of a lithium bromide-water single effect absorption chiller. Experimental designs and variance analysis are used to measure the effects of the variation of the heat exchangers areas on the performance of an absorption machine. To this end, the inlet cooling water temperature, the chilled water and the hot water of the generator are maintained respectively at 29.4 °C, 11.5 °C and 82.2 °C. Thus, for a machine whose nominal COP equals 0.717, they obtained 0.786, representing an improvement of 9.6 %, without varying nominal capacity and total heat transfer area.

Lostec and al. [6] introduced the simulation of a single stage solar absorption chiller operating with an H₂O-NH₃ mixture under steady state conditions. This simulation is based on heat and mass balances for each component. A parametric study is conducted to investigate the effect of evaporator and desorber temperature on the absorption chiller's performance. The numerical model is compared and validated with experimental data obtained with a solar absorption chiller operating at an evaporation temperature of 16 °C, heat source temperature of 75 °C and inlet cooling water temperature of 24 °C. The COP decreases by 25 % with a decrease of 10 °C in evaporator temperature and the COP increases by 4 % with an increase of 10 °C in desorber temperature.

Adewusi and Zubair [7] made an entropy analysis of H₂O-NH₃ absorption chillers single-stage and two-stage in order to reduce the entropy generated. They computed some parameters such as the COP of the machine and the total entropy generated flow in the system. This study is performed with an evaporation temperature of -10 °C, condensation temperature of 40 °C, and heat source temperature of about 135 °C and 200 °C respectively for single and two stage systems. The two-stage system with a COP of 0.734 is more efficient than the single-stage system with a COP of 0.598. Moreover, the total entropy generated for the two-stage system is greater than that for the single stage system. The authors showed that the increase in total entropy generated two-stage level is due to the irreversibility in the desorber as it produces about 50 % of the total entropy generated in the system. To correct this, they advocated reducing the heat to the generator so as to have a better performance factor.

Bazzo et al. [8] worked on experimental study of combining a natural gas micro turbine, a heat recovery steam generator (HRSG) and an H₂O-NH₃ pair absorption chiller fired by steam. The system is tested under different turbine loads, steam pressures and chiller outlet temperatures. According to the first law of thermodynamics, at the ambient temperature of around 24 °C and micro turbine at full load, the plant is able to provide 19 kW of saturated steam at 5.3 bar (161 °C), corresponding to 9.2 kW of refrigeration at -5 °C (COP = 0.44). From a second law point-of-view, it is found that there is an optimal chiller outlet temperature that maximizes the chiller exergetic efficiency. They noted that the micro turbine presented the highest irreversibilities, followed by the absorption chiller and the HRSG. In order to reduce the plant exergy destruction, a new design is recommended for the HRSG. Nevertheless, the performance chiller operating in cogeneration is 25 % less than the nominal value of 0.59 for the direct firing system.

Aman and al. [9] conducted energy and exergy analyses to evaluate the performance of the H₂O-NH₃ absorption chiller for residential air conditioning application under steady state conditions. The system operates at an evaporation temperature of 2 °C, condensation temperature of 30 °C, and heat source temperature of 80 °C. One of the aims of their study is to maximize the exergetic efficiency of an absorption chiller with a low temperature driving source such as solar thermal energy. The analyses uncovered that the absorber is where the most exergy loss occurs (63 %) followed by the generator (13 %) and the condenser (11 %). Furthermore, the exergy losses of the condenser and absorber greatly increase with temperature, the generator less so, and the exergy loss in the evaporator is the least sensitive to increasing temperature. In order to improve cycle efficiency, the highest efforts should be given to improving the absorber while the generator may be considered as the second priority. This literature review shows that the second law approach is widely used in the analysis of absorption cooling machines. Second law approaches and exergy analysis are currently gaining increased attention because of the additional information they provide on the quality of the energy conversion processes. However, only relatively few works are available on exergy analysis of simple effect absorption using H₂O-NH₃ and operating with evaporation temperature below 0°C. To the authors' knowledge, no published work is available detailing the interaction between the

different internal temperatures of the absorption chiller to improve the exergetic efficiency.

During absorption chiller operation, four external temperatures can be defined which are: the heat source temperature, the cold source temperature, and the temperatures of the cooling mediums for the absorber and the condenser. To these four external temperatures, correspond four internal temperatures which are respectively, the desorber, evaporation, absorber and condensation temperatures. In this work, in order to improve the performance of a H₂O-NH₃ single stage absorption machine (Fig. 1), the exergetic efficiency, irreversibility in each heat exchanger is calculated. The simulation is run with Matlab. The problem to be solved can be summarized as follows: with the four external temperatures and fixed cooling capacity, what are the values of the established internal temperatures that minimize irreversible losses in heat exchangers? This is an optimization problem, where the exergetic efficiency is the objective function to be maximized; the independent variables are the four internal temperatures of the system.

ANALYSIS AND MODELLING

A simulation program, with Matlab, is developed for the assessment of thermodynamic performance of the single-stage absorption chiller. The mass, energy and exergy balances of each component are carried out by following the Fig. 1 model. The thermodynamic properties of H₂O-NH₃ are used to determine the physical parameters of each system point [1, 12-17]. The mass balance of the mixture, the refrigerant enthalpy and entropy components are obtained from the following equations:

- Mass balance of the mixture

$$\sum \dot{m}_{in} = \sum \dot{m}_{out} \quad (1)$$

- Mass Balance of the refrigerant

$$\sum \dot{m}_{in} X_{in} = \sum \dot{m}_{out} X_{out} \quad (2)$$

- Energy balance

$$\dot{Q} = \sum \dot{m}_{in} h_{in} - \sum \dot{m}_{out} h_{out} \quad (3)$$

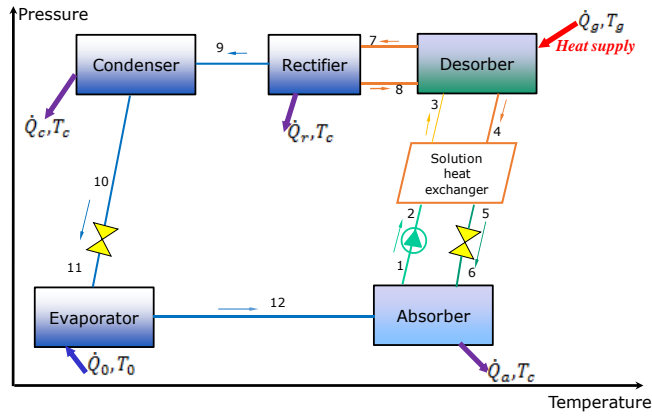


Figure 1. Absorption chiller single-stage

- Entropy balance

$$\dot{S} = \sum \dot{m}_{out} s_{out} - \sum \dot{m}_{in} s_{in} + \frac{\dot{Q}}{T}$$

where \dot{m} is the mass flow rate, h and s are the specific enthalpy and entropy respectively at temperature T and \dot{Q} is the heat transfer rate.

The COP is the ratio of the useful energy gained from the evaporator to the primary energy supply to the generator and mechanical work absorbed by the pump of the system.

$$COP = \frac{\dot{Q}_0}{\dot{Q}_g + \dot{W}} \quad (5)$$

The second law of thermodynamics can be expressed assuming reversible transformation as follows:

$$\frac{Q_0}{T_0} + \frac{Q_g}{T_g} + \frac{Q_c}{T_c} = 0 \quad (6)$$

From Eq. (6), one can express the ratio $\frac{\dot{Q}_0}{\dot{Q}_g}$ based on the temperatures involved in the system.

$$\frac{\dot{Q}_0}{\dot{Q}_g} = \frac{T_0}{T_g} \cdot \frac{T_g - T_c}{T_c - T_0} \quad (7)$$

- Exergetic balance

$$I_r = \sum (\dot{m}_{in} \psi_{in} - \dot{m}_{out} \psi_{out}) + \dot{Q} \left(1 - \frac{T_a}{T}\right) \quad (8)$$

where ψ the specific exergy and T_a environmental temperature. In this analysis, T_a is set to 298.15 K.

The exergy balance system gives us:

$$\dot{\theta}_g \cdot Q_g + \dot{\theta}_c \cdot Q_c + \dot{\theta}_0 \cdot Q_0 - e_{xD} + \dot{W} = 0 \quad (9)$$

with :

$$\theta_g = 1 - \frac{T_a}{T_g} \quad (10)$$

$$\theta_c = 1 - \frac{T_a}{T_c} \quad (11)$$

$$(12)$$

$$\theta_0 = 1 - \frac{T_a}{T_0}$$

\dot{W} is the pump power consumption and e_{xD} is the exergy destroyed by the process.

The maximum thermal performance of an absorption refrigeration system is determined by assuming that the entire cycle is totally reversible (i.e., the cycle involves no irreversibilities nor any heat transfer through a differential temperature difference) [8], it is possible to obtain:

$$COP_E = \left(1 - \frac{T_a}{T_g}\right) \left(\frac{T_0}{T_a - T_0}\right) \quad (13)$$

The second law efficiency of the absorption system leads to computing the exergetic efficiency, which is defined as the ratio of the useful exergy gained from a system to that supplied to the system [18]. The ratio between the two COP definitions in Eq. (5) and (13) is the exergetic efficiency of the machine, and gives an extent of the thermodynamic irreversibilities associated with the absorption cooling process:

$$ECOP = \frac{COP}{COP_E} \quad (14)$$

By using Eq. (5), (7) and (13), the exergetic efficiency of the system can be calculated as follows with \dot{W} negligible:

$$ECOP = \frac{|T_0 - T_a|}{T_g - T_a} \cdot \frac{T_g - T_c}{T_c - T_0} \quad (15)$$

In order to simulate the single effect absorption cooling system, several assumptions are made [13] :

- the analysis is made under steady conditions;
- the temperatures in components (desorber, condenser, evaporator and absorber) are uniform throughout the volume considered;
- the mixture at the outlet of the absorber and the desorber is in the saturated state. the coolant leaving the evaporator and the condenser is in the saturated state;
- the process through the pump is isenthalpic;
- the heat exchange with the environment surrounding and the pressure losses are assumed to be negligible;

RESULTS AND DISCUSSION

Fig. 2 shows that, for a given heat source temperature, the increase of the condensation temperature decreases the exergetic efficiency. Indeed, the increase of the condensation temperature leads to the increase of the temperature difference between the coolant and the refrigerant in the condenser. Thus for an evaporation temperature of 0 °C the exergetic efficiency is maximal for a condensation temperature below 33 °C.

The analysis of the curves Fig.3 shows that the reduction of evaporation temperature leads to the exergetic efficiency increase. This shows that H₂O-NH₃ pair is very favorable for very low evaporation temperatures. Decreasing the evaporation temperature causes an increase in the temperature of the heat source. For an evaporation temperature of 0 °C, the exergetic efficiency is maximal for a heat source temperature equal to 90 °C while the temperature increases to 105 °C for an evaporation temperature of -5 °C. In fact, the temperature of the heat source greatly varies depending on the refrigerating need. The heat demand increases with the need for cold.

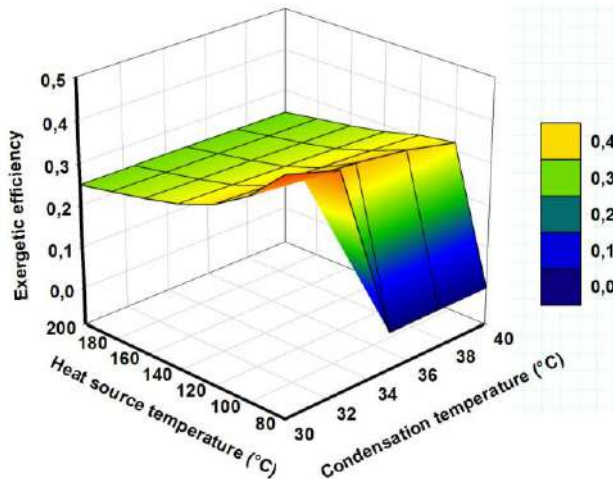


Fig.2. Exergetic efficiency depending on the heat source and condensation temperature for a fixed evaporation temperature T_0 : $T_0 = 0$ °C

According to those results, the temperature of the heat source varies depending on the refrigeration demand for maximum ECOP. It increases with the decrease of the evaporation temperature. Minimizing loss being our goal, it should be noted that increasing the temperature of the heat source more promotes the creation of entropy. So for evaporation temperatures of -10 °C and -15 °C, the system should work in heat source

temperatures respectively of 90 °C and 100 °C. This will reduce on the one hand the heat input to the desorber and on the other hand the heat extraction from the absorber.

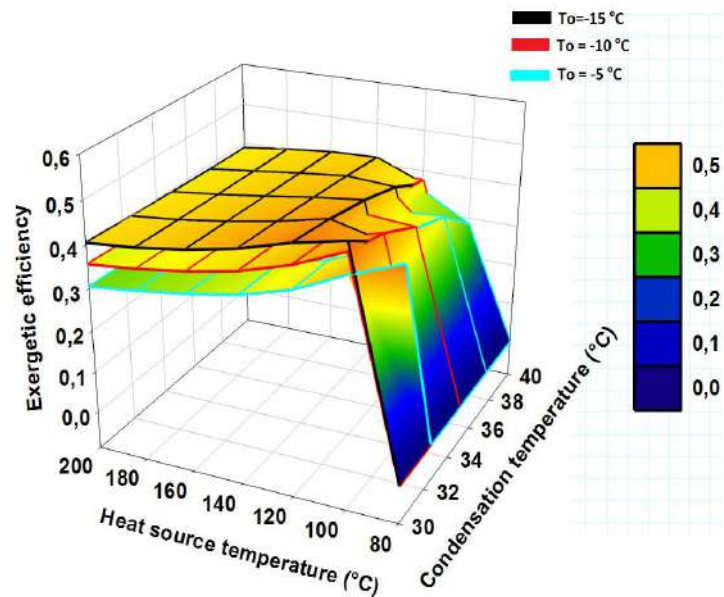


Fig.3. Comparison of exergetic efficiency depending on the heat source and condensation temperature with evaporation temperature variation

CONCLUSIONS

The second law efficiency of the system is investigated and compared under different system operating conditions. The results show that the exergetic efficiency of the system decreases with increasing absorption and condensation temperatures. Increasing the heat source temperature makes the exergetic efficiency reach a maximum before decreasing. The analysis reveals that the cycle is more thermodynamically efficient when the absorption cooling system is operated at a low evaporation temperature rather than a high evaporation temperature. Indeed, the exergy efficiency varies from 0.46 to 0.52 for an evaporation temperature ranging from 0 to -15 °C.

ACKNOWLEDGMENTS

We are grateful to the ICTP (The International Centre for Theoretical Physics) and ANSOLE (African Network for Solar Energy) for financial support in the frame of the ANSOLE SUR-PLACE Fellowship Program (ANSUP)

REFERENCES

1. G. Gershon, E. Michelson, Absorption Heat Pump Simulation and Studies: A Modular Computer

- Simulation of Absorption Systems, 1986. [cited May 16, 2015], http://btrc.ornl.gov/eere_research_reports/thermally_activated_technologies/absorption/modeling_and_simulation/ornl_sub_83_43337_2/ornl_sub_83_43337_2.pdf.
2. K.E. N'Tsoukpoe, D. Yamegueu, J. Bassole, Solar sorption refrigeration in Africa, *Renewable and Sustainable Energy Reviews* 35 (2014) 318–335.
 3. J. M. Gordon, K. C. Ng, A general thermodynamic model for absorption chillers: Theory and experiment, *Heat Recovery Systems and CHP* 15 (1995) 73–83.
 4. Z.-G. Sun N.L. Xie, Experimental studying of a small combined cold and power system driven by a micro gas turbine, *Applied Thermal Engineering* 30 (2010) 1242–1246.
 5. P.J. Martínez, J.M. Pinazo, A method for design analysis of absorption machines, *International Journal of Refrigeration* 25 (2002) 634–639.
 6. B. Le Lostec, N. Galanis, J. Millette, Simulation of an ammonia–water absorption chiller, *Renewable Energy* 60 (2013) 269–283.
 7. S.A. Adewusi, S.M. Zubair, Second law based thermodynamic analysis of ammonia–water absorption systems, *Energy Conversion and Management* 45 (2004) 2355–2369.
 8. E. Bazzo, A. Nacif de Carvalho, J.A. Matelli, Experimental results and thermodynamic analysis of a natural gas small scale cogeneration plant for power and refrigeration purposes, *Applied Thermal Engineering* 58 (2013) 264–272.
 9. J. Aman, D.S.K. Ting, P. Henshaw, Residential solar air conditioning: Energy and exergy analyses of an ammonia–water absorption cooling system, *Applied Thermal Engineering* 62 (2014) 424–432.
 10. R. Gomri, Investigation of the potential of application of single effect and multiple effect absorption cooling systems, *Energy Conversion and Management* 51 (2010) 1629–1636.
 11. S. Gong, K. Goni Boulama, Parametric study of an absorption refrigeration machine using advanced exergy analysis, *Energy* 76 (2014) 453–467.
 12. J.K. Pátek, Simple functions for fast calculations of selected thermodynamic properties of the ammonia-water system, *International Journal of Refrigeration* 18 (1995) 228–234.
 13. Ashrae Handbook, ASHRAE HVAC 2001, Fundamentals Handbook, 2001.
 14. G. Soleimani Alamdari, Simple functions for predicting thermodynamic properties of ammonia-water mixture, *International Journal of Engineering transaction* 20 (2007) 94-104.
 15. M. Conde Engineering, Thermophysical properties of H₂O-NH₃ solutions for the industrial design of absorption refrigeration equipment, 2004. [cited June 15, 2015] Available from <http://www.mrc-eng.com/Downloads/NH3&H2O%20%20Props%20English.pdf>.
 16. L. Zhu, J. Gu, Thermodynamic analysis of a novel thermal driven refrigeration system, *World Academy of Science, Engineering and Technology* 3 (2009) 330–334.
 17. C. A. Infante Ferreira, Thermodynamic and physical property data equations for ammonia-lithium nitrate and ammonia-sodium thiocyanate solutions, *Solar Energy* 32 (1984) 231-236.
 18. N.B. Ezzine, M. Barhoumi, K. Mejbri, S. Chemkhi, A. Bellagi, Solar cooling with the absorption principle: first and Second Law analysis of an ammonia-water double-generator absorption chiller, *Desalination* 168 (2004) 137–144.

PERFORMANCE IMPROVEMENT OF COMBINED ORGANIC RANKINE-VAPOR COMPRESSION CYCLE USING A SERIAL CASCADE EVAPORATION IN THE ORGANIC CYCLE

Oumayma Bounefour, Ahmed Ouadha*

Laboratoire des Sciences et Ingénierie Maritimes, Faculté de Génie Mécanique, Université des Sciences et de la Technologie Mohamed BOUDIAF d'Oran, Oran El-Mnouar, 31000 Oran, Algérie

*Corresponding author: Fax: + 213 4129 0466 Email: ah_ouadha@yahoo.fr

ABSTRACT

This paper describes an improvement solution for ORC-VCC systems. The solution consists in using cascade evaporation in the ORC subsystem in order to increase its power on the expander shaft. The heat source is divided into high temperature and low temperature ranges, a solution allowing the utilization of all kinds of heat sources (engine exhaust gas, jacket water and charge air) which are at different temperature levels. The paper also discusses performance of hydrocarbon refrigerants in such systems. The performance of the system using a cascade evaporation in the ORC subsystem are compared to those using a basic ORC subsystem.

INTRODUCTION

Over 90% of global trade is carried by sea, making the shipping industry as a key component of the world economy. Like the others transport modes, ships are powered using fossil fuels whose combustion produces greenhouse gases and others harmful pollutants such as nitrogen oxides (NO_x) and sulfur oxides (SO_x). It is recognized that fuel expenses account between 30 and 55 % of the total operational costs for large vessels [1]. Fuel is mainly consumed to generate the necessary power for propulsion and to produce electricity needs. Although that significant gain in the efficiency of propulsion engines has been achieved over the years, there is a little potential for further improvements. Recently, heat recovery concepts have attracted much interest from ship owners interested in emissions and ship operating costs reduction. Traditionally, high-temperature waste heat from main Diesel propulsion engines is utilized in an exhaust gas economizer and a steam turbine generation system. However, low-temperature heat such as engine jacket water has been rarely used. A path of increase of the overall efficiency of ship can be the heat recovery using technical solutions able to exploit low-temperature waste heat from Diesel engines. Among these solutions, the organic Rankine solution is probably the most reliable and mature technology. It is widely implemented in several fields including the geothermal energy, the solar energy, the biomass combustion and the heat recovery from industrial processes.

Many recent studies have focused on the subject of applying of ORC technology to exploit low-grade waste heat from marine Diesel engines [2-10]. All these studies have applied ORC systems to produce additional mechanical energy or to drive electric generator. Alternatively the waste heat from the Diesel engine can be used to operate an organic Rankine cycle (ORC), which in turn produces the energy necessary to drive the compressor of a vapor compression cycle (VCC). The VCC unit can produce refrigeration effect at different temperatures. The advantage of a combined ORC-VCC system compared to absorption refrigeration systems is that when refrigeration is not needed, all the thermal energy can be converted to power and used for others applications. Although that thermally driven refrigeration cycles that combine organic Rankine cycle and vapor compression refrigeration cycle have been studied for several applications [11-22], their use in marine applications has received less attention [23]. This paper aims to verify thermodynamically the improvement of the performance of a combined ORC-VCC system in order to explore the feasibility of such system in marine applications. It is the first step to start a preliminary design of the proposed system. It serves also as an initial screening of some promising hydrocarbon refrigerants, namely propane (R290), butane (R600), isobutane (R600a) and propylene (R1270) in ORC-VCC systems in order to investigate the thermodynamic performance that can be attained using these substances.

ENGINE ENERGY BALANCE

An energy balance can be used to identify the heat sources from a marine Diesel engine such as exhaust gases, cooling water or engine oil. It is interesting to mention that these heat sources present different level of quality and quantity. While exhaust gases produce large amount of energy at high temperatures (up to 400°C), the other sources produce less energy with lower temperatures. There is no doubt that recovering these heat sources yields to higher fuel savings. However, linking these systems with marine Diesel engines is a challenging task for the design of their components.

Figure 1 shows an example of an energy balance of a modern marine Diesel engine. The heat transferred to coolants includes charge air cooling (17.8%), jacket water cooling (4.8%) and lubricating oil cooling (3.2%). In addition, 25.1% of the total energy is lost, released into the atmosphere during the exhaust outlet. Finally, a small part of the energy (0.6%) is released by radiation. At first glance, the analysis of heat flows shows that there are three engine waste heat streams, at different temperature levels, that have potential to be recovered: exhaust gas (300-600°C); charge air (200°C); jacket water (80-100°C).

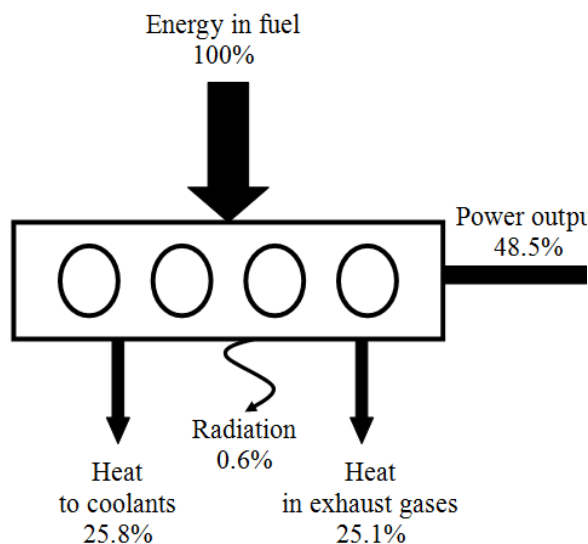


Figure 1

Typical heat balance of a marine Diesel engine.

WORKING FLUIDS SELECTION

The main advantage of ORC systems is simplicity due to limited number of components, in addition to their ability to use a large variety of working fluids. Several fluids have been used in ORC systems as reported in the review papers by Bao and Zhao [24] and Juhasz and Simoni [25].

During the CFCs and HCFCs phase out periods, natural refrigerants such as ammonia, carbon dioxide and some hydrocarbons have been reintroduced as a sustainable solution for refrigeration systems. Abandoned in the 30th in favor of more competitive refrigerants at that time, these substances are, nowadays, the most realistic solution which associates high performance, economy and environment protection.

In the present study, some hydrocarbons, namely propane (R290), butane (R600), isobutane (R600a) and propylene (R1270) are selected as the working fluids for the ORC-VCC system to be studied. Some common properties of the selected fluids are summarised in Table 1. Refrigerants used here are fully friendly environment fluids. They are natural and have not undesirable effects on environment. However, although that R134a presents a high global warming potential, it has been kept as reference fluid due its large application nowadays.

Working fluids for organic Rankine cycles can be classified according to the slope of the saturated vapor line in a $T-s$ diagram into wet, isentropic or dry fluids. Figure 2 indicates that wet fluids have high critical temperatures and large latent heat compared to dry fluids. A large latent heat involves smaller mass flow rates. However, dry fluids which are characterized by a positively sloped saturation curve in the $T-s$ diagram have better thermal performance because the fluid does not condense after its expansion in the expander unlike wet fluids which partially condense after their expansion. For wet working fluids, it is important to make sure that the vapor at the expander exit is dry to prevent the expander from liquid-hit. Control of the vaporization pressure of the ORC cycle can avoid the above issue.

Table 1

Thermophysical, security and environmental properties of the selected working fluids

Substance	Thermophysical data					Security group	Environmental properties	
	Type	M (g/mol)	T_b (°C)	T_c (°C)	p_c (bar)		ODP	GWP
R134a	i	102.0	-26.1	101.1	40.6	A1	0	1430
R290	w	44.1	-42.1	96.7	42.5	A3	0	-20
R600	d	58.1	-0.5	152.0	38.0	A3	0	-20
R600a	d	58.1	-11.7	134.7	36.3	A3	0	-20

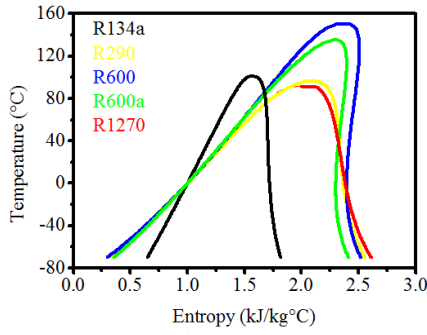


Figure 2

T-s saturated curves comparison of the working fluids.

Thermodynamic properties including enthalpy and entropy at different states have been obtained using a set of equations of state. The computational model adopted in this study is based on four local equations of state presented below [23]:

- an equation of state for the gas state,

$$Z = Z(T, \rho) \quad (2)$$

- a correlation for the saturated vapor pressure,

$$p_s = p_s(T) \quad (3)$$

- a correlation for the saturated liquid density,

$$\rho_L = \rho_L(T) \quad (4)$$

- an equation of the specific heat capacity at constant pressure in the ideal gas state.

$$c_p^0 = c_p^0(T) \quad (5)$$

Using the above equations and the differential equations of thermodynamics [26], it is possible to calculate the other essential thermodynamic functions necessary for the thermodynamic analysis, namely, the enthalpy, the entropy and the exergy.

THERMODYNAMIC ANALYSIS

Figure 3 shows combined ORC-VCC systems mounted on a marine Diesel engine. The system is linked to the engine heat source using the boiler of the ORC sub system. Vapors formed are expanded in the expander producing mechanical work on its shaft to drive the compressor of the vapor compression sub system. A condenser is used to condense the working fluid after expansion. The liquid obtained is pumped to the boiler to absorb heat from the engine jacket water and repeat a new cycle. The two subsystems are linked by coupling the expander of the ORC subsystem to the compressor of the VCC subsystem. The first system is referred to as ORC-VCC (basic system) while the second one is referred to as SCORC-VCC (serial cascade system).

Habitually, thermodynamic cycles are analyzed using the energy analysis method which is based on the first law of thermodynamics, i.e. the energy conservation concept. Unfortunately, this method cannot locate the degradation of the quality of energy. Instead, exergy analysis which is based on both the first and second laws of thermodynamics can overcome easily the limitations of the energy analysis. It permits to quantify the magnitude and the location of exergy losses within the system. Furthermore, the total exergy losses can be considered as an optimization criteria which, by minimization, provide optimum processes configuration. The concept and the methodology of exergy analysis are well-documented in the literature [27-29]. Bosnjakovic [30] has defined exergy as the theoretically gainful amount of work obtained by bringing materials into equilibrium with the surroundings in a reversible process. The surroundings can be defined in terms of temperature, pressure and chemical composition.

Combined systems, displayed in Figure 3, have been modeled using the common simplifying assumptions listed below:

- all processes are marked by steady state and steady flow,
- kinetic and potential energy have negligible effects,
- heat and friction losses are neglected,
- the working fluid leaving the condenser and the evaporator is saturated,
- the temperature and pressure of the environment are 25°C and 1 atm, respectively.

Mass, energy and exergy balances for any control volume at steady state with negligible kinetic, potential and chemical energy changes can be expressed, respectively, by

$$\sum \dot{m}_in = \sum \dot{m}_out \quad (6)$$

$$\dot{Q} + \dot{W} = \sum \dot{m}_out h_{out} - \sum \dot{m}_in h_{in} \quad (7)$$

$$\dot{E}x_{heat} + \dot{W} = \sum \dot{E}x_{out} - \sum \dot{E}x_{in} + \Delta \dot{E}x \quad (8)$$

where subscriptions *in* and *out* denote inlet and outlet states, \dot{Q} and \dot{W} the net heat and work inputs, \dot{m} the mass flow rate, h the enthalpy, $\dot{E}x$ the rate of exergy and $\Delta \dot{E}x$ is the rate of exergy losses.

The rate of exergy transfer by heat, $\dot{E}x_{heat}$, at a temperature T , is given by

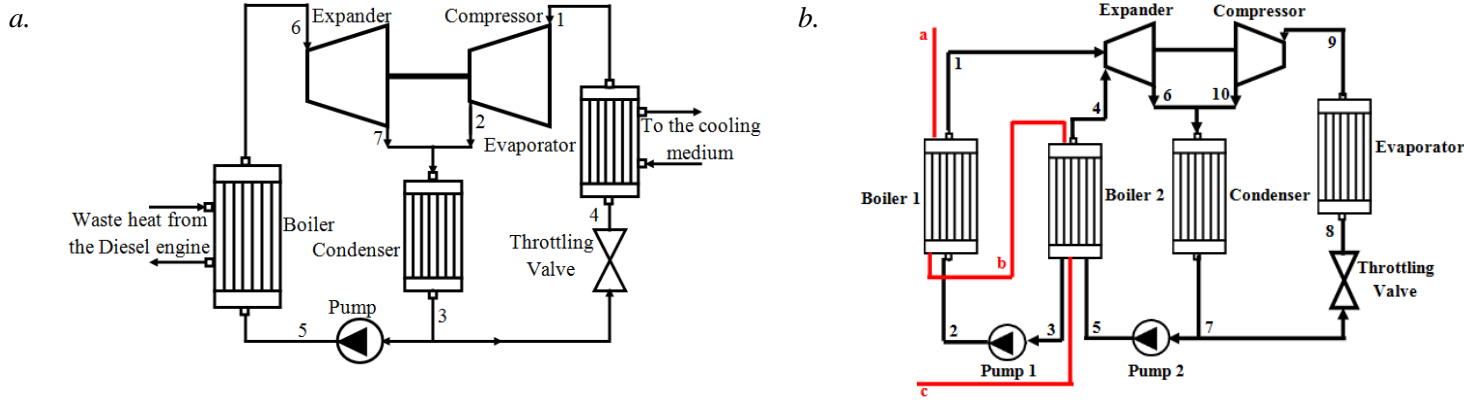


Figure 3

Schematic of the combined organic Rankine cycle - vapor compression cycle: *a.* ORC-VCC; *b.* SCORC-VCC.

$$\dot{E}x_{heat} = \left(1 - \frac{T_0}{T}\right) \dot{Q}$$

(9)

The rate of exergy, $\dot{E}x$, is given by

$$\dot{E}x = \dot{m} \cdot ex$$

(10)

Table 2
Energy and exergy balances equations

	Component	Energy balance	Exergy balance
ORC	Pump	$\dot{W}_{pump} = \dot{m}_{ORC} (h_5 - h_3)$	$\Delta \dot{E}x_{pump} = \dot{E}x_3 - \dot{E}x_5 + \dot{W}_{pump}$
	Boiler	$\dot{Q}_{boil} = \dot{m}_{ORC} (h_6 - h_5)$	$\Delta \dot{E}x_{boil} = \dot{E}x_5 - \dot{E}x_6 + \dot{Q}_{boil} (1 - T_0/T_{boil}^*)$
	Expander	$\dot{W}_{exp} = \dot{m}_{ORC} (h_6 - h_7)$	$\Delta \dot{E}x_{tur} = \dot{E}x_6 - \dot{E}x_7 - \dot{W}_{exp}$
	Condenser	$\dot{Q}_{cond} = \dot{m}_{ORC} (h_7 - h_3)$	$\Delta \dot{E}x_{cond} = \dot{E}x_7 + \dot{E}x_2 - \dot{E}x_3 - (h_3 - h_7 - h_2)/T_{cond}^*$
SCORC	Pump 1	$\dot{W}_{pump1} = \dot{m}_{ORC1} (h_2 - h_3)$	$\Delta \dot{E}x_{pump1} = \dot{E}x_3 - \dot{E}x_2 + \dot{W}_{pump1}$
	Pump 2	$\dot{W}_{pump2} = (\dot{m}_{ORC1} + \dot{m}_{ORC2})(h_5 - h_7)$	$\Delta \dot{E}x_{pump2} = \dot{E}x_7 - \dot{E}x_5 + \dot{W}_{pump2}$
	Boiler 1	$\dot{Q}_{boil1} = \dot{m}_{ORC1} (h_1 - h_2)$	$\Delta \dot{E}x_{boil1} = \dot{E}x_2 - \dot{E}x_1 + \dot{Q}_{boil1} (1 - T_0/T_{boil1}^*)$
	Boiler 2	$\dot{Q}_{boil2} = \dot{m}_{ORC1} (h_3 - h_5) + \dot{m}_{ORC2} (h_4 - h_5)$	$\Delta \dot{E}x_{boil2} = \dot{E}x_5 - \dot{E}x_4 + \dot{Q}_{boil2} (1 - T_0/T_{boil2}^*)$
	Expander	$\dot{W}_{exp} = \dot{m}_{ORC1} (h_1 - h_6) + \dot{m}_{ORC2} (h_4 - h_6)$	$\Delta \dot{E}x_{exp} = \dot{E}x_4 + \dot{E}x_1 - \dot{E}x_6 - \dot{W}_{exp}$
Condenser	$\dot{Q}_{cond} = (\dot{m}_{ORC1} + \dot{m}_{ORC2})(h_6 - h_7)$	$\Delta \dot{E}x_{cond} = \dot{E}x_6 + \dot{E}x_{10} - \dot{E}x_7 - (h_7 - h_6 - h_{10})/T_{cond}^*$	
VCC (a)	Evaporator	$\dot{Q}_{evap} = \dot{m}_{VCC} (h_1 - h_4)$	$\Delta \dot{E}x_{evap} = \dot{E}x_4 - \dot{E}x_1 + \dot{Q}_{evap} (1 - T_0/T_{evap}^*)$
	Compressor	$\dot{W}_{comp} = \dot{m}_{VCC} (h_2 - h_1)$	$\Delta \dot{E}x_{comp} = \dot{E}x_1 - \dot{E}x_2 + \dot{W}_{comp}$
	Throttling valve	$h_3 = h_4$	$\Delta \dot{E}x_{throt} = \dot{E}x_3 - \dot{E}x_4$
	Cycle ORC_VCC	$COP = \left[\frac{\dot{W}_{tur} - \dot{W}_{pump}}{\dot{Q}_{boil}} \right] \left[\frac{\dot{Q}_{evap}}{\dot{W}_{comp}} \right]$	$\eta_{ex} = 1 - \Delta \dot{E}x_{tot ORC_VCC} / \dot{E}x_{in}$
		η_{ORC}	COP_{VCC}

$$\text{Cycle}_{\text{SCORC_VCC}} \quad COP = \underbrace{\left[\frac{\dot{W}_{\text{exp}} - \dot{W}_{\text{pump1}} - \dot{W}_{\text{pump2}}}{\dot{Q}_{\text{boil1}} + \dot{Q}_{\text{boil2}}} \right]}_{\eta_{\text{SCORC}}} \underbrace{\left[\frac{\dot{Q}_{\text{evap}}}{\dot{W}_{\text{comp}}} \right]}_{COP_{\text{VCC}}} \quad \eta_{\text{ex}} = 1 - \frac{\Delta \dot{E}x_{\text{totSCORC_VCC}}}{\dot{E}x_{\text{in}}}$$

where, ex is the specific exergy defined as

$$ex = h - h_0 - T_0 (s - s_0)$$

(11)

The subscript 0 is related to the reference state.

From a second law point of view, it is important to quantify the exergy losses in each component in order to assess the overall performance of the system. Mass, energy and exergy balance equations are applied to each component of the system. The mathematical model for both ORC and VCC subsystems is given by the equations summarized in Table 2.

The exergy supplied to the system, $\dot{E}x_{\text{boil}}$, and the total exergy losses, $\Delta \dot{E}x_{\text{tot}}$, can be expressed as

$$\dot{E}x_{\text{boil}} = \dot{Q}_{\text{boil}} \left(1 - T_0 / T_{\text{boil}}^* \right)$$

(12)

$$\Delta \dot{E}x_{\text{totORC_VCC}} = \Delta \dot{E}x_{\text{pump}} + \Delta \dot{E}x_{\text{boil}} + \Delta \dot{E}x_{\text{exp}} + \Delta \dot{E}x_{\text{cond}} + \Delta \dot{E}x_{\text{evap}} + \Delta \dot{E}x_{\text{comp}} + \Delta \dot{E}x_{\text{throt}}$$

$$\Delta \dot{E}x_{\text{totSCORC_VCC}} = \Delta \dot{E}x_{\text{pump1}} + \Delta \dot{E}x_{\text{pump2}} + \Delta \dot{E}x_{\text{boil1}} + \Delta \dot{E}x_{\text{boil2}} + \Delta \dot{E}x_{\text{exp}} + \Delta \dot{E}x_{\text{cond}} + \Delta \dot{E}x_{\text{evap}} + \Delta \dot{E}x_{\text{comp}} + \Delta \dot{E}x_{\text{throt}}$$

(13)

T_{boil}^* , T_{evap}^* , T_{cond}^* are the heat source mean temperature in the boiler, evaporator and condenser respectively.

The exergy inlet to the system can be expressed as

$$\begin{cases} \dot{E}x_{\text{inORC_VCC}} = \dot{E}x_{\text{boil}} + \dot{E}x_{\text{evap}} \\ \dot{E}x_{\text{inSCORC_VCC}} = \dot{E}x_{\text{boil1}} + \dot{E}x_{\text{boil2}} + \dot{E}x_{\text{evap}} \end{cases}$$

(14)

RESULTS AND DISCUSSION

Simulation results have been obtained based on 1.46 kg/s hot fluid mass flow rate in the boiler. The boiler exit temperatures range from 60 to 90, which corresponds to heat source temperatures ranging from 70 to 100°C. The hydrocarbon fluids critical temperatures which are larger than 90°C allow the use of subcritical cycles for both power and refrigeration subsystems. Generally, the isentropic efficiency of a turbine ranges from 80 to 90% whereas the isentropic efficiency of compressor ranges from 70 to 90%.

Table 3

Design and operating parameters of the system

Hot fluid mass flow rate, kg/s	1.46
Evaporation temperature, °C	5
Boiler exit temperature, °C	60–90
Condensation temperature, °C	35
Expander isentropic efficiency, %	75
Compressor isentropic efficiency, %	80
Pump isentropic efficiency, %	60

In absence of relevant suitable model to validate such configuration of the whole combined system, the validation has been conducted for both the two subsystems separately. Thus, the accuracy of simulation results have been checked by comparing calculated values using the developed code to values obtained using the free code SOLKANE. Computations have been carried out according to the parameters listed in Table 4. Compression and expansion processes are assumed isentropic.

Table 4

Validation case operating parameters

Fluid	R134a
Mass flow rate in ORC, kg/s	1
Boiler temperature, °C	90
Condenser temperature, °C	30
Evaporation temperature, °C	-10
Refrigeration effect, kW	1

Table 5 presents comparisons between the two codes. It is clear that the model proposed is reliable in predicting the performance of both systems. The relative error for all parameters considered remains below 2.7%. In addition, the program developed has the advantage to be used more flexibly in order to determine the cycle performance for different operating conditions.

Table 5

Validation case results

	Parameter	Model	Solkane	δ (%)
ORC	Pump power, kW	1.4	1.4	0
	Turbine power, kW	12.7	12.7	0
	Mass flow rate, g/s	505.9	512.0	-1.2
	Thermal efficiency, %	11.3	11.0	2.7
VCC	Compressor power, kW	0.19	0.19	0
	Pressure ratio	3.83	3.84	-0.26

Mass flow rate, g/s	6.623	6.633	-0.15
COP	5.40	5.40	0

Figure 4 illustrates the effect of using cascade evaporation on the power produced on the shaft of the ORC expander. Obviously, the SCORC-VCC system produces more power compared to the ORC-VCC system. For both, R600 is the more suitable working fluid. However, the elevation of the boiler exit temperature is not always advantageous.

Results based on energy analysis, in terms of refrigerating effect and COP, the standard criterions of performance analysis of a refrigeration cycles, are plotted versus the boiler exit temperature in Figure 5.

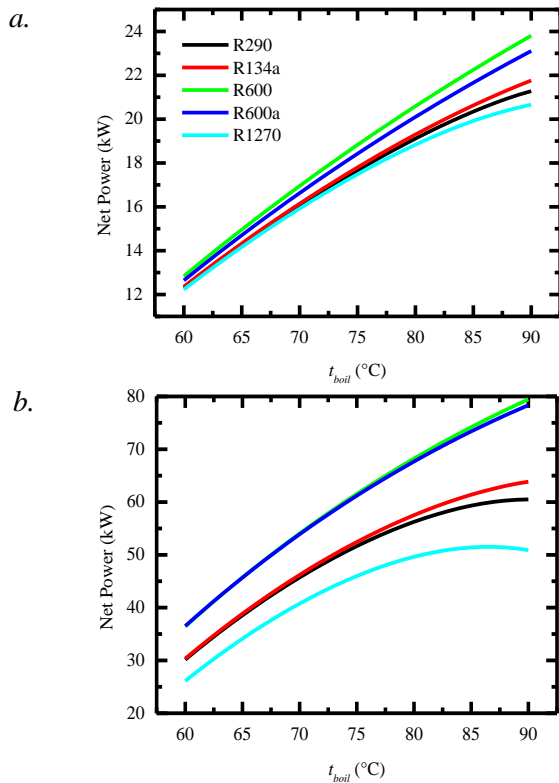


Figure 4

Net Power as function of the boiler exit temperature: *a.* ORC-VCC; *b.* SCORC-VCC.

Whatever the refrigerant used, the increase of the boiler exit temperature enhances the performance of the system. As expected, butane and isobutane give better refrigerating effect than R134a. However, propane and propylene give comparable results to R134a. Butane is the best refrigerant considering the COP. Although that the performance of the ORC subsystem are improved using the serial cascade, the

performance of the whole system are comparable for both cases under the conditions considered.

Figure 6 depicts the effect of the boiler exit temperature on the exergetic efficiency for both systems. The ORC-VCC system produce comparable exergetic efficiencies of all refrigerants mainly for boiler exit temperatures lower than 70°C. They range from 15 to 21%. However, for the SCORC-VCC system, the difference between refrigerants is clear. From an exergy point of view, R600 and R600a still the best.

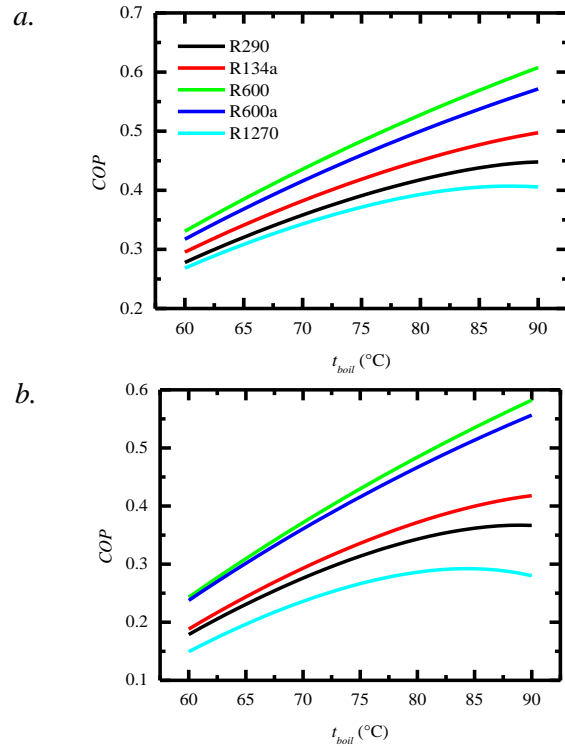
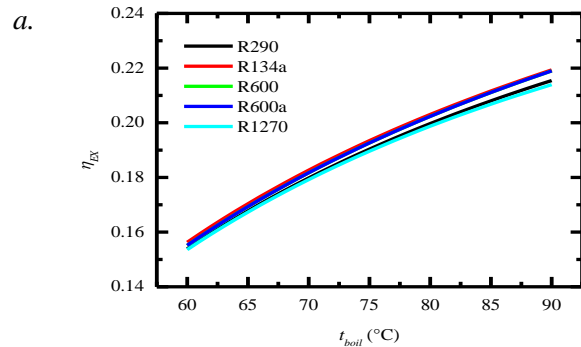


Figure 5

COP as function of the boiler exit temperature: *a.* ORC-VCC; *b.* SCORC-VCC.



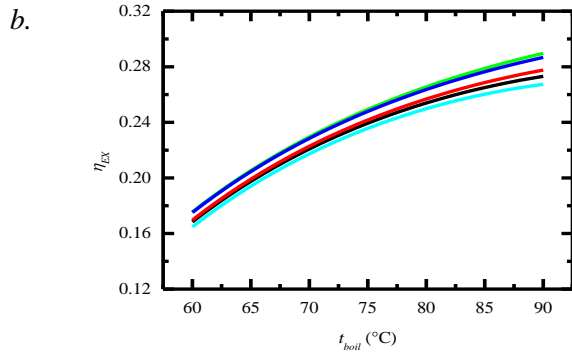


Figure 6

Exergetic efficiency as function of the boiler exit temperature: *a.* ORC-VCC; *b.* SCORC-VCC.

Figure 7 illustrates the percentage of the exergy destroyed in each component with respect to the total system exergy loss for each refrigerant. For all refrigerants, the highest exergy losses occur in the boiler (58-75%) followed by the evaporator (6.5-27%), the expander (2.5-11%) and the condenser (4.1-8.8%). Exergy losses in the compressor, the

throttling valve and the pump are negligible comparatively to the above exergy losses.

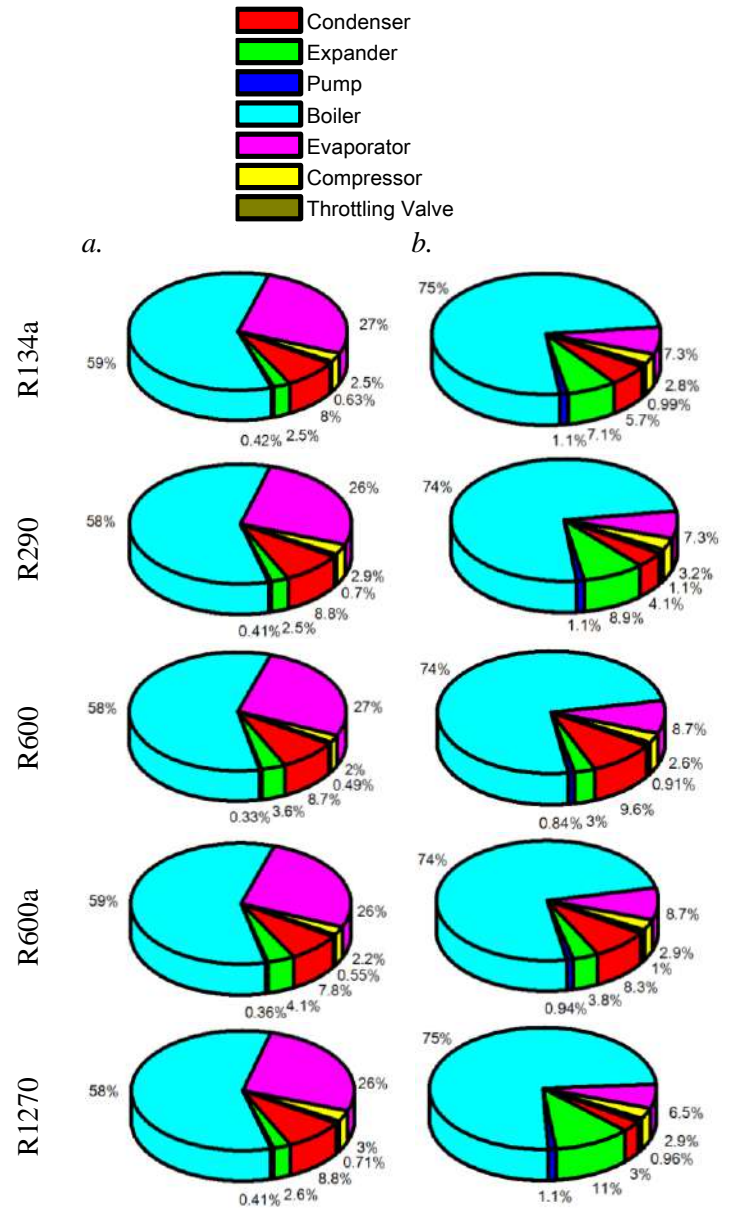


Figure 7

Exergy losses distribution in the system for $t_{boil} = 60^{\circ}\text{C}$; $t_{cond} = 35^{\circ}\text{C}$; $t_{evap} = 5^{\circ}\text{C}$: *a.* ORC-VCC; *b.* SCORC-VCC.

CONCLUSIONS

This paper includes a comprehensive thermodynamic analysis of a vapor compression refrigeration system driven by an organic Rankine Cycle. The later uses waste heat from a marine Diesel engine to produce the power that drives the compressor of the refrigeration system. Commonly operating data have been used to quantify exergy losses in each component of the system and the overall

performances of the system at a reference temperature of 25°C have been determined. Results

show that isobutane and butane yield excellent performance compared to R134a.

REFERENCES

1. Kalli, J., Karvonen, T., Makkonen, T., 2009, Sulphur content in ships bunker fuel in 2015, Technical Report, Helsinki, Finland: Ministry of Transport and communications.
2. Jin, J., Lee, H., Park, G. et al., 2012, Thermodynamic Analysis of the Organic Rankine Cycle as a Waste Heat Recovery System of Marine Diesel Engine, Transactions of the Korean Society of Mechanical Engineers B, **36**, no. 7: pp. 711-719.
3. Yu, G., Shu, G., Tian, H. et al., 2013, Simulation and Thermodynamic Analysis of a Bottoming Organic Rankine Cycle (ORC) of Diesel Engine (DE), Energy, **51**, pp. 281-290.
4. Kalikatzarakis, M., Frangopoulos, C.A., 2014, Multi-criteria selection and thermo-economic optimization of an organic Rankine cycle system for a marine application, In: Proceedings of the 27th International Conference on Efficiency, Cost, Optimization, Simulation, and Environmental Impact of Energy Systems (ECOS), Turku, Finland.
5. Yang, M., Yeh, R., 2015, Thermo-economic Optimization of an Organic Rankine Cycle System for Large Marine Diesel Waste Heat Recovery, Energy, **82**, pp. 256-268.
6. Song, J., Song Y., Gu, C., 2015, Thermodynamic Analysis and Performance Optimization of an Organic Rankine Cycle (ORC) Water Heat Recovery System for Marine Diesel Engines, Energy, **82**, pp. 976-985.
7. Soffiato, M., Frangopoulos, C. A., Manente, G. et al., 2015, Design Optimization of ORC Systems for Waste Heat Recovery onboard an LNG Carrier, Energy Conversion and Management, **92**, pp. 523-534.
8. Sung, T., You, S., Kim, K.C., 2015, A dual loop organic Rankine cycle utilizing boil-off gas in LNG tanks and exhaust of marine engine, 3rd International Seminar on ORC Power Systems, Brussels, Belgium.
9. Yuksek, E.L., Mirmobin, P., 2015, Waste heat utilization of main propulsion engine jacket Water in marine application, 3rd International Seminar on ORC Power Systems, Brussels, Belgium.

10. Baldi, F., Larsen, U., Gabrielli, C., 2015, Comparison of different procedures for the optimisation of a combined Diesel engine and organic Rankine cycle system based on ship operational profile, *Ocean Engineering*, **110**, Part B, pp. 85-93.
11. Wiley.Nazer, M.O., Zubair, S.M., 1982, Analysis of Rankine cycle air-conditioning systems, *ASHRAE J.*, **88**, pp. 332–334.
12. Egrican, A.N., Karakas, A., 1986, Second law analysis of a solar powered Rankine cycle/vapor compression cycle, *J. Heat Recovery Systems*, **6**, pp. 135–141.
13. Kaushik, S.C., Dubey, A., Singh, M., 1994, Thermal modelling and energy conservation studies on freon rankine cycle cooling system with regenerative heat exchanger, *Heat Recovery Systems & CHP*, **14**, pp. 67–77.
14. Kaushik, S.C., Singh, M., Dubey, A., 1994, Thermodynamic modelling of single/dual organic fluid Rankine cycle cooling systems: A comparative study, *Int. J. Ambient Energy*, **15**, pp. 37–50.
15. Jeong, J., Kang, Y.T., 2004, Analysis of a refrigeration cycle driven by refrigerant steam turbine, *Int. J. Refrig.*, **27**, pp. 33–41.
16. Dubey, M., Rajput, S.P.S., Nag, P.K., Misra, R.D., 2010, Energy analysis of a coupled power – refrigeration cycle, *Proceedings of the Institution of Mechanical Engineers Part A: J. Power Energy*, **224**, PP. 749–759.
17. Aphornratana, S., Sriveerakul, T., 2010, Analysis of a combined Rankine–vapour–compression refrigeration cycle, *Energy Conversion Management*, **51**, pp. 2557-2564.
18. Wang, H., Peterson, R., Herron, T., 2011, Design study of configurations on system COP for a combined ORC (organic Rankine cycle) and VCC (vapor compression cycle), *Energy*, **36**, pp. 4809-4820.
19. Wang, H., Peterson, R., Harada, K., Miller, E., Ingram-Goble, R., Fisher, L., Yih, J., Ward, C., 2011, Performance of a combined organic Rankine cycle and vapor compression cycle for heat activated cooling, *Energy*, **36**, pp. 447-458.
20. Demierre, J., Henchoz, S., Favrat, D., 2012, Prototype of a thermally driven heat pump based on integrated Organic Rankine Cycles (ORC), *Energy*, **41**, pp. 10–17.

21. Li, H., Bu, X., Wang, L., Long, Z., Lian, Y., 2013, Hydrocarbon working fluids for a Rankine cycle powered vapor compression refrigeration system using low-grade thermal energy, *Energy Buildings*, **65**, pp. 167-172.
22. Bu, X., Wang, L., Li, H., 2013, Performance analysis and working fluid selection for geothermal energy-powered organic Rankine-vapor compression air conditioning, *Geothermal Energy*, **1**, pp. 1-14.
23. Bounefour, O., Ouadha, A., 2014, Thermodynamic analysis and thermodynamic analysis and working fluid optimization of a combined ORC-VCC system using waste heat from a marine diesel engine, Proceedings of the ASME 2014 International Mechanical Engineering Congress and Exposition IMECE2014, Montreal, Quebec, Canada.
24. Bao, J., Zhao, L., 2013, A Review of Working Fluid and Expander Selections for Organic Rankine Cycle, *Renewable & Sustainable Energy Rev.*, **24**, pp. 325-342.
25. Juhasz, J.R., Simoni, L.D., 2015, A review of potential working fluids for low temperature organic Rankine cycles in waste heat recovery, 3rd International Seminar on ORC Power Systems, Brussels, Belgium.
26. Sytchev, V.V., 1983, *Les Equations Différentielles de la Thermodynamique*, Edition Mir, Moscou.
27. Kotas, T.J., 1985, *The exergy method of thermal plant analysis*, 1st ed. London: Butterworth.
28. Rodyansky, V.M., Sorin, M.V., Le Goff, P., 1994, *The efficiency of industrial processes: Exergy analysis and optimization*, New York: Elsevier.
29. Moran, M.J., Shapiro, H.N., 2000, *Fundamentals of engineering thermodynamics*, 4th ed. New York: John Wiley & Sons.
30. Bosnjakovic, F., 1965, *Technical thermodynamics*, Holt, Rinehart and Winston, New York.

COMPARATIVE ASSESSMENT OF LNG AND LPG IN HCCI ENGINES

Mohammed Djermouni, Ahmed Ouadha*

Laboratoire des Sciences et Ingénierie Maritimes, USTO-MB, B.P. 1505 Oran El M'naouar,
31000 Oran, Algérie

*Corresponding author: Fax: +213 41290461 Email: ah_ouadha@yahoo.fr

ABSTRACT

A recent paper by the authors [1] detailed a thermodynamic model for HCCI engines fuelled by natural gas. The present paper continues in the same direction by proposing to compare the performance of natural gas fuel to LPG fuel in HCCI engines. Operating parameters such as compressor pressure ratio and equivalence ratio are discussed as to their effect on the overall system performance.

INTRODUCTION

Economic and environmental pressure on internal combustion engines designers is increasing in order to build more efficient engines. In addition to environmental restrictions, it is expected that, in the near future, energy efficiency measures and policies will be increased.

Due to their high energy efficiency, Diesel engines are extremely attractive solution for many applications such as transport, marine propulsion and power station. However, in terms of NO_x emissions, it is difficult to make them able to meet stringent emissions standards. Methods proposed for emissions control include improved combustion processes, after-treatment techniques and alternative fuels. In this context, interest is growing in the performance and emissions benefits of HCCI engines. This technology combined with alternative fuels presents the potential to meet stringent requirements to limit pollutant emissions. First introduced in 1979 [2], the concept of homogeneous charge compression ignition has recently received great attention. In an HCCI engine, a homogeneous premixed fuel-air mixture, as in spark ignition engines, is auto-ignited by the temperature increase accompanying the compression as in compression ignition engines. The amalgamation of these technologies allows HCCI engines to offer diesel-like efficiency with low NO_x and particulates emissions. The auto-ignition is achieved by controlling its temperature, pressure, and composition, which makes the combustion in HCCI engines more sensitive to fuel chemistry compared to conventional engines.

HCCI engines can operate using a large variety of fuels. In addition to gasoline [3] and Diesel fuel [4], various alternative fuels such as iso-octane, acetylene, methanol, DME, ethanol, wet ethanol,

natural gas, hydrogen, biogas and some fuel blends have been investigated for HCCI applications [5-16]. Driven by energy security and concerns, the interest in alternative fuels is rapidly growing around the world. Alternative fuels such as natural gas, LPG, hydrogen and biofuels are potential candidates for many applications. However, availability and economic aspects make natural gas, LPG and Hydrogen more realistic solutions compared to biofuels. Although that internal combustion engines operating on hydrogen offer weight and cost advantages, they suffer from a serious drawback: the low efficiency. Consequently, for the present and the near future, natural gas and LPG as fuels are the best solution to meet upcoming emission regulations. Indeed, natural gas and LPG, thanks to their composition, are clean burning fossil fuels that produce much fewer pollutant emissions compared to traditional fuels.

Although that intense research efforts have been expended since the first study by Onishi et al. [2], studies on HCCI engines still lower than that dedicated to spark ignition and compression ignition engines. A review paper published recently by Sharma et al. [17] outlines progress and development of the concept of HCCI engines. The reviewed studies are reported and categorized in several topics including, the HCCI engine technology, parameters affecting the HCCI engine Performance, emissions and combustion characteristics.

The body of literature on HCCI engines includes several approaches to evaluate their performance. Basically, they are classified in three groups: the first is based on experimental approach, the second one uses computational fluids dynamics modelling and the third one is based on thermodynamic equations. The latter is useful for optimal design purposes. It can, in some cases, minimize tests on real models by

guiding experimental research and engine development.

Thus, it is necessary to carry out thermodynamic studies in order to calculate and compare engine performance using alternative fuels in HCCI applications. The present paper aims to offer a tool that allows a quick comparison between natural gas and LPG fuels using thermodynamic laws. The exergy balance equation is applied to each process of the system allowing the detection of inefficiency sources, in terms of exergy losses, and effort directions for improvement. The analysis is carried out for several operating conditions including compressor pressure ratio and equivalence ratio.

THERMODYNAMIC PROPERTIES

For the purpose of making cycle calculations, combustion products composition and their thermodynamic properties are required. These properties are necessary to investigate both design-point and off-design performances, and to determine optimum design parameters. Generally, the in-cylinder working fluid is considered as simply air. However, more rigorous thermodynamic studies require taking into account changes in the gas composition by tracking several chemical species.

In real processes, the specific heat of gases varies with temperature. However, for engine applications, its variation is negligible with pressure. The later is moderate. In the present model, it is assumed that the specific heat of gases varies with temperature according to the following polynomials form:

$$c_p = \sum_{i=1}^{11} a_i T^i \quad (1)$$

The numerical coefficients a_i , for each species, have been determined by a regression analysis method using literature data for temperature ranging from 300 to 3000 K [18].

Enthalpy and entropy can be derived from the specific heat capacity using the following relations:

$$\begin{cases} h = h_{00} + \int c_p(T) dT \\ s = s_{00} + \int \frac{c_p(T)}{T} dT - r \ln(p) \end{cases} \quad (2)$$

where h_{00} and s_{00} are the integration constants calculated according to an arbitrary reference state. For each gas, the enthalpy constant of integration is the sum of two parts: a part calculated by adjusting $h = 0$ at 298 K and a part representing the enthalpy of formation of the gas. For entropy, the integration

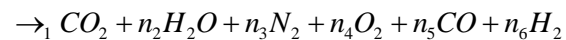
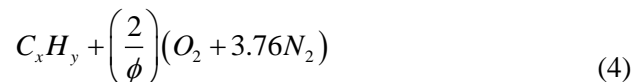
constant is calculated by adjusting $s = 0$ at 298 K and 1.01325 bar.

Thermodynamic properties of the combustion products have different dependencies on temperature. Therefore, it is more appropriate to calculate the thermodynamic properties of their mixture as a sum of the properties of individual species:

$$\Phi_m = \sum_{i=1}^n \Phi_i x_i \quad (3)$$

Alternative fuels considered in the present study have different physical and chemical properties. Thanks to their simple molecule structures, the combustion of these fuels produces much lower pollutant emissions compared to traditional fuels. More particularly, emissions of particulates and hydrocarbons are considerably reduced using these fuels.

Under ideal conditions, the combustion of fuels produces only water (H_2O) and carbon dioxide (CO_2), in addition to the nitrogen (N_2) from the air. However, in a real combustion, in addition to these main combustion products, the engine exhaust gases also contain many others compounds. In the present work, the following species are considered as combustion products: CO_2 , CO , H_2O , N_2 , O_2 and H_2 . The equation for combustion of fuels with air is written below:



The mole fractions, n_i , of the combustion products have been determined under equilibrium conditions by solving a nonlinear system of seven equations.

THERMODYNAMIC ANALYSIS

Habitually, thermal systems are analyzed using the energy analysis method which is based on the first law of thermodynamics, i.e. the energy conservation concept. Unfortunately, this method cannot locate the degradation of the quality of energy. Instead, exergy analysis which is based on both the first and second laws of thermodynamics can overcome easily the limitations of the energy analysis. It permits to quantify the magnitude and the location of exergy losses within the system. Furthermore, the total exergy losses can be considered as an optimization criteria which, by minimization, provides optimum processes configuration. The concept and the methodology of exergy analysis are well-documented in the literature.

For both energy and exergy analysis, the thermodynamic model is based on the following assumptions:

- All processes are marked by steady state and steady flow,
- Kinetic and potential energy have negligible effects,
- The temperature and pressure of the environment are 25°C and 1 atm, respectively.

SYSTEM DESCRIPTION

The system considered in the present study is depicted in Figure 1. The system consists of a compressor, a regenerator, a mixer, an HCCI engine, a catalytic converter and a turbine. Ambient air enters the compressor where its pressure and temperature rise to reach p_2 and T_2 . The compressed air passes through a generator where it is heated to T_3 at constant pressure. The hot air exiting the regenerator is mixed with the fuel injected into a mixer to form homogeneous mixture. Thus, the homogeneous gas mixture formed enters the combustion chamber where conditions of temperature and pressure reached during the compression process ensure an auto-ignition of the charge by approaching the top dead centre. Then, the exhaust gases flow through a catalytic converter where the temperature increases from T_6 to by T_7 due to the conversion of unburned particles. The gas leaving the catalytic converter enters a turbine to generate the power needed to drive the compressor. Finally, the exhaust gases leave the turbine at atmospheric pressure and temperature T_9 after having exchanged heat with compressed air in the regenerator.

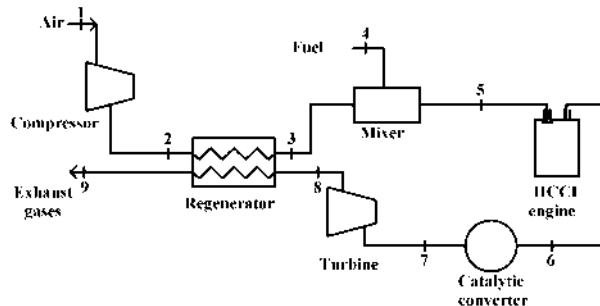


Figure 1
Scheme of the system studied

ENERGY ANALYSIS

After the determination of the working fluid properties at each point of the system represented in Figure 1, the energy analysis can be carried out. Mass and energy balances for any control volume at steady state with negligible kinetic and potential energy changes can be expressed respectively by the following expressions:

$$\begin{cases} \sum \dot{m}_i - \sum \dot{m}_o = 0 \\ Q - W = \sum \dot{m}_o h_o - \sum \dot{m}_i h_i \end{cases} \quad (5)$$

To carry out an energy analysis, the above balance equations should be applied to each component of the system.

The compressor is required to provide a compressed air supply for the engine in order to improve the power and efficiency. The compressor inlet properties (state 1) are calculated knowing T_1 and p_1 . For a given pressure ratio, r_p , the compressor outlet properties (state 2) are calculated in two steps:

- First, the temperature at the end of the isentropic compression is determined by the numerical solution of the following equation :

$$s_{2s} = s_1 \quad (6)$$

- Then, the properties at state 2 are calculated using the compression efficiency definition:

$$\eta_{comp} = (h_{2i} - h_1) / (h_2 - h_1) \quad (7)$$

Here again, temperature T_2 is obtained by a numerical inversion method.

An energy balance on the compressor yields

$$w_c = h_2 - h_1 \quad (8)$$

The regenerative heat exchanger (regenerator) is used to heat the compressed air using the exhaust gases. The effectiveness of this heat exchanger is given by:

$$\varepsilon_h = \left[(\dot{m} \cdot c_p)_2 (T_3 - T_2) \right] / \left[(\dot{m} \cdot c_p)_{\min} (T_8 - T_2) \right] \quad (9)$$

Temperature at the exit of the regenerative heat exchanger, T_3 , is calculated assuming $(\dot{m} \cdot c_p)_2 = (\dot{m} \cdot c_p)_{\min}$ by the following relation:

$$T_3 = T_8 \varepsilon_h + T_2 (1 - \varepsilon_h) \quad (10)$$

The application of energy balance on the regenerator yields

$$H_3 - H_2 = H_8 - H_9 \rightarrow H_9 = H_8 - H_3 + H_2 \quad (11)$$

Temperature at the exit of the mixer is calculated using energy balance equation :

$$H_5 = H_3 + H_4 \quad (12)$$

The gaseous mixture exiting the mixer enters the HCCI engine whose thermodynamic cycle is modelled by a turbocharged Otto cycle.

Temperature at the end of the intake process ($i-1'$) is calculated using the following expression [7]:

$$T_r = \frac{T_i(1-f)}{1-1/\left[(n \cdot r_c) p_e/p_i + (n-1)\right]} \quad (13)$$

where, f is the residual gases fraction fixed to 0.03 according to the reference cited.

The pressure remains unchanged:

$$p_r = p_i \quad (14)$$

During the compression process ($1'-2'$), the gaseous mixture is heated up to ignition and combustion. For a fixed pressure ratio ($r_c = 16$), properties at state $2'$ can be calculated in a similar manner to state 2 using compression isentropic efficiency.

Properties at the end of the heat supply process ($2'-3'$) are determined using an inversion numerical method of the following equation:

$$\dot{Q}_{in} = \dot{Q}_{fuel} - \dot{Q}_l \quad (15)$$

where \dot{Q}_{fuel} is the heat supplied to the cycle given by:

$$\dot{Q}_{fuel} = \eta_{comb} \dot{m}_{fuel} Q_{LHV} \quad (16)$$

The losses inside the combustor are taken into account by introducing combustion efficiency [19]:

$$\eta_{comb} = 100 - V_{\%c} - (1.26 + 0.25C_{e2} + 0.4C_{e2}^2) + (\phi - 0.2486)8.1 \quad (17)$$

where $C_{e2} = \ln(V_{\%c})/\ln(2)$

The heat losses \dot{Q}_l are calculated using:

$$\dot{Q}_l = h_c \cdot 10^{-3} (A_{ch} + A_{cyl})(T_{avr} - T_w)/(2 \cdot \dot{m}_a) \quad (18)$$

where, h_c is the heat transfert coefficient [20]:

$$h_c = (3.26L^{-0.2} p^{0.8} T_{avr}^{-0.73} \omega^{0.8}) \quad (19)$$

and ω is the mean gas velocity within the cylinder:

$$\omega = 2.28\bar{S}_p + (3.24e^{-3}/6) \left(V_d T_{ref} (p - p_{mot}) / (p_{ref} V_{ref}) \right) \quad (20)$$

where p_{mot} is the pressure at motored conditions [21]:

$$p_6 = p_r (V_r/V)^{\gamma} \quad (21)$$

p_r and V_r are the pressure and the volume at a reference state.

The parameters of the working fluid at the end of the expansion process ($3'-4'$) can be calculated also in similar manner to the compression process ($1'-2'$).

For a turbocharged engine, the exhaust process ($4'-1'$) is substituted by an expansion process ($4'-5'$). The final state parameters of this process are calculated again in a similar manner to the compression ($1'-2'$).

Finally, temperature and pressure at the end of the exhaust process ($5'-6$) are:

$$T_e = T_5 \quad (22)$$

$$p_6 = p_5 = p_e \quad (23)$$

The heat released by friction is evaluated using the relation of Wu and Ross [22]:

$$\dot{Q}_f = \dot{m}_t \left(183 + 2.3 \left(\left(\frac{N}{60} \right) - N_0 \right) * V_D \right) \quad (24)$$

with,

$$N_0 = 30 \sqrt{3/(1000V_d)} \quad (25)$$

The heat rejected is calculated using:

$$\dot{Q}_{out} = \dot{m}_t [(h_4 - r \cdot T_4) - (h_5 - r \cdot T_5)] \quad (26)$$

The net power produced by the cycle can be calculated using the following equation:

$$\dot{W}_{net} = \dot{Q}_{in} - \dot{Q}_{out} - \dot{Q}_f \quad (27)$$

The thermal efficiency of the engine, η_{th} , is defined as the ratio of the power produced by the cycle to total energy supplied to the cycle:

$$\eta_{th} = \dot{W}_{net} / \dot{Q}_{in} \quad (28)$$

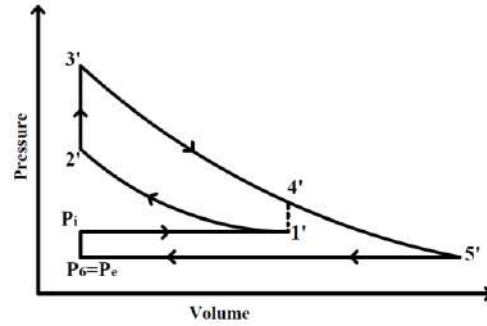


Figure 2

Otto turbocharged cycle

EXERGY ANALYSIS

Traditionally, thermodynamic cycles are analyzed using the energy analysis method which is based on the first law of thermodynamics, i.e. the energy conservation concept. Unfortunately, this method cannot locate the degradation of the quality of energy. Instead, exergy analysis which is based on both the first and second laws of thermodynamics can overcome easily the limitations of the energy analysis. Exergy analysis is considered by several researchers as powerful tool for thermodynamic cycles because it helps to determine the true magnitudes of losses and their causes and locations, showing thus where efforts should concentrated to improve the overall system and its components. Furthermore, the total exergy losses can be considered as an optimization criteria which, by minimization, provides optimum processes configuration. The concept and the methodology of exergy analysis are well-documented in the literature [23-25].

In absence of nuclear, magnetic, electric and superficial effects, the exergy of a system is composed of four components : physical, chemical, potential and kinetic.

$$ex = ex^k + ex^p + ex^{ph} + ex^{ch} \quad (29)$$

For engines applications, kinetic and potential contributions are assumed to be negligible compared to physical and chemical exergies. Physical exergy results from temperature and pressure differences from the dead state:

$$ex^{ph} = (h - h_0) - T_0(s - s_0) \quad (30)$$

On the other hand, chemical exergy takes into account deviations in chemical composition from reference substances present in the environment:

$$ex^{ch} = \sum x_i (\mu_i^* - \mu_{i,0}) \quad (31)$$

Exergy is always evaluated with respect to a reference environment (dead state).

The exergy destroyed in a system originate from the internal irreversibilities. It can be calculated using the global exergy balance in steady state [26]:

$$\Delta \dot{E}x = \sum \dot{E}x_i - \sum \dot{E}x_o = \sum \left(1 - \frac{T_0}{T_j} \right) \dot{Q}_k - \dot{W}_{cv} + \sum \dot{m}_i ex_i - \sum \dot{m}_o ex_o \quad (32)$$

where $\sum \dot{E}x_i$ and $\sum \dot{E}x_o$ are the destroyed, input and output exergy rates, respectively, \dot{m} is the mass flow rate of a stream of matter, and \dot{Q}_k and \dot{W}_{cv} the energy rates transfer by heat and work. The subscripts i and o denote inlet and outlet and the subscript k the boundary of the component of interest.

Instead, the exergy destruction rate can be determined using the Gouy-Stodola formula:

$$\Delta \dot{E}x = T_0 \dot{S}_{gen} \quad (33)$$

where \dot{S}_{gen} is the entropy generation rate.

From a second law point of view, it is important to quantify the exergy losses in each component in order to assess the overall performance of the system. To assess the contribution of each component of the system in the total exergy losses, exergy balance equation is applied to each component. The expressions allowing the calculation of individual exergy losses of each component of the system and their exergy efficiencies are summarized in Table 1.

Table 1
Individual exergy losses and efficiencies of the system components

Component	Exergy loss	Exergy efficiency
Compressor	$\dot{W}_{comp} + \dot{m}_a (ex_1^{ph} - ex_2^{ph})$	$\dot{m}_a (ex_2^{ph} - ex_1^{ph}) / (-\dot{W}_{comp})$
Regenerator	$\dot{m}_a (ex_2^{ph} - ex_3^{ph}) + \dot{m}_t (ex_8^{ph} - ex_9^{ph})$	$[\dot{m}_a (ex_3^{ph} - ex_2^{ph})] / [\dot{m}_t (ex_8^{ph} - ex_9^{ph})]$
Mixer	$\dot{m}_a ex_3^{ph} + \dot{m}_f ex_4^{ph} - \dot{m}_i ex_5^{ph}$	$(\dot{m}_a ex_3^{ph}) / (\dot{m}_f ex_4^{ph} - \dot{m}_i ex_5^{ph})$
HCCI engine	$\dot{m}_t (\Delta ex_{comp} + \Delta ex_{comb} + \Delta ex_{det} + \Delta ex_{echapp} + \Delta e_{gaz}^{ch})$	$\dot{W}_{net} / \dot{E}x_{fuel}$
Turbine	$\dot{m}_t (ex_7^{ph} - ex_8^{ph}) - \dot{W}_{tur}$	$\dot{W}_{tur} / [\dot{m}_a (ex_7^{ph} - ex_8^{ph})]$
Catalytic converter	$\dot{m}_t (ex_6^{ph} - ex_7^{ph} + ex_{cat}^{ch})$	$(\dot{m}_t ex_7^{ph}) / [\dot{m}_t (ex_6^{ph} + ex_{cat}^{ch})]$

Exergy losses are generated in all the components of the system, namely the compressor, the regenerator, the mixer, the HCCI engine, the turbine and the catalytic converter. Thus, the total exergy losses $\Delta \dot{E}x_{tot}$ may be written as the sum of individual losses occurring in these components, i.e.,

$$\Delta \dot{E}x_{tot} = \Delta \dot{E}x_{comp} + \Delta \dot{E}x_{reg} + \Delta \dot{E}x_{mix} + \Delta \dot{E}x_{HCCI} + \Delta \dot{E}x_{tur} + \Delta \dot{E}x_{cat} \quad (34)$$

The exergy efficiency is a criterion for thermodynamic perfection of a process and can be defined as the ratio of the product of a process to the

required input of fuel, both of which are expressed in exergy units:

$$\eta_{ex} = \frac{\dot{E}x_{product}}{\dot{E}x_{fuel}} \quad (35)$$

The term “product” represents the desired output of a process and “fuel” refers to the resource that is used to generate this output, which only in some cases is an actual fuel. The exergy efficiency shows the percentage of the fuel exergy that is transferred to product exergy.

RESULTS AND DISCUSSIONS

The model described in the previous sections has been used to develop a Fortran program for calculating the system performance using natural gas and LPG as fuels. Using appropriate operating data, energetic efficiency, exergetic efficiency and exergy losses in each device of the system at a reference temperature of 25°C have been determined. Results have been obtained based on engine compression ratio equal to 16. Table 2 shows the main operating conditions of the system shown in Figure 1.

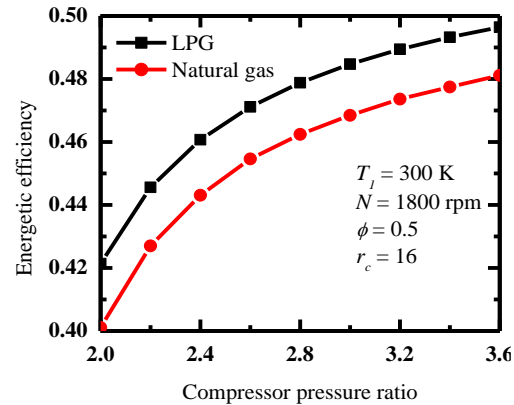
Table 2
Operating conditions

Ambient temperature, K	280-310
Ambient pressure, kPa	101.325
Compressor efficiency	0.8
Turbine efficiency	0.8
Engine compression ratio	16
Residual gases fraction	0.03
Equivalence ratio	0.3-0.7
Compressor compression ratio	2.1-3.6
Wall temperature, K	400

Thermal and exergetic efficiencies have been calculated for each fuel as function of the compressor pressure ratio for an ambient temperature fixed at 300 K as shown in Figure 3. At first glance, it is shown that there is slight difference among the fuels regarding thermal and exergetic efficiencies. While this difference is unchanged for energetic efficiency, it increases with increasing the compressor pressure ratio for exergetic efficiency. LPG fuel exhibits higher energetic and exergetic efficiencies than natural gas. For both fuels, the increase of the compressor compression ratio improves energy and exergy efficiencies. This increase is due to the increased density of the fuel-

air mixture, which causes an increase in the useful work produced by the engine.

a.



b.

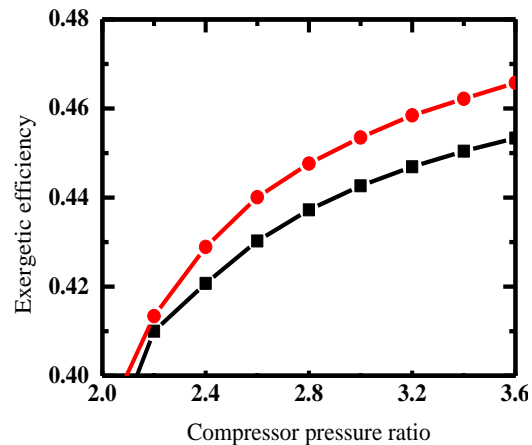


Figure 3

Effects of compressor pressure ratio *a* on the system performance: *a*. Energetic efficiency; *b*. Exergetic efficiency

The effects of changing fuel-air equivalence ratio on energetic and exergetic efficiencies are examined in Figure 4. Energetic and exergetic efficiencies behave similarly: both increase with increasing the fuel-air equivalence ratio. The increase of the engine efficiencies with regard to the equivalence ration is due the increase of the temperature at the end of the combustion process which increases the heat input. Again, the system fuelled with LPG presents higher energetic efficiency, while its exergetic efficiency is equal or lower than that of a system using natural gas as the fuel.

a.

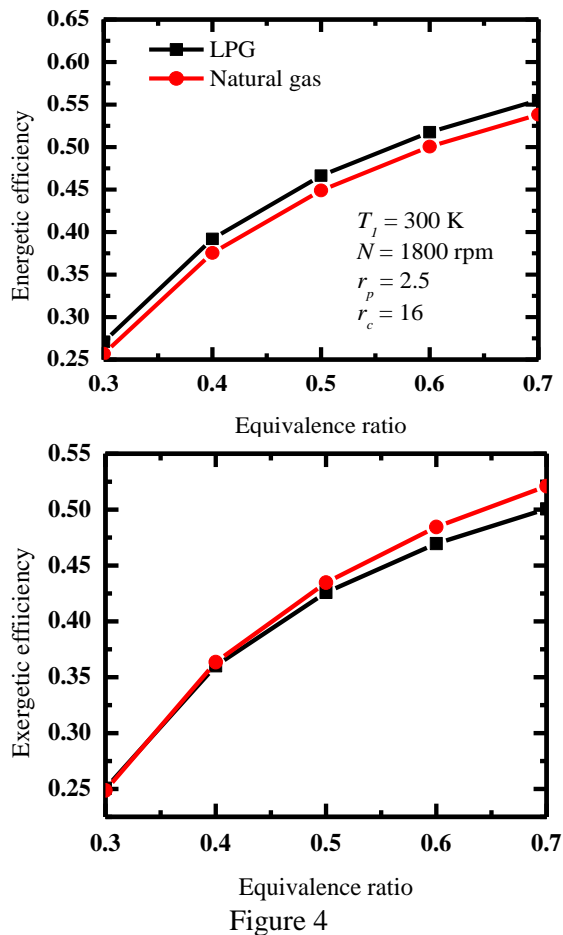


Figure 4

Combined effects of equivalence ratio and engine speed on the system performance: *a.* Energetic efficiency; *b.* Exergetic efficiency

Exergy losses of the components of the system for the fixed operating conditions indicated on Figure 5 have been calculated. The results show that for both fuels the greatest exergy losses occur in the HCCI engine. Irreversible processes occurring in the HCCI engine causes more than 85 % of total exergy losses in the system. Exergy losses in the HCCI engine originate mainly from the irreversible combustion process. During this process, an increased internal heat exchange occurs to raise the temperature of increased amounts of non-reactive species. Losses in the others components of the system are minimums, indicating that there is no potential for improvement under the operating parameters considered. The magnitude of exergy losses produced during the processes in the components of a system fuelled with LPG are lower than that produce in a system that uses natural gas as fuel.

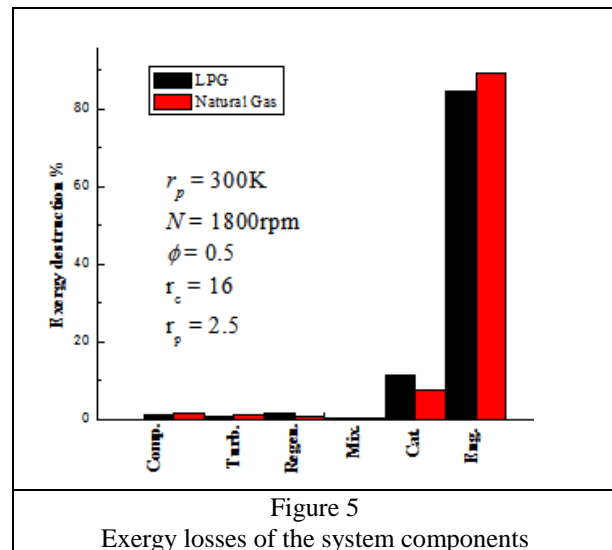


Figure 5

Exergy losses of the system components

CONCLUSIONS

Thermodynamic analysis of a thermal system based on a turbocharged HCCI engine fuelled with natural gas and LPG has been carried out. The working fluid is considered as a mixture of gases with variable specific heats.

The system performance have been determined and analyzed by numerical examples as a function of the compressor pressure ratio and the equivalence ratio. The results showed that the LPG fuel exhibits higher performance compared to natural gas.

REFERENCES

1. Djermouni, M., Ouadha, A., 2014, Thermodynamic analysis of an HCCI engine based system running on natural gas, Energy Conversion Management, **88**, pp. 723-731.
2. Onishi, S., Jo, S.H., Shoda, K., Jo, P.D., Kato, S., 1979, Active thermo-atmosphere combustion (ATAC)—a new combustion process for internal combustion engines SAE Paper.
3. Lavy, J., Dabadie, J., Angelberger, C., Duret, P. et al., 2000, Innovative Ultra-low NO_x Controlled Auto-Ignition Combustion Process for Gasoline Engines: the 4-SPACE Project, SAE Technical Paper 2000-01-1837.
4. Hasegawa, R., and Yanagihara, H., 2003, HCCI Combustion in DI Diesel Engine, SAE Technical Paper 2003-01-0745.
5. Christensen, M., Johansson, B., Einewall, P., 1997, Homogeneous charge compression ignition (HCCI) using iso-octane, ethanol and natural gas – a comparison with spark ignition operation, SAE Paper 971676.

6. Nathan, S.S., Mallikarjuna, J., Ramesh, A., 2010, Effects of charge temperature and exhaust gas re-circulation on combustion and emission characteristics of an acetylene fuelled HCCI engine, *Fuel*, **89**, pp. 515–521.
7. Zheng, Z., Yao, M., Chen, Z., and Zhang, B., 2004, Experimental Study on HCCI Combustion of Dimethyl Ether(DME)/Methanol Dual Fuel, SAE Technical Paper 2004-01-2993.
8. Yap, D., Megaritis, A., Wyszynski, M.L., 2004, An Investigation into Bioethanol Homogeneous Charge Compression Ignition (HCCI) Engine Operation with Residual Gas Trapping, *Energy & Fuels*, **18**, pp. 1315-1323.
9. Yap, D., Megaritis, A., Wyszynski, M.L., 2005, An Experimental Study of Bioethanol HCCI, *Combustion Science and Technology*, vol. **177**, n°11, pp. 2039-2068.
10. Mack, J.H., Aceves, S.M., Dibble, R.W., 2009, Demonstrating direct use of wet ethanol in a homogeneous charge compression ignition (HCCI) engine, *Energy*, **34**, pp. 782–787.
11. Jun, D. and Iida, N., 2004, A Study of High Combustion Efficiency and Low CO Emission in a Natural Gas HCCI Engine, SAE Technical Paper 2004-01-1974.
12. Ibrahim, M.M., Ramesh, A., 2014, Investigations on the effects of intake temperature and charge dilution in a hydrogen fueled HCCI engine, *Int. J. Hydrogen Energy*, **39**, pp. 14097–14108.
13. Wyszynski, M.L., Megaritis, A., Karlovsky, J., Yap, D., Peucheret, S., Lehrle, R. S., Xu, H., Golunski, S., 2004, Facilitation of HCCI Combustion of Biogas at Moderate Compression Ratios by Application of Fuel Reforming and Inlet Air Heating, *J. KONES Internal Combustion Engines*, **11**, (3-4).
14. Stenlääs, O., Christensen, M., Egnell, R., Johansson, B. et al., 2004, Hydrogen as Homogeneous Charge Compression Ignition Engine Fuel, SAE Technical Paper 2004-01-1976.
15. Chen, Z., Konno, M., Oguma, M., and Yanai, T., 2000, Experimental Study of CI Natural-Gas/DME Homogeneous Charge Engine, SAE Technical Paper 2000-01-0329.
16. Shioji, M., Kitazaki, M., Mohammadi, A., Kawasaki, K. et al., 2004, Knock Characteristics and Performance in an SI Engine With Hydrogen and Natural-Gas Blended Fuels, SAE Technical Paper 2004-01-1929.
17. Sharma, T.K., Rao, G.A.P., Murthy, K.M., 2015, Homogeneous Charge Compression Ignition (HCCI) Engines: A Review, *Arch. Computat. Methods Eng*, pp. 1-35.
18. Glassman, I., Yetter, R.A., 2008, *Combustion*. 4th ed. USA: Elsevier.
19. Mo, Y., 2002, HCCI heat release rate and combustion efficiency: a coupled kiva multi-zone modeling study. PhD Thesis, University Michigan, USA.
20. Soyhan, H.S., Yasar, H., Head, B., Kalghatgi, G.T., Sorusbay, C., 2009, Evaluation of heat transfer correlations for HCCI engine modeling, *Appl. Thermal Eng.*, **29**, pp. 541-549.
21. Heywood, J.B., 1988, *Internal Combustion Engine Fundamentals*, McGraw-Hill, New York.
22. Olof, E., 2002, Thermodynamic simulation of HCCI engine systems, PhD Thesis, Lund University, Sweden.
23. Kotas, T.J., 1985, *The exergy method of thermal plant analysis*, 1st ed. London: Butterworth.
24. Brodyansky, V.M., Sorin, M.V., Le Goff, P., 1994, *The efficiency of industrial processes: exergy analysis and optimization*, New York: Elsevier.
25. Moran, M.J., Shapiro, H.N., 2000, *Fundamentals of engineering thermodynamics*, 4th ed. New York: Wiley.
26. Bejan, A., Tsatsaronis, G., Moran, M., 1996, *Thermal design & optimization*, New York, USA: John Wiley & Sons.

MODELLING OF AN RDC EXTRACTION COLUMN USING THE DIFFERENTIAL MAXIMUM ENTROPY METHOD (DMaxEntM)

Menwer Attarakih^{*a}, Abdelmalek Hasseine^b, Hans-Joerg Bart^c

^aFaculty of Eng. &Tech., Chem. Eng. Dept. The University of Jordan 1942-Amman, Jordan

^bLaboratory LAR-GHYDE, University of Biskra, Algeria

^cChair of Separation Science and Technology, Center for Mathematical Modeling, TU Kaiserslautern, Germany

*Corresponding author: Fax: +962 6 5300 813 Email: attarakih@yahoo.com

ABSTRACT

Modelling of extraction columns in general and the RDC column in particular calls for detailed description of the dispersed phase. The population balance equation (PBE) proves to be the proper transport equation which respects the dispersed phase transport properties and accommodates droplet- droplet interactions. For such complex models, the PBE has no analytical solution. Therefore, we propose a converging sequence of continuous approximations to the number density function which maximizes the Shannon entropy functional as a solution to the PBE. The solution is an optimal and least biased functional subject to the available information. This constrained entropy maximization problem is solved by introducing a set of transport equations in terms of Lagrange multipliers instead of solving a NLP. Since differential form of the Lagrange multipliers is used, the method is referred to as the Differential Maximum Entropy Method (DMaxEntM). The DMaxEntM method is tested using analytical cases and even complex five-compartment RDC liquid-liquid extraction model.

Keywords Differential Maximum Entropy, Population Balance, RDC, Extraction.

NOMENCLATURE

C_1, C_2	Coalescence parameters, -, m^{-2}
$f^*(x, \lambda)$	Maximum entropy distribution function, $mm^{-1}m^{-3}$
$g(x)$	Particle breakage frequency, s^{-1}
$M(\lambda)$	Coded information matrix
t	Time, s
$\langle \mathbf{u} \rangle$	Mean particle velocity vector, ms^{-1}
x	Particle diameter, mm
σ	Standard deviation, mm
$\omega(x, y)$	Particle aggregation frequency, m^3s^{-1}
λ	Lagrange multipliers

INTRODUCTION

Liquid—liquid extraction equipment has attracted widespread interest as one of the key process equipment in major chemical engineering, petroleum, pharmaceutical industries and environmental protection [1, 2]. In spite of this, the design of extraction columns is still based on experimental pilot plant data with the help of steady state flowsheet simulators [3]. On the other hand, the population balance modelling approach with a focus

on the discontinuous dispersed phase, had been a growing area of research in the last two decades [1, 4]. In liquid-liquid extraction columns the population balance equation takes into account droplet growth, coalescence, breakage and accommodates the dependence of droplet velocity on droplet size and concentration. Being a transport equation with geometrical dependencies and nonlinear integral source terms, the solution methods for the PBE rely either on stochastic Monte Carlo methods, sectional methods or the Quadrature Method of Moments (QMOM) [4, 5, 6]. The QMOM and its variants proved to be an accurate and fast PBE solver, where a finite set of population moments is conserved. However; the QMOM cannot reproduce droplet size distribution. For example, this size distribution is required to evaluate the negative particle fluxes at zero particle size as in the case of droplet evaporation, for online droplet size monitoring [7] or to extract model parameters from the full size distribution [8].

Motivated by solving the PBE moment problem with distribution reconstruction, the mathematical problem at hand lends itself to the maximum

entropy method. With its numerous applications in statistical mechanics and its theoretical foundation based upon probability theory, the Maximum Entropy method (MaxEntM) has provided an extremely successful variation principle to address this type of reconstruction and closure problems [9, 17, 20, 21]. In this regard, Sobrino et al. (2015) [20] used the MaxEntM to convert the probability density functions of chord length distributions in terms of bubble diameters in fluidized beds. Attarakih et al. (2015) [21] used a novel idea based on the MaxEntM to solve the PBE by estimating the Lagrange multipliers using direct distribution sampling. In this work, we follow the work of Attarakih and Bart (2014) [17] to find the probability density distribution for the solution vector of the PBE subject to priori moment information which are evolved by the solution of the moment form of the PBE. The Solution consistency with respect to the continuous population balance equation is preserved by maximizing the Shannon entropy function under the condition that the first $N + 1$ moments of the approximate continuous function be equal to that derived from the continuous PBE. As a result of this, the sequence of continuous approximations to the exact number concentration function are found to converge both at the pointwise (in the sense of Kullback-Leibler distance) and mean (weak convergence) levels. In this work, we introduce the idea to extract the optimal Lagrange multipliers based on the Differential MaxEntM (DMaxEntM), instead of solving a convex nonlinear optimization problem (NLP) at each point in the space-time domain. As a practical case study, we solved the PBE using the DMaxEntM, which describes the hydrodynamics of a laboratory scale (DIN 150 mm) RDC extraction column. This column finds many applications in petrochemical and pharmaceutical industries [2] and attracted the attention of many researchers (see the review given in [4, 18]). Using this laboratory scale short segment of an RDC column, rapid and relatively inexpensive experimental data can be gathered. These experimental data were used to determine droplet rise velocity, breakage probability and extract the droplet-droplet coalescence model parameters based on the measured inlet and outlet droplet size distribution [8,15].

EXTRACTION COLUMN MODELLING

The least-biased maximum entropy approximation of the number density function subject to limited

information (the first N low-order moments of f) about f is given by [10,17]:

$$f_N^*(x, \lambda) = \exp \left(\sum_{r=0}^N \lambda_r x^r \right) \quad (1)$$

Where λ is a set of Lagrange multipliers. Classically, these can be found by solving a convex NLP by minimizing the potential function [10,17]. The disadvantage here is the solution of this NLP at each point in space and time with the need for proper initialization. To overcome this problem, we propose the DMaxEntM, which avoids the solution of this NLP by finding the optimal Lagrangian multipliers using a set of transport equations. The PBE (w.r.t. droplet size) can be written using the DMaxEntM by deriving a set of transport equations (with mean convective velocity vector $\langle \mathbf{u} \rangle$) in terms of the optimal Lagrange multipliers vector $\lambda = [\lambda_0 \ \lambda_1 \ \dots \ \lambda_N]^T$ [17]:

$$\frac{\partial \lambda}{\partial t} + \langle \mathbf{u} \rangle \cdot \nabla \lambda = \psi_N \quad (2)$$

In the above equation the source term ψ_N is the solution of the following linear system of equations:

$$M(\lambda)\psi_N = R_N - \nabla \cdot \langle \mathbf{u} \rangle \mu(\lambda) \quad (3)$$

Where the moment vector is defined as $\mu(\lambda) = [\mu_0 \ \mu_1 \ \dots \ \mu_N]^T$ and the coded information matrix $M(\lambda)$ is real, symmetric and positive definite matrix [17]. In fact, since the moments forming this matrix form a completely monotone set, then the Hankel determinants (Hankel minors) are all positive and hence the solution of the linear system of Eqs.(2) is unique [11]. This can be effectively solved using the Cholesky decomposition or any equivalent method. The initial and boundary condition vectors of Eq.(2) are found by a relaxation procedure similar to that used in solving the Bhatnagar–Gross–Krook of the Boltzmann equation instead of solving a convex NLP [10]. The source term R_N is an integral source term, which is closed using Eq.(1):

$$\begin{aligned} R_N = & \int_{\Omega} g(x') x'^r f_N^*(x') [\pi_r - 1] dx' \\ & + \int_{\Omega} \int_{\Omega} [\omega^* f_N^*(x) f_N^*(x')] [x^3 + x'^3]^{r/3} dx dx' \\ & - \int_{\Omega} \int_{\Omega} [x^r + x'^r] dx dx' \end{aligned} \quad (4)$$

In the above equation, g and ω are the droplet breakage and coalescence frequencies respectively,

and π_r is the r th moment of the daughter droplet distribution. Note that the present moment problem is a typical Hausdorff finite moment problem, where the particle size boundaries $\Omega = [x_{\min}, x_{\max}]$ are to be controlled for accurate and stable numerical integration. As a control procedure, we propose a set of moving boundaries in terms of the low-order moments (normalized population mean and variance) and a user controlled positive parameter. This is chosen such that negligible number of particles lies outside the interval $[x_{\min}, x_{\max}]$. Our computational experience shows that a value that lies between 5 and 6 is sufficient to produce accurate moments and distribution reconstruction.

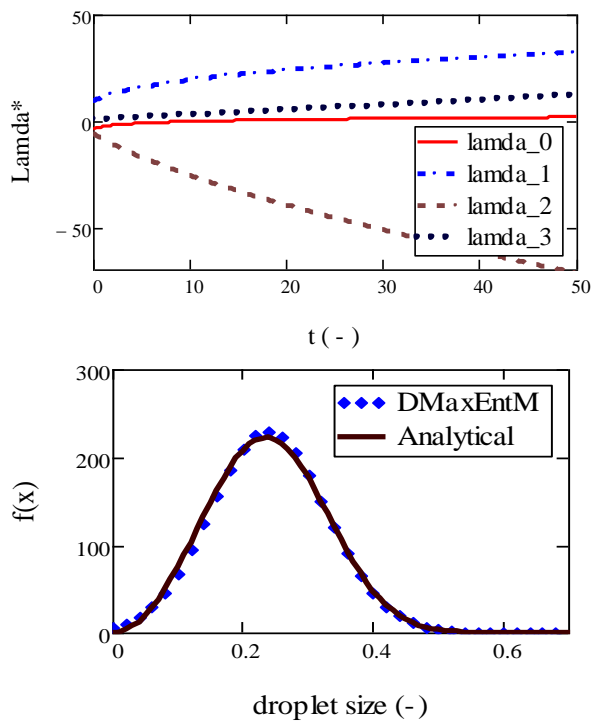


Figure 1

(Upper): Evolution of the optimal Lagrange multipliers for the case of homogeneous batch droplet breakage. (Lower): Reconstructed density function using the DMaxEntM at dimensionless time = 50 as compared to the analytical solution [12].

RESULTS AND DISCUSSION

In the present section we introduced a hierarchical approach for the exploration and validation of the DMaxEntM for the solution of the PBE. The first hierarchy is devoted to the homogeneous PBE to avoid the interaction of space and and time solvers. Accordingly, the effect of spatial domain discretization error on the DMaxEnt approach is eliminated. Firstly, we tested The DMaxEntM using

available standard analytical solutions for different cases of the homogeneous PBE with particle breakage, aggregation and coupled aggregation and growth. Due to space limitation, we present only one case due to particle breakage in homogenous system with respect to space while other cases can be found in Attarakih and Bart [17].

Analytical validation: The first case is the solution of the population balance equation of binary droplet breakage in a homogeneous system with frequency $g = x^3$, daughter droplet distribution $\beta(x|x') = 6x^2/x'^3$ and an initial condition $f = 3x^2 \exp(-x^3)$ with dimensionless particle mean ~ 0.9 . An adaptive Runge-Kutta method of orders 4 and 5 was used to solve the set of ODEs as given by Eq.(2). The linear system given by Eq.(3) was solved using Cholesky decomposition. The initial values for the λ -vector were obtained by a relaxation procedure similar to that used in solving the Bhatnagar–Gross–Krook (BGK) of the Boltzmann equation.

Fig.(1- upper panel) shows the time evolution of the optimal Lagrange multipliers using the DMaxEntM with four low-order moments starting from an initial state (λ^0) as predicted by the BGK equation. The smooth transition of Lagrange multipliers from the initial state to the final one indicates that the system of ODEs is not stiff and therefore any standard fixed or adaptive time step solver can be used. Here the coded information in this distribution is extracted successfully at any instant of time using the available optimal Lagrange multipliers. The accuracy of the predicted moments is also high, which is comparable to that obtained from the QMOM with two quadrature points. Actually, the relative error between the targeted and predicted moments is low using double precision arithmetic ($\sim 10^{-4}$ - 10^{-5}). This high accuracy is attributed to the unbiased maximum entropy solution $f_N(x)$. Fig.(1- lower panel) shows the extracted distribution $f_N(x)$ as function of dimensionless droplet size ($N=3$). Despite the small errors in the reconstructed distribution, the targeted moments (and even beyond that) are predicted with a very good accuracy. This depends on the accuracy with which the integrals in the source term are resolved. In this work an adaptive Gauss integration was used with an accuracy of 10^{-4} . Following Gzyl and Tagliani [13], the pointwise convergence is measured using Kullback-Leibler distance, where the decrease in

error is rapid until $N = 6$. Beyond this level, round-off errors start to weight the results [17].

Experimental validation: At the second hierarchy level, the DMaxEntM is validated using a laboratory scale RDC extraction column with 150 mm diameter and five compartments each of 30 mm height. The chemical system is n-butyl acetate-water (no mass transfer) which has relatively low interfacial tension. The simulation conditions and model specifications are the same as those reported in Attarakih et al. [14], where the n-butyl acetate is the dispersed (light) phase. The single droplet rise velocity is estimated using Kley and Traybal law as recommended in [1] for systems of relatively low interfacial tension. The breakage probability of droplet in the RDC column is due to the turbulent structure of the continuous phase which depends on the energy input, physical properties (mainly interfacial tension) and liquid droplet motion [18].

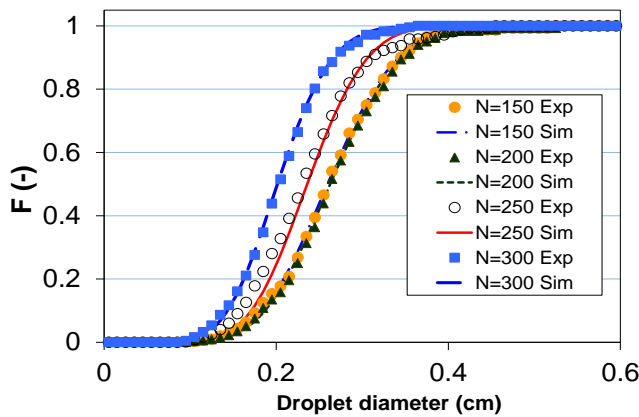


Figure 2

Steady state cumulative densities of the number concentration function in an RDC column at different rotor speeds. The experimental data is from [15].

Based on this, Schmidt et al. (2003) [18] proposed a breakage probability correlation based on single droplet experiments for RDC extraction column similar to that used in this work. This correlation was used to estimate droplet breakage probability as function of column geometry and rotor speed.

Numerical resolution: The numerical solution of the DMaxEnt model for the RDC column was accomplished by converting Eq.(2) into a set of ODEs in each RDC column compartment with first-order approximation of the spatial derivative ($\partial\lambda/\partial z$) where z is the spatial coordinate. The resting set of ODEs was solved using an adaptive Runge-Kutta method of order 4 & 5 using MATLAB software. For

the sake of numerical validation, the PBE was discretized with respect to droplet diameter using the EFPT (Extended Fixed-Pivot Technique), while the column space is resolved using the finite volume method with first-order upwind scheme [14].

Parameter identification: Unlike droplet breakage probability, the droplet-droplet coalescence frequency (ω see Eq.(4)) could not be easily determined based only on single droplet experiments due to the interaction between droplet breakage and coalescence at high dispersed phase concentration. Accordingly, a parameter identification algorithm is used to estimate the adjustable parameters which appear in nearly all of the published droplet coalescence models. Among these models is the model of Coualaloglou and Tavlarides (1977) [16] which has two adjustable parameters (C_1 and C_2). By estimating these parameters based on measured droplet size distribution, we are confronted by two types of errors: The systematic error (attributed to the PBE solver) and the measurement noise (attributed to the measured size distribution of the dispersed phase).

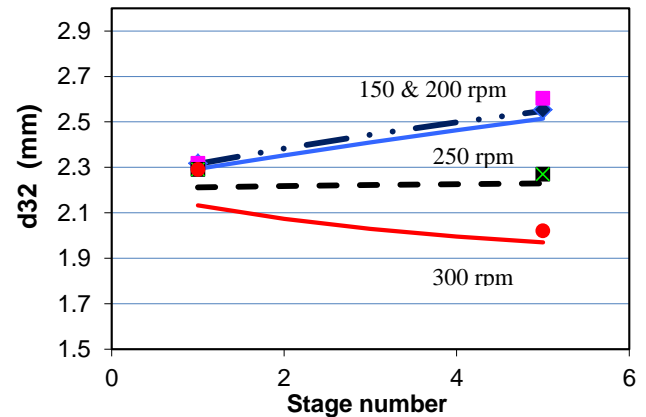


Figure 3

Steady state mean droplet diameter as compared to the experimental data [15] in an RDC column.

The systematic error can be dealt with by controlling the order of the DMaxEntM, the space discretization method and the time solver performance. On the other hand, regularization techniques (with empirically adjustable parameter) are the most common approaches used in parameter identification in the presence of measurement noise [19]. In [19], these authors used a regularization technique due the noise coming from using the Monte Carlo method as a PBE solver in addition to the measurement noise. For the measurement noise,

they used integral droplet properties (mean droplet diameter and dispersed phase holdup) as reference solution in their parameter identification of C_1 and C_2 . One drawback of this approach is the destruction of the droplet size distribution and hence the losses of detailed information about droplet distribution (in particular bimodal distributions). In this work, we used two combined integral approaches, as noise-filtering techniques, without losing any significant experimental information to cope up with the measurement noise in the droplet size distribution. Firstly, the measured droplet size distribution (at the outlet of the RDC column) is converted to a cumulative number density function where the integral operator damps significantly the measurement noise. Secondly, instead of using the cumulative distribution based on the experimental data, we use again the MaxEnt distribution as a smooth and continuous function to represent the cumulative droplet size distribution. In this case, the need for the complete size distribution is obvious, where the outlet droplet distribution is matched with the experimental data by adjusting the coalescence model parameters C_1 and C_2 . The inlet and outlet droplet size distribution properties are summarized in Table (1) at different rotor speeds and phase flow rates as 100 l/h for both phases using a set of experimental data from [15].

Table 1
Calculated parameters of measured droplet size distribution [15].

Rotor speed (min ⁻¹)	Inlet distribution		Outlet distribution	
	Mean (mm)	σ (mm)	Mean (mm)	σ (mm)
150	2.06	0.51	2.66	0.62
200	2.08	0.49	2.67	0.63
250	2.06	0.47	2.33	0.58
300	2.04	0.50	2.08	0.49

As an optimization technique, we used a rigorous optimization algorithm based on the constrained nonlinear SQP using the MATLAB function “fmincon”. The relative change in the elements of the \mathbf{C} vector is set equal to 10^{-6} and relative maximum constraint violation of order 10^{-6} . The objective function was set as the $\|F^{\text{exp}} - F^{\text{num}}\|_2$ with constraints on $\mathbf{C}^{\text{cons}} = (0, \infty)$. The first estimated values of these parameters, using the Coualoglou and Tavlarides (1977) [16], are summarized in Table (2) with a confidence level of 95 percent. A sample of

results is presented here at four different rotor speeds: 150, 200, 250 and 300 rpm. Firstly, the DMaxEntM was found to converge to the EFPT (Extended fixed-pivot technique) with 200 pivots using 4 and 6 moments. Secondly, Figure 2 shows the prediction capability of the DMaxEntM with its ability to follow the experimental data at different rotor speeds using the identified parameters shown in Table 2. It is noticed that the estimated parameters have the same order of magnitude at the two rotor speeds 150 and 200 rpm. This is because the critical rotor speed is near 200 rpm which is clear by referring to the mean droplet diameter profiles in Figure 3. As the rotor speed increases, the droplet breakage increases, where the droplet mean diameter is shifted to the left as indicated by the shift of mean standard deviation (σ) in Table 1.

Table 2

Estimated coalescence model parameters with an error corresponds to 95 percent confidence level.

Rotor speed (rpm)	C_1	C_2 (m ²) $\times 10^{-10}$	Error in C_1	Error in C_2 $\times 10^{-6}$
150	0.0617	1.526	0.0019	1.07
200	0.0693	8.965	0.0001	1.11
250	0.0470	7.437	0.0027	1.67
300	No coalescence is needed			
mean	0.0593	5.976	0.0016	1.28

At 250 rpm rotor speed it seems that a dynamic equilibrium between droplet breakage and coalescence is achieved (see Figure 3). On the other hand, at 300 rpm rotor speed, droplet breakage becomes dominant where the outlet droplet distribution and mean droplet diameter were predicted without including droplet coalescence model. The accuracy of the results is shown in Figures 2 and 3. Therefore, despite the complexity of the nonhomogeneous PBE, the predictability of the RDC model using the DMaxEntM is remarkable even when the distribution becomes unsymmetric and distorted by droplet breakage.

SUMMARY AND CONCLUSIONS

In this work, the DMaxEntM based on tracking the optimal Lagrange multipliers is introduced and transport equations of these multipliers are presented. The DMaxEntM relaxed the dependence of the MaxEntM on solving nonlinear optimization problem which requires specialized numerical optimization methods. The remarkable accuracy and flexibility of the DMaxEntM are addressed. It is

applied successfully to a standard case of homogeneous PBE with droplet breakage. As a real application, the DMaxEntM is applied to model the hydrodynamics of a short segment RDC extraction column. The simulation results show that the DMaxEntM is accurate enough to predict the number concentration of droplets population. As a final conclusion, the DMaxEntM is proved to be as an effective solver for the the PBE. This is in particular whenever the full size distribution is required.

ACKNOWLEDGMENTS

This work was accomplished during the summer stay of the lead author at the Chair of Separation Sciences & Technology/ University of Kaiserslautern.

REFERENCES

- [1] Godfrey, J. C. and Slater, M. J., 1994, *Liquid-liquid extraction equipment*, New York, John Wiley.
- [2] Kislik, V. S., 2012, *Engineering development of solvent extraction processes*, Elsevier.
- [3] Grinbaum, B., 2006, The existing models for simulation of pulsed and reciprocating columns—how well do they work in the real world? *Solvent Extraction and Ion Exchange*, **24**, pp. 795-822.
- [4] Attarakih, Abu-Khader, M. and Bart, H.-J., 2013, Modelling and dynamic analysis of an RDC extraction column using OPOSPM. *Chem. Eng. Sci.*, **9**, pp. 180-196.
- [5] Lage, P. L. C., 2011, On the representation of QMOM as a weighted-residual method—The dual-quadrature method of generalized moments. *Comp. Chem. Eng.*, **35**, pp. 2186–2203.
- [6] Santos, F. P., Senocak, I., Favero, J. L. and Lage, P. L. C., 2013, Solution of the population balance equation using parallel adaptive cubature on GPUS. *Comp. Chem. Eng.*, **55**, pp. 61-70.
- [7] Mickler, M. , Jildeh, H. B., Attarakih, M. and Bart, H.-J., 2014, Online monitoring, simulation and prediction of multiphase flows. *Can. J. Chem. Eng.*, **92**, pp.307-317.
- [8] Jildeh, H. B., Attarakih, M. and Bart, H.-J., 2014, Parameter optimisation and validation for droplet population balances. *Can. J. Chem. Eng.*, **92**, pp. 2010-2019.
- [9] Andre, F. and Vaillon, R., 2012, Generalization of the k-moment method using the maximum entropy principle. Application to the NBKM and full spectrum SLMB gas radiation models. *J. of Quantitative Spectroscopy and Radiative Transfer*, **113**, pp. 1508-1520.
- [10] Mead, L. R. and Papanicolaou, N., 1984, Maximum entropy in the problem of moments, *J. Math. Phys.*, **25**, pp. 2404 -2417.
- [11] Tagliani, A., 1999, Hausdorff moment problem and maximum entropy: A unified approach. *App. Math. Comp.*, **105**, pp. 291-305.
- [12] Ziff, R. M. and McGrady, E. D., 1985, The kinetics of cluster fragmentation and depolymerisation. *J. Phys. A:Math. Gen.*, **18**, pp. 3027-3037.
- [13] Gzyl, H. and Tagliani, A., 2010, Stieltjes moment problem and fractional moments. *Applied Mathematics and Computation*, **216**, pp. 3307–3318.
- [14] Attarakih, M., Bart, H.-J and Faqir, N., 2006 , Numerical solution of the bivariate population balance equation for the interacting hydrodynamics and mass transfer in liquid-liquid extraction columns. *Chem. Eng. Sci.*, **61**, pp.113-123.
- [15] Simon, M.,2004, *Koaleszenz von tropfen und tropfenschwärmen*. PhD thesis, The University of Kaiserslautern, Kaiserslautern.
- [16] Coulaloglou, C. A. and Tavlarides, L. L., 1977, Description of interaction processes in agitated liquid-liquid dispersions. *Chem. Eng. Sci.*, **32**, pp. 1289-1297.
- [17] Attarakih, M. and Bart, H.-J., 2014, Solution of the population balance equation using the differential maximum entropy method (DMaxEntM): An application to liquid extraction columns. *Che. Eng. Sci.*, **108**, pp. 123-133.
- [18] Schmidt, S., Simon, M. and Bart, H.-J., 2003, Tropfenpopulationsmodellierung – einfluss von stoffsystem und technischen geometrien, *Chem. Ing. Tech.*, **75**, pp. 62-68.
- [19] Vikhansky, A., Kraft, M., Simon, M., Schmidt, S. and Bart, H.-J.,2006, Droplets population balance in a rotating disc contactor: An inverse problem approach. *AIChE Journal*, **52**, pp. 1441-1450.
- [20] Sobrino, C., Acosta-Iborra, A., Izquierdo-Barrientos, M. A. & De Vega, M., 2015, Three-dimensional two-fluid modeling of a cylindrical fluidized bed and validation of the maximum entropy method to determine bubble properties. *Chem. Eng. J.*, **262**, pp. 628-639.
- [21] Attarakih, M., Hasseine, A. & Bart, H.-J., 2015, A meshfree maximum entropy method for the solution of the population balance equation, *Computer Aided Chemical Eng.*, **37**, pp. 197-202.

PERFORMANCE OPTIMIZATION FOR ABSORPTION REFRIGERATION MACHINE

Ridha Ben Iffa*, NahlaBouaziz and LakdarKairouani

Unité de RechercheEnergétique&Environnement, EcoleNationale d'Ingénieurs de Tunis. Université de Tunis El Manar, BP37, le Belvédère 1002, Tunisie

*Ridha Ben Iffa: Email: r.iffa@yahoo.fr

ABSTRACT

The objective of this work is to present an energy analysis of different absorption refrigerating systems operating with diverse refrigerants. We focus on both acceptable COP and low operating temperature. Therefore, a computer program is developed. An investigation of the thermodynamic properties is presented. Results show the COP evolution versus respectively the evaporator temperature, the temperature of condensation and the generator temperature. A particular interest is accorded to the intermediate pressure effect on the performance of the different systems. In order to better converge in the selection of the configuration and the refrigerant, which can ensure a good COP associated to relatively low operating temperature we have developed an experiments design, taking in account all parameters influencing the system performance and the operating function temperature. Result show that the refrigerating machine containing a compressor between the evaporator and the absorber has a coefficient of performance quite acceptable and that it can work at low generator temperature about 60 ° C and using the NH₃/LiNO₃ refrigerant.

Keywords Absorption, COP, Evapo-compression, Refrigeration.

NOMENCLATURE

COP	Coefficient of performance
f	circulation ratio
h	specific enthalpy, J/kg
H ₂ O	water
LiBr	Lithium bromide
LiNO ₃	lithium nitrate
\dot{m}	mass flow rate, kg/s
NaSCN	sodium thiocyanate
NH ₃	ammonia
P	pressure, bar, Pa
Q	heat-transfer rate, J/kg
S	Entropie, J/kg.K
T	temperature, °C,K
W	Work, J
x	mass fraction, %

Subscripts

1	first stage
2	second stage
AB	Absorber
CD	condenser
COM	compressor
Ent	Entrée d'un élément de la machine
EV	evaporator
GE	generator
ECH	Inter-exchange solution
in	inlet
out	outlet
L	Liquid
V	vapor

INTRODUCTION

Absorption machines have several advantages such as protecting the environment and the nature, this type of refrigerating machine does not use CFCs fluids (chlorofluorocarbons), which attack the ozone layer (Kang et al.2000 ;Boer et al.1987 ; Göktun 2000 ; Laouir et al. 2002). Besides they are quiet compared to vapor compression machines (Riffat and Guoquan 2004).

There are several models of absorption machines, can be found by a simple compound machines stage which consider a single absorber, an evaporator, a condenser and a single generator, which are the conventional absorption machine. This machine is working between two pressure levels (P_{EV} evaporator pressure and P_{CD} condenser pressure) has been the subject of several studies (Alvares and Trepp 1987; Misra et al. 2002; Mumah et al. 1994 ;Kouremenos 1985;Hulten and Berntsson 2002; Selahattin 1999).

Other models composed of different stages with different associations between the system components; they worked at three pressure levels (Saghiruddin and Siddiqui 2001; Bouaziz et al.2011; Charia et al.1991 ; Kumar 1993 ; Sun 1998). There is a wide range of torque that can be used for the refrigerating machine such as NH₃/H₂O, NH₃/NaSCN and NH₃/LiNO₃ (Sun 1998 ;Rodakis and Antonopoulos 1995; Linghui and Junjie 2010; Kairouani et al. 2005).

DESCRIPTION AND ANALYSIS OF THE SYSTEMS

Description of the systems

A single effect absorption refrigeration cycle, for which details are provided elsewhere (Bouaziz et al., 2011), is shown in Figure 1, the cascade cycle and double stage cycle represented respectively in Figure 2 and Figure 3 are developed by (Bouaziz et al., 2011), and the new cycle ECA (evaporator -compressor-absorber) is composed by an evaporator, an absorber, a generator, a condenser and a compressor inserted between the evaporator and the absorber. The cycle is represented in Figure 4.

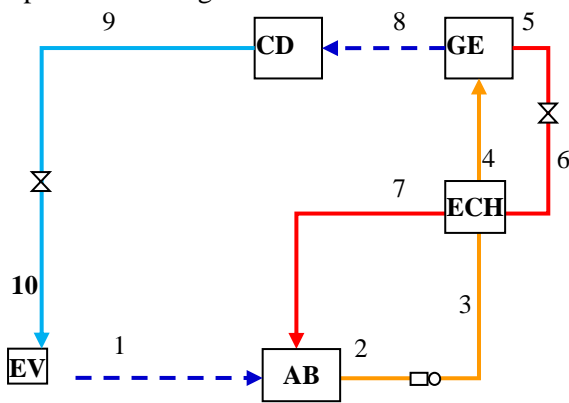


Figure 1 Single effect absorption refrigeration system

exchanger before entering the absorber ; the refrigerant condensate passes through expansion valve and enters the evaporator where it vaporizes, producing a cooling effect. Vapor exiting the compressor for enriches the solution into the absorber, the strong solution exiting the absorber passes through the solution heat exchanger on its way to the generator.

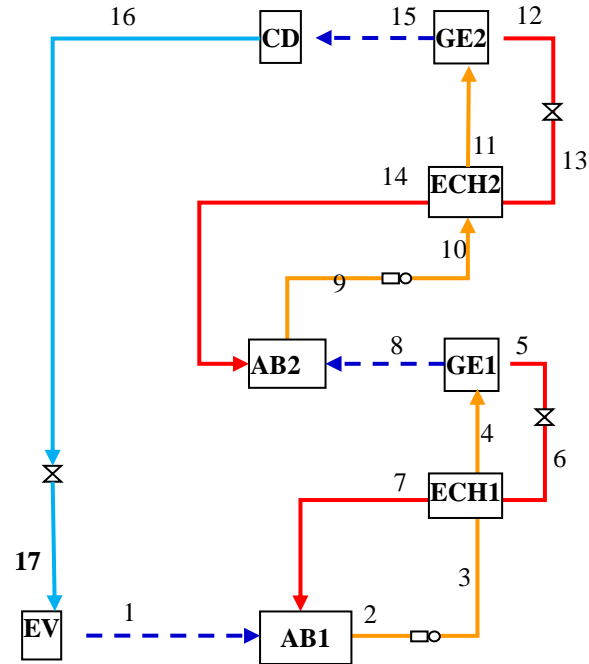


Figure 3 cascade 2

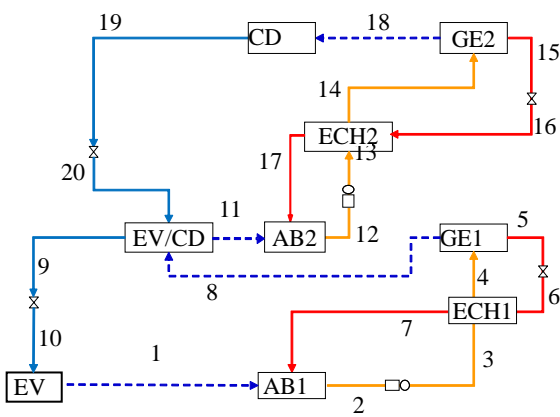


Figure 2 cascade 1

Three pressure levels are present in this configuration: the generator and the condenser works at high pressure and the evaporator at low pressure, while the absorber operates at an intermediate pressure. The refrigerant (NH_3 for $\text{NH}_3/\text{H}_2\text{O}$, NH_3/NaSCN , $\text{NH}_3/\text{LiNO}_3$ and H_2O for $\text{H}_2\text{O}/\text{LiBr}$) vapor from the generator enters the condenser and The weak solution exiting the generator passes through the solution heat

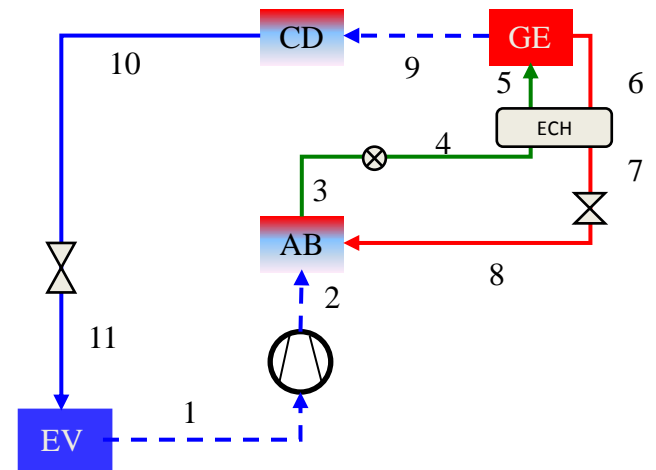


Figure 4 Cycle of evapo-compression (ECA)

Energy and mass balances

The mass balance governing the three present substances: weak solution, rich solution and refrigerant gas give:

$$\dot{m}_{FF} + \dot{m}_{xp} - \dot{m}_{xr} = 0 \quad (1)$$

$$\dot{m}_{FF} + x_p \times \dot{m}_{xp} - x_r \times \dot{m}_{xr} = 0 \quad (2)$$

$$f = \frac{(1-x_p)}{(x_r-x_p)} \quad (3)$$

The specific solution circulation factor f represents the mass of solution per kg of refrigerant vapor evaporated in the generator.

The rich and poor solution flow rates are given by Equations (4) And (5):

$$\dot{m}_{xr} = \dot{m}_{FF} \cdot f \quad (4)$$

$$\dot{m}_{xp} = \dot{m}_{FF} \cdot f \quad (5)$$

Energy balance for each installation component is presented by Equations

$$Q_{CD} = \dot{m}_{FF}(h_v - h_{out}) \quad (5)$$

$$Q_{AB} = \dot{m}_{FF}(h_v + (f - 1) \cdot h_{in} - f \cdot h_{out}) \quad (6)$$

$$Q_{GE} = \dot{m}_{FF}h_v + (f - 1) \cdot h_{out} - f \cdot h_{in} \quad (7)$$

$$Q_{EV} = \dot{m}_{FF}(h_v - h_{in}) \quad (8)$$

For an isentropic process, Laplace relation gives:

$$T_{in} \cdot P_{in}^{(1-\gamma)/\gamma} = T_{out} \cdot P_{out}^{(1-\gamma)/\gamma} \quad (9)$$

where:

T_{in} , P_{in} and, T_{out} , P_{out} , are the compressor temperature and pressure at the inlet and outlet, respectively.

Under the assumption of isentropic processes (ideal case), the consumed power is given by

$$Q_{is} = \dot{m}_{FF} \cdot C_{pFF} \cdot (T_{out} - T_{in}) \quad (10)$$

Taking into account the isentropic efficiency η_{is} , the real power is given by:

$$Q_{réel} = \frac{Q_{is}}{\eta_{is}} \quad (11)$$

$$Q_{is} = \dot{m}_{FF} \cdot (h_{out} - h_{in}) \quad (12)$$

Were the isentropic efficiency his is given by (Bouaziz et al., 2011; Brunin et al., 1997)

$$\eta_{is} = 0.874 - 0.0135 \cdot \tau \quad (13)$$

with

$$\tau = \frac{P_{AB}}{P_{EV}} \quad (14)$$

Coefficient of performance (COP) is given by the following expression:

$$COP = \frac{Q_{EV}}{Q_{GE} + Q_{COM}} \quad (15)$$

RESULTS AND DISCUSSION

Several studies have been devoted to determine the COP and limitations of absorption system operating conditions (Laouir et al. 2002). In order to evaluate the refrigeration absorption system performance, relative to different previously presented configuration, we have developed a numerical program. The calculating procedures of the fluid thermodynamic properties and the performance coefficient were obtained using MAPLE computer tools. The numerical simulation, developed in the present investigation carries out a comparative study of the referents systems performances.

Simple stage

Figure 5 shows the COP's evolution versus the generator temperature, for an evaporator temperature and a condenser temperature fixed respectively to 10 and 40°C.

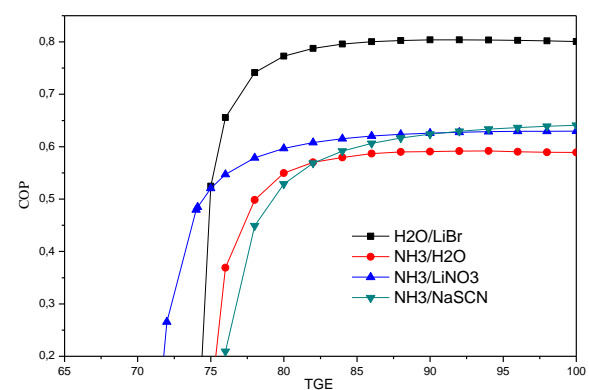


Figure 5 COP, of the simple stage system, evolution versus TGE with TEV= 10 °C and TCD=40°C.

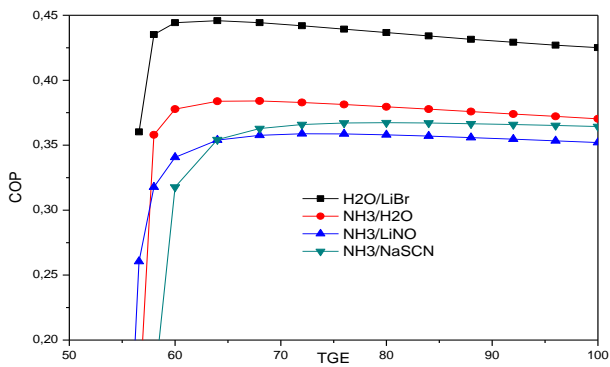


Figure 6 COP, of the cascade 1 system, evolution versus TGE with TEV= 10 °C and TCD=40°C.

Cascade 1

The temperature of the evapo-condenser is fixed at 25°C. Figure 6 shows the COP evolution versus TGE for different fluid, with TEV = 10°C and TCD=40°C.

Cascade 2

Figure 7 show the operating temperature is relatively low then to the classic system, less than 70 for all fluids. Where TEV, TCD and Pint are fixed respectively at 10 °C, 40°C and 3kPa for H₂O/LiBr, 750 kPa for the other fluid.

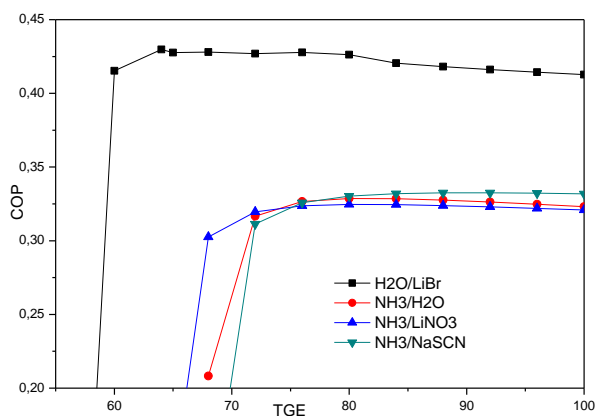


Figure 7 COP, of the cascade 1 system, as a function of aTGE with TEV= 10 °C and TCD=40°C.

New cycle

In the following, we fix the evaporator temperature and condenser temperature for each family of curve. The numerical results illustrate the evolution of the performance coefficient for different generator temperatures (see Figure 8).

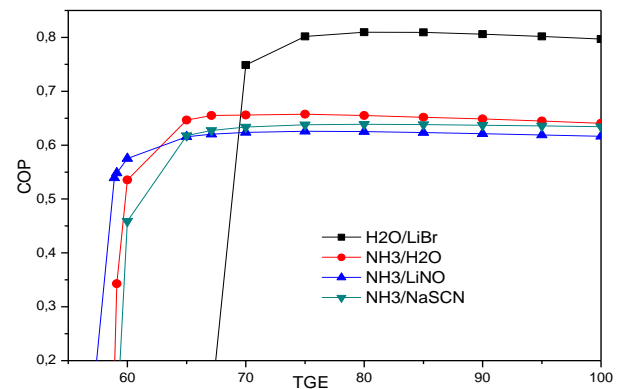


Figure 8 COP, of the Novel system, as a function of a TGE with TEV= 10 °C and TCD=40°C.

Figure 5-8 show that the H₂O/LiBr are a performing fluid, but their operating temperature is higher relative to other fluid. The cascade cycles decrease operating temperatures to levels generator but it has a low COP. The novel configuration has the advantage of single stage because the COP is almost the same and the advantage of cascade cycles because they are operating at low temperature.

Following the large number of results, we used an experimental design to determine the right combination.

EXPERIMENTS DESIGN

The objective of this research is to maximize the COP by maintaining a minimal value of the operating temperature (TGE).

It should be noted that the COP depends on three basic parameters:

- Generator temperature (TGE)
- Evaporator temperature (TEV)
- Condenser temperature (TCD)

The pair/couple used in the research and the installation affect the COP. For a minimal value of TCD or TGE or a maximal value of TEV, the COP is optimal.

In our investigation we have 5 factors with 4 levels (see table 1).

Table1 Factor and levels

Factor	Levels	Factor	levels	Factor	levels
Cycle	Ev-comp	T _{EV}	5°C	T _{GE}	65°C
	Casc 1		10°C		75°C
	Casc 2		15°C		85°C
	Simple		20°C		100°C
Fluid	H ₂ O	T _{CD}	25°C		
	LiNO ₃		30°C		
	NaSCN		35°C		
	LiBr		40°C		

There are two types of experimental plans: factorial, which require a high number of experiments (in our case, for example, five factors of four levels give $4^5 = 1024$ experiments) and fractional plans which can reduce the number. In our study, we are using a Carré Hyper Greco-Latin plan consisting of 16 experiments. The possible combinations are drawn in table 2.

In figure 9, we deduce that all the factors have a significant effect, and to obtain an acceptable COP with low temperature of the generator, the Evapo-comp cycle can be used.

Table 2 Le désigne du plan d'expérience

Cycle	Fluid	TEV	TCD	TGE	COP
Ev-comp	H2O	10	30	65	0,71
Ev-comp	LiNO3	15	35	75	0,68
Ev-comp	NaSCN	20	40	85	0,69
Ev-comp	LiBr	25	45	100	0,84
Cascade 1	H2O	15	40	100	0,38
Cascade 1	LiNO3	10	45	85	0,35
Cascade 1	NaSCN	25	30	75	0,39
Cascade 1	LiBr	20	35	65	0,47
Cascade 2	H2O	20	45	75	0,45
Cascade 2	LiNO3	25	40	65	0,46
Cascade 2	NaSCN	10	35	100	0,35
Cascade 2	LiBr	15	30	85	0,34
Simple	H2O	25	35	85	0,73
Simple	LiNO3	20	30	100	0,71
Simple	NaSCN	15	45	65	0,00
Simple	LiBr	10	40	75	0,52

Figures 10 and 11 confirm that the new cycle can operate in difficult conditions on the level of the condenser (high TCD) with low temperatures of the generator while the classical machine cannot operate unless the temperature is above a 75°C and temperatures lower than 40°C to provide the same COP than the new installation for TGE=65°C and TCD=45°C.

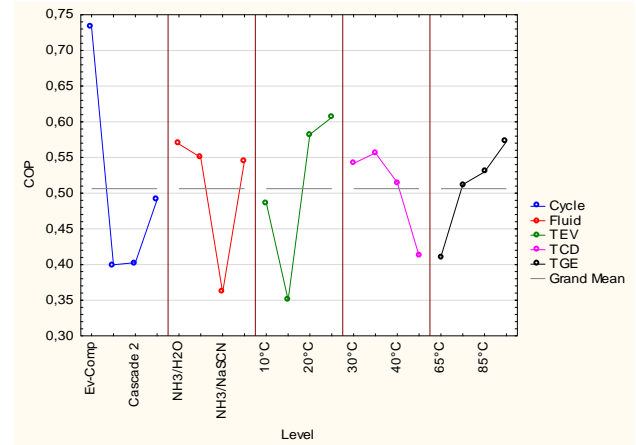


Figure 9 Graph of Main Effects

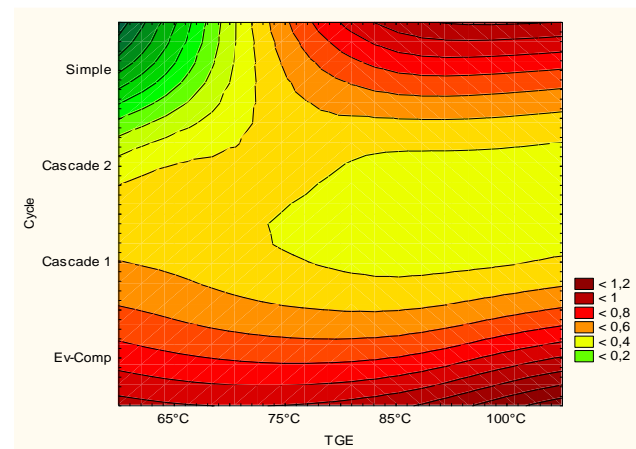


Figure 10 COP is function of TGE and Cycle

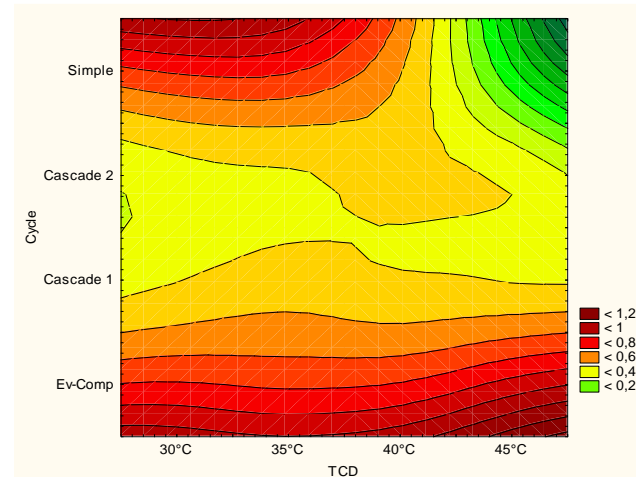


Figure 11 COP is function of TCD and Cycle

CONCLUSIONS

The conventional machine provides a COP considered as acceptable. It operates with an operating temperature on the level of the generator around 75°C for a condensation temperature of 40°C and an evaporation temperature of 10°C.

The cascade cycles 1 and 2 operate with a low T_{GE} but their COP is half of the simple machine. They have an operating problem in the first and second levels and this is due to the difference of Δx .

The new configuration produced a COP higher than the cascade cycle and the simple machine.

Besides, it operates with a T_{GE} lower than the one in cascade cycle or the simple level lower than 60 pour NH_3/H_2O , $NH_3/NaSCN$ and $NH_3/LiNO_3$ with the same temperatures of the evaporator and condenser.

REFERENCES

- Y. T. Kang, Y. Kunugi, T. Kashiwagi (2000) Review of advanced absorption cycles: performance improvement and temperature lift enhancement. *Int J. Refrig.* 23:388-401.
- D. Boer, M. Valles and A. Coronas (1998) Performance of double effect absorption compression cycles for air-conditioning using methanol-TEGDME and TFE-TEGDME systems as working pairs. *Int J. Refrig.* 21:542-555.
- S. Göktun (2000) Performance analysis of a heat engine driven combined vapor compression-absorption-ejector refrigerator. *Energy Convers. Mgmt* 41:1885-1895.
- A. Laouir, P. Legoff, J. M. Hornt (2002) Cycle de frigopompes à absorption en cascades matérielles-détermination du nombre d'étages optimal pour le mélange ammoniac-eau. *Int J. Refrig.* 25:136-148.
- S.B. Riffat, Guoquan Qiu (2004) Comparative investigation of thermoelectric air-conditioners versus vapour compression and absorption air-conditioners. *App. Th. Eng.* 24:1979-1993
- S. G. alvares and Ch. Trepp (1987) simulation of solar driven aqua-ammonia absorption refrigeration system. *Int J. Refrig.* 10:40-49
- Misra R D, Sahoo P K, Gupta A (2002) Application of the exergetic cost theory to the LiBr/H₂O vapour absorption system. *Energy* 27:1009-1025
- S. N. Mumah, S. S. Adefila and E. A. Arinze (1994) First law thermodynamic evaluation and simulation of ammonia-water absorption heat pump systems. *Energy convers. Mgmt.* 35:737-750
- D. A. Kouremenos (1985) A tutorial on reversed NH₃/H₂O absorption cycles for applications. *Solar energy* .34:101-115.
- Hulten M, Berntsson T (2002) The compression/absorption heat pump cycle-conceptual design improvements and comparisons with the compression cycle. *Int J. Refrig.* 25:487-497
- Selahattin Göktun (1999) Optimal performance of an irreversible, heat engine-driven combined vapour compression and absorption refrigerator. *Applied Energy* 62:67-79
- Saghiruddin, M. Altamush Siddiqui (2001) Economic analysis of two stage dual fluid absorption cycle for Optimizing generator temperatures. *Energy Conversion and Management* 42:407-437
- N. Bouaziz, R. Ben Iffa et L. Kairouani (2011) Performance of a water ammonia absorption system operating at three pressure levels. *JMER* 3:120-127
- N. Bouaziz, R. Ben Iffa et L. Kairouani (2011) Avantage d'une configuration de machine à absorption opérant à trois niveaux de pression. *Mécanique & Industries* 12:103-107
- M. Charia, A. Pilatte et M. Boudida (1991) Machine frigorifique à absorption (eau-ammoniac) fonctionnant avec des capteurs plans sur le site de Rabat. *Rev.Int.Froid* 14:297-303
- S. Kumar (1993) Experimental studies of a three-pressure absorption refrigeration cycle. *Rev.Int.Froid* 16:31-39
- E. D. Rodakis and K. A. Antonopoulos (1995) Thermodynamic cycle, correlations and nomograph for NH₃-NaSCN absorption refrigeration systems. *Heat Recovery Systems & CHP* .15:591-599
- Linghui Zhu, Junjie Gu (2010) Second law-based thermodynamic analysis of ammonia/sodium Thiocyanate absorption system. *Renewable Energy* 35:1940-1946
- L. Kairouani, E. Nahdiet R. Ben Iffa (2005) thermodynamic investigation of two stage absorption refrigeration system connected by a compressor. *Am. J. App. Sc* 2, 6:1036-1041
- Bouaziz N, Ben Iffa R, Nehdi E, Kairouani L (2011). Conception of an absorption refrigerating system operating at low enthalpy sources. In: Moreno-Pirarajan Juan Carlos, editor. *Thermodynamics systems in equilibrium and nonequilibrium*; ISBN: 978-953-307-283-8, InTech.
- Brunin O, Feidt M, Hivet B (1997). Comparison of the working domains of some compression heat pumps and a compression-absorption heat pump. *Int J Refrig*; 20:308e18. 417.

EXPERIMENTAL INVESTIGATION OF SYNGAS AND HYDROGEN PRODUCTION FROM STEAM BIOMASS GASIFICATION

Borisut Chantrawongphaisal¹, Zeghmati Belkacem², Satta Watanatham¹, Pravit Thapnui¹,
Phongsak Hongcharoensri¹, Pichai Wongharn¹

*Corresponding author: Fax: +66 2 577 9514 Email: borisut@tistr.or.th

ABSTRACT

An experimental study on biogasification is carried out on a semi-pilot scale fixed bed downdraft gasifier. The Eucalyptus chips is used as feedstock (diameter 2.54 to 3.81 cm and length 2.54 cm). Two oxidizing agent have been used : oxygen from air and steam. Saturated steam is injected into the oxidation and the reduction zone of the gasifier when the steady state conditions are reached. The objectives of the present study are to understand the effects of direct injection of steam in the combustion and reduction zone of the gasifier on products gas composition and temperature profile. The gases composition were determined using a Gas chromatograph (Varian 450-GC) equipped with a thermal conductivity detector to analyze the permanent gases H₂, CO, CH₄ and CO₂. Results revealed that the gas composition in producer gas are composed of carbon monoxide (CO) about 16 percent, hydrogen (H₂) about 30 percent, methane (CH₄) about 12 percent, nitrogen (N₂) about 33 percent, carbon dioxide (CO₂) about 9 percent. The high heating value of syngas is about 9.76 MJ per cubic meter.

KEYWORDS: Biomass gasification, steam gasification, steam reforming, pyrolysis, combustion.

INTRODUCTION

Biomass gasification is an effective and attractive method for converting biomass into combustible gases as syngas by partial oxidation at high temperatures in the range of 800°C-1200°C [1]. It is a technology applicable to all kinds of residues produced in agriculture, food processing industry, wood furnishing industrial and fast growing trees for energy. This technology is promising for Thailand which imported oil for more than 60 percent of its energy consumption. In traditional biomass gasification technologies as fixed bed, entrained bed, fluidized bed, an amount of pure oxygen is required as gasifying agent [2-4] In these traditional biomass gasifiers, the syngas production is low and the CO₂ emission is high during the gasification[5-8]. The quality and yield of syngas in biomass gasification is depending of the gasifier operating conditions as temperature, pressure, biomass feed rate, size of feed stock and the oxidizing agent such as air, oxygen and steam. The use of steam as oxidizing agent leads to high H₂ content in syngas production [9]. In order to increase the amount of hydrogen yield and the amount of H₂/CO content of the producer gas, the steam is used instead of air in the gasifier. Many researchers

investigated hydrogen production from biomass gasification in fluidized bed and few studies are concerning hydrogen production from oxygen/steam gasification in a downdraft gasifier [10] which is characterized by a higher H₂ content of gaseous product. In addition, the steam biomass gasification process can solve tar problem and increase the efficiency of biomass gasifier. Therefore this experimental study on steam biomass gasification with a downdraft gasifier.

The aim of this experimental study is to determine how to increase the high heating value of syngas in a fixed bed downdraft biomass gasification and lead to increase the temperature in ceramics kiln using eucalyptus chips as feedstock. The steam as oxidizing agent is injected into combustion and reduction zones.

Experimental set up and material

Experimental set up

The experimental set-up were performed in a co-current fixed bed downdraft gasifier pilot scale with 240 cm total height. This gasifier consists of the two concentric cylinders whose inner and outside

diameters are respectively equal to 20 cm and 35 cm. The lower part of the reactor is composed of a cone in which a barrel collects the ash. The cone and the upper cylinder are connected with a vertical cylinder of non-uniform section. The steam at 65 °C and pressure 0.250 bar is internal heat generate from water which pass through the gaseous pipeline with temperature 400 to 600 °C. The gas cleaning system installed after the cyclone. At the exit of the cleaning chamber the gases are sucked with a blower, 3 hp, placed between the cleaning chamber and the gas holder. The produce gas is stored in the gas holder and pass to the pottery kiln which has dimension 1 x 1 x 1 m³. The wood chips were feed to the top of the gasifier and were supplied into the reactor by manual system. The velocity of producer gas is measured inside the gas pipeline at the sampling port with a Pitot tube model Testo 512. Temperature was measured at several points (drying zone, combustion zone, reduction zone, outlet tube, pottery kiln) of the gasifier using thermocouples of type K connected to a data logger.

Experimental procedure

Each run was started using liquid petroleum gas (LPG) in order to ignite the feedstocks and to warm up the gasifier reactor. The temperature in the gasifier reactor was controlled by air (O₂) injected into the combustion zone with flow rate 18 m³per hour. The overall process of biomass gasification can be divided into four steps. The first step is drying where the moisture evaporates from the feedstock; the drying temperature is varying between 100°C to 200°C. The next step is the pyrolysis at the temperatures in a range 400- 700 °C. This was followed by the devolatilization, the step where evaporative compounds in biomass evaporate, consisting of hydrocarbon gases, hydrogen, carbon monoxide, carbon dioxide, tars and vapor. In this step, the major part of carbon content of the biomass is converted into char. The third step is the gasification process. During this process, carbon produced from the pyrolysis process reacted with oxygen from air. This combustion or oxidation reaction releases heat into the surrounding media, resulting in the changing temperature ranging from 700 °C to 1100 °C. The last step is the production of hydrogen and carbon monoxide by reforming of carbon and carbon dioxide.

After startup and warm up the gasifier, with air, the outlet temperature of the gaseous is about 400 °C

generate steam at temperature of 65 °C, a pressure of 0.250 bar with flow rate of 3.5 kg/hr . The air flow is immediately stop as soon as the steam is injected into the oxidation and reduction zone.

The steam addition promotes the water gas shift reaction and increases the hydrogen content in the producer gas. The unreacted chars and bottom ash are removed by a screw located at the bottom of the reactor and discharged into the water. The fly ashes in the producer gas are separated by the cyclone so that the clean production gas is sent to generate heat.

The wood chips were conveyed by manual into the top of the gasifier with a feed rate of 20 kg /hr.

Material

Eucalyptus chips (diameter 2.54 to 3.81 cm and length 2.54 cm) was used as biomass feedstocks for the experiments. The proximate and ultimate analysis were performed using TGA (America Society for Testing) and CHNS analyzer (Leco TruSpec CHN) and High Heating Value by Parr 6300 calorimeter. The gas composition was determined by a Gas Chromatograph Varian 450-GC.

The proximate analysis, ultimate analysis and heating values were carried out based on ASTM D7582, ASTM D 5373, and ASTM D 5865, respectively. The equipment used for these analysis is the TGA for the proximate analysis, the Leco TruSpec CHN for the ultimate analysis and the Parr 6300 calorimeter for the high heating values.

In air steam gasification, the major reactions contributing to the high H₂ yield are water-gas, water gas-shift reaction and the methane reforming reaction [10].

The major chemical reaction that occur during gasification are reported in table 1 [11].

Table 1: Chemical reaction during air steam gasification

Reactions	Heat of reaction	Type of reaction
$C+CO_2 \leftrightarrow 2CO$	172.5 kJ mol ⁻¹	Boudouard
$C+H_2O \leftrightarrow CO+H_2$	131.3 kJ mol ⁻¹	Water gas primary
$C+2H_2O \leftrightarrow CO_2+2H_2$	90.2 kJ mol ⁻¹	Water gas secondary
$C+2H_2 \leftrightarrow CH_4$	-74.9 kJ mol ⁻¹	Methanation

$2\text{CO} + \text{H}_2\text{O} \leftrightarrow \text{CO}_2 + \text{H}_2$	-41.2 kJ mol ⁻¹	Water gas shift
$\text{CH}_4 + \text{H}_2\text{O} \leftrightarrow \text{CO} + 3\text{H}_2$	-206.2 kJ mol ⁻¹	Steam reforming
$\text{CH}_4 + \text{CO}_2 \leftrightarrow 2\text{CO} + 2\text{H}_2$	247.4 kJ mol ⁻¹	Dry reforming

The heat necessary to the reaction is provided by partial oxidation of the gasified materials or is supplied externally.

RESULTS AND DISCUSSION

The properties of chips wood.

During the experimental tests, this moisture content was 11 %. (tables 2 and 3).

Table 2: Proximate analysis of eucalyptus wood

(wt, dry basis %)	
water content	11.12
Volatile mater	72.62
Ash	0.62
Fixed carbon	15.64
HHV,MJ/kg	16.9

It will noted that the eucalyptus water content is about 11 % . Furthermore, almost 70 % of eucalyptus wood chips is composed of high volatile matter components , low the fixed carbon and low ash content. Then the heat input to gasification system is quite high.

The chemical composition of eucalyptus wood chips expressed on. The ultimate analysis shows that the ash content is very low (Table 3). In addition there is no trace of nitrogen and sulfur and carbon and oxygen has high levels.

Table 3 : Ultimate analysis of feedstock (eucalyptus wood) %

(wt,%)	
carbon	45.05
Hydrogen	6.86
Oxygen	39.06
Nitrogen	0
Sulfur	0
Ash	9.03

Temperature distribution in the gasifier. As it can be seen in figure 1, the temperature in the gasifier describes four reactive zones namely drying, pyrolysis, oxidation and reduction describe below. It will be noted that the carbon in oxidation zone was oxidized with oxygen from air with exothermic reaction at temperature of about 1000 °C after the steam was feeded into oxidation zone and the carbon in oxidation zone was oxidized with oxygen from steam at temperature of about 800 °C.

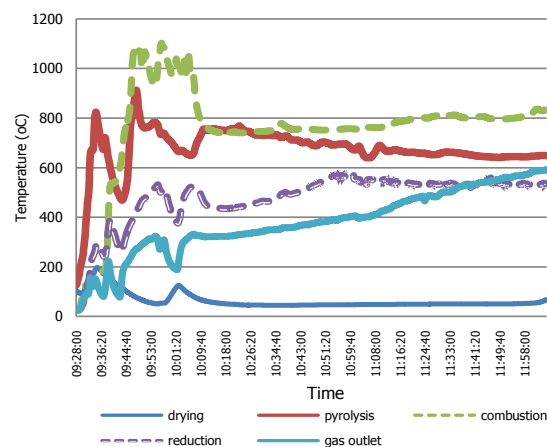


Figure 1

The temperature distribution in gasifier reactor **Effect of steam on biomass gasification** Generally, the steam has effects on reforming the light hydrocarbon and tar formed during biomass gasification to increase hydrogen in producer gas.

The producer gas composition produces by conventional biomass gasification and steam hydrogasification are presented in Table4.

Table 4 : Composition of the producer gas by gasification with two oxidizing agents : oxygen from air ; steam water.

Producer gas	air	steam
Hydrogen ,H ₂	15	30
Carbon monoxide, CO	18	16
Methane,CH ₄	0	12
Carbon dioxide ,CO ₂	12	9
Nitrogen,N ₂	55	33

The results reported in Table 4 illustrate the effectiveness of gasification with steam as oxidizing agent. Indeed, the hydrogen content obtained with the steam is equal to twice that obtained using the oxygen from air as oxidant agent. We also note that the use of steam as oxidizing agent leads to an increase in the methane content and to significant reduction of CO₂ and N₂ content in producer gas. The high heating value of syngas is about 9.76 MJ per cubic meter.

CONCLUSIONS

An experimental study of a steam gasification in a fixed bed downdraft gasifier is reported. We showed that the use of steam as oxidizing agent increases considerably the hydrogen and methane content in the gas produced by this process. In comparison to gasify biomass with two oxidizing agents between oxygen from air and steam. The composition of both are different. The nitrogen gas from air is presented in the producer gas which is directly effects on the temperature reduction. The hydrogen from steam also balance hydrogen in substance and lead to increase hydrogen and methane in syngas production.

Acknowledgments

The author would like to thank to Thailand Institute of Scientific and Technological Research, TISTR, who is funding the research

REFERENCES

- [1] Sheth PN, Babu BV. Experimental studies on producer gas generation from wood waste in a downdraft biomass gasifier. *Bioresour Technol* 2009;100 (12):3127–33.
- [2] Colomba Di Blasi, Dynamic behaviour of stratified downdraft gasifiers. *Chem Eng Sci*, 2000; 55 p. 2931, 2044
- [3] Beenackers AACM. Biomass gasification in moving beds, a review of European technologies. *Renew Energy*, 1999, 16, p. 1180-1186
- [4] Li XT, Grace JR, LIM CJ, Watkinson AP, Chen HP, Kim JR, Biomass gasification in a circulating fluidized bed. *Biomass Bioenergy*, 2004, 26, p. 171-193
- [5] Sergio, R., 2014, Hydrogen Rich Gas from Catalytic Gasification of Biomass in a Fluidized Bed Catalytic Filters, CHEMICAL

ENGINEERING

TRANSACTIONS, vol.37, pp.157-162.

- [6] Morteza, S. and Ahmad, T., 2014, Hydrogen and Syngas Production via Pyrolysis and Steam Gasification of Bagasse in a Dual Bed Reactor, *Petroleum and Coal*, Vol.56(3), pp.307-313.
- [7] Gallucci F., Hamers H.P., Zanten M., Experimental demonstration of chemical looping combustion of syngas in packed bed reactors with limonite, *Chem. Eng. J.* 274 (2015) 156–168.
- [8] Crnomarkovic N., Repic R., Mladenovic R., Neskovic O., Veljkovic M., Experimental investigation of role of steam in entrained flow coal gasification, *Fuel* 86 (2007) 194–202
- [9] LV PM, Chang J., Wang TJ, Chen Y., Zhu JX, Hydrogen -rich gas production from biomass catalytic gasification. *Energy Fuels* 2004, 18, p; 228-233.
- [10] Ashokkumar M. Sharma, Ajay Kumar, Raymond L. Huhnke, Effect of steam injection location on syngas obtained from an air -steam gasifier.
- [11] L. Emami Taba, M. Faisal Irfan; W.A.M. Wan Daud, M. Harun Chakrabarti, The effect of temperature on various parameters in coal, biomass and co-gasification: a review, *Ren Sustainable Energy Rev.* 16, (2012)p. 5584-5596

NUMERICAL MODELING OF A REFRESHING BURIED TANK

Auteurs : Karim DEHINA¹, Abderrahmane Medjdoub MOKHTARI¹, Bernard SOUYRI²

¹Laboratoire LMST université des sciences et de la technologie Mohamed BOUDIAF d'Oran

²Laboratoire (LOCIE) - Université de Savoie

karimdehina@yahoo.fr, am_mokhtari@yahoo.fr, Bernard.Souyri@univ-savoie.fr

ABSTRACT

We present in this paper an energy behaviour study of a horizontal water tank buried in the ground for the need to refresh buildings. This study aims to develop a model for energy simulation system to evaluate its energy efficiency and its relevance to improve summer comfort in Mediterranean climate buildings.

There is provided a one-dimensional model layers in the radial section of the tank, taking into account the stratification. The ground is represented by a two-dimensional finite element domain coupled to the tank that allows studying the soil / tank system under varying conditions.

Initially, the tank is studied separately ground by considering isothermal boundary conditions and a constant feed rate. The comparison of results obtained by this model with those obtained using a CFD model in ANSYS FLUENT is satisfactory.

A case study is then modelled as well by the model proposed by Fluent; the article shows the good agreement between the numerical results.

Finally, the model is implemented in the software TRNSYS where a simulation of the underground tank coupled to a building is achieved.

The results of this simulation show that a shallow underground tank can contribute to buildings cooling during the summer, and offers the prospect of a parametric study to optimize the system under different operating conditions.

NOMENCLATURE

Symbol	Name,	unity
A	surface of contact between nodes	m^2
A_c	Shell Surface node	m^2
C_p	Specific heat	$J/kg.K$
h	Convective heat coefficient	$W/m^2.K$
H	Height of node	m
G	Solar radiation	W/m^2
k	Thermal conductivity	W/mK
M	Weight	kg
\dot{m}	Mass flow rate	kg/s
q	Thermal Unit Flow	W/m^2
Q	Heat flow	W
P	Electric power	W
T	Temperature	K
T_s	Average soil surface temperature	K
t	Time	s
t_{min}	Time corresponding to minimal T_s	<i>day</i>

U Global heat transfer coefficient W/m^2K

Greek symbols

α_{sol}	Albedo	-
β	Flow signal entering	<i>1 or 0</i>
δ_1	Rising flow signal value	<i>1 or 0</i>
δ_2	Dropping flow signal	<i>1 or 0</i>
α	thermal diffusivity	$m^2.s^{-1}$

Indices

amb	Ambient
f	frigorific
i	Layer number
in	Entry
out	Exit
pl	Floor
sur	Surface
z	Depth axis

1. INTRODUCTION

Géosolar systems such as Canadian or Provencal wells and geothermal heat pumps are enjoying great success and attracting increasing interest due to their implementation simplicity and energy efficiency. In recent years a new geothermal storage system is studied in the laboratory LMST at the University of Science and Technology of Oran (Algeria) where a horizontal tank buried at shallow depth, coupled with a hydraulic floor, should contribute to the refreshment of 'a building. We are interested in this communication to the numerical simulation of this system to assess its energy efficiency. The tank coupled to the ground is integrated in a module running under Trnsys 16.0 software where it is possible to simulate the system coupled to a building under realistic weather conditions.

Studies on the thermal storage tanks are mainly relate to solar tanks, which several models have been proposed based on discretisation level of of water volume. Duffie and Beckman [1] present three-configurations of a monodimensional storage tank, fully mixed, stratified and piston model. Nelson & al. [2] found that stratification varies in refreshing thermal storage tanks with the modified Biot number. Csordas & al. [3] studied the effect of vertical jet on stratification in the entry region of vertical tanks. The penetration of a horizontal jet was studied by Pantokratoras [4] where he proposed a modified Froude number to calculate jet trajectory. A tridimensional zonal model proposed by Blandin [5] highlights the importance of localized physical phenomena such as jets and internal heat exchangers.

Determination of the temperature field influenced by the tank can be done by the model Kasuda et al. [6] for which the floor surface temperature can be obtained from the relationship of Mihalakakou [7].

Unlike solar tanks, buried refreshing tank we study has only an input and an output, and the temperature gradients are relatively weaker. A three-dimensional model would be very costly in time and memory due coupling to ground and building.

A one-dimensional model with a limited number of layers, and taking into account the particularities of the injection area seems to be a good compromise between reliability and the computation time.

2. MODELING

2.1. CFD model of the tank

Under ANSYS FLUENT 12.0, we simulate steady flow water entering in a horizontal commercial tank of 1m diameter and 2.2m lengt. We apply an isothermal condition on the shell face $T_s = 25^\circ \text{C}$. The water is

injected at a temperature $T_{in} = 30^\circ \text{C}$ and a flow rate = 0.1 l/s in the top of the tank at a height $h = 0,95\text{m}$ from the base, and exits through the bottom at a height $h = 0.05\text{m}$. The physical characteristics of the water are assumed to be constant.

Figure 1 shows a sharp drop in temperature at the entry region where most of heat exchange occurs in the upper layers. The velocity profile is shown in Figure 2. We can see mixing lower layers. This result is consistent with studies referenced [3], [4] and [5].

It can be concluded that the tank has two distinct zones, the upper portion being located at and above the jet where the bulk product to the heat exchange with the external environment and the bottom characterized by low exchange .The transitional regime in the case of an charging/discharging cycle, the upper part ensures rapid cooling of the water while the bottom stop mode allows unloading the tank.

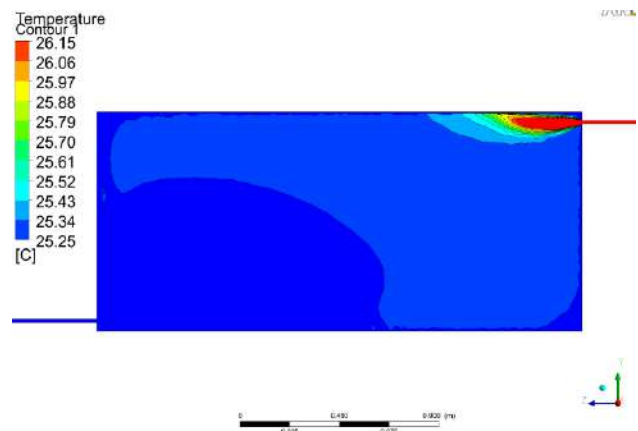


Figure 1: isothermal profile in the tank - longitudinal section

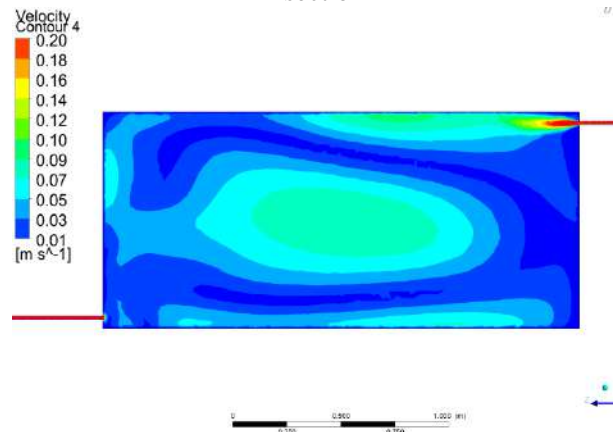


Figure 2: speed profile in the tank - longitudinal section

2.2. Monodimensional model of the tank

The proposed monodimensional model is based on the distinction between the upper and lower parts mentioned in paragraph 2.1 above. The upper part is

designated in Figure 3 by the node 4 while the lower part is divided into three segments 1,2 and 3. The temperature of the node 2 is considered as the outlet temperature T_{out} .

At each time step dt we solve a system of four differential equations (1) corresponding to the number of nodes.

$$M_i C_p \frac{dT_i}{dt} = \beta \dot{m} C_p (T_{in} - T_i) + \delta_1 \dot{m} C_p (T_{i-1} - T_i) + \delta_2 \dot{m} C_p (T_{i+1} - T_i) + k A_{i-1} (T_{i-1} - T_i) + k A_i (T_{i+1} - T_i) + U A_{c,i} (T_s - T_i) \quad (1)$$

$$\beta = 1 \text{ si } \sum_{i=1}^n H_i = h_{in} , \text{ if not } \beta = 0$$

$$\delta_1 = 1 \text{ if } H_{in} < H_{out} \text{ et } H_{in} < \sum_{i=1}^n H_i \leq H_{out}, \text{ if not } \delta_1 = 0$$

$$\delta_2 = 1 \text{ if } H_{in} > H_{out} \text{ and } H_{in} > \sum_{i=1}^n H_i \geq H_{out}, \text{ if not } \delta_2 = 0$$

Coefficients δ_1 et δ_2 indicate the direction of flow in the general case where the injection water is either at the top or bottom of the tank

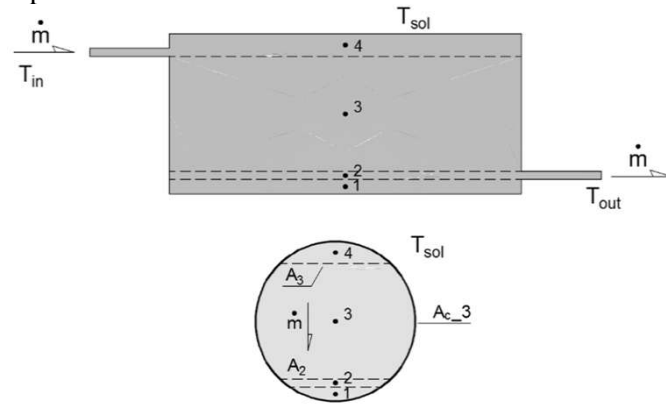
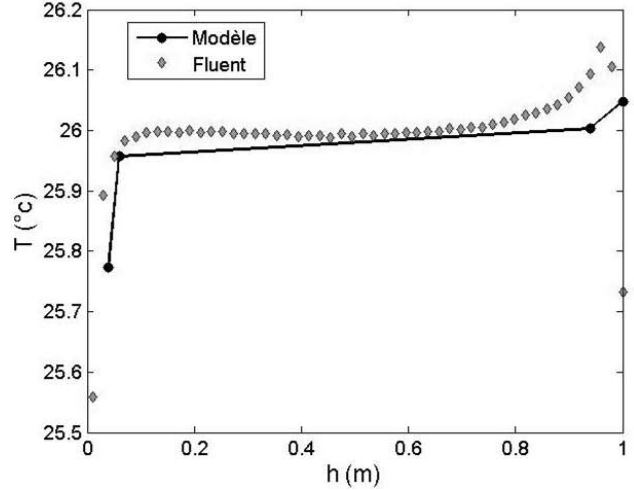


Figure 3: monodimensional model of the refreshing tank

Figure 4 shows the change in average temperatures by node in the tank bottom upward. The temperature $T_{in} = 30^\circ \text{C}$ input is not shown for readability. There has been a satisfactory agreement between the CFD model and the proposed one-dimensional model.

Figure



4: Water temperature in the tank - Compare CFD model and simplified model

2.3. Ground tank model coupling

The ground is represented by a rectangular area in finite elements - Figure 5 -including the tank. The surface temperatures T_{sur} the bottom and T_z vary according to time. It is considered that the side walls are adiabatic.

The temperature at the surface of the ground T_{sur} is given by Mihalakou [7] on the basis of heat balance between the convective flow and radiative \mathcal{O}_{rad} et \mathcal{O}_{conv} shown in Figure 6, the conduction within the soil being neglected. Thiers [8] provides a reformulated expression of this temperature given by equation (2)

$$T_{sur} = \frac{(1 - \alpha_{sol}) \cdot G + h_r \cdot T_{amb} + (h_r - h_e) \cdot \frac{b_{lat}}{a_{lat}}}{h_e} \quad (2)$$

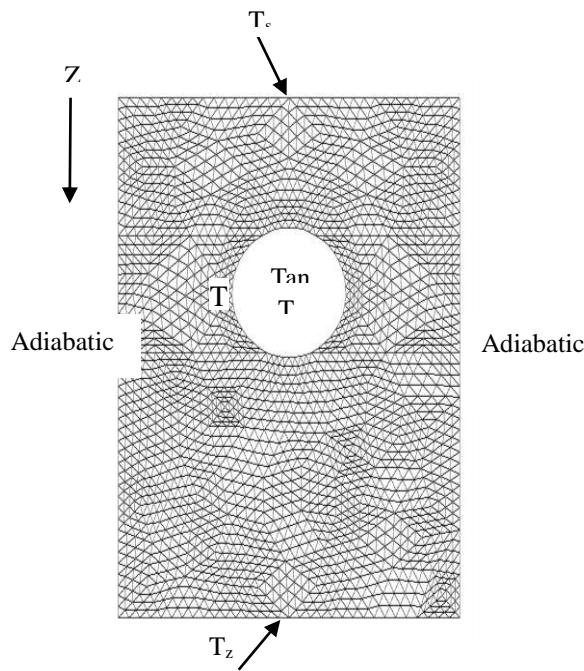


Figure 5: Section soil in contact with the tank finite element

Where α_{sol} and G represent the albedo and solar radiation, h_r, h_e convective parameters, and b_{lat}, a_{lat} are empirical constants. [8]

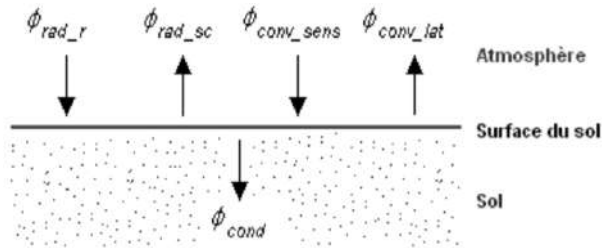


Figure 6: Ground surface energy balance [8]

The temperature T_z at a given depth is given by equation (3) Kasuda [6]

$$T(Z, t) = \bar{T}_s - A \cdot e^{\left(-z \cdot \sqrt{\frac{\pi}{365\alpha}}\right)} \cdot \cos\left(\frac{2\pi}{365}\left(t - t_{min} - \frac{Z}{2} \cdot \sqrt{\frac{365}{\pi\alpha}}\right)\right)$$

Coupling with ground is possible by calculating each time $t^{(n)}$ the flows exchanged between the tank i node and the adjacent ground node (4)

$$q = U \left(T_i^{(n)} - T_s^{(n)} \right) \quad (4)$$

At step $t^{(n+1)}$ soil interface temperature T_s is obtained by numerical solution of the diffusion equation (5) on the thermal field representing the ground

$$\frac{\partial^2 T}{\partial x^2} + \frac{\partial^2 T}{\partial z^2} = \frac{1}{\alpha} \frac{\partial T}{\partial t} \quad (5)$$

3. Study of the complete system building - refreshing buried tank

3.1. Simulation parameters

Under Trnsys 16.0 we simulate the energy behaviour of a room equipped with a hydraulic floor coupled with a buried refreshing tank in Oran. The system initialization begins 1st May in continuous operation. Table 1 summarizes the most simulation important parameters.

Tank	Diameter (m)	1.00
	Length (m)	2.20
	Axis depth (m)	2.50
Soil	Thermal diffusivity α (m ² /s)	5.88 x 10 ⁻⁷
	Room	
	Floor area (m ²)	20.00
	Height (m)	3.00
	Level	R.D.C
	Window	Double glazing 2m ²
	External walls U (W/m ² .K)	0.615
	Roof U (W/m ² .K)	1.08
	Hydraulic floor U (W/m ² .K)	0.77
	Wood isoplane door U (W/m ² .K)	3.00
Circuit	Pump Q (l/s)	0.20
	Tubing P.E.R Ø 20mm L(m)	10.00
	Pump electric power P(W)	60.00

3.2. RESULTS AND DISCUSSION

Operating tank allows according to Figure 7 to lower the indoor temperature 1 to 2 ° C during the period of July 10 to 31. The heat flux absorbed by the hydraulic floor designated in Figure 8 by the refrigerating gain is calculated by equation (6)

$$q_f = h_{pl}(T_{air} - T_{pl}) \quad (6)$$

In this case the mean cooling flow obtained over this period is $q_f = 10.5$ W / m² therefore a total flow $Q_f = 210$ W for an area of 20 m². Performance coefficient COP of the system is obtained by relation (7)

$$COP = \frac{q_f}{P} = 3.5 \quad (7)$$

Finally, it would be useful to define a volume ratio of storage per floor area. For this case, it is 87 liters / square meter of floor.

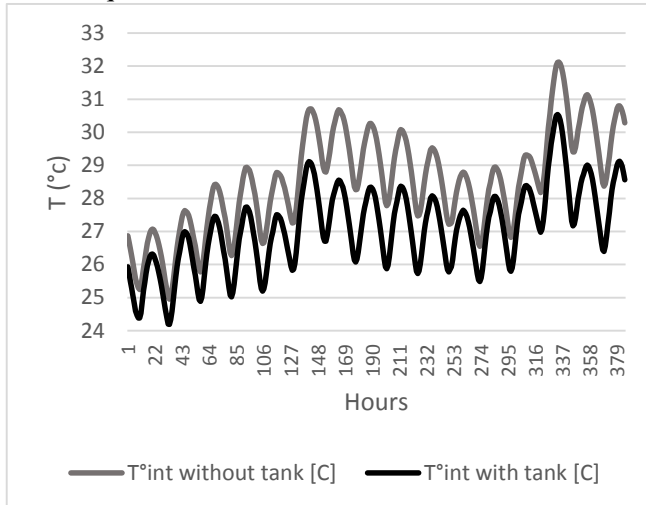


Figure 7: Internal temperature in the room with and without refreshing tank of 10 to 31 July

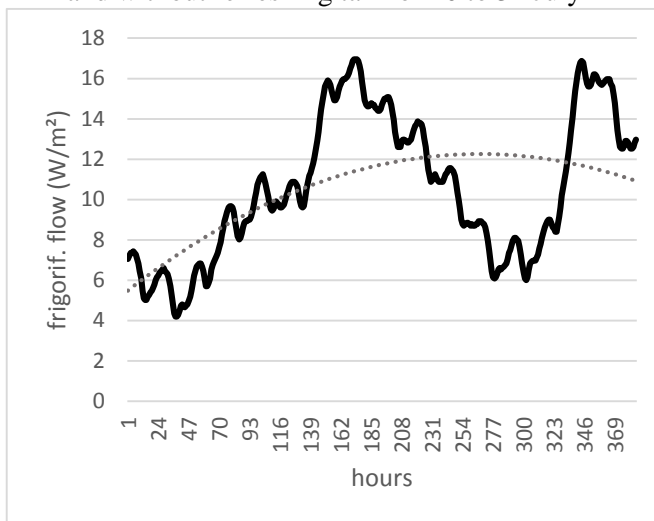


Figure 8: Frigorific flow of hydraulic floor July 10 to 31

CONCLUSIONS

The numerical model of a buried refreshing tank, developed in this paper, allows coupling with a building hydraulic floor for a global simulation under Mediterranean weather.

The results for a case study has shown that this system has a good energy efficiency with a performance coefficient greater than 3, and can contribute to building refreshment, lowering the average air temperature within 1.5 ° c. Thermal comfort remains to be assessed according to considered climate region.

In order to optimize the system, this model opens the way for a more detailed parametric study where the influence of the storage volume, the exchange surface and tank depth should be appreciated.

Finally it would be interesting to study this system in combination with other renewable energy systems to achieve a degree of permanent thermal comfort during the summer depending on the climate.

KEYWORDS Numerical modelling, geothermal storage, cooling, energy efficiency

REFERENCES

1. J.A. Duffie et W.A. Beckman, 2013, *Solar Engineering of Thermal processes*, WILEY, 4ème edition, Pages 375-384.
2. J. Nelson, A. Balakrishnan. 1999, Parametric studies on thermally stratified chilled water storage systems. *Applied Thermal Engineering* 19. 89-115.
3. G.F. Csordas, A.P. Brunger, K.G.T. Hollands, et M.F. Lightstone, 1192, *Solar Energy* Volume 49, No. 6, pages 497-505.
4. A. Pantokratoras, 1998, Horizontal penetration of inclined thermal buoyant jets, *International Communication, Heat Mass Transfer*, Volume. 25. No. 4, pages 561-569.
5. D. Blandin, Modélisation et validation expérimentale de nouveaux concepts de ballons solaires à forte stratification, 2010, *thèse de doctorat*, INSA de Lyon, pages 58-87,
6. T. Kasuda, , P.R. Archenbach, "Earth Temperature and Thermal Diffusivity at Selected Stations in the United States", 1965, *ASHRAE Transactions*, Volume 71, Part 1.
7. G. Mihalakakou, On estimating soil surface temperature profiles, 2002, *Energy and buildings* 34, Pages 251-259.
8. S. Thiers, Bilans énergétiques et environnementaux de bâtiments à énergie positive, 2008, *Thèse de doctorat, paris école supérieure des Mines*, Pages 58-60.

DESIGN ANALYSIS OF A MVC DESALINATION UNIT POWRED BY A GRID CONNECTED PHOTOVOLTAIC SYSTEM

M. Ibrahimi *, A. Arbaoui, Y. Aoura, ENSAM

ENSAM, BP 40 24, UMI, Meknes, MAROC

*Corresponding author: Fax: (+212)05 35467163/64 Email: ibrahimi.mouhsine@hotmail.fr

ABSTRACT

The Mechanical Vapor Compression (MVC) technology offers an interesting alternative for small scale desalination of seawater to produce high quality distilled water with competitive cost. The use of solar energy especially for desalination of seawater is well adapted for the Saharan region where the fresh water is scarce and solar energy potential is high. This paper presents a design analysis of a single-effect mechanical vapor compression (MVC) desalination unit powered by a grid connected photovoltaic (PV) solar system. The aim of this work is to define, as function of the freshwater needs and site specificity, the embodiment of the MVC components and the PV panels' size. The proposed approach is based on MVC components models coupled with a solar energy estimation model. The results are illustrated using a case study in Dakhla city sited at the south of Morocco. They show that the embodiment of the global system depends greatly on the temperature of brine and distillate streams. A large gap between these design variables reduces the heat transfer area, but increases the size of the PV system.

Keywords : Mechanical Vapor Compression, solar irradiance, photovoltaic panels, Desalination, evaporator, South of Morocco.

NOMENCLATURE

M : Mass flow rate, kg/s
 A : Area, m²
 X : Concentration of the wastewater
 Q : Heat exchange capacity, kW
 C_p : Specific heat capacity, kJ/(kg °C)
 T : Temperature, °C
 λ : Latent heat for evaporation, kJ/kg
 U : Overall heat transfer coefficient, kW/m² °C
 ΔT : Temperature drop, °C
 P : Pressure, kPa
 P_d : Power, W
 γ : Compressibility factor
 η : Efficiency
 H : Enthalpy, kJ/kg
 W : Specific power consumption, kWh/m³

Subscripts

f : Feed
 b : Brine
 d : Distillate
 o : Outlet temperature

c^w : Intake seawater
 e : Evaporator
 c : Condensate
 vp : Saturated vapor below demister
 s : Superheated compressed vapor
 v : Saturated vapor above demister
 is : Isentropic compressed vapor
 $cell$: Solar cell
 cmp : Compressor

INTRODUCTION

As freshwater scarcity continues to increase with the increasing continuous of population, desalinating seawater is becoming a necessity for meeting freshwater needs especially in the North Africa and other regions. Water scarcity is a threat to over 40% of the global population [1]. Several researchers focused on studying photovoltaic cell and solar thermal collectors in order to favor either the thermal or electric generation.

The two major types of technologies that are used around the world for desalination can be broadly classified as either membrane such as reverse osmosis (RO) or thermal including single effect evaporation (SEE), multiple effect evaporation

(MEE), multi-stage flash (MSF), thermal vapor compression (TVC) and mechanical vapor compression (MVC) [2,3]. Both technologies need energy to operate and produce fresh water.

The inception of commercial mechanical vapor compression (MVC) units dates back to the early 1970s [4,5]. MVC units have been evolved to become a mature technology over past decades. However, initial costs, system design and energy consumption remain challenging problems. Efficient use of energy in such energy-intensive operations is crucial to reduce the net energy consumption and to compete with other desalination technology. The MVC process remains to be attractive and competitive for production capacities less than 5000 m³/d [6].

MVC literature studies include system modeling and design as well as field data and performance evaluation [4]. An early report by Matz and Fisher [5] in 1981 showed that either the RO or MVC system has a definitive edge regarding total production cost. However, expansion of the MVC process remained limited. In 1994, only 200 MVC units with very small unit capacity are reported by Zimmerman [7].

Several water desalination plants driven by solar energy are in operation. In Abu Dhabi, a solar desalination plant has been successfully operated since 1984. It consists of a multi-effect stack evaporator with an average yearly production of 85 m³/d. In Almeria (Spain), a Multi Effect Distillation (MED) solar seawater desalination plant of 72 m³/d was tested and a Wind/PV/RO of around 3 m³/d for seawater desalination in Lavrio, Greece [8].

A photovoltaic solar panels powered a MVC unit equipped is believed to present the best possible design combination.

The detailed MVC and solar models are quite complex to solve, since it contains many coupled variables and many constraints corresponding to complex physics phenomena.

In this study, we describe a thermodynamic model of a combination of photovoltaic (PV) solar system and a single-effect mechanical vapor compression (MVC) desalination unit. The model is solved for a typical day in each season in Dakhla-Morocco city (23° 41' 5 N -15° 57' 28 O) which is poor in water resources, and rich in solar sources. The solar energy is converted into electrical energy to power the compressor and circulation pumps.

SYSTEM DESCRIPTION

Solar radiation received at the surface is of primary importance for the purpose of building solar energy devices, estimating crop etc. However, direct measuring is not available in many cases, so numerical technique becomes an effective alternative to estimate global irradiance through observed meteorological data.

In our case, the solar energy is converted into electrical energy using the photovoltaic panels to power the compressor and other components

Fig. 1 shows the sequence of operations in an MVC system. Electricity is needed for compressor, circulation pumps and for water treatment processes. The main components of the MVC unit are: the mechanical vapor compressor, evaporator/condenser heat exchanger, and a circulation pumps. The demister serves to filter the water vapor before joining the compressor. The feed preheater is a plate type heat exchanger, which recovers part of the sensible heat found in the distillate and brine stream to heat the intake seawater. The thermal energy recovered is then sprayed over the evaporator tubes of the evaporator/condenser. The feed temperature is further increased to the brine boiling temperature and subsequently evaporation commences. The produced steam is drawn through the demister to the compressor which is powered using the PV solar panels and electric network in order to add an additional amount of superheat, increases the pressure and temperature of the steam by compression. The superheated vapor that has passed through the condenser heat exchanger tube releases its latent heat, which can be the heat source of the evaporator. At the same time, the vapor is condensed into purified water. The condensed distillate product and the brine stream flow through the preheaters where it exchanges heat with the intake stream. And distilled water is treated before being transported to the consumer.

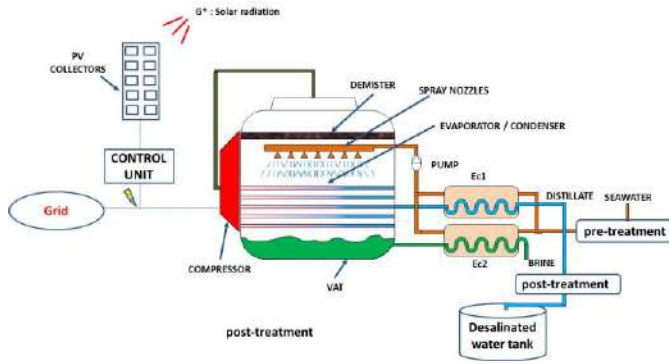


Figure 1

Schematic diagram of MVC desalination unit combined with grid/photovoltaic panels.

The MVC and PV panels design model is based on the design step in the product lifecycle. More detailed of this approach is presented in previous work [13]

Some simplifications are made on several components, whereas others are more detailed. In this context, we don't take into account:

- Interactions between components (pipes, cables...).
- Spray nozzles, pumps.

The power produced by the PV module can be directly used to feed the needs of the MVC unit, but in case of insufficiency the electrical grid offers the ability of compensation to ensure the stability of the production.

The models are based on equations for solar, energy and mass conservation. The following assumptions have been made during modeling:

- The system operates under steady-state.
- Negligible energy losses are assumed for the evaporator, preheaters, pipelines and pumping system.
- Assuming zero salinity for the product water is validated by the very high salinity of the feed or brine stream.
- Salt balance that takes into account the product salinity has a very small effect on the material balance accuracy.
- The physical properties for the product in vapor and liquid phases depend on the stream temperature.
- The physical properties of the feed seawater and brine depend on the stream temperature and salinity.

- The driving force for heat transfer in the evaporator is assumed constant and equal to the difference between the condensation saturation temperature and the brine boiling temperature.
- The influence of ambient temperature on the photovoltaic cell is negligible
- The relative humidity in Dakhla is taken equal to 50% and assumed constant throughout the day.
- the site is located in an urban area with a coefficient of atmospheric turbidity $B = 0.1$
- The saturation vapor pressure of water is calculated for a constant ambient temperature.

PROCESS MODELING

The system consists of the following subsystems: the MVC unit and the solar models.

Solar modeling

The solar constant E_{Sol} received according to day (j) of the year can be calculated with the following formula:

$$E_{Sol} = 1367 \times \left(1 + 0.0334 \times \frac{\cos(j - 2.7206)}{365.25} \right) \quad (1)$$

The incidence coefficient (CI) is defined in part by the height and azimuth of the sun and on the other hand by the direction (θ) and the inclination (i) of the receiving solar collector:

$$CI = \sin(i) \times \cos(h) \times \cos(\theta - \alpha) + \cos(i) \times \sin(h) \quad (2)$$

The Direct solar irradiance on a receiver plane (θ , i) is given by:

$$G = CI \times E_{Sol} \times e^{(-E_R \times m \times T_L)} \quad (3)$$

(m) is the atmospheric masse defined by :

$$m = \frac{P_{atm}}{\left(101325 \times \sin(h) + 15198.75 \times (3.885 + h)^{-1.253} \right)} \quad (4)$$

E_R is the integral Rayleigh optical thickness given by:

$$E_R = \frac{1}{(0.9 \times m + 9.4)} \quad (5)$$

T_L Defined the Linke disorder factor:

$$T_L = 2.4 + 14.6 \times B + 0.4 \times (1 + 2 \times B) \times \ln(P_v) \quad (6)$$

B depends on location, in our case $B = 0.10$, an urban location and P_v is the partial pressure of water vapor.

The sunshine duration is giving by:

$$D_{in} = \frac{2}{15} \times \text{Arcos}(-\tan(Lat) \times \tan(Dec)) \quad (7)$$

The MVC unit modeling

The mass flow rates of seawater M_d and brine M_b are obtained from the following system of equations:

$$M_f = M_d + M_b \quad (8)$$

$$M_b = \frac{X_f}{X_b} M_f \quad (9)$$

The amount of heat given by the distillate and the brine in the heat exchanger is given by equations (10) and (11):

$$Q_{E1} = M_d C_{pd} (T_d - T_o) \quad (10)$$

$$Q_{E2} = M_b C_{pb} (T_b - T_o) \quad (11)$$

The amount of heat acquired by the evaporator and the condenser are given by:

$$Q_{ev} = M_d \lambda_{vp} + M_f C_p (T_b - T_f) \quad (12)$$

$$Q_{con} = M_d \lambda_d + M_d C_{pv} (T_s - T_d) \quad (13)$$

The following equation translates the interaction between the evaporator and the condenser

$$Q_{ev} = Q_{con} = A_e U_e (T_d - T_b) \quad (14)$$

The temperature of the steam produced below the demister T_{vp} is lower than the brine boiling temperature T_b because of two factors which are determined from the characteristic of the demister [9, 10]:

- The boiling point elevation (BPE).
- The nonequilibrium allowance (NEA).

$$T_{vp} = T_b - \text{BPE} - \text{NEA} \quad (15)$$

The temperatures of the steam above T_v and below T_{vp} demister is given by:

$$T_v = T_{vp} - \Delta T_p \quad (16)$$

The isentropic superheated temperature of compressed vapor is obtained in terms of the inlet vapor temperature T_v and the compression ratio [9]:

$$T_{is} = (T_v + 273.15) \left(\frac{P_d}{P_v} \right)^{\frac{(\gamma-1)}{\gamma}} - 273.15 \quad (17)$$

The enthalpy of the superheated steam H_s is expressed in terms of the saturation enthalpy of the compressed vapor H_d , isentropic temperature T_{is} , and the inlet vapor enthalpy H_v according to the following equation [9]:

$$H_s = [H_d + C_{pv} (T_{is} - T_d) - H_v] \times \left[\frac{\left(\frac{P_d}{P_v} \right)^{\frac{(\gamma-1)}{\gamma \eta_{comp}} - 1}}{\left(\frac{P_d}{P_v} \right)^{\frac{(\gamma-1)}{\gamma} - 1}} \right] + H_v \quad (18)$$

At the outlet of the compressor, the temperature of the superheated steam is given by:

$$T_s = \frac{(H_s - H_d)}{C_{pv}} + T_d \quad (19)$$

The specific power consumption of the compressor can be expressed by:

$$W = (H_s - H_d)(1000/3600) \quad (20)$$

The specific heat transfer area of the evaporator is calculated from the following relationship:

$$A_e = \frac{M_d \lambda_d + M_d C_{pv} (T_s - T_d)}{U_e (T_d - T_b)} \quad (21)$$

The daily electric energy consumed by MVC unit must be met to respond to the need for safe water:

$$En_{el} = W \times (Md \times 3600 \times 24) \quad (22)$$

The area of PV panels to fulfill the need of potable water:

$$A_{pv} = \frac{En_{el}}{G \times \eta_{cell} \times D_{in}} \quad (23)$$

MODEL IMPLEMENTATION

A desalination unit supplied by photovoltaic panels is considered. The main objective of this study is to define, the power consumption of the compressor, the heat transfer area of the evaporator, the daily solar irradiance received by a sensor, the inclination of the solar sensor and total area of the PV panels as a function of the need for freshwater. In a MVC solar desalination unit, freshwater is only produced over the insolation duration. Also on cloudy days, water need is covered by using the electric network. Water production must be without interruption mainly during hot and moderate seasons. The sizing depends on site characteristics (solar irradiation, ambient temperature, insolation duration, wind velocity...), plant energy need, and the well characteristics. Also the MVC unit is mainly defined in terms of ΔT which represents the difference between the saturation temperatures of compressed steam and the brine boiling temperature. This parameter allows determining both the energy consumption and the heat transfer area of the evaporator. The proposed approach is illustrated using the software 'SCILAB' [11].

The input variables which determine the need via the global model are listed in Tab1.

Table 1

Input variables of the global model

Input variables	Values
Water demand, L/j	1000
Intake seawater temperature, °C	25
Xf/Xb	0.2
Heat transfer coefficient of evaporator, kW/m ² °C	3.37
Efficiency of the vapor compressor, %	70
Efficiency of the silicon cells, %	16
Latitude of the location (Dakhla)	23° 41' 5 N
Altitude of the local point, m	10
Coefficient of atmospheric turbidity	0.1

The calculation results are made as a function of the brine boiling temperature T_b (70°C-100°C), the temperature difference ΔT (1°C –10°C), the distillate flow rate M_d (0-30008 L/d) and the inclination i (0° -90°).

The solution algorithm of the SOLAR-MVC models is shown in Fig.2. The algorithm starts with definition of design parameters.

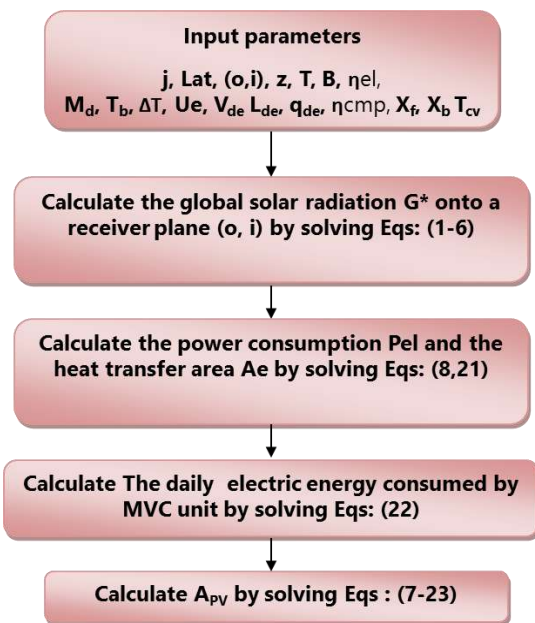


Figure 2
Schematic of solution procedure

RESULTS AND DISCUSSION

A systematic approach has been carried out to study the effect of different factors on the performance of

the considered SOLAR-MVC desalination system. The results are given for a case study in the Dakhla city sited at the south of Morocco. Predictions of the mathematical model are shown in Figs. 3–7.

The evolution of the daily solar irradiation G^* in the typical days is given in Fig. 3 for a direction sensor $\alpha = 0^\circ$ and the inclination $i = 30^\circ$. It is expected that the maximum solar intensity under these conditions found equal to 942 W/m² on 21 March [12].

Solar irradiation received by a sensor during a given day varies according to the orientation, inclination, location etc. The electric power produced by PV panels is covered by the power grid in such way to have an instantaneous quite stable power at the inlet of the MVC unit equal to the maximum solar intensity. The influence of the inclination (i) on the surface of solar panels (A_{PV}) to produce an amount of freshwater $M_d=1000$ l/day, is shown in Fig. 4 for a boiling temperature $T_b=90^\circ\text{C}$ and temperature difference $\Delta T=5^\circ\text{C}$. As shown, with the change of the inclination (i), the surface of PV panels varies differently in each typical day, this is because of the change in the solar height. However the lower value of (A_{PV}) in June 21 is obtained at the inclination (i) = 2°. Fig. 5 shows the PV area versus the produced freshwater. This sizing defines the PV surface whose are able to fulfill water need. It is found that to meet the demand of 1000 l/day on 21 June and for an inclination sensor $i = 30$, $T_b= 80^\circ\text{C}$, and $\Delta T=8^\circ\text{C}$ it is desirable to bring an area of PV panels higher than or equal to 13 m². In fact, surfaces range defined two zones: acceptable and discarded PV surfaces.

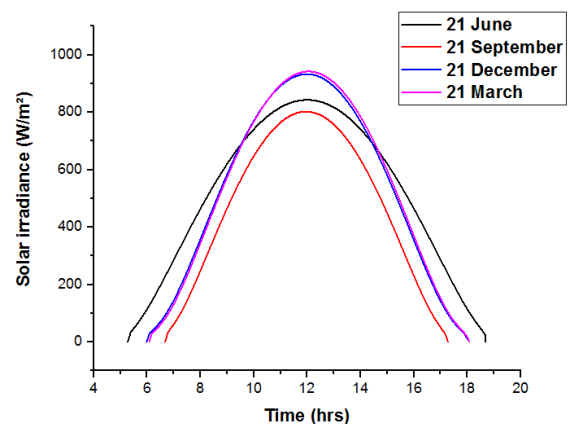


Figure 3
Hourly solar irradiance of Dakhla.

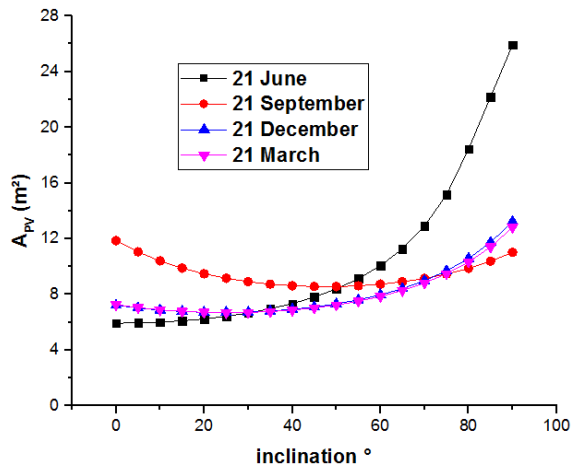


Figure 4

Influence of the inclination on the maximum solar irradiance.

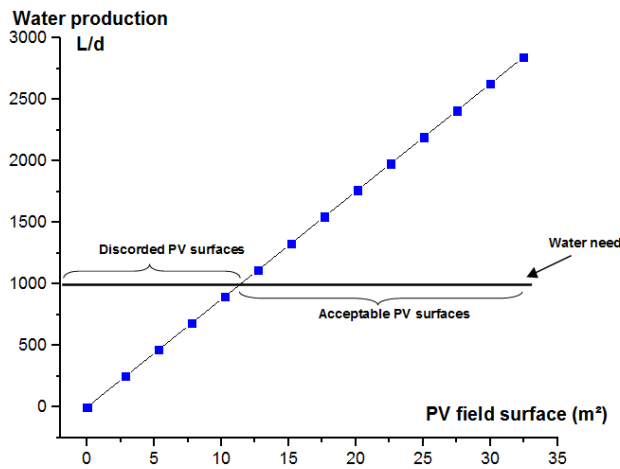


Figure 5

PV surface range able to cover water need.

Figs 6, 7 show the influence on the heat transfer area of the evaporator and the surface of solar panels as a function of T_b and ΔT . In fig. 6, for $\Delta T=5^\circ\text{C}$, the heat transfer area of the evaporator decreases slightly with the increase of evaporation temperature, and in the same time the surface of solar panels decreases as the brine boiling temperature rise increases because the specific volume decreases when brine temperature rise is greater. This implies that the operation in the high value of T_b is desirable. In the other hand, as can be seen in fig. 7, for a boiling temperature $T_b=90^\circ\text{C}$, the operation with a large gap between the temperature difference (ΔT) decrease the heat transfer area of evaporator, but increase the surface of solar panels. This inferred that there is an optimum value of temperature difference that will lead to the optimum system with lower PV area and smaller heat transfer area [13].

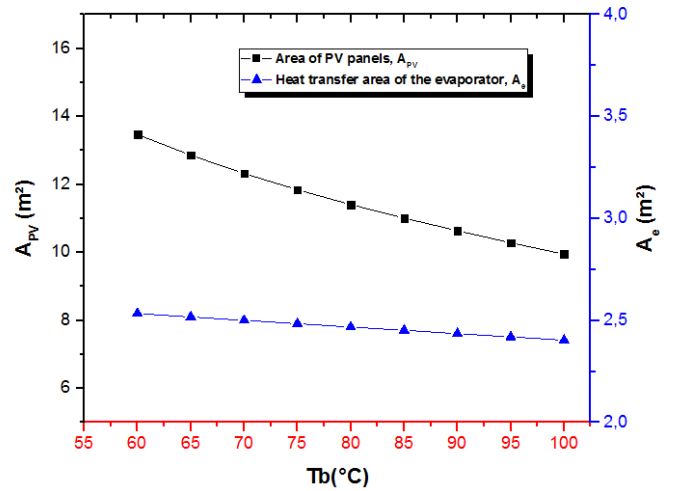


Figure 6

Influence of the boiling temperature T_b on the PV size and the heat transfer area.

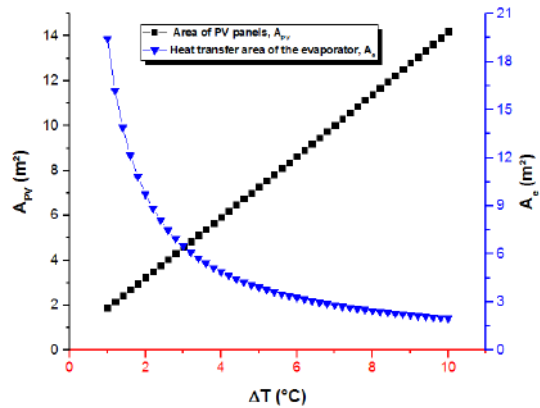


Figure 7

Influence of the temperature difference ΔT on the PV size and the heat transfer area.

CONCLUSIONS

An investigation on the sizing of a MVC desalination system coupled with solar grid/photovoltaic panels is presented. In order to provide the size for all key components required to ensure successful implementation of the main function of the MVC unit. The results show that:

- The freshwater productivity increases linearly with the increase of the PV area, which is 13 m^2 , and the use of PV panels saves approximately 61 % of electrical energy, for the considered desalination case.

- With the increasing of the inclination, the maximum value of the solar irradiation varies differently in each typical day, which means that a well-studied inclination will be beneficial.

-The operations with an elevated brine boiling temperature is desirable since it reduces the energy consumption of the compressor.

-The operations with a high value of ΔT reduce the heat exchange area, therefore the cost of the evaporator reduced too, but increase the power consumption. This inferred that an optimization study is needed to find a compromise between the congestion (investment cost) and electric energy consumption to design an efficient desalination unit.

REFERENCES

1. International Water Management Institute. In Water for food, water for life: a comprehensive assessment of water management in agriculture, Earthscan, 2007; 57.
2. O. Lefebvre, R. Moletta, Treatment of organic pollution in industrial saline wastewater: a literature review, *Water Res.* 40 (2006) 3671–3682.
3. D.F. Zhao, J.L. Xue, S. Li, H. Sun, Q.D. Zhang, Theoretical analyses of thermal and economical aspects of multi-effect distillation desalination dealing with high salinity wastewater, *Desalination* 273 (2011) 292–298.
4. Matz R, Fisher U. A comparison of the relative economics of sea water desalination by vapor compression and reverse osmosis for small to medium capacity plants. *Desalination* 1981;36:137–51.
5. Matz R, Zimerman Z. Low-temperature vapour compression and multi-effect distillation of seawater. Effects of design on operation and economics. *Desalination* 1985;52:201–16.
6. Al-Sahali M, Ettouney H. Developments in thermal desalination processes: design, energy, and costing aspects. *Desalination* 2007;214:227–40.
7. Z. Zimerman, Development of large capacity high efficiency mechanical vapor compression (MVC) units, *Desalination*, 96 (1994) 51–58.
8. Zejli, D., Ouammi, A., Sacile, R., Dagdougui, H., & Elmidaoui, A. (2011). An optimization model for a mechanical vapor compression desalination plant driven by a wind/PV hybrid system. *Applied Energy*, 88(11), 4042-4054.
9. H. Ettouney “Design of single-effect mechanical vapor compression” *Desalination* 190 (2006) 1 15.
10. A. Cipollina, G. Micale and L. Rizzuti “Investigation of flashing phenomena in MSF chambers” *Desalination* 216 (2007) 273-300.
11. Campbell, Stephen L., Jean-Philippe Chancelier, and Ramine Nikoukhah. *Modeling and Simulation in SCILAB*. Springer New York, 2006.
12. Bekkouche, S. M. A., et al. "Practical installation methods of thermal insulation in a residential building in hot climate." *Power Engineering, Energy and Electrical Drives (POWERENG)*, 2013 Fourth International Conference on. IEEE, 2013.
13. M. Ibrahim, A. Arbaoui, Y. Aoura, L. Ouzizi. (2015). Embodiment design of a mechanical vapor compression desalination unit, presented at the IEEE IRSEC15 Conference, Marrakech, Morocco

THERMAL ANALYSIS OF A 3.9 MWTH PARABOLIC TROUGH SOLAR COLLECTOR OPERATING WITH AIR AT 600°C

R. AIT EL CADI^{1,2,*}, N. SELHAOUI¹, K. BOUABID², L. GOURDO¹, A. IHLAL², L. BOUIRDEN¹, B. ABNAY³

¹ Laboratory of Thermodynamics and Energy (LTE), ² Laboratory of Materials and Renewable Energy (LMER), University IBN ZOHR, faculty of science BP 8106 - City Dakhla, Agadir, Morocco

³ Ciment du Maroc, Ait Baha, Agadir, Morocco

* radia.aitelcadi@edu.uiz.ac.ma

ABSTRACT

In this paper is presented a novel solar trough concentrating system, the concentrator is based on pneumatic polymer membrane mirrors, mounted on a rigid and durable concrete support structure. The novel receiver design, which uses air as the heat transfer fluid at ambient pressure, is based on an array of absorber cavities coupled to secondary concentrating optics for operating temperatures exceeding 600 °C. The first commercial solar plant with this technology, with a maximum thermal power output of 3.9 MWth, is currently under construction in Ait Baha, Morocco.

In this study, a mathematical model for the efficiency of the parabolic trough solar collector was established. The performance characteristics of cosine effect, shadowing effect, end loss effect were calculated by using the mathematical model.

KEYWORDS: Solar energy, Parabolic trough collectors, Solar concentration, Efficiency, Optical performance.

INTRODUCTION

In recent years, concentrated solar power (CSP) for electricity production promises to be one of the most viable options to replace fossil fuel power plants. In the technology field of concentrated solar thermal power generation, parabolic trough solar collector (PTC) plants are the most developed ones of all commercially operating plants.

The performance of parabolic trough over the last 25 years has proven that this technology is an excellent alternative for the commercial power industry. However, conventional solar parabolic trough plants suffer from several technical and economical disadvantages. These include especially a maximum operating temperature limited to 450 °C, and a difficulty in creating rigid metallic support structures with large trough apertures. This has impelled the development of a novel parabolic trough comprising a 9 m aperture, based on inflated metallized polymer films mounted on a concrete support structure, coupled to a solar receiver based on air as heat transfer

fluid [1], A photograph of the inflated solar trough collector is shown in Fig. 1.1.



Fig. 1.1: Photograph of the novel parabolic trough collector [1]

The new receiver (Fig 1.2) implements a cross-flow design where the full temperature gain is achieved in each absorber cavity [1].

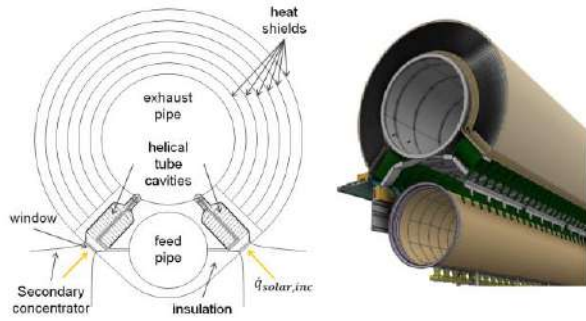


Fig 1.2: Schematic of the novel receiver design [1]

ANALYSIS AND MODELLING

1. Geometry model for PTC

A PTC consists of a linear parabolic mirror which reflects and concentrates the received solar energy onto a receiver positioned along the focal line, only the beam radiation (DNI) that is directly normal to the collector surface can be focused and thus be available to warm the receiver. Fig. 2 shows the angle of incidence between the collector normal and the beam radiation on the PTC. The angle of solar incidence results from the relationship between the sun's position in the sky and the orientation of the collectors for a given location [2]. The angle of solar incidence is not equal to 0° and the reason is that the parabolic trough solar collector is generally horizontal layout, single axis tracking the sun.

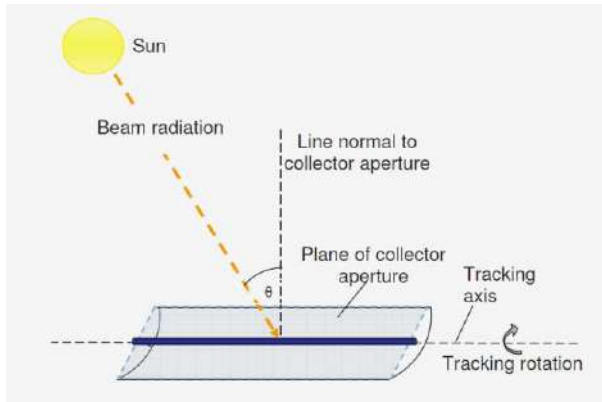


Fig. 2: Angle of incidence on a parabolic trough collector [4]

2. Efficiency of PTC

Power absorbed by the receiver of the PTC can be written as:

$$Q_{abs} = A_c \cdot I_{DNI} \cdot \cos \theta_i \cdot IAM \cdot \eta_{opt,mirr} \cdot \eta_{Shadow} \cdot \eta_{end,loss} \cdot \eta_{track}$$

Where:

I_{DNI} : is the Direct Normal Irradiance,

θ_i : is the angle of solar incidence,

A_c : is the collector aperture area,

η_{shadow} : is the factor for solar shading,

$\eta_{end,loss}$: is the factor for the calculation of the relative end loss,

IAM : is the Incident Angle Modifier;

η_{track} : is the tracking error,

$\eta_{opt,mirr}$: optical efficiency that accounts for losses due to mirror optics and imperfections,

The field efficiency for parabolic trough solar collector is defined as:

$$\eta_{field} = \frac{Q_{abs}}{A_c \cdot I_{DNI}} = \cos \theta_i \cdot IAM \cdot \eta_{opt,mirr} \cdot \eta_{Shadow} \cdot \eta_{end,loss} \cdot \eta_{track}$$

As parabolic trough solar concentrators accept only DNI, diffuse irradiation is subtracted from the global irradiation to obtain the beam irradiation, the global solar irradiance can be written as:

$$G_h = D_h + I_{DNI} A_c \cos(\theta_i)$$

The incidence angle modifier (IAM) corrects for some additional reflection and absorption losses.

The incidence angle modifier is defined for this work as the incidence angle modifier defined by Dudley and al [3], divided by the cosine of the incidence angle:

$$IAM = \frac{K}{\cos(\theta)}$$

The equation for the incidence angle modifier used in the solar field model is:

$$IAM = 1 + 0.000884 \cdot \frac{\theta}{\cos(\theta)} - 0.00005369 \cdot \frac{\theta^2}{\cos(\theta)}$$

The positioning and geometry of the collector troughs and the receiver can introduce further losses, due to shading of parallel rows in the morning and evening as well as end losses from the receiver.

End losses occur at the ends of the receiver, where, for a nonzero incidence angle, some length of the absorber tube is not illuminated by solar radiation reflected from the mirrors. Fig 3

shows the occurrence of end losses for a receiver with a nonzero angle of incidence.

The end losses are the function of the focal length of the collector, the length of the collector, and the incident angle. The factor for the end loss is:

$$\eta_{end.loss} = 1 - \frac{f \tan(\theta_i)}{L_{PTC}}$$

Where:

- f : focal length of the collectors
 θ_i : incident angle
 L_{PTC} : length of a single solar collector.

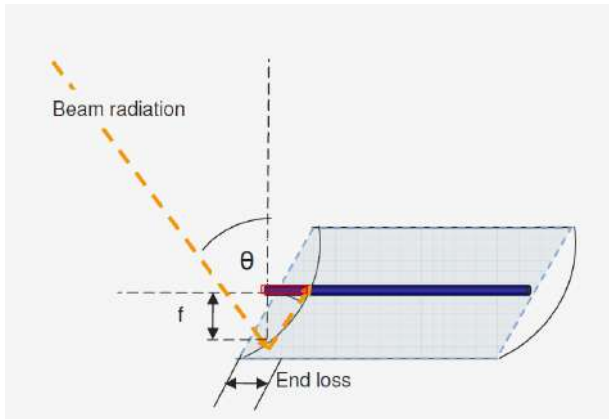


Fig 3: End losses from a receiver.[4]

3. Solar Incidence Angle

The angle of incidence θ_i represents the angle between the beam radiation on a surface and the plane normal to that surface. It's the results from the relationship between the sun's position in the sky and the orientation of the collectors for a given location.

The angle of incidence will vary over the course of the day (as well as throughout the year) and will heavily influence the performance of the collectors [4].

Once the declination angle, hour angle, and zenith angle are known, the angle of incidence on the collectors and the sun-tracking angle can be calculated. The incidence angle for a plane rotated about a horizontal north-south axis with continuous east-west tracking to minimize the angle of incidence and the sun-tracking angle is given by [5]

$$\cos(\theta_i) = \sqrt{\cos^2(\theta_z) + \cos^2(\delta) \sin^2(\omega)}$$

Where ω is the hour angle; δ is the declination of the sun; θ_z is the zenith angle.

The position of the sun depends on the hour angle (ω), ω comes as a result of the rotation on the earth, which spins on its axis at a rate of 15° per hour.

The calculation formula of hour angle and the declination angle is:

$$\delta = 23.45 \sin\left(360 \frac{284 + n}{365}\right)$$

$$\omega = (\text{SolarTime} - 12) \cdot 15^\circ /_{hr}$$

Where n is the day number of the year (1 for January 1, 365 for December 31) and SolarTime is the solar time angle.

There is an important distinction between standard time and solar time. In solar time, the sun aligns with the local meridian ($\omega = 0$) at exactly 12:00 or "solar noon." However, standard time is not based on the local meridian but on a standard meridian for the local time zone. The standard time must be adjusted to reflect the current time of day in solar time. The relationship between solar time and standard time, in hours, is:

$$\text{SolarTime} = \text{StandardTime} - \text{DST} + \frac{L_{st} - L_{Loc}}{15} + E \cdot \frac{1h}{60 \text{min}}$$

where DST is daylight saving time adjustment; L_{st} is standard meridian for the local time zone; L_{loc} is the local meridian of the collector site, E is the equation of time that determines the deviation in local time from solar time as a function of the day of the year; the calculation process of equation of time is [4]:

$$E = 229.18(0.00075 + 0.001868 \cos(B) - 0.032077 \sin(B) - 0.014615 \cos(2B) - 0.04089 \sin(2B))$$

Where:

$$B = \frac{360}{365}(n-1)$$

The final angle required to solve for the angle of incidence is the zenith angle. The zenith angle is related to both the declination angle and the hour angle by the following relationship [4]:

$$\cos \theta_z = \cos \delta \cos \phi \cos \omega + \sin \delta \sin \phi$$

Where:

- δ :Declination angle
- ω :Hour angle
- ϕ :Latitude location of the plant

4. Thermal Performance and Losses

The heat transfer model of the PTC is given by:

$$Q_{abs} - Q_{reradiation} - Q_{convection} - Q_{conduction} - Q_{gain,HTF} = 0$$

Where Q_{abs} is the solar radiation reflected by the primary concentrator and absorbed by the receiver, $Q_{reradiation}$ and $Q_{convection}$ are energy losses from the system by emitted radiation and convection, $Q_{conduction}$ is the energy lost through the receiver end plates and receiver supports by conduction, and Q_{HTF} is the useful energy removed from the receiver by the HTF.

Energy balance for an absorber section of length dy yields [6]:

$$dQ_{HTF} = \dot{m}_{HTF} C_{p,HTF} dT_{HTF}$$

The HTF temperature $T_{HTF}(y)$ along the receiver axis is calculated by numerical integration [7]:

$$T_{HTF}(y) = T_{HTF,in} + \int_0^y \frac{dQ_{HTF}(y)}{\dot{m}_{HTF} \cdot C_{p,HTF}(T_{HTF}(y))}$$

The overall thermal efficiency is defined as:

$$\eta_{th} = \frac{Q_{HTF}}{Q_{abs}} = 1 - \frac{Q_{heat,losses}}{Q_{abs}}$$

Where:

$$Q_{heat,losses} = Q_{reradiation} - Q_{convection} - Q_{conduction}$$

RESULTS AND DISCUSSION

A commercial solar plant is currently under construction in Ait Baha, Morocco for the purpose of boosting electricity production from waste heat of a cement factory.

The parameters for the collector were shown at Table 2, prototype as shown in Fig 1.

Table 1: Computing site

Regions	Geographic coordinates
AIT BAHA, Agadir, Morocco	30°13'1,0" North 9°8'6.0" West

Table 2: Parameters of the parabolic trough solar collector [1].

Parameters	Data
Focus length	3.5 m
Aperture width	9 m
Length of collector	211.68 m
Geometric concentration ratio	73 sun
Cleanliness factor	0.92
Mirror reflectance	0.93
Tracking error	0.94

Fig 4 and 5 show variation of $(DNI \cos(\theta_i))$ throughout the day, as calculated for Ait Baha collector location, orientation, and tracking capability. For reference, the direct normal insolation and cosine of the incidence angle are shown on the graphs as well. The summer solstice (June 21, 2015) is shown in Fig 4; the winter solstice (December 21, 2014) is shown in Fig 5.

The impact of the lower solar altitude angle in the winter is clearly seen in comparing Fig 4 to Fig 5. There is also a noticeable sag in $DNI \cos(\theta)$ around noon in Fig 5.

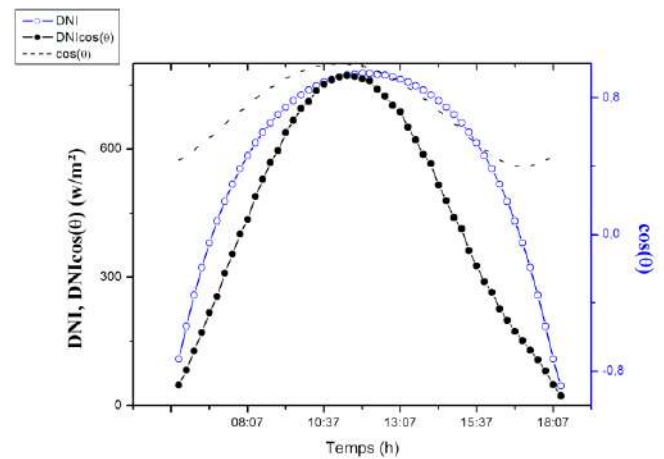


Fig 4 : DNI and DNI cos (θ) at AIT BAHA on June 21, 2015

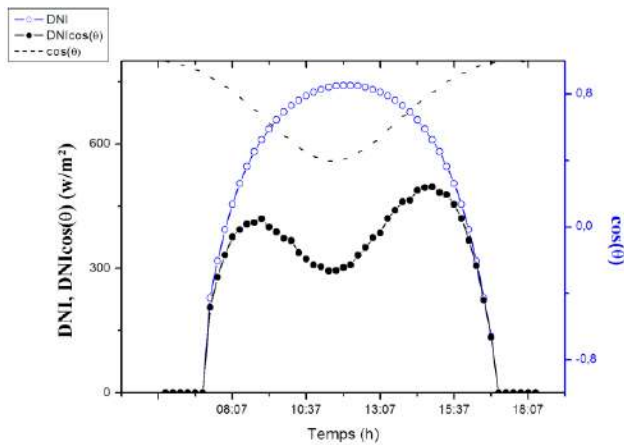


Fig 5 : DNI and DNI $\cos(\theta)$ at AIT Baha on December 21, 2014

CONCLUSIONS

A parabolic trough concentrator is a complex system which demands thorough knowledge of structural, optical, thermal instrumentation and controls engineering.

The instantaneous efficiency of a parabolic trough concentrator can be calculated from an energy balance on the receiver tube, a model will be developed under the TRNSYS environment and confirmed with the experimental results, which will allowed us to evaluate the performance of the plant under transient conditions in Ait Baha.

ACKNOWLEDGMENTS

This work is financially supported by IRESEN (Institut de Recherche en Energie Solaire et Energies Nouvelles, MOROCCO) in the framework of the project InnoRherm1:

“EVALUATION DES PERFORMANCES DES SITES THERMOSOLAIRES (Application au site CSP de la Cimenterie d’Ait Baha)

REFERENCES

1. P. Good, G. Zanganeh, G. Ambrosetti, M.C. Barbato, A. Pedretti, A. Steinfeld, 2014 , Towards a commercial parabolic trough CSP system using air as heat transfer fluid, Energy Procedia, 49 381 – 385.
2. W. B. Stine and R. W. Harrigan, 1985, Solar Energy Fundamentals and Design: With Computer Applications, John Wiley & Sons, Hoboken, NJ, USA.
3. Dudley, V., Kolb, G.J., Mahoney, A.R., Mancini, T.R., Matthews, C.W., Sloan, M., and Kearney, D, 1994, Test Results: SEGS LS-2 Solar Collector. Sandia National Laboratories, SAND94-1884.
4. A. M. Patnode, 2006 ,Simulation and performance evaluation of parabolic trough solar power plants, University of Wisconsin-Madison, Madison, Wis, USA.
5. J. Duffie and W. Beckman, 2006, Solar Engineering of Thermal Processes, John Wiley & Sons, Hoboken, NJ, USA, 3rd edition.
6. ROMAN BADER, thesis, 2011, Optical and thermal analyses of an air-based solar trough concentrating system, DISS. ETH NO. 19772, ETH ZURICH.
7. Munson, B. R., Young, D. F., and Okiishi, T. H, 1994, Fundamentals of Fluid Mechanics, 2nd ed., Wiley, New York.

SIMULATION OF PHOTOVOLTAIC INSTALLATION CONNECTED TO THE GRID WITH STORAGE SYSTEM

S. Ben Mabrouk* ⁽¹⁾, H.Oueslati ⁽¹⁾, A. Ben Mabrouk ⁽¹⁾, G. Zizzo ⁽¹⁻²⁾, D. La Cascia ⁽¹⁻²⁾, L. Dusonchet ⁽²⁾, S. Favuzza ⁽²⁾, F. Massaro ⁽²⁾

1- CRTEn – Research and Technology Centre of Energy. LPT - Laboratory of Thermal Processes, P.Box : 95 Hammam-Life 2050, Tunisia.

*Corresponding author: Fax: +21679 325825 Email: salah.benmabrouk@crten.rnrt.tn

2- DEIM – Department of Energy, Engineering Information and Mathematical models University of Palermo, Italy.

ABSTRACT

In the present paper, we present a renewable energy sustainable micro-system installed upon a platform located on the Research and Technology Centre of Energy (CRTEn in Borj Cerdia Tecnopark-Tunisia). This prototype has been conceived through the ENPI (European Neighborhood and Partnership Instrument) cross-border cooperation Italy – Tunisia. 2007-2013 DE.DU.ENER.T. Project.

The aim of this project is to improve energy efficiency order to minimize the electricity cost consumed at the laboratory. Therefore, we targeted to install several microsystems using renewable sources to reduce these electricity consumption by using other sustainable, green and clean resources and store it with storage systems (traditional and innovative batteries).

A theoretical study of the PV system sizing was carried out in order to evaluate the compatibility between the different equipment of this installation and to compare the results with those found by the SMA Sunny Design software. In addition, a simulation study of our installation using a PV*SOL simulation software was reported.

We designed and managed these systems optimally to promote the self-consumption of the electric energy in the building of our Research Laboratory. We will focus on the use of the PV system by evaluating the impacts of electricity generation using renewable energy levied on electricity grid and economy rates that can be achieved during operating hours.

Key words: *Renewables energies, Simulation, Sustainable development, Photovoltaic panel.*

NOMENCLATURE

Symbol	Description	Unit			
E	Integer Part	No unit	βV_{OC}	Temperature coefficient	%/°C
$U_{mppt,max}$	Maximum input Dc voltage to the inverter	V	V_{string}	String voltage	V
$U_{mppt,min}$	Minimum input Dc voltage to the inverter	V	ΔT	Temperature difference	°C
U_{mpp}	Maximum voltage of the PV panel	V	V_{max}	Maximum input voltage to the inverter	V
U	DC Voltage drop	V	$I_{string\ input}$	Maximum input current per string	A
I, I_{Mpp}	Maximum current of the panel	A	Greek Symbols		
L	Cable length	m	ρ, ρ_l	Resistivity of the conductive wire	$\Omega \cdot mm^2/m$
u	AC Voltage drop	V			
s	Cable section	mm ²			
$cos\phi$	Power factor	No unit			
λ	Linear reactance	Ω/m			
I_b	Maximum output current of the inverter	A			
Δu	Relative voltage drop	V			
U_0	Nominal voltage	V			
ΔV	Voltage difference	V			

INTRODUCTION

The expected increase in energy demand, along with the predominance of coal in the energy mix, highlights the significance of promoting energy efficiency. Higher rate of urbanization with increased floor space for both residential and commercial purposes has imposed enormous pressure on the existing sources of energy. Increased

energy consumption will lead to more greenhouse gas emissions with serious impacts on the global environment. Also, limited availability of energy the existing energy resources and highly transient nature of renewable energy sources have enhanced the significance of energy efficiency and conservation in various sectors.

Hybrid Energy System (HES) is an electric energy system, which is made up of a single or many electric sources [2, 1]. These sources could be renewable, traditional, or mixed and works in off-grid or connected to the grid. If this HES system contain only the renewable energy sources it will be name by a Hybrid Renewable Energy System (HRES) such as the photovoltaic, the wind turbine and so they can address emissions, reliability, efficiency, and economical limitations of single renewable energy source [3, 2].

The HRES systems are becoming famous for standalone power generation in not isolated and isolated area due to the growing, the improvement and efficiency in renewable energy technologies [3]. This hybrid system have many advantages for our country such as protect the environmental, reduce the emission of gas especially CO₂ and other pollutants emissions. The cost of solar and wind energy can be competitive with the classical grid installation and the diversity of natural resources who are renewable, clean and inexhaustible [4]. Most of these equipments can be easily installed and deployed for another utilizations. Financially, these sources are free and there costs are predictable and not influenced by fuel price [5-8]. However, the most disadvantage of the hybrid system photovoltaic PV–Wind is there dependence on climatic changes and weather. Then they must be oversized to make their standalone systems reliable and to satisfy the load [9].

A various hybrid renewable energy system have been installed in different countries because many domains are concerned with the uses of the HRES. One of this area is the researches [1,10] witch have focused on the performance analysis of demonstration systems, the development of efficient power photovoltaic panel and the innovation of new types of PV panel and wind turbine. [6].

This work will focus only on the study and the sizing of the PV installation for this DE .DU.ENER.T. project [8].

TUNISIAN PROTOTYPE

Description of the prototype

The Tunisian prototype of the DE.DU.ENER.T. installed near the Laboratory of Thermal Processes a part of the Research and Technology Centre of Energy CRTEn to reduce the energy consumption consumed from the grid by this laboratory, and it composed by a 12KW of photovoltaic field and a 1KW of wind turbine.



Figure 1. Laboratory Site and the platform of our installation.

Table 1. Geographical and Climatic Data of Borj Cedria Site.

Reference Location for climatic Data	Borj Cedria
Latitude	36.71°
Longitude	10.41°
Altitude	2 m
Maximum summer outdoor temperature	42 °C
Minimum winter outdoor temperature	10 °C
Solar Irradiation	From Meteonorm 7 Software
Wind Speed	From Meteonorm 7 Software
Average wind speed	2.9 m/s

The geographic and climatic data of the site are reported in Table I.



Figure 2. Site of Tunisian and Italian implantations.

Work methodology and laboratory equipments

Because of the unavailability of an electrical consumption meter dedicated to the laboratory (LPT), we made an estimation of the energy consumption of the LPT. To make this estimation, we conducted census of electrical equipment used by one local of this laboratory.

This local contain three type of equipment:

- Laboratory equipment such as drying oven, desiccator and precision balance.
- Workstations and printers.
- Lighting equipment.

Then we extrapolated this consumption for the remainder of locals and offices for this laboratory.

Finally, we have refined our extrapolation by an error margin of 10%.

STUDY OF THE ELECTRICAL ENERGY CONSUMPTION

After identifying the different equipment of the laboratory, we tried to identify the optimal operating mode (number of unit, operating hours ...) and identified the different electrical characteristics (current, voltage, power ...) for each appliance to determine the real power consumption in this laboratory and the higher energy consuming equipment.

The power consumed by each equipment is calculated as follows:

$$\text{Total Power} = \text{Unit power} \times \text{Quantity}$$

$$\text{Daily Power} = \text{Total Power} \times \text{Hours Operating} / \text{day}$$

$$\text{Monthly Power} = \text{Daily Power} \times \text{Number of day per month}$$

$$\text{Annualy Power} = \text{Mounthly Power} \times \text{Number of mounth}$$

Consequently after determining these powers, the photovoltaic power to install is determined by the following expression:

$$\text{PV Power} = \frac{\sum \text{Annualy Power}}{\text{Basic Consumption}}$$

The basic consumption is equal 1800 Kwh/year.

SIZING OF THE EQUIPMENTS

PV Pannel

We have chosen to install Yingli Solar monocrystalline photovoltaic panels of 250 Wp, tinted in black because in this case it becomes more selective and we will have a maximum yield of 15.3%.

Table 2. Electrical characteristics of PV Panels.

Characteristics PV Panel			
Characteristics	Units	STC Conditions	NOCT Conditions
Maximum Power	W	250	181.6
Voltage at PElectrical cmx	V	28.9	26.4
Current at Pmax	A	8.66	6.91
Open circuit voltage	V	37.6	34.8
Short circuit cuurent	A	9.29	7.50

Table 3. Thermal characteristics of PV Panels

Characteristics	Symbol	Units	Value
Nominal Temperature of cell		°C	46 +/- 2
Temperature coefficient for Pmax	γ	%/°C	-0.42
Temperature coefficient for Voc	β_{Voc}	%/°C	-0.31
Temperature	α_{Isc}	%/°C	0.04

<i>Characteristics</i>	<i>Symbol</i>	<i>Units</i>	<i>Value</i>
coefficient for I_{sc}			
Temperature coefficient for V_{mpp}	$\beta_{V_{mpp}}$	%/°C	-0.41

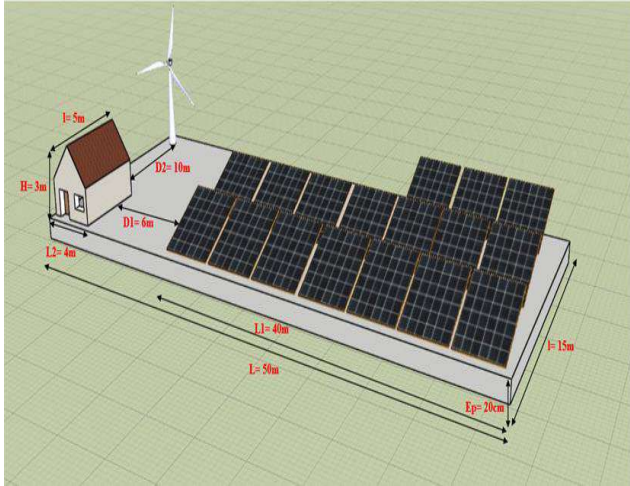


Figure 3.
Platform of installation.

Converter

For our installation of 12 Kw with a type of exposure and incline of 36°, using a single inverter is sufficient. But, for larger installation the installation of multiple inverters can reduce the risk of outages.

The selected inverter is a Sunny Tripower 12000 TL-20 whose technical characteristics are presented in the following tables:

We must make sure that voltage delivered by the PV field belongs to the MPPT voltage range of the inverter. This MPPT voltage range will also have an impact on the number of PV panels in string.

The following equations are used to determine the minimum and maximum number of PV panels in string [11]:

$$\text{Maximum number of panels} = E \left(\frac{U_{mppt, \max}}{U_{mpp} * 1,15} \right)$$

$$\text{Minimum number of panels} = E \left(\frac{U_{mppt, \min}}{U_{mpp} * 0,95} \right)$$

The theoretical calculation has given us a minimum number of 16 panels and a maximum number of 24 panels, and we will connect to the A input of the inverter 32 panels

according to 2 strings and to the B input 16 panels into a single string.

The sizing of an inverter per string is based on three criteria: power compatibility, Maximum voltage compatibility, current compatibility [12].

Table 4.
Electrical Characteristics of Inverter

<i>Characteristics</i>	<i>Symbol</i>	<i>Units</i>	<i>Value</i>
Maximum DC Power	P_{\max}	W	12 275
Maximum Input Voltage	V_{\max}	V	1 000
MPP Voltage range	U_{mppt}	V	400- 800
Maximum Input Current A/ B	I_{\max}	A	18 A / 10 A
Number of independent Input A/ B	MPP		A : 2 / B : 2
Grid Frequency		Hz	50-60
Maximum Output current		A	17.4

SIMULATION BY SMA SUNNY DESIGN SOFTWARE

In this part we realized a simple simulation for our photovoltaic installation by the SMA Sunny Design which is a photovoltaic software for SMA inverters like our inverter [14].

Compatibility of the electric characteristics

The important object for this sizing is to compare the results for the power, voltage and the current compatibility, which are found theoretically with those found by this software.

The following figure presents the compatibility for the voltage range and the input current between the out photovoltaic field and the input of the inverter.

	Input A:	Input B:
Number of strings:	2	1
PV modules per string:	16	16
Peak power (input):	8.00 kWp	4.00 kWp
Typical PV voltage:	432 V	432 V
Min. PV voltage:	387 V	387 V
Min. DC voltage (Grid voltage 220 V):	150 V	150 V
Max. PV voltage:	647 V	647 V
Max. DC voltage:	1000 V	1000 V
Max. current of PV array:	17.3 A	8.7 A
Max. DC current:	18 A	10 A

Figure 4.

Compatibility of the electrical characteristics of our sizing.

Performance Ratio

The performance ratio (PR) is indicated in percentage and is the ratio between the real and the theoretical yield of the photovoltaic system.

If the value of this ratio approaches of 100%, we consider that this photovoltaic system has an efficient operation. However, it is not possible to reach the value of 100% in practice because the operation of the photovoltaic system always generates inevitable losses such as the thermal and conduction losses. The performance ratio is calculated as follows [13]:

$$\text{Performance Ratio} = \frac{\text{Real yield}}{\text{Theoretical yield}}$$

In the following figure, we present the profile of this performance ratio.

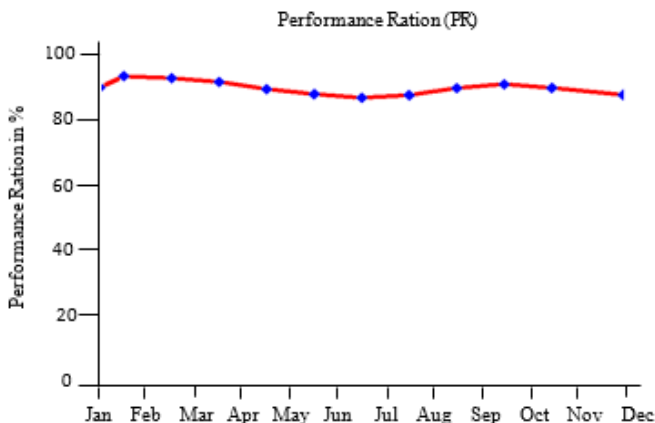


Figure 5.

Performance ratio.

We noted that our installation is effective because it have a higher performance ratio (more than 80%) and we deduct that this value is fluctuating because of some conditions such as panel temperature, shading, solar irradiation and the energy losses.

Production Forecast with consumption

In the following figure, we present the quantity of the energy produced by the PV installation, the energy consumed from the grid and a little quantity of energy stored by using batteries.

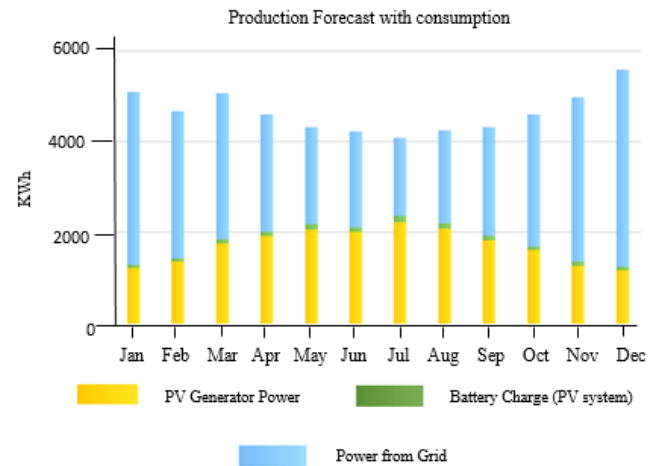


Figure 6.

Production forecast with consumption.

We noted that by summing each monthly power produced or purchased we find a very similar value to that found previously by using the SMA Sunny Design software (fig.7). This small variation is due to the difference between the values of each weather databases [15].

ANALYSIS AND MODELLING

At the meantime, the total energy consumption of our laboratory will be monitored in order to compare it to the consumption of the laboratory before the installation this micro-system of renewable energy system.

Self consumption profile

The following figure presents the consumption profile for our system by using some battery to storage some energy for lighting at night, and the effect of this installation to reduce the quantity of electricity purchased from the grid.

We know that the energy consumed by our laboratory per year is equal 49505 kWh and with results of this profile of self-consumption, we can conclude that the self-sufficiency quota is equal 32.2% of PV Energy and the self-consumption quota is equal 82.4% of Energy Consumption per year.

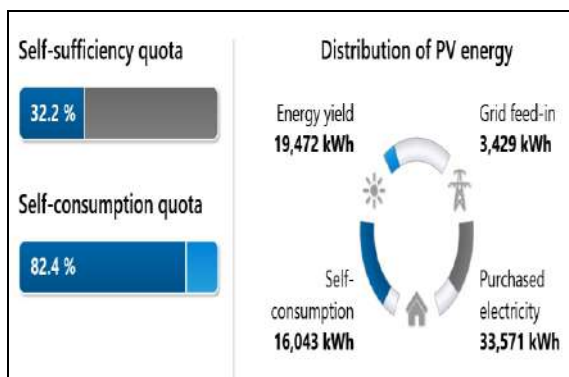


Figure 7.
Self Consumption profile.

SIMULATION BY PV*SOL SOFTWARE

In this part we realized a simulation for our photovoltaic installation by the PV*SOL software to have some idea about the efficiency for this system and to compare some results with the others results given by SMA Sunny Design software.

RESULTS AND DISCUSSION

After the connection of our system of installation to the electricity distribution grid, some measurements and data will be extracted to use it for the step of Capitalization and monitoring.

At the meantime, the total energy consumption of our laboratory will be monitored in order to compare it to the consumption of the laboratory before the installation of this micro-system of renewable energy system.

CONCLUSIONS

The paper has presented the prototype considered by the DE.DU.ENER.T. project that has been installed near the LPT Laboratory in Borj Cerdia Tecnopark (Tunisia).

Some result of simulation realized by some industrial software such as Sunny Design and PV*SOL indicate that the hybrid electric system could provide about 38% of the total consumption of the electricity for our laboratory.

In a future work, the result of the measurement campaign will be presented together with the results of the research.

ACKNOWLEDGMENTS

The project has been funded by “Programme Instrument Européen de Voisinage et de Partenariat (IEVP) Coopération Transfrontalière (CT) - Programme ENPI Italie-Tunisie 2007- 2013 Projet DE.DU.ENER.T. “ Le Développement durable dans la production énergétique dans le territoire” Ps 2.3.005 CUP : C17D13000000006 - Progetto cofinanziato dall’Unione Europea - “Sfide comuni, obiettivi condivisi” - Assistenza Tecnico-scientifica Ares s.r.l. - Soggetti: Comune di Valderice, Centre de Recherches et des Technologies de l’Energie (CRTE) - Technopole de Borj Cedria -Tunisia, Consorzio Universitario della Provincia di Trapani, Libero Consorzio Comunale di Trapani”.

REFERENCES

- [1] Sudhakar K, Tulika S, Kavali J. Matlab Modeling and Simulation of Solar Photovoltaic Panel; LAMBERT Academic Publishing.
- [2] Bajpai P, Dash V. Hybrid renewable energy systems for power generation in stand-alone applications: A review. *Renew Sustain Energy Rev* 2012;16:2926– 39.
- [3] Erdinc O, Uzunoglu M. Optimum design of hybrid renewable energy systems: Overview of different approaches. *Renew Sustain Energy Rev* 2012;16:1412– 25.
- [4] Marques AJ, Boccaletti C, Ribeiro EFF. Uninterruptible Energy Production in Standalone Power Systems for Telecommunications presented at the International Conference on Renewable Energies and Power Quality (ICREPQ’09) Valencia (Spain), 2009.
- [5] W.T. Chong, M.S. Naghavi, S.C. Poh, T.M.I. Mahlia, K.C. Pan. Techno-economic analysis of a wind-PV hybrid renewable energy system with rain water collection feature for urban high-rise application. *Appl Energy* 2011; 88:4067–77.

- [6] Kazem HA. Renewable energy in Oman: status and future prospects. *Renew Sustain Energy Rev*2011; 15:3465–9.
- [7] Zachariah Iverson, Ajit Achuthan, Pier Marzocca, Daryush Aidun. Optimal design of hybrid renewable energy systems (HRES) using hydrogen storage technology for data center applications. *Renew Energy* 2013; 52:79–87.
- [8] S. Ben mabrouk, A. Ben Mabrouk, K.Harzli, D. La Cascia , H.Oueslati, G. Zizzo, L. Dusonchet, S. Favuzza, M.G. Ippolito, F. Massaro. Experimentation of Sustainable Energy Microsystems : the DE.DU.ENER.T. Resaerch Project. 4th International Conference on Renewable Energy Research and Applications (ICRERA2015) , 22-25 November 2015 Palermo, Italy.
- [9] Kazem HA, Khatib T. Techno-economical assessment of grid connected photovoltaic power systems productivity in Sohar, Oman. *Sustain Energy Tech- nol Assess* 2013;3:61–5.
- [10] Kabalci E. Design and analysis of a hybrid renewable energy plant with solar and wind power. *Energy Convers Manag* 2013;72:51–9.
- [11] Harish V.S.K.V, Kumar A. A review on modeling and simulation of building energy systems. *Renewab and Sustain Energy Reviews*, 2016; 56: 1272 – 1292.
- [12] Paiva JE, Carvalho AS. Controllable hybrid power system based on renewable energy sources for modern electrical grids. *Renew Energy* 2013; 53: 271–279.
- [13] A. Labouret, M. Viloz , Installations photovoltaïques :Conception et dimensionnement d’installations raccordées au réseau , 5ed,Edition le Monter, DUNOD : Paris, 2012, pp.127-139.
- [14] Unio Technique de l’Electricité (UTE), UTE C 15-105 Guide Pratique : Detemination des sections de conducteurs et choix des dispositifs de protection, Méthodes pratiques , Edition UTE, CEDEX , 2003, pp.83-91.
- [15] SMA Solar Technology AG, Perfratio UFR100810 : Indice de performance, version 1.0, pp.1-9

A NUMERICAL INVESTIGATION OF A DIFFUSION-ABSORPTION CHILLER BASED ON PROPYLENE-NONANE MIXTURE

Nessrine SOLI

Department of Genius Chemical-Processes, UR11ES83, Environnement, Catalyses and Analyzes Processes,
National school of Engineers of Gabès, Street Omar Ibn El Khattab - Zrig - 6029 - Gabès, Tunisia

Email : nesrine.soli.tn@gmail.com

ABSTRACT

We propose in this work a numerical investigation of a diffusion-absorption refrigeration cycle working with a hydrocarbon mixture. It is about a machine of low refrigerating power (300 W) .the level of temperature in the generator is about 150 °C (fossil energy or solar energy) and it working with a no harmful mixture for the environment. We used a cooling medium temperature in the condenser and absorber at 35° C. Helium is used as inert gas. The total pressure of operation is about 17.5 bar. A modeling on suitable software was made for the system. The mixture of propylene/nonane was considered. The validation of our model was made by comparison with the results of literature. Parametric studies are also undertaken to analyze the effects of the temperature of the generator, and also the temperature of evaporator on the performance of the system .Generally, we can conclude that the mixture of hydrocarbon proposed is a rather promising refrigerant as for the technical advantages which they offer, such as the use potential of a heat source at a temperature not exceeding 150°C.

KEYWORDS

Diffusion-absorption refrigeration cycle; Propylene; Nonane; Helium, Coefficient of performance.

NOMENCLATURE

T: temperature

P: pressure

I: index of component i

Y: Molar fraction in the phase vapor

X: molar fraction in the liquid phase

P: pressure of operation of system

GEN: generator

COND: condenser

GHX: exchanger gas gas

EVAP: evaporator

ABS: absorber

SHX: exchanger of solution

vari: variance of body i

Var Cycles: variance of cycle

mi: molar flow of flow I

hi: molar enthalpy of flow I

QG: driving energy provided to the generator

Q Cond: heat released on the level of condenser

Q abs: heat released on the level of the absorber

Q evap: power of refrigeration

ΔT : thermal pinching

COP: Coefficient of performance

INTRODUCTION

One of largest challenge that the world meeting today is to guarantee an acceptable level of comfort while controlling the continuous exhaustion of fossil energies and the protection of our environment. In this context production of cold and the development of the systems guaranteeing these objectives of which spoken different refrigerating machines.

The search for powerful refrigerants for the refrigerating machines is thus of great importance. But, demolished of them efforts of research, only two mixtures remain used exclusively: lithium aqueous bromide solutions and those of ammonia. However, these two mixtures present certain disadvantages which limit their use.

With the passing of years, a certain number of researchers have studies and describes the

performances of various absorption-diffusion refrigeration cycles, graphically, in experiments and numerically:

Koyfman and al. [1] carried out an experimental study of the pump with bubbles by absorption - diffusion. According to Koyfman, the performances of the pump with bubbles mainly depend on the driving temperature and the contribution of heat to the pump with bubbles.

The study showed that the maximum average temperature of the generator is lower than 90°C. Consequently, the complete system with absorption-diffusion which functions with organic solvents and HCFC us refrigerant can use weak potential heat sources to make the cycle functional.

Karamangil and al. [2], presented a review on the systems of refrigeration at absorption, the pairs of cooling agent - absorbing currently used and their substitutes.

Moreover, they carried out a thermodynamic analysis of the systems of refrigeration with absorption using of the pairs of solutions usually met in the literature. Les numerical results showed that the system with the LiBr - H₂O mixture has values of high COP (0, 55).

Thus, the system NH₃ - LiNO₃ is more advantageous at particularly low temperatures of generator (Temperature of generator < 75°C).

Muñoz and al. [3] worked out a review of technologies of diffusion-absorption refrigeration. Indeed, they summarized the working fluids used in absorption - diffusion systems of refrigeration.

Kherris and al. [4] carried out a theoretical study of a refrigerating system of absorption - diffusion functioning with the couple ammonia - water and hydrogen like inert gas.

The results obtained highlight the influence of the various parameters on the performance of the installation.

It appears clearly that the coefficient of performance is not a sufficient criterion for the best alternative of the machine but, other essential parameters having a great influence on the performance of the machine such as:

- The temperature of the condenser
- The temperature of the absorber
- The temperature of the evaporator

We consider in this work the mixture of hydrocarbons us working fluids for our installation. They are thermally stable fluids in the field of the temperatures of use, nontoxic and not corrode [5, 7]

The most volatil fluid, the propylene is selected like refrigerant and nonane like absorbent.

The studied configuration (fig. 1) is a refrigerating machine with absorption - diffusion.

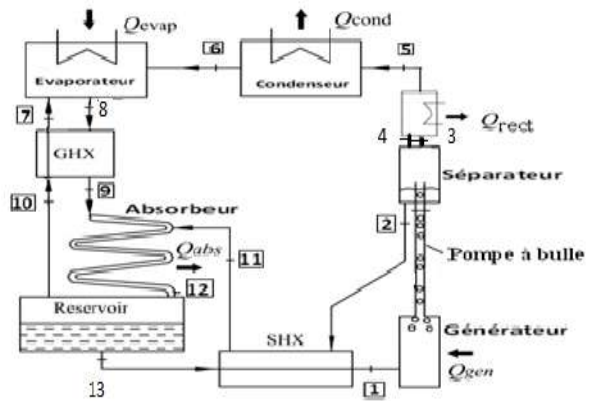


Fig.1. refrigerating machine with absorption - diffusion.

MATERIALS AND METHODS

Refrigerating machine with absorption-diffusion:

1. Description of a refrigerating machine with absorption-diffusion [5]:

The refrigerating machine with absorption-diffusion was invented by Von Platen and al[10].

It uses three fluids of operation: the ammonia (cooling agent), water (absorbent) and hydrogen like an inert gas.

In the operation of a machine with absorption-diffusion, one uses a gas of support which balances the pressures between the condenser and the evaporator while allowing the evaporation of the cooling agent and thus the refrigeration.

Since there is no moving part in the unit, the system with absorption-diffusion is quiet and reliable. It is thus often employed in rooms, offices, and in the arid and isolated regions.

2. Thermodynamic investigation of a refrigerating machine with absorption-diffusion [8]:

2.1. Modelisation of the various machine's parts: While using the following figure (figure 1) one will determine the assessments matters and the

energy balances of all the components of the installation:

2.1.1 Generator + Separator:

Total mass assessment:

$$\dot{m}_3 + \dot{m}_2 = \dot{m}_1 + \dot{m}_4$$

Partial assessment on the refrigerant:

$$\dot{m}_3 Y_3 + \dot{m}_2 X_2 = \dot{m}_1 X_1$$

Energy balance:

$$\dot{m}_2 H_2 + \dot{m}_3 h_3 - \dot{m}_1 h_1 - \dot{m}_4 h_4 = Q_{Gen}$$

2.1.2.Grinding-machine operator:

Total mass assessment:

$$\dot{m}_5 + \dot{m}_4 = \dot{m}_3$$

Partial assessment on refrigerant:

$$\dot{m}_3 Y_3 = \dot{m}_5$$

Energy balance:

$$\dot{m}_3 h_3 - \dot{m}_5 h_5 - \dot{m}_4 h_4 = Q_{Rec}$$

2.1.3.Condenser:

Total mass assessment:

$$\dot{m}_5 = \dot{m}_6$$

Partial assessment on refrigerant:

$$\dot{m}_5 Y_5 = \dot{m}_6 X_6$$

Energy balance:

$$\dot{m}_5 h_5 - \dot{m}_6 h_6 = Q_{Con}$$

2.1.4.Evaporator:

Total mass assessment:

$$\dot{m}_7 + \dot{m}_6 = \dot{m}_8$$

Partial assessment on refrigerant:

$$\dot{m}_6 X_6 + \dot{m}_7 Y_7 = \dot{m}_8 Y_8$$

Partial assessment on helium:

$$\dot{m}_7 Y_{7he} = \dot{m}_8 Y_{8he}$$

Energy balance:

$$\dot{m}_8 h_8 - \dot{m}_6 h_6 - \dot{m}_7 h_7 = Q_{Evap}$$

2.1.5.Exchanger gas-gas:

Total mass assessment:

$$\dot{m}_9 + \dot{m}_7 = \dot{m}_{10} + \dot{m}_8$$

Partial assessment on refrigerant:

$$\dot{m}_9 Y_9 + \dot{m}_7 Y_7 = \dot{m}_{10} Y_{10} + \dot{m}_8 Y_8$$

Partial assessment on helium:

$$\dot{m}_9 Y_{9he} + \dot{m}_7 Y_{7he} = \dot{m}_{10} Y_{10he} + \dot{m}_8 Y_{8he}$$

Energy balance:

$$\dot{m}_9 h_9 + \dot{m}_7 h_7 - \dot{m}_8 h_8 - \dot{m}_{10} h_{10} = Q_{EGG}$$

2.1.6.Absorber:

Total mass assessment:

$$\dot{m}_9 + \dot{m}_{11} = \dot{m}_{12}$$

Partial assessment on refrigerant:

$$\dot{m}_9 Y_9 + \dot{m}_{11} X_{11} = \dot{m}_{12} X_{12}$$

Partial assessment on helium:

$$\dot{m}_9 Y_{9he} = \dot{m}_{12} Y_{12he}$$

Energy balance:

$$\dot{m}_9 h_9 + \dot{m}_{11} h_{11} - \dot{m}_{12} h_{12} = Q_{Abs}$$

2.1.7.Exchanger liquid-liquid:

Total mass assessment:

$$\dot{m}_{13} + \dot{m}_2 = \dot{m}_1 + \dot{m}_{11}$$

Partial assessment on refrigerant:

$$\dot{m}_{13} X_{13} + \dot{m}_2 X_2 = \dot{m}_1 X_1 + \dot{m}_{11} X_{11}$$

Energy balance:

$$\dot{m}_{13} h_{13} + \dot{m}_2 H_2 - \dot{m}_1 h_1 - \dot{m}_{11} h_{11} = 0$$

$$\dot{m}_1 h_1 - \dot{m}_{13} h_{13} = Q_{ELL}$$

2.2. Variance calcul of the installation: A cyclic heat engine is consisted a whole of element which is presented as being open systems [7, 8]. For the determination of his total variance V_G , it is necessary to take account of the number of variables repeated between two consecutive elements R_i , than it should be then cut off from the sum of the elementary variances of each element V_i :

$$V_g = \sum_i V_i - \sum_i R_i$$

The calculation of the variance for the various machine parts is detailed on table 1.

Table 1
Variance of the various element of the cycle

Element	Variance
Generator + Separator	8
Condenser	1
Grinding-machine operator	3
Evaporator	5
Absorber	9
Exchanger gas-gas	8
Exchanger liquid-liquid	9

The variance of cycle = 43-33 = 10 thus, it is thus appropriate to take 10 independent variables.

3. Principe of the operation of a machine with absorption - diffusion:

3.1.Description of the cycle [5]:The basic components of the machine are the generator, the condenser, the evaporator and the absorber.

The refrigerating effect required is produced by the difference of the pressures partial of the cooling agent between the condenser and the absorber.

In order to maintain a pressure equal in all the apparatus helium circulates in the loop evaporator-absorber.

The liquid cooling agent leaving the condenser is conveyed in the evaporator where reign a high helium pressure.

So its partial pressure falls until the pressure which corresponds to a minimal temperature of evaporation in this point (T_{min}).

While evaporating, by contribution of a thermal power of the exterior (Q_{Evap}), the partial pressure of the cooling agent increases until the pressure which corresponds to the temperature of end of evaporation and the maximum pressure partial of the cooling agent in the gas circuit circulating between the absorber and the evaporator.

The produced vapor is forwarded to the absorber then it returns to current counter of the poor solution coming from the generator.

Having absorbed the vapor of the cooling agent, the solution now known as rich outgoing at the bottom of the absorber will supply the pump with bubbles.

This last master key then in the generator when the cooling agent is illustrated in the form of vapor forwarded to the condenser whereas the poor solution streams is going towards the head of the absorber by gravity.

Two exchangers with counter-current ensure a better use of provided energy. In the exchanger of solution (ELL), laid out between the absorber and the generator, the poor solution turning over of the generator is cooled by the rich solution which warms up its share before entering the pump to bubbles.

A second exchanger (EGG), between the absorber and the evaporator, ensures the cooling of gas coming from the absorber before introducing it into the evaporator.

3.2. Fundamental input and assumptions:

- The installation is considered for a refrigerating power of 300 Watt.
- Cooling with the ambient air at an average temperature of 35°C,
- Generator: Driving heat provided to the generator can have several origins: solar collector, thermal discharge, water vapor, combustion gas. One fixes a maximum temperature of this source at 130°C.

- The machine is supposed in constant operating condition and the pressure losses are considered negligible.

- The purity of the vapor of refrigerant on the outlet side of the generator is higher than 99 %.

- The vapor of the refrigerant leaving the generator towards the condenser is supposed to be saturated. The poor solution on the outlet side of the generator is saturated at the driving temperature with the cycle.

- The two exchangers of heat are supposed to be adiabatic and characterized each one by a thermal pinching; That of the pre-cooler (vapor/vapor exchange) is fixed at 10°C and that of the exchanger of solution (liquid/liquid exchange), with 5°C.

RESULTS AND DISCUSSION

Simulation of the refrigerating machine with absorption-diffusion: Simulations on a software adapts machine operating with absorption-diffusion cycle in stationary regime are carried out taking into account the assumptions and operating conditions mentioned front, the results of the simulation of the machine in C3H6/n-C9H20/He are presented in the table 3.

In literature, very few results were obtained with hydrocarbons like working fluid in a machine with absorption - diffusion cycle.

In a study, Chekir and al. [7] used binary mixtures, alkanes as working liquids for the machines with absorption. The refrigerants considered are propane, n-butane and isobutane, and absorbents, pentane, hexane, heptane and octane. Among the twelve possible combinations, ten mixtures only are possible in absorption (C3-c5;C3-c6;C3-c7;C3-c8;iC4-C6;iC4-C7;iC4-C8;C4-c6;C4-c7;C4-c8).

While being based of a comparison of the pressures, flows of the solutions and COP of the machines functioning with these mixtures, to chekir and al. the C4-C8 couple is chosen to be the optimal couple.

Table 3
Results of simulation of machine absorption-diffusion
for $Q_e=300\text{watt}$

Reference	Chiller	Working liquid	Q_e (kw)	COP	T generator (°C)	T evaporator (°C)	Results	Inert gas
Our work (2015)	diffusion	C3H6/nC9H20	0.308	0,2213	130	0	simulation	helium
Zaitseff et al. (1995)	diffusion	NH3/H2O	1	0.22	140	-15	simulation	helium
Mazouz et al. (2014)	diffusion	NH3/H2O	0.02	0.12	185	-20;-10	experimental	hydrogen

Table 4
Validation of results

Referenc e	Chiller	Working liquid	Q_e (kw)	COP	T generator (C)	T evaporator (C)	Results	Inert gas
Dardour and al(2013)	diffusion	C3/C9 C3H8/C9H20	1	0.20	120	2	Simulation (with water cooling in condenser and the absorber)	Hydrogen
Our work (2015)	diffusion	C3/C9 C3H8/C9H20	1	0.197	120	2	simulation	Hydrogen
Sayadi and al(2013)	Diffusion adapted to the solar	C3/C6 C3H8/nC6H1 4	1	0,24	121	0	Simulation (with water cooling in the condenser and the absorber)	helium
Our work (2015)	diffusion	C3/nC6 C3H8/nC6H1 4	1	0.239	121	0	simulation	helium
Referenc e	Chiller	Working liquid	Q_e (kw)	COP	T generator (C)	T evaporator (C)	Results	Inert gas
Dardour and al(2013)	diffusion	C3/C9 C3H8/C9H20	1	0.20	120	2	Simulation (with water cooling in condenser and the absorber)	Hydrogen
Our work (2015)	diffusion	C3/C9 C3H8/C9H20	1	0.197	120	2	simulation	Hydrogen
Sayadi and al(2013)	Diffusion adapted to the solar	C3/C6 C3H8/nC6H1 4	1	0,24	121	0	Simulation (with water cooling in the condenser and the absorber)	helium
Our work (2015) Soli	diffusion	C3/nC6 C3H8/nC6H1 4	1	0.239	121	0	simulation	helium

This last couple conduit to the best COP (0,37) in the case of an installation air cooled, value 29% lower than an installation functioning with the ammoniac/eau mixture under the same conditions. Sayadi and al. [9] studied theoretically a machine of absorption/diffusion water-cooled and of a capacity of 1kw using the software HYSYS, the fluids used are binary mixtures of light hydrocarbons (C3/nC6, C3/C6, propylene/C5, propylene/iC4, propylene/iC5) in combination with helium like inert gas.

The heat of drive is supposed to be provided by a field of vacuum solar collector whose heat proved to be of 121°C for a temperature of exit of evaporator of 0° C.

The rate of flow of cooling water between the coolers and the tower of cooling is of 140 l/hr.

Dardour and al. [5] carried out the study and performances of a machine with absorption - diffusion analyzes using the propane mixture/n-nonane like working liquid and hydrogen like inert gas.

The results of the study showed that in mode of water cooling and in an interval of temperature of the driving heat which change between [110°C, 125°C], the coefficient of performance is about 0.51, this value makes this couple competitive compared to certain working liquids used in marketed machines with absorption and allows it to be presented in the form of a possible substitute.

Of another hand, Dardour and al. carried out a parametric study, which is in bond with the effect of the temperature of driving heat: they showed that, under the specified operating conditions, the system is of more powerful with COP of about 0.44 for a temperature of driving heat not exceeding 120°C.

According to Dardour and al. the use of a mixture of alkane like working liquid in combination with an inert gas like hydrogen or helium in a machine with absorption-diffusion is promising.

Validation of the results:

To validate our simulation related to our flowsheet, we compared our results respectively for the couple propane/nonane, with those of H. Dardour and al. [5] and for the couple propane/hexane, with those of Sayadi and al. [9] These results are deferred in table 4.

Parametric study:

Effect of the temperature of evaporation: On figure (2) is traced the variation of the COP according to different temperature of exit of evaporator (-6,-4,-2, 0, 2, 4, 6).

The figure shows that the COP is a decreasing function of the temperature of exit of evaporator for temperatures lower than zero dismantles Celsius but this variation is negligible for positive values.

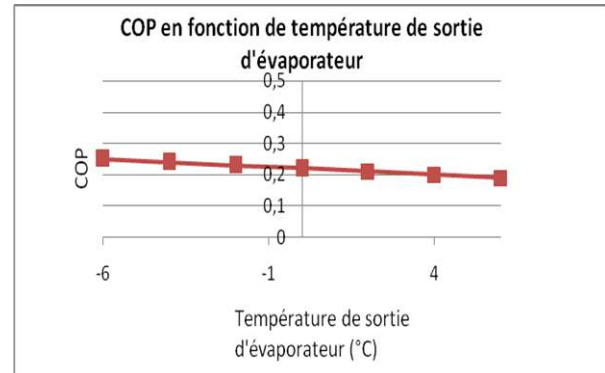


Figure 2

COP according to Temperature of exit of evaporator

Effect of the driving temperature: We illustrate in Figure (3) the variations of the refrigerating coefficient of performance according to the driving temperature in the interval [120°C - 160 °C].

The examination of this figure makes it possible to identify a decreasing variation of the COP according to driving temperature: the COP gradually decreases to leave 0.22 with T=120°C and reached 0.17 with T=150°C. In the interval [150°C - 160° C] the COP is nearly constant, it is about 0.17.

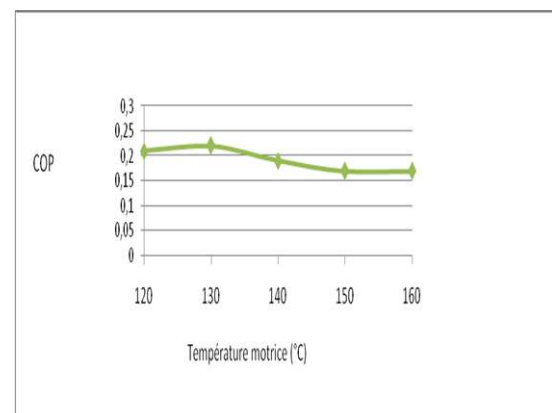


Figure 3

COP according to driving Temperature

CONCLUSIONS

In this work, we proposed a binary mixture of hydrocarbon very little used, until now, like working liquids for the refrigerating machines with absorption-diffusion.

The installation functions under a pressure moderated about 17 bar; with propylene like refrigerant and n-nonane like absorbent.

By using the air as medium of cooling, the system propylene/nonane gives a coefficient of performance of about 0.22, value definitely comparable with that of an installation functioning with the couple ammoniac/water under the same conditions.

The simulation of the refrigerating machines with absorption-diffusion cycle and the calculated performances offer promising prospects for these mixtures in the field for the refrigeration to absorption-diffusion cycle.

REFERENCES

1. U.Koyfman ,M.Jelinek ,U.Levy,J.Borde, An experimental study of the performance of the pump with bubbles for system of refrigeration by absorption -diffusion with organic fluids, *Thermal Genius applied* ,Volume 23, Numéro 15 , Octobre 2003, pages 1881-1894
2. M.Karamangil ,S.Coskun ,O.Kaynaklı ,N. Yamankaradeniz , A study of simulation of the performance evaluation of a system of refrigeration with absorption in only one stage by using working liquids and the conventional solutions , *Renewable & Sustainable Energy Reviews* , Volume , September 2010, Pages 1969-1978
3. J.Rodríguez-Muñoz ,J.Belman-Flores, Examination of technologie of refrigeration diffusion of absorption, *Renewable & Sustainable Energy Reviews* , Volume 30 , February, 2014, Pages 145-153
4. S. Kherris , R. Chadouli et A. Asnoun, Improvement of the performance of a refrigerating cycle with absorption-diffusion NH₃-H₂O-H₂, *Renewable & Sustainable Energy Reviews* Vol. 12 N°2 (2009) 215 – 224.
5. H.Dardour ,H.Mhiri, S.Gabsi, A,Bellagi , thesis :Study of the refrigerating machines has absorption diffusion using a systematic mixture of alkanes : study and rigorous modeling of the absorber, 2012
6. N. Chekir ,A. Bellagi , Study of a refrigerating machine with absorption: thermodynamic modeling, calculation of liquid-vapor balances and study of the binary cases of mixtures of n-alkanes, ,2000,pages 10-12
7. N. Chekir, Kh. Mejbri ,A. Bellagi, Simulation of a cooler with absorption functioning with mixtures of alkanes, *International Review of the Cold* , Volume 29, number 3 , may 2006, Pages 469-475
8. B. Chaouachi and S. Gabsi ,Design and Simulation of an Absorption Diffusion Solar Refrigeration Unit *American Journal of Applied Sciences* 4 (2): 85-88, 2007
9. Z.Sayadi , N.Ben Thameur , M. Bourouis ,A.Bellagi , Optimization of the performances of solar energy leads small-coolers to absorption-diffusion to work with light hydrocarbons, *Conversion and Energy economy* ,Volume 74 , October 2013, Pages 299-307
10. Von Platen, C.G. Munters, Refrigerator, US Patent 1 (1928) 685-764.

ANALYZE THE ENERGETIC PERFORMANCE OF A NEW COMBINED SYSTEM ORC-VCC FOR THE COGENERATION

NoureddineTOUJENI ^{a,1}, Nahla BOUAZIZ ¹, Lakdar KAIROUANI ¹

¹Unité de Recherche Énergétique & Environnement, Ecole Nationale des Ingénieurs de Tunis,
Université Tunis EL Manar, BP 37 Le Belvédère 1002, Tunis, TUNISIE

^a Email: toujeninoureddine@gmail.com Fax: 216 71 872 729

ABSTRACT

This paper presents a new system which combines a Rankine-vapor compression cycle for the cogeneration of electricity and refrigeration. The proposed system uses low-temperature heat sources such as solar energy, industrial waste heat and biomass. The proposed new system is studied and analyzed. Great interest is paid on system performance, versus different operating parameters. We focus specially on the effect of the evaporation temperature, the mass flow, the temperature and the heating source pressure on the performance of the novel configuration object of this work.

KEYWORDS

Low-grade energy, low condensing temperature, organic Rankine cycle, evaporator-condenser, cogeneration, vapor-compression cycle.

NOMENCLATURE

COP_{vcc} : Coefficient of performance for VCC
 η_{orc} : Organic Rankine cycle efficiency
 h : Enthalpy (kJ/kg)
 m : Mass flow rate for ORC (kg/s)
 Q_b : Boiler heat input (kW)
 Q_{exh1} : Regenerator1 heat input (kW)
 Q_{exh2} : Regenerator2 heat input (kW)
 Q_{ev1} : The power of the evaporator to the condenser ORC fluid (kW)
 Q_{ev2} : The power of the evaporator2 provided to the user (kW)
 Q_{ev} : The overall power evaporated by the VCC cycle (kw)
 W_{com} : Compressor work input (kW)
 W_{exp} : Expander work output (kW)
 W_{net} : Net work output for Overall system (kW)
 W_{pump} : working fluid pump power consumption (kW)
 η_{com} : Compressor isentropic efficiency
 η_{exp} : Expander isentropic efficiency
 η_{pump} : Working fluid pump isentropic efficiency
 T : Temperature (°C)

a: Fluid for ORC
 b: Fluid for VCC
 E: effectiveness of the system

Index:

1: pump inlet
 2: pump outlet
 3 : regenerator 1 Output for the orc cycle fluid
 4: regenerator 2 Output for the orc cycle fluid
 5: expander inlet
 6: expander outlet
 7: compressor inlet
 8: compressor outlet
 9: condenser inlet
 10: condenser outlet
 11: regenerator 1 outlet
 12: evaporator2 inlet
 13: evaporator 2outlet

INTRODUCTION

Nowadays, the world is facing multiple energy challenges resulting from the increasing need for fossil energy that is insufficient and more environmental problems including the greenhouse

effect produced by waste heat from the industry. Therefore, the exploitation of renewable energy becomes crucial even a vital need to support unsustainable energy requirements of the industry.

The sources of renewable energy are potential sources, such as solar, biomass, geothermal and waste heat from the industry, which however cannot be converted into electricity or cool without a great economy and autonomy.

In terms of power generation, several dynamic cycles are used as the Rankine cycle the Kalina cycle and Gosswami cycle . Among them, the organic Rankine cycle is the less complex and the most powerful prompting many researchers for lost years [1-5] to focus study and improve the cycle.

This paper is aiming to develop new combined-ORC-VCC with a working fluid R600a for ORC and ammonia for the VCC whose goal is to get cogeneration to produce electrical power and cooling capacity. This study reveals for the influence of system parameters such as the temperature of the hot source, evaporation temperature and mass flow rate on the performance of the system including the cooling capacity, net working coefficient performance for both of the ORC and VCC cycles ,and the overall COP of the system.

1. ANALYSIS AND MODELLING

The considered system in this work is an organic Rankine cycle (ORC) which is combined with a vapor compressor cycle (VCC) and its schematic diagram is shown in Fig. 1.

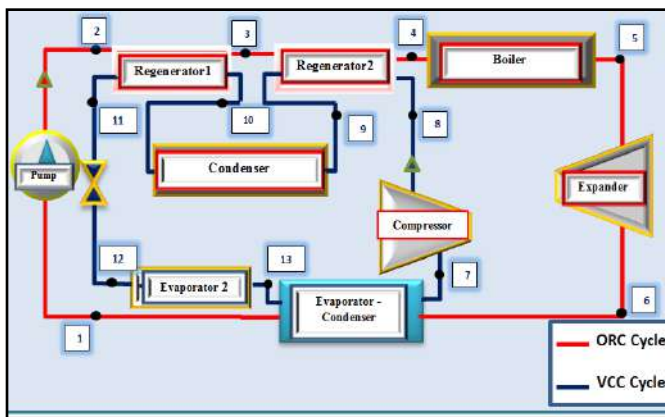


Figure 1. System schematic

The system consists in a pump, a boiler, a turbine, two regenerators, a condenser, an expansion valve, an evaporator and an evaporator- condenser system. The working principle of this system is as follows:

Pumping from 1 to 2 of refrigerant (a) that increase the pressure to reach the heating pressure.

A part of utilized heat where the temperature is very low and cool (less than 10°C) will be recovered to the VCC using the regenerator1.

Then, the fluid will enter in the second recuperator (regenerator 2) to be reheated while exploiting the heat output VCC cycle compressor. The fluid will be passed immediately to the boiler (2-3) to determine the heating and evaporation at constant pressure.

Once the fluid (a) is vaporized, it will be passed directly for the expander that given birth a mechanical power. Then, after the expansion phase at the turbine level, the working fluid condenses in condenser-evaporator system with using a quantity of the flow generated by VCC evaporation.

Concerning the VCC cycle; The compression phase (6-7) allow the augment of the pressure till of condensation pressure. Once the fluid completely condensed (7-8), the fluid will pass in the next stage to regenerator 1 in purpose to benefit its heat to cool the fluid and circulate in an expansion valve (8-5) to lower their pressure until reach the vaporization pressure. The first part of refrigeration capacity is produced by the evaporator 2 is used to be exploited. The second evaporation will be made in the evaporator-condenser serving for the condensation of ORC.

The working fluid considered in this study is R600 for ORC and ammonia for VCC.

2. Thermodynamic models

For ORC:

$$W_{exp} = \dot{m}_1 (h_5 - h_{6s}) \cdot \eta_{exp} \tag{1}$$

$$W_{pump} = \dot{m}_1 \frac{(h_{2s} - h_1)}{\eta_{pump}} \tag{2}$$

$$Q_b = \dot{m}_1 (h_5 - h_4) \tag{3}$$

$$\eta_{orc} = \frac{(W_{exp} - W_{pump})}{Q_b} \tag{4}$$

For VCC:

$$W_{comp} = \dot{m}_2 \frac{(h_{8s} - h_7)}{\eta_{comp}} \tag{5}$$

$$Q_{ev1} = \dot{m}_2 (h_7 - h_{13}) \tag{6}$$

$$Q_{ev2} = \dot{m}_2 (h_{13} - h_{12}) \tag{7}$$

$$Q_{ev} = \dot{m}_2 (h_7 - h_{12}) \tag{8}$$

$$\tag{9}$$

$$COP_{VCC} = \frac{(Q_{ev1} + Q_{ev2})}{W_{comp}}$$

The overall performance of ORC/VCC is defined as follows :

$$Q_{exh1} = \dot{m}_1(h_3 - h_2) = \dot{m}_2(h_{10} - h_{11}) \quad (10)$$

$$Q_{exh2} = \dot{m}_1(h_4 - h_3) = \dot{m}_2(h_8 - h_9) \quad (11)$$

$$W_{net} = W_{exp} - W_{comp} - W_{pump} \quad (12)$$

$$E = W_{net}/Q_{ev2} \quad (13)$$

3. RESULTS AND DISCUSSION

3.1. System performance analysis and operating parameters effect

The Figure 4 displays the curve pattern effectiveness (E) of the system in function between the temperature in expander inlet(T5) , temperature of output regenerator 1 (T3) and temperature of output regenerator 2 (T4) at $T_{ev}=10^\circ\text{C}$. We note that the elevation of the Temperature T5 leads to the elevation of E. This is due to the augmentation of the turbine Work W_{exp} which is proved with the equation [1] and diagram (T,s) of the fluid R600a as well.

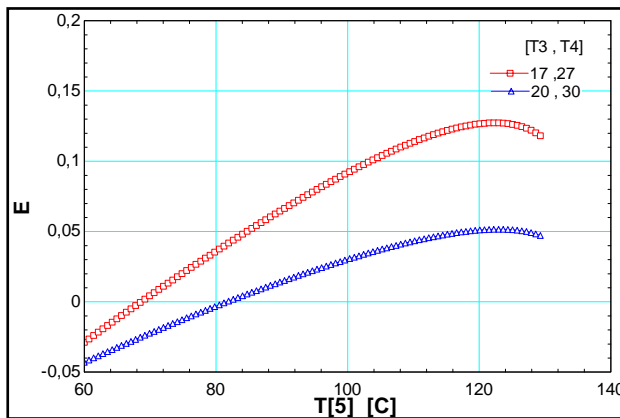


Figure 2.
variation in efficiency(E) as a function of T(5),T(3)and T(4)

Regarding the effect of (T1,T4) on(E), It is well noted that these two factors have a remarkable impact and mostly when T[5] increases. This means that both recovery systems (generator 1 and 2) have an

effect and an added value on the performance of the system. This effect appears on the Figure 3 and 4, where Figure 5 represents the effect of T3 and T4 with T5 on the cop of CVV cycle. It is clear that T3 and T4 have a large effect on the COP whereas the transition from condition 1 (red curve) toward condition 2 (Blue curve) allows the cycle improvement by almost 0.12 on T5 band.

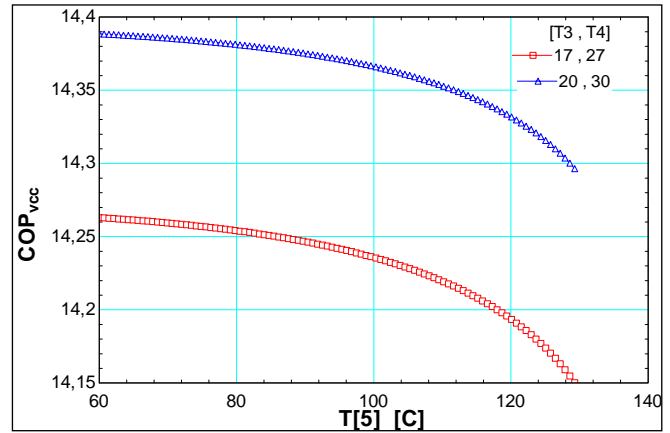


Figure3.
Variation in (COP vcc)as a function of T(5),T(3)

In addition, the effect of the second recovery systems and T5 on η_{orc} (figure 6), we notice that T3,T4 effect is lower than VCC cycle. Contrary, T5 has a great impact on the η_{orc} which expressed on the equation (4).

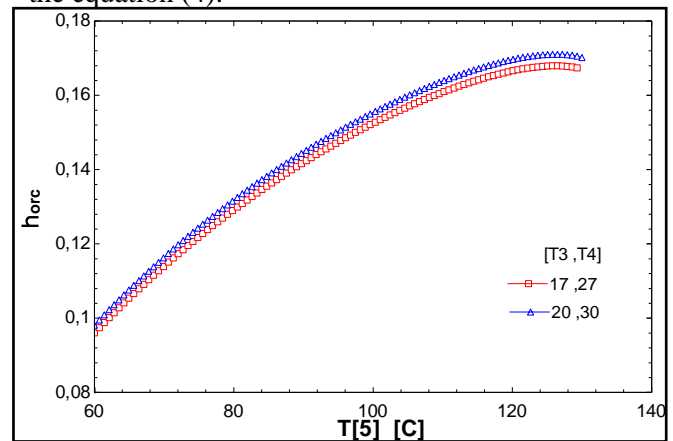


Figure 4
Variation in η_{orc} as a function of T(5),T(3)and T(4)

To achieve the performances of the cycle, Figure 8 displays an iso-answer surface that includes globally the three terms of performance (ORC , COP VCC and E).

Both Figures 6 and 2 show clearly that the efficiency value may take negative values, where our system becomes unable to produce the electricity and to cover the energetic need of the compressor.

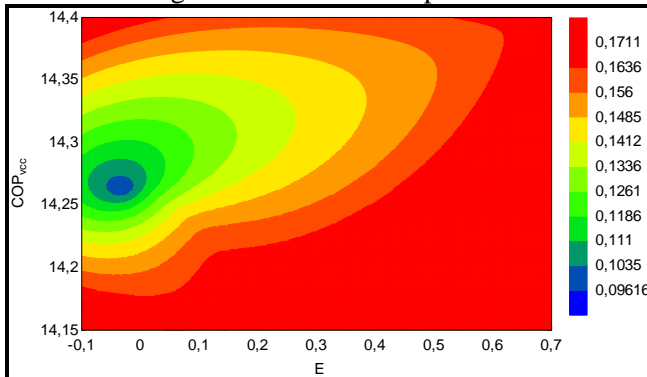


Figure 5. Performing surface (E), COP_{vcc} and η_{orc}

As a result, it is necessary to study closely the operating parameters (T3, T4, T7 and T5) on the system efficiency E in purpose to frame the confidence interval.

3.2.. Study of the system efficiency (E) and the impact of effective parameters (using the experiment plan tool)

The methodology of experiment plans is a very powerful tool and largely employed in all the experimental approach in the modeling of the industrial processes (6). This is noted in the previous paragraph and signaling that influential factors on the efficiency of E are: T3, T4, T5 and T7.

The table 1 illustrates the selected levels of each factor. We have established a factorial and complete plan, forasmuch the experiments are purely digitals. Additionally, it is unnecessary to reduce the number of runs because we can obtain more precise results.

Table 1
Selected levels of factor.

factors	Levels		
	1	2	3
T5	80	90	100
T7	5	10	15
T3	17	20	23
T4	27	30	33

The Table 2 displays the impact values of these factors on the outputted response. The factors with a direct impact and more significant are T3 and T7 and

the highest interaction coefficient is (T7*T4) which is proved on the interaction's graph Figure 6.

Table 2
Impact values of factors

Source	Log Worth
T7*T3	3,707
T3*T4	2,494
T3	2,158
T4	0,964
T5*T3	0,449
T5*T4	0,253
T5	0,241
T5*T7	0,070
T7	0,017
T7*T4	0,007

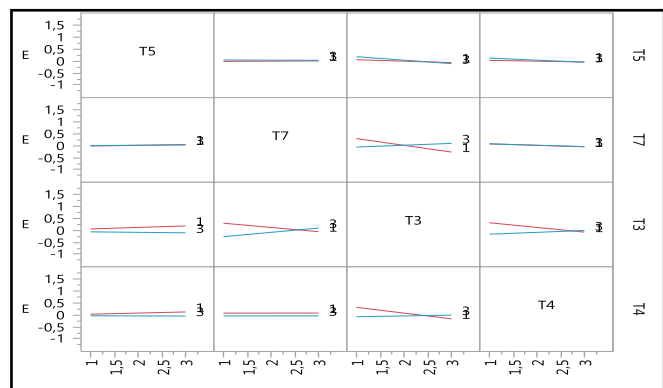


Figure 6
Interaction values between the factors

After illustrating the graphical curve of the response with different factors levels (Figure 7), we found out that (E) has positive value on T4=1 level and this allows to set it and determinate the optimum T3 value with a positive response whatever the value of T5 and T7 is. T5 and T7 are extrinsic parameters belong to the available source (T5) and the client need to cold (T7).

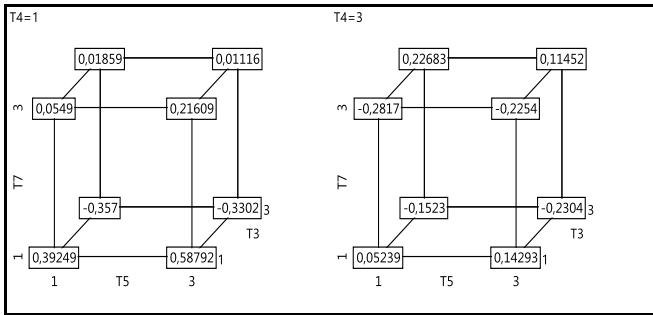


Figure 7

Curve of the response with different factors levels

The Figure 8 illustrates the iso-response that satisfies these constraints. As result, we find that we can manage a functioning interval with T=17 and T4=27.

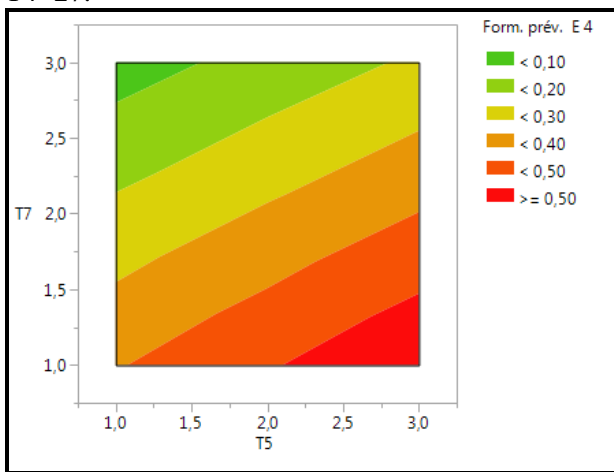


Figure 8

Schematic of T-s plots of the selected work fluids for ORC

CONCLUSIONS

In this study, the performance of a new combined organic rankine cycle and vapor compression cycle is thermodynamically investigated. The main numerical

results show that the use of two generators under appropriate conditions, improves the system performance. besides, the performance of the new system depend closely on the condenser temperature.

REFERENCES

[1]: D. Casartelli, M. Binotti, P. Silva, E. Macchi, E. Roccaro, T. Passera. Power block off-design control strategies for indirect solar ORC cycles. Energy Procedia 69 (2015) 1220 – 1230

[2]: Sylvain Quoilin, Martijn Van Den Broek, Sébastien Declaye, Pierre Dewallef. Techno-economic survey of Organic Rankine Cycle (ORC) systems. Renewable and Sustainable Energy Reviews 22 (2013) 168–186

[3]: Villarini M., Bocci E., Moneti M., Di Carlo A., Micangeli A. State of art of small scale solar powered ORC systems: a review of the different typologies and technology perspectives. Energy Procedia 45 (2014) 257 – 267

[4]: E.H. Wang, H.G. Zhang, B.Y. Fan, M.G. Ouyang, Y. Zhao, Q.H. Mu. Study of working fluid selection of organic Rankine cycle (ORC) for engine waste heat recovery

[5]: WANG Zhiqi, ZHOU Naijuna, Guo Jing. Performance analysis of ORC power generation system with low-temperature waste heat of aluminum reduction cell. Physics Procedia 24 (2012) 546 – 553

[6]: Montgomery, « Introduction to Statistical Quality Control ». New York: John Wiley and Sons D.C. (2001).

TRANSIENT ANALYSIS OF AN ABSORPTION SOLAR REFRIGERATOR WITH EXTERNAL AND INTERNAL IRREVERSIBILITIES

Boukhchana Yasmina^{1*}, Fellaf Ali², Ben Brahim Ammar¹

¹ Research Unit of Applied Thermodynamics, Department of Chemical and Processes Engineering, National School of Engineers of Gabes, University of Gabes, St Omar Ibn El-Khattab, 6029 Gabes, Tunisia Affiliation

² Research Unit of Applied Thermodynamics, Technology Department, High Institute of Applied Sciences and Technology

University of Gabes, 6029 Gabes, Tunisia

*Corresponding author: Fax: + 216 75 392 190 Email: Yasmina.Boukhchana@enig.rnu.tn

ABSTRACT

The transient analysis of a solar absorption refrigeration cycle with external and internal irreversibilities is presented in this paper. The model consists of a flat plate solar collector, a refrigerator with three finite-size heat exchangers, namely, the evaporator between the refrigeration load and refrigerant, the condenser between the refrigerant and the ambient, and the generator between the solar collector and the refrigerant, and finally the refrigerated space. The total thermal conductance of the three heat exchangers is fixed.

An empirical function is used to model the internal entropy generation of the cycle. The parameters of this function are estimated by fitting data obtained by simulation to the predictions of the THR model. The model is based on the first and second laws of thermodynamics, heat transfer equations at finite thermal source and sink capacities and entropy generation terms in order to consider the internal and external irreversibilities of the cycle.

A thermodynamic analysing and optimization of the absorption cycle is then performed, reporting the operating conditions for minimum time to reach a prescribed cold-space temperature, thus maximum refrigeration rate, specifically, the optimal temperature of hot space and the optimal way of allocating the thermal conductance inventory.

The results are presented in normalized charts for general applications. The collector temperature presents major influence on the conceptual and functional characteristics compared to the stagnation temperature influence. On the other hand the thermal load in the refrigerated space and the thermal conductance of the walls has analogous effects, therefore important to be considered in actual design. As a result, the model is expected to be a useful tool for simulation, design, and optimization of solar collector based energy systems.

Key words:

NOMENCLATURE

A : Area, (m²)
 a, b : Constant in Eq.(5)
 B : Dimensionless collector size parameter
 C : Specific heat, (kJ/kg K)
 G : Irradiance on collector surface, (W/m²)
 M : Mass of air in the refrigerated space, (kg)
 Q : Heat transfer rate, (W)
 S : Entropy generation rate, (kJ/K)
 t : Time, (s)
 T : Temperature, (K)
 U : Global heat transfer coefficient, (W/m² K)
 W, y, z : Conductance fraction
 Greek letters
 Γ : Dimensionless temperature

θ : Dimensionless time
 η : Efficiency of a flat plate collector
 Superscripts
 0 : Ambient
 air : Air
 H : Heat source
 L : Refrigerated space
 load : Cold space thermal load
 opt : Optimum
 SC : Solar collector
 Set : Setpoint
 St : Collector stagnation temperature.

INTRODUCTION

Absorption refrigeration systems that could be used with solar energy or other sources of thermal energy

such as waste heat are being developed for application in air-conditioning systems. The performance of absorption systems were studied extensively by detailed computer simulation [1-3]. The development of such computer codes require considerable effort and they also need as input the thermophysical properties of the working fluids. For preliminary design studies and for performance data representation it is useful to develop simplified models for absorption cooling systems. Such models can be used to represent performance characteristics of absorption machines when they form sub-components of a larger thermal system simulation programme.

Several idealized models were developed recently using the three-heat-reservoir (THR) configuration of the absorption cycle [4-6]. These models which take into account the external heat transfer irreversibilities of the cycle are able to provide realistic performance limits for the coefficient of performance (COP) and the cooling capacity of absorption refrigeration systems [6].

However, if the THR models are to predict the performance of real absorption machines closely, the internal irreversibilities of the cycle in addition to the external irreversibilities have to be included in the analysis. Such models were used to obtain the optimum performance of commercial absorption chillers [7, 8]. Also by using a few fitting parameters, these models were able to reproduce performance data for absorption chillers [7].

Nevertheless, all those studies focus on the systems steady state properties and ignore completely their dynamic behavior. Steady-state models are useful under many conditions although under strongly dynamic conditions that are often seen in real-life operation, these models can become unacceptably inaccurate [9]. However, steady state models do not provide time dependent information on the thermal behavior of absorption refrigerators and are therefore not suitable for transient system simulations.

In contrast, the model presented in this work allows the simulation of the dynamic absorption refrigerator behavior. It extends the range of applicable models for transient system simulations, where the time constants of the refrigerator significantly influence the system performance. The dynamic model of an irreversible absorption refrigerator allows the simulations of its transient behavior for changing input conditions or design parameters. This is important because absorption refrigerators usually have a high thermal mass, consisting of their internal

heat exchangers, the absorbing solution and the externally supplied heat transfer media.

The contribution of this work is the analysis of the transient irreversible three heat reservoir absorption heat transformers with Newton's heat transfer law. Thus, a transient mathematical model for a solar collector driven refrigeration plant is introduced. Finding an optimum heat transfer rate received from the solar collector to the generator and investigating the effect of time in solar collector stagnation temperature and collector temperature and heat rate are derived by minimizing the time required to reach a certain operation temperature in the refrigerated space. This issue becomes more important in large scale cooling applications in which the thermal inertia of the refrigerated space becomes very large.

THE TRANSIENT MODEL

The main features of the absorption refrigerator–refrigerated space model are shown in Figure 1. The cycle has negligible work input. The cycle is driven by the heat transfer rate Q_H received from the source temperature T_H , which is determined by the operation temperature of the generator. The refrigeration load Q_L is removed from the refrigerated space, at T_L , and the heat transfer rate Q_0 is rejected to the ambient, T_0 . The refrigerator shown in Figure 1 operates irreversibly due to the entropy-generation mechanisms that are present (for example, heat transfer, mixing, and throttling).

The irreversible model takes into account the internal and external irreversibilities, which are fundamental features that will be present in the design of real absorption refrigerators.

The instantaneous heat transfer interactions are given by

$$Q_H = (UA)_H (T_H - T_{HC}) \quad (1)$$

$$Q_L = (UA)_L (T_L - T_{LC}) \quad (2)$$

$$Q_0 = (UA)_0 (T_{0C} - T_0) \quad (3)$$

Additionally, \dot{Q}_H is proportional to the collector efficiency, where, without loss of generality, and negligible heat loss between the solar collector and the generator, as follows:

$$Q_H = \eta_{SC} A_{SC} G \quad (4)$$

where A_{SC} represents the collector area, G is the irradiance at the collector surface.

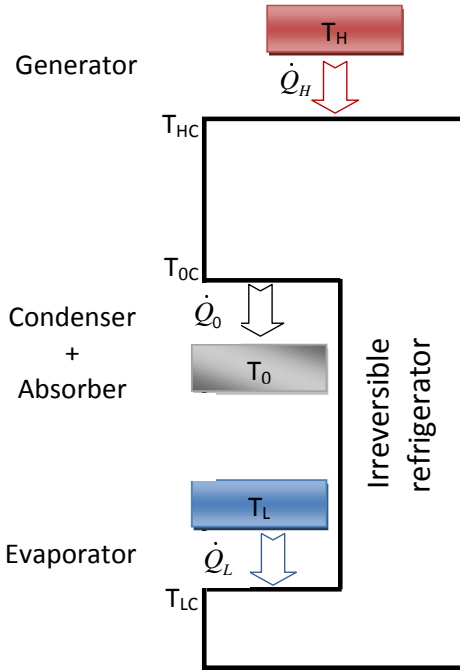


Figure 1
Problem sketch

The efficiency of a flat plate collector can be calculated as [10, 11]:

$$\eta_{SC} = a - b(T_H - T_0) \quad (5)$$

where a and b are two constants that can be calculated, as discussed by Sokolov and Hershgal [10, 12]. Eq. (5) can be rewritten by introducing the collector stagnation temperature T_{st} as follows:

$$\eta_{SC} = b(T_{st} - T_H) \quad (6)$$

where T_{st} (for which $\eta_{SC} = 0$) is given by:

$$T_{st} = T_0 + a/b \quad (7)$$

The equation for heat input Q_H can be rewritten by combining Eqs. (4) and (6) as follows:

$$Q_H = A_{SC} G b (T_{st} - T_H) \quad (8)$$

The first and second law read:

$$Q_H + Q_L - Q_0 = 0 \quad (9)$$

$$\frac{dS_{in}}{dt} = \frac{Q_0}{T_{OC}} - \frac{Q_H}{T_{HC}} - \frac{Q_L}{T_{LC}} \quad (10)$$

We account for the transient cooling of the refrigerated space by writing the first law,

$$M_{air} C_{v,air} \frac{dT_L}{dt} = (UA)_w (T_0 - T_L) + Q_{load} - Q_L \quad (11)$$

where $(UA)_w (T_0 - T_L)$ accounts for the rate of heat gain from the ambient through the walls of the refrigerated space and Q_{load} is the thermal load or rate of heat generated inside the refrigerated space. By writing the set of Eqs. (1)–(10) for the absorption refrigerator and (11) for the refrigerated room, we

take into account the fact that the thermal inertia of the refrigerated space is large enough such that the transient operation of the refrigerator can be neglected when compared to the time evolution of the temperature inside the refrigerated space.

Generally, it is difficult to model all internal entropy generation sources in order to get an analytical variation law. We have chosen to consider the following approaches [13, 14].

The entropy of the working fluid is represented by using linear variation law with temperature:

$$\frac{dS_{in}}{dt} = \beta_1 (T_{HC} - T_{OC}) + \beta_2 (T_{OC} - T_{LC}) \quad (12)$$

where the parameters β_1, β_2 are to be estimated by fitting detailed simulation data to predictions.

To obtain the best estimates of the parameters β_1 and β_2 from simulated performance data [15, 16] the following least-square procedure is used.

According to the cycle model mentioned above, the rate of entropy generated by the cycle is described quantitatively by the second law as:

$$\frac{dS_{Tot}}{dt} = \frac{Q_0}{T_0} - \frac{Q_H}{T_H} - \frac{Q_L}{T_L} \quad (13)$$

The factors $(UA)_H$, $(UA)_L$, and $(UA)_0$ represent the overall thermal conductances of the heat exchangers. The overall thermal conductance of the walls of the refrigerated room is given by $(UA)_w$.

Since $(UA)_H$, $(UA)_L$, and $(UA)_0$ are commodities in short supply, it makes sense to recognize the total external conductance inventory, UA (hardware), as a constraint:

$$UA = (UA)_H + (UA)_L + (UA)_0 \quad (14)$$

In addition, we define the ratio w , which accounts for the “size” of the heat transfer area of the refrigerated room, as follows:

$$w = \frac{(UA)_w}{UA} \quad (15)$$

The nondimensional version is

$$\bar{Q}_H = y(\Gamma_H - \Gamma_{HC}) \quad (16)$$

$$\bar{Q}_L = z(\Gamma_L - \Gamma_{LC}) \quad (17)$$

$$\bar{Q}_0 = (1 - y - z)(\Gamma_{OC} - 1) \quad (18)$$

$$\bar{Q}_H = B(\Gamma_{st} - \Gamma_H) \quad (19)$$

$$\bar{Q}_H + \bar{Q}_L - \bar{Q}_0 = 0 \quad (20)$$

$$\frac{d\bar{S}_{in}}{d\theta} = \frac{\bar{Q}_0}{\Gamma_{OC}} - \frac{\bar{Q}_H}{\Gamma_{HC}} - \frac{\bar{Q}_L}{\Gamma_{LC}} \quad (21)$$

$$\frac{d\bar{S}_m}{d\theta} = \bar{\beta}_1 (\Gamma_{HC} - \Gamma_{OC}) + \bar{\beta}_2 (\Gamma_{OC} - \Gamma_{LC}) \quad (22)$$

$$\frac{d\bar{S}_{tot}}{d\theta} = \bar{Q}_0 - \frac{\bar{Q}_H}{\Gamma_H} - \frac{\bar{Q}_L}{\Gamma_L} \quad (23)$$

$$\frac{d\Gamma_L}{d\theta} = w(1-\Gamma_L) + \bar{Q}_{load} - \bar{Q}_L \quad (24)$$

where we have appropriately defined the following nondimensional groups:

$$\Gamma_i = \frac{T_i}{T_0}, \bar{Q}_i = \frac{Q_i}{UAT_0}, \quad (25)$$

$$\theta = \frac{tUA}{M_{air}C_{v,air}}, B = \frac{A_{sc}Gb}{UA}, \bar{S} = \frac{S}{M_{air}C_{v,air}} \quad (26)$$

The conductance allocation ratios are

$$y = \frac{(UA)_H}{UA}, z = \frac{(UA)_L}{UA} \quad (27)$$

We are interested in how the imperfect features (finite temperature differences) identified in the model influence the overall performance of the refrigeration plant.

NUMERICAL METHOD AND RESULTS

The problem consists of integrating Eqs. (23) and (24) in time and solving the non-linear system (16)–(22) at each step time. The objective is to minimize the time θ_{set} to reach a specified refrigerated space temperature, $\Gamma_{L,set}$, in transient operation. To generate the results shown in Fig. 2–7 some selected parameters were held constant and others were varied. The numerical method calculates the transient behavior of the system, starting from a set of initial conditions, then the solution is marched in time and checked for accuracy until a desired condition is achieved (temperature set points or steady state). The equations are integrated in time explicitly using an adaptive time step, 4th–5th order Runge–Kutta method [17]. Newton–Raphson’s method with appropriate initial guesses was employed for solving the above set of non-linear equations.

During the integration of the ordinary differential equations, one time the set of fixed parameters $\Gamma_H, \Gamma_{st}, B, y, z, w$ and \bar{Q}_{load} is defined Eqs (16) and (19) give Γ_{HC} . The system of Eqs (16)–(22), at each time step of integration of Eqs (23) and (24), deliver $\bar{Q}_0, \bar{Q}_L, \Gamma_{OC}$ and Γ_{LC} .

To test the model and for conducting the analysis presented in this section, we assuming a small absorption refrigeration unit with a low total thermal conductance ($UA = 400$ W/K), we considered a total heat exchanger area $A = 4\text{m}^2$ and an average global heat transfer coefficient $U = 0.1$ kW/m² K in the heat exchangers and $U_w = 1.472$ kW/m² K across the

walls, which have a total surface area $A_w = 54\text{m}^2$, $T_0 = 25^\circ\text{C}$ and $Q_{load}=0.8$ kW. Considering a typical air conditioning application, the refrigerated space temperature to be achieved was established at $T_{L,set} = 16^\circ\text{C}$.

Thus, the resulting dimensionless parameters that were kept fixed initially were: $\bar{Q}_{load}=0.007$, $w=0.2$, $\Gamma_{L,set}=0.97$.

Fig. 2 shows that the temperature of the evaporator starts to decrease linearly then it decreases very slowly. Here, the reaction of the evaporator is seen strongly affected by the generator behavior. His temperature starts rising linearly, then it becomes stable. As the temperature of the generator is higher causing more heat is absorbed in the evaporator. While, the temperature of the evaporator is decreasing very slowly the temperature of the generator still maintained quit constantly, indicating that the equilibrium state has reached [18]. Also, there is an intermediate value of the collector size parameter B , between 0.04 and 0.1, such that the temporal temperature gradient is maximum, minimizing the time to achieve prescribed set point temperature ($\Gamma_{L,set} = 0.97$).

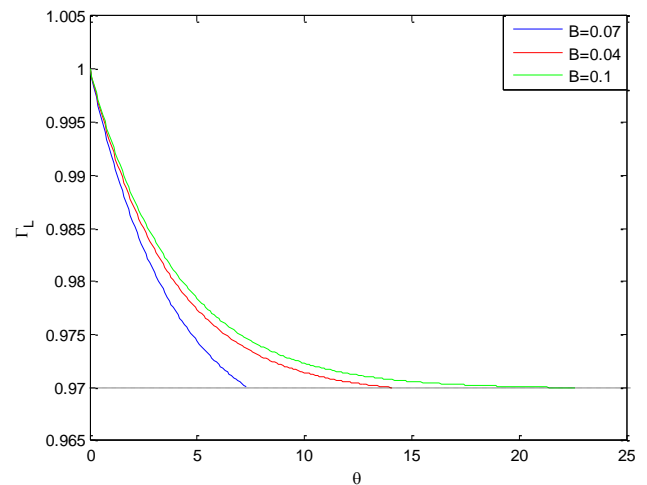


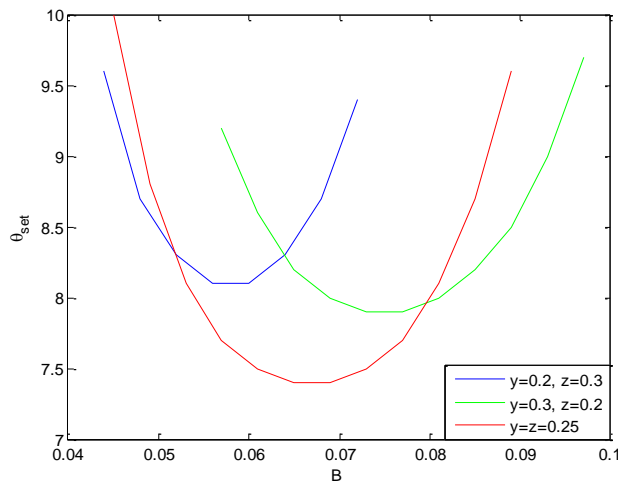
Figure 2. The behavior refrigeration space temperature, Γ_L in time ($\Gamma_H = 1.3$, $\Gamma_{st} = 1.6$)

Fig. 3 shows the behavior of θ_{set} versus B , while varying y and Γ_H . The results stress the importance of identifying B_{opt} , mainly for lower values of Γ_H . For $\Gamma_H = 1.3$, there is a narrower range of values for B where the system operates in optimal conditions, outside of which the performance deteriorates dramatically. This effect is reduced as Γ_H increases, as is demonstrated with the results for $\Gamma_H = 1.4$.

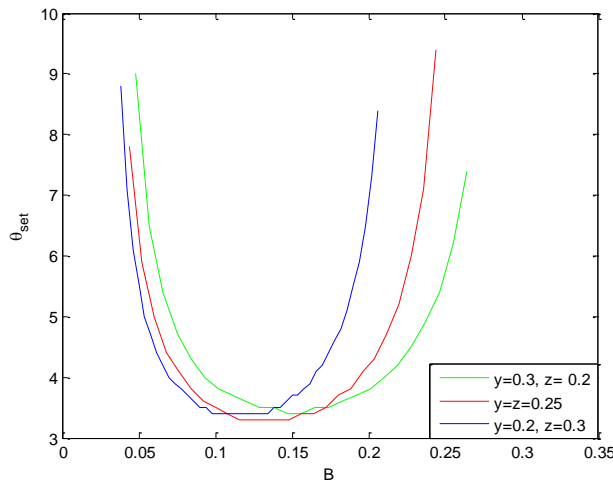
During the transient operation, to reach the desired $\Gamma_{L,set} = 0.97$, there is an internal and a total entropy

generated by the cycle, which is obtained by integrating Eqs. (21-23) in time. Fig. 4 and 5 show the internal and total entropy generated by the cycle up to θ_{set} , versus B , while varying y and Γ_H . We see that there are a minimum for internal and total entropy generated by the cycle for a certain dimensionless collector size parameter B . Note that B_{opt} , identified for minimum time to reach $\Gamma_{L,set}$, does not coincide with the B_{opt} where minimum internal and total entropy occurs, although the values are close.

B_{opt} is simply the optimal collector size for which in the presence of a finite UA— θ_{set} is minimum, which represents neither maximum efficiency nor minimum total entropy generated by the cycle.

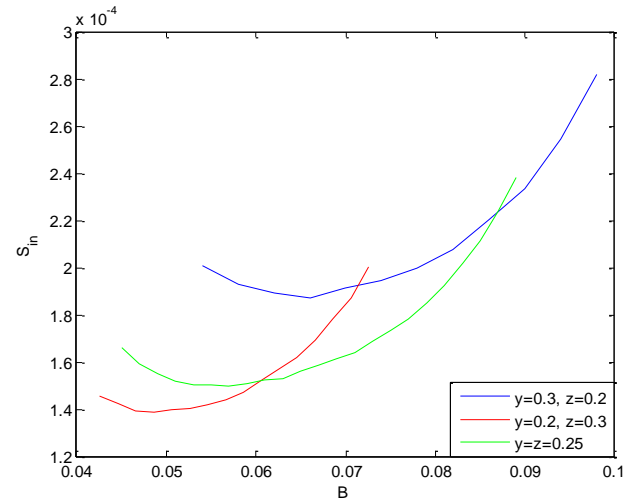


(a) : $\Gamma_H=1.3$

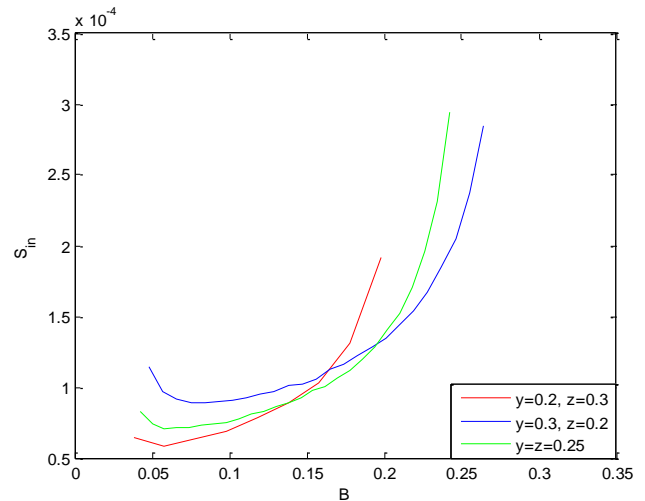


(b) : $\Gamma_H=1.4$

Figure 3. Time to reach a refrigerated-space temperature setpoint for different coupling temperatures and thermal conductance allocations.

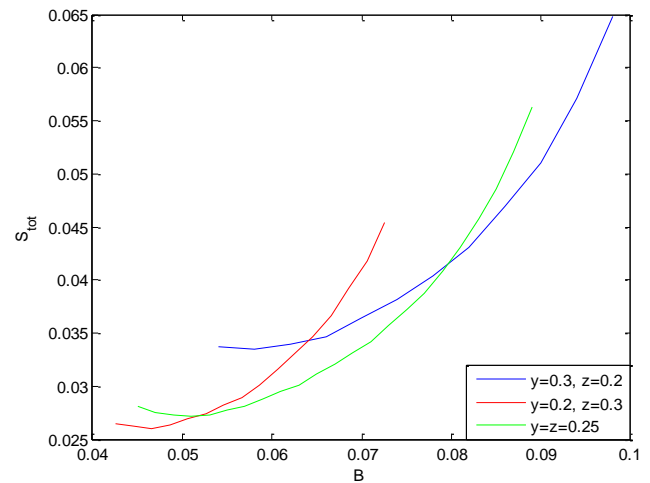


(a) : $\Gamma_H=1.3$

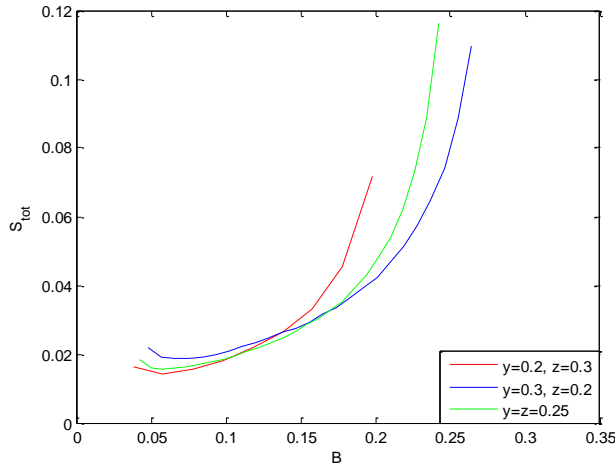


(b) : $\Gamma_H=1.4$

Figure 4. Internal entropy generated during the time to reach a refrigerated-space temperature setpoint for different coupling temperatures and thermal conductance allocations.



(a) : $\Gamma_H=1.3$



(b) : $\Gamma_H=1.4$

Figure 5. Total entropy generated during the time to reach a refrigerated-space temperature setpoint for different coupling temperatures and thermal conductance allocations.

According to our initial proposition, we seek the set of optimal values (B_{opt} , y_{opt}) that minimize θ to reach $\Gamma_{L,set}$, thus maximizing \bar{Q}_L in the transient regimes. Figures 6 and 7 illustrate the behavior of $\theta_{set,min}$ and B_{opt} ($\theta_{set,min}$) versus y , while varying Γ_H , therefore identifying the set (B_{opt} , y_{opt}) which corresponds to our original set of fixed parameters \bar{Q}_{load} , w , and $\Gamma_{L,set}$. The results show that the thermal conductance should be divided equally between the generator and evaporator for maximum \bar{Q}_L ($y = 0.25$).

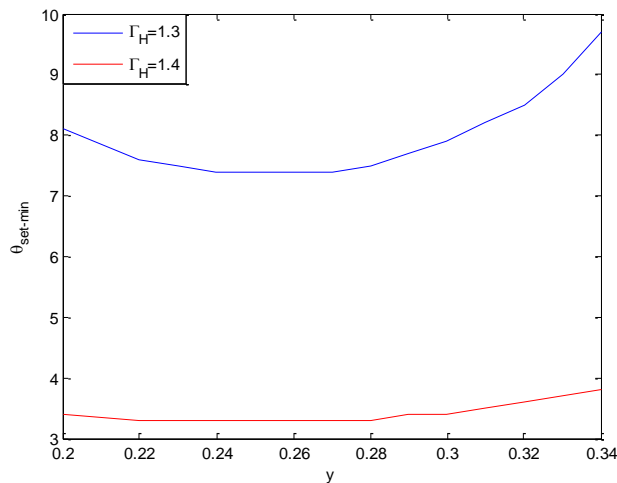


Figure 6. Minimum time to reach a refrigerated-space temperature setpoint for different coupling temperatures, with respect to the variation of the thermal conductance allocation.

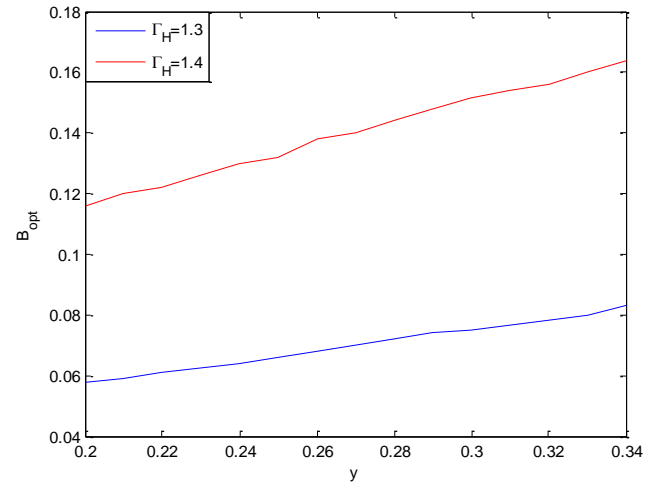


Figure 7. Optimal collector size to reach a refrigerated-space temperature setpoint for different coupling temperatures, with respect to the variation of the thermal conductance allocation

CONCLUSIONS

In this article, a transient irreversible model to study the absorption refrigeration cycle was presented and used to demonstrate the existence of an optimal way of allocating the thermal conductance inventory and an optimal collector size for maximum refrigeration rate. The model accounts for the internal and external irreversibilities. Appropriate dimensionless groups were identified and the generalized results reported in charts using dimensionless variables. The importance of the analysis of the absorption refrigeration system in the transient regime is this stressed.

The most important conclusion is that

- The Optimal collector size and minimum time to reach a specified refrigerated-space temperature are influenced analogously by the thermal conductance of the walls.
- In general, half of the total supply of thermal conductance has to be divided equally between the generator and evaporator, for maximum refrigeration rate.
- Optimal size collector identified for minimum time to reach set point temperature in the refrigerated space does not coincide with B_{opt} where minimum total entropy occurs.

REFERENCES

- Linden M.O. and Klein S. A. 1985, Steady state modeling of absorption heat pumps with a

- comparison to experiments. ASHRAE Trans. **2**, pp. 1793-1807.
2. Grossman G., Gommed K. and Gadoth D. 1987, A computer model for simulation of absorption systems in flexible and modular form. ASHRAE Trans. **93**(2), pp.2389-2428.
 3. Gommed K. and Grossman G. 1990, Performance analysis of staged absorption heat pumps: water-lithium bromide systems. ASHRAR Trans., pp. 1590-1598.
 4. Chen J. and Yan Z. 1989, Equivalent combined systems for three-heat-source heat pumps. J. Chem. Phys. **90**(9), pp. 4951-495.
 5. Chen J. and Yan Z. 1989, An optimal endoreversible three-heat-source refrigerator. J. Appl. Phys. **65**(1), pp. 1-4.
 6. Wijesundera N. E. 1996, Performance limits of absorption cycles with external heat-transfer irreversibilities. Appl. Thermal Engng, **16**(2), pp. 175-181.
 7. Gordon J. M. and Ng K. C. 1995, A general thermodynamic model for absorption chillers: theory and experiment. Heat Recovery CHP, **15**(1), pp. 73-83.
 8. Tong Chua H., Han Q., Choon Ng K., and Gordon J.M. 1996, Thermodynamic modeling and experimental evidence for the optimization and maximum-efficiency operation of absorption chillers. ECOS'96, Efficiency, Cost, Optimization, Simulation and Environmental Aspects of Energy Systems, June 25-27, Stockholm, 157-166.
 9. Browne M.W., Bansal PK. 2002, Transient simulation of vapour-compression packaged liquid chillers. Int J Refrige, **25**, pp. 597-610.
 10. Bejan A., Vargas J.V.C. and Sokolov M. 1995, Optimal Allocation of a Heat Exchanger Inventory in Heat Driven Refrigerators, International Journal of Heat and Mass Transfer, **38**, pp. 2997-3005.
 11. Sokolov M., Hershgal D. 1993, Optimal coupling and feasibility of a solar powered year-round ejector air conditioner, Solar Energy, **50**(6), pp. 507-516.
 12. Sokolov M., Hershgal D. 1993, Solar-powered compression-enhanced ejector air conditioner, Solar Energy, **51**, pp.183-194.
 13. Wijesundera NE. 1997, Performance of three-heat-reservoir absorption cycles with external and internal irreversibilities, Applied Thermal Engineering, **17**(12), pp. 1151-1161.
 14. Gordon J.M., Ng K.C. 2000, Cool Thermodynamics, Cambridge Int. Science Publishers, Cambridge.
 15. Boukhchana Y., Fellah A. and Ben Brahim A. 2014, Numerical Study of Entropy Generation in an Irreversible Solar-Powered Absorption Cooling Systems, 9ème Congrès Francophone de Génie des Procédés, Agadir, Maroc, April 28-30,.
 16. Boukhchana Y., Fellah A. and Ben Brahim A. 2015, Transient modeling and simulation of an ammonia-water absorption solar refrigerator, International Journal of Mechanics and Energy, **3**(1), pp. 33-43.
 17. Yang W.Y., Cao W., Chung T.S., Morris J. (2005), Applied numerical methods using MATLAB, Wiley-Interscience, A John Wiley & Sons, Inc.;
 18. Abdullah M.O., Hien T.C. 2010, Comparative analysis of performance and technoeconomics for a H₂O-NH₃-H₂ absorption refrigerator driven by different energy sources. Applied Energy, **87**, pp. 1535-1545.

Constructive Materials: Mechanical Optimisation

INFLUENCE OF THE POZZOLANIC REACTIVITY OF THE BLAST FURNACE SLAG (BFS) AND METAKAOLIN ON MORTARS

Kamal ABDELLI¹, Mahfoud TAHLAITI², Rafik BELARBI³, Mohamed Nadjib OUDJIT¹

¹Laboratoire du Bâti dans l'Environnement (LBE), Faculté de Génie Civil, USTHB, BP 32, El Alia – Alger, Algérie. Fax : +213 21 24 72 24, Email : kabdelli@usthb.dz

²ICAM, School of Engineering, Nantes, France

³Laboratoire des Sciences de l'Ingénieur pour l'Environnement (LASIE), Université de La Rochelle, France

ABSTRACT

The objectives of this study is to evaluate the pozzolanic reactivity of mortars with tow mineral admixtures (Metakaolin and BFS) in substitution of cement. The rate of substitution is fixed after optimization of the mechanical results. Metakaolin and the BFS from blast furnaces have been used with 10% and 40% respectively to the replacement of the cement. At long time, The use of two admixtures provides better results to those of the reference mortar at early age, The mortar containing metakaolin provides results better than the reference one, while mortar containing BFS gives inferior results up to 70% of the reference mortar. Metakaolin by its important specific surface area and reactivity improve the mechanical behavior at early ages. However, the BFS reacts very late. In order to improve the mechanical results at early and long time, a new mortar were casted with 10% of MK and 40% of BFS in substitution of the cement. Isothermal calorimetry and compressive strength tests were performed. Hydration phenomena were analyzed.

Keywords Metakaolin, BFS, Mortar, Reactivity, pozzolanic

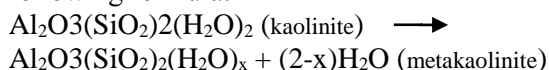
INTRODUCTION

The most interesting way to reduce pollution caused by the cement industry is the substitution of part of the clinker with less polluting materials and proven pozzolanic hydraulic properties. Among the most used alternative materials, there is the blast furnace BFS, a byproduct of the industry of the steel industry, the latent hydraulic properties, and metakaolin, derived from dehydroxylation of kaolin, and from very interesting the pozzolan properties.

The granulated blast furnace BFS is obtained by rapid cooling and by quenching, of the smelting rests of Smelting at 1450 ° C, which allows to obtain a vitrified and granulated material [1].

The physicochemical properties of blast furnace BFS confer interesting hydraulic properties to be used as an addition in partial substitution of cement. In addition to its environmental qualities, the blast furnace BFS has other qualities such as resistance to sulphate attack, low permeability, resistance to aggressive environments and resistance to freeze thaw, low heat of hydration, which leads to an excellent durability. [2]

The metakaolin is obtained by dehydroxylation of the kaolin by calcination according to the following formula:



These physicochemical properties confer pozzolan qualities more important than any other mineral additives. Its reactivity with portlandite, after cement hydration, enables the manufacture of an additional CHS to the cement one, associated to its high finesse which allows it to fill voids and reduce porosity, and thus make it more resistant to aggressive agents, thereby increasing the durability of concrete.

The objective of this study is to compare the activity of the BFS and pozzolan metakaolin, used alone or combined. The evolution of the compression behavior of mixtures cement / metakaolin was carried out on mortar. The microstructure portion showing and explaining the performance increase in the compression of the mortars compared with the control mortar was carried out on the paste. The balance of these two parts has allowed us to see the influence of the physicochemical properties of the two materials on pozzolanic activity on the quality of mortars.

MATERIALS AND EXPERIMENTAL TECHNIQUES

Metakaolin used in this study was manufactured in our laboratory whose original kaolin comes from a city of Jijel (east part of Algeria). After calcination at the optimum temperature and time,

it has been summered and finely ground to achieve a fineness of 18m² / g.

The blast furnace slag was recovered from the steel plant in El Hadjar (Annaba, Algeria). The cement used is CEM 1 42.5. Their properties, chemical analysis, BET and D50 are shown in Table 1.

Normal mortar (1/3 liant – 2/3 sand) used for the compression tests part, is designed according to standard NF P 15-403. Substitution of 5, 10, 15, 20 and 25% of the mass of cement by the only MK, 20, 40, 60 and 80% of only dairy and a combination of the best results in the compression of the two materials, the 10% occurrence for MK and 40% for LT summers have studied. A water/binder ratio of 0.4 and a superplasticizer has been used.

The mortar specimens (4x4x16 cm³) designed, have been kept in water at 20°C until to perform the tests.

The paste used for the microstructure part have been done in the same conditions as mortars and stored in an air conditioned room (20°C, 50% RH) until to perform the tests.

Two methods of investigation on the microstructure have been implemented. These tests have been performed on powder issued from the crushed cement pastes and sieved to 80µm. The diffraction X-ray analysis (XRD) is used to visualize the crystallized phases (anhydrous or hydrated) present in the cement matrix. It also keeps track of developments in the pozzolanic reaction by consuming the Portlandite following the heights of the characteristic lines of the latter. Thermogravimetric analysis (TGA) is used to quantify certain hydrated phases through the mass loss caused by the loss of water from hydrates at increased temperature. Positioning ATG curves between them, gave information about the reactivity of the mixtures studied.

Choice and characteristics of materials

Table 1 : materials properties

Components (%)	BFS	MK	cement
SiO ₂	33,26	38,32	21,83
Al ₂ O ₃	10,00	33,23	3,76
Fe ₂ O ₃	1,06	14,63	4,83
CaO ₂	44,58	0,48	63,47
K ₂ O	-	11,64	0,48
Ti	-	1,08	-
MgO	4,66	-	2,20
SO ₃	0,20	-	1,89
Fire loss	0,44	1,00	0,91
BET (m ² /g)	6,00	18,00	3,25
D50 (µm)	9,65	9,08	9,50

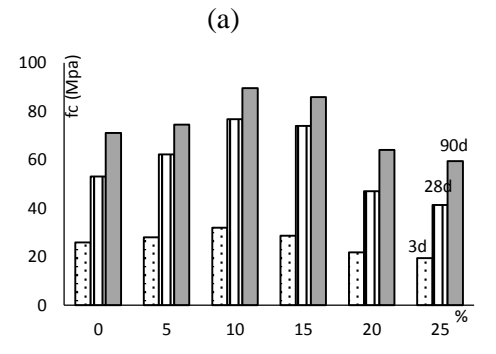
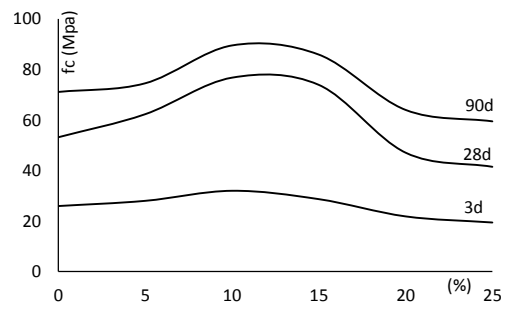


Figure 1 : Compressive strength of mortars containing 5, 10, 15, 20 and 25% of metakaolin

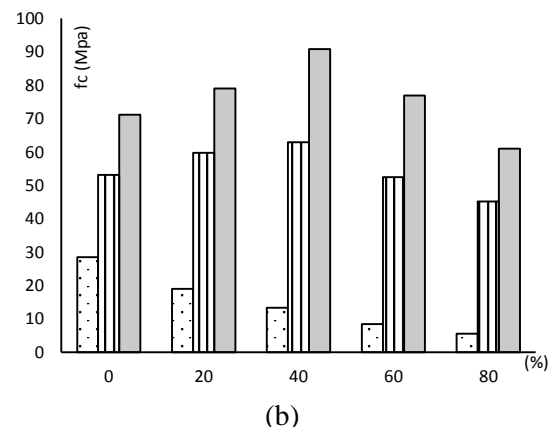
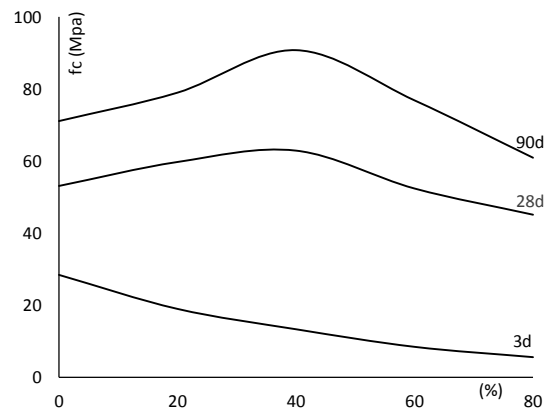


Figure 2 : Mechanical strength of mortars containing 20, 40, 60 and 80% of BFS

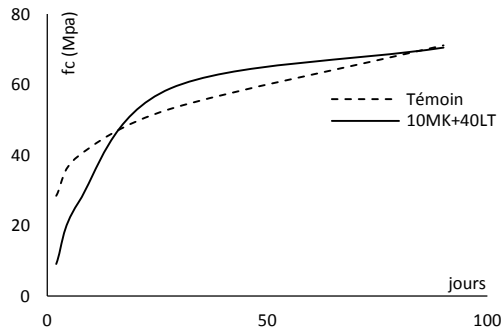


Figure 3 : Mechanical strength of mortars containing 40% of BFS and 10% of MK

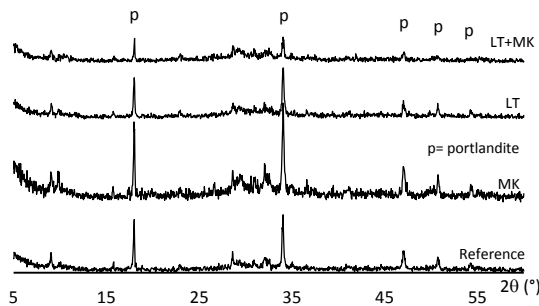


Figure 4 : Diffractometrics of X rays of the studies pastes at 90 days

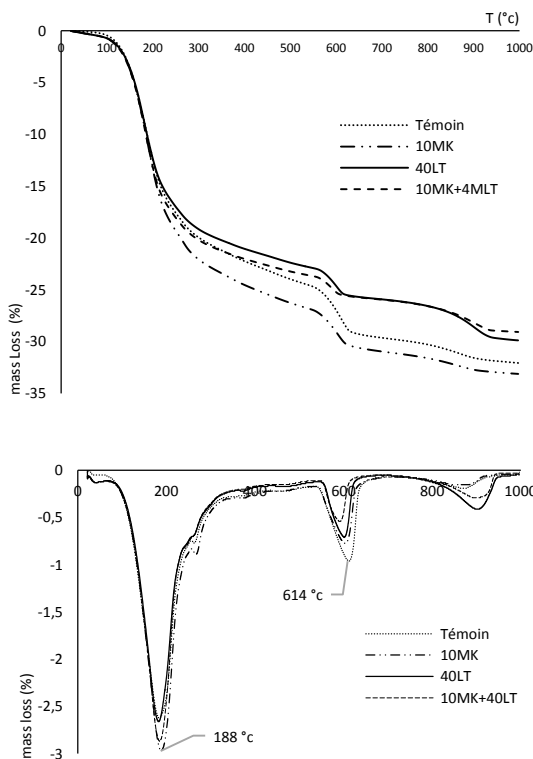


Figure 5 : Thermogravimetric Analysis of the studied pastes at 90 days

RESULTS AND DISCUSSION

Influence of BFS

The evolution of the compressive strength of mortars containing 20%, 40%, 60% and 80% of BFS is shown in Figure 2. At an early age, the compressive strengths of mortars containing 20, 60 and 80% BFS are lower than the witnessed one. The mortar containing 40% of BFS, by cons, has an equivalent or superior result than the mortar witness to approximately 7 days. Beyond 28 days, the mortars containing 20, 40 and 60% of BFS all have better results than the witnessed one. The mortar containing 80% of BFS is lower, which is consistent with the literature [3]. These results show the latent behavior of the BFS that needs to be activated to be reactive with water, in order to have a basic medium to enable the hydration of the BFS.

The hydration of clinker occurs due to hydrolytic attack (H₂O), the hydratation of the BFS occurs due to the reaction of glass dissolution attack by hydroxyl (OH⁻). [4] At a young age, the BFS does not instantly reacts with portlandite produced by the hydration of C₃S and C₂S cement, it takes a few days to have the ideal conditions to allow this activity. The chemical effect, or pozzolanic, BFS occurs over the duration.

Increased mechanical results at about 7 days, the mortar containing 40% BFS, are mainly due to the physical effect given the high fineness of BFS (Table 1). This causes a heterogeneous nucleation, which is based on surface phenomena [1].

Figures 4 and 5 showing the X-ray diffraction and thermogravimetric analysis mortars to 90 days of age confirmed the mechanical results found.

Thus, from curves of figure 4, the characteristic lines of portlandite of witness mortars are more important than those of mortars containing BFS. The hydration process of the BFS has reached its optimum rate, consumed portlandite produced by the hydration of cement in order to form new CSH which gives the mortar the high mechanical resistance recorded.

Figure 5 of the TGA analysis complete the X-ray diffractometry analysis, it logs water's loss associated with the hydration products (CSH and Portlandite mainly) during the increase in temperature experienced by the sample. The positioning of the curves in the intervals corresponding to the CSH (80–220°C), following the broad endotherm located at about 188°C, and

the portlandite (400–600°C), the endotherm located at about 614°C, of our samples, indicates their level of dehydration, hence their quantification. The curve relative to the mortar containing the ATG of the BFS (without metakaolin) is positioned above that of the reference mortar in the dehydration interval portlandite and in the same position of the dehydrating interval CSH. This confirms the role played by the smoothness of the BFS and therefore its physical effect, besides its latent effect of the BFS and slowly to hydrate.

Influence metakaolin

Figure 1 shows the development of the compressive strength of mortars containing 5%, 10%, 15%, 20% and 25% of MK, replacing partially the cement. The results show that the mechanical strength increases at all ages for replacements below 15% compared to the reference mortar. Beyond these values, strengths are lower than the reference mortar. The incorporation of metakaolin causes substantial pozzolanic activity between 14 and 28 days of age [5], wherein the compressive strength is greater than that of the controlled one. In addition, the compressive strength is not growing at the same rate as the first days [3].

In addition to the filling effect and C₃S grains accelerator due to its smoothness [6], metakaolin is very responsive to the very young age. It begins to react with the free lime produced by the hydration of cement following the dissolution-precipitation of C₃S that offers the ideal conditions for the dissolution of the metakaolin to form CSH, this reaction consumes 30 to 40% in the amount of metakaolin present in the [6] mortar. Beyond 28 days, the pozzolanic activity slowed metakaolin due to the decrease in the rate of portlandite in mortars. [7]

From the diffraction of X-ray curve mortar containing 10% metakaolin and that of the reference mortar at 90 days of age, we note that the characteristic lines of portlandite of the witness mortar are more important than those of mortars containing metakaolin. Metakaolin having a pozzolanic significant power consumed a maximum of portlandite during the hydration reaction.

The complete thermogravimetric analysis that analyzes the positioning of the mortar curve containing metakaolin is below that of the control

in the intervals corresponding to the CSH and CH. This confirms the mechanical strengths results found.

Influence of BFS and metakaolin in a ternary mortar

The results of the compressive strength of mortar containing both 40% of BFS and 10% of metakaolin, in weight replacement of cement, are shown in Figure 3. Note that the presence of metakaolin did not have the desired effect at a young age. From 2 to 7 days, mortars exhibit inferior resistance to controlled one. At 28 days, the compressive strength of the mixture exceeds that of the controlled one. At 90 days, it is equivalent to that of the controlled one.

XRD curve shows the intensity of the lines corresponding to the portlandite, is less than those of the controlled.

The TGA curve of mortar containing 40% of LT and 10% of MK is positioned above the controlled one.

Metakaolin reacts with the free lime, produced by the hydration of cement to form CSH at young age, thereby reducing the concentration of hydroxyls in the pore solution which are necessary to hydrate the vitreous phase of BFS. Accordingly, some components of the BFS cannot react, which leads to a reduction in mechanical strength [5].

CONCLUSION

The use of partial replacement BFS cement in mortars produced an increase in long-term strengths. Even at 80% substitution, the results are very encouraging with 45 MPa at 28 days and 60 MPa at 90 days.

By cons, for metakaolin, the results are more interesting at the young age where pozzolanic activity is intense.

The substitution of cement by metakaolin and BFS together does not give the expected results. Specially with the substitutions percentages used. The intense activity pozzolan metakaolin at young age is a part of the cause. Perhaps by reducing the quantities of both materials would give better results.

REFERENCES

1. Behim Mourad, 2005 «Sous produits industriels et développement durable : Réactivité, rôle et durabilité des laitiers d'El

- Hadjar dans les matériaux à matrice cimentaire», Université de Annaba, Algérie.
2. Mladenka Saric-Coric et Pierre-Claude Aïtcin, 2003 « Bétons à haute performance à base de ciments composés contenant du laitier et de la fumée de silice », *Canadian Journal of Civil Eng.* Vol. 30.
 3. Khatib J.M., Hibbert J.J., 2004 «Selected engineering properties of concrete incorporating BFS and metakaolin» *Construction and Building Materials*, 19, 460–472.
 4. Van Rampaey Gilles, 2006 «Etude de la réactivité des ciments riche en laitier, à basse température et à temps court, sans ajouts chloruré», Université Libre de Bruxelles, 2006.
 5. Khatib J.M., Sabir B.B., Wild S., 1996 «Some properties of metakaolin past and mortar», *Concrete for Environment enhancement and Protection*, Ed. Dhir R.K. and Dyer T.D., Spon press, London.
 6. Wu Z. and Young J.F. 1984 «The hydration of tricalcium silicate in the presence of colloidal silica», *Journal of materials Sciences*, Vol 19, 3477-3486.
 7. Sha W. and Pereira G.B., 2001 «Differential scanning calorimetry study of ordinary portland cement paste containing metakaolins and theoretical approach of metakaolins activity» *Cement and Concrete Research*, 23, 455-461.

INFLUENCE OF THE ORIGIN OF METAKAOLIN ON POZZOLANIC REACTIVITY OF MORTARS

Kamal ABDELLI¹, Mahfoud TAHLAITI², Rafik BELARBI³, Mohamed Nadjib OUDJIT¹

¹Laboratoire du Bâti dans l'Environnement (LBE), Faculté de Génie Civil, USTHB, BP 32, El Alia – Alger, Algérie. Fax : +213 21 24 72 24, Email : kabdelli@usthb.dz

²ICAM, School of Engineering, Nantes, France.

³Laboratoire des Sciences de l'Ingénieur pour l'Environnement (LASIE), Université de La Rochelle, France.

ABSTRACT

Cement is one of the main sources of environmental impacts of concrete use. It is thus recognized that the most pragmatic solution for minimizing environmental impacts of concrete is the reduction of the cement content. This could be achieved by replacing a part of cement with mineral additions such as fly ash, blast-furnace slag or metakaolin (MK) during concrete mixing.

In recent years, the incorporation of MK in building materials is growing. Metakaolin (Al₂Si₂O₇) is a material obtained by calcination of kaolinite between 500°C and 800°C.

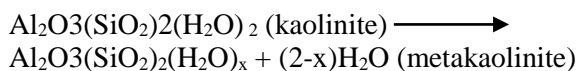
In this study, Three MK issued from three different regions in Algeria were tested. The regions are, Jijel (MKJ), Gulema (MKG) and Béchar (MKB). This study aims to investigate the effects of the origin of MK blended at early age. The chemical and mineralogical analysis (XRD, BET, SSB and SEM) show a difference in their metakaolinite content. One mortar prepared with 15% substitution rates of cement with different MK. The early-age reactivity of metakaolin-blended cement mortar was investigated. Isothermal calorimetry and compressive strength tests were performed. The hydration rate and the evolution of Ca(OH)₂ content of mortars were monitored using thermogravimetric analysis (ATG). The early age reactivity of the three MKs is very different.

Key words Metakaolin, reactivity, pozzolanic, portlandite, mortar.

INTRODUCTION

Cement is the most essential building material in the modern world because of its low manufacturing cost and the diversity of its use. The decomposition of limestone CaCO₃ CaO and CO₂ generates a very important pollution, which is the biggest failure of the cement. Substitution by other cement based materials such as allumino silicate is necessary.

Metakaolin is an adequate solution for this use. The energy generated by calcination of kaolin is derived from dehydroxylation of the kaolin by calcination according to the following formula:



This dehydroxylation generates only water evolution, which is an important asset. In addition, the metakaolin has very interesting pozzolanic properties that can improve the performance of concretes [1].

The pozzolanic activity is the reaction between the silica from the dissolution of MK and calcium hydroxide (Ca (OH) ₂) produced by cement hydration. This reaction gives rise to CSH and CASH [2].

The objective of this study was to compare the activity of three pozzolan metakaolin produced in our laboratory through the index of pozzolanic activity. The evolution of the compression behavior of mixtures cement/metakaolin was carried out on mortar. The microstructure portion showing and explaining the increase in the mechanical performance of mortars containing metakaolin compared to the controlled mortar was carried out on paste. The balance of these two parts allowed us to see the influence of the properties of pozzolan metakaolin and their activity on the quality of concrete

MATERIALS AND EXPERIMENTAL TECHNIQUES

The three metakaolins used in our study have been made in our laboratory. They came from three kaolin whose origin and properties are completely different. After calcination at an optimal temperatures and time, those elements were grinding with the same grinding time and determine their fineness to assess the energy consumption required to manufacture them. Chemical analysis, mineralogical and SEM imaging tests were performed to complete the properties of these metakaolins.

Table 1. Metakaolins properties

Components (%)	MKB	MKJ	MKG
Si	38,63	54,33	49,42
Al	21,85	34,87	41,89
Fe	3,92	4,65	0,24
Ca	24,62	0,21	3,66
K	2,85	5,53	0,28
Ti	1,20	0	0
Mg	1,98	0	0
S	4,06	0	1,32
Mn	0	0	2,75
PAF	9	1	5
BET (m ² /g)	-	18	-
Content metakaolinite	27,4	60,42	80,9
D50 (µm)	20,1	9,08	27,67

Normal mortar used for the compression test, is designed according to standard NF P 15-403. A substitution of 15% of the mass of cement by the MK and a water / cement ratio of 0.4 has been used. A superplasticizer, polycarboxylate, was used and estimated in the order of 0.8% of the weight of cement, to improve the workability of the mixture.

The mortar specimens (4x4x16 cm³) which have been implemented have been kept in water at 20 °C to perform the tests.

The results obtained in terms of mechanical strengths are used to obtain the index of pozzolanic activity of different metakaolins. This index is the weight ratio of the compressive strength of mortars containing metakaolin at the "j" day on the compressive strength of the controlled mortar witness at the same day [3].

$$I_{ap} = \frac{RC_j}{RC_{Référence}} \quad \text{Eq 1}$$

This parameter gives an indication of the potential gain or loss of the mechanical resistance, generated by the pozzolan properties of the metakaolins, and its progression over the time. Figure 4 summarizes the results.

The paste used for the microstructure part have been used in the same conditions as mortars and stored in an air conditioned room (20 ° C, 50% RH) to perform the tests.

Two methods of investigation on the microstructure have been implemented. These tests are performed on a powder that come from the grinding cement pastes and sieved to 80 µm. The diffraction X-ray analysis (XRD) is used to visualize the crystallized phases (anhydrous or

hydrated) present in the cementitious matrix. It also keeps track of developments in the pozzolanic reaction by consuming the Portlandite by comparing the heights of the characteristic lines of the latter.

Thermogravimetric analysis (TGA) is used to quantify certain hydrated phases through dehydration of hydration products with increasing sample temperature. It is characterized by the mass loss caused by the departure of water hydrates. The positioning of TGA curves in between provides information about the reactivity of the studied mixtures.

Mortar compressive strength tests (EN 196-1) are made using a press 2 000 kN.

RESULTS AND DISCUSSION

The chemical analysis reveals a disparity in the levels of oxides mainly represented in metakaolins. Silicon oxides and aluminum oxides are the main indicators of the quality of metakaolins and are more present in MKG than MKJ and MKB. It is very important to report a low alumina in MKB as mentioned in Table 1. The mineralogical composition gives a clear idea on the metakaolins reactivity ability. Thus, according to Diaz Garcia [4], in general metakaolins consist of 65 to 85% of metakaolinite, 5 to 25% of muscovite and 7 to 13% of quartz. Our metakaolins have dispersed proportions in metakaolinite with 80% of kaolinite for KG, 60% for KJ and 27% for KB. This is due to the geological origins of kaolin. MEB images of three metakaolins allowed us to observe the morphology of their platelets. They are shown in Figure 2. From the image (b) which represents the kaolin Guelma characteristics of the hexagonal faces of the kaolinite structure. The images (a) and (c) representing the kaolin from Bechar and Jijel respectively, show random structure, which demonstrates that both kaolins have disorganized structures [5].

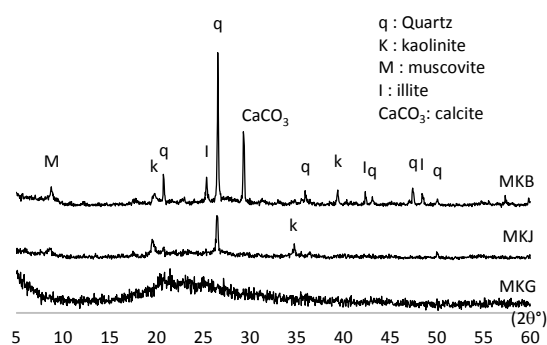


Figure 1. Mineralogic Analyses of MKB, MKG and MKJ.

The mechanical results show an extra resistance to all ages of all mortars containing metakaolin compared to the reference mortar. In Figure 4 we see clearly the difference with the evolution of the progression of strength mortars depending on the nature of metakaolin.

However, at 14 days, the increase of the mechanical strength with respect to the reference mortar varies from 25 to 44%. This significant gain is due to the intense activity engendered pozzolan metakaolin at young age. [6] For MKB and MKG, this increase is more important compared to 28 and 90 days of the order of 15 and 14% for MKG and 38 and 25% for MKB. A report, by cons for MKJ, the progression of strength is optimal at 28 days compared to the controlled one. Thus, the 14 days strength gain is 33% changing to 39% at 28 days and drops to 21% at 90 days. These results are consistent with the literature for a degree of substitution of between 15 and 20% by weight of metakaolin in cement replacement [7]. In the other hand, we can see a high results of the compressive strength of mortars containing metakaolin MKB despite its lack in metakaolinite. The original kaolin is rich in quartz and kaolinite contained therein is poorly crystallized, which indicates that the latter react completely with portlandite produced by the hydration of cement, in addition to the role played by the filler is quartz the other components of metakaolin which by their fineness and fill the empty part in increasing the compactness and thus strength. Analyzes by X-ray diffraction shows the pozzolanic reaction by consuming portlandite $\text{Ca}(\text{OH})_2$. Replacing part of the cement with metakaolin allows the formation of the hydration products comprised of a crystallized portion: CH, CAH and CASH represented by C_2ASH_8 , C_4AH_{13} , C_3AH_8 detectable by XRD, and an amorphous portion CSH undetectable by XRD [8]. Figure 5 confirms the results of the compressive strength. Thus, the reference mortar portlandite peaks are higher than other mortars. In other mortars, the presence of metakaolin, which reacts one consuming portlandite, have lower peaks. The mortar containing MKG consumed the most portlandite due to its high capacity in metakaolin, followed by one containing KJ and end MKB in accordance with the results of mechanical strength obtained.

C-S-H and portlandite, responsible for the resistance of the material can be estimated by other analyzes such as thermogravimetric analysis. The measurement of the mass loss, corresponding to the dehydration of CSH and portlandite, evaluates the share of water reacted with the cement

quantifying chemically water. Figure 3 shows a broad endotherm located at about 229°C , corresponding to the dehydration reaction of CSH. All curves of metakaolin containing mortars are positioned below that of the reference mortar, which implies additional manufacturing CSH induced by the presence of metakaolin. In addition, the positioning of MKB curves, KJ and MKG informs us about the CSH amount produced by each metakaolin. In mortar containing MKJ, is greater than that of MKB and MKG, which is consistent with the index of pozzolan activity and the results of compressive strength.

Assessment of consumer portlandite (CH) gives us an indication of the progress of the pozzolanic reaction.

The endotherm located at about 655°C , corresponding to the dehydration reactions of portlandite, the positioning of the curves is similar to that of HSCs, which confirms a larger portlandite produced by the cement consumption, which is consistent with results of the compressive strength.

Thus, all the mortars containing metakaolin are below the reference mortar, which indicates the presence of an additional amount of C-S-H formed by the presence of metakaolin in the cementitious matrix.

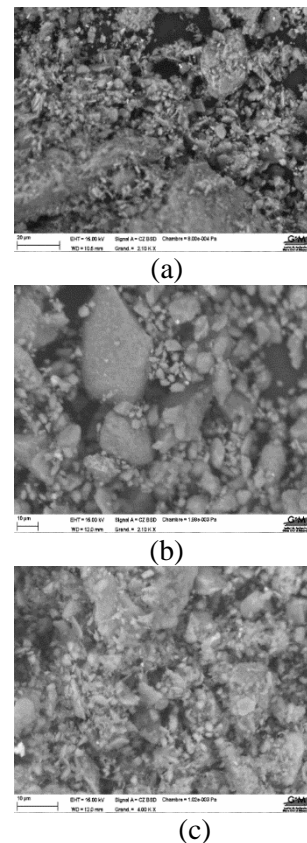


Figure 2. SEM of MKB (a), MKG (b) and MKJ (c)

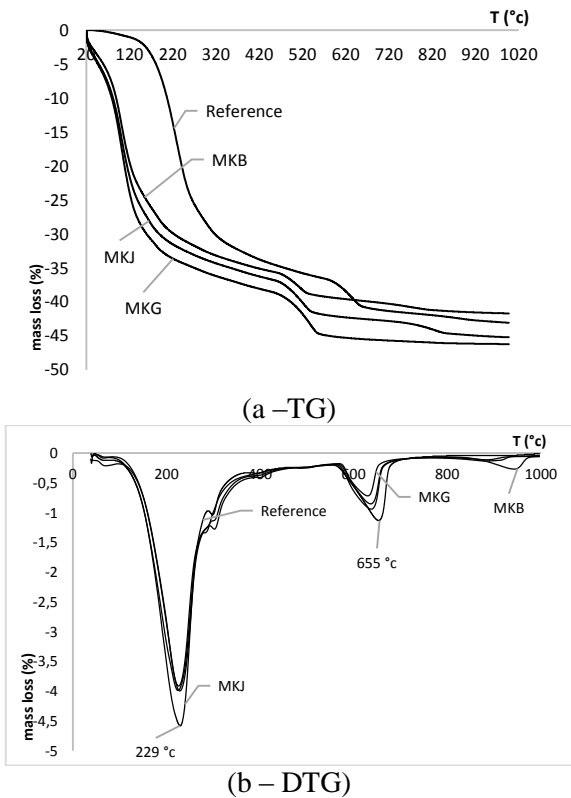


Figure 3. TGA of pastes containing metakaolins at 28 days

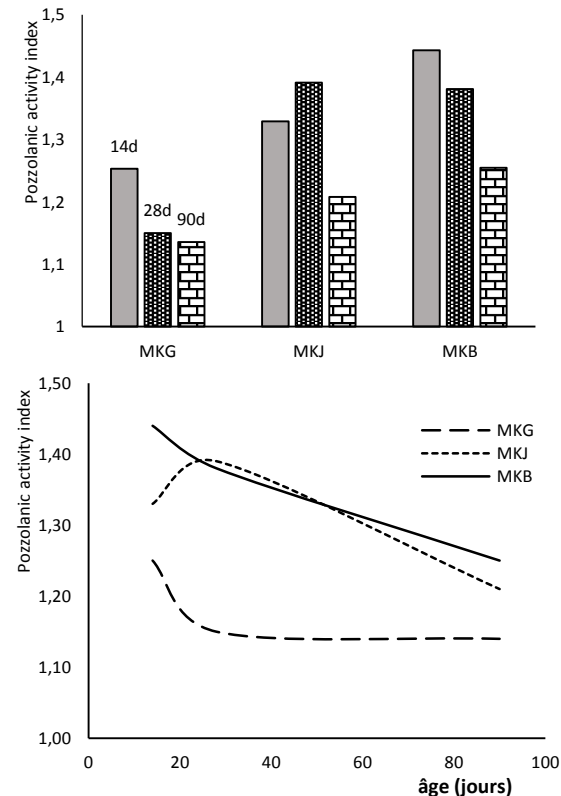


Figure 4. Pozzolanic activity index of the three metakaolins

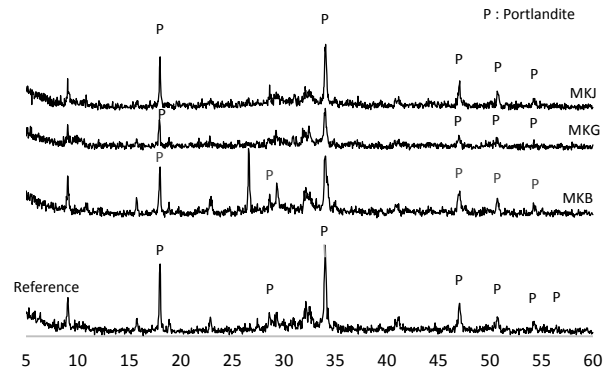


Figure 5. XRD of pastes containing metakaolins at 28 days

CONCLUSION

The increase in reactivity and mechanical performance can be partly explained by the increased amount of hydrates formed, in addition, by the pozzolanic reaction when the addition of metakaolin in the cementitious matrix.

The results obtained by mortars containing our metakaolins are conform to literature. The compressive strength increases at early age to exceed the reference mortar between 7 and 28 days. In addition, the increase in mechanical strength diminishes.

The nature of the physical and chemical properties metakaolins are responsible for these results. The grain size (> 10µm) which gives the metakaolin this ability to fill voids thereby reducing porosity, and the ability to react with portlandite is consuming the maximum at a young age, and additional training to the CSH the only cement.

REFERENCES

1. Sabir B.B., Wild S., Bai J., 2001 «Metakaolin and calcined clays as pozzolans for concrete. A review», *Cement and Concrete Research*, 23, 441–454.
2. Meller N., Hall C., Kyritsis K., Girit G., 2007 «Synthesis of cement based on CaO–Al₂O₃–SiO₂–H₂O (CASH) hydroceramics at 200 and 250 °C: Exsitu and in-situ diffraction», *Cem. Concr. Res.* 37, 823–833.
3. Cassagnabère F., 2007 «Produits préfabriqués en béton fillé : vers l'amélioration des performances du matériau pour mieux gérer le procédé de fabrication», *XXV^{èmes} Rencontres Universitaires de Génie Civil*.
4. Garcia-Diaz Eric, 1995 «Réactivité pouzzolanique des métakaolinites : Corrélation avec les caractéristiques

- minéralo-gitologiques des kaolinites», Thèse de Doctorat, Ecole Nationale Supérieure des Mines de Saint Etienne et de l'Institut National Polytechnique de Grenoble.
5. Bich C., 2005 «Contribution à l'étude de l'activation thermique du kaolin : évolution de structure cristallographique et activité pouzzolanique», Thèse de Doctorat, INSA de Lyon.
 6. Khatib J.M., Sabir B.B., Wild S., 1996 «Some properties of metakaolin past and mortar», Concrete for Environment enhancement and Protection», Ed. Dhir R.K. and Dyer T.D., Spon press, London.
 7. Vu D.D., Stroeven P., Bui V.B., 2001 «Strength and durability aspects of calcined kaolin-blended portland cement mortar and concrete», Cement and Concrete Research, 23, 471–478.
 8. De Silva P.S. and Glasser F.P., 1993 «Phase relations in the system $\text{CaO-Al}_2\text{O}_3\text{-SiO}_2\text{-H}_2\text{O}$ Relevant to metakaolin calcium hydroxyde hydration», Cement and Concrete research. Vol. 23, pp. 627-639.

A COMPARATIVE STUDY OF THE DURABILITY OF CONCRETE BASED ON OPC CEMENT AND BLENDED CEMENT SUBJECTED TO ACCELERATED CARBONATION

Merah AHMED¹, Khenfer MOHAMED MOULDI², Quéneudec Michèle³

1, 2 University of Laghouat, Civil Engineering Research Laboratory, Laghouat-ALGERIA

3 Université de Picardie France ; Unité de Recherche EPROAD /IMaP

BP 37G Street of Ghardaia, Laghouat , Algeria

*Corresponding author: Fax: +213 29 10 34 83 Email: a.merrah@yahoo.fr

ABSTRACT

Reinforced concrete as structural material is used in most civil engineering structures, and exposed to several aggressions (physical, chemical, and mechanical).

Among one of these chemical attacks, we cite the phenomenon of carbonation, which depends mainly on the type and class of cement.

The two main classes of used cement for the concrete formulation in Algeria are ordinary portland cements and blended cements.

This phenomenon affects greatly the durability and limit the lifetime of additional costs of repair, which can sometimes exceed the original cost of realization.

This work is part of the sustainable development option, by studying the behavior of the two classes of cements mentioned above, it revolves around the phenomenon of carbonation of concrete, which once the cover is carbonated, reinforcement corrosion has beginning.

This approach focuses, on both concrete formulations(based on ordinary Portland cements and blended cements), according to both concrete formulations results , samples were made in order to subject them to the accelerated carbonation in a chamber enriched with CO₂ as recommended by AFPC- AFREM.

The obtained results show clearly that the concretes based on Portland cements (OPC) are less sensitive to carbonation phenomenon compared with concrete-based on blended cements.

KEY WORDS: Reinforced concrete, OPC cement, blended cement, durability, accelerated carbonation.

1. INTRODUCTION

Reinforced concrete is sensitive to atmospheric conditions and more particularly to the carbonation phenomenon, which it due to the penetration of carbon dioxide. This gas reacts with the cement hydrates and causes a decrease in the pH of the pore solution. Once, the concrete cover is carbonated, steel reinforcements initially protected are likely to corrode. Associated disorders of this phenomenon correspond to cracks and degradation of the concrete cover, by the formation of iron oxides and hydroxides on the armatures. These can have serious consequences on the reduction of the bearing capacity of the structures elements.

As reinforced concrete structures, this material is widely used around the world for the realization of structures in all field, the absolute need is the protection of this material against atmospheric attack

and therefore ,the increase of its life .Among of these attacks, is the phenomenon of carbonation.

Carbonation is a natural phenomenon which is manifested by the penetration of atmospheric CO₂ in concrete through the pores, the latter reacts with the cement hydrates, mainly portlandite which gives to concrete the basic pH. This phenomenon decreases the Ph, once, the concrete cover is carbonated, the corrosion of steel reinforcement is initiated.

Furthermore, most of civil engineering structures in Algeria were made by reinforced concrete, witch is mainly based on two classes of cements, Ordinary Portland cements OPC, and blended cement.

Many researchers have been interested in the effect of cement additions on the concrete carbonation, [1] developed a mathematical model that controls the evolution of carbonation in time with 50% relative

humidity; this model has been extended to cover the case of carbonation of the coating system (lime cement) and concrete, this model has been validated for concrete based on ordinary Portland cement (OPC) and on blended cement with pozzolanic additions. Elsewhere [2] show that the carbonation depth of concrete samples decreases if additions (silica fume and fly ash with a high and low calcium content) replace a quantity of aggregates, increases if additions replace a quantity of cement.

Moreover [2] concludes that the carbonation depth in mortars based on blended cement is higher than the depth of carbonation mortars based on OPC cements. In the same context, [3] shows that additions in volume (pozzolan materials) increases the carbonation rate with increasing W / C ratio, and concluded that the depth of accelerated carbonation (chamber riched of 3% CO₂) is 10 times higher than under natural exposure conditions. According to [4], a rate higher than 10% additions in silica fume increases the potential for carbonation. [5] studied the effect of limestone fillers on the microstructure and permeability due to carbonation of cement pastes conditionally controlled CO₂ pressure, it shows that the carbonation samples (RH = 65%) is fast during the first hours while it decreases significantly if the relative humidity increases, this study shows that on the additional carbonation of portlandite, CSH are also carbonated.

Otherwise [6] shows that the fly ash additions (about 30%) to ordinary Portland cement with a ratio of W / C in order of 0.6, the cement pastes develop coarse capillary pores which for extensive drying occur even if the total porosity decreases.

This work inscribed in a sustainable development approach, which is to study the behaviour of concretes based on OPC cement and blended cements (42.5 CEM II / B) produced in Algeria, subjected to the accelerated carbonation. This work studies the effect of the class of cement on the evolution of the accelerated carbonation depth, two concrete formulations [1], [9] were made based on both classes of cement (OPC cement 42.5 and blende cements CEM II / B) from the two concrete formulations, prismatic test samples 7x7x28 cm were made, and they were subjected to the accelerated carbonation test in a chamber enriched in CO₂ as recommended by AFPC- AFREM, carbonation depth measurements were carried out by spraying phenolphthalein at 4, 7,14, 28, 42 and 56 days

For this study, the choice is oriented for the cements produced in Algeria, the OPC CEM I and cement CEM II 42.5 / B [1, 10-15]

2. Experimental Procedure

2.1 Concrete formulation.

The used method for the two concrete formulations is the Dreux Gorisse method. Two classes of gravel (3-8mm, 8-15 mm) are used, with absolute density equal to 2700kg/m³, and a sand used with absolute density of 2400 kg / m³ are used. Table 2 shows the results of two concrete formulations.

The cement used for the 1st concrete formulation is ordinary Portland cement (OPC) CEM I 42.5, **Table 1 shows** the chemical and physical characteristics of this cement.

Cement used for the 2nd concrete formulation is the blended cement CEM II 42.5 / B, **Table 2** shows the chemical and physical characteristics of this cement.

The concrete cement content is 408 kg / m³ for the both concrete formulations, the slump cone is 11cm. The compressive strength at 28 days of the formulated concrete is 30MPa (the most used concrete in Algeria). The W / C ratio is around 0.52.

Table 1: Physical and chemical characteristics of the OPC CEM I 42.5 cement used

CEMI 42.5	SiO ₂	Al ₂ O ₃	Fe ₂ O ₃	CaO	MgO	K ₂ O	Na ₂ O	SO ₃	S.s cm ² /g
	20-23	4.07-4.80	4.70-5.40	62-65	0.71-1.22	0.35-0.50	0.07-0.18	1.00-1.45	2500-3263

*S.s : Specific surface

Table 2: Chemical and physical characteristics of the blended cement

CEM II/B	SiO ₂	Al ₂ O ₃	Fe ₂ O ₃	CaO	MgO	K ₂ O	Na ₂ O	SO ₃	S.s cm ² /g
42.5	20.58	4.90	4.70	62.8	0.63	0.42	0.07-0.18	2.28	3700

The clinker content of the used blend cement is about 80%, about 16% of limestone, and 4% of gypsum

*S.s : Specific surface

Tables 3 and 4 include the results of two concrete formulations.

Table 3: results of the concrete composition of the 1st formulation (OPC cement CEM I 42.5)

Sand (0-5)(kg)	Gravel 3-8 (kg)	Gravel 8-15 (kg)	Ciment CEM I 42.5 (kg)	Water(l)	E/C
708	115	933	408	225	0.57

Table 4: Results of the concrete composition of the 2nd formulation (CEM II 42.5 / B)

Sand (0-5) kg	Gravel 3-8(kg)	Gravel 8-15(kg)	Ciment CEM I 42.5 (kg)	water(l)	E/C
708	115	933	408	211	0.52

The compressive strength at 28 days of the formulated concrete is 30 MPa

Figure 1: Represents the DRX mineralogical composition of used limestone gravel

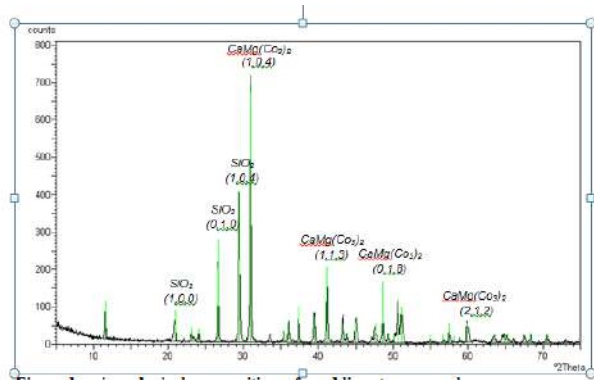


Figure 1: mineralogical composition of used limestone gravel

This analysis allowed to identify the nature of the component elements limestone gravel, they are all dolomite CaMg (CO₃)₂ and some quartz elements SiO₂.

2.2 Preparation of samples and conservations conditions for accelerated carbonation test:

The prismatic samples 7x7x28 cm are made in such a way as to apply the procedure recommended by AFPC-AFREM [16].

For both formulations, samples were made to undergo accelerated carbonation test, and they will be used for the carbonated concrete depth measurements, other samples will be used to monitor evolution in the mass during the test.

All these samples were cured in water for 28 days

Before initiating accelerated carbonation test, the procedure specified in AFREM recommendations in the first phase is to saturate samples in the water. At the end of this phase, the samples will be weighed, dried for two days in an oven set at a temperature of 40 ± 2 C °, then they are still weighed, once before their introduction into the chamber of the accelerated carbonation.

2.3 Accelerated carbonation test

The test procedure adopted is the one recommended by the AFPC AFREM [16] which consist to place (after 28 days of curing and drying) the prismatic samples 7x7x28cm (**Figure 2**) of two concrete formulations in the chamber of accelerated carbonation(**50 % CO₂+50 % Air**)(**Figure 3**), , Regulated at a temperature of 20 ° C and a relative humidity of 65 ± 5%.

All these samples are maintained in the chamber of accelerated carbonation for a period of 90 days.

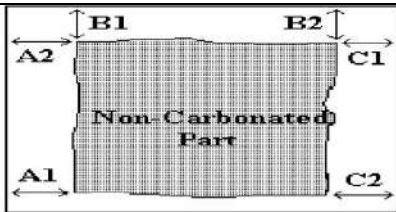
For each formulations, samples are removed from the chamber of accelerated carbonation at different intervals: 4, 7, 14, 28, 42, 56 and 90 days, and they were sliced in two parts (**figure 5**), and a measurements of carbonation depth (by spraying the solution of phenolphthalein, (1% phenolphthalein in 70% ethyl alcohol) were executed with according to RILEM CPC-18 recommendations [17].

Carbonated depth corresponds to the distance between the outer surface of the concrete and the coloring front (**Figure 3**), the uncarbonated concrete takes a pink color and the carbonated concrete is not colored (**Figure 5**) . This method is based on the change of the PH value, initially around 13for the uncarbonated concrete and passes to 9 for the carbonated concrete, five distances are determined

for each side of the test samples. The values of carbonation depth are given in mm.



Figure 2 : Prismatic samples 7x7x28cm



$$D = \frac{A1 + A2 + B1 + B2 + C1 + C2}{6}$$

Figure 3 : Measuring of the carbonation depth with spraying phenolphthalein VILLAIN [18]



Figure 4 : Samples into the chamber



Figure 5 : detection of the carbonated zone

3. Results and discussion

3.1 DRX test

This technique essentially qualitative, used to differentiate varieties of the same crystallographic mineral such as portlandite and calcium carbonate (calcite). However, it does not identify the semi-crystalline or amorphous compounds such as amorphous portlandite or amorphous newly formed calcium carbonates.

This method involves bombarding a sample (isotropic homogeneous powder consisting of tiny crystals welded together) with X-rays and recording the X-ray intensity which is redistributed according to the orientation in space. The scattered X-rays interfere with each other, the intensity then has maxima in certain directions. There is talk of diffraction phenomenon.

The detected intensity is then recorded as a function of the beam deflection angle. The curves thus obtained are called diffractograms

Figures 6 and 7, show diffractograms for an angle range (0 to 26 degrees), for each types of carbonated concrete and after 90 days in the carbonation chamber.

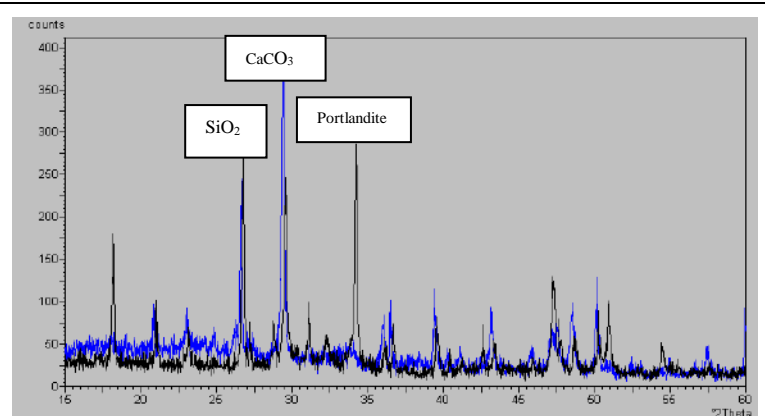


Figure 6 : DRX analyzes on the carbonated and uncarbonated samples for the 2nd concrete formulation (based on Blended cement)

*Carbonated samples: blue color
*Carbonated samples: black color

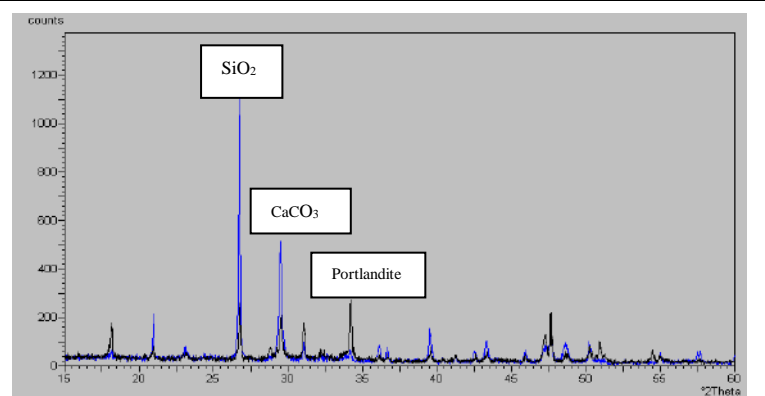


Figure 7 : DRX analyzes on the carbonated and uncarbonated samples for the 1st concrete formulation (based on OPC cement)

In order to confirm the carbonation depth measures obtained by means of the spraying phenolphthalein, the x-ray diffraction was used for the detection of the depth of carbonation of the samples from the two concrete formulations.

For both concrete formulations of carbonated samples, we observe that the peaks of portlandite, ettringite and aluminates, clearly present in uncarbonated concrete, almost disappear for the both concrete formulations

3.2 Impact of the concrete formulation on the accelerated carbonation

Figure 8 shows the results of the accelerated carbonation test for the test samples of the two concrete formulations. From this figure, we see that the 1st concrete formulation based on the OPC cement is less sensitive to carbonation phenomenon than the second one.

The 1st concrete formulation gives a better protection for the concrete against the carbonation phenomenon compared with the 2nd concrete formulation. These results are in agreement with those obtained by Kritsada Sisomphon et al. [3]

In addition, for concrete samples of the 1st formulation, it was found that the depth of carbonation is low during the first days and increase from the 7th day, but it is still inferior to the depth of carbonation samples of the 2nd concrete formulation; This is due to the fact that during the first days the relative humidity is not stable within the chamber due to water exchange between the concrete and the relative humidity inside the chamber of accelerated carbonation.

3.3 Evolution of mass during the accelerated carbonation test

Figure 9: shows the evolution of the mass during accelerated carbonation test for samples of the two concrete formulations.

From this figure, it was found that in the early days of the test a mass gain, especially for the samples of the 2nd concrete formulation; this can be explained by the fact that in the early days the relative humidity varies depending on the water exchange between the concrete and the atmosphere in the accelerated carbonation chamber. Then the relative humidity stabilizes at a value of $65 \pm 5\%$. Moreover,

this figure has the same looks for the two concrete formulations, which agree with the results of AFREM crossover tests. We also note that the mass gain during the accelerated carbonation test is less important for samples from the 1st formulation of concrete, this is due that the cement CEMII / 42.5 B of the second formulation contains t additions.

These results confirm that the use of the 1st formulation of concrete based on cement CEM I 42.5 OPC gives a supplementary protection against the carbonation than the 2nd concrete formulation based on blended CEM II 42.5 /B

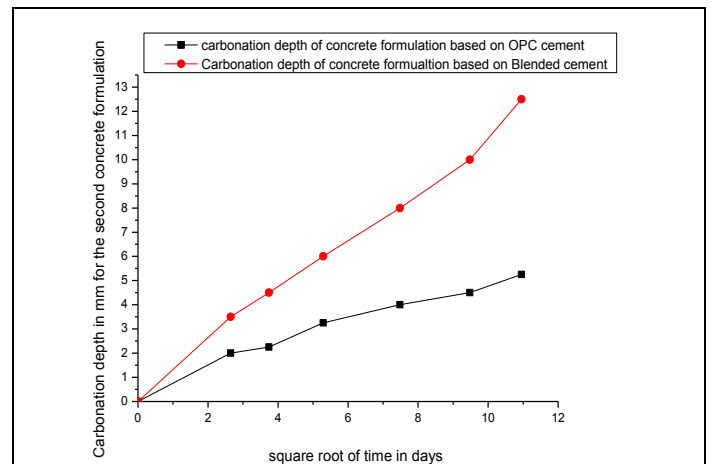


Figure 8 : carbonation depth (concrete based on OPC cement and concrete based on blended cement)

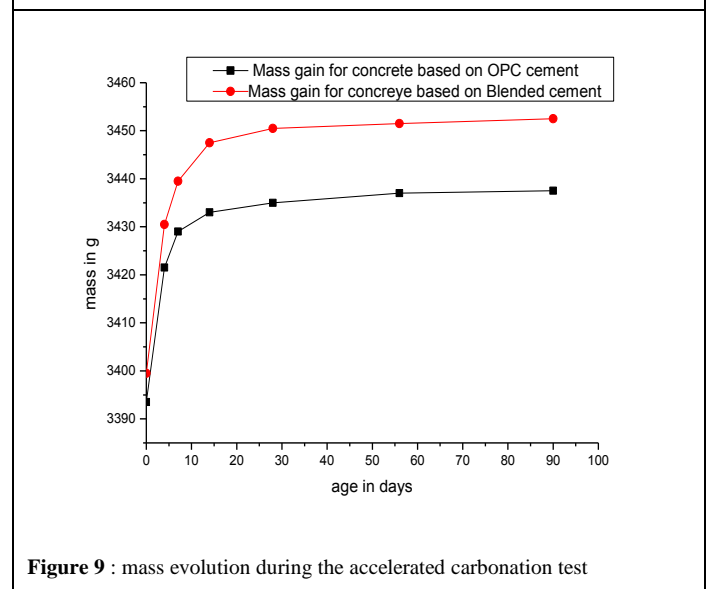


Figure 9 : mass evolution during the accelerated carbonation test

4. Conclusion

In the present work, a concrete composition B30 was made (2 fractions of gravel). Samples from both concrete formulations were made and submitted to the accelerated carbonation test,

We can draw the following conclusions:

1. The use of OPC cement for the realization of reinforced concrete structures minimizes carbonation phenomenon compared to concretes based on cement CEM II / B 42.5,
2. We have found that a low mass change for concrete samples based cements CEM I / 42.5, compared to concretes based cements CEM II / 42.5 B.
3. As regards the accelerated carbonation test, it was also found that the water exchange between the concrete and the atmosphere in the chamber do not stabilize after the 7th days.
4. The results show that the formulation of concrete-based OPC cement is less sensitive to carbonation phenomenon compared to the concrete formulation based on cements CEM II / 42.5 B.

5. Bibliographie

1. **Marlova P, KulakowskFernanda M, Pereiraenise C.C, Dal Molin.** Carbonation-induced reinforcement corrosion in silica fume concrete. 2009, Vol. 23, pp. 1189-1195.
2. **DAKHMOUCHE, Fatima-Zohra.** *Carbonatations de betons adjuvantés à base de ressources locales algériennes.* s.l.: université d'Orléans et l'Université Mentouri de Constantine, 2009. Thèse de doctorat.
3. **V.G. PAPANAKIS, M. N. FARDIS, C.G. VAYENS.** effect of composition, environmental factors and cement-lime mortar coating on concrete carbonation. 1992, Vol. 25, pp. 293-304.
4. **H.Beushausen.N.Burmeister.** The use of surface coatings to increase the service life of reinforced concrete structures for durability class XC. *Materials and structures, Rilem.* 2013.
5. **K.K. Sideris, A.E. Savva, J. Papayianni.** Sulfate resistance and carbonation of plain and blended cements. *Cement and Concrete Composites.* 2006, Vol. 28, pp. 47-56.
6. **A.M.G Senviratne, G. Sergi, C.L Page, Vol 14, 2000, pp 55-59.** Performance Characteristics of surface coatings applied to concrete for control of

reinforced corrosion. *Construction and Building Materials vol 14.* 2000, pp. 55-59.

7. **Committee, Concrete Permanent.** Measurement of hardened Concrete carbonation Depth CPC 18. 1988, Vol. 21, pp. 453-455.
8. **A. Brenna, F. Bolzoni, S. Bretta, M. Ormellesse.** Long-term chloride-induced corrosion monitoring of reinforced concrete coated with commercial polymer-modified mortar and polymeric coatings. *Construction and Building Materials vol 48.* 2013, pp. 734-744.
9. *La carbonatation des bétons aux fortes additions calcaires.* **Falih Raffie Moro, Fouad Ghomari, Mohamed Amine Boukli Hacène, Omar Taleb, Ahmed Loukili, Emmanuel Rosière.** [éd.] 21-31. Tlemcen ALGERIE : s.n., 2011. XXIXe Rencontres Universitaires de Génie Civil.
10. **A. Morandea, M.Thiéry, P.Dangla.** Impact of accelerated carbonation on OPC cement paste blended with fly ash. *Cement and Concrete Research.* 2015, Vol. 67, pp. 226-236.
11. *Essai de carbonatation accéléré mesure de l'épaisseur de béton carbonaté.* **BETONS, AFPC-AFREM-DURABILITE DES BETONS.** 1997, pp. 153-158.
12. **Quoc Tri Phung, Norbert Maes, Diederik Jacques, Els Bruneel, Isabel.** Effect of limestone fillers on microstructure and permeability due to carbonation of cement pastes under controlled CO₂ pressure conditions. *Construction and Building Materials.* 2015, Vol. 82, pp. 376-390.
13. **Miguel. Angel. Sanjuan, Cesar del olmo.** Carbonation resistance of one industrial mortar used as a concrete coating. *Elsevier, Building and Environment, vol 36.* 2001, pp. 949-953.
14. **Kritsada Sisomphon, Lutz Franke.** Carbonation rates of concrete containing high volume of pozzolanic materials. *Cement and Concrete Research.* 2007, Vol. 37, pp. 1647-1653.
15. **Park, D.C.** Carbonation of concrete in relation to Co₂ permeability and degradation of coatings. *Construction and building Materials , Vol 22.* 2008, pp. 2260-2268.
16. **Fattuhi, N. I.** Carbonation of concrete as affected by mix constituents and initial water curing period. *N° 110 vol 19 issue 2 Materials and Structures.* March – April 1986, pp. 131-136.
17. **A.A. Almusallam, F.M. Khan, SU. Dulaijan, O.S.B Al-Amoud.** Effectiveness of surface coatings in improving concrete durability. *Cement and concrete composites, vol 25.* 2003, pp. 473-481

MESO-SCALE ANALYSIS OF THE AGGREGATE SIZE INFLUENCE ON THE MECHANICAL PROPERTIES OF HETEROGENEOUS MATERIALS USING THE BRAZILIAN SPLITTING TEST

AL-KHAZRAJI Hayder*, BENKEMOUN Nathan, CHOINSKA Marta, KHELIDJ Abdelhafid
LUNAM Université, GeM, UMR CNRS 6183
IUT de Saint Nazaire, Université de Nantes, France

*Corresponding author: Email: hayder.al-khazraji@univ-nantes.fr

ABSTRACT

The effect of the aggregate size on the behavior of the hardened concrete under splitting tensile loading is studied in this paper. The studies of Tasdemir et al., 2001, Appa et al., 2011, Li et al., 2014 show that the behavior of heterogeneous materials which are subjected to loading depends on many parameters such as volume fraction, aggregate type, and aggregate size, etc. In this paper an investigation was made to study the effect of aggregate size on the mechanical properties of heterogeneous materials such as concrete in the context of the Brazilian splitting test. Five finite element simulations have been carried out in this research to study the behavior of concrete under diametral compression load. Cylinder specimens of concrete with 50 mm of thickness and 110 mm of diameters have been regarded. Five diameters of aggregate have been employed in the analyses, ranging from 4 to 16 mm. This study has employed a meso-scale model (mechanical model) based upon a 3D lattice approach, representing with explicitly heterogeneity and failure mechanism of the concrete. This model considers the concrete to be a two-phase material in which aggregates are melt within the cement paste. Because of using a non-adapted meshing process to mesh the microstructure, a weak discontinuity (jump in the deformation field) is introduced in the kinematics. Three sets of bar elements are thus present: one being completely located into the aggregate (no weak discontinuity). The second set of element is located within the cement paste (no weak discontinuity) and the last set of elements is splitted into two parts by a physical interface (weak discontinuity activated); each part having different elastic properties. The second enhancement of kinematics introduced here is a strong discontinuity representing crack opening (discontinuous displacement field). The results of the numerical simulations show the ability of the meso-scale model to evaluate the mechanical failure in the context of the Brazilian splitting test. Also, the results show that (1) the maximum tensile stress, (2) the fracture energy and (3) the maximum crack opening are all have been increased when the aggregate diameter was increased.

Keywords Meso-scale analysis, Aggregate, Mechanical properties

INTRODUCTION

The concrete is a widely used material in concrete structures, it is considered to be a heterogeneous material which is consisting of aggregate melts into cement paste or mortar. Designed structures need the information about the factors that influence crack initiation and propagation in the concrete. Prediction modulus of the elasticity of concrete depends on two materials: the aggregate and the cement paste. The volume of the aggregate occupies most of the concrete, therefore these information are needed for the numerical investigation of concrete behaviour.

The mechanical behaviour of concrete depends on many characteristics such as, volume fraction; aggregate type and aggregate size, etc. The aim of this study is to investigate the influence of aggregate size on the mechanical properties of heterogeneous material such as concrete in the context of the Brazilian splitting test.

Previous studies like Tasdemir et al. [19] and Burcu et al. [4] investigated the influence of the

volume fraction of aggregate on mechanical properties of concrete depending on the meso-mechanical approach and the experimental work. App et al. [2] pointed out to the influence of the surface type of aggregate on fracture behaviour of heterogeneous materials. Another study was made by Li et al. [13] reported that the splitting tensile strength of concrete had been increased with the roughness of coarse aggregate.

Hillerborg's research [12] demonstrated that the fracture energy of mortars are lower than those in the concretes. Furthermore the increasing of the aggregate size is caused by the increasing of the fracture energy according Li et al. [15] study. Elices et al. [9] concluded in their research that the average values of the initial crack opening w_1 and the average values of the critical opening w_c are increasing with the aggregate size.

ANALYSIS AND MODELLING

Splitting tensile test (Brazilian test)

In order to investigate the behavior of concrete during splitting tensile test, the tensile tests of concrete are classified into direct and indirect tensile tests. A direct tensile test is executed by applying an axial tension force to the concrete specimens. Cunha et al. [8] developed this test (direct tensile) by molding specimen with embedded steel bars. The bars were used to apply the tensile force to the concrete. Also, Mechtcherine et al. [16] developed this test by using (dog-bone) specimen as un-notched element and prism as notched one. The experimental results compared with the notched specimens by the other studies [6, 14].

As a result of the constricts as pointed out, most of the researchers changed the test method to use the indirect tensile test techniques, i. e. flexural test and Brazilian splitting test. These tests are less complicated than other type of tests that are considered to be the test set-up procedure that has been standard in several Codes, ASTM and the Euro Code.

The Brazilian splitting test set-up can be seen in the figure 1. A test strategy consists of a concrete cylinder specimen placed horizontally and loaded in compression (diametral load) by the loading platens of the compression testing machine along the length of the cylinder.

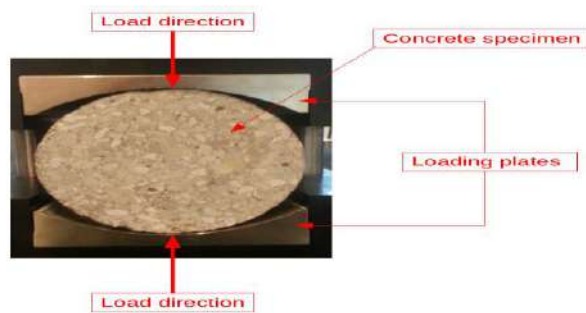


Figure 1. The test set-up of the Brazilian splitting test.

As shown in figure 2, the distribution of the loading (applied load and tensile stress) are according to ASTM C496 [1], and equation 1 is the formula to be used to calculate the splitting tensile strength under diametral loading for concrete cylinder specimen. Where, f_{st} is the splitting tensile strength in (MPa) at the failure due to the ultimate diametral loading P_u in (N), and D is the diameter of the cylinder specimen in (mm), B is the specimen thickness in (mm).

$$f_{st} = 2P_u / \pi BD \quad (1)$$

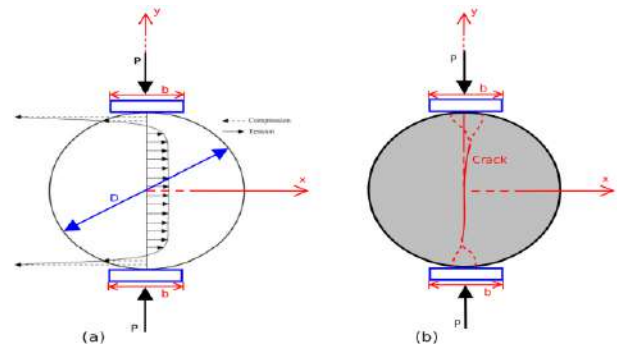


Figure 2. The description behaviour of specimen cylinder under loading, distribution stress [ASTM C496] [1] (a) and applied load with crack pattern (b).

Meso-scale model mechanical-numerical model

This study is based on a meso-scale model with enhanced kinematics for representing the failure of the heterogeneous materials. This type of enhancement kinematics is classified to two types of kinematics: weak discontinuity (jump in the deformation field) without any mesh adaptation and strong discontinuity (discontinuous displacement field) for measuring crack value.

Furthermore, this model was considered that the concrete consists of a multi-phases material (aggregates melt into cement paste) and that the concrete is quasi-brittle material. For discretization 3D heterogeneous multi-phases material by using Enhanced Finite Element Method (E-FEM). Three sets of elements have been obtained. Figure 3 shows three types of elements for representing the specimen cylinder concrete.

The first set of elements colored in blue represents the cement paste and the second set of elements colored white are the inclusions (aggregates). The last set is colored in red, which is placed between aggregates and cement paste, and this type of elements consists of two parts; the first part has the properties of the cement paste, while the second part has the properties of the aggregates (inclusions).

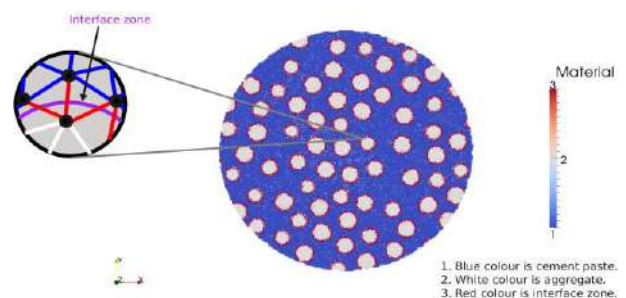


Figure 3. 3D representation of two-phase heterogeneous materials.

Weak discontinuity

Due to the heterogeneity of materials and do not need change adapted meshes caused by splitting into parts for third set elements which placed at interface position between the aggregate and the cement paste, each part has different elastic properties. Figure 4 shows the first enhanced kinematics with two subdomains; the first one represents the elastic properties of the cement paste, and the second one represents the elastic properties of the aggregate. Equation 2 offers the first enhancement of the elements bar at the interface between the two subdomains (two elastic properties), also by function calculates jump in the deformation field, where l is the length of the element bar, and θ is the scalar dimensionless.

$$G_1 = -1/\theta l, x \in [0, \theta l] \tag{2a}$$

$$G_1 = 1/l(1-\theta), x \in [\theta l, l] \tag{2b}$$

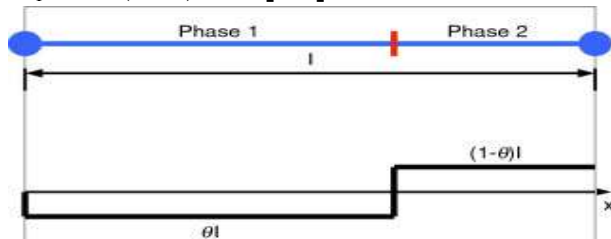


Figure 4. Split truss element with weak discontinuity and G_1 function [3].

Strong discontinuity

The concrete is considered to be a quasi-brittle material for representing the softening behavior with crack width introduced second kinematic enhancement (strong discontinuity). Thanks to the strong discontinuity, approach can be measured the opening crack value, figure 5 shows element bar with strong discontinuity and G_2 function, which consists the Dirac function δ_r placed within the interface zone and $-1/l$. The elements in this enhancement place in the interface zone and cement paste or aggregate. The function G_2 can be written as:

$$G_2 = -1/l + \delta_r \tag{3}$$

Table 1

Geometry Properties of Materials, (E, σ_u, G_u) Modulus of Elasticity, Tensile Stress and Fracture Energy.

Cement paste	Aggregate	Interface	Volume of fraction
$E_{mor}=35$ GPa	$E_{agg}=100$ GPa	-	
$\sigma_u =3$ MPa	-	$\sigma_u =3$ MPa	20 %
$G_u =80$ J/m ²	-	$G_u =80$ J/m ²	

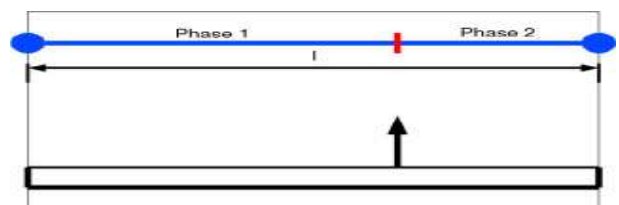


Figure 5. Split truss element with strong discontinuity and G_2 function [3].

Tension-softening relation

The mechanical meso-scale model that deals with quasi-brittle materials to represent this feature must be determined relation between the applied tensile load and softening behavior of concrete. This relation based on yield function to activate the strong discontinuity. Yield function is written by:

$$\Phi = t_r - (\sigma_u - q) \tag{4}$$

$$q = \sigma_u (1 - \exp(-\sigma_u / G_u [l/u/l])) \tag{5}$$

where t_r is the tensile stress at the discontinuity, and σ_u is the fracture stress. This equation depends on fracture energy G_u which is based on the total area under the tensile stress-crack opening curve in figure 6b.

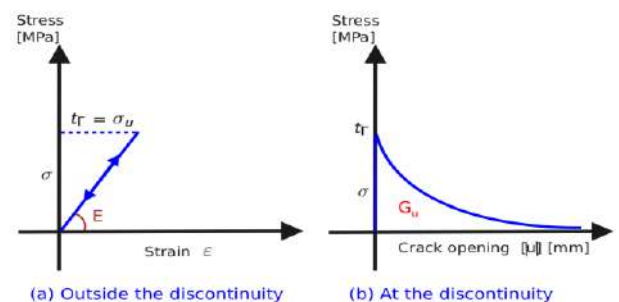


Figure 6. The elastic-quasi-brittle behaviour.

RESULTS AND DISCUSSION

Numerical simulations and results

In this section, the description of the numerical simulations and the results for the five cylinder specimens under the Brazilian splitting test will be given.

Discretization of two-phase materials

Five cylinder specimens with the size 110 x 50 mm diameter and thickness respectively have been simulated. The parameter variable in this study is the aggregate diameter (simulated with mono-sizes aggregate) while the volume of the fraction has kept constant 20% for the five specimens. The aggregate diameters are 4, 8, 10, 14 and 16 mm respectively, also each simulation consists of one diameter. The geometry properties for each phase (cement paste, aggregate and interface zone) are summarized in table 1. As shown in figure 7, 3D isometric view for five cylinder specimens are simulated with different aggregate diameters.

Maximum crack opening

The focus of this study is to describe the effect of aggregate size on the mechanical behavior of concrete in context of Brazilian splitting tensile test. The numerical results show the influence of aggregate diameter on the crack opening without changes in the volume of fraction. On the other hand, the increasing in the aggregate diameter leads to an increase in the maximum crack opening, figure 8 shows this relation for five cylinder specimens are simulated. In addition, the results show that the orientation of the cracking became more isotropic in the specimens with larger aggregate diameters.

The previous study offered that the crack open is decreasing when the interface zone is strong, and this decrease is depending on the properties of cement paste and rough of crack [11], while other authors presented the increase of the critical opening w_c with the aggregate size [10, 15, 17].

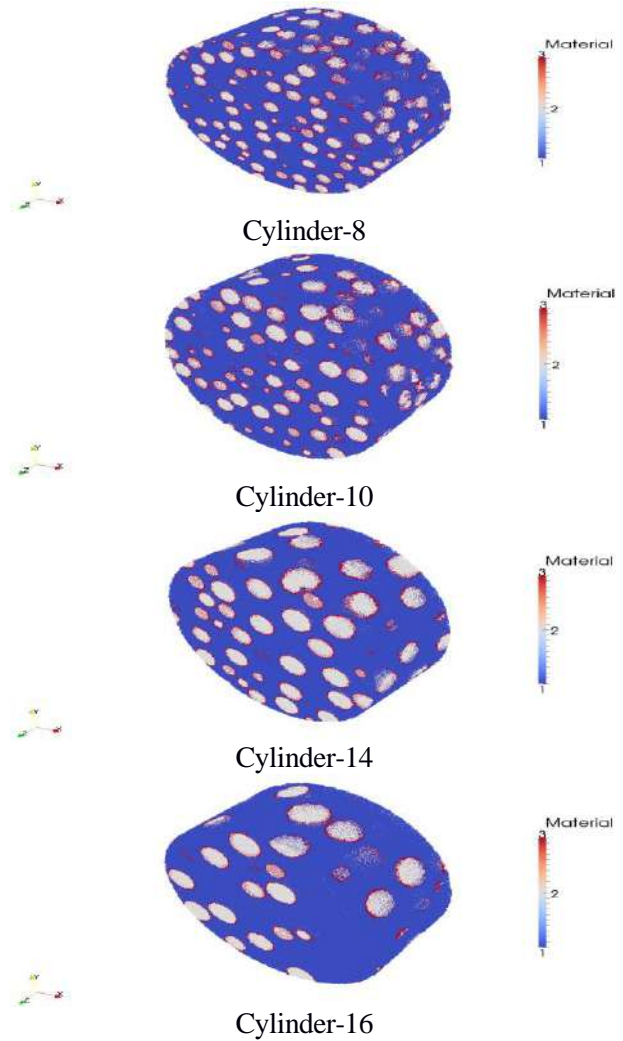
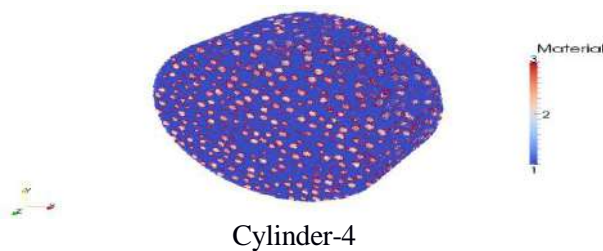


Figure 7. 3D isometric view section in the five simulated cylinders.

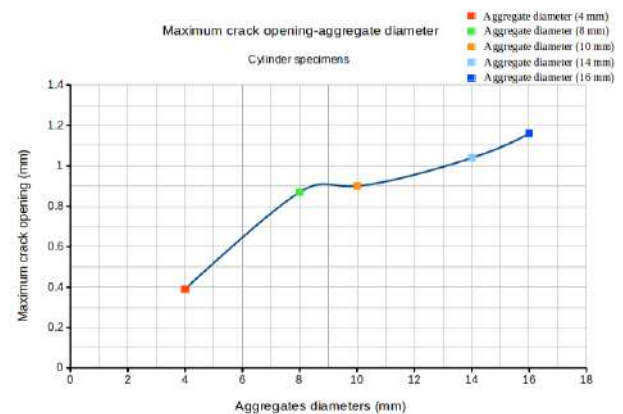


Figure 8. Maximum crack opening versus aggregate diameter.

Splitting tensile stress

The numerical results show the relation between aggregate diameters with the maximum splitting tensile stress. Therefore the increasing of aggregate diameter tends to cause an increase in

the maximum tensile stress. Otherwise, figure 9 shows the maximum tensile stress is a function of aggregate diameter for five cylinder specimens are simulated. One noticeable point is that the total surface area of the interface zone between the aggregate and the cement paste depends on the aggregate diameter, see table 2.

Concerning the effect of aggregate diameter, many studies have recently shown the influence of aggregate size on the mechanical behavior of concrete under loading. The increasing in the tensile stress resulted from the increasing of aggregate size [18], in addition, tensile strength for high-strengthed concrete is increasing with the aggregate size [7].

Table 2
Surface Area of Aggregates for Five Cylinder Specimens.

Specimen	Surface area of aggregates mm ²	Ultimate tensile stress σ_u MPa
Cylinder-4	43178.1	1.7
Cylinder-8	7489.6	1.9
Cylinder-10	5943.9	1.953
Cylinder-14	2764.6	2.01
Cylinder-16	1420.0	2.11

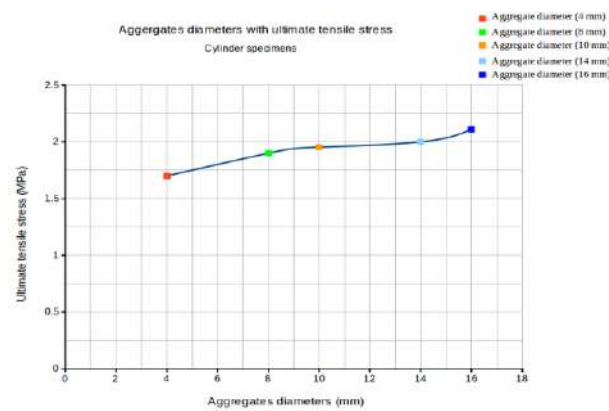


Figure 9. Ultimate tensile stress versus aggregates diameters.

Fracture energy

By integrating the area under the curve (stress-crack opening) relation in figure 6, the total energy can be calculated for each simulation. Figure 10 gives a clear representation of 3D heterogeneous materials mechanism that occurs during the splitting tensile loading, which is a representative of a softening behavior.

The results obtained show that the fracture energy, as a function of aggregate diameter, it seems to increase as the aggregate diameter increases, which is confirmed with the standard of CEB-FIP model code [5].

As shown in table 4, the fracture energy for many studies, which compared with the fracture energy is obtained from numerical simulations, it shows the influence of the volume of fraction and aggregate sizes on the fracture energy, i. e. the increasing of aggregate size leads to an increase in the fracture energy.

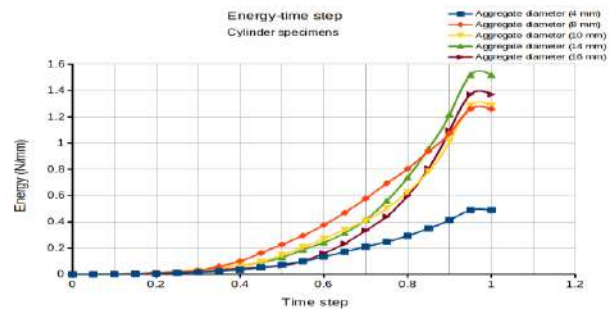


Figure 10. Energy versus time step for five cylinder specimens are simulated.

Table 4
Increasing of Fracture Energy with Aggregate Size.

Authors	Volume of fraction %	Increasing of fracture energy %
Petersson, 1980	50	13
Mihashi, 1989, 1991	40	50
Tasdemir et al., 1996	49	34
Rao and Prasad, 2002	44	35
Numerical simulations	20	68

REFERENCES

1. ASTM C496, Test Method for Splitting Tensile Strength of Cylindrical Concrete Specimens, ASTM Book of Standards.
2. App Rao, G. and Raghu Prasad, B. K., 2011, Influence of interface properties on fracture behaviour of concrete, Indian Academy of Sciences, Res 36 (2) pp. 193-208.
3. Benkemoun N., Hautefeuille M., Colliat JB., Ibrahimbegovic A., 2010, Failure of heterogeneous materials: 3D meso-scale FE models with embedded discontinuities. International Journal of Numerical Methods in Engineering 82: 1671-1688.
4. Burcu A., Ayda S. A., Fikret B., Hakan N. A., Cengiz S., 2012, Interpretation of aggregate volume fraction effects on fracture behavior of concrete, Construction and Building Materials 28 pp. 437-443.
5. CEB-FIP Model Code, 1990, Comité Euro-International du Béton (CEB), Bulletin d'Information 195, Lausanne, Switzerland.
6. Cedolin L., Poli S.D., Iori I., 1987, Tensile behavior of concrete, ASCE J. Eng. Mech. 113 pp. 431-449.

7. Chen B., Liu J., 2004, Effect of aggregate on the fracture behavior of high strength concrete. *Construction and Building Materials* ;18 pp. 585–90.
8. Cunha V.M.C.F., Barros J.A.O., Senna-Cruz J.M., 2011, An integrated approach for modeling the tensile behavior of steel reinforced self-compacting concrete, *Cement and Concrete Research* 41 pp. 64–76.
9. Elices A., and Rocco C. G., 2008, Effect of aggregate size on the fracture and mechanical properties of a simple concrete, *Engineering Fracture Mechanics* 75 pp. 3839-3851.
10. Grassl P., Wong H.S., Buenfeld N.R., 2010, Influence of aggregate size and volume fraction on shrinkage induced micro-cracking of concrete and mortar. *Cement Concrete Research* 40(1) pp. 85–93.
11. Guinea G.V., El-Sayed, Rocco C.G., Elices M., Planas J., 2002, The effect of the bond between the matrix and the aggregates on the cracking mechanism and fracture parameters of concrete, *Cement and Concrete Research* 32 pp. 1961– 1970.
12. Hillerborg A., 1985, results of three comparative test series for determining the fracture energy G_f of concrete, *Materials and Structures* 18 (107) pp. 407-13.
13. Li H., Xianglin G., Feng L., 2014, Influence of aggregate surface roughness on mechanical properties of interface and concrete, *Construction and Building Materials* 65 pp. 338-349.
14. Li Q., Ansari F., 2000, High-strength concrete in uniaxial tension, *ACI Mat. J.* 97 pp. 49–55.
15. Li Q., Deng Z., Fu H., 2004, Effect of aggregate type on mechanical behavior of dam concrete, *ACI materials Journal* 101 (6) pp. 483-92.
16. Mechtcherine V., Muller H.S., 1998, Effect of test set-up on fracture mechanical parameters of concrete, in: *Proc. FRAMCOS-3 Fracture Mech and Concrete Struct.*, Germany , pp. 377-386.
17. Mihashi H., Nomura N., Izumi M., 1989, Influence of matrix strength and gravel size on fracture properties of concrete. In: Shah SP, Swartz SE, Barr B, editors. *Fracture of concrete and rock*. Elsevier;. pp. 503–12.
18. Rao G. A., Raghu Prasad B. K., 2002, Fracture energy and softening behavior of high-strength concrete. *Cement Concrete Research*, 32 pp. 247–52.
19. Tasdemir C., Tasdemir M.A., Lydon F.D., Barr B.I.G., 1996, Effects silica fume and aggregate size on the brittleness of concrete. *Cement Concrete Research* ;26(1) pp. 63–8.

PREDICTION OF THE STIFFNES MODULUS OF A POLYMER MODIFIED ASPHALT VIA THE EXPERIMENTAL DESIGN METHOD

Amine Meksen and Mahmoud Bensaïbi
Ecole Nationale Supérieure des Travaux Publics
National School of Built and Ground Works Engineering
BP 16051 rue Sidi Garidi, BP 32, Vieux Kouba, Algiers, Algeria
Fax: +213 21 28 87 61; Email: amine7my@hotmail.fr

ABSTRACT

The modified asphalt mixtures obtained by adding a polymer have a high resistance to rutting and fatigue. This makes their use desirable in achieving long life pavements. Studying the behavior of these mixtures requires a large number of experiments. We propose in this work a mathematical model to predict the stiffness modulus of a modified asphalt by addition of PR Plast Sahara according to the most influential parameters (the binder content, the additive percentage and the production temperature). This is to establish a mathematical relationship that determines by calculations its stiffness modulus, depending on the given parameters.

However, to develop the model, it is necessary in a first stage, to perform an important number of experiments. A Box-Behknen experimental design has been exploited to reduce this number and thus obtain maximum information by performing a minimum of experiments, thereby resulting in savings in cost and time.

INTRODUCTION

Rutting and fatigue cracking are the main forms of road damage. Adding polymers to asphalt is a promising technique to enhance the pavements resistances to these defects, thus increasing their service life [1][2][3].

Studies have shown that the contribution of binder's stiffness to the rutting resistance is about 50% and that asphalt mixes modified with SBS (Styrene-Butadiene-Styrene) and SBR (Styrene-Butadiene-Rubber) were significantly more resistant to fatigue and rutting, while aggregates internal structure have low influence on these characteristics. Therefore bitumen modification by polymers addition significantly improves the mechanical proprieties of the asphalt mix [4][5].

There are two main types of polymers for bitumen modification [6]:

- Elastomers
- Plastomers

Elastomers absorb the oil fractions from the bitumen and swell up to nine times their initial volume. At an appropriate concentration, a continuous polymer

phase is formed throughout the bitumen matrix and modifies its proprieties, increasing its resistance to deformations[7][8]. SBS is the most widely used elastomer. According to many authors, it is the most suitable polymer for bitumen modification [9]. The plastomers are a class of linear polymers, derived from ethylene. They increase the viscosity and stiffness of the bitumen by forming rigid network structures, resistant to deformation. Plastomers under the action of a stress, may undergo elastic and plastic deformations. EVA (Ethylene Vinyl Acetate) are the most used plastomers [10]. The pavement performance depends on the rheological behavior of the bitumen polymer mix, because of the polymers high molecular weight. This makes the formation of a uniform system within the bitumen matrix, difficult, thus causing compatibility problems [11] [12][13]. At low dosages, the polymers are distributed in the continuous bitumen matrix. At high temperatures, the stiffness modulus of the polymer is greater than that of the bitumen, resulting in improved resistance to rutting. Regarding low temperatures the polymer stiffness modulus is lower than bitumen's and thus prevents cracking. Medium

dosage of polymers creates microstructures in which the two phases are connected. They are unstable and highly dependent on the temperature. In the presence of large amounts of additive, the polymer becomes the continuous phase of the mixture. The mixture takes on the characteristics of the plasticized polymer with the bitumen oils and can't be used as pavement material [14].

The purpose of this study is to model the stiffness modulus of asphalt mixtures modified by PR Plast Sahara which is a mixture of polyolefins, based on the most influential parameters which are the percentage of additive, the binder content and the production temperature.

OBJECTIVE AND EXPERIMENTAL PROCEDURE

In order to study the characteristics of the modified asphalt depending on the parameters that are considered most influential, a mathematical model is developed. This is to establish a mathematical relationship that determines its characteristics (outputs) depending on the given parameters (inputs). Figure 1 illustrates the system modelling.

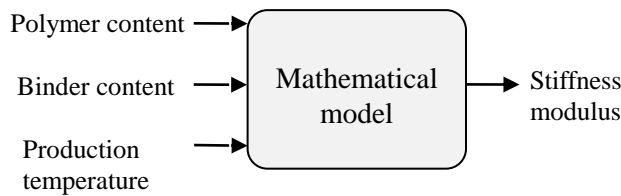


Figure 1
Modelling of the stiffness modulus

In order to develop the model, stiffness modulus measurement will be conducted using the Nottingham Asphalt Tester. To minimize the number of trials, experimental design method was exploited.

Experimental design: An experimental design is an ordered sequence of experiments, each to acquire new information by varying one or more parameters while performing the least possible trials [15]. The steps of the experimental design study are as follows:

- 1) Selection of representative responses of the system.
- 2) Identification of potentially influencing factors.
- 3) Choosing the study field of the factors.

- 4) Determination of experiments to be performed as well as their execution order.
- 5) Analysis of the factors influence and their interactions.
- 6) Establishment of the mathematical model.

The Box-Behnken design was selected. It is used to establish second order polynomial models [16].

In a previous study, Harizi and al. allowed the identification of the most influential parameters on the stiffness modulus [17]. Table 1 lists them.

Table 1
Experimental Design Factors

Factor	Type
Binder content	Quantitative
Polymer content	Quantitative
Production temperature	Quantitative

The stiffness modulus E is expressed by a second order polynomial with interactions between the parameters as shown by Equation 1.

$$E = c_0 + c_1B^2 + c_2B + c_3P^2 + c_4P + c_5T^2 + c_6T + c_7BP + c_8BT + c_9BT \tag{1}$$

- B : Binder content
- P : Polymer content
- T : Production temperature
- c_i : Coefficients to determine (i=1...9).

EXPERIMENTATION

Materials: The tested material is a modified bituminous concrete. It is composed of aggregates supplied from Keddara quarry in Boumerdes, Algeria, bitumen with a penetration grade of 40/50 and PR Plast Sahara in the form of 0/2mm polyolefines granules pre-stuffed with bitumen whose role is to improve the stiffness modulus and resistance to rutting.

Samples preparation: Weight percentages of each aggregate fraction used in the samples making are listed in the following table:

Table 2
Fractions Weight Percentages

Fraction (mm)	Weight percentage
---------------	-------------------

8\15	33%
3\8	25%
0\3	42%

The grading curve of the bitumen concrete used in this study is given in figure 2.

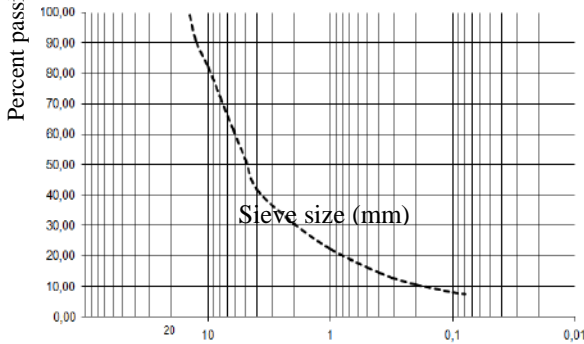


Figure 2
Aggregates grading curve

The specimens for testing are cylindrical samples of diameter 100 mm and thickness of 65 mm on average. They were made for binder contents, additive and different temperatures depending on the experimental design.

Characterisation: The stiffness modulus is determined by the Nottingham Asphalt Tester which is an indirect tensile test. This device uses cylindrical samples taken from the pavement by coring, or prepared in the laboratory. These samples are repeatedly subjected to a vertical compression load causing a measured horizontal deformation from which the stiffness modulus is calculated.

RESULTS AND INTERPRETATIONS

The trials results are shown in table 3

Table 3
Experimental Design and Test Results

Trial	Binder content	Polymer content	Production Temperature	Stiffness Modulus
1	4.5%	0.2%	180° C	7891
2	6.5%	0.2%	180° C	4431
3	4.5%	0.8%	180° C	6036
4	6.5%	0.8%	180° C	6380
5	4.5%	0.5%	170° C	5840
6	4.5%	0.5%	190° C	6434

7	6.5%	0.5%	170° C	7138
8	6.5%	0.5%	190° C	6687
9	5.5%	0.2%	190° C	7583
10	5.5%	0.8%	170° C	10538
11	5.5%	0.2%	170° C	6875
12	5.5%	0.8%	190° C	6450
13	5.5%	0.5%	180° C	8990
14	5.5%	0.5%	180° C	8591
15	5.5%	0.5%	180° C	8326

For each trial, three specimens were manufactured to determine the average of the results. Using this plan allowed the establishment of the model after 45 trials instead of 81 (45% less specimens).

Model determination: The model coefficients were calculated using the polynomial regression method. Equation 1 becomes:

$$M=8635 - 1894L^2 - 195L - 557A^2 + 320A - 217T^2 - 404T + 950LA - 261LT - 1199AT \tag{2}$$

The highest coefficients correspond to the most influential parameters. In this case it is the binder content, the binder / additive interaction and the additive / temperature interaction.

The response surfaces for a fixed temperature value (figure 3) clearly show that the optimal binder content is 5.5%. For lower values of binding, the aggregates are not sufficiently coated, resulting in a low adhesion and a large void ratio. In addition, an excessive amount of binder is also a problem in limiting the contact forces between aggregates. This leads the bitumen matrix to ensure the resistance to deformation which depresses the asphalt mix stiffness. The effect of the polymer is highly dependent on the production temperature. Its stiffening proprieties diminish with the increasing of the temperature until producing the opposite effect by depressing the stiffness modulus.

The response surfaces for fixed binder content (Figure 4) show the interaction between the polymer content and the production temperature.

The maximum values of the stiffness modulus are achieved for high percentages of polymer content and low temperatures. It is therefore assumed that high temperatures have a negative impact on the polymer.

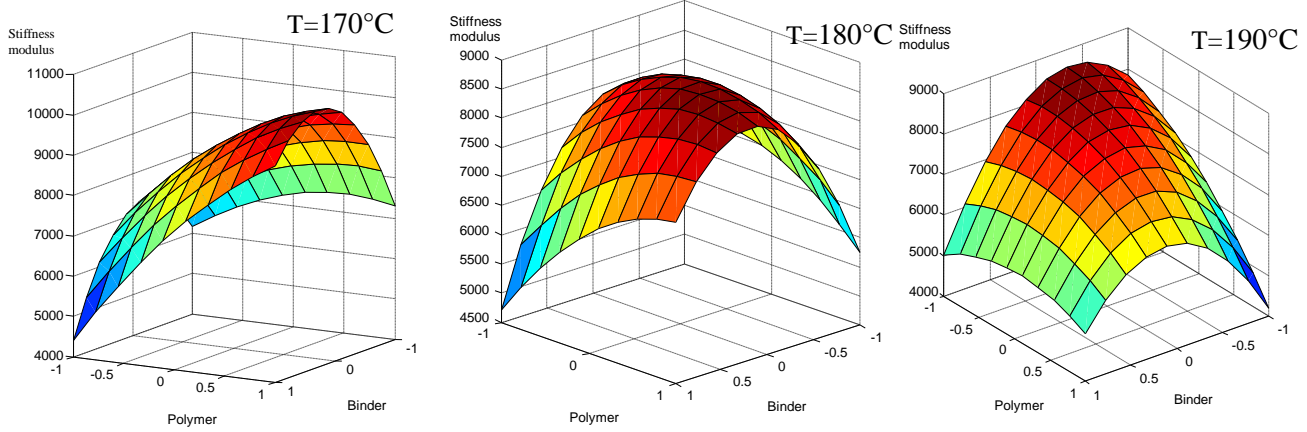


Figure 3
Response surfaces for different production temperatures

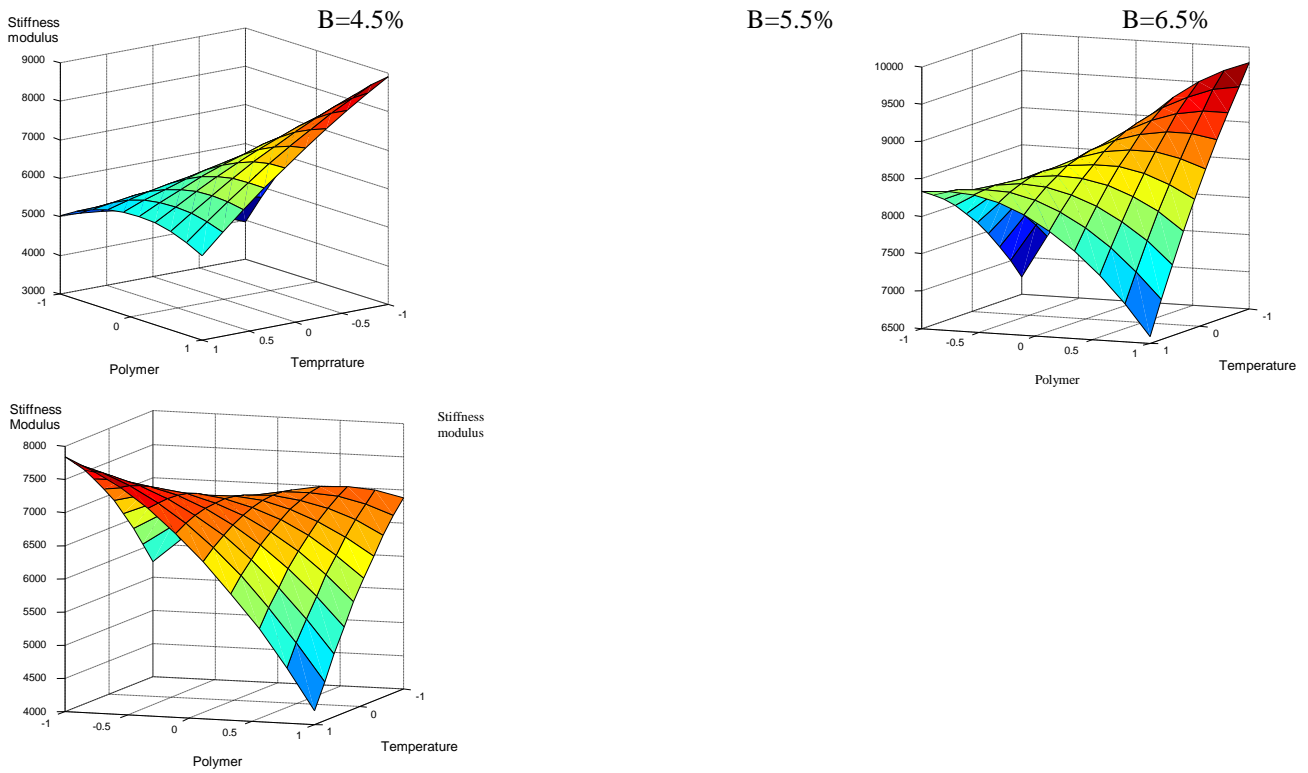


Figure 4
Response surfaces for different binder contents

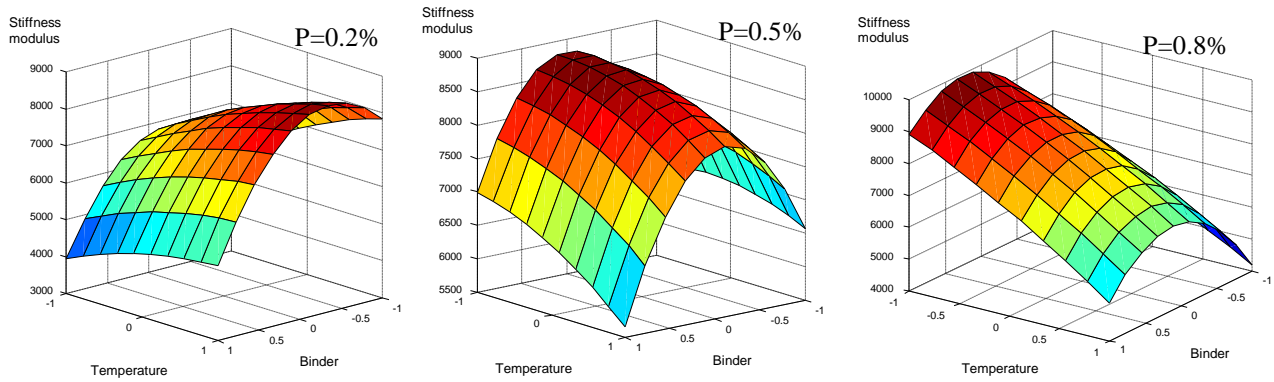


Figure 5
 Response surfaces for different polymer contents

- The optimal binder content is 5.5%.
- For high production temperature, the polymer has negative effect on the stiffness modulus.
- The highest values of stiffness modulus are achieved for high polymer content and low production temperature.

The response surfaces for fixed polymer content (Figure 5) express the interaction between the binder content and the production temperature. For the minimum value of polymer content, it is observed that this interaction is low because the temperature variation area stays below temperatures that could damage the bitumen. For larger polymer content, the temperature increase has a deleterious effect on the stiffness modulus of the mix. This is due to the discussed interaction between the polymer and the temperature.

CONCLUSIONS

This work was dedicated to the development of a mathematical model determining the stiffness modulus of a polymer modified asphalt, based on the most influential parameters namely binder content, polymer content and production temperature.

The using of an experimental design has reduced the number of trials needed by half, allowing saving in cost and time.

The resulting model has led to the following conclusions:

- The most influential parameters on the stiffness modulus of a polymer modified asphalt are the binder content, the binder / additive interaction and additive / temperature interaction.

REFERENCES

1. Lee, H. J., Lee, J. H., & Park, H. M., 2007. Performance evaluation of high modulus asphalt mixtures for long life asphalt pavements. *Construction and Building Materials*, 21(5), 1079-1087.
2. Cao, W., Liu, S., Li, Y., & Xue, Z., 2016. Rutting-Resistance Performance of SBS and Anti-Rutting Additive Composite-Modified Asphalt-Concrete Mixtures.
3. Huang, M., & Huang, W., 2016. Laboratory investigation on fatigue performance of modified asphalt concretes considering healing. *Construction and Building Materials*, 113, 68-76.
4. Radziszewski, P. 2007. Modified asphalt mixtures resistance to permanent deformations. *Journal of Civil Engineering and Management*, 13(4), 307-315.
5. Sargand, S. M., & Kim, S. S., 2001. Performance evaluation of polymer modified and unmodified Superpave mixes. In *2nd Int. Symp. on Maintenance and Rehabilitation of Pavements and Technological Control. Segundo Simposio Sobre Manutencao e Rehabilitacao de Pavimentos e Controle Tecnolologico* (No. 01-147).
6. Brovelli, C., Crispino, M., Pais, J., & Pereira, P., 2015. *Using polymers to improve the rutting resistance of asphalt concrete*. *Construction and Building Materials*, 77, 117-123.

7. Sengoz, B., & Isikyakar, G, 2008. Evaluation of the properties and microstructure of SBS and EVA polymer modified bitumen. *Construction and Building Materials*, 22(9), 1897-1905.
8. Kim, S., Sholar, G., Byron, T., & Kim, J, 2009. Performance of polymer-modified asphalt mixture with reclaimed asphalt pavement. *Transportation Research Record: Journal of the Transportation Research Board*, (2126), 109-114.
9. Liang, M., Liang, P., Fan, W., Qian, C., Xin, X., Shi, J., & Nan, G, 2015. Thermo-rheological behavior and compatibility of modified asphalt with various styrene-butadiene structures in SBS copolymers. *Materials & Design*, 88, 177-185.
10. Alataş, T., & Yilmaz, M, 2013. Effects of different polymers on mechanical properties of bituminous binders and hot mixtures. *Construction and Building Materials*, 42, 161-167.
11. Becker, Y., Mendez, M. P., & Rodriguez, Y, 2001. Polymer modified asphalt. In *Vision Tecnologica*.
12. Airey, G. D, 2004. Styrene butadiene styrene polymer modification of road bitumens. *Journal of Materials Science*, 39(3), 951-959.
13. Liang, M., Xin, X., Fan, W., Luo, H., Wang, X., & Xing, B. (2015). Investigation of the rheological properties and storage stability of CR/SBS modified asphalt. *Construction and Building Materials*, 74, 235-240.
14. Zhu, J., Birgisson, B., & Kringos, N, 2014. Polymer modification of bitumen: Advances and challenges. *European Polymer Journal*, 54, 18-38.
15. Goupy, J., & Creighton, L. 2006. *Introduction aux plans d'expériences-3ème édition-Livre*. Dunod.
16. Ferreira, S. C., et al. 2007. Box-Behnken design: An alternative for the optimization of analytical methods. *Analytica chimica acta*, 597(2), 179-186.
17. Harizi, I., Morsli, M., & Bensaibi, M, 2013. Laboratory Evaluation of the Stiffness Modulus of a Modified Bituminous Concrete with PR PLAST Sahara. *Journal of Civil Engineering and Architecture*, 7(2), 132.

EFFECT OF THE GLASS POWDER AND THE POLYPROPYLENE FIBERS ON THE CHARACTERISTICS OF HIGH-PERFORMANCE CONCRETES

M. Belkadi^{1,2(*)}, R. Chaid², A.Perrot³, A.Djeridi², N .Saoudi⁴

¹ Mohamed El Bachir El Ibrahimi University, Bordj Bouariridj – Algeria

²UR-MPE, M'Hamed Bougara University, Boumerdes – Algeria

³ UBS – LIMATB, Research Centre, Saint Maudé, BP 92116 56321 Lorient – France

⁴LRME, Mohand Oulhadj, Bouira University, Algeria

(*)E-mail: mouradlsilb@hotmail.fr

ABSTRACT

The Ultra-High Performances Fiber-Reinforced Concrete (UHPFC) come to answer in projects of the current events, that is their complexity of forms, implemented or speed, this material having exceptional mechanicals properties quality guaranteeing a high compactness and an optimal resistance. The present study investigates the properties of Ultra Performances Fiber-Reinforced concretes successful (UPFC), by the study of the incorporation effect of the glass powder on the physical, mechanical properties and the durability of concretes, as well as the influence of the various types of fibers reversed forecast the effect of Superplasticizer on the characteristics of the UPFC to the fresh and hardened state. The results of the tests show that the formulated UPFC with the contents of 0,5 and 1 % of the glass powder presents of better.

Key words : Concret, HUPFC, Superplasticizer, Glass powder, Durability.

INTRODUCTION

The development of concretes in high and in ultra-high performances (HPC and UHPC) is a topical subject, for the multiple advantages using these materials allows towards the structural and economic performances. knowing the reduction of the heterogeneousness, obtained by the improvement of the matrix quality, so as to increase the density by it and minimize the differences of rigidity and resistance with regard to the aggregates. Our study licence the formulation, the characterization of the UPFC, the action of both types of glass powder (transparent and

smoked) on the physical and mechanical properties. As well as the influence of incorporation of polypropylenes fibers.

MATERIALS

Cement : The class of cement used is CPJ CEMII 42,5N MATINE , with grinding finesse (SSB) about 3555 cm²/g. with addition of 18% of limestone coming from ACC of LAFARGE Algeria.

Physic-Mechanical characteristics of the cement used are in the table 1.

Table 1

Physico-mecanique characteristics of cement

<i>Physical characteristics</i>		<i>mechanical characteristics (MPa)</i>	
Beginig of setting	150 - 180 min	Compressive strenth	
End of setting	3 h 30 ~ 4 h 30	7days	36,74
Masse spécifique	3,1 g /cm ³	14days	41,07
Heat of hydratation	456,60 (j/g)	28days	45,07

Sand

We have used the sand dune (Oued Suf). After the granulometric analysis (fig 1) and

the measurement of fineness modulus table 2 (Mf = 2) , so we used Boussada sand (Mf = 0,95) to correct the finesse modulus.

Table 2
Characteristics of sands

Types of sands	Mv_{ap} (kg/m ³)	Mv_{ab} (g/cm ³)	ESP (%)	M_f
Sand dune	1 566	2,5	87,31	2
Sand Boussaâda	1 480	2.66	68	0.95

The Sand is siliceous

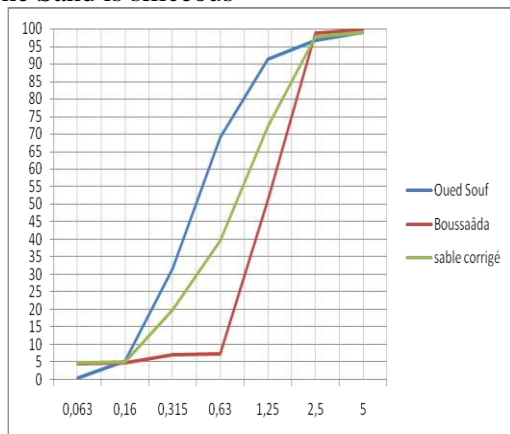


Figure 1

Granulometric analysis of sands

Table 3
Analysis of the glass powder made by X-ray fluorescence

Composants(%)	SiO ₂	Al ₂ O ₃	Fe ₂ O ₃	CaO	MgO	SO ₃	K ₂ O	Na ₂ O	P ₂ O ₅	TiO ₂	PAF
glass Tr	72,21	1,5	0,36	11,54	0,54	0,24	0,25	12,74	0,01	0,04	0,57
glass Sm	72,64	1,13	0,59	10,00	1,90	0,26	0,44	12,58	0,01	0,04	0,41

Table 4

Physical characteristics of *smoked* glass powder

Characteristic s	Mv_{ap} (kg/m ³)	Mv_{ab} (g/cm ³)	SSB (cm ² /g)	Activity pouzzolanique	Color
Glass powder	2330	2,63	4641	14g (Ca(OH) ₂ /g	White grisâtre

Different formulations were tested and characterized at fresh and hardened state, successive adjustment of the quantities of components, until obtaining the final formulation table 5.

superplasticizer : Viscocrete TEMPO 12 provided from group SIKA.

Brawn liquid clearly, PH : 6 ± 1 , Density : $1,06 \pm 0,01$, Cl : $\leq 1\%$. Na₂O E : $\leq 1\%$

Fibers : coming from SIKA and TEKNACHEM SIKAfiber: polypropylène with 12mm length and 34 μ m diameter.

FIBRETEK PP : polypropylène length : 18 mm

Glass powder : In this work we have used two type of glass, Transparent glass and Smoked glass, obtained after crushing collected fragments for 1 hour ,The physicochemical characteristics of the glass powder illustrated in table 3and 4,

Table 5
Formulations of UPFC with sand dunes

<i>Glass powder</i>	<i>Transparent glass powder</i>				<i>Smoked glass powder</i>			
% fiber	F 0,5%	F 1%	F 1,5%	F 2%	F 0,5%	F 1%	F 1,5%	F 2%
Cement (Kg)	800	800	800	800	800	800	800	800
Sand dune (Kg)	1065	1065	1065	1065	1065	1065	1065	1065
Glass Powder (Kg)	240	240	240	240	240	240	240	240
Water (l)	224	224	224	224	224	224	224	224
Fiber polypropylène (Kg)	4,5	9	13,5	18	4,5	9	13,5	18
Superplasticizer (Kg)	12	12	12	12	12	12	12	12
Masse volumique (kg/m ³)	2345,5	2350	2354,5	2359	2345,5	2350	2354,5	2359
W/C	0,28	0,28	0,28	0,28	0,28	0,28	0,28	0,28
% PV / C	30	30	30	30	30	30	30	30

The workability of concretes is appreciably improved by smoked glass in comparison to the transparent glass. The use of the Superplasticizer allows a stability of the maneuverability during one hour.

RESULTS AND CONCLUSION

The mechanical behavior of UHPFC (Ultra-High performance Fiber-Reinforced

Concrete) at the static charge was studied all in flexion strength (3 points) and in uniaxial compression on prismatic test cubes 40×40×160 mm.

Compressive Strength

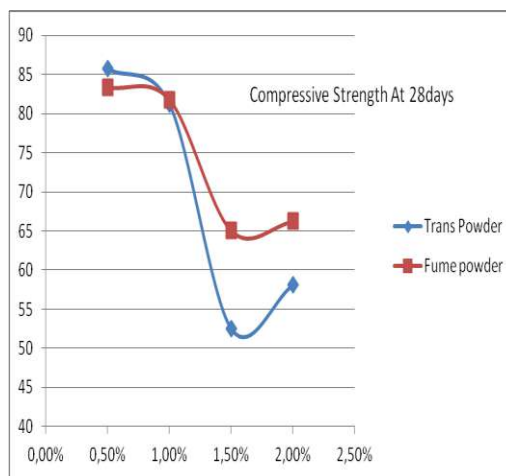
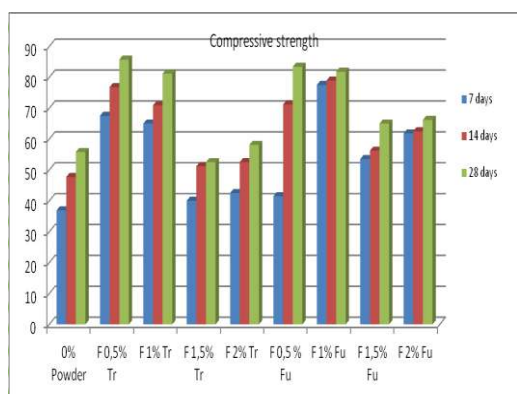


Figure 2 (a,b)
Compressive strength of glass powder (Transparent Tr and Smoked Sm)

The first remarks from graph (Fig 2) shows that;

- The compressive strength resistance varies between 52,5MPa to 85,7 MPa.
- The Powder have physical and chemical roles [7].
- The interests resultants at 28 days of compressive resistance are (0,5% and 1%) for Transparent Glass Powder Tr, and for Smoked Glass Powder Sm:
- the smoked glass powder is important in comparison to the transparent powder.

Flexion Strength

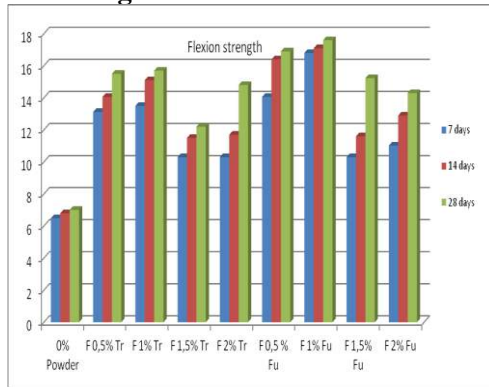


Figure 3 Flexion strength of glass powder (transparent Tr and smoked Sm) [MPa]

The smoked glass powder percentage are very important at 28 days , all them are better than the transparent powder

The percentage interesting for the two type of glass is 1% even for fume and transparent.

Sound Auscultation

The measurement permit to characterize the physical homogeneity of concrete, and to locate the defects.

Table 6
Results of sound auscultation

	0% powder	F 0,5% Tr	F 1% Tr	F 1,5% Tr	F 2% Tr	F 0,5 % Sm	F 1% Sm	F 1,5% Sm	F 2% Sm
V (m/s)	4685	5058	4868	4972	4868	5029	5117	4937	5080
T (μ s)	74,7	69,4	71,9	70,4	71,9	69,6	68,4	70,9	68,9

All the Glass powder improve the homogeneity of concrete compare it to ordinary concrete

CONCLUSION

The workability is improved in concrete with smoked glass powder better then transparent powder.

mechanical Characteristics behavior increased with addition off the glass powder (transparent and smoked)

The acoustics properties improved with glass powder, confirm their quality and homogeneity.

Finally, valorization of the waste even the glass powder is important to preserve our environnement. en substitution 30% of cement in weight with waste glass, in an economic and environnemental contribution, because of reduction of CO₂ let out by commentary.

REFERENCES

- [1] The French Standards (AFNOR) (French National Organization for Standardization).
- [2] Taфраoui Ahmed " Contribution to the valuation of the sand of dune of the western erg (Algeria). Application in new concretes " Doctoral thesis University of Toulouse, France.
- [3] Richard P., Cheyrezy M, Mars-April 1995, Concretes of Reactive Powders, Annals of the ITBTP, n°532, puts into series Concrete 320 pp. 85-102.
- [4] French association, of Civil engineering, AFGC (Recommendation AFGC).
- [5] Behloul M in March-April, 1995, Definition of a law of behavior of the BPR. Annals of the ITBTP, no.532, p. 122-127.

THE TOTAL REPLACEMENT EFFECT OF LIMESTONE POWDER BY MARBLE POWDER ON THE FREEZE-THAW RESISTANCE OF THE SELF-COMPACTING CONCRETE.

S. Bensalem^{1,2(*)}, C. Amouri¹, H. Houari¹, M. Belachia², A. Belkadi¹

¹ Laboratory Materials and Durability of Constructions, University of Mentouri, Constantine, Algeria.

² Laboratory of Materials, Geotechnics, Habitat and Urban, University of 20 Août 1955, Skikda, Algeria

*Corresponding author: Fax: + 213 31 81 89 67 Email: Bensalem.sara2@gmail.com

ABSTRACT

This paper aims to study the behavior of self-compacting concrete under freeze and thaw cycles, mainly the effect of the total replacement of limestone powder by marble powder on the performance of SCC.

The mixtures were subjected to freeze/thaw test according to ASTM C 666 Procedure B, air freezing and water thawing. The test methods used to evaluate durability were weight change, length change, compressive and tensile strength loss.

The results show that the total replacement of limestone powder by marble powder has a positive effect on the freeze-thaw resistance of self-compacting concrete.

Key words:

INTRODUCTION

Since its invention, the self-compacting concrete has revolutionized the field of construction; its use provides a multitude of benefits [1]. The mineral admixtures have greatly confirmed their use and provide an improvement of its mechanical properties and durability. Recently, marble powder is used as an admixture in the self-compacting concrete in alternative to limestone fillers and other costly mineral admixtures [1-5]. Some authors have found that the addition of about 20% of marble powder gives a decrease in density while improving the flowability and the compressive strength [1][5]. Currently many studies are interested in durability in particularly aggressive environments.

The studies deal with the sustainability of SCC based on marble powder has been relatively few. The data from the literature in this area and specially that concern their resistance to freeze - thaw are rare.

This paper is a contribution of our experimental research on marble powder in field of sustainable self-compacting concrete in aggressive environments such as freeze-thaw cycles.

This work aims to study the behavior of self-compacting concrete under freeze and thaw cycles, mainly the effect of the total replacement of limestone powder by marble powder on the performance of SCC.

The mixtures were subjected to freeze/thaw test according to ASTM C 666 Procedure B, air freezing and water thawing. The test methods used to evaluate

durability were weight change, length change, compressive and tensile strength loss.

MATERIALS AND MIXTURES

Materials: In production of SCC, Portland Cement CEM II/42.5, a sand 0/3 mm, coarse calcareous aggregate 3/8 mm and 8/15 mm, were used. Besides, limestone powder (LP) and marble powder (MP) were used. The properties of cement and by-products used in this study are presented in Table 1.

Table 1.

The characteristics of cement and by-products used.

Component (%)	Cement	LP	MP
SiO ₂	27.83	0.06	0.15
Fe ₂ O ₃	3.12	0.02	0.04
Al ₂ O ₃	6.21	0.09	0.08
CaO	57.22	51.97	54.86
MgO	0.94	0.01	1.03
SO ₃	2.02	0.01	0.07
Specific gravity	3.15	2.7	2.75
Blaine (cm ² /g)	3891	3900	3500

A superplasticizer high range water reducing admixture (HRWRA) based on modified polycarboxylic ether (Conforms with the standard EN 934) was also used. Tap water used was obtained from the laboratory for the production of concrete mixtures.

Mixture proportions: The design method used is the Chinese method developed by Nan Su et al [7].

Table 2 presents the composition and labeling of the SCC mixture.

Table 2
The composition of SCC in 1m³.

Materials (kg/m ³)	SCC MP	SCC LP
Cement CPJ 42.5	410	410
Sand 0/3	850	850
Gravel 3/8	298	298
Gravel 8/15	428	428
SP	9.72	9.72
Water	204	204
MP	130	-
LP	-	130
W/C	0.50	0.50

The quality of fresh SCCs was verified according to tests recommended by the EFNARC European recommendations [8].

All the Mixtures properly meet the required specifications for such concrete. Concerning the mechanical proprieties, the total replacement of limestone powder by marble powder gives satisfactory results.

Test procedure: After demolding, the specimens were kept in water, at a temperature of about 23 ± 2%, until testing.

Freezing and thawing was performed according to ASTM C 666 “Standard Test Method for Resistance of Concrete to Rapid Freezing and Thawing, procedure B – rapid freezing in air and thawing in water.”[9] the closest to our local winter conditions.

After 14 day curing, the specimens were subjected to 30 moderated freeze/thaw cycles in an F/T chamber where temperatures ranged from + 20°C to -18°C with a constant speed for all mixtures. The weigh change, length change, cubic compressive strength (70×70×70 mm) and flexural tensile strength (70×70×280 mm) were recorded at 10, 20 and 30 cycles.

RESULTS AND DISCUSSION

Weight change: Weight changes of SCC specimens after different cycles of freeze-thaw are presented in Figure 1.

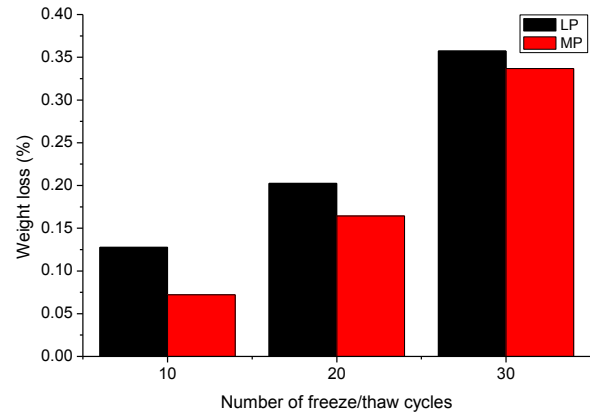


Figure 1
Weight changes of SCC specimens after different cycles of freeze-thaw.

The specimen's weight after 30 freeze-thaw cycles did not show a dramatic reduction. The weight change during the freeze-thaw cycles is due to water movement in and out of the specimen and cracking. As seen in Figure 1, all the specimens cured in water undergo a weight loss of 0.34% and 0.37% for MP and LP specimens respectively.

Length changes: Length changes of SCC specimens after different cycles of freeze-thaw are represented in Figure 2. All mixtures undergo lengthening in freeze thaw testing, if we refers to the criterion defined by ASTM C 666, all carried concrete resistant to freeze thaw i.e. the lengthening is less than 500 µm/m.

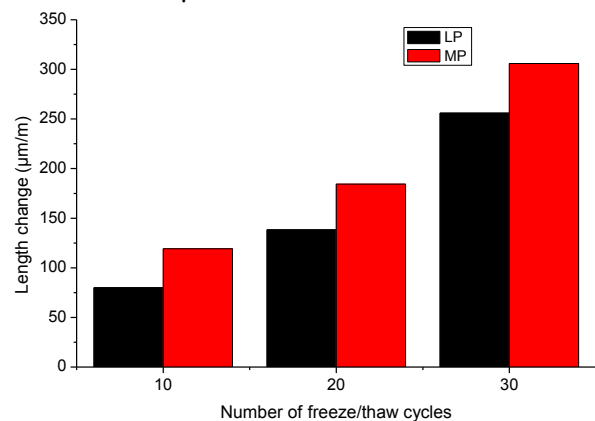


Figure 2
Length changes of SCC specimens after different cycles of freeze-thaw.

The results show that the samples take up relatively high amount of water and the dilation measurements indicate that the sample expanding. From the Figure 2 we noticed that the length change is more

important for the MP specimens compared to LP specimens, which act as a control concrete.

Compressive strength loss: Cubic compressive strength loss of SCC subjected to freeze-thaw cycles are represented in Figure 3. A continues compressive strength loss was recorded for all SCC mixtures but with different degrees, if we refers to the strength criterion defined by PN-88/B-06250 standard, all carried concrete resistant to freeze thaw i.e. the strength loss is less than 20%.

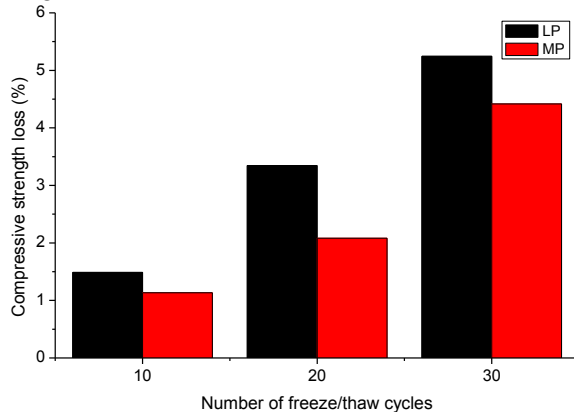


Figure 3

Cubic compressive strength loss of SCC subjected to freeze-thaw cycles.

As seen in Figure 3, all SCCs had lost strength in cycling. The highest compressive strength loss is around 5.24% for LP samples. This result is consistent with Xie et al. [10]. This loss is related to the water absorption of the samples. Micro-cracks mainly exist at cement paste-aggregate interfaces within concrete even prior to any loading and environmental effects. When the number of freeze-thaw cycles increases the degree of saturation in pore structures increases by sucking in water near the concrete surface during the thawing process at temperatures above 0°C. Some of the pore structures are filled fully with water. Below the freezing point of those pores, the volume increase of ice causes tension in the surrounding concrete. If the tensile stress exceeds the tensile strength of concrete, micro-cracks occur. By continuing freeze-thaw cycles, more water can penetrate the existing cracks during thawing, causing higher expansion and more cracks during freezing. The load carrying area will decrease with the initiation and growth of every new crack. Necessarily the compressive strength will decrease with freeze-thaw cycles [11-13].

Flexural tensile strength loss: Flexural tensile strength loss of SCC subjected to freeze-thaw cycles are represented in Figure 4. It can be seen that in general the specimens matured in water are more sensitive to freeze thaw action than the specimens matured in ambient temperature.

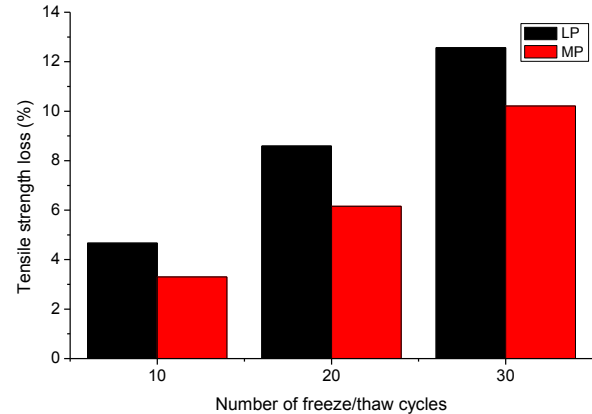


Figure 4

Flexural tensile strength loss of SCC subjected to freeze-thaw cycles.

As seen in Figure 4, the tensile strength decreased sharply under the action of freeze-thaw cycles; it gave about a 12.6% and 10.2% decrease over the initial tensile strength after 30 cycles of freeze-thaw for LP and MP specimens respectively.

Further, it can be seen that after the same cycles number, the tensile strength loss is larger than the cubic compressive strength loss. The reason is as follows: when the specimen is under the action of compressive loads, the cracks are caused in the action parallel to the compressive load. It means the damage is caused by the concentration of tensile stress vertical to the compressive load. So the influence of freeze-thaw cycles on tensile strength is larger than the compressive strength [14].

CONCLUSION

This study focuses on assessing the impact of limestone powder total replacement by marble powder on self-compacting concrete performance subjected to moderate freeze-thaw cycles according to ASTM C 666 standard by adapting the test roughness to Algerian context using a small number of cycles and without salt deicer. Based on the performed experiments, the following conclusions can be drawn:

SCC based on marble powder present characteristics very comparable with those of SCC mixture with limestone powder.

The loss of compressive strength and tensile strength after the action of freeze-thaw cycles was evident. However, it can be stated that the freeze-thaw cycles negatively influenced the value of the flexural tensile strength.

REFERENCES

1. Uysal, M., Yilmaz K., 2011. Effect of mineral admixtures on properties of self-compacting concrete. *Cement & Concrete Composites*, 33, 771–776.
2. Bensalem, S., Amouri, C., A., Houari, H., Belachia. M., 2014. Elaboration and characterization of self-compacting concrete based on local by-products. *International Journal of Engineering, Science and Technology*, Vol. 6, No. 1, 98-105.
3. Gesoglu, M., Güneyisi, E., Kocabag, MÖE., Bayram, V., Mermerdas, K., 2012. Fresh and hardened characteristics of self compacting concretes made with combined use of marble powder, limestone filler, and fly ash. *Construction and Building Materials*, 37, 160–170.
4. Topcu, I.B., Bilir, T., and Uygunoglu, T., 2009. Effect of waste marble dust content as filler on properties of self-compacting concrete. *Construction and Building Materials*, 23 , 1947–1953.
5. Boukhelkhal, A., 2012. Rhéologie caractérisation physico mécanique et durabilité des bétons autoplaçants à base de la poudre de marbre poudre de marbre. *Magister thesis*, University of Ammar Telidji, Laghouat.
6. Amouri, C., Bensalem, S., Belkadi, A., Houari, H., Belachia. M., 2014. Evaluation of the performances of self-compacting concretes based on byproducts subject to freeze thaw in local conditions. *International Journal of Engineering, Science and Technology*, Vol. 6, No. 4, 45-51.
7. Nan Su, Kung-Chung Hsu, His-Wen Chai., 2001. A simple mix design method for self-compacting concrete. *Cement and Concrete Research*, 31, 1799–1807.
8. EFNARC., 2002. Specification and guidelines for self-compacting concrete. UK: EFNARC.
9. American Society for Testing and Materials, ASTM C 666, 1997. Standard Test Method for Resistance of Concrete to Rapid Freezing and Thawing. *ASTM International*, West Conshohocken, PA, USA.
10. Xie Y, Liu B, Yin J, Zhou S., 2002. Optimum mix parameters of high strength self-compacting concrete with ultra-pulverized fly ash. *Cement & Concrete Research*, 32, 477–80.
11. Shang, H.S., Song, Y.P., Qin, L.K., 2008. Experimental study on strength and deformation of plain concrete under triaxial compression after freeze-thaw cycles. *Building and Environment*, 43, 1197-1204.
12. Gencil O, Brostow W, Ozel C, Filiz M., 2010. Concretes containing hematite for use as shielding barriers. *Materials Science-Medziagotyra*, 6 (3), 249-256.
13. Gencil Osman, Cengiz Ozel, Fuat Koksai, Ertugrul Erdogmus, Gonzalo Martínez-Barrera, Witold Brostow., 2012. Properties of concrete paving blocks made with waste marble. *Journal of Cleaner Production*, 21, 62-70.
14. Huai-Shuai Shang, Ting-Hua Yi, Yu-Pu Song, 2012. Behavior of Plain Concrete of a High Water-Cement Ratio after Freeze-Thaw Cycles. *Materials*, 5, 1698-1707.

EFFECT OF SAND TYPE ON PERFORMANCES OF SELF-COMPACTING CONCRETE

Lakhdar Azzouz^a, Benchaa Benabed^a, El-Hadj Kadri^b, Said Kenaic

^a Civil Engineering Laboratory, University of Laghouat, Algeria

^b Laboratory L2MGC, University of Cergy-Pontoise, France

^c Geomaterials Laboratory, University of Blida, Algeria

Corresponding author: +213 29145847 Email: l.azzouz@lagh-univ.dz

ABSTRACT

Self-compacting concretes (SCC) are known to be very fluid concretes, homogeneous, that take place by the only mean of gravity without segregation and bleeding. Higher cement and fines content is needed in SCC to increase their flowability and stability. The use of sands rich in fines may be a cost effective alternative source of filler. These sands may also improve the performance and cost effectiveness of SCC. It should be noted that no detailed investigation has been done to study the effect of type and quality of sand on the rheological and mechanical properties of SCC. Hence, the main objective of this research work is to examine the influence of various types of sand with different morphologies and origins on the fresh and hardened properties of SCC. Various types of sand were used: crushed sand (CS), river sand (RS), dune sand (DS) and a mixture binary or ternary of these sands. The mixture proportions were based on Okamura's method, with improvements made on the methods of selecting the sand–mortar (S/M) ratio and the superplasticizer content. For all mixtures the sand/mortar and water/cement ratios were kept constant. The experimental results indicate that the rheological and mechanical performances of mortars and concretes improve with mixtures of crushed and river sands but decrease with mixtures of crushed and dune sands especially for higher dune sand content. This effect was also observed with mortar and concrete containing ternary sands

Keywords: crushed sand, river sand, dune sand, rheology, mechanical strength

INTRODUCTION

Self-compacting concrete (SCC) is a new generation of concrete that fits well with the current state of development of the structures facing a labor less qualified. This range of concrete is characterized by a high workability and a high deformability, while being stable and ensures durable structures. The SCC can be implemented without vibration, through confined areas only under the effect of gravity, while developing good compactness without requiring skilled labor during the consolidation. These properties contribute to a sustainable concrete quality. Depending on the density and complexity of the reinforcement of structural elements, the need for vibration can decrease significantly and even be eliminated, which is a labor-intensive economy [1-2]. SCC is characterized, in general, by a formulation containing various chemical and mineral additives in precise proportions to meet the requirements of the specifications for workability and stability. The incorporation of supplementary cementitious materials improves the rheological, physical, mechanical and durability properties of SCC [3-4]. For example, the limestone fillers are generally used to increase the amount of powder in the composition of SCC [5]. In the production of crushed sand, there is a significant proportion of fines in the sand, this proportion of fines is

approximately 10-15% of the total weight of crushed sand. The use of sands rich in fines may be regarded as an alternative source of fillers. These sands enhance the cost of SCC by reduction of the high demand for fillers on the one hand, and secondly obtaining a SCC with good physical and mechanical properties of BAP such as permeability, absorption and strength [6-17]

Moreover, the abundance of fine sand dunes, particularly in Sahara desert of Algeria, the idea of promoting its value in the manufacturing of concrete represents a great economic importance. With the depletion of aggregate resources in Algeria and the high cost of transportation, it becomes economic and environmental interest that could present the valuation of abundant local sands such as crushed sand and dunes sand for manufacturing of concretes. It is in this context that the present work is part and it aims to use different types of sand for the manufacturing of SCC. In this regard, three types of sand with different origin and morphology are used; crushed sand, dune sand and river sand. Binary and ternary mixtures of these sands were also used in this study. Hence, the main objective of this study is to provide more information about the effects of various types of sand on fresh and hardened properties of self-compacting concrete.

Tests used to characterize the rheological and mechanical properties of mortars include: slump

flow, flow time, L-box test, segregation test and compressive strength.

MATERIALS AND TESTS

Materials: The cement used in the present study was a CEM I 42.5. The chemical and physical properties of cement are given in Table 1. A polycarboxylic-ether type superplasticizer (SP) with a specific gravity of 1.07 and a solid content of 30% was used.

Continuously graded coarse aggregates (CA) (3/8 and 8/15 mm) were used in this study with a specific gravity and water absorption of 2.7% and 2.52% respectively. Various types of sand were used: crushed sand (CS), river sand (RS), dune sand (DS) and a mixture of these sands. The physical properties and sieve analysis results of these sands are given in Table 2 and Figure 1 respectively.

Mixture proportions: SCC mixes were made, which had total cement content of 475 kg/m³ for. Coarse aggregates content was maintained at 31% by volume of cement for concrete and fine aggregates content at 50% by volume of mortar in concrete. The W/P was fixed at 0.4 by weight with air-content being assumed to be 1%.

SCC mixes were prepared with different types of sand: crushed sand, river sand, dune sand and binary or ternary sands. The SCC mixture proportions are summarized in Table 3.

Table 1. Chemical and physical properties of cement

Chemical component	(%)
SiO ₂	21.7
CaO	65.7
MgO	0.7
Al ₂ O ₃	5.2
Fe ₂ O ₃	2.7
SO ₃	0.6
MnO	-
K ₂ O	0.4
TiO ₂	-
Na ₂ O	0.7
Cl	0.01
Loss of Ignition	0.3
Physical properties	
Specific density	3.15
Fineness (m ² /kg)	300
Compressive strength at 28 days (MPa)	44

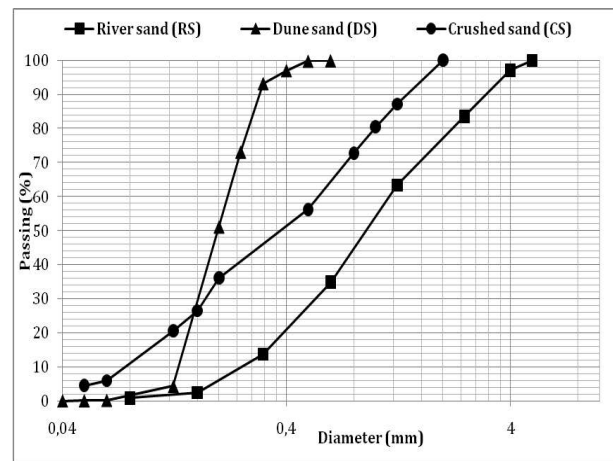


Figure 1. Particle size distributions of different sands

Mixing procedure: The mixing procedure and time are very important, thus the mixing process was kept constant for all concrete mixtures. The batching sequence consisted of homogenizing the powder and aggregates for 30 s in a rotary planetary mixer, then adding 70% of water and mixed for 1 min. Thereafter remaining water (30%) with SP was introduced, and the concrete was mixed for 5 min, then the mixing was stopped for 2 min and again the concrete was further mixed for 30 sec before it was discharged from the mixer

Table 2. Physical properties of the investigated sands

Properties	Sand type		
	CS	RS	DS
Specific gravity	2.68	2.67	2.65
Unit weight (kg/m ³)	1541	1758	1520
Fineness modulus	2.21	2.45	0.78
Sand equivalent (%)	71	87	83

Concrete testing : In this investigation the filling ability was evaluated by slump flow and V-funnel tests for SCC [8]. The passing ability was measured by L-Box tests [8]. The resistance to segregation was measured by GTM sieve stability test.

For compressive strength tests, from each concrete mixture three prisms of 70x70x280 mm were cast. Specimens were left covered with a plastic sheet. After removal from moulds, at 24 h of age, concrete specimens were immersed in water saturated with lime at 20 °C until the age of testing. The compression test was conducted at the age of 28 according to NFP 15-451 on the half samples obtained after the flexural test.

Table 3. SCC mixture proportions

Mix N°	Cement (kg/m ³)	CS (%)	CS (kg/m ³)	RS (%)	RS (kg/m ³)	DS (%)	DS (kg/m ³)	CA (kg/m ³)	SP (kg/m ³)	Water (kg/m ³)
SCC1	475	100	886	0	0	0	0	830	2.9	190
SCC2	475	75	665	25	222	0	0	830	2.9	190
SCC3	475	50	443	50	443	0	0	830	2.9	190
SCC4	475	25	222	75	665	0	0	830	2.9	190
SCC5	475	75	665	0	0	25	222	830	2.9	190
SCC6	475	50	443	0	0	50	443	830	2.9	190
SCC7	475	25	222	0	0	75	665	830	2.9	190
SCC8	475	0	0	0	0	100	886	830	7.1	190
SCC9	475	0	0	100	886	0	0	830	4.2	190
SCC10	475	0	0	75	665	25	222	830	4.2	190
SCC11	475	0	0	50	443	50	443	830	4.2	190
SCC12	475	0	0	25	222	75	665	830	4.2	190
SCC13	475	50	443	25	222	25	222	830	2.9	190
SCC14	475	25	222	50	443	25	222	830	2.9	190
SCC15	475	25	222	25	222	50	443	830	2.9	190

RESULTS AND DISCUSSION

Slump flow test: The results of slump flow are presented in Figure 2. We note that the slump flow values of SCC: 3, 4, 8, 9, 10, and 13 are in the range of SF3 class (760-850 mm). Whereas SCC: 1, 2, 5, 6, 7 and 11 are in the range of the SF2 class (660-750 mm) defined by the AFGC recommendations [9]. We note an increase in the slump flow of SCC with mixture sand of river and crushed sand, this increase becomes very important when the percentage of river sand exceeds 50%. As against a decrease in slump flow was observed in SCC with mixture sand of crushed and dune sand or river and sand dune, this decrease also becomes very important when the sand dune percentage is very high. Therefore, the addition of dune sand up to 25% improves the slump flow of SCC. Beyond this content of dune sand, the slump spread decreases and does not meet the criteria for self-compacting concrete and behaves like an ordinary concrete. From this, we can conclude that the river sand has a beneficial effect on the slump spread, unlike the dune sand which reduces remarkably the slump spread of SCC.

V-funnel flow time: The results of variation of the flow time using the V-Funnel test are shown in Figure 3. This test indicates the filling capacity of mixture. The test of the flow through the funnel in V is a way to evaluate the viscosity and resistance to segregation of concrete. From figure 3 it can be noted that the values of the flow time through V-funnel are included in the interval (6-12 sec) proposed by Domone [20-24]. The addition of sand dunes increases the flow time of SCC compared to river sand, but the recorded values of the flow time meet the recommendations of SCC production. One

can say that even with moderate dosages in sand dunes, the measured flow time shows that incorporation of dune sand increases the viscosity of SCC and this is due to the increase of the specific surface area of fine aggregate.

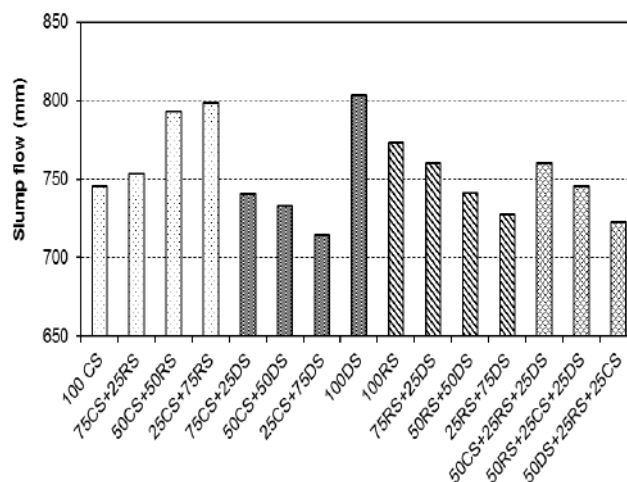


Figure 2. Slump flow of SCC with different types of sand

L-box test: The results of variation of H_2 / H_1 using L-box test are shown in Figure 4. It is seen that all results comply with the requirements of AFGC recommendations [19] ($H_2 / H_1 > 0.8$). We also notice a decrease in H_2 / H_1 in SCC with binary and ternary mixtures sands when the sand dune percentage is above 50%. The partial incorporation of sand dunes in the mixtures increases the filling capacity of SCC, and therefore the mobility of SCC in confined areas.

The use of binary and ternary mixtures sands improves the rheological properties of SCC. R'mili et al [21] have studied the effect of the incorporation of crushed sand and desert sand on properties of

self-compacting concrete. The results show that the ability to fill in L-box, is improved when the crushed sand is partially replaced by the desert sand.

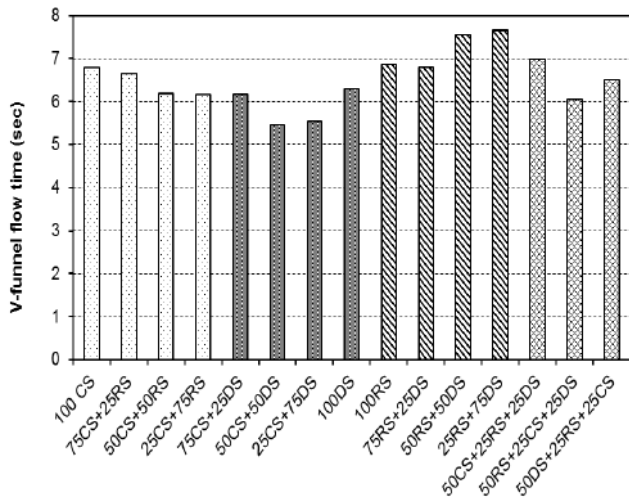


Figure 3. V-funnel flow time of SCC with different types of sand

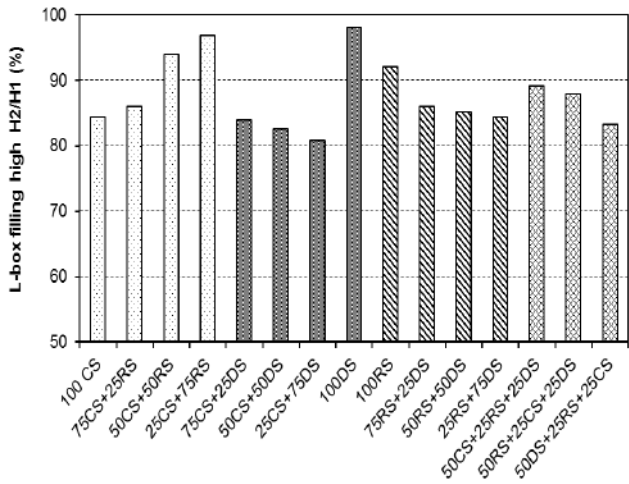


Figure 4. L-box filling high of SCC with different types of sand

Sieve stability test GTM: Sieve stability results are shown in Figure 5. It is noted that the percentages of milt passing through the sieve are between 6 and 15% according to recommendations ENFRAC [18], except for SCC: 7 8, 12 and 15, which are slightly above than the recommended values for SCC. This is due to high percentage of sand dune used in blends, since the latter has a fine particle size that passes through the sieve with the amount of milt. Generally, we can say that the results obtained show that all SCC have good resistance to segregation and bleeding. Further, visual examination of SCC reveals that they are homogeneous and stable. The use of calcareous sand with river or sand dune increases the volume of the paste and therefore improves the stability of the SCC.

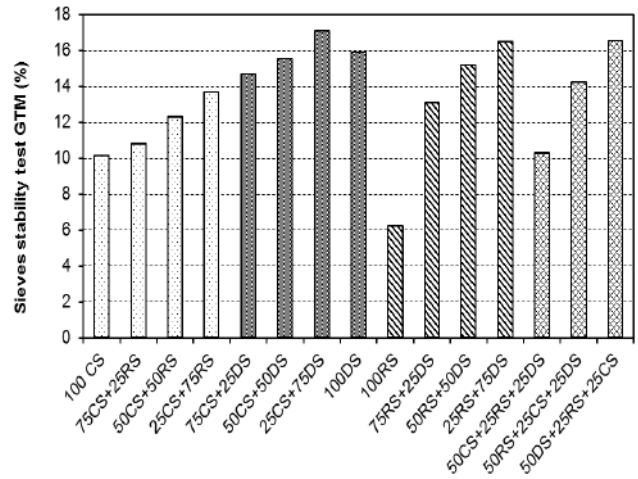


Figure 5. Sieve stability GTM of SCC with different types of sand

Compressive strength: Figure 6 shows the variation of the compressive strength of different SCC at 28 days. We note that the best strengths achieved after 28 days are obtained with SCC made with mixture sand of river and crushed sand. It is shown that the river sand has a beneficial effect on the compressive strength of SCC due to its continuous particle size. However, the strength gain for SCC containing crushed sand appears to be linked to the existence of limestone fines in sand. A reduction in the compressive strength was observed in SCC with binary and ternary mixtures of crushed-dune sand, river - dune sand and crushing- river - dune sand. This means that the dune sand decreases compressive strength of SCC due to its fine particle size and high porosity, which gives less compactness of SCC than those made with river and crushed sand

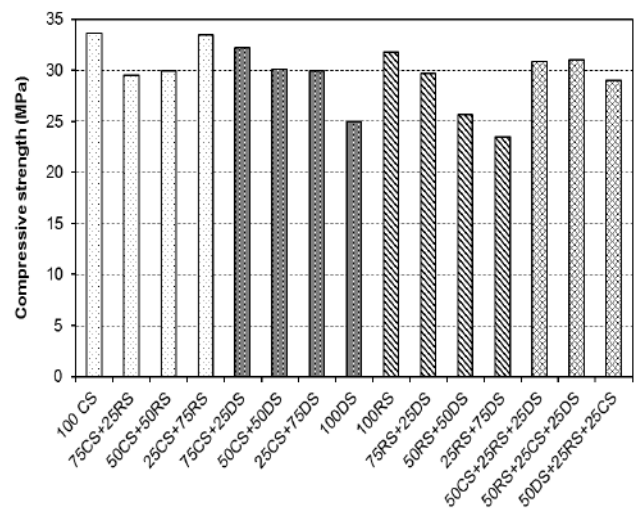


Figure 6. Compressive strength of SCC with different types of sand

CONCLUSION

The assessment of the behavior of SCC at fresh and hardened state leads to the following:

- The use of binary and ternary mixtures sands improves the rheological and mechanical properties of SCC.

- At different contents of river and crushed sand, the rheological and mechanical characteristics are met and comply with recommendations of the manufacturing of SCC. However, the use of high dosages of sand dunes reduces the rheological parameters of SCC. Therefore, to meet the self-compacting properties, additional amounts of water and superplasticizer are strongly required.

- The best strengths are obtained for SCC made with crushed and river sand. This is due to the good size distribution of these sands. The mechanical strengths decreased by adding a high content of dune sand but they reach acceptable values.

Based on the obtained results, it can be argued that the use of locally available materials in the manufacturing of concrete can be an economic and technological important alternative in some developing countries. The partial incorporation of the sand dune in the composition of self-compacting concrete can provide a solution for some work in the southern regions of the country where this material is very abundant. Moreover, crushed limestone sands are interesting alternative source to replace the river sand (rolled) for making any kind of concrete.

REFERENCES

- Okamura H., Ouchi M., Self-compacting concrete, development, present use and future, in: A. Skarendahl, O. Petersson (Eds.), *Self-Compacting Concrete*, RILEM Symposium Stockholm, RILEM Publications, 3-14 (1999).
- Okamura H., Ouchi M., Self-compacting concrete, *Journal of Advanced Concrete Technology*, 1: 5-15 (2003).
- Sonebi M., Medium strength self-compacting concrete containing fly ash: modeling using factorial experimental plans, *Cement and Concrete Research*, 34:1199-208 (2004).
- Sonebi M., Bartos P.J., Hardened SCC and its bond with reinforcement, In *Proceeding of First International RILEM Symposium on Self-Compacting Concrete (PRO 7)*, Stockholm, Sweden (1999).
- Uysal M., Yilmaz K., Ipek M., The effect of mineral admixtures on mechanical properties, chloride ion permeability and impermeability of self-compacting concrete, *Construction and Building Materials*, 27: 263-70, (2011).
- Felekoglu B., A comparative study on the performance of sands rich and poor in fines in self-compacting concrete, *Construction and Building Materials*, 22: 646-654 (2008).
- Bosiljkov V.B., SCC mixes with poorly graded aggregate and high volume of limestone filler, *Cement and Concrete Research*, 33:1279-1286 (2003).
- Ho DWS, Sheinn AMM, Ng CC, Tam CT. The use of quarry dust for SCC application, *Cement and Concrete Research*, 32: 505-511 (2002).
- Felekoglu B. Utilisation of high volumes of limestone quarry waste in concrete industry (SCC case), *Resources Conservation and Recycling*, 51: 770-791 (2007).
- Menadi B, Kenai S, Khatib J, Ait Mokhtar A. Strength and durability of concrete incorporating crushed limestone sand, *Construction and Building Materials*, 23: 625-33 (2009).
- Guimaraes MS, Valdeo JR, Palomino AM, Santamarina JC. Aggregate production: fines generation during rock crushing, *International Journal of Mineral Process*, 81: 237-47 (2007).
- Johansen K, Mortsell E, Lindgard J. Effect of adding natural fine sand rich in fines on the fresh concrete properties, *Nordic concrete Research Publications*, 22 (2000).
- Donza H, Cabrera O, Irrassar EF. High strength with different fine aggregate, *Cement and Concrete Research*, 32: 1755-1761 (2002).
- Johansen K, Busterud L. Low grade SCC with secondary natural sand rich in fine. In: Ozawa K, Ouchi M, editors, *Second International RILEM Symposium on SCC*, Japan, (2001).
- Topoçu IB, Ugurlu A. Effect of the use of mineral filler on the properties of concrete, *Cement and Concrete Research*, 33: 1071-1075 (2003).
- Topoçu IB. Effects of using crushed stone dust on concrete properties. In: *Tenth engineering symposium, Civil Engineering'99*, Suleyman Demirel University, Isparta, Turkey (1999).
- Okamura H, Maekawa K, Ozawa K. High performance concrete, 1st edition: Gihoudou Publication, Tokyo (1993).
- EFNARC, *Specification and Guidelines for Self-Compacting Concrete* (2002).
- AFGC, *Association française de Génie Civil, Bétons Autoplaçants: Recommandations provisoires, documents scientifiques et techniques*, (2002).
- Domone P.L., Jin J., Properties of mortar for Self-Compacting Concrete, *Proceedings of the 1st International Symposium on SCC*, , RILEM Proceedings PRO 7, Sweden (1999).
- R'mili A., Ben Oueddou M., Incorporation du sable de concassage et du sable de désert dans la composition des bétons autoplaçants, *Séminaire international, Innovation et Valorisation en génie civil et matériaux de construction*, N10-271, Rabat, Maroc, (2011).
- Tayeb Bouziani, Assessment of fresh properties and compressive strength of self-compacting concrete made with different sand types by mixture design modelling approach, *Construction and Building Materials*, 49: 308-314, (2013).
- Benchara Benabed, Lakhdar Azzouz, El-Hadj Kadri, Said Kenai & Akram Salah Eddine Belaidi, Effect of fine aggregate replacement with desert dune sand on fresh properties and strength of self-compacting mortars, *Journal of Adhesion Science and Technology*, Volume 28, Issue 21, 2182-2195, (2014).
- Benchara Benabed, El-Hadj Kadri, Lakhdar Azzouz, Said Kenai, Properties of self-compacting mortar made with various types of sand, *Cement and Concrete Composites*, 34, 1167-1173, (2012).

THERMO-MECHANICAL BEHAVIOR OF UNFIRED CLAY BRICKS AND FIRED CLAY BRICKS MADE FROM A MIXTURE OF CLAY AND LATERITE

Séckou BODIAN*¹, Mactar FAYE¹, Ndeye Awa SENE¹, Vincent SAMBOU², Oualid LIMAM³,
Jean E. AUBERT⁴, Harouna BAL¹

¹*Laboratoire d’Énergétique Appliquée (LEA), Université Cheikh Anta Diop, BP:5085 Dakar-Fann, Sénégal*

²*Centre International de Formation et de Recherche en Energies Renouvelables, Université Cheikh Anta Diop, BP 5085*

³*Laboratoire Génie Civil (LGC), Ecole Nationale d’Ingénieurs de Tunis, Université El Manar, Tunis-Tunisie*

⁴*Laboratoire Matériaux et Durabilité des Constructions (LMDC), Université Paul Sabatier, Toulouse-France*

*Corresponding author: Fax: +221 33 825 55 94 Email: bodianeckou@yahoo.fr

ABSTRACT

The objective of this paper is to determine the mechanical and thermal properties of unfired and fired clay bricks made from a mixture of clay and laterite. In this study, we first investigate the physical properties of the raw materials. Then, experiments were conducted with six compositions of clay bricks prepared by adding laterite to study the effect on mechanical and thermal properties. Our experiments demonstrate that for use as building material, clay brick with 30 % of laterite is the optimal mixture both for unfired and fired bricks.

Key words: Clay; Laterite; Unfired clay bricks; Fired clay bricks; Mechanical properties.

NOMENCLATURE

c	specific heat capacity (J.kg ⁻¹ .K ⁻¹)
e	thickness (m)
E	thermal effusivity (J.m ⁻² .K ⁻¹ .s ^{-1/2})
m	mass (g)
P	Laplace parameter
PI	plasticity index (%)
R _C	thermal contact resistance between the heating element and the sample (m ² .K.W ⁻¹)
W _{dried}	weight of the dried sample (g)
W _{fired}	weight of the fired sample (g)
W _L	liquidity limit (%)
W _P	plasticity limit (%)

Greek letters

Ψ	Quadratic error between experimental and theoretical curves
λ	thermal conductivity (W.m ⁻¹ .K ⁻¹)
ρ	density (kg.m ⁻³)
φ	heat flux density (W.m ⁻²)
Φ	Laplace transform of the heat flux density

θ Laplace transform of the temperature

Subscripts

exp	experimental
mod	model

INTRODUCTION

Population growth in Africa leads to uncontrolled urbanization. This has many consequences such as access to decent housing. To address this issue, many governments have opted for the construction of social housing.

A thorough analysis of the building sector shows that construction materials as concrete contribute significantly to the cost of construction. The high energy consumption and the pollution caused by the production of concrete materials as well as the low financial capability of population in developing countries push to find alternative construction materials. The clay and the laterite are often used as alternative materials because they are locally available.

There are several authors who are interested in these two materials [1-8]. In the literature, many

¹ LEA, Université Cheikh Anta Diop, Dakar, Sénégal BP:5085

works on physical and mechanical properties of laterite materials are presented [1-3]. Kasthurba et al. [1] have showed that the physical and mechanical properties of laterite are dependent on the location of the quarry as well as the depth of the quarry. Mbumbia et al. [2] have studied the effect of firing temperature on mechanical properties of lateritic soil bricks. The test results have revealed that the compressive strengths of fired lateritic soil bricks at a very low temperature 550°C are higher than those of the same bricks stabilized with lime or cement. The mixture of lateritic and cement for rural housing has analysed by Akinmusuru [3]. He has showed that the firing temperature significantly affects the crushing strength of the laterite-cement bricks.

Many studies have been published regarding the characterization of thermal proprieties of laterite based materials [4, 5]. Bal et al. [4] have studied the evolution of the thermal conductivity of laterite based bricks with millet waste additive. The authors have showed that adding millet waste may strongly decrease the thermal conductivity of the bricks. Sindanne et al. [5] have studied the thermal conductivity of laterite stabilized by cement, sawdust and lime. Results indicate that thermal conductivity increases when the percentage of cement and lime increases. However, it decreases when the rate of the sawdust increases.

With regard the works on clay bricks, some authors [6-8] have investigated the unfired clay bricks and other [9] the fired clay bricks. Among the authors who have worked on the unfired clay bricks, we can mention Oti et al. [6]. Indeed, Oti and co-authors have studied the physical and mechanical properties of unfired clay bricks stabilized by lime. The laboratory results demonstrate that the compressive strength, moisture content, water absorption rate, percentage of void, density and durability assessment are within the acceptable engineering standards for clay masonry units. Miqueleiz et al. [7] have investigated the alumina filler wastes and coal ash waste for unfired brick production. The laboratory results show that the compressive strength of the unfired bricks decreases when increasing the amount of waste. Mounir et al. [8] have investigated the thermal properties of clay by combining it with cork, using the asymmetrical hot plate and the flash methods. The authors have showed that the thermal conductivity of the clay with additives of cork is reduced relative to that of the sample without additive.

Many studies have been published concerning the fired clay bricks. Sutcu et al. [9] have studied the physical, thermal and mechanical properties of the fired clay bricks with waste marble powder addition as building materials. The authors have showed that the waste marble powder at certain ratios can be utilized to lighten and to make porous the body in production of fired clay bricks. Consequently, these bricks produced with addition of waste marble can be used as a heat insulation construction material.

The works presented above show that some authors have focused on laterite while others worked on the clay. Few authors, however, are interested in the mixture of clay and laterite. Ngon Ngon et al. [10] have studied the physical and mechanical properties of the lateritic and alluvial clayey mixtures of Yaoundé in view to manufacture of fired bricks for the fulfilment buildings. The results show that there is an optimal amount of alluvial clay material that should be added to lateritic clays Yaounde.

As shown in this literature review, there is little work on the clay laterite mixture. To our knowledge there is no study on the thermal and mechanical properties of unfired and fired bricks made with a mixture of clay and laterite.

The objective of this paper is to compare the thermomechanical properties of unfired and fired bricks made with a mixture of clay and laterite.

This paper begins with the presentation of materials and methods, in the second section the results and discussions are presented on the physical properties, the mechanical properties and the thermal properties.

MATERIALS AND METHODS

Raw materials

The study is carried out on a mixture of clay materials and laterite. These raw materials come from the region of Thiès (Sénégal).

Preparation of brick samples

Clay is used in the manufacture of bricks because it is a binding agent. However, it has large shrinkage characteristics upon drying. To reduce shrinkage the laterite is added. In this work, a series of experiments was made to measure the impact of adding laterite on thermophysical and mechanical properties of unfired and fired clay bricks. Six compositions of different percentage of laterite per weight were detailed in Tab 1.

Table 1
Composition of specimens.

Brick sample	B0	B10	B20	B30	B40	B50
Proportion of Laterite (%)	0	10	20	30	40	50

Figure 1a and Figure 1b show respectively the samples for mechanical test and for thermal test. The dimensions of sample for mechanical test are 16 cm x 4 cm x 4 cm and those for thermal test are 11 cm x 11 cm x 3.3 cm.

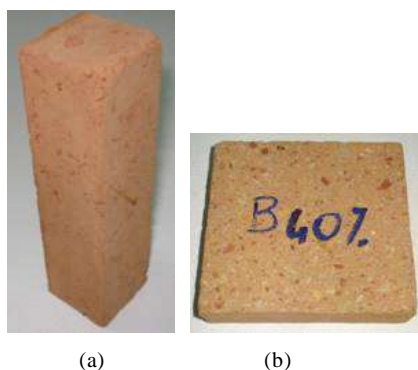


Figure 1

Clay bricks samples: (a) sample for mechanical test and (b) sample for thermal test.

The amount of water used to make the samples is determined by the equation:

$$m_{\text{water}} = W_{P(\text{Clay})} \times m_{\text{Clay}} + W_{P(\text{Laterite})} \times m_{\text{Laterite}} \quad (1)$$

Our study is focused on unfired and fired clay bricks. Firing is an essential step for improving the mechanical resistance of clay bricks. For firing bricks samples, we used an electric furnace whose maximum temperature is 1200 °C. The dried samples are fired about 1 h 37 min at 900 °C.

Physical tests

The physical properties of the raw materials as Atterberg limits and the density are first determined. Then, the linear shrinkage of unfired bricks is studied. The liquidity limit was measured by the method of the dish of Casagrande (W_L) and the

plasticity limit by the method of the roller (W_P). These measures were realized according to NF P94-051 standard [11]. The Atterberg limits were used to determine the plasticity index (PI) of the studied materials. Thus,

$$PI = W_L - W_P \quad (2)$$

where PI is the plasticity index; W_L is the liquidity limit and W_P represents the plasticity limit.

A pycnometer was used to determine the densities of the raw materials according to NF P94-054 standard [12].

The linear shrinkage was determined by measuring the length of the sample before and after drying. The linear shrinkage is expressed as a percentage and is calculated according to the following formula [13]:

$$\text{Linear shrinkage (\%)} = \frac{L_{\text{before drying}} - L_{\text{after drying}}}{L_{\text{before drying}}} \times 100 \quad (3)$$

where $L_{\text{before drying}}$ is the length of the sample before drying and $L_{\text{after drying}}$ is the length of the sample after drying.

Mechanical tests

The compressive strength of clay bricks is measured as described in NF EN 12390-3 [14]. For unfired clay bricks, tests are done after 28 days. The testing machine is presented in the Figure 2.



Figure 2

Machine testing compression-flexure 50 kN Class 1.

Thermal tests

Thermal conductivity and thermal effusivity are measured by the Asymmetric Hot Plate method which uses transient technique to study the heat conduction of samples [4]. The asymmetrical experimental device described in detail by Laaroussi et al. [15], is presented in Figure 3.

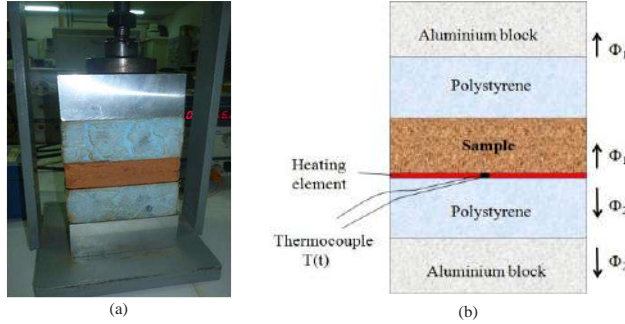


Figure 3

View (a) and schema (b) of the experimental hot plate device [4].

A plane heating element having the same section (10 cm x 10 cm) as the sample is placed under the sample. A thermocouple is stuck on the lower face of the heating element. This disposal is placed between two extruded polystyrene blocks with a thickness 5 cm set between two aluminum blocks with a thickness 4 cm. A heat flux step is sent into the heating element and the transient temperature $T(t)$ is recorded. Since the thermocouple is in contact with polystyrene that is a deformable material, the presence of the thermocouple does not increase the thermal contact resistance between the heating element and the polystyrene. Furthermore, since polystyrene is an insulating material, this thermal contact resistance will be neglected.

The theoretical model originates from the integral transform treatment of the heat equation [16] is modeled with the hypothesis that the heat transfer remains unidirectional 1D at the center of the sample during the experiment. The recording processing of $T(t)$ is realized by supposing that the heat transfer at the center of the heating element is 1D. Considering the very low value of the heat flux reaching the aluminum blocks through the polystyrene and their high thermal capacity, their temperatures are supposed equal and constant. Within these hypotheses, one can write:

$$\begin{bmatrix} \theta \\ \Phi_1 \end{bmatrix} = \begin{bmatrix} 1 & 0 \\ C_p & 1 \end{bmatrix} \begin{bmatrix} 1 & R_c \\ 0 & 1 \end{bmatrix} \begin{bmatrix} A_e & B_e \\ C_e & D_e \end{bmatrix} \begin{bmatrix} A_i & B_i \\ C_i & D_i \end{bmatrix} \begin{bmatrix} 0 \\ \Phi'_1 \end{bmatrix} = \begin{bmatrix} A & B \\ C & D \end{bmatrix} \begin{bmatrix} 0 \\ \Phi'_1 \end{bmatrix} \quad (4)$$

$$\begin{bmatrix} \theta \\ \Phi_2 \end{bmatrix} = \begin{bmatrix} A_i & B_i \\ C_i & D_i \end{bmatrix} \begin{bmatrix} 0 \\ \Phi'_2 \end{bmatrix} \quad (5)$$

with

$$\Phi_0 = \Phi_1 + \Phi_2 = \frac{\phi_0}{p} \quad (6)$$

θ is the Laplace transform of the temperature $T(t)$, Φ_1 the Laplace transform of the heat flux density leaving the heating element (upstream), Φ_2 the Laplace transform of the heat flux density leaving the heating element (downstream), Φ_0 the Laplace transform of the total heat flux density produced in the heating element, ϕ_0 the heat flux density produced in the heating element, R_c the thermal contact resistance between the heating element and the sample, Φ'_1 the Laplace transform of heat flux density input on the upper aluminum block, Φ'_2 is the Laplace transform of heat flux density input on the lower aluminum block. p is the Laplace parameter.

$$\begin{bmatrix} A_e & B_e \\ C_e & D_e \end{bmatrix} = \begin{bmatrix} \cosh(qe) & \frac{\sinh(qe)}{\lambda q S} \\ \lambda q S \sinh(qe) & \cosh(qe) \end{bmatrix} \quad \text{with } q = \frac{E}{\lambda} \sqrt{p} \quad (7)$$

$$\begin{bmatrix} A_i & B_i \\ C_i & D_i \end{bmatrix} = \begin{bmatrix} \cosh(q_i e_i) & \frac{\sinh(q_i e_i)}{\lambda_i q_i S} \\ \lambda_i q_i S \sinh(q_i e_i) & \cosh(q_i e_i) \end{bmatrix} \quad \text{with } q_i = \frac{E_i}{\lambda_i} \sqrt{p} \quad (8)$$

λ is the Sample thermal conductivity, e the Sample thickness, λ_i the Polystyrene thermal conductivity, e_i the Polystyrene thickness, E the sample thermal effusivity, E_i the Polystyrene thermal effusivity. The system leads to:

$$\theta(p) = \frac{\Phi_0(p)}{\frac{D}{B} + \frac{D_i}{B_i}} \quad (3)$$

The principle of the method is to estimate the value of the thermal effusivity E and the thermal conductivity λ of the sample that minimize the sum

of the quadratic error

$$\Psi = \sum_1^N [T_{exp}(t_i) - T_{mod}(t_i)]^2$$

between the

experimental curve and the theoretical curve calculated with relation (3). The inverse Laplace transformation is performed using the De Hoog algorithm [17].

RESULTS AND DISCUSSION

Physical properties

The Atterberg limits of the clay and the laterite are reported in

Table 2. The plasticity index shows that the clay is moderately plastic [18] and the laterite is weakly plastic.

Table 2

Atterberg limits of the raw materials.

Atterberg limits	Clay	Laterite
Liquidity limit, W_L (%)	77.62	33.07
Plasticity limit, W_P (%)	22.51	16.02
Plasticity index PI (%)	55.11	17.05

The absolute density of raw materials is respectively 2381 kg/m^3 for clay and 2564 kg/m^3 for laterite. The two materials have densities of the same order of magnitude.

The linear shrinkage is an important parameter for bricks manufacturers. In order to obtain the brick desired geometry after the drying process, we study the total linear shrinkage. The result of linear shrinkage is presented in Figure 4. These results show that the highest shrinkage is obtained for clay brick with 0 % of laterite and the lowest shrinkage is obtained for clay brick with 30 % of laterite.

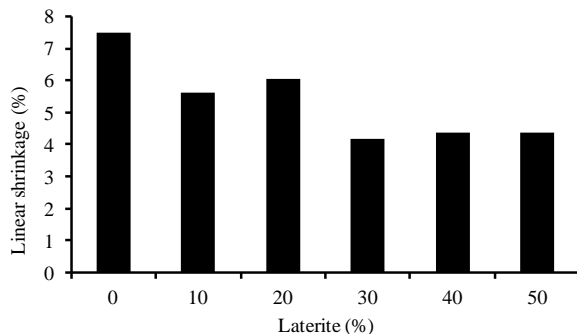


Figure 4

Variation of linear shrinkage by percentage of laterite.

Mechanical properties

To ensure the engineering quality of a material, especially for building construction use, mechanical testing is the essential criteria. The compressive strength is the mechanical property measured.

The Figure 5 presents the results of the compressive strength of unfired and fired clay bricks. The results show that clay brick with 30 % of laterite has the greatest compressive strength in both cases. The highest values of 4.98 MPa and 22.93 MPa are obtained respectively for unfired and fired clay bricks with 30 % of laterite. The firing allowed to increase the compressive strength by a factor of about 4.

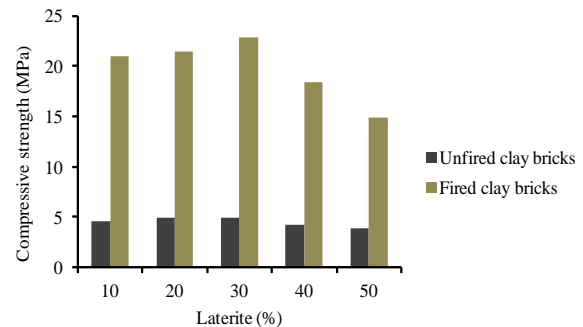


Figure 5

Variation of the compressive strength of unfired and fired clay bricks versus percentage of laterite.

Thermal properties

Figure 6 presents the results of the thermal conductivity of unfired and fired clay bricks. The results show that the variation of thermal conductivity with laterite Percentage has the same shape for unfired and fired clay bricks. The thermal conductivity curves present a minimum of 0.64 W/m.K and 0.34 W/m.K respectively for unfired and fired clay brick when percentage of laterite is about 30 %. The firing decreases the thermal conductivity by a factor about 2.

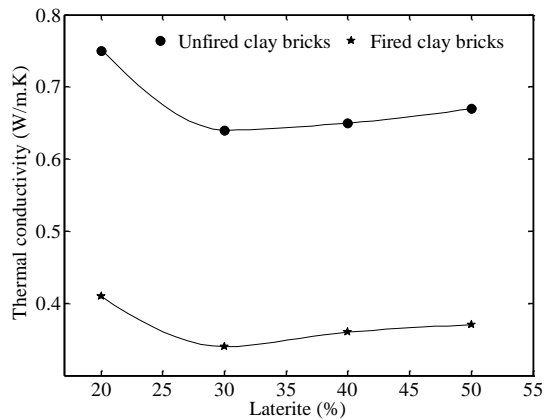


Figure 6

Variation of the thermal conductivity of unfired and fired clay bricks versus percentage of laterite.

Figure 7 presents the results of the thermal effusivity of unfired and fired clay bricks. The results show that the variation of thermal effusivity with laterite Percentage has the same shape for unfired and fired clay bricks. The thermal effusivity curves present a minimum of $1280 \text{ J.K}^{-1}.\text{m}^{-2}.\text{s}^{-1/2}$ and $804 \text{ J.K}^{-1}.\text{m}^{-2}.\text{s}^{-1/2}$ respectively for unfired and fired clay brick when percentage of laterite is about 30 %. The firing decreases the thermal effusivity of clay material.

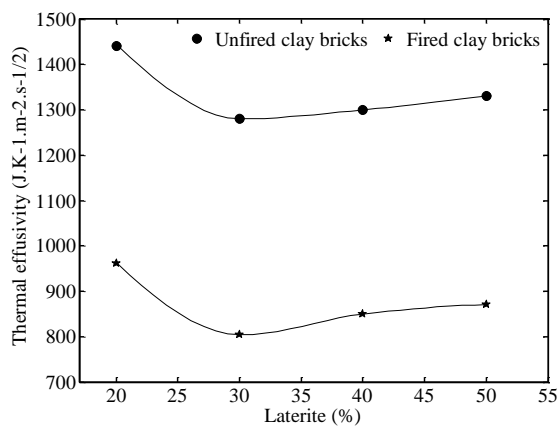


Figure 7

Variation of the thermal effusivity of unfired and fired clay bricks versus percentage of laterite.

CONCLUSIONS

The aim of this work is to determine the thermophysical and mechanical properties of unfired clay bricks and fired clay bricks made from a mixture of clay and laterite. In the light of this experimental

investigation, the following conclusions can be drawn:

- The unfired clay brick with 30 % of laterite presents the lowest shrinkage after drying.
- The unfired and fired clay bricks with 30 % of laterite present the optimum of compression strength.
- The firing increases the compressive strength by a factor about 4.
- The unfired and fired clay bricks with 30 % of laterite present the lowest thermal conductivity and the lowest effusivity.
- The firing decreases the thermal conductivity by a factor about 2.
- Our experiments demonstrate that for use as building material, clay brick with 30 % of laterite is the optimal mixture both for unfired and fired bricks.

REFERENCES

- 1 A. Kasthurba, M. Santhanam et M. Mathews, «Investigation of laterite stones for building purpose from Malabar region, Kerala state, SW India – Part 1: Field studies and profile characterisation,» *Construction and Building Materials*, vol. 21, p. 73–82, 2007.
- 2 L. Mbumbia, A. M. d. Wilmaris et J. Tirlocq, «Performance characteristics of lateritic soil bricks fired at low temperatures: a case study of Cameroon,» *Construction and Building Materials*, vol. 14, pp. 121-131, 2000.
- 3 J. O. Akinmusuru, «Lateritic soil-cement bricks for rural housing,» *The International Journal of Cement Composites and Lightweight Concrete*, vol. 6, 1984.
- 4 H. Bal, Y. Jannot, S. Gaye et F. Demeurie, «Measurement and modelisation of the thermal conductivity of a wet composite porous medium: Laterite based bricks with millet waste additive,» *Construction and Building Materials*, vol. 41, p. 586–593, 2013.
- 5 A. Sindanne, G. Ntamack, L. Sanga, C. Moubeke, K. Sallabou, H. Bouabid, K. Mansour et S. D'Ouazzane, «Thermophysical characterization of earth blocks stabilized by

- cement, sawdust and lime,» *Journal Building Materials and Structures*, vol. 1, pp. 58-64, 2014.
- 6 J. Oti, J. Kinuthia et J. Bai, «Engineering properties of unfired clay masonry bricks,» *Engineering Geology*, vol. 107, p. 130–139, 2009.
- 7 L. Miqueleiz, F. Ramirez, J. Oti, A. Seco, J. Kinuthia, I. Oreja et P. Urmeneta, «Alumina filler waste as clay replacement material for unfired brick production,» *Engineering Geology*, vol. 163, p. 68–74, 2013.
- 8 S. Mounir, Y. Maaloufa, A. Cherki et A. Khabbazi, «Thermal properties of the composite material clay/granular cork,» *Construction and Building Materials*, vol. 70, p. 183–190, 2014.
- 9 M. Sutcu, H. Alptekin, E. Erdogmus, Y. Er et O. Gencil, «Characteristics of fired clay bricks with waste marble powder addition as building materials,» *Construction and Building Materials*, vol. 82, p. 1–8, 2015.
- 10 G. F. N. Ngon, R. Y. Fouateu, G. L. L. Nana, D. L. Bitom, P. Bilong et G. Lecomte, «Study of physical and mechanical applications on ceramics of the lateritic and alluvial clayey mixtures of the Yaoundé region (Cameroon),» *Construction and Building Materials*, vol. 31, p. 294–299, 2012.
- 11 «NF P94-051. Détermination des limites d'Atterberg,» AFNOR, Mars 1993.
- 12 «NF P94-054. Détermination de la masse volumique des particules solides des sols - Méthode du pycnomètre à eau,» AFNOR, Octobre 1991.
- 13 C. Bories, M. Borredon, E. Vedrenne et G. Vilarem, «Development of eco-friendly porous fired clay bricks using pore-forming agents: A review,» *Journal of Environmental Management*, vol. 143, pp. 186-196, 2014.
- 14 «NF EN 12390-3. Essai pour béton durci- Partie 3 : Résistance à la compression des éprouvettes,» AFNOR, Février 2003.
- 15 N. Laaroussi, A. Cherki, M. Garoum, A. Khabbazi et A. Feiz, «Thermal properties of a sample prepared using mixtures of clay bricks,» *Energy Procedia*, vol. 42, p. 337 – 346, 2013.
- 16 D. Maillet, S. André, J. Batsale, A. Degiovanni et C. Moyne, «Thermal quadrupoles: solving the heat equation through integral transforms,» *Chichester (PA): John Wiley & Sons Ltd*, 2000.
- 17 F. De Hoog, «An improved method for numerical inversion of Laplace transforms.,» *Soc Ind Appl Math*, vol. 3(3), p. 357–66, 1982.
- 18 H. Mahtali, «Identification du potentiel de gonflement d'un sol de la région de Souk-Ahras,» Colloque International Sols Non Saturés et Environnement « UNSATlemcen09 » Tlemcen , 27 et 28 Octobre 2009.

ABRASION RESISTANCE OF CONCRETE AND HIGH STRENGTH CONCRETE REINFORCED WITH STEEL FIBERS

Fatima SETTI ^{1,*}, Karim EZZIANE ¹, Bakhti SETTI ²,

¹ Geomaterials Laboratory University of Hassiba Ben-Bouali Chlef
BO: 151, Chlef, 02000, Algeria.

² Laboratory Materials Science and Environment, University of Hassiba Ben-bouali, Chlef, Algeria.

*Corresponding author: Fax: 00 213 27 72 72 34, Email:
setti_fati@yahoo.fr

ABSTRACT

The aim of this study is to quantify the effect of incorporating steel fibers in the cement matrix on the abrasion resistance of concrete and high strength concrete. For this purpose four mixtures were used for each type, a concrete without fibers serving as a control concrete, and a metal fiber-reinforced concrete with metallic fibers three assays measured at 0.5, 1 and 1.5% of the concrete volume. The experimental study was conducted on samples having substantially the same weight, with one abrasive filler, thereby obtaining the weight decrease in the effect of abrasion of each sample for different percentages of fiber versus time (2, 4, 6 and 8 hours). The results show a remarkable improvement in the abrasion resistance when the dosage of fibers increases. The abrasion resistance of concrete is highly dependent on its resistance to compression, and can be expressed by a simple linear relationship for all concretes described in this study.

KEYWORDS

Abrasion resistance; High-strength concrete; Steel fibers.

INTRODUCTION

The concrete remains a modern material, but its low tensile strength, fragility and its ability to micro cracking that it must be reinforced in the majority of applications. Reinforcing metal fiber main objective is to improve the behavior of concrete to delay, limit or prevent brittle fracture [1]. The use of fibers has a long history going back at least 3500 years. In more recent times, different

types of fibers such as asbestos, cellulose, steel, polypropylene and glass have been used to reinforce cement products [1, 2]. Introduction of fibers in concrete can help to improve the plastic cracking characteristics, the tensile or flexural strength, the impact strength and toughness and to control cracking and the mode of failure by means of postcracking ductility and to improve durability [3, 4].

Improving the strength of concrete reinforced with metallic fibers allows to not only improve the behavior in bending and tension, also the compression resistance of concrete [5]. Compressive strength of concrete recognized as the most important mechanical property of structural concrete. The relationship between concrete composition and compressive strength has long been a matter of interest for researchers [6]. The factors influencing the strength of concrete are: the amount and type of cement, w/c ratio, aggregate type and grading, workability of fresh concrete, mineral admixtures used, chemical additives, curing condition and time, etc [7]. These compressive strength parameters is generally reported as the most important factor that influences the abrasion resistance of concrete [8, 9]. Atis [10] reported that the increase in compressive strength and a decrease in porosity resulted in a decrease in the abrasion of fly ash concrete. abrasion is influenced also in this way. Yazici and Inan [11] with high strength concretes (HSC) having compressive strength between 65 and 85 MPa concluded that wear damage of high strength concrete can be estimated from compressive and splitting tensile strength results. Yen et al. [12] investigated the abrasion-erosion resistance of high-strength concrete (HSC) mixtures in which cement was partially replaced by four kinds of replacements (15%, 20%, 25% and 30%) of Class F fly ash. They concluded that abrasion-erosion resistances of fly ash concrete mixtures were improved by increasing

compressive strength and decreasing the ratio of water-to-cementitious materials. The objective of this study was to quantify the effect of the presence of metal fibers in the concrete on the mechanical behavior of the latter including resistance to compression and abrasion.

EXPERIMENTAL STUDY

Materials and mix proportions:

The materials used in this research include cement CEM II 42.5A and its properties are presented in Table 1. silica fume, a rolled sand from Oued Rasse whose fineness modulus $M_f = 2.02$, an apparent density of 1.63 and a sand equivalent $E_s = 78 \%$; This allows you to say that the sand is clean and that the adhesion properties and the plasticity of the clay are not to be feared. The gravel used is a crushed gravel of the career of Oued Fodda to the region of Chlef (Algeria), and that is usually used in the current concrete. Impurities are the order of 1.2% and a Los Angeles LA coefficient = 24%. The type of silica fume used is an "S 95 DS" manufactured by the Canadian company SKW, marketed by the company "SIKA". Its chemical oxide composition given in Table 2.

The fibers used are steel fibers DRAMIX RC-45/50-BN to a high carbon content. They are manufactured from drawn wire cold and are presented in cylindrical form and provided with end hooks. Table 3 represents the type and the geometrical characteristics of the fibers used. In order to check the workability of the

concrete and to keep an even consistency while inserting the steel fibers, it was used superplasticizer, high range water reducer, manufactured by Algerian Granitex, marketed under the name «MEDAFLOW 30» Yellowish color, density of 1.07 and 30% dry extract. The water used in this case is supposed potable water from the tap and contains none harmful impurity. Two types of concrete were prepared, a concrete of an average compressive strength of 30 MPa S30 with water cement ratio W/C= 0,6 and a high strength concrete of an average compressive strength of 60 MPa of strength supposed S60 with W/C= 0,4 and 8% of silica fume (8% of cement mass). All mixtures were prepared with constant cement content of 400 kg/m³, and with volume fractions of 0.5, 1, and 1.5% fibers (relative to the total volume of the concrete).

Table 1
Composition of the cement used

Chemical composition (%)							
SiO ₂	Al ₂ O ₃	Fe ₂ O ₃	CaO	MgO	SO ₃	K ₂ O	Loi
20.58	4.90	4.70	62.8	0.63	2.28	0.42	1.00
Mineralogical composition (%)							
C ₃ S	C ₂ S	C ₃ A	C ₄ AF				
41.8	33.3	5.1	10.7				
Composition of cement (%)							
Clinker	Limestone	Gypsum					
86.5	10	3.5					


Sample preparation and testing procedure: In order to determine the effect of steel fibers on compression strength and abrasion resistance, cube specimens with dimension of 100 mm were prepared. Mixing was carried out using a mixer whose total mixing time is 3 minutes; to ensure homogeneous distribution of the fibers during mixing

of the mixture, they are introduced at the end, after the water and superplasticizer were added.

Table 2
Technical data from the silica fume

Apparent density	0,65 ± 0,10
real density (helium)	2,24
SiO ₂ content	95% (≥ 92%)
Na ₂ O content eq.	0,60% (≤ 1,0%)
SiC content	1,50% (≤ 3,0%)
C content free	1,50% (≤ 3,0%)
total S content	0,10% (≤ 0,20%)
BET specific surface area (m ² / g)	23 (20 à 26)
Content in oxides (Fe, Al, Mg, Ca)	1,00% (≤ 1,50%)
Cl content	0,06% (≤ 0,20%)

Table 3
Characteristics of metallic fibers

Form 				
Length (mm)	Diameter (mm)	Slenderness Ratio (l/d)	Tensile strength (MPa)	Nb of fiber per kg
50	1.05	48	1000	2800

The abrasion test is passed on micro Duval device where each compartment, a test sample is prepared which is composed of: 1 concrete cube, 1kg of small spherical balls of stainless steel (D = 10 ± 0.5 mm), sand 500g and 2 liter of water. The test begins by performing machine 12,000 rotations (for 2 hours) at a constant speed of 100 ± 5 revolutions / min. Is thus obtained the weight decrease as a result of abrasion of each specimen for different percentages of fibers as a function of time such as 2, 4, 6, 8 hours.

RESULTS AND DISCUSSION

Compression strength: The compressive strength of the mixtures with 0.4 w/c ratio varied between 50 and 66.1 MPa, the concrete with 1.5% of fibers, possessing the highest value (Fig. 1).

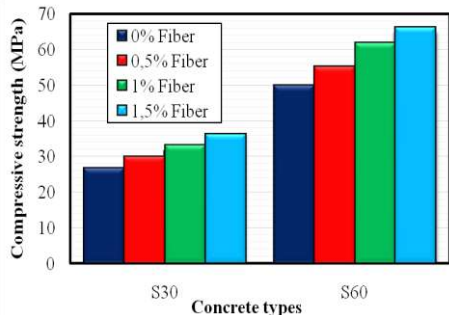


Figure 1

Compressive strength results of concrete mixtures at 28 days.

The mixtures with 0.60 w/c ratio had compressive strengths between 27 and 36.2 MPa, the concrete with 1.5% of fibers, again, possessing the highest value. The addition of steel fiber resulted in gain of strength, equal 10.4, 23.6, and 32.2% for concrete with 0.5, 1, and 1.5% of volume fiber respectively for concretes with w/c ratio of 0.4. Moreover gain of strength equal 12.3, 23.8, and 35% for concrete with 0.5, 1, and 1.5% of volume fiber respectively for concretes with w/c ratio of 0.6 (Fig. 2). This result is compliance with the results found by Song and Hwang [13] found that these of steel fiber at 1.5% volume fraction, resulted in a 15.3% improvement in compressive strength of high strength concrete.

On the other side, Altun et al. [14] reported that the use of steel fiber caused a slight decrease in the

compressive strength of normal strength concretes. Sun and Xu [15] reported that the use of polypropylene fiber at 0.9 kg/m^3 improved concrete's compressive strength about 7% and that 1.35 kg/m^3 fiber addition adversely affected the strength and caused a 6% decrease when compared to the reference. Nihat Kabay [16] reported that the addition of basalt fiber BF resulted in decrease in compressive strength. Although doubling the fiber length contributed to compressive strength, the achieved strengths were below the references.

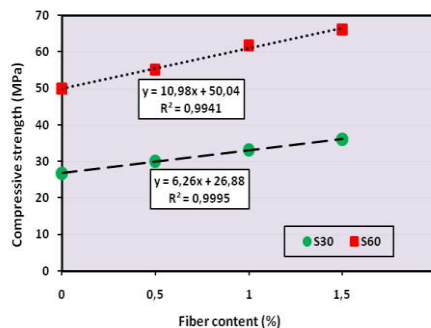


Figure 2

Compressive strength versus fiber content (%)

Abrasion resistance: The variation of abrasive wear values versus time per hours of concretes shown in Figures 3 and 5. It can be clearly noticed from this result that concrete mixtures having higher compressive strength, in general, possessed lower abrasion values. It can be seen that the abrasion resistance of concretes containing steel fibers is significantly improved for any type of concrete used. As the dosage fiber content increases, the weight loss due to

abrasion decreases. The abrasion by the abrasive filler was very aggressive in the beginning, only the skin of concrete has deteriorated, but as soon as abrasion reached the coarse aggregate, a slowing down of the weight loss of concrete is felt.

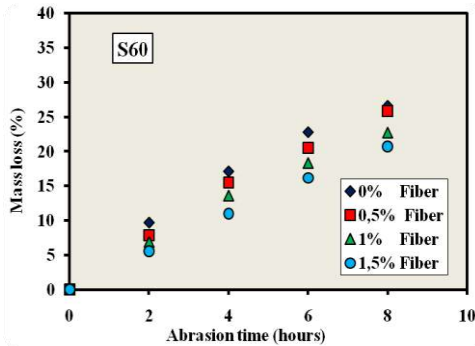


Figure 3

Abrasive resistance versus time of concretes with average compressive strength 60 MPa.

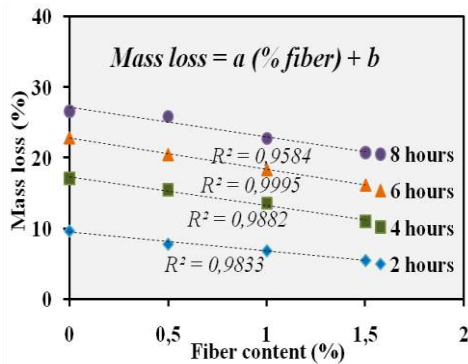


Figure 4

Abrasive resistance versus fiber content for 60 MPa compressive strength.

The difference in the loss due to abrasion can be visibly seen by the shape of the specimens after the test. It is interesting to note that the fibers do not only reduce the abrasion, but they

also improve the consistency of the matrix. This improvement increases with time. So the use of higher fiber content provided decreases in abrasive wear values when compared to the reference concretes (Figs. 4, 6).

This result is similar to that found by other studies [17], where the incorporation of 0.5 and 1% fiber reduces abrasion of 2 and 9%, respectively; on samples subjected to a rotation of 2000 rpm the unit to Los Angeles. The contribution of polypropylene and steel fibers on abrasion have also been reported [15, 18].

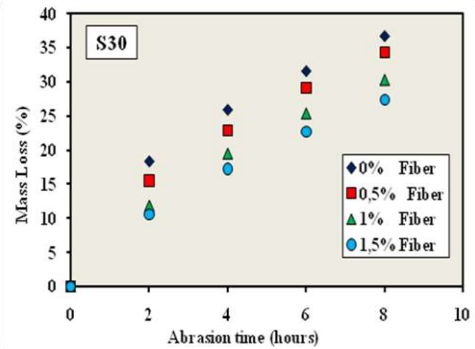


Figure 5

Abrasive resistance versus time of concretes with average compressive strength 30 MPa.

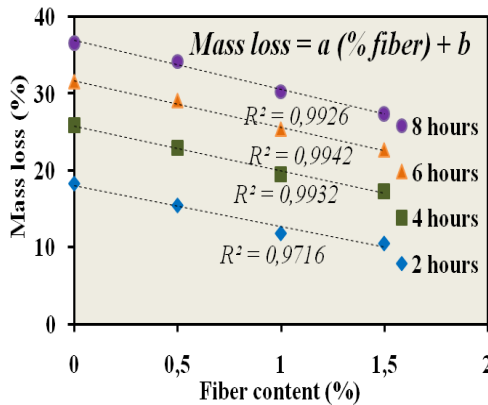


Figure 6

Abrasive resistance versus fiber content for 30 MPa compressive strength.

CONCLUSIONS

This study aims to quantify the effect of adding metal fibers on mechanical properties of concrete, in particular the compressive strength, and abrasion resistance.

We can conclude that:

- The compressive strength at 28 days evolves according to the dosage of used fibers. The gain depends on the concentration and the geometry of the fibers.
- The fibers reduce the abrasive effect and improve the consistency of the matrix.
- The abrasion resistance of the concrete is highly dependent on its resistance to compression for all types of concretes mentioned in this study.

REFERENCES

1. Rossi, P, 1998, Les bétons de fibres métalliques, Press ENPC.
2. Hannant, D.J, 2003, Fibre reinforced concrete, in, Newman J,

Choo B.S, editors, Advanced concrete technology-processes, Oxford: An Imprint of Elsevier, pp. 146–63.

3. Banthia, N, Sappakittipakorn, M, 2007, Toughness enhancement in steel fiber reinforced concrete through fiber hybridization, Cement and Concrete Research, 37, pp. 1366–1372.
4. Felekoglu, B, Tosun, K, Baradan, B, 2009, Effects of fibre type and matrix structure on the mechanical performance of self-compacting micro-concrete composites, Cement and Concrete Research, 39, pp.1023–1032.
5. Damgir, R.M, Ghugal, Y.M, 2010, Prediction of compressive strength by Incorporating steel fiber, 35th Conference on Our World in Concrete & Structures, Singapore, pp. 25–27.
6. Wu K.R, Chen B, Yao W, Zhang D, 2001, Effect of coarse aggregate type on mechanical properties of high-performance concrete, Cement and Concrete Research, 31, pp. 1421–1425.
7. Kilic, A, Atis, C.D, Teymen, A, Karahan, O, Ozcan, F, Bilim, C, Ozdemir, M, 2008, The influence of aggregate type on the strength and abrasion resistance of high strength concrete, Cement and Concrete Composites, 30, pp. 290–296.
8. Grdic, Z.J, Curcic, G.A.T, Ristic, N.S, Despotovic, I.M, 2012, Abrasion resistance of concrete micro-reinforced with polypropylene fibers, Construction and Building Materials, 27, pp. 305–312.

9. Siddique, R., Kapoor, K., Kadri, E.H, 2012, Bennacer R, Effect of polyester fibres on the compressive strength and abrasion resistance of HVFA concrete, *Construction and Building Materials*, 29, pp.270–278.
10. Atis, C.D, 2003, Abrasion-porosity-strength model for fly ash concrete, *Journal of Materials in Civil Engineering*, 15, pp. 408–410.
11. Yazici, S, Inan, G, 2006, An investigation on the wear resistance of high strength concretes, *Wear*, 260, pp. 615–618.
12. Yen, T, Hsu, T.H, Liu, Y.W, Chen, S.H, 2007, Influence of Class F fly ash on the abrasion– erosion resistance of high-strength concrete, *Construction and Building Materials*, 21, pp. 458–463.
13. Song, P.S, Hwang, S, 2004, Mechanical properties of high-strength steel fiber reinforced concrete, *Construction and Building Materials*, 18, pp. 669–673.
14. Altun, F, Haktanir, T, Ari, K, 2007, Effects of steel fiber addition on mechanical properties of concrete and RC beams, *Construction and Building Materials*, 21, pp. 654–661.
15. Suna, Z, Xu, Q, 2009, Microscopic, physical and mechanical analysis of polypropylene fiber reinforced concrete, *Materials Science and Engineering A*, 527, pp.198–204.
16. Nihat Kabay, 2014, Abrasion resistance and fracture energy of concretes with basalt fiber, *Construction and Building Materials*, 50, pp. 95–101.
17. Nicholas, J.P, 2002, Abrasion wear, abrasion resistance, and related strength characteristics in concrete, with special reference to concrete pavers, PhD thesis, University of the Witwatersrand, 300 p.
18. Felekog, L.B, Türkel, S, Altuntas, Y, 2007, Effects of steel fiber reinforcement on surface wear resistance of self-compacting repair mortars, *Cement and Concrete Composites*, 29, pp. 391–396.

SEISMIC VULNERABILITY CLASSIFICATION OF ROADS

Sonia ADAFER^a and Mahmoud BENZAIBI^a

^(a)Ecole Nationale Supérieure des Travaux Publics –ENSTP

National School of Built and Ground Works Engineering Algiers, Algeria

(1, Rue Garidi BP 32, Vieux Kouba , Alger Algérie)

*Corresponding author: Fax: +213 21 28 87 61 Email: adafersonia@gmail.com

ABSTRACT

Experience from past earthquakes all over the world showed that the road network could undergo heavy damages. To prevent these damages, vulnerability studies must be carried out.

The purpose of this study is to develop a seismic vulnerability assessment method for roads. The methodology is based on the determination of a numerical indicator called Vulnerability Index (VI). To achieve this, the main parameters that influence the seismic behaviour of roads are identified on the basis of the worldwide seismic feedback experience and data from past Algeria earthquakes. Furthermore, the Analytical Hierarchy Process (AHP) is used to quantify the identified parameters and to define an analytical expression of the 'VI'. A classification of the seismic vulnerability of road sections is proposed, according to the obtained Vulnerability Index (VI) value.

To exhibit the efficiency of the developed method, several road sections are studied and the obtained results are in good adequacy with in-situ observations). Moreover, in order to assess the seismic vulnerability of an urban city road network, the developed model is combined to a GIS (Geographical Information system) to perform several earthquake scenarios and the results of Tipaza city are presented.

NOMENCLATURE

C_{ijkl} : Score of category

LP : liquefaction Potential

MMI: Mercalli Modified Intensity

RSVI : Road Seismic Vulnerability Index program

VI : Vulnerability Index

VR : Vulnerability Range

W_i : weighting coefficient of structural or hazard parameters,

W_{ij} : weighting coefficient of items,

W_{ijk} : weighting coefficient of factors

INTRODUCTION

Among lifelines, road network play an important role in the daily life. It assures services such as transportation and socio-economic exchanges. Moreover, during major disasters such as earthquakes, it allows emergency response, repair operations and recovery activities. Nevertheless, the road network may as well as other structures suffer heavy damages due to seismic event. As a result, these damages induce delay in the rescue operations and extensive socio-economic losses.

In order to reduce road seismic vulnerability, several studies have been carried out [1-5]. Methods for

performing seismic scenario have been developed taking into consideration road networks [6-11].

Among vulnerability assessment methods, the vulnerability index method is used for different lifelines [12]. It consists in determining a value resulting from an analytical expression that contains several parameters. These parameters are either qualitative or quantitative which differentially affect the system vulnerability. Furthermore, the expression of the VI generally contains weighting coefficients. These weights may be calculated by applying MCDM (Multi Criterion Decision Making) methods. These ones allow to take into account many parameters with different nature and unequal importance [13].

Among the MCDM methods, the Analytical Hierarchy Process (AHP) is commonly used. It was developed by Saaty [14] and is used in different fields. Recently, many researchers have applied this method to assess seismic vulnerability of tunnels [15], bridges [16], roads [17, 18], buildings [19], buildings construction site [20], lifelines [21] and urban areas [22].

In this study, the vulnerability index method is applied to assess the seismic vulnerability of roads. Based on feedback from past earthquakes over the world [23-28], and Algerian observations from Ain Temouchent and Zemmouri earthquakes [29, 30],

most important parameters that have an influence on seismic behaviour of road network are identified. Moreover, to take into account their relative importance, the AHP method is used to derive weighting coefficient for each identified parameter.

BACKGROUND OF THE PROPOSED METHOD

The developed method is based on the following main stages.

Stage 1. Identification of the vulnerability parameters: Roads vulnerability depends on their geometric and structural characteristics as well as geotechnical and seismic proprieties of the location site. Factors that affect the seismic behaviour of the road are defined on the basis of seismic experience of past earthquakes all over the world and in Algeria, so two types of parameters are identified : Structural and Seismic ones. These parameters are divided into items. In turn, the identified items are divided into factors and factors are subdivided in categories, as given in (Table 1).

Stage 2. Quantification of identified parameters: Using the AHP method, a hierarchical structure is built in order to model the problem. The hierarchical structure is established through the defined parameters and their characteristics.

Then, pairwise comparisons are performed and the validated weighting coefficients are determined for each parameter, item and factor (Table 2).

The VR1 range associated to the green colour classifies the road section as safe; it suffers a little or no damages. No requirement to any repairs is necessary.

The VR2 range associated to the orange colour classifies the road section as moderately resistant; it suffers moderate damages. Some components need retrofitting operations.

The VR3 range associated to the red colour classifies the road section as weak with low resistant; it suffers heavy damages. Many components need retrofitting or rebuilding operations.

Table 1
Identified Parameters

Parameter	Item	Factor	Category
Structural	Pavement	Number of lanes	> 2 lanes
			≤ 2 lanes
		Pavement Type	Paved
			Unpaved
		Height	H ≤ 2m
			2m < H ≤ 5m
			5m < H ≤ 8m
			H > 8m
	Embankment	Compaction quality	Compliant with standards
			Compliant with technical provisions
	Slope	Other	
		< 2/3	
		= 2/3	
Ground conditions	Ground type	> 2/3	
		Rock	
		Hard soil	
		Soft soil	
		Very soft soil	
	Landslide potential	Low	
		Medium	
		High	
Maintenance conditions	Pavement conditions	High	
		Medium	
		Low	
			Slope protection measures
Compliant with technical provisions			
Without any protections			
Hazard	Seismic intensity	-	MMI < VIII
			VIII ≤ MMI < IX
			IX ≤ MMI < X
			X ≤ MMI < XI
			XI ≤ MMI
			LP = 0
Liquefaction potential	-	0 < LP ≤ 5	
		5 < LP ≤ 15	
		15 < LP	
Intersection with fault	-	No intersection	
		Intersection	

Table 2
Weighting coefficients

Parameter Weight	Item Weight	Factor Weight
Structural 0.250	Pavement 0.108	Number of lanes 0.667
		Pavement Type 0.333
	Embankment 0.283	Height 0.648
		Compaction Quality 0.122
		Slope 0.230
		Ground type 0.200
	Ground conditions 0.561	Landslides potential 0.800
		Pavement conditions 0.667
	Maintenance conditions 0.048	Slope protection measures 0.333
		Seismic intensity 0.633
Hazard 0.750	Liquefaction Potential 0.106	-
	Intersection with fault 0.261	-

Stage 3 - Definition of the vulnerability index ‘VI’: The vulnerability index (VI) expression is developed as follows:

$$VI = \sum_{i=1}^2 W_i \sum_{j=1}^{3 \text{ or } 4} W_{ij} \sum_{k=1}^{2 \text{ or } 3} W_{ijk} C_{ijkl} \quad (1)$$

With:

W_i the weighting coefficient of structural or hazard parameters,

W_{ij} the weighting coefficient of items,

W_{ijk} the weighting coefficient of factors, where $W_{ijk}=1$ if $i=2$

and C_{ijkl} the score of category, where $l = 2$ or 3 or 4 or 5 .

Stage 4 - Proposal of a vulnerability classification of road: According to the value obtained for the vulnerability index, three vulnerability ranges VR1, VR2 and VR3 are proposed (Table 3):

Table 3
Vulnerability index ranges

Range	VR1	VR2	VR3
VI value	10 – 20	20 – 35	35 – 50
Assigned color	Green	Orange	Red

DEVELOPED PROGRAM

A program under Matlab software is developed in order to compute the vulnerability index. This program is called RSVI ‘Road Seismic Vulnerability Index’. The flow chart of this program is given in Figure 1.

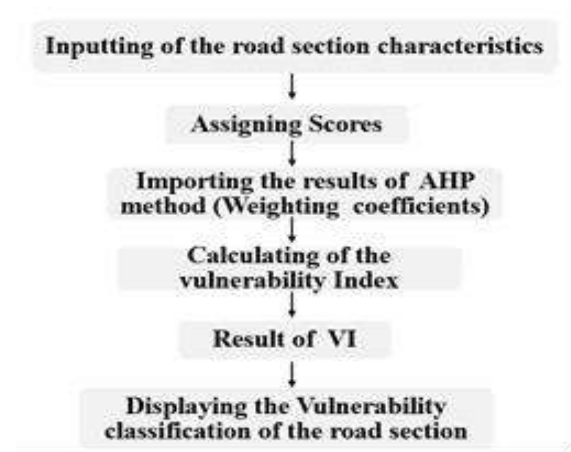


Figure 1
Flow Chart of the RSVI program

APPLICATIONS

To show the efficiency and to validate the developed model, using the RSVI program, several road sections have been studied. Furthermore, this model can be used to achieve seismic scenarios in order to predict the behaviour of roads under seismic event.

Post-earthquake assessment: Several road sections have been treated and two case studies are presented in this paper.

Case Study 1: It is about a road in Ain Temouchent a town located in West of Algiers (about 360 km). It is a section of the national road (RN35) located in Ain

Temouchent at the kilometer marker 19+500. This road section crosses a soft soil and includes a high embankment ($H=7\text{m}$).

Using the RSVI program, the obtained vulnerability index (VI) is equal 13.58. This value is included in range VR1, hence the road section is classified green.

On 22 December 1999, the North of Algeria was struck by a shallow earthquake, namely Ain Temouchent earthquake [31]. Its Mercalli Modified Intensity was VII and caused considerable damages to Ain Temouchent and its suburb [29].

The results of this study are in a good adequacy with in-situ observations. In fact, this road section did not suffer any damages after the quake [29].

Case Study 2: The studied road is situated nearby the town of Boumerdes in East Algiers (about 70 km). It is related to a section of the national road (RN68) located in the suburb of Boumerdes. This road section crosses a liquefiable silts and sand and includes a low embankment ($H=4\text{m}$).

Using the RSVI program, the obtained vulnerability index (VI) is equal 28.99. This value is included in range VR2, hence the road section is classified orange.

The seismic vulnerability of this section road is mainly due to the liquefaction phenomenon in the area.

On 21 May 2003 Boumerdes earthquake struck Zemmouri region in the north of Algeria ($\text{MMI}=\text{X}$). It damaged many structures, bridges and roads through the town and the region nearby [32].

The result of this study is in a good adequacy with in-situ observations. In fact, this road section needed recovery operations after the quake [30].

Seismic scenarios: The road network of Tipaza city has been chosen to be investigated. This town is located in the North of Algeria. This region experienced some moderate to strong earthquakes and is well-known for its active faults [33].

In order to assess the seismic vulnerability of the main road network of Tipaza, several earthquake scenarios were performed. The road network about 9518 meters was decomposed into 73 road sections according to their features. Then, using the RSVI program, a VI was obtained for each road section. Using a GIS, a vulnerability map of the road network was carried out for each seismic scenario.

Hereafter, the results of two performed seismic scenarios are presented.

Seismic scenario 1: It corresponds to a seismic intensity $\text{MMI}=\text{VIII}$. As it can be noticed in figure 2, the 73 road sections are classified in VR1 (green class). Accordingly, the whole of the road network has a low seismic vulnerability. These results are in a good adequacy with in-situ observations after the Chenoua Earthquake of 1989, the road network of the city had undergone no damages [34].

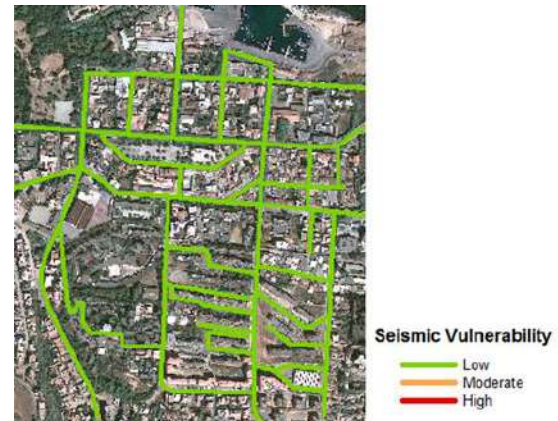


Figure 2
Vulnerability Map of the road network
(Seismic scenario 1)

Seismic scenario 2: It is for seismic intensity $\text{MMI}=\text{IX}$. As it can be seen in figure 3, all the road sections are classified in VR2 (orange class). Accordingly, the whole of the road network has a moderate seismic vulnerability. This is due to the features of the road network: location on hard soil, no high embankments, no landslides, no liquefaction phenomenon and the latest retrofitting in 2009 was compliant with the standards.

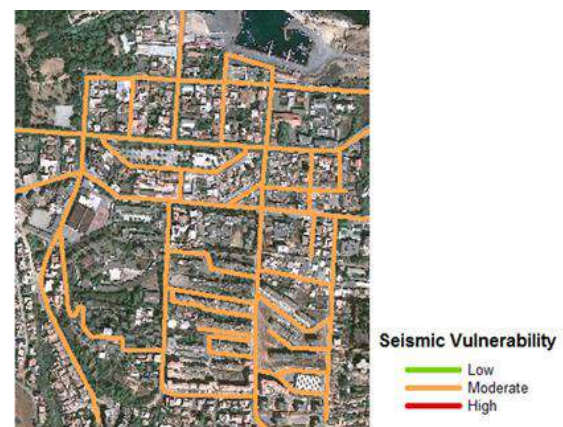


Figure 3
Vulnerability Map of the road network
(Seismic scenario 2)

CONCLUSION

From this study, it can be drawn that a seismic vulnerability classification for roads is developed on the basis of a defined Vulnerability Index (VI). Its efficiency is established in several studies. This method allows defining the prioritization of the retrofiting operations during an earthquake to safeguard the functionality of the road network.

The developed model is also used to perform seismic scenario that is very useful to highlight which seismic event could seriously damage a given road. Moreover, the outcomes of this pre-earthquake assessment enable to propose recommendations or actions to improve weak features of studied roads in order to ensure their performance against future earthquakes. Additionally, this tool is very useful for emergency management and urban planning.

REFERENCES

- Argyroudis, S. A., Pitilakis, K. D., and Anastasiadis, A. I., 2005, Roadway Network Seismic Risk Analysis in Urban Areas : The case of Thessaloniki - Greece, in Geoline: Lyon, France.
- Arsik, I., and Sibel Salman, F., 2013, Modeling Earthquake Vulnerability of Highway Networks. Electronic Notes in Discrete Mathematics 41 (1): pp.319-326.
- D'Andrea, A., Cafiso, S., and Condorelli, A., 2005, Methodological Considerations for the Evaluation of Seismic Risk on Road Network. Pure and Applied Geophysics. 162(4): 767-782.
- Shoji, G., and Nakamura, T., 2014, Development of Damage Functions on Road Infrastructures Subjected to Extreme Ground Excitations by Analyzing Damage in the 2011 off the Pacific Coast of Tohoku Earthquake. Journal of Disaster Research Vol.9 No.2, 2014. pp.121-122.
- Yang, L., and Qian, D., 2012, Vulnerability Analysis of Road Networks. Journal of transportation systems engineering and information technology. 12 (1): pp.105.
- ATC-25, 1991, Seismic Vulnerability and Impact of Disruption of Lifelines in the Conterminous United States, Applied Technology Council, in Federal Emergency Management Agency (FEMA): USA.
- FEMA-NIBS, 2004, Hazard US Earthquake Loss Estimation Methodology. National Institute of Building Sciences: NIBS document 5200-03, Washington, DC.
- JICA, 2002, The study on earthquake disaster mitigation in the Kathmandu Valley: Nippon Koei Co LTD, Final report, Kingdom of Nepal.
- RADIUS, 1996, Assessment Tools for Diagnostic of Urban Areas against Seismic Disasters: Secrétariat IDNDR (International Decade for Natural Disaster Reduction), United Nations
- RISK-UE, 2003, Vulnerability assessment of lifelines and essential facilities (WP06): methodological handbook - Appendix 1: Roadway transportation system: Report n°GTR-RSK 0101-152av7/Geo Ter, UE.
- Syner-G D3.7, 2009, Systemic Seismic Vulnerability and Risk Analysis for Buildings, Lifeline Networks and Infrastructures Safety Gain, Deliverable D3.7 - Fragility functions for roadway system elements: Norwegian Geotechnical Institute (NGI) - Seventh Framework Programme, UE
- Pitilakis, K., Alexoudi, A., Argyroudis, S., Monge, O., and Martin, C., 2005, Chapter 9: vulnerability assessment of lifelines. In: GoulaX, Oliveira CS, Roca A (eds) Assessing and Managing Earthquake in Risk Springer Publications, I. 1-4020-3524-1, Editor.
- Bhushan, N., and Rai, K., 2004, *Strategic Decision Making - Applying the Analytic Hierarchy Process*. 183.
- Saaty, T. L., 1980, *The analytic hierarchy processess : planning, priority setting resource* Mc Grew, Hill, New York.
- Wang, Z. Z., and Zhang, Z., 2013, Seismic damage classification and risk assessment of mountain tunnels with a validation for the 2008 Wenchuan earthquake. Soil Dynamics and Earthquake Engineering. 45: pp.45-55.
- Mohammadreza, Y., Mohammad Zin, R., and Mohammadreza, V., 2012, A Model for Seismic Vulnerability Score Assignment of Road Infrastructure Using Linear Regression Technique. Applied Mechanics and Materials 147: pp.266-269.
- Adafer, S., and Bensaibi, M., 2014, Seismic vulnerability assessment of road networks, in Second European Conference on Earthquake Engineering and Seismology, Istanbul Aug 25-29.: Turkey. p. p 1-9.
- Adafer, S., and Bensaibi, M., 2015, Seismic Vulnerability Index for Road Networks. Proceedings of International Conference on Industrial Technology and Management Science

- (ITMS 2015)- Beijing, March 27-28. pp.1233-1236.
19. Panahi, M., Rezaie, F., and Meshkani, S., 2013, Seismic vulnerability assessment of school buildings in Tehran city based on AHP and GIS. *Nat. Hazards Earth Syst. Sci. Discuss.* 1: pp.4511-4538.
 20. Zahaf, A., and Bensaibi, M., 2014, Seismic Vulnerability of Building Construction Site. *Journal of Civil Engineering and Architecture.* 8(1): pp.37-46.
 21. Jia, Q., Bai, P., and Duan, Q., 2013, Risk Assessment on Beijing Urban Infrastructure Vulnerability. *Proceedings of the 2nd International Conference On Systems Engineering and Modeling (ICSEM-13).* pp.45-50.
 22. Sarvar, H., Amini, J., and Laleh-Poor, M., 2011, Assessment of Risk Caused By Earthquake in Region 1 of Tehran Using the Combination of RADIUS, TOPSIS and AHP Models. *Journal of Civil Engineering and Urbanism.* 1(1): pp.39-48
 23. Anbazhagan, P., Srinivas, S., and Chandran, D., 2011, Classification of road damage due to earthquakes. *Natural Hazards.* 60(2): pp.425-460.
 24. Edwards, C. L., 2004, *Zemmouri, Algeria, Mw 6.8 Earthquake of may 21, 2003* Technical Council of lifeline Earthquake Engineering TCLEE Monographs 27,USA. pp.120.
 25. EERI, 2003, Earthquake of Boumerdes May, 21 2003- Learning from Earthquakes, Reconnaissance Report.
 26. EERI/CTC, 1980, Preliminary Reconnaissance Report El Asnam Earthquake, Algeria 10th 1980: Earthquake Engineering Research Institute,USA
 27. FHWA, 2004, Seismic Retrofitting Manual for Highway Structures: Federal Highway Administration Part 2,US Departement of transportation,USA.
 28. O'Connor, J. S., Mesa, L., and Nykamp, M., 2007, Damage to the highway system from the Pisco, Peru earthquake of August 15,2007: Technical report MCEER-07-0021,New York,USA.
 29. CTTT, 1999, Road networks expertise of Ain Temouchent following the earthquake of 22/12/99: Algeria.
 30. CTTT, 2003, Road networks diagnosis of Boumedes following the earthquake of 21/05/2003: Algeria.
 31. Yelles, C., A. K., Djellit, H., Beldjoudi, H., Bezzeghoud, M., and Buforn, E., 2004, The Ain Temouchent (Algeria) Earthquake of December 22 nd , 1999. *Pure and Applied Geophysics.* 161: 607-621.
 32. JRT, 2004, Boumerdes Earthquake May 21, 2003 - Japanese Reconnaissance Team-.
 33. Bounif, A., Bezzeghoud, M., Dorbath, L., and Legrand, D., 2003, Seismic source study of the 1989 , October 29 , Chenoua (Algeria) earthquake from aftershocks , broad-band and strong ground motion records. *Annals of Geophysics.* 46.
 34. Ambraseys, N. N., Elnashai, A. S., Bommer, J. J., Haddar, F., Madas, P., Elghazouli, A., et al.,1989. *Chenoua earhquake (Algeria).pdf.*

MECHANICAL BEHAVIOUR OF A STRUCTURE REINFORCED BY CARBONE FIBERS

T. AYAD¹, T. KADRI*, A. REZIGUA²

*Professeur Tahar Kadri Laboratoire Méthode et Procédé de Construction Département d'Architecture et Génie Civil Université de Mostaganem Algérie

1,2 Laboratoire Méthode et Procédé de Construction Département d'Architecture et Génie Civil Université de Mostaganem Algérie

*T. KADRI: Tel: +21377657228 Email: kadritahar59@hotmail.fr

ABSTRACT

In this paper, an analytic study is presented to investigate the effect of crack length on the single lap shear joint under tensile load and analyze the distribution of the adhesive shear stress. A parametric study was conducted according to the change of the dimensions, of the position of the pre crack in order to evaluate the shear stress along the bonded joint, A finite element analysis was proposed for the validation of our analytic model and also for determining the stress concentration points of the pre-crack and the two edges of the bonded assembly, the results in this paper show good agreement between analytic study and FEA model for shear stress at both free edges of adhesive, but less satisfactory agreement at the interface of adhesive.

Keywords Composite, shear stress, bonded assembly, crack, adhesive, carbon fiber, structure.

NOMENCLATURE

M_1	Bending moment at x1 position
P	Applied load
w_1	Lap shear joint deflection at x1 position
R_A	Crack tip A reaction
M_A	Bending moment at crack tip A
M_0	Bending moment at x0 position
α_n	Eccentricity ratio
l_A	Overlap length of single lap shear joint
l_B	Free lap length of single lap shear joint
w_0	Lap shear joint deflection at x0 position
h_1	Upper adherend thickness (strap)
h_2	Lower adherend thickness (lap)
t_1	Adhesive thickness
c	Overlap length of single lap shear joint
Δ	Undimensional quantity
η	Thickness ratio of h1, h2
Σ	Young modulus ration of adherends
\hat{R}_A	Undimensional reaction force
\hat{M}_A	Undimensional bending moment
Q_1	Shear force at x1 position
Q_2	Shear force at x2 position
D_0	Adherend bending stiffness
D_1	Adherend bending stiffness
E_1	Young modulus of adherend
ν_{12}	Poisson ratio max
ν_{21}	Poisson ratio min
D_{1L}	Lap adherend bending stiffness at left hand side
D_{2L}	Lap adherend bending stiffness at right hand side
D_U	Strap adherend bending stiffness
τ_{xy}	Adhesive shear stress
x_A	Half crack length at crack tip A

INTRODUCTION

The adhesive bonding has many advantages over traditional techniques such as riveting or welding. First it is very fast to implement, especially since its application is often automated.

It fits together when you have different materials, fragile or thin. The blend between materials which is continuous to produce a uniform effort to avoid stress concentrations. This results in higher mechanical strength than that produced by riveting. It does not require significant local heating, as for welding, and so does not alter the properties of materials to be assembled. Weight gain is important; adhesives absorb some vibration and provide both thermal insulation, acoustic and electric. However, the bonding is a technique for assembling complex surface preparation must be meticulous. Many models for adhesive bonded joints were developing using single lap joint geometries. This configuration has been adopted by the American Society of Testing Materials as a standard mechanical test for the determination of distribution shear stress. Goland and Reissner [1] were the first to include the effect of the eccentric load path by applying moments at the edges of the joint. Erdogan F and Ratwani M [2] Single lap joint configurations have been studied for about sixty years and numerous analytic and numerical models have been developed. Hart-Smith L.J [3] provided a considerable amount of work on glued joints in a single layer, double overlap, stepped and

chamfered. Analytic solutions have incorporated thermal effects and the effects of imbalance rigidity. In addition, he is interested in the non-linear behavior of the adhesive, where he developed an approach to perfect elastic-plastic. The analysis method has been developed to investigate the size of crack in adherents near overlap ends on failure behavior of adhesive single lap joint by Tong L [4, 6]. Numerical methods can be used to analyze models with arbitrary geometries and load conditions; the two dimensional finite element analyses of adhesive bonded joints was adopted by many searcher Tong L and Steven GP [5] The problem to study here is the existence of a crack length that significantly redistributes the stresses in the adhesive layer and thus changes the stresses resultants in both adherends The objective of this work is to study the effect of crack length on the stress distributions in adhesive layer by introducing a corrector factor with combination of Goland and Reissner study and Tong L analysis.

ANALYSIS AND MODELLING

An analytic model was proposed to calculate the forces and moments resulting in different sections of the specimen, including the cracked zone and interface. The solution procedure involves a comprehensive analysis of the joint. Figure.1 shows the joint with an imposed crack in the adherend. A concentrated load P is applied to the center line of each edge. Crack length c is imposed on the surface of the adhesive at distance t1. The thickness of the substrate is equal to h, while the thickness of the adhesive is η. Two coordinate systems are involved; the first is located at the free edge (x0, z (w0)) and the other is located to the middle of the adhesive layer (x1, z (w1)). The crack is bounded on both sides left and right by two sections A and B. the crack has a crack tip at section A inside the overlap and a crack tip at section B outside the joint. As shown in figure.1, the crack has a length of xA + xB, where xA is the length of the crack part inside the overlap and xB is the length of the crack part outside the overlap.

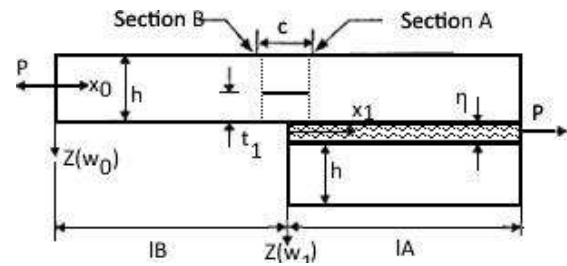


Figure.1: A single lap shear joint under tensile load.

Pre-cracked bonded assembly under tensile load

Single lap shear joint

Following the approach of Goland and Reissner [1], can be fixed equal to M0 and M1 bending moment at the position x0 and x1 by each unit of width,

$$M_1 = P \left(\alpha_n x_n - w_1 + \frac{R_A}{P} x_1 + \frac{M_A}{P} \right) \quad [1]$$

for $0 \leq x_0 \leq l_B$

$$M_0 = P \left[\alpha_n (x_0 + l_A) - w_0 - \left(\frac{h_1}{2} + h_2 - \Delta h_1 \right) + \frac{R_A}{P} (x_0 + l_A) + \frac{M_A}{P} \right] \quad [2]$$

Similar to the thin plate’s cylindrical bending theory, the differential equations for the cross section, w1 and w0 are given by:

$$\frac{d^2 w_1}{dx_1^2} = -\frac{M_1}{D_1} = -\frac{P}{D_1} \left(\alpha_n x_1 - w_1 + \frac{R_A}{P} x_1 + \frac{M_A}{P} \right) \quad (3)$$

And

$$\frac{d^2 w_0}{dx_0^2} = -\frac{M_0}{D_0} = -\frac{P}{D_0} \left[\alpha_n (x_0 + l_A) - w_0 - \left(\frac{h_1}{2} + h_2 - \Delta h_1 \right) + \frac{R_A}{P} (x_0 + l_A) + \frac{M_A}{P} \right] \quad (4)$$

$$D_0 = \frac{Q_{11} h^3}{12} ; D_1 = \frac{2Q_{11} h^3}{3} ; Q_{11} = \frac{E_1}{1 - \nu_{12} \nu_{21}}$$

D0 and D1 are the adherents bending stiffness. Solving differential equations (3) and (4), we get:

$$\frac{w_1}{L} = A_1 \cosh(\lambda_1 x_1) + B_1 \sinh(\lambda_1 x_1) + \left(\alpha_n + \widehat{R}_A \right) \frac{x_1}{L} + \widehat{M}_A \quad (5)$$

$$\frac{w_0}{L} = A_0 \cosh(\lambda_0 x_0) + B_0 \sinh(\lambda_0 x_0) + \left[(\alpha_n + \hat{R}_A) \frac{(x_0 + l_A)}{L} - \alpha_n + \hat{M}_A \right] \quad (6)$$

The global bending moments M_A and M_B obtained as follow:

At crack tip A $x_1 = x_A$

$$M_A = \frac{P \cdot t \cdot \cosh(\lambda_1 \cdot x_A)}{2} \cdot \left(-1 + k \left(1 + \frac{(\mu_1 \cdot \tanh(\lambda_1 \cdot x_A))}{(\mu_2 \cdot \tanh(\lambda_0 \cdot l))} \right) \right) \quad (7)$$

At crack tip B $x_0 = x_B$

$$M_B = \frac{k \cdot P \cdot t \cdot \sinh \lambda_0 (l - x_B)}{2 \cdot \sinh(\lambda_0 \cdot l)} \quad (8)$$

Adhesive shear stress analysis

Bending moment factor according Goland and Reissner

In this case, the bending moment and shear force are not collinear. If the imposed load P is rather weak, the rotation in the overlap region is negligible; the bending moment at the edge is expressed by:

$$M_0 = \frac{Pt}{2} \quad (9)$$

When the load is increased, the rotation in the overlap region is quite important. This rotation is transmitted to the edges of the bonded assembly. It is in this case that Goland and Reissner introduce the correction factor k; hence the bending moment at the edges of the bonded assembly is expressed again by:

$$M_0 = k \frac{Pt}{2} \quad (10)$$

The factor k in expression (10) is always smaller than 1.

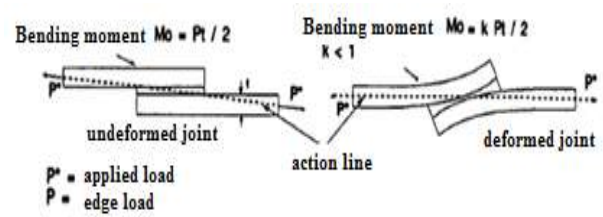


Figure. 3: Bending moment in a deformed and undeformed joint under tensile load.

Because of the change in stiffness along the bonded assembly, Goland and Reissner divide their analysis into the joint in three plates: the two members and the overlap region (Figure 3). Equality between two expressions (9) and (10) we can write:

$$M_0 = D \cdot \left[\frac{d^2 w}{dx^2} \right]_{\text{at edge}} = k \frac{Pt}{2} = \frac{1}{1 + 2\sqrt{2} \tanh \frac{\lambda c}{2\sqrt{2}}} \frac{Pt}{2} \quad (11)$$

With k, the correction factor of Goland and Reissner bending moment by:

$$k = \frac{1}{1 + 2\sqrt{2} \tanh \frac{\lambda c}{2\sqrt{2}}} \quad (12)$$

Where

$$\lambda = \sqrt{12(1 - \nu^2)} \frac{\sqrt{P/tE}}{t} = \sqrt{\frac{P}{D}} \quad (13)$$

E, t, ν are adherend properties and c is half the overlap length.

The derivation of these equations is based on the following assumptions:

- the joint is symmetrical (identical adherends),
- joint width is large compared to the adherend thickness,
- adhesive thickness is neglected,
- the angle α of the line of action is negligible in calculation of the edge tension

The shearing force Q at the edge of the joint, takes the form as follow:

$$Q = -D \left[\frac{d^3 w}{dx^3} \right]_{\text{au bord}} = k \frac{Pt}{2} \sqrt{\frac{P}{D}} \quad (14)$$

The shearing force in the overlap zone is determined by the equilibrium of the relative moment (Figure 4):

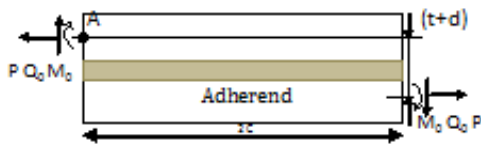


Figure. 4: The adhesive joint cross section.

$$Q_{equilibrium} = \frac{(t+d)P-2M_0}{2c} \quad (15)$$

The shear stress is given by the ratio between the shear force and the cross-section. By solving the differential equation of second order, Goland and Reissner led to the general expression for the shear stress.

$$\tau(m) = \left[\frac{\beta \cdot c}{t} \cdot (1 + 3 \cdot k) \cdot \frac{\cosh \left[c \cdot \frac{\beta}{t} \cdot m \right]}{\sinh \left[\frac{\beta \cdot c}{t} \right]} + 3 \cdot (1 - k) \right] \cdot p \cdot \frac{t}{\beta \cdot c} \quad (16)$$

$$\beta = \sqrt{8 \cdot \frac{Ga \cdot t}{E \cdot d}}$$

Combination between study of Liyong Tong and approach of Goland and Reissner

According to L.Tong [4], it is possible to express the bending moment MA in the presence of the crack with expression (7), but the existence of a crack length that significantly redistributes the stresses in the adhesive layer and thus changes the stresses resultants in both adherends.

RESULTS AND DISCUSSION

Lot of work has been done to understand and predict failure behavior of adhesive bonded single lap joints, based on many search in this case there are two important studies as follow:

Failure load increase by increasing the crack length results predicted by L.Tong [4].

k factor decrease by increasing the applied load results predicted by Goland and Reissner [1] and Hart-Smith L.J [3].

By both important studies, when crack length increase the k factor decrease.

From expression (7), we can extract the factor k:

$$k = \frac{\left(\frac{2 \cdot M_A}{P \cdot t} + \cosh(\mu_2 \cdot x_A) \right)}{\left(1 + \left(\frac{\mu_1 \cdot \tanh(\mu_2 \cdot x_A)}{\mu_2 \cdot \tanh(\mu_2 \cdot l)} \right) \right)} \quad (17)$$

So, for the calculation of the shear stress at the adhesive layer in the presence of crack, we can use the expression (16) of Goland and Reissner. To see the crack length effect on the values of shear stresses at the free edge of single lap shear joint, we focus only on the crack length xA in the expression (17). The shear stress in the adhesive layer of single lap shear joint as shown in the table. 1.

Table.1: Shear stress at free edge of overlap with k factor.

Half crack length xA [mm]	Factor k	Shear stress at free edge $\tau(m)_{max}$ [MPa]
0	0.3060	48.7997
1	0.2718	46.4079
2	0.2464	44.6336
3	0.2275	43.3085
4	0.2134	42.3215
5	0.2030	41.5962

This theory is based on differential equations for the stresses of adhesive:

Mechanical properties of adherends same as T300/934

Young's modulus E=Mpa 57226

In plane Poisson ratio = 0.05

Out of plane Poisson ratio = 0.28

Mechanical properties of FM300K film adhesive (nominal bondline thickness 0.16 mm)

Young modulus Ea=Mpa 2400

Poisson ratio = 0.32

Table. 2: Parameters of the geometric adhesive bonded.

Geometrical parameters	Values	Unit
c : half-length covering	25	mm
b : width of the joint	25.4	mm
t : thickness of adherends	1.72	mm
d : Adhesive thickness	0.16	mm

I Effect of crack length on adhesive shear stress

The shear stress along the bondline (adhesive mid-layer) was calculated and plotted against the overlap length for lap shear joint models with different crack lengths. Figure.5 shows the shear stress distribution in adhesive layer. We evaluated the shear stress at the edge in terms of

a gradual increase in crack length of 0-4 mm. From this figure, it is obvious that this stress decreases as a function of crack length, Because the presence of the crack absorbs some of the energy dissipated to both edges. The distribution of shear stress for different crack length $x_A=2\text{mm}$ and $x_A=4\text{mm}$ have the same distribution as model without crack only difference for the maximum shear stress at the end of free edge of the overlap part of single lap shear joint .

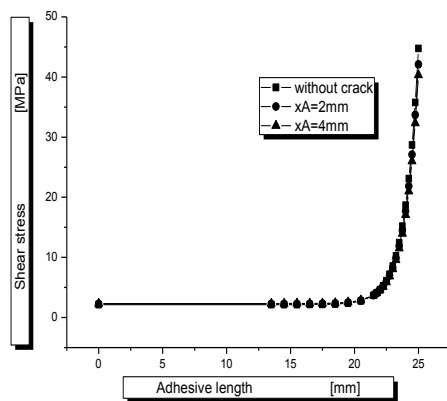


Figure. 5: Variation of the shear stress along the bonded joint according to the variation in the length of the half crack.

Results

III Effect of crack position

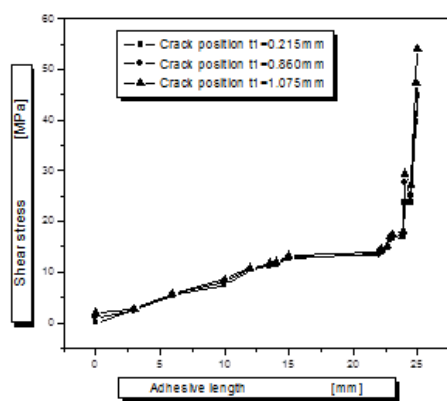


Figure. 6: Variation of the shear stress as a function of the crack position $x_A=2\text{mm}$.

To evaluate the shear stress along the adhesive area, we varied the crack location from 0.215 to 1.075 mm of the bonded joint (Figure 6). From this figure, it is clear that the three curves follow the same pace, with the exception of a

remarkable difference appears on the edge of the bonded joint. The presence of the crack generates a small perturbation of the stresses in the adhesive layer and this perturbation or stress concentration decrease or disappears when the distance between the crack position and the adhesive layer increase.

IV Correlation between analytic and numerical results

Figures. 5 and 7 show the effect of half crack length on distribution of shear stress in the adhesive layer with analytic and FEA model, comparing the results we found that the shear stresses with different crack length predicted by analytic model have the same curve as model with no crack and the only difference is the maximum shear stresses, but in the FEA model the shear stresses with different crack length have not the same curve as model without crack because the shear stress in the adhesive layer of a different crack length is smaller between the overlap end and the crack tip and is larger between the overlap center and a point slightly away from the crack tip.

A good agreement between analytic and numerical results as shown in table.3, maximum shear stress (at free edge) of adhesive layer are presented with different crack length, when the crack length increases from 2 to 10mm, the maximum shear stress predicted by FEA and analytic model decreases, and there is small difference between both model as shown in table. 3.

Table.3: Maximum shear stress [MPa] comparison between analytic and FEA results (Applied load: 410.22 N/mm).

Crack length [mm]	Analytical model τ_{xy}	FEA model τ_{xy}	Absolute relative difference	K factor
No crack	74.6336	71.692	3.94%	0.6757
2mm	69.4567	68.561	1.29%	0.6016
4mm	65.4372	64.675	1.16%	0.5441
6mm	62.2691	62.450	0.29%	0.4988
8mm	59.7458	60.583	1.40%	0.4627
10mm	57.7237	58.083	0.62%	0.4337

CONCLUSIONS

An analytic study was carried out to investigate and validated results by FEA (ANSYS) of the evolution of stresses in a bonded joint at interface and free edge with a crack. The analytic model was proposed for the determination of bending moment in the cracked zone. The balance of this moment has been transferred to the interface to calculate the shear stress along the adhesive layer of bonded joint. From the present results, the following is concluded.

- The presence of a crack has a significant effect on the shear stress distribution in adhesive layer.
- The presence of distant crack has no effect on the distribution of shear stresses in the adhesive.
- The results of the finite element modeling (ANSYS) have shown that there is also a second peak in the shear stress over the edge.
- Compared results showed good agreement between the maximum shear stress of the cracked section calculated by FEA (ANSYS) and those of the analytic model at free edge of adhesive layer

This study presented an investigation of the crack effect and a mechanic behavior on a composite repaired structure, which is very important to prepare perfectly a material composite for repairing damaged structure.

REFERENCES

- [1]. Goland M., Reissner E. 1944, The stress in cemented joints, *Journal of Applied Mechanics*, Vol. 11, N° 1, pp. A-17-27.
- [2]. Erdogan F., Ratwani M. 1971, Stress Distribution in Bonded Joints, *Journal of Composite Materials*, Vol. 5, pp. 378-393.
- [3]. Hart-Smith L.J. 1973, Adhesive-Bonded Double-Lap Joints, NASA, TR CR-112235.
- [4]. Tong L. 1998, Failure of adhesive-bonded composite single lap joints with embedded cracks *AIAA Journal*; 36(3):448-56.
- [5]. Tong L, Steven GP. 1999, Analysis and design of structural bonded joints Boston (USA): Kluwer Academic;.
- [6]. Cheuk PT, Tong L. 2002, Failure of adhesive bonded composite lap shear joints with embedded precrack» *Compos Sci Technol*; 62:1079–95.
- [7]. Luo Q., Tong L. 2009, Analytical solutions for nonlinear analysis of composite single-lap Adhesive joints *International Journal of Adhesion & Adhesives* 29 (2009) 144– 154

FRP PROPERTIES EFFECT ON NUMERICAL DEFORMATIONS IN FRP BARS- REINFORCED CONCRETE ELEMENTS IN HOT ZONE

Ali Zaidi¹, Mohammed Moulay Brahim¹, Kaddour Mouattah¹, and Radhouane Masmoudi²

¹Structures Rehabilitation and Materials Laboratory (SREML), University of Laghouat, Algeria

²Department of civil engineering, Sherbrooke University, QC, Canada

*Corresponding author: Email: Ali.Zaidi@USherbrooke.ca or a.zaidi@mail.lagh-univ.dz

ABSTRACT

Fiber reinforced polymer (FRP) bars exhibit higher thermal properties in transverse direction with respect to concrete. This difference in transverse thermal properties between FRP and concrete may affect transverse thermal deformations and consequently cracking thermal loadings producing failure of concrete cover. This paper presents a numerical study to investigate the effect of thermal and mechanical properties of FRP bars on circumferential thermal deformations of concrete cylinders axially reinforced with FRP bars under temperature increase up to 60°C using nonlinear finite element models. For concrete in tension, a stress–strain relationship with tension softening is used. Whereas, unidirectional FRP bars is considered linear elastic/brittle. The numerical simulation results show significant effects of FRP bars-transverse elasticity modulus on the evolution of transverse thermal deformations in concrete cylinders reinforced with FRP bars under the temperature increase.

NOMENCLATURE

QUANTITY	SYMBOL
Concrete cover thickness;	c
Bar diameter;	d_b
Modulus of elasticity of concrete;	E_c
Transverse modulus of elasticity of FRP bar;	E_{tb}
Compressive strength of concrete;	f_c
Tensile strength of concrete;	f_{ct}
Radius of concrete cylinder reinforced axially reinforced with FRP bar	r_2
Coefficient of thermal expansion of concrete;	α_c
Transverse coefficient of thermal expansion of FRP bar;	α_{tb}
Transverse Poisson's ratio of FRP bar;	ν_{tt}
Poisson's ratio of concrete;	ν_c
Temperature variation (thermal load);	ΔT
Thermal load producing the first radial cracks in concrete at FRP bar/concrete interface;	ΔT_{cr}
Thermal load producing the splitting failure of concrete cover	ΔT_{sp}

INTRODUCTION

The research in advanced composite material field has permitted to use fiber reinforced polymer (FRP) in concrete structures as a reinforcement substituting steel bars because of their sensibility to the corrosion phenomenon. FRP is considered as an effective solution to eradicate the corrosion problem and reduce the repair cost of concrete structures such as bridges and parking garages. However, the transverse thermal incompatibility between FRP bars and concrete is a major problem in concrete structures exposed to high temperatures in hot climate regions. Because the coefficient of thermal expansion of FRP bars in the transverse direction is 3 to 5 times greater than that of concrete [1-4]. This difference in transverse thermal expansion induces circumferential tensile stresses in concrete which may cause splitting cracks and eventually the spalling of concrete cover. Further studies are necessary to determine the minimum concrete cover thickness to avoid the failure of concrete cover under high temperatures. Extension research works were carried out by Zaidi et al. (2013) [1], Masmoudi et al. (2005) [2], and Aiello et al (2001) [3] to investigate the thermal effect on FRP bars-

reinforced concrete structures varying the concrete cover thickness and the FRP bar diameter. These previous studies did not take into account the effect of the transverse elastic modulus of FRP bars. For this reason, a numerical investigation was carried out on concrete cylinders axially reinforced with FRP bars subjected to temperature increase to evaluate the influence of FRP transverse elastic modulus on the performance of concrete elements reinforced with FRP bars. The study proves that the circumferential thermal deformations within concrete cover surrounding FRP bars are affected by thermo-mechanical properties of FRP bars in hot regions.

NUMERICAL SIMULATIONS

Main hypothesis:

Finite element simulations for concrete cylinder axially reinforced with FRP bar under high temperatures were carried out to investigate the effect of thermo-mechanical properties of concrete and FRP bars on the behavior of concrete cover. The nonlinear behavior was considered for concrete material while the linear elastic/brittle behavior was assumed for FRP bar. A hypo-elastic model is implemented in the finite element ADINA software to simulate the concrete behavior. The stress-strain relationship of concrete in tension exhibits a linear elastic response up to the concrete tensile strength, which is followed by a linear descending branch down to the ultimate tensile strain. The numerical investigation was performed assuming plane stress conditions. Due to the geometrical symmetry of the problem and loading conditions, only a quarter of the cross section was modeled. Both concrete and FRP bars were meshed using triangular finite elements with six nodes. A perfect bond was assumed for the modeling of the interface between FRP bar and concrete.

Various design parameters effects have been considered in the characterization of cracking's initiation from the interface of concrete/bar up to its arrival at the outer surface of concrete cover. To study the influence of concrete parameters, a concrete cover to FRP bar diameter ratio (c/d_b) between 1 and 2.5 was considered. The problem is considered to be static whilst the thermal loading ΔT was increased steadily by an increment of 5°C, and the maximum temperature variation ΔT was 60°C ($T=80^\circ\text{C}$ since the reference temperature $T=20^\circ\text{C}$). In order to study only the concrete confining action contribution to sustain tensile stresses, no transverse

reinforcement was used. The main parameters considered in this study were the effects of FRP transverse elastic modulus and concrete cover thickness on the delay of the concrete cracks propagation.

Materials:

FRP bar:

The main thermoelastic parameters of FRP bar are reported in Table 1 wherein the transverse elastic modulus (E_{tb}) is ranged from 4 to 10 GPa, and the transverse coefficient of thermal expansion of FRP bar (α_{tb}) is equal to $33 \times 10^{-6} / ^\circ\text{C}$ and $58 \times 10^{-6} / ^\circ\text{C}$. Whereas, the transverse Poisson's ratio of FRP bar (ν_{tt}) is assumed equal to 0.38. The concrete cover thickness surrounding FRP bar is considered to be equal 20, 30, and 40 mm as recommended by the canadian code CSA-S6-06 [6].

Table 1
FRP bar Properties used

FRP bar diameter, d_b (mm)	E_{tb} (GPa)	α_{tb} ($\times 10^{-6}/^\circ\text{C}$)
13; 16; 19; 25	4; 7; 10	33; 58

Concrete:

Four concrete classes namely C30, C40, C50, and C60 were considered. The corresponding mechanical properties of the four concrete classes were estimated according to the design code CEB-FIP Model Code [7]. The tensile strength and Young's modulus are reported in Table 2.

Table 2
Concrete Mechanical Properties used

Concrete class	C30	C40	C50	C60
Compressive strength f_c (MPa)	30	40	50	60
Tensile strength f_{ct} (MPa)	2.9	3.5	4.1	4.6
Young's Modulus E_c (GPa)	29	31	33	35

The coefficient of thermal expansion and the Poisson's ratio of concrete have been considered equal to $\alpha_c = 11 \times 10^{-6} / ^\circ\text{C}$ and $\nu_c = 0.17$, respectively.

RESULTS AND DISCUSSION

Cracks propagation and failure modes:

Table 3 presents typical critical depths of radial cracks l_{cr} , from which the concrete cover is completely cracked, versus the ratio of concrete cover thickness to FRP bar diameter c/d_b and transverse elasticity modulus of FRP bars E_{tb} for a concrete cylinder reinforced with FRP bar of 25 mm diameter having a compressive concrete strength $f_c = 40$ MPa, and a coefficient of thermal expansion (CTE) of FRP bars in transverse direction $\alpha_{tb} = 33 \times 10^{-6}/^\circ\text{C}$. It can be observed that the ratio of cracking critical depth to concrete cylinder radius (l_{cr}/r_2) increases with the increase in the transverse elasticity modulus of FRP (E_{tb}), as shown in figure 1 for $c/d_b = 1.5$. While, this ratio l_{cr}/r_2 decreases with the increase in the ratio c/d_b , this is due to the reduction of the radial pressure exerted by FRP bar on concrete cover when the ratio c/d_b increased. Also, it is noted that for a concrete cylinder having $c/d_b=1.9$ and $E_{tb} = 4$ GPa, radial cracks do not reach the outer surface of concrete cover (that means not entirely cracked) under temperature variation up to $+60$ °C. The same remark can be noted for concrete cylinders having $c/d_b=2.5$ and $E_{tb} = 4$; 7; and 10 GPa. From these numerical simulation results, it can be concluded that the splitting failure of concrete cover is occurred when the radial cracks reach the cracking critical depth $l_{cr} = (0.45 - 0.63)r_2$ depending on the ratio c/d_b .

Table 3

Critical depth of radial crack l_{cr} through concrete cover versus (Concrete class C40; FRP bar N°25; $\alpha_{tb}=33 \times 10^{-6}/^\circ\text{C}$)

c/d_b	r_2^* (mm)	E_{tb} (GPa)	l_{cr} (mm)	l_{cr}/r_2	Average l_{cr}/r_2
1.0	38.10	4	20	0.52	0.63
		7	25.3	0.66	
		10	27	0.71	
1.5	50.80	4	23.4	0.46	0.52
		7	23.3	0.46	
		10	32.7	0.64	
1.9	60.96	4	-	-	0.45
		7	24.8	0.41	
		10	29.2	0.48	

* r_2 : Radius of concrete cylinder reinforced axially with FRP bar.

Figure 1 shows the main typical crack patterns found in the numerical simulations for a concrete cylinder reinforced with FRP bar of 25 mm diameter having a ratio $c/d_b=1.5$ and various FRP transverse elasticity modulus E_{tb} .

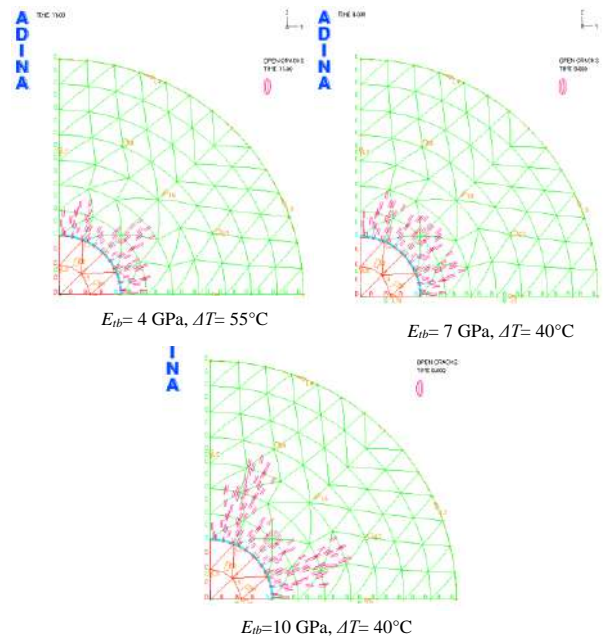


Figure 1

Typical radial crack patterns through concrete cover (C40; FRP N°25; $\alpha_{tb}=33 \times 10^{-6}/^\circ\text{C}$; $c/d_b=1.5$)

Figure 2 and Table 4 illustrate thermal loadings ΔT_{sp} producing the splitting failure of concrete cover. The whole rupture is produced immediately after that the radial crack depth reaches the cracking critical depth l_{cr} . It can be seen that thermal loadings ΔT_{sp} increase proportionally with the ratio c/d_b and the concrete strength class. However, these thermal loads decrease with the increase in the transverse elasticity modulus (E_{tb}) and the transverse coefficient of thermal expansion (α_{tb}) of FRP bars. From Table 4, it can be suggested that for Saharan regions (Arabian Gulf, Northern Africa) where the climate temperature is about 60°C in summer ($\Delta T=40^\circ\text{C}$ since the reference temperature is about 20°C), a ratio $c/d_b \geq 2$ with concrete and FRP materials having respectively compressive concrete strength $f_c = 40$ MPa and FRP transverse coefficient of thermal expansion $\alpha_{tb} = 33 \times 10^{-6}/^\circ\text{C}$, is sufficient to avoid the failure of concrete cover.

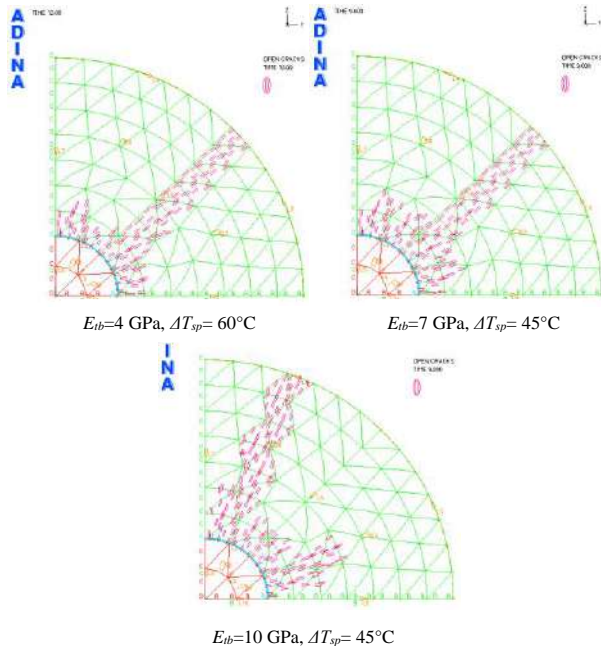


Figure 2

Splitting failure of concrete cover for different E_{ib} (C40; FRP N°25; $\alpha_{ib}=33 \times 10^{-6}/^{\circ}\text{C}$; $c/d_b=1.5$)

Table 4

Thermal loadings ΔT_{sp} ($^{\circ}\text{C}$) producing the splitting failure of concrete cover of reinforced concrete cylinders

c/d_b E_{ib} (GPa)	$\alpha_{ib}=33 \times 10^{-6}/^{\circ}\text{C}$					$\alpha_{ib}=58 \times 10^{-6}/^{\circ}\text{C}$				
	1.0	1.2	1.5	1.9	2.5	1.0	1.2	1.5	1.9	2.5
	C30	45	50	55	>60	>60	20	25	25	30
	7	35	35	45	50	55	15	20	20	25
	10	30	30	40	40	50	15	15	20	25
C40	4	50	60	60	>60	>60	25	30	35	40
	7	40	40	45	55	>60	20	20	25	30
	10	35	35	45	45	60	15	20	25	35
C50	4	60	60	>60	>60	>60	30	30	35	40
	7	45	50	55	>60	>60	20	25	30	35
	10	40	40	50	>60	>60	20	20	25	40
C60	4	>60	>60	>60	>60	>60	35	35	40	55
	7	50	55	>60	>60	>60	25	25	35	40
	10	45	45	60	>60	>60	20	25	30	45

FRP bar-transverse elastic modulus effect on thermal deformation:

Figures 3 and 4 show circumferential thermal deformations, at the interface of FRP bar/concrete, versus temperature variation ΔT and FRP transverse elasticity modulus for a concrete cylinder reinforced with FRP bar of 25 mm diameter having a compressive concrete strength $f_c = 40$ MPa, a coefficient of thermal expansion (CTE) of FRP bars in transverse direction $\alpha_{ib} = 33 \times 10^{-6}/^{\circ}\text{C}$, and a ratio $c/d_b=1$. It can be observed that the thermal strains curves are linear and the similar trend until the thermal loads, producing the circular crown of cracking concrete, from which the strain curves change their trend because of the presence of the deep radial cracks that reach the cracking critical depth, as shown in Figure 1. Also, it can be seen that the circumferential thermal strains increase significantly with the increase in the transverse elasticity modulus of the FRP bar E_{ib} particularly for high temperatures.

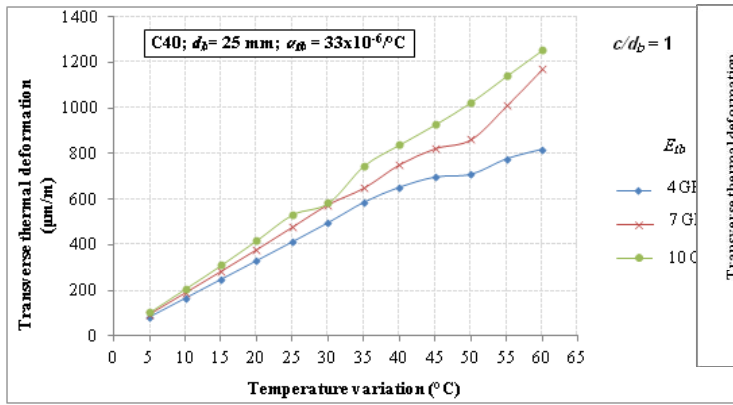


Figure 3

Transverse thermal deformations at the interface of FRP bar/concrete for different E_{tb} (C40; $d_b=25$ mm; $c/d_b=1$; $\alpha_{tb}=33 \times 10^{-6}/^\circ\text{C}$).

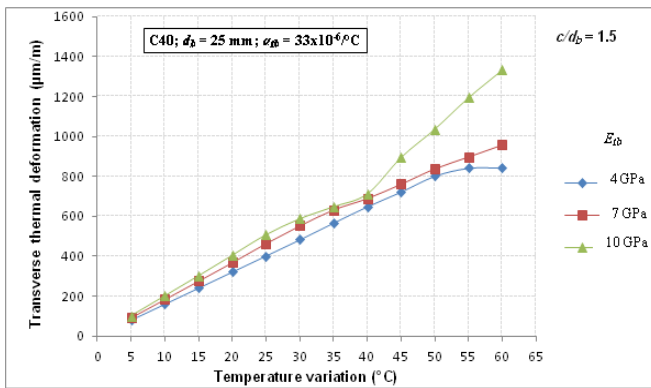


Figure 4

Transverse thermal deformations at the interface of FRP bar/concrete for different E_{tb} (C40; $d_b=25$ mm; $c/d_b=1.5$; $\alpha_{tb}=33 \times 10^{-6}/^\circ\text{C}$).

Figure 5 presents circumferential thermal deformations, at the interface of FRP bar/concrete, versus temperature variation ΔT and c/d_b ratio for a concrete cylinder reinforced with FRP bar of 25 mm diameter having a compressive concrete strength $f_c=40$ MPa, a transverse coefficient of thermal expansion of FRP bars $\alpha_{tb}=33 \times 10^{-6}/^\circ\text{C}$, and FRP transverse elasticity modulus $E_{tb}=4$ GPa. This figure proves that thermal strain curves are linear and similar until thermal loads, corresponding to the development of the circular crown of cracks within concrete, from which the curves exhibit clearly their divergence. It can be concluded that the concrete cover thickness has no big influence on the transverse thermal deformations of FRP bar-reinforced concrete cylinders.

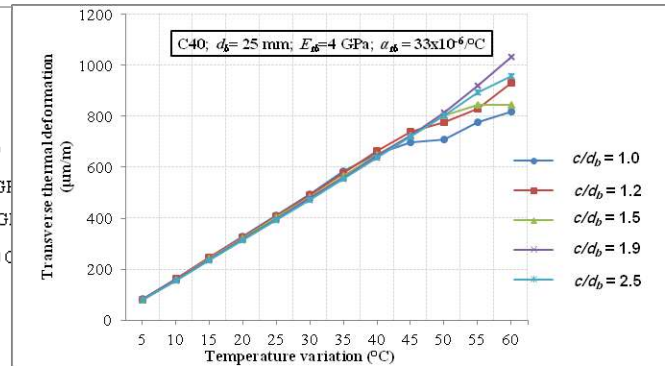


Figure 5

Thermal deformations at the interface of FRP bar/concrete (C40; $d_b=25$ mm; $E_{tb}=4$ GPa; $\alpha_{tb}=33 \times 10^{-6}/^\circ\text{C}$) for different ratio c/d_b .

CONCLUSIONS

The numerical analysis of the FRP thermo-mechanical properties effect on circumferential thermal deformations of concrete cover surrounding FRP bars under temperature increase up to 60°C , permits to draw the following conclusions:

- The circumferential thermal deformations increase significantly with the increase in the FRP transverse elasticity modulus E_{tb} particularly for high temperatures.
- The concrete cover thickness has no big influence on the circumferential thermal deformations of FRP bar-reinforced concrete cylinders.
- For Saharan regions (Arabian Golf, Northern Africa) where the climate temperature is about 60°C in summer ($\Delta T=40^\circ\text{C}$ since the reference temperature is about 20°C), a ratio of concrete cover thickness to FRP bar diameter $c/d_b \geq 2$ is sufficient to avoid the failure of concrete cover using concrete and FRP materials that have respectively compressive concrete strength $f_c=40$ MPa and FRP transverse coefficient of thermal expansion $\alpha_{tb}=33 \times 10^{-6}/^\circ\text{C}$.
- Thermal loadings ΔT_{sp} producing the splitting failure of concrete cover increase proportionally with the ratio c/d_b and the concrete strength class.

ACKNOWLEDGMENTS

The writers would like to acknowledge the support of the Civil Engineering Department of Sherbrooke University (Canada) and also the Structures Rehabilitation and Materials Laboratory (SREML) of Laghouat University (Algeria). The opinion and

analysis presented in this paper are those of the authors.

REFERENCES

1. Zaidi, A., Masmoudi, R., and Bouhicha, M., 2013, Numerical analysis of thermal stress deformation in concrete surrounding FRP bars in hot region, *Construction and Building Materials*, **38**, pp. 204–213.
2. Masmoudi, R., Zaidi, A., and Patrick, G., 2005, Transverse thermal expansion of FRP bars embedded in Concrete, *Journal of Composites for Construction*, ASCE, **9**, pp. 377-387.
3. Aiello, M.A., Focacci, F., and Nanni, A., July-August 2001, Effects of Thermal Loads on Concrete Cover of Fiber-Reinforced Polymer Reinforced Elements: Theoretical and Experimental Analysis, *ACI Materials Journal*, **98**, pp. 332-339.
4. Gentry, T.R., Husain, M., 1999, Thermal compatibility of concrete and composite reinforcements, *Journal of Composite for Construction*, **3**, pp. 82-86
5. ADINA, 2012, *Theory and Modelling Guide Volume I: ADINA Solids & Structures*, ADINA R & D Inc., USA.
6. Canadian Standards Association, 2006, *Canadian highway bridge design code. CAN/CSA-S6-06*, Toronto, Ontario, Canada.
7. Comité Euro International du béton, 2003, *CEB-FIP Model code 1990 : Design code, 1990*, Thomas Telford House, London, 437 p.
8. American Concrete Institute, 2003, *Guide for the Design and Construction of Concrete Reinforced with FRP Bars, 440.1R03*, Reported by ACI Committee 440.

TIME-DEPENDENT BEHAVIOR OF COMPOSITE STEEL-CONCRETE BEAMS WITH CREEP ACCORDING EUROCODE 4

RAHAL Nacer^{1,a,*}, BEGHADAD Houada^{2,a}, TEHAMI Mohamed^{2,a}, SOUICI Abdelaziz^{1,a}

¹Civil Engineering department, University of Mascara, Algeria

²Civil Engineering department, USTO BP 1505 M'Naouer, Oran 31000 Algeria

^aLaboratory of mechanical structure and construction stability (LM2SC), USTO, Oran 31000 Algeria

*N. RAHAL: Email: rahnac2002@yahoo.fr

ABSTRACT

As well known, the deformation of concrete elements subjected to permanent loads increases with time due to creep. So connecting concrete with steel, as in composite structures, considerable stress redistributions between the two materials occur along the time. Generally this variation consists in a reduction of stress in the concrete slab and an increase in the steel element. In the steel-concrete composite beams, the interaction between the two materials is characterized by the concept of the degree of connection (N/N_f) represents the ratio of the connector's number in partial connection and the connector's number in perfect connection. The effect of creep on the behaviour of composite beams has been studied analytically by Tehami et al and numerically by Partov et al. The two proposed methods are to determine the solicitations and the additional stresses provided by the creep of concrete in the steel-concrete composite beams having perfect connection only ($N/N_f=1$). To overcome to the drawback of this model, the objective of this work is to formulate the effects of concrete creep on behavior of steel-concrete composite beams regardless the employed degree of connection. Results obtained from our suggested model are completely satisfactory.

KEYWORDS Composite beam, creep, time, degree of connection, deformation, Volterra integral equations, steel, concrete

1. INTRODUCTION

The steel-concrete composite system comprehends the structures obtained joining, through particular connection devices, steel members, with different shapes (steel profiles, plates, trusses, etc.), to reinforced concrete slabs.

The most frequent use of the composite system is in the construction of floors in steel industrial or office buildings [1] and in the construction of bridges and viaducts [2]. In some cases, the composite system is also used for the columns of buildings [1, 3].

When a constant compressive load is applied to a concrete specimen, the specimen is immediately deformed and then continues to deform gradually over time when the load is maintained [4,5,6]. This phenomenon discovered in 1907 by Hatt [7]. The effect of this gradual deformation for constant applied load is called concrete creep. The strain which is produced in the course of a creep test at the end of loading may be three or four times the initial elastic strain [8].

The behavior of the composite system is significantly different with respect to concrete structures and steel structures, because of the interaction of the two materials. This interaction emphasizes considerably the effects of time dependent phenomena because creep interest only the concrete; the steel, that is

solidarized to the concrete, contrasts the deformation variations causing significant changes in the stress distribution [9, 10, 11, 12].

The effect of creep on the behaviour of steel-concrete composite beams has been studied analytically by Tehami et al [13]. Numerically, it was analyzed by Partov et al [12]. The two proposed methods are to determine, at any time t , the solicitations and the additional stresses provided by the creep of concrete in the steel-concrete mixed beams having perfect connection only ($N/N_f = 1$).

In reality, most connectors used in steel-concrete composite beams, such as studs, are discrete elements. This type of elements induces the steel concrete interface, a lower slip sliding of the same beam connectionless. This concept is called partial interaction wherein the rigidity of such a beam is less than that of the same beam with full connection. This concept is represented in the calculations codes, by report degree of connection (N/N_f).

N : number of partial connection, N_f : number of total connection and N/N_f : is the degree of shear connection in % ($N/N_f \geq 0,4$) [14].

$$Si \begin{cases} N/N_f = 1 & : \text{Perfect connection} \\ 0 < N/N_f \leq 1 & : \text{Partial connection} \\ N/N_f = 0 & : \text{No connection} \end{cases}$$

Since the degree of connection (N/N_f) effect's is a real fact, its introduction into the analysis of composite steel and concrete beams behavior is essential.

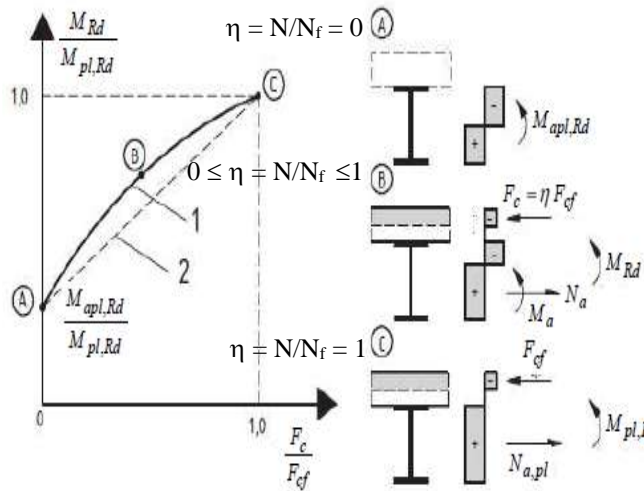


Figure 1: Effect of N/N_f in bending moment.

By introducing the influence of the degree of connection (N/N_f) on the steel-concrete interface (in which: $N/N_f < 1$), our present contribution is therefore to develop and enrich the model developed by Tehami et al [13] which was designed only for composite beams with full connection (in which: $N/N_f = 1$). Hence, our methodology is more general and applicable to composite beams regardless of the degree of connection (N/N_f) employed.

The work introduced in this article is a theoretical study of the behavior of composite beams with respect to the phenomenon of concrete creep. In fact, our contribution through this work resides essentially in consideration of the degree of connection between the slab and steel beam. While using the theory of the linear viscoelasticity of the concrete, and on the basis of the rate of creep method of concrete, in proposing an analytical model, made up by a system of two linear differential equations, emphasizing the effects caused by creep on the resistance of a steel-concrete composite section.

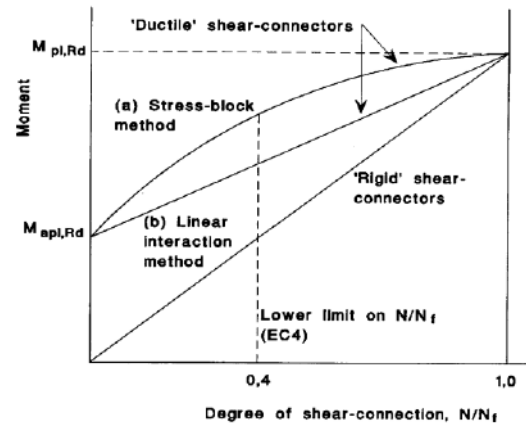


Figure 2 : minimum of N/N_f in composite beams [14].

The well stocked results, by the use of formulation proposed, are satisfactory while confronting them to those given by Tehami et al [13] and Partov et al [12]. They also show that the variation of the efforts, in normal efforts and in bending moments, soliciting the slab made of concrete and the metallic beam is in the beginning important and so that it decreases, continually, during the time until the stabilization. They also show that new local constraint redistribution will be developed in the slab made of concrete and in the metallic beam.

The relative deformation at time t , is calculated by using the two following equations [15, 16, 17, 18, 19]:

$$\varepsilon(t) = \frac{\sigma(t)}{E_c(\tau_1)} + \frac{1}{E_c(\tau_1)} \int_{\tau_1}^t \sigma(\tau) \frac{\partial \varphi(t, \tau)}{\partial \tau} d\tau \quad (1)$$

$$\frac{d\varepsilon(t, \tau)}{d\varphi} = \frac{1}{E_c(\tau_1)} \frac{d\sigma(t)}{d\varphi} + \frac{\sigma(t)}{E_c(\tau_1)} \quad (2)$$

2. USE OF THE CONCRETE AGEING FOR THE STEEL-CONCRETE MIXED BEAMS

Let's consider that a cross section of a steel-concrete mixed beam is subjected to a normal force N_0 and a bending moment M_0 , applied at the centre of gravity of its cross section made homogeneous (Fig. 3).

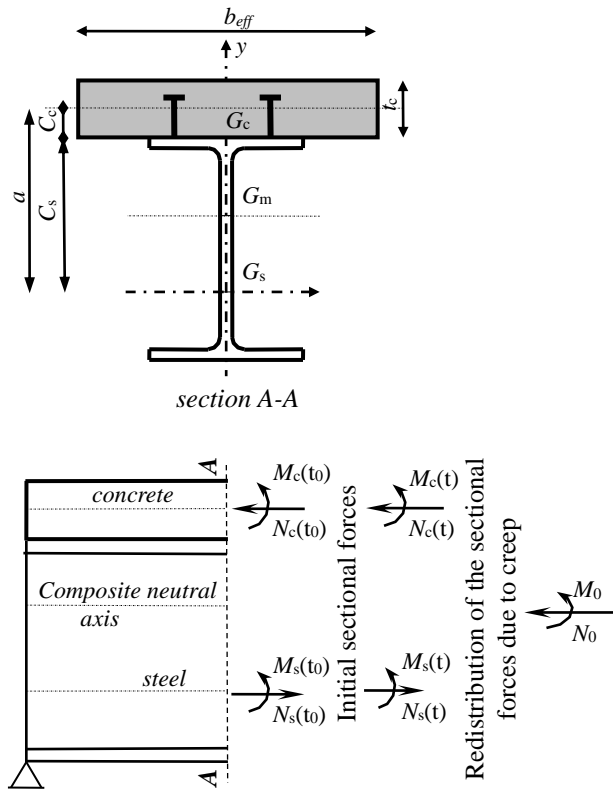


Figure 3 : Internal efforts in steel-concrete composite beams subjected to creep

2.1 Basic equations of equilibrium

Let us denote both the normal forces and the bending moments in the cross-section of the plate and the girder after the loading in the time $t = 0$ with $N_c(t_0)$, $M_c(t_0)$, $N_s(t_0)$, $M_s(t_0)$ and with $N_c(t)$, $M_c(t)$, $N_s(t)$, $M_s(t)$ a new group of normal forces and bending moments, arising due to creep of concrete.

In a steel-concrete composite cross section, the creep will affect in time, the diagram of stress distribution but the equilibrium conditions must be preserved [22]. By introducing the effect of the degree of connexion, we can write the static equilibrium of the composite cross section, as follows:

$$\begin{cases} N_s(t) - N_c(t) \left[\left(\frac{A_s}{A_m} - \frac{A_c \cdot C_c^2}{I_m} \right) \left(1 - \frac{N}{N_f} \right) - 1 \right] = N_0 \\ M_s(t) - N_c(t) a \left[1 - \left(\frac{A_s}{A_m} - \frac{A_c \cdot C_c^2}{I_m} \right) \left(1 - \frac{N}{N_f} \right) \right] + M_c(t) = M_0 \end{cases} \quad (3)$$

A_c : concrete slab area ($A_c = b_{eff} \times t_c$).

A_m : area of homogeneous composite section.

A_s : Metallic beam area.

I_m : Moment of inertia of the homogeneous composite section.

2.2 Compatibility equations

Due to the fact that the problem is internally statically indeterminate system, the equilibrium equations (Eq. 15) are not sufficient to solve it. It is necessary to produce two additional equations in the sense of compatibility and deformations of both steel girder and concrete slab in time t .

The behavior of the mixed beams is characterized by the interaction between steel and concrete. The use of the connection that prevents slip and lifting of the two materials allows us writing the interface condition at which the curvatures and deformations of the concrete slab and the steel beam are equal, then we can write:

2.2.1 Compatibility of curvatures concrete/steel

$$\chi_c(t) = \frac{M_c(t)}{E_c I_c} = \frac{M_s(t)}{E_s I_s} \quad (4)$$

E_s : longitudinal deformation modulus of steel.

2.2.2 Compatibility of deformations concrete/steel

$$\varepsilon_c(t) = \frac{N_c(t)}{E_c A_c} + \frac{M_c(t)}{E_c I_c} C_c = \frac{N_s(t)}{E_s A_s} + \frac{M_s(t)}{E_s I_s} C_s \quad (5)$$

I_c : Moment of inertia of the concrete slab.

I_s : Moment of inertia of the metallic beam.

In accordance with the irreversible law of concrete (Eq.1), by using the relations (Eqs.3) of the equilibrium conditions, by using the compatibility equations (Eqs. 4 and 5) and by expressing the efforts $N_s(t)$ and $M_s(t)$ as a function of $N_c(t)$ and $M_c(t)$, one obtains the following system of differential equations.

$$A_1 \frac{dM_c(t)}{d\varphi} + A_2 \frac{dN_c(t)}{d\varphi} + M_c(t) = 0 \quad (6)$$

$$A_3 \frac{dM_c(t)}{d\varphi} + A_4 \frac{dN_c(t)}{d\varphi} + A_5 M_c(t) + A_6 N_c(t) = 0 \quad (7)$$

Where:

$$A_1 = \left(1 + \frac{I_c}{nI_s}\right) \left[1 - \left(\frac{A_s}{A_m} - \frac{A_c \cdot C_c^2}{I_m}\right) \left(1 - \frac{N}{N_f}\right)\right]$$

$$A_2 = -\frac{a \cdot I_c}{n \cdot I_s} \left[1 - \left(\frac{A_s}{A_m} - \frac{A_c \cdot C_c^2}{I_m}\right) \left(1 - \frac{N}{N_f}\right)\right]$$

$$A_3 = \left(\frac{C_c}{I_c} - \frac{C_s}{nI_s}\right) \left[1 - \left(\frac{A_s}{A_m} - \frac{A_c \cdot C_c^2}{I_m}\right) \left(1 - \frac{N}{N_f}\right)\right]$$

$$A_4 = \left(\frac{1}{A_c} + \frac{1}{nA_s} + \frac{C_s \cdot a}{nI_s}\right) \left[\left(\frac{A_s}{A_m} - \frac{A_c \cdot C_c^2}{I_m}\right) \left(1 - \frac{N}{N_f}\right) - 1\right]$$

$$A_5 = \frac{C_c}{I_c} \left[1 - \left(\frac{A_s}{A_m} - \frac{A_c \cdot C_c^2}{I_m}\right) \left(1 - \frac{N}{N_f}\right)\right]$$

$$A_6 = -\frac{1}{A_c} \left[1 - \left(\frac{A_s}{A_m} - \frac{A_c \cdot C_c^2}{I_m}\right) \left(1 - \frac{N}{N_f}\right)\right]$$

If we consider in the equations (Eqs.6 and 7), that $N=N_f$ (beams with full connection), we obtain the system of differential equations developed by Tehami et al [13]. The general solution of the system of differential equations (Eqs.6 and 7) [23], and which constitutes the relations giving the variation, in time, of the loadings, i.e: bending moments $M_c(t)$ and normal efforts $N_c(t)$, are given respectively by the following matrix expression :

$$\begin{Bmatrix} M_c(t) \\ N_c(t) \end{Bmatrix} = \begin{bmatrix} C_1 & C_2 \cdot a_1 \\ C_1 \cdot a_2 & C_2 \end{bmatrix} \begin{Bmatrix} e^{\lambda_1 \varphi} \\ e^{\lambda_2 \varphi} \end{Bmatrix} \quad (8)$$

C_1 and C_2 : after setting of the concrete condition, the constants are determined. The application of the load, at time t_0 , generates a bending moment $M_c(t_0)$ and axial force $N_c(t_0)$ on the slab of concrete.

3. NUMERICAL RESULTS

To validate this model, we have examined the composite beam that has been treated by Partov et al [12] using our proposed method. The geometric and physical characteristics of the discussed example are: $b_{eff} = 2940$ mm, $t_c = 300$ mm, $b_{fit} = 300$ mm, $t_{fit} = 15$ mm, $b_{fb} = 400$ mm., $t_{fb} = 30$ mm, $h_w = 1455$ mm, $t_w = 15$ mm., $A_c = 8820$ cm², $A_s = 383.25$ cm², $A_m = 2543.05$ cm², $I_c = 661500$ cm⁴, $I_s = 1217963.7$ cm⁴, $I_m = 4536360.758$ cm⁴, $C_c = 15.0$ cm, $C_s = 88.87$ cm, $a = 103.87$ cm, $E_c = 33 \times 10^4$ MPa, $E_s = 2.1 \times 10^5$ MPa, n

$= 6.56$, $M_0 = 1237$ KN.m, $N_c(t_0) = 846.60$ KN, $M_c(t_0) = 27.56$ KN.m

The initial time of the loading is expected to be $t_0 = 28$ days.

The work was done by varying the degrees of connection $N/N_f = (100\%, 80\% \text{ and } 60\%)$. Calculate the bending moments $M_c(t)$ and the normal efforts $N_c(t)$ in the concrete slab, were carried out until the loadings stability was observed.

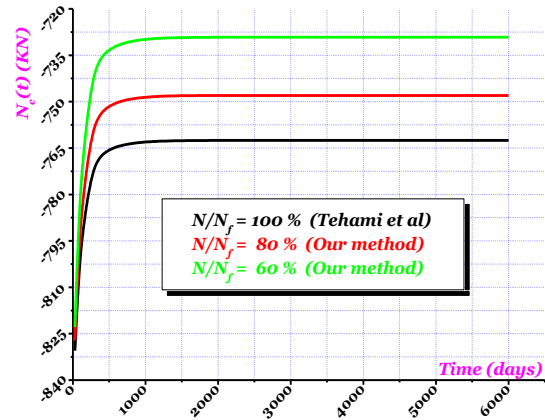


Figure 4: Reduction, in time, of the concrete slab normal effort $N_c(t)$

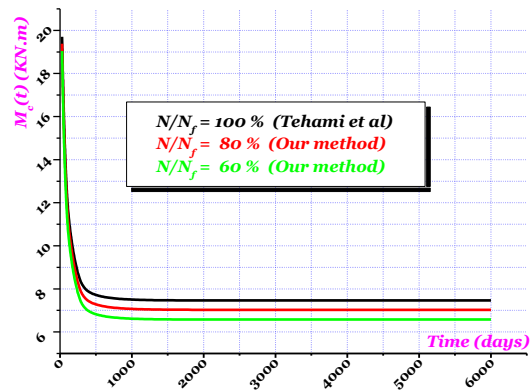


Figure 5: Reduction, in time, of the concrete slab moment $M_c(t)$

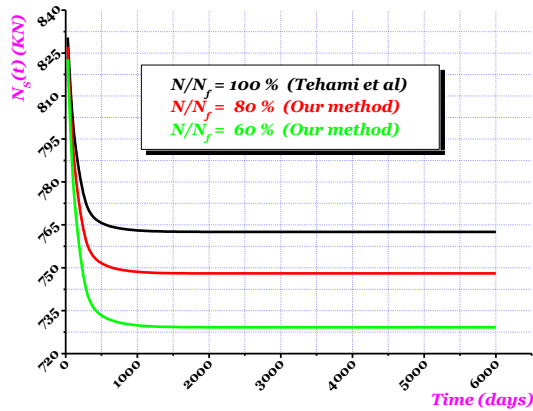


Figure 6: Increase, in time, of the normal effort $N_s(t)$ recovered by the

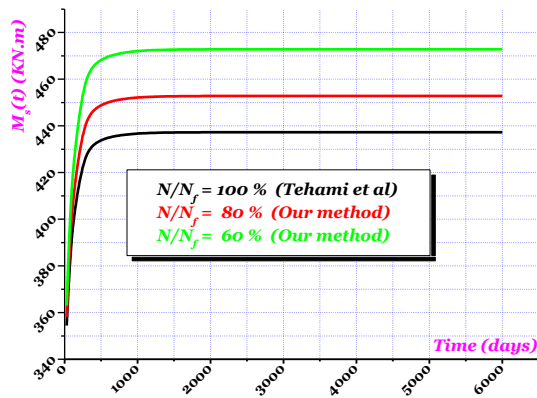


Figure 7: Increase, in time, of the moment $M_s(t)$ recovered by the steel section

4. CONCLUSION

The objective of this work is to formulate the effects of concrete creep on the service behavior of composite steel and concrete beams with consideration of the variation in the degree of connection (N/N_f) used in steel-composite beams concrete. In this context, a framework for analytical formulation was developed in this paper.

The model developed in this paper is to extend and generalize the one proposed by Tehami et al [13] (designed only for composite beams with full connection: $N/N_f = 1$), by introducing a new variable that is the degree of connection (N/N_f), which will give the new stress redistribution due to creep and which correspond to the case of complete connection and the partial connection. Hence, with respect to time t this research supports the conclusion that:

1- In steel-concrete beams, the effects of creep can cause significant changes in the deformations and in the internal stresses.

2- The effects of creep are expressed by the decrease of the stresses in the concrete plate and in the increase of stresses in the steel beam.

3- In a mixed steel-concrete beam, the degree of connection (N/N_f), with consideration of concrete creep, has the effect:

3.1 To increase progressively over time, its curvature.

3.2 To change the position of its neutral axis.

4- The results obtained by this analytical method, are completely comparable with the results derived by Partov et al [12] and Tehami et al [13].

5- Our present methodology is more general and applicable to composite beams regardless the employed degree of connection (N/N_f).

The results obtained by this analytical method, are completely comparable with the results derived by Partov et al [12] and Tehami et al [13].

Depending on the degree of connection (N/N_f) and the direct application of our formulas, this model will be a working tool and a simple way to predict in terms of the local redistribution of stresses due to flow regardless the used type of connection.

REFERENCES

1. Johnson R P. Composite structures of steel and concrete - beams, slabs, columns, and frames for buildings. blackwell scientific Editions Third Edition; 2004.
2. Johnson R.P., Buckby R.J., (1994), Composite Structures of Steel and Concrete, Volume 2: Bridges, Blackwell Scientific Publications, Oxford, U.K.
3. Dezi L., Gattesco N., (2006), Composite Structures – New Buildings, Restoration, Bridges, CISM Press, Udine, Italy.
4. Hashim A R., Time dependent effects in reinforced concrete sections subjected to flexure, University of Surrey. A Thesis Submitted for the Degree of Doctor of Philosophy, 1986.
5. Mosley W H and Bungey J H., Reinforced concrete design, Fourth edition. Macmillan Education LTD, 1990.
6. Svetlana M Kostić, Biljana Deretić-Stojanović, Saša Stošić, Redistribution effects in linear elastic analyses of continuous composite steel-concrete

- beams according to eurocode 4. *Architecture and Civil Engineering* 2011; 9(1): 133-145.
7. Hatt W K., Notes on the effect of time element in loading reinforced concrete beams. *ASTM Proc* 1907; 7: 421-433.
 8. Setra : Eurocodes 3 et 4. Application aux ponts-routes mixtes acier-béton. Guide méthodologique Service d'Etudes Techniques des Routes et Autoroutes; 2007.
 9. Gilbert, R. I., and Bradford, M. A. (1995). "Time-dependent behavior of continuous composite beams at service load." *Journal of Structural Engineering, ASCE*, 121(2), 319-327.
 10. Macorini, L., Fragiaco, M., Amadio, C., and Izzuddin, B.A. (2006). "Long term analysis of steel-concrete composite beams: FE modelling for effective width evaluation." *Engineering Structures*, 28(8), 1110-1121.
 11. Dezi, L., Leoni, G., and Tarantino, A. M. (1995). "Time-dependent analysis of prestressed composite beams." *Journal of Structural Engineering, ASCE*, 121(4), 621- 633.
 12. Partov D and Kantchev V. Time-dependent analysis of composite steel-concrete beams using integral equation of volterra, according eurocode 4. *Journal of Engineering Mechanics*, Vol.16, N°5, 2009, p.2-26.
 13. Tehami M and Ramdane K E. Creep behaviour modelling of a composite steel-concrete section. *Journal of Constructional Steel Research* 65 (2009) 1029-1033
 14. Eurocode 4, " Design of composite steel and concrete structures, Part 1.1: General rules and rules for buildings", Revised draft February 2005. Prepared for the commission of the European communities and the European committee for standardisation, 2005.
 15. Kumar M P and Paulo J M M. *Concrete, Microstructure, Properties and Materials*. Third Edition. McGraw-Hill Companies; 2006.
 16. Gilbert R I. *Time effects in concrete structures. Developpements in Civil Engineering, N° 23*, Elsevier (1991).
 17. Gilbert R I and Ranzi G. *Time dependent behaviour of concrete structures*. Spon Press, New York – USA; 2011.
 18. Bažant Z P. *Mathematical modeling of creep and shrinkage of concrete*. Wiley Interscience publication John Wiley and Sons Chichester; 1988.
 19. Eurocode 2. *Design of concrete structures - Part 1: General rules and rules for Buildings*. together with United Kingdom National Application Document. British standard DD ENV; 1992.
 20. Jiansheng F, Xin N, Quan L and Quanwang L., Long-term behavior of composite beams under positive and negative bending. II: Analytical study. *Journal of structural engineering* 2010; 136(7): 858-865.
 21. Favre R, Jaccourd J P, Burdet O et Hazem C. *Dimensionnement des structures en béton - Aptitude au service et éléments de structures*, TGC, V8. Presses Polytechniques et Universitaires Romandes, Lausanne; Avril 1997.
 22. Rüsç H, Jungwirt D et Hilsdorf H. *Kritische Sichtung der Verfahren zur Berücksichtigung der Einflüsse von Kriechen und Schwinden des Betons auf das Verhalten der Tragwerke*. *Beton und Stahlbetonbau*, West Berlin, Vol. 68, (1973), pp. 49–60

DYNAMIC ANALYSIS OF FIBER REINFORCED COMPOSITE BEAM CONTAINING A TRANSVERSE CRACK

Y. Hammou¹, Y. Adjal¹, R. Benzidane¹ and Z. Sereir¹

¹ Laboratoire Structure en Composite et Matériaux Innovants – LSCMI,
Faculté de Génie Mécanique, BP 1505 El M'Naouer, UST-MB, Oran, Algérie
yh.usto@gmail.com

ABSTRACT

The present research article deals with the effect of a transverse crack on the flexural vibration of fiber reinforced composite beam based on Euler-Bernoulli beam theory. The presence of a crack in structural elements leads to an energy concentration near to cracks region and introduced a local flexibility which affect the dynamic response of such structures. Linear fracture mechanic theory has been used for crack modeling by introducing the stress intensity factors expressions. A parametric study has carried out in order to investigate the influence of fiber orientation, crack depth and crack location on the natural frequencies and theirs corresponding shape modes

KEYWORDS: Flexural vibration, cracks, composite beam, Natural frequency, mode shapes.

NOMENCLATURE

L	beam length
b	beam breadth
a	crack width
x	crack position
P	bending loads
U	strain energy
A	crack surface
K_I, K_{II}, K_{III}	stress intensity factors
D_1, D_2, D_{12}	coefficients depending
σ	Stress
c_{ij}	flexibility coefficients
J	elastic strain energy
EI	the flexural rigidity
m	mass per unit length
$\Theta(x)$	cross-sectional rotation
$M(x)$	bending moment
$S(x)$	shear force
ω	natural frequency

INTRODUCTION

The Fiber Reinforced composite materials have been attracted many engineering industry, such as aerospace, naval construction and civil building. The increasing of their utilizations, due mainly to excellent various properties, including high rigidity, resistance to environmental conditions and high fatigue strength. The Fiber-reinforced composite beams have used in the construction of many

structural elements, such as robot arms, rotating machine parts, and turbine blades.

The existing cracks in structural elements may affect their mechanical behavior and lead to damage failures. Due to this fact, many researchers have focused their studying in the amelioration of mechanical proprieties of these structures. The presence of cracks can be introducing a local flexibility which has an influence on their dynamic characteristics. However, the evaluation of dynamical behavior of cracked structures can be used as robust technique in predicting a presence of cracks. This research subject has been tackled in many papers.

The deriving of crack formulation was based on fracture mechanic theory including the stress intensity factors which considered as important parameters for identifying the flexibility matrix. Relating to this subject area. Krawczuk [7] have determined the flexibility coefficients matrix of composite beam containing a single crack. According to literature, it can be found a range of analytical and numerical methods adopted for studying the influence of existing cracks on dynamic characteristic of composite beam. Concerning the analytical methods, the works have done by Wang et al.[10], focused in the developing a new mathematical model for evaluating the natural frequencies and theirs corresponding mode shape of

unidirectional cracked composite beam under coupled flexural–torsion vibrations. Semi-analytical method titled ‘Generalized Differential Quadrature’, used by Daneshmehr et al. [4] for free vibration analysis of cracked composite beam, based on first order shear theory. Ghoneam [5] have proposed a new analytical model to study the effect of fiber orientation and various boundary conditions in dynamic behavior of cracked and uncracked laminate composite beam. A transfer matrix method related to state vector has been used by Mostafa [9] for free vibration analysis and crack identification of stepped beams with multiple edge cracks and different boundary conditions.

Several researchers have interested in the using of numerical method like finite element method, for example. Krawczuk [8] have proposed new finite element for identification the dynamical characteristic of cracked composite beam. Behera et al.[3] used finite element method for free vibration of laminate composite beam with a transverse crack, based on first shear deformation. Kisa [6], studied the effect of crack on natural frequencies and their corresponding mode shape of a cantilever composite beam, using finite element associated with component mode synthesis methods. Other authors interested in the using of finite element analysis by means a numerical code[1] investigated the variations in the eigen-nature of cracked composite beams due to different crack depths and locations using numerical and experimental investigation.

This present paper in devoted for studying the effect of an edge crack on the flexural vibration of unidirectional composite beam. A Parametric study has carried out in order to investigate the influence of fiber orientation, crack depth and crack location on the natural frequencies and theirs corresponding shape modes. The dynamic analysis of cracked composite beam used as technique for prediction the fatigue damage.

CRACK FORMULATION THEORY

The presence of a crack in structure leads to energy concentration in the region near to the crack and introduce a local flexibility which affect the dynamic characteristics of these structures, considering a composite beam containing a transversal edge crack, shown in Figure 1, the beam is subjected to pure bending loads P .

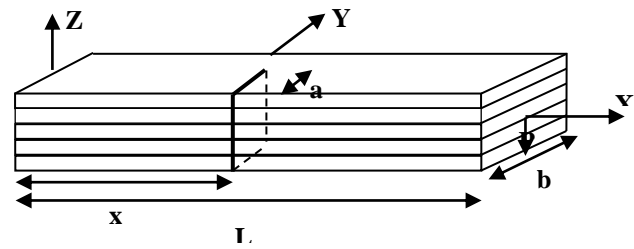


Figure 1

Geometry of cracked composite beam

Based on linear fracture mechanic theory, the crack formulation have been derived in which, the flexibility coefficients are expressed as a function of stress intensity factors and crack form.

The additional displacement due to presence of a crack in rectangular cross section, under the acting of load P , determined by the Castigliano’s theorem

$$u_i = \frac{\partial U}{\partial P_i} \quad (1)$$

where U is the strain energy of a cracked structure, defined as follows :

$$U = \int_A \left(D_1 \sum_{i=1}^{i=N} K_{II}^2 + D_{12} \sum_{i=1}^{i=N} K_{II} \sum_{i=1}^{i=N} K_{III} + D_2 \sum_{i=1}^{i=N} K_{III}^2 \right) dA \quad (2)$$

where A denotes the cracked surface, K_{In} , K_{IIIn} , et K_{IIIIn} are the stress intensity factors for fracture mode I, II and III, respectively, these factors were used to evaluate the stress field around the cracks region , D_1 , D_2 and D_{12} are coefficients depending on the materials parameters, are taken from [7]

The stress intensity factors for cracked composite beam, given as [2]

$$K_{ij} = \sigma_n \sqrt{\pi a} Y_j(\zeta) F_{jn}(a/b) \quad (3)$$

where σ_n is the stress of cracked area which relating to corresponding fracture mode, is the the correction function dependent in geometry, $Y_j(\zeta)$ is the correction factor for the anisotropic material [10], a is the crack depth and, L and b are the length and the breadth of beam respectively. The stress intensity factor corresponding to cracked beam under bending loading about z -axis , given as follows

$$K_I = \sigma_4 \sqrt{\pi a} Y_1(\zeta) F_1(a/b), \sigma_4 = \frac{12P}{bh^3} z; \quad (4)$$

Where

$$Y_1(\zeta) = 1 + 0.1(\zeta - 1) - 0.016(\zeta - 1)^2 + 0.002(\zeta - 1)^3;$$

The flexibility coefficients of cracked composite beam under loading are expressed in the following form

$$c_{ij} = \frac{\partial^2}{\partial P_i \partial P_j} \int_{-h/2}^{h/2} \int_0^a J(\alpha) d\alpha dz \quad (5)$$

where

$J(\alpha) = \partial U / \partial \alpha$ is the elastic strain energy release rate
 J , a is the crack depth .

The coefficient flexibly parameter used in the case of pure bending load, which considered herein, is c_{44} and given as [10].

$$c_{44} = \frac{24\pi D_1}{b^2 h^3} \int_0^a \alpha [F_1(\alpha/b)]^2 d\alpha; \quad (6)$$

Equation of Motion for flexural vibration The free flexural vibration of an Euler-Bernoulli beam with constant cross-section is expressed in the following differential equation

$$EI \frac{\partial^4 h}{\partial y^4} - m \frac{\partial^2 h}{\partial t^2} = 0 \quad (7)$$

where EI represents the flexural rigidity of unidirectional composite beam, m is the mass per unit length, given as [7].

$$EI = b \left(D_{22} - \frac{D_{12}^2}{D_{11}} \right) \quad (8)$$

$$m = b\rho h \quad (9)$$

By using separation of variable $h(y, t) = H(y)e^{i\omega t}$

the Eq. 8 will yield

$$EI H^{iv} - m\omega^2 H = 0 \quad (10)$$

where $\lambda = (m\omega^2 L^4 / EI)^{1/4}$,

The general solution of the above equation is

$$H(x) = A_{k1} \cosh \lambda x + A_{k2} \sinh \lambda x + A_{k3} \cos \lambda x + A_{k4} \sin \lambda x \quad (11)$$

The expressions for cross-sectional rotation $\Theta(x)$, the bending moment $M(x)$ and the shear force $S(x)$ become

$$\Theta(x) = \left(\frac{1}{L} \right) (A_{k1} \lambda \sinh \lambda x + A_{k2} \eta \cosh \lambda x - A_{k3} \eta \sin \lambda x + A_{k4} \eta \cos \lambda x) \quad (12)$$

$$M(x) = \left(\frac{EI}{L^2} \right) (A_{k1} \lambda^2 \cosh \lambda x + A_{k2} \lambda^2 \sinh \lambda x - A_{k3} \lambda^2 \cos \lambda x - A_{k4} \lambda^2 \sin \lambda x) \quad (13)$$

$$S(x) = - \left(\frac{EI}{L^3} \right) (A_{k1} \lambda^3 \sinh \lambda x + A_{k2} \lambda^3 \cosh \lambda x + A_{k3} \lambda^3 \sin \lambda x - A_{k4} \lambda^3 \cos \lambda x) \quad (14)$$

The cracked composite is divided in two sub-beams at cracked section. Thus, the continuity conditions for

an edge crack located at distance $x = x_c$ can be expressed as [10]

$$M_i(x_c) = M_{i+1}(x_c) \quad (15)$$

$$S_i(x_c) = S_{i+1}(x_c) \quad (16)$$

$$H_i(x_c) = H_{i+1}(x_c) \quad (17)$$

Moreover, a discontinuity cross-sectional rotation due to an existing crack can be expressed as follows

$$\Theta_i(x_c) = \Theta_{i+1}(x_c) - c_{44} M_i(x_c) \quad (18)$$

where c_{44} is the crack-sectional flexibility coefficient parameter, using in the case of cracked beam under bending load in vertical direction. The subscript (i) and (i+1) in Eqs 15,16,17 and 18 refers to left and right of sub-beam at cracked section.

The boundary conditions of clamped composite beam are :

$$H_i(0) = \Theta_i(0) = 0 \quad (19)$$

$$M_{i+1}(1) = S_i(1) = 0 \quad (20)$$

Substitution of Eqs 11- 14 into Eqs 15-20 will yield the characteristic equation of the cracked composite beam

$$[B]\{A\} = \{0\} \quad (21)$$

where

$\{A\} = \{A_{11}, A_{12}, A_{13}, A_{14}, A_{21}, A_{22}, A_{23}, A_{24}\}^T$ is a vector

composed of 8 unknowns and $[B]$ represents a

characteristic matrix given as function of natural frequency .Setting the determinant

$\det[B(w)] = B(w) = 0$ yields the natural

frequencies. The corresponding mode shapes are obtained by substituting each natural frequency back into eq

RESULTS AND DISCUSSION

Consider a cracked composite beam clamped at left end and free at right end, having length L , height t and width b , containing an edge crack located at a distance x from the left end, as shown in Figure 2 . The composite beam considered herein is made of unidirectional graphite fiber-reinforced, where its physical and geometrical characteristics are chosen similarly to [7].

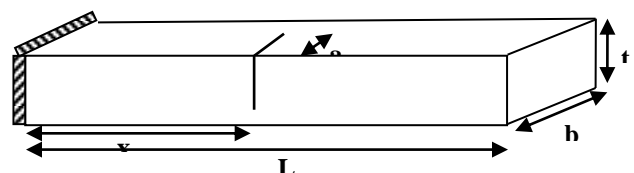


Figure 2.

A cantilever cracked composite beam

The material properties of the graphite fiber-reinforced composite beam are given in Table. 1. The geometrical characteristics, the length (L), height (t) and width (b) of the composite beam, are taken as 0.5m, 0.005m and 0.1m respectively.

Table 1. The material properties of the graphite fiber-reinforced composite beam

E_f (GPa)	E_m (GPa)	G_f (GPa)	G_m (GPa)
275.6	2.76	114.8	1.036
ρ_f (Kg/m ³)	ρ_m (Kg/m ³)	ν_f	ν_m
1900	1600	0.2	0.33

The numerical results have been adopted for evaluating the effect of fiber fraction volume, crack depth ration and crack locations on the dynamic characteristic of a cracked composite beam, which are presented graphically. The influence of the fiber orientation on flexural rigidity of composite beam for different values of the fiber volume fraction ($V=0.2, 0.4, 0.6, 0.8$) is shown in Figure 3. As can be observed, the bending stiffness having higher values, when the angle of fiber is greater than 45° . In the same figure, the increasing of fiber volume fraction affects considerably the bending stiffness of composite beam. Therefore, it can be concluded that the rigidity of composite beam is a function of fiber volume fraction and fiber orientation.

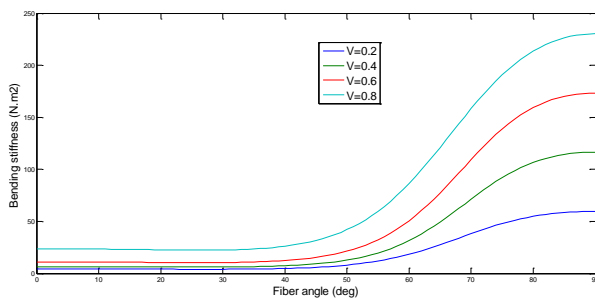


Figure 3:

Variation of bending stiffness of composite beam for different values of fiber volume fraction $V= 0.2, 0.4, 0.6, 0.8$

Figure 4 shows the effect of fiber orientation on fundamental natural frequency for various crack depth ($a/b=0.2, 0.4, 0.6, 0.8$), the fiber volume fraction considered herein is ($V=0.5$) and the crack is located at a distance ($x/L=0.3$). Based on graphically results shown in this figure, the changes in fundamental natural frequency are appeared due to the variation of fiber angle from 0° to 90° , when the

fiber angle is greater than 45° , these changes become more sensitive, this due to fact, the change in flexural rigidity which is a function of fiber angle. In Figure5, it is noticeable also the increasing in crack depth led to reduction in fundemntal natural frequencies.

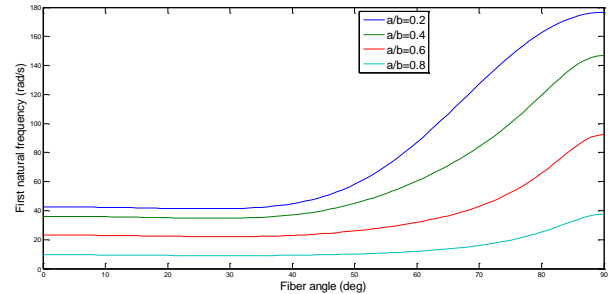


Figure 4

Effect of angle of fiber on fundamental natural frequency of the cracked composite beam for different crack depth ($a/b=0.2, 0.4, 0.6, 0.8$)

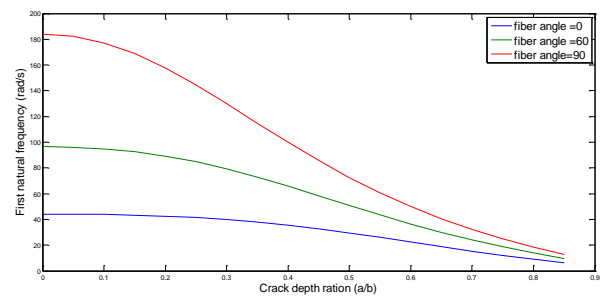


Figure 5

Effect of crack depth on fundamental natural frequency of the cracked composite beam for different angle of fiber

The variation of first natural frequency of cracked composite beam for range of crack position is illustrated in Figure 6.

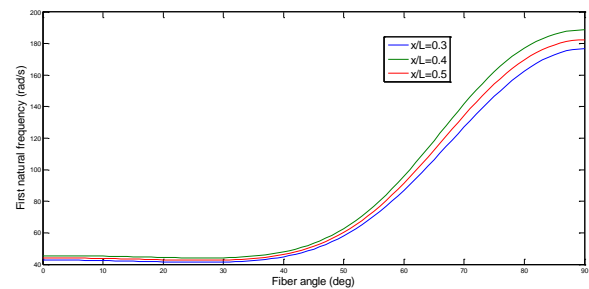


Figure 6.

Effect of angle of fiber on fundamental natural frequency of the cracked composite beam for different crack location $x/L=0.3, 0.4, 0.6$

As observed from results that, these changes due to variation of fiber angle for a crack located at distance ($x/L=0.3$) from the fixed end of composite beam is lower compared to those located at 0.4 0.5, therefore, the crack position has also affect the variation of natural frequencies.

The Figure 7 shows the variation of the first natural frequency as a function of crack depth ratio for different values of fiber volume fraction ($V=0.2, 0.4, 0.6, 0.8$). It can be seen that the reduction in the natural frequency is caused by the increasing of crack depth, it is also observed from this figure, that the natural frequencies having higher values when the fiber volume fraction is ($V=0.8$).

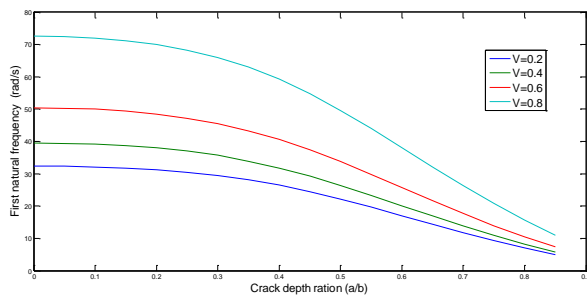


Figure 7.

Effect of crack depth on fundamental natural frequency of the cracked composite beam for different values of volume fraction ($V=0.2, 0.4, 0.6, 0.8$)

In Figure 8 demonstrates the variation of fundamental natural frequency as a function of crack depth ratio, the increasing of crack depth reduces the first natural frequency. the results show also that these variations of natural frequency to crack position at a distance ($x/L=0.2$) from the fixed are less sensitive compared to other cracks positions ($x/L=0.4, 0.6$).

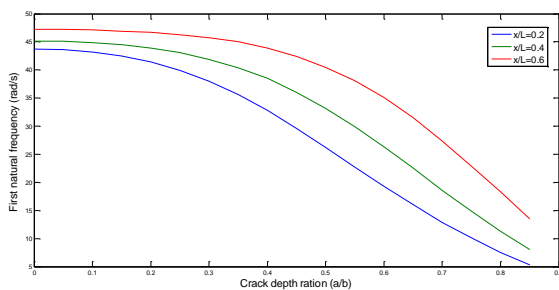


Figure 8.

Effect of crack depth on fundamental natural frequency of the cracked composite beam for different crack location ratio $x/L=0.2, 0.4, 0.6$

The effect of crack location on first natural frequency of cracked composite beam for various values of crack depth ratio is illustrated in Figure. 9. The angle of fiber is assumed to be zero degree, As can be seen, the changes in crack positions have a considerable effect on natural frequency variation, the crack located near to fixed end of composite beam has a smaller effect.

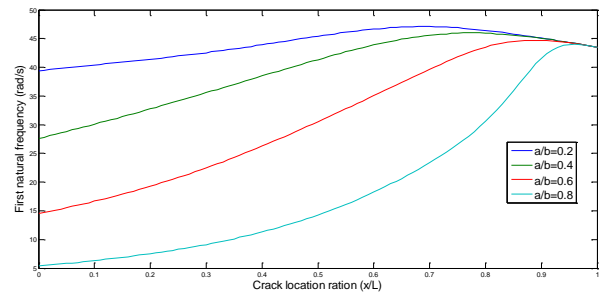


Figure 9.

Effect of crack location on fundamental natural frequency of the cracked composite beam for different crack depth ratio $a/b=0.2, 0.4, 0.6$

The effect of crack depth on first and second mode shape is illustrated in Figure. 10.

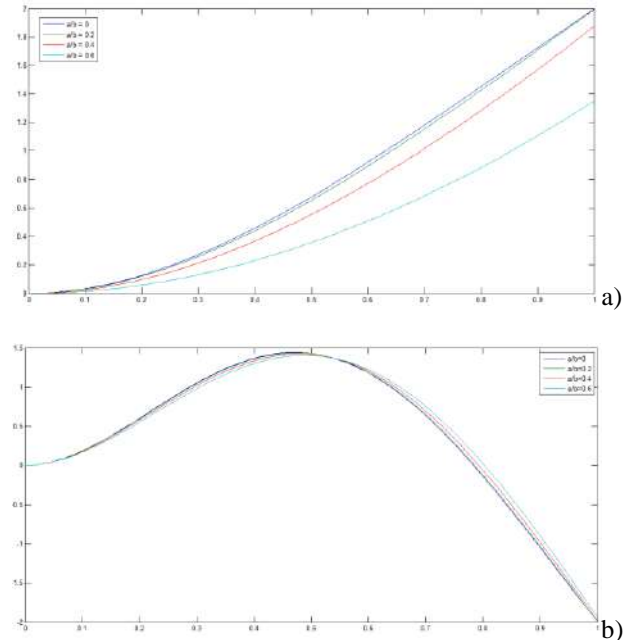


Figure 10.

The mode shapes for a crack located at ($x_c=0.5$) and fiber angle 60° as a function of crack depth ratio changes. a) First mode shape of flexural vibration, b) Second mode shape of flexural vibration

As observed in this figure, it is evident that the changes in mode from is caused by the presence of a crack, these changes are more significantly, when the crack depth is greater than ($a/b=0.4$) for the first mode shape, therefore, it can be concluded that the modification in mode shape will be used as technique for predication the damage in structures.

CONCLUSIONS

The flexural vibration of fiber reinforced composite containing an edge crack, based on Euler-Bernoulli theory is studied. The obtained results show the influence of several parameters, such as fiber angle, crack depth ration and crack positions on natural frequencies; however, the reduction in natural frequency values is more sensitive when the crack depth increase. Also, the dynamic behavior of unidirectional cracked composite beam with a lower flexural rigidity is more sensitive to presence of a crack. In addition to these numerical results, the natural frequencies variation is more significantly when the crack located at middle of beam, due to fact, that bending moment is higher at this position. Finally, the evaluation of dynamical behavior of cracked composite beam can be used as robust technique in predicting a presence of cracks.

REFERENCES

1. Abd El-Hamid (1998). "An investigation into the Eigen-nature of cracked composite beams". *Composite Structures* Vol. 38, No. 1 - 4, pp. 45-55.
2. Bao and Suo (1992). "The role of material orthotropy in fracture specimens for composites". *Journal of Applied Mechanics* 29, 1105-1116.
3. Behera S., Sahu S.K., Asha A. V. (2015) "Vibration Analysis of Laminated Composite Beam with Transverse Cracks" *Advances in Structural Engineering*, pp. 67-75.
4. Daneshmehr, A.R. , Nateghi, A, Inman, D.J (2013). "Free vibration analysis of cracked composite beams subjected to coupled bending-torsion loads based on a first order shear deformation theory". *Applied Mathematical Modelling* Vol 37, pp. 10074-10091.
5. Ghoneam S. M. (1995). "Dynamic analysis of open cracked laminated composite beams". *Composite Structures*, 32, 3-11.
6. Kisa (2003). "Free vibration analysis of a cantilever composite beam with multiple cracks". *Composites Science and Technology* 64 (2004) 1391–1402.
7. Krawczuk M., and Ostachowicz W.M., (1995). "Modeling and Vibration analysis of a cantilever composite beam with a transverse open crack". *Journal of Sound and Vibration* 183(1), 69-89.
8. Krawczuk, M., Ostachowicz, W. and Zak, A., 1997a, "Dynamics of cracked composite material structures," *Computational Mechanics*, 20, 79-83.
9. Mostafa A. (2012) "A transfer matrix method for free vibration analysis and crack identification of stepped beams with multiple edge cracks and different boundary conditions" *International Journal of Mechanical Sciences*, 57 , pp.19-33.
10. Wang, K., Inman, D.J, Farrar, C.R,(2005). "Modeling and analysis of a cracked composite cantilever beam vibrating in coupled bending and torsion" *Journal of Sound and Vibration* Vol 284, pp. 23-49.

Inner and Outer Flows

RESUSPENSION OF INDOOR PARTICLES DUE TO HUMAN FOOT MOTION

AHMED BENABED¹, KARIM LIMAM¹

¹LaSIE, UMR 7356 CNRS University of La Rochelle,
Avenue Michel Crépeau 17042 cedex 1, La Rochelle, France

*Corresponding author: Fax: +33546458200 Email: ahmed.benabed@univ-lr.fr

ABSTRACT

Particle resuspension from flooring due to indoor human activities is believed to be one of the most important sources of particulate matter compared to other indoor sources. In this work, particle resuspension due to human foot motion was studied in a 50×25×25 cm environmentally controlled experimental chamber. Only the stepping down motion of the foot during the gait cycle is considered. The motion was modelled using an 8×22 cm rectangular plate, which performs a rotation motion toward the floor. Temporal tracking of resuspended particles from representative samples of flooring materials is carried out with an Optical Particle Counter (Grimm 1.108). Resuspension source strengths estimated using the mass balance equation ranged from 0.05±0.005 s⁻¹ to 0.5±0.05 s⁻¹ and from 0.07±0.005 s⁻¹ to 0.6±0.05 s⁻¹ for smooth and rough linoleum, respectively. Results showed that resuspension source strengths increased with particle size. For all particle sizes, rough linoleum exhibited higher resuspension source strengths.

Key words:

INTRODUCTION

As the world's climate changes, new regulations have been imposed to improve buildings energy efficiency and to reduce greenhouse gas emissions. Therefore, buildings that were designed to operate under the old climatic conditions may not function well under the new conditions, consequently affecting Indoor Air Quality (IAQ) by increasing inhalable particle matter (PM) concentration. In fact, the confinement of buildings following the insulation works has led to an increase in temperature and indoor humidity, which encourages the production of indoor allergens. In addition, as a result of ventilation airflow diminution, the air speed in big closed volume has slowed and it is more difficult to remove the settled PM.

As reported in [1], indoor PM are dominated by particles smaller than 500 µm. Particles inside building can be generated from either indoor sources (skin, hair, plant, pets, cooking, smoking, building materials) or out-door sources (soil and rock debris, forest fires, sea salt, volcanic debris, fuel combustion, industrial process) [2].

High concentration of particulate pollutants creates health problems and impairs the ability of occupants to work or to learn [3], [4], [5]. Since people spend a lot of their time in numerous different indoor environments like residences, public buildings, offices [6], they are more exposed to indoor air pollutants. Thus, indoor air quality has become a matter of growing concern over the last decades.

Indoor PM concentration is affected by several factors including direct emissions from indoor sources, ventilation conditions, outdoor environment, interior materials, deposition onto indoor surfaces, removal from indoor surfaces by means of ventilation and indoor human activities. Of the different factors quoted above, human activities such as walking, contributes substantially to increase concentration of inhalable particles [7], [8], [9], [10], [11]. Thus, this subject has recently drawn increased attention. However, despite numerous studies carried out, many uncertainties remain. This partly due to the complex nature of particles, in terms of their source, mechanism of formation and their chemical composition, on another hand, is due to the complexity of particle resuspension process itself. Therefore, further work in this area is still necessary to solve some crucial outstanding difficulties.

In order to understand better particle resuspension process, attention is drawn to one human gait cycle instead of a real activity. However, the style, the intensity and the frequency of the human footstep are parameters that greatly influence particle resuspension. Thus, in order to improve experimental reproducibility and to eliminate the variability caused by these parameters on particle resuspension, researchers often use models to mimic the human walking, rather than real human footstep. In the next part of this work, the different models of

the human footstep used in this area will be presented.

In Zhang et al. [12], to study the particles detachment, resuspension, and transport due to human walking, the foot stepping motions down and up in a gait cycle were modeled using a combination of two effective circular disks. In Kubota et Higuchi work [13], the foot was modeled as either an elongated plate or a prosthetic foot wearing a slipper, moving in normal to the floor, downward or upward. The experimental methods used were particle visualizations and particle image velocimetry (PIV) measurements in air, supplemented by dye flow visualization in water. The flow visualizations with human foot tapping and stomping were performed to elucidate the particle resuspension in real situations. Goldasteh et al. [14] used a mechanical foot that mimics human walking, equipped with a real shoe to estimate resuspension rate. Khalifa et Elhadidi [15] studied the flow resulting from a horizontal circular disk moving downward at a constant velocity toward a horizontal floor seeded with spherical micro-particles. The effect of this flow on particle detachment and levitation was investigated. In the work of Tian et al. [16], the resuspension mechanism is comprised of heel and toe plates equipped with a real human shoe and controlled by electric actuators to simulate the human footstep. Gomes et al. [17], reproduced the human foot effects by applying aerodynamic and mechanical disturbances in an environmentally controlled experimental chamber.

Those different studies at a small scale clarify some points concerning resuspension mechanism during the walking process. First, the complete particle resuspension process of deposited particle includes its detachment from the surface after the break-up of the particle-surface contact and then its transport by the flow. Detachment of particle from surface occurs with two mechanisms: rolling motion for small particles and burst-type resuspension for large particles [18]. On one hand, results indicate that aerodynamic disturbances created under the foot during its motion, dominate the particle resuspension behavior [17]. This aerodynamic disturbance appeared as a high velocity region created under the foot which is sufficiently large to detach deposited particles. On another hand, it appears clearly that the amount of resuspended particles from a substrate increase with increasing fluid velocity regardless of the flow conditions [18], [19]. The foot motion far from the substrate plays an important role in the

dispersion and transport of particles in the environment after their detachment [14].

Particle resuspension from substrate depends on numerous parameters including particle properties, substrate morphology, substrate loading, environment conditions and human activity factors. Among those different parameters, surface morphologies have a significant impact on particle detachment [20], [21], [22], [23]. In particular, the two main characteristics of surface morphology are roughness and surface charge heterogeneities. Surface roughness can extend over several length scale, thus, an apparently smooth surface at a macroscopic scale, could lead to rough surface at a smaller scale. Microscopic surface roughness of particle and substrate creates imperfect contact between them, thereby affecting significantly the adhesion force [21], [22]. Moreover, macroscopic roughness of substrate surface affects initial particle rolling motion before lifted off [18], [23]. In Soltani et Ahmadi [21] and Goldasteh et al [24], particle and substrate surfaces roughness was modeled using hemispherical bumps. They found that number and repartition of asperities on surfaces play an important role on particle detachment process. In Yang et al. [23], effect of surface roughness on particle-substrate interaction was studied by the airflow method. They show that low roughness about 0.2-0.4 μm is associated with the lowest critical air velocity (velocity needed to detach 50% of 11-41 μm particle), and increased air velocities for roughness $<0.2 \mu\text{m}$ or $>0.4 \mu\text{m}$. This is due to the fact that particle size, contact area and number of contact influence simultaneously on adhesion force [25]. Furthermore, macroscopic roughness modifies fluid motion generated by the foot in the near-wall region [18], consequently affects the flow velocity.

The aim of the present study was to characterize walking-induced dust resuspension as function of particle size and flooring type. Only the downward motion of the foot during the gait-cycle was considered. A rectangular rotating plate was used to mimic a foot motions instead of a real human foot to improve experimental reproducibility of the resuspension mechanism, and facilitate study of the influence of parameters cited above. PM concentration elevation in a chamber due to the plate downward motion was evaluated. The chamber decay rates were estimated for two types of hard flooring. Eventually, resuspension source strengths were estimated using the mass balance equation.

MATERIAL AND METHODS

In this study, a 22x8cm rectangular wooden plate was used to mimic the stepping down motion of the foot during a gait cycle. The plate performed free rotation on an axis toward the floor. The axis is screwed to the floor; thereby the plate rotates only in a well-defined direction. Downward motion is achieved from an angle $\varphi=20^\circ$. Experiments were conducted in a 50x25x25 cm environmentally controlled experimental chambers with RH=40% throughout the whole study. The chamber was wooden and exchanges with outside environment only through an opening equipped with a filter. The chamber was placed in a cleanroom to reduce external environment influence during the experiments. Two types of hard flooring commonly used in residence were tested: rough and smooth linoleum. In order to control surface loading, only an elementary area was seeded. The seeding system is comprised of a dust disperser TOPAS SAG 410, which ensures constant and continuous dosing of powders with high accuracy and over long operational periods. Dust used in this study was Orgasol microsphere powders with sizes ranging from 0.5 to 20 μm . An Optical Particle Counter (Grimm 1.108) monitored the real time PM concentration inside the resuspension chamber before and after the plate motion. This portable counter offers 15 size channels capturing particles within size ranges from 0.3 μm to 20 μm and larger. During the resuspension experiment, particle concentration was measured at different points around the plates, and then spatial averages were calculated to facilitate the use of mass balance model to estimate source strengths.

RESULTS AND DISCUSSION

In order to compare results for the different sizes, concentration of each particle size was normalized to the concentration of corresponding particle size during the injection process. Fig. 1 illustrates variation of particle concentration inside the chamber as a function of time for different particles sizes. After the resuspension event, particle concentration increases sharply to orders of magnitude higher than the background level. After about one minute, concentration decayed exponentially. The results are in agreement with previous works. Indeed, a single activity can increase by several orders of magnitude the concentration of particle matter (PM) in a closed volume. In the next part of this work, the effects of floor roughness and particle size on particle

resuspension were investigated using the resuspension source strengths approach. Two types of flooring commonly used in residences were tested: smooth and rough linoleum.

SOURCE STRENGTHS ESTIMATION

To estimate resuspension source strengths, a mass balance approach was used [26]. At time t , and for particle in a given size range i , the mass balance equation can be written as follows:

$$V \frac{dC_{i,in}(t)}{dt} = faVC_{i,out}(t) - (a + \lambda_{i,d})VC_{i,in}(t) + \lambda_{i,R}AC_{i,di}(t) + S'_i(t) \quad (1)$$

$C_{i,in}$: Concentration inside the chamber ($\#/m^3$)

$C_{i,out}$: Concentration outside the chamber ($\#/m^3$)

$C_{i,di}$: Floor loading ($\#/m^2$)

A : Resuspension surface area (m^2)

V : Resuspension chamber volume (m^3)

a : Air exchange rate (s^{-1})

f : Penetration factor (dimensionless)

$\lambda_{i,d}$: Deposition rate (s^{-1})

$\lambda_{i,R}$: Resuspension rate (s^{-1})

S'_i : Indoor source emission ($\#/s^{-1}$)

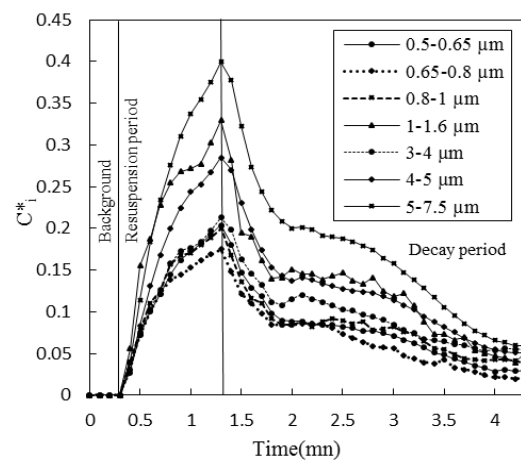


Fig. 1 Normalized particle concentration versus time profile of one representative experiment (flooring type: rough linoleum, RH =40%)

The deposition rate $\lambda_{i,d}$ is embedded in the decay rate $(a + \lambda_{i,d})$ to calculate the resuspension source

strengths. The method for the decay rate estimation is described below. Since resuspension study has been conducted in a cleaned room, the first term of eq1 is removed. The term $S'_i(t)$ is also removed because there are no other indoor sources during the study. We put the term corresponding to the resuspension by indoor activities as a source term $S_i(t)$. With these considerations, eq1 becomes:

$$V \frac{dC_{i,in}(t)}{dt} = -(a + \lambda_{i,d})VC_{i,in}(t) + S_i(t) \quad (2)$$

Without indoor activities and particle sources, particle concentration decays exponentially in the chamber. Decay rates were obtained as the slope of the regression line of natural logarithm of particle concentration along time axis.

Fig. 2 represents the decay rates estimated for the chamber as a function of particle size in two cases. Flooring types in the case 1 and case 2 are smooth and rough linoleum, respectively; however, the walls and the ceiling textures are identical. Results show that decay rates for the two cases are identical. In fact, this is probably due to the small flooring areas of the chamber, which affects slightly the decay rates. For the two cases and for particles $< 4 \mu\text{m}$, decay rate is almost constant, however, it increases sharply with particle size for particles larger than $4 \mu\text{m}$.

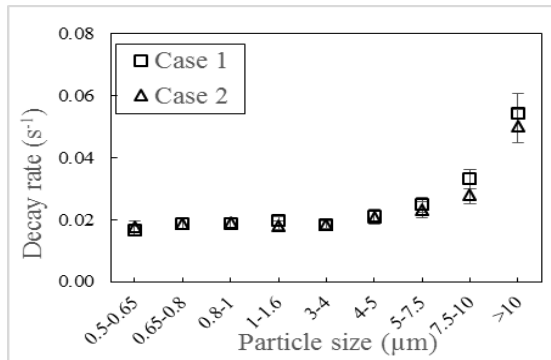


Fig. 2 Experimental decay rates for the chamber with two flooring types. Case 1: smooth linoleum, case 2: rough linoleum. The error bars represent the standard deviation of the mean

Once the decay rates are determined, resuspension source strengths can be estimated by solving the mass balance equation (eq 2). Integration this equation, from t_i to t_f , where t_i and t_f , are times corresponding the beginning and the end of resuspension event gives:

$$V \int_{t_i}^{t_f} \frac{dC_{i,in}^*(t)}{dt} dt = -V \int_{t_i}^{t_f} (a + \lambda_{i,d})VC_{i,in}^*(t) dt + \int_{t_i}^{t_f} S^*(t) dt \quad (3)$$

he superscript * refers to normalized variables. The average of resuspension source strengths for particle in a given size range i over the resuspension time $T = t_f - t_i$ is:

$$\overline{S_i^*(T)} = V \left[\frac{C_{i,in}^*(t_f) - C_{i,in}^*(t_i)}{T} + (a + \lambda_{i,d})\overline{C_{i,in}^*(T)} \right] \quad (4)$$

$C_{i,in}^*(t)$ is the average of normalized indoor concentration for particle in the size range i during the resuspension period. This term was evaluated using numerical integration with trapezoidal rule.

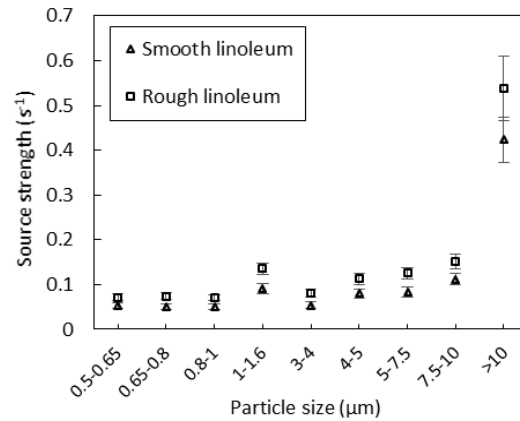


Fig. 3 Resuspension source strength for two types of flooring: smooth and rough linoleum. The error bars represent the standard deviation of the mean.

Fig. 3 shows resuspension source strengths versus particle size estimated for two flooring types. Firstly, for all particle sizes, surface roughness improves particle resuspension. This finding can be explained by the fact that surface roughness increases strongly the velocity near the floor surface; increasing in turn the lift and drag forces. Secondly, for the two flooring types, resuspension source strengths for particle in the size range 1-10 μm are larger than those obtained for particles with sizes smaller than $1 \mu\text{m}$. Eventually, resuspension source strengths for particles larger than $10 \mu\text{m}$, is almost 4 times greater than those for PM10

(particles with size $< 10 \mu\text{m}$). This finding is likely due to the fact that electrostatic force effects for larger particles are marginal compared to lift and drag forces.

CONCLUSIONS

In this study, particle resuspension due to human foot motion was investigated experimentally. The study was conducted using a rectangular plate, which rotates toward the floor to mimic the downward motion of the foot during a gait cycle. Orgasol microsphere powders in the size range $0.5\text{--}20 \mu\text{m}$ were used. The study was conducted in an environmentally controlled experimental chamber ($\text{RH} \approx 40\%$). Decay rates for the chamber with two flooring types were evaluated. Source strengths for two flooring types and different particle sizes using mass balance equation were estimated. Results show that for the two flooring types, particles larger than $10 \mu\text{m}$ are associated with greater resuspension source strengths. Resuspension source strengths for particles in the size range $1\text{--}10 \mu\text{m}$ are larger than those for particles lower than $1 \mu\text{m}$. This study displays unequivocally that surface roughness improves particles resuspension.

REFERENCES

- [1] P. J. Liroy, N. C. G. Freeman, and J. R. Millette, "Dust: a metric for use in residential and building exposure assessment and source characterization," *Environ. Health Perspect*, vol. 110, no. 10, pp. 969–983, Oct. 2002.
- [2] L. Morawska and T. Salthammer, *Indoor Environment: Airborne Particles and Settled Dust*. John Wiley & Sons, 2006.
- [3] M. J. Mendell, "Indoor residential chemical emissions as risk factors for respiratory and allergic effects in children: a review," *Indoor Air*, vol. 17, no. 4, pp. 259–277, 2007.
- [4] G. Viegi, M. Simoni, A. Scognamiglio, S. Baldacci, F. Pistelli, L. Carrozzi, and I. Annesi-Maesano, "Indoor air pollution and airway disease [State of the Art]," *Int. J. Tuberc. Lung Dis*, vol. 8, no. 12, pp. 1401–1415, 2004.
- [5] B. Brunekreef and S. T. Holgate, "Air pollution and health," *The Lancet*, vol. 360, no. 9341, pp. 1233–1242, Oct. 2002.
- [6] N. E. Klepeis, W. C. Nelson, W. R. Ott, J. P. Robinson, A. M. Tsang, P. Switzer, J. V. Behar, S. C. Hern, W. H. Engelmann, and others, "The National Human Activity Pattern Survey (NHAPS): a resource for assessing exposure to environmental pollutants," *J. Expo. Anal. Environ. Epidemiol.* vol. 11, no. 3, pp. 231–252, 2001.
- [7] J. Qian and A. R. Ferro, "Resuspension of Dust Particles in a Chamber and Associated Environmental Factors," *Aerosol Sci. Technol.*, vol. 42, no. 7, pp. 566–578, May 2008.
- [8] T. L. Thatcher and D. W. Layton, "Deposition, resuspension, and penetration of particles within a residence," *Atmos. Environ.*, vol. 29, no. 13, pp. 1487–1497, 1995.
- [9] J. A. Rosati, J. Thornburg, and C. Rodes, "Resuspension of Particulate Matter from Carpet Due to Human Activity," *Aerosol Sci. Technol.*, vol. 42, no. 6, pp. 472–482, Apr. 2008.
- [10] N. M. Lefcoe and I. I. Incullet, "Particulates in domestic premises. II. Ambient levels and indoor-outdoor relationships," *Arch. Environ. Health*, vol. 30, no. 12, pp. 565–570, Dec. 1975.
- [11] J. A. Sagona, S. L. Shalat, Z. Wang, M. Ramagopal, K. Black, M. Hernandez, and G. Mainelis, "Evaluation of particle resuspension in young children's breathing zone using stationary and robotic (PIPER) aerosol samplers," *J. Aerosol Sci.*, vol. 85, pp. 30–41, Jul. 2015.
- [12] X. Zhang, G. Ahmadi, J. Qian, and A. Ferro, "Particle Detachment, Resuspension and Transport Due to Human Walking in Indoor Environments," *J. Adhes. Sci. Technol.*, vol. 22, no. 5–6, pp. 591–621, Jan. 2008.
- [13] Y. Kubota and H. Higuchi, "Aerodynamic Particle Resuspension Due to Human Foot and Model Foot Motions," *Aerosol Sci. Technol.*, vol. 47, no. 2, pp. 208–217, Feb. 2013.
- [14] I. Goldasteh, Y. Tian, G. Ahmadi, and A. R. Ferro, "Human induced flow field and resultant particle resuspension and transport during gait cycle," *Build. Environ.*, vol. 77, pp. 101–109, Jul. 2014.
- [15] H. E. Khalifa and B. Elhadidi, "Particle Levitation Due to a Uniformly Descending Flat Object," *Aerosol Sci. Technol.*, vol. 41, no. 1, pp. 33–42, Feb. 2007.
- [16] Y. Tian, K. Sul, J. Qian, S. Mondal, and A. R. Ferro, "A comparative study of walking-induced dust resuspension using a consistent test mechanism," *Indoor Air*, vol. 24, no. 6, pp. 592–603, Dec. 2014.

- [17] C. Gomes, J. Freihaut, and W. Bahnfleth, “Resuspension of allergen-containing particles under mechanical and aerodynamic disturbances from human walking,” *Atmos. Environ.*, vol. 41, no. 25, pp. 5257–5270, Aug. 2007.
- [18] C. Henry and J.-P. Minier, “Progress in particle resuspension from rough surfaces by turbulent flows,” *Prog. Energy Combust. Sci.*, vol. 45, pp. 1–53, Dec. 2014.
- [19] B. Zuo, K. Zhong, and Y. Kang, “An experimental study on particle resuspension in a room with impinging jet ventilation,” *Build. Environ.*, vol. 89, pp. 48–58, Jul. 2015.
- [20] A. S. Kassab, V. M. Ugaz, M. D. King, and Y. A. Hassan, “High Resolution Study of Micrometer Particle Detachment on Different Surfaces,” *Aerosol Sci. Technol.*, vol. 47, no. 4, pp. 351–360, Apr. 2013.
- [21] M. Soltani and G. Ahmadi, “On particle adhesion and removal mechanisms in turbulent flows,” *J. Adhes. Sci. Technol.*, vol. 8, no. 7, pp. 763–785, Jan. 1994.
- [22] I. Goldasteh, G. Ahmadi, and A. Ferro, “A Model for Removal of Compact, Rough, Irregularly Shaped Particles from Surfaces in Turbulent Flows,” *J. Adhes.*, vol. 88, no. 9, pp. 766–786, Sep. 2012.
- [23] Y. Jiang, S. Matsusaka, H. Masuda, and Y. Qian, “Characterizing the effect of substrate surface roughness on particle–wall interaction with the airflow method,” *Powder Technol.*, vol. 186, no. 3, pp. 199–205, Sep. 2008.
- [24] I. Goldasteh, G. Ahmadi, and A. R. Ferro, “Monte Carlo simulation of micron size spherical particle removal and resuspension from substrate under fluid flows,” *J. Aerosol Sci.*, vol. 66, pp. 62–71, Dec. 2013.
- [25] J. Qian, J. Peccia, and A. R. Ferro, “Walking-induced particle resuspension in indoor environments,” *Atmos. Environ.*, vol. 89, pp. 464–481, Jun. 2014.
- [26] A. R. Ferro, R. J. Kopperud, and L. M. Hildemann, “Source Strengths for Indoor Human Activities that Resuspend Particulate Matter,” *Environ. Sci. Technol.*, vol. 38, no. 6, pp. 1759–1764, Mar. 2004.

EXPERIMENTAL INVESTIGATION OF SOIL PARTICLES FILTRATION PROCESS THROUGH GRANULAR POROUS MEDIA

Samira AZIROU^{a,b}, Ahmed BENAMAR^a, Abdelkader TAHAKOURT^b

^aLOMC UMR 6294 CNRS- Havre university (France) Waves and Complex Media Laboratory (LOMC), UMR 6294 CNRS, Havre university, France.

^bEngineering Construction and Architecture Laboratory (LGCA), Faculty of Technology, Bejaia University, 06000 Bejaia, Algeria.

Email: azirousamira@gmail.com

ABSTRACT

The term filtration as used with reference to civil engineering works, describes the restriction of particles migration from a soil into or through a granular medium. In geotechnical engineering, presence of filters in hydraulic structures is essential for soil protection from erosion. The main design criteria against which performance is assessed are a criterion for retention of fine particles. The characteristic size of filter medium influences the size distribution of the pore and hence the capacity for the retention of the flowing particles, and the hydraulic conductivity of the filter itself. Porosity is one of the important parameters governing transport and particle deposition in porous media. It represents the voids between the solid matrixes of a granular media. The particles size distribution of inlet particles and retained ones within the filter were analyzed and related to the filter opening size. The choice of this filter is based on several parameters, mainly the porous media opening size. The filter porosity variation was assessed and correlated with clogging particles volume. The evolution of such parameter may be an indicator of likely filter clogging. In this paper we report the results of a laboratory study devoted to investigating the behaviour of granular filters during the filtration of silt particles. Two kinds of silts involving different plasticity are used and a filter F_1 was designed according to the criteria of USBR (US Bureau of Reclamation 1986). In order to attempt to explain the effect of grain shape in the filtration mechanism, a second filter F_2 collected from Seine River (France) providing the same grain-size distribution that of the filter F_1 but with rounded grains shape was selected.

KEYWORDS: *Porous Media, Filter, Particles, Flow, Silt, Grain shape.*

INTRODUCTION

The construction of hydraulic structures (dams, levees) needs impermeable base soil (core) protected by a downstream filter. Filters are used to prevent movement of soil particles from or between various zones and foundations of embankment dams. Such movement, if not controlled, can result in the development of concentrated leaks that can lead to serious consequences and, in extreme cases, failure of dam embankments [10]. With high hydraulic pressure, particles from base soil could be detached and transported through the filter bed [3, 4, 5, 6, 7]. Particles that are larger than the opening pore in the filter bed will be trapped. The suspended particles slowly fill the pores, resulting in an increase of hydraulic resistance and a decrease of the porosity in

the medium. As water flows through the soil, fine particles of the core can be washed out under hydraulic loading, leading to internal erosion and likely failure of the structure. So, a correctly designed filter must retain loose soil particles and thus prevent piping, while it will be able to allow seepage water to flow and avoid the development of high internal pore pressures [3, 4, 5, 6, 7, 8, 9, 16]. The detachment of fine particles and their subsequent transport throughout the porous network of the filter requires that the pore space is sufficient. This space is conditioned by the granular distribution, which in turn depends on the size of the grains, their form and their contact conditions [16, 19]. The main filter design criteria are empirical relationships based essentially on the representative size d_{85} (85% finer than $75\mu\text{m}$) of the soil to protect and the opening of filter pore D_{15}

(sieve size for which 15% of the weighed filter material is finer). A series of laboratory observations on sets of base soil-filter combination has usually led the researchers to recommend empirical relationships. Terzaghi (1922) was the first to suggest empirical criteria describing the importance of the grain size in the design of granular filters. This criterion was improved by other authors like Vaughan and Soars (1982), Sherard & Dunnigan (1985), Kenney & Lau (1985) and recently Foster & Fell (2001) and Reddi & al (2002) [23, 20, 15, 12, 19]. In order to design a filter it is recommended to consider the most critical situation [21], the presence of a concentrated flow through the base soil. In this case the particles are eroded when the hydraulic load exceeds the critical value of shear stress of the internal surface cracks. The filter behaviour depends on the geometric requirements (grain size and pore distribution, fine particles size and concentration), water (velocity or gradient) and physicochemical processes. Benamar & al (2004, 2009) [1, 2] and Marot & al (2012) [17] reported that deposition processes depend on the grain angularity which contributes to increase the suffusion resistance and high filtration. According to previous studies, higher concentration of particles in the flowing suspension involves important deposition rate [3, 19]. Large concentration of particles causes increased capture rate and so rapid clogging. In this paper we have investigated various parameters affecting filtration behaviour including: hydraulic conductivity, porosity, size of eroded particles, the grains shape and their influence on the filter efficiency was evaluated.

MATERIAL AND METHODS:

Experimental set up and test procedure

The device used for erosion test in vertical flow conditions is already described by Sherard & Dunnigan (1985) [20] for the No Erosion Test (NET). It is devoted to simulate the filtration of cohesive soils in granular filter with the presence of a crack. The apparatus is shown schematically in figure 1. The so-called NEF test (No Erosion Filter) uses a permeameter (cell made of Plexiglas) which is 140 mm of diameter and 280 mm high. Within the cell a sample of base soil (representing the core) of 25 mm thickness is compacted above the layer of granular

filter (150 mm thickness) previously selected. A 10 mm diameter pinhole was drilled through the base soil in order to induce a concentrated flow through the hole towards the filtering layer. The cell was connected to a water supply which provides a selected pressure in a range from 25 kPa to 120 kPa, the pressure was increased by steps of 25 kPa. The cell is equipped with a pressure gauge and the outlet is directed to a turbidity-meter and a flow-meter providing continuous record of measured values. A flow induced with a very low pressure is applied through the soil-filter system and once saturation reached, the water pressure is increased gradually by steps corresponding to selected pressure test values. A particle concentration is derived using a previous correlation between fines concentration and turbidity (NTU). The performance of the soil-filter combination is observed during a processing time close to 10 minutes.

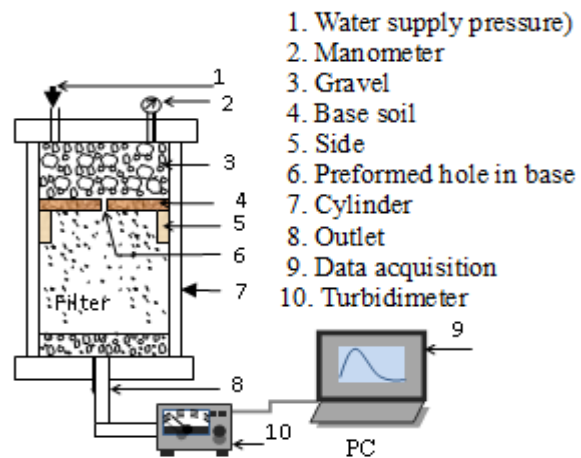


Figure 1

General view of experimental apparatus

Materials

The parametric study involves samples made of silt for the base soil and sand for the filters. The particle size distributions of the two materials are shown in Figure 2. Two base soils were selected for erosion: silt 1 with a maximum particle size of 120 μm and silt 2 (quite finer) whose maximal size is close to 106 μm . The two silts involve the same size d_{85} (45.5 μm), which leads to the same ratio (D_{15} / d_{85}) of 11. For lower size than d_{50} , silt 2 contains more fines than silt 1. The intrinsic characteristics of the two tested silts are listed in Table 2. The geotechnical characterization provides a liquidity limit of 37% and a plastic index $I_p = 20$ for the silt 1 (very plastic),

while Silt 2 provides a liquidity limit of 33%, it was classed as a slightly plastic ($I_p = 12$).

Table 1 shows the analysis of different existing criteria; the comparison reveals that the design criteria proposed by Sherard and Dunnigan (1985) was the most conservative. The choice of filters for fine soils prone to suffusion or internal erosion is essentially based on the grain-size distribution properties of materials. In our case the filter design was done in a way to meet the USBR (US Bureau of Reclamation 1986) criteria. The both filters used in the present study have the same grains size distribution but an angular grain shape for the filter F_1 and a rounded grain shape for the filter F_2 (FHWA NHI-06-088, [11]). The selected filters are efficient if fines grading involves a d_{85} size larger than 62 μm . The diameter d_{85} (45.5 μm) of the two investigated silts was strictly smaller than the required dimension given in Table (2) (right column), showing that filtration may be not efficient.

Table 1

Granulometric criteria applied to the designed filter [13]

AuthorS	Filter Criteria	Filter parameters	Fines size (μm)
Terzaghi (1922)	$(D_{15F}/d_{85B}) \leq 4$	$0.25D_{15F}$	140
Karpoff (1955)	$5 < (D_{50F}/d_{50B}) \leq 10$ (sable fin)	$M_{ax}=0.2D_{50F}$ $M_{in}=0.1 D_{50F}$	300 150
Kenney & al (1985)	$(D_{15F}/d_{85B}) \leq 5$	$0.20D_{15F}$	112
Sherard & al (1985)	$(D_{15F}/d_{85B}) \leq 9$	$0.11D_{15F}$	62
Honjo & al (1989)	$(D_{15F}/d_{85B}) \leq 5.5$	$0.18D_{15F}$	101

Table 2

Intrinsic characteristics of fine materials

	Plasticity		
	$W_L(\%)$	$W_p(\%)$	$I_p(\%)$
Silt 1	37	17	20 (Very plastic)
Silt 2	33	21	12 (Slightly Plastic)

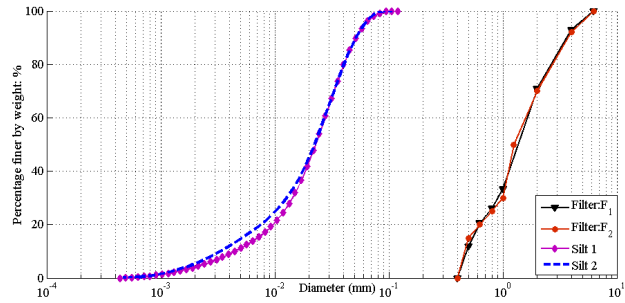


Figure 2

Grain size distributions of used materials

RESULTS AND DISCUSSION

Evaluation of the hydraulic conductivity change in filter F_1

After saturation of the filter in the cell, the measurement of the initial hydraulic conductivity is performed by a flowmeter placed at the outlet of the column. This device enables us to save flow values throughout the test. The hydraulic conductivity is determined using Darcy's law presented by equation (1).

$$Q = -k \frac{A\Delta h}{L} \quad (1)$$

Where:

Q is the volume of flow, l/s,

k is the hydraulic conductivity of the medium, m/s

A is the apparent area of the material, m^2 ,

Δh is the difference of the hydraulic gradient.

To compare very easily the different parameters with several loads, curves of results are presented in dimensionless form (k/k_0). Figure 3 and 4 show the evolution of the hydraulic conductivity in the filter F_1 according to the type of silt and the pressure applied to the inlet cell. So, comparing two silts indicates that for a plastic soil (silt 1) erodibility is less than that of a slightly plastic soil (silt 2) which clogs the pores and leads to a drastic reduction of hydraulic conductivity. The hydraulic conductivity reduction observed in the filter (close to 40 %) when used with silt 2 at a water pressure of 25 kPa is almost the same than that measured at 50 kPa when the filtration is processed for silt 1. The hydraulic load impacts heavily the internal stability of fine soils. Figure 4 shows that under a water pressure of 50 kPa

the hydraulic conductivity evolve significantly compared to the hydraulic conductivity reduction obtained with previous pressure of 25 kPa (Fig. 3). The reduction reaches 40% with silt 1 and then becomes 60 % with silt 2 under a water pressure of 50 kPa.

Such results suggest that silt 2 is more filtered than silt 1 under similar hydraulic conditions. The erodibility of silt 1 can be assumed to be lower, inducing less particles flowing through the filter. The effect of water pressure on hydraulic conductivity reduction is due to previous deposition of particles within the filter and which not detached by the occurring higher pressure. This latter leads also to more particles removed from the core hole owing to increased shear stress on the hole-surface. The curves from Figure 3 and 4 illustrate that once hydraulic conductivity falls down in the beginning of filtration; its value remains constant, leading to a steady-state flow through the filter. So, no clogging risk occurs.

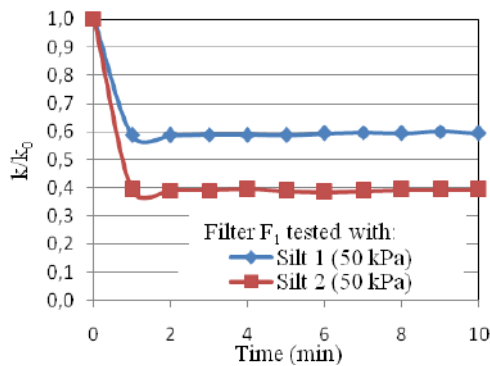


Figure 3

The hydraulic conductivity of the filter F_1 tested under a pressure of 25 kPa.

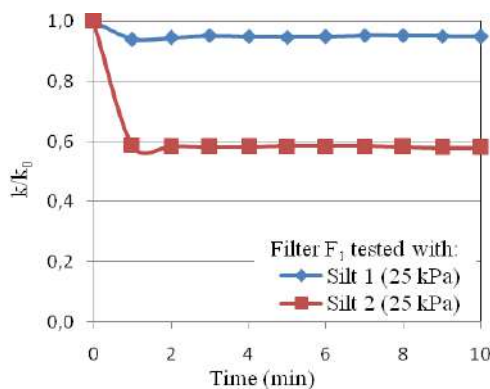


Figure 4

The hydraulic conductivity of the filter F_1 tested under a pressure of 50 kPa.

Porosity in the filters

Porosity is one of the most important parameters of concern in filtration process which includes the transport and deposition of particles in a porous medium. So, it is therefore important to investigate its evolution. Based on the experimental evaluation of the hydraulic conductivity of the filter for different silts tested, we were able to approximate the porosity n reduction according to the Equation 2 of Kozeny, Carman, [18]:

$$k = k_0 \frac{n^3 (1-n_0)^2}{n_0^3 (1-n)^2} \quad (2)$$

Where k_0 is the initial hydraulic conductivity of the filter; k is the measured hydraulic conductivity; n_0 is the initial porosity; n is the porosity corresponding to the hydraulic conductivity k ;

The evolution of porosity was computed for different pressure ranges from 25 kPa to 120 kPa.

Influence of the plasticity index

Fellow & al (1991) [9], described that clay shale with the lowest plasticity was the most susceptible to piping. Delgado & al (2012) [7] conclude that the base soil plasticity has influence in the boundary filter. Figure 5 shows the erosion tests of the two kinds of silt show that the porosity decreases during loading and the effect of applied pressure decreases slightly when its amplitude increases. The porosity decreases considerably when using silt 2 than silt 1. These results can be related to clogging process in many pores by the flowing suspension containing a large amount of silt 2 particles, which reduces the hydraulic conductivity. If comparing the two silts, we conclude that during the first pressure steps the filter porosity in the presence of slightly plastic base soil (silt 2) is affected by a reduction ten percent greater than that calculated with very plastic base soil (silt 1).

Influence of the Grain Shape of the Filter

The detachment of fines particles and their transport throughout the filter is conditioned by the granular distribution, but also depend on the grain shape of the filter. Figure 6 shows the results of the porosity reduction in the two filters F_1 and F_2 for the silt 1 (very plastic), the results are quite similar in both

filters. The grain shape had not influence on the porosity reduction if the base soil was very plastic.

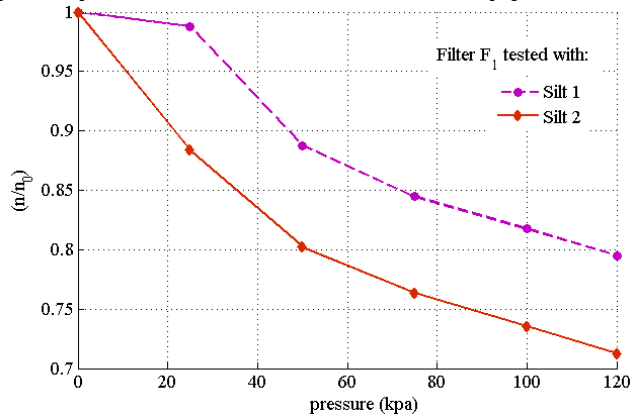


Figure 5

Filter porosity reduction in the filter F₁ for two base soils at different loads.

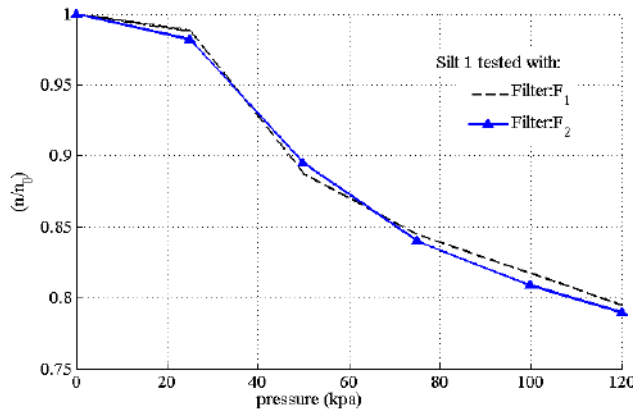


Figure 6: Porosity reduction comparison in filter F₁ and F₂ tested with Silt 1.

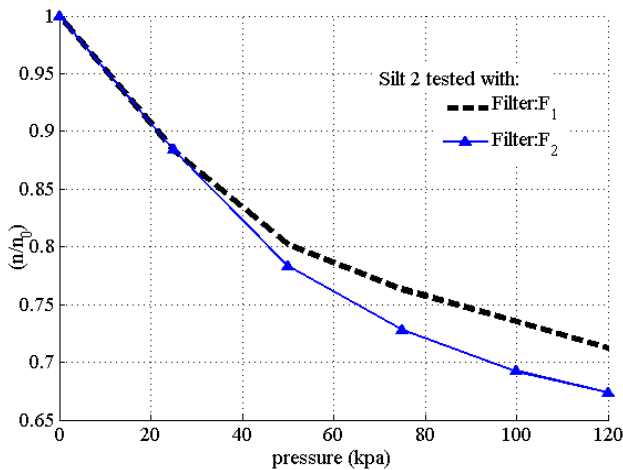


Figure 7:

Porosity reduction comparison in filter F₁ and F₂ tested with Silt 2.

Figure 7 shows the results of the porosity reduction in filter F₁ and F₂ tested with the base soil Silt 2 (slightly plastic). The same reduction was shown at 25 kPa but the gap increases at a pressure of 120 kPa to a difference of 5%. The damage caused in the filter F₂ was more important than in the filter F₁. The grain shape influences the porosity of the filter if the base soil was a slightly plastic.

Assessment of filter criteria

During the filtration tests we have separately collected samples of eroded particles through the filter for various water pressures for subsequent particle size analysis. The results can bring some knowledge about the maximal particle size which can flow through the filter without trapping.

In order to understand the filtration mechanism the distribution of sizes d_{85} for recovered and trapped particles was plotted with respect to the grading curve of silt 2 (Fig. 8). The results indicate that the fine fraction of silt particles are infiltrated (recovered) since the size of particles collected (<35 μm) is widely smaller than that of silt (45 μm). The increase of the applied pressure generates increased size of eroded particles owing to higher shear stress applied on the internal surface of the hole. The d_{85} size (ranging between 28 μm and 38 μm) of the infiltrated portion of fine particles is widely less than the filter opening. These results confirm the criteria based on the filter size D_{15} but it remains that particle whose size is greater than d_{85} core soil requires larger opening filter.

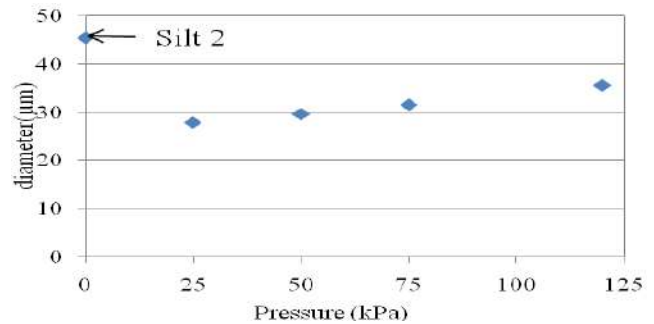


Figure 8

d_{85} particle size of recovered fines versus applied pressure (Silt 2 tested with filter F₁).

During filtration particles trapped and recovered depend on the relative size of flowing particles and filter opening (constrictions distribution and pore size). In order to investigate the qualitative

performance of the filter, the particle size distribution of filtered particles (in both upper and lower sides of the filter) and recovered ones at each hydraulic pressure at the outlet of the filter is carried out (Figs. 9 and 10).

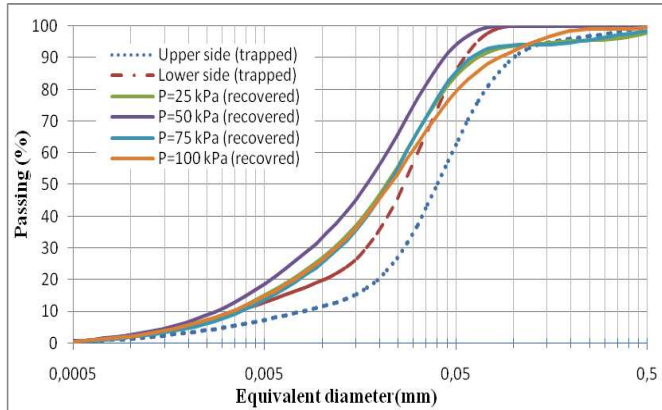


Figure 9

Particle size distribution of the recovered samples
(Silt 1 tested with filter F_1)

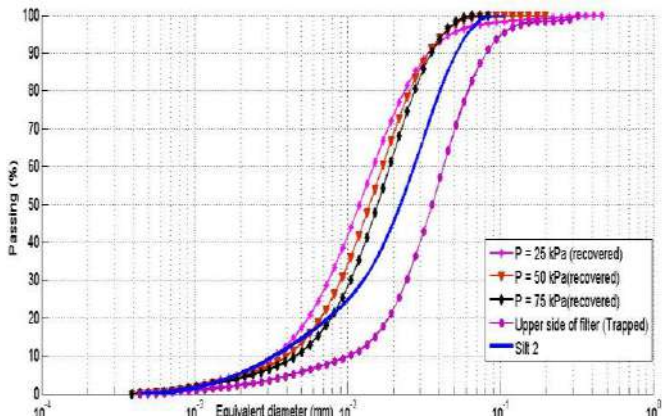


Figure 10

Particle size distribution of the recovered samples
(silt 2 tested with filter F_1)

For filtered particles (Fig. 9) (dashed lines) it is shown that particles retained by the filter upstream are coarser than that retained downstream, as reported in several filtration studies. As regards to the recovered particles (solid lines) seems to have a similar shape and d_{90} size is the same in the different cases of water pressure.

However, particles recovered under a pressure of 50 (second step of loading) stands out from other curves, indicating the recovery of finer particles. The recovered samples are finer than the initial size of base soil. The effect of applied pressure is evident on the size distribution of recovered particles, since

increasing pressure leads to recover coarser particles, at least during the two first hydraulic gradients. The size d_{50} of eroded particles is finer than that of collected from the filter (trapped particles). The analysis of the size distribution of retained particles within the filter at the end of the test shows that large size particles (coarser fraction) are retained by the filter. The grain size distribution of the filter material advocates the blocking of large silt particles in the voids formed by the grains.

CONCLUSION

Two materials representing the base soil have been selected and tested with the aim of filtration mechanism investigation. The soil-filter system was subjected to increasing water pressure, geometric and hydraulic parameters were measured during and after filtration. The results of this experimental study lead to following main results:

Although the ratio (D_{15} / d_{85}) provided by the two silts is similar the filtration mechanism generates different results with the two samples.

Comparison of filter design criteria reveals that the relation proposed by Sherard and Dunnigan (1985) was the most conservative.

The plasticity of the base soil influences greatly the filtration since slightly plastic soils (silt 2) are more erodible than plastic soils (silt 1).

The hydraulic conductivity in the filter is of a great concern and leads to understand the filtration process but it remains a global parameter and knowing its spatial evolution along the filter becomes a necessity.

The hydraulic conductivity fall involves systematically a reduction in filter porosity. The damage caused in the rounded filter (F_2) was more important than in the angular filter (F_1). The grain shape influences the porosity of the filter if the base soil was a slightly plastic but it had not influence on the porosity reduction if the base soil was a very plastic.

The comparison of existing criteria in relation with d_{85} size of the recovered particles indicates that the large particles were filtered while the fines were infiltrated. Even if tested materials do not meet checked criteria, the filtration operates.

REFERENCES

1. Benamar Ahmed, Hua Qing Wang, Nasredine Ahfir, Abdellah Alem, Nicolas Masséi,

- Jean-Paul Dupont. 2004." Effets de la vitesse d'écoulement sur le transport et la cinétique de dépôt de particules en suspension en milieu poreux saturé". *Comptes Rendus Géoscience*. Volume 337, n° 5 pages 497-504, Doi 10.1016/j.crte.2004.12.002.
2. Benamar A., Ahfir N., Wang H., (2009) Particle transport and Deposition in Porous Media, "Porous media: Heat and Mass Transfer, Transport and Mechanics", Nova Science Publishers, New York. ISBN 978-1-60692-437-2, pp. 171-186.
 3. Benamar, A. 2013. Clogging Issues Associated With Managed Aquifer Recharge Methods: Soil Clogging Phenomena In Vertical Flow. IAH Commission On Managing Aquifer Recharge. Australia. 77 p.
 4. Correia, Ricardo Neves Dos Santos, Laura Maria Mello Saraiva Caldeira And Emanuel Maranh Das Neves. "Laboratory Test For Evaluating Limitation Of Flows During Internal Erosion In Zoned Dams". *Geotechnical Testing Journal*. 2014.
 5. Correia, Ricardo Neves Dos Santos, Laura Maria Mello Saraiva Caldeira And Emanuel Maranh Das Neves. "Laboratory Test For Evaluating Crack Filling During Internal Erosion in Dams". *Geotechnical Testing Journal*. 2015.
 6. Correia, Ricardo Neves Dos Santos, Laura Maria Mello Saraiva Caldeira And Emanuel Maranh Das Neves. "Experimental Study On Crack Filling By Upstream Fills In Dams ". *Geotechnique*. 2014.
 7. Delgado-Ramos, José Manuel Poyatos And Francisco Osorio. "Internal Erosion Of Clayey Soils Protected By Granular Filters". *A Houille Blanche* · October 2012.
 8. Delgado-Ramos. "Internal Erosion Risk Analysis in Embankment Dams with Granular Filters". *Semana International Sobre La Aplicacion*. Valencia March 07-11 2005.
 9. Fellow Leonard, G.A.V, ASCE, A.B. Huang, and Jose Ramos, Members, ASCE. "Piping and Erosion Tests at Conner Run Dam" *Journal of Geotechnical Engineering*, Vol.117, No 1, January, 1991, ASCE.
 10. FEMA P 1032. May 2015. "Evaluation and Monitoring of Seepage and Internal Erosion ". Interagency Committee on Dam Safety (ICODS).
 11. FHWA NHI-06-088, 2006: Federal Highway Administration US Department, Transportation. Publication, NHI., Vo. I, No. 132012, pp. 2-14.
 12. Foster, Mark and Robin Fell. "Assessing Embankment Dam Filters That Do Not Satisfy Design Criteria". *Journal of Geotechnical and Geoenvironmental Engineering*. Mai 2001. Gao.C.
 - 2007." Factors Affecting Particle Retention In Porous Media". *Emirates Journal for Engineering Research*.
 13. Honjo, Y., Veneziano, D. 1989. Improved filter criterion for cohesionless soils." *J. Geotech. Engrg.*, 115(1), pp. 75–94.
 14. Karpoff, K. P. 1955. The Use of Laboratory Tests to Develop Design Criteria for Protective Filters. *American Society for Testing Materials*, Vol. 55, pp. 1183-1198.
 15. Kenney. T.C., Lau. D. 1985. Internal Stability Of Granular Filters. *Can. Geotech. J.*, Vol. 22.
 16. Locke. Marke R. 2001. Analytical and Laboratory Modelling of Granular Filters for Embankment Dams. Doctor of Philosophy Thesis. University of Wollongong. Faculty of Engineering.
 17. Marot Didier, Fateh Bendahmane and Hong Hai Nguyen. 2012." Influence of angularity of coarse fraction grains on internal erosion process". *La Houille Blanche*, pp. 47 - 53. DOI: <http://dx.doi.org/10.1051/lhb/2012040>
 18. Nguyen. Q. T. 2011. Analyse Expérimentale et Numérique de la Compaction des Renforts Fibreux. Application pour la Perméabilité. Thèse de Doctorat. INSA de Lyon. France.
 19. Reddi Lee I. M., Park Y. J., L. A. 2002. Particule Transport Characteristics and Filtration of Granitic Residual Soils from the Korean Peninsula. *Can. Geotech. J.* 39: 472-482 p.
 20. Sherard. J. L., Dunnigan L. P. 1985. Filters and Leakage Control in Embankments Dams. *American Society of Civil Engineers*.
 21. Terzaghi, K. Peck. R. B. Mersi. G. "Soil mechanics in engineering practice". Wiley interscience publication third edition. 1940.
 22. USACE 1971. Dewatering and Groundwater Control for Deep Excavations. Technical Memorandum No. 5-818-5 (April), Office of Chief of Engineers, US Army, Washington D.C.
 23. Vaughan, P. R., Soares, H. F. 1982. Design of filters for clay cores of dams. *ASCE Journal of Geotechnical Engineering Division*, January, Vol. 108 (GT1) pp. 17-31.
 24. Wan Chi Fai and Fell Robin. 2004. "Investigation of Rate of Erosion of Soils in Embankment Dams". *Journal of Geotechnical and Geoenvironmental Engineering*, Vol. 130, No. 4. ISSN 1090-0241/ 2004/4-373–380.

A CFD COMSOL MODEL FOR SIMULATING COMPLEX URBAN FLOW

Saddok Houda¹, Rafik Belarbi², Abdelmalek Hasseine³, Nouredine Zemmouri⁴,

¹Laboratoire de Génie Mécanique University of Biskra, B.P. 145 R.P. 07000 Biskra, ALGERIA ²Laboratory LASIE, University of La Rochelle, France

³Laboratory LARGHYDE University of Biskra, ALGERIA

⁴Laboratory Iacomofa University of Biskra

¹Corresponding author: Saddok.houda@univ-biskra.dz

ABSTRACT

Flow modeling around buildings can be achieved either by using wind-tunnel studies or via the utilization of Computational Fluid Dynamics (CFD) techniques. Conducting wind-tunnel studies may be expensive and time consuming, /or environmental configurations. On the other hand, CFD can provide significant cost benefits for assessing and optimizing engineering design solutions related to environmental concerns and appear attractive as a potential alternative tool.

The experiments in the wind tunnel is time consuming and expensive, especially in the case of the urban complexes configurations where it is often necessary to do many tests changes of parameters and configuration of the environment, which has oriented us towards the use of simulation. To do so Google Earth image of the fabric structure was used as a backdrop in the AC3D software. The outlines of the buildings were then traced to create polygons, which were then extruded to produce the 3D individual buildings. This study shows the feasibility of applying a COMSOL CFD model to simulate the airflow behavior in a vernacular urban area. The computational fluid dynamics software COMSOL is used to determine velocity field flow in complex morphological street network .

KEYWORDS: COMSOL CFD model, Complex urban fabrics, Buildings, Urban Flow

INTRODUCTION

Building physics aims to study the built environment. The classification of urban scales based on a number of considerations weather and geography. Our scale study in this work is the microclimate scale. It corresponds to a horizontal spatial scale wherein the transverse dimension of the studied urban fragments does not exceed a few hundred meters and a vertical scale corresponding to the sub-layer roughness figure 1.

In this paper, we present a methodology to build 3D urban area models; objects that will be included in the simulation must be prepared in a step-by-step procedure starting with the capture of the area of investigation using Google Earth 4.2 Professional [2] as shown in figures2 and 3

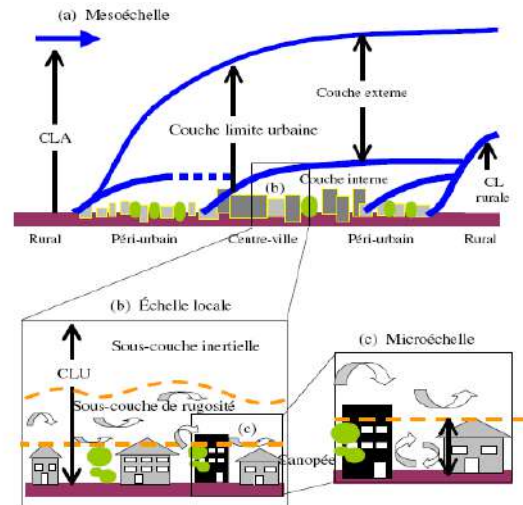


Figure 1

Representation of Climate and Atmospheric scales, mesoscale (a), locally (b) and micro (c) Oke[1].



Figure 2
Ghardaia complex urban morphology



Figure 3
Tracing the complex urban morphology using AC3D

The image is then imported in the AC3D software where the outlines of the buildings were traced and then extruded to produce the individual buildings [3]. The dimensions and the geometry of the objects are scaled to fit the real size of the configuration. Magics12.0 software [4] has been used to correct the file containing the urban geometry of the case study as shown in figures 4 and 5.

This specific built environment with its complex and organic geometry will help to demonstrate the ability of CFD COMSOL [4] software to tackle the most complicated situations.

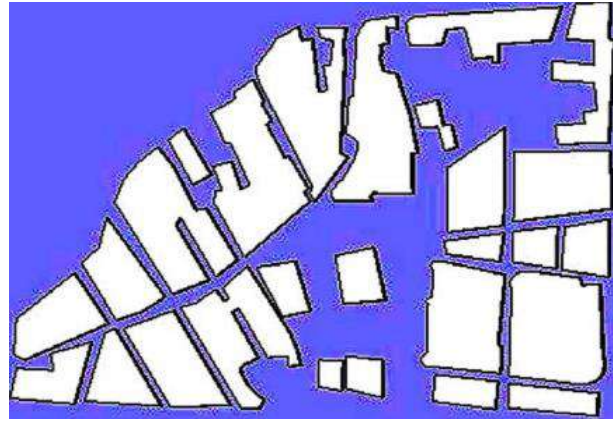


Figure 4
Defective 3D urban configuration tracing result using AC3D

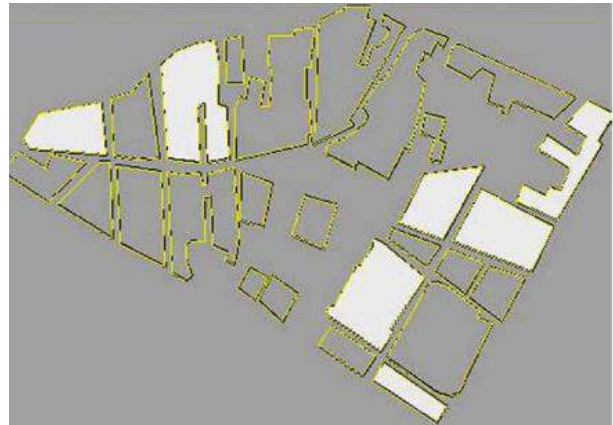


Figure 5
Repaired 3D urban configuration tracing result using Magics

ANALYSIS AND MODELLING

The governing equations of incompressible turbulent wind flow around buildings are continuity and the Reynolds-averaged Navier–Stokes equations, expressed as follows:

$$\rho(\mathbf{u} \cdot \nabla)\mathbf{u} =$$

$$\nabla \cdot \left[-\rho\mathbf{I} + (\mu + \mu_T)(\nabla\mathbf{u} + (\nabla\mathbf{u})^T) - \frac{2}{3}(\mu + \mu_T)(\nabla \cdot \mathbf{u})\mathbf{I} - \frac{2}{3}\rho k\mathbf{I} \right] + \mathbf{F}$$

$$\nabla \cdot (\rho\mathbf{u}) = 0$$

$$\rho(\mathbf{u} \cdot \nabla)k = \nabla \cdot \left[\left(\mu + \frac{\mu_T}{\sigma_k} \right) \nabla k \right] + P_k - \rho\epsilon$$

$$\rho(\mathbf{u} \cdot \nabla)\epsilon = \nabla \cdot \left[\left(\mu + \frac{\mu_T}{\sigma_\epsilon} \right) \nabla \epsilon \right] + C_{\epsilon 1} \frac{\epsilon}{k} P_k - C_{\epsilon 2} \rho \frac{\epsilon^2}{k}, \quad \epsilon = \epsilon_p$$

$$\mu_T = \rho C_\mu \frac{k^2}{\epsilon}$$

$$P_k = \mu_T \left[\nabla \mathbf{u} : (\nabla \mathbf{u} + (\nabla \mathbf{u})^T) - \frac{2}{3}(\nabla \cdot \mathbf{u})^2 \right] - \frac{2}{3}\rho k \nabla \cdot \mathbf{u}$$

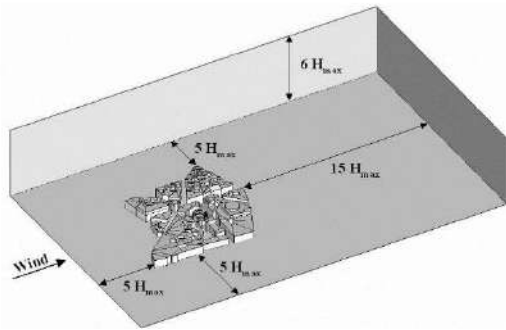


Figure 6

Recommended computational domain size where Hmax refers the maximum height of the building, adapted after Franke et al. [6] and Tominaga et al. [7].

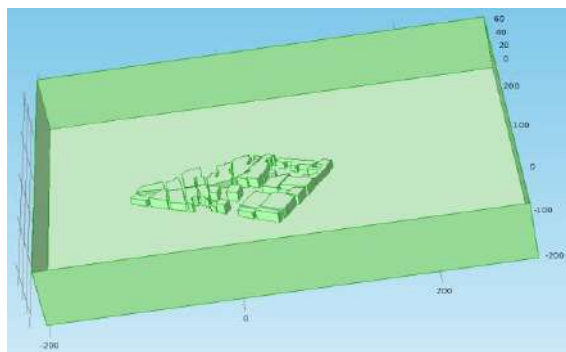


Figure 7

Domain size of the case study

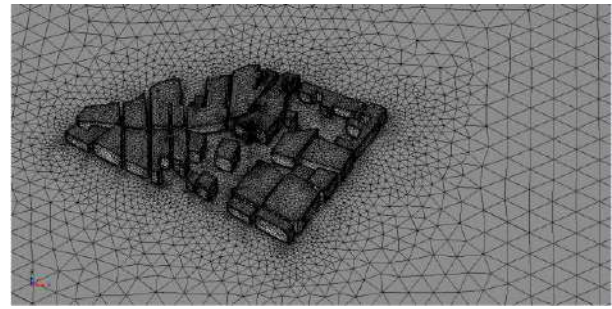


Figure 8
The mesh

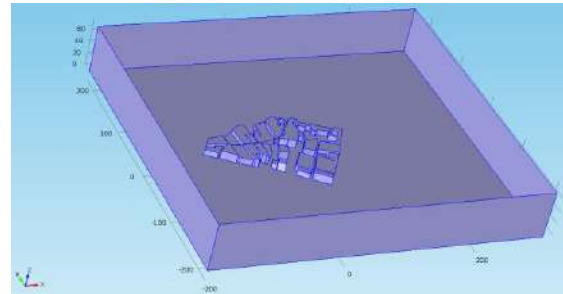


Figure 9

Setup of the 3D urban configuration for simulation

The size of the domain has been taken as a multiple of the characteristic height of the tallest building which is in this case 18 meters, as recommended by Hall [5] who suggests that the distance between any edge of the domain and the buildings must be at least five times of the characteristic height of the building, as shown in figure 6 and 7. The downstream distance is 15 times height, and the height of the domain is 6 times height. The domain covers the entire area of 450 m x 350 m, including all the buildings and surrounding areas. The height of 90 m from the ground in the vertical direction of the calculation domain provides about 75m of open space above the tallest building. Complete mesh consists of 671798 domain elements, 48172 boundary elements, and 4374 edge elements.

The most important thing is to correctly reproduce the characteristics of separating flows near the roof and the walls. Therefore, a fine grid arrangement is required to resolve the flows near the corners as shown in figure 8.

BOUNDARY CONDITIONS

An inflow condition was applied at the leftmost (upwind) side (y-z plane) of the domain as given in

Figure 9. An inlet wind speed of 3 m/s has been chosen as representing the average wind conditions in the region. In addition the orientation of the urban configuration has been selected according to the prevailing wind direction. A pressure outlet condition was applied at the rightmost (downwind) side (y-z plane) of the domain.

RESULTS AND DISCUSSION

The 3D steady RANS equations are solved with k-ε turbulence model because it does perform well for external flow problems around complex geometries. The k-ε model solves for two variables: k; the turbulent kinetic energy, and ε; the rate of dissipation of kinetic energy. Wall functions are used in this model, so the flow in the buffer region is not simulated. It should be noted that Wall functions ignore the flow field in the buffer region, and analytically compute a non-zero fluid velocity at the wall. To achieve a numerical solution, the nonlinear solver solves the equations iteratively.

Figure 10 and 11 show respectively the velocity magnitude and the corresponding streamlines and contour velocity magnitude.

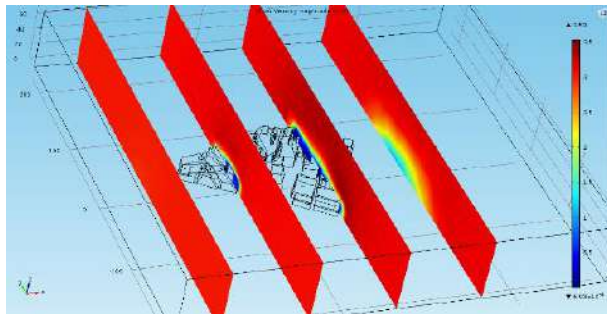


Figure 10
The velocity magnitude

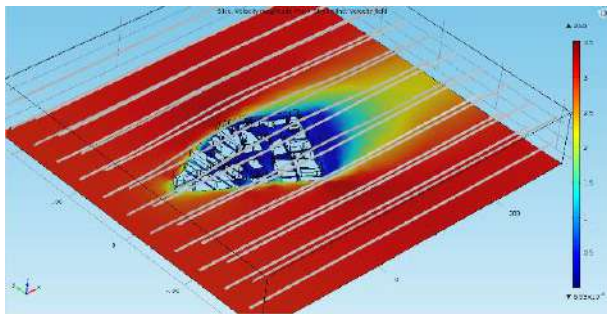


Figure 11
The streamlines.

In Figure 11 we can see that the Air streams are brutally separated from their initial trajectory approaching obstacles of constructions.

Detachment points are often absent, due to the organic form constructions and they appear at the contact of the flow with the sharp edges of certain other constructions downstream of which there is an increase in speed wind and pressure drop figure 12.

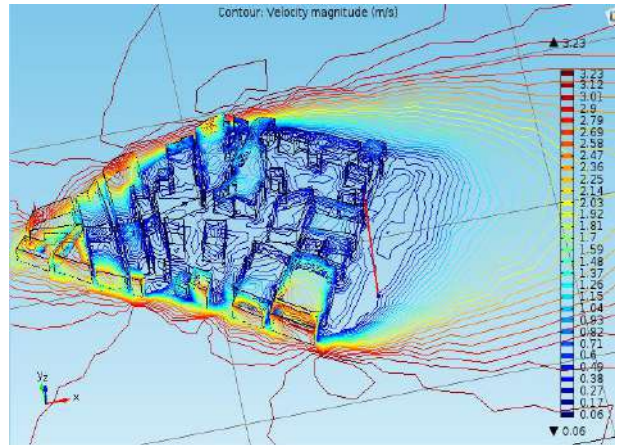


Figure 12
Contour velocity magnitude.

Houses of this kind of urban fabric behave like baffles that create a rotating flow which constitute the recirculation zones. It is seen from Figures 11 and 12 that the velocity of air flux varies drastically with urban density. In the present case the urban configuration acts as a wind shield reducing the air velocity inside the urban fabric, whereas the maximum velocities are observed at the boundaries of the lot. In the wake zone the velocities are low but is characterized by strong turbulence.

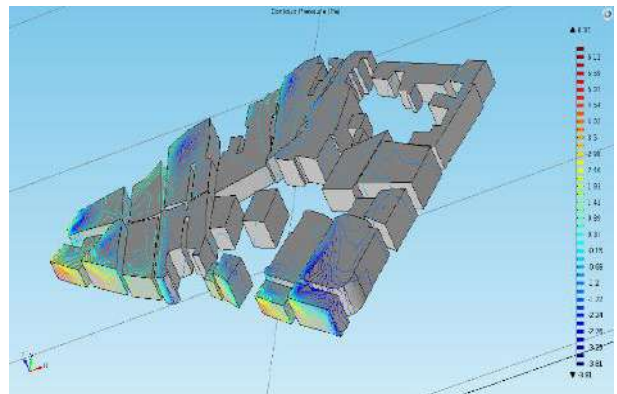


Figure 13
Contour pressure.

Figure 12 and 13 show respectively the Surface wall lift in viscous units and Contour pressure.

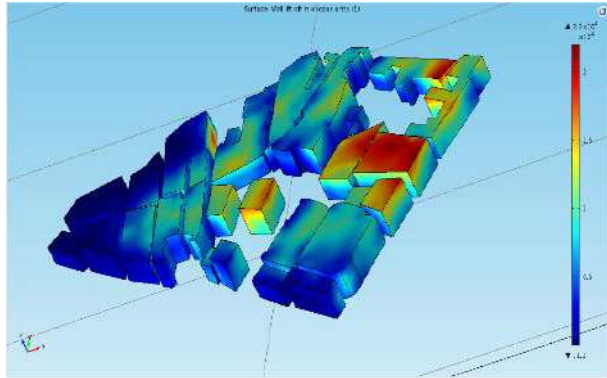


Figure14
Surface wall lift in viscous units.

CONCLUSIONS

A numerical study of wind velocities in a vernacular, complex urban area has been undertaken and discussed in the present study. It was found that the velocity distribution could considerably change with the building shape and urban configuration. By using COMSOL-CFD tool, useful information can be drawn and used by urban developers, architectural designers and environmental planners to promote natural ventilation, a good measure for reducing energy use in buildings and providing better outdoor air quality. It should be kept in mind that the main objective of this research is to improve the understanding of the behavior of a system, rather

than obtaining results readily comparable with regulatory standards.

REFERENCES

1. Oke, T.R, Initial guidance to obtain representative meteorological observations at urban cities. Instruments and observing methods WMO/TD, no.81, 2006.
2. Software, 'Google Earth Version 4.2', 2007
3. 3D Design Software, 'AC3D 6.5.28' copyright © 2009 Inivis ltd.
4. Software, 'Materialise Magics Version 12.0.1.2', 2007.
4. Comsol (2012), CFD Module User'Guide, www.comsol.com
5. Franke, J, Hellsten, A, Schlünzen, H, and Carissimo, B, 2007: Best Practice Guideline for the CFD simulation of flows in the urban environment: COST Action 732: Quality Assurance and Improvement of Microscale Meteorological Models. Tech. Rep. ISBN 3-00-018312-4, COST Office Brussels.
6. Tominaga, Y, Mochida, A, Yoshie, R, Kataoka, H, Nozu, T, Yoshikawa, M, and Shirasawa, T, 2008: AIJ guidelines for practical applications of CFD to pedestrian wind environment around buildings. *J. Wind Eng. Ind. Aerodyn.*, 96 (10-11), 1749–1761.
7. Hall, R.C, 1996, Evaluation of modeling uncertainty –CFD modeling of near-field atmospheric dispersion. .Project EMU final report.WS Atkins Consultants Ltd, UK.

DYNAMICS OF A PLANE IMPINGING JET IN THE PRESENCE OF SELF-SUSTAINING SOUND: CORRELATION BETWEEN THE ACOUSTIC FIELD AND THE TRANSVERSE VELOCITY

H. H. Assoum¹, M. El Hassan¹, J. Hamdi², M. Ali¹, K. Abed-Meraïm² and A. Sakout²

¹ Beirut Arab University-Tripoli Campus, Corniche El Meena, next to the Olympic Stadium, Tripoli, Lebanon

² Laboratoire des Sciences de l'Ingénieur pour l'Environnement (LaSIE), University of La Rochelle, Avenue Michel Crépeau, Pôle Sciences et Technologies, 17000 La Rochelle, France

*Corresponding author: Fax: + 961 6 218400 Email: h.assoum@bau.edu.lb

ABSTRACT

Ventilation strategies play an important role of enhancing energy conservation, Indoor Air Quality (IAQ) and acoustic comfort in any conditioned space. Impinging jets are used in such application and should be understood to be controlled. This paper focuses on the flow physics and the aero-acoustic coupling of an impinging jet ventilation system. Experimental data coupling are obtained thanks to simultaneous measurements of the velocity and the acoustic fields using respectively time-resolved particle image velocimetry (PIV) and a microphone. Spatio-temporal cross-correlations between the transverse velocity and the acoustic signals give us a better understanding of the self-sustained tones generated in impinging jets. A pre-whitening technique is used to investigate the coupling between the acoustic and the velocity signals. This method is useful for analyzing small random signals superimposed on a high amplitude pure tone

Keywords: Self-sustained tones, PIV, Aero-acoustics

INTRODUCTION

Impinging jets on a surface with an edge geometry (slot, grid, etc...) are widely used in ventilation systems of commercial and residential rooms to improve the mixing and diffusion of air flow and ensure the necessary air quality and comfort. These jets may, under certain conditions, be a source of noise due to self-sustaining tones which lead to discomfort and thus should be reduced or suppressed. Since the source of these tonal noises are strongly related to the vortex dynamics in the jet, cross-correlations between both the velocity and the vorticity fields with the acoustic signals are helpful in order to understand the underlying physical mechanisms. For example, the understanding of the vortex dynamics involved in the production of these tones, its synchronization with the sound field is of high interest in order to define control strategies that aim at decreasing the acoustic level generated in such configurations. In addition, the simultaneous investigation of the quasi-periodic dynamics of the most energetic modes of the large-scale vortical structures and the pressure variation of the radiated acoustic waves is useful to build reduced order models that capture the main mechanism involved in the noise generation. In this paper we consider a

plane jet impinging on a slotted plate. The acoustic field and the vortices trajectories between the outlet and the surface of the slotted plate are investigated simultaneously for several number of Reynolds based on the dimension of the nozzle $Re = U_0.H / \nu$ (where U_0 is the average stream-wise velocity at the exit of the convergent and ν is the kinematic viscosity of air).[1,2,3,4,5,6,7]

EXPERIMENTAL APPARATUS AND PROCEDURES

A schematic of the experimental set-up is presented in Figure 1. A compressor (1) creates an air flow in the installation. This compressor is isolated from the experimental room and is commanded by a frequency controller (2) to regulate the air flow (the speed of air flow). The air flow is generated through a damping space (3) of 1m³ and a tube (4) of 1250 mm in length with a rectangular section (90×200 mm²) extended by a rectangular convergent (5), which provides a free jet of height $H = 10$ mm and width $Ly = 200$ mm. A 4 mm thick aluminum plate (6) (250×250 mm²) is fitted with a beveled slot (7) of the same dimension as the convergent outlet and

is carefully aligned with the convergent using a gauge and a displacement system. The distance from the impinging surface to the exit of the convergent section is denoted L . In this paper, the nozzle-to-plate distance is equal to 40 mm ($L/H = 4$). The origin is taken at the jet exit.

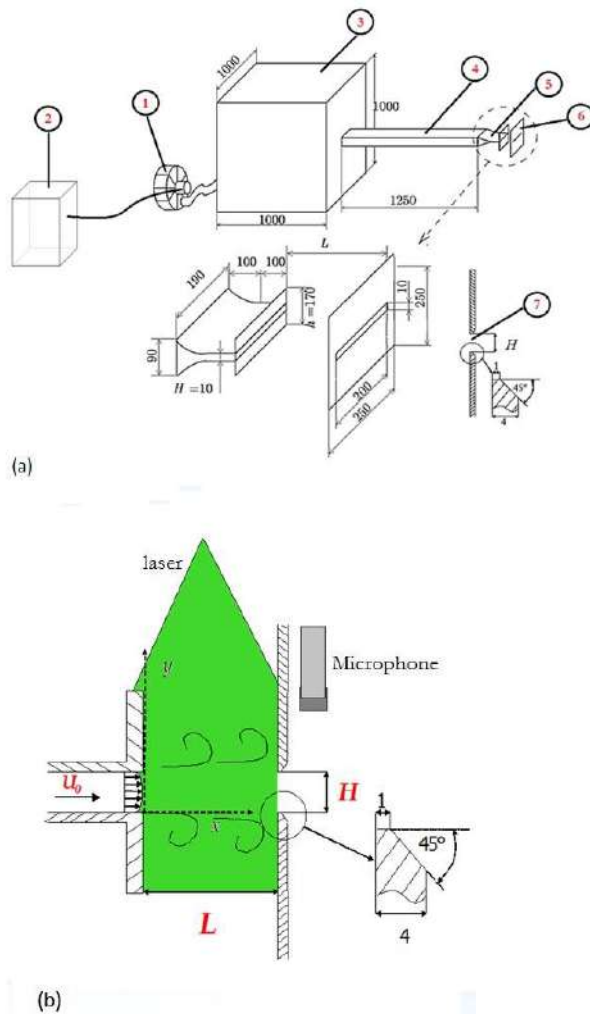


Figure 1: Schematic of the experimental set-up (dimensions in mm). a: The flow leaves the convergent section after entering a rectangular cross-section from a large settling chamber. b: The geometry of the impinged plate

Simultaneous measurements of the acoustic pressure and velocity field were performed. A microphone was placed behind the plate, (away from the hydrodynamic disturbances) to measure the radiated sound pressure. The microphone was a B&K Free-Field 1/2 Type 4189, which has a sensitivity range from 7 Hz to 20 kHz.

The PIV system [15] used for this study is composed of one Phantom V9 camera of 1200×1632 pixels²

mounted normally to the direction of the light sheet plane generated from a Nd: YLF NewWave Pegasus laser of 10mJ energy per pulse and 527 nm wavelength, the laser sheet obtained by a system of lenses has a minimal thickness of 0.5 mm in the measurement section. The acquisition frequency of the PIV system is 1500 Hz. The air jet flow was seeded with small olive oil droplets, 1 to 2 μ m in diameter, provided by a liquid seeding generator.

RESULTS AND DISCUSSION

The self-sustained tones are accompanied by levels of sound which can reach very high values. The sound pressure levels obtained in the studied jet here are shown in Figure 2 for different Reynolds number and a confining ratio $L/H=4$. The frequencies of self-sustained sounds (F) are also plotted on this figure. The evolution of the self-sustained tones frequencies has a succession of stages with abrupt jumps. The acoustic level increases when the Reynolds number increases with a peak at certain Reynolds numbers. The sound level peaks coincide with abrupt jumps of the frequencies of self-sustained tones.

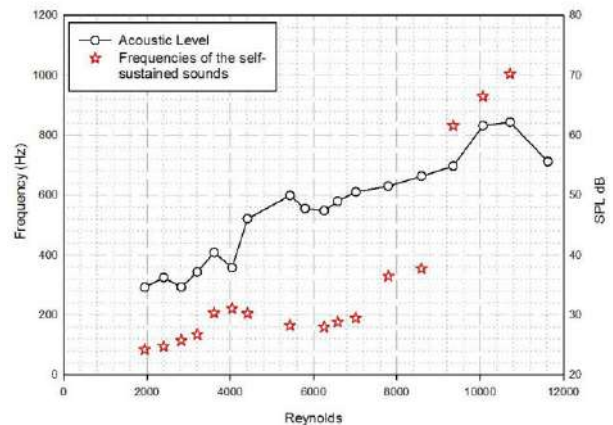


Figure 2: Acoustic level and frequencies of self-sustained sounds versus Reynolds number for $L/H = 4$

The feedback loop and the transfer of energy from the dynamic field to the acoustic one are optimized when a jump of frequency of the self-sustained tones occurs. These abrupt jumps are often associated with an aerodynamic changing in the flow.

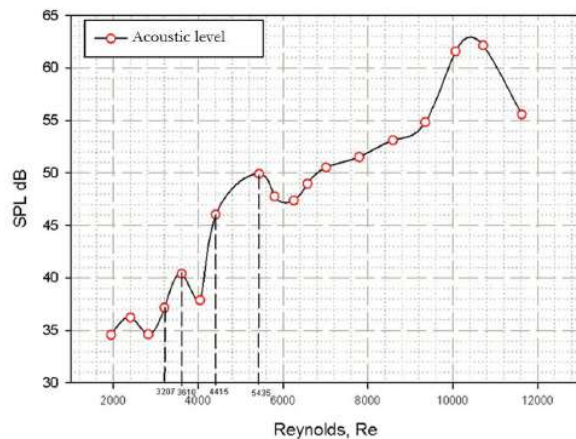


Figure 3: Sound level for different Reynolds. $L/H = 4$

The positions of the vortices centers are shown in Figure 4 for $Re = 5435$ and $Re = 4415$ presenting respectively a peak of the acoustic level and the Reynolds which precedes it (Figure 3). As it is shown in Assoum [1] for a plane jet impinging on a slotted plate, when an acoustic peak occurs, vortices have two paths when they are travelling from the outlet to the plate. A first path where vortices are deviated in the transverse direction close to the wall and a second path where vortices escape by the slot when they approach the surface of the plate. The acoustic signal reaches a maximum in amplitude when vortices are close to the slot and strangling the flow creating self-sustained sounds.

The cross-correlations between the vortex dynamics and the acoustic signals give a better understanding regarding the generation of noise. The phase relation between the acoustic signal and the vortex dynamics is of high interest for the development of theoretical and semi-empirical models. To observe the trajectory of vortices, several mathematical tools have been proposed for the identification and the characterization of vortices. Vorticity, the simplest tool, still used but known for its sensitivity for a shear layer. Other criteria, such as the Q criterion (developed by Hunt and Wray (1998)), λ_2 [12] or D [8] have been suggested to overcome this problem. The swirling-strength criterion (λ_2) is used in this paper to identify the vortices. This method of vortex identification allows the detection of the position of the center of rotary structures, it can also distinguish between the shear and rotation in the assumption that the center of a vortex corresponds to a minimum of local pressure.

To understand the difference between configurations with a low and high levels of noise (for respectively

$Re = 4045$ and $Re = 5435$), the cross-correlations between the transverse velocity of the jet (representing the passage of the vortices) and the acoustic signals are presented here. At first we consider the Reynolds number $Re = 4045$, which has relatively a low level of noise (Figure 3). The correlations between the acoustic signal and the transverse velocities are shown in Figure 5 along the line $Y/H = 0.6$ for $L/4 = H$. A peak of correlation which is centered at $t = 0$ ms exists close to the plate $X/H = 3.9$ but with a low coefficient of correlation (about 0.32) what explain the low acoustic level at this Reynolds number.

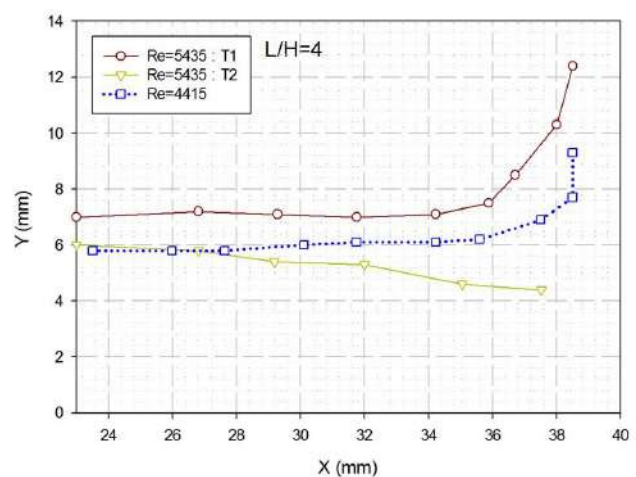


Figure 4: Positions of the vortices centres for different Reynolds number. $L/H=4$

Now we consider the Reynolds number $Re = 5435$ which represents a peak of the acoustic level (Figure 5). The dynamics of the vortices is presented in Figure 6(a). Vortices hit the plate then they follow a first path along the wall of the plate. Vortices according to the second path escape through the slot of the plate. The correlations between the acoustic signal and the transverse velocities are shown in Figure 6(b) along the line $Y/H = 0.6$ for $L/4 = H$. One can see that there are two peaks of correlation near the wall at $X/H = 3.9$, the first peak is positive and centered at $t = 0$ ms and the second peak is negative delayed by about 3ms. This distribution of the cross-correlation between the transverse velocity and the acoustic signal is due to two vortices which arrive successively at the plate; the first vortex is deviated in the transverse direction and responsible for the first peak of correlation and the second

which arrives after this latter escape through the slot of the plate and is responsible for the second peak of correlation. For $Y/H = 2$ (Figure 7(a)) and close to the wall, a phase jump of the correlation is observed at $X/H = 3.6$. This phase shift is explained by the fact that the acoustic signal becomes correlated with the secondary vortices closer to the wall as presented in Figure 7(b) at $Y/H = 2$.

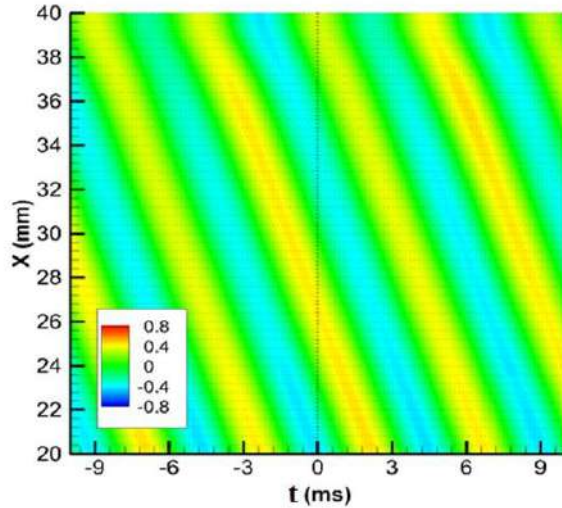


Figure 5: Cross-correlations between the acoustic signal and the transverse velocity along $Y/H=0.6$ for $Re=4045$

In order to calculate the cross-correlations between the acoustic signal and the transverse velocity U_y , we firstly used the signal of U_y directly extracted from the PIV field. In this signal, Kelvin-Helmholtz vortices are the dominant structures, the passage of these primary structures may hide other information belonging to other physical phenomena. Therefore, the pre-whitening technique proposed by Ho and Nosier [9] is used. This technique also used by Assoum et al. [1] allows to other frequency peaks not directly related to the passage of the dominant Kelvin-Helmholtz vortices to be shown. It consists in replacing the high resonant peaks in the cross-spectrum of two considered signals with the average value of the two neighboring frequency components, and then to calculate the cross-correlation using the inverse Fourier transform of the resulting spectrum. For the Reynolds number $Re=4045$ which represent a low level of the acoustic level, the planar cross-correlation between the pre-whitened signals of U_y extracted along $Y/H = 0.6$ and the acoustic one is presented (Figure 8). Cross-correlations are shown for all positions starting from the nozzle exit ($X/H=0$) toward to the impinging wall ($X/H = 40$).

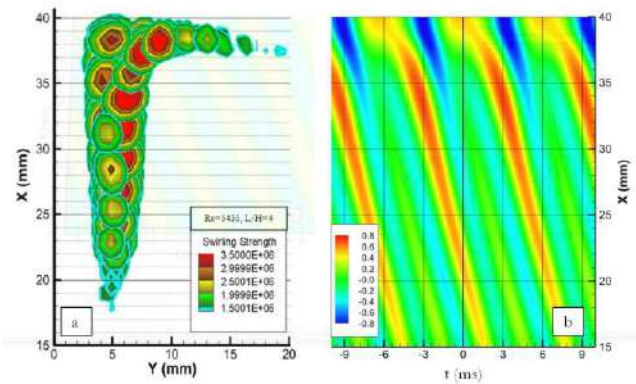


Figure 6: (a): Vortices using λ_2 criterion showing the paths of vortices on the half of the jet ($Y > 0$) for $R = 5435$. (b): Cross-correlations between the acoustic signal and the transverse velocity along $Y/H = 0.6$ for $Re = 5435$

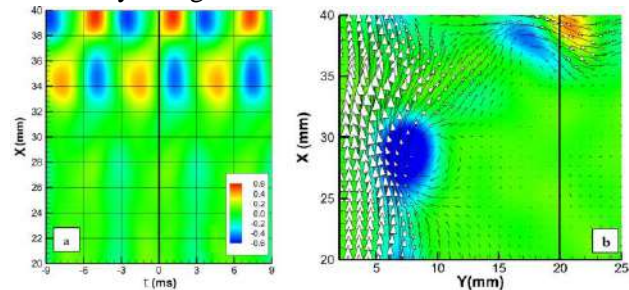


Figure 7: (a): Cross-correlations between the acoustic signal and the transverse velocity along $Y/H = 2$ for $Re = 5435$. (b): Vorticity field showing the secondary vortices near the wall at $Y/H = 2$ for $Re=5435$.

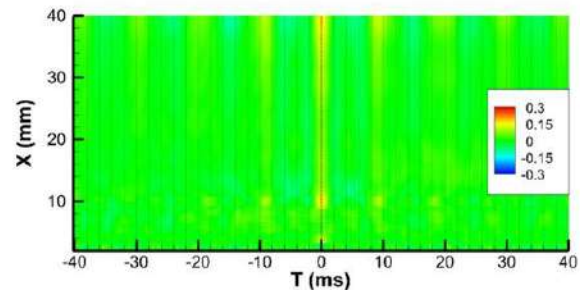


Figure 8: Pre-whitened signals: Cross-correlations between the acoustic signal and the transverse velocity along $Y/H = 0.6$ for $Re = 4045$

One can see that no significant correlation could be found. For this Reynolds number, the self-sustained sounds are relatively low, and the feedback loop is not well installed. For $Re=5435$ representing the peak of the acoustic level in Figure 3, one can note that a periodic correlation exists on the Figure 9(a).

The period of this correlation is related to the Kelvin-Helmholtz structures, but the correlation map does not present a slope (which reflects the progress of the vortices) as it was the case before pre-whitening. The peak of correlation is independent from the position where U_y is extracted along the line $Y/H = 0.6$ and is centered at $t = 0$ ms along the X-axis.

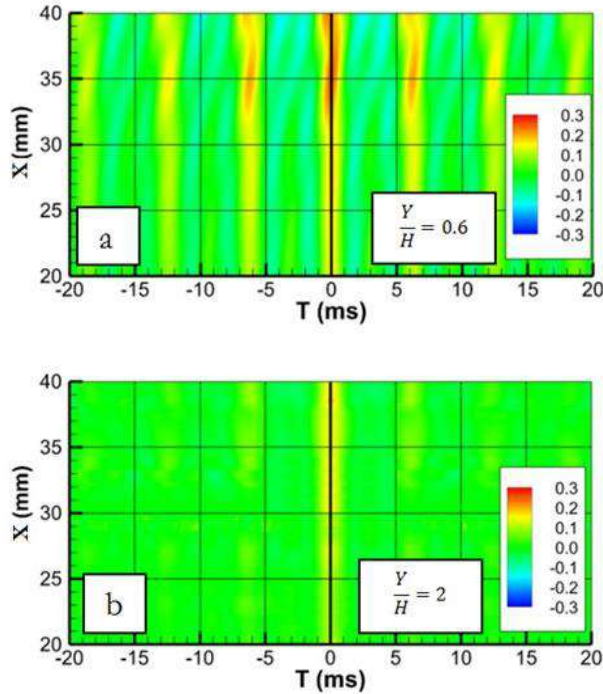


Figure 9: Pre-whitened signals: Cross-correlations between the acoustic signal and the transverse velocity along $Y/H = 0.6$ (a) and $Y/H = 2$ (b) for $Re = 4045$

Since the jet shear layer near the nozzle was controlled by a direct feedback loop for $Re \leq 10000$ [14], and as it was shown in [1], the generated perturbation at the impact of the jet could trigger an instability which is set along the axis of the jet from the plate to the birth of the primary instabilities in the shear layer of the flow.

Figure 9(b) shows the planar cross-correlation of the acoustic signal with U_y , after pre-whitening at the distance of $2*H$ from the axis of the jet. Far from the jet axis, we can observe that the correlation observed when $Y/H = 0.6$ along the X-axis (Figure 13(a)) does not exist. Non-significant coefficient of correlation exists very near from the wall.

CONCLUSIONS

The dynamics of vortices in a plane jet impinging on a slotted plate and the generated acoustic field are

investigated experimentally using time-resolved PIV measurements and a microphone. It was found that when a peak of the acoustic level is reached, a jump of the self-sustained tones frequencies occurs and a change of the aerodynamic mode takes place. This implies that the change of the aerodynamic mode which is directly related to the self-sustained frequency amplify the sound intensity and promotes the transfer of energy to the acoustic field. It was found that in self-sustained configurations, vortices have two paths when they are travelling from the outlet to the plate. A first path where vortices are deviated in the transverse direction close to the wall and a second path where vortices escape by the slot when they approach the surface of the plate. The planar cross-correlation presentation between the acoustic signal and the transverse velocity shows that the acoustic wave created by the considered impinging jet is instantaneously generated with the impact of the Kelvin-Helmholtz vortices on the surface of the plate. A pre-whitening technique is used to investigate more deeply the coupling between the acoustic field and the velocity one. This method shows that a centered peak of correlation is set along the X-axis at the center of the jet. This peak of correlation revealed an instability which is set along in the jet from the plate to the birth of the primary instabilities in the shear layer of the flow. This instability is related to the feedback loop of the self-sustained sounds.

REFERENCES

1. Assoum, H. H., El Hassan, M., Abed-Meraïm, K., Martinuzzi, R. and Sakout, A.: 2013, Experimental analysis of the aero-acoustic coupling in a plane impinging jet on a slotted plate, *Fluid Dynamics Research* 45(4), 045503
2. Assoum H.H., El Hassan, M, Abed-Meraïm, K. and Sakout, A. 2014, The vortex dynamics and the self-sustained tones in a plane jet impinging on a slotted plate, *European Journal of Mechanics-B/Fluids*, V 48 p 231-235
3. Assoum, H.H., Abed-Meraïm, Sakout, A. The acoustic production and the vortices dynamics involved in a plane impinging jet. (2013) *Congrès Français de Mécanique*.

4. Assoum, H.H., Sakout, A., Abed-Meraïm, K., Alia, A., Hassan, M.E., Vetel, J. Experimental investigation of the vibration of a slotted and a non-slotted plates and the acoustic field in a plane impinging jet. (2012) Proceedings - European Conference on Noise Control, pp. 801-806.
5. Assoum, H.H., Sakout, A., Hassan, M.E., Vetel, J., Alia, A., Abed-Meraïm, K. Experimental investigation of the vibration of a slotted plate and the acoustic field in a plane impinging jet. (2012) Acoustics 2012, France (2012). hal-00810574
6. Billon, A. and Sakout, A.: 2005, Two feedback paths for a jet-slot oscillator, *Journal of Fluids and Structures* 21, 121–132.
7. Billon, A., Valeau, V. and Sakout, A.: 2004, Instabilités de l'écoulement produisant le bruit de fente, *C. R. Mécanique* 332, 557–563.
8. Chong, M. S., Perry, A. E. and Cantwell, B. J.: 1990, A general classification of three-dimensional flow fields, *Physics of Fluids A: Fluid Dynamics* 2(5), 765–777.
9. Ho, C. and Nosseir, N.: 1980, Large coherent structures in an impinging turbulent jet, *Turbulent Shear Flows* 2, p 297. Springer.
10. Ho, C. and Nosseir, N.: 1981, Dynamics of an impinging jet. Part 1. The feedback phenomenon, *Journal of Fluid Mechanics* 105, 119 – 142.
11. Howe, M.: 1975, Contributions to the theory of aerodynamic sound, with application to excess jet noise and the theory of the flute, *Journal of Fluid Mechanics* 71(04), 625–673.
12. Jeong, J. and Hussain, F.: 1995, On the identification of a vortex, *J. Fluid Mech.* 285, 69–94.
13. Nosseir, N. and Ho, C.: 1982, Dynamics of an impinging jet. Part 2. The noise generation, *Journal of Fluid Mechanics* 116, 379–391.
14. Powell, A.: 1961, On the edgetone, *J. Acoust. SOCA* 33, 395–409.
15. Raffel, M., Willert, C. and Kompenhans, J.: 2002, Particle image velocimetry : a practical guide, Springer, New York .
16. Rockwell, D. and Naudascher, E.: 1979, Self-sustained oscillations of impinging free shear layer, *Ann. Rev. Fluid Mech* 11, 67–94.
17. Rossiter, J.: 1964, Wind tunnel experiments on the flow-over rectangular cavities at subsonic and transonic speeds, Technical Report 64037, Royal Aircraft Establishment
18. Walker, J. D. A., Smith, C. R., Cerra, A. W. and Doligalski, T. L.: 1987, The impact of a vortex ring on a wall, *Journal of Fluid Mechanics* 81, 99–140.

THE TURBULENT KINETIC ENERGY AND THE ACOUSTIC FIELD IN A RECTANGULAR JET IMPINGING A SLOTTED PLATE

H. H. Assoum^{1*}, M. El Hassan¹, J. Hamdi², A. Hammoud¹, K. Abed-Meraïm² and A. Sakout²

¹ Beirut Arab University-Tripoli Campus, Corniche El Meena, next to the Olympic Stadium, Tripoli, Lebanon

² Laboratoire des Sciences de l'Ingénieur pour l'Environnement (LaSIE), University of La Rochelle, Avenue Michel Crépeau, Pôle Sciences et Technologies, 17000 La Rochelle, France

*Corresponding author: Fax: + 961 6 218400 Email: h.assoum@bau.edu.lb

ABSTRACT

Ventilation systems are of vital importance for buildings, not only to provide acceptable thermal conditions and air quality for occupants, but also with regards to energy usage. Impinging jets can be encountered in many ventilation strategies which have major impacts on the acoustic environment and energy performance. The self-sustaining tones can be generated in such applications where a feedback loop is installed in the system. This phenomenon is explained by the corollary of Howe who shows that the origin of noise in such configurations can be attributed to fluid rotations. Howe highlights the role of phase conditions between the vorticity, the velocity of the flow and the acoustic velocity for the optimization of energy transfers between the turbulent kinetic energy and the sound field. In this work, we use 2D-PIV technique and a microphone respectively to measure the kinematic fields simultaneously with the acoustic generation for a rectangular jet impinging on a slotted plate. This study aims to investigate the transfers between the turbulent kinetic energy and the sound field for two Reynolds numbers presenting a high and a low noise levels. It is shown that phase conditions are necessary for the optimization of energy transfer which allows the installation of the self-sustained loop in the flow. It was found also that the change of the aerodynamic mode which is directly related to the self-sustained frequency.

KEYWORDS

Self-sustained tones, PIV, Turbulent kinetic energy

INTRODUCTION

Several configurations in which a shear layer interacts with an obstacle can generate self-sustained tones. Self-sustained tones are generated due to a feedback loop which was described by [11, 12]. Self-sustaining sounds related to aero-acoustic coupling occurs in impinging jets when a feedback loop is present between the jet exit and a slotted plate: the downstream-convicted coherent structures and upstream-propagating pressure waves generated by the impingement of the coherent structures on the plate are phase locked at the nozzle exit. The upstream-propagating waves excite the thin shear layer near the nozzle lip and result in periodic coherent structures. The period is determined by the convection speed of the coherent structures and the distance between the nozzle and the plate [1,2,3,4,5,6,7,8,9,10]. Actually, in this case, the

interaction between the flow and the obstacle generates an aero-acoustic source and the perturbation which is fed back upstream leads to a direct feedback path inducing an amplification of the flow fluctuations [16, 18, and 19]. This feedback loop optimizes the transfer of energy between the aero-dynamic fluctuations, essentially incompressible, and the acoustic fluctuations [13, 14, and 15]. The acoustic energy such created is principally distributed over well-defined frequency peaks. In this paper we consider a plane jet impinging on a slotted plate. The two-dimensional turbulent kinetic energy is calculated for different cases presenting low and high levels of the acoustic generation.

EXPERIMENTAL APPARATUS AND PROCEDURES

A schematic of the experimental set-up is presented in Figure 1. A compressor (1) creates an air flow in the installation. This compressor is isolated from the experimental room and is commanded by a frequency controller (2) to regulate the air flow (the speed of air flow). The air flow is generated through a damping space (3) of 1m³ and a tube (4) of 1250 mm in length with a rectangular section (90×200 mm²) extended by a rectangular convergent (5), which provides a free jet of height $H = 10\text{mm}$ and width $L_y = 200\text{mm}$. A 4 mm thick aluminum plate (6) (250×250 mm²) is fitted with a beveled slot (7) of the same dimension as the convergent outlet and is carefully aligned with the convergent using a gauge and a displacement system.

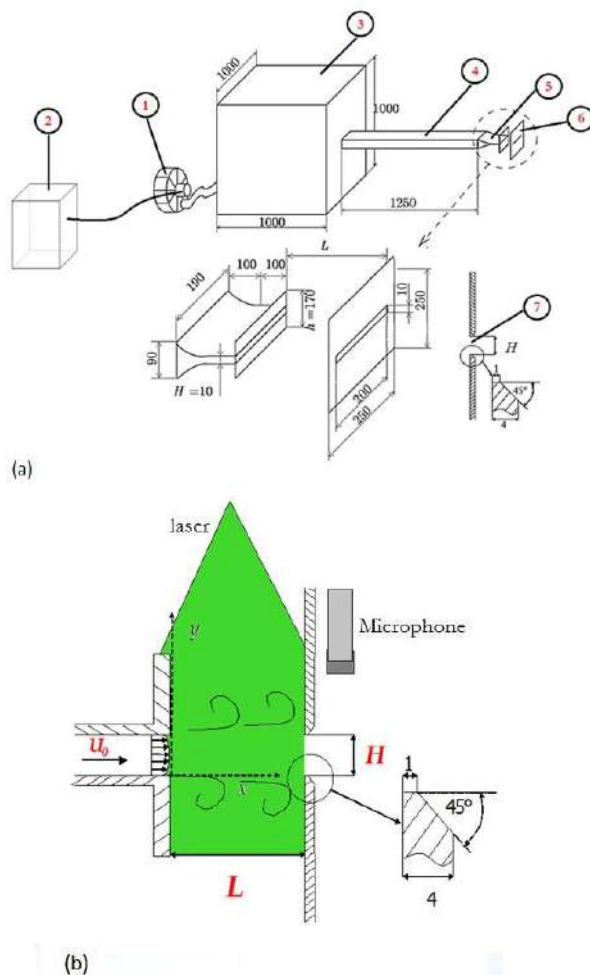


Figure 1: Schematic of the experimental set-up (dimensions in mm). a: The flow leaves the convergent section after entering a rectangular cross-section from a large settling chamber. b: The geometry of the impinging plate

The distance from the impinged surface to the exit of the convergent section is denoted L . In this paper, the nozzle-to-plate distance is equal to 40 mm ($L/H = 4$). The origin is taken at the jet exit.

Simultaneous measurements of the acoustic pressure and velocity field were performed. A microphone was placed behind the plate, (away from the hydrodynamic disturbances) to measure the radiated sound pressure. The microphone was a B&K Free-Field 1/2 Type 4189, which has a sensitivity range from 7 Hz to 20 kHz.

The PIV system [17] used for this study is composed of one Phantom V9 camera of 1200×1632 pixels² mounted normally to the direction of the light sheet plane generated from a Nd: YLF New Wave Pegasus laser of 10mJ energy per pulse and 527 nm wavelength, the laser sheet obtained by a system of lenses has a minimal thickness of 0.5 mm in the measurement section. The acquisition frequency of the PIV system is 1500 Hz. The air jet flow was seeded with small olive oil droplets, 1 to 2 μm in diameter, provided by a liquid seeding generator.

RESULTS AND DISCUSSION

The self-sustained tones are accompanied by levels of sound which can reach very high values. The sound pressure levels obtained in the studied jet here are shown in Figure 2 for different number of Reynolds and a confining ratio $L/H=4$. The frequencies of self-sustained sounds (F) are also plotted on this figure. The evolution of the self-sustained tones frequencies has a succession of stages with abrupt jumps. The acoustic level increases when the Reynolds number increases with a peak at certain Reynolds numbers. The sound level peaks coincide with abrupt jumps of the frequencies of self-sustained tones.

The feedback loop and the transfer of energy from the dynamic field to the acoustic one are optimized when a jump of frequency of the self-sustained tones occurs. These abrupt jumps are often associated with an aerodynamic changing in the flow. To illustrate the aerodynamic change, we consider, for example, the peak of the sound level and the frequency jump which take place at $Re = 3610$ for $L/H = 4$ (Figure 4). Thus, in Figure 3 two fields of the vorticity are shown for two Reynolds number at two arbitrary instants; the first Reynolds number corresponds to the peak of the acoustic level at

Re = 3610 and the second Reynolds precedes it at Re = 3207 for L/H = 4.

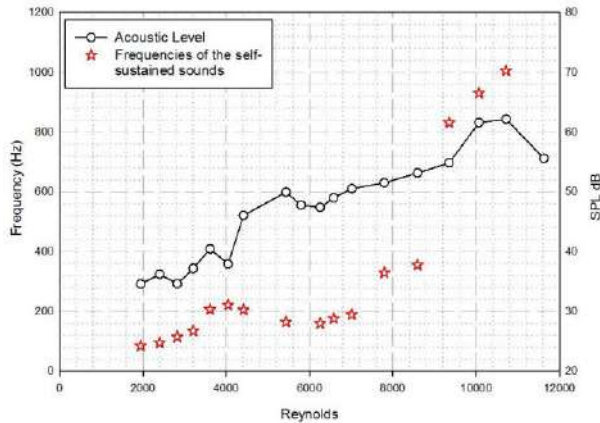


Figure 2: Acoustic level and frequencies of self-sustained sounds versus Reynolds number for L/H = 4

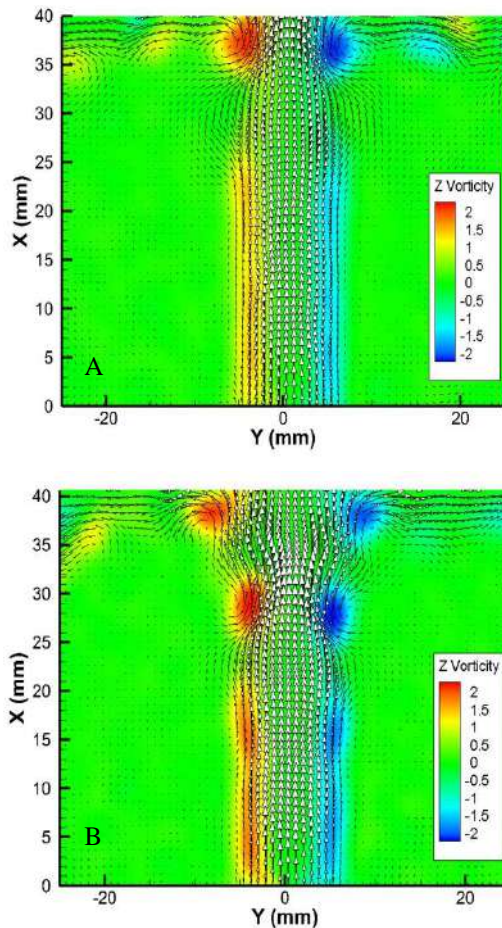


Figure 3: Vorticity fields for Re = 3207 (A) and Re = 3610 (B). L/H=4.

The vorticity fields ω_z are calculated in the plane (XY). When the Reynolds number increases from Re

= 3207 to Re = 3610, one can see that the number of vortices between the convergent and the plate doubled (it passes from 2 to 4 vortices). The frequency of the self-sustained sounds is associated with the vortex shedding frequency and the aerodynamic changing mode. The peak of the sound level which occurs with the jump of the self-sustained tones frequencies implies that the change of the aerodynamic mode amplify the sound intensity and promotes the transfer of energy to the acoustic field. A similar conclusion is obtained for other peaks of the sound level.

When the self-sustained loop is optimized, the transfer of energy from the aerodynamic field to the acoustic one occurs in configurations which allows an optimum interaction of the acoustic fields with the aerodynamic fluctuations. In the corollary of Howe [13] of energy, to evaluate the acoustic power exchanged with the flow, it requires three quantities; the vorticity, the flow velocity and the acoustic velocity. Acoustic velocity is a very sensitive quantity that requires a very specific metrology. With 2D PIV measurements, we can evaluate the turbulent kinetic energy (TKE) of the aerodynamic field and analyze its correlation with the acoustic level.

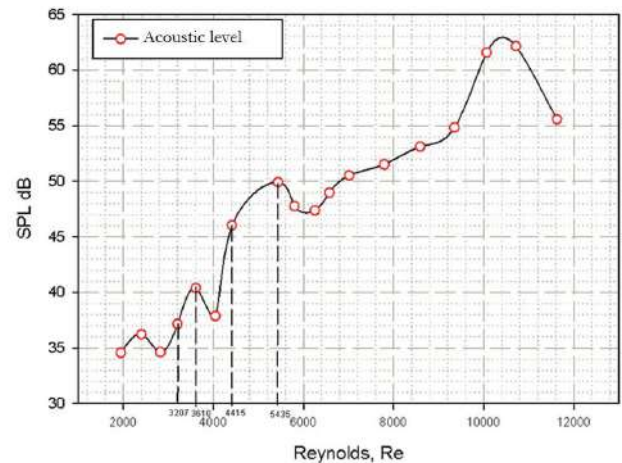


Figure 4: Sound level for different Reynolds. L/H = 4

Thus, in this section, the mean two-dimensional turbulent kinetic energy is considered (the mean of the turbulent kinetic energy calculated in the plane (X,Y)) for different Reynolds number and L/H = 4. The evolution of the turbulent kinetic energy is important to be quantified simultaneously with the acoustic level to have a better understand of its role in this phenomenon of the energy transfer between

these quantities in the case of a high level of the acoustic generation.

The two-dimensional turbulent kinetic energy (TKE) is calculated for each pixel of the PIV images in the plane (X, Y) and then normalized by the mean stream-wise velocity at the outlet. The two-dimensional turbulent kinetic energy (TKE) is given by $TKE = (u'^2 + v'^2) / \langle U_0^2 \rangle$, where u' and v' are respectively the longitudinal and the transverse fluctuations.

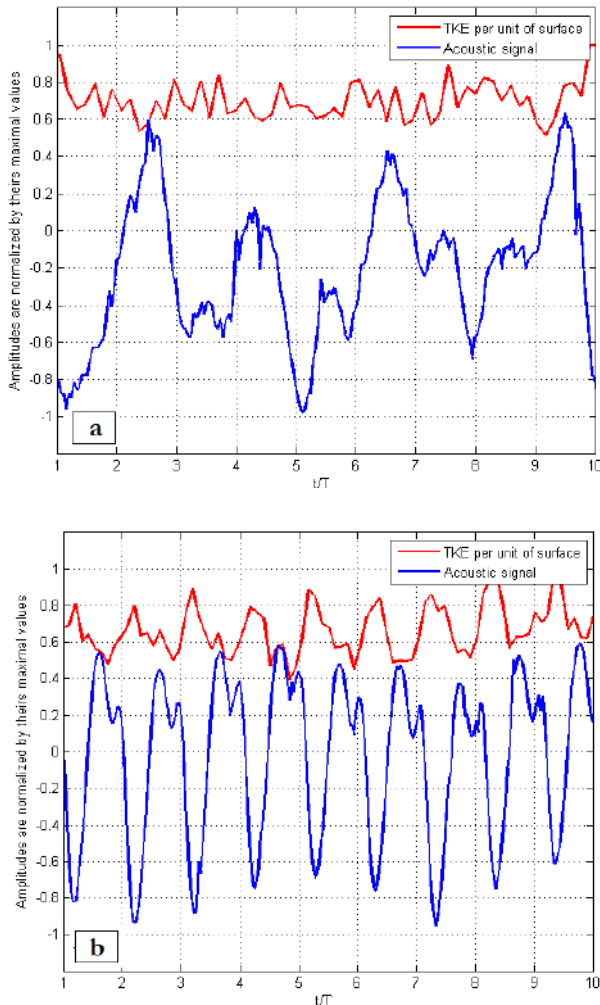


Figure 5: The acoustic signal and the two-dimensional Turbulent Kinetic Energy (TKE) per unit of surface for $L/H = 4$. (a) : $Re = 4045$, (b) : $Re = 5435$. Amplitudes are normalized by their maximal values.

In a second calculation, the sum of the turbulent kinetic energy (TKE) over of all the pixels of the image is divided by the surface on which the sum done. This calculation is applied for successive instants (successive PIV images) and thus we obtain the evolution of the two-dimensional TKE per unit of surface and over the time. Then the time of acquisition is normalized by the period (T) of the

self-sustained tones found in the acoustic signal. By this way the two-dimensional TKE per unit of surface is obtained as a function of the acoustic cycle of the self-sustained sounds.

We consider here two Reynolds number $Re = 4045$ and $Re = 5435$ (with convergent-to-plate ratio $L/H = 4$) which represent two configurations; the first (for $Re = 4045$) for a low acoustic level and the second for a peak of the acoustic level (Figure 4). For each case, the evolution of the TKE is presented simultaneously with the acoustic signal in Figure 6. One can observe that for $Re = 4045$ presented in Figure 5(a), the acoustic signal is not well organized. Actually, organized self-sustained sounds are not well installed in this case. The TKE evolution is similar to a random noise signal. In Figure 5(b) when $Re = 5435$, the acoustic signal is well organized as well as the evolution of the TKE contrary to the case when $Re = 4045$. In fact, for $Re = 5435$ a peak of the acoustic level is obtained and self-sustained sounds are installed at specific frequencies. There is an opposition of phase between the turbulent kinetic energy and the acoustic signals which have, both of them, the same frequency. As it will be presented in the next section, the peak of the acoustic signal corresponds to the impact of vortices on the plate, this implies that the energy transfer from the fluctuating field to the acoustic one is optimized and becomes maximal when the vortices reach the slot of the plate. Thus, when the feedback loop is optimized the same frequency is imposed and the turbulent kinetic energy is minimal as it is transferred to the acoustic field and thus they are in opposition of phase. When the vortices get close to the slot, a partial blockage of the passage of the flow by the slot takes place due to these vortices what increases the intensity of whistling through this slot; at the same time the TKE is transferred to the acoustic field.

In order to check the evolution of the two-dimensional TKE versus the Reynolds numbers in high and low acoustic level configurations for $L/H = 4$, the average of the TKE obtained over one period (T) of the self-sustained tones is calculated. Thus, in Figure 6, the mean TKE is presented per unit of surface and over one period T for different Reynolds number. In this figure, the TKE has two main peaks, the first at $Re = 3610$ and the second between $Re = 4415$ and $Re = 5435$. The two peaks of the TKE coincide with two peaks of the acoustic level. As explained previously, the feedback loop of the self-sustained sounds is optimal when a maximum of

energy passes from the fluctuating field to the acoustic one. This energy transfer is favored when the fluctuating energy is available for these energy exchanges. In addition, this favored condition occurs when we have a jump of the self-sustained tones frequencies what corresponds to the change of the aerodynamic mode. If we do the same calculation of the TKE for a Reynolds number which is relatively of a low acoustic level, the acoustic signal is not structured and its comparison with the TKE shows that there is no synchronization between them and signals are similar to a random fluctuations.

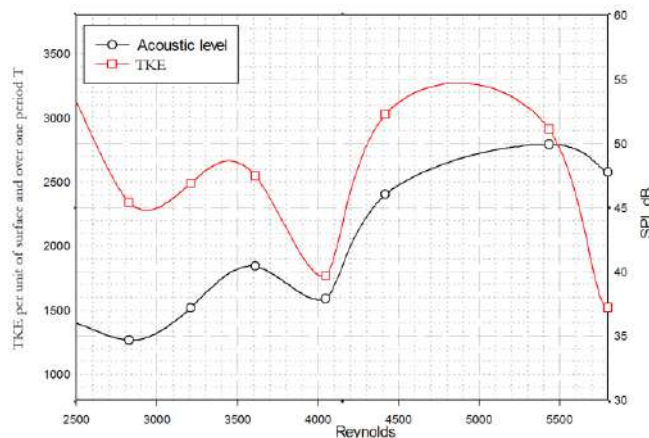


Figure 6: Evolution of the acoustic level and the two-dimensional Turbulent Kinetic Energy (TKE) for $L/H = 4$.

CONCLUSIONS

The dynamics of vortices in a plane jet impinging on a slotted plate and the generated acoustic field are investigated experimentally using time-resolved PIV measurements and a microphone. It was found that when a peak of the acoustic level is reached, a jump of the self-sustained tones frequencies occurs and a change of the aerodynamic mode takes place. This implies that the change of the aerodynamic mode which is directly related to the self-sustained frequency amplify the sound intensity and promotes the transfer of energy to the acoustic field. When the feedback loop is optimized and installed in the jet, the evolution of the two-dimensional turbulent kinetic energy is as well organized as the acoustic signal and is disposed to be transferred to the acoustic field. Actually, when the vortices approach from the slotted plate, a partial blockage of the passage of the flow by the slot due to these vortices

increases the intensity of the self-sustained tones and at the same time the turbulent kinetic energy is transferred to the acoustic field.

REFERENCES

1. Assoum, H. H., El Hassan, M., Abed-Meraïm, K., Martinuzzi, R. and Sakout, A.: 2013, Experimental analysis of the aero-acoustic coupling in a plane impinging jet on a slotted plate, *Fluid Dynamics Research* 45(4), 045503
2. Assoum H.H., El Hassan, M., Abed-Meraïm, K. and Sakout, A. The vortex dynamics and the self-sustained tones in a plane jet impinging on a slotted plate, *European Journal of Mechanics-B/Fluids*, V 48 p 231-235
3. Assoum, H.H., Abed-Meraïm, Sakout, A. The acoustic production and the vortices dynamics involved in a plane impinging jet. (2013) *Congrès Français de Mécanique*.
4. Assoum, H.H., Sakout, A., Abed-Meraïm, K., Alia, A., Hassan, M.E., Vetel, J. Experimental investigation of the vibration of a slotted and a non-slotted plates and the acoustic field in a plane impinging jet. (2012) *Proceedings - European Conference on Noise Control*, pp. 801-806.
5. Assoum, H.H., Sakout, A., Hassan, M.E., Vetel, J., Alia, A., Abed-Meraïm, K. Experimental investigation of the vibration of a slotted plate and the acoustic field in a plane impinging jet. (2012) *Acoustics 2012, France (2012)*. hal-00810574
6. Billon, A. and Sakout, A.: 2005, Two feedback paths for a jet-slot oscillator, *Journal of Fluids and Structures* 21, 121-132.
7. Billon, A., Valeau, V. and Sakout, A.: 2004, Instabilités de l'écoulement produisant le bruit de fente, *C. R. Mécanique* 332, 557-563.
8. Chong, M. S., Perry, A. E. and Cantwell, B. J.: 1990, A general classification of three-dimensional flow fields, *Physics of Fluids A: Fluid Dynamics* 2(5), 765-777.
9. Glessier, M., Valeau, V. and Sakout, A.: 2008, Vortex sound in unconfined flows: Application to the coupling of a jet-slot oscillator with a resonator, *Journal of Sound and Vibration* 314, 635-649.
10. Gutmark, E., Wolfshtein, M. and Wygnanski, I.: 1978, The plane turbulent impinging jet, *J. Fluid Mech.* 88, 737-756.

11. Ho, C. and Nasseir, N.: 1980, Large coherent structures in an impinging turbulent jet, *Turbulent Shear Flows* 2, p 297. Springer.
12. Ho, C. and Nasseir, N.: 1981, Dynamics of an impinging jet. Part 1. The feedback phenomenon, *Journal of Fluid Mechanics* 105, 119 – 142.
13. Howe, M.: 1975, Contributions to the theory of aerodynamic sound, with application to excess jet noise and the theory of the flute, *Journal of Fluid Mechanics* 71(04), 625–673.
14. Orlandi, P. and Verzicco, R.: 1993, Vortex rings impinging on walls: axisymmetric and three-dimensional simulations, *Journal of Fluid Mechanics* 256, 615–646.
15. Powell, A.: 1961, on the edgetone, *J. Acoust. SOCA* 33, 395–409.
16. Preisser, J. and Block, P.: 1976, An experimental study of the aeroacoustics of a sub-sonic jet impinging normal to a large rigid surface, *A.I.A.A Paper no. 76-520*.
17. Raffel, M., Willert, C. and Kompenhans, J.: 2002, *Particle image velocimetry: a practical guide*, Springer, New York.
18. Rockwell, D. and Naudascher, E.: 1979, Self-sustained oscillations of impinging free shear layer, *Ann. Rev. Fluid Mech* 11, 67–94.
19. Walker, J. D. A., Smith, C. R., Cerra, A. W. and Doligalski, T. L.: 1987, The impact of a vortex ring on a wall, *Journal of Fluid Mechanics* 81, 99–140.

FINITE ELEMENT MODELING OF POLYDISPERSE FLOWS USING THE DIRECT QUADRATURE METHOD OF MOMENTS

Bart Janssens^{1*}, Walter Bosschaerts¹, Karim Limam²,

¹Royal Military Academy, Department of Mechanics, Avenue de Renaissance 30, 1000 Brussels, Belgium

²La Rochelle University, LaSIE, Avenue Michel Crépeau, 17042 La Rochelle Cedex 1, France

*Corresponding author: Fax: +32 2 4414 100 Email: bart.janssens@rma.ac.be

ABSTRACT

We present an Eulerian method to compute polydisperse flow, using a stabilized finite element method for the flow and particle transport equations, an equilibrium approach to compute the particle velocity field and a Direct Quadrature of Method of Moments to take into account polydispersity and particle coagulation. For the coagulation, a kernel that can be used in direct numerical simulation is derived.

The method is tested on the Taylor-Green vortex and a Burgers vortex.

NOMENCLATURE

St: Stokes number

c : Particle number concentration

k_i : $-\lambda_i/\lambda_3$

n : Particle number concentration

$R_{\alpha\gamma}$: Collision radius

\mathbf{u} : Fluid velocity

\mathbf{v} : Particle velocity

\mathbf{x} : Position

v_p : Particle volume

β : Density ratio parameter or collision kernel

λ_i : i -th eigenvalue of the rate-of-strain tensor

ρ_f : Fluid density

ρ_p : Particle density

σ : Collision rate

τ : Generalized particle relaxation time

τ_p : Particle relaxation time

INTRODUCTION

The presence of small particles constitutes an important factor in determining air quality in our buildings and cities. This kind of pollution is typically consists of a wide distribution of particles, with sizes ranging from a few nanometers to 10 μm [1]. The size distribution of the particles need not be constant in time, and can in fact be influenced by effects such as coagulation between particles.

The aim of the present paper is to show a recent implementation [2] and verification of a combined

flow and Eulerian particle transport model, based on the finite element method for the transport equations, and the Direct Quadrature Method of Moments [3] to account for polydispersity and coagulation. The idea of this method is to approximate the size distribution using Dirac delta functions, resulting in variables for the abscissa and weights that need to be transported through the solution domain. The advantage of this approach is that the size distribution can be described using only a few (< 6 , typically) variables and the shape of the size distribution does not need to be known in advance. We combine this method with a locally implicit formulation for the particle velocity, resulting in a more accurate solution for the particle dispersion and an extension of the applicable size range [4]. The techniques explained here are valid for small Stokes numbers up to about 0.25. For a detailed overview of alternative methods, we refer to [5,6].

Paper overview: The next section of this paper is dedicated to the modeling techniques that we have applied. After that, the model is applied to test cases and the results are shown. Finally, we draw our conclusions and present our ideas for future work.

MODELLING METHOD

The presented method combines three different models: a stabilized finite element method for solving the Navier-Stokes equations governing the fluid flow; an equilibrium Euler method for calculating particle

property transport and velocity calculation; the DQMOM method to account for the particle size distribution and coagulation. For details on the fluid model, we refer to [2]. The results of the equilibrium Euler and DQMOM methods will be presented, with full derivations again available in [2].

Equilibrium Euler approach: The idea of the equilibrium Euler approach [4] is that we can write a transport equation for a particle property such as the number concentration n as follows:

$$\frac{\partial n}{\partial t} + \nabla \cdot (n\mathbf{v}) = 0$$

The velocity \mathbf{v} is the particle velocity, and the above equation is valid only if we suppose that the particle velocity can be represented as an Eulerian field. This is a strong hypothesis, since the particle velocity not only depends on the fluid velocity but also on the particle initial conditions. Two particles with different initial velocities might still have different velocities at the same time and position. If the particle relaxation time τ_p is sufficiently small with respect to the fluid velocity time scale, it can be shown (see [6]) that the effect of particle initial conditions decreases exponentially fast, and an Eulerian velocity field may be used. This approximation is also called the mono-kinetic assumption [7].

In the above equation, the particle velocity is extracted from the Maxey and Riley particle equation of motion [8]. The approximate analytical solution as derived in [2] yields:

$$\mathbf{v} = \mathbf{u} - \tau(1 - \beta)(\mathbf{I} + \tau\nabla\mathbf{u})^{-1} \left(\frac{D\mathbf{u}}{Dt} - \mathbf{g} \right)$$

The parameters β and τ represent the density ratio parameter and generalized particle relaxation time, respectively:

$$\beta \equiv \frac{3}{\frac{2\rho_p}{\rho_f} + 1}$$

$$\tau \equiv \tau_p \left(1 + \frac{\rho_f}{2\rho_p} \right)$$

The “locally implicit” term appears in the form of the matrix inverse $(\mathbf{I} + \tau\nabla\mathbf{u})^{-1}$. In the unmodified equation, this is replaced by the identity matrix. In the monodisperse case, the computational cost comes down to the solution of one additional transport equation for the particle concentration. For the velocity, a 3x3 system needs to be solved at each node, due to the locally-implicit term. This approach has been shown to be accurate up to $St = 0.25$ [4], although a more rigorous criterion for determining the validity will be discussed in the results section.

Polydisperse flow: For polydisperse flow, the particle size becomes an additional variable that may evolve under the influence of phenomena such as particle coagulation. Instead of just transporting a single number concentration, we need to transport a particle distribution function $f(v_p, \mathbf{x}, t)$. This can be thought of as a particle size distribution function in terms of particle volume, defined at every point in the domain and at every time. Due to the time-space discretization already employed for the solution of the Navier-Stokes equations, it remains to discretize this function in terms of the particle volume. The DQMOM method [3] proposes to do this by using a weighted sum of Dirac delta functions:

$$f(v_p, \mathbf{x}, t) \approx \sum_{\alpha=1}^N f_{\alpha} \delta(v_p - v_{\alpha})$$

The set of weights f_{α} and abscissas v_{α} associated with each Dirac function form different particle “phases”, each with a number density function value f_{α} and particle volume v_{α} . They depend on time and position, though we will omit this from the notation to avoid the clutter. We can now write transport equations for f_{α} and the weighted particle volume $\zeta_{\alpha} = f_{\alpha}v_{\alpha}$:

$$\frac{\partial f_{\alpha}}{\partial t} + \nabla \cdot (f_{\alpha}\mathbf{v}_{\alpha}) = a_{\alpha}$$

$$\frac{\partial \zeta_{\alpha}}{\partial t} + \nabla \cdot (\zeta_{\alpha}\mathbf{v}_{\alpha}) = b_{\alpha}$$

The source terms a_{α} and b_{α} that appear here are used to model particle coagulation. They are obtained as the solution of the linear system:

$$(1 - k) \sum_{\alpha=1}^N v_{\alpha}^k a_{\alpha} + k \sum_{\alpha=1}^N v_{\alpha}^{k-1} b_{\alpha} = \bar{S}_k^+ - \bar{S}_k^-$$

Here, \bar{S}_k^+ and \bar{S}_k^- are the birth and death rates due to coagulation, respectively. These are expressed in terms of the coagulation kernel $\beta(v_{\alpha}, v_{\gamma})$:

$$\bar{S}_k^+ = \frac{1}{2} \sum_{\alpha=1}^N \sum_{\gamma=1}^N (v_{\alpha} + v_{\gamma})^k \beta(v_{\alpha}, v_{\gamma}) f_{\alpha} f_{\gamma}$$

$$\bar{S}_k^- = \sum_{\alpha=1}^N \sum_{\gamma=1}^N v_{\alpha} \beta(v_{\alpha}, v_{\gamma}) f_{\alpha} f_{\gamma}$$

The coagulation kernel depends on the physical driving force of the coagulation phenomenon. It can be influenced by Brownian motion, or fluid turbulence, for example. In a direct numerical simulation (DNS), where the instantaneous fluid velocity is fully described, the kernel can be broken down into a part due to particle size difference on the one hand:

$$\beta_1(v_\alpha, v_\gamma) = |v_\alpha - v_\gamma| \pi \left(\left(\frac{3}{4\pi} v_\alpha \right)^{\frac{1}{3}} + \left(\frac{3}{4\pi} v_\gamma \right)^{\frac{1}{3}} \right)^2$$

On the other hand we have the effect of non-uniform flow, which depends on the eigenvalues $(\lambda_1, \lambda_2, \lambda_3)$ of the rate of strain tensor, and the expression needs to be chosen from the following 3 options:

$$\beta_2 = 8(-\lambda_3)R_{\alpha\gamma}^3 \left(\int_0^{\frac{\pi}{2}} \frac{2(k_1 \cos^2 \phi + k_2 \sin^2 \phi)^{\frac{3}{2}}}{3\sqrt{k_1 \cos^2 \phi + k_2 \sin^2 \phi + 1}} d\phi - \frac{\pi}{6}(k_1 + k_2 - 1) \right)$$

$$\beta_3 = 8\lambda_3 R_{\alpha\gamma}^3 \int_0^{\frac{\pi}{2}} \frac{2(k_1 \cos^2 \phi + k_2 \sin^2 \phi)^{\frac{3}{2}}}{3\sqrt{k_1 \cos^2 \phi + k_2 \sin^2 \phi + 1}} d\phi$$

$$\beta_4 = 8(-\lambda_3)R_{\alpha\gamma}^3 \left(\frac{1}{3}(\sqrt{k_1} + (k_1 - 1) \arctan(\sqrt{k_1})) - \frac{\pi}{6}(k_1 - 1) \right)$$

$$\beta_5 = -\frac{4\pi R_{\alpha\gamma}^3}{3}(\lambda_1 + \lambda_2 + \lambda_3)$$

In the above equations, $R_{\alpha\gamma} = r_\alpha + r_\gamma$ is the collision radius between two particles and $k_i = -\lambda_i/\lambda_3$. The choice of equation depends on the signs of the eigenvalues. Table 1 summarizes all the possibilities.

Table 1
Choice of collision kernel

λ_1	λ_2	λ_3	$\beta_{\alpha\gamma}$
> 0	> 0	< 0	$\beta_1 + \beta_2$
< 0	< 0	> 0	$\beta_1 + \beta_3$
> 0	0	< 0	$\beta_1 + \beta_4$
≤ 0	≤ 0	≤ 0	$\beta_1 + \beta_5$
> 0	> 0	> 0	β_1

Collision efficiency: The above theory assumes that every collision leads to coagulation of the particles involved. In reality, this is not the case, and a collision efficiency needs to be taken account [9, 10]. For the verification performed in this work, we simplify the model and assume that the collision efficiency is always one.

Solution algorithm: Using the above equations, the complete solution algorithm for a polydisperse flow with coagulation can be formulated as follows:

1. Choose a set of N particle volumes v_α and distribution function values f_α

2. Compute the fluid flow field
3. **for all** α in $1..N$ **do**
 - a. Compute the velocity field v_α
 - b. Compute the particle velocity field gradients at the nodes, using the average of surrounding elements
4. **for all** nodes in the mesh **do**
 - a. Compute the moment source terms \bar{S}_k^+ and \bar{S}_k^-
 - b. Solve the linear system for a_α and b_α
5. Solve the transport equations for the weights and weighted abscissa.
6. Next timestep: go to 2.

RESULTS

For verification of the method, we use two test cases: periodic Taylor-Green vortices are used to verify the implementation of the locally implicit extension to the equilibrium Eulerian approach, and polydisperse flow through a Burgers vortex is used to verify the collision kernel.

Taylor-Green vortices: We track bubbles (density ratio $\beta = 3$) through a periodic field of Taylor-Green vortices with diameter D and maximal swirl velocity V_s . This computation was previously performed in [11], but without the locally implicit modification. Figure 1 presents contours of particle concentrations along with particle streamlines at dimensionless time $tV_s/2D = 2$, allowing us to visualize an overview of the flow field.

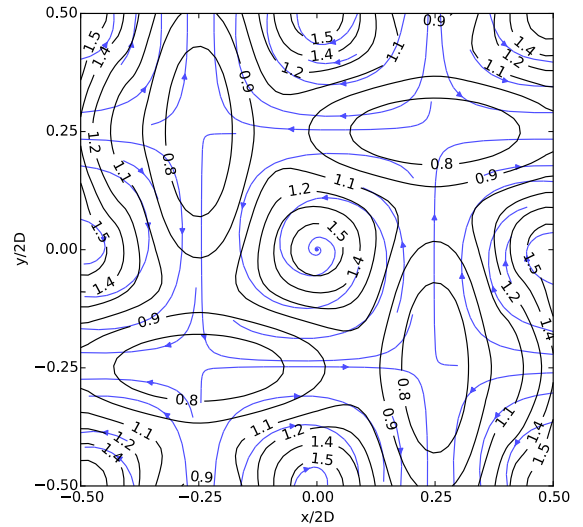


Figure 1: Contours of particle concentrations along with particle streamlines at dimensionless time $tV_s/2D = 2$ and with $St = 0.25$

Depending on the Stokes number, the bubble concentration peak at the center of the vortices is more or less pronounced. To illustrate this, Figure 2 presents a logarithmic plot of the concentration (normalized by the initial concentration) as a function of dimensionless time.

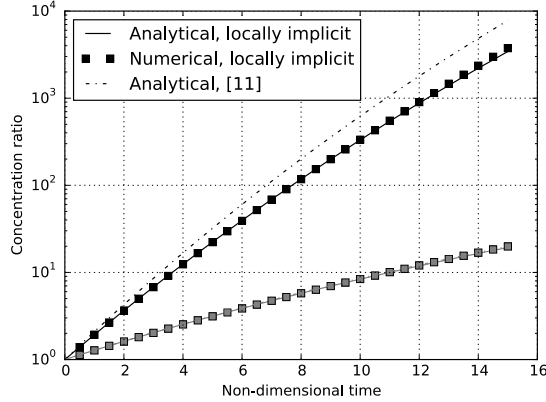


Figure 2: Concentration ratio as a function of dimensionless time. Gray: $St = 0.25$, black: $St = 0.75$.

We plotted the numerical solution along with two analytical solutions: one from [11], excluding the locally implicit term, and one obtained from the particle velocity equation with locally implicit term, derived in [2]. At the lower Stokes number, the locally implicit term has no influence and all graphs overlap, but at $St = 0.75$, the unmodified approach from [11] overpredicts the peak concentration by a factor of 2. To verify the validity of the equilibrium approach, we used the criterion derived in [6]: The eigenvalues of $\frac{1}{2}(\nabla\mathbf{v} + \nabla\mathbf{v}^T)$ should be greater than $-1/\tau$ at every node in the domain. This was confirmed for both Stokes numbers considered.

Burgers vortex: In [12], the trajectories of rain droplets through a Burgers vortex are computed, along with geometrical collision rates between particles of different sizes. Their method is Lagrangian in nature, but the Stokes numbers employed permit the use of an equilibrium Euler approach. We repeated the calculation, to obtain contours of the collision rate, defined as:

$$\sigma = \frac{n_\alpha(\mathbf{x}, t)n_\gamma(\mathbf{x}, t)}{n_{\alpha 0}n_{\gamma 0}}\beta_{\alpha\gamma}$$

The velocity components of the imposed Burgers vortex are:

$$u = -\frac{r_0^2 y \omega_0}{2(x^2 + y^2)} \left(1 - e^{-\frac{x^2 + y^2}{r_0^2}} \right)$$

$$v = \frac{r_0^2 x \omega_0}{2(x^2 + y^2)} \left(1 - e^{-\frac{x^2 + y^2}{r_0^2}} \right)$$

We run the test with a “weak” and “strong” vortex, with respective properties $\omega_0 = 18 \text{ s}^{-1}$, $r_0 = 1 \text{ cm}$ and $\omega_0 = 180 \text{ s}^{-1}$, $r_0 = 1/3 \text{ cm}$. The properties of the particles are summarized in Table 2.

Table 2
Particles for the Burgers vortex test

Diameter (μm)	τ_p (ms)	St, weak (10^{-3})	St, strong (10^{-3})
20	1.3	2.5	25
40	5.2	1.0	10
80	21	40	400

Figures 3 and 4 show the collision rates between the 40 μm and 80 μm particles, for the weak and strong vortices, respectively.

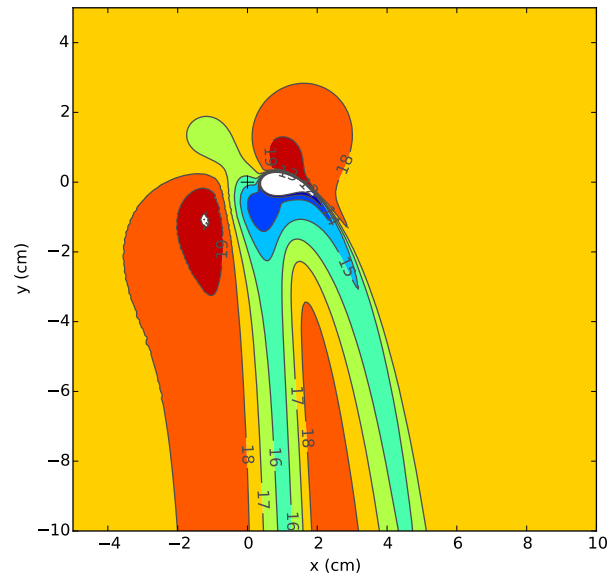


Figure 3: Collision rate between 40 μm and 80 μm particles in the weak vortex, in $10^{-9} \text{ m}^3 \text{ s}^{-1}$.

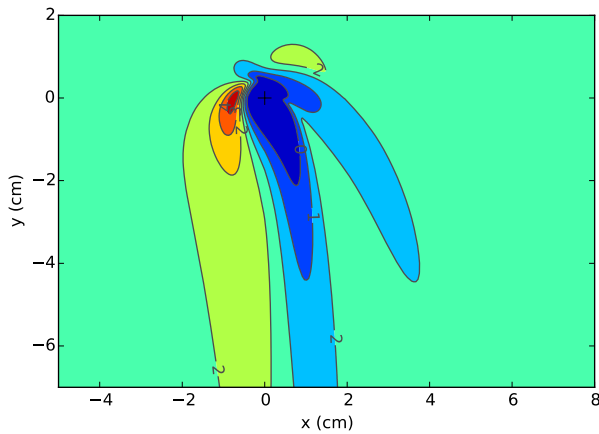


Figure 4: Collision rate between 40 μm and 80 μm particles in the strong vortex, in $10^{-9} \text{ m}^3\text{s}^{-1}$.

In the strong vortex, more particles are cleared away from under the vortex, resulting in lower collision rates under the vortex center. Further from the vortex, the collision rate is dominated by gravity, since the particles of different size have a different settling velocity. The contours we obtain visually match the values presented in [12]. Even though a direct comparison remains difficult due to the fact that in [12] the values are only given along particle trajectories, the values appear to be in the same range. This reinforces our confidence in the correctness of our implementation.

In Figure 5, we present the result for the collision rate between particles with a diameter of 20 μm .

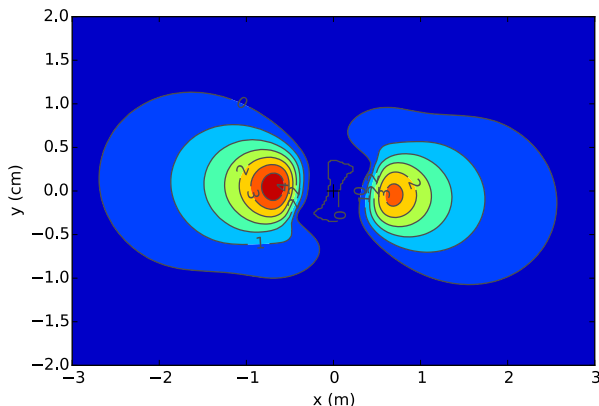


Figure 5: Collision rate among 20 μm particles in the strong vortex, in $10^{-13} \text{ m}^3\text{s}^{-1}$.

The collision rate in Figure 5 is 4 orders smaller than the rates in Figure 3 and 4, indicating that the effect of the additional terms from Table 1 is much smaller than the effect of β_1 . Nonetheless the additional terms must be accounted for, otherwise simulations starting from a monodisperse distribution would never exhibit coagulation.

CONCLUSIONS AND FUTURE WORK

We presented a method to compute dilute polydisperse flows under equilibrium conditions, accounting for the effect of coagulation of particles. By using the DQMOM technique to account for polydispersity, only two additional transport equations need to be solved per transported Dirac function, and no assumptions need to be made on the shape of the particle size distribution.

The concentration transport equation was first tested on periodic Taylor-Green vortices. This demonstrated that the inclusion of the locally implicit term in the particle velocity equation allows for a better approximation of the particle velocity as the Stokes number increases.

The second test case involved polydisperse flow through a Burgers vortex and indicates that the results from our (Eulerian) implementation agree with results in literature obtained using a Lagrangian method.

Future work involves further validation of the method by comparison with experiments in order to evaluate the influence of turbulence characteristics on particle coagulation.

On the theoretical level, extension of the method to higher orders must be studied, to permit steeper particle concentration gradients.

ACKNOWLEDGMENTS

The software developed in this work is part of the Coolfluid 3 framework, freely available under LGPL v3 license at <http://coolfluid.github.io>. We thank the Coolfluid 3 development team for the many hours of work and helpful discussions, without which this work would not have been possible. In particular: Tiago Quintino for laying out the basic framework; Willem Deconinck for the work on the mesh structure; Tamás Bányai for his help with the solvers and linear systems interface; and Quentin Gasper for the work on the GUI.

REFERENCES

1. C. A. Pope and D. W. Dockery. “Health Effects of Fine Particulate Air Pollution: Lines that Connect”. In: *J. Air & Waste Manage. Assoc.* 56 (2006), pp. 709–742.
2. B. Janssens. “Numerical modeling and experimental investigation of fine particle coagulation and dispersion in dilute flows”. PhD thesis. Université de La Rochelle, 2014.

3. D. L. Marchisio and R. O. Fox. "Solution of population balance equations using the direct quadrature method of moments". In: *Journal of Aerosol Science* 36.1 (2005), pp. 43–73.
4. J. Ferry, S. L. Rani, and S. Balachandar. "A locally implicit improvement of the equilibrium Eulerian method". In: *International journal of multiphase flow* 29.6 (2003), pp. 869–891.
5. S. Balachandar and J. K. Eaton. "Turbulent dispersed multiphase flow". In: *Annual Review of Fluid Mechanics* 42 (2010), pp. 111–133.
6. J. Ferry and S. Balachandar. "A fast Eulerian method for disperse two-phase flow". In: *International Journal of Multiphase Flow* 27.7 (2001), pp. 1199–1226.
7. R. O. Fox, F. Laurent, and M. Massot. "Numerical simulation of spray coalescence in an Eulerian framework: direct quadrature method of moments and multi-fluid method". In: *Journal of Computational Physics* 227.6 (2008), pp. 3058–3088.
8. M. R. Maxey and J. J. Riley. "Equation of motion for a small rigid sphere in a nonuniform flow". In: *Physics of fluids* 26 (1983), p. 883.
9. A. Renoux and D. Boulaud. *Les aérosols, physique et métrologie*. Ed. by. Lavoisier. 1998.
10. F. Laurent, M. Massot, and P. Villedieu. "Eulerian multi-fluid modeling for the numerical simulation of coalescence in polydisperse dense liquid sprays". In: *Journal of Computational Physics* 194.2 (2004), pp. 505–543.
11. O. Druzhinin and S. Elghobashi. "Direct numerical simulations of bubble-laden turbulent flows using the two-fluid formulation". In: *Physics of Fluids* 10 (1998), p. 685.
12. R. J. Hill. "Geometric collision rates and trajectories of cloud droplets falling into a Burgers vortex". In: *Physics of Fluids* 17.3 (2005), p. 037103.

NUMERICAL STUDY OF TRANSPORT AND PARTICLE DEPOSITION INSIDE BUILDINGS

Limam K.¹, El Hamdani S², M. Abadie¹, G. Lindner¹, Bendou A.²
1 LaSIE FRE-CNRS 3474, av. M. Crépeau 17042 La Rochelle Cedex 1 France
2 LMPEE, ENSA d'Agadir, BP 1136, Agadir, Maroc

*Karim LIMAM: Fax: +33 5 46 45 82 41 Email: klimam01@univ-lr.fr

ABSTRACT

Increasingly, we must reduce our energy consumption related to the ventilation system of habitable environments while improving the indoor air quality. Our work concerns the study of particulate matter inside buildings and more specifically the pollution transport phenomena. A numerical study of particle transport inside a ventilated room (30m³ room) was made using STAR CD software to solve the airflow in the domain and an in-house code to calculate the trajectories of solid particles in a three-dimensional turbulent flow. We analyze then the influence of ventilation systems (filtration, flow rate, inlet and outlet positions) on the concentration of indoor air particles. By using prediction tools, we carried out several numerical simulations, and then summarized the results. The main objective of this numerical study is to present the potential of this type of predictive tool that, in addition to determining the trajectories of particles, allow us to address the residence time of particles in the atmosphere, monitor particle-wall deposition and to study the spatial heterogeneity of particle concentrations.

INTRODUCTION

The industrial development is accompanied by a significant deterioration of the environment that keeps getting more and more polluted. In addition to the solid and liquid pollution, air pollution gives great concern to citizens, politicians and governments. The current lifestyle requires citizens to live on average 20 to 22 hours a day in confined spaces (homes, workplaces ...). These confined places suffer from the accumulation of pollution due to poor ventilation and the use of insulation materials [1-9].

Among the major health risks induced by air pollution, we quote the one related to the presence of sufficient quantities of suspended particles in the air, commonly called dust. The "fine" particles whose diameter is less than or equal to 10 microns are inhaled easily. They penetrate deep into the lungs (particulate matter <2.5µm reach the alveoli) and are causing serious heart and respiratory disorders.

In this study, we will address the influence of ventilation systems (filtration, airflow, inlet and outlet positions) on concentrations of

particulate air inside of a real room in the house MARIA CSTB from Marne-la-Vallée (30m³), where the flow is strongly three-dimensional.

MARIA, Automated House for Innovative Research on Air, from the French "*Maison automatisée pour des recherches innovantes sur l'air*" is a full-size house built near ARIA (the new research center of the Scientific and Technical Centre for Construction (CSTB) located in Marne-la-Vallée. It is dedicated to the sanitary quality of buildings, products and technologies, and specially their impact on the quality of indoor air. Numerical modeling of the transport and deposition of pollutants will be made using the Lagrangian approach.

The numerical study of the dispersion and deposition of particles in the 30m³ room will be made using the STAR CD software to solve the airflow in the area. After, we will use a code to calculate the trajectories of solid particles in three-dimensional turbulent flows developed by LaSIE during the PhD work of Abadie [1] and Sandu [5].

NUMERICAL MODELLING

The governing equations for the fluid flows are deduced from general conservation laws of mass and momentum (Navier-Stokes).

Continuity equation :

$$\operatorname{div}(\vec{u}) = 0 \quad (1)$$

Equations of motion :

$$\frac{\partial \vec{u}}{\partial t} + \operatorname{div}(\vec{u} * \vec{u}) = -\frac{1}{\rho} \operatorname{grad} p + \operatorname{div}(\nu (\operatorname{grad} \vec{u} + (\operatorname{grad} \vec{u})^t)) + \vec{g} \quad (2)$$

To determine the trajectories of particles in an airflow we chose the Lagrangian model. The particles are followed along their trajectory through the resolution of the dynamic equation of motion, written according to Abadie [1]:

$$\underbrace{\frac{\pi}{6} d_p^3 \rho_p \frac{dU_p}{dt}}_I = \underbrace{C_D \frac{\pi}{8} \rho d_p^2 |U - U_p| (U - U_p)}_{II} + \underbrace{\frac{\pi}{6} d_p^3 \rho \frac{dU}{dt}}_{III} + \underbrace{C_a \frac{\pi}{6} d_p^3 \rho \left(\frac{dU}{dt} - \frac{dU_p}{dt} \right)}_{IV} + \underbrace{C_h d_p^2 \sqrt{\pi \rho \mu} \int_0^t \frac{dt'}{\sqrt{t-t'}} dt'}_V + \underbrace{F_e}_{VI} \quad (3)$$

with

- I* : force acceleration of the particle,
- II* : drag force (viscous resistance) of the particle,
- III* : term due to the pressure gradient around the particle induced by its movement,
- IV* : force of "added mass" of the particle,
- V* : historical term from Basset,
- VI* : external forces,
- d_p : particle diameter (m),
- ρ, ρ_p : densities of the fluid and the particle (kg m^{-3}),
- μ : dynamic viscosity of the fluid ($\text{kg m}^{-1} \text{s}^{-1}$),
- U, U_p : total velocity of the fluid and the particle (m s^{-1}),
- C_D : drag coefficient,
- C_a : added mass coefficient, and
- C_h : Basset coefficient.

We show that the III and V terms can be neglected when the velocity gradients between the particle and the fluid are low. The equation to solve becomes:

$$\frac{\pi}{6} d_p^3 \rho_p \frac{dU_p}{dt} = C_d \frac{\pi}{8} \rho d_p^2 |U - U_p| (U - U_p) + C_a \frac{\pi}{6} d_p^3 \rho \left(\frac{dU}{dt} - \frac{dU_p}{dt} \right) + F_e \quad (4)$$

The external forces that can be taken into account in the numerical code are: the drag force, the added mass force, gravity, thrust force and thermophoresis force. Thermophoresis force arises when a temperature gradient exists in the gas. The value of this force depends on the gas and the properties of the particle. However, in this study the treated flows are isothermal, so it is not necessary to take this force into account.

SOLVING METHOD FOR THE FLUID FLOW

For the numerical study of the dispersion of particles in the air, we considered that the particles are sufficiently diluted and do not influence the air flow. Thus, this will be a permanent characteristic in this study. For the prediction of airflow; our choice fell on the statistical approach for both the correct results that it can offer and the expertise available within the laboratory. The geometries used in CFD studies of indoor deposition are generally of the scale of a single room or two adjacent rooms [9]. They tend to be simple and symmetrical, frequently allowing the use of structured meshes.

The software used is STAR CD, a commercial version from CD-Adapco. The flow is calculated using the k- ϵ model, that gives the temporal average values of the speed variables, pressure, turbulent kinetic energy and turbulent kinetic energy dissipation rate in each of the mesh points. The k- ϵ model is a two equation model, that means, it includes two extra transport equations to represent the turbulent properties of the flow. This allows a two equation model to account for history effects like convection and diffusion of turbulent energy. We used the in-house code PARDIFF that was developed by Adrian Sandu [5] and Marc Abadie [1]. This simulation code uses the particle dynamics relationship as a dispersed phase in the carrier fluid in a

turbulent flow. The geometries used in CFD studies of indoor deposition are generally of the scale of a single room or two adjacent rooms [1,3,5,9,11,12]. They tend to be simple and symmetrical, frequently allowing the use of structured meshes.

NUMERICAL SIMULATION OF DISPERSION AND DEPOSITION IN THE MARIA CSTB ROOM

The Figure 1 (below) show the geometry of the studied domain. This room is mechanically ventilated by two openings: inlet 34.5x2.3 cm and outlet 3.3x3.3 cm.

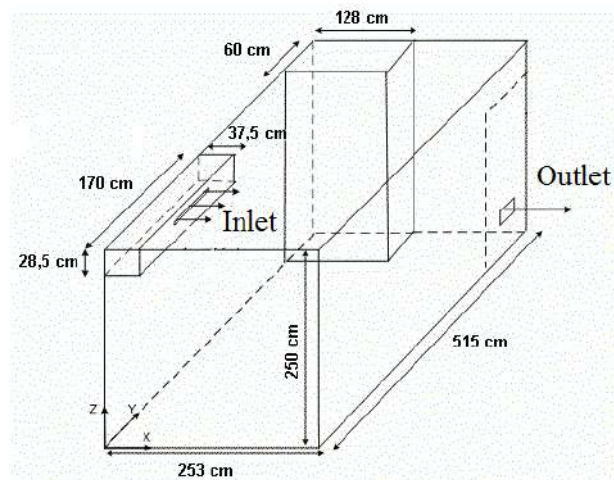


Figure 1

Geometry of the studied domain

The determination of the flow requires a very fine mesh in most of the domain. To accurately track any changes in mass and aerodynamic fields, particularly in the area where the gradients are important, we have adopted a non-uniform mesh, strongly tightened near the walls and vents. A better mesh quality provides a more accurate solution. For example, one can refine the mesh at certain areas of the geometry where the gradients are high, thus increasing the fidelity of solutions in the region. Also, this means that if a mesh is not sufficiently refined then the accuracy of the solution is more limited. Thus, mesh quality is dictated by the required accuracy.

Several tests were conducted to optimize the mesh near the walls to allow the use of the $k-\epsilon$ model at low-Reynolds number calculated for the air flow. The value of the dimensionless distance y^+ is less than 1 for all the sides of the field. The airflow inside the chamber was

obtained using the STARCD code, using the K -epsilon model for low Reynolds number. The convergence criteria chosen imply that the sum of the normalized residues in each volume control and for each variable (speed, pressure and turbulent quantities) must be less than 10^{-5} . The numerical scheme was the Quick scheme. For this study, we simulated two cases of air renewal: 1 vol/h and 0.5 vol/h.

Inlet speed is uniform, the turbulent kinetic energy (equation 5) is determined from the intensity of the turbulence which is a function of the standard deviation of velocity fluctuations (The turbulence rate that was determined from measurements is 6.9 %) and the velocity at the inlet. The dissipation rate is expressed as a function of the turbulent kinetic energy and a characteristic length scale of the flow inlet (equation 6).

$$K = \frac{3}{2} (IU)^2 \quad (5)$$

$$\tilde{\epsilon} = C_{\mu}^{3/4} \frac{K^{3/2}}{L} \quad (6)$$

The inlet velocity of air in the room is calculated by the following equation:

$$U = \frac{Q}{S} \quad (7)$$

with $Q = V\lambda_r$, where U : the inlet velocity ($\text{m}\cdot\text{s}^{-1}$), Q : airflow ($\text{m}^3\cdot\text{s}^{-1}$),

λ_r : room air change rate (s^{-1}),

V : volume of the ventilated room and

S : the inlet surface (m^2).

For $\lambda_r = 0.5 \text{ vol/h}$, we obtained an inlet velocity of $0.5333 \text{ m}\cdot\text{s}^{-1}$.

For $\lambda_r = 1 \text{ vol/h}$, the inlet velocity is $1.0667 \text{ m}\cdot\text{s}^{-1}$.

The characteristic length scale of the flow was approximated by the following relationship:

$L = 0.09d_H$, where d_H is the hydraulic diameter of the vent. The walls are considered to be impermeable to air, which the speed is zero. The limit boundary conditions for turbulence are $k = 0$ and $\epsilon = \infty$.

RESULTS AND DISCUSSION

Fluid phase

This first part is to introduce the airflow that prevails inside the chamber. Figures 2 and 3 are the average field of air velocities in the study room. Everywhere in the room, the

velocities are very low. They are of the order of 0.1955 m/s for 1 vol/h and 0,051 m/s for 0.5 vol/h. Near the air inlet, the velocity is 0.272 m/s for 1 vol/h and 0.1365 m/s for 0.5 vol/h.

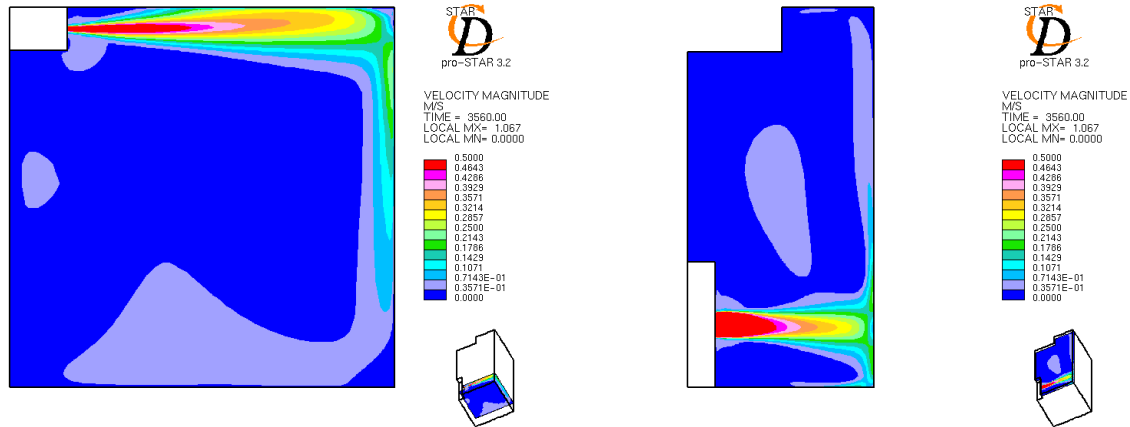


Figure 2

Velocity fields for the XZ plan (left) and XY (right) at the center of the inlet (1 vol/h)

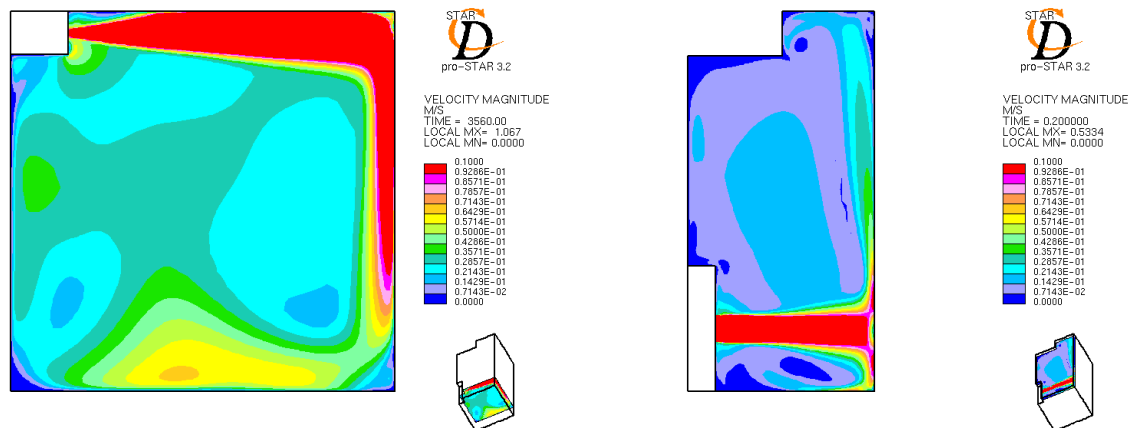


Figure 3

Velocity fields for the XZ plan (left) and XY (right) at the center of the inlet (0,5 vol/h)

Dispersed phase: Trajectories and residence time

This second part aims to present the transport and distribution of particles initially introduced in the field of study. After obtaining the fluid flow, particles are injected at the inlet, blowing to the center of the room. The dispersion of the particles, their eventual deposition or extraction by the outlet is then studied. The simulated particles have $2\mu\text{m}$ of diameter, they cannot coagulate with each other and they

adhere to the walls they encounter. The forces acting on the particles are essentially the forces of gravity and drag. The injection speed of the particles is considered equal to that of the fluid. Under the effect of the airflow and the various forces, the particles follow different trajectories that lead to the extraction mouth by which they leave the room or to the walls to which they adhere. Figure 4 shows the location

of the place of particle deposition in the chamber. Most particles were adhered on the

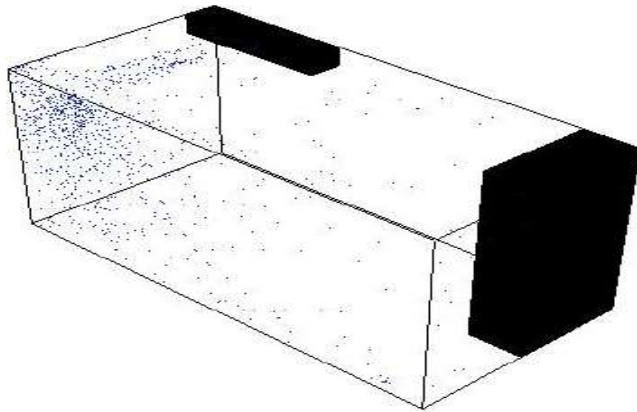


Figure 4

Deposition location of the particles

An injection simulation at the center of the room was made to reproduce the experimental protocol. Generally, the particles move in a first step from the center of the room to the ventilation inlet where they are strongly scattered by the air jet. This first particle motion is strongly linked to transportation by air in the first zone that is at low turbulence and low turbulent dispersion. Thus, the streamlines of the fluid field from the injection position of the particles, shown in Figure 5, are practically coincident with the start of the particle trajectories. Secondly, the particles reaching areas with higher turbulence (near the jet), will depart from the movement of air by turbulent dispersion and acquire their own paths. Figure 5 below shows the evolution of the final location of the particles. Should be noted that nearly 6 minutes elapsed before the particles begin to drop. Between 6 and 7.5 min, particle deposition is performed only on the wall opposite the jet (P5) and the block on the side opposite to the output (P3). Between 7.5 and 13 min, no particles being deposited or leaving the room and during this time the majority of particles are dispersed in the entire volume. At this time, the concentration in the room becomes more homogeneous and the deposition of particles (and extraction outlet) follows an increasing trend. After one hour, 53% of injected particles are deposited on the room walls while 18% have left the room by the extraction and 28.5% remain in the air. 24% of the injected particles are deposited on the wall opposite the jet (P5), 9% on the

wall opposite the flow which shows the influence of the air flow.

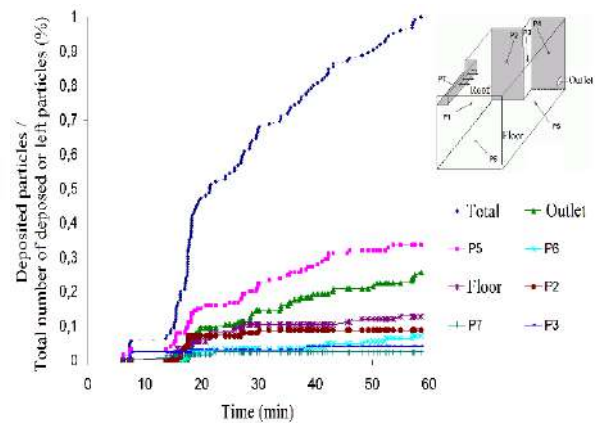


Figure 5

Evolution of particle deposition (2 μ m)

ground and the remaining 20% on the other walls. The particle residence time is difficult to assess since become nearly 28.5% of particles remains uncertain. Nevertheless, based on the 18% who leave the room, the average residence time of 2 μ m particles is 32 min with a minimum residence time of 17 min.

CONCLUSIONS

The main objective of the numerical study of the room from MARIA CSTB was to present the potential of numerical simulation software for the problems associated with particulate pollutants in indoor environments. This study allow us to better understand the influence of ventilation on particulate pollution, showing that the movement of particles in indoor air depends not only on the injection site of the pollutant (despite an injection of blowing away, the pollutant can be sucked by the jet blowing), but also and mainly the path taken by the airflow in the atmosphere (venting strategy). We showed also, through the numerical study of MARIA room, how it was possible to arrive at an assessment of trajectories and residence time (particle injection by the blower port and the center of the cell) of particles within the domain. Heat sources [10] or varying inclination of deposition surfaces [11-12] and the related change of the adjacent air flow may increase the deposition velocity and be source of enhanced local soiling.

ACKNOWLEDGEMENT

This study has been funded by the French Agency of the Environment and the Energy Management (ADEME), the French Ministry of Ecology and Sustainable Development (MEDD) and the French National Institute for Industrial Environment and Risks (INERIS) in the framework of the project PRIMEQUAL 2: French Program on Atmospheric Pollution and its Impacts.

REFERENCES

1. ABADIE M., “Contribution à l'étude de la pollution particulaire : rôle des parois, rôle de la ventilation”. Thèse Université de La Rochelle, LaSIE (2000).
2. AKOUA A., “Appréciation de l'efficacité de la ventilation pour l'étude de la qualité de l'air intérieur”. Thèse Université de La Rochelle, LaSIE, 2004
3. Bouilly J., “Étude de l'Impact de la Pollution Particulaire sur la Qualité de l'Air Intérieur en Site Urbain”. Thèse Université de La Rochelle, LaSIE, 2003
4. Hinds, W.C., “Aerosol Technology : Properties, Behaviour, and Measurement of Airborne Particles”. Edited by John Wiley & Sons, Inc, 1982.
5. Sandu, A., “Contribution à l'Etude Numérique du Transport Turbulent de Polluants Particulaires en Cavités”. Thèse de doctorat des universités de La Rochelle (France) et de Bucarest (Roumanie), décembre 1999.
6. Byrne, M.A., “An Experimental Study of the Deposition of Aerosol on Indoor Surfaces”. Thesis for the degree of Doctor of Philosophy of the University College of London and the Diploma of Imperial College, 1995.
7. Chan, L.Y., Kwok, W. S. et al. and Chan, C. Y., “Human exposure to respirable suspended particulate and airborne lead in different roadside microenvironments”. *Chemosphere*, Vol. 41, pp. 93-99, 2000.
8. Etkin, D. S., “Particulates in Indoor Environments: Characterization and Health Effects”. *Indoor Air Quality Update*, Cutter Information Corp., 1994.
9. Z. Zhang, Q. Chen, Comparison of the Eulerian and Lagrangian methods for predicting particle transport in enclosed spaces, *Atmos. Environ.* 41 (25) (2007)5236–5248.
10. X. Chen, A. Li, An experimental study on particle deposition above near-wall heat source, *Build. Environ.* 81 (2014) 139-149.
11. S. Shi, Y. Li, B. Zhao, Deposition velocity of fine and ultrafine particles onto manikin surfaces in indoor environment of different facial air speed, *Build. Environ.* 81 (2014) 388-395.
12. Mleczkowska, A, et al, Particle penetration and deposition inside historical churches *Building and Environment* 95, pp 291-298, (2016).

EXPERIMENTAL STUDY OF PARTICLE CONCENTRATIONS IN AN UNDERGROUND MAGENTA METRO STATION OF PARIS

A. Fortain^{1,2}, K.Limam^{*2}, C.Cremezi Charlet¹, G.Lindner²

1 SNCF, Direction de l'Innovation et de la Recherche 45 rue de Londres 75379 Paris cedex 8

2 LaSIE FRE-CNRS 3474, av. M. Crépeau 17042 La Rochelle Cedex 1 France

*Karim LIMAM: Fax: +33 5 46 45 82 41 Email: klimam01@univ-lr.fr

ABSTRACT

Two experiments were carried out in an underground station of Paris. The aim was to evaluate the influence of two parameters on particle number concentrations: ventilation and the movement of trains (braking and departing). These experiments took place by night when traffic stopped to allow the study of all the three parameters individually. Different measurements have been performed: particle number concentrations, air velocity, CO₂ concentration and particle mass concentration (PM₁₀).

First results do not show any influence of ventilation when turned off and on during one night. Passengers' activity and especially trains pass-by have a stronger influence on particle concentration. Due to the fact that fine particle concentration levels are not reproducible, results should be interpreted very carefully. But as influences can be observed, this study could be completed by another one that could permit to distinguish emission and transport of particles, especially particles with a diameter less than 1 μ m that represent the major part of particle number concentrations.

INTRODUCTION

Indoor air quality in offices, schools and houses has been studied for years. It is not the case of the indoor air quality in underground train stations, which is still not well understood. Different studies have been carried out in several underground stations (Stockholm [1], Helsinki [2], London, New York, Rome,..) to evaluate mass concentration level. Measurements performed in Helsinki also mentioned particle number concentrations (10 nm<Diameter<500 nm) in the station. All these studies have been carried out to better investigate personal exposure. But it is also interesting to understand what kind of phenomenon influences particle concentrations in order to better appreciate station particle's sources.

To this end, three experiments have been carried out, in order to find the influence of two different parameters, namely ventilation and trains on the pollutant concentrations. These experiments took place by night when public access is forbidden in order that these three parameters could be individually investigated.

METHODS

The measurements were performed in Magenta station (RER line E) at the same place at the end of one platform. The ventilation system of the station is described on Figure 1, arrows schematize the air circulation. This air circulation is the least favorable mode in terms of particles concentration.



Figure 1 Arrangement of the material
Three particles counter were arranged at three different heights (0.50, 1.10 and 1.70m) and another one were arranged at 1.70m height 1m further. An anemometer was also placed 1m from the three counters. Measurements of particle mass concentration (PM₁₀) and CO₂ concentration were also performed.

Measurement devices were placed as shown on

Figure 1.

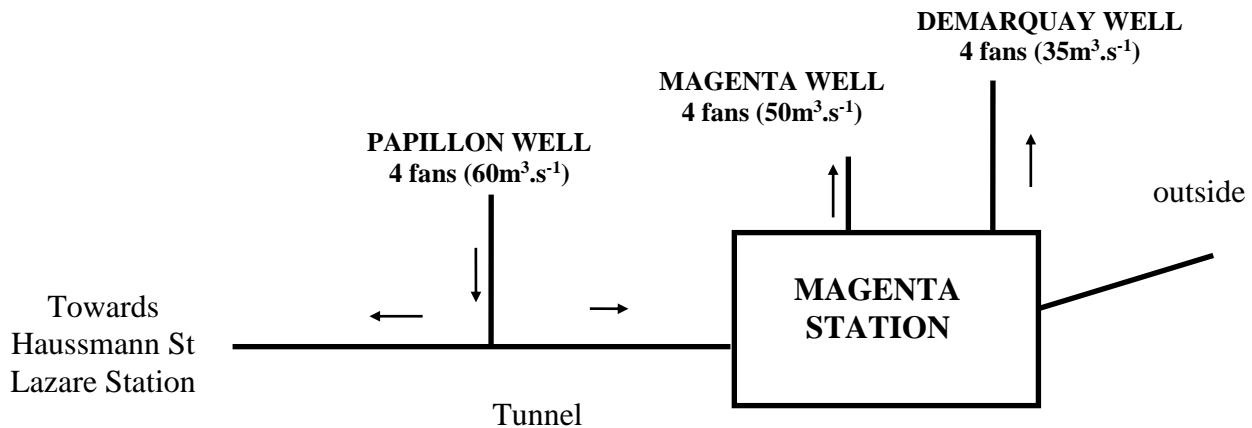


Figure 2 Description of the ventilation system.

During the first experiment, Demarquay, Papillon and Magenta fans were turned off between 11:05pm and 11:35pm. Those fans were turned on between 2:55am and 4:50am. During the second experiment, to study the influence of train pass-by on particle concentrations, two scenarios were repeated: pass-by without stopping and pass-by with braking and stopping.

To better validate the current results, a comparison was made with the Nazaroff model [5]. The Nazaroff model allows to calculate the evolution of the overall concentration, with the assumption of a homogeneous distribution of concentrations set for the study of confined ventilated spaces. The model's equations is described as follows:

$$\frac{dC_i(t)}{dt} = \underbrace{f\lambda_r C_{ext}(t)}_I - \underbrace{\lambda_r C_i(t)}_{II} - \underbrace{\lambda_d C_i(t)}_{III} + \underbrace{\frac{s(t)}{V}}_{III}$$

Where the first part (I) of the equation represents the exchanges between the inside and outside, the second (II) refers to the deposition and the third (III) being the source term. A theoretical flow is used for the extraction ($170\text{m}^3.\text{s}^{-1}$) and insuflation ($120\text{m}^3.\text{s}^{-1}$). The decay used for the Nazaroff model is indicated in Figure 3 (deposition part (II)).

RESULTS AND DISCUSSION

Ventilation

During the measurement period the relative humidity ranged from 47% to 57% and the temperature from 11.4 to 13.4°C.

Firstly, measurements of particle concentrations show higher concentrations for particles ranged between 0,3 and 0,4 μm than those for bigger height classes. During the night, fine particle (0,3 to 0,4 μm) concentrations part increase whereas the others decrease (**Erreur ! Source du renvoi introuvable.** **Erreur ! Source du renvoi introuvable.** and **Erreur ! Source du renvoi introuvable.**). Globally, air becomes impoverished in particles and PM_{10} concentration in the station reduces to the urban level.

Disturbances due to trains pass-by have an important effect on particle concentrations (less than 1 μm). As one can see on Figure 3 and, between 00:00am and 01:00am and after traffic started, the particle concentrations variations fit with trains pass-by. When considering air velocity (that also fits with trains pass-by), ranged from 1.0 to 2.2 $\text{m}.\text{s}^{-1}$ on nearest track of measurement's one before traffic stopped and up to 4 $\text{m}.\text{s}^{-1}$ after traffic start on measurement's track, it is easier to understand that particles are under high trains' disturbances. When there is no traffic in the station, air velocity ranged from 0.02 to 0.6 $\text{m}.\text{s}^{-1}$. Then, particle concentrations

decrease to lower level on 45', as shown on Figure 3.

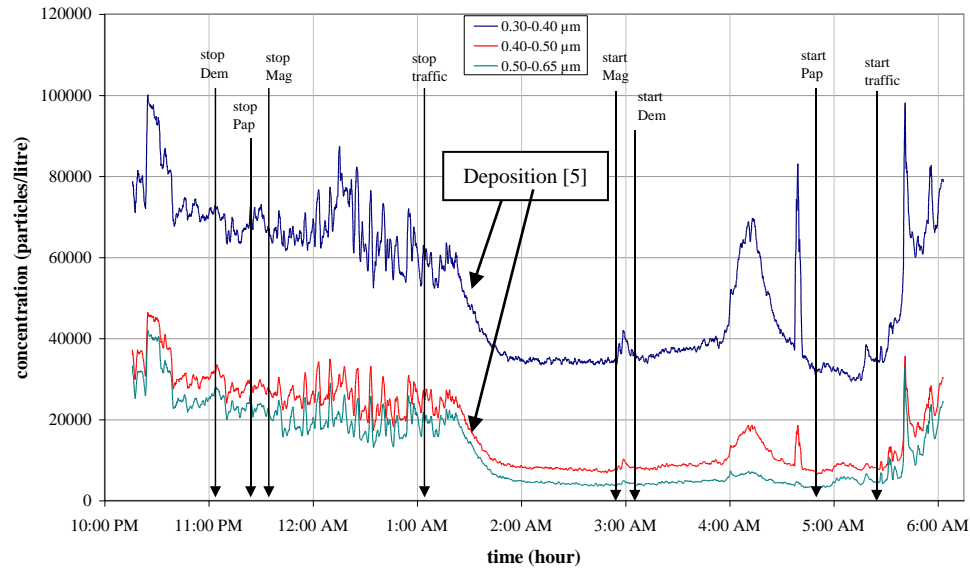


Figure 3
Particle concentrations variations at 1.70m.

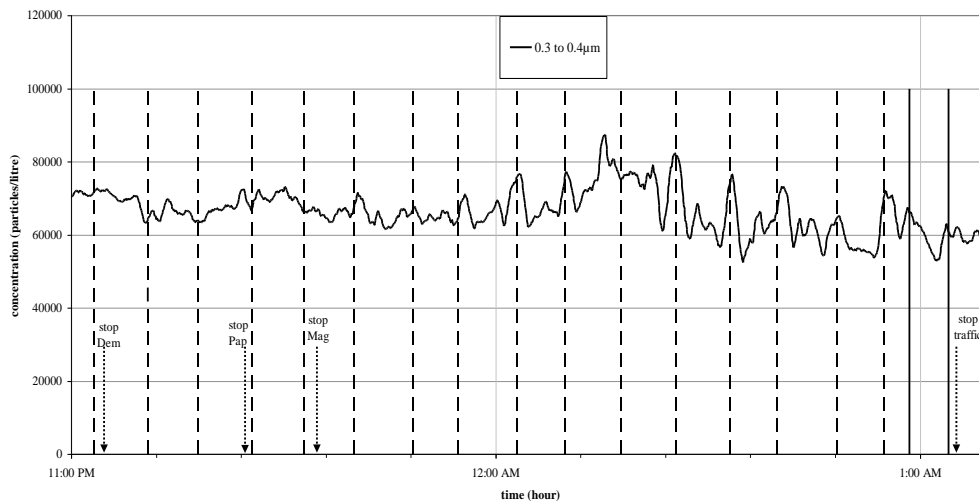


Figure 4
Trains entry on nearest track of measurement's one and particle concentration at 1.70m between 11:00pm and 1:15am

In Figure 4, the stop Dem, stop Pap and stop Mag, represents the interruption of the ventilation from Demarquay, Papillon and Magenta respectively. When looking on a smallest period during the night (on Figure 4), after 11:30 pm, 1' after each train entry on nearest track of measurement's one (when train sets in motion represented by the dashed vertical line) corresponds to a particle concentrations decrease. This can be explained by the fact that particles move outside the station with train's movement. As fine particle concentrations are relatively close for each measurement's height, only fine particle

concentrations at 1.70m is represented on Figure 4. Before traffic stopped, measurements also show that relative humidity increase (approximately 3%) when trains enter in the station. This can be due to passengers when coming-out from trains or to trains if outside relative humidity is higher than inside one. Because of low variations of CO₂ concentrations, we cannot conclude on the passengers' influence on relative humidity.

The results for the particle concentration at 1,7m (Figure 4) are analyzed with the Nazaroff model, presented in Figure 5. Figure 6 which is given by [6] allows for the last

deposition rate of assessment obtained in the literature with the Nazaroff model [5].

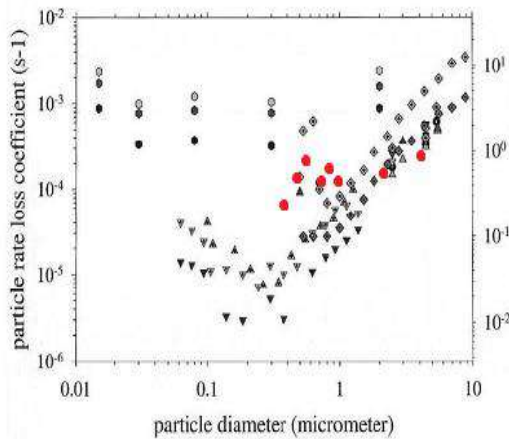


Figure 5
Comparison of results (red dot deposition model) with the Nazaroff model [5].

Trains During the measurement period the relative humidity ranged from 56% to 64% and the temperature from 16 to 18°C. Four pass-by were performed during this test: two when braking and stopping, and two other without stopping. Measurements give four different

signatures for the four pass-by. Fine particles are one more time present in majority, even during pass-by trains. The timetable of the different pass-by is shown in Table 1.

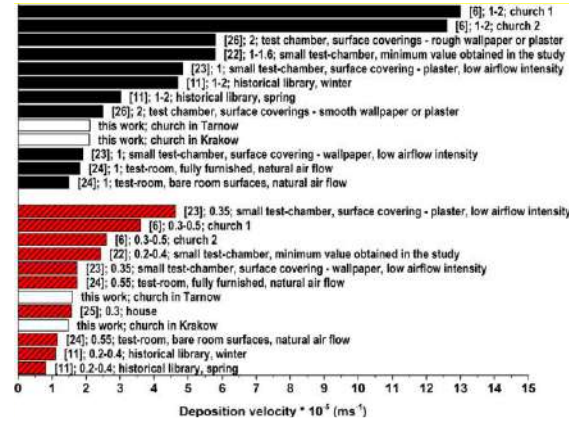


Figure 6
Particle deposition velocities obtained in various studies for coarse (black) and fine (hatched) particle size modes [6].

Table 1: Timetable of the different pass-by.

	braking 1	stop 1	braking 2	stop 2
entry	2h18min57s	3h02min40s	3h47min34s	4h32min31s
stop	2h19min24s	/	3h48min03s	/
Setting in motion	2h20min30s	/	3h49min04s	/
Departure	2h20min56s	3h03min07s	3h49min33s	4h32min57s

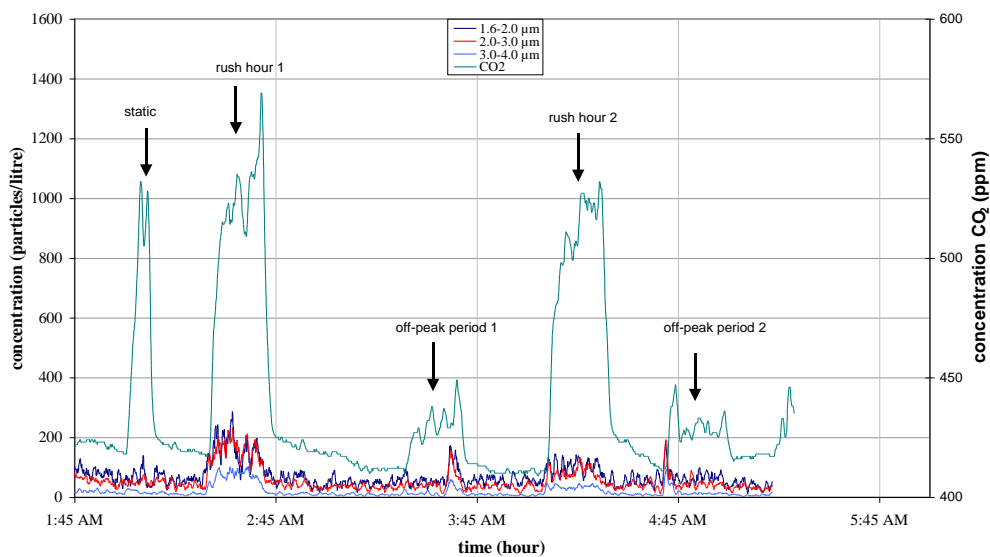


Figure 7.a
Particles concentrations variations at 0.50m

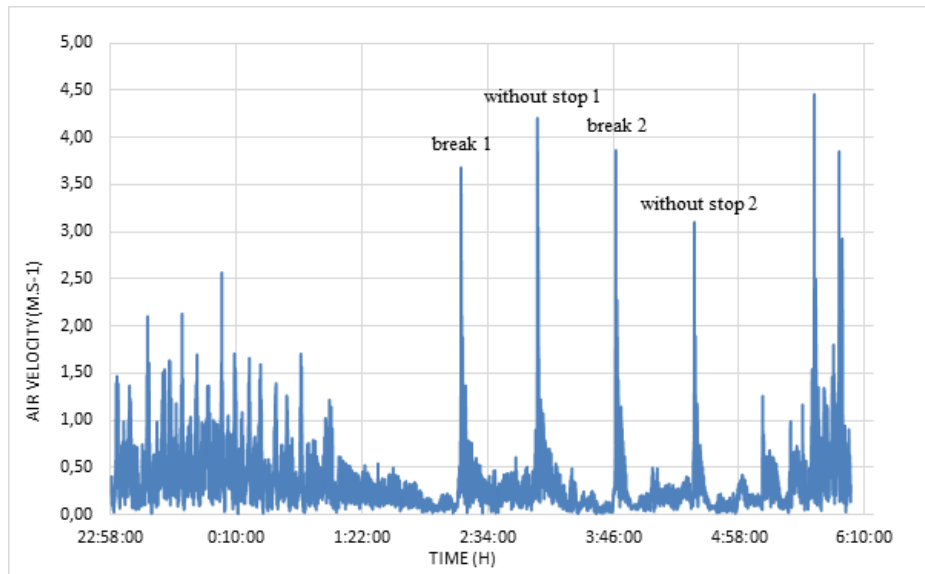


Figure 6.b

Changes in velocity caused by brakage.

During this last experiment, the concentrations of particles ranged between 0.3 and 0.65µm are approximately two times lower than during the first one.

Table 2 gives granulometric distribution during this third experimentation. It shows, as during the first one, fines particles represent the major part of particles numbers.

As we can see on Figure 7.a,b trains' signatures due to the four pass-by are not reproducible two by two in spite of the same conditions (same operator, same speed...). One pass-by, the first without stopping, does not cause an important signature. The other three pass-by cause fast increase and decrease particle concentrations. These variations can

be observed for the whole particles' height and are probably due to the transport caused by trains' air mixing, as air velocities are up to 4.5m.s-1 on measurement's track, as during the first experiment. The difference which can be observed between the two last pass-by in term of maximum concentrations represents approximately 5400 part/L for particles ranged between 0.3 and 0.4µm.

Figure 8.a,b shows the impact of trains braking and speed reduction, showing a high burst of velocity caused by the displacement of air.

We note that for fine particles <1.6µm, the speed reduction from the braking is the source of pollution compared to a non-stop passage (Figure 8.a,b).

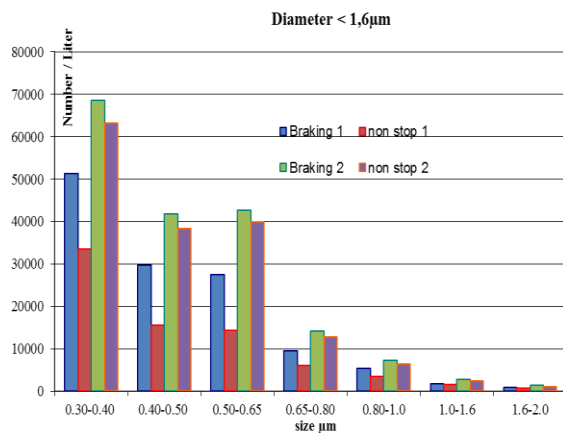


Figure 8.a
Impact braking

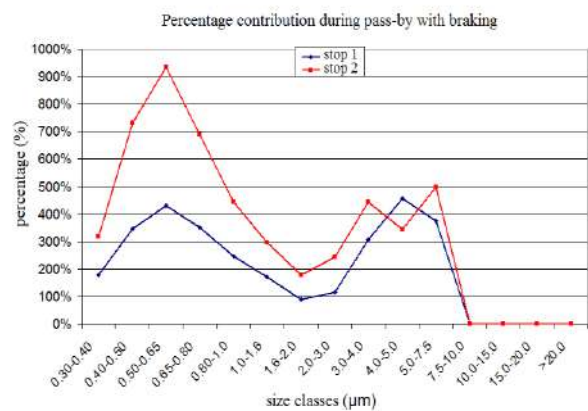


Figure 8.b
Impact braking

Table 2: Granulometric distribution during the experimentation at 00h

size (μm)	0.30-0.40	0.40-0.50	0.50-0.65	0.65-0.80	0.80-1.0	1.0-1.6	1.6-2.0	2.0-3.0
Concentration(part/L)	24984	9632	7940	3350	2120	790	337	362
Repartition (%)	50.33%	19.41%	16.00%	6.75%	4.27%	1.59%	0.68%	0.73%
size(μm)	3.0-4.0	4.0-5.0	5.0-7.5	7.5-10.0	10.0-15.0	15.0-20.0	>20.0	total
Concentration(part/L)	78	31	8	4	0	0	0	49636
Repartition (%)	0.16%	0.06%	0.02%	0.01%	0.00%	0.00%	0.00%	100%

As during the previous experiments, the same relative humidity variations (approximately 3% to 4%) have also been observed during the period of trains pass-by. As there were no passengers in the station during this test, we can conclude that this variation is due to trains pass-by.

CONCLUSION

The first experiment did not show an effect of ventilation on particle concentration. Ventilation may not have a significant influence on resuspended particles but it may have an impact on the accumulation of particle concentration. So it could be interesting to turn off the station's ventilation during several days or weeks if it's possible.

The last experiment gave an idea of trains pass-by influence on particle concentration. This source is probably the most important in the station. But it is also the most complex because it is difficult to estimate the part of emission, transport and resuspension. Many studies have been carried out to determine PM_{10} and $\text{PM}_{2.5}$ levels in underground stations. Particle number concentrations are rarely performed. Such measurements have been done by P.Aarnio [2] to compare it to urban level. In our study, such measurements have been carried out to characterize different particle sources. To have more information on particle transport, it could be interesting to measure the concentration level in tunnel to compare respective pollution of tunnels and station. But punctual measurements could not be sufficient to understand such difficult phenomenon as particle transport and resuspension.

Nevertheless, these two experiments show particles less than $1\mu\text{m}$ representing the major

part of particle number concentration in the underground station. In order to reduce their concentrations, it is very important to better understand their origins and behavior.

ACKNOWLEDGEMENT

Personnel of Magenta station, Personnel of "Agence d'Essais Ferroviaires" from SNCF are acknowledged for technical help in arranging this campaign.

REFERENCES

1. Johansson, C, Particulate matter in the underground of Stockholm, Atmospheric Environment 37, october 2002
2. Aarnio P, The concentrations and composition of and exposure to fine particles ($\text{PM}_{2.5}$) in the Helsinki subway system, Atmospheric Environment 39, may 2005
3. Limam, K (LaSIE) "Etude du Transport des Particules à l'Intérieur des Locaux", PRIMEQUAL II, 2006.
4. Alloul-Marmor, L, Réentrainement par écoulement d'air d'une contamination particulaire déposée sur une surface. Application au cas d'un tas de poudre. Thesis doctoral, University of ParisXII April 2002.
5. Nazaroff, W W, Cleaning products and air fresheners: exposure to primary and secondary air pollutants, Atmospheric Environment 38, June 2004.
6. Mleczkowska, A, et al, Particle penetration and deposition inside historical churches Building and Environment 95, pp 291-298, (2016)

AN APPROACH USING LATTICE BOLTZMANN METHOD TO SIMULATE FLUID-STRUCTURE-INTERACTION

M. Benamour*, E. Liberge, and C. Béghein

LaSIE, La Rochelle University, Avenue Michel Crépeau, 17000 La Rochelle cedex 1, FRANCE

*Corresponding author: Fax: +33 5 4645 8241 E-mail: malek.benamour@univ-lr.fr

ABSTRACT

A numerical approach based on the Lattice Boltzmann method (LBM) and volume penalization technique is proposed to tackle the problem of the interaction of a moving rigid cylinder with an incompressible fluid flow. The present methodology was applied to an oscillating rigid cylinder in a fluid flow, which is a classical benchmark of Fluid-Structure Interaction (FSI). Two cases were considered: flow around a cylinder undergoing forced harmonic oscillations, and flow around a cylinder in free oscillations due to the fluid forces at Reynolds number 20. Our results have been validated and compared with those obtained using a classical CFD approach. To compare the results of the LBM and classical approach, and to ensure that the resolution of the structure would be the same in both simulations, the Shiels et al. [1] structure adimensionalisation has been used. The simulations of LBM have been implemented for a two level refined grid around the cylinder, with the grid refinement technique proposed by Lagrava et al. [2]. The flow characteristics, the oscillation frequency, the lift and drag coefficients values associated have been investigated. A good agreement was found between the results computed with the volume penalization method applied to the lattice Boltzmann equation, and those obtained with the classical approach. The same approach has been used in our previous works to simulate incompressible flows around obstacles [3].

Keywords Lattice Boltzmann method, Volume Penalization technique, Fluid Structure Interaction, CFD.

NOMENCLATURE

f_α	Density distribution function
f_α^{eq}	Equilibrium distribution function
Δx	Space step
Δt	Time step
c_s	Speed of sound
\mathbf{u}	Fluid velocity
\mathbf{u}_s	Solid velocity
F_α	Forcing term
D	Diameter of cylinder
m	mass of cylinder
Re	Reynolds number
k	Stiffness of the spring
y_{eq}	Position at equilibrium
f	Oscillation frequency
F_y	Lift force
C_l	Lift coefficient
$C_{l_{rms}}$	Mean square of the lift coefficient
$C_{l_{max}}$	Maximum of the lift coefficient
C_d	Drag coefficient
<i>LBM</i>	Lattice Boltzmann Method
<i>BGK</i>	Bhatnagar Gross Krook
<i>CFD</i>	Computational Fluid Dynamics
<i>FSI</i>	Fluid-structure interaction
<i>IBM</i>	Immersed boundary method
<i>ALE</i>	Arbitrary Lagrangian Eulerian
<i>Lu</i>	Lattice unit

Greek symbols

τ	Single relaxation time
ν	kinematic viscosity
α	Direction
ρ	Fluid density
ξ	Particle velocity
ω	Weighting coefficients
χ	Mask function
η	Permeability coefficient
Ω_f	Fluid domain
Ω_s	Solid domain

INTRODUCTION

Flows around moving bodies are the subject of various numerical and experimental studies. FSI occurs when fluid in contact with structure, makes it move and deform. Furthermore, the deformation or the displacement of the structure changes the velocity field and pressure of the fluid flow. The FSI problems have a lot of important applications in many different branches of engineering such as, aerodynamics, hydrodynamics, sedimentation, flow in porous media, turbulence, biomechanics, etc. Several techniques have been developed to model bodies moving in fluids, using the lattice Boltzmann method. Ladd [4], used the bounce back rule to model the no-slip boundary condition between the particle and fluid, and he also proposed the momentum exchange method to calculate the fluid force exerted on the solid particle. The

drawback of this technique was that it requires the use of a large number of solid nodes in order to represent correctly the physical boundaries of the solid structure. Based on the work of Ladd, many efforts have been made to simulate flows around complex geometries and moving objects (Filippova and Hänel [5], Mei et al [6], Bouzidi et al [7], etc).

Noble and Torczynski [8] presented another model to simulate flows with moving solids. A source term that depends on the percentage of the cell saturated with fluid is introduced into the lattice Boltzmann equation. With this term, the conventional lattice Boltzmann equation was recovered for fluid regions, and the bounce back condition developed by Zou and He [9] was applied when the lattice node was occupied only by the solid. This method is relatively simple to implement for two-dimensional cases, but it is not easy to apply for three-dimensional cases. In addition, this method is valid only for the Bhatnagar-Gross-Krook (BGK) collision operator model.

A popular method used for simulating fluid-structure interaction is the immersed boundary method (IBM), which was originally introduced by Peskin [10] to model blood flow in the heart. This technique employs a fixed regular mesh for the flow domain, and a Lagrangian points attached to the moving boundary, and adds a forcing term in the Navier-Stokes equations to model the influence of the boundary on the fluid flow. Feng and Michaelides [11], and Ten Cate et al. [12], were the first ones to combine the LBM and the IBM for the simulation of flows around rigid particles. The forcing term was modeled by Feng and Michaelides with a restoration force acting on the particle boundary. Ten Cate et al. used for this term a variant developed by Goldstein et al. [13], where the restoration force on the boundary can be due, from a physical point of view, to a damped oscillator. The disadvantage of this method was that results depended on one or two empirical parameters. To overcome this problem, Dupuis et al. [14], introduced into the Immersed Boundary-lattice Boltzmann method, the direct forcing approach proposed by Fadlun et al. [15]. In this approach, the forcing point was located in the fluid region in the immediate vicinity of the solid boundary, and an interpolation between the solid points and the fluid points was used to evaluate the forcing term. With this approach, the no-slip condition is not exactly satisfied at the solid boundary, and some streamlines may penetrate in the solid obstacle. To enforce the no-slip condition at the solid boundary, Wu and Shu [16], by using the

forcing term proposed by Guo et al. [17], developed an implicit procedure, where a velocity correction was calculated for all Lagrangian points at the boundary.

In parallel with the immersed boundary method, the Lagrange multipliers method has been implemented with the LBM by Shi and Phan-Thien [18] to model flows around moving obstacles. This approach is based on the work of Yu [19] which is an extension of the Glowinski et al [20] formulation. The idea of this approach is that the fluid equation was solved on a fictitious domain including the fluid domain and the solid domain, and a force (the Lagrange multiplier) was introduced to force the velocity of the fictitious fluid inside the solid domain to be the same as the solid velocity. The solid domain was followed with a Lagrangian description. With this method, the remeshing procedure, which is computationally time consuming, was avoided.

Recently the Arbitrary Lagrangian-Eulerian (ALE) approach was applied to the Lattice Boltzmann method by Meldi et al. [21]. This method use a fixed grid, and a moving one which follows for example the flow around a moving obstacle. The communication between the fixed and the moving grid is performed using interpolations. The nodes of the moving grid are displaced arbitrarily using a Lagrangian description. In this region, the Navier-Stokes equations are solved on the moving grid [22]. Meldi et al. used Chapman-Enskog procedure to develop the lattice Boltzmann formulation for a moving grid. Non-deforming grids were chosen.

The purpose of the present work is to present a new approach that combines the Lattice Boltzmann method and a volume penalization technique to treat the problem of the interaction between a moving rigid cylinder and an incompressible fluid flow. The paper is structured as follows: the governing equations and the proposed method are described first. Next we present the numerical results of flow around a cylinder undergoing forced harmonic oscillations, and flow around a cylinder in free oscillations due to the fluid forces at Reynolds number 20. Finally, the conclusions and perspectives are drawn.

NUMERICAL METHODS

This section describes the formulation employed to simulate fluid-structure interaction using our present approach.

Lattice Boltzmann Method

The LBM, which is accurate, easy to implement, and natural to parallelize has been successfully applied in fluid mechanics during the last decades [23]. It was thus chosen in the present work, for flow computation. The lattice Boltzmann equation (LBE) with the Bhatnagar-Gross-Krook (BGK) collision operator can be expressed as:

$$f_\alpha(\mathbf{x} + \Delta t, \xi_\alpha t + \Delta t) = f_\alpha(\mathbf{x}, t) - \frac{1}{\tau} \left(f_\alpha(\mathbf{x}, t) - f_\alpha^{eq}(\mathbf{x}, t) \right) + \Delta t F_\alpha \quad (1)$$

Where $f_\alpha(\mathbf{x}, t)$ is the density distribution function along α direction and $f_\alpha^{eq}(\mathbf{x}, t)$ is its corresponding equilibrium distribution function, ξ_α is the particle velocity, τ is the non-dimensional relaxation time, Δx and Δt are the lattice spacing and time step. The nine-velocity square lattice model $D2Q9$ was used, in this model the lattice velocities are:

$$\begin{aligned} \xi_0 &= (0, 0), & \xi_\alpha &= c \left(\cos((\alpha - 1)\pi/2), \right. \\ & & & \left. \sin((\alpha - 1)\pi/2) \right) \quad \text{for } \alpha = 1, 2, 3, 4, & \xi_\alpha &= \\ & & & c\sqrt{2} \left(\cos((\alpha - 5)\pi/2 + \pi/4), \sin((\alpha - 5)\pi/2 + \right. \\ & & & \left. \pi/4) \right) \quad \text{for } \alpha = 5, 6, 7, 8. \end{aligned}$$

Where $c = \Delta x / \Delta t = 1$, the equilibrium distribution function is given by:

$$\begin{aligned} f_\alpha^{eq}(\mathbf{x}, t) &= \omega_\alpha \rho \left[1 + \frac{\xi_\alpha \cdot \mathbf{u}}{c_s^2} \right. \\ & \left. + \frac{\mathbf{u} \mathbf{u} : (\xi_\alpha \xi_\alpha - c_s^2 I)}{2c_s^4} \right] \quad (2) \end{aligned}$$

ω_α are the weighting coefficients (for the $D2Q9$ model: $\omega_0 = 4/9$, $\omega_\alpha = 1/9$ for $\alpha = 1, 2, 3, 4$, $\omega_\alpha = 1/36$ for $\alpha = 5, 6, 7, 8$, c_s is the speed of sound). For our numerical simulations, the forcing term F_α in the lattice Boltzmann equation (1) was modelled using the forcing term proposed by Guo et al [17]:

$$F_\alpha = \left(1 - \frac{1}{2\tau} \right) \omega_\alpha \left[\frac{\xi_\alpha \cdot \mathbf{u}}{c_s^2} + \frac{(\xi_\alpha \cdot \mathbf{u})}{c_s^4} \xi_\alpha \right] \cdot \mathbf{F} \quad (3)$$

The macroscopic properties such as the fluid density ρ and velocity \mathbf{u} can be evaluated as follows:

$$\rho = \sum_\alpha f_\alpha(\mathbf{x}, t) \quad (4)$$

$$\rho \mathbf{u} = \sum_\alpha \xi_\alpha f_\alpha(\mathbf{x}, t) + \frac{\Delta t}{2} \mathbf{F} \quad (5)$$

The incompressible Navier–Stokes equations can be obtained from Eq.1, using the Chapman–Enskog expansion, with a kinematic viscosity given by:

$$\nu = c_s^2 \Delta t (\tau - 0.5) \quad (6)$$

Volume penalization method

This method was first presented by Angot [24]. It consists in introducing a volume penalization term into the equation that needs to be solved in order to take into account the influence of the obstacle on the fluid domain. Since this equation is solved on both fluid and solid domains, the boundary conditions at the fluid–solid interface are naturally applied. In this work, the volume penalization technique was applied to the incompressible Navier–Stokes equations into the lattice Boltzmann framework. The same combination was successfully used in our previous work to simulate incompressible flows around fixed obstacles [3].

The Navier–Stokes equations with a volume penalization term read [24]:

$$\begin{aligned} \rho \frac{\partial \mathbf{u}}{\partial t} + \rho \mathbf{u} \cdot \nabla \mathbf{u} &= -\nabla p + \mu \nabla \cdot [(\nabla \mathbf{u} + (\nabla \mathbf{u})^T)] \\ & - \frac{\rho}{\eta} (\chi(\mathbf{u} - \mathbf{u}_s)) \quad (7) \end{aligned}$$

$$\nabla \cdot \mathbf{u} = 0 \quad (8)$$

where μ and p are the dynamic viscosity and the pressure of the fluid considered, $F = -\frac{\rho}{\eta} (\chi(\mathbf{u} - \mathbf{u}_s))$ is the penalization term, χ is a mask function, which is equal to 0 in the fluid domain Ω_f , and to 1 in the solid domain Ω_s , η is a permeability coefficient that is very high in the fluid domain and very small in the solid domain, and \mathbf{u}_s is the desired solid velocity.

In the fluid domain, the ratio χ/η is null, hence the penalization term has no influence. In the solid domain, the ratio χ/η is very high, the velocity is thus equal to \mathbf{u}_s , and the physical equation becomes negligible. The penalization term \mathbf{F} is introduced into the lattice Boltzmann equation Eq. (1), using the forcing term proposed by Guo and al. [17]. The fluid velocity was calculated according to the following expression (deduced from equation 5):

$$\mathbf{u} = \frac{\sum_\alpha \xi_\alpha f_\alpha + \frac{\Delta t}{2} \frac{\chi}{\eta} \rho \mathbf{u}_s}{\rho + \frac{\Delta t}{2} \frac{\chi}{\eta} \rho} \quad (9)$$

RESULTS AND DISCUSSION

In this section, the volume penalization method coupled with the LBM have been tested on the configuration described in Fig.1, a cylindrical rigid solid, attached to a spring, has been immersed in a fluid flow at Reynolds number 20.

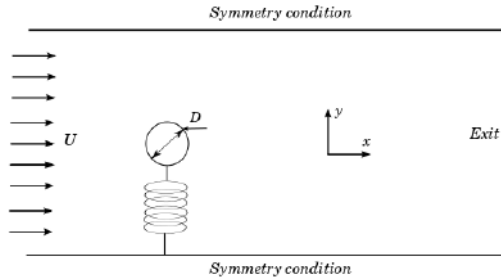


Figure 1 Configuration studied

For the LBM parameters, we consider the inlet velocity $U_{max} = 0.0229$, the diameter of the cylinder $D = 29$ and $\tau = 0.6$. To adapt an accurate mesh around the moving cylinder, our simulations were performed with a two level refined grid where the grid refinement technique proposed by Lagrava et al. [2] based on multi-domain approach was chosen. The initial grid-size is 580×290 , the first refinement grid-size is 353×353 and the last one 349×349 . Thus, in the fine grid, the obstacle contains 116 nodes along its diameter. Two cases were considered: flow around a cylinder undergoing forced harmonic oscillations, and flow around a cylinder in free oscillations. Our results were validated and compared with those obtained from Code_Saturne [25], an open source finite volume CFD software using the Arbitrary Lagrangian Eulerian method for solving Navier-Stokes equations on a moving mesh, and an implicit coupling for the displacement of the structure. The flow characteristics, the oscillation frequency, the lift coefficient C_l and drag coefficient C_d values associated were investigated.

Structure adimensionalisation

To compare the results of the LBM and Code_Saturne, and to ensure that the resolution of the structure would be the same in both simulations, we used the Shiels et al. structure adimensionalisation. The displacement of the structure along the vertical axis is governed by the following equation:

$$m\ddot{y} + k(y - y_{eq}) = F_y \quad (10)$$

Where m is the mass of cylinder, k is the stiffness of the spring, y_{eq} the position at equilibrium and F_y is the lift forces. The Shiels et al. structure adimensionalisation has been used:

$$y^* = \frac{y}{D}, \quad m^* = \frac{m}{0.5\rho D^2}, \quad k^* = \frac{k}{0.5\rho U_\infty^2}, \quad t^* = t \frac{U_{max}}{D}$$

Thus, the dimensionless equation for the structure becomes:

$$m^* \ddot{y}^* + k^* (y^* - y_{eq}^*) = C_l \quad (11)$$

In the present study the chosen parameters are:

$$m^* = 10 \text{ and } k^* = 3.56$$

Cylinder in forced oscillations

Flow around a cylinder undergoing forced harmonic oscillations is the first test carried out. In this case the fluid force F_y acting on the body in equation 10 is null. Initially the cylinder-oscillating amplitude was fixed at $D/4$, the solid movement equation is given as follows:

$$y(t) = \left(y_0 - \frac{D}{4}\right) + \frac{D}{4} \cos(\omega t) \quad (12)$$

Where $y_0 = y(t)$. Fig 2, compares the dimensionless velocity field obtained by the LBM with volume penalization (a) and by Code_Saturne (b) after 10 oscillations of the cylinder. A satisfactory agreement can be noticed.

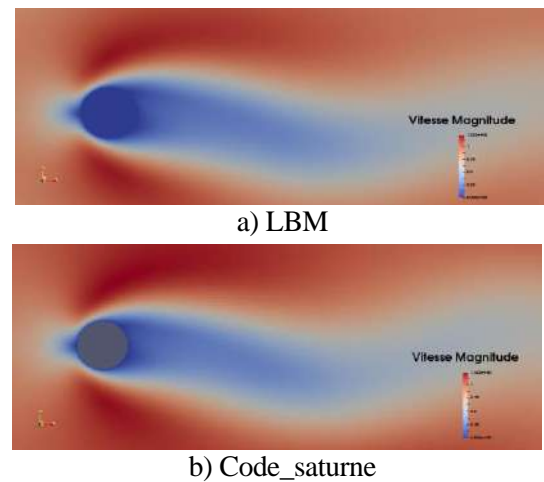


Figure 2 Comparison of dimensionless velocity fields obtained by a) LBM and b) Code_Saturne

The mean drag coefficient, the root mean square and the maximum of the lift coefficient are listed in Table 1. A good agreement is obtained between the compared results.

Table 1 Comparison of lift and drag coefficients

	LBM	Code_saturne
$\langle C_d \rangle$	2.26	2.26
C_{lrms}	0.12	0.11
C_{lmax}	0.17	0.17

Figure 3 shows the comparison of the lift coefficient obtained by our approach and Code_Saturne. We can see that the results are superimposed. The amplitudes and the time period of oscillations are substantially the same. However we can observe the oscillation of the results obtained by combination of the LBM and the volume penalization method, this is due to the changes of the mask function when the cylinder moves.

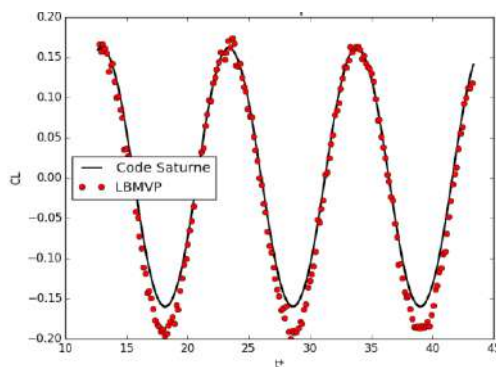


Figure 3 Comparison of the lift coefficient obtained by LBM and Code_Saturne

Cylinder in free oscillations

In this second case, the computations were made following the previous calculation. After imposing 10 oscillations, the fluid forces are taken into account in equation (10). The two domains fluid and solid are coupled by an explicit asynchronous scheme. This simple coupled algorithm was retained because in the current example, $1 \Delta t$ in LBM corresponds to a $\Delta t = 8 \cdot 10^{-4} s$ in physical equation. In addition, the time step in each level of refinement is divided by 2. As our simulations have been carried out with 2 degrees of refinement, the structure was resolved with a time step divided by 4 which is very small.

The results between the two compared simulations are in a good agreement as shown in figure 4. We can see that the flow induces a damping of the structure oscillations (a decrease in the amplitude), and a change of the oscillation frequency. In fact, while the dimensionless frequency $f_0^* = 2\pi\omega_0$ of the spring-mass system is equal to 0.095, the cylinder under the effect of fluid forces, oscillates at a frequency $f^* = 0.09$. The effects of flow are transmitted identically on both methods of resolution. We can also observe a slight

difference on the minimum and maximum displacement of the cylinder, this difference remains in the margin of error that may exist when comparing two codes.

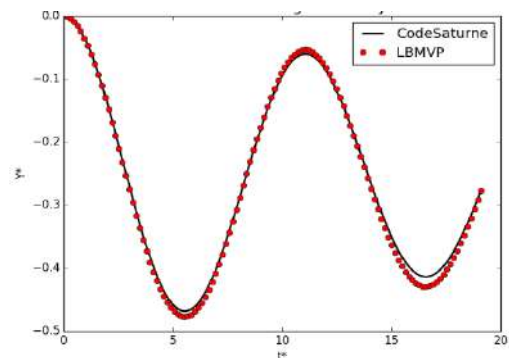


Figure 4 The position of the gravity center according to time obtained by the LBM and Code_Saturne

CONCLUSIONS

In this paper, a volume penalization technique applied for fluid–structure interaction problem using lattice Boltzmann method has been presented. This approach was applied to simulate incompressible flow around oscillating rigid cylinder. Our results presented were validated with those computed using CFD Code_Saturne. The results of the cylinder in forced oscillations show that there is a good agreement in velocity fields between the two compared simulations. The same remark may be done concerning the mean drag coefficient, the root mean square and the maximum of the lift coefficient. However slight oscillations of the results obtained by our present approach can be observed, this is due to the changes of the mask function when the cylinder moves. In the case where the cylinder is in free oscillations, the fluid forces taken into account are transmitted identically on both methods of resolution. In future work we would like to extend our present approach to high Reynolds numbers.

REFERENCES

1. D. Shiels, A. Leonard et A. Roshko, « Flow-induced vibration of a circular cylinder at limiting structural parameters », Journal of Fluids and Structures, vol. 15, no. 1, p. 3–21, 2001.
2. D. Lagrava, O. Malaspinas, J. Latt et B. « Advances in multi-domain lattice Boltzmann grid refinement », Journal of Computational

- Physics,
vol. 231, p. 4808–4822, mai 2012.
3. M. Benamour, E. Liberge, and C. Béghin. Lattice Boltzmann method for fluid flow around bodies using volume penalization. *The Int Journal of Multiphysics*, 9(3) :299- 316, 2015.
 4. Anthony J. C. Ladd. Numerical simulations of particulate suspensions via a discretized Boltzmann equation. Part 2. Numerical results. *J. of Fluid Mechanics*, 271: 311–339, July 1994.
 5. O. Filippova et D. Hänel, « Grid refinement for lattice-BGK models », *Journal of Computational Physics*, vol. 147, p. 219–228, nov. 1998.
 6. R. Mei, L.-S. Luo et W. Shyy, « An accurate curved boundary treatment in the Lattice Boltzmann Method », *Journal of Computational Physics*, vol. 155, p. 307–330, nov. 1999.
 7. M. Bouzidi, M. Firdaouss et P. Lallemand, « Momentum transfer of a Boltzmann lattice fluid with boundaries », *Physics of Fluids*, vol. 13, p. 3452–3459, nov. 2001.
 8. D. Noble et J. Torczynski, « A lattice-boltzmann method for partially saturated computational cells », *International Journal of Modern Physics C*, vol. 9, no. 8, p. 1189–1201, 1998.
 9. Qisu Zou and Xiaoyi He. On pressure and velocity boundary conditions for the lattice Boltzmann BGK model. *Physics of Fluids (1994-present)*, 9(6):1591–1598, June 1997.
 10. Charles S Peskin. Numerical analysis of blood flow in the heart. *Journal of Computational Physics*, 25(3) :220–252, November 1977.
 11. Z.G. Feng and E.E. Michaelides. The immersed boundary lattice boltzmann method for solving fluid-particles interaction problems. *J. Comput. Phys.*, 195:602–628, 2004.
 12. Ten Cate, A. Nieuwstad, C., Derksen, J. and Van den Akker, H. Particle imaging velocimetry experiments and lattice-Boltzmann simulations on a single sphere settling under gravity. *Phys. Fluids.*, 14, 11. (2002), 4012–4025.
 13. Goldstein, D. and Handler, R. and Sirovich, L. Modeling a no-slip flow boundary with external force field. *J. Comput. Phys.* 105(93), 354-366.
 14. Alexandre Dupuis, Philippe Chatelain, and Petros Koumoutsakos. An immersed boundary-lattice-boltzmann method for the simulation of the flow past an impulsively started cylinder. *Journal of Computational Physics*, 227(9) :4486-4498, April 2008.
 15. E. A. Fadlun, R. Verzicco, Y. P. Orl and J. Mohd-yusof. Combined immersed boundary finite difference methods for three-dimensional complex flow simulations. *Journal of Computational Physics*, pages 35–60, 2000.
 16. J. Wu and C. Shu. Implicit velocity correction-based immersed boundary-lattice Boltzmann method and its applications. *J. Comput. Phys.*228(6):1963-1979, 2009.
 17. Zhaoli Guo, Chuguang Zheng and Baochang Shi. Discrete lattice effects on the forcing term in the lattice boltzmann method. *Physical Review E*, 65(4):1–6, April 2002.
 18. X. Shi et N. Phan-Thien, « Distributed Lagrange multiplier/fictitious domain method in the framework of lattice Boltzmann method for fluid-structure interactions », *Journal of Comput Physics*, vol. 206, p. 81–94, juin 2005.
 19. Z. Yu, « A DLM/FD method for fluid/flexible body interactions », *Journal of Computational Physics*, vol. 207, p. 1–27, juil. 2005.
 20. R. Glowinski, T. W. Pan, T. I. Hesla et D. D. Joseph, A distributed Lagrange multiplier/fictitious domain method for particulate flows, *International Journal of Multiphase Flow*, vol. 25, p. 755–794, août 1999.
 21. M. Meldi, E. Vergnault et P. Sagaut, « An arbitrary Lagrangian–Eulerian approach for the simulation of immersed moving solids with Lattice Boltzmann Method », *Journal of Comput Physics*, vol. 235, p. 182–198, fév. 2013.
 22. Jean Donea, Antonio Huerta, J.-Ph. Ponthot and A. Rodríguez-Ferran. Arbitrary Lagrangian-Eulerian Methods. In *Encyclopedia of Computational Mechanics*. John Wiley & Sons, Ltd, 2004.

23. R. Mei, L.-S. Luo et W. Shyy, « An accurate curved boundary treatment in the Lattice Boltzmann Method », *Journal of Computational Physics*, vol. 155, p. 307–330, nov. 1999.
24. Philippe Angot, Charles-Henri Bruneau, and Pierre Fabrie. A penalization method to take into account obstacles in incompressible viscous flows. *Numerische Mathematik*, 81(4) :497-520, February 1999.
25. Archambeau F, Méchitoua N, Sakiz M. Code_Saturne: a Finite Volume Code for the Computation of Turbulent Incompressible Flows. *International Journal on Finite Volumes*. 2004 ;1.

VALIDATION OF TURBULENCE MODELS FOR SIMULATION OF TURBULENT FLOW OF AIR AROUND AN OBSTACLE SQUARE SECTION

ALLICHE Mounir^{1*}, REBHI Redha¹, MAMOU Mahmoud², KORICHI Abdelkader¹

1- *Laboratoire de Mécanique Physique et Modélisation Mathématique (LMP2M), Université de Médéa, Quartier Ain Dheb, Medea, 26000, Medea, Algeria*

2- *Aerodynamics Research Laboratory, National Research Council Canada, Ottawa, Ontario, Canada*

*Corresponding author: Fax: +213 25 78 52 53 Email: alliche.mounir@univ-medea.dz

ABSTRACT

In this work was studied numerically a two-dimensional 2D flow around an obstacle using computational fluid dynamics techniques (CFD). The aim of this study is to evaluate the ANSYS CFX v12.1 performance for simulation of turbulent flows of the wind by using the Navier-Stokes equations with several turbulence models. The assessment is based on comparing the predicted results with those obtained experimentally Cedval 1-3. The experimental results were generated in a wind tunnel at the Metrological Institute of the University of Hamburg. Our main objective in this study is to find the appropriate turbulence model for simulating complex flow in the presence of separation and attachment. We considered five turbulence models, namely the standard $k-\varepsilon$ model, the $k-\varepsilon$ model feasible, model RNG $k-\varepsilon$, the standard model $k-\omega$ and $k-\omega$ SST model. Suitable meshes were used to meet the criteria required by each turbulence model.

KeyWords: Dynamic computational fluid CFD, turbulent flows, turbulence models, separation and attachment

NOMENCLATURE

H	building height, m
Re	Reynolds Number
u	Air Velocity, $m\ s^{-1}$
u^+	dimensionless velocity near the wall
k	turbulent kinetic energy, $m^2\ s^{-2}$
ε	dissipation rate of k, $m^2\ s^{-3}$
κ	Von Karman Constant
ω	turbulent Frequency
ν	kinematic Viscosity of air $Kg\ (m\ s)^{-1}$
y^+	dimensionless distance to the wall

INTRODUCTION

Different turbulence models have been proposed in the field of CFD to improve the conditions of the turbulent flow of air around a two-dimensional obstacle (2D). CFD engineering applications also increased with the development of different models of turbulence such as the turbulence model $k-\varepsilon$ standard turbulence model $k-\varepsilon$ Realizable, RNG $k-\varepsilon$, $k-\omega$ SST $k-\omega$, etc. The efficiency and accuracy of these models have been clearly confirmed when

applied to these simple flow fields that the flow in a channel. Recently, many computer simulation studies of turbulent flow structure of the air around an obstacle were conducted, including the study of Murakami and Mochida [1] where a three-dimensional numerical simulation (3D) of 'airflow around a cubic model with turbulence model $k-\varepsilon$. The numerical simulation of the airflow around a cubic obstacle is to estimate the influence of a mesh division system and the boundary conditions on the simulated results. Vardoulaskis et al. [2] A comparison study to evaluate the ability of four RAMS CFD models (Shensi, MIMO, and Fluent VADIS) to simulate wind flow and turbulence building around a single block with insulated use of $k-\varepsilon$ turbulence closure system. In particular, the four models overestimated the turbulent kinetic energy generated in the impact area near the wall. Shmidit and Theile [3] studied numerically unstable flow around an obstacle square dimensional (3D) by applying turbulence models DNS, LES and RANS. The main objective of this study was to evaluate the performance of DNS turbulence models compared to models LES and RANS on a coarse mesh. The

case considered is the turbulent flow at a Reynolds number $Re = 1.3 \times 10^4$. Tominaga and Stathopoulos [4] present a study on the accuracy of prediction of flow and pollutant dispersion around a cubic building using different turbulence models $k-\varepsilon$ and the numerical results were compared with wind tunnel data. This study was compared to four kinds of turbulence model, $k-\varepsilon$ standard, RNG $k-\varepsilon$, realizable $k-\varepsilon$ and $k-\varepsilon$ modified by Kato and Launder. Iaccarino and Durbin [5] interested in XR / h and the second recirculation zone in the case of unsteady and steady. They compare several results based on experimentation and others based on turbulence models such as LES and RANS. Castro [6] interested in the influence of the connecting length of the laminar boundary layer, it shows that for $0.34 < \delta / h < 0.80$ the connecting length decreases along δ / h , δ being the thickness of the laminar boundary layer. Xiang Li et al [7] uses the turbulence model $k-\varepsilon$ to determine the air change rate for an urban canyon. The $k-\varepsilon$ turbulence model was applied to different aspect ratios ($H / W = 0.5, 1, 2$) this model was validated against the modeling (simulations of large scale and THE (RNG) $k-\varepsilon$) and results in the wind tunnel. Average speeds and intensities of turbulence calculated by the $k-\varepsilon$ model are in good agreement with the results in the wind tunnel available in the literature (Place et al., 2004. Jeong and Andrews, 2002. Baik et al. 2000). Tominaga and Stathopoulos [8] compared the wind tunnel measurements with numerical simulations by a CFD code on pollutant dispersion around buildings with a point source located between the central buildings. They used to study two modeling approaches, a RANS approach with a closed model RNG $k-\varepsilon$ and the second approach SLE model to study the influence of speed and concentration camps. Louriero et al. [9] A detailed comparison of some numerical calculations and laboratory data to flow on a hill in two dimensions with six 2D turbulence models ($k-\varepsilon$, RNG $k-\varepsilon$, $k-\omega$ SST $k-\omega$) and two models moments (SSG-RSM- ε , BSL-RSM- ω). Experimental results include complete profiles of the components of the average velocity and Reynolds tensor. The $K-\omega$ model were observed much more efficient than the base model $k-\varepsilon$. The turbulence properties in the reverse flow zone were the best simulated by the BSL-RSM model. Ratnam et al. (2008) studied the performance of turbulence models to predict the flow and heat transfer on the wall of a cube. The Reynolds number $Re = 1870$ is considered. Calculations are performed using five models of turbulence: Standard $k-\varepsilon$, $k-\varepsilon$

low Reynolds number, non-linear $k-\varepsilon$ standard $k-\omega$ and $k-\omega$ model improvement to solve the shutdown problem. The results showed that the improved model $k-\omega$ gives a better agreement with the experimental study. The model non-linear $k-\varepsilon$ gives a better prediction compared to the turbulence model $k-\varepsilon$ low Reynolds number and $k-\varepsilon$ standard. Lateb et al. [10] studied the dispersion of pollutants in a configuration with two buildings using different turbulence models RANS (standard $k-\varepsilon$, realizable $k-\varepsilon$ and RNG $k-\varepsilon$) to determine the best model of turbulence to reproduce the dispersion the pollutant plume when the digital results were compared to wind tunnel experiment, it was found that the model of realizable $k-\varepsilon$ turbulence gives a better agreement with the results for a lower height, while for height maximum, the turbulence model RNG $k-\varepsilon$ provided a great agreement with the experimental results. The realizable $k-\varepsilon$ turbulence model was the only model capable of providing good trend for the concentration distribution in the lower area between the two buildings, but no turbulence model observed in the upper region. The turbulence model $k-\varepsilon$ was generally considered insufficient for the reproduction of distribution of vertical concentration.

MATHEMATICAL MODELING

The computational domain is shown in Fig. 1. A fully turbulent flow at a Reynolds number of $ReH = 4 \times 10^5$ was considered. The computational domain is defined by the planché blower and the barrier (Wall), where the grip conditions were applied, a symmetry plane in mid-height of the test section (Symmetry) the inlet (inlet) upstream and the outlet (outlet) downstream. A velocity profile was measured at the input and zero relative pressure was applied to the output.

MESHING

Fig. 1 shows the topology of the mesh which consists of five blocks of non-uniform structured grids. A mesh refinement near the solid walls was considered for an accurate simulation of the effects of walls. To demonstrate the sensitivity of the solution mesh size, mesh three have been considered; namely a coarse mesh 60000 nodes, refined way to 127500 nodes and 240000 Dense mesh nodes. The block sizes of the mesh are

presented in Table 1. The distribution of the nodes of the three meshes is shown in Fig. 2.

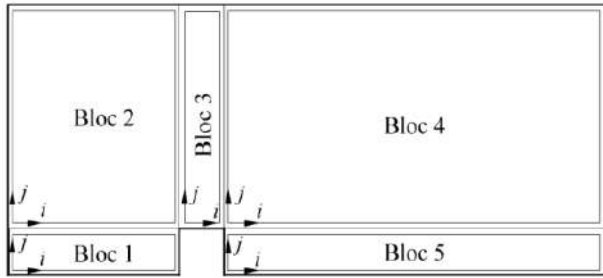


Figure 1. Mesh topology

TABLEAU 1. Nodes Number in different Mesh blocks

Mesh for k-ε , RNG k-ε , SST k-ω, k-ω models			
	coarse	fine	dense
Block 01	101×76	151×101	201×151
Block 02	101×101	151×151	201×201
Block 03	76×101	101×151	151×201
Block 04	201×101	301×151	401×201
Block 05	201×76	301×101	401×151

The ICEM preprocessor associated with ANSYS12.1 is used for the construction of the computational domain and mesh generation. Close attention was paid to the treatment near the wall before the choice of the grid; making this important step in the validation of the model for future analysis. In all cases, the choice of the configuration of the mesh, as regards the chosen turbulence model is based on the value of the dimensionless distance from the wall y^+ + calculated using the following equation:

$$u^+ = \frac{u}{u_*}, \quad y^+ = \frac{u_* y}{\nu} \tag{1}$$

The grid was adjusted several times on the basis of the value of y^+ of cells near the wall until the values of y^+ were in the range of limitation. After the first node near the wall, the mesh is refined to capture the high gradient of velocity, pressure and the amount of turbulence in the vicinity da wall. For each model of turbulence used, a study of the independence of the mesh was conducted to find the mesh which allows a compromise between the desired accuracy and the cost of the solution in time and memory.

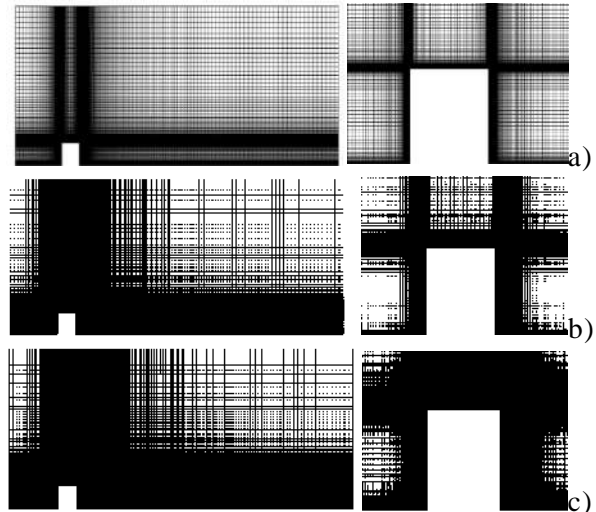


Figure 2. Mesh Distribution
a) : Coarse, b) : Fine, c) : Dense

Boundary conditions

At the inlet, located at $x / H = -2.7$, a fully developed velocity profile is imposed. This is directly extracted from the prior calculation of a ride height and length $7H$ $18H$, which is long enough to allow the velocity profile to grow, more so than an approximation of a profile turbulent velocity was imposed entry. Using a preliminary calculation for the entry requirements avoids use for each simulation a long dominates upstream of the geometry and reduces power and computing time required in obtaining a solution. Downstream, the condition is a static pressure output whose average value is relative $\bar{P}_{stat} = 0$ Pa.

This boundary condition does not allow the fluid to enter the area in case of recirculation in the output plane and, therefore, no speciation is to be made in relation to turbulent quantities in this map because they are then calculated by the solver. This type of boundary condition is quite appropriate since the output plane is located far downstream of geometry and no recirculation is expected at this position. To ensure the flow conditions at the entrance of the experience Cedval 1-3, the measured velocity profile was viewed as a condition of entry. U The velocity profiles, kinetic energy k and turbulent dissipation ϵ turbulent frequency ω . The measured velocity profile is given in Fig. 3. A good representation of the speed profile is given by the following expression:

$$u = ay^b \tag{2}$$

with : $a = e^B$ and $b = A$.

A and B are constants ($A = 3.00547, B = 1.69502$).

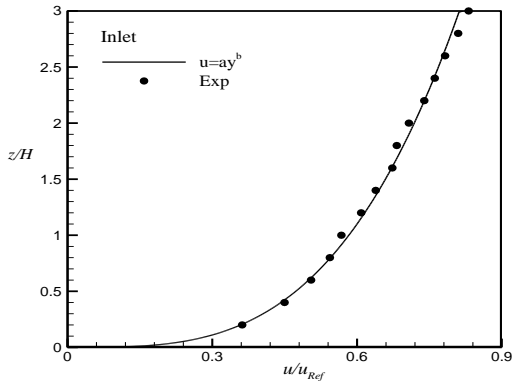


Figure 3. Velocity Profile in the Inlet

The turbulent kinetic energy k was calculated from the fluctuation in speed values measured in the wind tunnel Cedval 1-3. [13] It is given by the following equation:

$$k = \frac{1}{2}(\overline{u'^2} + \overline{w'^2}) \quad (3)$$

The dissipation of turbulent ε (square cubic meter per second) is defined by the following relationship:

$$\varepsilon = C_{\mu}^{3/4} \frac{k^{3/2}}{kz} \quad (4)$$

where z is the height of the channel, constant κ Von Karman $\kappa = 0.4$ and C_{μ} is a numerical constant $C_{\mu} = 0.09$.

Turbulent frequency is calculated as:

$$\omega = \frac{k}{\nu(\mu_t / \mu)} \quad (5)$$

where ν is the kinetic viscosity et (μ_t / μ) is the turbulente viscosity ratio, that is fixed at 10.

RESULTS

The convergence test analysis of the mesh should identify some situations that may affect the convergence of flow calculations around an obstacle. Nevertheless, despite the unfavorable discretizations, all simulations have been brought very regularly with RMS residuals of 1×10^{-8} for all the different equations. A typical convergence curve is shown in Fig. 4 to show the regularity of convergence. All

calculations are performed in steady state conditions (steady state).

For turbulence models that use wall functions (k- ε and RNG k- ε), the first cell is placed in the turbulent (log law region) right after the buffer layer that satisfies the condition. For turbulence models k- ω SST k- ω and the first cell is placed in the region of the viscous layer, very close to the wall to capture the viscous flow effects. Thus, the three meshes were generated with the same distance from the first node of the wall (the height of the cell near the wall) of $0.04H$ for the k- ε family and 4×10^{-4} for family k- ω . The evolution of y^+ near the wall obtained by the standard k- ε model and k- ω SST model for the considered meshes are presented graphically in Fig. 5. The sharp decline y^+ is expected due to the presence of the obstacle in the direction of flow.

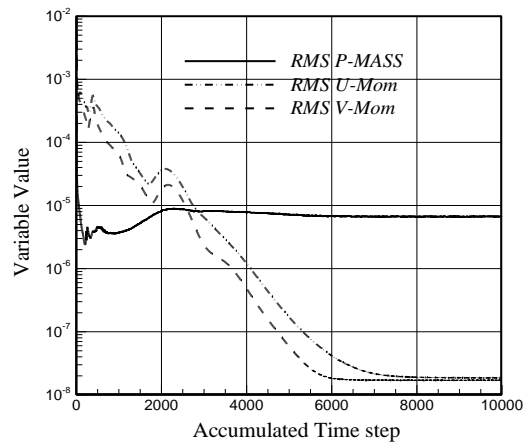


Figure 4. Convergence curves for the refined mesh and turbulence model SST k- ω .

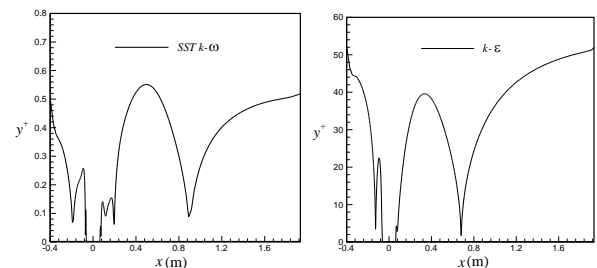


Figure 5. Y + profile for turbulence models

To assess the sensitivity of the results presented to the mesh, additional calculations on a progressive refined mesh were performed. In each case the mesh was obtained by multiplying the number of the points by a factor of 1.5, in the two directions x and z . The comparison between the results obtained with a coarse mesh, fine and dense, using the turbulence model SST k- ω , is shown in Fig. 6.

We can show that, in terms of average speed profiles, the convergence of the solution has been reached and the solution becomes independent of the mesh size. We can see that the coarse mesh gives results close to the experimental and faster in the simulation. To be more careful and more specific, the average mesh size was chosen (Refined) for simulations.

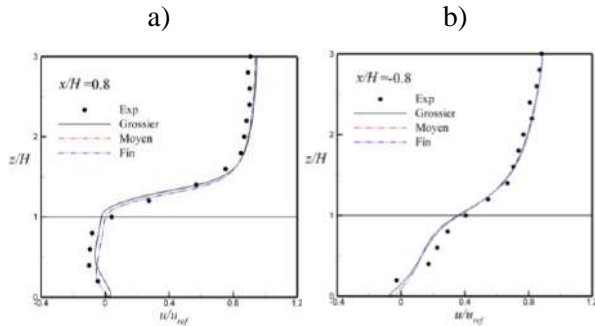


Figure 6. L'effet de maillage sur le profil de vitesse u pour modèle de turbulence SST $k-\omega$.

Fig. 7a shows the profiles of the two velocity components in different sections upstream, above and below the obstacle obtained with five turbulence models (standard $k-\epsilon$, realizable $k-\epsilon$, RNG $k-\epsilon$, standard $k-\omega$ and SST $k-\omega$) plot with the experimental data. One can show that, upstream of the obstacle, the velocity components u and w profiles obtained with the different turbulence models are comparable and they are close to those experimental.

The regions where the turbulence models start, we could not estimate the correct speed corresponding to the appearance of the recirculation vortex that forms on the front base of the obstacle. The rapid change of the high pressure gradient, caused by the stagnation point, prevents adequately capture the flow field in this region. Over the obstacle, the two models of turbulence RNG $k-\epsilon$ and $k-\omega$ SST predict more accurately the velocity profiles u w and especially near the wall. Downstream of the obstacle, a slight deviation from the experimental data was observed at about half the height of the obstacle. Above the roof of the obstacle, the turbulence models RNG $k-\epsilon$ and SST $k-\epsilon$ show a better agreement with the experimental data. For the velocity component w (Fig. 7b), it is only correctly predicted by both turbulence models RNG $k-\epsilon$ and $k-\omega$ SST, above the obstacle. As can be expected in this area in a small recirculation bubble leading vertical flow. Because of its small size, the speed w component is provided elsewhere around the area.

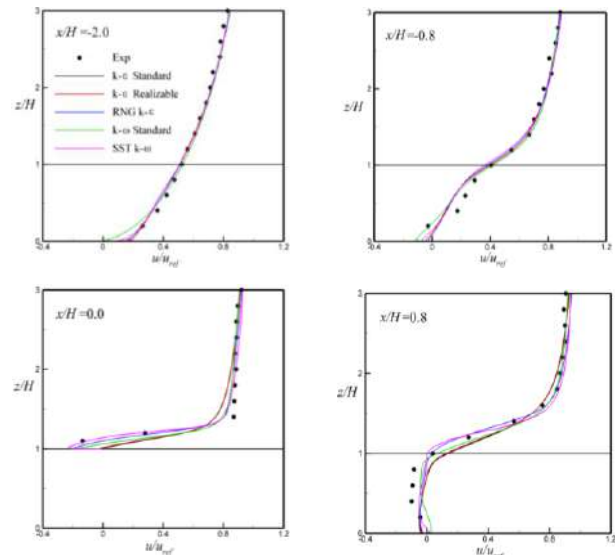


Figure 7a. Comparison of predicted velocity profiles u with the experimental Cedval 1-3.

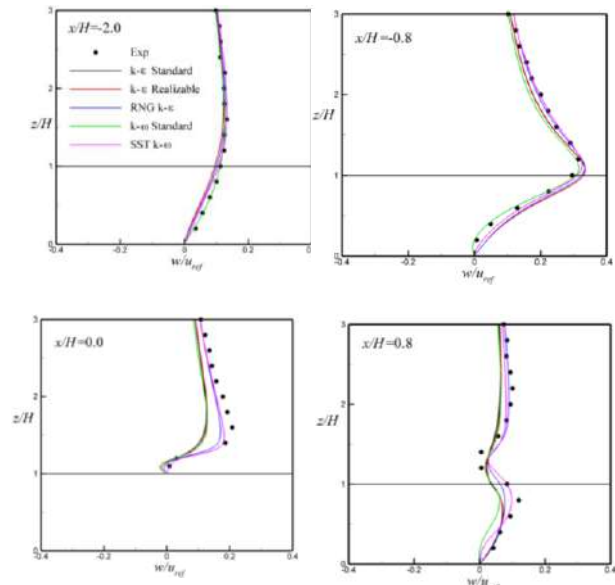


Figure 7b. Comparison of predicted velocity profiles w with the experimental Cedval 1-3

The streamlines and pressure distribution are used to visualize the flow structure in the field. The lines of the currents obtained by the five turbulence models are shown in Fig. 8. Generally, in terms of overall qualitative form, all models can predict the structure of the flow formed by the separation and recirculation connection. It can be shown with the five turbulence models, the general characteristics of the flow and the overall prediction modes front, top and back of the vortex is similar, although some differences are visible. The description of the common behavior is: close to the obstacle, the flow stagnates in front of the obstacle directly receiving

the impact of the flow of air. A part of the flow flows downward and forms a small vortex at the front base of the obstacle. The fluid flowing to the roof between the roof edge level forming a small recirculation bubble above the obstacle. Behind the barrier, which is dominated by a vortex in an arc in the wake region. For the evolution of the pressure, to satisfy the momentum equation, static pressure increases substantially in the front part of the recirculation zone and decreases above the obstacle. Fig. 8 shows that the point upstream vortex separation of the obstacle is under-provided for in the standard $k-\varepsilon$ models and achievable $k-\varepsilon$, the underestimation is more pronounced in the RNG $k-\varepsilon$ models. However, it is slightly overestimated by SST $k-\omega$. The prediction given by standard $k-\omega$ is different from experimental results. The stagnation point is predicted by the $k-\varepsilon$ standard models, achievable $k-\varepsilon$ and $k-\omega$ SST. The separation flow formed by the bubble above the obstacle, a connection of the flow is observed in the results obtained by the standard $k-\varepsilon$ model, realizable $k-\varepsilon$ and $k-\omega$ standard. However, in the experimental results as well as those predicted by turbulence models RNG $k-\varepsilon$ and SST $k-\omega$, this attachment is not obtained and the recirculation downstream extending over the block face. The same phenomenon is obtained by using the DNS turbulence model (Hattori and Nagano 2012). The results of turbulence models of the $k-\varepsilon$ family in a structure are very different than those of turbulence models of the $k-\omega$ family. Indeed, the decomposition of the recirculation zone downstream of the barrier formed by two vortices rotating against, primary and secondary, it is expected that by models of the $k-\omega$ family and gives a better agreement with experimental measurements. The presence of this secondary flow is consistent with the experimental measurement by Cedval A1-3 and it seems to be characteristic of the actual flow. The flow recirculation zone behind the obstacle is overestimated resulting in a greater attachment length thus underestimates the recovery flow models by RNG $k-\varepsilon$, $k-\omega$ and SST $k-\omega$. A similar underestimation flow recovery is obtained by Lakehal and Rodi [11] using different versions of model $k-\varepsilon$ and Ferziger and Shah [12] using the LES model.

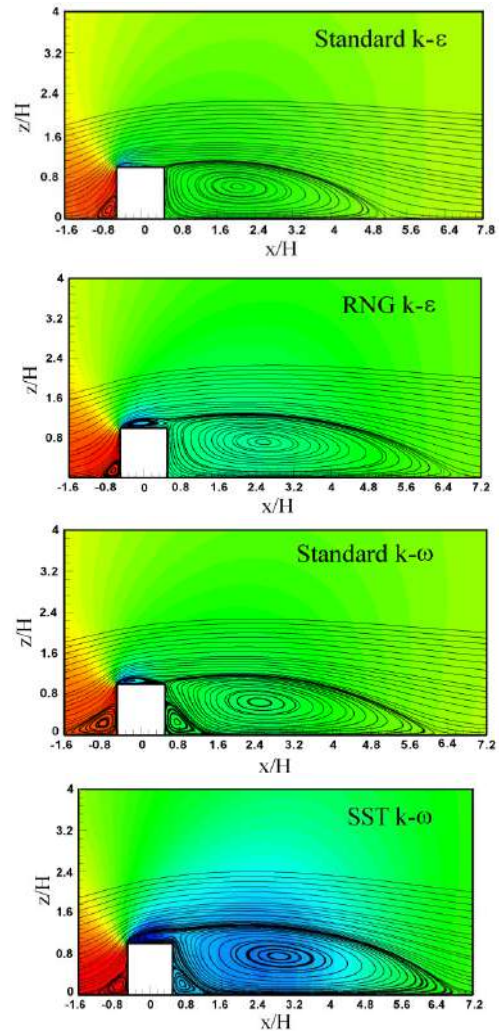


Figure 8. Comparison of streamlines in the plane of symmetry $z/H = 0$: $k-\varepsilon$ standard model, RNG $k-\varepsilon$ model, standard $k-\omega$ and $k-\omega$ SST (Shear Stress Transport).

Fig. 9a shows the velocity vector measured along the centerline of the xz plane of the blower Cedval 1-3, while Fig. 9b shows the velocity vector obtained by numerical simulation of the turbulence model using SST corresponding $k-\omega$. The structure of the flow obtained by SST $k-\omega$ compatible with the physics of turbulent flows obtained in the wind tunnel in the same conditions

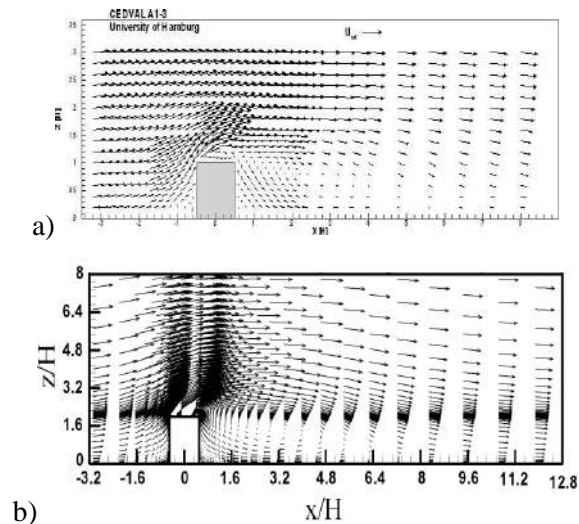


Figure 9. Comparison of velocity Fields a) Cedval A1-3 data, b) numerical simulation using SST k- ω model of turbulence.

CONCLUSIONS

In this work, a numerical simulation of the turbulent flow around a two-dimensional cubic obstacle (2D) in a channel with a value of Reynolds number $Re = 4 \times 10^4$ was performed. To validate the results of the numerical simulation by those in the experimental Cedval 1-3 [13], we considered five models of turbulence (model k- ϵ standard model k- ϵ Realizable model RNG k- ϵ model k- ω and k- ω SST model). Results are obtained for both cases many local Reynolds: 1) for low Reynolds number turbulence models $\sim y^+ 1$ and 2) for the turbulence models to many local Reynolds $y^+ > 30$.

The results generally indicate a consistent behavior on all model despite that there's an acceptable deviation from the set of experimental data Cedval 1-3. It was also shown that the results of turbulence models of the k- ϵ family are very different turbulence models of the k- ω family. Indeed, the decomposition of the recirculation zone downstream of the barrier consists of two vortices rotating against, primary and secondary. It is expected that the models of the k- ω family give better agreement with experimental measurements. The presence of this secondary flow is consistent with the

experimental measurement by Cedval A1-3 and it seems to be characteristic of the actual flow. It can be concluded that, although the turbulence model SST k- ω overestimates the connecting length of the flow, it may provide enough all recirculation zones, for example upstream zone, above and below the obstacle, better than all the other models.

REFERENCES

1. S. Murakami and A. Mochida, 3-D Numerical simulation of airflow around a cubic model by means of the k- ϵ model, *Journal of Wind Engineering and Industrial Aerodynamics*, 31, 283-303, 1988.
2. S. Vardoulakis, D. Reneta, K. Richards, D. Hamlyn, G. Camilleri, M. Weeks, J. F. Sini, R. Britter, C. Borrego, M. Schatzmann and N. Moussiopoulos, Numerical model inter-comparison for wind flow and turbulence around single-block buildings, *Environmental Modeling & Assessment*, Volume 16, Issue 2, pp 169-181, 2011.
3. S. Schmidt and F. Thiele, Comparison of numerical methods applied to the flow over wall-mounted cubes, *International Journal of Heat and Fluid Flow*, 23, 330–339, 2002.
4. Y. Tominaga, and D. Stathopoulos, Numerical simulation of dispersion around an isolated cubic building: comparison of various types of k- ϵ models, *Atmospheric Environment*, 43, 3200–3210, 2009.
5. G. Iaccarino and P. Durbin, Unsteady 3D RANS simulations using the v2-f model, center for turbulence Research, *Annual Research Briefs*, 263-269, 2000.
6. I. P. Castro, Measurements in shear layers separating from surface-mounted bluff bodies, *J. Wind Eng. And Ind. Aero*, vol. 7, 253-257, 1981.
7. X. Xiang Li, C. H. Liu and D. Y. C. Leung, Development of a k- ϵ model for the determination of air exchange rates for street canyons, *Atmospheric Environment*. 39, 7285–7296, 2005.
8. Y. Tominaga and T. Stathopoulos, CFD modeling of pollution dispersion in building array: evaluation of turbulent scalar flux modeling in RANS model using LES results. *J. Wind Eng. Ind. Aerodyn.* 104–106, 484–491, 2012.

-
9. J. B. R. Loureiro, A. T. P. Alho and A. P. S. Freire, The numerical computation of near-wall turbulent flow over a steep hill. *Journal of Wind Engineering and Industrial Aerodynamics*, 96, 540–561, 2008.
 10. M. Lateb, C. Massona, T. Stathopoulos and C. Bédard, Comparison of various types of $k-\epsilon$ models for pollutant emissions around a two-building configuration, *J. Wind Eng. Ind. Aerodyn.* 115, 9–21, 2013.
 11. D. Lakehal, W. Rodi, Calculation of the flow past a surface mounted cube with 2 layer turbulence models, *J. Wind Eng. Aerodyn.* 67-68, 66-78, 1997.
 12. K. B. Shah, J. H. Ferziger, A fluid mechanics view of wind engineering: Large eddy simulation of flow past a cubic obstacle. *Journal of Wind Engineering and Industrial Aerodynamics*, 67-68, 211-224, 1997.
 13. B. Leidl, Compilation of experimental data for validation of micro scale dispersion models, <http://www.mi.uni-hamburg.de/cedval/>, 2003.

CFD-BASED ENTROPY GENERATION ANALYSIS OF MULTIPLE JETS

M. Boussoufi^{1,*}, A. Sabeur-Bendehina¹, A. Ouadha¹, M. El Ganaoui²

¹Laboratoire des Sciences et Ingénierie Maritimes, Faculté de Génie Mécanique, Université des Sciences et de la Technologie Mohamed Boudiaf d'Oran, B.P. 1505 Oran El M'naouer, 31000 Oran, Algérie

²Institut Universitaire de Technologie de Longwy, Université Henri Poincaré, Nancy 1, 186 Rue de Lorraine, 54 400 Cosnes et Romain, France

*Corresponding Authors: boussoufi-mustapha@hotmail.fr

ABSTRACT

The present study aims to associate the second law of thermodynamics using the concept of entropy generation in order to study numerically the flow and the interaction of multiple jets. Several configurations of a single jet surrounded by equidistant 3, 5 and 9 circumferential jets have been studied. The turbulent incompressible Navier-Stokes equations have been solved numerically using the commercial CFD code Fluent. The standard $k-\epsilon$ model has been selected to assess the eddy viscosity. The domain has been reduced to a quarter of the geometry due to symmetry. Results for axial and radial velocities have been compared to experimental measurements from the literature. Furthermore, additional results involving entropy generation rate have been presented and discussed.

KEYWORDS CFD, multiple jets, entropy generation

NOMENCLATURE

C_p Specific heat at constant pressure (kJ/kg)

S Spacing between two nozzles axis

Re Reynolds number, $Re = \bar{U}D/\nu$

u_c Axial velocity component

U_e Velocity at nozzle exit

d Peripheral jet diameter

D Diameter of nozzle, m

L Dimensionless range, $L = x/D$

H Mean enthalpy

K turbulent kinetic

P pressure

U mean velocity

x, y Cartesian coordinates, m

$\dot{S}_{gen,vis}^m$ Volumetric entropy generation rate due to viscous dissipation, $W m^{-3} k^{-1}$

$\dot{S}_{gen,therm}^m$ Volumetric entropy generation rate due to heat transfer, $W m^{-3} k^{-1}$

\dot{S}_{gen} Total entropy generation, $W K^{-1}$

T Static temperature, k

T_e Temperature at nozzle exit

V volume, m^3

Greek letters

μ Dynamic viscosity, $kg m^{-1}s^{-1}$

μ_{eff} Effective Dynamic viscosity

μ_t Turbulent viscosity

λ Thermal conductivity of gas, $Wm^{-1} K^{-1}$

λ_{eff} Effective thermal conductivity, $Wm^{-1} K^{-1}$

ν Viscosity of the gas,

ρ Fluid density, $kg m^{-3}$

ϵ Dissipation rate

τ_{ij} Stress tensor

INTRODUCTION

Multiple jets are commonly used for several engineering processes. Nowadays, researchers normally associate Computational Fluid Dynamics (CFD) simulations to experimental tests in order to develop and optimize these processes. CFD is a powerful tool that can be used by engineers to better understand the flow features of multiple jets. Recently, due to computational resources development, CFD techniques have been applied to design and study several engineering processes. CFD simulations allow more flow details which are costly obtained using experimental tests. Furthermore, CFD can be useful in guiding processes development and experimental measurements.

Due to their practical applications, single and multiple jets have been extensively studied using experimental and numerical approaches. Ball et al. [1], in a review paper, traced the history and the

major advances in round jets. The review has included both experimental and computational studies carried out since 1926. However, most of the previous studies focused on the flow and jet interactions phenomena analysis using global and local parameters such as velocity, pressure and kinetic turbulent energy using different configurations of nozzles.

Alternatively, the flow of jets can be analysed using the concept of entropy generation analysis which is based on the second law of thermodynamics. Since its establishment by Bejan [2], entropy generation analysis has received a growing interest in optimization of thermal processes. Entropy generation is directly related to thermodynamic irreversibilities, which characterize any real process. Hence, methods based on entropy generation minimization can be considered as a robust tool in the optimization of thermal processes.

The entropy analysis concept applied to jets flows has received less attention. Among studies, Shuja et al. [3] have evaluated numerically the effect of turbulence models on the local entropy generation rate in an impinging jet. The results showed that the low-Reynolds number $k-\epsilon$ model predicts a smaller value of the volumetric entropy generation compared to the second order closure model RSM in the stagnation region. Cervante and Solorio [4] have investigated the entropy generation in a plane turbulent oscillating jet. They showed that the entropy generation increases along the flow direction and depend directly on the entrainment of the still ambient fluid. Shuja et al. [5] have studied a confined laminar swirling jet and entropy generation with different jet exit velocity profiles. They found that the swirling expands the jet in the radial direction and reduces the jet length in the axial direction. Hence, when the swirl velocity increases the entropy generation rate decreases. In a second paper Shuja et al. [6], the authors have examined the effects of the outer cone angle of the annular nozzle on the entropy generation in an impinging jet. They concluded that the volumetric entropy generation rate increases at the nozzle exit due to the velocity gradients of the flow emerging from the nozzle. Chu and Liu [7] have analyzed the entropy generation in a two-dimensional high-temperature confined jet flow. They observed that the total entropy generation number decreases when the jet Reynolds number and Boltzmann number increase. Gazzah and Belmabrouk [8] have studied numerically the directed co-flow effects on local entropy generation rate in turbulent

and heated round jets. The results obtained show that the directed co-flow with a positive angle enhances the mixing. Consequently, the local entropy generation rate increases progressively with the deviation angle.

The purpose of this study is to investigate the flow features and entropy generation of multiple jets. Computations have performed for several configurations of a single jet surrounded by equidistant 3, 5 and 9 circumferential jets.

MATHEMATICAL MODELING AND SIMULATION METHOD PHYSICAL DOMAIN

This study uses the case designed and studied by Manohar *et al.* [9]. The experiment measured centerline velocity for five jets. In addition to this configuration, computations have been carried out for single, 3 and 9 jets. Figure 1.a shows the arrangement of nozzles in the case of 9 jets. Due to symmetry, only a quarter of the geometry has been considered as illustrated in Figure 1.b

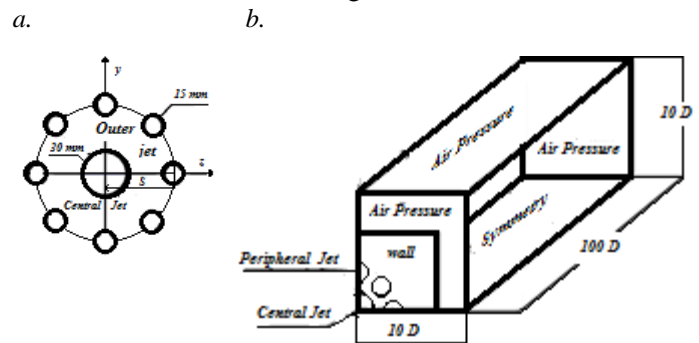


figure 1

schematic representation of the physical domain:
a. nozzles arrangement; b. computational domain

GOVERNING EQUATIONS AND BOUNDARY LAYERS

Air is the working fluid and it is considered as an incompressible ideal gas. The flow field is obtained by solving the three-dimensional steady state incompressible Reynolds Averaged Navier-Stokes equations for continuity, momentum and energy, given, in Cartesian coordinates, by

$$\frac{\partial(\rho U_i)}{\partial x_i} = 0 \quad (1)$$

$$\frac{\partial}{\partial x_j}(\rho U_j U_i) = -\frac{\partial P}{\partial x_i} + \frac{\partial}{\partial x_i} \left[\mu \left(\frac{\partial U_i}{\partial x_j} + \frac{\partial U_j}{\partial x_i} \right) - \rho \overline{u'_i u'_j} \right] \quad (2)$$

$$\rho C_p U_i \frac{\partial T}{\partial x_i} = \frac{\partial}{\partial x_i} \left[\lambda \frac{\partial T}{\partial x_i} - \rho C_p \overline{u'_i T'} \right] \quad (3)$$

Where U_i , T and P denote mean quantities for velocity, temperature and pressure, respectively. The average Reynolds stresses and turbulent heat fluxes, $-\rho \overline{u'_i u'_j}$ and $-\rho C_p \overline{u'_i T'}$, resulting from the averaging operation, are modeled using a turbulence model. τ_{ij} is the viscous stress tensor, μ the viscosity, C_p the heat capacity and λ is the thermal conductivity. To take into account the density variation versus temperature, the ideal gas law is used,

$$P = \rho r T \quad (4)$$

A turbulence model is needed to model the unknown Reynolds stresses through turbulent eddy viscosity, μ_t . Miltner et al. [10] have compared several RANS-turbulence models to predict turbulent free jets. They concluded that the simple and inexpensive Standard- k - ε model serves very well for the description of most effects in most regions of the considered free jets, hence the choice of the standard k - ε turbulence model [11] to compute the turbulent eddy viscosity:

$$\mu_t = C_\mu \rho \frac{k^2}{\varepsilon} \left(\frac{\partial u_i}{\partial x_j} + \frac{\partial u_j}{\partial x_i} \right) - \frac{2}{3} \mu \frac{\partial u_i}{\partial x_i} \delta_{ij} \quad (5)$$

Where C_μ is a constant, ρ is the fluid density, and k and ε are two additional independent variables, which need to be modeled and solved in a similar way as velocities.

Unlike all natural processes, jets flows are irreversible. The thermodynamic irreversibility in a process is characterized by its entropy generation. Entropy generation originates from viscous dissipation and heat transfer through finite temperature difference. Irreversibility predictions in jets flows can be obtained by solving the entropy generation equation. In absence of chemical reactions, the local rate of entropy generation per unit volume, \dot{S}_{gen}^m , can be expressed as

$$\dot{S}_{gen}^m = \dot{S}_{gen,vis}^m + \dot{S}_{gen,therm}^m \quad (6)$$

The first term on the right side of Eq. (6) represents the entropy generation due to fluid friction, while the

second term denotes the entropy generation by the heat transfer. Bejan [2] established analytical expressions for entropy generation through fluid flow and heat transfer which are expressed in three-dimensional cartesian coordinates as

$$\dot{S}_{gen,vis}^m = \frac{\mu_{eff}}{T} \left\{ \begin{aligned} & \left(\frac{\partial u}{\partial x} \right)^2 + \left(\frac{\partial v}{\partial y} \right)^2 + \left(\frac{\partial w}{\partial z} \right)^2 + \left(\frac{\partial u}{\partial z} + \frac{\partial w}{\partial x} \right)^2 \\ & + \left(\frac{\partial u}{\partial y} + \frac{\partial v}{\partial x} \right)^2 + \left(\frac{\partial v}{\partial z} + \frac{\partial w}{\partial y} \right)^2 \end{aligned} \right\} \quad (7)$$

$$\dot{S}_{gen,therm}^m = \frac{\lambda_{eff}}{T^2} \left\{ \left(\frac{\partial T}{\partial x} \right)^2 + \left(\frac{\partial T}{\partial y} \right)^2 + \left(\frac{\partial T}{\partial z} \right)^2 \right\} \quad (8)$$

Where k and μ are the thermal conductivity and dynamic viscosity of the fluid, respectively. The terms u and T denote the velocity and temperature of the fluid.

BOUNDARY CONDITIONS

The jets are generated with a velocity U_e and a temperature T_e . The outlet is specified as ambient pressure. A turbulence intensity of 5% is indicated at the inlet and outlet.

SOLUTION PROCEDURE

CFD codes, such as Fluent, provide wide computational flexibility and several options for turbulent incompressible flow simulations. Structured hexahedral cells have been used to mesh the computational domain. The mesh is refined in the region closed to the nozzles. Fluent solves the three-dimensional Navier-Stokes equations using a control volume approach for flow, pressure, temperature and turbulence. Reynolds stress terms are modeled using one of several turbulence models available in the code. The pressure-based implicit solver, has been adopted. SIMPLE Algorithm is used pressure – velocity coupling and a second order upwind scheme has been used to discretize the convective terms. The solution is considered converged when all the residuals are lower than 10^{-5} .

RESULTS AND DISCUSSIONS

Numerical results have obtained for single, three, five and nine jets. The simulation results are presented as follows; first, a mesh study has been carried out to guarantee a grid independent solution, then the model predictions have been compared with

experimental data. In addition, the velocity and temperature profiles have been plotted for the configurations studied. Finally, the entropy generation has been presented as profiles and contours.

MESH STUDY

The mesh quality and resolution play a significant role in the numerical solution accuracy and stability. Thus, a mesh study has been carried out to guarantee a grid independent solution. The latter is assessed by the analysis of three different mesh sizes of 300,000, 450,000 and 1,000,000 cell volumes for the case of five jets configuration. The three meshes have been compared quantitatively by considering numerical uncertainties in predicting the centreline velocity as illustrated in Figure 2. It is clear that the centreline velocity values are almost identical. Hence, computations have been performed for a mesh containing 450,000 control volume cells.

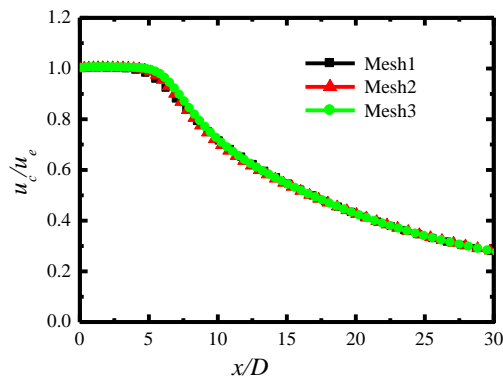


Figure 2

Influence grid on the centerline velocity variation in a five jets configuration

NUMERICAL MODEL VALIDATION

The results obtained using the computational model have been compared to the experimental results published by Manohar et al. (2004). Experiments have been performed for two configurations representing single jet and five jets. In Figure 3, the comparison between the calculated and measured centerline velocity curves for single jet and five jets is shown. For single jet, the overall trend of the centerline velocity curve is matched, but the

computed values are overpredicted mainly for x/D greater than 5. However, for 5 jets, it can be seen that the general behavior of the calculated centerline velocity curve follows quite well the experimental one as shown in Figure 3.b.

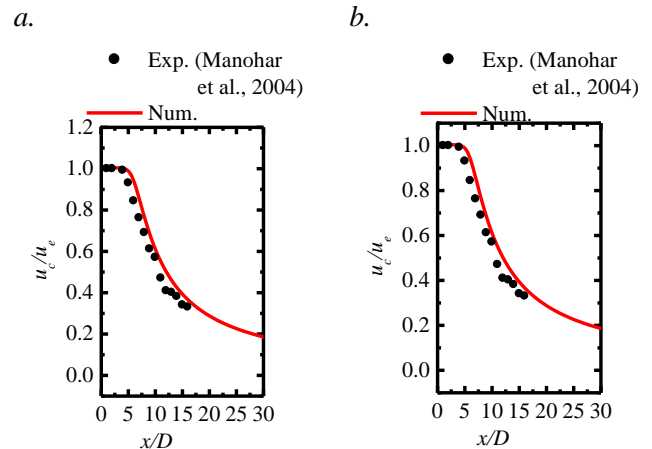


Figure 3

Comparison of numerical and experimental centerline velocities: *a.* Single jet; *b.* 5 jets

For five jets, the computed mean radial velocities have been compared to experimental measurements for axial positions x/D equal to 4, 7, 9, 12, 14 and 16 as illustrated in Figure 4. A good agreement is noted for all data.

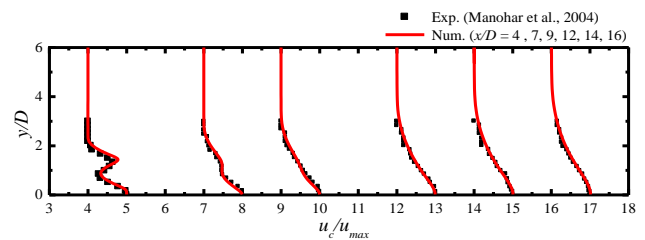


Figure 4

Comparison of mean velocities for five jets configuration ($S/D = 1.5$)

CENTERLINE VELOCITY PROFILES

Figure 5 illustrates the dimensionless centerline velocity as function of the dimensionless length of jets for single, 3, 5 and 9 jets for a temperature of 500 K. The centerline velocity is related to the inlet velocity U_e , while the jet length is related to the nozzle diameter D . For all cases, the centerline velocity profile is divided into two regions: a

constant velocity region for x/D lower than 6 and decreasing region for x/D greater than 6. In the first region, the centerline velocity is equal to the inlet velocity for all configurations. However, in the second region, the increase of the number of nozzles increases the centerline velocity.

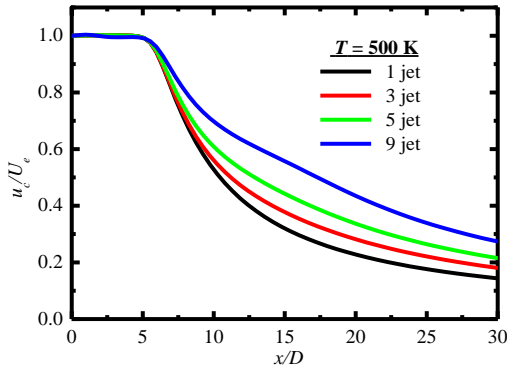


Figure 5
Centerline velocity as function of jet length

To better illustrate the variation of the temperature gradients along the jet, the evolution of the temperature along the the jet is plotted in Figure 6. It is shown that the large temperature gradients occur between $x/D = 6$ and 12. The increase of the number of nozzles considerably reduces the temperature gradients

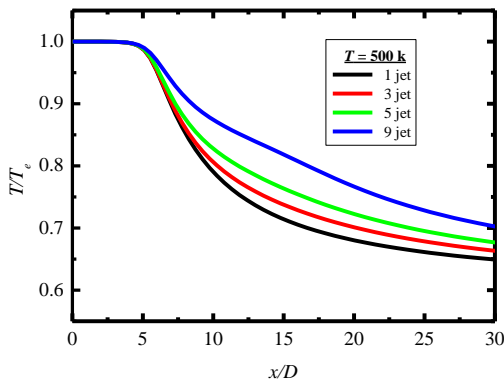


Figure 6
Temperature as function of jet length

ENTROPY GENERATION

The profiles of axial entropy generation rate by volume unit, for single, 3, 5 and 9 jets, are given in Figure 7 for an inlet temperature fixed to 500 K. For x/D lower than 5, the velocity gradients are negligibles involving a negligible entropy generation rate. However, for x/D equal to 7, the entropy generation presents a maximum value. This value decreases by increasing the the number of nozzles. Afeter the pic values, the entropy generation decreases. For x/D greater than 15, the entropy generation remains constant for all configurations.

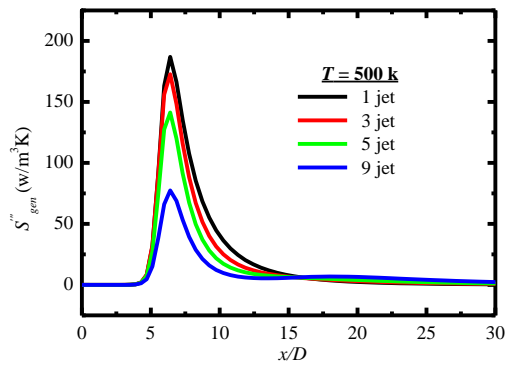


Figure 6
Entropy generation rate as function of jet length

Table 1 exhibits the total entropy generation and its visous and heating parts for single, 3, 5 and 9 jets. The total values are obtained by integrating the local entropy generation vaules on the computational domain. The large temperature gradients contribute significantly in the increase of the entropy generation due to heat transfer. The last column represents the Bejan number which compares the dominance of entropy generation due to heat transfer to that due to fluid friction.

Table 1

Compares the four configuration jets with the asymptotic entropy generation rate at different temperature

	T (K)	$\dot{S}_{gen} (W.K^{-1})$	$\dot{S}_{gen,vis} (W.K^{-1})$	$\dot{S}_{gen,therm} (W.K^{-1})$	Bejan number
Single Jet	298	0.2925	0.2925	0	
	320	0.4015	0.2928	0.1087	0.27
	500	4.4783	0.1451	4.3332	0,9676
	1000	15.7560	0.0544	15.7016	0.9965
3 Jets	298				
	320	0.5683	0.4048	0.1636	0.2878
	500	6.7383	0.2210	6.5172	0.9670
	1000	23.7065	0.0831	23.6234	0.9965
5 Jets	298	0.5996	0.5996		
	320	0.7640	0.5452	0.2187	0.2862
	500	9.0092	0.2981	8.7112	0.967
	1000	31.5844	0.1120	31.4725	0.9964
9 Jets	298				
	320	1.1296	0.8081	0.3215	0.2846
	500	13.1883	0.4388	12.7495	0.9667
	1000	45.8850	0.1600	45.7249	0.9965

CONCLUSIONS

in the present study, the second law of thermodynamics using the concept of entropy generation has been used to study numerically the flow and the interaction of multiple jets. Several configurations of a single jet surrounded by equidistant 3, 5 and 9 circumferential jets have been studied. The main conclusions are listed below:

- The CFD model can properly predict the flow patterns in multiple jets. The agreement between the CFD predictions and the experimental results is very good. The discrepancies are less than 5% in most regions.
- Most irreversibilities are due to heat transfer since the entropy rate due to heat transfer dominates.

ACKNOWLEDGMENTS

The first author acknowledges his training period in the University of Lorraine (IUT of Longwy) permitting the achievement of the present work

REFERENCES

- [1] Ball, C.G., Fellouah, H., Pollard, A., 2012, The flow field in turbulent round free jets, *Progress Aerospace Sciences*, 50, pp. 1-26.
- [2] Bejan A. 1982, Entropy generation through heat and fluid flow. New York: Wiley.
- [3] Shuja SZ, Yilbas BS, Budair MO. 2001, Local entropy generation in an impingement jet: minimum entropy concept evaluating various turbulence models. *Comput Methods Appl Eng*; 190:3623–44.
- [4] J. Cervante et F.Solorio. 2002, Entropy generation in a plane turbulent oscillating jet, *International Journal of Heat and Mass Transfer*, vol 45, pp 3125-3129.
- [5] Shuja SZ, Yilbas BS, Budair MO. 2002, Investigation into a confined laminar swirling jet and entropy production. *Int J Numer Meth Heat Fluid Flow*; 12:870–87.
- [6] Shuja SZ, Yilbas BS, Budair MO. 2007, Entropy generation due to jet impingement on a surface. Effect of annular nozzle outer angle. *Int J Numer Methods Heat Fluid Flow*; 17:677–91.
- [7] Chu SX, Liu LH. 2009, Entropy generation analysis of two-dimensional hightemperature confined jet. *Int J Therm Sci*; 48:998–1006.
- [8] M.H. Gazzah et H. Belmabrouk, 2014, Local entropy generation in co flowing turbulent

jets with variable density, *International Journal of Numerical Methods for Heat and Fluid*, Vol 24, pp 1679 – 1695.

- [9] Manohar, and al. 2004, A Numerical and experimental investigation of the interactions between a non uniform planar array of incompressible free jets, *Int. J. Numer. Meth. Fluids*, 44:431-446.
- [10] Miltner and al. 2015, have compared several RANS-turbulence models to predict turbulent

free jets. They concluded that the simple and inexpensive Standard-k- ϵ model serves very well for the description of most effects in most regions of the considered free jets.

- [11] Launder and Spalding. 1974, the Numerical Computation of Turbulent Flows. *Computer Methods in Applied Mechanics and Engineering*, 3:269-289.

A GEOMETRICAL APPROACH FOR SIMULATING STATIC CONTACT ANGLES IN MULTIPHASE FLOWS WITH A LATTICE BOLTZMANN METHOD

Sébastien Leclaire^{1,2,3,*}, Kamilia Abahri¹, Rafik Belarbi², Jonas Latt^{3,4},
Bastien Chopard³ and Rachid Bennacer¹

¹École Normale Supérieure de Cachan, LMT, 61 avenue du Président Wilson, 94230 Cachan, France

²LaSIE UMR 7356, Université de La Rochelle, A. Michel Crépeau 17042 cedex 1, La Rochelle, France

³Department of Computer Science, University of Geneva, 7 route de Drize, 1227 Carouge, Switzerland

⁴FlowKit Sàrl, Route d'Oron 2, 1010 Lausanne, Switzerland

*Corresponding author: Email: sebastien.leclaire@etu.unige.ch

ABSTRACT

Nowadays, computational fluid dynamics (CFD) is frequently used in many engineering design processes as it may give insights that could not be accessible otherwise. However, a great variety of complex flows, and in particular multiphase flow, remain difficult to model through computer simulations. While the lattice Boltzmann method has shown to be well-adapted for multiphase flow simulations, fluid-structure interaction at a solid wall appears to be difficult to achieve with this method. All numerical methods need to respect at the solid wall Young's law for static contact angles. The standard approach to model contact angles in the lattice Boltzmann method is to impose fictitious densities in the solid lattice sites. This approach is shown to be clearly deficient. To improve upon this approach, we propose a geometrical wetting boundary condition that is similar to Dirichlet boundary conditions.

KEYWORDS: *Computational fluid dynamics, lattice Boltzmann method, multiphase flow, wetting boundary condition, static contact angle.*

NOMENCLATURE

θ_i	Angle of the velocity vectors
\mathbf{c}_i	Velocity vectors
c	Velocity of the distribution functions
Δx	Lattice spacing
Δt	Time step
N_i^k	Distribution functions
Ω^k	Collision operator.
F	Gradient
F^*	Predicted gradient
\mathbf{n}_{b1}	Theoretical normal boundary vector 1
\mathbf{n}_{b2}	Theoretical normal boundary vector 2
\mathbf{n}^*	Normalized predicted gradient
\mathbf{n}_b	Interpolated normal boundary vector
D_{b1}	Euclidian distance $ \mathbf{n}^* - \mathbf{n}_{b1} $
D_{b2}	Euclidian distance $ \mathbf{n}^* - \mathbf{n}_{b2} $
r	Interpolation weight
\mathbf{n}^{**}	Normalized corrected gradient
F^{***}	Corrected gradient

INTRODUCTION

The lattice Boltzmann method for multiphase flows may be classified in various categories, but there are three types of methods that are used most frequently: the color-gradient approach from Gunstensen et al. [1], the pseudo-potential approach from Shan and Chen [2], and the free-energy approach from Swift et al. [3]. A book about multiphase flow modeling with the lattice Boltzmann method has been recently published by Huang et al. [4]. It gives a good overview of the current state of the art and also encompasses most of the available lattice Boltzmann model. It is a good guide for newcomers that are interest in that research field.

In multiphase flow modeling, the imposition of wetting boundary conditions has always been a real challenge from a numerical point of view. The objective of wetting boundary conditions is to provide the user of the multiphase flow solver with means of imposing an exact contact angle, and

consequently to avoid an undefined behavior of the flow solver near a solid boundary. Among other reasons, such a condition is difficult to model because the contact line at the wall leads to a numerical singularity. Therefore, and given that laboratory experiments show that the contact angle are very sensitive to the properties of the solid wall [5], very special care needs to be given to the wetting boundary condition.

The standard approach in the lattice Boltzmann method consists of imposing fictitious densities on solid lattice sites. Those fictitious densities are usually implemented using ghost lattice sites which form a belt around the lattice sites that are considered pure fluid. For example, in presence of two fluid components denoted by the colors red and blue, a solid wall can become wetting for the red fluid if the ghost sites contain more a higher red than blue fluid density. Up to a certain extent, this technique produces the desired results, because the fictitious densities at the ghost lattice sites impact the computation of density gradients near solid wall, and in this way emulate the behavior of different types of wetting fluids near a solid boundary.

However, although this standard approach is very simple to implement, it suffer from a great deal of numerical artifacts. Indeed, near the contact line, fictitious mass transfer can occur along the boundary and spoil the numerical results [6,7]. In this work, we show how it is possible to alleviate these numerical difficulties by implementing the wetting boundary condition following a geometrical approach [6]. The idea consists of directly imposing the contact angle at the boundaries in much the same way Dirichlet boundary conditions are generally imposed.

NUMERICAL METHODS

In this work, an appropriate modeling of static contact angles at a solid boundary in a multiphase flow simulation is achieved with the help of two methodologies: a color-gradient based multiphase lattice Boltzmann method for fluid-fluid interface interactions and a suitable wetting boundary condition near the solid boundary to impose the desired contact angle at the contact line.

Multiphase Lattice Boltzmann Method:

The full description of the numerical method is available in Ref. [6]. We only provide a short

summary, as this conference paper focuses on the wetting boundary condition.

The present two-phase lattice Boltzmann model uses two sets of distribution functions moving on a D2Q9 lattice, one set per fluid phase. The velocity vectors \mathbf{c}_i are defined with respect to the discrete angles $\theta_i = \pi(4-i)/4$:

$\mathbf{c}_i = [0,0]$	$i=1$
$\mathbf{c}_i = [\sin(\theta_i), \cos(\theta_i)]c$	$i=2,4,6,8$
$\mathbf{c}_i = [\sin(\theta_i), \cos(\theta_i)]c\sqrt{2}$	$i=3,5,7,9$

where $c=\Delta x/\Delta t$, Δx is the lattice spacing and Δt is the time step.

The distribution functions are denoted by $N_i^k(\mathbf{x}, t)$, where the superscript k for identifies the "color" of the fluids. For example, the superscript k can adopt the value $k=r$ for the red fluid and the value $k=b$ for the blue fluid. The color-blind distribution function $N_i(\mathbf{x}, t) = N_i^r(\mathbf{x}, t) + N_i^b(\mathbf{x}, t)$ is used to represent the sum of the colored distribution functions. The algorithm follows the following evolution equation:

$$\begin{aligned} |N^k(\mathbf{x} + \mathbf{c}_i \Delta t, t + \Delta t)\rangle \\ = |N^k(\mathbf{x}, t)\rangle + \Omega^k(|N^k(\mathbf{x}, t)\rangle) \end{aligned}$$

where the symbol $|*\rangle$ uses the "bra" Dirac notation in velocity space. The collision operator Ω^k combines three operators, which are explicated as follows:

- 1) Single-phase collision operator Ω_1^k :
 $|N^k(\mathbf{x}, t^*)\rangle = \Omega_1^k(|N^k(\mathbf{x}, t)\rangle)$
- 2) Multiphase collision operator (perturbation) Ω_2^k :
 $|N^k(\mathbf{x}, t^{**})\rangle = \Omega_2^k(|N^k(\mathbf{x}, t^*)\rangle)$
- 3) Multiphase collision operator (recoloring) Ω_3^k :
 $|N^k(\mathbf{x}, t^{***})\rangle = \Omega_3^k(|N^k(\mathbf{x}, t^{**})\rangle)$
- 4) Streaming operator:
 $|N^k(\mathbf{x} + \mathbf{c}_i \Delta t, t + \Delta t)\rangle = |N^k(\mathbf{x}, t^{***})\rangle$

The details of the sub-operators Ω_1^k , Ω_2^k and Ω_3^k are given in Ref. [6]. The wetting boundary condition only influences the multiphase operators Ω_2^k and Ω_3^k .

Geometrical Wetting Boundary Condition:

To describe the numerical method, we refer to groups of lattice sites and boundary nodes shown in Figure (1).

- 3) Using the fact that we know \mathbf{n}_b on the *large square* lattice sites and that we know exactly \mathbf{n}^* on the *large circle* lattice sites. A linear least-square interpolation using these points is performed on each component x and y to correct \mathbf{n}^* at the *large diamond* lattice site.

Since this least-square interpolation does not guarantee a vector of unit norm, this vector has to be normalized, to obtain the unitary vector \mathbf{n}^{**} .

- 4) The corrected gradient F^{***} is finally given by:

$$F^{***} = F^* / \mathbf{n}^{**}$$

Overall, this methodology can be used to impose the contact angle at the contact line. Indeed, the wetting boundary condition can modify the density gradients near the solid boundary and take into account the contact angle which is prescribed at the solid boundary nodes.

RESULTS AND DISCUSSION

This geometrical wetting boundary condition has first been tested on the lattice Boltzmann model in Ref. [6]. Figure (3) shows visually how the model behaves with the standard approach compared to the geometrical approach.

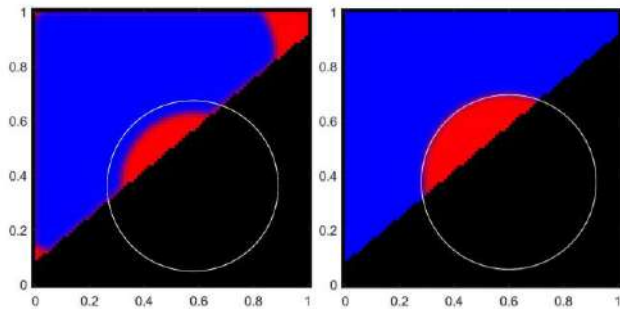


Figure 3: Standard approach (left) and geometrical approach (right). The solid boundary is tilted by an angle of 40 degrees while the fluid-solid contact angle is 120 degrees. The analytical solution is given by the white circle.

It is this clear that the standard approach has numerical deficiencies, while the geometrical approach is able to capture the analytical solution. Indeed, in the standard approach there is a “leak” of fluid along the boundary. Although his “leak”, could

in principle be associated with a thin physical boundary layer, it has, in the present case, no valid physical interpretation, as it occurs in a completely unpredictable manner. The geometrical approach leads to more expected results if the solid wall is modeled as an “ideal” boundary. Note that the standard approach never reaches a steady state (up to the time we simulate) because the leak is continuous in time and continue until the entire droplet mass has been moved away from the analytical white circle

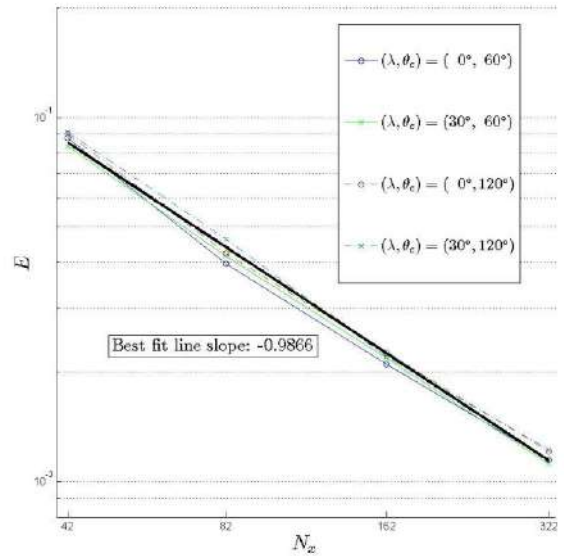


Figure 4: Error between the analytical and numerical solutions as a function of the lattice size, different contact angles and tilt inclination angles for the boundary. The numerical approach is first-order accurate.

Figure (4) shows the error between the analytical solution and the numerical solution at steady state for various lattice sizes, different contact angles and tilt inclination angles for the boundary. The error is decreasing with lattice refinement, and this is expected. The overall lattice Boltzmann method coupled with the geometrical wetting boundary condition is also first order accurate. Indeed, the best fit line slope of the logarithm of the error versus the number of lattice sites is equal to -0.9866. This clearly indicates first-order accuracy, as perfect first-order accuracy would yield a slope equal to -1.

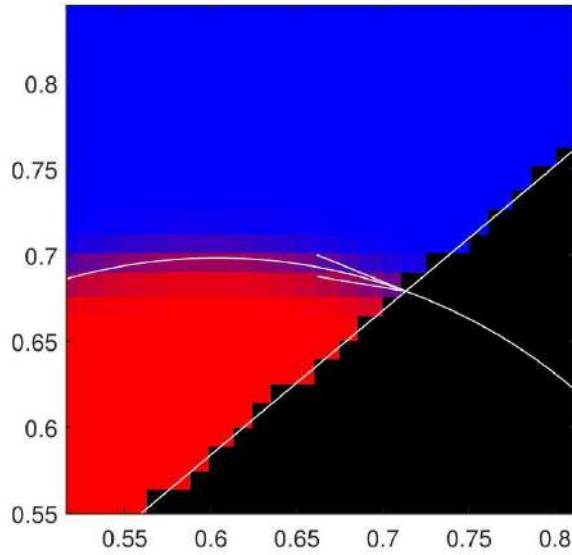


Figure 5: Zoom of Figure (3) with the geometrical approach. A visual representation of the error estimate with $N_x=82$ is shown with white lines.

Figure (5) shows an error estimate with the geometrical approach when fluid-solid contact angle is 120 degrees and when the boundary is tilted by an angle of 40 degrees. This estimation indicates an error of ± 6 degrees. Overall, this would give approximately an error of approximately ± 1.5 degrees on the finest grid. This level of accuracy is satisfactory.

PRELIMINARY RESULTS IN 3D

The idea of imposing the contact angle at the solid boundary is similar for 3D flows. We do not elaborate the detailed methodology here, as it is slightly different from the 2D one. Nevertheless, some preliminary results are encouraging and also presented here. Figure (6) shows a capillary fall between two plates executed with a three-dimensional multiphase lattice Boltzmann solver. The bottom fluid is the non-wetting fluid. The white horizontal lines show the theoretical heights predicted by Jurin's law [8]. The agreement between the theory and the numerical results are satisfactory.

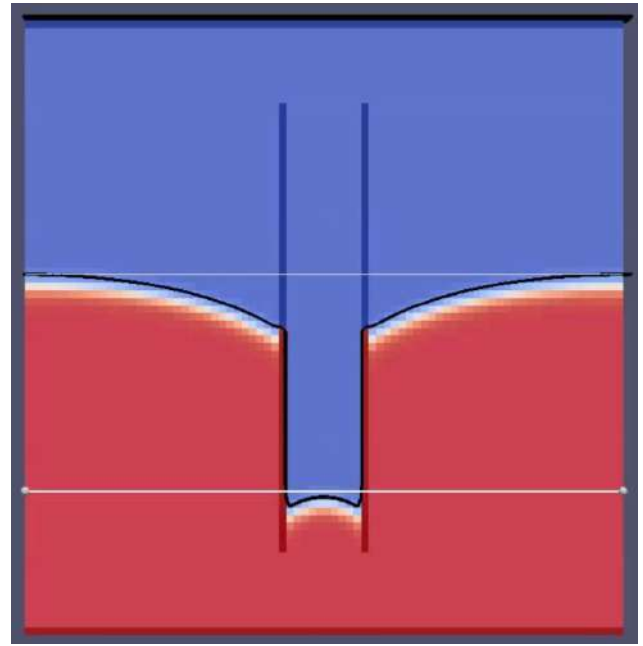


Figure 6: Capillary fall between two parallel plates. The analytical positions of the heights predicted by Jurin's law are given by the white horizontal lines.

Figure (7) shows a three-dimensional capillary rise inside a cylindrical tube as predicted by Jurin's law if the bottom fluid is the wetting fluid. The solid geometry and the lattice Boltzmann solver are fully three-dimensional. The interface deformation outside the tube is also clearly visible. More investigations of these types of 3D flows are still needed, but the results are encouraging.

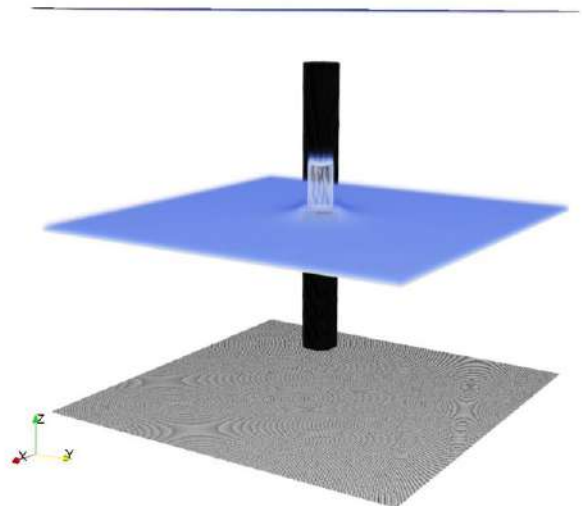


Figure 7: Three-dimensional capillary rise inside a cylindrical tube.

CONCLUSIONS

We propose a new geometrical wetting boundary condition for the lattice Boltzmann method. The proposed method is showed to avoid numerical difficulties occurring in the standard approach and also to be numerically compatible with analytical solutions. Overall, this a step forward in the numerical modeling of multiphase flows.

ACKNOWLEDGMENTS

Sébastien Leclaire thanks the FRQNT “Fonds de recherche du Québec – Nature et technologies” for financial support. This work has been partially supported by French Research National Agency (ANR) through "Habitat intelligent et solaire photo voltaïque Program" (project HYGRO-BAT n°ANR-10-HABISOL-005).

REFERENCES

1. Gunstensen, A. K., Rothman, D. H., Zaleski, S., & Zanetti, G. (1991). Lattice Boltzmann model of immiscible fluids. *Physical Review A*, 43(8), 4320–4327. doi:10.1103/PhysRevA.43.4320
2. Shan, X., & Chen, H. (1993). Lattice Boltzmann model for simulating flows with multiple phases and components. *Physical Review E*, 47(3), 1815–1820. doi:10.1103/PhysRevE.47.1815
3. Swift, M. R., Orlandini, E., Osborn, W. R., & Yeomans, J. M. (1996). Lattice Boltzmann simulations of liquid-gas and binary fluid systems. *Physical Review E*, 54(5), 5041–5052.
4. Huang, H., Sukop, M., & Lu, X. (2015). *Multiphase Lattice Boltzmann Methods: Theory and Application* (p. 392). Wiley-Blackwell.
5. Grate, J. W., Dehoff, K. J., Warner, M. G., Pittman, J. W., Wietsma, T. W., Zhang, C., & Oostrom, M. (2012). Correlation of oil-water and air-water contact angles of diverse silanized surfaces and relationship to fluid interfacial tensions. *Langmuir : The ACS Journal of Surfaces and Colloids*, 28(18), 7182–8. doi:10.1021/la204322k
6. Leclaire, S., Abahri, K., Belarbi, R., & Bennacer, R. (2016). Modeling of static contact angles with curved boundaries using a multiphase lattice Boltzmann method with variable density and viscosity ratios. *International journal for numerical methods in fluids*. (In press)
7. Otomo, H., Fan, H., Li, Y., Dressler, M., Staroselsky, I., Zhang, R., & Chen, H. (2016). Studies of accurate multi-component lattice Boltzmann models on benchmark cases required for engineering applications. Fluid Dynamics. Retrieved from <http://arxiv.org/abs/1601.01237>
8. https://en.wikipedia.org/wiki/Jurin%27s_law

NUMERICAL STUDY OF HEAT TRANSFER AND FLOW CHARACTERISTICS OF AIR JET IN A SEMI-CONFINED CAVITY

Tovondrainy NORBERT*, Stéphane ABIDE**, Belkacem ZEGHMATI**,
Chrysostôme RAMINOSOA*, Michel Aimé RANDRIAZANAMPARANY *

* : Univ. Antsirananana, Laboratoire de Thermique Appliquée (LTA), B.P.O, 201 Antsirananana

** : Univ. Perpignan via Domitia, Laboratoire de MATHématiques et PhySique (LA.M. P.S.),
EA4217, F66860 Perpignan Cedex

*norbertovondrainy@gmail.com, stephane.abide@univ-perp.fr, zeghmati@univ-perp.fr,
chrysostome.raminosa@gmail.com, michel.randrianamparany@gmail.com*

ABSTRACT

A numerical study of heat transfer and flow characteristics of an air jet 2D turbulent and unsteady in a semi-confined cavity is presented. The bottom wall is divided into two thermal zones while the other walls are adiabatic: the wall part of the confined zone, located between the impingement jet and the vertical wall is maintained at a temperature T_f while the other wall part is a constant temperature $T_c > T_f$. T_c is equals to the air jet temperature. Transfers are described by RANS and the energy equation; the turbulence model is the first order SST $k-\omega$ model (Standard and Shear-Stress Transport). Simulations have been performed with the FLUENT software. Computational are conducted for Reynolds number ranging from 10000 to 20000 based on jet width, jet to target plate distance, h/e , from 4 to 12 (h being the impact height and e the nozzle size). Results reveal that, whatever the value of the Reynolds number, the air jet separates the cavity into two areas. Concerning the heat transfer, results show notably that, for whatever the value of each Reynolds number and for impact height considered in this study, the most intensive thermal exchanges are situated in the vicinity of the impact area of the jet on the bottom wall.

KEYWORDS: Turbulent plane jet, Nusselt number, turbulence modeling.

NOMENCLATURE

C_f - skin friction coefficient
 e - slot nozzle width, [m]
 H - impingement distance, [m]
 k - kinetic energy of turbulent, [m^2s^{-2}]
 L - length of the impingement plate, [m]
 Nu - local Nusselt number, [-]
 P_k - production of turbulent kinetic energy, [$kg \cdot m^{-1} \cdot s^{-3}$]
 Re - Reynolds number, [-]
 T - temperature, [K]
 \bar{u}_j - mean velocity components, [ms^{-1}]
 V_{in} - inlet jet velocity, [ms^{-1}]
 x_j - coordinate directions [m]

Greek symbols

α, β, β^* turbulent model constants
 μ - dynamic viscosity of fluid, [$kg \cdot m^{-1} \cdot s^{-1}$]
 ν - kinetic viscosity, [m^2s^{-1}]
 ν_t - turbulent kinetic viscosity, [m^2s^{-1}]
 ρ - fluid density, [$kg \cdot m^{-3}$]
 σ_k - turbulent Prandtl number for k , [-]
 σ_ω - turbulent Prandtl number for ω , [-]

ω - specific dissipation rate, [s^{-1}]

τ_w - shear stress ($N \cdot m^{-2}$)

Subscripts

c - cold temperature
 h - warm temperature
 in - inlet

1. INTRODUCTION

The study of the jets is of particular importance for heat transfer and mass phenomena in turbulent flows because of their multiple industrial applications. Thus, impinging jets are used in heating or drying processes for production of paper, textiles, glass, annealing of metal sheets, cooling of electronic components and turbine blades. Impinging jets can be also used to reduce the heat and mass transfer across the open door in the tertiary or industrial premises, while enabling the passage of people, vehicles and other transportation. In other application areas, they behave like a light curtain limiting the propagation of heat, smoked and toxic gases during a fire.

Impinging jets present a normal straining due to the nearly irrotational behavior of the flow in the stagnation region [1,2]. Therefore, a correct prediction of heat transfer in impinging situations is of great importance in many industrial applications. Moreover, an accurate prediction of this quantity requires a good prediction and a detailed understanding of the characteristics and the structure of the impinging jet flow. That's why many experimental [3-9] and numerical [10-15] works are devoted to the study of impinging jets. Generally, computations of impinging jet flow are performed either to gain fundamental insight of the structures of the flow or to validate a computational model, which could be further useful for designing complex jet, using different turbulence models. Simulations using Reynolds averaged Navier-Stokes (RANS) have been widely used to predict wall-bounded flows due to its simplicity and, to some extent, of its capability of prediction. Numerical studies using these models have been published by Heyerichs and Pollard [10], who examined an impinging slot jet at a Reynolds number of 10000. Wang and Mujumdar [12] analyzed the effectiveness of five low Reynolds RANS models for two Reynolds numbers of 5200 and 10400 and two dimensionless jet-to-surface spacing of 2.6 and 6. Zuckerman and Lior [13] compared the accuracy in predicting Nusselt number distribution of impinging flows by different RANS based turbulence models and concluded that of all turbulence models, the SST k- ω model is the best in predicting both second peaks in the Nusselt number and the Nusselt number profile. Kubacki and Dick [14] have previously shown that the latest version of the k- ω model, with the inclusion of the stress limiter term in the definition of the eddy viscosity and the cross diffusion term in the equation of specific dissipation rate, can accurately predict the flow and heat transfer in the stagnation region of a circular impinging jet. Then, Kubacki and Dick [15] used the same k- ω model in their hybrid RANS/LES simulations of plane impinging jet.

This study focuses on numerical analysis of heat transfer and flow characteristics of an air jet in a semi-confined cavity. The main objective of this work is to determine the parameters that can influence the structures of the flows, the isotherms and the heat transfer between the flat plate and the impinging air jet.

2. MATHEMATICAL FORMULATION

2.1. Physical model and assumptions: Figure 1 shows the computational domain and coordinate system for the two-dimensional semi-confined impinging air jet considered. The bottom wall is divided into two thermal zones while the other walls are adiabatic: the wall part of the confined zone, located between the impingement jet and the vertical wall is maintained at a cold temperature $T_c = 278K$ while the other wall part is at a constant temperature $T_h > T_c$, equal 293K, which is equal to the air jet temperature.

The air is assumed to be an ideal gas, the Boussinesq approximation is used and transfers are described by turbulent forced convection equations.

2.2. Transfer equations: In the present study, the turbulent air jet flow is predicted using RANS model. For an incompressible; the RANS and the energy equation are, in Cartesian coordinates, using the Einstein summation convention:

$$\frac{\partial \bar{u}_i}{\partial x_i} = 0 \quad (1)$$

$$\frac{\partial \rho \bar{u}_i}{\partial t} + \frac{\partial \rho \bar{u}_j \bar{u}_i}{\partial x_j} = -\frac{\partial P}{\partial x_i} + \frac{\partial}{\partial x_j} \left(\mu \frac{\partial \bar{u}_i}{\partial x_j} - \overline{\rho u_i u_j} \right) \quad (2)$$

$$\rho C_P \left(\frac{\partial \bar{T}}{\partial t} + \frac{\partial \bar{u}_j \bar{T}}{\partial x_j} \right) = \frac{\partial}{\partial x_j} \left(\alpha \frac{\partial \bar{T}}{\partial x_j} - \overline{\rho u_j T'} \right) \quad (3)$$

Where $(-)$ denotes the modeled Reynolds averaged quantities. The Reynolds stress tensor is approximated by various turbulence models provided in the software fluent. In this study, we use the SST k- ω model because it provides results in good agreement with experimental data [16].

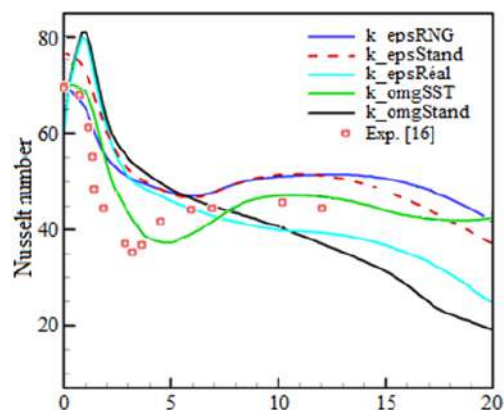


Figure1: Local Nusselt number evolution along the impingement plate. Effect of turbulence model [16]

The equations of this model read [17]:

$$\frac{\partial k}{\partial t} + \frac{\partial \bar{u}_j k}{\partial x_j} = \frac{\partial}{\partial x_j} \left[\left(\nu + \frac{\nu_k}{\sigma_k} \right) \frac{\partial k}{\partial x_j} \right] + P_k - \beta^* k \omega \quad (4)$$

$$\frac{\partial \omega}{\partial t} + \frac{\partial \bar{u}_j \omega}{\partial x_j} = \frac{\partial}{\partial x_j} \left[\left(\nu + \frac{\nu_t}{\sigma_\omega} \right) \frac{\partial \omega}{\partial x_j} \right] + \alpha \frac{\omega}{k} P_k - \beta \omega^2 \quad (5)$$

Where, P_k represents the production of turbulent kinetic energy k and ω is the specific dissipation rate. The closure coefficients and the associated relations are:

$$\alpha = 0.52 ; \beta = 0.082 ; \beta^* = 0.09 ; \sigma_\omega = 0.5 ; \sigma_k = 0.6$$

2.3. Initial and boundary conditions: The initial conditions ($t = 0$ s) throughout the computational domain are:

$$U = 0 ; V = V_{in} ; T = T_{in} ; k = 1 ; \omega = 1.$$

The boundary conditions are reported in figure 1. The bottom wall is divided into two isothermal zones while the other walls are adiabatic.

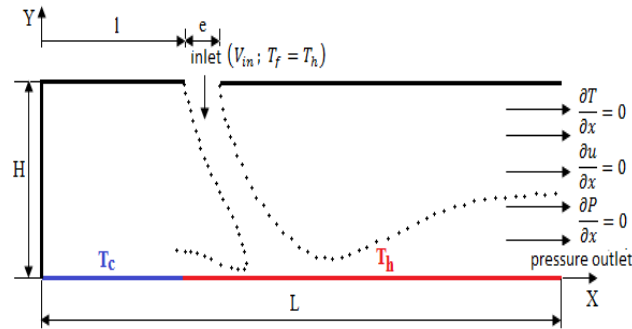


Figure 2: Sketch of the computational domain.

For the need of physical analysis, the local Nusselt number and the skin friction coefficient (C_f) are defined by:

$$Nu(X) = \frac{\partial \theta}{\partial y} \Big|_{wall} \quad C_f = 2 \cdot \tau_w / (\rho v_m^2) \quad (6)$$

3. NUMERICAL PROCEDURE

The governing equations were computationally solved numerically using FLUENT software and the mesh was generated using the commercial software GAMBIT. The link between the pressure and velocity field is assumed by the SIMPLE algorithm. The inlet

jet condition is given by a constant velocity profile $V_{in} = (\mu/\rho) \cdot (Re/e)$. At the exit, pressure-outlet boundary condition is imposed, while null gradient is assumed for the scalar variables. The solution is considered converged when the normalized residual falls below 10^{-11} for the energy equation and below 10^{-8} for all other variables within 3750 iterations.

4. RESULTS AND DISCUSSION

First, we determine the length of the cavity for that the flow is fully developed at its exit. Three lengths have been considered: $L=15, 20$ and 30 m. Figure 3 shows that, for a cavity length $L=30$ m, the outflow can be considered fully developed.

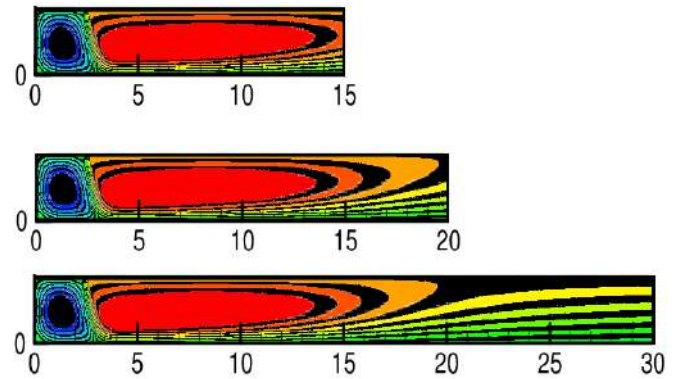


Figure 3: Flow structure: Effect of the cavity length

Figure 4 shows the streamlines for different Reynolds numbers of 10000 – 20000 and different impingement plate distance of $4e - 12e$. It can be seen that the flow induced by the air jet in the semi-confined cavity is described by two asymmetric recirculating cells located on either side of the air jet flowing from the top bottom to the impingement area. This flow structure is induced by the combination of the air jet and the confining effects due to the vertical wall and one part of the top wall. Furthermore, the size of the main re-circulating cell elongate along the direction of outlet flow increases on the one hand, with the augmentation of Reynolds number and the other hand, with the distance jet to plane plate.

The distribution of isotherms shows a similar shape, which is two asymmetric re-cells located on either side of the air jet (Figure 5). When the Reynolds number increases to 20000, the effect of convection on fluid flow and heat transfer in the enclosure was slightly larger than that at $Re=10000$ but its

magnitude remains weak. Then, figure 6 shows the influence of the Reynolds number on the temperatures profile, plotted at $y = 1.2e$, in the confined area, with an impingement plate distance $H = 12e$. It will be noted a monotonic increase of the temperatures up to a distance from the vertical wall $x = 0.3$. Beyond $x = 0.3$ the temperature reaches a maximum; stabilizes until $x = 1.9$ and then decreases slightly when approaching the air jet flow.

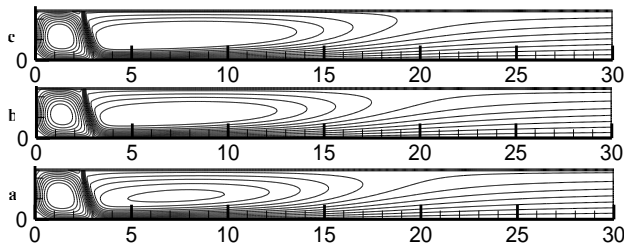


Figure 4: Streamlines pattern. $H = 12e$. Effects of Reynolds number; (a) $Re = 10000$; (b) $Re = 15000$ and (c) $Re = 20000$

The temperatures increase with the Reynolds number due to the intensification of transfer by convection between the warm part of the bottom wall and the air flow.

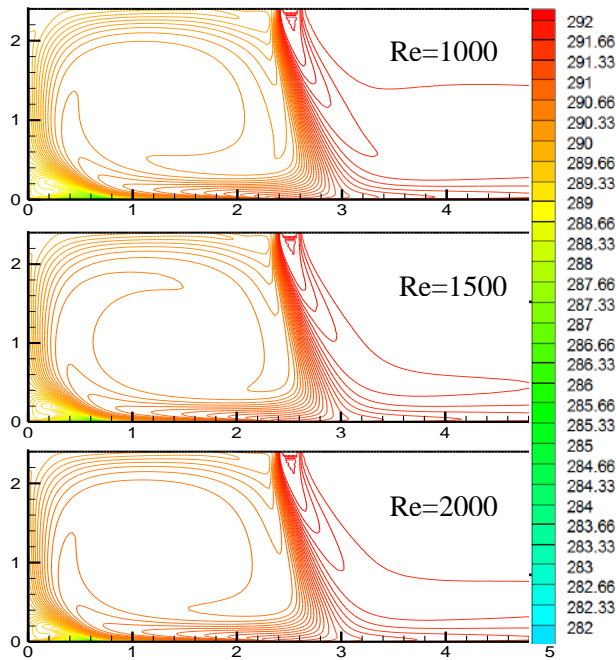


Figure 5: Isotherms for $H = 12e$ for various Reynolds numbers.

The evolution of the local Nusselt number along the bottom wall presents two peaks for values of H superior to $4e$. The first peak is located in the impact area of the jet on the cold wall and the second in the impact area of the jet on the hot wall. It will be noted that the second peak appears for a jet exit to impingement plate distance H greater than $4e$.

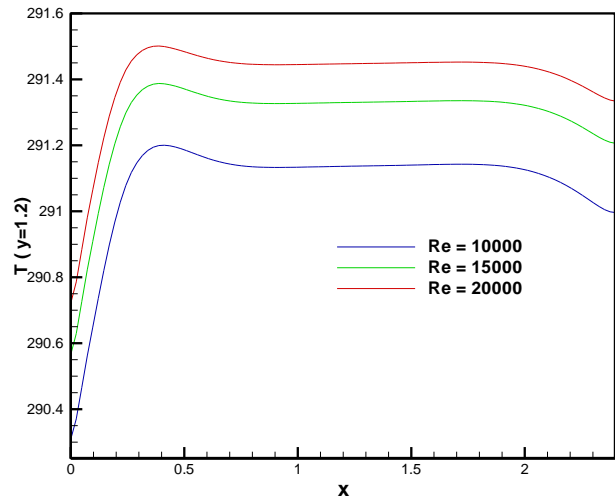


Figure 6: Evolution of the air temperature along the bottom wall. $y = 1.2$ for $H = 12e$. Effect of Re number

The evolutions of the local Nusselt number along the bottom wall are plotted in figure 7 for different Reynolds numbers and height ratios. It can be seen that for whatever the value Reynolds number and for impact height considered in this study, the most intensive thermal exchanges are located in the vicinity of the impact area of the jet. For a height impingement $H = 4e$, the local Nusselt number increases sharply to reach a maximum value in the vicinity of the impact area of the jet then decreases gradually as the flow approaches the exit of the cavity.

The evolution along the bottom wall of the local skin friction coefficient defined by is plotted in figure 9. This evolution is similar to the one of the local Nusselt Number. The local skin friction coefficient reaches its maximum values in the impingement area and is even higher than the air jet velocity is large.

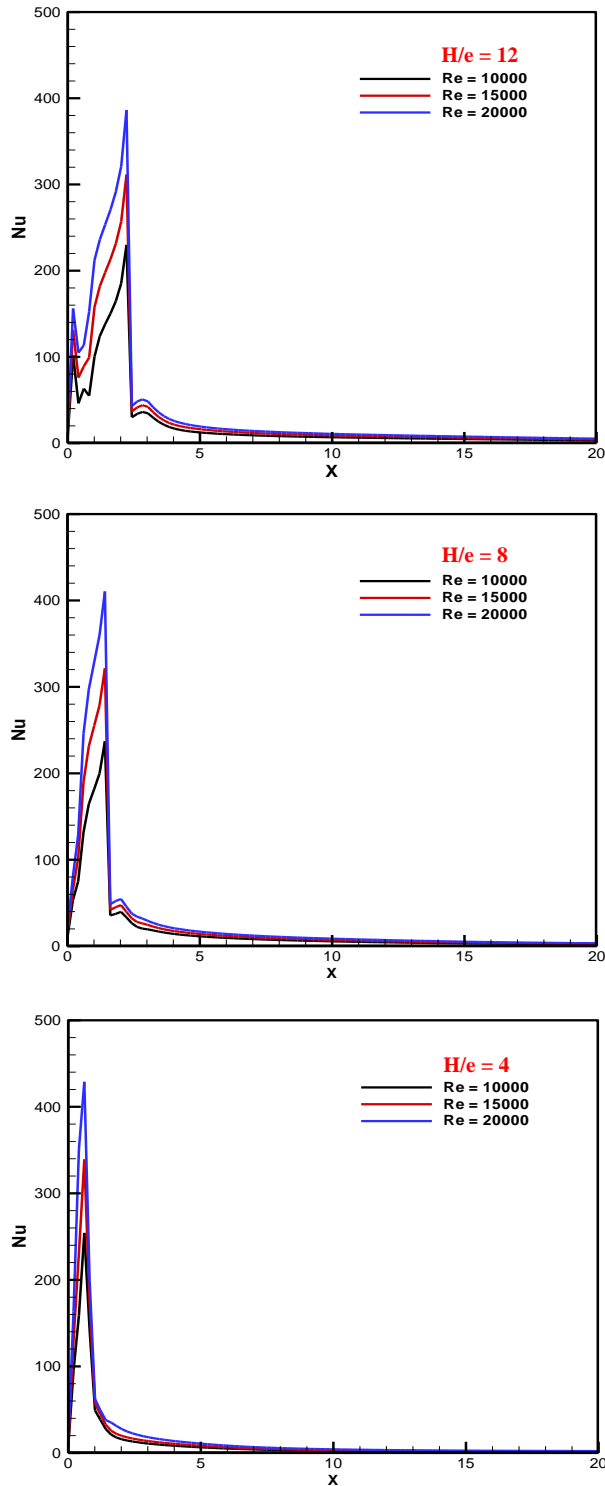


Figure 7: Evolution of the local Nusselt along the bottom wall

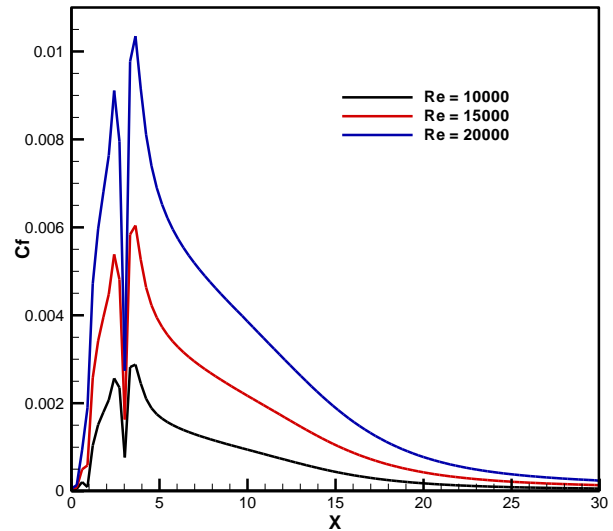


Figure 8: Distribution of local skin-friction at different Reynolds numbers for H/e = 12

CONCLUSIONS

Heat transfer and flow characteristics of an air jet in a semi-confined cavity have been investigated numerically for Reynolds numbers ranging from 10000 to 20000 and three to plane plate distances: 4, 8 and 12. The following conclusions may be drawn from this study:

- the flow is described by two asymmetric re-circulating cells located on either side of the air jet flowing from the top bottom to the impingement area. The re-circulating cell elongate along the outlet air flow direction of flow increases on the one hand, with the augmentation of Reynolds number and the other hand with the distance jet to plane plate,

- the increase of the Reynolds number leads to an improvement of the heat transfer exchange between the impingement area and the air flow. An increase of the local skin friction coefficient and the temperatures in the confined zone is observed,

- in the impingement area, the Nusselt number increases respect to a decrease of the jet-to-plate distance.

ACKNOWLEDGMENTS

This work was been financially supported by the French Government (BGF). The authors gratefully acknowledge this institution.

REFERENCES

1. Y.J.Jang, M.A. Leschziner, K.Abe, L. Temmerman, 2002, Investigation of anisotropy resolving turbulence models by reference to highly-resolved LES data for separated flow, *Flow, Turbulence combust*, **69**, pp. 161-203.
2. T.J.Craft, H. Lacovides, J.H. Yoon, 1999, Progress in the use of non-linear two-equation models in the computation of convective heat transfer in impinging and separated flow, *Flow, Turbulence combust*, **63**, pp. 59-81
3. R.Gardon, J.C. Akfirat, 1966, Heat transfer characteristics of impinging two dimensional air jets, **88**, pp. 101-108.
4. A.R.P. Van Heiningen, 1982, Heat transfer under impinging slot jet. Ph.D. Thesis, McGill University.
5. R. Viskanta, 1993, Heat Transfer to impinging isotherm gas and flame jets, **6**, pp.111-134.
6. H. Hofmann, M.Kind, H.Martin, 2007, Measurements on steady state heat transfer and flow structure and new correlations for heat and mass transfer in submerged impinging jets, **50**, pp.3957-3965.
7. S. Ashforth-Frost, K. Jambunathan, C.F. Whitney, 1997, Velocity and turbulence characteristics of a semi-confined orthogonally impinging slot jet, **14**, pp.60-67.
8. J. Zhe, V. Modi, 2001, Near wall measurements for a turbulent impinging slot jet, **123**, pp.112-120.
9. V. Narayanan, J. Seyed-Yagoobi, R.H. Page, 2004, An experimental study of fluid mechanics and heat transfer in an impinging slot jet flow, **47**, pp.1827-1845.
10. K. Heyerichs, A. Pollard, 1996, Heat transfer in separated and impinging turbulent flows, **39**, pp.2385-2400.
11. S.M. Hosseinalipour, A.S. Mujumdar, 1995, Comparative evaluation of different turbulence models for confined impinging and opposing jet flows, Part A **28**, pp.647-666.
12. S.J. Wang, A.S. Mujumdar, 2005, A comparative study of five low Reynolds number k-epsilon models for impingement heat transfer, flow, turbulence combust, **25**, pp.31-44.
13. N. Zuckerman, N. Lior, 2006, Jet impingement heat transfer: physics, correlations, and numerical modeling, *Advances in Heat Transfer*, **39**, pp.565-631.
14. S. Kubacki and E. Dick, 2009, Convective heat transfer prediction for an axisymmetric jet impinging onto a flat plate with an improved k- ω model. *International Journal of Numerical Methods for Heat and Fluid Flow*, **19**, pp.960-981.
15. S. Kubacki and E. Dick, 2010, Simulation of plane impinging jets with k- ω based hybrid RANS/LES models. *International Journal of Heat and Fluid Flow*, **31**, 862-878.
16. J.E. Jaramillo, F.X. Trias, A. Gorobes, C.D. Pérez-Segarra, A. Oliva, 2012, DNS and RANS modelling of a turbulent plane impinging jet, **55**, pp. 789-801.
17. F.R. Menter, 1993, Zonal two equation k-omega turbulence models for aerodynamic flows, pp.1993-2906.
18. S. Poncet, T.D. Nguyen, S. Harmand, J. Pellé, R. D. Soghe, C. Bianchini, S. Viazzo, 2013, Turbulent impinging jet flow into an unshrouded rotor-stator system: Hydrodynamics and heat transfer, **44**, pp. 719-734.
19. X. Wang, 2009, Numerical predicting and analysis of turbulent flows in heat transfer cavities disaggregated using an elliptical relaxation model, Ph.D. Thesis, Lille1 University.

EFFECTS OF THE IMPELLER BLADE DIAMETER AND ITS ORIENTATION ON THE MIXING EFFICIENCY IN CYLINDRICAL TANKS

Youcef KAMLA¹, Ilies Moahmed ARAB², Houari AMEUR³, Mohamed BOUZIT² and Khadidja KAMLA⁴

¹Université Hassiba Ben Bouali Hay Salem, route nationale N° 19, 02000 Chlef, Algérie, Laboratoire des sciences et ingénieries maritimes.

²Université des sciences et de la technologie USTO-MB, 1505 El M'nouar, Oran, Algeria. Laboratoire des sciences et ingénieries maritimes.

³Institut des Sciences et Technologies, Ctr Univ Naâma, BP 66, 45000, Algeria

⁴Université IBN Khaldoun, BP P 78 zaâroua 14000, Tiaret, département de physique, solide de la matière

*Corresponding author: Email: youcef.kamla@univ-usto.dz

Kamla_youcef@yahoo.fr

ABSTRACT

The present study focuses on the effects of different geometrical parameters on the flow structure and the energy consumption in mixing vessels. To do so, we used a two-blade impeller to validate our numerical model against the experiment using the Ansys CFX code, and then we modified the diameter of the stirrer and the number of blades. Finally, we gradually modified the blade curvature angle until we reached a helical screw configuration. The numerical validation was in a good agreement and the obtained results showed that the importance the edge effect at the extremity of the blades is proportional to the diameter. The results also showed that the variation in the blade twist enhances the mixing by transformation of the tangential flow into an axial flow. We also noticed an increase in the energy consumption.

NOMENCLATURE

d: Blade diameter (m)

D: Tank diameter (m)

T: Tank height (m)

N_p: Power number (dimensionless)

[α]: Angle of blade twist (°)

INTRODUCTION

Agitators with wide blades are generally used for highly viscous fluids in the laminar regime. One of the commonly used is the two blades impeller. Several studies have been achieved, among others, the work of Bertrand and Couderc [1] who studied the 2D flows of pseudoplastic fluids. Youcefi [2] studied experimentally the hydrodynamics of the mechanically agitated viscoelastic fluids. These studies showed that for a low rotational velocity, the flow rate is essentially tangential.

CFD techniques are widely applied in studies of mixing systems; Hiraoka et al. [3] studied viscous Newtonian and Non-Newtonian flows for a 2D classical bladed impeller. Abid et al. [4] studied numerically the 3D laminar flow of a Newtonian fluid (glycerol solution) mixed by a two-blade stirrer.

Bouzit and Ameer [5] interested to Newtonian and non-Newtonian shear thinning fluids with the same kind of impeller. Ameer and Bouzit [6] proposed a correlation for predicting the power required in the agitation of complex fluids by two-flat-blade impellers. Vakili and Nasr Esfahany [7] studied numerically the 3D Newtonian fluid flow induced by a two-blade impeller but this time within the turbulent regime.

Haruki Furukawa et al. [7] gave new power number correlations for different types of impellers (paddle, Rushton turbine, anchor and pitched paddle). Then Ameer H and Al. [8] made a comparative study of the flow structure and the power consumption between simple and double helical-ribbon impellers. Ming et al. [9] studied the power consumption in a stirred tank equipped with different impeller. The effect of the Reynolds number, the fluid rheology and the impeller blade curvature on the minxing performances were studied by Ameer. H et al. [10], the effects of blade curvature angles on power consumption in a stirred tank were evaluated by Reza .A et al. [11].

1. DISCUSSION ON THE STUDIED GEOMETRY

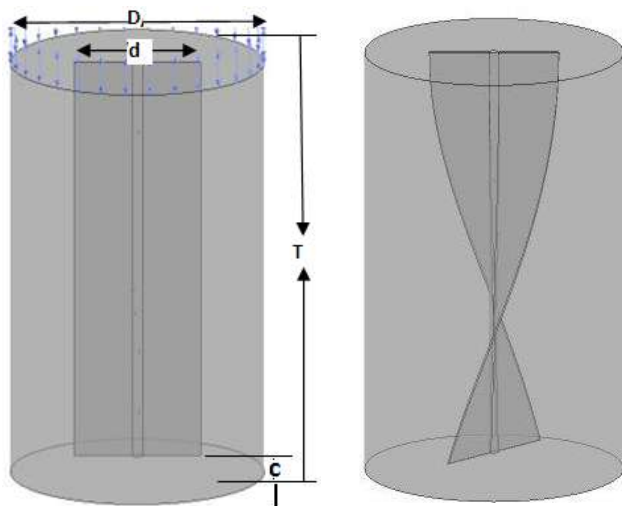
The studied domain is composed by a cylindrical tank with a flat plat bottom with a diameter D and a height T (equal to $1.5D$). The stirrer contains two blades with a height equal to the liquid height. The impeller diameter is $d = 0.5 D$, it is placed vertically at a clearance $C = 0.066 * D$ to avoid the scrapping with the tank bottom.

To solve the numerical problem we used a tetrahedral unstructured grid with 133,169 and 670,744 elements for the two studied impellers, respectively. The convergence criterion was set to 10^{-5} .

Several geometries with different ratios d/D , and different numbers of blades are realized, as summarizes in Table 1.

Table 1
Dimensions of different geometries

	$D/T=1.5$		$C/D=0.066$	
d/D	0.5	0.66	0.82	0.98
Blade Number	2	4	6	8



(Twin-Bladed) $\alpha = 135^\circ, d/D = 0.5$
Fig.1. Configuration of the mixing system

2. RESULTS AND DISCUSSION

2.1. VALIDATION OF THE NUMERICAL MODEL

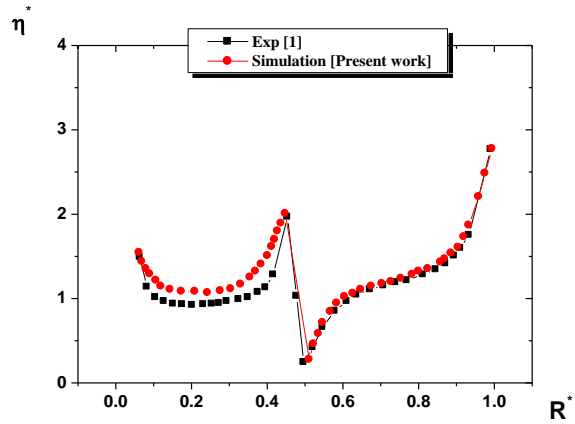


Fig.2. Validation of the shear stress for $Re = 0.1, n = 0.7, h/T = 1, D/T = 0.508, Z^* = 0.503$

Fig. 2 presents the validation of our numerical results against the experimental data of Bertrand and Couderc [1]: our results are in a good agreement.

2.2. EFFECTS OF THE RATIO d/D

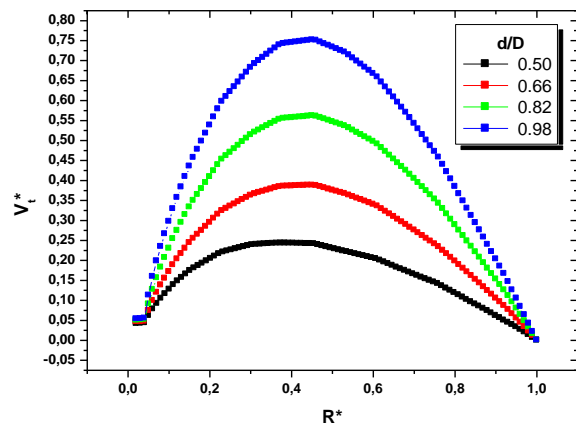


Fig. 3. Tangential velocity (effect of the diameter), $Z^*=0.87, Re=4, \theta=90^\circ$

Several values of the ratio d/D were used to deduce the effect of this last on the fluid circulation and therefore on the mixing efficiency (Table 2).

Table 2
Diameter of the different geometries realized

d/D	0.5	0.66	0.82	0.98
-------	-----	------	------	------

D : Tank diameter
 d : impeller diameter

The axial and tangential velocities are strongly proportional to the ratio d/D (Fig. 3). So for the same thickness of the blade, the flow intensity increases

by increasing the ratio d/D , giving then a more efficient mixing.

3. EFFECT OF THE NUMBER OF BLADES ON THE FLOW STRUCTURE AND THE ENERGY CONSUMPTION

3.1. THE FLOW STRUCTURE

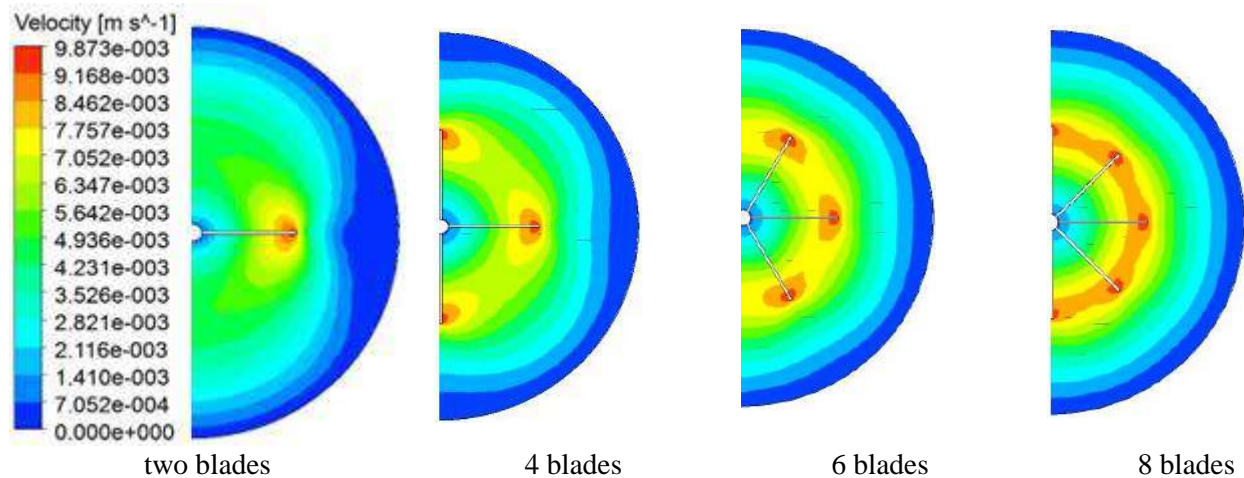


Fig.4. Velocity distribution for $d/D = 0.5$, $Re = 10$

3.2. ENERGY CONSUMPTION FOR DIFFERENT NUMBER OF BLADES

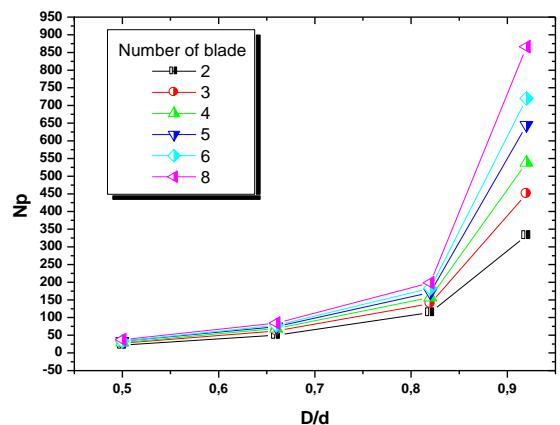


Fig.5. Power number for different values of d/D and the number of blades with $Re = 10$

4. EFFECTS OF THE BLADE TWIST ON THE FLOW STRUCTURE AND THE ENERGY CONSUMPTION

4.1. FLOW STRUCTURE

The results of Figs. 4 and 5 show that the well-mixed region size increases by increasing the number of

blades. It is the desired purpose, however, it requires more power consumption .

Figs. 6 & 7 show the effect of the blade twist. The variation of the tangential velocity has been studied for different angles (0° , 45° , 135° , 180°). We remark that the extremity of the blade is the most active region of the flow; this last gradually decreases when approaching the vertical walls of the tank where the fluid circulation is neglected. We also notice that the decrease of the tangential velocity is more rapid for an angle of 45° .

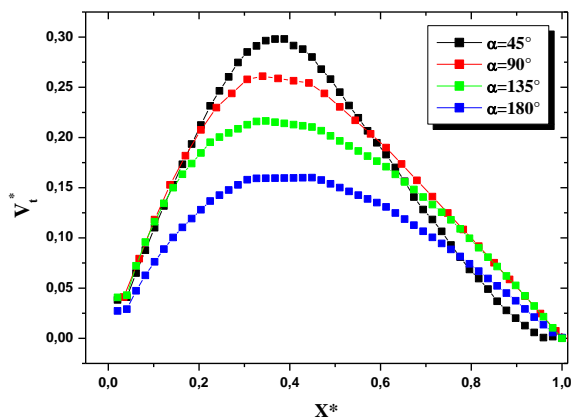


Fig.6. Tangential velocity for $Re=10$, $d/D=0.5$, $Z^*=0.5$

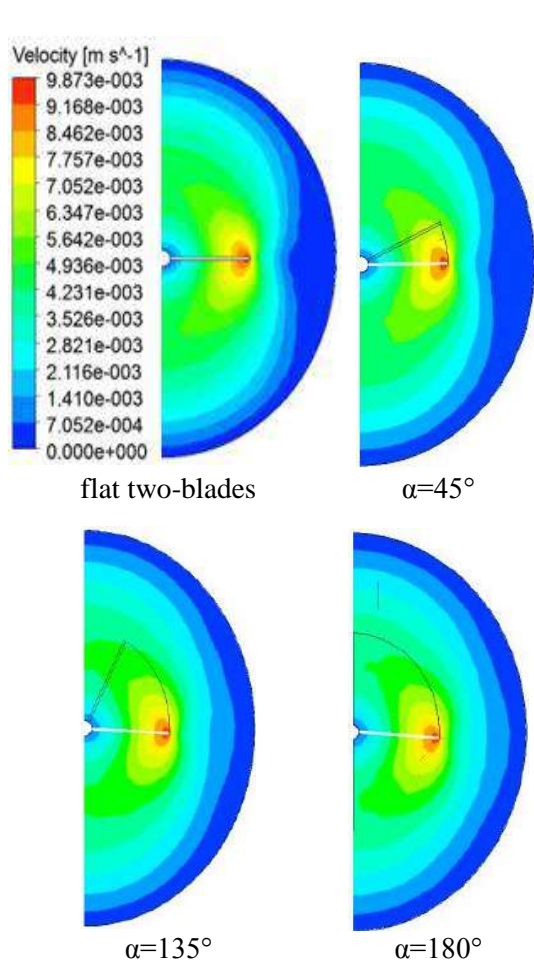


Fig.7. Velocity distribution for $Re = 10$, $d/D = 0.5$, $Z^* = 0.5$

4.2. POWER CONSUMPTION

Table 3
Power consumption for different bladed with differences orientation angle

	$d/D = 0.5, Re = 10$			
Orientation angle [deg]	45	90	135	180
Np	22.99	22.23	21.96	21.71
	$d/D = 0.82, Re = 10$			
Orientation angle [deg]	45	90	135	180
Np	113.4	112.7	111.90	111.0

Table 3 summarizes the values of the power number for all the twist angles studied. Results showed that the twist angle is inversely proportional to the power consumption.

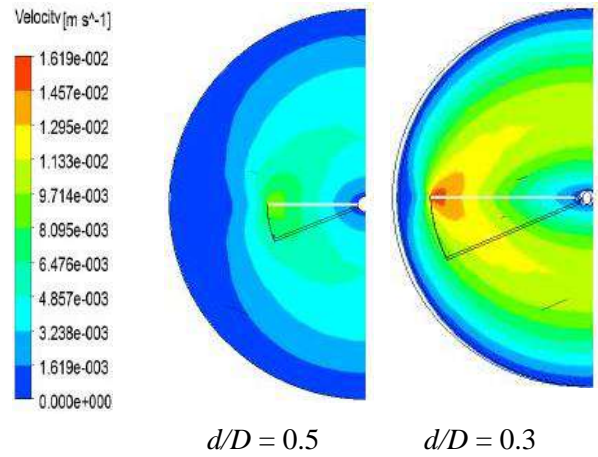


Fig.8. Velocity distribution for different blade diameters, at $\alpha = 45^\circ$

Conclusion

The present study focused on the effects of the blade diameter (d/D), the blade twist (α) and the blade number on the flow structure and the power consumption. The results found permitted us to withdraw the following conclusions:

The increase of d/D and the number of blades enhances quantitatively the mixing, but with a dramatically increased power consumption.

The twist of the blades is an interesting parameter to study in the future, its increase permits to partially eliminate the dead zones near the tank walls with a slight decrease in the power consumption.

KEYWORDS

ANSYS (CFD), 2-paddle impeller; power Number; cavern.

REFERENCES

- Bertrand, J. Couderc, J.P. 1982, Agitation de fluides pseudoplastiques par un agitateur bipale. Can. J. Chem. Eng. 60, 738-747.
- Youcefi A, 1993. Etude expérimentale de l'écoulement d'un fluide viscoélastique autour d'un agitateur bipale en cuve agitée. Ph.D. Thesis, Institut National Polytechnique, Toulouse.
- Hiraoka, S. Yamada, I, 1979, Mizoguchi, K. Two dimensional model analysis of flow behavior of highly viscous non Newtonian fluid in agitated vessel with paddle impeller. Chem. Eng. Japan, 12, 56-62.

4. Abid, M. Catherine, X. Bertrand, J. 1994, Modeling of the 3Dhydrodynamics on 2-blades impellers in stirred tanks filled with a highly viscous fluid, *Can. J. Chem. Eng.*, 72, pp. 184-193.
5. Bouzit, M. Simulation numérique de l'écoulement de fluides newtoniens autour d'un agitateur bipale. 2007, Thèse Doctorat d'état, USTO
6. Vakili, M.H. Nasr, Esfahany M. 2009, CFD analysis of turbulence in a baffled stirred tank: a three-compartment model, *Chem. Eng. Sci.*, 64, 351-362.
7. Furukawa. H, Kato. Y, Inoue. Y, Kato. T, Tada. Y, Hashimoto. S. 2012, Correlation of Power Consumption for Several Kinds of Mixing Impellers, *International Journal of Chemical Engineering.* 1-6.
8. Ameer. H, Bouzit. M, Ghenaim. A. 2013, Hydrodynamics in a vessel stirred by simple and double helical ribbon impellers, *Cent. Eur. J. Eng.*, 3(1), 87-98.
9. Ming-hui. X, Jian-ye. X, Zhen. Z, Guo-zhong. Z, J. C, Ying-ping. Z, Si-liang. Z, Henk. N.2014, Power consumption, local and average volumetric mass transfer coefficient in multiple-impeller stirred bioreactors for Xanthan gum solutions *Chemical Engineering Science*, 106. 144–156.
10. Ameer, H., Bouzit, M. 2013, Numerical investigation of flow induced by a disc turbine in unbaffled stirred tank, *Acta Scientiarum*, 469-476.
11. Reza, A. G. Abdul Aziz, A.R, Shaliza. I, Saeid. B, Arami-Niya. A. 2013, Study of various curved-blade impeller geometries on power consumption in stirred vessel using response surface methodology, *Journal of the Taiwan Institute of Chemical Engineers*, 44, 192-201.

NUMERICAL INVESTIGATION AND ANALYSIS OF INDOOR AIR QUALITY IN A ROOM BASED ON IMPINGING JET VENTILATION

L. KOUFI ^{1,2,3}, Z. YOUNSI ^{2,3}, Y. CHERIF ^{1,3}, H. NAJI ^{1,3,*}

¹ Univ. Artois, EA 4515, Laboratoire de Génie Civil et géo-Environnement (LGCgE), F-62400 Béthune, France

² FULP, Hautes Etudes d'Ingénieur (HEI), 13 Rue de Toul, F-59000 Lille, France

³ Univ. Lille, F-59000 Lille, France

* Corresponding author: Email: hassane.naji@univ-artois.fr; Tél: +33 3 21 63 71 41

ABSTRACT

This study presents numerical investigation and analysis of carbon dioxide transport (CO₂) within an isothermal three-dimensional room using impinging jet ventilation (IJV). The IJV is an effective strategy for use in buildings. The study is carried out under turbulent and transient flow regime. The URANS equations supplemented with energy and concentration equations are solved using the Stream code. We are targeting primarily the efficiency of the ventilation ε_C and the index of indoor air quality I_{IAQ} . The ventilation flow rate is $50 \text{ m}^3 \cdot \text{h}^{-1}$. Here, our ultimate aim is to analyze the behavior of the flow and repartition of CO₂ inside the room. The RNG $k-\varepsilon$ model was adopted to handle the turbulence. CFD simulations were systematically checked, through available experimental and/or numerical results. The obtained results indicated that the IJV ensures a homogeneous concentration distribution and a velocity of the ambient air less than $0.25 \text{ m} \cdot \text{s}^{-1}$. This is in agreement with the recommendations of ASHRAE 55. The comparative results demonstrate that the IJV evacuates sufficiently the CO₂ and ensures good air quality in an acceptable time.

KEY WORDS: CFD simulation / impinging jet ventilation / indoor air quality / ventilation efficiency / Turbulence

NOMENCLATURE

C	Chemical species' concentration (<i>ppm</i>)	Re	Reynolds number ($Re = \rho D_n D_h / \mu$)
C_m	Average concentration (<i>ppm</i>)	t	Time (<i>s</i>)
C_0	Reference concentration (<i>ppm</i>)	T	Temperature (<i>K</i>)
C_{in}	Chemical species' concentration at inlet (<i>ppm</i>)	T_0	Temperature reference (<i>K</i>)
C_{out}	Chemical species' concentration at outlet (<i>ppm</i>)	u_i	Velocity components ($\text{m} \cdot \text{s}^{-1}$)
C_{th}	Threshold concentration (<i>ppm</i>)	U_{in}	Velocity inlet ($\text{m} \cdot \text{s}^{-1}$)
C_p	Specific heat ($\text{J} \cdot \text{Kg}^{-1} \cdot \text{K}^{-1}$)	x_i	Coordinates (<i>m</i>)
D	Diffusion coefficient of chemical species ($\text{m}^2 \cdot \text{s}^{-1}$)	<i>Greeks symbols</i>	
I_{IAQ}	Index of Indoor air quality	α	Thermal diffusivity ($\text{m}^2 \cdot \text{s}^{-1}$)
g	Gravity acceleration ($\text{m} \cdot \text{s}^{-2}$)	β_T	Thermal expansion coefficient ($\beta_T = T_0^{-1}, \text{K}^{-1}$)
k	Turbulent kinetic energy ($\text{m}^2 \cdot \text{s}^{-2}$)	β_C	Concentration expansion coefficient ($\beta_C = C_0^{-1}$)
L	Characteristic length (<i>m</i>)	ε	Turbulent energy dissipation ($\text{m}^2 \cdot \text{s}^{-3}$)
n	Normal direction	ε_C	Ventilation effectiveness coefficient
N	Buoyancy ratio ($N = \beta_C \Delta C / \beta_T \Delta T$)	λ	Thermal conductivity ($\text{W} \cdot \text{m}^{-1} \cdot \text{K}^{-1}$)
p	Fluid pressure (<i>Pa</i>)	μ	Dynamic viscosity ($\text{kg} \cdot \text{m}^{-1} \cdot \text{s}^{-1}$)
\dot{Q}	Ventilation rate ($\text{m}^3 \cdot \text{h}^{-1}$)	ρ	Density of the mixture ($\text{kg} \cdot \text{m}^{-3}$)

INTRODUCTION

It is now accepted that ventilation systems, thermal comfort, and air quality within the built environment are important issues as they are related to both energy conservation, occupants' health, and productivity. Indeed, today, users spend more time inside the premises (homes, schools, offices, transports, stores, etc.) [1]. It is obvious that proper distribution of air is an important issue for the comfort and air quality of

indoor spaces. Many pollutants from a variety of sources may be present in this environment and sometimes at higher concentrations than outside. For a question of energy saving, the exchanges between the outside and inside buildings were greatly reduced what could drive a containment situation thus leading to deterioration in air quality.

To overcome the problems related to the health of occupants and to reduce energy consumption, the

ventilation has been used. It is the primary mechanism for removing contaminants from within buildings. Thereby, the ventilation is now considered as a promising solution to ensure a good indoor air quality. Its role is to renew sufficiently stale air by fresh air unpolluted and evacuate pollutants of the occupation zones. However, this technique can result in significant energy costs. Indeed, the introduction of fresh air causes important temperature gradients that affect the thermal comfort of occupants. These temperature gradients can be negative or positive depending on the climate. For this, different ventilation strategies have been adopted to ensure a good quality of indoor air firstly, and limit energy losses on the other hand.

Since many decades, the impinging jet ventilation (IJV) is used for ventilated rooms [2,3]. Indeed, this system is capable to provide a better distribution of flow parameters (velocity, temperature and concentration) and as well as its flexibility for both cooling and heating purposes. In the IJV system, a high momentum air jet is discharged downwards, strikes the floor and spreads over it, thus distributing the fresh air along the floor in the form of a very thin shear layer [4]. This method allows the airflow to overcome buoyancy forces due to temperature and concentration gradients generated by the sources. Therefore, it promotes the evacuation of stale air and ensures better ventilation efficiency in the occupied zone [5]. However, high velocities can take place in the occupied zone. Therefore, the flow of IJV system must be properly sized to allow proper design ensuring better indoor environment.

Several studies have been conducted to deepen understanding of the behavior of air flow and distribution of heat and pollutants inside the ventilated rooms using IJV. Below, we briefly describe some work on the topic discussed here. Karimipannah and Awbi [3] among the first to raise the IJV. They performed a numerical and experimental study of performance evaluation of this method. They considered a three-dimensional room equipped with a ventilation system with impingement jet. The authors compared its performance with another system “displacement ventilation”. The results they presented are part of an extensive research program to develop alternative and effective ventilation systems. They found that the IJV system has slightly higher performance than the displacement ventilation system. Cao *et al.* [6] conducted an experimental study of the IJV inside a large-scale room upstairs. The air jet is introduced perpendicularly to the ceiling. Then, the flow is deflected and becomes parallel. They considered several Reynolds numbers ($Re=1000, 2000$

and 4000) to determine the jet velocity to ensure a certain comfort inside the room. The results show that the flow behavior is different from earlier studies in a relatively small room. Chen and Moshfegh [7] performed a numerical study of the IJV in an office room. They compared the performance of the Standard $k-\varepsilon$ [8], the Renormalization Group (RNG) $k-\varepsilon$ [9], and the Realizable $k-\varepsilon$ [10], for the prediction of the mean velocity field and the temperature pattern. The validation of the model is performed via an experimental study inside a room with dimensions of $4.2 \times 3.6 \times 2.5 \text{ m}^3$. The authors found that the three models provide favorable predictions of velocities and temperature compared to the measurements. Also, the RNG $k-\varepsilon$ model gave the best performance. Chen *et al.* [11] presented a numerical study of the IJV under various heat loads from $17-65 \text{ W.m}^{-2}$ in an office room. They performed measurements of velocities and temperature to validate the numerical model. They tested three turbulence models: RNG $k-\varepsilon$, SST $k-\omega$ [12] and $\overline{v^2} - f$ [13]. They found that these models give good agreement with the measurements. The $\overline{v^2} - f$ model has provided the best performance, especially on the overall temperature prediction. Next, the authors used the latter model to study the effect of several parameters such as position heat sources, number of occupants. In terms of results, the authors found that the fields of flow and temperature are greatly influenced by the parameters studied here.

Since the ventilation effectiveness is typically used in building, we conducted a numerical study to predict the aero-solutal behavior inside a three-dimensional ventilated room. To achieve this, the unsteady Reynolds averaged Navier-Stokes (URANS) equations are solved via the Stream Code. To handle the turbulence, the RNG $k-\varepsilon$ model is used, due its reliability according to references [4,11].

The main purpose of this study is to assess the IJV in terms of behavior flow, indoor air quality (IAQ), and air exchange efficiency for the inside of a room.

The remainder of this paper is organized as follows. In Section 2, the physical model and the governing equations supplemented by specific boundary conditions are described. In section 3, key parameters of this study are presented. After, the Section 4 is devoted to a brief description of the numerical approach while emphasizing its validation. In Section 5, results are presented and discussed. Finally, the major conclusions are summed up in in Section 6.

PROBLEM DESCRIPTION AND FORMULATION

Figure 1 shows a schematic of the physical system with inlet and outlet conditions. It is a ventilated chamber of dimensions $4 \times 3 \times 2.5$ m³ (i.e. length, width and height) filled with an *air-CO₂* mixture. It is provided with two openings for the supply of fresh air and the evacuation of contaminated air. The ventilation rate was 50 m³.h⁻¹. The walls are adiabatic and impermeable. Note that inlet and outlet air are positioned in the middle plane $Y=1.5$ m.

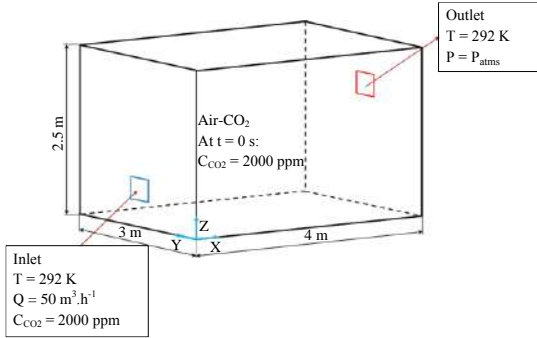


Fig. 1. Schematic drawing of the ventilated room.

Mathematical modeling

An unsteady state 3D-model is considered to analyze the flow in the whole room. The fluid is assumed to be Newtonian, incompressible under the Boussinesq approximation (and neglecting viscous heating). Besides, the airflow is turbulent. Note that the level of concentration of CO₂ is considered low (the amount of CO₂ is much lower than air (0.02%)). Based on these assumptions, the RANS equations are given by:

$$\frac{\partial \rho}{\partial t} + \nabla \cdot (\rho \mathbf{U}) = 0 \quad (1)$$

$$\frac{\partial (\rho \bar{\mathbf{U}})}{\partial t} + \nabla \cdot (\rho \bar{\mathbf{U}} \otimes \bar{\mathbf{U}}) = -\nabla p + \nabla \cdot (\mu \nabla \bar{\mathbf{U}} - \overline{u_i u_j}) + \rho [g \beta_T (T - T_0) + g \beta_C (C - C_0)] \mathbf{e}_3 \quad (2)$$

$$\frac{\partial (\rho C_p T)}{\partial t} + \nabla \cdot (\rho C_p T \bar{\mathbf{U}}) = \nabla \cdot (\lambda \nabla T - \rho C_p \overline{u_i T}) \quad (3)$$

$$\frac{\partial (\rho C)}{\partial t} + \nabla \cdot (\rho C \bar{\mathbf{U}}) = \nabla \cdot (\rho D \nabla C - \rho \overline{u_i C}) \quad (4)$$

where $\overline{\rho u_i u_j}$, $\overline{\rho u_i T}$ and $\overline{\rho u_i C}$ are the average Reynolds stresses, turbulent heat and mass fluxes, respectively, which are modeled as follows:

$$\overline{\rho u_i u_j} = -\mu_t S_{ij} + (2/3) \rho k \delta_{ij} \quad (5)$$

$$\overline{\rho u_i T} = -\alpha_t \nabla T \quad (6)$$

$$\overline{\rho u_i C} = -D_t \nabla C \quad (7)$$

where $k = \overline{u_i u_i} / 2$ is the turbulent kinetic energy, δ_{ij} is the Kronecker tensor, μ_t is the eddy viscosity, α_t and D_t are the turbulent thermal diffusivity and turbulent mass diffusivity, respectively. The eddy viscosity μ_t is computed by:

$$\mu_t = C_\mu \rho k^2 / \varepsilon \quad (8)$$

where ε is the turbulent dissipation rate, and C_μ is a constant model.

The *RNG* $k-\varepsilon$ model is employed to close the system (1)-(4). The *RNG* $k-\varepsilon$ model is an example of two equation models that use the Boussinesq hypothesis. It is based on the following equations:

$$\partial (\rho k) / \partial t + \nabla \cdot (\rho k \bar{\mathbf{U}}) = \nabla \cdot [\mu + (\mu / \sigma_k)] \nabla k + G_s + G_b + \rho \varepsilon \quad (9)$$

$$\partial (\rho \varepsilon) / \partial t + \nabla \cdot (\rho \varepsilon \bar{\mathbf{U}}) = \nabla \cdot [\mu + (\mu / \sigma_\varepsilon)] \nabla \varepsilon + C_1 (G_s + G_b) (1 + C_3 R_f) (\varepsilon / k) - C_2 (\rho \varepsilon^2 / k) \quad (10)$$

with $G_s = \mu_t S_{ij} \nabla \bar{\mathbf{U}}$, $G_b = g_i \beta_T (\mu_i / Pr_i) \nabla T + g_i \beta_C (\mu_i / Sc_i) \nabla C$, $R_f = -G_b / (G_s + G_b)$, $S_{ij} = (\partial \bar{u}_i / \partial x_j) + (\partial \bar{u}_j / \partial x_i)$, and σ_k , σ_ε , C_1 , C_2 , C_3 , C_μ are the model constants whose values are given in Table 1.

Table 1. Model constants of the *RNG* $k-\varepsilon$ model

σ_k	σ_ε	C_1	C_2	C_3	C_μ
0.719	0.719	$C_1(\eta)$	1.68	0.0	0.085

with $C_1(\eta) = 1.42 - (\eta(1 - \eta / 4.38) / (1 + 0.012\eta^2))$, $\eta = kS / \varepsilon$ and $S = (S_{ij} S_{ij})^{1/2}$.

Boundary conditions

The system of equations (1)-(10) are subjected to the following boundary conditions (BCs). $U=0$ on all solid surfaces, $U=U_{in}$ at the air inlet, $\partial U / \partial n = 0$ at the air outlet. As for thermal BCs, the room is supposed isotherm at 292 K and its walls are adiabatic. For the CO₂, we assumed that its concentration is 2000 ppm at $t=0$ s, while the air enters at a concentration of 350 ppm. At the outlet, we set $\partial C / \partial n = 0$. Regarding the turbulent quantities, their values are those advocated by Henkes *et al.* [14].

CHARACTERISTIC PARAMETERS

Ventilation effectiveness

The efficiency of a ventilation (ε_C) to remove a contaminant element can be defined as [5]:

$$\varepsilon_C = \frac{C_{out} - C_m}{C_m - C_{in}} \quad (11)$$

This quantity allows assessing the ability of a ventilation system to remove pollutants in a ventilated domain. Note that $\varepsilon_C > 1$ translates an effective ventilation.

Index of indoor air quality

The index of indoor air quality (I_{IAQ}) can be calculated from the following relationship:

$$I_{IAQ} = \frac{C_m - C_{out}}{C_{Th} - C_{out}} \quad (12)$$

Such expression is used to evaluate the quality of indoor air with respect to a pollutant. Note that when $I_{IAQ} < 1$, the quality of indoor air is good.

NUMERICAL MODELING

Discretization

The computational analysis is performed using the general purpose finite-volume CFD code Stream. A quadratic structured mesh is used with a coefficient of geometric expansion of 1.05. The terms of advection and diffusion are discretized using first-order upwind scheme. The SIMPLEC algorithm [15] was used for the pressure-velocity coupling. The resolution of the resulting algebraic system is achieved using multiple-iteration constrained conjugate gradient (MICCG).

Before the targeted simulations, we have checked the independence of the mesh with respect to results. For this, we built four mesh grids with a time step of 0.01 s ($21 \times 26 \times 31$, $41 \times 46 \times 51$, $61 \times 66 \times 71$ and $81 \times 86 \times 91$). The obtained results indicated that the last two grids provide similar velocity and concentration profiles plotted at different points of the area. Therefore, we chosen the grid $61 \times 66 \times 71$ for all calculations implemented here. Similarly, we examined the temporal evolution of velocity and concentration considering different time steps (0.5, 0.1, 0.05 and 0.01 s). It was found that a time step less than 0.05 s gives satisfactory results. Normalized residuals required for convergence has been 10^{-8} for the energy, and 10^{-5} for the remaining equations that correspond to 1% of the default tolerance settings of stream.

Validation and verification

To check and validate our approach, different problems were considered. For not overload the text, we present only the problem addressed by Chung and Hsu [16]. It concerns a ventilated three-dimensional room filled with an air- CO_2 mixture. At $t=0$ s, the CO_2 concentration is at 2000 ppm and the mixture temperature is at 300 K. Fresh air is introduced at a temperature of 300 K and at a concentration of 350 ppm. The ventilation flow rate is $391.7 \text{ m}^3 \cdot \text{h}^{-1}$. The comparisons achieved are shown in Figure 2 for the temporal evolution of the concentration at the occupation zone (2, 2, 1.2). Based on these comparisons, it can be concluded that the numerical approach, for the case of this study, provides satisfactory results.

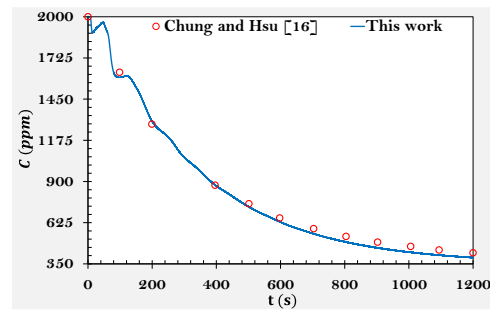


Fig. 2. Temporary evolution of the concentration at point (2, 2, 1.2); comparison with [16].

RESULTS AND DISCUSSIONS

In the following, we present the results of impinging jet ventilation system. We show streamlines, iso-velocity and temporal evolution of the CO_2 concentration for different measurement points at three levels ($Z=0.8$, 1.2 and 1.7 m). The coordinates of these points are gathered in Table 2.

Figure 3 presents the streamlines plotted when steady state is established. We found that the jet air changes direction at floor level, it allows the distribution of fresh air at the bottom and adjacent side walls. Then, the air tends to rise upwards to reach the exit causing recirculation zones in the occupation area. Also, we note that the flow is symmetrical about the middle plane ($Y=1.5$ m). From these results, we can conclude that the air is evenly distributed in the room.

In order to control the airflow distribution in the room, we have plotted the contours of iso-velocity with two values 0.25 and $0.15 \text{ m} \cdot \text{s}^{-1}$. These contours are showed in Figure 4. We found that the jet propagates in an equivalent manner in the longitudinal and lateral directions. The velocity of the jet decreases as one moves away from the air inlet diffuser. The velocity in the vicinity of the diffuser is well above $0.5 \text{ m} \cdot \text{s}^{-1}$. Note that around the exhaust opening, the velocity is higher than $0.5 \text{ m} \cdot \text{s}^{-1}$. It should be noted that the velocity of the airflow in the zone of occupancy is less than $0.25 \text{ m} \cdot \text{s}^{-1}$. This is consistent with the recommendations of the ASHRAE 55.

Figure 5 depicts the temporary evolution of the concentration of CO_2 of each measuring points. It is found that the concentration at the local center is almost homogeneous. It decreases with time. This indicates that the ventilation removes progressively the contaminant (CO_2). At $t=100$ min, the concentration level is very low, the CO_2 is at 410 ppm only. Also, we observe that, for a given time, the concentration is almost constant regardless of the level of sampling.

Table 2. Measurement points

Points	Z=0.8 m		Points	Z=1.2 m		Points	Z=1.7 m	
	X (m)	Y (m)		X (m)	Y (m)		X (m)	Y (m)

P01	3.0	1.5	P11	3.0	2.0	P21	3.0	1.5
P02	2.0	1.5	P12	3.0	1.0	P22	2.0	1.5
P03	1.0	1.5	P13	2.0	2.0	P23	1.0	1.5
P04	3.0	2.0	P14	2.0	1.0	P24	3.0	2.0
P05	3.0	1.0	P15	1.0	2.0	P25	3.0	1.0
P06	2.0	2.0	P16	1.0	1.0	P26	2.0	2.0
P07	2.0	1.0	P17	3.0	1.5	P27	1.0	1.0
P08	1.0	2.0	P18	2.0	1.5	P28	1.0	2.0
P09	1.0	1.0	P19	1.0	1.5	P29	1.0	1.0



Fig. 3. Streamlines: front view (*left*) and perspective view (*right*).



Fig. 4. Contour plots of iso-velocity with: 0.25 m.s^{-1} (*left*) and 0.15 m.s^{-1} (*right*)

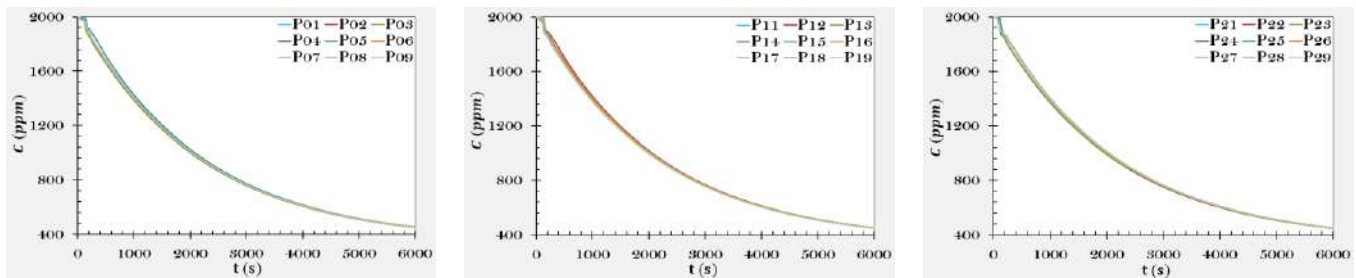


Fig. 5. Temporary evolution of the concentration (*ppm*): $Z=0.8 \text{ m}$ (*left*), $Z=1.2 \text{ m}$ (*middle*), $Z=1.7 \text{ m}$ (*right*).

Figure 6 shows the time evolution of ε_c and I_{IAQ} . We note that the IJV present good efficiency that is close to unity. This indicates that the IJV evacuate sufficiently the CO_2 contaminant. Regarding the index of indoor air quality, we get an index $I_{IAQ} < 1$ after only 33 min . This period corresponds to the time where the concentration of CO_2 falls below 1000 ppm . This value corresponds to the limited risks value fixed by French regulations. We conclude that the IJV puts only 33 min

to avoid dangerous exposure. We believe this time is widely appreciated.

Following these results, it is clear that the IJV provides better comfort environment ventilation, i. e. good ventilation effectiveness to remove pollutant ($\varepsilon_c \approx 1$), good air quality ($I_{IAQ} < 1$) in an acceptable time (33 min only), and favorable airflow distribution inside the room (0.25 m.s^{-1}). It should be noted that the IJV ensures a perfect homogeneity inside the room



Fig. 6. Temporary evolution of ε_C (left) and I_{IAQ} (right).

CONCLUDING REMARKS

This study deals with the numerical simulation of a turbulent contaminated flow in a 3D room. The emphasis has been on the influence of ventilation on the behavior flow and indoor air quality in a ventilated room. Computations have been performed with Reynolds number of $5 \cdot 10^3$. In URANS framework, the RNG $k-\varepsilon$ turbulence model is used. The remarks summarizing the present study are:

- According to the results of the behavior of the airflow, the IJV ensures good distribution of fresh air inside the room. The air is spreading in an equivalent manner in the longitudinal and lateral directions. The velocity of flow in the zone of occupancy is less than

- [1] Q. H. Deng, J. Zhou, C. Mei, and Y.-M. Shen, 2004, Fluid, heat and contaminant transport structures of laminar double-diffusive mixed convection in a two-dimensional ventilated enclosure, *Int. J. Heat Mass Transf.*, 47, pp. 5257–5269.
- [2] T. Karimipناه, 1996, Turbulent jets in confined spaces, Centre for Built Environment Royal Institute of Technology, Sweden, Gävle.
- [3] T. Karimipناه and H. B. Awbi, 2002, Theoretical and experimental investigation of impinging jet ventilation and comparison with wall displacement ventilation, *Build. Environ.*, 37, pp. 1329–1342.
- [4] H. J. Chen, B. Moshfegh, and M. Cehlin, 2012, Numerical investigation of the flow behavior of an isothermal impinging jet in a room, *Build. Environ.*, 49, pp. 154–166.
- [5] H. B. Awbi, 2003, *Ventilation of Buildings*, 2nd ed. London; New York: Routledge.
- [6] G. Cao, M. Ruponen, and J. Kurnitski, 2010, Experimental investigation of the velocity distribution of the attached plane jet after impingement with the corner in a high room, *Energy Build.*, 42, pp. 935–944.
- [7] H. Chen and B. Moshfegh, 2011, Comparing $k-\varepsilon$ models on predictions of an impinging jet for ventilation of an office room, 12th Int. Conf. on Air Distribution in Rooms, Trondheim, June 19-22.
- [8] B. E. Launder and D. B. Spalding, 1974, The numerical computation of turbulent flows, *Comput. Methods Appl. Mech. Eng.*, 3, pp. 269–289.

$0.25 \text{ m}\cdot\text{s}^{-1}$. This is in line with recommendations from the ASHRAE 55.

- Regarding the ventilation effectiveness to remove CO_2 , the IJV provides favorable efficiency ($\varepsilon_c \cong 1$). This indicates that the *air-CO₂* mixture is greatly diluted. The concentration at the outlet air is substantially equal to the average concentration of the room. This proves that the *air-CO₂* mixture is homogeneous inside the room.
- Finally, the IJV ensure good air quality after 33 min. Such a delay is acceptable to minimize CO_2 exposure to concentration greater than 1000 ppm.

REFERENCES

- [9] V. Yakhot, S. A. Orszag, S. Thangam, T. B. Gatski, and C. G. Speziale, 1992, Development of turbulence models for shear flows by a double expansion technique, *Phys. Fluids Fluid Dyn.*, 4, pp. 1510–1520.
- [10] W. W. L. T. -H. Shih, 1994, A New $k-\varepsilon$ Eddy Viscosity Model for High Reynolds Number Turbulent Flows - Model Development and Validation, *Comp. Fluids*, 24.
- [11] H. J. Chen, B. Moshfegh, and M. Cehlin, 2013, Investigation on the flow and thermal behavior of impinging jet ventilation systems in an office with different heat loads, *Build. Environ.*, 59, pp. 127–144.
- [12] F. Menter, 1993, Zonal Two Equation $k-\omega$ Turbulence Models For Aerodynamic Flows, 23rd Fluid Dyn., Plasmadynamics, and Lasers Conf., American Institute of Aeronautics and Astronautics.
- [13] P. A. Durbin, 1991, Near-wall turbulence closure modeling without ‘damping functions,’ *Theor. Comput. Fluid Dyn.*, 3, pp. 1–13.
- [14] R. A. W. M. Henkes, F. F. Van Der Vlugt, and C. J. Hoogendoorn, 1991, Natural-convection flow in a square cavity calculated with low-Reynolds-number turbulence models, *Int. J. Heat Mass Transf.*, 34, pp. 377–388.
- [15] G. D. R. J. P. van Doormaal, 1984, Enhancements of the SIMPLE Method for Predicting Incompressible Fluid Flows, *Numer. Heat Transf.*, 7, pp. 147–163.
- [16] K. C. Chung and S.-P. Hsu, 2001, Effect of ventilation pattern on room air and contaminant distribution, *Build. Environ.*, 36, pp. 989–998.

Safety, Reliability and Durability

INFLUENCE DE REFROIDISSEMENT DES SURFACES D'UN HABITAT SUR LA TEMPERATURE DE L'AIR INTERIEUR

* Abdelmadjid KADDOUR^a, S.M.A BEKKOUCHE^a

^aUnité de Recherche Appliquée en Energies Renouvelables, URAER, Centre de Développement des Energies Renouvelables, CDER, 47133, Ghardaïa, Algeria

*Corresponding author: Fax: +213 29 87 01 52 Email: kaddour.majid@gmail.com

RESUME

Cette étude examine comment le refroidissement par évaporation intégré de bâtiment peut contribuer à la réduction de la température dans de grands espaces vitrés. Le principe de refroidissement est basé sur le changement de phase de l'eau; c'est à dire la variation de la phase liquide à la phase vapeur de l'eau. Le refroidissement par évaporation des bâtiments est la technique la plus ancienne pour l'amélioration des conditions intérieures du confort. Récemment, l'intérêt dans ses perspectives d'application a été fortement renouvelé en raison des coûts de l'électricité augmentés pour la climatisation et les problèmes environnementaux associés de la combustion de combustibles fossiles. La capacité de refroidissement et la température interne de l'air intérieur semblent plus sensibles pour le taux de ventilation naturelle et la résistance au transfert de chaleur à la surface interne.

La conception d'un système de refroidissement par évaporation de la construction intégrée en combinaison avec le grand espace vitré est un processus complexe. Les solutions résultant de cette méthode de conception méthodique sont évalués sur critères concernant le fonctionnement et la réalisation par la méthode Kesselring. En conséquence, un procédé est proposé par le maintien d'un film mince d'eau sur les surfaces hydrophiles de construction de super-TiO₂ revêtu pour réduire les températures de surface de la libération de chaleur latente due à l'évaporation de l'eau. Les températures de surface inférieures contribuent à la réduction de la température de l'air ambiant depuis l'intensité du transfert de chaleur à travers la surface froide.

Les variables qui affectent largement ce processus d'évaporation sont les différences de pression de vapeur d'eau dans l'air, la taille de la surface de contact et le coefficient de transfert de masse spécifique (renforcée par convection).

INTRODUCTION

Dans la pratique, les grands espaces vitrés sont pour la plupart désignés comme désignés comme des zones où les gens restent seulement pour de courtes périodes de temps. Le climat dans une telle zone de circulation peut être autorisé à varier, ce qui exclut la nécessité des mesures importantes.

Les personnes qui utilisent effectivement cet espace dans la pratique ne seront pas conscientes de cela, cependant, si la zone est attrayante, les gens seront généralement enclins à utiliser de façon plus intensive. Les sièges seront installés, éventuellement une réception, et peut-être même une salle de cantine ou au collège.

Cela laisse le problème de lacunes inévitables en termes de climat intérieur. De nombreuses techniques

de refroidissement passif ont été proposées pour diminuer la température l'air ambiant par exemple de vitrage de haute réflectance solaire, matériau d'isolation thermique, refroidissement par évaporation, etc. Entre ces techniques de refroidissement passif, le refroidissement par évaporation semble le seul qui peut être adopté sans compromettre indûment la toiture de verre. Par conséquent, cette étude examinera comment le refroidissement par évaporation intégré d'une construction (directe ou indirecte) peut contribuer à la réduction de la température dans les grands espaces vitrés. L'objectif principal de cette étude est de concevoir et modéliser une solution passive de refroidissement par évaporation intégrée en se concentrant sur les flux d'énergie et le bilan thermique global.

Méthodologie : Cette étude comprend plusieurs processus parallèles et série. D'abord une analyse sera faite du grand espace vitré lui-même, qui est principalement axée sur l'application de verre, les flux d'énergie et l'équilibre global de la chaleur. Deuxièmement une analyse est réalisée selon la technique de refroidissement par évaporation avec une revue de la littérature récente. La conception d'un système de refroidissement par évaporation en combinaison avec les grandes espaces recouvertes de verre est un processus complexe. Pour appuyer ce processus de la conception méthodique est utilisé. La méthode de conception méthodique est une méthodologie pour la structuration et la documentation des étapes du processus de conception [1]. Les fonctions à remplir et les fonctionnalités pour créer sont répertoriées dans un tableau morphologique. Dans un schéma morphologique des sous-fonctions de refroidissement par évaporation sont répertoriés verticalement. Les solutions possibles pour ces sous-fonctions sont énoncées horizontales. De cette façon, il devient clair que la solution différente est pour chaque sous-fonction.

Cette vue d'ensemble des fonctions et leurs solutions rend en combinant différentes sous solutions à des solutions globales plus faciles.

SYSTEME ET MODELISATION

Aujourd'hui, le photo catalyse est devenu un mot commun et de nombreux produits utilisant des fonctions photo-catalytiques ont été commercialisés. Parmi les nombreux candidats à catalyseur de photo, TiO₂ est presque le seul matériau approprié pour une utilisation industrielle à l'heure actuelle et sans doute aussi à l'avenir. A titre précision, TiO₂ a l'activité plus efficace, et la stabilité la plus élevée et le moindre coût. De manière plus significative, il a été utilisé depuis les temps anciens, et donc, sa sécurité pour l'homme et l'environnement est garantie par l'histoire. [1]

Comme mentionné précédemment, le maintien d'une fine pellicule d'eau sur les surfaces d'un bâtiment, une stratégie de refroidissement efficace pour réduire sensiblement les températures de surface. Dans cette étude une méthode de fixation est proposée de surfaces d'eau par aspersion continue de l'eau sur les surfaces de la construction qui seront couverts avec un photo catalyseur TiO₂.

Dû à la lumière UV, la surface devient très hydrophile et joue un rôle important dans la minimisation de la

quantité d'aspersion d'eau nécessaire pour former un film d'eau. En d'autres termes, l'irradiation de la lumière solaire provoque alors l'angle de contact à diminuer progressivement, jusqu'à ce que finalement l'angle de contact devient 0°. Par conséquent, la surface revêtue de TiO₂ entière est couverte avec de l'eau. [2]

Récemment un scientifique a prouvé qu'une très fine couche d'eau d'environ 0,1 mm d'épaisseur peut couvrir l'ensemble des substances hautement hydrophiles. L'eau peut être alimentée en continu en petites quantités pour un bâtiment vertical. Il est très important de noter que les bâtiments ne sont pas refroidis par l'eau elle-même, mais par le flux de chaleur latente lorsque l'eau s'évapore. En fait, il est possible que la température de la surface de paroi soit inférieure à celle de l'eau d'arrosage. La couche d'eau la plus mince, la température de surface plus efficace des bâtiments et la diminution de la température de l'air ambiant comme la quantité de flux de chaleur latente diminue pour refroidir le film mince d'eau. Le taux d'évaporation et la chute de température associée dépendent de la couleur et / ou le matériau de construction de type (coefficient d'absorption solaire), la vitesse du vent sur la surface du bâtiment, la température ambiante et l'humidité relative. Le refroidissement de la surface du bâtiment peut conduire à la réduction de la quantité d'électricité consommée pour la climatisation. [3]

Sur la figure 1, le principe de l'évaporation de la pellicule d'eau sur une paroi externe / construction est représentée schématiquement, l'hypothèse est que l'ensemble du TiO₂ revêtu surface est recouverte d'un film mince d'eau.

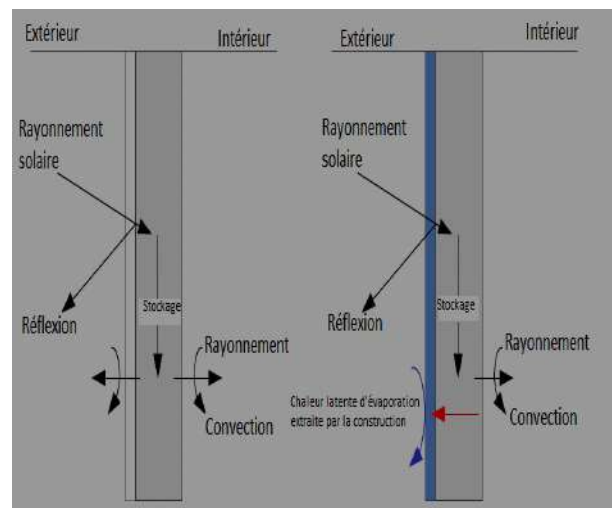


Figure 1
Vue schématique de la couche d'eau sur la construction [4]

$$C_3 \frac{dT_{s,i}}{dt} = \underbrace{\frac{T_{s,e} - T_{s,i}}{R_3}}_{\text{Conduction}} - \underbrace{\frac{T_{s,i} - T_i}{R_4}}_{\text{Convection}} \quad [W] \quad (3)$$

Les rayonnements solaires direct et diffus augmentent à la fois la température de surface de la construction selon l'absorption et la réflexion du matériau de construction. Pour l'évaporation du film mince d'eau, la chaleur absorbée dans la construction sera utilisé. Il en résulte une température de surface externe décroissant ($T_{s,e}$). Le réseau thermique de la couche d'eau est représentée sur la figure 2.

Les équations de transfert de chaleur 1-dimensionnelles pour la construction de bâtiments y compris le film mince d'eau sont présentés dans les équations (1) à (3).

Le second terme de l'équation (1) est le transfert de chaleur par convection de l'air ambiant à la pellicule d'eau. Le coefficient de transfert de chaleur par convection est considéré comme une fonction de la vitesse du vent est donnée par l'équation (5) : Jürges. [4]

$$R_1 = \frac{1}{\alpha_c * A} \quad [K/W] \quad (4)$$

$$\alpha_c = 4.2 * w + 6.2 \quad [W/m^2K] \quad (5)$$

Le troisième terme de l'équation (1) est le transfert de chaleur par convection à partir de la pellicule d'eau à la surface du bâtiment de TiO2 revêtu. Le coefficient de transfert de chaleur par convection est déterminé comme suit, voir l'équation (7). Le nombre de Nusselt est calculé suivant l'équation Johnson-Rubensin [7].

$$R_2 = \frac{1}{\alpha_w * A} \quad [K/W] \quad (6)$$

$$\alpha_w = \frac{Nu \lambda_w}{z} \quad [W/m^2K] \quad (7)$$

$$Nu = 0.0296 R_e^{0.8} P_r^{0.6} \quad (8)$$

$$R_e = \frac{U_w z}{\nu} \quad (9)$$

$$P_r = \frac{\nu}{\alpha} \quad (10)$$

$$\alpha = \frac{\lambda_w}{w * c_w} \quad [W/m^2K] \quad (11)$$

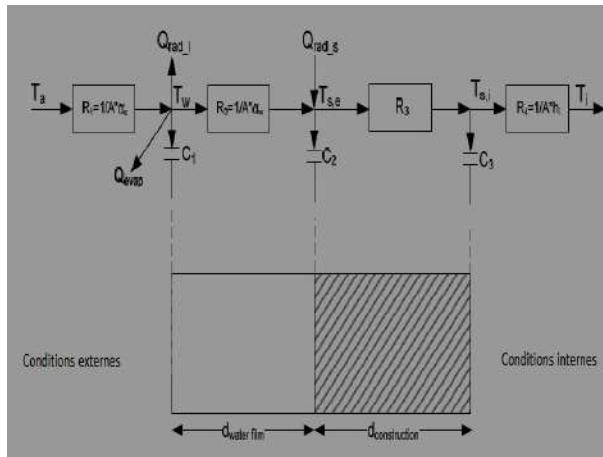


Figure 2
Réseau thermique de la pellicule d'eau sur une construction

$$C_1 \frac{dT_w}{dt} = \frac{T_a - T_w}{R_1} - \frac{T_w - T_{s,e}}{R_2} - Q_{rad} - Q_{evap} \quad (1)$$

$$C_1 \frac{dT_w}{dt} = \frac{T_a - T_w}{R_1} - \frac{T_w - T_{s,e}}{R_2} - A * \epsilon \sigma (T_w^4 - T_{sky}^4) - A * l \frac{\alpha_c}{c_m} (X_{s,e} - X_a) \quad [W]$$

Convection Rayonnement (ondes longues)

$$C_2 \frac{dT_{s,e}}{dt} = \frac{T_w - T_{s,e}}{R_2} + Q_{rad} - \frac{T_{s,e} - T_{s,i}}{R_3}$$

$$C_2 \frac{dT_{s,e}}{dt} = \underbrace{\frac{T_w - T_{s,e}}{R_2}}_{\text{Convection}} + A * \underbrace{\frac{T_w - T_{s,e}}{R_2} \alpha R_s}_{\text{Rayonnement (ondes courtes)}} - \underbrace{\frac{T_{s,e} - T_{s,i}}{R_3}}_{\text{Conduction}} \quad [W] \quad (2)$$

Le quatrième terme de l'équation (1) est le rayonnement net longueur d'onde entre le ciel et le film d'eau et le cinquième terme est la chaleur latente de l'évaporation. La surface externe du bâtiment est refroidie par le flux de chaleur latent en fonction de la différence de pression de vapeur du mélange de vapeur d'eau dans l'air et la pression de vapeur d'eau à la surface, la taille de la zone de contact et le coefficient de transfert de masse et non pas par un flux de chaleur sensible.

Pour déterminer l'humidité absolue de l'air ambiant (X_a) et de l'humidité absolue de la pellicule d'eau sur la surface du bâtiment ($X_{s,e}$) la pression de vapeur des mélanges sont nécessaire. Le calcul de la pression de vapeur saturante est selon Künzel. Il convient de noter que les températures T dans la formule (12) sont en degrés Celsius.

$$P_{sat} = 611 * e^{\left(\frac{17.08 * T}{234.18 + T}\right)} \quad [Pa] \quad (12)$$

$$P_v = RH * P_{sat} \quad [Pa] \quad (13)$$

$$x = f * \frac{P_v}{P_T - P_v} = f * \frac{(RV * P_{sat})}{P_T - (RV * P_{sat})} \quad \left[\frac{kg}{kg}\right] \quad \text{with } f = 0.622 \quad (14)$$

L'humidité absolue de l'air ambiant et l'humidité absolue des surfaces de l'immeuble peuvent être déterminés selon la formule (14).

$$x_a = 0.622 * \frac{(RV * P_{sat@T_a})}{P_T - (RV * P_{sat@T_a})} \quad \left[\frac{kg}{kg}\right] \quad (14a)$$

$$x_{s,e} = 0.622 * \frac{(RV * P_{sat@T_{s,e}})}{P_T - (RV * P_{sat@T_{s,e}})} \quad \left[\frac{kg}{kg}\right] \quad (14b)$$

Le flux de chaleur entrant dans l'enceinte du bâtiment peut être déterminé par la formule (15). Dans le cas du refroidissement, le flux de chaleur sera négatif dû au fait que la température de surface interne est inférieure à la température de l'air intérieur.

$$\dot{q} = \frac{T_{s,i} - T_i}{R_4} \quad [W] \quad (15)$$

Le flux de chaleur entrant dans l'enceinte du bâtiment par le revêtement de verre n'est pas seulement par conduction, mais surtout par le rayonnement solaire à travers la feuille de verre semi-transparent. Un mécanisme lié à l'absorption du verre, contribue à la charge thermique en dessous. En effet, le rayonnement solaire absorbé par la feuille de verre est ensuite libéré à la fois par rayonnement et par convection thermique à l'environnement, tant à l'intérieur qu'à l'extérieur. (Voir figure 3)

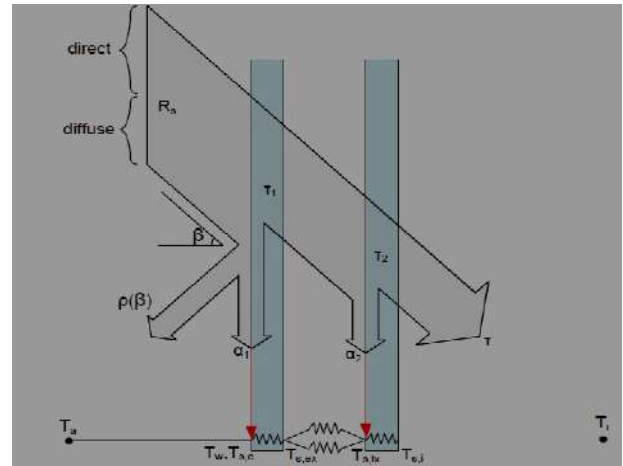


Figure 3
Rayonnement solaire sur un système de vitrage semi-transparent

Le rayonnement solaire à la fois diffuse et directe est généralement limitée à $0,25 < \lambda < 3$ gamme de longueurs d'onde pm. Pour chaque longueur d'onde, la somme des fractions de la somme d'énergie réfléchi, transmise et absorbée par le verre est égale à un. C'est l'une des lois fondamentales de la conservation de l'énergie: $\alpha(\lambda) + \rho(\lambda) + \tau(\lambda) = 1$. Le coefficient d'absorption (α) est divisé en deux fractions, l'une pour la vitre extérieure (α_1) et l'autre pour le panneau de verre intérieur (α_2). Le rayonnement solaire qui entre directement dans l'espace sous-jacent est définie comme la combinaison des transmittances τ_1 et τ_2 .

$$\tau = \tau_1 \tau_2 A R_s \quad [W] \quad (16)$$

Les résistances au transfert de chaleur entre les plaques de verre dans la cavité sont données par les résistances R_R et R_c pour respectivement rayonnement et par convection. Ces résistances individuelles sont remplacées par une résistance totale de la cavité, appelé R_{cav} (R_4). Le coefficient de transmission thermique totale (valeur U) pour le double vitrage (sans film d'eau) peut être calculé comme suit:

$$U_{gl} = \left(2 \left(\frac{d_{gl}}{\lambda_{gl}} \right) + R_i + R_{cav} + R_e \right)^{-1} \quad [W/m^2K] \quad (17)$$

Dans le cas d'un film d'eau sur le double vitrage, la résistance R_e externe sera remplacée par des résistances de transfert de chaleur de l'air extérieur (R_1) et le film d'eau (R_2). Dans la figure 4, le réseau thermique du film mince d'eau sur double vitrage est montré.

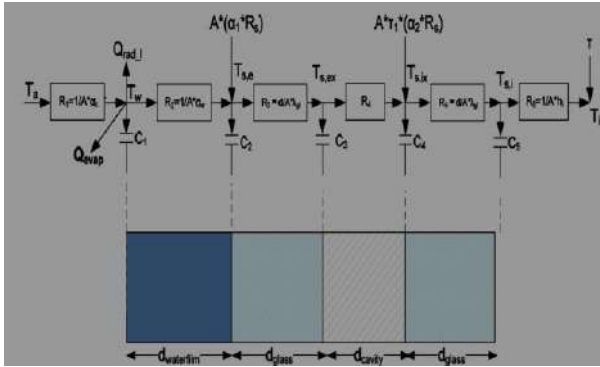


Figure 4

Réseau thermique du film d'eau sur double vitrage

Les équations différentielles pour ce réseau thermique peuvent être écrites comme suit :

$$C_1 \frac{dT_w}{dt} = \frac{T_a - T_w}{R_1} - \frac{T_w - T_{s,e}}{R_2} - A * \varepsilon \sigma (T_w^4 - T_{sky}^4) - A * l \frac{\alpha_c}{c_m} (X_{s,e} - X_a) \quad [W] \quad (18)$$

$$C_2 \frac{dT_{s,e}}{dt} = \frac{T_w - T_{s,e}}{R_2} + A(\alpha_1 R_s) - \frac{T_{s,e} - T_{s,i}}{R_3} \quad [W] \quad (19)$$

$$C_3 \frac{dT_{s,i}}{dt} = \frac{T_{s,e} - T_{s,i}}{R_3} - \frac{T_{s,i} - T_i}{R_4} \quad [W] \quad (20)$$

$$C_4 \frac{dT_{s,ix}}{dt} = \frac{T_{s,e} - T_{s,ix}}{R_4} + A\tau_1(\alpha_2 R_s) - \frac{T_{s,ix} - T_{s,i}}{R_5} \quad [W] \quad (21)$$

$$C_5 \frac{dT_{s,i}}{dt} = \frac{T_{s,ix} - T_{s,i}}{R_5} - \frac{T_{s,i} - T_i}{R_6} \quad [W] \quad (22)$$

Le flux de chaleur entrant dans l'espace peut être déterminé par l'équation (23).

$$\dot{q} = \left(\frac{T_{s,i} - T_i}{R_6} + \tau \right) \quad [W] \quad (23)$$

Comme mentionné précédemment est le gain de chaleur solaire Coefficient (CGS) la fraction de éclairement incident (de rayonnement solaire incident sur le vitrage) qui pénètre dans le bâtiment et devient une chaleur dans l'espace. Il comprend à la fois la

partie directement transmis (τ) et la partie absorbée et réémise du rayonnement solaire.

Lorsque la valeur U du système de vitrage est connue, la résistance thermique combinée de la cavité pour à la fois le rayonnement et la convection peut être calculée comme suit:

$$R_{cav} = R_4 = \left(\frac{1}{U_{gl}} - 2 \left(\frac{d_{gl}}{\lambda_{gl}} \right) - R_1 - R_2 - R_6 \right) \quad [W/m^2K] \quad (24)$$

HABITAT DE REFERENCE

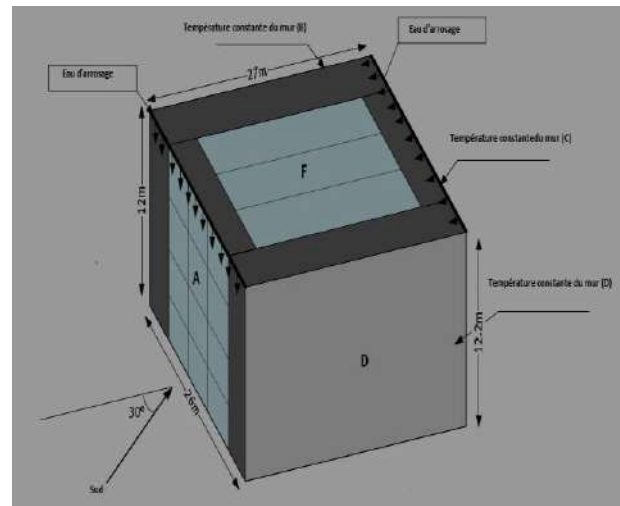


Figure 5

Habitat de référence

Ce grand espace vitré est conçu comme «espace de circulation»: une zone où les gens ne restent que pour de courtes périodes de temps. En pratique, cette oreillette est utilisée plus intensivement, car un grand nombre d'activités, comme des «Jeux-de-boules», sont organisées (voir figure5). Cela laisse le problème de lacunes inévitables en termes de climat intérieur.

Par conséquent, la paroi extérieure orientée au sud (A) et le toit vitré (F) sont équipé d'un revêtement de TiO2. Le système de refroidissement est une application de la super hydrophile de ce revêtement de TiO2. Par conséquent, un film mince d'eau peut être formé en continu par aspersion d'eau sur la surface et l'évaporation de l'eau à travers la surface peut ainsi être réalisée.

Les propriétés spécifiques du projet sont présentées dans le tableau 1. Les parois internes (B à D) seront modélisées comme des murs de température constants dus à des espaces adjacents climatisés. Pour la surface de la terre adjacente à la construction

de plancher une température constante de 10 ° C sera supposée.

Tableau 1

Propriétés de l'édifice de l'atrium de référence

Paramètre	Composition	Symbole	Surface [m ²]	Orienteation
Mur extérieur	Béton (30%) Verre (70%)	A	317.2	[90.0, 30.0]
Mur intérieur	Béton léger	B	329.4	[90.0, 120.0]
		C	317.2	[90.0, 210.0]
		D	329.4	[90.0, -60.0]
Etage	Béton (isolé)	E	702	[0.0, 30.0]
Toit	Béton (30%) Verre (70%)	F	702	[0.0, 30.0]
Autres	Calendrier d'utilisation Taux de ventilation Gains de chaleur interne	8h-18h 1[1/hr] 1000 [W]		

Au cours des simulations de l'écoulement d'air de ventilation à travers l'atrium et la chaleur interne gains seront maintenues constantes pendant les heures de fonctionnement de 8-18h. De ce fait l'effet de refroidissement par évaporation de l'eau est mieux prévisible et indépendant de ces variables.

RESULTAS ET DISCUSSION

Le modèle d'air et l'humidité d'air est capable de simuler la température intérieure, l'humidité de l'air et la consommation d'énergie intérieure pour le chauffage et le refroidissement d'un bâtiment multi-zone. Pour résoudre les équations 1 dimensions de transfert de chaleur, des données climatiques détaillées, en tant que en fonction du temps est nécessaire. La température ambiante (T_a), par l'humidité relative (Rh_e), la vitesse du vent (w) et le rayonnement solaire à la fois diffus ($Q_{sol-dir}$) et ($Q_{sol-dir}$) directe sont des paramètres d'entrée importants.

L'azimut (0-360°) et l'inclinaison (0-90°) des différentes surfaces de construction seront entré dans le modèle. Après avoir défini les propriétés des différents matériaux de construction (épaisseur, la conductivité thermique, d'absorption solaire, la capacité, etc.) et le film d'eau (épaisseur, la vitesse de l'eau, etc.) les

unidimensionnels équations de bilan de chaleur sont résolues pour toutes les surfaces de construction. Le transfert de chaleur à une dimension correspond aux formules (1-3) et (18 à 22) respectivement pour les pièces de construction et des systèmes de vitrage. Les flux de chaleur (formules 15 et 23) à travers la façade du bâtiment et le toit sont additionnés et serviront comme paramètre d'entrée pour l'ensemble du bâtiment dans le modèle de HAMBBase. La température de l'air ambiant de sortie résultant du modèle de HAMBBase est réinjecté à l'entrée des 1D équations de transfert de chaleur. Sur la base des flux thermiques avec ou sans évaporation de la capacité de refroidissement peut être calculée:

$$q_{cooling} = q_{in} - (q_{in})^* [W] \quad (25)$$

* : sans évaporation

Tout d'abord un aperçu a été créé de paramètres d'entrée qui sont nécessaires pour spécifier un modèle de HAMBBase dans l'environnement MATLAB. D'autre part, les paramètres d'entrée qui sont susceptibles d'avoir un impact sur l'effet de refroidissement de l'ensemble du système ont été sélectionnés et énumérés dans le Tableau 2.

Tableau 2

Vue d'ensemble des valeurs maximales et minimales des paramètres sélectionnés

Paramètre	Symbole	Unité	Valeur	
			Minimal	Maximal
Conditions externes				
Vitesse du vent	w	[m/s]	2	10
Humidité relative	RH	[%]	40	90
Film mince d'eau			Minimal	Maximal
Vitesse d'écoulement d'eau	U_w	[m/s]	0.1	0.5
Epaisseur du film mince d'eau	d_w	[m]	0.0001	0.001
Couche de construction			Minimal	Maximal
Epaisseur de couche	d	[m]	0.05	0.30
Facteur d'absorption	α	[-]	0.40	0.90
Couche de verre			Minimal	Maximal
absorption solaire de la vitre extérieure	α_{glass}	[-]	0.05	0.4
Valeurs de U du verre	U_{glass}	[W/m ² K]	1	4

Le système d'équations d'énergie (1) à (25) a été résolu pour la semaine d'été typique du 1 au 7 juin 2014. Les températures des surfaces de toit (T_s) à la fois pour la construction et le système de vitrage sont représentées sur les figures 6 et 7 respectivement.

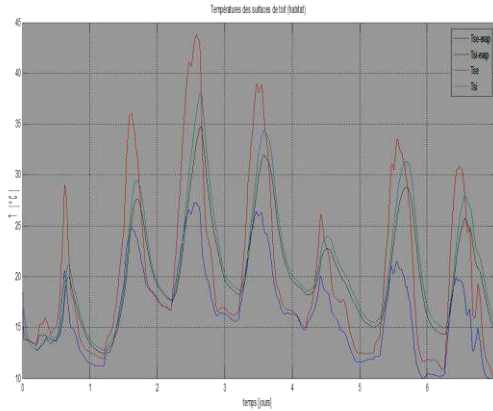


Figure 6

Les températures de surface (avec ou sans évaporation) de la construction en fonction du temps

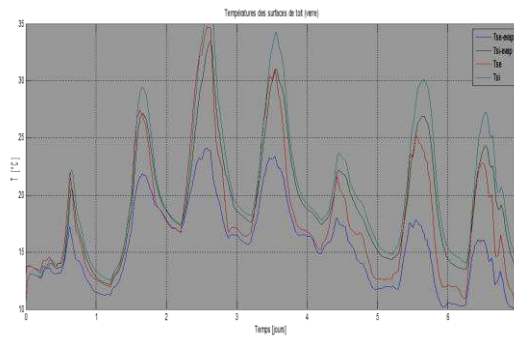


Figure 7

Les températures de surface (avec ou sans évaporation) de l'enveloppe de verre ($\alpha = 0,35$) en fonction du temps

Sur la figure 7, les températures de surface du revêtement de verre (avec ou sans évaporation en surface) sont montrées pour un coefficient d'absorption solaire constante de $\alpha = 0,35$.

La capacité de refroidissement et les effets sur la température de l'air intérieur du système de refroidissement proposé sur le toit de TiO₂-couché et façade sud sont présentés dans les figures 8 et 9.

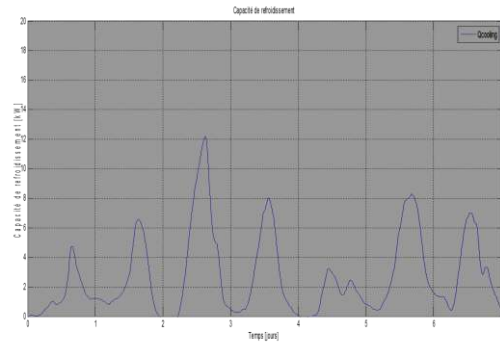


Figure 8

Capacité de refroidissement du système en fonction du temps

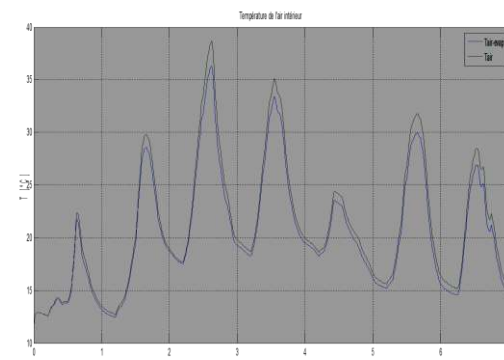


Figure 9

Températures de l'air intérieur en fonction du temps

Les réductions de température simulées dans le grand espace vitré en raison de l'effet de l'évaporation du film mince d'eau sont entre 1K pour moins de jours ensoleillés et 3K pour les beaux jours (pour $U = 1.5W / m^2K$). Le nombre de jours 3, l'humidité relative est diminuée jusqu'à 45% et le rayonnement solaire est maximal. Pour cette raison de la différence de pression de vapeur du mélange de vapeur d'eau dans l'air et la pression de vapeur d'eau à la surface du bâtiment est maximale. Cela permet plus d'eau pour évaporer, ce qui entraîne une augmentation du flux de chaleur latente et une capacité de refroidissement plus élevée. Ainsi, le système fonctionne de refroidissement optimal sur la partie la plus chaude de la journée, lorsque le refroidissement est souhaitable.

En prenant en compte l'énergie totale qui est nécessaire pour maintenir la température intérieure inférieure à 24 ° C, la réduction de la charge de

renforcement de refroidissement peut être déterminée. Les économies d'énergie d'environ 15% sont possibles pour le simulée grand verre couverte espace avec l'air conditionné.

CONCLUSIONS

Le refroidissement par évaporation est considéré comme un moyen approprié pour atténuer l'extrême environnement thermique des grands espaces vitrés. Utilisation de la conception méthodique méthode, les concepts issus comme matériaux poreux et TiO₂-super-hydrophile pour les surfaces de bâtiments revêtus montrent le plus grand potentiel pour les grands espaces vitrés. Les variables qui affectent largement le processus d'évaporation de ces concepts:

- La Taille de la surface de contact;
- Le coefficient de transfert de masse spécifique.

Les résultats des simulations montrent que le taux d'évaporation dépend fortement de la extérieure la température de la toiture ou de façade surface. En raison du taux élevé d'absorption solaire du verre, le rayonnement solaire direct transmis dans l'espace vitré est réduite. Cet effet est opposé de ce qui se passe sur les murs et les toits opaques, où le faible rayonnement solaire absorbé est souhaitable de réduire le flux de chaleur par conduction vers l'enceinte.

Les températures de surface externe de la toiture de verre sont réduites par 3-9K due à la libération de la chaleur latente de l'évaporation de l'eau. Les réductions de température simulées dans le grand espace vitré sont entre 1K et 3.5K pour les jours respectivement moins ensoleillées et ensoleillées.

Enfin, on peut conclure que le renforcement de catalyseur revêtu super-hydrophile photo surfaces avec film mince d'eau sont en mesure de contribuer de manière significative à l'air intérieur la réduction de la température. Aussi, l'augmentation d'absorption du rayonnement solaire en verre ($\alpha = 0,3$) est nécessaire, parce que l'efficacité du processus de refroidissement par évaporation est basée sur sa capacité à évacuer la chaleur absorbée à partir du toit ou de façade, avant son entrée dans l'espace situé derrière.

MOTS-CLES: modèle de La chaleur et de l'humidité d'air (HAM), Modélisation, refroidissement, températures des surfaces, ventilation

REFERENCES

1. Zeiler, W, Methodical Design 1972-2006: A historical Overview about a Design model, Design Principles and Practices: An International Journal, Vol..1, 2007.
2. P. Blesgraaf (1996) Grote Glasoverkapte Ruimten – Atria, serres, passages. Novem.
3. M. Dubois (1998) Solar-protective glazing for cold climates. A parametric study of energy use in offices. Department of Building Science, Lund University Sweden.
4. Zeiler, W., Savanovic, P., Boxem, G. (2009). Nanotechnology for sustainable building facades. In J.-L. Scartezzini (Ed.), Proceedings of the CISBAT 2009 International Scientific Conference "Renewables in a Changing Climate: from Nano to Urban Scale" (pp. 167-172). Lausanne.

RISK-EU METHOD APPLIED TO THE ALGERIAN CITY OF ARZEW TO ASSESS EXPOSURE TO EARTHQUAKES

AOUANE Abderrahim^{1*}, RAHAL D. Driss², A.H. Mohammed Belhadj¹, HAMOU Kada¹

¹PhD student at the University of Sciences and technology of Oran. «Department of Civil Engineering» BP 1505 Oran El - Menouar Algeria and engineer a HYPROC SC.

²Professor, University of sciences and technology of Oran «Department of Civil Engineering» BP 1505 Oran El - Menouar Algeria.

*Corresponding author: +213 6 70 19 01 00 Email: aouane_rahim@yahoo.fr

ABSTRACT

In order To mitigate the adverse consequences of an earthquake, determining the vulnerability of buildings is imperative and crucial for saving human lives and buildings.

So far, a good review / assessment of the RISK-EU method appears, as opposite to the other methods (more than a dozen) vulnerability assessment methods, to be by far the most suitable and applicable to the Context and seismographic configuration of Algeria,

This tentative case study will review and evaluate, in particular, the RISK-EU method for Arzew city with due consideration to the following parameters:

-Geographical position: North West of Algeria

-Classified in Zone II, average seismicity area, in accordance with the Algerian seismic Rule - RPA99 version 2003-

-She suffered several earthquakes, the most recent one happened last 21 Mars 2014 ($M_s=4.3$; equivalent to $VI \approx VII$ as per EMS 98),

-The whole town is sitting on the rim between two tectonic plates and next to the Mediterranean Sea grand rifts

This study is based on the results of a survey assessing the exposure of the Arzew city buildings with a cross check and comparison with results obtained through the use of another method, widely used in Algeria, named « CTC ». This latter method is based on the assessment of the extent of the damages.

For clarity sake and better understanding of our results, we have included in this study a « seismic risk map » Such map has been developed using a « SIG method » (Geographical information system)

This study contains proposals to enhance the protection of the Arzew city buildings and reduce the overall risk and exposure to the frequent seismic activity in the Mediterranean area.

Keywords RISK EU; CTC; ARZEW; vulnerability; GIS

INTRODUCTION

Arzew city situated in Algeria's North West, has been shaken by many earthquakes, the most recent one are those of March 21th 2014 ($M=4.3$) and February 2nd 2014 ($M=2.9$). Last ones listed were from July the 24th to august the 4th "25 shakes". The entire city is prone to earthquakes because of the collision between the two tectonic plates and existence of many breaks at the north of the city (Mediterranean Sea).

Buildings are more exposed to earthquake's danger than citizens, this influence directly on its longevity. It's difficult to master this risk because of its amplification and lack of maintenance. In order to mitigate the harmful consequences of a possible earthquake, it's imperative to determinate the vulnerability of buildings to preserve human lives, buildings and hydrocarbon complexes.

There are two different methods to evaluate buildings vulnerability, these methods exist since

the 70's "GNDT, AFPS2005, ATC 13, Vulniralp 1 and 2, RISK-EU", these methods are not used in Algeria for many reasons (typological and no qualifications). The methods used are derived from the Italian method GNDT, based on vulnerability index.

Our presentation will be about practicing the European method "RISK-EU" and the CTC one "Control Technique Center – constructions diagnosis" for Arzew's city, also about rapprochement between the two methods.

To perform and display the impact of seismic vulnerability on Arzew's city, a risk map has been created with a geographic information system (GIS) as a support to help taking decisions by elected assemblies administrators, civil protection, police and other public services taking care of citizen protection and welfare.

METHODS APPROACH (RISK-EU AND CTC)

RISK-EU method

Developed by University Gènes (UNIGE) from vulnerability model exposed in **EMS 98** and guides **GNDT** (*Gruppo Nazionale Difesa dai Terremoti*).

It includes two levels:

- **Level 01:** Based on vulnerability index evaluation, vulnerability and fragility curve for a certain type of buildings.
- **Level 02:** Mechanic method based on dynamic modeling.

Our study will be about the first level, depending on the building typology and the factors that can alter its behavior.

Vulnerability index V_1 varies from 0 to 1, the maximal value represents extreme vulnerability; it's obtained by adding these 4 indexes:

V_1^* : Based in typology.

ΔV_m : Factors aggravating vulnerability

$$\Delta V_m = \sum V_m .$$

ΔV_r : Expert judgment. (Value which takes into properties of specific typologies at a regional level).

ΔV_f : Uncertainty of typology reading and vulnerability factors.

$$V_1 = V_1^* + \Delta V_m + \Delta V_r + \Delta V_f$$

The method expressing vulnerability is obtained with the damages probability matrix (DPM), this is the result of statistical correlation between intensity EMS 98 and caused damages degree.

Average damage estimation u_d

$$\mu_d = 2.5 x \left(1 + \tanh \left(\left(\frac{(I + 6.25 V_1 - 13.1)}{2.3} \right) \right) \right)$$

CTC Method

It's a technical investigate record about construction diagnosis, a method used by Technical Control Center « CTC » which determines the habitability by ranking the following buildings on a five levels scale (1,2,3,4,5) corresponding to the colors (green 1, green 2, orange 1, orange 2 and finally red).

Analysis sheet of the CTC method contains:

- General identification in formations, use and number of levels.
- Observation of soil problems, foundation and infrastructures.

- Damage evaluations of structural and secondary elements.
- Comments on probable causes of damages.
- Global evaluation of the general level of damages.
- Emergency measures recommendation.

After these steps, the engineers rank the following buildings following the damages to assign.

Table 1: classification of buildings following the damage (method CTC)

Level	Color	Damages severity	Description
1	Green 1	No damages	Except furniture and broken windows
2	Green 2	Light weight damages	Cracked interior partitions, ceilings, piping damages and isolated non structural damages
3	Orange 1	modest damages	Important damages for non structural parts and small damages for structural ones
4	Orange 2	Important damages	Very important non structural damages, and important structural damages. X cracks in the bracing sails, bursting nodes « P/P ».
5	Red	Very important damages	Fallen buildings or to condemn

CREATING A GEOGRAPHIC INFORMATION SYSTEM

To achieve a geographic information system (SIG), a combination of data related to different buildings must be extracted from the database (already designed) destined for taking decisions for specific interventions.

Database creation

A mission field has allowed us to assess the actual condition of the buildings.

Throughout our field research, field forms were indicated for each building. (According to both methods).

The survey form has four main components of the two methods:

- Description sheet of the book,
- Environmental evaluation sheet,
- Structural evaluation sheet.
- Functional evaluation sheet.

The main data collected are shown in Table 1.

Note that all the appraised buildings are reinforced concrete.

Thematic analysis

Thematic analysis is the principal step of a SIG. It translates the meaning of a representation. Our analysis will be done based on u_d (RISK EU) and N (CTC).

Table 2: Estimation of buildings proportions analyzed by districts.

District studied	Number of studied buildings	Construction years	Damage degree RISK – EU	Damage degree CTC
chevrier	4	1956 -1980	D2	N2
Ahmed ZABANA	10	1988	D1@D2	N2 @ N3
Amir Abdelkader	6	1982	D2	N3
	3	1988	D3	N3 @ N4
	8	1988	D1	N2
Tour ville	8	Before 1962	D0	N1
Cité Ben Boulaid	22	1978	D1 @ D3	N1 @ N4
Cité Complexe	6	1982	D2 @ D3	N3

RESULTS ANS INTERPRÉTATIONS

According to the analysis made on the basis of the CLC method, $\approx 50\%$ of the analyzed buildings are green class 1 and 2. This shows a good seismic resistance. Furthermore, 40% of buildings are orange 1 (N3) and 13% orange 2 (N4)

This is explained by the influence of social settings (construction of a railway station with "Ben-Boulaid City "), lack of maintenance for the neighborhoods " City Complexe " and " Amir Abdelkader city ", the apartments in these neighborhoods built in the 80's since they received no planning and are devoid of any maintenance system, even worse, they are rent rent.

According to the EU RISK-method analysis, it shows that 45% of the analyzed buildings are D0 and D1 it means they incur no risk. The classified buildings D2 represent 40% (Slight damage) and 18% with moderate damage or D3.

Table 3: Comparison of Arzew’s results in %

RISK EU		CTC	
D0	17%	N1	17%
D1	28%	N2	30%
D2	40%	N3	40%
D3	18%	N4	13%
D4	0%	N5	0%
D5	0%		



Figure 1: Thematic analysis of the methods RISK-EU (Ben-Boulaid district)



Figure 2: thematic analysis of the methods CTC (Ben-Boulaid district)

If we compare the results of the two methods, there is an almost perfect similarity between the levels N1, N2 and N3 degrees compared to D0, D1 and D2, with the exception of a few buildings N4 and D3 where the basis of the similarity no longer applies.

This difference may be justified by the accuracy of the damage estimation formula comparing with the CTC method mainly based on visual observation.

This difference in the two levels (N4 and D3), guided us to design a new method RISK-DZ, which takes into account the existing parameters in a method and not the other (vice-versa), all that to get similar and convincing results.

PROPOSALS

Due to the structural complexity of Arzew’s buildings, vulnerability estimation became difficult, to moderate this problem, works and discussions were done to promote the new

method (quick and easy) not yet experienced (ongoing research), a fusion of two RISK-EU CTC methods to generate the new method RISK-DZ.

We will use the same settings as the two proposed methods, with perfect adaptation, adjustments and removal of certain items.

Example: hardening the vulnerability index (Bad maintenance, RPA code level (PS54, RPA81, RPA88, RPA99, and RPA2003 following year of construction) consideration of delimited constructions soil nature (soil morphology: sagging, flick, slip, uniform compaction) and the supporting and bracing elements, influence of adjacent buildings, sealingetc.

CONCLUSION

This study has shown that the exposure of Arzew City to Seismic risk is not insignificant, because of its peculiarity. The testing of assessment methods about the vulnerability that are developed on the basis of a post-seismic examination informed us that intervention in advance will be more judicious.

Despite the historical seismicity in Algeria, the seismic risk is always a detrimental frequent phenomenon, for a better assessment of the buildings, it was essential to create a new method (RISK-DZ) adapted to the Algerian context, that will allow us a more realistic and plausible estimate.

The use of risk map (SIG) with the method, provides information on the attention to be given to buildings, is still a powerful support to managers, decision makers and local officials for a deeper insight on eventual rehabilitation.

Also, it would be interesting to amend this method from now, by the assessment of some important buildings in order to estimate the cost of a probable rehabilitation and estimate the eventual human losses. All decisions taken by governments for any possible rehabilitation project, will allow the reduction of seismic risk in the city of Arzew

REFERENCES

1. Lestuzzi P (2006); Cours parasismique école polytechnique fédéral de lausanne.
2. Pellissier V.; Badoux 2004 « Evaluation des stratégies pour la gestion du risque sismique du bâtiment » thèse doctorat : Laboratoire de construction en béton.
3. Lucien CHIROIU, séminaire AFPS 2001 « Estimation de dommages sismiques post catastrophe à l'aide de l'imagerie satellite. Application au séisme de Gujarat, Inde, 2001 ».
4. Aouane A. ; Touati H (2007) « **Risque sismique** « **Exemple ville d'ARZEW** ».colloque international « La communication dans les stratégies de gestion des risques ».
5. Ministre de l'habitat et de l'urbanisme : Mission CTC « guide pour le maître de l'ouvrage » fiche d'enquête relative au diagnostic des constructions.
6. Milan ZACEK (2004) : vulnérabilité et renforcement, cahier 2 « collection conception parasismique ».
7. BRGM (2004) Projet européen RISK-UE : application à la ville de Nice « rapport final ».
8. BRGM (2008) Scénario départemental de risque sismique méthodologie et processus de réalisation.
9. BRGM (2008) Mise en œuvre d'une base de données du bâti aux Antilles « rapport final ».
10. BRGM (2008) Comparaison de méthodes qualitatives d'évaluation de la vulnérabilité des constructions aux séismes « Plan séisme - action 2.4.7. Guide des méthodes de diagnostics de la résistance des bâtiments aux séismes ».
11. A. SENOUCI & co (2012) colloque international 15 WCEE portugale lisboa "classification of buildings of oran city (algeria) based on their seismic vulnerability"
12. CGS, 2010. Etude d'aléa sismique de la région d'Oran-Arzew, Rapport Final. CGS, Alger.
13. Thèse baba Ahmed 2011 évaluation du risque des bâtiments algériens en milieu urbain: simulation et prédiction.
14. Pellissier V. 2004. "évaluation de stratégie pour la gestion du risque sismique du bâtiment" thèse de doctorat es-science, école polytechnique fédérale de Lausanne, suisse.

COMPOSITE MATERIALS CONTAINING DIFFERENT POLYMER LEVELS: DESIGNING & ESTIMATING DURABILITY INDICATORS

N. Latroch^{1,4}, A.S. Benosman^{1,2,3*}, N. Bouhamou⁴, B. Belbachir^{1,3}, H. Taïbi³, M. Mouli¹

¹ Department of Civil Engineering, Laboratory of Materials LABMAT, ENPO, Oran, Algeria.

² Department of Chemistry, Preparatory School of Science and Technology EPST,
BP 165 RP, 13000 Bel Horizon, Tlemcen, Algeria.

³ Faculty of Exact Sciences and Applied, Lab. of Polymer Chemistry, University of Oran 1, A. Benbella,
Oran; Algeria.

⁴ Department of Civil Engineering, University of Mostaganem, Algeria.

*Corresponding author: Email: amre20022000@yahoo.fr

ABSTRACT

The growing need for building material resources, and the requirements to preserve the environment, in a vision of sustainable development, has become necessary to study reinforcement techniques, using composite materials. Using local organic or inorganic materials in construction fields and public works is particularly important. Polymer-Mortar Composites (PMCs) are usually employed in the building industry as finishing materials, tile adhesive (mortar-adhesive) or façade coating. In repair applications, the addition of soluble polymer (latex) allows improving the adhesion properties of the materials used as coating. The use of mineral additives as partial substitutes for cement, in construction sites as well as in ready-to-use mortars, is an unknown practice in our country. For this reason, we thought it is crucial to study and assess the influence of these additions on the properties of cured composite. The mineral additives used in this study are silica fume and natural pozzolan, which necessarily need to be valorized.

The present research work aims to use a specific experimental methodology that is able to identify the relationship between the degree of substitution by the mineral additives, the polymer and the modifications to the properties of fresh and hardened cement mixtures. Therefore, five PMC combinations were formulated from different percentages of additions, i.e. natural pozzolan (NP: 25%^w), silica fume (Sf: 5%^w) and polymer latex (P: 0, 5, 7.5, 10, 12.5 and 15%^w). Their durability factors, such as the porosity accessible to water and capillary absorption rate (sorptivity), were characterized, at different maturities. The results obtained were compared with those of the reference mortars, made with Portland cement (CEMI). They showed that the decrease in porosity and sorptivity depends on the pair “mineral addition/polymer”. But overall, the addition of polymer latex and pozzolanic additions have a beneficial effect on the durability of the composite materials (PMCs).

KEYWORDS

Durability; Composite Materials PMC; Mineral/Polymer additions; Porosity; Sorptivity

INTRODUCTION

Mortars are certainly used to assemble materials, but also to equalize or confer a consistent finish to walls and floors as well. They can be used for insulation, repair and renovation. For decades, formulators of concrete have developed ever more effective mortars in order to meet the market requirements. For this reason, the building materials industry manufactures nowadays polymer-mortar composites (PMCs) [1]. The cement industry uses a lot of raw material, and this has a harmful effect on the environment. From there, several techniques have emerged and still

continue to develop in order to partially replace cement by local mineral additions [2-5].

This work presents an experimental study, performed in the laboratory, on composite materials (PMC) containing different concentration levels of polymers, and based on mineral additions, such as natural pozzolan and silica fume. This paper aims to find the optimal percentage of these additions as well as that of polymer latex, while investigating the impact of these additions on the physical characteristics of mortars, such as the porosity accessible to water and the evaluation of the rate of capillary absorption (sorptivity), at different maturities. The results obtained are compared with

those of unmodified mortars; they indicate that the reduction in sorptivity and porosity depends on the mineral additions and polymer used. Thus, adding the polymer latex and pozzolanic additions have a beneficial effect on the durability of modified composite materials. Moreover, promising outcomes have been revealed, and this requires particular attention which should open up new prospects for sustainable development in the future.

MATERIALS USED

Cement: The cement used in all tests is a CEM I 32.5N cement, from the cement plant of Beni-Saf, which comes in 50 kg bags. It is characterized by a number of conventionally measured criteria, which conform to the Algerian standard NA 442. The Blaine specific surface area was measured at the plant, according to standard EN 196-6 [6]. This cement has a fineness equal to 3139 cm²/g and an absolute density of 3.09. The initial and final setting times of cement are 1h 50 min and 3 hours 25 minutes, respectively, according to standard EN 196-3 [7]. The chemical composition of cement and the mineralogical one of clinker are given in Tables 1 and 2.

Natural pozzolan (Pz): This is a natural volcanic pozzolan, extracted from the deposit of Bouhamidi in the region of Beni-Saf (North West of Algeria). The natural pozzolan used in all tests is in the form of powder, resulting from crushed pozzolanic slag, previously steamed for 24 hours at a temperature of 50 °C, to remove moisture; they were then ground until the resulting powder can pass through a sieve with an 80-micron mesh [8]. The chemical composition of ground natural pozzolan is shown in Table 1.

Silica fume (Sf): The silica fume used in our study is a Ferro-silicon type additive for concrete in aggressive environments, from TECKNACHEM Company (Sidi Bel-Abbes). Its chemical composition is given in Table 1.

Table 1
Elementary Chemical Composition of CEM I 32.5 Cement

Elements	Cement	Pz	Sf
SiO ₂	21.35	44.85	79.0
Al ₂ O ₃	4.59	16.32	-
Fe ₂ O ₃	5.52	9.49	-
CaO	63.89	10.1	20.0
MgO	1.37	4.2	-
K ₂ O	0.41	-	-
SO ₃	2.72	1.05	-
L.O.I	2.47	4.1	-
I.R	0.22	-	-
Cl	-	-	-
Na ₂ O ₃	-	3.0	-

Table 2
Mineralogical composition of clinker

C ₃ S	C ₂ S	C ₃ A	C ₄ AF	CaO libre
47.15	25.69	2.84	16.78	2.32

Polymer (P): The polymer used, known as TEKWELD from TECKNACHEM Company, is a synthetic resin (Latex) in the form of a high density aqueous solution, stable in an alkaline medium, and especially designed to be added to the mixing water of cement mortars or plaster. The main characteristics of the polymer used are summarized in Table 3.

Table 3
Characteristics of the polymer used

Characteristics	Shape	Color	Density	pH
Polymer	Liquid	White (Milk)	1.05±0.01	6

Sand: In this experimental study, the silica sand used was of fraction 0/5, and came from the quarry of Nedroma, 60km northwest of Tlemcen. Before use, a granular correction of this sand was conducted by *sea sand* in order to have a continuous *granulometry*, according to the granulometric analysis of standardized sand (Fig. 1).

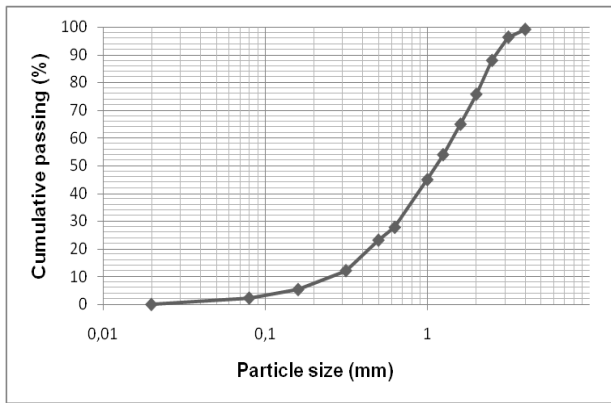


Figure 1
Particle size distributions of Sand

EXPERIMENTAL CONDITIONS

It was decided to produce composites based on mineral additives (PMC) with different polymer contents, i.e. $P/C = 0.5, 7.5, 10, 12.5$ & 15% , where P is the soluble polymer P and C the cement. The mineral additives used are silica fume and natural pozzolan which must necessarily be realized with percentages of 25% natural pozzolan and 5% silica fume. The mortar used in the present study, consists of the following proportions by mass: 1 cement and 3 sand, with a constant water to cement ratio $W/C = 0.5$, superplasticizer/cement = 1.3% and antifoam/polymer = 1% for all composites mortars (Table 4).

Table 4
Summary of experimental program

Code	C (%)	SCMs (%)		P (%)	E/C	SP (%)	AM (%)
		Pz	Sf				
C_M (0,0,0)	100	-	-	-	0.5	1.3	1
$Pz^{25}Sf^5P^5$ (25,5,5)	70	25	5	5	0.5	1.3	1
$Pz^{25}Sf^5P^{7.5}$ (25,5,7.5)	70	25	5	7.5	0.5	1.3	1
$Pz^{25}Sf^5P^{10}$ (25,5,10)	70	25	5	10	0.5	1.3	1
$Pz^{25}Sf^5P^{12.5}$ (25,5,12.5)	70	25	5	12.5	0.5	1.3	1
$Pz^{25}Sf^5P^{15}$ (25,5,15)	70	25	5	15	0.5	1.3	1

C_M : Control Mortar; Pz: pozzolan; Sf: Silica fume; P: Tekweld; SP: Superplasticizer; AM: antifoam.

Mortars and/or composites were cast and compacted mechanically with a shock table (NF EN 196.1 [9]). The molds containing the specimens were covered with a plastic film and stored in the laboratory environment. After the cure period of one day in water saturated with lime, the specimens were removed and they were kept in an environment with a temperature of $20 \pm 2^\circ\text{C}$ and a relative humidity of $60 \pm 5\%$ up to 28 days and to 56 days.

TEST METHODS

The actual study consists in the characterization of the durability factors, such as the sorptivity and the porosity accessible to water, at different maturities, of unmodified mortars (control mortars) and polymer-mortar composites (PMCs). This is done for the sake of comparison only.

The capillary absorption (sorptivity): The capillary absorption measures the rate of water absorption by capillary suction of unsaturated mortar specimens, brought into contact with water without hydraulic pressure (Fig. 2). In this study, the test is performed according to the procedure AFPC-AFREM [10]. The increase in the mass of the specimen is then measured as a function of time at 1, 4, 9, 16, 25, 36 and 49 minutes. The capillary absorption test is carried out after 28 and 56 days of curing of the specimens in order to examine the effect of the pozzolanic reaction, which is a slow reaction, and also to see the possibility of forming the latex polymer film.

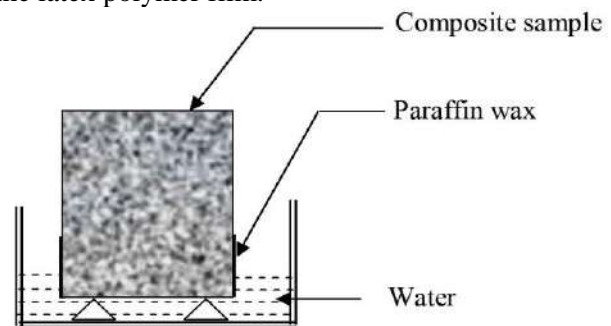


Figure 2
Measurement of composite sorptivity

Porosity accessible to water: The porosity accessible to water measures the percentage of voids connected with the surface, within the mass of mortar. The test is performed according to standard NF EN 18-459 [11], also at 28 and 56 days of curing.

RESULTS AND DISCUSSION

Capillary absorption: Figure 3 presents the influence of polymer latex and mineral additives on capillary absorption of mortars, containing ternary cements, at the age of 28 and 56 days.

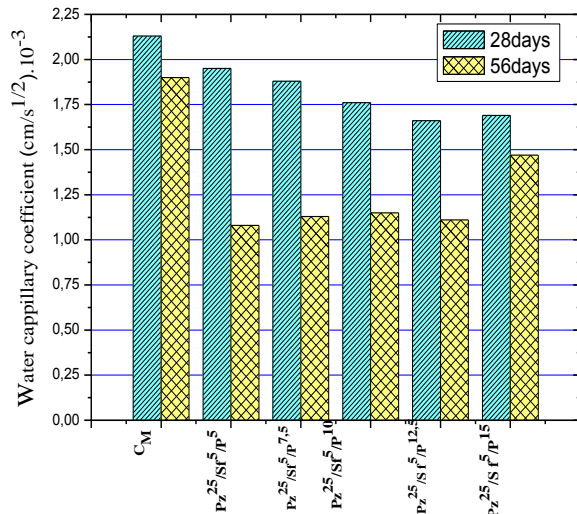


Figure 3

Capillary absorption of polymer-mortar composites, at 28 and 56 days.

Figure 3 exhibits the influence of polymer latex addition on the absorptivity of mortar specimens, containing (25% Pz / 5% Sf). The sorptivity coefficient decreases proportionally with the rate of polymer additions, at 28 days. A decrease in the absorption rate, of 40% at 28 days and 26% at 56 days, relative to control mortar, is noted for the composite (Pz²⁵ Sf⁵ P⁵).

From these results, it can be stated that the pores in the hardened paste and the interfaces between hardened cement paste and aggregates are filled with these inorganic and organic additions. Therefore, the capillary pores are reduced compared to the unmodified mortar (CEMI). According to Ghrici et al. [12], the capillary pores are reduced by the formation of secondary C-S-H gel due to the pozzolanic reaction. In addition, Siad et al. [13] reported that the significantly lower sorptivity of the SCC mixtures with Pozzolan from a natural source in Algeria or fly ash may be attributed to their less porous interfacial zone, and also the refined pore structure of the paste matrix.

The absorption is further reduced, at 56 days, due to the activation of the pozzolanic reaction of mineral additions, natural pozzolan and silica fume, over time (formation of 2nd generation C-S-H gel), with a moderate percentage (5% - 12.5%) of the polymer. When the mortar containing latex is mixed with water, cement hydration and the formation of a pure polymer occur simultaneously, which corresponds to the coalescence of polymer particles, while the cement matrix is losing water. A polymer-cement co-matrix is also formed, hence giving a network where the two phases (cement and polymer) overlap and thus bind to aggregates [14].

Porosity accessible to water: Figure 4 presents the ratio of the total volume of open pores within the composites to their *total apparent volume*, at 28 and 56 days.

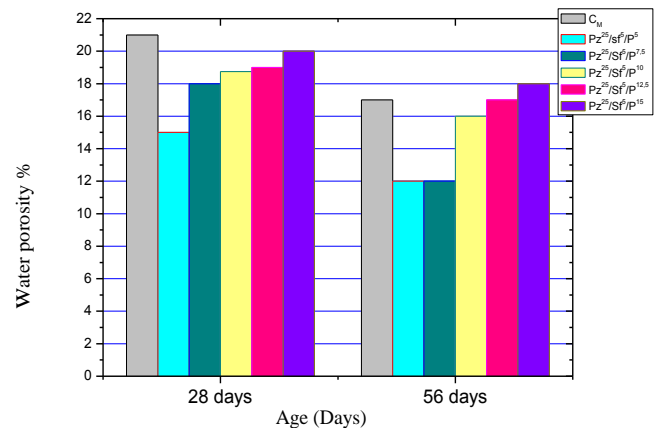


Figure 4

Porosity accessible to water of polymer-mortar composites, at 28 and 56 days.

It can be seen, on Figure 4, that polymer-mortar composites have lower porosity compared to the control mortar, especially for the composites (Pz²⁵Sf⁵P⁵) and (Pz²⁵Sf^{7.5}P⁵) that generally show the lowest porosity accessible to water. The low porosity of these two composites, at 28 and 56 days, is certainly due to the combination of the two positive effects of mineral admixtures as well as the addition of the polymer latex. Therefore, a 2nd generation C-S-H gel is produced through the pozzolanic reaction and a polymer latex film is formed as well.

CONCLUSIONS

This work aimed to investigate the influence of two mineral additions, i.e. natural pozzolan and silica fume, and the polymer latex of organic origin, on the physical characteristics of mortar composites. These characteristics are the capillary absorption (the sorptivity coefficient) and the porosity accessible to water of composites, at different maturities. The results obtained clearly showed that the polymer additions and mineral admixtures (25%NP+ 5%Sf) can contribute to the reduction of the capillary absorption and porosity of composites, as compared to the unmodified mortar (control mortar). The beneficial effect of adding natural pozzolan, silica fume and the polymer to the ternary cement, on the physical characteristics, is mainly due to the combination of two positive effects which are the 2nd generation C-S-H gel generated through pozzolanic reaction and also the formation of a cement-polymer co-matrix.

One of the major advantages of polymer-based composite materials is the ability to valorize a large amount of natural pozzolan in order to enhance the sustainability of buildings in an aggressive environment [15].

ACKNOWLEDGMENTS

We would like to express our gratitude for the financial support of the Algerian CNEPRU project CNEPRU E01820120116. We are also grateful to Mr M.T. Gouasmi and Mr O. Hasnaoui General Director of HASNAOUI Companies Group, The TEKNACHEM Algeria.

REFERENCES

- Ohama, Y., 1995, *Hand Book of Polymer-Modified Concrete and Mortars, Properties and Process Technology*. Noyes Publications: USA, pp.236.
- Shannag, M.J., 2000, High strength concrete containing natural pozzolan and silica fume, *Cem. Concr. Compos.* **22**, pp. 399-406.
- Turanli, L., Uzal, B. and Bektas, F., 2005, Effect of large amounts of natural pozzolan addition on properties of blended cements, *Cem. Concr. Res.* **35**, pp. 1106-1111.
- Latroch, N., Belbachir, B., Benosman, A.S., Bouhamou, N., Taïbi, H., and Mouli, M., 2015, In Proceedings of 2nd International Symposium on Materials and Sustainable Development CIMDD'2015, University M'hamed Bougara Boumerdes, Algeria, 9-10 November, pp. 157-161, (ISBN: 978-9931-9090-6-2).
- Belbachir, B., Benosman, A.S., Taïbi, H., Mouli, M., Senhadji, Y. and Belbachir, M., 2016, Behavior of composite mortars based on SCMs in acidic media. *J. Mater. Environ. Sci.* **7** (2), pp.187-195.
- NF EN 196-6, 2012, in: Méthodes d'essai des ciments - Partie 6: détermination de la finesse, (CEN), AFNOR, Paris, France.
- NF EN 196-3, 2006, Méthodes d'essais des ciments – Partie 3: Détermination du temps de prise et de la stabilité, European Committee for Standardization, AFNOR, CEN.
- Ghrici, M., 2006, Etude des propriétés physico Mécaniques et de la durabilité des ciments à base de pouzzolane naturelle, Thèse de Doctorat d'état, USTMB d'Oran, Algérie.
- EN 196-1, 2005, Methods of testing cement - Part 1: determination of strength. European Committee for Standardization, CEN.
- AFPC-AFREM, 1997, Méthodes recommandées pour la mesure des grandeurs associées à la durabilité, Compte rendu des Journées Techniques AFPC-AFREM «Durabilité des Bétons», 11-12 décembre, Toulouse, France, pp. 283.
- Norme, NF EN 18-459, 2010 : Béton - Essai pour béton durci - Essai de porosité et de masse volumique.
- Ghrici, M., Kenai, S. and Said-Mansour, M., 2007, Mechanical properties and durability of mortar and concrete containing natural pozzolana and limestone blended cements. *Cem. Concr. Compos.* **29**, pp. 542-549.
- Siad, H., Mesbah, H.A., Mouli, M., Escadeillas, G. and Khelafi, H., 2014, Influence of Mineral Admixtures on the Permeation Properties of Self-Compacting Concrete at Different Ages. *Arab. J. Sci. Eng.* **39**, pp. 3641-3649.
- Ohama, Y., 1998, Polymer based admixtures. *Cem. Concr. Compos.* **20**, pp. 189-212.
- Benosman, A.S., Latroch, N., Belbachir, B., Taïbi, H., Ayed, K. and Mouli, M., 2015, *Matériaux Composites Mortier-Polymère à Bases des Additions Minérales : Durabilité dans un Environnement à Tendence Acide*. Rencontres Universitaires de Génie Civil AUGC'15, 27-29 May, Bayonne, France. <hal-01167753>.

EXPERIMENTAL AND COMPUTER MODELING STUDY OF THE DIFFUSIVITY IN CEMENT-SILICA FUME BASED MATERIALS

Z. Bajja^{1,2,*}, W. Dridi¹, A. Darquennes², R. Bennacer²

¹CEA, DEN, DPC, SECR, Laboratoire d'Etude du Comportement des Bétons et des Argiles, F-91191 Gif-sur-Yvette, France

²LMT-Cachan/ENS-Cachan/CNRS/Université Paris Saclay, 61, Avenue du Président Wilson, 94235 Cachan, France

*Corresponding author: phone: +33 65 207 0343 Email: bajjazineb@gmail.com

ABSTRACT

Concrete durability continues to be a subject of considerable interest since the use of cementitious materials in the construction of several structures. In particular, cement based materials are largely used in the nuclear industry for the building of nuclear power plants and the infrastructures dedicated to the storage of the radioactive waste. Concrete durability is mainly explained by the resistance of concrete to the penetration of aggressive agents principally by diffusion. The latter is closely related to the mineral composition and the porosity of the material. Therefore, the knowledge of the relationship between microstructure and transport properties is a point of major importance. This work proposes a combination of computer models able to estimate the diffusion coefficients of SFC pastes and mortars, from a single investigation of the microstructure by nitrogen adsorption. The approach used consists firstly in manufacturing SFC mortars by varying sand volume fraction from 30 to 65% while silica fume replacement and water to binder ratio were respectively set at 10% and 0.4. Nitrogen adsorption tests were then performed and collected data on C-S-H nature are introduced into a SFC pastes hydration model. The latter provides the mineral composition which is an input parameter in the multilayer transport model that estimates the effective diffusion coefficient (D_e) of cement pastes. For mortars, a 3D biphasic model (sand and cement matrix) was used to compute the (D_e) of mortars at different inclusion volume fractions. The numerical results were approved by comparison to experimental data obtained from tritiated water (HTO) diffusion tests performed on manufactured mortars.

Keywords: Modeling; Diffusion; cement paste; Mortars; Silica fume; Microstructure

INTRODUCTION

Cementitious materials are omnipresent in civil and infrastructure constructions, from small components to huge buildings. Besides their classical use in construction, these materials are also envisaged for use both as encapsulation of radioactive waste and as engineered barriers for disposal of radioactive waste. In particular, silica fume cement based materials are mainly used in surface repositories for low-level and intermediate-level waste management. For these applications, the effective diffusion coefficient (D_e) is a key parameter for characterizing the resistance of such materials to the penetration of aggressive ions or radionuclides release [1] [2]. Tritium is one of the radionuclides often encountered in the nuclear industry, especially under the form of tritiated water (HTO) [3] and [4]. It is also the tracer chosen to assess the confinement ability of matrices for nuclear waste storage [5] [6].

HTO Diffusion coefficients are determined in steady state by means of through-out diffusion cells. However, these tests are usually very long and require several months to many years especially for concretes.

The objective of this paper is to estimate the effective diffusion coefficients of silica fume cement pastes, mortars and concrete using numerical models.

MODELING APPROACH

To estimate the diffusion coefficient of mortars and concretes, several steps must be followed. Indeed, the modeling approach is a combination of three different models summarized in Figure 1. Each model has input and output parameters.

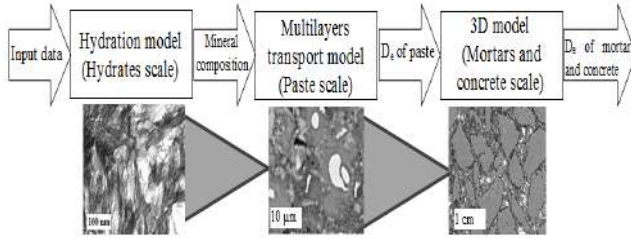
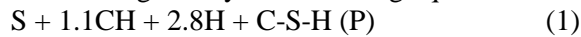


Figure 1

Calculation steps to estimate the diffusivity of mortars and concretes.

Hydration model: hydration model used for SFC pastes is the Tennis and Jennings model [7], in which the addition of silica fume (SF) was considered. The basic model which assumes stoichiometric reactions for the hydration of the four dominant compounds in Portland cement, C3S, C2S, C3A, and C4AF, has been modified taking into account the pozzolanic reaction of SF given by the following equation:



With S, CH, H and C-S-H (P) represent respectively silica (SiO₂), portlandite (Ca(OH)₂), water (H₂O) and pozzolanic C-S-H. This latter type of C-S-H is added to the two other types of C-S-H existing in a Portland cement matrix: the C-S-H (HD) for High Density and C-S-H (LD) for Low Density. The C-S-H (LD) has a low dry density of 1440 kg/m³ [7] unlike the C-S-H (HD) and C-S-H (P) have two close dried density of respectively 1750 [7] and 1805 kg/m³ [8] and then probably a quite similar nanostructure. Hereafter, we choose not to make any distinction between C-S-H (HD) and C-S-H (P), and assume that they have comparable nanostructure, intrinsic porosity and an identical intrinsic diffusion coefficient. The assembly of these C-S-H will be called C-S-H (HD&P). Concerning hydration degrees, the reaction rates chosen for the Portland cement components are approximations based on Avrami equations [7], while the pozzolanic reaction degree was calculated based on Jander's equation [9]. To estimate the mineral compositions of SFC pastes, this model requires as input data: the mass composition of the Portland cement used, the SF content, the water to binder ratio w/b and finally Mr, the ratio of the mass of C-S-H (LD) to the total mass of C-S-H, used to calibrate the model. This ratio is determined by assuming that the C-S-H (LD) is the only component of the microstructure that contributes appreciably to the surface area as

measured by nitrogen. It is defined as [7]:

$$M_r = \frac{S_{N_2} M_D}{S_{LD} M_t} \quad (2)$$

Where S_{N₂} is the specific surface area of the dried paste (determined from nitrogen sorption isotherms), M_D is the mass of dried paste, S_{LD} is the surface area per gram of D-dried C-S-H LD, and M_t is the total mass of C-S-H.

The model outputs an estimation of the phases' volume fractions ie. C-S-H (LD), C-S-H(HD), C-S-H(P), capillary porosity, anhydrous products and other hydrates (AFm, AFt and CH).

Multilayers transport model: This model is inspired by those developed by Bejaoui & Bary in [10], and Dridi in [11]. It is based on the concept that in cement pastes, the phases which contribute to the diffusive transport of dissolved species in pore water are the capillary porosity and the C-S-H (because of their intrinsic porosities) [10]. It is proposed here to distinguish the two types of C-S-H: C-S-H (LD) and C-S-H (HD&P). Three diffusive phases have thus to be considered to apply the composite model to SFC pastes: capillary porosity, LD and HD&P C-S-H. The self-diffusion coefficient (for a given diffusing species) of capillary porosity is higher than the one of C-S-H phases, and because of their higher porosity, the self-diffusion coefficient of C-S-H (LD) is supposed to be greater than the one of C-S-H (HD&P). The cement paste is represented by an assemblage of multilayers spheres and its diffusion coefficient is calculated by homogenization. Three configurations can be represented depending on which diffusive phase or mixed components are percolating in the system (see [10]). The percolation threshold of the diffusive phases is set at 15%.

To summarize, by providing as input data, the phases' volume fractions as well as the values of self-diffusion coefficients of each specie (D_{cp} for capillary porosity, D_{LD} and D_{HD+P} respectively for LD and HD&P C-S-H), the model estimates the equivalent diffusivity of the whole system (SFC paste).

3D model for mortars: This model is a computation chain composed of several steps. Its objective is to calculate the equivalent diffusivity of mortars and concretes. The first step is to generate a representative geometry of a mortar or a concrete using a numerical platform called SALOMÉ [19]. In

fact, mortar or concrete is considered as a cementitious matrix in which are embedded inclusions of aggregates surrounded by an ITZ layer (Interface Transition Zone). For materials with SF addition, The ITZ is non-existent or negligible [13, 14]. The mortar's volume contains then, in the context of this study, only two phases (sand and cement matrix). The number and size of grain sand are determined from the sand size distribution (the sand used here is a standardized sand CEN EN 196-1 0.08 /2 mm) and the sand volume fraction in each mortar. Inclusion rates can be varied from 0 to 65%, the maximum level reached by the model. Figure 2 shows an example of a representative volume for SFC mortar (a scale of $1500 \mu\text{m}^3$).

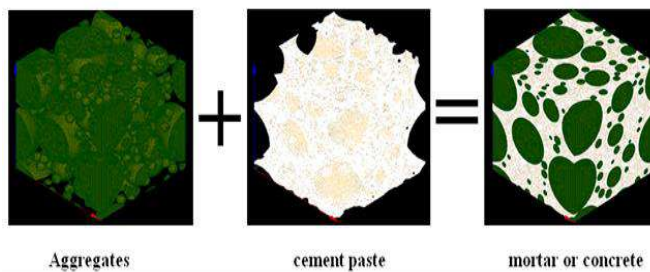


Figure 2

Volume of SFC mortar with 50% inclusions rate
(Standardized sand size distribution)

The created volume of mortar is then meshed and finite element simulations with mixed boundary conditions -applying a temperature gradient- were performed on the 3D structures of mortar. The resolution of this problem provides an estimation of the equivalent diffusion coefficient of mortars and concrete, starting from the value of the diffusion coefficient of the cement matrix. The siliceous sand is considered as non-diffusive.

EXPERIMENTAL TESTS

In this work, four SFC mortars were manufactured by varying sand volume fraction from 30 to 65% while silica fume replacement and water to binder ratio were respectively set at 10% and 0.4. Raw materials used were: ordinary Portland cement (European grade CEM I 52, 5 N CE PM-ES-CP2 NF), siliceous standardized sand (EN 196-9) with a particle size distribution ranging from 0.08 to 2mm labeled SN, water and slurried silica-fume (SF). 24h after their manufacture, the mortars were demolded and immersed in a saturated lime solution for 6-month period at $20 \pm 1^\circ\text{C}$. Then samples were sectioned from

the center to produce 6 mm thick discs. One disc was used for diffusion tests and the other for nitrogen adsorption test necessary to determine M_r , the ratio of the mass of C-S-H (LD) to the total mass of C-S-H, previously defined by Eq. 2. Samples were tested by the through-out diffusion method [15; 16]. It consists on putting a sample disc between two compartments. The downstream compartment is filled with an alkaline solution ($\text{NaOH} = 0.1 \text{ mol/L}$; $\text{KOH} = 0.1 \text{ mol/L}$; $\text{CaO} = 2 \text{ mmol/L}$) in order to prevent cement pore solution from leaching. The same alkaline solution doped with radioactive tritium water (HTO) was incorporated in the upstream compartment. The concentration of tritiated water in the downstream compartment was followed over time until the steady state has been reached. By adjusting experimental and analytical curves based on the resolution of Fick's laws, the effective diffusion coefficient D_e can be obtained.

RESULTS AND DISCUSSION

The four mortars manufactured were crushed and sieved to extract the powder corresponding to the SFC paste contained in mortars. This powder was tested by Nitrogen sorption apparatus (called also BET) in the dry and ignited state. The average value obtained for the ratio M_r is 0.24 ± 0.03 . In addition to the value of M_r , have been introduced into the hydration model, the chemical composition of cement, a water/binder ratio of 0.4 and a silica fume content of 10% by weight of cement. This model estimates the mineral compositions of the SFC paste contained in the tested mortars as shown in Table 1.

Table 1:

Estimation of phases' volume fractions in the SFC paste contained in tested mortars

Capillary porosity	11.03%
C-S-H (LD)	14.73%
C-S-H (HD&P)	42.43%
Other hydrates (CH, Aft, Afm..)	24.34%
Anhydrous	7.46%

Knowing the mineral composition and the intrinsic diffusivity of each phase, the multilayers homogenization model calculates the diffusion coefficient of the paste. For capillary porosity, the intrinsic diffusivity is described -as a first approximation- by that of the tritium in an aqueous

solution at 25°C ($2.27 \cdot 10^{-9} \text{ m}^2/\text{s}$) [17]. Hydrates such as CH, AFm or others, are considered as non-diffusive and their intrinsic diffusivities almost zero. However at this stage, the diffusivity of C-S-H (LD) and (HD&P) remains unknown.

These two unknowns' factors can be determined by reverse analysis using experimental values of HTO diffusion coefficients and the mineral compositions of some cement pastes.

A previous study [18] found experimental values of HTO diffusion coefficients of $1.44 \cdot 10^{-12}$; $2.56 \cdot 10^{-12}$ and $5.36 \cdot 10^{-12} \text{ m}^2/\text{s}$, respectively for Portland cement pastes with a water/binder ratio of 0.3, 0.4 and 0.5.

Here also, the mineral composition estimation of these pastes was given using the same hydration model and by varying the w/b ratio between 0.3; 0.4 and 0.5, by filling out the chemical composition of Portland cement used (the same cement as that used for SFC mortars) [18] and finally by considering a M_r ratio for Portland cement based materials expressed as follows (Eq. 3) [7]:

$$M_r = 3.017(w/c)\alpha - 1.347\alpha + 0.538 \quad (3)$$

Where w/c is the water to cement ratio and α is the degree of hydration.

Table 2 shows the volume percentages of each phase contained in Portland cement pastes (SF content of 0%).

Table 2:
Estimation of phases' volume fractions in Portland cement pastes tested in [18]

w/c	0.3	0.4	0.5
Capillary porosity	7.08%	12.72%	19.21%
C-S-H (LD)	11.95%	22.6%	34.84%
C-S-H (HD&P)	37.39%	28.32%	14.60%
Other hydrates (CH, Aft, Afm..)	14.68%	14.49%	13.94%
Anhydrous	13.74%	6.36%	2.99%

HTO intrinsic diffusivities of LD and HD C-S-H are adjusted on experimental diffusion coefficients and the mineral composition given by Table 2. Here we find intrinsic diffusivities of $3.6 \cdot 10^{-12}$ and $6.510^{-13} \text{ m}^2/\text{s}$ respectively for LD and HD C-S-H. Table 3 compares experimental diffusion coefficients D_e with numerical D_e estimated by the multilayers

homogenization model when LD and HD C-S-H were assigned their relative diffusivities.

Table 3:
Data for tritiated water diffusion in Portland cement pastes

w/c	Experimental D_e $\times 10^{-12}(\text{m}^2/\text{s})$	Model $D_e \times$ $10^{-12}(\text{m}^2/\text{s})$
0.3	1.44	1.25
0.4	2.56	2.32
0.5	5.36	5.15

As can be seen in Table 3, a good agreement was observed between the experimental and computer model values for Portland cement paste (the error doesn't exceed 15%).

Coming back to SFC paste contained in mortars tested, and since the relative diffusivities of all phases are now known, it is possible to estimate a computer modeling diffusion coefficient of $6.90 \cdot 10^{-13} \text{ m}^2/\text{s}$ for the silica fume cement matrix contained in mortars with 10% SF.

With 10% SF addition, the diffusion coefficient of SFC paste has been estimated at $6.90 \cdot 10^{-13} \text{ m}^2/\text{s}$, almost four times less than the effective diffusion coefficient obtained without SF addition of $2.56 \cdot 10^{-12} \text{ m}^2/\text{s}$. This gap seems in agreement with data available in literature [5].

The final step of the calculation chain is to evaluate the diffusion coefficients of mortars with different sand volume fractions. Sand content was varied from 0 to 65%. The numerical D_e were compared to the effective diffusion coefficient obtained experimentally at steady-state of diffusion tests. Figure 3 shows the values obtained from computer modeling and through-out diffusion tests.

As can be seen in Figure 3, an excellent agreement is observed between the experimental and computer model values of HTO diffusion coefficients for SFC mortars with 10% SF addition. The maximum error obtained is around 15%.

The modeling approach suggested in this work is therefore efficient to estimate diffusion coefficients of silica fume cement pastes, mortars and concretes from a simple characterization of the cementitious matrix microstructure by nitrogen sorption and using a succession of computation steps.

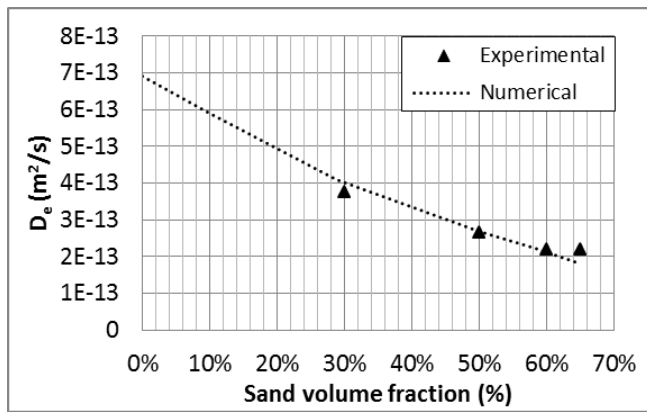


Figure 3

Comparison of experimental and numerical diffusion coefficients.

CONCLUSION

A numerical model approved by experimental results is presented in this paper. It aims first to assess the volume fractions of dissolved chemical species diffusing in saturated SFC paste by introducing the water and silica fume content, the cement composition, and a ratio M_r obtained from a simple characterization using nitrogen sorption. Then, the model considers the system at the scale of the mineralogical assemblage. Its purpose is to estimate the equivalent diffusivity of the paste by accounting for the self-diffusion coefficients (for a given species) of the various components of the microstructure and the way in which the latter are arranged in the space. Finally, a three-dimensional modeling is applied to up-scale diffusive properties from the scale of cement paste and aggregates to the one of mortar and concretes.

REFERENCES

- [1] P. Faucon, F. Adenot, J.F. Jacquinet, J.C. Petit, R. Cabrillac, M. Jorda . Long-term behaviour of cement pastes used for nuclear waste disposal: review of physico-chemical mechanisms of water degradation *Cem Concr Res*, 28 (6), pp. 847–857 (1998),
- [2] C. Galle, H. Peycelon, P. Le Bescop, S. Bejaoui, V. L’Hostis, B. Bary, et al. Concrete long-term behaviour in the context of nuclear waste management: experimental and modelling research strategy *J Phys Iv*, 136, pp. 25–38 (2006).
- [3] D. Kim, I.W. Croudace, P.E. Warwick. The requirement for proposer storage of nuclear and related decommissioning samples to safeguard accuracy of tritium data, *J Hazard Mater*, 213–214, pp. 292–298 (2012)
- [4] M.-H. Li, T.-H. Wang, S.-P. Teng , Experimental and numerical investigations of effect column length on retardation factor determination: a case study of cesium transport in crushed granite *J Hazard Mater*, 162 pp. 530–535 (2009).
- [5] A. Delagrave, J. Marchand, M. Pigeon Influence of microstructure of the tritiated water diffusivity on mortars *Adv Cem Based Mater*, 7 pp. 60–65 (1998).
- [6] E. Tevissen, J.M. Soler, P. Montarnal, A. Gautschi, L.R. Van Loon Comparison between in situ and laboratory diffusion studies of HTO and halides in Opalinus clay from the Mont Terri *Radiochim Acta*, 92, pp. 781–786 (2004).
- [7] P.D Tennis, H.M. Jennings. A model for two types of calcium silicate hydrate in the microstructure of Portland cement pastes, *Cement and Concrete Research Volume 30, Issue 6*, pp. 855–863 (2000).
- [8] H.F.W. Taylor, *Cement Chemistry*, Thomas Telford, London, (1997).
- [9] P. Barnes, *Structure and Performance of cements*, applied Science Publishers, London and New York, (1983).
- [10] B. Bary, S. Bejaoui. Assessment of diffusive and mechanical properties of hardened cement pastes using a multi-coated sphere assemblage. *Cem. Concr. Res.*, Vol 36, p. 245-258 (2006).
- [11] W. Dridi, Analysis of effective diffusivity of cement based materials by multi-scale modelling, *Journal of Materials and Structures* 46:313-326 (2013)
- [12] D.P. Bentz, O.M. Jensen, A.M. Coats, F.P. Glasser , Influence of silica fume on diffusivity in cement based materials, I Experimental and computer modeling studies on cement pastes, *Cem. Concr. Res.* 30 pp. 953-962 (2000).
- [13] A. Goldman, A. Bentur. Effects of pozzolanic and non-reactive microfillers on the transition zone in high strength concretes. In: Maso JC, editor. *Interfaces in cementitious composites*, RILEM Proceedings 18. E and FN Spon; pp. 53–61 (1992).
- [14] D.P. Bentz, Influence of silica fume on diffusivity in cement-based materials: II. Multi-scale modeling of concrete diffusivity, *Cem. Concr. Res.*, 30 pp. 1121-1129 (2000).
- [15] C. Richet, « Etude de la migration des radioéléments dans les liants hydrauliques – Influence du vieillissement des liants sur les mécanismes et la cinétiques des transferts »

Université d'Orsay: France, 1992 (PhD manuscript in French)

[16] F. Nugue, M.P. Yssorche-Cubaynes, J.P.Ollivier, Innovative study of non-steady-state tritiated water diffusion test, *Cem. Concr. Res.* 37 pp. 1145-1151 (2007).

[17] P. Vanysek, *CRC Handbook of Chemistry and Physics* . 81st edition Revision of tables of Diffusion

Coefficients and ionic conductivities. CRC Press Boca Raton (2000).

[18] B. larbi. « Caractérisation du transport diffusif dans les matériaux cimentaires : influence de la microstructure dans les mortiers » . PhD manuscript in French, Université Paris-Est 2013.

[19] <http://www.salome-platform.org/>

SEISMIC SCENARIOS OF TIPAZA NETWORK SUPPLY

Fatma Zohra Halfaya¹, Hadj Idris Djillali², Mahmoud Bensaibi², Luc Davenne³

¹Department of Civil Engineering, University Blida1, Algeria

²Department of Materials and Structures, Ecole Nationale Supérieure des Travaux Publics, National High School of Public Works, Kouba, Algiers, Algeria

³LEME, IUT Ville d'Avray, University Paris X, France.

*Corresponding author: Fatma Zohra Halfaya: Email: fz_halfaya@yaoo.fr

ABSTRACT

The present study deals with the seismic vulnerability of buried pipelines.

First the vulnerability index of water supply network is assessed using the vulnerability index method "VI". This method is a reliable tool allowing diagnosis and localized intervention to reduce losses of a water supply network after an earthquake. A Geographical Information System (GIS) is used also in this study.

Then using seismic scenarios and vulnerability curves which describe the seismic behavior of the buried pipes the water network of Tipaza city is studied and the rates of damage of the network are calculated

KEYWORDS

NOMENCLATURE

VI: vulnerability index

GIS: Geographical Information system (GIS)

N: number of pipe breaks and joint failure

L: extended length of pipeline (km).

$R_{fm}(x)$: damage rate (breaks/km)

X: ground motion parameter such as PGA, PGV, or SI (spectral intensity)

$R_f(x)$: standard damage rate (breaks/km) as a function of ground motion parameter x

C: correction factors

PGV: Peak Ground Velocity

MMI: Modified Mercaly Intensity

INTRODUCTION

In large cities, several thousand kilometer of water supply network spread over expanded urban areas. Because of the huge stock, the majority of these pipes are highly vulnerable to strong ground motions and large ground deformations. In major events, repair works of a number of pipe breaks and joint failures are time-consuming. From the point of view of seismic risk management, it is of great importance to evaluate seismic vulnerability of existing pipelines.

Several methods of vulnerability assessment do exist. The first one was elaborated by the ATC (Applied Technology Council) in the ATC-25 report in 1991. It gives the damage risk (number of breaks per kilometer) under the form of damage probability matrices (DPM) in which the earthquake intensity is characterized by the Modified Mercaly Intensity (MMI). An addenda, the ATC-25-1[1] report, is dedicated to water supply. The FEMA (Federal Emergency Management Agency)[4] and the NIBS (National Institute of Building Sciences) financed a project to develop a tool for estimating the damage under earthquake hazard. The methodology was implemented in the software HAZUS[5] using a geographic information system (GIS). The European project RISK-UE[14] had the objective to propose a methodological manual, adapted to the European context, for the realization of seismic risk scenarios.

The RADIUS (Risk Assessment Tools for Diagnosis of Urban Areas against Seismic Disaster)[13] method was initiated by the UN Secretariat and aimed to provide developing countries by an efficient tool to assess the vulnerability of their cities.

Other vulnerability assessment methods were developed, all aims to reduce the seismic effect

on pipelines. For instance, Ueno et al.[15] and Nojiima [12], introduce a vulnerability factor (V-factor) for the evaluation of seismic vulnerability of lifeline network facilities.

STATISTICAL MODEL FOR ESTIMATION OF PIPELINE DAMAGE

The main elements that have an influence on the seismic vulnerability of buried pipelines[9][12] are: Ground Shaking, Landslides, Liquefaction, Settlement, Fault Crossings, Material pipe, Pipes diameters and Soil conditions. Based on this factors, statistical method is widely used for estimation of damage to pipes subjected to strong ground shaking and ground deformations.

Typical method for estimating number of pipe breaks and joint failure is to multiply extended length of pipeline by damage rate representing the average number of pipe breaks and joint failure per unit length.

$$N = L \cdot R_{fm}(x) \quad (1)$$

Where N: number of pipe breaks and joint failure, L: extended length of pipeline (km), x: ground motion parameter such as PGA, PGV, or SI (spectral intensity), and $R_{fm}(x)$: damage rate (breaks/km).

Damage rate $R_{fm}(x)$ is given by the following equation:

$$R_{fm}(x) = C_d \cdot C_p \cdot C_g \cdot R_f(x) \quad (2)$$

Where $R_f(x)$: is the standard damage rate (breaks/km) as a function of ground motion parameter x , C_d is the correction factor for pipe diameter, C_p : is the correction factor for pipe material/joint type, C_g : is the correction factor for ground and liquefaction. Standard damage $R_f(x)$ (breaks/km) is defined for a combination of a particular type of pipe material, joint, and pipe diameter on the basis of damage statistics from past earthquakes.

Although the framework of Eqns. (1) and (2) are common to various models of statistical estimation methods, different models have different sets of correction factors and standard damage rate function.

VULNERABILITY INDEX OF PIPELINES

A simple method termed ‘‘Vulnerability Index (VI) method’’ to quantify relative vulnerability of buried pipeline is proposed (Table 1). As equation (3) shows, the VI is evaluated by considering number of parameters influencing the behavior of the pipe with

weighting factor derived from past Algerian earthquakes (Ain Temouchent 1999 and Zemouri 2003), note that some correction factors may be unreliable due to statistical insufficiency:

$$VI = C_m \cdot C_d \cdot C_p \cdot C_f \cdot C_s \cdot C_g \cdot C_i \cdot C_l \quad (3)$$

C_m : is the correction factor for pipe material

C_d : is the correction factor for pipe diameter

C_f : is the correction factor for fault crossings

C_s : is the correction factor for settlement and landslide

C_g : is the correction factor for ground type

C_i : is the correction factor for the seismic intensity

C_l : is the correction factor for liquefaction

Table 1
Weighting factors

Parameter	Category	Weighting Factor
Materials	Ductile cast iron	0.30
	Cast iron	1.00
	PVC	1.00
	Steel	0.30
	Galvanized steel	1.75
	Asbestos cement	2.50
	PEHD	0.10
Diameter (mm)	$\phi < 75$	1.6
	$75 < \phi < 150$	1.0
	$150 < \phi < 250$	0.9
	$250 < \phi < 450$	0.7
	$450 < \phi < 1000$	0.5
	$\phi > 1000$	0.4
Fault Crossing	No Intersection	1.0
	One Intersection	2.0
	Several Intersections	2.4
Settlement/Landslide	No risk	1.0
	Average risk	2.0
	Important risk	2.4
Ground Type	Deposit Soil :	4.7
	Alluvium: very soft	
	Deposit Soil :	2.9
	Diluvium: soft	
	Weathered Rock:	2.0
	Medium	
	Moderate Weathered Rock: Medium	1.0
	Slightly / No Weathered Rock:	0.5
Stiff / Hard		
Liquefaction	$0 \leq PL < 5$	1.0
	$5 \leq PL < 15$	2.0

	15≤PL	2.4
Ground Shaking	MMI<8	1.0
	8≤MMI<9	2.1
	9≤MMI<10	2.4
	10≤MMI<11	3.0
	11≤MMI	3.5

In this method, the pipe diameters are those commonly used in Algeria. The fault crossings pipe is considered with no crossings, one crossing and more than one crossing. Settlement and/or landslide are considered also through a geological conclusion (if there is no risk, an average risk or an important risk) on the soil movement. The ground conditions are considered with respect to the soil type. The seismic intensity is considered using the MMI scale. Finally the liquefaction is considered through the calculation of a potential of liquefaction (PL) (In this work, the method of Iwasaki is used). Based on previous study, Halfaya and al, and on past Algerian earthquakes (Ain Temouchent 1999 and Zemouri 2003) a classification for pipeline according the VI is proposed in Table 2.

Table 2
Pipe Classification

Range VI	Evaluation	Colour
0 < VI < 5	Low vulnerability	Green
5 ≤ VI < 12	Medium vulnerability	Orange
12 ≤ VI	High vulnerability	Red

In this classification when the vulnerability index ranges between zero and five the vulnerability of the pipe is low and the green color is associated. When it is more than twelve it means a critical situation and the pipe is vulnerable so the red color is associated. Then for intermediate situation (VI ranges between five and twelve) the orange color is associated. These values are for Algerian case; despite the fact they need more statistical data to be checked, they will be used here.

VULNERABILITY CURVES

Isoyama et al.[16] proposed the following equation to assess the number of damages per kilometer in water pipeline.

$$Rm(v) = C_p \cdot C_d \cdot C_g \cdot C_l \cdot R(v) \quad (4)$$

With v the PGV (peak ground velocity) and $R(v)$ expressed by Isoyama et al. after Kobe earthquake as:

$$R(v) = 2.24 \times 10^{-3} (v-20)^{1.51} \quad (5)$$

In this work an expression to assess vulnerability curves for Algerian case is proposed in equation 6.

$$Rm(v) = VI^c \cdot R(v) \quad (6)$$

With $VI^c = VI / C_i$ in order to do not consider the seismic effect twice.

APPLICATION

Study area:

The area under study is Tipaza which is an agglomeration located west Algiers (Algeria). The growth of the population of the city is represented on Table 3.

Table 3
Evolution of the population of 1998 to 2026

	Population (inhabitant)			
Years	1998	2004	2011	2026
Population	21915	25080	31210	43690

Tipaza is an area prone to seismicity. It is classified zone 3 according to the seismic code in use (RPA, 1999, version 2003).

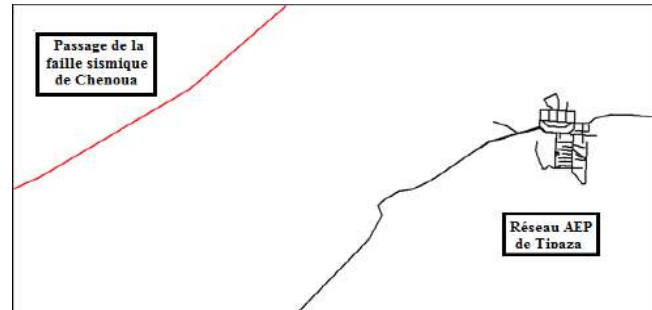


Figure 1

Seismic fault of Chenoua (in red) and Tipaza water supply network (in black)

The fault of Chenoua (figure 1) is located at 3.8 Km to the North-West of the city, it does not cut the network in any point. The soil is considered as a Rock.

Water supply network:

The water system network of Tipaza is represented by its diameters, from diameter 40mm to diameter 400mm. The total length of the network is approximately 19 km. Table 4 shows the length of the network according to materials and diameters.

Table 4
Length according material and diameter

Diameter (mm)	Abestos Cement (m)	Cast Iron (m)	PVC (m)	Galvanized Steel (m)	PEHD (m)	Steel (m)	Total (m)
40		92		327			419
50				138			138
63			1032		138		1170
80				76			76
90					424		424
100		1429					1429
125	188						188
150						466	466
200	615	2643					3258
250	445	1294					1739
300	675						675
400	8349						8349
Total (m)	10271	5459	1032	541	562	466	18331

Vulnerability index:

A program was developed to give the classification of the different section pipe of Tipaza network. The result of the present study is given in Table 5. A representation of this result on a GIS (Geographic Information System) is given in figure 2.

Table 5
Pipes classification

Range	Length (m)	Percentage %	Color
[0-5]	2322.3	12.67%	Green
[5-12]	14343.4	78.24%	Orange
[12 >]	1665.5	9.09%	Red



Figure 2

Tipaza pipe classification represented on a GIS

As it can be seen, the majority of the network is vulnerable, more than 80% of the network is classified orange and red, which means in case of a

strong earthquake, the population will be thirsty, inducing health problems. Table 6 shows that pipes with galvanized steel have strong vulnerability while PEHD pipes have low vulnerability.

Table 6
Classification of pipes according materials

Materials (ml)	Abestos cement %	Cast iron %	PVC %	Galvanized steel %	PEHD %	Steel %
Green	0	3	0	0	100	100
Orange	35	97	100	0	0	0
Red	65	0	0	100	0	0

Vulnerability curves:

Vulnerability curves according different materials are developed and given here after.

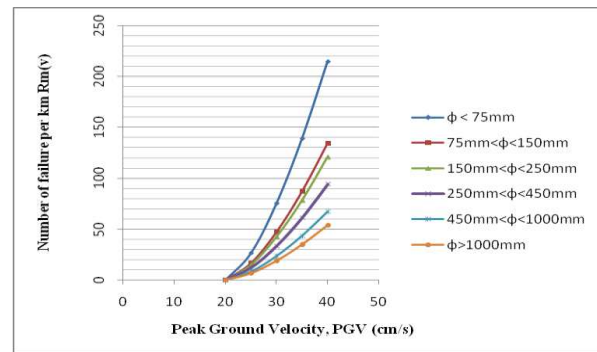


Figure 3

Cast iron and PVC vulnerability curves.

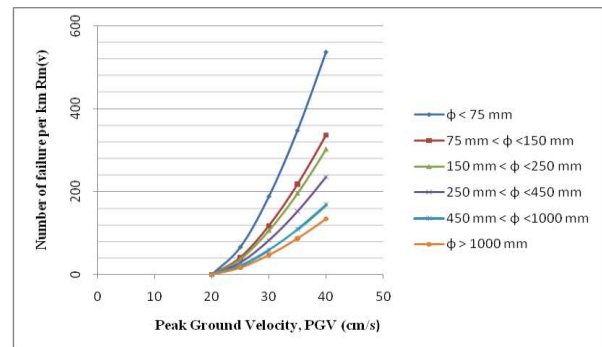


Figure 4

Abestos cement Vulnerability curves

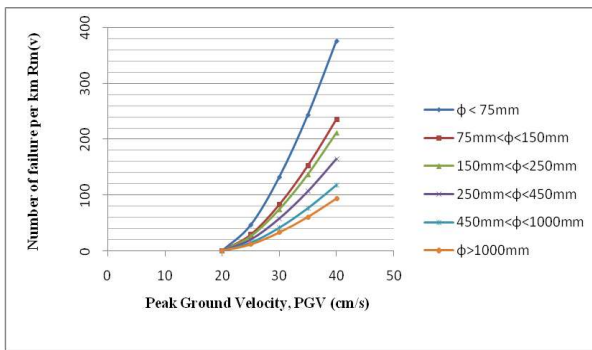


Figure 5
Galvanized steel vulnerability curves

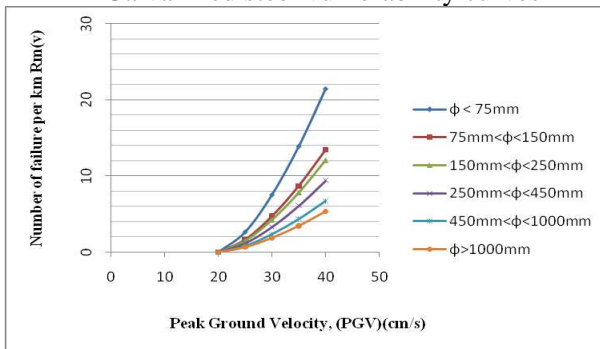


Figure 6
PEHD vulnerability curves

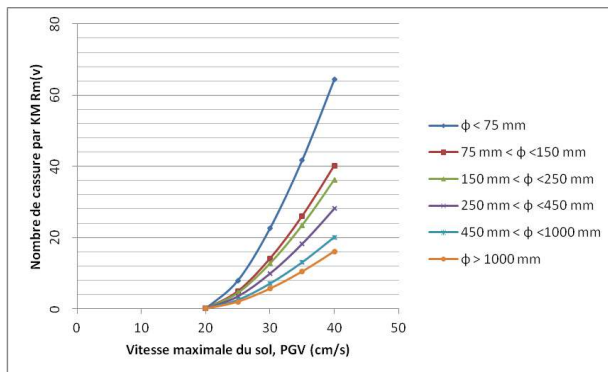


Figure 7
Steel vulnerability curves

The vulnerability curves show that small diameter pipelines suffer more important damages than large diameter pipes, they are more vulnerable than great ones.

Pipelines with lower C_p coefficient have better seismic behavior than those with a high C_p coefficient. This is due to material ductility which allows important displacements without any breaks or failures. As it can be seen, the best material is PEHD and the worst is Abestos ciment.

LOSS ASSESSMENT

The main hypothesis is that pipes classified orange must be repaired and those classified red must be replaced so in the lost assessment study, these two categories will be considered. Table 7 gives the length of pipes classified orange and red according the material.

Table 7
Length of buried pipes to repair and replace

Material	Abestos cement (ml)	Cast iron (ml)	PVC (ml)	Galvanized steel (ml)
Orange	3595	5295	1032	0
Red	6676	0	0	541

The estimate of the cost of repair and replacement of the pipes of this network after an earthquake is given in the table 8:

Table 8
Cost of repair and replacement

Works	Length (ml)	Cost/ml/ DA
Repair	9922	7000
Replacement steel pipe	6676	30000
	541	60000

In Table 9 the cost assessment for the Tipaza water supply network is given. As it can be seen, the total cost is more than 2.5 Million euro which is very huge.

Table 9
Cost assessment

Works	Cost in DA	Cost in Euro
Repair	69 454 000	578 783
Replacement	232 740 000	1 939 500
TOTAL COST	302 194 000	2 518 283

CONCLUSION

Vulnerability assessment for the water supply network of Tipaza under seismic motion was treated through the use of a vulnerability index method. This one allows the diagnosis of the different section pipe according a proposed classification. Based on this index, vulnerability curves were

derived. These ones allow performing seismic scenarios in order to establish priority setting. Coast assessment for the water network of Tipaza city was derived also. It highlights the vulnerability of the network since this coast is huge. The priority setting was also derived in order to help decision maker city.

References

1. ATC 25, Applied Technology Council, Seismic Vulnerability and Impact of Distribution of Lifelines in the Conterminous United States, 1991.
2. ATC 25-1 Applied Technology Council, Seismic Vulnerability and Impact of Disruption of Lifelines in the Conterminous United States. ATC-25, Redwood City, CA 25-1, 1991.
3. Centre de Recherche en Astronomie Astrophysique et Géophysique (CRAAG), Étude géologique géophysique et géotechnique des piémonts Est et Ouest de la ville de Blida, CRAAG Report, 2005.
4. Federal Emergency Management Agency (FEMA), Earthquake loss estimation methodology HAZUS technical volumes, NIBS Document number 5201, National Institute of Building Sciences, 1997.
5. Federal Emergency Management Agency (FEMA), Estimating earthquake losses with HAZUS, Federal Emergency Management Agency, 2000.
6. Hadj Idris D., « Vulnérabilité sismique de la ville de Tipaza », mémoire de magister, Département Génie Civil, Université Blida1, 2014.
7. Halfaya FZ., Bensaibi M., Davenne L., « Indice de Vulnérabilité Sismique des Conduites Enterrées en Béton », *Colloque International Caractérisation et Modélisation des Matériaux et Structures* CMMS1, 12 & 13 novembre 2014.
8. Halfaya FZ., Bensaibi M., Davenne L., « Seismic Safety Assessment of Existing Buried Pipelines », *International Journal of Water & Hydro Constructions-IJWHC*, Volume 1: Issue 2, pp. 1-5, June 2014
9. Halfaya FZ., Bensaibi M., Davenne, L., « Vulnerability assessment of water supply network », *Energy Procedia*, Vol. 18, 2012, p. 772 – 783.
10. Halfaya FZ., Bensaibi M., Davenne, L., « Seismic vulnerability of buried water pipes », *Advanced Materials Research*, Vols. 518-523, pp 3740-3743, 2012.
11. Iwasaki T, Tokida K, Tatsuoka F, Watanabe S, Yasuda S, Sato H, « Microzonation for soil liquefaction potential using simplified methods », *Proc 3rd Int, Conference on Microzonation, USA*, 1982.
12. Nojima, N., « Seismic vulnerability index for lifeline facilities », *The 14th World Conference on Earthquake Engineering*, China, 2008.
13. OYO Corporation. RADIUS methodology. IDNDR, 1999.
14. Risk-ue, Geo-Ter, Vulnerability assessment of lifelines and essential facilities (WP06) :methodological handhook, Potable water utility system, Report n° GTR-RSK 0101-152av7, February, 2003.
15. Ueno J, Takada S, Kuwata Y, « Performance of water supply system during the 2003 Tokachi-Oki earthquake », *NCREE Workshop*, 2004.
16. Isoyama et al., “Damage estimation of water distribution pipes following recent earthquakes in Japan”, 7th International Conference on Urban Earthquake Engineering and 5th International Conference on Earthquake Engineering, Tokyo Institute of Technology, Tokyo, Japan, 2010.

CHLORIDE TRANSPORT ON PARTIALLY SATURATED CONCRETE MEDIA: THE INFLUENCE OF THE HYDRIC STATE

Hayet CHALABI^{1,*} . Abdelillah BEZZAR⁽¹⁾ . Abdelhafid KHELIDJ⁽²⁾

¹ Department of civil engineering, faculty of technology, university of Tlemcen, Algeria

² LUNAM, GeM, IUT of Saint-Nazaire, university of Nantes, France

* Corresponding author: hayet.cha@hotmail.com

ABSTRACT

Transport of chloride in unsaturated concrete media is largely controlled by various phenomena occurring during the kinetics of the penetration of the ions chlorides within this media. This article studies the influence of the hydric rate of cementitious material on the penetration of chlorides. This transfer test was performed which insures an optimal contact of the material with a chloride solution without perturbing the hydric state of the material during these tests and by taking into account the fixation of chlorides on the matrix materiel. The results showed the important effect of the rate of saturation on the chlorides transfer and fixation.

NOMENCLATURE:

WS: water saturation

Mh: mass at natural water contents

Md: mass after oven dry (at 65 °C)

Ms: mass in water saturation

W: water

C: cement

C_B: bound chloride

C_F: Free chloride

A,B: constants

INTRODUCTION

Reinforced concrete structures in seaboard are exposed to aggressive environments, chloride transfer within concrete is often responsible on corrosion of structural steel [1]. This parameter, was frequently studied in saturated cementitious media in this case the movement of chloride ions occur by diffusion under a concentration gradient, but in reality the construction is not always saturated; e.g. of a structure subjected de-icing agent or a construction in marine

environment which can have various rate of saturation (tidal zone), inside this media the transport of chlorides arises by other mechanisms. Few experimental approaches are used in this purpose. [2] Use an innovative method which consists to insure a limited rate of chloride in the form of gas on the surface of the sample the chloride of hydrogen HCl gaz obtained by the combustion of the PVC. [3] Studied the effect of drying and moistening on the transfer of chlorides in a concrete partially saturated by means of a device which feigns the cycles of drying / moistening automatically. [4] test samples

already immersing in a salt solution after that conditioned in 65 and 85 % humidity a duration of 2 hours follow-up by a drying to take back the same initial conditions. In the works [5,6] to avoid perturbing the state of saturation, the sample is submitted to chlorides under a solid state. All the experimental approaches used in the works quoted previously showed the strong dependence between the state of saturation of the material and the transfer of chlorides in spite of the difficulty controlling the hydric state of the material during the test.

In this present work, we proceeded to the study of the effect of the hydric state on the transfer of chlorides within a disk of the ordinary concrete (W/C=0.5) conditioned in various hydric states. The evolution of the concentration of chlorides within the material was presented by chlorides concentration profiles.

MATERIALS AND METHODS

Materials

A CEMII 42.5 cement is used, and calcareous sand 0/4 fraction. Three fractions of calcareous gravel are used 3/8, 8/16 and 16/20.

Concrete mixtures

The composition of concrete and the mechanical characteristics obtained cylindrical specimens (22*11) cm are presented in the table 1. The specimens were exposed 24 hours in the ambient air then they are immersed in the water during 3 months

in an ambient temperature to assure a complete hydration of cement.

Table 1
Concrete mixtures and properties

Concrete mixtures (Kg/m ³)		
Gravel	16-20 mm	533
Gravel	8-16 mm	432
Gravel	3-8 mm	144
Sand		660
Cement		350
Water		175
W/C		0.5
Concrete properties		
28 Day water porosity (%)		11.3
90 Day water porosity (%)		10.90
28 Day compressive strength (MPa)		39.14
90 Day compressive strength (MPa)		44

A disk of 5 cm height is sliced in the middle of the specimen, this thickness often used as coatings applied Reinforced concrete structures in marine environment. Two layers of epoxy resin covered the surface sample for to assure a unidirectional transfer. In this present study, the hydric rate of the material is defined by four degrees of saturation 30, 45, 70 and 90 %.

The degree of water saturations for concrete sample was measured by weighing representative samples with their naturel water contents M_h , after water saturation (AFRC AFREM modify) M_s and after oven drying at 65° C, M_d .

$$WS (\%) = \frac{M_h - M_d}{M_s - M_d} \times 10 \quad (1)$$

Chloride test Transfer

The transfer of chlorides is assured by the optimal contact of the base of the sample with the salt solution 30 g/l concentration of NaCl. This contact is assured by glass supports. The samples are placed in a closed desiccator. The renewal of the solution is regularly made to assure a constant concentration must in all the duration of the experiment.

Dosage of ions chlorides

The content of chloride for all samples is determined after 15 days of exposure, the specimen tank to be ground every 3 mm thick layers by means of grinding instrument, which allows us to get back a very fine

powder from the centre of the sample. The collected powder spends by a step of extraction of chlorides by the nitric acid diluted with 20 % for the total chlorides and without acid for the free chlorides. After a step of filtration, the content of chloride is determined by potentiometric titration [7].

Chloride sorption isotherms

Chlorides in the concrete are in two forms: fixed physically or chemically in the cementitious matrix and freed in the interstitial solution of the concrete, the free are is responsible on corrosion of structural steel. The sorption isotherm can be obtained by several experimental methods. In this work, we proceeded to measure of the sorption isotherms by profiles method.

RESULT AND DISCUSSION

The figures 01-04 illustrates the evolution of the content in chlorides total, free and fixed according to the depth of penetration for an exposure time of 15 days and for various degrees of saturation. The first remark which can we do that in spite of the short duration of the experiment de the porous network is important. We also note that for a degree of 45 % saturation the content in chloride is important and that the increase of degree of saturation from 45 % to 90 % increase of the content in chlorines and also the decrease 45 % to 30 % causes a decrease of the content in chloride consequently.

The figure 05 shows the diagram of the evolution of the content in total chlorides, on one hand we noticed that all the depths present a peak of concentration of the chlorides which corresponds to the degree of saturation 45 %. On the other hand, we notice that the depth of penetration of chlorides is important in samples its degree of low saturation.

Seen the importance of the fixation of chlorides on the transfer, we presented the total, free and fixed chlorides. The fixation of chlorides is more important for higher degrees of saturation (90 and 70 %).

The results obtained shows that in concrete who present high degree of saturation the penetration rate of chlorides is lesser comparing it with the other materials which present an important gaseous phase. For that purpose, we can say that transfer of chlorides occur by other mechanisms in the porous media in parallel with the diffusion of chlorides. The convection under the gradient of the capillary

pressure [8] and also the transfer of the humidity [9] quoted by [10]. The peak, which presents the graph, is generally defined in the literature by percolation threshold [1] where the porous media becomes not interconnected and the transfer becomes unimportant in case with water saturation is low than the saturation threshold, but always there is a possibility of the transfer by the effect of the transfer of the humidity [6].

In the media not saturated the speed of convective flow bothers the fixation of chlorides consequently the chloride migrates preferentially towards the biggest pore [11].

The figure 06 shows the experimentally derived isotherm corresponding to test with WS of 70 %, were plotted and fitted to the Langmuir isotherm:

$$C_B = A \frac{BC_F}{1+BC_F}$$

Data fitting to this equation yielded the constants $A=125.87$ et $B=0.0061$ with a $R^2=0.96$. Langmuir isotherm was found at low free chloride concentrations

CONCLUSIONS

In the unsaturated media, the transport of the ions and the hydric transfer interact, the flow of the water accelerates widely the transport of the ions because the convective transport governed by the gradient of pressure of the liquid is much faster than the diffusive transport of in the gradient of the concentration. Nevertheless, the transfer of chlorides also requires high one degree of saturation of a threshold of saturation to formulate continuous paths allow the chlorides to migrate within the porous middle.

The penetration of chlorides is the result of the transport of chlorides and its fixation, the binding of chlorides depends several parameters bound to the composition and the microstructure of the material cementitious but not only, it also depends the saturation of the material.

KEYWORDS: Diffusion, Transport, Convection, Chloride, Humidity and Degree of saturation.

ACKNOWLEDGMENTS

A part of this work was realized within laboratory GEM UMR_C 6183 (laboratory GEM, Nantes university in Saint-Nazaire). I thank Pr Abdelhafid Khelidj for her reception in the laboratory and Ms Stéphanie Bonnet for her technical support.

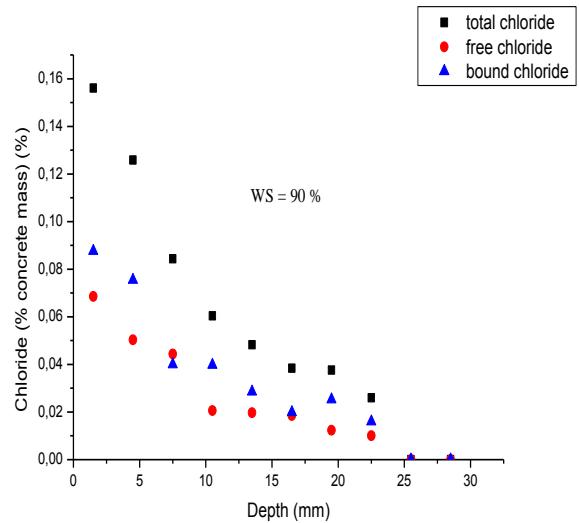


Figure 1

Experimental total, free and bound chloride profiles
WS=90% (15 days)

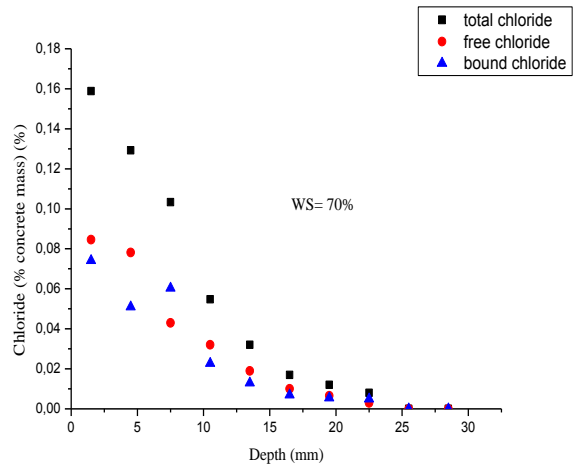


Figure 2

Experimental total, free and bound chloride profiles
WS=70 % (15 days)

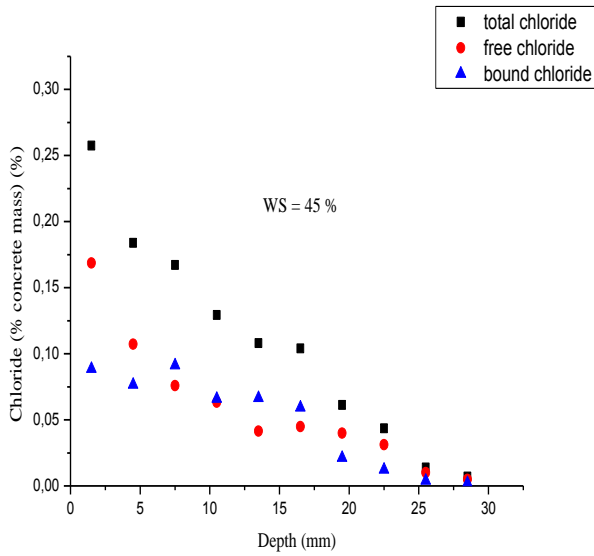


Figure 3

Experimental total, free and bound chloride profiles
WS=45% (15 days)

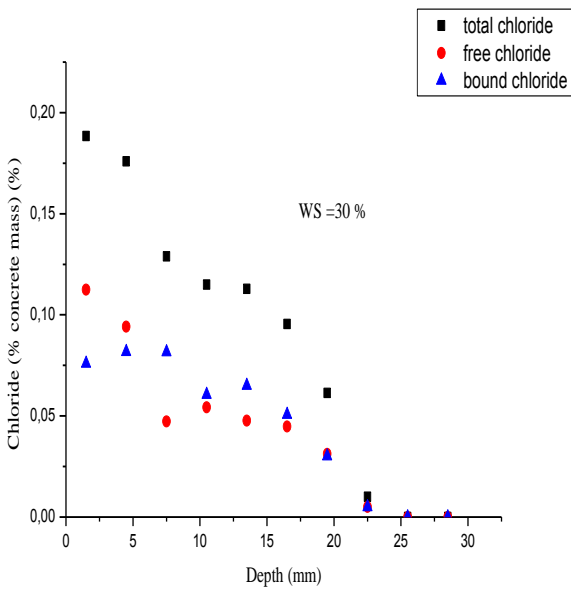


Figure 4

Experimental total, free and bound chloride profiles
WS=30% (15 days)

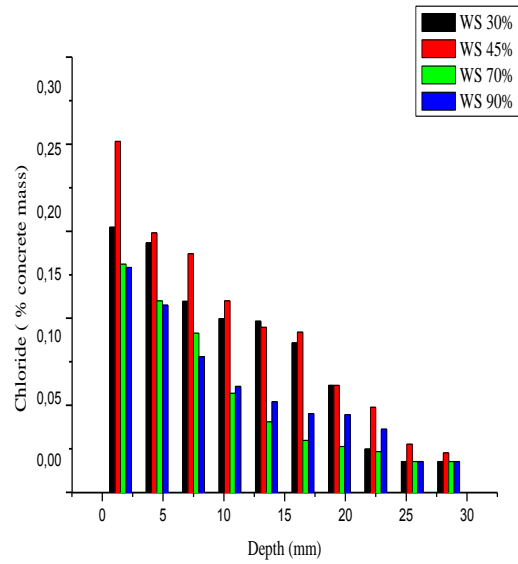


Figure 5

Total chloride profile measured at 15 days

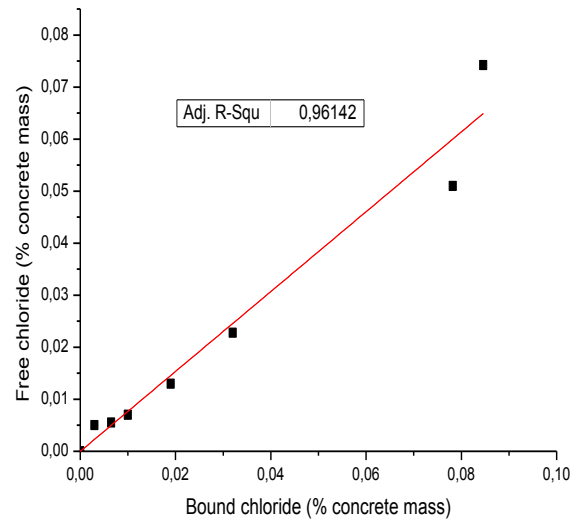


Figure 6

Isotherm derived from experimental data of WS 70% line shows the fitted Langmuir isotherm

REFERENCES

- [1] Ollivier, J.P and Vichot, A. 2008, "La durabilité des bétons : bases scientifiques pour la formulation de bétons durables dans leur environnement", Presses de l'école nationale des ponts et chaussées, France.
- [2] Climent, M.A., Vera, G. and all, 2002, "A test method for measuring chloride diffusion coefficients through nonsaturated concrete. Part I: The instantaneous plane source diffusion case", *Cement and Concrete Research*, 32, pp. 1113-1123.
- [3] Ben Fraj, A., Bonnet, S., and Khelidj, A., 2012, "New approach for coupled chloride/moisture transport in non-saturated concrete with and without slag", *Construction and Building Materials*, 35, pp. 761-771.
- [4] Nielsen, E.P. and Geiker, M.R., 2003, "Chloride diffusion in partially saturated cementitious material", *Cement and Concrete Research*, 33, pp. 133-138.
- [5] Guimarães, A.T.C., Climent, M.A., and all, 2011, "Determination of chloride diffusivity through partially saturated Portland cement concrete by a simplified procedure", *Construction and Building Materials*, 25, pp. 785-790.
- [6] Daian, J.F. and François, R., 2001, "Diffusion de sels dans les matériaux humides : analyse des processus couplés et étude expérimentale", *Revue française de génie civil*, 5, pp. 331-355.
- [7] Nilsson, L.O., Poulsen, E., and all, 1996, "HETEK Chloride penetration into concrete state of the art: transport processes, corrosion initiation, test methods and prediction models", Road Directorate, Report No.53.
- [8] Wang, X., 2012, "Modélisation du transport multi-espèces dans les matériaux cimentaires saturés ou non saturé et éventuellement carbonatés", PhD thesis of Paris-Est university.
- [9] Francy, O., 1998, "Modélisation de la pénétration des ions chlorures dans les mortiers partiellement saturés en eau", PhD thesis of Paul Sabatier university.
- [10] François, R., Francy, O., and all, 2001, "Mesure du coefficient de diffusion des chlorures : comparaison entre régime permanent et régime transitoire", *Revue française de génie civil*, 5, pp. 309-329.
- [11] Vera, G de., Climent, M.A., and all, 2007, "A test method for measuring chloride diffusion coefficients through partially saturated concrete. Part II: The instantaneous plane source diffusion case with chloride binding consideration", *Cement and Concrete Research*, 37, pp. 714-724.

REHABILITATION STUDY OF CONSTRUCTION BUILT IN SEISMIC ZONE IN ALGERIA

Imane DJAFAR HENNI*, Amar KASSOUL

(Hay Es Salam, B.P 151, Laboratory Structures, Geotechnics and Risks, Hassiba Benbouali University of Chlef, Algeria)

*Corresponding author: Email: djh-im@hotmail.fr

ABSTRACT

The rehabilitation of damaged buildings is a domain which remains a challenge after each earthquake. From there, several studies have been launched in this domain in order to develop solutions that can prolong the durability, improve the seismic resistance of constructions and reduce the cost of their maintenance. The objective of this work is to achieve a rehabilitation study of an administrative building built in a low seismicity zone according to the old Algerian earthquake rules (RPA83). Moreover, after the earthquake of Boumerdes in 2003, modifications have been made to this regulation, and this zone was changed into a high seismicity zone. However, after diagnosis and various investigations, it is always hard to make a radical choice about the preferred method of rehabilitation, and to facilitate the approval of such method to future designers, a comparative study of the rehabilitation of an old building in seismic zone in Algeria will be performed by proposing two models of bracing members, knowing that the first model concerns the strengthening by adding new reinforced concrete shear walls and the second is about the integration of new steel braced frames. Finally, we will highlight the performance of the proposed solutions for the strengthening by nonlinear static analysis of push-over type. The results obtained in terms of capacity curve and performance point showed a large performance of the structure by the two proposed reinforcing models.

KEYWORDS

Rehabilitation, Vulnerability, Strengthening, Shear wall, Braced frame, Pushover analysis.

NOMENCLATURE

V: Shear force.

Δ : Top displacement.

S_a : Spectral acceleration.

S_d : Spectral displacement.

RC: Reinforced concrete.

INTRODUCTION

Many existing buildings in Algeria, built according to the old codes, do not possess the necessary seismic resistance, and can seriously compromise occupant safety during a moderate seismic event. These buildings are characterized by the following nonconforming works: little shear resistance columns, inadequate recovery bars for longitudinal reinforcement, structural systems of strong beams and weak columns and little shear resistance in beam-column junctions. Losses due to earthquakes are

usually significant, but they can become gravest due to ignorance or the lack in the application of an efficient and integrated rehabilitation. In fact, precipitated or incorrect conception as well as poor execution of the repair works can lead to greater damages and even to loss of human life in case future quakes [1]. Numerous studies have been conducted on the rehabilitation of vulnerable structures. Hassaballah and al. [2] conducted a strengthening of weak columns of an existing hospital in Sudan by inserting reinforced concrete shear walls and the proposed solution has completely solved the problem and all columns were secured. And, this same technique was adopted by Davidovici [3, 4] on the rehabilitation of existing hospitals and schools reinforced concrete. On the other hand, several configurations of bracing systems may be installed within the bays of a reinforced concrete frame aiming to provide a

significant increase of the horizontal capacity of the structure, as have demonstrated Farmisano and al. [5,6], who have validated this reinforcement technique on an existing structure in Italy. In Algeria, several practical studies have been conducted on the rehabilitation of structures after El Asnam earthquake in 1980 and Boumerdes earthquake in 2003. We mention KASSOUL and al. [7] who conducted a study on the performance and strengthening of a construction of seven floors with resisting frame systems designed according to the old Algerian earthquake rules, whose shear wall system proposed for strengthening of the structure has largely improved its performance. Moreover, despite the existence of recommendations [8] and a technical guide of repair or strengthening methods for structures [9], there is a lack of regulatory support for the study of rehabilitation. The purpose of this study concerns the rehabilitation of an administrative building dimensioned according to the version of Algerian earthquake rules RPA81/v1983, which the bracing system is provided by the resisting frame systems, in a transitory period where the seismic code has not known its true application in low seismicity zones. Currently, this zone was changed to a high seismicity zone (zone IIb) in the present version of the Algerian earthquake rules (RPA99/v2003) [10]. First, a summary of the rehabilitation method of Eurocode 8-3 [11] is presented. Then two rehabilitation models are proposed for reinforcement. Finally, the paper highlights the performance of the proposed solutions for the reinforcement using the capacity spectrum method (CSM) applied according to the ATC40 code, which is a non-linear static analysis.

2. METHOD OF REHABILITATION ACCORDING TO THE EUROCODE 8-3

2.1 Information for structural assessment:

According to the steps described by Eurocode 8-3 [10], the first step governing the structural rehabilitation begins with the collection of the general and historical information of the building, especially the required input data to begin the rehabilitation methodology.

2.1.1 General and Historical Information: In order to assess the earthquake resistance of existing structures, the input data shall be collected from a variety of sources, including:

- Specific available documentation to the building in question,
- Relevant sources of generic data (e.g. contemporary codes and standards),
- Field investigations and, in most cases, in-situ and/or laboratory measurements and tests, as described in the following steps.

It should be checked between the data collected from different sources to minimize uncertainties.

2.1.2 Required Input data: The minimum input data required for the evaluation of the structure according to Eurocode 8-3 [10] are summarized as follows:

- a. Classification and identification of the structural system and its compliance with the regularity criteria in EC8-1 [11].
- b. Identification of the type of building foundations.
- c. Identification of the ground conditions as categorized in EC8-1 [11].
- d. Information about the overall dimensions and cross-sectional properties of the building elements and the mechanical properties and condition of constituent materials.
- e. Information about identifiable material defects and inadequate detailing.
- f. Information on the seismic design criteria used for the initial design, including the value of the force reduction factor (q).
- g. Description of the present and/or the planned use of the building (with identification of its importance category, as described in EC8-1) [11].
- h. Re-assessment of imposed actions on the building, considering its use.
- i. Information about the type and extent of previous and present structural damage, if any, including earlier repair measures.

The different types of analysis and different values of the confidence coefficients must be adopted according to the volume and quality of the gathered information.

2.2 Definition and identification of knowledge levels:

The type of allowable analysis and the appropriate confidence factor values, according to EC8-3 [10] is based on three knowledge levels, namely limited knowledge (KL1), normal (KL2) and full (KL3). The factors determining the appropriate knowledge level are: the geometry of the structural system and non-structural elements, detailing of reinforcement in reinforced concrete and the mechanical properties of

the constituent materials. The identification of the knowledge level of these factors is necessary to examine the following aspects:

- i. Physical condition of reinforced concrete elements and presence of any degradation, due to carbonation, steel corrosion, etc.
- ii. Continuity of loads downhill between lateral resisting elements.

2.3 Confidence factors: To determine the properties of existing materials used in the calculation of capacity, and when this one must be compared with demand for safety verification, the average values obtained from in-situ tests and the additional sources of information shall be divided by the coefficient of confidence, CF, given by the EC8-3 [10], which is the appropriate knowledge level that complies with the requirements. However, in order to compute the force capacity in terms of the ductile components, intended to be used in the safety checks, the mean value properties of existing materials shall be multiplied by the confidence factor CF for the appropriate knowledge level.

2.4 Vulnerability assessment: Assessment is a quantitative procedure for checking whether an existing undamaged or damaged building will satisfy the required limit state appropriate to the seismic action under consideration, as specified in EC8-1 [11].

3. DESCRIPTION OF THE BUILDING

The existing building selected for reinforcement is an administrative structure of high importance of five floors braced by resisting frame systems with a concrete compression stress measured about $f_{ck} = 15$ MPa, and a yield strength of steel $f_{cy} = 400$ MPa. This building was built in 1984 in a low seismicity zone (zone I), according to Algerian earthquake rules (RPA81/v1983). After the earthquake of Boumerdes in 2003, the zoning of the site has been changed to a high seismicity zone (zone IIb) according to Algerian earthquake rules (RPA99/v2003) [10]. The plan view of the building containing the different quotations is illustrated in Figure 1. The dimensions and quantity of reinforcement of beams and columns are shown in Table 1 and Figure 2.

Table 1
Dimensions of beams and columns.

Elements	Directions and stories	Dimension (cm x cm)
Columns	Ground floor & 1 st floor 2 nd , 3 rd & 4 th floors	40x40 35x35
Beams	All levels	30x40

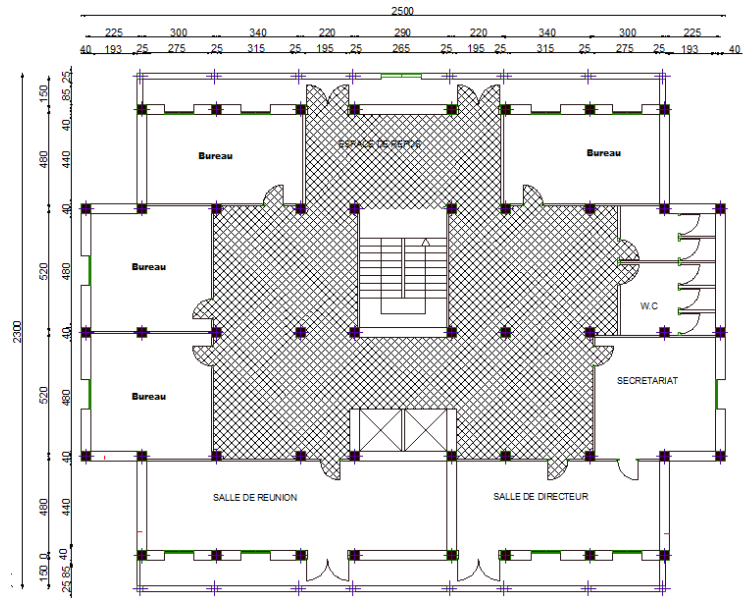


Figure 1
Scheme of the initial plan building

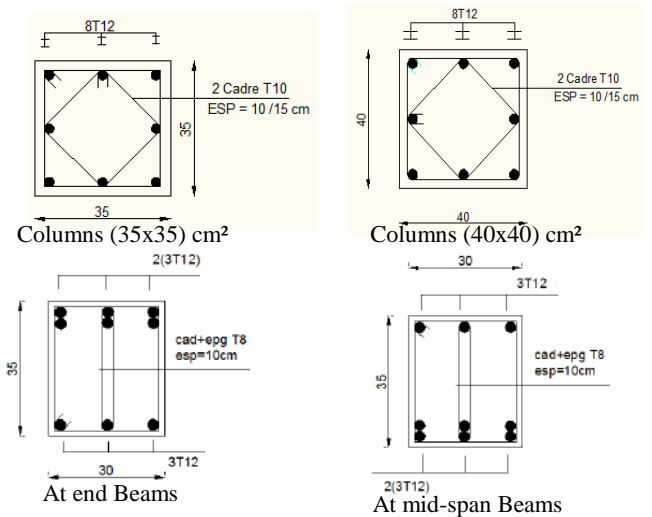


Figure 2
Detailing of structural elements.

Accordingly, after vulnerability assessment of the Eurocode8-3 rehabilitation method [11] on one hand, and by the linear dynamic analysis using the Sap2000v15 software [14] on the other, the building showed a flagrant inadequacy in the period, the base seismic force and the relative inter-story drift, which

more, till it reaches a value of 10342,17 KN for the structure reinforcing by RC shear walls, so three times more than the force before strengthening. Concerning the roof displacement, from Figure 6, the capacity curve of the initial structure shows that the corresponding ultimate displacement reached values of 14, 42 cm which is decreased at 10, 87 cm for the structure reinforced by RC shear walls, until 9.36 cm for the structure with the metal braced frames, which represent a decrease of about 32% and 54% respectively. Consequently, it can be deduced that strengthening by adding reinforced concrete shear walls increases the capacity of shear strength three more than times. Furthermore, the rehabilitation by integrating metal braced frames provides a remarkable improvement in terms of deformation.

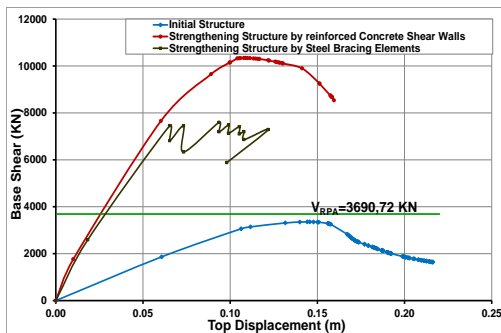


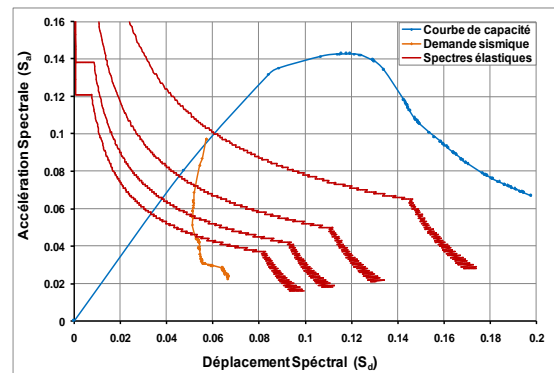
Figure 6
Capacity Curves (pushover)

5.2 Fragility curves: The performance point allows the making of several considerations on the behavior of the structure to the earthquake from the integration of a regulatory response spectrum, corresponding to the current seismic zone (IIb), on the capacity curve of the structure. In our case, the crossing is practically at the limit of the elastic behavior of the initial structure and for both rehabilitation models, this performance point is located in the middle of the elastic domain as shown in Figure 7. From this Figure and Table 2, it is also clear that the reinforcement models adopted in this study improve the behavior of the structure, because for 3062,65KN of shear force for strengthening by shear walls, the roof displacement reaches 2.1 cm. However, for the force obtained of rehabilitation by metal braced frames which represents 85% of the latter, the roof displacement is of 1.8 cm which represents an improvement of 17% compared to the RC shear walls. Consequently, for a similar seismic spectrum (IIb zone), the reinforced structure by adding reinforced concrete shear walls and

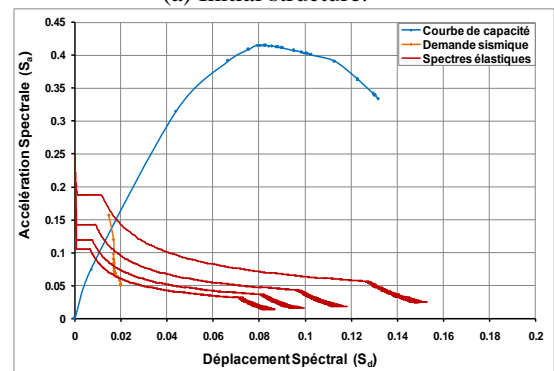
integrating steel braced frames, shows a significantly improved performance in terms of shear in the base and displacement at the roof respectively.

Table 2
Comparison of performance point coordinates of structures

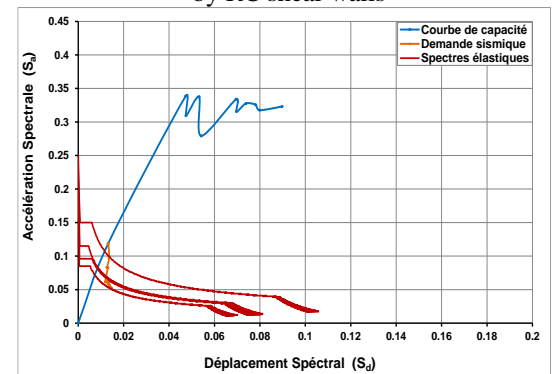
	Initial Structure	Strengthening structure by RC shear walls	Strengthening structure by steel braced frames
V (KN)	2171,41	3062,65	2596,12
Δ (m)	0,072	0,021	0,018



(a) Initial structure.



(b) Strengthening structure by RC shear walls



(c) Strengthening structure by steel braced frames.

Figure 7
Fragility curves and performance point.

6. CONCLUSION

The rehabilitation study adopted in this work, consists on evaluating comparative seismic vulnerability between two reinforcement models applied to a vulnerable structure, dimensioned according to the old Algerian earthquake rules, by the SAP2000/v15 software, knowing that the first model concerns the strengthening by adding new reinforced concrete shear walls and that the second is about the integration of new steel braced frames. The capability study of the building's performance by push-over analysis shows that:

- The two rehabilitation models chosen in this study show a greatly improved performance in terms of shear force at the base and roof displacement.
- The strengthening by adding reinforced concrete shear walls increases a shear capacity from a rate of 36% compared to the other model.
- The rehabilitation by integration of steel braced frames ensures an improvement of 16% in terms of deformation compared to that obtained by the addition of shear walls.

REFERENCES

1. Penelis G.G., Kappos A.J, Earthquake resistant concrete structures. London, Edition E & FN SPON, 1997.
2. Hassaballa A. E., Ismaeil M. A., Fathelrahman M. A., 2014, Seismic Evaluation and Retrofitting of Existing Hospital Building in the Sudan, Open Journal of Civil Engineering, 4, 159-172.
3. DAVIDOVICI Victor, Strengthening by reinforced concrete shear walls, 2006.
4. DAVIDOVICI Victor, Rehabilitation of existing hospitals, 2007.
5. A. Formisano, G. De Matteis, S. Panico and F. M. Mazzolani, 2008, Seismic Upgrading of Existing RC Buildings by Slender Steel Shear Panels: a Full-Scale Experimental Investigation. Advanced Steel Construction Vol. 4, No. 1, pp. 26-45 (2008).
6. Antonio Formisano (2007). Seismic upgrading of existing RC buildings by means of metal shear panels: design models and full-scale tests. Doctoral thesis, Université degli Studi di Napoli 'Federico II'.
7. A. Kassoul, A. Zerrouk and I. Djafar henni 2015, Rehabilitation of an Edified Building in a Seismic Zone in Algeria According to the Eurocode 8-3. 5th ECCOMAS Thematic Conference on

SEISMIC FRAGILITY CURVES FOR UNREINFORCED MASONRY STRUCTURES

Fouzia Djaalali and *Mahmoud Bensaibi

(Ecole Nationale Supérieure des Travaux Publics, National School of Built and Ground Works Engineering, 1
rue Sidi Garidi, Algiers, Algeria,

University Mohamed Bougarra, Boumerdes, Algeria)

*Corresponding author: Fax: +213 21288761 Email: bensaibim@yahoo.co.uk

ABSTRACT

Low and mid-rise unreinforced masonry (URM) buildings are the most common structures types in Algerian historical urban nuclei. Past earthquake reconnaissance reports showed that such structures have high seismic vulnerability. In order to avoid heavy damages in URM structures, the seismic performance level should be quantitatively measured through risk assessment of such structures. Fragility functions are an effective tool for risk assessment of structural systems as it can be used for probabilistic estimation of seismic losses. Within this paper fragility curves are derived for Algerian URM buildings using a log-normal probability distribution and vulnerability curves obtained by performing the vulnerability index method. Seismic scenarios of different intensities (VII to X) were performed for the district of Belouizdad of Algiers. The obtained results were integrated into a Geographical Information System (GIS) tool and the damage distributions of URM buildings for the district are given.

Key words:

NOMENCLATURE

- VI = vulnerability index
- D = damage
- \ln = natural Logarithm
- k_i = weighting factor
- C_i = vulnerability classes
- $\mu_{ln D}$ = log-normal mean
- $\sigma_{ln D}$ = standard deviation
- ϕ = standard normal cumulative distribution function
- Σ = sum
- I = intensity
- MDR = mean damage ratio
- MMI = Mercalli Modified Intensity
- CDF = cumulative density function

INTRODUCTION

Several seismic events stroke many regions in Algeria causing heavy damages such as Ain-Temouchent (1999) and Boumerdes (2003) earthquakes. Post-seismic investigations have shown extensive damages to unreinforced masonry structures (URM). Knowing that such structures are commonly found in Algerian urban nuclei, seismic risk assessments must be carried out on this population of buildings to identify the buildings most

likely to undergo losses during an earthquake. The results of such studies are important in the mitigation of losses under future seismic events as they allow strengthening intervention and disaster management plans to be drawn up [1, 2, 3]. Vulnerability and fragility curves [4, 5] are derived to assess the damage distribution of all buildings with similar characteristics in relation to the event intensity. Then, seismic scenarios can be performed [6-18]. It means that, vulnerability curves are used to obtain synthetic results of the mean damage to buildings in a selected territory [19-24] and fragility curves are an effective tool for risk assessment of structural systems as it can be used for probabilistic estimation of seismic losses [25-30].

Within this paper, fragility curves for Algerian low and mid-rise URM buildings are derived based on vulnerability functions developed in a previous study [24]. Seismic scenarios of different intensities (VII to X) are performed for masonry buildings of Belouizdad district.

BASIC ASSUMPTIONS

The vulnerability curves express the average damage rate which a stock of buildings belonging to various vulnerability classes with respect to various seismic intensities could undergo. These curves are

a function of the constructive system, of the site on which the city is built as well as certain numbers of local parameters. So each city has its own vulnerability curves. Algerian vulnerability curves for URM buildings were developed in [23, 24]. These curves were built based on the vulnerability index method and serve here as a basis to derive fragility curves.

Vulnerability index method: The method consist in attributing a numerical value to each studied building, representing its "seismic quality". This number is called "Vulnerability Index (VI)", it is obtained by a sum of weighting value expressing the "seismic quality" of the structural and non-structural parameters which are deemed to play a significant role in the seismic response of the considered building. Twelve (12) parameters were identified. For each parameter, the numerical value may be ranged in four classes. Class C1 refers to situation considered conform to Algerian seismic code in use. C2 and C3 refer to situation considered conform to ancient Algerian code and C4 refers to unsafe configurations. The obtained values are given in Table 1.

Table 1
Weighting parameters values [23, 24]

Parameter	Coefficient k_i			
	C1	C2	C3	C4
1. Total shear resistance of walls	0	0.05	0.12	0.21
2. Plan regularity	0	0.01	0.04	0.07
3. Elevation regularity	0	0.01	0.04	0.07
4. Walls connection	0	0.03	0.07	0.10
5. Walls type	0	0.01	0.03	0.05
6. Floor	0	0.01	0.03	0.05
7. Roof	0	0.01	0.03	0.05
8. Soil conditions	0	0.02	0.06	0.10
9. Pounding effect	0	0.01	0.04	0.07
10. Modifications	0	0.01	0.04	0.07
11. Details	0	0.00	0.02	0.03
12. General maintenance conditions	0	0.03	0.08	0.13

The weighting values are obtained by a statistical survey, based on Algerian past earthquake data. The vulnerability index is expressed as:

$$VI = \sum_{i=1}^{12} k_i \quad (1)$$

Vulnerability function: The methodology defined in [19] allows the translation of the buildings vulnerability functions from region to region by systematically considering the differences in buildings design codes. So, Algerian vulnerability functions of URM buildings were deduced from those obtained after Friuli (Italy) earthquake, an area which has same kind of masonry structures. These vulnerability curves are given on Figure 1 [23, 24]. They are function on the Mercally Modified Intensity (MMI) versus the Mean Damage Ratio (MDR) in percentage. These curves depend on the vulnerability index of the considered building. This vulnerability index (VI) is set varying from zero (no damage) to one (collapse). A step of 0.1 is taken in order to represent this vulnerability finely (Figure 1) [23, 24].

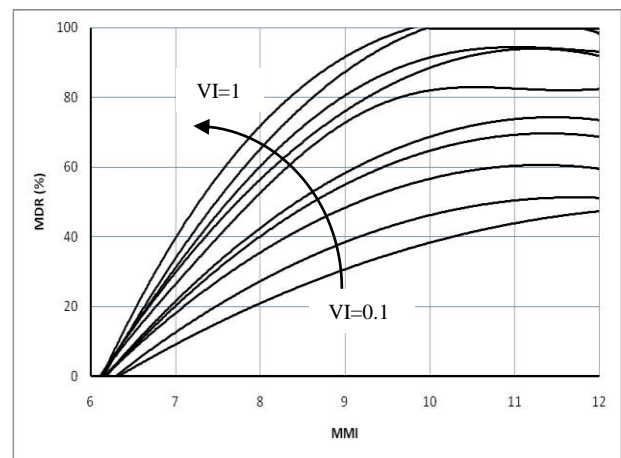


Figure 1
Algerian vulnerability curves
for URM buildings [24]

To link the MDR given by the developed vulnerability curves to the damage level, the definitions given by Park and Ang in [31] are used. These definitions are summarized in Table 2 and will be used to build fragility functions.

FRAGILITY CURVES ASSESSMENT

Fragility curves provide the probability of reaching or exceeding a given damage state as a function of the intensity of the natural event, and they are usually modelled by lognormal functions. A very important point is that fragility curves clearly take into account that not all buildings of the same type

will suffer the same level of damage for a given event intensity [22].

Table 2
Limit states damages

Damage categories	Damage Level
Negligible	Non structural = 0.01 – 0.1
Minor	Light structural damage = 0.1 – 0.2
Moderate	Moderate structural damage = 0.2 – 0.5
Severe	Severe structural damage = 0.5 – 0.85
Collapse	Collapse = 0.85 -1.

Damage measure and performance levels:

Defining a measure for quantifying the buildings seismic damage is the first important step of fragility analysis. In the case of URM buildings, three performance levels are defined in FEMA 356. In HAZUS [21] four limit states - Slight damage, moderate damage, extensive damage and collapse damage- are defined. In this study the limit states defined by Park and Ang. are adopted and the fragility curves are developed accordingly. Figure 2 shows the mean damage ratio (MDR) distribution for URM structures for different earthquake intensity levels. According to Park et al. [28], a log-normal distribution for the statistical description of the building response is a reasonable assumption. The log-normal mean ($\mu_{\ln D}$) and the standard deviation ($\sigma_{\ln D}$), necessary to describe the log-normal distribution, can be estimated from the log-normal probability plot of the data points (Figure 2).

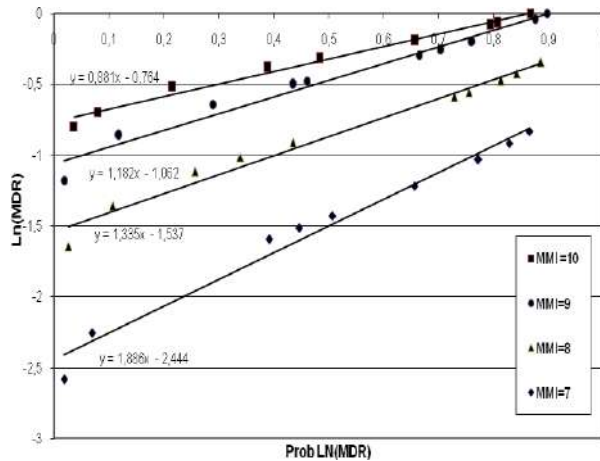


Figure 2
Log-normal fitting of fragility

The log-normal mean and the standard deviation is estimated from the y-intercept and the slope of the

fitted line respectively. The Log-normal parameters for description of fragility curves are given in Table 3.

Table 3
Log-normal parameters

MMI	$\mu_{\ln D}$	$\sigma_{\ln D}$
7	-2,444	1,886
8	-1,537	1,335
9	-1,062	1,182
10	-0,764	0,881

The variance of MMI 7 is higher than that of MMI 10 for instance, as the slope of MMI 7 is steeper than that of MMI 10.

The probability of exceedance different limit states damage (None Damage = 0.01, Light Damage = 0.1, Moderate Damage = 0.2, Sever Damage = 0.5, Collapse = 0.85) of the structure can then be calculated using the obtained log-normal parameters.

Construction of fragility curves: The probability of exceedance corresponding to a given limit state is calculated according following equation:

$$P(D > D_{limstate} / I) = 1 - \Phi\left(\frac{\ln(D_{limstate}) - \mu_{\ln D}}{\sigma_{\ln D}}\right) \quad (2)$$

where $\phi(\cdot)$ denotes standard normal cumulative distribution function (CDF).

For example, the log-normal mean and standard deviation of the mean damage ratio (MDR) corresponding to the seismic intensity MMI = 8 are -1,537 and 1,335, respectively.

The fragility curves of URM structures corresponding to different limit states can then be generated by plotting the seismic level in term of MMI intensity and the probability of exceeding limit state (Figure 3).

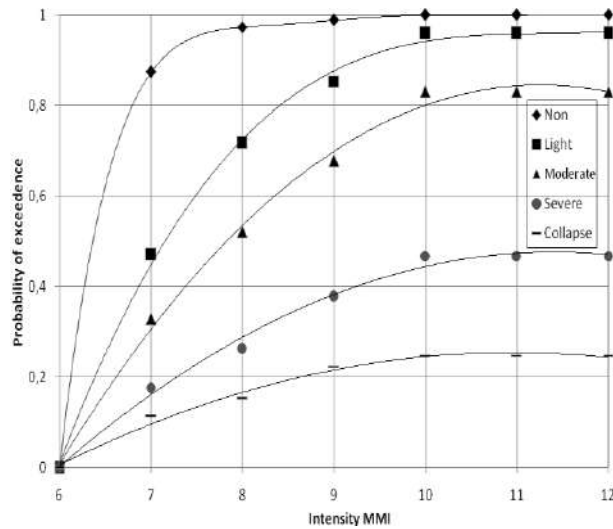


Figure 3
Fitted fragility curves for Algerian URM masonry buildings

Figure 3 shows, for instance, for an earthquake of intensity 10, the probability of exceeding a damage state “collapse” is 25%, it is 50% for the damage state “severe” and it is 100% for the state no damage.

Discussion: It appears that, the probability of exceeding a given limit state increase with the seismic intensity.

According to seismic code, the inelastic behavior of URM buildings starts at about MMI = 7 and several structural damage at about MMI = 10 [19]. So, the analysed buildings have more than 30% probability of exceeding the moderate damage state and around 18% probability of exceeding the severe damage state for MMI=7.

For MMI=10, these buildings have more than 80% probability of exceeding the moderate damage state and more than 40% probability of exceeding the severe damage state.

Even for low seismic intensity (between 7 and 8), the damage state "collapse", has a significant probability of exceedance (more than 10%).

So, it can be derived, that Algerian URM structures have low seismic performance, this is due to the fact that most of the such structures are designed without consideration of seismic loadings.

SEISMIC SCENARIOS

Seismic scenarios of different intensities (VII to X) are performed for the district of Belouizdad of Algiers using fragility curves developed above. The obtained results for 645 buildings are integrated into

a Geographical Information System (GIS) tool and the damage distributions of URM buildings for the district are given in Figure 4.



Figure 4
Seismic scenarios for intensities (VII to X)

Regarding the seismic scenarios for intensity VII, 57% of the buildings stocks present a light damage state with 0.47 probability of exceedance. Only 9.4% of the buildings expected a moderate damage state. 33% of buildings have no damage with 0.87

probability of exceeding this damage state. For the seismic scenario of the intensity $I = VIII$, the probability of exceeding moderate damage state is 0.52 with a rate of 72.62%. Moreover, rates of masonry buildings of 23.68% are expected to suffer a light damage with 0.72 probability of exceedance. Only 1.7% of buildings stocks suffer a severe damage with 0.26 probability of exceedance. The results shows that for seismic scenario $I = IX$, the majority of masonry buildings (90.11%) expected a moderate damage state with the probability of exceedance of 0.68. Only 9.89% suffer severe damage. Regarding the last seismic scenario of intensity X , the probability of exceeding severe damage state is 0.47 representing 37.8% of the analyzed buildings. The probability of exceeding moderate damage state is 0.83 for 62.8% of URM masonry constructions of the Belouizdad district. Therefore, the obtained results correlate with the vulnerability of the URM buildings of the Belouizdad district of Algiers.

CONCLUSIONS

Fragility curves are derived for unreinforced low and mid-rise masonry buildings in Algeria based on vulnerability index method and developed vulnerability functions. Vulnerability curves are used to obtain a synthetic result of mean damage to buildings in a given region, however fragility curves may be used to assess the damage distribution of all buildings in the study area. Fragility curves give the probability of exceeding a damage limit state for a given seismic intensity. The obtained functions show the vulnerability of Algerian URM buildings to seismic action, this is due to several parameters such as the lack of maintenance, the intensive use of such buildings due to grow of population and the no compliance design with seismic code. These facts emphasize the importance of developing such functions for accurate seismic risk analysis to perform seismic plans mitigation.

REFERENCES

1. Coburn, A., and Spence, R. 1992, *Earthquake Protection*. Chichester, Great Britain: John Wiley and Sons.
2. Cole, S.W., Xu, Y., and Burton, P.W. 2008, Seismic hazard and risk in Shanghai and estimation of expected building damage. *Soil Dynamics and Earthquake Engineering*, 28, 778–794.
3. ATC-13 1985, *Earthquake damage evaluation data for California*. ATC-13. Applied Technology Council. Redwood city, California.
4. S.M., and Kayhan, A.H. 2010, Fragility based damage assessment in existing precast industrial building: A case study for Turkey. *Structural Engineering and Mechanics*, 341, 39-60.
5. Lagomarsino, S. and Magenes, G. 2009. Evaluation and reduction of the vulnerability of masonry buildings. The state of Earthquake Engineering Research in Italy: the ReLUIS-DPC 2005-2008 Project. G. Manfredi and M. Dolce eds, 1-50.
6. Dolce, M., Kappos, A., Masi, A., Penelis, G., and Vona, M. 2006, Vulnerability assessment and earthquake damage scenarios of the building stock of Potenza (Southern Italy) using Italian and Greek methodologies. *Engineering Structures*, 28, 357–371.
7. Giovinazzi, S., Lagomarsino, S. and Penna, A. 2003, Seismic Risk Scenarios: Typological and Mechanical Approach in Vulnerability Assessment. *Geophysical Research Abstract*, 5, 09910.
8. Risk-UE 2003, An advanced approach to earthquake risks scenarios with to applications different European towns, WP4: Vulnerability of current buildings. Evk4-ct-2000-00014.
9. Srikanth, T., Kumar, R. P., Singh, A. P., Rastogi, B. K., and Kumar, S. 2010, Earthquake vulnerability assessment of existing buildings in Gandhidham and Adipur cities Kachchh, Gujarat (India). *European Journal of Scientific Research*, 41 (3), 336-353.
10. Vicente, R., Parodi, S., Lagomarsino, S., Varum, H., Mendes, D.A., and Silva, J.A.R. 2008, Seismic vulnerability assessment, damage scenarios and loss estimation case study of the old city centre of Coimbra, Portugal. 14th World Conference on Earthquake Engineering. Beijing, China.
12. Dolce, M., Kappos, A., Masi, A., Penelis, G., and Vona, M. 2006, Vulnerability assessment and earthquake damage scenarios of the building stock of Potenza (Southern Italy) using Italian and Greek methodologies. *Engineering Structures*. 28, 357–371.
13. Martinelli, A., Cifani, G., Cialone, G., Corazza, L., Petracca, A., and Petrucci, G. 2008, Building vulnerability assessment and damage scenarios in Celano (Italy) using a quick survey data-based

- methodology. *Soil Dynamic and Earthquake Engineering*. 28, 875– 889.
14. Barbat, A.H., Pujades, L.G., and Lantada, N. 2008, Seismic damage evaluation in urban areas using the capacity spectrum method: Application to Barcelona. *Soil Dynamic and Earthquake Engineering*. 28, 851–865.
 15. Ansal, A., Kurkulus, A., and Tonuk, G. 2010, Seismic Microzonation and earthquake damage scenarios for urban areas. *Soil Dynamic and Earthquake Engineering*. 30, 1319-1328.
 16. Vida I, F., Feriche, M., Ruiz, A., and Ontiveros, A. 2010, Seismic vulnerability assessment of traditional unreinforced masonry buildings. The case of Granada city (Spain). Ninth International Workshop on Seismic Microzoning Risk Reduction. Cuernavaca, México.
 17. Ansal, A., Akinci, G., Cultrera, M., Erdik, V., and Pessin, G. 2009, Loss estimat in Istambul based on deterministic earthquake scenario. *Soil Dynamic and Earthquake Engineering*. 29(4), 699-709.
 18. Erdik, M., Sesetyan, K., Demircioglu, M.B., Hancilar, U., and Zulfikar, C. 2011, Rapid earthquake loss assessment after damaging earthquakes. *Soil Dynamic and Earthquake Engineering*. 31, 247–266.
 19. Huo, J.R., Lawson, R.S., and Kishi, N.G. 1998, Translation of earthquake vulnerability functions. Eleventh European Conference one Earthquake Engineerin. Balkema.
 20. Whitman, R.V., Reed, J.W., and Hong, S.T. 1974, Earthquake damage probability matrices. Proceedings of the Fifth World Conference on Earthquake Engineering. Rome, Italy. 25-31.
 21. NIBS-National Institute of building Sciences 1999, HAZUS 99 earthquake loss estimation methodology. Technical manual. Washington, DC.
 22. Saeidi, A., Deck, O., and Verdel, T. 2009, Development of building vulnerability functions in subsidence regions from empirical methods. *Journal of Engineering Stuctures*, 31, 2275-2286.
 23. Djaalali, F. 2013, Détermination des courbes de vulnérabilité pour le bâti en maçonnerie de la capitale Alger (Algérie). Doctorat Thesis. National School of Built and Ground Works Engineering, Algiers, Algeria.
 24. Djaalali, F., Bensaibi, M., Bourahla,N., and Davene, L. 2012, Vulnerability curves for masonry constructions Algiers case study. *Structural Engineering and Mechanics*, 42(5), 609-629.
 25. Lagomarsino, S., and Giovinazzi, S. 2006, Macroseismic and mechanical models for the vulnerability and damage assessment of current buildings. *Bulletin of Earthquake Engineering*, 4, 415-443.
 26. Rota, M., Penna, A., and Magenes, G. 2010, A methodology for deriving analytical fragility curves for masonry buildings based on stochastic nonlinear analyses. *Engineering Structures*. 32, 1312-1323.
 27. Pagnini, LC., Vicente, R., Lagomarsino, S., and Varum, H. 2011, A mechanical model for the seismic vulnerability assessment of old masonry buildings. *Earthquakes and Structures*, 2(1), 25-42.
 28. Park, J., Towashiraporn, P., Craig, J.I., and Goodno, B.J. 2009, Seismic fragility analysis of low-rise unreinforced masonry structures. *Journal of Engineering Stuctures*, 31, 125-137.
 29. Wen, Y.K., Ellingwood, B.E., Veneziano, D., and Bracci, J. 2003. Uncertainty modeling in earthquake engineering. Mid-America Earthquake Center Poject FD-2 Report.
 30. Rota, M., Penna, A., and Magenes, G. 2010, A methodology for deriving analytical fragility curves for masonry buildings based on stochastic nonlinear analysis. *Journal of Engineering Structures*, 32, 1312-1323.
 31. Williams, M.S., and Sexsmith, R.G. 1995, Seismic damage indices for concrete structures A state-of-the-Art. *Earthquake Spectra*, 11(2), 319-349.

SEISMIC VULNERABILITY INDEX FOR BRIDGES

Mohamed Chérif DJEMAI ^{1*}, Mahmoud BENSAIBI ²

¹University Blida1, Blida, Algeria.

Email: djmai.medcherif@gmail.com

²National School of Built and Ground Works Engineering,
Ecole Nationale Supérieure des Travaux Publics, Algiers, Algeria

Email: bensaibim@yahoo.co.uk.

ABSTRACT

Bridges play an important role in transportation network. After an earthquake, bridges must remain functional. To reach this goal, vulnerability study must be conducted.

The aim of this study is to develop a vulnerability index method for bridges. The most important parameters influencing the seismic behavior of bridges are identified, and a seismic vulnerability assessment model is developed using the analytical hierarchy process (AHP) to quantify the contribution of each parameter.

Using the developed model, several bridges are treated and the obtained results show a good adequacy with in situ observations.

INTRODUCTION

Natural disasters such as earthquakes can cause severe damage to transportation network, which affect rescue and emergency operations. Therefore, the seismic vulnerability assessment of critical infrastructure in transportation network must be investigated.

In last decade, different empirical, analytical and hybrid approaches are developed to estimate the seismic vulnerability of bridges and help project managers and decision makers to intervene before and after an earthquake.

The available current procedures in United States are developed by the Applied Technology Council (ATC) [1], the Federal Highway Administration (FHWA) [2, 3], The California Department of Transportation (CALTRANS)[4, 5], for the others States of America, there are Nevada and Missouri [6], Washington [7, 8], Illinois [9], New York [10], Tennessee [11], and Oregon [12], procedures.

In Japan, three methods are used, "JHPC" (Japan Highway Public Corporation), "MOC"(Japanese Ministry of Construction) [13, 14], and KUBO - KATAYAMA method [15]. Many other approaches do exist, among them, the "FEDRO" (Federal Roads Office) method applied in Switzerland [16], "SISMOA" method applied in France, [17, 18], and

"QMT" (Quebec Ministry of Transportation) method applied in Canada (Quebec) [19].

In the present study, a seismic vulnerability assessment for bridges is performed using the vulnerability index (VI) method. In this method, the most important parameters that play a role in the seismic behavior of bridges are identified, and then weighting coefficients for each parameter are determined using the Analytical Hierarchy Process (AHP). A classification based on the obtained "VI" is also proposed.

DEVELOPED APPROACH

The developed method is based on the vulnerability index method, which combines several parameters that have an influence on the seismic behavior of bridges. It allows calculating the seismic vulnerability index "VI".

Identification of the parameters: Various parameters are defined from post-seismic observations and seismic experience feedbacks, [20 - 22].

The parameters selected for this model are configured on two groups, structural and hazard parameters. The structural parameters describe structural aspects that make systems more or less vulnerable. The aim of hazard parameters is to consider the influence of seismicity.

Selected parameters of the evaluation model are declined in items; each item is divided to a number of factors; these factors are also composed of several categories (Table 1).

Each parameter, item and factor has a related weight W_i, W_{ij}, W_{ijk} respectively, which reflect its relative importance. The aim is to determine the weighting coefficients value.

Table 1
Hierarchy of Parameters, Items, Factors and Score of each Category.

Parameter	Item	Factor	Category	Scores	
Structural	Superstructure	Girder type	Arch or rigid frame	10	
			Continuous Girder	30	
			Simple Girder	50	
		Number of spans	1 Span	20	
			2 Spans or more	40	
			Skew	Straight deck (No skewed)	10
		Low		20	
		Medium		30	
		Curvature	High	40	
	Min. bridge seat width		Straight deck (No curvature)	10	
			Low	20	
		Medium	30		
	Bearings	Min. bridge seat width	High	40	
			Wide 70cm or wider	10	
			Narrow less than 70cm	40	
		Bearing type	No seat: 0cm	20	
			With specific device	10	
			Bearing (with clear design concept)	20	
		Ground and Foundation	Ground type	Movable bearing	40
				Others (no bearing, etc)	20
Stiff/Hard				0	
Foundation type	Medium		10		
	Soft		40		
	Very soft		50		
Expanded	Pile Bent	40			
	Others Pile	20			
Expanded	30				

Piers and Abutments	Max. height of Abutment / Pier (m)	Less than 5m	10
		Between 5 to 10m	30
		More than 10m	50
Construction Materiel of Abutment / Pier		Reinforced Concrete	40
		Masonry	30
		Others	20
Pier type		No piers for masonry structure	10
		No piers for other than masonry structure	40
		Columns piers	20
Abutment type		Massive piers	10
		Backfilled abutment	40
		Buried abutment	30
Seismic intensity	-	Abutment Superficially Founded	20
		MMI < VIII	10
		VIII ≤ MMI < IX	20
		IX ≤ MMI < X	30
		X ≤ MMI < XI	40
		XI ≤ MMI	50
Liquefaction potential	-	No liquef.	10
		Low 0 < PL ≤ 5	20
		Medium 5 < PL ≤ 15	30
		High 15 < PL	50

Quantification of the identified parameters:

To derive the weighting coefficients, the Analytical Hierarchy Process (AHP) method is applied. The AHP was developed by Thomas L. Saaty [23] in the 1970s and has been extensively studied and refined since then. It is a robust and flexible multi-criteria decision analysis methodology.

It is a modelling technique which reduces a system to a sequence of pair-wise comparisons of identified components [24].

Several application models for assessing seismic vulnerability of infrastructures was developed using AHP process [25 - 27].

The model based on AHP allowed determining the relative contribution of each parameter. The pairwise comparisons are entered in a reciprocal comparison matrix for each level of the hierarchy. The obtained

weights for each level (parameters, items and factors are summarized in Table 2.

Table 2
Weighting Factors, Items and Parameters.

Parameter	W*	Item	W*	Factors	W*	
Structural	0.250	Superstructure	0.512	Girder type	0.574	
				Number of spans	0.232	
				Skew	0.097	
				Curvature	0.097	
		Bearings	0.120	Min. bridge seat width	0.667	
				Bearing type	0.333	
		Ground and Foundation	0.281	Ground type	0.750	
				Foundation type	0.250	
		Piers and Abutments	0.086	Max. height of Abutment / Pier (m)	0.491	
					Construction Materiel of Abutment / Pier	0.268
					Pier type	0.160
					Abutment type	0.081
Hazard	0.750	Seismic intensity	0.800	-	-	
		Liquefaction potential	0.200	-	-	

*Weight.

A numeric worth score S_{ijkl} from 0 to 50 is assigned to every category. This reflects the one-dimensional value of the performance level of each category. The last column of Table 1 shows the score values of all categories.

Determination of vulnerability index: the vulnerability index "VI" is defined as:

$$VI = \sum_{i=1}^2 W_i \sum_{j=1}^{2or4} W_{ij} \sum_{k=1}^{2or4} W_{ijk} S_{ijkl}$$

Where:

W_i : The weighting coefficient of structural or hazard parameters.

W_{ij} : The weighting coefficient of items.

W_{ijk} : The weighting coefficient of factors.

S_{ijkl} : the score.

According to the values obtained for the vulnerability index, three classes are proposed to classify bridges. The three risk levels, low, medium and high and their range are summarized in Table 3.

Table 3
Risk Levels of Bridges.

Risk Level	VI
Low Risk	0 < VI < 35
Medium Risk	35 ≤ VI < 50
High Risk	VI ≥ 50

CASE STUDIES

Validation of the proposed approach: To investigate the sensitivity of the proposed methodology, seven bridges are considered.

First, The Damous Bridge is situated in the western boundary of the Tipaza province, in the national road N°11. It was built in 1987, and it having a total length of 280.0m and a total width of 13.5m with nine spans.

Second, the highway bridge named Mazafran Bridge is the longest one in Tipaza region, 420m length and 27,5m width. The bridge is situated in the eastern boundary and crosses Mazafran River, it has eleven spans.

Fadjana, Boukadir and Bouyaghsane Bridges are situated respectively in the national road N°65, N°66 and N°67.

Finally, El Harrach and Sabdou Bridges are located in Algiers and Boumerdes provinces, respectively.

The obtained results are compared to those provided by Kubo Katayama method [15] Table 4. As it can be seen the obtained results are in good agreement.

Table 4
Comparison between the results obtained by Kubo-Katayama and Developed Methods.

Bridges	Developed Method	Kubo-Katayama Method
Damous Bridge (Tipaza)	High Risk	High Probability of Damage
Mazafran Bridge (Tipaza)	High Risk	High Probability of Damage
Fadjana Bridge (Tipaza)	Medium Risk	Medium Probability of Damage
Boukadir Bridge (Tipaza)	Low Risk	Low Probability of Damage
Bouyaghsane Bridge (Tipaza)	Medium Risk	Medium Probability of Damage

El Harrach Bridge (Algiers)	Medium Risk	Medium Probability of Damage
Sabdou Bridge (Boumerdes)	High Risk	High Probability of Damage

Applications of the proposed approach: In order to apply the proposed method, a number of bridges located in Tipaza region have been chosen. Tipaza is situated in the north of Algeria, West of Algiers (capital of Algeria). The road network in this wilaya contains ninety two (92) bridges; Fifty seven (57) of them are studied.

The study area illustrated in Figure 1 is located south of the seismogenic basin of Mitidja, beside several active faults. The seismic movements caused by those faults can be felt with different intensities. The strongest events are the Chenoua (Tipaza) and Zemmouri (Boumerdes) earthquakes. They were occurred on October 29th, 1989 (6.0) and on May 21st, 2003 (M 6.8) respectively.



Figure 1
Tipaza bridges locations.

The seismic risk assessment was performed for three different scenarios; the seismic intensities of those scenarios are VIII, IX and X on MMI scale (Modified Mercalli Intensity Scale). The distribution of expected risk for the three hazard levels is shown in Figure 2.

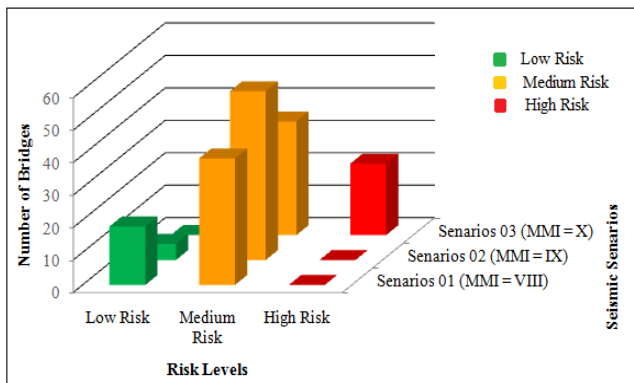


Figure 2
Distribution of Expected Risk as a function of Seismic Scenarios.

Discussion of results: It can be noticed that the most of studied bridges have a medium risk level. No high risk level was observed for the first and second scenarios. Whereas nearly 40% of studied bridges have a high risk for the third scenario (MMI=X).

The bridges that have a medium risk level need detailed investigations to be reinforced or rebuilt.

According to above results, it can be drawn that in addition to structural parameters, the seismic intensity plays an important role in bridge vulnerability. This role is more or less important depending on the epicenter location of the seismic event.

At least, the results of this study are in good adequacy with in situ observations.

CONCLUSION

To evaluate the seismic vulnerability and risk levels of existing bridges, a new developed method is presented in this paper. This approach is used to calculate a vulnerability index for bridges and classify them.

The proposed model was carrying out using AHP method through identifying and quantifying the most important parameters and factors affecting the seismic vulnerability of bridges.

The provided results can be used to prioritize retrofitting intervention on bridges. Also a preparedness plan can be given to local authorities in order to reduce the impact of a future earthquake.

REFERENCES

1. ATC, Applied Technology Council, 1983, Seismic Retrofitting Guidelines for Highway Bridges, Report No.ATC 6-2.
2. Buckle, I.G., Mayes, R.L., and Button, M.R., 1987, Seismic Design and Retrofit Manual for Highway Bridges, Report No. FHWA-IP-87-6, Washington, USA.
3. Buckle, I.G., 1990, The preliminary screening of bridges for the seismic retrofit, Proceedings: Second Workshop on Bridge Engineering Research in Progress, University of Nevada, Reno.
4. Maroney B., Gates J., 1990, *Seismic risk identification and prioritization in the Caltrans seismic retrofit program*, Proceeding of the 59th Annual Convention Structural Engineering Association of California, pp. 321– 341.

5. Gilbert, A.D., 1993, *Developments in seismic prioritisation of bridges in California*, Proceedings: Ninth Annual US/Japan Workshop on Earthquake and Wind Design of Bridges. Tsukuba Science City, Japan.
6. Maffei, J., and Park, R., 1994, *A review of seismic evaluation and retrofit technology for bridges*, Proceedings, Annual Technical Conference, New Zealand National Society for Earthquake Engineering, New Zealand.
7. Babaei K., Hawkins N., August 1991, *Bridge seismic retrofit prioritization*, In Proceedings of the third US conferences on lifeline earthquake engineering, Los Angeles, California, , p.149 – 155.
8. Babaei K., Hawkins N., 1993, Bridge seismic retrofit planning program, Washington State Department of Transportation, Olympia, Washington, Report No. WA-RD 217.1.
9. Cooling, T.L., 1990, *Illinois department of transportation, seismic condition studies*, Proc. Seminar Assessing and Managing Earthquake Risk in the Central United States, Cosponsored by Woodward-Clyde and EQE Consultants, St. Louis.
10. Buckle, I.G., 1990, A Prioritization Plan for Seismic Bridge Retrofit: Issues and Recommendations, Report to New York State Department of Transportation, NY.
11. Pezeshk, S., Chang, T.S., Yiak, K., and Kung, H., 1993, Seismic vulnerability evaluation of bridges in Memphis and Shelby county, Tennessee, Earthquake Spectra, Vol. 9.
12. Larsson A., Groff, R., December 1995, *Prioritization of Oregon bridges for seismic retrofitting*, National seismic conference on bridges and highways, San Diego, California.
13. PIARC, January 1994, *Synthesis report on natural disaster reduction of roads*, 5th meeting of PIARC/Working group G2, Washington DC, 2nd Report.
14. Légeron F., 2001, Seismic vulnerability and retrofit of bridges, Technical Report SETRA, France.
15. Kubo K., Katayama T., 1977, *A simple method for evaluating seismic safety of existing bridge structures*, Proceedings of 6th WCEE, New Delhi, 1951–1956.
16. Wenk T., 2005, *Evaluation parasismique des ponts - routes existants*, Office fédéral des routes, OFROU, Division réseaux routiers, Berne.
17. Marchand P., Davi D., Schmitt P., Thibault C., Duval A.M., Criado D., 2006, *SISMOA: a simplified method to assess the seismic vulnerability of existing bridges*, First European conference on earthquake engineering and seismology, Geneva, Switzerland.
18. Gueguen Ph., 2013, *Seismic vulnerability of structures*, ISTE Ltd and John Wiley & Sons, Inc, Great Britain.
19. Nollet M. J., LeBoeuf D., Khaled A., (Mai 2007), *Microzonage et vulnérabilité sismique des ponts de la Ville de Québec*, 14^{ème} Colloque sur la progression de la recherche québécoise sur les ouvrages d'art, Université Laval, Canada.
20. Gimez Soberon C., Oller S., Barbat A. H., 2002, *Seismic Vulnerability of Bridges Using Simplified Models*, Monografia CIMNE IS-47, Spain.
21. Adaffer S., Bensaibi M., 2015, Seismic Vulnerability Index for Road Networks, International Conference on Industrial Technology and Management Sciences (ITMS 2015), March 27-28. Tianjin, China.
22. Bensaibi M., Djemai M.C., Décembre 2011, Estimation de l'indice de vulnérabilité pour les ponts, Algérie Equipement N° 50, Algérie.
23. Saaty T. L., 1980, *The Analytic Hierarchy Process*, New York, McGraw-Hill.
24. Sharma, V., Al-Hussein, M., Safouhi H. and Bouferguene A., 2008, Municipal Infrastructure Asset Levels of Service Assessment for Investment Decisions Using Analytic Hierarchy Process, Journal of Infrastructure Systems, Vol. 14, No. 3.
25. Yadollahi M., Rosli M., and Vafaei M., 2012, A Model for Seismic Vulnerability Score Assignment of Road Infrastructure Using Linear Regression Technique, Applied Mechanics and Materials, Switzerland, Vol. 147 (2012) pp 266-269.
26. Rashidi M., Gibson P., 2012, A methodology for bridge condition evaluation, Journal of Civil Engineering and Architecture, Wollongong, 6(9), 1149-1157.
27. Zayed T., Edward Minchin Jr. R., Andrew J. Boyd, Gary R. S., and Michael C. McVay, February 2007, Model for the Physical Risk Assessment of Bridges with Unknown Foundation, Journal Of Performance Of Constructed Facilities, ASCE, pp 44-52.

COMBINED EFFECT OF TEMPERATURE AND SULFATE ATTACK ON THE DURABILITY OF REPAIR MORTAR BASED ON MIXTURE OF DUNE-ALLUVIAL SAND

Mohammed Fatah LAKHDARI*, Ali ZAIDI, Mohammed BOUHICHA and Benharzallah KROBBA
Structures Rehabilitation and Materials Laboratory (SREML), Laghouat University, Algeria

*Corresponding author Email: mf_lakhdari@yahoo.com

ABSTRACT

The objective of this experimental research is to study the combined effect of temperature and sulfate attack effect on the durability of dune –alluvial sand mortar. 4x4x16mm Specimens of this mortar were exposed to sulfate solutions $MgSO_4$ and solutions Na_2SO_4 then exposed to 50 °C temperature in oven for three months and were tested. Results showed that the mechanical strengths of the dune –alluvial sand mortars, either in compression or in tensile, decrease with time. Dune alluvial sand mortar with Superplasticizer exhibits the best behavior under sulfate attack.

Keywords: Dune-Alluvial Sand Mortar, Durability, Magnesium Sulfate attack, Sodium Sulfate attack, temperature effect, Superplasticizer effect.

INTRODUCTION

The possibility of using dune sand, existing in abundance in the Algerian Sahara, as a building material was the subject of many researches. This interest finds its justification in economic and environmental considerations. The results obtained by different authors agree on the possibility to use dune sand in mortars or concretes [1]. However, certain aspects related to the durability of such types of mortars or concrete require more studies. One of these aspects relates to durability with respect to frequent sulfates subsisting in Saharan soil. Our contribution consists to investigate the durability of dune and alluvial sand mortars subjected to the combined effect of temperature and sulfate attacks. We present in this investigation characteristics of the two studied mortars namely: MSDA4 (Dune and alluvial sand mortar), MSDA4P (Dune and alluvial sand mortar with super-plasticizer). The both formulated mortars were studied in previous works [2]. Then, we exhibit the results obtained from the durability tests carried out on 4x4x16mm mortar specimens immersed in sulfate solutions under temperature of 50 °C. The concentration of sulfate solutions used was 10% Magnesium sulfate ($MgSO_4$) and 10% of Sodium sulfate (Na_2SO_4). The results obtained show the reduction of mechanical properties, in terms of compressive and flexural strengths of dune and alluvial sand mortars subjected

to the combined effect of temperature and sulfate solutions attacks.

DUNE-ALLUVIAL SAND MORTARS PROPERTIES

Procedures followed to formulate the repair mortar MSDA4 which is constituted of dune sand, stream sand, and cement and also to formulate the repair mortar MSDA4P which is similar to MSDA4 but with Super-plasticizer were published in previous work [3].

Material used:

Alluvial and dune sands:

Two types of sands were used in this study:

- A sand of dune extracted from the northern area of the town of Laghouat (South of Algeria) named SD.
- A sand of stream (alluvial sand) named SA extracted from Wad M'Zi situated at Laghouat city.

Cement:

Cement used is the type CPJ CEM II 42.5. Standards tests were conducted to determine physical, chemical and mechanical properties of the cement used

Mixing water:

Water used in this experimental study is the laboratory tap water of Laghouat University (Algeria).

Mortars description

Both Mortars MSDA4 and MSDA4P had ratios of water/Cement W/C = 0.6 and 0.55, respectively, and a ratio of Cement/Sand C/S equal to 1/3. It is noted that the cement content is about 350kg/m³. Percentages values of dune sand (SD) and alluvial sand (SA) used in this study were equal to 60% and 40%, respectively. The additive used in the MSDA4P mortar is the type of Super-plasticizer SP40 with a percentage of 1.9% of the cement content.

Experimental results of dune- alluvial sand mortars mechanical properties:

Results of the compressive and flexural strength as a function of the age for dune-alluvial sand mortar specimens (MSDA4 and MSDA4P) stored at the free air inside the laboratory are presented in figures 1 and 2. These figures show the additive effect on the mortar strength. It is noted that compressive strengths of MSDA4 and MSDA4P mortars have been found equal to 30 MPa and 40 MPa, respectively. Mortars with Superplasticizer exhibit stronger strength than mortars without Superplasticizer. This fact is in accordance with results reported by Prince et al. (2002) [4] and can be explained by the acceleration effect of the Superplasticizer on the development rate of Hydrated Calcium Silicate in the cement paste.

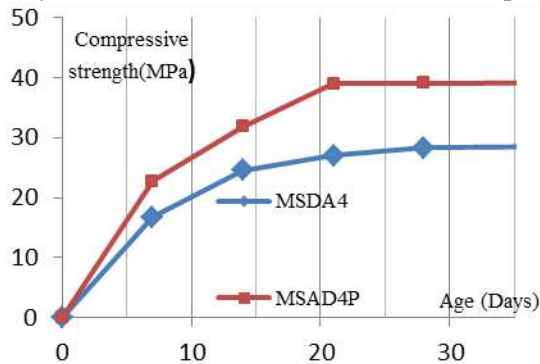


Figure 1
Compressive strength of Mortars

In Flexural, figure 2 shows that MSDA4P mortar reaches a strength value of 7.5 MPa due to effect of Superplasticiser. While, for MSDA4 mortar the flexural strength is about 6.0 MPa.

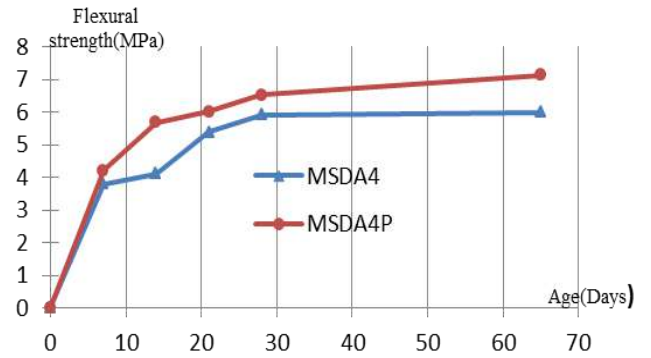


Figure 2
Flexural strength of Mortars

DURABILITY OF DUNE-ALLUVIAL SAND MORTARS IN AGGRESSIVE ENVIRONMENT

Test procedures:

The mortar specimens are kept in free air inside the laboratory until 28 days and then they are immersed in two different environments (attack solutions):

- Attack solutions 1: Immersion in sulfate (Mg SO₄) 10% at 50 °C. The solution sulfate attack used is the Magnesium sulfate (MgSO₄) with a concentration of 10% (accelerated attack).

- Attack solutions 2: Immersion in sulfate (Na SO₄) 10% at 50 °C. The solution sulfate attack used is the Sodium sulfate (NaSO₄) with a concentration of 10% (accelerated attack).

Results and discussion

Compressive strength

a) Magnesium Sulfate attack:

Figure 3 shows the combined effect of temperature and magnesium sulfate attack on the compressive strength.

It can be observed that the compressive strength decreases for all mortars immersed in sulfate solutions, particularly, for MSDA4 in which the strength show a reduction from 30 MPa to 14.5 MPa after 45 days immersion in magnesium sulfate with a reduction rate more greater than 50%. This result is in good accordance with that obtained by Amin et al. (2008) [5], which is due to the substitution of

Ca²⁺existing in C-S-H by Mg²⁺ ions of MgSO₄. For MSDA4P mortar, the effect of the additive seems to reduce the damage of attack effects with reduction rate of compressive strength to 30%, this value is more moderate than the MSDA4 one. Prince et al. (2003) [6] and Kim et al. (2000) [7] reported that molecules of Superplasticizer were adsorbed in the non hydrated phase of the cement. This inhibits the germination and the growth of ettringite crystals. This result shows that the additive could improve the durability of the mortar in the Saharan environment characterized by high temperature and high MgSO₄ content.

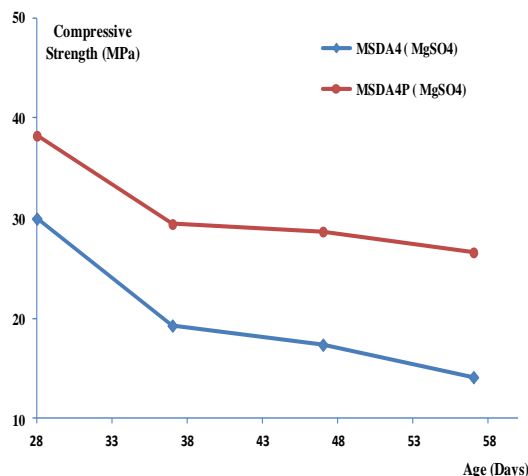


Figure 3
Compressive strength of mortars in magnesium sulfate solution (MgSO₄)

b) Sodium Sulfate attack:

In Sodium Sulfate attack the decrease of compressive strength is about 30% and 20% for MSDA4 mortar and MSDA4P mortar, respectively, as shown in figure 4.

Figure 5 shows that the reduction rate of compressive strength is very low in sodium sulfate solution compared to that of specimens immersed in magnesium sulfate solution. It can be concluded that the magnesium sulfate attack has more influence on the compressive strength of mortars than the sodium sulfate for alluvial-dune sand mortars under combined effect of temperatures and sulfate attacks.

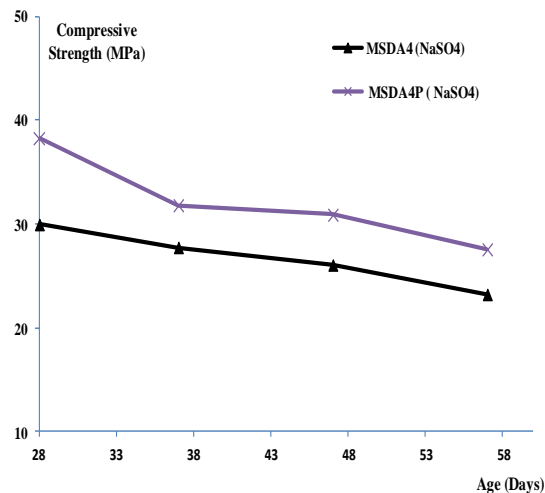


Figure 4
Compressive strength of mortars in sodium sulfate solution (NaSO₄)

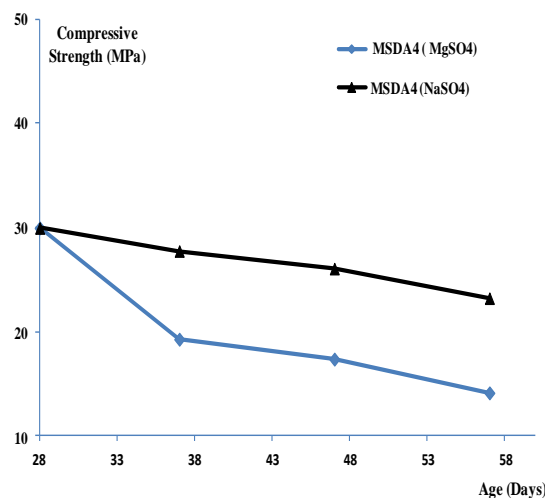


Figure 5
Effect of sulfate type on compressive strength of mortars without super-plasticizer

Flexural strength:

a) Magnesium Sulfate attack:

Figure 6 shows that the flexural strength of MSDA4P mortar exhibits a notable fall in the sulfate solution. This strength decreases from its maximum value of 6.4 MPa to a minimum value less than 3.4 MPa with a reduction rate of 50% for the first 30 days immersion. In the case of MSDA4 the figure shows a gradual reduction during attacks. At the end of 45 days, the strength values are similar for both mortars.

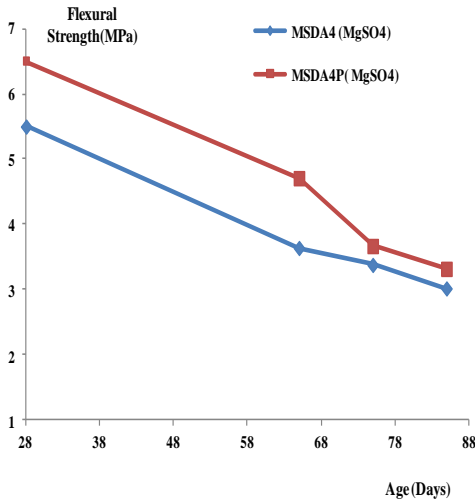


Figure 6

Flexural strength of Mortars in magnesium sulfate solution (MgSO4)

b) Sodium Sulfate attack:

In Sodium Sulfate attack, as shown in figure 7, the flexural strength decreases with reduction rates of 42% and 39% for MSDA4 and MSDA4P mortars, respectively. As noted in the compressive strength section, the degradation of the flexural strength in the Magnesium Sulfate solution is more important compared to that in the Sodium Sulfate solution, as shown in figure 8. The decrease of strength is due, as explained by Wee et al. (2000) [8], to the reaction carried out between Sulfate Ions provided by the Sodium Sulfate and the Portlandite to form the Gypsum.

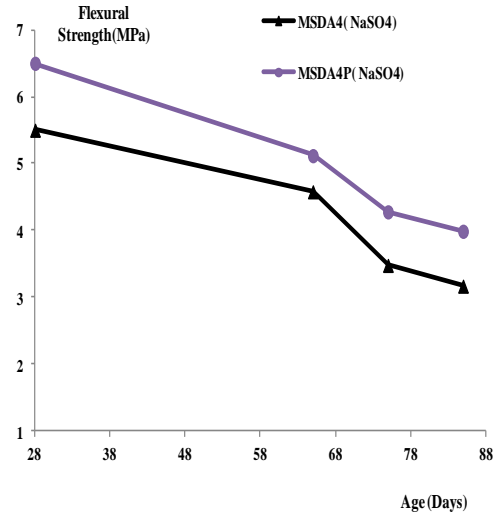


Figure 7

Flexural strength of Mortars in sodium sulfate solution (NaSO4)

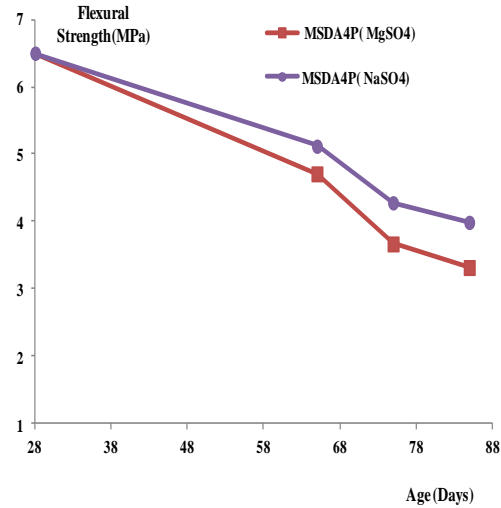


Figure 8

Effect of sulfate type on flexural strength of mortars with super-plasticizer

CONCLUSIONS

From analysis of experimental results on the durability of dune-alluvial sand mortars subjected to the combined effect of high temperature and Sulfate attacks, the following conclusions can be drawn:

-The reduction in compressive and flexural strengths of mortars without Super-plasticizer is more than 50% for dune-alluvial sand mortars immersed in both sulfate solutions ($MgSO_4$ and $NaSO_4$) under high temperature of 50 °C during 45 days.

- The Magnesium sulfate attack has a big influence on the strength degradation of dune-alluvial sand mortars with respect to the Sodium sulfate attack under high temperature of 50 °C.

-The Super-plasticizer added to dune-alluvial sand mortars could enhance the durability of mortars in the Saharan environments characterized by high temperature of 50 °C and high sulfate content.

ACKNOWLEDGMENTS

The writers would like to acknowledge the support of the Structures Rehabilitation and Materials Laboratory (SREML) and also the Civil Engineering Department of Laghouat University (Algeria). The opinion and analysis presented in this paper are those of the authors.

REFERENCES

1. Benchaa, B., Azzouz, L., Kadri, E., Belaidi, A. S.E., Soualhi, H., Juin 2012, Propriétés physico-mécaniques et durabilité des mortiers à base de sable de dune, XXX^e Rencontres AUGC-IBPSA Chambéry, Savoie.
2. Lakhdari, M.F., Zaidi, A., 2015, Formulation of repair mortar based on mixture of dune sand and alluvial sand, ISBS, 2nd International Sustainable Building Symposium, Proceeding-ISBS-2015, Ankara, Turkey, pp. 674-678.
3. Lakhdari, M.F., Zaidi, A., Bouhicha, M., and Krobba, B., October 2015, Physical-Mechanical Performances of a Dune-Alluvial Sand Mortar, 2nd International Conference on Computational and Experimental Science and Engineering (ICCESEN-2015), Antalya, Turkey.
4. Prince, W., Edwards-Lajnef, M., Aitcin P.-C., 2002, Interaction between ettringite and a polynaphthalene sulfonate Superplasticiser in cementitious paste, *Cement and Concrete Research*, **32**, pp.79-85
5. Amin, M.M., Jamaludin, S.B., Pa, F.C., Chuen, K.K., 2008, Effects of Magnesium Sulfate Attack on Ordinary Portland Cement Mortars, *Portugaliae Electrochimica Acta*, **26**, pp. 235-242
6. Prince, W., Espagne, M., Aitcin, P.-C., 2003, Ettringite formation: A crucial step in cement Superplasticiser compatibility, *Cement and Concrete Research*, **33**, pp. 635-641
7. Kim Byung-Gi, Jiang Shiping, Jolicoeur Carmel, Aitcin, P.-C., 2000, The adsorption behavior of PNS superplasticizer and its relation to fluidity of cement paste, *Cement and Concrete Research*, **30**, pp. 887-893
8. Wee, T.H., Suryavanshi, Arvind K., Wong, S.F., and Anisur Rahman, K.M., 2000, Sulfate Resistance of Concrete Containing Mineral Admixture, *ACI Materials Journal*, **97**, pp. 536-549

EFFECT OF SAND NATURE AND RATE OF NATURAL POZZOLANA ON THE DURABILITY OF MORTARS

Mohammed ROUBI^{a,*}, Hamid KHELAFI^a, Nouria KAID^a, Mustapha Lotfi GHOMARI^a

^a Civil Engineering Department, Faculty of Architecture and Civil Engineering, University of Sciences and Technology Mohamed BOUDIAF, BP.1505, El Menaouar, 31000 Oran, Algeria.

*Corresponding author: Fax: +213 665 444 417 Email: rouibi.med@gmail.com

ABSTRACT

Deterioration of concrete and mortars in natural environments is more often the result of degradation of the cementitious matrix, as aggregates are considered inert and durable materials. However, there are several important cases where the aggregates themselves directly contribute to the deterioration of concrete or are sensitive to severe external environments. This paper is concerned experimental investigations to study the durability of mortars-based natural pozzolana using two different types of sand (river limestone and siliceous crushed sands). This property was evaluated for mortar samples stored in different curing conditions (distilled water and a sulfate solution with 5% MgSO₄) and for different curing periods. The various properties studied consist of compressive and flexural strengths, mass variation and X-ray diffractometer analysis. The results obtained indicated that the sulfate of magnesium adversely affect the durability of pozzolanic mortars. Besides mortars made with limestone sand slow or delay the attack of magnesium sulfates and mortars made with siliceous sand accelerates the attack.

INTRODUCTION

Aggregates have a significant influence on the rheological and mechanical properties of mortars and concrete. It was reported that density, distribution of the particle sizes, form and texture of surface clearly influence the properties of these mixtures in terms of water requirements and workability [1;2]. It was also stated that mineralogical composition, hardness, elastic modulus and degree of aggregate variation can affect the properties of mortars and concretes in the hardened state, in general, and angular form and texture of the rough surface may improve the bending strength [3] with respect to compression strength.

Aggregates are more resistant to an external aggressive attack and generally less permeable than the cementitious matrix. However, some aggregates may present properties which make them vulnerable to deterioration and therefore compromise the durability of concrete. In some cases, aggregates can be sensitive to attacks of external agents. Studies conducted by Skrapoulou et al. [4;5] showed that concrete containing limestone sand are likely sensitive to thaumasite formation at low temperatures (5°C).

Incorporation of mineral additions such as natural pozzolana, as a mineral addition in cement, is one of

the solutions to increase durability of concrete to sulfate attacks [6]. Attack of sulfates is one of the environmental deteriorations most aggressive which affects the durability of concrete structures. Sulfates can very significantly deteriorate concrete in a relatively short period of time (10 to 15 years) [14]. Concrete deterioration in sulfatic environment is generally a consequence of degradation of the cementitious matrix, since aggregates are regarded as inert and more durable materials. The question which then arises is twofold: (i) Are aggregates really inert or (ii) do they not affect the durability of concrete in sulfatic environments?

In Algeria, natural pozzolana constitutes the raw materials in several branches of industries. The pozzolana used is a natural rock of siliceous volcanic origin and extracted from the plants of Bouhamidi (Beni-Saf). Abundance of this material continue to constitute an opening towards use of alternative mortars that are less pollutant as construction industry is still significant and mortars are still used worldwide. Although it has been previously considered in various research studies [7-13] and knowledge of its use and studies of its properties exist in literature review, this pozzolana, like those materials used in mortars and concretes,

still has potential technological benefits to promote mortars as far as environmental impact, sustainability and economic valorization are concerned.

The main objective of this research work is to report results of an experimental survey relating on the influence of two different natural sands on the physical and mechanical properties and durability of pozzolanic mortars when high magnesium sulfates environment (MgSO_4) is used.

MATERIALS USED AND TEST METHODS

In this section, materials used in the preparation of mortars and test procedures are outlined. The chemical, mineralogical as well as compressive and flexural strengths of samples were examined to study the durability of mortars-based natural pozzolana using two different types of sand (river limestone and siliceous crushed sands) and the samples of which were stored in different curing conditions (distilled water and sulfate solution with 5% MgSO_4) and for different curing periods.

Sand: two natural sands obtained from two different deposits: river sand from Oued El Sobha, Chlef (LS) and crushed sand of the quarry from Djebbala (SS) were used. Both sands were prepared in accordance with EN 196-1 [15] and provided in bags of $1350 \pm 5\text{g}$. The physical and mechanical properties and mineralogical composition of the two sands are shown in Table 1.

Cement: CEM I/42.5 of the Lafarge manufacture was used. This cement was characterized in terms of Blaine's specific surface using a Blaine device. This analysis revealed a specific surface area of $3384 \text{ cm}^2/\text{g}$ and a real density of 3.11 g/cm^3 . The mineralogical properties of this cement are reported in Table 2.

Natural pozzolana (NP): the absolute density of the used pozzolana is 2.85 g/cm^3 . The chemical and mineralogical properties of the used pozzolana are reported in Table 2.

Test methods: preparation of mortars was carried out according to EN 196-1 [15], using Portland cement CEM I and three binder combinations obtained by partial replacement of cement in terms of weight with different proportions of natural pozzolana (10%, 20% and 30%). Samples were stored in a moist environment for 24 hours. After this

period, samples were immersed in saturated lime water for 27 days. After this duration of cure, some samples were stored in distilled water and the left samples were stored in sulfate solution (5% MgSO_4).

Four types of mortars, reflecting various compositions, were considered. These mortars are named according to the nature of sand. The percentage of natural pozzolana and its composition are given in Table 3.

Table 1
Physical and mechanical properties of sands.

Tests	Value	
	LS	SS
Fineness modulus (FM)	2.78	
Apparent density (g/cm^3)	1.540	1.320
Absolute density (g/cm^3)	2.780	2.950
Absorption coefficient Ab (%)	0.335	0.930
Value of blue (VB)	0.913	0.833
Equivalent sands (Piston)	92.263	89.897
Friability coefficient FS (%)	38.040	48.200

Table 2
Chemical composition of pozzolana and cement.

Composition	Pozzolana	Cement
SiO_2	46.8	21.75
CaO	9.2	62.86
Fe_2O_3	10.5	4.60
MgO	3.8	1.25
Al_2O_3	18.8	3.94
SO_3	0.2	1.85
K_2O	0.5	-
Na_2O	0.8	-
Insoluble Residues	-	0.48
P.F	6.5	3
C_3S	-	57.5
C_2S	-	19
C_3A	-	2.65
C_4AF	-	14

Table 3
Mortars composition.

	C (g)	NP (g)	Sand (g)		W/C
			LS	SS	
MLS0	450	0	1350	-	0.56
MLS10	405	45	1350	-	0.56
MLS20	360	90	1350	-	0.57
MLS30	315	135	1350	-	0.57
MSS0	450	0	-	1350	0.70
MSS10	405	45	-	1350	0.71
MSS20	360	90	-	1350	0.72
MSS30	315	135	-	1350	0.72

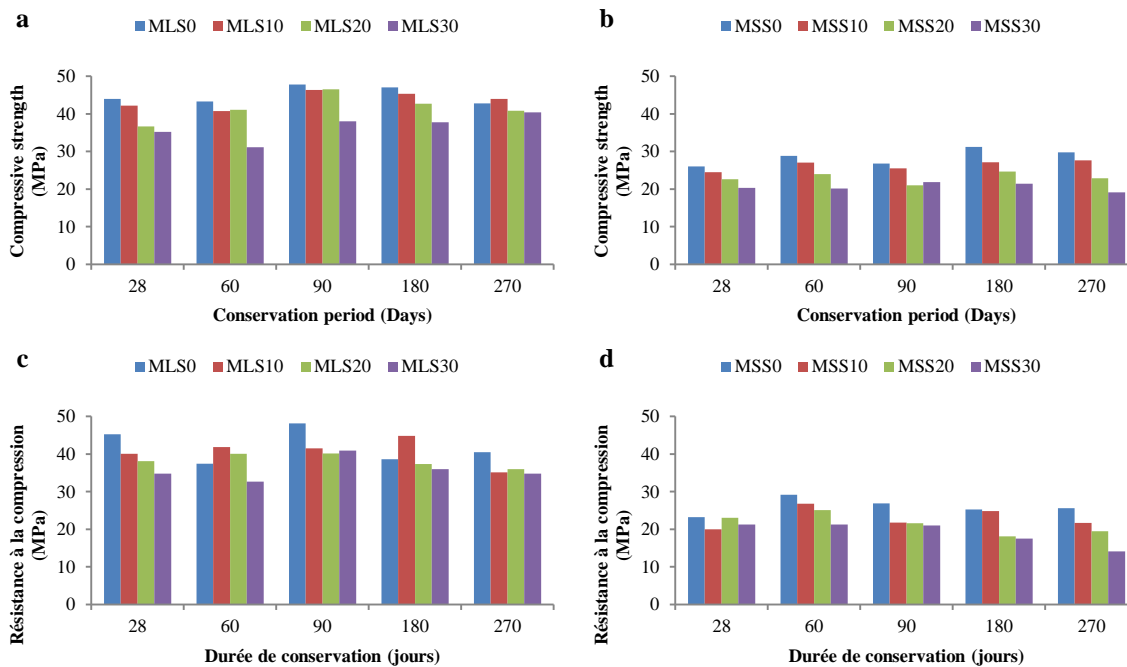


Figure 1

Evolution of the compressive strength of the mortars, (a): MLS conserved in Dw, (b): MSS conserved in Dw, (c): MLS conserved in Ms, (d): MSS conserved in Ms, during 270 days.

Sulfate solutions were prepared according to ASTM 1012 [16] and NF P 18-837 [17]. The pH of the solution was maintained at 7 ± 2 by the addition of a sulfuric acid solution H_2SO_4 and a concentration of 0.01 mol/l [18]. The durability of the mortars was evaluated by visual analysis, variation of mass, variation of bending strength, compression strength and by XRD analysis, after 28, 60, 90, 180 and 270 days of conservation, in distilled water (Dw) and solution of magnesium sulfate (Ms).

RESULTS AND DISCUSSIONS

In this study, emphasis was put on compressive and flexural strengths, mass variation and X-ray diffractometer analysis. To start with, compressive and flexural strength tests were undertaken to provide the basic mechanical properties of the formulated mortars and give a first insight into their applicability. With this intension in mind, all samples, using limestone sand (LS) and silica sand (SS), were submitted to compressive and flexural strength tests and testing was performed at the ages of 28, 60, 90, 180 and 270 days.

Compressive strength: Based on these results, the compression strength of all the mortars, stored in distilled water (Dw) and shown in Figs. 1a & 1b, was achieved by the continuity of both formation and

activity of hydrates such as CSH, which play important role in the improvement of compression strength of mortars. These results confirm those reported by Said et al. [14]. Mortars using limestone sand (LS) have higher compressive strength in comparison to results obtained for mortars using silica sand (SS). In (SS) mortars the water/cement (W/C) ratios may have been responsible for the low strength as they adversely affect the compressive strength and the duration of hydration [19]. The compressive strength of the control mortar (no additives) was higher than the compressive strength of pozzolanic mortars. The decrease in the strength of pozzolanic mortars may also be due to the higher W/C ratios and for which we believe that they require increased demand of water, as previously reported [7].

Further tests were also carried out to determine compressive strength for mortars stored in magnesium sulfate solution, at the ages of 28, 60, 90, 180 and 270 days. Considering these results, a clear tendency for increase in compression strength at different ages was visible (Figs. 1c and 1d) for all the samples. The achievement of higher compressive strength may be due to the formation of expansive products such as gypsum, ettringite and brucite. Generally, these mortars are accompanied by a decrease in the compression strength which may be the result of micro-fissuring engendered by the long

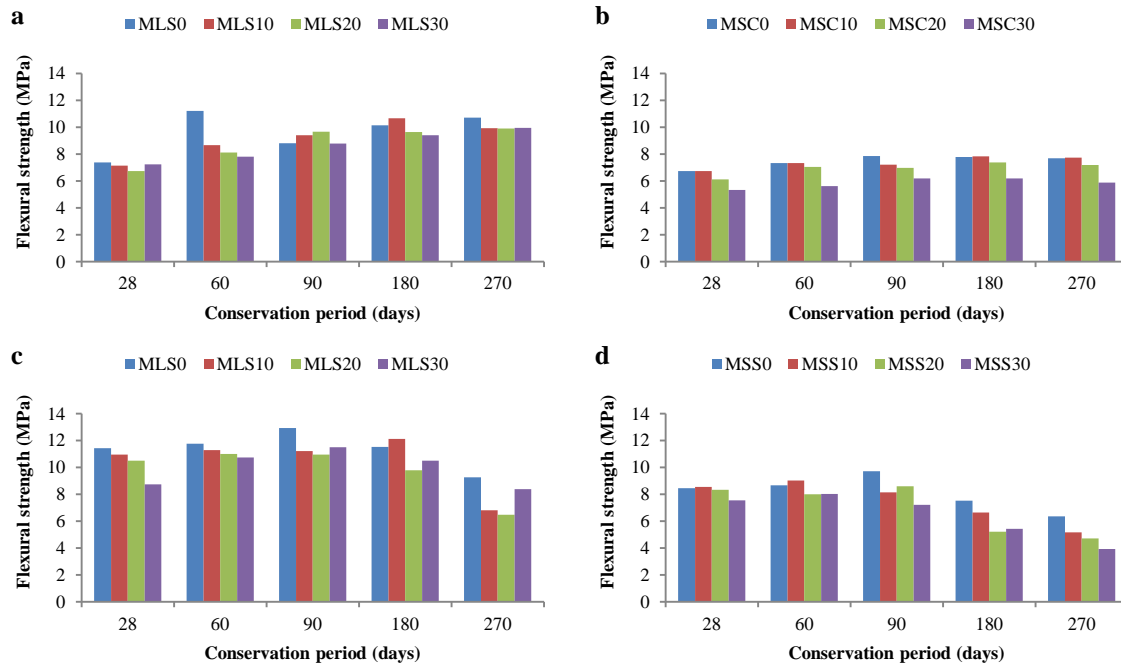


Figure 1

Evolution of the flexural strength of the mortars, (a): MLS conserved in Dw, (b): MSS conserved in Dw, (c): MLS conserved in Ms, (d): MSS conserved in Ms, during 270 days.

term expansive products. Once again, control mortars showed higher compression strength in comparison to mortars with natural pozzolana and limestone sand (LS) and (SS) mortars. However, the low strength of these mortars was proportional to the percentages of additions and because of the less quantity in portlandite consumed by reaction of the pozzolana. In this context, both Lee et al. [20;21] and Ganjian et al. [22] reported that the presence of portlandite was beneficial as long as it decreases the sulfate action of magnesium allowing its retention in the brucite. Therefore the residual quantity of magnesium, suited to the attack of the CSH, was inversely proportional to the quantity of portlandite in the cement paste. However, this enabled the authors to conclude that natural pozzolana has a fatal effect against sulfate of magnesium attacks.

The decrease in the compression strength of (LS) and (SS) mortars, stored in the sulfate solution (5% $MgSO_4$), was observed after 90 days (Fig. 1c) and 60 days, respectively. This confirmed the results reported by Skarapoulou et al. [5-6] and the reason was twofold. This may be due (i) to the difference in (W/C) ratios used for the two mortars and because the mortar with limestone sand slows or delays the attack of magnesium sulfate at room temperature and (ii) to the reaction of limestone (LS) with the cementitious matrix which produces additional

portlandite. Unlikely, the (SS) mortars can accelerate the attack of magnesium sulfate, because of the less quantity of hydrated paste in portlandite and which was prevented by the reaction of silica in (SS) mortars.

Flexural strength: Similarly, (LS) mortars (Figs 2a and 2c) have higher flexural strength in comparison to (SS) mortars (Figs. 2b and 2d) for both curing conditions (distilled water and solution of magnesium sulfate), respectively. The low strengths may probably due to the variation of w/c ratios for (SS) mortars. Improvement of the flexural strength for mortars in sulfatic conditions, which also confirmed by Çavdar et al. [23], may be due to the filling of the pores by products formed during the reaction of the cement hydrates with the solution of magnesium sulfate (gypsum, brucite and ettringite).

The decrease in flexural strength for (LS) mortars (Fig. 2c) was noticed after 80 days of conservation in the solution of magnesium sulfate (Ms) and flexural strength drop of (SS) mortars (Fig. 2d) was visible after 90 days. In this case, the attack of magnesium sulfates on (LS) mortars was delayed by the reaction of the cementitious matrix with limestone (LS) to produce additional portlandite. These findings complied with those reported by Skarapoulou et al. [4;5]. In addition, reaction of

portlandite with silica may have been responsible for the accelerated attack of magnesium sulfate on (SS)

mortars and the achievement of deterioration of the mortars in short terms.

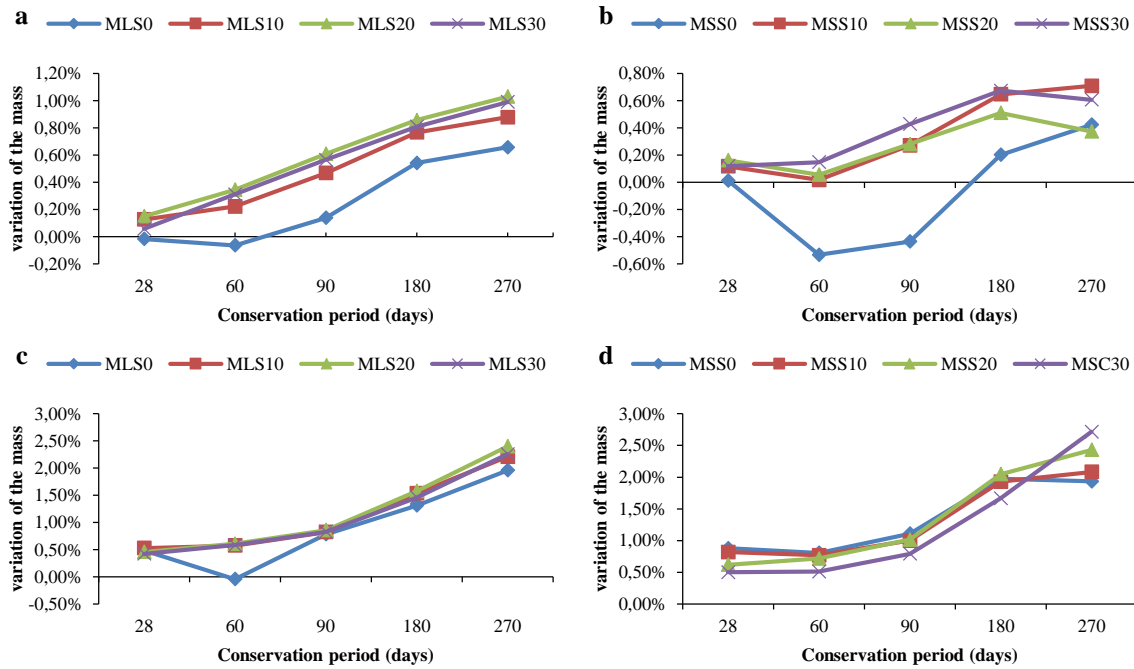
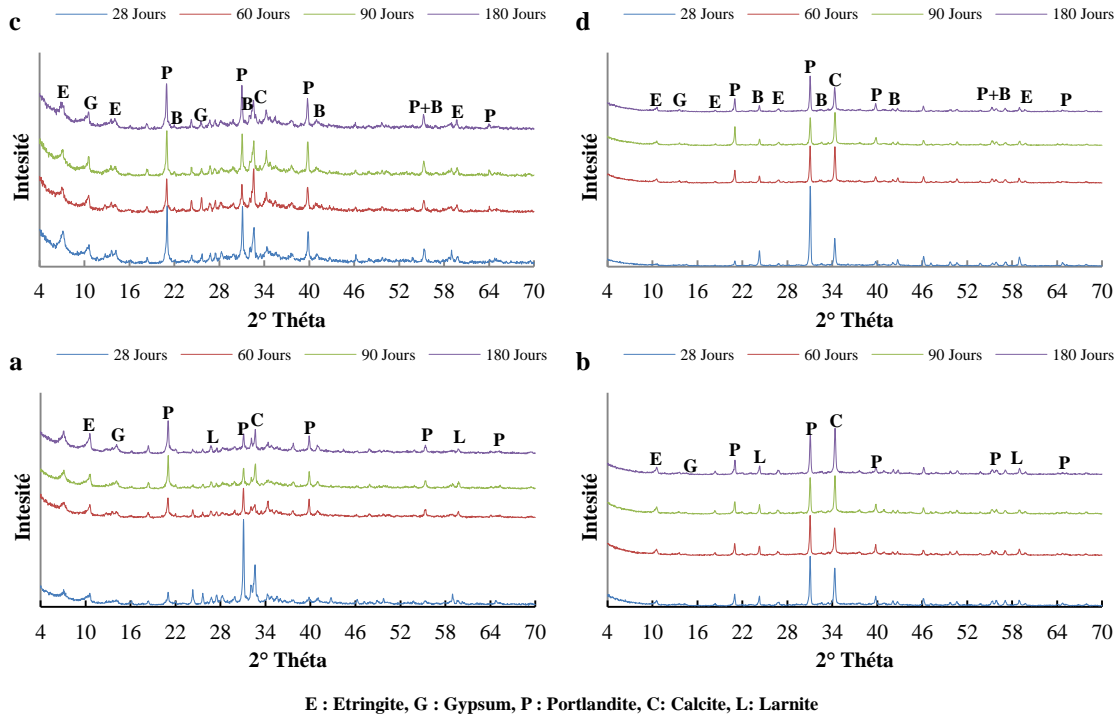


Figure 3

Variation of the mass of the mortars (a): MSL conserved in Dw, (b): MSS conserved in Dw, (c): MSL conserved in Ms, (d): Mss conserved in Ms, during 270 days.



E : Etringite, G : Gypsum, P : Portlandite, C : Calcite, L : Larnite

Figure 4

XRD of mortar (a) : MLS10 conserved in Dw, (b) : MSS10 conserved in Dw, (c) : MSC10 conserved in Ms, (d) : MSS10 conserved in Ms, during 270 days.

Mass variations: A further study was conducted to determine the evolution of the mass of (LS) and (SS) mortars, stored in distilled water (Dw) and the

solution of magnesium sulfate (Ms), as shown in Figs. 3a to 3d. The evolution of the mass for the two mortars stored in the distilled water solution (Figs.

3a and 3b) was caused by hydrate formation. This is explained by the swelling caused by the formation of expansive products such as brucite, gypsum and ettringite in the solution of sulfate magnesium (Figs. 3c and 3d). One can notice that there was higher improvement in mass for (LS) mortars than recorded by (SS) mortars, stored in the (Dw) solution. This improvement was provided by the additional amount of portlandite (reaction of cementitious matrix with limestone) which dissolved during leaching. With the dissolution of portlandite, the cement paste became porous and allowed transport of distilled water within the cementitious matrix. Unlikely (SS) mortars have a small amount of portlandite.

Microstructure analysis: Figs. 4a to 4d show the results obtained by the use of X-ray diffractometer analysis. This technique provided additional data which further elucidated the behavior of mortar samples prepared with limestone (LS) and siliceous (SS) sands and stored in distilled water (Dw) and magnesium sulfate solution (Mg).

The use of XRD spectra proved the progress of hydration in mortars in distilled water prepared and incorporating limestone and siliceous sands, as shown in Figs. 4a and 4b. This may be due to the formation of the peaks of gypsum, portlandite and the ettringite. The density peak of ettringite was higher compared with that of gypsum. Intensity peaks of portlandite seem to be more important in mortars with limestone sand, a result which was well established with the mass loss for these mortars.

Comparing the XRD spectra of the samples before and after the attack (see Figs. 4c and 4d), the analysis revealed the formation of gypsum, portlandite, ettringite and brucite following sulfatic attack (MgSO_4). Portlandite peaks are more visible and intense for (LS) mortars than for (SS) mortars. This confirms the decrease in mechanical strengths in short term.

CONCLUSIONS

The main purpose of this study was to evaluate the effect of the nature of two sands and the rate of natural pozzolana on mortar samples stored in magnesium sulfate (5% of MgSO_4), using a natural pozzolana extracted in Beni Saf (Algeria).

Experiments on mortars stored in different curing conditions and periods permitted to draw the following results:

- Compressive and flexural strengths were higher for the control mortars (no additives) than for mortars incorporating natural pozzolana;

- Mortars using natural pozzolana (10%) have compressive and flexural strengths similar to that of control mortars;
- Pozzolanic reaction started since the period of maturation. This reaction produced formation of second generation CSH and contributed in improving the compressive strength;
- Mortars using limestone sand have higher compressive and flexural strengths than mortars prepared with siliceous sand;

Regarding durability, results of experimental investigation of magnesium sulfate attack (5% MgSO_4) showed that:

- Sulfate environment adversely affect the properties of cementitious materials due to the formation of expansive products such as gypsum, ettringite and brucite;
- Natural pozzolana has a fatal effect against sulfate of magnesium attacks.
- Mortars incorporating limestone sand lead to delayed attack by sulfates of magnesium;
- Unlike, mortars using siliceous sand lead to accelerated attack by sulfates of magnesium;

REFERENCES

1. Nanthagopalan P, Santhanam M, Fresh and hardened properties of self-compacting concrete produced with manufactured sand, *Cem. Conc. Comp* 33, 2010,353-358.
2. Cortes D D, Kim H K, Palomino A M, Santamarina J C, Rheological and mechanical properties of mortars prepared with natural and manufactured sands, *Cem. Concr. Res* 38, 2008,1142-1147.
3. Li Beixing, Guoju K, Mingkai Z, Influence of manufactured sand characteristics on strength and abrasion resistance of pavement cement concrete, *Constr Build Mater* 25, 2011, 3849-3853.
4. Skarapoulou A, Tsvivilis S, Kakali G, Sharp J H, Swamy R N, Long term behavior of Portland Limestone cement mortars exposed to magnesium sulfate attack, *Cem. Conc. Comp* 31, 2009,628-636.
5. Skaropoulou A, Kakali G, Tsvivilis S, Thaumassite form of sulfate attack in limestone cement concrete: The effect of cement composition, sand type and exposure temperature, *Constr Build Mater* 36, 2012, 527-533.
6. Petrov N, Thibault M, Tagnit-Hamou A, Attaques externes et internes par les sulfates; similarités et différences, 1er Congrès International sur la

- technologie et la durabilité du béton, U.S.T.H.B, Alger 24-25 et 26 Mai 2004.
7. Ghrici M, Kenai S, Said Mansour M. Mechanical properties and durability of mortar and concrete containing natural pozzolana and limestone blended cements. *Cem. Conc. Comp* 29,2007, 542–9.
 8. Ezziane K, Bougara A, Kadri A, Khelafi H, Kadri E. Compressive strength of mortar containing natural pozzolan under various curing temperature, *Cem. Conc. Comp* 29, 2007, 587–93.
 9. Mouli M, Khelafi H, Strength of short composite rectangular hollow section columns filled with lightweight aggregate concrete, *Eng. Struct* 29, 2007, 1791–1797.
 10. Mouli M, Khelafi H, Performance characteristics of lightweight aggregate concrete containing natural pozzolan, *Build Environ* 43, 2008, 31-36.
 11. Kaid N, Cyr M, Julien S, Khelafi H, Durability of concrete containing a natural pozzolan as defined by a performance based approach, *Constr Build Mater* 23, 2009, 3457–3467.
 12. Ayed K, Benaissa A, Vidal T, Pons G, Étude du retrait et du fluage des bétons autoplaçants à base de pouzzolanes naturelles et de fines siliceuses algériennes, *Can J Civil Eng* 29, 2012, 10–19.
 13. Siad H, Kamali-Bernard S, Mesbah H A, Escadeillas G, Mouli M, Khelafi H, Characterization of the degradation of self-compacting concrete in sodium sulfate environment: Influence of different mineral admixtures, *Constr Build Mater* 47, 2013, 1188-1200.
 14. Gagne R., Durabilité et réparation des bétons (GCI 714). Chapitre 2 : la durabilité des bétons. Université de Sherbrooke, Canada, p160-185, www.civil.usherbrooke.ca/cours/gci714/PDF/Chap2_4.Pdf, 2002.
 15. NF EN 196-1, Méthodes d'essais des ciments- Partie 1 : Détermination des résistances mécaniques, AFNOR, Paris, 2006.
 16. ASTM.C1012, Standard Test Method for Length Change of Hydraulic-Cement Mortars Exposed to a Sulfate Solution”, ASTM, USA, 2004.
 17. NF P 18-837, Produits de calage et/ou scellement à base de liants hydrauliques, Essai de tenue à l'eau de mer et : ou à l'eau à haute teneur en sulfates, AFNOR, Paris, 1993.
 18. Rozière E, 2007, Etude de la durabilité des bétons par une approche performantielle, thèse doctorat, L'École Centrale de Nantes et l'Université de Nantes, Nantes, France, 2007.
 19. Ollivier J. P & Vichot A, Durabilité des bétons, Presse de l'école Nationale Des Ponts Et Chaussées, Paris, 2007.
 20. Lee S T, Moon H Y, Swamy R N, Sulfate attack and role of silica fume in resisting strength loss, *Cem. Conc. Comp* 27, 2005, 65-76.
 21. Lee S T, Moon H Y, Hooton R D, Kim J P, “Effect of solution concentrations and replacement levels of metakaolin on the resistance of mortars exposed to magnesium sulfate solutions”, *Cem. Concr. Res* 35, 2005, 1314–1323.
 22. Ganjian E, Pouya H S, Effect of magnesium and sulfate ions on durability of silica fume blended mixes exposed to seawater tidal zone, *Cem. Concr. Res* 35, 2005, 1332-1343.
 23. Çavdar A, Yetgin S, Investigation of mechanical and mineralogical properties of mortars subjected to sulfate, *Constr Build Mater* 24, 2010, 2331-22.

IMPACT OF FIBER TREATMENT ON THE FIRE REACTION AND THERMAL DEGRADATION OF BUILDING INSULATION STRAW COMPOSITE

Naima Belayachi*¹, Dashnor Hoxha¹, Brahim Ismail¹

¹ Université d'Orléans, INSA-CVL, PRISME, EA 4229, 8 Rue Léonard de Vinci, 45072 Orléans cedex 2, France

*Corresponding author: Fax: +33 02 38 41 70 63 Email: naima.belayachi@univ-orleans.fr

ABSTRACT

In this paper, both treated and untreated straw fibers are used to manufacture the light-weight composite for building insulation. The main objective of this work is to investigate the effect of the treatment on the thermal degradation and flammability of the material in order to examine his fire behavior. The selected wheat and barley straws are mixed with lime or gypsum plaster in this experimental investigation. In order to improve the mechanical properties of the composite, the straw fibers are treated with linseed oil and boiled water for decreasing their water absorption and increasing their compatibility and adhesion with the binder respectively. The treatment is carried out by total impregnation in the boiled water and linseed oil. The different composites are manufactured using mixture procedure optimized in previous works of the authors. Then the treated and untreated composite specimens are analyzed and compared through TG-DSC analysis to study their combustion process at microscopic level, and flammability test to study their fire reaction at macroscopic level. The properties of composites based on the fibers treated with linseed oil vary significantly.

KEYWORDS *Straw, lime, gypsum, Fire reaction, TG-DSC analysis, Linseed oil treatment, Flammability.*

INTRODUCTION

Addition of low density biodegradable natural fibers to mineral or polymer matrix present attractive alternatives to synthetic fibers for different applications with various performances, and low environmental impact. Most of these composites have been developed in order to reduce weight and produce environmentally friendly materials in particular in building sector resulting in a decrease of energy consumption of the building and the reduction of the GHG emission. In the recent years, several research have been undertaken on the production of innovative materials with specific properties and mechanical performance [1, 2]. However, many major difficulties limit the large use of natural fibers for structural applications, like their low strength compared to metals and polymers, water absorption and low fire resistance. These factors results inadequate properties for many purposes. Then, the treatment of fibers is an area of research more important for improve the properties of the natural fiber composites [3, 4]. These treatments improve significantly the mechanical properties but it is difficult to find a single effective treatment for all properties. Few analysis are carried out for example to examine the effect of these treatments used

generally for mechanical properties on the thermal degradation and fire behavior. This is an important point to establish the use conditions and performance criteria of the natural fiber composites in building applications [5, 6]. The fire risk is defined as the potential factor for structure and materials design [5]. The majority of the existing studies in the literature is on the polymer composites or natural fibers reinforcing polymer matrix [7-12]. The more used test for understanding the fire behavior in these investigations is the flammability test according UL94 (ASTM D3801), and TG-DSC-FTIR thermal analysis.

In this context, the present paper aims to study the fire behavior of the straw lime and straw-plaster composite proposed in the framework of a previous research program PROMETHE on the materials with low environmental impact based on the cereal straw fibers for thermal insulation rehabilitation. Samples were manufactured for the different experiments in laboratory without compaction with barley or wheat straw and lime and gypsum plaster binders [13, 14].

For thermal degradation and fire behavior, the study combines microscopic and macroscopic methods respectively, thermal analysis (thermogravimetric and differential scanning calorimetry) and reaction

to fire tests ignitability in accordance with test methods and Euro-class system defined by European standardization [15]. The flammability test described in this European standards is equivalent to the UL 94 test widely used for polymer materials. For reaction fire and flammability tests, the samples were exposed to a gas small flame. Time, occurrence of burning droplets and reached height flame are registered for classification criteria [15, 16]. In most investigations on composite materials used in building applications, the fire behaviour is studied by flammability test, TG-DSC analysis [16, 17] and fire resistance test [18] or only PCFC calorimeter [19].

The effect of fiber treatment, the fiber variety and binder natures are examined. The fibers are treated by total immersion in boiled water and linseed oil for different times.

The comparison of the results with the non-treated composite shows that the linseed oil treatment has a significant effect on the degradation and flammability. However, the boiled water treatment has a little influence on the properties of the straw-composite in the exposure conditions of this work.

EXPERIMENTAL INVESTIGATION

In this laboratory experiments, the fire behavior is studied by flammability test for small flame. It is the first step to analyze the fire behavior but it is not sufficient to give the final fire classification of the composite. In this section, the brief description of the experimental work is given.

Materials: The bio-composite studied in this investigation is a new innovative material based on wheat and barley straw. The straw-concrete is made with two types of binders lime and gypsum plaster. The selection of the used natural fibers and the binder was carried out in previous studies [13, 14] in the framework of research program PROMETHE. In this work, an attention is focused on the treatment of straw fibers and the change of the thermal degradation of the bio-composite. Then, the fibers are treated before their mixture with the lime or gypsum-plaster binders. There are a significant number of studies on different treatments in order to improve the compatibility between the natural fibers and the binders and increase the tensile or compressive strength, like alkali treatment [3] or boiled water treatment [4]. In this work, two treatments are selected, boiled-water to improve the straw-surface

and linseed treatment to decrease the water absorption.

Straw treatment: For linseed treatment the crushed wheat/barley fibers have been firstly immersed in the linseed oil for different times (10s, 5, 10, 15 minutes, 1h). Then, fibers have been dried at 60 °C during 48 hours before their use in the mixture. For the second treatment, the straw fibers were impregnated (Figure 1) for the same times in the boiled water at 100°C beforehand. Fibers have been dried at 60 °C in the oven in the same way.

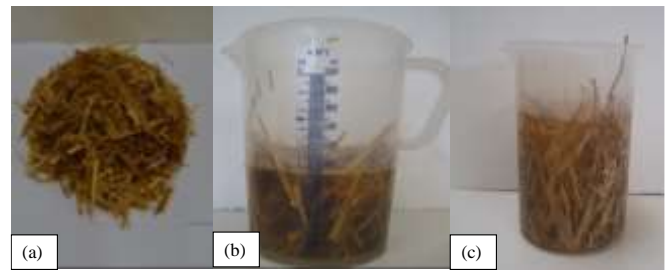


Figure 1

Straw fibers treatment: (a) crushed straw, (b) linseed oil immersion, (c) boiled water immersion.

Composite manufacture: In order to limit the number of tested samples, only optimal time of impregnation is used (10 minutes), determined before the composite manufacture based on a comparison of Young modulus and the water absorption coefficients not presented here. The mixture procedure, the introduction in the molds and the curing conditions are the same of previous works [13] in order to compare the behavior and to keep the same thermal and mechanical compromise. The samples used for flammability are cut according the standard NF EN 11925-2 [15]. They measure 250 mm of height, 90 mm of length and 60 mm of width.

According to the type of straw (wheat and barley), of binder (lime and plaster) and the treatment, eight composites with treated fibers are studied and compared with four composites prepared with non-treated fibers (Table 1).

Flammability test: In this work only flammability test for small flame is performed, in order to examine the reaction to fire of the straw composite and his fire classification according to the European standards. The

flammability test has been conducted as described by EN 11925-2 [15]. For each straw-composite, the test is carried out for three specimens. The test consists to expose the material to a single flame for 15 s in class E and 30 s in class D. The burner was angled at 45° with the flame length of 20 mm. The distance between the burner and the tested surface is 5 mm. A plate is disposed below the tested surface to collect the burning droplets. Figure 2 present the flammability test performed in this work.

After removing the flame, the flame spread and the droplet occurrence are examined. For the class E and D, the flame spread should be less than 150 mm after 15 s and 30 s of flame exposure respectively. Infrared camera is installed for the temperature examination during and after the flame exposure.

Table 1
Different manufacturing straw-composites

Composites	Designation
Wheat-Plaster- NonTreated	W-P-NT
Wheat-Plaster-Boiled water	W-P-BW
Wheat-Plaster-Linseed Oil	W-P-LO
Wheat - lime - Non Treated	W-L-NT
Wheat- lime - Boiled Water	W-L-BW
Wheat - lime - Linseed Oil	W-P-LO
Barley-Plaster- Non Treated	B-P-NT
Barley-Plaster-Boiled water	B-P-BW
Barley -Plaster - Linseed Oil	B-P-LO
Barley - lime - Non Treated	B-L-NT
Barley - lime - Boiled Water	B-L-BW
Barley - lime - Linseed Oil	B-L-LO

Thermal analysis: Thermogravimetric analyzer coupled to a differential scanning calorimetry was used to follow both the mass loss and the heat flow exchange during the thermal degradation of the different composites. These analysis are performed by LINSEIS STA PT-1000 apparatus under inert atmosphere. Powder samples of about 20 mg were placed in an alumina crucible and heated from ambient temperature to 1000 °C with a heating rate of 20 °C/min.

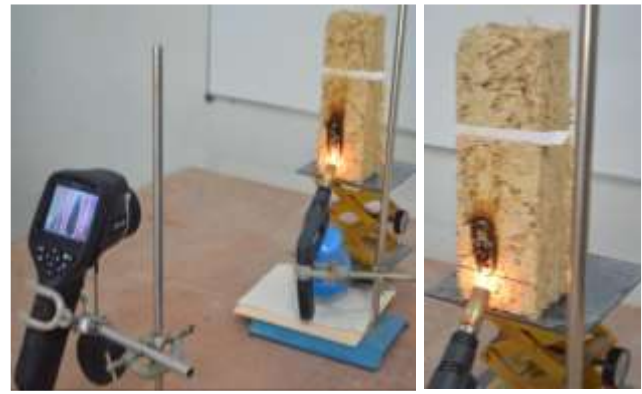


Figure 2
Experimental flammability test under small flame of straw concrete.

RESULTS AND DISCUSSION

Small flame test: Table 2 summarizes the flame propagation height and the observation of the occurrence of the flaming droplets for the different straw composites. The flame spread has been measured after 20s after removing the burner. We can observed that for the different composites, the flame does not exceed 15 cm. The results shows also that the composites based on treated fibers with linseed oil record the smallest flame propagation.

Table 2
Flame spread for 15 s of exposure after 20s removal burner

Composites	Flame height (cm)	Droplets Yes/No
W-P-NT	8.5	No
W-P-BW	9.1	No
W-P-LO	6.1	No
W-L-NT	7.9	No
W-L-BW	6.7	No
W-P-LO	5.7	No
B-P-NT	13.1	Yes
B-P-BW	7.5	No
B-P-LO	4.5	No
B-L-NT	8.2	No
B-L-BW	6.3	No
B-L-LO	3.4	No

The linseed oil treatment behaves as a flame retardant. It was observed a few flaming droplets on the horizontal plate only for the composite based on non- treated barley straw. The boiled water treatment showed an effect on the flame spread in the case of the barley composite.

Figure 3 shows an example of the exposed surface to burner flame and the temperature during burning and after 5 minutes of exposure for barley lime composite.

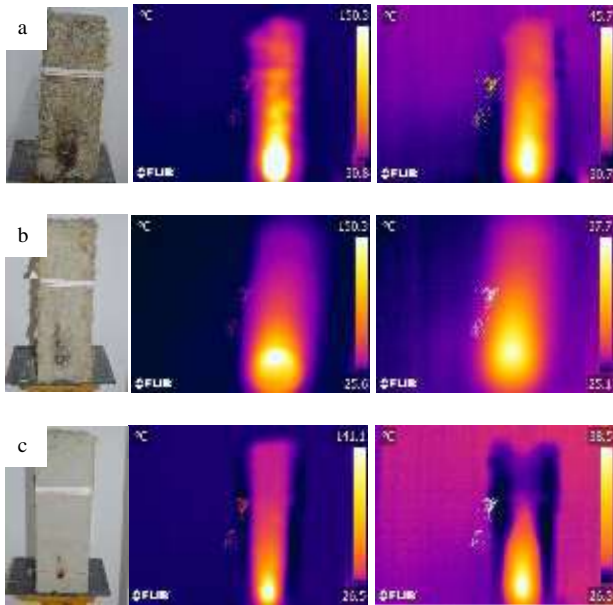


Figure 3

State of exposed surface and temperature field after at 15 s and 5 min after flame for barley lime composite: (a) B-L-NT, (b) B-L-BW, (c) B-L-LO.

This figure demonstrate the fire performance of the straw composite, there is no spread flame after removing the burner with this time exposure. The exposure surface is not degraded material without dripping during this time ignition. The temperature decreases greatly after removal of the burner. Table 3 shows the results of flame spread and droplets occurrence for a time of flame exposure more important.

We can observed that the flame spread heights are larger but still less than 15 cm. For the same barley-lime composite, the flame spreads is larger for the non-treated and treated composites than the previous case (Figure 4).

The droplets occurrence is present for this time of flame exposure in the case of the non-treated wheat straw composite. It is observed also that the composite based on the lime binder have the smallest flame spread in the two times exposure for the two types of straw fibers.

Table 3

Flame spread for 30 s of exposure after 60 s the flame removal

Composites	Flame height (cm)	Droplets Yes/No
W-P-NT	13.4	Yes
W-P-BW	10.5	No
W-P-LO	10.2	No
W-L-NT	8.6	No
W-L-BW	8.1	No
W-P-LO	7.2	No
B-P-NT	14.2	Yes
B-P-BW	9.3	No
B-P-LO	6.7	No
B-L-NT	8.5	No
B-L-BW	9.3	No
B-L-LO	4.1	No

As can be seen from these results in the conditions of flame exposure studied here for the two criteria of flame spread and droplets occurrence, we can say that the linseed oil treatment used for the reduction of water absorption improves significantly the fire performance at macroscopic level for the different bio-composites.

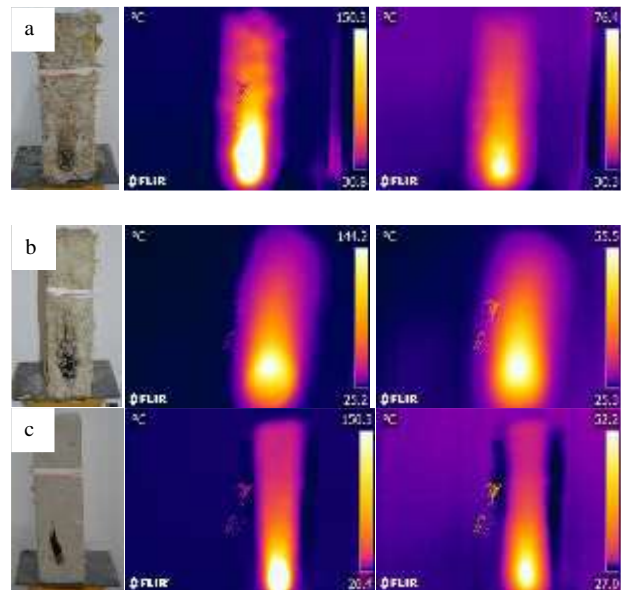


Figure 4

State of exposed surface and temperature field after at 30 s and 5 min after flame for barley lime composite: (a) B-L-NT, (b) B-L-BW, (c) B-L-LO.

Mass loss and heat flow: The composites based on gypsum-plaster and lime using treated and non-treated fibers are studied. The first result represented on Figure 5, shows the effect of the treatment on mass loss of the composites. It is clear

on the TG curves that the two treatment showed an important effect on the composite degradation which reached 50 % for the linseed oil treatment.

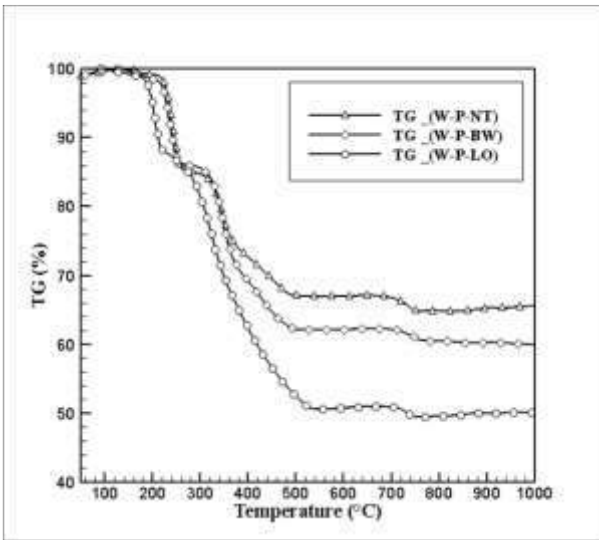


Figure 5

TG curve of wheat-plaster composites with treated and non-treated fibers

For treated and non-treated fibers, the degradation is characterized by three stages achieved at temperatures about: 220, 500 and 750 °C. The highest mass loss about (30 %, 35% and 50%) respectively for non-treated, boiled water treated fibers and linseed oil treated fibers occurs in temperature interval of 260-500°C. The mass loss for the two stages occurs first for the composite based on linseed oil treated fibers with differences of about 40°C. The last stage at 700°C, shows a very low mass loss about 2%.

The important mass loss is accompanied by endothermic peak for the three composites with a difference for the linseed oil treated fibers. The exothermic peak presented on the DSC curve is occurs for the plaster binder due to a reaction which the molecular structure of the anhydrite rearranges to an insoluble anhydrite.

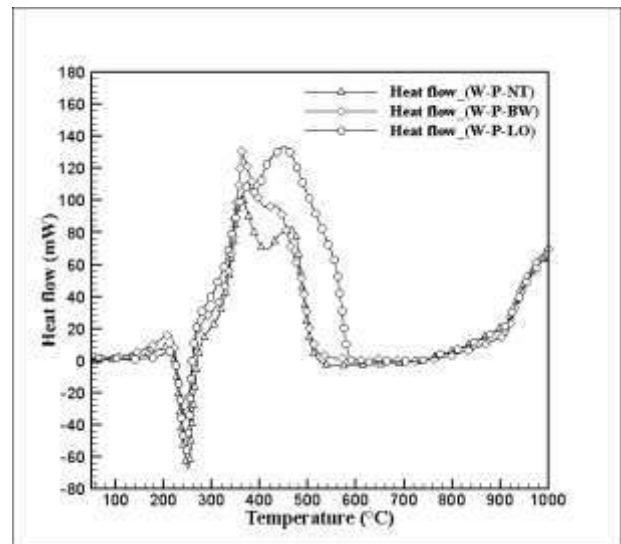


Figure 6

Heat flow exchange given by DSC analysis for the wheat-plaster composite for non-treated and treated fibers

The effect of binder nature is showed on Figure 7. The heat flow curve does not show an exothermic peak in the case of lime based composite with heat generation. In addition, it is clearly observed that the mass loss is more important in the barley based composite with a shift of temperature from the beginning of degradation stages.

The results of this part shows also, a significant effect of linseed oil treatment at the microscopic level with important mass loss. However, this effect is different for macroscopic level where his role was rather to spread flame retardant. So, the question remains open for the representative volume of TG-DSC tests for this type of highly heterogeneous material with high fibers content with multidirectional orientation.

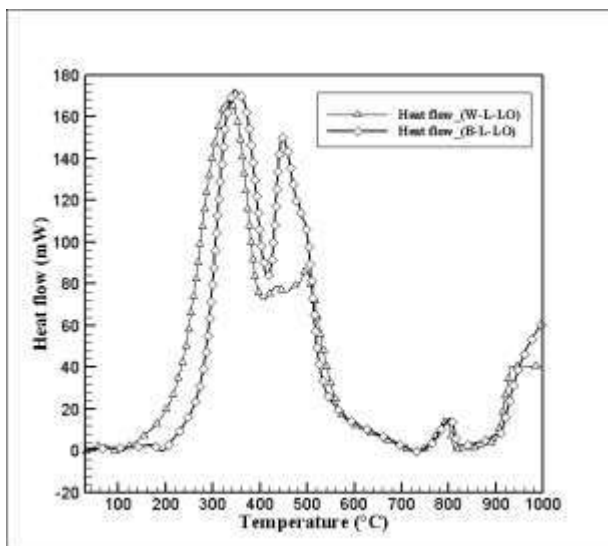
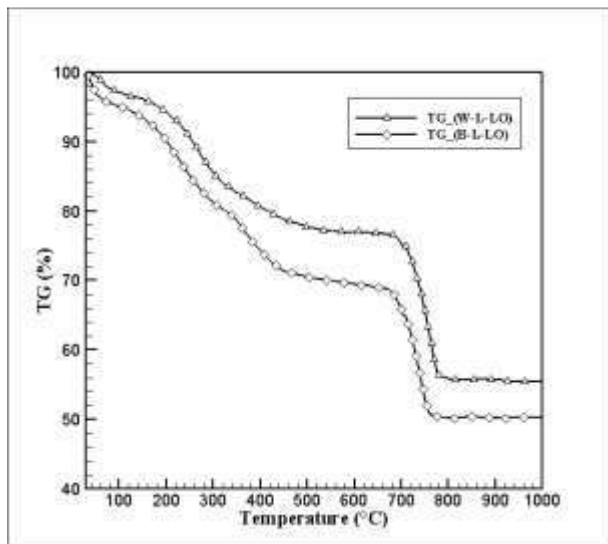


Figure 7

TG curve and Heat flow exchange of DSC analysis for the wheat-lime and barley lime composite based on linseed oil treated fibers

CONCLUSION

This paper investigates the effect of fiber treatment on the fire behavior and thermal degradation of the new bio-composite based on straw proposed for building insulation. The performed tests of the flammability and TG-DSC analysis in this work is a first attempt to understand the fire behavior of the straw based composite materials.

The major conclusion of this investigation is the significant effect of the linseed oil treatment at macroscopic level by flammability test and microscopic level by TG-DSC analysis. The linseed oil

treatment retards the flame spread and prevents the composite degradation. The flame spread is stopped after removing the flame burner for all composites. Barley based composite show a delicate fire behaviour than the wheat-composite.

In order to clarify the difference between macroscopic and microscopic level, further investigation is proposed by using the cone calorimeter test with representative samples to provide a better understanding of the fire performance of the proposed straw composite.

ACKNOWLEDGMENTS

The authors express their special thanks to Alain Bret for his help in performing the flammability tests.

REFERENCES

1. Wei, J, Meyer, C, 2014, Degradation rate of natural fiber in cement composites exposed to various accelerated aging environment conditions. *Corrosion science*, 88, pp. 118-132.
2. Ali, M, Chouw, N, 2013, Experimental investigations on coconut-fibre rope tensile strength and pullout from coconut fibre reinforced concrete. *Construction building materials*, 41, pp. 681-690.
3. Gomes, A, Matsuo, T, Goda, K, Ohgi, J, Development and effect of alkali treatment on tensile properties of curaua fiber green composites *Composites : Part A*, 38, pp. 1811–1820.
4. Sellami, A, Merzoud, M, Amziane, S, 2013, Improvement of mechanical properties of green concrete by treatment of the vegetals fibers, *Construction and Building Materials* 47, pp. 1117–1124.
5. Hidalgo, J. P, Welch, S, Torero, J. L, 2015, Performance criteria for the fire safe use of thermal insulation in buildings, *Const. and Build. Mat*, 100, pp. 285-297.
6. Naughton, A, Fan, M, Bregulla, J, 2014, Fire resistance characterization of hemp fibre reinforced polyster composites for use the construction industry, *Comp. part B*, 60, pp. 546-554.
7. Bocz, K, Szolnoki, B, Marosi, A, Tabi, T, Wladyka-Przybylak, M, Marosi, G, 2013, Flax fibre reinforced PLA/TPS biocomposites flame retarded with multifunctional additive system, *Poly. Degrad. And Stab*, 106, pp. 63-73.

8. Chattopadhyay, D. K, Webster Dean C, 2009, Thermal stability and flame retardancy of polyurethanes, *Prog. Poly. Scien*, 34, pp. 1068-1133.
9. Fox, D. M, Novy, M, Brown, K, Zammarano, M, Harris, R. H, Murariu, M, McCarthy, E, Seppala, J. E, Gilman, J. W, 2009, Flame retarded poly(lactic acid) using POSS-modified cellulose:2. Effect of intumescent flame retardant formulations on polymer degradation and composite physical properties, *Poly. Degrad. And Stab*, 106, pp. 54-62.
10. Laoutid, F, Bonnaud, L, Alexandre, M, Lopez-Cuesta, J. M, Dubois, Ph, 2009, New prospects in flame retardant polymer materials: from fundamentals to nanocomposites, *Mat. Sci. and Eng R*, 63, pp. 100-125.
11. Monti, M, Tsampas S. A, Fernberg, S. P, Blomqvist, P, Cuttica, F, Fina, A, Camino, G, 2015, Fire reaction of nanoclay-doped PA6 composites reinforced with continuous glass fibers and produced by commingling technique, *Poly. Degrad. & Stab*. 121, pp. 1-10.
12. Ju, Y, Liao, F, Dai, X, Cao, Y, Li, J, Wang, X, 2016, Flame-retarded biocomposites of poly(lactic acid): distiller's dried grains with solubles and resorcinol di (phenyl phosphate), *Composites A*, 81, pp. 52-60.
13. Belayachi, N, Bouasker, M, Hoxha, D, Al-mukhtar, M, 2013, Thermo-mechanical behaviour of an innovative straw lime composite for thermal insulation applications, *Applied. Mechan. and Mat*, 390, pp. 542-546.
14. Bouasker, M, Belayachi, N, Hoxha, D, Al-Mukhtar, M, 2014, Physical characterization of natural straw fibers as aggregates for construction materials applications, *Materials*, 7, pp. 3034-3048.
15. EN ISO 11925-2, Reaction to fire tests, Ignitability of building products subjected to direct impingement of flame-Part 2: single flame source test.
16. Younis, A. A, 2015, Evaluation the flammability and thermal properties of a new flame retardant coating applied on polyester fabric, *Egypt. J. Petrol*.
<http://dx.doi.org/10.1016/j.ejpe.2015.04.001>
17. Garcia, M, Hidalgo, J, Garmendia, I, Garcia-Jaca, J, 2009, Wood-plastics composites with better fire retardancy and durability performance, *Comp. part B*, 40, pp. 1772-1776.
18. Haurie, L, Mazo, J, Delgado, M, Zalba, B, 2014, Fire behavior of a mortar with different mass fractions of phase change material for use in radiant floor systems, *Energy. Build.*, 84, pp. 86-93.
19. Palumbo, M, Formosa, J, Lacasta, A, M, 2015, Thermal degradation and fire behavior of thermal insulation materials based on food crop by-products, *Const. and Build. Mat.*, 79, pp. 34-39.

FRACTAL DIMENSION OF AGGREGATE COMBINED GRADATION: A QUANTITATIVE PARAMETER FOR SOME PHYSICAL PROPERTIES OF THE CONCRETE MIX

Soumia Kheira SEBSADJI*, Kaddour CHOUICHA

Dept. of Civil Engineering - Univ. of Sciences and Technology of Oran Med Boudiaf (USTO-MB)
BP 1505, El Mnaouer, 31000 Oran, Algeria

*Corresponding author: Fax: + 00213 41 29 06 53 - Email: soumia.sebsadji@univ-usto.dz

ABSTRACT

This study is based upon the fractal nature of ideal Particle Size Distributions (PSD) suggested by numerous concrete mix designs, i.e. ideal PSD can be shown to be equivalent to power law distributions $E_c(\phi \geq \phi_i) \propto \phi_i^{-DF}$, where $E_c(\phi \geq \phi_i)$ is the number of grain of size greater than ϕ_i and DF is a non-whole number called fractal dimension. This fact allows us to analyze the solid skeleton of a concrete (i.e. all components of concrete mixture except water) as a fractal structure, thus to determine some of physical properties of the concrete mixture.

For DF ranging from 2.5 to 3 and based upon many geometrical parameters of the concrete as the granular range d/D and the volumetric fraction of all solids in the concrete mixture, analytical formulas have been proposed relating DF and some physical properties of concrete, as the coarse/fine aggregate ratio, the fineness modulus of the sand fraction, the average grain size and the specific surface area of grains.

The focus of this research is the development of simple formulas by which concrete properties can be predicted knowing the concrete mix gradation, i.e. the mix design method used.

KEYWORDS: PSD – fractal dimension – grain number – coarse/fine aggregate ratio – fineness modulus – average grain size – specific surface area

INTRODUCTION

Fractals can be defined as disordered systems. One of the main properties of fractals is their power law behavior of the form: $N(L > r) \propto r^{-DF}$, such as N is the number of objects in the system with size greater than r , DF is a non integer dimension referred to as *Fractal Dimension* and the symbol \propto stands for ‘proportional to’ [7;12].

Concrete mixtures can be considered as fractal objects because their corresponding solid particle size distributions (PSD), since they must be as close as possible to one of the ideal grading curves, they can be transformed to “grain number E_c ” versus “grain size ϕ_i ” distribution, following a fractal power law of type $E_c \propto \phi_i^{-DF}$ [3;7;10;12]. To get a better understanding of this, we give an example. First, we transform an ideal grading curve according to Fuller & Thompson [1], on fitted straight line $E_c(\phi \geq \phi_i) = f(\phi_i)$ in log-log scale (see Figure 1).

The data points will be obtained by the following expressions:

$$E_c(\phi \geq \phi_i) = \sum_{j=1}^i E_{\phi_j} \quad (1)$$

such as: $E_{\phi_j} = R_{\phi_j} / (\rho v_{\phi_j})$ & $v_{\phi_i} = \pi \phi_i^3 / 6$

where $E_c(\phi \geq \phi_i)$ denotes the grain number of size greater than ϕ_i ; E_{ϕ_i} the grain number of one size class ϕ_i ; R_{ϕ_i} the weight residue on sieve ϕ_i mesh; v_{ϕ_i} the volume per grain of size ϕ_i and ρ the mass density of aggregates.

in Figure 1, using linear regression, fitting results show a good linear fit between $E_c(\phi \geq \phi_i)$ and ϕ_i ($R^2 \approx 1$). The equation of the best linear fit is:

$$\log E_c(\phi_i) = a + (-DF) \log \phi_i \Rightarrow E_c(\phi_i) = \mathcal{C} \phi_i^{-DF} \quad (2)$$

$\mathcal{C} = 10^a$ is a constant depending on some properties of concrete [3], the slope of the best-fitted line representing the relationship between E_c and ϕ_i is the fractal dimension DF .

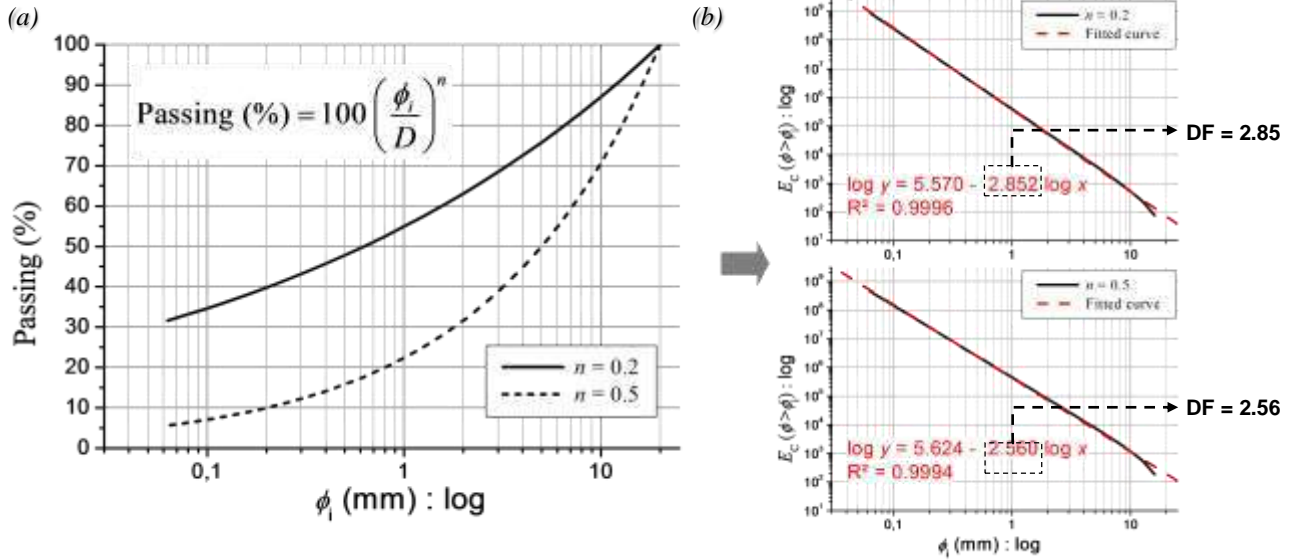


Figure 1

(a) Fuller-Thompson ideal grading curve (b) The corresponding fitted curves: $E_c(\phi \geq \phi_i) = f(\phi_i)$

One can achieve the same result whatever the method of concrete composition (see [3;7;10]), that enables us to assume PSDs of real concrete mixtures as fractals, which allows identifying them by knowing two parameters: DF value and the total particle size range d/D .

GRADING CURVE OF A FRACTAL GRANULAR MIXTURE

The solid concrete mixes will be noted $\mathcal{M}_{d/D}^{DF}$, meaning that the grain size distribution of the mix is fractal and that the grain size is ranging from d to D . Each concrete mixture will be constituted by particles of n monosized classes, numbered from ϕ_1 for the largest to ϕ_n for the smallest ones, according to a geometric progression of reason $\sqrt[10]{10}$, such as grains belong to a class 'i' will be the set of particles of number E_{ϕ_i} , retained between two successive sieves with a mesh size of ϕ_i and ϕ_{i+1} , as shown in the following expressions:

$$\forall i \in [1, n]: \begin{cases} \phi_i > \phi_{i+1} \text{ (such as: } \phi_1 = D \text{ \& } \phi_n = d) \\ \phi_i / \phi_{i+1} = \lambda = \sqrt[10]{10} \end{cases} \quad (3)$$

from which we can obtain:

$$\left. \begin{aligned} \phi_2 &= \phi_1 / \lambda = D / \lambda \\ \phi_3 &= \phi_2 / \lambda = D / \lambda^2 \dots \end{aligned} \right\} \Rightarrow \phi_i = D / \lambda^{i-1} \quad (4)$$

E_{ϕ_i} the grain number of one size class ϕ_i ;

From Eq. (2), the grain number of grain of size greater than ϕ : $E_{C\phi}(\phi) = \mathcal{C} \phi^{-DF}$, thus E_{ϕ_i} the grain number of one size class ϕ_i can be obtained as follows:

$$E_{\phi_i} = \begin{cases} \mathcal{C} \phi_i^{-DF}, & \text{if } i = 1 \\ \mathcal{C} (\phi_i^{-DF} - \phi_{i-1}^{-DF}), & \forall i \in [2, n] \end{cases} \quad (5)$$

By replacing $\phi_i = D / \lambda^{i-1}$ in the above equation we obtain:

$$E_{\phi_i} = \begin{cases} \mathcal{C} D^{-DF}, & \text{if } i = 1 \\ \mathcal{C} D^{-DF} (\lambda^{DF(i-2)})(\lambda^{DF} - 1), & \forall i \in [2, n] \end{cases} \quad (6)$$

On the basis of these equations, one can obtain grading curve of a fractal granular mixture $R_c(\phi) = f(\phi)$ or $T_c(\phi) = f(\phi)$ (resp. %cumulative retained or passing), obtained by transformation of the fractal straight line $E_c(\phi) = f(\phi)$. First, the the percentage of material retained on each sieve $R_{\phi_i}(\%)$ can be expressed as:

$$R_{\phi_i}(\%) = 100 R_{\phi_i} / \sum_{j=1}^n R_{\phi_j} \quad (7)$$

Such as R_{ϕ_i} , the weight retained on ϕ_i mesh sieve, will be equal to:

$$R_{\phi_i} = E_{\phi_i} m_{\phi_i} = E_{\phi_i} (\rho v_{\phi_i}) \quad (8)$$

Where $\begin{cases} E_{\phi_i} : \text{number of grains of size } \phi_i \\ m_{\phi_i} : \text{weight of a grain of size } \phi_i \end{cases}$

Therefore, combining equations (4), (7) & (8) gives:

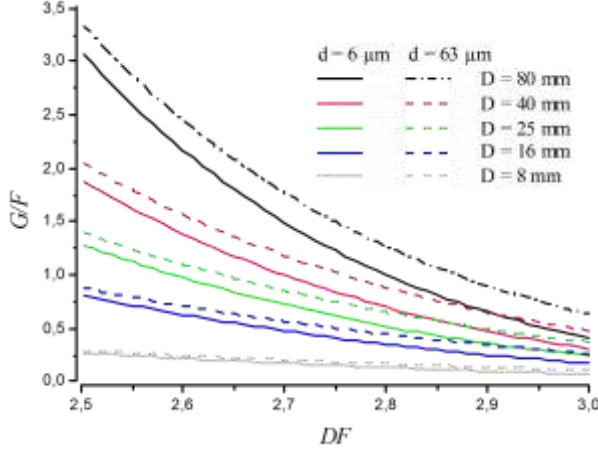


Figure 2

G/F ratio for granular mixtures $\mathcal{M}_{d/D}^{DF}$ related to d , D and DF ($\phi_{GF} = 5$ mm)

$$R_{\phi_i}(\%) = 100 E_{\phi_i}(\rho v_{\phi_i}) / \sum_{j=1}^n E_{\phi_j}(\rho v_{\phi_j})$$

$$\Rightarrow R_{\phi_i}(\%) = A \begin{cases} 1, & \text{if } i=1 \\ (\lambda^{DF} - 1) \lambda^{3-2DF} \lambda^{i(D-3)}, & \forall i \in [2, n] \end{cases} \quad (9)$$

and $A = 100 / \left(1 + (\lambda^{DF} - 1) \lambda^{3-2DF} \sum_{j=2}^n \lambda^{j(D-3)} \right)$

A further development of the above equations yields to the equations of a fractal grading curves (for further details see reference [11]):

$$R_{C\phi}(\%) \approx 100 \begin{cases} \frac{D^{3-DF} - \phi_i^{3-DF}}{D^{3-DF} - d^{3-DF}} \Rightarrow \text{if } DF < 3 \\ \frac{\log D - \log \phi_i}{\log D - \log d} \Rightarrow \text{if } DF = 3 \end{cases} \quad (10)$$

PHYSICAL PROPERTIES OF CONCRETE MIXTURE

Using equations in (10) we will determine grading curves for some granular mixes $\mathcal{M}_{d/D}^{DF}$, regarded as the dry mixes of concrete. That will enable us to determine some physical properties of concrete mixes. The fractal dimension considered in these mixes will be in the range of 2.5 to 3 [10;11].

Ratio of fine-to-coarse fractions: The ratio of fine-to-coarse fractions of the dry concrete mix, noted G/F , can be determined by the use of the following expression, where ϕ_{GF} represents the particle size cut between fine and coarse fractions:

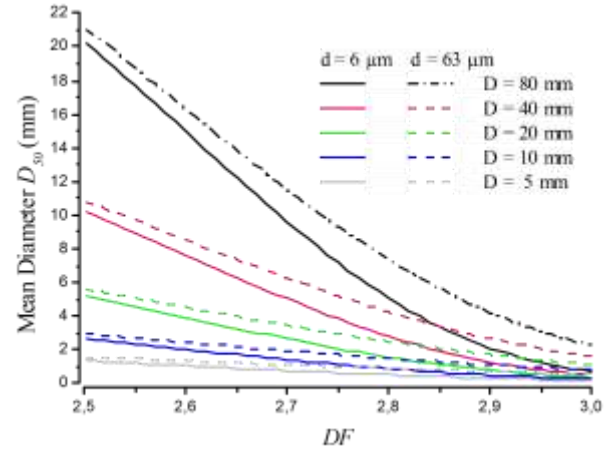


Figure 3

Mean diameter D_{50} for granular mixtures $\mathcal{M}_{d/D}^{DF}$ related to d , D and DF

$$G/F = \frac{\text{weight of coarse fraction } (\phi_i > \phi_{GF})}{\text{weight of fine fraction } (\phi_i \leq \phi_{GF})}$$

$$= \frac{M_T R_{C\phi_{GF}}(\%)}{M_T [100 - R_{C\phi_{GF}}(\%)]} = \frac{R_{C\phi_{GF}}(\%)}{T_{C\phi_{GF}}(\%)} \quad (11)$$

By replacing $R_{C\phi_i}(\%)$ from Eq.(10), Eq. (11) can be rewritten as follows, such as $d < \phi_{GF} < D$:

$$G/F = \begin{cases} \frac{D^{3-DF} - \phi_{GF}^{3-DF}}{\phi_{GF}^{3-DF} - d^{3-DF}} \Rightarrow \text{if } DF < 3 \\ \frac{\log D - \log \phi_{GF}}{\log \phi_{GF} - \log d} \Rightarrow \text{if } DF = 3 \end{cases} \quad (12)$$

Figure 2 illustrates an example of calculation of the ratio G/F for some dry concrete mixes by using Eqs in (12). In this example, considered variables are: d , D and DF .

Average diameter of grains: Characteristic diameters of grains as the average grain diameter are relevant parameters involved in the description of size distribution of granular mixtures. The average particle diameter, denoted D_{50} , is defined as the size for which 50% of the material of larger particles, i.e. the cumulative weight percent of material passing a sieve size of D_{50} noted $P_{50\%}$ is 50% [9].

According to this definition, the average grain size D_{50} of a dry concrete mix $\mathcal{M}_{d/D}^{DF}$, can be expressed as follows (by using Eqs in (10)):

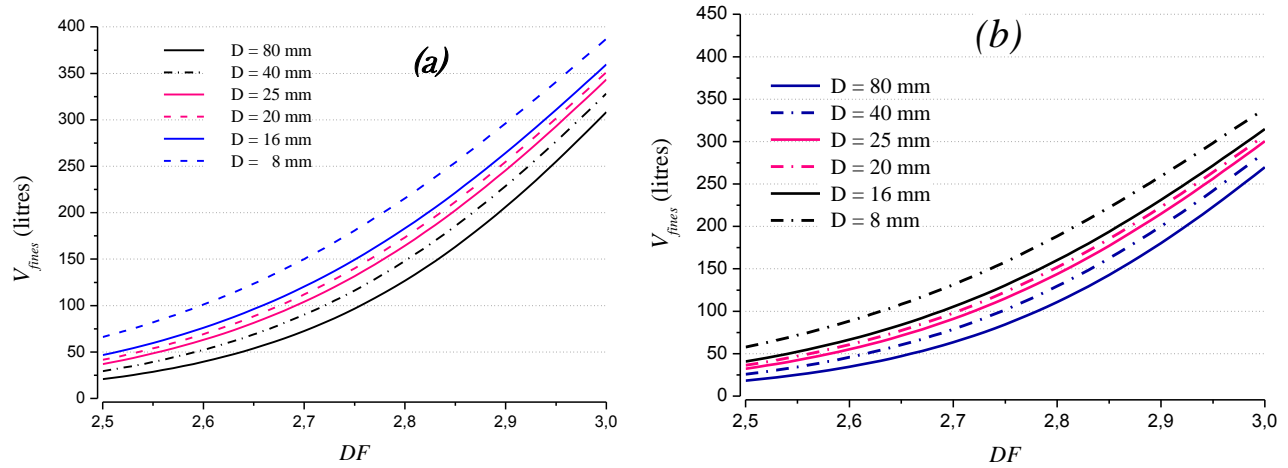


Figure 4

Amount of fines of concrete mixes, such as $M_T = 2350 \text{ kg}/1 \text{ m}^3$: (a) Fines = 100% fines of sand ($\rho_G = 2,5 \text{ g}/\text{cm}^3$) (b) Fines = 100% cement ($\rho_C = 3,2 \text{ g}/\text{cm}^3$).

$$P_{50\%} = 100 \begin{cases} \left(\frac{D_{50}^{3-DF} - d^{3-DF}}{D^{3-DF} - d^{3-DF}} \right) & \Rightarrow \text{if } DF < 3 \\ (\log D_{50} - \log d) / (\log D - \log d) & \Rightarrow \text{if } DF = 3 \end{cases}$$

from which we can obtain D_{50} :

$$\begin{cases} D_{50}^{3-DF} = (P_{50})D^{3-DF} + (1-P_{50})d^{3-DF} & \Rightarrow \text{if } DF < 3 \\ \log D_{50} = (P_{50})\log D + (1-P_{50})\log d & \Rightarrow \text{if } DF = 3 \end{cases} \quad (13)$$

Or in simplified form:

$$D_{50} = \begin{cases} \left[P_{50}D^{3-DF} + (1-P_{50})d^{3-DF} \right]^{\frac{1}{3-DF}} & \Rightarrow \text{if } DF < 3 \\ D^{P_{50}} d^{1-P_{50}} & \Rightarrow \text{if } DF = 3 \end{cases} \quad (14)$$

Such as: $P_{50} = P_{50\%}/100$

Figure 3 illustrates an example of calculation of D_{50} for some dry concrete mixes by using Eqs in (14). In this example, considered variables are: d , D and DF .

Amount of fines in a concrete mix: Fines are beneficial in a concrete mix, because they fill voids, reduce bleeding and improve workability [2;4;5]. Fines in the concrete mix must fill the voids of the bigger aggregates; hence the optimum content of

fines is related to the granular extent d/D and to the PSD of the mix, i.e. DF .

In this work, amount of fines will be considered consisting of aggregate fines and cement with most particles passing through a $63 \mu\text{m}$ sieve, this sieve opening will be denoted ϕ_{fines} . In this section, we derive will equations that can be used to determine the amount of fines ($\leq \phi_{fines}$) in a granular mix $\mathcal{M}_{d/D}^{DF}$ as follows, such as the amount of fines (in %) in the concrete mix is denoted $A_{fines}(\%)$:

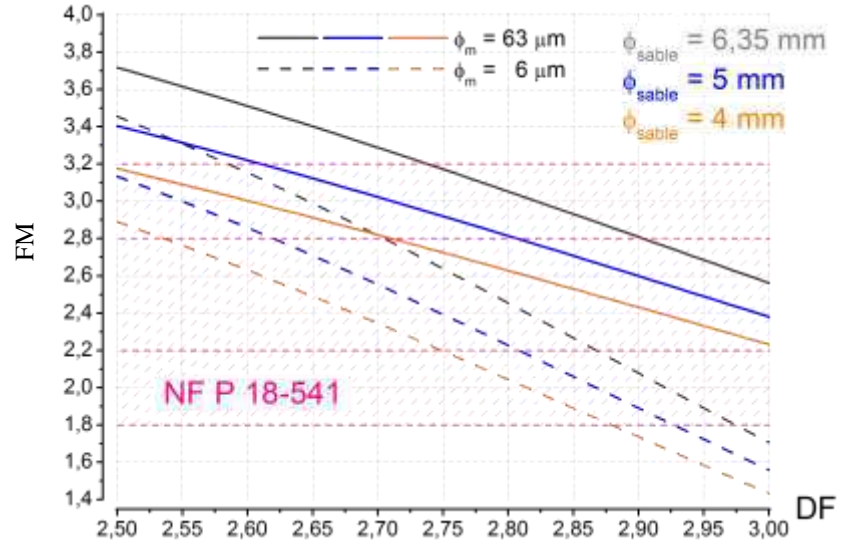
$$A_{fines}(\%) = 100 \begin{cases} \frac{(\phi_{fines}/d)^{3-DF} - 1}{(D/d)^{3-DF} - 1} & \Rightarrow \text{if } DF < 3 \\ \frac{\log(\phi_{fines}/d)}{\log(D/d)} & \Rightarrow \text{if } DF = 3 \end{cases} \quad (15)$$

M_T is the total mass of the concrete ingredients (except water), hence M_{fines} , the mass of fines in this mix that can be composed of sand fines (G_1), cement (G_2) and mineral addition (G_3), can be given as follows:

$$\begin{aligned} M_{fines} &= (A_{fines}(\%)/100)M_T \\ &= G_1 + G_2 + G_3 = P_1M_T + P_2M_T + P_3M_T \end{aligned} \quad (16)$$

Such as P_1, P_2 & P_3 are the volumetric proportions of fines and $P_1 + P_2 + P_3 = 1$. By using Eq. (16), we can determine the fines content, denoted V_{fines} , as follows:

Figure 5
Fineness Modulus of sand
fraction of granular mixes
 $\mathcal{M}_{d/D}^{DF}$, related to DF and
sizes: ϕ_{sand} & ϕ_m .
In pink, recommended FM
values (range is 1.8 to 3.2)
according to NF P 18-541
standard



$$V_{fines} = G_1/\rho_{G_1} + G_2/\rho_{G_2} + C/\rho_C \quad (17)$$

ρ_{G_1} , ρ_{G_2} & ρ_C are respectively the absolute densities of each type of fines: sand fines, mineral addition and cement. By replacing Eq. (16) in (17), we obtain:

$$V_{fines} = M_T \frac{A_{fines}(\%)}{100} \left(\frac{P_1}{\rho_{G_1}} + \frac{P_2}{\rho_{G_2}} + \frac{P_3}{\rho_C} \right) \quad (18a)$$

Or, for m types of concrete fines, of the absolute densities: ρ_1, \dots, ρ_m ; V_{fines} can be expressed as follows:

$$V_{fines} = M_T \frac{A_{fines}(\%)}{100} \left(\frac{P_1}{\rho_1} + \frac{P_2}{\rho_2} + \dots + \frac{P_m}{\rho_m} \right) \quad (18b)$$

The mean density of all concrete fines ρ_{fines} , can be expressed as:

$$\rho_{fines} = \frac{M_{fines}}{V_{fines}} = \frac{1}{P_1/\rho_1 + P_2/\rho_2 + \dots + P_m/\rho_m} \quad (19)$$

By combining Eqs (15)-(19), we obtain the following equations, allowing the determination of the amount of fines by unit mass of concrete mix:

$$V_{fines} = M_{fines} / \rho_{fines}$$

$$V_{fines} = \frac{M_T P}{100} \begin{cases} \frac{(\phi_{fines}/d)^{3-DF} - 1}{(D/d)^{3-DF} - 1} & \Rightarrow \text{if } DF < 3 \\ \frac{\log(\phi_{fines}/d)}{\log(D/d)} & \Rightarrow \text{if } DF = 3 \end{cases} \quad (20)$$

and $P = P_1/\rho_1 + P_2/\rho_2 + \dots + P_m/\rho_m$

Figure 4 illustrates an example of calculation of the

amount of fines for some dry concrete mixes by using Eqs in (20). In this example, considered variables are: D and DF .

Fineness modulus: The fineness modulus (FM) is an empirical factor used to estimate the proportions of fine and coarse aggregates in concrete mixtures.

According to NF P 18-541, fineness modulus can be obtained by adding the cumulative percentages of aggregate retained on each of the standard sieves ranging from 80 to 0.16 mm and dividing this sum by 100. Generally, fineness modulus of sand of concrete shall not be less than 1.8 or more than 3.2 to make good concrete.

According the above definition, FM of the sand fraction ($\phi_m < \phi < \phi_{sand}$) in a granular mix $\mathcal{M}_{d/D}^{DF}$, can be write as follow:

$$FM = \frac{1}{100} \sum_{i=1}^t \bar{R}_{C_{\phi_i}} (\%) \quad (21)$$

$$\text{and : } \phi_{i_{FM}} \in \left\{ [\phi_m; \dots; \phi_{sand}] \cap \left[\phi_j \right] \right\}$$

Such as:

$$\phi_{i_{FM}} \in \left\{ [\phi_m; \dots; \phi_{sand}] \cap \left[\phi_j \right] \right\}; \left[\phi_j \right]_{FM} = [0.16; \dots; 80] :$$

sieves considered in FM definition ; t : number of sieve ϕ_i ; such as $\phi_i \in [\phi_m; \dots; \phi_{sand}]$ and

$$\phi_{i_{FM}} \in \left[\phi_j \right]_{FM}; \bar{R}_{C_{\phi_i}} \text{ cumulative weight percent}$$

passing of the sand fraction in the mix, such as:

$$\bar{R}_{C\phi_i}(\%) = 100 \begin{cases} \frac{\phi_{\text{sand}}^{3-DF} - \phi_i^{3-DF}}{\phi_{\text{sand}}^{3-DF} - \phi_m^{3-DF}} & \Rightarrow \text{if } DF < 3 \\ \frac{\log \phi_{\text{sand}} - \log \phi_i}{\log \phi_{\text{sand}} - \log \phi_m} & \Rightarrow \text{if } DF = 3 \end{cases}$$

By substituting the above expressions in Eq. (21), we obtain the following expressions allowing the determination of FM:

$$FM = \begin{cases} \frac{t \phi_{\text{sand}}^{3-DF} - \sum_{i=1}^t \phi_i^{3-DF}}{\phi_{\text{sand}}^{3-DF} - \phi_m^{3-DF}} & \Rightarrow \text{if } DF < 3 \\ \frac{t \log \phi_{\text{sand}} - \sum_{i=1}^t \log \phi_i}{\log \phi_{\text{sand}} - \log \phi_m} & \Rightarrow \text{if } DF = 3 \end{cases} \quad (22)$$

Figure 5 illustrates an example of calculation of FM for some dry concrete mixes by using Eqs in (22). In this example, considered variables are: DF and the sand fraction sizes: ϕ_{sand} and ϕ_m .

ANALYSIS AND CONCLUSION

The key point of this study is to consider ideal size gradations for concrete, hence concrete mix gradations as almost fractal. This allowed us first, to propose a general fractal gradation curve which would describe any concrete mix gradation with the help of two parameters: the granular extent d/D and the fractal dimension DF . Second, to propose simple analytical formulas allowing the calculation of some physical properties of the dry concrete mixes.

According to our analytical results, DF values varying from 2.5 to 3 indicate that the concrete mix gradation is coarser for small DF values and finer for more DF values, thus we can see decreasing G/F ratio, fineness modulus FM and average particle size D_{50} ; and a significant increase of the amount of fines V_{fines} in the concrete mix. These results are in agreement with others in the literature, for instance, some researchers have proposed an optimal gradation curve $\% \text{Passing} = 100(\phi_i/D)^q$, such as $q=0.37$ (corresponding to $DF=2.69$) to achieve maximum compactness for ordinary concrete and $q=0.30$ (corresponding to $DF=2.76$) for Self Consolidating Concrete that the mix must be finer [6].

Therefore, the fractal dimension can be a good characterization parameter to be adjusted to obtain some required properties of concrete.

REFERENCES

1. Amirjanov A. et Sobolev K., 2008, Optimization of a computer simulation model for packing of concrete aggregates, *Particulate Science and Technology*, **26**, pp. 380-395.
2. Baron J. et Ollivier J.P., 1996, *Les Bétons : Bases et Données pour leur Formulation*, Eyrolles, Paris, France.
3. Chouicha K., 2006, La dimension fractale et l'étendue granulaire comme paramètres d'identification des mélanges granulaires, *Materials and Structures*, **39**, pp. 665-681.
4. De Larrard F., 2000, *Structures granulaires et formulation des bétons*, Volume OA34, Laboratoire Central des Ponts et Chaussées, Paris, France.
5. Dreux G. et Festa J., 1998, *Nouveau guide du béton et de ses constituants*, Eyrolles, Paris, France.
6. He H., 2010, *Computational modelling of particle packing in concrete*, PhD, Univ. de Technol. de Delft, Delft, Pays-Bas.
7. Lecomte A. et Thomas A., 1992, Caractère fractal des mélanges granulaires pour bétons de haute compacité", *Materials and Structures*, **25**, pp. 255-264.
8. NF P 18-541, 1994, Granulats - Granulats pour béton hydrauliques. Association Française de Normalisation (AFNOR), France.
9. Paderno C., 2010, *Comportement du ballast sous l'action du bourrage et du trafic ferroviaire*, Thèse de Doctorat, EPFL, Lausanne, Suisse.
10. Sebsadji S.K. et Chouicha K., 2012, Determining periodic representative volumes of concrete mixtures based on the fractal analysis, *International Journal of Solids and Structures*, **49**, pp. 2941-2950.
11. Sebsadji S., 2013, *Application du modèle fractal à l'étude des propriétés du béton*, Thèse de Doctorat, Univ. des Sc. et de la Technol. d'Oran (USTO), Oran, Algérie.
12. Wang Z., Cheng Q., Cao L., Xia Q. et Chen Z., 2007, Fractal modelling of the microstructure property of quartz mylonite during deformation process, *Mathematical Geology*, **39**, pp. 53-68

SEISMIC VULNERABILITY ASSESSMENT OF BLIDA CITY

Khalida TADJER ¹, Bensaïbi MAHMOUD ²,

¹ Department of Civil Engineering, University Blida 1, Algeria.

² Department of Material and Structures High National School of Public Works Algiers, Algeria.

*Corresponding author : Email: khalidatadjer@yahoo.fr

ABSTRACT

The seismic vulnerability of an urban area is of a great deal for local authorities especially those facing earthquakes. So, it is important to have an efficient tool to assess the vulnerability of existing buildings. Blida is located in the north part of Algeria, an area prone to seismicity, classified zone III according to the Algerian Seismic Code (RPA99 version 2003) [12]. The town is among the oldest cities in the north. Built especially during the colonial period, Blida is characterized by vulnerable urban conditions with dense buildings and narrow roads. Using geographic information systems (GIS), the seismic vulnerability of Blida is assessed. First the vulnerability indexes of buildings are calculated, then making seismic scenarios. Damage rates are determined taking into account the seismotectonic aspect of the region and vulnerability curves of structures commonly found in Blida. The results show a relatively high rate of damage in buildings and considerable losses.

KEYWORDS

seismic vulnerability index, geographic information systems (GIS)

INTRODUCTION

Earthquakes are natural catastrophes that defy man's power, but seismic vulnerability of urban centers is produced by human activity [1]. Throughout the last thirty years scientific and technical action has been oriented towards the definition of new building-methods that tend to increase buildings' seismic resistance, [4], [5], [15]. However, the old structures vulnerability that represent the majority of these buildings, is also quite worrying and its assessment is a considerable task as regards the diversity of the materials used, the variety of the building- methods, the number of a town's or a territory's buildings which has to be studied, the state of the old buildings' conservation, etc. [7].

The evolution of the seismic vulnerability's study in the world has given birth to several methods, [4]. The method's type chosen depends on the evaluation's goal and also on data's availability, on the material and the technology used, [16], [17].

In Algeria, the last earthquakes show that the seismic activity is important. In fact, this activity is linked to faults that illustrate compression movements along the limit of Algeria-Europe's plates mostly touches

the north of the country where the biggest towns are situated. The town of Blida as regards its location in a high seismic activity region (south of the Mitidja's seismogene basin), its high population's condensation, its generally very old buildings and its administrative importance in the region requires a particular attention concerning its protection against that natural phenomenon that highly threatens it and that may hit the town at any moment.

We have assessed the seismic vulnerability of Blida city by carrying out seismic scenarios. To do this, the different data of the study's zone have been structured under a geographic information system (GIS) [2]. The scenarios' carrying out consists in crossing the data of the seismic hazard of the studied zone, the stakes (the buildings) and the stakes' vulnerability confronted to seismic aggression.

The value of the buildings' seismic vulnerability's index of the zone of study has been calculated by the VIP (Vulnerability Index Program), [6], [10], [11], and the damages provoked by the earthquake taken into account in the scenarios have been calculated by a GIS established program.

STUDY AREA

The situation of the city of Blida, its geographic and tectonic context highly requires a vulnerability analysis of its existing buildings.

The zone under study includes the historical centre considered as the oldest district where most of the buildings date from the colonial era. This area is mostly composed of single or two storied buildings of which most are in an advanced state of decay. We may find, in the same surroundings, some recent buildings and some others dating from the Ottoman era, figure 1 and figure 2.



Figure 1
Zone under study



Figure 2
Didouche Mourad Street (town-centre)

SECTORS DIVISION

To make the inventory draw up of the study-zone structures easier, it is better to divide the study zone into identified sectors inside the soils occupation plan as base-sectors composing the town-centre. In our case, we have chosen a sectors division including 20 analysis units each representing one area identified with a number, figure 3.

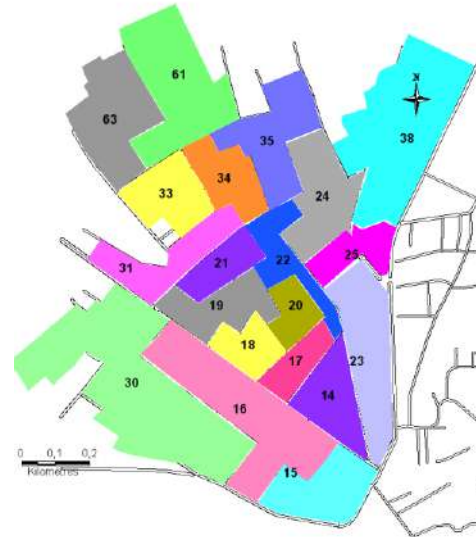


Figure 3
Sectors division of the study zone in 20 analysis units on GIS

GENERAL POPULATION AND HOUSING CENSUS

The analysis of the population’s and accommodation’s data made for the needs of the downtown’s seismic vulnerability is based on the population and accommodation general census (RGPH-2008) established by the National Office of Statistics in 2008 (ONS, 2008), [3]. To make the exploitation of the study-zone’s census results more rapid, a data base on a geographic information system has been created. The zone of study’s total constructions’ number is 2512 for a population of 14997 inhabitants.

SCENARIOS

Seismicity-analysis: The different studies of the seismic hazard in the region of Blida have shown the presence of many active sources that may provide more or less important earthquakes. For the study’s needs, the fault of Blida also called Soumaa Bouinan fault has been considered as the one that could generate most damages because it crosses Blida’s downtown, figure 4. The maximum magnitude generated by this fault has been

estimated by the CRAAG (Astronomy, Astrophysics and Geophysics’ research Centre) at 7.08 on Richter scale.

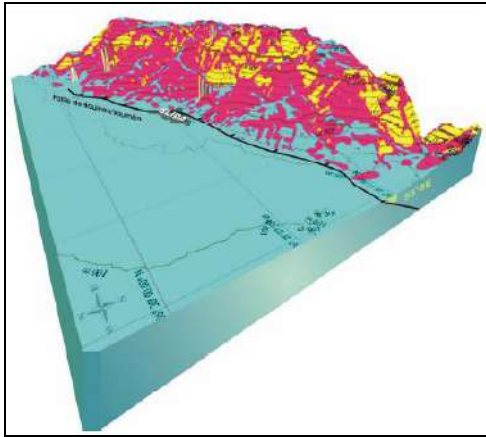


Figure 4
Active fault of Soumâ / Bouinan

In our study, we have considered two seismic scenarios. The characteristics of these latter are summed up in table 1 and table 2:

Table 1
First scenario

Seismic source	Magnitude	Epicenter	Attenuation law
Blida fault	7.08	Downtown	Joyner-Boor (1981)

Table 2
Second scenario

Seismic source	Magnitude	Epicenter	Attenuation law
Blida fault	7.08	15 km from downtown	Joyner-Boor (1981)

Analysis of the urban system: The data collected for each structure recorded are treated by the VIP program (Vulnerability Index Program) in order to determine the vulnerability index, [11]. All the data are treated and analyzed afterwards with a geographic information tool (GIS). The total number of analyzed buildings reaches 370 of which 300 are built in masonry and 70 in reinforced concrete.

Assessment of rate of damages: The damages provoked by the earthquake considered in the scenarios are assessed through the use of seismic vulnerability functions programmed under SIG, [8], figures 5 and 6. These curves are defining the relation between seismic intensity and the damages’ rates for various Algerian structural types and they appear as an acceleration function/ MMI (Modified Mercalli Intensity). The value of the intensity is obtained by converting the PGA (Peak Ground Acceleration) to MMI.

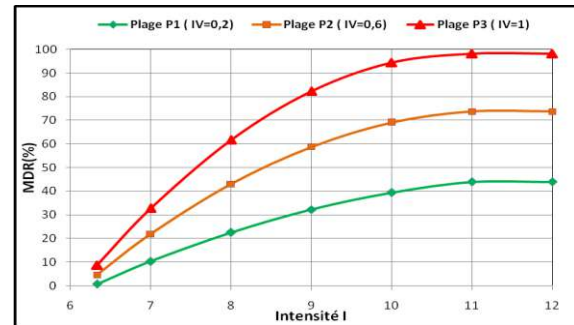


Figure 5
Vulnerability curves of Masonry structures [14]

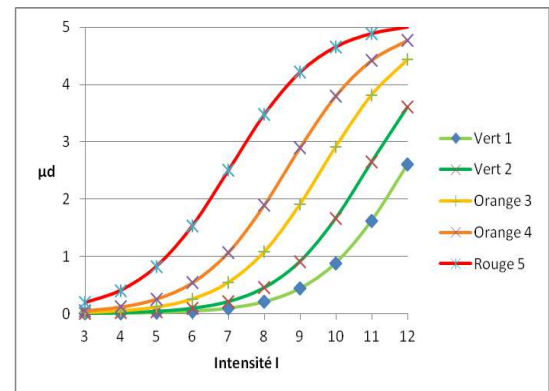


Figure 6
Vulnerability curves of Reinforced concrete structures [13]

RESULTS

Concerning results, we have considered the following damages’ rates’ classification, tables 3 and 4.

Table 3
Masonry structure [9]

Damages’ rate	0 – 20%	20% - 60%	60% - 100%
classification	green	orange	red

Table 4
Reinforced concrete structure

Damages' rate	0 – 40%	40% - 70%	70% - 100%
classification	green	orange	red

First scenario: After a GIS analysis, on a total number of 370 buildings of which 300 in masonry and 70 in reinforced concrete, we have numbered 69 classified ‘green’, 10 classified ‘orange’ and 291 classified ‘red’, figures 7 et 8.



Figure 7
Classification of the buildings according to their damage's rates

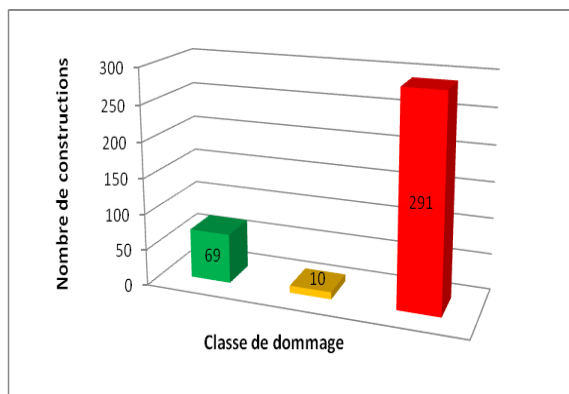


Figure 8
Damage-classes and number of constructions

The proportion of the number belonging to each class according to the total number of constructions is given in figure 9.

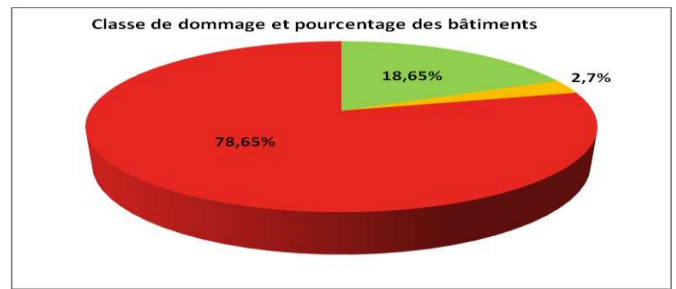


Figure 9
Buildings' proportion for each class

The proportion of the buildings classified ‘orange’ represents nearly 81 % of the total number of building, an extremely important proportion. Moreover, almost 79 % of the constructions are classified ‘red’ which leads to assert that this zone’s estate-park shows big vulnerability to earthquake. The total number of the study’s results shown in figure 7 stresses on the high, the moderate and the weak zones. Thus, the external risk appears to be a weak risk-zone but the risk gets bigger the more we approach the central core.

Second scenario: For this second scenario, we have numbered 71 buildings classified ‘green’, 192 classified ‘orange’ and 07 classified ‘red’. The damage’s rate has seriously decreased, the number of ‘red’ classified buildings has lowered as compared to the first scenario to 64 %, figure 10. This damage-decrease in the second scenario is obviously due to the remoteness from the study-zone’s epicenter.



Figure 10
Classification of the buildings according to their damage's rates

The vulnerability of the study-zone’s different districts is geared by the constructions damage-class

and by the number of inhabitants as well. A GIS request has allowed us to carry out this analysis. The result is shown in figure 11.

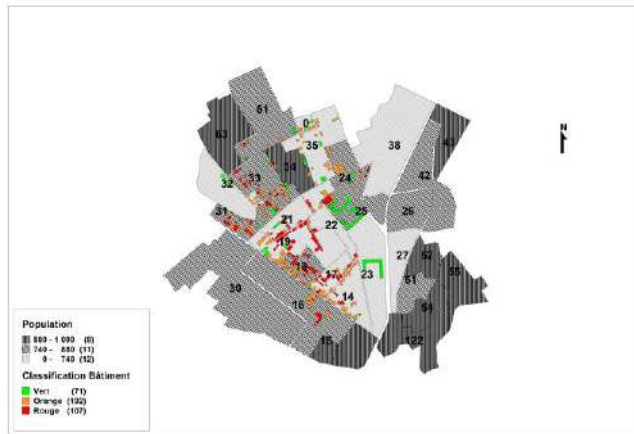


Figure 11
Districts' vulnerability

Therefore, we are to retain the four most vulnerable districts according to the percentage of the buildings classified "red" and according to the population-number (figure 11). The district 19 is thus considered as being the most vulnerable with a percentage of 51,16 % for the "red" classified buildings, and a population of 639 inhabitants. This one is followed by district 33 with a percentage of 48,14% and a population of 832 inhabitants. Then comes in the third position district 18 with a red buildings' percentage of 37,5% and a population of 780 inhabitants. The last one is district 77 with 36,66 % of "red" buildings and a population of 736 inhabitants.

So, it would be advisable to centre reinforcement or rehousing actions towards these districts which include a population of 2987 inhabitants that is to say 20% of our study-zone's.

CONCLUSION

The carrying out of Blida town's seismic scenario has permitted to quantify the local risk. The use of GIS in this work has allowed the exploitation of the data collected in situ and the diagnosis of the most vulnerable zones.

In fact, the results clearly demonstrate the high vulnerability of the city of Blida and the fragility of its urban fabric.

The carrying out of the scenarios on GIS has allowed us to approach the seismic vulnerability of the zone

of study from both the analytic and spatial points of view.

Through this study, we can know now the weak points of the town which are downtown districts.

We have noticed that the most vulnerable buildings are located inside the district's core which is characterized by a big buildings' concentration and very narrow streets.

Finally, a spatial analysis has permitted to locate geographically the structures and their damage's rate, their typology and their number of floors.

Therefore, for Blida downtown, the districts (19), (18), (33) and (17) are shown as the most vulnerable ones.

These results may help in decision-making concerning Blida's development. They may also be useful in the organization of the first aids, the state of readiness, the reinforcement of buildings and reconstruction's actions particularly if we consider that the available budget and efforts in case of a catastrophe are often limited or even non-available in a town like Blida submitted to earthquakes.

REFERENCES

1. AFPS (Association Française du Génie Parasismique), 2005, Vulnérabilité sismique du bâti existant, Approche d'ensemble, Cahier technique n° 25. France.
2. URBA (Centre d'étude et de réalisation en urbanisme). 2004, PDEAU du grand Blida analyse et diagnostic phase1, Algeria.
3. ONS (office national des statistiques), 2008, Recensement Général de la population et de l'Habitat (RGPH), Algeria.
4. Lantada, N. Pujades, L.G. and A.H. Barbat. 2004, Risk Scenarios for Barcelona, Spain. 13th World Conference on Earthquake Engineering. paper N°. 423, Canada.
5. Silvia del Carmen MOQUERA MACHADO. 2002, Analyse multi-aléas et risque naturels dans le département du Chocó (nord-ouest de la Colombie). Doctorate thesis N° 3351. Genève.
6. Bensaïbi, M., Djaalali, F., Belheouane, F I., Amellal, O., and Yousfi, N. 7-8 Mars 2011. Seismic Vulnerability Index Method - Algerian case studies. 9. *th International Conference on Urban Earthquake Engineering, Tokyo Institute of Technology, Tokyo, Japon,*
7. Tadjer , K, 2007, Scenario Catastrophe Sismique du Centre Ville de Blida. Master thesis. University Saad Dahlab Blida. Algeria.

8. Bensaïbi, M., Djaalali, F., Belheouane, F I., and Bourahla, Nourredine, 2011, Vulnerability Index Method – Algeriers case study. *Seventh National Conference of Earthquake Engineering*.
9. Fatma Imene Belheouane, 2006, Détermination De L'indice De Vulnérabilité Pour Les Bâtiments En Béton Armé. Master thesis, University Saad Dahlab Blida, Algérie.
10. Amellal, O, 2008, Évaluation De L'indice De Vulnérabilité Pour Les Structures En Charpente Métallique. Master thesis University Saad Dahlab Blida, Algérie.
11. Yousfi, N, 2010, Estimation De L'indice De Vulnérabilité Des Structures Mixtes. Master thesis University Saad Dahlab Blida, Algérie.
12. RPA, Règlement Parasismique Algérien (RPA99 version 2003), CGS Centre Génie Parasismique, 2003, Algeria.
13. Belheouane , F I., Bensaïbi, M, 2011, Evaluation De l'Indice De Vulnérabilité Sismique Des Structures En Béton Armé, Cas D'étude : Structures En Béton Armé En Algérie. Actes du 8^{em} Colloque National AFPS, Paris, France.
14. Boukri, M., 2003, Détermination de l'Index de Vulnérabilité Pour les Constructions en Maçonnerie de la Ville d'Alger. Master thesis. University Saad Dahlab Blida. Algérie
15. Lang, K., 2002, Seismic Vulnerability of existing Buildings. Doctorate thesis, Swiss Federal Institute of technology, Zurich, Swiss.
16. Ishita R. P, Khandaker S, Application of Analytical Hierarchical Process and GIS in Earthquake Vulnerability Assessment: Case Study of Ward 37 and 69 in Dhaka City Journal of Bangladesh Institute of Planners ISSN 2075-9363, Vol. 3, pp. 103-112, Bangladesh Institute of Planners December 2010,
17. Sarvar H, Amini J , Laleh-Poor M, Assessment of Risk Caused By Earthquake in Region 1 of Tehran Using the Combination of RADIUS, TOPSIS and AHP Models, *Journal of Civil Engineering and Urbanism, Volume 1, Issue 1: 39-48 ,2011.*

Sponsors



Communauté
d'Agglomération de
La Rochelle



UNIVERSITÉ
DE LORRAINE

UNIVERSITÉ
PERPIGNAN
VIA
DOMITIA

